

# **ENGINEERING MECHANICS 2017**

**23<sup>rd</sup> INTERNATIONAL CONFERENCE**

**MAY 15 - 18, 2017, SVRATKA, CZECH REPUBLIC**



## **BOOK OF FULL TEXTS**

**Editor: Vladimír Fuis**

---

**Institute of Solid Mechanics, Mechatronics and Biomechanics,  
Faculty of Mechanical Engineering, Brno University of Technology**

**Institute of Thermomechanics,  
Academy of Sciences of the Czech Republic, v.v.i. – branch Brno**

**Association for Engineering Mechanics**

**Institute of Theoretical and Applied Mechanics,  
Academy of Sciences of the Czech Republic, v.v.i.**

**ŽĐAS, a.s., Žďár nad Sázavou**

**Czech Society for Mechanics**

**IFTToMM Member Committee of Czech Republic**



**Text may be copied and used freely, but credit should be given to this Proceedings.**

**Copyright © 2017 Brno University of Technology**

**Institute of Solid Mechanics, Mechatronics and Biomechanics**

**1<sup>st</sup> edition, 2017**

**ISBN 978-80-214-5497-2**

**ISSN 1805-8248**

**The Conference is hosted by the hotel Svratka.**

All the papers were reviewed by members of the international scientific committee.

## SCIENTIFIC COMMITTEE

### *Chairman:*

Assoc. Prof. Vladimír Fuis, PhD.

Brno University of Technology & IT AS CR, Brno, CZ

### *Members:*

Prof. Ivan Baláž, PhD.

STU, Bratislava, SK

Prof. Dr. Pavol Bauer

Delft University of Technology, NL

Prof. Ján Benčat, PhD.

University of Žilina, SK

Dr. Ouadie Bennouna

ESIGELEC, FR

Prof. Jiří Burša, PhD.

Brno University of Technology, Brno, CZ

Prof. Radim Čajka, PhD.

VSB - Technical University of Ostrava, CZ

Prof. Miloš Drdácký, DrSc.

ITAM AS CR, Prague, CZ

Prof. Paola Forte

University of Pisa, IT

Assoc. Prof. Karel Frydryšek, PhD.

VSB - Technical University of Ostrava, CZ

Prof. Ardeshir Guran, PhD.

Institute of Structronics, Ottawa, Canada

Jaromír Horáček, DSc.

Institute of Thermomechanics AS CR, Prague, CZ

Assoc. Prof. Lidia Ilieva-Mitutsova, PhD.

Bulgarian Academy of Sciences, Sofia, BG

Prof. Přemysl Janíček, DSc.

Brno University of Technology, CZ

Prof. Miroslav Jícha, PhD.

Brno University of Technology, CZ

Prof. Milan Jirásek, DSc.

Czech Technical University in Prague, CZ

Assoc. Prof. Jiří Kala, PhD.

Brno University of Technology, CZ

Prof. Zdeněk Kala, PhD.

Brno University of Technology, CZ

Prof. Zbyněk Keršner, PhD.

Brno University of Technology, CZ

Prof. Juraj Králik, PhD.

STU, Bratislava, SK

Assoc. Prof. Jiří Krejsa, PhD.

Brno University of Technology & IT AS CR, Brno, CZ

Prof. Anne-Maria Laukkanen, PhD.

University of Tampere, FI

Prof. Dušan Maga, PhD.

Czech Technical University in Prague, CZ

Prof. František Maršík, DSc.

Institute of Thermomechanics AS CR, Prague, CZ

Prof. Arkadiusz Mężyk

Silesian University of Technology, Gliwice, PL

Prof. Dr. Damijan Miljavec

University of Ljubljana, Ljubljana, SI

Jiří Minster, DSc.

ITAM AS CR, Prague, CZ

Jiří Náprstek, DSc.

ITAM AS CR, Prague, CZ

Prof. Bořek Patzák, PhD.

Czech Technical University in Prague, CZ

Prof. Michail Pavlenko

Moscow State Mining University, Moscow, RU

Prof. Dr. Paolo Pennacchi

Politecnico di Milano, Milan, IT

Prof. Kazimierz Peszynski, PhD.

Univ. of Technol. and Life Science, Bydgoszcz, PL

Prof. Jindřich Petruška, PhD.

Brno University of Technology, CZ

Jiří Plešek, PhD.

Institute of Thermomechanics AS CR, Prague, CZ

Prof. František Pochylý, PhD.

Brno University of Technology, CZ

Assoc. Prof. Stanislav Pospíšil, PhD.  
 Prof. Jaromír Příhoda, PhD.  
 Assoc. Prof. Tomáš Profant, PhD.  
 Ladislav Půst, DSc.  
 Prof. Ján Sládek, DSc.  
 Prof. Vladimír Sládek, DSc.  
 Prof. Milan Sokol, PhD.  
 Prof. Pavel Šafařík, PhD.  
 Prof. Michal Šejnoha, DSc.  
 Prof. Alexander Tesár, DSc.  
 Prof. Václav Tesař, PhD.  
 Prof. Tomasz Topoliński  
 Prof. Michael Valášek, DSc.  
 Prof. Pavel Vlasák, DSc.  
 Prof. Yuri Sergeevich Voribiev  
 Prof. Jaroslav Zapoměl, DSc.  
 Prof. Vladimír Zeman, DSc.  
 Prof. Anatoly P. Zinkovskii, DSc.  
 Prof. Rudolf Žitný, PhD.  
 Prof. Milan Žmíndák, PhD.

ITAM AS CR, Prague, CZ  
 Institute of Thermomechanics AS CR, Prague, CZ  
 Brno University of Technology, CZ  
 Institute of Thermomechanics AS CR, Prague, CZ  
 ICA, SAS, Bratislava, SK  
 ICA, SAS, Bratislava, SK  
 STU, Bratislava, SK  
 Institute of Thermomechanics AS CR, Prague, CZ  
 Czech Technical University in Prague, CZ  
 ICA, SAS, Bratislava, SK  
 Institute of Thermomechanics AS CR, Prague, CZ  
 Univ. of Technol. and Life Science, Bydgoszcz, PL  
 Czech Technical University in Prague, CZ  
 Institute of Hydrodynamics AS CR, Prague, CZ  
 NAS of Ukraine, Kharkov, UA  
 Institute of Thermomechanics AS CR, Ostrava, CZ  
 University of West Bohemia in Pilsen, CZ  
 National Academy of Sciences of Ukraine, Kiev, UA  
 Czech Technical University in Prague, CZ  
 University of Žilina, SK

## HONOURARY COMMITTEE

Pavel Cesnek, MSc.  
 František Mládek

Managing Director of ŽĎAS Inc.  
 Mayor of Svratka

## List of Sections:

**KEY** Keynote Lectures  
**BIO** Biomechanics  
**DYN** Dynamics  
**FLU** Fluid Mechanics  
**FRA** Fracture Mechanics  
**KIN** Kinematics  
**MCT** Mechatronics  
**REL** Reliability  
**SOL** Mechanics of Solids  
**TER** Thermomechanics

## **Main Headings**

<b>Table of Contents (by the first Author's Name) .....</b>	<b>6</b>
<b>Table of Contents (by Sections) .....</b>	<b>23</b>
<b>Keynote Lectures .....</b>	<b>41</b>
<b>Papers .....</b>	<b>65</b>
<b>Authors Index .....</b>	<b>1142</b>

## Table of Contents

### KEYNOTE LECTURES

<b>Jebáček I., Matějů J.:</b> <i>AEROBATIC SPECIAL IN-FLIGHT TESTS AT INSTITUTE OF AEROSPACE ENGINEERING .....</i>	<b>42</b>
<b>Juračka J.:</b> <i>SPECIFICS OF AEROSTRUCTURES EXPERIMENTAL TESTING .....</i>	<b>46</b>
<b>Peszynski K., Olszewski L., Smyk E., Kasprowicz T.:</b> <i>DEVELOPMENT OF NEW TYPE VENTILATION DUCTS SYSTEM .....</i>	<b>50</b>
<b>Porteš P., Kučera P., Pištěk V., Fojtášek J., Zháňal L.:</b> <i>MODERN TOOLS FOR VEHICLE DEVELOPMENT .....</i>	<b>54</b>
<b>Šafařík P.:</b> <i>SHOCK WAVES IN AN IDEAL GAS AND ENTROPY ANALYSIS.....</i>	<b>58</b>

### PAPERS

<b>Adamczak S., Zmarzły P., Koziar T., Gogolewski D.:</b> <i>ANALYSIS OF THE DIMENSIONAL ACCURACY OF CASTING MODELS MANUFACTURED BY FUSED DEPOSITION MODELING TECHNOLOGY .....</i>	<b>66</b>
<b>Adamczak S., Zmarzły P., Koziar T., Gogolewski D.:</b> <i>ASSESSMENT OF ROUNDNESS AND WAVINESS DEVIATIONS OF ELEMENTS PRODUCED BY SELECTIVE LASER SINTERING TECHNOLOGY.....</i>	<b>70</b>
<b>Aizikovich S., Vasiliev A., Volkov S., Mitrin B.:</b> <i>MATHEMATICAL MODELING OF MICRO INDENTATION OF A TRANSVERSELY ISOTROPIC HALF-SPACE WITH FUNCTIONALLY GRADED COATING BY A CONICAL INDENTER .....</i>	<b>74</b>
<b>Aleksandrowicz P.:</b> <i>ANALYSIS OF VEHICLE COLLISIONS WITH THE SDC METHOD .....</i>	<b>78</b>
<b>Aleksandrowicz P.:</b> <i>VERIFYING THE APPLICATION OF THE MODELS OF CRASH AND COLLISION DETECTION OF INCOMPATIBLE VEHICLES.....</i>	<b>82</b>
<b>Anweiler S.:</b> <i>VIDEOGRAMMETRY IN FLUIDIZED BEDS ANALYSIS.....</i>	<b>86</b>
<b>Appel M., Grepl R.:</b> <i>PARAMETER ESTIMATION FOR ENGINEERS: A NEW TOOL FOR EFFECTIVE SEARCH FOR SIMULINK MODEL PARAMETERS.....</i>	<b>90</b>
<b>Augustín T., Fillo I.:</b> <i>INFLUENCE OF GROUND STRESS DISTRIBUTION ON PUNCHING RESISTANCE .....</i>	<b>94</b>
<b>Aydin E., Öztürk B., Dutkiewicz M.:</b> <i>OPTIMAL PASSIVE CONTROL OF SHEAR BUILDINGS .....</i>	<b>98</b>

<b>Baláž I., Koleková Y.:</b> <i>PLASTIC RESISTANCE OF ALUMINUM I-PROFILE UNDER BENDING AND TORSION ACCORDING TO CONTINUOUS STRENGTH METHOD</i> .....	<b>102</b>
<b>Bang N. V., Rozehnal D.:</b> <i>AERODYNAMIC HYSTERESIS OF OSCILLATING AIRFOIL</i> .....	<b>106</b>
<b>Baranovskii E. S., Artemov M. A.:</b> <i>STEADY FLOWS OF SECOND-GRADE FLUIDS SUBJECT TO STICK-SLIP BOUNDARY CONDITIONS</i> .....	<b>110</b>
<b>Baranowski L., Kaczmarek W., Panasiuk J., Prusaczyk P., Besseghieur K.:</b> <i>INTEGRATION OF VISION SYSTEM AND ROBOTIC ARM UNDER ROS</i> .....	<b>114</b>
<b>Baranowski L., Panasiuk J., Siwek M.:</b> <i>USE OF A RASPBERRY PI TO BUILT A PROTOTYPE WIRELESS CONTROL SYSTEM OF A MOBILE ROBOT</i> .....	<b>118</b>
<b>Bayer J.:</b> <i>A CONCEPT FOR TESTING AND MONITORING OF BUILDING STRUCTURES – THEORETICAL CASE STUDY</i> .....	<b>122</b>
<b>Bęczkowski R., Cebulski J., Pasek D., Gucwa M.:</b> <i>PRODUCING A LAYER OF IRON FE-CR-C-NB UNDER CONDITIONS OF INTENSE HEAT RECEPTION</i> .....	<b>126</b>
<b>Bednář L., Tajč L., Miczán M., Mrózek L., Hoznedl M.:</b> <i>POSSIBILITY OF DAMPING PRESSURE PULSATIONS IN BALANCING CONTROL VALVES</i> .....	<b>130</b>
<b>Benešovský M., Návrát T., Petruška J.:</b> <i>VERIFICATION OF FAST ALGORITHM FOR CROSS-ROLL STRAIGHTENING</i> .....	<b>134</b>
<b>Besseghieur K., Kaczmarek W., Panasiuk J., Prusaczyk P.:</b> <i>FORMATION CONTROL OF MOBILE ROBOTS UNDER ROS</i> .....	<b>138</b>
<b>Bienioszek G., Kciuk S.:</b> <i>DETERMINATION OF BOUNDARY CONDITIONS FOR THE OPTIMIZATION PROCESS OF BLAST MITIGATION SEAT SHOCK ABSORBERS</i> .....	<b>142</b>
<b>Blasiak M., Blasiak S.:</b> <i>APPLICATION OF FRACTIONAL CALCULUS IN HARMONIC OSCILATOR</i> .....	<b>146</b>
<b>Blasiak M., Blasiak S.:</b> <i>THE APPLICATION OF INTEGRAL TRANSFORMS TO SOLVING PARTIAL DIFFERENTIAL EQUATIONS OF THE FRACTIONAL ORDER</i> .....	<b>150</b>
<b>Blasiak S.:</b> <i>HEAT TRANSFER IN NON-CONTACTING FACE SEALS USING FRACTIONAL FOURIER LAW</i> .....	<b>154</b>
<b>Blasiak S.:</b> <i>HEAT TRANSFER MODEL FOR THE WAVY-TILT-DAM MECHANICAL SEALS USING GREEN'S FUNCTION METHOD</i> .....	<b>158</b>
<b>Blatnická M., Blatnický M., Sága M., Kubiak M.:</b> <i>STRESS ANALYSIS OF PART OF THE WELDED STRUCTURE</i> .....	<b>162</b>

<b>Blatnický M., Dižo J., Blatnická M., Svoboda M.: DESIGN OF A ROBOT MANIPULATOR WORKING SCREW REVOLUTIONS .....</b>	<b>166</b>
<b>Bochat A., Zastempowski M.: KINEMATICS AND DYNAMICS OF THE MOVEMENT OF THE SELECTED CONSTRUCTIONS OF THE DISC CUTTING ASSEMBLIES .....</b>	<b>170</b>
<b>Bochnia J.: MECHANICAL PROPERTIES OF MATERIALS OBTAINED BY 3D-PRINTING TECHNOLOGY .....</b>	<b>174</b>
<b>Bochnia J.: RELAXATION OF MATERIALS OBTAINED USING POLYJET TECHNOLOGY .....</b>	<b>178</b>
<b>Bojarczak P., Nowakowski W., Łukasik Z.: VISUAL DIAGNOSTICS OF RAIL FASTENING SYSTEM AS A METHOD TO IMPROVE SAFETY .....</b>	<b>182</b>
<b>Bojczuk D., Szteleblak W.: OPTIMAL REPAIR AND REINFORCEMENT OF BAR STRUCTURES USING FINITE TOPOLOGY VARIATIONS .....</b>	<b>186</b>
<b>Borák L., Marcián P.: INHOMOGENEOUS MATERIAL PROPERTIES ASSIGNMENT TO FINITE ELEMENT MODELS OF BONE: A SENSITIVITY STUDY .....</b>	<b>190</b>
<b>Borkowski K., Janecki D., Zwierzchowski J.: ACCURACY OF THE VISUAL MEASUREMENT SYSTEM OF BENT PIPES .....</b>	<b>194</b>
<b>Borowski S., Rama R., Knopik L., Kaszkowiak J.: ASSESSMENT OF THE VOLUME OF CROP BY THE WINDROW'S MEASUREMENT .....</b>	<b>198</b>
<b>Borsuk G., Wydrych J., Pochwała S.: COMPARING TURBULENCE MODELS FOR GAS-PARTICLE MIXTURE PNEUMATIC CONVEYING .....</b>	<b>202</b>
<b>Bošanský M., Patzák B.: ON PARELLELIZATION OF LINEAR SYSTEM EQUATION SOLVER IN FINITE ELEMENT SOFTWARE .....</b>	<b>206</b>
<b>Brabec P., Reichrt K.: MODIFICATION OF THE INTAKE MANIFOLD OF A COMBUSTION ENGINE .....</b>	<b>210</b>
<b>Brezina L., Losak P.: MODEL OF CAR SUSPENSION WITH PARAMETRIC UNCERTAINTY .....</b>	<b>214</b>
<b>Brózda K., Major M., Selejdak J.: COMPUTATIONAL ANALYSIS OF SERVICEABILITY LIMIT STATE OF BEAMS REINFORCED WITH FRP BARS .....</b>	<b>218</b>
<b>Bucci V., Marino A., Mauro F., Sandron C., Mattiazzo G.: REDESIGN OF A WAVE ENERGY CONVERTER IN FERROCEMENT .....</b>	<b>222</b>
<b>Cabová K., Lišková N., Novotná P., Benýšek M., Zeman F., Wald F.: MODELLING OF STANDARD FIRE TEST .....</b>	<b>226</b>
<b>Cebulski J., Bęczkowski R., Pasek D.: THE USE OF WELDING FOR FORMING FEAL COATING ON S235 .....</b>	<b>230</b>
<b>Čečrdle J., Raška J.: AIRCRAFT WING FLUTTER ASSESSMENT CONSIDERING DAMAGE TOLERANCE - BASED FAILURE STATES .....</b>	<b>234</b>

<b>Cekus D., Skrobek D.:</b> <i>THE INFLUENCE OF THE LENGTH OF TRAJECTORY OF SCARA MANIPULATOR DUTY CYCLE ON ELECTRICITY CONSUMPTION</i> .....	<b>238</b>
<b>Černý M., Dzurilla M., Musil M.:</b> <i>ELECTROMAGNETIC ENERGY HARVESTER WITH MECHANICAL AMPLIFIER FOR TRANSLATIONAL KINETIC</i> .....	<b>242</b>
<b>Červ J., Valeš F., Adámek V.:</b> <i>A SHORT WAVE LIMIT OF THE FREQUENCY EQUATION FOR PLANE-STRESS NONAXISYMMETRIC DISC MOTIONS</i> .....	<b>246</b>
<b>Chatys R., Miśków G., Miśków J.:</b> <i>STRUCTURAL MODELLING OF THE STRENGTH PROPERTIES OF POLYMER COMPOSITES STRUCTURAL MODELLING OF THE STRENGTH PROPERTIES OF POLYMER COMPOSITES</i> .....	<b>250</b>
<b>Chatys R., Piernik K.:</b> <i>NUMERICAL ANALYSIS OF POLYMER COMPOSITE BEND TESTS MADE BY VACUUM BAGGING</i> .....	<b>254</b>
<b>Cienciala J., Frydryšek K., Podešva J.:</b> <i>NONLINEAR VIBRATION – STOCHASTIC APPROACH</i> .....	<b>258</b>
<b>Ćwiklak J., Krasuski K., Jafarnik H.:</b> <i>DESIGNATION THE VELOCITY OF CESSNA 172 AIRCRAFT BASED ON GPS DATA IN FLIGHT TEST</i> .....	<b>262</b>
<b>Dabrowski A., Balcerzak M., Pikunov D.:</b> <i>APPLICATIONS OF THE NEW METHOD OF THE LYAPUNOV EXPONENTS ESTIMATION</i> .....	<b>266</b>
<b>Dindorf R., Wos P., Pawelec K.:</b> <i>STUDY OF THE POSSIBILITY OF USE OF BIOELECTRIC SIGNALS TO WIRELESS REMOTE CONTROL OF THE ELECTRO-PNEUMATIC POSITIONING SYSTEMS</i> .....	<b>270</b>
<b>Dočkal K., Šperka P., Křupka I., Hartl M.:</b> <i>FLUID FLOW MEASUREMENTS OF 5P4E BY PARTICLE TRACKING VELOCIMETRY</i> .....	<b>274</b>
<b>Drahorádová L., Moravec J., Andrlík V.:</b> <i>TESTING THE POSITIONING ACCURACY AND REGULARITY OF THE MOTION THREADED MECHANISM FEED DRIVE</i> .....	<b>278</b>
<b>Duda S., Gembalczyk G., Jureczko P.:</b> <i>THE EFFECT OF BODY WEIGHT UNLOADING ON KINEMATIC GAIT PARAMETERS DURING TREADMILL WALKING</i> .....	<b>282</b>
<b>Dudek D., Kazala R., Straczynski P.:</b> <i>JITTER ANALYSIS OF MQTT PROTOCOL FRAMES IN MOBILE ROBOT CONTROL SYSTEM</i> .....	<b>286</b>
<b>Dvořáková E., Patzák B.:</b> <i>COMPUTATIONAL PERFORMANCE OF A DSG-BASED ISOGEOMETRIC BEAM ELEMENT</i> .....	<b>290</b>
<b>Dzierżek K., Rečko M., Pietrala D. S.:</b> <i>QUICK PROTOTYPING OF MANIPULATOR CONTROL SYSTEM WITH PLC CONTROLLER</i> .....	<b>294</b>
<b>Dziopa Z., Nyckowski M.:</b> <i>THE DYNAMICS OF THE GUIDE ARRANGEMENT BEING AN ELEMENT OF THE LAUNCHER INSTALLED ON A COMBAT VEHICLE</i> .....	<b>298</b>



<b>Eliáš J., Le J. -L.:</b> <i>MITIGATION OF MESH DEPENDENCY IN PROBABILISTIC FINITE ELEMENT SIMULATION OF QUASIBRITTLE FRACTURE</i> .....	<b>302</b>
<b>Fiedler J., Koudelka T.:</b> <i>CALCULATION OF SHELL STRUCTURES BY USING LAYERED MODEL</i> .....	<b>306</b>
<b>Fischer C., Náprstek J.:</b> <i>LYAPUNOV EXPONENTS – PRACTICAL COMPUTATION</i> .....	<b>310</b>
<b>Frydryšek K., Drábková S., Plášek M.:</b> <i>BIOMECHANICS - AIRFLOW IN THE NASAL CAVITY AND THE NASAL SEPTUM PERFORATION</i> .....	<b>314</b>
<b>Frydryšek K., Dvořák L.:</b> <i>BIOMECHANICS - TESTING OF MECHANICAL AND UTILITY PROPERTIES OF BOTTLES FOR REDON DRAINAGE</i> .....	<b>318</b>
<b>Gajdosova K., Sonnenschein R.:</b> <i>ENDURANCE LIMIT OF FRP COMPOSITES USED FOR REINFORCEMENT OF CONCRETE STRUCTURES</i> .....	<b>322</b>
<b>Gapiński D., Szmidt P.:</b> <i>THE CONTROL PROCESS OF A SCANNING AND TRACKING IR SEEKER USING INVERSE DYNAMICS</i> .....	<b>326</b>
<b>Gidlewski M., Jemioł L., Żardecki D.:</b> <i>SENSITIVITY INVESTIGATIONS OF THE LANE CHANGE AUTOMATED PROCESS</i> .....	<b>330</b>
<b>Gierz Ł.:</b> <i>VALIDATION OF THE FEM-BASED STRESS ANALYSIS OF AN INNOVATIVE LOAD-BEARING STRUCTURE OF AIR-ASSISTED SEED DRILLS WITH ELECTRONIC SEEDING CONTROL</i> .....	<b>334</b>
<b>Gilewski W., Obara P.:</b> <i>EXACT 3-NODED TIMOSHENKO BEAM FINITE ELEMENT WITH ENHANCED STRAIN FIELD – A MAGIC ROLE OF GAUSS POINTS</i> .....	<b>338</b>
<b>Gilewski W., Pelczyński J.:</b> <i>THE INFLUENCE OF ORTHOTROPY LEVEL FOR PERPENDICULAR TO GRAIN STRESSES IN GLULAM DOUBLE TAPERED BEAMS</i> .....	<b>342</b>
<b>Goethel F. M., Mrozowski J., Awrejcewicz J.:</b> <i>COORDINATIVE PATTERNS AND GAIT STABILITY ACCESSED BY NONLINEAR DYNAMICS APPROACH: A PRELIMINARY STUDY</i> .....	<b>346</b>
<b>Golebiowska I., Dutkiewicz M.:</b> <i>EXPERIMENTAL ANALYSIS OF EFFICIENCY OF MASS DAMPERS</i> .....	<b>350</b>
<b>Golebiowska I., Dutkiewicz M., Usewicz B.:</b> <i>MECHANICAL DAMPERS ON OVERHEAD POWER LINES</i> .....	<b>354</b>
<b>Grzyb M., Stefański K.:</b> <i>TURBULENCE IMPACT ON THE CONTROL OF GUIDED BOMB UNIT</i> .....	<b>358</b>
<b>Had J.:</b> <i>IMPLEMENTATION OF INTERACTING CREEP AND FATIGUE UNDER THERMO-MECHANICAL LOADING</i> .....	<b>362</b>
<b>Hájek P., Švancara P., Horáček J., Švec G. J.:</b> <i>EFFECTS OF TURBULENCE IN FE MODEL OF HUMAN VOCAL FOLDS SELF-OSCILLATION</i> .....	<b>366</b>
<b>Havelka J., Sýkora J., Kučerová A.:</b> <i>CALDERÓN'S INVERSE PROBLEM IN CIVIL ENGINEERING</i> .....	<b>370</b>

<b>Hejnova M.:</b> <i>PRINCIPLE OF THE ROLLING CONTACT FATIGUE FORMATION</i> .....	<b>374</b>
<b>Hollý I., Sonnenschein R.:</b> <i>GFRP REINFORCEMENT IN CONCRETE – FACTORS AFFECTING BOND PROPERTIES</i> .....	<b>378</b>
<b>Horáček J., Radolf V., Bula V., Košina J.:</b> <i>EXPERIMENTAL MODELLING OF PHONATION USING ARTIFICIAL MODELS OF HUMAN VOCAL FOLDS AND VOCAL TRACTS</i> .....	<b>382</b>
<b>Hubova O., Konecna L.:</b> <i>WIND FLOW AROUND HIGH-RISE BUILDINGS AND ITS INFLUENCE ON THE PEDESTRIAN COMFORT</i> .....	<b>386</b>
<b>Hynek P., Vampola T.:</b> <i>EXAMINATION OF THE BASIC GEOMETRICAL PARAMETERS OF THE LOWER RESPIRATORY TRACT OF THE HUMAN AND ITS SIMPLIFIED COMPUTATIONAL MODEL</i> .....	<b>390</b>
<b>Ivankova O., Meri D., Vojtekova E.:</b> <i>DESIGN AND OPTIMIZATION OF SUPPORTING STRUCTURE OF A MULTIPURPOSE HIGH-RISE BUILDING WITH RESPECT TO THE WIND LOAD</i> .....	<b>394</b>
<b>Ivankova O., Valasik A., Konecna L.:</b> <i>A HIGH-RISE BUILDING - INFLUENCE OF CHANGE OF SOIL STIFFNESS ON HORIZONTAL AND VERTICAL DEFLECTIONS</i> .....	<b>398</b>
<b>Janiček P.:</b> <i>SYSTEMS CONCEPTION OF PROBLEM-SOLVING</i> .....	<b>402</b>
<b>Janiček P., Fuis V.:</b> <i>MODELLING – A TOOL FOR PROBLEM-SOLVING</i> .....	<b>406</b>
<b>Janouchová E., Kučerová A., Sýkora J.:</b> <i>ROLE OF RANDOM FACTORS IN NONLINEAR REGRESSION: A CASE STUDY FOR ESTIMATION OF THERMOPHYSICAL PARAMETERS</i> .....	<b>410</b>
<b>Jarzyna T.:</b> <i>DETERMINATION OF RIGIDITY AND DAMPING PARAMETERS OF HYDRODYNAMIC BEARINGS</i> .....	<b>414</b>
<b>Jegla Z., Reppich M.:</b> <i>VERIFICATION OF A NEW THERMAL CALCULATION METHOD BY INDUSTRIAL RADIANT CHAMBER MEASUREMENTS</i> .....	<b>418</b>
<b>Jirásko J., Max A., Bezdekova J.:</b> <i>STATIC NUMERICAL ANALYSIS OF A HYDRAULIC CURING PRESS</i> .....	<b>422</b>
<b>Jureczko M., Jureczko P.:</b> <i>ANALYSIS OF RELATIONSHIP BETWEEN POSTURAL STABILITY AND DEGREE OF VISUAL IMPAIRMENT</i> .....	<b>426</b>
<b>Kadlíček T., Janda T., Šejnoha M.:</b> <i>THE CALIBRATION PROGRAM FOR THE HYPOPLASTIC SAND MODEL</i> .....	<b>430</b>
<b>Karoľ M., Chlupová A., Mazánová V., Kruml T.:</b> <i>FATIGUE CRACK INITIATION AND GROWTH IN 316L STEEL IN TORSIONAL CYCLIC LOADING</i> .....	<b>434</b>
<b>Kaszkowiak J., Markiewicz-Patalon M., Borowski S., Dorszewski P.:</b> <i>IMPACT OF SUPERCHARGING ON THE NOISE LEVEL IN BIOGAS ENGINES</i> .....	<b>438</b>
<b>Katrňák T.:</b> <i>DESIGN OF NEW PARAMETERS FOR EVALUATION OF LOAD CAPACITY OF SEMI-SHELL STRUCTURES</i> .....	<b>442</b>

<b>Kawlewska E., Zarwańska M., Larysz D., Wolański W., Gzik M.: PREOPERATIVE PLANNING OF CORRECTION OF CRANIAL DEFORMATIONS USING DISTRACTORS.....</b>	<b>446</b>
<b>Kebli B., Baka Z.: AXISYMMETRIC DEFORMATION OF AN ELASTIC MEDIUM WEAKENED BY AN ANNULAR CRACK .....</b>	<b>450</b>
<b>Keckstein T., Bezděková J., Votápek P.: STATIC CHECKING COMPUTATION OF A LATHE TAILSTOCK .....</b>	<b>454</b>
<b>Kilinc O., Vágner J.: WAYSIDE DIAGNOSIS OF METRO WHEELSETS USING ACOUSTIC SENSOR DATA AND ONE-PERIOD ANALYSIS .....</b>	<b>458</b>
<b>Klečková J., Hamza J.: NUMERICAL SIMULATION OF STEAM FLOW AROUND VIBRATING TURBINE BLADES.....</b>	<b>462</b>
<b>Kłosowiak R., Bartoszewicz J., Urbaniak R.: ENERGY TRANSFORMATION IN TURBULENT FLOW INSIDE REVERSIG CHAMBER.....</b>	<b>466</b>
<b>Knopik L., Migawa K., Peszyński K., Wawrzyniak S.: SOME REMARKS ON PREVENTIVE REPLACEMENT MODEL.....</b>	<b>470</b>
<b>Kolman R., Cho S. S., Gonzalez J. G., Park K. C., Berezovski A.: AN EXPLICIT TIME SCHEME WITH LOCAL TIME STEPPING FOR ONE-DIMENSIONAL WAVE PROPAGATION IN A BIMATERIAL BAR.....</b>	<b>474</b>
<b>Konopelska A., Jureczko M.: EVALUATION OF KNEE JOINT STIFFNESS IN CHILDREN WITH CEREBRAL PALSY.....</b>	<b>478</b>
<b>Kořínek T., Petříková M.: AN INVESTIGATION OF MASS TRANSFER IN A VORTEX SHEDDING PAST SQUARE CYLINDER.....</b>	<b>482</b>
<b>Koruba Z., Krzysztofik I.: A CONTROL WITH THE USE OF LQR MODIFIED METHOD IN THE GYROSCOPE SYSTEM OF TARGET TRACKING .....</b>	<b>486</b>
<b>Kostek R., Aleksandrowicz P.: EFFECT OF CONTACT PARAMETERS ON THE PATTERN OF VEHICLE COLLISIONS WITH A ROUND PILLAR.....</b>	<b>490</b>
<b>Kostek R., Aleksandrowicz P.: IDENTIFICATION OF THE PARAMETERS OF VEHICLE CONTACT WITH A RIGID BARRIER FROM A CRASH TEST.....</b>	<b>494</b>
<b>Košťal R., Janhuba L., Hlinka J.: INTELLIGENT SCHEDULED MAINTENANCE METHODOLOGY FOR GENERAL AVIATION STRUCTURES BASED ON MSG-3 AND MULTIPLE- CRITERIA DECISION MAKING ANALYSIS .....</b>	<b>498</b>
<b>Koudelka T., Krejčí T., Kruis J.: NUMERICAL MODELLING OF EXPANSIVE CLAYS.....</b>	<b>502</b>
<b>Koukal M.: ANALYSIS OF THE MANUFACTURE PERTURBATIONS OF THE TOTAL HIP REPLACEMENT.....</b>	<b>506</b>
<b>Kovář J.: THE INFLUENCE OF CONTACT REGION ON PROBABILITY OF CERAMICS FRACTURE .....</b>	<b>510</b>

<b>Králík J.:</b> <i>PROBABILITY NONLINEAR ANALYSIS OF THE FAILURE OF THE NPP HERMETIC STEEL DOOR DUE TO ACCIDENTAL EXTREME OVERPRESSURE</i> .....	<b>514</b>
<b>Krejsa J., Sýkora M.:</b> <i>PROBABILISTIC ESTIMATION OF A BRIDGE FATIGUE LIFE IN ACCORDANCE TO fib MODEL CODE 2010</i> .....	<b>518</b>
<b>Krejsa J., Vechet S.:</b> <i>THE EVALUATION OF HOKUYO URG-04LX-UG01 LASER RANGE FINDER DATA</i> .....	<b>522</b>
<b>Kriváček J., Sadovský Z.:</b> <i>ON THE CHOICE OF GEOMETRICAL IMPERFECTIONS IN GMNIA STRENGTH CALCULATIONS OF THIN-WALLED STRUCTURES</i> .....	<b>526</b>
<b>Krzysztofik I., Koruba Z.:</b> <i>APPLICATION OF THE SLIDING CONTROLLER FOR THE GYROSCOPE SYSTEM OF THE ANTI-AIRCRAFT MISSILE</i> .....	<b>530</b>
<b>Kšica F., Vetiška J., Hadaš Z.:</b> <i>METHODOLOGY FOR PREDICTING DYNAMIC BEHAVIOUR OF MACHINE TOOLS BASED ON A VIRTUAL MODEL</i> .....	<b>534</b>
<b>Kubík M., Macháček O., Strecker Z., Roupec J., Mazůrek I.:</b> <i>DYNAMIC VISCOSITY OF COMMERCIALY AVAILABLE MAGNETORHEOLOGICAL FLUIDS</i> .....	<b>538</b>
<b>Kubík P., Petruška J., Hůlka J., Šebek F.:</b> <i>SIMULATION OF THE SMALL PUNCH TEST OF AISI 316L AUSTENITIC STEEL</i> .....	<b>542</b>
<b>Kučera P., Píštěk V.:</b> <i>SHAFT VIBRATION OF THE TRUCK</i> .....	<b>546</b>
<b>Kucíková L., Vorel J., Sýkora J., Šejnoha M.:</b> <i>EFFECTIVE HEAT AND MOISTURE TRANSPORT PROPERTIES OF SPRUCE</i> .....	<b>550</b>
<b>Kukielka K., Kukielka L.:</b> <i>THERMOMECHANICAL MODELING AND ANALYSIS OF THE THREAD ROLLING PROCESS WITH ELECTROCONTACT HEATING</i> .....	<b>554</b>
<b>Kulesza Z., Trochimeczuk R.:</b> <i>DYNAMICS OF MULTIBODY SURGICAL ROBOTIC SINGLE INCISION LAPAROSCOPIC SURGERY TOOL</i> .....	<b>558</b>
<b>Kulhavý P., Srovátková M., Petrů M.:</b> <i>ALTERNATIVE POSSIBILITIES OF BIAXIAL TESTING OF FIBER AND FABRIC MATERIALS IN NONSTANDARD CONDITIONS</i> .....	<b>562</b>
<b>Kumpán P.:</b> <i>SEGMENTATION OF HUMAN MOTION ACCELERATION WITH PROBABILISTIC CLASSIFIER</i> .....	<b>566</b>
<b>Kupireddi K. K., Sai Sudheer S. V., Balasubramanian K.:</b> <i>EFFECT OF LOOP DIAMETER ON TWO-PHASE NATURAL CIRCULATION LOOP PERFORMANCE</i> .....	<b>570</b>
<b>Kurzawa A., Bocian M., Jamroziak K., Pyka D.:</b> <i>ANALYSIS OF CERAMIC-METALLIC COMPOSITES OF BALLISTIC RESISTANCE ON SHOTS BY 5.56 MM AMMUNITION</i> .....	<b>574</b>
<b>Kyncl M., Pelant J.:</b> <i>ATMOSPHERIC GAS FLOW AROUND AND INSIDE HIGH HALLS SUPPORTED WITH THE SIMULATION OF THE FANS</i> .....	<b>578</b>

<b>Laco K., Borzovič V.:</b> <i>SHEAR FORCES OF THE APPROACH SLABS OF THE ROAD BRIDGES</i> .....	<b>582</b>
<b>Laski P. A.:</b> <i>KINEMATICS AND WORKSPACE ANALYSIS FOR A 6-DOF PARALLEL MANIPULATOR WITH COAXIAL CTUATED ARMS</i> .....	<b>586</b>
<b>Löffelmann F.:</b> <i>FAILURE INDEX BASED TOPOLOGY OPTIMIZATION FOR MULTIPLE PROPERTIES</i> .....	<b>590</b>
<b>Macháček O., Kubík M., Novák P.:</b> <i>A NEW METHOD OF MAGNETORHEOLOGICAL DAMPER QUALITY EVALUATION</i> .....	<b>594</b>
<b>Maćkowiak P., Ligaj B.:</b> <i>DAMAGE TO ADHESIVE SINGLE LAP JOINT MADE OF MATERIALS WITH DIFFERENT PROPERTIES UNDER STATIC LOADING CONDITIONS</i> .....	<b>598</b>
<b>Major M., Kuliński K., Major I.:</b> <i>INNOVATIVE CONCRETE-POLYURETHANE COMPOSITE BLOCKS LOCATED IN THREE-LAYER WALL – THERMAL NUMERICAL ANALYSIS</i> .....	<b>602</b>
<b>Malínek P.:</b> <i>STABILITY MARGINS EXPERIMENTAL SEARCH OF AN AEROELASTIC SYSTEM</i> .....	<b>606</b>
<b>Mališ M., Šplíchal J.:</b> <i>SIMULATION OF PILOT LOAD DURING EMERGENCY LANDING CONDITIONS</i> .....	<b>610</b>
<b>Mallick A., Ranjan R.:</b> <i>THERMO-MECHANICAL ANALYSIS OF A FUNCTIONALLY GRADED ANNULAR FIN</i> .....	<b>614</b>
<b>Marcián P., Florian Z., Horácková L., Borák L.:</b> <i>ANALYSIS OF BOUNDARY CONDITIONS IN FINITE ELEMENT SUB-MODELS OF INTERACTION OF HUMAN MANDIBLE WITH DENTAL IMPLANT</i> .....	<b>618</b>
<b>Mašek J., Brožek P., Horák M.:</b> <i>THERMO-VACUUM TEST CHAMBER DEVELOPMENT FOR HEAT SWITCH TESTING IN SIMULATED MARTIAN CONDITIONS</i> .....	<b>622</b>
<b>Mat’as M., Frydryšek K.:</b> <i>RELIABILITY ASSESSMENT OF THE PRETENSIONED BOLTS BASED ON PROBABILITY</i> .....	<b>626</b>
<b>Mauro F., Cerni P., Nabergoj R.:</b> <i>RANS CALCULATIONS ON SUBMERGED BODIES</i> .....	<b>630</b>
<b>Mauro F., Nabergoj R.:</b> <i>DETERMINATION OF NON-LINEAR ROLL DAMPING COEFFICIENTS FROM MODEL DECAYTEST</i> .....	<b>634</b>
<b>Max A., Hynek M., Řehounek L.:</b> <i>ANALYSIS OF A BOOM CONVEYOR</i> .....	<b>638</b>
<b>Mazurkiewicz A.:</b> <i>IMPACT OF MINERAL CONTENT IN HUMAN TRABECULAR BONE ON ITS ELASTIC PROPERTIES</i> .....	<b>642</b>
<b>Mazurkiewicz A.:</b> <i>IMPACT OF MINERAL CONTENT IN HUMAN TRABECULAR BONE ON ITS STATIC AND FATIGUE PROPERTIES</i> .....	<b>646</b>

<b>Menshykov O., Menshykova M., Guz I. A.:</b> <i>THICK-WALLED COMPOSITE PIPES UNDER BENDING</i> .....	<b>650</b>
<b>Migawa K., Knopik L., Neubauer A., Perczyński D.:</b> <i>SIMULATION OF THE MODEL OF TECHNICAL OBJECT AVAILABILITY CONTROL</i> .....	<b>654</b>
<b>Migawa K., Knopik L., Soltysiak A., Kolber P.:</b> <i>THE METHOD OF RISK ASSESSMENT IN TRANSPORT SYSTEMS</i> .....	<b>658</b>
<b>Mikeš K., Jirásek M.:</b> <i>ON EFFICIENCY OF QUASICONTINUUM SIMULATION OF CRACK PROPAGATION IN ELASTIC-BRITTLE DISORDERED LATTICES</i> .....	<b>662</b>
<b>Mochar D., Gabriel D., Masák J., Kopačka J., Kolman R., Plešek J., Hynek P., Vtípil J.:</b> <i>EXPLICIT DYNAMIC FINITE ELEMENT ANALYSIS OF A FIRING PIN ASSEMBLY</i> .....	<b>666</b>
<b>Morávková Z., Tomečková I., Frydryšek K.:</b> <i>BEAM RESTED ON UNILATERAL ELASTIC FOUNDATION – (THEORY, EXPERIMENTS AND FINITE ELEMENT APPROACH)</i> .....	<b>670</b>
<b>Mrozik Ł.:</b> <i>SHAPING THE STRUCTURE OF LOW WATER-BINDER RATIO CEMENT PASTES</i> .....	<b>674</b>
<b>Muraszkowski A., Szrek J.:</b> <i>THE CONCEPT OF MOBILE SYSTEM OF ANALYSIS AND VISUALIZATION OF HUMAN GAIT PARAMETERS</i> .....	<b>678</b>
<b>Murín J., Goga V., Kutiš V., Hrabovský J., Sedlár T., Paulech J.:</b> <i>MODELLING AND MEASUREMENT OF NON-UNIFORM ELASTOSTATIC TORSION OF HOLLOW CROSS-SECTION BEAMS</i> .....	<b>682</b>
<b>Musil M., Sivý M.:</b> <i>PARAMETRIC INSTABILITY OF THE PLANE FREE SURFACE OF THE LIQUID IN CYLINDRICAL STORAGE TANKS</i> .....	<b>686</b>
<b>Myšáková E., Lepš M.:</b> <i>SHIFTING OF LHS DESIGN FOR SURROGATE MODELING</i> .....	<b>690</b>
<b>Nagireddy P. D., Rao Srinivasa Ch.:</b> <i>EXPERIMENTAL STUDIES ON FE304 NANOFLUID FLOWING THROUGH A CIRCULAR TUBE</i> .....	<b>694</b>
<b>Náprstek J., Fischer C.:</b> <i>NON-HOLONOMIC PLANAR AND SPATIAL MODEL OF A BALL-TYPE TUNED MASS DAMPING DEVICE</i> .....	<b>698</b>
<b>Němec M., Jelínek T., Klíma J.:</b> <i>TESTING OF FULL STAGE MIXED-FLOW TURBINE FOR AUTOMOTIVE APPLICATIONS</i> .....	<b>702</b>
<b>Němec Z., Nevrlý J.:</b> <i>MODELING OF ROAD ROLLER DRIVE EQUIPPED WITH HYDROSTATIC RECOVERY OF KINETIC ENERGY</i> .....	<b>706</b>
<b>Němeček J., Kruis J., Koudelka T.:</b> <i>MODELING OF CHLORIDE MIGRATION IN CONCRETE</i> .....	<b>710</b>
<b>Nocoň L., Koruba Z.:</b> <i>MODIFICATIONS OF CONTROL ACTUATION SYSTEMS OF ATGM</i> .....	<b>714</b>

<b>Nowakowska K., Michnik R., Myśliwiec A., Chrzan M.:</b> <i>IMPACT OF STRENGTHENING OF THE ERECTOR SPINAE MUSCLE ON THE VALUES OF LOADS OF THE MUSKULOSKELETAL SYSTEM IN THE LUMBAR SPINE SECTION.....</i>	<b>718</b>
<b>Nowakowski Ł., Miko E., Skrzyniarz M.:</b> <i>DESIGNATION OF THE MINIMUM THICKNESS OF MACHINED LAYER FOR THE MILLING PROCESS OF DURALUMIN PA6.....</i>	<b>722</b>
<b>Nowakowski Ł., Miko E., Skrzyniarz M.:</b> <i>MILLING WITH A TOOL WITH UNEVENLY DISTRIBUTED CUTTING PLATES.....</i>	<b>726</b>
<b>Nowakowski L., Skrzyniarz M., Miko E.:</b> <i>THE ANALYSIS OF RELATIVE OSCILLATION DURING FACE MILLING .....</i>	<b>730</b>
<b>Nowakowski L., Skrzyniarz M., Miko E.:</b> <i>THE ASSESSMENT OF THE IMPACT OF THE INSTALLATION OF CUTTING PLATES IN THE BODY OF THE CUTTER ON THE SIZE OF GENERATED VIBRATIONS AND THE GEOMETRICAL STRUCTURE OF THE SURFACE.....</i>	<b>734</b>
<b>Osiński P., Stosiak M.:</b> <i>SHAPING THE STARTING OF A HYDROSTATIC TRANSMISSION WITH PROPORTIONALLY CONTROLLED ELEMENTS.....</i>	<b>738</b>
<b>Osowski P., Wolski M., Piatkowski T.:</b> <i>VERYFICATION OF VELOCITY MESURMENT METHODS BY HIGH SPEED CAMERA AND ACCELEROMETER ON EXAMPLE OF IMPACT TESTER.....</i>	<b>742</b>
<b>Paczkowski T., Sawicki J.:</b> <i>EXPERIMENTAL STUDIES OF VIBRATION OF THE TECHNOLOGICAL DEVICE FOR ELECTROCHEMICAL MACHINING OF CURVILINEAR SURFACES.....</i>	<b>746</b>
<b>Pásek M., Bébarová M., Christé G.:</b> <i>A MODIFIED MATHEMATICAL MODEL OF HUMAN VENTRICULAR CARDIOMYOCYTE INCORPORATING SEPARATE T-TUBULAR AND SURFACE DYADS AND SUBMEMBRANE SPACES.....</i>	<b>750</b>
<b>Patyk S., Patyk R., Kukielka L., Kalduński P., Chojnacki J.:</b> <i>NUMERICAL METHOD FOR DETERMINING THE MAIN FORCE OF BURNISHING ROLLING OF ROUGH CYLINDRICAL SURFACE WITH REGULAR PERIODICAL OUTLINES ASPERITIES .....</i>	<b>754</b>
<b>Pavlenko M.:</b> <i>THE FORMATION OF ZONES OF THE COAL ARRAY VOLUMETRIC IMPREGNATION AS A RESULT OF THE VIBRATION IMPACT .....</i>	<b>758</b>
<b>Pejkowski Ł.:</b> <i>DETERMINATION OF THE NUMBER OF CYCLES FOR ASYNCHRONOUS PERIODIC MULTIAXIAL LOADINGS USING ENERGY BASED CUMULATIVE DAMAGE THEORY.....</i>	<b>762</b>
<b>Perz K., Rewolińska A.:</b> <i>IMPACT OF FILTER CONTAMINATION ON EFFICIENCY AND EFFECTIVENESS OF AIR FILTER .....</i>	<b>766</b>
<b>Peszyński K., Perczyński D., Smyk E., Kolber P.:</b> <i>EXPERIMENTAL VERIFICATION OF VELOCITY DISTRIBUTION IN DIFFERENT CROSS-SECTIONAL VENTILATION DUCTS.....</i>	<b>770</b>

<b>Pichal R., Machacek J.: EXPERIMENTAL AND NUMERICAL STUDY OF STAYED STEEL COLUMNS.....</b>	<b>774</b>
<b>Pietrala D. S., Laski P. A., Bracha G. F., Dzierzek K.: APPLICATION OF WOLFRAM MATHEMATICA PACKAGE TO CONTROL THE 6-DOF PARALLEL ROBOT.....</b>	<b>778</b>
<b>Piwowarski D., Anweiler S., Ulbrich R., Tańczuk M.: UNMANNED AIRCRAFT VEHICLE DESIGN FOR TEMPERATURE FIELD ANALYSIS .....</b>	<b>782</b>
<b>Plánička S., Vimmr J.: NUMERICAL SIMULATIONS OF FREE SURFACE FLOWS USING A THREE-EQUATION MODEL .....</b>	<b>786</b>
<b>Pochwała S., Wydrych J., Borsuk G.: THE EFFECT OF VELOCITY PROFILE DEFORMATION OF AN AVERAGING PITOT TUBE THE EFFECT OF VELOCITY PROFILE DEFORMATION OF AN AVERAGING PITOT TUBE.....</b>	<b>790</b>
<b>Polach P., Hajžman M., Byrtus M., Dyk Š., Smolík L.: MATHEMATICAL MODELLING OF ROTOR SYSTEMS WITH JOURNAL BEARINGS IN LIMIT CASES.....</b>	<b>794</b>
<b>Prachar A., Hospodář P., Vrchota P.: GUST ALLEVIATION OF NASA COMMON RESEARCH MODEL USING CFD.....</b>	<b>798</b>
<b>Pravdová I., Eliášová M.: INFLUENCE OF AN INTIAL IMPERFECTION ON THE LATERAL AND TORSIONAL BUCKLING OF A HYBRID BEAM.....</b>	<b>802</b>
<b>Profant T., Hrstka M., Klusák J., Keršner Z.: ON THE ENERGY RELEASE RATE OF THE CRACK EMANATING FROM THE INCLUSION INTERPHASE .....</b>	<b>806</b>
<b>Prokop A., Řehák K.: VIRTUAL PROTOTYPE APPLICATION TO HEAVY-DUTY VEHICLE GEARBOX CONCEPT.....</b>	<b>810</b>
<b>Půst L., Pešek L.: RUNNING FLUTTER WAVES IN BLADES CASCADE .....</b>	<b>814</b>
<b>Řehounek L., Jíra A., Denk F.: MECHANICAL BEHAVIOR OF A TITANIUM ALLOY TRABECULAR STRUCTURE .....</b>	<b>818</b>
<b>Reut O. V.: THE ANTIPLANE PROBLEM FOR A STRIP WEAKENED BY A CRACK.....</b>	<b>822</b>
<b>Romańczyk M., Elsner W.: NUMERICAL ANALYSIS FOR OPTIMAL LOCALIZATION OF GAS INLET IN A VENTURI MIXER.....</b>	<b>826</b>
<b>Roupec J., Mazůrek I., Strecker Z., Kubík M., Macháček O.: TENSILE STRENGTH OF PURE IRON SAMPLES MANUFACTURED BY SELECTIVE LASER MELTING METHOD .....</b>	<b>830</b>
<b>Runt D., Novotný J., Pruška J.: SPECIAL ELEMENT FOR NUMERICAL MODELLING OF THE ROCK BOLT REINFORCEMENT .....</b>	<b>834</b>
<b>Sądej M., Gierz Ł.: POLYURETHANE COMPOSITES WITH IMPROVED MECHANICAL PROPERTIES.....</b>	<b>838</b>



<b>Sant Z., Mifsud L., Muscat C.:</b> <i>SIMULATION OF DAILY LIFE ACTIVITIES IN BIOMECHANICS</i> .....	842
<b>Sapietová A., Šulka P., Sapieta M., Domański T.:</b> <i>VERIFICATION OF MECHANISM'S FUNCTIONALITY FOR POSITIONING THE CAR SEAT USING MSC.ADAMS</i> .....	846
<b>Schmidt J., Janda T., Šejnoha M., Valentin J.:</b> <i>EXPERIMENTAL DETERMINATION OF VISCO-ELASTIC PROPERTIES OF LAMINATED GLASS INTERLAYER</i> .....	850
<b>Šebek F., Petruška J., Kubík P.:</b> <i>DUCTILE FRACTURE CRITERIA IMPLEMENTATION AND CALIBRATION USING THE TENSION–TORSION TESTS</i> .....	854
<b>Semkło Ł., Frąckowiak A., Ciałkowski M.:</b> <i>LOCATION OF LEAKS IN THE WATER SUPPLY NETWORK</i> .....	858
<b>Ševeček O., Majer Z., Kotoul M.:</b> <i>INFLUENCE OF CERAMIC FOAM PARAMETERS ON THE FRACTURE BEHAVIOUR UPON THE TENSILE TEST</i> .....	862
<b>Shatskyi I., Makoviichuk M., Perepichka V., Dalyak T.:</b> <i>EFFECT OF CRACKS CLOSURE IN PLATES AND SHELLS UNDER COMBINED TENSION AND BENDING</i> .....	866
<b>Shatskyi I., Popadyuk I., Velychkovych A.:</b> <i>MODELLING OF ENERGY DISSIPATION IN SHELL DAMPERS</i> .....	870
<b>Siwulski T., Warzyńska U.:</b> <i>THE ADVANTAGES OF A NEW HYDRAULIC CYLINDER DESIGN WITH A CONTROL SYSTEM</i> .....	874
<b>Sławski S., Duda S., Machoczek T.:</b> <i>THIN WALLED PIPE CRUSHED IN JAWS</i> .....	878
<b>Smyk E., Mrozik D., Wawrzyniak S., Peszyński K.:</b> <i>TUBULAR AIR DEFLECTOR IN VENTILATION DUCTS</i> .....	882
<b>Smyk E., Wawrzyniak S., Perczyński D., Kolber P.:</b> <i>AXISYMMETRIC VALVE WITH SYNTHETIC JET ACTUATOR</i> .....	886
<b>Sobotka J.:</b> <i>FORCED VIBRATION ANALYSIS OF PRESTRESSED EULER-BERNOULLI BEAM WITH DISCONTINUITIES BY MEANS OF DISTRIBUTIONS WITHOUT USING MODAL ANALYSIS</i> .....	890
<b>Sokół K.:</b> <i>INSTABILITY OF A STEPPED COLUMN LOADED BY THE EXTERNAL FOLLOWER FORCE</i> .....	894
<b>Sokol M., Lamperová K., Venglar M., Hernández Carrasco L. H.:</b> <i>OPTIMUM DESIGN OF TUNED LIQUID COLUMN DAMPER FOR HIGH-RISE BUILDING</i> .....	898
<b>Sokol Z., Fila J., Eliášová M.:</b> <i>LOAD BEARING TEST OF WALL FROM HOLLOW GLASS BLOCKS USING VITRALOCK INSTALLATION SYSTEM</i> .....	902

<b>Sokolski M., Sokolski P.:</b> <i>ACOUSTIC CLIMATE IN THE CABINS AS A FACTOR OF REBUILDING EFFECTIVENESS OF LONG TERM OPERATED BUCKET WHEEL EXCAVATORS – A CASE STUDY</i> .....	<b>906</b>
<b>Sokolski P.:</b> <i>ON WEAR PROCESSES IN PIN JOINTS IN CATERPILLARS OF LARGE-SIZE WORKING MACHINES</i> .....	<b>910</b>
<b>Sosnowski M.:</b> <i>COMPUTER AIDED OPTIMIZATION OF A NOZZLE IN AROUND-THE-PUMP FIRE SUPPRESSION FOAM PROPORTIONING SYSTEM</i> .....	<b>914</b>
<b>Stefański K., Chatys R., Stefańska A.:</b> <i>THE USE OF GYROSCOPIC EXECUTIVE SYSTEM FOR HOMING OF THE MISSILE ON THE AERIAL TARGET</i> .....	<b>918</b>
<b>Stopel M., Cichański A., Skibicki D.:</b> <i>MODELING OF PRESTRESSED BOLT CONNECTION IN LS-DYNA CRASH TEST ANALYSIS OF ROAD INFRACTURE</i> .....	<b>922</b>
<b>Štorkán J., Vampola T., Horáček J.:</b> <i>COMPUTATIONALLY EFFICIENT MODEL OF THE HUMAN VOCAL FOLD</i> .....	<b>926</b>
<b>Straka P., Příhoda J.:</b> <i>MODELLING OF FLOW IN LINEAR BLADE CASCADE WITH THICK TRAILING EDGE AT A LOWER REYNOLDS NUMBER</i> .....	<b>930</b>
<b>Strecker Z., Strmiska T., Roupec J., Kubík M., Macháček O.:</b> <i>DESIGN OF FAST MAGNETORHEOLOGICAL DAMPER USING SOFT MAGNETIC COMPOSITES</i> .....	<b>934</b>
<b>Strzelecki P.:</b> <i>RETESTED RUNOUT SPECIMENS IN FATIGUE RESEARCH</i> .....	<b>938</b>
<b>Šulc P., Pešek L., Bula V., Košina J., Cibulka J.:</b> <i>PROPOSAL OF HYPERELASTIC PROPORTIONAL DAMPING AS DISSIPATED ENERGY MODEL OF HARD RUBBERS</i> .....	<b>942</b>
<b>Šulc S., Šmilauer V., Wald F.:</b> <i>COUPLED SIMULATION FOR FIRE-EXPOSED STRUCTURE USING CFD AND THERMO-MECHANICAL MODELS</i> .....	<b>946</b>
<b>Šulka P., Sapietová A., Dekýš V., Sapieta M.:</b> <i>ANALYSIS OF NON-STATIONARY VIBRATION MODE MECHANICAL DEVICE</i> .....	<b>950</b>
<b>Svojanovský T., Trtík L.:</b> <i>STRESS ANALYSIS OF THE TOTAL REPLACEMENT OF THE TRAPEZIOMETACARPAL JOINT</i> .....	<b>954</b>
<b>Sýkora J., Kučerová A., Zeman J.:</b> <i>CONSTRUCTION OF RANDOM FIELD BASED ON IMAGE ANALYSIS</i> .....	<b>958</b>
<b>Szews M., Perczyński D., Knopik L., Wawrzyniak S.:</b> <i>TEMPERATURE ANALYSIS DEPENDENCE IN THE VICINITY OF THE BRAKE DISK</i> .....	<b>962</b>
<b>Szkoda K., Gałąska P., Źak M., Pezowicz C.:</b> <i>BIOMECHANICAL STUDY OF THE CERVICAL SPINE WITH DISC IMPLANTS: A FINITE ELEMENT ANALYSIS</i> .....	<b>966</b>

<b>Szmidt P., Gapiński D., Koruba Z.:</b> <i>THE ANALYSIS OF SELECTION OPTIMAL PARAMETERS OF PID CONTROLLERS FOR A MODIFIED ARTILLERY-MISSILE SYSTEM</i> .....	970
<b>Szrek J., Bałchanowski J.:</b> <i>MODELLING AND SIMULATION RESEARCHES OF DYNAMICS OF TRANSLATIONAL PARALLEL MECHANISM</i> .....	974
<b>Takosoglu J. E.:</b> <i>DYNAMIC CHARACTERISTICS OF PNEUMATIC ARTIFICIAL MUSCLES</i> .....	978
<b>Tomaszewski T.:</b> <i>ANALYSIS OF SIZE EFFECT FOR NOTCHED MINI SPECIMENS MADE OF STAINLESS STEEL</i> .....	982
<b>Topolinski T., Ligaj B., Mazurkiewicz A., Miterka S.:</b> <i>EVALUATION OF DEFORMATIONS OF THICK-LAYER GLUED JOINTS APPLIED IN CONSTRUCTION OF RAIL VEHICLES</i> .....	986
<b>Tůma J., Šuránek P., Mahdal M.:</b> <i>ALL-PASS FILTERS AS A TOOL FOR CONVERTING A POSITIVE FEEDBACK TO A NEGATIVE FEEDBACK WHEN CONTROLLING WEAKLY DAMPED SYSTEMS</i> .....	990
<b>Učeň O., Frydryšek K., Fojtík F., Bialý L., Pleva L.:</b> <i>BIOMECHANICS – VERIFICATION OF FORCE CHARACTERISTICS OF A DEVICE FOR REDUCTION OF BONE FRAGMENTS IN PATIENTS WITH FINGER FRACTURES</i> .....	994
<b>Uhříčik M., Oravcová M., Palček P., Chalupová M., Kuchariková L.:</b> <i>THREE-POINT BENDING FATIGUE DAMAGE MECHANISMS ASSOCIATED WITH THE DIFFERENT STRUCTURE OF AL-MG CAST ALLOYS</i> .....	998
<b>Úradníček J., Kraus P., Musil M., Bachratý M.:</b> <i>MODELING OF FRICTIONAL STICK SLIP EFFECT LEADING TO DISC BRAKE NOISE VIBRATION AND HARSHNESS</i> .....	1002
<b>Uzny S., Osadnik M.:</b> <i>INFLUENCE OF LONGITUDINAL ELASTIC SUPPORT ON STABILITY OF A PARTIALLY TENSIONED COLUMN</i> .....	1006
<b>Valentová S., Vorel J., Šejnoha M.:</b> <i>EFFECTIVE ELASTIC AND STRENGTH PROPERTIES OF UNIDIRECTIONAL FIBROUS CERAMIC COMPOSITES</i> .....	1010
<b>Valeš J., Kala Z.:</b> <i>WEAK AXIS BUCKLING - ELASTIC RESISTANCE OF A COLUMN</i> .....	1014
<b>Vampola T., Horáček J.:</b> <i>INFLUENCE OF THE NASAL CAVITIES TO HUMAN VOICE QUALITY</i> .....	1018
<b>Vechet S., Krejsa J., Chen K.-S.:</b> <i>EXPERT SYSTEM SHELL ARCHITECTURE BASED ON DECISION NETWORK</i> .....	1022
<b>Vida R., Halvonik J.:</b> <i>INFLUENCE OF COMPRESSIVE STRESS ON SHEAR FORCE DISTRIBUTION IN BRIDGE DECK SLABS</i> .....	1026

<b>Világi F., Knížat B., Urban F., Olšiak R., Mlkvik M., Ridzoň F., Mlynár P.:</b> <i>ESTIMATION OF MINOR LOSSES IN A NATURAL CIRCULATION HELIUM LOOP .....</i>	<b>1030</b>
<b>Vlasák P., Chára Z., Konfršt J.:</b> <i>CONCENTRATION DISTRIBUTION AND SLIP VELOCITY OF COARSE-PARTICLE-WATER MIXTURE IN HORIZONTAL AND INCLINED PIPE SECTIONS.....</i>	<b>1034</b>
<b>Vlček V., Zolotarev I., Kozánek J., Šidlof P., Štěpán M.:</b> <i>SOME ENERGY RELATIONS OF THE SELF-EXCITED PROFILE VIBRATION IN FLOWING FLUID .....</i>	<b>1038</b>
<b>Vorel J., Kabele P.:</b> <i>BACK ANALYSIS FOR DETERMINATION OF TENSION-SOFTENING DIAGRAM.....</i>	<b>1042</b>
<b>Votrubec R.:</b> <i>PLATFORM STABILIZED BY MEANS OF TWO GYROSCOPES AND DAMPED WITH MAGNETORHEOLOGICAL DAMPER“.....</i>	<b>1046</b>
<b>Vrchota P., Prachař A., Hospodář P., Dolgopyat D., Seifert A.:</b> <i>SIMPLIFIED OSCILLATORY BOUNDARY CONDITION FOR EFFICIENT CFD SIMULATION OF AFC EFFECT .....</i>	<b>1050</b>
<b>Wirwicki M., Andryszczyk M., Andrzejewska A., Topoliński T.:</b> <i>TESTING THE STRENGTH OF THE ADHESIVE CONNECTION IN SPECIMEN - MONOTONIC TENSILE AND SHEAR WITH UNDER VARIABLE LOAD .....</i>	<b>1054</b>
<b>Wodarski P., Michnik R., Gzik M., Jurkojc J., Bieniek A., Nowakowska K.:</b> <i>VARIANTS OF UPPER LIMB MOTION INDEX CALCULATIONS IN THE ASSESSMENT OF UPPER LIMB MOTION DYSFUNCTION .....</i>	<b>1058</b>
<b>Wolski M., Piatkowski T., Osowski P.:</b> <i>ROTARY MOTION SELECTED CONTROL METHODS ANALYSIS FOR PADDLE SORTERS ARMS .....</i>	<b>1062</b>
<b>Woś P., Dindorf R.:</b> <i>A SEMI-ACTIVE PNEUMATIC SUSPENSION OF THE WORKING MACHINE SEAT.....</i>	<b>1066</b>
<b>Woś P., Dindorf R.:</b> <i>LEAK MEASURING SYSTEM OF COMPRESSED AIR IN PIPELINE.....</i>	<b>1070</b>
<b>Wydrych J., Borsuk G., Pochwała S.:</b> <i>ANALYSIS OF THE EROSION WEAR MODELING RESULTS OF THE PNEUMATIC CONVEYING SYSTEMS .....</i>	<b>1074</b>
<b>Zachar M., Guzej M., Horský J.:</b> <i>NUMERICAL THERMAL COMPARISON OF HEAT SINK MATERIALS FOR AUTOMOTIVE LED HEADLAMPS.....</i>	<b>1078</b>
<b>Zachwieja J., Peszyński K.:</b> <i>DETERMINATION OF THE STRESS - STRAIN STATE FOR INDUSTRIAL PIPELINE BASED ON ITS VIBRATION.....</i>	<b>1082</b>
<b>Záda V.:</b> <i>APPLICATION OF HAMILTONIAN MECHANICS IN EXPONENTIALLY STABLE CONTROL OF ROBOTS .....</i>	<b>1086</b>
<b>Zajac P., Kowalczyk L.:</b> <i>COMPREHENSIVE SERVICE OF CONFERENCE PARTICIPANTS USING AUTOMATIC IDENTIFICATION .....</i>	<b>1090</b>

<b>Zajac P., Kwasniowski S.:</b> <i>MODELLING FORKLIFT TRUCK MOVEMENT IN THE VDI CYCLE AND THE POSSIBILITY OF ENERGY RECOVERY</i> .....	<b>1094</b>
<b>Zajac P., Kwasniowski S.:</b> <i>RELIABILITY OF AUTOMATIC IDENTIFICATION SYSTEMS IN LOGISTICS SYSTEMS</i> .....	<b>1098</b>
<b>Žák J.:</b> <i>FULL WIDTH WARP TENSION SENSOR</i> .....	<b>1102</b>
<b>Žak M., Filipiak J., Plonek T.:</b> <i>A FINITE ELEMENT STRESS ANALYSIS TO PREDICT THE RISK FACTORS OF AORTIC DISSECTION - PRELIMINARY STUDIES</i> .....	<b>1106</b>
<b>Zapoměl J., Ferfecki P., Kozánek J.:</b> <i>REDUCTION OF THE ENERGY LOSSES BY APPLICATION OF CONTROLLABLE SQUEEZE FILM DAMPERS</i> .....	<b>1110</b>
<b>Zastempowski M.:</b> <i>DYNAMICS OF MOVEMENT IN SCISSOR-FINGER CUTTING ASSEMBLY</i> .....	<b>1114</b>
<b>Zeman V., Hlaváč Z.:</b> <i>FRICTION FORCES AND FRETTING WEAR IN REACTOR CORE BARREL COUPLINGS</i> .....	<b>1118</b>
<b>Zemanová A., Zeman J., Janda T., Šejnoha M.:</b> <i>FREE VIBRATION ANALYSIS OF LAMINATED GLASS BEAMS USING DYNAMIC EFFECTIVE THICKNESS AND OTHER APPROACHES</i> .....	<b>1122</b>
<b>Zhuravlova Z., Kozachkov D., Pliusnov D., Radzivil V., Reut V., Shpynarov O., Tarasova E., Nerukh D., Vaysfeld N.:</b> <i>MODELLING OF VIRUS VIBRATION WITH 3-D DYNAMIC ELASTICITY THEORY</i> .....	<b>1126</b>
<b>Ziolkowska J.:</b> <i>POLYURETHANE COATINGS AND METHODS OF EXAMINATION OF THEIR PROPERTIES</i> .....	<b>1130</b>
<b>Zvolský T.:</b> <i>MATHEMATICAL MODEL OF ENGINE VALVE MECHANISM</i> .....	<b>1134</b>
<b>Zwierzchowski J.:</b> <i>A DEVICE FOR AUTOMATIC ROBOT TOOL CENTER POINT (TCP) CALIBRATION ADJUSTMENT FOR THE ABB INDUSTRIAL ROBOTS</i> .....	<b>1138</b>

## Table of Contents (by Sections)

### KEY - KEYNOTE LECTURES

<b>Jebáček I., Matějů J.:</b> <i>AEROBATIC SPECIAL IN-FLIGHT TESTS AT INSTITUTE OF AEROSPACE ENGINEERING</i> .....	<b>42</b>
<b>Juračka J.:</b> <i>SPECIFICS OF AEROSTRUCTURES EXPERIMENTAL TESTING</i> .....	<b>46</b>
<b>Peszynski K., Olszewski L., Smyk E., Kasprowicz T.:</b> <i>DEVELOPMENT OF NEW TYPE VENTILATION DUCTS SYSTEM</i> .....	<b>50</b>
<b>Porteš P., Kučera P., Pištěk V., Fojtášek J., Zháňal L.:</b> <i>MODERN TOOLS FOR VEHICLE DEVELOPMENT</i> .....	<b>54</b>
<b>Šafařík P.:</b> <i>SHOCK WAVES IN AN IDEAL GAS AND ENTROPY ANALYSIS</i> .....	<b>58</b>

### BIO - BIOMECHANICS

<b>Borák L., Marcián P.:</b> <i>INHOMOGENEOUS MATERIAL PROPERTIES ASSIGNMENT TO FINITE ELEMENT MODELS OF BONE: A SENSITIVITY STUDY</i> .....	<b>190</b>
<b>Duda S., Gembalczyk G., Jureczko P.:</b> <i>THE EFFECT OF BODY WEIGHT UNLOADING ON KINEMATIC GAIT PARAMETERS DURING TREADMILL WALKING</i> .....	<b>282</b>
<b>Frydryšek K., Drábková S., Plášek M.:</b> <i>BIOMECHANICS – AIRFLOW IN THE NASAL CAVITY AND THE NASAL SEPTUM PERFORATION</i> .....	<b>314</b>
<b>Frydryšek K., Dvořák L.:</b> <i>BIOMECHANICS - TESTING OF MECHANICAL AND UTILITY PROPERTIES OF BOTTLES FOR REDON DRAINAGE</i> .....	<b>318</b>
<b>Goethel F. M., Mrozowski J., Awrejcewicz J.:</b> <i>COORDINATIVE PATTERNS AND GAIT STABILITY ACCESSED BY NONLINEAR DYNAMICS APPROACH: A PRELIMINARY STUDY</i> .....	<b>346</b>
<b>Hájek P., Švancara P., Horáček J., Švec G. J.:</b> <i>EFFECTS OF TURBULENCE IN FE MODEL OF HUMAN VOCAL FOLDS SELF-OSCILLATION</i> .....	<b>366</b>
<b>Horáček J., Radolf V., Bula V., Košina J.:</b> <i>EXPERIMENTAL MODELLING OF PHONATION USING ARTIFICIAL MODELS OF HUMAN VOCAL FOLDS AND VOCAL TRACTS</i> .....	<b>382</b>
<b>Hynek P., Vampola T.:</b> <i>EXAMINATION OF THE BASIC GEOMETRICAL PARAMETERS OF THE LOWER RESPIRATORY TRACT OF THE HUMAN AND ITS SIMPLIFIED COMPUTATIONAL MODEL</i> .....	<b>390</b>

<b>Jureczko M., Jureczko P.:</b> <i>ANALYSIS OF RELATIONSHIP BETWEEN POSTURAL STABILITY AND DEGREE OF VISUAL IMPAIRMENT</i> .....	<b>426</b>
<b>Kawlewska E., Zarwańska M., Larysz D., Wolański W., Gzik M.:</b> <i>PREOPERATIVE PLANNING OF CORRECTION OF CRANIAL DEFORMATIONS USING DISTRACTORS</i> .....	<b>446</b>
<b>Konopelska A., Jureczko M.:</b> <i>EVALUATION OF KNEE JOINT STIFFNESS IN CHILDREN WITH CEREBRAL PALSY</i> .....	<b>478</b>
<b>Koukal M.:</b> <i>ANALYSIS OF THE MANUFACTURE PERTURBATIONS OF THE TOTAL HIP REPLACEMENT</i> .....	<b>506</b>
<b>Kulesza Z., Trochimeczuk R.:</b> <i>DYNAMICS OF MULTIBODY SURGICAL ROBOTIC SINGLE INCISION LAPAROSCOPIC SURGERY TOOL</i> .....	<b>558</b>
<b>Marcián P., Florian Z., Horáčková L., Borák L.:</b> <i>ANALYSIS OF BOUNDARY CONDITIONS IN FINITE ELEMENT SUB-MODELS OF INTERACTION OF HUMAN MANDIBLE WITH DENTAL IMPLANT</i> .....	<b>618</b>
<b>Mazurkiewicz A.:</b> <i>IMPACT OF MINERAL CONTENT IN HUMAN TRABECULAR BONE ON ITS ELASTIC PROPERTIES</i> .....	<b>642</b>
<b>Mazurkiewicz A.:</b> <i>IMPACT OF MINERAL CONTENT IN HUMAN TRABECULAR BONE ON ITS STATIC AND FATIGUE PROPERTIES</i> .....	<b>646</b>
<b>Nowakowska K., Michnik R., Myśliwiec A., Chrzan M.:</b> <i>IMPACT OF STRENGTHENING OF THE ERECTOR SPINAE MUSCLE ON THE VALUES OF LOADS OF THE MUSKULOSKELETAL SYSTEM IN THE LUMBAR SPINE SECTION</i> .....	<b>718</b>
<b>Pásek M., Bébarová M., Christé G.:</b> <i>A MODIFIED MATHEMATICAL MODEL OF HUMAN VENTRICULAR CARDIOMYOCYTE INCORPORATING SEPARATE T-TUBULAR AND SURFACE DYADS AND SUBMEMBRANE SPACES</i> .....	<b>750</b>
<b>Řehounek L., Jíra A., Denk F.:</b> <i>MECHANICAL BEHAVIOR OF A TITANIUM ALLOY TRABECULAR STRUCTURE</i> .....	<b>818</b>
<b>Sant Z., Mifsud L., Muscat C.:</b> <i>SIMULATION OF DAILY LIFE ACTIVITIES IN BIOMECHANICS</i> .....	<b>842</b>
<b>Štorkán J., Vampola T., Horáček J.:</b> <i>COMPUTATIONALLY EFFICIENT MODEL OF THE HUMAN VOCAL FOLD</i> .....	<b>926</b>
<b>Svojanovský T., Trtík L.:</b> <i>STRESS ANALYSIS OF THE TOTAL REPLACEMENT OF THE TRAPEZIOMETACARPAL JOINT</i> .....	<b>954</b>
<b>Szkoda K., Gałąska P., Źak M., Pezowicz C.:</b> <i>BIOMECHANICAL STUDY OF THE CERVICAL SPINE WITH DISC IMPLANTS: A FINITE ELEMENT ANALYSIS</i> .....	<b>966</b>
<b>Učeň O., Frydryšek K., Fojtík F., Bialý L., Pleva L.:</b> <i>BIOMECHANICS – VERIFICATION OF FORCE CHARACTERISTICS OF A DEVICE</i>	

<i>FOR REDUCTION OF BONE FRAGMENTS IN PATIENTS WITH FINGER FRACTURES.....</i>	<b>994</b>
<b>Vampola T., Horáček J.:</b> <i>INFLUENCE OF THE NASAL CAVITIES TO HUMAN VOICE QUALITY.....</i>	<b>1018</b>
<b>Wirwicki M., Andryszczyk M., Andrzejewska A., Topoliński T.:</b> <i>TESTING THE STRENGTH OF THE ADHESIVE CONNECTION IN SPECIMEN - MONOTONIC TENSILE AND SHEAR WITH UNDER VARIABLE LOAD .....</i>	<b>1054</b>
<b>Wodarski P., Michnik R., Gzik M., Jurkojc J., Bieniek A., Nowakowska K.:</b> <i>VARIANTS OF UPPER LIMB MOTION INDEX CALCULATIONS IN THE ASSESSMENT OF UPPER LIMB MOTION DYSFUNCTION .....</i>	<b>1058</b>
<b>Żak M., Filipiak J., Plonek T.:</b> <i>A FINITE ELEMENT STRESS ANALYSIS TO PREDICT THE RISK FACTORS OF AORTIC DISSECTION - PRELIMINARY STUDIES.....</i>	<b>1106</b>
<b>Zhuravlova Z., Kozachkov D., Plusnov D., Radzivil V., Reut V., Shpynarov O., Tarasova E., Nerukh D., Vaysfeld N.:</b> <i>MODELLING OF VIRUS VIBRATION WITH 3-D DYNAMIC ELASTICITY THEORY .....</i>	<b>1126</b>

## **DYN - DYNAMICS**

<b>Aleksandrowicz P.:</b> <i>ANALYSIS OF VEHICLE COLLISIONS WITH THE SDC METHOD .....</i>	<b>78</b>
<b>Aydin E., Öztürk B., Dutkiewicz M.:</b> <i>OPTIMAL PASSIVE CONTROL OF SHEAR BUILDINGS .....</i>	<b>98</b>
<b>Bayer J.:</b> <i>A CONCEPT FOR TESTING AND MONITORING OF BUILDING STRUCTURES – THEORETICAL CASE STUDY.....</i>	<b>122</b>
<b>Bienioszek G., Kciuk S.:</b> <i>DETERMINATION OF BOUNDARY CONDITIONS FOR THE OPTIMIZATION PROCESS OF BLAST MITIGATION SEAT SHOCK ABSORBERS .....</i>	<b>142</b>
<b>Bochat A., Zastempowski M.:</b> <i>KINEMATICS AND DYNAMICS OF THE MOVEMENT OF THE SELECTED CONSTRUCTIONS OF THE DISC CUTTING ASSEMBLIES .....</i>	<b>170</b>
<b>Brezina L., Losak P.:</b> <i>MODEL OF CAR SUSPENSION WITH PARAMETRIC UNCERTAINTY.....</i>	<b>214</b>
<b>Chatys R., Miśków G., Miśków J.:</b> <i>STRUCTURAL MODELLING OF THE STRENGTH PROPERTIES OF POLYMER COMPOSITES STRUCTURAL MODELLING OF THE STRENGTH PROPERTIES OF POLYMER COMPOSITES.....</i>	<b>250</b>



<b>Chatys R., Piernik K.:</b> <i>NUMERICAL ANALYSIS OF POLYMER COMPOSITE BEND TESTS MADE BY VACUUM BAGGING</i> .....	<b>254</b>
<b>Cienciala J., Frydryšek K., Podešva J.:</b> <i>NONLINEAR VIBRATION – STOCHASTIC APPROACH</i> .....	<b>258</b>
<b>Čečrdle J., Raška J.:</b> <i>AIRCRAFT WING FLUTTER ASSESSMENT CONSIDERING DAMAGE TOLERANCE - BASED FAILURE STATES</i> .....	<b>234</b>
<b>Červ J., Valeš F., Adámek V.:</b> <i>A SHORT WAVE LIMIT OF THE FREQUENCY EQUATION FOR PLANE-STRESS NONAXISYMMETRIC DISC MOTIONS</i> .....	<b>246</b>
<b>Dabrowski A., Balcerzak M., Pikunov D.:</b> <i>APPLICATIONS OF THE NEW METHOD OF THE LYAPUNOV EXPONENTS ESTIMATION</i> .....	<b>266</b>
<b>Dziopa Z., Nyckowski M.:</b> <i>THE DYNAMICS OF THE GUIDE ARRANGEMENT BEING AN ELEMENT OF THE LAUNCHER INSTALLED ON A COMBAT VEHICLE</i> .....	<b>298</b>
<b>Fischer C., Náprstek J.:</b> <i>LYAPUNOV EXPONENTS – PRACTICAL COMPUTATION</i> .....	<b>310</b>
<b>Gapiński D., Szmidt P.:</b> <i>THE CONTROL PROCESS OF A SCANNING AND TRACKING IR SEEKER USING INVERSE DYNAMICS</i> .....	<b>326</b>
<b>Golebiowska I., Dutkiewicz M.:</b> <i>EXPERIMENTAL ANALYSIS OF EFFICIENCY OF MASS DAMPERS</i> .....	<b>350</b>
<b>Golebiowska I., Dutkiewicz M., Usewicz B.:</b> <i>MECHANICAL DAMPERS ON OVERHEAD POWER LINES</i> .....	<b>354</b>
<b>Grzyb M., Stefański K.:</b> <i>TURBULENCE IMPACT ON THE CONTROL OF GUIDED BOMB UNIT</i> .....	<b>358</b>
<b>Ivankova O., Meri D., Vojtekova E.:</b> <i>DESIGN AND OPTIMIZATION OF SUPPORTING STRUCTURE OF A MULTIPURPOSE HIGH-RISE BUILDING WITH RESPECT TO THE WIND LOAD</i> .....	<b>394</b>
<b>Ivankova O., Valasik A., Konecna L.:</b> <i>A HIGH-RISE BUILDING - INFLUENCE OF CHANGE OF SOIL STIFFNESS ON HORIZONTAL AND VERTICAL DEFLECTIONS</i> .....	<b>398</b>
<b>Jarzyna T.:</b> <i>DETERMINATION OF RIGIDITY AND DAMPING PARAMETERS OF HYDRODYNAMIC BEARINGS</i> .....	<b>414</b>
<b>Kilinc O., Vágner J.:</b> <i>WAYSIDE DIAGNOSIS OF METRO WHEELSETS USING ACOUSTIC SENSOR DATA AND ONE-PERIOD ANALYSIS</i> .....	<b>458</b>
<b>Kolman R., Cho S. S., Gonzalez J. G., Park K. C., Berezovski A.:</b> <i>AN EXPLICIT TIME SCHEME WITH LOCAL TIME STEPPING FOR ONE-DIMENSIONAL WAVE PROPAGATION IN A BIMATERIAL BAR</i> .....	<b>474</b>
<b>Kostek R., Aleksandrowicz P.:</b> <i>EFFECT OF CONTACT PARAMETERS ON THE PATTERN OF VEHICLE COLLISIONS WITH A ROUND PILLAR</i> .....	<b>490</b>

<b>Kostek R., Aleksandrowicz P.:</b> <i>IDENTIFICATION OF THE PARAMETERS OF VEHICLE CONTACT WITH A RIGID BARRIER FROM A CRASH TEST</i> .....	<b>494</b>
<b>Krzysztofik I., Koruba Z.:</b> <i>APPLICATION OF THE SLIDING CONTROLLER FOR THE GYROSCOPE SYSTEM OF THE ANTI-AIRCRAFT MISSILE</i> .....	<b>530</b>
<b>Kučera P., Píštěk V.:</b> <i>SHAFT VIBRATION OF THE TRUCK</i> .....	<b>546</b>
<b>Macháček O., Kubík M., Novák P.:</b> <i>A NEW METHOD OF MAGNETORHEOLOGICAL DAMPER QUALITY EVALUATION</i> .....	<b>594</b>
<b>Major M., Kuliński K., Major I.:</b> <i>INNOVATIVE CONCRETE-POLYURETHANE COMPOSITE BLOCKS LOCATED IN THREE-LAYER WALL – THERMAL NUMERICAL ANALYSIS</i> .....	<b>602</b>
<b>Malínek P.:</b> <i>STABILITY MARGINS EXPERIMENTAL SEARCH OF AN AEROELASTIC SYSTEM</i> .....	<b>606</b>
<b>Mališ M., Šplíchal J.:</b> <i>SIMULATION OF PILOT LOAD DURING EMERGENCY LANDING CONDITIONS</i> .....	<b>610</b>
<b>Mauro F., Nabergoj R.:</b> <i>DETERMINATION OF NON-LINEAR ROLL DAMPING COEFFICIENTS FROM MODEL DECAYTEST</i> .....	<b>634</b>
<b>Mochar D., Gabriel D., Masák J., Kopačka J., Kolman R., Plešek J., Hynek P., Vtípil J.:</b> <i>EXPLICIT DYNAMIC FINITE ELEMENT ANALYSIS OF A FIRING PIN ASSEMBLY</i> .....	<b>666</b>
<b>Musil M., Sivý M.:</b> <i>PARAMETRIC INSTABILITY OF THE PLANE FREE SURFACE OF THE LIQUID IN CYLINDRICAL STORAGE TANKS</i> .....	<b>686</b>
<b>Náprstek J., Fischer C.:</b> <i>NON-HOLONOMIC PLANAR AND SPATIAL MODEL OF A BALL-TYPE TUNED MASS DAMPING DEVICE</i> .....	<b>698</b>
<b>Nocoń Ł., Koruba Z.:</b> <i>MODIFICATIONS OF CONTROL ACTUATION SYSTEMS OF ATGM</i> .....	<b>714</b>
<b>Paczkowski T., Sawicki J.:</b> <i>EXPERIMENTAL STUDIES OF VIBRATION OF THE TECHNOLOGICAL DEVICE FOR ELECTROCHEMICAL MACHINING OF CURVILINEAR SURFACES</i> .....	<b>746</b>
<b>Polach P., Hajžman M., Byrtus M., Dyk Š., Smolík L.:</b> <i>MATHEMATICAL MODELLING OF ROTOR SYSTEMS WITH JOURNAL BEARINGS IN LIMIT CASES</i> .....	<b>794</b>
<b>Prokop A., Řehák K.:</b> <i>VIRTUAL PROTOTYPE APPLICATION TO HEAVY-DUTY VEHICLE GEARBOX CONCEPT</i> .....	<b>810</b>
<b>Půst L., Pešek L.:</b> <i>RUNNING FLUTTER WAVES IN BLADES CASCADE</i> .....	<b>814</b>
<b>Sapietová A., Šulka P., Sapieta M., Domański T.:</b> <i>VERIFICATION OF MECHANISM'S FUNCTIONALITY FOR POSITIONING THE CAR SEAT USING MSC.ADAMS</i> .....	<b>846</b>

<b>Schmidt J., Janda T., Šejnoha M., Valentin J.:</b> <i>EXPERIMENTAL DETERMINATION OF VISCO-ELASTIC PROPERTIES OF LAMINATED GLASS INTERLAYER</i> .....	<b>850</b>
<b>Shatskyi I., Popadyuk I., Velychkovych A.:</b> <i>MODELLING OF ENERGY DISSIPATION IN SHELL DAMPERS</i> .....	<b>870</b>
<b>Sobotka J.:</b> <i>FORCED VIBRATION ANALYSIS OF PRESTRESSED EULER-BERNOULLI BEAM WITH DISCONTINUITIES BY MEANS OF DISTRIBUTIONS WITHOUT USING MODAL ANALYSIS</i> .....	<b>890</b>
<b>Sokol M., Lamperová K., Venglar M., Hernández Carrasco L. H.:</b> <i>OPTIMUM DESIGN OF TUNED LIQUID COLUMN DAMPER FOR HIGH-RISE BUILDING</i> .....	<b>898</b>
<b>Stefański K., Chatys R., Stefańska A.:</b> <i>THE USE OF GYROSCOPIC EXECUTIVE SYSTEM FOR HOMING OF THE MISSILE ON THE AERIAL TARGET</i> .....	<b>918</b>
<b>Šulc P., Pešek L., Bula V., Košina J., Cibulka J.:</b> <i>PROPOSAL OF HYPERELASTIC PROPORTIONAL DAMPING AS DISSIPATED ENERGY MODEL OF HARD RUBBERS</i> .....	<b>942</b>
<b>Šulka P., Sapietová A., Dekýš V., Sapieta M.:</b> <i>ANALYSIS OF NON-STATIONARY VIBRATION MODE MECHANICAL DEVICE</i> .....	<b>950</b>
<b>Szmidt P., Gapiński D., Koruba Z.:</b> <i>THE ANALYSIS OF SELECTION OPTIMAL PARAMETERS OF PID CONTROLLERS FOR A MODIFIED ARTILLERY-MISSILE SYSTEM</i> .....	<b>970</b>
<b>Szrek J., Bałchanowski J.:</b> <i>MODELLING AND SIMULATION RESEARCHES OF DYNAMICS OF TRANSLATIONAL PARALLEL MECHANISM</i> .....	<b>974</b>
<b>Úradníček J., Kraus P., Musil M., Bachratý M.:</b> <i>MODELING OF FRICTIONAL STICK SLIP EFFECT LEADING TO DISC BRAKE NOISE VIBRATION AND HARSHNESS</i> .....	<b>1002</b>
<b>Zachwieja J., Peszyński K.:</b> <i>DETERMINATION OF THE STRESS - STRAIN STATE FOR INDUSTRIAL PIPELINE BASED ON ITS VIBRATION</i> .....	<b>1082</b>
<b>Zapoměl J., Ferfecki P., Kozánek J.:</b> <i>REDUCTION OF THE ENERGY LOSSES BY APPLICATION OF CONTROLLABLE SQUEEZE FILM DAMPERS</i> .....	<b>1110</b>
<b>Zastempowski M.:</b> <i>DYNAMICS OF MOVEMENT IN SCISSOR-FINGER CUTTING ASSEMBLY</i> .....	<b>1114</b>
<b>Zeman V., Hlaváč Z.:</b> <i>FRICTION FORCES AND FRETTING WEAR IN REACTOR CORE BARREL COUPLINGS</i> .....	<b>1118</b>
<b>Zemanová A., Zeman J., Janda T., Šejnoha M.:</b> <i>FREE VIBRATION ANALYSIS OF LAMINATED GLASS BEAMS USING DYNAMIC EFFECTIVE THICKNESS AND OTHER APPROACHES</i> .....	<b>1122</b>
<b>Zvolský T.:</b> <i>MATHEMATICAL MODEL OF ENGINE VALVE MECHANISM</i> .....	<b>1134</b>

## FLU - FLUID MECHANICS

<b>Anweiler S.:</b> <i>VIDEOGRAMMETRY IN FLUIDIZED BEDS ANALYSIS</i> .....	<b>86</b>
<b>Bang N. V., Rozehnal D.:</b> <i>AERODYNAMIC HYSTERESIS OF OSCILLATING AIRFOIL</i> .....	<b>106</b>
<b>Baranovskii E. S., Artemov M. A.:</b> <i>STEADY FLOWS OF SECOND-GRADE FLUIDS SUBJECT TO STICK-SLIP BOUNDARY CONDITIONS</i> .....	<b>110</b>
<b>Bednář L., Tajč L., Miczán M., Mrózek L., Hoznedl M.:</b> <i>POSSIBILITY OF DAMPING PRESSURE PULSATIONS IN BALANCING CONTROL VALVES</i> .....	<b>130</b>
<b>Borsuk G., Wydrych J., Pochwała S.:</b> <i>COMPARING TURBULENCE MODELS FOR GAS-PARTICLE MIXTURE PNEUMATIC CONVEYING</i> .....	<b>202</b>
<b>Cabová K., Lišková N., Novotná P., Benýšek M., Zeman F., Wald F.:</b> <i>MODELLING OF STANDARD FIRE TEST</i> .....	<b>226</b>
<b>Dočkal K., Šperka P., Křupka I., Hartl M.:</b> <i>FLUID FLOW MEASUREMENTS OF 5P4E BY PARTICLE TRACKING VELOCIMETRY</i> .....	<b>274</b>
<b>Hubova O., Konecna L.:</b> <i>WIND FLOW AROUND HIGH-RISE BUILDINGS AND ITS INFLUENCE ON THE PEDESTRIAN COMFORT</i> .....	<b>386</b>
<b>Klečková J., Hamza J.:</b> <i>NUMERICAL SIMULATION OF STEAM FLOW AROUND VIBRATING TURBINE BLADES</i> .....	<b>462</b>
<b>Kłosowiak R., Bartoszewicz J., Urbaniak R.:</b> <i>ENERGY TRANSFORMATION IN TURBULENT FLOW INSIDE REVERSIG CHAMBER</i> .....	<b>466</b>
<b>Kořínek T., Petříková M.:</b> <i>AN INVESTIGATION OF MASS TRANSFER IN A VORTEX SHEDDING PAST SQUARE CYLINDER</i> .....	<b>482</b>
<b>Kubík M., Macháček O., Strecker Z., Roupec J., Mazůrek I.:</b> <i>DYNAMIC VISCOSITY OF COMMERCIALY AVAILABLE MAGNETORHEOLOGICAL FLUIDS</i> .....	<b>538</b>
<b>Kupireddi K. K., Sai Sudheer S. V., Balasubramanian K.:</b> <i>EFFECT OF LOOP DIAMETER ON TWO-PHASE NATURAL CIRCULATION LOOP PERFORMANCE</i> .....	<b>570</b>
<b>Kyncl M., Pelant J.:</b> <i>ATMOSPHERIC GAS FLOW AROUND AND INSIDE HIGH HALLS SUPPORTED WITH THE SIMULATION OF THE FANS</i> .....	<b>578</b>
<b>Mauro F., Cerni P., Nabergoj R.:</b> <i>RANS CALCULATIONS ON SUBMERGED BODIES</i> .....	<b>630</b>
<b>Nagireddy P. D., Rao Srinivasa Ch.:</b> <i>EXPERIMENTAL STUDIES ON FE3O4 NANOFLUID FLOWING THROUGH A CIRCULAR TUBE</i> .....	<b>694</b>
<b>Němec M., Jelínek T., Klíma J.:</b> <i>TESTING OF FULL STAGE MIXED-FLOW TURBINE FOR AUTOMOTIVE APPLICATIONS</i> .....	<b>702</b>

<b>Osiński P., Stosiak M.:</b> <i>SHAPING THE STARTING OF A HYDROSTATIC TRANSMISSION WITH PROPORTIONALLY CONTROLLED ELEMENTS</i> .....	<b>738</b>
<b>Perz K., Rewolińska A.:</b> <i>IMPACT OF FILTER CONTAMINATION ON EFFICIENCY AND EFFECTIVENESS OF AIR FILTER</i> .....	<b>766</b>
<b>Peszyński K., Perczyński D., Smyk E., Kolber P.:</b> <i>EXPERIMENTAL VERIFICATION OF VELOCITY DISTRIBUTION IN DIFFERENT CROSS-SECTIONAL VENTILATION DUCTS</i> .....	<b>770</b>
<b>Plánička S., Vimmr J.:</b> <i>NUMERICAL SIMULATIONS OF FREE SURFACE FLOWS USING A THREE-EQUATION MODEL</i> .....	<b>786</b>
<b>Pochwała S., Wydrych J., Borsuk G.:</b> <i>THE EFFECT OF VELOCITY PROFILE DEFORMATION OF AN AVERAGING PITOT TUBE THE EFFECT OF VELOCITY PROFILE DEFORMATION OF AN AVERAGING PITOT TUBE</i> .....	<b>790</b>
<b>Prachař A., Hospodář P., Vrchota P.:</b> <i>GUST ALLEVIATION OF NASA COMMON RESEARCH MODEL USING CFD</i> .....	<b>798</b>
<b>Romańczyk M., Elsner W.:</b> <i>NUMERICAL ANALYSIS FOR OPTIMAL LOCALIZATION OF GAS INLET IN A VENTURI MIXER</i> .....	<b>826</b>
<b>Semkło Ł., Frąckowiak A., Ciałkowski M.:</b> <i>LOCATION OF LEAKS IN THE WATER SUPPLY NETWORK</i> .....	<b>858</b>
<b>Siwulski T., Warzyńska U.:</b> <i>THE ADVANTAGES OF A NEW HYDRAULIC CYLINDER DESIGN WITH A CONTROL SYSTEM</i> .....	<b>874</b>
<b>Smyk E., Mrozik D., Wawrzyniak S., Peszyński K.:</b> <i>TUBULAR AIR DEFLECTOR IN VENTILATION DUCTS</i> .....	<b>882</b>
<b>Smyk E., Wawrzyniak S., Perczyński D., Kolber P.:</b> <i>AXISYMMETRIC VALVE WITH SYNTHETIC JET ACTUATOR</i> .....	<b>886</b>
<b>Sosnowski M.:</b> <i>COMPUTER AIDED OPTIMIZATION OF A NOZZLE IN AROUND-THE-PUMP FIRE SUPPRESSION FOAM PROPORTIONING SYSTEM</i> .....	<b>914</b>
<b>Straka P., Příhoda J.:</b> <i>MODELLING OF FLOW IN LINEAR BLADE CASCADE WITH THICK TRAILING EDGE AT A LOWER REYNOLDS NUMBER</i> .....	<b>930</b>
<b>Világi F., Knížat B., Urban F., Olšiak R., Mlkvik M., Ridzoň F., Mlynár P.:</b> <i>ESTIMATION OF MINOR LOSSES IN A NATURAL CIRCULATION HELIUM LOOP</i> .....	<b>1030</b>
<b>Vlasák P., Chára Z., Konfršt J.:</b> <i>CONCENTRATION DISTRIBUTION AND SLIP VELOCITY OF COARSE-PARTICLE-WATER MIXTURE IN HORIZONTAL AND INCLINED PIPE SECTIONS</i> .....	<b>1034</b>
<b>Vlček V., Zolotarev I., Kozánek J., Šidlof P., Štěpán M.:</b> <i>SOME ENERGY RELATIONS OF THE SELF-EXCITED PROFILE VIBRATION IN FLOWING FLUID</i> .....	<b>1038</b>

<b>Vrchota P., Prachař A., Hospodář P., Dolgopyat D., Seifert A.: SIMPLIFIED OSCILLATORY BOUNDARY CONDITION FOR EFFICIENT CFD SIMULATION OF AFC EFFECT .....</b>	<b>1050</b>
--	-------------

<b>Wydrych J., Borsuk G., Pochwała S.: ANALYSIS OF THE EROSION WEAR MODELING RESULTS OF THE PNEUMATIC CONVEYING SYSTEMS .....</b>	<b>1074</b>
---	-------------

## **FRA - FRACTURE MECHANICS**

<b>Eliáš J., Le J. -L.: MITIGATION OF MESH DEPENDENCY IN PROBABILISTIC FINITE ELEMENT SIMULATION OF QUASIBRITTLE FRACTURE .....</b>	<b>302</b>
---	------------

<b>Had J.: IMPLEMENTATION OF INTERACTING CREEP AND FATIGUE UNDER THERMO-MECHANICAL LOADING.....</b>	<b>362</b>
---	------------

<b>Hejnova M.: PRINCIPLE OF THE ROLLING CONTACT FATIGUE FORMATION .....</b>	<b>374</b>
---	------------

<b>Karoľ M., Chlupová A., Mazánová V., Kruml T.: FATIGUE CRACK INITIATION AND GROWTH IN 316L STEEL IN TORSIONAL CYCLIC LOADING.....</b>	<b>434</b>
---	------------

<b>Kubík P., Petruška J., Hůlka J., Šebek F.: SIMULATION OF THE SMALL PUNCH TEST OF AISI 316L AUSTENITIC STEEL.....</b>	<b>542</b>
---	------------

<b>Kurzawa A., Bocian M., Jamroziak K., Pyka D.: ANALYSIS OF CERAMIC-METALLIC COMPOSITES OF BALLISTIC RESISTANCE ON SHOTS BY 5.56 MM AMMUNITION .....</b>	<b>574</b>
---	------------

<b>Maćkowiak P., Ligaj B.: DAMAGE TO ADHESIVE SINGLE LAP JOINT MADE OF MATERIALS WITH DIFFERENT PROPERTIES UNDER STATIC LOADING CONDITIONS.....</b>	<b>598</b>
---	------------

<b>Menshykov O., Menshykova M., Guz I. A.: THICK-WALLED COMPOSITE PIPES UNDER BENDING .....</b>	<b>650</b>
---	------------

<b>Profant T., Hrstka M., Klusák J., Keršner Z.: ON THE ENERGY RELEASE RATE OF THE CRACK EMANATING FROM THE INCLUSION INTERPHASE .....</b>	<b>806</b>
--	------------

<b>Reut O. V.: THE ANTIPLANE PROBLEM FOR A STRIP WEAKENED BY A CRACK.....</b>	<b>822</b>
---	------------

<b>Roupec J., Mazůrek I., Strecker Z., Kubík M., Macháček O.: TENSILE STRENGTH OF PURE IRON SAMPLES MANUFACTURED BY SELECTIVE LASER MELTING METHOD .....</b>	<b>830</b>
--	------------

<b>Šebek F., Petruška J., Kubík P.: DUCTILE FRACTURE CRITERIA IMPLEMENTATION AND CALIBRATION USING THE TENSION–TORSION TESTS .....</b>	<b>854</b>
--	------------

<b>Ševeček O., Majer Z., Kotoul M.: INFLUENCE OF CERAMIC FOAM PARAMETERS ON THE FRACTURE BEHAVIOUR UPON THE TENSILE TEST .....</b>	<b>862</b>
--	------------

<b>Shatskyi I., Makoviichuk M., Perepichka V., Dalyak T.:</b> <i>EFFECT OF CRACKS CLOSURE IN PLATES AND SHELLS UNDER COMBINED TENSION AND BENDING.....</i>	<b>866</b>
<b>Strzelecki P.:</b> <i>RETESTED RUNOUT SPECIMENS IN FATIGUE RESEARCH.....</i>	<b>938</b>
<b>Tomaszewski T.:</b> <i>ANALYSIS OF SIZE EFFECT FOR NOTCHED MINI SPECIMENS MADE OF STAINLESS STEEL.....</i>	<b>982</b>
<b>Topolinski T., Ligaj B., Mazurkiewicz A., Miterka S.:</b> <i>EVALUATION OF DEFORMATIONS OF THICK-LAYER GLUED JOINTS APPLIED IN CONSTRUCTION OF RAIL VEHICLES .....</i>	<b>986</b>
<b>Uhříčik M., Oravcová M., Palček P., Chalupová M., Kuchariková L.:</b> <i>THREE-POINT BENDING FATIGUE DAMAGE MECHANISMS ASSOCIATED WITH THE DIFFERENT STRUCTURE OF AL-MG CAST ALLOYS.....</i>	<b>998</b>
<b>Valentová S., Vorel J., Šejnoha M.:</b> <i>EFFECTIVE ELASTIC AND STRENGTH PROPERTIES OF UNIDIRECTIONAL FIBROUS CERAMIC COMPOSITES .....</i>	<b>1010</b>
<b>Vorel J., Kabele P.:</b> <i>BACK ANALYSIS FOR DETERMINATION OF TENSION-SOFTENING DIAGRAM.....</i>	<b>1042</b>

## **KIN - KINEMATICS**

<b>Ćwiklak J., Krasuski K., Jaferník H.:</b> <i>DESIGNATION THE VELOCITY OF CESSNA 172 AIRCRAFT BASED ON GPS DATA IN FLIGHT TEST.....</i>	<b>262</b>
<b>Drahorádová L., Moravec J., Andrlík V.:</b> <i>TESTING THE POSITIONING ACCURACY AND REGULARITY OF THE MOTION THREADED MECHANISM FEED DRIVE .....</i>	<b>278</b>
<b>Osowski P., Wolski M., Piatkowski T.:</b> <i>VERYFICATION OF VELOCITY MESURMENT METHODS BY HIGH SPEED CAMERA AND ACCELEROMETER ON EXAMPLE OF IMPACT TESTER.....</i>	<b>742</b>
<b>Zajac P., Kwasniowski S.:</b> <i>MODELLING FORKLIFT TRUCK MOVEMENT IN THE VDI CYCLE AND THE POSSIBILITY OF ENERGY RECOVERY .....</i>	<b>1094</b>

## MCT - MECHATRONICS

<b>Adamczak S., Zmarzły P., Koziar T., Gogolewski D.: ANALYSIS OF THE DIMENSIONAL ACCURACY OF CASTING MODELS MANUFACTURED BY FUSED DEPOSITION MODELING TECHNOLOGY .....</b>	<b>66</b>
<b>Adamczak S., Zmarzły P., Koziar T., Gogolewski D.: ASSESSMENT OF ROUNDNESS AND WAVINESS DEVIATIONS OF ELEMENTS PRODUCED BY SELECTIVE LASER SINTERING TECHNOLOGY .....</b>	<b>70</b>
<b>Appel M., Grepl R.: PARAMETER ESTIMATION FOR ENGINEERS: A NEW TOOL FOR EFFECTIVE SEARCH FOR SIMULINK MODEL PARAMETERS.....</b>	<b>90</b>
<b>Baranowski L., Kaczmarek W., Panasiuk J., Prusaczyk P., Besseghieur K.: INTEGRATION OF VISION SYSTEM AND ROBOTIC ARM UNDER ROS .....</b>	<b>114</b>
<b>Baranowski L., Panasiuk J., Siwek M.: USE OF A RASPBERRY PI TO BUILT A PROTOTYPE WIRELESS CONTROL SYSTEM OF A MOBILE ROBOT.....</b>	<b>118</b>
<b>Besseghieur K., Kaczmarek W., Panasiuk J., Prusaczyk P.: FORMATION CONTROL OF MOBILE ROBOTS UNDER ROS .....</b>	<b>138</b>
<b>Blasiak M., Blasiak S.: APPLICATION OF FRACTIONAL CALCULUS IN HARMONIC OSCILATOR .....</b>	<b>146</b>
<b>Blasiak M., Blasiak S.: THE APPLICATION OF INTEGRAL TRANSFORMS TO SOLVING PARTIAL DIFFERENTIAL EQUATIONS OF THE FRACTIONAL ORDER .....</b>	<b>150</b>
<b>Borkowski K., Janecki D., Zwierzchowski J.: ACCURACY OF THE VISUAL MEASUREMENT SYSTEM OF BENT PIPES .....</b>	<b>194</b>
<b>Borowski S., Rama R., Knopik L., Kaszkowiak J.: ASSESSMENT OF THE VOLUME OF CROP BY THE WINDROW'S MEASUREMENT.....</b>	<b>198</b>
<b>Cekus D., Skrobek D.: THE INFLUENCE OF THE LENGTH OF TRAJECTORY OF SCARA MANIPULATOR DUTY CYCLE ON ELECTRICITY CONSUMPTION .....</b>	<b>238</b>
<b>Černý M., Dzurilla M., Musil M.: ELECTROMAGNETIC ENERGY HARVESTER WITH MECHANICAL AMPLIFIER FOR TRANSLATIONAL KINETIC .....</b>	<b>242</b>
<b>Dindorf R., Wos P., Pawelec K.: STUDY OF THE POSSIBILITY OF USE OF BIOELECTRIC SIGNALS TO WIRELESS REMOTE CONTROL OF THE ELECTRO-PNEUMATIC POSITIONING SYSTEMS .....</b>	<b>270</b>
<b>Dudek D., Kazala R., Straczynski P.: JITTER ANALYSIS OF MQTT PROTOCOL FRAMES IN MOBILE ROBOT CONTROL SYSTEM.....</b>	<b>286</b>
<b>Dzierżek K., Rećko M., Pietrala D. S.: QUICK PROTOTYPING OF MANIPULATOR CONTROL SYSTEM WITH PLC CONTROLLER.....</b>	<b>294</b>
<b>Gidlewski M., Jemioł L., Żardecki D.: SENSITIVITY INVESTIGATIONS OF THE LANE CHANGE AUTOMATED PROCESS.....</b>	<b>330</b>



<b>Koruba Z., Krzysztofik I.:</b> <i>A CONTROL WITH THE USE OF LQR MODIFIED METHOD IN THE GYROSCOPE SYSTEM OF TARGET TRACKING</i> .....	<b>486</b>
<b>Krejca J., Vechet S.:</b> <i>THE EVALUATION OF HOKUYO URG-04LX-UG01 LASER RANGE FINDER DATA</i> .....	<b>522</b>
<b>Kšica F., Vetiška J., Hadaš Z.:</b> <i>METHODOLOGY FOR PREDICTING DYNAMIC BEHAVIOUR OF MACHINE TOOLS BASED ON A VIRTUAL MODEL</i> .....	<b>534</b>
<b>Kumpán P.:</b> <i>SEGMENTATION OF HUMAN MOTION ACCELERATION WITH PROBABILISTIC CLASSIFIER</i> .....	<b>566</b>
<b>Laski P. A.:</b> <i>KINEMATICS AND WORKSPACE ANALYSIS FOR A 6-DOF PARALLEL MANIPULATOR WITH COAXIAL CTUATED ARMS</i> .....	<b>586</b>
<b>Muraszkowski A., Szrek J.:</b> <i>THE CONCEPT OF MOBILE SYSTEM OF ANALYSIS AND VISUALIZATION OF HUMAN GAIT PARAMETERS</i> .....	<b>678</b>
<b>Němec Z., Nevrlý J.:</b> <i>MODELING OF ROAD ROLLER DRIVE EQUIPPED WITH HYDROSTATIC RECOVERY OF KINETIC ENERGY</i> .....	<b>706</b>
<b>Nowakowski Ł., Miko E., Skrzyniarz M.:</b> <i>DESIGNATION OF THE MINIMUM THICKNESS OF MACHINED LAYER FOR THE MILLING PROCESS OF DURALUMIN PA6</i> .....	<b>722</b>
<b>Nowakowski Ł., Miko E., Skrzyniarz M.:</b> <i>MILLING WITH A TOOL WITH UNEVENLY DISTRIBUTED CUTTING PLATES</i> .....	<b>726</b>
<b>Nowakowski L., Skrzyniarz M., Miko E.:</b> <i>THE ANALYSIS OF RELATIVE OSCILLATION DURING FACE MILLING</i> .....	<b>730</b>
<b>Nowakowski L., Skrzyniarz M., Miko E.:</b> <i>THE ASSESSMENT OF THE IMPACT OF THE INSTALLATION OF CUTTING PLATES IN THE BODY OF THE CUTTER ON THE SIZE OF GENERATED VIBRATIONS AND THE GEOMETRICAL STRUCTURE OF THE SURFACE</i> .....	<b>734</b>
<b>Pietrala D. S., Laski P. A., Bracha G. F., Dzierżek K.:</b> <i>APPLICATION OF WOLFRAM MATHEMATICA PACKAGE TO CONTROL THE 6-DOF PARALLEL ROBOT</i> .....	<b>778</b>
<b>Piwowarski D., Anweiler S., Ulbrich R., Tańczuk M.:</b> <i>UNMANNED AIRCRAFT VEHICLE DESIGN FOR TEMPERATURE FIELD ANALYSIS</i> .....	<b>782</b>
<b>Strecker Z., Strmiska T., Roupec J., Kubík M., Macháček O.:</b> <i>DESIGN OF FAST MAGNETORHEOLOGICAL DAMPER USING SOFT MAGNETIC COMPOSITES</i> .....	<b>934</b>
<b>Takosoglu J. E.:</b> <i>DYNAMIC CHARACTERISTICS OF PNEUMATIC ARTIFICIAL MUSCLES</i> .....	<b>978</b>
<b>Tůma J., Šuránek P., Mahdal M.:</b> <i>ALL-PASS FILTERS AS A TOOL FOR CONVERTING A POSITIVE FEEDBACK TO A NEGATIVE FEEDBACK WHEN CONTROLLING WEAKLY DAMPED SYSTEMS</i> .....	<b>990</b>

<b>Vechet S., Krejsa J., Chen K.-S.: EXPERT SYSTEM SHELL ARCHITECTURE BASED ON DECISION NETWORK .....</b>	<b>1022</b>
<b>Votrubec R.: PLATFORM STABILIZED BY MEANS OF TWO GYROSCOPES AND DAMPED WITH MAGNETORHEOLOGICAL DAMPER" .....</b>	<b>1046</b>
<b>Wolski M., Piatkowski T., Osowski P.: ROTARY MOTION SELECTED CONTROL METHODS ANALYSIS FOR PADDLE SORTERS ARMS .....</b>	<b>1062</b>
<b>Woś P., Dindorf R.: A SEMI-ACTIVE PNEUMATIC SUSPENSION OF THE WORKING MACHINE SEAT .....</b>	<b>1066</b>
<b>Woś P., Dindorf R.: LEAK MEASURING SYSTEM OF COMPRESSED AIR IN PIPELINE.....</b>	<b>1070</b>
<b>Záda V.: APPLICATION OF HAMILTONIAN MECHANICS IN EXPONENTIALLY STABLE CONTROL OF ROBOTS .....</b>	<b>1086</b>
<b>Zajac P., Kowalczyk L.: COMPREHENSIVE SERVICE OF CONFERENCE PARTICIPANTS USING AUTOMATIC IDENTIFICATION .....</b>	<b>1090</b>
<b>Zwierzchowski J.: A DEVICE FOR AUTOMATIC ROBOT TOOL CENTER POINT (TCP) CALIBRATION ADJUSTMENT FOR THE ABB INDUSTRIAL ROBOTS.....</b>	<b>1138</b>

## **REL - RELIABILITY**

<b>Augustín T., Fillo L.: INFLUENCE OF GROUND STRESS DISTRIBUTION ON PUNCHING RESISTANCE .....</b>	<b>94</b>
<b>Bęczkowski R., Cebulski J., Pasek D., Gucwa M.: PRODUCING A LAYER OF IRON FE-CR-C-NB UNDER CONDITIONS OF INTENSE HEAT RECEPTION .....</b>	<b>126</b>
<b>Bojarczak P., Nowakowski W., Łukasik Z.: VISUAL DIAGNOSTICS OF RAIL FASTENING SYSTEM AS A METHOD TO IMPROVE SAFETY.....</b>	<b>182</b>
<b>Cebulski J., Bęczkowski R., Pasek D.: THE USE OF WELDING FOR FORMING FEAL COATING ON S235.....</b>	<b>230</b>
<b>Gajdosova K., Sonnenschein R.: ENDURANCE LIMIT OF FRP COMPOSITES USED FOR REINFORCEMENT OF CONCRETE STRUCTURES.....</b>	<b>322</b>
<b>Gierz Ł.: VALIDATION OF THE FEM-BASED STRESS ANALYSIS OF AN INNOVATIVE LOAD-BEARING STRUCTURE OF AIR-ASSISTED SEED DRILLS WITH ELECTRONIC SEEDING CONTROL.....</b>	<b>334</b>
<b>Gilewski W., Pelczyński J.: THE INFLUENCE OF ORTHOTROPY LEVEL FOR PERPENDICULAR TO GRAIN STRESSES IN GLULAM DOUBLE TAPERED BEAMS.....</b>	<b>342</b>

<b>Hollý I., Sonnenschein R.: GFRP REINFORCEMENT IN CONCRETE – FACTORS AFFECTING BOND PROPERTIES.....</b>	<b>378</b>
<b>Janouchová E., Kučerová A., Sýkora J.: ROLE OF RANDOM FACTORS IN NONLINEAR REGRESSION: A CASE STUDY FOR ESTIMATION OF THERMOPHYSICAL PARAMETERS.....</b>	<b>410</b>
<b>Knopik L., Migawa K., Peszyński K., Wawrzyniak S.: SOME REMARKS ON PREVENTIVE REPLACEMENT MODEL.....</b>	<b>470</b>
<b>Košťal R., Janhuba L., Hlinka J.: INTELLIGENT SCHEDULED MAINTENANCE METHODOLOGY FOR GENERAL AVIATION STRUCTURES BASED ON MSG-3 AND MULTIPLE- CRITERIA DECISION MAKING ANALYSIS .....</b>	<b>498</b>
<b>Kovář J.: THE INFLUENCE OF CONTACT REGION ON PROBABILITY OF CERAMICS FRACTURE .....</b>	<b>510</b>
<b>Králik J.: PROBABILITY NONLINEAR ANALYSIS OF THE FAILURE OF THE NPP HERMETIC STEEL DOOR DUE TO ACCIDENTAL EXTREME OVERPRESSURE.....</b>	<b>514</b>
<b>Krejša J., Sýkora M.: PROBABILISTIC ESTIMATION OF A BRIDGE FATIGUE LIFE IN ACCORDANCE TO fib MODEL CODE 2010 .....</b>	<b>518</b>
<b>Laco K., Borzovič V.: SHEAR FORCES OF THE APPROACH SLABS OF THE ROAD BRIDGES .....</b>	<b>582</b>
<b>Migawa K., Knopik L., Neubauer A., Perczyński D.: SIMULATION OF THE MODEL OF TECHNICAL OBJECT AVAILABILITY CONTROL.....</b>	<b>654</b>
<b>Migawa K., Knopik L., Soltysiak A., Kolber P.: THE METHOD OF RISK ASSESSMENT IN TRANSPORT SYSTEMS.....</b>	<b>658</b>
<b>Mrozik Ł.: SHAPING THE STRUCTURE OF LOW WATER-BINDER RATIO CEMENT PASTES.....</b>	<b>674</b>
<b>Pichal R., Machacek J.: EXPERIMENTAL AND NUMERICAL STUDY OF STAYED STEEL COLUMNS.....</b>	<b>774</b>
<b>Pravdová I., Eliášová M.: INFLUENCE OF AN INTIAL IMPERFECTION ON THE LATERAL AND TORSIONAL BUCKLING OF A HYBRID BEAM .....</b>	<b>802</b>
<b>Sokolski M., Sokolski P.: ACOUSTIC CLIMATE IN THE CABINS AS A FACTOR OF REBUILDING EFFECTIVENESS OF LONG TERM OPERATED BUCKET WHEEL EXCAVATORS – A CASE STUDY.....</b>	<b>906</b>
<b>Sokolski P.: ON WEAR PROCESSES IN PIN JOINTS IN CATERPILLARS OF LARGE-SIZE WORKING MACHINES.....</b>	<b>910</b>
<b>Stopel M., Cichański A., Skibicki D.: MODELING OF PRESTRESSED BOLT CONNECTION IN LS-DYNA CRASH TEST ANALYSIS OF ROAD INFRACTURE.....</b>	<b>922</b>

<b>Vida R., Halvonik J.: INFLUENCE OF COMPRESSIVE STRESS ON SHEAR FORCE DISTRIBUTION IN BRIDGE DECK SLABS .....</b>	<b>1026</b>
<b>Zajac P., Kwasniowski S.: RELIABILITY OF AUTOMATIC IDENTIFICATION SYSTEMS IN LOGISTICS SYSTEMS.....</b>	<b>1098</b>

## **SOL - MECHANICS OF SOLIDS**

<b>Aizikovich S., Vasiliev A., Volkov S., Mitrin B.: MATHEMATICAL MODELING OF MICRO INDENTATION OF A TRANSVERSELY ISOTROPIC HALF-SPACE WITH FUNCTIONALLY GRADED COATING BY A CONICAL INDENTER.....</b>	<b>74</b>
<b>Aleksandrowicz P.: VERIFYING THE APPLICATION OF THE MODELS OF CRASH AND COLLISION DETECTION OF INCOMPATIBLE VEHICLES.....</b>	<b>82</b>
<b>Baláž I., Koleková Y.: PLASTIC RESISTANCE OF ALUMINUM I-PROFILE UNDER BENDING AND TORSION ACCORDING TO CONTINUOUS STRENGTH METHOD.....</b>	<b>102</b>
<b>Benešovský M., Návrát T., Petruška J.: VERIFICATION OF FAST ALGORITHM FOR CROSS-ROLL STRAIGHTENING.....</b>	<b>134</b>
<b>Blatnická M., Blatnický M., Sága M., Kubiak M.: STRESS ANALYSIS OF PART OF THE WELDED STRUCTURE.....</b>	<b>162</b>
<b>Blatnický M., Dižo J., Blatnická M., Svoboda M.: DESIGN OF A ROBOT MANIPULATOR WORKING SCREW REVOLUTIONS.....</b>	<b>166</b>
<b>Bochnia J.: MECHANICAL PROPERTIES OF MATERIALS OBTAINED BY 3D-PRINTING TECHNOLOGY.....</b>	<b>174</b>
<b>Bochnia J.: RELAXATION OF MATERIALS OBTAINED USING POLYJET TECHNOLOGY.....</b>	<b>178</b>
<b>Bojczuk D., Sztelblak W.: OPTIMAL REPAIR AND REINFORCEMENT OF BAR STRUCTURES USING FINITE TOPOLOGY VARIATIONS.....</b>	<b>186</b>
<b>Bošanský M., Patzák B.: ON PARELLELIZATION OF LINEAR SYSTEM EQUATION SOLVER IN FINITE ELEMENT SOFTWARE .....</b>	<b>206</b>
<b>Brabec P., Reichrt K.: MODIFICATION OF THE INTAKE MANIFOLD OF A COMBUSTION ENGINE .....</b>	<b>210</b>
<b>Brózda K., Major M., Selejdak J.: COMPUTATIONAL ANALYSIS OF SERVICEABILITY LIMIT STATE OF BEAMS REINFORCED WITH FRP BARS.....</b>	<b>218</b>

<b>Bucci V., Marino A., Mauro F., Sandron C., Mattiazzo G.: REDESIGN OF A WAVE ENERGY CONVERTER IN FERROCEMENT .....</b>	<b>222</b>
<b>Dvořáková E., Patzák B.: COMPUTATIONAL PERFORMANCE OF A DSG-BASED ISOGEOMETRIC BEAM ELEMENT.....</b>	<b>290</b>
<b>Fiedler J., Koudelka T.: CALCULATION OF SHELL STRUCTURES BY USING LAYERED MODEL .....</b>	<b>306</b>
<b>Gilewski W., Obara P.: EXACT 3-NODED TIMOSHENKO BEAM FINITE ELEMENT WITH ENHANCED STRAIN FIELD – A MAGIC ROLE OF GAUSS POINTS.....</b>	<b>338</b>
<b>Havelka J., Sýkora J., Kučerová A.: CALDERÓN'S INVERSE PROBLEM IN CIVIL ENGINEERING.....</b>	<b>370</b>
<b>Janiček P.: SYSTEMS CONCEPTION OF PROBLEM-SOLVING .....</b>	<b>402</b>
<b>Janiček P., Fuis V.: MODELLING – A TOOL FOR PROBLEM-SOLVING.....</b>	<b>406</b>
<b>Jirásko J., Max A., Bezdekova J.: STATIC NUMERICAL ANALYSIS OF A HYDRAULIC CURING PRESS .....</b>	<b>422</b>
<b>Kadlíček T., Janda T., Šejnoha M.: THE CALIBRATION PROGRAM FOR THE HYPOPLASTIC SAND MODEL .....</b>	<b>430</b>
<b>Katrňák T.: DESIGN OF NEW PARAMETERS FOR EVALUATION OF LOAD CAPACITY OF SEMI-SHELL STRUCTURES.....</b>	<b>442</b>
<b>Kebli B., Baka Z.: AXISYMMETRIC DEFORMATION OF AN ELASTIC MEDIUM WEAKENED BY AN ANNULAR CRACK .....</b>	<b>450</b>
<b>Keckstein T., Bezděková J., Votápek P.: STATIC CHECKING COMPUTATION OF A LATHE TAILSTOCK .....</b>	<b>454</b>
<b>Koudelka T., Krejčí T., Kruis J.: NUMERICAL MODELLING OF EXPANSIVE CLAYS.....</b>	<b>502</b>
<b>Kriváček J., Sadovský Z.: ON THE CHOICE OF GEOMETRICAL IMPERFECTIONS IN GMNIA STRENGTH CALCULATIONS OF THIN-WALLED STRUCTURES .....</b>	<b>526</b>
<b>Kucíková L., Vorel J., Sýkora J., Šejnoha M.: EFFECTIVE HEAT AND MOISTURE TRANSPORT PROPERTIES OF SPRUCE.....</b>	<b>550</b>
<b>Kukielka K., Kukielka L.: THERMOMECHANICAL MODELING AND ANALYSIS OF THE THREAD ROLLING PROCESS WITH ELECTROCONTACT HEATING .....</b>	<b>554</b>
<b>Kulhavý P., Syrovátková M., Petrů M.: ALTERNATIVE POSSIBILITIES OF BIAxIAL TESTING OF FIBER AND FABRIC MATERIALS IN NONSTANDARD CONDITIONS .....</b>	<b>562</b>
<b>Löffelmann F.: FAILURE INDEX BASED TOPOLOGY OPTIMIZATION FOR MULTIPLE PROPERTIES.....</b>	<b>590</b>

<b>Maťas M., Frydryšek K.: RELIABILITY ASSESSMENT OF THE PRETENSIONED BOLTS BASED ON PROBABILITY .....</b>	<b>626</b>
<b>Max A., Hynek M., Řehounek L.: ANALYSIS OF A BOOM CONVEYOR.....</b>	<b>638</b>
<b>Mikeš K., Jirásek M.: ON EFFICIENCY OF QUASICONTINUUM SIMULATION OF CRACK PROPAGATION IN ELASTIC-BRITTLE DISORDERED LATTICES .....</b>	<b>662</b>
<b>Morávková Z., Tomečková I., Frydryšek K.: BEAM RESTED ON UNILATERAL ELASTIC FOUNDATION – (THEORY, EXPERIMENTS AND FINITE ELEMENT APPROACH) .....</b>	<b>670</b>
<b>Murín J., Goga V., Kutiš V., Hrabovský J., Sedlár T., Paulech J.: MODELLING AND MEASUREMENT OF NON-UNIFORM ELASTOSTATIC TORSION OF HOLLOW CROSS-SECTION BEAMS .....</b>	<b>682</b>
<b>Myšáková E., Lepš M.: SHIFTING OF LHS DESIGN FOR SURROGATE MODELING .....</b>	<b>690</b>
<b>Němeček J., Kruis J., Koudelka T.: MODELING OF CHLORIDE MIGRATION IN CONCRETE.....</b>	<b>710</b>
<b>Patyk S., Patyk R., Kukielka L., Kalduński P., Chojnacki J.: NUMERICAL METHOD FOR DETERMINING THE MAIN FORCE OF BURNISHING ROLLING OF ROUGH CYLINDRICAL SURFACE WITH REGULAR PERIODICAL OUTLINES ASPERITIES .....</b>	<b>754</b>
<b>Pavlenko M.: THE FORMATION OF ZONES OF THE COAL ARRAY VOLUMETRIC IMPREGNATION AS A RESULT OF THE VIBRATION IMPACT .....</b>	<b>758</b>
<b>Runt D., Novotný J., Pruška J.: SPECIAL ELEMENT FOR NUMERICAL MODELLING OF THE ROCK BOLT REINFORCEMENT .....</b>	<b>834</b>
<b>Sądej M., Gierz Ł.: POLYURETHANE COMPOSITES WITH IMPROVED MECHANICAL PROPERTIES.....</b>	<b>838</b>
<b>Sławski S., Duda S., Machoczek T.: THIN WALLED PIPE CRUSHED IN JAWS.....</b>	<b>878</b>
<b>Sokół K.: INSTABILITY OF A STEPPED COLUMN LOADED BY THE EXTERNAL FOLLOWER FORCE .....</b>	<b>894</b>
<b>Sokol Z., Fila J., Eliášová M.: LOAD BEARING TEST OF WALL FROM HOLLOW GLASS BLOCKS USING VITRALOCK INSTALLATION SYSTEM.....</b>	<b>902</b>
<b>Sýkora J., Kučerová A., Zeman J.: CONSTRUCTION OF RANDOM FIELD BASED ON IMAGE ANALYSIS .....</b>	<b>958</b>
<b>Uzny S., Osadnik M.: INFLUENCE OF LONGITUDINAL ELASTIC SUPPORT ON STABILITY OF A PARTIALLY TENSIONED COLUMN.....</b>	<b>1006</b>
<b>Valeš J., Kala Z.: WEAK AXIS BUCKLING - ELASTIC RESISTANCE OF A COLUMN.....</b>	<b>1014</b>
<b>Žák J.: FULL WIDTH WARP TENSION SENSOR .....</b>	<b>1102</b>

<b>Ziolkowska J.:</b> <i>POLYURETHANE COATINGS AND METHODS OF EXAMINATION OF THEIR PROPERTIES</i> .....	<b>1130</b>
---	-------------

## **TER - THERMOMECHANICS**

<b>Blasiak S.:</b> <i>HEAT TRANSFER IN NON-CONTACTING FACE SEALS USING FRACTIONAL FOURIER LAW</i> .....	<b>154</b>
<b>Blasiak S.:</b> <i>HEAT TRANSFER MODEL FOR THE WAVY-TILT-DAM MECHANICAL SEALS USING GREEN'S FUNCTION METHOD</i> .....	<b>158</b>
<b>Jegla Z., Reppich M.:</b> <i>VERIFICATION OF A NEW THERMAL CALCULATION METHOD BY INDUSTRIAL RADIANT CHAMBER MEASUREMENTS</i> .....	<b>418</b>
<b>Kaszkowiak J., Markiewicz-Patalon M., Borowski S., Dorszewski P.:</b> <i>IMPACT OF SUPERCHARGING ON THE NOISE LEVEL IN BIOGAS ENGINES</i> .....	<b>438</b>
<b>Mallick A., Ranjan R.:</b> <i>THERMO-MECHANICAL ANALYSIS OF A FUNCTIONALLY GRADED ANNULAR FIN</i> .....	<b>614</b>
<b>Mašek J., Brožek P., Horák M.:</b> <i>THERMO-VACUUM TEST CHAMBER DEVELOPMENT FOR HEAT SWITCH TESTING IN SIMULATED MARTIAN CONDITIONS</i> .....	<b>622</b>
<b>Šulc S., Šmilauer V., Wald F.:</b> <i>COUPLED SIMULATION FOR FIRE-EXPOSED STRUCTURE USING CFD AND THERMO-MECHANICAL MODELS</i> .....	<b>946</b>
<b>Szews M., Perczyński D., Knopik L., Wawrzyniak S.:</b> <i>TEMPERATURE ANALYSIS DEPENDENCE IN THE VICINITY OF THE BRAKE DISK</i> .....	<b>962</b>
<b>Zachar M., Guzej M., Horský J.:</b> <i>NUMERICAL THERMAL COMPARISON OF HEAT SINK MATERIALS FOR AUTOMOTIVE LED HEADLAMPS</i> .....	<b>1078</b>

# **KEYNOTE LECTURES**



## **AEROBATIC SPECIAL IN-FLIGHT TESTS AT INSTITUTE OF AEROSPACE ENGINEERING**

**I. Jebáček<sup>\*</sup>, J. Matějů<sup>\*\*</sup>**

**Abstract:** *The article provides information about real flight tests of an aircraft at Institute of Aerospace Engineering. Application of methodology is presented on attractive Red Bull Air Race aerobatic aircraft. DAQ system and sensors (used for testing response of an aircraft on control surface deflection) and control forces measurement is briefly described as well as calibration and testing procedure. Only very few results (maximum forces) are provided as the rest of data is not allowed to publish.*

**Keywords:** Measurement, Force, Control, Calibration, In-flight, Airplane.

### **1. Introduction**

Aircraft testing is an inseparable part of the development of any flying vehicle regarding safety and reliability strict rules. The purpose of the tests can be divided into several groups such as: development, certification or verification tests. All of them lead to the creation of the best possible technical production. For this reason, it is necessary to give a proper attention to these experiments since the appropriate tests give a feedback to engineers. Based on the results they can refine their theoretical practices.

Each day the engineers of Aircraft Testing Facility at Institute of Aerospace Engineering (IAE) solve interesting problems linked to an industry's research and development. A lot of in-flight tests have been performed at IAE. VUT-001, VUT-061, C172T or Dornier 28, EV-55 are common aircraft tested at IAE. Test of the aerobatic special for Red Bull Air Race (Fig. 1) is different in some aspects and set up a new challenge for our team at IAE.



*Fig. 1: EDGE 540V3 aerobatic airplane.*

---

<sup>\*</sup> Assoc. Prof. Ivo Jebáček, PhD.: Institute of Aerospace Engineering, Brno University of Technology; Technická 2896/2; 616 69, Brno; CZ, jebacek@fme.vutbr.cz

<sup>\*\*</sup> Ing. Jiří Matějů.: Institute of Aerospace Engineering, Brno University of Technology; Technická 2896/2; 616 69, Brno; CZ, jiri.mateju.vut@gmail.com

## 2. In flight measurement of control stick forces at EDGE 540 aerobatic aircraft

Martin Šonka is a famous Red Bull Air Race and aerobatic pilot (sitting in EDGE 540 V3 in Fig. 1) as well as the Czech aerobatic representative in the category "Unlimited".

Travelling to Red Bull Air Race competitions is very time consuming. Moreover, weather is not always good for flight tests and thus the pilots do not have enough time for adequate training of a race track. That is the reason why the racing pilots use training flight simulators.

The simulators are important for training and pilot's progress and set up the requirement for better mathematical model of simulation. For example, the control forces feedback can help to simulate the flight more realistic. These forces can be determined analytically, but it is preferable and more accurate to perform flight tests.

## 3. Measured parameters, DAQ, sensors and calibration

The aim of this measurement was to determine the control stick forces for typical aerobatic manoeuvres. The main goal was to measure deflections and forces in a control stick. It was necessary to define several flight parameters to define precise simulation model.

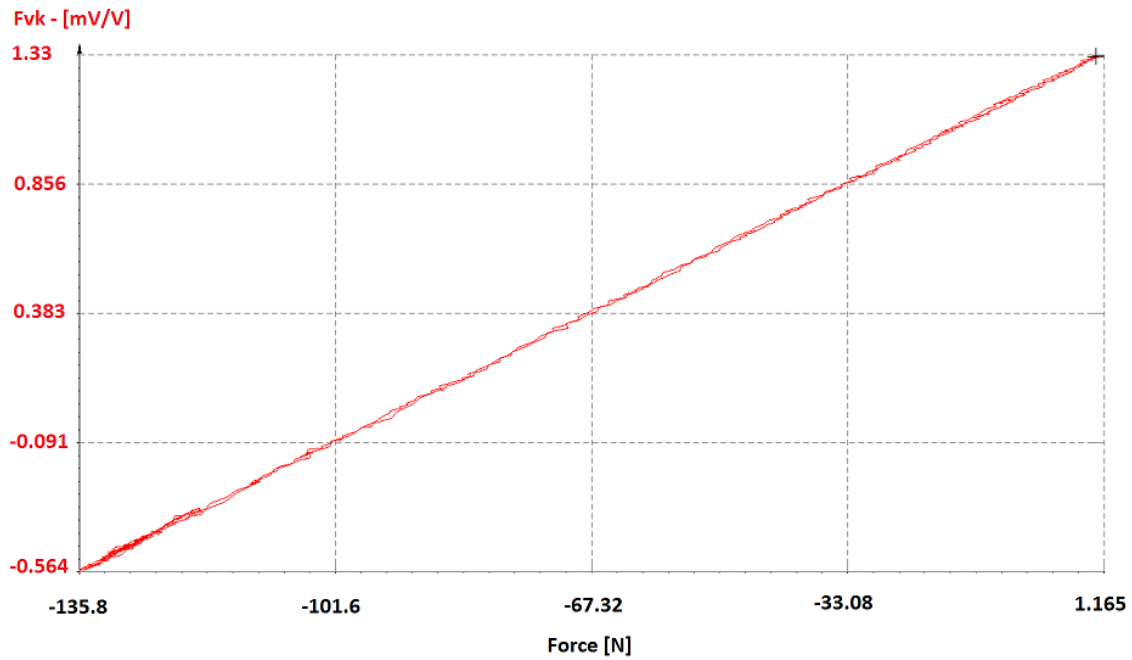
Acceleration and positional angles in flight were measured by inertial unit. Speed, altitude and motor parameters were taken from data log in inner data acquisition (DAQ) unit of the aircraft. It was also important to know the weight of the plane before and after the flight test. Forces in pedals were omitted (rudder control forces are less important).

The aircraft achieves load factor around 10 G during aerobatic manoeuvres, special attention had to be therefore paid to fit the measuring device Dewetron Minitaur and all sensors as potentiometers for the elevator and aileron deflections, inertial measurement unit, GPS antenna and so on. The fixing of potentiometer is shown in Fig. 2. The potentiometer is directly connected to the steel frame of fuselage. The connection to the control system is visible too.



*Fig. 2: Connection of elevator deflection sensor.*

A lot of methods exist for forces measurement, but installation of strain gauges directly on the stick was the most convenient. To avoid all negative influences a full bridge of strain gauge was installed on control stick in longitudinal and lateral force directions. From mathematical point of view, the calibration process is searching of relation between internal load in specific cross section of the structure (strain due to bending moment on control stick) and response of strain gauge bridge located in this section (Jebáček, et al, 2015). Fig. 3 shows linear dependence of voltage (on strain gauge bridge) on force read on calibrated load cell. Coefficients of linear regression were sufficient for force stick determination. For better accuracy second order polynomial dependence was used for aileron stick force.



*Fig. 3: Graph response - force.*

Deflections were calibrated with mechanical deflection meter (Fig. 4), which is faster and more reliable than standard digital level.



*Fig. 4: Calibration of control surface deflection.*

#### 4. Test procedure

All the preparations and tests had to be done within a few days, when the plane and pilot were available.

The aerobatic manoeuvres (steep turns, rolls, stalls and so on) were defined first.

Before the flight, the stick forces and control surface deflections were calibrated.

After all the preparations the aircraft was weighted and M. Šonka performed aerobatic flight plan. All data were continuously recorded during the flight in a rate of 100 samples per second.

Because the flight consisted of many manoeuvres, separated parts for evaluation of maximal forces were used. The aircraft trajectory was measured precisely and manoeuvre recognizing was carried out and

required waveform of each flight manoeuvre was defined. Typical measuring window of measured parameters is in Fig. 5.

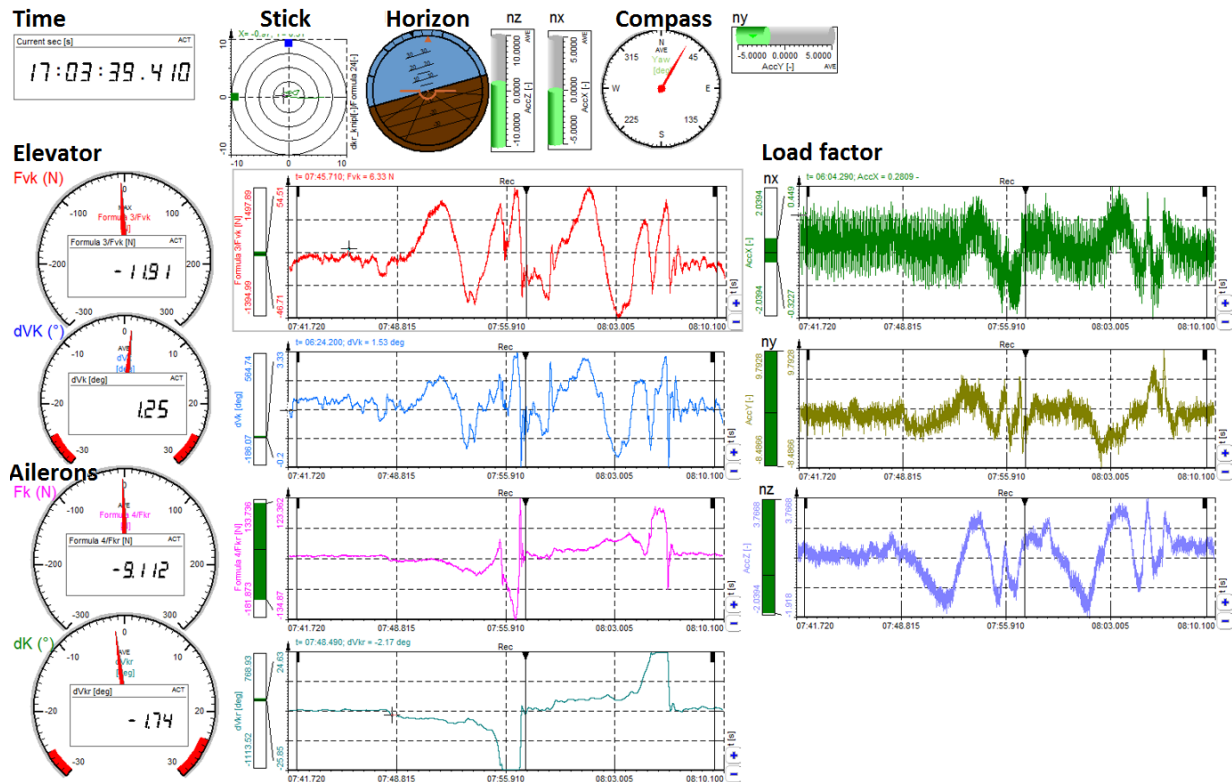


Fig. 5: Measuring window.

The maximal values 270 N in longitudinal and 209 N in lateral control system were measured.

Not only the maximal forces in control stick were defined, but also their time dependency with respect to flight conditions. This will help to get flight simulator closer to the real aircraft and improve the pilot's effective training.

## 5. Conclusion

The article describes practical experimental measurement of a real aircraft in flight. This procedure is standard for large transport airplanes, but it's unique for light aerobatic aircraft. Stick forces, control deflections and its dependency on flight conditions in various aerobatic manoeuvres were defined. The tests helped to understand the behaviour of an aircraft and improved mathematical model of the simulator. It can improve the placing of M. Šonka in Red Bull Air Race. Unfortunately, not all results can be published.

## Dedication (Acknowledgement)

The research leading to these results has received funding from the Ministry of Education, Young and Sport under the National Sustainability Programme I (Project LO1202).

Flight tests were finished in cooperation with Assoc. Prof. D. Rozehnal, and Assoc. Prof. P. Františ.

## References

Jebáček, I. and Horák, M. (2015) Measuring of a Nose Landing Gear Load during Take-Off and Landing. Applied Mechanics and Materials, 2015, Vol. 821, No. 821, pp. 325-330. ISSN: 1662-7482.



## SPECIFICS OF AEROSTRUCTURES EXPERIMENTAL TESTING

**J. Juračka\***

**Abstract:** *The article provides information about ground tests of aircraft structures at Institute of Aerospace Engineering, Brno University of Technology. The paper presents some of the specifics of the testing.*

**Keywords:** Aircraft, Structure, Testing.

### 1. Introduction

Generally, the experimental verification of aircraft structures is similar to other engineering works, nevertheless it has some specifics, which are described in this paper. Essentially, the tests are divided into the ground (laboratory) tests and flight tests. Other division defines the tests for the development and certification, i.e. they are proving the entire set of requirements of aeronautical standards defined the aviation authority, which confirms individual requests with their methods of proof.



*Fig. 1: Composite wing structure test.*

### 2. Load definition and conditions

The first steps for the structures testing is its definition and design of arrangement. Based on the geometry and weight, where the aircraft take-off weight is significantly dominating, there are defined the aerodynamic and inertial forces acting on the structure during the flight and each of the maneuvers. Subsequently these forces are expressed in the form of normal and shear forces and bending and torsional

---

\* Assoc. Prof. Jaroslav Juračka, PhD.: Institute of Aerospace Engineering, Brno University of Technology; Technická 2896/2; 616 69, Brno; CZ, juracka@fme.vutbr.cz

moments along the construction of the wing, tail and fuselage. There is also defined the maximum load for each load cases and it is declared as the **limit load**.

Subsequently, with regard to the type of construction, there is defined the **ultimate load**, i.e., limit load multiplied by the safety factor that is at least 1.5 and it is properly increased if all "normal conditions" are not fully complied, or there is a certain doubts level about the quality of production technology (e.g. castings, etc.)

From this perspective, it can be pointed out, for example, the influence of temperature and dispersion of production quality for composite structures that may cause a further increase of the required safety factor about 1.5 times.

Similarly, as in other branches, there are also significantly evaluated the fatigue characteristics of the structure, where it is also necessary to define the loading. It is prepared on the basis of a long-term collection of spectrum data about the particular amplitudes of load and their cumulative frequency and on the basis of the typical flight profile. Then the defined spectrum is ready for the planned life-time of the structure, based on the range of the test sample multiplied by the safety factor (3 for complete part), and subsequently it is applied to the structure.

### 3. Slim composite wing tests

A special chapter of the tests is to prove the static strength of composite wing structure. The wings are tested by application of local forces into collets for reaching of prescribed shear force, bending moment and torque moment. Unlike the metal structures, however, a significant deflection of the structure (see Fig. 1) has to be reflected, and it brings a significant accumulated energy, which is released during structure fail, and it destroyed the whole structure significantly. Another phenomenon of large deflection is the displacement of loading forces compared to the unloaded condition, i.e. thanks to the deformation, the resultant total force distributed over load system moves closer to the root of the wing, and it causes the necessity to shift this total force during the test procedure. The distance of the loading tree arms is also changing by the deformation of structure. Therefore, this phenomenon requires a special process in the design of the loading tree system, using the expected deformation and imaginary location of forces on the radials of circumscribing circle. By this step the result forces have got effect of perpendicular acting on the wing plane during the ultimate load.

Another specification of composites is the impact of the requirements of the regulations, which require "normal operating conditions". While, in case of the metal structures increased temperature due to surface coating is not considered significantly, in case of composite structures it is necessary to demonstrate ultimate strength according to the expected temperature. The regulation condition requires a hot summer day when the aircraft is exposed to direct sunlight. According to the surface color, the tests are realized in the temperature range from 54 Celsius degrees (for white surfaces) up to 90 Celsius degrees (for black or dark blue colors). This temperature difference is very important because the polymer resins with enhanced temperature can be getting close of the glass transition temperature, and it is significant for the technological process and the types of matrix. When approaching this temperature there are changes of viscosity and creep of structure. Generally, it can be said that each temperature increase compared to the room temperature during tests, means the higher structure deformation.

For conclusive tests at higher temperatures is a specific test of aircraft structures, where is the necessity of construction of the "heating boxes" that allow maintaining the temperature and heating of structure. For these cases, the Institute of Aerospace Engineering developed the Heating Chamber of Polystyrene, which was protected as the utility model.

Another phenomenon is also the effect of humidity, which requires a considerable number of validation tests of the material due to moisture.

### 4. Fatigue tests

Part of the aircraft structures proving is also proving of the operational reliability, which covers the effects of operational damage (impacts) and fatigue life (durability). In the context of aviation, first the safe life philosophy was applied, which required proof of ability to carry all the load cycles throughout life without any fault. Here are applied appropriate safety factors in accordance to the range of the

specimen. Nowadays applied approach is the philosophy of Damage tolerance, which assumes potential defect of the structure, and together with maintenance system and structure design there is secure the timely detection before it reaches a critical size. These approaches are of course linked to the NDT methods and inspection systems. The optical methods are used in many cases, but there are also used more advanced methods, for example, the acoustic emission (Cejpek et al., 2015, Juračka et al., 2011) (see Fig. 2) or surface waves.

The significant proportion of aeronautical testing is also partial development tests, where dominate tests for the determination of growth curves of cracks (Klement et al., 2015), strain energy release rate (Matejak et al., 2012), etc.

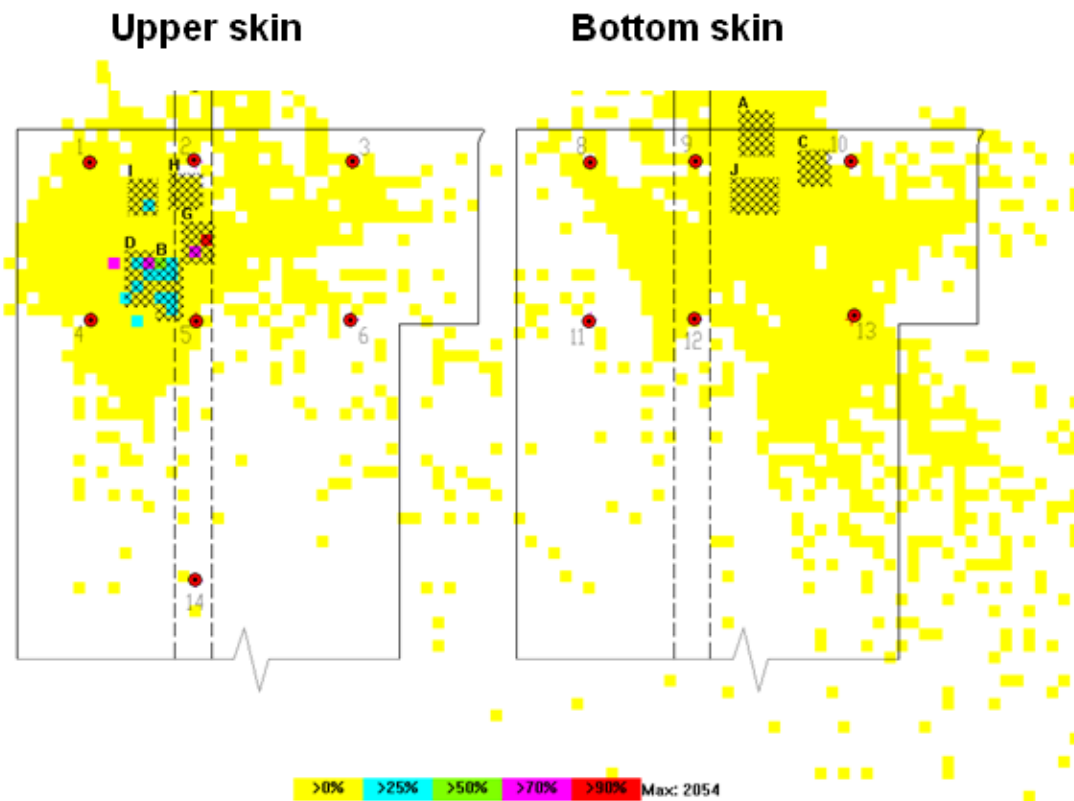


Fig. 2: Structure diagnostic during fatigue test by acoustic emission.

## 5. Dynamic tests

The last chapter of tests are tests of structures under dynamic load. A typical example is the resistance of the dynamic impact of small particles (stones), but also resistance, for example, the impact of the bird. In the framework of the development tests it may be, for example, impact of dynamic load on the panel (Splichal et al., 2015) with the evaluation of buckling or integrity (separation or delamination of the reinforcements from the skin).

Specific tests are drop tests of undercarriage (see Fig. 3), where the behavior of landing gear during the landing impact (Jebacek et al., 2015) is evaluated. Requirement is to absorb the energy of dynamic impact and minimally springing-back, which is given the aircraft mass and descending speed. Here are successfully used the drop test on the measuring platform with the evaluation of forces, acceleration and landing gear compression. In the case of tests of larger aircraft, it is necessary to simulate also the forward speed of the aircraft, mainly by using impact of the spinning wheel on hard surface.

The last mentioned type of dynamic tests are cockpit tests that prove the emergency load cases. There are either the direct impact of the glider to the Earth's surface at an angle of 45 (which can be simulated as well as quasi-static) or dynamic tests of seats of the larger aircraft.

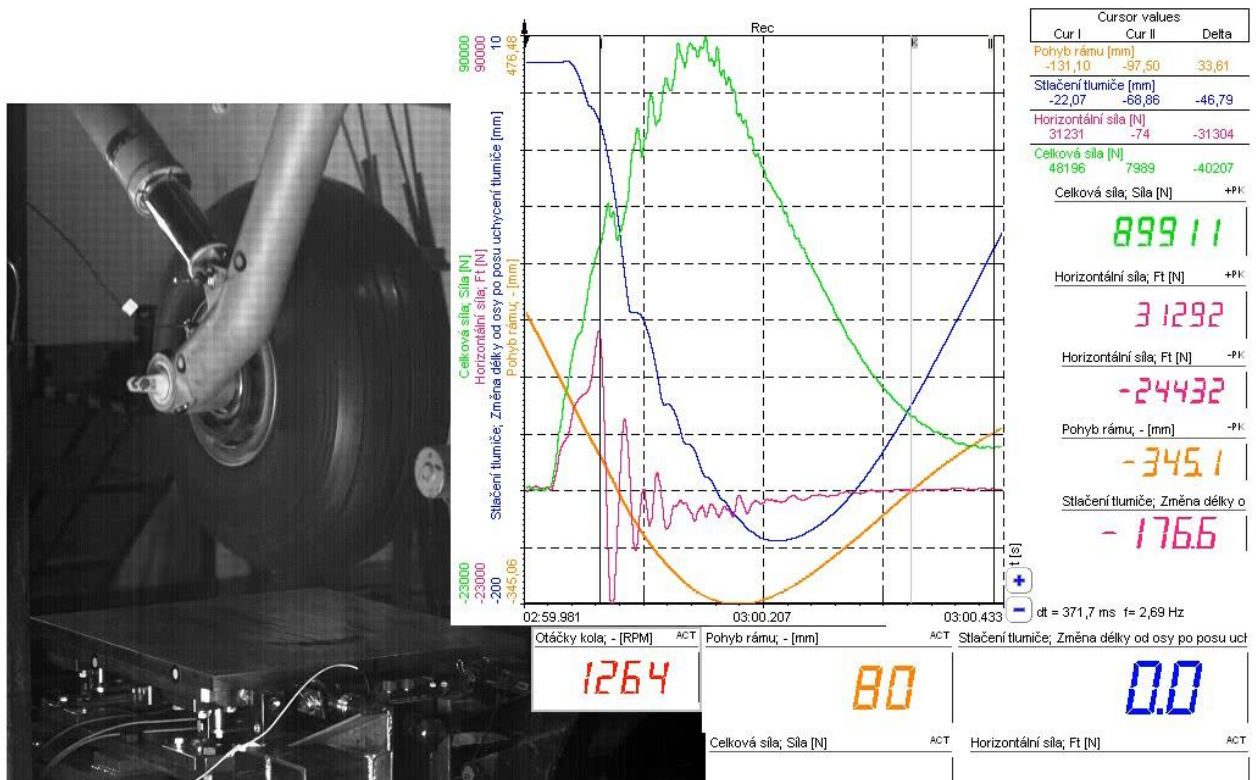


Fig. 3: Landing gear drop test.

## 6. Conclusion

The article mentions limited extend of some tests of aircraft technology, that were realized by the Institute of Aerospace Engineering, Brno University of Technology, and assist in the development or certification of a number of domestic and foreign aircrafts. The article does not mention any flight tests, which are also carried out to demonstrate the aircraft that are mentioned by my colleagues in another paper.

## Dedication (Acknowledgement)

The research leading to these results has received funding from the Ministry of Education, Young and Sport under the National Sustainability Programme I (Project LO1202).

## References

- Jebacek, I. and Horak, M. (2015) Measuring of a Nose Landing Gear Load during Take-Off and Landing. Applied Mechanics and Materials, Vol. 821, No. 821, pp. 325-330. ISSN: 1662-7482.
- Klement, J. and Augustin, P. (2015) Damage tolerance of high-speed machined integral panels made from 2024-T351 aluminium alloy. In XIII Expert Seminar Materials and technologies in the production of special techniques, University of Defense, Brno, pp. 52-59. ISBN: 978-80-7231-999- 2.
- Cejpek, J., Weis, M. and Juračka, J. (2015) Acoustic Emission Localization in Testing of Composite Structures. Svatka, ČR.
- Jebacek, I. and Horak, M. (2012) Possibilities and methods of in-flight loading measurement. Aviation, Vol. 16, No. 2, pp. 47-50, ISSN: 1648-7788.
- Juračka, J. and Weis, M. (2011) Fatigue Testing of Composite Structure and Monitoring of Acoustic Emissions. Letecký zpravodaj, Vol. 2011, No. 2, p. 37-42, ISSN: 1211-877X.
- Matejak, V. and Juracka, J. (2012) The determination of delamination energy release rate of composite bi- material interface. In Proc. ICAS 2012, International Council of the Aeronautical Sciences (ICAS), Brisbane, pp. 1-7. ISBN: 978-0-9565333-1- 9.
- Splichal, J., Pistek, A. and Hlinka, J. (2015) Dynamic tests of composite panels of an aircraft wing. Progress in aerospace sciences, Vol. 2015, No. 78, pp. 50-61. ISSN: 0376-0421.



## DEVELOPMENT OF NEW TYPE VENTILATION DUCTS SYSTEM

K. Peszynski<sup>\*</sup>, L. Olszewski<sup>\*\*</sup>, E. Smyk<sup>\*\*\*</sup>, T. Kasprowicz<sup>\*\*\*\*</sup>

**Abstract:** The paper presents a way of basic parameters measurement – local losses coefficient  $\zeta$  and line resistance coefficient  $\lambda$  – which determining pressure losses in ducts of ventilation systems. There was taken into consideration wide scope of cross-sectional areas from  $A = 0.051 \text{ m}^2$  to  $A = 2.323 \text{ m}^2$ . All measurements were provided for constant Reynolds number  $Re = 100000$ .

**Keywords:** Ventilation, Rounded rectangular cross-sectional area, Minor (local) losses coefficient, Line resistance coefficient.

### 1. Introduction

Air flow in circular and rectangular ducts is commonly encountered in ventilation and air-conditioning systems. Both of them have their advantages and disadvantages. Circular systems have better flow and strength properties but they are characterized by worse use of space. The air in a typical ventilation system passes through various fittings, bends, elbows, inlets, exits, enlargements, and contractions in addition to the ducts. Flow through fittings is very complex, and a theoretical analysis is generally not plausible. Therefore, local losses are usually experimentally determined by the manufacturers of the components. The Polish manufacturer, "Nucair Technologies Sp. z o.o." develops new ventilation system based on rounded rectangular cross-sectional area. Examination of the system air-flow properties was commissioned to Mechatronics and Working Machines Group of FME, UTP University of Technology and Life Sciences in Bydgoszcz, Poland.

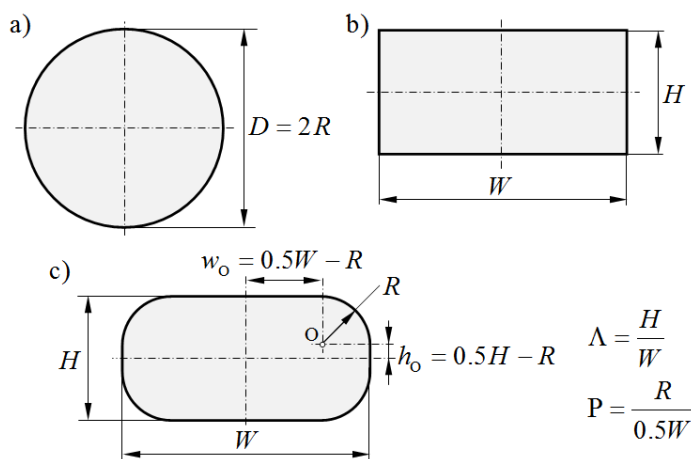


Fig. 1: Characteristic parameters of ducts: a) circular; b) rectangular; c) rounded rectangular.

<sup>\*</sup> Assoc. Professor Kazimierz Peszynski, PhD.: Faculty of Mechanical Engineering, UTP University of Science and Technology in Bydgoszcz, Al. Prof. S. Kaliskiego 7, Bydgoszcz; PL, kazimierz.peszynski@utp.edu.pl.

<sup>\*\*</sup> Lukasz Olszewski, MSc.: Faculty of Mechanical Engineering, UTP University of Science and Technology in Bydgoszcz, Al. Prof. S. Kaliskiego 7, Bydgoszcz; PL, lukasz.olszewski@utp.edu.pl.

<sup>\*\*\*</sup> Assist. Prof. Emil Smyk, MSc.: Faculty of Mechanical Engineering, UTP University of Science and Technology in Bydgoszcz, Al. Prof. S. Kaliskiego 7, Bydgoszcz; PL, emil.smyk@utp.edu.pl.

<sup>\*\*\*\*</sup> Assist. Prof. Tomasz Kasprowicz, MSc.: Faculty of Mechanical Engineering, UTP University of Science and Technology in Bydgoszcz, Al. Prof. S. Kaliskiego 7, Bydgoszcz; PL, tomasz.kasprowicz@utp.edu.pl.

Cross-sectional area is characterized by three parameters: width  $W$ , height  $H$ , and fillet radius  $R$  (Fig. 1). These parameters, during the analysis, are used in two non-dimensional forms: flatness of rectangle  $\Lambda = H/W$  and relative rounding  $P = R/0.5W$ , where width  $W$  is the basic parameter.

Fillet radius  $R$  is substantial. Therefore, the knowledge of rectangular cross-section cannot be directly used. The new type of ducts mixes various properties of ducts with circular cross-section (best theoretically recognised) and rectangular cross-section (most used).

From the dimensional point of view, the system consists of 50 recommended, 20 permissible, and 7 not recommended cross-sections (Fig. 2), where white cells are recommended, 5 % of grey cells are permissible, 25 % of grey cells are not recommended, and 35 % of grey cells are impossible.

		Cross-sectional area $A$ [m <sup>2</sup> ]								
		$H$ [mm]								
$A$		200	250	300	400	500	600	800	1000	1200
$R$ [mm]	100	0.051	0.066	0.081	0.111	0.141	0.171	0.231	0.291	0.351
	100	0.071	0.091	0.111	0.151	0.191	0.231	0.311	0.391	0.471
	100	0.091	0.116	0.141	0.191	0.241	0.291	0.391	0.491	0.591
	100	0.111	0.141	0.171	0.231	0.291	0.351	0.471	0.591	0.711
	200	0.151	0.191	0.231	0.311	0.391	0.471	0.631	0.791	0.951
	200				0.366	0.466	0.566	0.766	0.966	1.166
	200				0.446	0.566	0.686	0.926	1.166	1.406
	200				0.526	0.666	0.806	1.086	1.366	1.646
	200				0.606	0.766	0.926	1.246	1.566	1.886
	300						1.003	1.363	1.723	2.083
	300						1.123	1.523	1.923	2.323
		recommended	permissible		not recommended			impossible		

Fig. 2: Dimensions of new system.

The cross-sectional area  $A$  varies from  $A_{min} = 0.051 \text{ m}^2$  to  $A_{max} = 2.423 \text{ m}^2$ . This wide scope of areas imposes high demands relating to the measurement stand.

## 2. Measurements

The study of new components flow properties consists of determination of two basic parameters: (a) line resistance coefficient  $\lambda$  and (b) local losses coefficient  $\zeta$ , both are dimensionless. These parameters are used to calculate the pressure loss in ventilation system composed of serial connected  $i$  straight ducts and  $j$  components (e.g. elbows, fittings) (Orzechowski et al., 1997)

$$P_{los} = \frac{\rho V_{avg}^2}{2} \left( \sum_i \lambda_i \frac{l_i}{D_{h,i}} + \sum_j \zeta_j \right) \quad (\text{Pa}) \quad (1)$$

where  $\rho$  is the air density(kg/m<sup>3</sup>),  $V_{avg}$  is the air average velocity(m/s),  $l_i$  is the length of straight ducts (m),  $D_{h,i}$  is hydraulic diameter of straight ducts (m),  $\lambda_i$  and  $\zeta_i$  as mentioned above.

Hydraulic diameter was calculated from the formula

$$D_h = \frac{4A}{p} = \frac{2(\Lambda - (4 - \pi)P^2)}{1 + \Lambda - (4 - \pi)P} W \quad (2)$$

where  $A$  is a cross-sectional area of duct (m<sup>2</sup>),  $p$  is its perimeter (m), other nomenclature discussed above.

Number of components must be reduced to  $i = 2$  and  $j = 1$  for measurements of properties  $\lambda$  and  $\zeta$ . As a result, we obtain system presented in Fig. 3. In this figure  $Q_{in} = Q_{out}$  means air flow rate (m<sup>3</sup>/s) through

examined duct. After reduction and rearranging equation (1), we obtain formula to determine local losses coefficient  $\zeta$

$$\zeta = \frac{2P_{\text{los}}(l)}{\rho v_{\text{avg}}^2} - \lambda \frac{l_{\text{in}}}{D_h} - \lambda \frac{l_{\text{out}}}{D_h} \quad (3)$$

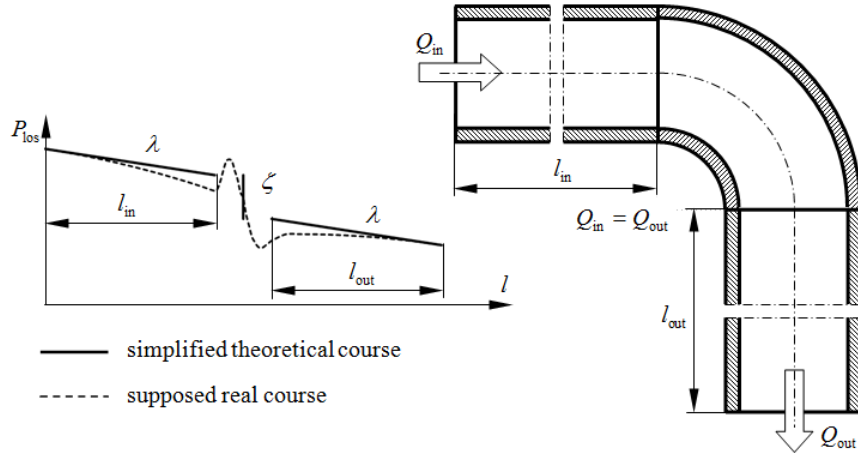


Fig. 3: The idea of experimental minor (local) losses determination.

The actual image of the laboratory stand is presented in Fig. 3. Part a) shows duct with  $W = 0.6 \text{ m}$ ,  $H = 0.2 \text{ m}$  and  $R = 0.1 \text{ m}$ . Part b) shows supply system, which consists of fan controlled by power inverter and flow straightener (cuboid in the foreground) located in the background in the left side of part a). Part c) shows measurement point, which consists of Prandtl probe with digital pneumo-electric transducer and it is connected to a computer located in the main part of Fig.4a). Part d) of Fig. 4 shows main part of flow straightener in a honeycomb shape with length 0.5 m. Dimensions of flow straightener are 0.18 m x 0.12 m. Hexagon side is 35 mm.



Fig. 4: Laboratory stand a) duct with supply system, b) view of supply system, c) measurement point, d) flow straightener.

It is necessary to determine  $\lambda$  for calculations  $\zeta$ , as we can see in the formula (3). Line resistance coefficient  $\lambda$  can be determined after substitution of  $\zeta = 0$  into the equation (3), and after rearranging we obtain

$$\lambda = \frac{2P_{\text{los}}}{\rho V_{\text{avg}}^2} \cdot \frac{D_h}{l_{\text{in}} + l_{\text{out}}} \quad (4)$$

A new configuration of laboratory stand is a result of substitution  $\zeta = 0$  and it is presented in Fig. 5.

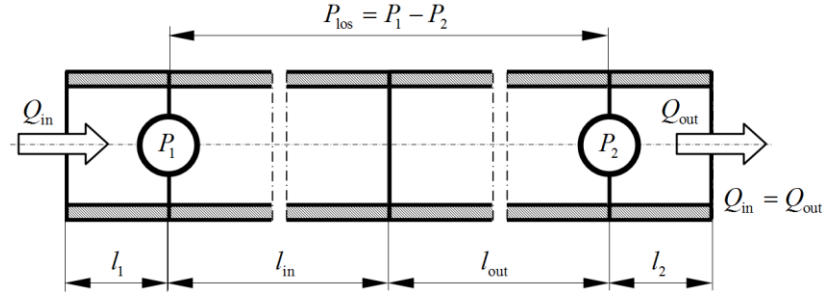


Fig. 5: Idea of laboratory stand for determination of line resistance coefficient  $\lambda$ .

In Fig. 5,  $l_1$  and  $l_2$  are inlet and outlet parts of the duct and they are necessary for smoothing the flow, both about  $3D_h$ .  $l_{in}$  and  $l_{out}$  are bigger than  $10D_h$ .

All tests are performed for  $Re = 100000$ . This number results from analysis  $V_{avg}$

$$Re = \frac{V_{avg} D_h}{\nu} \rightarrow V_{avg} = \frac{Re \cdot \nu}{D_h} \quad (5)$$

For standard  $\nu = 1.5 \cdot 10^{-5} \text{ m}^2/\text{s}$  for air, we obtain very simple formula  $V_{avg} = 1.5/D_h$ . For  $D_h \in \langle 0.248; 1.579 \rangle (\text{m})$ , we obtain scope of average velocity  $V_{avg} \in \langle 6.041; 0.926 \rangle (\text{m/s})$ . The maximum permissible average velocity in ventilation ducts is  $V_{avg} = 10 \text{ m/s}$ . Maximum of average velocity is limited by noise produced by ventilation system. The next step is to calculate average velocity at a maximum velocity  $V_C$  in the center of the duct (Peszyński et al., 2016)

$$V_C = V_{avg} \frac{\Lambda - (4 - \pi)P^2}{\Lambda \frac{n}{n+1} \left( \frac{n}{n+1} \left( 1 - \left( \frac{4P^2}{\Lambda} \right)^{\frac{n+1}{n}} \right) + \pi 4^{\frac{1}{n}} \left( \frac{P^2}{\Lambda} \right)^{\frac{n+1}{n}} \right)} \quad (6)$$

where  $1/n$  is exponent Prandtl power-law velocity profile. Velocity at the central point of cross-sectional area is measured by Prandtl probe and tuned to correct value using power inverter.

### 3. Conclusions

Presented studies show that smaller maximum velocities ( $V_C < 2.0 \text{ m/s}$ ) for bigger ducts sizes, where Reynolds number  $Re = 100000$ , cause measurement problems of low pressures ( $P_{C, dyn} < 3.0 \text{ Pa}$ ). Instead of Prandtl probe, the thermo-anemometer is used for these cross-sectional areas to measure maximum velocity. The quality of individual connections of duct segments has significant effect on line resistance coefficient  $\lambda$

### Acknowledgement

The authors would like to kindly thank the company Nuair Technologies Sp. z o.o., SolecKujawski, Poland for the performance of tested ducts and the delivery of air supply system. Authors also received institutional support BS 16/2013 granted by Faculty of Mechanical Engineering of UTP University.

### References

- Orzechowski, Z., Prywer, J. and Zarzycki, R. (1997) Fluid Mechanics in Environmental Engineering, WNT, Warsaw (in Polish).
- Peszyński, K., Olszewski, L., Smyk, E. and Perczyński, D. (2016) Analysis of the Velocity Distribution in Different Types of Ventilation System Ducts, International Conference Experimental Fluid Mechanics 2016, Nov. 15th – 18th, 2016, Mariánské Lázně, Czech Republic, pp. 577-580.

## MODERN TOOLS FOR VEHICLE DEVELOPMENT

P. Porteš<sup>\*</sup>, P. Kučera<sup>\*\*</sup>, V. Pištěk<sup>\*\*\*</sup>, J. Fojtášek<sup>\*\*\*\*</sup>, L. Zhaňal<sup>\*\*\*\*\*</sup>

**Abstract:** *The development of vehicles is constantly advancing, therefore, it is required to have more sophisticated tools for the development of a complete vehicle or its individual parts. This article describes modern tools used at the Institute of Automotive Engineering in Brno for vehicle development, i.e. simulation multibody software MSC ADAMS/Car or tools for MIL and HIL testing of mechatronic systems. Furthermore, the article presents tools enabling the use of multibody models for analysing data obtained from driving tests and software for processing and analysing the measured or calculated data obtained during all phases of vehicle development.*

**Keywords:** Multibody models, Dynamics, MIL, HIL, Simulink, NI VeriStand, C, C++, Adams/Car, Data analysis, Vehicle dynamics testing.

### 1. Introduction

The development of vehicles is constantly advancing, therefore, it is required to have more sophisticated tools for the development of a complete vehicle or its individual parts. Thus, this article describes not only the commercial tools, but also the primary custom tools for the development and testing of vehicle dynamics and mechatronic systems at the Institute of Automotive Engineering in Brno.

Simulations using a detailed multi-body model significantly contribute to the development of the vehicle in the pre-prototype stages and are widely used during all developmental stages. Currently, it is possible to use one of the commercial software such as MSC ADAMS, SIMPACK, and LMS Virtual.Lab Motion (LMS DADS). Chapter 2 describes the use of MSC ADAMS software and its module ADAMS/Car.

The third chapter deals with tools used for the testing and development of mechatronic systems. Here mainly the developing custom tools for MIL and HIL testing are described. Therefore, the library was developed to assemble different configurations of vehicles and also for a vehicle simulator to test ECU prototype. These tools are continuously expanded and used for fast and parallel development of mechatronic applications in cooperation with automotive manufacturers.

After the simulation of vehicle and component testing it is required to take a test drive of the vehicle. These tests verify the function and mutual co-operation of all subsystems and also perform a synchronisation of all setting elements – the final setting. For these purposes, it is important to have a means which would simplify the data analysis, either with their effective processing or by providing quantities which are essential for the analysis processes. In many cases, these quantities cannot be measured or it is very difficult. Therefore, a method and software tools are created to effectively build a detailed multibody model which could be linked with the measured signals and calculate dynamic states of the vehicle while tested (see Chapter 4).

---

<sup>\*</sup> Assoc. Prof. Ing. Petr Porteš, PhD.: Institute of Automotive Engineering, Brno University of Technology, Technická 2896/2; 616 69, Brno; CZ, portes@fme.vutbr.cz

<sup>\*\*</sup> Ing. Pavel Kučera, PhD.: Institute of Automotive Engineering, Brno University of Technology, Technická 2896/2; 616 69, Brno; CZ, kucera@fme.vutbr.cz

<sup>\*\*\*</sup> Prof. Ing. Václav Pištěk, DrSc.: Institute of Automotive Engineering, Brno University of Technology, Technická 2896/2; 616 69, Brno; CZ, pistek.v@fme.vutbr.cz

<sup>\*\*\*\*</sup> Ing. Jan Fojtášek: Institute of Automotive Engineering, Brno University of Technology, Technická 2896/2; 616 69, Brno; CZ, fojtasek@iae.fme.vutbr.cz

<sup>\*\*\*\*\*</sup> Ing. Lubor Zhaňal, PhD.: Institute of Automotive Engineering, Brno University of Technology, Technická 2896/2; 616 69, Brno; CZ, zhanal@fme.vutbr.cz



The last chapter details a tool for general data processing of measurements and calculations which is used in all developmental stages of the vehicle.

## 2. Tools for vehicle dynamics – Adams

Through the multibody method of mechanism analysis it is possible to perform static, kinematic and dynamic simulations of individual subsystems and the whole vehicle and thus analyse the resulting properties using the virtual prototype. MSC ADAMS Car software is the world's most widely used solution in the field of linking multibody system and the vehicles dynamics theory. Modelling using this system, however, requires numerous input parameters and interdisciplinary experience. Based on the sophisticated databases of the already verified models of individual subsystems, it is possible to significantly shorten the time needed to build the basic and also more advanced analyses, while achieving sufficient robustness of calculation. To simulate the various events the predefined and also custom test rigs for axles, drivetrain and the entire vehicle are used. During driving simulations, it is possible to use a variety of standardized manoeuvres and multiple levels of feedback driver algorithm. These allow to find and analyse the situations that are the stability limit of the vehicle. Finished models offer virtual testing and analysis of the impact of the construction changes on the vehicle characteristics before the production of the physical prototype (Fojtášek, 2016). Of course, it is possible to replace the individual rigid parts with flexible bodies and the direct calculation of the deformation and tension under static and dynamic loading, or export of load states may be further used in subsequent strength and endurance calculations.

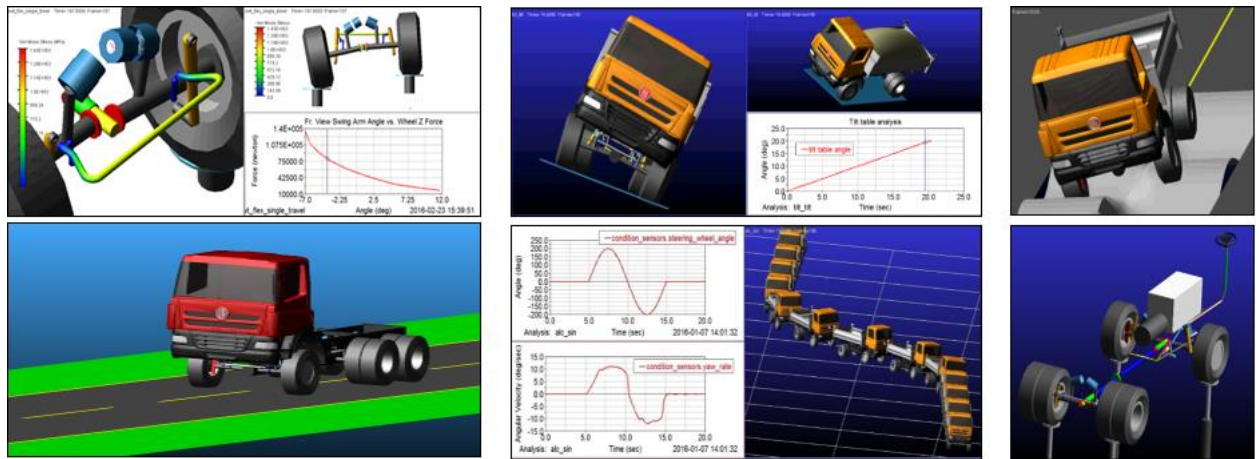


Fig. 1: Adams/Car applications.

## 3. Tools for development of mechatronics system - HIL

Custom applications for mechatronic systems are developed in C, C++, or in a Simulink software. To verify the design of the control algorithm in the MIL testing, own library with blocks describing individual parts of the vehicle is developed in Simulink software. More detailed description can be found in (Kučera, 2014). Users of this library can assemble the whole vehicle. This can test the vehicle dynamics, vibration and especially the different mechatronic systems. After the verification of algorithm by MIL testing, hardware for HIL testing is used. For this purpose, the National Instruments hardware NI 3110 RT is used. This device is a substitution for the control unit used for testing on a real vehicle. The control algorithm is compiled into the appropriate language and it is placed using NI VeriStand software into the hardware processor. Using the I/O interface the user can connect the necessary sensors and actuators. A sample of application is a developed mechatronic system used for automatic control of the lock differential in cooperation with the truck manufacturer. It is described by (Kučera, 2016). In the first phase of the development it is possible to test the control algorithms in the laboratory, as shown in Fig. 2 on the left, and then also on the actual vehicle. An advantage is the parallel development of the ECU prototype. Another tool is a vehicle simulator in real time described in (Kučera, 2015). It is a tool for simulation and visualization of a vehicle driving which is controlled by a real driver. This is illustrated in Fig. 2 on the right. These tools are used and can effectively and parallelly develop and test the mechatronic system.



Fig. 2: HIL applications.

#### 4. Data Analysis Using Multibody Model of Vehicle

This chapter describes the resources by which it is possible to enclose the driver – test vehicle – mathematical model into one computational loop. These resources are used during test drives to analyse the dynamic behaviour of the vehicle, its subsystems and final optimization of their settings. For this purpose, a measuring system that is able to provide all the necessary quantities for calculating the vehicle dynamic state is assembled. SAMS multibody software is also created (Porteš, 2014). Based on the 3D topology of the mechanism the software generates the model equations in symbolic form (the programming language C++), generally for solving kinematics, statics and dynamics (direct and inverse problems). In order to interconnect the measured data with the computational model, its formalism is adapted and supplemented by modelling elements, allowing the model to include forces and torques of unknown size (Porteš, 2014). Measured and calculated data are analysed, processed and animated using data analysis software TeleMatrix. This approach will get results from the measurements which are comparable in complexity and detail to the simulation calculations and to the user is comfort comparable to current multibody simulation software. Another advantage of this approach is that with the right set of measured signals, it is not necessary to include models of all subsystems, as it would be the case with conventional simulation. For example, it is not necessary to include the tire model with over 50 parameters. On the other hand, the calculation of the vehicle states could provide force effects and kinematic quantities which allow us to obtain parameters of the tire model during data post processing or to adapt the parameters to conditions corresponding to the drive test. Fig. 3 shows the principle of the method of connecting the measured values with the mathematical model.

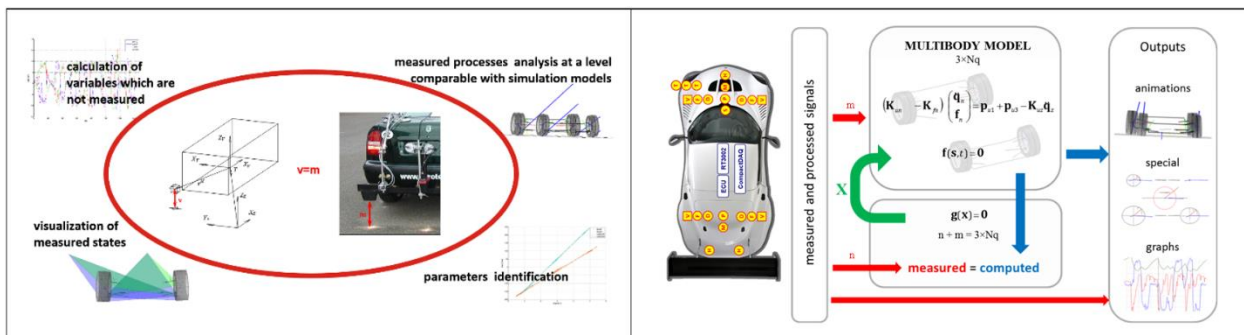


Fig. 3: The principle of linking the measured values with a mathematical model.

#### 5. Data Analysis – TeleMatrix

TeleMatrix program is composed as an extension of Matlab development environment. The main purpose is to concentrate and interconnect various analytical tools that can then be easily and quickly applied in the analysis and processing of heterogeneous data. The program also allows to create automated procedures, which can then be advantageously applied during all developmental stages of the vehicle. It is important for comparison of the results, e.g. from partial developmental stages – the pre-prototype

simulation, verification measurements of the prototype, or test drives during the final tuning of the vehicle. In addition to the wide range of traditional tools for data analysis and the ability to import from many different formats and data loggers, the program also allows to work with events, commentaries, intelligent search of conditions, compiling final reports, and an overall management of large projects.

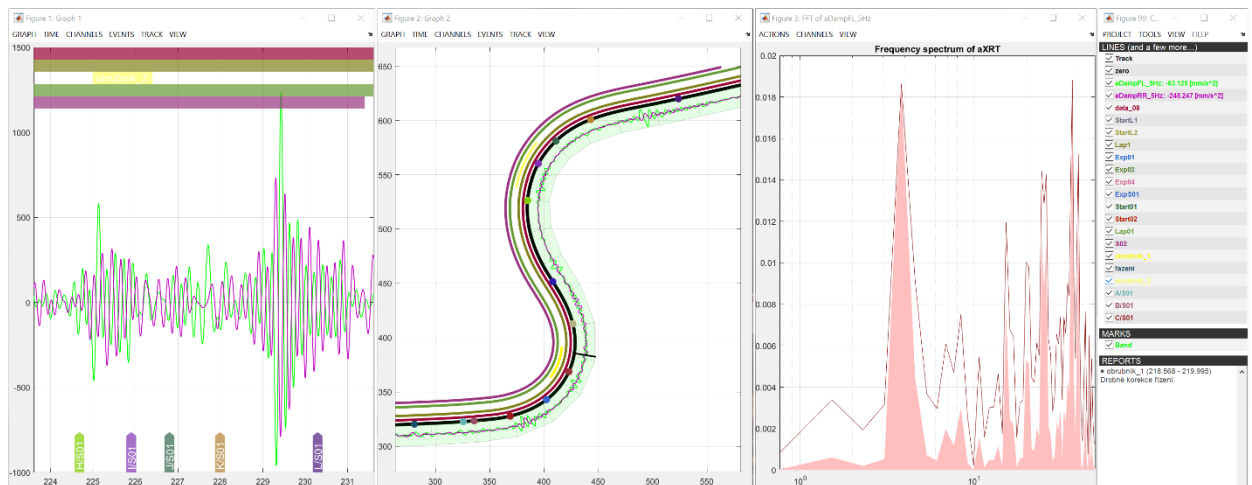


Fig. 4: TeleMatrix – example of analysed data.

## 6. Conclusions

The aim of all automotive institutions is to have sophisticated tools for fast and efficient development. Therefore, this article described a combination of commercial and custom made tools for development and testing of vehicle dynamics and mechatronic systems.

For the simulation of a vehicle drive and optimization of its parameters, MSC ADAMS/Car software is used, particularly in pre-prototype stages, but also in other stages if there is a need to predict the characteristics of the vehicle after the application of the proposed changes.

For MIL testing, commercial tools are extended by the libraries of the vehicle computational models. For HIL testing of the ECU, the vehicle simulator tool has been continuously extended.

To analyse the behaviour of the actual vehicles during test drives more effectively, tools which enable to utilize the multibody models for direct analysis of measured data are created.

Simple assessment and comparison of data from all individual stages of the project are then performed by TeleMatrix program which includes a number of integrated general and also specialized tools.

These contemporary tools are widely used in automotive technology and significantly contribute to rapid and sophisticated new product development.

## Acknowledgement

This work is an output of the internal BUT research project Reg. No. FSI-S-17-4104.

## References

- Fojtášek, J. (2016) Lane Change Manoeuvre of Virtual Heavy Vehicle Equipped with Yaw Moment Control. *Perners' Contacts*, 4, XI, pp. 24-31, ISSN: 1801-674X.
- Kučera P. and Pištěk V. (2016) Mechatronic System of Automatic and Manual Differential Lock Control - Vehicle Turning, in: *17th International Conference on Mechatronics*, Czech Technical University in Prague, Prague, pp. 307-310.
- Kučera, P. (2015) Mechatronic approach to vehicle dynamics. Doctoral thesis, BUT Brno.
- Kučera P. and Pištěk V. (2014) Virtual prototype of a heavy duty off-road truck driveline in Simulink software, in: *Conference Transport Means 2014*, Kaunas University Technology Press, Kaunas, pp. 5-8.
- Porteš, P. (2014) Utilisation of mathematical vehicle models in analysis of measured data. Habilitation thesis, Brno University of Technology (in Czech).



## SHOCK WAVES IN AN IDEAL GAS AND ENTROPY ANALYSIS

P. Šafařík\*

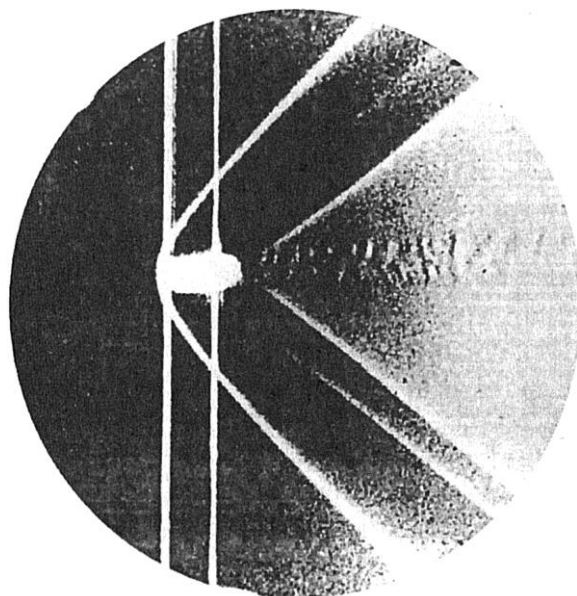
**Abstract:** *In the paper, theories of normal and oblique shock waves will be presented. Principles of fluid mechanics and thermodynamics of an ideal gas are applied. Properties of shock waves will be discussed in connection with ambiguous solutions. Entropy analysis enables to determine conditions of occurrence of shock waves. An optimization task for shock wave parameters is formulated and solved.*

**Keywords:** Shock waves, Entropy analysis, Optimization task.

### 1. Introduction

Theory of shock waves is introduced in many textbooks of gas dynamics, for instance (Shapiro, 1953). Primary theoretical works on shock waves were achieved (Rankine, 1870 and Hugoniot, 1887). Experimental evidence of existence of shock waves was carried out in the year 1886. Mach and Salcher (1887) published the schlieren picture (see Fig. 1) where shock waves upstream and downstream of the projectile in flight are evident. Further experimental and theoretical investigations made possible development of theory of shock waves, for instance (Prandtl, 1907). The shock wave theory enables to solve parameters of fluid flow on shock waves. For numerical solutions in aerodynamic practice, auxiliary (subsidiary) tables (AMES Research Staff, 1948) and diagrams (AMES Research Staff, 1948) were prepared. Modern internet aids offer accessible calculators, for instance (Compressible Aerodynamic Calculator, 2014). A detail historical overview of investigations of shock waves is given in the book (Krehl, 2009).

The aim of this paper is to present theoretical approach and description of flow structure in experimental results at occurrence of shock waves.



*Fig. 1: Schlieren picture of the projectile in flight.*

---

\* Prof. Pavel Šafařík, PhD.: Department of Fluid Mechanics and Thermodynamics, Faculty of Mechanical Engineering, CTU in Prague, Technická 4; 166 07, Prague; CZ, pavel.safarik@fs.cvut.cz

## 2. Shock wave theory

Shock waves are adiabatic abrupt physical phenomena. They are surfaces with discontinuity of fluid flow parameters. Basic theoretical approach is based on balances of mass, momentum and energy fluxes. The condition of adiabatic process is defined by constant value of total specific enthalpy  $h_{01} = h_{02} = h_0$ . A control volume is chosen very thin in a part of the shock wave.

In following paragraphs, only substantial knowledge will be presented.

### 2.1. Normal shock wave theory

The scheme of control volume for normal shock wave is shown in Fig. 2. Following system of equations is based on balance of mass

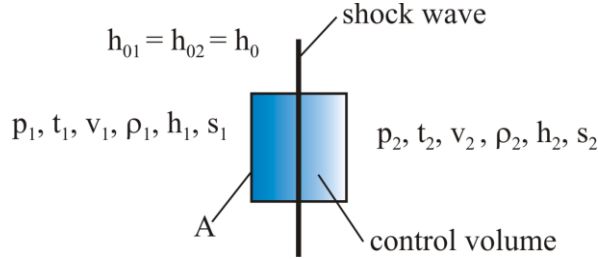


Fig. 2: The scheme of control volume for normal shock wave.

$$\frac{\dot{m}}{A} = \rho_1 v_1 = \rho_2 v_2, \quad (1)$$

balance of momentum

$$p_1 - p_2 = \frac{\dot{m}}{A}(v_2 - v_1) \Rightarrow p_1 + \rho_1 v_1^2 = p_2 + \rho_2 v_2^2, \quad (2)$$

balance of energy

$$h_1 + \frac{v_1^2}{2} = h_2 + \frac{v_2^2}{2} \quad (3)$$

and equation of state of an ideal gas

$$p = \frac{\kappa - 1}{\kappa} \rho h. \quad (4)$$

One of solutions of the system Eqs. (1 – 4) is Rankine-Hugoniot equation – relation between ratio of pressures downstream  $p_2$  and upstream  $p_1$  and ratio of densities downstream  $\rho_2$  and upstream  $\rho_1$  of the shock wave

$$\frac{p_2}{p_1} = \frac{\frac{\kappa + 1}{\kappa - 1} \cdot \frac{\rho_2}{\rho_1} - 1}{\frac{\kappa + 1}{\kappa - 1} - \frac{\rho_2}{\rho_1}}, \quad (5)$$

which is depicted in diagram in Fig. 3 in comparison with isentropic relation  $\frac{p}{\rho^\kappa} = \text{const}$ . From the

system of Eqs. (1 – 4) it is also possible to derive dependence of ratio of pressures downstream  $p_2$  and upstream  $p_1$  of shock wave on upstream Mach number  $M_1$

$$\frac{p_2}{p_1} = \frac{2\kappa}{\kappa + 1} M_1^2 - \frac{\kappa - 1}{\kappa + 1}. \quad (6)$$

Prandtl relation for values of non-dimensional velocities upstream  $\lambda_1$  and downstream  $\lambda_2$  of a normal shock wave is well-known

$$\lambda_1 \cdot \lambda_2 = 1. \quad (7)$$

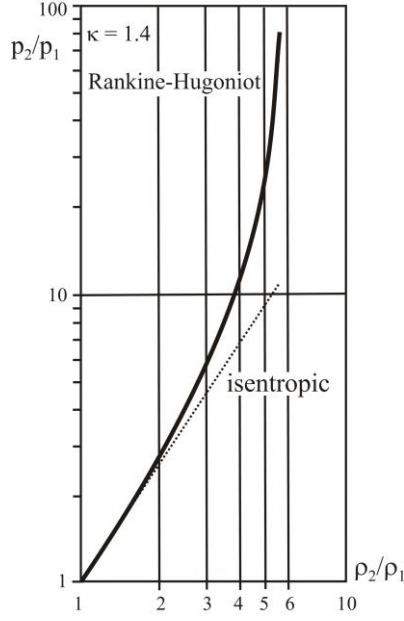


Fig. 3: Dependence of ratios of pressures and densities, Eq. (5).

## 2.2. Oblique shock wave theory

The scheme of control volume for oblique shock wave is shown in Fig. 4 where geometric parameters of the shock wave angle  $\beta$  and the deflection angle  $\delta$  are depicted. Velocity vectors  $v_1$  and  $v_2$  are distinguished. Their normal  $v_n$  and tangential  $v_t$  components are used in balances of mass and momentum. The system of equations consists of balances mass, momentum in normal direction, momentum of tangential direction, energy and equation of state.

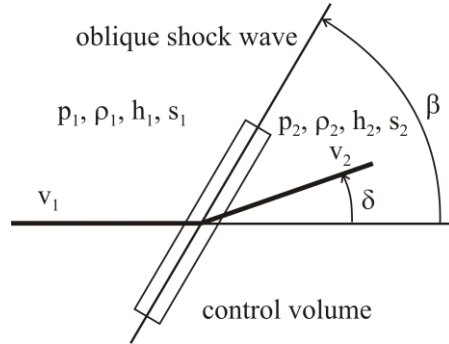


Fig. 4: The scheme of control volume for normal shock wave.

The solution of the system confirms that Rankine-Hugoniot equation, Eq. (5), holds also for oblique shocks. Ratio of pressures depends not only on upstream Mach number  $M_1$  but also second independent variable – the shock angle  $\beta$  - appears

$$\frac{p_2}{p_1} = \frac{2\kappa}{\kappa + 1} M_1^2 \sin^2 \beta - \frac{\kappa - 1}{\kappa + 1}. \quad (8)$$

Prandtl equation for oblique shock waves is not so easy as in the case of normal shock waves, Eq. (7), but beside normal velocity components  $v_{n1}$  and  $v_{n2}$  tangential velocity component  $v_{t1} = v_{t2} = v_t$  takes place

$$v_{n1} \cdot v_{n2} = a_*^2 - \frac{\kappa - 1}{\kappa + 1} v_t^2, \quad (9)$$

where  $a_*$  is critical speed of sound. For computation of the deflection angle  $\delta$ , following equation was derived

$$\tan \delta = 2 \cot \beta \left[ \frac{M_1^2 \sin^2 \beta - 1}{M_1^2 (\kappa + \cos 2\beta) + 2} \right]. \quad (10)$$

From working formulas for parameters of oblique shock wave different tables and charts were prepared. The shock polars in hodograph plane proved to be very useful. In Fig. 5 shock wave polars are depicted and sonic conditions downstream of the oblique shock wave are indicated.

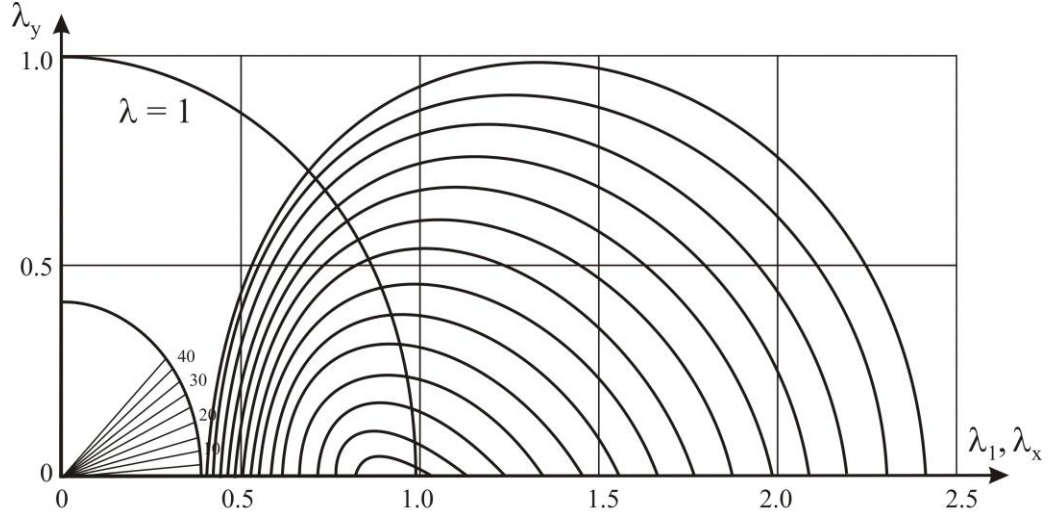


Fig. 5: Shock wave polars in hodograph plane,  $\kappa = 1.4$ .

### 3. Entropy analysis of shock waves

From aerodynamic equations for oblique shock waves and from thermodynamic relations it is possible to derive relation for entropy increase

$$\frac{s_2 - s_1}{r} = \ln \left\{ \left( \frac{2\kappa}{\kappa + 1} M_1^2 \sin^2 \beta - \frac{\kappa - 1}{\kappa + 1} \right)^{\frac{1}{\kappa - 1}} \cdot \left[ \frac{(\kappa - 1)M_1^2 \sin^2 \beta + 2}{(\kappa + 1)M_1^2 \sin^2 \beta} \right]^{\frac{\kappa}{\kappa - 1}} \right\}. \quad (11)$$

The analysis of the Eq. (11) confirms that the existence of shock waves can be only in supersonic flow field of an ideal gas,  $M_1 > 1$ . For oblique shock waves the shock wave angle is in the region

$\mu_1 = \arcsin \frac{1}{M_1} \leq \beta \leq \frac{\pi}{2}$ . When  $\beta$  is positive the oblique shock wave is left-running. If it is negative

the oblique shock wave is right-running. Maximum value of the deflection angle  $\delta_{\max}$  on oblique shock waves exists and can be derived as a function of Mach number  $M_1$  upstream of the oblique shock wave  $0 \leq \delta \leq \delta_{\max}(M_1)$ . For given value of the deflection angle  $\delta$  two solutions of parameters of oblique shock wave exist. The dividing regime corresponds to the condition maximum of the deflection angle.

### 4. Optimal parameters of oblique shocks

Achieved knowledge on parameters of shock waves enables to formulate and solve optimization tasks. One of them has the criterion of optimum minimum entropy increase for given deflection angle  $\delta = \text{const.}$ , Šafařík (1993)

$$\left( \frac{d(s_2 - s_1)}{dM_1} \right)_{\delta = \text{const}} = 0. \quad (12)$$

The solution of the optimization task offered interesting results

the optimal Mach number  $M_{1\text{opt}}$  upstream of the oblique shock wave

$$M_{1\text{opt}} = \sqrt{\frac{2}{1 - \kappa \cdot \sin \delta}} \quad (13)$$

the optimal shock wave angle

$$\beta = \frac{\pi}{4} + \frac{\delta}{2} \quad (14)$$

the optimal ratio of static pressures

$$\left( \frac{p_2}{p_1} \right)_{opt} = \frac{1 + \kappa \cdot \sin \delta}{1 - \kappa \cdot \sin \delta} = M_{1opt}^2 - 1. \quad (15)$$

In Fig. 6, parameters for maximum deflection angle and for sonic flow downstream of the oblique shock wave (see in book by Maršík, 2015) are compared with optimal parameters of oblique shock waves.

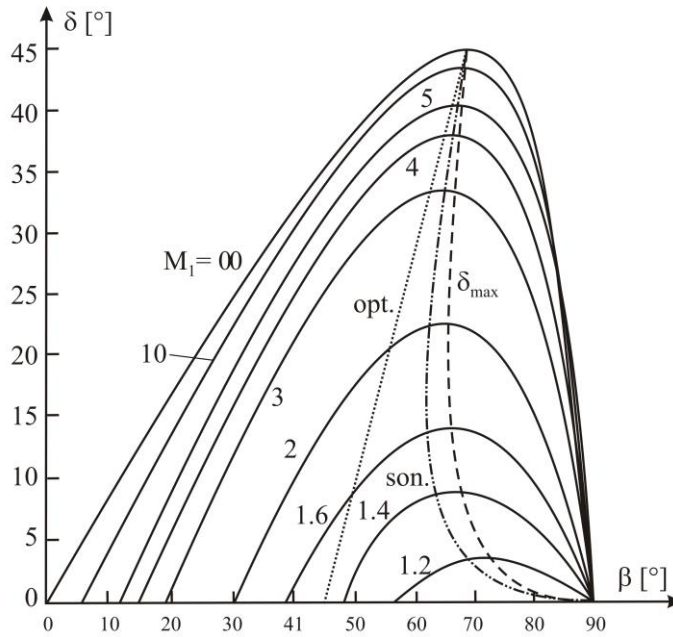


Fig. 6: Diagram the deflection angle  $\delta$  versus the shock wave angle  $\beta$ ,  $\kappa = 1.4$ .

## 5. Conclusions

High-speed flow investigations have to prepare new knowledge and data for reliable and effective design and operation of machines. Classical gas dynamics proposes important and interesting topics for study of compressible fluid flow. Their solutions can give new experience and instruments for understanding of complex processes in flow systems.

## Acknowledgement

The support from the Technology Agency of the Czech Republic in the frame of the Competence Centre Advanced Technology of Heat and Electricity Output, No.TE01020036 is gratefully acknowledged.

## References

- AMES Research Staff (1948) Equations, Tables, and Charts for Compressible Flow, NACA Report 1135, Washington.
- Compressible Aerodynamic Calculator (2014) <http://www.dept.aoe.vt.edu/~devenpor/aoe3114/calc.html>.
- Hugoniot, H. (1887) Memoir on the Propagation of Movements in Bodies, Especially Perfect Gases, Journal de l'Ecole Polytechnique, Vol. 57, pp. 3-97, (in French).
- Krehl, P.O.K. (2009) History of Shock Waves, Explosions and Impacts, Springer-Verlag, Berlin.
- Mach, E. and Salcher, P. (1887) Photographical fixation of the processes introduced by projectile in the air, Sitzungsberichte der Kaiserlichen Akademie der Wissenschaften. Mathematisch-Naturwissenschaftliche Classe, Vol. 95, Abteilung II, pp. 764-780, (in German).
- Maršík, F. (2015) Propagation of Waves and Nonlinear Phenomena in Dissipative Systems, VŠB-TU, Ostrava (in Czech).

- Prandtl, L. (1907) New study on the flow of gases and vapors, *Physicalische Zeitschrift*, Vol. 8, No. 1, pp. 23-30, (in German).
- Rankine, W.J.M. (1870) On the Thermodynamic Theory of Waves of Finite Longitudinal Disturbances, *Philosophical Transactions of the Royal Society of London*, Vol. 160, pp. 277-288.
- Rosenhead, L. (1954) *A Selection of Graphs for Use in Calculations of Compressible Airflow*, The Claderon Press, Oxford.
- Šafařík, P. (1993) On Optimal Shock Wave Parameters, *IT NEWS*, Vol. 2, No. 3, pp. 9-14.
- Shapiro, A.H. (1953) *The Dynamics and Thermodynamics of Compressible Fluid Flow*, Ronald Press, New York.



# PAPERS



## ANALYSIS OF THE DIMENSIONAL ACCURACY OF CASTING MODELS MANUFACTURED BY FUSED DEPOSITION MODELING TECHNOLOGY

S. Adamczak<sup>\*</sup>, P. Zmarzły<sup>\*\*</sup>, T. Kozior<sup>\*\*\*</sup>, D. Gogolewski<sup>\*\*\*\*</sup>

**Abstract:** *The main purpose of the research was to assess the dimensional accuracy of models manufactured by additive technology Fused Deposition Modeling (FDM). The shape of the samples have been designed in a way which allow to take into account all typical geometrical characteristics of casting models, i.e. linear and angular dimensions. Machine "Dimension 1200es" has been used to build the samples using ABS P430 material. Due to the effect of anisotropy in both the mechanical properties, shape and dimensional accuracy, authors decided to analyze the effect of building direction on the dimensional accuracy of the above mentioned samples. For this purpose, have been manufactured appropriate physical models which were placed on the working platform of the machine in three typical angles: 0 °, 45 °, 90 °. Measurements of geometric dimensions have been performed on the CMM Prismo Navigator machine. Research results confirmed that the printing direction has a significant impact on the dimensional accuracy of manufactured parts. It can be conclude that Fused Deposition Modeling technology can be used to build precise casting models.*

**Keywords:** Technological heredity, Additive technologies, FDM, Casting draft, CMM.

### 1. Introduction

The dynamic development of modern, unconventional manufacturing technologies, among others, additive technologies determines the possibility of their implications in many industries, i.e. for building static sealing rings (Błasiak, 2016 and Kundera, 2014a), in foundry industry (Chhabra, 2011) or in prototyping (Takosoglu, 2016a and Takosoglu et al., 2016b). Generative technologies allow for the manufacturing of prototypes and fully functional elements of machines and mechanisms directly from the mathematical 3D CAD model. Due to the layered nature of the process it is possible to produce complex-shape physical model which are difficult to obtain by conventional methods or even impossible in some cases (Kundera, 2014b). One of the areas, where additive technologies can be widely used is foundry industry. They can be used for both, to build casting patterns and molds. Due to the low melting point of most of FDM materials, this technology can be used especially in the lost material casting method. In the case of construction of casting patterns, which shape is often impossible to perform by traditional methods, authors decided to examine the possibility of adapting FDM additive technology, to produce accurate, durable and wear resistant casting models.

Analyzing the current state of art it can be noted that preliminary studies on the possibilities of the application of FDM technology in some industries have been conducted. These works, however, does not describe in a comprehensive way the influence of technological parameters on the dimensional-shape accuracy of manufactured components. It was found that the dimensional-shape accuracy of casting patterns is very important, because the resulting inaccuracies will move through the technological

---

<sup>\*</sup> Prof. Stanisław Adamczak: Chair of Mechanical Technology and Metrology, Kielce University of Technology, Al. 1000-lecia P. P. 7, 25-314 Kielce; PL adamczak@tu.kielce.pl

<sup>\*\*</sup> Ph.D. Paweł Zmarzły: Chair of Mechanical Technology and Metrology, Kielce University of Technology, Al. 1000-lecia P. P. 7, 25-314 Kielce; PL pzmarzly@tu.kielce.pl

<sup>\*\*\*</sup> MSc. Tomasz Kozior: Chair of Mechanical Technology and Metrology, Kielce University of Technology, Al. 1000-lecia P. P. 7, 25-314 Kielce; PL tkoziior@tu.kielce.pl

<sup>\*\*\*\*</sup> MSc. Damian Gogolewski: Chair of Mechanical Technology and Metrology, Kielce University of Technology, Al. 1000-lecia P. P. 7, 25-314 Kielce; PL dgogolewski@tu.kielce.pl

heredity on the obtained casts. Due to the intensive development of the foundry industry it is necessary to create high-quality products, castings, which will not need to be subjected to further finishing processes. Therefore production of high accuracy casting patterns and molds is a key aspect. This processes involves the developing of measurement methods that allow to meet the requirements of modern foundry industry (Adamczak, 2016 and Nowakowski, 2016).

The possibilities of application of FDM technology in engineering are described, inter alia, in the work (Bartkowiak et al., 2015), wherein the authors examined the effects of selected process parameters, such as the orientation of layers on 3D roughness parameters of curved sample surface. The study also applied the further finishing processes by using acetone.

In the paper (Griffiths et al., 2016) authors determined the influence of layer thickness and orientation of models on the working platform on the tensile strength of samples made by FDM technology in accordance with ISO 527 standard. The material used for the construction of samples was bio-degradable polylactide PLA.

## 2. Research procedure

The aim of the study was to evaluate the effect of the location of the models on the working platform on the samples dimensions which represented the typical casting patterns. Due to the availability of the technology, authors were chosen FDM technology. Samples were manufactured at the Laboratory of Reverse Engineering using machine "Dimension 1200es" produced by Stratasys Company. Measurements of geometric dimensions have been performed on the CMM Prismo Navigator, which is equipped at Laboratory for Computer-Based Measurement of Geometrical Quantities located in the Department of Manufacturing Engineering and Metrology at Kielce University of Technology.

### 2.1. FDM Technology

Fused Deposition Modeling technology (FDM) is based on a layered construction of physical models directly from three-dimensional CAD model. In this method input plastic material in a form of string is heats locally to obtain semi-liquid state and then through the printing nozzle is distributing into the current building cross-section of the model. An important advantage of this technology is the availability of low cost building materials and low complexity of the process, but due to the relatively thick constructed layer equal at least of 0.1 mm and a heat shrinkage, mechanical properties and dimensional accuracy significantly depends on the orientation of models on the working platform.

### 2.2. Samples

The samples were located on the working machine platform on three different angles:  $0^\circ$  (No. 1),  $45^\circ$  (No. 2),  $90^\circ$  (No. 3). For each type of direction have been made a five pieces of the samples. Fig. 1a is an example of a typical casting model with marked geometrical dimensions, while Fig. 1b shown the real physical samples with measured dimensions. The draft of the side wall at an angle of  $1^\circ$  is the typical angle used in pattern construction that allow to remove pattern from the sand mold easily.

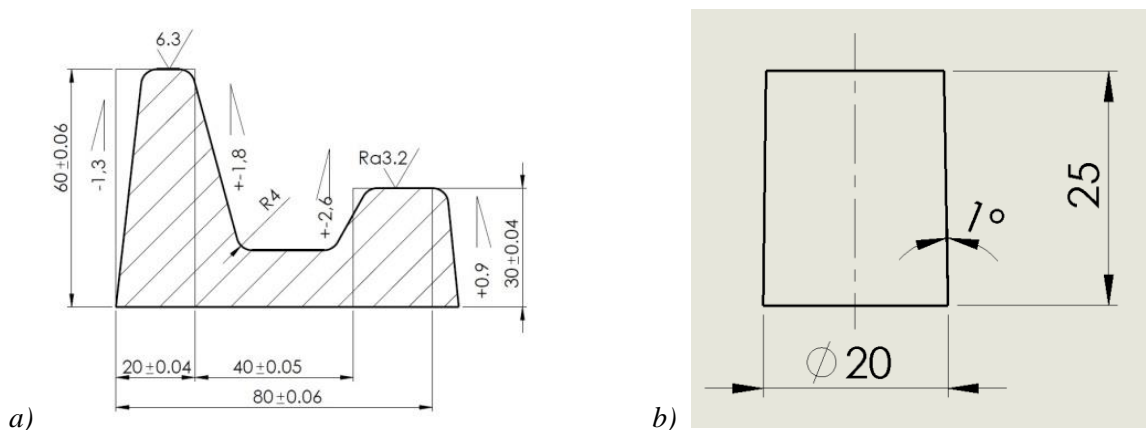


Fig. 1: Testes samples: a) example of typical casting model; b) tested samples.

### 3. Results analysis

Measurement strategy was based on active scanning probe VAST Gold S-ACC, where linear measurement accuracy is equal  $0.9 + L / 350 \mu\text{m}$ . The research results of the draft angle of side wall and the height of the samples are shown in Tab. 1, where the symbol "s" means deviation. In order to better visualize the results of calculations the mean value of relative error are presented in Fig. 2.

Tab. 1: Research results.

No. sample		high, mm	relative error, %	angle, °	relative error, %
1 (0°)	a	25.037	0.15	1.056	5.6
	b	25.015	0.06	1.060	6
	c	25.071	0.28	1.083	8.3
	d	25.033	0.13	1.067	6.7
	e	25.061	0.24	1.068	6.6
	<b>mean</b>	<b>25.043</b>	<b>0.17</b>	<b>1.067</b>	<b>6.7</b>
	s	0.023		0.01	
2 (45°)	a	25.146	0.58	1.032	3.2
	b	25.159	0.63	0.981	1.9
	c	25.165	0.66	0.995	0.5
	d	25.175	0.7	0.946	5.4
	e	25.148	0.59	0.947	5.3
	<b>mean</b>	<b>25.159</b>	<b>0.63</b>	<b>0.98</b>	<b>2</b>
	s	0.012		0.036	
3 (90°)	a	25.171	0.68	1.257	25.7
	b	25.245	0.98	1.076	7.6
	c	25.154	0.62	1.055	5.5
	d	25.194	0.78	1.057	5.7
	e	25.286	1.14	1.068	6.8
	<b>mean</b>	<b>25.21</b>	<b>0.84</b>	<b>1.103</b>	<b>10.3</b>
	s	0.055		0.087	

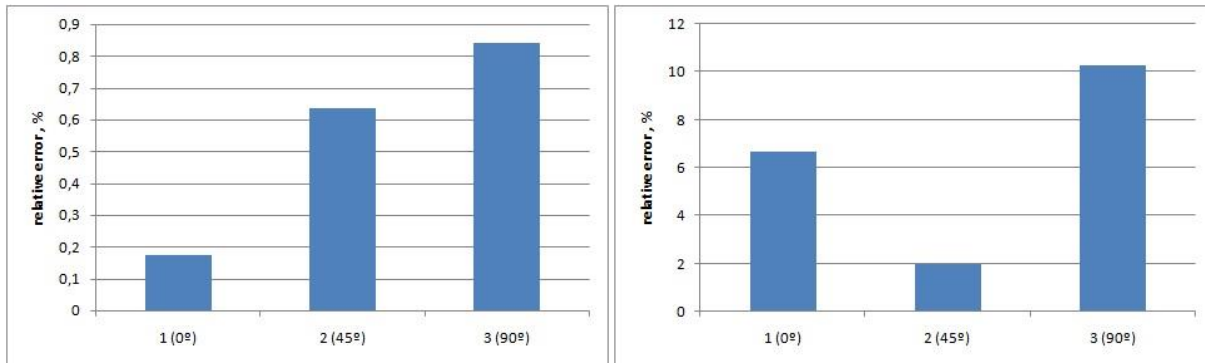


Fig. 2: Relative error of representation the nominal value a) linear dimension; b) angular dimensions.

Analyzing the research results of the linear dimension, i.e. the height of the elements, it can be noted that there is a relation between the orientation of models on the virtual platform and dimensional deviations. The relative error for samples placed at an angle of  $0^\circ$  reached the lowest value, equal to 0.17 %. In the case of the samples No. 2 the value of relative error has increased. This value was equal 0.63 %. The least favorable results were obtained for the samples produced at an angle of  $90^\circ$ . The calculated value was equal 0.84 %.

A similar analysis was performed for the draft angle of side-wall. The most favorable value was achieved for the samples No. 2. The resulting value was equal 2 %. In the case of samples No. 1 the value of relative error had increased, reaching the value equal 6.7 %. The highest value of the relative error was calculated for the samples No. 3 - 10.3 %. The largest relative error was noted for sample 3a (25.7 %). For the rest of samples No. 3 (b-e) were obtained similar values as in the case of samples No. 1 and No. 2.

#### 4. Conclusions

Analyzing the research results and the current state of art related to adaptation of additive technology into the foundry industry, it can be concluded that the FDM technology can be used in industrial practice. Moreover based on the research results it can be concluded:

1. The samples orientation on the virtual platform has directly influence on the dimensional accuracy of the model. The obtained angular dimensions were less accurate in compare to the linear dimensions.
2. The most favorable representation of the nominal value for linear dimension was achieved for samples No. 1, meanwhile the least favorable values were calculated for samples placed at an angle of 90 °.
3. By analyzing the representation of the nominal value for angular dimensions, it can be noted that the calculated value of the samples No. 2 reached the lowest value. The most inaccurate results were obtained for samples No. 3.
4. Based on the result of measurements it can be noted that almost all types of samples indicated positive material shrinkage. In all cases, the measured linear dimension value was greater than nominal value. Analogous results were obtained for angular dimension. Only for samples No. 2 the measured value was lowest than nominal value.
5. Complex analysis of the research results indicated that engineers should take into account during the design stage the geometrical deviation of manufactured parts.

#### Acknowledgement

The study was conducted using research facilities purchased with EU funds in the framework of the 2007-2013 Development of Eastern Poland Operational Programme, LABIN Project – Support for Innovative Research Facilities of the Kielce University of Technology in Kielce. Priority 1 – Innovative Economy, Measure 1.3 – Support for R&D Projects.

Therefore, the authors would like to thank to leaders the LABIN program.

#### References

- Adamczak, S., Zmarzły, P. and Stępień, K. (2016) Identification and analysis of optimal method parameters of the V-block waviness measurements. *Bulletin of the Polish Academy of Sciences Technical Science*, 64, 2, pp. 45-52.
- Bartkowiak, T., Lehner, J.T., Hyde, J., Wang, Z., Bue P.D., Norgaard, H.H. and Brown, C.A. (2015) Multi-Scale areal curvature analysis of fused deposition surfaces. *Proceedings - Achieving Precision Tolerances in Additive Manufacturing*, pp. 77-82.
- Błasiak, S. and Zahorulko, A. (2016) A parametric and dynamic analysis of non-contacting gas face seals with modified surfaces. *Tribology International*, 94, pp. 126-137.
- Chhabra, M. and Singh, R. (2011) Rapid casting solutions: a review. *Rapid Prototyping Journal*, 17, 5, pp. 328-350.
- Griffiths, C.A., Howarth, J., de-Almeida R.G. and Rees, A. (2016) Effect of build parameters on processing efficiency and material performance in fused deposition modelling. *Procedia CIRP* 49, pp. 28-32,
- Kundera, Cz. and Bochnia, J. (2014a) Investigating the stress relaxation of photopolymer O-ring seal models. *Rapid Prototyping Journal*, 20, 6, pp. 533-540.
- Kundera Cz., and Kozior, T. (2014b) Research of the elastic properties of bellows made in SLS technology. *Advanced Materials Research* 874, pp. 77-81.
- Nowakowski, L., Miko, E. and Skrzyniarz, M. (2016) The analysis of the zone for initiating the cutting process of X37CrMoV51 steel. *Engineering Mechanics* 2016, 426-429.
- Takosoglu, J.E. (2016a) Control system of delta manipulator with pneumatic artificial muscles. *Engineering Mechanics* 2016, 546-549.
- Takosoglu, J.E., Laski, P.A., Błasiak, S., Bracha, G., and Pietrala, D. (2016b) Determination of flow-rate characteristics and parameters of piezo valves, in: *Proc. Int. Conf. Exp. Fluid Mech. 2016* (ed. Dancova, P.), Techn. Univ. Liberec, pp. 814-818.

## ASSESSMENT OF ROUNDNESS AND WAVINESS DEVIATIONS OF ELEMENTS PRODUCED BY SELECTIVE LASER SINTERING TECHNOLOGY

S. Adamczak<sup>\*</sup>, P. Zmarzły<sup>\*\*</sup>, T. Kozior<sup>\*\*\*</sup>, D. Gogolewski<sup>\*\*\*\*</sup>

**Abstract:** *This paper presents preliminary research results of the influence of process parameters of the selective laser sintering technology (SLS) on the roundness and waviness parameters of cylindrical elements. The excessive values of these deviations impact on the further manufacturing process and reduce the functional properties of final products. The samples were designed in cylindrical shape and it were produced in the Laboratory of Unconventional Manufacturing Technology. The Formiga P100 machine was employed to build samples, using polyamide powder PA2200, which based on polyamide PA12. Due to the heterogeneity of the surface structure which is caused by layered nature of process, the samples were located on the virtual platform in three characteristic orientations. Measurement of the geometric deviations were performed on the Talyrond 365, which is located in the Laboratory for Computer-Based Measurement of Geometrical Quantities at the Department of Manufacturing Engineering and Metrology at Kielce University of Technology. The analysis of the research result showed that the building direction has a significant impact on the above mentioned parameters.*

**Keywords:** Additive technology, SLS, Roundness deviation, Waviness deviation, Technological heredity.

### 1. Introduction

Conventional manufacturing technologies which allow to produce precise machine and mechanisms parts have some limitations. One of them is the difficulty of building complex shapes machine parts with both internal and external dimensions. Application of traditional technology also entails large investment of time and work related with the preparation of technological documentation or tools, for example, casting molds and patterns, injection molds or specialized machining tools. Moreover, the production of some types of elements, particularly hollow is often difficult or sometimes even impossible (Kundera, 2014b). An alternative way of production in compare to traditional technologies are becoming the non-conventional manufacturing techniques, among other additive technologies (Błasiak, 2016 and Leu 2013), electro-erosion technology, laser technology (Nowakowski, 2016c), or application the high-pressure water jet cutter (Spadło, 2015). Additive technologies are based on a layered construction of physical models using three-dimensional CAD models. The development of these technologies creates opportunities for their adaptation, among others in: aerospace, foundry or mechanical industry (Kundera, 2014a and Nowakowski, 2016b) or pneumatic muscles (Takosoglu, 2016).

The selective laser sintering technology, which is one of the most complicated additive technologies, was used to build samples in this paper. The mechanical properties, shape and dimensional accuracy of final product depends on the technological parameters, among others, printing direction, layer thickness, laser speed and power, cooling time or even temperature in building chamber (Pilipović, 2010).

---

<sup>\*</sup> Prof. Stanisław Adamczak: Chair of Mechanical Technology and Metrology, Kielce University of Technology, Al. 1000-lecia P. P. 7, 25-314 Kielce; PL adamczak@tu.kielce.pl

<sup>\*\*</sup> Ph.D. Paweł Zmarzły: Chair of Mechanical Technology and Metrology, Kielce University of Technology, Al. 1000-lecia P. P. 7, 25-314 Kielce; PL pzmarzly@tu.kielce.pl

<sup>\*\*\*</sup> MSc. Tomasz Kozior: Chair of Mechanical Technology and Metrology, Kielce University of Technology, Al. 1000-lecia P. P. 7, 25-314 Kielce; PL tkoziior@tu.kielce.pl

<sup>\*\*\*\*</sup> MSc. Damian Gogolewski: Chair of Mechanical Technology and Metrology, Kielce University of Technology, Al. 1000-lecia P. P. 7, 25-314 Kielce; PL dgogolewski@tu.kielce.pl

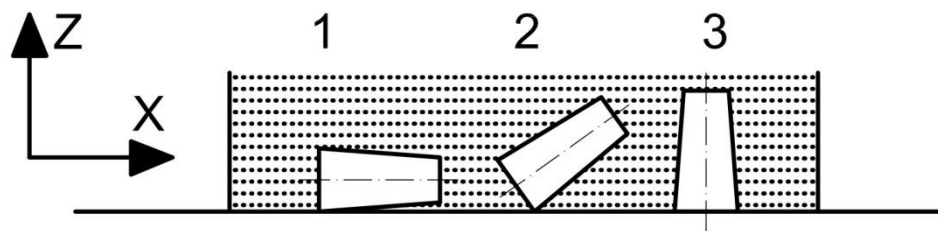
According to Whitehouse (2010) it can be note that about 70 % of all mechanical parts have a cylindrical shape. One of the basic parameter describing manufacturing accuracy of cylindrical parts is roundness deviation (Stępień, 2014). For cylindrical elements manufactured by rapid technologies, analysis of the roundness profile allow to assess the defects which arising during the operation of sintering. Excessive values of roundness deviation causes difficulties in assembly of components, what is very important in casting technology. In this cases, deviations result from production process of casting patterns or casting molds can be transferred on the final products within phenomena so-called "technological heredity". Moreover, considering the evaluation of production accuracy of high quality mechanical components, the geometrical deviation of cylindrical surface should be examined in range that included surface waviness (Adamczak et al., 2016). The high values of waviness deviation of rotational elements is important source of vibration(Adamczak, 2017 and Nowakowski, 2016a). Therefore, presented research related to assessment the impact of technological parameters of SLS technology on the geometrical accuracy of cylindrical components are reasonable.

## 2. Study design

The first step of research procedure was designed a cylindrical samples and manufactured it using additive technology, known as Selective Laser Sintering (SLS). This technology based on a layered nature of building physical models. The layer of material in a form of powder is distributed to building platform. Then a selected cross-section of a currently building layer is sintering using CO<sub>2</sub> laser. The polyamide powder PA2200 was used to build the samples. The selected technological parameters used in research were presented in Tab. 1 (EOS COMPANY, 2008). The examinations were carried out for samples placed on the virtual platform with three different positions, i.e. at an angle of 0 ° (No. 1), 45 ° (No. 2), 90 ° (No. 3). The main goal of the presented research was to assess the influence of printing direction on the samples roundness and waviness deviation.

*Tab. 1: Selected properties and technological parameters of SLS Technology.*

Selected properties of PA2200				Technological parameters		
	Value	Unit	Standard		Value	Unit
Young's modulus	1700	MPa	EN ISO 527	Laser power	21	W
Shore hardness	75	Skala D	ISO 864	Laser velocity	2500	mm/s
Impact strength (23°C)	4.4	kJ/m <sup>2</sup>	ISO 180/1A	Energy density	0.056	J/mm <sup>2</sup>
Tensile strength	48	MPa	EN ISO 527	Focus beam diameter	0.42	mm
Powdered density	0.45	g/cm <sup>3</sup>	EN ISO 60	Printing direction	0/45/90	°
Sintered powder density	0.93	g/cm <sup>3</sup>	EOS metod	Layer thickness	0.1	mm



*Fig. 1: Samples with support material.*

The next step of the research procedure was to measure the roundness and waviness deviations of components manufactured by SLS technology. The examinations were carried out using measuring device Talyrond 365 Taylor Hobson Company. The principle of the device work based on radial method with rotary table. The high accuracy of Talyrond 365 provides a measuring head with resolution of 1.3 nm for measuring range 0.08 mm and Ultra Roundness 5.17 software. The roundness and waviness profiles were measured in a half-way of height of the manufactured samples i.e. 12.5 mm. The parameters used to analyzed were roundness deviation RONt measured in range of 2 – 15 upr (undulation per revolution) as well as a waviness deviation measured in a range of 16 – 50 upr. In order to calculated desired deviations, the primary profile was filtered using Gaussian filter.



### 3. Analysis of the research results

The research results of the geometrical structure of cylindrical surfaces represented by roundness and waviness deviations were presented in Tab. 2. Symbols a-e indicate the consecutive number of samples manufactured including their different location on the virtual platform.

Tab. 2: Research results.

No. sample		RONt, $\mu\text{m}$		No. sample		RONt, $\mu\text{m}$		No. sample		RONt, $\mu\text{m}$	
		2 – 15, upr	16 – 50, upr			2 – 15, upr	16 – 50, upr			2 – 15, upr	16 – 50, upr
1 (0°)	a	171.78	50.23	2 (45°)	a	51.94	29.70	3 (90°)	a	42.05	20.01
	b	155.49	55.14		b	37.97	28.61		b	51.35	27.09
	c	163.52	71.04		c	47.80	20.47		c	40.65	27.07
	d	169.05	60.09		d	72.83	22.96		d	35.95	20.52
	e	127.20	43.45		e	51.89	27.75		e	40.79	21.56
mean		157.41	55.99	mean		52.49	25.90	mean		42.16	23.25

Analyzing the results presented in Tab. 2 it can be concluded that the roundness and waviness deviations of elements manufactured by SLS technology reach unfavorable high values. The highest mean value of roundness deviation was obtain for samples produced at an angle of 0°, however the lowest value was measured for samples manufactured at an angle of 90°. Similar results were obtain for waviness deviation measured in range of 16 – 50 undulation per revolution. Based on research results it can be noted that the cross-section of the samples printed for angle 90° have more cylindrical shape. On the other hand for samples produced for angle 0° this shape was elliptical.

Detailed harmonic analysis of measured roundness and waviness profiles indicated that the second harmonic was dominant in all measured samples. This showed that the cylindrical elements manufactured using SLS technology have oval shape. The cool down process in most rapid technologies is very complex. A large temperature gradient and location on the working platform may impact on shrinkage, which results in production an oval shape of elements (Fig. 2).

Furthermore, in order to better illustrate the measurement results, the Fig. 2 shows roundness profile of measured samples, while the Fig. 3 presents the waviness deviations.

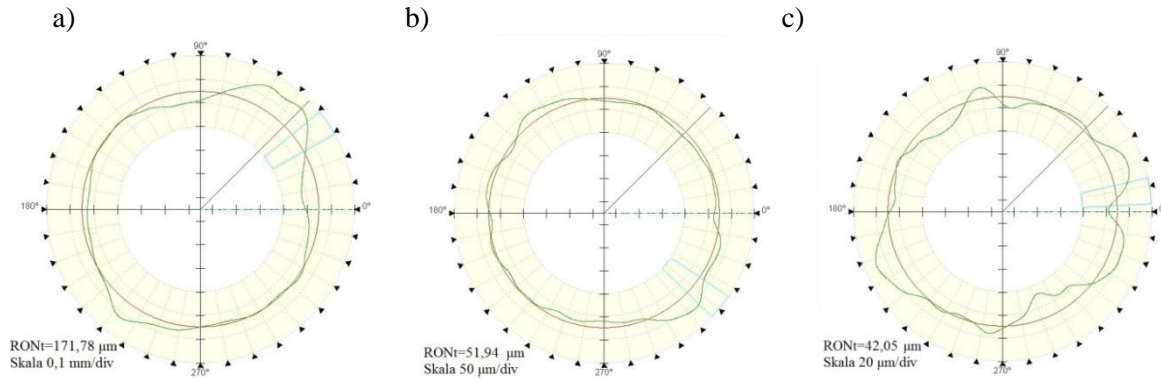


Fig. 2: Roundness profile of samples: a) No. 1a b) No. 2a c) No. 3a.

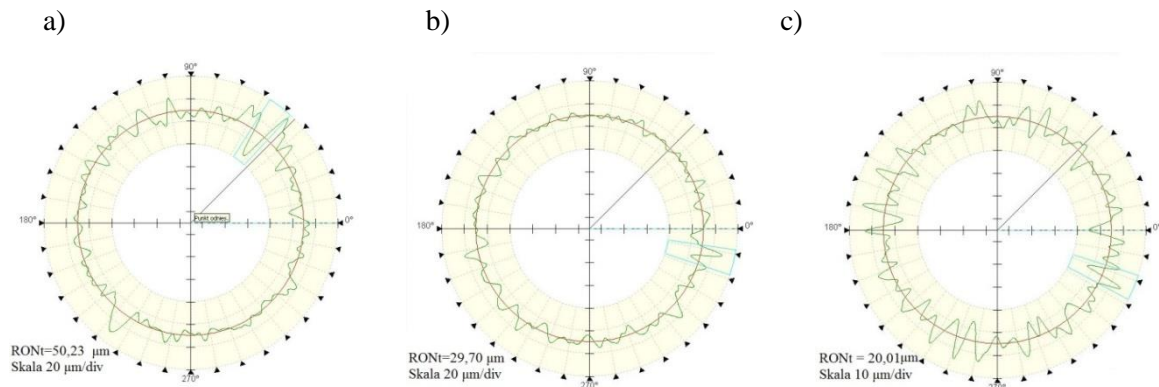


Fig. 3: Waviness profile of samples: a) No. 1a b) No. 2a c) No. 3a.

#### 4. Conclusions

1. Based on research results it can be concluded that the values of roundness deviations for all examined cylindrical samples were significantly greater than the values of waviness deviations. Excessive values of roundness deviations effect on the principle of error transferring to the next stage of production as a part of phenomena known as "technological heredity". This kinds of deviations result from layer building nature, which is a characteristic disadvantage of rapid technologies.
2. In order to achieve the smallest values of roundness and waviness deviations of a cylindrical parts produced using SLS technology, the model building axis should be located in parallel direction to main printer axis (axis Z). Therefore the angle of printed direction should be equal 90 °.
3. The results obtained in this paper indicated that application of rapid technology called as Selective Laser Sintering request subjected manufacturing models to further processes.

#### Acknowledgement

The study was conducted using research facilities purchased with EU funds in the framework of the 2007-2013 Development of Eastern Poland Operational Programme, LABIN Project – Support for Innovative Research Facilities of the Kielce University of Technology in Kielce. Priority 1 – Innovative Economy, Measure 1.3 – Support for R&D Projects.

Therefore, the authors would like to thank to leaders the LABIN program.

#### References

- Adamczak, S., Zmarzły, P. and Stępień, K. (2016) Identification and analysis of optimal method parameters of the V-block waviness measurements. *Bulletin of the Polish Academy of Sciences Technical Science*, 64, 2, pp. 45-52.
- Adamczak, S. and Zmarzły, P. (2017) Influence of raceway waviness on the level of vibration in rolling-element bearings. *Bulletin of the Polish Academy of Sciences Technical Science*, in press.
- Błasiak, S. and Zahorulko, A. (2016) A parametric and dynamic analysis of non-contacting gas face seals with modified surfaces. *Tribology International*, 94 pp. 126-137.
- Eos Company (2008) Formiga P100 - User Manual, Monachium.
- Kundera, C. and Bochnia, J. (2014a) Investigating the stress relaxation of photopolymer O-ring seal models. *Rapid Prototyping Journal*, 20, 6 pp. 533-540.
- Kundera, C. and Koziar, T. (2014b) Research of the elastic properties of bellows made in SLS technology. *Advanced Materials Research* 874 pp. 77-81.
- Leu, M.C. and Guo, N. (2013) Additive manufacturing: technology, applications and research needs, *Frontiers of Mechanical Engineering*, 8, 3, pp. 215-243.
- Nowakowski, Ł., Miesikowska, M. and Błasiak, M. (2016a) Speech intelligibility in the position of CNC machine operator. *Engineering Mechanics*, pp. 422-425.
- Nowakowski, Ł., Miko, E. and Skrzyniarz, M. (2016b) The analysis of the zone for initiating the cutting process of X37CrMoV51 steel. *Engineering Mechanics*, pp. 426-429.
- Nowakowski, Ł. and Wijas, M. (2016c) The evaluation of the process of surface regeneration after laser cladding and face milling. *Engineering Mechanics*, pp. 430-433.
- Pilipović, A., Valentan, B., Brajlili, T., Haramina, T., Balić, J., Kodvanj, J., Sercer, M. and Drstvenšek, I. (2010) Influence of laser sintering parameters on mechanical properties of polymer products, *International Conference on Additive Technologies ICAT 2010*.
- Stępień, K. (2014) In situ measurement of cylindricity—Problems and solutions. *Precision engineering-journal of the international societies for precision engineering and nanotechnology*, 38,3 pp. 697-701.
- Spadło, S., Hlavac, L., Hlavacova, I.M. and Krajcarz, D. (2015) Influence Traverse Speed on Surface Quality after Water-jet Cutting for Hardox Steel. *Proceedings of 24th International Conference on Metallurgy and Materials METAL 2015*, pp. 723-728.
- Takosoglu, J.E., Laski, P.A., Błasiak, S., Bracha, G. and Pietrala, D. (2016) Determining the static characteristics of pneumatic muscles, *Measurement and Control*, 49, 2, pp. 62-71.
- Whitehouse, D.J. (2010) *Handbook of Surface and Nanometrology*, Second Edition, CRC Press.



## MATHEMATICAL MODELING OF MICRO INDENTATION OF A TRANSVERSELY ISOTROPIC HALF-SPACE WITH FUNCTIONALLY GRADED COATING BY A CONICAL INDENTER

S. Aizikovich<sup>\*</sup>, A. Vasiliev<sup>\*\*</sup>, S. Volkov<sup>\*\*</sup>, B. Mitrin<sup>\*\*\*</sup>

**Abstract:** *The paper considers rigid punch with conical tip which is indented into a surface of an elastic transversely-isotropic half-space with a functionally-graded transversely-isotropic coating. Elastic moduli of the coating vary independently with depth according to arbitrary positive continuously differentiable functions. Integral transformation technique is used to construct a dual integral equation of the problem. Cases of free and fixed boundaries of the contact area are considered. Fixed boundaries of the contact correspond to the case when the cylindrical punch with conical tip is indented on a depth greater than height of the punch tip. Bilateral asymptotic method is used to construct the approximated analytical expressions for the contact stresses, indentation force and radius of the contact area (in case of free boundaries). Some aspects of modeling of micro- and nano- indentation experiments are discussed. Numerical examples are provided for a case of a hard homogeneous or functionally graded transversely isotropic coating.*

**Keywords:** Indentation, Conical indenter, Functionally graded coating, Transversely isotropic material, Contact problem, Analytical solution.

### 1. Introduction

Improvement of the service life of various structural elements is one of the most important tasks facing the modern industry. Various types of protective coatings which have a complex functionally graded or layered structure are used for this purpose. To characterize strength and elastic properties of these coatings nanoindentation experiments are widely used. Most of widely adopted nanoindentation analysis methods rely on solutions of classical contact problems for isotropic homogeneous materials (Oliver and Pharr, 2004). Increasing usage of complex functionally graded and composite anisotropic coatings requires development of more accurate mathematical models for analysis of experimental results. Recent results on mathematical simulation of deformation of functionally-graded materials can be found in (Alinia et al., 2016; Kudish et al., 2016a, 2016b, 2017; Su et al. 2016; Tokovyy and Ma, 2015).

Indenters of different sizes and shapes are used for indentation of samples. The most common shapes of the indenter's tip are spherical, pyramidal and conical. It is known that in mathematical simulation of the widely used Berkovich pyramid a conical punch with an appropriate opening angle can be successfully used. This paper is focused on mathematical simulation of indentation of an elastic transversely isotropic half-space with a functionally graded transversely isotropic coating by a conical punch.

### 2. Formulation of the problem

A nondeformable conical punch is pressed into a surface of an elastic transversely isotropic half-space consisting of a functionally graded layer (coating) of thickness  $H$ , and a homogeneous half-space (substrate). A cylindrical system of coordinates  $r', \varphi, z$  is chosen with the  $z$  axis being normal to the surface of the half-space and passing through the center of the punch. The  $z$  axis is the axis of symmetry

---

<sup>\*</sup> Prof. Sergey Aizikovich, DSc.: Research and Education Center "Materials", Don State Technical University, 1 Gagarin sq., Rostov-on-Don, Russia, saizikovich@gmail.com

<sup>\*\*</sup> Research Fellows Andrey Vasiliev and Sergey Volkov, PhD.: Research Institute of Mechanics, National Research Lobachevsky State University of Nizhni Novgorod, 23 Gagarin av., Nizhni Novgorod, Russia; andre.vasiliev@gmail.com

<sup>\*\*\*</sup> Junior Researcher Boris Mirin, PhD.: Research and Education Center "Materials", Don State Technical University, 1 Gagarin sq., Rostov-on-Don, Russia, boris.mitrin@gmail.com

for all elastic moduli. The punch is pressed into the surface  $z = 0$  of the half-space by the action of a normal centrally applied force  $P$  and moves distance  $\delta$  downward the  $z$ -axis. It is assumed that there are no friction forces between the punch and the half-space.

Cone angle  $-2\alpha$  is obtuse enough, i.e.  $\pi - 2\alpha \ll 1$ ;  $\chi = a \operatorname{ctg} \alpha$  stands for a length of the projection of the segment connecting the edge of a contact area with the apex of the cone to  $z$  axis. The projection of the contact area is a circle of radius  $a$ . Elastic moduli  $c_{11}, c_{12}, c_{13}, c_{33}, c_{44}$  of the half-space vary with depth according to the following:

$$c_{kj} = \begin{cases} c_{kj}^{(c)}(z) & -H \leq z \leq 0, \\ c_{kj}^{(s)} = \text{const} & -\infty < z < -H, \end{cases} \quad (kj) = 11, 12, 13, 33, 44, \quad (1)$$

where  $c_{kj}^{(c)}(z)$  are arbitrary continuously differentiable positive functions,  $c_{kj}^{(s)}$  are positive constants. Hereafter, superscripts (c) and (s) correspond to the coating and to the substrate, respectively. The coating and the substrate are glued without sliding. Outside of the punch, the surface is traction-free.

### 3. Solution of the problem

Using the integral transformation technique the problem can be reduced to the following dual integral equation, see (Aizikovich et al., 2015) for details:

$$\begin{cases} \int_0^\infty \bar{p}(\gamma) L(\lambda\gamma) J_0(r\gamma) d\gamma = E_{ef}^{(c)} \frac{(\delta - r\chi)}{2a}, & r \leq 1, \\ \int_0^\infty \bar{p}(\gamma) J_0(r\gamma) \gamma d\gamma = 0, & r > 1, \end{cases} \quad (2)$$

where  $r = r'/a$  is the dimensionless radial coordinate;  $\lambda = H/a$  is the relative thickness of the coating;  $J_0$  is the Bessel's function of the first kind;  $E_{ef}^{(c)}$  is the effective elastic modulus on the surface of the coating;  $L(\lambda\gamma)$  is the kernel transform of the integral equation or the compliance function of the elastic half-space with functionally graded coating;  $\bar{p}(\gamma)$  is the Hankel transform of the contact stresses  $p(r) = -\sigma_z|_{z=0}$ ,  $r \leq 1$ .

The kernel transform  $L(\lambda\gamma)$  for arbitrary variation of elastic moduli can be calculated only numerically from the two point boundary value problem for a system of ordinary differential equations with variable coefficients, see (Aizikovich et al., 2015) and (Vasiliev et al., 2016a) for details.

Solution of the dual integral equation (2) is constructed using bilateral asymptotic method. The method is based on an idea of approximation of the kernel transform  $L(\lambda\gamma)$  by the following expression:

$$L(\lambda\gamma) \approx L_N(\lambda\gamma) = \prod_{i=1}^N (\lambda^2 \gamma^2 + A_i^2) / (\lambda^2 \gamma^2 + B_i^2), \quad A_i, B_i \in C. \quad (3)$$

Replacing kernel transform  $L$  by its approximation  $L_N$  we get the approximated dual integral equation which can be solved in closed analytical form, see (Aizikovich et al., 2015) for details. Thus, the contact stresses has the form:

$$\begin{aligned} p(r) = & \frac{E_{ef}^{(s)} \chi}{2a} \left[ \ln \frac{1 + \sqrt{1 - r^2}}{r} + \left( \frac{2\delta}{\pi\chi} - 1 \right) \frac{1}{\sqrt{1 - r^2}} + \right. \\ & \left. - \sum_{i=1}^N \left( \frac{\lambda}{A_i} \frac{C_i \operatorname{ch}(A_i \lambda^{-1}) + D_i \operatorname{sh}(A_i \lambda^{-1})}{\sqrt{1 - r^2}} - C_i \int_r^1 \frac{\operatorname{sh}(A_i \lambda^{-1} t) dt}{\sqrt{t^2 - r^2}} - D_i \int_r^1 \frac{\operatorname{ch}(A_i \lambda^{-1} t) dt}{\sqrt{t^2 - r^2}} \right) \right] \end{aligned} \quad (4)$$

Here  $E_{ef}^{(s)} = E_{ef}(-H - 0)$  is the effective elastic modulus of the substrate. Expression (4) describes the contact pressure for the fixed contact boundaries, i.e. than the edges of the cylindrical punch with conical

tip are cut into the material. For free boundaries we should satisfy the following condition:  $p(1) = 0$ . Satisfying it we get contact stresses for the case of free contact boundaries:

$$p(r) = \frac{E_{ef}^{(s)} \chi}{2a} \left( \ln \frac{1 + \sqrt{1 - r^2}}{r} + \sum_{i=1}^N \left( C_i \int_r^1 \frac{\text{sh}(A_i \lambda^{-1} t)}{\sqrt{t^2 - r^2}} dt + D_i \int_r^1 \frac{\text{ch}(A_i \lambda^{-1} t)}{\sqrt{t^2 - r^2}} dt \right) \right). \quad (5)$$

Coefficients  $C_i$ ,  $D_i$  can be obtained from a system of linear algebraic equations. For the case of free boundaries, this system has the form:

$$\begin{aligned} \sum_{i=1}^N \frac{D_i}{A_i^2 - B_k^2} &= B_k^{-2}, \quad k = 1, \dots, N; \\ \sum_{i=1}^N C_i \frac{A_i \text{ch}(A_i \lambda^{-1}) + B_k \text{sh}(A_i \lambda^{-1})}{A_i^2 - B_k^2} &= B_k^{-1} - \sum_{i=1}^N D_i \frac{B_k \text{ch}(A_i \lambda^{-1}) + A_i \text{sh}(A_i \lambda^{-1})}{A_i^2 - B_k^2}. \end{aligned} \quad (6)$$

Radius of the contact area can be found from the equation:

$$\delta = \frac{\pi \chi}{2} \left( 1 + \lambda \sum_{i=1}^N \left[ \frac{C_i}{A_i} \text{ch}(A_i \lambda^{-1}) + \frac{D_i}{A_i} \text{sh}(A_i \lambda^{-1}) \right] \right) \quad (7)$$

Using the conditions of the equilibrium of the punch  $P = 2\pi a^2 \int_0^1 p(r) r dr$  we get the expression for the indentation force for the case of free boundaries:

$$P = \frac{\pi a E_{ef}^{(s)}}{2} \chi \left( 1 + 2\lambda \sum_{i=1}^N \left( \frac{C_i}{A_i} \left[ \text{ch} \frac{A_i}{\lambda} - \frac{\lambda}{A_i} \text{sh} \frac{A_i}{\lambda} \right] + \frac{D_i}{A_i} \left[ \frac{\lambda}{A_i} - \frac{\lambda}{A_i} \text{ch} \frac{A_i}{\lambda} + \text{sh} \frac{A_i}{\lambda} \right] \right) \right). \quad (8)$$

For determination of mechanical properties of materials with coating from the results of nanoindentation it is convenient to consider the contact stiffness (Pharr et al., 1992):  $S = dP/d\delta$ . It can be obtained from (7) and (8) as a function of parameter  $\lambda$ .

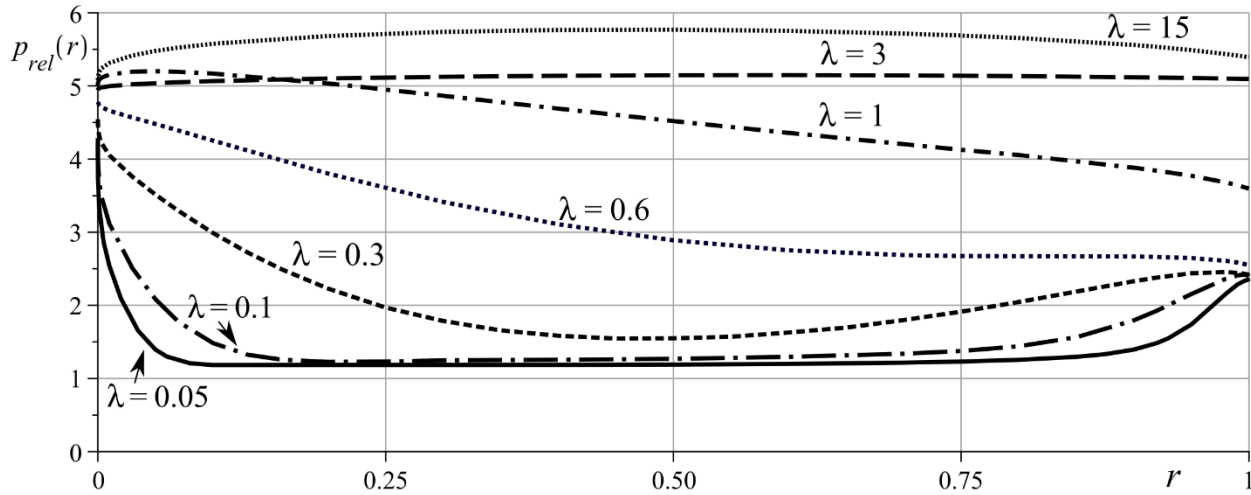


Fig. 1: Relative contact stresses  $p_{rel}$  on surface of the functionally graded coating.

As an illustration of the obtained results let us consider an isotropic glass fiber as a substrate material, Young's modulus and Poisson's ratio are  $E^{(s)} = 21$  GPa and  $\nu^{(s)} = 0.15$ . Coating is assumed to be transversely isotropic with elastic moduli on its surface:  $c_{11} = 213.5$  GPa,  $c_{13} = 138.67$  GPa,  $c_{33} = 222.67$  GPa and  $c_{44} = 23.67$  GPa corresponding to the single crystal of gold with all the crystallites having a  $\langle 111 \rangle$  axis parallel to each other and oriented normal to the substrate surface. We consider a coating with linearly varying elastic moduli to values corresponding to pure platinum  $c_{11} = c_{33} = 314.5$  GPa,  $c_{13} = 192.75$  GPa,  $c_{44} = 60.87$  GPa. To illustrate the behavior of the contact normal pressure, let us designate the dimensionless relative function  $p_{rel}^{(c)}(r) = p(r)/p_{hom}^{(c)}(r)$ , where

$$p_{\text{hom}}(r) = E_{\text{ef}}^{(s)} \chi / (2a) \ln \left( \left( 1 + \sqrt{1 - r^2} \right) / r \right) \quad (9)$$

Relative contact pressure  $p_{\text{rel}}$  for various values of  $\lambda$  are presented in Fig. 1.

#### 4. Conclusions

The present research continues the study of contact mechanics for functionally-graded (FG) materials made by authors earlier. Approximated analytical solutions was previously constructed for: plane contact problem on indentation of an isotropic (Kudish et al., 2016a) and transversely isotropic (Vasiliev et al., 2017) FG half-plane; axisymmetric torsion of a transversely isotropic FG half-space (Vasiliev et al., 2016b) and axisymmetric indentation of an isotropic FG half-space by a conical punch (Aizikovich et al., 2015), etc. Analytical expression for the contact stiffness which takes into account the inhomogeneity of the elastic material can be used in the analysis of nano- or micro-indentation experiments.

#### Acknowledgement

Authors acknowledge the support of the Russian Foundation for Basic Research (RFBR) grants nos. 16-07-00958-a, 17-07-00969-a and Ministry of Education and Science of Russia through Governmental Assignment. A.S. Vasiliev and S.S. Volkov acknowledge the support of the President of the Russian Federation through grant no. MK-5342.2016.1.

#### References

- Aizikovich, S.M., Vasil'ev, A.S. and Volkov, S.S. (2015) The axisymmetric contact problem of the indentation of a conical punch into a half-space with a coating inhomogeneous in depth. *J. Appl. Math. Mech.*, 79, 5, pp. 500-505.
- Alinia, Y., Beheshti, A., Guler, M.A., El-Borgi, S. and Polycarpouc, A.A. (2016) Sliding contact analysis of functionally graded coating/substrate system. *Mech. Mater.*, 94, pp. 142-155.
- Kudish, I.I., Volkov, S.S., Vasiliev, A.S. and Aizikovich, S.M. (2016a) Some criteria for coating effectiveness in heavily loaded line elastohydrodynamically lubricated contacts-Part I: Dry contacts. *J. Tribol.*, 138, 2, 21504.
- Kudish, I.I., Volkov, S.S., Vasiliev, A.S. and Aizikovich, S.M. (2016b) Some criteria for coating effectiveness in heavily loaded line elastohydrodynamically lubricated contacts-Part II: Lubricated contacts. *J. Tribol.* 138, 2, 21505.
- Kudish, I.I., Volkov, S.S., Vasiliev, A.S. and Aizikovich, S.M. (2017) Effectiveness of coatings with constant, linearly, and exponentially varying elastic parameters in heavily loaded line elastohydrodynamically lubricated contacts. *J. Tribol.*, 139, 2, 021502.
- Oliver, W.C. and Pharr, G.M. (2004) Measurement of hardness and elastic modulus by instrumented indentation: Advances in understanding and refinements to methodology. *J. Mater. Res.*, 19, 1, pp. 3-20.
- Pharr, G.M., Oliver, W.C. and Brotzen, F.R. (1992) On the generality of the relationship among contact stiffness, contact area and elastic modulus during indentation. *J. Mater. Res.*, 7, 3, pp. 613-617.
- Su, J., Ke, L.-L. and Wang, Y.-S. (2016) Axisymmetric frictionless contact of a functionally graded piezoelectric layered half-space under a conducting punch. *Int. J. Solids Struct.*, 90, pp. 45-59.
- Tokovyy, Yu. and Ma, C.-C. (2015) Analytical solutions to the axisymmetric elasticity and thermoelasticity problems for an arbitrarily inhomogeneous layer. *Int. J. Eng. Sci.*, 92, pp. 1-17.
- Vasiliev, A.S., Volkov, S.S. and Aizikovich, S.M. (2016a) Normal point force and point electric charge in a piezoelectric transversely isotropic functionally graded half-space. *Acta Mech.*, 227, pp. 263-273.
- Vasiliev, A.S., Swain, M.V., Aizikovich, S.M. and Sadyrin, E.V. (2016b) Torsion of a circular punch attached to an elastic half-space with a coating with periodically depth-varying elastic properties. *Arch. Appl. Mech.*, 86, pp. 1247-1254.
- Vasiliev, A.S., Volkov, S.S., Aizikovich, S.M. and Mitrin, B.I. (2017) Plane contact problem on indentation of a flat punch into a transversely-isotropic half-plane with functionally graded transversely-isotropic coating. *Z. Angew. Math. Phys.* 68, 1, doi: 10.1007/s00033-016-0746-8.

## ANALYSIS OF VEHICLE COLLISIONS WITH THE SDC METHOD

P. Aleksandrowicz\*

**Abstract:** *The article covers the problem of verifying vehicle crashes with the use of research procedures referred to as the SDC method. Performing research following that procedure facilitates verifying the crashes of vehicles which result in damage to the car body and elements of the vehicle, infrastructure in terms of extortion of undue damages. Simplifications in the process of vehicle damage claim management lead to potential abuses and more and more sophisticated extortion methods require a development and improvement of engineering tools to verify the claims notified. To facilitate the SDC method analysis, there has also been developed a dedicated IT tool automating the decision-making process for verifying the vehicle crashes with the method proposed. The author's research, with actual damage-inflicting incidents, has demonstrated a practical application of the SDC research method and, at the same time, the problem of a lack of effective research procedures in case of frauded damage claims in insurance companies and a lack of verification before such claims are referred to court proceedings.*

**Keywords:** SDC method, Crash verification, Fraud, Damage claim verification.

### 1. Introduction

Every year insurance companies in Poland manage, on average, about 1 700 000 motor insurance claims under the obligatory third-party civil-liability insurance policies held by the owners of motor vehicles and optional comprehensive-cover insurance (<http://piu.org.pl>). All that results in the payment of damages to restore the damaged property. And the vehicle repair costs provide the grounds for the extortions of damages for the costs to be covered most frequently under the insurance policy of the offender indicated. Interestingly, the average vehicle damage claim in which passive safety systems, in a form of gas bags were started, can make the repair of a few-year average-class vehicle non-cost-effective (Aleksandrowicz, 2015). Insurance companies see the problem of insurance crime, however, they do not introduce any research methods to verify the vehicle crashes which would use the accomplishments of post-accident engineering and newly-developed methods. Neither is the actual scale of the insurance crime known. Scientific theories concerning high values of the so-called dark figure of crime (the ratio of the undisclosed to disclosed acts) in financial crimes point to an expected high rate of unknown irregularities (<http://piu.org.pl>). With that in mind, this study presents the procedures developed and the author's research the results of which focus on enhancing the effectiveness of identifying fake incidents in motor insurance claims. Therefore the problem covered here is valid both in practical and cognitive approach. The research methods have been broken into three groups; the static analysis (S), the major objective of which is geometrical verification of damage in terms of their compliance on the study objects, dynamic analysis (D) the objective of which is to verify the circumstances of the car crash applying simulation programs used in the reconstruction of car accidents as well as the analysis of characteristic damage (C) to verify the marks of a mutual contact of the objects during the crash declared (Aleksandrowicz, 2016, [https://www.youtube.com/watch?v=T0Bkum\\_8A64&feature=youtu.be](https://www.youtube.com/watch?v=T0Bkum_8A64&feature=youtu.be)).

### 2. Static analysis (S)


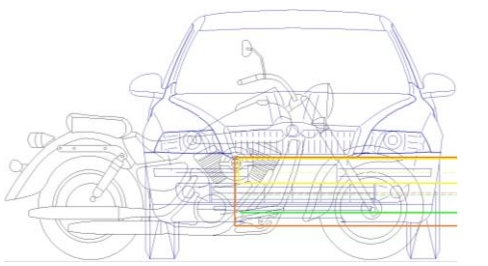


The best results of verification in terms of determining whether there is a geometric matching of the damage of vehicles is provided by a comparison of real objects participating in the vehicle damage claim notified. However, the possibilities of such comparisons are usually limited; hence a proposal of alternative research methods; the above-mentioned comparison of real objects, a comparison of one of the

---

\* Piotr Aleksandrowicz, PhD.: Machine Maintenance Department, Institute of Machinery Operation and Transport, University of Science and Technology, Al. prof. S. Kaliskiego 7; 85 796, Bydgoszcz; Poland, [p.aleksandrowicz@utp.edu.pl](mailto:p.aleksandrowicz@utp.edu.pl)

objects with disassembled elements of the other one, the use of photographs of both objects to make the transparent superposition involving the placement of scaled photographs on each other and the breakdown of vertical stylings of both vehicles (<http://www.autoview.at>). Tab. 1 illustrates the research methods proposed.

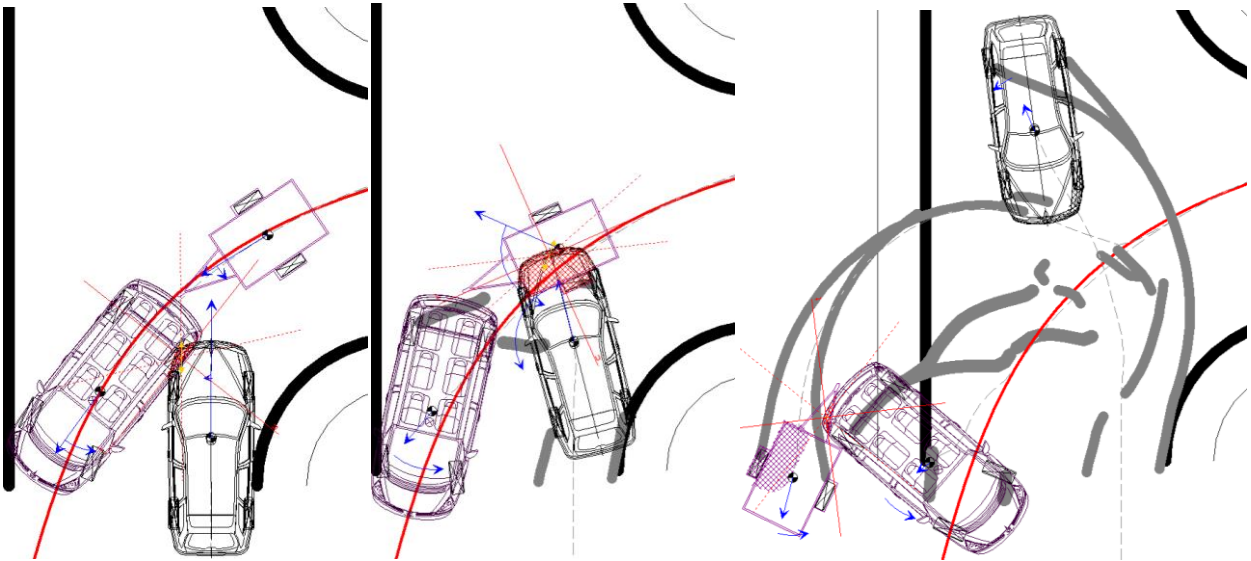
*Tab. 1: Static (S) research methods.*

Comparison of real objects	Comparison of vertical stylings
	
Comparison with vehicle elements	Transparent superposition
	

### 3. Dynamic analysis (D)

To perform a dynamic analysis, the potential of simulation programs applied in road accident reconstruction, including Multi Body Systems (MBS) modelling IT tools, e.g. PC Crash, Virtual Crash and VSIM is used (<http://www.pc-crash.com>, <http://www.vcrashusa.com>, <http://www.cyborgidea.com.pl>). The simulation programs are applied to verify the crashes of vehicles and their post-collision positions and the time and space relations of the objects necessary for the occurrence of such crash.

Due to the availability of data for calculations, the procedure was divided into material- and human-based evidence procedures (Aleksandrowicz, 2016). Fig. 1 presents a crash verification analysis result sample ([https://www.youtube.com/watch?v=T0Bkum\\_8A64&feature=youtu.be](https://www.youtube.com/watch?v=T0Bkum_8A64&feature=youtu.be)).



*Fig. 1: Dynamic analysis result recorded.*



#### 4. Characteristic damage analysis (C)

To perform the characteristic damage analysis, site inspection of the objects damaged or the photographs taken at the resolution allowing for multiple magnification are used. The analysis aims at identifying the marks of contact between the vehicles in a form of paint layers, shape mapping, etc. (Aleksandrowicz, 2016). Fig. 2 presents a sample mark of the mapping of a part of vehicle registration number of the crashing vehicle on the bumper of the claimant's vehicle.



Fig. 2: Characteristic damage identified.

#### 5. The IT tool developed to support the decision-making process with the SDC method

To enhance the effectiveness of the research methods applied, an IT tool has been developed which offers decision variants once the results of procedures S, D, C of a given damage verified are entered. Figs 3 and 4 present the dialog boxes of the program ([http://wim.utp.edu.pl/dok/wyklady/analiza\\_sdc.xlsm](http://wim.utp.edu.pl/dok/wyklady/analiza_sdc.xlsm)).

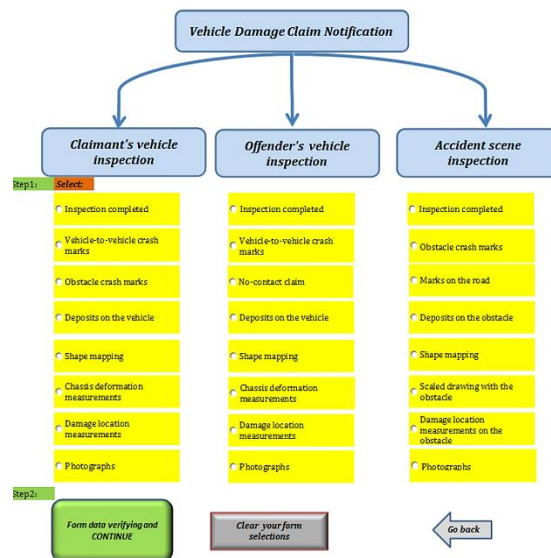


Fig. 3: Program dialog box - entering the input data.

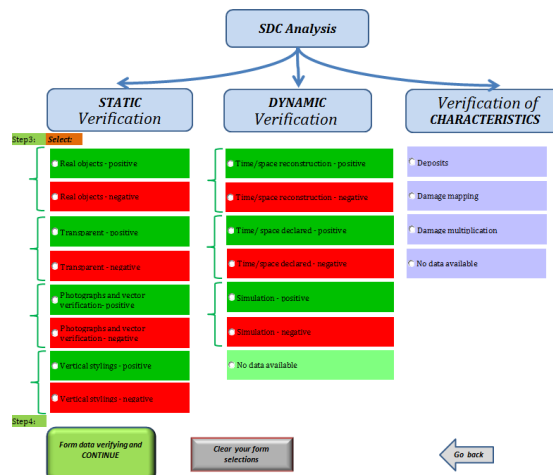


Fig. 4: Program dialog box - entering the results of procedures S, D, C.

## 6. Case study – own research

The research was performed in 72 vehicle damage claim cases in which the payment of damages was refused and damages were claimed by the parties already in court. To verify the position of the insurance company in each of the cases, the SDC method was applied. The analysis was made following the procedure S, D, C and then data was entered into the program developed to support the decision-making process (Aleksandrowicz, 2016, [https://www.youtube.com/watch?v=T0Bkum\\_8A64&feature=youtu.be](https://www.youtube.com/watch?v=T0Bkum_8A64&feature=youtu.be)). Letters **P** and **N** stand for a positive or negative result of each research procedure separately, as compared with the total result provided with the SDC method. Fig. 5 presents the research results.

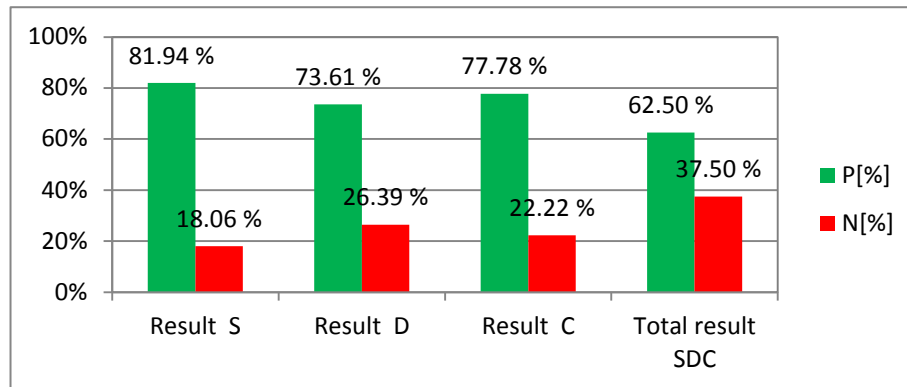


Fig. 5: Results of the research performed with the SDC method.

## 7. Conclusions

The SDC method can be used not only in the process of damage management to eliminate unjustifiable claims (extorted, frauded damages) but also by law departments of insurance companies to evaluate the justifiability of a dispute which, if lost, generates considerable costs. It is that functionality of the SDC method which has been applied for researching the cases analysed. The results of research have demonstrated that 62.5 % of the cases qualified by insurance companies as extortions and referred to court as a result of the claim of the claimants' for payment of damages turned out to be the claims which should have been accepted already at the stage of damage claim management. The results point to a problem faced in insurance companies related to an adequate claim verification at the stage of claim management. The proposed research method, SDC, together with the tool supporting the decision-making process, could find a practical application by optimising the process of damage claim management and cutting the costs of insurance companies' operation. Besides the research has shown that S and C procedures confirm only the contact of vehicles, however they do not determine the occurrence of the crash in the circumstances declared, which can be verified by applying procedure D since it facilitates the evaluation of the relations between objects in time and space as well as the very crash and its effects. Applying that procedure, one should remember, however, about a careful evaluation of the input data affecting the simulation result, which has been described in other papers (Aleksandrowicz, 2016 and Wach, 2015).

## References

- Aleksandrowicz, P. (2016) Post-accident engineering for verifying damage claims. Press of the University of Science and Technology in Bydgoszcz, Bydgoszcz (in Polish).
- Aleksandrowicz, P. (2015) Optimization of post-accident vehicle repair costs . Part 1. Rail Transport Technology, Vol. 12, pp. 1768-1774 (in Polish).
- Wach, W. (2015) Structural road accident reconstruction credibility. Court Expertise Institute, Kraków (in Polish).



## VERIFYING THE APPLICATION OF THE MODELS OF CRASH AND COLLISION DETECTION OF INCOMPATIBLE VEHICLES

**P. Aleksandrowicz\***

**Abstract:** *The article covers the incompatible vehicle crashes. Today computer programs are widely applied in the analysis of vehicle crashes. However, it is the expert's responsibility to select the right collision model in terms of the application of the right IT tool or a selection of the right option in the computer program. Such selection must be adequate to the incident analysed, also in terms of the limitations of the models of contact between the simulation objects. The problem has been presented based on a case study a head on truck-to-car collision. The research has involved the use of VSIM simulation program. The experimental verification has demonstrated a practical application of the impact (force) crash model with the volumetric (3D) collision detection model, as most adequate to the collision analysis of incompatible vehicles.*

**Keywords:** VSIM, Crash model, Collision detection, Crash compatibility.

### 1. Introduction

The accident reconstruction identifies a problem of an applicable selection of the crash model and the detection of collision of the simulation objects in calculations. It is especially clear in the case of the incompatible vehicle crash. Papers (Gabler et al., 1996, Mendis et al., 2002, Van der Sluis, 2000 and Wicher, 2012) discuss the analytical grounds of the compatibility laws, crash test types and the term of the vehicle aggressiveness, while another paper (Yang et al., 2012) covers experimental results of crash-incompatible vehicles. Compatibility is mostly related to geometrical relationships between the bodies (shape, height) as well as mass and rigidity, which has been discussed in e.g. another paper (Aleksandrowicz, 2014) for crashes of vehicles of different categories. Truck designing strives for installing devices which would prevent a passenger car driving under a truck, which is demonstrated in other papers (Lambert et al., 2002 and Zou et al., 2001). So far there has been developed no universal crash model the application of which would be adequate in each crash case. For study reasons, vehicle crashes are usually simulated with the use of FEM (Finite Element Method). The application of such models for the reconstruction of road accidents is sporadic. In property valuer's practice the programs modelling the crash in MBS (Multi Body Systems) are most frequently applied; e.g. PC Crash, Virtual Crash. For instance, in other papers (Dima et al., 2014 and Semela et al., 2007) those programs have been validated receiving a satisfactory convergence with tests and video-recordings. One should, however, underestimate neither the simulation program model simplifications nor the effect of uncertain input data on the simulation results, which has been discussed e.g. in other papers (Bułka et al., 2007 and Wach, 2008). In Poland the most commonly applied simulation program for the vehicle crash analysis is VSIM. Its experimental verification in terms of incompatible vehicle crash modelling is not found and, with that in mind, this topic has been covered in the present article due to its cognitive and functional values.

### 2. Selected collision detection methods

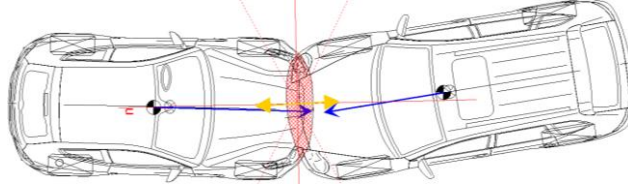
Object-to-object crash modelling is one of the most essential elements of the simulation program. It is a vast problem, which will not be discussed here. Crash detection both identifies the collision of its objects and provides geometrical data indispensable for the IT tool to make calculations.

---

\* Piotr Aleksandrowicz, PhD.: Machine Maintenance Department, Institute of Machinery Operation and Transport, University of Science and Technology, Al. prof. S. Kaliskiego 7; 85 796, Bydgoszcz; Poland, p.aleksandrowicz@utp.edu.pl

## 2.1. 2D Model

A 2D detection model is the simplest model to study the contact between the objects of simulation. It verifies the occurrence of a common part of the objects; the areas which are projections of their stylings on the horizontal plane. The simulation objects in that model are considered vertical cuboids with the base being the projection of their styling. In general the shapes of styling projections are downloaded by the program from an external database, e.g. AutoView. Fig. 1 presents a 2D collision detection.



*Fig. 1: 2D collision detection.*

## 2.2. Superellipsoid – superellipsoid model

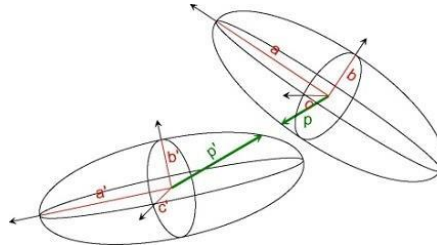
The 3D object-to-object contact model based on superellipsoids describes the simulation object or its element with a general formula (Bulka et al., 2011):

$$\left| \frac{x}{a} \right|^n + \left| \frac{y}{b} \right|^n + \left| \frac{z}{c} \right|^n = 1 \text{ for } n \geq 2 \quad (1)$$

where:

a, b, c – length of the semiaxis and n – the order of superellipsoid corresponding to its rounding.

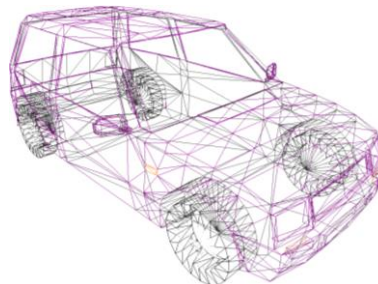
The contact detection involves a comparison of the distance between the centres of ellipsoid with the sum of the distance between the centre of each of them and the point on its surface and a line joining the centres of those ellipsoids. If the sum of those distances is greater than the distance between the centres, the ellipsoids analysed are in contact. Fig. 2 presents a 2D collision detection.



*Fig. 2: Collision detection between ellipsoids.*

## 2.3. 3D model

In the 3D model, to detect the contact of objects, three-dimensional networks of the body shape are applied, using the Gilbert-Johnson-Keerthi algorithm (GJK) (Gilbert et al., 1988). VSIM offers a unique solution with a three-dimensional map of points included in the vehicle body interior. However, the map is the same for each body type, which is a simplification in terms of the body shapes of various vehicle makes, even within the same type. Collision detection involves verifying which of the body network interior points of the simulation object are contained in the network interior of the other one. Fig. 3 presents the body network made up of VSIM program triangles.



*Fig. 3: Body network applied in VSIM4.*

### 3. Case study – own research

The study objects include Opel Corsa and Mercedes Actros 1840 the post-accident positions of which have been documented in photographs and the site description. The positions symbolise red rectangles and the model evaluation measure assumes the best post-accident position matching (%) to that position of the angle of rotation  $\emptyset$  and S distance of the centre of gravity of the simulation object. Fig. 4 presents the objects of the study.

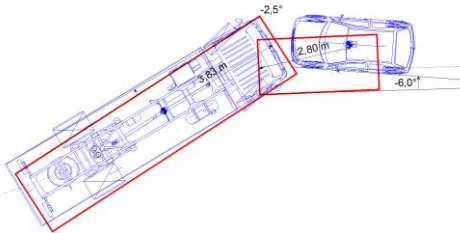
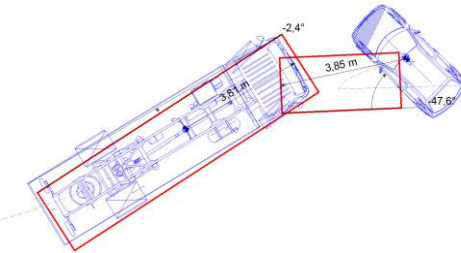
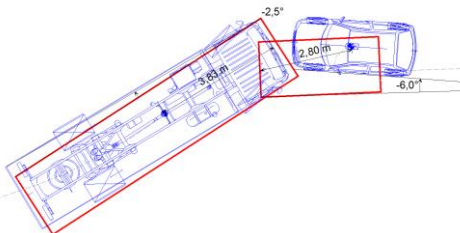
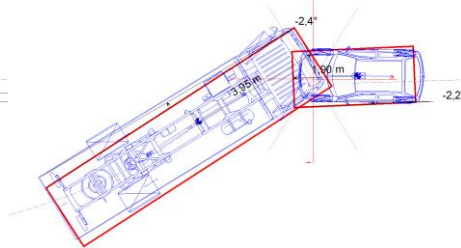
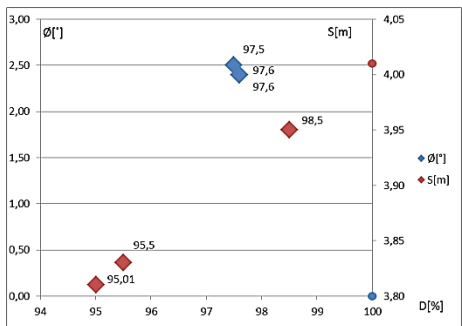
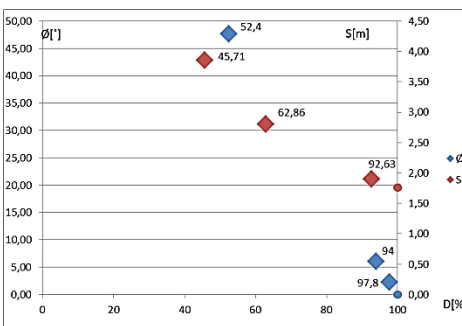


Fig. 4: Objects of the study and their position assumed in simulation calculations.

The crash was analysed with the use of the available crash models and the collision detection in VSIM4, and vehicle stylings have been derived from AutoView database (<http://www.cyborgidea.com.pl>).

Tab. 1 illustrates the study results (<https://www.youtube.com/watch?v=bLe0VoPvtOo>, <https://www.youtube.com/watch?v=O8BOxVlokSQ>).

Tab. 1: Results of verifying the models of crash and collision detection in VSIM4.

Impulse crash model	Impact (force) crash model																																							
2D collision detection model	2D collision detection model																																							
																																								
3D collision detection model	3D collision detection model																																							
																																								
Mercedes matching positions $\emptyset$ , S	Opel matching positions $\emptyset$ , S																																							
 <table border="1"><thead><tr><th>D[%]</th><th>Ø[°]</th><th>S[m]</th></tr></thead><tbody><tr><td>95.01</td><td>95.01</td><td>3.80</td></tr><tr><td>95.5</td><td>95.5</td><td>3.85</td></tr><tr><td>97.5</td><td>97.5</td><td>4.00</td></tr><tr><td>97.6</td><td>97.6</td><td>4.00</td></tr><tr><td>98.5</td><td>98.5</td><td>3.95</td></tr></tbody></table>	D[%]	Ø[°]	S[m]	95.01	95.01	3.80	95.5	95.5	3.85	97.5	97.5	4.00	97.6	97.6	4.00	98.5	98.5	3.95	 <table border="1"><thead><tr><th>D[%]</th><th>Ø[°]</th><th>S[m]</th></tr></thead><tbody><tr><td>45.71</td><td>45.71</td><td>3.80</td></tr><tr><td>52.4</td><td>52.4</td><td>4.00</td></tr><tr><td>62.86</td><td>62.86</td><td>3.95</td></tr><tr><td>92.63</td><td>92.63</td><td>3.85</td></tr><tr><td>94</td><td>94</td><td>3.80</td></tr><tr><td>97.8</td><td>97.8</td><td>3.80</td></tr></tbody></table>	D[%]	Ø[°]	S[m]	45.71	45.71	3.80	52.4	52.4	4.00	62.86	62.86	3.95	92.63	92.63	3.85	94	94	3.80	97.8	97.8	3.80
D[%]	Ø[°]	S[m]																																						
95.01	95.01	3.80																																						
95.5	95.5	3.85																																						
97.5	97.5	4.00																																						
97.6	97.6	4.00																																						
98.5	98.5	3.95																																						
D[%]	Ø[°]	S[m]																																						
45.71	45.71	3.80																																						
52.4	52.4	4.00																																						
62.86	62.86	3.95																																						
92.63	92.63	3.85																																						
94	94	3.80																																						
97.8	97.8	3.80																																						

#### 4. Conclusions

The analysis has demonstrated that the 2D collision detection model for incompatible vehicle crash should not be applied irrespective of the vehicle crash model selected. Especially the impact model gave a result far from the actual post-accident vehicle positions. Selecting the impulse crash model, irrespectively of the collision detection, the program generates the same result and it is also divergent from the actual state identified at the site. The impulse crash model is therefore not useful for the incompatible vehicle crash simulation. The best matching results for post-accident incompatible vehicle crash position were produced by the application of the crash (force) impact model with the 3D collision detection model: Mercedes  $\emptyset = 97.6\%$  and  $S = 98.5\%$  as well as Opel  $\emptyset = 97.8\%$  and  $S = 92.63\%$ . The discrepancies for the 2D detection model result from the assumption of considering the simulation objects as vertical cuboids with the base being a projection of their styling. The differences in the crash impact (force) model and the 3D collision detection model should be related to a simplified application of universal 3D vehicle type networks and not individually dedicated for each of them. Additionally the program simplification includes non-deformability of the 3D network of the vehicle during the crash, which should direct its development towards modelling solutions as e.g. in DyMesh convection (York et al., 1999).

#### References

- Aleksandrowicz, P. (2014) Biomechanics in road accident analysis. The Press of the University of Science and Technology in Bydgoszcz, Bydgoszcz (in Polish).
- Bułka, D. and Duś, S. (2011) Methods of detecting a collision between objects in 3D space applied in road accident reconstruction. The 12th Conference Road Accident Reconstruction Problems, 26-28.10.2011, Zakopane, pp. 45-55 (in Polish).
- Bułka, D., Walczak, S. and Wolak, S. (2007) Uncertainty of modeling of typical defense maneuvers with the road accident reconstruction models as an example. The 16th Conference EVU Road accident reconstruction uncertainty, 08-10.11.2007, Kraków, pp. 1-11 (in Polish).
- Dima D.S., Covaciu, D. and Chiru, A. (2014) Validation of simulation and optimization reconstruction in PC Crash with video recorded sample. 3rd International Congress Science and Management of Automotive and Transportation Engineering, 23-25.10.2014 Craiova, Romania, SMAT Paper no 2014-MTSRT51, pp. 207-212.
- Gabler, H.C. and Hollowel, W.T. (1996) NHTSA'S Vehicle Aggressivity and Compatibility Reaserch Program, Of the 15th International Technical Conference on the Enhanced Safety of Vehicles, Vol. 1, pp. 576-592.
- Gilbert, E.G., Johnson, D.W. and Keerthi, S.S. (1988) A fast procedure for computing the distance between complex objects in three-dimensional space. In IEEE Journal of Robotics and Automation, Vol. 4, pp. 193-203.
- Lambert, J. and Rechnitzer, G. (2002) Review of Truck Safety, Stage 1: Frontal, Side and Rear Underrun Protection. MONASH University, Accident Reasearch Centre. Raport No. 194. Victoria.
- Mendis, K., Mani, A. and Prasad, A.K. (1996) Concepts to Reduce Hevy Truck Aggressivity in Truck-to-car Collisions. Proc. Of the 15th International Technical Conference on the Enhanced Safety of Vehicles, 13-16.05.1996, Melbourne, Australia Vol. 1, pp. 674-677.
- Semela, M. and Bradac, A. (2007) Procedure of collision solving in the system of Virtual Crash and options for results validation. The 12th International conference of experts - analytics of road accidents, 09.06.2007, Brno, The Czech Republic, pp. 1-19 (in Czech).
- Van der Sluis, J. (2000) Vehicle compatibility in car-to-car collisions. Literature review in the framework of the European research project Improvement of crash compatibility between cars, Workpackage 1, SWOV, Leidschendam, pp. 1-39.
- Wach, W. (2008) Vehicle crash analysis in terms of modeling uncertainty. Scientific Papers of the Kielce University of Technology, Technical Sciences, Vol. 8, pp. 273-285 (in Polish).
- Wicher J. (2012) Vehicles. Vehicle and road traffic safety. Publishing House of Communications, Warsaw (in Polish).
- Yang, Na., Zhao G. and Zhu Y. (2012) Analysis of Vehicle Crash Compatibility. 3rd International Conference on Digital Manufacturing & Automation, 31.07-02.08.2012, Guilin, China, Vol. 2, pp. 230-232.
- York, A. and York, R. (1999) The DyMesh method for three-dimensional multi-vehicle collision simulation. SAE Paper No. 1999-01-0104.
- Zou R., Rechnitzer, G. and Grzebieta, R. (2001) Simulation of Truck Rear Underrun Barrier Impact, SAE, Paper No. 2001-06-0225, pp. 1-7.

## VIDEOGRAMMETRY IN FLUIDIZED BEDS ANALYSIS

S. Anweiler\*

**Abstract:** *Developed videogrammetric research technique is an optical method for analysis and estimation of gas fluidized bed hydrodynamics. Videogrammetry consists of process visualization, image analysis and stochastic process analysis. The two-phase flow pattern is described by the fluctuation of grey level parameter. Research focuses on the statistical analysis of the behavior of a fluidized bed operating under bubbling to turbulent conditions. Experimental data are collected by the means of a developed dynamic image analysis technique. Study was conducted in transparent, narrow fluidization apparatus. Results show that profiles of the grey level fluctuations and its stochastic parameters are correlated with particular flow pattern. The conformity of the digital flow pattern recognition method gives 82 % reliability.*

**Keywords:** Fluidization, Two-Phase Flow Pattern, Dynamic Image Analysis, Stochastic Process.

### 1. Introduction

Specific features of gas-fluidized beds are the exceptional solid mixing rate or distinctive heat and mass transfer properties. They can be related to the presence of certain flow pattern and are dominated by its behavior. Detailed information on two-phase flow pattern of gas-solid mixture is a need everywhere fluidization technology is applied, particularly in industrial processes. Therefore, leading and modernization of industrial system processes or design and development of fluidization devices, require wide range of experimental data according various flow characteristics. This causes the need for multiphase system measurement methods and flow structure estimation, capable of giving particular information about condition of given fluidization system. The most commonly used approach for fluidized bed simulations is Eulerian–Eulerian continuum modelling (Busciglio et al., 2008). In this model of multiphase flows the fluid and solid phases are treated as interpenetrating continuum phases. The balances of continuity, momentum and energy for both phases need to have appropriate boundary conditions and jump conditions for phase interfaces. Even until now the resultant continuum approximation for the solid phase has no equation of state and lacks variables such as viscosity and normal stress (Pain et al., 2001). Therefore certain averaging techniques and assumptions are required to obtain a complete momentum balance for the solids phase. Almost a half of century was not enough to fully develop a theory of particle collision based on the kinetic theory approach (Chapman and Cowling, 1970). The solid-phase momentum equation contains an additional term to account for momentum exchange due to particle–particle collisions (Sinclair and Jackson, 1989). The absence of the stress term of the particle phase in the particulate momentum equation has led to different models adopting different closure methods for local structures (Molerus, 1993), including the kinetic theory model (Gidaspow, 1994) and (Hrenya and Sinclair, 1997). All these problems comes from the lack of experimental data (Anweiler and Ulbrich, 2004). Digital visualization of two-phase flow and dynamic image analysis offers unique possibility for uncovering complexity of the flow pattern, without invading the delicate multiphase equilibrium inside the apparatus (Agarwal et al., 1996). Different image analysis methods allow CFD model verifications (Anweiler and Masiukiewicz, 2016). The aim of presented research work is to draw up digital optical method for two-phase flow structure estimation inside fluidization apparatuses. To obtain the aim, the advantage of high speed video camera and own PC software for image processing and analysis was taken. Developed method - videogrammetry - is based on dynamic analysis of digital image sequences, representing the fluidization process and stochastic analysis of the process (Ulbrich et al., 2002).

---

\* Stanisław Anweiler, PhD.: Environmental Engineering Department, Opole University of Technology, Mikołajczyka 5; 45-271, Opole; PL, s.anweiler@po.opole.pl



## 2. Experimental set-up

The experiment was held in vertical, narrow, transparent model of fluidization apparatus, which is shown in Fig. 1a. Visualization of two-phase flow structures was done with the use of high speed ( $F_{\max} = 1800$  fps) and high resolution ( $1024 \times 1024$  pix), digital CMOS camera. Schematic view of visualization technique is shown in Fig. 1b.

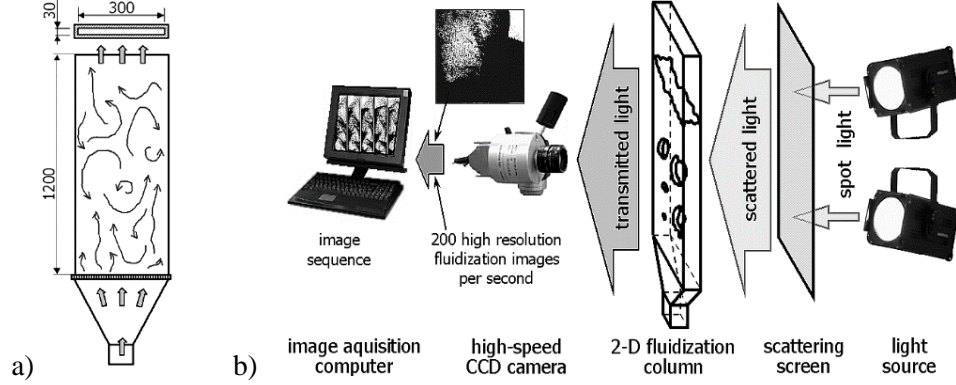


Fig. 1: Experimental setup: a) the dimensions of the fluidized bed chamber; b) two-phase flow pattern visualization technique.

The column was filled with polyethylene spherical particles ( $d = 6.0$  mm;  $\rho_s = 1050$  kg/m<sup>3</sup>;  $Ar = 7.84 \times 10^6$ ;  $u_{mf} = 1.4$  m/s; Geldart group D). Geldart particle groups are one of the criteria of physical similarity for solid particles. Archimedes number ( $Ar$ ) is one of the criteria of hydrodynamic similarity for solid particles and is given according to (Lim et al., 1995). Modified Archimedes number ( $Ar^{1/3}$ ) was used and another criterion of similarity – dimensionless gas velocity ( $u_G^*$ ) according to (Bi et al., 1995).

## 3. Methods

The experiment consisted of three steps. First – visualization of the fluidization process. Second – dynamic image analysis of obtained fluidization images. Third – stochastic analysis of grey level fluctuations. Dynamic image analysis is the key feature of described method and consists of average brightness level of pixel calculation ( $M_k$ ) in the specified area of the image according to Eq. (1).

$$M_k = \frac{1}{(n-l)(o-m)} \sum_{j=l}^n \sum_{i=m}^o p_{j,i}^k \quad k = 1, 2, \dots, N \quad (1)$$

where: ( $l, m, n, o$ ) – examination area coordinates,  $p_{j,i}^k$  – grey level value for single pixel with ( $j, i$ ) coordinates for the ( $k$ ) image number, which is a part of sequence with ( $N$ ) images.

Stochastic analysis of the brightness fluctuation is made to find stochastic character of the process. This allows determination of periodic and random events and was done using autocorrelation function (ACF) according to Eq. (2) and probability density function (PDF) according to Eq. (3)

$$R_{xxr} = \frac{\frac{1}{N-1} \sum_{i=0}^{N-1} (x_i - \bar{x})(x_{i+r} - \bar{x})}{R_{xx0}} \quad r = 0, 1, \dots, N-1 \quad (2)$$

$$P(x) = \lim_{\Delta x \rightarrow 0} \lim_{T \rightarrow \infty} \frac{\frac{T_x}{T}}{\Delta x} \quad (3)$$

## 4. Results and discussion

The result of two-phase flow pattern investigation, is precise visualization of fluidization pattern, as shown in Fig. 2, which demonstrates partial sequences of acquired images for turbulent fluidization. For each frame of the sequence (movie), dynamic image analysis gives a set of instantaneous grey level values. With the use of different measuring areas, the flow structure can be analyzed in various modes.

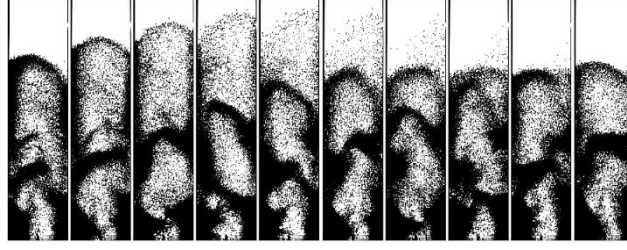


Fig. 2: Image sequence (visualization) of plug flow pattern in classical fluidized bed ( $\Delta\tau = 0.05$  s).

The area can act as a local or global event tracking device. The result of that analysis is set of grey level fluctuation time courses, as shown in Fig. 3. Various placement of measuring areas ( $L_1$ ,  $L_2$ ,  $L_3$ ) generates different grey level fluctuation signals. The profile of grey level changes is basis for flow regime estimation and two-phase structure recognition. Further data processing is grounded on the theory of stochastic process.

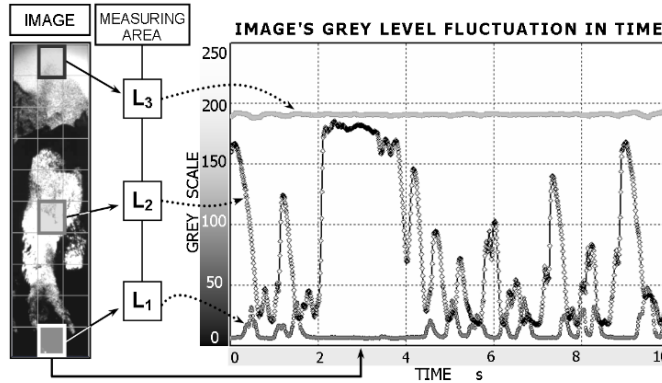


Fig. 3: Dynamic image analysis (pixel brightness) in specified area of the image, generates different grey level fluctuation time signals (depend on used area, i.e.  $L_1$ ,  $L_2$ ,  $L_3$ ).

The results of stochastic analysis are shown in Fig. 4. The profiles of the fluctuation courses and values of the functions are correlated with particular flow pattern.

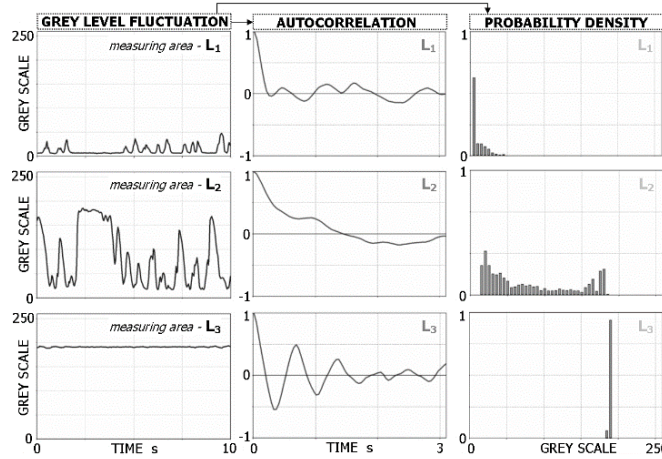


Fig. 4: Example results of stochastic analysis of grey level fluctuations obtained from image analysis.

## 5. Conclusions

The analysis of presented results provides many detailed information about the two-phase flow pattern, such as the intensity of bubbling, size, shape and speed of the bubbles, void fraction, coalescence/dispersion of gas/solids and more. Final step of the research work and summary of the investigation is compatibility analysis of the method. The proper identification of the two-phase gas-solid flow pattern according to visualized flow structures was done by correlation of the visualization results with measurements and recognition data. The analysis of method's detection efficiency is shown in Tab. 1. For each two-phase pattern the stochastic functions and parameters were determined in time, space and gas velocity domain. For each case there is also a video recording of real flow pattern. From

one side there are visually observed structures, from the other side there are recognized flow structures. Recognition was based on digital image analysis. Tab. 1 shows the efficiency analysis with the use of stochastic parameters technique for classical fluidization. The conformity of the digital recognition method is high and gives 82 % reliability.

Behavior of the fluidized bed depends on many factors. To estimate it's condition, there is a need for a versatile, non-invasive and operational safe measurement technique. Videogrammetry, as optical method for two-phase, gas-solid flow pattern estimation has all these advantages. Dynamic image analysis meets general requirements for investigation of fluidized bed condition. This method is also suitable for design and troubleshooting of new devices or process monitoring. The results could be used for comparison of different processes, which will allow creation of automated monitoring system for process analysis and maintenance, i. e. preservation of desired flow pattern in various types of fluidized beds and other multiphase flow devices.

*Tab. 1: Example of the conformity test for elaborated optical estimation method for two-phase flow pattern – correlation of observed (visualized) flow pattern and identified flow structure with the use of dynamic image analysis.*

Classic fluidization						
	No. of identified objects	Observed flow structure				
		Filtration	Bubble	Plug	Turbulent	$\Sigma$
Identified flow structure	Filtration	3				3
	Bubble		5	3		8
	Plug		1	8	1	10
	Turbulent		1		5	6
	$\Sigma$	3	7	11	6	27
Efficiency		100%	71%	73%	83%	82%

## References

- Agarwal, P.K., Hull, A.S. and Lim, K.S. (1996) Digital Image Analysis Techniques for the Study of Bubbling Fluidized Beds, in: Non-Invasive Monitoring of Multiphase Flows (eds. Chaouki, J., Larachi, F. and Duduković, M.P., Elsevier, New York.
- Anweiler, S. and Masiukiewicz, M. (2016) Application of stereology for two-phase flow structure validation in fluidized bed reactors. *Thermal Science*, 20(4), pp. 1199-1208.
- Anweiler, S. and Ulbrich, R. (2004) Flow pattern for different fluidization apparatuses. *Inżynieria Chemiczna i Procesowa*, 25(3), pp. 577-582.
- Bi, H. T., Grace, J. R. and Zhu, J. (1995) Regime transitions affecting gas-solids suspensions and fluidized-beds. *Chemical engineering research & design*, 73(2), pp. 154-161.
- Busciglio, A., Micale, G., Rizzuti, L. and Vella, G. (2008) Study of bubbling fluidization dynamics via Digital Image Analysis Technique. *Advances in Fluid Mechanics VII, WIT Transaction on Engineering Science*, 59, pp. 213-222.
- Chapman, S. and Cowling, T.G. (1970) The mathematical theory of non-uniform gases: an account of the kinetic theory of viscosity, thermal conduction and diffusion in gases. Cambridge university press.
- Gidaspow, D. (1994). Multiphase flow and fluidization: continuum and kinetic theory descriptions. Academic press.
- Hrenya, C.M. and Sinclair, J.L. (1997) Effects of particle-phase turbulence in gas-solid flows. *AIChE Journal*, 43(4), pp. 853-869.
- Lim, K.S., Zhu, J.X. and Grace, J.R. (1995) Hydrodynamics of gas-solid fluidization. *International journal of multiphase flow*, 21, pp. 141-193.
- Molerus, O. (1993) Principles of flow in disperse systems (Vol. 4). Springer.
- Pain, C.C., Mansoorzadeh, S. and De Oliveira, C.R.E. (2001) A study of bubbling and slugging fluidised beds using the two-fluid granular temperature model. *International Journal of Multiphase Flow*, 27(3), pp. 527-551.
- Sinclair, J.L. and Jackson, R. (1989) Gas-particle flow in a vertical pipe with particle-particle interactions. *AIChE Journal*, 35(9), pp. 1473-1486.
- Ulbrich, R., Krótkiewicz, M., Szmolke, N., Anweiler, S., Masiukiewicz, M. and Zajac, D. (2002) Recognition of two-phase flow patterns with the use of dynamic image analysis. *Proceedings of the Institution of Mechanical Engineers, Part E: Journal of Process Mechanical Engineering*, 216(4), pp. 227-233.



## PARAMETER ESTIMATION FOR ENGINEERS: A NEW TOOL FOR EFFECTIVE SEARCH FOR SIMULINK MODEL PARAMETERS

M. Appel<sup>\*</sup>, R. Grepl<sup>\*\*</sup>

**Abstract:** *An estimation of Simulink model parameters is very important problem in field of system identification in mechatronics. This paper describes features and advantages of the New Parameter Estimation Tool developed with respect to particular engineering needs. Among other things, the tool allows to use the arbitrary combination of a model and a measured data for the construction of cost function of the optimization process. This enables to formulate various tasks briefly outlined in this paper including comparison of several candidate models or performing estimations of models with shared parameters. Furthermore, all temporary simulation results are stored and later can be browsed and viewed by user. This enables to get very clear visual insight into the estimation problem and especially increases the usefulness of the Brute force method use. Finally, the tool allows to cope actively with the problem of initial guesses of an optimization method. As a result, user can automate and control parameter estimations for time-consuming and demanding problems.*

**Keywords:** Parameter estimation, Simulink, Optimization, Software tool.

### 1. Introduction

The field of system identification is very important in many specific areas of modelling, testing, signal processing and control design in mechatronics. In engineering practice, many problems are formulated through creation of simulation models with given structure and system identification is then reduced to the parameter estimation. Typically, these models are implemented in MATLAB/Simulink and consequently the Simulink Parameter Estimation (SPE) tool is used to search for parameters based on measured data.

The SPE does not analyze in any way the structure of a simulation model and uses it as a black box with mathematical optimization to find the set of parameters. Selected parameters in simulation blocks are adjusted by the optimization algorithm and simulation is performed. Next, the cost function is calculated expressing the difference (MSE) between simulated and measured data. Further, the parameters are again modified by algorithm and simulation runs again. Finally, if optimization converges, the minimum of parameter vector is found. An example of simulation model with highlighted parameters is shown in Fig. 1. Generally, the estimated parameters can also include initial states of the model.

Although the SPE is very useful and widely used tool, from the practical point of view, it lacks several important features. In this paper, a New Parameter Estimation Tool (NPET) is introduced and briefly described.

The rest of the paper is organized as follows: first, the motivation for the use of several models in one optimization problem definition is described in Sec. 2. Next, in Sec. 3, other important features are mentioned. Finally, the GUI is shown in Sec. 4.

### 2. The parameter estimation problem: mass-spring-damper system with dry friction example

To demonstrate several aspects of practical approach to parameter estimation, a linear mechanical mass-

---

<sup>\*</sup> Ing. Martin Appel, MECHLAB, ISMMB, FME, Brno University of Technology, Technická 2; 616 69, Brno; CZ, martin.appel@mechlab.cz

<sup>\*\*</sup> Assoc. Prof. Robert Grepl, PhD., MECHLAB, ISMMB, FME, Brno University of Technology, Technická 2; 616 69, Brno; CZ, robert.grepl@mechlab.cz

spring-damper system with nonlinear (dry) friction is used. The simulation model of this system is shown in Fig. 1. The equation of motion

$$m\ddot{x} + kx + b\dot{x} + T \operatorname{sgn}(\dot{x}) = cu \quad (1)$$

contains five unknown parameters (mass  $m$ , stiffness  $k$ , viscous damping  $b$ , dry friction  $T$ , actuator constant  $c$ ). Input system variable  $u$  is known.

### 2.1. How many parameters can be estimated?

The  $n = 5$  parameters above have specific physical meaning and from engineering point of view it would be beneficial to be able to estimate all of them. However, only four ( $n - 1$ ) parameters in this equation can be estimated independently, typically the equation should be rewritten in the form:

$$p_1\ddot{x} + p_2x + p_3\dot{x} + p_4 \operatorname{sgn}(\dot{x}) = u \quad (2)$$

These redefined parameters can be estimated but with lost physical meaning.

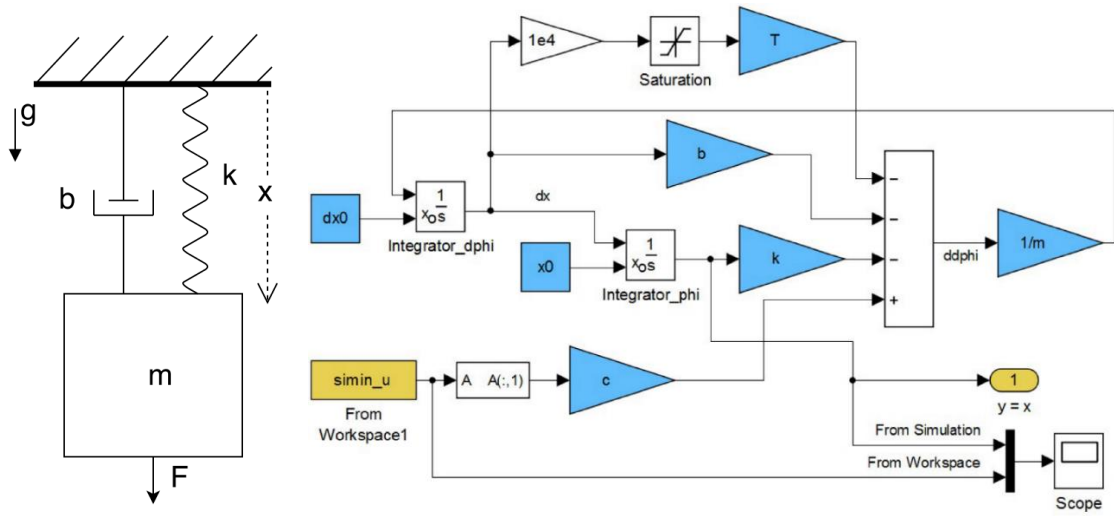


Fig. 1: Schematic and Simulink model of mass-spring system.

### 2.2. Modification of experimental setup

To solve the described problem, a certain modification of real experimental setup can often be done. The simplest example is to add an extra mass  $M$  (known) to the system:

$$(m + M)\ddot{x} + kx + b\dot{x} + T \operatorname{sgn}(\dot{x}) = cu \quad (3)$$

Such experimental arrangements provide in fact two different physical systems with five shared parameters ( $m, k, b, c, T$ ). Combining these two systems (1) and (3) all five parameters can be estimated.

The procedure of the estimation can be clearly shown on simplified example:

$$\begin{aligned} m \ddot{x} &= cu \\ (m + M) \ddot{x} &= cu \end{aligned} \quad (4)$$

By minimizing the number of parameters, the (4) can be rewritten in the form:

$$\begin{aligned} p_1 \ddot{x} &= u \\ p_2 \ddot{x} &= u \end{aligned} \quad (5)$$

With known input  $u$  and measured  $\ddot{x}$ , both parameters  $p_1$  and  $p_2$  can be uniquely determined. Next, the calculation of  $m$  and  $c$  is just solution of two equations (with  $p_1, p_2$  and  $M$  known):

$$\begin{aligned} p_1 c &= m \\ p_2 c &= m + M \end{aligned} \quad (6)$$

leading to result:

$$c = \frac{M}{p_2 - p_1} \quad (7)$$

Obviously, in real-world examples, the derivation of resulting parameters will not be so clearly understandable. To automate this process (4)-(7), the two independent systems (4) can simply be estimated using optimization methods while parameters  $m$  and  $c$  are shared. The SPE tool can utilize described approach only if the user includes both systems (4) into one Simulink model.

### 3. Overview of main NPET features

#### 3.1. Estimation using combination of several models and measured data

Previous section shows the potential usefulness of the combination of several simulation models (M) and measured data set (D) in one optimization. Generally, the NPET allows arbitrary combination of several Simulink models (independent files) with sets of measured data. The cost function  $e$  of the optimization method can be constructed according to the user's needs.

There are two basic applications:

- 1) **Combination of several modified experimental setups with shared parameters** (previous Section describes it in details). In such example, the cost function can have following form:

$$e = w_1 m_1(p_1, p_2, p_3) + w_2 m_2(p_3, p_4) \quad (8)$$

- 2) **Testing of several model candidates for the best fidelity:** In real life, the structure of the system model is never exactly known. Considering the example of mass-spring system, user can create many variants of simulation model including (3), model without dry friction ( $T = 0$ ), model with quadratic damping and many others. The parameters of these candidate models can then be estimated and the model with the best fitting parameters (measuring the fidelity by MSE) can be selected. In such case, there are several competing cost functions:

$$\begin{aligned} e_1 &= m_1(p_1, p_2, p_3) \\ e_2 &= m_2(p_3, p_4) \end{aligned} \quad (9)$$

In the SPE tool the (M, D) couples can be arbitrarily combined using weights, logical and algebraic functions which allow very rich possibilities of task formulation.

#### 3.2. Automated repetitive start from different initial condition

One of the most typical problems of the gradient (but also gradient-free) optimization methods use is the freezing in local minimum. Because avoiding this problem is very difficult (despite the optimism of GA fans), it is much easier to simply overcome the problem with repetitive starting of the algorithm from different (random) initial condition. The NPET allows to define the conditions to restart the optimization with respect to computation time and precision.

#### 3.3. Storing temporary simulation results in memory

One of the best engineering approaches to optimization is Brute force method. It can of course be utilized only in case of middle-size problems, but then it could be very useful. In NPET, user can start the Brute force search which takes several days, all results (not necessary the simulated trajectories but the set parameter – MSE) are stored and available for later browsing. Such starting search can also be useful to get an overview of the properties of parameter state space.

Not only Brute force but all optimization methods store their results in NPET. Very often, the evaluation of model with specific set of parameters is computationally costly. In such case, it is better to search for already performed simulations in a database than calculate it again.

From the engineering perspective, the ability to explore the searched space visually (see Fig. 2) is one of the crucial advantages of NPET. The right side of GUI shows the plot of measured and simulated data with the possibility to limit the number of plots via MSE. On the left side, the corresponding parameter

sets are drawn. User can clearly see how intense the performed search was in particular part of an optimization state space. This allows to analyze the stored simulation results with high level of comfort.

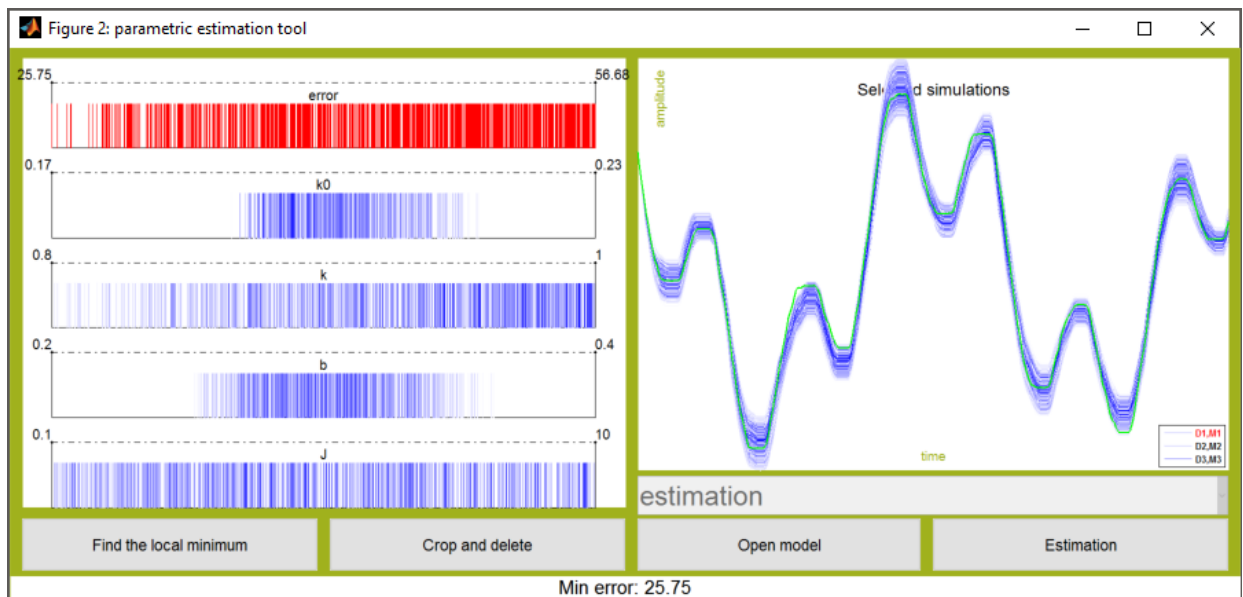


Fig. 2: Main GUI of NPET.

#### 4. Conclusions

The NPET described briefly in this paper was used for estimating several nonlinear system models including nonlinear systems such as BLDC pump, electromagnetic levitation experimental setup and electronic throttle (Grepl, 2010). The estimated results, insensitivity to wrong initial guess and general user comfort of the use were very satisfactory and promising.

The software was implemented in MATLAB using object oriented programming as a result of a thesis (Appel, 2016). Besides the main estimation engine, several optimization methods were implemented or adapted for use in the NPET which allows to use the tool without the need of MATLAB Optimization Toolbox or Global Optimization Toolbox.

#### Acknowledgement

This work is an output of cooperation between FME Brno University of Technology and NETME Centre, regional R&D centre built with the financial support from the Operational Programme Research and Development for Innovations within the project NETME Centre (New Technologies for Mechanical Engineering), Reg. No. CZ.1.05/2.1.00/01.0002 and, in the follow-up sustainability stage, supported through NETME CENTRE PLUS (LO1202) by financial means from the Ministry of Education, Youth and Sports under the „National Sustainability Programme I”.

#### References

- Appel, M. (2016) Application of Optimization Methods for Parameters Estimation of Simulation Models, master thesis, FME, Brno University of Technology, (in Czech).
- Grepl, R. and Lee, B. (2010) Modeling, parameter estimation and nonlinear control of automotive electronic throttle using a Rapid-Control Prototyping technique Int. J. of Automotive Technology, Vol. 11, pp. 601-610.
- Nelles, O. (2001) Nonlinear System Identification, ISBN 978-3-662-04323-3.
- Ljung, L. (2010) Perspectives on system identification, Annual Reviews in Control. Vol. 34, pp. 1-12.

## INFLUENCE OF GROUND STRESS DISTRIBUTION ON PUNCHING RESISTANCE

T. Augustín<sup>\*</sup>, L. Fillo<sup>\*\*</sup>

**Abstract:** The presented paper brings new aspects of ground stress distribution influence on punching resistance for two types of subsoil. After the analysis of punching phenomena, paper continues with a comparison of the uniform ground stresses and software numerical model ground stresses distribution and their influence on the calculation of three types of footings and their punching resistance.

**Keywords:** Ground Stresses, Footings Stiffness, Punching, Shear Resistance.

### 1. Introduction

Punching as dangerous phenomenon in structural engineering needs two steps of verification. The first one is a diagonal strut failure verification (crushing of concrete) at control perimeter  $u_0$  of a column and the second one is the shear-tension failure verification of concrete or transverse reinforcement in circumference of area surrounded by control perimeters  $u_i$ , which are analysed in distances from  $0.5d$  to  $2.0d$  (if possible) from face of column (Fig. 1).

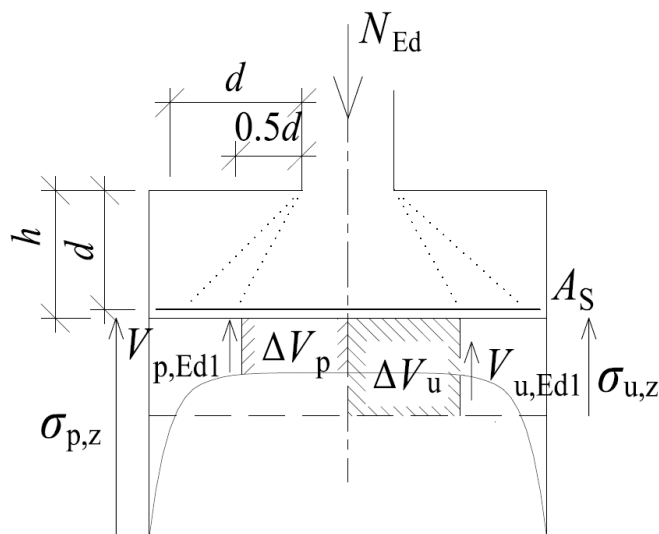


Fig. 1: Shear-tension failure verification of footing in control perimeters.

### 2. Soil Parameters

Two types of subsoil were used for calculation, according to geology of Bratislava. The first subsoil consisted of three soil layers. The second subsoil consisted of one soil layer. The properties of the soils are described in Tab. 1. For each subsoil the design resistance calculation ( $R_d$ ) was done, after (1) (EN 1997-1:2004, 2010 and Cajka, 2016).

$$R_d = (c'_d N_c s_c d_c i_c j_c + q' N_q s_q d_q i_q j_q + \gamma' B / 2 N_\gamma s_\gamma d_\gamma i_\gamma j_\gamma) / \gamma_R \quad (1)$$

<sup>\*</sup> Ing. Tomáš Augustín: Faculty of Civil Engineering, STU in Bratislava, Radlinského 11; 810 05, Bratislava; SK, tomas.augustin@stuba.sk

<sup>\*\*</sup> Prof. Ing. Ľudovít Fillo, PhD.: Faculty of Civil Engineering, STU in Bratislava, Radlinského 11; 810 05, Bratislava; SK, ludovit.fillo@stuba.sk

Tab. 1: Soil Parameters.

Parameters	Subsoil 1			Subsoil 2
	1. Layer	2. Layer	3. Layer	Layer
$E_{\text{def}}$ [MPa]	5	70	5	100
$\nu$ [-]	0.4	0.25	0.4	0.25
$c_{\text{ef}}$ [kPa]	14	-	10	-
$\varphi_{\text{ef}}$ [°]	18	33	15	33
$\gamma$ [kN/m <sup>3</sup> ]	21	19	20	19
$h$ [m]	4	4	10	20

### 3. Verification of Punching

The maximum shear force is limited by compressive capacity of the struts at the column perimeter. Crushing of the struts at column perimeter is controlled by reduced compressive strength of concrete (2) according to (EN 1992-1-1:2004/AC, 2010).

$$v_{\text{Ed,max}} = \frac{\beta V_{\text{Ed}}}{u_0 d} \leq v_{\text{Rd,max}} = 0.4 \nu f_{\text{cd}} \quad (2)$$

$$\nu = 0.6 \left[ 1 - \frac{f_{\text{ck}} [\text{MPa}]}{250} \right] \quad (3)$$

Another limit for the punching resistance is also derived from concrete shear resistance (4) according to (EN 1992-1-1:2004/AC, 2010). Requirements concerning the maximum punching shear resistance are based on the  $k_{\text{max}}$  factor (Hanzel et al., 2014) and punching shear resistance without shear reinforcement  $v_{\text{Rdc}}$  (4) and (5).

$$v_{\text{Rdc}} = \frac{0.18}{\gamma_c} k (100 \rho_1 f_{\text{ck}})^{1/3} \frac{2d}{a} \geq 0.035 k^{3/2} f_{\text{ck}}^{1/2} \frac{2d}{a} \quad (4)$$

$$v_{\text{Rd,cs}} = 0.75 v_{\text{Rd,c}} + \left( \frac{1.5d}{s_r} \right) \frac{A_{\text{sw}} f_{\text{ywd,ef}}}{u_1 d} \leq k_{\text{max}} v_{\text{Rd,c}} \quad (5)$$

Latest experiments have also shown that the  $k_{\text{max}}$  value depends on many factors. The first and the most important factor is the type of shear reinforcement and particularly conditions for their anchoring. For this analysis  $k_{\text{max}} = 1.46$  ( $200 < d < 700$  mm) was used (Fingerloos et al., 2012).

Calculation of the punching shear force  $V_{\text{Ed}}$  depends on influence of ground resistance distribution (Fig. 1). If we take into account uniform distributed ground stresses,  $\Delta V_u$  is bigger than a part of force  $\Delta V_p$ , which comes from a more precise distribution of ground stresses and therefore this simpler design of footings brings the unsafe solution, because the punching shear force on the load side is lower.

$$V_{\text{Ed}} = N_{\text{Ed}} - \Delta V_u \quad (6)$$

This shear force enters into the condition of reliability similarly as in equation (1).  $\Delta V_u$  is the result of the uniform ground resistance distribution (Fig. 1). If we consider a more precise distribution of ground stresses,  $\Delta V_p$  (Fig. 1) is less than  $\Delta V_u$  and therefore brings the bigger punching shear force and the verification of punching is more conservative but the safe side.

The more precise analysis of ground stresses comes from a numerical model, created in Sofistik – software, based on FEM (Finite Element Method) with Boussinesq subsoil.

The two types of footings were analyzed for the subsoil 1 – the thickness - 360 mm for the footing with shear reinforcement and the thickness 510 for the footing without shear reinforcement.

For the subsoil 2 only a footing with a thickness – 900 mm was analyzed, because in this case the limiting criterion for punching was the crushing of a concrete strut. All footings were made from the concrete C25/30, with column 500 x 500 mm.

Tab. 2: Footings parameters.

	1. Footing (1. subsoil)	2. Footing (1. subsoil)	3. Footing (2. subsoil)
Dimensions [mm]	2800 x 2800 x 360	2800 x 2800 x 510	2800 x 2800 x 900
$\rho$ [kN]	0.0052	0.0021	0.0018
$N_{Ed}$ [kN]	1850	1800	5400
$\Delta V_p$ [kN]	267	410	2856
$\Delta V_u$ [kN]	148	226	1555
$v_{p,Ed}$ [kN/m <sup>2</sup> ]	1679	835	723
$v_{u,Ed}$ [kN/m <sup>2</sup> ]	1562	736	479
$v_{Rd,c}$ [kN/m <sup>2</sup> ]	1055	753	635
$v_{Rd,cs}$ [kN/m <sup>2</sup> ]	1562	-	-

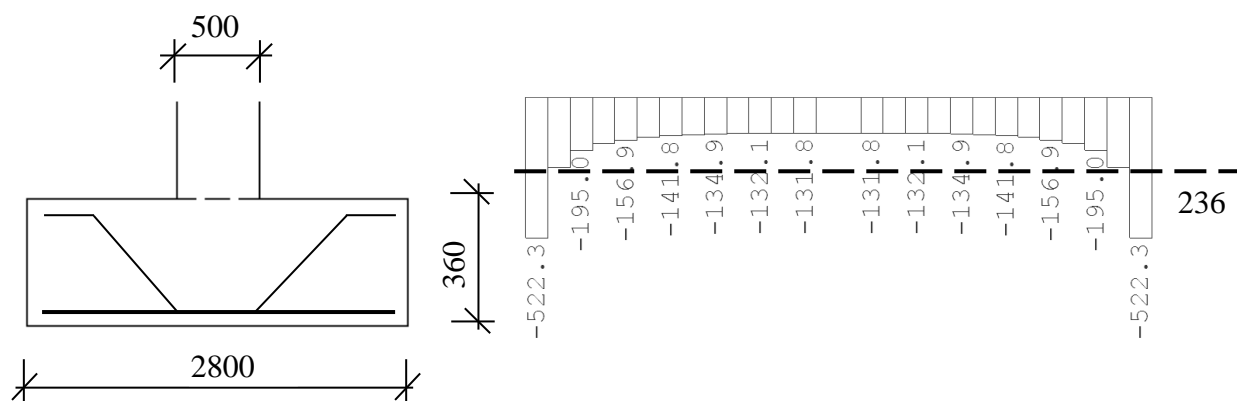


Fig. 2: Footing with shear reinforcement (left), ground stress [kPa] (right) – Subsoil 1.

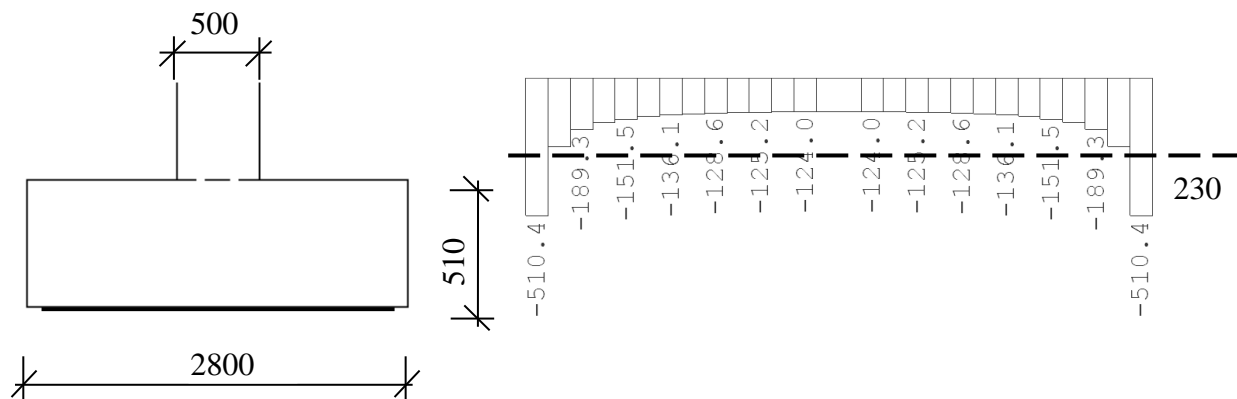


Fig. 3: Footing without shear reinforcement (left), ground stress [kPa] (right) – Subsoil 1.

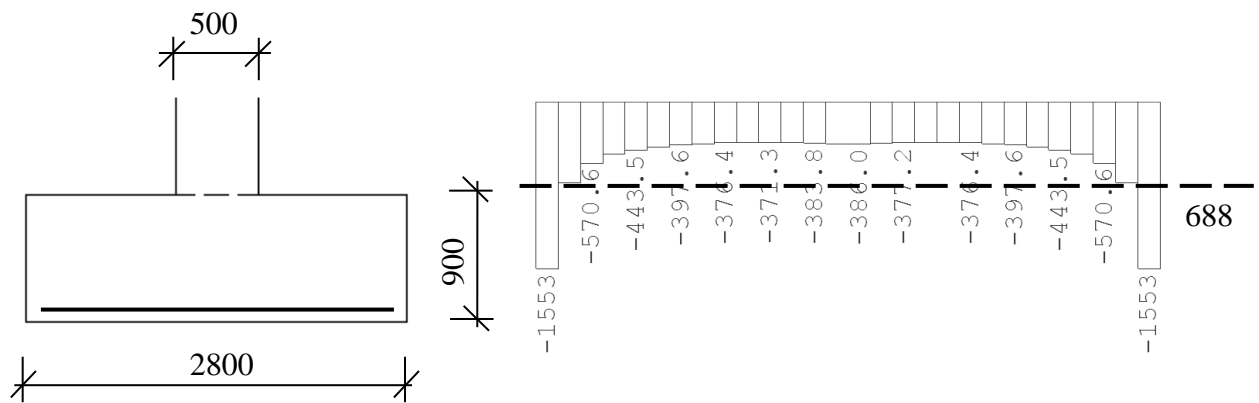


Fig. 4: Footing without shear reinforcement (left), ground stress [kPa] (right) – Subsoil 2.

#### 4. Conclusions

The paper presents results of two types of subsoil and three types of footing analysis and their influence on punching resistance. After the analysis of punching phenomena, paper continues with a comparison of the uniform ground stresses and more precise - software numerical model ground stresses distribution and their influence on the calculation of the punching phenomenon. Tab. 2 confirms that suggestion of uniform stresses distribution brings results on unsafe side for all considered types of footings and subsoils, respectively.

#### Acknowledgement

This work was supported by the Slovak Research and Development Agency under the contract APVV-15-0658 and Slovak Grand Agency under the contract VEGA 1/0456/17.

#### References

- Cajka, R., Labudkova, J. and Mlynarcik, P. (2016) Numerical solution of soil-foundation interaction and comparison of results with experimental measurements. *International Journal of GEOMATE* 11(1) pp. 2116-2122.
- Hanzel, J., Majtánová, L. and Halvonik, J. (2014) Punching Resistance of Flat Slabs without Shear Reinforcement. In 21. Concrete Days 2014. Proceedings of Conference. Prague, 6 p.
- EN 1992-1-1:2004/AC (2010), Eurocode 2: Design of concrete structures – Part 1-1: General rules and rules for buildings.
- EN 1997-1:2004 (2010) Eurocode 7: Geotechnical – general requirements.
- Fingerloos, F., Hegger, J. and Zilch K. (2012) EUROCODE 2 für Deutschland. Ernst & Sohn, 387 p.



## OPTIMAL PASSIVE CONTROL OF SHEAR BUILDINGS

E. Aydin<sup>\*</sup>, B. Öztürk<sup>\*\*</sup>, M. Dutkiewicz<sup>\*\*\*</sup>

**Abstract:** *In the paper, the analysis of damping parameters for vibration reduction of buildings with use of optimization algorithm is presented. Optimal values of damping coefficients are determined at fundamental structural mode of shear buildings in order to attain desired added damping ratios. The cost function is defined as the sum of damping coefficients of the dampers to be minimized. Proposed optimization problem is solved by using three different numerical algorithms that are namely: Simulated Annealing, Nelder Mead and Differential Evolution algorithms, respectively. Numerical example is presented to prove the validity of the proposed method. The changes of optimal distributions of the dampers with respect to target damping ratios and structural periods in a particular range are investigated for two-story shear building model. The numerical results show that the proposed damper optimization method is easy to apply and efficient to find optimal damper distribution for a target damping ratio.*

**Keywords:** Optimal dampers, Target damping ratio, Added dampers, Optimal passive control, Optimal design of dampers.

### 1. Introduction

The concept of supplemental dampers within a structure suggests that part of the input energy will be absorbed, not by the structure itself, but rather by supplemental damping elements. The usage of the added dampers can increase the damping level of buildings ranging from 20 % to 40 %.

The effects of variations support member stiffness of dampers upon the optimal damper allocation problem were investigated (Takewaki and Yoshitomi 1998). A procedure for obtaining the optimal stiffness and damping distributions based upon the optimality criteria was presented by Takewaki (1999a, 1999b). An optimal damper placement method was proposed to minimize the dynamic compliance of a building frame (Takewaki 2000a, Shukla et al. 1999, Fujita et al. 2010, Aydin et al. 2007) and beam (Takewaki 1998). A new objective function for finding optimal size and location of the added viscous dampers was proposed based on the elastic base moment in planar steel building frames (Aydin 2012). In this studies, a cost function that is the sum of damping coefficients of the added dampers is minimized to find optimal damping coefficients of the added dampers under a specified added damping ratio and both lower and upper bounds of each damping coefficient of the added dampers. Differential Evolution, Nelder Mead and Simulated Annealing are used to solve the simple optimization problem. Moreover, in the numerical examples, the effects of the changes of desired target damping ratio and the period of the structures above the optimal damper designs are investigated.

### 2. Theoretical background of the analysed problem

For the analysed model the equation of motion can be written as:

$$\mathbf{M}\ddot{\mathbf{u}}(t) + (\mathbf{C} + \mathbf{C}_{ad})\dot{\mathbf{u}}(t) + \mathbf{K}\mathbf{u}(t) = -\mathbf{M}\mathbf{r}\ddot{\mathbf{u}}_g(t) \quad (1)$$

where  $\mathbf{M}$ ,  $\mathbf{C}$  and  $\mathbf{K}$  present mass, structural damping and stiffness matrices, respectively  $\ddot{\mathbf{u}}(t)$ ,  $\dot{\mathbf{u}}(t)$  and  $\mathbf{u}(t)$  are acceleration, velocity and displacement vectors, respectively. The  $\mathbf{r}$  denotes influence

---

<sup>\*</sup> Assoc. Prof. Ersin Aydin, Faculty of Engineering, Department of Civil Engineering, Ömer Halisdemir University, Nigde, Turkey, eaydin@ohu.edu.tr

<sup>\*\*</sup> Assoc. Prof. Baki Öztürk, Faculty of Engineering, Department of Civil Engineering, Hacettepe University, Ankara Turkey, bakiozturk@hacettepe.edu.tr

<sup>\*\*\*</sup> Dr. Eng. Maciej Dutkiewicz, Faculty of Civil, Architecture and Environmental Engineering, Department of Building Construction, University of Science and Technology in Bydgoszcz, Al. Prof. S. Kaliskiego 7, 85-796 Bydgoszcz PL, e-mail: macdut@utp.edu.pl

vector that all elements is equal to one.  $\ddot{u}_g(t)$  is defined as ground acceleration. The structural damping matrix,  $\mathbf{C}$  can be calculated in proportion to only mass matrix, only stiffness matrix or linear combination of mass and stiffness matrices. It is given as

$$\mathbf{C} = \alpha \mathbf{M} \quad (2),$$

$$\mathbf{C} = \beta \mathbf{K} \quad (3),$$

$$\mathbf{C} = \alpha \mathbf{M} + \beta \mathbf{K} \quad (4),$$

where  $\alpha$  and  $\beta$  are generally calculated in terms of first normal mode of vibration in Eqs. (2) - (3). In general,  $\alpha$  and  $\beta$  in Rayleigh damping matrix, given in Eq. (4), are determined by using the first and second normal modes of vibration. While this is called as proportional damping matrix,  $\mathbf{C}_{ad}$  is the non-proportional damping matrix that should be designed optimally to minimize an objective. The matrix,  $\mathbf{C}_{ad}$  can be decomposed into corresponding added viscous dampers and is written as

$$\mathbf{C}_{ad} = c_1 \mathbf{C}_1 + c_2 \mathbf{C}_2 + \dots + c_n \mathbf{C}_n \quad (5),$$

where  $c_i$  ( $i = 1, \dots, n$ ) corresponds to the damping coefficient of  $i^{\text{th}}$  added damper; and  $\mathbf{C}_i$  ( $i = 1, \dots, n$ ) denotes the location matrix of the  $i^{\text{th}}$  added damper. Moreover, the location matrix is also equal to the partial differential of  $\mathbf{C}_{ad}$  with respect to  $i^{\text{th}}$  added damping coefficient of dampers as

$$\mathbf{C}_i = \frac{\partial \mathbf{C}_{ad}}{\partial c_i} \quad (6).$$

Two ends of the viscous dampers have different velocity since one end is attached to one building storey and the other end to a different storey. These devices produce damping forces in proportion to relative velocity between each one of the ends. These elements achieve the energy dissipation during an external vibration such as a wind and an earthquake excitation. The damping force of a linear viscous damper is given as

$$F_{ad} = c_{ad} \cdot \dot{u} \quad (7),$$

where  $c_{ad}$ ,  $\dot{u}$  denote the damping coefficient of manufactured viscous damper and relative velocity between each one of the ends of damper, respectively

In the fundamental mode, the damping ratio is calculated as follows

$$2\zeta_1 \omega_1 = \frac{\phi_1^T (\mathbf{C} + \mathbf{C}_{ad}) \phi_1}{\phi_1^T \mathbf{M} \phi_1} = \frac{\phi_1^T \mathbf{C} \phi_1}{\phi_1^T \mathbf{M} \phi_1} + \frac{\phi_1^T \mathbf{C}_{ad} \phi_1}{\phi_1^T \mathbf{M} \phi_1} \quad (8),$$

where  $\zeta_1$  denotes damping ratio after dampers are inserted to the structure,  $\phi_1$  is the normalized fundamental mode vector and  $\omega_1$  is the undamped natural circular frequency of the model structure. The first term on the right side of Eq. (8) covers proportional damping matrix, and therefore there are no couplings between first mode and any of the other modes. This situation is expressed as

$$\frac{\phi_1^T \mathbf{C} \phi_i}{\phi_1^T \mathbf{M} \phi_i} = \begin{cases} 2\zeta_s \omega_1 & i = 1 \\ 0 & i \neq 1 \end{cases} \quad (9),$$

where  $\zeta_s$  denotes structural damping ratio for the fundamental mode. The second term on the right side of Eq. (8) include non-proportional damping matrix. However, only for purposes of a simplified design it is convenient to assume that

$$\frac{\phi_1^T \mathbf{C}_{ad} \phi_i}{\phi_1^T \mathbf{M} \phi_i} = \begin{cases} 2\zeta_{ad} \omega_1 & i = 1 \\ 0 & i \neq 1 \end{cases} \quad (10),$$

where  $\zeta_{ad}$  denotes added damping ratio for the fundamental mode. The Eq. (8) can be rewritten using Eqs. (9) - (10) as follows

$$2\zeta_1 \omega_1 = 2(\zeta_s + \zeta_{ad}) \omega_1, \quad (11), \quad \zeta_1 = \zeta_s + \zeta_{ad} \quad (12).$$

Structural damping ratio  $\zeta_s$  is generally assumed to be constant as 0.02 in steel structures or 0.05 in RC structures. The parameter  $\zeta_1$  denotes the desired value of the damping ratio when the dampers are inserted to the structure. The parameter  $\zeta_{ad}$ , which occurs due to the effects of the added dampers, is the added damping ratio. The desired  $\zeta_{ad}$  is determined from Eq. (12), if the structural damping ratio and the desired total damping ratio are known. Therefore, the desired added damping ratio is calculated as

$$\zeta_{ad} = \zeta_1 - \zeta_s \quad (13).$$

The Eq. (8) can be rewritten for only added damping ratio as

$$2\zeta_{ad} \omega_1 = \frac{\phi_1^T \mathbf{C}_{ad} \phi_1}{\phi_1^T \mathbf{M} \phi_1} = c_1 \frac{\phi_1^T \mathbf{C}_1 \phi_1}{\phi_1^T \mathbf{M} \phi_1} + c_2 \frac{\phi_1^T \mathbf{C}_2 \phi_1}{\phi_1^T \mathbf{M} \phi_1} + \dots + c_n \frac{\phi_1^T \mathbf{C}_n \phi_1}{\phi_1^T \mathbf{M} \phi_1} \quad (14),$$

where the coefficients ( $\mu_i$ ) of the  $c_i$  can be written as follows

$$\mu_i = \frac{\phi_1^T c_i \phi_1}{\phi_1^T M \phi_1} \quad (15).$$

The formula of the desired added damping ratio for fundamental mode is written as below using Eqs. (14) - (15)

$$\zeta_{ad} = \frac{1}{2\omega_1} (\mu_1 c_1 + \mu_2 c_2 + \dots + \mu_n c_n) = \frac{1}{2\omega_1} \sum_{i=1}^n \mu_i c_i \quad (16).$$

In this study, design variables are considered as the damping coefficients of the added dampers. Optimal damper problem is based on minimization of total cost of the dampers that is expressed as the sum of damping coefficients of the added dampers which is given as

$$\text{Min. } f = \sum_{i=1}^n c_i \quad (17).$$

The cost function to be minimized in Eq. (17) indicates total damping coefficient of the added dampers. Eq.(16) can be rewritten as an equality constraint in terms of the added damping ratio

$$\zeta_{ad} = \frac{1}{2\omega_1} (\mu_1 c_1 + \mu_2 c_2 + \dots + \mu_n c_n) = \frac{1}{2\omega_1} \sum_{i=1}^n \mu_i c_i \quad (18),$$

where  $\zeta_{ad}$  is a fixed damping ratio that can be given as a desired damping ratio. The fundamental natural circular frequency and the parameter  $\mu_i$  are known parameters from the vibration characteristics of the structure. Both objective function and equality constraint are the linear function of the design parameters. Taking into account the inequality constraints on the upper and lower bounds of the damping coefficients of each added damper gives the following

$$0 \leq c_i \leq \bar{c}_i \quad (i=1,2,\dots,n) \quad (19),$$

where  $\bar{c}_i$  is the upper bound of damping coefficient of the damper in  $i^{\text{th}}$  story. In practical applications, a damper capacity and size which corresponds to the upper bound of the added damper should be restricted because of commercial and manufacturing limitations.

### 3. Numerical analysis and discussion

Analysed 2-storey shear building model such as linear manufactured viscous dampers that are added to each story is shown in Fig. 1.

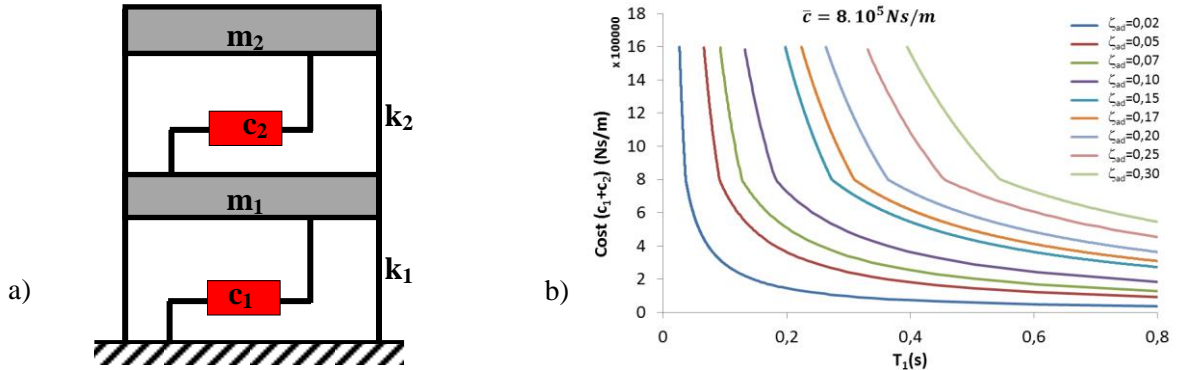


Fig. 1: a) 2-storey shear buildings with supplemental dampers; b) Variation of minimum values of cost function according to period of the structure for different added damping ratios.

The three various numerical minimization methods such as Differential Evolution, Nelder Mead and Simulated Annealing, which are well known in the optimization literature, are used to solve the optimization problem. The aim of using these three optimization methods is to verify the results obtained from a method with the other methods. The used optimization methods in the numerical minimization module of the Mathematica 5.0 (2003) are expressed in the following paragraph.

Optimization problem is applied to 2-story shear building to find optimal damping coefficient of added dampers under the upper and lower limits of the design variables and the target value of the damping ratio in the first mode. The target damping ratio is considered as  $\zeta_{ad} = 0.20$ . The change of the period depends on the structural stiffness. The story stiffness coefficients are equal in all stories. The stiffness coefficient is selected such that the period is fixed to 1.04305 s. For this period and target added damping ratio  $\zeta_{ad} = 0.20$ , the optimization is performed. While the period of the structure is decreased by increase of the

stiffness, optimization is performed using three different method for fixed damping ratio  $\zeta_{\text{ad}} = 0.20$ . The target added damping ratio is taken as 0.02, 0.05, 0.10, 0.20, 0.15, 0.25 and 0.30, respectively. For each one of the added damping ratios, optimization is performed for these cases and the variations of the optimal damping coefficients ( $c_1$ ,  $c_2$ ) according to period of the structure are plotted in Fig. 2.

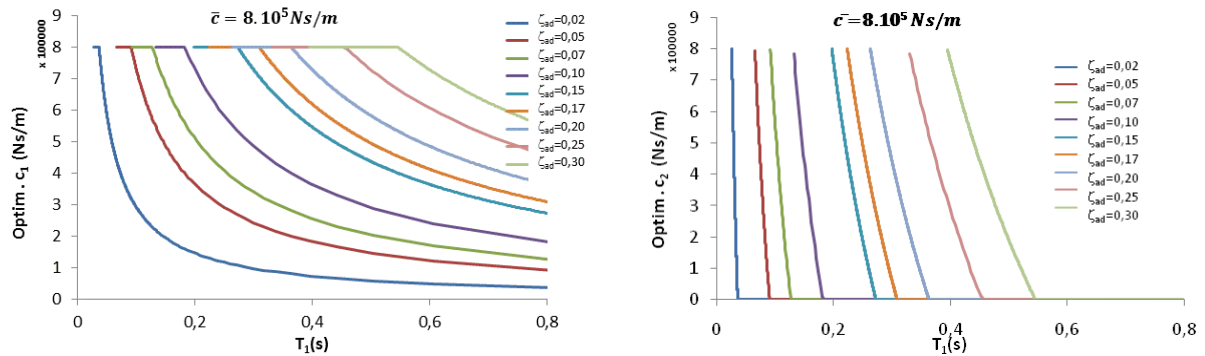


Fig. 2. The variation of optimal values of  $c_1$  and  $c_2$  according to period of the structure for different added damping ratios.

The variations of the minimum values of cost function for different added damping ratios are also presented in Fig. 1. It can be seen that the increase of the period results in decrease of the minimum values of the cost function.

#### 4. Conclusions

A simple optimization method is proposed to find optimal damper placement. The optimization problem is constructed based on minimizing the sum of the damping coefficients of the added dampers under a target added damping ratio in the first mode and both upper and lower bounds of the added dampers. Both the cost function and the constraint functions are linear function of the design variables. Three different numerical minimization methods are used for justification in this study. The results obtained from minimization methods match with each other. The effects of variation of the fundamental period and the target added damping ratio above the optimal designs are also investigated. The numerical results reveal that the increase of the fundamental period results in the decrease of cost function value for a fixed upper bound of added damping coefficient and a specified target added damping ratio. The more added damping ratio is needed, the more the cost function value occurs. In the numerical examples, the upper bound of the added damping coefficients is taken as a fixed value. The numerical results state explicitly that the proposed method is effective in order to minimize the total damping coefficient and to attain a desired damping ratio in the first mode.

#### References

- Aydin, E. (2012) Optimal Damper Placement Based on Base Moment in Steel Building Frames, Journal of Constructional Steel Research, 79, pp. 216-225.
- Aydin, E., Boduroglu, M.H. and Guney, D. (2007) Optimal damper distribution for seismic rehabilitation of planar building structures, Eng. Struct, 29, pp. 176-185.
- Fujita, K., Yamamoto, K., Takewaki, I. (2010) An evolutionary algorithm for optimal damper placement to minimize interstorey-drift transfer function in shear building, Earthquakes and Structures, 1(3):289-306.
- Shukla, A.K., Datta, T.K. (1999) Optimal use of viscoelastic dampers in building frames for seismic force, J. of Struct. Eng, 125(4), 401-409.
- Takewaki, I. (1999a) Non-monotonic optimal damper placement via steepest direction search, EarthqEng&StructDyn, 28, 655-670.
- Takewaki, I. and Yoshitomi, S. (1998) Effects of support stiffnesses on optimal damper placement for a planar building frame, The Struct Design of Tall Build, 7, 323-336.
- Takewaki, I. (1998) Optimal damper positioning in beams for minimum dynamic compliance, Comput Methods in Appl Mech and Engng, 156, 363-373.
- Takewaki, I. (1999b) Displacement-acceleration control via stiffness-damping collaboration, Earthq Eng Struct Dyn, 28:1567-1585.
- Takewaki, I. (2000a) Optimum damper placement for planar building frames using transfer functions, Structural and Multidisciplinary Optimization, 20, 280-287.

## PLASTIC RESISTANCE OF ALUMINUM I-PROFILE UNDER BENDING AND TORSION ACCORDING TO CONTINUOUS STRENGTH METHOD

I. Baláž\*, Y. Koleková\*\*

**Abstract:** *The continuous strength method (CSM) is a deformation-based design approach that allows a rational exploitation of strain hardening. This paper describes the development of the method and its application to aluminium structural elements. The key design concepts are expressed through a set of straightforward design equations, while the range of stress-strain responses is allowed for through material specific coefficients in the adopted bi-linear (elastic, linear hardening) material model. The design method enables enhancements in structural efficiency and, unlike traditional approaches, provides the designer with information on the level of plastic deformation that the structure is undergoing at the ultimate limit state. Plastic bending moment resistance utilizing strengthening in stress-strain diagram. Investigation of 6 stress-strain diagrams. Resistance of I-profile under combination of major axis bending moment and bimoment.*

**Keywords:** Aluminium, Deformation-based, Local buckling, Stainless steel, Steel, Strain hardening, Structures,  $\sigma$ - $\epsilon$  diagrams. I-profile resistances, Bending moment, Bimoment interaction.

### 1. Introduction

The cross-section and member design rules given in Eurocode EN 1993 and Eurocode EN 1999 are based on the assumption of elastic, perfectly plastic material behaviour leading to the concept of cross-section classification, the use of elastic and plastic moment capacities and plastic hinge design. In reality, structural steel and other structural metallic materials such as stainless steel and aluminium do not exhibit this form of idealised stress-strain response. Instead, the stress-strain curves of these materials display differing degrees of nonlinearity, roundedness in the region of the yield stress, a range of plateau lengths and often the absence of a plateau altogether, varying strain hardening slopes and so on. The idealisation of elastic, perfectly plastic material behaviour is generally reasonable for hot-finished structural steel with a long yield plateau, while for other materials, the idealisation is more questionable.

For the case of the traditional elastic, perfectly plastic material model, post-yield strains do not result in any increase in stress. However, for a hardening material model, increasing post yield strains do lead to an increase in stress, and hence the strength of a cross-section is related to the level of strain it can endure prior to failure, typically by inelastic local buckling. In such circumstances (i.e. design of structures composed of strain hardening materials), since strength is dependent on deformation, a deformation-based design approach becomes desirable. Recent research into such an approach, referred to as the continuous strength method (Gardner, 2008), is outlined in (Gardner, 2016).

The continuous strength method (CSM) is a deformation-based design approach that accounts for strain hardening. The method has been shown to give a high level of accuracy and consistency in predicting the resistance of structural steel (Gardner, 2008, Liew and Gardner, 2015), stainless steel (Afshan and Gardner, 2013, Zhao et al, 2015), and aluminium (Su et al, 2014) cross-sections under compression, bending and combined loading. The method has also been applied to the determination of cross-section resistances in fire (Theofanous et al, 2016).

The CSM has two key components: (i) a ‘base curve’ that defines the limiting strain  $\epsilon_{CSM}$  for a cross-section (i.e. the deformation capacity) based on its local slenderness and (ii) a strain hardening material

---

\* Prof. Ing. Ivan Baláž, PhD.: Department of Metal and Timber Structures, Faculty of Civil Engineering, Slovak University of Technology in Bratislava, Slovak Republic, Radlinského 11; 810 05, Bratislava; SK, ivan.balaz@stuba.sk

\*\* Assoc. Prof. Ing. Yvona Koleková, PhD.: Department of Structural Mechanics, Faculty of Civil Engineering, Slovak University of Technology in Bratislava, Slovak Republic, Radlinského 11; 810 05, Bratislava; SK, yvona.kolekova@stuba.sk

model, which enables stresses greater than the yield stress  $f_y$  to be achieved. These two key components are described in (Gardner, 2016) and applied in this paper.

Since the continuous strength method is a deformation-based design approach, it requires the determination of a relationship between the maximum limiting strain that a cross-section can endure prior to reaching its ultimate capacity and its local slenderness. This relationship is equivalent to the process of cross-section classification used in many structural metallic design codes, but instead of placing a cross-section into a discrete behavioural class, a normalized limiting strain is assigned (Gardner, 2016). For slender cross-sections, the limiting strain is below the yield strain and there is therefore no benefit to be gained from strain hardening, except in the case of non-doubly-symmetric cross-sections that can have limiting strains on the compression side less than the yield strain yet take benefit from strain hardening on the tensile side; for non-slender sections, the limiting strain is beyond the yield strain and benefit can be derived from strain hardening. Cross-sections comprising flat plates and circular hollow sections (CHS) are described in (Gardner, 2016).

## 2. Stress-strain relationships of aluminium alloys

The models for the idealization of the stress-strain relationship of aluminium alloys are provided by the Annex E (EN 1999-1-1, 2007). These models are conceived in order to account for the actual elastic-hardening behaviour of such materials. The analytical characterization of the stress  $\sigma$  – strain  $\varepsilon$  relationship of an aluminium alloy can be done by means of one of the following models: (i) piecewise models, (ii) continuous models.

All models defined in (EN 1999-1-1, 2007) were analyzed and compared with CSM model (Gardner, 2016). In this investigation the officially published Amendments A1 (2009) and A2 (2013) were taken into account together with proposal for Amendment (N 503, 2017). The results of the investigation for the wrought aluminium alloy EN AW-5083-O/H111 are given in Fig. 1. The aluminium alloy 5083 is known for exceptional performance in extreme environments. It is highly resistant to attack by both seawater and industrial chemical environments. The aluminium alloy 5083 also retains exceptional strength after welding. It has the highest strength of the non-heat treatable alloys but it is not recommended for use in temperatures in excess of 65 °C. It is typically used in: shipbuilding, rail cars, vehicle bodies, tip truck bodies, mine skips and cages, pressure vessels.

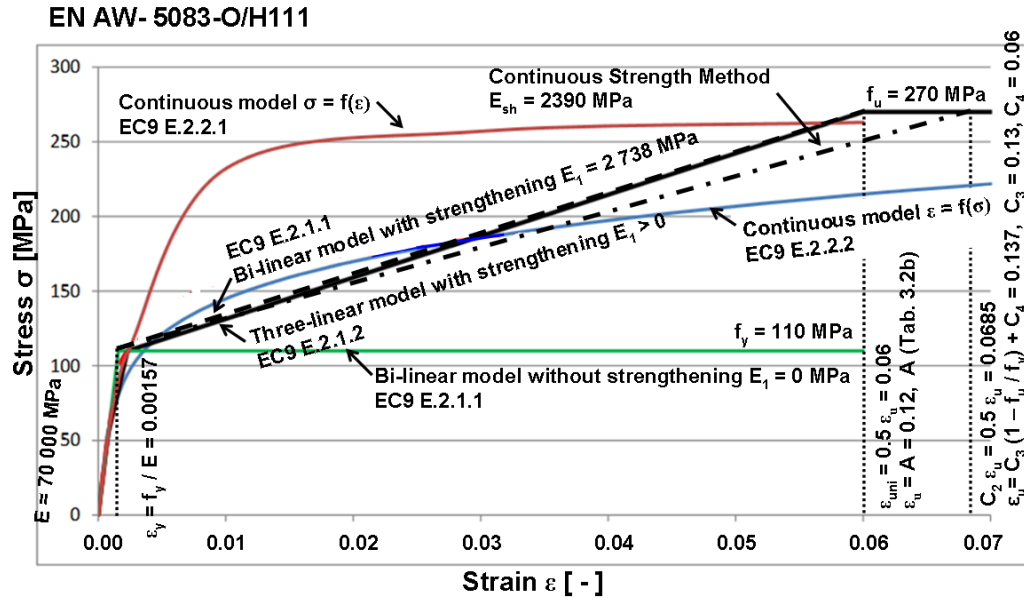


Fig. 1: Comparisons of the five stress-strain relationships given in EN 1999-1-1 with CSM one defined in (Gardner, 2016) for the non-heat treatable wrought aluminium alloy EN AW-5083-O/H111.

From the obtained results (Fig. 1) it is clear that: (i) the continuous model  $\sigma = f(\varepsilon)$  defined in the clause E.2.2.1 have to be corrected (Baláž 2017b,c), (ii) end part of the CSM diagram defining  $\varepsilon_u$  should be verified by more experiments (Baláž, 2017d, Mei-Ni et al, 2016), (iii) there is acceptable agreement between CSM model (dot-and-dashed line) and bi-linear model with strengthening defined in the clause E.2.1.1 (dashed line).



### 3. Continuous Strength Method (Gardner, 2016)

Within the continuous strength method (CSM), the base curve defines the relationship between cross-section deformation capacity and cross-section slenderness. For non-slender cross-sections, the base curve for cross-sections comprising flat plated elements (e.g. I-sections and square and rectangular hollow sections – SHS and RHS) is given by Equation 1 and shown with corresponding test data in Fig. 1. The test data have been collected from the literature and include results for steel, stainless steel and aluminium stub columns and beams (in-plane four-point bending). The transition between non-slender and slender cross-sections is defined at a local slenderness value of 0.68. Cross-sections with a local slenderness below 0.68 are deemed to be non-slender and have failure strains greater than the yield strain and can thus benefit from strain hardening; cross-sections with a local slenderness greater than 0.68 are slender and have limiting strains below the yield strain.

### 4. Application of Continuous Strength Method (CSM)

The method (Vlasov, 1936, Strelʹbickaja, 1947, 1958) together with CSM (Gardner, 2016) was applied by (Baláž, 2017a) for calculation of the resistance of I-section and channel section under combination of major axis bending moment  $M_y$  and bimoment  $B$  using: (i) elastic theory, (ii) plastic theory without strengthening (see model E.2.1.1 in Fig. 1), (iii) plastic theory with strengthening (see CSM model in Fig. 1).

The following numerical example was calculated for input values: extruded I-profile with dimensions  $h = 200$  mm,  $b_f = 100$  mm,  $t_f = 11.4$  mm,  $t_w = 7$  mm, made of wrought aluminium alloy EN AW-5083-O. The below values were calculated according to (Gardner, 2016). The local slenderness of the web and of the flange show that I-section is non-slender:

$$\bar{\lambda}_{p,w} = 0.216, \bar{\lambda}_{p,f} = 0.259, \bar{\lambda}_p = \max(0.216, 0.259) = 0.259 < 0.68 \quad (1)$$

$$f_y = 110 \text{ MPa}, f_u = 270 \text{ MPa}, \varepsilon_y = f_y / E = 110 \text{ MPa} / 70\,000 \text{ MPa} = 0.00157 \quad (2)$$

$$\varepsilon_u = C_3 (1 - f_y / f_u) + C_4 = 0.13 (1 - 110 \text{ MPa} / 270 \text{ MPa}) + 0.06 = 0.137 \quad (3)$$

$$E_I = (f_u - f_y) / (C_2 \varepsilon_u - \varepsilon_y) = (270 \text{ MPa} - 110 \text{ MPa}) / (0.5 \times 0.137 - 0.00157) = 2\,390 \text{ MPa} \quad (4)$$

$$\frac{0.25}{\bar{\lambda}_p^{3.6}} = 32.2, C_1 \frac{\varepsilon_u}{\varepsilon_y} = 0.5 \frac{0.137}{0.00157} = 43.6, \varepsilon_{CSM} = \min(15, 32.2, 43.6) \varepsilon_y = 15 \times 0.00157 = 0.02357 \quad (5)$$

CSM bi-linear diagram in Fig. 1 is defined by 3 points with coordinates as follows: the bottom point (0, 0), the middle point ( $\varepsilon_y, f_y$ ), the top point ( $C_2 \varepsilon_u = 0.5 \times 0.137 = 0.06852, f_u$ ). There is acceptable difference comparing with EN 1999-1-1 bi-linear diagram according to clause E.2.1.1, which differs only in a coordinate of top point ( $\varepsilon_{uni} = 0.5 A = 0.5 \times 0.12 = 0.6, f_u$ ). Limiting values according to CSM and EN 1999-1-1, respectively are:

$$\varepsilon_{CSM,max} = \min(15 \varepsilon_y, C_1 \varepsilon_u) = \min(0.02357, 0.06852) = 0.02357 \quad (6)$$

$$\varepsilon_{uni,max} = 0.30 - 0.22 f_y / 400 \text{ MPa} = 0.2395 \text{ for } f_y < 400 \text{ MPa}, \text{ and } 0.08 \text{ for } f_y \geq 400 \text{ MPa} \quad (7)$$

The characteristic value of the plastic bending moment resistance calculated for bi-linear model without strengthening (Fig. 1) is

$$M_{y,pl,Rk} = W_{y,pl} f_y = 277.251 \text{ cm}^3 \times 110 \text{ MPa} = 30.5 \text{ kNm} \quad (8)$$

The characteristic value of the plastic bending moment resistance calculated for bi-linear model with strengthening (Fig. 1):

- a) according to formula (F.2) and Table F.2 in EN 1999-1-1 is  $M_{EC9} = 31.44 \text{ kNm}$ ,
- b) according to formula (37.9) in (Strelʹbickaja, 1958) is  $M_{Str} = 39.10 \text{ kNm}$ ,
- c) according to CSM formula (13) in (Gardner, 2016) is  $M_{CSM} = 43.97 \text{ kNm}$ .

### 5. Conclusions

Application of CSM in resistance calculation of I-profile under interaction of bending moment and torsion. Comparisons of five strain-strain diagrams given in EN 1999-1-1 with CSM one (Gardner, 2016).

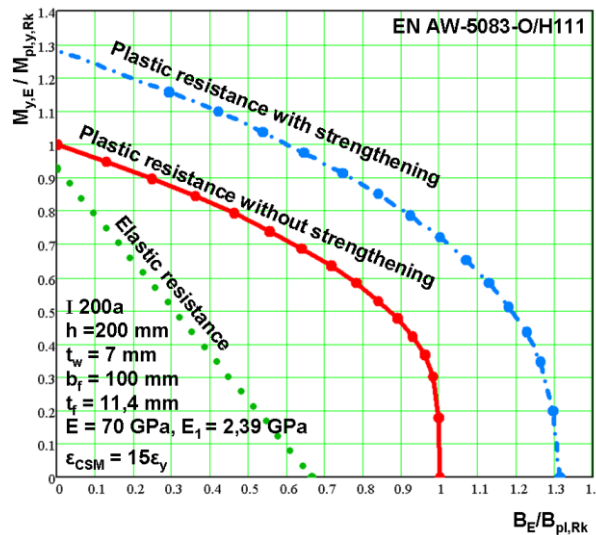


Fig. 2: Resistance of I-section under interaction of bending moment and bimoment.

## Acknowledgement

Project No. 1/0603/17 was supported by the Slovak Grant Agency VEGA.

## References

- Afshan, S. and Gardner, L. (2013) The continuous strength method for structural stainless steel design. *Thin-Walled Structures*, 68, pp. 42-49.
- Baláž, I. (2017a) Resistance of I- and Channel Sections According to Continuous Strength Method. *Proceedings of the 22<sup>nd</sup> Conference of Structural Engineers*. March 16.-17. 2017. Piešťany. (in Slovak).
- Baláž, I. (2017b) Correspondence with Prof. Torsten Höglund, chairman of WG1 EN 1999-1-1. March 28. 2017.
- Baláž, I. (2017c) Correspondence with Dipl.-Ing. Reinhold Gitter, member of WG1 EN 1999-1-1. March 28. 2017.
- Baláž, I. (2017d) Correspondence with Prof. Leroy Gardner, member of WG EN 1993-1-1. March 28. 2017.
- CEN/TC250/SC 09 – N 503 (2017) AM EC9-1-1-2016 – 15, January 19, 2017, pp. 40-49.
- EN 1999-1-1 (2007) and Amendment A1 (2009) and Amendment A2 (2013) Eurocode 9 - Design of aluminium structures. Part 1-1: General structural rules.
- Gardner, L. (2008) The Continuous Strength Method. *Proceedings of the Institution of Civil Engineers - Structures and Buildings*, 161(3), pp. 127-133.
- Gardner, L. (2016) The Continuous Strength Method for Steel, Stainless Steel and Aluminium Structural Design. *Proceedings of the Eight International Conference on Steel and Aluminium Structures*. Hong Kong, China December 7.-9.2016, pp. 1-11.
- Liew, A. and Gardner, L. (2015) Ultimate capacity of structural steel cross-sections under compression, bending and combined loading. *Structures*, 1, pp. 2-11.
- Mei-Ni, S., Young, B. and Gardner, L. (2016) The continuous strength method for the design of aluminium alloy structural elements. *Engineering Structures* 122, pp. 338-348.
- Strel'bickaja, A.I. (1947) St Venant torsion of thin-walled profile in limit state. *DAN SSR*. No. 4. (in Ukrainian).
- Strel'bickaja, A.I. (1958) Investigation of strength of thin-walled beams in elastic-plastic state. Publishing AN USSR. Kijev. (in Russian).
- Su, M.N., Young, B. and Gardner, L. (2014) Deformation-based design of aluminium alloy beams. *Engineering Structures*. 80, pp. 339-349.
- Vlasov, V.Z. (1936) New method of calculation of prismatic beams made of thin-walled profiles under combination of axial force, bending and torsion. *Proceedings of VIA RKKA*. No. 20. Projekt i standard. No. 8, 9, 10.
- Zhao, O., Rossi, B., Gardner, L. and Young B. (2015) Behaviour of structural stainless steel crosssections under combined loading – Part II: Numerical modelling and design approach. *Engineering Structures*. 89, pp. 247-259.
- Theofanous, M., Prosper, T., Knobloch, M. and Gardner, L. (2016) The continuous strength method for steel cross-section design at elevated temperatures. *Thin-Walled Structures*. 98, pp. 94-102.



## AERODYNAMIC HYSTERESIS OF OSCILLATING AIRFOIL

N. V. Bang<sup>\*</sup>, D. Rozehnal<sup>\*\*</sup>

**Abstract:** *In the aerodynamic calculations, the steady aerodynamic data, which contain the coefficients in form of a function dependent only on the angle of attack (AoA) are used. However, the airfoil aerodynamic characteristics are always unsteady in the real conditions at the same AoA can be different because of the time delay, which occurs in dynamic state. The unsteady approach can improve the aerodynamic calculation process of propellers and wind turbines in the yaw (in the crosswind) or helicopter rotors at high forward speed. This paper contains the results of wind tunnel test of the oscillating airfoil which demonstrate hysteresis properties of airfoil aerodynamics and the dependency of aerodynamic hysteresis on the angular frequency.*

**Keywords:** Oscillating airfoil, 2D airfoil, Aerodynamic hysteresis, Angular frequency, Dynamic stall.

### 1. Introduction

The unsteady behavior of airfoils has been known as a cause of the undesirable aerodynamic phenomenon in helicopter main rotors, wind turbine blades, aircraft propellers, and wings. It is directly related to the dynamic properties of airfoil sections when they perform rapid pitching and plunging motion against inflow direction.

This report presents, in graphical form, some experimental aerodynamic data from the wind tunnel test of oscillating airfoils at the same flow condition, but at various angular frequencies. Test results show that lift and drag characteristics of airfoil section feature typical hysteresis loop shape which depends clearly on the frequency of pitching motion.

### 2. Theoretical analysis

The static pre-stall data of airfoils used in the aircraft industry is usually obtained from wind tunnel tests when the AoA of the airfoil section increases very slowly to minimize the influence of the rotation on the measured data. In the range of small AoA, the flow through the airfoil can be described by potential flow model and the static lift curve can be considered as a linear. When the AoA of airfoil increases to high-enough value, the flow around airfoil behaves like a separated flow. The so-called “pre-stall data” appear only in a certain range limited by a stall angle. Below this stall angle, the airfoil dramatically stops producing lift.

Dynamic stall is the delay of stall existence at high AoA. It is characterized by the shedding and passage over the upper surface of the airfoil. The typical aspect of this phenomenon is the increase of stall coefficients and stall angle (McCroskey, 1981 and Åhlund, 2004). In some cases, the lift coefficient in the dynamic stall can increase for about 50 to 100 % in comparison with its static value (Sharma, 2010).

There are many studies on the dynamic stall of airfoils, and the focus of this paper is on the cases of dynamic changes. During dynamic changes, the stall phenomenon does not appear, because the AoA of airfoil section changes around a relatively small value  $\alpha_o$ , which is much lower than the static stall angle (Fig. 1). An example of dynamic change is the harmonic oscillating blade section of non-pitching propellers or wind turbines in steady yaw (Guntur, Sorensen, Schreck and Bergami, 2016). The vortex-

---

<sup>\*</sup> Ing. Nguyen Van Bang: Department of Air Force and Aircraft Technology, University of Defence, Kounicova 65, 662 10 Brno, CZ, phone: +420 770 662 887, vanbang.nguyen@unob.cz

<sup>\*\*</sup> Assoc. Prof. Dalibor Rozehnal, PhD.: Department of Air Force and Aircraft Technology, University of Defence, Kounicova 65, 662 10 Brno, CZ, dalibor.rozehnal@unob.cz

shedding shows different shapes when airfoil rotates up or down and the aerodynamic curves look like closed hysteresis loops (McCroskey, 1981).

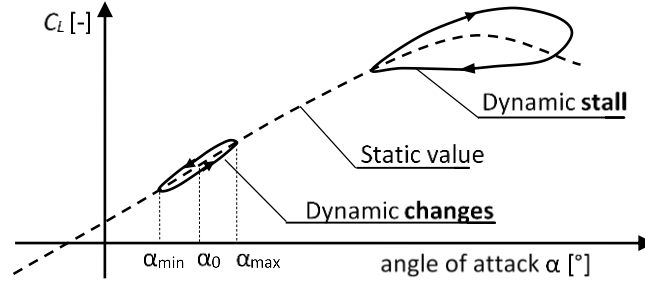


Fig. 1: Comparison of the dynamic stall and the dynamic change (Åhlund, 2004).

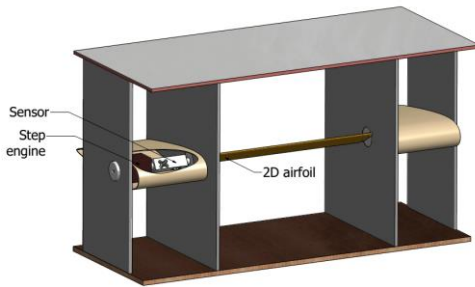
The AoA of airfoil section is changed from  $\alpha_{min}$  to  $\alpha_{max}$  and then returns to the minimum value with constant angular frequency  $\omega$ . During one revolution of the rotor, the blade section operates harmonically with the oscillated movement. This movement can be described by the mean value  $\alpha_0$  of the AoA with the amplitude  $\Delta\alpha = (\alpha_{max} - \alpha_{min})/2$  and angular frequency  $\omega$ . The static curve can be noted as a special case of the dynamic change in the same range of AoA when the angular frequency is zero.

$$\alpha = \alpha_0 + \Delta\alpha \cdot \sin(\omega t) \quad (1)$$

The necessary condition of unsteady behavior on the airfoil is the non-zero angular frequency  $\omega$  of the oscillating movement. The angular frequency  $\omega$  can be estimated through the largest and smallest values of AoA  $\omega = \Delta\alpha / \Omega$ . If  $b$  is the chord of the airfoil and  $V$  is the onset flow velocity, the ratio between these two parameters defines reduced frequency  $k = \omega b / (2 V)$ . In this paper, experimental results with different values  $\omega$  are compared under the same test conditions.

### 3. Test setup

Test equipment used for the measurements of unsteady aerodynamic characteristics of wing section is shown in Fig. 2. Lift and drag forces acting on the airfoil section are measured by two two-component strain gauge balances, which are mounted on both ends of the airfoil section. The body of balance is milled from duralumin and each balance contains four strain gauges, which are connected to the full Wheatstone bridge with a total resistance of 700  $\Omega$ .



a) scheme of the test stand.



b) placement of test stand in the wind tunnel.

Fig. 2: Test set-up in wind tunnel.

The airfoil section has the same airfoil with chord  $b = 58 \text{ mm}$  along the span  $l = 60 \text{ mm}$ . Both sides of the airfoil section are fixed and kept in position by sliding bearings, where the axis of rotation is at the 44 % of the chord (Tab. 1). One end can freely rotate while the second is fixed in the sensor. The position of this oscillating axis and the tested free flow velocity are limited by the holding moment of the stepper motor. Stepper motor is also used to generate the oscillation. This motor is connected to the NI stepper motion controller which has been programmed in LabVIEW software. At higher oscillating frequency, it is necessary to perform the correction for deviation of AoA at the boundary values. Symbol of rotating direction CCW indicates counterclockwise rotation, which is related to the side view of the test

equipment. Measurement equipment is located in the open measurement section of a low-speed return-flow wind tunnel.

Tab. 1: Main parameters of test.

<b>Test section size</b>	600 mm x 58 mm x 10 mm	<b>Mean AoA <math>\alpha_o</math></b>	10 °
<b>Wind velocity V</b>	15 [m/s]	<b>Amplitude of AoA <math>\Delta\alpha</math></b>	15 °
<b>Maximum Re</b>	128 000	<b>Mechanical tolerance</b>	$\pm 0.45$ °

#### 4. Result and discussion

The AoA changes regularly around  $\alpha_o = 10^\circ$  with an angular amplitude of  $\Delta\alpha = 15^\circ$ . The total AoA can be theoretically described by equation  $\alpha = 10 + 15 \sin(\omega.t)$ . The value of angular frequency  $\omega$  is changed differently due to the speed regulation of electric stepper motor. In this paper, lift and drag coefficients of the measured section are compared in 5 various values of angular frequency  $\omega$ . Both lift and drag data have been graphically displayed in Fig. 3.

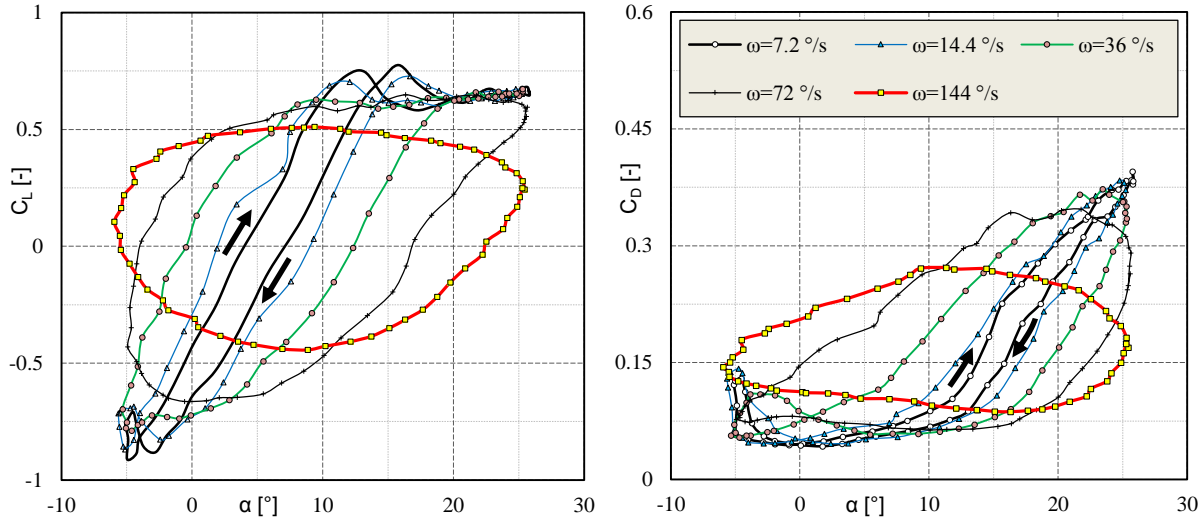


Fig. 3: The lift and drag characteristics with  $\alpha = 0^\circ \pm 15^\circ$ , direction CCW.

The real amplitude of the movement is slightly increased because of the mechanical tolerance of the system and deformation of measured airfoil due to aerodynamic and inertial forces. Furthermore, the stepper motor used has full-step of  $1.8^\circ$  and the motor shaft can be precisely positioned only in discrete positions, which are separated by this step. The real angle of the stepper motor at high loads must be calculated with an error of approximately  $0.9^\circ$ . As a result of the cyclic motion, the AoA can increase for about  $0.21^\circ$  to  $1.08^\circ$ .

#### Hysteresis share of aerodynamic curves

In every oscillating cycle, the lift curve is divided into two parts when values go up and down. The dependency of the lift coefficient on AoA when the AoA is increased from  $-15^\circ$  to  $15^\circ$  can be described by the left part of the curve shown in Fig. 3 (arrow pointing up). At the beginning is the AoA decreased from  $15^\circ$  to  $-15^\circ$  and the change of lift coefficient is shown in the right part of the curve (with a digit down). At the smallest frequency ( $\omega = 7.2^\circ/\text{s}$ ), both parts of the lift curve have very similar shape. However, the first part (arrow pointing up) appears to be shifted to the left for a certain distance in comparison to the second part. With the  $\omega$  increasing, the difference between both parts of the hysteresis loop becomes more apparent.

#### The dependency of the shape of the hysteresis on angular frequency

With the increased angular frequency  $\omega$ , the “thickness” (distance between lower and upper part) of lift loop increases too, yet the height (distance between maximum and minimum value) of lift curve

decreases (Fig. 4). Absolute value of lift coefficient decreases approximately to a half from  $C_L = -0.91 \div 0.78$  for  $\omega = 7.2$  °/s to  $C_L = -0.44 \div 0.51$  for  $\omega = 144$  °/s (red solid curve, Fig. 4). In this limiting case, the lift characteristic occurs an elliptic shape (red solid curve, Fig. 3).

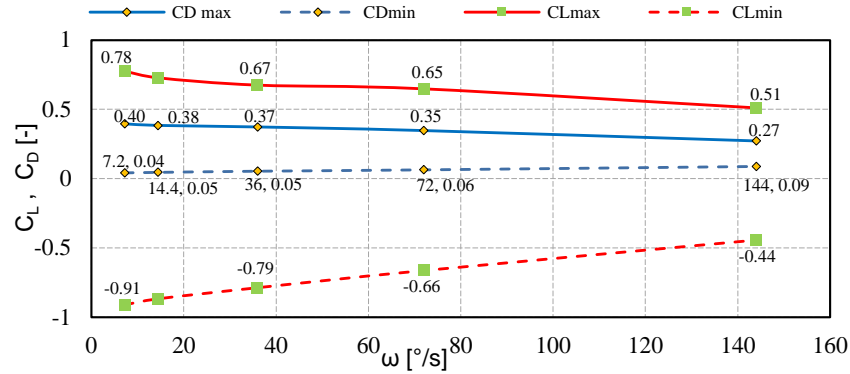


Fig. 4: The dependent of hysteresis shape on angular frequency.

The minimum value of drag coefficient increases proportionally with angular frequency. In limiting case, when  $\omega = 144$  °/s, the minimum drag coefficient is 2.5 times higher than for  $\omega = 7.2$  °/s and the maximum drag coefficient decreases for about 30 % (blue solid curve, Fig. 4). It is possible to confirm the hypothesis that aerodynamic coefficient of the oscillating wing section is related to the oscillation.

## 5. Conclusion

In the aerodynamic calculation of propellers or wind turbines in yaw, the oscillation of blade sections is usually ignored and only static data are used. Nonetheless, the blade element model and vortex theory show all blades of yawed propeller and wind turbines oscillate (Munduate, 2002) and the static data is not enough to calculate precisely the efficiency of such rotors. Therefore, a new method is proposed, in which the aerodynamic data must include the unsteady effect of oscillating movement. The value of the aerodynamic coefficient of current airfoil must be a function not only of the AoA but also of the angular frequency  $\omega$  (represented by reduced frequency  $k$ ). The experimental results can be used to perform interpolation to obtain aerodynamic coefficients, which include the effect of oscillating state  $C_L, C_D = f(\alpha, \omega)$ .

## Acknowledgement

The paper has been prepared thanks to the support of project SV16-FVT-K205-PET “Improvement of the experimental methods in aircraft technologies”, University of Defence Brno, Czech Republic.

## References

- McCroskey, W.J. (1981) The phenomenon of dynamic stall. NASA-A-8464, 1981.
- Sharma, M. (2010) Experimental Investigations of Dynamic Stall for an Oscillating Airfoil. PhD. Thesis. Indian Institute Of Technology, Kanpur, 2010.
- Guntur, S., Sorensen, N.N., Schreck, S. and Bergami, L. (2016) Modeling dynamic stall on wind turbine blades under rotationally augmented flow fields. Wind Energy, 19(3), 383-397, 2016.
- Åhlund, K. (2004) Investigation of the NREL NASA/Ames Wind Turbine Aerodynamics Database. Aeronautics, FFA, Swedish Defense Research Agency, 2004.
- Munduate, X. (2002) The prediction of unsteady three-dimensional aerodynamics on wind turbine blades. PhD. Thesis. University of Glasgow, 2002.

## STEADY FLOWS OF SECOND-GRADE FLUIDS SUBJECT TO STICK-SLIP BOUNDARY CONDITIONS

E. S. Baranovskii<sup>\*</sup>, M. A. Artemov<sup>\*\*</sup>

**Abstract:** This paper is devoted to analyzing steady flows of second-grade fluids in a plane channel with impermeable walls under the assumption that the flows are driven by constant pressure gradient. We use various boundary conditions, namely, no-slip, stick-slip, free-slip, and mixed boundary conditions, assuming that the solid walls may include two parts differing by their physical properties. For each of the considered boundary value problems, we present the exact solutions, which characterize the velocity field and the pressure in the channel. Moreover, for model parameters we establish explicit relationships that guarantee the slip (no-slip) regime on the solid walls.

**Keywords:** Non-Newtonian fluids, Second-grade Fluids, Plane channel flows, Stick-slip boundary conditions, Exact solutions.

### 1. Introduction

Many of the materials used in practice belong to the class of fluids of complexity  $N$  (Rivlin, 1955 and Dunn, 1995). For such fluids, the Cauchy stress tensor  $\mathbf{T}$  is given by

$$\mathbf{T} = -p\mathbf{I} + \mathbf{F}(\mathbf{A}_1, \dots, \mathbf{A}_N),$$

where  $p$  is the pressure,  $\mathbf{F}$  is a frame indifferent response function, and  $\mathbf{A}_1, \mathbf{A}_2, \dots, \mathbf{A}_N$  are the first  $N$  Rivlin–Ericksen tensors:

$$\begin{aligned}\mathbf{A}_1 &= \nabla \mathbf{v} + (\nabla \mathbf{v})^T, \\ \mathbf{A}_j &= D_t \mathbf{A}_{j-1} + \mathbf{A}_{j-1} \nabla \mathbf{v} + (\nabla \mathbf{v})^T \mathbf{A}_{j-1}\end{aligned}$$

for  $j = 2, 3, \dots, N$ . Here,  $\mathbf{v}$  is the velocity and  $D_t$  is the material time derivative.

If  $\mathbf{F}$  is a polynomial of degree  $N$ , then the appropriate fluid is called a *fluid of grade  $N$* .

The classical incompressible Newtonian fluid  $\mathbf{T} = -p\mathbf{I} + \nu\mathbf{A}_1$  is a fluid of grade 1. Well-studied nonlinear-viscous fluids, for which the constitutive equation is given by fluid  $\mathbf{T} = -p\mathbf{I} + \nu(\mathbf{A}_1)\mathbf{A}_1$ , are belong to the class of fluids of complexity 1.

In this work, we deal with the second-grade fluids

$$\mathbf{T} = -p\mathbf{I} + \nu\mathbf{A}_1 + \alpha_1\mathbf{A}_2 + \alpha_2\mathbf{A}_1^2, \quad (1)$$

where  $\nu$  is the viscosity coefficient,  $\alpha_1$  and  $\alpha_2$  are the normal stress moduli. It was shown in the paper Dunn (1974) that  $\nu \geq 0$ ,  $\alpha_1 \geq 0$ , and  $\alpha_1 + \alpha_2 = 0$ . Using the notation  $\alpha = \alpha_1 = -\alpha_2$ , we rewrite (1) as follows

$$\mathbf{T} = -p\mathbf{I} + \nu\mathbf{A}_1 + \alpha\mathbf{A}_2 - \alpha\mathbf{A}_1^2. \quad (2)$$

We are interested in finding exact solutions for steady flows of the fluid (2) in a plane infinite channel. The main feature of this paper is that the different types of boundary conditions on solid walls are used. In addition to the classical no-slip condition  $\mathbf{v} = \mathbf{0}$ , we consider stick-slip, free-slip, and mixed boundary conditions, assuming that the channel walls may differ in their physical properties. Such models are

<sup>\*</sup> Assoc. Prof. Evgenii S. Baranovskii, PhD.: Department of Applied Mathematics, Informatics and Mechanics, Voronezh State University, Universitetskaya Ploshchad 1, Voronezh 394018, Russia, esbaranovskii@gmail.com

<sup>\*\*</sup> Prof. Mikhail A. Artemov, DSc.: Department of Applied Mathematics, Informatics and Mechanics, Voronezh State University, Universitetskaya Ploshchad 1, Voronezh 394018, Russia, artemov\_m\_a@mail.ru

interesting both in theoretical research and in dealing with applied problems. The importance of wall slip effect and its impact on different characteristics of fluid flows, especially in the case of non-Newtonian fluids, is noted in many studies (see, e.g., the recent papers Rajagopal (2003), Kazatchkov (2010), Hatzikiriakos (2012) and the references cited therein). Significant contribution to the study of the causes and mechanisms of slipping of fluids and disperse systems on solid surfaces was made by Tolstoy (1953).

In this paper for each of the considered boundary value problems we present exact solutions, which determine the velocity field and the pressure in the flow region. Moreover, for model parameters we establish explicit relationships that guarantee the slip (no-slip) regime on the solid walls of the channel.

It should be mentioned that Hron et al. (2008) investigate steady flows of fluids of complexity 2 in a plane channel and a cylindrical pipe and flows between two rotating concentric cylinders subject to the Navier slip boundary condition, which is a special case (or more precisely, a limit case) of the stick-slip condition. Existence, uniqueness and qualitative properties of the solutions to motion equations of second-grade fluids in arbitrary bounded domains with Navier's slip boundary condition are studied in the papers Le Roux (1999), Busuioc (2003), Tani (2005), and Baranovskii (2015).

## 2. Statement of the problems

It is well known that the steady motion of a homogeneous incompressible fluid is governed by the following system of equations:

$$\rho(\mathbf{v} \cdot \nabla)\mathbf{v} = \operatorname{div} \mathbf{S} - \nabla p + \rho \mathbf{g}, \quad \operatorname{div} \mathbf{v} = 0, \quad (3)$$

where  $\rho$  is the density of the fluid,  $\mathbf{v}$  is the velocity,  $\mathbf{S}$  is the deviator of the stress tensor  $\mathbf{T}$ ,  $p$  is the pressure, and  $\mathbf{g}$  is the body force per unit mass. The operators  $\operatorname{div}$  and  $\nabla$  are the divergence and the gradient, respectively, with respect to the space variables  $x, y, z$ .

Let us consider fluid flows between (infinite) parallel plates  $z = -h$  and  $z = h$ . We assume that the flows are driven by constant pressure gradient

$$\frac{\partial p}{\partial x} = -\xi, \quad \xi > 0, \quad (4)$$

and  $\mathbf{g}^T = (0, 0, -g)$ . Thus, we deal with the plane Poiseuille flow. For such flow, we obviously have  $v_1 = u(z)$ ,  $v_2 = 0$ ,  $v_3 = 0$ , where  $u = u(z)$  is a function. This yields that  $(\mathbf{v} \cdot \nabla)\mathbf{v}$  and  $\operatorname{div} \mathbf{v} = 0$ . Hence system (3) is reduced to

$$\operatorname{div} \mathbf{S} = \nabla p - \rho \mathbf{g}. \quad (5)$$

Assume that the fluid obeys the constitutive relation (2). Taking into account  $\mathbf{T} = -p\mathbf{I} + \mathbf{S}$ , we can rewrite (5) in the form

$$\operatorname{div}(\nu \mathbf{A}_1 + \alpha \mathbf{A}_2 - \alpha \mathbf{A}_1^2) = \nabla p - \rho \mathbf{g}. \quad (6)$$

We shall use this equation for handling second-grade fluid flows in the channel  $-h \leq z \leq h$ . Note that the unknowns of (6) are  $u$  and  $p$ .

Of course, (6) must be supplemented with appropriate boundary conditions in order to take into account physically important solutions. Experimental data and theoretical works point to various possibilities for the behaviour of fluid flows on solid walls, see for example the paper Rajagopal (2003).

In this paper, we examine the three boundary value problems describing flows of second-grade fluids in the plane channel with impermeable walls.

**Problem (A)** Find functions  $u$  and  $p$  that satisfy (4), (6) subject to the no-slip conditions  $\mathbf{v} = \mathbf{0}$  on  $z = \pm h$ .

**Problem (B)** Find functions  $u$  and  $p$  that satisfy (4), (6) subject to the impermeability condition  $\mathbf{v} \cdot \mathbf{n} = 0$  and the stick-slip boundary condition on  $z = \pm h$ :

$$\begin{aligned} \|(\mathbf{Tn})_{\tan}\|_{\mathbf{R}^3} \leq \sigma &\Rightarrow \mathbf{v}_{\tan} = \mathbf{0}, \\ \|(\mathbf{Tn})_{\tan}\|_{\mathbf{R}^3} > \sigma &\Rightarrow (\mathbf{Tn})_{\tan} = -(\sigma + k \| \mathbf{v}_{\tan} \|_{\mathbf{R}^3}) \frac{\mathbf{v}_{\tan}}{\| \mathbf{v}_{\tan} \|_{\mathbf{R}^3}}. \end{aligned}$$

In this formulas,  $\mathbf{n}$  is the exterior unit normal vector on the channel walls,  $\mathbf{v}_{\tan}$  denotes the tangential

component of  $\mathbf{v}$ ,  $k > 0$  is the slip coefficient, and  $\sigma \geq 0$  is the slip threshold.

**Problem (C)** Find functions  $u$  and  $p$  that satisfy (4), (6) subject to the impermeability condition  $\mathbf{v} \cdot \mathbf{n} = 0$  on  $z = \pm h$  and the mixed boundary conditions:

$$\|(\mathbf{Tn})_{\tan}\|_{\mathbf{R}^3} \leq \sigma \Rightarrow \mathbf{v}_{\tan} = \mathbf{0}, \text{ for } z = h,$$

$$\|(\mathbf{Tn})_{\tan}\|_{\mathbf{R}^3} > \sigma \Rightarrow (\mathbf{Tn})_{\tan} = -(\sigma + k_1 \|\mathbf{v}_{\tan}\|_{\mathbf{R}^3}) \frac{\mathbf{v}_{\tan}}{\|\mathbf{v}_{\tan}\|_{\mathbf{R}^3}}, \text{ for } z = h,$$

$$(\mathbf{Tn})_{\tan} = -k_2 \mathbf{v}_{\tan} \text{ on } z = -h,$$

where  $k_1 > 0$  and  $k_2 \geq 0$ .

*Remark.* The last equality is the free-slip boundary condition, also known as Navier's slip law.

### 3. Results

Our main results are given in the following tables.

Tab. 1: Overview of solution to problem (A).

Velocity	$u(z) = -\frac{\xi}{2\nu}(z^2 - h^2)$
Pressure	$p(x, z) = -\xi x + \alpha(u'(z))^2 + \rho g(h - z)$

Tab. 2: Overview of solution to problem (B).

	The case $\xi h \leq \sigma$	The case $\xi h > \sigma$
Velocity	$u(z) = -\frac{\xi}{2\nu}(z^2 - h^2)$	$u(z) = -\frac{\xi}{2\nu}(z^2 - h^2) + \frac{\xi h - \sigma}{k}$
Pressure	$p(x, z) = -\xi x + \alpha(u'(z))^2 + \rho g(h - z)$	$p(x, z) = -\xi x + \alpha(u'(z))^2 + \rho g(h - z)$
Regime on the channel walls	<i>the no-slip regime</i>	<i>the slip regime</i>

Tab. 3: Overview of solution to problem (C).

	The case $\xi h \leq \sigma \left(1 - \frac{\nu}{2(\nu + k_2 h)}\right)$	The case $\xi h > \sigma \left(1 - \frac{\nu}{2(\nu + k_2 h)}\right)$
Velocity	$u(z) = -\frac{\xi}{2\nu}(z^2 - h^2) - \frac{\xi h}{\nu + 2k_2 h}(z - h)$	$u(z) = -\frac{\xi}{2\nu}(z^2 - h^2) - \frac{\xi h(k_1 - k_2) + \sigma k_2}{2hk_1 k_2 + \nu(k_1 + k_2)}z + \frac{\xi h^2(k_1 + k_2) + 2\xi h\nu - \sigma h k_2 - \nu\sigma}{2hk_1 k_2 + \nu(k_1 + k_2)}$
Pressure	$p(x, z) = -\xi x + \alpha(u'(z))^2 + \rho g(h - z)$	$p(x, z) = -\xi x + \alpha(u'(z))^2 + \rho g(h - z)$
Regime on the wall $z = -h$	<i>the slip regime</i>	<i>the slip regime</i>
Regime on the wall $z = h$	<i>the no-slip regime</i>	<i>the slip regime</i>

#### 4. Conclusions

In this note we present exact solutions of some boundary value problems describing the steady flows of second-order fluids in a plane channel under the no-slip boundary condition as well as stick-slip and mixed boundary conditions.

These solutions show that the pressure in the channel significantly depends on the normal stress coefficient  $\alpha$ , especially in those subdomains, where the change of flow velocity is large (in the transverse direction of the channel). At the same time, the velocity field is independent of  $\alpha$ , and therefore coincides with the velocity field that occurs in the case of a Newtonian fluid ( $\alpha = 0$ ).

In a description of stick-slip flows, the key point is value of  $\xi h$ , where  $\xi$  is module of the gradient pressure,  $h$  is the half-channel height. If  $\xi h$  exceeds some threshold value, then the slip regime holds at solid surfaces, otherwise the fluid adheres to the walls of the channel.

If it is assumed that on one part of the boundary the free-slip condition (Navier's condition) is provided, while on the other one the stick-slip condition holds, then for the slip regime the corresponding threshold value is reduced to a certain extent, but not more than twice.

#### Acknowledgement

This work was supported by the Russian Foundation for Basic Research, project no. 16-31-00182.

#### References

- Baranovskii, E.S. (2015) Existence results for regularized equations of second-grade fluids with wall slip, *Electronic Journal of Qualitative Theory of Differential Equations*, 91, pp. 1-12.
- Busuioc, A.V., Ratiu, T.S. (2003) The second grade fluid and averaged Euler equations with Navier-slip boundary conditions. *Nonlinearity*, 16, pp. 1119-1149.
- Dunn, J.E. and Fosdick, R.L. (1974) Thermodynamics, stability, and boundedness of fluids of complexity 2 and fluids of second grade, *Archive for Rational Mechanics and Analysis*, 56, pp. 191-252.
- Dunn, J.E. and Rajagopal, K.R. (1995) Fluids of differential type: Critical review and thermodynamic analysis. *International Journal of Engineering Science*, 33, 5, pp. 689-729.
- Hatzikiriakos, S.G. (2012) Wall slip of molten polymers. *Progress in Polymer Science*, 37, 4, pp. 624-643.
- Hron, J., Le Roux, C., Malek, J. and Rajagopal, K.R. (2008) Flows of incompressible fluids subject to Navier's slip on the boundary, *Computers and Mathematics with Applications*, 56, p. 2128-2143.
- Kazatchkov, I.B. and Hatzikiriakos, S.G. (2010) Relaxation effects of slip in shear flow of linear molten polymers, *Rheologica Acta*, 49, 3, p. 267-274.
- Le Roux, C. (1999) Existence and uniqueness of the flow of second-grade fluids with slip boundary conditions, *Archive for Rational Mechanics and Analysis*, 148, pp. 309-356.
- Rajagopal, K.R. (2003) On some unresolved issues in non-linear fluid dynamics, *Russian Mathematical Surveys*, 58, pp. 319-330.
- Rivlin, R.S. and Ericksen, J.L. (1955) Stress-deformation relations for isotropic materials. *Journal of Rational Mechanics and Analysis*, 4, 2, pp. 323-425.
- Tani, A., Le Roux, C. (2005) Steady-state solutions to the equations of motion of second-grade fluids with general Navier type slip boundary conditions in Hölder spaces. *Journal of Mathematical Sciences*, 130, 4, pp. 4899-4909.
- Tolstoy, D.M. (1953) Slipping of fluids and disperse systems on solid surfaces, *Doctoral dissertation in Mathematics and Physics*, Moscow, (in Russian).



## INTEGRATION OF VISION SYSTEM AND ROBOTIC ARM UNDER ROS

L. Baranowski<sup>\*</sup>, W. Kaczmarek<sup>\*\*</sup>, J. Panasiuk<sup>\*\*\*</sup>, P. Prusaczyk<sup>\*\*\*\*</sup>, K. Besseghieur<sup>\*\*\*\*\*</sup>

**Abstract:** *The paper presents the conception of integrating a three-dimensional image sensor device with the robotic arm manipulator via Robot Operating System. Using a 3D camera, the position of user's arm is retrieved. Selected angles are replicated into desired robotic joints. The authors focused their attention on ability of implementing this using online available libraries.*

**Keywords:** Robot teleoperation, Kinova, Robotic arm, Kinect, Human tracking.

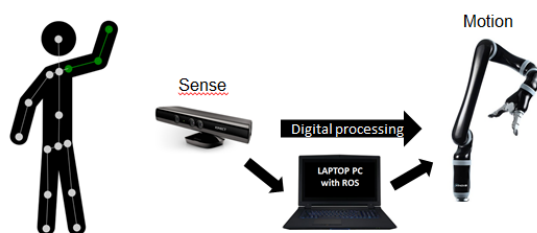
### 1. Introduction

Although artificial intelligence starts being used for decision-making in many areas in our lives, human intelligence is still necessary to make decision and manipulate the robot in unstructured changing environments.

Usually teleoperation require complicated knowledge of various modes of control. Task can be performed using joysticks and dials. According to (Du et al., 2016), recently lot of research have been conducted in the area of the robot teleoperation using human hand gesture. New developed methods were able to tracks motion of user's hand-arm using inertial sensors placed in gloves and exoskeleton systems. Processed user motion after translation becomes robot's motion.

However, this equipment may cause difficulty in natural human-limb motion. Scientists found the solution for that in contactless technology based on vision and markers tracking. Markerless, contactless approach came in with the next step of development.

According to (Marić et al., 2016), a complete replication of human arm movement with robotic arms is impossible because of the complexity of shoulder and finger joints. Even the most advanced robotic arms cannot match human ability, and as a consequence impossibility of direct mapping of human arm joint positions to a robotic arm. The alternative could be a dynamic transform of the measured angles to acceptable ranges as explained in section 3.2 (Implementation of control).



*Fig. 1: Conceptual drawing.*

<sup>\*</sup> Prof. Leszek Baranowski, PhD.: Faculty of Mechatronics & Aerospace, Military University of Technology, Kaliskiego 2, 00-908, Warsaw, PL, leszek.baranowski@wat.edu.pl

<sup>\*\*</sup> Wojciech Kaczmarek, PhD.: Faculty of Mechatronics & Aerospace, Military University of Technology, Kaliskiego 2, 00-908, Warsaw, PL, wojciech.kaczmarek@wat.edu.pl

<sup>\*\*\*</sup> Jarosław Panasiuk, PhD.: Faculty of Mechatronics & Aerospace, Military University of Technology, Kaliskiego 2, 00-908, Warsaw, PL, jaroslaw.panasiuk@wat.edu.pl

<sup>\*\*\*\*</sup> Piotr Prusaczyk, MS.: Faculty of Mechatronics & Aerospace, Military University of Technology, Kaliskiego 2, 00-908, Warsaw, PL, piotr.prusaczyk@wat.edu.pl

<sup>\*\*\*\*\*</sup> Khadir Besseghieur, MS.: Faculty of Mechatronics & Aerospace, Military University of Technology, Kaliskiego 2, 00-908, Warsaw, PL, besseghieurkh@hotmail.fr

In this paper, the aim of the authors is to present an integration of Image sensor with the robotic arm in ROS environment using existing libraries. The result of this project is a simple robot teleoperation based on joint angle copying. Robotic arm will respond to a human hand motion, replicating simplified selected human joints described in Fig. 1. The rest of this paper is organized as follows: the next section is dedicated for hardware implementation of the system. Section 3 contains a short introduction to ROS and software implementation.

## 2. Hardware Integration

For this project both devices, Kinect and Kinova arm, communicate by USB interface. Producer provides required drivers for both devices. Personal computer is responsible for handling those devices.

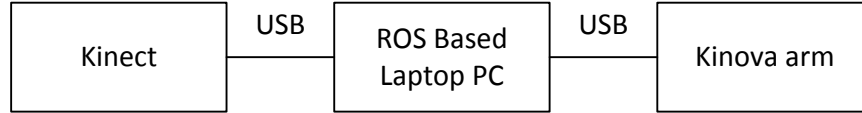


Fig. 2: Block diagram.

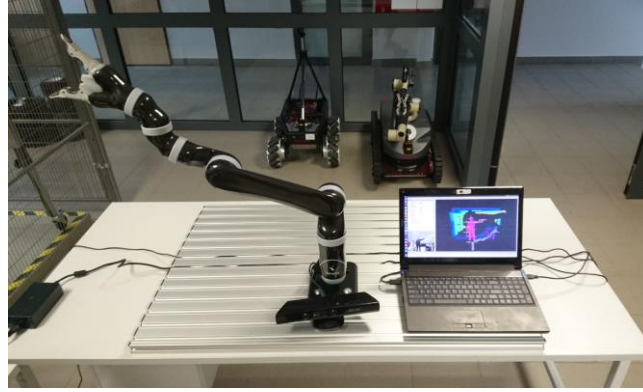


Fig. 3: Workbench.

### 2.1. Kinova arm

The Kinova arm is a light-weight robot composed of six inter-linked segments, the last of which is a two-fingered hand. The arm has a weight of 5 kg and can reach approximately 70 cm in all directions. It can be mounted on any mobile platform or to a fixed station. The arm can be controlled by user through the controller or though the computer. The objects can be grasped or released with the hand of this device. The arm lifts objects up to 750 g in the long-range and 1250 g in the mid-range. (Kinova, User Manual)

Below, parameters for kinematics of the Kinova arm are presented.

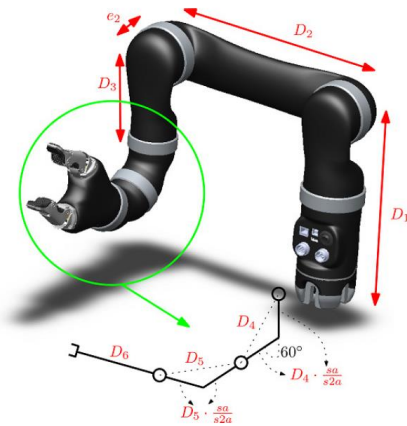


Fig. 4: DH Parameters of the Kinova arm.

Tab. 1: Classic DH Parameters of the Kinova arm.

DH Parameters				
i	alpha(i-1)	a(i-1)	di	teta1
1	pi/2	0	D1	q1
2	pi	D2	0	q2
3	pi/2	0	-e2	q3
4	2*aa	0	-d4b	q4
5	2*aa	0	-d5b	q5
6	pi	0	-d6b	q6

Current position of the arm is obtained by absolute encoders implemented in each servo which also has torque, current, acceleration and temperature sensors for better monitoring.

The Kinova arm comes with libraries called Kinova API ([www.github.com/Kinovarobotics/kinova-ros](http://www.github.com/Kinovarobotics/kinova-ros)) which allows the arm to be controlled via user's own application in two different control modes. The first one is joint mode. It provides direct access to each joint of the robot arm. Desired angular position or angular speed can be set in each joint. The another one, Cartesian mode, gives ability to control position and orientation of the robot's hand.

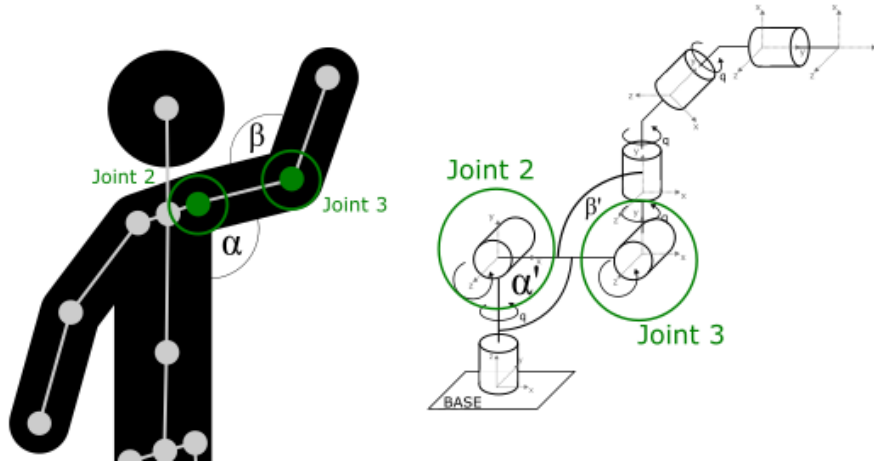


Fig. 5: Simplified conception of joints control.

## 2.2. Kinect

In this project, Kinect is used for sensing the environment. This is a complex input device which contains several sensors like RGB camera, depth sensor and microphone array (Keen et al., 2011). RGB camera can provide image in VGA resolution (640 x 480 pixels) with 30 Hz frame rate. Depth sensor uses IR camera and IR structured-light laser projector to get the infrared image which is transformed into point cloud by the built-in algorithm. We can derive the exact position in space of everything in the room it occupies.

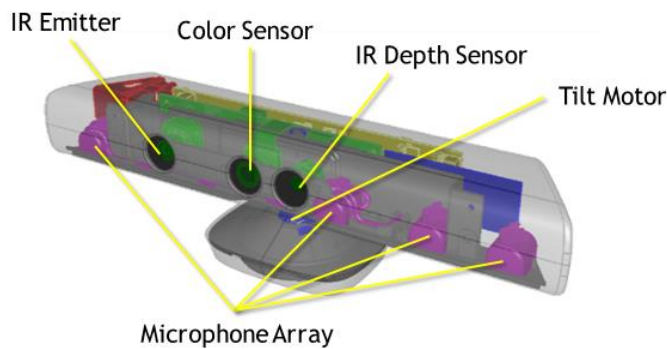


Fig. 6: Parts of the Kinect sensor. Source: MSDN Microsoft.

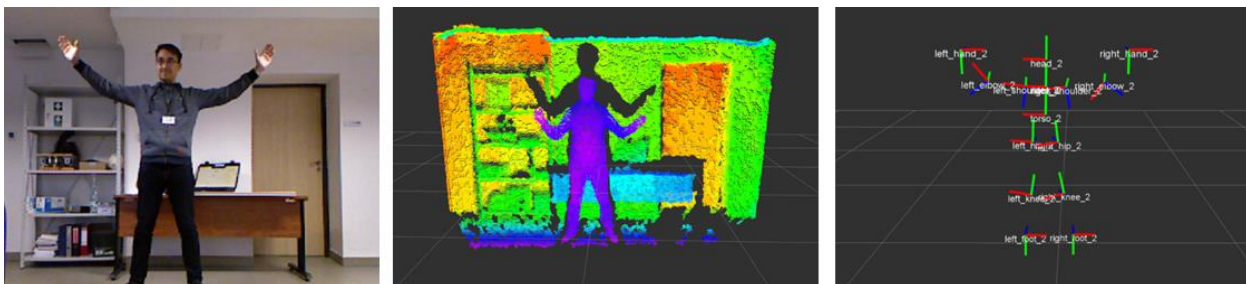
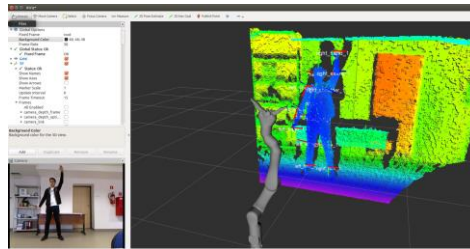


Fig. 7: Kinect data input (from left): a) RGB Image; b) Pointcloud image; c) Joints positions.

### 3. ROS

ROS is a Linux-based, open source, meta-operating system which allows user to low-level device control, passing messages between processes, and package management. The distributed nature of ROS gives rise to specific concepts that allow many independent computational processes to interact with each other, and together create the overall behavior of a robotic system. The communication structure of ROS is designed around the concept of nodes, messages, topics, services, and parameters. In ROS system, the main organizational component is the package. It consists of executable programs called nodes, libraries, data-sets, and configurational files. Inside the system, nodes process data and communicate with each other. The communicated data are called messages. The nodes exchange data over the topics, which is a simple string. More information is available in (Quigley et al., 2015)



*Fig. 8: RVIZ application.*

#### 3.1. OpenNI Kinect Package

For human detection and tracking OpenNI Kinect package ([www.wiki.ros.org/openni\\_kinect](http://www.wiki.ros.org/openni_kinect)) has been used. The package allows to interact with digital devices. This is ready solution, with minimal time spent on configuration, user can focus on further integration with other devices, such as manipulators. After detection of a human, for human tracking, quick initialization is needed. Initialization procedure looks like 'surrender sign' shown in Fig. 7. After successful initialization, tracking script provides axes coordinate (transforms) of each part of users body (Fig. 7c).

#### 3.2. Implementation of control

The program computes the angles between the right shoulder, right elbow, and right hand transforms then the manipulator's joint 2 and 3 will be controlled to move so that the calculated angles are reached (Fig. 5). Because of limitations on the robotic joints and for safety reasons, the arm's joints are required to move only in specified ranges which are prescribed in the program.

### 4. Conclusions

This paper presents a method of creating a link between an image sensor and a robotic arm using robot operating system and public available libraries. A simple robot teleoperation system has been designed. User can control the robotic joints using his right hand. Future works will be conducted to implement under ROS complete Cartesian control to check the possibilities of markerless contactless methods of robot teleoperation.

### References

- Du, G., and Zhang, P. (2016). A novel human-manipulators interface using hybrid sensors with Kalman filter and particle filter. In *Robotics and Computer-Integrated Manufacturing*, 2016, pp. 93-101.
- Du, G., and Zhang, P. (2014) Markerless human-robot interface for dual robot manipulators using Kinect sensor. In *Robotics and Computer-Integrated Manufacturing* 2014, pp. 150-159.
- Kaczmarek, W., and Tomaszuk, M. (2016) Use of the vision system to control industrial robot with gestures. Volume 89 sheet 7 of the series *Mechanik*, pp. 712-713.
- Kean, S., Hall, J., and Perry, P. (2011) *Meet the Kinect – An Introduction to Programming Natural User Interfaces*. Apress.
- Marić, F., Jurin, I., Marković, I., Kalafatić, Z., and Petrović, I. (2016) Robot arm teleoperation via RGBD sensor palm tracking. In *MiPro Computer in technical sciences* 2016, pp. 1300-1305.
- Quigley M., Gerky B., and Smart W.D. (2015) *Programming Robots with ROS, a Practical Introduction to the Robot Operating System*. First. O'Reilly Media, Inc.

## USE OF A RASPBERRY PI TO BUILT A PROTOTYPE WIRELESS CONTROL SYSTEM OF A MOBILE ROBOT

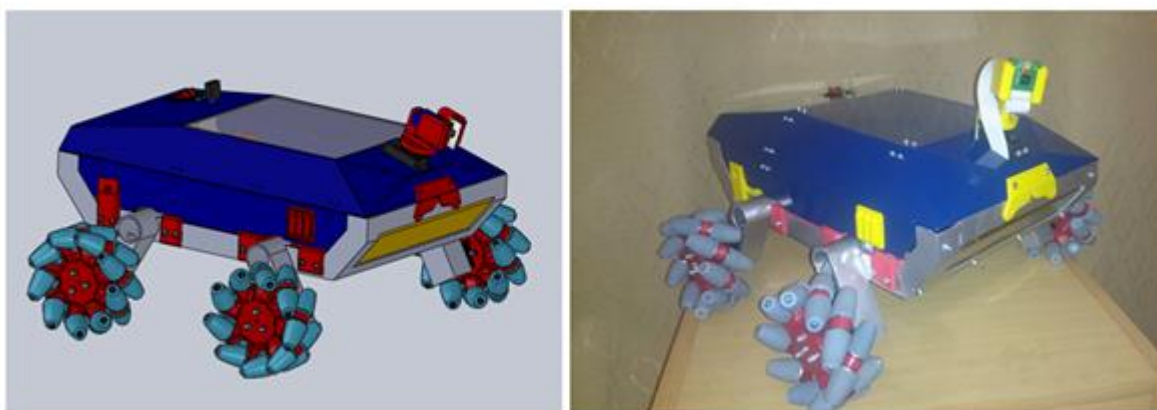
L. Baranowski<sup>\*</sup>, J. Panasiuk<sup>\*\*</sup>, M. Siwek<sup>\*\*\*</sup>

**Abstract:** *The main aim of this article is to present the design and build wireless control system for the mobile robot with omnidirectional wheel. The system uses popular Raspberry Pi microcomputer with dedicated hardware and operator PC. The drive's control is supported by Arduino Mega 2560. The control application was developed using free software tool. The article presents the step by step guide to system configuration and startup.*

**Keywords:** Raspberry Pi, Mobile robot control system, Wireless mobile robot control system, Omnidirectional wheels.

### 1. Introduction

The design of mobile robots can be considered in terms of three of the most notable aspects: the way of moving, the transmission medium, the method of controlling a robot. The wheel drive that is most commonly used in robotics, allows very fast movement. Its simple structure makes it reliable and easy to control. Low drive's energy consumption follow a small rolling resistance. Because of these properties, wheeled mobile robots are cheap to build, operation and servicing. In the case of wheeled robots, an interesting solution is to use a special omnidirectional wheels in order to achieve an off-road platform, while reducing the resistance occurring in the system (relative to the track drive) and simplifying the structure (in the case of a drive with a pair of steered wheels). This solution is not without drawbacks. Robots using omnidirectional wheels are less efficient in the field and have worse traction on flat surfaces. The model of a robot equipped with omnidirectional wheels was designed based on the diagrams described in the literature and in the Internet (Panasiuk et al., 2015). Omnidirectional system allows the robot to move linearly forward, backward, right, left, at fixed angles and rotate in place. The Fig. 1 shows the CAD model and the real model.



*Fig. 1: CAD model and real model of mobile robot with omnidirectional wheels.*

---

<sup>\*</sup> Prof. Leszek Baranowski, PhD.: Faculty of Mechatronics & Aerospace, Military University of Technology, Kaliskiego 2, 00-908, Warsaw, PL, [leszek.baranowski@wat.edu.pl](mailto:leszek.baranowski@wat.edu.pl)

<sup>\*\*</sup> Jarosław Panasiuk, PhD.: Faculty of Mechatronics & Aerospace, Military University of Technology, Kaliskiego 2, 00-908, Warsaw, PL, [jaroslaw.panasiuk@wat.edu.pl](mailto:jaroslaw.panasiuk@wat.edu.pl)

<sup>\*\*\*</sup> Michał Siwek, MS.: Faculty of Mechatronics & Aerospace, Military University of Technology, Kaliskiego 2, 00-908, Warsaw, PL, [michal.siwek@wat.edu.pl](mailto:michal.siwek@wat.edu.pl)



The analysis of the mobile robots design indicates a huge versatility of control systems. Way data transfer control robot and feedback to the operator is one of the most important parts of the devices. Until recently it was believed that the use of wired connections is the safest, relatively inexpensive solution that provides the smallest transmission errors.. However, such solution limits significantly the possibilities of mobile robot. Attention should be paid to the technique of wireless communication.

## 2. Methods

When designing a control system for the mobile robot with omnidirectional wheels one should put the emphasis on the launching simplicity and low cost of construction. It should also be fairly easy to control such system from a PC. The developed system consist of wireless control system and video transmission based on Raspberry Pi, HD camera (image source), Arduino Mega 2560 as a microcontroller implements driver control system and Windows PC with wireless network adapter (as operator PC)(Robotics forum Forbot). System is shown in Fig. 2.

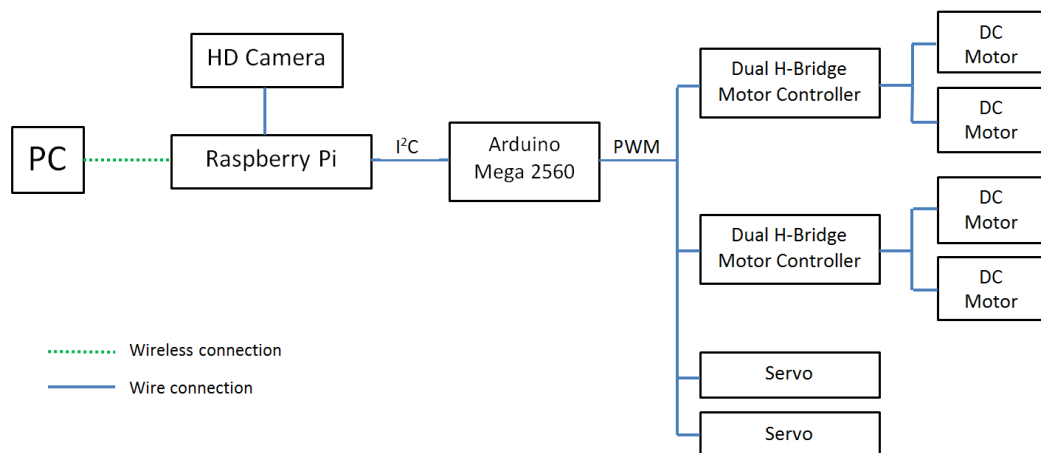


Fig. 2: Block diagram of the robot control system.

### 2.1. The hardware implementation

Raspberry Pi microcomputer in the B version is equipped with a 700 MHz processor and 512 MB RAM. SD cards up to 64GB are used as data carriers. This solution has reduced the weight of the Raspberry Pi board and the risk of failure associated with traditional hard disk. Raspberry Pi is equipped with basic connections and interfaces: two USB, Ethernet socket, SPI, I2C and UART. Linux-Raspbian is installed on the SD card. Electronics companies offer a variety of circuits used in vision systems.

The choice of the camera was dictated by: minimalism, the possibility of quick implementation in the system and the price. The module with the HD camera compatible with Raspberry Pi was chosen based on the aforementioned features. The camera is equipped with a 5 Mpx CCD matrix, which allows recording in 1080 p. The connection of the camera with Raspberry Pi is performed by connecting tape. The system installed in the memory of microcomputer supports selected camera module.

Due to the knowledge of the Wi-Fi communication between robot and PC built using this transmission standard. Among the many commercially available devices for wireless transmission of data, the chosen LB-LINK wireless network adapter. The adapter has a 150 Mbps transmission speed, frequency band 2.4 GHz and 17 dBm antenna power. The LB-LINK adapter is an extension dedicated to the Raspberry Pi and does not require installing additional drivers (Fried, 2013).

To obtain a full functionality, omnidirectional chassis requires four independent control signals used to control the drives. In addition, the projected vision system should have rotational motion control of the camera. This task requires two independent PWM signal outputs. Raspberry Pi B is equipped with only one PWM signal output. Additionally, CPU resources will largely be used to support wireless communication and video streaming. Therefore, Arduino Mega 2560 equipped with ATmega microcontroller was selected as the drive control signals forming unit. Data transmission between Arduino and Raspberry Pi is done by I2C bus.

## 2.2. The software implementation

Implementation of the control system required the implementation of several tasks: connection of the operator PC to on-board robot computer, development of application that provides video streaming, development of application enabling drives control via Arduino.

The first step to configure of the Raspberry Pi as access point and create a robot network, to which the operator PC will be able to connect. To do this, after logging in connect LB-LINK adapter to the USB and Internet through Ethernet connector. Next step is to check LB-LINK adapter visibility in Raspbian using Linux command `ifconfig -a` and install the drivers for working Raspberry Pi as a DHCP server by typing in the terminal `sudo apt-get install hostapd isc-dhcp-server`. After driver installation open dhcp configuration file using command `sudo nano /etc/dhcp/dhcpd.conf`. Changes in the configuration file related settings would allow to obtain IP and DNS address, network mask and range of allocated IP addresses.

Next configuration steps to investigate the static IP address for the Raspberry Pi. It necessary to open another configuration file using the command `sudo nano /etc/network/interfaces` and add information about the static IP address for connecting wlan0.

The final step of DHCP server configuration is to open the host configuration file using the command `sudo nano /etc/hostapd/hostapd.conf` and enter the name of the LB-LINK adapter driver, the network name, password and other network parameters. After properly configuring the network, rebooting Raspbian, the robot Wi-Fi was visible in the networks available on PC. The wireless connection robot-operator PC was implemented by the SSH protocol, which is a communication protocol used in TCP/IP for terminal connection to the computer. SSH works in client-server architecture on default port 22. To connect operator PC to the on-board robot computer uses the popular and free software PuTTY, which is a client in network connections. After downloading and installing the software on operator PC the first step was to connect with the local robot Wi-Fi. Then, in the PuTTY address field one should enter robot IP address (Fig. 5, no. 1), select the port number (Fig. 5, no. 2), and communication protocol type (Fig. 5, no. 3). The program also allows to enter the name of configuration (Fig. 5, no. 4). After initializing the connection by pressing Open, the terminal appeared from which one can log in to Raspbian and start video streaming and robot control application (Engst, 2003, Sosna, 2008 and Fried, 2013).

Wireless communication control application is written in Python using the available in Raspbian development environment Geany (Sosna, 2008). The application allows to control the movements of a robot, robot speed and rotation of the head with a camera using the PC keyboard. Pressing a key starts the algorithm checking the binary code key pressed. When the control key is pressed- the algorithm processes the information in accordance with the assigned function key, forms a control data frame and sends to the ATmega microcontroller by I<sup>2</sup>C bus. The microcontroller encodes frame and forms PWM drives control signal according to the received information.

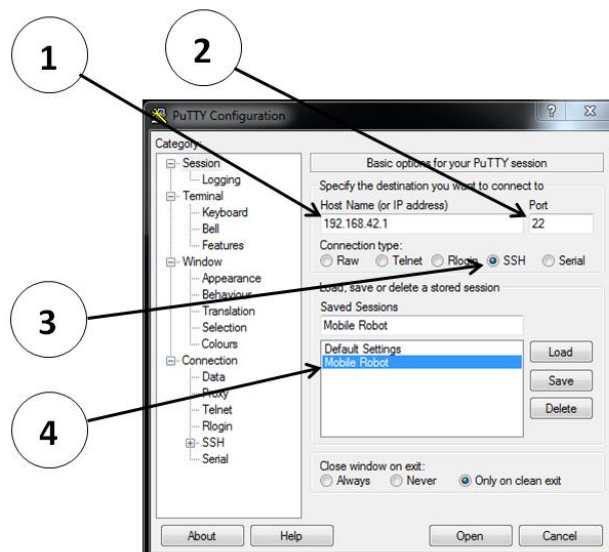


Fig. 3: PuTTY configuration window.

Video streaming was realized by running on the computer raspberry Pi server sends video data (Robotics forum Forbot). This task uses the *vlc* library, which was downloaded and installed on the Raspberry Pi as an additional package. To start the video streaming one should open another terminal window, log in to Raspbian and enter the *raspivid* command with appropriate parameters of streaming. Once so configured video streaming operator can preview the data on VLC Media Player installed on PC, running option program *Open Network Stream...* and typing the IP address of the on-board robot computer. The view of the operator PC screen with open application shown in the Fig. 4.

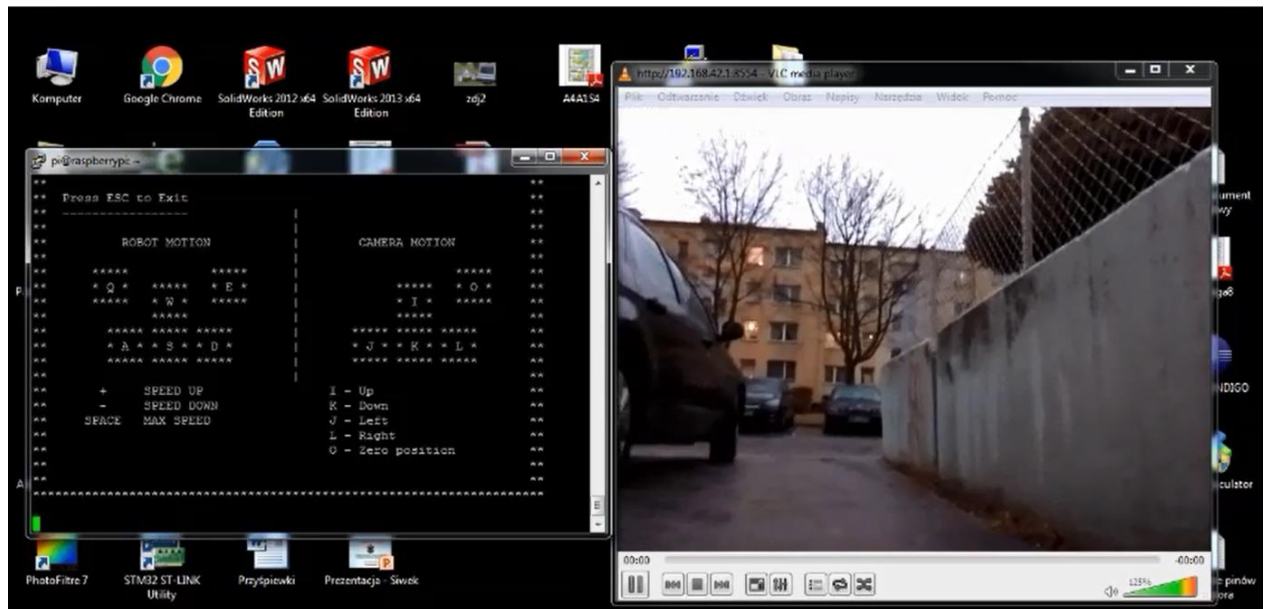


Fig. 4: Operator PC screen.

### 3. Conclusions

The result of the work is universal control system for mobile platforms. The user can set it up and adapt to any design of mobile robot. This solution allows for quick and cheap start prototype of the mobile robot to check its functional and driving parameters. Tests of the control system have shown that the video streaming has a 1.5 s delay, and control data transmission has 1s delay. Transmission range in open space is 55 m, in a confined space 40 m. Designated transmission parameters are imposed by the capabilities of Raspberry Pi. At the stage of construction of the control system shown in this paper, the security issues was not considered. The main problem is loss of the control and in this case robot stops. Reliability issues of the robot control system will be resolved at next stage of project development.

### References

- Engst, A. and Fleishman, G. (2003) *The Wireless Networking Starter Kit*, Second Edition. Peachpit, San Francisco.
- Fried, L. (2013) Setting up a Raspberry Pi as a WiFi Access point. [Online] Available: <https://cdn-learn.adafruit.com/downloads/pdf/setting-up-a-raspberry-pi-as-a-wifi-access-point.pdf> [Accessed 3 October 2015].
- Panasiuk, J., Kaczmarek, W. and Siwek, M. (2015) Design and build of mobile robot with omnidirectional wheels, *MECHANIK*, 7, pp. 621-630 (in Polish).
- Sosna, Ł. (2008) *Linux. Commands and orders*. Helion, Gliwice (in Polish).
- Robotics forum Forbot <http://www.forbot.pl/forum/index.php> (Accessed 10 January 2017).



## A CONCEPT FOR TESTING AND MONITORING OF BUILDING STRUCTURES – THEORETICAL CASE STUDY

J. Bayer<sup>\*</sup>

**Abstract:** *A mere comparison of measured and analytical deformations, natural frequencies and mode shapes provides us with just a small part of the information contained in the data, especially when component-level damage prevention is needed. The presented analysis studies in detail a few criteria for evaluation of measured data, with the example of simulated plane trusses in respect to the ultimate limit state. It demonstrates the high potential of a systematic approach, while combining several criteria, particularly when using simultaneous strain and deformation measurements, as it documents the proposed Relative Mode Difference (RMD) criterion. On the other hand, the study points out the major limitation of practical applications that is caused by unknown inherent uncertainties of various kinds, providing us with the incentive for further experimental research.*

**Keywords:** Testing, Monitoring, Building structures, Ultimate limit state, Mode shapes, Strains.

### 1. Introduction

The motivations for Structural Health Monitoring (SHM) and its state-of-the-art are discussed in detail in (Brownjohn, 2006). It is obvious that SHM (Li, 2016) is a quite complex topic embracing many disciplines, such as system identification (Ewins, 1984), reliability (Gao, 2012), uncertainty estimation [ISO 2394], measurement technologies (e.g. Ye, 2014), data processing, etc.

It is well known that many structural faults are accompanied by a change in the transfer properties of structures, as reflected by measurable changes of deformations, natural frequencies and mode shapes. In the case of the ageing process, these faults quite often have a gradual character. It has been a matter of research in recent years that monitoring can help to assess more precisely the actual condition of building structures. Another sub-problem not yet being resolved satisfactorily is component-level structural information, which is the focus of this case study.

Generally, many load cases must be analysed to assess whether a building structure accommodates the ultimate limit states (further ULS). A final number of critical sections can be determined from this process. By knowing the initial state of a completed structure, the reliabilities or the utilization ratio can be estimated for each of these critical sections. An efficient meaningful SHM presumes that the fault tolerance is clearly observable with the aid of the measured or monitored parameters.

It is not the goal of this study to deal with the observability of various kinds of damage, because it is the matter of individual conditions, depending on applied methods, equipment and environment. However, it is the aim of the study to review a few concepts for the evaluation of measured data and to point out what benefit may be obtained from their combination.

The secondary aim of this study was the testing of the new RMD-criterion for localising damage from mode shapes. The experimental verification is planned during the future years.

### 2. Analytical models

Plane truss models (cantilever, simple supported beam, and continuous beam) were chosen to save computer time for numerous calculations and because they are well suited for tracing the bending and

---

<sup>\*</sup> Ing. Jan Bayer, CSc.: ITAM AS CR, v.v.i., Prosecká 809/76, 190 00 Praha 9, Czech Republic, e-mail: bayer@itam.cas.cz

shear effects separately. The numerical results do not have a practical meaning, because mere assumed, fictive uncertainties were always applied to introduce the evaluation method in its complexity.

The Cantilever and Simply Supported Truss models were loaded with the Point Load and dimensioned so that all elements were utilised to 75 % of the ULS. The same applies for the Continuous Truss with the difference that the elements were grouped into five groups of elements out of which only the mostly stressed one was utilised to 75 % of the ULS.

### **3. Evaluation criteria**

There are several types of static and dynamic loading tests that can be applied repeatedly and various types of quantities that can be continuously monitored and of course also numerous analytical procedures to process or evaluate the measured results. A set of experimentally obtained and conceivably analytically evaluated quantities is understood in this article as an evaluation criterion and can also be understood as a point of view on the condition of the structure. The goal is to choose a suitable combination of different evaluation criteria to be able to check or observe all the necessary parts of the structure.

In the following paragraphs, by “damage” is understood the reduction of the cross section of an element so that the stress in this element reaches the ULS.

#### **Influence line:**

The influence line, usually in the form of measured displacements or strains at one point of the structure, can easily be measured e.g. by a vehicle crossing a bridge. The change of the influence line is a suitable parameter that can be obtained from repeated loading tests which reflect the changes of stiffness along the structure. A change of the influence line always occurs at the location of the damage. In the case of a change of shear stiffness, there is a step in the influence line, while changes in the bending stiffness cause a change of its inclination. The situation may be less transparent in the case of multiple damage and statically indeterminate structures, especially around the supports.

If we know the precision of measurements, including all kinds of uncertainties, we can also estimate the extent of “observable or identifiable damage”. This can be tuned to the current needs by using more measuring points and / or measured quantities. Considering the assumed (fictive) uncertainty of measurements of 2 %, the identifiable extent of damage was less than on half of the elements at any of the three models.

#### **Natural frequencies:**

Natural frequencies – it is the frequently used parameter in structural health monitoring (SHM). They can be used for indication of damage and, under special conditions, also for the assessment of its location or its extent. As in the previous case, the analysis was carried out considering the damage of each of its structural elements under the assumption that only 5 natural bending modes can be identified experimentally. If it is further assumed that the average drop of 5 natural frequencies of 0.5 % can be clearly distinguished and the drop of a single frequency can be measured with an uncertainty of 1 %, the identifiable extent of damage could also be estimated.

It should be noted that the minimum changes that can indicate the damage of one of the elements were considered. There is, of course, also the possibility that the cross section of all the structural elements will be reduced, for example, by just 10 % and therefore the ULS will not be exceeded anywhere. The structure will be safe, but the drop of natural frequencies will be considerably greater than the assumed tolerance of 1 %. This implies that monitoring could provide a warning at a safe level, but the condition would need to be checked visually on the site in any case.

Not all the elements could be checked only with aid of natural frequencies under the assumed conditions on the considered analytical models.

#### **Flexibility change derived from the mode shapes:**

In this study, it was assumed that the mode shapes could be measured at the nodes of the upper flange only in the vertical direction. According to (Padney, 1994), the flexibility matrix  $F$  can be computed from the following equation:

$$\mathbf{F} = (\mathbf{\Omega})^{-1} \cdot \mathbf{\Phi} \cdot \mathbf{\Phi}^T, \quad (1)$$

where  $\mathbf{\Omega}$  is the diagonal matrix of eigenvalues and  $\mathbf{\Phi}$  is the matrix of the natural mode shapes scaled to the mass matrix. The negative changes of the main diagonal of the flexibility matrix show maxima at the location of damage analogically to the influence line and the integral of this function reflects the extent of the damage.

Theoretical estimation of the uncertainty of the flexibility changes is even more dubious than in the previous cases, because it will always depend on local conditions. Nevertheless, for our purposes, the value of 0.005 m/N for the global extent of the damage (the integral value!) was assumed to be the resolvable limit.

The flexibility changes resemble very much the character of the changes of the influence. The Flexibility changes could provide the damage indication at another set of elements than in the case of the previous criteria, but again some elements were rather unsensitive to this criterion.

#### Relative change of the relation between deformations and strains derived from the mode shapes:

If there are elements whose damage does not cause a significant change of the previously discussed criteria, there is still the possibility of local monitoring. The amplitudes of the measured mode shapes can be scaled in respect to strain amplitudes at critical points on the structure. The change caused by local damage can then easily be expressed as the relation of modes on intact and damaged structure, e.g. with the aid of the Modal Scale Factor (MSF) (Ewins, 2000; Allemang, 2003). Measurements of strains are a more demanding task than measuring accelerations or velocities in general (Bayer, 2016). However, new technologies provide us with promising new solutions like Fibre Bragg Grating optical sensors (Ye, 2014).

Thus we suppose that a reference measurement  $Vr_{i,j}$  of  $m$  modes using  $n$  degrees of freedom ( $i = 1...n$ ;  $j = 1...m$ ) is available from the intact structure and another corresponding set of modes  $Vd_{i,j}$  from the damaged structure. The measurement is also available of strains at a single critical point  $\varepsilon_r$  and  $\varepsilon_d$  coming from the intact and damaged structures. The relative change of modes can then be defined as

$$RMD_j = \frac{\sum_{i=1}^n \frac{Vr_{i,j}}{\varepsilon_r} * \frac{Vd_{i,j}}{\varepsilon_d}}{\sum_{i=1}^n \frac{Vr_{i,j}}{\varepsilon_r} * \frac{Vr_{i,j}}{\varepsilon_r}} - 1 \quad (2)$$

If the damage of an element was not noticed by the previous criteria, but the strain between its nodes could be measured, the critical condition of this element could easily be identified by the RMD criterion.

Using assumed uncertainty of the RMD criterion of 10 % the damage on the continuous truss would be observable on all the elements when applied together with the previous criteria (see Fig. 1).

#### 4. Conclusions

Focusing on the ULS, the case study presents an approach to component-level damage prevention. It demonstrates on a few simple truss structures that it is theoretically possible for the monitoring of static and dynamic deformations to be used as a collapse prevention in the case of gradually progressing damage. An efficient combination of available measured data and appropriate evaluation criteria can be obtained from a systematic analysis of damage scenarios. The reviewed criteria are merely an example for “data mining”. It is, of course, possible to propose or invent others (e.g. Wu, 2004 or Whelan, 2015), with respect to monitoring the goals in individual cases.

It is also obvious that a successful application on real structures depends on inherent uncertainties (concerning the analytical model, local and global environmental effects, measurement equipment, etc.) whose reliable estimation is still a problem that requires further experimental research.

A relative mode difference criterion for damage localisation was proposed, using measured vibration mode shapes and corresponding strains at a few critical points. This implies that monitoring of dynamic strains at low or ambient levels could be a promising field of application.

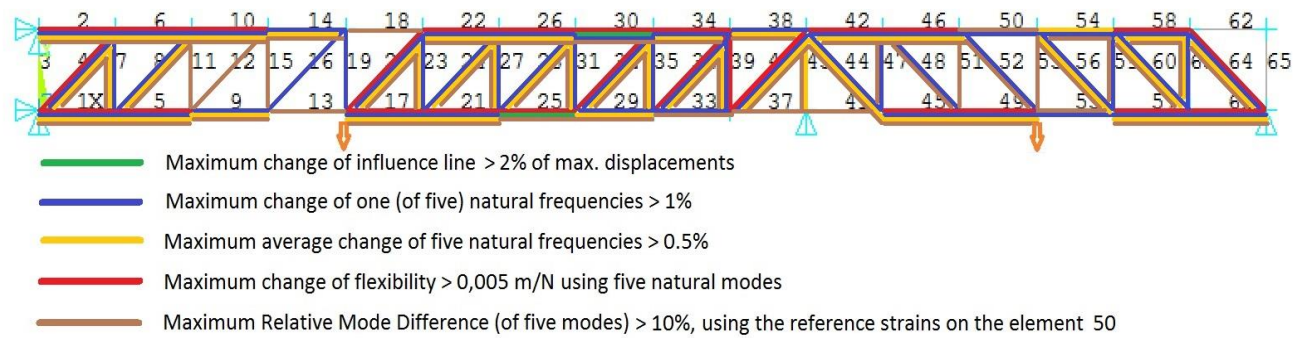


Fig. 1: Observable damage under assumed, fictive uncertainties on the continuous truss.

## Acknowledgement

The supports of grants GA CR 17-26353J (identification code AVOZ 68378297) and the institutional support RVO 68378297 are greatly appreciated.

## References

- Allemang, R.J. (2003) The Modal Assurance Criterion (MAC) Twenty Years of Use and Abuse, Sound and Vibration.
- Bayer, J., Urushadze, S. and Zima, P. (2016) Health monitoring of building structures: Preliminary considerations on a case study, Proc. of conf. Engineering Mechanics 2016, pp. 49-52.
- Brownjohn, J.M.W. (2007) Structural health monitoring of civil infrastructure, Phil. Trans. R. Soc. A 365, 589-622, doi:10.1098/rsta.2006.1925.
- Ewins, D.J. (1984) Modal Testing, Theory, Practice, and Application, ISBN-10: 0863802184, Mechanical Engineering Research Studies: Engineering Dynamics Series, 2nd Edition, 1984.
- Ewins, D.J. (2000) Model validation: Correlation for updating. Sadhana. Vol. 25, Part 3, June 2000, pp. 221-234.
- Gao, L. (2012) Reliability-based evaluation of bridge live load carrying capacity in the United States, 28th US-Japan Bridge Engineering Workshop, Portland, Oregon, US.
- Li, H.N., Ren, L., Jia, Z.G., Yi, T.H. and Li, D.S. (2016) State-of-the-art in structural health monitoring of large and complex civil infrastructures, Journal of Civil Structural Health Monitoring 6, pp. 3-16, DOI 10.1007/s13349-015-0108-9.
- Pandey, A.K. and Biswas, M. (1994) Damage detection in structures using changes in flexibility, Journal of Sound and Vibration 169, (1994), pp. 3-17.
- Whelan, M.J. and Gangone M.V. (2015) Effect of measurement uncertainties on strain-based damage diagnostics for highway bridges, Journal of Civil Structural Health Monitoring, 2015(5), pp. 321-335, DOI 10.1007/s13349-015-0110-2.
- Wu, D. and Law, S.S. (2004) Damage localization in plate structures from uniform load surface curvature, JSV 276, pp. 227-244.
- Ye, X. W., Su, Y. H. and Han, J.P. (2014) Structural Health Monitoring of Civil Infrastructure Using Optical Fiber Sensing Technology: A Comprehensive Review, Hindawi Publishing Corporation, Scientific World Journal, Volume 2014, Article ID 652329, <http://dx.doi.org/10.1155/2014/652329>.

## **PRODUCING A LAYER OF IRON FE-CR-C-NB UNDER CONDITIONS OF INTENSE HEAT RECEPTION**

**R. Bęczkowski<sup>\*</sup>, J. Cebulski<sup>\*\*</sup>, D. Pasek<sup>\*\*\*</sup>, M. Gucwa<sup>\*\*\*\*</sup>**

**Abstract:** *The paper analyzes the influence of the quality of the new flux cored wire intended for cladding process by one set cladding parameters such as welding speed, thermal conductivity coefficient of aluminum, power source setting, the length of projecting portion of the electrode, wire speed and speed of oscillation on the hardness distribution and structure in bead. The results of hardness distribution analysis allows to illustrate the nature of the impact of the examined input variables on parameters of generated surface. The most important parameters here are the hardness distribution and structure of bead. The cladding process was conducted by Flux Cored Arc Welding (FCAW). As additional material for cladding Fe-Cr-C-Nb was used. To describe the properties of the layers Vickers hardness, optical microscope (OM) and scanning electron microscope (SEM) were used.*

**Keywords:** Cladding, FCAW, Hardness, Structure, SEM.

### **1. Introduction**

Special materials are available for production of hard plates with high abrasive resistance. Cored wires belong to welding materials that are often used to deposit cladding with high resisting. The problem to solve in industrial practice is the correct setting of the flux-cored self-shielding arc welding parameters and their impact on the final desired surface parameters such as hardness, structure and lifespan (Bęczkowski, 2017 and Kejžar, 2003).

The use of core wire in the production of clad with different chemical composition and good quality has a great potential. The problem is to determine which of the surfacing parameters have a significant impact on the final characteristics of clad (Pernis et al., 2013 and Mendez et al., 2014).

Hardness distribution and structure are one of the most important parameters of abrasion plates. The producer allows possibility to choose plate in the configuration for example 10+5. The first number gives the information about the thickness of the parent material. Mostly S235 material grade is used. And the second number describes the thickness of hard layer. This number gives the information about the length of the lifespan. Hardness distribution and structure are responsible for durability and adhesive (Bęczkowski et al., 2015 and Bęczkowski et al., 2016 and Dwivedi, 2004).

The development of new materials as cored wire and technologies as flux cored arc welding in the process leads to improvement of tribological properties of deposited coatings designed for protection against wear. Special cored wires belong to cladding materials that are often used to deposit surface with high wear resistance. Special hardfacing alloys of high-chromium white irons with carbides in the deposited structure using cladding are well known for their wear resistance (Adamiak et al., 2010 and Dwivedi, 2004 and Kejžar, 2003).

---

<sup>\*</sup> Robert Bęczkowski, PhD.: Institute of Mechanical Technology, Częstochowa University of Technology, Armii Krajowej Street 21; 42-201, Częstochowa; PL, rbeczkowski@spaw.pcz.pl

<sup>\*\*</sup> Janusz Cebulski, PhD.: Faculty of materials engineering and metallurgy, Silesian University of Technology; Krasińskiego Street 8, 40-019; Katowice; PL, Janusz.Cebulski@polsl.pl

<sup>\*\*\*</sup> Dorota Pasek, M.Sc., Eng.: Faculty of materials engineering and metallurgy, Silesian University of Technology; Krasińskiego Street 8, 40-019; Katowice; PL, Dorota.Pasek@polsl.pl

<sup>\*\*\*\*</sup> Marek Gucwa, PhD.: Institute of Mechanical Technology, Częstochowa University of Technology, Armii Krajowej Street 21; 42-201, Częstochowa; PL, mgucwa@spaw.pcz.pl

High-chromium white irons with carbides in the structure are commonly used for the hardfacing plate in the different sector in industry. Hardfacing alloys consist of  $\text{Cr}_7\text{C}_3$ ,  $\text{Cr}_{23}\text{C}_6$ ,  $\text{Cr}_3\text{C}$ ,  $\text{NbC}$ ,  $\text{Nb}_2\text{C}$  primary and eutectic carbides and eutectic austenite or martensite. To make hardfacing layers many cladding technologies were used. Using the cored wire gives additional possibility to change the properties of clads. In the wire core different kind of carbides like chromium, niobium with hardness over 1000 HV can be found. Using the flux cored arc welding against wear is one of the most common technology to develop the hard layer (Bęczkowski et al., 2015 and Mendez et al., 2014 and Niagaj, 2011 and Orłowicz, 2009 and Winczek, 2016).

## 2. Methods

Workplace with a water-cooled table was used in the sample welding and additionally the pad receiving heat from the space surfacing made of aluminum was laid. As the parent material S235JR steel with a thickness of 10 mm and dimensions of 200 x 400 mm was used, wire (C = 5.4 %, Cr = 29 %, Si = 1.2 %, Nb = 3.0 %, Mn = 0.4 %, B < 1 %) was used for the cladding. For the test the input factors were defined by: cladding speed, (160 mm/min), coefficient of thermal conductivity of aluminum, (2.15 W/mK), power source setting, (11480 W), the length the projecting portion of the electrode, (30 mm), the frequency of oscillation (2.4 m/min), wire feed speed (5.8 m/min), diameter of cored wire (2.8 mm) and width of amplitude of bead (35 mm).

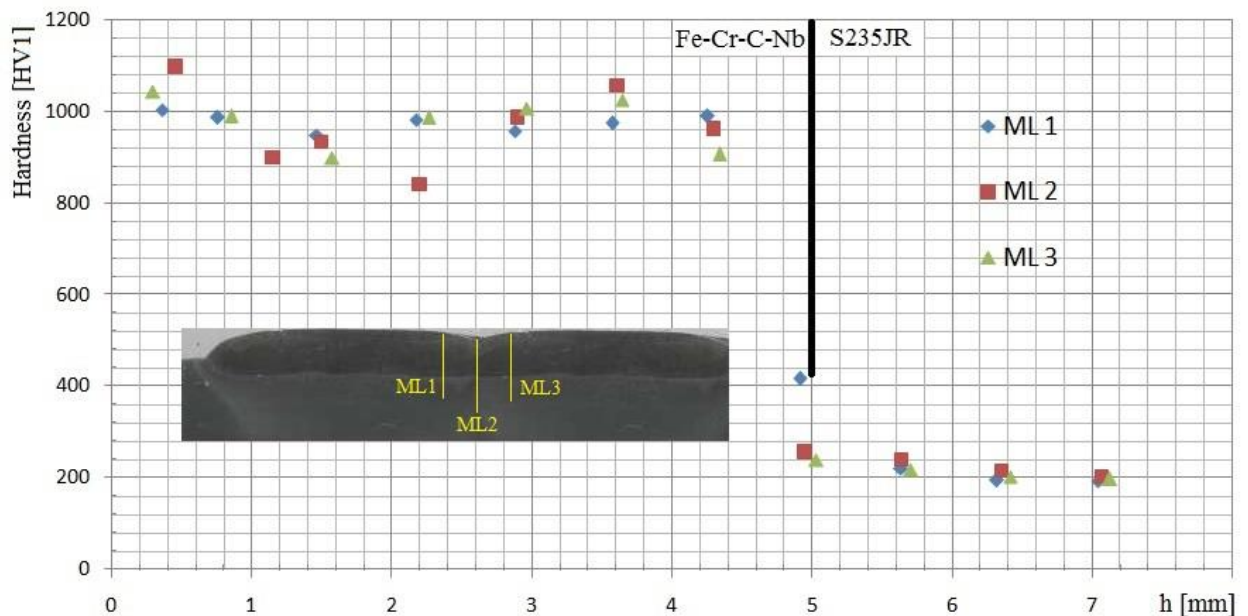
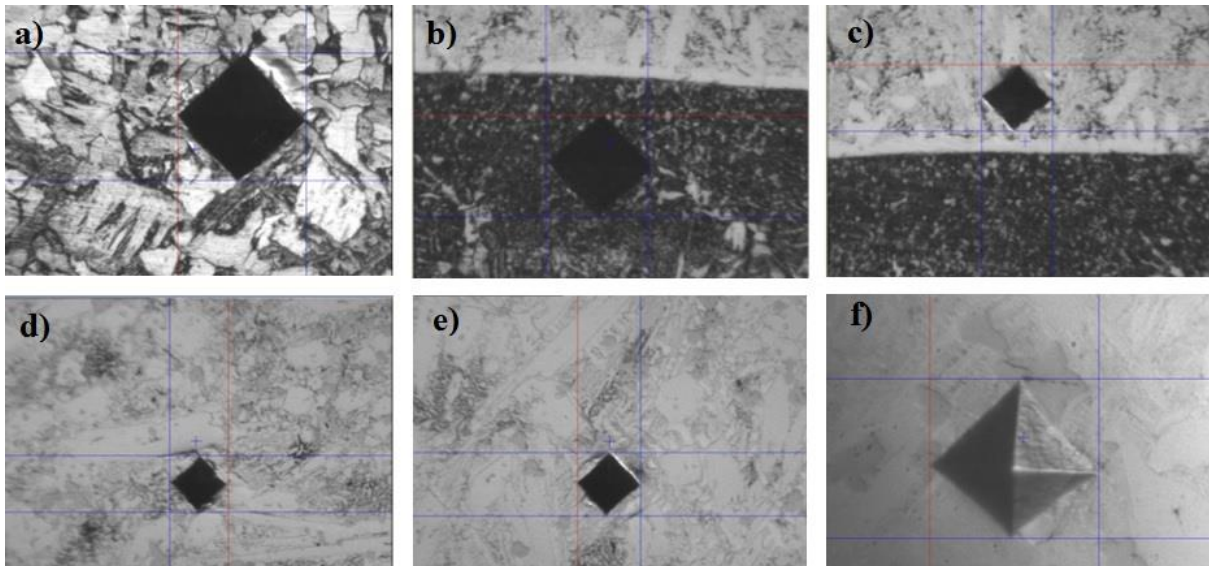


Fig. 1: Hardness distribution of the distance from the top surface of the bead.

Hardness measurement was conducted on cross-section material. Hardness was measured with Vickers method according to a norm PN-EN ISO 6507-1 with a load 9.81 N (HV1) the device type ZWICK. Fig. 1 shows the results of measure hardness distribution HV1 of the distance [mm] from the top surface of the bead. Hardness was done in three lines of measurement (ML), which were denoted by ML1, ML2 and ML3.

Fig. 2 shows cross-section of all the layers: parent material (a), line fusion: under (b) and over (c), bead (d-f).

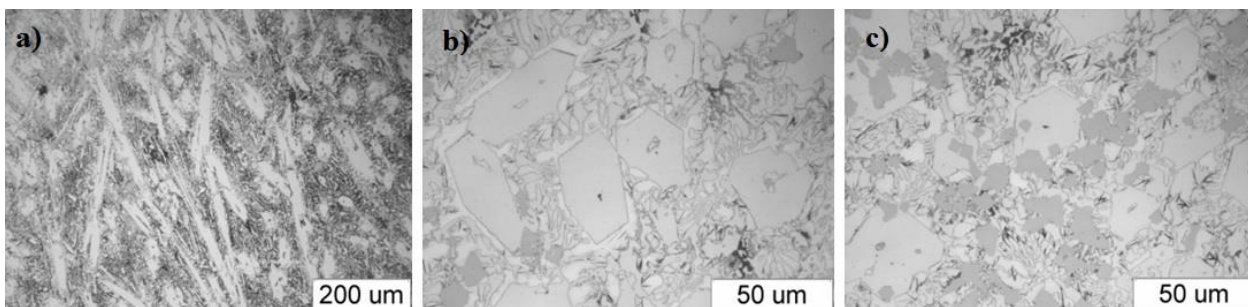




*Fig. 2: View of hardness distribution from the parent material to the top of the bead.*

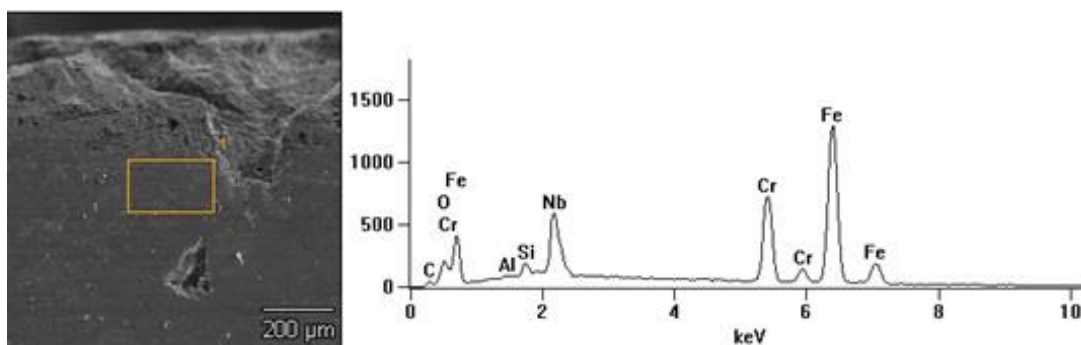
Metallographic tests were conducted on polished micro-sections etched in 3% alcohol solution of nitric acid (nital). Microstructure observations were conducted with the use of metallographic microscope Olympus GX51.

Fig. 3 shows the distribution of carbides in the clad. Fig. 3a shows general view of structure. The distribution of carbides with low (Fig. 3b) and high (Fig. 3c) participation of niob carbides is showed.



*Fig. 3: Structure of bead with distribution of the carbides.*

The chemical composition was determined by X-ray microanalysis EDS using a scanning electron microscope equipped with a Hitachi S4200 ray EDS detector. Fig. 4 shows the SEM surface analysis of hardfacing layers, with the presence of Fe, Cr, Nb and C. Given the chemical affinity it should be assumed that in the material are niobium and chromium carbides. Due to the methodology research, share of coal should be considered approximately.



*Fig. 4: SEM analysis of the microscope together with an indication of the chemical composition.*

Tab. 1: Number of Weight %.

<i>C</i>	<i>O</i>	<i>Al</i>	<i>Si</i>	<i>Cr</i>	<i>Fe</i>	<i>Nb</i>
1.5	4.3	0.3	1.0	19.6	61.7	11.7

Tab. 2: Number of Atom %.

<i>C</i>	<i>O</i>	<i>Al</i>	<i>Si</i>	<i>Cr</i>	<i>Fe</i>	<i>Nb</i>
6.1	13.1	0.5	1.8	18.4	54.1	6.1

### 3. Conclusions

Hardness distribution was checked in several lines and the results of this test show that on the top of specimen the hardness is the highest, in the middle section hardness goes down and by the parent material value of hardness goes up. Surprisingly, in the middle section of clad, hardness is lower than in the top and bottom section. Normally, the bottom section made by mixed clad with parent material has the lowest hardness. In this case using additional aluminum plate gives the quickest heat dissipation.

Observations under the optical microscope (Fig. 3) show the principal axes of the distribution of carbides in the direction of heat dissipation. The location of niobium carbides is not uniform. There are places with small areas of niobium carbides (Fig. 3b) and areas with a high proportion (Fig. 3c) of niobium carbides. Their presence depends on the area of the bead. The increase of the share of niobium carbides was observed over the line of fusion, which proved by hardness measurements.

Tests performed using a scanning electron microscope (SEM) with X-ray and chemical composition allow to conclude that the multiphase layer is deposited, and it is composed of chromium and niobium carbides. This information is confirmed in studies of surface distribution of elements included in the weld hardfacing layers and forming areas with different phase composition.

### References

- Adamiak, M., Górka, J. and Kik, T. (2010) Structure analysis of welded joints of wear resistant plate and constructional steel, Archives of Materials Science and Engineering, 56, 2, pp. 108-114.
- Bęczkowski, R. (2017) Effect of cladding parameters on the hardness of bimetal plates. Metalurgija, 56, 1-2, pp. 59-62.
- Bęczkowski, R., Gucwa, M., Wróbel, J. and Kulawik, A. (2015) The Impact of the Bead Width on the Properties of the AntiAbrasion Surfacing Weld. International Conference of Numerical Analysis and Applied Mathematics 2015 (ICNAAM 2015), AIP Conf. Proc. 1738, 480095-1–480095-4; doi: 10.1063/1.4952331.
- Bęczkowski, R. and Gucwa, M. (2016) Defects Appearing in the Surfacing Layers of Abrasion Resistant, Archives of foundry engineering, 16 ,4, pp. 23-28.
- Dwivedi, D.K. (2004) Microstructure and abrasive wear behaviour of iron base hardfacing, Materials Science and Technology, 20, pp. 1326-1330.
- Kejžar R. (2003) Study of the alloying of a surfacing weld in the surfacing of wear-resistant deposits with alloyed welding fluxes. Materiali in Tehnologije, 37, 3-4, pp. 167-172.
- Mendez, P.F., Barnes, N., Bell, K., Borle, S.D., Gajapathi, S.S., Guest, S.D., Izadi, H., Gol, A.K. and Wood, G. (2014) Welding processes for wear resistant overlays. Journal of Manufacturing Processes, 16, pp. 4-25.
- Niagaj, J., (2011) Effect of niobium on properties of hardfaced layers surface welded by Fe-Cr-C open arc flux-cored wire electrodes, Welding technology review, 10, pp. 67-72.
- Orłowicz, W., Shevelaya, V., Trytek, A. and V. Kirilov, V. (2009) Effect of the concentrated heat flow treatment on the structure and the antiwear properties of cast iron, Archives of foundry engineering, 9, 2, pp. 185-188.
- Pernis, I., Kasala, J. and Žabecká, D. (2013) Resistance of weldclads made by flux-cored arc welding technology against erosive wear. Metalurgija, 52, 3, pp. 352-354.
- Winczek, J. (2016) Modeling of heat affected zone in multipass GMAW surfacing S235 steel element. Procedia Engineering, 136, pp. 108-113.



## POSSIBILITY OF DAMPING PRESSURE PULSATIONS IN BALANCING CONTROL VALVES

L. Bednář<sup>\*</sup>, L. Tajč<sup>\*\*</sup>, M. Miczán<sup>\*\*\*</sup>, L. Mrózek<sup>\*\*\*\*</sup>, M. Hoznedl<sup>\*\*\*\*\*</sup>

**Abstract:** *The cone shape alterations are given for balanced control valves of steam turbines and their influence is assessed on the flow field in the valve outlet diffuser. Suitable solutions are searched for, which will guarantee the stability of the boundary layer on the diffuser wall in all operating modes of the turbine. It is verified whether using steam flow from the bypass valve can prevent separation of the main steam flow from the diffuser wall. Various variants of the steam outlet from the valve cone are considered.*

**Keywords:** Steam turbine, Valve, Vibration.

### 1. Introduction

The maximum lifting force of an unbalanced valve is proportional to the inlet pressure and the valve seat diameter squared. If the lifting force exceeds the possibilities of the servo drive, it is necessary to use a higher number of unbalanced valves or to regulate the turbine using balanced valves. With a more complicated construction of balanced valves their operating reliability is lower than that of traditional control valves. Here a part of the spindle is formed by a bypass valve, from which the big cone is suspended. It is lifted from the seat after the initial balancing caused by the steam flow through the bypass valve. In balanced valves it is necessary to guarantee positive snub force on the freely suspended cone for all turbine modes with a sufficient margin for abrupt step increase of pressure under the cone. The valves work in a wide range of lift and pressure ratios. A complex flow field occurs under the valve cone. A flow vortex or possible separation from the diffuser wall or cone wall appears. Pressure vibrations are generated in a broad range of frequencies. Vibration of the natural frequencies of the valve part or the pipe system with the corresponding spectrum frequency can cause mechanical damage. Especially in valves with higher flow area problems with high frequency pulsations and corresponding vibrations fully appeared. The aim of the paper is to show the character of flow field under the cone for selected operating modes and the connection between the shape of the cone and the diffuser and the steam flow from the bypass valve. Ways of damping or limiting fluctuational components causes by pressure pulsations are searched for.

### 2. Summary of findings of the balanced valve variants

In many cases attempts appear to use a shaped valve cone. It is supposed that in specific operating modes of the turbine and a fully open valve fewer pressure losses occur than in the valve with a perforated cone. For partial opening of the valve Laval's nozzle occurs between the cone profile and the seat and diffuser wall. A step pressure change in the shock wave occurs for higher value Mach number than for the flat bottom cone.

In Fig. 1 a computational study is presented for the flow in the valve with the shaped cone. Mach number is up to 2.46. The rotationally symmetrical computation variant is used (Matas, 2001). 3D calculation confirms the existence of unordered velocity field with unbalanced pressure distribution on the cone

---

<sup>\*</sup> Ing. Lukáš Bednář: Doosan Škoda Power s.r.o., Tylova 1/57, 301 28 Plzeň; CZ, lukas.bednar@doosan.com

<sup>\*\*</sup> Ing. Ladislav Tajč, CSc.: University of West Bohemia, Univerzitní ul. 8, 306 14 Plzeň; CZ, ladislav.tajc@doosan.com

<sup>\*\*\*</sup> Ing. Martin Miczán, Ph.D.: Doosan Škoda Power s.r.o., Tylova 1/57, 301 28 Plzeň; CZ, martin.miczan@doosan.com

<sup>\*\*\*\*</sup> Ing. Lukáš Mrózek: University of West Bohemia, Univerzitní ul. 8, 306 14 Plzeň; CZ, lukas.mrozek@doosan.com

<sup>\*\*\*\*\*</sup> Ing. Michal Hoznedl, Ph.D.: Doosan Škoda Power s.r.o., Tylova 1/57, 301 28; CZ, michal.hoznedl@doosan.com

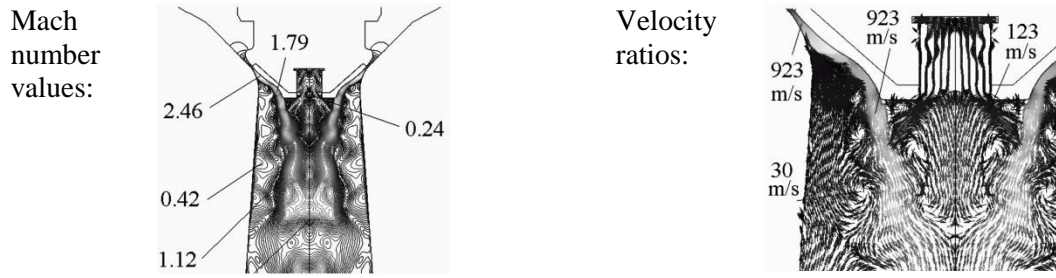


Fig. 1: Mach numbers and velocities distribution in the valve diffuser with a shaped cone.

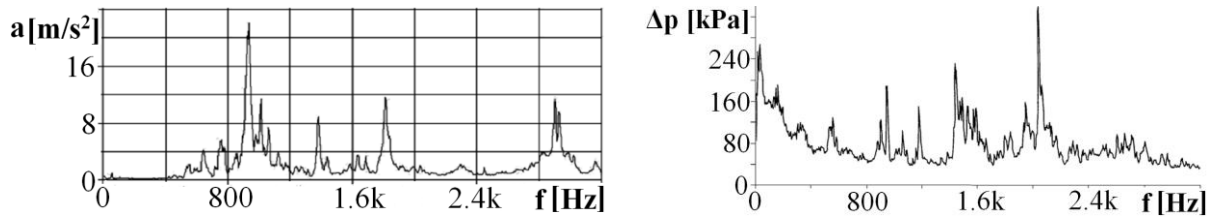


Fig. 2: Spindle acceleration and pressure pulsations behind the shaped cone in dependence on frequency.

surface. Pressure pulsations occur on the cone and a spectrum of pulsations of different frequencies appear in the flow. In Fig. 2 an example is given of acceleration in the valve spindle and the course of pressure pulsations on the diffuser outlet. Frequency spectra are similar, but not identical. Pressure pulsations reach up to 8 % of the inlet pressure value. The cause of low frequency vibrations is related with flow separation and vortex structures occurrence. High frequency vibrations appear for small lift of the valve cone and large pressure drops. Provided there are in the piping system supersonic speeds with excess kinetic energy, it results in its obstruction in the system of shock waves. Interaction of various waves with vortex areas in the diffuser is related with the so-called trans-sonic unsteadiness, which is the source of high frequency pressure pulsations of steam.

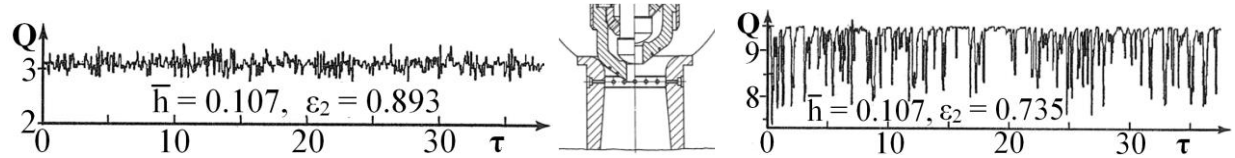


Fig. 3: Oscillograms of forces operating on the spindle with a shaped cone and a central opening.

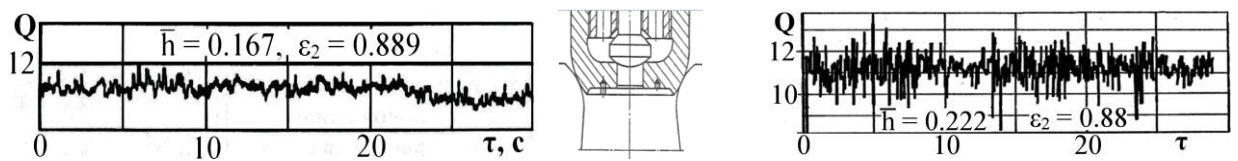


Fig. 4: Oscillogram of forces operating on the valve spindle with the flat bottom transition cone.

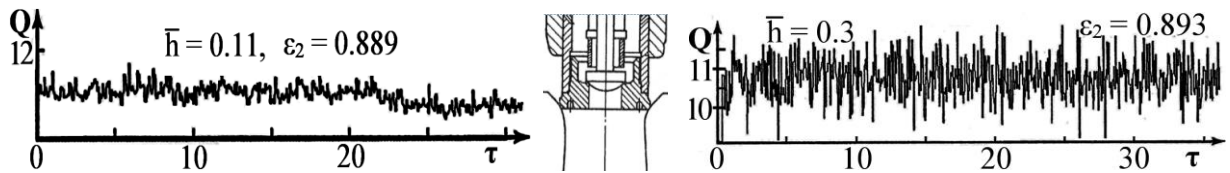


Fig. 5: Oscillograms of forces operating on the flat bottom cone and a central opening.

The influence of pressure pulsation on the cone can be mapped using time records of force operating on the valve spindle. It shows that the load force can vary in the range up to 10 ÷ 15 % of mean force on the cone. From the records of load force on the spindle given in Figs. 3, 4 and 5 it is evident that force fluctuations are not directly related to the cone shape. For the shaped cone, the cone with a flat bottom transition and for the flat bottom cone similar amplitudes of load force are calculated. Pressure pulsations are related with vortex and possible flow separation from the diffuser wall. The central inlet opening can contribute to the diffuser wall separation.

### 3. Possibilities of damping pressure pulsations

Damping pressure pulsations and thus vibrations of the balanced valve is enabled by using a muffler (damper) installed in the valve. Its placement and characteristic flow is evident from Fig. 6. Experimentally lowering pressure pulses and vibrations on the valve was confirmed (Šťastný at all, 2003). Using the damper velocity ratios under the cone changed. In the original valve – see Fig. 1, flow separation from the diffuser wall under the cone occurred. After damper installation stream flow separation from the diffuser wall does not occur. It is confirmed by distribution of Mach numbers in the diffuser neck.

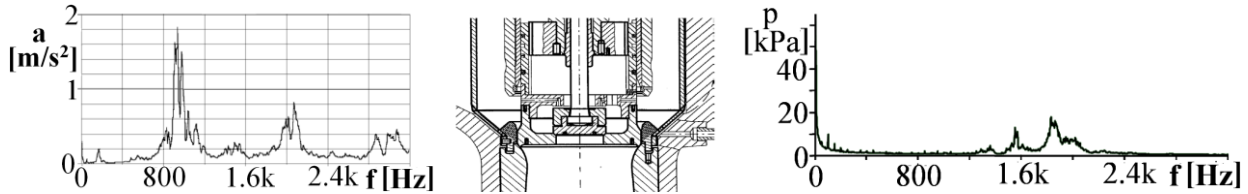


Fig. 6: Vibrations on the spindle and pressure pulsation under the cone with damper.

Stream flow separation from the diffuser wall can considerably contribute to the existence of intensive pressure pulsations. When the flow follows a curved surface effects known as Coanda effect are applied. Flow separation occurs at a certain pressure and curve of the wall ratio. The Coanda pressure ratio is shown in Fig. 7. Here also the valve construction is given with corresponding pressure and wall curves.

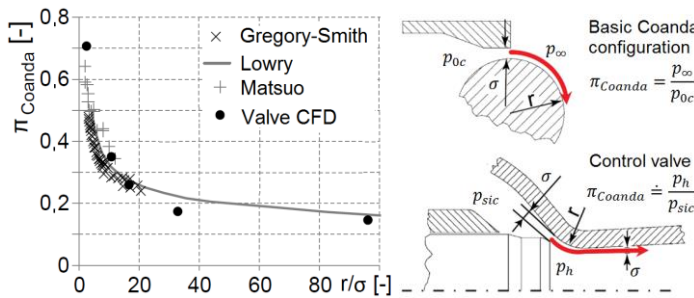


Fig. 7: Coanda pressure ratio.

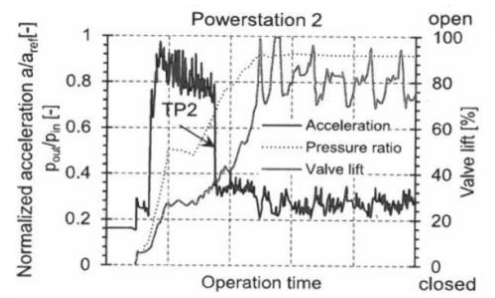


Fig. 8: Acceleration on the valve under Coanda effect.

Corresponding pressure ratio is given by the operating parameters of the turbine. To the pressure ratio a corresponding mass steam flow is assigned and thus the lift of the cone. The only parameter that can influence the separation and non-separation states is the radius of curved surface  $r$ . It is desirable to be as large as possible, but it is impossible to increase it limitlessly. The fact that in flow separation pressure pulsations and also vibrations increase is confirmed by experiment carried out by the Siemens company (Domicich at all, 2015). In Fig. 8 cone lifts are recorded as well as pressure ratios and acceleration on the valve during the start of turbine operation. The step change in acceleration for certain lift of the cone and pressure ratio is evident.

Widening the diffuser can influence the pressure loss and the location of possible flow separation. Experiments on valves with the diffuser opening angle of  $7^\circ$  and  $10^\circ$  confirmed lower intensity of vibrations for valves with smaller widening. For seven-stage diffuser also the value of pressure loss is more favourable. The main reason for valve construction with a seven-stage diffuser is operating reliability and vibration and noise damping. However, it cannot fully prevent the flow separation from the diffuser wall.

It is possible to test whether, for balanced valves, the steam from the bypass valve can be used to stabilize the flow field in the diffuser. Instead of central opening, a perforated bottom could be use. It is desirable to limit the vortex influence under the cone and guarantee flow in the positive direction in the whole cross section of the diffuser throat. From the flow computational study it is evident that this requirement is not met. In the valve flow separation from the diffuser wall appears and backward flow occurs. Another adjustment can be done by directing the steam flow from the bypass valve to the diffuser wall using holes drilled sidelong in the cone bottom. In the 2D model of the cone several operating modes were tested. In the variant with balancing, attaching the flow to the diffuser wall was confirmed. Positive results are

also achieved for the valve with a shaped cone and steam outlet from the bypass valve directed to the diffuser wall. Its flow and the resulting load force for two lifts of the cone are shown in Fig. 9. In the experiment for the steady lift of the load force pressure ratio on the valve was gradually decreasing. The step change in the load force occurs during transition to the transonic flow. The fluctuational component of tensile force did not increase significantly. There is a strong vibration damping compared to valves with central outlet opening (Fig. 3).

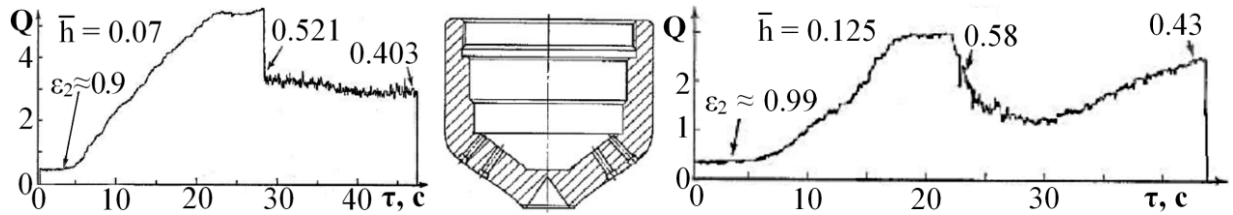


Fig. 9: Oscillogram of shaped cone vibrations with wall perforation for variable pressure ratio  $\varepsilon_2$ .

Also the flow calculations in valves with a flat bottom cone and with slots for steam from the bypass valve show lower sensibility to flow separation from the diffuser wall. The version with two rows of slots is given in Fig. 10. Calculations for the one-row slot version are found in Fig. 11. It is evident that location of outlet openings, direction of steam flow, mass flow and steam dynamics from the bypass valve are vital. It is related with pressure distribution inside the valve and thus with the resulting force necessary for separating the big cone from the seat. Besides the flow in the diffuser it is necessary to consider the steam flow through the inner parts of the valve.

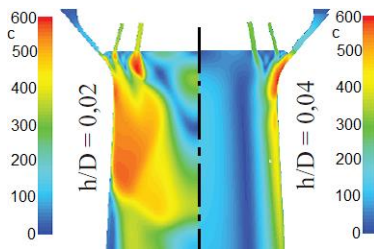


Fig. 10: Velocity distribution in the diffuser, two rows of slots.

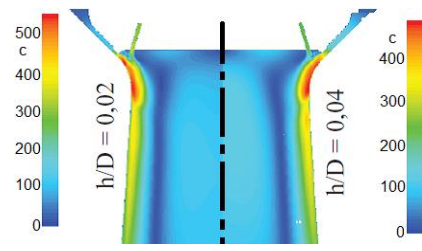


Fig. 11: Velocity distribution in the diffuser, one row of slots.

#### 4. Conclusions

As a result of the vortex under the cone, turbulent and unsteady velocity field occurs in the valves. Pressure pulsations appear in the broad range of frequencies. • The central outlet opening in balanced valves contributes to the existence of flow separation from the diffuser wall as well as to the increase of fluctuational force operating on the valve spindle. • Flow separation from the diffuser wall is also a result of Coanda effect for a specific pressure ratio on the valve. • Pressure pulsations can be damped using special dampers or by using steam flow from the bypass valve. It is also necessary to consider pressure ratios in the inner parts of the valve. • A positive influence of steam from the bypass valve is demonstrated in valves with a shaped cone as well as in valves with flat-bottom cones.

#### Acknowledgement

This work has been supported by the project SGS-2016-045 (Increasing the efficiency, reliability and service life of power system machines and devices 4).

#### References

- Matas, R. (2001) Numerical Solution of Axisymmetric Models of the Steam Turbine Control Valves at off Design Conditions. Proceedings of the Colloquium Fluid Dynamic 2001, pp. 51-54, Prague.
- Šťastný, M., Bednář, L., Tajč, L., Kolář, P., Martinů, P. and Matas, R. (2003) Pulsating Flows in the Inlet of a Nuclear Steam Turbine, 5th European Conference on Turbomachinery, Prague.
- Domicich, C.B., Bendra F., Brillert D., Dahmen, H.J. and Musch, C. (2015) Improving the Design of Steam Turbine Inlet Valves by Numerical Method for Enhanced Part Load Operation, 11th European Conference on Turbomachinery.



## VERIFICATION OF FAST ALGORITHM FOR CROSS-ROLL STRAIGHTENING

M. Benešovský<sup>\*</sup>, T. Návrat<sup>\*\*</sup>, J. Petruška<sup>\*\*\*</sup>

**Abstract:** *This paper describes a computational model to simulate cross-roll straightening of rods. This model is based on the Lagrangian approach to the description of the continuum. The implementation of the model was performed in the ANSYS software. In the other part of the work results are presented, which are then compared with the fast algorithm for cross-roll straightening based on the Euler approach.*

**Keywords:** Computational simulation, Cross-roll straightening, FEM, Hyperbolic rollers, Curvature, Rod bending, Residual stress.

### 1. Introduction

Rolled rods can be inappropriately deformed after a heat treatment and therefore they can wobble unacceptably during machining. For this purpose, cross-roll straightener is used, reducing the curvature and unacceptable wobble of the rod. In practice, there are different types of rods with different geometrical and material properties. Each type of rod requires particular settings of straightener's parameters, e.g. offset of upper deflection rollers, angle of roller. Values of these parameters can be estimated with experience or with virtual simulation of cross-roll straightening.

Despite the fact that the technology of cross-roll straightening is relatively old, virtual simulations of cross-roll straightening are only at the beginning. This confirms fact, that only few authors deal with this issue. One of them is Mutrux et al. (2008), where the collective of authors perform simulations of cross-roll straightening on a straightener with two rollers. The upper roller is concave and the lower roller is convex. The problem is solved in the LS-DYNA software. Authors use bilinear material model with kinematic hardening. The rod was 10 m long and its model is divided into two parts, the outer being modeled using beam elements and the middle one modeled using solid elements. During the simulation the beam elements never touch the rollers. Outputs are displacements in planes XY and XZ. Huang et al. (2011), another relevant team of authors focused on cross-roll straightening on a straightener with 10 rollers. This straightener has 5 upper and 5 lower rollers. Each upper roll is above the lower roll and there is no deflection roller. The simulation of straightening has been done in MSC.MARC software. The model of geometry is not the rod but it is a pipe. Outputs are Von Mises stress and strain and circularity. In Feng et al. (2013), team of authors simulated cross-roll straightening for a straightener with 7 rollers. The shape of the roller was created in software CATIA and MATLAB. Numerical simulation was solved in Abaqus.

Since the virtual simulation of cross-roll straightening is a very time consuming, a fast algorithm of cross-roll straightening has been developed by Petruška et al. (2016a). The final version of the fast algorithm should be used to adjust the position of hyperbolic rollers in real time. In order to make the predictions fast enough, it was necessary to use the Euler approach to description the continuum. Due to low computer time requirements, optimization of vertical offset of rollers could be made as shown in Petruška

---

<sup>\*</sup> Ing. Marek Benešovský: Institute of Solid Mechanics, Mechatronics and Biomechanics, Brno University of Technology, Antonínská 548/1; 601 90, Brno; CZ, marek.benesovsky@vutbr.cz

<sup>\*\*</sup> Assoc. Prof. Ing. Tomáš Návrat, PhD.: Institute of Solid Mechanics, Mechatronics and Biomechanics, Brno University of Technology, Antonínská 548/1; 601 90, Brno; CZ, navrat@fme.vutbr.cz

<sup>\*\*\*</sup> Prof. Ing. Jindřich Petruška, CSc.: Institute of Solid Mechanics, Mechatronics and Biomechanics, Brno University of Technology, Antonínská 548/1; 601 90, Brno; CZ, petruska@fme.vutbr.cz

et al. (2016b). The fast algorithm can be used also for non-circular profile as presented in Návrat et al. (2014).

Many experiments are needed to be performed for the sufficient verification of the fast algorithm, which is too expensive. For these reasons, the main aim of the work was to create a standard Lagrangian FEM model to be used for the verification of the fast algorithm for cross-roll straightening.

The above-mentioned papers demonstrate that the simulation of cross-roll straightening has been solved in FEM software, such as LS-DYNA, MSC.MARC, Abaqus. Due to accessibility of ANSYS at the Institute of Solid Mechanics, Mechatronics and Biomechanics, the simulation will be solved in this software. As some results like the curvature per meter cannot be obtained directly from the FEM model, macros and m-scripts must be used to evaluate those. Then a curvature and residual stress from the fast algorithm can be verified by the curvature and residual stress from the standard FEM model.

## 2. Method

Based on the findings obtained from literature, an analysis model was created for the required straightener with nine rollers (Fig. 1). Rotation and translation of the rod was not driven by the rotation of rollers, but it was caused by the boundary conditions prescribed on the rod.

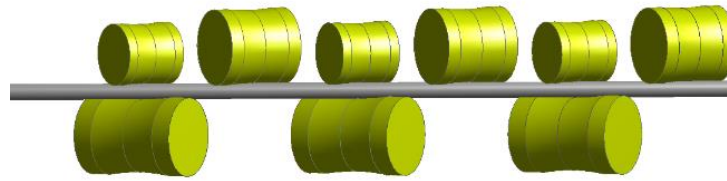


Fig. 1: Cross-roll straightener with nine rollers.

### 2.1. Model of material

Homogeneous, isotropic and ideally elastoplastic model of the steel material was used for the rod with the following parameters: Young's modulus 206 GPa, Poisson's ratio 0.3 and tensile yield strength 900 MPa.

### 2.2. Model of geometry

Model of geometry consists of two basic parts - hyperbolic rollers and the straightened rod.

**Hyperbolic rollers:** The cross-roll straightener with nine rollers has three types of rollers. There are lower rollers, upper pressure rollers and upper deflection roller (Fig. 1). The hyperboloid (work space of the roller) can be described by the length of the major semi-axis  $r$  and the minor semi-axis  $c$ . Other important parameters of the roller are the length of the work space  $L_1$  and the total length of the roller  $L$ . Values for the above-mentioned parameters of the three types of rollers are shown in Tab. 1.

Tab. 1: Parameters of the rollers.

Type of rollers	$r$ [mm]	$c$ [mm]	$L_1$ [mm]	$L$ [mm]
lower	160	379	310	480
upper pressure	130	379	190	276
upper deflection	160	379	220	340

**The rod:** The diameter of the rod was determined to be 70 mm and the initial curvature per meter<sup>1</sup> was 4 mm/m.

<sup>1</sup> The following relationship applies for the curvature per meter and radius of curvature:  $k_m = r - \sqrt{r^2 - 10^6/4}$

### 2.3. Connections

In this standard FE model interaction can be only between the rod and rollers. The surface of rollers is rigid and the rod is modeled as a flexible body. The type of the contact was chosen “Frictionless” and the algorithm was chosen “Augmented Lagrangian” because the convergence is the best for this settings.

### 2.4. Mesh

Following elements were used for the mesh: BEAM188, CONTA175 and TARGE170. As the rod was meshed by BEAM188, it was not possible to prescribe the contact on the surface of the rod. The contact was prescribed in nodes that were placed on the midline of the rod. For this reason, the geometry of the rod penetrates the geometry of rollers as shown in Fig. 2.

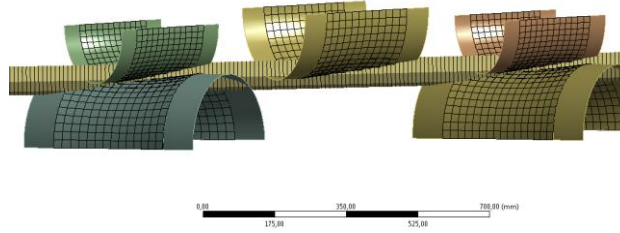


Fig. 2: Penetration.

### 2.5. Boundary conditions

The simulation was divided into two load steps. In the first step, the first part of the rod was loaded by the vertical displacement of upper deflection rollers as shown in Fig. 3. Displacements of other rollers remained zero in all directions. Due to convergence problems in the first load step, it was necessary to prescribe zero  $x$  and  $z$  displacements of the global coordinate system at the end of the rod. Boundary conditions that were applied on rollers in the first step stay unchanged in the second step with upper deflection rollers remaining in the same position as at the end of the first step. A new boundary condition is applied at the end of the rod in the second step. It is a displacement in the  $x$  direction and rotation around the  $x$  axis as shown Fig. 4. As the second part of the rod (the part for evaluation of results) must be affected by all the rollers and because the helix pitch is 110 mm, the displacement in the  $x$  direction must be 4800 mm and the rotation around the  $x$  axis  $15709^\circ$  (i.e., about 44 revolutions).

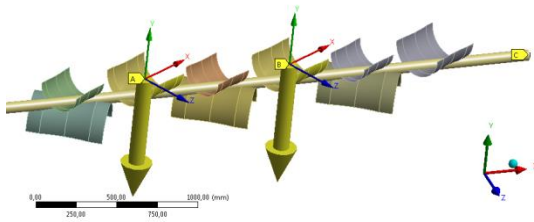


Fig. 3: The first load step.

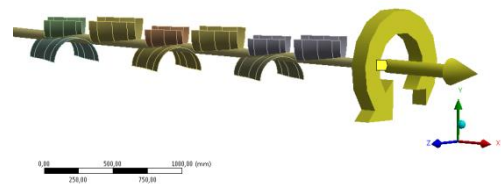


Fig. 4: The second load step.

## 3. Results

In this section, the fast straightening algorithm results are compared to standard Lagrangian FE analysis model.

Fig. 5 shows a graph in which the output curvature is dependent on the offset of upper deflection rollers. The blue curve represents results for the fast algorithm and a red curve represents results for the standard FE model. Both curves have the same trend and the minimum output curvatures are different by only a few percent. The offset of upper deflection rollers is different for the minimum output curvatures. It is 8 mm for the fast algorithm and 9 mm for the ANSYS model. Difference is about 11 %. ANSYS model has a greater stiffness.

Fig. 6 demonstrates a relationship between the residual stress and the offset of upper deflection rollers. Trends of both curves are similar again. The offset of upper deflection rollers are 7.4 mm for the fast

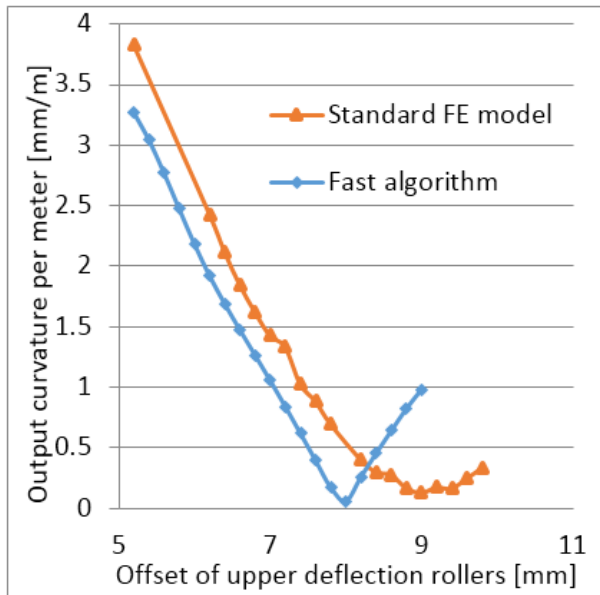


Fig. 5: Verification output curvature.

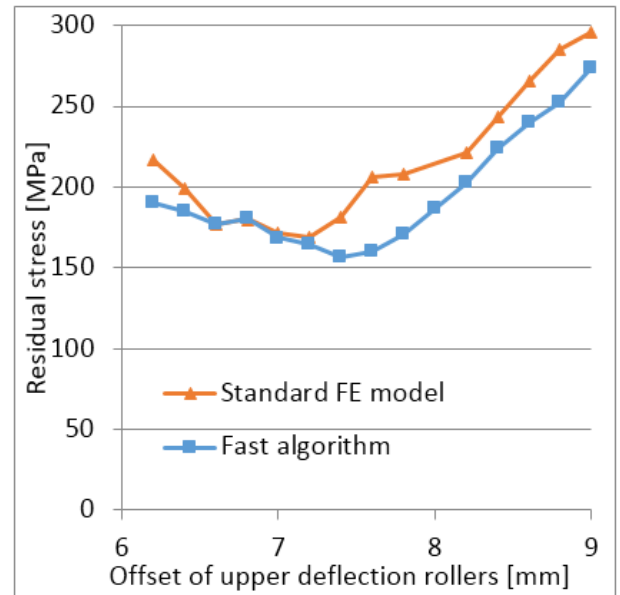


Fig. 6: Verification residual stress.

algorithm and 7.2 mm for the ANSYS model. Difference is less than 3 %. The value of residual stress for these offsets is 155 MPa for the fast algorithm and 170 MPa for the ANSYS model. Difference is less than 9 %.

The last important parameter is the calculation time. The calculation time of one standard FE model is about 10 hours. This simulation is a very time consuming because a real cross-roll straightening takes about 10 seconds. The calculation time of the fast algorithm is many times lower than the calculation time of the standard FE model. It is about 140 seconds for one simulation.

#### 4. Conclusions

Although the fast algorithm is much faster than standard FE model, the application of fast algorithm for real-time control straightener will be probably not possible. This is caused by the fact, that we have to perform an optimization for each type of rod, which leads to a wide range of calculations. This problem could be solved with previously performed optimization and subsequent implementation of obtained parameters into the straightener control system.

In conclusion we can say that presented differences are (particularly in Figs. 5 and 6) greater than we expected. So the problem of the cross-roll straightening cannot be closed. Therefore, further research should be focused on creating a new FE model that will be based on solid elements.

#### Acknowledgment

This work is an output of project NETME CENTRE PLUS (LO1202) created with financial support from the Ministry of Education, Youth and Sports under the „National Sustainability Programme I“.

#### References

- Huang, H.G., Zheng, H.P., Du, F.S. and Wang, W.Z. (2011) Numerical simulation analysis on the ten cross rolls straightening process of the heavy calibre seamless steel tube. *Advanced Materials Research*, 421, pp. 56-59.
- Feng, J.-C., Chen, M.-H., Liang, W.-M. and Hu, X. (2013) Application program design and numerical simulation of seven-cross-roller straightener. *Journal of Plasticity Engineering*, 1, pp. 16-20.
- Mutrux, A., Berisha, B., Hochholdinger, B. and Hora, P. (2008) Numerical modelling of cross roll straightening. *Proceedings of the 7th LS-Dyna Anwederforum, Bamberg, Germany*.
- Navrat, T. and Petruska, J. (2014) Eulerian description of rail straightening process, *Applied Mechanics and Materials*, 624, pp. 213-217.
- Petruška, J., Návrát, T. and Šebek, F. (2016) Novel approach to computational simulation of cross roll straightening of bars. *Journal of Materials Processing Technology*, 233, 7, pp. 53-67.
- Petruška, J., Návrát, T., Šebek, F. and Benešovský, M. (2016) Optimal intermeshing of multi roller cross roll straightening machine, *Aip Conference Proceedings*, 1769.



## FORMATION CONTROL OF MOBILE ROBOTS UNDER ROS

K. Besseghieur<sup>\*</sup>, W. Kaczmarek<sup>\*\*</sup>, J. Panasiuk<sup>\*\*\*</sup>, P. Prusaczyk<sup>\*\*\*\*</sup>

**Abstract:** *In this paper, a new framework is proposed for implementing the formation control laws on nonholonomic mobile robots based on ROS (Robot Operating System). To achieve the desired formation, mobile robots need to localize themselves within the environment, to communicate their positions to each other and to measure their corresponding velocities. ROS provides some convenient packages that make the formation problem easier to solve. We describe each of these packages and how they can be used to solve the formation control problem under ROS.*

**Keywords:** Mobile robots, Formation control, Robot Operating System (ROS).

### 1. Introduction

Multi-robot systems present a more robust and cheaper solution to certain tasks that are better performed using several low-cost robots rather than single, complex ones. A multi-robot system may be required to travel over large distances in order to reach a site related to a mission or task. While traversing the distances, it may be desirable for the robots to move in a rigid formation with fixed inter-robot distances. This gives rise to the formation control problem. Moreover, the latter has several potential applications for mine sweeping, boarder patrolling and for cooperative mapping to name a few.

The formation problem has been regarded as an important problem in multi-robot systems where the objective is to make a team of vehicles move toward and maintain a desired geometric pattern, while maintaining a featured motion. According to the survey presented in (Guanghua et al., 2013), and the references therein, formation structure can be divided into three strategies: the leader–follower strategy, the behavioral and the virtual structure approaches. Several approaches have been proposed in the literature to solve this problem. However, most of the existing literature tackle the theoretical side of the problem mainly the controller design is considered where several control strategies are adopted to make the formation errors converge to zero. Nevertheless, some of them have carried on real experiments to prove the effectiveness of their proposed controller. Furthermore, multi robots systems implementation on ROS has rarely been considered except in few works like (Muddu et al., 2015) about multi robots coverage and (Hennes et al., 2012) about multi robot collision avoidance.

In this paper, we propose a new framework for all the mobile robots based on ROS so that real experiments for the formation control problem can be conducted effectively. This allows all the researches in this area to assess the performance and effectiveness of their controllers throughout the experiments. Due to its simplicity and scalability, the leader-follower approach is considered in this paper. However, the proposed framework can be extended so that other formation strategies can be implemented. The remainder of the paper is organized as follows: the next section is dedicated for a small introduction about ROS concepts and their use in the formation problem. In section 3, formation control framework is sketched where each part of the latter is detailed and the needed ROS packages are presented. In the last section, we conclude our work and draw some future work directions.

---

<sup>\*</sup> Khadir Besseghieur, MS.: Faculty of Mechatronics & Aerospace, Military University of Technology, Kaliskiego 2, 00-908, Warsaw, PL, besseghieurkh@hotmail.fr

<sup>\*\*</sup> Wojciech Kaczmarek, PhD.: Faculty of Mechatronics & Aerospace, Military University of Technology, Kaliskiego 2, 00-908, Warsaw, PL, wojciech.kaczmarek@wat.edu.pl

<sup>\*\*\*</sup> Jarosław Panasiuk, PhD.: Faculty of Mechatronics & Aerospace, Military University of Technology, Kaliskiego 2, 00-908, Warsaw, PL, jaroslaw.panasiuk@wat.edu.pl

<sup>\*\*\*\*</sup> Piotr Prusaczyk, MS.: Faculty of Mechatronics & Aerospace, Military University of Technology, Kaliskiego 2, 00-908, Warsaw, PL, piotr.prusaczyk@wat.edu.pl

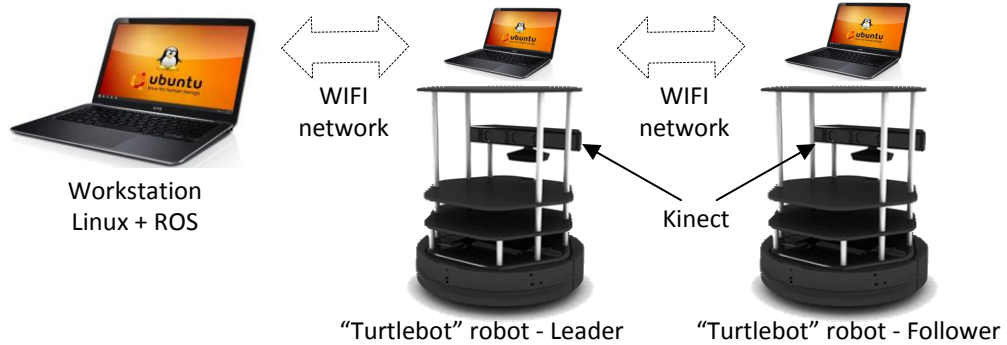
## 2. ROS background

ROS is a Linux-based, an open source software package that provides a software framework to aid in the development of complex robotic applications (Quigley et al., 2015). It is based on the concepts of nodes, topics, messages and services. A node is an executable program that performs computation. Nodes need to communicate with each other to complete the whole task. The communicated data are called messages. ROS provides an easy way for passing messages and establishing communication links between nodes, which are running independently. They pass these messages to each other over a Topic, which is a simple string. However, topics are asynchronous, synchronous communication is provided by services. Services act in a call-response manner where one node requests that another node execute a one-time computation and provide a response. For more details about ROS, the reader can refer to (Quigley et al., 2015).

We can see how these concepts help to solve the formation control problem in ROS. Nodes for instance are responsible for launching several algorithms to control, localize the robot and to transmit the data. The topic “/tf” is the holder of the robot’s postures. Therefore, when a node needs a robot position, it has to subscribe to this topic. In our framework, services are essentially used in communication between robots where the control node solicits the communication node to transmit postures to another robot.

The presented formation implementation relies on several operational assumptions to narrow the implementation goal to a specific scope which is about testing the formation control laws with real experiments. First, it is assumed an occupancy grid representation of the static map is available to all robots. This removes the requirement for multi-robot SLAM and map merging, which are outside the scope of this work. Second, each robot knows its initial position and possesses the required sensors in order to maintain an accurate estimation of its pose within the two dimensional map using the navigation stack. A wireless communication network is assumed to be available over the entire coverage region.

Our test bench includes “Turtlebot” robots equipped with the Kinect camera sensor and with embedded laptops. The robots communicate over an 802.11n WIFI network (Fig. 1).



*Fig. 1: A general view of the system.*

## 3. Formation control framework on ROS

To build a robust formation control framework on ROS, we need before to know how each robot contributes to realize the whole formation. We decided to set up our framework according to what is needed in the leader-follower approach. Note that this framework can be extended to implement different formation control strategies.

In the leader-follower approach, each robot takes another neighboring robot as a leader to determine its motion. The leader robot moves along predefined trajectory while the follower robots keep track of the leader robot and maintain desired distance and bearing angle.

Most of the control laws proposed in the literature show that the leader’s relative coordinates and velocities are needed in the control laws implemented on the followers. Therefore, the complete multi-robot formation control strategy can be divided into three phases that each robot must be able to carry out on its own. Each robot must be able to:

- Localize itself within the map.
- Communicate data with other robots. The communication direction is from the leader to its followers.

- Execute the implemented formation control laws. Only for the followers. Note that the leader can be directly controlled from the workstation keyboard using the “Teleoperation” ROS package.

In addition to the basic nodes needed for running the robot, three additional nodes are indispensable for controlling the robots to achieve formation. AMCL node for localization, Ad Hoc Communication node for data transmission and the control node that executes the control algorithm. The nodes are running simultaneously and thus they have to communicate to each other through ROS topics or ROS services as depicted in fig.2. Note that on each robot, all the nodes are executed under a specific namespace for the robot. The ROS parameter ‘tf\_prefix’ is exclusive for each robot as well.

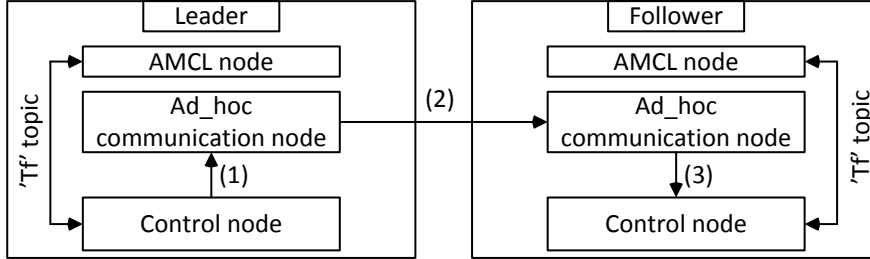


Fig. 2: Formation control framework.

### 3.1. Localization

The ROS navigation stack is used to provide the localization of the robot. The Localization method uses the Adaptive Monte-Carlo Localization (AMCL) approach presented in (Hennes et al., 2012), it is based on a weighted particle system in which each particle represents an estimated pose of the robot and consists of two phases of calculation: the prediction and update phases. AMCL combines the onboard encoders' measurements and the data provided by the Kinect sensor to provide an accurate estimation of the robot position. The AMCL node publishes the robot's postures into the 'tf' topic.

### 3.2. Data communication

Several ROS packages have been proposed to transmit data between several machines based on ROS. The multimaster\_fkie package (Tiderko et al., 2016) allows the discovery and synchronization of robots as well as unicast and multicast transmissions based on UDP where two additional nodes need to be run. Master\_discovery node connects to its local master and broadcasts the time stamp of the last change to the network and master\_sync node connects to all known master\_discovery nodes then it registers or unregisters the remotely available topics and services with the local ROS master. SocRob Multicast package is proposed in (Reis et al., 2013) based on Reconfigurable and Adaptive TDMA (RA-TDMA) communication protocol. The Ad Hoc Communication package considered in (Ander et al., 2014) is preferred in our framework where an Ad hoc On-Demand Distance Vector (AODV) for unicast and Multicast transmission is implemented. It uses automatic repeat request (ARQ) on data link and transport layers for unicast and multicast allowing reliable transmissions. Comparing with the multimaster\_fkie package, the ad\_hoc communication package provides more reliable transmission of data and the communication is only established on demand.

The communication between robots is mainly used for transmitting the leader's postures and velocities to its followers. These data are essential for controlling the follower to keep the desired separation and bearing with the leader. However, the two control nodes do not communicate directly, they utilize the intermediate Ad Hoc Communication node as depicted in Fig. 2. (1) represents a service call which includes the hostnames of the sender and the recipient robots, data to be transmitted and the topic where the data will be published at the destination. The Ad Hoc Communication package wraps the data into an extended MAC frame and transmits the frame using a raw socket (2). When the data has successfully been received at the destination, it will be published in the predefined topic. Note that, a custom ROS msg file that includes the variables definitions for the data to be transmitted must be defined as well as a new ROS srv file, which holds that custom msg file, is necessary in the service call for data transmission.

### 3.3. The control node

The control nodes are considered as the main part in the robots control. However, the algorithms differ when it comes to a leader or a follower robot control. As sketched in Fig. 3, after the initialization phase, the program goes into the control loop. The nodes then listen to their corresponding ‘/tf’ topics and subscribe to the topic where the robot’s velocities are being published as well as subscribing to the topics published by the ad hoc communication node to get the leader’s postures and the workstation order. A test is held where only a received character from the workstation interrupts an endless wait loop. This order is transmitted using the same package Ad Hoc Communication. After receiving the order, each follower executes the implemented control laws, which are based on nonlinear system control theory. The obtained velocities are then published to the corresponding velocity command topics. Whereas for the leader, it is controlled from the workstation using the ‘Teleoperation’ ROS package.

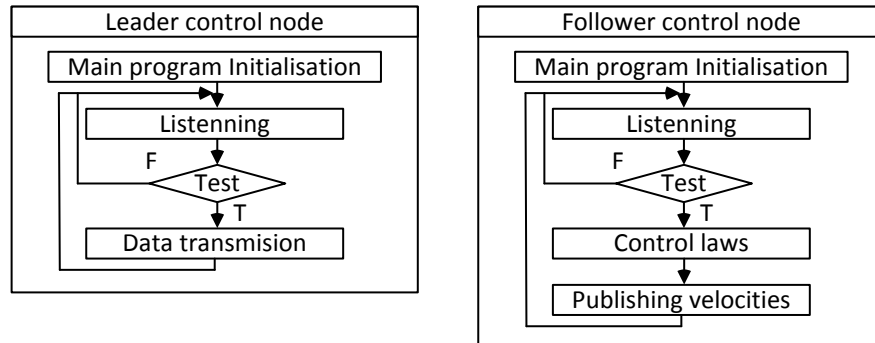


Fig. 3: Control nodes algorithms.

## 4. Conclusion

In this work, a ROS framework for implementing formation control algorithms on mobile robots based on ROS is designed that can be exploited by researches in this area to assess their control algorithms performances. The proposed framework is divided into three phases where the localization and communication phases are functionalities provided by existing ROS packages whereas the control phase indicates the custom ROS node. The framework has been tested on our test-bench, the communication is reliable but the localization can be more accurate, this will be tackled in our future work by improving the localization algorithm or employing better sensors than the Kinect camera where the Hokuyo Lidar is considered to be a better alternative. Future works include extending this framework for other formation control strategies than the leader-follower approach.

## Acknowledgement

My acknowledgements are directed to the co-authors of this paper for providing me with the necessary equipment to carry on this research and to the anonymous reviewers of this paper.

## References

- Andre, T., Neuhold, D. and Bettstetter, C. (2014) Coordinated multi-robot exploration: Out of the box packages for ROS. In Globecom Workshops (GC Wkshps), pp. 1457-1462, IEEE.
- Guanghua, W., Deyi, L., Wenyan, G. and Peng, J. (2013) Study on formation control of multi-robot systems. In Intelligent System Design and Engineering Applications, 2013 3 rd Int. Conf on pp. 1335-1339, IEEE.
- Hennes, D., Claes, D., Meeussen, W. and Tuyls, K. (2012) Multi-robot collision avoidance with localization uncertainty. In Proc. 11th Int. Conf. on Autonomous Agents and Multiagent Systems-Volume 1, pp. 147-154.
- Muddu, R.S.D., Wu, D. and Wu, L. (2015) A frontier based multi-robot approach for coverage of unknown environments. In Robotics and Biomimetics (ROBIO), 2015 IEEE Int. Conf on pp. 72-77, IEEE.
- Quigley M., Gerky B. and Smart W.D. (2015) Programming Robots with ROS, a Practical Introduction to the Robot Operating System, First. O'Reilly Media, Inc.
- Reis, J.C., Lima, P.U. and Garcia, J. (2013) Efficient distributed communications for multi-robot systems. In Robot Soccer World Cup, pp. 280-291, Springer Berlin Heidelberg.
- Tiderko, A., Hoeller, F. and Röhling, T. (2016) The ROS Multimaster Extension for Simplified Deployment of Multi-Robot Systems, chapter in Robot Operating System (ROS) Volume 625 of the series Studies in Computational Intelligence pp. 629-650.

## DETERMINATION OF BOUNDARY CONDITIONS FOR THE OPTIMIZATION PROCESS OF BLAST MITIGATION SEAT SHOCK ABSORBERS

G. Bienioszek<sup>\*</sup>, S. Kciuk<sup>\*\*</sup>

**Abstract:** *The aim of this study was to define the boundary conditions existing during examination of the seat on a drop-tower. Within the work, the basic information about mine blast phenomenon and its influence on the crew of special vehicles were gathered and discussed. The necessary use of blast mitigation seats was indicated and the basic methods for testing their efficiency were presented. A seat without shock attenuation system was examined. The conducted research allowed for determination of the acceleration levels measured at selected points. It was noticed that even without shock absorbing system, the seat is capable of mitigating some amount of incoming energy due to plastic deformation. However, it was not enough to lower the acceleration to a human tolerable level. This highlights the need for shock attenuation system implementation and optimization in order to minimize the acceleration transferred to the passenger. The obtained results provide a basis for further work in this area. The gathered signals were compared with literature data describing vehicle acceleration during mine blasts. The drop-tower used during the study proved to be suitable for explosion impact simulations.*

**Keywords:** Drop-tower, Acceleration sensor, Blast mitigation seat, Protection of military vehicle crew.

### 1. Introduction

Experiences gained during military conflicts in Iraq and Afghanistan showed that explosions of improvised explosive devices (IEDs) were the most common cause of death and injury of soldiers (Krzyształa et al., 2012). According to the current state of knowledge the physics of a mine blast process and its impact on the vehicle can be divided into four phases (Ramasamy et al., 2010). The first one is the formation of a explosion shock wave, which causes damage to the hearing and internal organs of passengers. The second stage relates to penetration of fire debris through the hull of the vehicle. During the third phase, rapid vertical acceleration is applied to the vehicle and local bending of the floor may occur. The fourth and last state is associated with the heat and toxic gases transferred into the interior.

Each of these stages is connected to a different kind of threat. Therefore, it is necessary to use diverse protective measures in order to keep the crew alive (Krzyształa et al., 2012). These include the appropriate shape of the hull and armor of the vehicle (Krzyształa et al., 2016). These measures allow the for partial dispersion of explosion energy and protection of passengers from mine and soil fragments. However, they do not provide sufficient protection during the third phase. The rapid acceleration causes permanent spinal injuries and involves the risk of head injury (Krzyształa et al., 2012).

Nowadays, anti-explosive seats have become essential pieces of equipment in mine-resistant vehicles. They allow for significant reduction of shock impulses to 20-25 g, which is considered to be the maximum limit of human tolerance for acceleration in a vertical axis (Krzyształa et al., 2012). Research on these types of seats are carried out around the world by governments of various countries and private companies (Kargus et al., 2008). According to the standard NATO AEP-55 Vol. 2 (2011), the newly designed seats shall be validated during field blast-off tests. However, at an early stage of product development, they are too expensive and do not provide sufficiently reproducible results (Cheng et al., 2010).

---

<sup>\*</sup> MSc. Eng. Grzegorz Bienioszek: Institute of Theoretical and Applied Mechanics, Silesian University of Technology, Konarskiego 18a; 44-100, Gliwice; PL, grzegorz.bienioszek@polsl.pl

<sup>\*\*</sup> PhD. Eng. Sławomir Kciuk: Institute of Theoretical and Applied Mechanics, Silesian University of Technology, Konarskiego 18a; 44-100, Gliwice; PL, slawomir.kciuk@polsl.pl

Drop-tests have become a widely-used method during research on blast mitigation seats. Their operating principle consists of dropping the object from a desired height, which is then rapidly decelerated during impact with the ground or a special pulse-shaper (Kargus et al., 2008). It has been proved that these tests can be characterized with different boundary conditions than those occurring during the actual mine blast (Cheng et al., 2010). The main difference is the relative displacement between the seat and the dummy which exists during drop-tests and which is not present in real explosions under a vehicle. Consequently, this generates decompression of the spine and seat cushions. These phenomena lead to overestimation of the seat's effectiveness. Despite this, drop-tower tests can be successfully used to obtain reliable conclusions. The condition is that the above mentioned differences must be taken into account during the analysis of results (Cheng et al., 2010).

The application of drop-tests has great practical importance during the optimization and verification of the effectiveness of a designed seat (Kargus et al., 2008). An important issue is to determine the boundary conditions present during the study. The choice of the proper initial height and pulse-shaper construction has a large influence on the characteristics of the generated acceleration (Cheng et al., 2010). Moreover, a test of the un-damped seat shall be conducted and the obtained data can be used later for a comparison of different shock absorbing system solutions.

## 2. Methods

Accelerations were recorded using an automatic measuring system for the acquisition of rapidly changing voltage signals (Szmidski et al., 2011). The experiment setup consisted of a drop-tower, an un-damped seat and three ADXL001-500 accelerometers (Fig. 1a). They were placed on the falling carriage, the seatback and the seat cushion. According to NATO AEP-55 Vol. 2 (2011), the sampling frequency was set to 100 kHz. The signal was calibrated for zero offset error with the use of 100 ms pre-trigger data.

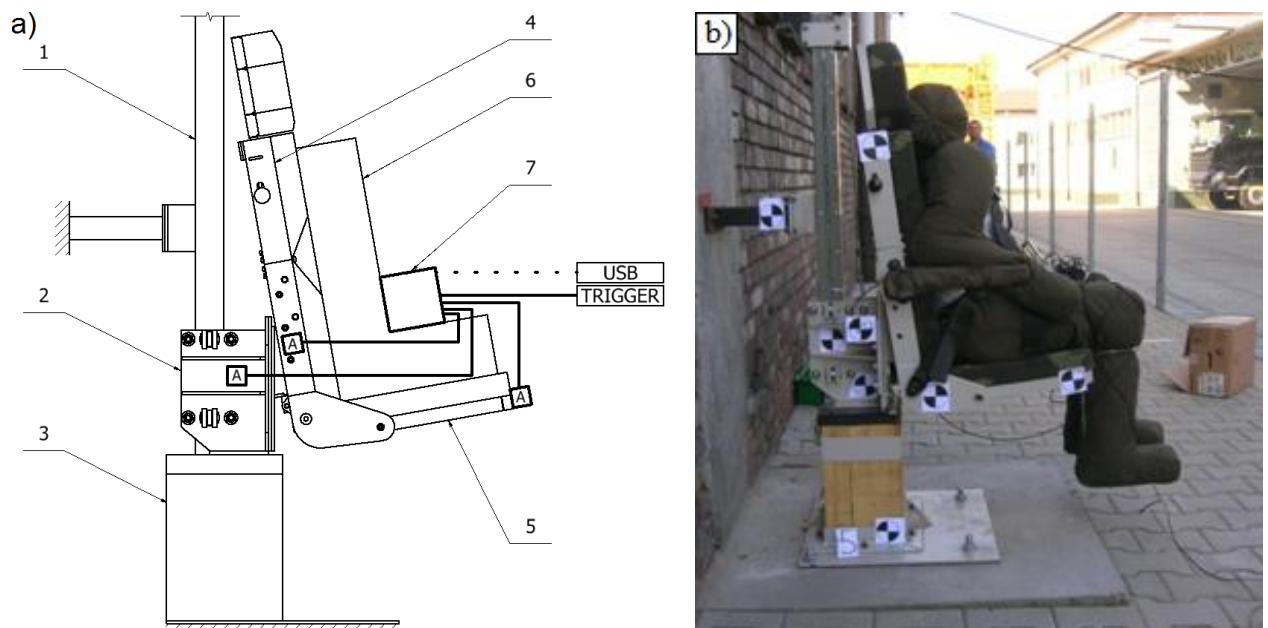


Fig. 1: Experiment setup: a) physical model, b) real object (1 – rail, 2 – carriage, 3 – bumper, 4 – seatback, 5 – seat cushion, 6 – 80kg load, 7 – analyzer, A - accelerometers).

The test stand consisted of a carriage, which moves along a vertical sliding guide (Fig. 1b). The mounting method of the seat to the carriage was the same as in a real vehicle. After dropping, the whole assembly was decelerated on a bumper made of wood and rubber. The purpose of this element was to shape the input acceleration pulse whose duration, according to Cheng et al. (2010), should not exceed 10 ms.

The initial height of the carriage was set to 3 m. This height was chosen to provide the input acceleration value of at least 300 g (Krzyształa et al., 2012). Interaction between the seat and the passenger was modeled in a simplified manner by placing weights on the seat with a total mass of 80 kg. The use of a more advanced anthropomorphic test device (ATD) was not possible due to the considerable risk of damage caused by the lack of a shock absorbing system.



The results were compared by calculation with the use of FEM model prepared in LS-Dyna software. It consisted of approximately 800 000 elements. In order to simplify calculation following assumptions were made. The dummy was replaced with lumped mass of 80kg connected to seat cushion, so it was assumed to be a rigid body. Only 80 ms of simulation was performed. The carriage and seat were placed 100 mm above the bumper. The initial velocity of system was set to 7.5 m/s. It was calculated according to energy conservation principle, assuming that carriage was falling from 3 m. The piecewise linear plasticity material model with bilinear stress-strain interpolation was used for all metallic parts.

### 3. Results and discussion

The dependence of the acceleration from its time measured at selected points of the system was presented in Fig. 2. In order to analyse the results of data only linked directly to impact deceleration, all signals were processed with the use of a filter CFC-180 Hz recommended by the SAE standard J211-1 (1995). This enabled filtering out the part of the signals associated with the mechanical vibration on high frequency, which were not investigated.

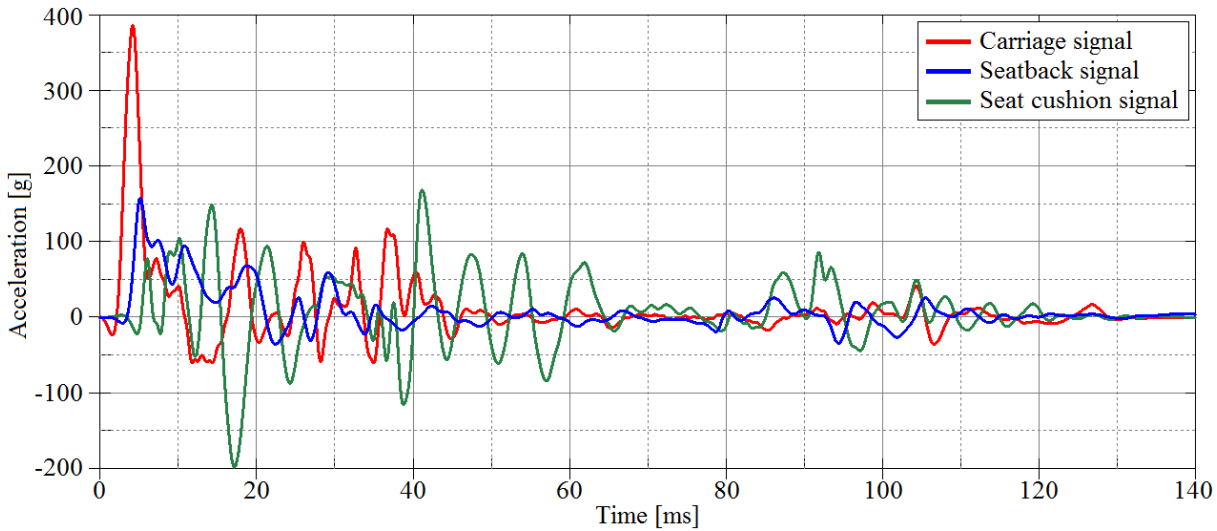


Fig. 2: Acceleration recorded during experiment at selected points of the system.

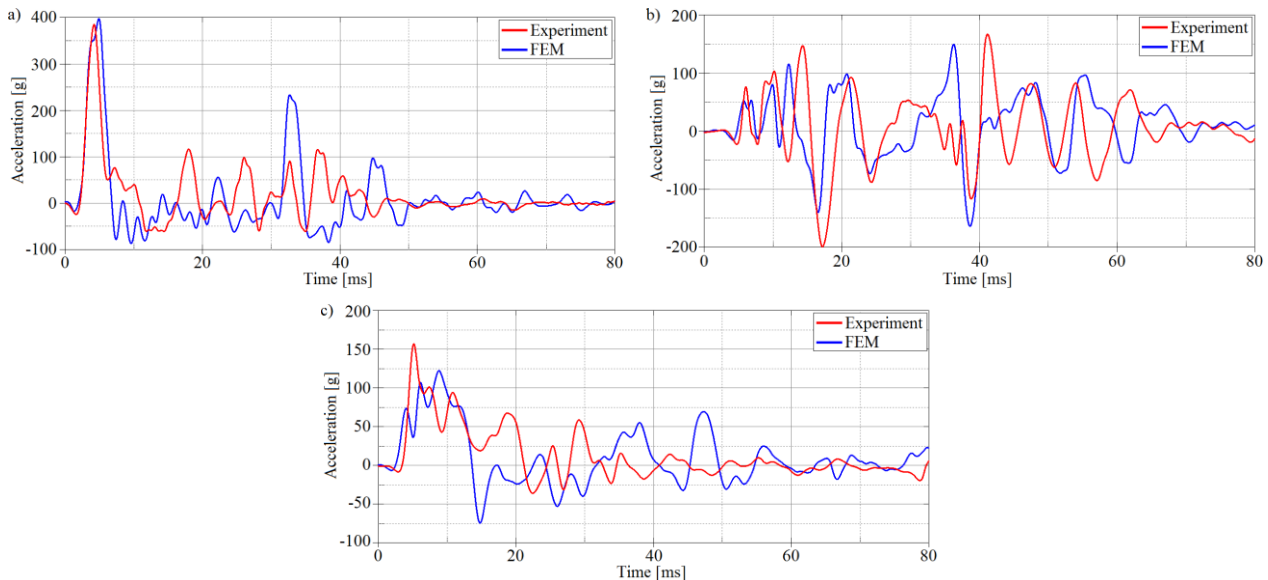


Fig. 3: Comparison of experimental and FEM results for: a) carriage, b) seat cushion, c) seatback.

Comparison of FEM and experimental results (Fig. 3) showed a good convergence between them. Divergence for input signal recorded for the carriage (Fig. 3a) did not exceed 10 % for initial, highest peak. The acceleration amplitude range and signal shape obtained during numerical simulation for another two measuring points (Fig. 3b-c) were in satisfactory correlation with the experimental data.



Simplifying assumptions and not taking into account the energy loss due to friction between drop-tower guide and carriage were the main reasons of differences between results.

Carriage acceleration reached 380 g, which thus exceeded the assumed minimum value of 300 g. This proved there had been an accurate choice of initial height. The pulse duration of platform acceleration did not exceed 10ms. Thus showing, the drop-tower allowed for the generation of acceleration impulses similar to those occurring during a mine explosion under the vehicle.

Acceleration recorded for the seatback did not exceed 160 g. Despite the lack of a shock attenuation system, partial reduction of input acceleration occurred. The reason for this was the presence of relative displacements between elements, which were caused by strains in bolted connections and small deformations of the seat construction.

Oscillations of the seat flap, with an approximate amplitude of  $\pm 200$  g, were observed. This was due to the design of the seat bottom part, which is fixed to the seatback by means of two rotational kinematic pairs. They increase functionality of the seat, but also lead to greater displacements, and thus the acceleration, recorded during impact.

#### **4. Conclusions**

The acceleration characteristics of a carriage during an impact correlates well enough with the basic parameters of impulse generated by a mine blast. Therefore, a drop-tower can be successfully used for testing anti-explosion seats.

The chosen value of initial height allowed for achievement of an input acceleration of 380 g, which is well above the assumed minimum. This indicates the possibility of a reduction in initial height during further research.

The identified acceleration of the seatback turned out to be lower than the input pulse. This implies that despite the lack of a shock absorbing system, the seat construction provides a partial reduction of acceleration transmitted to the passenger. However, obtained values are still an order of magnitude larger than the level of human tolerance to the acceleration in the horizontal axis. Therefore, implementation and optimization of the shock attenuation system is a necessary condition, so that the seat can ensure a sufficient level of protection during mine explosion.

#### **Acknowledgement**

The authors wish to express gratitude to the Rosomak S.A. company for their permission and cooperation during the experimental research.

#### **References**

- Cheng, M., Dionne, J. and Makris, A. (2010) On drop-tower test methodology for blast mitigation seat evaluation. *International Journal of Impact Engineering*, 37, pp. 1180-1187.
- Kargus, R., Li, T., Frydman, A. and Nesta, J. (2008) Methodology For Establishing The Mine/IED Resistance Capacity of Vehicle Seats, in: *Proc. 26th Army Science Conference*, Army Research Laboratory, Orlando.
- Krzyształa, E., Kciuk, S. and Mężyk A. (2012) Identification of hazards to the crew of special vehicles during an explosion. *Scientific Publishing House of The Institute for Sustainable Technologies*, Gliwice.
- Krzyształa, E., Kciuk, S. and Mężyk A. (2016) Minimisation of the explosion shock wave load onto the occupants inside the vehicle during trinitrotoluene charge blast. *International Journal of Injury Control and Safety Promotion*, 23:2, pp. 170-178.
- NATO AEP-55, Volume 2 (2011) *Procedures For Evaluating The Protection Level of Armoured Vehicles - Mine Threat*.
- Ramasamy, A., Masouros, S., Newell, N., Hill, A., Proud, W., Brown, K., Bull, A. and Clasper J. (2010) In-vehicle extremity injuries from improvised explosive devices: current and future foci. *Philosophical Transactions of The Royal Society B*, 366, pp. 160-170.
- SAE J211-1 (1995) *Instrumentation for Impact Test, Part 1, Electronic Instrumentation*.
- Szmidt, P., Kciuk, S., Mężyk, A. and Krzyształa E. (2011) Autonomous measurement system for the acquisition of rapidly changing voltage signals. *PL Patent*, 219525.

## APPLICATION OF FRACTIONAL CALCULUS IN HARMONIC OSCILATOR

M. Blasiak<sup>\*</sup>, S. Blasiak<sup>\*\*</sup>

**Abstract:** *This paper presents two models of the vibrating system derived from the classical equation of harmonic oscillator, which were reduced to a single model. For the description of the reduced model one used the Fractional Calculus and the concept of derivative-integral defined by Caputo.*

**Keywords:** Harmonic oscillator, Caputo derivative, fractional calculation, Kelvin – Voight model.

### 1. Introduction

The developing industry and new technologies of components and systems manufacture led to the development of new mathematical tools for describing dynamic processes occurring in these systems or components. Such a new mathematical tool that caught the attention of scientists in recent years is the Fractional Calculus. The use of fractional calculus consists in the generalization of the classic derivatives (and integrals which are directly connected to derivatives) in the real numbers. The basic concept of this calculus is the notion of derivative-integral of fractional order. The most popular and most commonly used (also in this paper) is the concept of derivative - integral defined by Caputo. Although the derivatives of non-total order and differential equations of fractional order are known in the mathematical areas (Blasiak, S., 2016), recently they are used in the field of mechanics and physics. Differential equations of fractional order are used among others to describe physical phenomena occurring in electromagnetism, propagation of energy, thermal stresses (Blasiak, S. et al., 2014), relaxation vibrations (Blasiak, M., 2016; Blasiak, S. and Zahorulko, 2016; Nowakowski et al., 2016), viscoelasticity, thermoelasticity and pneumatic systems (Laski et al., 2014; Takosoglu et al., 2016; Zwierchowski, 2016). Compared to the classical calculus, the main advantage of fractional calculation is the possibility of investigation of the nonlocal response of mechanical systems. In the papers (Stanislavsky, 2005; Yonggang and Xiu'e, 2010) the authors defined the mechanical oscillators replacing the total derivatives with derivatives of fractional order. These equations were solved numerically and analytically using Laplace transform. In (Kaczorek, 2013) the author by using the Caputo derivative presented analytical solution of the fractional damped oscillator equation.

Harmonic oscillators appear in different areas of classical mechanics, electronics, experimental physics and quantum physics. Harmonic oscillators are defined by ordinary differential equations.

The following paper presents two models of the vibrating system derived from the classical equation of harmonic oscillator, which was reduced to a single model described by differential equation of fractional order.

### 2. Methods

Classical damped harmonic oscillator has three main components: the mass  $m$  (kg), the damping factor  $c$  (Ns/m), rigidity factor  $k$  (N/m):

---

\* Malgorzata Blasiak, PhD.: Kielce University of Technology, al. Tysiaclecia Panstwa Polskiego 7, 25-314, Kielce, Poland  
mdrab@tu.kielce.pl

\*\* Slawomir Blasiak, PhD.: Kielce University of Technology, al. Tysiaclecia Panstwa Polskiego 7, 25-314, Kielce, Poland  
sblasiak@tu.kielce.pl

$$m \frac{d^2 x(t)}{dt^2} + c \frac{dx(t)}{dt} + k x(t) = v(t) \quad (1)$$

for extortion  $v(t) = A_0 \cdot \sin(\omega t)$

Two cases were concerned:

The first model for  $m=0$  and the following initial condition:  $x(0)=0$

$$c \frac{dx(t)}{dt} + k x(t) = v(t) \quad (2)$$

Second model for  $c=0$  and the following initial conditions:  $x'(0)=0, x(0)=0$

$$m \frac{d^2 x(t)}{dt^2} + k x(t) = v(t) \quad (3)$$

Caputo's fractional derivative of a function  $f(t)$  is defined as:

$$\frac{d^\alpha}{dt^\alpha} f(t) \equiv {}^C D_t^\alpha f(t) = \frac{1}{\Gamma(n-\alpha)} \int_0^t (t-\tau)^{n-\alpha-1} \frac{d^n f(\tau)}{d\tau^n} d\tau \quad (4)$$

$$t > 0, n-1 < \alpha < n$$

In this definition, both the derivative and integral are defined on the interval, rather than at a point, as seen from the classical definition of a derivative.

Taking into account the relations of (4) to (1) and (2) equations and introducing replacement coefficients  $a$  and  $b$ , one brought them to a fractional equation of general form

$$a {}^C D_t^\alpha x(t) + b x(t) = v(t) \quad (5)$$

By applying the Laplace transform to (5) equation, one received:

$$g(s) = \frac{\bar{v}(s)}{as^\alpha + b} = \frac{1}{a} \frac{1}{s^\alpha + \frac{b}{a}} \cdot \bar{v}(s) \quad (6)$$

After applying the inverse Laplace transform in (6) equation, one obtained:

$$G(t) = \frac{1}{a} t^{\alpha-1} E_{\alpha,\alpha} \left( -\frac{b}{a} t^\alpha \right) \quad (7)$$

where  $E_{\alpha,\alpha}(t)$  is the Mittag-Leffler function, defined as follows:

$$E_{\alpha,\beta}(z) = \sum_{k=0}^{\infty} \frac{z^k}{\Gamma(\beta + \alpha k)} \quad z \in C, \beta \in C, \alpha > 0, \beta > 0 \quad (8)$$

In case when  $\alpha = \beta = 1$ , ML function has the following form  $E_{1,1}(z) = e^z$  and for  $\alpha = \beta = 2$ :

$$E_{2,2}(z) = \cosh(\sqrt{z}).$$

Using the general dependence on the inverse Laplace transform, and the Green's function, one wrote

$$x(t) = \mathcal{L}^{-1} \left\{ \frac{1}{s^\alpha + \omega^2} \cdot \bar{f}(s) \right\} = \int_0^t G(t-\tau) f(\tau) d\tau \quad (9)$$

and received the equation describing the oscillations of the system:

$$x(t) = \frac{1}{a} \int_0^t (t-\tau)^{\alpha-1} E_{\alpha,\alpha} \left( -\frac{b}{a} (t-\tau)^\alpha \right) v(\tau) d\tau \quad (10)$$

The results of numerical analysis of the current model are presented later in this article.

### 3. Results

For calculations one adopted the values of substitute coefficients  $a = b = 1$  in equation (5).

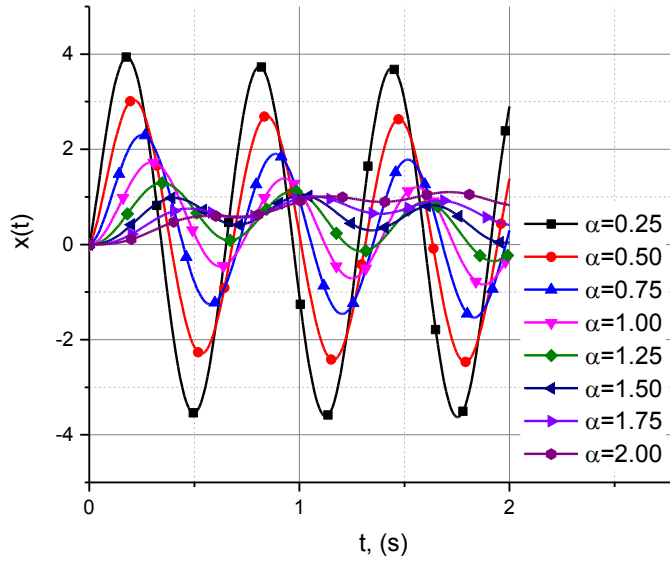


Fig. 1: Progression of vibrations of the system for  $0 < \alpha \leq 2$ .

The charts show the analysis of the course of vibrations for different values of  $\alpha$  describing the order of equation (5) of fractional order.

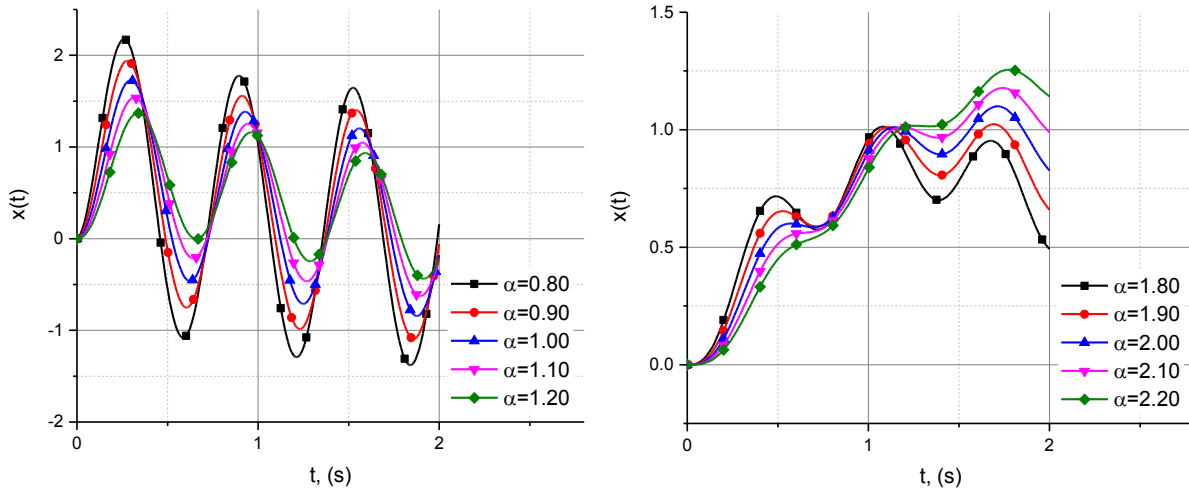


Fig. 2: Progression of vibrations of the system for  $\alpha \approx 1$  and  $\alpha \approx 2$ .

The obtained results for  $\alpha=1$  and  $\alpha=2$  are compliant with the results of analytical calculations described by the following dependencies

$$x(t) = \frac{a\omega A0}{a^2\omega^2 + b^2} e^{-\frac{b}{a}t} + \frac{A0(b\sin(\omega \cdot t) - a\omega\cos(\omega \cdot t))}{a^2\omega^2 + b^2} \quad (11)$$

$$x(t) = \frac{A0\omega}{\sqrt{\frac{b}{a}(\omega^2 a - b)}} \sin\left(\sqrt{\frac{b}{a}} \cdot t\right) - \frac{A0}{(\omega^2 a - b)} \sin(\omega \cdot t) \quad (12)$$

where (11) dependency presents the solution of the first model ( $m = 0$ ), and equation (12) is the solution of the second model ( $c = 0$ ).

The topic of ordinary differential equations is one of the most important subjects in mathematics and other sciences. However, there are no general methods to solve such equations. One of the most known methods to solve ordinary differential equations is the integral transform method. In this paper presented the Laplace transform were used to solve harmonic oscillator equations.

#### 4. Conclusion

In the paper one replaced the two models of oscillating systems described by classical equations of harmonic oscillator, by one reduced model of fractional order. For the description of the above mentioned model one used the concept of derivative-integral of fractional order defined by Caputo. It is significant that both the derivative and integral are defined on the interval, in contrast to the classical definition of a derivative, which is defined at a point. Therefore, the applied mathematical model allows to determine the whole set of the courses of vibrations of the system, and not only, as it does in the classical theory of vibrations, for an equation of 1 or 2 order.

#### Reserences

- Blasiak, M. (2016) Parametric analysis of piezoelectric transducer used for signal processing, in: Proc. Int. Conf. on Engineering Mechanics 2016 (ed. Zolotarev, I and Radolf, V.), Svratka, pp. 66-69.
- Blasiak, S. (2016) Time-fractional heat transfer equations in modeling of the non-contacting face seals, International Journal of Heat and Mass Transfer, 100, , pp. 79-88. doi:10.1016/j.ijheatmasstransfer.2016.04.040
- Blasiak, S., Takosoglu, J.E. and Laski, P.A. (2014) Heat transfer and thermal deformations in non-contacting face seals, Journal of Thermal Science and Technology, 9, 2, pp. JTST0011-JTST0011. doi:10.1299/jtst.2014jtst0011
- Blasiak, S. and Zahorulko, A.V. (2016) A parametric and dynamic analysis of non-contacting gas face seals with modified surfaces, Tribology International, 94, , pp. 126-137. doi:10.1016/j.triboint.2015.08.014
- Kaczorek, T. (2013) Application of the drazin inverse to the analysis of descriptor fractional discrete-time linear systems with regular pencils, International Journal of Applied Mathematics and Computer Science, 23, 1, pp. 29-33. doi:10.2478/amcs-2013-0003
- Laski, P.A., Takosoglu, J.E. and Blasiak, S. (2014) A delta type closed kinematics chain with pneumatic muscle actuator manipulator, in: Proc. Int. Conf. on Engineering Mechanics 2014 (ed. Fuis, V.), Svratka, pp. 360-363.
- Nowakowski, L., Miesikowska, M. and Blasiak, M. (2016) Speech intelligibility in the position of cnc machine operator, in: Proc. Int. Conf. on Engineering Mechanics 2016 (ed. Zolotarev, I and Radolf, V.), Svratka, pp. 422-425.
- Stanislavsky, A.A. (2005) Twist of fractional oscillations, Physica A: Statistical Mechanics and Its Applications, 354, 1-4, pp. 101-110. doi:10.1016/j.physa.2005.02.033
- Takosoglu, J.E., Laski, P.A., Blasiak, S., Bracha, G. and Pietrala, D. (2016) Determination of flow-rate characteristics and parameters of piezo valves, in: Proc. Int. Conf. Exp. Fluid Mech. 2016 (ed. Dancova, P.), Techn. Univ. Liberec, pp. 814-818.
- Yonggang, K. and Xiu'e, Z. (2010) Some comparison of two fractional oscillators, Physica B: Condensed Matter, 405, 1, pp. 369-373. doi:10.1016/j.physb.2009.08.092
- Zwierzchowski, J. (2016) Industrial robot vision system for moving spherical elements, in: Proc. Int. Conf. on Engineering Mechanics 2016 (ed. Zolotarev, I and Radolf, V.), Svratka, pp. 626-629.

## THE APPLICATION OF INTEGRAL TRANSFORMS TO SOLVING PARTIAL DIFFERENTIAL EQUATIONS OF THE FRACTIONAL ORDER

M. Blasiak<sup>\*</sup>, S. Blasiak<sup>\*\*</sup>

**Abstract:** *The authors presented a description of the mathematical model of the string vibrations with the use of a partial differential equation of the fractional order. They applied the Caputo fractional derivative in their deliberations. The following integral transforms were used in order to solve this problem: the Laplace transform for  $t$  time and finite sine transform for  $x$  displacement.*

**Keywords:** Integral Transform, Fractional Wave Equation, Caputo Fractional Derivative, Mittag-Leffler Function.

### 1. Introduction

Over the last decades, partial differential equations of the fractional order have been applied in the modelling of various processes, such as energy propagation, thermal stresses, relaxation vibrations, nonlinear control system theory or robotics. Derivatives and integrals of fractional order became an attractive area of mathematics, being widely applied in various fields of science, especially physics, astrophysics, nuclear physics, chemistry, classical mechanics, quantum mechanics, vibration (Nowakowski, Miko, et al., 2016) or engineering (Blasiak, M., 2016; Laski, 2016; Laski et al., 2014; Nowakowski, Miesikowska, et al., 2016; Takosoglu et al., 2016; Zwierzchowski, 2016). A very important model is the fractional wave equations, which has been used in the theory of vibrations of smart materials in media where the memory effects cannot be neglected (Herzallah et al., 2010). The authors of papers (Blasiak, S., 2016; Stanislavsky, 2005) replaced the classical wave equation with the derivative of the fractional order.

This paper presents the fractional generalization of the wave equation describing the propagation of a wave in the string for the set initial and boundary conditions. The main advantage of the fractional calculation is the possibility of the investigation of the nonlocal response of mechanical systems, contrary to the classical calculation. The Caputo fractional derivative, as well as the Laplace transform for  $t$  time (Schiff, 1999) and finite sine transform for  $x$  displacement were applied in order to describe the problem in question.

### 2. Methods

The considerations apply to a uniform, flexible string of finite  $l$  length, with the height difference of mounting of two ends along  $y$  axis amounting to  $a$ . The physical properties of the system are determined by the following parameters:  $\rho$  - mass of the string section with a unit length and  $T$  - tensile strength. A wave causing vibrations perpendicular to the string length was taken into consideration. A case of low string vibrations, where the string deflections from the balance point are low in comparison with the string length, was considered.

The time-fractional wave equation (1) was presented below.

---

\* Malgorzata Blasiak, PhD.: Kielce University of Technology, al. Tysiaclecia Panstwa Polskiego 7, 25-314, Kielce, Poland  
mdrab@tu.kielce.pl

\*\* Slawomir Blasiak, PhD.: Kielce University of Technology, al. Tysiaclecia Panstwa Polskiego 7, 25-314, Kielce, Poland  
sblasiak@tu.kielce.pl

$$\rho \frac{\partial^\alpha y}{\partial \tau^\alpha} = T \frac{\partial^2 y}{\partial x^2} \quad 0 < x < l, t > 0 \quad (1)$$

By substituting  $t = \frac{T}{\rho} \tau = \nu \tau$ , the following equation was formulated:

$$\frac{\partial^\alpha y}{\partial t^\alpha} = \frac{\partial^2 y}{\partial x^2} \quad 0 < x < l, t > 0 \quad (2)$$

The following boundary and initial conditions were considered:

$$\begin{aligned} a) & y(0, t) = 0, \quad t > 0, \\ b) & y(l, t) = a, \quad t > 0, \\ c) & y(x, 0^+) = 0, \quad 0 < x < l, 0 < \alpha \leq 2, \\ d) & y_t(x, 0^+) = 0, \quad 0 < x < l, 1 < \alpha \leq 2. \end{aligned} \quad (3)$$

By substituting the finite sine transform in the general form  $f^*(n, t) = \int_0^L f(x, t) \sin\left(\frac{n\pi x}{L}\right) dx$  to equation (2), the following equation was formulated:

$$\mathfrak{T}_s \left[ \frac{\partial^2 y}{\partial x^2} \right] = \frac{n\pi}{l} \left[ y(0, t) - (-1)^n y(l, t) \right] - \frac{n^2 \pi^2}{l^2} y^* = \frac{n\pi}{l} \left[ -(-1)^n a \right] - \frac{n^2 \pi^2}{l^2} y^* \quad (4)$$

The left side in equation (2) describes the Caputo fractional derivative in the general form (Parsian, 2012):

$$\frac{\partial^\alpha}{\partial t^\alpha} f(t) \equiv D_C^\alpha f(t) \quad (5)$$

where:

$$\begin{aligned} D_C^\alpha f(t) &= I^{n-\alpha} D^n f(t) = \frac{1}{\Gamma(n-\alpha)} \int_0^t (t-\tau)^{n-\alpha-1} \frac{d^n f(\tau)}{d\tau^n} d\tau \\ t &> 0, \quad n-1 < \alpha < n \end{aligned} \quad (6)$$

$\Gamma$  - Euler gamma function.

the Laplace transform rule for fractional derivative

$$\mathcal{L} \{ D_C^\alpha f(t) \} = s^\alpha \bar{f}(s) - \sum_{k=0}^{n-1} f^{(k)}(0^+) s^{\alpha-1-k}, \quad n-1 < \alpha < n \quad (7)$$

$$\mathcal{L} \{ D_C^\alpha y(t) \} = s^\alpha \bar{y}(s) - \underbrace{y^{(0)}(0^+) s^{\alpha-1-0}}_{=0} - \underbrace{y^{(1)}(0^+) s^{\alpha-1-1}}_{=0}, \quad n-1 < \alpha < n$$

Equation (2), after applying the Laplace transform and boundary condition (3)b  $\bar{y}(l, s) = \frac{a}{s}$ , might be recorded as follows:

$$\bar{y}^*(s) = -(-1)^n \frac{al}{n\pi} \left( \frac{1}{s} - \frac{s^{\alpha-1}}{(s^\alpha + \omega^2)} \right) \quad (8)$$

For the second element from the brackets in equation (8), the inverse Laplace transform was used:



$$\mathcal{L}^{-1}\left[\frac{s^{\alpha-1}}{(s^{\alpha} + \omega^2)}\right] = t^{1-1} E_{\alpha,1}(-\omega^2 t^{\alpha}) = E_{\alpha}(-\omega^2 t^{\alpha}) \text{ for } \omega^2 = \left(\frac{n\pi}{l}\right)^2$$

where  $E_{\alpha,\beta}(z)$  means Mittag-Leffler type function defined by the series

$$E_{\alpha,\beta}(z) = \sum_{v=1}^{\infty} \frac{z^v}{\Gamma(\alpha v + \beta)} \quad \alpha > 0, \beta > 0 \quad (9)$$

That is why, after applying the inverse Laplace transform, equation (8) takes the following form:

$$y^*(n) = -(-1)^n \frac{n\pi a}{l} \frac{1}{\omega^2} (1 - E_{\alpha}(-\omega^2 t^{\alpha})) \quad (10)$$

After using the inverse sine transform, the following equation was obtained:

$$y(x,t) = -\frac{2a}{l} \sum_{n=1}^{\infty} (-1)^n \frac{l}{n\pi} (1 - E_{\alpha}(-\omega^2 t^{\alpha})) \cdot \sin\left(\frac{n\pi x}{l}\right) \quad (11)$$

By using the following dependency:

$$\frac{2a}{l} \sum_{n=1}^{\infty} \frac{l}{n\pi} (-1)^n \cdot \sin\left(\frac{n\pi x}{l}\right) = -\frac{a x}{l}$$

The dependency describing the string vibrations takes its final form

$$y(x,\tau) = \frac{a x}{l} + \frac{2a}{\pi} \sum_{n=1}^{\infty} \frac{(-1)^n}{n} E_{\alpha}(-v\omega^2 \tau^{\alpha}) \cdot \sin\left(\frac{n\pi x}{l}\right) \quad (12)$$

For  $E_2(-z) = \cos(\sqrt{z})$

$$y(x,\tau) = \frac{a x}{l} + \frac{2a}{\pi} \sum_{n=1}^{\infty} \frac{(-1)^n}{n} \cos\left(\sqrt{v} \frac{n\pi \tau}{l}\right) \cdot \sin\left(\frac{n\pi x}{l}\right) \quad (13)$$

## Results

The following data was adopted for the calculations: the string length  $l = 20 \text{ m}$ , the height difference of mounting of two string ends  $a = 0.1 \text{ m}$ , the velocity of transverse waves  $v = 0.25 \text{ m/s}$ .

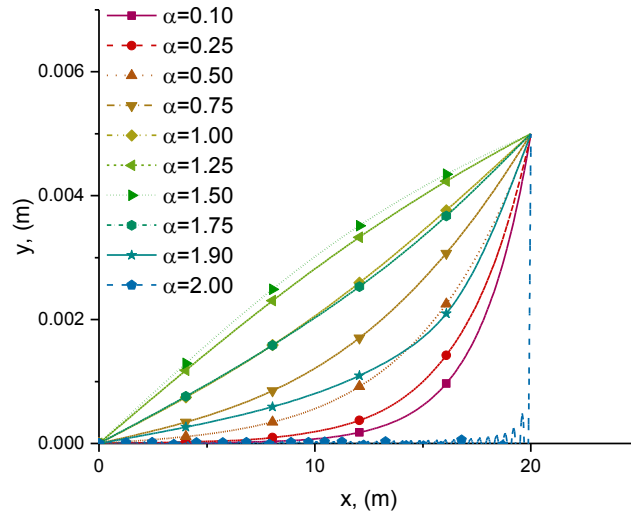


Fig. 1: Wave propagation in the string for different  $\alpha$ .

### 3. Conclusions

This paper describes the mathematical model of string vibrations of a finite length with the use of a partial differential equation of the fractional order. The application of fractional calculus for the calculation of the presented model makes it possible to determine the whole set of the waveforms of the string vibrations, and not only as it is found in the classical theory of vibrations, equations 1 or 2. The Laplace transform for  $t$  time and finite sine transform for  $x$  displacement were applied in order to solve the presented model. The main advantage of using the integral transforms is the solution of partial differential equations by transforming them into algebraic equations as well as automatic consideration of the initial and boundary conditions in the solving process.

### References

- Blasiak, M. (2016) Parametric analysis of piezoelectric transducer used for signal processing, in: Proc. Int. Conf. on Engineering Mechanics 2016 (ed. Zolotarev, I and Radolf, V.), Svratka, pp. 66-69.
- Blasiak, S. (2016) Time-fractional heat transfer equations in modeling of the non-contacting face seals, International Journal of Heat and Mass Transfer, 100, , pp. 79-88. doi:10.1016/j.ijheatmasstransfer.2016.04.040
- Herzallah, M.A.E., El-Sayed, A.M.A. and Baleanu, D. (2010) On the fractional-order diffusion-wave process, Romanian Reports of Physics, 55, 3-4, pp. 274-284.
- Laski, P.A. (2016) The design of a proportional slit valve with a piezoelectric actuator, in: Proc. Int. Conf. on Engineering Mechanics 2016 (ed. Zolotarev, I and Radolf, V.), Svratka, pp. 350-353.
- Laski, P.A., Takosoglu, J.E. and Blasiak, S. (2014) A delta type closed kinematics chain with pneumatic muscle actuator manipulator, in: Proc. Int. Conf. on Engineering Mechanics 2016 (ed. Fuis, V.), Svratka, pp. 360-363.
- Nowakowski, L., Miesikowska, M. and Blasiak, M. (2016) Speech intelligibility in the position of cnc machine operator, in: Proc. Int. Conf. on Engineering Mechanics 2016 (ed. Zolotarev, I and Radolf, V.), Svratka, pp. 422-425.
- Nowakowski, L., Miko, E. and Skrzyniarz, M. (2016) The analysis of the zone for initiating the cutting process of x37crmov51 steel, in: Proc. Int. Conf. on Engineering Mechanics 2016 (ed. Zolotarev, I and Radolf, V.), Svratka, pp. 426-429.
- Parsian, H. (2012) Time fractional wave equation: caputo sense, Adv. Stud. Theor. Phys, 6, 2, pp. 95-100. Retrieved from <http://www.doaj.org/doi/func=fulltext&aId=1379100>.
- Schiff, J. (1999) The laplace transform: theory and applications, The Mathematical Gazette, 85, 502, pp. 178. doi:10.2307/3620536.
- Stanislavsky, A.A. (2005) Twist of fractional oscillations, Physica A: Statistical Mechanics and Its Applications, 354, 1-4, pp. 101-110. doi:10.1016/j.physa.2005.02.033.
- Takosoglu, J.E., Laski, P.A., Blasiak, S., Bracha, G. and Pietrala, D. (2016) Determination of flow-rate characteristics and parameters of piezo valves, in: Proc. Int. Conf. Exp. Fluid Mech. 2016 (ed. Dancova, P.), Techn. Univ. Liberec, pp. 814-818.
- Zwierzchowski, J. (2016) Industrial robot vision system for moving spherical elements, in: Proc. Int. Conf. on Engineering Mechanics 2016 (ed. Zolotarev, I and Radolf, V.), Svratka, pp. 626-629.

## HEAT TRANSFER IN NON-CONTACTING FACE SEALS USING FRACTIONAL FOURIER LAW

S. Blasiak<sup>\*</sup>

**Abstract:** *The paper presents a mathematical model of the heat transfer process in non-contacting face seals. A time fractional Fourier law, obtained from fractional calculus, was applied for a slewing ring (rotor). Heat transfer in a stator was described by Laplace's equation. The fractional heat conduction equation (for the rotor) was considered in the case  $0 < \alpha \leq 2$ .*

**Keywords:** Time Fractional Fourier Law, Mechanical Seal, Non-Contacting Face Seal, Heat Transfer, Integral Transform.

### 1. Introduction

The paper presents a model based on time fractional Fourier law, where a derivative of temperature becomes fractional over time. Most of the scientific papers relating to the transfer of heat in non-contacting face seals are based on the classical Fourier law. One of the first studies illustrate mathematical models which contain an explicit reference to heat transfer in one direction (Pascovici and Etsion, 1992) and do not include changes in temperature over time. Other works include a much more advanced thermo-hydrodynamic and thermo-elasto-hydrodynamic models of non-contacting face seals (Blasiak, S., 2015; Blasiak, S. et al., 2014). In the field of non-contacting face seals one can see a broader aspect of research. It concerns vibration analysis of sealing rings based on models presented in the works (Blasiak, M., 2016; Blasiak, S. and Zahorulko, 2016; Koruba and Krzysztofik, 2013; Krzysztofik and Koruba, 2014), but also experimental studies including measurements of geometrical dimensions and surface structure, materials (Adamczak and Bochnia, 2016; Bochnia, 2012; Koruba and Krzysztofik, 2013; Krzysztofik and Koruba, 2014) and protective layers (Nowakowski, Miesikowska, et al., 2016; Nowakowski, Miko, et al., 2016; Nowakowski and Wijas, 2016), or studies aimed at obtaining temperature measurements on different test rigs. Another aspect of ongoing research work, which has become extremely popular in the last thirty years, is the differential and integral calculus conducted on derivatives of fractional order. An example may be the new rheological model, heat transfer and mass flow (Blasiak, S., 2016), dynamic processes (Kaczorek, 2013), phenomena taking place in electrical networks, robotics (Janecki et al., 2015; Janecki and Zwierzchowski, 2009, 2015; Laski, 2016; Laski et al., 2014; Laski Pawel et al., 2015; Pietrala, 2016; Takosoglu, J E et al., 2014; Takosoglu, J E, 2016) or properties of viscoelastic materials. This paper presents a model of heat transfer in non-contacting face seals. Integral transform was used to solve differential equations involving partial derivatives. Results concerning the solution of time fractional Fourier law were presented and discussed.

### 2. Theoretical Model

A part of the theoretical model was presented and solved in previous work (Blasiak, S., 2016), while describing the stationary issues of heat transfer in the following system: fluid film – sealing rings for non-contacting face seals. A conduction equation (9) for a non-rotating ring will be fixed (steady state), while the rotor will take into account the changes in temperature over time (10) and it will be a fractional equation with respect to time.

$$\frac{1}{r} \frac{\partial \theta^s}{\partial r} + \frac{\partial^2 \theta^s}{\partial r^2} + \frac{\partial^2 \theta^s}{\partial z^2} = 0 \text{ for } r_i \leq r \leq r_o; 0 \leq z \leq L, \quad (1)$$

---

<sup>\*</sup> Sławomir Blasiak, PhD.: Kielce University of Technology, al. Tysiąclecia Państwa Polskiego 7, 25-314, Kielce, Poland  
sblasiak@tu.kielce.pl

$$\frac{\partial^\alpha \theta^r}{\partial t^\alpha} = \kappa \left( \frac{1}{r} \frac{\partial \theta^r}{\partial r} + \frac{\partial^2 \theta^r}{\partial r^2} + \frac{\partial^2 \theta^r}{\partial z^2} \right), \text{ for } r_i \leq r \leq r_o; 0 \leq z \leq L^r; t > 0. \quad (2)$$

The exact transition to time fractional heat conduction equation was presented in the work of (Povstenko, 2015). The left side of the equation (2) is the Caputo fractional derivative in the general form:

$$\frac{\partial^\alpha}{\partial t^\alpha} f(t) \equiv D_C^\alpha f(t) = I^{n-\alpha} D^n f(t) = \frac{1}{\Gamma(n-\alpha)} \int_0^t (t-\tau)^{n-\alpha-1} \frac{d^n f(\tau)}{d\tau^n} d\tau \quad (3)$$

$$t > 0, \quad n-1 < \alpha < n$$

with initial conditions:

$$\begin{aligned} t=0 \quad \theta &= 0, \quad 0 < \alpha \leq 2, \\ t=0 \quad \frac{\partial \theta}{\partial t} &= 0, \quad 1 < \alpha \leq 2. \end{aligned} \quad (4)$$

The solution of equations (1) and (2) for the sealing ring – fluid film system is possible using the analytical methods including boundary conditions specified in the paper (Blasiak, S., 2016).

### 3. Analytical solution of the model

Marchi–Zgrablich integral transform, Fourier finite cosine transform and Laplace transform for time-fractional differential equations were used to solve the (2) equation for a rotor. After performing the algebraic transformations and applying three integral transforms, the equation (2) has the following form:

$$\hat{\theta}^{r*}(s) = -\frac{\kappa \bar{q}}{\lambda^r (s^\alpha + \omega^2)}. \quad (5)$$

Temperature of the rotor is described by the following equation:

$$\begin{aligned} T^r = T_o - \frac{\kappa}{\lambda^r L^r} \sum_{n=1}^{\infty} \frac{\bar{q} \cdot S_p(\lambda^r, \alpha^f, k_n \cdot r)}{\int_{r_i}^{r_o} r [S_p(\lambda^r, \alpha^f, k_n \cdot r)]^2 dr} \sum_{m=1}^{\infty} t^{\alpha-1} E_{\alpha,\alpha}(-\omega_0^2 t^\alpha) + \\ - \frac{2\kappa}{\lambda^r L^r} \sum_{n=1}^{\infty} \frac{\bar{q} \cdot S_p(\lambda^r, \alpha^f, k_n \cdot r)}{\int_{r_i}^{r_o} r [S_p(\lambda^r, \alpha^f, k_n \cdot r)]^2 dr} \sum_{m=1}^{\infty} t^{\alpha-1} E_{\alpha,\alpha}(-\omega^2 t^\alpha) \cdot \cos\left(\frac{m\pi z}{L^r}\right). \end{aligned} \quad (6)$$

A similar calculation procedure aimed at solving equation (1) was carried out for a stationary ring.

$$T^s = T_0 + \sum_{n=1}^{\infty} \frac{\cosh(k_n z) \int_{r_i}^{r_o} r \cdot \theta^f \cdot S_p(\lambda^s, \alpha^f, k_n \cdot r) dr}{\cosh(k_n L^s) \int_{r_i}^{r_o} r [S_p(\lambda^s, \alpha^f, k_n \cdot r)]^2 dr} \cdot S_p(\lambda^s, \alpha^f, k_n \cdot r). \quad (7)$$

### 4. Results and discussion

Numerical calculations were performed based on physico-chemical properties of the materials used for sealing rings and the medium to be sealed, gathered in the table below.

Tab. 1: The properties of materials used for rings.

	Young's modulus E	Poisson's coefficient ν	Thermal conductivity λ	Thermal Expansion τ
<b>Silicon carbide</b>	380 (GPa)	0.18	130 (W/mK)	$5 \times 10^{-6} (^{\circ}\text{C}^{-1})$
<b>Carbon</b>	25 (GPa)	0.20	15 (W/mK)	$4 \times 10^{-6} (^{\circ}\text{C}^{-1})$

The calculations also assume, as in the work:(Pascovici and Etsion, 1992), that the height of the radial slot is  $1\text{ }\mu\text{m}$ .

Tab. 2: Geometric and operating reference parameters.

Geometric parameters		Operating parameters	
Inner radius $r_i$	0.040 (m)	Angular velocity $\omega$	500 (rad/s)
Outer radius $r_o$	0.045 (m)	Nominal slot $h_o$	$1 \times 10^{-6}$ (m)
Thickness of rings $L^s$ and $L^r$	0.010 (m)	Medium temperature $T_o$	20 ( $^{\circ}\text{C}$ )
Thermal conductivity $\lambda^f$	0.65 (W/mK)	Heat transfer coefficient (water) $\alpha^f$	18000 ( $\text{W}/\text{m}^2\text{ K}$ )

Fig 1. shows temperature distribution for  $t = 0.25(\text{s})$  and the order of fractional derivative  $\alpha$  in the range of  $\alpha = 0.5 - 2$ .

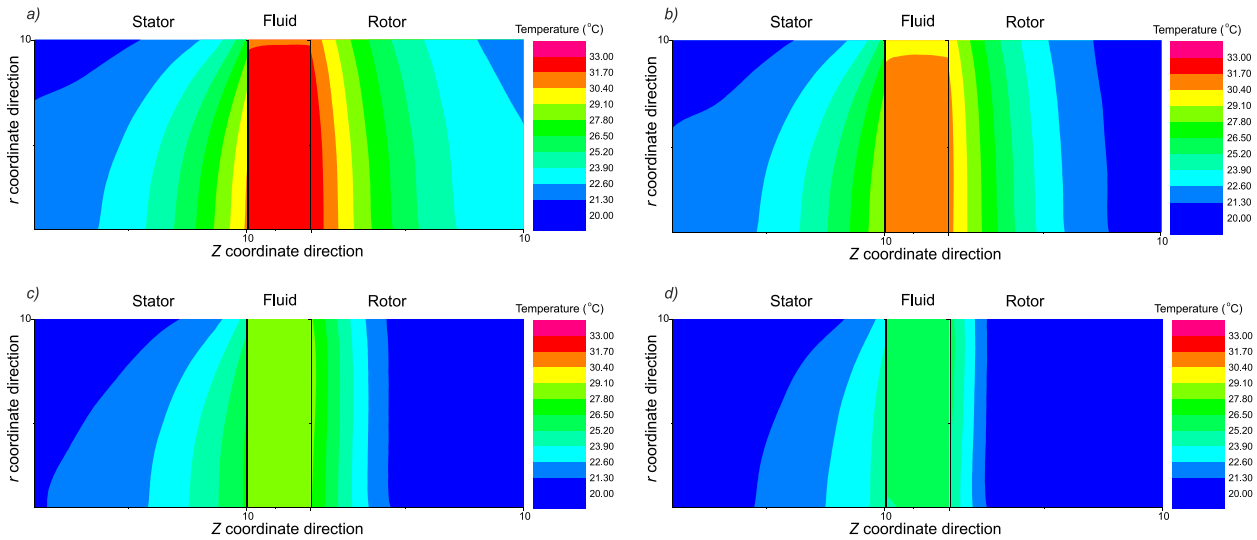


Fig. 1: Temperature distribution in the fluid film and sealing rings for: a)  $\alpha = 0.50$ , b)  $\alpha = 1.00$ , c)  $\alpha = 1.50$ , d)  $\alpha = 2.00$ .

The use of fractional heat conduction equation reflects the whole spectrum of heat conduction. If we assume  $\alpha = 1$ , we will receive the classical form of Fourier's equation. In case of  $\alpha = 2$ , it will be the ballistic heat conduction.

## 5. Conclusion

The use of differential equations of fractional order has expanded the possibilities for the analysis of thermal phenomena occurring in the slot, on the surface and subsurface layer of the stator and rotor. The friction heat caused by shear stresses occurring in the medium layer affects the local changes in temperature of the seal. After exceeding the boiling point in fluid film, the working medium is discharged, which in turn leads to dry friction and drastic wear of sealing rings. In addition, it may also result in the allowable temperature being exceeded for the used materials, lead to their destruction due to the occurrence of defects related to cracking or obliterating of rings resulting from thermal stresses.

## References

- Adamczak, S. and Bochnia, J. (2016) Estimating the approximation uncertainty for digital materials subjected to stress relaxation tests, *Metrology and Measurement Systems*, 23, 4, SI, pp. 545-553.
- Blasiak, M. (2016) Parametric analysis of piezoelectric transducer used for signal processing, in: *Proc. Int. Conf. on Engineering Mechanics 2016* (Eds. Zolotarev, I., Radolf, V.), Svratka, Czech Republic, pp. 66-69.

- Blasiak, S. (2015) The two dimensional thermohydrodynamic analysis of a lubrication in non-contacting face seals, *Journal of Thermal Science and Technology*, 10, 1, pp. JTST0016-JTST0016. doi:10.1299/jtst.2015jtst0016
- Blasiak, S. (2016) Time-fractional heat transfer equations in modeling of the non-contacting face seals, *International Journal of Heat and Mass Transfer*, 100, pp. 79-88. doi:10.1016/j.ijheatmasstransfer.2016.04.040
- Blasiak, S., Takosoglu, J.E. and Laski, P.A. (2014) Heat transfer and thermal deformations in non-contacting face seals, *Journal of Thermal Science and Technology*, 9, 2, pp. JTST0011-JTST0011. doi:10.1299/jtst.2014jtst0011
- Blasiak, S. and Zahorulko, A. V. (2016) A parametric and dynamic analysis of non-contacting gas face seals with modified surfaces, *Tribology International*, 94, pp. 126-137. doi:10.1016/j.triboint.2015.08.014
- Bochnia, J. (2012) Ideal material models for engineering calculations, *Procedia Engineering*, 39, 0, pp. 98-110.
- Janecki, D., Cedro, L. and Zwierzchowski, J. (2015) Separation of non-periodic and periodic 2d profile features using b-spline functions, *Metrology and Measurement Systems*, 22, 2, pp. 289-302.
- Janecki, D. and Zwierzchowski, J. (2009) The bird-cage method used for measuring cylindricity. a problem of optimal profile matching, in: XIX IMEKO WORLD Congr. Fundam. Appl. Metrol. Proc. IMEKO, PO BOX 457, H-1371 5 Budapest, Hungary, pp. 1784-1789.
- Janecki, D. and Zwierzchowski, J. (2015) A method for determining the median line of measured cylindrical and conical surfaces, *Measurement Science and Technology*, 26, 8.
- Kaczorek, T. (2013) Application of the Drazin inverse to the analysis of descriptor fractional discrete-time linear systems with regular pencils, *International J. of Applied Mathematics and Computer Science*, 23, 1, pp. 29-33.
- Koruba, Z. and Krzysztofik, I. (2013) An algorithm for selecting optimal controls to determine the estimators of the coefficients of a mathematical model for the dynamics of a self-propelled anti-aircraft missile system, *Proceedings of the Institution of Mechanical Engineers Part K-J. Of Multi-Body Dynamics*, 227, K1, pp. 12-16.
- Krzysztofik, I. and Koruba, Z. (2014) Mathematical model of movement of the observation and tracking head of an unmanned aerial vehicle performing ground target search and tracking, *Journal of Applied Mathematics*.
- Laski, P.A. (2016) The design of a proportional slit valve with a piezoelectric actuator, in: *Proc. Int. Conf. on Engineering Mechanics 2016* (Eds. Zolotarev, I., Radolf, V.), Svratka, Czech Republic, pp. 350-353.
- Laski, P.A., Takosoglu, J.E. and Blasiak, S. (2014) A delta type closed kinematics chain with pneumatic muscle actuator manipulator, in: *Proc. Int. Conf. on Engineering Mechanics 2014* (Ed. Fuis, V.), Svratka, Czech Republic, pp. 360-363.
- Laski P.A., Takosoglu J.E. and Blasiak, S. (2015) Design of a 3-dof tripod electro-pneumatic parallel manipulator, *Robotics and Autonomous Systems*, 72, pp. 59-70. doi:10.1016/j.robot.2015.04.009
- Nowakowski, L., Miesikowska, M. and Blasiak, M. (2016) Speech intelligibility in the position of CNC machine operator, in: *Proc. Int. Conf. on Engineering Mechanics 2016* (Eds. Zolotarev, I., Radolf, V.), Svratka, Czech Republic, pp. 422-425.
- Nowakowski, L., Miko, E. and Skrzyniarz, M. (2016) The analysis of the zone for initiating the cutting process of x37crmov51 steel, in: *Proc. Int. Conf. on Engineering Mechanics 2016* (Eds. Zolotarev, I., Radolf, V.), Svratka, Czech Republic, pp. 426-429.
- Nowakowski, L. and Wijas, M. (2016) The evaluation of the process of surface regeneration after laser cladding and face milling, in: *Proc. Int. Conf. on Engineering Mechanics 2016* (Eds. Zolotarev, I., Radolf, V.), Svratka, Czech Republic, pp. 430-433.
- Pascovici, M.D. and Etsion, I. (1992) A thermohydrodynamic analysis of a mechanical face seal, *ASME Journal of Tribology*, 1992, vol.114, pp. 639-645.
- Pietrala, D.S. (2016) Parallel manipulator with pneumatic muscle drive, in: *Proc. Int. Conf. on Engineering Mechanics 2016* (Eds. Zolotarev, I., Radolf, V.), Svratka, pp. 458-461.
- Povstenko, Y. (2015) *Fractional Thermoelasticity*. Springer International Publishing.
- Takosoglu, J.E. (2016) Experimental research of flow servo-valve, in: *Proc. Int. Conf. Exp. Fluid Mech. 2016* (ed. Dancova, P.), Techn. Univ. Liberec, pp. 819-823.
- Takosoglu, J.E., Laski, P.A. and Blasiak, S. (2014) Innovative modular pneumatic valve terminal with self-diagnosis, control and network communications, in: *Proc. Int. Conf. on Engineering Mechanics 2014* (Ed. Fuis, V.), Svratka, Czech Republic, pp. 644-647.

## HEAT TRANSFER MODEL FOR THE WAVY-TILT-DAM MECHANICAL SEALS USING GREEN'S FUNCTION METHOD

S. Blasiak \*

**Abstract:** *The paper presents a two-dimensional model of heat transfer for Wavy Tilt Dam (WTD) of mechanical face seal. This model includes both the heat transfer in liquid, and in sealing rings. It has been also assumed that the stationary ring is completely isolated from the environment. All the heat generated in the radial gap is discharged to the surrounding medium on the process side, by the rotor. The comparison of temperature distributions for a smooth surface and a surface with a wave, clearly indicates that the introduction of surface modification has a big influence on the temperature distribution in a fluid-film sealing rings. The research has also revealed that the maximum temperature of the fluid-film is reduced with increasing amplitude of the undulations of the surface.*

**Keywords:** Green's Function method, Mechanical seal, Non-contacting face seal, Heat transfer.

### 1. Introduction

High reliability, high tightness and flexibility are just some of the range of benefits offered by the non-contact face seals. Development of this type of construction was possible thanks to the wider research conducted over those critical components of machinery and equipment (Laski, Takosoglu, and Blasiak, 2014; Laski, 2016; Nowakowski, Miesikowska, and Blasiak, 2016; Nowakowski, Miko, and Skrzyniarz, 2016; Takosoglu, Laski, Blasiak, Bracha, and Pietrala, 2016a, 2016b). These studies within their scope included the dynamic of vibration of sealing rings and control (Zhang and Zhao, 2014; Lee and Zheng, 2013; Koruba and Krzysztolik, 2013; Krzysztolik and Koruba, 2014) and heat transfer in a fluid-film sealing rings. These studies are particularly important because of the wide range of temperatures in which there are working non-contact face seals. Manufacturers declare temperature ranges of these components from -20 to 220 °C for gas-dynamic seals, and from -54 to even 650 °C for non-contact face seals working with other media (Meng, Bai, and Peng, 2014) and with various operating parameters (Kavinprasad, Shankar, and Karthic, 2015). Such a large range of operating temperature poses a number of problems for scientific researchers. Evaporation of the working medium forces the conduction of research and development of mathematical models describing the phenomenon of two-phase flow through the radial gap (Nyemeck, Brunetiere, and Tournerie, 2015) and bench research on this phenomenon, (Wang, Huang, Liu, Li, and Wang, 2014). When making a further analysis of the literature in the field of heat transfer in a non-contact face seals, both for the fluid layer and cooperating rings, one can find works including thermo-hydrodynamic models (THD) and thermo-elastohydrodynamic models (TEHD) as in the works: (Blasiak, 2015) and (Brunetiere, 2010), and the work of numerical solution of models of heat transfer and thermo deformation of sealing rings (Blasiak, Takosoglu, and Laski, 2014). New technologies allow for the development of materials with physical properties (Bochnia, 2012; Adamczak and Bochnia, 2016) allowing to discharge into the environment the large heat fluxes, as well as to perform certain microstructures on the sliding surfaces of rings. In addition, conducted research aim at developing scientific solutions reducing the leakage of the working fluid to the environment. This is particularly important if the non-contact face seals work in devices pumping dangerous and aggressive media, which leakage might contaminate the environment. The presented work aims to present the solution of the heat exchange model using Green's Function Method for Wavy Tilt Dam (WTD) mechanical face seal and to illustrate the results of analyzes for specific operating conditions.

---

\* Slawomir Blasiak, PhD.: Kielce University of Technology, al. Tysiaclecia Panstwa Polskiego 7, 25-314, Kielce, Poland  
sblasiak@tu.kielce.pl



## 2. Formulation of the problem

The non-contact face seal consists of two rings: the fixed (1) and rotating (2), between which there is a fluid film. Diagram of such a seal is shown in Fig. 1a.

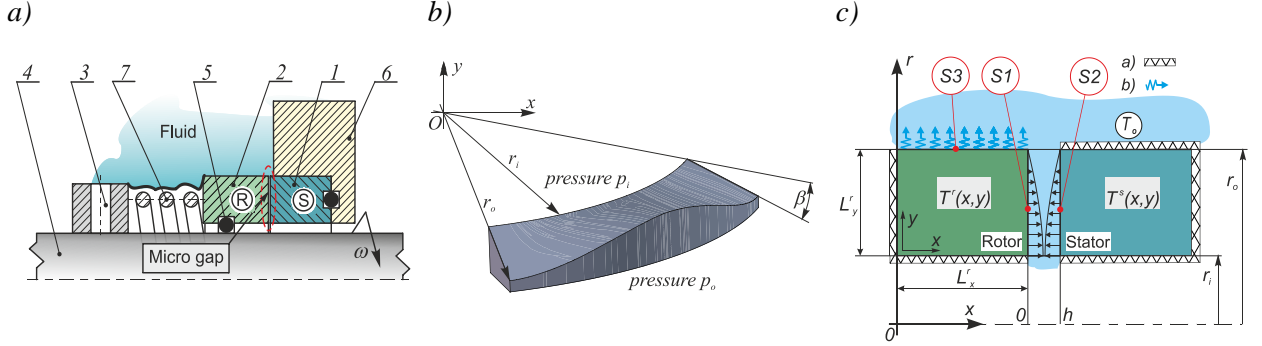


Fig. 1: a) diagram of non-contact face seal. 1 - stator 2 - rotor 3 - steady pin, 4 - shaft, 5 - O-ring 6 - housing, 7 - spring; b) ring surface profile; c). conditions of heat transfer in the non-contact face seal, a) isolated surfaces, b) heat transfer by convection.

The height of the radial gap for the wavy-tilt-dam mechanical seal, is described by this relationship, similarly as in the work of (Liu, Liu, Li, Liu, and Wang, 2015):

$$h = h(r) = \begin{cases} h_o + (1 + \cos(N_g \cdot \theta)) \cdot (y - y_d) \cdot \beta & y > y_d \\ h_o & y \leq y_d \end{cases} \quad (1)$$

The temperature distribution in the fluid film was determined by solving the simplified equation of energy, as:

$$\mu \left( \frac{\partial v_\phi}{\partial x} \right)^2 + \lambda^f \frac{\partial^2 T^f}{\partial x^2} = 0 \quad (2)$$

Where  $v_\phi$  describes the linear variation of fluid velocity along the height of fluid film (Couette flow).

Assumed boundary conditions are referenced as in Fig. 1c:

On the surface S1 it is assumed that  $T^r(y) = T^f(y)$  and  $\lambda^r \left( \frac{\partial T^r}{\partial x} \right) = \lambda^f \left( \frac{\partial T^f}{\partial x} \right) \Big|_{x=0}$ . On the surface S2 -it is

assumed the equality of temperatures,  $T^f(y) = T^s(y)$  for  $x = h$  and  $\left( \frac{\partial T^f}{\partial x} \right) \Big|_{x=h} = 0$ , which means that the

entire heat of the radial gap is discharged to the surrounding medium practically by the rotating ring. On the surface S3, it is assumed the heat transfer by convection according to the formula:

$-\lambda^r \frac{\partial T^r}{\partial y} \Big|_{y=L_y} = \alpha^r (T^r - T_o) \Big|_{y=L_y}$ . Mathematical model is solved, using the Green's function method.

## 3. Analytical solution

In the first step of the considered issue, there has been fixed the distributions of temperature in the sealing rings by specifying a general form of a function satisfying the Laplace's equation (5), both for the stationary ring (stator), as well as the rotor, taking into account the boundary conditions set out above. In the present model there has been assumed a rectangular coordinate system in order to simplify analytical calculations.

$$\frac{\partial^2 \theta}{\partial x^2} + \frac{\partial^2 \theta}{\partial y^2} = 0 \quad (3)$$

Finally, the relationship describing the temperature distribution in the stator takes the form:

$$\begin{aligned} \theta^s(x, y) = & \frac{2}{L_y} \sum_{n=1}^{\infty} \cos\left(\frac{n\pi}{L_y} y\right) \frac{\sinh\left(\frac{L_x n \pi}{L_y} \left(1 - \frac{x}{L_x}\right)\right)}{\sinh\left(\frac{L_x n \pi}{L_r}\right)} \int_0^{L_y} \left(\theta(x', y')\Big|_{x'=0} \cos\left(\frac{n\pi}{L_y} y'\right)\right) dy' + \\ & + \frac{2}{L_y \pi} \sum_{m=1}^{\infty} \frac{2 \sin\left(\frac{(2m-1)\pi}{2L_x} x\right)}{(2m-1)} \int_0^{L_y} \left(\theta(x', y')\Big|_{x'=0}\right) dy' \end{aligned} \quad (4)$$

The dependence describing the temperature distribution in the rotor takes the form used for numerical calculations in the form of:

$$\begin{aligned} \theta^r(x, y) = & \frac{2}{L_x} \sum_{m=1}^{\infty} \sum_{n=1}^{\infty} \frac{2 \left( \gamma_n^{r^2} + \left( \frac{\alpha^r}{\lambda^r} \right)^2 \right)}{L_y \left( \gamma_n^{r^2} + \left( \frac{\alpha^r}{\lambda^r} \right)^2 \right) + \left( \frac{\alpha^r}{\lambda^r} \right)} \frac{\cos(\beta_m^r x) \cos(\beta_m^r L_x) \cos(\gamma_n^r y)}{(\gamma_n^{r^2} + \beta_m^{r^2})} \int_0^{L_y} \left( \frac{d\theta(x', y')}{dx} \Big|_{x'=L_x} \cos(\gamma_n^r y') \right) dy' + \\ & + \frac{1}{L_x} \sum_{n=1}^{\infty} \frac{2 \left( \gamma_n^{r^2} + \left( \frac{\alpha^r}{\lambda^r} \right)^2 \right)}{L_y \left( \gamma_n^{r^2} + \left( \frac{\alpha^r}{\lambda^r} \right)^2 \right) + \left( \frac{\alpha^r}{\lambda^r} \right)} \frac{\cos(\gamma_n^r y)}{(\gamma_n^{r^2})} \int_0^{L_y} \left( \frac{d\theta(x', y')}{dx} \Big|_{x'=L_x} \cos(\gamma_n^r y') \right) dy' \end{aligned} \quad (5)$$

In the following part of the paper, there has been conducted the analysis of the results of numerical calculations obtained, based on the presented mathematical model of non-contact face seal taking into account the geometrical parameters and consumables.

#### 4. Results and discussion

Numerical calculations for the wavy-tilt-dam mechanical seals have been performed for the parameters. Water at a temperature  $T_o$  of  $20^\circ C$  has been assumed as the working medium. It has been assumed that the outer and the inner radius is respectively 45 mm and 40 mm for the two cooperating rings. It has been also assumed that the rotor is rotating at an angular speed of 300 rad/s, its thermal conductivity is  $\lambda^r = 16.4$  (W/m·K). The calculations assume the height of radial gap at level of 1  $\mu m$  and wavy number  $Ng = 6$ . In this part of the paper there are collected results of simulation research on the influence of parameters related to the topography of the surface of the rotor in wavy-tilt-dam mechanical seals. In the following figures there are presented in graphical form temperature changes in the radius  $r_m = 0.5 \cdot (r_i + r_o)$ , along the thickness of the rings and the radial gap in the direction of the  $OZ$  axis. Height of the rings and the fluid film is shown in a dimensionless form, as further control nodes.

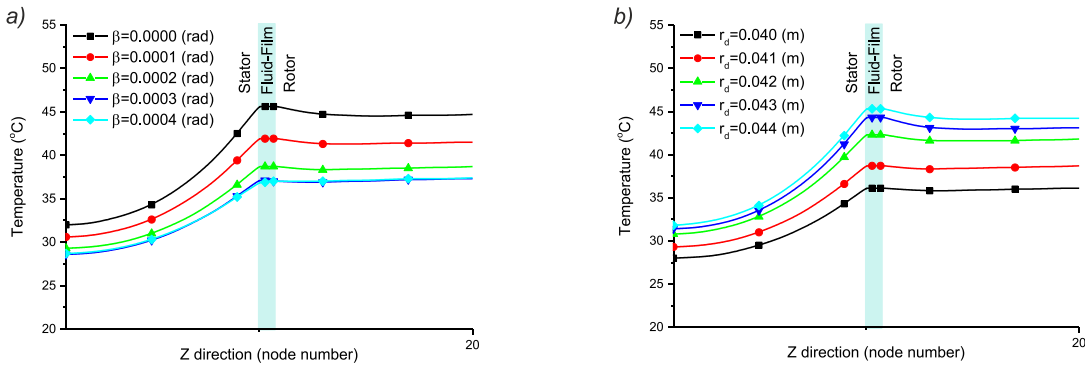


Fig. 2: Temperature distribution in the fluid film and sealing rings for  $r_m$  under different a) taper angle  $\beta$ , b) dam radius  $r_d$ .

After analyzing the results shown in Fig. 2a it can be noted that increasing the value of the angle  $\beta$  by the value of  $0.0001$  rad does not cause systematic changes in temperature in the considered set of rings fluid film on the radius  $r_m$ . For the angle of  $\beta = 0.0003$  rad and  $\beta = 0.0004$  rad temperature distributions are practically overlapping. This fact indicates the existence of a certain optimum associated with geometry of the wavy face, for which heat transfer is most effective.

## 5. Conclusion

The main task to be met by non-contact face seals is the maintenance of tightness, regardless of the external factors affecting. There is a close relationship between the geometry of the radial gap and leak. The main factors binding these parameters are deformations caused by uneven distribution of temperature in the seal rings of the wavy-tilt-dam mechanical seals. Developing more accurate mathematical models and computational devices shall allow the appointment during the design process of temperature distributions in system of rings-fluid film. This will allow researchers and engineers to estimate the temperature range and selection of appropriate materials for the sealing rings. This knowledge, in turn, will allow to achieve high reliability and service life of created constructions.

## References

- Adamczak, S. and Bochnia, J. (2016) Estimating The Approximation Uncertainty For Digital Materials Subjected To Stress Relaxation Tests. *Met. And Measurement Systems*, 23, 4, SI, pp. 545-553.
- Blasiak, S. (2015) The two dimensional thermohydrodynamic analysis of a lubrication in non-contacting face seals. *Journal of Thermal Science and Technology*, 10, 1, pp. JTST0016-JTST0016, doi: 10.1299/jtst.2015jtst0016.
- Blasiak, S., Takosoglu, J. E. and Laski, P. A. (2014) Heat transfer and thermal deformations in non-contacting face seals. *Journal of Thermal Science and Technology*, 9, 2, pp. JTST0011-JTST0011, doi: 10.1299/jtst.2014jtst0011.
- Bochnia, J. (2012) Ideal Material Models for Engineering Calculations. *Procedia Engineering*, 39, 0, pp. 98-110.
- Brunetiere, N. (2010) An analytical approach of the thermoelastohydrodynamic behaviour of mechanical face seals operating in mixed lubrication. *Proc. of the Ins. Of Mech. Eng. Part J-J. Of Eng. Trib.*, 224, J12, pp. 1221-1233.
- Kavinprasad, S., Shankar, S. and Karthic, M. (2015) Experimental and CFD investigations of carbon/SS316 mechanical face seals under different lubricating conditions. *Ind. Lub. And Trib.*, 67, 2, pp. 124-132.
- Koruba, Z. and Krzysztofik, I. (2013) An algorithm for selecting optimal controls to determine the estimators of the coefficients of a mathematical model for the dynamics of a self-propelled anti-aircraft missile system. *Proceedings of the Institution Of Mechanical Engineers Part K-J. Of Multi-Body Dynamics*, 227, K1, pp. 12-16.
- Krzysztofik, I. and Koruba, Z. (2014) Mathematical Model of Movement of the Observation and Tracking Head of an Unmanned Aerial Vehicle Performing Ground Target Search and Tracking. *Journal Of Applied Mathematics*.
- Laski, P.A. (2016) The Design Of A Proportional Slit Valve With A Piezoelectric Actuator. In: *Proc. Int. Conf. on Engineering Mechanics 2016* (Eds. Zolotarev, I., Radolf, V.), Svratka, pp. 350-353.
- Laski, P. ., Takosoglu, J. E. and Blasiak, S. (2014) A Delta Type Closed Kinematics Chain With Pneumatic Muscle Actuator Manipulator. In: *Proc. Int. Conf. on Engineering Mechanics 2014* (ed. Fuis, V.), Svratka pp. 360-363.
- Lee, S.C. and Zheng, X.L. (2013) Analyses of both steady behavior and dynamic tracking of non-contacting spiral-grooved gas face seals. *COMPUTERS & FLUIDS*, 88, pp. 326-333
- Liu, Y., Liu, W., Li, Y., Liu, X. and Wang, Y. (2015) Mechanism of a wavy-tilt-dam mechanical seal under different working conditions. *Tribology International*, 90, pp. 43-54
- Meng, X.-K., Bai, S.-X. and Peng, X.-D. (2014) An efficient adaptive finite element method algorithm with mass conservation for analysis of liquid face seals. *Journal Of Zhejiang University-Science A*, 15, 3, pp. 172-184
- Nowakowski, L., Miesikowska, M. and Blasiak, M. (2016) Speech Intelligibility In The Position Of Cnc Machine Operator. In: *Proc. Int. Conf. on Engineering Mechanics 2016* (Eds. Zolotarev, I., Radolf, V.), Svratka, pp. 422-425.
- Nowakowski, L., Miko, E. and Skrzyniarz, M. (2016) The Analysis Of The Zone For Initiating The Cutting Process Of X37crmov51 Steel. In: *Proc. Int. Conf. on Engineering Mechanics 2016* (Eds. Zolotarev, I., Radolf, V.), Svratka, pp. 426-429.
- Nyemeck, A. P., Brunetiere, N. and Tournier, B. (2015) A Mixed Thermoelastohydrodynamic Lubrication Analysis of Mechanical Face Seals by a Multiscale Approach. *Tribology Transactions*, 58, 5, pp. 836-848.
- Takosoglu, J. E., Laski, P. A., Blasiak, S., Bracha, G. and Pietrala, D. (2016a) Determination of flow-rate characteristics and parameters of piezo valves. In: *Proceedings of the International Conference Experimental Fluid Mechanics 2016*. (ed. Dancova, P.), Techn. Univ. Liberec, pp. 814-818.
- Takosoglu, J. E., Laski, P. A., Blasiak, S., Bracha, G. and Pietrala, D. (2016b) Determining the Static Characteristics of Pneumatic Muscles. *MEASUREMENT & CONTROL*, 49, 2, pp. 62-71, doi: 10.1177/0020294016629176.
- Wang, T., Huang, W., Liu, X., Li, Y. and Wang, Y. (2014) Experimental study of two-phase mechanical face Seals with laser surface texturing. *Tribology International*, 72, pp. 90-97.
- Zhang, G.-y. and Zhao, W.-g. (2014) Design and Experimental Study on the Controllable High-Speed Spiral Groove Face Seals. *Tribology Letters*, 53, 2, pp. 497-509.

## STRESS ANALYSIS OF PART OF THE WELDED STRUCTURE

M. Blatnická\*, M. Blatnický\*\*, M. Sága\*\*\*, M. Kubiak\*\*\*\*

**Abstract:** *This paper deals with strength analysis of a part of the welded steel structure of the test device that will be used to calibrate vehicle axle scales with a loading capacity up to ten tons. The analysis is carried out in ADINA software. This analysis results will be used to check the safety of the design and structure. In the case of exceeding the permissible stress, deformation, displacement, etc., this analysis results will form a benchmark material for optimization of the structure.*

**Keywords:** Strength analysis, ADINA software, Welded structure.

### 1. Introduction

Weight measurement is one of the most widely used laboratory and technical activities. New types of scale designs have been developed and widely used in practice, increasing the accuracy and speed of measurement. In order to ensure measurement accuracy over the entire technical life of the scales, these require regular calibration with precisely defined recalibration intervals whose time step is defined in standards.

A testing device has been designed in order to enable carrying out experimental measurements to determine suitability of a scale for vehicle axles with a loading capacity up to ten tons. Since, currently, great emphasis is placed on efficiency, cost reduction and economically advantageous performance; this structure will be subjected, prior to a prototype manufacture, to strength analysis with software support in order to determine whether the structure is able to withstand the given load with a certain degree of safety (Murín, 1999, Žmindák et al., 2013). Based on the above-mentioned analysis (Gerlici et al., 2014) we are able to say in advance whether a given structural design is satisfactory or, conversely, it needs further optimisation in order to prevent potential loss of life or property.

### 2. Analyzed welded steel structure

This steel structure will be gradually loaded with a burden weighting from 2 tons up to 10 tons, including its own weight, so as the structure will gradually lift the boxes containing weights, located inside the structure.

The boxes with weights are stockpiled, and each box contains four weights. The burden consists of 16 weights – 500 kg each, own weight, and additional lighter weights so that the total weight is 10 tons. The main part of the structure consists of two parallel angle girders – side plates, to which suspension means of thick metal sheet are welded and which will be analyzed in this paper. Here will be fitted suspension tubes of the boxes in which the load (weight) is situated. The load chronology is guaranteed by different sizes of holes for hanging tubes. On this support structure, a hydraulic cylinder is placed that will lift the whole structure and transmit the compressive force derived from the burdens onto a scale placed on a platform, through the girder, in order to calibrate the scale (Fig. 1-left).

---

\* Ing. Mária Blatnická: Department of Applied Mechanics, Faculty of Mechanical Engineering, University of Žilina, Univerzitná 1; 010 26, Žilina; SK, maria.blatnicka@fstroj.uniza.sk

\*\* Ing. Miroslav Blatnický, PhD.: Department of Transport and Handling Machines, Faculty of Mechanical Engineering, University of Žilina, Univerzitná 1; 010 26, Žilina; SK, miroslav.blatnický@fstroj.uniza.sk

\*\*\* Prof. Dr. Ing. Milan Sága: Department of Applied Mechanics, Faculty of Mechanical Engineering, University of Žilina, Univerzitná 1; 010 26, Žilina; SK, milan.saga@fstroj.uniza.sk

\*\*\*\* PhD. Eng. Marcin Kubiak: Czestochowa University of Technology, Institute of Mechanics and Machine Design Foundations, Dabrowskiego 73, Czestochowa, Poland, kubiak@imipkm.pcz.pl

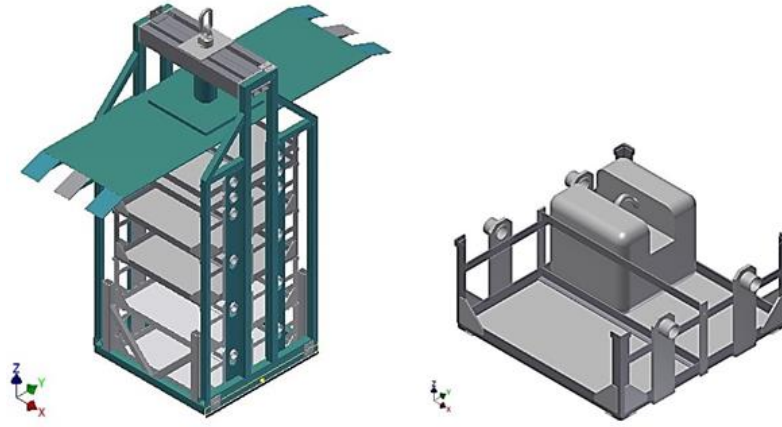


Fig. 1: Steel structure for vehicle axle scale calibration (left) and box for weights (right).

The analysis will result in comparison of the observed values of stress, displacement and strain (deformation) of the steel structure with the permissible values that depend on the type of material used (strength, stiffness, etc.) (Handrik et al., 2016, Sapieta et al., 2016, Žmindák et al., 2004). Since we are dealing with a welded structure consisting of thin-walled sections, it will be modelled as a shell body using central line planes, with a subsequent thickness assignment. The structure is made of EN S355 (STN 11 523) steel that has the yield strength  $R_e = 320 \div 360 \text{ MPa}$ , and the ultimate strength  $R_m = 520 \div 640 \text{ MPa}$  (Bajla et al., 2014). The safety coefficient is  $k = 2$  (-). At the weld sites we must take into account a reduced permissible stress by the recommended 30 %, through introducing the welding effect coefficient  $c = 0.7$  (-).

The permissible stress for the material chosen, with consideration of the relevant coefficients, will be as follows:

$$\sigma_{dov} = \frac{R_e}{k} \quad (1)$$

$$\sigma_{dov} = \frac{320}{2} = 160 \text{ MPa}$$

and the permissible stress at the weld site will be as follows:

$$\sigma_{dov}^w = c \cdot \sigma_{dov} \quad (2)$$

$$\sigma_{dov}^w = 0.7 \cdot 160 = 112 \text{ MPa}$$

### 3. Side plate stress analysis

In this paper the simulation analysis of side plates is described. The computer model of side plates is shown in Fig. 2-left.

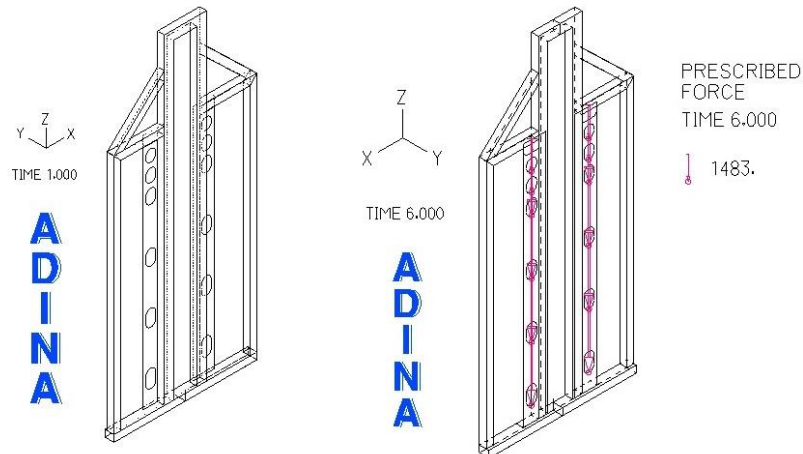


Fig. 2: Model of the side plate (left) and its load at time  $t = 6 \text{ s}$  (right).

By reason that the request of the stepwise loading is demanded on the structure regarding the exact calibration of scale, the load was applied by several time functions (Tab. 1).

The load is applied in the form of single forces entered in points (Fig. 2-right). Values of these forces are listed in Tab. 2.

Tab. 1: Time functions 1 – 6 for the gradual lifting of boxes 1 – 6.

Time [s]	Function value 1	Function value 2	Function value 3	Function value 4	Function value 5	Function value 6
0	0	0	0	0	0	0
1	1	0	0	0	0	0
2	1	1	0	0	0	0
3	1	1	1	0	0	0
4	1	1	1	1	0	0
5	1	1	1	1	1	0
6	1	1	1	1	1	1

Tab. 2: Values of the forces applied at the time.

Force	Value [N]	Time function
$F_1$	1483	1
$F_2$	1483	2
$F_3$	5140	3
$F_4$	5140	4
$F_5$	5140	5
$F_6$	5140	6

It follows from Tabs. 1 and 2, that the side plate is subjected at time  $t = 6$  s to the force  $F'$ . Its value is given (side plate has two parallel suspensions):

$$F' = 2 \cdot (F_1 + \dots + F_6) = 47052N, \quad (3)$$

The values of individual forces are determined as the sum of the forces from the weight mass and the box mass, where the box mass (weight) was calculated in ADINA software. Furthermore, we prescribe to the structure also a load resulting from its own weight, namely  $m = 204.05$  kg:

$$F'' = m \cdot g = 204.05 \cdot 9.81 = 2001.7N. \quad (4)$$

Then, the total loading force is:

$$F = F' + F'' = 47052 + 2001.7 = 49053.7N. \quad (5)$$

The results from numerical analysis show (Fig. 3), that the largest reduced stress is at the site No 1 and it reaches the value of 184.5 MPa and exceeds the permissible stress of 112 MPa.

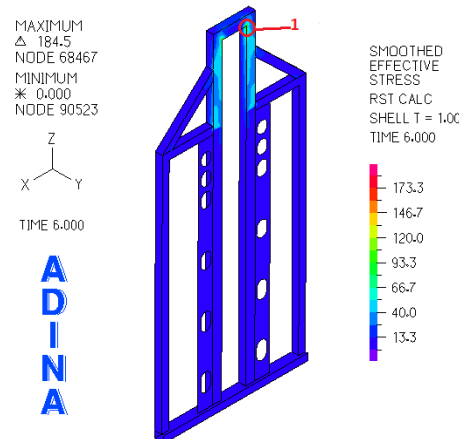


Fig. 3: Distribution of HMM reduced stress in the side plate.

For stress reduction in the site No 1 we propose the thickness modification from the original 5 mm to 10 mm.

This proposed structural modification caused a reduction of the stress at the site No. 7 on the value of 55.63 MPa (Fig. 4).

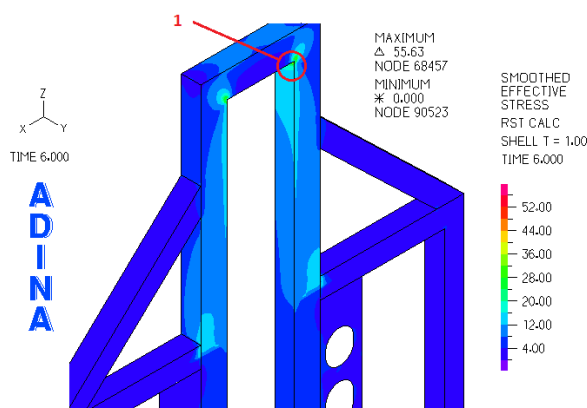


Fig. 4: Distribution of HMM reduced stress in the side plate following the structural modification.

#### 4. Conclusion

The aim of this paper was to perform strength analysis of a part of the welded steel structure of the testing device. Using the structure's draft modelled in the CAD software, the part of the considered structure was modelled in ADINA Software (Bathe, 1996). Then the strength analysis was carried out and the stress value was compared to the permissible stress. It was found that the part of the structure does not meet the requirements of the selected safety level. The thin-walled sections' thickness increased at the site where stress exceeded the permissible value. Subsequently, the device was reanalysed to assess the strength. This reanalysis resulted in the fact that the part analyzed complies with safety requirements, and is thus suitable for manufacture and use, when applying the conditions corresponding with the initial task – that is the maximum loading mass with a total weight of 10 tons.

#### Acknowledgement

This work has been supported by the Slovak Research and Development Agency under the contract | No. APVV-14-0096.

#### References

- Bajla, J., Bronček, J., Antala, J., Sekerešová, D. (2014) Mechanical Engineering Tables. Selection Standard. Slovak Office Standards, Metrology and Testing. ISBN 978-80-8130-039-4, (In Slovak).
- Bathe, K. J. (1996) Finite element procedures. Prentice-Hall, Inc. New Jersey. ISBN 0-13-301458-4.
- Gerlici, J., Lack, T., Harušinec, J. (2014) Development of test stand prototype for rail vehicles brake components testing. *Komunikácie*, 16, 3A, pp. 27-32.
- Handrik, M., Vaško, M., Kopas, P., et al. (2016) The linear and nonlinear stability loss of structures due to thermal load. *Procedia Engineering*, 136, pp. 359-364.
- Murín, J. (1999) Finite Element Method for Beam and Frame Constructions. (In Slovak). Bratislava: STU Bratislava. 130 p. ISBN 80-227-1287-6.
- Sapieta, M., Dekýš, V., Sapietová, A. (2016) Thermal-stress analysis of beam loaded by 3 point bending. *Procedia Engineering*, 136, pp. 216-219.
- Žmindák, M., Novák, P., Dekýš, V., et al. (2013) Finite Element Thermo-mechanical Transient Analysis of Concrete Structure. *Procedia Engineering*, 65, pp. 224-229.
- Žmindák, M., Grajciar, I., Nozdrovický, J. (2004) Modeling and Computation in Finite Element Method, Žilina. ISBN 80-968823-5, (in Slovak).



## DESIGN OF A ROBOT MANIPULATOR WORKING SCREW REVOLUTIONS

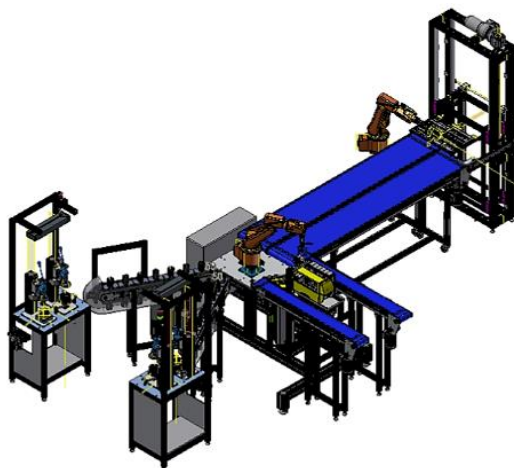
M. Blatnický\*, J. Dižo\*, M Blatnická\*\*, M. Svoboda\*\*\*

**Abstract:** *The paper deals with a constructional design of a versatile adaptive gripper for a robot manipulator. More specifically, it is a constructional design of a motional kinematics of fingers, which are controlled by a working screw, and also there is a design of a belt gear from the engine to the gripper working screw. This solution has its base in previous analytical computation of forces and is substantial for the further correct selection of an engine transmission and gearing considered for achievement of required manipulator fingers kinematics.*

**Keywords:** Handling machinery, Belt gear, Kinematics, Gripper.

### 1. Introduction

An important role of engineers is to analyse used and new-designed working processes for finding an optimal way of execution of an existing operation. In the development, design and production process of machines and their subsystems there are nowadays used various methods and approaches. In these processes computational simulations are utilized, which allow to identify structural and dynamic properties of structures by means of virtual reality tools (Lack, 2014a, Lack, 2014b, Lack 2013, Soukup, 2014), measurements and experimental methods on prototypes or finished products) or also by special equipment in laboratories (Gerlici, 2013, Gerlici, 2014). The best working process is generally considered that one, at which the costs on output are minimalized, what can be achieved by mechanisation (Besekerskij, 1970).



*Fig. 1: Locating of designed robot on the automatic line.*

---

\* Ing. Miroslav Blatnický, PhD., Ing. Ján Dižo, PhD.: Department of Transport and Handling Machines, Faculty of Mechanical Engineering, University of Žilina, Univerzitná 1; 010 26, Žilina; Slovak Republic, miroslav.blatnický@fstroj.uniza.sk, jan.dizo@fstroj.uniza.sk,

\*\* Ing. Mária Blatnická: Department of Applied Mechanics, Faculty of Mechanical Engineering, University of Žilina, Univerzitná 1; 010 26, Žilina; Slovak Republic, maria.blatnicka@fstroj.uniza.sk,

\*\*\* Ing. Martin Svoboda, PhD.: Department of Machines and Mechanics, Faculty of Production Technology and Management, Jan Evangelista Purkyně University in Ústí nad Labem, Pasteurova 3334/7; 400 96, Ústí nad Labem; Czech Republic, svoboda@fvmtm.ujep.cz.

Mechanisation is an important means of increasing productivity, quality and production competitiveness. For successful introduction of mechanisation is necessary to know and understand physical dependencies of executed operations. Operations are executed by transfer of mechanical, electrical, pneumatic or hydraulic energy. The aim is to make individual working processes as short and simple as possible, easy to learn and at the same time minimal man-power consuming. Mechanisation significantly relieves the man of heavy manual labour for instance in dangerous or harmful environment. These days can be characterised by developed production and automation (Fig. 1). Automation is a process of a replacement of a man control function by operation of various machines and devices.

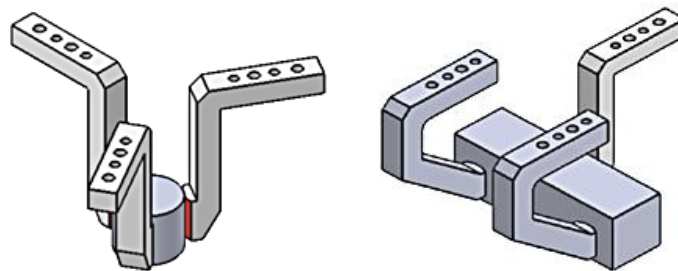
Automation is a highly complex process including very simple control operations, which are performed automatically at a relatively simple device, as well as very complicated control of big production units. Control is a purposeful action of valuation and processing of information about controlled object or process, actions in the process (these may include measurement device data, signalling equipment states) and according to them related machines are controlled so that prescribed aim is reached – handling piece loads of maximal weight  $m = 25 \text{ kg}$  in this instance.

## 2. Requirements imposed on manipulator

Basic imposed requirement is a simple control, a necessity of a control by an operator, provided compatibility with operative system. Appliance load capacity is 25 kg and gripping force results from it according to material contact. A number of gripping fingers is 3. Mechanism drive is electrical (AC servomotor) for two mechanisms, because of the fact that one of the fingers has one degree of freedom and the remaining two fingers have two degrees of freedom. Required operative finger range is  $0 - 60^\circ$  (depends on a size of load) and 1.05 rad when rotating of two fingers at change of load shape. Permitted finger length at maximal gripping force is 150 mm. Maximal finger folding pace is  $25 \text{ mm.s}^{-1}$  and finger rotation speed  $1.57 \text{ rad.s}^{-1}$ . Designed robot manipulator will be a part of an automatic line in Fig. 1. Function of the robot is loading movable containers with ready products.

## 3. Manipulator working screw

A selection of the manipulator working screw results from the loads imposed on the screw at robot operation. Computation of the gripping force and an engine output was designed for gripping two basic objects i.e. circle shaped objects and direct planed objects (Fig. 2) (blocks, cubes).



*Fig. 2: Orientation of the gripping fingers at manipulating the rotational shaped objects (left) and the direct planed objects (right).*

When body equilibrium conditions and friction condition between normal and friction forces were taken into account, we found out in previous calculations that normal force  $F_{N1}$  acting on the most loaded finger (in Fig. 2 right - non-rotating finger, i.e. the finger acting by a reaction against a force action of the oppositely oriented pair of fingers) is  $F_{N1} = 1\,720 \text{ N}$ . After evaluation of the gripping forces sizes of both gripped objects was found that at gripping the object of non-circle shape, the force acting on the non-rotating finger is greater. Hence each next computation was realized at gripping such loads. Subsequently, a constructional design of the robot manipulator finger with components allowing achievement of the required movement possibilities was created (Fig. 3 left). Gripper motion kinematic is provided by knuckle mechanism of joint sphere with thread. At mechanism motion kinematic is necessary to provide two degrees of freedom at two active fingers. This motion was assured by usage of articulation (Fig. 3 right). At mechanism motion in vertical direction, there is a curve motion. This motion was ensured by acceptable slope of connecting ball with thread, which is at ball-joint type: RBL 10D –  $40^\circ$ , RBIDL –

25°. For part of finger that makes only vertical motion, there is a fixed arm suspension assured by a screw connection. This way, just one degree of freedom of this part was provided.

For a working screw design is necessary to know a loading force size. In the previous calculations it was found that the resultant loading force acting in the working screw axis is  $F_s = 16\,780\text{ N}$ . For a correct option of the screw is needed to choose a screw with a higher dynamic load rating than the computed force  $F_s$ .

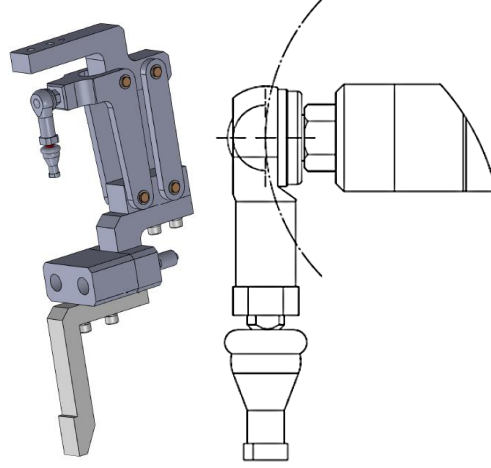


Fig. 3: Constructional design of one of the robotic manipulator finger (left) and Knuckle motion curve (right).

The next condition is that chosen working screw has high efficiency so we select a ball screw for example by company Bosch. Selected screw with dynamic load rating  $C = 27.5\text{ kN}$ , thread effective diameter  $d_0 = 32\text{ mm}$  and thread pitch  $t = 5\text{ mm}$  meets requirements, which will be made on it in operation.

#### 4. Calculation of working screw revolutions

Revolutions of the selected working screw have to reach the specific value in order to meet the condition imposed on the manipulator that the pace of the fingers folding is  $v_x = 25\text{ mm.s}^{-1}$ . Since, between the finger folding pace  $v_x$  and the speed of nut moving on the screw  $v_y$ , there is a lever transmission according to the Fig. 4, it can be written that (1):

$$v_y = \frac{a}{c} \cdot v_x \quad (1)$$

By solving the equation for the speed of the nut motion in the vertical direction we get  $v_x = 17.0833\text{ mm.s}^{-1}$ .

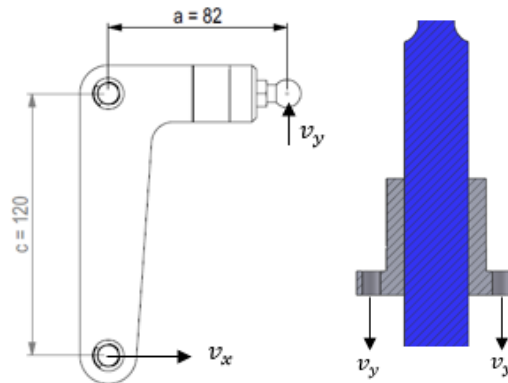


Fig. 4: Lever arm of the mechanism (left) and kinematics of the working screw nut (right).

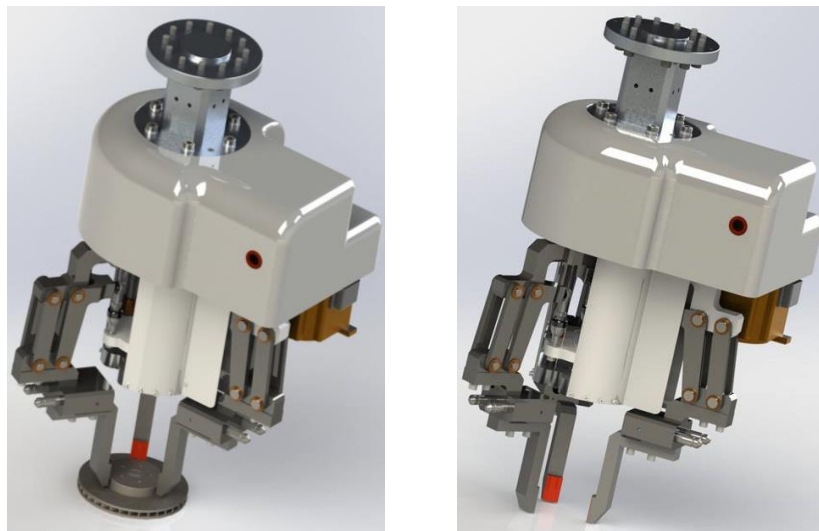
With acquired value of the nut speed  $v_y$  it is possible to calculate correct screw revolutions  $n$  according to the screw pitch  $t$  (2):

$$n = \frac{v_y}{t} \quad (2)$$

By solving the equation (2) we find the number of rotations per second, i.e.  $n = 3.4166\text{ s}^{-1}$ .

## 5. Conclusion

The aim of this paper is a partial solution of a robot manipulator design. It consists of constructional design of gripping fingers for operation with piece loads of maximal weight 25 kg, of selection of the working screw ensuring mechanism drive and determination of its revolutions needed. It is possible to state that this aim was accomplished. Overall solution of the issue is to reach theoretically function equipment, ready for implementation to the real production. So it is needed a next solution of a knuckle mechanism selection for assurance of a working motion, calculation of fingers speed, transmission design, drive mechanism design, belt gear of rotating fingers design etc.



*Fig. 5: 3D model of a versatile gripper for a robot manipulator.*

## Acknowledgement

This paper was created during the processing of the project “RAILBCOT - RAIL Vehicles Brake Components Test Stand”, ITMS Code 26220220011 based on the support of Research and Development Operational Program financed by European Fund of a Regional Development. The work was also supported by the Scientific Grant Agency of the Ministry of Education of the Slovak Republic in project No. APVV-0842-11: “Equivalent railway operation load simulator on the roller rig.

Research-Educational Center of Rail Vehicles (VVCKV)

## References

- Besekerskij, V. A. et al. (1970). Collection of automatic control tasks. STNL Prague. ISBN 04-016-70, (in Czech).
- Gerlici, J., Lack, T. and Harušinec, J. (2013). The test stand load modulus implementation for the realistic railway operation in the laboratory conditions. In: Manufacturing Technology. Vol. 13, Issue 4, 2013, pp. 444-449. ISSN 1213-2489.
- Gerlici, J., Lack, T. and Harušinec, J. (2014). Realistic simulation of railway operation on the RAILBCOT test stand. In: Applied Mechanics and Material. Vol. 486, 2014, pp. 387-395. ISSN 1660-9336.
- Gerlici, J. and Lack, T. (2011). Railway wheel and rail head profiles development based on the geometric characteristics shapes. In: Wear Vol. 271, 2011. Issue 1-2. pp. 246-258.
- Lack, T. and Gerlici, J. (2014a). A modified strip method to speed up the tangential stress between wheel and rail calculation. In: Applied Mechanics and Material. Vol. 486, 2014, pp. 359-370. ISSN 1660-9336.
- Lack, T. and Gerlici, J. (2014b). A modified strip method to speed up the calculation of normal stress between wheel and rail calculation. In: Applied Mechanics and Material. Vol. 486, 2014, pp. 371-378. ISSN 1660-9336.
- Lack, T. and Gerlici, J. (2013). The FASTSIM method modification to speed up the calculation of tangential contact stresses between wheel and rail. In: Manufacturing Technology. Vol. 13, Issue 4, 2013, pp. 486-492. ISSN 1213-2489.
- Soukup, J., Žmindák, M., Skočilas, J. and Rychlíková, L. (2014). Application of mesh-free methods in transient dynamic analysis of orthotropic plates. In: Manufacturing Technology. Vol. 14, Issue 3, 2014, pp. 441-447. ISSN 1213-2489.

## KINEMATICS AND DYNAMICS OF THE MOVEMENT OF THE SELECTED CONSTRUCTIONS OF THE DISC CUTTING ASSEMBLIES

A. Bochat<sup>\*</sup>, M. Zastempowski<sup>\*\*</sup>

**Abstract:** *The mathematical dependencies describing the kinematics and dynamics of the movement of the disc cutting assemblies used in agrarian mowing machines for cutting of the plant material for windrow are described in this study.*

**Keywords:** Mowing machines, Disc cutting assemblies, Kinematics, Dynamics, Plant material.

### 1. Introduction

The cutting assemblies of the disc type are commonly used in agrarian mowing machines for cutting of plant material for windrow. Cutting of plants takes place with the use of inertia of plants' blades, that is without the use of the crosscut edge. The discs of the discussed cutting assemblies are equipped with straight knives ( $\alpha = 0^\circ$ ). Knives are fastened to discs self-aligning with the use of clevis pins (Bochat, 2010).

From the analysis of the commonly available literature it results, that the subject area of kinematics and dynamics of movement of the machines' has been presented only by Bochat and Zastempowski (2013) in their publications. Other authors, within the frames of machines' construction, have mainly dealt with the subject matter connected with the rules of designing and the analysis of a construction's strength (Piatkowski et al., 2014, Tomaszewski et al., 2014), with the rules of the use of MES and the numerical analysis (Szala, 2014; Knopik et al, 2016; ) with mathematic modeling and a construction's optimization (Knopik et al., 2016; Peszynski et al., 2016; Ligaj and Szala, 2010, Zastempowski and Bochat, 2014, 2015) as well as the interaction of technical devices on the environment (Karwowska et al., 2013, 2014).

Correct designing of the cutting assemblies, that is disc with knives, is the basic problem that a disc mowing machines' constructor has been facing. It shall be possible on condition of thorough getting to know the dependencies between the geometric and kinematic parameters of the construction of discs with knives and the operating parameters of the machine – mowing machine. That is why, in this study, there is an attempt to describe the movement of the cutting discs of the mowing machine's mathematically.

### 2. Analysis of the issue

The discs with knives in agrarian mowing machines, make a movement composed of a rotational movement around its own axis and the translational movement resulting from the movement of the machine – mowing machine. The trajectories of movement of the two neighbouring knives are presented in Fig. 1. The individual knives cut the plants from the surface limited by two cycloids, that is the cycloid determining the path of movement of the external knife's edge and the cycloid determining the path of movement of the internal knife's edge. Both the pairs of cycloids intersect what means, that a knife shifting as the second runs in the part of its idle movement above the area cut by the first knife (double hatched area). Between the cycloids there may also remain the area from which the plants shall not be cut down (unshaded area).

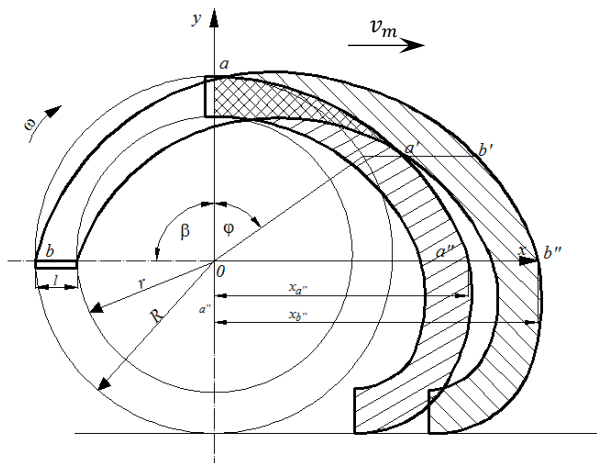
---

<sup>\*</sup> Prof. Andrzej Bochat, PhD.: Faculty of Mechanical Engineering, UTP University of Science and Technology, Poland. Al. Prof. Kaliskiego 7, 85-796 Bydgoszcz, e-mail: bochat@utp.edu.pl

<sup>\*\*</sup> Marcin Zastempowski, PhD.: Faculty of Mechanical Engineering, UTP University of Science and Technology, Poland. Al. Prof. Kaliskiego 7, 85-796 Bydgoszcz, e-mail: zastemp@utp.edu.pl

- For the point  $a'$

$$y_{a'} = R \cos \omega t \quad (2)$$



- For the point  $b'$

$$y_{h'} = R \cos(\omega t - \beta), \quad (4)$$

$\varphi, \beta$ - appropriate angles (according to Fig. 2), where  $\varphi = \omega t$ .

$$x_{h''} - x_{a''} = h = l \cos \alpha, \quad (5)$$

$$\varphi = \frac{\pi}{2} = \omega t \quad (6)$$

$$t = \frac{\pi}{2\omega}. \quad (7)$$

$$x_{a''} = v_m \frac{\pi}{2\omega} + R. \quad (8)$$

$$\omega t = \frac{\pi}{2} + \beta, \text{ and after the transformations } t = \frac{\pi+2\beta}{2\omega}. \quad (9)$$



So:

$$x_{b''} = v_m \frac{\pi+2\beta}{2\omega} + R \sin\left(\frac{\pi}{2} + \beta - \beta\right) = v_m \frac{\pi+2\beta}{2\omega} + R, \quad (10)$$

from where:

$$l = v_m \frac{\pi+2\beta}{2\omega} + R - \left(v_m \frac{\pi}{2\omega} + R\right) = v_m \frac{\beta}{\omega}. \quad (11)$$

Substituting to the formula (11):

$$\beta = \frac{2\pi}{z}, \quad (12)$$

where:  $z$  - number of knives on a disc,

we receive:

$$l = \frac{2\pi v_m}{\omega z}. \quad (13)$$

To ensure cutting of plants with the whole length of a knife, the below condition has to be fulfilled:

$$\frac{v_{nz}}{v_m} \geq \frac{2\pi R}{4l \cos\alpha}, \quad (14)$$

where:  $v_{nz}$  - knife's peripheral speed.

In order to determine the resultant speed  $v$  and acceleration  $a$  of a knife, the equations (1) and (2) have to be correctly differentiated and an appropriate mathematical operation be performed. Differentiating the equations (1) and (2) once, there has been received:

$$v_{xa} = \frac{dx_{a'}}{dt} = v_m + R \omega \cos\omega t, \quad (15)$$

$$v_{ya} = \frac{dy_{a'}}{dt} = -R \omega \sin\omega t. \quad (16)$$

Taking into account the fact, that the resultant knife's speed is described by the dependency:

$$v = \sqrt{v_{xa}^2 + v_{ya}^2}. \quad (17)$$

We have received following conversions:

$$v = \sqrt{v_m^2 + 2v_m R \omega \cos\omega t + R^2 \omega^2}. \quad (18)$$

However differentiating the equations (1) and (2) twice, we have received:

$$a_{xa} = \frac{dv_{xa}}{dt} = -R \omega^2 \sin\omega t, \quad (19)$$

$$a_{ya} = \frac{dv_{ya}}{dt} = -R \omega^2 \cos\omega t. \quad (20)$$

So:

$$a = \sqrt{(-R\omega^2 \sin\omega t)^2 + (-R\omega^2 \cos\omega t)^2} = R\omega^2. \quad (21)$$

Dynamic equation of the rotational movement of a disc with knives may be described with the use of the equation:

$$M = J\varepsilon, \quad (22)$$

where:  $M$  - turning moment on the shaft driving a disc with knives,

$J$  - mass inertia moment of a disc with knives,

$\varepsilon$  - angular acceleration of the disc with knives,  $\varepsilon = \frac{a}{R}$ .



### 3. Final conclusions

In the light of the conducted analysis of this issue, the following conclusions may be formed:

1. The mathematical dependencies describing the kinematics and dynamics of the movement of the disc cutting assemblies applied in mowing machines presented in the study, constitute the first attempt of the comprehensive issue's presentation.
2. Derived dependencies make it possible to establish the relations between the geometrical and kinematic parameters of construction of disc with knives and the operating parameters of the machine – mower, in the aspects of its operation's effectiveness.
3. The established dependencies may be applied in the phase of simulation tests concerning new mowers' constructions.

### Reference

- Bochat, A. (2010) Theory and design of cutting units for agricultural machines. Publishing house - UTP University of Sciences and Technology Bydgoszcz.
- Bochat, A. and Zastempowski, M. (2013) Modeling the Dynamics of the Vegetable Material Detachment Process from Undisturbed Areas to Improve the Design of Selected Agricultural Machines. Transactions of the ASABE, vol. 56(4), pp. 1309-1314.
- Karwowska, M., Mikolajczak, J., Dolatowski, Z. and Borowski, S. (2013) The effect of varying distances from the wind turbine on meat quality of growing finishing pigs. Annals of Animal Science, 15, 4. pp. 1043-1054.
- Karwowska, M., Mikolajczak, J., Borowski, S., Dolatowski, Z., Marc-Pienkowska, J. and Budzinski, W. (2014) Effect of noise generated by the wind turbine on the quality of goose muscles and abdominal fat. Annals of Animal Science, 14, 2. pp. 441-451.
- Knopik, L., Migawa, K. and Kolber, P. (2016). Statistical analysis of parameters of rail vehicles. In Proc of 22nd International Conference on Engineering Mechanics (Eds. Zolotarev, I., Radolf, V.), Svratka, Czech Republic, pp. 286-289.
- Knopik, L., Migawa, K. and Wdzieczny, A., (2016). Profit optimalization in operation systems. Polish Maritime Research, 23, 1. pp. 93-98.
- Piatkowski, T., Sempruch, J. and Tomaszewski, T. (2014) Dynamics of a sorting process with a stream of discrete impact loads. Transactions of the Canadian Society for Mechanical Engineering, 38, 1, pp.139-154.
- Peszynski, K., Szmyt, W., Wawrzyniak, S. and Perczynski, D. (2016) Mathematical model of selected object thermal properties. In Proc of 22nd International Conference on Engineering Mechanics (Eds. Zolotarev, I., Radolf, V.), Svratka, Czech Republic, pp.454-457.
- Ligaj, B. and Szala, G. (2010) Experimental verification of two-parametric models of fatigue characteristics by using the tests of S55J0 steel as an example. Polish Maritime Research, 17, 1. pp. 39-50.
- Szala, G. (2014) Comments on linear summation hypothesis of fatigue failures . Polish Maritime Research. 21, 3. pp. 77-85.
- Tomaszewski, T., Sempruch, J. and Piatkowski, T (2014) Verification of selected models of the size effect based on high-cycle fatigue testing on mini specimens made of EN AW-6063 aluminum alloy. Theor. App. Mech., 52, pp. 883–894.
- Zastempowski, M., Bochat, A. (2014) Modeling of cutting process by the shear-finger cutting block. ASABE Applied Engineering in Agriculture. Vol. 30, No. 3, pp. 347-353.
- Zastempowski, M., Bochat, A. (2015) Mathematical model of elastic deflection of a tubular cross-section. Polish Maritime Research, No. 2 (86), Vol. 22, pp. 93-100.

## MECHANICAL PROPERTIES OF MATERIALS OBTAINED BY 3D-PRINTING TECHNOLOGY

J. Bochnia \*

**Abstract:** *This paper discusses the results of the static compression tests of cylindrical samples made from ceramic powders using incremental forming method with application of 3D-Printing technology. The analysis of tests results has been conducted. Anisotropy of the mechanical properties of the material, depending on the direction of the elements on the build tray of 3D printer, has been observed.*

**Keywords:** Additive technologies, Compressive strength, Mechanical properties of materials.

### 1. Introduction

Building a model with an incremental technique involves additions of layers of the material, where each subsequent layer is an exact reflection of the model cross-section in a given plane. The resulting model assumes a predetermined shape, which is designed using a CAD computer program for three-dimensional designing. The materials from which the models are made differ from materials used in other technologies. Usually in such technologies as waste or plastic machining etc., we use semi-finished products, which were produced previously in other processes, e.g. in the ironworks (Nowakowski et al., 2016). Additive technology is used both for shaping the model geometry and the properties of the material created. Therefore, it is reasonable to perform tests of the properties (Adamczak and Bochnia, 2016) of the produced materials. The characteristics of 3D-printing technology and the materials used are shown in the works of (Brett et al., 2014), (Goulas et al., 2016). With the development of the materials used in additive technologies, there are more and more studies on their properties (Lee et al., 2007), (Pilipović et al., 2009).

One of the incremental technologies is the adhesive bonding of ceramic powders referred to as 3D-printing. For the execution of this method, machines with printing nozzles can be used, similar to those in the inkjet printers. The binder is applied by the nozzles onto the powder spread on the build tray of the machine. The build tray changes its position down in the Z axis direction by increments of the value of thickness of distributed powder. The binder initially joins the powder building so called uncured model, which in order to achieve performance after printing is cured by for example an epoxy resin.

This paper presents the results of the compression tests of samples produced with 3D-Printing technology, in different directions of print. The results may be useful for engineers who design various models. Moreover, molds obtained with this technology can also be used in various types of modeling of engineering calculations (Bochnia, 2012) and construction works (Takosoglu et al., 2016) or research works (Blasiak, 2015).

### 2. Methods

Solid model of the sample was drawn using CAD 3D program and saved in a digital file with .stl extension using triangulation parameters in the export options: resolution – adjusted, deviation - tolerance 0.016 mm, angle - tolerance 5°. Using a computer program that comes with the 3D printer, the sample models were placed (virtually) on the build tray in two different orientations, in order to enable horizontal and vertical printing.

---

\* Eng. Jerzy Bochnia, PhD.: Kielce University of Technology, al. Tysiąclecia Państwa Polskiego 7, 25-314 Poland; Department of Machine Technology and Metrology jbochnia@tu.kielce.pl

Samples for the research were made of ceramic powders with 3D-Printing technology, using ZPrinter 650 (current name ProJet 660) and materials from 3D Systems. Cylindrical samples of the following dimensions were made: height 15 mm and diameter of 10 mm.

Samples were printed in the orientation:

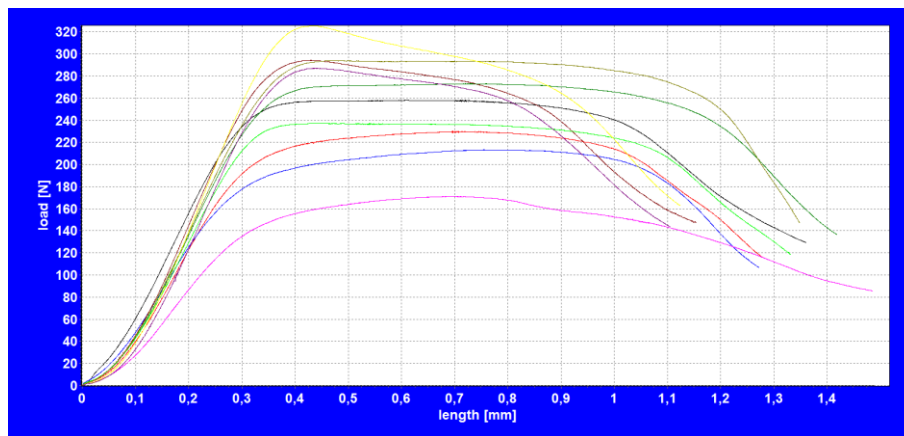
- horizontal, print direction X – 20 pcs.
- vertical, print direction Z – 20 pcs.

Then, after cleaning the samples from the remaining powder, 10 pieces from each of the printing directions were selected, and cured with the epoxy resin. In this way, there were obtained four series of samples, 10 pcs each. In each series: printed horizontally - cured and uncured by the resin, and printed vertically - cured and uncured by the resin. The samples were prepared to perform the compression tests by appropriate markings.

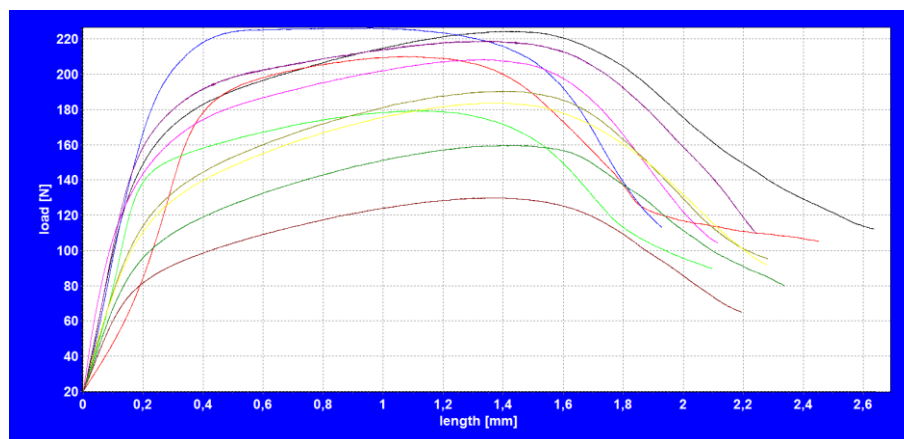
The test was made using the Inspect mini (Hegewald & Peschke MPT GmbH) testing machine with range of 3 kN, equipped with a flat compression plates. Measurement, data acquisition and setting the parameters of the test was performed in the LABMASTER program (Version 2.5.3.21), which is supplied with the Inspect mini machine.

### 3. Results

Examples of collective graphs compressive force versus displacement obtained directly from the computer of testing machine were shown in Figs. 1, 2, 3 and 4.



*Fig. 1: The stress-strain dependency for the uncured samples of 10 mm diameter printed in a horizontal position - direction X.*



*Fig. 2: The stress-strain dependency for the uncured samples of 10 mm diameter printed in a vertical position - direction Z.*

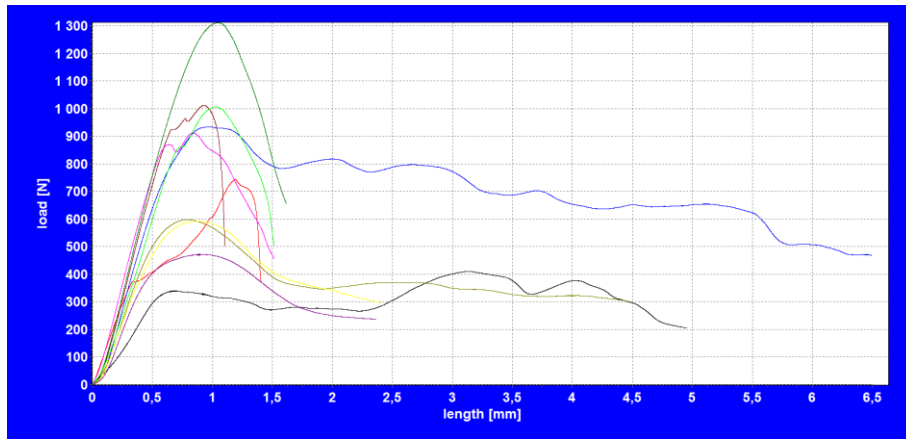


Fig. 3: The stress-strain dependency for the samples cured with epoxy resin having a diameter of 10 mm printed in a horizontal position - direction X.

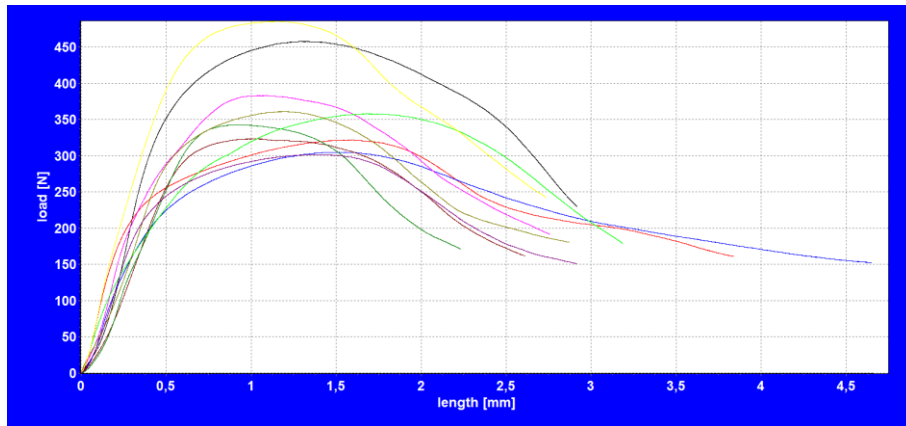


Fig. 4: The stress-strain dependency for the samples cured with epoxy resin having a diameter of 10 mm printed in a vertical position - direction Z.

Compressive strength was calculated with the formula:

$$\sigma = \frac{F_m}{S} \quad (1)$$

where:  $F_m$  – the maximum compressive force,

$S$  – surface area of the sample onto which the compressive force is applied.

The deformation of individual samples was calculated using the following formula:

$$\varepsilon = \frac{L_0 - L}{L_0} \cdot 100\% \quad (2)$$

where:  $L_0$  – initial height of the roll sample,

$L$  – sample length after compression.

Test results: compressive strength  $\sigma$  and deformation of individual samples  $\varepsilon$  was presented in table 1. The table presents average values calculated for each measurement series.

Tab. 1: Results of compressive strength tests.

	Direction X, uncured samples	Direction X, cured samples	Direction Z, uncured samples	Direction Z, cured samples
<b>Average compressive strength <math>\sigma</math> [MPa]</b>	$\bar{\sigma} = 3.29$	$\bar{\sigma} = 9.95$	$\bar{\sigma} = 2.46$	$\bar{\sigma} = 4.64$
<b>Average deformation <math>\varepsilon</math> [%]</b>	$\bar{\varepsilon} = 8.6$	$\bar{\varepsilon} = 18.6$	$\bar{\varepsilon} = 15.1$	$\bar{\varepsilon} = 20.5$

Based on the presented compression graphs 1 ÷ 4 one may state a large dispersion of results. Although curing the samples with the resin has increased the average compressive strength, it has not improve the

reproducibility of the results. This type of phenomenon can be observed in the majority of composite materials.

#### 4. Conclusions

The conducted research shows that the material built with additive technology 3D-Printing has clear anisotropic properties determined by the orientation of the element on the build tray of the machine, thus by the printing direction. The samples printed in vertical direction, both uncured and cured with resin, have a respectively smaller compressive strength than the samples printed in the horizontal direction. Curing with resin increases the compressive strength from two to three times. The tests of the compressive strength showed a large dispersion of results which may indicate a considerable heterogeneity of materials received with this technology.

#### Acknowledgement

The paper was prepared with the use of both facilities and equipment purchased for European Union funds within the scope of the Development of Eastern Poland Operational Program for 2007 – 2013, Project LABIN Apparatus Support for Innovative Scientific Laboratories of the Kielce University of Technology, Priority axis I – Modern Economy, Measure 1.3 – Support for Innovations and research project No. POIG 02.02.00-26-023/08-00.

#### References

- Adamczak, S. and Bochnia, J. (2016) Estimating the approximation uncertainty for digital materials subjected to stress relaxation tests, *Metrology and Measurement Systems*, 23, 4, SI, pp. 545-553. doi:10.1515/mms-2016-0048.
- Blasiak, S. (2015) An analytical approach to heat transfer and thermal distortions in non-contacting face seals, *International Journal of Heat and Mass Transfer*, 81, pp. 90-102. doi:10.1016/j.ijheatmasstransfer.2014.10.011
- Bochnia, J. (2012) Ideal material models for engineering calculations, *Procedia Engineering*, 39, 0, pp. 98-110. doi:http://dx.doi.org/10.1016/j.proeng.2012.07.013.
- Goulas, A. (2016) Additive manufacturing of physical assets by using ceramic multicomponent extra-terrestrial materials, *Additive Manufacturing Jou*, 10, pp. 36-42. doi:10.1016/j.addma.2016.02.002.
- Lee, C.S., Kim, S.G., Kim, H.J. and Ahn, S.H. (2007) Measurement of anisotropic compressive strength of rapid prototyping parts, *Journal of Materials Processing Technology*, 187-188, pp. 627-630. doi:10.1016/j.jmatprotec.2006.11.095.
- Conner, B.P., Manogharan, G.P., Martof, A.N., Rodomsky, L.M., Rodomsky, C.M., Jordan, D.C. and Limperos, J.W. (2014) Making sense of 3-d printing: creating a map of additive manufacturing products and services, *Additive Manufacturing*, 1, 4, pp. 64-76. doi:10.1016/j.addma.2014.08.005.
- Nowakowski, L., Miko, E. and Skrzyniarz, M. (2016) The analysis of the zone for initiating the cutting process of x37crmov51 steel, in: *Proc. of Int. Conf Engineering Mechanics 2016* (ed. Zolotarev, I. and Radolf, V.), Svratka, Czech Republic, pp. 426-429.
- Pilipović, A., Raos, P. and Šercer, M. (2009) Experimental analysis of properties of materials for rapid prototyping, *International Journal of Advanced Manufacturing Technology*, 40, 1-2, pp. 105-115. doi:10.1007/s00170-007-1310-7.
- Takosoglu, J.E., Laski, P.A., Blasiak, S., Bracha, G. and Pietrala, D. (2016) Determining the static characteristics of pneumatic muscles, *Measurement and Control*, 49, 2, pp. 62-71. doi:10.1177/0020294016629176.

## RELAXATION OF MATERIALS OBTAINED USING POLYJET TECHNOLOGY

J. Bochnia \*

**Abstract:** *The paper presents the results of stress-relaxation test on materials which has been produced using PolyJet printing technology. The test has been described and a rheological model has been fit to the relaxation curve determined in the experiment. Values of the parameters of the rheological model has been estimated.*

**Keywords:** Additive technologies, Material relaxation, Rheological model.

### 1. Introduction

Development of printing technologies also impacts on development of materials used in these types of technologies. On the market, there are more and more new materials with various physical and mechanical characteristics that are objects of research. These materials include photocured resins used in PolyJet printing technology (Paz et al., 2016). Building models by using PolyJet printing technology consists of spraying layers of resin with a special head and every new layer accurately reflects a model section in the given working plane. This way of building models and at the same time creating material that models are made of, causes the anisotropy of mechanical characteristics. That problem was presented by many studies (Bass et al., 2016)(Beyer and Figueroa, 2016). This is, for sure, a disadvantage of the technology in comparison to e.g. injection moulding or mechanical operations (Nowakowski and Wijas, 2016) where the anisotropy does not exist or is slightly less.

Printed materials are characterised by, like most of polymers, stress relaxation which causes the need of research on the subject. Stress relaxation in polymer materials was described in many studies, e.g. (Blanco et al., 2014)(Chivers et al., 2014) but there are not many research results concerning stress-relaxation for printed materials (Adamczak and Bochnia, 2016). Worth mentioning are the studies on stress-relaxation of rheological models which are also known as models of ideal bodies (Hernandez-Jimenez et al., 2002)(Del Nobile et al., 2007). The relations of the stress changes in the function of time  $\sigma = f(t)$  are particularly interesting. This paper presents the results of a stress relaxation test performed for a material created using PolyJet technology and Connex 350 printer. Created specimens and the relaxation test with adapting selected rheological model to a relaxation curve determined by experimentation were described. The rheological model parameters were also estimated. The test results can be needful in various modelling projects for engineering calculations (Bochnia, 2012), construction works (Takosoglu et al., 2016) or research (Błasiak and Zahorulko, 2016).

### 2. Methods

The specimens were made of photocured resin, Vero White, by means of an Connex 350 3D printer based on PolyJet technology. The solid model of the test pieces was generated in a 3D CAD program and saved as an .stl file. The settings determining the model accuracy selected in the STL Mesh Export Options dialogue box were as follows: resolution – adjusted, deviation – 0.015 mm tolerance, angle – 5° tolerance. Then, the Objet Studio program was used to arrange the models horizontally on the build tray of the Connex350 printer. The specimens were printed in the Glossy mode to achieve smooth surfaces. Printed specimens on a build tray of the printer are presented in Fig. 1.

---

\* Eng. Jerzy Bochnia, PhD.: Kielce University of Technology, al. Tysiąclecia Państwa Polskiego 7, 25-314 Poland; Department of Machine Technology and Metrology jbochnia@tu.kielce.pl

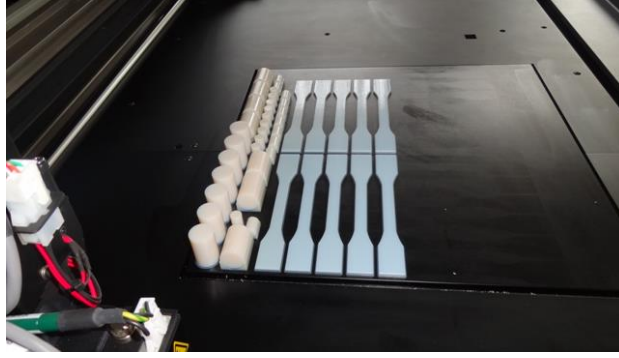


Fig. 1: Printed specimens on a build tray of Connex 350 printer.

A flat specimen of dimensions complied with ASTM D638 standard was chosen for the relaxation test: width of the narrow section,  $13 \pm 0.02$  mm; length of the narrow section,  $57 \pm 0.02$  mm; overall width,  $19 \pm 0.025$  mm; overall length,  $165 \pm$  no max; gauge length,  $50 \pm 0.01$  mm; distance between the grips,  $115 \pm 0.02$  mm; fillet radius,  $76 \pm 0.04$  mm; and thickness,  $4 \pm 0.4$  mm. The test of relaxation was made using the Ispect mini (Hegewald & Peschke MPT GmbH) testing machine with range of 3 kN. Measurement, data acquisition and setting the parameters of the test was performed in the LABMASTER program (Version 2.5.3.21), which is supplied with the Ispect mini machine.

It is very difficult to describe the relaxation process mathematically using a solid model as the description needs to have some physical significance. The Maxwell-Wiechert model for the second order was used for a description. The generalized Maxwell model, also known as the Maxwell-Wiechert model, is shown in Fig. 2.

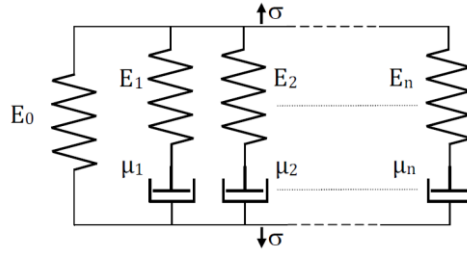


Fig. 2: Generalized Maxwell model (Maxwell-Wiechert model).

The model consists of  $n$  simple Maxwell models assembled in parallel and Hooke's law, where  $E_0, E_1, E_2 \dots E_n$  are the elastic moduli and  $\mu_1, \mu_2, \dots \mu_n$  are the coefficients of viscosity of the simple models. The equation describing this model is written as:

$$\sigma(t) = \varepsilon_0 \left( \sum_{i=1}^n E_i e^{\frac{-t}{t_i}} + E_0 \right) \quad (1)$$

where:  $\varepsilon_0$  – predetermined displacement,  
 $n$  – number of simple Maxwell models,  
 $i$  – number of the subsequent model.

For  $n = 2$ , i.e. for two simple Maxwell models and Hooke's law assembled in parallel, Equation (1) can be written as:

$$\sigma(t) = \sigma_0 + \sigma_1 e^{\frac{-t}{t_1}} + \sigma_2 e^{\frac{-t}{t_2}} \quad (2)$$

where:  $\sigma_0$  – initial stress at  $t = 0$ ,  
 $t_1$  – relaxation time.

The relaxation time, defined as the ratio of the properties of a Newtonian fluid and a Hookean solid, can be written as:

$$t_1 = \frac{\mu_1}{E_1}, \quad t_2 = \frac{\mu_2}{E_2} \quad (3)$$

where:  $\mu_1, \mu_2$  – coefficients of viscosity,  
 $E_1, E_2$  – elastic modulus.



### 3. Results

The relaxation test was conducted using block programming. The given displacement value was 0.1 mm. In this stage the displacement value of an arm of a tensile testing machine was 0.1 mm causing specimen stress. Next, the displacement value of 0.1 mm was kept for 300 s and during that time the stress decreased what means that the stress relaxation occurred. The last stage was specimen offloading. The chart of loading and relaxation is presented in Fig. 3.

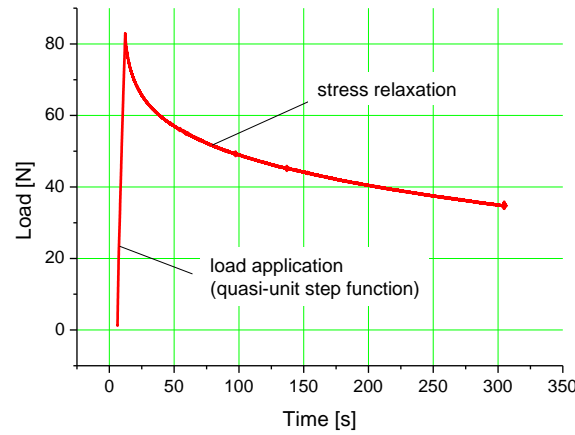


Fig. 3: A stress relaxation plot for Vero White.

Next, only a part of the chart with stress relaxation was analysed. The curve obtained experimentally for the equation (2) was fitted with the approximation method. Origin computer programme was used for approximation performing. The results of curve fitting are presented in Fig. 4.

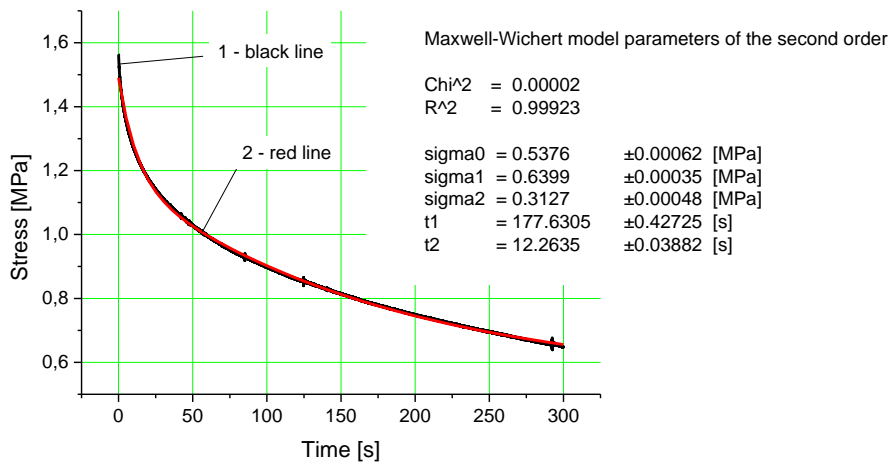


Fig. 4: Experimental curve compared with the approximation curve. 1 – experimental curve for specimen made of Vero White, 2 – approximation curve obtained using Equation (2) for two Maxwell models and Hooke's law connected in parallel, Chi<sup>2</sup> - a chi-squared test, also written as  $\chi^2$  test, is any statistical hypothesis test wherein the sampling distribution of the test statistic is a chi-squared distribution, R<sup>2</sup> (R squared) - the coefficient of determination, is a number that indicates the proportion of the variance in the dependent variable that is predictable from the independent variable.

For the experimental relaxation curve, the approximation was conducted using equation (2) to determine  $\sigma_0$ ,  $\sigma_1$ ,  $\sigma_2$ ,  $t_1$ ,  $t_2$  parameters and values for Chi2 test and R2 coefficient. The parameters values are presented in Fig. 4. The conclusion of Fig. 4 quality assessment is: a high fitting level of the approximation curve to the real curve (experimental) using the equation (2) was obtained.

This paper presents only one experiment but procedures for further research are also determined, so the research will be continued and described in a more voluminous publication.

#### 4. Conclusions

Estimating parameters of the relaxation function using approximation (2) shows full overview of curves fitting and confirms suitability of the adapted model of an ideal body for describing real materials. The description of the experimental relaxation curve with determined approximation accuracy is very important because of physical characteristics of the obtained parameters.

The conducted experiment widens knowledge on new materials characteristics made using printing technologies- in this case using PolyJet technology.

#### Acknowledgement

The paper was prepared with the use of both facilities and equipment purchased for European Union funds within the scope of the Development of Eastern Poland Operational Program for 2007 – 2013, Project LABIN Apparatus Support for Innovative Scientific Laboratories of the Kielce University of Technology, Priority axis I – Modern Economy, Measure 1.3 – Support for Innovations and research project No. POIG 02.02.00-26-023/08-00.

#### References

- Adamczak, S. and Bochnia, J. (2016) Estimating the approximation uncertainty for digital materials subjected to stress relaxation tests, *Metrology and Measurement Systems*, 23, 4, SI, pp. 545-553. doi:10.1515/mms-2016-0048.
- Bass, L., Meisel, N.A. and Williams, C.B. (2016) Exploring variability of orientation and aging effects in material properties of multi-material jetting parts, *Rapid Prototyping Journal*, 22, 5, pp. 826-834. doi:10.1108/RPJ-11-2015-0169.
- Beyer, C. and Figueroa, D. (2016) Design and analysis of lattice structures for additive manufacturing, *Journal of Manufacturing Science and Engineering-Transactions of the ASME*, 138, 12. doi:10.1115/1.4033957.
- Blanco, D., Fernandez, P. and Noriega, A. (2014) Nonisotropic experimental characterization of the relaxation modulus for polyjet manufactured parts, *Journal of Materials Research*, 29, 17, pp. 1876-1882. doi:10.1557/jmr.2014.200.
- Blasiak, S. and Zahorulko, A.V. (2016) A parametric and dynamic analysis of non-contacting gas face seals with modified surfaces, *Tribology International*, 94, , pp. 126-137. doi:10.1016/j.triboint.2015.08.014.
- Bochnia, J. (2012) Ideal material models for engineering calculations, *Procedia Engineering*, 39, 0, pp. 98-110. doi:http://dx.doi.org/10.1016/j.proeng.2012.07.013.
- Chivers, R.A., Bonner, M.J., Hine, P.J. and Ward, I.M. (2014) Shape memory and stress relaxation behaviour of oriented mono-dispersed polystyrene, *Polymer*, 55, 4, pp. 1055-1060. doi:10.1016/j.polymer.2014.01.002
- Del Nobile, M.A., Chillo, S., Mentana, A. and Baiano, A. (2007) Use of the generalized maxwell model for describing the stress relaxation behavior of solid-like foods, *Journal of Food Engineering*, 78, 3, pp. 978-983. doi:10.1016/j.jfoodeng.2005.12.011.
- Hernandez-Jimenez, A., Hernandez-Santiago, J., Macias-Garcia, A. and Sanchez-Gonzalez, J. (2002) Relaxation modulus in pmma and ptfe fitting by fractional maxwell model, *Polymer Testing*, 21, 3, pp. 325-331. doi:10.1016/S0142-9418(01)00092-7.
- Nowakowski, L. and Wijas, M. (2016) The evaluation of the process of surface regeneration after laser cladding and face milling, in: *Proc. Int. Conf. on Engineering Mechanics 2016* (eds. Zolotarev, I and Radolf, V.), Svratka, Czech Republic, pp. 430-433.
- Paz, R., Monzon, M.D., Benitez, A.N. and Gonzalez, B. (2016) New lightweight optimisation method applied in parts made by selective laser sintering and polyjet technologies, *International Journal of Computer Integrated Manufacturing*, 29, 4, pp. 462-472. doi:10.1080/0951192X.2015.1066033.
- Takosoglu, J.E., Laski, P.A., Blasiak, S., Bracha, G. and Pietrala, D. (2016) Determination of flow-rate characteristics and parameters of piezo valves, in: *Proc. Int. Conf. Exp. Fluid Mech. 2016* (ed. Dancova, P.), Techn. Univ. Liberec, pp. 814-818.

## VISUAL DIAGNOSTICS OF RAIL FASTENING SYSTEM AS A METHOD TO IMPROVE SAFETY

P. Bojarczak<sup>\*</sup>, W. Nowakowski<sup>\*\*</sup>, Z. Łukasik<sup>\*\*\*</sup>

**Abstract:** *The safety in railway transport is a very important aspect. Safety depends mainly on the state of railway infrastructure. Hence, the methods allowing for the assessment of the infrastructure should be developed. In the paper, authors present visual method allowing for diagnostics of rail fastening system. This method uses wavelet transform to extract feature and neural network to detect (classify) defect occurring in this system.*

**Keywords:** Visual diagnostics, Rail fastening system, Neural network, Safety.

### 1. Introduction

The state of railway track has an immense impact on the safety of railway traffic. The railroad spike is an important element of railway track. Until now in Poland, diagnostics of railroad spikes has been carried out in visual form by inspectors. This method is ineffective and inaccurate. One person is able to check very limited section of railway track. Needless to say that the weariness of inspector has also an influence on the effectiveness. Hence authors proposed the method based on visual algorithms which allows for automation of diagnostics and elimination of people.

### 2. Research problem

All images used in the development of the algorithm presented here come from visual system installed on an ultrasonic flaw detecting carriage. The goal of this system was to enable to the operator to “manually” verify if the defects registered by the ultrasonic equipment were not caused by rail joints or turnouts. This visual system does not perform any image processing and analysis, it just records images of the left and right rails of the track. One video frame of the size 1294 x 964 pixels covers a constant section of the rail, 0.5 meter in length, independently of the speed of the carriage. The visual system records a section of the rail and its vicinity. Therefore, it is necessary to narrow the image under analysis to a fragment containing railroad spikes. It can be realized by the Region of Interest procedure (ROI). Railroad spike lies on the intersection of the rail and railroad tie, therefore ROI should detect both the rail and the spike. Such ROI is presented in (Bojarczak, 2013). Once the fragment of image with spike is extracted, the algorithm for automatic visual diagnostics has to be applied. Fig. 1 presents a block diagram of the proposed algorithm.

It consists of two main components. The first part, called feature extraction, serves to detect the most informative (salient) features describing spikes under analysis. The second, called the detector (classifier), classifies the image under analysis into two classes on the basis of the features extracted. The first and second classes comprise images of spike without and with defects, respectively.

---

<sup>\*</sup> Assoc. Prof. Ing. Piotr Bojarczak, PhD.: Faculty of Transport and Electrical Engineering, Kazimierz Pulaski University of Technology and Humanities in Radom, Malczewskiego 29; 26-600, Radom; PL, p.bojarczak@uthrad.pl

<sup>\*\*</sup> Ing. Waldemar Nowakowski, PhD.: Faculty of Transport and Electrical Engineering, Kazimierz Pulaski University of Technology and Humanities in Radom, Malczewskiego 29; 26-600, Radom; PL, w.nowakowski@uthrad.pl

<sup>\*\*\*</sup> Prof. Ing. Zbigniew Łukasik, PhD.: Faculty of Transport and Electrical Engineering, Kazimierz Pulaski University of Technology and Humanities in Radom, Malczewskiego 29; 26-600, Radom; PL, z.lukasik@uthrad.pl

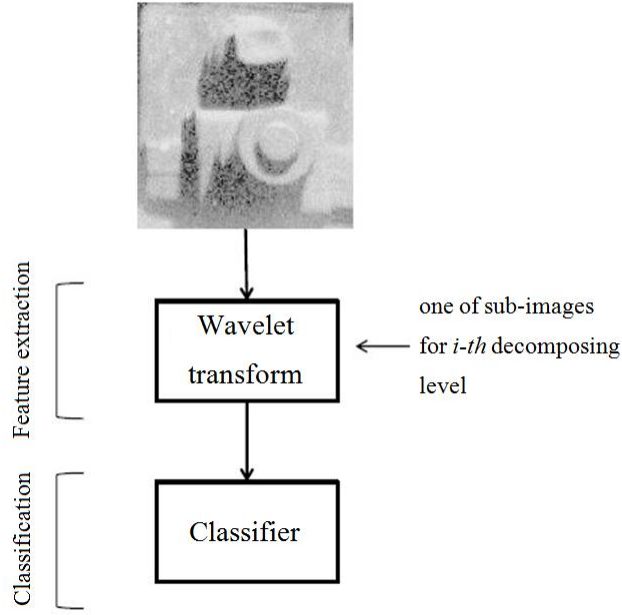


Fig. 1: Block diagram of the proposed algorithm.

Two-dimensional Discrete Wavelet Transform (2D DWT) was used to feature extraction. 2D DWT is the extension of one-dimensional Discrete Wavelet Transform (1D DWT). 1D DWT decomposes the analyzed function  $f(t)$  on finite lasting components called  $\Psi(t)$  wavelets (Mallat, 1989 and Daubechies, 1988).

$$W(a,b) = \int_{-\infty}^{+\infty} f(t) * \Psi_{a,b}(t) dt \quad (1)$$

where:

$$\Psi_{a,b}(t) = \frac{1}{\sqrt{a}} \Psi\left(\frac{t-b}{a}\right) \quad (2)$$

is a wavelet function of time scale (dilatation) equal to  $a$  and time shift (translation) described by  $b$ . If wavelets functions are only chosen for  $a=2^k$  and  $b=2^n$  where  $k$  and  $n$  are integer number, then formula describes discrete wavelet transform of original function  $f(t)$ . DWT can split original function  $f(t)$  into two parts:  $f_o(t)$  corresponding to coarser approximation of  $f(t)$  and  $g_o(t)$  corresponding to high frequency detail function, defined as a difference between  $f(t)$  and its approximation version. The approximated version  $f_o(t)$  can be further split into two parts – coarse approximation  $f_l(t)$  and the detail part  $g_l(t)$ . This process can be continuously performed up to some assumed level. The splitting process is also called decomposition level. In case of 2D DWT the wavelet decomposition is performed twice: first on the rows of the image and then on its columns thus 2D DWT generates 4 sub-images:  $f_{LL}(x,y)$ ,  $f_{LH}(x,y)$ ,  $f_{HL}(x,y)$  and  $f_{HH}(x,y)$  corresponding to smooth sub-image, horizontal details sub-image, vertical details sub-image and diagonal details sub-image, respectively.

Support Vector Machine (SVM) has been used to classify (detect) railroad spikes with and without defects - Classifier block in Fig. 1. While designing the SVM classifier, the hyper-plane separating the data into two classes (one containing a spike with defect and one containing a spike without defect) is constructed in  $M$ -dimensional input space (Burges, 1998 and Cristianini, 2000). SVM is a linear system performing linear separation in  $R$ -dimensional feature space created by nonlinear projection of  $M$ -dimensional input space ( $R>M$ ) with the use of the function  $\phi(x)$ . The main advantage of the SVM is the maximal-margin separation between data of the two classes, which in turn ensures maximum classification rate. In practice, if instead of function  $\phi(x)$  the kernel function  $K(x, x_i) = \phi^T(x_i)\phi(x)$  is applied. There are three types of kernels: linear, polynomial and Gaussian. If the kernel is of the linear form, then the hyper-plane is constructed in the original  $M$ -dimensional input space. However, if the kernel is of polynomial or Gaussian form the hyper-plane is constructed in a higher dimensional space.

### 3. Results

The crucial issue is the right choice of the wavelet, decomposing level and the type of sub-image. Hence authors examined  $f_{LL}(x,y)$ ,  $f_{LH}(x,y)$  and  $f_{HL}(x,y)$  sub-images for up to fourth decomposing level and nine wavelets. Fig. 2 presents example of sub-images of spike for 2-th level of decomposition with bior1.1 wavelet.

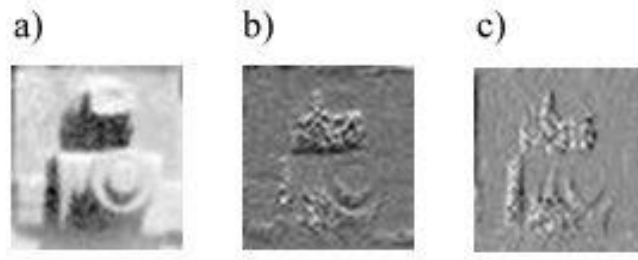
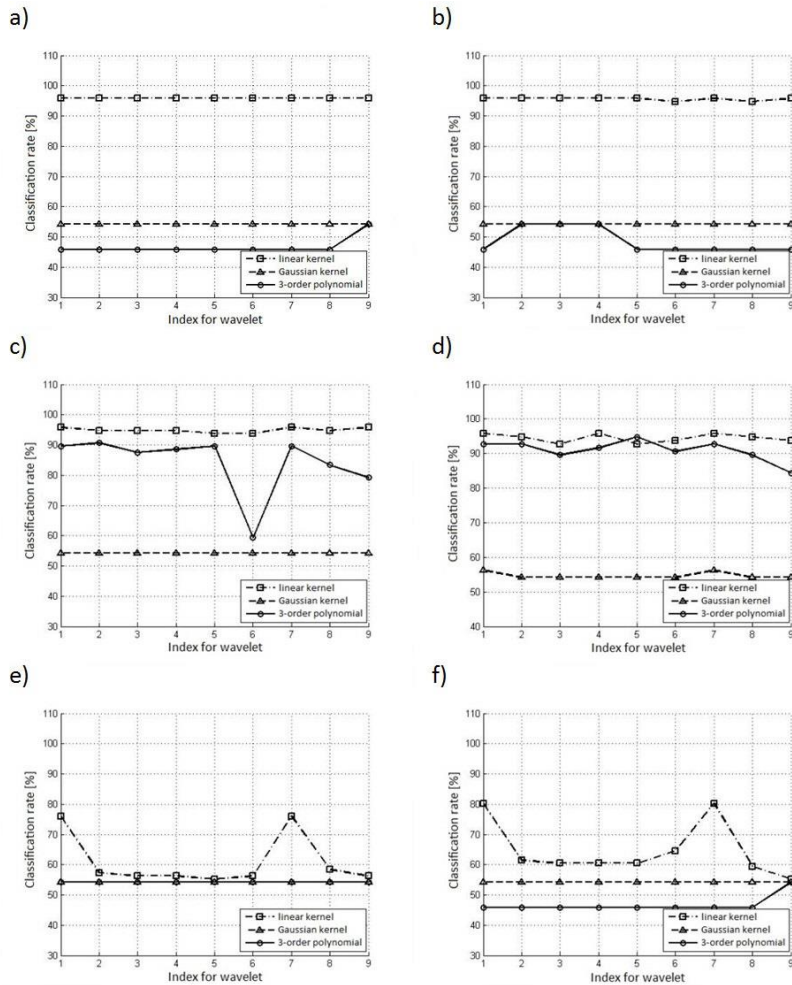


Fig. 2: 2DWT a)  $f_{LL}(x,y)$  sub-image; b)  $f_{HL}(x,y)$  sub-image; c)  $f_{LH}(x,y)$  sub-image for 2 decomposing level and bior1.1 wavelet.

First, the SVM classifier was trained on 160 images of spike without defect and 115 images of spike with defect. These images correspond to appropriate sub-images obtained after performing  $n$ -th decomposition. Next, the operation of proposed algorithm was checked on testing set including 160 images of spike without defect and 115 images of spike with defect. This set did not take part in training process. Fig. 3 presents the relationship between classification rate and the type of wavelet. Numbers on horizontal axis corresponds to type of wavelet: 1- db1; 2 - db3; 3 - db3; 4 - coif1; 5 - coif2; 6 - coif3; 7 - bior.1.1; 8 - bior2.3 and 9 - bior3.1. Classification rate is defined as ratio of the number of correctly classified images to total number of testing images.



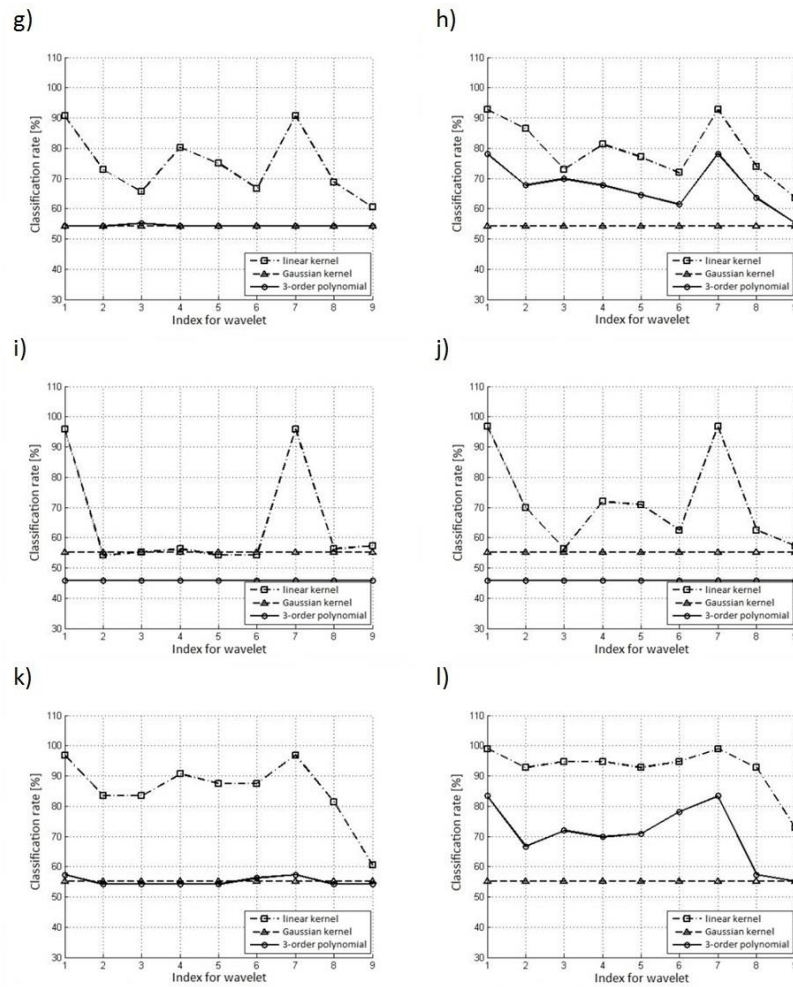


Fig. 3: Relationship between classification rate and type of wavelet for a), b), c), d)  $f_{LL}(x,y)$  sub-image; e), f), g), h)  $f_{LH}(x,y)$  sub-image; i), j), k), l)  $f_{HL}(x,y)$  sub-image for up to 4 decomposing level.

#### 4. Conclusions

According to Figs. 3a and 3b for  $f_{LL}(x,y)$  sub-image and first and second decomposing level, the classification rate is equal to 96 % (for SVM with linear kernel) and does not depend on the type of wavelet used in decomposition. It depends only on the form of kernel used in SVM classifier. Therefore the feature extraction part of the presented algorithm can be omitted and the image of spike can be directly given to SVM with linear kernel. The presented algorithm is able to detect defect occurring in spike based on its image.

#### Acknowledgement

This material is based upon work supported by Polish National Centre for Research and Development under Grant No. PBS3/A6/29/2015.

#### References

- Bojarczak, P. (2013) Visual algorithms for automatic detection of squat flaws in railway rails, Insight Non-Destructive Testing and Condition Monitoring, The Journal of The British Institute of Non-Destructive Testing, Vol. 55, No 7, pp. 353-359.
- Mallat, S. (1989) A theory for multiresolution signal decomposition: the wavelet representation, IEEE Trans PAMI, Vol. 11, pp. 674-693.
- Daubechies, I. (1988) Ten lectures on wavelets, SIAM Press.
- Burges, C.J.C. (1998) A tutorial on Support Vector Machines for pattern recognition, Data Mining and Knowledge Discovery. Vol. 2, pp. 121-167.
- Cristianini, N. (2000) Support Vector Machines and other kernel based learning methods, Cambridge University Press.



## OPTIMAL REPAIR AND REINFORCEMENT OF BAR STRUCTURES USING FINITE TOPOLOGY VARIATIONS

D. Bojczuk<sup>\*</sup>, W. Szteleblak<sup>\*\*</sup>

**Abstract:** *The problem of optimal repair and/or optimal reinforcement of bar structures by introduction of new elements is considered in this paper. The corresponding optimization problem is formulated as the maximization of the global stiffness increment induced by repair (reinforcement) under the cost constraint. The potential energy is assumed as the measure of the global structure stiffness, while the cost constraint corresponds to condition imposed on the maximal cost of the repair and/or reinforcement. The method of determination of the structure global stiffness increment induced by finite topology modification is proposed and the optimization algorithm is presented. Numerical examples of optimal repair and/or reinforcement of some structures illustrate the theoretical considerations.*

**Keywords:** Bar Structures, Optimal Repair, Optimal Reinforcement, Finite Topology Variations, Global Stiffness.

### 1. Introduction

Global stiffness and load capacity of a structure due to operation of certain factors, for example atmospheric, biological, chemical, etc., may significantly decrease. Moreover, need of taking into account additional loads sometimes occurs. In these and similar situations appears necessity of repair and/or reinforcement of the structure in the current state.

In the present paper, at first general approach for determination of finite increments of the global stiffness caused by finite topology modifications (cf. Mróz and Bojczuk, 2003) is adjusted to the bar structures. Next, assuming that the structure is weakened or damaged, the problem of optimal repair or reinforcement is formulated. The method of solving this problem using finite topology modifications corresponding to introduction of substructures or structural elements is presented.

The hitherto existing papers usually apply probabilistic approach to the damage processes and focus attention on optimal inspection and maintenance (cf. Jido et al., 2008 and Ortega-Estrada et al. 2013), in contrary to this paper, which is devoted to optimal repair or optimal reinforcement of weakened structures.

### 2. Formulation of problem of optimal repair (reinforcement)

The problem of optimal repair and/or optimal reinforcement of the fixed primary structure in order to maximize global stiffness, admitting finite topology modifications, can be presented in the form

$$\max \Delta \Pi \quad \text{subject to} \quad C \leq C_0, \quad (1)$$

where  $\Delta \Pi$  denotes increment of the potential energy caused by introduction of stiffening substructures or structural elements subjected to optimal design,  $C$  is the global cost of the structure after this finite modification and  $C_0$  denotes the upper bound on the global cost. Here, the potential energy  $\Pi$  is assumed as the measure of the structure global stiffness.

---

<sup>\*</sup> Dr hab. Dariusz Bojczuk, PhD.: Faculty of Management and Computer Modelling, Kielce University of Technology, Al. Tysiąclecia Państwa Polskiego 7, 25-314 Kielce; PL, mecdb@tu.kielce.pl

<sup>\*\*</sup> Dr Wojciech Szteleblak, PhD.: Faculty of Mechatronics and Mechanical Engineering, Kielce University of Technology, Al. Tysiąclecia Państwa Polskiego 7, 25-314 Kielce; PL, wszteleblak@tu.kielce.pl



### 3. Determination of finite changes of global stiffness

Let us consider, on the example of a frame, determination of finite increment of the potential energy induced by finite topology modification. We assume that the primary structure 1 will be connected with a new additional substructure 2 (Fig. 1), which position and stiffness parameters are the design variables. In view of Betti's reciprocity theorem separately for the structures 1 and 2, before and after connection, we get

$$\begin{aligned} \mathbf{P}_1 \cdot \mathbf{u}_1 &= \mathbf{P}_1 \cdot \mathbf{u}_1^0 + T_C w_{1C}^0 + N_C u_{1C}^0 + M_C \theta_{1C}^0, \\ \mathbf{P}_2 \cdot \mathbf{u}_2 &= \mathbf{P}_2 \cdot \mathbf{u}_2^0 - T_C w_{2C}^0 - N_C u_{2C}^0 - M_C \theta_{2C}^0, \end{aligned} \quad (2)$$

where  $\mathbf{P}_1, \mathbf{P}_2$  are the vectors of generalized loads,  $\mathbf{u}_1^0, \mathbf{u}_2^0$  and  $\mathbf{u}_1, \mathbf{u}_2$  denote the vectors of generalized displacements before and after connection, while  $\mathbf{P}_C(N_C, T_C, M_C)$ ,  $\mathbf{u}_{1C}^0(u_{1C}^0, w_{1C}^0, \theta_{1C}^0)$ ,  $\mathbf{u}_{2C}^0(u_{2C}^0, w_{2C}^0, \theta_{2C}^0)$  are the vectors of internal forces and generalized displacements of the structures at the connection point. Now, the increment of the potential energy can be presented as follows

$$\begin{aligned} \Delta \Pi &= \Pi - \Pi^0 = -\frac{1}{2}(\mathbf{P}_1 \cdot \mathbf{u}_1 + \mathbf{P}_2 \cdot \mathbf{u}_2) + \frac{1}{2}(\mathbf{P}_1 \cdot \mathbf{u}_1^0 + \mathbf{P}_2 \cdot \mathbf{u}_2^0) = \\ &= \frac{1}{2}[N_C(u_{2C}^0 - u_{1C}^0) + T_C(w_{2C}^0 - w_{1C}^0) + M_C(\theta_{2C}^0 - \theta_{1C}^0)] = \\ &= \frac{1}{2}\mathbf{P}_C \cdot (\mathbf{u}_{2C}^0 - \mathbf{u}_{1C}^0) = \frac{1}{2}\mathbf{P}_C \cdot [\mathbf{u}_C^0], \end{aligned} \quad (3)$$

where  $[\mathbf{u}_C^0]$  denotes discontinuity of generalized displacement vectors at the connection point. Taking into account that  $[\mathbf{u}_C] = \mathbf{u}_{2C} - \mathbf{u}_{1C} = \mathbf{0}$  and  $\mathbf{u}_{1C} = \mathbf{u}_{1C}^0 + \mathbf{D}_{1C}\mathbf{P}_C$ ,  $\mathbf{u}_{2C} = \mathbf{u}_{2C}^0 - \mathbf{D}_{2C}\mathbf{P}_C$ , we get that  $[\mathbf{u}_C^0] = \langle \mathbf{D}_C \rangle \mathbf{P}_C$ , where  $\langle \mathbf{D}_C \rangle = \mathbf{D}_{1C} + \mathbf{D}_{2C}$  is the sum of the local compliance matrices related to the interface. Therefore, finally the equation (3) can be rewritten as follows (cf. Mróz and Bojczuk, 2003)

$$\Delta \Pi = \frac{1}{2}\mathbf{P}_C \cdot [\mathbf{u}_C^0] = \frac{1}{2}\mathbf{P}_C \cdot \langle \mathbf{D}_C \rangle \mathbf{P}_C = \frac{1}{2}[\mathbf{u}_C^0] \cdot \langle \mathbf{D}_C \rangle^{-1} [\mathbf{u}_C^0]. \quad (4)$$

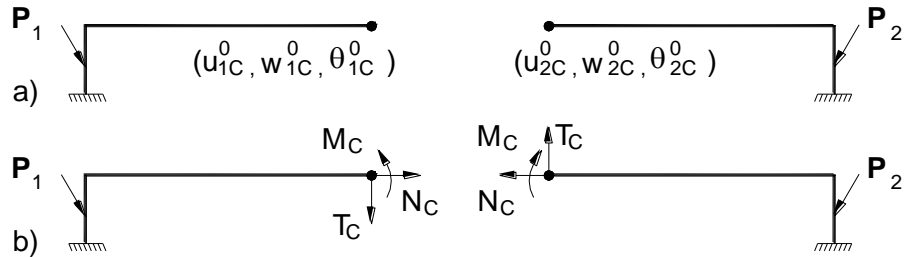


Fig. 1: Connection of a primary structure 1 with reinforcing substructure 2:  
a) the structures before connection; b) the structures after connection.

So, the stiffness increment depends on, easy to determine, vector of initial displacements discontinuity  $[\mathbf{u}_C^0]$  and inverse of the matrix  $\langle \mathbf{D}_C \rangle$ . In order to calculate  $\langle \mathbf{D}_C \rangle$ , at first stiffness matrices of the primary structure and additional substructure  $\mathbf{K}_1, \mathbf{K}_2$  and their inverses  $\mathbf{D}_1 = \mathbf{K}_1^{-1}$ ,  $\mathbf{D}_2 = \mathbf{K}_2^{-1}$  are determined. Now  $\mathbf{D}_{1C}, \mathbf{D}_{2C}$  can be easily specified as the submatrices of  $\mathbf{D}_1, \mathbf{D}_2$  of considerably smaller dimensions. It is important to notice that during optimization matrices  $\mathbf{K}_1, \mathbf{D}_1$  do not change, so only  $\mathbf{K}_2$  and  $\mathbf{D}_2$  should be separately calculated in each step of optimization.

### 4. Optimal design algorithm

In order to determine optimal repair or reinforcement by introduction of an additional substructure the following algorithm, which combines FEM analysis and any gradient optimization method, can be used:

1° Determine plan of the primary structure repair or reinforcement.

- 2° Using information from the topological derivative (cf. Bojczuk and Mróz, 1998; Mróz and Bojczuk, 2003) or by direct decision of designer, choose, under the constraint of the maximal cost, initial location and stiffness of the finite reinforcing modification.
- 3° Applying any gradient optimization method, where  $\Delta \Pi$  is calculated from (4), as it was described in Section 3, determine optimal values of the design parameters for the substructure.
- 4° Terminate the procedure or propose another method of repair or reinforcement and return to 1°.

## 5. Illustrative examples

Numerical examples of optimal repair and reinforcement of bar structures presented in this Section illustrate applicability and usefulness of the proposed approach.

### 5.1. Example 1: Optimal repair (reinforcement) of symmetric truss

The symmetric truss made of steel, which global stiffness is not sufficient, should be reinforced. All bars of the truss have cross-section of circular tube shape and their areas respectively are  $A_1 = 8 \cdot 10^{-4} \text{ m}^2$ ,  $A_2 = 5 \cdot 10^{-4} \text{ m}^2$ ,  $A_3 = 3 \cdot 10^{-4} \text{ m}^2$  (Fig. 2). It is assumed that reinforcement can be performed by adding symmetrically located one or two pairs of new bars, but only in tension.

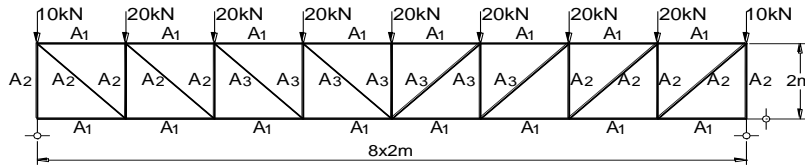


Fig. 2: Static scheme of the truss.

The problem of optimal design has the form (1), where it is assumed that the cost is proportional to the volume and the volume of the additional bars should not exceed  $V_0 = 10^{-2} \text{ m}^3$ . Due to symmetry only half of the truss is analyzed. Possible initial locations of new bars are chosen, as these lines between two nodes, so far not connected by bars, where virtual strains are positive (because of tension) and the biggest (cf. Mróz and Bojczuk, 2003). During optimization optimal pairs (pair) of bars are selected and their cross-section areas are determined.

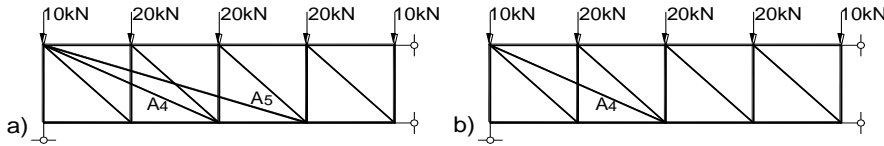


Fig. 3: The optimal designs.

The primary structure (Fig. 2) has the potential energy  $\Pi = -2.200 \text{ kJ}$ . The optimal designs are shown in Fig. 3. In the case of introduction of two pairs of bars (Fig. 3a) the potential energy increased to  $\Pi = -1.929 \text{ kJ}$  and the cross-section areas of the bars are  $A_4 = 6.24 \cdot 10^{-4} \text{ m}^2$  and  $A_5 = 3.49 \cdot 10^{-4} \text{ m}^2$  respectively. When only the one pair of bars is introduced optimal solution is shown in Fig. 3b. In this case the potential energy of the truss increased to  $\Pi = -1.948 \text{ kJ}$ . The cross-section areas of the pair of bars are  $A_4 = 11.18 \cdot 10^{-4} \text{ m}^2$ .

### 5.2. Example 2: Optimal repair (reinforcement) of frame

Now, let us consider frame structure made of steel, which is shown in Fig. 4. Both, columns and cross-beam are double-T bars of cross-section areas  $A = 10^{-2} \text{ m}^2$ . It is assumed that the frame can be reinforced by adding two or one column. The optimization problem consists in maximization of the total potential energy increment under cost constraint. Here we assume that the cost is proportional to material volume and the maximal volume of additional columns is  $V_0 = 5 \cdot 10^{-2} \text{ m}^3$ . The design parameters are

locations of columns  $s_i$  and their cross-section areas  $A_i$ . Here, two types of connections of additional columns to foundation and to the cross-bar denoted by  $k$  are considered, namely either pinned or fixed.

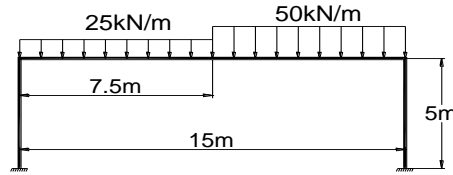


Fig. 4: Static scheme of the frame

The primary structure (Fig. 4) has the potential energy  $\Pi = -25.45 \text{ kJ}$ . For the case of introduction of two columns, these columns are initially located symmetrically in relation to the point of cross-beam maximal deflection, while the optimal solution is shown in Fig.5a. Tab.1 contains optimal values of the design parameters and potential energy for three types of optimization problems considered here, namely introduced columns are simply supported, clamped or clamped but with equal cross-section areas. In the case of introduction of one column (Fig. 5b), this column is initially located at the point of the maximal deflection of cross-beam (cf. Bojczuk and Mróz, 1998). Optimal values of design parameters are in the fixed case:  $s = 8.22 \text{ m}$ ,  $\Pi = -0.8335 \text{ kJ}$ , and in the pinned case:  $s = 8.35 \text{ m}$ ,  $\Pi = -0.8489 \text{ kJ}$ .

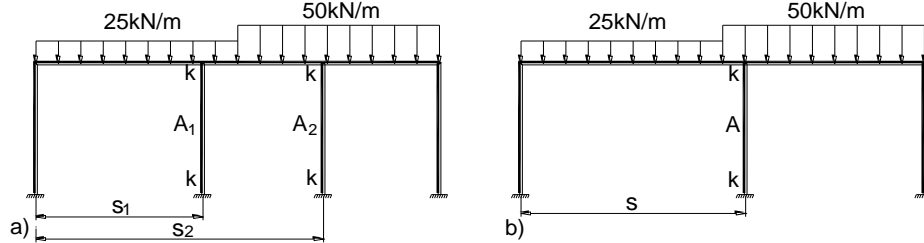


Fig. 5: Optimal design of the frame: a) the case with two additional columns, b) the case with one additional column

Tab. 1: Optimal values of design parameters

Connection type	Design parameters				
	$s_1[\text{m}]$	$s_2[\text{m}]$	$A_1 \cdot 10^{-4}[\text{m}^2]$	$A_2 \cdot 10^{-4}[\text{m}^2]$	Poten. en.[kJ]
fixed	6.21	10.69	43.1	56.9	-0.3349
pinned	6.18	10.68	42.8	57.2	-0.3353
fixed, constant $A_1, A_2$	6.40	10.82	50	50	-0.3375

## 6. Conclusions

The problem of optimal repair and/or reinforcement of bar structures in order to maximize global stiffness under cost constraint is analyzed in this paper. The algorithm of optimization, in which, initially, finite topology variations corresponding to new elements and substructures are introduced into the structure, is presented and successfully applied in some illustrative examples. The formulated approach can be also used for other types of finite modifications like replacement or removal of structural elements.

## References

- Bojczuk, D. and Mróz, Z. (1998) On optimal design of supports in beam and frame structures. *Structural Optimization*, 16, 1, pp. 47-57.
- Jido, M., Otazawa, T. and Kobayashi, K. (2008) Optimal repair and inspection rules under uncertainty. *Journal of Infrastructure Systems*, 14, 2, pp. 150-158.
- Mróz, Z. and Bojczuk, D. (2003) Finite topology variations in optimal design of structures. *Structural and Multidisciplinary Optimization*, 25, 3, pp. 153-173.
- Ortega-Estrada, C., Trejo, R., De Leon, D. and Campos, D. (2013) Optimal plan for inspection and maintenance of structural components by corrosion, in: *Proceedings of the World Congress on Engineering*, Vol. I, WCE 2013, July 3-5, 2013, London, U. K.

## INHOMOGENEOUS MATERIAL PROPERTIES ASSIGNMENT TO FINITE ELEMENT MODELS OF BONE: A SENSITIVITY STUDY

L. Borák\*, P. Marcián\*\*

**Abstract:** *The present work deals with a strain intensity sensitivity to finite element mesh density in computational models of skull bone sample with an inhomogeneous distribution of Young's modulus. Computational experiments on models with various mesh density were conducted to test the hypothesis that the strain intensity distribution along the bone sample thickness is significantly influenced by the mesh density when material properties of bone obtained from the computer tomography are assigned to the finite element model. The results indicate that the mesh quality matters.*

**Keywords:** Computer tomography, Finite element method, Material mapping, Patient-specific.

### 1. Introduction

There are two major features that helps to define the contemporary musculoskeletal biomechanics. “A patient specific approach” and “in silico medicine”. The first feature is based on a general trend in today's health-care for personalized medicine (Zadpoor, 2015). In such cases, the patient-specific approach requires additional information pertaining to individual patients. As for bone-related problems, a good start for creating a reliable and effective personalized model is to acquire a set of images from the computer tomography (CT). These images, which differ for each patient, provide not only a necessary insight into the patient's state of health but also the information necessary for building the model. CT systems are based on a principle of measuring X-ray attenuation of tissues which can be transformed into the Hounsfield units (HU). Using an appropriate calibration, HU can provide information on the apparent density ( $\rho$ ) of bone tissue. It has been proved many times that elastic properties of bones are correlated to  $\rho$  (Helgason, 2016); therefore, from the CT-based distribution of  $\rho$ , an inhomogeneous Young's modulus (E) distribution in the bone might be obtained as well using an appropriate E- $\rho$  relationship.

The second feature might be defined as the use of computer simulations for medical purposes. Finite element method has become a strong tool for many biomechanicians of today. This tool enables relatively accurate predictions and provides a good insight into behavior of living systems without necessity of invasive procedures. Combining those two features, high-level computational models might be created and used for a wide range of research as well as for helping the treatment of actual clinical cases. However, there is still a big amount of unresolved problems pertaining to the methodology. For instance, the inhomogeneous material assignment to FE models is still not common routine and not all limits of the method have been identified and investigated.

In the most popular approach, a mapping of CT-based  $\rho$  into FE models is performed by association of CT-numbers with corresponding nodes of the FE model (Taddei, 2004). A practical implementation is mostly often based on in-house software applications or on publicly available software such as Bonemat (Zannoni, 1998). However, suitability of concrete implementation might depend on the specific problem as no universal approach exists. In any case, the accuracy of the mapping is still questionable and using of FE models with the inhomogeneous material properties distribution is still under scrutiny.

The aim of the work is to present our approach to the material assignment and to study strain intensity sensitivity to mesh density when the inhomogeneous material distribution in a skull bone is assumed.

---

\* Ing. Libor Borák, PhD.: Institute of Solid Mechanics, Mechatronics and Biomechanics, Faculty of Mechanical Engineering, Brno University of Technology, Technická 2896/2, 616 69 Brno, Czech Republic; CZ, liborborak@seznam.cz

\*\* Ing. Petr Marcián, PhD.: Institute of Solid Mechanics, Mechatronics and Biomechanics, Faculty of Mechanical Engineering, Brno University of Technology, Technická 2896/2, 616 69 Brno, Czech Republic; CZ, marcian@fme.vutbr.cz

## 2. Material and Methods

### 2.1. Geometry and material properties

For the purposes of this study, a skull from actual patient (male, 31 yo) was CT-scanned (resolution 0.4 x 0.4 x 0.7 mm). The images were processed using an in-house software application STL Model Creator (Matlab 2010, MathWorks, Natick, MA, USA) to obtain a digitized geometry. The geometry was treated in a CAD software (SolidWorks, Dassault Systems, Velizy-Villacoublay, France) and then imported into a FE software (Ansys 17.2, Swanson Analysis Systems Inc., Houston, PA, USA). Afterwards, positions of nodes of the discretized geometry along with the CT images were imported into another in-house software application CTPixelMapper (Python 3.4) to perform a mapping of CT-numbers into the FE model and a conversion into Young's moduli (Fig. 1 and 2). For the conversion, a general eq. (1) was used for three different types of material assumed to be contained in the CT data depending on specific CT-numbers. Material coefficients for those tissues are listed in Tab. 1. Eq. (1) combines a CT- $\rho$  conversion based on a phantom calibration of CT device with E- $\rho$  conversion taken from literature (Helgason et al., 2008). Poisson's ratio for bone was assumed to be 0.3.

$$E = a \cdot (b \cdot CT^c + d)^e + f \quad (1)$$

Tab. 1: Material coefficients associated with Eq. 1.

Note	CT number range	a [mm <sup>2</sup> /s <sup>2</sup> ]	b [g/cm <sup>3</sup> ]	c [-]	d [g/cm <sup>3</sup> ]	e [-]	f [MPa]
Soft tissue	(0-1280>	0	1	1	1	1	5
Cancellous bone	(1280-1500>	2.5x10 <sup>-7</sup>	0.9756	1	-975.6	3	0
Cortical bone	(1500-4095>	1.25x10 <sup>-6</sup>	0.9756	1	-975.6	3	0

### 2.2. FE Model

For the study, only a beam-like sample was retrieved from the whole skull (Fig. 3). The sample with dimensions of 5x7x25 mm and with the assigned material was encastered and loaded by an arbitrary linear force of 15 N/mm concentrated in the middle of the sample length (Fig. 4). Seven variants of the FE mesh were tested to show how the combination of the mesh density and the inhomogeneous material assignment affects the strain fields in the regions of interest. In these variants, uniform free mesh consisted of tetrahedral quadratic elements (SOLID187) sized 0.1; 0.2; 0.4; 0.7; 1.0; 1.5; 2.0 mm. Therefore, the geometry discretization as well as the material mapping were carried out seven-times to obtain seven FE models of "testing" bone sample. See Fig. 4 for exemplification of the finest and roughest meshes. To confirm that the governing factor in the presumed strain variability is the material assignment, seven "control" FE models were recalculated under the same condition as the testing ones with the only exception that a homogeneous Young's modulus of 5 GPa was assumed.

### 2.3. Sensitivity study

Strain intensity distributions were evaluated along four paths indicated in Fig. 4. Preliminary testing calculations proved that the paths were in a sufficient distance from the constraints or loading and were not influenced by them. The finest mesh was considered as a reference one and results from models with this mesh were compared to results from models of other mesh densities. The non-parametric Wilcoxon rank-sum test was used for the comparison.

## 3. Results and Discussion

Typical strain intensity distributions along the paths are shown in Fig. 5. The control models did not account for the presence of less stiff cancellous bone; therefore, the total strains were generally lower than those at the same position when more accurate inhomogeneous material properties were used. The comparisons of control model results prove that even the roughest mesh is sufficient to provide satisfactory results when the homogeneous material properties are assumed. Fig. 6 shows typical result of

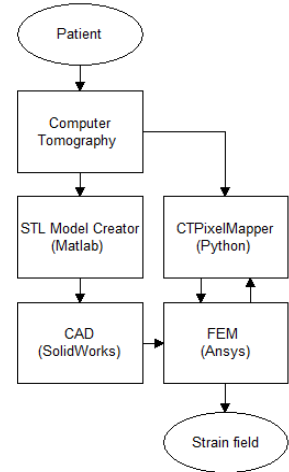


Fig. 1: Procedure flowchart.

such comparison. The results of different mesh densities are virtually the same (correlation of  $R^2 = 0.96$  to 1.00) and small deviations might be attributed to the free mesh variability and related numerical issues.

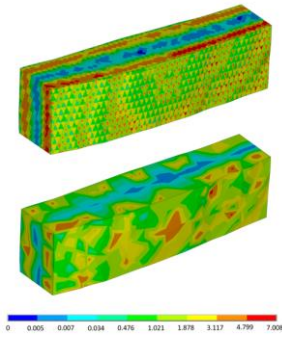


Fig. 2: Typical distribution of  $E$  within the sample (in GPa). Up: The finest mesh. Down: The roughest mesh.

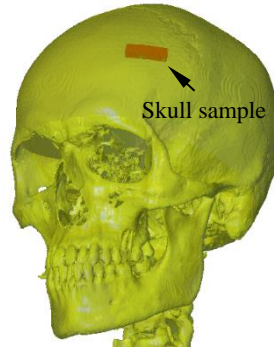


Fig. 3: CT-scanned human skull and the position of the sample.

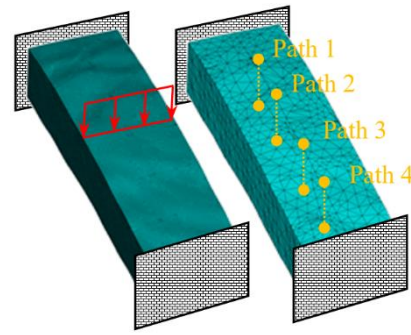


Fig. 4: FE Models of skull bone samples. Left: The finest mesh with depicted boundary conditions and loading. Right: The roughest mesh with depicted evaluation paths.

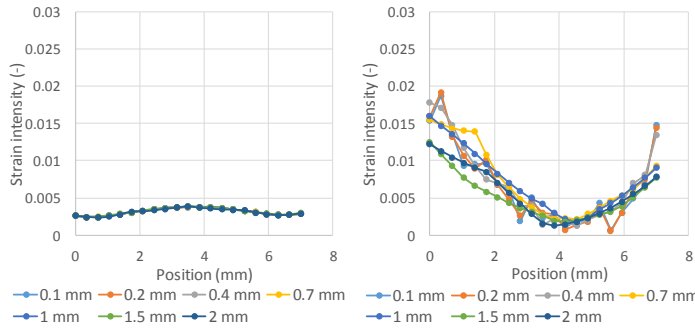


Fig. 5: Typical distribution of strain intensity along the path. Left: Results on Path 4 of control models (homogeneous distribution of  $E$ ). Right: Results on Path 4 of testing models (inhomogeneous distribution of  $E$ ).

The testing models show much greater result differences than the control models. This was due to strong dependency of material assignment on the mesh density. From Fig. 7 it is evident that linear trends in the comparisons deviate from the identity when the element size increases. While the worst correlation between models with the fine meshes was observed to be  $R^2 = 0.97$ , the worst finest vs. roughest mesh result correlation was  $R^2 = 0.43$ . In order to decide what deviation is already unacceptable, the Wilcoxon test was used to test a null hypothesis that the median difference between pairs of the calculated strain intensity distributions is zero. For all pairs, the z-score was calculated and the results are listed in Tab. 2. The critical z-score for a 95 % confidence interval is  $\pm 1.96$ . Therefore, if the calculated z-score is outside the  $\pm 1.96$  interval, the null hypothesis must be rejected. Results in Tab. 2 indicate that all meshes with the element sizes lower than 1.0 mm (i.e.  $\leq$  image voxel size) produce strain intensity distributions that are not significantly different from those of the reference one. Finer mesh with element size similar or smaller than CT voxel satisfactorily reproduce the source images. Whether this accuracy is beneficial in terms of biomechanical simulation should be further investigated. However, it seems that the mesh quality is a significant factor that affect the results from models with the inhomogeneous material properties.

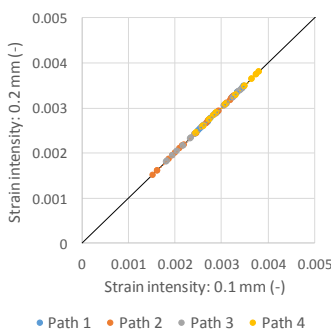
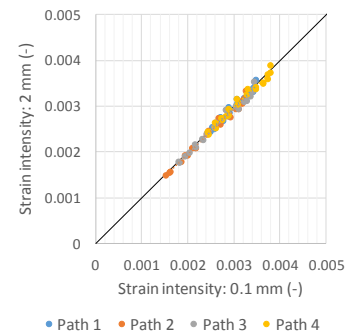


Fig. 6: Comparison of strain intensity distribution between the control models (homogeneous distribution of  $E$ ).



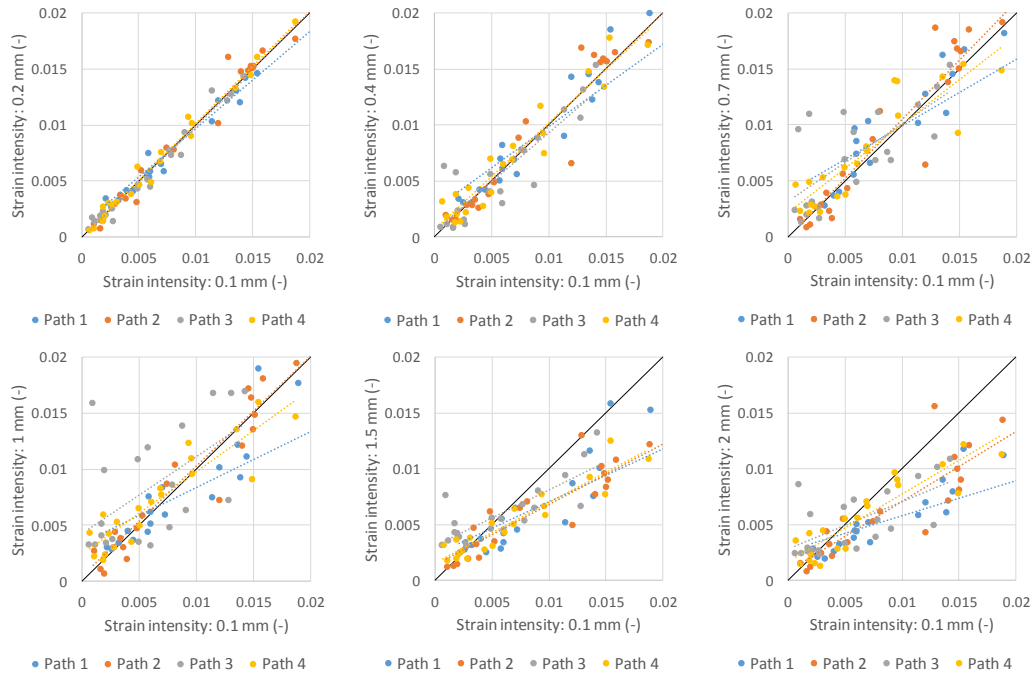


Fig. 7: Comparison of strain intensity distribution between testing models.

#### 4. Conclusion

The calculations indicated that FE mesh quality matters when it comes to material properties assignment to the FE models, especially when a free mesh of tetrahedral elements is used. Unfortunately, many questions remain and further detailed investigations should be performed to find an optimal methodology that would ensure reliable patient-specific models. In any case, the difference between homogeneous and inhomogeneous distribution of material properties is evident and it should be preferable to use the second one for patient-specific models if strain fields within the bone is in question.

Tab. 2: Z-scores of Wilcoxon test.

Element size	Path 1	Path 2	Path 3	Path 4
0.2 mm	-1.13	-0.05	-1.20	-0.61
0.4 mm	-0.19	-0.50	-0.85	-0.85
0.7 mm	-0.16	-0.89	-1.76	-1.86
1.0 mm	-2.00 <sup>▲</sup>	-0.57	-2.17 <sup>▲</sup>	-2.07 <sup>▲</sup>
1.5 mm	-3.53 <sup>▲</sup>	-3.25 <sup>▲</sup>	-0.40	-2.21 <sup>▲</sup>
2.0 mm	-3.94 <sup>▲</sup>	-3.08 <sup>▲</sup>	-0.92	-1.48

<sup>▲</sup> Null hypothesis is rejected.

#### Acknowledgement

The research was supported by the Czech Science Foundation by Grant No. 16-08944S.

#### References

- Helgason, B., Gilchirst, S., Ariza, O., Vogt, P., Enns-Bray, W., Widmer, R.P., Fitze, T., Palsson, H., Pauchard, Y., Guy, P., Fergusson, S.J. and Cripton, P.A. (2016) The influence of the modulus-density relationship and the material mapping method on the simulated mechanical response of the proximal femur in side-ways fall loading configuration. *Medical Engineering and Physics*, 38, pp. 679-689.
- Marcián, P., Konečný, O., Borák, L., Valášek, J., Řehák, K., Krpalek, D. and Florian, Z. (2011) On the Level of Computational Models in Biomechanics Depending on Gained Data from Ct/Mri and Micro- Ct, in: *MENDEL 2011 - 17th International Conference on Soft Computing*. 1. Brno: Brno University of Technology, pp. 255-267.
- Taddei, F., Pancanti, Al. and Viceconti, M. (2004) An improved method for the automatic mapping of computed tomography numbers onto finite element models. *Medical Engineering & Physics*, 26, pp. 61-69.
- Zadpoor, A.A. and Weinans, H. (2015) Patient-specific bone modeling and analysis: The role of integration and automation in clinical adoption. *Journal of Biomechanics*, 48, pp. 750-760.
- Zannoni C., Mantovani, R. and Viceconti, M. (1998) Material properties assignment to finite element models of bone structures: A new method. *Medical Engineering & Physics*, 20, pp. 735-740.



## ACCURACY OF THE VISUAL MEASUREMENT SYSTEM OF BENT PIPES

K. Borkowski<sup>\*</sup>, D. Janecki<sup>\*\*</sup>, J. Zwierzchowski<sup>\*\*\*</sup>

**Abstract:** *The paper presents a solution designed to increase the measurement accuracy of the vision system for the large-sized bent pipes with one fixed camera. For this purpose, a model of perspective distortions has been developed for the outline of the object's shape observed by the camera. Efficacy of the model was examined through a series of experimental measurements and their comparison with the model measurements of the pipe made on the coordinate measuring machine. During research, two versions of the program were used in parallel, where only one took into account the perspective distortions. The studies have confirmed the legitimacy and effectiveness of the used model improving the accuracy and repeatability of the measurement.*

**Keywords:** Vision system, Measurement, Pipes, Camera, Measurement accuracy.

### 1. Introduction

Modern vision systems are successfully widely used in our lives. They help us get to work through the traffic analysis (Beymer et al., n.d.) and control of the road signalling. They inform us about the amount and location of free parking spaces. They enable the autonomous car drive, and they watch over our security while shopping and they lead the shopping cart behind us.

As a result of the dynamic development of the machine vision, cameras replace an increasing number of sensors on the production lines. They are used for identifying materials, tools and products, recognising the presence, quality control of the products (Hongbin Jia et al., 2004), or correctness of technological operations. They support engineers while conducting research (Takosoglu et al., 2016) and experiments (Błasiak et al., 2014). They are also successfully used for the dimension and shape control of the produced elements. This work has described the measurement and control system for the large-sized bent pipes. Their measurement while using other alternative methods, due to the size and weight, is a complex and laborious task. The following sections describe the concept of the measurement stand, applied solutions and they present the results of preliminary measurements.

### 2. Methods

The examined measurement stand has been designed for the requirements of the company dealing with the manufacturing of bent pipes with diameters up to 1 meter. Between the successive stages of processing, the pipes are moved between the positions using a gantry. The prepared position will be placed over the existing measuring table in the factory. The application of a contactless, optical measurement method will not affect the reduction of the transport and working space. The measurement part used for the data acquisition will be placed over the mechanism of the gantry. Measurement data sent through Ethernet will be analysed by the software installed on the personal computer located in the design department, where the reports from the conducted measurements will also be generated. Fig. 1 shows the

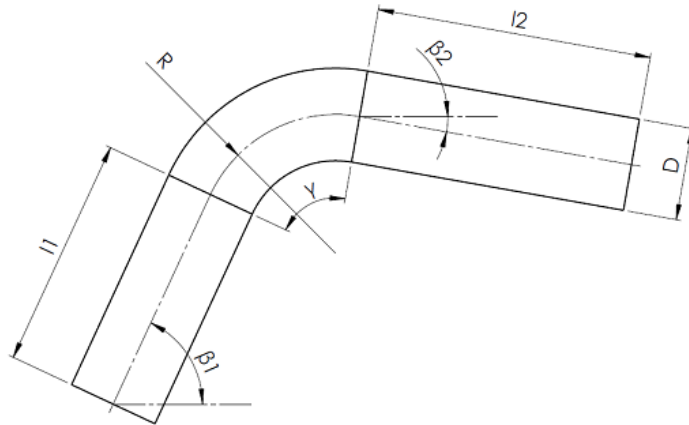
---

<sup>\*</sup> mgr inż. Krzysztof Borkowski: Department of Automation and Robotics, Kielce University of Technology, al. Tysiąclecia Państwa Polskiego 7; 25-314 Kielce; Poland, kborkowski@tu.kielce.pl

<sup>\*\*</sup> prof. dr hab. inż. Dariusz Janecki: Department of Automation and Robotics, Kielce University of Technology, al. Tysiąclecia Państwa Polskiego 7; 25-314 Kielce; Poland, djanecki@tu.kielce.pl

<sup>\*\*\*</sup> dr inż. Jarosław Zwierzchowski: Department of Automation and Robotics, Kielce University of Technology, al. Tysiąclecia Państwa Polskiego 7; 25-314 Kielce; Poland, j.zwierzchowski@tu.kielce.pl

following parameters of the bent pipe subjected to control: pipe diameter  $D$ , bending angle  $\gamma$ , bending radius  $R$ , length of the straight sections  $l_1, l_2$ .

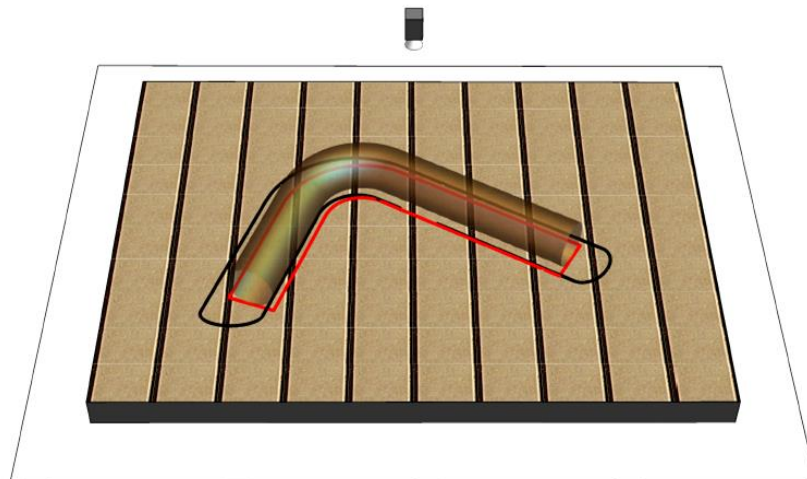


*Fig. 1: Controlled parameters of the bent pipe.*

### Modelling the sources of distortion

The high-class stationary industrial camera with a lens with a fixed focal length matched to the working conditions is the measurement element. Parameters of the pipe are calculated from data obtained from a digital photography, which is processed and analysed by the prepared algorithms.

Numerous non-linearities associated with the geometry of the measuring system, the optical system of the camera and light-sensitive matrix and perspective distortions of the observed outline of the object have a negative impact on the accuracy and repeatability of the measurement results (Remondino and Fraser, 2006). In order to eliminate them, two mathematical models were developed. The first one, described in (Borkowski et al., 2016) allows the determination of the perspective projection of the edge of the perfect curved pipe on the table surface of the camera point. Due to the complexity, the analytical model is used after the appointment of the initial values. Fig. 2 shows a difference between a simple projection (red line) and a perspective projection (black line) on the table surface. Along with increasing the distance of the pipe from the centre of the table (optical axis of the camera) and its growing dimensions, the differences between contours are growing.



*Fig. 2: The calculated contours of the pipe after the simple and perspective projections.*

By matching the calculated projection of the pipe to the points of the pipe's edge in the picture, the algorithm obtains a higher accuracy and repeatability of the results on the entire surface of the measuring table.

The second mathematical model determines the relationship between the pixel coordinates of the digital image and the coordinate system associated with the measuring table. Its description included the

inclination of the actual optical axis of the camera relative to the measuring table and the image sensor, different height and width of pixels in the matrix, as well as the lens aberrations, that is the radial and tangential distortion (Hartley and Zisserman, 2000). The process of determining the parameters of the model is called the calibration of the camera. The paper model has been prepared in order to perform the calibration, on which the squares with the same lengths of the sides were printed. Based on the points read out from the model placed in several positions, so that the entire surface of the measuring table was covered, the parameters of the model are calculated. Fig. 3 shows the straightened image along with the selected and adjusted contour of the pipe.

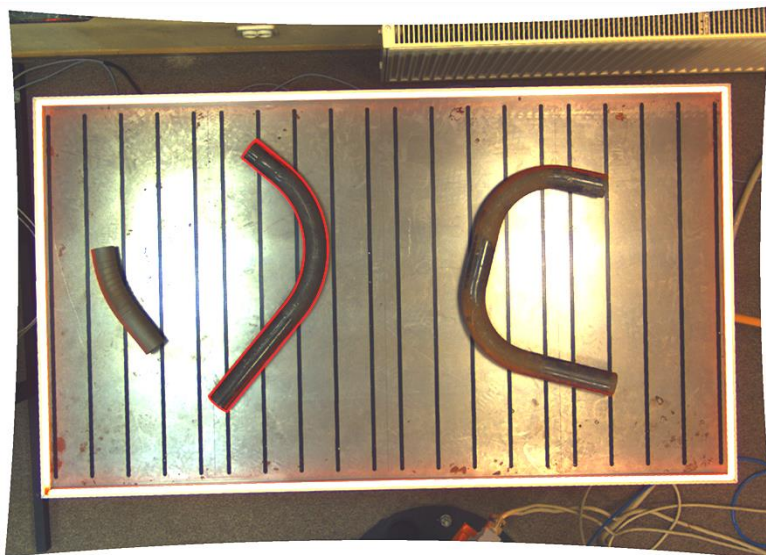


Fig. 3: The image straightened with the calibration camera model.

### Comparative studies

For the purpose of the preliminary measurement accuracy assessment of the position, the model measurement of the curved pipe was conducted on the Prismo Navigator coordinate measuring machine of the Zeiss company. Based on the collected outlines of the pipe's edges, the surface model of a perfect pipe has been adjusted in the middle of its height. Then, a series of 10 measurements for this pipe with different position and orientation on the measuring table was performed, during which two versions of the program were used at the same time for data processing. The first one has additionally used the model describing the perspective distortion of the projection of the pipe's edge with respect to the camera point. The measurement results are presented in Tab 1.

Tab. 1: Summary of the measurement results for the bent pipe.

Measured parameter	Model measurement	Series of measurements with the perspective model		Series of measurements without the perspective model	
		Average value	Standard deviation	Average value	Standard deviation
Pipe diameter [mm]	60.8	60.1	0.2	60.2	0.7
Bending angle [°]	89.9	90.1	0.3	90.1	0.3
Bending radius [mm]	238.6	238.9	0.7	242.2	1.6
Length of the 1 straight section [mm]	296.4	295.9	1.1	304.2	2.7
Length of the 2 straight section [mm]	100.9	100.4	1.9	104.4	1.0
Length of the centre line [mm]	771.5	772.1	1.7	789.4	2.4

When analysing the parameters, it should be taken into account that the pipes during the bending process becomes oval, and the actual bending radius is a composite of many different arcs. Therefore, the length of the pipe's centre line was calculated on the basis of the measured values, which can be interpreted as the total length of the pipe.

### 3. Conclusions

The obtained results confirm the validity of the application of the perspective model. For the measurement series, parameters such as: the bending angle, or the length of the straight section were determined with the accuracy of about 1mm, while without taking into account the perspective distortion, the mean error was 4 times greater. In the case of the pipe's diameter, the smallest dispersion of results of the measurements was observed and almost a constant amount of errors, which may indicate the inaccurate determination of the pipe's edge points. The biggest differences were shown by an additional parameter – the length of the centre line, for which the mean error, after taking into account the perspective distortions, proved to be even several times smaller. In addition, this indicator has shown a high efficiency and repeatability of the measuring system, despite the lack of possibilities to clearly determine the beginning and ending of the arc.

The developed system is competitive towards other modern methods, it offers a fully automated, contactless and fast measurement process, it does not require proper orientation and referencing of the object, as well as it allows the simultaneous measurement of several pipes located on the scribing table. The measurement errors obtained by the system in the conversion into image coordinates amounted to about 2–4 pixels. The use of the vision systems on technological lines as control and measurement devices will enable the introduction of quality control as a continuous, automated, comprehensive and integral production stage.

### References

- Beymer, D., McLauchlan, P., Coifman, B. and Malik, J. (n.d.) A real-time computer vision system for measuring traffic parameters, in: Proc. IEEE Comput. Soc. Conf. Comput. Vis. Pattern Recognit. IEEE Comput. Soc, pp. 495-501. doi:10.1109/CVPR.1997.609371.
- Blasiak, S., Takosoglu, J.E. and Laski, P.A. (2014) Heat transfer and thermal deformations in non-contacting face seals, *Journal of Thermal Science and Technology*, 9, 2, pp. JTST0011-JTST0011. doi:10.1299/jtst.2014.jtst0011.
- Borkowski, K., Janecki, D. and Zwierzchowski, J. (2016) A vision system for measuring large-scale bent pipes. Selected problems in mechatronics and material engineering. Kielce University of Technology Publishers M80, pp. 34-37.
- Hartley, R. and Zisserman, A. (2000) Multiple view geometry in computer vision second edition, Cambridge University Press.
- Hongbin J., Murphey, Y. L., Jinajun S. and Tzyy-Shuh Ch. (2004) An intelligent real-time vision system for surface defect detection, in: Proc. 17th Int. Conf. Pattern Recognition, 2004. ICPR 2004. IEEE, pp. 239-242 Vol. 3. doi:10.1109/ICPR.2004.1334512.
- Remondino, F. and Fraser, C. (2006) Digital camera calibration methods: considerations and comparisons, *International Archives of Photogrammetry, Remote Sensing and Spatial Information Sciences*, 36, 5, pp. 266-272.
- Takosoglu, J.E., Laski, P.A., Blasiak, S., Bracha, G. and Pietrala, D. (2016) Determination of flow-rate characteristics and parameters of piezo valves, in: Proc. Int. Conf. Exp. Fluid Mech. 2016 (ed. Dancova, P.), Techn. Univ. Liberec, pp. 814-818.

## ASSESSMENT OF THE VOLUME OF CROP BY THE WINDROW'S MEASUREMENT

S. Borowski<sup>\*</sup>, R. Rama<sup>\*\*</sup>, L. Knopik<sup>\*\*\*</sup>, J. Kaszkowiak<sup>\*\*\*\*</sup>

**Abstract:** *The construction's solution of the preservatives' applicator used during the biomass' harvesting is presented in this work. There have also been described own studies, the purpose of which is drawing up of an operation's algorithm of applicators' controller making it possible to change the dope of a preserving preparation in the function of collected mass' volumes. As a result of the conducted experiments it has been determined, that the analysed data is consistent with the gamma distribution. Identification of the probability distribution shall make it possible to accept certain assumptions concerning the construction of the costs' optimization model and drawing up of the applicator's steering algorithms.*

**Keywords:** Steering with applicators, Green fodder's harvesting, Biomass ensiling.

### 1. Introduction

In the agrarian practice, conducting of field works with the use of the best available methods is an important element making it possible to achieve high crops. It is also very important in case of harvests (Bochat and Zastempowski 2013, Zastempowski and Bochat 2014). Mistakes made at that time may result in getting increased losses, getting a low quality product, increase of problems related to storage and later post-harvesting treatment. In case of harvested green fodders designed for silages to be used as fodder or a biogas plant's substrate, incorrect harvesting may drive even to the harvested material's damaging. Energy losses occurring as a result of natural processes occurring in a pile are another crucial element in case of harvesting fodders preserved by ensiling.

Lactic fermentation is a common method of preservation of plant material designed for fodder's production and substrate's acquisition for a biogas plant. (Kalač 2011; Köfinger et al. 2012; Pakarinen et al. 2011; Weissbach 2009). The technology of preparing silages to be used as batch – coenzyme for biogas production at agrarian biogas plants is similar, like in case of ensilaging of fodders for ruminants. That is why, bad quality ensilages are also not fit for biogas production due to the volume of obtained gas and biomethane comprised in it (Węglarzyk and Podkowska 2010). Due to the required volume of acetic acid and acetic acid, preferred is the use of additives comprising heterofermentative lactic bacteria, in particular of *Lactobacillus buchneri*, which shall not result in excessive acidification with acetic acid but with acetic acid (Kalač 2011; Oude Elferink et al. 1999). However, the heterofermentative process leads to fermentation losses (Banemann et al. 2008, 2009; Nussbaum 2012; Ruser et al. 2009).

Getting good ensilage depends on many variable factors such as the quality of harvested plant material, adding of an appropriate preservative in an appropriate volume. The volume of the dope (volume) should depend on temporary machine's efficiency. At present on the market there are available many systems supporting the work of agrarian machines, which are characterized by high reading precision of the harvested material in real time. However, not so many solutions are designed for adjustment of temporary

---

<sup>\*</sup> Sylwester Borowski, PhD.: Faculty of Mechanical Engineering, UTP University of Science and Technology, Poland. Al. Prof. Kaliskiego 7, 85-796 Bydgoszcz, e-mail: sylwester.borowski@utp.edu.pl

<sup>\*\*</sup> R. Rama MSc.: Faculty of Mechanical Engineering, UTP University of Science and Technology, Poland. Al. Prof. Kaliskiego 7, 85-796 Bydgoszcz, e-mail: roksana.rama@utp.edu.pl

<sup>\*\*\*</sup> Leszek Knopik DSc.: Faculty of Management, UTP University of Science and Technology, Poland. Al. Prof. Kaliskiego 7, 85-796 Bydgoszcz, e-mail: leszek.knopik@utp.edu.pl

<sup>\*\*\*\*</sup> Jerzy Kaszkowiak, PhD.: Faculty of Mechanical Engineering, UTP University of Science and Technology, Poland. Al. Prof. Kaliskiego 7, 85-796 Bydgoszcz, e-mail: kaszk@utp.edu.pl

capacity of applicators assembled on harvesting materials. It is in particular noticeable in case of trailers and harvesting presses.

That is why, the analysis of commercial solutions existing on the market of systems for automatic adjustment of applied additives' volumes in the function of temporary efficiency of a harvesting machine and presentation of own studies the effect of which is drawing up of an algorithm of a applicators' controller operation making it possible to change the dope of preservative in the function of harvested mass of plant material to be ensilaged, constitutes the purpose of the study.

Well known world concerns specializing in production of machines for harvesting green fodders, have in their offer many solutions easing work with their machines. These systems, often based on the GPS technology, make it possible to obtain information which may be used for adjustment of temporary applicators' efficiency.

## 2. Material and methods

The following machines constituted the test bed: a tractor, a rotating mowing machine, a carrousel tedder, a carrousel rake. Lucerne (*Medicago media*) from the second swath in the beginning of blooming phase was the plant material used in the tests.

Following cutting, the plant material was redried in the field up to the humidity of 45 %. Then, from the material redried like that, rollers were formed. All the activities were conducted pursuant to the rules of good agrarian practice.

Having formed the rollers, the intermediate measurements of a roller's height were made with the use of a controller's model developed at the Faculty of Mechanical Engineering, UTP in Bydgoszcz. In the tests there was used the information from the ultrasonic sensor making it possible to measure the distance within the range 0 - 1500 mm. The applicator is made of a central unit equipped with a touch display unit making it possible to change the setpoints. Applicators' steering is possible thanks to the applied proportional valve or the PWM signal for solid materials' applicators. The input information comes from the sensors (ultrasonic sensor 1) and an impulse generator located on a collecting machine's land wheel. The block diagram of the applicator's controller used for the tests is presented in Fig. 1.

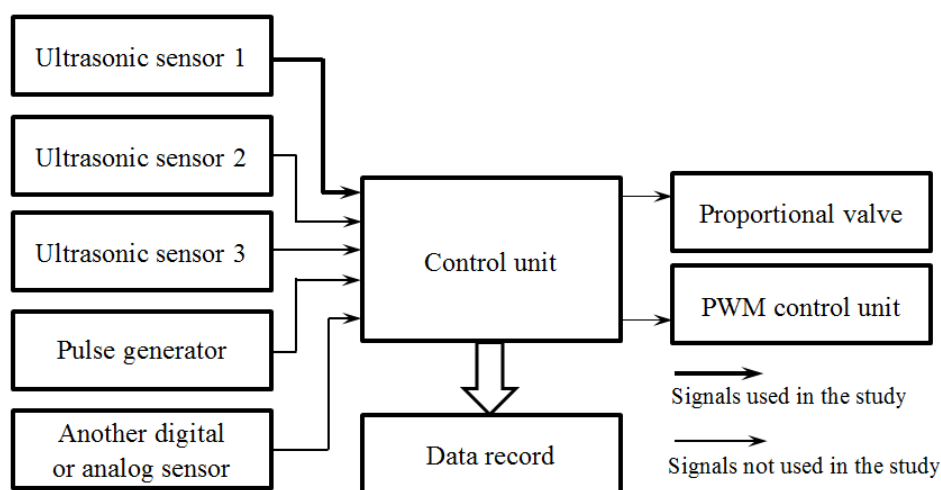


Fig. 1: Block diagram of the applicator's controller.

## 3. Conducted tests

N = 4120 of measurement data obtained in the course of measurements have been subject to statistical analysis. As a result of the conducted analysis, the following has been obtained:

- Mean value = 525.98 mm
- Standard deviation  $\sigma = 73.57$  mm
- Variation coefficient  $V = 0.14$



- xmin = 395 mm
- xmax = 773 mm

The basic purpose of that stage of statistical analysis was to find the probability distribution of the analysed real data (Bobrowski and Lybacka, 1995). The preliminary analysis of data showed, that in the analysed case the examples with „a shift” should be considered. The minimum measurement value obtained is equal to Min = 395 mm, that is why from each value the value of 390 mm has been deducted. For the data prepared like that, the attempt was made to match the gamma distribution of the probability density function of the form:

$$f(x) = \frac{1}{\beta^\alpha \Gamma(\alpha)} x^{\alpha-1} e^{-x/\beta} \quad (1)$$

for  $x > 0$ ,  $\alpha > 0$ ,  $\beta > 0$ .

$\Gamma(\alpha)$  means the gamma function determined with the formula:

$$\Gamma(\alpha) = \int_0^{\infty} x^{\alpha-1} e^{-x} dx \quad (2)$$

Values of invariable parameters were estimated with the maximum likelihood method and the following has been calculated:

$$\alpha = 3.16$$

$$\beta = 43.24$$

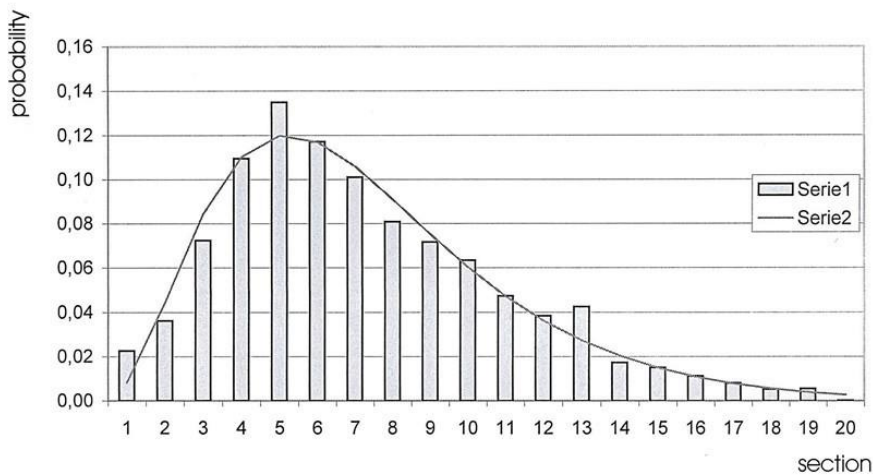


Fig. 2: The histogram of distribution: series1 – of empirical data, series 2 - theoretical data.

The consistency of the empirical distribution with the gamma distribution has been tested with the use of the Kolmogorov compliance test (for big statistical samples). Empirical and theoretical density is presented in Fig. 2. The calculated value of statistics  $\lambda = 0.91$ . The value of the significance level  $p\text{-value} = 0.66$ , points at the absence of grounds to reject the hypothesis that the analysed data are consistent with gamma distribution. The diagram of density presented in Fig. 1 shows, that gamma distribution is a good model for the examined empirical distribution.

#### 4. Conclusions

As it results from the analysis of the selected literature sources, the preserved biomass designed for power purposes, stored in the form of silage, requires adding of silage additives. Appropriately selected formulations allow to decrease the losses of energy at the time of storage and allow to increase the biogas' yield. However, the use of additives at present takes place in most of the cases, without automatic change of dose during harvesting. Only few harvesting chaff cutters are equipped with appropriate systems controlling the work of applicators.



The conducted preliminary tests showed the usability of ultrasonic sensors for the windrow's height measurement. Obtaining of that type of results makes it possible to take up works on a controller, which may control the applicator's capacity in a simple manner. As it results from the conducted analysis of constructional solutions, on the market there are no constructions designed for use in trailers and collecting presses.

Identification of the probability distribution shall make it possible to assume appropriate assumptions for construction of the costs optimization model and the algorithm of applicators' steering.

## Reference

- Agro Biogas Plant (Agrobiogazownia). (2010). Red. Węglarzyk K. and Podkówka W. IZ PIB, Grodziec Śląski, Zespół Wydawnictw i Poligrafii Instytutu Zootechniki PIB.
- Banemann D., Mayrhuber E., Schein H. and Nelles M. (2008) Effect of homo- and hetero-fermentative silagen additive on the methane yield of mais silage. Proc. of 13th Int. Conf. Fooder conservation, Nitra, Slovak Republic, 156-157.
- Banemann D., Nelles M. and Thaysen J. (2009) Silages as feedstock for biogas: Novel perspectives for silage additives. Proc. of XVth Int. Silage Conf., Madison, Wisconsin, USA, 355-356.
- Bobrowski D. and Łybacka K. (1995) Selected methods of statistical inference, Wyd. Politechniki Poznańskiej, Poznań, (in Polish).
- Bochat, A. and Zastempowski, M. (2013) Modeling the Dynamics of the Vegetable Material Detachment Process from Undisturbed Areas to Improve the Design of Selected Agricultural Machines. Transactions of the ASABE, vol. 56(4), pp. 1309-1314.
- Kalač P., 2011. The required characteristics of ensiled crops used as a feedstock for bio-gas production: a review. J. Agrobiol. 28, 85-96.
- Köfinger P., Grabherr R., Eikmeyer F.G., Zakrzewski M., Schlütter A., Mayrhuber E. and Schwab H. (2012) Metagenomic analysis of a microbial community isolated from silage. Proc. of XVIth Int. Silage Conf., Hämmenlinna, Finland, 350-351.
- Nussbaum HJ. (2012) Effects of silage additives based on homo- and heterofermentative lactic acid bacteria on methane yields in the biogas processing. Proc. of XVIth Int. Silage Conf., Hämmenlinna, Finland, 452-453.
- Oude Elferink S.J.W.H., Dreihuis F., Krooneman J., Gottschal J.C. and Sierk F. (1999) *Lactobacillus buchneri* can improve the aerobic stability of silage via a novel fermentation pathway: the anaerobic degradation of lactic acid to acetic acid and 1,2-propanediol. Proc. 12th Int. Silage Conf., Uppsala, Sweden, 266-267.
- Pakarinen A., Maijala P., Jaakkola S., Stoddard F.L., Kymäläinen M. and Viikari L. (2011) Evaluation of preservation methods for improving biogas production and enzymatic conversion yields of annual crops. Biotechnol. Biofuels 4:20.
- Ruser B., Pahlow G., Kräft A. and Rutherford W. (2009) Improved biogas production from silage treated with an esterase producing inoculant. Proc. of XVth Int. Silage Conf., Madison, Wisconsin, USA, 455-456.
- Weissbach F. (2009) Prediction of biogas production potential of silages. Proc. of XVth Int. Silage Conf., Madison, Wisconsin, USA, 189-190.
- Zastempowski, M. and Bochat, A. (2014) Modeling of cutting process by the shear-finger cutting block. ASABE Applied Engineering in Agriculture. Vol. 30, No. 3, pp. 347-353.

## COMPARING TURBULENCE MODELS FOR GAS-PARTICLE MIXTURE PNEUMATIC CONVEYING

G. Borsuk<sup>\*</sup>, J. Wydrych<sup>\*\*</sup>, S. Pochwała<sup>\*\*\*</sup>

**Abstract:** *The system of transport tertiary air in cement kiln installation is one of the elements, which has the very large influence on production processing. This paper analyses numerical calculation in the installation for tertiary air in a cement plant. The operation condition of the installation is to ensure transport of gas with the smallest number of particles. By comparing several turbulence models used for calculation gas phase motion and Lagrangian model for discrete phase one can find an optimal solution. The particle trajectories depend on velocity field in researched models. For analyzed examples, the same pressure drop between inlet and outlet to the tertiary air duct were set.*

**Keywords:** Pneumatic conveying, Turbulence models, Two-phase flow, CFD.

### 1. Introduction

The purpose of the tertiary air duct of kiln installation is to supply stream of hot gas with a minimum number of particles carried away from the kiln head (Lain et al., 2011). For optimization of the kiln, it is necessary to understand the detailed processes occurring in the installation. The specific requirements of process on design stage the burner system is to provide a burner design that will deliver efficient and reliable combustion (Lederer, 1996). Yet, extensive use of this form of transportation may bring about some problems that need to be eliminated. During pneumatic conveying we can observe uncontrolled particles segregation (Akili et al., 2001). These phenomenon influenced at flow direction changed by gravity and centrifugal force. As an effect, it forms, so called, the ‘rope’ of particles inside the gas stream, which distorts the conveying process and conducts to the premature erosion of the system elements (Wydrych, 2010). There are many references, on both theoretical and experimental research on homogeneous fluid flow through a single bend, especially focusing on energy losses (Grabavic et al., 1995, Hu et al., 2006).

### 2. Methods

In this work, the object of analysis is to study involving optimization of the design of the installation for supply hot gasses from the clinker cooler section to decarbonizator, where low-calorific fuel is burned (Saidura et al., 2011). The system of tertiary air pipe is designed as an element of the cement kiln installation (Fidaros et al., 2007). The problem to solve is separation particles from a gas, to reduce the deposition of particles in a horizontal channel (Levy et al., 1998).

In work (Borsuk et al., 2016) one alternative design was presented. Fig. 1 presents a general view of the rotary kiln. An integral part of this installation is a connection between kiln head and precalciner. The inlet to this installation is located at the outflow from clinker cooler. This work presents calculations results applied to the determination of construction of pneumatic installations for tertiary air. Researches were made for several turbulence models.

---

<sup>\*</sup> Adjunct prof. Grzegorz Borsuk, PhD.: Department of Thermal Engineering and Industrial Facilities, Opole University of Technology, 76 Prószkowska str., 45-758, Opole; Poland, g.borsuk@po.opole.pl

<sup>\*\*</sup> Adjunct prof. Jacek Wydrych, PhD.: Department of Thermal Engineering and Industrial Facilities, Opole University of Technology, 76 Prószkowska str., 45-758, Opole; Poland, j.wydrych@po.opole.pl

<sup>\*\*\*</sup> Adjunct prof. Sławomir Pochwała, PhD.: Department of Thermal Engineering and Industrial Facilities, Opole University of Technology, 76 Prószkowska str., 45-758, Opole; Poland, s.pochwała@po.opole.pl

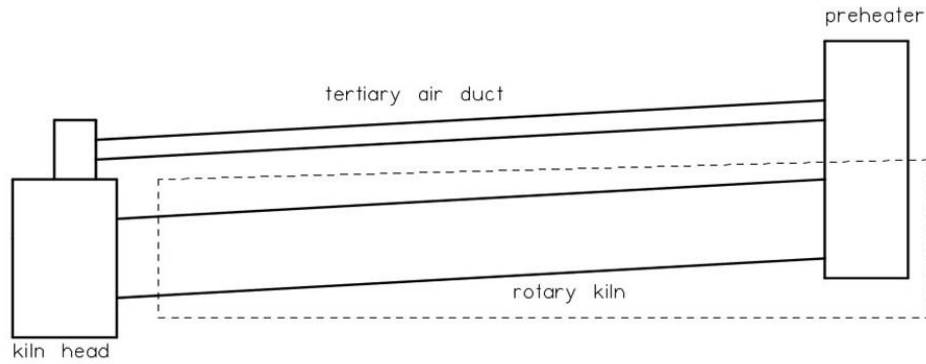


Fig. 1: Rotary kiln with the tertiary air installation.

## 2.1. Boundary conditions

The purpose of calculation domain development was describing the complex process of cement production. Due to this, only flow distribution through the kiln head was included for subsequent analysis. Consequently, authors decided to consider a design of the cement kiln installation using only those elements which are necessary to bring correct results of pneumatic transport in the tertiary air duct. For the calculations, there were set the same boundary conditions for each turbulence model. From the cement plant, there was an information about the flow rate of incoming air to the head of rotary kiln. Boundary conditions in the exits it was set -12 Pa for the kiln and -900 Pa for the tertiary air pipe for each example.

For the particle calculation, Rosin-Rammler-Sperling distribution was used and 10 fractions of particles with the range from 15 to 600  $\mu\text{m}$  were determined. Table 1 presents the distribution of particles in each fraction determined as a part of the total mass flow rate. The same number of intake points for all particle fractions was assumed in the calculations. The adopted boundary conditions gave the expected calculations of the pressure drop values. Calculations were performed using ANSYS Package (Ansys Inc. 2015).

The first result of the calculation it was the velocity profile. In next stage, the same number of particles were injected to the domain and calculation included interaction between gas and particles. Simultaneously quantity of particles transported in the tertiary air installation was counted.

Tab. 2 presents results of velocity calculation at the outlet to the cement kiln and tertiary air pipe for analyzed turbulence models.

Tab. 1: Particle ratios.

$d$ [ $\mu\text{m}$ ]	percentage
15	7.51
35	9.39
55	10.32
75	14.12
110	17.16
150	18.66
220	16.67
350	5.15
450	0.95
600	0.07

Tab. 2: Turbulence model.

Model	type	velocity [m/s]		$v/v_{av}$ [%]	
		kiln	pipe	kiln	pipe
Standard k - $\omega$ Model	T01	3.37	29.60	-3.9	5.3
Transition k - $\omega$ Model	T02	5.42	16.42	54.7	-41.6
Shear-Stress Transport (SST) k - $\omega$ model	T03	3.31	29.57	-5.5	5.2
Linear Pressure-Strain Model	T04	3.13	30.72	-10.8	9.2
Stress-Omega Model	T05	3.07	31.13	-12.4	10.7
Spalart-Allmaras Model	T06	3.46	28.11	-1.1	0.0
Standard k - $\epsilon$ Model	T07	3.31	29.28	-5.4	4.1
RNG k - $\epsilon$ Model	T08	3.20	29.31	-8.8	4.3
Realizable k - $\epsilon$ Model	T09	3.26	28.93	-6.8	2.9
	av	3.50	28.12		

Comparing the results of average velocity in the exit of kiln and pipe in the installation with vertical pipe there is a significant difference for model T02 (k -  $\omega$  Transition model). The velocity is lower more by 40 % in the pipe than average value. It has an influence on the number of particles transported in tertiary air pipe. Fig. 2 presents particle trajectories for all alternative models for particles with a diameter in range  $110 \div 450 \mu\text{m}$ . For turbulence model T02 small number of particles is transported to the tertiary air pipe as a result of the small gas velocity.

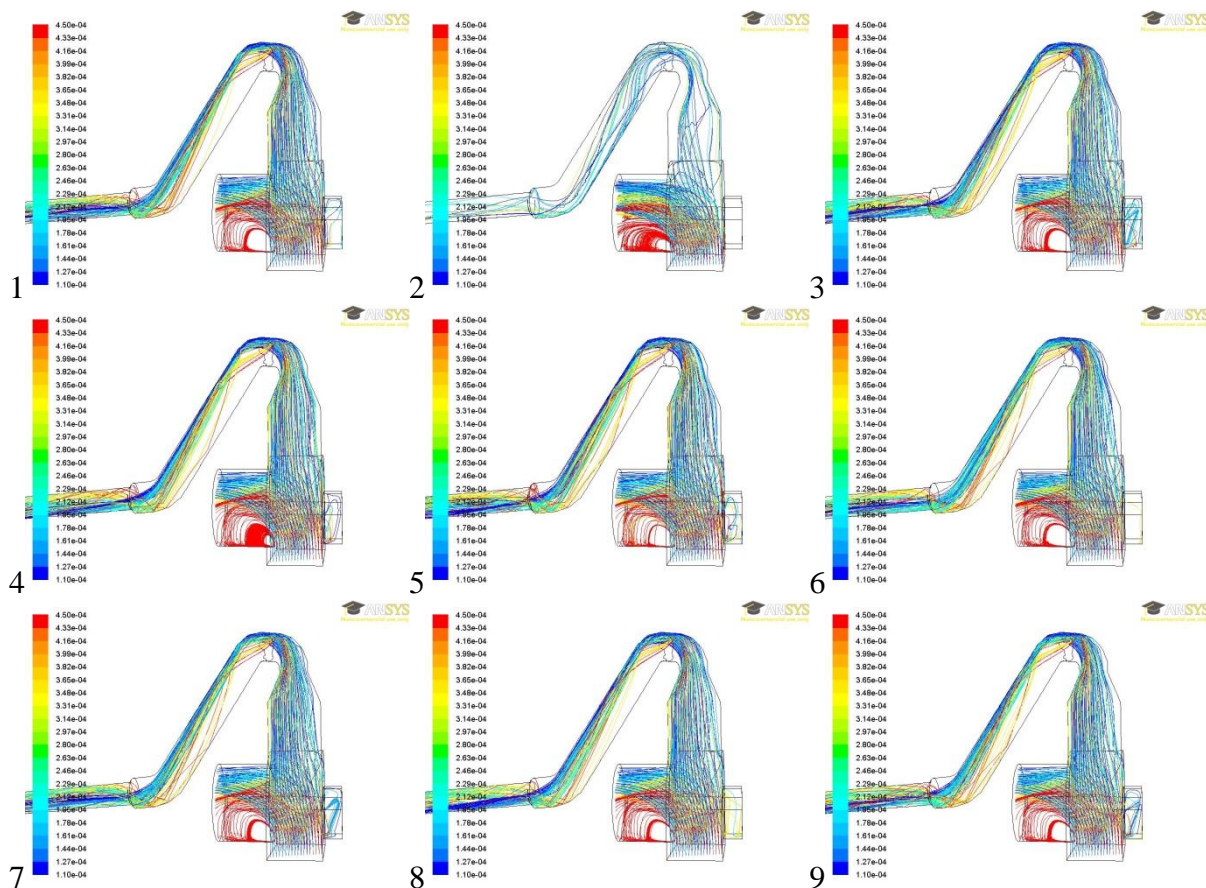


Fig. 2: Particle trajectories for different alternative turbulent model ( $d_{110} - d_{450} \mu\text{m}$ ).

Figs. 3 and 4 show the percentage of particles transported to the tertiary air duct. There is some difference between the number of particles for all diameters. In those pictures, eight alternative models are presented, without model T02.

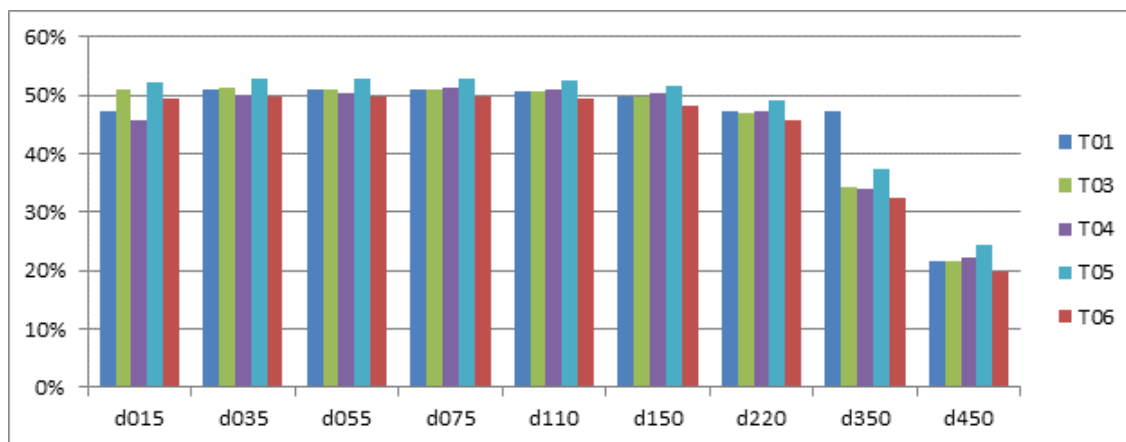


Fig. 3: The percentage of particles transported to the tertiary air pipe for selected models.

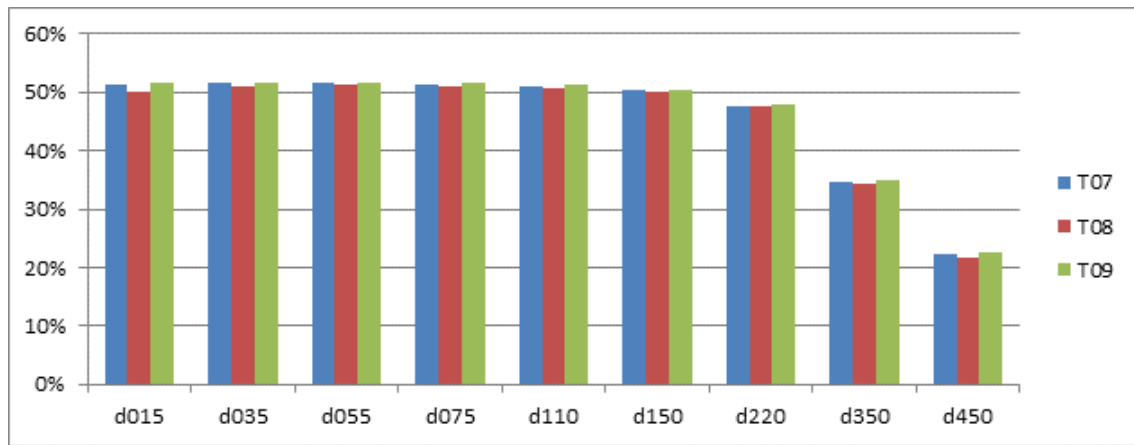


Fig. 4: The percentage of particles transported to the tertiary air pipe for models T07 ÷ T09.

### 3. Conclusions

In this work, different turbulence models were tested in order to find the most suitable solution to use as a part of the numerical model for particle conveying. Installation with a vertical pipe from the kiln head was researched for each turbulence model. Pressure values at the inlet and two outlets were always the same and treated as the boundary conditions for all sets.

Initially, velocity vectors for each alternative domain were calculated. In next stage particle tracks for each turbulence model was calculated. From that part of the calculations, there are some conclusions.

In an installation with a vertical pipe, almost all turbulence model bring similar velocity at the exit of the pipe. From that, the same numbers of particles are going to the pipe and kiln. Only for the model type T02, there is a very small number of particles transported through the tertiary air pipe. The best particle reduction in the tertiary air is for alternative model type T06, it is for all diameters. Model type T04 is better than others only for small particles. In model type T05 the reduction of particles in tertiary air duct was less effectively.

The comparison of the results proves that the choice of the proper turbulence model is very important. The final results of modeling should be compared with experimental data.

### References

- Akili H., Levy E.K., Sahin B. (2001) Gas-solid flow behavior in a horizontal pipe after a 90° vertical-to-horizontal elbow. *Powder Technology*, 116, 43-52.
- Borsuk G., Wydrych J., Dobrowolski B. (2016) Modification of the inlet to the tertiary air duct in the cement kiln installation, *Chemical and Process Engineering*, 37 (4), 517-527.
- Fidaros D.K., Baxevanou C.A., Dritselis C.D., Vlachos N.S. (2007). Numerical modelling of flow and transport processes in a calciner for cement production. *Powder Technology*, 171, 81-95.
- Grbavcic Y.B., Vukowic D.V. (1995) Effect of particle diameter, particle density and loading ratio on the effective drag coefficient in steady turbulent gas-solids transport, *Powder Technology*, 84.
- Hu Z., Lu J., Huang L., Wang S. (2006). Numerical simulation study on gas-solid two-phase flow in pre-calciner. *Communications in Nonlinear Science and Numerical Simulation*, 11, 440-451.
- Lain S., Sommerfeld M. (2012). Numerical calculation of pneumatic conveying in horizontal channels and pipes: Detailed analysis of conveying behaviour. *International Journal of Multiphase Flow*, 39, 105-120.
- Lederer H. (1996). A new rotary kiln burner technology. *World cement*, 27 (12), 45-48.
- Saidura R., Hossaina M.S., Islama M.R., Fayazb H., Mohammed H.A. (2011). A review on kiln system modelling. *Renewable and Sustainable Energy Reviews*, 15, 2487-2500.
- Wydrych J. (2010). Comparative analysis of the methods of simulation of flow in boiler dust systems. *Chemical and Process Engineering*, 31 (4), 603-656.

## ON PARELLELIZATION OF LINEAR SYSTEM EQUATION SOLVER IN FINITE ELEMENT SOFTWARE

M. Bošanský\*, B. Patzák\*\*

**Abstract:** Numerical modelling using high performance computers brings in new opportunities in finite element computations. The contribution focuses on comparing the efficiency of different existing libraries to solution of large, sparse, non-symmetric systems of linear equations, based on direct or iterative algorithms. In particular, the direct solver from SuperLU library (X.S. Li, 1999), iterative solver from Portable, Extensible Toolkit for Scientific Computation (PETSc) are compared. Additionally, the performance and scalability of parallel SuperLU solver is studied, using OpenMP (Chapman, 2008, Barney, 2014) and POSIX threads (Nicols, 1996) based on shared memory model. Also, the scalability of PETSc solver on distributed memory model using Message passing interface (MPI) (Pacheco, 1997) is evaluated. The paper shows that parallelization can efficiently exploit the power of modern available hardware and significantly reduce the computation time.

**Keywords:** Parallel computing, Memory, Direct solver, Iterative solver.

### 1. Introduction

Recent developments in computer hardware bring in the new opportunities in computational science. Traditional codes run sequentially on a computer with a single processing unit. The future of scientific computing seems to be in parallel computing, that allows to overcome limitations of traditional sequential processing units, where permit us to run simulation codes only sequentially. Parallelization can significantly reduce computational time by more efficient use of available hardware.

Parallel computing is based on an idea of dividing the work into the smaller tasks, which are solved concurrently by the simultaneous use of multiple computing resources (Barney, 2010). Parallel programs are more difficult to design, because parallelism introduces new sources of complexity. Communication, synchronization between the tasks, and load balancing are one of the most important problems to getting scalable parallel performance. Parallel computers can be classified, for example, by type of memory architecture. The main types of memory systems are shared, distributed, and hybrid memory systems (Hughes, 2003).

The Finite Element Method (FEM) actually represents a broad spectrum of techniques that share common features. The FEM is numerical method for finding solution to boundary value problems described by ordinary differential equations. The original differential equation or system of differential equations is converted to the algebraic system of equations. For the case of linear elasticity, the resulting system has a form

$$\mathbf{K} * \mathbf{r} = \mathbf{F} \quad (1)$$

where  $\mathbf{K}$  and  $\mathbf{F}$  are global stiffness matrix and load vector, and  $\mathbf{r}$  is vector of unknown displacements. One of the key feature of the FEM is that the stiffness matrix is typically positive definite symmetric matrix with sparse structure.

A system of linear equations is called sparse if only relatively small number of stiffness matrix values are non-zero. An efficient algorithm for solving linear system must exploit this property. There are different

---

\* Ing. Michal Bošanský, Department of Mechanics, Faculty of Civil Engineering, CTU in Prague, Thákurova 7/2077; 166 29, Prague; CZ, [michal.bosansky@fsv.cvut.cz](mailto:michal.bosansky@fsv.cvut.cz)

\*\* Prof. Bořek Patzák, Department of Mechanics, Faculty of Civil Engineering, CTU in Prague, Thákurova 7/2077; 166 29, Prague; CZ, [borek.patzak@fsv.cvut.cz](mailto:borek.patzak@fsv.cvut.cz)

schemes for efficient storage of sparse matrices and solution of related linear problem. The problem is about solve equation (1) where  $\mathbf{r}$  and  $\mathbf{F}$  are just vectors,  $\mathbf{K}$  is a sparse matrix, and even storing a dense matrix of  $\mathbf{K}$  's size would be prohibitively expensive. There are a number of different libraries out there that solve a sparse linear system of equations. This paper compares SuperLU library as a representative of shared memory model and PETSc as a distributed memory model representative. SuperLU contains a set of sparse direct solvers for solving large sets of linear equations. The kernel algorithm in SuperLU is sparse Gaussian elimination. First step of solution algorithm is a triangular factorization. In addition to complete factorization, SuperLU library also has limited support for incomplete factorization (ILU) preconditioner which approximately solves equation (1). Permutation matrices can be set up to improve sparsity, numerical stability and parallelism. The SuperLU routines appear in three different variants: sequential, multi-threaded (shared memory systems) and parallel (distributed memory systems).

PETSc consists of a variety of libraries similar to classes in C++ (Stroustrup, 1997) with an abstract interface to provide clean and effective implementations for solving partial differential equations. Different algorithms, for example Krylov subspace methods (KSP) or truncated Newton methods are provided. After creating the matrix and vectors that define linear system (1) the user can then use KSP to solve system of linear equations. PETSc supports MPI as a distributed memory parallelism.

The speed-up of computation is one of the most important goals of parallel computing (Patzak, 2010). Effective parallel algorithm is considered as scalable, where with increasing number of processing threads the execution time is monotonically decreasing, ideally in a linear trend. However, when individual computing threads are mutually dependent, the ideal scalability is difficult to obtain due to the overhead of parallel algorithm (synchronization, locking) and due to the fact that some parts are essentially serial.

## 2. Implementation

Comparison of different existing libraries developed to the solution of sparse linear systems is the subject of presented paper. In this contribution, we compare efficiency of serial direct and iterative solvers on selected benchmark problems. The comparison was made using OOFEM finite element solver (Patzak, 2000). The interface to SuperLU library has been implemented, consisting of new classes to represent SuperLU solver and sparse matrix storage. The interface to PETSc already exists. SuperLU is used with expert driver based on OpenMP or POSIX threads. The driver advantageously uses symmetry of matrix in linear system. Ordering of the columns of matrix is optimized using as multiple minimum degree applied to the structure of  $\mathbf{A}^T + \mathbf{A}$ . PETSc parallel solver based on distributed memory has been configured to use conjugated gradient solver from KSP to solve linear system of equations.

## 3. Results

The individual approaches have been evaluated using a benchmark problem of a 3D finite element model of nuclear containment (Jete 250k) and a benchmark problem representing 3D finite element model of porous microstructure (Micro 250k). The nuclear containment mesh consists of 87320 nodes and 959700 tetrahedral elements with linear interpolation. The total number of equations was 260322. The model of porous microstructure mesh consist of 85184 nodes and 79507 brick elements with linear interpolation. The total number of equations was 255552. Both structures has been loaded with self-weight, resulting in nonzero contribution of every element to the external load vector. The benchmark problems are characterized by different sparsity of system matrix. The model of porous microstructure has significantly more nonzeros members than model of nuclear containment, which is really sparse problem. Number of nonzeros members in model of nuclear containment is 433555173 and to solve the problem with direct solver required 4.3 Gb of system memory. Number of nonzeros members in the model of porous microstructure is 1528773527 and to solve the problem with direct solver required 15.3 Gb of system memory. The PETSc solver needed 4673 iterations to solve problem of nuclear containment and 14687 iterations to solve porous microstructure. The relative solution relevance used was  $1.e^{-6}$ . The individual approaches have been tested on two Linux workstations (running Ubuntu 14.04 OS) with the two CPU Intel(R) Xeon(R) CPU E5-2630 v3 @ 2.40GHz and 126GB RAM. The two CPU units consists of eight physical and sixteen logical cores, allowing up to thirty-two threads to run simultaneously on one workstation. All the tests fit into a system memory.



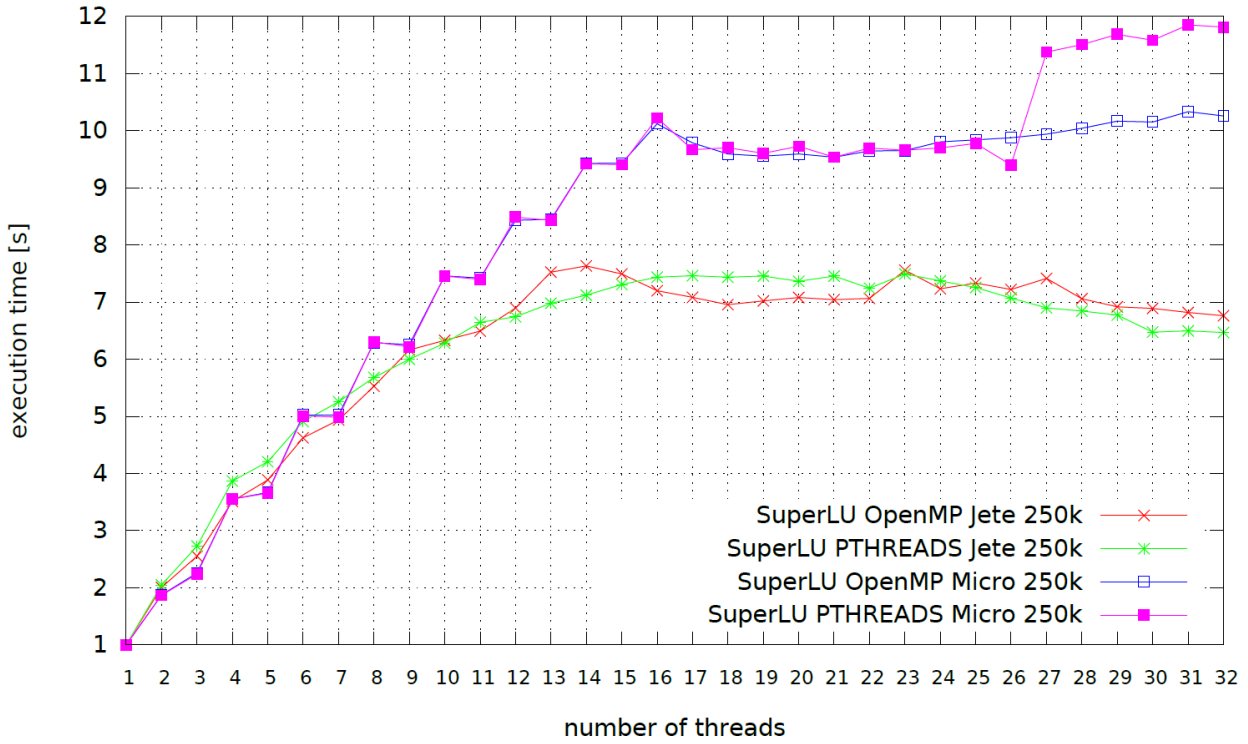


Fig. 1: Speed-up of linear system solution of direct SuperLU solver based on shared memory.

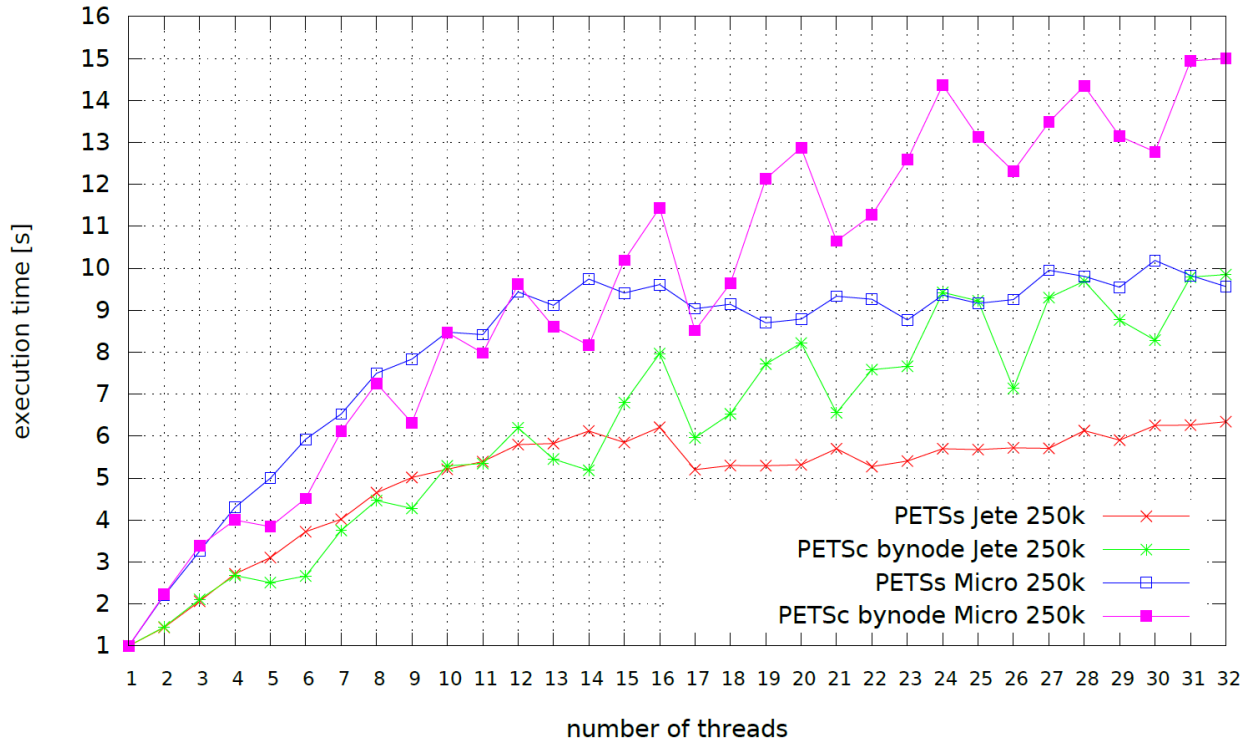
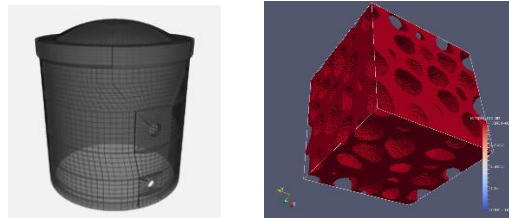


Fig. 2: Speed-up of linear system solution of iterative PETSc solver based on distributed memory.

Speed-up to solve linear system of equations using direct solver based on shared memory model (SuperLU with using OpenMP and POSIX threads) and iterative solver based on distributed memory (PETSc with using MPI) are presented in Fig. 1 and Fig. 2. The reported executions times have been obtained as an average of five consecutive runs. It can be clearly observed, that time needed for the execution is reduced with increasing number of threads. This can be caused by reading the local memory bus limits on single workstation.

For the direct solver SuperLU needed considerably more time to solve problem than iterative solver PETSc on both benchmark problems. The computational times for 17 threads and more are similar and no significant speed-up progress is achieved.

The results of PETSc solver executed on one workstation (32 threads with hyper-threading) and on two workstations (16 threads on workstation 1 and 16 threads on workstation 2 marked bynode keyword in Fig. 2) show that there are slight differences between using the solver on one or two computers caused by an additional overhead due to communication over network. PETSc solver using communication over the network on two workstations (by node) show better speed-up proportionally for higher number of threads (17 - 32 threads) than solving the same problem only on one computer. However, using both parallel solvers one can achieve better performance compared to serial code.



*Fig. 3: Benchmarks problems: on the left 3D finite element model of nuclear containment (Jete 250k) and on the right of 3D finite element model of porous microstructure cube (Micro 250k).*

#### 4. Conclusions

Different approaches to solve system of linear equations with direct and iterative solvers have been implemented and their efficiency compared on tests examples. Results show that there are significant differences between performance of direct and iterative solvers for considered benchmarks. The PETSc iterative solver based on distributed memory has the better performance than SuperLU direct solver based on shared memory. However, the presented conclusions are related to selection of benchmark problems. In general, the possibility to have both iterative and direct parallel solvers can be an advantage. It is therefore important to have different possibilities available in general purpose finite element code.

#### Acknowledgement

This work was supported by the Grant Agency of the Czech Technical University in Prague, grant No. SGS15/038/OHK1/1T/11 “Advanced algorithms for numerical modelling in mechanics of structures and materials”.

#### References

- Li, X.S., Demmel, J.W., Gilbert, J.R., Grigori, L., Shao, M. and Yamazaki, I. (1999) Lawrence Livermore National Laboratory, SuperLU Users' Guide Program Interface, September 1999, LBNL-44289, <http://crd.lbl.gov/xiaoye/SuperLU/>.
- Balay, S., Abhyankar, S., Adams, M.-F., Brown, J., Brune, P., Buschelman, K., Dalcin, L., Eijkhout, V., Gropp W.-D., Kaushik, D., Knepley, M.-G., Curfman McInnes, L., Rupp, K., Smith, B.-F., Zampini, S. and Zhang, H. (2016) Argonne National Laboratory, ANL-95/11 - Revision 3.7, <http://www.mcs.anl.gov/petsc>.
- Chapman, B., Jost, G., Pas, R.V.D. (2008) Using OpenMP - portable shared memory parallel programming. Morgan Kaufmann Publishers, Inc.
- Barney, B., Lawrence Livermore National Laboratory (2014) OpenMP - An Application Program Interface. <https://computing.llnl.gov/tutorials/openMP/>.
- Nicols, B., Buttler, C. and Farrell, J.P. (1996) Pthreads Programming, ISBN 1-56592-115-1, O'Reilly and Associates.
- Pacheco, P.P. Univ. of San Francisco, Univ. of San Francisco, A User's Guide to MPI, 1997
- Hughes, C., Hughes T. (2003) Parallel and Distributed Programming Using C++. ISBN 0-13-101376-9, Pearson Education.
- Barney, B. (2010) Task scheduling for parallel systems. <https://computing.llnl.gov/tutorials/parallel comp/>.
- Stroustrup, B. (1997) The C++ programming language. Murray Hill, AT Labs Murray Hill, New Jersey.
- Patzak, B. (2010) Parallel computations in structural mechanics. ISBN 978-80-01-04565-7, Czech Technical University in Prague.
- Patzak, B. OOFEM, 2000, <http://www.oofem.org>.

## MODIFICATION OF THE INTAKE MANIFOLD OF A COMBUSTION ENGINE

P. Brabec<sup>\*</sup>, K. Reichrt<sup>\*\*</sup>

**Abstract:** *This paper deals with the issue of the variable length of the intake manifold for combustion engines. The part of it is also a demonstration of used constructions of mass-produced vehicles. The aim was to optimise the length of the intake manifold for the submitted combustion engine using the Ricardo Wave software and then to design its possible construction solution.*

**Keywords:** SI Engine, Intake manifold, Variable length, CAD design.

### 1. Introduction

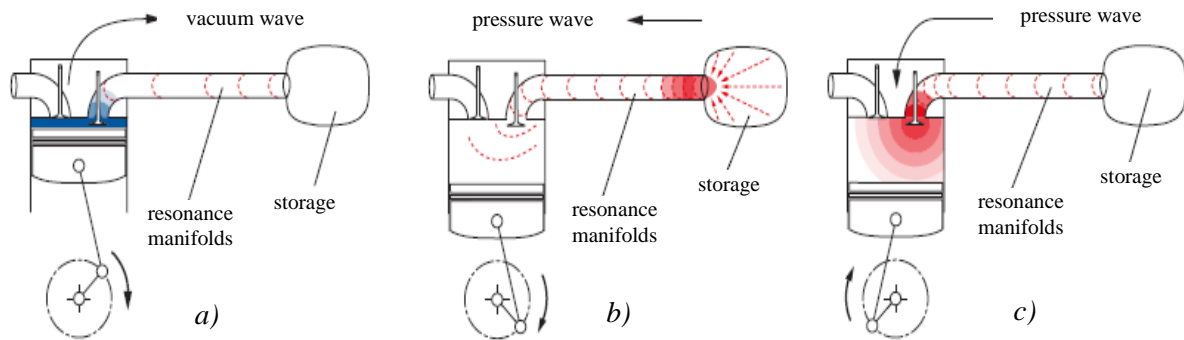
When constructing the engine, the aim is both to reach high torque when the speed is low, and high rated power when the speed is maximum. The engine torque flow is adequate to absorbed air weight depending on the engine speed. An assisting means for influencing the torque is the geometric design of the intake manifold. The easiest way of supercharging lies in using the intake air dynamics. A standard intake manifold of multipoint injection systems consists of individual intake manifolds and a collection (intake) manifold with an air throttle. In this case, too, the short manifold enables high rated power at the same time with losses of torque in low speed; and the long manifold shows the opposite characteristics. Big capacity of the collection manifold produces (at certain torque) a partial resonance effect which improves the filling. However, it results in possible dynamic errors (deviations in mixture composition when there are fast changes in load). Almost ideal torque characteristics are obtained by using by the intake manifold with switching between different lengths (Bausshuysen, Schäfer, 2002), (Vlk, 2002). Resonance supercharging with an individual manifold for each cylinder means that each cylinder has its own separate manifold of a certain length usually connected to the collection manifold by the storage one. Energy balance is characterized by changing the intake piston movement to kinetic energy of the air column in front of the intake valve and its following change into pressure energy. For charging the column, vacuum and pressure waves are used. Let us describe what happens inside the intake manifold when charging. The intake valve opens, piston moves down and creates vacuum wave in the area of the intake manifold. It spreads in the resonance manifold towards its other end which leads to a storage. The size of the air pressure inside the storage is equal (approximately) to the atmospheric pressure. This is considerably higher than the air pressure size of the intake valve (Fig. 1a). The vacuum which, in the meantime, reached the storage takes with it the air which is situated inside the storage. The air then flows into the resonance manifold creates – in the place of the vacuum wave – a pressure wave of the same size which goes towards the intake valve. It can also be concluded that the vacuum wave at the end of the resonance manifold bounced back from the storage (Fig. 1b). The pressure wave goes through the resonance manifold and pushes the air towards the intake valve which is still open. This process takes until the pressure in front of the intake valve and the pressure inside the cylinder are equal. The reverse flow will be prevented from by closing the intake valve (Fig. 1c). To overcome the distance between the storage and the intake valve, the vacuum wave (or pressure wave respectively) needs some specific time (milliseconds). Both vacuum and pressure waves move at a speed of sound. Considering that the speed of sound does not change, neither the distance changes and the time is still constant. However, the time interval in which the intake valve is open (and depending on the motor speed) changes in a way that the more the motor speed increases the more this time interval shortens. It means that when the speed is higher, the pressure wave would reach the intake valve once it is already closed. In order to be able to

---

<sup>\*</sup> Ing. Pavel Brabec, PhD.: Technical University of Liberec, Studentská 2; 461 17, Liberec 1; CZ, pavel.brabec@tul.cz

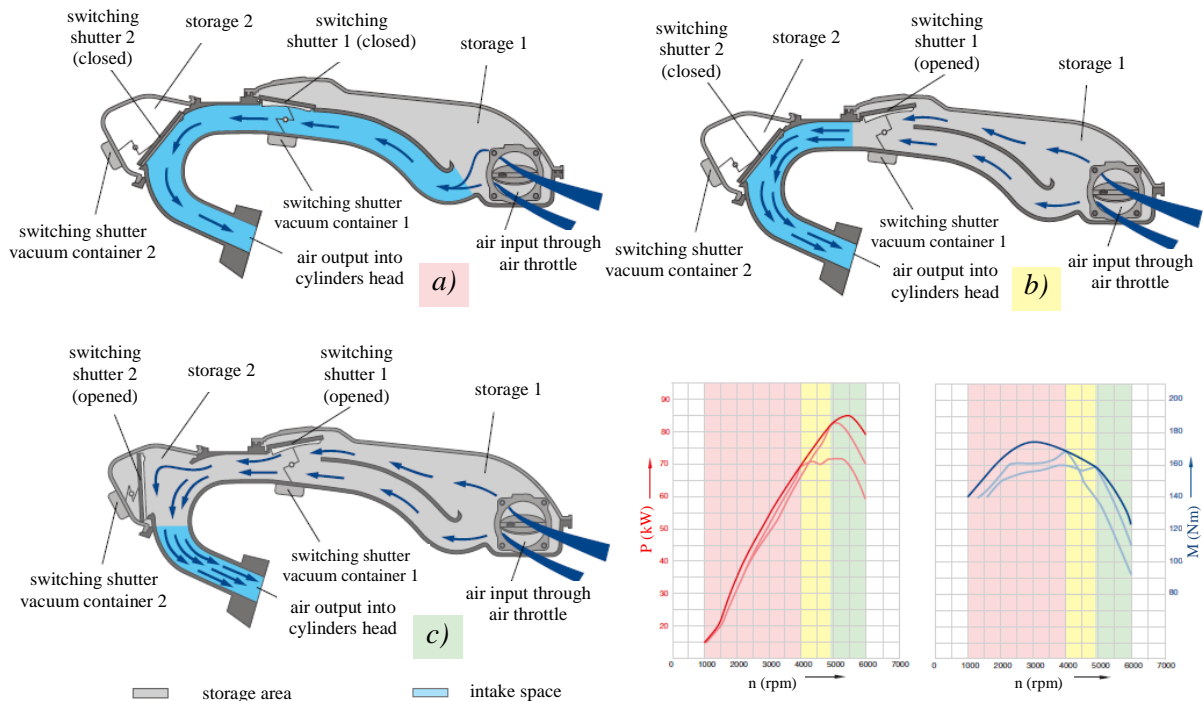
<sup>\*\*</sup> Ing. Kamil Reichrt: Technical University of Liberec, Studentská 2; 461 17, Liberec 1; CZ, kamil.reichrt@tul.cz

shorten the time  $t$  (so that the pressure wave would reach the intake valve when it is still open) it would be necessary to shorten the distance (space)  $s$ . The waves movement speed cannot be changed and shortening the distance  $s$  means to shorten the resonance manifold.



*Fig. 1: Principle of resonance charging: a) creation of vacuum wave;  
b) pressure wave which moves towards intake valve;  
c) pressure wave going into the cylinder through open intake valve (Škoda Auto, 2001).*

Overall, it can be concluded that the higher the motor speed is the shorter the resonance manifold must be – it means that a long resonance manifold (torque position) is suitable for low and medium speed and a short resonance manifold (power position) is suitable for high speed. Resonance charging in the resonance area causes increasing of charging pressure by 15-30 kPa, therefore increasing the motor power is usually by 10 to 35 %. In 2005, this principle was used for example by the automobile manufacturer Porsche for Boxster S, Cayman S, 911 Carrera Coupe (the resonance charging and variable timing system VarioCam) where brake mean effective pressure was about 1.25 MPa. In the Fig. 2 there is an illustration of a technical solution of an intake manifold with a variable length of intake for a spark ignition non-supercharged motor (volume 2.0 l, power 85 kW) by Škoda.



*Fig. 2: Intake manifold with variable length of intake for spark ignition non-supercharged motor by Škoda: a) torque position (increasing of torque, speed range 780 – 4000 min<sup>-1</sup>);  
b) power position – long space of intake (switching shutter 1 of intake manifold opens at 4000 min<sup>-1</sup>);  
c) power position – short space of intake (switching shutter 2 of intake manifold opens at 4800 min<sup>-1</sup>)  
(Škoda Auto, 2001).*

## 2. Simulation calculation of a combustion engine

For making a modification of the intake manifold, the ŠA 1.2 HTP motor was chosen. This drive unit was chosen mainly because of knowing its simulation parameters which were already experimentally verified when doing the previous project. For making a simulation calculation, the Ricardo Wave software was used. This software uses the access 0-D for simulation of a motor cylinder and 1-D for modelling an intake and an exhaust manifolds. To reach results which are as close to reality as possible, it is necessary to create a simulation model as a complete scheme beginning with solid intake and ending with an exhaust including its equipment. The quality of the model input data significantly affects the results; therefore, the model was verified with the experiment.

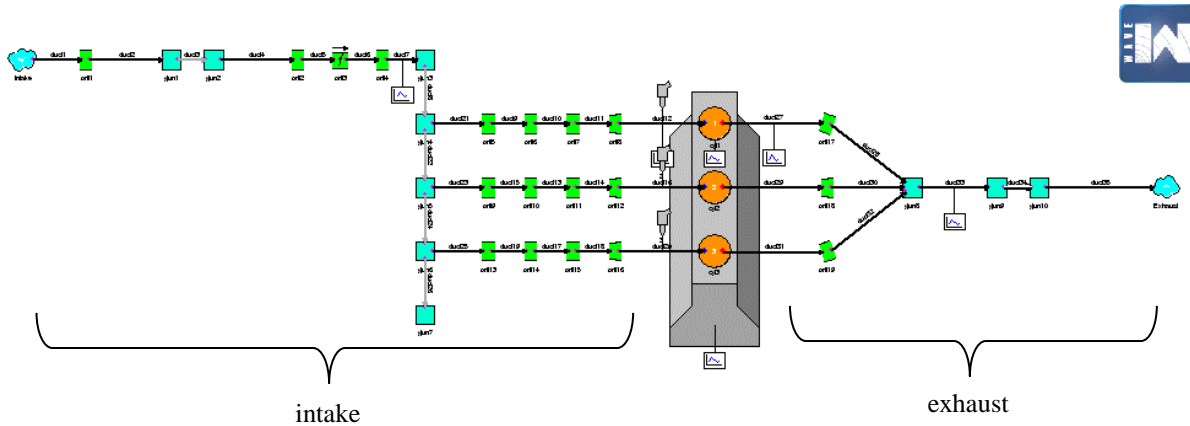


Fig. 3: Simulation model of combustion engine.

The length of the intake was calculated in estimated realisable range which means from 100 to 800 mm. First, the dependence of authoritative motor parameters (such as torque, effective power, and also volumetric efficiency) was performed on the length of the manifold in various modes (speed) of the motor. Then, the most suitable lengths of the intake manifold were chosen. The next step was to discover the optimal cross-section area. The conception of an intake manifold with continuous-variable length was rejected by reason of a required larger installation area. Finally, the simplest two-stage variant of the intake manifold was chosen because according to the simulation calculations the three-stage variant would not lead to a more substantial improvement of the motor cylinder charging. From the results of the simulation and by reason of production the choice was as follows: the suitable length of the long branch of the intake is 690 mm and the diameter of the circular cross-section area is 30 mm; the suitable length of the short branch of the intake is 326 mm and the cross-section is 35 mm (Reichrt, 2015). These pieces of knowledge were also used when creating the construction design of the intake manifold.

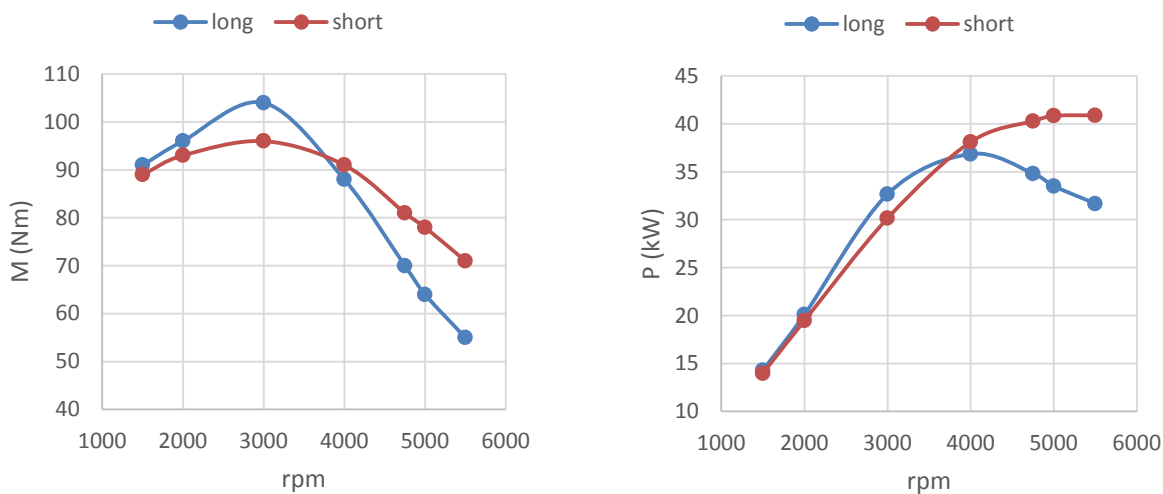


Fig. 4: Graph of torque and power of combustion engine in dependence of speed for both of the chosen values of intake manifold length.



### 3. Construction solution design of a variable intake manifold

The resulting 3D model of the intake manifold was made of three main parts by reason of manufacturability. An important aspect is the choice of dividing planes. These main parts are stuck together and for precise fitting are used grooves in individual parts which fit together. The change of the length of the intake manifold is covered by a rotating gate valve which is located in the short branch of the manifold. An electromagnetic valve would be used to control the gate valve.



*Fig. 5: 3D model of designed variable intake manifold (Reichrt, 2015).*

### 4. Conclusions

The simulation results show visible advantages of a variable intake manifold. The torque value when the speed is lower was increased and also the power when the operational speed of the combustion engine is higher rose. The charging efficiency values in full range of engine speed was also increased and the specific consumption of fuel when the speed is high decreased slightly. This positive effect only appears when taking into consideration the full load characteristic of the engine; when taking into consideration a partial load, dynamic in the intake manifold is not used because of using the air throttle. If a variable intake manifold was used in a motor with higher swept volume, even larger improvement of power parameter would appear.

### Acknowledgement

This publication was written at the Technical University of Liberec, Faculty of Mechanical Engineering with the support of the Institutional Endowment for the Long Term Conceptual Development of Research Institutes, as provided by the Ministry of Education, Youth and Sports of the Czech Republic in the year 2017.

### References

- Baushuysen, R. and Schäfer, F. (2002) Internal Combustion Engine Handbook - Basic, Components, Systems, and Perspectives. Vieweg Verlag, Wiesbaden, Germany.
- Vlk, F. (2002) Accessories of vehicle engines. Publishers and publishing VLK, Brno (in Czech).
- Reichrt, K. (2015) Design adjustment of the intake manifold of the engine to the variable. Diploma work, Technical University of Liberec, Liberec (in Czech).
- Documents of the company Škoda Auto.

## MODEL OF CAR SUSPENSION WITH PARAMETRIC UNCERTAINTY

L. Brezina<sup>\*</sup>, P. Losak<sup>\*\*</sup>

**Abstract:** A quarter model of a car suspension is the simplest possible model for entry analysis of a suspension behavior. However, such a model is very rough typically without modelled suspension nonlinearities or other effects influencing the model dynamics significantly. The paper proposes approach where a given suspension parameter is modelled as uncertain. It is consequently investigated the amount of the uncertainty of a given parameter which covers the given nonlinearity. The advantage of the approach is that the model with parametric uncertainty has still very simple structure possibly in a form of linear state-space model with possible utilization in robust control design.

**Keywords:** Multi-body model, Car suspension, Parametric uncertainty.

### 1. Introduction

Multi-body model of a car suspension is in its simplest form represented by a quarter model with two degrees of freedom (Fig. 1) which is constituted by two ordinary differential equations. Such a model can be considered as entry level for analysis of a car suspension behavior. However, it contains neither nonlinearities in the suspension nor other significant influences such as wear and tear of suspension elements projecting directly into the behavior of the system.

Introducing all of mentioned influences makes the model substantially more complicated which especially in a case of full suspension car model leads to increased computational demands and also to its lower readability.

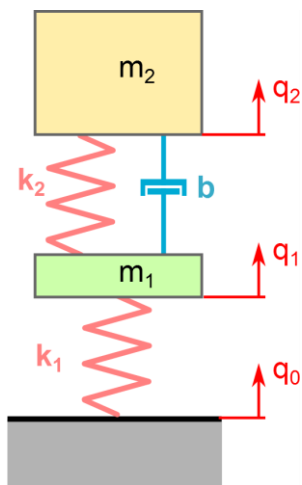


Fig. 1: Quarter model scheme.

The possible way how to overcome complicated introducing of details influencing the dynamics of the model and yet keeping it simple is to utilize apparatus of modeling with given amount of uncertainty (Green, 1994). The model containing an uncertainty (for example in some of parameters such as stiffness or mass) has still quite simple structure, possibly in a form of state linear time invariant model. This allows working with the model efficiently. Let's also note that models with uncertainty are generally utilized in robust control design (Gu et al., 2005).

The goal of the paper is to find out whether the simple quarter model with parametric uncertainty defined for a given suspension parameter is able to cover a behavior of more complicated suspension model with a nonlinearity. In the positive case will be investigated needed amount of uncertainty of the parameter.

<sup>\*</sup> Ing. Lukas Brezina, PhD.: Institute of Solid Mechanics, Mechatronics and Biomechanics, Brno University of Technology, Technická 2896/2; 602 00, Brno; CZ, brezina.l@fme.vutbr.cz

<sup>\*\*</sup> Ing. Petr Losak, PhD.: Institute of Solid Mechanics, Mechatronics and Biomechanics, Brno University of Technology, Technická 2896/2; 602 00, Brno; CZ, losak@fme.vutbr.cz



## 2. Suspension model

### 2.1. Quarter model

The quarter model of the car suspension (Fig. 1) generally describing oscillating system with two degrees of freedom is defined by two well-known ordinary differential equations

$$\begin{aligned} m_1 \ddot{q}_1 &= b(\dot{q}_2 - \dot{q}_1) + k_2(q_2 - q_1) - k_1(q_1 - q_0) \\ m_2 \ddot{q}_2 &= -b(\dot{q}_2 - \dot{q}_1) - k_2(q_2 - q_1) \end{aligned}, \quad (1)$$

where  $m_1$  means unsprung mass,  $m_2$  sprung mass,  $k_1$  stiffness of the tire,  $k_2$  stiffness of the coil spring,  $b$  damping of the damper,  $\ddot{q}_1$ ,  $\dot{q}_1$ ,  $q_1$  are kinematics quantities of the unsprung mass,  $\ddot{q}_2$ ,  $\dot{q}_2$ ,  $q_2$  are kinematics quantities of the sprung mass and finally  $q_0$  is the excitation from the road surface.

### 2.2. Model of damping nonlinearity

The damping characteristic of a car damper is intentionally nonlinear. The main reason is the requirement of different intensity of the damping for the lifting and lowering of a wheel. Nonlinear damping characteristics used in the paper is obtained from (Pražák, 2006). It is linearized in the sense of least square method for obtaining of parameter  $b$  nominal value. Both, nonlinear and linear damping are shown in Fig. 2.

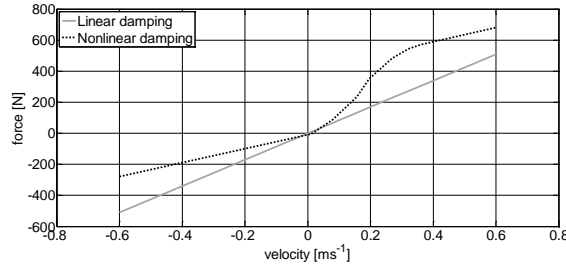


Fig. 2: Linear and nonlinear damping characteristics.

### 2.3. Quarter model with parametric uncertainty

For the sake of simplicity will be modeled as uncertain only parameter  $b$ , which means that

$$b_{\Delta} = b \pm \Delta, \quad (2)$$

where  $b_{\Delta}$  is the damping with parametric uncertainty,  $b$  represents the nominal value of the damping and  $\Delta$  is the uncertainty value (in this case as percentage of  $b$ ). In a same way can be defined uncertainties in other parameters.

For more comfortable work with the model, it was transformed into state-space form

$$\begin{aligned} \dot{\mathbf{x}} &= \mathbf{A}\mathbf{x} + \mathbf{B}\mathbf{u} \\ \mathbf{y} &= \mathbf{C}\mathbf{x} + \mathbf{D}\mathbf{u} \end{aligned}, \quad (3)$$

where  $\mathbf{x} = [q_2 \quad \dot{q}_2 \quad q_1 \quad \dot{q}_1]^T$  is vector of states,  $\mathbf{u} = q_0$  is the input to the system and  $\mathbf{y} = [q_2 \quad q_1]^T$  represents outputs of the system (displacement of the both masses). Matrices  $\mathbf{A}$ ,  $\mathbf{B}$ ,  $\mathbf{C}$ ,  $\mathbf{D}$  are defined as

$$\mathbf{A} = \begin{bmatrix} 0 & 1 & 0 & 0 \\ -\frac{k_2}{m_2} & -\frac{b_{\Delta}}{m_2} & \frac{k_2}{m_2} & \frac{b_{\Delta}}{m_2} \\ 0 & 0 & 0 & 1 \\ \frac{k_2}{m_1} & \frac{b_{\Delta}}{m_1} & \frac{-k_2 + k_1}{m_1} & -\frac{b_{\Delta}}{m_1} \end{bmatrix}, \quad \mathbf{B} = \begin{bmatrix} 0 \\ 0 \\ 0 \\ \frac{k_1}{m_1} \end{bmatrix}, \quad \mathbf{C} = \begin{bmatrix} 1 & 0 & 0 & 0 \\ 0 & 0 & 1 & 0 \end{bmatrix}, \quad \mathbf{D} = \begin{bmatrix} 0 \\ 0 \end{bmatrix}.$$

## 2.4. Model of excitation from the road surface

Input to the quarter model as an excitation from the smooth terrain is generated using function (4). The function is defined by summing several sinusoids of appropriate amplitude and frequency as follows.

$$q_0 = (-0.143\sin(1.75(x+1.73)) - 0.180\sin(2.96(x+4.98)) - 0.012\sin(6.23(x+3.17)) + 0.088\sin(8.07(x+4.63))) / 5 \quad (4)$$

## 3. Numerical experiments

The scope of numerical experiments was to compare output displacement of the sprung and unsprung mass of the linear quarter model (1) with the corresponding outputs of the model containing the nonlinear damping defined according to Fig. 2 (for results see Figs. 3 – 6) and consequently to compare outputs of the nonlinear model with outputs of the uncertain one.

The values of parameters for the linear model were used as follows:  $m_1 = 33 \text{ kg}$ ,  $m_2 = 400 \text{ kg}$ ,  $k_1 = 125000 \text{ N.m}^{-1}$ ,  $k_2 = 50000 \text{ N.m}^{-1}$  and from the linearization obtained  $b = 849 \text{ N.s.m}^{-1}$ .

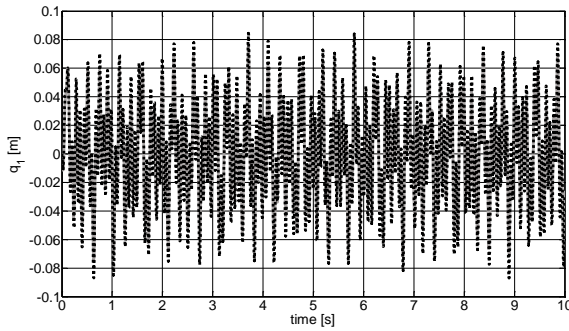


Fig. 3: Unsprung mass displacement, linear vs nonlinear (dashed) damping.

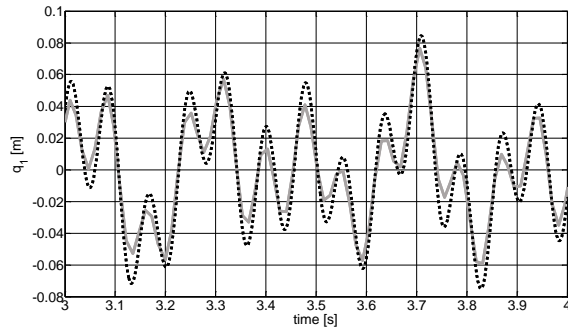


Fig. 4: Unsprung mass displacement, linear vs nonlinear (dashed) damping-detail.

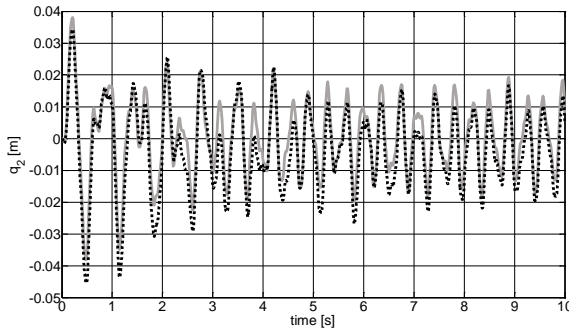


Fig. 5: Sprung mass displacement, linear vs nonlinear (dashed) damping.

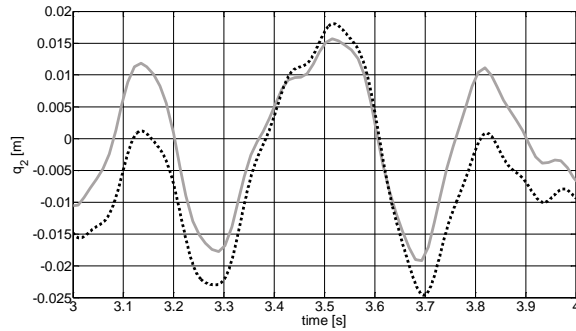


Fig. 6: Unsprung mass displacement, linear vs nonlinear (dashed) damping-detail.

The difference (according to Kullback-Leibler) between the outputs of the linear and nonlinear model is approximately 22.4 %, thus the linear model can be in some situations insufficient. The following simulation results (Figs. 7 and 8) compare outputs of the model with uncertainty on the damping according to (3) with the model containing the nonlinearity in the damping. The uncertainty was changed from  $\pm 10 \%$  to  $\pm 100 \%$  of  $b$ , the increment was 10 %.

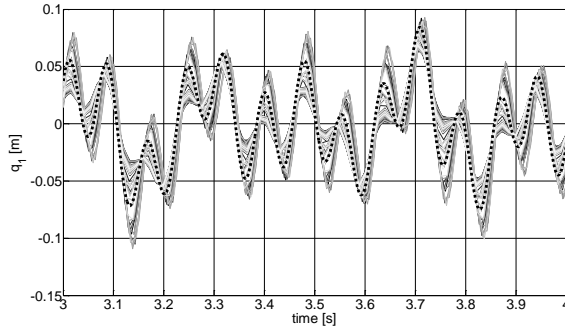


Fig. 7: Unsprung mass displacement, samples of the model with uncertainty  $\pm 100\%$  vs nonlinear (dashed)-detail.

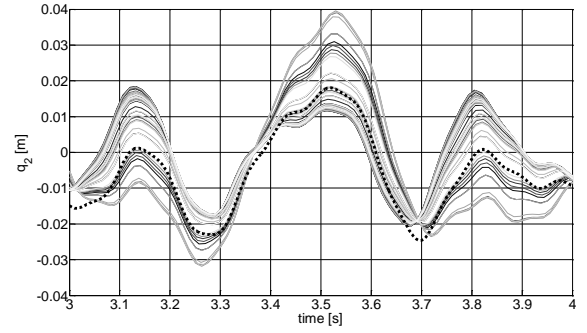


Fig. 8: Sprung mass displacement, samples of the model with uncertainty  $\pm 100\%$  vs nonlinear (dashed)-detail.

The difference between outputs of the uncertain model samples (50 samples for every 10 %) and nonlinear model was evaluated by Kullback-Leibler method and it is represented by following boxplots (Figs. 9 and 10).

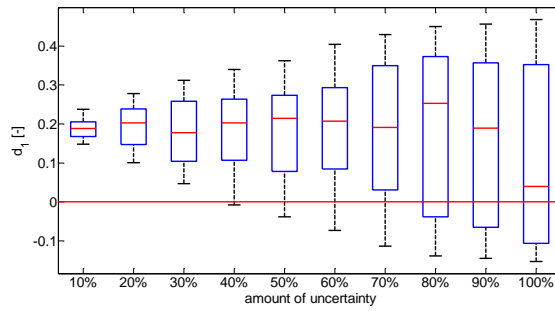


Fig. 9: Difference between  $q_1$  of the uncertain model samples and nonlinear model.

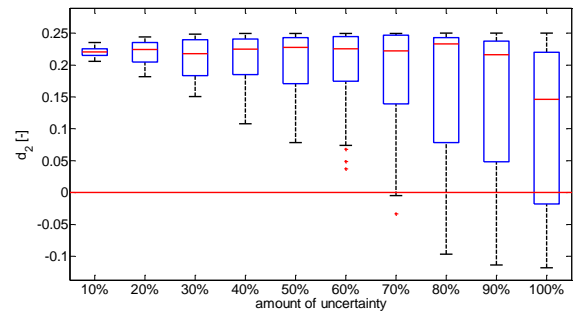


Fig. 10: Difference between  $q_2$  of the uncertain model samples and nonlinear model.

#### 4. Conclusions

The difference between outputs of the linear quarter model and the model with nonlinear damping is approximately 22.4 % thus in some cases might be the linear model insufficient. The introduced parametric uncertainty of the damping was changed gradually by 10 % from  $\pm 10\%$  to  $\pm 100\%$  of  $b$ . It was investigated that outputs of the nonlinear model will be covered by outputs of the uncertain model for the uncertainty at least  $\pm 40\%$  (for  $q_1$ ), respectively at least  $\pm 70\%$  (for  $q_2$ ). Such a model with modeled uncertainty is able to cover behavior of the nonlinear model and due to its simple structure it is computationally efficient and suitable for consequent robust control design. In a similar way can be modelled different types of nonlinearities or other influences such as wear and tear of the elements which can be difficult to model or predict in classical way.

#### Acknowledgement

This work is supported by project NETME Centre PLUS. The results of this project NETME CENTRE PLUS (LO1202) were co-funded by the Ministry of Education, Youth and Sports within the support programme „National Sustainability Programme I“.

#### References

- Green, M. and Limebeer, D.J.N. (1994) Linear robust control. Prentice-Hall, Upper Saddle River.
- Gu, D.W., Petrov, P.H. and Konstantinov, M.M. (2005) Robust Control Design with Matlab, Springer, London.
- Pražák, F. (2006) Suspension damper as an element influencing driving qualities of a car, PhD Thesis, BUT, Brno (in Czech).

## COMPUTATIONAL ANALYSIS OF SERVICEABILITY LIMIT STATE OF BEAMS REINFORCED WITH FRP BARS

K. Brózda<sup>\*</sup>, M. Major<sup>\*\*</sup>, J. Selejdak<sup>\*\*\*</sup>

**Abstract:** Fiber Reinforced Polymers (FRP) reinforcement are increasingly common as internal reinforcement of Reinforced Concrete (RC) members, because of their excellent properties as high tensile strength, corrosion resistance and non-magnetization. However, the flexural and mechanical characteristics of FRP bars such as low modulus of elasticity or non-yielding characteristics, results in large values of deflection and wide crack of FRP RC element. This paper investigates and compares the Serviceability Limit State (ULS) of simply supported beam subjected to various values of flexural stresses. The beams reinforced with Carbon Fiber Reinforced Polymer (CFRP) and Aramid Fiber Reinforced Polymer (AFRP) bars were examined. The computational analysis of beams static work was based on American guide for the design (ACI 440.1R-06), with taking into consideration all reduction factors. The influence of various parameters as the reinforcement ratio or load level were analyzed.

**Keywords:** FRP reinforcement, Beam, Deflection, Crack width, Flexural strength.

### 1. Introduction

The fibre reinforced polymers (FRP) bars offer an attractive alternative to conventional steel reinforcement. Their good physical and mechanical properties as low density and thermal expansion coefficient, high corrosion resistance in aggressive environments, high tension strength-to-weight ratio and very good fatigue properties cause the development of investigation of FRP reinforced concrete members. However, no discernible yield point, relatively low modulus of elasticity and different flexural strength depending on the FRP type result in large crack widths and deflections. These characteristics are the reason that the serviceability limit states, primarily deflection and cracking, is one of the critical issues necessary to be examined during design of concrete structural elements reinforced with FRP bars. In the investigation the beam under different level of live load, with various reinforcement ratio of two types of FRP bars was considering. This research evaluate the relation between deflection and crack width to nominal moment capacity of concrete member reinforced with FRP bars (Abdalla, 2002 and Gravina, 2008).

### 2. Available design recommendations

Many years of designers and researchers experience contributed to development of the guides based on among others design equations which predict flexural strength, crack widths and deflections of concrete beams reinforced with FRP bars. The design recommendations are available in four elaborations: American (ACI 440.1R-06), Canadian (CSA-S806-02, 2002), Japanese (JSCE No.23, 1997) and Italian (CNR-DT 203/2006).

The guidelines for cracking and deflection based on standards for typical reinforced concrete, because of significant differences in modulus of elasticity, tensile strength and deformation characteristics cannot be directly applied for FRP rebar (Toutanji, 2003). However, the recommendations for design FRP

---

<sup>\*</sup> M.Sc., Eng. Kinga Brózda.: Faculty of Civil Engineering, Czestochowa University of Technology, Akademicka 3; 42 200, Czestochowa; PL, kbrozda@bud.pcz.czyst.pl

<sup>\*\*</sup> Assoc. Prof. Eng. Maciej Major, PhD.: Faculty of Civil Engineering, Czestochowa University of Technology, Akademicka 3; 42 200, Czestochowa; PL, mmajor@bud.pcz.czyst.pl

<sup>\*\*\*</sup> Assoc. Prof. Eng. Jacek Selejdak, PhD.: Faculty of Civil Engineering, Czestochowa University of Technology, Akademicka 3; 42 200, Czestochowa; PL, jselejdak@bud.pcz.czyst.pl

reinforced concrete (RC) include following assumptions (Bywalski, 2014): perfect adhesion between FRP bars and concrete surface, the applicable flat cross-section condition, linear relation  $\varepsilon$ - $\sigma$  for FRP in tension until destruction of member and neglected expandable concrete zone.

### 3. Computational analysis

#### 3.1. Calculation model

The simply supported exterior beams with rectangular cross-section sized 350 x 180 mm are calculated. A superimposed service dead load of  $w_{SDL} = 3.0$  kN/m and three levels of service live load  $w_L$  (3.0, 4.5 and 6.0 kN/m) are assumed. Beams are reinforced with AFRP and CFRP bars, with various reinforcement ratio: 0.61 % (3 $\Phi$ 12), 0.42 % (3 $\Phi$ 10) and 0.24 % (3 $\Phi$ 7.5). The concrete is specified by class C20/25 ( $f'_c = 14.3$  MPa) and concrete cover thickness  $c = 35$  mm is assumed. The  $L_{eff}/240$  limitation for long-term deflection and maximum crack width of 0.4 mm are taken into consideration. The span of the beam is constant for each of the analyzed case ( $L_{eff} = 3.0$  m).

Design procedure follows the ultimate and serviceability limit states according to ACI 440.1R-06. The tensile strength  $f'_{fu}$  and modulus of elasticity of FRP  $E_f$  of the bars are reported by the manufacturers (Sireg Geotech S.r.l) - AFRP:  $f'_{fu} = 1400$  MPa,  $E_f = 60$  GPa, and CFRP:  $f'_{fu} = 2300$  MPa (CFRP),  $E_f = 130$  GPa.

#### 2.2. The results of computations

During analysis the three various reinforcement depend on the diameter of the bar were considered. Depend on levels of service live load  $w_L$  following values of the ultimate moments  $M_u$  were achieved: 12.01 kN·m for  $w_L = 3$  kN/m, 14.52 kN·m for 4.5 kN/m and 17.07 kN·m for 6 kN/m. The deflection limitation equal 12.5 mm and the limit of crack width equal 0.4 mm was controlled according to available standards for design RC (ACI 318M-05 and EN 1992-1-1:2004).

Results of computational analysis of flexural strength  $\Phi \cdot M_n$ , ( $\Phi$  – reduction factor) long-term deflection  $\Delta_{LT}$  and crack width  $w$  are presented in the Tabs. 1 – 2.

*Tab. 1: Result of computational analysis of AFRP RC beam.*

Property	3 $\Phi$ 12 AFRP			3 $\Phi$ 10 AFRP			3 $\Phi$ 7.5 AFRP		
Flexural strength $\Phi \cdot M_n$ [kN·m]	29.80			26.22			21.08		
Service live load level $w_{LL}$ [kN/m]	3.0	4.5	6.0	3.0	4.5	6.0	3.0	4.5	6.0
deflection $\Delta_{LT}$ [mm]	0.98	1.82	2.97	1.41	2.62	4.24	2.52	4.64	7.46
crack width $w$ [mm]	0.30	0.36	0.42	0.42	0.51	0.59	0.74	0.88	1.03

*Tab. 2: Result of computational analysis of CFRP RC beam.*

Property	3 $\Phi$ 12 CFRP			3 $\Phi$ 10 CFRP			3 $\Phi$ 7.5 CFRP		
Flexural strength $\Phi \cdot M_n$ [kN·m]	38.35			34.42			28.40		
Service live load level $w_{LL}$ [kN/m]	3.0	4.5	6.0	3.0	4.5	6.0	3.0	4.5	6.0
deflection $\Delta_{LT}$ [mm]	0.60	1.11	1.77	0.87	1.59	2.51	1.56	2.80	4.37
crack width $w$ [mm]	0.14	0.17	0.20	0.20	0.24	0.28	0.35	0.42	0.49

The results of analysis indicate that the effect of reducing modulus of elasticity is significant for Serviceability Limit State (SLS). The reserve of flexural strength is very large – in analyzed cases the ultimate moment did not exceed the nominal moment capacity with strength reduction factor  $\Phi \cdot M_n$ . In almost each of the analyzed cases variant  $\rho \geq 1.4 \cdot \rho_{fb}$  were found (where  $\rho_{fb}$  – FRP reinforcement ratio producing balanced strain conditions). Thus, there were a cases of damage mechanism as concrete crushing failure (ACI 440.1R-06). Therefore, the strength reduction factor  $\Phi$  decreased the nominal moment capacity of 35 %. The long-term deflection of analyzed beams are lower than limitation: 0.98 – 7.46 mm for AFRP RC and 0.60 – 4.37 mm for CFRP RC. However, the crack limit equal 0.4 mm is fulfilled in only two of analyzed cases of beams reinforced with AFRP bars and in seven cases of beams reinforced with CFRP bars. The results were presented as dependency graphs. The relation between level of the ultimate moment (thereby the level of live load) and long-term deflection is presented in Fig. 1, while the dependence of crack width – in Fig. 2.

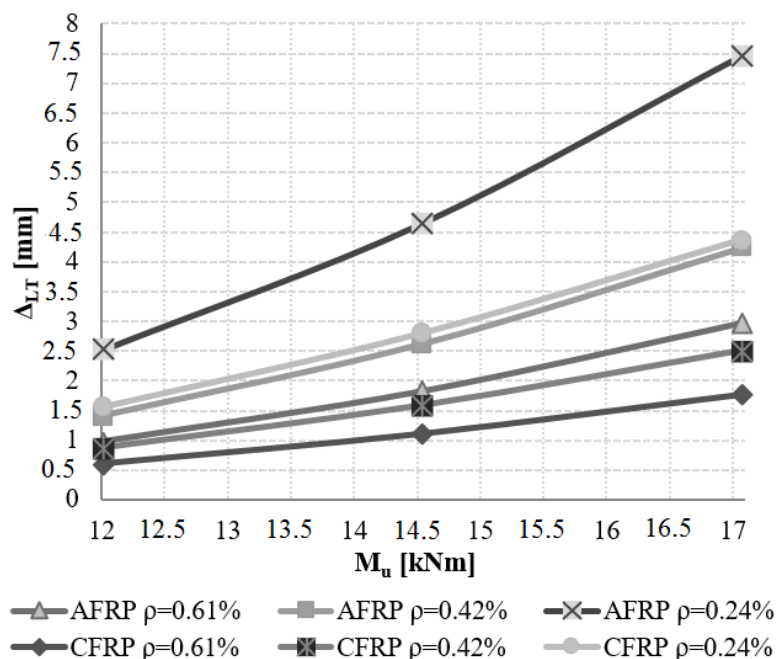


Fig. 1: Dependency graph of the long-term deflection and increasing ultimate moment.

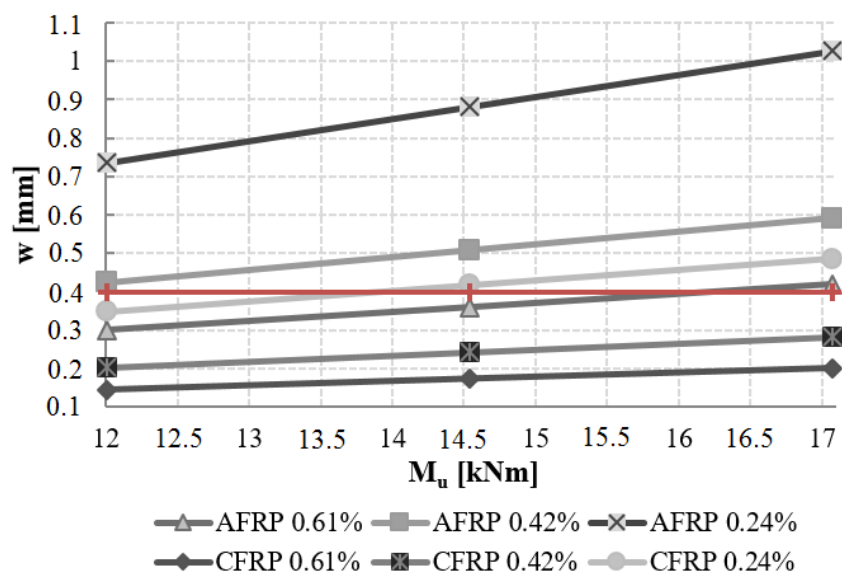


Fig. 2: Dependency graph of the crack width and increasing ultimate moment.

### 2.3. The analysis of the results

Based on the graph in Fig. 1, it can be estimated that depending on the level of the live load the values of long-term deflection increase exponentially. By estimating the trend line it is expected that limitation of

deflection of beam with the lowest load-capacity index (AFRP RC,  $\rho = 0.24\%$ ) can reach at the ultimate moment approximately equal to  $20 \text{ kN}\cdot\text{m}$  – which also indicates the fulfillment of the condition of flexural strength. However, in this case the crack width exceeds almost double limit value at the live load  $w_L = 3.0 \text{ kN/m}$  ( $M_u = 12.01 \text{ kN}\cdot\text{m}$ ). The crack width would be equal approximately  $1.2 \text{ mm}$  for  $M_u = 20 \text{ kN}\cdot\text{m}$  (it means triple exceeded condition).

In turn, based on the estimated trend line the beam with a highest load-capacity index (CFRP RC,  $\rho = 0.61\%$ ) can reach the deflection limitation in the value of ultimate moment nearly  $M_u = 47 \text{ kN}\cdot\text{m}$ . Whereas the crack width increases practically linear, it can be estimated that at a given  $M_u$  value, the crack width can reach slightly more than  $0.5 \text{ mm}$ .

Considering these conclusions the reduced value of modulus of elasticity makes the limit crack condition as crucial during designing the FRP RC members. At the assumed value of  $L_{\text{eff}}$ , achieving deflection limitation is practically proportional to achieving the maximum flexural strength. However, the assumed limit of cracking significantly limits the possibility of increasing the level of live load or length of beam span. Accordingly, during designing the FRP RC members it is important to consider that the influence of the relatively low modulus of elasticity is significant for Serviceability Limit State (SLS). Assuming that the modulus of elasticity of CFRP bars is about  $50\%$  higher than modulus of AFRP bars, the values of long-term deflection in CFRP RC beams are approximately  $40\%$  lower than in AFRP RC beams, while the cracks width of CFRP RC beams are lower by about  $50\%$ .

#### 4. Conclusions

The computational analysis of beams under static work, based on ACI 440.1R-06 guide for the design allowed the conclusion that influence of relatively low modulus of elasticity of FRP reinforcement is significant for Serviceability Limit State (SLS), especially crack width. Due to the very good tensile strength of FRP reinforcement, the flexural strength of beams had high load-capacity index in each of analyzed cases. However, the analysis of Serviceability Limit State is indispensable for faultless operation of beams. It is expected that in the analyzed cases under the assumed load level achieving the Ultimate Limit State for bending is almost synonymous with achieving the Serviceability Limit State for deflection. Despite this, the mechanical properties of FRP reinforcement have significantly influence on increasing the value of crack width. Having more than twice value of modulus of elasticity, the long-term deflections are reduced by almost  $40\%$ , and cracks width more than  $50\%$ .

#### References

- Abdalla, H.A. (2002) Evaluation of deflection in concrete members reinforced with fibre reinforced polymer (FRP) bars. *Composite Structures*, 56 (2002), pp. 63-71.
- ACI 440.1R-06 (2006) Guide for the design and construction of concrete reinforced with FRP bars.
- ACI 318M-05 Building code requirements for structural concrete and commentary.
- Bywalski, C., Drzazga, M. and Kamiński, M. (2014) Calculation of bending elements reinforced with FRP bars. *Materiały budowlane*, 6(2014), pp. 72-73, (in Polish).
- CSA-S806-02 (2002) Design and Construction of Building Components with Fibre Reinforced Polymers.
- CNR-DT 203/2006 Guide for the Design and Construction of Concrete Structures Reinforced with Fiber-Reinforced Polymer Bars.
- EN 1992-1-1:2004 Design of concrete structures. General rules and rules for buildings.
- Gravina, R.J. and Smith, S.T. (2008) Flexural behavior of indeterminate concrete beams reinforced with FRP bars. *Engineering Structures*, 30 (2008), pp. 2370-2380.
- JSCE (1997) Recommendation for design and construction of concrete structures using continuous fiber reinforcing materials, *Concrete Engineering Series No. 23*.
- Sireg Geotech S.r.l. product data sheet, available at: [www.sireggeotech.it/en](http://www.sireggeotech.it/en) (22.12.2016).
- Toutanji, H. and Deng, Y. (2003) Deflection and crack-width prediction of concrete beams reinforced with glass FRP rods. *Construction and Building Materials*, 17 (2003), pp. 69-74.



## REDESIGN OF A WAVE ENERGY CONVERTER IN FERROCEMENT

V. Bucci<sup>\*</sup>, A. Marinò<sup>\*\*</sup>, F. Mauro<sup>\*\*\*</sup>, C. Sandron<sup>\*\*\*\*</sup>, G. Mattiazzo<sup>\*\*\*\*\*</sup>

**Abstract:** *The case study for the redesign of a floating device able to produce electric energy from sea waves is presented. In particular, the steel hull of the ISWEC set up by the spin off "Wave for Energy" of the Politecnico di Torino has been converted in ferrocement without changing the total mass displacement and the position of the centre of gravity. Moreover, the essential ferrocement technology is illustrated, stressing the main differences with respect to the reinforced concrete. A reference guide useful for the early stage design scantling of small ferrocement crafts has been adopted for the specific case studied.*

**Keywords:** Wave Energy Converter, WEC, ISWEC, Ferrocement, Gyroscopic floating device.

### 1. Introduction

Over 70 % of the globe is covered by water containing a large amount of energy, which constitutes one of the largest unexploited source of renewable energy. Comparing the various technologies for the exploitation of this renewable energy, the capacity of devices for wave energy conversion is significantly greater than wind and solar farms. This stems from the fact that water is a high density source of energy, in fact, the potential energy of waves, in terms of energy transport, is about five times higher than the one generated by the wind and 10 ÷ 30 times higher than solar one. Over the years a wide range of Wave Energy Converters (WEC) has been developed, and more than one thousand of prototypes among Japan, North America and Europe (Clément et al., 2002) has been installed. As it is known, steel is the main ship construction material, which over the years has been improved in its mechanical characteristics. Such a material has no processing problems, but presents high costs of maintenance. In order to overcome the maintenance costs of WECs ferrocement can be used as hull construction material. In this paper, a case study regarding the redesign in ferrocement of the ISWEC, which is a WEC built by "Wave for Energy" a spin off Company of the Politecnico di Torino and installed offshore from Pantelleria, is presented.

### 2. Wave Energy Converters

The classification of WECs can be done according to both the distance from the shore of the installation location and its working principle. Considering the distance, they can be:

- *Onshore devices:* installed on the seabed in shallow waters, or integrated into breakwaters or cliffs.
- *Nearshore devices:* installed in moderate water depths (10 ÷ 25 m) a few hundred meters from the shore, can be either floating structures or rested on the seabed without mooring.
- *Offshore devices:* installed in deep water (> 40 m), are floating or submerged structures moored to the seabed. These are the devices exploiting the more powerful waves far from the shore.

---

<sup>\*</sup> Aggr. Prof. Vittorio Bucci: Dept. of Engineering and Architecture, University of Trieste, via Valerio 10; 34127, Trieste; I, vbucci@units.it

<sup>\*\*</sup> Assoc. Prof. Alberto Marinò: Dept. of Engineering and Architecture, University of Trieste, via Valerio 10; 34127, Trieste; I, marino@units.it

<sup>\*\*\*</sup> Ir. Francesco Mauro: Dept. of Engineering and Architecture, University of Trieste, via Valerio 10; 34127, Trieste; I, fmauro@units.it

<sup>\*\*\*\*</sup> Ing. Cristiano Sandron: Dept. of Mechanical and Aerospace Engineering, Politecnico di Torino, Corso Duca degli Abruzzi, 24; 10129, Torino; I, cristiano.sandron@marefvg.it

<sup>\*\*\*\*\*</sup> Assoc. Prof. Giuliana Mattiazzo: Dept. of Mechanical and Aerospace Engineering, Politecnico di Torino, Corso Duca degli Abruzzi, 24; 10129, Torino; I, giuliana.mattiazzo@polito.it

If the working principle is considered the WECs can be collected as follows:

- *Attenuators*: use the oncoming waves energy to induce an oscillatory motion between two (or more) adjacent structural components. The energy can be captured by hydraulic motors or direct drive Power Take Off (PTO).
- *Point absorbers*: are floating structures that can absorb energy from all directions. They use buoyant forces to induce heaving motion of the top body with respect to the fixed base. The base can be moored to the seabed, or held in place by gravitational forces through a large foundation mass.
- *Oscillating wave surge converters*: energy is obtained from the wave motion and the movement of water inside the device by means of an arm mounted on a pivot coupling that swings like a pendulum.
- *Oscillating water columns*: the wave generates a water column oscillating inside a closed vessel and compresses the contained air, which in turn moves a turbine connected to an electric generator.
- *Overtopping/terminator devices*: the device is floating or fixed to the shore. They have a reservoir which is filled by overtopping waves, so accumulating potential energy. Then the water is released back to the sea through a conventional low-head turbine coupled with an electric generator.
- *Submerged pressure differential devices*: attached to the seabed, have a top component, which rises and falls when waves move over it, so capturing energy from the hydrodynamic pressure changes.
- *Rotating mass devices*: electricity is produced by the rotation of an eccentric mass or a gyroscope connected to an electric generator inside a floating device oscillating with waves.

### 3. Inertial Sea Wave Energy Converter (ISWEC)

ISWEC (Bracco et al., 2011) is an *active* floating system where pitch motion produces electric energy by means of a gyroscope. The system is defined *active* because it requires the presence of a rotating mechanical member powered by an electric motor. The energy produced by an ISWEC can be estimated equal to 250 MWh/year, with a saving of 68 t of CO<sub>2</sub> if the same energy had been produced by fossil fuels. Therefore, considering that the average consumption of a family is about 3000 kWh/year, a single device would be able to meet the energy needs of more than 50 families (Bracco et al., 2015). Currently, the hull of ISWEC system contains two 130 kW gyroscopic groups having a mass equal to 25 tons each. The steel hull has the following dimensions.

Tab. 1: Main dimension ISWEC

Main Dimension	
Length	15.33 m
Width	8.04 m
Depth	4.5 m
Draft	3.25 m
Displacement	313 t

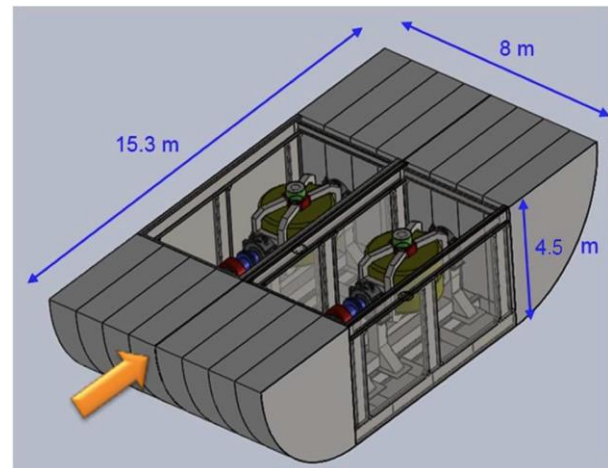


Fig. 1: ISWEC.

### 4. Ferrocement

Ferrocement is a composite material consisting of mortar reinforced by a number of steel wire meshes and bars. The mechanical properties of such a composite material are determined by the individual properties of matrix (mortar) and reinforcements (meshes and bars).

The mortar used for ferrocement is a mixture of cement, additives, aggregates and water. The cement must comply with either the ASTM C150-85a (Portland cement), the ASTM C 595-85 (blended hydraulic cement), or other equivalent Standards. Mineral additives, such as Pulverised Fly Ash (PFA), silica fume or blast furnace slag, may be used in order to improve workability and long-term mechanical properties

(Housing and Building Research Institute, 2015). If mineral additives are used, they must be in accordance with either ASTM C 618-85 or ASTM C 989-85a Standards. The aggregate used for ferrocement is sand, which must comply with the ASTM C33-86 Standard or equivalent. The maximum sand particle size depends on the constructional criteria, i.e., the size of the metal meshes and the distance between them. However, the most used sand size is the Sieve Number 16 (equivalent to 1.19 mm). The suggested mix proportion ranges of mortar for ferrocement are: sand-cement ratio by weight  $1.4 \div 2.5$  and water-cement ratio by weight  $0.3 \div 0.5$  (Balaguru et al., 1997). In most cases, the compression resistance evaluated by a cylindrical test after 28 days of curing, it was found to be not less than  $35 \text{ N/mm}^2$ .

The reinforcing mesh can be of different kinds, but the main required property is the flexibility. The meshes most commonly used are:

- *Hexagonal wire mesh*, is the most easy and cheap to be used, but is not efficient as much as meshes with square opening, because the wires cannot be oriented along the direction of tensions.
- *Square welded wire mesh*, is more rigid than the previous reinforcement and has got an increased resistance to cracking.
- *Square woven wire mesh*, is similar to the previous one, but is a bit more flexible and easy to work.
- *Expanded metal lath*, has the same strength of the welded mesh, but is stiffer, providing greater resistance to impact and a better control of cracking. It is difficult to be used in corners.
- *Bars*, may be used in combination with wire mesh, complying with ASTM A615-86, A616-86 or A617-84. Bars must be made of steel with minimum yield strength  $410 \text{ N/mm}^2$  and tensile strength  $615 \text{ N/mm}^2$ .
- *Fibers*, added to the mortar mix, are short steel wires or other fibrous materials used to control cracking and to increase impact resistance.

The substantial difference between reinforced concrete and ferrocement is the presence in the latter of steel wire meshes. As findings of experiments (Alwash, 1982) comes out that both crack spacing and width decrease with a greater number of wire meshes layer, Fig. 2. Moreover, by ferrocement it is possible to reduce the thickness of plates with respect to reinforced concrete.

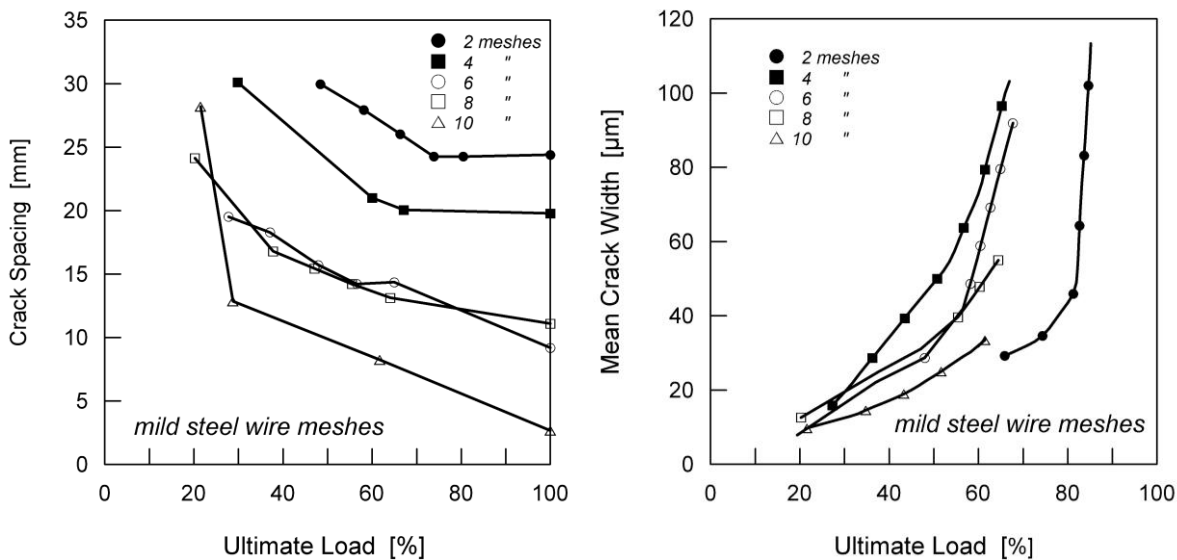


Fig. 2: Spacing and width of cracks vs percentage of the ultimate load.

## 5. Case study

The main advantages in using ferrocement in shipbuilding are the low costs of raw materials, the low level of skills required for manufacturing and the reduced maintenance due to the good resistance to rot and corrosion. Despite these advantages, currently ferrocement has found few applications in shipbuilding (mainly fishing vessels and pleasure crafts), consequently also the building regulations are few and quite dated (ABS, 1969). However, there is an evidence of their application in 1995 in relation to a FAO project for the construction of small fishing boats in India (Riley, 1995). In the early stage of the redesign

of ISWEC in ferrocement has been used the guide for scantling of fishing boat reported in the above-mentioned FAO Technical Paper. Such a guide is valid for crafts having frame spacing in the range 600÷700 mm and mesh size between 18÷22 gauge. In particular, for a craft about 15 m long comes out a minimum thickness for hull and deck equal to 30 mm, 6 layers of square welded wire mesh (size  $13 \times 13$  mm and wire gauge 19), longitudinal and transversal reinforcing rods with diameter 6 mm and spacing 50 mm. Fig. 3 shows the scantling plans of the ISWEC.

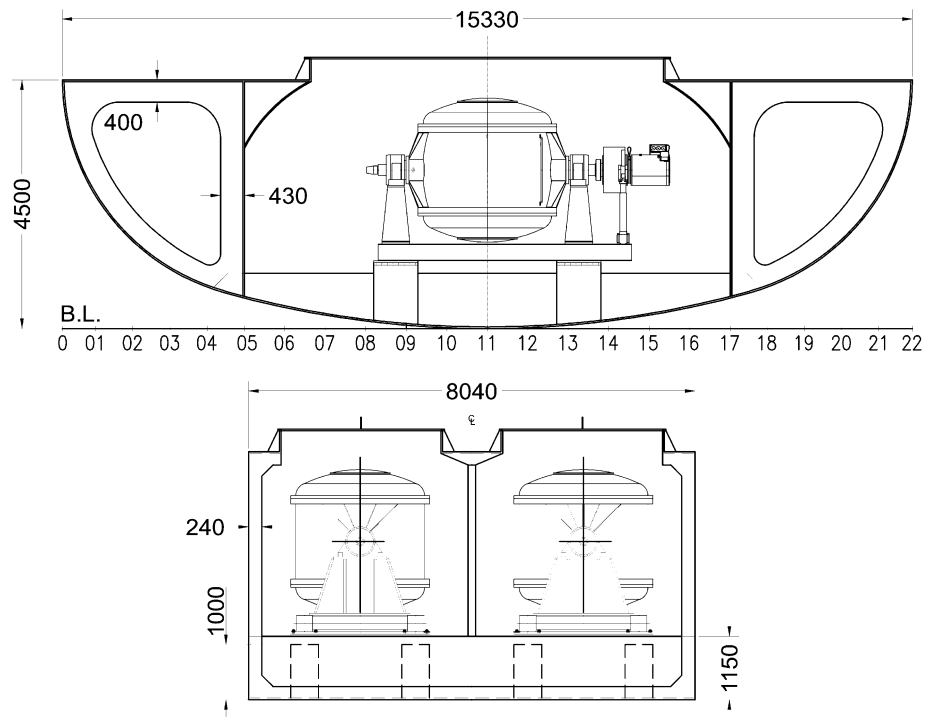


Fig. 3: Longitudinal and transversal sections of ISWEC in ferrocement.

## 6. Conclusions

Renewable energy from the sea represents a promising technological trajectory of European Development Strategy until 2030, aimed at reducing the greenhouse gas emissions by the use of conversion devices like the WECs. Great attention must be paid on the WECs construction, taking into account that they are constantly exposed to harsh marine environment and that it is to minimize the maintenance costs. Ferrocement, as hull construction material, would seem able to meet such requirements as well as low first costs and low skill capacity. In the case study presented the hull weight turns to be greater (196 t) than the steel solution (63 t), but this is not a problem because the ballast can be reduced without compromising the performance of the device in terms of centre of gravity and total mass displacement.

## References

- ABS (1969) Guidelines for the construction of ferrocement vessels.
- Alwash, A. (1982) Flexural behaviour of ferrocement, University of Sheffield.
- Balaguru, P. N. et al. (1997) State of the art report on ferrocement, Reported by ACI Committee 549.
- Bracco, G., Giorcelli, E. and Mattiazzo, G. (2011) ISWEC: a gyroscopic mechanism for wave power exploitation. Mechanism and Machine Theory, vol. 46, no. 10, pp. 1411-1424.
- Bracco, G., Giorcelli, E., Giorgi, G., Mattiazzo, G., Passione, B., Raffero, M. and Vissio, G. (2015) Performance assessment of the full scale ISWEC system, in. Proc. of the IEEE International Conference on Industrial Technology 2015, pp. 2499-2505.
- Clément, A. et al. (2002) Wave energy in Europe: current status and perspectives. renew. sust. energy rev., pp. 405-431.
- Housing and Building Research Institute, (2015), Bangladesh National Building Code, Vol. 2 of 3.
- Riley, R. and Turner, J. (1995), Fishing boat construction: building a ferrocement fishing boat, FAO Fisheries Technical Paper n. 354.

## MODELLING OF STANDARD FIRE TEST

**K. Cabová<sup>\*</sup>, N. Lišková<sup>\*\*</sup>, P. Novotná<sup>\*\*\*</sup>, M. Benýšek<sup>\*\*\*\*</sup>, F. Zeman<sup>\*\*\*\*\*</sup>, F. Wald<sup>\*\*\*\*\*</sup>**

**Abstract:** *The paper describes an application of Computational Fluid Dynamics to the simulation of a furnace for fire-resistance tests following standard fire conditions. The model is based on an accurate representation of a real fire furnace of fire laboratory PAVUS a.s. located in the Czech Republic. It includes geometry of the real furnace, material properties of the furnace linings, burners, ventilation conditions and measurement devices. The model allows controlling of gas temperature and the static over pressure in the volume of the furnace as it is specified in requirements of European standard for fire resistance tests. The accuracy of the model is validated on results of a fire test executed in a horizontal furnace. The results of the virtual furnace illustrate the great potential for investigating the thermal behaviour of fire-resistance tests.*

**Keywords:** Fire-resistance test, Numerical model, Virtual furnace, FDS, Furnace.

### 1. Introduction

Testing by standard fire test is a common method of obtaining fire-resistance rating of structural elements, see (Buchanan, 2001). Fire resistance of a structural element is quantified as the time for which the element can meet certain criteria during exposure to a standard fire-resistance test. Despite fire-resistance tests are very common they can be quite time consuming regarding their planning, preparation and analysis of results of a test. The cost of the test is also very high. Because of these drawbacks, numerical model of a horizontal furnace is developed. The model takes advantage of great possibilities of Computational Fluid Dynamics (CFD) code Fire Dynamics Simulator (FDS).

First attempts to apply CFD modelling in standard testing are described in (Welch et al., 1997, Cayla et al., 2011, Auguin et al., 2013 and Cuffe et al., 2014).

### 2. Fire resistance furnace

A horizontal furnace of fire laboratory PAVUS a.s. of dimensions 3.0 m x 4.0 m and 2.2 m high was chosen. The furnace is heated by 8 natural gas burners. Flue gas exhaust system is performed using a frequency fan placed in a conduit which is connected to the opening (500 mm x 800 mm) in the floor of the furnace. Ground plan and vertical section of the furnace are shown in Fig. 1a and Fig. 1b. Then, there is a sensor to control the furnace pressure and 14 holes 100 mm below the ceiling to place plate thermometers. The plate thermometers cooperate with gas burners and regulate the temperature inside the furnace. Walls of the furnace are made of blocks and mats of fire-resistant ceramic fibers, with the total thickness of 230 mm. Floor is composed of bricks of thickness of 256 mm. The ceiling may be closed by concrete panels or by a steel welded structure insulated with ceramic fibers.

---

<sup>\*</sup> Ing. Kamila Cábová, PhD.: Department of Steel and Timber Structures, Faculty of Civil Engineering, Czech Technical University in Prague, Thákurova 7; 166 29, Prague; CZ, kamila.cabova@fsv.cvut.cz

<sup>\*\*</sup> Ing. Nikola Lišková: Department of Steel and Timber Structures, Faculty of Civil Engineering, Czech Technical University in Prague, Thákurova 7; 166 29, Prague; CZ, nikola.liskova@fsv.cvut.cz

<sup>\*\*\*</sup> Ing. Petra Novotná: Faculty of Civil Engineering, Czech Technical University in Prague, Thákurova 7; 166 29, Prague; CZ, petra.novotna.1@fsv.cvut.cz

<sup>\*\*\*\*</sup> Ing. Martin Benýšek: Department of Concrete Structures, Faculty of Civil Engineering, Czech Technical University in Prague, Thákurova 7; 166 29, Prague; CZ, martin.benysek@fsv.cvut.cz

<sup>\*\*\*\*\*</sup> Bc. Filip Zeman: Faculty of Civil Engineering, Czech Technical University in Prague, Thákurova 7; 166 29, Prague; CZ, filip.zeman@fsv.cvut.cz

<sup>\*\*\*\*\*</sup> Prof. Ing. František Wald, CSc.: Department of Steel and Timber Structures, Faculty of Civil Engineering, Czech Technical University in Prague, Thákurova 7; 166 29, Prague; CZ, wald@fsv.cvut.cz

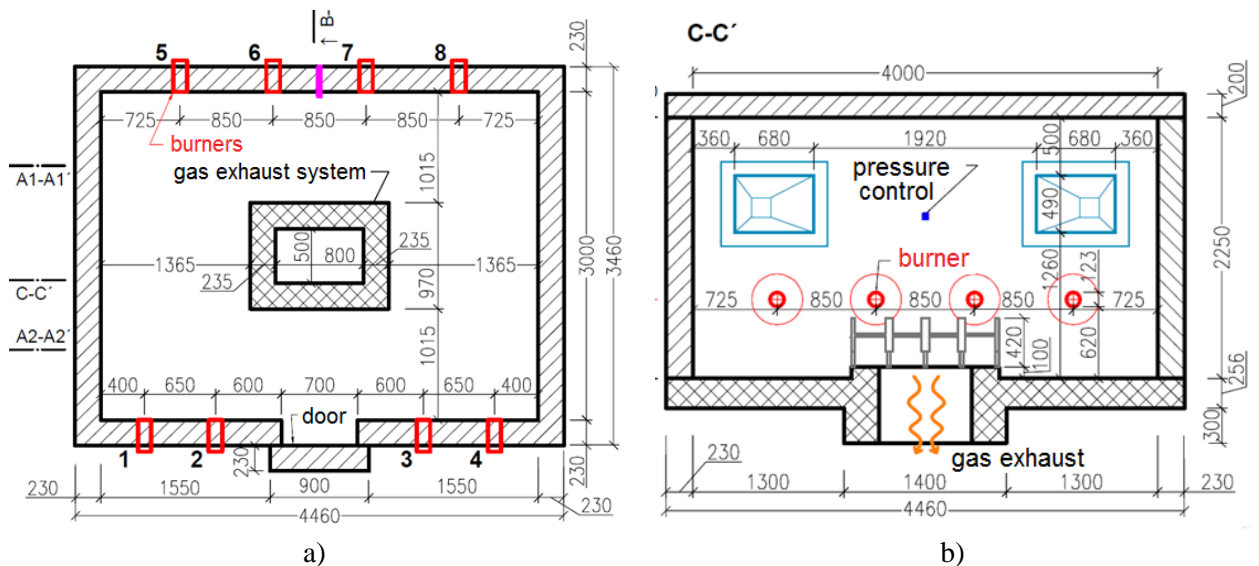


Fig. 1: a) Ground plan of the furnace; b) Section of the furnace.

For standard fire testing it is important to meet requirements of European standard EN 1363-1:2013, which defines the conditions of fire resistance tests. Two constraints must be achieved in the real furnace as well as in the model:

1. The average temperature in the furnace is monitored and controlled to follow the relationship:

$$T = 345 \log_{10} (8t + 1) + 20 \quad (1)$$

with T is the average temperature in °C, t is time in min.

According to Czech standard CSN EN 1363-1 tolerances for the temperature distribution in the furnace may vary up to  $\pm 100$  °C.

2. The furnace pressure relative to the pressure outside the furnace at the same height must be constantly monitored. The pressure in the furnace should not exceed 20 Pa. Sensor placement and the requirements for it are given in standard EN 1363 - 1.

## 2.1. Model of the furnace

The model is created in the computational fluid dynamics code FDS (Fire Dynamics Simulator) version 6.4.0 (McGrattan et al., 2013). Geometry of the furnace, material properties of furnace linings, burners and ventilation conditions are created to correspond to the horizontal furnace of fire laboratory PAVUS a.s. described above.

Considering dimensions of the real furnace, time needed for numerical solution and sufficient level of accuracy of results, mesh size of 250 mm x 250 mm x 250 mm was selected. In the bottom part of the model the mesh is enlarged to simulate the conduit of the gas exhaust system, see Fig. 2a. In reality a hole leading into the conduit is protected with welded steel structures, while in the model there is a steel plate placed 250 mm above the hole. The plate can be seen in Fig. 2a. In Fig. 2a burners and niches of four visors may be also observed.

Material properties of the furnace linings are taken from data sheets of manufacturers. These include: density, specific heat capacity and thermal conductivity of high alumina bricks, thermally insulating bricks, calcium silicate boards, blocks of refractory ceramic fibres, steel and insulating refractory concrete. For detailed material properties see (Novotná, 2017 and Lišková, 2017).

In the model burners are simulated as eight square surfaces of type VENT of dimension 250 mm x 250 mm, which are located 0.5 m above the floor. The fuel in the real furnace is composed of the mixture of natural gas and air, just as it is in the case of virtual furnace, with the prescribed reaction of burning of this mixture. Power of the burners in the model is gradually increased in dependence on time according to the power of burners measured in a pilot fire test. In the model it is defined by a ramp function of heat



release rate per surface area (HRRPUA). Details of reaction of burning and power of the burners are given in (Novotná, 2017 and Lišková, 2017).

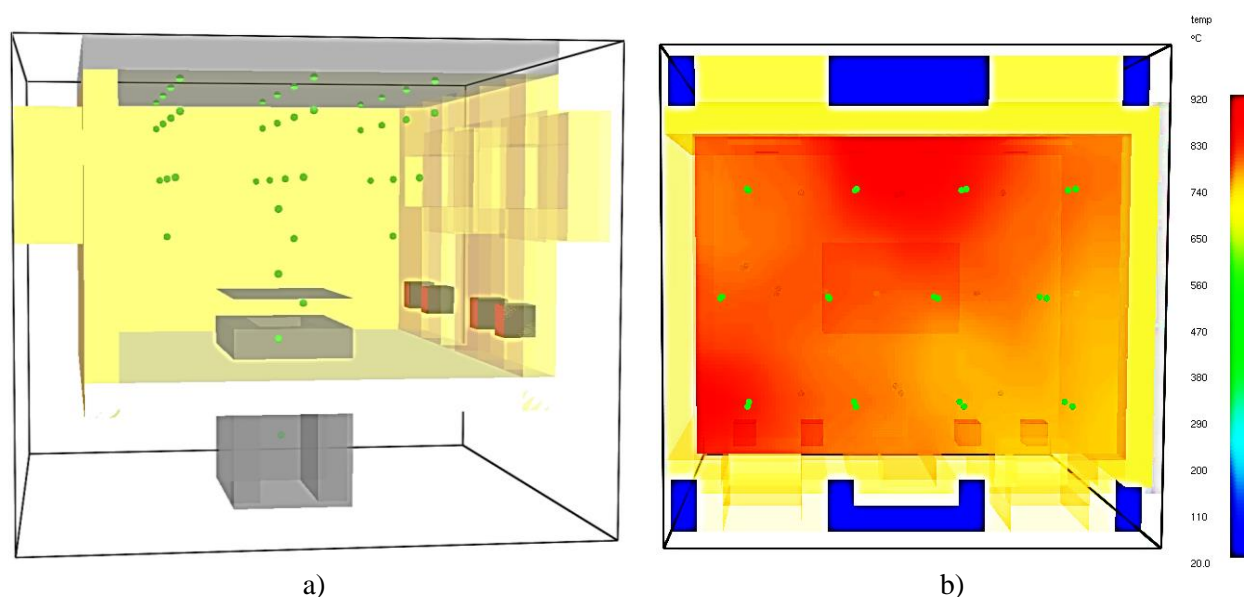


Fig. 2: a) Model of the furnace; b) Temperature resolution 100 mm below the ceiling in 15 min.

Unlike in the real furnace ventilation system in the model is simulated only by the rectangular concrete conduit with an opening at the border of the computational domain. This opening is created as a VENT of type OPEN, which allows natural exhaust of gases.

In the model gas temperature is calculated by devices of type THERMOCOUPLE and ADIABATIC SURFACE TEMPERATURE which allow later comparison with gas temperature measured during the fire test at coated thermocouples and plate thermometers. In visualization of the model location of temperature devices are displayed as green points, see Fig. 2a and Fig. 2b. Pressure in the virtual furnace is also calculated to control the requirement of EN 1363 – 1.

## 2.2. Results and validation

Spatial resolution of gas temperature below the ceiling of the virtual furnace in 15 min of the calculation is presented in Fig. 2b. A gradient in red colour indicates non-uniform temperature resolution ranging from 700 °C to 750 °C. Development of average gas temperature calculated from all devices simulating plate temperatures (PT), which were placed 100 mm below the ceiling, is shown in Fig. 3a. The development is compared with the standard temperature curve according to EN 1363 - 1. Based on the diagram it may be stated that after 5 min the temperature is within the acceptable tolerance given in EN 1363 – 1 ( $\pm 100$  °C).

The furnace pressure calculated in the virtual furnace is compared to development of the pressure during the real fire test in Fig. 3b. Before 5 min big fluctuation may be observed. Then, the pressure evolution in the real furnace is maintained around level of 20 Pa. Despite this, in the model values are higher in range from 5 Pa to 10 Pa. This may be caused by simplified attitude of ventilation in the model. When improving the gas exhaust system with addition of forced vent, the temperature evolution in time may be in better correlation.

## 3. Conclusions

The paper presents the model of the horizontal furnace for fire-resistance tests. The model allows controlling gas temperature and the static over pressure in the volume of the furnace, so it can meet the requirements of European standard EN 1363-1:2013, which defines the conditions for fire resistance tests.

The accuracy of the model is validated to fire test executed in the horizontal furnace of fire laboratory PAVUS a.s. located in Czech Republic. The test of empty horizontal furnace helped to adjust the burners and check the total functionality of the model.



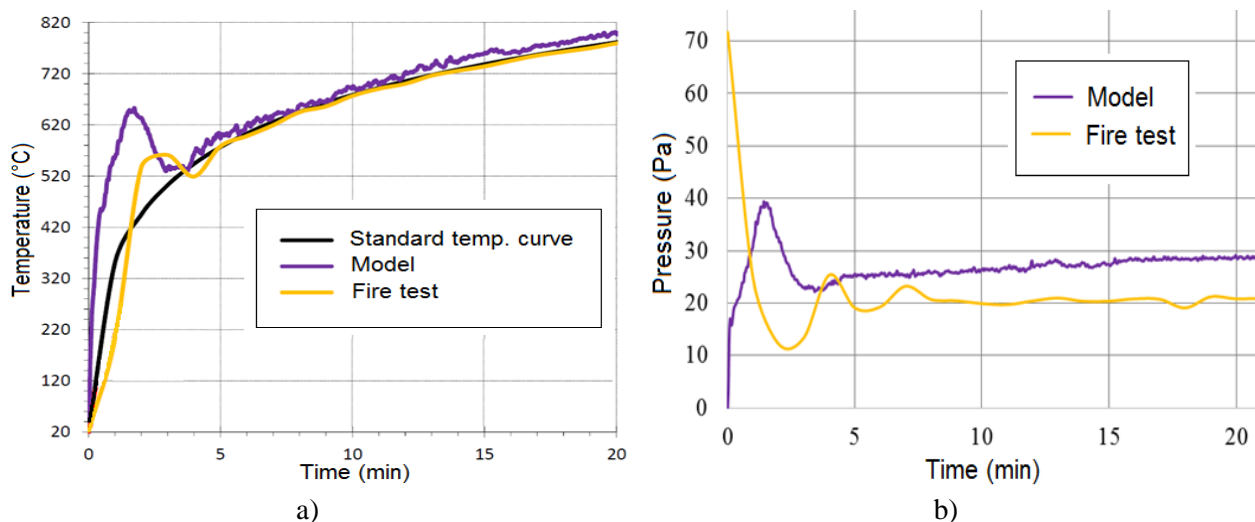


Fig. 3: a) Gas temperature development 100 mm below the ceiling in the virtual furnace;  
b) Comparison of pressure in the virtual furnace and the fire test.

Certainly, further development is needed to improve the model. Namely, to improve the system of ventilation – in the real furnace a frequency fan placed in an exhaust duct draws hot gases out. Natural flue gas exhaust, which is used in this model, is not sufficient and therefore the pressure in the furnace is too high. Another point of planned improvement lies in material testing. These tests should provide accurate values of physical properties of materials that are used in the furnace. Finally, it is necessary to study sensitivity of mesh density in the model. With improved ventilation system, accurate material properties and finer mesh, more accurate results may be achieved.

In conclusion, the virtual furnace has a great potential for investigating the thermal behaviour of fire-resistance tests. A huge advantage inheres in the evaluation of the thermal effect throughout the volume of the furnace, which allows an accurate prediction of fire-resistance tests and evaluation of large number of technical alternatives and boundary conditions. It may be also used for optimization of settings of the real furnace in order to reach as uniform temperature resolution across the volume of the furnace as possible.

### Acknowledgement

Research presented in this paper was supported by project n. 16-18448S in the frame of Czech science foundation (GA CR).

### References

- Auguin, G., et al. (2013) FLACOMARE, Fire resistance of composite materials: Application to a sandwich panel, 21st French Congress on Mechanics, Bordeaux, France (in French).
- Buchanan, A. H. (2001) Structural Design for Fire Safety. University of Canterbury, New Zealand.
- Cayla, F., Leborgne and H., Joyeux, D. (2011) Application of a virtual resistance furnace: fire resistance test simulation of a plasterboard membrane, Proc. of ASFE Conf., Prague, pp. 343-348.
- Cueff, G., et al. (2014) Thermomechanical behaviour of cellulose-based materials: application to a door under fire resistance test, Proc. of Conf. on Structures in Fire, Shanghai, pp. 1055-1062.
- Lišková, N. (2017) Adiabatic surface temperature in horizontal furnace, Diploma thesis, Czech Technical University in Prague (in Czech).
- McGrattan, K., et al. (2013) Fire Dynamics Simulator (Version 6) - User's Guide. Gaithersburg, Maryland, USA: National Institute for Standards and Technology, Special Publication 1019 - Sixth Edition.
- Novotná, P. (2017) Modelling of fire test in furnace, Diploma thesis, Czech Technical University in Prague (in Czech).
- Welch, S. and Rubini, P. (1997) Three-dimensional Simulation of a Fire-Resistance Furnace, Fire Safety Science – Proc. of the Fifth International Symposium, Melbourne, Australia, pp. 1009-1020.

## THE USE OF WELDING FOR FORMING FEAL COATING ON S235

**J. Cebulski<sup>\*</sup>, R. Bęczkowski<sup>\*\*</sup>, D. Pasek<sup>\*\*\*</sup>**

**Abstract:** Implementation of new materials into industrial practice allows to build more durable and reliable machine parts suitable to operate at high temperature and other special conditions. The paper analyzes implementation of welding method to make intermetallic surface Fe40Al5CrTiB on material grade S235JR. The process was made with tungsten inert gas (TIG) and with the use of reserved polarity direct current (DC-). Welded sample was made as: single bead, multi bead and as multilayer. After the welding process, samples were tested with geometric measurement, Vickers hardness (HV), light microscopy (LM) and scanning electron microscopy (SEM). This technology can be used to develop resistance surfaced in the power industry in the future.

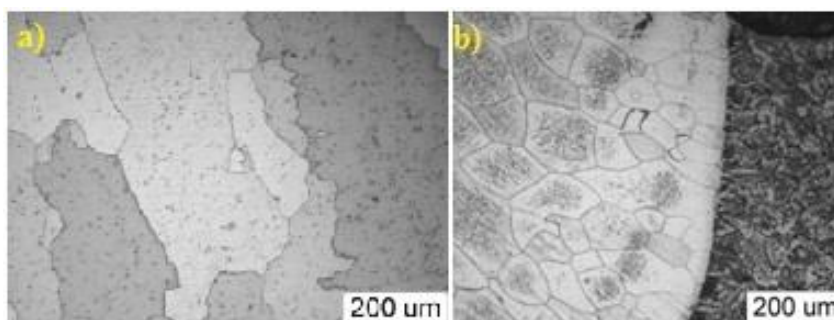
**Keywords:** Coating, FeAl, Intermetallic, Imperfection, TIG.

### 1. Introduction

Currently, in order to increase the lifespan of equipment used outside special working surfaces welded with electrodes or wires of specifications are applied. Surfacing is one of the modern processes of machines parts and devices regeneration. Obtaining layer material that fulfils the criteria specified for the construction will meet the market demand, thereby it can solve the problem of their durability. The innovatory method of obtaining the coating of improved properties is modifying the surface layer by welding wire made of alloy based on intermetallic phase Fe40Al5Cr0,2TiB. Changing the properties of the material depends on the dimensions (thickness) of the welded layer. The alloys based on intermetallic phase matrix FeAl are characterized by very good resistance to high-temperature corrosion, and also good corrosion resistance in both oxidizing and carburization atmosphere and in sulfur-containing compounds.

The alloys based on intermetallic phase matrix FeAl have many advantages, for example low density, relatively low price of raw materials, and good resistance to oxidation. There are also some disadvantages, like the lack of ductility at ambient temperature.

With the use of welding process intermetallic alloys FeAl properties can be changed. The Fig. 1 shows the microstructure alloy after crystallization (a) and after welding (b).



*Fig. 1: Microstructure of the Fe40Al5CrTiB alloy: a) additional material for cladding; b) after welding.*

<sup>\*</sup> Janusz Cebulski, PhD.: Faculty of materials engineering and metallurgy, Silesian University of Technology; Krasińskiego Street 8, 40-019; Katowice; PL, Janusz.Cebulski@polsl.pl

<sup>\*\*</sup> Robert Bęczkowski, PhD.: Institute of Mechanical Technology, Częstochowa University of Technology, Armii Krajowej Street 21; 42-201, Częstochowa; PL, rbeczkowski@spaw.pcz.pl

<sup>\*\*\*</sup> Dorota Pasek, MSc.: Faculty of materials engineering and metallurgy, Silesian University of Technology; Krasińskiego Street 8, 40-019; Katowice; PL, Dorota.Pasek@polsl.pl

## 2. Methods

Material used in the research consists of Fe40Al5CrTiB alloy samples after crystallization. The chemical composition of the alloy is shown in Tab. 1

Tab. 1: Chemical composition of the Fe40Al5Cr0.2TiB alloy.

Fe40Al5Cr0.2TiB	Fe	Al	Cr	Ti	B
% mass	68.21	23.66	5.77	0.15	0.015

The paper analyzes implementation of welding method to make intermetallic surface Fe40Al5CrTiB on material grade S235JR. Welding process was conducted by tungsten inert gas (TIG). Parameters of welding process were described in Tab. 2 with the use of reserved polarity direct current (DC-).

Tab. 2: Parameters of welding process.

TIG	Thickness [mm]	Shielding gas	Current [A]	Flow rate [l/min]	Position of welding	Welding speed [mm/s]
DC- WTh 2,4	5	Argon II	100	10	PA, Flat -Down hand	1.0 - 2.5

Tests were made for a single bead (SB), multi bead (MB) and multilayer (ML). Fig. 2 shows location of the bead.

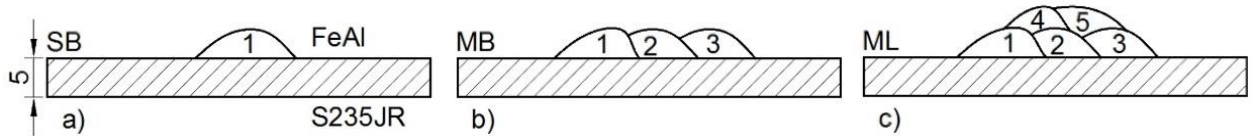


Fig. 2: Hardness distribution of the distance from the top surface of the bead.

Alloy microstructure based on intermetallic phase FeAl after welding process was analyzed by light microscope OLYMPUS GX51. The tests were made for three samples: single (SB), multi bead (MB) and multi layer (ML).

Processing of welding alloy matrix intermetallic FeAl removes casting defects (Fig. 3) but not completely. On the cross-section surface of intermetallic bead some imperfection of welding was seen. Fe-Al intermetallic alloy on S235JR steel is characterized by microstructure of columnar grains occurring in the zone from the melting point and by the presence of equilateral grains in the outer part of the clad.

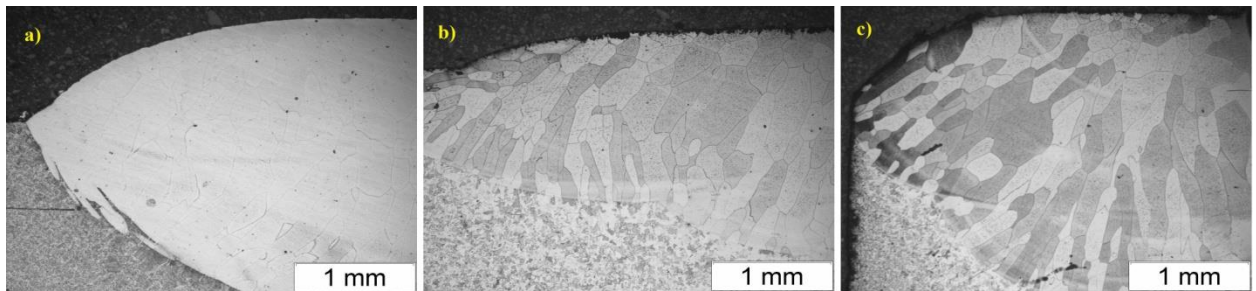


Fig. 3: View of welding samples with imperfection.

Hardness measurement was conducted on cross-section material. Hardness was measured with Vickers method according to a norm PN-EN ISO 6507-1 with a load 9.81 N (HV1) the device type ZWICK.

The Fig. 4 shows the results of hardness distribution HV1 measurement for specimens: SB, MB, ML.

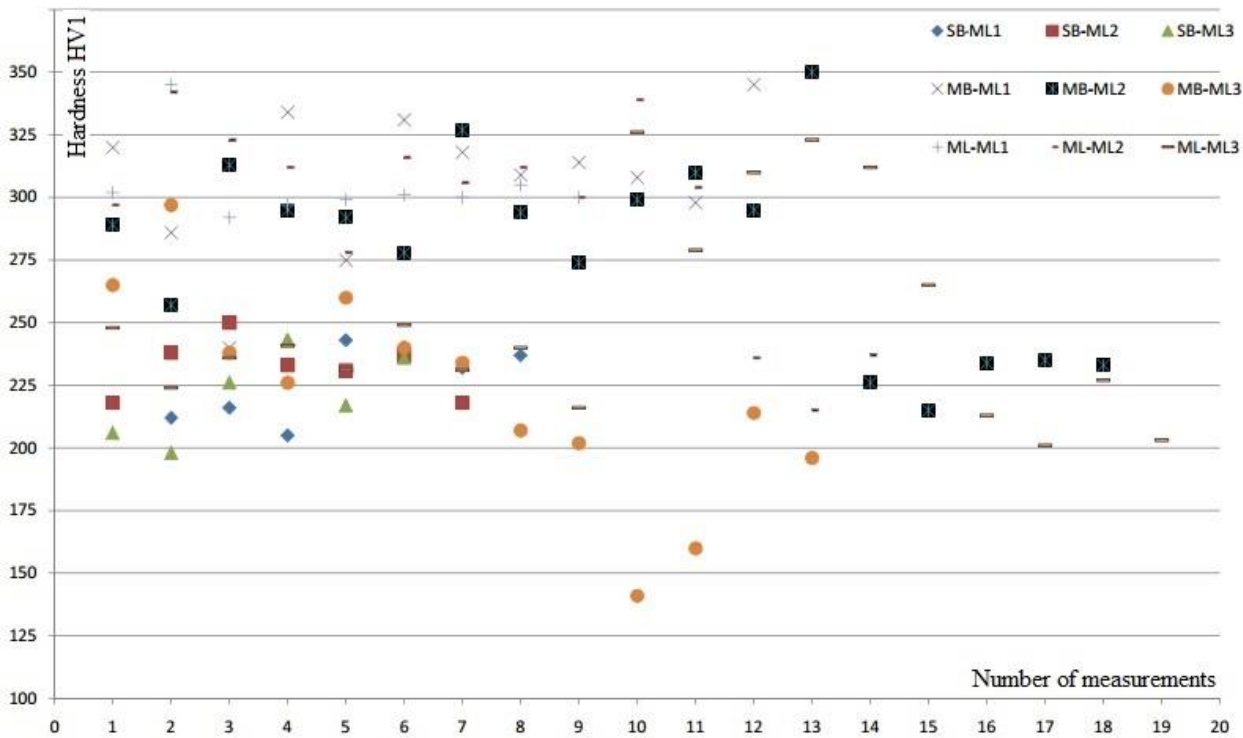


Fig. 4: View of hardness distribution from the parent material to the top of the bead.

Metallographic tests were conducted on polished micro-sections etched in ferric chloride. Microstructure observations were conducted with the use of metallographic microscope Olympus GX51.

Fig. 5 shows the coating structure for single bead (SB) (Fig. 5a), multi bead (MB) (Fig. 5b) and multi layer (ML) (fig.5c).

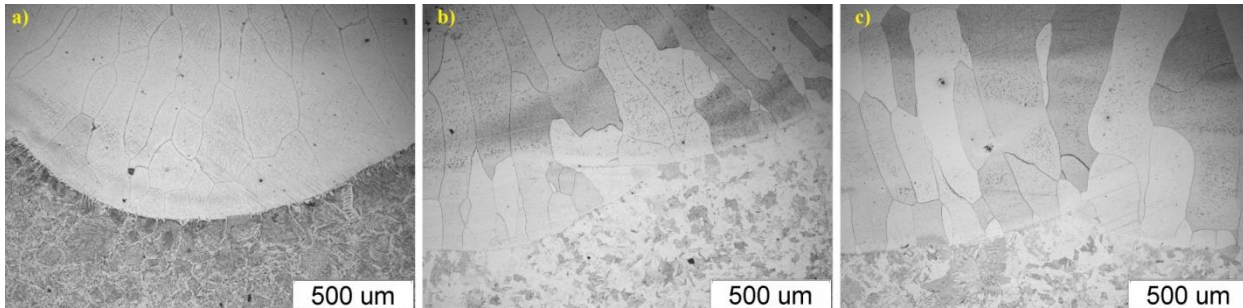


Fig. 5: Microscopic view fusion line of clad.

The chemical composition was determined by X-ray microanalysis EDS using a scanning electron microscope equipped with a Hitachi S4200 ray EDS detector. Fig. 6 shows the SEM surface analysis coating layers, in which, based on studies the presence of Al, Si, Cr, Fe is shown. Tab. 1 shows chemical analysis of intermetallic layers FeAl. Observations made using a scanning electron microscope of the deposit FeAl intermetallic alloy showed a coarse-grained structure of the weld layer and a clear line of separation of the base material and weld material (FeAl). The study of the chemical composition made with X-ray microanalysis EDS method showed reduced content of aluminium in the weld pad and unchanged chemical composition of the steel in the heat affected zone. The content of aluminium in the weld pad is 12 - 20 at %, indicating a substantial aluminium evaporation when melting during welding. The reduction in aluminium content of less than 37 at % results in formation of  $\text{Fe}_3\text{Al}$  intermetallic alloy. Conducting the welding with reserved polarity direct current (100 A), intermetallic alloy  $\text{Fe}_{40}\text{Al}$  obtained welding layer  $\text{Fe}_3\text{Al}$  has different properties from the alloy used for welding. Despite the good corrosion resistance in high temperature compared to heat resisting steels, the corrosion resistance of FeAl intermetallic alloy is much higher.



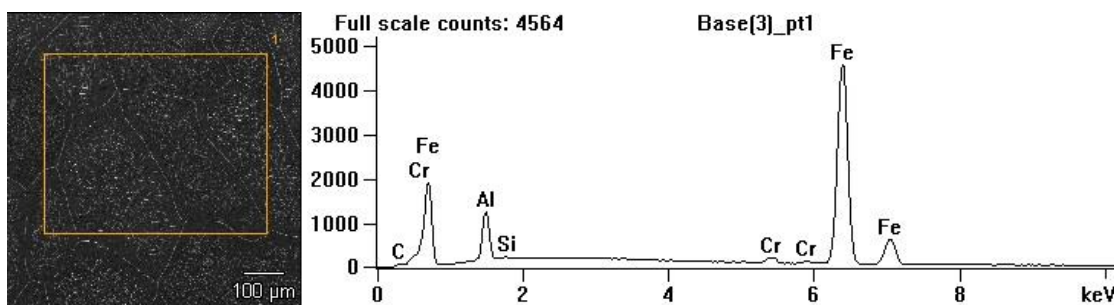


Fig. 6: SEM analysis of the microscope together with an indication of the chemical composition.

Tab. 1: Number of Weight % (a) Number of Atom % (b).

(a)	Al	Si	Cr	Fe	(b)	Al	Si	Cr	Fe
	6.1	0.2	1.3	92.3		11.8	0.4	1.3	86.4

### 3. Conclusions

Microstructure of the Fe40Al5CrTiB alloy was changed after welding process. The microscopic grains grew and formed a coarse-grained structure of the material. Gas tungsten arc welding process is possible to make intermetallic surface FeAl. The test results show, that DC current can be used to burn this kind of material, but in cross section of pad several kinds of welding imperfection can be seen, such as pores, lack of fusion. This kind of imperfection is located on or near to fusion line. While making multi bead or multi layer this kind of imperfection is reduced. The imperfection occurs only in the first layer. Next bead or layer was without this kind of defects. Hardness distribution is checked in several line and results of these test show that; if it is the first or the last bead, the hardness is about 200 to 250 HV1; if there is more than one bead the hardness increases from 275 to 350 HV1. Observing by light microscopy (Fig. 4), it can be concluded that the microstructure of the weld layer of an alloy based on intermetallic phase FeAl has a heterogeneous grain size. In the boundary fused, where the speed of heat dissipation is larger, columnar crystals crystallize, whereas above they form more equated grains. This phenomenon is related to the conditions of crystallization of the weld layer. Grain between successive bead was melted and combined.

The welding layer made of an intermetallic alloy FeAl is characterized by coarseness and reduced aluminium content comparing to the content of this element in the material used for welding. The welding layer is homogeneous without the presence of welding defects such as emptiness, or discontinuity on the border of fusion.

### References

- Bęczkowski, R. and Gucwa, M. (2016) Defects Appearing in the Surfacing Layers of Abrasion Resistant. Archives of Foundry Engineering, 16 ,4, pp. 23-28.
- Białucki, P. and Derlukiewicz, W. (2011) Surfing In the aluminium die-casting metal mould regeneration. Welding Technology Review, 10, pp. 44-49, (in Polish).
- Cebulski, J. and Lalik, S. (2010) Research of the structure welded of Fe-Al intermetallic phase based alloys. Welding Technology Review, 1, pp. 24-26, (in Polish).
- Cebulski, J., Fornalczyk, A. and Pasek, D. (2016) The kinetic of corrosion of the FeAl intermetallic phase-based alloys. Journal of Achievements in Materials and Manufacturing Engineering, 70, 2, pp.53-59.
- Dobrzański, L.A. (2002) Elementary material and metallurgy science. Gliwice, (in Polish).
- Kupka, M. (2005) Structure and properties of the FeAl phase based alloys obtained by metallurgical processing. Wyd. Uniwersytet Śląski, Katowice, (in Polish).
- Tasak, E., Ziewiec, A. and Parzych, S. (2011) The influence of the heat treatment on the properties of welded joints made with use of submerged arc welding and the GTAW method of the 7CrMoVTiB10-10 steel. Power welding Conference; pp. 179-188.
- Gontarz, G., Golański, D. and Chmielewski, T. (2013) Properties Fe-Al type intermetallic layers produced by AC TIG method. Advances in Materials Science, 13, 3 (37), pp. 5-16.
- Chmielewski, T. and Golański, D. (2011) The new method of in-situ fabrication of protective coatings based on FeAl intermetallic compounds. Proceedings of the Institution of Mechanical Engineers, Part B, Journal of Engineering Manufacture, 4, 225, pp. 611-616.

## AIRCRAFT WING FLUTTER ASSESSMENT CONSIDERING DAMAGE TOLERANCE - BASED FAILURE STATES

J. Čečrdle<sup>\*</sup>, J. Raška<sup>\*\*</sup>

**Abstract:** *This paper deals with aircraft wing flutter analysis considering the failure states, originated by the application of the damage - tolerance design philosophy on the wing structure. Such damages may influence the integral stiffness of a wing structure and, as a consequence, to influence its flutter characteristics. Therefore, airworthiness regulation standards require flutter analysis of these failure states. The paper presents the simple method of the wing stiffness transformation. The source model is the detailed static FE model, applicable to include the mentioned damages. Target model is the aeroelastic stick FE model, applicable for aeroelastic analyses. The method of assessment of the influence of damage on the wing flutter is shown. The methodology is demonstrated on the example of a commuter aircraft wing bending - torsional flutter. The method is applicable for compliance with FAR / CS 23.629(g)(h) requirements.*

**Keywords:** Aeroelasticity, Flutter, Damage Tolerance, Reglementary Damage.

### 1. Introduction

Aeroelastic flutter certification analyses of an aircraft structure must include the assessment of many parameters, which may influence flutter behaviour of a structure. Provided that the damage tolerance design philosophy is applied on a structure, the influence of specific failure states must be also analysed (FAR / CS 23.629(g)(h)). The reason is that damage tolerance assumes damages even on a new structure. Damages that are growing during an aircraft lifetime may then influence the integral stiffness of a structure and influence its flutter behaviour.

The proposed method of compliance is based on the usage of standard aeroelastic stick model with the modified stiffness characteristics. These modified stiffnesses are determined for the specific (so called reglementary) damages, representing the damages, which are large enough and cannot occur during an aircraft lifetime. Thus, the proposed approach is conservative. The modified characteristics are obtained from the detailed FE model used for static analyses. The method is good compromise taking into account the accuracy, necessary effort and available means, models and data.

### 2. Transformation of stiffness characteristics

Aeroelastic stick model, which is ordinarily used for flutter analyses include beam-like elements to model stiffness (vertical bending, in-plane bending and torsional) of structural parts (e.g., wing). Beam-like description, which is based on the slender beam theory, is applicable for the undamaged structure with the gentle changes in the spanwise stiffness. However, considering the failure states with the sharp changes in the stiffness between the undamaged section, damaged section and back, the slender beam theory is not applicable. Due to the damage, strain and stress distribution round about the damaged section are completely different, compare to the slender beam theory.

Therefore, the detailed model (Fig. 1) used usually for static analyses was used for determination of the damaged structure stiffness. Damages were modelled on the detailed shell element model (see example in Fig. 2). Then the static analyses under the unity load (vertical bending, in-plane bending and torsional) were performed.

---

<sup>\*</sup> Ing. Jiří Čečrdle, PhD.: Strength of Structures Dept., Aeronautical Research and Test Institute (VZLU), Beranovych 130; 199 05, Prague - Letnany; CZ, cecrdle@vzlu.cz

<sup>\*\*</sup> Ing. Jan Raška, PhD.: Strength of Structures Dept., Aeronautical Research and Test Institute (VZLU), Beranovych 130; 199 05, Prague - Letnany; CZ, raska@vzlu.cz

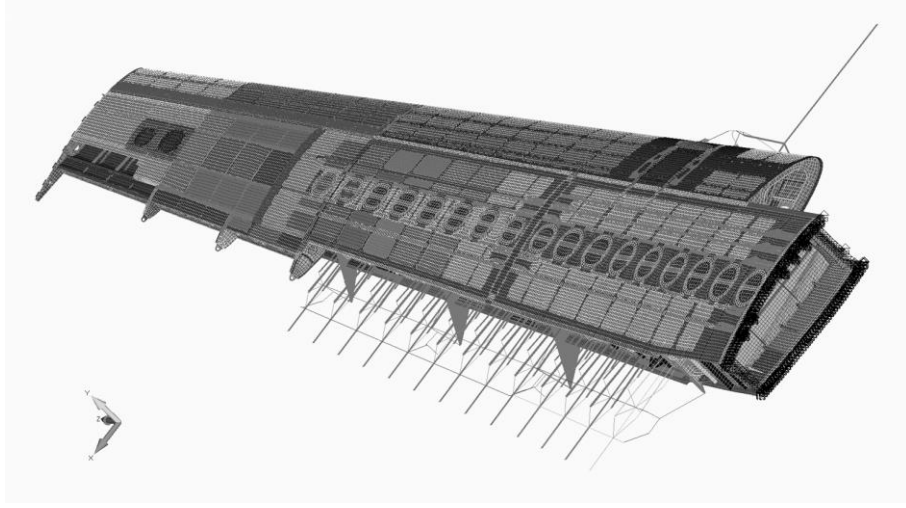


Fig. 1: Detailed static shell element FE model of a wing structure.

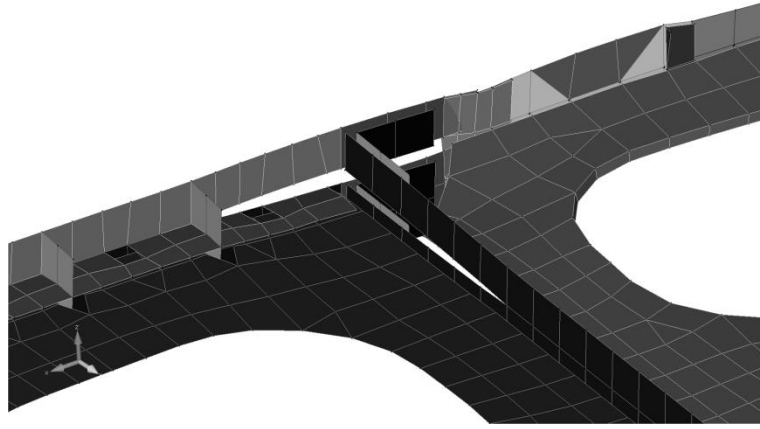


Fig. 2: Example of analysed damage - front spar damage (complete detachment of bottom flange, crack of web up to 1/3 of height), crack of skin under spar up to the closest stringer.

For the purpose of transformation to the stick model, displacements of the shear centre line are required. Therefore, the points of the appropriate sections were selected and the displacements (translational and rotational) were transformed using method of regression (root mean square method - RMS). This approach is applicable considering the slender beam theory deformation model, i.e., assuming the rigid section with no in-plane deformation and with no deplanation. Provided that the reference point is placed on the shear axis, only the deformation terms  $u_{x0}/F_x$ ,  $u_{y0}/F_y$ ,  $\alpha_y/F_x$ ,  $\alpha_x/F_y$  and  $\alpha_z/M_z$  should be non-zero. Obviously, in the real case, other terms are non-zero as well. The reasons are following: 1) the elastic axis is not coincident with the shear axis, 2) real wing does not fulfil the slender beam theory (especially at the damaged section) and, 3) discretization and numerical character of the solution. Nevertheless, assessing the RMS deviation of deformation values, the proposed approximation can be considered as acceptable in terms of accuracy.

For the beam bending moment ( $M$ ) and displacement angle ( $\alpha$ ) we can write:

$$\frac{d\alpha_{bend}}{dz} = \frac{\pm M_{bend}}{EJ_{bend}} \quad (1)$$

Equation (1) can be discretized between sections  $i$  and  $i+1$  as:

$$\frac{\alpha_{(i+1)bend} - \alpha_{(i)bend}}{z_{(i+1)} - z_{(i)}} = \frac{\pm M_{bend}}{EJ_{(i;i+1)bend}} \quad (2)$$

where cross-sectional inertia  $J$  between sections  $i$  and  $i + 1$  is considered as constant. Analysis was performed on the damaged structure ( $p$ -index) as well as on the undamaged structure (no index). Both



analyses were performed using the same geometry ( $z$ -coordinates) and the same load ( $M_{bend}$ ). Eliminating these terms we obtain the final equation:

$$\frac{\alpha_{(i+1)bend} - \alpha_{(i)bend}}{{}^p\alpha_{(i+1)bend} - {}^p\alpha_{(i)bend}} = \frac{{}^pEJ_{(i;i+1)bend}}{EJ_{(i;i+1)bend}} \quad (3)$$

Equation (3) characterises the decrease in the bending stiffness due to the damage between sections  $i$  and  $i + 1$ . By analogy, for the torsion we can write:

$$\frac{d\alpha_{tor}}{dz} = \frac{M_{tor}}{GJ_{tor}} \quad (4)$$

$$\frac{\alpha_{(i+1)tor} - \alpha_{(i)tor}}{z_{(i+1)} - z_{(i)}} = \frac{M_{tor}}{GJ_{(i;i+1)tor}} \quad (5)$$

$$\frac{\alpha_{(i+1)tor} - \alpha_{(i)tor}}{{}^p\alpha_{(i+1)tor} - {}^p\alpha_{(i)tor}} = \frac{{}^pGJ_{(i;i+1)tor}}{GJ_{(i;i+1)tor}} \quad (6)$$

Despite the inaccuracies, which have been described, the proposed method was found as acceptable. Although the target beam model does not have the correct strain and stress distribution in the damaged section, it has very accurate spanwise translational and rotational displacement in the reference points. Therefore, the model can be considered as enough accurate for the follow-on flutter analysis.

### 3. Flutter analysis

Aeroelastic stick model is characterised by the stiffness characteristics of the structural parts modelled using massless beam elements placed at the elastic axes of the particular structural part. Inertia characteristics are modelled using concentrated masses with appropriate mass moments of inertia. Engine attachment stiffness as well as connections of structural parts is modelled using spring elements. Various conditions, multi-point constrains, e.g., for the attachment of control surfaces, visualization, connections, etc. are also used.

For the purpose of the described analyses, the stiffness model was modified using the tapered-beam elements allowing specifying the cross-sectional inertia characteristics in the several spanwise sections. This allowed keeping the initial grid positions regardless the spanwise stations of the available stiffness data of the damaged structure. Stiffness model was prepared for both the failure states including damages and the undamaged state (see example in Fig. 3).

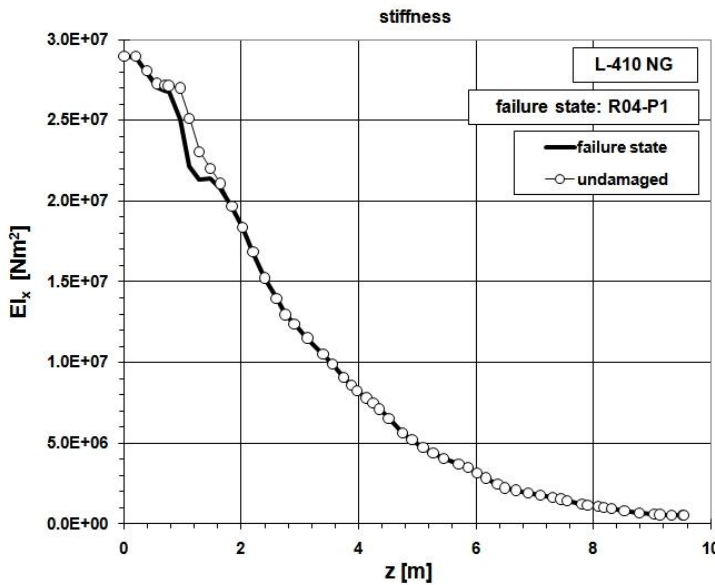


Fig. 3: Stick model bending stiffness example (failure state and undamaged state).

The higher influence of the damages was found on the bending stiffness characteristics while the influence on the torsional stiffness was very low.

Flutter analyses were performed as usual using pk-based method. Aerodynamic matrix is included into the stiffness matrix (real part) and into the damping matrix (imaginary part). The method generates directly total damping of the vibrating system for the selected velocities (true air speed). Flutter analysis is performed as non-matched analyses, i.e., aerodynamic matrices are generated only for

the reference Mach number ( $M_{REF}$ ) and for the selected values of reduced frequency ( $k$ ). The velocity and Mach number values do not match, and therefore, the results have reference character. Such an approach is usually employed in the subsonic aeroelastic analysis to evaluate the rate of reserve in terms of the stability with respect to the specific (certification) velocity. Structural damping was set using viscous model. The common value of  $g = 0.02$  was used. Analyses included mode shapes up to the frequency of  $f = 100 \text{ Hz}$ .

Analysed mass configuration include that one on which the bending torsional flutter (Fig. 4) with the critical mode combination of wing 2<sup>nd</sup> symmetric bending and wing 1<sup>st</sup> symmetric torsion mode was found. The reason is that this type of flutter instability is sensitive to the characteristics of the wing bending and torsional modes, which may be influenced by the change in the stiffness.

Compare to the undamaged state, the critical flutter speed of the failure states slightly increased while the flutter frequency slightly decreased. The reason is an increase in the difference between the frequencies of the critical modes (2<sup>nd</sup> symmetric bending and wing 1<sup>st</sup> symmetric torsion).

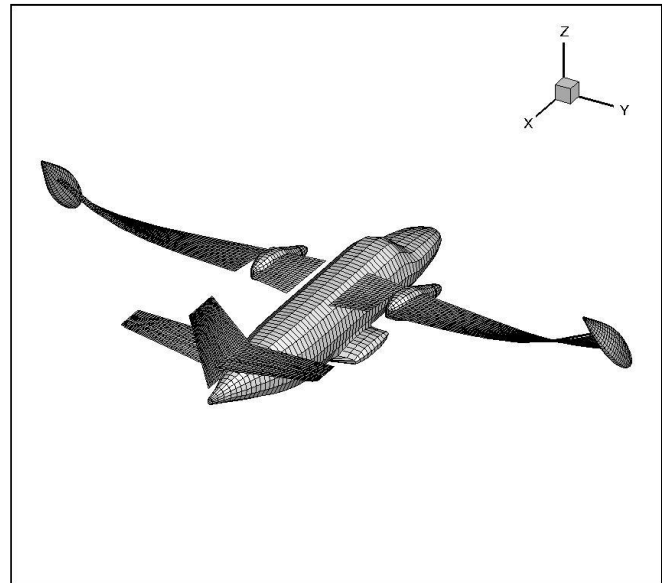


Fig. 4: Aircraft wing bending - torsional flutter shape.

#### 4. Conclusion

The paper presents the methodology of the aircraft wing flutter analysis considering the failure states, originated by the application of the damage - tolerance design philosophy on the wing structure. The main problem of the solution is obtaining of the stiffness characteristics of the damaged structure and its transformation from the detailed static model to the target aeroelastic stick model. The proposed method is simple and enough accurate. The application example includes the analysis of bending torsional flutter considering a single specific damage (reglementary damage).

The method is applicable for compliance with FAR / CS 23.629(g)(h) regulation requirements. We can formulate the following statements:

- 1) Failure state analyses must be performed using the model that includes the stiffness characteristics updated with respect to the results of the ground vibration test.
- 2) Failure state analyses according FAR / CS 23.629(g) may be performed with regard to those flutter cases with the low reserve towards the certification margin. Application of reglementary damages represent conservative approach with respect to the requirements of FAR / CS 23.629(g).
- 3) Analysis of the state required by FAR / CS 23.629(h), i.e., the state, for which the residual strength is demonstrated, may be performed analogously. In this case, multiple damages representing the mentioned state of a structure must be taken into account.

#### References

- CS-23, Amdt.3 (2012), Certification Specifications for Normal, Utility, Aerobatic, and Commuter Category Aeroplanes, CS-23, Amendment 3, European Aviation Safety Agency, 20.7.2012.
- FAR-23, Amdt.62 (2012), Federal Aviation Regulations, Part 23: Airworthiness Standards: Normal, Utility, Acrobatic and Commuter Category Airplanes, FAR-23, Amendment 62, US. Department of Transportation, Federal Aviation Administration, 31.1.2012.
- AC-23.629-1B (2004), Means of Compliance with Title 14 CFR, Part 23 §23.629, Flutter, Advisory Circular, AC-23.629-1B, US. Department of Transportation, Federal Aviation Administration, 28.9.2004.

## THE INFLUENCE OF THE LENGTH OF TRAJECTORY OF SCARA MANIPULATOR DUTY CYCLE ON ELECTRICITY CONSUMPTION

D. Cekus<sup>\*</sup>, D. Skrobek<sup>\*\*</sup>

**Abstract:** The paper presents the using of Particle Swarm Optimization (PSO) method to determine the shortest trajectory of the end-effector of SCARA manipulator. It has been assumed that the obstacles occur in the workspace, but the transfer above them is impossible, therefore the problem is considered in two-dimensional space. In the PSO algorithm the impact of the inertia weight of the length of the searched minimal trajectory has been shown. For found out trajectory the electricity consumption required to execute a duty cycle of SCARA manipulator has been determined. Only theoretical considerations were conducted.

**Keywords:** PSO, SCARA, Manipulator, Optimization, Electricity consumption.

### 1. Introduction

Lots of engineering problems have the form of optimization tasks. So-called heuristic methods are helpful for complex optimization problems. In this paper, using the Particle Swarm Optimization (PSO) method (Kennedy et al., 1995), the optimal trajectory between two defined points for the SCARA manipulator (Fig. 1a) has been determined. In the analyzed problem, the manipulator has to perform a duty cycle consisting in the movement of the end-effector between two points, but obstacles appear on the path (Fig. 1b). It was assumed that the height of the obstacles prevents the transfer of the elements above them which the problem reduced to the two-dimensional space.

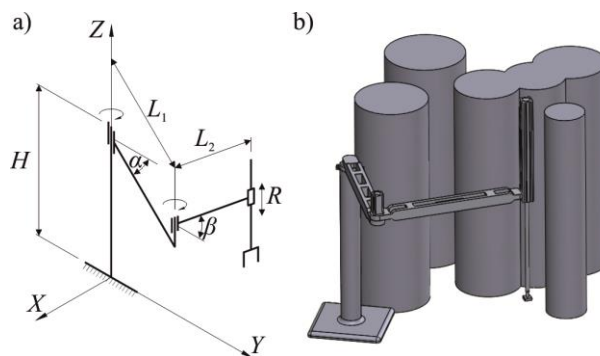


Fig. 1: SCARA manipulator: a) kinematic diagram; b) exemplary working environment.

Determination of the minimal path allows for shortening the time of working cycle, but not to minimize energy consumption, as shown in subsequent chapters of this paper.

### 2. Formulation and solution of the problem

The first stage of the work is to determine the shortest trajectory of the duty cycle. For this purpose, the PSO method has been used. The following parameters of the PSO algorithm have been adopted: the number of iterations ( $It$ ) = 200, the population size = 150, the number of points creating the path (without the start and end point) = 10. Using the PSO method, the results also depend on the so-called

<sup>\*</sup> Assoc. Prof. Dawid Cekus Phd. Eng., Institute of Mechanics and Machine Design Foundations, Czestochowa University of Tehnology, Street Dąbrowskiego 73; 42-201, Czestochowa; PL, cekus@imipkm.pcz.pl

<sup>\*\*</sup> M.Sc. Eng. Dorian Skrobek., Institute of Mechanics and Machine Design Foundations, Czestochowa University of Tehnology, Street Dąbrowskiego 73; 42-201, Czestochowa; PL, skrobek@imipkm.pcz.pl

"the inertia weight". In this work, the inertia weight was calculated according to the equation (Ao et al., 2010, Ting et al., 2012, Lin et al., 2003, Storn et al., 1997):

$$w = w_0 \exp\left(-a\left(\frac{It}{MaxIt}\right)^b\right), \quad (1)$$

where:  $w_0 = 0.9$ ;  $It$  - the current iteration,  $MaxIt$  - the maximum number of iterations,  $a$  - local search attractor,  $b$  - global search attractor. In the present study, the optimal trajectory has been determined for three different values of the parameter  $a$  and  $b$  (Fig. 2).

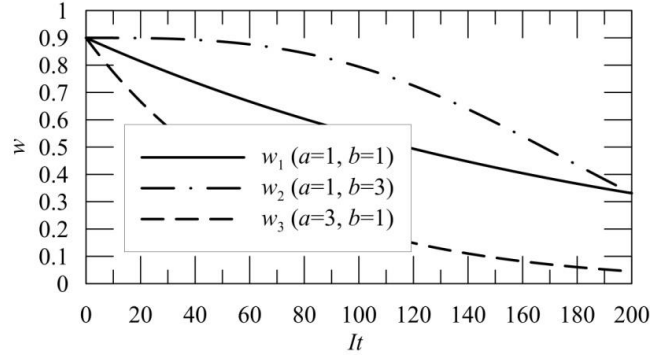


Fig. 2: The value of the inertia weight during subsequent iterations of the PSO algorithm.

For the accepted value of parameters of inertia weight, the following lengths of trajectory have been obtained: 1407.0379 mm (for  $w_1$ ), 1407.0066 mm (for  $w_2$ ) and 1406.8273 mm (for  $w_3$ ). The shortest trajectory (for  $w_3$ ) with the selected positions of arms  $L_1$  and  $L_2$  is shown in Fig. 3. The position of manipulator arms has been calculated on the basis of inverse kinematics (Cekus et al., 2015).

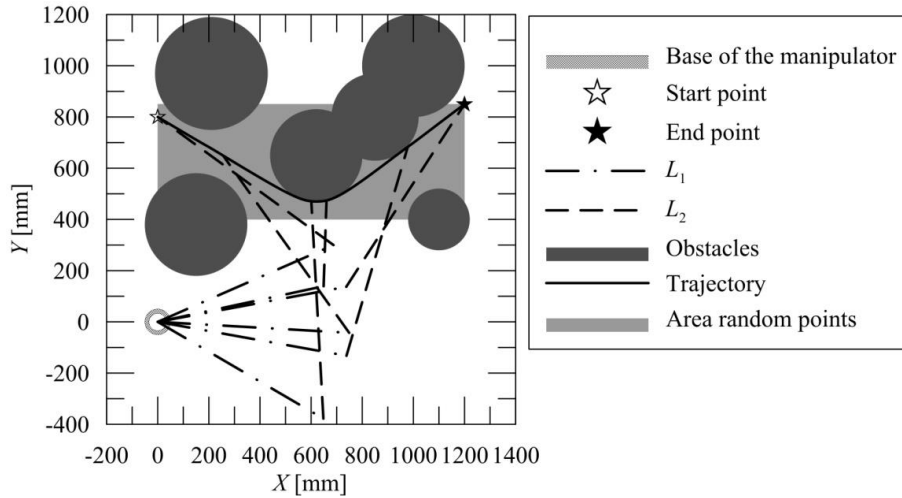


Fig. 3: The determined shortest trajectory with the selected positions of arms  $L_1$  and  $L_2$ .

The next stage of the research was to determine the electricity consumption of manipulator drives for the calculated trajectories. It was assumed that for the initial time  $t = 0$  s, the electricity consumption is equal to zero ( $E_c = 0$  J). Total electricity consumption (Kucuk, 2013, Posiadala et al., 2015, Ur-Rehman et al., 2010) is integral of function of total instantaneous power ( $P_T$ ) within the limits of the considered time  $<0, t_k>$ :

$$E_C = \int_0^{t_k} P_T dt. \quad (2)$$

It is accepted that the execution time ( $t_k$ ) each operating cycle is equal to 100 s, despite the different lengths of trajectories.

The total instantaneous power is the sum of the momentary power of individual drives:

$$P_T = \sum_{i=1}^2 P_i. \quad (3)$$

When the drive is in motion, i.e. the angular velocity exists, the momentary power of a single drive is defined as follows:

$$P_i = P_i^{(R)} + P_i^{(L)} + P_i^{(EM)}. \quad (4)$$

Otherwise, the instantaneous power is constant.

The first component of the sum (4) is responsible for losses arising from the winding resistance of the drive. The second component of the sum (4) defines the losses caused by self-induction. The third component of the sum (4) determines the power used to generation of electromotive force.

$$P_i^{(R)} = R_i I_i^2, \quad P_i^{(L)} = |L_i I_i \dot{I}_i|, \quad P_i^{(EM)} = |I_i U_i|, \quad (5)$$

where:  $R$  - resistance,  $L$  - inductance,  $U$  - electromotive force.

Values occurring in equations (5) characterizing the electric current are functions of time and depend linearly on the instantaneous angular velocity of the drive (Fig. 4b) and the instantaneous torque on the motor shaft (Fig. 4b):

$$I_i = k_i^{(I)} \frac{M_i}{u_i}, \quad U_i = k_i^{(U)} \dot{\phi}_i u_i, \quad (6)$$

where:  $u_i$  - axle ratio,  $k_i^{(I)}$  - torque sensitivity factor,  $k_i^{(U)}$  - back emf. constant,  $\dot{\phi}_i$  - the angular velocity,  $M_i$  - moment of motor.

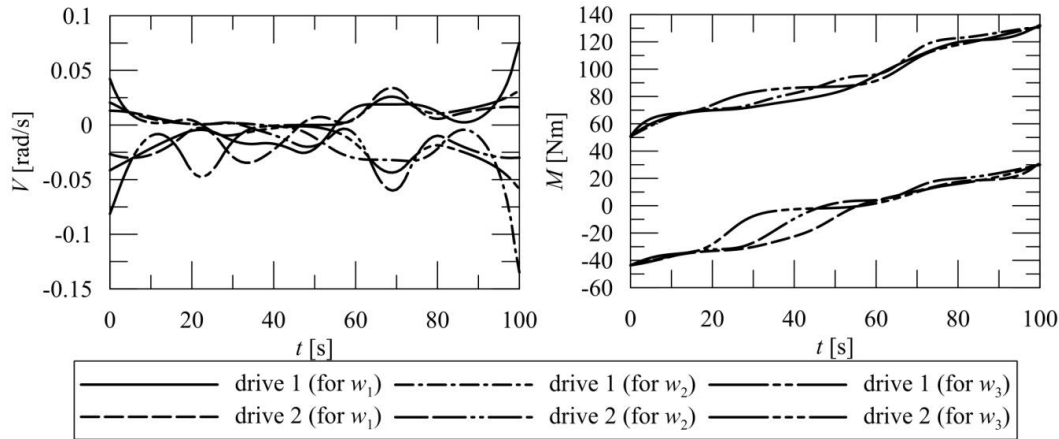


Fig. 4: The angular velocity (on the left), torque on the motor shaft (on the right).

The electric energy consumption of manipulator for adopted the inertia weights is presented in Fig. 5. Aside from drive parameters, the center of gravity position of each arm has the influence on the electricity consumption of manipulator. The change of center of gravity of manipulator arms causes the change of angular position, angular velocity and angular acceleration, which has the impact on the change of torque on individual drive (Fig. 4).

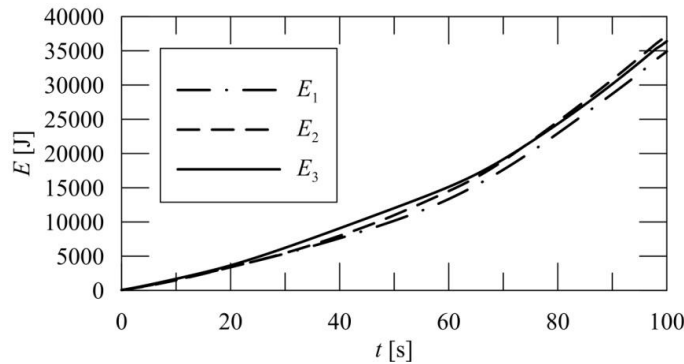


Fig. 5: Electricity consumption.

Total electricity consumption in the examined time (100 s) is equal to: 34915.78 J (for w1), 37222.13 J (for w2), and 36400.73 J (for w3). Based on these results, it can be stated that the minimum energy consumption is not the smallest for the shortest trajectory. It is associated with the change of the center of gravity of manipulator members during of the duty cycles. Therefore, for minimizing the consumption of electricity apart from seeking the optimal trajectory should pay attention to the value of moments of motors.

### 3. Conclusions

The use of one of the heuristic algorithms - the Particle Swarm Optimization method - to determine the optimal trajectory of SCARA manipulator end-effector has been presented in the work. The task was to calculate the shortest path connecting two defined points avoiding obstacles.

In the calculations the influence of changes of the inertia weight parameters adopted in PSO algorithm on the length of the determined trajectory has been presented. For the obtained trajectories the electricity consumption has been computed. The demonstrated results allowed to conclude that the inertia weight does not significantly impact on the length of the trajectory, while the length of the trajectory has the influence on the energy consumption. However, the lowest electricity consumptions does not occur when the trajectory is minimal. Therefore, the minimization of length of the trajectory to cover by the end-effector of manipulator cannot be the sole determinant during the optimization of the electricity consumption. In this case, first of all, pay attention on the displacement of the center of gravity of arms manipulator during the working cycle.

This work contains only theoretical considerations, but the results of subsequent works will be verified experimentally on four degrees of freedom manipulator that is mounted on a Mars rover (Pierzgalski et al., 2017). Optimization problems will concern a duty cycle in three-dimensional space and will analyze the solutions obtained by other heuristic methods, e.g. the genetic algorithm (Cekus et al., 2015).

### References

- Ao, Y. and Chi, H. (2010) An adaptive Differential Evolution to Solve Constrained Optimization Problem in Engineering Design, *Scientific research* 2, pp. 65-77.
- Cekus, D., Skalik, A., Skrobek, D. and Waryś, P. (2015) Kinematic analysis of four degrees of freedom manipulator, *Solid State Phenomena, Volume: Mechatronic Systems and Materials VI*, pp. 277-282.
- Cekus, D. and Waryś, P. (2015), Identification of parameters of discrete-continuous models, *AIP Conf. Proc.* 1648, 850055, <http://dx.doi.org/10.1063/1.4913110>.
- Kennedy, J. and Eberhart, R.C. (1995) Particle Swarm Optimization, *Proceedings of the. IEEE International Conference on Neural Networks*, Volume 4, pp. 1942-1948.
- Kucuk, S. (2013) Energy minimization for 3-RRR fully planar parallel manipulator using particle swarm optimization, *Mechanism and Machine Theory*, 62, pp. 129-149.
- Lin, W., Lee, W. and Hong, T. (2003) Adapting crossover and mutation rates in genetic algorithms, *Journal of information science and Engineering*, 19, pp. 889-903.
- Posiadala, B., Tomala, M., Cekus, D. and Waryś, P. (2015) Work cycle optimization problem of manipulator with revolute joints, *International Journal of Dynamics and Control*, March 2015, Volume 3, Issue 1, pp. 94-99.
- Pierzgalski, M., Ptak, P., Cekus, D. and Sokół, K. (2017) Modeling and stress analysis of a manipulator mounted on a Mars rover, *Procedia Engineering*, Volume 177, pp. 121-126, <http://dx.doi.org/10.1016/j.proeng.2017.02.199>
- Storn, R. and Price, K. (1997) Differential evolution - a simple and efficient heuristic for global optimization over continuous spaces, *Journal of Global Optimization*. 11, pp. 341-359. DOI:10.1023/A:1008202821328.
- Ting, T.O., Shi, Y., Cheng, S. and Lee, S. (2012) Exponential Inertia Weight for Particle swarm Optimization, *Advances in Swarm Intelligence*, vol. 7331, Springer, Berlin, Heidelberg, DOI: 10.1007/978-3-642-30976-2\_10.
- Ur-Rehman, R., Caro, S., Chablat, D. and Wegner, P. (2010) Multi-objective path placement optimization of parallel kinematics machines based on energy consumption, shaking forces and maximum actuator torques, *Application to the Orthoglide*, *Mechanism and Machine Theory*, 45, pp. 1135-1141.

## ELECTROMAGNETIC ENERGY HARVESTER WITH MECHANICAL AMPLIFIER FOR TRANSLATIONAL KINETIC

M. Černý\*, M. Dzurilla\*\*, M. Musil\*\*\*

**Abstract:** *This paper deals with the design and construction of a mechanical amplifier coupled to an electromagnetic energy harvester to generate power from low-amplitude ( $\pm 2$  mm) and low-frequency ( $\leq 8$  Hz). Design and simulation guidance of magnetic flux to achieve an effective changes of the polarity.*

**Keywords:** Harvester, Amplifier, Electromagnetism, Mechanism, Guidance.

### 1. Introduction

Today's level of minimization allows many devices to be used in places that were unthinkable until now. Particularly, given the wireless data transmission, sensors are limited by the necessity of electric power supply. When using the cable system to power the devices, the advantages of wireless communication are considerably reduced. Using batteries is not the best solution because of their life expectancy and limited working conditions. To push the boundaries of the possibilities for technical control and management, the scientists have recently been exploring new alternatives based on the inexhaustible energy sources in the close distance around the powered system.

One of the most effective alternative ways to supply power to consumer electronic devices seems to be the exploitation of the surrounding vibrations. However, kinetic parameters of standard environment, including human movement, vibration of bridges, buildings and many devices and machines, are low-frequency. To solve this problem, many solutions were designed, such as exploitation of resonance oscillation (Sardini et al., 2011), mechanical frequency, or rotating movement with eccentric mass. Performance of many of these systems goes down out of the range of appropriate conditions, whenever there are big static displacement, non-periodic vibrations and low amplitude. The range is usually narrow, which is a huge disadvantage. The opposite approach to this solution is "direct force", where vibrations are transmitted only by transfer multiplying amplitude and frequency (Shahosseini et al., 2014). Although these solutions tend to create less energy compared to resonance harvesters, they have the advantage of a wider excitation band. Their disadvantage, however, is that they might not be applicable everywhere, especially, as far as vehicles are concerned. That is why this paper is focused on harvester with mechanical amplifier.

### 2. Harvester design

The core of the phenomenon explored is an oscillating body which is able to amplify small amplitude  $0.325R$ -times thanks to an amplifying gear connected to a coil on a crank. System of magnets in the trajectory of the coil multiplies the frequency 4 times, given a maximum oscillation. Oscillating body with mass " $m$ " with a crest secured on a base is shown in Fig. 1. There is a pendulum connected to the base with a mass " $m_2$ " with its center of gravity in a position " $R$ " from the rotation axis, with a gear of inertia " $I$ " and a gear radius " $r$ ". The gear ratio is  $1 \text{ mm} = 18^\circ$ .

---

\* Ing. Michal Černý: Faculty of Mechanical Engineering STU in Bratislava; Námetie Slobody 17; 812 31 Bratislava 1; SK, michal.cerny@stuba.sk

\*\* Ing. Michal Dzurilla: Faculty of Mechanical Engineering STU in Bratislava; Námetie Slobody 17; 812 31 Bratislava 1; SK, michal.dzurilla@stuba.sk

\*\*\* Prof. Ing. Miloš Musil, CSc.: Faculty of Mechanical Engineering STU in Bratislava; Námetie Slobody 17; 812 31 Bratislava 1; SK, milos.musil@stuba.sk



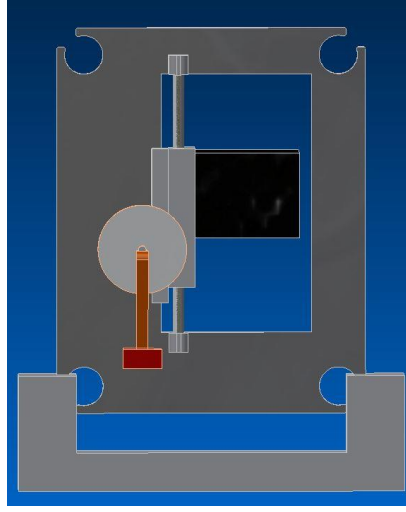


Fig. 1: Simplified model of mechanism.

Basic description of dynamic mechanism:

$$x = r \sin \varphi \rightarrow \dot{x} = \dot{\varphi} r \cos \varphi \quad (1)$$

$$E_k = \frac{1}{2} m \dot{x}^2 + \frac{1}{2} I \dot{\varphi}^2 = \frac{1}{2} m r^2 \dot{\varphi}^2 \cos^2 \varphi + \frac{1}{2} I \dot{\varphi}^2 \quad (2)$$

$$E_p = \frac{1}{2} m_2 g R (1 - \cos \varphi) \quad (3)$$

$$\frac{d}{dt} \left( \frac{\partial E_k}{\partial \dot{\varphi}} \right) - \frac{\partial E_k}{\partial \varphi} + \frac{\partial E_p}{\partial \varphi} + \frac{\partial D}{\partial \dot{\varphi}} = Q_j \quad (4)$$

$$\frac{\partial E_k}{\partial \dot{\varphi}} = \frac{\partial}{\partial \dot{\varphi}} \left( \frac{1}{2} m r^2 \dot{\varphi}^2 \cos^2 \varphi + \frac{1}{2} I \dot{\varphi}^2 \right) = m r^2 \dot{\varphi} \cos^2 \varphi + I \dot{\varphi} \quad (5)$$

$$\frac{d}{dt} \left( \frac{\partial E_k}{\partial \dot{\varphi}} \right) = m r^2 \ddot{\varphi} \cos^2 \varphi - 2 m r^2 \dot{\varphi} \cos \varphi \sin \varphi + I \ddot{\varphi} = m r^2 (\ddot{\varphi} \cos^2 \varphi - \dot{\varphi} \sin(2\varphi)) + I \ddot{\varphi} \quad (6)$$

$$\frac{\partial E_k}{\partial \varphi} = \frac{\partial}{\partial \varphi} \left( \frac{1}{2} 2 m r^2 \dot{\varphi}^2 \cos \varphi \sin \varphi + \frac{1}{2} I \dot{\varphi}^2 \right) = - 2 m r^2 \dot{\varphi}^2 \cos \varphi \sin \varphi = - \frac{1}{2} m r^2 \dot{\varphi}^2 \sin(2\varphi) \quad (7)$$

$$\frac{\partial E_p}{\partial \varphi} = + \frac{1}{2} m_2 g R \sin \varphi \quad (8)$$

$$m r^2 (\ddot{\varphi} \cos^2 \varphi - \dot{\varphi} \sin 2\varphi) + I \ddot{\varphi} + \frac{1}{2} m r^2 \dot{\varphi}^2 \sin(2\varphi) + \frac{1}{2} m_2 g R \sin \varphi = 0 \quad (9)$$

$$\ddot{\varphi} [m r^2 \cos^2 \varphi + I] + \dot{\varphi}^2 \frac{1}{2} m r^2 \sin 2\varphi - \dot{\varphi} m r^2 \sin 2\varphi + \frac{1}{2} m_2 g R \sin \varphi = 0 \quad (10)$$

As shown in Fig. 2, pairs of the magnets are located on the both sides of the corridor track. Corridor track is an air gap, where the coil is moving. Each pair of magnets has same orientation. Every pair is oppositely oriented as its nearby pair. For more effective guidance of magnetic flux is using steel slabs with higher-order value permeability than air. Description of Fig. 2, red: steel material, blue: magnets, orange: Polylactic acid (PLA)

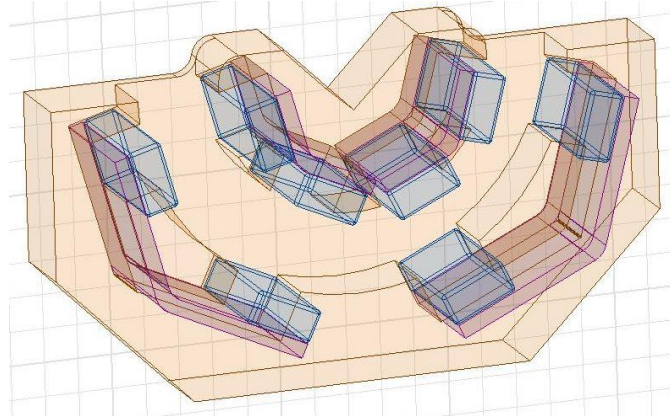
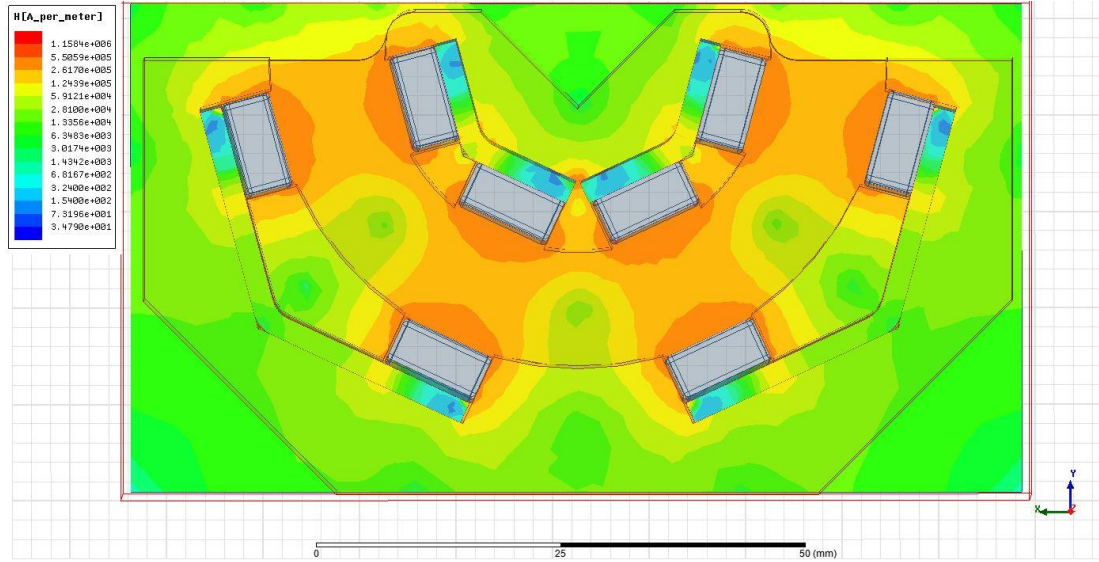


Fig. 2: Corridor for the coil.

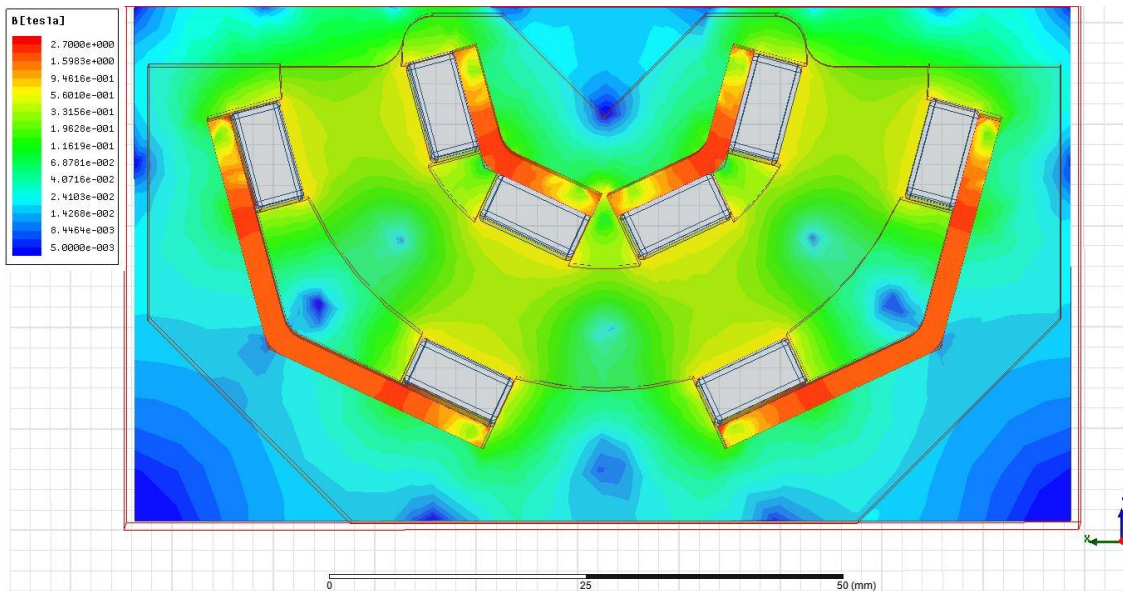
Field distribution of magnetic induction in the air gap is the most important parameter, which decides the parameter of the generator. In particular the dependence of magnetic induction, which passes through the coil, thus the size if the induced voltage.

Between the magnets is the moving coil. The exact value depends on specific constructive solution. Due to the construction and location of the permanent magnets, the magnetic induction is not constant. Its assembly, they used method of finite element method and magneto-static analysis. A shown in Fig. 3, we can see magnetic circuit and distribution of magnetic induction.



*Fig. 3: Magnetic field distribution of inductance in the air gap and steel between the magnets.*

As shown in Fig. 4, magnetic flux density in closed circuit, where steel has main effect on accuracy direction of magnetic flux.



*Fig. 4: Field distribution of magnetic flux density in the air gap and steel between the magnets.*

As shown in Fig. 5, there are two sets of corridor track coils. The assembly is designed for easy handling and visual control during the measurement. Measurement was carried out both horizontally and vertically. Vertically compiled harvester as shown in Fig. 3a), have partially common phase. Fig. 3b), weight and coil in a phase.

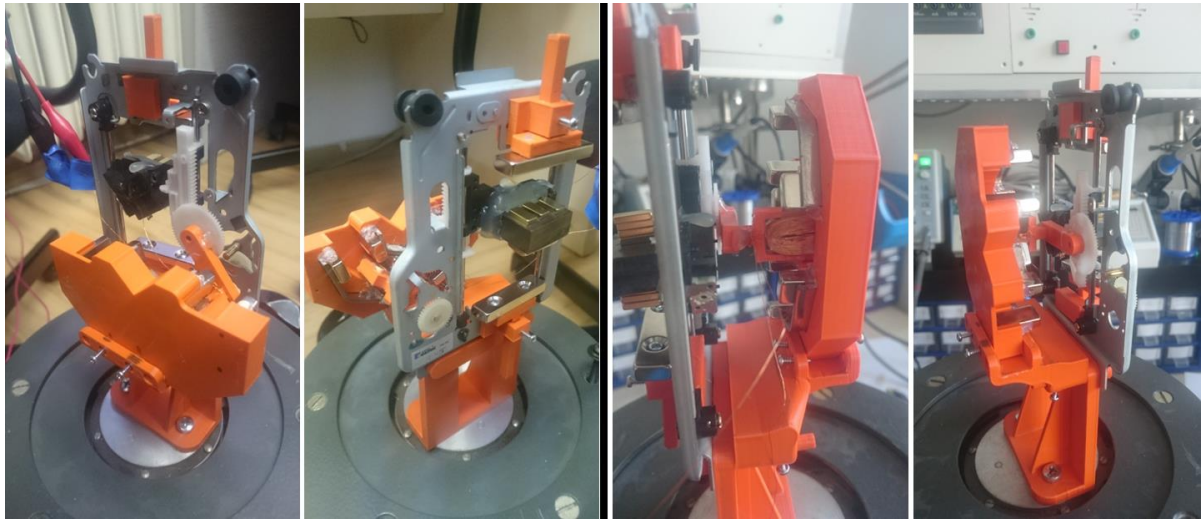


Fig. 5: a) Partially common phase;

Fig. 5: b) Common phase.

The third way of harvester assembly is horizontal, which is excited by oscillation sideways. Weight and coil are in the phase where earth gravity affect just the coil. Losses in the plastic rack, the pinion and total motion cause big losses to mechanism, which they will display outside of the weight and coil.

As shown in Fig. 6, captures a voltage at the resistance of  $240\ \Omega$ , excitation frequency 7 Hz and amplitude  $\pm 2$ ,  $U_{Pk-Pk} = 3.42\text{ V}$ . Resistor has a lower value due to the simulation load. Asymmetric progress of generating voltage is caused by incomplete track of the coil between the magnets and their non - linear velocity in the given sections between the magnetic pairs. Fig. 7, captures a progress of a voltage at the resistance of  $240\ \Omega$ , excitation frequency 3 Hz and amplitude  $\pm 3$ ,  $U_{Pk-Pk} = 4.04\text{ V}$ .

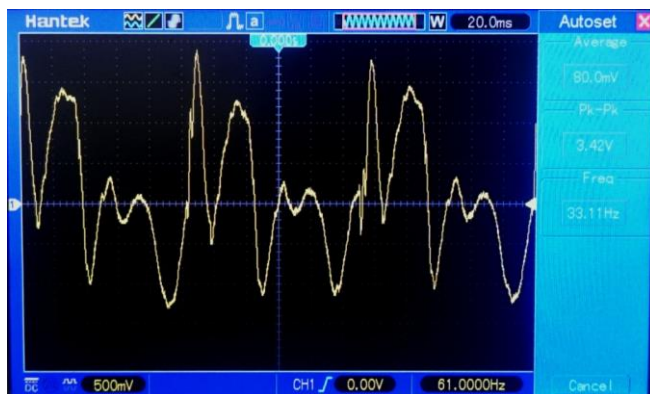


Fig. 6: The waveform of the voltage at 7 Hz.

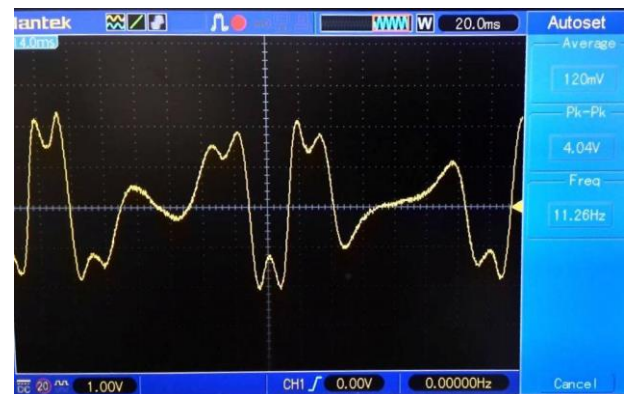


Fig. 7: The waveform of the voltage at 3 Hz.

### 3. Conclusion

This work studies design of a mechanical amplifier for low frequencies. The variety in the results creates a range of possibilities for optimization of the harvester. Measurements have shown the best results when keeping the dynamic parameters in a range of 3 – 8 Hz. To gain electric energy, however, excitation amplitude of  $\pm 2\text{ mm}$  is necessary.

### Acknowledgement

This work was supported by the grant from the Grant Agency of VEGA no. 1/0742/15 and by the Slovak Research and Development Agency under the contract no. APVV-15-0630.

### References

- Sardini, E. and Serpelloni, M. (2011) An efficient electromagnetic power harvesting device for low-frequency applications. Sensors and Actuators A 172 pp. 475-482.
- Shahosseini, I. and Najafi, K. (2014) Mechanical Amplifier for Translational Kinetic Energy Harvester. Center for Wireless Integrated MicroSensing and Systems, University of Michigan, USA.



## A SHORT WAVE LIMIT OF THE FREQUENCY EQUATION FOR PLANE-STRESS NONAXISYMMETRIC DISC MOTIONS

J. Červ\*, F. Valeš\*\*, V. Adámek\*\*\*

**Abstract:** *It is proved that the general frequency equation for plane-stress nonaxisymmetric disc motions tends for the first mode of propagation and for wavelengths very short when compared with the disc radius to the secular equation for Rayleigh waves.*

**Keywords:** Frequency equation, Elastic disc, Rayleigh waves.

### 1. Introduction

The frequency equation for plane-stress nonaxisymmetric motions of an elastic disc (the disc boundary  $r = r_1$  is assumed to be free of tractions) can be written as, see Cerv (1988),

$$\left\{ \left[ \frac{y^2}{2} - 1 + \frac{1}{\kappa} \right] J_{\kappa}(\kappa y \varphi) - \frac{y \varphi}{\kappa} J_{\kappa+1}(\kappa y \varphi) \right\} \cdot \left\{ \left[ \frac{y^2}{2} - 1 + \frac{1}{\kappa} \right] J_{\kappa}(\kappa y) - \frac{y}{\kappa} J_{\kappa+1}(\kappa y) \right\} - \left\{ \left[ \frac{1}{\kappa} - 1 \right] J_{\kappa}(\kappa y) + y J_{\kappa+1}(\kappa y) \right\} \cdot \left\{ \left[ \frac{1}{\kappa} - 1 \right] J_{\kappa}(\kappa y \varphi) + y \varphi J_{\kappa+1}(\kappa y \varphi) \right\} = 0. \quad (1)$$

The symbols  $y$  and  $\varphi$  represent the dimensionless ratios

$$y = \frac{c}{c_2}, \quad \varphi = \frac{c_2}{c_3} = \sqrt{\frac{1-\mu}{2}}, \quad (2)$$

where  $c_2$  and  $c_3$  are the velocities of shear and dilatational waves, respectively. Poisson's ratio is denoted by  $\mu$ ,  $c$  is the phase velocity. The parameter  $\kappa$  is the dimensionless wavenumber and it can be written as

$$\kappa = \frac{2\pi}{\lambda} r_1, \quad (3)$$

where  $r_1$  is the disc radius,  $\lambda$  is the wavelength. The symbol  $J_{\kappa}$  denotes the Bessel function of the first kind, order  $\kappa$ . The frequency equation (1) has an infinite number of discrete roots  $y = c / c_2$ , each corresponding to a particular mode of propagation. In the paper Cerv (1988) it is shown by means of a numerical procedure that the first mode which belongs to the first dispersion curve represents Rayleigh-type waves.

The aim of the paper is to find a simpler form of the equation (1) which could approximate the first mode of propagation for wavelength very short when compared with the disc radius.

---

\* Assoc. Prof. Jan Červ, PhD.: Institute of Thermomechanics AS CR, v.v.i.; Dolejškova 5; 182 00, Prague; CZ, cerv@it.cas.cz

\*\* František Valeš, PhD.: Institute of Thermomechanics AS CR, v.v.i.; Veleslavínova 11; 301 14, Pilsen; CZ, vales@it.cas.cz

\*\*\* Vítězslav Adámek, PhD.: NTIS – New Technologies for the Information Society, University of West Bohemia; Univerzitní 8; 306 14, Pilsen; CZ, vadamek@kme.zcu.cz

## 2. Problem solution

Let  $\kappa$  be a sufficiently large number ( $\kappa = 2\pi r_l / \lambda \gg 1$ ). For these short wavelengths ( $r_l$  being arbitrary but fixed) and for the first mode of propagation it holds, see Cerv (1988),

$$0 < y < 1 . \quad (4)$$

From (2) it also follows

$$0 < \varphi < 1 . \quad (5)$$

The equation (1) may be rewritten into the form

$$\begin{aligned} & \left\{ \left[ \frac{y^2}{2} - 1 + \frac{1}{\kappa} \right] - \frac{y\varphi}{\kappa} \frac{J_{\kappa+1}(\kappa y \varphi)}{J_{\kappa}(\kappa y \varphi)} \right\} \cdot \left\{ \left[ \frac{y^2}{2} - 1 + \frac{1}{\kappa} \right] - \frac{y}{\kappa} \frac{J_{\kappa+1}(\kappa y)}{J_{\kappa}(\kappa y)} \right\} = \\ & = \left\{ \left[ \frac{1}{\kappa} - 1 \right] + y \frac{J_{\kappa+1}(\kappa y)}{J_{\kappa}(\kappa y)} \right\} \cdot \left\{ \left[ \frac{1}{\kappa} - 1 \right] + y\varphi \frac{J_{\kappa+1}(\kappa y \varphi)}{J_{\kappa}(\kappa y \varphi)} \right\} . \end{aligned} \quad (6)$$

It is evident that estimates of the ratios of the Bessel functions in (6) have to be determined.

### 2.1. Asymptotic representation of $J_{\kappa+1}(\kappa y) / J_{\kappa}(\kappa y)$ , $J_{\kappa+1}(\kappa y \varphi) / J_{\kappa}(\kappa y \varphi)$

If  $\alpha$  is any fixed and positive number and  $\kappa$  is large and positive, the following asymptotic expansion of  $J_{\kappa}(\kappa \cdot \text{sech} \alpha)$  is valid, see Watson (1966),

$$J_{\kappa}(\kappa \cdot \text{sech} \alpha) \approx \frac{\exp[\kappa(\tanh \alpha - \alpha)]}{\sqrt{2\pi\kappa} \cdot \tanh \alpha} \sum_{m=0}^{\infty} \left\{ \frac{\Gamma\left(m + \frac{1}{2}\right)}{\Gamma\left(\frac{1}{2}\right)} \cdot \frac{A_m}{\left(\frac{1}{2}\kappa \cdot \tanh \alpha\right)^m} \right\}, \quad (7)$$

where  $A_0 = 1$ ,  $A_1 = \frac{1}{8} - \frac{5}{24} \coth^2 \alpha$ , .... Taking only the first term of this expansion and writing

$$\text{sech} \alpha = \frac{1}{\cosh \alpha} = y, \quad (8)$$

we have for  $\kappa \gg 1$

$$J_{\kappa}(\kappa y) \approx \frac{\exp\left[\kappa\left(\sqrt{1-y^2} - \text{arcsech } y\right)\right]}{\sqrt{(2\pi\kappa)} \cdot \left(\sqrt{1-y^2}\right)^{1/2}}. \quad (9)$$

From (8) it is clear that for  $\alpha > 0$  it holds  $0 < y < 1$ , i.e., the condition (4) is fulfilled. The corresponding formula for  $J_{\kappa+1}([\kappa+1]y)$  can be then derived from (9). We obtain

$$J_{\kappa+1}([\kappa+1]y) \approx \frac{\exp\left[(\kappa+1) \cdot \left(\sqrt{1-y^2} - \text{arcsech } y\right)\right]}{\sqrt{[2\pi(\kappa+1)]} \cdot \left(\sqrt{1-y^2}\right)^{1/2}}. \quad (10)$$

Let  $\hat{y}$  be a new variable which is given by

$$\hat{y} = \frac{(\kappa+1)}{\kappa} y. \quad (11)$$

For any fixed  $y$ ,  $0 < y < 1$ , we can assign a number  $\kappa_0 \gg 1$  such that for every  $\kappa > \kappa_0$  we have

$$0 < \hat{y} < 1. \quad (12)$$

Substituting (11) into (10) leads to

$$J_{\kappa+1}(\kappa\hat{y}) \approx \frac{\exp \left[ (\kappa+1) \cdot \left( \sqrt{1 - \left( \frac{\kappa}{\kappa+1} \right)^2 \hat{y}^2} - \operatorname{arcsech} \left( \frac{\kappa}{\kappa+1} \hat{y} \right) \right) \right]}{\sqrt{2\pi} \sqrt{(\kappa+1)} \cdot \left( \sqrt{1 - \left( \frac{\kappa}{\kappa+1} \right)^2 \hat{y}^2} \right)^{1/2}}. \quad (13)$$

Denoting denominator in (13) as D one gets after a small algebra  $D = \sqrt{2\pi\kappa} \left( \sqrt{1 + \frac{2}{\kappa} + \frac{1}{\kappa^2} - \hat{y}^2} \right)^{1/2}$ .

Neglecting  $2/\kappa, 1/\kappa^2$  in D we receive for a sufficiently large  $\kappa$  the asymptotic expression for D

$$D \cong \sqrt{2\pi\kappa} \left( \sqrt{1 - \hat{y}^2} \right)^{1/2}. \quad (14)$$

Let P be the exponent in numerator of (13). For P we get

$$P = \kappa \left( \sqrt{1 + \frac{2}{\kappa} + \frac{1}{\kappa^2} - \hat{y}^2} \right) - \kappa \cdot \operatorname{arcsech} \left( \frac{1}{1+1/\kappa} \hat{y} \right) - \operatorname{arcsech} \left( \frac{1}{1+1/\kappa} \hat{y} \right), \text{ and for a sufficiently large } \kappa \text{ it may be written as}$$

$$P \cong \kappa \left[ \sqrt{1 - \hat{y}^2} - \operatorname{arcsech} \hat{y} \right] - \operatorname{arcsech} \hat{y}. \quad (15)$$

In view of the expressions (14) and (15), the approximation (13) may be rewritten in the form

$$J_{\kappa+1}(\kappa\hat{y}) \approx \frac{\exp \left[ \kappa \left[ \sqrt{1 - \hat{y}^2} - \operatorname{arcsech} \hat{y} \right] \right]}{\sqrt{2\pi\kappa} \left( \sqrt{1 - \hat{y}^2} \right)^{1/2}} \cdot \exp(-\operatorname{arcsech} \hat{y}), \text{ and by using the approximation (9),}$$

we obtain

$$J_{\kappa+1}(\kappa\hat{y}) \approx J_{\kappa}(\kappa\hat{y}) \cdot \exp(-\operatorname{arcsech} \hat{y}). \quad (16)$$

Taking the expression (8) and using the following identity for the inverse hyperbolic functions, as may be seen in the book of Rektorys (1968), we get for arbitrary  $z, 0 < z \leq 1$

$$\operatorname{arcsech} z = \operatorname{arccosh} \frac{1}{z} = \ln \left( \frac{1 + \sqrt{1 - z^2}}{z} \right). \quad (17)$$

The substitution of (17) into (16) yields (for  $z = \hat{y}$ )  $J_{\kappa+1}(\kappa\hat{y}) \approx J_{\kappa}(\kappa\hat{y}) \cdot \left( \frac{1}{\hat{y}} + \left[ \frac{1}{\hat{y}^2} - 1 \right]^{1/2} \right)^{-1}$  and after

a simple algebra we have

$$\frac{J_{\kappa+1}(\kappa\hat{y})}{J_{\kappa}(\kappa\hat{y})} \approx \frac{1 - \sqrt{1 - \hat{y}^2}}{\hat{y}}. \quad (18)$$

The approximation (18) is true for a sufficiently large  $\kappa$  and for any fixed  $\hat{y}, 0 < \hat{y} < 1$ . It is evident that terms having the argument  $\kappa y \varphi$  (see (6)) can be treated in the same manner. Therefore, one gets the similar approximation

$$\frac{J_{\kappa+1}(\kappa\hat{y}\varphi)}{J_{\kappa}(\kappa\hat{y}\varphi)} \approx \frac{1 - \sqrt{1 - (\hat{y}\varphi)^2}}{\hat{y}\varphi}. \quad (19)$$

Now we may return to the equation (6). If we substitute (18) and (19) (with original variable  $y$ ) into the equation (6), and then neglect small quantities as  $\kappa \rightarrow +\infty$ , we obtain

$$\left[ \frac{y^2}{2} - 1 \right]^2 - \sqrt{1 - y^2} \cdot \sqrt{1 - \varphi^2 y^2} = 0 . \quad (20)$$

The equation (20) may be considered to be an approximation of the general equation (1) (or (6)) for the first mode of propagation as  $\kappa \rightarrow +\infty$ . In view of (2), the equation (20) may have the form

$$\left[ \left( \frac{c}{c_2} \right)^2 - 2 \right]^2 - 4 \left[ 1 - \left( \frac{c}{c_2} \right)^2 \right]^{1/2} \cdot \left[ 1 - \left( \frac{c}{c_3} \right)^2 \right]^{1/2} = 0 . \quad (21)$$

The equation (21) is the well-known secular equation for Rayleigh waves in isotropic elastic 2D continuum, see Graff (1975). Secular equations for Rayleigh waves in anisotropic media are studied in the paper by Cerv & Plešek (2013).

### 3. Conclusions

It is proved that the general frequency equation (1) for plane-stress nonaxisymmetric disc motions tends to the secular equation for Rayleigh waves for the first mode of propagation and for wavelength very short when compared with the disc radius  $r_1$ . The former results reached in Cerv (1988) by a numerical procedure were corroborated by this study.

### Acknowledgement

The work was supported by the projects 17-22615S (GA CR), TH01010772 (TA CR) with institutional support RVO: 61388998 and by the project LO1506 of the Czech Ministry of Education, Youth and Sports.

### References

- Cerv, J. (1988) Dispersion of elastic waves and Rayleigh-type waves in a thin disc. *Acta Technica CSAV*, 33, 1, pp. 89-99.
- Watson, G.N. (1966) *A Treatise on the Theory of Bessel Functions*. At the University Press, Cambridge.
- Rektorys, K. et al. (1968) *Overview of applied mathematics*. SNTL, Prague (in Czech).
- Graff, K.F. (1975) *Wave Motion in Elastic Solids*. Clarendon Press, Oxford.
- Cerv, J. and Plešek, J. (2013) Implicit and explicit secular equations for Rayleigh waves in two-dimensional anisotropic media. *Wave Motion*, 50, pp. 1105-1117.



## STRUCTURAL MODELLING OF THE STRENGTH PROPERTIES OF POLYMER COMPOSITES

R. Chatys<sup>\*</sup>, G. Miśków<sup>\*\*</sup>, J. Miśków<sup>\*\*\*</sup>

**Abstract:** This paper analyses the relationship between the structural complexity and the strength properties of fibrous composite materials fabricated by vacuum bag moulding. It shows that the mathematical model based on the critical volume fraction provides relatively good results. The materials under study were three- and five-layer sandwich-structured composites. Composite A consisted of a fibreglass core and two carbon fibre fabric skins. In composite B there was a polyester core between two fibreglass layers and two carbon fibre fabric skins. The results obtained for the materials suggest that this method can be used by design engineers working with a wide variety of polymer composites.

**Keywords:** Composite, Strength properties, Critical volume fraction, Vacuum bag, Modelling.

### 1. Introduction

The development of new composites, e.g. sandwich-structured composites, with specific properties different from those of traditional structural materials, has led to an increased interest in polymer-matrix composite materials. The materials have a wide range of potential applications. They are particularly suitable where innovative solutions are required. Because of their high strength properties (Reifsnider, 2005 and Chatys, 2013), they can be used in various controlled mobile systems (Stefański et al., 2014), including unmanned aerial vehicles (Gapinski, 2014 and Koruba, 2010), where properties superior to those of traditional structural materials not containing reinforcing particles are necessary. A vital characteristic of composite materials is that their structure can be designed in such a way as to obtain desirable properties to suit the needs of any industry (Pavelko, 2007); hence extensive research is a prerequisite.

### 2. Description of an executive anti-aircraft missile control element

The model verifying the strength properties of the composites under study assumed that the distribution of stresses in the volume was uniform. The fibre failure was considered using the critical volume fraction (Fig. 1) for components differing in the physical and mechanical properties (Fig. 2) (Paramonov, 2012).

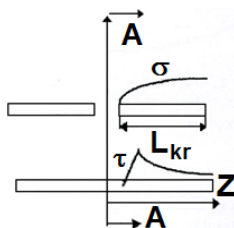


Fig. 1: Transfer of stress to the adjacent reinforcement (Blumbergs et al., 2010) resulting from tangential stress ( $\tau$ ).

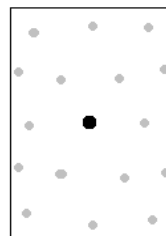


Fig. 2: Volume fraction of the laminate with a damaged fibre (•) (Blumbergs et al., 2010).

<sup>\*</sup> Assistant Prof. Rafał Chatys, Post-doctoral degree Eng.: Faculty of Mechatronics and Mechanical Engineering, Kielce University of Technology, al. 1000-lecia P.P. 7; 25-345, Kielce; PL, chatys@tu.kielce.pl

<sup>\*\*</sup> Gracjan Miśków, MSc: Phoenix Equipment Polska, ul. Jodłowa 54, 77-200 Miastko; PL, biuro@phoenixequipment.pl

<sup>\*\*\*</sup> Jerzy Miśków, MSc: Bielsko Aviation, Entrepreneurship and Innovation Park, ul. Stefana Kości 43, 43-512 Kaniów, PL opticup@opticup.com.pl

It is quite difficult to determine the exact location of the damaged fibres (reinforcement) (•) because of their random distribution. Moreover, the damage process increases with increasing load between the fibres. The fibre failure in a composite is connected with the mechanism of distribution of stresses between the neighbouring fibres. The area and volume of this zone are dependent on the ineffective length ( $l$ ) along which the damaged fibre transfers stress to adjacent fibres through tangential stresses (2) (Tab. 1).

Tab. 1: Model parameters.

Model parameters	Relationships
ineffective length	$L_{kr} = d_j \left[ \left( \frac{1 - v^{0.5}}{v^{0.5}} \right) \cdot \frac{E_f}{G_m} \right]^{0.5} \arccos h \left[ \frac{1 - (1 - \varphi)^2}{2 \cdot (1 - \varphi)} \right] \quad (1)$ <p>where: <math>d_f</math> – fibre diameter; <math>v</math> – fibre volume; <math>E_f</math> – Young's modulus for the fibre; <math>G_m</math> – matrix shear modulus; <math>\varphi</math> – level of interaction between the reinforcement and the matrix (<math>\varphi = 0.97\%</math>).</p>
tangential stress	$\tau_{lok} = \frac{\beta r}{2} \cdot \varepsilon E_i \tanh \left( \frac{\beta l}{2} \right) \quad (2)$ <p>where: <math>\beta</math> – const. (<math>\beta = 1 / B</math>); <math>r</math> – fibre radius; <math>\varepsilon</math> – elongation; <math>l</math> – fibre length (critical length).</p>
maximum stress	$\sigma_{max} = \frac{2\tau_{lok}}{\beta r} \left[ \frac{1}{\tanh \left( \frac{\beta l}{2} \right)} - \frac{1}{\sinh \left( \frac{\beta l}{2} \right)} \right] \quad (3)$ <p>where: <math>\beta</math> – const. (<math>\beta = 1 / B</math>); <math>r</math> – fibre radius; <math>l</math> – fibre length (critical length); <math>\tau_{lok}</math> – tangential stress.</p>

The failure process continues since the loading of the fibre increases by the value of stress transferred from the damaged fibre. The ultimate tensile strength of the laminate (fibre bundles) is exceeded, which leads to a redistribution of the local stresses  $\tau_{lok}$  in the adjacent components. If the stress is lower than the ultimate tensile stress, the volume fraction will continue to transfer stresses to the adjacent fibres. Knowing the tangential stress of the  $i$ -th volume fraction, we can calculate the maximum stress ( $\sigma_{max}$ ) in the damaged area. Its lowest value will indicate the strength of the composite.

### 3. Materials and methods

The sandwich-structured composites fabricated by vacuum bagging consisted of a polymer reinforcement in the form of fibreglass fabric [ $0^\circ / -90^\circ$ ] (Fig. 3a) and Rymatex biaxial carbon woven cloth (Fig. 3b) with a basis weight of  $600 \text{ g/m}^2$  and  $400 \text{ g/m}^2$ , respectively. The vacuum bag moulding process involved using vacuum pressure generated in the closed mould to press the laminate components (Paramonov et al., 2012). Before the gelcoat - a resin/hardener mixture - was applied, the reinforcement layers were degreased with Spacewax 300 wax and the mould surface was polished (Fig. 3d) to make the separation of the cured composite easier. Then, the mould edges were covered with double-sided tape to which a flexible bag was attached in order to ensure that the system was well-sealed and constant vacuum pressure could be maintained throughout the process.

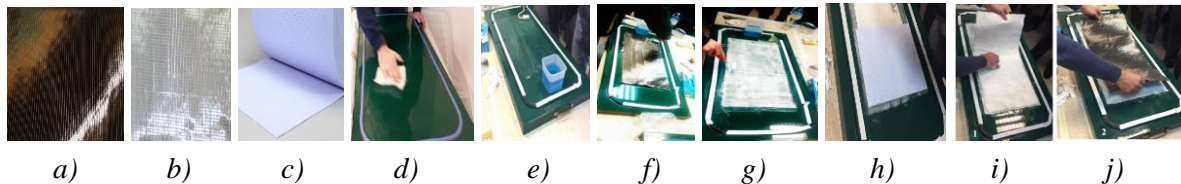


Fig. 3: Stages of fabrication of composite A and composite B.

The next stage required coating the mould with a first layer of epoxy resin (Fig. 3e). The resin-to-hardener ratio was 3-to-1 (100 g of LH 289 resin to 33 g of L 289 hardener), as recommended in the operation sheet. In composite A there were three layers: two carbon fibre fabric skins and fibreglass as the core material (Fig. 3f). The surface of the laminate was wet out with epoxy resin (Fig. 3g). Composite B

was formed in a similar way but the core material was Lantor Coremat®) Soric XF (Fig. 3c), which is characterised by high resin absorption when impregnated. The honeycomb plate (Fig. 3h) was placed in between two layers of resin-soaked fibreglass fabric (Fig. 3i) with carbon fibre fabric skin (Fig. 3j) on both sides. The top layer was also wetted with epoxy resin. The other materials required to complete the vacuum system and assist in the laminating process included peel ply (release fabric), breather fabric and perforated film. A control valve was incorporated in the breather fabric to control the volume of vacuum pressure in the envelope. The air was removed from the system through a flexible hose connected to a vacuum pump. The laminating process was completed at a pressure of -0.9 bars. The materials were heat treated at a temperature of 600 °C for 5.5 hours. The sandwich panels fabricated at the Laboratory of Composite Materials of the Kielce University of Technology were cut into testpieces with dimensions specified in the PN-EN 10002-1+ACI standard using an A.P.W2010BB waterjet cutting system (Nowakowski, 2016). Composite A and composite B were cut with a speed of 2.0 and 0.8 m/s, respectively. The next stage was quasi-static tensile tests carried out on composite A specimens in accordance with the ISO 14129:1997 standard; the experimental data were obtained using an INSTON 8501 universal testing machine operating at a speed of 2 mm/min. Composite B in the form of unnotched specimens with dimensions of 100 x 10 x 3 mm was tested to determine its Charpy impact resistance in accordance with the PN-EN ISO 179-2 standard using an Instron CEAST 9050 impact pendulum with an energy of 25 J.

#### 4. Results and discussion

The strength parameters obtained for composite A were characterised by a slight scatter of results with an average of 537.30 MPa (Tab. 2). The three-ply composite failed by shear at the interphase boundary and the resin layer containing the fibreglass fabric between the two carbon fibre layers, which was due to the occurrence of defects in the laminate structure and the cutting parameters applied during cutting.

Tab. 2: Mechanical properties of composite A fabricated by vacuum bagging.

Specimen number	$F_{\max}$ [N]	$\epsilon$ [mm]	$\sigma_{\max}$ [MPa]	E [MPa]
A1	1197.5	1.44	532	4.9
A2	1286.0	1.68	542	5.0
A3	1208.0	1.38	538	4.9
Average value	1230.5	1.50	537.30	4.93

The modelled values of strength (failure at the lowest volume fraction) in composite A and composite B (with the Soric XF core) were found to be 612.60 and 552.48 MPa, respectively (Tab. 3). The experimental value of  $\sigma_{\max}$  reported for composite A was 20 % lower than the modelled value. The structural complexity and a larger number of defects in the structure (scale effect) of composite B resulted in a greater decrease in the modelled value of  $\sigma_{\max}$  (of about 10 %).

Tab. 3: Modelled parameters of the sandwich-structured composites.

Material	$L_{kr}$ [mm]	$\tau_{lok}$ [MPa]	$\sigma_{\max}$ [MPa]
Composite A	0.590	6.047	612.60
Composite B	0.494	5.938	552.48

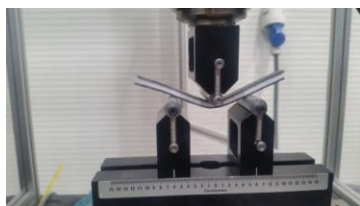


Fig. 4. Specimen under three-point bending.

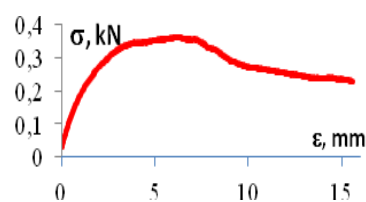


Fig. 5. Load vs. elongation for composite B.

The modifications to the structure of composite A aimed at extending its use in lightweight load-carrying structures. The laminate was modified by adding a polyester core in between the fibreglass reinforcement and carbon fibre skins (composite B). The results obtained for composite B during the three-point

bending tests (Fig. 4) were used to determine the adhesive strength at the interface between the carbon fibre and glassfibre reinforcement and the polyester core (Fig. 5). The analysis of the  $\sigma - \varepsilon$  relationship revealed that it was a ductile material because the curve had no clear yield point at which adhesion at the interface between the core and the glass and carbon reinforcement failed. Apart from the three-point bending test, composite B was subjected to impact loading, which lightweight load-carrying structures may be exposed to. The results of the impact resistance tests ( $R_e$ ) for composite B with a honeycomb core showed that there was a fracture (delamination) of the core with separation of the reinforcement from the core on one side. The average value of the impact resistance of composite B obtained from three tests was  $133.75 \text{ kJ/m}^2$  (Tab. 4).

*Tab. 4: Impact resistance of composite B.*

Specimen number	Specimen dimensions	$R_e \text{ [kJ/m}^2\text{]}$
B1	120 x 10.5 x 7.8	137.99
B2		130.58
B3		132.68
<b>Average value</b>	<b>120 x 10.5 x 7.8</b>	<b>133.75</b>

## 5. Conclusions

The strength properties of polymer composites with different arrangements of their constituents to be used in different applications are analysed using various tests and calculation methods, which help estimate more or less approximately these parameters for a designed structure. This paper has discussed two materials that can be used in structures where light weight and high strength are required. When a new material is approved (and certified) for a specific use, calculation and simulation results are not taken into account. However, structural engineers involved in design rely on data obtained from methods of estimation. This paper has dealt with experiments on composite materials with specifically arranged fibres, which exhibits different strength properties. The inaccuracy of the common calculation methods used to determine the strength of composite structures is due to the quality of the lamination process (Chatys, 2013). Composite materials fabricated by vacuum bag moulding are very compacted; bundles of continuous fibres (differing in weight) are arranged into arrays according to the number and stacking sequence of layers where stress concentrations are present.

## References

- Chatys, R. (2013) Investigation of the Effect of Distribution of the Static Strength on the Fatigue Failure of a Layered Composite by Using the Markov Chains Theory. *Mechanics of Comp. Materials*, 48, 6, pp. 629-63.
- Blumbergs, I., Chatys, R. and Kleinhofs, M. (2010) Experimental Research of Carbon Fiber Composite Material Characteristics. *Proc. Of IV Int. Conf. on Scientific Aspects of Unmanned Aerial Vehicle – SAUAV'2010*, May, 5-7, Suchedniów, Poland, pp. 46-51.
- Gapinski, D. and Krzysztofik, I. (2014) The process of tracking an air target by the designed scanning and tracking seeker, in: *Proc. 2014 15th Int. Carpathian Control Conf.* (eds. Petras, I., Podlubny, I., Kacur, J., and Farana, R.), IEEE, pp. 129-134.
- Koruba, Z., Dziopa, Z. and Krzysztofik, I. (2010) An analysis of the gyroscope dynamics of an anti-aircraft missile launched from a mobile platform. *Bulletin of the Polish Academy of Sciences – Technical Sciences*, 58, 4, pp. 651-656.
- Nowakowski, L. and Wijas, M. (2016) The evaluation of the process of surface regeneration after laser cladding and face milling, in: *Proc. 22th Int. Conf. Eng. Mech. 2016* (eds. Zolotarev, I. and Radolf, V.), Inst. Thermomechanics, Acad. Sci. Czech Republic, Prague, pp. 430-433.
- Paramonov, J., Chatys, R., Anderson, J. and Kleinhofs, M. (2012) Markov Model of Fatigue of a Composite Material with Poisson Process of Defect Initiation, *Mechanics of Composite Materials*, 48, 2, pp. 217-228.
- Pavelko, I., Pavelko, V. and Chatys, R. (2007) Strength of Fibrous Composites with Impact Damage, *Journal Mechanika*, 219, pp. 187-198.
- Reifsnider, K.L. and Stinchcomb, W.W. (2005) A Critical-Element Model of the Residual Strength and Life of Fatigue-Loaded Composite Coupons, *Composite Materials: Fatigue and Fracture*, Astm stp 907, pp. 298-313.
- Stefański, K., Grzyb, M. and Nocoń, Ł. (2014) The analysis of homing of aerial guided bomb on the ground target by means of special method of control, in: *Proc. 2014 15th Int. Carpathian Control Conf.* (eds. Petras, I., Podlubny, I., Kacur, J., and Farana, R.), IEEE, pp. 551-556.

## NUMERICAL ANALYSIS OF POLYMER COMPOSITE BEND TESTS MADE BY VACUUM BAGGING

R. Chatys<sup>\*</sup>, K. Piernik<sup>\*\*</sup>

**Abstract:** *The paper presents in a very detailed way the technology of production of polymer composite by vacuum bag method. Subsequently, a three-point bending test was performed on ABAQUS. To conduct a thorough analysis of the behavior of materials in the angle of pose: 0 °, 90 °, 45 °. Models were made using Sold. Numerical analysis was carried out to obtain the initial results needed to produce a polymer composite with the specified number of layers and the amount of pavement required to achieve the best strength properties*

**Keywords:** Modelling, Composite, MES (ABAQUS), Technology, Three-point bending.

### 1. Introduction

Impact is often used to influence the objects of the outside world, used by most living beings. Instinctively or consciously they use the fact that the forces formed at the moment of impact in the bodies in contact repeatedly (sometimes even thousands of times) exceed the weight of these bodies. All this made the basic strike by destroying, destroying, and altering the shape of external objects. Hence, there is a direct link between scientific research on the effects of impact as a physical process and the mechanics of fracture (Rokach, 2005). Vacuum bag method is one of the most popular forms of polymer composite production in the world. This method is relatively cheap and allows for the production of very high quality composites. Finite element methods are numerical methods that can be applied to the exact solution of complex technical problems (Rao, 2005). Thanks to this, very accurate results of displacements and analyzes can be obtained in the whole area of the sample, and it allows to model multi-axis stretching of materials which will be the subject of subsequent articles.

### 2. Methods

Plate made of polymer composite was made by the vacuum bag method in the Laboratory of the Technical University of Świętokrzyska. Prior to the actual bending test, the FEM simulation was performed. To verify the theoretical stresses and deformations with the real ones that will appear in subsequent publications.

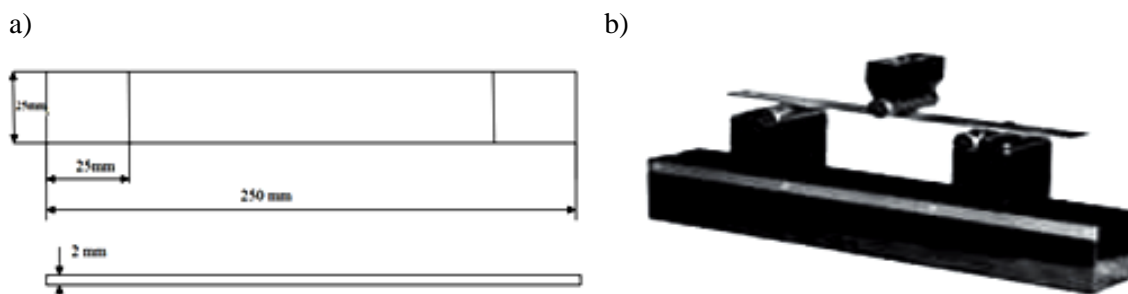


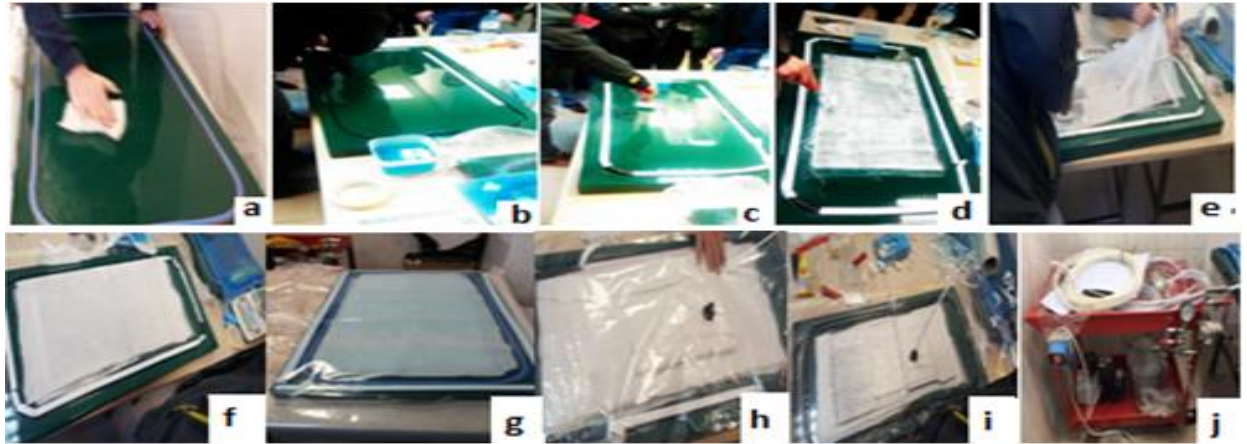
Fig. 1: a) Geometrical dimensions of the sample; b) Device for bending laminates (Suwak, 2010).

<sup>\*</sup> Assistant Prof. Rafał Chatys, Post-doctoral degree. Faculty of Mechatronics and Mechanical Engineering, Kielce University of Technology, al. 1000-lecia P.P. 7; 25-345, Kielce; PL, chatys@tu.kielce.pl

<sup>\*\*</sup> Krzysztof Piernik, PhD-student: Faculty of Mechatronics and Mechanical Engineering, Kielce University of Technology, al. 1000-lecia P.P. 7; 25-345, Kielce; PL, piernikkrzysztof@gmail.com



Tab. 1: Stages of manufacture of polymer composite vacuum bag method: a - polishing mold; b - attaching the double sided tape mounting; c - the imposition of the first layer of resin; d - overlap the first layer fibreglass fabric; e - imposition of layer peel ply; f - fabric breathable perforated foil; g, h - vacuum bag attachment along with a hole with extraction; i - material subjected to pressure; j- vacuum unit.



Prepare a three point bend test in ABAQUS according to the actual model shown in Fig. 1b. Due to the difficulty of performing composite stretching tests, three or four point bending tests (Fig. 1b) are used in a large-scale study of these materials. In ISO-EN ISO178 standard it is intended to use rectangular samples with a height-to-distance ratio of  $l/h = 16$ . This ensures that damage due to normal stresses  $\sigma$  associated with the bending moment occurs due to delamination caused by tangential stresses (Laboratory of Materials Strength).

The ABAQUS program has been modeled in three-point bending mode in the ASSEMBLY module, 3 contact connections have been made (Fig. 2).

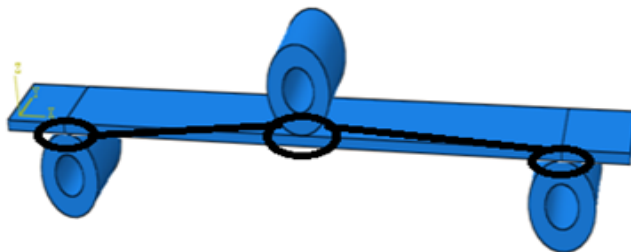


Fig. 2: Model three-bend made in module ASSEMBLY.

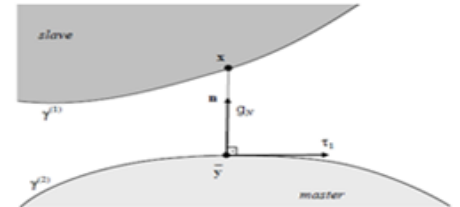


Fig. 3: Kinematic variables in contact in the three-point bending (Supkiewicz, 2014).

Formulation of contact conditions requires the introduction of kinematic variables determining the relative position and the relative movement of the contact surfaces (Fig. 3). A master-slave approach in which arbitrarily assigns slave and master roles, respectively, and relative motion is described with respect to the configuration associated with the master body (Lengiewicz, 2008).

Tab. 2: Average strength of laminates (Chatys, 2015).

angle [°]	average $F_{\max}$ [kN]	average $\sigma_{\max}$ [MPa]	average E [GPa]
0	7.31	122.90	11.27
45	8.63	174.60	14.18
90	4.36	73.67	9.62

Very important role in the design of dynamic composite materials tests is the selection of the grid (Fig. 4) because we use contact links for two different metals of different structures (in this case steel composite).

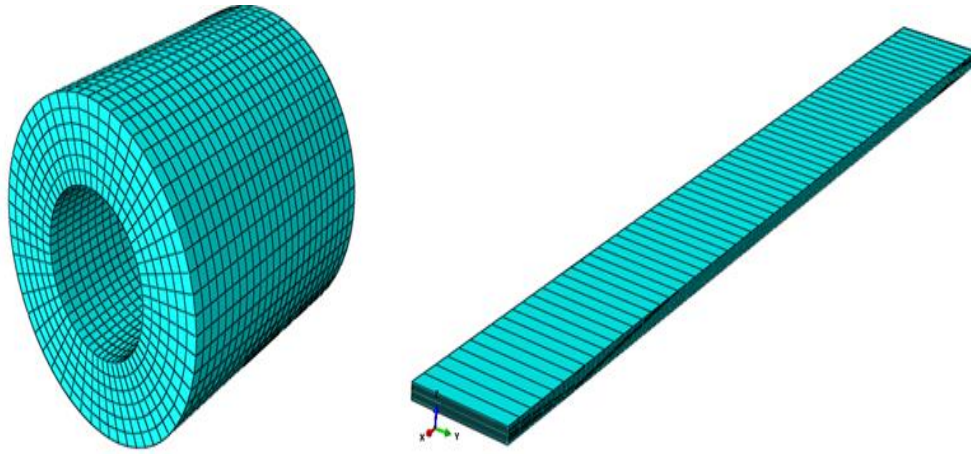


Fig. 4: Finite element mesh selection for stamp and composite.

## 2.1. Analysis of the results

The analytical methods for determining the strength of the polymer composites taking account of shock loads, observed a decrease in strength in research materials as a result of exceeding the threshold energy. In the literature discusses only the quality of the process of the destruction of and provides assessment of the likely size of damage by analysis (e.g., linear), as the equivalent of Tresca and Von Misesa (Chatys, 2013). The distribution of such equivalent stresses under specified impact hypothesis Huber (Bohdar, 2004 and Rokach, 2005) for the above data contained in Tab. 2 (obtained from the five tests). Hypothesis Huber von Misses ( $W_{C-T-G}$ ) very well coincide with the experimental data for elastic and according to her: work ratio bigger material at a given point of the body dictates the strain energy density, regardless of the type of stress state saved the above dependencies:

$$W_{C-T-G} = \left( \left| \frac{\sigma_1 - \sigma_2}{2} \right|, \left| \frac{\sigma_1 - \sigma_3}{2} \right|, \left| \frac{\sigma_2 - \sigma_3}{2} \right| \right) \quad (1)$$

$$\max = \left( \left| \frac{\sigma_1 - \sigma_2}{2} \right|, \left| \frac{\sigma_1 - \sigma_3}{2} \right|, \left| \frac{\sigma_2 - \sigma_3}{2} \right| \right) = \left| \frac{\sigma}{2} \right| \leq \frac{R_k}{2} \quad (2)$$

where:  $\sigma_1, \sigma_2, \sigma_3$  - values of principal stresses.

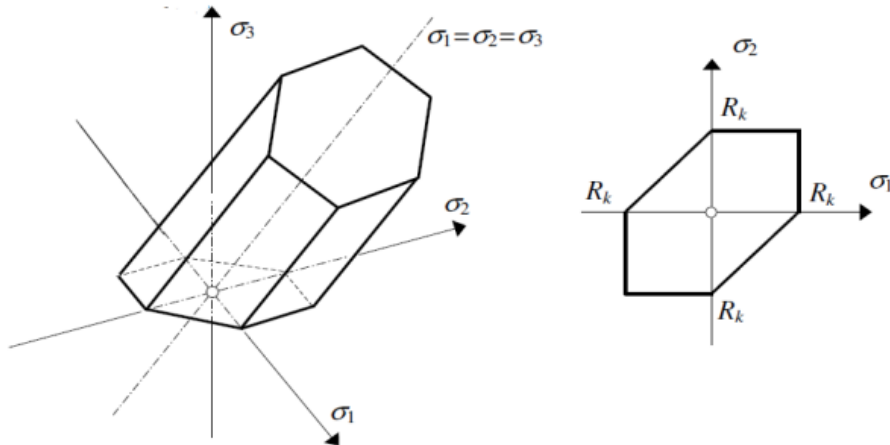


Fig. 5: Graphical interpretation of Huber's hypothesis (Bohdar, 2004).

In the Haigh-Becker three-dimensional space, the above condition defines the space within an infinitely long cylinder with an axis that coincides with the axis of the axes and in a two-dimensional space - an area bounded by an ellipse (Bohdar, 2004).

The graphs below (Fig. 6) can be analyzed in detail for the stress distribution of Huber von Misses. Only the stresses of the sample measurement base are taken into account.



### 3. Conclusions

During bending tests, many problems can provide a compression strength that accurately reflects the FEM analysis. Taking into account the positive and negative aspects of stretching and bending, they are used equally often. These tests are designed not only to determine the strength and elasticity modules but also the fracture behavior of the material (fig) as it is of great importance for the various types of collisions exposed to already finished composite products (e.g tram elements or car bumpers). Polymeric unidirectional characterizes high anisotropy of strength modules and elasticity.

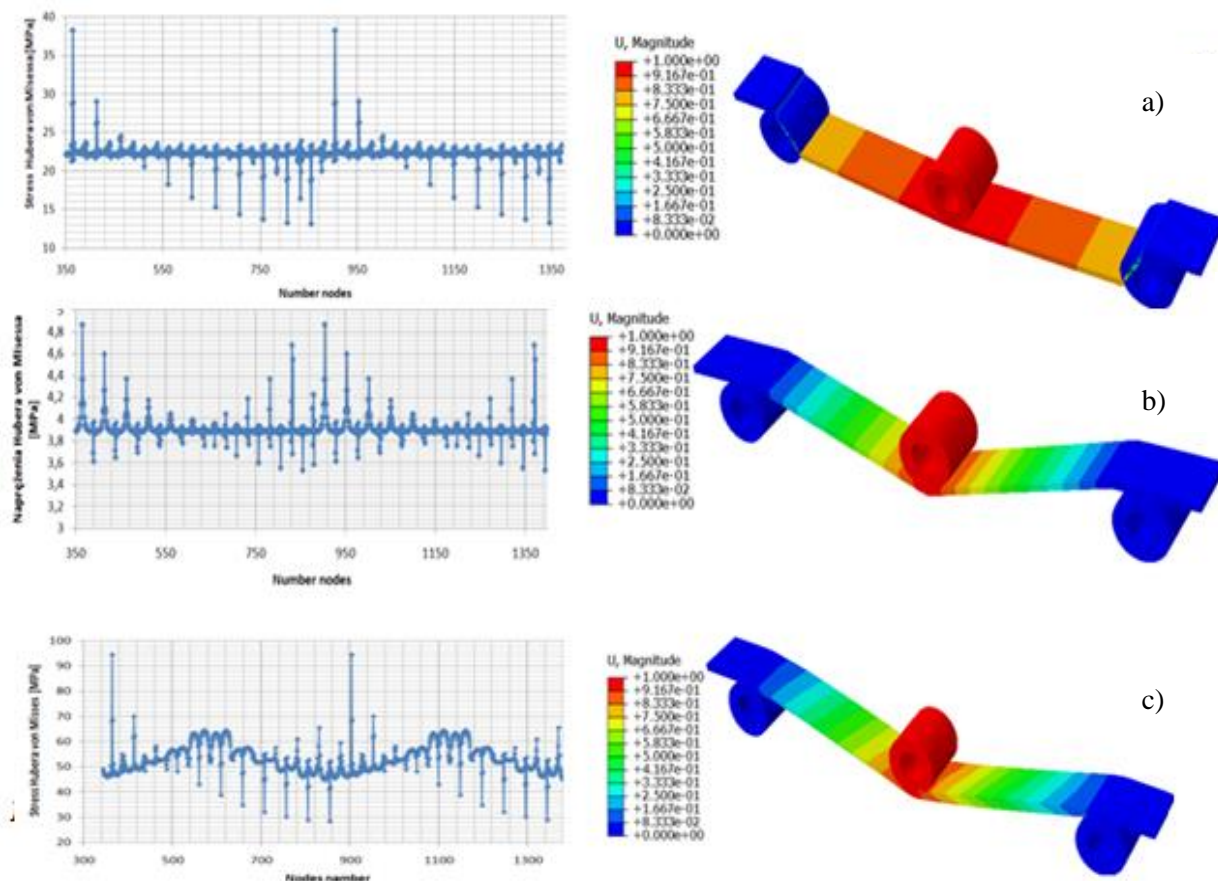


Fig. 6: Chart Missesa von Huber stress destroying composite installation:  
a) Destroying composite installation 0 °; b) Destroying composite installation 90 °;  
c) Destroying composite installation 45 °.

### References

- Rokach, I. (2005) Numeric-Analytical Impact Modeling, Kielce (in Polish).
- Rao, S.S. (2005) The Finitement Method IN Engineering.
- Langiewicz J. (2008) Department of Materials Engineering Unassisted, Department of Materials Mechanics, IPPT PAN, PhD. Thesis, [http://www.ippt.pan.pl/\\_download/doktoraty/Lengiewicz\\_doktorat.pdf](http://www.ippt.pan.pl/_download/doktoraty/Lengiewicz_doktorat.pdf), (in Polish).
- Chatys, R. and Piernik, K. Modeling of mechanical properties of aerospace products made of fiber reinforced composites (in Polish).
- Chatys, R. (2013) A Statistical Analysis of Strength Parameters of Fibrous Composites at Failure using the Markov Process, Monogrhy M52, Ed. Kielce of Technology University, Kielce, pp. 174.
- Suwak, R. and Rawluk, M. (2010) Application of Three-point Bending to Study the Course of Deformation of Refractory Concrete at High Temperature. Scientific Works of Institute of Ceramic and Construction Materials. 6, 3, pp. 90-103.

## NONLINEAR VIBRATION – STOCHASTIC APPROACH

J. Cienciala<sup>\*</sup>, K. Frydrýšek<sup>\*\*</sup>, J. Podešva<sup>\*\*\*</sup>

**Abstract:** *This paper presents a stochastic approach to the free vibration of a solid body with nonlinear damping. Simulations were conducted in MATLAB and Anthill, using the Monte Carlo method. The results of practical damping tests were used and approximated to create a mathematical model of vibration. For the stochastic calculations, the input parameters of the mathematical model were assigned deviations using a histogram of probability distribution reflecting real operational situations.*

**Keywords:** Vibration, Nonlinear damping, Dynamics, Stochastic mechanics, Monte Carlo.

### 1. Introduction

This paper describes a solution for the technical free vibration of a solid body taking into account the influence of nonlinearity in viscous dampers. The calculations are based on motion equations of technical vibration including nonlinearity of damping via the mathematical expression of the characteristics of the damping elements. As it is very problematic to find a closed-form solution, the vibration is solved numerically. An integral part of the paper is a stochastic calculation of vibration incorporating variance in input values. The stochastic calculations are conducted using the Monte Carlo method in Anthill software. The resulting curves for the investigated parameters can find practical application in the optimization of products such as rotary machines, where the parameters of mass, centre of gravity position etc. change during operation. An ideal example is a washing machine, whose mass and centre of gravity vary depending on the quantity of water or clothing inside it, meaning that stochastic variance realistically represents the normal operation of the machine. Variables also include the characteristics of suspension springs or damping, as shown in the probability calculations. For more details see Brousil (1989), Juliš (1987), Timoshenko (1960) and Frydrýšek (2011), Frydrýšek (2012).

### 2. Nonlinear free vibrations

In order to determine the curves for the vibration of a body, it is necessary to specify the damping function  $F_b$  [N], see Fig. 1b, which best corresponds with real data. The appropriate power function was specified in the following form:

$$F_b(v) = \text{sign}(v) \cdot p_1 \cdot (|v|)^{p_2}, \quad (1)$$

where the coefficients  $p_1 = 140$  kg/s,  $p_2 = 1/5$  and  $v$  [m/s] is the velocity of linear motion of the damper.

It is very difficult, if not impossible, to find a closed-form solution for self-induced or externally-induced vibration with the given nonlinear damping function. Possible variants therefore include the linearization of the damping function or numerical calculation. From our observations, initial conditions and measuring follows the simplification based on the 1D model (i.e. the other 5 generalized coordinates can be neglected).

---

<sup>\*</sup> M.Sc. Jakub Cienciala: Department of Applied Mechanics, Faculty of Mechanical Engineering, VSB - Technical University of Ostrava, 17. listopadu 2172/15; 708 33, Ostrava; CZ, jakub.cienciala@vsb.cz

<sup>\*\*</sup> Assoc. Prof. M.Sc. Karel Frydrýšek, Ph.D.: Department of Applied Mechanics, Faculty of Mechanical Engineering, VSB - Technical University of Ostrava, 17. listopadu 2172/15; 708 33, Ostrava; CZ, karel.frydrysek@vsb.cz

<sup>\*\*\*</sup> Assoc. Prof. M.Sc. Jiří Podešva, Ph.D.: Department of Applied Mechanics, Faculty of Mechanical Engineering, VSB - Technical University of Ostrava, 17. listopadu 2172/15; 708 33, Ostrava; CZ, jiri.podesva@vsb.cz

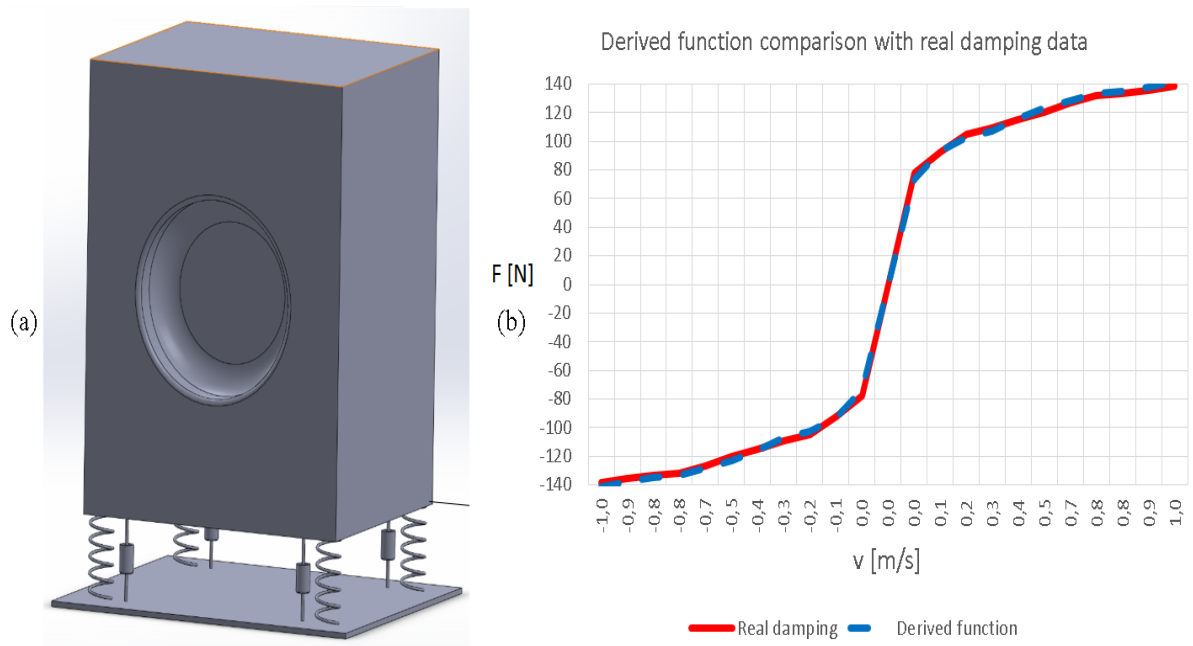


Fig. 1: a) Illustration of the solid body; b) comparison of derived damping function with real data.

The advantage of numerical calculation is the option of using nonlinear damping characteristics, which better represent reality than the linearization of the damping function. The calculation assumes an even acceleration of motion at very short intervals  $dt = 0.0001$  s. The solution is thus performed by iteration, with the initial displacement  $x_0$  [m] and the initial velocity  $v_0$  [m/s]. The relation for acceleration is derived from the motion equation as follows:

$$a = \frac{-F_k - F_b}{m_t} = \frac{-k_c \cdot x - \text{sign}(v) \cdot p_1 \cdot (|v|)^{p_2}}{m_t} \left[ \frac{m}{s^2} \right], \quad (2)$$

where  $F_k$  [N] is the directional force of the suspension springs,  $F_b$  [N] is the directional force of the dampers,  $m_t$  [kg] is the mass of the body,  $k_c$  [N/m] is the total suspension spring stiffness, and  $x$  [m] is the trajectory of motion.

After introducing the initial values  $x_0$  [m] and  $v_0$  [m/s], we obtain the initial acceleration  $a_0$  [m/s<sup>2</sup>]. It is then necessary to select an appropriate number of integration steps for the numerical solution dependent on the time step  $dt$ .

The numerical calculation can be carried out using the loop “for” in MATLAB software; see Fig. 2:

```

1 - mt=173;kc=27200;x0=0.03;v0=0;
2 - p1=140;p2=0.2;
3 - dt=0.0001;
4 - n=20000;
5
6 - for i=1:n
7 -     a0(i)=-(kc*x0(i)+sign(v0(i))*p1*abs(v0(i))^p2)/mt;
8 -     v(i+1)=v(i)+a(i)*dt;
9 -     x(i+1)=x(i)+v(i)*dt+0.5*a(i)*dt^2;
10 -    a(i+1)=-(kc*x(i+1)+sign(v(i+1))*p1*abs(v(i+1))^p2)/mt;
11 - end;
```

Fig. 2: Numerical calculation of vibration (MATLAB program).

The resulting curves for nonlinear vibration (trajectory, velocity and acceleration) are shown in Fig. 3.

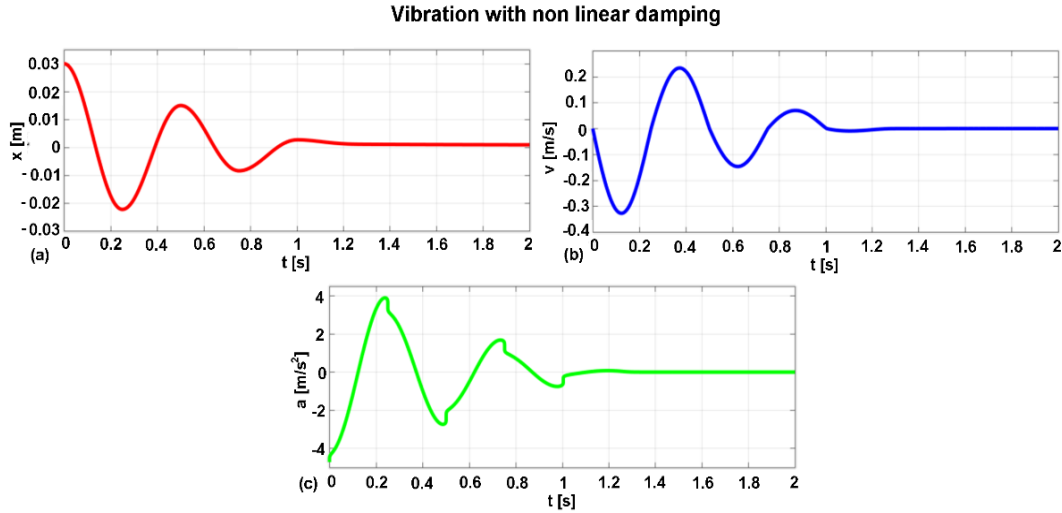


Fig. 3: Vibration with nonlinear damping: a) trajectory; b) velocity; c) acceleration.

### 3. Stochastic inputs

The stochastic approach (Monte Carlo method) is explained in the references Frydryšek (2010), Frydryšek (2011) and Frydryšek (2012).

In order to solve the vibration of a body with a certain probability value (the stochastic approach), the individual inputs were assigned probability distributions. This corresponds sufficiently with reality. Three basic parameters were used with the specified variance ( $m_t = 173.13 \pm 0.8$  kg,  $k_c = 27199.603 \pm 415.331$  N/m,  $x_0 = 0.03 \pm 0.006$  m).

Probability distributions of the individual parameters can be depicted using histograms. For example, the histogram for the probability distribution of the total mass of the body is shown in Fig. 4a, and the histogram for suspension spring stiffness is shown in Fig. 4b.

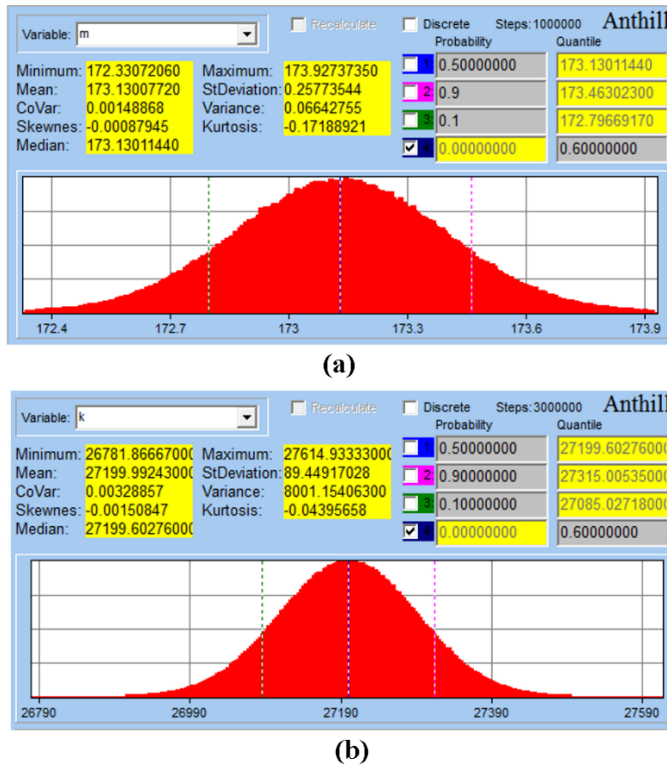


Fig. 4: Probability distribution histogram for: a) total mass  $m_t = 173.13 \pm 0.8$  kg; b) suspension spring stiffness  $k_c = 27199.603 \pm 415.331$  N/m.

#### 4. Stochastic outputs

The resulting vibration curves for  $3 \times 10^6$  Monte Carlo simulations show a variance that is best illustrated in graphic form, e.g. depicting the time dependence of trajectory and velocity; see Fig. 5.

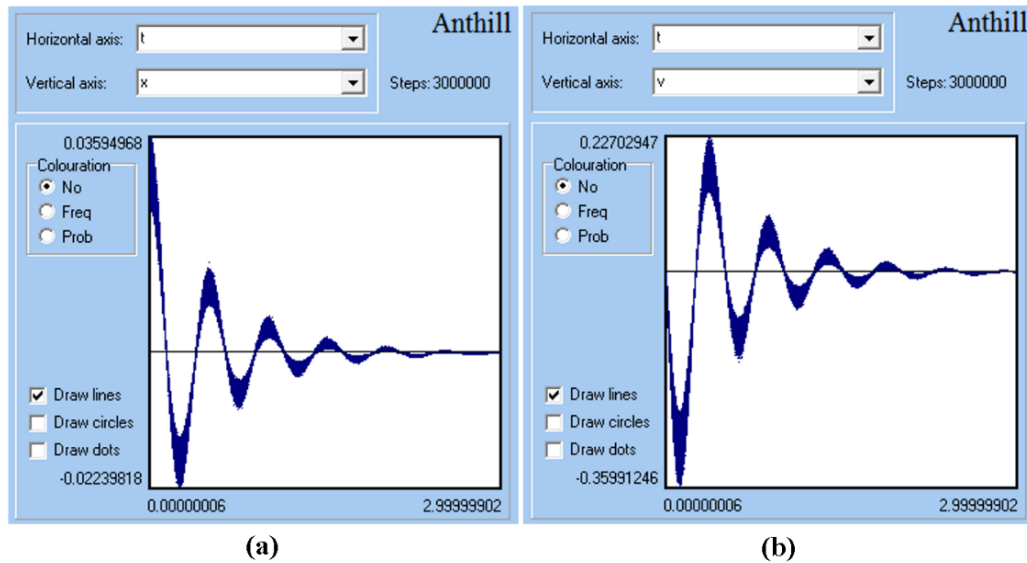


Fig. 5: a) time dependence of trajectory; b) time dependence of velocity.

#### 5. Conclusion

The data characterizing the damping of a body in motion were interpolated by means of a nonlinear function that was incorporated into the vibration calculation. As it was not possible to find a closed-form solution, the problem was solved numerically on a simple 1D model. The calculation used stochastic inputs (histograms) in the Monte Carlo method. The individual input parameters were assigned probability distributions corresponding with reality; the solution thus describes real variance. The advantage of using stochastic calculations is the ability to determine the interval of values in which an observed parameter occurs with a specified level of probability. In the case of the vibration of a body with rotating unbalance, this method brings significant benefits especially in determining the resonance area which must be overcome as rapidly as possible when the machine is starting or finishing its rotary motion. The calculations using Anthill software (Monte Carlo method) were conducted with  $3 \times 10^6$  random simulations. The stochastic approach is a modern trend in science and technology which enables engineers to respect the reality of random parameters that are typical of random vibration.

#### Acknowledgement

This paper is an output of the project SP 2017/136.

#### References

- Brousil, J., Slavík, J. and Zeman, V. (1989) Dynamics, SNTL, Prague (in Czech).
- Frydrýšek, K. (2010) Stochastics calculations in mechanics 1, VSB – Technical University of Ostrava, Faculty of Mechanical Engineering, ISBN 978-80-248-2314-0, pp. 1-149 (in Czech).
- Frydrýšek, K. (2011) Probabilistic approaches applied in the solution of problems in mining and biomechanics, 17<sup>th</sup> International Conference on Engineering Mechanics, Svratka, Czech Republic, ISBN 978-80-87012-33-8, pp. 151-154.
- Frydrýšek, K. (2012) Monte Carlo approach applied in the design of machine parts and structures, International Journal of Mechanics, Vol. 6, Issue 4, ISSN 19984448, pp. 222-229.
- Juliš, K., Brepta, R. (1987) Mechanics, Part II, Dynamics, SNTL, Prague (in Czech).
- Timoshenko, S. (1955) Vibration Problems in Engineering, Van Nostrand Company.

## DESIGNATION THE VELOCITY OF CESSNA 172 AIRCRAFT BASED ON GPS DATA IN FLIGHT TEST

J. Ćwiklak<sup>\*</sup>, K. Krasuski<sup>\*\*</sup>, H. Jafernik<sup>\*\*\*</sup>

**Abstract:** *In recent years the GPS satellite receiver is a basic equipment of avionics onboard of aircraft. Especially, the GPS receiver is utilized for designation the component of PV (Position-Velocity) model of the aircraft in kinematic mode in air navigation. The mathematical scheme of recovery the velocity of aircraft in local frame ENU (East-North-Up) is presented in this article. As part of research works a values of velocity of motion of the aircraft were appointed and showed.*

**Keywords:** GPS, Velocity, ENU frame, Aircraft.

### 1. Introduction

The GPS receiver is usually placed on the board the platform of plane that allows to recovery the position of the aircraft in three-dimensional space. The typical accuracy of determine the position of the aircraft for GPS receiver is presented in ICAO instruction in Annex 10 (Grunwald et al., 2016). Set coordinates of the aircraft are related by the GPS receiver to the geocentric XYZ or the geodetic BLh frame or the local ENU frame (Wierzbicki et al., 2016). The GPS receiver built in into the navigational system of the aircraft also allows for determining the navigational parameters such as coordinates, velocity or attitude. Components of the vector speed are determined along each coordinate axis ENU and determine the relative rate of movement of platform.

Exploiting the technical infrastructure of the GPS receiver for determining navigational parameters of velocity of the platform of the aircraft is the aim of the study. In paper the relative velocity of motion of Cessna 172 plane were presented and described. The GPS data for research experiment are obtained from dual-frequency Topcon HiperPro receiver. The GPS receiver was installed onboard Cessna 172 plane at during the flight test on military aerodrome in Dęblin in 1<sup>st</sup> June of 2010. The article was divided into 3 sections and references were added at the end of this paper.

### 2. Methods and Results

The relative velocity of the flight of the aircraft was determined in the local ENU frame and is expressing the change of ENU coordinates in the determined interval of the time, according to equations:

$$V_E = \frac{\Delta E}{\Delta t} \quad (1)$$

$$V_N = \frac{\Delta N}{\Delta t} \quad (2)$$

$$V_U = \frac{\Delta U}{\Delta t} \quad (3)$$

---

<sup>\*</sup> Assoc. Prof. Janusz Ćwiklak, PhD.: Faculty of Aviation, Polish Air Force Academy; Dywizjonu 303 nr 35; 08 521, Dęblin; PL, j.cwiklak@wsosp.pl

<sup>\*\*</sup> Msc. Ing. Kamil Krasuski, PhD. candidate: Faculty of Geodesy, Cartography and Cadastre, District Office of Ryki, Wyczółkowskiego 10A; 08 500, Ryki; PL, kk\_deblin@wp.pl

<sup>\*\*\*</sup> Assist. Prof. Henryk Jafernik, PhD.: Faculty of Transport, Silesian University of Technology, Krasińskiego 13; 40 019, Katowice; PL, henryk.jafernik@polsl.pl



where  $V_E$  - velocity along to East (E) axis,  $V_N$  - velocity along to North (N) axis,  $V_U$  - velocity along to Up (U) axis,  $\Delta t$  - time interval.

The coordinates of aircraft in local frame ENU are designated using formula (Sanz Subirana et al., 2013):

$$\Delta E = -\sin L \cdot \Delta X + \cos L \cdot \Delta Y + 0 \cdot \Delta Z \quad (4)$$

$$\Delta N = -\cos L \cdot \sin B \cdot \Delta X - \sin L \cdot \sin B \cdot \Delta Y + \cos B \cdot \Delta Z \quad (5)$$

$$\Delta U = \cos L \cdot \cos B \cdot \Delta X + \sin L \cdot \cos B \cdot \Delta Y + \sin B \cdot \Delta Z \quad (6)$$

where  $(E, N, U)$  - the coordinate of aircraft position in navigational frame ENU,  $(X, Z, Y)$  - geocentric coordinates of aircraft,  $(B, L)$  - geodetic coordinates of aircraft,  $B$  - Latitude,  $L$  - Longitude.

The geocentric coordinates  $(X, Z, Y)$  are determined based on navigation solution of user position in GPS system. In this paper, the geocentric coordinates of aircraft were designated using SPP (Single Point Positioning) method for C/A code observations. The GPS kinematic observations were collected by dual-frequency Topcon HiperPro receiver, which was located into pilot's cabin in Cessna 172 plane (Ćwiklak et al., 2010). The flight test was conducted close to military aerodrome in Dęblin in Poland at time of 1<sup>st</sup> June of 2010 (see Fig. 1). The flight trajectory of Cessna 172 plane was calculated into RTKLIB software in RTKPOST numerical module. The mathematical scheme of solution of SPP method in RTKPOST module is focused on least square estimation in stochastic model. The input data such as GPS observations and ephemeris parameters must be implemented in SPP method in RTKPOST module (Takasu, 2013). The final geocentric coordinates of aircraft can be also transformed using Helmert's formula into geodetic frame  $(B, L)$ . The results of trajectory in geodetic frame  $(B, L)$  are presented into Fig. 1. The geodetic coordinates  $(B, L)$  expressed the aircraft's position in global WGS-84 datum.

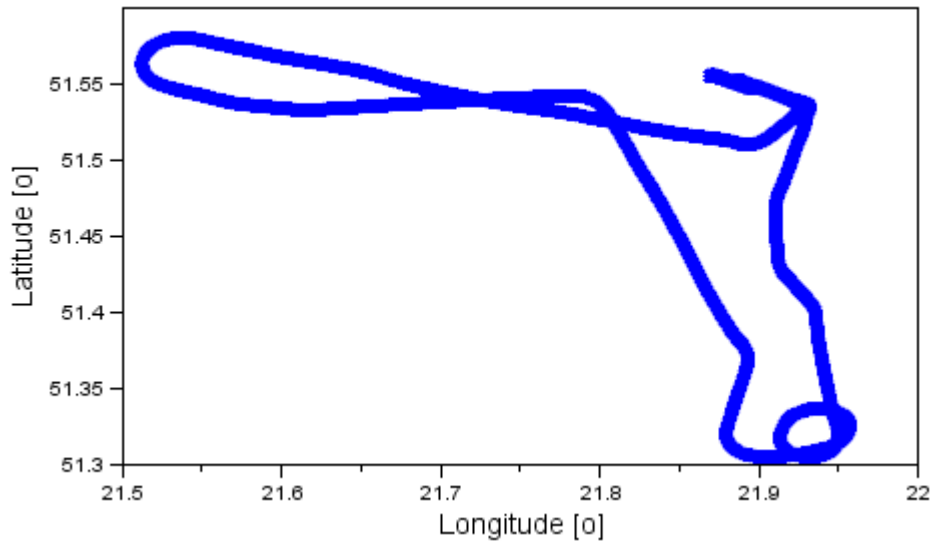


Fig. 1: The horizontal trajectory of flight of Cessna 172 plane.

Fig. 2 presents relative velocity of the flight of the Cessna 172 aircraft related to the local ENU frame. The value of the velocity along the E axis fluctuates -30.01 m/s to 31.35 m/s, in addition the average of absolute velocity is 11.85 m/s. One should be underline that the dispersion of results for the velocity along E and N axis is biggest of results presented in Fig. 2. The results of velocity parameter along the N axis are between -37.89 m/s and +31.07 m/s. The average of absolute value of  $V_N$  velocity equals 12.13 m/s, whereas the median for this parameter equals 6.92 m/s. The value of velocity for  $V_U$  parameter amounts between -5.14 m/s and 8.29 m/s. Moreover the average of absolute value of  $V_U$  parameter equals 0.52 m/s, whereas the median 0.29 m/s, accordingly. Additionally the  $V_U$  parameter has the smallest scattering of results in comparing to the  $V_E$  and  $V_N$  velocities. Moreover the results of  $V_E$  and  $V_N$  velocities are not exceeded the value of  $\pm 50$  m/s.



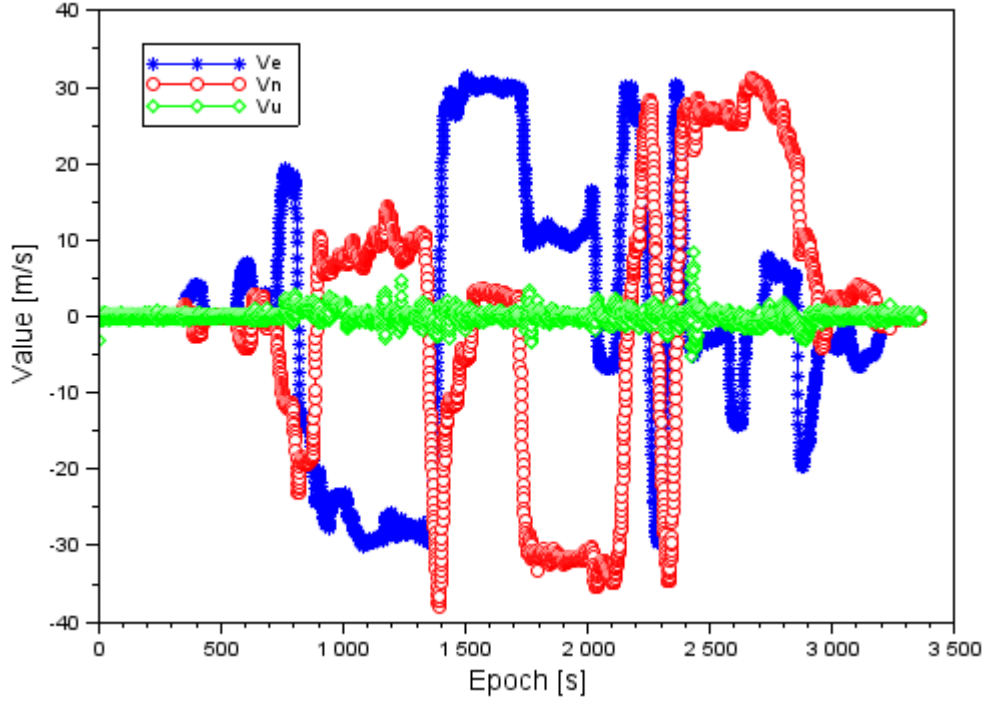


Fig. 2: The relative velocity of flight of Cessna 172 plane.

By identifying the velocity of the aircraft along each axis of the local ENU model, determination of the total velocity of flight of the Cessna 172 plane is possible, as below:

$$V_0 = \sqrt{V_E^2 + V_N^2 + V_U^2} \quad (7)$$

where  $V_0$  - total velocity of aircraft.

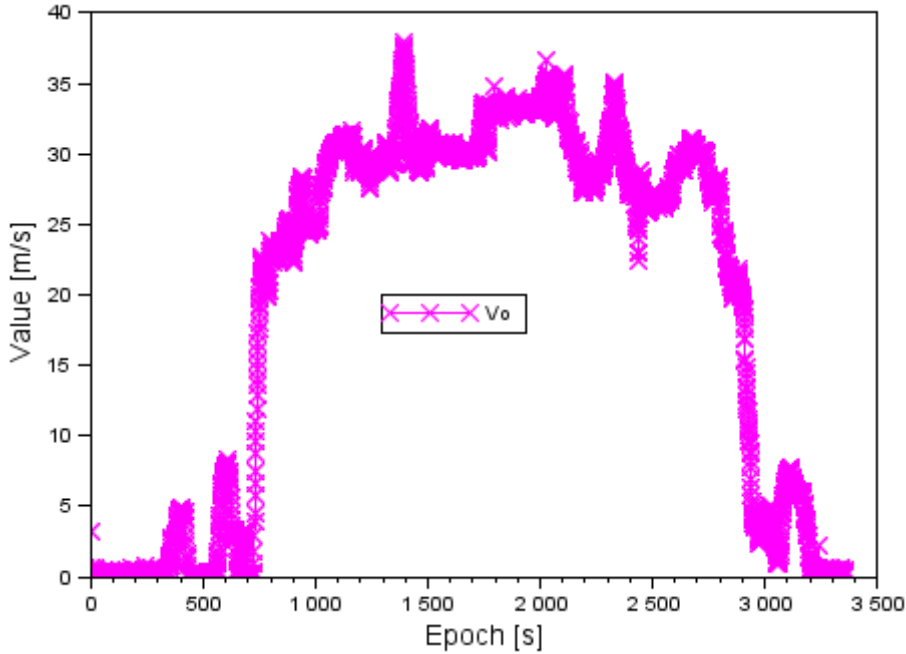


Fig. 3: The total velocity of flight of Cessna 172 plane.

Fig. 3 presents graph of the total velocity of the aircraft in the function of measured epoch. The average value of the velocity of an aircraft equals 19.57 m/s. It should be added that scattering of results for the parameter of the total movement speed of Cessna 172 plane equals between 0.02 m/s and 37.91 m/s. In addition median parameter for total velocity parameter equals 27.02 m/s. It is worthwhile to note that  $V_0$  velocity parameter is less than 10 m/s for 34 % of obtained results and 72 % of results are less than 30 m/s, accordingly. In middle phase of flight, the total velocity can reach up to 38 m/s.

### 3. Conclusions

The practical application of the satellite GPS technique in the technology of aircraft, particularly in the aspect of the determination of position and velocity were presented in this article. In this paper, results of determination of coordinates the velocity in local frame ENU for the Cessna 172 aircraft were presented. The coordinates of the aircraft were expressed in the local frame ENU on the basis of the transformed method between geocentric, geodetic and local frame in GPS system. The nominal position of the aircraft was designated using GPS code observations for SPP positioning method in kinematic mode. Moreover the total velocity of motion of the Cessna 172 plane was also determined also in paper. The input data for research experiment was registered through dual-frequency Topcon HiperPro receiver at during the flight experiment close to military aerodrome in Dęblin in Poland. The flight test was realized using Cessna 172 plane in day of 01.06.2010.

### References

- Ćwiklak, J. and Jafernik, H. (2010) The monitoring system for aircraft and vehicles of public order services based on GNSS. *Annual of Navigation*, No. 16, pp. 15-24.
- Grunwald, G., Ciećko, A., Bakula, M. and Kaźmierczak, R. (2016) Examination of GPS/EGNOS integrity in north-eastern Poland. *IET Radar, Sonar & Navigation*, 10 (1), pp. 114-121, doi: 10.1049/iet-rsn.2015.0053.
- Sanz Subirana, J., Juan Zornoza, J.M. and Hernández-Pajares, M. (2013) *GNSS Data Processing, Vol. I: Fundamentals and Algorithms*. ESA Communications, ESTEC, Noordwijk, Netherlands, ISBN: 978-92-9221-886-7, pp. 186-187.
- Takasu, T. (2013) *RTKLIB ver. 2.4.2 Manual*, RTKLIB: An Open Source Program Package for GNSS Positioning.
- Wierzbicki, D. and Krasuski, K. (2016) Utilization GPS technics for determination Heading, Pitch and Roll angles – part I. *Problems of Mechatronics*, 7, 1 (23), pp. 113-126, (in Polish).

## APPLICATIONS OF THE NEW METHOD OF THE LYAPUNOV EXPONENTS ESTIMATION

Dabrowski<sup>\*</sup>, M. Balcerzak<sup>\*\*</sup>, D. Pikunov<sup>\*\*\*</sup>

**Abstract:** In this article we show the new simple and effective method of Lyapunov Exponents (LE) estimation, based on the perturbation vector and its derivative dot product analysis. We show that presented method can be applied in different aspects of the nonlinear systems control. Moreover, our method is based on very simple computations, involving only basic mathematical operations, such as summing, subtracting, multiplying, dividing, thus it can be easier to apply than other methods. As the actual Lyapunov exponent value is calculated before the next integration step it does not involve an integration errors.

**Keywords:** Stability, Lyapunov exponents, Nonlinear dynamics, Control system optimization.

### 1. Introduction

Controlling system dynamics with use of Lyapunov Exponents (LE) is employed in many different areas of the scientific research and is used in controlling dynamics of increasingly complex dynamical systems. LE are employed in scientific research of materials (Aniszewska, 2008), electric power systems (Wadduwage, 2013), non-continuous systems (Serweta, 2015), systems with time delay (Stefański, 2005), aerodynamics (Hu, 2012), time series analysis (Yang, 2012), optimal control (Zhu, 2004), chaotic encryption and secure communication (Chunbiao, 2012), multi-objective optimization (Fraga, 2014), parametric oscillations and fluctuating parameters (Stefanski, 2008), neuronal models investigations (Soriano, 2012). Thus, there is still need to elaborate fast and simple methods of LE calculation. The new method of LE estimation is presented in this paper.

### 2. Method

Generally presented method bases on the analysis of the disturbance changes  $dz(t)$  in the direction of the general disturbance vector  $z(t)$  (Fig. 1) and was discussed in (Dabrowski, 2012, 2012, 2014).

Fig. 1 shows two perturbations of  $z$  in the phase space. Assume that  $z$  for the dynamical state  $x(t)$  evolves according to linear transformation assigned  $U(x(t))$ .

Let  $z^*$  be the component of  $z$  in the direction of eigenvector  $w^*$  of linear transformation  $U(x(t))$ . In that case:

$$\frac{dz^*}{dt} = U(x(t))z^* = \lambda^* z^* \quad (1)$$

where  $\lambda^*$  is the eigenvalue of  $U(x(t))$ , corresponding to eigenvector  $w^*$ . After transformation of (1) to scalar form one can obtain:

$$\frac{|dz^*|}{|z^*|} = \lambda^* dt \quad (2)$$

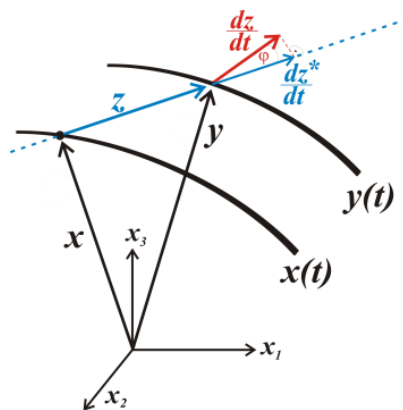


Fig. 1: Scheme of perturbation vector and its derivative.

<sup>\*</sup> Assoc. Prof. Artur Dabrowski, PhD.: Division of Dynamics Dept of Mechanical Engineering, Lodz University of Technology, Stefanowskiego 1/15; 90-924, Lodz; Poland, Ar2rDe@p.lodz.pl

<sup>\*\*</sup> Marek Balcerzak, MSc.: Division of Dynamics Dept of Mechanical Engineering, Lodz University of Technology, Stefanowskiego 1/15; 90-924, Lodz; Poland, marek.blck@gmail.com

<sup>\*\*\*</sup> Danylo Pikunov, MSc.: Division of Dynamics Dept of Mechanical Engineering, Lodz University of Technology, Stefanowskiego 1/15; 90-924, Lodz; Poland, dpikunov@gmail.com

Integration of (2) yields:

$$|\mathbf{z}^*| = |\mathbf{z}_0^*|e^{\lambda^* t} \quad (3)$$

where  $\mathbf{z}_0^*$  is the initial state of  $\mathbf{z}^*$ . Equation (3) describes evolution of the disturbance  $\mathbf{z}^*$  in the direction of  $\mathbf{w}^*$ . One can notice that the formula (3) describes an averaged evolution of perturbation length. This shows a connection between largest eigenvalue of  $\mathbf{U}(\mathbf{x}(t))$  and LLE of the considered dynamical system. Such connection stands the base of our new method and can be utilized further in estimation of LE spectrum.

### 3. Method applications

This section considers application of the method in estimation of the Lyapunov exponents in analysis of different types of dynamical systems. In the first case (Figs. 2a, 2b) perturbation  $\mathbf{z}(t)$  was derived from the linearized equations and Largest Lyapunov exponent (LLE) was analysed. Mathematical model of the system is as follows:

$$\ddot{x} + \beta\dot{x} + \alpha x^3 = q \cos(\eta t) \quad \ddot{z} + \beta\dot{z} + \alpha z^2 x = 0 \quad (4)$$

Application of the method in the bifurcational analysis can be seen in (Fig. 2a). One can see different types of system dynamics and values of LLE confirming chaotic, periodic dynamics existence. Zero LLE values which determine period doubling bifurcation points are visible as well. Comparison of the results with the Stefanski method (Stefanski, 2005) is shown in (Fig. 2b).

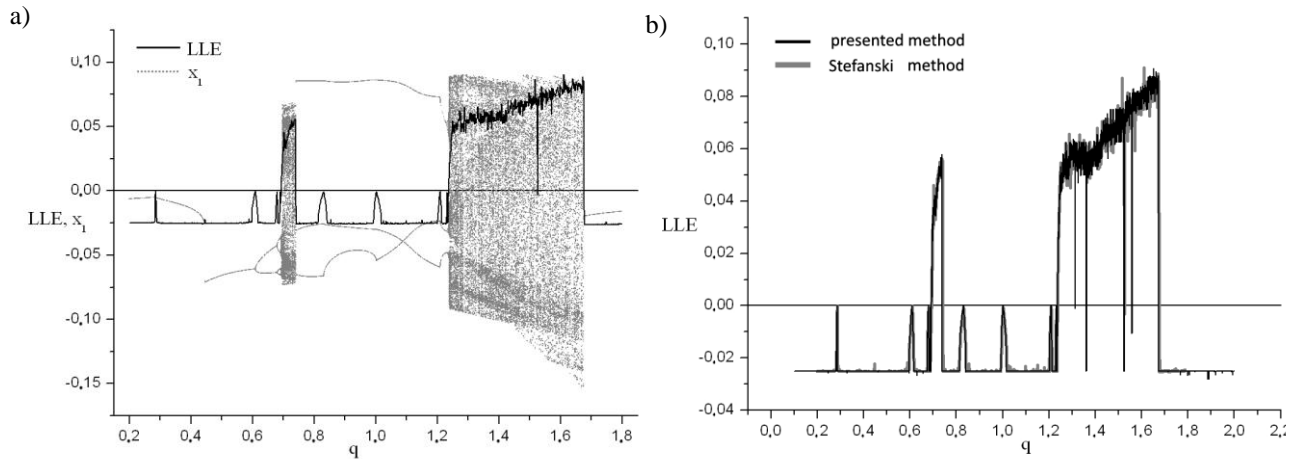


Fig. 2: Bifurcation diagrams for linearized equations of the perturbation analysis.

The next case considers studies of Duffing system dynamics where perturbation  $\mathbf{z}(t)$  was derived from the differences of actual dynamical states of two identical systems with different initial states.

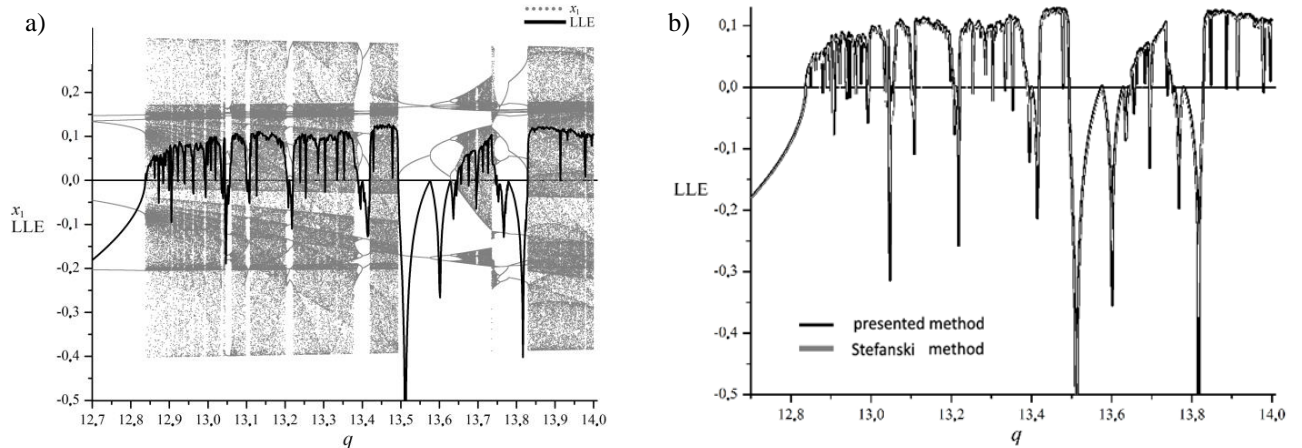


Fig. 3: Bifurcation diagrams for two systems perturbation analysis.

Similarly to the previous case application of the method in the bifurcational analysis has been presented. It can be seen in (Fig. 3a). One can see different types of the system dynamics and values of LLE confirming chaotic, periodic dynamics existence. Zero LLE values which determine period doubling bifurcation points are visible as well. Comparison of the results with the Stefanski method is shown in (Fig. 3b).

#### Application of the method in dynamical systems with desired controlled behaviour



Fig. 4: Scheme of the control system.

In this section we investigate application of the method in analysis of dynamics of the controlled inverted pendulum (Fig. 5a) and optimization of its control systems parameters. Our method is applied to estimate the Largest Lyapunov Exponent (LLE) as a criterion for control performance assessment (CPA) in a simulated control system. As any control system can be analyzed as a dynamic system, disturbance acting on the system in time  $t = 0$  can be treated as a change of initial conditions of the dynamic system. Thus behaviour of the error of regulation contains all the data necessary to the estimation of the Lyapunov exponents of the system. Scheme of the control system is presented in (Fig. 4).

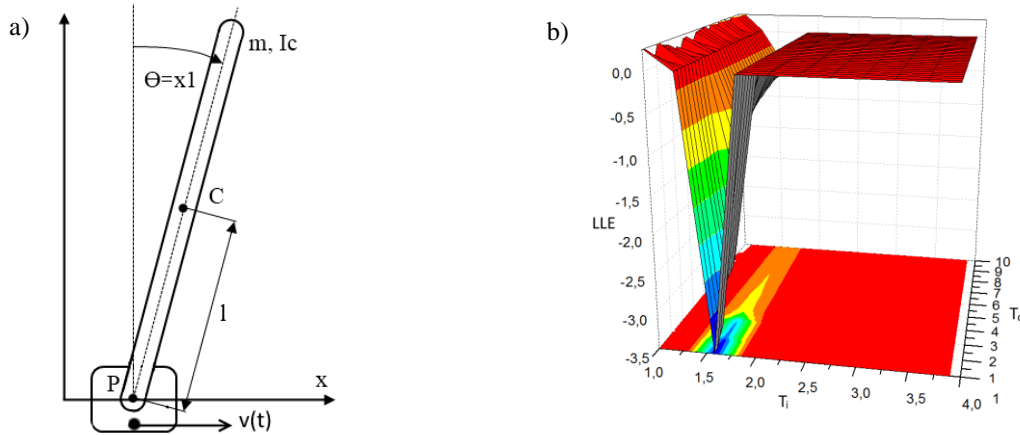


Fig. 5: a) Inverted pendulum; b) its bifurcational analysis.

During the experiment action of the control system was tested for different coefficients of PID regulator ( $k_p$ ,  $T_I$ ,  $T_D$ ). For each combination of PID coefficients values of LLE were calculated. Based on that parameters ranges for each pendulum three dimensional bifurcational diagrams were obtained (Fig. 5b). It shows dependence of the LLE on the regulator parameters, and map of the parameters showing ranges of the LLE values in different colours. These investigations allowed us to choose optimal values of the regulator with taking into account the range of its best effectiveness. Finally values  $k_p$ ,  $T_I$  and  $T_D$  were chosen for the lowest LLE values. Time series of the system regulation error  $e(t)$  for optimized parameters are presented in (Fig. 6). One can see fast decay of the oscillations proving big efficiency of optimized regulators.

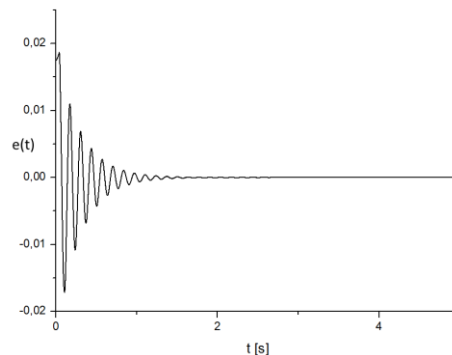


Fig. 6: Time series of the system regulation error  $e(t)$ .

#### 4. Conclusions

We have investigated the new method of LE estimation. We have presented theoretical description showing mathematical simplicity of the method and simplified background of the basic idea. We have introduced proofs of our method effectiveness based on results of simulations for different types of nonlinear dynamical systems. The next step of development of the method can be considered in estimation of LE from a real time series, systems with discontinuities, with time delay and others. It can be also extended onto multidimensional control.

#### Acknowledgement

This study has been supported by Polish Ministry of Science and Higher Education under the program Diamond Grant, project No. D/2013 019743.

#### References

- Aniszewska, D. and Rybaczuk, M. (2008) Lyapunov type stability and Lyapunov exponent for exemplary multiplicative dynamical systems, *Nonlinear Dyn* vol. 54, pp. 345-354.
- Chunbiao, L., Wang, J. and Wen, H. (2012) Absolute term introduced to rebuild the chaotic attractor with constant Lyapunov exponent spectrum, *Nonlinear Dyn* vol. 68, pp. 575-587.
- Dabrowski, A. (2012) Estimation of the largest Lyapunov exponent from the perturbation vector and its derivative dot product, *Nonlinear Dyn* vol. 67, pp. 283-291.
- Dabrowski, A. (2012) The largest Transversal Lyapunov Exponent and Master Stability Function from the perturbation Vector and its derivative Dot Product (TLEVDP), *Nonlinear Dyn* vol. 69, pp. 1225-1235.
- Dabrowski, A. (2014) Estimation of the the Largest Lyapunov exponent-like (LLEL) stability measure parameter from the perturbation vector and its derivative dot product (part 2) experiment simulation, *Nonlinear Dynamics* vol. 78, pp. 1601-1608.
- Fraga, L.G. and Tlelo-Cuautle, E. (2014) Optimizing the maximum Lyapunov exponent and phase space portraits in multi-scroll chaotic oscillators, *Nonlinear Dyn* vol. 76, pp. 1503-1515.
- Hu, D.L., Huang, Y. and Liu, X.B. (2012) Moment Lyapunov exponent and stochastic stability of binary airfoil driven by non-Gaussian colored noise, *Nonlinear Dyn* vol. 70, pp. 1847-1859.
- Serweta, W., Okolewski, A., Blazejczyk-Okolewska, B., Czolczynski, K. and Kapitaniak, T. (2015) Mirror hysteresis and Lyapunov exponents of impact oscillator with symmetrical soft stops, *International Journal of Mechanical Sciences* vol. 101-102, pp. 89-98.
- Soriano, D.C., Fazanaro, F.I., Suyama, R., Oliveira, J., Marconi, R.A. and Madrid, K. (2012) A method for Lyapunov spectrum estimation using cloned dynamics and its application to the discontinuously-excited FitzHugh–Nagumo model, *Nonlinear Dyn* vol. 67, pp. 413-424.
- Stefanski, A. (2008) Lyapunov exponents of the systems with noise and fluctuating parameters, *Journal of Theoretical and Applied Mechanics* vol. 46(3), pp. 665-678.
- Stefanski, A., Dabrowski, A. and Kapitaniak, T. (2005) Evaluation of the largest Lyapunov exponent in dynamical systems with time delay, *Chaos, Solitons and Fractals* vol. 23, pp. 1651-1659.
- Wadduwage, D.P. and Annakkage, U.D. (2013) Power system transient stability analysis via the concept of Lyapunov Exponents, *Electric Power Systems Research* vol. 104, pp. 183-192.
- Yang, C., Wu, C.Q. and Zhang, P. (2012) Estimation of Lyapunov exponents from a time series for n-dimensional state space using nonlinear mapping, *Nonlinear Dyn* vol. 69, pp. 1493-1507.
- Zhu, W.Q. (2004) Feedback Stabilization of Quasi Nonintegrable Hamiltonian Systems by Using Lyapunov Exponent, *Nonlinear Dynamics* vol. 36, pp. 455-470.

## STUDY OF THE POSSIBILITY OF USE OF BIOELECTRIC SIGNALS TO WIRELESS REMOTE CONTROL OF THE ELECTRO-PNEUMATIC POSITIONING SYSTEMS

R. Dindorf<sup>\*</sup>, P. Wos<sup>\*\*</sup> K. Pawelec<sup>\*\*\*</sup>

**Abstract:** *The aim of the study was to perform bioelectric signal analysis focusing on its applicability to wireless remote control of the electro-pneumatic servo-systems. The test-stand was constructed to wireless remote control of the electro-pneumatic servo-drive by means of bioelectric signals generated by the operator. The natural bioelectric signals generated by brain, facial muscles and eye muscles read by the NIA (Neural Impulse Actuator) are translated into control commands in the controller of electro-pneumatic servo-drive. Bioelectric signals (EEG, EMG and EOG) detected by means of special forehead band with three sensors are sent to the actuator box, where they are interpreted as control signals. The control signals from the actuator box are transmitted via a wireless WiFi network to the controller of pneumatic system. This paper proposes a novel Wireless Network Interface Controller (WNIC) for the control of pneumatic position system using bioelectric signals.*

**Keywords:** Bioelectrical signals, Wireless remote control, Electro-pneumatic positioning system.

### 1. Introduction

The brain and body provide a wealth of information about a person's physiological, cognitive and emotional states. There is an increasing trend to use physiological signals in computerised systems as an input control, and since entry level physiological sensors have become more widespread, physiological interfaces are liable to become pervasive in our society (e.g., through mobile phones). The three main components of the brain are cerebellum, cerebrum and brain stem (pons and medulla oblongata). Cerebellum is located between brain stem and cerebrum. Cerebellum controls facial muscle coordination, thus affecting signals (eye movements and muscle movements) by Brain-Body Interface (BBI) (Fairclough et al., 2011). Various devices read bioelectrical signals (e.g. electrocorticographic signals, skin biopotential or facial muscle tension) and translate them into computer understandable input. The concept of Brain-Computer Interaction (BCI) involves communication between a human brain, and an external computer device. Stimulating muscles, eyeball movement or a bioelectrical change in the brain's activity causes a change in people biopotentials, which may be measured and used as a control signal. Human-Computer Interface (HCI) enables people to control computer applications using bio-electric signals recorded from the body. Bioelectrical potentials (bio-potentials) are made up of four different signals (Gnanayutham et al., 2007): Galvanic Skin Response (GSR), Electrooculography (EOG), Electromyography (EMG), Electroencephalography (EEG). Bioelectrical signals may be also used for operating pneumatic servo system. The machine operator's reaction time may be significantly reduced if become equipped with an appropriate interface which measures and analyses bioelectric signals. Then sends appropriate control signals to the operated pneumatic servo system. A good example is an emergency stop of a device activated by pressing the emergency stop button using "thoughts", which would contribute to the safety of the pneumatic control systems. The use of wireless communication will also contribute to improvements in safety, particularly if the operator is right next to the operated

---

<sup>\*</sup> Prof. Ryszard Dindorf: Kielce University of Technology, al.Tysiaclecia Panstwa Polskiego 7, 25-314 Kielce, PL, dindorf@tu.kielce.pl

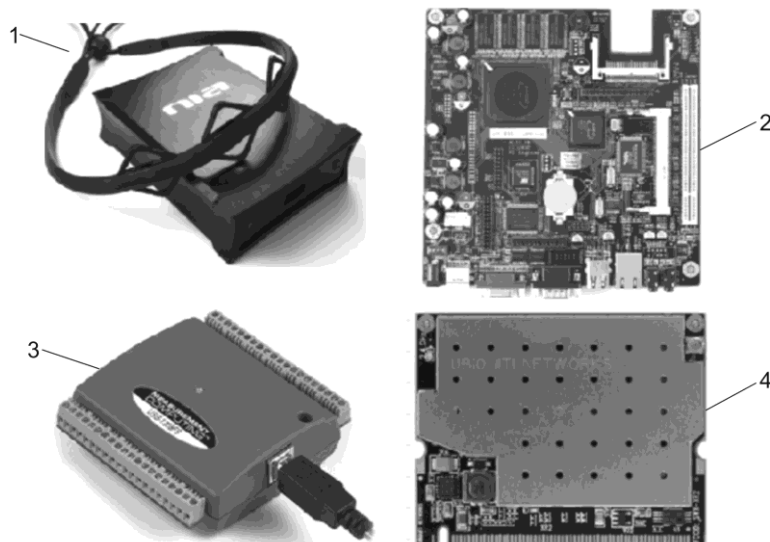
<sup>\*\*</sup> EngD. Piotr Wos: Kielce University of Technology, al.Tysiaclecia Panstwa Polskiego 7, 25-314 Kielce, PL, wos@tu.kielce.pl

<sup>\*\*\*</sup> PhD. student Katarzyna Pawelec: Kielce University of Technology, al.Tysiaclecia Panstwa Polskiego 7, 25-314 Kielce, PL, katarzyna.pawelec20@wp.pl





Ziegler-Nichols method. The current actuator position is sent to the operator in order to verify the intended position. The wireless remote controller builds on a biosignal reader - Neural Impulse Actuator (NIA), microcomputer board ALIX.1D PC, data acquisition device MicroDAQ USB-1208FS, wireless card Ubiquiti XR2 and wireless network interface controller (WNIC) (Fig. 2). The ALIX.1D system board is equipped with an AMD Geode 500 MHz processors and 256 MB of RAM. It is powered by a 12V supply and has low power consumption, in the range of 0.4 to 0.5 A. The software for the servo drive and controller was written using the LabVIEW environment (Mazur et al., 2013).



*Fig. 2: Elements used for the controller construction: 1 – Neural Impulse Actuator (NIA), 2 – microcomputer board, 3 – module of the acquisition data, 4 - wireless network interface controller (WNIC).*

The NIA device by OCZ is a BCI (Brain-Computer Interface) type interface equipped with a neurosignal reader (Hagedoorn et al., 2016), (Reynolds et al., 2009). The signals originating from the neural activity of the brain are captured by NIA in the form of electrical biopotentials which occurred as a result of Alpha and Beta brain waves, movement of the facial muscles and eye lids. Effective control of technical devices with the use of NIA requires a snug fit of the brain wave reader sensors to the forehead, calibration of the device and training. A dedicated application analysis of EEG, EMG and EOG biosignals together with one basing on appropriate bioelectric signal values as defined by the user, generate signals for pressing keys in the keyboard. The key to be pressed at a given bioelectric signal level is defined by the user in the application settings.

### 3. Control result

All available application level bio-electrical signals: muscle tension measurement, eyeball movement as well as Alfa and Beta waves were used in the experiment. Events simulating pressing appropriate keys on a keyboard were assigned to defined signal levels. Page Up - increase the actuator position value, Page Down - decrease the actuator position value, End - pressing of the emergency stop button. As a result of the conducted experiment, it was confirmed that the use of electromyography signals (EMG), for example by regulating the pressure of the tongue on the upper palate or clenching teeth with a larger or smaller force provides the best control signal generating effects. During the tests it was very difficult to precisely define the requested position of the actuator. Other bioelectrical signals did not facilitate determination of the pneumatic actuator (rodless cylinder) position, as it was difficult to obtain their appropriate level. The precision of position control of the electro-pneumatic servo drive may be increased by the operator undergoing appropriate training. As a result of the experiment the positional control characteristics of electro-pneumatic servo mechanism for different input signals were obtained (Dindorf et al., 2017). In Figs. 3 position control results of electro-pneumatic systems for ramp signal and follow-up signal are depicted. From analysis of above graphs it results that there is a delay between the value of set signal and actuator position. This delay is implemented by acquisition data module, since it results from the analysis program action that the most time take to generate voltage by the system. The second reason of

acquisition data module delays is that communication with module takes place via USB interface, which isn't a real time interface.

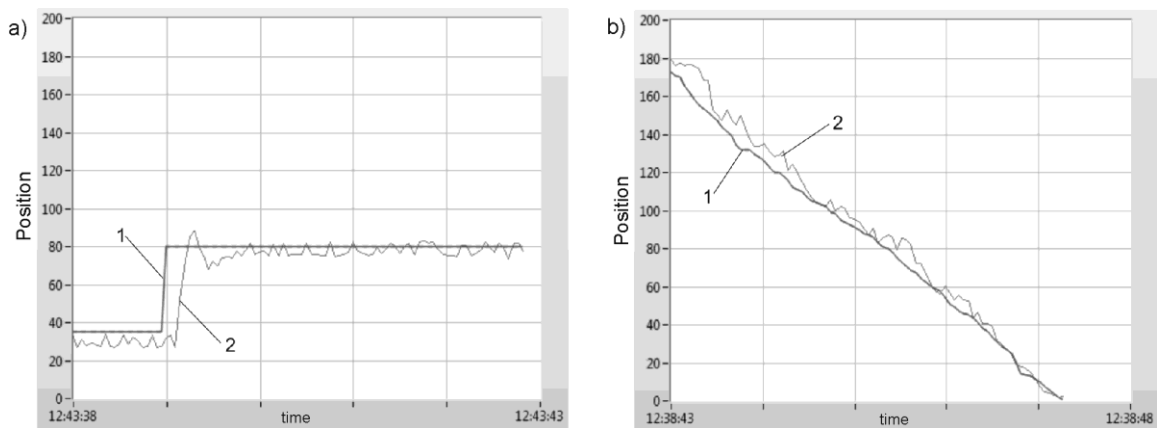


Fig. 3: Experimental position control results of electro-pneumatic system for: a) ramp signal; b) follow-up signal: 1 – setpoint position, 2 – current position.

## Acknowledgement

The test stand of electro-pneumatic positioning systems remotely wireless controlled by bioelectric signals was awarded a medal at the 6th Fair of Pneumatics, Hydraulics, Drives and Controls PNEUMATICON'2013 in Kielce Trade Fair (Poland).

## 4. Conclusions

The conducted laboratory tests confirm that various bio-electrical signals may be used in the control process. It is easiest to use electrical activity signals generated by muscle movements (eyeball movement, clenching of teeth). This paper proposes a novel Wireless Network Interface Controller (WNIC) for the control of pneumatic position system using bioelectric signals. The bioelectrical signals subjected to appropriate training control may be used in systems not requiring significant position precision of pneumatic positioning system. They can also improve safety of a device by reducing operator's reaction time to sudden events, e.g.: emergency stop or faster operation of a break. In the NIA actuator the actual reaction times are about 30 % to 60 % shorter than what one can realistically achieve with emergency stop. The use of wireless communication increases operator's safety during device operation, as he does not have to be in the direct vicinity of the device. It also improves the mobility and reduces the cost of network infrastructure development and expansion. The control system using bioelectrical signal and remote wireless communication network was constructed and practically applied in pneumatic positioning systems.

## References

- Dindorf, R and Wos, P. (2015) Brain computer interface for wireless remote control. MCSB'2015 – International Conference Cybernetic Modelling of Biological Systems. 14-15 May 2015, Krakow, DOI: 10.1515/bams-2015-0011, pp. 15-16.
- Dindorf, R., Takosoglu, J. and Wos, P. (2017) Development of Pneumatic Control Systems. Monograph. Kielce University of Technology, Kielce.
- Fairclough, S.H., Gilleade, K., Nack, L.E. and Mandryk, R.L. (2011) Brain and body interfaces: Designing for meaningful interaction. The ACM CHI Conference on Human Factors in Computing Systems, 7–12 May 2011, Vancouver, Canada, pp. 65-68.
- Gnanayutham, P. and George J. (2007) Inclusive design for Brain Body Interfaces. in: D.D. Schmorow, L.M. Reeves (Eds.), Foundations of Augmented Cognition, Springer Verlag, pp. 102-111.
- Hagedoorn, H. (2016) OCZ NIA Review – Neural impulse actuator. Available at: <http://www.guru3d.com/articles-pages/ocz-nia-review-neural-impulse-actuator,1.html>.
- Mazur, S., Dindorf, R. and Wos, P. (2013) Remote control of the electro-pneumatic servo drive using biosignals. Technical Transactions, Mechanics, Z. 1-M, pp. 245-256.
- Reynolds, B. and Waechter A. (2009) Brain computer interfacing using the Neural Impulse Actuator. A usability and statistical evaluation. California Polytechnic State University.

## FLUID FLOW MEASUREMENTS OF 5P4E BY PARTICLE TRACKING VELOCIMETRY

K. Dočkal\*, P. Šperka, I. Křupka, M. Hartl

**Abstract:** Lubricant flow in an elastohydrodynamic contact is investigated by new methodology based on particle tracking velocimetry. Measurement method provides positions of silver nanoparticles dissolved in the lubricant through several images captured by high speed camera. These are connected, in places of high probability of correct detection of identical particle on multiple images. Connected positions are linearly fitted to get average speed and after that statistically processed to obtain velocity profile. This method was applied on 5P4E base fluid, characterized by high viscosity and pressure sensitivity. Experimental results provide evidence about slide to roll ratio influence on the velocity profiles under piezoviscous conditions. At low slide to roll ratios the profile shape match plug flow model with highly viscous core and slip on the solid-liquid interfaces. As the slide to roll ratio increases, corresponding velocity profile curvature is reduced.

**Keywords:** Elastohydrodynamic Lubrication, Rheology, Fluid Flow, Particle Tracking Velocimetry.

### 1. Introduction

Elastohydrodynamic lubrication (EHL) taking place in many mechanical parts, where the geometry is highly non-conform (Fig. 1). In such regime, the film separating contact bodies usually reach up to 1  $\mu\text{m}$  and is subjected to high pressures (up to 3 GPa), along with shear rates up to  $10^8 \text{ s}^{-1}$ . Conditions like these, usually lead to different behavior of lubricant from one under ambient conditions, given by pressure-viscosity, temperature-viscosity and shear rate-viscosity relationships.

Because of difficulties associated with predictions implementing all these relationships at once, a lot of studies are currently based on modified Reynolds equation, which is sufficient for film thickness. Film thickness is given by the processes ongoing in the inlet region, where the pressure is small enough. However, for those taking place in central region (friction, fluid flow), where the lubricant is exposed to high pressures, temperatures and shear rates, the Reynolds equation is inadequate. Phenomena such as limiting shear stress, wall slip or glassy transition are needed to be considered.

Estimation of lubricant behavior in Hertz area can be based on molecular dynamics phase diagram, like the one discussed by Martinie (2016). This diagram summarizes several proposed models of film behavior with respect to the pressure and shear rate, complemented by experimental data. For EHL are essential three of them. First one is solid like behavior of the lubricant caused by increase of the viscosity due to high pressures and low shear rates. Flow profile is expected to be linear. In higher shear rates one of two possible mechanism can occur. Wall slip respective plug flow model (Ehret, 1998), where the slip occurs on the solid- liquid interface and the core is solidified (Fig. 2) or last possible case derived from assumption of uneven temperature distribution along film thickness (Bair, 1994). The shear is presumed to be localized in plane of maximum temperature therefore lower viscosity (Fig. 2).

Only a little experimental evidence is available about fluid flow, most likely because an appropriate measuring method didn't exist. Lately, approach employing fluorescence microscopy (Reddyhoff, 2010) was used to study lubricant rheology inside point contact. This one was modified (Ponjavic, 2013) for using, in field of fluorescence specific technique, fluorescence recovery after photobleaching (FRAP), allowing to study through film thickness flow profile. This method is however limited by the diffusion of the fluorescence tracer to lubricants with high Péclet number. Flow profiles measured by this method for

---

\* Ing. Kryštof Dočkal: Institute of Machine and Industrial Design, Brno University of Technology, Technická 2896/2; 616 69, Brno; CZ, dockal@fme.vutbr.cz

polybutene correspond to the Ehret plug flow model. Further investigations with 5P4E polyphenyl ether base fluid (Galmiche, 2016) clearly shows the importance of the pressure effect on the shape of velocity profile. At isoviscous rigid conditions, the profile is almost linear as expected. However, as the pressure rises the shear banding starts to prevail.

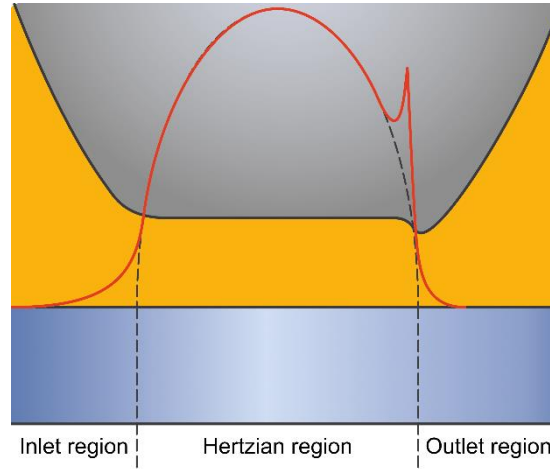


Fig. 1: EHL contact regions with pressure profile (red).

Alternative approach to study fluid flow (Šperka, 2014), employed in this study, is the particle tracking velocimetry (Fig. 3). Methods using particles have certain limitation in direct determination of particle position along film thickness, commonly requiring modification of an experimental rig (Kikuchi, 2015; Byeon, 2016). This could be overcome by statistical processing of the data set. The aim of present study is to investigate response of flow profile on different slide to roll ratios under piezoviscous conditions. The lubricant used in this study is 5P4E for its high viscosity and for which the flow behavior under high pressures has been shown.

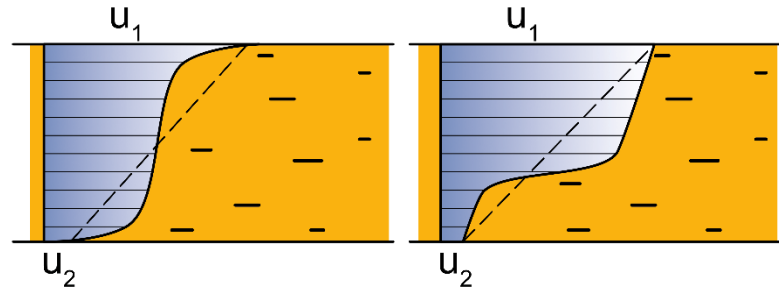


Fig. 2: Plug flow and shear banding.  $U_1$  and  $U_2$  are speeds of contacting surfaces.

## 2. Methods

The lubricant flow profile measurements were conducted on ball-on-disc optical tribometer, capable of precision thickness measurement. EHL contact is formed between 25.4 mm bearing steel ball and borosilicate BK7 glass disc. Applied load is 15 N through the liver, giving a maximum pressure around 401 MPa falling under piezoviscous regime. The slide to roll ratio (SRR) is defined as  $2(u_1 - u_2)/(u_1 + u_2)$  and varies between 100 % and -100 %. Contact is captured by the CMOS camera at 6000 fps along with 120  $\mu$ s exposition time. The lens has magnification 50 $\times$ .

For a flow analysis, the silver nanoflakes with diameter up to 10  $\mu$ m (Sigma Aldrich) and thickness in nanometers were added to the 5P4E with a viscosity around 2.63 Pa s at 25  $^{\circ}$ C. Amount of nanoparticles dispersed in the lubricant was increased until in the central region were approximately 10 of them during experiment. Solution was mixed in ultrasonic cleaner, then mechanically using spatula. Before experiments, layer of lubricant was applied on disc, followed by loading the contact and putting it's into pure rolling for 5 minutes to ensure better dispersion of particles. From every experiment 400 images were captured. When needed, a median filter with radius 2 pix were applied to reduce outliers and noise.

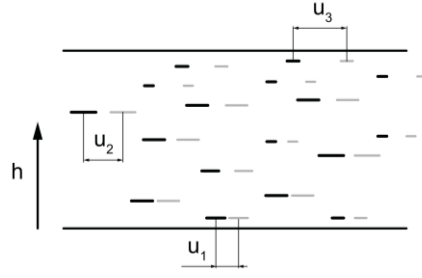


Fig. 3: Particle tracking: black lines – particles, grey lines – particles captured on subsequent image.  
 $U_x$  are speeds of particles at different heights of film

The actual particle tracking consists of three steps. First one is the particle detection, which was done by multiscale detection algorithm (Olivo-Marin, 2002) in Hertzian region. Second step is joining individual detections together (Chenouard, 2013), so the average velocity could be calculated from the change of position between subsequent images by linear fit. Number of created connections between spots is limited by uncertainty, which increases with tracking distance. Third step (Fig. 4) consists of velocity profile evaluation from tracked displacements of particles. This is done under certain assumption that the through film distribution of particles is uniform. Then the cumulative histogram of measured speeds should describe the flow profile. Velocities lying outside the interval  $15\text{--}45\text{ mm s}^{-1}$  could be caused by insensitivity of the technique.

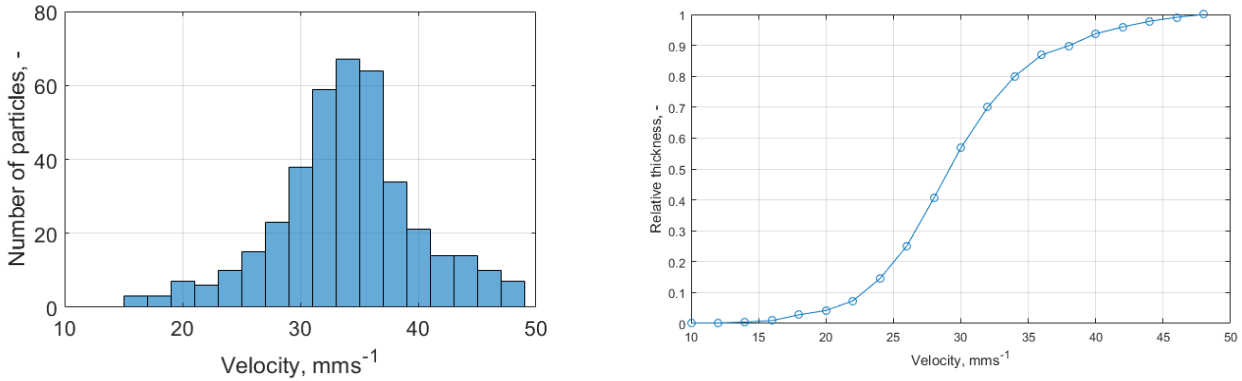


Fig. 4: Speed profile evaluation fort SRR -100 %.

### 3. Results and discussion

Experiments were conducted at mean speed  $30\text{ mm s}^{-1}$  for a range of SRR from -100 % to 100. Speed of ball respectively disc varies from 15 to  $45\text{ mm s}^{-1}$ . Velocity profile was evaluated from limited number of particles inside relatively flat central region. Film thickness is estimated by Homrock&Dowson prediction to 745 nm. Experiments are conducted under piezoviscous conditions in the region of plug flow or shear banding (Martinie 2016). Therefore, shape of the velocity profiles should correspond to plug flow model for low shear rates and for higher one the shear banding should occur.

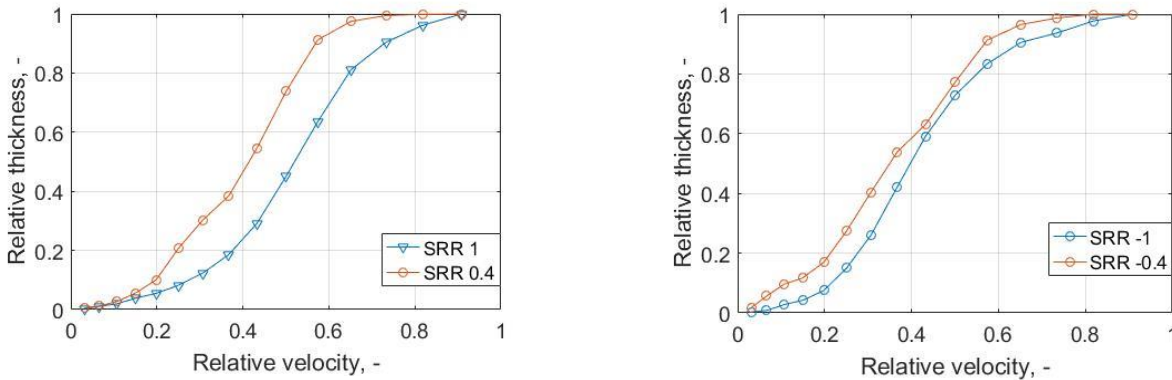


Fig. 5: Speed profile evaluation.

As can be seen from Fig. 5, velocity profiles for both positive and negative SRRs have shape of the S curve divided into three regions. Two regions where major shear take a place are near the surfaces of

contact bodies. They're thicknesses are around 10 % of film thickness. These two are separated with thick core, where the speed changes only a little. This description corresponds to the plug flow model.

With increasing the SRR, the boundary regions getting thicker and the transition between central and boundary regions are smoother. Near the slower surface, it seems, that the transition to the plug is longer, especially for positive SRRs. This may be related to temperature gradient, since the surface with lower speed remains in contact longer thus, it's temperature should be higher. Similar temperature distribution was concluded by (Galmiche, 2016), for the shear banding, where the layer with localized shear was approximately at height of 20 % of film thickness. Profiles however do not show any signs of shear banding as it was in the previous study. Central part of profile doesn't seem to change. The tilt remains constant.

Changes in profile shape are more likely caused by viscosity changes inside the lubricant. Viscosity variations could be caused by pressure or temperature change. Since the applied load is constant, and thus the pressure should be as well. It suggests that the viscosity is influenced by the temperature. Temperature increase could lower the viscosity of the core of lubricant. At a higher slide to roll ratios, profile could become even more linear. However, at some value of SRR, approaching to the linear profile should stop accompanied by transition to shear banding regime caused by temperature gradient.

#### **4. Conclusion**

Particle tracking velocimetry method was used to study nanometer thick fluid film inside EHL contact. Velocity profiles of 5P4E for several values of SRR were measured. With higher SRR the profiles become smoother and the curvature is slightly reduced. Shape changes were attributed to viscosity decrease caused by temperature gradient through film thickness. Although velocity profiles were obtained for a range of SRRs, it would be great benefit to be able to investigate fluid flow at higher shear rates, where is the shear banding transition likely to occur. Further work will focus on the estimation of fluid flow under such conditions.

#### **Acknowledgement**

This research was supported by Czech Science Foundation, project No. 14-31139P.

#### **References**

- Bair, S., Quershi, F. and Khonsari, M. (1994) Adiabatic shear localization in a liquid lubricant under pressure. *Journal of Tribology-Transactions of the Asme*, 116, 4, pp. 705-708.
- Byeon, H., J. et.al. (2016). Hybrid bright-field and hologram imaging of cell dynamics. *Scientific Reports*, 6, 33750.
- Chenouard, N., Bloch, I. and Olivo-Marin, J.C. (2013) Multiple Hypothesis Tracking for Cluttered Biological Image Sequences. *Ieee Transactions on Pattern Analysis and Machine Intelligence*, 35, 11, pp. 2736-2750.
- Ehret, P., Dowson, D. and Taylor, C.M. (1998) On lubricant transport conditions in elastohydrodynamic conjunctions. *Proceedings of the Royal Society a-Mathematical Physical and Engineering Sciences*. 1971, 454, pp. 763-787.
- Galmiche, B., Ponjavic, A. and Wong, J.S.S. (2016) Flow measurements of a polyphenyl ether oil in an elastohydrodynamic contact. *Journal of Physics-Condensed Matter*, 28, 13, 134005.
- Kikuchi, K. and Mochizuki, O. (2015) Velocity profile of thin film flows measured using a confocal microscopy particle image velocimetry system with simultaneous multi depth position. *Measurement Science & Technology*, 26, 2, 25301.
- Martinie, L. and Verge, P. (2016) Lubrication at Extreme Conditions: A Discussion About the Limiting Shear Stress Concept. *Tribology Letters*, 63, 2, 21.
- Olivo-Marin, J. C. (2002) Extraction of spots in biological images using multiscale products. *Pattern Recognition*, 35, 9, pp. 1989-1996.
- Ponjavic, A., Chennaoui, M. and Wong, J.S.S. (2013) Through-Thickness Velocity Profile Measurements in an Elastohydrodynamic Contact. *Tribology Letters*, 50, 2, pp. 261-277.
- Reddyhoff, T., et.al. (2010) Lubricant Flow in an Elastohydrodynamic Contact Using Fluorescence. *Tribology Letters*, 38, 3, pp. 207-215.
- Sperka, P., Krupka, I. and Hartl, M. (2014) Evidence of Plug Flow in Rolling-Sliding Elastohydrodynamic Contact. *Tribology Letters*, 54, 2, pp. 151-160.



## TESTING THE POSITIONING ACCURACY AND REGULARITY OF THE MOTION THREADED MECHANISM FEED DRIVE

L. Drahorádová<sup>\*</sup>, J. Moravec<sup>\*\*</sup>, V. Andrlík<sup>\*\*\*</sup>

**Abstract:** *This paper introduces linear feed drives and design of the innovative motion threaded mechanism. The motion threaded mechanism use rolling elements in a similar way as the ball screw. It has sheaves instead of balls which circulate inside the nut. The paper continues by description of the test bed and measuring method of positioning accuracy and regularity. Next part of the paper includes results and discussion of the measurement. At the end outline of future research continuation is presented.*

**Keywords:** Motion Threaded Mechanism, Position Error, Positioning Accuracy, Amplitude Spectrum.

### 1. Introduction

Linear feed drive is a standard part of the mechanical equipment, for example machine tools, drives in additive technologies or manipulators and it is used for positioning the components. Ball screws are usually used in accurate mechanical linear positioning mechanisms. Ball screw changes the direction of motion, from rotational to linear. Whole mechanism consists of a screw, a nut and balls between them which reduce friction. The nut consists of a solid with grooves for the balls, segments transferring the balls, seals and end flange. A cutaway through the nut is shown in Fig. 1b.

Qualities of the ball screw are very good - high efficiency, long lifetime, high load capacity and preload endurance. The motion of the ball screw is smooth in comparison with a classical lead screw. The ball screw can change direction of motion not only from rotational motion to linear motion but also from linear motion to rotational motion. For example, that advantage can be useful for emergency opening of an automatic gate (Souček, 2004 and Souček, 2015).

### 2. Design and qualities of a motion threaded mechanism

An innovative mechanism – motion threaded mechanism (Fig. 1a) change the direction of motion, from rotational motion to linear motion in a similar way as ball screw. It consists of a screw, three rings and end flanges which are clipped by four rods. The number of rings can be higher or lower depending on requirements on the linear feed drive. Four small rollers with sheaves at 90° angle are placed inside each of the rings and fixed by threaded stoppers. Sheaves are fixed in the rollers with pins. Sheaves copy the groove of the thread like balls inside the nut of the ball screw but sheaves keep at the same position with respect to the nut in comparison with balls which circulate inside the nut.

The production of the nut prototype was very simple in comparison with the ball screw nut because it doesn't need any special machining technologies for grooves of thread inside the nut and the transferring segments. Then price of the nut could be much lower with no specialization on production of ball screw. The motion threaded mechanism has more silent and smoother running because of absence of the ball circulation which can produce vibrations and noise. Further advantages are possibility of very high pitch for high linear speed or variable pitch in additional change. Disadvantages are bigger size of the nut and

---

<sup>\*</sup> Ing. Lucie Drahorádová: Faculty of Mechanical Engineering, Czech Technical University in Prague, Horská 3; 128 00, Prague; CZ, Lucie.Drahoradova@fs.cvut.cz

<sup>\*\*</sup> Ing. Jan Moravec, PhD.: Faculty of Mechanical Engineering, Czech Technical University in Prague, Horská 3; 128 00, Prague; CZ, J.Moravec@fs.cvut.cz

<sup>\*\*\*</sup> Assoc. Prof. Ing. Vladimír Andrlík, CSc.: Faculty of Mechanical Engineering, Czech Technical University in Prague, Horská 3; 128 00, Prague; CZ, Vladimír.Andrlík@fs.cvut.cz

lower static stiffness because number of contacts between the nut and screw is lower. These are the main features in comparison with ball screw. (Drahorádová, Andrlík, 2016, CTU in Prague, 2013 and CTU in Prague 2014).

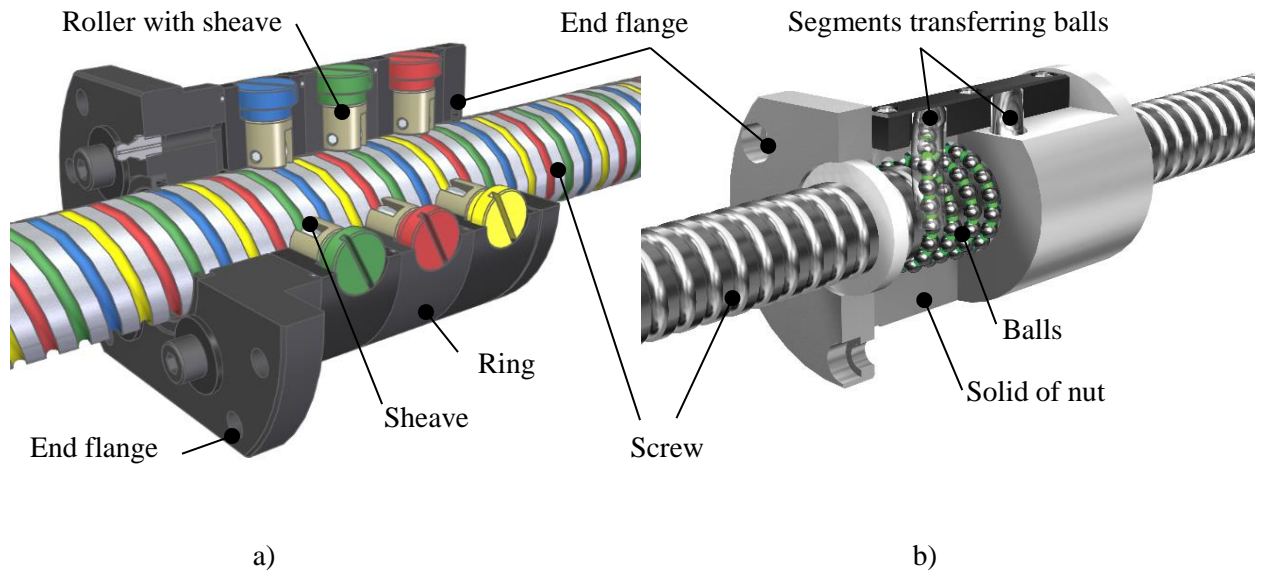


Fig. 1: a) Cutaway through the nut of motion threaded mechanism, (Drahorádová, Andrlík, 2016);  
b) Cutaway through the nut of THK SBN ball screw. (Motion Control Tips, 2011).

### 3. Description of the experiment

The motion threaded mechanism has a screw with gothic profile of grooves. The four starts screw diameter is 40 mm and pitch is 40 mm too. The screw is put in the axial-radial bearing and radial bearing in the test bed housing and connected with the servomotor by the jaw coupling (Fig. 2). The length of the screw between the centres of bearings  $L$  is 1200 mm and the active length is 800 mm. The position of the table is scanned by a rotary encoder in the motor and linear encoder on the table. It is labelled as  $y$ .

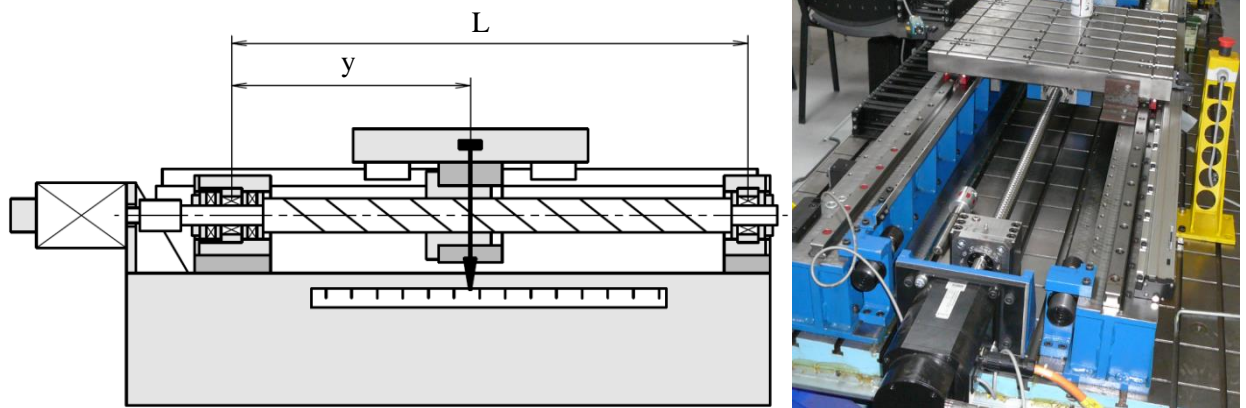


Fig. 2: The schematic picture and photo of test bed.

The experimental test bed with the motion threaded mechanism feed drive axis was assembled and prepared. Programs for motion control and data evaluation was written in the software Matlab with Real Time Toolbox. The experimental feed drive axis was equipped with a direct and indirect measuring system. Position and velocity feedbacks were enclosed from the motor encoder and both cascade control loops were embodied in PC. The direct measuring system was used only for comparison with main motor encoder and e. g. for evaluation of an appropriate backlash. Current control was enclosed in Control Techniques converter. Communication between PC with Matlab Real Time Toolbox and frequency converter Control Techniques was analog via AD card Humusoft MF614. Basic experiments with regularity of motion were carried out.

Testing speeds of the table were from 0.1 m/s to 0.5 m/s (from 150 rev/min to 750 rev/min at the motor) and desired/actual position, velocity and current were monitored. The motion of the table was performed on a 750 mm long track with positive and negative rotation of the motor.

#### 4. Results and discussion

The position error was calculated as a difference of the desired position  $p_{des}$  and the actual position  $p_{act}$  from motor encoder  $\Delta_{me}$  and linear encoder  $\Delta_{le}$ :

$$\Delta_{me} = p_{desme} - p_{actme} \quad (1)$$

$$\Delta_{le} = p_{desle} - p_{actle} \quad (2)$$

The position error (for velocities 0.1 m/s, 0.15 m/s and 0.28 m/s – Fig. 3) was rising with the velocity of the table in the interval 0.02 – 0.095 m and with mismatch between motor encoder and linear encoder which can be up to 0.85 mm. On the detail is shown small mismatch between them. This is due to the backlash in mechanism.

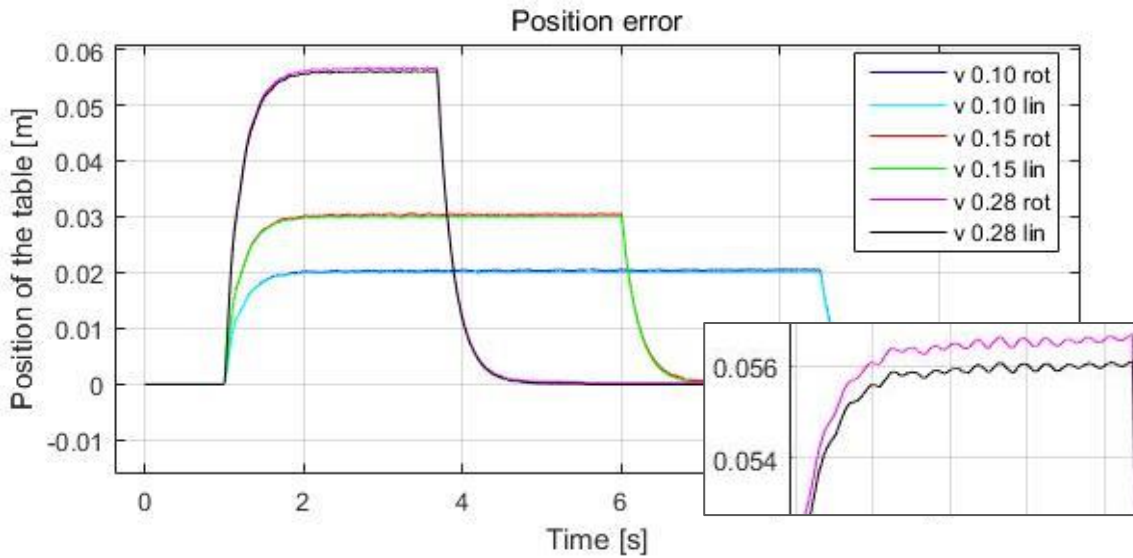


Fig. 3: The graph of position error for velocities 0.1 m/s, 0.15 m/s and 0.28 m/s.

Monotonous vibrations which are in higher resolution in Fig. 4 below, are caused mainly by mounting imperfections between the motor and the screw. This implies the frequency spectrum of vibrations (Fig. 5), where the first harmonic of the screw is dominant. Other harmonics are negligible in comparison with it. Harmonics and proportions of frequency spectrum were similar in all measures.

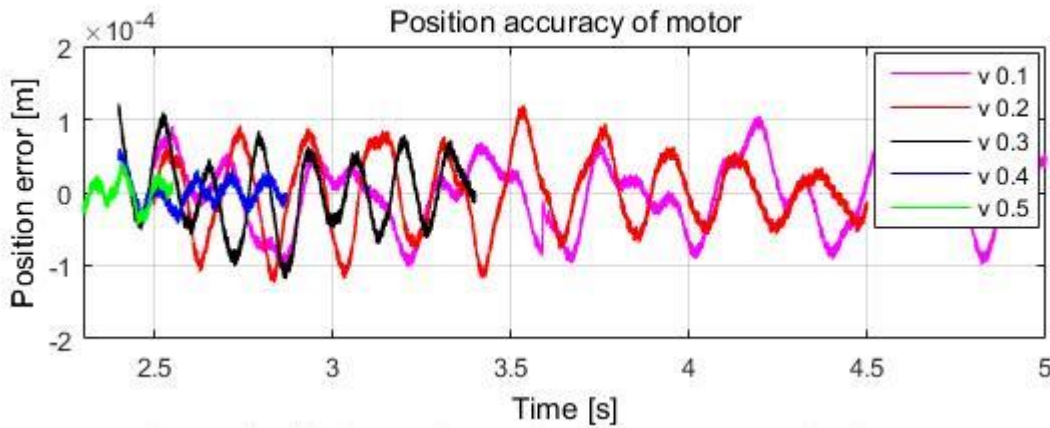


Fig. 4: The graph of position accuracy for velocities 0.1 – 0.5 m/s.

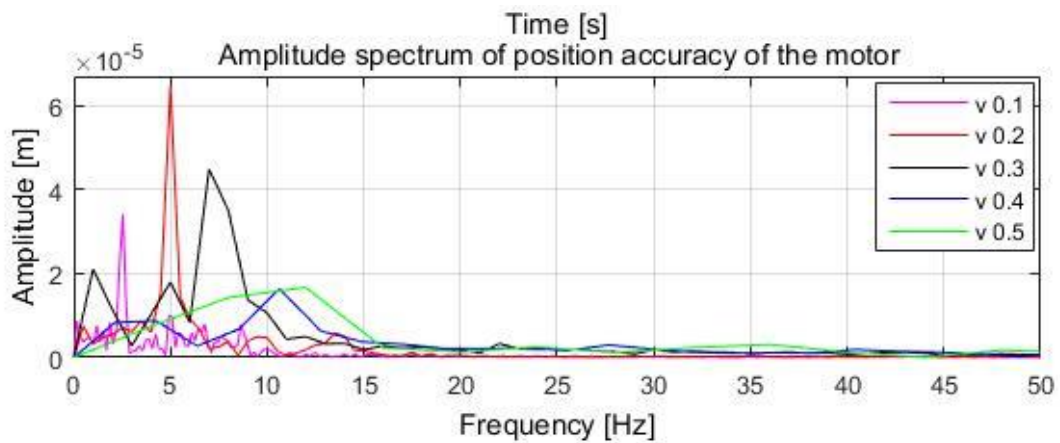


Fig. 5: The graph of amplitude spectrum of position accuracy for velocities 0.1 – 0.5 m/s.

## 5. Conclusions

The experimental test bed and appropriate HW and SW was commissioned and first experiments were carried out. Experiments shows assembly imperfections in mechanism which are caused presumably by mounting and backlash in the mechanism and coupling. Because the nut consists of rings it can be preloaded by using a very thin spacer. Now the mechanism is being disassembled and setting-up of these imperfections as backlash and shaft misalignment are in focus. Other experiments will be done and compared with the ball screw.

## Acknowledgement

The research is supported by the grant SGS13/189/OHK2/3T/12.

The nut was made by Ing. Petr Konečný, PhD, Final Hlinsko, s.r.o. and ZPS Modřany, a.s.

The threaded shaft was made by the company Kuličkové šrouby Kuřim, a.s.

## References

- Drahorádová, L. and Andrlík, V. (2016) Design and Production of the Motion Threaded Mechanism, in: 22nd International Conference Engineering Mechanics 2016, Prague: Institute of Thermomechanics, Academy of Sciences of the Czech Republic, pp. 134-137, available at: <http://www.engmech.cz/2016/im/im/page/proc>
- Souček, P. (2004) Servomechanisms in Production Machines of the Monograph. Czech Technical University in Prague, ISBN 80-01-02902-6 (in Czech)
- Souček, P. (2015) Didactic text: Submitted Transfers in Drive of NC Machines. Department of Production Machines and Equipment, Faculty of Mechanical Engineering, Czech Technical University in Prague, pp. 1-70 (in Czech)
- Czech Technical University in Prague, Faculty of Mechanical Engineering, Department of Production Machines and Equipment. Motion Threaded Mechanism. Inventor: Andrlík, V. National utility model application. CZ, registration number: 24842, 21.1.2013
- Czech Technical University in Prague, Faculty of Mechanical Engineering, Department of Production Machines and Equipment. Multiple Motion Threaded Mechanism. Inventors: Andrlík, V., Kolář, M. National utility model application. CZ, application number: 2014-30202, 3.11.2014
- Motion Control Tips (2011) What are Ballscrew? Summary for Motion Engineers, in: Motion Control Tips, available at: <http://www.motioncontroltips.com/ballscrews/>

## THE EFFECT OF BODY WEIGHT UNLOADING ON KINEMATIC GAIT PARAMETERS DURING TREADMILL WALKING

S. Duda<sup>\*</sup>, G. Gembalczyk<sup>\*\*</sup>, P. Jureczko<sup>\*\*\*</sup>

**Abstract:** *Body weight unloading (BWU) has become a typical strategy of gait training for patients with neurological and musculoskeletal disorders. However, the unloading system has an impact on the gait parameters. The aim of this study was to investigate kinematic gait parameters of healthy person during treadmill walking by manipulating BWU and treadmill speed. The two type of unloading strategies has been studied - with stationary unloading system and with application of algorithm controlling a follow-up the movement of unloading system in horizontal axis.*

**Keywords:** Body weight unloading, Kinematic gait parameters, Rehabilitation, Treadmill walking.

### 1. Introduction

The use of mechatronic devices in gait rehabilitation field has increased substantially. In the recent years a gait rehabilitation with systems for body weight unloading (BWU) has become increasingly popular (Lee and Hidler, 2008; Patiño et al., 2007; Threlkeld et al., 2003). Because of the high reproducibility of exercises a body weight unloading (BWU) carried on treadmills is a high effective method of gait rehabilitation for patients with neurological and musculoskeletal disorders. The main premise behind this method is that the additional support of patients' body weight realized by a BWU system with suspension harness during treadmill walking will reduce the load applied on the lower joints. It is especially helpful when patients start walking and allowing them to generate the locomotor patterns (Fischer and Wolf, 2015; Sousa et al., 2009).

Gait rehabilitation with treadmills and supported by BWU system is usually recommended early after injury to induce sensory stimulation (Threlkeld et al., 2003) and improve locomotor ability (Dickstein, 2008; Lamontagne and Fung, 2004; Schmid et al., 2007; Sousa et al., 2009; Van Hedel et al., 2006).

The general assumptions of gait rehabilitation on treadmills was that treadmill and overground gait patterns were similar enough and gait corrections on treadmills could replace a conventional overground walking training. However, research comparing treadmill and overground gait showing that treadmill training introduces habits different from those assumed to be correct in walking (Fischer and Wolf, 2015).

Because of the many advantages (e.g. small area of training, reduction of hard physiotherapists work) the devices with BWU systems and treadmills should be improved continuously. Currently used devices of this type have a stationary unloading system, mounted in one position without any possibility of movement. This article presents an attempt to determine the effect of follow-up the movement of unloading system in horizontal axis (over the patient) on the kinematic gait parameters.

### 2. Methods

This studies was conducted with the device for the re-education of locomotion functions, which was developed in the Institute of Theoretical and Applied Mechanics of the Silesian University of

---

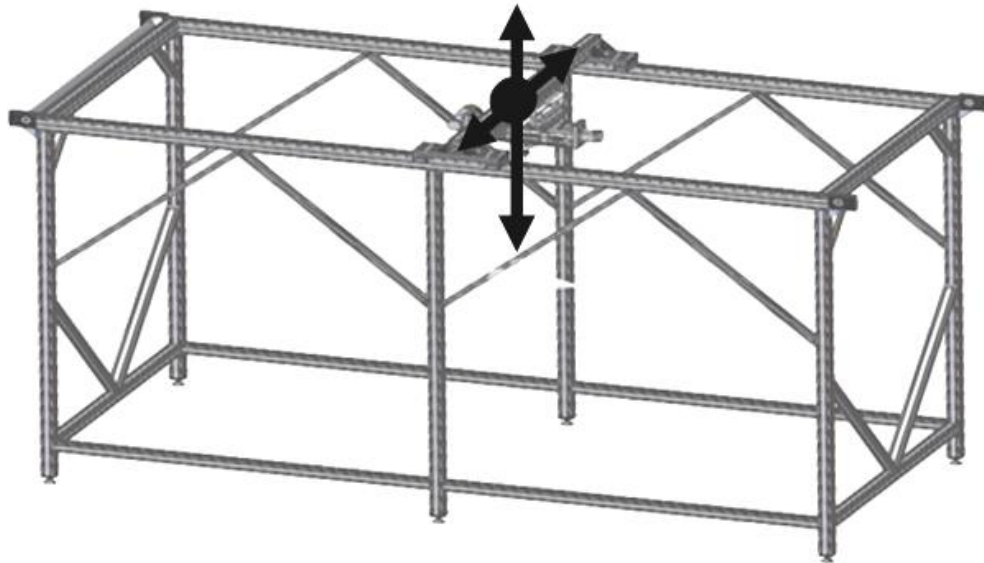
<sup>\*</sup> Assoc. Prof. Slawomir Duda, PhD.: Institute of Theoretical and Applied Mechanics, Silesian University of Technology, Akademicka 2A; 44-100, Gliwice; PL, Slawomir.Duda@polsl.pl

<sup>\*\*</sup> M.Sc. Eng. Grzegorz Gembalczyk: Institute of Theoretical and Applied Mechanics, Silesian University of Technology, Akademicka 2A; 44-100, Gliwice; PL, Grzegorz.Gembalczyk@polsl.pl

<sup>\*\*\*</sup> PhD. Eng. Pawel Jureczko: Institute of Theoretical and Applied Mechanics, Silesian University of Technology, Akademicka 2A; 44-100, Gliwice; PL, Pawel.Jureczko@polsl.pl

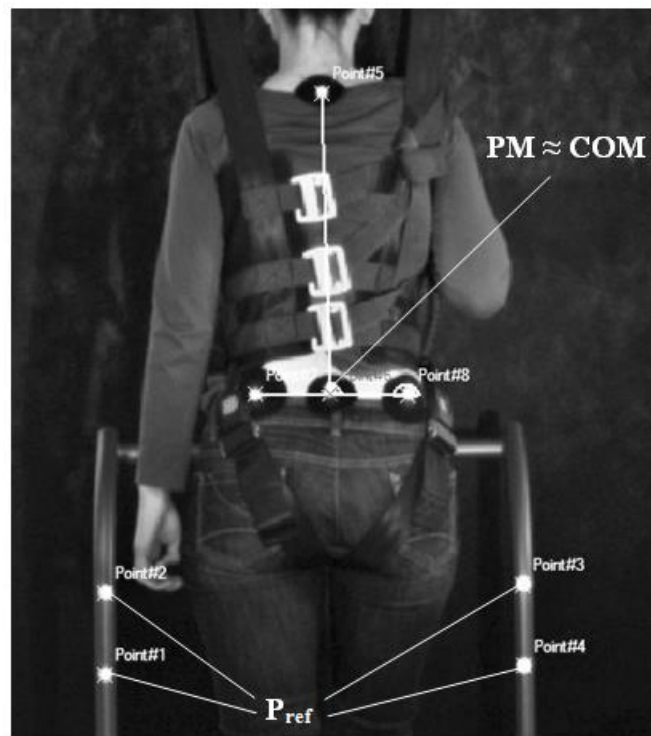


Technology. The structure of the device is based on the structure of an overhead travelling crane. As a result of installing three drives, the movement of the sling of the person in rehabilitation is possible in all axes. In the experiment only the unloading system with rehabilitation harness and a drive winch relative to the girder were used as indicated in Fig. 1 (Duda et al., 2015). The treadmill was located directly under the BWU system and it worked independently.



*Fig. 1: Mechatronic device for locomotor training.*

While testing with the TEMA motion analysis system, the movement of the point near to the centre of the subject mass (PM) has been established. The movement of the subject has been registered using two digital video cameras manufactured by Basler with a sampling frequency of 100 Hz. Reflective markers have been placed on anthropometric points on the body of the subject (Fig. 2), which allowed to estimate the trajectory of the movement of the centre of mass (Nordin and Frankel, 2001). Additionally, four reference points have been placed on fixed plane, parallel to the patients coronal plane.



*Fig. 2: Video camera image with measurement point marked.*

### 3. Measurements and results

The tests have been conducted with the participation of a healthy person during treadmill walking with a different unloading conditions:

- without unloading,
- with unloading implemented by a stationary unloading system,
- with unloading implemented by a unloading system with a movement follow-up in patients coronal plane.

In modes b and c, unloading at the levels of 100 N (20 % of subjects body weight), 150 N (26 % BW) and 200 N (35 % BW) has been applied. In each cases the treadmill speed equaled 1 km/h, 2 km/h and 3 km/h. The treadmill speed was increased after at least 15 seconds. The value of unloading has been controlled by closed-loop control system with strain gauges force sensor and the maximum error between the reference and measured unloading force was smaller than 25 N, what is presenting in the figure below (Fig. 3).

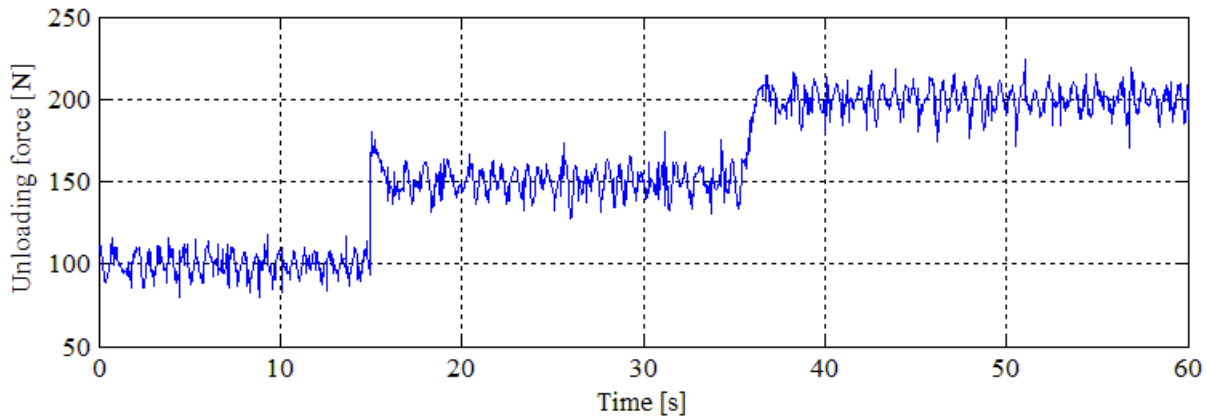


Fig. 3: The value of unloading force as a function of time.

The displacements of the centres of subjects mass established in the tests in each of the modes were used to determine the average displacement ranges in relation to the frontal and longitudinal axes of the subjects.

Tab. 1 presents the mean values of the range of displacement of the centre of the subject's mass in the normal treadmill walking and with three experimental BWU conditions. The BWU was realized by stationary winch. Tab. 2 contains the same values but obtained for devices with a follow-up movement of the winch in the horizontal axis, parallel to subjects frontal axis. The follow-up movement has been realized with PID controller in feedback with rope inclination angle (Mężyk et al., 2016).

As we can see, for a slow speed and low value of unloading force, kinematic gait parameters were comparable with a case without unloading. Increasing levels of BWU resulted in a significant increase in displacement of the centre of the subject's mass. The application of follow-up movement system in unloading winch allowed to decrease the excessive displacements in relation to the horizontal axis and to improve the range of movement in relation to the vertical axis.

Tab. 1: The range of displacement of the centre of the subject's mass- mean values.

	Unloading force [N]				Unloading force [N]			
	0	100	150	200	0	100	150	200
	Range of displacement in horizontal axis [mm]				Range of displacement in vertical axis [mm]			
Vt = 1 [km/h]	63.88	63.49	67.99	87.47	8.70	4.18	5.31	4.64
Vt = 2 [km/h]	48.14	49.47	64.87	71.12	14.13	13.13	18.16	16.32
Vt = 3 [km/h]	32.02	56.64	62.15	63.78	25.38	28.97	31.87	32.48



*Tab. 2: Ranges of displacement of the centre of the subject's mass with - mean values (test with follow-up movement in frontal axle).*

	Unloading force [N]				Unloading force [N]			
	0	100	150	200	0	100	150	200
	Range of displacement in horizontal axis [mm]				Range of displacement in vertical axis [mm]			
<b>Vt=1 [km/h]</b>	63.88	63.65	54.21	61.54	8.70	4.54	5.18	5.39
<b>Vt=2 [km/h]</b>	48.14	47.78	58.88	62.99	14.13	18.49	18.71	15.35
<b>Vt=3 [km/h]</b>	32.02	50.38	53.56	56.06	25.38	25.62	29.86	31.45

#### 4. Conclusions

The article presents the results of empirical research on kinematic gait parameters while walking on a treadmill with different cases of body weight unloading. During the experiment a typical and new strategy of unloading, with follow-up movement of unloading system in patients coronal plane, has been tested.

The use of high value of BWU resulted in significant changes on kinematic gait parameters in relation to the normal treadmill walking. The application of follow-up movement allowed to decrease the excessive ranges of displacement of the centre of the subject's mass. This confirms the efficiency of the applied unloading strategy, ensuring a greater reflection of the correct walk.

During the study also other parameters like the angle of rope inclination have been registered but a range of displacement has been considered the most representative.

The main limitation of the measurements was the participation of a healthy person since the effectiveness of the proposed unloading strategy should be verified with the participation of people with the gait disabilities.

#### References

- Dickstein, R. (2008) Rehabilitation of Gait Speed After Stroke: A Critical Review of Intervention Approaches. *Neurorehabilitation and Neural Repair*, 22, pp. 649-660.
- Duda, S., Gąsior, D., Gembalczyk, G., Kciuk, S. and Mężyk, A. (2015) Mechatronic device for locomotor training. *Acta Mechanica et Automatica*, 10, 4, pp. 310-315.
- Fischer, A.G. and Wolf, A. (2015) Assessment of the effects of body weight unloading on overground gait biomechanical parameters. *Clinical Biomechanics*, 30, pp. 454-461.
- Lamontagne, A. and Fung, J. (2004) Faster is better implications for speed-intensive gait training after stroke. *Stroke*, 35, pp. 2543-2548.
- Lee, S.J. and Hidler, J. (2008) Biomechanics of overground vs. treadmill walking in healthy individuals. *Journal of Applied Physiology*, 104, 3, pp. 747-755.
- Mężyk, A., Czapla, T., Klein, W. and Mura, G. (2016) Numerical simulation of active track tensioning system for autonomous hybrid vehicle. *Mechanical Systems and Signal Processing*, 89, pp. 108-118.
- Nordin, M. and Frankel, V.H. (2001) Basic biomechanics of the musculoskeletal system. Lippincott Williams & Wilkins, Philadelphia.
- Patiño, M.S., Gonçalves, A.R., Monteiro, B.C., Santos, I.L., Barela, A.M. and Barela, J.A. (2007) Kinematic, kinetic and electromyographic characteristics of young adults walking with and without partial body weight support. *Brazilian Journal of Physical Therapy*, 11, 1, pp. 19-25.
- Schmid, A., Duncan, P.W., Studenski, S., Lai, S.M., Richards, L., Perera, S. and Wu, S.S. (2007) Improvements in speed-based gait classifications are meaningful. *Stroke*, 38, pp. 2096-2100.
- Sousa, C.O., Barela, J.A., Prado-Medeiros, C.L., Salvini, T.F. and Barela, A.M. (2009) The use of body weight support on ground level: an alternative strategy for gait training of individuals with stroke. *Journal of NeuroEngineering and Rehabilitation*, 6, 43.
- Threlkeld, A.J., Cooper, L.D., Monger, B.P., Craven, A.N. and Haupt, H.G. (2003) Temporospatial and kinematic gait alterations during treadmill walking with body weight suspension. *Gait Posture*, 17, 3, pp. 235-245.
- Van Hedel, H., Tomatis, L. and Müller, R. (2006) Modulation of leg muscle activity and gait kinematics by walking speed and bodyweight unloading. *Gait Posture*, 24, 1, pp. 35-45.

## JITTER ANALYSIS OF MQTT PROTOCOL FRAMES IN MOBILE ROBOT CONTROL SYSTEM

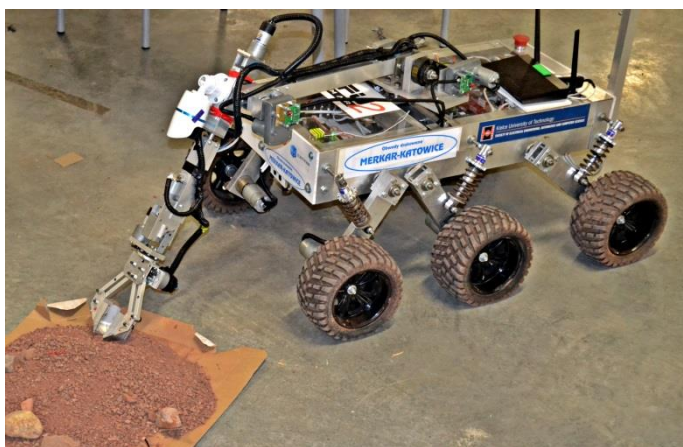
D. Dudek<sup>\*</sup>, R. Kazala<sup>\*\*</sup>, P. Straczynski<sup>\*\*\*</sup>

**Abstract:** *The paper presents a control system of the mobile handling robot which uses Internet of Things concept. Then a problem with jitter in communication between devices is shown. Based on the analysis a method which reduces the problem is proposed. It uses two instances of message broker. The first one for very important messages and the second for other information. Finally, the conclusions of the usability of the proposed method are presented.*

**Keywords:** Mobile robot, Internet of Things, Communication protocols, Control.

### 1. Introduction

Internet of Things is a relatively new concept in which objects can exchange information over the Internet (Chooruang, 2016 and Pingle et al., 2016 and Kazala et al., 2015). Access to the data is possible from any place, which is covered by the Internet network. Such idea can be used during the design of control systems of various mechatronic devices. On the basis of this idea has been developed in preparation for the European Rover Challenge competition and for projects (Dudek, 2016 and Straczynski, 2016) a mobile handling robot FUMAR shown in Fig. 1.



*Fig. 1: Mobile robot FUMAR.*

During testing of the robot control system, some problems were encountered related to the implementation of the MQTT protocol brokers which were used in the robot. They caused delays in the transmission of messages. The purpose of the paper is analysis of delays in the transmission of messages in robot control system. The relationship between occupancy level of the broker and the message sending time were investigated. Method of improving the system based on the introduction of a hierarchy of messages and double the broker has been presented. Finally the conclusions of the usability of the proposed method are presented.

---

<sup>\*</sup> Damian Dudek, MSc.: Department of Industrial Electrical Engineering and Automatics, Kielce University of Technology, Aleja Tysiąclecia Państwa Polskiego 7; 25-314 Kielce; PL, damiand@tu.kielce.pl

<sup>\*\*</sup> Robert Kazala, PhD.: Department of Industrial Electrical Engineering and Automatics, Kielce University of Technology, Aleja Tysiąclecia Państwa Polskiego 7; 25-314 Kielce; PL, rkazala@tu.kielce.pl

<sup>\*\*\*</sup> Pawel Straczynski, MSc.: Department of Industrial Electrical Engineering and Automatics, Kielce University of Technology, Aleja Tysiąclecia Państwa Polskiego 7; 25-314 Kielce; PL, pstraczynski@tu.kielce.pl

## 2. Mobile robot architecture

Mobile robot analyzed in the paper consists of six not steerable wheels powered by DC geared motors and platform with mounted a manipulating arm. The design of the robot is shown in Fig. 1. The robot arm has six degrees of freedom. To move each of arm links, DC motors equipped with gearboxes are also used (Dudek et al., 2016). For measuring the position and velocity determination, magnetic absolute encoders from AMS are used.

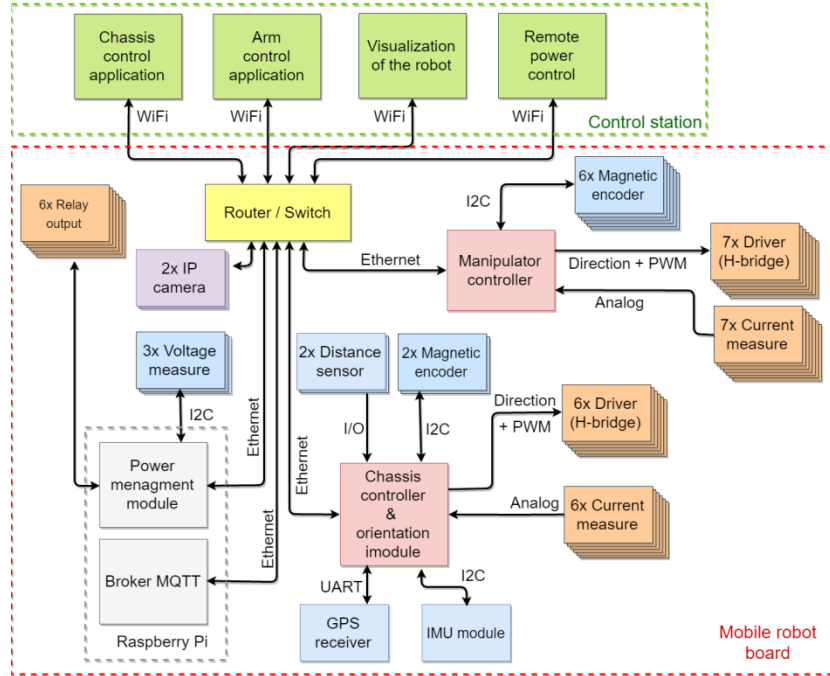


Fig. 2: Robot control system.

To ensure the greatest possible reliability and scalability, modular control system was developed. It enables redundancy of individual subsystems. In order to be able to control from a distance, the communication system is based on the idea of the Internet of Things. In the system, Ethernet and MQTT protocol are used which utilizes publish-subscribe communication model. Hardware architecture of the control system of the robot is shown in Fig. 2.

As the main onboard computer, single board computer Raspberry Pi with Ubuntu Mate operating system is used. It handles MQTT message broker. In addition, the computer which acts as a supervisory module allows disabling the other subsystems and monitoring the status of the lithium-polymer batteries. Other modules are managed by TM4C1294 microcontrollers from Texas Instruments, equipped with modern and efficient ARM Cortex-M4F core.

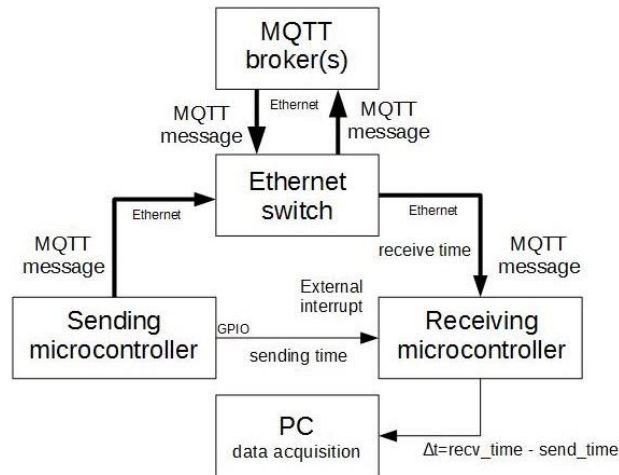


Fig. 3: Configuration of the broker test system.

### 3. Analysis of the impact of occupancy of broker on the data transfer time

One of the main problems in designing systems based on MQTT protocol is a fact that they use TCP/IP stack. Typically, in order to optimize the throughput, it employs Nagle algorithm which performs aggregation of frames (Nagle 1984). This is particularly undesirable in the systems which often exchange small portion of information. Nagle's algorithm should be disabled when additional latency is unacceptable. In subsystems which are based on microcontroller and LwIP TCP/IP stack implementation it can be forced to immediately send frames with use of `tcp_output()` function. This solution makes that each frame contains one MQTT protocol message. A bigger problem is in the case of MQTT brokers because it is not always possible turning off the Nagle algorithm. Initially, in the robot control system, popular open source MQTT broker called Mosquitto were used. To analyze latency in communication between two devices a special measurement unit shown in Fig. 3 were prepared.

During testing, it was noticed that the Nagle algorithm is enabled in the Mosquitto broker instance. The effect of MQTT frame aggregation caused by the algorithm is shown in Fig. 4. This broker does not allow to disable this mechanism using the configuration file. Therefore, it was decided to use Erlang MQTT broker (EMQ) that does not use this algorithm.

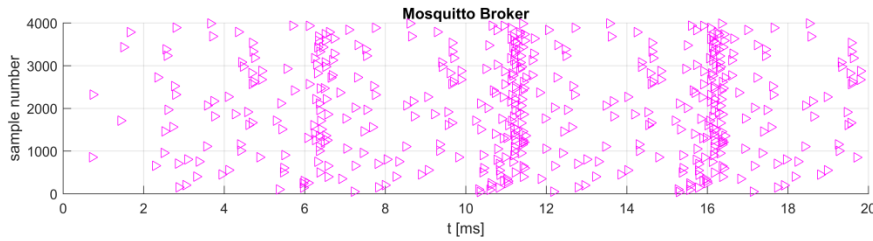


Fig. 4: Frame aggregation effect for Mosquitto broker.

Each of mechatronic communication systems contain at least few priorities of transmitted messages. The robot communication system, presented in this paper, has different kinds of MQTT protocol frames. They can be divided into high priority control messages and normal priority information messages. In order to minimize the transmitting time for high-priority messages, instead of a single instance of the broker, the two broker system was introduced. The first instance of the broker processes only most important MQTT topics, while the second one forwards others. Proposed priorities are presented in Fig. 6. Reducing occupancy of main broker through separation of messages positively affect the speed of high-priority packets. Results of the experiment are shown in Fig. 5.

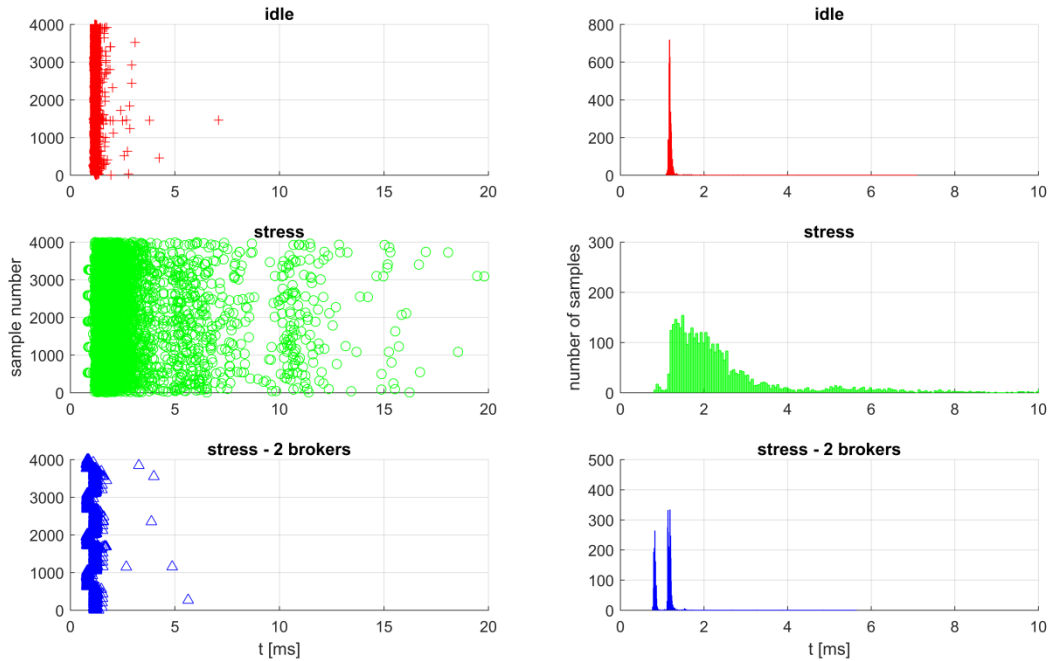
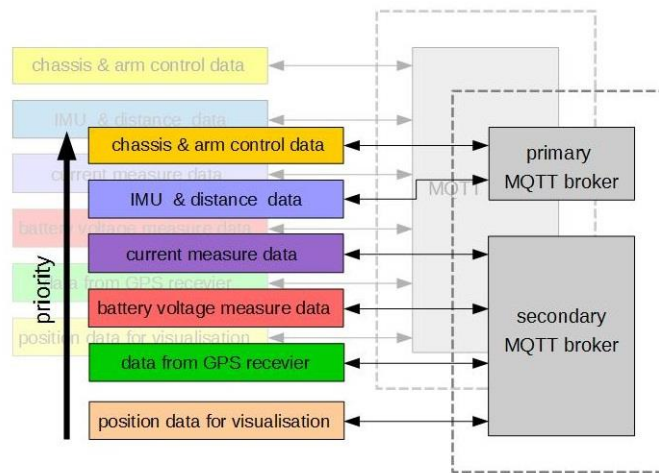


Fig. 5: Analysis of high priority frames end-to-end time.



*Fig. 6: Proposed priorities in two broker robot communication system.*

Fig. 5 idle shows the times of transmission of priority frames in the absence of information frames for one broker configuration. Fig. 5 stress presents the same configuration with lots of information frames. Stress – 2 brokers shows configuration with two brokers with the same amount of information frames. It is clearly evident that the two brokers configuration even with a heavy load provides a low jitter of priority frames.

#### 4. Conclusions

The use of IoT technologies in control systems of robots and other mechatronic devices, greatly simplifies the exchange of information between modules and between the operator and the controlled device. Using MQTT protocol enables the development of modular and scalable control systems. It can be easily integrated with the Internet network and used in systems consistent with the concept of Industry 4.0. For small installations with few transmitted messages, the control system can use a single broker. However, in the case of systems in which there is an intensive exchange of data and information transferred have different validity, the use of a single broker is not effective. This is due to the occurrence of delays in the transmission of the priority information. The solution to this problem is to use two or more brokers, each support information with different priority. Additional improvement can be obtained by assigning operating system priorities to broker processes. However, this does not give a significant reduction of a jitter of transmitted messages. In the future it will be possible to set priorities for each of the MQTT topics in the broker since it is planned to extend the MQTT protocol. Currently, there are implementations of brokers that use priorities, but efficiency of these solutions, particularly in multi-core systems is smaller than the use of separate brokers.

#### References

- Chooruang, K. and Pongpat, M. (2016) Wireless Heart Rate Monitoring System Using MQTT. *Procedia Computer Science* 86, pp. 160-163.
- Dudek, D. (2016) Robotic arm control system utilizing ARM microcontroller and MQTT protocol. Master Thesis, Kielce University of Technology.
- Dudek, D., Kazała, R. and Strączyński, P. (2016) Mobile Manipulation Robot Utilizing Internet Technologies Things In Control And Monitoring System. *Pomiary Automatyka Robotyka* 20 (4), pp. 37-45, (in Polish).
- Kazała, R., Taneva, A., Petrov, M. and Penkov, S. (2015) Wireless Network for Mobile Robot Applications. *IFAC-PapersOnLine*, Vol. 48, No. 24, pp. 231-236.
- Nagle, J. (1984) Congestion Control in IP/TCP Internetworks. *ACM SIGCOMM Computer Communication Review*, Volume 14 Issue 4, October 1984, pp. 11-17.
- Pingle, Y., Dalvi, S.N., Chaudhari, S.R. and Bhatkar, P. (2016) Electricity Measuring IoT Device. 3rd International Conference on Computing for Sustainable Global Development (INDIACom), pp. 1423-1426. IEEE.
- Strączyński, P. (2016) Mobile robot navigation and control system using ARM microcontroller. Master Thesis, Kielce University of Technology.

## COMPUTATIONAL PERFORMANCE OF A DSG-BASED ISOGEOMETRIC BEAM ELEMENT

E. Dvořáková<sup>\*</sup>, B. Patzák<sup>\*\*</sup>

**Abstract:** An application of Discrete shear gap (DSG) method to the isogeometric Timoshenko beam element with variable curvature is presented. A locking-removal capability of DSG is compared to the reduced integration. While the reduced integration does not remove stress or strain oscillations, DSG provides results matching exact solution. The application of DSG method results in full stiffness matrix of a patch and compared to reduced integration is computationally more demanding. This possibly leads to a deterioration of overall time efficiency of the isogeometric approach. Thus the computational performance of the element is compared to the standard straight beam element. Results proved the enormous time efficiency of isogeometric element over standard FEA and excellent convergence properties of DSG method.

**Keywords:** Beam element, Discrete shear gap, Isogeometric analysis, NURBS, Shear locking.

### 1. Introduction

Isogeometric analysis (Hughes et al., 2005) is a recently developed alternative of standard finite element method, which has been proposed to bridge the gap between CAD (Computer Aided Design) and FEA (Finite Element Analysis). In practice, CAD models are mostly represented by the splines, while the standard FEA is usually based on polynomial basis functions. Isogeometric analysis uses the spline basis for both CAD and FEA data representations.

The switch of basis functions from polynomials to splines in FEA offers great benefits. The same geometry representation can be shared by both CAD and FEA systems and thus no transformation from one to another is needed. Moreover spline functions enable exact description of the shapes which cannot be exactly described by polynomials (e.g. conic sections). These aspects can significantly improve computational efficiency and accuracy.

An exact geometry representation in isogeometric analysis can be especially profitable for structures of curved geometries. Main focus of this paper is placed on structural analysis of curved beams. Timoshenko beam element based on work of Bouclier (2012) is presented. The formulation of the element suffers from locking phenomena and DSG method is used to unlock the element. Finally, the computational efficiency over classical straight beam element is studied.

### 2. Isogeometric beam element

The presented element formulation uses NURBS (Non-Uniform Rational B-Splines) as a basis functions for both geometry description and unknown approximations. A  $p^{th}$  degree NURBS functions  $N_i^p$  are generated from B-splines as

$$N_i^p(\xi) = \frac{S_i^p(\xi)w_i}{\sum_{i=1}^n S_i^p(\xi)w_i}, \quad (1)$$

where  $S_i^p$  are  $p^{th}$  degree B-spline functions,  $w_i$  are the weights associated with the corresponding basis function and  $\xi \in (0, 1)$  is a parametric coordinate running through the entire patch (subdomain of knot

---

<sup>\*</sup> Ing. Edita Dvořáková: Department of Mechanics, Faculty of Civil Engineering, CTU in Prague; Thákurova 7, 166 27, Prague; CZ, edita.dvorakova@fsv.cvut.cz

<sup>\*\*</sup> Prof. Dr. Ing. Bořek Patzák: Department of Mechanics, Faculty of Civil Engineering, CTU in Prague; Thákurova 7, 166 27, Prague; CZ, borek.patzak@fsv.cvut.cz



spans which are seen as “elements” in isogeometric analysis). See Piegl (1997) for better understanding of NURBS geometry.

A curved Timoshenko beam element with three independent unknowns, tangential displacement  $u_t(s)$ , normal displacement  $u_n(s)$  and rotation  $\theta(s)$ , is being considered. Membrane, transverse shear and bending strains are given by

$$\varepsilon_m(s) = u'_t(s) - \frac{u_n(s)}{R(s)}, \quad \gamma_s(s) = \frac{u_t(s)}{R(s)} + u'_n(s) - \theta(s), \quad \chi_b(s) = \theta'(s), \quad (2)$$

where curvilinear coordinate  $s$  runs along the midline of the beam, the prime indicates a derivation with respect to the  $s$  and  $R$  is a radius of a curvature. For simplicity, the dependence on  $(s)$  will be omitted in the following text. The stiffness matrix is evaluated using

$$\mathbf{K} = \int_0^L \mathbf{B}^T \mathbf{D} \mathbf{B} ds, \quad (3)$$

where strain-displacement matrix  $\mathbf{B}$  is derived using formulas for strain components (2) and  $\mathbf{D}$  is a material matrix resulting from

$$N = EA\varepsilon_m, \quad Q = GA\gamma_s, \quad M = EI\chi_b, \quad (4)$$

where  $N, Q$  and  $M$  are axial force, transverse shear force and bending moment, respectively. Young's modulus  $E$ , shear modulus  $G$ , area  $A$  and moment of inertia  $I$  are the material and cross-section characteristics.

### 3. Numerical locking

Due to the independent approximation of displacements and rotation the element suffers from shear locking. The formula for bending strain results in lower order term than formula for shear strain (2), but actually this should be vice-versa. Moreover from the formula for the shear strain it is obvious that zero shear strain cannot be satisfied along entire patch when the same order interpolation of unknowns is used because of field-inconsistency (Adam et al., 2014). In this paper the performance of Discrete Shear Gap (DSG) method, originally developed for unlocking the standard finite elements (Bletzinger, 2000) and further extended also for isogeometric elements (Echter, 2010), is examined.

The DSG approach can be divided into several steps yielding the modified strain-displacement matrix  $\mathbf{B}$  used to evaluate stiffness matrix  $\mathbf{K}$ . The main idea of the method is to satisfy the equation for shear strain (2) in integral sense (instead of pointwise). The shear contributions  $u_n^{\gamma^{hi}}$  (so called “shear gaps”) to the deflection  $u^n$  in the collocation points are calculated by integration of  $\gamma_s^h$  (2) as

$$u_n^{\gamma^{hi}} = \int_0^{s_i} \gamma_s^h ds = \int_0^{s_i} \frac{u_t}{R} + u'_n - \theta ds = \mathbf{B}^{DSG} \mathbf{r}, \quad (5)$$

where the collocation points  $s_i$  are given as Greville abscissa of the control points (Piegl, 1997). The modified shear displacements  $u_n^{\gamma^{modh}}$  are interpolated using NURBS basis functions

$$u_n^{\gamma^{modh}} = \sum_{i=1}^n N_i \tilde{u}_n^{\gamma^{hi}}. \quad (6)$$

In case of isogeometric analysis, the discrete shear gaps  $\tilde{u}_n^{\gamma^{hi}}$  are non-interpolatory, therefore they need to be expressed using values in the control points. For this purpose, the transformation matrix  $\mathbf{A}$  is derived

$$\{u_n^{\gamma^h}\} = \mathbf{A} \{\tilde{u}_n^{\gamma^h}\}, \quad A_{ij} = N_j(s_i), \quad (7)$$

where  $\{u_n^{\gamma^h}\}$  are interpolatory values of shear gaps at control points and  $N_j(s_i)$  is the  $j^{th}$ -basis function evaluated at  $i^{th}$ -collocation point. The modified shear strain is then given as



$$\gamma_s^{mod^h} = \sum_{i=1}^n N_i' \tilde{u}_n^{\gamma_{hi}} \quad (8)$$

and the modified part of the strain-displacement matrix  $\mathbf{B}$  corresponding to shear component is obtained by combining (5)-(8) as

$$\mathbf{B}^\gamma = \mathbf{N}' \mathbf{A}^{-1} \mathbf{B}^{DSG}. \quad (9)$$

It is important to note, that this modification has to be performed on the patch level, as the collocation points are located along the entire patch. Moreover the inverse of  $\mathbf{A}$  introduce a full global patch stiffness matrix. This leads to the higher computational cost which could possibly reduce the advantages of isogeometric approach and therefore should be further analysed.

#### 4. Numerical examples

The presented isogeometric beam element has been implemented into OOFEM finite element code (Patzák, 2017) and its performance has been tested on the circular cantilever beam subjected to the tip force load (Fig. 1). Ability of reduced integration and DSG method to unlock the element with cubic approximation is illustrated in Fig. 1. For reduced integration, the scheme proposed by Bouclier (2012) has been used (i.e. two Gauss points per each knotspan + 2 additional Gauss points per patch). Both methods (DSG and reduced integration) show good results when the convergence of normal displacement at the tip of the beam is studied, nevertheless the reduced integration still suffers from the oscillations in strains along the beam (Fig. 1). The DSG method proven itself to successfully unlock the element and provide results in agreement with exact solution.

In order to document the benefits of IGA over standard FEA, the computational performance of isogeometric element using DSG approach has been compared to classical straight Timoshenko beam element with cubic approximation which does not suffer from locking (Bittnar, 1992). To demonstrate the quality of solution, the  $L^2$  norm of normal displacement error  $\|e\|$

$$\|e\| = \sqrt{\int_0^L (u_n^{exact} - u_n^h)^2 ds}, \quad u_n^{exact} = \left( \frac{R^3}{2EI} + \frac{R}{kGA} + \frac{R}{2EA} \right) \varphi \sin(\varphi) \quad (10)$$

is used. To illustrate the convergence, the solution time consumed with respect to the error  $\|e\|$  is plotted in Fig. 2. The obtained results document the enormous time efficiency of isogeometric element over standard FEA. Moreover, it is obvious, that degree elevation can reduce the error while the computational time is kept low.

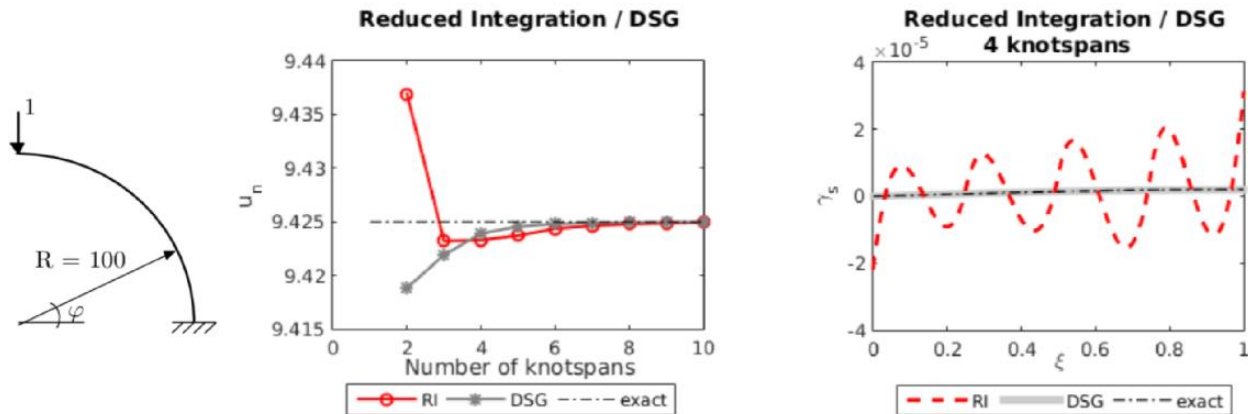


Fig. 1: Circular cantilever beam: (left) problem setup,  $E = 10^6$ ,  $h = 1.0$ ,  $b = 1.0$ ,  $\nu = 0.0$ , (centre) convergence of the normal displacement at the tip of the beam with cubic NURBS approximation using reduced integration (2 Gauss points per knotspan + 2 additional Gauss points per patch), (right) oscillations in shear strain when the reduced integration is used while the use of DSG matches the exact solution.

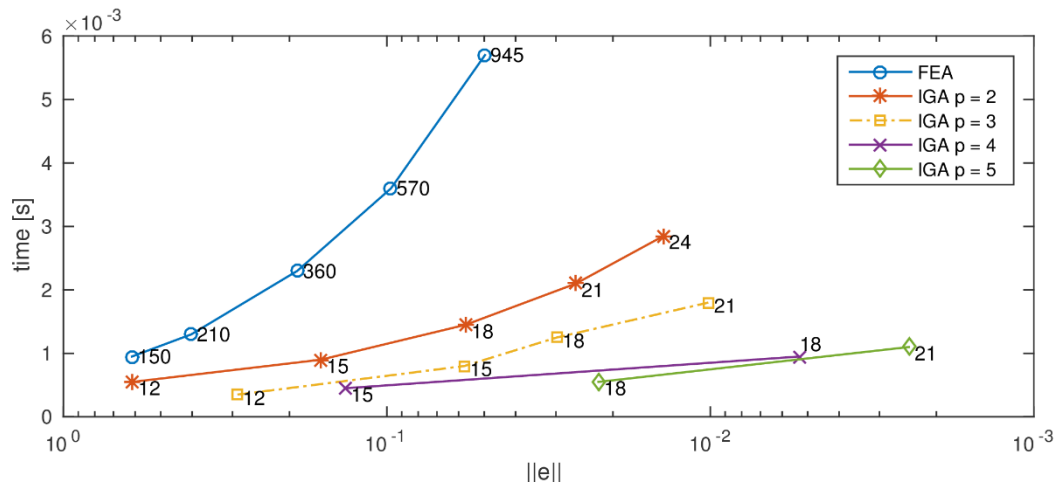


Fig. 2: Circular cantilever beam: Comparison of solution time in OOFEM with respect to the error of normal displacement using Timoshenko beam elements with cubic approximation (FEA) and isogeometric beam elements with different approximation orders. The numbers in the plot indicate the required number of degrees of freedom for specific simulation.

## 5. Conclusions

The isogeometric Timoshenko beam element has been implemented into existing finite element code. It has been shown, that the reduced integration does not remove the oscillations in strains, while the satisfactory results are obtained in case of use of DSG method.

The significant time efficiency of isogeometric element over standard straight beam element has been proven. The performance of standard FEA could be enhanced using suitable curved beam element formulation, however such is not currently available in OOFEM. Also these formulations have usually some assumptions, such as constant curvature. On the contrary, isogeometric formulation enable exact description of arbitrarily curved geometries.

## Acknowledgement

The financial support of this research by the Grant Agency of the Czech Technical University in Prague (SGS project No. SGS17/043/OHK1/1T/11) is gratefully acknowledged.

## References

- Adam, C., Bouabdallah, S., Zarroug, M. and Maitournam, H. (2014) Improved numerical integration for locking treatment in isogeometric structural elements, Part I: Beams. *Comput. Methods Appl. Mech. Engrg.*, 279, pp. 1-28.
- Bittnar, Z. and Šejnoha, J. (1992) *Numerical methods of mechanics 1*, Vydavatelství ČVUT, Praha (in Czech).
- Bletzinger, K.U., Bischoff, M. and Ramm, E. (2000) A unified approach for shear-locking-free triangular and rectangular shell finite elements, *Computers and Structures*, 75, pp. 321-334.
- Bouclier R. and Elguedj, T. (2012) Locking free isogeometric formulations of curved thick beams. *Comput. Methods Appl. Mech. Engrg.*, 245-246, pp. 144-162.
- Echter, R. and Bischoff, M. (2010) Numerical efficiency, locking and unlocking of NURBS finite elements. *Comput. Methods Appl. Mech. Engrg.* 199, pp. 374-382.
- Hughes, T.J.R., Cottrell, J.A. and Bazilevs, Y. (2005) Isogeometric analysis: CAD, finite elements, NURBS, exact geometry and mesh refinement. *Comput. Methods Appl. Mech. Engrg.* 194, pp. 4135-4195.
- Patzák, B. (2017) OOFEM project home page, <http://www.oofem.org>, 2017.
- Piegl, L. and Tiller, W. (1997) *The NURBS Book*. Springer-Verlag Berlin Heidelberg, New York.

## QUICK PROTOTYPING OF MANIPULATOR CONTROL SYSTEM WITH PLC CONTROLLER

K. Dzierżek<sup>\*</sup>, M. Rećko<sup>\*\*</sup>, D. S. Pietrala<sup>\*\*\*</sup>

**Abstract:** Presented article depicts new approach to the industrial manipulator's control that simplifies new control algorithms implementation. A prototyping setup consists of RXi BOX IPC and input/output modules RSTi distributed I/O, which are fully compatible with PLC controllers. Control algorithm optimisation is performed on a Box IPC in a high-level programming language that drastically accelerates implementation. Following implementation, a Box IPC and distributed I/O, are substituted with a real-time operating PLC. After algorithm optimisation and programming of the PLC, system is ready to work

**Keywords:** PLC controller, Robotic arm, Phantom device, Control, IPC.

### 1. Introduction

Many kinds of manipulators found implementation in a variety of fabrication lanes. However, robotic arm's use is not only limited to industry. Growing number of mobile platforms is currently equipped with a manipulator. The most arduous task, regarding use scenario, is to implement optimal control algorithm. Authors' goal is to address this problem in this paper.

System's output (execution device) is a Hyperion 2 Mars rover analogue. It was created to compete in an international competition University Rover Challenge 2014. During this challenge, the rover had to perform several tasks, which required the use of an onboard manipulator. Use of joystick to control its robotic arm was imprecise. An optimal control algorithm was a result of numerous experiments and gradual improvements. Currently, it consists of the Phantom device equipped with encoders for precise angle reads and industrial PC. Such setup allows feedforward as well as control in Cartesian cordite system.

### 2. Robotic arm – Phantom system

System for rapid prototyping of robotic arm controllers (Fig. 1) consists of the Phantom device (1), RXI\_IPC\_EP, model ICRXIFC7E111A controller (2) with modular input/output interface RSTi I/O, communication devices, a set of 2, SATELLINE-3AS 869 (3), mobile robot fitted out with a robotic arm (4). The computer (5) with Linux operating is used to control drive unit by means of radio modems (6) are additional equipment.

The system can operate in two modes: feed-forward and Cartesian. In the feed-forward mode, the robotic arm recreates temporary positions of individual phantom's joints. Need to create robotic arm's kinematic equivalent in the form of a phantom device is a disadvantage of this method. The Cartesian coordinates system mode requires calculation of end effector's global position, following, calculations of temporary angles between each joint using inverse kinematics on robot's side of the system.

---

<sup>\*</sup> Kazimierz Dzierżek, DSc, PhD, Eng.: Faculty of Mechanical Engineering, Białystok University of Technology, str. Wiejska 45c; 15-351, Białystok; PL, k.dzierzek@pb.edu.pl

<sup>\*\*</sup> Maciej Rećko, MSc, Eng.: Faculty of Mechanical Engineering, Białystok University of Technology, str. Wiejska 45c; 15-351, Białystok; PL, maciej.recko@outlook.com

<sup>\*\*\*</sup> Dawid Sebastian Pietrala, MSc.: Department of Automation and Robotics, Kielce University of Technology, Aleja Tysiąclecia Państwa Polskiego 7; 25-314 Kielce; PL, dpietrala@tu.kielce.pl

Fig. 2 depicts the phantom device, that consists of the base (1), three rotational joints (2, 4, 6), three rigid links (3, 5, 7) an encoder (8) and simulated end effector's tip (9). The device has four additional encoders. Each in every joint and one embedded in the base.

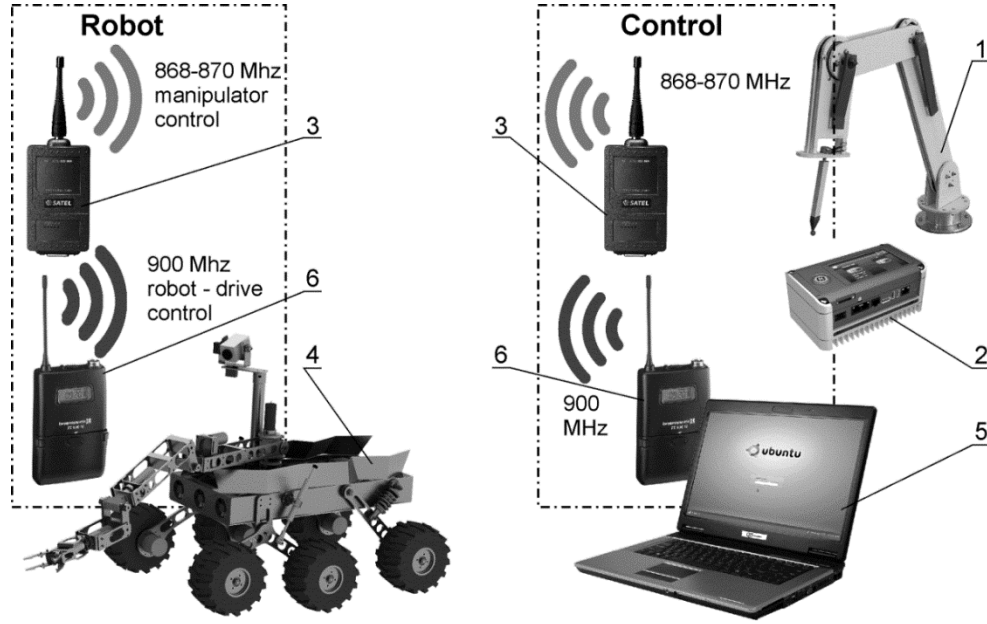


Fig. 1: System scheme.

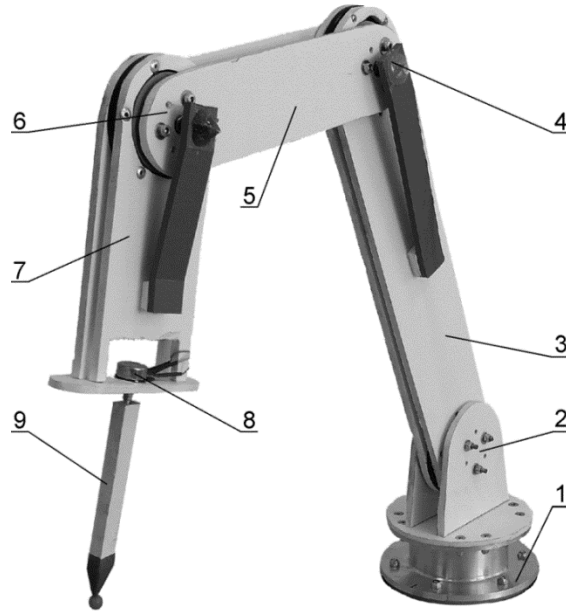


Fig. 2: The phantom device.

### 3. Robotic arm's and phantom's kinematics

The robotic arm and the phantom device are kinematic “twins”. This feature allows easy implementation of feed-forward control mode as well as consideration of Cartesian manipulation scenarios. To calculate the position of the end effector's tip (point P) a forward kinematics calculation is required (Pietrala 2016).

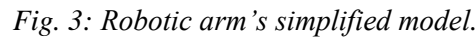
Using a Denavit- Hartenberg parameters, local transformation matrices were obtained that were used to create global transformation matrix. There are numerous methods of calculating forward and inverse kinematics of the robot's chain (Craig, 1999).

$${}^0_P T = {}^0_1 T \cdot {}^1_2 T \cdot {}^2_3 T \cdot \dots \cdot {}^{i-1}_i T \cdot \dots \cdot {}^{P-1}_P T \quad (1)$$

That results in position vector (3).

$$P = \begin{bmatrix} f_{14} \\ f_{24} \\ f_{34} \end{bmatrix} \quad (3)$$

However, to recreate the position on robot's side of the system, an inverse kinematics calculations are required. To simplify calculations, let's consider manipulator as a kinematic chain in XY-Z plane (Fig. 3).


$$\theta_1 = \text{atan}(P_y, P_x). \quad (4)$$
$$\cos\theta_3 = \frac{P_{cx}^2 + P_{cy}^2 + (P_{cz} - l_1)^2 - l_2^2 - l_3^2}{2 \cdot l_2 \cdot l_3}. \quad (5)$$
$$\theta_3 = \text{atan}(\sqrt{1 - M^2}, M). \quad (6)$$
$$\theta_2 = -\frac{\pi}{2} + \alpha + \beta, \quad (6)$$
$$\alpha = atan2(l_3 \cdot \sin\theta_3, l_2 + l_3 \cdot \cos\theta_3), \quad (7)$$

296

Finally:

$$\theta_4 = \eta - \theta_2 - (\pi - \theta_3). \quad (9)$$

Having  $\theta_1, \theta_2, \theta_3$  i  $\theta_4$ , a proper setup of the robotic arm is dependent on the robot's on-board.

In order to lower a number of possible solutions to those calculations and also eliminate unobtainable configurations a  $\eta$ - nutation angle is used. It is an angle between X-Y plane and last link. It determines inclination of the last link thus end effector. This approach was inspired by graphical solution of the inverse kinematics found in literature (Spong and Vidyasagar, 1997, and Tchoń et. al., 2000).

#### 4. Conclusions

The considered solution proved to step in a direction leading towards more reliable and precise control of the robotic arm. During series of experiments, proposed system performed above expectations. It not only accelerated control algorithm implementation but also allowed to detect several minor faults that occurred during the design process. The essential advantage of proposed system is its ease of programming and modularity. Performed tests consisted of repeating actions performed using direct connection between phantom and robot controllers.

The main computer, an IPC Box, is connected to the I/O module using MODBUS Protocol. This solution ensures quick access to sensory data and very easy use of this information in prototyped algorithm. Any inconsistencies in system's performance can be easily detected and corrected giving a programmer a sophisticated tool to create optimal algorithms.

Thanks to considered solution, an algorithm that proved to perform correctly can be implemented in a PLC controller operating in real time. Even inputs and outputs can be reused following prototyping phase. This approach reduces the time needed for new equipment implementation and assures its proper functioning.

Development of individual systems would take more time, including fine tuning the algorithm. Moreover, this solution is not only time saving thus cost-efficient, but also guarantees the best possible performance.

Future development of the project may bring even further improvement of usability and increased algorithm prototyping speed. Necessary modifications are currently implemented and will certainly benefit in our further research.

#### Acknowledgement

Research conducted under the S/WM/1/2016 and financed from the resources for science of the Ministry of Science and Higher Education

#### References

- Craig, J.J. (1995) Introduction to Robotics, Wydawnictwa Naukowo-Techniczne, Warsaw (in Polish).
- Czaplicki, P. Rećko M. and Tołstoj-Sienkiewicz, J. (2016) Robotic Arm Control System for Mars Rover Analogue, in proc. 21st International Conference on Methods and Models in Automation and Robotics, Międzyzdroje, pp. 1122-1126.
- Spong, M.W. and Vidyasagar, M. (1997) Dynamics and Robot Control, Wydawnictwa Naukowo-Techniczne, Warsaw (in Polish).
- Tchoń, K. et. al. (2000) Manipulators and Mobile Robots, Akademicka Oficyna Wydawnicza PLJ, Warsaw (in Polish).
- Hardware Reference Manual. (2014) RXi Box IPC-EP, General Electric Company.
- PACSystems RSTi (2012) Network Adapter Manual, GE Intelligent Platforms.
- PACSystems\* RXi. (2013) Distributed IO Controller, User's Manual, GE Intelligent Platforms.
- Pietrala, D. S. (2016) Parallel manipulator with pneumatic muscle drive, in: Proc. Int. Conf. on Engineering Mechanics 2016 (eds. Zolotarev, I and Radolf, V.), Svratka, Czech Republic, pp. 458-461.
- Laski, P. A., (2016) The design of a proportional slit valve with a piezoelectric actuator, in: Proc. Int. Conf. on Engineering Mechanics 2016 (eds. Zolotarev, I and Radolf, V.), Svratka, Czech Republic, pp. 350-353.

## THE DYNAMICS OF THE GUIDE ARRANGEMENT BEING AN ELEMENT OF THE LAUNCHER INSTALLED ON A COMBAT VEHICLE

Z. Dziopa<sup>\*</sup>, M. Nyckowski<sup>\*\*</sup>

**Abstract:** *The guide arrangement is an element of the self-propelled anti-aircraft missile set. The disturbance which is transferred onto the assembly is generated during the motion of the short-range target homing missiles along the guide. The aim of the paper is to discuss how the input generated within the assembly affects the motion of the guide arrangement.*

**Keywords:** Guides arrangement, Launcher, Operator, Combat vehicle, Missile, Dynamics.

### 1. Introduction

The key role in the functioning of the self-propelled anti-aircraft missile set belongs to the arrangement of guides, Fig. 1. Before and at the initial stage of the launching the missile contacts the guide via two directing rings. The missile moves along the guide simultaneously revolving around the longitudinal axis. At this stage the missile has two points of contact with the launcher guide. These points are represented by two supports. The placement of the directing rings on the missile body determine the location of the supports. The structure of the arrangement results from the accepted assumption and determines missile mobility. The two-point support is binding until the instant the first directing ring of the missile abandons the guide. From that moment the kinematic pair: guide-missile, previously a set with a two-degree freedom, becomes a set with a three-degree freedom of movement. The structure of the arrangement changes as the missile moves along the guide. The support is reduced to one point. In the general case the support leads to the lack of co-linearity of the points located on the longitudinal axis of the missile compared to the points located on the longitudinal axis of the guide. This particular property is characteristic of the arrangement: guide-missile with a three-degree freedom. The fact that the longitudinal axis of the missile and the longitudinal axis of the guide do not overlap all the time is typical of the structure.

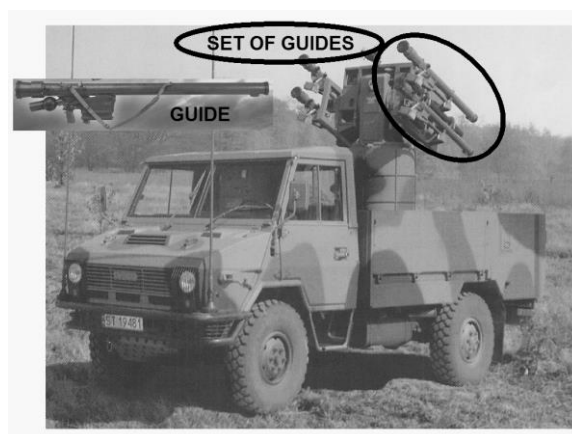


Fig. 1: Self-propelled anti-aircraft missile set.

<sup>\*</sup> Prof. Zbigniew Dziopa, PhD. Eng.: Faculty of Mechatronics and Mechanical Engineering, Kielce University of Technology, al. 1000-lecia P.P. 7; 25-314, Kielce; PL, zdziopa@tu.kielce.pl

<sup>\*\*</sup> Research Assistant Maciej Nyckowski, MSc. Eng.: Institute of Aviation, al. Krakowska 110/114, 02-256 Warsaw; PL, nyckowski@gmail.com



The guide arrangement consists of two guides located one under the other and links the platform and the missile. It is necessary for the guide arrangement, with maximum efficiency, to insulate the missile against undesirable platform vibrations and disturbance generated by launching missiles as well as providing conditions for proper localization of the target by missiles (Dziopa, 2015).

## 2. Physical model

The model of the self-propelled anti-aircraft missile assembly consists of five elements (Dziopa, et al 2015). These elements are: a combat vehicle, an operator seated in the chair, a launcher and two missiles and a target. The launcher, which consists of a platform and a set of guides, is installed on the vehicle, Fig. 2.

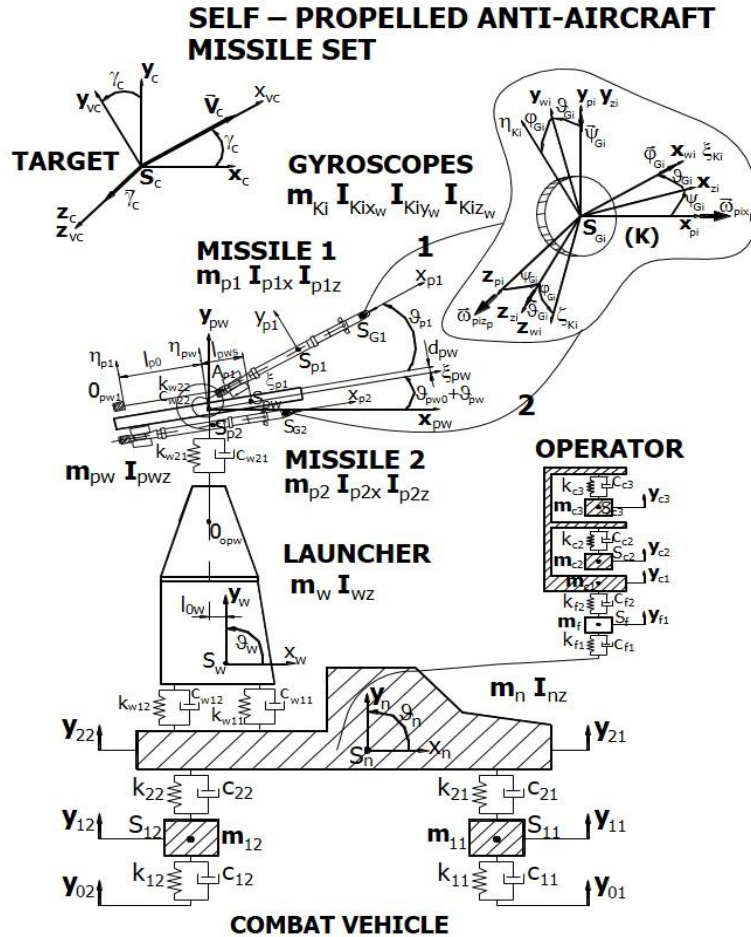


Fig. 2: Physical model of the self-propelled anti-aircraft missile set.

The launcher does not change its configuration after the guide arrangement has been set into the position of intercepting the target (Dziopa, 2013). At this instant the guide arrangement is turned towards the platform in accordance with the elevator angle:  $\vartheta_{pw0}$ . The  $\vartheta_{pw0}$  angle is the initial angle of inclination of the set of guides. The guide arrangement is a perfectly rigid body with mass:  $m_{pw}$  and the moment of inertia:  $I_{pwz}$  (Chatys, 2013). The object is placed on the platform with the use of two passive elastic-damping elements with linear parameters  $k_{w21}$  and  $c_{w21}$  respectively and  $k_{w22}$  and  $c_{w22}$ . Two independent generalized coordinates were used to determine the position of the guide arrangement at any moment:

- $y_{pw}$  - vertical relocation of the rotation centre  $O_{opw}$  of the guide arrangement,
- $\vartheta_{pw}$  - angle of rotation of the guide arrangement around the  $O_{opw} z_{pw}$  axis.

## 3. Mathematical model

The studied arrangement is described by differential equations with ordinary derivatives represented by twenty-four independent generalized coordinates (Baranowski et al., 2016). On account of the limited

number of pages and a lengthy notation of the equations, only the dependences describing the guide arrangement motion will be presented.

The equations representing the motion of the guide arrangement:

$$\begin{aligned}
& (m_{pw} + m_{p1} + m_{p2})\ddot{y}_{pw} + [m_{pw}l_{03} + m_{p1}(l_{15} - l_{06} - l_{14} + l_{11}) + \\
& + m_{p2}(l_{25} + l_{06} + l_{24} + l_{21})]\ddot{\vartheta}_{pw} + m_{p1}(l_{11} - l_{14})\ddot{\vartheta}_{p1} + m_{p2}(l_{21} - l_{24})\ddot{\vartheta}_{p2} + \\
& + m_{p1}l_{02}\ddot{\xi}_{p1} + m_{p2}l_{02}\ddot{\xi}_{p2} + [m_{pw}l_{04} + m_{p1}(l_{16} + l_{05} + l_{13} + l_{12}) + \\
& + m_{p2}(l_{26} - l_{05} - l_{23} + l_{22})]\dot{\vartheta}_{pw}^2 - m_{p1}(l_{12} + l_{13})\dot{\vartheta}_{p1}^2 - m_{p2}(l_{22} - l_{23})\dot{\vartheta}_{p2}^2 + \\
& - 2m_{p1}(l_{13} + l_{12})\dot{\vartheta}_{pw}\dot{\vartheta}_{p1} + 2m_{p2}(l_{23} - l_{22})\dot{\vartheta}_{pw}\dot{\vartheta}_{p2} + 2m_{p1}l_{01}\dot{\vartheta}_{pw}\dot{\xi}_{p1} + \\
& + 2m_{p2}l_{01}\dot{\vartheta}_{pw}\dot{\xi}_{p2} + k_{w21}\lambda_{w21} = (P_{ss1}\sin\vartheta_{p1} + P_{ss2}\sin\vartheta_{p2})\cos(\vartheta_{pw0} + \vartheta_{pw}) + \\
& - (m_{pw} + m_{p1} + m_{p2})g
\end{aligned} \tag{1}$$

$$\begin{aligned}
& (m_{pw}l_{pws}^2 + I_{pw} + m_{p1}a_{11} + I_{p1} + m_{p2}a_{21} + I_{p2})\ddot{\vartheta}_{pw} + [m_{pw}l_{03} + \\
& + m_{p1}(l_{15} - l_{06} - l_{14} + l_{11}) + m_{p2}(l_{25} - l_{06} - l_{24} + l_{21})]\ddot{y}_{pw} + (m_{p1}a_{13} + I_{p1})\ddot{\vartheta}_{p1} + \\
& + (m_{p2}a_{23} + I_{p2})\ddot{\vartheta}_{p2} - m_{p1}a_{12}\ddot{\xi}_{p1} + m_{p2}a_{22}\ddot{\xi}_{p2} - m_{p1}a_{14}\dot{\vartheta}_{p1}^2 - m_{p2}a_{24}\dot{\vartheta}_{p2}^2 + \\
& - 2m_{p1}a_{14}\dot{\vartheta}_{pw}\dot{\vartheta}_{p1} - 2m_{p2}a_{24}\dot{\vartheta}_{pw}\dot{\vartheta}_{p2} + 2m_{p1}a_{15}\dot{\vartheta}_{pw}\dot{\xi}_{p1} + 2m_{p2}a_{25}\dot{\vartheta}_{pw}\dot{\xi}_{p2} + \\
& + k_{w22}\lambda_{w22} = P_{ss1}(\xi_{p1} - l_{p0})\sin\vartheta_{p1} + P_{ss2}(\xi_{p2} - l_{p0})\sin\vartheta_{p2} + \\
& + m_{p1}g(l_{06} - l_{15} + l_{14} - l_{11}) - m_{p2}g(l_{06} + l_{25} + l_{24} - l_{21}) - m_{pw}gl_{03}
\end{aligned} \tag{2}$$

where:

$$\begin{aligned}
\lambda_{w21} &= y_{pw} + y_{pws} + l_{0w}(\vartheta_w + \vartheta_{ws}) - (y_w + y_{ws}), \quad \lambda_{w22} = \vartheta_{pw} + \vartheta_{pws} - (\vartheta_w + \vartheta_{ws}) \\
l_{01} &= \cos(\vartheta_{pw0} + \vartheta_{pw}), \quad l_{02} = \sin(\vartheta_{pw0} + \vartheta_{pw}), \quad l_{03} = l_{pws} \cos(\vartheta_{pw0} + \vartheta_{pw}), \quad l_{04} = l_{pws} \sin(\vartheta_{pw0} + \vartheta_{pw}) \\
l_{05} &= d_{pw} \cos(\vartheta_{pw0} + \vartheta_{pw}), \quad l_{06} = d_{pw} \sin(\vartheta_{pw0} + \vartheta_{pw}), \quad l_{11} = l_{ps1} \cos(\vartheta_{pw0} + \vartheta_{pw} + \vartheta_{p1}) \\
l_{12} &= l_{ps1} \sin(\vartheta_{pw0} + \vartheta_{pw} + \vartheta_{p1}), \quad l_{13} = d_p \cos(\vartheta_{pw0} + \vartheta_{pw} + \vartheta_{p1}), \quad l_{14} = d_p \sin(\vartheta_{pw0} + \vartheta_{pw} + \vartheta_{p1}) \\
l_{15} &= (\xi_{p1} - l_{p0})\cos(\vartheta_{pw0} + \vartheta_{pw}), \quad l_{16} = (\xi_{p1} - l_{p0})\sin(\vartheta_{pw0} + \vartheta_{pw}), \quad l_{21} = l_{ps2} \cos(\vartheta_{pw0} + \vartheta_{pw} + \vartheta_{p2}), \\
l_{22} &= l_{ps2} \sin(\vartheta_{pw0} + \vartheta_{pw} + \vartheta_{p2}), \quad l_{23} = d_p \cos(\vartheta_{pw0} + \vartheta_{pw} + \vartheta_{p2}), \quad l_{24} = d_p \sin(\vartheta_{pw0} + \vartheta_{pw} + \vartheta_{p2}) \\
l_{25} &= (\xi_{p2} - l_{p0})\cos(\vartheta_{pw0} + \vartheta_{pw}), \quad l_{26} = (\xi_{p2} - l_{p0})\sin(\vartheta_{pw0} + \vartheta_{pw}) \\
a_{11} &= d_{pw}^2 + d_p^2 + l_{ps1}^2 + (\xi_{p1} - l_{p0})^2 + 2d_w d_p \cos\vartheta_{p1} - 2d_p(\xi_{p1} - l_{p0})\sin\vartheta_{p1} + 2d_{pw}l_{ps1}\sin\vartheta_{p1} + \\
& + 2l_{ps1}(\xi_{p1} - l_{p0})\cos\vartheta_{p1} \\
a_{12} &= d_{pw} + d_p \cos\vartheta_{p1} + l_{ps1} \sin\vartheta_{p1}, \quad a_{22} = d_{pw} + d_p \cos\vartheta_{p2} + l_{ps2} \sin\vartheta_{p2} \\
a_{13} &= d_p^2 + l_{ps1}^2 + d_{pw}d_p \cos\vartheta_{p1} - d_p(\xi_{p1} - l_{p0})\sin\vartheta_{p1} + d_{pw}l_{ps1}\sin\vartheta_{p1} + l_{ps1}(\xi_{p1} - l_{p0})\cos\vartheta_{p1} \\
a_{14} &= d_{pw}d_p \sin\vartheta_{p1} + d_p(\xi_{p1} - l_{p0})\cos\vartheta_{p1} - d_{pw}l_{ps1}\cos\vartheta_{p1} + l_{ps1}(\xi_{p1} - l_{p0})\sin\vartheta_{p1} \\
a_{15} &= \xi_{p1} - l_{p0} - d_p \sin\vartheta_{p1} + l_{ps1} \cos\vartheta_{p1} \\
a_{21} &= d_{pw}^2 + d_p^2 + l_{ps2}^2 + (\xi_{p2} - l_{p0})^2 + 2d_{pw}d_p \cos\vartheta_{p2} - 2d_p(\xi_{p2} - l_{p0})\sin\vartheta_{p2} + 2d_{pw}l_{ps2}\sin\vartheta_{p2} + \\
& + 2l_{ps2}(\xi_{p2} - l_{p0})\cos\vartheta_{p2} \\
a_{22} &= d_{pw} + d_p \cos\vartheta_{p2} + l_{ps2} \sin\vartheta_{p2}, \quad a_{25} = \xi_{p2} - l_{p0} - d_p \sin\vartheta_{p2} + l_{ps2} \cos\vartheta_{p2} \\
a_{23} &= d_p^2 + l_{ps2}^2 + d_{pw}d_p \cos\vartheta_{p2} - d_p(\xi_{p2} - l_{p0})\sin\vartheta_{p2} + d_{pw}l_{ps2}\sin\vartheta_{p2} + l_{ps2}(\xi_{p2} - l_{p0})\cos\vartheta_{p2} \\
a_{24} &= d_{pw}d_p \sin\vartheta_{p2} + d_p(\xi_{p2} - l_{p0})\cos\vartheta_{p2} - d_{pw}l_{ps2}\cos\vartheta_{p2} + l_{ps2}(\xi_{p2} - l_{p0})\sin\vartheta_{p2}
\end{aligned}$$

#### 4. Numerical simulation

The exemplary courses of linear acceleration variation of the guide arrangement are presented in Figs. 3, 4 (two-degree freedom) and 5, 6 (three-degree freedom). The generated disturbance results from the drive

of the assembly along a rough road at the speed of 30[km/h] and launching two missiles (Gapiński, 2014). The characteristics for three cases of inclination of the guide arrangement are compared. It is possible to determine such instants of time which represent physical phenomena of mechanical reaction nature in the course of three seconds of the assembly operation (Koruba, 2013 and Stefański, 2012).

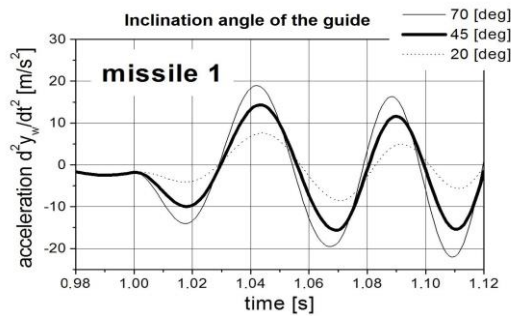


Fig. 3: Take-off missile 1.

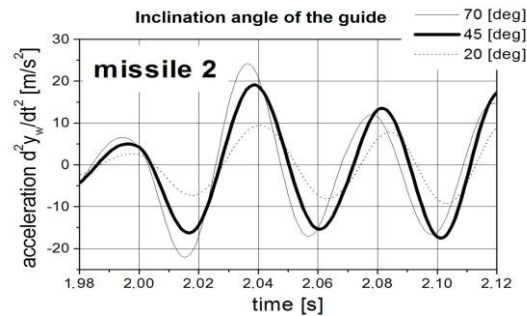


Fig. 4: Take-off missile 2.

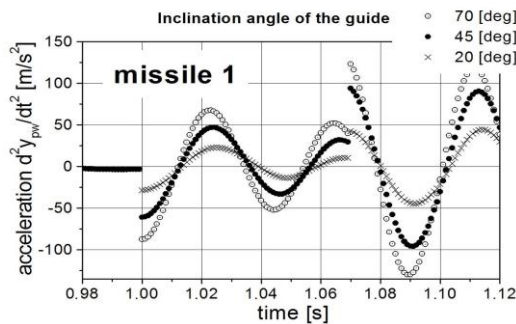


Fig. 5: Take-off missile 1.

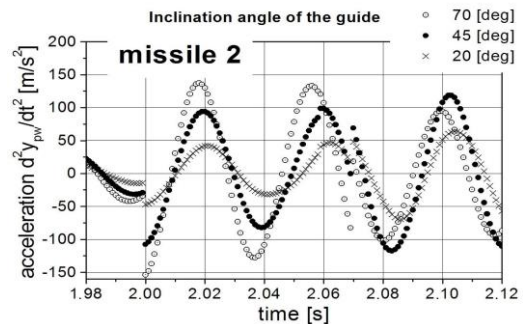


Fig. 6: Take-off missile 2.

## 5. Conclusions

The guide arrangement suffers from a distinct induction during the movement of the assembly along an uneven road and launching both missiles. The dynamic characteristic of the guide arrangement and their inclination angle determine the level of disturbance which affects the launching missile. A distinct change in the course of alteration of physical quantities describing the motion of the guide arrangement, e.g. the abrupt change of linear acceleration, occurs when the structure of the assembly or its mass is changed.

## References

- Baranowski, L., Gadowski, B., Majewski, P. and Szymonik, J. (2016) Explicit “ballistic M-model”: a refinement of the implicit “modified point mass trajectory model”. *Bulletin of the Polish Academy of Sciences - Technical Sciences*, 64, 1, pp. 81-89, DOI: 10.1515/bpasts-2016-0010.
- Chatys, R. (2013) Investigation of the Effect of Distribution of the Static Strength on the Fatigue Failure of a Layered Composite by Using the Markov Chains Theory. *Mechanics of Composite Materials*, Vol. 48, No. 6, pp. 629-638, (DOI: 10.1007/s11029-013-9307-9, Springer, ISSN 0191-5665).
- Dziopa, Z., (2013) Elements of Dynamics Analysis of the Warship Launcher of Anti-Aircraft Short Range Homing Missiles. *Solid State Phenomena*, vol.196, *Mechatronics System, Mechanics and Materials*, Trans Tech Publications Ltd, Switzerland, ISBN-13: 978-3-03785-274-3, pp. 28-42.
- Dziopa, Z., Buda, P., Nyckowski, M. and Pawlikowski, R. (2015) Dynamics of an unguided missiles launcher. *Journal of Theoretical and Applied Mechanics*. No. 1, Vol. 53, ISSN 1429-2955, pp. 69-80.
- Dziopa, Z. and Koruba, Z. (2015) The impact of launcher turret vibrations control on the rocket launch. *Bulletin of the Polish Academy of Sciences – Technical Sciences*, Vol. 63, No. 3, pp. 717-728.
- Gapiński, D. and Krzysztofik, I. (2014) The process of tracking an air target by the designed scanning and tracking seeker. 15th International Carpathian Control Conference (ICCC), Velke Karlovice, Czech Republic, pp. 129-134, IEEE Catalog Number: CFP1442L-CDR, ISBN 978-1-4799-3528-4.
- Koruba, Z. and Krzysztofik, I. (2013) An algorithm for selecting optimal controls to determine the estimators of the coefficients of a mathematical model for the dynamics of a self-propelled anti-aircraft missile system. *Proceedings of the Institution of Mechanical Engineers, Journal of Multi-Body Dynamics*, 227, 1, pp. 12-16.
- Stefański, K. and Koruba, Z. (2012) Analysis of the Guiding of Bombs On Ground Targets Using a Gyroscope System. *Journal of Theoretical And Applied Mechanics*, Vol. 50, Iss. 4, pp. 967-973.

## MITIGATION OF MESH DEPENDENCY IN PROBABILISTIC FINITE ELEMENT SIMULATION OF QUASIBRITTLE FRACTURE

J. Eliáš\*, J.-L. Le\*\*

**Abstract:** *The contribution introduces probabilistic variant of the crack band model to mitigate mesh dependency issues in probabilistic finite element simulations of quasibrittle fracture. The probabilistic crack band model is limited to the element size larger than the localization band. It introduces transition from the weakest link theory (crack may choose freely where to initiate and propagate within the element) to standard crack band model with only one possible crack band position within the element. The transition is driven by level of localization reached by the element and its surroundings. The probability density function of the elemental strength and energy dissipation is modified accordingly. The model is applied in simulations of prisms loaded under tension, bending and three-point-bending. The obtained statistical characteristics of the results are nearly mesh independent proving applicability of the probabilistic crack band model.*

**Keywords:** Localization, Finite elements, Mesh dependency, Crack band, Spatial randomness.

### 1. Introduction

Concrete, composites, tough ceramics, etc. are examples of quasibrittle materials widely used in nowadays engineering structures. The tensile post-peak constitutive response of quasibrittle materials can be characterized by a gradual loss of load-carrying capacity. This phenomenon gives rise to the strain localization. Localization instability causes spurious mesh sensitivity in the finite element (FE) simulations, because the damage localizes into a single layer of elements and energy needed to cause material damage depends on the mesh discretization. Possible remedy is to introduce a material length scale into the model. These models with the internal length are usually referred to as the localization limiters. The simplest of them is the crack band model developed by Bažant and Oh (1983), in which the post-peak branch of the stress-strain curve is adjusted to keep constant fracture energy. Special care needs to be taken for the proper definition of the element size under a multi-axial stress (Jirásek and Bauer, 2012). The localization limiters were developed for deterministic analysis. The strain localization has, however, great importance in the reliability of structural design (Bažant et al. 2009, Le et al., 2011). So far, there is still a lack of understanding of the effect of the strain localization on the stochastic FE analysis of quasibrittle fracture (Strack et al., 2014).

The conventional crack band (CBM) model modifies the material constitutive relationship in order to preserve the fracture energy for localized damage. Following this concept, we attempt to investigate how to adjust the probability distributions of the constitutive parameters to ensure the mesh objectivity of probabilistic FE simulations. This contribution presents a probabilistic crack band model (PCBM) that involves a probabilistic treatment of damage evolution. It is limited to the case where the finite element size is larger than the crack band width. It is based on previously published paper of Le and Eliáš (2016).

### 2. Probabilistic crack band model

The fracturing occurs under tensile straining, where the stress-strain response is governed by three material parameters: the elastic modulus  $E$ , the tensile strength  $f_t$  and the energy dissipation density  $\gamma$ . In this study we consider that the tensile strength and the energy dissipation density are random and independent for each element and also mutually independent. The objective is to determine what

---

\* Jan Eliáš: Institute of Structural Mechanics, Faculty of Civil Engineering, Brno University of Technology; Veveří 331/95, 60200, Brno, CZ, elias.j@fce.vutbr.cz

\*\* Jia-Liang Le: Civil, Environmental, and Geo- Engineering, University of Minnesota, Minneapolis, MN, USA, jle@umn.edu

modification of the probability distribution of  $f_t$  and  $\gamma$  would ensure independence of the simulation results on mesh discretization.

Tensile loading induces a damage band of fixed width  $h_0$  (usually referred to as the crack band width) with size of approx. two to three times the maximum aggregate size. (Bažant and Planas, 1998, Bažant and Pang, 2007). In probabilistic analysis, another probabilistic length scale related to the spatial correlation of the material properties emerges. However, recent studies have shown that material properties of finite elements of size equal to the crack band width can be considered as statistically independent (Bažant and Pang, 2007). Assuming  $h_e > h_0$ , we can treat the material properties of each element as statistically independent, and omit completely the internal probabilistic length scale.

Three stages of fracture process can be distinguished: damage initiation, localization, and propagation. These three stages have very different implications on the regularization of energy dissipation as well as on the probabilistic treatment of localized damage. In the context of FE simulations, we propose a parameter for each Gauss point that measures the level of localization

$$\kappa_c = \begin{cases} \frac{1}{(n_i + n_o)} \left[ \frac{(n_i + n_o + 1) \max_{k \leq n_o + n_i} (\phi_k)}{\sum_{k=0}^{n_i + n_o} \phi_k} - 1 \right] & \text{if } \phi_0 > 0 \\ 0 & \text{if } \phi_0 = 0 \end{cases} \quad (1)$$

where  $n_i$  is the number of surrounding Gauss points within the element of interest (i.e. inner neighbors in Fig. 1b),  $n_o$  is the number of surrounding Gauss points within the neighboring elements (outer neighbors),  $\phi_0$  is the damage level of the Gauss point of interest,  $\phi_k$  is the damage level of the  $k$ th surrounding Gauss point. In addition to the strain localization level of each Gauss point, it is also necessary to determine the localization level of the surrounding Gauss points, which is described by

$$\kappa_w = \frac{1}{n_o - 1} \left[ \frac{n_o \cdot \max_{k=n_i+1}^{n_i+n_o} \phi_k}{\sum_{k=n_i+1}^{n_i+n_o} \phi_k} - 1 \right] \quad (2)$$

Since the damage localization is an irreversible process, both localization parameters  $\kappa_c$  and  $\kappa_w$  are treated as non-decreasing.

The modification of the energy dissipation density in conventional CBM assumes fully localized crack and yields:  $\gamma h_e = G_f$  where  $G_f$  is the fracture energy. Let us define the reference energy dissipation density  $\gamma_0$  that corresponds to element size equal to crack band width:  $\gamma_0 = G_f/h_0$ . The CBM does not explicitly address the transition from damage initiation to localization. At the damage initiation stage, in contrast to fully localized crack, the total energy dissipation of the material should be proportional to the element size because the entire material element would suffer distributed damage. We propose a smooth transition based on additional model parameter  $\kappa_{0c}$  using the localization parameter  $\kappa_c$

$$\gamma = \gamma_0 f(\kappa_c) \quad \text{where} \quad f(\kappa_c) = \frac{h_0}{h_e} + \left( 1 - \frac{h_0}{h_e} \right) \exp \left( - \frac{\kappa_c}{\kappa_{0c}} \right) \quad (3)$$

The random nature of considered solid implies variability of the crack band location within the element. We consider that the random onset of the damage band in the material element is reflected by the statistics of the tensile strength. Since independent strength at possible locations of the damage band are considered, one may use the weakest link model to describe the overall elemental strength distribution

$$F_{f_t}(\sigma) = 1 - [1 - P_1(\sigma)]^{n_e} \quad (4)$$

where  $n_e$  is the number of potential crack bands in one element and  $P_1(x)$  is cumulative distribution function of strength of the single crack band. The number of potential crack bands is largely dependent on the localization level in the surrounding material elements. Fig. 1a shows two material elements, one with

localized damage. Such situation would lead to stress concentration and would dictate the location of the localization band in the upper element. Therefore, the number of potential crack bands would be  $n_e = 1$ . The transition from unconstrained to fully constrained location of the crack band is expressed by an empirical function dependent on additional model parameter  $\kappa_{0w}$

$$n_e = 1 + \left( \frac{h_e}{h_0} - 1 \right) \exp \left( - \frac{\kappa_w}{\kappa_{0w}} \right) \quad (5)$$

### 3. Simple examples

Concrete specimens with length  $L = 4$  m, depth  $D = 0.5$  m and thickness  $b = 0.1$  m under three different loading configurations are simulated using the proposed PCBM, see Fig. 1c. The distribution of the maximal nominal stress,  $\sigma_{N,\max}$ , is calculated. The nominal stress is expressed as the maximum principal stress based on the elastic analysis  $\sigma_N = P/bD$  for uniaxial tension,  $6M/bD^2$  for pure bending and  $3PL/2bD^2$  for three-point-bending, where  $P$  and  $M$  are the applied force and moment. The performance of the PCBM is compared to (i) the conventional crack band model (CBM) without adjusting the probability distribution of tensile strength (i.e.  $n_e = 1$  in Eq. 4) and (ii) the crack band model with considering the weakest link model of tensile strength (WLM) regardless of the localization level (i.e.  $n_e = h_e/h_0$  in Eq. 4).

A simple isotropic damage model with Mazar's equivalent strain and linear softening is used. Specimens are discretized using linear quadrilateral elements with four integration points assuming a 2D plane stress condition. The solver is developed as a modification of the OOFEM software (Patzák, 2012 and Patzák and Rypl, 2012).

The material parameters are following: elastic modulus  $E = 30$  GPa, Poisson's ratio  $\nu = 0.2$ , mean tensile strength  $\bar{f}_t = 3$  MPa, and mean fracture energy  $\bar{G}_f = 80$  J/m<sup>2</sup>. The probabilistic distribution for both strength and fracture energy is the Gaussian-Weibull grafted distribution (Bažant and Pang, 2007) with the coefficient variation 0.15, the grafting point  $P_{gr} = 10^{-3}$ , and the Weibull modulus  $m = 26$ . Three different mesh sizes are modeled:  $50 \times 50$  mm,  $100 \times 50$  mm, and  $200 \times 50$  mm, where the first number is the width and the second the depth of the element, respectively. The crack band width  $h_0$  is 50 mm. The PCBM parameters  $\kappa_{0c} = 0.19$  and  $\kappa_{0w} = 0.283$  are found by minimization of the difference between results computed on different mesh sizes.

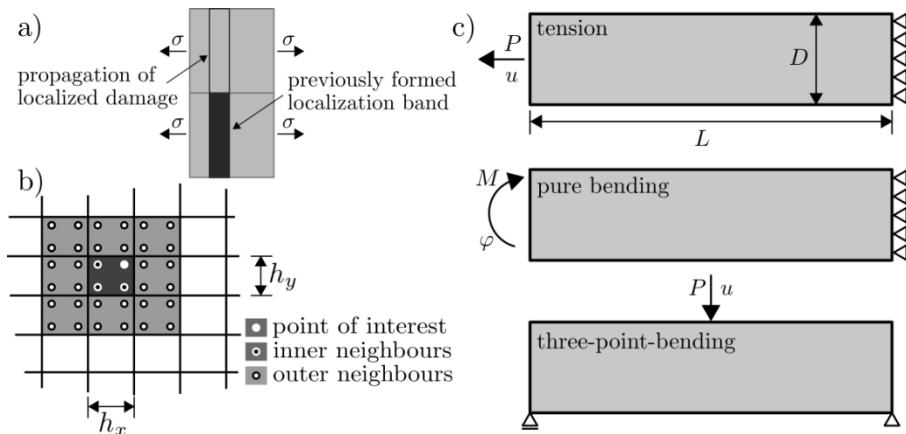


Fig. 1: a) Propagation of localized damage; b) determination of localization levels using information of neighboring Gauss points; c) loading configurations: uniaxial tension, pure bending, and three-point bending.

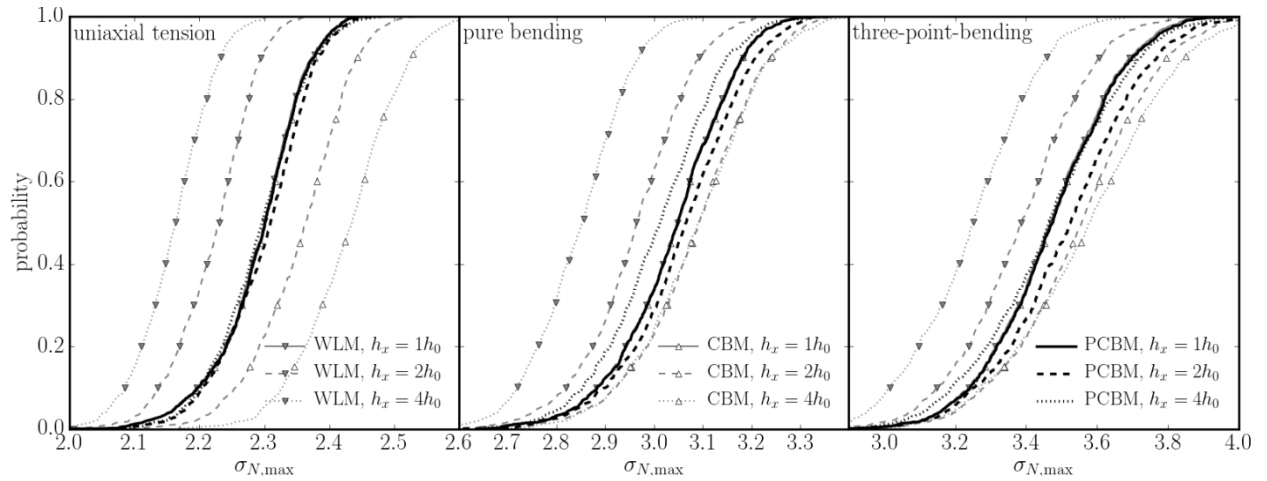


Fig. 2: Cumulative distribution function of the simulated maximal nominal stress.

#### 4. Results and discussion

Fig. 2 presents the cumulative distribution function of the nominal strength obtained from 1000 realizations. For the reference size,  $h_e = h_0$ , all three methods yield the same result. For larger elements, the CBM overestimates the structural strength and the WLM underestimates it. Only the proposed PCBM shows reasonable mesh independence.

This study demonstrates that the conventional crack band model suffers from mesh sensitivity in the probabilistic simulations. The developed probabilistic crack band model improves the formulation by consideration of the random onset of localization band inside the material element. Besides, the regularization of fracture energy during the transition from damage initiation to localization is presented.

#### Acknowledgement

Jan Eliáš acknowledges support from the Czech Science Foundation under project No. 15-19865Y. Jia-Liang Le acknowledges support under grant W911NF-15-1-0197 to the University of Minnesota from the U.S. Army Research Office.

#### References

- Bazant, Z.P., Le, J.-L. and Bazant, M.Z. (2009) Scaling of strength and lifetime distributions of quasibrittle structures based on atomistic fracture mechanics. *Proceedings of the National Academy of Sciences of the United States of America*, 106, pp. 11484-11489.
- Bazant, Z.P. and Oh, B.-H. (1983) Crack band theory for fracture of concrete. *Materials and Structures*, 16, pp. 155-177.
- Bazant, Z.P. and Pang, S.D. (2007) Activation energy based extreme value statistics and size effect in brittle and quasibrittle fracture. *Journal of Mechanics and Physics of Solids*, 55, pp. 91-134.
- Bazant, Z.P. and Planas, J. (1998) *Fracture and Size Effect in Concrete and Other Quasibrittle Materials*. CRC Press, Boca Raton and London.
- Jirásek, M. and Bauer, M. (2012) Numerical aspects of the crack band approach. *Computers and Structures*, 110, pp. 60-78.
- Le, J.-L., Bazant, Z.P. and Bazant, M.Z. (2011) Unified nano-mechanics based probabilistic theory of quasibrittle and brittle structures: I. strength, crack growth, lifetime and scaling. *Journal of Mechanics and Physics of Solids*, 59, pp. 1291-1321.
- Le, J.-L. and Eliáš, J. (2016) A probabilistic crack band model of quasibrittle fracture. *Journal of Applied Mechanics – ASCE*, 83, 5, pp. 051005-7.
- Patzák, B. (2012) OOFEM - an object-oriented simulation tool for advanced modeling of materials and structures. *Acta Polytechnica*, 52, pp. 59-66.
- Patzák, B. and Rypl, D. (2012) Object-oriented, parallel finite element framework with dynamic load balancing. *Advances in Engineering Software*, 47, pp. 35-50.
- Strack, O.E., Leavy, R.B. and Brannon, R.M. (2014) Aleatory uncertainty and scale effects in computational damage models for failure and fragmentation. *International Journal for Numerical Methods in Engineering*, 102, 3-4, pp. 468-495.



## CALCULATION OF SHELL STRUCTURES BY USING LAYERED MODEL

J. Fiedler<sup>\*</sup>, T. Koudelka<sup>\*\*</sup>

**Abstract:** *The DKT plate element and the plane element with rotational degrees of freedom are employed to define a shell element. Moreover, layered model is taken into account to include possible nonlinear behaviour across a cross-section of a shell. The paper explains principles of layered model and interaction between the elements used. The model and the shell element are implemented into the SIFEL solver using finite element method.*

**Keywords:** Shell element, DKT plate element, Plane element with rotational degrees of freedom, Layered model, Finite element method.

### 1. Introduction

When the topic of shell structures is concerned, nonlinear behaviour of a material is often desirable to be taken into consideration. Although this subject can be resolved by using 3D elements together with a nonlinear material model, with respect to the planar character of shell structures, it is preferred to use 2D modelling tools to find a solution to the problem. In this regard, a possible way to involve nonlinearity in a calculation is by adding layered model to the process (Hu and Schnobrich, 1991).

The authors have continued to explore the topic of layered model within the SIFEL environment (Krejčí, Koudelka and Kruis, 2011) and are now extending the work from previous years focused on the application of layered model solely on plate structures to the application on shell elements.

For purpose of this application, a triangle shell element was created by combining two separate elements – the DKT plate element and the triangle plane element with rotational degrees of freedom. The idea behind the shell element was to use two, in SIFEL already developed, separate elements without any changes and to form an interaction between them so they could simulate the shell behaviour. Although the idea itself seems very simple, several subsidiary issues has emerged, especially with regard to integration points.

The first part of the paper is dedicated to basic description of layered model. Principles of the DKT and the rotational plane element are then explained followed by the examination of the elements' interaction. At the end, several issues that have been dealt with are mentioned in detail.

### 2. Layered model

When describing deformation of a shell structure, the following vectors can be adopted

$$\boldsymbol{\varepsilon}_0 = \{\varepsilon_{0,x}, \varepsilon_{0,y}, \gamma_{0,xy}\}^T, \quad \boldsymbol{\kappa} = \{\kappa_x, \kappa_y, \kappa_{xy}\}^T, \quad (1)$$

where  $\boldsymbol{\varepsilon}_0$  is the vector of middle plane strain and  $\boldsymbol{\kappa}$  represents the vector of curvatures. If the statement, that straight lines normal to the middle plane remain straight and normal to the middle plane after deformation, is accepted, the development of deformation  $\boldsymbol{\varepsilon} = \{\varepsilon_x, \varepsilon_y, \gamma_{xy}\}^T$  across the  $z$ -coordinate can be expressed as follows

---

<sup>\*</sup> Ing. Josef Fiedler: Faculty of Civil Engineering, Czech Technical University in Prague, Thákurova 7/2077; 166 29, Prague; CZ, josef.fiedler@fsv.cvut.cz

<sup>\*\*</sup> Ing. Tomáš Koudelka, Ph.D.: Faculty of Civil Engineering, Czech Technical University in Prague, Thákurova 7/2077; 166 29, Prague; CZ, koudelka@cml.fsv.cvut.cz

$$\boldsymbol{\varepsilon}(z) = \boldsymbol{\varepsilon}_0 + z\boldsymbol{\kappa}. \quad (2)$$

When layered model is employed, a shell structure is decomposed into small layers (Fig. 1) and Eq. 2 can be rewritten into the following form

$$\boldsymbol{\varepsilon}_j = \boldsymbol{\varepsilon}_0 + z_j\boldsymbol{\kappa} \quad (3)$$

where  $\boldsymbol{\varepsilon}_j$  represents strain components of the  $j$ -th layer and  $z_j$  is the distance of the  $j$ -th layer from the middle plane. Each layer is considered to be in the plane stress state and by using the appropriate stiffness matrix  $\mathbf{D}_j$ , stress components of the  $j$ -th layer  $\boldsymbol{\sigma}_j$  can be obtained

$$\boldsymbol{\sigma}_j = \mathbf{D}_j \boldsymbol{\varepsilon}_j \quad (4)$$

The integration of the stress components over the layer thickness yields resultant forces

$$\mathbf{n} = \{n_x, n_y, n_{xy}\}^T, \quad \mathbf{m} = \{m_x, m_y, m_{xy}\}^T \quad (5)$$

that are obtained as the summation of contributions from all layers. The single contribution from the  $j$ -th layer to the stress resultant forces is formulated as follows

$$\mathbf{n}_j = t_j \boldsymbol{\sigma}_j, \quad \mathbf{m}_j = z_j t_j \boldsymbol{\sigma}_j \quad (6)$$

And by combining all contributions and substituting Eq. 3 and Eq. 4 into Eq. 5, the final stress resultant forces are attained

$$\begin{Bmatrix} \mathbf{n} \\ \mathbf{m} \end{Bmatrix} = \sum_j \begin{bmatrix} t_j \mathbf{D}_j & z_j t_j \mathbf{D}_j \\ z_j t_j \mathbf{D}_j & z_j^2 t_j \mathbf{D}_j \end{bmatrix} \begin{Bmatrix} \boldsymbol{\varepsilon}_0 \\ \boldsymbol{\kappa} \end{Bmatrix} \quad (7)$$

It is important to notice here that layered model enables to use various stiffness matrices for layers. For even distribution of stiffness across a cross-section, off-diagonal members of the matrix in Eq. 7 are equal to zero. Only when stiffness is distributed unequally, off-diagonal members are taken into account.

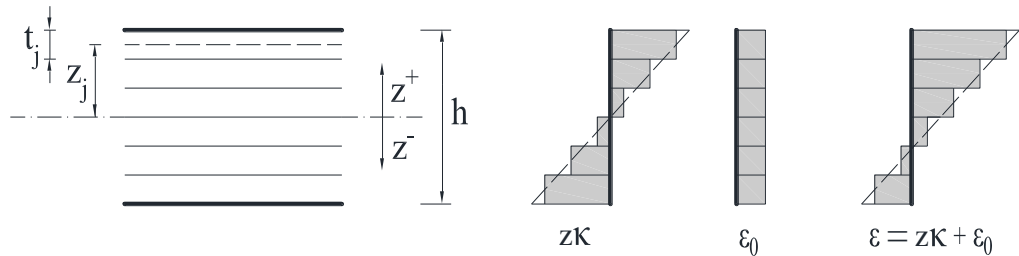


Fig. 1: Decomposition of a structure into layers.

### 3. Elements used and their interaction

A general shell element holds 6 degrees of freedom at each node – 3 displacements  $u, v, w$  and 3 rotations  $\varphi_x, \varphi_y, \varphi_z$ . In the case of layered model, it is assumed that the triangle shell element is assembled from the DKT element and the plane element with rotational degrees of freedom (Jirásek and Bažant, 2002), (Bittnar and Šejnoha, 1996).

In this interaction, the DKT element is intended to represent plate behaviour of a shell and the distribution of deflection  $w$  and rotations  $\varphi_x, \varphi_y$  is from the element obtained. The plane element is employed to calculate the remaining displacements  $u, v$  and the rotation  $\varphi_z$ . In addition, the curvatures  $\kappa_x, \kappa_y, \kappa_{xy}$  are computed within the DKT element and the strains  $\varepsilon_x, \varepsilon_y, \gamma_{xy}$  are received from the plane element, which are then used, with regard to Eq. 1, as the middle plane strains.

The class of the shell element (primary element) is in SIFEL created in the form of a coordinator between the plate element and the plane element (secondary elements). The idea is to take already developed plate and plane elements and use them in the algorithm as individual units without any changes. The work done by the shell element can be summarized into the following points:

- assembles the stiffness matrix
- transforms values from global to local character and vice versa
- collects data from the core calculation and redistributes them into the secondary elements and vice versa
- gathers calculation data from the secondary elements and generate the final output

Although these are fairly obvious procedures, the authors would like to introduce some difficulties that have come out through the implementation of the shell element.

#### 4. Stiffness matrix

The stiffness matrix of an element can be expressed in finite element method as

$$\mathbf{K} = \int_V \mathbf{B}^T \mathbf{D} \mathbf{B} dV \quad (8)$$

where  $\mathbf{B}$  represents the matrix of shape functions derivations and  $\mathbf{D}$  is the matrix of material stiffness. Let us focus only on the expression after the integration mark in Eq. 8. While considering a shell element assembled by one plate element and one plane element, it can be stated that

$$\mathbf{B}^T \mathbf{D} \mathbf{B} = \begin{bmatrix} \mathbf{B}_N^T & \mathbf{0} \\ \mathbf{0} & \mathbf{B}_M^T \end{bmatrix} \begin{bmatrix} \mathbf{D}_N & \mathbf{D}_{NM} \\ \mathbf{D}_{MN} & \mathbf{D}_M \end{bmatrix} \begin{bmatrix} \mathbf{B}_N & \mathbf{0} \\ \mathbf{0} & \mathbf{B}_M \end{bmatrix} \quad (9)$$

where  $\mathbf{B}_N$  is the matrix of shape functions derivations for a plane element and  $\mathbf{B}_M$  for a plate element.  $\mathbf{D}_N$  then represents the material stiffness matrix of a plane element and  $\mathbf{D}_M$  of a plate element. The off-diagonal members  $\mathbf{D}_{NM}$  and  $\mathbf{D}_{MN}$  can be interpreted as a relation between the two elements. If linear elasticity is considered, the off-diagonal members are neglected and Eq. 9 can be, after multiplication, rewritten into the following form

$$\begin{bmatrix} \mathbf{B}_N^T \mathbf{D}_N \mathbf{B}_N & \mathbf{0} \\ \mathbf{0} & \mathbf{B}_M^T \mathbf{D}_M \mathbf{B}_M \end{bmatrix} \quad (10)$$

which is exactly as a plate and a plane element are simply put together. However, when some form of nonlinearity across a cross-section is employed, the off-diagonal members cannot be ignored and Eq. 9 is possible to modify into

$$\begin{bmatrix} \mathbf{B}_N^T \mathbf{D}_N \mathbf{B}_N & \mathbf{B}_N^T \mathbf{D}_{NM} \mathbf{B}_M \\ \mathbf{B}_M^T \mathbf{D}_{MN} \mathbf{B}_N & \mathbf{B}_M^T \mathbf{D}_M \mathbf{B}_M \end{bmatrix}. \quad (11)$$

To fit this idea on layered model, the material stiffness matrices  $\mathbf{D}_N$ ,  $\mathbf{D}_M$ ,  $\mathbf{D}_{NM}$  and  $\mathbf{D}_{MN}$  can be interpreted in regards of Eq. 7 as follows

$$\mathbf{D}_N = \sum t_j \mathbf{D}_j; \quad \mathbf{D}_M = \sum z_j^2 t_j \mathbf{D}_j; \quad \mathbf{D}_{NM} = \mathbf{D}_{MN} = \sum z_j t_j \mathbf{D}_j. \quad (12)$$

After the numerical integration, it is possible to achieve the stiffness matrix of the shell element that is created by a plate and a plane element and equipped with layered model.

#### 5. Integration points and nonlinear calculation

When performing a calculation on integration points, it is necessary to be aware of the fact that the chosen plane element includes more integration points than the DKT plate element. Although both elements use the 3-point integration system, the plane element performs the integration twice therefore possesses two sets of the same 3 integration points. Given that layered model determines stress resultant forces on every integration point and at the same time uses both middle plane strains and curvatures, the so-called artificial integration points are established to deal with the issue. These integration points collect both strain vectors and perform calculation of stress resultant forces. The results are then distributed to the appropriate integration points on particular elements. The artificial integration points hold only the

composition of an integration point but they are not used for the integration of nodal forces involved in the equilibrium equations. They just perform the calculation of stress resultant forces and further generated data inside are eventually used for creating the output. It should be also noted that the artificial points are created in respect of the 3-point integration system. Instead of performing calculation of stress resultant forces 3 times (once on the DKT element and twice on the plane element), it is done only once and results are spread over the remaining integration points.

As mentioned at the beginning, adopting layered model can be a suitable way to include nonlinearity. When a shell structure is imaginarily divided into layers, each layer is assigned its own strain components according to Eq. 3. While the plane stress state is considered, any material model can be attached to every layer, thus creating space for involving nonlinearity and at the same time keeping the problem in 2D. As stated above, all calculations are done on the artificial integration points where all nonlinear parameters for layers are stored and printed out to the output in case of a successful calculation.

As an example of a nonlinear calculation using layered model, the results from a concrete rectangular slab considering plastic yielding in layers are shown in Fig. 2. The slab is supported simply alongside the upper and the side edges while the lower edge is fixed. The slab is loaded uniformly and the values of plastic multiplier  $\gamma$ , that indicate the amount of plastic yielding at the area, can be observed from Fig. 2.

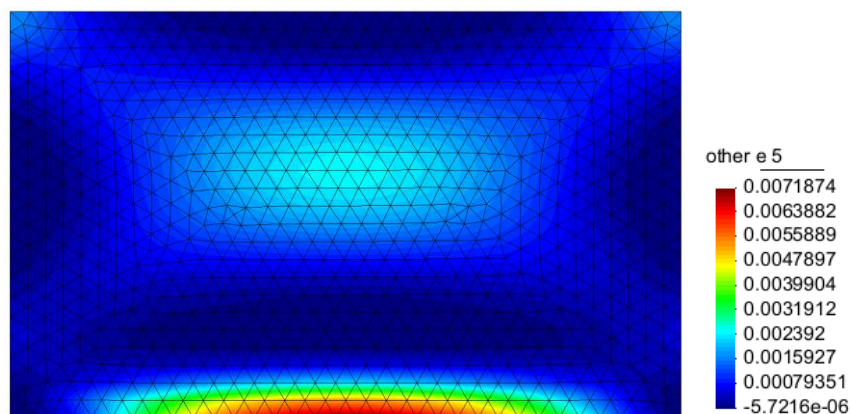


Fig. 2: Development of plastic multiplier  $\gamma$  in a rectangular slab [-].

## 6. Conclusions

The application of layered model to the shell element assembled from the DKT plate element and the plane element with rotational degrees of freedom has been presented in the paper. Difficulties and principles regarding the implementation of layered model and the shell element itself has been mentioned.

## Acknowledgement

The paper was supported by project SGS17/043/OHK1/1T/11 - Advanced numerical modeling in mechanics of structures and materials.

## References

- Bittnar, Z. and Šejnoha, J. (1996) Numerical methods in structural mechanics. ASCE Press, New York, Thomas Telford, co-publisher, London.
- Hu, H.T. and Schnobrich, W.C. (1991) Nonlinear finite element analysis of reinforced concrete plates and shells under monotonic loading. Computers & structures, Vol. 38, No. 5/6, pp. 637-651.
- Jirásek, M. and Bažant, Z.P. (2002) Inelastic Analysis of Structures. 1st ed. Wiley, Chichester.
- Krejčí, T., Koudelka, T. and Kruis, J. (2011) Modeling of building constructions in SIFEL environment. Czech Technical University in Prague, 1. ed., Prague.

## LYAPUNOV EXPONENTS – PRACTICAL COMPUTATION

C. Fischer<sup>\*</sup>, J. Náprstek<sup>\*\*</sup>

**Abstract:** *The Lyapunov exponents serve as numerical characteristics of dynamical systems, which measure possible divergence of nearby trajectories of the solution. In this way they express dependence of the dynamical system on initial conditions. However, the value of Lyapunov exponents consists in their ability to characterise deterministic chaos. The limiting process intrinsic in the definition of Lyapunov exponents, unfortunately, seriously complicates their computation. The short paper presents an overview of difficulties in numerical approaches to enumeration of Lyapunov exponents or at least the largest one and shows a promising method based on QR decomposition of the system Jacobian.*

**Keywords:** Lyapunov exponent, Dynamical system, Non-linear system.

### 1. Introduction

The collocation “deterministic chaos” seems to be a contradiction in itself. However, in the theory of dynamical systems it refers to systems whose results are reproducible but (almost) unpredictable. No mathematical definition of the term deterministic chaos is universally accepted yet and chaos is usually characterised by its properties. The reasonably simple working definition due to Strogatz (2000) states: Chaos is aperiodic long-term behaviour in a deterministic system that exhibits sensitive dependence on initial conditions. The Lyapunov exponents (LE) provide a numerical measure of the last condition of the Strogatz’s definition: sensitivity on initial conditions. Thus, a strictly positive LE in dissipative systems can be, under additional conditions, regarded as an indicator of deterministic chaos (Politi 2013, Dieci 2011). For other examples of their applications see, e.g., (Ott 1993). It is worth noting that in most applications it is sufficient to approximate only a subset of LE, e.g., the largest one.

Consider the  $m$  dimensional non-linear differential system

$$\dot{x} = f(x), \quad x(0) = x_0. \quad (1)$$

Let the right-hand side  $f$  is a smooth function and solution  $x_{x_0}$  of (1) exists for given initial condition  $x_0$  and  $t \geq 0$ . Using two terms of Taylor expansion of  $f(x)$  can be easily derived that the infinitesimal perturbations  $\delta$  to a trajectory  $x_{x_0}$  are described by the linearized equation

$$\dot{\delta} = Jf(x_{x_0})\delta, \quad (2)$$

where  $Jf(x)$  be the Jacobian of the right-hand side  $f$  in (1). Eq. (2) is linear ordinary differential equation and its stability can be examined using traditional means. In dynamical systems, evolution of size of the perturbation  $\delta$  is governed by the relation

$$\|\delta(t)\| = e^{\lambda_1 t} \|\delta(0)\|, \quad (3)$$

where  $\lambda_1$  is the largest LE. The relation (3) is usually supposed to serve as a formula for calculation of  $\lambda_1$ :

$$\lambda_1 = \lim_{t \rightarrow \infty} \frac{1}{t} \ln \|\delta(t)\|, \quad (4)$$

Regarding the whole spectrum of LE, the exact definition is more complicated. Dieci et al. (2011) define upper and lower LE as follows. Let  $A(t) = Jf(x_{x_0})$  and define numbers  $\mu_i, \nu_i, i = 1, \dots, m$  such that

<sup>\*</sup> RNDr. Cyril Fischer, PhD., Institute of Theoretical and Applied Mechanics AS CR, v.v.i., Prosecká 76, 190 00 Praha 9, fischer.c@itam.cas.cz

<sup>\*\*</sup> Ing. Jiří Náprstek, DrSc., Institute of Theoretical and Applied Mechanics AS CR, v.v.i., Prosecká 76, 190 00 Praha 9, naprstek@itam.cas.cz

$$\mu_i = \limsup_{t \rightarrow \infty} \frac{1}{t} \ln \|Y(t)e_i\|, \quad v_i = \limsup_{t \rightarrow \infty} \frac{1}{t} \ln \|Z(t)e_i\|, \quad (5)$$

where  $m \times m$  matrices  $Y(t), Z(t)$  are the solutions of

$$\dot{Y}(t) = A(t)Y(t), Y(0) = Y_0, \quad \dot{Z}(t) = -A(t)^T Z(t), Z(0) = Z_0, \quad Y_0, Z_0 \in \mathbb{R}^{m \times m} \text{ regular} \quad (6)$$

and  $e_i$  is the  $i$ -th standard unit vector. Such  $\mu_i, v_i$ , which minimize  $\sum_{i=1}^m \mu_i, \sum_{i=1}^m v_i$  for all possible initial conditions  $Y_0, Z_0$  are called *upper* or *lower Lyapunov exponent* and denoted  $\lambda_i^u, \lambda_i^l$ , respectively. If  $\lambda_i^u = \lambda_i^l = \lambda_i$  for all  $i$  the system is called regular. Politi (2013) uses slightly different yet equivalent definition. Vast majority of publications assumes regularity of the underlying system. This assumption, e.g., enables validity of the basic computational rule (4). Also the present work will follow this practice.

## 2. Numerical methods

Numerical approximation of LE is often introduced using discrete maps instead of continuous dynamical system. The discretized continuous system can be usually regarded as a discrete map; however, such an approach imposes restrictions on discretization parameters and, moreover, changes properties of the original dynamical system.

Most of the introductory texts start and end with estimation of the largest Lyapunov exponent  $\lambda_1$  using the limiting approach similar to Eq. (4). Danger of this simple approach is illustrated in Fig. 1, inspired by Strogatz (2000). It shows typical evolution of separation of two adjacent trajectories,  $\|\delta_0\| = 10^{-3}$  for the Lorenz system  $\sigma = 10, b = 8/3, r = 28$ . The correct value  $\lambda_1 \approx 0.9$  is well approximated by the slope the line  $\ell$ . Fig. 1 points out two weaknesses of the approach (4). For  $t < 10$  is the mean slope of  $\|\delta\|$  shown as  $\ell_1$  and for  $t > 20$  as  $\ell_2$ . The line  $\ell_1$  reflects influence of initial conditions, for different initial conditions can be either almost horizontal or disappear at all. It can be eliminated in the real computation by selecting the initial condition on the attractor. The plateau  $\ell_2$ , on the other hand, appears when separation of the trajectories is comparable to the size of the attractor and cannot be eliminated. Fig. 1 shows that algorithmization of the method based on (4) could be a cumbersome task.

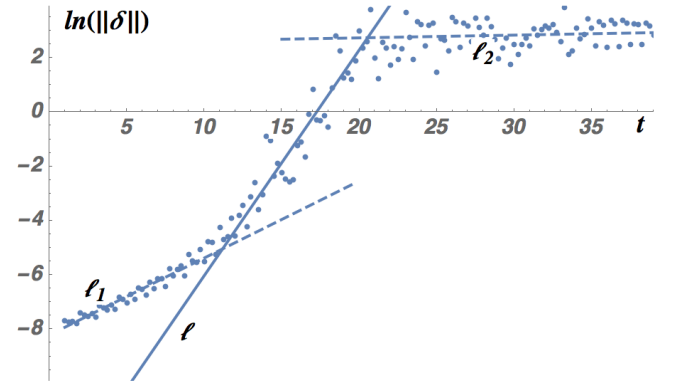


Fig. 1: Numerical approximation of largest LE of the Lorenz attractor.

For  $t < 10$  is the mean slope of  $\|\delta\|$  shown as  $\ell_1$  and for  $t > 20$  as  $\ell_2$ . The line  $\ell_1$  reflects influence of initial conditions, for different initial conditions can be either almost horizontal or disappear at all. It can be eliminated in the real computation by selecting the initial condition on the attractor. The plateau  $\ell_2$ , on the other hand, appears when separation of the trajectories is comparable to the size of the attractor and cannot be eliminated. Fig. 1 shows that algorithmization of the method based on (4) could be a cumbersome task.

Besides the initial condition, other factors influencing estimation of the largest LE can be: discretization parameter of the differential solver, size of initial separation of trajectories  $\|\delta_0\|$  and number of averaged trials for random initial perturbations of size  $\|\delta_0\|$ . The discretization parameter or choice of (stable!) integration method does not seem to influence results too much, the procedure works well even with adaptive methods provided the samples of individual trajectories match. On the other hand, size of initial perturbation influences results significantly. From Tab. 1 can be seen that too large  $\delta_0$  results in an underestimated value of  $\lambda_1$ . The second row of the table shows values determined from a single random perturbation and rows 3 and 4 list average values and variances computed from 100 different initial perturbations of size  $\|\delta_0\|$ , respectively.

Tab. 1: Influence of size of initial perturbation on the estimation of the largest LE.

$\ \delta_0\ $	0.1	0.01	0.001	0.0001	0.00001	$10^{-6}$
single $\lambda_1$	0.48004	0.68527	0.72202	0.96167	0.93266	0.95062
mean $\lambda_1$	0.27817	0.56540	0.81150	0.93027	0.94803	0.94875
variance $\lambda_1$	0.02018	0.01525	0.00700	0.00050	0.00053	0.00004

The same approach can be practically used when several or all LE are to be determined. The procedure has to be augmented by regular reorthogonalization, in the similar manner as in the well-known subspace iteration method for computing eigenvalues. A large variety of methods is based this approach, mainly based on theoretical and practical papers by Galgani et al. (1980) and Benettin et al. (1980). Example of a



good practical implementation is available due to Sandri (1996). When using this approach, the computation can easily exploit parallel architecture of current computers (Tange 2011).

The approach based on Eq. (4) can be also used in the case when there are available only the experimental or other discrete data. The simple implementation accompanying paper (Wolf 1985) or the monograph (Kantz and Schreiber 2004) provide basic functionality only and cannot distinguish chaotic and stochastic data. The more advanced procedure described by Rosenstein et al. (1993) is similarly based on identifying of different yet similar sections in the experimental data, which are used subsequently to simulate separating of close trajectories. Although the algorithm is relatively simple, its application depends on several more or less heuristic parameters. These are namely embedded dimension  $\mathcal{M}$ , reconstruction delay  $\mathcal{J}$  and number of data available  $\mathcal{N}$ . While the parameter  $\mathcal{N}$  is usually fixed, determination of optimal values for  $\mathcal{M}$  and  $\mathcal{J}$  can be tricky, for discussion and hints see the cited paper.

The example results for the  $x$ -coordinate of the Lorenz system from the previous page for three different values of  $\mathcal{M}$  are shown in Fig. 2. Data were obtained using a fixed step fourth order RK integrator with  $\Delta t = 0.01$  and delay was set to  $\mathcal{J} = 18 \cong 0.18s$ . The solid curves show time dependency of the averaged values of  $\ln\|\delta\|$ . As in Fig. 1, the curves for  $\mathcal{M} = 2, 3$  exhibit linear growth for ca.  $1 < t < 3.5$ , giving a good estimate of  $\lambda_1$ . In accordance with Rosenstein's results the case  $\mathcal{M} = 1$  gave no usefull result. However, presence of false linear slope  $\ell_1$  for both  $\mathcal{M} = 2, 3$  lowers credibility of obtained results.

The recent and advanced approaches to stability assessment are based on the idea of maintaining the orthogonal transformation of the perturbation coordinates during integration, e.g., Náprstek (2014). Lyapunov (1992) showed in his thesis that for regular systems the LE may be extracted as the limit of the time average of the diagonal elements of the upper triangular coefficient matrix. If the coefficient matrix (denoted  $\mathbf{B}$ ) in the (regular) system (2) is triangular, then its LE can be determined as

$$\lambda_i = \lim_{t \rightarrow \infty} \frac{1}{t} \int_0^t B_{ii}(s) ds . \quad (7)$$

The main idea of the work presented by Dieci et al. (2011) is based on transformation of the general Jacobian  $\mathbf{J}f(x_{x_0})$  to an upper triangular matrix  $\mathbf{B}$  using a time-dependent orthogonal QR transformation. The algorithms developed by Dieci et al. offer computation of several or all LE of a (not necessarily regular) system. The authors claim that their packages LESLIS, LESLIL, LESNLS and LESNLL are mature enough to provide a scientific community with a mean for reliable, yet cautious, estimation of LE. All methods implemented in the package start from a full rank initial condition  $Y_0 \in \mathbb{R}^{n \times m}$ , where  $n \leq m$  is a number of LE to be computed. It is advised to select the  $Y_0$  at random, this is needed to guarantee that all possible growth behaviour is represented in the columns of  $Y(t)$  and that the  $n$  most dominant exponents will emerge. In each step  $t_i \rightarrow t_{i+1}$ , the methods perform (i) integration, (ii) orthogonalization, (iii) update of LE estimates. This division of the general procedure is simple and allows a free hand in implementation of individual tasks. The package offers several special integration schemes, including those which preserve orthogonality. Unlike the traditional methods, this package uses adaptive steplength based on local error estimate for both increased efficiency and accuracy. The time-variable orthogonalization is implemented as either discrete or continuous QR factorization. The both methods are equivalent in case of exact arithmetic, however, their performance will depend on a particular problem. As an alternative solution strategy, the user is enabled to use his own particular integrator (e.g., a stiff one), approximate each step the solution trajectory using polynomials and let the linear version of the code to evaluate the LE estimates. This latter approach could be also used for estimation of LE of a discrete (experimental) data series.

To illustrate the method, the non-linear version of the code was employed to compute the LE of the same Lorenz system as above. Namely, the procedure LESNLS was used, which require explicit formulation of

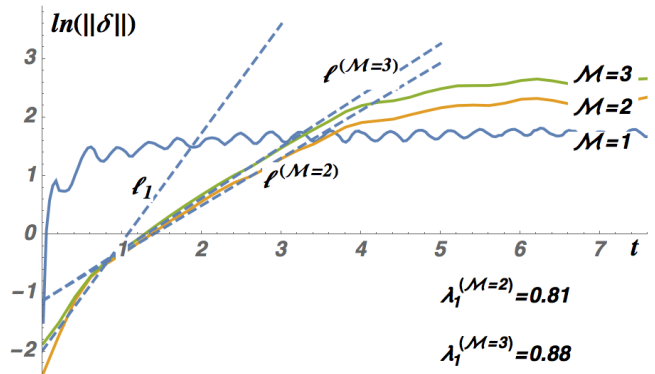


Fig. 2: Approximation of largest LE of the Lorenz attractor using discrete data for three values of the embedded dimension  $\mathcal{M} = 1, 2, 3$ .



the Jacobian of the system. The computed LE were:  $\lambda_1 = 0.9095$ ,  $\lambda_2 = -0.000696$ ,  $\lambda_3 = -14.5755$  and this values correspond well with other sources. The computed Lyapunov exponents as a function of time in a semilog scale are shown in Fig. 3.

### 3. Conclusions

The Lyapunov exponents play an irreplaceable role in characterization of dynamical systems behaviour. By the very nature of the limiting process intrinsic in the definition of Lyapunov exponents, their approximation is bound to be limited in extent, and perhaps the approximations themselves may be considered of dubious validity. This fact was shown in the first part of the text, where several definition-based approaches were discussed. Although there exist good implementations of such methods, stress was put upon illustrative examples of difficulties present in the nature of estimation of Lyapunov exponents for continuous systems and experimental data. On the other hand, it seems that the approach based on the orthogonal QR factorization of the Jacobian can serve as a reasonable and robust method.

### Acknowledgement

The kind support of the Czech Science Foundation project No. 15-01035S and the institutional support RVO 68378297 are gratefully acknowledged.

### References

- Benettin, G., Galgani, L., Giorgilli, A. and Strelcyn, J.-M. (1980) Lyapunov Characteristic Exponents for smooth dynamical systems and for hamiltonian systems; A method for computing all of them. Part 2: Numerical application. *Meccanica*, 15 (1), pp. 21-30.
- Dieci, L., Jolly, M.S. and Van Vleck, E.S. (2011) Numerical Techniques for Approximating Lyapunov Exponents and their Implementation. *Journal of Computational and Nonlinear Dynamics*, 6(1), 011003-7.
- Galgani, L., Giorgilli, A., Strelcyn, J.M. and Benettin, G. (1980) Lyapunov Characteristic Exponents for smooth dynamical systems and for Hamiltonian systems; a method for computing all of them. Part 1: Theory. *Meccanica*, 15 (1) pp. 9-20.
- Kantz, H. and Schreiber, T. (2004) *Nonlinear time series analysis*. Cambridge University Press, Cambridge.
- Lyapunov, A.M. (1992), *The general problem of the stability of motion*, translated by A. T. Fuller. Taylor & Francis, London.
- Náprstek, J. and Fischer, C. (2014) Stability of limit cycles in autonomous nonlinear systems. *Meccanica*, 49 (8) pp. 1929-1943.
- Ott, E. (1993) *Chaos in Dynamical Systems*. Cambridge University Press, New York.
- Politi, A. (2013) Lyapunov exponent. *Scholarpedia*, 8(3):2722.
- Rosenstein, M.T., Collins, J.J. and De Luca, C.J. (1993) A practical method for calculating largest Lyapunov exponents from small data sets. *Physica D: Nonlinear Phenomena*, 65 (1) pp. 117-134.
- Sandri, M. (1996) Numerical calculation of Lyapunov exponents. *Mathematica Journal*, 6 (3), pp. 78-84.
- Strogatz, A.H. (2000) *Nonlinear Dynamics and Chaos: With Applications to Physics, Biology, Chemistry, and Engineering (Studies in Nonlinearity)*. Westview Press, Cambridge.
- Tange, O. (2011) GNU Parallel-The Command-Line Power Tool.; login: *The USENIX Magazine*, 36(1), pp. 42-47.
- Wolf, A., Swift, J.B., Swinney, H.L. and Vastano, J.A. (1985) Determining Lyapunov exponents from a time series. *Physica D*, 16(3), pp. 285-317.

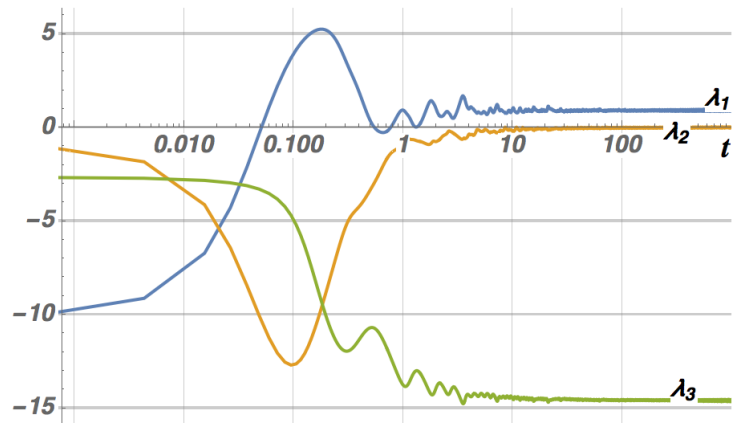


Fig. 3: Convergence of all three LE of the Lorenz attractor using the QR procedure LESNLS.

## **BIOMECHANICS - AIRFLOW IN THE NASAL CAVITY AND THE NASAL SEPTUM PERFORATION**

**K. Frydryšek<sup>\*</sup>, S. Drábková<sup>\*\*</sup>, M. Plášek<sup>\*\*\*</sup>**

**Abstract:** *In addition to olfactory, reflective and immune activities, respiration is one of the physiological functions of the nose. The article deals with biomechanical research into the influence of pathological and anatomical effects of the nasal septum perforation on the character of flow during respiration. This is related to subsequent changes of flow in the nasal cavity from predominantly laminar to turbulent flow, i.e. undesirable changes in physiological functions of the nasal cavity occur. The objective of the present study was to examine the influence of the septal perforation and its position. For this purpose, numerical simulation using CFD was carried out on the simplified box model, bringing the comparison of the flow pattern both for an intact and perforated septum. The results can help towards better understanding of the given problem and underlie the further investigation in this field.*

**Keywords:** Respiration, Nasal airflow, Septal perforation, Airflow patterns, Numerical modelling.

### **1. Introduction**

Respiration is one of the basic physiological functions of the nose. Other functions include the olfactory function, as well as reflective activity ensuring protective reflexes (e.g. sneezing) and the immune function. Pathological-anatomical changes, such as the deviation of the nasal septum, septal perforation, hypertrophy of the lower nasal concha, accidents of the external nose, etc., often result in changes in the physiological functions of the nasal cavity, pathophysiological changes in the dynamics and characteristics of airflow in the nasal cavity – from mostly laminar airflow to turbulent flow and the consequent negative effect on the mucous membranes of the nasal cavity. These changes often lead to the drying of the nasal mucosa, formation of nasal crusts, recurrent epistaxis, decreased immunity, pain and obstruction of nasal breathing due to an increase in nasal resistance, with a direct impact on the quality of patients' lives.

Therefore, it is important to address the biomechanics of the problem (i.e., a multidisciplinary medical-engineering view of the flow during respiration in the nasal cavity with a normal and perforated septum). Numerical modelling is performed using the finite volume method (the program ANSYS/Fluent).

### **2. Anatomy of the Nose and the Nasal Cavity**

The external nose has the shape of a triangular pyramid; we distinguish the nasal dorsum (dorzum nasi) which ends in the nasal root (radix nasi) at the top and the nasal tip (apex nasi) at the bottom. Lateral walls of the nose form the nasal wings (alae nasi). In the front part of the nasal wings and nasal septum, cartilages – cartilago alaris major, nasi lateralis and septi nasi – are the basis of the nasal bone. For the nasal dorsum and root, nasal bones and frontal projections of the upper jaw are the osseous base. The lateral, upper and middle wall of the nasal cavity, and simultaneously the base of the anterior cranial fossa and medial wall of the eye socket are formed by the ethmoid bone (os ethmoidale), which is inserted into

---

<sup>\*</sup> Assoc. Prof. M.Sc. Karel Frydryšek, Ph.D., ING-PAED IGIP: Department of Applied Mechanics, Faculty of Mechanical Engineering, VSB-Technical University of Ostrava; 17. listopadu 15/2172; 708 33, Ostrava; CZ, karel.frydrysek@vsb.cz

<sup>\*\*</sup> Assoc. Prof. M.Sc. Sylva Drábková, Ph.D.: Department of Hydromechanics and Hydraulic Equipment, Faculty of Mechanical Engineering, VSB-Technical University of Ostrava; 17. listopadu 15/2172; 708 33, Ostrava; CZ, sylvia.drabkova@vsb.cz

<sup>\*\*\*</sup> M.D. Marek Plášek, Department of Otorhinolaryngology, University Hospital Ostrava, Faculty of Medicine, University of Ostrava, 17. listopadu 1790, 708 52 Ostrava, CZ

incisure of the frontal bone. The side wall of the ethmoid bone is supplemented by the upper jaw, lacrimal bones and lower nasal conchae, see Hybášek et al. (2013).

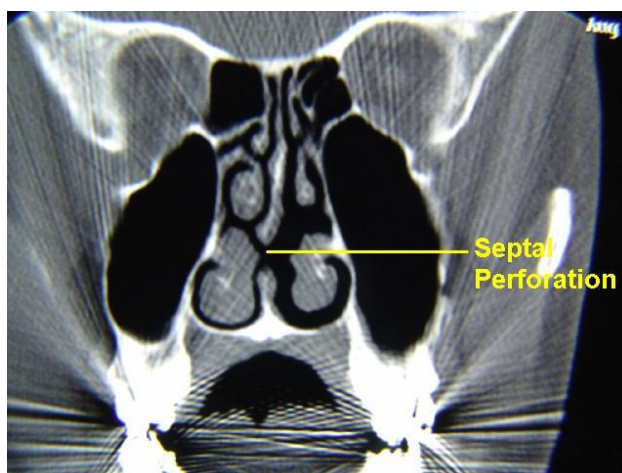
The nasal septum (septum nasi) divides the nasal cavity into two, under physiological conditions, nearly symmetrical halves. The nasal septum that is not deviated has a role in physiological predominantly laminar airflow. It is divided into three parts – the membranous, cartilaginous and osseous part. The base of the cartilaginous part is the cartilago septi nasi; the osseous part consists of the vomer and the vertical lamella of the ethmoid bone (lamina perpendicularis ossis ethmoidalis), see Hybášek et al. (2013) and Kennedy et al. (2012). At the front, the nasal cavity is surrounded by the nostrils, at the transition to the nasopharynx through choanas, in front of the nasal cavity (cavum nasi proprium), the nasal vestibule (vestibulum nasi) is located, which is lined with skin with adnexa. The nasal cavity is lined with respiratory epithelium (double columnar ciliated epithelium), and it is divided by nasal conchae (lower, middle, upper) passing from the lateral nasal wall to the individual nasal passages – the common one (meatus nasi communis) located in the nasal septum, and three side levels – lower, middle and upper nasal passage (meatus nasi inferior, medius and superior), see Hybášek et al. (2013).

### 3. Physiological Functions of the Nose

The essential function of the nasal cavity is the respiratory function. In the process of breathing, the nasal cavity plays an important part; it has three basic functions – cleaning, heating and humidifying the inhaled air. At rest, air flows through the nasal cavity at the speed of about 5 litres/minute at a load of up to 70 litres/minute. Slot-like cross-section of the nasal cavity shows that it is adapted for the laminar flow of air – a significant role in this process is played by the nasal septum without deviation. The turbulent flow occurs at places of extending the space beyond the narrowed areas, e.g. beyond the rear ends of the nasal conchae, beyond the nasal valve, beyond the deviation of the nasal septum, and also in the area of the perforation of the nasal septum. During respiration, the resistance of the nasal cavity is about 8 - 20 mm of the water column; if increased air exchange is needed, the area of the nasal valve is widened by the external nose muscles by opening the nostrils; if the resistance rises above 40 mm of the water column, we also need to start breathing through the mouth to cover higher claims for air exchange (e.g. in sports). At inspiration, the air temperature is 31 - 36 °C, namely even at sub-zero temperatures of the air of the external environment; this constant temperature significantly protects mucosa of the lower airways. The nasal mucosa moisturizes the air to a value of 75 – 80 % in the nasopharynx; the air is further humidified during the passage through the airways up to 95 – 100 %. The mucous membrane of the nasal cavity is protected from drying by mucus produced by seromucous and cup-shaped cells, see Kennedy et al. (2012). Other functions of the nose are the olfactory and immune function.

### 4. Septal Perforation

Perforation of the nasal septum, see Fig. 1 is a relatively frequent clinical problem in rhinology. Patients with this disease suffer from dryness of the nasal mucous membranes, increased formation of nasal crusts, recurrent epistaxis, nasal breathing pain and obstruction; an annoying whistling sound often occurs when



*Fig. 1: Septal perforation (CT image in the frontal projection).*

breathing in, see Romo et al. (1999). Perforations are often iatrogenic after interventions on the nasal septum (septoplasty, bipolar electrocoagulation). Another cause may be systemic inflammatory diseases (e.g. granulomatosis with polyangiitis), abuse of anemization drops, sprays, cocaine, etc. The cause often remains undetected; these perforations are then idiopathic, see Kharoubi (1998). Generally, the pathophysiologic mechanism of alteration of the nasal mucosa and the development of clinical symptoms is characterized as a change in the laminar flow of air in the nasal cavity to turbulent flow, see Fairbanks (1980).

## 5. Numerical Modelling

The simplified box model was defined based on a physical experiment presented by Grützenmacher et al. (2005). The basic dimensions of the so-called Mink's box were:  $L = 100\text{ mm}$ ,  $w = 30\text{ mm}$  and  $h = 10\text{ mm}$ . The septum was represented by the partition  $80 \times 4\text{ mm}$ . Simulations of incompressible transient flow were run in double precision using the two-dimensional turbulent viscous solver ANSYS/Fluent Release 16.2. The discretized Navier–Stokes equations were solved on unstructured meshes using the finite volume approach. The renormalization group (RNG)  $k-\epsilon$  model, adapted for turbulent flow of low Reynolds numbers, was applied. Viscosity and density of air were set to  $1.7894 \times 10^{-5}\text{ kg.m}^{-1}.\text{s}^{-1}$  and  $1.225\text{ kg.m}^{-3}$ . The walls were modelled as rigid with no-slip boundaries. Pressure condition with zero gauge pressure was defined at inflow and the boundary condition at the exit from the domain was set to mass flow inlet with the desired mass flow rate. Three values of the flow rate were assumed:  $50\text{ mls}^{-1}$ ,  $250\text{ mls}^{-1}$  and  $500\text{ mls}^{-1}$ .

Four series of simulations were carried out, firstly without the septum perforation, followed by three different locations of  $15\text{ mm}$  septum perforation illustrated below (see Fig. 2 and Fig. 3). Velocity, pressure field and turbulence parameters were evaluated for each geometry modification.

## 6. Results

In all cases the flow was symmetrical and turbulence in the domain increased with the increasing flow rate. To illustrate the influence of the perforation, a filled contours plot is presented for the flow rate of  $500\text{ mls}^{-1}$ . Effective viscosity was evaluated. The laminar viscosity  $1.7894 \times 10^{-5}\text{ kg.m}^{-1}.\text{s}^{-1}$  can be observed at the inflow. In the case of intact septum, the flow along the septum walls exhibits a low value of turbulence. The amplitude of  $1.21 \times 10^{-3}\text{ kg.m}^{-1}.\text{s}^{-1}$  can be observed in the sharp corners at the top of the model.

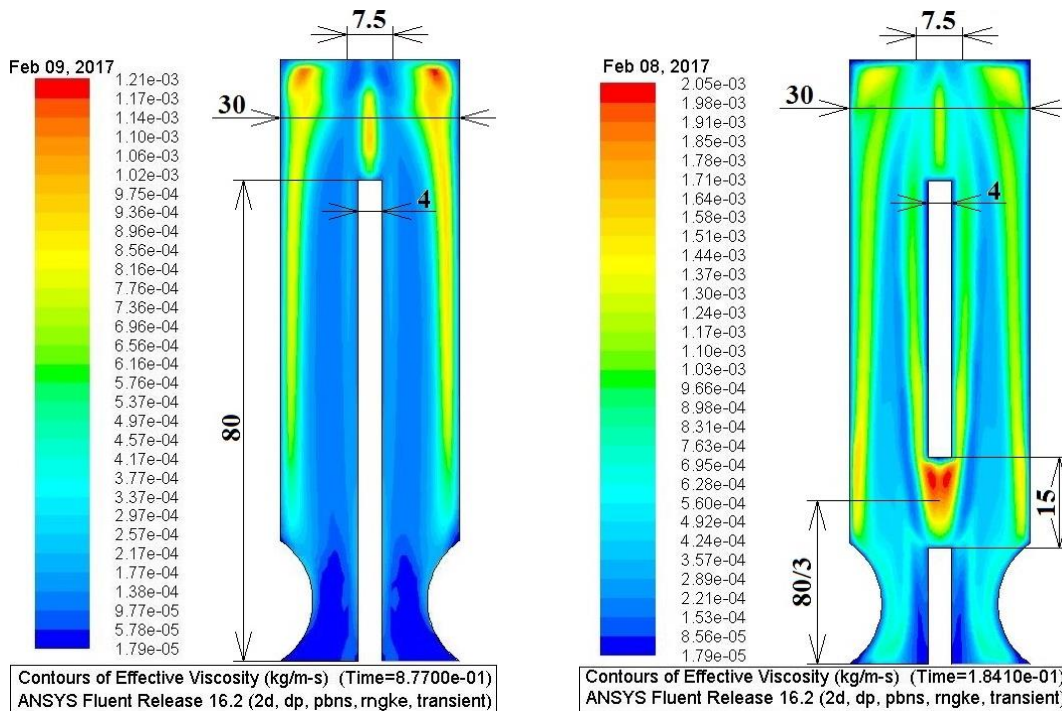


Fig. 2: Evaluation of effective viscosity for: a) intact septum; b) perforation located at 1/3 of septum length.



Effective viscosity distribution and airflow patterns within the model change in the case of perforation. In a gap the flow stagnates and two counter-rotating vortices develop. In the case of perforation, the effective viscosity increases by about 70 %. Turbulence increase can be observed also along the septum walls mainly above the perforation (see Fig. 2b and Fig. 3).

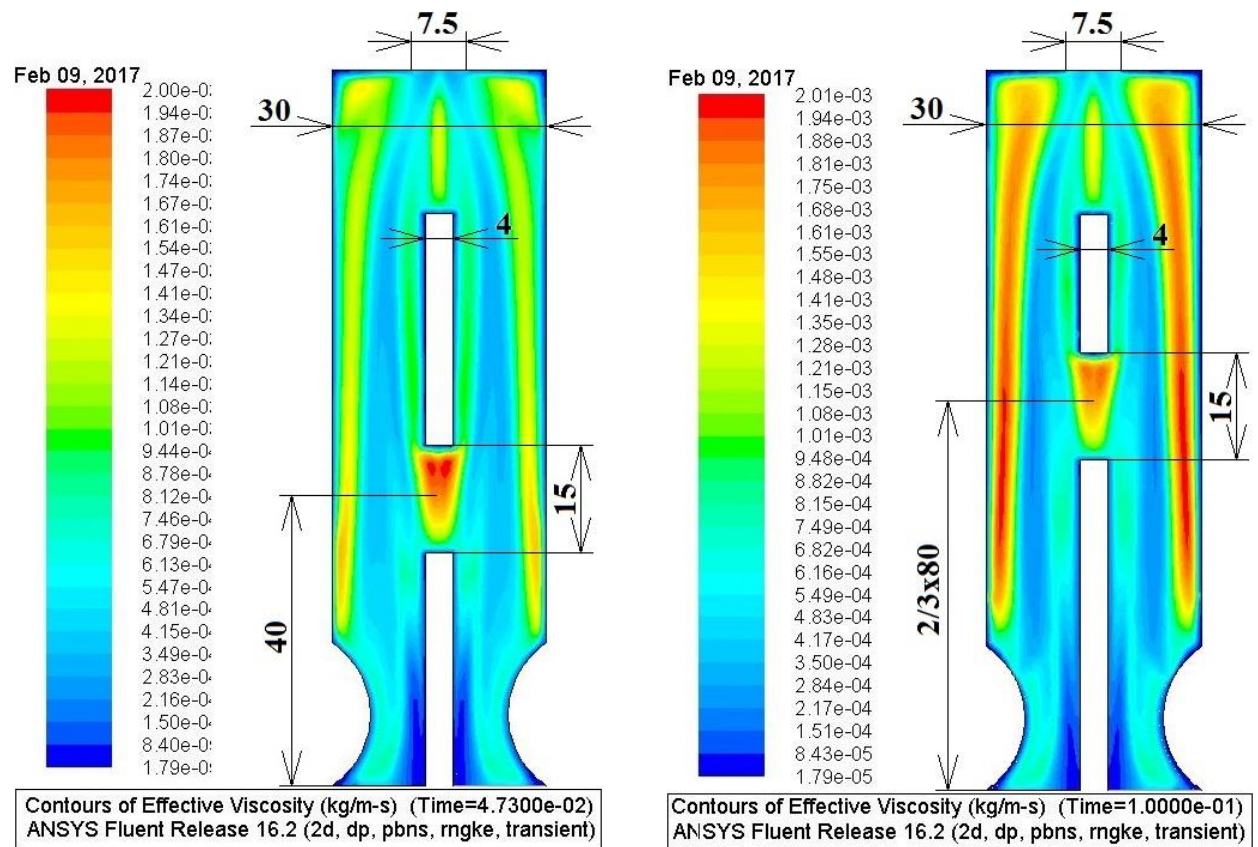


Fig. 3: Evaluation of effective viscosity for perforation located at: a) 1/2 and b) 2/3 of septum length.

## 7. Conclusions

Septal perforations are avoidable complications of septal surgery, but they can also occur because of a variety of traumatic, iatrogenic, caustic, inflammatory etc. reasons.

The results of numerical modelling of respiration in the nasal cavity show an undesirable increase in effective viscosity by about 70 % in cases of septal perforation. The results can serve as a basis in the decision-making in treating patients.

## Acknowledgments

This work was supported by Czech projects SP2017/136 and SP2017/103.

## References

- Fairbanks, D.N. (1980) Closure of nasal septal perforations, *Arch Otolaryngol*; 106, pp. 509-513.
- Grützenmacher, S. Mlynski, R., Lang, C., Scholz, S., Saadi, R. and Mlynski, G. (2005) The Nasal Airflow in Noses with Septal Perforation: A Model Study, DOI: 10.1159/000085958, *ORL* 2005, 67, pp. 142-147.
- Hybášek, I. et al. (2013) *eOtorinolaryngologie*, online, verze I.2017, <http://mefanet.lfhk.cuni.cz/clanky.php?aid=18>, ISSN 1803-280X.
- Kharoubi, S. (1998) Rhinolithiasis associated with septal perforation. A case report. *Acta Otorhinolaryngol Belg*; 52, pp. 241-245.
- Romo, T. Sclafani, A.P., Falk, A.N. and Toffel, P.H. (1999) A graduated approach to the repair of nasal septal perforations, *Plast Reconstr Surg*, 103 (1), pp. 66-75.
- Kennedy, D.W. et al. (2012) *Rhinology: Diseases of the Nose, Sinuses, and Skull Base*, Thieme Medical Publishers (DVD included), Inc., New York, USA, ISBN 978-1604060607, pp. 1-800.

## BIOMECHANICS - TESTING OF MECHANICAL AND UTILITY PROPERTIES OF BOTTLES FOR REDON DRAINAGE

K. Frydryšek<sup>\*</sup>, L. Dvořák<sup>\*\*</sup>

**Abstract:** *The article deals with biomechanical research of properties of bottles for Redon drainage, which is used in treatment for removal of unwanted fluids from the human body. Several measurements were made of vacuum, tightness and the amount of drained fluid and also a stress analysis of bottle walls using the finite elements method. The results (operating characteristics, mechanical properties) are important basis for the introduction of the product in normal medical practice. The collected data can be used to deduce the correct use of drains during treatment.*

**Keywords:** Redon drainage, Measurements, Calculations, Removal of fluids, Mechanical stress.

### 1. Introduction

Drain is a commonly and widely used medical device for removal of unwanted physiological or pathological fluids from the body (such as blood, lavage fluid, pus, intestinal contents, air etc.), see Fig. 1. There are various types of drainage. Our article deals with the vacuum/suction (i.e. Redon drainage), see the product in Fig. 1b. Redon drainage is a system based on the principle of vacuum extraction of fluid into a collection bottle through a suction tubing with a terminal connection to the drain, which is inserted into the patient body, see references Frydryšek (2016), Carruthers (2013) and Williams (2003).



Fig. 1: Vacuum drainage: a) application; b) examined Redon vessel.

At the request of the manufacturer of medical devices, our workplace tested a device for extracting air from Redon bottle drains, Fig. 1b. After reaching the desired vacuum in the bottle, the rubber neck is secured with a locking clasp and the Redon bottle is ready for use. The bottle vacuum allows draining of fluids e.g. after a surgery.

In addition to verification of the vacuum device, parameters of the Redon bottles themselves were measured (pressures and the amount of drained fluid), see Figs. 1b to 3. Finally, also the strength and deformation analysis was performed using FEM. The results will serve as an important basis for product recommendation to common medical practice. The collected information also gives an overview of the characteristics of the Redon drainage, which doctors can utilize in improving patient care.

---

<sup>\*</sup> Assoc. Prof. M.Sc. Karel Frydryšek, Ph.D., ING-PAED IGIP: Department of Applied Mechanics, Faculty of Mechanical Engineering, VSB-Technical University of Ostrava; 17. listopadu 15/2172; 708 33, Ostrava; CZ, karel.frydrysek@vsb.cz

<sup>\*\*</sup> M.Sc. Lukáš Dvořák, Ph.D.: Department of Hydromechanics and Hydraulic Equipment, Faculty of Mechanical Engineering, VSB-Technical University of Ostrava; 17. listopadu 15/2172; 708 33, Ostrava; CZ, lukas.dvorak@vsb.cz

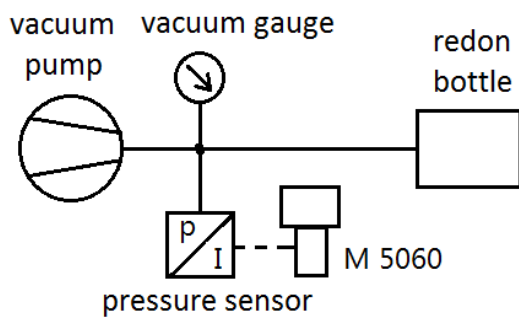


Fig. 2: Measurement of air vacuum during aspiration of a Redon bottle.

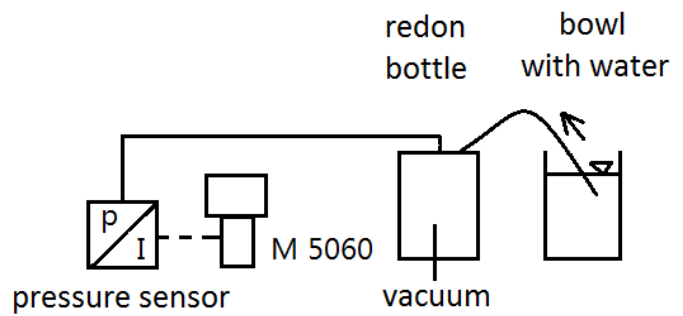


Fig. 3: Measurement of draining of fluid.

## 2. Measurement

The actual evacuating device is relatively simple; it consists only of a mechanical vacuum pump Busch R5, vacuum gauge and port for connection of the bottle. For measurement of vacuum the PR15 sensor was used, with measurement range  $-1$  to  $6$  bar and a measurement device M5060, both from Hydrotechnik. Multi-system M5060 is designed to measure pressure, temperature, flow, force, torque, and other variables. According to the manufacturer, the measurement uncertainty is  $\pm 0.15\%$  of the maximum measured value.

First, the calibration of the vacuum indicator located on the vacuum pump was performed. This was followed by verification of the aspiration rate of air from the bottle of volume  $400$  ml. The measurement schematic is in Fig. 2.

Fig. 4 shows the measured course of pressure in a bottle of an effective volume  $400$  ml (the calibrated volume of the bottle, above the max. volume line there is still approx.  $50$  ml). The aspiration of air started at  $1$  s and the required vacuum, i.e. min  $-0.9$  bar was reached approx. in  $2$  s. After this time the bottle can be closed.

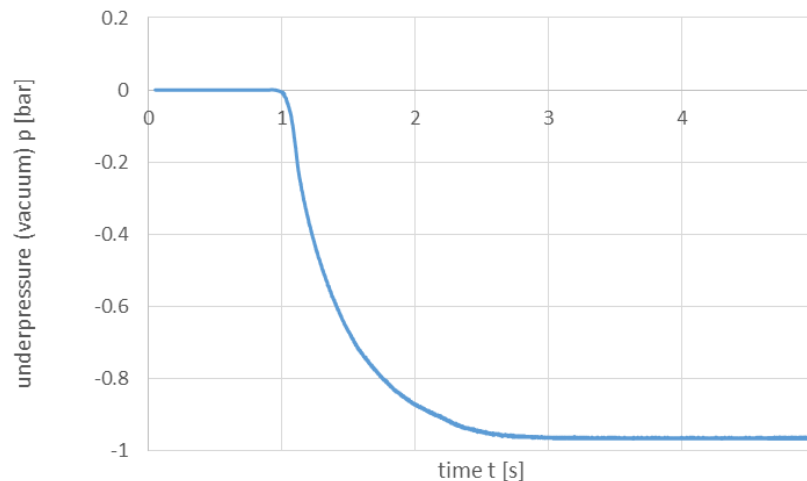


Fig. 4: Measurement - course of air vacuum during aspiration.

Another measurement was to determine the changes in vacuum, depending on the amount of drained liquid. During the measurements the bottle was connected through a tube to a pressure sensor, and through a second tube, after the release of the clasp, water was drained into the bottle, see diagram in Fig. 3. During filling of the bottle the vacuum has been recorded, and the value of the volume of drained liquid was read from the scale on the bottle. Measurements were performed on two bottles. From the course of pressure in Fig. 5 it is evident that after the effective volume  $400$  ml is filled, the remaining vacuum in the bottle is min.  $-0.8$  bar.



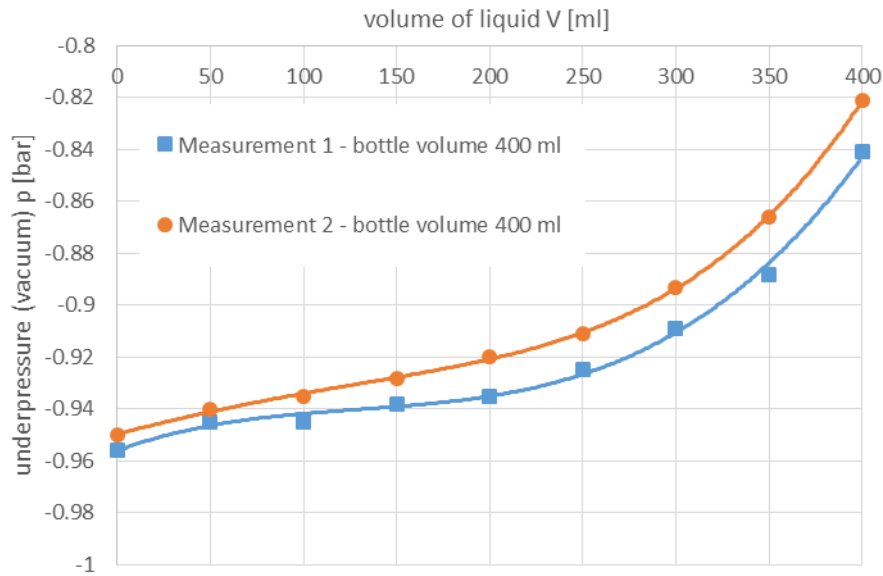


Fig. 5: Two measurement records - course of pressure during drainage.

The next measurement verified the amount (level) of vacuum in bottles ready for shipment. 10 samples of 200 ml and 10 samples of 400 ml were examined. Results are shown in Tab. 1.

Tab. 1: Vacuum in Redon bottles ready for use.

measurement	1	2	3	4	5	6	7	8	9	10	mean
bottles 400 ml	-0.898	-0.888	-0.878	-0.888	-0.895	-0.892	-0.878	-0.898	-0.885	-0.868	<b>-0.8868</b>
bottles 200 ml	-0.777	-0.75	-0.777	-0.754	-0.757	-0.744	-0.761	-0.758	-0.761	-0.785	<b>-0.7624</b>

Apart from the above measurements, also e.g. tightness of the bottles, tightness of clasps for closing bottles, tightness of hose connections were determined.

### 3. Finite Element Analysis of Redon bottles

The subject of the FEM calculation was verification of the strength of the collection vacuum Redon bottle when comparing various shape versions (imperfections) that are commonly encountered during the production process. The vessel is made of hard PVC. The vacuum in the bottle is 0.9 bar.

The measurements of randomly selected bottles and the adopted simplifications showed 8 variants of simple geometries of symmetrical vessels (plane strain formulation), see Fig. 6. Variants 7 and 8 correspond to the bottle with a notch (extremely damaged bottle). The bottle material is considered isotropic and homogeneous. Finally, the calculations of deflections and stresses were performed, see e.g. Fig. 7.

### 4. Conclusions

From experiments (pressure measurement and measurement of the quantity of drained fluid) and stress analysis (calculations of deflections and stress) it is evident that the disposable Redon bottles are properly designed and can be used in conventional medical practice.

Knowledge gained from measuring of fluid drainage is important finding for physicians and serves to improve the patient care.

### Acknowledgments

This work was supported by Czech projects SP2017/136 and SP2017/103.

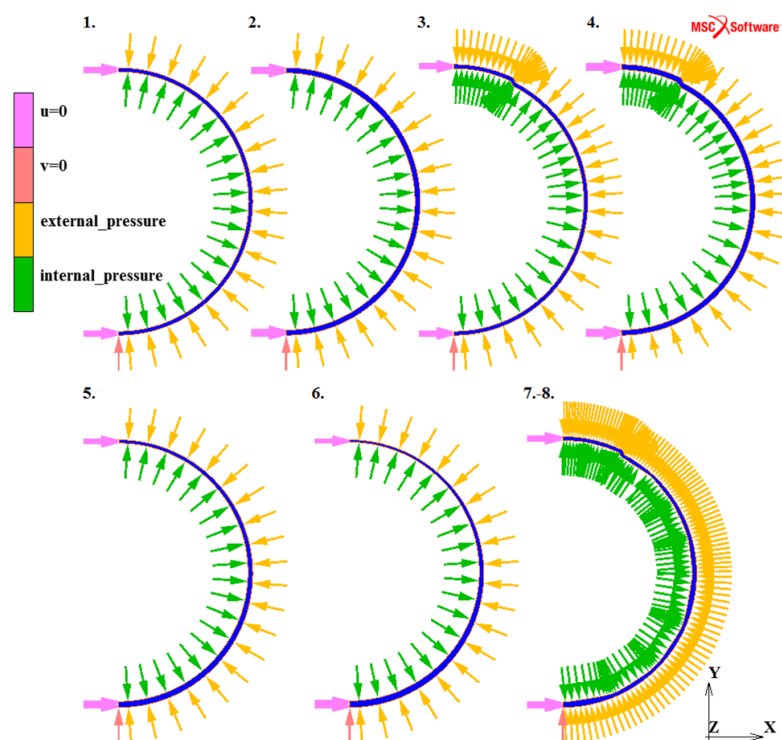


Fig. 6: FEM - Variants of Redon bottle calculations (plain strain, planar symmetry and boundary conditions, SW MSC.MARC/MENTAT).

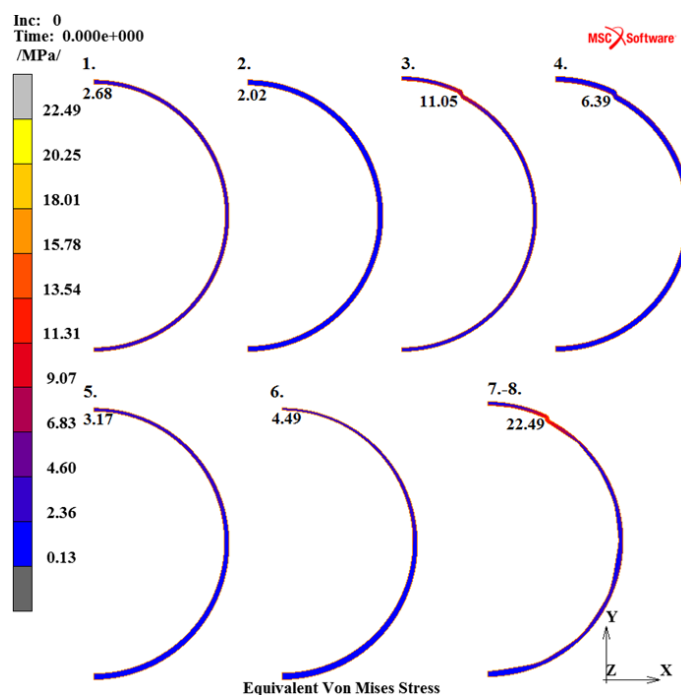


Fig. 7: FEM - Variants of Redon bottle calculations (Equivalent von Mises Stress).

## References

- Carruthers, K.H., Eisemann, B.S., Lamp, S. and Kocak, E. (2013) Optimizing the closed suction surgical drainage system, *Plast Surg Nurs*, 2013, 33(1), pp. 38-42.
- Frydrýšek, K. and Dvořák, L. (2016) Redon bottles - Calculation and Measure Report, 218, 5, pp. 1-35.
- Williams, J., Toews, D. and Prince M. (2003) Survey of the use of suction drains in head and neck surgery and analysis of their biomechanical properties, *J. Otolaryngol* 2003, 32(1), pp.16-22.

## ENDURANCE LIMIT OF FRP COMPOSITES USED FOR REINFORCEMENT OF CONCRETE STRUCTURES

K. Gajdosova<sup>\*</sup>, R. Sonnenschein<sup>\*\*</sup>

**Abstract:** FRP reinforcement subjected to a constant load over time can suddenly fail after a time period called the endurance time. This phenomenon is known as creep rupture. Carbon fibers have a very good resistance to creep rupture. Aramid fibers are more susceptible to this phenomenon and glass and basalt fibers are the most susceptible ones. Results of various previous experimental programs showed the ratios of stress level at creep rupture to the initial strength to be in range of 0.18 to 0.93 for different types of FRP reinforcement. Simple example was chosen to calculate supposed stresses in reinforcement and according to results, only calculated values for CFRP reinforcement are lower than the 50-years residual stresses according to aforementioned experiments. The values of residual stresses are only extrapolated from short-term tests and real experience in time is needed to decide about real long-term degradation of these materials.

**Keywords:** FRP reinforcement, Creep rupture, Stress limitations.

### 1. Introduction

During renovation and execution of concrete structures, non-metallic reinforcing materials are increasingly used considering their appealing advantages like low weight, high strength and easy application. The significant difference between steel and composite reinforcement is the long-term behavior. FRP composites can be subjected to creep rupture. That is why stress level under sustained load should be limited as the portion of the short-term strength of FRP reinforcement. Long-term properties depend both on fibers and matrix used in FRP. The best long-term properties are reported for carbon FRP, the worst ones for glass and basalt FRP.

### 2. FRP reinforcement

FRP reinforcement is anisotropic in nature and can be manufactured using a variety of techniques such as pultrusion, braiding and weaving. The characteristics of FRP reinforcement are dependent on factors such as fiber volume, type of fiber, type of resin, fiber orientation, dimensional effects and quality control during manufacturing. (ACI 440.1R-03) The resin acts as a matrix bonding the fibers together and transferring the load applied to the composite between each of the individual fibers. The resin also protects the fibers from abrasion and impact damage as well as severe environmental conditions (water, salts, alkalis) which affect the durability of FRP products. (Benmokrane, 2015) To the commonly used fibers carbon (CFRP), glass (GFRP), aramid (AFRP) and basalt (BFRP) fibers belong.

Glass fibers are the cheapest ones but the less durable due to high chemical sensibility to alkali environment. Carbon fibers tend to show the best resistance. CFRP and AFRP reinforcement is also insensitive to chloride ions. Carbon and glass fibers do not absorb water which affects in better fatigue strength. The most discussed problem of non-metallic reinforcement is the behavior during elevated temperature – which is the problem of resin. Carbon fibers themselves are not sensitive to high temperature and that is why CFRP shows the most favorable behavior. CFRPs are in addition not affected by ultraviolet rays.

---

<sup>\*</sup> Ing. Katarina Gajdosova, PhD.: Faculty of Civil Engineering, Department of Concrete Structures and Bridges, Slovak University of Technology, Radlinskeho 11; 810 05 Bratislava; SK, katarina.gajdosova@stuba.sk

<sup>\*\*</sup> Ing. Robert Sonnenschein, PhD.: Faculty of Civil Engineering, Department of Concrete Structures and Bridges, Slovak University of Technology, Radlinskeho 11; 810 05 Bratislava; SK, robert.sonnenschein@stuba.sk

Durability of FRP reinforcement is not only influenced by component properties but also by the interface between them. The transfer of shear and transverse forces at the interface between reinforcement and concrete, influencing the bond, and between individual fibers within the composite are the resin-dominated mechanisms. Fiber-dominated mechanisms control properties such as longitudinal strength and stiffness of FRP reinforcement. (Ceroni, 2006)

### 3. Long-term properties of FRP reinforcement

FRP reinforcement subjected to a constant load over time can suddenly fail after a time period called the endurance time. This phenomenon is known as creep rupture. The endurance time of FRP reinforcement decreases as the ratio of the sustained tensile stress to the short-term strength increases. The endurance time also decreases with the effects of high temperature, ultraviolet radiation exposure, high alkalinity, wet and dry cycles, and freezing-thawing cycles. (ACI 440.1R-03) Carbon fibers have a very good resistance to creep rupture. Aramid fibers are more susceptible to this phenomenon and glass and basalt fibers are the most susceptible ones. Nevertheless, the susceptibility of the resin is the biggest problem.

The viscoelastic response and temperature sensitivity of polymeric resins make an FRP material more sensitive to creep and other rate-dependent phenomena than metallic materials. A typical creep history of a structure reinforced with FRP composites consists of three different regions, as it is shown in Fig. 1. In the primary region, creep grows faster in time. In secondary region, the creep strains do not grow and structure remains serviceable. The tertiary region means a damage of material in structure. (Banibayat, 2014)

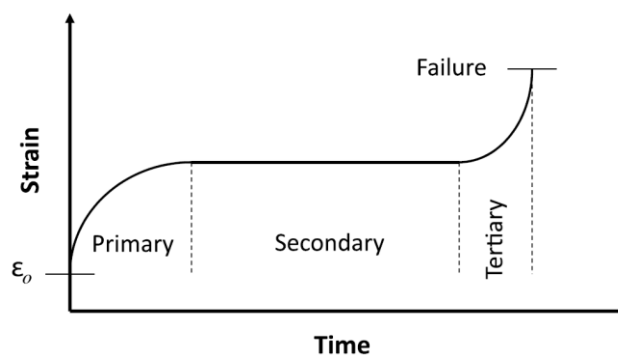


Fig. 1: Creep strain of FRP reinforcement (Banibayat, 2014).

A few series of creep rupture tests were conducted on FRP reinforcement with different fibers (carbon, aramid, glass, basalt). Usually the tests lasted for a time of 100 h and the results were linearly extrapolated to 500,000 h (more than 50 years).

Results of the experimental program of Yamaguchi et al. (1997) showed the ratios of stress level at creep rupture to the initial strength to be 0.29 for GFRP, 0.47 for AFRP and 0.93 for CFRP. In another extensive investigation (Ando et al. 1997) the percentage of stress at creep rupture versus the initial strength after 50 years was found to be 0.79 for CFRP and 0.66 for AFRP. Seki et al. (1997) reported the ratio of 0.55 for GFRP. A 50-year ultimate creep rupture strength coefficient of 0.18 was found by Banibayat and Patnaik (2014) to be suitable for BFRP reinforcement.

There are two possibilities to avoid creep rupture – adjust the material resistance of FRP reinforcement or limit the stress level in FRP reinforcement under sustained stresses.

### 4. SLS – stress limitations

High levels of creep can cause unacceptable effect on the function of the structure. That is why codes used in current practice limit stress levels in materials. To avoid non-linear creep behavior of concrete, the compressive stress in concrete under quasi-permanent combination of actions is limited to 45 % of concrete compressive strength in Eurocode 2. Under this value linear creep can be assumed.

The durability of FRP composite materials is generally good until the fibers are protected by the resin. At high stress levels, however, micro-cracks can appear in the resin. This is a very uncertain situation for

fibers, in particular glass, because they can be damaged by moisture and the alkaline concrete environment. (*fib* Bulletin 40, 2007)

Recommendations on sustained stress limits imposed to avoid creep rupture are provided in design section of ACI 440.1R (2003).

*Tab. 1: Allowable stresses in FRP reinforcement to avoid creep rupture (ACI 440.1R-03).*

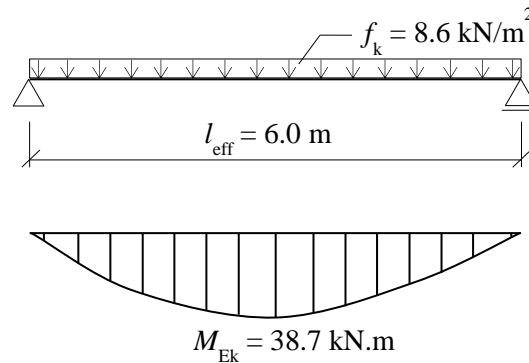
Fiber type	GFRP	AFRP	CFRP
Creep rupture stress limit $f_{f,s}$	$0.20 f_{fu}$	$0.30 f_{fu}$	$0.55 f_{fu}$

## 5. Example

For illustration of FRP composite reinforcement action in a simply supported one-way reinforced concrete slab, the example shown in Fig. 2 was chosen.

The input parameters:

- slab thickness: 250 mm
- reinforcement bars diameter: 6 mm
- reinforcement characteristics: see Tab. 2
- concrete cover: 20 mm
- concrete class: C25/30
- effective span of a slab: 6000 mm



*Fig. 2: Example of a one-way slab.*

In serviceability limit state, from characteristic combination of action, the stresses in reinforcement were calculated and compared with allowed values stated before (Tab. 3).

*Tab. 2: Properties of FRP reinforcing bars.*

	CFRP	GFRP	AFRP	BFRP
Tensile strength [MPa]	3100	1000	2100	1500
Modulus of elasticity [GPa]	170	50	83	41
Limit strain [%]	1.20	2.20	2.90	2.50

## 6. Conclusions

FRP reinforcement subjected to a constant load over time can suddenly fail after a time period called the endurance time. This phenomenon is known as creep rupture. The viscoelastic response and temperature sensitivity of polymeric resins make an FRP material more sensitive to creep and other rate-dependent phenomena than metallic materials. To avoid creep rupture of FRP composite, the stress level in FRP reinforcement under sustained stresses should be limited. From the results of the chosen example it can be seen that only calculated values of stresses in CFRP reinforcement are lower than the 50-years residual

stresses according to ACI code and other authors` experimental investigations. Nevertheless, it cannot be stated that other FRP composites will not reliably satisfy their function in the structure and that structures with other FRP reinforcement types will fail before reaching their service life because the values of residual stresses are only extrapolated from short-term tests and we need real experience in time to decide about real long-term degradation of these materials.

*Tab. 3: Comparison of calculated stresses in reinforcement and the creep rupture stress limits according to various authors.*

	CFRP		GFRP		AFRP		BFRP	
Calculated stress in reinforcement:	1638.5		592.2		1280.5		892.8	
	Stress limits [MPa]							
ACI 440.1R-03 (2003)	1705.0	+4.1 %	200.0	−66.2 %	630.0	−50.8 %	−	
Yamaguchi et al. (1997)	2883.0	+76.0 %	290.0	−51.0 %	987.0	−23.6 %	−	
Ando et al. (1997)	2449.0	+49.5 %	−		1386.0	+8.2 %	−	
Seki et. al (1997)	−		550.0	−7.1 %	−		−	
Banibayat and Patnaik (2014)	−		−		−		270.0	−69.8 %

### Acknowledgements

This work was supported by the Slovak Research and Development Agency under the contract No. APVV-15-0658 and the University Science Park (USP) of the Slovak University of Technology in Bratislava (ITMS: 26240220084).

### References

- ACI 440.1R-03 Guide for the Design and Construction of Concrete Reinforced with FRP Bars, 2003.
- Banibayat, P. and Patnaik, A. (2014) Creep Rupture Performance of Basalt Fiber-Reinforced Polymer Bars, Journal of Aerospace Engineering, Vol.04014074, pp. 1-6.
- Benmokrane, B., Elgabbas, F., Ahmed, E. and Cousin, P. (2015) Characterization and Comparative Durability Study of Glass/Vinylester, Basalt/Vinylester, and Basalt/Epoxy FRP bars. J Compos Const 2015. ASCE ISSN 1090e0268/04015008(12).
- Ceroni, F., Cosenza, E., Gaetano, M. and Pecce, M. (2006) Durability Issues of FRP Rebars in Reinforced Concrete Members, Cement & Concrete Composites, Vol. 28, pp: 857.
- fib Bulletin 40: FRP reinforcement in RC structures, 2007.

## THE CONTROL PROCESS OF A SCANNING AND TRACKING IR SEEKER USING INVERSE DYNAMICS

D. Gapiński\*, P. Szmidt\*\*

**Abstract:** The paper presents a control method of a designed detecting and tracking head for seeking short-range missiles. The problem of inverse dynamics in relation to different types of external interferences was used to control an optical axis of the seeker head. The research includes an analysis of impact of the mentioned interferences on accuracy of head axis control, shapes of its spatial displacements trajectories and values of generated control torques. Numerical simulations were performed using special software written in C++ and results of some research were presented graphically.

**Keywords:** IR seeker, Dynamics, Homing, Control.

### 1. Introduction

The subject of the research is an optical detecting and tracking head (Gapiński, 2008) for seeking, anti-aircraft, homing missiles. The main task of the device is detecting and tracking air targets that emit infrared radiation (aircraft, helicopters, etc.). The paper presents control procedures for the abovementioned device by using, so-called, the inverse dynamics problem and, at the same time, considering the impact of interferences resulted from angular displacements of a missile launcher.

### 2. Interferences model

Despite of the fact that the interferences resulted from movements of a missile launcher are impossible to predict and have random character, there is a possibility of modelling this type of phenomenon to reflect natural phenomenon in a sufficient way (Stefański, 2012). The above research study presents one of the analysed types of interferences that impacts on the detecting and tracking head and comes from angular displacements of a missile launcher held by a shooter (an anti-aircraft shooter).

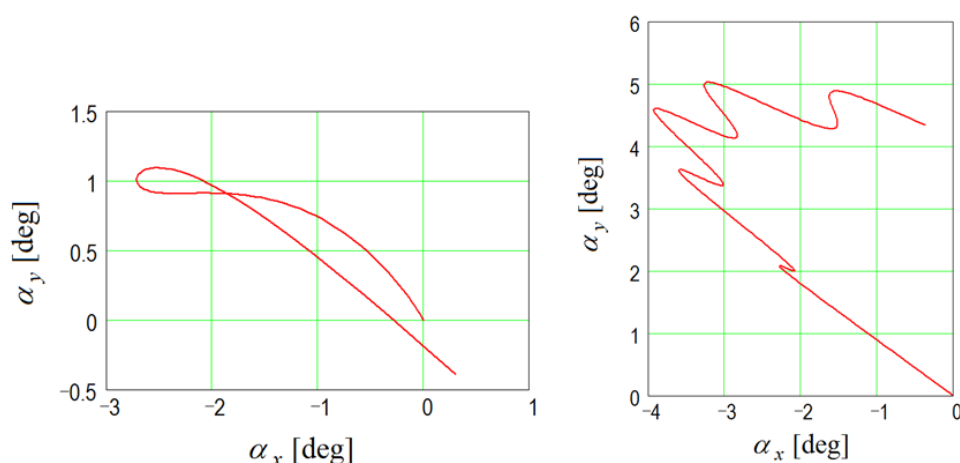


Fig. 1: Examples of axis angular movements simulations of a missile in a missile launcher.

\* Research Assistant Daniel Gapiński, PhD. Eng.: Faculty of Mechatronics and Mechanical Engineering, Kielce University of Technology, al. 1000-lecia P.P. 7; 25-345, Kielce; PL, dgapinski@tu.kielce.pl

\*\* PhD. student Piotr Szmidt, M.Sc. Eng.: Faculty of Mechatronics and Mechanical Engineering, Kielce University of Technology, al. 1000-lecia P.P. 7; 25-345, Kielce; PL, petersz@wp.pl



To prepare mathematical description of the interference phenomenon which consists of the abovementioned angular displacements of a missile launcher, the basic mathematical functions like sine or cosine were used in a way that allows for obtaining trajectories of missile launcher axis movements that correspond with real movements when shooting in a battlefield (Dziopa et al., 2015). The movement of a missile axis in a missile launcher was marked using angular displacements:  $\alpha_x, \alpha_y$ , represented in a plane perpendicular to a longitudinal axis of a missile (Koruba et al., 2013). Examples of numerical simulations of the above interferences are presented in Fig. 1. The total duration of the tracking air target before start the missile is on average 5 seconds (Gapiński et al., 2016).

### 3. Analysis of controlling possibilities of a head optical axis

In Fig. 2 there is 3D visualisation of the designed seeker head and a comparison of coordinate systems with equations of motion for its specified elements.

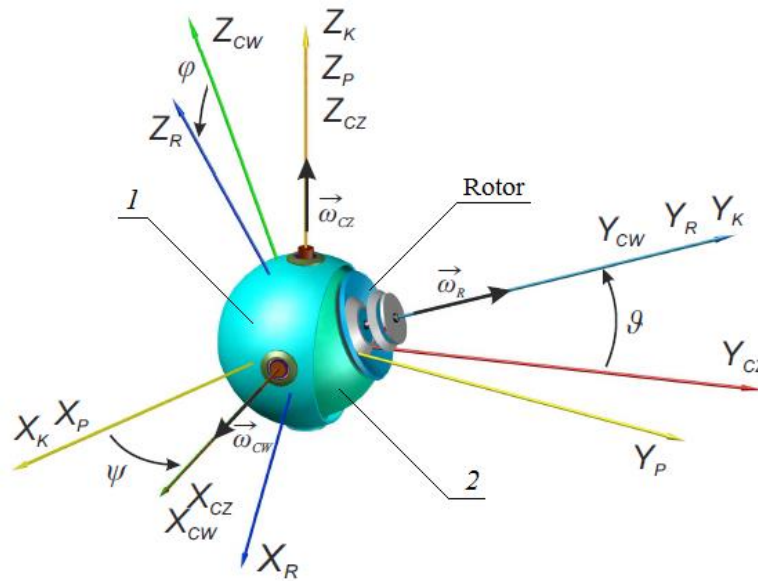


Fig. 2: 3D visualisation of the seeker head with chosen coordinate systems.

The following systems of coordinates were introduced:

- $OX_K Y_K Z_K$  – system of coordinates connected with the set direction in space;
- $OX_P Y_P Z_P$  – moving coordinate system connected with the missile;
- $OX_{CZ} Y_{CZ} Z_{CZ}$  – moving coordinate system connected with the outer housing;
- $OX_{CW} Y_{CW} Z_{CW}$  – moving coordinate system connected with the inner housing;
- $OX_R Y_R Z_R$  – moving coordinate system connected with the rotor.

The following markings of angles of rotation and the order of measuring them were adopted:

- $\psi$  – angle of rotation  $OX_{CZ} Y_{CZ} Z_{CZ}$  in relation to  $OX_P Y_P Z_P$  around axis  $Z_{CZ}$ ,
- $\vartheta$  – angle of rotation  $OX_{CW} Y_{CW} Z_{CW}$  in relation to  $OX_{CZ} Y_{CZ} Z_{CZ}$  around axis  $X_{CW}$ ,
- $\varphi$  – angle of rotation  $OX_R Y_R Z_R$  in relation to  $OX_{CW} Y_{CW} Z_{CW}$  around axis  $Y_R$ ,
- 1, 2 – outer and inner housing made of reinforcement polymer composites (Chatys, 2013).

Controlling by using, so-called, the inverse dynamics problem consists of calculating control torques (Takosoglu, 2016) of specified seeker head caps that cause required axis movements determined by the angles:  $\vartheta_z(t)$  and  $\psi_z(t)$ . So, the inverse dynamics problem allows for programming the changes in time of both angles of a seeker head axis deviation (Krzysztofik et al., 2014).  $M_Z$  and  $M_W$  control torques are calculated using the correlation:

$$\begin{aligned}
M_Z = & \left[ J_{z_{CZ}} + J_{z_{CW}} + J_{z_R} + (J_{y_{CW}} - J_{z_{CW}} - J_{z_R}) \sin^2 \vartheta_z \right] \dot{\omega}_{z_{CZ}} + \\
& + \frac{1}{2} (J_{y_{CW}} - J_{z_{CW}} - J_{z_R}) \sin 2\vartheta_z (\omega_{z_{CZ}} \dot{\vartheta}_z + \dot{\omega}_{y_{CZ}}) + \\
& - \left[ J_{z_{CW}} + J_{z_R} - (J_{y_{CW}} - J_{z_{CW}} - J_{z_R}) \sin^2 \vartheta_z \right] \omega_{y_{CZ}} \dot{\vartheta}_z + \\
& - (J_{z_{CW}} + J_{z_R}) \omega_{z_{CW}} \omega_{x_{CW}} \sin \vartheta_z - J_{y_{CW}} \omega_{y_{CW}} \omega_{x_{CW}} \cos \vartheta_z + \\
& + J_{y_R} n \omega_{x_{CW}} \cos \vartheta_z - (J_{x_{CZ}} - J_{y_{CZ}}) \omega_{x_{CZ}} \omega_{y_{CZ}} + \\
& - (J_{x_{CW}} + J_{x_R}) \omega_{x_{CW}} \omega_{y_{CZ}} + c_z \dot{\psi}_z
\end{aligned} \tag{1}$$

$$\begin{aligned}
M_W = & (J_{x_{CW}} + J_{x_R}) \ddot{\vartheta}_z + (J_{x_{CW}} + J_{x_R}) \dot{\omega}_{x_{CZ}} + \\
& - (J_{y_{CW}} - J_{z_{CW}} - J_{z_R}) \omega_{y_{CW}} \omega_{z_{CW}} - J_{y_R} n \omega_{z_{CW}} + c_w \dot{\vartheta}_z
\end{aligned} \tag{2}$$

where:

$$\begin{aligned}
\omega_{x_{CZ}} &= \omega_{x_P} \cos \psi + \omega_{y_P} \sin \psi, \\
\omega_{y_{CZ}} &= -\omega_{x_P} \sin \psi + \omega_{y_P} \cos \psi, \\
\omega_{z_{CZ}} &= \dot{\psi} + \omega_{z_P}, \\
\omega_{x_{CW}} &= \omega_{x_{CZ}} + \dot{\vartheta}, \\
\omega_{y_{CW}} &= \omega_{y_{CZ}} \cos \vartheta + \omega_{z_{CZ}} \sin \vartheta, \\
\omega_{z_{CW}} &= -\omega_{y_{CZ}} \sin \vartheta + \omega_{z_{CZ}} \cos \vartheta.
\end{aligned}$$

As given quantities the following were adopted:

$J_{x_{CZ}}, J_{y_{CZ}}, J_{z_{CZ}}$  – moments of inertia of the complete outer housing;

$J_{x_{CW}}, J_{y_{CW}}, J_{z_{CW}}$  – moments of inertia of the complete inner housing;

$J_{x_R}, J_{y_R}, J_{z_R}$  – moments of inertia of the rotor;

$\vec{\omega}_P(\omega_{x_P}, \omega_{y_P}, \omega_{z_P})$  – missile angular velocity;

$M_Z$  – moment of missile forces interacting on the outer housing;

$M_W$  – moment of forces of the outer housing interacting on the inner housing;

$M_R$  – moment of forces of the inner housing interacting on the rotor;

$M_{TR}$  – moment of friction forces in rotor bearings and aerodynamic resistance;

$M_{TW}, M_{TZ}$  – moments of friction forces in the bearings of respectively: inner and outer housing,

provided that  $M_{TW} = c_w \dot{\vartheta}$ ,  $M_{TZ} = c_z \dot{\psi}$ ,

where:

$c_w$  – friction coefficient in the bearing of the inner housing,

$c_z$  – friction coefficient in the bearing of outer housing.

The law of scanning the air space by the optoelectronic system of the device was presented in (Gapiński, 2008) and we will write it in the following way:

$$\beta_x(t) = \arctg(\tg(\beta(t))) \cdot \cos \left( \arcsin \left( \frac{z_{zp}(t)}{\sqrt{x_{zp}(t)^2 + z_{zp}(t)^2}} \right) \right) \tag{3}$$

$$\beta_z(t) = \arctg(\tg(\beta(t))) \cdot \sin \left( \arcsin \left( \frac{z_{zp}(t)}{\sqrt{x_{zp}(t)^2 + z_{zp}(t)^2}} \right) \right) \tag{4}$$

where:

$\beta_x(t), \beta_z(t)$  – angular coordinates of the detected target in relation to the scanning seeker axis,

$\beta(t)$  – the resultant angle of deflection of a light beam from the optical axis,

$x_{zp}, z_{zp}$  – components of the location of a light beam on the surface of the primary mirror,

$x_c, z_c$  – components of the location of a target on the surface of the scanning plane,  
 $x_s, z_s$  – components of the location of a light beam on the surface of the scanning plane.

Controlling the seeker head axis was evaluated, among others, by programming it for searching the airspace, first on the cone plane, and, after scanning the whole chosen space, searching the airspace along a developing spiral. A computer simulation of airspace searching with chosen trajectories and tracking a manoeuvring air target (moving with the speed of 200 m/s) are presented in Fig. 3. The target trajectory is described by the equation described in (Koruba et al., 2010) Fig. 4.

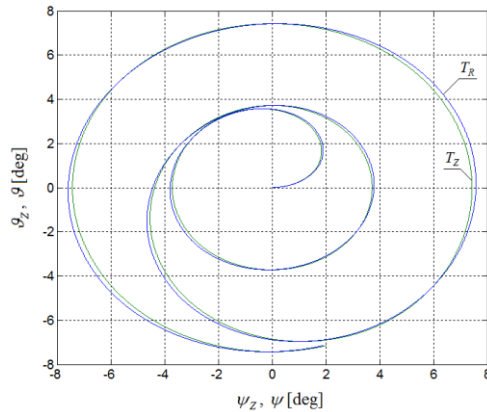


Fig. 3: The trajectory of  $T_Z$  set and actual  $T_R$  movement of the seeker head axis.

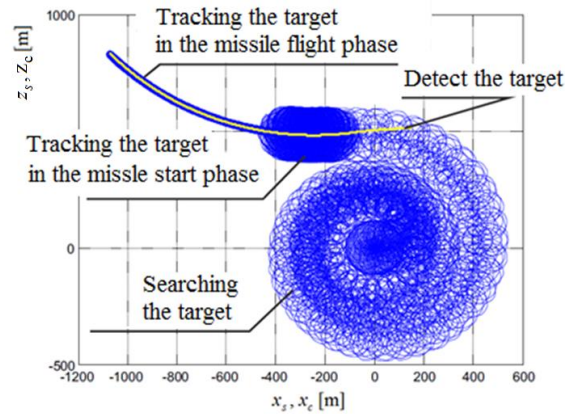


Fig. 4: Target searching, detecting and tracking.

#### 4. Conclusions

The results of the computer simulations presented in the paper show that, despite of the impact of different external interferences, the tested seeker head can track detected targets very precisely. Controlling the seeker head axis by using the inverse dynamics is performed with precision appropriate for homing. The non-linearity of equations (1, 2) of the mathematical model should be considered because it is caused, among others, by unspecified parameters of external forces. Considering the non-linearity of the system, all calculations should be performed in, so-called, real-time in relation to current measurements from all sensors – obviously, it will force using additional numeric processors for calculating.

#### References

- Chatys, R. (2013) Investigation of the Effect of Distribution of the Static Strength on the Fatigue Failure of a Layered Composite by Using the Markov Chains Theory. *Mechanics of Composite Materials*, 48, 6, pp. 629-638.
- Dziopa, Z., Buda, P., Nyckowski, M. and Pawlikowski, R. (2015) Dynamics of an unguided missiles launcher. *Journal of Theoretical and Applied Mechanics*. No. 1, Vol. 53, pp. 69-80.
- Gapiński, D. and Koruba, Z. (2016) Analysis of reachability areas of a manoeuvring air target by a modified maritime missile-artillery system ZU-23-2MRE. *Dynamical Systems: Theoretical and Experimental Analysis*, Springer Proceedings in Mathematics & Statistics, Vol. 182, pp. 125-144.
- Gapiński, D. (2008) Optical scanning seeker, Patent PL 199721 B1 (in Polish).
- Koruba, Z. and Krzysztofik, I. (2013) An algorithm for selecting optimal controls to determine the estimators of the coefficients of a mathematical model for the dynamics of a self-propelled anti-aircraft missile system. *Proceedings of the Institution of Mechanical Engineers, Part K: Journal of Multi-body Dynamics*, 227, 1, pp. 12-16.
- Koruba, Z. and Ładyżyńska-Kozdraś, E. (2010) The dynamic model of a combat target homing system of an unmanned aerial vehicle. *Journal of Theoretical and Applied Mechanics*, 48, 3, pp. 551-566.
- Krzysztofik, I. and Koruba, Z. (2014) Mathematical Model of Movement of the Observation and Tracking Head of an Unmanned Aerial Vehicle Performing Ground Target Search and Tracking. *Journal of Applied Mathematics*, 2014, Article ID 934250, 11 p.
- Stefanski, K. and Koruba, Z. (2012) Analysis of the guiding of bombs on ground targets using a gyroscope system. *Journal of Theoretical and Applied Mechanics*, 50, 4, pp. 967-973.
- Takosoglu, J.E. (2016) Control system of delta manipulator with pneumatic artificial muscles, in: *Proc. 22th Int. Conf. Eng. Mech. 2016* (eds. Zolotarev, I. and Radolf, V.), Svratka, Czech Republic, pp. 546-549.

## **SENSITIVITY INVESTIGATIONS OF THE LANE CHANGE AUTOMATED PROCESS**

**M. Gidlewski<sup>\*</sup>, L. Jemioł<sup>\*\*</sup>, D. Żardecki<sup>\*\*\*</sup>**

**Abstract:** *The lane change automation is one of fundamental problems of vehicle control. In the paper we report selected fragments of our research, focused on sensitivity investigations of the controller. This controller is based on a simple reference model of the vehicle lateral dynamics with steering servomechanism inertia effects neglected. Sensitivity studies are implemented by comparative numerical simulations, with the real object (medium capacity semi-autonomic truck) modeled as a 3D multi-body non-linear system. Presented in the paper exemplary results demonstrate the effects of variations of the time constant parameter of the steering servomechanism. The results show the benefits of the vehicle's automated control for the lane change.*

**Keywords:** Lane change automation, Simulation, Modeling, Sensitivity investigations, Inertia effects.

### **1. Introduction**

The lane-change maneuver is one of the basic vehicle's operations out of which sequences of complex maneuvers can be assembled (e.g., avoiding obstacles, vehicle passing). Therefore, this maneuver is a subject of many research papers related to vehicle automation (e.g. Bevan et al., 2010, Gao et al., 2010, Moshuk et al., 2013, Park et al., 2009, Shiller and Sundar, 1996).

Within our research project, analytical and simulation studies were undertaken on the application of the active steering system EPS (Electric Power System equipped with special controller) for automated driving of a semi-autonomous vehicle (truck of medium load capacity). Results of those studies were partially reported in authors' publications (Gidlewski and Żardecki 2015 a, b, 2016 a, b, Gidlewski et al. 2016). So far unpublished results presented in this paper involve sensitivity analysis of the controller action due to inertia effects neglected in the reference model (small time constant of the steering servomechanism).

### **2. Control system for lane change automation**

The lane change process refers to two variables – the displacement of the centre of mass and the angular orientation of the vehicle body with respect to the trajectory of the centre of mass. According to the driving practice as well as the control theory, the steering system signal should have the “bang-bang” form, and the control process can be divided into two phases - transposition and stabilization (Fig. 1).

The steer in the first phase of the process can be carried out partially in an open system (“blindly”, “quickly”) by generating an appropriate profile of the steering wheel rotation angle. Accuracy of this phase of the manoeuvre should be ensured by the reference model. An additional correcting signal is present during this phase of control. Then, a correction of the steering wheel rotation angle is carried out in a closed loop system based on the principle of regulation, by comparing the displacement of the vehicle computed according to the reference model with its measured value. The steer in the second phase has to be carried out completely in the closed loop system, based on comparison of the angular orientation of the vehicle with respect to the roadway axis.

---

<sup>\*</sup> Dr eng. Mirosław Gidlewski, Automotive Industry Institute (PIMOT), University of Technology and Humanities in Radom, miroslaw.gidlewski@uthrad.pl

<sup>\*\*</sup> M.Sc. eng Leszek Jemioł, University of Technology and Humanities in Radom, leszek.jemiol@uthrad.pl

<sup>\*\*\*</sup> Dr hab. eng. Dariusz Żardecki, Military University of Technology (WAT), Automotive Industry Institute (PIMOT), dariusz.zardecki@wat.edu.pl

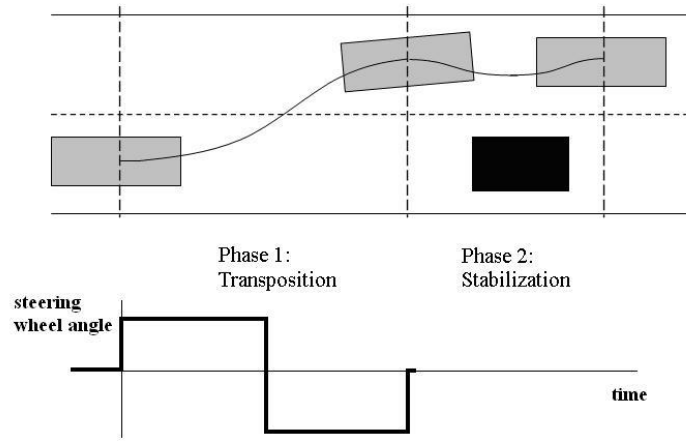


Fig. 1: Concept of time decomposition of the lane change control.

The controller (Fig. 2) generates the steering system signal  $\delta_H(t)$  which is an input signal for the vehicle's steering system (EPS-type servomechanism). This input signal consists of the reference "bang-bang" type signal  $\delta_{HR}(t)$  modified by corrective signals  $\Delta\delta_H(t)$  from two regulators. Parameters of the reference signal generator as well as parameters of the regulators are based on the reference mathematical model of the lane change process. The reference model is a simplified linear dynamical model of the vehicle motion based on the well known "bicycle model" of vehicle lateral dynamics. For the analytical synthesis of the controller algorithm small dynamical inertia effects (producing small time constants) are neglected. Owing to such simplifications, the controller requires only several main vehicle parameters (speed, mass, etc). In practical implementation, the signal  $\delta_H(t)$  has the limitation of its derivative (max 10 rad/s). Therefore, it practically assumes a trapezoidal form.

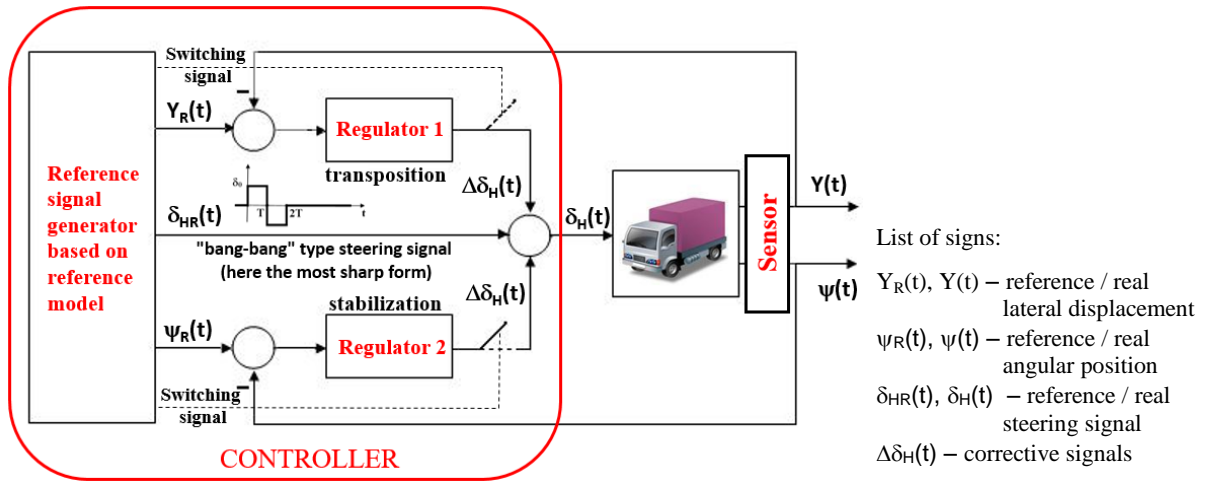


Fig. 2: Block diagram of the automatic control system.

Note that because of the inertia effects, the real steering signal acting on the steered wheels takes a smoothed form. Thus, the real steering signal  $\delta_H^*(t)$  can be treated as the result of transformation of the signal  $\delta_H(t)$  by a typical linear inertia block characterized by the time constant  $T$ . To analyze that effect on the control system action, sensitivity investigations are necessary.

### 3. Sensitivity investigations of the control system

In order to evaluate the performance of the control system, extensive simulations of the lane change process have been conducted with the use of a comprehensive model of the STAR 1142 medium truck (3D multi-body non-linear system) as a virtual plant to be controlled in accordance with the developed algorithms. The tests carried out to assess controller's sensitivity to various possible model inaccuracies have been performed in accordance with the schematic diagram shown in Fig. 3. In those tests, two simulations have been carried out for each case: one based on the nominal (initial) model and another based on the model modified by detuning its parameters, adding some disturbances, etc. Based on those simulation results, numerical indexes  $W_X$  are additionally introduced as relative sensitivity measures.

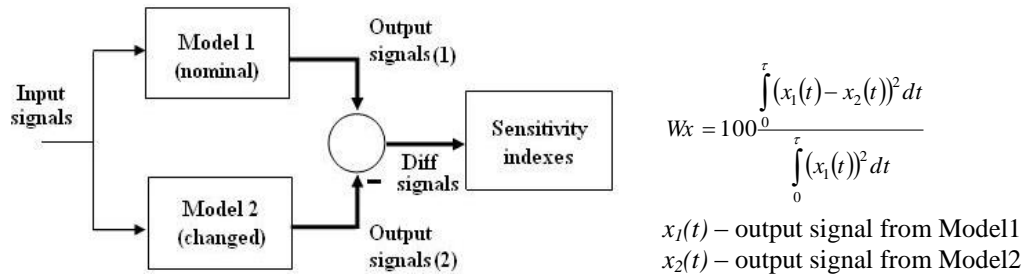


Fig. 3: Block diagram visualizing the simulation tests for the sensitivity analysis purposes.

In the studies, when the subject of the sensitivity analysis concerns the time constant effect, the nominal model works with  $T = 0$ , while the modified model works with  $T > 0$ . For given  $T$ , the sensitivity indexes, especially  $W_{\delta H^*}$ ,  $W_Y$ , and  $W_{\psi}$ , express the effect and significance of the time constant.

Exemplary simulation results presented in Fig. 4 and indexes values demonstrate the effects of variations of the time constant on the lane change process. In this study, the vehicle (here fully loaded truck) was driven on a wet asphalt road ( $\mu = 0.3$ ) with the constant speed  $V = 70$  km/h. For better understanding the role of regulators, the results are presented for the controller working without and with the regulators.

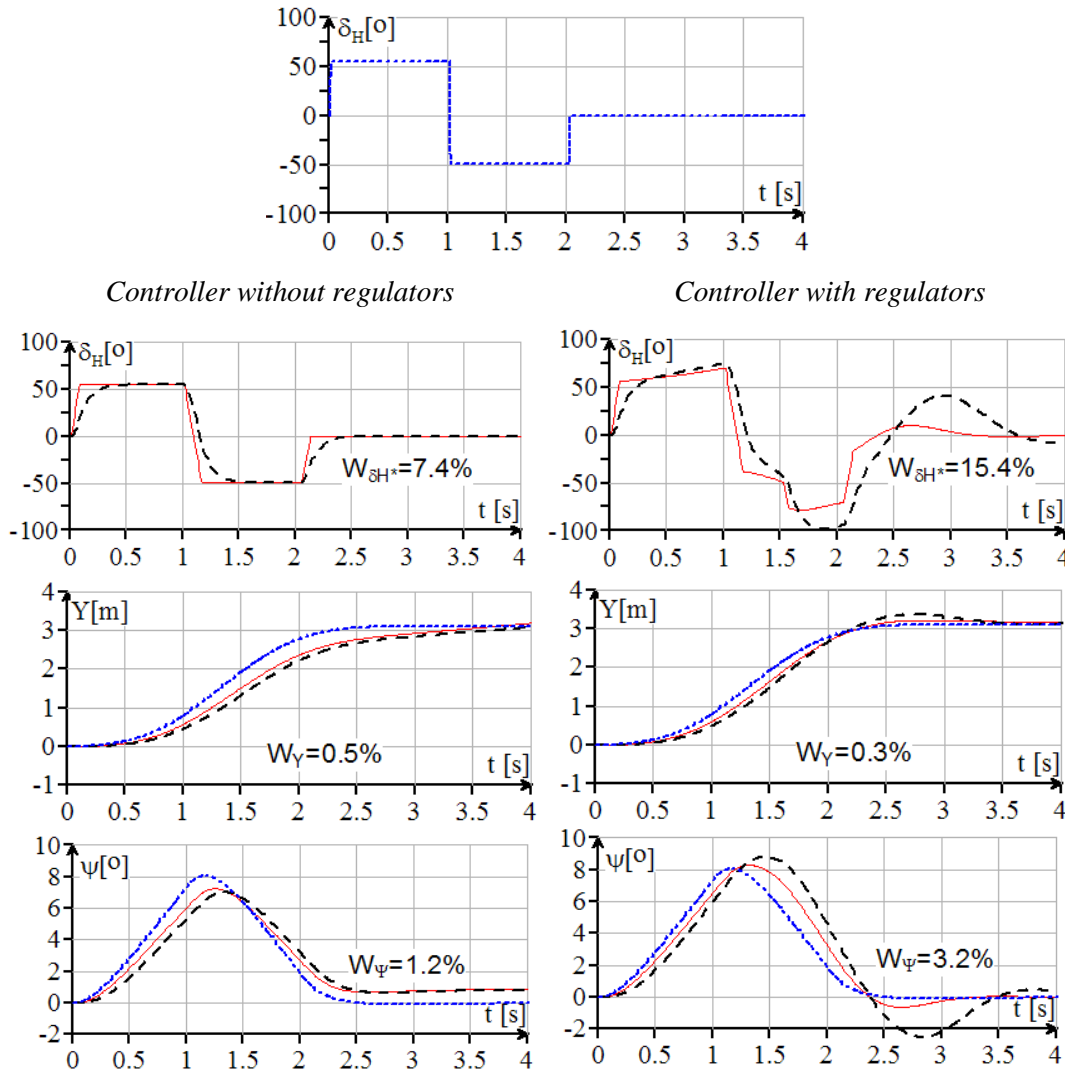


Fig. 4: Effects of time constant  $T$  variation.

Dotted line – for reference signals, solid line – when  $T = 0$  s, dashed lines – when  $T = 0.1$  s.

The values of indexes  $W_{\delta H^*}$ ,  $W_Y$ ,  $W_{\psi}$  presented in Tab. 1 have been computed from the signals obtained for various conditions of vehicle motion (3 different speeds  $V$ , 3 different tire-road friction coefficients  $\mu$ ). In those studies the truck was loaded, and the controller was working with the regulators.

Tab. 1: Values of sensitivity indexes for various speeds and tire-road friction coefficients.

	$\mu = 0.1$	$\mu = 0.2$	$\mu = 0.3$
$V = 16.67 \text{ m/s}$ (60 km/h)	$W_{\delta H^*} = 10.8 \%$ $W_Y = 0.3 \%$ $W_\psi = 1.7 \%$	$W_{\delta H^*} = 13.3 \%$ $W_Y = 0.3 \%$ $W_\psi = 2.4 \%$	$W_{\delta H^*} = 15.3 \%$ $W_Y = 0.3 \%$ $W_\psi = 3.1 \%$
$V = 19.44 \text{ m/s}$ (70 km/h)	$W_{\delta H^*} = 11.0 \%$ $W_Y = 0.3 \%$ $W_\psi = 1.8 \%$	$W_{\delta H^*} = 13.6 \%$ $W_Y = 0.3 \%$ $W_\psi = 2.5 \%$	$W_{\delta H^*} = 15.4 \%$ $W_Y = 0.3 \%$ $W_\psi = 3.2 \%$
$V = 22.22 \text{ m/s}$ (80 km/h)	$W_{\delta H^*} = 13.0 \%$ $W_Y = 0.3 \%$ $W_\psi = 2.0 \%$	$W_{\delta H^*} = 14.3 \%$ $W_Y = 0.2 \%$ $W_\psi = 2.5 \%$	$W_{\delta H^*} = 15.2 \%$ $W_Y = 0.2 \%$ $W_\psi = 3.2 \%$

#### 4. Conclusions

The results of simulations and the sensitivity analysis show that:

- The regulators are necessary for the proper operations of the controller.
- The algorithm of the controller with regulators functions well even with the small inertia effects of the EPS steering system neglected.
- The algorithm of the controller with regulators operates well for various conditions of vehicle motion.
- The method of automatic control of the lane change manoeuvre based on the controller equipped with regulators can be an attractive idea for developers of active steering systems that enhance active safety of cars and trucks.

#### References

- Bevan, G.P., Gollee, H. and O'Reilly, J. (2010) Trajectory generation for road vehicle obstacle avoidance using convex optimization. Proceedings of the Institute of Mechanical Engineers Part D – Journal of Automobile Engineering, Vol. 224 (4).
- Gao, Y., Lin, T., Borrelli, F., Tseng, E. and Hrovat, D. (2010) Predictive control of autonomous ground vehicles with obstacle avoidance on slippery roads. Dynamic Systems and Control Conference, available on the Internet.
- Gidlewski, M. and Żardecki, D. (2015a) Automatic Control of Steering System During Lane Change. Proceedings of ESV'2015 Conference in Gothenburg, Sweden, available on the Internet.
- Gidlewski, M. and Żardecki, D. (2015b) Influence of Nonlinearity Simplifications in a Reference Model of a Motor Vehicle on the Automatic Control of the Vehicle Steering System During a Lane-change Manoeuvre. Proceedings of 13th International Conference Dynamical Systems - Theory and Applications DSTA'2015 (Dynamical Systems, Control and Stability), Lodz, Poland.
- Gidlewski, M., Jemioł L. and Żardecki, D. (2016) Simulation Investigation of the Dynamics of the Process of Sudden Obstacle Avoiding by a Motor Vehicle. The Archives of Automotive Engineering, Vol. 73, No. 3,
- Gidlewski, M. and Żardecki, D. (2016a) Simulation-Based Sensitivity Studies of a Vehicle Motion Model. Proceedings of 20<sup>th</sup> International Scientific Conference Transport Means 2016, Juodkrante, Lithuania, available on the Internet.
- Gidlewski, M. and Żardecki, D. (2016b) Investigation of vehicle motion control process due to the linearization of the lateral dynamics reference model used in the controller. Mechanics Research Communications, Elsevier, to be published, now available on the Internet.
- Moshchuk, N., Shih-Ken Chen, Zagorski, C. and Chatterjee A. (2013) Path planning for collision avoidance maneuver. Proceedings of the ASME 2013 International Mechanical Engineering Congress and Exposition IMECE2013, San Diego, California.
- Park, J.M., Kim, D.W., Yoon, Y.S., Kim, H.J. and Yi, K.S (2009) Obstacle avoidance of autonomous vehicles based on model predictive control. Proceedings of the Institute of Mechanical Engineers Part D – Journal of Automobile Engineering, Vol. 223.
- Shiller, Z. and Sundar, S. (1996) Optimal Emergency Maneuvers Of Automated Vehicles. Research Reports California Partners for Advanced Transit and Highways (PATH) – UC Berkeley.



**VALIDATION OF THE FEM-BASED STRESS ANALYSIS OF AN INNOVATIVE  
LOAD-BEARING STRUCTURE OF AIR-ASSISTED SEED DRILLS WITH  
ELECTRONIC SEEDING CONTROL**

**L. Gierz\***

**Abstract:** *The paper presents a validation of the FEM analyses based on the tensometric method. The model of the load-bearing frame used in the research has been described with detailed location of the tensometers. The analysis includes the development of the load characteristics based on the operating conditions data. The comparative analysis of the results has provided information related to the distribution of stresses in the frame and has confirmed the significance of the results of the simulation with an acceptable level of error. The authors specifically focused on the presentation of the implementation of loads for the case of field sowing.*

**Keywords:** Modeling, Load-bearing frame, FEM analysis, Tensometry.

## **1. Introduction**

Reaching high efficiency of sowing as well as other farming activities is possible only through increasing of the cruising speed and the operating width of the machinery. Increasing the cruising speed is, however, limited by dynamic phenomena that deteriorate the quality of the machine operation, increase equipment loads and unit consumption of energy. Hence, in order to achieve high efficiency, machines of increasingly greater operating width are designed. With the operating width exceeding 3 meters, it is necessary to apply a folded frame system, widely used in large air-assisted seeding equipment (Rutkowski et al., 2005, Markowski et al., 2013).

The folded frames pose a variety of durability-related problems. In an experimental mechanical-pneumatic seed drill of the operating width of 4 m, developed by our team within the NR03-0021-06/2009 development project, a special frame of patented design was applied PL 395969 (2014). The drill coulter beam in this model is divided into two segments folded for transport in the horizontal plane on the side of the seeding drill (Kęska et al., 2012). Two beamed coulters are designed in such a manner that in each of them a pressure accumulator is located with a patented system of coulter pressure system PL 396735 (2013).

This type of design has not yet been applied in the seeding equipment, which is why before it was manufactured, its durability was precisely validated with the finite elements method. This method is currently the most widely applied and the most effective method of durability calculations of load-bearing machinery structures. It allows analyses of a variety of load-bearing structures of complex geometry subjected to loads in the form of concentrated forces, loads originating in reciprocal influence of components as well as the inertia forces and gravity (Chodurski et al., 2015, Szczepaniak, 2008, Łodygowski et al. 1994). When analyzing previous achievements related to the discussed design, the authors also dealt with the problem of principles of design and durability analysis of the equipment (Zienkiewicz & Taylor, 2005) using FEM and numerical analysis (Karayel et al., 2004, Kukielfka et al., 2014) with mathematical modeling and optimization (Keska et al., 2011, and Zastempowski et al., 2014).

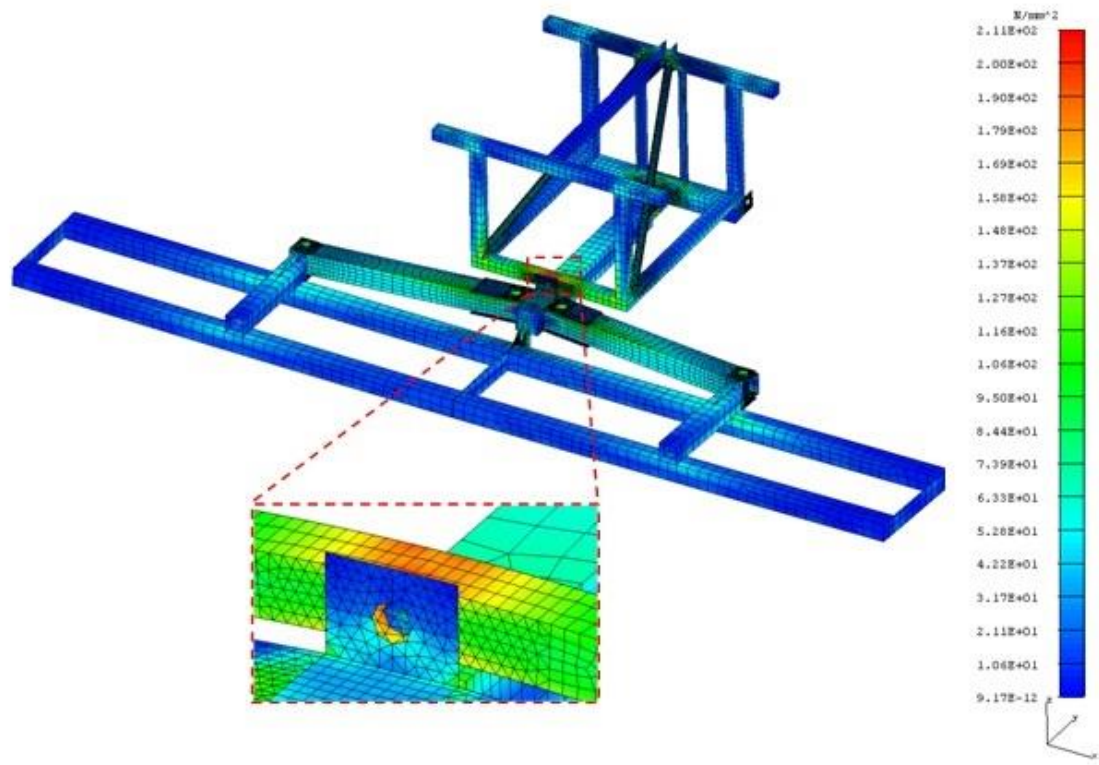
Despite the fact the finite elements method is getting increasingly accurate, the results obtained from the simulation may include a significant level of error. The error may result from the adopted assumptions such as: loads or lack of accuracy in the development of the model etc. Therefore, there is a significant margin of uncertainty of the results of the calculations. This can be reduced by performing empirical

---

\* Assist. Prof. Łukasz Gierz, PhD.: Poznań University of Technology, ul. Piotrowo 3, 60-965Poznan, Poland, Institute of Machines and Motor Vehicles lukasz.gierz@put.poznan.pl

research validating the calculations. When analyzing the works performed thus far, one may encounter a variety of methods validating the strength of the equipment: preliminary strength calculations already at the stage of conceptual design, simulation research utilizing mathematical modeling (Zastempowski et al., 2015) or tensometric measurements of physical objects.

The first stage for the works were the FEM calculations, for which the renowned I-DEAS software was utilized. Example stresses reduced according to the Huber von Mises hypothesis (Ellobody et al., 2014, Zienkiewicz et al., 2005) have been shown in Fig. 1.



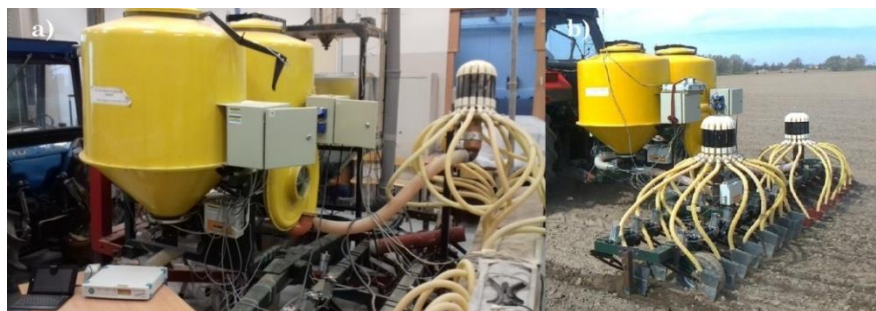
*Fig. 1: Stresses reduced according to the Huber von Mises hypothesis.*

In the field tests of the seeding equipment no visible damage or plastic deformations of the frame were observed.

In order to increase the level of confidence regarding the theoretical calculations, an empirical validation of the FEM calculations was carried out by measuring the actual frame deformations at selected points with the tensometric equipment.

## 2. Methods

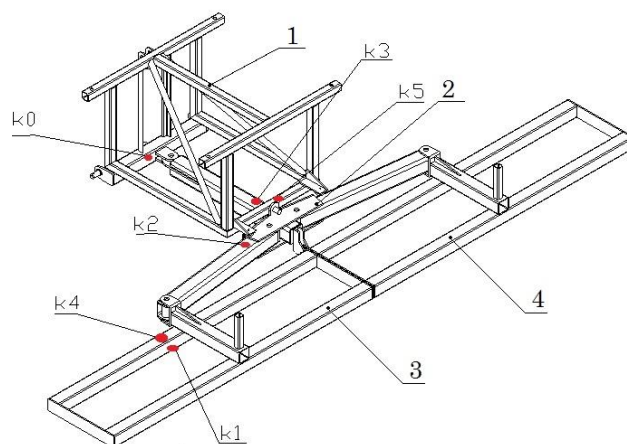
The experimental research was carried out in the laboratory at Poznan University of Technology and under field conditions. The test seeding was performed in the spring of 2013 on a farm in Gwarzewo near Poznan on a sandy soil prepared for seeding of oat and wheat. Fig. 2 presents the seeding equipment a) on the test stand and b) under field tests.



*Fig. 2: Tensometric measurements of the load-bearing frame: a) laboratory; b) field.*

The tensometers were placed on the outer walls of the load-bearing frame profiles at six points most exposed to the load. A diagram of the location of the tensometers has been shown in Fig. 3. The points were selected based on previously performed FEM simulations on the original version of the frame (Gierz et al., 2011).

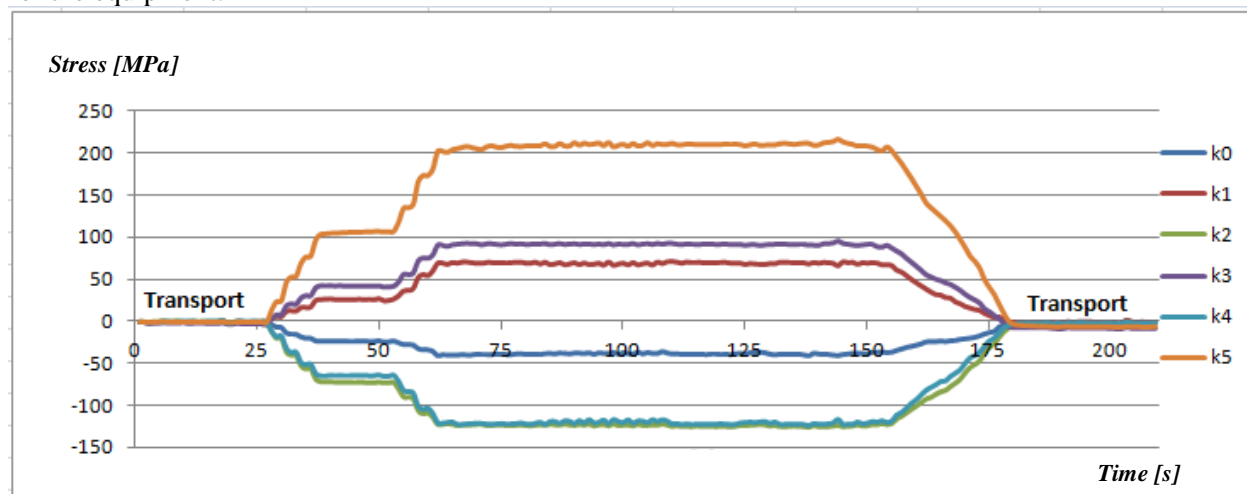
The measurements were carried out with an 8 channel Spider 8 by HBM connected with a portable computer via an RS232 cable. The measurement equipment was fitted on the seeder and powered from the power generator located in the front of the tractor serving the purpose of providing power to the seeder blower and all of its electronic components. For the operation of the tensometric bridges, proprietary software was used that supported HBM systems. The software was developed by Institute of Machines and Motor Vehicles of Poznan University of Technology.



*Fig. 3: The model support frame and the diagram of the arrangement of the strain gauges:  
1 - backbone, 2 - main frame, 3 - right coulter frame, 4 - left coulter frame,  
k0 - k5 – another set of strain gauges.*

### 3. Results

The result of the empirical research was the determination of the longitudinal deformations and stresses at 6 selected points of the load-bearing seeder frame. The loads exerted on the load-bearing seeder frame during the field test originated from the resistance of the coulters and their pneumatic force as well as the loads coming from the seed accumulators. As can be seen in Fig. 4, the loads coming from the weight of the components hung on the frame are very small and do not exceed 10 MPa for all 6 tensometers (transport). Significant loads, however, reaching 220 MPa for the most exposed fragment of the frame, occur during seeding. Significant stress of the frame was observed at point k2 and at point k4 of the beam where the clamping stresses reach 125 MPa. The stresses at the other points are low and are not hazardous for the equipment.



*Fig. 4: Curves of the stresses for the load-bearing frame of a mechanical-pneumatic seeder in the operating and transport modes.*

#### 4. Conclusions

The presented results of stress measurements obtained with the tensometric method are very close to the analogical results obtained in the FEM simulations, which renders the presented mathematical model of the equipment and the loads exerted on the frame sufficiently adequate. The greatest difference between the results of the FEM calculations and the tensometric measurements remains in the range of 14 %. The analyses and measurements performed within this work have confirmed that the tested object has sufficient durability and has a significant stress reserve at many points, which enables its further optimization. The field tests have also confirmed the above. As the results indicate, none of the 6 measurement points recorded an excess of admissible stress in both the material and the welded joints. The results of the measurements will be of particular use in the optimization of the design of the seeder frame, and generally, for further improvement of seeders

#### Acknowledgements

The research was supported by statutory resources appropriated to Institute of Machines and Motor Vehicles, Poznań University of Technology as “The Grant for Young Researchers” No.05/51/DSMK/3477.

#### References

- Chodurski, M., Dębski, H., Samborski, S. and Teter, A. (2015) Numerical strength analysis of the load-bearing frame of a palletizing robot's universal head. *Eksplotacja i Niezawodność – Maintenance and Reliability*; 17 (3): 374–378, <http://dx.doi.org/10.17531/ein.2015.3.7>.
- Gierz, Ł., Kęska, W., Gierz, Sz. and Gierz, K. (2011) Modelling and computer analysis of superstructure frame strength of prototype pneumatic seed drill adapted for precision agriculture. *Journal of Research and Applications in Agricultural Engineering*, Poznań, Vol. 56(3), pp. 92-96, (in Polish).
- Karayel, D., Barut, Z.B. and Ozmerzi, A. (2004) Mathematical modeling of vacuum pressure on a precision seeder. *Biosystems Engineering*. 87: 437-444.
- Kęska, W. and Gierz, Ł. (2011) Mathematical Modeling and Komputer Simulation of Sowing, *Proceedings of 69 International Conference on Agricultural Engineering Land TECHNIK AgEng 2011 nt. “Solutions for Intelligent and Sustainable Farming”*, VDI\_Berichte Nr 2124.2011, Hannover, Germany, pp. 459-464.
- Kęska, W., Feder, S., Kośmicki, Z., Włodarczyk, K., Gierz, Ł. and Selech, J. (2012) Experimental mechanical-pneumatic seed drill for sowing grain with electronic sowing control. *Journal of Research and Applications in Agricultural Engineering*, Poznań, Vol. 57(2), pp. 113-115, (in Polish).
- Kukielka, L., Kukielka, K., Kulakowska, A., Patyk, R., Malag, L. and Bohdal, L. (2014) Incremental modelling and numerical solution of the contact problem between movable elastic and elastic/visco-plastic bodies and application in the technological processes. *Applied Mechanics and Materials*, Vol. 474, pp. 159-164.
- Łodygowski, T. and Kąkol, W. (1994) Finite element method in selected issues of mechanical engineering structures, *The script Poznan University of Technology*, (in Polish).
- Markowski, P., Rawa, T., Akielewicz, A., Golder, M., Lipiński, A. and, Anders, A. (2013). Comparative analysis of Longitudinal irregularity of wheat seeding with a Universal seeder and cultivation-seeding aggregate. *Agricultural Engineering* 3(145) T.1, pp. 233-241, (in Polish).
- Rutkowski, J. and Szczepaniak, J. (2005) Simulations and analysis of virtual computer models in application to series of types of agricultural rollers. *Journal of Research and Applications in Agricultural Engineering*, Vol. 50(1). pp. 5-9, (in Polish).
- Szczepaniak, J. (2008) Contemporary tools aiding projecting of agricultural machinery. *Agricultural Technology Horticultural and Forest*. Nr 1. pp. 20-24, (in Polish).
- Zienkiewicz, O.C. and Taylor R.L. (2005) *The Finite Element Method For Solid And Structural Mechanics*, Butterworth-Heineman. pp. 440-450.
- Zastempowski, M. and Bochat, A. (2014) Modeling of cutting process by the shear-finger cutting block. *ASABE Applied Engineering in Agriculture*. Vol. 30, No. 3, pp. 347-353.
- Zastempowski, M. and Bochat, A. (2015) Mathematical model ling of elastic deflection of a tubular cross-section. *Polish Maritime Research* No.2 (86), Vol. 22, pp. 93-100.
- Gierz, Ł., Kęska, W. and Gierz, Sz. (2014) Folding beam. PL 395969.
- Gierz, Ł., Kęska, W., Selech, J. and Zakrzewska, G. (2013) The team to press the coulter on the ground. PL 396735.

## EXACT 3-NODED TIMOSHENKO BEAM FINITE ELEMENT WITH ENHANCED STRAIN FIELD – A MAGIC ROLE OF GAUSS POINTS

W. Gilewski\*, P. Obara\*\*

**Abstract:** *The present paper is dedicated to the idea of enhanced strain field in development of multi-node Timoshenko beam finite element. It is proved that it is possible to obtain exact stiffness matrix for 3-noded beam element with carefully selected substitute strain field and enrichment points. The selection can be recommended for more sophisticated analysis of plates and shells.*

**Keywords:** Timoshenko beam, Finite element, Enhanced strain, Gauss points.

### 1. Introduction

Beams, plates and shells are widely applied in engineering structures. However, there are several difficulties with discretization procedures employed to calculate such elements – among others, locking phenomena and spurious strains (Gilewski, 2005), which are of major importance. Development of high-performance finite elements for moderately thick beams, plates and shells dates back to 1970. It was followed by hundreds of publications concerning different conceptions for finite elements that were supposed to deal with the appearing difficulties.

According to the present state of the art, one of the best conception is a formulation of the finite element with enhanced strain field (Bathe et al., 1989; Brezzi et al., 1989; Dvorkin and Bathe, 1984; Simo and Rifai, 1990). In this formulation, spurious strains are approximated independently of displacements, and after that they are “sewed” with strains resulting from displacements in the selected amount of points. The conception has now reliable mathematical foundations in the form of theorems of solution existence and uniqueness, or several variational formulations (Bathe et al., 1989; Borja, 2008; Brezzi et al., 1989; Militello and Felippa, 1990). The idea of enhanced strain fields is still developed for shell elements (Cesar, 2002; Chościelewski and Witkowski, 2006).

The present study deals with construction of three-noded finite elements with enhanced strain fields as a base study for plate/shell multi-node elements. Arbitrary enrichment points are applied. It has been proved that using Gauss-Legendre points, an exact three-noded finite element is obtained.

### 2. Algorithm

Taking into consideration a Timoshenko beam problem, the following values may be defined: displacements  $\mathbf{u}(\xi) = \{w(\xi), \phi(\xi)\}$ , strains  $\boldsymbol{\varepsilon}(\xi) = \{\kappa(\xi), \gamma(\xi)\}$  and stresses (internal forces)  $\boldsymbol{\sigma}(\xi) = \{M(\xi), Q(\xi)\}$ . In the above notation, a dimensionless coordinate system is used:  $\xi = x/a$ , where  $a$  is a characteristic dimension (equal to the half of the element length in further considerations). The geometric relations between strains and displacements are as follows:

$$\kappa = -\frac{1}{a} \frac{d\phi}{d\xi} = \mathbf{D}_1 \mathbf{u}; \quad \mathbf{D}_1 = \begin{bmatrix} 0 & -\frac{1}{a} \frac{d}{d\xi} \end{bmatrix}, \quad (1)$$

---

\* Prof. dr hab. inż. Wojciech Gilewski: Institute of Building Engineering, Warsaw University of Technology, Al. Armii Ludowej 16; 00-637 Warsaw; PL, w.gilewski@il.pw.edu.pl

\*\* Dr inż. Paulina Obara: Faculty of Civil Engineering and Architecture, Kielce University of Technology, Al. Tysiąclecia PP 7; 25-314 Kielce; PL, paula@tu.kielce.pl

$$\gamma = \frac{1}{a} \frac{dw}{d\xi} - \phi = \mathbf{D}_2 \mathbf{u}; \quad \mathbf{D}_2 = \begin{bmatrix} \frac{1}{a} \frac{d}{d\xi} & -1 \end{bmatrix}, \quad (2)$$

and the constitutive equations are:  $M = EJ\kappa$ ,  $Q = kGA\gamma$ , where  $M$  is a bending moment,  $Q$  is a shear force,  $E$  is Young's modulus,  $J$  is a moment of inertia,  $k$  is a shear correction factor,  $G$  is a shear modulus,  $A$  is a cross-sectional area.

A standard approximation of an element displacement field  $\mathbf{u}(\xi) = \mathbf{N}(\xi) \mathbf{q}$  and a strain field:

$$\kappa(\xi) = \mathbf{B}_1(\xi) \mathbf{q}, \quad \mathbf{B}_1 = \mathbf{D}_1 \mathbf{N}, \quad \gamma(\xi) = \mathbf{B}_2(\xi) \mathbf{q}, \quad \mathbf{B}_2 = \mathbf{D}_2 \mathbf{N} \quad (3)$$

are used. Transverse shear strains (3), as a function of dimensionless coordinates  $\alpha_i$ , can be calculate at enrichment points:  $x_i = \alpha_i a$  for  $i = 1, 2, \dots, N$ :

$$\gamma(\alpha_i) = \mathbf{B}_2(\alpha_i) \mathbf{q}. \quad (4)$$

An independent interpolation of the enhanced transverse shear strain field is applied:

$$\gamma_{enhanced} = C_1 + C_2 \xi + C_3 \xi^2 + \dots + C_N \xi^{N-1} = \mathbf{p}^T(\xi) \mathbf{C}, \quad (5)$$

where  $\mathbf{p}(\xi) = \{1, \xi, \xi^2, \dots, \xi^{N-1}\}$ ,  $\mathbf{C} = \{C_1, C_2, C_3, \dots, C_N\}$ .

Assuming equality of strain fields at each enrichment point:

$$\mathbf{p}^T(\alpha_i) \mathbf{C} = \mathbf{B}_2(\alpha_i) \mathbf{q}; \quad i = 1, 2, \dots, N, \quad (6)$$

for all of the following enrichment points we obtain:

$$\mathbf{P} \mathbf{C} = \tilde{\mathbf{B}} \mathbf{q}, \quad (7)$$

where

$$\mathbf{P} = \begin{bmatrix} \mathbf{p}^T(\alpha_1) \\ \mathbf{p}^T(\alpha_2) \\ \dots \\ \mathbf{p}^T(\alpha_N) \end{bmatrix}, \quad \tilde{\mathbf{B}} = \begin{bmatrix} \mathbf{B}_2(\alpha_1) \\ \mathbf{B}_2(\alpha_2) \\ \dots \\ \mathbf{B}_2(\alpha_N) \end{bmatrix}. \quad (8)$$

Now the interpolation constants  $\mathbf{C}$  may be calculated as:

$$\mathbf{C} = \mathbf{P}^{-1} \tilde{\mathbf{B}} \mathbf{q}. \quad (9)$$

The enhanced transverse shear strain field can be presented in the following form:

$$\gamma_{enhanced}(\xi) = \mathbf{p}^T(\xi) \mathbf{P}^{-1} \tilde{\mathbf{B}} \mathbf{q} = \mathbf{B}_2^{enhanced}(\xi) \mathbf{q}, \quad (10)$$

where

$$\mathbf{B}_2^{enhanced}(\xi) = \mathbf{p}^T(\xi) \mathbf{P}^{-1} \tilde{\mathbf{B}}. \quad (11)$$

The total strain field is constructed as follows:

$$\boldsymbol{\varepsilon} = \begin{bmatrix} \kappa \\ \gamma_{enhanced} \end{bmatrix} = \begin{bmatrix} \mathbf{B}_1(\xi) \\ \mathbf{B}_2^{enhanced}(\xi) \end{bmatrix} \mathbf{q} = \mathbf{B}_{enhanced} \mathbf{q}. \quad (12)$$

As a next step, one can construct an element stiffness matrix according to the standard procedure employed in a displacement formulation of FEM, with the integration over the element length:

$$\mathbf{K} = \int_{\Omega} \mathbf{B}_{enhanced}^T \mathbf{E} \mathbf{B}_{enhanced} d\Omega. \quad (13)$$

### 3. Three-noded exact beam finite element

A three-noded beam finite element,  $2a$  in length, with natural degrees of freedom is considered:

$$\mathbf{q} = \{w_1 \quad \phi_1 \quad w_2 \quad \phi_2 \quad w_3 \quad \phi_3\}. \quad (14)$$



Applying polynomial interpolation, the shape function matrix can be define as follows:

$$\mathbf{N}(\xi) = \begin{bmatrix} N_1 & 0 & N_2 & 0 & N_3 & 0 \\ 0 & N_1 & 0 & N_2 & 0 & N_3 \end{bmatrix}, \quad (15)$$

where:  $N_1(\xi) = \frac{1}{2}\xi(\xi-1)$ ,  $N_2 = 1 - \xi^2$ ,  $N_3(\xi) = \frac{1}{2}\xi(\xi+1)$ .

For two symmetrically located enrichment points  $\alpha_1 = -\alpha$ ,  $\alpha_2 = \alpha$  and linear enhanced strain field  $\gamma_{enhanced} = C_1 + C_2\xi$ , the following element stiffness matrix is obtained:

$$\mathbf{K} = \begin{bmatrix} \frac{7H}{6a} & -H\frac{3\alpha^2+2}{6} & -\frac{4H}{3a} & H(\alpha^2-1) & \frac{H}{6a} & -H\frac{3\alpha^2-2}{6} \\ -H\frac{3\alpha^2+2}{6} & \frac{7EJ + Ha^2(3\alpha^4+1)}{6a} & \frac{2H}{3a} & \frac{-4EJ - 3Ha^2\alpha^2(\alpha^2-1)}{3a} & H\frac{3\alpha^2-2}{6} & \frac{EJ + Ha^2(3\alpha^4-1)}{6a} \\ -\frac{4H}{3a} & \frac{2H}{3a} & \frac{8H}{3a} & 0 & -\frac{4H}{3a} & -\frac{2H}{3a} \\ H(\alpha^2-1) & \frac{-4EJ - 3Ha^2\alpha^2(\alpha^2-1)}{3a} & 0 & \frac{8EJ + 6Ha^2(\alpha^2-1)^2}{3a} & -H(\alpha^2-1) & \frac{-4EJ - 3Ha^2\alpha^2(\alpha^2-1)}{3a} \\ \frac{H}{6a} & H\frac{3\alpha^2-2}{6} & -\frac{4H}{3a} & -H(\alpha^2-1) & \frac{7H}{6a} & H\frac{3\alpha^2+2}{6} \\ -H\frac{3\alpha^2-2}{6} & \frac{EJ + Ha^2(3\alpha^4-1)}{6a} & -\frac{2H}{3a} & \frac{-4EJ - 3Ha^2\alpha^2(\alpha^2-1)}{3a} & H\frac{3\alpha^2+2}{6} & \frac{7EJ + Ha^2(3\alpha^4+1)}{6a} \end{bmatrix} \quad (16)$$

The crucial aspect is to select the location of enrichment points. A criterion applied in this study consists in comparing maximum deflection of a cantilever beam loaded with a concentrated force (Fig. 1a), obtained using one finite element with the enhanced strain field, and an exact solution from the Timoshenko beam theory.

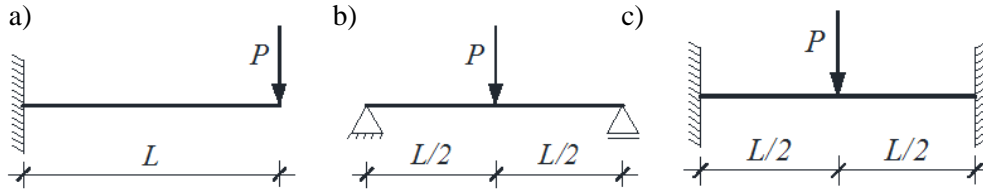


Fig. 1: Timoshenko beam: a) Cantilever; b) Simply supported; c) Clamped.

The results are as follows:

- exact solution:

$$w_{\max}^{exact} = \frac{2Pa^3(4-3\mu)}{3EJ(1-\mu)}, \quad \mu = \frac{3\gamma}{1+3\gamma}, \quad \gamma = \frac{EJ}{Ha^2}, \quad (17)$$

- enhanced solution – 1 finite element:

$$w_{\max}^{enhanced} = \frac{2Pa}{H} + \frac{Pa^3(7-6\alpha^2+3\alpha^4)}{2EJ}. \quad (18)$$

Comparison of the received solutions, (17) and (18), leads to biquadratic equation:

$$3\alpha^4 - 6\alpha^2 + \frac{5}{3} = 0. \quad (19)$$

Solutions of the Eq. (19) are superconvergence points of transverse shear strains enrichment:

$$\alpha^{1,2} = \pm\sqrt{\frac{1}{3}}, \quad \alpha^{3,4} = \pm\sqrt{\frac{5}{3}}. \quad (20)$$

The first two solutions correspond to the location of Gauss-Legendre points. The third and the fourth solution are located outside the finite element. In all cases, we obtain the exact solution of a cantilever beam problem, using one finite element with the enhanced strain field. Mesh refining does not influence on solution.

The exact stiffness matrix is following:



$$\mathbf{K}_{e2} = \begin{bmatrix} \frac{7H}{6a} & -H\frac{1}{2} & -\frac{4H}{3a} & -H\frac{2}{3} & \frac{H}{6a} & H\frac{1}{6} \\ -H\frac{1}{2} & \frac{21EJ+4Ha^2}{18a} & \frac{2H}{3} & \frac{-108EJ-4Ha^2}{81a} & -H\frac{1}{6} & \frac{3EJ-2Ha^2}{18a} \\ \frac{4H}{3a} & \frac{2H}{3} & \frac{8H}{3a} & 0 & -\frac{4H}{3a} & -\frac{2H}{3} \\ -H\frac{2}{3} & \frac{-108EJ-4Ha^2}{81a} & 0 & \frac{72EJ+24Ha^2}{27a} & H\frac{2}{3} & \frac{-12EJ-6Ha^2}{9a} \\ \frac{H}{6a} & -H\frac{1}{6} & -\frac{4H}{3a} & H\frac{2}{3} & \frac{7H}{6a} & H\frac{1}{2} \\ H\frac{1}{6} & \frac{3EJ-2Ha^2}{18a} & -\frac{2H}{3} & \frac{-12EJ-6Ha^2}{9a} & H\frac{1}{2} & \frac{21EJ+4Ha^2}{18a} \end{bmatrix}. \quad (21)$$

It is possible to check that the calibration of enrichment points on the cantilever beam (matrix (21)) gives also exact results for other boundary conditions. One can receive exact solution for simply supported (Fig. 1b) as well as clamped (Fig. 1c) beams with the use of single finite element.

#### 4. Conclusions

The present paper presents construction of stiffness matrix for a 3-noded finite element of a moderately thick beam with enhanced strain fields. Applying linear substitute strains and enrichment points:  $\alpha^{1,2} = \pm\sqrt{1/3}$  or  $\alpha^{3,4} = \pm\sqrt{5/3}$ , the exact three-noded finite element is received. The enrichment points can be recommended for more sophisticated analysis of plates and shells.

#### References

- Bathe, K.J., Brezzi, F. and Cho, S.W. (1989) The MITC7 and MITC9 plate bending elements. *Computers & Structures*, 32, pp. 797-814.
- Borja, R. (2008) Assumed enhanced strain and the extended finite element methods: A unification of concepts. *Computer Methods in Applied Mechanics and Engineering*, 197, 2789-2803.
- Brezzi, F., Bathe, K.J. and Fortin, M. (1989) Mixed interpolated elements for Reissner - Mindlin plates. *International Journal for Numerical Methods in Engineering*, 68, pp. 1137-1179.
- Cesar de Sa, J.M.A. et al. (2002) Development of shear locking-free shell elements using an enhanced assumed strain formulation. *International Journal for Numerical Methods in Engineering*, 53, pp. 1721-1750.
- Chróścielewski, J. and Witkowski, W. (2006) Four-node semi-EAS element in six-field nonlinear theory of shells. *International Journal for Numerical Methods in Engineering*, 29, pp. 1595-1638.
- Davis, P.J. and Rabinowitz, P. (2007) *Methods of numerical integration*. 2nd ed. Dover Publ., Inc., Mineola, New York.
- Dvorkin, E.N. and Bathe, K.J. (1984) A continuum mechanics based four – node shell element for general non-linear analysis. *Engineering Computations*, 1, pp. 77-88.
- Gilewski, W. (2005) *Correctness of finite elements. From Timoshenko beam to moderately thick plate*. Warsaw University of Technology Publishing House, Warsaw, (in Polish).
- Militello, C. and Felippa, C.A. (1990) A variational justification of the assumed natural strain formulation of finite elements. Part I: Variational principles. *Computers & Structures*, 34, 3, pp. 431-438.
- Militello, C. and Felippa, C.A. (1990) A variational justification of the assumed natural strain formulation of finite elements. Part II: The C-0 four-node plate element. *Computers & Structures*, 34, 3, pp. 439-444.
- Simo, J.C. and Rifai, M.S. (1990) A class of mixed assumed strain methods and the method of incompatible modes, *International Journal for Numerical Methods in Engineering*, 29, pp. 1595-1638.

## THE INFLUENCE OF ORTHOTROPY LEVEL FOR PERPENDICULAR TO GRAIN STRESSES IN GLULAM DOUBLE TAPERED BEAMS

W. Gilewski<sup>\*</sup>, J. Pelczyński<sup>\*\*</sup>

**Abstract:** This paper presents parametric analysis of distribution of the delamination normal stress perpendicular to the grain in double tapered, simply supported beams made of glued laminated timber. The parameters are height of the beam in the apex area and the level of diversity of orthotropic material properties from the isotropy to orthotropy according to the standards of design. The calculations are performed by the finite element method (FEM) in terms of the linear theory of elasticity with plane stress assumption. The results of the FEM calculations are referred to the indications of the design standards.

**Keywords:** Orthotropy, Glulam, Perpendicular to grain stress.

### 1. Introduction

One of the most important feature of the design of double tapered simply supported beams (see Fig. 1) with a glued-laminated timber is a need to consider delaminating action of stress perpendicular to the wood fibers and the possible reinforcement against this stress (Franke et al., 2015; Thelanderson and Larsen, 2003; Vratusa et al., 2011). In traditional calculations of beams this stress is neglected. Design standards provide formulae for normal stresses perpendicular to grain (dependent on the value of bending moment and slope of the beam in apex area) and the extent of their occurrence in the apex zone – the width of the zone is equal to twice the height of the beam (see Fig. 1). In real design the values and the distribution of these stresses depend on the geometry of the beam, the load (including the way of load application on the beam height), and material parameters. The purpose of this study is to evaluate the effect of variation of orthotropic properties of the beam on both the level and distribution of delaminating stresses.

### 2. Modeling

Modeling of the beam is based on a 2D linear theory of elasticity in plane stress condition for seven cases of orthotropic physical properties (Tab. 1). Geometry, load and boundary conditions are shown in Fig. 1.

*Tab. 1: Material parameters.*

Material	E <sub>1</sub> [MPa]	E <sub>2</sub> [MPa]	$\nu_{12}$	G <sub>12</sub> [MPa]
Ort-1 (EN)	12600	420	0.35	780
Ort-2	12600	2450	0.35	1428
Ort-3	12600	4480	0.35	2076
Ort-4	12600	6510	0.35	2724
Ort-5	12600	8540	0.35	3371
Ort-6	12600	10570	0.35	4019
Ort-7 (Isotropy)	12600	12600	0.35	4667

<sup>\*</sup> Prof. Wojciech Gilewski, PhD., DSc.: Institute of Building Engineering, Warsaw University of Technology, Al. Armii Ludowej 16; 00-637, Warszawa; PL, w.gilewski@il.pw.edu.pl

<sup>\*\*</sup> Jan Pelczyński, MSc: Institute of Building Engineering, Warsaw University of Technology, Al. Armii Ludowej 16; 00-637, Warszawa; PL, j.pelczynski@il.pw.edu.pl

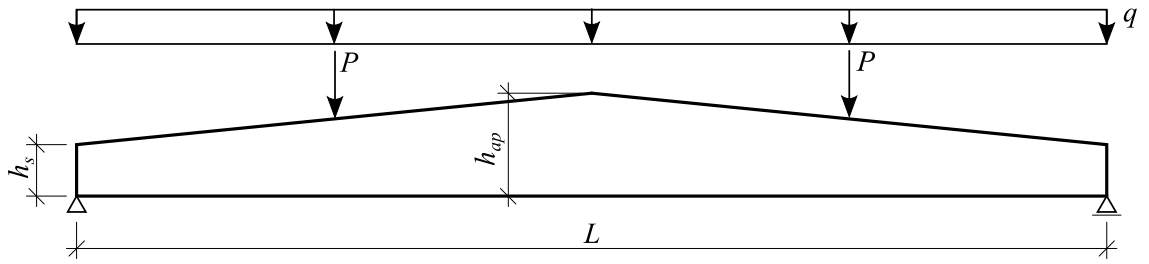


Fig. 1: Geometry, boundary conditions and loads.

The calculations were performed using the Abaqus FEM software (ABAQUS documentation, 2017, Zienkiewicz and Taylor, 2000). Two dimensional 8-node biquadratic solid plane stress elements (CPS8R) with reduced integration were used (Abaqus documentation 2017).

Figs. 2 – 5 present examples of distributions of tensile stresses perpendicular to the fibers for both the largest and lowest beam height considered in the analysis and for four of seven considered material properties loaded with either concentrated forces or distributed load.

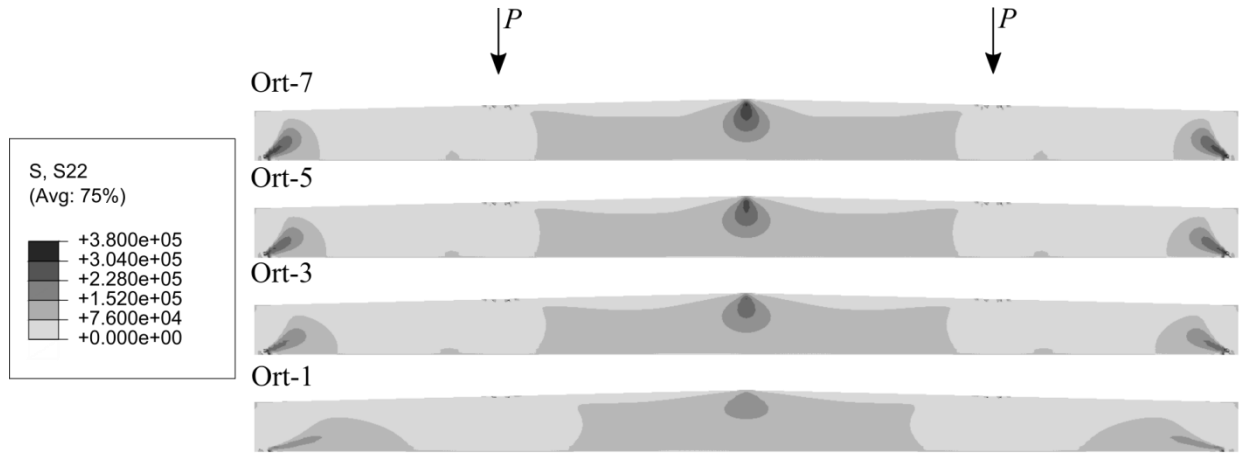


Fig. 2: Positive stress perpendicular to the grain.

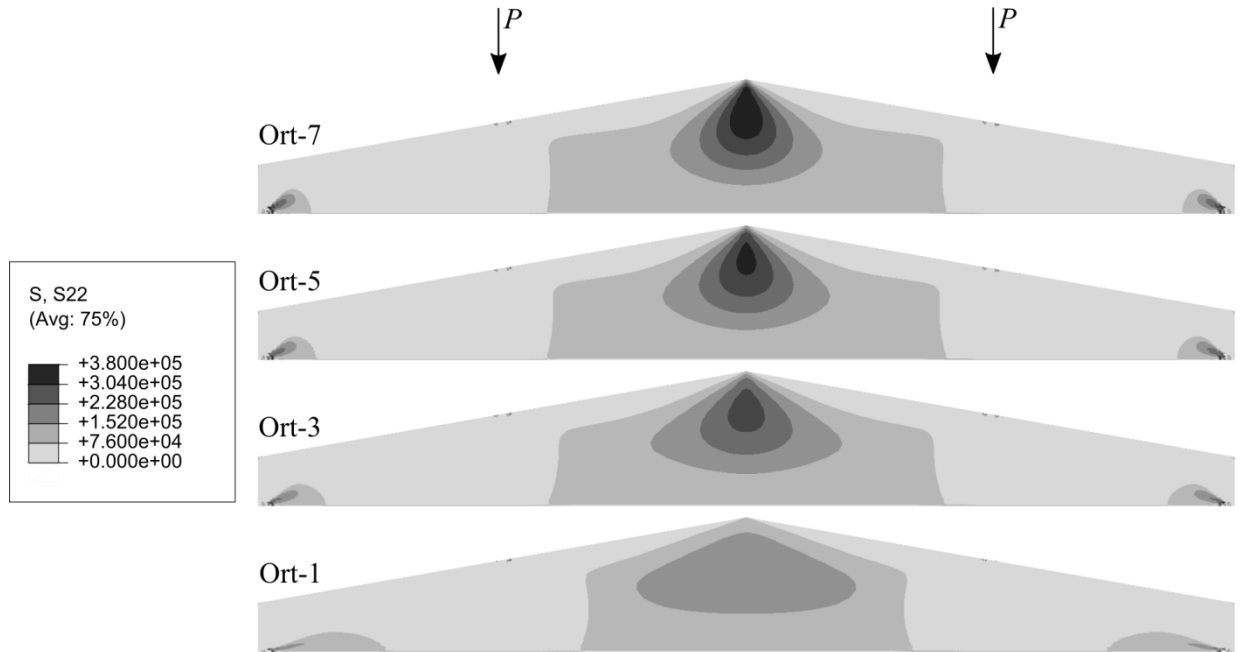


Fig. 3: Positive stress perpendicular to the grain.

The area of strictly positive tensile stress for the beam loaded with two concentrated forces is much wider than twice the height of standard design in the apex area (Figs. 2 and 3). This is particularly noticeable for low apex height. However, the level of the analyzed stresses deserves attention – from this point of view, the area of the zone in the beam of higher apex is wider. The width of the zones of significant stress is similar for different levels of orthotropy. The depth of the zone of significant stress is bigger for materials close to isotropy and is less than half the apex height. Strongly orthotropic properties lead to the lowest stress values. Tensile stresses in the boundary zones are not examined in this study.

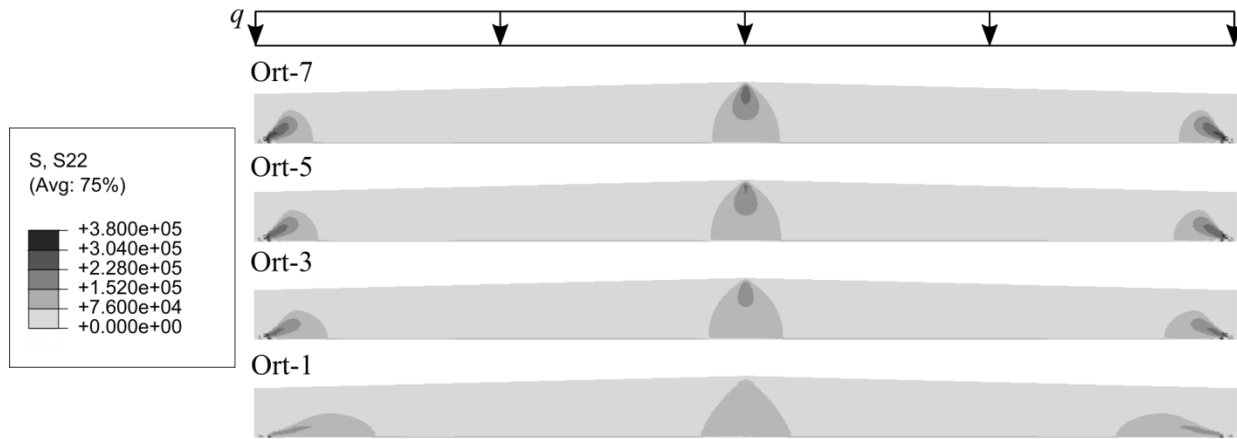


Fig. 4: Maximum stress perpendicular to the grain.

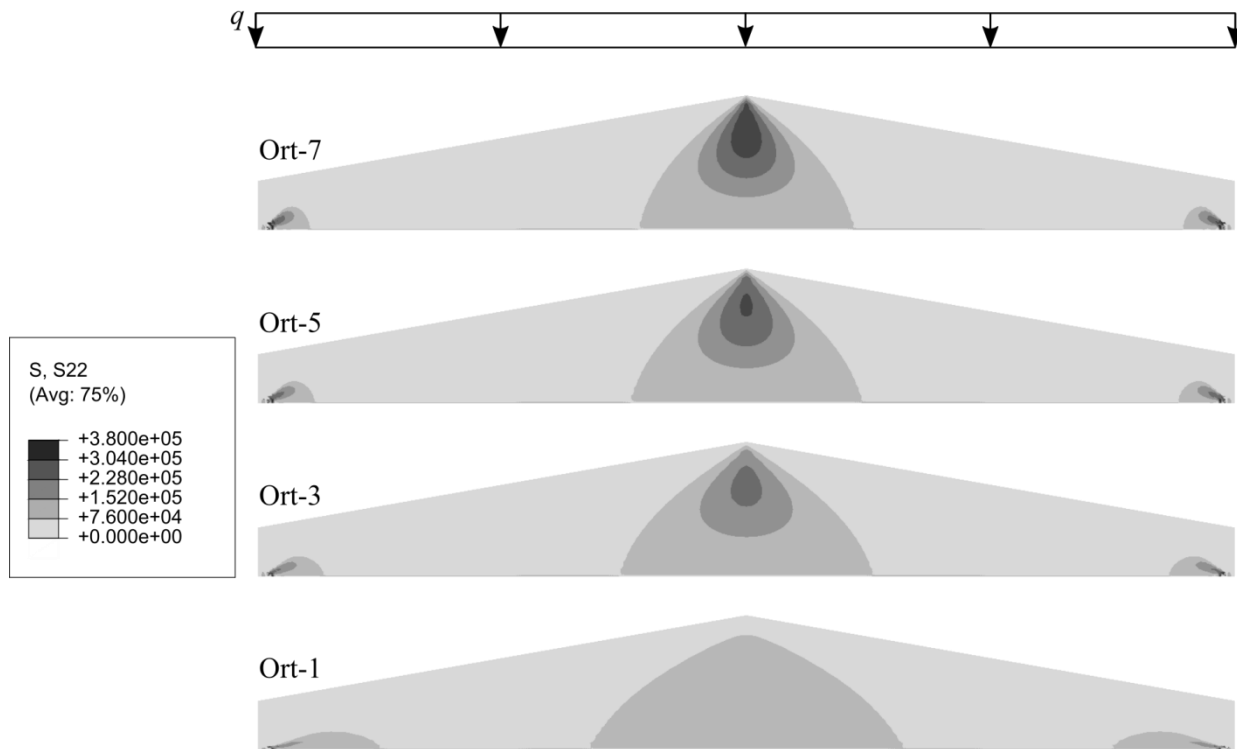


Fig. 5: Maximum stress perpendicular to the grain.

The zone of tensile stresses for uniformly distributed load is smaller than for the concentrated load. For distributed load the width of the zone in both higher and lower beams is close to doubled apex height, what is assumed in design codes. The depth of the relevant stress is smaller the case of uniformly distributed load – the stress is concentrated on the apex. Strong variation of the orthotropic properties leads to the reduction of gradients of stresses perpendicular to grain of the beam.

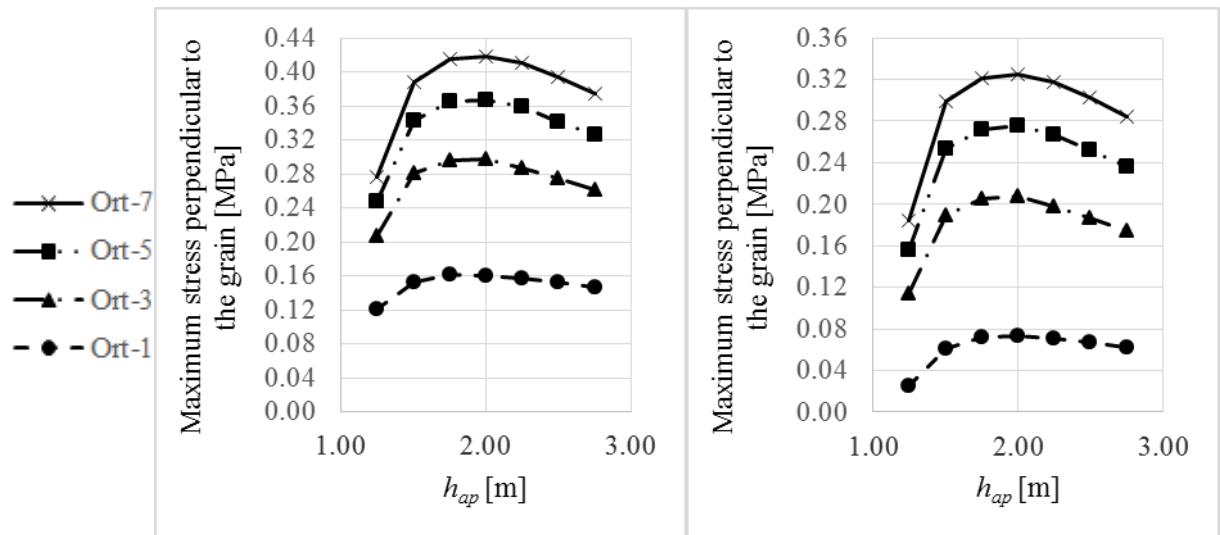


Fig. 6: Maximum stress perpendicular to the grain for a) concentrated forces; b) distributed load.

The maximum values of normal stress perpendicular to the fibers depend on the height of the apex and differentiation of the properties of orthotropy (see Fig. 6). Higher stress values are obtained for materials close to isotropy. Strong orthotropic material properties results in smaller stress variation according to the apex height. It is worth to mention that the greatest value for isotropy occur when the apex height is two times larger than the height in the boundary zone – the extreme moves in the direction of 1.75 for beams with different orthotropic properties, regardless of the type of load (see also Danielsson, 2010).

### 3. Conclusions

The paper presents parametric analysis of values and zones of normal stresses perpendicular to the grain of double tapered simply supported beams made of glued laminated timber. The width of the areas of stresses in the apex area depends on a small extent on diversity of orthotropic properties of the beam. In the extent relevant to the design the width corresponds to the area of standard design. Strong orthotropic material properties reduce the value of positive normal stress gradients and reduces their distribution. A visible impact of the beam geometry on the stress concentrations leads to the conclusion that in the beams with geometry not considered in design codes computational methods within the theory of elasticity are to be applied. The maximum values of normal stress perpendicular to the fibers are much higher for materials close to isotropy. Strong orthotropic material properties result in smaller stress variation according to the apex height.

### References

- ABAQUS Documentation 2017
- Danielsson, H. (2010) Design and perpendicular to grain tensile stress in double-tapered glulam beams, Report of Division of Structural Mechanics, Lund University, Lund, Sweden, 21 p.
- Franke, S., Franke, B. and Harte, A.M. (2015) Failure modes and reinforcement techniques for timber beams – State of the art, Construction and Building Materials, 97, pp. 2-13.
- Thelandersson, S. and Larsen, H.J. (2003) Timber Engineering, John Wiley & Sons, Chichester, England.
- Vratusa, S., Kitek, M. and Kilar, V. (2011) Structural particulars of glued laminated beams of variable height, Drewno, 54 (185), pp. 19-38.
- Zienkiewicz, O.C. and Taylor, R.L. (2000) The finite element method. Vol. 1. The basis, Butterworth-Heinemann, New Jersey.
- EN 1995-1-1:2004, Eurocode 5: Design of timber structures – Part 1-1: General – Common rules and rules for buildings.

## COORDINATIVE PATTERNS AND GAIT STABILITY ACCESSED BY NONLINEAR DYNAMICS APPROACH: A PRELIMINARY STUDY

M. F. Goethel<sup>\*</sup>, J. Mrozowski<sup>\*\*</sup>, J. Awrejcewicz<sup>\*\*\*</sup>

**Abstract:** *The relationship between the trajectories of the pressure center (CoP) and the Mass Center (CoM) is determinant for the human stability during gait. To understand the relationship between these trajectories it is necessary to access the coordinating pattern that is maintained during the performance of this daily activity. Nonlinear dynamics and dynamical systems approaches and methodologies are increasingly being implemented in biomechanics and human movement coordination research. Therefore, the aim of this preliminary study was to investigate the coordinative patterns between the movements of the CoP and the CoM during the human gait, so that in the near future it is possible to propose a new gait stability criterion based on this approach. Using the kinematics and dynamometry, the CoP and CoM trajectories were calculated and then using the continuous relative phase method (CRP) the coordinative patterns of one subject were obtained in 3 gait attempts. The phenomena analyzed showed similarity of amplitude and in the temporal location. The variability of the coordinative patterns was also calculated and this variable inspires the continuity of the study with different samples.*

**Keywords:** Nonlinear dynamics, Coordination, Variability, Stability, Gait.

### 1. Introduction

Harmony is an essential feature of human gait warranting for efficient and smoothed movements during walking (Menz et al., 2003). Gait harmony has been defined as the capacity to transfer the symmetry of human body into alternated, synchronized, symmetric, coordinated and rhythmic movements (Menz et al., 2003).

When we examine the trajectories of the Center of Pressure (CoP) under the feet and the Center of Mass (CoM) of the total body, we see the challenge to the human control system to manage the relationship between these two points (Winter, 2009) (Fig. 1).

Relevant to identifying the nature of coordination changes is the distinction in the dynamical systems approach between order and control parameters (Turvey, 1990). Order parameters identify low-dimensional qualitative states (“macro states”) of the system dynamics, in which changes between states can be induced by manipulating an specific control parameter, such as frequency or velocity (Turvey, 1990). The relative phase between body segments has been identified as an order parameter because of its fundamental reflection of cooperativity between components in the system (“micro states”) (Van Emmerik and Van Wegen, 2000). Relative phase between component oscillators can identify different qualitative states of the system dynamics on which basis changes in coordinative patterns can be evaluated and discontinuous transitions are characterized by abrupt jumps between different coordinative modes (such as the transition from bipedal walking to running) (Hamill et al., 2005). Under a continuous scaling of a control parameter, preservation of the pattern is maintained for a wide range of control parameter values. However, when the pattern becomes unstable, these abrupt changes can occur for very small increments or decrements in the control parameter (nonlinearity) (Van Emmerik et al., 2004). Continuous phase transitions are more or less smooth and can occur over a larger interval of control

---

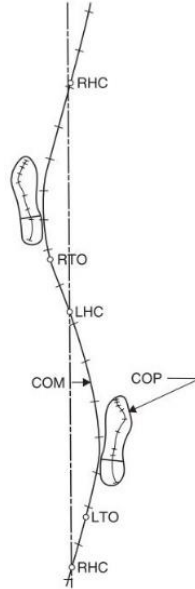
<sup>\*</sup> Márcio Fagundes Goethel, PhD.: Department of Automation, Biomechanics and Mechatronics, Politechnika Łódzka, Street Stefanows 1/15; 90-924, Łódź; PL, gbiomech@gmail.com

<sup>\*\*</sup> Dr. hab. inż. Jerzy Mrozowski, PhD.: Department of Automation, Biomechanics and Mechatronics, Politechnika Łódzka, Street Stefanows 1/15; 90-924, Łódź; PL, jan.awrejcewicz@p.lodz.pl

<sup>\*\*\*</sup> Prof. dr. hab. inż. Jan Awrejcewicz, PhD.: Department of Automation, Biomechanics and Mechatronics, Politechnika Łódzka, Street Stefanows 1/15; 90-924, Łódź; PL, jan.awrejcewicz@p.lodz.pl

parameter values. Critical in distinguishing these two types of transitions is the stability of the order parameter: In abrupt transitions, instability occurs before the transition point. This instability can be measured by means of critical fluctuations (increase in standard deviation) in relative phase or the relaxation time after a transient perturbation (Hamill et al., 2005).

Therefore, the objective of this preliminary study is to investigate the coordinative patterns between the movements of the Center of Pressure (CoP) and the Center of Mass (CoM) during the human gait, so that in the continuity of this study it is possible to propose a new criterion of gait stability.



*Fig. 1: Trajectories of the CoM and CoP. LTO – left toe off, LHC – left heel contact, RTO – right toe off, RHC –right heel contact. Note that the COM never passes within the base of support of either foot.*

*Adapted from Winter (2009, pp. 291).*

## 2. Methods

To collect the data was used 07 camera T10 with 250 fps (Vicon®) with kinematics software Vicon Nexus (Vicon®) and one force plate model OR6-6 (AMTI®). For the motion reconstruction, basic reflective markers (Vicon®) are fixed bilaterally according to the PluginGait model for whole body (Vicon®).

One young man (24 years, height of 170 cm and a body mass of 74 kg) performed 3 gait trials with a distance of 20 meters and at the chosen speed of the subject. The force plate was located 10 meters from the start of the gait and so that the subject performed the step with the dominant lower limb on the force plate. The analysis interval comprised the entire stance phase of the dominant lower limb (from the heel contact to the toe off over the force plate).

The data were processed and analyzed by specific routines developed in Matlab (Mathworks®, Inc.). The establishment of the optimal cut-off frequencies for signal filtering was performed using residual analysis (Winter, 2009), wherein the signal of the kinematic data was filtered with a recursive Butterworth lowpass 4th order with cutoff frequency of 6 Hz and the data of dynamometry with a recursive Butterworth lowpass 4th order with cutoff frequency of 95 Hz.

The medio-lateral displacement and velocity of the CoM were calculated from the position data from the reflective markers and the medio-lateral displacement and velocity of the CoP were calculated from the forces and moments obtained with the force plate using the function (Lafond, Duarte, & Prince, 2004)

$$CoP_x = \frac{-M_y + F_x \cdot Z_0}{F_z} + X_0, \quad (1)$$

where  $M$  is the moment,  $F$  the reaction force,  $x$ ,  $y$  and  $z$  are the mediolateral, anteroposterior and vertical direction, respectively, and  $X_0$ ,  $Z_0$  are the offsets from the geometric center of the force platform.

For the phase graphics construction, first, the data of the CoM and CoP of each trial, were interpolated to 2500 points using Spline Cubic functions. The interpolation procedure was realized to standardize the different amount of samples of the files.



Phase graphics were constructed from the velocity as function of displacement, with the displacement in the horizontal axis and the velocity in vertical axis. Prior to calculating the phase angle ( $\varphi$ ), the data of displacement and velocity for each trial were normalized (Li et al., 1999). The goal of normalizing the data is to transform the phase graphics in such a way that both displacement of the signal and its first derivative are limited to the range between  $-1$  and  $1$ . First, normalization is accomplished for any input signal  $y(t)$  by the function

$$f(y(t_i)) = \frac{y(t_i)}{\max(|y(t)|)} . \quad (2)$$

This technique limits the input signal of the function to either  $-1$  or  $1$  depending on the maximum absolute value of  $y(t)$ . This method is used for velocity normalization because the zero value has qualitative meaning and, arguably, should be preserved. In other words, after normalization the zero value represents the zero value in the original signal. A second normalization technique is based on the function

$$g(y(t_i)) = 2 \left( \frac{y(t_i) - \min(y(t))}{\max(y(t)) - \min(y(t))} \right) - 1 . \quad (3)$$

This function transforms the original values  $y(t)$  in such a way that the minimum value of  $g(y(t))$  equals  $-1$  and the maximum value of  $g(y(t))$  equals  $1$ . Here the zero value is midway between the maximum and minimum and can, therefore, be arbitrary.

After normalization, the phase angle of the signal at time  $t_i$  is calculated based on the normalized phase graphic (Li et al., 1999)

$$\varphi(t_i) = \tan^{-1} \left( \frac{\dot{x}_{norm}(t_i)}{x_{norm}(t_i)} \right) . \quad (4)$$

Finally, the continuous relative phase, CRP( $t_i$ ), at time  $t_i$  between two signals  $x_1(t)$  and  $x_2(t)$  is calculated as

$$\begin{aligned} CRP(t_i) &= \varphi_1(t_i) - \varphi_2(t_i) \\ &= \tan^{-1} \left( \frac{\dot{x}_{1,norm}(t_i)x_{2,norm}(t_i) - \dot{x}_{2,norm}(t_i)x_{1,norm}(t_i)}{x_{1,norm}(t_i)x_{2,norm}(t_i) + \dot{x}_{1,norm}(t_i)\dot{x}_{2,norm}(t_i)} \right) . \end{aligned} \quad (5)$$

CRP was set in the range of  $-180^\circ \leq \varphi \leq 180^\circ$ , as the difference between the phase angles of the CoP ( $\varphi_{CoP}$ ) and of the CoM ( $\varphi_{CoM}$ ) for each data sample. A larger phase angle of one point in relation to each other may be interpreted as that the same plays a slower movement or with lower amplitude, or a combination of both factors. From the CRP curves, were obtained the positive peak (maximum value), negative peak (minimum value), and the percentage time of the stance phase in which these values occurred. A CRP mean curve of the 3 trials was calculated (Fig. 3). The variability was calculated as the mean of the Standard Deviations (SD) of the CRP measures.

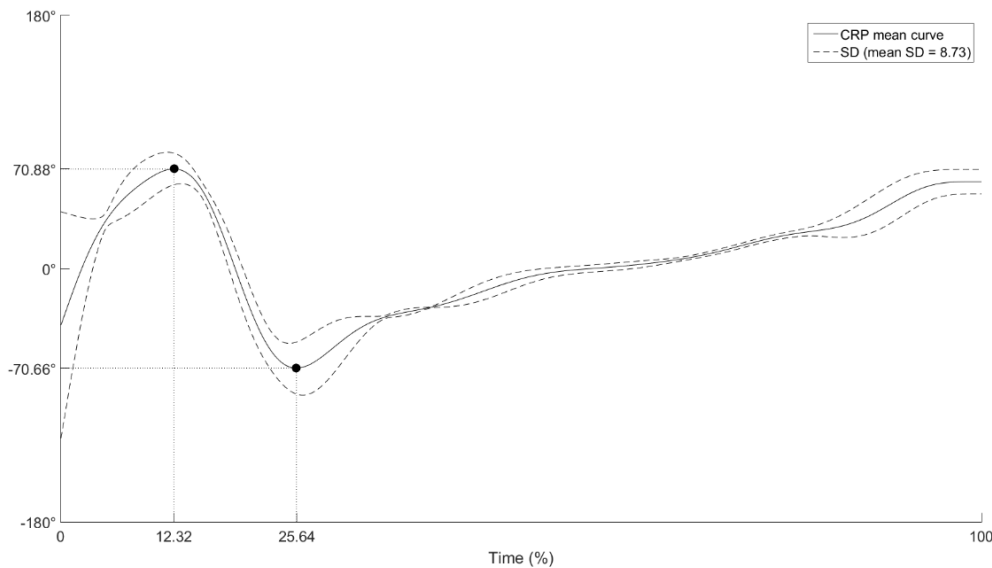


Fig. 2: CRP mean curve and Standart Deviation (SD); Positive Peak and Negative Peak, as well, the percentage time of the stance phase in which these values occurred.

### 3. Discussion and Conclusions

To discuss our results we can establish 3 hypotheses: 1. that the magnitudes of the anti-phase phenomena are similar in individuals without compromised stability; 2. that the anti-phase phenomena occur in specific moments in the stance phase of the gait in individuals without compromised stability; 3. that the variability of the coordinative patterns can be an index of stability.

The values of the positive peak ( $71.49^{\circ} \pm 10.89^{\circ}$ ) and the negative peak ( $-72.43^{\circ} \pm 19.75^{\circ}$ ) of the CRP curves are quite similar and lead us to accept the first hypothesis as true. Already the moment of occurrence of positive peaks ( $12.09\% \pm 1\%$ ) and negative peaks ( $25.47\% \pm 1.2\%$ ) appear to be repeated in the 3 trials, and still showing a very small variability, showing that these anti-phase phenomena have a temporal accuracy in the stance phase, and lead us to accept the second hypothesis as true.

According to Hamill et al. (2005), we can relate the increase of the standard deviation of the CRP curve with instability. However, as in this preliminary study we only have data from a subject without compromised stability, it is not possible to establish if this measure will have a higher value in subjects with an unstable gait, but we can verify a low value ( $\pm 8.7267^{\circ}$ ) when we analyze this healthy individual in 3 trials. In this way, we can show the tendency to accept the third hypothesis as true and establish as objective of the continuity of this study to investigate a sample that possesses individuals who do not have compromised stability and individuals who have unstable gait, such as elderly fallers and individuals with Parkinson's disease.

### Acknowledgement

The authors would like to thank the National Science Centre of Poland under the grant OPUS 9 No. 2015/17/B/ST8/01700 for years 2016–2018 for financially supporting this project.

### References

- Hamill, J., Haddad, J.M. and Van Emmerik, R.E.A. (2005) Using Coordination Measures for Movement Analysis. In XXIII International Symposium on Biomechanics in Sports, Beijing, China, pp. 33-38.
- Lafond, D., Duarte, M. and Prince, F. (2004) Comparison of three methods to estimate the center of mass during balance assessment. *Journal of Biomechanics*, 37, pp. 1421-1426.
- Li, L., Van Den Bogert, E.C.H., Caldwell, G.E., Van Emmerik, R.E.A. and Hamill, J. (1999) Coordination patterns of walking and running at similar speed and stride frequency. *Human Movement Science*, 18, 1, pp. 67-85.
- Menz, H.B., Lord, S.R. and Fitzpatrick, R.C. (2003) Acceleration patterns of the head and pelvis when walking on level and irregular surfaces. *Gait and Posture*, 18, 1, pp. 35-46.
- Turvey, M.T. (1990). Coordination. *The American Psychologist*, 45, 8, pp. 938-953.
- Van Emmerik, R.E.A., Rosenstein, M.T., McDermott, W.J. and Hamill, J. (2004) A nonlinear dynamics approach to human movement. *Journal of Applied Biomechanics*, 20, 4, pp. 396-420.
- Van Emmerik, R.E.A. and Van Wegen, E. E. H. (2000) On variability and stability in human movement. *Journal of Applied Biomechanics*, 16, 4, pp. 394-406.
- Van Emmerik, R.E.A. and Wagenaar, R.C. (1996) Effects of walking velocity on relative phase dynamics in the trunk in human walking. *Journal of Biomechanics*, 29, 9, pp. 1175-1184.
- Winter, D.A. (2009) *Biomechanics and Motor Control of Human Movement* (4th ed.). Wiley, Waterloo, Ontario, Canada.

## EXPERIMENTAL ANALYSIS OF EFFICIENCY OF MASS DAMPERS

I. Gołębiowska\*, M. Dutkiewicz\*\*

**Abstract:** *In the first part of the paper types of vibrations of overhead transmission lines have been presented indicating the need to reduce these vibrations with the use of different dampers. In the second part the results of the experiments with mass damper, called Stockbridge damper, and its efficiency are presented. Stockbridge dampers effectively reduce vibrations by absorbing the energy supplied from the outside. In the real cases the power input comes from the wind. The efficiency of vibration damping is analyzed in the frequency domain corresponding to aeolian frequencies. Two-mass dampers were analyzed and their dynamic characteristics were presented and described by the power function in the frequency domain. The additional parameter - phase angle between excitation force and the velocity of the vibrating damper was presented as well.*

**Keywords:** Stockbridge damper, Mass damper, Tuned vibrations, Dynamic absorber, Aeolian vibrations, Overhead transmission lines.

### 1. Introduction

Stockbridge dampers whose efficiency is the subject of this paper play a significant role in the reducing the aeolian vibration of overhead transmission lines (OTL) (Vecchiarelli et al., 2000). Among different types of vibrations caused by the wind, particularly these vibrations are dangerous as they lower the ultimate and serviceability states of power transmission lines. Besides aeolian vibrations, wind may cause the galloping or wake induced vibrations (Holmes, 2001). Aeolian vibrations may cause the damages of transmission lines because of fatigue of steel or aluminum, the materials from which the lines are made. Various dampers, type of Stockbridge, torsional or spiral dampers are often attached to the transmission lines to minimize these vibrations (Gołębiowska, 2015). Among the Stockbridge dampers, the asymmetrical damper is a multi-resonance system with dissipation of energy by friction between strands of messenger. Stockbridge dampers may dissipate the energy in every direction and this is the main advantage of application them. Furthermore these dampers may be used on transmission lines of large diameter and properly optimized may attenuate vibrations in wide frequency range.

### 2. Application of tuned mass dampers attached to transmission lines

Aeolian vibrations of transmission lines due to wind actions are characterized by high frequency and small amplitudes of vibrations (Diana et al., 1993). Apart from them, oscillations of high amplitude and low frequency called galloping and wake induced vibrations of average amplitude but lower than aeolian frequency are also observed. Aeolian vibrations are in the range of 3 to 150 Hz at wind speed from 1 to 7 m/s acting perpendicular to the line, which usually happens in open plots, in the area without buildings and infrastructure. The amplitude of oscillation does not exceed diameter of the conductor. These vibrations are difficult to observe due to the fact that transmission lines diameters are from 6 to 50 mm, which exceeds the amplitudes of vibrations. The maximum amplitude of vibrations occurs at resonance, when the natural frequency of conductor is close to the vortex frequency. These vibrations can be controlled by the use of different dampers (Wang et al., 1997, Scanlan 1978, Uno 1991). Attaching the damper ( $m_D$ ) to the vibrating mass ( $m$ ) causes a reduction of vibration of this mass (Fig. 1).

---

\* Prof. Dr Eng. Irena Gołębiowska: Department of Building Construction, University of Science and Technology, ul. Prof. S. Kaliskiego 7, 85-796 Bydgoszcz, Poland; tel.: +48 052 340 85 79, fax: +48 052 340 82 25; igolebio@utp.edu.pl

\*\* Dr. Eng. Maciej Dutkiewicz: Department of Building Construction, University of Science and Technology, ul. Prof. S. Kaliskiego 7, 85-796 Bydgoszcz, Poland; tel.: +48 510 035 090, fax: +48 052 340 82 25; macdut@utp.edu.pl

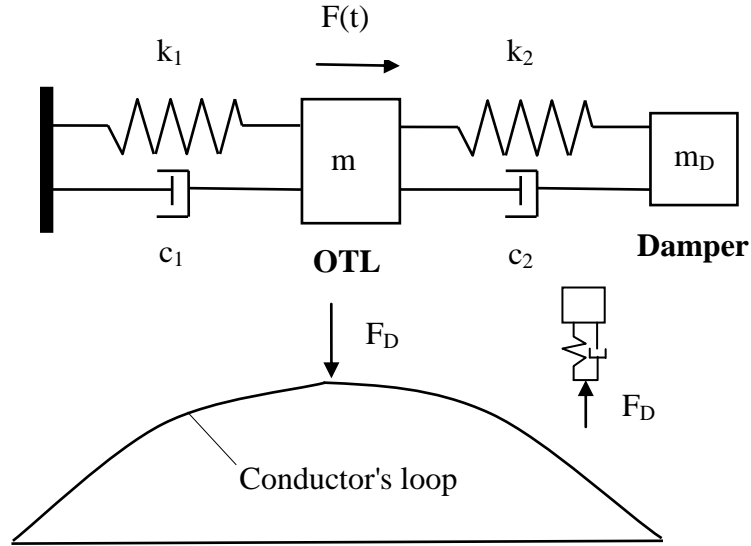


Fig. 1: Principle of tuned mass damper attached to the transmission line.

The use of Stockbridge damper is still very popular solution. Stockbridge damper is constructed from a flexible cable or rod (messenger) and the masses at its ends (Fig. 2) (Krispin et al., 2007). The vibrations of the line are passed through the clamp mounted the damper's messenger to the conductor and consequently the masses on the ends of the damper begin to vibrate. By careful selection of parameters of the damper such as mass at the ends of the messenger, stiffness and length of the damper's messenger, one can design the optimal damping of the transmission energy line (Gimsing et al., 2012). First Stockbridge damper held at the ends of the messenger masses made of concrete blocks. Nowadays steel masses at end of the damper's rod are used and galvanized steel is applied for damper's rod. From the point of reduction of vibrations, the location of damper on the cable is significant.

The purpose of the dampers is reduction of vibration by absorbing energy from the wind and stabilization of the movement of the conductor to avoid deformation that can cause the damage. According to analysis performed in the paper (Meynen et al., 2005) the value of safe limit deformation of the conductor is 200 microns/m.

### 3. Principle of damper behaviour

Principle of the damper behaviour refers to the vibrating transmission line that causes the vibrations of the masses of the damper and movement of the messenger. Movement of the masses and messenger bending cause the interstrands frictions and dissipation of energy (Fig. 2.).

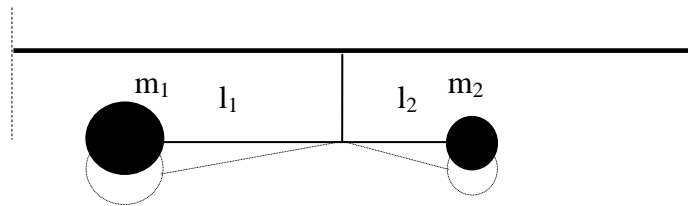


Fig. 2: Model of Stockbridge damper.

Nowadays the messengers are designed with several individual strands, with numbers up to 19, to better dissipate the energy. During the optimization of the damper, the appropriate cross section, length of the messenger, number of strands and the size of the masses at the ends of messenger are designed.

Symmetrical dampers have two degrees of freedom, which correspond to the first and second mode of vibrations. Asymmetric dampers have four modes of vibrations, alternately for larger and smaller mass of the damper giving a wider range of effective frequencies of vibration damper. Basically, two dampers are attached to the span of the line in the place of an anti-node where the amplitude of the standing wave is maximum. More than two dampers are connected to the line in the case of longer spans.

#### 4. Determination of the effectiveness of vibration dampers and the parameters of the experiment

Effectiveness of dampers were measured as the value of dissipation energy through the damper. The exciting force was input to the damper through the connection clamp.

Experiment stand consists of shaker, force sensor, accelerometer, amplifier, postprocessing analyser. Target frequencies were in the range of 4 to 100 Hz, that can happen in real conditions in the case of aeolian vibrations. The aim of the experiment was to measure the acceleration/velocity and control the exciting force acting on the damper to determine the value of the total energy dissipated by the damper. The experiments were performed for fix damper's parameters:  $m_1=1.6$  kg,  $m_2 = 1.3$  kg, messengers length  $l_1= 230$  mm,  $l_2 = 180$  mm, 19 was the number of individual innerstrands of messenger. During the experiment the phase angle between the excited force and response velocity of vibration are determined.

Accelerometer and force transducer were mounted close to the clamp of the damper. The parameters of the measurements were fixed. A sweep rate of 0.2 decade / min was used. Clamp velocity was held constant at 0.1 m / s. The damper power is determined as (IEC 61897, 1998):

$$P = 0.5 \times F \times V \times \cos \phi \quad (1),$$

where: P is the power [W], F is the exciting force [N] - peak value, V is the velocity of the damper clamp [m/s],  $\phi$  is the phase value between the velocity and the force [degree].

#### 5. Results and discussion

During the experiments of forced vibration of two-mass dampers, the maximum of energy dissipation were observed: peaks no. 1 and 3 corresponding to the vibration of mass  $m_1$  and peaks 2 and 4 for the mass  $m_2$  (Fig. 3). Fig. 3 shows the curves of energy dissipation in the frequency domain for three dampers of the same type. Maximum value of power dissipation is 0.8 W at frequency 7 Hz, 0.7 W at 20 Hz, 1.4 at 36 Hz and 2.5 Hz at 67 Hz.

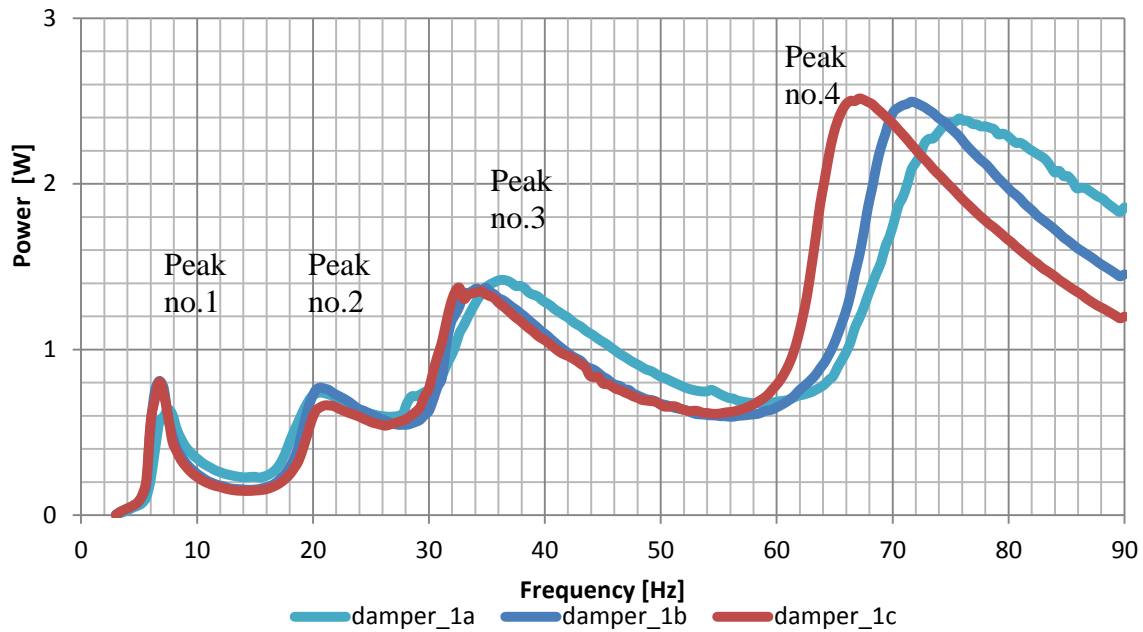
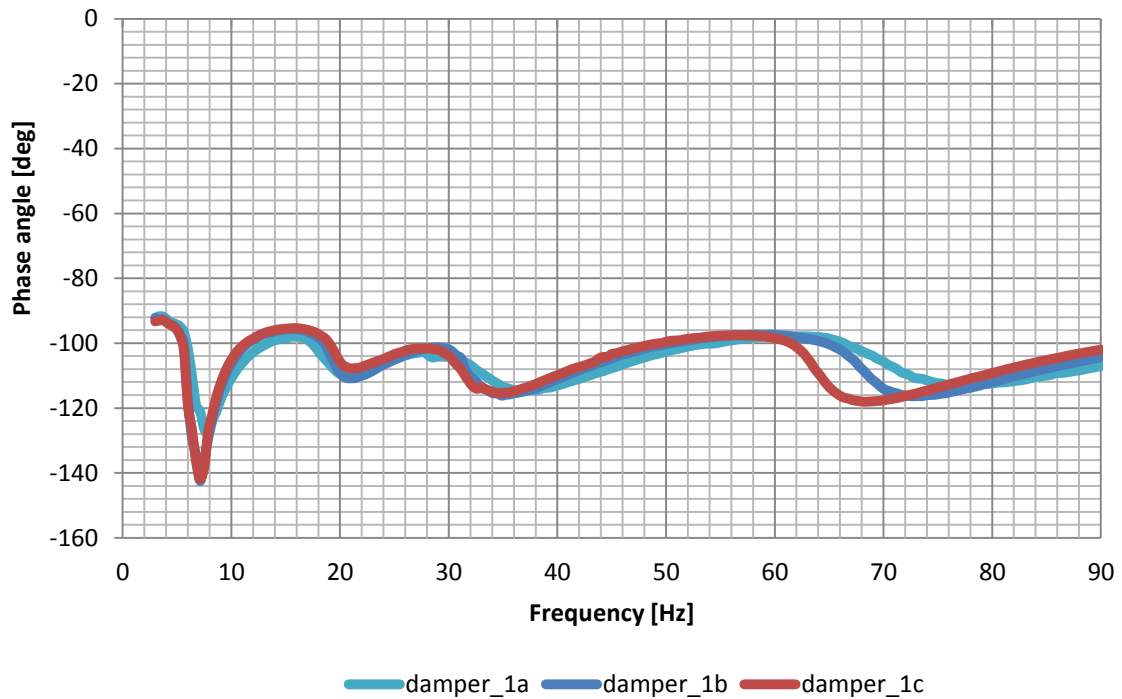


Fig. 3: Damper power curves.

Fig. 4 shows the curves of phase angle between the force and response velocity of vibration, which present the conformity of received results.



*Fig. 4: Phase angle between force and velocity.*

## 6. Conclusions

In the paper the efficiency of asymmetrical Stockbridge dampers was analysed. The efficiency of vibration damping was analyzed in the frequency range corresponding to aeolian vibrations. Dampers were analysed and their dynamic characteristics were determined by power function in the frequency domain. Phase angle between force and response velocity was determined. Received results confirm the efficiency of the tested dampers in the analyzed range of frequencies.

The choice of parameters of the damper such as weights, length, stiffness and damping of messenger, location of the damper on the line is one of the steps carried out the research to optimize the vibration of overhead transmission lines in the field of mechanical damping. This research also will cover issues related to the aerodynamic damping e.g. selection of the shape of the damper and results will be performed in the future papers.

## References

- Diana, G., Cheli, F., Fossati, F. and Manenti, A. (1993) Aeolian vibrations of overhead transmission lines: computation in turbulence conditions, *J. Wind Eng. Ind. Aerodyn.*, vol. 46-47, pp. 639-648.
- Gimsing, N. and Georgakis, Ch. (2012) *Cable Supported Bridges: Concept & Design*, Wiley, 3rd Edition.
- Gołębiewska, I., Dutkiewicz, M. and Usewicz, B. (2015) *Methods of damping of overhead transmission lines*, TTS, 12, pp.2544-2548, (in Polish).
- Holmes, J.D. (2001) *Wind Loadings of Structures*, Spon Press, New York.
- IEC 61897 Ed. 1.0 (1998) *Requirements and Tests for Stockbridge Type Aeolian Vibration Dampers*.
- Krispin, H.J., Fuchs, S. and Hagedorn, P. (2007) Optimization of the efficiency of aeolian vibration dampers," *IEEE PES PowerAfrica Conference and Exposition, PowerAfrica*.
- Meynen, H., Verma, P., Hagedorn, P. and Schafer, M. (2005) On the numerical simulation of vortex-induced vibrations of oscillating conductors, *J. of Fluids and Struct.*, 21(1).
- Scanlan, R.H. (1978) The action of flexible bridges under wind, I: flutter theory. *J Sound Vib*;60(2):187-199.
- Uno, K., Kitagawa, S., Tsutsumi, H., Inoue, A., Nakaya, S. (1991) A simple method of designing cable vibration dampers of cable-stayed bridges, *J. of Struct. l Eng., JSCE*, Vol. 37A, pp.789-798.
- Vecchiarelli, J., Curie, I.G. and Havard D.G. (2000) Computational analysis of aeolian conductor vibration with a stockbridge-type damper, *J. of fluids and struct.* 14, 489-509.
- Wang, H.Q., Miao, J.C., Luo, J.H., Huang, F. and Wang, L.G. (1997) The free vibration of long-span transmission line conductors with dampers, *Journal of Sound and Vibr.*, 208(4):501.

## MECHANICAL DAMPERS ON OVERHEAD POWER LINES

I. Gołębiowska<sup>\*</sup>, M. Dutkiewicz<sup>\*\*</sup>, B. Usewicz<sup>\*\*\*</sup>

**Abstract:** *Conductors constitute important components of overhead power lines. They are characterised by low internal damping, low rigidity and low weight. Thus, they can reach high amplitudes of wind induced vibrations. As a result of such vibrations, conductors are subject to variable dynamic stresses which determine the durability of a power line. Limiting possible damage caused by wind is crucial, not only due to safety of the structure, but also for economic reasons. This paper briefly describes basic types of conductor vibration excitations caused by wind. Such aerodynamic phenomena as vortex excitation, galloping and wake induced vibrations, and selected mechanical dampers used on overhead power lines are presented.*

**Keywords:** Mechanical dampers, Vibration of conductors, Control of vibration.

### 1. Introduction

An overhead power line is a set of properly insulated conductors located next to each other on supporting structures. The crucial component of a power line is a current-leading conductor. In a power line, conductors are fixed to supporting structures with insulators. The aim of supporting structures is to support conductors and/or take their tension strength. Aluminium is generally used for designing such conductors. A typical structure of a conductor comprises a braided aluminium wire rope with steel wire core. Conductors are characterized by low rigidity, relatively low damping and low weight. Therefore, they are very susceptible to wind. One of the most important aspect, both when designing and installing power lines, is knowledge on vibration generation mechanisms. As a result of vibrations caused by wind, a conductor is subject to variable stresses which determine its durability. Amplitude and vibration frequency depend on numerous factors, such as line rated data, climatic and terrain conditions, etc. Vortex induced vibrations (aeolian vibrations), galloping and wake induced vibrations are predominant in overhead power line conductors. Reducing the level of such vibrations is very important, since undamped vibrations may lead to destruction of a conductor, equipment, power line or to a failure of a transmission network.

This paper presents basic types of overhead power line conductor vibrations caused by wind, damping of which is crucial for their safe operation and selected, effective mechanical dampers.

### 2. Types of vibrations

Overhead power lines are constantly subject to variable wind loads which may gradually lead to the impairment of their durability, resulting in the shortened service life. Wind forces are caused by three main types of conductor vibrations: aeolian vibrations with a frequency from 3 to 150 Hz and amplitudes lower than the conductor diameter, galloping with a frequency from 0.1 to 1 Hz and amplitudes from  $\pm 0.1$  to 1 of conductor sag, wake induced vibrations with a frequency from 0.15 to 10 Hz and amplitudes from 0.5 to 80 times the conductor diameter (Gołębiowska, 2015).

**Vortex induced vibrations (aeolian vibrations).** The majority of common wind induced vibrations are aeolian vibrations. These vibrations are generated as a result of vortices shed in the conductor wake under

---

<sup>\*</sup> Prof. Dr. Eng. Irena Gołębiowska, Department of Building Construction, University of Science and Technology in Bydgoszcz, Al. Prof. S. Kaliskiego 7, 85-796 Bydgoszcz PL, e-mail: irena\_golebiowska@wp.pl

<sup>\*\*</sup> Dr. Eng. Maciej Dutkiewicz, Department of Building Construction, University of Science and Technology in Bydgoszcz, Al. Prof. S. Kaliskiego 7, 85-796 Bydgoszcz PL, e-mail: macdut@utp.edu.pl

<sup>\*\*\*</sup> Eng. Bogdan Usewicz, Department of Building Construction, University of Science and Technology in Bydgoszcz, Al. Prof. S. Kaliskiego 7, 85-796 Bydgoszcz PL.



sustained wind of low speed from 1 to 7 m/s – they occur mainly in the vertical plane. Vibrations of conductors, both single and in a bundle, form standing waves with forced nodes and intermediate nodes located along the span at intervals depending on the frequency of free vibrations. When the conductor wind flow is laminar, alternately shedding vortices are formed in two points of the suction zone and make the conductor move perpendicularly towards the wind direction. The alternate shedding of vortices is regular. As a result, a so-called Karman vortex street is formed. When the frequency of the shedding of vortices is approximately equal to one of the frequencies of free vibrations of a conductor, a ‘lock-in’ phenomenon occurs. During this frequency synchronisation, the conductor is in the resonance state. Aeolian vibrations occur on single conductors and conductors in a bundle. Although these vibrations are hardly noticeable due to low amplitude values (lower than the conductor diameter), they are very important, since they can lead to fatigue destruction of a conductor in points of high stress concentrations.

**Galloping.** This phenomenon was observed for the first time on ice-covered power lines subject to strong wind. Galloping is an aeroelastic self-excitation phenomenon characterised by low frequencies and high amplitudes, and it refers to single conductors and conductors in a bundle, with one or two loops of standing and running waves, or their combination in a conductor span. Standing waves may have one or more loops (up to 10) over the span length. However, a small number of loops is predominant. In most cases, galloping is caused by sustained wind of an average and high speed ( $V > 15$  m/s), blowing on an asymmetrically loaded (e.g. with ice or wet snow) conductor. High amplitudes are observed in the vertical plane, whereas the frequencies depend on the type of a conductor and vibrations (EPRI Research project 792, 2005). Galloping is a typical instability caused by the coupling of aerodynamic forces which affect the conductor with its vibrations. Conductor vibrations change the wind angle of attack on a periodic basis. The change of the angle of attack results in a change of aerodynamic forces affecting the conductor, which consequently changes the conductor response. The first, simplified criterion (if a single degree-of-freedom system is applied) pertaining to the instability connected with galloping was presented by Den Hartog. A precondition for galloping (on the basis of the quasi-steady theory) is the presence of negative aeroelastic damping in the system. A conductor of a circular section cannot gallop due to its geometrical symmetry ( $dC_L/d\alpha = 0$ ), unless this section is changed. Icing of a conductor changes its cross-section, thus it leads to its aerodynamic instability (Farzaneh, 2008). Research works carried out by Hartog indicate that the aerodynamic instability is the main reason for the galloping phenomenon. His research was conducted with an assumption that the vertical motion of a conductor is predominant, and the effect of torsional and horizontal motions can be ignored. Further research proved that the torsional motion is an integral part of the galloping phenomenon. The effect of a coupled torsional-translational motion plays a crucial role in most cases of progressing galloping (Luongo, 2009).

### Wake induced vibrations

Unlike aeolian vibrations or galloping, wake induced vibrations can occur only on conductor bundles and only when one conductor lies within the wake of another conductor. Wake induced vibrations are caused by sustained wind of an average and high speed ( $V > 10$  m/s). As opposed to galloping, these vibrations may occur all year round. An amplitude of these vibrations is not that high as for galloping. However, they can lead to destruction of conductors, clamps or dampers. They are not as common as aeolian vibrations.

### 3. Methods of vibration control

Popular methods of reducing vibrations of power line conductors can be divided as follows: aerodynamic-structural methods (application of dual-conductors – twisted pair, oval cross-section conductors, self damping conductors) and mechanical methods (mechanical dampers mounted on conductors or conductor bundles). Commonly used equipment for damping overhead power line conductor vibrations includes: dampers of type Stockbridge, spiral dampers, torsional dampers, spacers with damping properties (for conductor bundles). Selected, effective mechanical dampers are described below.

**Stockbridge dampers** are most frequently used dampers on overhead power lines (Fig. 1a). A classic Stockbridge damper consists of two ‘inertial masses’ (metal weights) clamped at the ends of a specially designed short steel wire strand (messenger) attached with a clamp to the damped conductor. The energy of vibrations is dissipated through friction caused by slippage between the messenger wires. When the damper is positioned on a vibrating conductor, the vertical motion of the weights forces the steel conductor to bend, causing friction between the wires which dissipates the

energy. The size and shape of the weights and damper geometrics influence the quantity of energy dissipated for specific vibration frequencies. An improved version of the classic damper (an asymmetrical Stockbridge damper) features two different weights in the shape of a bell, located asymmetrically at the ends of a steel galvanised messenger of possibly the best energy dissipation properties. Such a design of the damper doubles the number of resonance peaks from two obtained with the classic version of the Stockbridge damper to four in the improved version. Modern Stockbridge dampers are intended for effective energy transfer and dissipation for the whole spectrum of frequencies within aeolian vibrations. To ensure effective damping, the first damper should be located next to the attachment (suspension), inside the shortest loop which is formed at the highest speed of wind (7 m/s) (Technical Report IEEE, 2015).

**The Spiral Damper** (impact type damper) has been applied on small diameter conductors ( $\leq 19$  mm) for over 30 years. It is made of rugged non-metal material in the form of spiral of length 1.2 – 1.5 m, with an internal diameter exceeding the conductor diameter. A spiral at the one end adheres tightly to the conductor (the supporting part). During aeolian vibrations, the damping part of this spiral impacts the conductor and causes formation of impulses which disrupt conductor vibrations (Technical Report IEEE, 2015). Another type of spiral damper is the **Air Flow Spoiler**. It can be used on conductors in order to balance aerodynamic lift forces which cause galloping. Usually, spoilers cover approx. 25 % of the span length and are used in two groups (Conductor Galloping Basics, 2016).

The **Detuning Pendulum** is used for single cables and cables in a bundle. A typical design of the damper is a weight attached to a cable or cable bundle. The length of the arm and weight depend mainly on the cable diameter and span length. Arm length and weight required to overcome moment of ice and wind load, thus minimizing or eliminating galloping. This damper separates frequencies of vertical vibrations from frequencies of torsional vibrations. In most cases, 3 - 4 dampers are installed along the span, using braids in order to decrease local cable tensions (EPRI Research project 792, 2005).

The **Torsional Damper and De-tuner** is a modern damping device. It combines properties of a torsional damper and detuner. This damper uses a torsional motion of a conductor during galloping to damper vibrations, and improves its effectiveness by separating frequencies of vertical vibrations from frequencies of torsional vibrations, as in pendulum dampers. This damper increases the value of a critical speed of wind, above which galloping occurs, and reduces its amplitudes. In most cases, 2 - 3 dampers are installed along the span (Vinogradov, 2012).

For controlling galloping for single conductors (shorter span), and for controlling aeolian vibrations (in conductors of small diameters and spans) can be used **AR Twister dampers**. Three types of AR Twisters are manufactured: Piston, Kanister and Slider (Fig. 1b) (AR Products LLC, 2015). Twisting is the main technique for galloping control in all these dampers. All AR Twister dampers reduce or eliminate galloping of a conductor by making the conductor rotate and – as a consequence – decrease the aerodynamic lift. The AR Twister is an inertial device made of aluminium (due to its weight and durability). Damping required to control aeolian vibrations is achieved by rubbing metal with metal, as a result of slight motions between the device body and its clamp. These devices are rigidly fixed to the conductor with standard vertical clamps (over the conductor) or clamps which are angled at  $45^\circ$  to  $60^\circ$ . Such an arrangement of dampers causes an initial torsion of the conductor under gravity forces. In the event of galloping, inertial forces affect the device making the conductor twist again, in the opposite direction to its initial position. When galloping, torsional oscillations increase, ice sediment is distributed over the greater surface of the conductor and the profile becomes smooth and less eccentric. At the same time, the aerodynamic lift force is reduced and the level of vibrations decrease (AR Products LLC, 2015).

A **damping spacer** combines the function of maintaining distance between conductors (preventing their damage caused by impacts) with the function of vibration damping. Depending on the arrangement of conductors in a bundle, different types of spacers are available. Rigid and spring spacers are usually used for controlling galloping. Early versions of rigid spacers comprised ceramic insulators connected with an aluminium tube and attached to conductors with standard suspension. At present, light polymer insulators are applied. A modern spacer for a conductor bundle consists of a rigid aluminium frame (body) and several jibs (clamps), the number of which is determined by the number of conductors in the bundle. The jibs are attached to the frame with special resilient joints. In addition to the basic function of maintaining spacing between the conductors, this damper provides vibration damping by means of damping pads in body-clamp connections, and is used to limit bending stresses and – consequently – to reduce deformations in bundle conductors.

**AR Spacer / Twister** can be mounted on a single conductor or conductor bundles in a vertical or horizontal position. This device is designed to reduce the level of vibrations in low unit weight conductors. AR Spacer/Twister combines the advantages of the twisting action of the AR Clamp with the features of the polymer insulators. AT Twister eliminates galloping by making the conductor twist, thus resulting in a decrease of the aerodynamic lift force (AR Products LLC, 2015).

**AR Mood 2 Spacer Damper** is mounted horizontally or vertically on conductor bundles in order to control galloping. This device consists of a steel spring rim and aluminium clamps. Articulated clamps rotate on the rim, allowing the conductor to rotate and twist, while maintaining distance between the individual conductors. The effective performance of this spacer/damper is ensured by large rotation angles which effectively change the wind angle of attack during galloping (AR Products LLC, 2015).

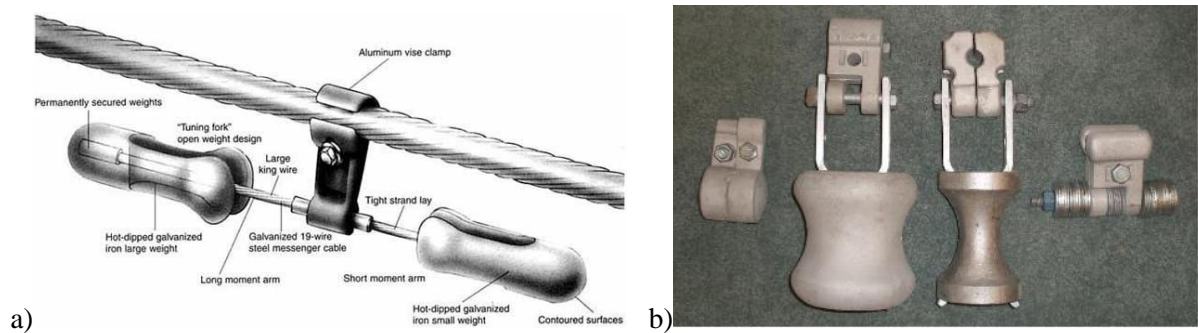


Fig. 1: a) Stockbridge damper (Hubbell Power Systems, 2016) and b) AR Twister dampers (AR Products LLC, 2015)

#### 4. Conclusions

Vibrations of overhead power line conductors caused by wind may lead to their destruction. Therefore, reducing the level of such vibrations is important due safety of the entire structure. Common methods of minimization of conductor vibrations are passive: proper shaping of the external surface of a conductor, a proper design of the conductor (self-damping) and use of special damping devices, depending on the type of excitations.

At present, there is no way to completely reduce vibrations during galloping, for which amplitudes may reach high values. According to the research literature, Air Flow Spoilers and torsional dampers are most effective in minimizing conductor galloping, whereas Stockbridge dampers are still the most efficient devices for aeolian vibrations and spiral dampers are excellent for very small diameter of conductors.

#### References

- Golebiowska, I., Dutkiewicz, M. and Usewicz, B. (2015) Methods of damping of overhead transmission lines, TTS, 12/2015, 5, pp. 2544-2548, (in Polish).
- State of the art of conductor galloping. A complementary document to "Transmission line reference book – Wind induced conduction motion Chapter 4: Conductor galloping", based on EPRI Research project 792. CIGRE ad hoc SC, 2005.
- Technical Report IEEE Power & Energy Society: An introductory discussion on Aeolian Vibration of Single Conductors, 2015.
- Farzaneh, M., (2008) Atmospheric icing of power networks. Springer.
- Luongo, A., Zulli, D. and Piccardo, G. (2009) On the effect of twist angle on nonlinear galloping of suspended cables. Computers and Structures 87 (15-16), pp. 1003-1014.
- Vinogradov, A., Iosif, I.S., and Jean-Louis, L. (2012) Highly efficient antigalloping device TDD for transmission lines with bundled conductors-development, test, design version. International Conference Energy of Moldova, pp. 223-228.
- Conductor Galloping Basics, Report prepared by Preformed Line Products, 2016.
- AR Products LLC 2015 (data per day 30.09.2016) <http://arproducts.org/> - product catalog.
- <http://www.hubbellpowersystems.com/connectors/trans/dampers/damper.asp> (data per day 30.09.2016).

## TURBULENCE IMPACT ON THE CONTROL OF GUIDED BOMB UNIT

M. Grzyb<sup>\*</sup>, K. Stefański<sup>\*\*</sup>

**Abstract:** *The study presents the method for the control of the guided bomb unit operating in turbulent atmosphere. The proportional navigation method was used to guide the bomb onto a ground target. The investigations included the analysis of the effect of atmospheric disturbances on target hitting accuracy and flight trajectory profile, and also of the values of generated control forces. Numerical simulations were conducted using Matlab software. The results of some investigations are presented in a graphic form.*

**Keywords:** Dynamics, Homing, Bomb, Control, Atmospheric turbulence.

### 1. Introduction

The guidance of target homing flying object of the guided bomb unit type occurs in the Earth's atmosphere in which different atmospheric phenomena are observed. They include turbulence, wind shear and wind gusts. Atmospheric disturbances that are random in character cannot be easily predicted, and the effect they produce may lead to the combat mission failure. Atmospheric phenomena can be described only in the approximate manner. In a flight, the flying object is subjected to different disturbances, including those originating from the medium in which the object moves. The task of the guided bomb unit is to perform the flight according to the implemented control algorithm developed in the automatic pilot (Baranowski et al., 2016 and Dziopa et al., 2015). The autopilot on the basis of data from scanning and seeking head (Gapiński et al., 2015) forces the deflections of aerodynamic control surfaces, on which control forces are generated. That control surfaces, as well as wings, to reduce mass, may be made of light composite materials (Paramonov et al., 2012).

The guidance method is intended to minimise the deviation of the current flight variables from the assigned ones, i.e. to compensate atmospheric disturbances in the best way.

### 2. The turbulence model

Although atmospheric phenomena cannot be predicted in advance and occur suddenly, it is possible to model them in such a manner so that models closely represent natural phenomena. The mathematical description of the turbulence phenomenon was based on the theory of stochastic processes. Dryden model of turbulence was applied (Moorhouse, 1982). The values of power spectral density in the coordinate system related to the bomb can be presented as follows:

$$\Phi_{u_g}(\omega) = \frac{2\sigma_u^2 L_u}{\pi V_{bu}} \frac{1}{1 + \left(L_u \frac{\omega}{V_{bu}}\right)^2}, \quad \Phi_{v_g}(\omega) = \frac{\sigma_v^2 L_v}{\pi V_{bu}} \frac{1 + 3\left(L_v \frac{\omega}{V_{bu}}\right)^2}{\left[1 + \left(L_v \frac{\omega}{V_{bu}}\right)^2\right]^2}, \quad \omega = V_{bu}\Omega \quad (1)$$

where:  $\Omega$  – spatial frequency;  $V_{bu}$  – velocity in steady flight of the bomb ;  $L_{u,v}$  – turbulence scale lengths;  $\sigma$  – turbulence intensities.

<sup>\*</sup> Research Assistant Marta Grzyb, MSc. Eng.: Faculty of Mechatronics and Mechanical Engineering, Kielce University of Technology, al. Tysiąclecia P.P. 7; 25-314, Kielce; PL, mgrzyb@tu.kielce.pl

<sup>\*\*</sup> Assistant Prof. Konrad Stefański, PhD. Eng.: Faculty of Mechatronics and Mechanical Engineering, Kielce University of Technology, al. Tysiąclecia P.P. 7; 25-314, Kielce; PL, kstefanski@tu.kielce.pl

Model each component of turbulence so that it would have zero mean value and white noise distribution. As a result, a random output signal with a specified power spectral density was produced. The dependence between power spectral density of the input signal obtained from the linear filter and power spectral density of the output can be written as follows:

$$\Phi_{u_g, v_g}(\omega) = |G(s)|_{s=j\omega}^2 \Phi_F(\omega) \quad (2)$$

For white noise having Gaussian distribution  $\Phi_F(\omega) = 1$ , turbulence signals were generated that take the following form:

$$G_{u_g}(s) = \sigma_u \frac{\sqrt{\frac{2}{\pi}} \tau_1}{s + \tau_1}, \quad \tau_1 = \frac{V_{bu}}{L_u}, \quad G_{v_g}(s) = \sigma_v \sqrt{\frac{3}{\pi}} \tau_2 \frac{s + \frac{\sqrt{3}}{3} \tau_2}{(s + \tau_2)^2}, \quad \tau_2 = \frac{V_{bu}}{L_v} \quad (3)$$

### 3. Bomb equations of motion

Figure 1 shows the set of coordinate systems for which flight equations for the hypothetical guided bomb unit were derived. An exemplary bomb assault on a ground moving target is shown in Fig. 2. The following notations were adopted (Koruba, 2016):  $\alpha, \beta$  – attack angle and sideslip angle [rad];  $\psi, \vartheta, \varphi$  – pitch angle, yaw angle and roll angle of the bomb [rad];  $\gamma, \chi$  – flight-path angle in vertical plane and horizontal plane – pitch angle and yaw angle of bomb velocity vector [rad],  $S\xi\eta\zeta$  – coordinate system for the bomb;  $Sxyz$  – velocity coordinate system;  $Sx'_gy'_gz'_g$  – coordinate system with the bomb as an origin, parallel with the starting system;  $\vec{V}_b$  – bomb velocity vector;  $\vec{V}_t$  – target velocity vector.

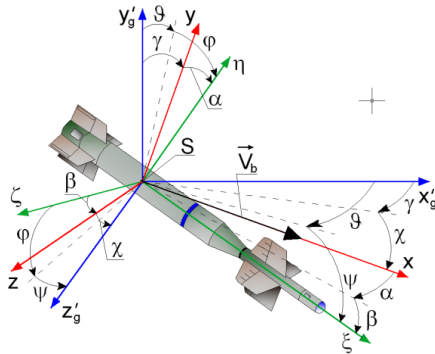


Fig. 1: Coordinate system with angles of rotation.

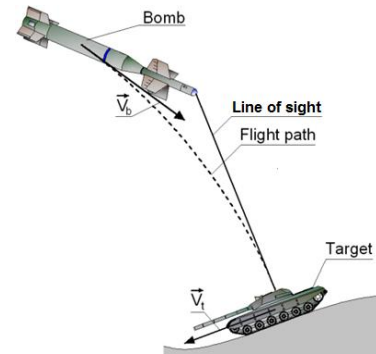


Fig. 2: Example of bomb attack on target.

In the study, it was assumed that the bomb is a rigid body that does not rotate around its longitudinal axis. The flight dynamics equations for the guided bomb unit are as follows (Grzyb, 2011 and Krzysztofik, 2014):

$$\dot{V}_b = -g \sin \gamma - \lambda_x V^2, \quad \dot{\gamma} = \frac{1}{V} \left( \frac{Q_y}{m} - g \cos \gamma \right) + \lambda_y V \alpha, \quad V = V_b - U_g \quad (4a)$$

$$\ddot{\gamma} = V \left( -D_1 \frac{V}{l_b} \alpha - D_2 \dot{\alpha} - D_3 \dot{\gamma} \right) + \frac{Q_y e}{J_k}, \quad \lambda_x = \frac{c_x S_x \rho}{2m}, \quad \lambda_y = \frac{c_y S_y \rho}{2m}, \quad D_{1,2,3} = \frac{C_i l_b}{J_k} \quad (4b)$$

where:  $l_b$  – length of the bomb body [m];  $\rho$  – air density [ $\text{kg}/\text{m}^3$ ];  $S_x$  – cross-sectional area of the bomb;  $S_y$  – lifting area [ $\text{m}^2$ ];  $m$  – mass of the bomb [kg];  $J_k$  – moments of inertia of the bomb in relation to its transverse axis [ $\text{kg} \cdot \text{m}^2$ ];  $Q_y$  – bomb flight control force [N];  $e$  – distance between control force and aerodynamic pressure centre [m];  $g$  – acceleration of gravity [ $\text{m}/\text{s}^2$ ];  $\lambda_x, \lambda_y, D_{1,2,3}$  – relative aerodynamic coefficients of aerodynamic forces and moments [ $1/\text{m}$ ] (Koruba, 1999 and Koruba, 2010);  $c_x, c_y$  – coefficients of aerodynamic forces;  $C_i$  – coefficients of moments of aerodynamic forces;  $U_g$  – velocity of turbulence [ $\text{m}/\text{s}$ ].

#### 4. Digital simulation results

Numerical simulations were conducted for the hypothetical guided bomb unit in backward hemisphere attack on a ground target. The following numerical values were used: starting bomb position:  $x_{b0} = 0$  m,  $y_{b0} = 5000$  m; starting target position:  $x_{t0} = 4000$  m,  $y_{t0} = 0$  m; angle of a bomb launch:  $\gamma_0 = 0$  rad; starting angle of pitch of a target velocity vector:  $\gamma_{t0} = 0.1$  rad; starting bomb velocity:  $V_{b0} = 250$  m/s; target velocity:  $V_c = \text{const} = 20$  m/s;  $l_b = 1.5$  m;  $m = 100$  kg;  $J_k = 18.75$  kg.m<sup>2</sup>;  $\lambda_x = 0.00044$  1/m;  $\lambda_y = 0.0067$  1/m;  $D_1 = 0.0551$  1/m,  $D_2 = 0.121$  1/m,  $D_3 = 0.061$  1/m;  $t$  – time. The flight path of the target was described as follows:  $\gamma_t(t) = \gamma_{t0} - 0.05 \cdot t$ .

For the bomb guidance to the target, a proportional navigation algorithm was used, whereas the control forces were determined using a classic PID controller (Takosoglu et al, 2016b). Graphical representation of the results is shown in Figs. 3 – 8.

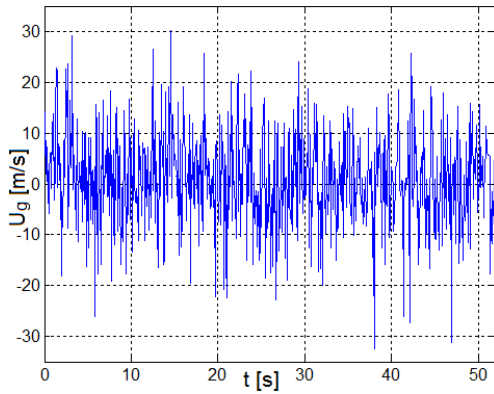


Fig. 3: Velocity of turbulences.

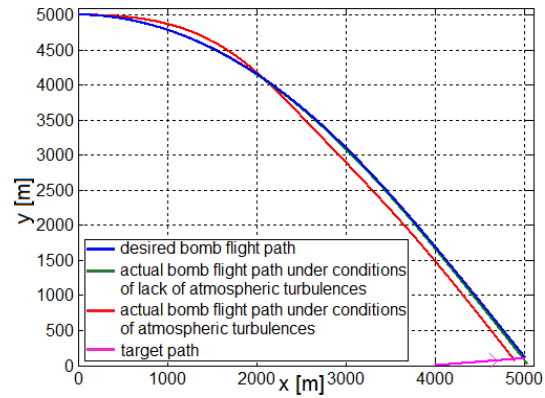


Fig. 4: The bomb flight path and target motion path.

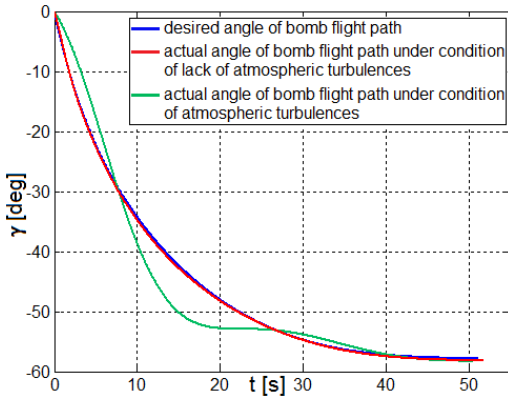


Fig. 5: Desired and actual angles of bomb flight path.

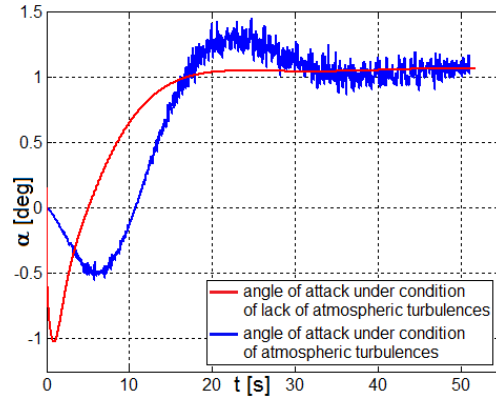


Fig. 6: The angle of attack realized during the bomb flight.

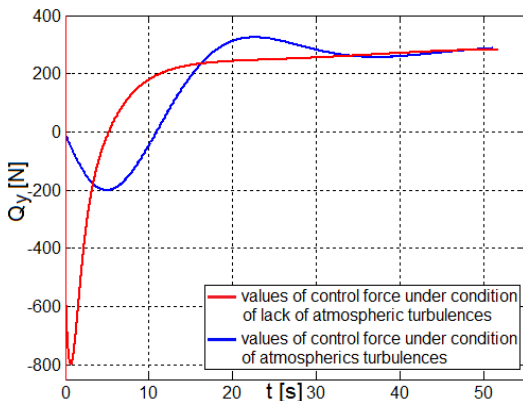


Fig. 7: Values of control forces required for homing the bomb on the target.

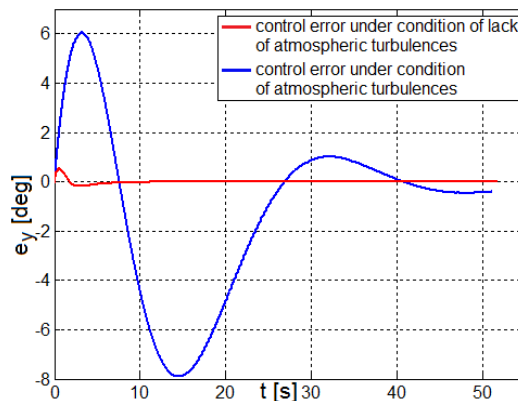


Fig. 8: Values of control errors.

## 5. Conclusions

The effect of atmospheric disturbances on the flight was analysed in many studies for flying objects of various types, including: a plane (Lungu et al. 2016), unmanned aerial vehicle (Jafar et al., 2016) and guided bomb (Kowaleczko, 2009).

This study focused on the modelling of random atmospheric phenomena, namely vertical turbulence and on the analysis of the effect produced by this phenomenon on the flight profile of the guided bomb unit. For that purpose, the spectral representation of turbulence, i.e. the Dryden model was employed. At the model input white noise was used. It was assumed that the level of turbulence intensity is the same regardless of the altitude of the guided bomb unit flight. Based on the investigations conducted for the study, it can be stated that atmospheric disturbances distort all the parameters of the guided bomb unit flight (Figs. 3 – 8). The control method proposed in the study allows delivering the bomb onto a ground target with the accuracy of 5 metres. The control force that is generated to compensate random disturbances takes on real values. In spite of the turbulence occurring throughout the guided bomb unit flight, all flight parameters have acceptable values.

It is assumed that in further studies spatial model of turbulence will be employed. It will be accompanied by a system for the system for reducing the effects of random disturbances in which Kalman filter, among others, will be used.

## References

- Baranowski, L., Gadomski, B., Majewski, P. and Szymonik, J. (2016) Explicit “ballistic M-model”: a refinement of the implicit “modified point mass trajectory model”. *Bulletin of the Polish Academy of Sciences - Technical Sciences*, 64, 1, pp. 81-89, doi: 10.1515/bpasts-2016-0010.
- Dziopa, Z., Buda, P., Nyckowski, M. and Pawlikowski, R. (2015) Dynamics of an unguided missiles launcher. *Journal of Theoretical and Applied Mechanics*, 53, 1, pp. 69-80.
- Gapiński, D., Krzysztofik, I. and Koruba, Z. (2014) Analysis of the dynamics and control of the modified optical target seeker used in anti-aircraft rocket missiles. *Journal of Theoretical and Applied Mechanics*, 52, 3, pp. 629-639.
- Grzyb, M. and Stefański, K. (2011) Guiding a smart bomb using a special algorithm for target identification and tracking (in polish). *Pomiary Automatyka Robotyka*, R 15, 2, pp. 668-676.
- Jafar, A., Fasih-UR-Rehman, S., Fazal-UR-Rehman, S., Ahmed, N. and Shehzad, M.U. (2016) A robust  $H_\infty$  control for unmanned aerial vehicle against atmospheric turbulence. *International Conference on Robotics and Artificial Intelligence (ICRAI)*, pp. 1-6.
- Koruba, Z. and Nocoń, Ł. (2016) Numerical analysis of the dynamics of automatically tracked anti-tank guided missile using polynomial functions. *Journal of Theoretical and Applied Mechanics*, 54, 1, pp. 13-25.
- Koruba, Z. and Osiecki, J.W. (1999) Constructions, dynamics and navigation of the short range rocket missile. 1-st part, *Academy Course Book*, 348, Kielce University of Technology, (in Polish).
- Koruba, Z. and Ładyżyńska-Kozdraś, E. (2010) The dynamic model of a combat target homing system of an unmanned aerial vehicle. *Journal of Theoretical and Applied Mechanics*, 48, 3, pp. 551-566.
- Kowaleczko, G. and Żyluk, A. (2009) Influence of atmospheric turbulence on bomb release. *Journal of Theoretical and Applied Mechanics*, 47, 1, pp. 69-90.
- Krzysztofik, I. and Koruba, Z. (2014) Mathematical model of movement of the observation and tracking head of an unmanned aerial vehicle performing ground target search and tracking. *Journal of Applied Mathematics*, Article ID 934250, 11 p.
- Lungu, M., Lungu, R., Grigorie, L. and Preotu, O. (2016) The influence of atmospheric turbulences on aircraft landing process. *International Conference on Applied and Theoretical Electricity (ICATE)*, pp. 1-5.
- Moorhouse, D.J. and Woodcock, R.J. (1982) Guide for MIL-F-8785C, Military specification flying qualities of piloted airplanes. *U.S. Military Specification MIL-F-8785C*, Washington, D.C.
- Paramonov, J., Chatys, R., Anderson, J. and Kleinhofs, M. (2012) Markov Model of Fatigue of a Composite Material with Poisson Process of Defect Initiation. *Mechanics of Composite Materials*, 48, 2, pp. 217-228, doi: 10.1007/s11029-012-9267-5.
- Takosoglu, J., Laski, P., Blasiak, S., Bracha, G. and Pietrala, D. (2016b) Determining the static characteristics of pneumatic muscles. *Measurement & Control*, 49, 2, pp. 62-71, doi: 10.1177/0020294016629176.



## IMPLEMENTATION OF INTERACTING CREEP AND FATIGUE UNDER THERMO-MECHANICAL LOADING

J. Had\*

**Abstract:** Presented work is dealt with thermo-mechanical fatigue analysis. Only elastic stress and temperature field are taken from FEM analysis. Strain components are calculated using nonlinear Maxwell model to cover both elastoplasticity and viscoplasticity. For stepwise stress history elastoplastic and viscoplastic strain component are gain independently solving one after another. For every point in loading history is consequently found closed hysteresis loop and damage increment corresponding to actual hysteresis loop is evaluated. Current damage is calculated by Prandtl-Ishlinskii model of hysteresis using iso-thermal fatigue curves.

**Keywords:** Thermo-mechanical fatigue, Hysteresis modeling, Viscoplasticity, Damage prediction.

### 1. Introduction

During the service of an engine, a multitude of material damage such as foreign object damage, erosion, high cycle fatigue, low cycle fatigue, fretting, hot corrosion/oxidation, creep, and thermo-mechanical fatigue is induced in these parts. The mechanical loading and effects based on the temperature gradient were stated as the most important factors.

Changing temperature during the loading cycles has influence on stress-strain state and therefore it causes closure problem of stress-strain hysteresis loop. Temperature dependent fatigue properties brings additional aspects to deal with. An approach for solving hysteresis loops closure problem as well as modeling of damage can be found in Nagode (2010).

Moreover real engine can operate in long-term conditions. Besides, loading spectra can contains specific loading type, dwell for instance, and they cannot be covered by traditional way of analysis. In additional, due to high temperature field time-dependent degradation mechanism has to be taken into consideration and its interaction with pure fatigue ( $\epsilon_{pl}$  induced mechanism). The way how creep and fatigue can be considered and interacted is described in further paragraphs.

### 2. Framework of coupling elastoplasticity and viscoplasticity

It is known that the fatigue and creep damages depend on elastoplastic strain and stress respectively. If the life prediction is based on the instantaneous values, both fatigue and creep damages should be overestimated for positive mean stress due to relaxation. For this purpose viscoplastic strain component must be evaluated and affected final elastoplastic strain and stress respectively. In order to cover viscoplasticity spring-slider model was extended to the nonlinear Maxwell model by adding nonlinear damper in series according to Nagode (2007), see Fig. 1.

Stress tensor and temperature field serve as inputs into fatigue analysis procedure. For this purpose elastic FEM analysis was performed and all necessary inputs for fatigue analysis are calculated from elastic stress tensor and temperature field. In fatigue analysis elastoplastic stress  $\sigma_{el-pl}(t_i)$  is calculated with Neuber's approximation from FEM elastic input. From calculated elastoplastic stress, total strain  $\epsilon_{total}(t_i)$  can be solved. For strain approximation stress-controlled Prandtl-Ishlinskii model can be used to cover elastoplasticity according to equation (1) and (2). Description of approximation of cyclic

---

\* Ing. Jiří Had, PhD.: VZLÚ a.s., Beranových 130 Praha 9, Prague; CZ, +420 225 115 593, had@vzlu.cz

deformation curve and calculation of parameters of spring-slider model  $C_r$  and  $r_r$  can be seen in Nagode (2010) and Grzesikiewicz (2012).

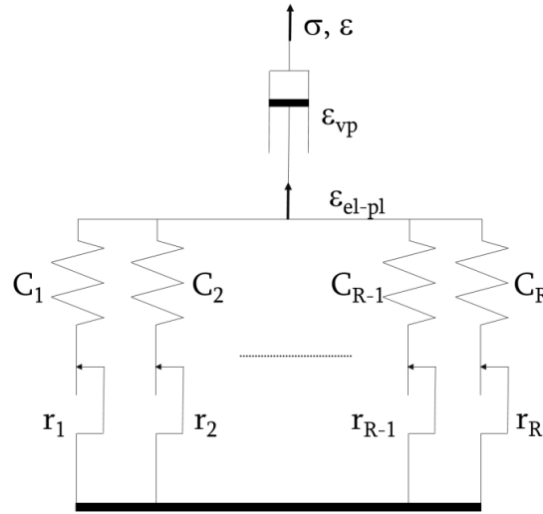


Fig. 1: Maxwell model of viscoplasticity.

$$\epsilon_{\text{total}}(t_i) = \sum_{r=1}^R C_r(T_i) * (\sigma_{\text{el-pl}}(t_i) - \sigma_r^{\text{pl}}(t_i)) \quad (1)$$

$$\sigma_r^{\text{pl}}(t_i) = \max \left\{ \begin{array}{l} \sigma_{\text{el-pl}}(t_i) - r_r \\ \min \left\{ \begin{array}{l} \sigma_{\text{el-pl}}(t_i) + r_r \\ \sigma_r^{\text{pl}}(t_{i-1}) \end{array} \right\} \end{array} \right\} \quad (2)$$

Total strain  $\epsilon_{\text{total}}$  can be divided into elastoplastic and viscoplastic part according to (3).

$$\epsilon_{\text{total}}(t_i) = \epsilon_{\text{pl}}(t_i) + \epsilon_{\text{vp}}(t_i) \quad (3)$$

For stepwise stress history elastoplastic  $\epsilon_{\text{pl}}$  and viscoplastic  $\epsilon_{\text{vp}}$  strain component are gain independently solving one after another. Viscoplastic strain component is approximately calculated from eq. (4).

$$\epsilon_{\text{vp}}(t_i) \approx \text{sgn}(\sigma_{\text{el-pl}}(t_{i-1})) \dot{\epsilon}_{\text{vp}}(t_{i-1})(t_i - t_{i-1}) + \epsilon_{\text{vp}}(t_{i-1}) \quad (4)$$

Visoplastic strain rate  $\dot{\epsilon}_{\text{vp}}$  in (4) is calculated from model proposed in Bina (1997) in the following form (5).

$$\log \dot{\epsilon}_{\text{vp}} = A_1 + A_2 \log \left| \frac{1}{T} - \frac{1}{A_5} \right| + A_3 \log \left| \frac{1}{T} - \frac{1}{A_5} \right| [\sinh(A_6 \sigma T)] + A_4 \log [\sinh(A_6 \sigma T)] \quad (5)$$

Unknown elastoplastic strain  $\epsilon_{\text{pl}}$  is then easily calculated from known total strain (1) and viscoplastic strain (4) from equation (3). Finally, stress  $\sigma_{\text{el-pl}}(t_i)$  can be solved from plastic strain controlled Prandtl-Ishlinskii model, see (6) and (7).

$$\sigma_{\text{el-pl}}(t_i) = \sum_{r=1}^R S_r(T_i) * (\epsilon_{\text{pl}}(t_i) - \epsilon_r(t_i)) \quad (6)$$

$$\epsilon_r(t_i) = \max \left\{ \begin{array}{l} \epsilon_{\text{pl}}(t_i)(t_i) - q_r \\ \min \left\{ \begin{array}{l} \epsilon_{\text{pl}}(t_i)(t_i) + q_r \\ \epsilon_r(t_{i-1}) \end{array} \right\} \end{array} \right\} \quad (7)$$

According presented procedure, plastic strain component and corresponding stress are calculated in every time step from whole loading history. Because every stress and strain variable are dependent on previous state, whole loading history should be repeated several times. In the case of presented coupled viscoplasticity and elastoplasticity several repetitions are recommendable. Into every repetition comes variables from previous run. Strain component and corresponding stress were calculated to contribute to pure fatigue damage. For that reason extrapolated stabilized cyclic deformation curve for strain rate  $\dot{\epsilon} \rightarrow \infty$  is used in hysteresis model. Example of simulation of two loading histories with five repetition is on following figures, see Fig. 2.

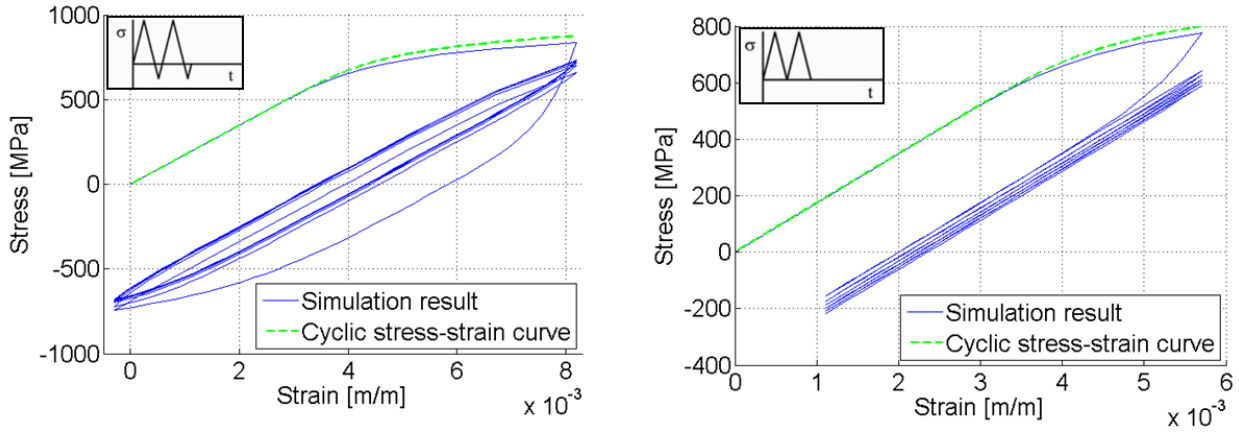


Fig. 2: Example of stress-strain simulation.

### 3. Damage prediction

Every step of loading history is analyzed sequentially and therefore growing damage is calculated starting from  $t = 0$  to the end of loading spectrum. Theoretical background of damage calculation is proposed in paper Nagode (2010). In every time step hysteresis loop is formed between current analyzed time step and certain point from previous loading. Actual stress amplitude and mean stress is calculated from this loop. Actual fatigue damage is evaluated with SWT damage operator. Prandtl-Ishlinskii model of hysteresis is applied on interpolated iso-thermal fatigue curves for current temperature. Actual fatigue damage is get as the sum of elemental contributions from each individual spring-slider sub-models of fatigue curve.

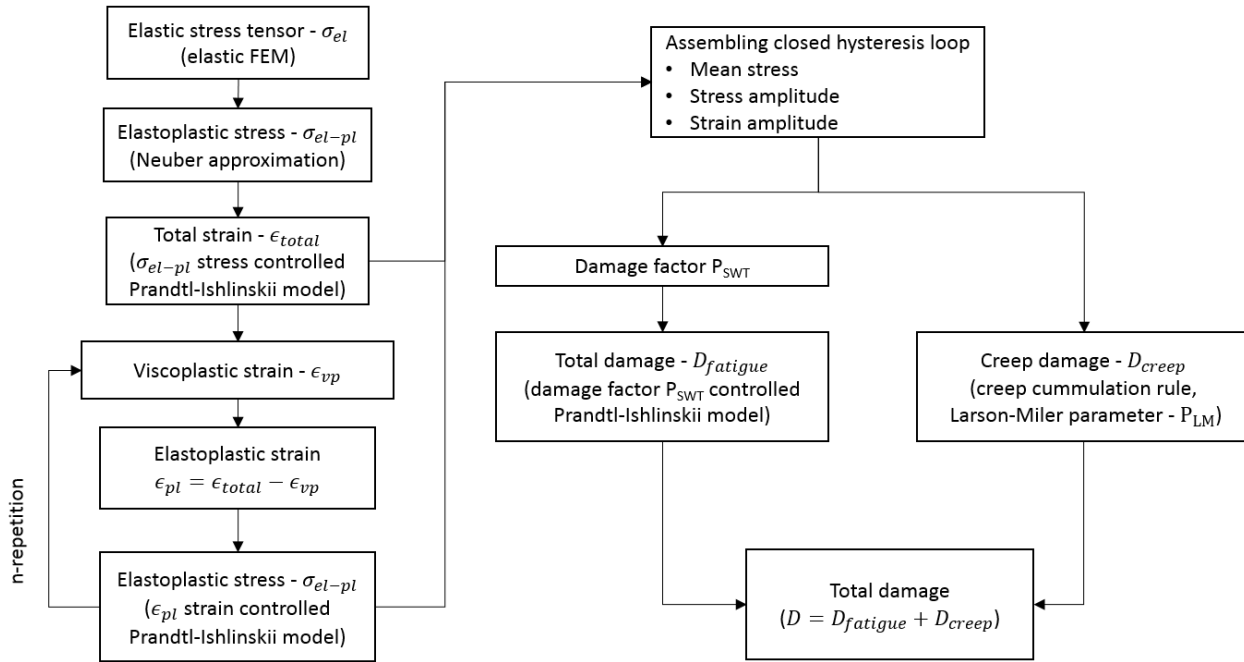


Fig. 3: Block scheme of consideration of both fatigue and creep damage mechanisms.

Creep damage is calculated according to (8).

$$D_c(t_i) = \sum \frac{t_i}{t_c} \quad (8)$$

Corresponding time to rupture  $t_c$  is calculated from creep master curve. For life time prediction where creep doesn't contribute to major part of life, Larson-Miller parameter is used to get time to rupture, see (9).

$$\log \sigma = A_1 + A_2 P_{LM} + A_3 P_{LM}^2$$

$$P_{LM} = T(\log(t_{cr}) + A_4) \quad (9)$$

Total damage is then supposed as the summation of fatigue and creep damage. Sequential block scheme of described approach is depicted in Fig. 3.

#### 4. Conclusions

Presented paper briefly described promising approach for continuous damage calculation during the non-isothermal loading. This concept is computational cheap and very effective using only widely available material data from isothermal tests. Coupling elastoplasticity and viscoplasticity mechanisms enables calculation both fatigue and creep damage. Whole analysis framework is suitable for those cases: low level of plastic strain, crucial point is localized inside of small area and stress-strain redistribution occurs only at small scale during the loading history.

#### Acknowledgement

This work was supported by Výzkumný a zkušební letecký ústav, a.s. in project TMF, project number IP4409.

#### References

- Nagode, M., Hack, M. and Fajdiga, M. (2010) Low cycle thermo-mechanical fatigue: damage operator approach. *Fatigue & Fracture of Engineering Materials & Structures*, 33, 3, pp. 149-160.
- Nagode, M. and Fajdiga, M. (2007) Coupled elastoplasticity and viscoplasticity under thermomechanical loading. *Fatigue & Fracture of Engineering Materials & Structures*, 30, 6, pp. 510-519.
- Bína, V. and Hakl, J. (1997) Relation between creep strength and strength for specific creep strain at temperatures up to 1200° C. *Materials Science and Engineering: A*, 234, pp. 583-586.
- Grzesikiewicz, W. and Zbiciak, A. (2012) Study of generalized Prandtl rheological model for constitutive description of elastoplastic properties of materials. *Journal of Achievements in Materials and Manufacturing Engineering*, 55, 2, pp. 501-510.

## EFFECTS OF TURBULENCE IN FE MODEL OF HUMAN VOCAL FOLDS SELF-OSCILLATION

P. Hájek<sup>\*</sup>, P. Švancara<sup>\*</sup>, J. Horáček<sup>\*\*</sup>, J. G. Švec<sup>\*\*\*</sup>

**Abstract:** *The purpose of the study is to determine whether a turbulence model in fluid flow calculation affects the vocal folds (VF) vibration and the acoustics of human vocal tract (VT). The objective is examined using a two-dimensional (2D) finite element (FE) model of the fluid-structure-acoustic interaction for self-sustained oscillations of the VF. The FE model consists of the models of the VF, the trachea and a simplified model of the human VT. The developed FE model includes large deformations of the VF tissue and VF contact interrupting the airflow during glottis closure. The airflow is modelled by the unsteady viscous compressible Navier-Stokes equations, without and with the Shear Stress Transport (SST) turbulence model. Fluid-structure interaction (FSI) and morphing of the fluid mesh are realized using Arbitrary Lagrangian-Eulerian (ALE) approach. The method is applied on the FE model of the VT shaped for the Czech vowel [a:]. Also effect of varying stiffness of the superficial lamina propria (SLP) is analyzed. The numerical simulations showed that considering of the turbulence affects mainly higher frequencies apparent in a frequency spectrum of the VT acoustics.*

**Keywords:** Simulation of phonation, SST turbulence model, Fluid-structure-acoustic interaction, Finite element method, Biomechanics of voice.

### 1. Introduction

Relatively large number of computational models were recently published in literature, however many of them do not cover the complete fluid-structure-acoustic interaction. FE model of the interaction between structure and airflow created by Alipour et al. (2000) was one of the first partial differential equation based models. The model was modified later to comprise acoustics of the vocal tract (Alipour et al., 2015). Zhang et al. (2004) take into account interaction between airflow and acoustics resolved by Ffowcs-Williams-Hawkings method. The fluid-structure-acoustic interaction is usually solved in two ways. Coupling of a structure and incompressible fluid flow solutions with acoustic analogy is more common (Link et al., 2009), on the other side if compressible fluid is considered (Suh et al., 2007), the acoustic solution can be obtained directly from the pressure field.

Previous studies of the authors concern of numerical simulations of self-sustained VF vibration (Švancara at al., 2011; Švancara at al., 2014) with emphasis on material properties of lamina propria (Hájek et al., 2016a; Hájek et al., 2016b). In this study a new FE model is presented and the solution of fluid flow without the turbulence model is compared to the solution with included SST turbulence model, one of the most advanced in the group of RANS (Reynolds-averaged Navier-Stokes) flow models.

### 2. Methods

The 2D FE model was created in the program system ANSYS 15.0 and is composed of 14389 linear elements; see Fig. 1a. Geometry of the four layered VF was created according widely used Scherer's M5

---

<sup>\*</sup> Ing. Petr Hájek: Institute of Solid Mechanics, Mechatronics and Biomechanics; Brno University of Technology; Technická 2896/2; 616 69, Brno; CZ, 126528@vutbr.cz

<sup>\*</sup> Ing. Pavel Švancara, PhD.: Institute of Solid Mechanics, Mechatronics and Biomechanics; Brno University of Technology; Technická 2896/2; 616 69, Brno; CZ, svancara@fme.vutbr.cz

<sup>\*\*</sup> Ing. Jaromír Horáček, DSc.: Institute of Thermomechanics; Academy of Sciences of the Czech Republic; Dolejškova 1402/5; 182 00, Prague; CZ, jaromirh@it.cas.cz

<sup>\*\*\*</sup> RNDr. Jan G. Švec, PhD.: Department of Biophysics; Palacky University Olomouc; 17. listopadu 12; 771 46, Olomouc; CZ, jan.svec@upol.cz

geometry (Scherer et al., 2001). Young's modulus of VF layers were used as follows: epithelium 25000 Pa, SLP 2000 – 5000 Pa, ligament 8000 Pa and muscle 65000 Pa. Poisson's ratio of 0.49 was considered for all layers except the muscle with 0.40. The material density of  $1040 \text{ kg}\cdot\text{m}^{-3}$  was used for all layers. Geometry of the VT was converted from magnetic resonance images (Radolf, 2010). Material properties of air corresponding to the human body temperature were used: density  $1.205 \text{ kg}\cdot\text{m}^{-3}$ , fluid viscosity  $1.81351 \cdot 10^{-5} \text{ kg}\cdot\text{m}^{-1}\cdot\text{s}^{-1}$ , speed of sound  $353 \text{ m}\cdot\text{s}^{-1}$ . Boundary conditions of the structural (VF) and fluid (VT and trachea) part of the model are shown in the Fig. 1a together with position of evaluation points. Other details of the model can be found for example in Hájek et al. (2016b).

At first VF are set to phonatory position by pushing them slightly into the contact. Solution algorithm for fluid-structure interaction is based on explicit coupling scheme with separate solvers for the structural and fluid part. More details can be found in Švancara et al. (2014). Computational algorithm of airflow with SST turbulence model is given in Fig. 1b.

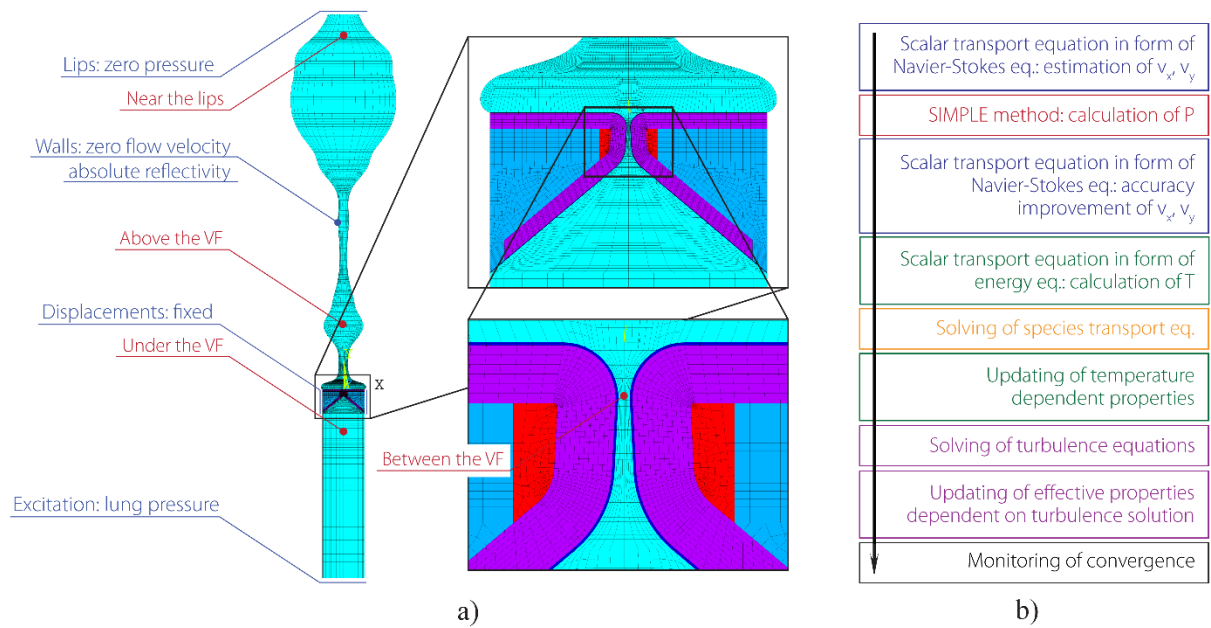


Fig. 1: a) Complete FE model with boundary conditions (blue), evaluation points (red) and with details of FE mesh; b) computational algorithm of airflow with SST turbulence model.

Typical computation of 0.1 s long phonation with turbulence model took approximately 13.5 hours on Intel i7-960 3.20 GHz (4 cores / 8 threads) and 12 GB of RAM. Equivalent solution without turbulence model took 3 hours less on the same PC.

### 3. Results and discussion

Comparison of the VF oscillation characteristics with and without turbulence model for increasing Young's modulus of the SLP ( $E_{\text{SLP}}$ ) is in Tab. 1. Evaluated parameters of VF oscillations were the maximal width of glottis  $WG_{\text{max}}$ , the open quotient OQ, the closed quotient CQ, the closing quotient CIQ, the speed quotient SQ, the speed index SI and the fundamental oscillation frequency. The lung pressure  $p_{\text{Lu}}$  was decreased by 5 Pa for simulations with turbulence model in order to initiate the self-sustained vibrations.

From the results we can observe the increase of the fundamental frequency for simulations with turbulence model. Maximal width of glottis  $WG_{\text{max}}$  remains more or less in the same limits. Duration of the open phase is slightly shorter compared to the closed phase when using the turbulence model (see open quotient OQ and closed quotient CQ in Tab. 1). The values of the quotients correspond to clinical results (Lohscheller et al., 2013).

Tab. 1: Characteristics of VF oscillation depending on turbulence model, Young's modulus of the lamina propria  $E_{SLP}$  and lung pressure  $p_{Lu}$ .

Turbulence model	$E_{SLP}$ [Pa]	$p_{Lu}$ [Pa]	$WG_{max}$ [mm]	OQ [-]	CQ [-]	CIQ [-]	SQ [-]	SI [-]	$f$ [Hz]
Yes	2000	270	0.56	0.38	0.62	0.09	3.14	0.52	132
	2500		0.49	0.46	0.54	0.09	4.00	0.60	132
	3000		0.42	0.50	0.50	0.06	7.20	0.76	122
	3500		0.38	0.57	0.43	0.06	8.83	0.80	97
No	2000	275	0.55	0.47	0.53	0.07	5.33	0.68	123
	2500		0.48	0.47	0.53	0.09	4.29	0.62	127
	3000		0.42	0.55	0.45	0.07	6.83	0.74	116
	3500		0.38	0.57	0.43	0.07	6.86	0.75	103

Fig. 2 shows an example of the vocal folds self-oscillations that are stabilized after several periods of transient regime both for simulation with and without the turbulence model. Comparing flow velocities in selected node between the VF one can observe a decrease of all peaks for simulation with SST turbulence model. Such a decrease could be caused by energy dissipation due to capturing smaller eddies by turbulence. Power spectral density of acoustic pressure in the node near the lips is not too affected by using the SST turbulence model for frequencies up to 3 kHz, see Fig. 3. For frequencies above 3 kHz, an amplitude decrease of resonance frequencies for simulation with the turbulence model can be observed.

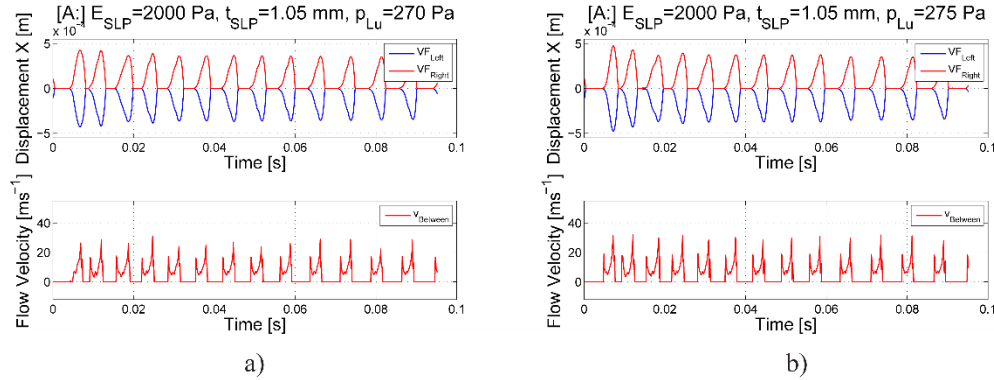


Fig. 2: Displacement in  $x$  direction of selected nodes on the face of the left and right VF located in the middle of the VF height and flow velocity in selected node between the VF: a) with turbulence model; b) without turbulence model.

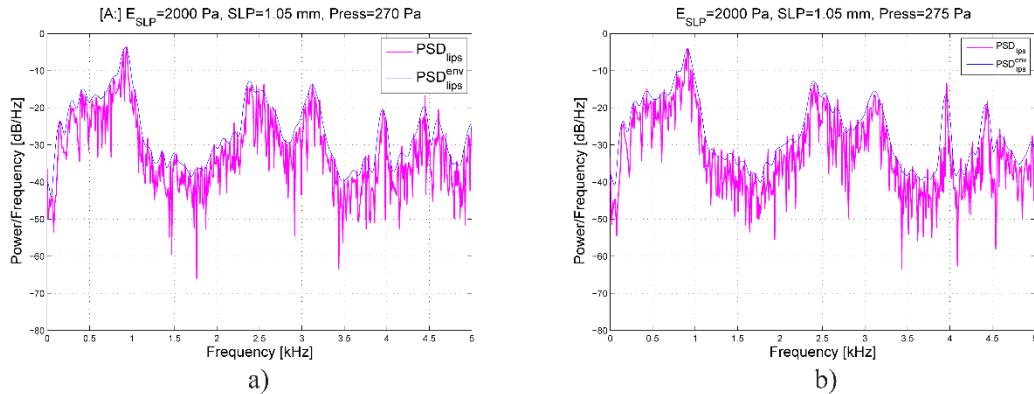


Fig. 3: Power spectral density of acoustic pressure in selected node near the lips a) with turbulence model; b) without turbulence model.



#### 4. Conclusion

The 2D FE model of the fluid-structure-acoustic interaction during self-sustained oscillation of the human vocal folds was created and effect of the SST turbulence model on the VF vibration and the acoustics of the VT was analyzed.

The computed results showed that use of SST turbulence model leads to slightly increase of the fundamental frequency even for smaller lung pressure used for excitation. For simulation with turbulence model also duration of the open phase is slightly shorter comparing to the case without turbulence model. Use of SST turbulence model leads also to decrease of peaks of flow velocities between the VF and to decrease of the peaks of acoustic resonances for frequencies above 3 kHz. Turbulence model is capable of capturing smaller eddies comparing to simulations without any turbulence model. Computation without any turbulence model is able to capture only eddies up to size of an element. Smaller eddies represent additional dissipation of energy in form of acoustic quadrupoles on higher frequencies (Williams, 1969). Larger eddies carry more energy than the relatively small ones (Williams, 1969) and for that reason larger eddies have dominant impact on interaction between fluid and acoustics and affect mainly lower frequencies.

#### Acknowledgement

This research is supported by Grant Agency of the Czech Republic by the project No 16-01246S „Computational and experimental modelling of self-induced vibrations of vocal folds and influence of their impairments on human voice.”

#### References

- Alipour, F., Berry, D.A. and Titze, I.R. (2000) A finite-element model of vocal-fold vibration. *Journal of the Acoustical Society of America*, 108(6), pp. 3003-3012.
- Alipour, F. and Scherer, R.C. (2015) Time-Dependent Pressure and Flow Behavior of a Self-oscillating Laryngeal Model With Ventricular Folds. *Journal of Voice*, 29(6), pp. 649-659.
- Hájek, P., Švancara, P., Horáček, J. and Švec, J.G. (2016a). Numerical Simulation of the Self-oscillating Vocal Folds in Interaction with Vocal Tract Shaped for Particular Czech Vowels. in: 15th International Conference on Global Research and Education (Inter-Academia), Springer Verlag, Warsaw, pp. 317-323.
- Hájek, P., Švancara, P., Horáček, J. and Švec, J.G. (2016b) Numerical Simulation of the Effect of Stiffness of Lamina Propria on the Self-sustained Oscillation of the Vocal Folds. in: *Engineering Mechanics*, Svratka, pp. 182-185.
- Link, G., Kaltenbacher, M., Breuer, M. and Döllinger, M. (2009) A 2D finite-element scheme for fluid-solid-acoustic interactions and its application to human phonation. *Computer Methods in Applied Mechanics and Engineering*, 198(41), pp. 3321-3334.
- Lohscheller, J., Švec, J.G. and Döllinger, M. (2013) Vocal fold vibration amplitude, open quotient, speed quotient and their variability along glottal length: kymographic data from normal subjects. *Logopedics. Phoniatrics. Vocology*, 38(4), pp. 182-192.
- Radolf, V. (2010). Direct and inverse task in acoustics of the human vocal tract. PhD Thesis, Czech Technical University in Prague.
- Scherer, R.C., Shinwari, D., De Wit, K.J., Zhang, C., Kucinski, B.R. and Afjeh, A.A. (2001) Intraglottal pressure profiles for a symmetric and oblique glottis with a divergence angle of 10 degrees. *Journal of the Acoustical Society of America*, 109(4), pp. 1616-1630.
- Suh, J. and Frankel, S.H. (2007) Numerical simulation of turbulence transition and sound radiation for flow through a rigid glottal model. *Journal of the Acoustical Society of America*, 121(6), pp. 3728-3739.
- Švancara, P., Horáček, J. and Hrůza, V. (2011) FE modelling of the fluid-structure-acoustic interaction for the vocal folds self-oscillation. in: *Vibration Problems ICOVP 2011* (Náprstek, J., Horáček, J., Okrouhlík, M., Marvalová, B., Verhulst, F., Sawicki, J.), Springer, Berlin, pp. 801-807.
- Švancara, P., Horáček, J., Martínek, T. and Švec J.G. (2014) Numerical simulation of videokymographic images from the results of the finite element model. in: *Engineering Mechanics*, Svratka, pp. 640-643.
- Williams, J.E.F. and Hawkins, D.L (1969). Sound Generation by Turbulence and Surfaces in Arbitrary Motion. *Philosophical Transactions of the Royal Society of London, Series A, Mathematical and Physical Sciences*, 264(1151), pp. 321-342.
- Zhang, Z., Mongeau, L., Frankel, S.H., Thomson, S. and Park, J.B. (2004) Sound generation by steady flow through glottis-shaped orifices. *Journal of the Acoustical Society of America*, 116(3), pp. 1720-1728.

## CALDERÓN'S INVERSE PROBLEM IN CIVIL ENGINEERING

**J. Havelka<sup>\*</sup>, J. Sýkora<sup>\*\*</sup>, A. Kučerová<sup>\*\*\*</sup>**

**Abstract:** *In specific fields of research such as treatment of historical structures, medical imaging, material science, geophysics and others, it is of particular interest to perform only a non-intrusive boundary measurement. The idea is to obtain a comprehensive information about the material properties inside the domain under consideration while maintaining the test sample intact. This contribution is focused on such problems i.e. synthesizing a physical model of interest with a boundary inverse techniques. The forward model is represented by a basic time dependent diffusion equation with Finite Element (FE) discretization and the parameters are subsequently recovered using a modified Calderon problem principle, numerically solved by a regularized Gauss-Newton method. We provide a basic framework, implementation details and modification of general constraints originally derived for a standard setup of Calderon problem. The proposed model setup was numerically verified for various domains, load conditions and material field distributions. Both steady-state and time dependent cases are studied.*

**Keywords:** Boundary inverse, Finite Element Method, Calderón's problem, Heat transfer.

### 1. Introduction

In this contribution we propose two linear models describing a heat transfer and an inverse method based on Neuman-to-Dirichlet (NTD) operator. Although the idea of boundary inverse method using electric current dates back to 1930s in geophysics it has gained more attention must later in 1980s as a medical imaging technique, i.e. Electrical Impedance Tomography (EIT). The first rigorous formulation of this problem is the most commonly attributed to Argentinian mathematician Alberto Calderón who formed his thoughts in his foundational paper (Calderón 1980). Further development and proofs of uniqueness of the solution were given in (Somersalo, et al., 1992 and Brown, 1997). The basic procedure in EIT is following: by stimulating electrodes attached on a body surface with different injection patterns and simultaneously measuring the resulting potentials on these electrodes, one can with the knowledge of domain shape, electrode impedance and applied current uniquely recover the isotropic conductivity field (Calderón 1980).

### 2. Forward models

The presented models will play a fundamental role since each will be repeatedly evaluated in the inverse process and will also substitute an experiment, i.e. will be used to generate artificial measurements. The steady-state model represents a straight forward, single-parameter model that closely relates to the classical concept of Calderón problem, while the time-dependent model is essentially a two-parameter based and has a wider spread of use in real world applications.

#### 2.1. Steady-state heat transfer

Following the same principles mentioned in (Calderón, 1980), one can obtain a similar set of equations for a steady-state heat transfer, allowing a more general boundary conditions. The governing equations may therefore take a following form

---

<sup>\*</sup> Ing. Jan Havelka: Department of Mechanics, Faculty of Civil Engineering, Czech Technical University in Prague, Thákurova 7/2077, 166 29 Prague, CZ, jan.havelka.1@fsv.cvut.cz

<sup>\*\*</sup> Ing. Jan Sýkora, PhD.: Department of Mechanics, Faculty of Civil Engineering, Czech Technical University in Prague, Thákurova 7/2077, 166 29 Prague, CZ, jan.sykora.1@fsv.cvut.cz

<sup>\*\*\*</sup> Ing. Anna Kučerová, PhD.: Department of Mechanics, Faculty of Civil Engineering, Czech Technical University in Prague, Thákurova 7/2077, 166 29 Prague, CZ, anicka@cml.fsv.cvut.cz

$$\left\{ \begin{array}{ll} \nabla \cdot (\lambda(x) \nabla u(x)) = 0, & x \in \Omega \\ \alpha^{(i)}(u_0^{(i)}(x) - u(x)) = f_T, & x \in \partial\Omega_T^{(i)} \setminus e_l \\ u(x) + r_l \lambda \frac{\partial u}{\partial n}(x) = T_l, & x \in e_l \\ \lambda \frac{\partial u}{\partial n}(x) = f_N, & x \in \partial\Omega_N^{(i)} \setminus e_l \end{array} \right. \quad (1)$$

where  $u$  is a temperature,  $\lambda$  is a thermal conductivity,  $L$  is the number of electrodes,  $r_l$  is an electrode resistance coefficient,  $e_l$  is  $l$ -th electrode and  $T_l$  is the  $l$ -th stimulation pattern. The environment factors are  $\alpha$  being the heat transfer coefficient,  $u_0$  is the outside temperature and  $f_N$  are prescribed fluxes with corresponding boundary subsets  $\partial\Omega_T$  and  $\partial\Omega_N$  respectively.

Contrary to electrostatics, the consequences of aforementioned conditions are following relaxed assumptions under which the solution can be proved (Somersalo, et al., 1992 and Cheng, et al., 1989):

**Assumption 1.** The conductivity  $\lambda$ , contact resistances  $r_l$  and transfer coefficients  $\alpha^{(i)}$  satisfy following

- (i)  $\lambda \in L^\infty(\Omega; \mathbb{R})$ ,  $\inf_{x \in \Omega} \lambda(x) = \lambda_- > 0$ ,
- (ii)  $0 < r_l^- \leq r_l \leq r_l^+ < \infty, l = 1, \dots, L$ ,
- (iii)  $0 < \alpha_-^{(i)} \leq \alpha^{(i)} \leq \alpha_+^{(i)} < \infty, \forall i$ .

In this settings, we assume the accessible boundary  $\Gamma_m$  is completely captured with a thermal camera or with an array of discrete thermometers. Each active electrode is then consecutively, one after each other, heated to temperature  $T_l$  resulting into  $L$  thermal images of the observed boundary  $\Gamma_m$ .

## 2.2. Time dependent heat transfer

In real conditions it is, however, not an easy task to maintain a stable and steady state conditions. Not only the surrounding temperature will fluctuate, but for standard building materials like bricks, wood, etc. the steady state, after changing the loading conditions, is reached after several hours or days depending on the volumetric capacity, heat conductivity, material thickness and temperature change. Therefore, we intend to apply the identical principles used in a Calderón problem for time dependent models.

To capture a time dependent heat transfer, one can adapt following set of equations

$$\left\{ \begin{array}{ll} \rho c_p \frac{\partial u}{\partial t} - \nabla \cdot (\lambda \nabla u) = f, & x \in \Omega \\ \alpha^{(i)}(u_0^{(i)}(x) - u(x)) = f_T, & x \in \partial\Omega_T^{(i)} \\ u = f_D, & x \in \partial\Omega_D^{(i)} \\ \lambda \frac{\partial u}{\partial n}(x) = f_N, & x \in \partial\Omega_N^{(i)} \end{array} \right. \quad (2)$$

where  $\rho$  is volumetric mass density,  $c_p$  is specific heat capacity and  $\partial\Omega_{N,T,D}^{(i)}$  are non-intersecting subsets of boundary  $\partial\Omega^{(i)}$  in  $i$ -th loading condition with corresponding environmental factors  $u_0$ ,  $\alpha^{(i)}$ ,  $f_{T,D,N}$ . In order to maintain NTD sensing, the set of equations in is subjected to following constrain

**Assumption 2.** Let  $\Gamma_m$  be a subset of boundary  $\partial\Omega$  that is being observed. Then

$$\Psi = \left( \partial\Omega_N^{(i)} \cup \partial\Omega_T^{(i)} \right) : (\Psi \cap \Gamma) \neq \emptyset, \forall i,$$

must hold, i.e. the boundary subjected to measurements must contain at least some Neumann conditions.

Conditions as indicated in assumption 1 must be also met, i.e. (ii,iii) have to be extended for  $\rho$  and  $c_p$ .

In this settings, the model is intended to only rely on the environment natural factors without stimulating electrodes. Also the data from thermal cameras are recorded continuously on the accessible boundary.

## 3. Numerical solution of the inverse problem

Results in section 4 share the following regularized Gauss-Newton iteration scheme (Holder, 2004)

$$\sigma_{k+1} = \sigma_k + \delta \sigma_k \quad (3)$$

$$\delta\sigma_k = (\mathbf{J}_k^T \mathbf{J}_k + \alpha_k \mathbf{L}^T \mathbf{L})^{-1} \left( \mathbf{J}_k^T (\mathbf{u}_r - F(\sigma_k)) - \alpha_k \mathbf{L}^T \mathbf{L} (\sigma_k - \sigma_r) \right) \quad (4)$$

where  $f(\sigma) \in R^{vw}$  represents a discrete NTD operator of a forward model with  $v$  being the number of measurement points and  $w$  is the number of experiments. The a priori measured quantity is stored in vector  $\mathbf{u}_r \in R^{vw}$  and the regularization operator  $L$  is a pre-calculated Laplacian. In all cases the reference field  $\sigma_r = \sigma_0 = 1$ . From our experience, the most reliable choice of hyper-parameter  $\alpha_k$  was the one used in Levenberg-Marquardt regularization in a following form

$$\alpha_k = \max(\max(\mathbf{J}_k^T \mathbf{J}_k)) \quad (5)$$

Jacobian  $\mathbf{J}_k$  was updated in each iteration and was calculated numerically in a following way

$$J_i^{(jkl)} = \frac{\partial u_{jk}}{\partial \sigma_l^i} \quad (6)$$

where  $\mathbf{J}_i$  is a third-order tensor in  $i$ -th iteration, indexes  $jk$  are representing measurement nodes in FE mesh and individual measurements respectively. Index  $l$  identifies a conductivity change on  $l$ -th element.

#### 4. Results

In this section we investigate the models under various conditions. Specifically, we consider partial data reconstruction and different material properties.

From Fig. 2 and Fig. 3 one can notice that the rightmost figures suffer from an insufficiency of data leading into major artefacts in reconstructed material fields. Also the non-smooth material field was more difficult to recover, which was most evident in the leftmost Fig. 2 and Fig. 3.

Results for a single parameter steady-state simulations were generated in approximately 10 Gauss-Newton iterations, whereas the two-parameter time-dependent problem took 72 iterations. Despite the inaccuracies in certain situations, e.g. insufficiency of data, non-smooth material field, the Gauss-Newton method proved to be stable and reliable solver for such tasks.

##### Steady-state heat transfer model

The foregoing results were generated for following boundary conditions:  $f_T = 10 \cdot (u_i - u)$ , where  $u_1 = 30^\circ\text{C}$ ,  $u_2 = 15^\circ\text{C}$ . The other parameters were chosen in a following way:  $T_l = 10^\circ\text{C}$ ,  $r_l = 0.01 \frac{^\circ\text{C m}^2}{\text{W}}$ .

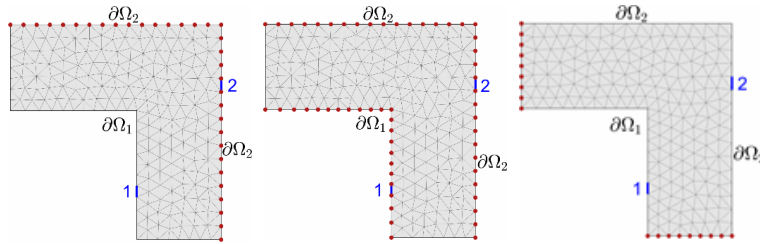


Fig. 1: A set of domains with different boundaries subjected to measurements.  
Red dots: measurement nodes, blue lines: electrodes.

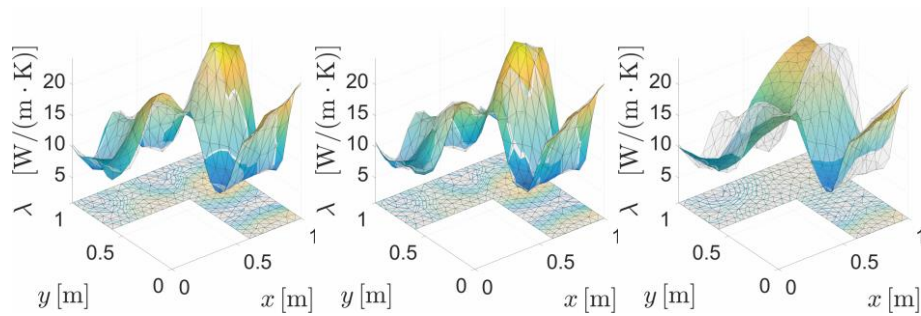


Fig. 2: Reconstruction: a smooth distribution. In grey: original field, in color: reconstructed field.

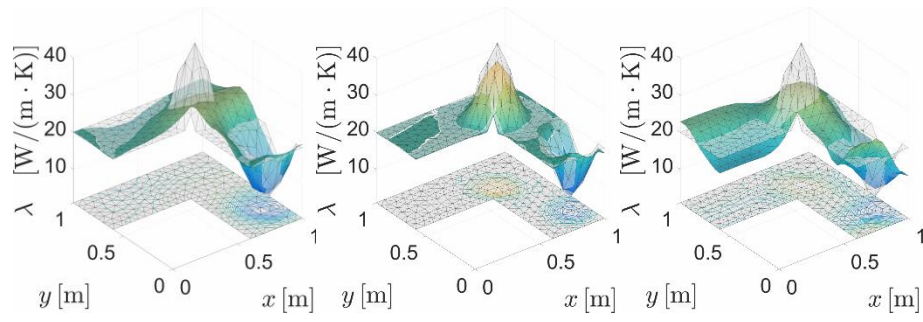


Fig. 3: Reconstruction: non-smooth distribution. In grey: original field, in color: reconstructed field.

### Time-dependent heat transfer model

Assumed boundary conditions are captured in Fig. 4 with a following meaning:  $f_T|_{\partial\Omega_i} = 10 \cdot (f_i - u)$

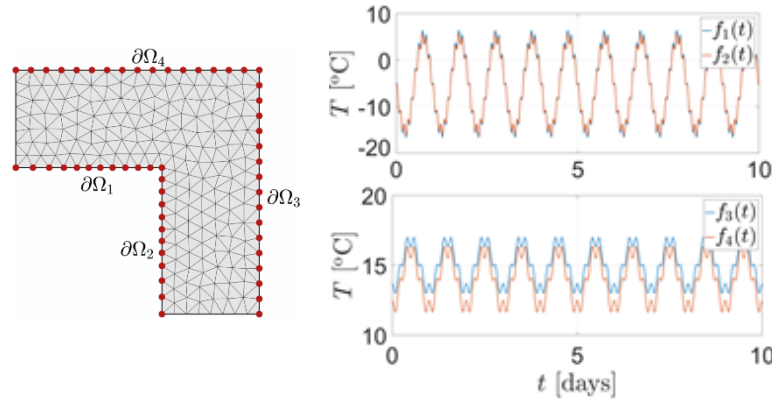


Fig. 4: Domain with boundary conditions.

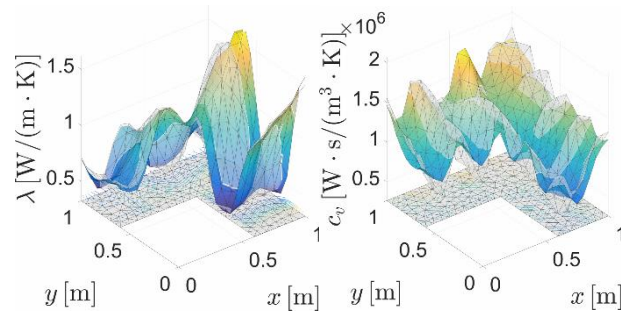


Fig. 5: Reconstruction: left: conductivity field, right: volumetric capacity.

### Acknowledgement

The financial support of this research by the GA15-07299S, GA16-11473Y and SGS17/038/OHK1/1T/11 is gratefully acknowledged.

### References

- Brown, R.M. and Uhlmann, G.A. (1997) Uniqueness in the inverse conductivity problem for nonsmooth conductivities in two dimensions. *Communications in Partial Differential Equations*, 22(5-6):1009-1027.
- Calderón, A.P. (1980) On an inverse boundary value problem. *Seminar on Numerical Analysis and Its Applications to Continuum Physics: Rio de Janeiro*, 12:67-73.
- Holder, D.S. (2004) *Electrical Impedance Tomography: Methods, History and Applications*. Series in Medical Physics and Biomedical Engineering. Taylor & Francis, 1st edition.
- Cheng, K.S., Isaacson, D., Newell, J.C. and Gisser D.G. (1989) Electrode models for electric current computed tomography. *IEEE Transactions on Biomedical Engineering*, 36(9):918-924.
- Somersalo, E., Cheney, M. and Isaacson, D. (1992) Existence and uniqueness for electrode models for electric current computed tomography. *SIAM Journal on Applied Mathematics*, 52(4):1023-1040.

## PRINCIPLE OF THE ROLLING CONTACT FATIGUE FORMATION

M. Hejnova\*

**Abstract:** *There is a lot of theoretical methods how to proceed at the service life assessment of the machine components like gears, bearings, cam mechanisms. This paper deals with principle of the rolling contact fatigue, which is necessary to take into account at the service life estimation. On the basis of these knowledge we can make experimental testing of the samples and from results we can determine relatively exactly the value of the service life of the chosen machine part.*

**Keywords:** Rolling contact fatigue, Pitting, Fracture mechanics.

### 1. Introduction

VÚTS, a.s. deals with the design of cam mechanisms and cams production more than thirty years. This provides us a lot of experience in design and calculation of both axial and radial cams. With designing is connected the methodology of the life prediction of the cam surface. On this basis, we can determine the life of the cam mechanism respectively time when damage occurs.

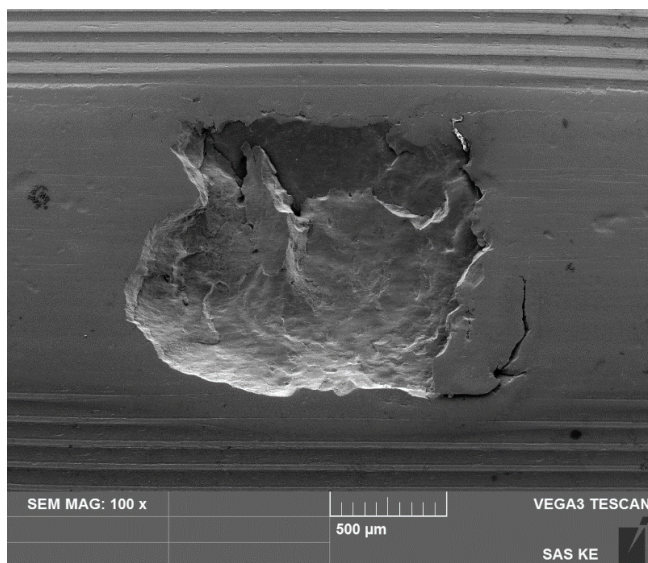


Fig. 1: Damaged surface (pitting) (acquired in own research).

The rolling contact fatigue (RCF) occurs in functional surfaces that are exposed to repeated loading (high local pressure) during movement of the functional surfaces of the machine components (see Fig. 4). It may be a relative rolling movement or a combination of sliding and rolling, what is more common in practice. Characteristic for RCF is gradual accumulation of the cracks in the surface layer at the repeated contact stress. The best known cases of the RCF are at the roller bearings, gears, cam mechanisms, railway wheels etc. Formation, progress and intensity of damage caused by fatigue wear are very dependent on the working conditions (e.g. lubrication, temperature).

There is more types of RCF. The most common (at cam mechanisms) is pitting (Fig. 1). We can observe micro- and macropitting by size of the pits on the damaged surface. Other types of RCF are e.g. spalling, galling, scuffing and scoring.

---

\* Ing. Monika Hejnová, PhD.: VÚTS, a.s., Svárovská 619, 460 01 Liberec; CZ, monika.hejnova@vuts.cz



## 2. Mechanical (mathematical) analysis of RCF

The commonly used theoretical models are based on the Hertz's contact theory. On its basic is given the value of the Hertzian pressure, which is decisive at the determining of the save load. At this load it will not occur damage of the functional surfaces of the cam and roller.

Assumptions of Hertz's theory are available in the literature Koloc (1988). There is a schematic view of the contact of the two cylinders in Fig. 2. There is a contact of cam and roller at the cam mechanism. The length of the contact area is denoted  $l$ , the radii of curvature at point of contact are  ${}^1\rho_y$ ,  ${}^2\rho_y$  and  $F$  defines normal reaction between the particular elements of the pair (Koloc, 1988).

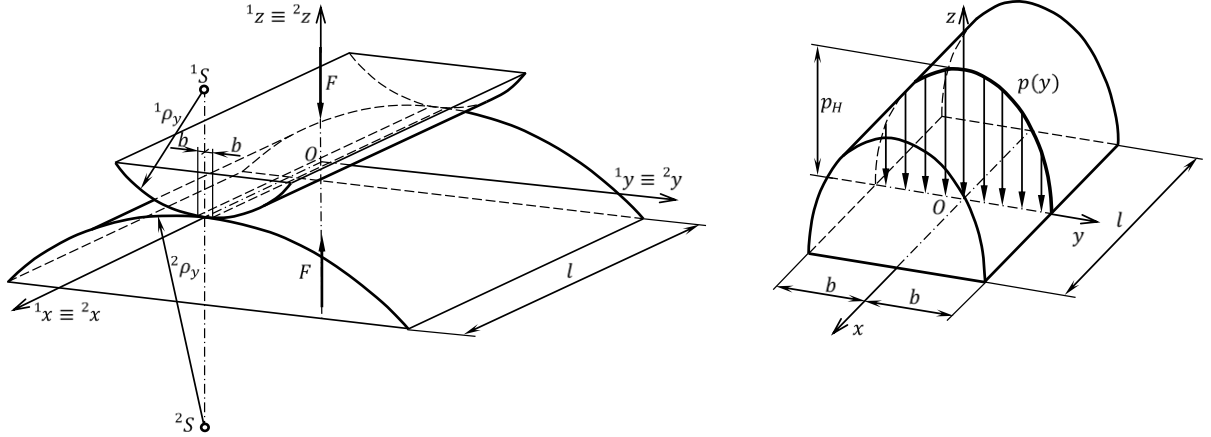


Fig. 2: Contact of cylindrical bodies with parallel axes and pressure distribution in contact.

Hertzian pressure is a maximum compressive stress  $p_H$  defined as (1), where  $f$  is the load in proportion to the length unit.

$$p_H = \frac{2f}{\pi b} = \sqrt{\frac{f(|{}^2\rho_y| \pm {}^1\rho_y)}{\pi(\delta_1 + \delta_2){}^1\rho_y|{}^2\rho_y|}} \quad (1)$$

Unlike the positive radius of curvature of the roller follower  ${}^1\rho_y$ , the radius of curvature of the cam surface in contact  ${}^2\rho_y$  may attain both, positive or negative values. Actually this fact is defined in relation (1) by quantity  $|{}^2\rho_y|$ .

$$\delta_{1,2} = \frac{1 - \mu_{1,2}^2}{E_{1,2}} \quad (2)$$

The quantities  $\delta_1$ ,  $\delta_2$  are the characteristics of elasticity of the elements in the pair (2), where the Poisson's ratio and the modulus of tension elasticity are denoted as  $\mu_{1,2}$  and  $E_{1,2}$  respectively. Rearranging relation (1) we get the bisected contact area (3).

$$b = 2 \sqrt{\frac{f(\delta_1 + \delta_2){}^1\rho_y|{}^2\rho_y|}{\pi(|{}^2\rho_y| \pm {}^1\rho_y)}} \quad (3)$$

The next step is to calculate a reduces stress (Koloc, 1988). The reduced stresses  $\sigma_{red}(\psi, \varsigma)$  are limited by the actual strength condition, written in the form (4), where  $\psi$  is an angular cam displacement and  $\psi \in (0, 2\pi)$  and  $\varsigma = |z|/b \geq 0$ .

$$\max \sigma_{red}(\psi, \varsigma) < \sigma_h \quad (4)$$

For steel are the usual values  $\sigma_c \approx 0.33 R_m$  and  $R_e \approx (0.55 \text{ to } 0.8) R_m$ . However, since the transitory stress limit is  $\sigma_h \approx 2\sigma_c \approx 0.66 R_m$ , the relation (4) may be replaced by the inequality (5), where  $\psi \in (0, 2\pi)$  and  $\varsigma = z/b \geq 0$ . This equation states that no destructive action of elastic deformation is produced in the general pair under operation.

$$\max \sigma_{red}(\psi, \varsigma) < R_e \quad (5)$$

The other view at the mathematical modelling is shown in the Fig. 3. We can see the course of the stress in dependence of the depth below surface. The most important information is, that the maximum of the stress is in the certain depth under the surface. This place is the most loaded and here may form cracks.



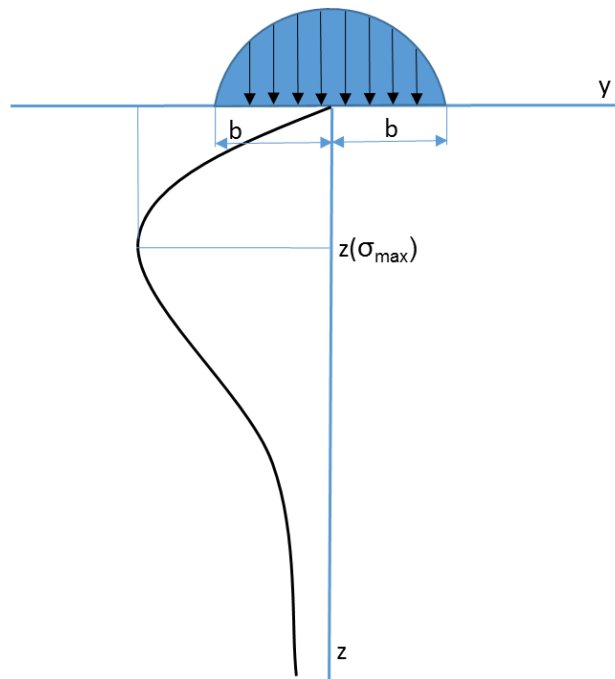


Fig. 3: Dependence between depth below the surface layer and stress.

### 3. Material analysis of RCF

As it has been written above, pitting is the often type of the RCF. From the material point of view we can RCF describe by 3 stages (Pekař, 2015):

1. Stage of the material mechanical properties changes
2. Stage of the cracks nucleation
3. Stage of the cracks propagation to fracture

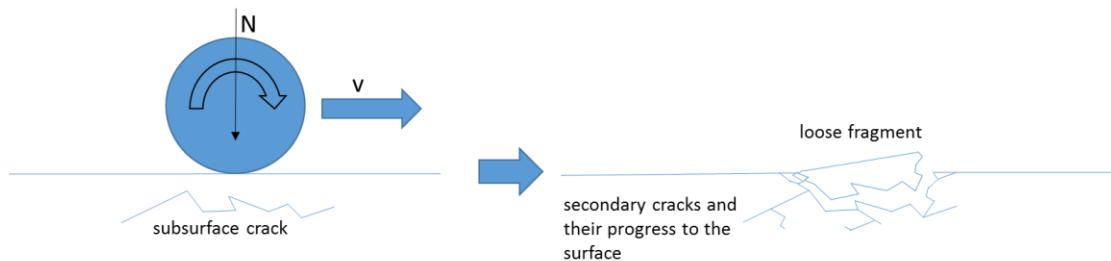


Fig. 4: Pitting formation.

The pitting formation is shown in the Fig. 4. Below the surface can be formed cracks. These cracks can join together with cracks on the surface and it leads to loosening of the small part of the surface (see also Fig. 6). The cracks formation below the surface is connected with the dependence shown in the Fig. 3. If the stress below the surface is high, there can occur the small plastic deformations in the material and repeated loading may lead to crack formation.

RCF is hard depend on the surface hardness, impurities and roughness of the surface (see Fig. 5) (Pošta, 2010)

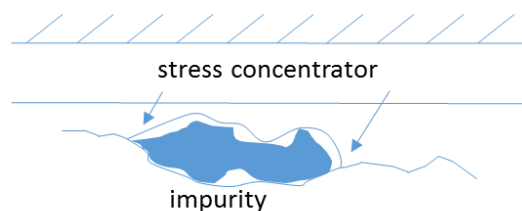
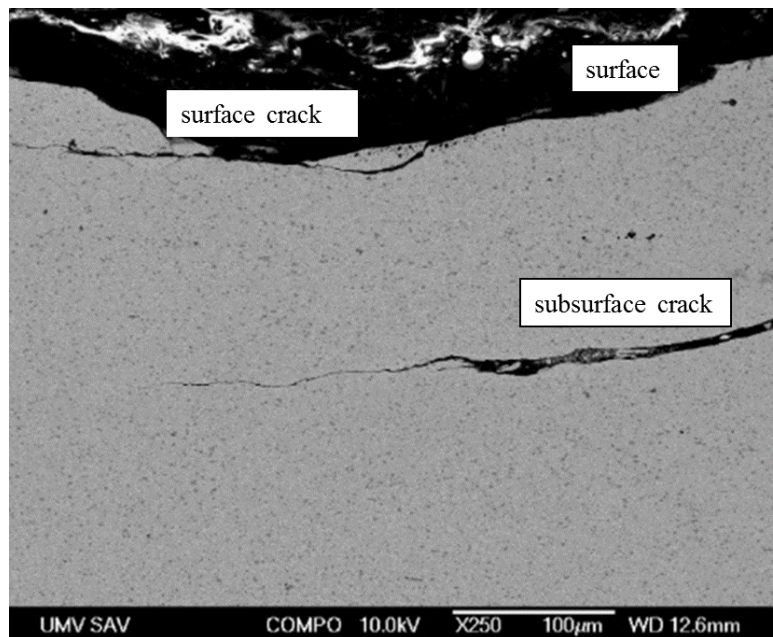


Fig. 5: Material imperfections.

It is important to mention influence of the lubrication on the RCF. At the motion of the contact surfaces penetrates oil to surface cracks. At the next movement of the contact surfaces is the oil closed in the cracks and his pressure increases. This leads to further distribution of cracks. (Pošta, 2010)



*Fig. 6: Detail of the damaged part (acquired in own research).*

We can say, that process of the service life estimation is not only theoretical, but we have to do a lot of tests before we obtain the concrete value. We need detailed information especially about material quality and these information we can obtain from macroscopic and microscopic analyses.

#### 4. Conclusions

We need to have knowledge not only about fracture mechanics but also about calculation of the pressure distribution under the surface. Then we may determine the service life of the examined machine component. RCF is close connected to properties of the concrete material. These properties specify range in which are calculations valid and service life estimation is correct.

The service life may be determined on the basis of the equations including empirically obtained coefficients. Accuracy of this estimation is given by more factors. These are mechanical properties of examined material, surface treatment quality, purity of the material. Of course, the role play working conditions, too.

#### Acknowledgement

The research work reported here was made possible by National Programme of Sustainability- project supported by Ministry of Education, Youth and Sports.

#### References

- Koloc, Z. and Václavík, M. (1988) Cam mechanisms. Prague: SNTL— Publisher of the technical literature. 379 p., (in Czech).
- Pošta, J. (2010) Wearing out. <http://www.gsxr.wz.cz/opotrebn.htm> (in Czech).
- Pekař, V. (2015) A new approach to models of failures and maintenance strategy. <http://www.reliability.estranky.cz/clanky/nektre-druhy-poruch/nektre-druhy-poruch---cyklicke-zatezovani-konstrukce-az-k-unavovemu-lomu.html> (in Czech).

## GFRP REINFORCEMENT IN CONCRETE – FACTORS AFFECTING BOND PROPERTIES

I. Hollý\*, R. Sonnenschein\*\*

**Abstract:** *Corrosion of steel reinforcement is the major cause of deterioration of existing RC structures. Combined effects of moisture, temperature, and chlorides reduce the alkalinity of concrete and exacerbate the corrosion of steel reinforcement, especially for concrete structures subjected to aggressive environments, such as marine structures and bridges and parking garages exposed to de-icing salts. Glass fiber reinforcement polymer (GFRP) bars are suitable alternatives to steel bars in reinforced concrete applications if durability, electromagnetic transparency, or ease of demolition in temporary constructions is sought, that have to be demolished partially by tunnel boring machines (TBMs). The bond of GFRP reinforcement is different from steel reinforcing bars. This paper presents factors affecting the bond strength between GFRP reinforcement and concrete.*

**Keywords:** Concrete, GFRP reinforcement, Bond, Temperature, Environmental conditions.

### 1. Introduction

It is known that, in well designed and quality concrete have high alkalinity of the concrete pore solution. At this high pH, the embedded reinforcing steel is protected against corrosion due to the formation of a sub-microscopically thin film. With time, the alkalinity becomes reduced in the concrete due to chemical reactions (Karlsson, 2014). A significant number of existing structures (buildings, bridges, park decks etc.) need strengthening, rehabilitation or replacement. Corrosion produces deep pitting and severe loss of cross section of the reinforcing steel. This normally leads to costly repair and catastrophic failures. Several approaches have been chosen to control the corrosion process such as improving the permeability of concrete by additives and admixtures and epoxy-coating steel bars. The latter has been widely used in bridges and parking garages. A completely different approach to control the corrosion process would be to use materials that are highly corrosion resistant, such as reinforcing bars constructed of composites materials. Glass fiber reinforced polymer (GFRP) bars (Fig. 1) that have been produced recently are considered to be ideal candidate and have great potential to fill such a need. While glass fibers are highly resistant to corrosion by acids, the combination of wrongly types of glass fibers and resins could lead to premature deterioration of GFRP bars in alkaline environment. However, many structures constructed with these bars have been in service for more than ten years in extremely aggressive environments (Eshani et al, 1996).



*Fig. 1: Composite GFRP reinforcement.*

---

\* Ing. Ivan Hollý, PhD.: Department of Concrete Structures and Bridges, Faculty of Civil Engineering SUT in Bratislava; Radlinskeho 11; 810 05, Bratislava; SK, ivan.holly@stuba.sk

\*\* Ing. Róbert Sonnenschein, PhD.: Department of Concrete Structures and Bridges, Faculty of Civil Engineering SUT in Bratislava; Radlinskeho 11; 810 05, Bratislava; SK, robert.sonnenschein@stuba.sk

The use of polymer composite materials instead of steel can be considered as a promising alternative. Glass fibers are a popular choice as reinforcement due to their low cost and many advantageous features. The advantages of GFRP include high strength, low density, and low cost. However, the relatively low elastic modulus of GFRP bars (compared with that of steel) generally leads to a higher deformability and greater crack widths in GFRP-reinforced structural elements. The design and construction guidelines for the use of GFRP bars are in many ways based on knowledge gained from steel reinforcement design (Karlsson, 2014).

## 2. Bond behavior of GFRP bars

Bond between reinforcement and concrete is necessary to ensure composite action of the two materials. The force in the steel bar is transmitted to the surrounding concrete by bond, which can be divided into three components: adhesion, mechanical interlocking and friction. The understanding of bond behavior of GFRP bars is important because most bond behavior models for studying the bond of GFRP bars have evolved from models that were previously developed for steel bars. Because these models for steel bars are well-established, they serve as convenient data to define the bond behavior of GFRP bars (Ganga et al. 2012). Generally, the resin used for the production of the bars is water resistant and therefore the formation of chemical bonds between the concrete and the bar is very limited unless special treatment is used. Results from experimental research have shown that there are two bond components for GFRP bars: mechanical interlocking and friction due to surface roughness (Zhou et al, 2012).

Trends in the literature have also shown that the average bond strength of GFRP bars is approximately 55 to 90 percent of steel reinforcement of the same diameter (Vint, 2012). Despite some research has been done in the evaluation of the bond behavior of FRP bar in concrete during the last decades, there is not yet a formulation that has a large acceptance of the technical and scientific communities for the prediction of the bond behavior between GFRP bars and surrounding concrete (Mazaheripour et al., 2013). Typical surface profiles used in GFRP bars to improve bond interaction include: sand coating, helical or braided wrapping with fibers to created indentations in the bar's surface, and deformations in the resin (surface indentations or ribs). The average bond strength is higher for bars that are ribbed or have helical strands wrapped around them than for bars that are purely sand coated (Fig. 2) (Vint, 2012).

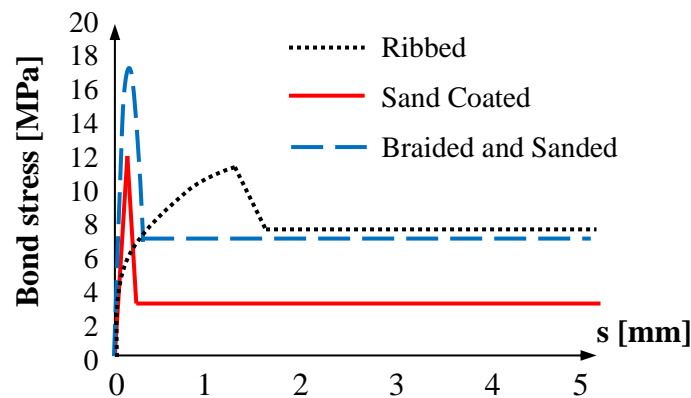


Fig. 2: Bond stress-slip relationship for GFRP bars with different surface (Vint, 2012).

### 2.1. Effect of different environmental conditions

Information from durability tests and life cycle analysis has to be established for the tested FRP reinforcement to determine the bond strength modification factor  $k_D$ , which should be related to environment and time. If the modification is in the code in form of a reduction of tensile strength of FRP, then a reduction of bond strength should not be necessary. If GFRP is used for the civil structures, the influence of water on the durability of GFRP is a critical issue since the civil structures are usually exposed to moisture during their service life. The influences of various environments such as moisture, alkali and chloride solutions, and wetting and drying cycles on the durability performance of GFRP composites have been investigated by numerous researchers. However, few long-term performance data are available for GFRP composites to date. Therefore, the durability performance of GFRP has been an important issue in recent years. Generally, an accelerated aging method with high temperature was used to accelerate the degradation process of GFRP (Kim et al., 2006).

The ACI 440.1R guide for internal GFRP reinforcement recommended an environmental reduction factor  $k_D$ , to represent the reduction in strength and strain properties of GFRP materials during their service life (Tab. 1). The environmental reduction factor  $k_D$  depends on the location and severity of exposure conditions. For GFRP the  $k_D$  varies from 0.75 to 0.50. Reduction factors are higher for external exposure conditions such as bridge decks, beams, and columns. Lower reduction factors are suggested for interior exposure conditions such as building beams and slabs because of the reduced severity and exposure to environmental elements (e.g., moisture, temperature fluctuations, and others) Ganga et al. 2012).

Tab. 1: Environmental reduction factor for GFRP bars at different exposure conditions (Ganga, 2012).

Exposure conditions	Environmental reductions factor ( $k_D$ )
Interior exposure	0.75
Exterior exposure (bridges, piers and unclosed parking garages)	0.65
Aggressive environment (chemical plants, waste water treatment plants)	0.50

## 2.2. Bond properties at elevated temperature

The bond between GFRP and concrete is essential to transfer loads. In the event of fire, changes in the mechanical properties of the matrix have the potential to cause loss of bond at modestly increased temperatures, and result in loss of interaction between FRP and concrete. The result could be catastrophic.

Tab. 2: Bond between GFRP bars and concrete at elevated temperature (Tepfers, 2004).

Temperature (°C)	Bond strength in % of values at 20°C	$k_T$ (-)
20	100	1.0
100	35 - 80	0.35 - 0.8
150	20 - 40	0.2 - 0.4
220	10 - 20	0.1 - 0.2

GFRP bars at elevated temperatures may experience significant transverse thermal expansion leading to cracking or spalling of the concrete cover or to the development of shear stresses in their adhesive layer. They may ignite and emit dense smoke and toxic gases. They can lose their bond with the substrate or surrounding concrete. All of these concerns have not been adequately studied or addressed by current design guidelines (Bisby et al., 2005). The use of GFRP reinforcement is not recommended for structures in which fire resistance is essential to maintain structural integrity. Because FRP reinforcement is embedded in concrete, the reinforcement cannot burn due to a lack of oxygen; however, the polymers will soften due to the excessive heat. The temperature at which a polymer will soften is known as the glass-transition temperature  $T_g$ . Beyond the  $T_g$ , the elastic modulus of a polymer is significantly reduced due to changes in its molecular structure. The value of  $T_g$  depends on the type of resin, but is normally in the region of 65 to 120 °C (ACI, 2006). Below zero temperatures can cause changes in mechanical properties and create additional micro cracks in GFRP materials (Mathieu et al., 2010).

## 3. Design bond stress for reinforcing bars

The design value of the ultimate bond stress  $f_{bd}$  for GFRP reinforcing bars may be taken as (Tepfers, 2004):

$$f_{bd} = \eta_0 \cdot \eta_1 \cdot \eta_2 \cdot k_D \cdot k_T \cdot f_{ctd} < f_{bd,FRP} \quad (1)$$

where:

-  $\eta_0$  is a coefficient related to the structure of the surface of the reinforcing bar.  $\eta_0 = 2.25$  for ribbed steel bars, for GFRP shall be defined by manufacturer for every type of GFRP rebar,

- $\eta_1$  is the coefficient related to the quality of the bond condition and the position of the bar during concreting according to STN EN 1992-1-1,
- $\eta_2$  is related to the bar diameter:  $\eta_2 = 1.0$  for  $\varnothing \leq 32$  mm,  $\eta_2 = (132 - \varnothing)/100$  for  $\varnothing > 32$  mm,
- $k_D$  is modification factor for durability (see Tab. 1),
- $k_T$  is modification factor for temperature (see Tab. 2),
- $f_{ctd}$  is the design value of concrete tensile strength ( $= f_{ctk,min}/\gamma_C$ ),
- $f_{bd,FRP}$  is the design bond strength in the surface of the FRP-bar/rod (determined in pull-out test with short bond length and central placement of bar/rod).

#### 4. Summary

For GFRP an extensive experimental work is needed in order to develop reliable and rational guidelines for design. One property of importance that has been studied for many years is the bond between steel reinforcing bars and the concrete interface. This property is crucial, as it has a major effect on the structural performance of a member with regards to cracking, deformability, internal damping and instability in concrete structures. It is critical that the bond interface does not deteriorate, thereby ensuring an adequate level of strength and ductility in the structure. While the bond characteristics of steel bars in concrete have been investigated extensively, such data are lacking for GFRP bars. It cannot be assumed similar responses for steel and GFRP bars due to their different mechanical and physical properties.

#### Acknowledgement

This work was supported by the Slovak Research and Development Agency under the contract No. APVV-15-0658 and by University Science Park (USP) of the Slovak University of Technology in Bratislava (ITMS: 26240220084).

#### References

- Karlsson, J. (2014) Alternative Reinforcement Approaches – Extended service life of exposed concrete structures, Master's thesis, Chalmers University of Technology, Göteborg, Sweden.
- Zhou, J., Chen, X. and Chen, S. (2012) Effect of Different Environments on Bond Strength of Glass Fiber-Reinforced Polymer and Steel Reinforcing Bars, in: Journal of Civil Engineering. 16(6), (2012) pp. 994-1002.
- Mazaheripour, H., Barros, J.A. O., Sena-Cruz, J.M., Pepe, M. and Martinelli, E. (2012) Experimental study on bond performance of GFRP bars in self-compacting steel fiber reinforced concrete, in: Composite Structures, Vol. 95 (2012), pp. 202-212.
- Eshani, M.R., Saadatmanesh, H. and Tao, S. (1996) Design recommendations for bond of GFRP rebars to concrete, in: Journal of Structural Engineering, Vol. 122, No. 3, (1996), pp. 247-254.
- Ganga Rao, H.V.S., Taly, N. and Vijay, P.V. (2007) Reinforced Concrete Design with FRP Composites, Taylor & Francis Group, Boca Raton.
- Vint, L.M. (2012) Investigation of Bond Properties of Glass Fibre Reinforced Polymer Bars in Concrete under Direct Tension, Master's thesis, Department of Civil Engineering, University of Toronto.
- Tepfers, R. (2004) Bond clause proposal for FRP-bars/rods in concrete based on CEB/FIP Model Code 90 with discussion of needed tests, Chalmers University of Technology, Göteborg, Sweden.
- Kim, H-Y., Park, Y-H., You, Y.-J. and Moon, Ch.-K. (2006) Durability of GFRP Composite Exposed to Various Environmental Conditions, KSCE Journal of Civil Engineering. Vol. 10, No. 4 (2006) 291-295.
- Bisby, L.A., Williams, V.R.K., Kodur, V.R.K., Green, M.F. and Chowdhury, E. (2005) Fire Performance of FRP Systems for Infrastructure: A State-of-the-Art Report, National Research Council, Ottawa.
- Mathieu, R. and Brahim, B. (2010) Behaviour of GFRP Reinforcing Bars Subjected to Extreme Temperatures, in: Journal of Composites for Construction. Vol. 14, No. 4, 53-360.
- ACI 440.1R-06 (2006) Guide for the Design and Construction of Structural Concrete Reinforced with FRP Bars, ACI.
- STN EN 1992-1-1 (2005) General rules and rules for buildings.



## EXPERIMENTAL MODELLING OF PHONATION USING ARTIFICIAL MODELS OF HUMAN VOCAL FOLDS AND VOCAL TRACTS

J. Horáček<sup>\*</sup>, V. Radolf<sup>\*</sup>, V. Bula<sup>\*</sup>, J. Košina<sup>\*</sup>

**Abstract:** *The study provides information on experimental research on a complete 1:1 scaled model of human phonation. The model includes human lungs, the trachea, the laryngeal part with artificial vocal folds and the vocal tracts designed for different vowels. The measurement set up enables modelling the time signals not easily measured in humans during phonation as for example fluctuations of the subglottic, laryngeal and oral pressures measured simultaneously with the glottis opening and the glottis area registered by a high-speed camera. The simulation of phonation is performed in the ranges of the airflow rate and the subglottic pressure typical for a normal humans' physiology.*

**Keywords:** Biomechanics of voice, Experimental simulation of human phonation in vitro.

### 1. Introduction

The contribution presents the special experimental facility designed for in vitro measurements of voicing performed on originally developed 1:1 scaled models of human vocal folds and vocal tract. The designed models are based on CT and MRI measurements of human subject during phonation. The measured phonation (aerodynamic, vibration and acoustic) characteristics are comparable with values found in humans; however, obtaining reliably some of such characteristics, like for example pulsations of air pressure in subglottal, intraglottal and supraglottal spaces, from in vivo measurements is usually very problematic or nearly impossible. The knowledge of these characteristics for the artificial vocal folds can be useful for experimental verification of 3D computational finite element models of phonation due to relatively exactly defined input aerodynamic, material and geometrical parameters, which is also problematic to know reliably and exactly in humans.

### 2. Methods

Comparing to the recent studies of the authors (Horáček et al., 2016a, b) the measurement set up was updated, especially for measurements of air pressures in the laryngeal part of the vocal tract near the vocal folds and in the oral cavity, see Fig. 1. The high speed camera had to be included in the measurement set up for analyses of the vocal folds vibration. The developed simplified model of the human lungs, which includes the splitting of the air spaces up to the fourth order branching, was also built-in in the experimental facility, see Fig. 2. The measurements presented in this study were performed with an innovative three layer vocal folds model, see Fig. 3. Silicon wedge, modelling a vocal fold body (3), was added inside the vocal fold reducing the space of the liquid layer modelling the lamina propria layer (2) positioned under the silicon cover (1). This modification substantially reduced the airflow rate of phonation onset below  $Q = 0.1$  l/s and the fundamental phonation frequency below  $F_0 = 80$  Hz. The plexiglass model of the vocal tract for the vowel [u:], designed on the basis of CT images measured during a subject phonation is attached to the larynx model at the bottom end, see Fig. 4. Installation of pressure transducers in the vocal tract cavity allowed obtaining more information on magnitudes of pressure fluctuations in laryngeal and oral parts of the vocal tract. Usage of the high-speed camera enabled to study vibration amplitudes of the vocal folds and to determine the glottis opening and closing phases in relation to the acoustic and pressure data measured synchronously in time domain. The all

---

<sup>\*</sup> Ing. Jaromír Horáček, DSc., Ing. Vojtěch Radolf, PhD., Ing. Vitězlav Bula, Ing. Jan Košina: Institute of Thermomechanics of the Czech Academy of Sciences, Dolejškova 1405/5, Prague; CZ, jaromirh@it.cas.cz, radolf@it.cas.cz, bula@it.cas.cz.



measured signals were simultaneously sampled by the frequency of 16.4 kHz and registered by the measurement system Brüel & Kjaer PULSE controlled by a personal computer (see Fig. 1).

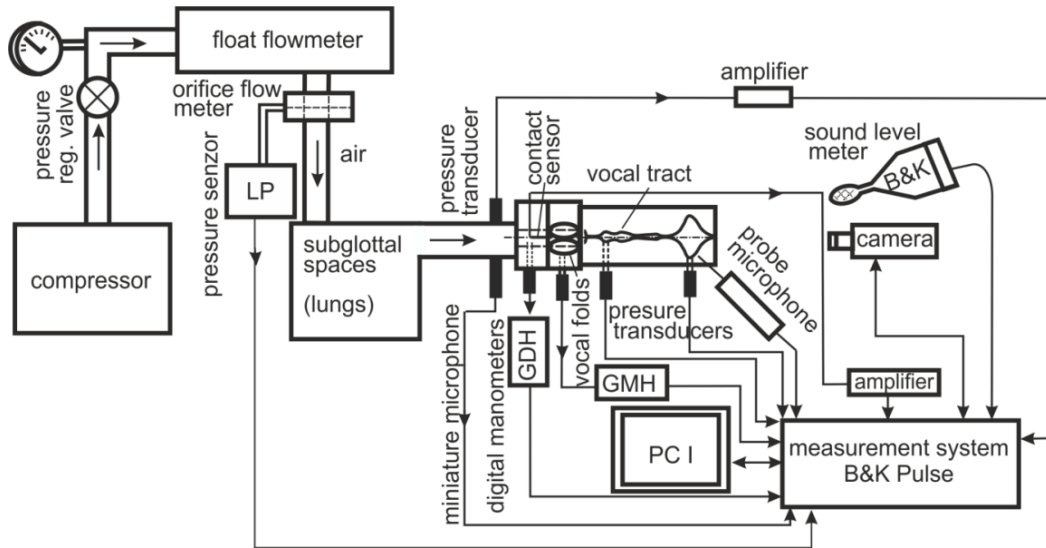


Fig. 1: Scheme of the measurement set up.

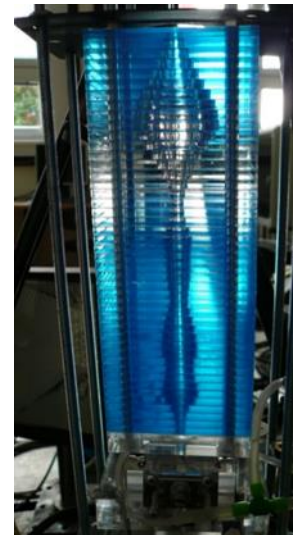
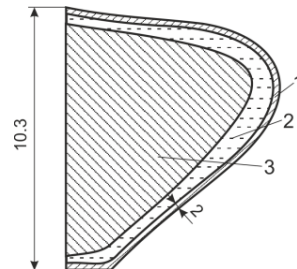
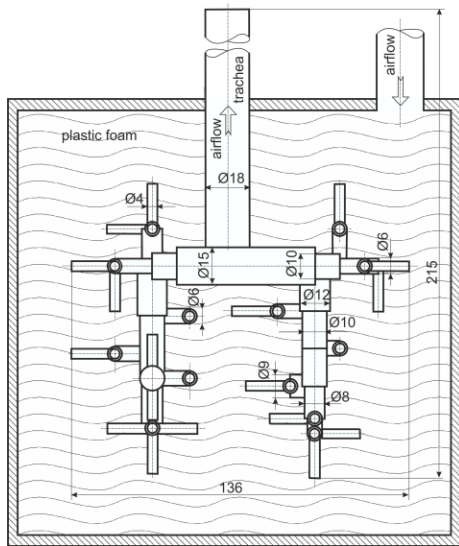


Fig. 2: Schema of the lungs model. Fig. 3: Schema of the vocal fold model. Fig. 4: Vocal tract model.

### 3. Some examples of results

The example of one measurement trial is demonstrated by Fig. 5. Each trial, which usually takes 10 s, is performed for a constant preset airflow rate. All measured time signals are monitored on the PC screen and the measurement starts when the phonation is stabilized. After about two seconds powerful lights, focused on the self-oscillating vocal folds, are switched on, which enables for about 0.5 s to register and later to visualize the vibrations of the vocal folds by the high speed camera. However, the light influences some pressure signals by a temperature drift due to an intensive heating of the pressure transducers positioned near the vocal folds. After about 2 s the lights are switched off which is followed by a sudden stop of the airflow, and the distorted signals are returning slowly back to zero or to a constant equilibrium value. The drifts of the pressure signals are corrected afterwards, during evaluation of the results.

Fig. 6 shows typical time records of the following measured signals: 1/ the subglottal pressure measured just below the vocal folds by two different pressure transducers for determination of the pressure fluctuations (the signal denoted by  $Mic_{Min}$ ) and the mean pressure value (the signal denoted by  $P_{sub}$ ), 2/ the laryngeal pressure ( $P_{larynx}$ ) measured just above the vocal folds, 3/ the oral pressure ( $P_{oral}$ ) measured in the mouth cavity of the vocal tract model, and 4/ the acoustic sound signal ( $Mic$ ) measured outside the vocal

tract of about 30 cm from the mouth. These signals are shown together with 5 images of the glottis taken during one period ( $T_{period} = 1 / F_0$ ) of the vocal folds vibration. The glottis was closed for 41 % of the period followed by the maximum of the glottis opening  $maxGO = 0.8$  mm.

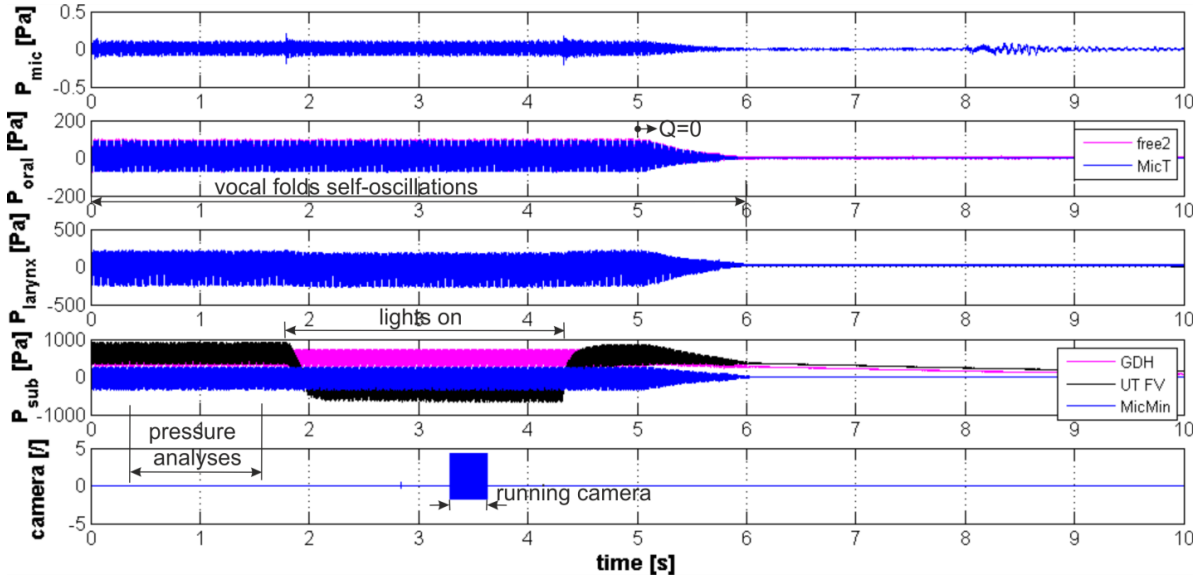


Fig. 5: Example of registered signals during one measurement procedure - airflow rate  $Q = 0.04$  l/s.

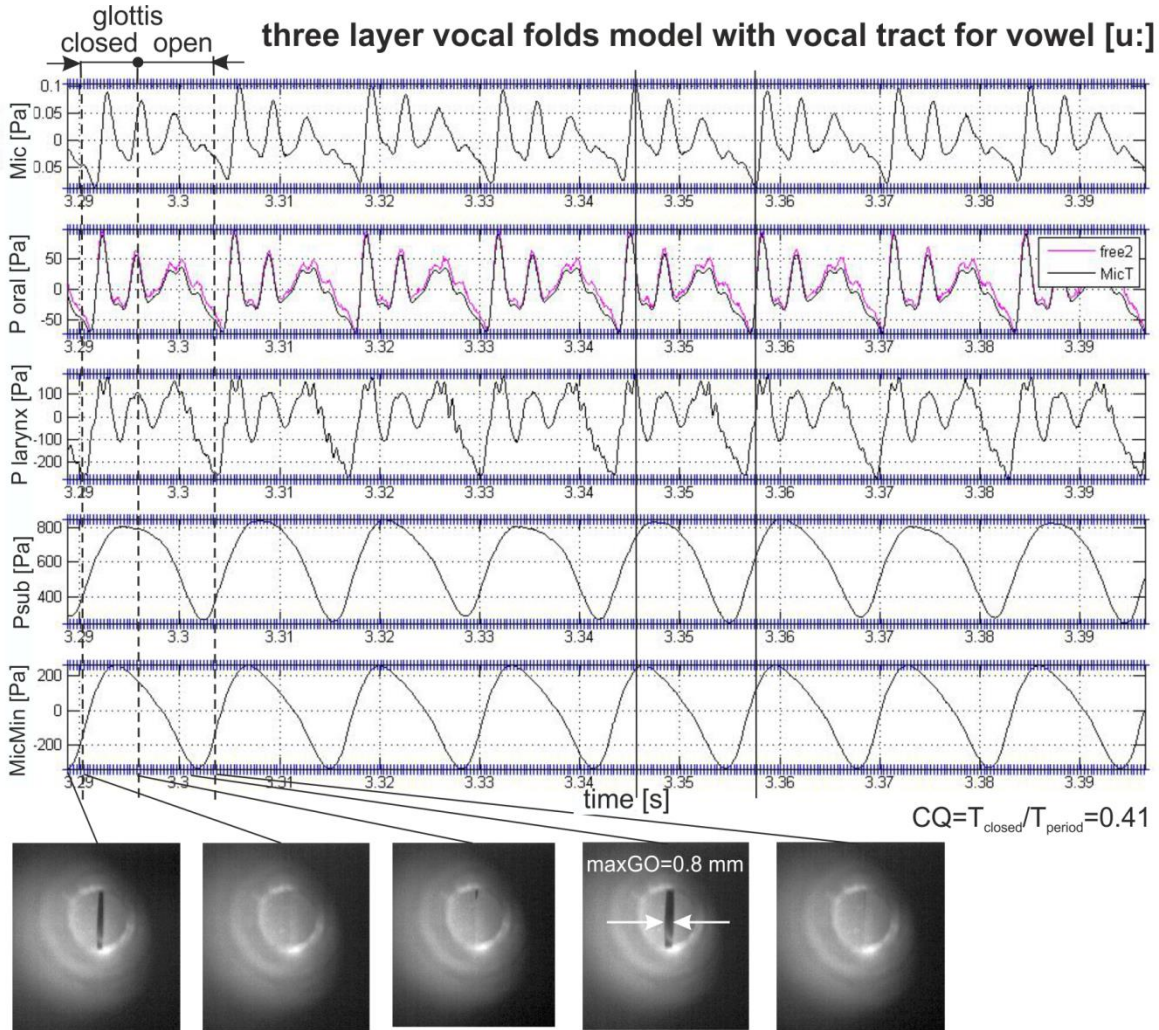


Fig. 6: Example of the measured pressure signals and snapshots of the vocal folds vibration (mean flow rate  $Q = 0.04$  l/s, closed quotient  $CQ = 0.41$ , maximum glottis opening  $maxGO = 0.8$  mm).

The maxima of peaks of the generated sound level ( $Mic$ ) appear after the glottis closure. The pressure waveforms inside and outside the vocal tract ( $P_{larynx}$ ,  $P_{oral}$ ,  $Mic$ ) are similar, only slightly time shifted due to the limited sound propagation velocity. These waveforms contain many higher harmonics of the fundamental phonation frequency and the resonance (formant) frequencies of the acoustic cavities of the vocal tract model for the vowel [u:], contrary to the signal ( $Mic_{Min}$ ) for the subglottic pressure fluctuations where the fundamental frequency  $F_0 = 76$  Hz principally dominates, see Fig. 6.

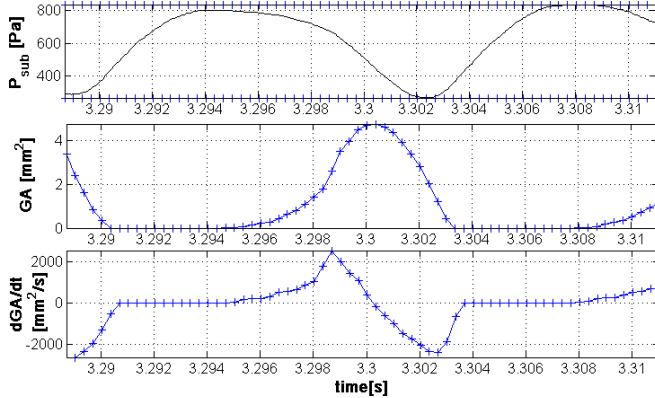


Fig. 7: Measured pressure signal and glottis area.

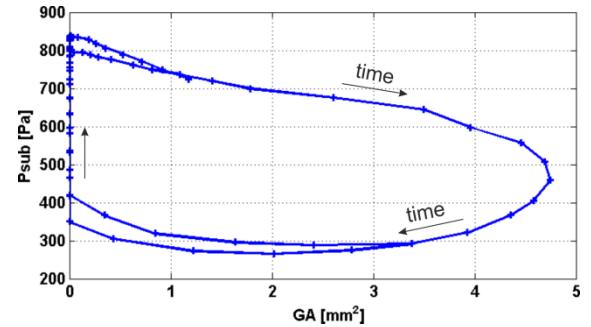


Fig. 8: Measured hysteresis loop.

Fig. 7 shows the evaluated glottis area  $GA(t)$  and the time derivative of the  $GA$  in relation to the measured subglottic pressure during of about one and half period of the vocal fold vibration. After the glottis closure for  $t > 3.29$  s ( $GA = 0$ ) the subglottic pressure increases and reaches the maximum value of about 800 Pa. Afterwards the glottis area increases during opening phase of the glottis and the subglottic pressure decreases to its mean value at the maximum opening of the glottis. During the closing phase of the glottis the subglottic pressure decreases to a minimum value. The maximum of the absolute value of the derivative  $dGA/dt$  appears before the glottis closure, i.e. shortly before the vocal folds collision. Interesting result is that this maximum negative value is practically identical with the positive maximum of the derivative  $dGA/dt$  observed in the opening phase. The derivative of the glottis area  $dGA/dt$  is an important parameter for estimating the impact stress between the colliding vocal folds.

Fig. 8 shows a nearly periodic dependence of the measured subglottic pressure on the glottis area. The time signals  $P_{sub}(t)$  and  $GA(t)$  create a hysteresis loop oriented in time domain in the clockwise direction. The loop corresponds to the instability of the aeroelastic system due to the vocal folds self-oscillations; the energy from the airflow is transferred to the viscoelastic structure of the vocal folds.

#### 4. Conclusions

Experimental modelling of phonation is important not only for understanding basic principles of voice production and for verification of mathematical models of phonation but also for detection of laryngeal pathologies and treatment of laryngeal disorders. The experimental modelling of phonation includes nearly all aspects of this complex physiological as well as physical process covering the fluid-structure-acoustic interaction phenomena.

#### Acknowledgement

The work has been supported by the grant project GACR No 16-01246S.

#### References

- Horáček, J., Bula, V., Košina, J. and Radolf, V. (2016a) Phonation characteristics of self-oscillating vocal folds replica with and without the model of the human vocal tract, in Proc. Int. Conf. on Engineering Mechanics 2016 (eds. Zolotarev, I. and Radolf, V.), Svratka, Czech Republic, pp. 214-217.
- Horáček, J., Vampola, T., Bula, V., Radolf, V. and Dušková, M. (2016b) Experimental investigation of airflow, acoustic and vibration characteristics of a liquid filled self-oscillating vocal folds model, in Proc. Flow-Induced Vibration & Noise: FIV 2016 (eds. Gonzalez Diez, N., Belfroid, S. and Golliard, J.), Delft: TNO, pp. 23-30.

## WIND FLOW AROUND HIGH-RISE BUILDINGS AND ITS INFLUENCE ON THE PEDESTRIAN COMFORT

O. Hubova<sup>\*</sup>, L. Konecna<sup>\*\*</sup>

**Abstract:** *The contribution deals with wind flow around two high-rise buildings standing close to each other with surrounding lower parts and the effects of these objects on the territory around the buildings, which is supposed to be a recreational zone. The configuration of the objects relative to the prevailing wind flow is not optimal; two tower blocks are in a “wind catching layout”. What is needed to improve is contribution to urban planning and cooperation with urban planners and architects in a collective research in the perception of urban space. The effect of considerably diversified parameters has to be quantified. The aim of the experimental measurements in the wind tunnel was to demonstrate the need for delay the high-rise buildings apart due to strong suction on leeward, as well as the Venturi-effect, which occurred in the space between the buildings.*

**Keywords:** Wind pressure coefficient, Local angle of wind attack, Wind environment, Roughness length, Reference wind speed, Effective wind velocity, Pedestrian wind comfort.

### 1. Introduction

In the aerodynamics of structures it is necessary to determine the wind load, which is represented by a simplified set of pressures or forces for the whole structure, or for the structural parts. The wind tunnel tests are used for the study of building complex and their surrounding and for some environmental problems, which depends on the turbulence intensity and integral length scale. In most urban areas, an important problem is the achievement of an acceptable wind comfort around the buildings, with aspects that concern the quality of life and the use of the area affected by the buildings, associated to social and economic impacts.

### 2. Wind load

The effect of wind load on a structure can be expressed by external wind pressure:

$$w_e(z) = c_{pe} \cdot q_p(z) = c_{pe} \cdot [1 + 7 \cdot I_v(z)] \cdot 1/2 \cdot \rho \cdot v_m^2(z) \quad (1),$$

where:

$$c_{pe} = \frac{\Delta p}{p_{dyn}(z_{ref})} = \frac{p(t) - p_0}{1/2 \cdot \rho \cdot \bar{v}^2(z_{ref})} \quad \text{is external wind pressure coefficient} \quad (2).$$

The value was calculated by Eq. 2, where  $p(t)$  is the wind pressure in measuring point on the surface of the model and  $p_0$  is static pressure of undisturbed flow measured by Prandtl probe. Dynamic pressure of the mean wind velocity was considered in reference height (in our case, reference height was equaled to the height of the top edge of examined model).

$q_p(z)$  is peak velocity pressure,  $v_m(z)$  is mean wind velocity at a height  $z$ ,  $I_v(z)$  is turbulence intensity at height  $z$ .

---

<sup>\*</sup> Assoc. Prof. Ing. Olga Hubova, PhD.: Faculty of Civil Engineering, Department of Structural Mechanics, Slovak University of Technology Bratislava; Radlinskeho 11; 810 05 Bratislava; SK, olga.hubova@stuba.sk

<sup>\*\*</sup> Ing. Lenka Konecna, PhD.: Faculty of Civil Engineering, Department of Structural Mechanics, Slovak University of Technology Bratislava; Radlinskeho 11; 810 05 Bratislava; SK, lenka.konecna@stuba.sk



The values of external wind pressure coefficients on the facade of high stand-alone building are specified in EN 1991-1-4. For two high buildings with weak interaction (Fig. 1) it is necessary to determine these values by experimental measurements. The experimental measurements were made in wind tunnel with boundary layer (BLWT) in Bratislava (see Hubova et al., 2014). New wind tunnel allows in its two measuring areas to simulate steady and turbulent wind flow. We tested the buildings configuration in the turbulent wind flow.

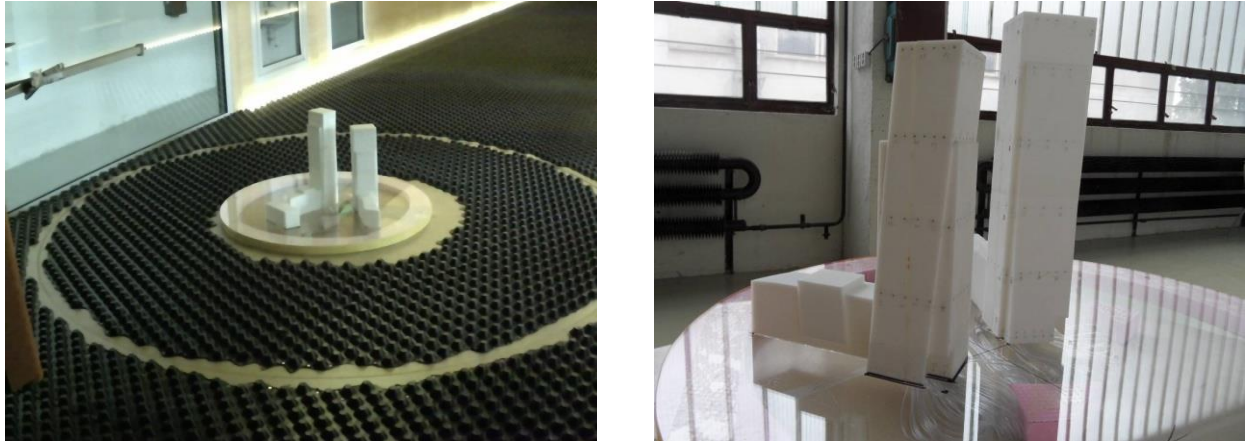


Fig. 1: Model of the high-rise buildings (SF 1:300) in turbulent wind flow and detail.

Reference wind speeds were selected so as to fulfill flow similarity of prototype and model. Velocities were chosen with regard to (ASCE Manuals 1999). In all positions measurements were made for 2 different velocities (9.255 m/s and 11.535 m/s). The model was rotated from initial positions ( $0^\circ$  = North wind) every  $22.5^\circ$  clockwise, thereby the changing of wind direction acting on the objects was simulated. We monitored the change of the wind flow on high buildings in sampling points for 6 height levels (see Fig. 2).

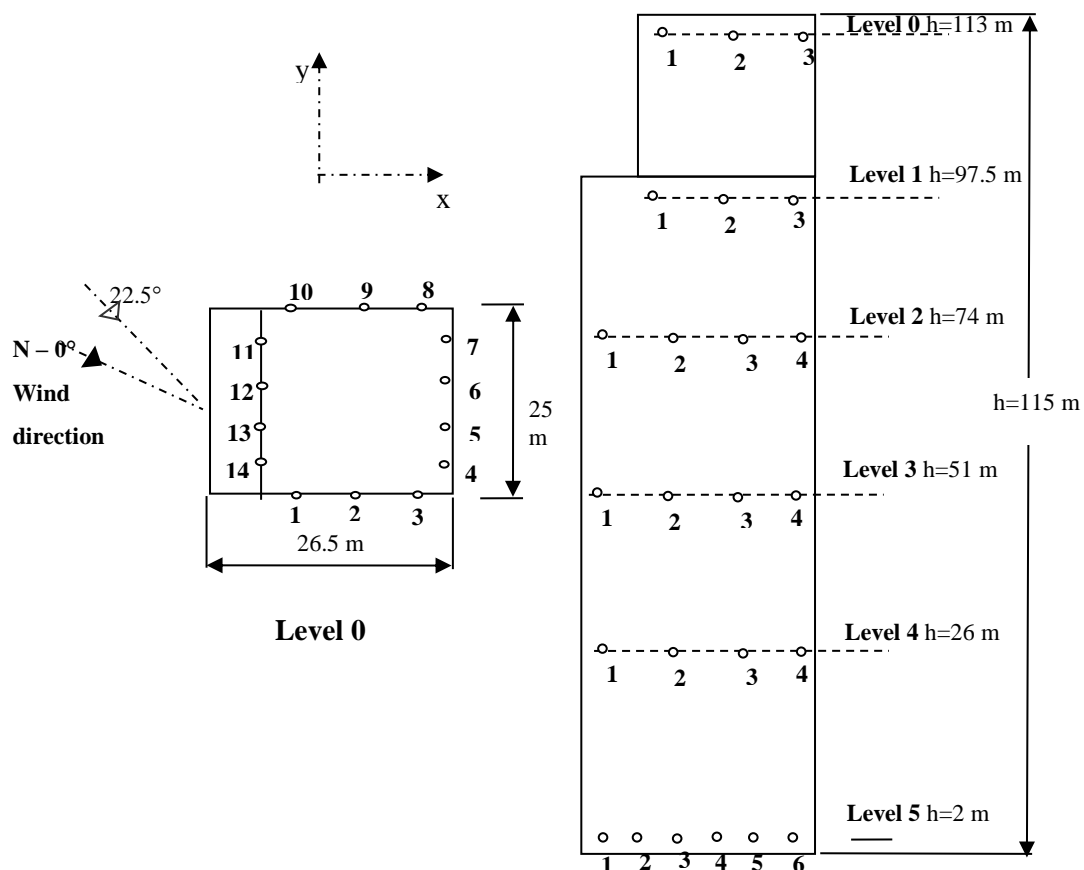


Fig. 2: Sampling points on the model of the higher building.

Measurements of local pressures under various wind directions using the turn table detected the direction in which we obtained the maximum values of wind pressures.

Comparison between the wind pressure on the facade of the 115 m high building obtained by calculation according to EN 1991-1-4 and the values obtained by experimental measurements (EXP) is shown in the graph in Fig. 3. The resulting values of wind suction obtained experimentally were significantly higher than values in accordance with EN standards. In the lower part of the building the suction values were twice as large as the standard values. The external wind pressure coefficients obtained from repeated experimental measurements made on model in turbulent wind flow indicate the local extremes of suction in certain directions.

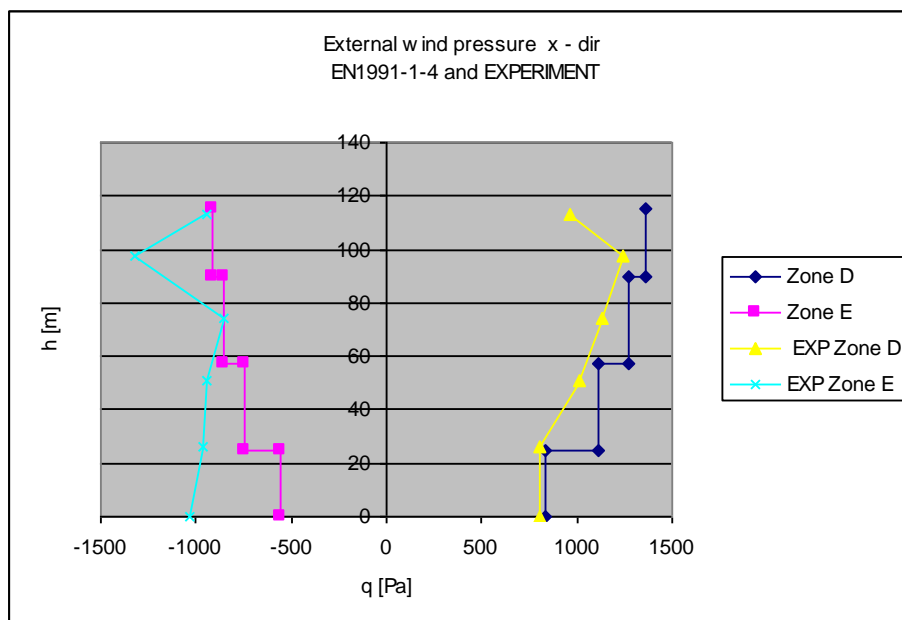


Fig. 3: Comparison of external wind pressure in windward D and leeward E zone.

### 3. Pedestrian wind comfort

Wind comfort criteria are based on the definition of the probability of exceedence  $P_{exc}$  of a given threshold effective wind speed  $V_{ef}$  at the pedestrian level ( $z = 1.7 \div 2.0$  m) (see Tab. 1) and were defined by several institutions participating in COST 14 and authors (see Stathopoulos et al., 1992).

$$V_{ef} = v_m(1.7 \div 2.0 \text{ m}) \cdot [1 + g \cdot I_v(1.7 \div 2.0 \text{ m})] \quad (3)$$

Tab. 1: The scale of discomfort.

$V_{ef}$ [m.s <sup>-1</sup> ]	Pedestrian comfort
4	Standing, sitting - long period
6	The first feelings Standing sitting – short period
8	Slow walking
9	Walking is influenced
15	Walking is difficult

Tab. 2: Pedestrian wind comfort.

$V_{ef}$ [m.s <sup>-1</sup> ]	Points
> 4 m/s	47 – 55, 61
> 6 m/s	19,20,21,22,23,25,29 - 38, 40 - 46
> 8 m/s	3,4,9,10,11,12,13,15,16,26,27,28, 39
> 9 m/s	A,B,C,E,F,G,O,N,M,H,I,J 0,1,2,5,6,7,8,16,17,18,

The effective speed at the pedestrian level was measured in 120 points (see Fig. 4), using a thermo-anemometer probe. The most unfavorable values are processed in Tab. 2.

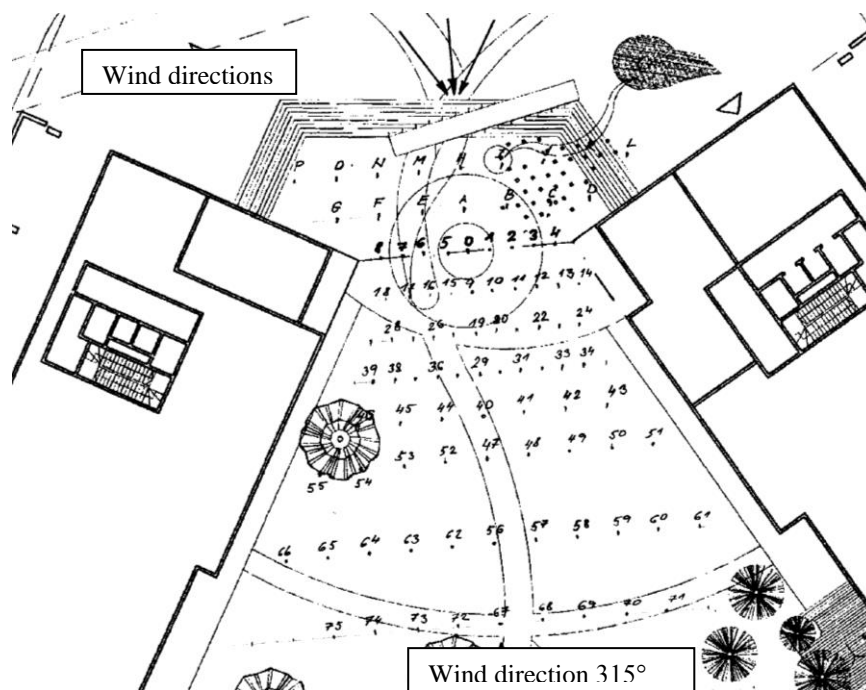


Fig. 4: Scheme of measurement points for determining the pedestrians wind comfort.

#### 4. Conclusions

We analyzed the wind flow and effect of the structures between pair of tall building situated in central area of Bratislava and tried to find best situation for pedestrian wind comfort.

The external wind pressure coefficients obtained from repeated experimental measurements made on model in turbulent wind flow indicate the local extremes of suction in lower part of the building and in corners. Coefficients of suction in the corners were greater than  $-2$ . The unfavorable situation is also the entry into the higher tower, where we measured suction  $-1\,050$  Pa. We recommend not oriented entries in Northwest wind direction. The biggest problems will cause a north-west wind, which is by lower and higher buildings channeled into a narrow neck between buildings and wind speed is rapidly increased. Speed between buildings is affected by the distance between them the value of projects proposed  $12.5$  m causes a significant increase of wind flow near the ground. We recommend greater distance between buildings, to alleviate this phenomenon (see Tsang et al., 2009).

#### Acknowledgement

This paper was created with the support of the Research and Development Operational Programme for the project "University Science Park of STU Bratislava", ITMS 26240220084 and VEGA grants No. 01/0544/15, 1/0265/16. This paper was created with the support of the TU1304 COST action "WINERCOST". Authors thank to the Slovak University of Technology for the support – grant No. 1651.

#### References

- ASCE Mannuals and Reports on Engineering Practice, no.67 (1999) Wind Tunnel Studies of Buildings and Structures. Library of Congress Catalog Card No. 98-44103, USA, ISBN 0-7844-0319-8.
- EN 1991-1-4: Eurocode 1: 2005. Action on structures – Part 1-4: General actions - Wind actions.
- Hubova, O., Lobotka, P. (2014) The Natural Wind Simulations in the BLWT STU Wind Tunnel, in: Proceedings of ATF 3rd Conference on Building Physics and Applied Technology in Architecture and Building Structures. E - Book of reviewed papers, May 6-7, 2014, Austria, Vienna, pp. 78-84, ISBN 978-3-200-03644-4.
- Stathopoulos, T., Wu, H., Bédant, C. (1992) Wind environment around buildings. Journal of Wind Engineering and Industrial Aerodynamics, pp. 41-44.
- Tsang, C.W., Kwok, K.C.S. and Hitchcock, P.A. (2009) Effects of building dimensions and separations on pedestrian – level environment, in: 5th European & African Conference on Wind Engineering, Florence, Italy, July 19-23, 2009.



## EXAMINATION OF THE BASIC GEOMETRICAL PARAMETERS OF THE LOWER RESPIRATORY TRACT OF THE HUMAN AND ITS SIMPLIFIED COMPUTATIONAL MODEL

P. Hynek<sup>\*</sup>, T. Vampola<sup>\*\*</sup>

**Abstract:** *This contribution deals with the examination of the basic parameters of the lower respiratory tract of a human. Among these parameters are the diameters (cross-section area) of the channels dependent on the remoteness from the Larynx, the length of the individual branches, angles etc. Further we propose a semi-automatic method to regenerate the simplified geometry of the lower respiratory tract of a human from very detailed input (described by a surface mesh) for the subsequent formation of a 3D computational model. The final simplified geometry can be adjusted by user intervention (e.g. changing the specific diameter). The key feature in the simplification is that the cross section areas and channel length of the lower respiratory tract are maintained. The final 3D computation model of lower respiratory tract is easy to connect with a simplified vocal tract model (Vampola et al., 2008) and the basic acoustic characteristic or fluid flow depends on the tract geometry may be examined.*

**Keywords:** Lower respiratory tract, Human lung parameters, Computational model, Trachea, Mainstem bronchus.

### 1. Introduction

The lungs are the primary organs of respiratory and they are situated within the thoracic cavity of the chest. Human lungs are split to the two parts – the left and right lungs. The right lung is bigger than the left, because the left lung shares more space in the chest with the heart. The main parts of the right lung are called the right lower, the middle and the upper lobes of the lung. The left lung has 3 parts too. They are called the left lower and the upper lobes of the lung and the Lingula.

The lower respiratory tract begins at the trachea and branches into the bronchi and bronchioles which receive air breathed in via the conducting zone. These divide until air reaches microscopic alveoli, where the process of gas exchange takes place.

The primary function of the lung is breathing, but the main cavity of the lower respiratory tract (e.g. Trachea) is connected with the vocal tract and together form the phonation space.

This paper describes the formation of a simplified computational model of the human lower respiratory tract, which come out from the geometry obtained by magnetic resonance imaging (MRI).

The base of our model is a triangular surface mesh, which contains all right and left lobes, Trachea, Primary and Secondary bronchi and several other levels of branching (Fig. 1). A certain publication (e.g.



*Fig. 1: Detail (cross-section) of surface mesh obtained by MRI.*

<sup>\*</sup> Ing. Petr Hynek: Department of Mechanics, Biomechanics and Mechatronics, Faculty of Mechanical Engineering, Czech Technical University in Prague, Technická 4, Praha 6, Czech Republic, hynek@fs.cvut.cz

<sup>\*\*</sup> prof. Dr. Ing. Tomáš Vampola.: Department of Mechanics, Biomechanics and Mechatronics, Faculty of Mechanical Engineering, Czech Technical University in Prague, Technická 4, Praha 6, Czech Republic, tomas.vampola@fs.cvut.cz

Rozanek et al.) presents, that branching inside human lungs is occurs up to the 23<sup>rd</sup> level. In view of the fact that the resolution of the scanner and following reconstruction of the surface mesh for our model contains just several first levels (until diameters of 1 mm, it corresponds with the 9<sup>th</sup> – 11<sup>th</sup> levels of branching).

The quality of the surface mesh is not sufficient for directly forming the computational model, because it contains a lot of poor quality elements. The channels of smaller diameters are formed by large surface elements (probably due to points set reconstruction) and a very small number, which greatly distort the real geometry of the channels (see Fig. 2). This surface mesh is also called “dead”, which is very difficult to modify (only by manual intervention).

Our goal is to map the basic geometrical parameters (cross-section area, length of individual branches, etc.) and form the computational model, which will be simply modifiable and is based on the real geometry. It allows to simply simulate various pathological phenomena and detect their influence on the quality of the human voice.

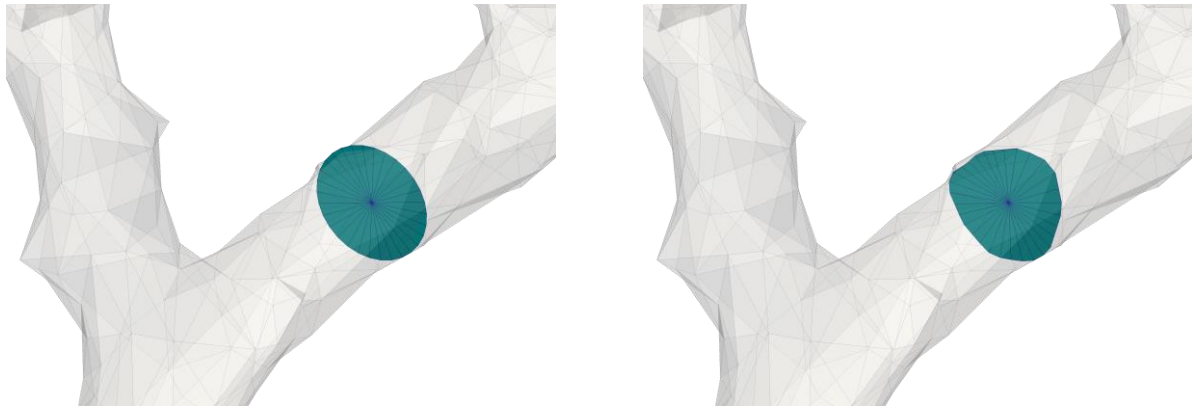


Fig. 2: Poor quality of the surface (remoteness from Larynx 230 mm). Comparison of reconstruction cross-section area (left) and original shape (right).

## 2. Mapping of basic parameters of the respiratory tract

For forming a computational model which faithfully describes the real geometry a thorough mapping of the basic parameters for the available surface mesh of the respiratory tract is necessary.

### 2.1. Cross – Section Area reconstruction

The first parameter (from which another can be found) is the minimal cross-section area of channel according to the remoteness. The minimal value of the area indicated, that the cross-section is perpendicular to the centerline of the channel. Our approach for minimal area searching inside the channel is based on the optimization process. A target function is the minimization of the cross-section area specified with number of triangles (see Fig. 2). The normal vector for each triangle can be determined by (5), where matrix (1) - (3) are the basic transformation matrix for rotation motion (Valášek et al., 2004). Optimization parameters for the cross-section minimization are 3 angles ( $\alpha$ ,  $\beta$  and  $\gamma$ ). The optimization process is controlled by the Octave software (Eaton et al., 2009) using the optimization toolbox.

$$T_{\varphi x}(\alpha) = \begin{bmatrix} 1 & 0 & 0 & 0 \\ 0 & \cos(\alpha) & -\sin(\alpha) & 0 \\ 0 & \sin(\alpha) & \cos(\alpha) & 0 \\ 0 & 0 & 0 & 0 \end{bmatrix} \quad (1) \quad T_{\varphi y}(\beta) = \begin{bmatrix} \cos(\beta) & 0 & \sin(\beta) & 0 \\ 0 & 1 & 0 & 0 \\ -\sin(\beta) & 0 & \cos(\beta) & 0 \\ 0 & 0 & 0 & 1 \end{bmatrix} \quad (2)$$

$$T_{\varphi z}(\gamma) = \begin{bmatrix} \cos(\gamma) & -\sin(\gamma) & 0 & 0 \\ \sin(\gamma) & \cos(\gamma) & 0 & 0 \\ 0 & 0 & 1 & 0 \\ 0 & 0 & 0 & 1 \end{bmatrix} \quad (3) \quad r = T_{\varphi x}(\alpha)T_{\varphi y}(\beta)T_{\varphi z}(\gamma) \begin{bmatrix} 0 \\ 0 \\ 1 \\ 1 \end{bmatrix} \quad (4) \quad n = \begin{bmatrix} r(1) \\ r(2) \\ r(3) \end{bmatrix} \quad (5)$$

## 2.2. Centerline of the channel

One of the basic parameters of the complex branching channels are so called centerlines of the channel, which describes the channel direction, diameter of the placed sphere inside a channel and the distance from entry into channel (in our case the Larynx). The centerline can be found as the gradual connection of the closest centers of gravity for a cross-sections from section 2.1. Searching for the minimal cross-section area inside the channel forming a centerline can be done in one step. Just enter the start and final point and the optimization algorithm will complete the whole journey. A flowchart of the centerline searching process is shown in Fig. 3. The new current point of the centerline is dependent on the surface normal – during the optimization process a turn off from the normal can happen and the next current point is the one that is the closest to the final (target) point.

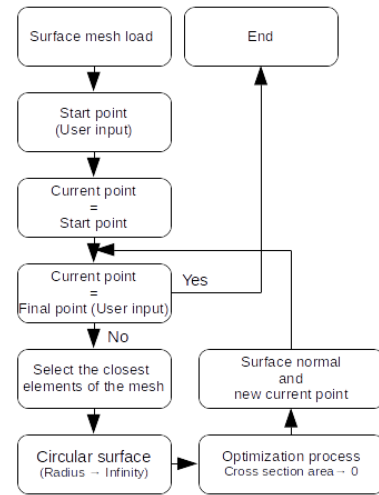


Fig. 3: Flowchart of optimization process.

## 2.3. Equivalent diameter

For forming of the simplified computational model, it is advantageous to replace the real cross-section of the channel with a regular shape, e.g. circular or elliptical section. In our case is we used a circular section, because it is close to the real shape, see Fig. 2. The regular shape is easy to parametrize for the easier formation of the computational model, as shown in section 2.4.

Dependence of the equivalent diameter of the channel to the remoteness from larynx is shown in Fig. 4. The graph shows, that equivalent diameter increases at the points of branching. The graph records the path from Larynx (0 mm) over the Trachea (0 – 100 mm), Left Main bronchus (100 – 150 mm), Left Upper Lobe Bronchus (150 – 200 mm) to the Tertiary Bronchi (black highlight area in Fig. 5 left).

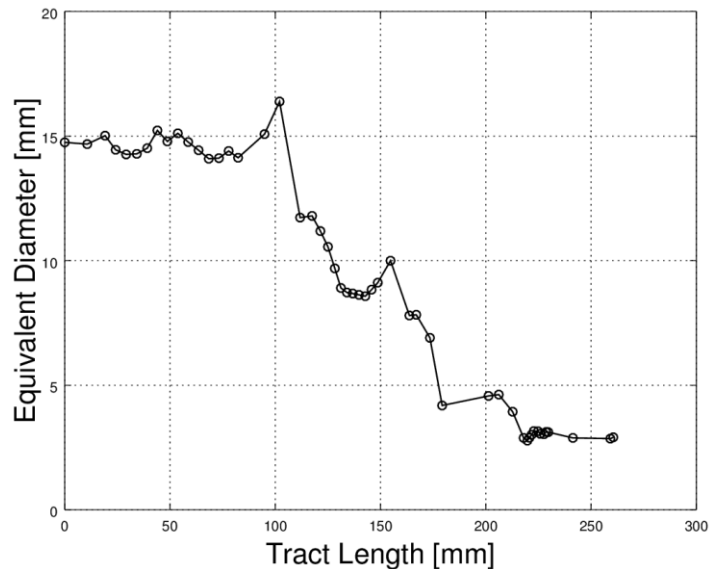
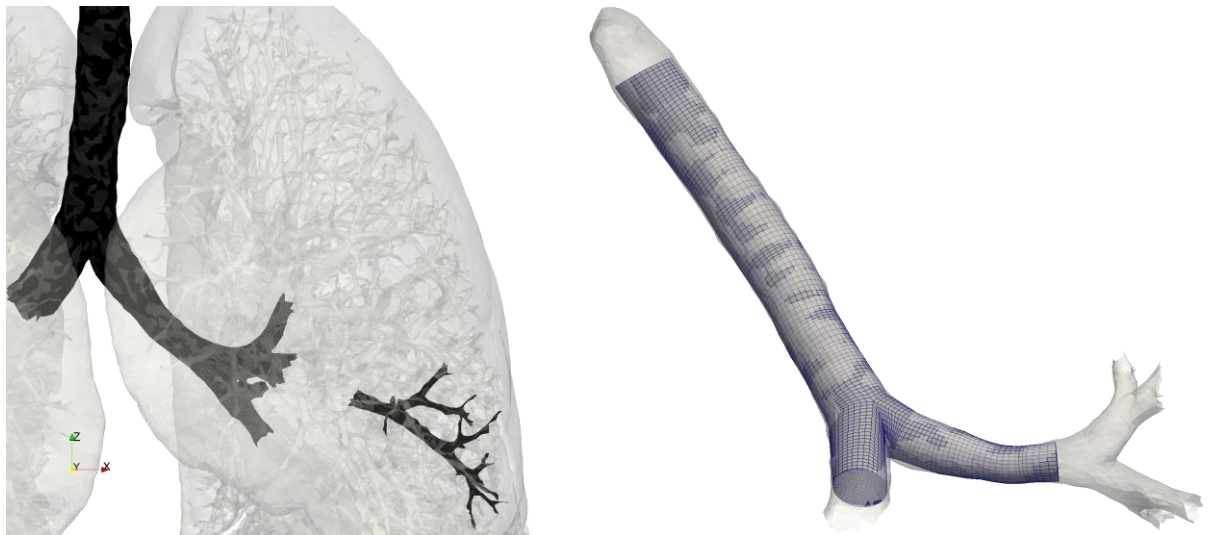


Fig. 4: Equivalent diameter for the investigated part of the channel

## 3. Forming of the 3D computational model

By careful examination of the geometry of the lower respiratory tract, it is obvious that even in these complex branching channels only 2 basic elements occur – straight parts and branching parts. This fact can be very helpful for the semi - automatic forming of the computational model. Also, for forming the 3D finite element model, both basic element (straight and branched) can be parametrized and produce the computation mesh based on hexahedrons elements (or only 2D elements), as shown in Fig. 5 on the right. The parameters are input diameters, normal of the cross-section area (from section 2.1.), branch lengths but also the number of elements (including boundary layer). One possibility is to use meshing free software GMSH (Geuzaine et al., 2009) which comprises own scripting language. The Fig. 5 right shows a geometry deviation of the reconstruction mesh (blue elements) and surface mesh obtained by MRI (grey surface).



*Fig. 5: Highlight of modeled parts (left) and 3D computational mesh of Trachea and left Main Bronchus (right).*

#### 4. Conclusions

This paper introduces the basic procedure for forming the computational model of the complex branching channel, which can be used as an input for the finite element method (FEM), and also the finite volume method (FVM). The model is based on the known surface mesh, which is inappropriate for directly creating the computational model (poor quality elements, impossible parametrization). The model is formed by the help of two basic construction elements (straight and branched part), which are gradually linked to the one whole. Both constructions elements are fully parametric (geometry and mesh) and are formed by the scripting language of the GMSH software (Geuzaine et al., 2009) and controlled by Octave (Eaton et al., 2009). Therefore it is possible to simply edit the model geometry and create a computation model for various pathologies.

#### Acknowledgement

The research is supported by the Grant Agency of the Czech Republic by project No 16-01246S Computational and experimental modelling of self-induced vibrations of vocal folds and influence of their impairments on human voice.

#### References

- Eaton, J.W., Bateman, D. and Hauberg, S. (2009) GNU Octave version 3.0.1 manual: a high-level interactive language for numerical computations. CreateSpace Independent Publishing Platform. ISBN 1441413006 URL <http://www.gnu.org/software/octave/doc/interpreter/>
- Geuzaine C. and Remacle, J.-F. (2009) Gmsh: a three-dimensional finite element mesh generator with built-in pre- and post-processing facilities. International Journal for Numerical Methods in Engineering, Vol. 79, Iss. 11, pp. 1309-1331.
- Rozanek, M. and Roubik, K. Modelling of the respiratory system in MATLAB.DOI: Modelling of the respiratory system in MATLAB.
- Valášek, M., Šika, Z. and Bauma, V. (2004) Mechanics B. Vydavatelství ČVUT, ISBN 8001029190, (in Czech).
- Vampola, T., Horáček, J. and Švec, J.G. (2008) FE Modeling of Human Vocal Tract Acoustics. Part I: Production of Czech Vowels. Acta Acustica united with Acustica [online]. 2008, 94(3), 433-447 [cit. 2017-02-11]. DOI:10.3813/AAA.918051. ISSN 16101928.

## DESIGN AND OPTIMIZATION OF SUPPORTING STRUCTURE OF A MULTIPURPOSE HIGH-RISE BUILDING WITH RESPECT TO THE WIND LOAD

O. Ivankova<sup>\*</sup>, D. Meri<sup>\*\*</sup>, E. Vojtekova<sup>\*\*\*</sup>

**Abstract:** *The subject of this article is the static analysis of a high-rise multipurpose building. The static analysis is focused on the structure subjected to effects of horizontal forces due to wind load and vertical forces of the own weight of the structure. The wind analysis is made for all four sides of the high-rise building, rotating the way of flowing by 90 degrees. Obtained results represent the maximal horizontal displacements of each model.*

**Keywords:** Static Analysis, Wind Load, Exoskeleton, Multipurpose High-Rise Building, Diagrid Tube Structure.

### 1. Introduction

When designing the high-rise building, it is always an important task to find the right proportion between the height of the building and its perceptive width from the various angles of street view. The perceptual width is dependent on the shape of floor plan and the whole shaping of the building's mass along its height. The article deals with static analysis of very slim high-rise building with effective arrangement of vertical communications and technological facilities and usable areas for functional use at the typical floor. The structure of the investigated building is composed of the reinforced core and the steel tube exoskeleton. The static analysis is focused on effects of lateral wind loads on the structural system (Zhou et al., 2002). The result of the analysis is the displacement of the highest (top floor) slab of the building. Final displacements have to comply with the Limit Serviceability State. From the results it is possible to define, which model of designed tube exoskeleton is the most ideal from the viewpoint of resistance to all vertical and lateral loads.

### 2. Architectural Design

The main task was to design a very slim high-rise building with efficient ratio between the utility of storey area to area of vertical communications and technological facilities in narrow corner of the lot, which is bordered by two traffic streets. Another demand for the design was to conceive a universal floor plan of high-rise building, where the functional use of the storey could be changed to apartments, hotel rooms, or open office spaces. The structure with central reinforced core and perimeter load bearing tube system is suitable for this type of high-rise building (Eisele et al., 2002). In architectural design there was no supposition for using of columns in internal disposition. The largest span between the core and perimeter tube system is in floor plan 20 m. The floor plan of the high-rise building changes along the height from regular square shape to rhomboidal shape with two rectangular edges to intensify the impression of visual slimness of the building. Two areas with non-planar surfaces arise on the spatial envelope of the building. The shaping of support perimeter tube structure could be realized by means of diagrid raster with slant orientation of load bearing beams. The tube structure with diagrid disposition

---

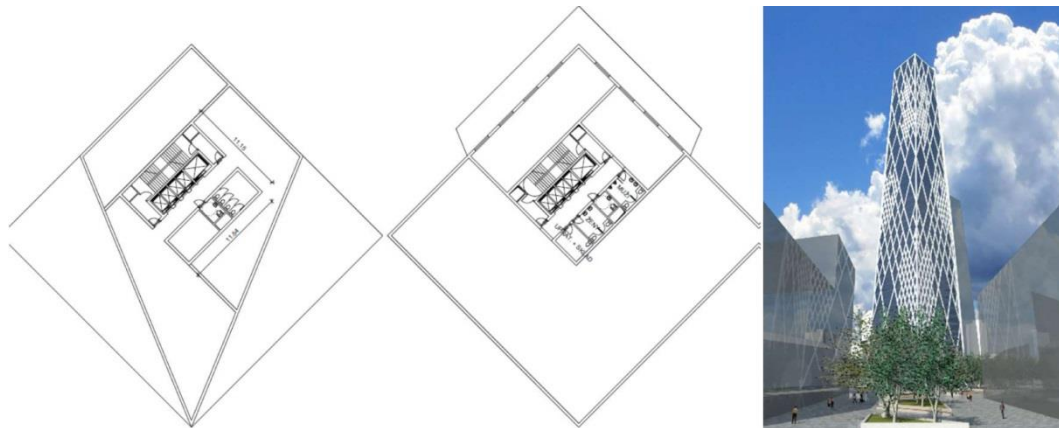
<sup>\*</sup> Assoc. Prof., Ing. Oľga Ivánková, PhD.: Department of Structural Mechanics, Faculty of Civil Engineering, Slovak University of Technology, Radlinského 11; 810 05, Bratislava; SK, olga.ivankova@stuba.sk

<sup>\*\*</sup> Ing. Dávid Méri : Department of Structural Mechanics, Faculty of Civil Engineering, Slovak University of Technology, Radlinského 11; 810 05, Bratislava; SK, david.meri@stuba.sk

<sup>\*\*\*</sup> Ing. arch. Eva Vojteková, PhD.: Institute of Architectural and Engineering Structures, Faculty of Architecture, Slovak University of Technology; Nám. Slobody 19; 812 45, Bratislava; SK, vojtekova@fa.stuba.sk



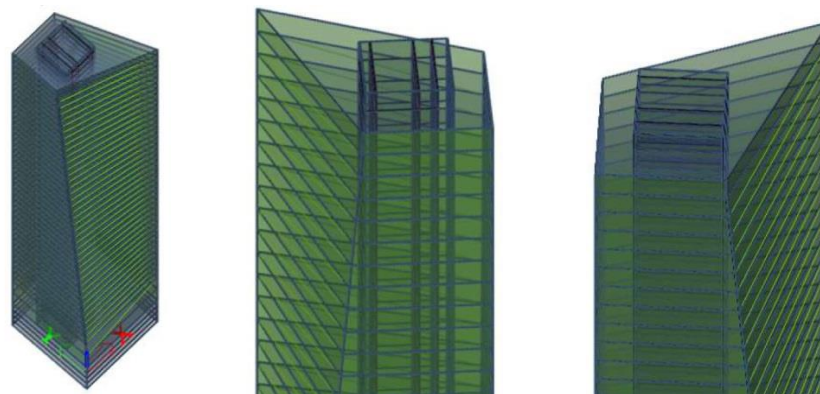
of support elements appears to be more suitable from the viewpoint of bearing vertical load. Architectural design was elaborated as model design for a universal high-rise building with multipurpose use Bc. Tomáš Heinsch also participated in the design of the high-rise building with the authors.



*Fig. 1: Top floor plan, Ground floor plan, Visualization of the high-rise building.*

### 3. High-Rise Building's Models

Particular models of the high-rise building were created by using spatial variant of FEM in program Scia Engineer. Seven models were created, which were different in exoskeleton design. The shape of high-rise building is based on square ground floor plan with proportions 30 x 30 m. Dimensions of two sides of floor plan decrease with increasing height of the building. The top ground floor plan's shape is an irregular tetragon. The height of all models is 165.4 m, consisting of 44 floors with structural height 3.6 m, first and second above-ground levels (7.4 m) and top (technological) level (3.0 m). Reinforced concrete core with stiffened walls having size of 300 mm (concrete C40/50) and steel exoskeleton, with various dimensions of cross sections in each model, create a vertical structural system of high-rise building. Reinforced concrete slabs with thickness of 200 mm (concrete C40/50) create horizontal support structure. For all models the loads from curtain wall skin with thickness of 200 mm and density of 300 kg/m<sup>3</sup> were considered. The models differ from one another by exoskeleton layout and dimensions. Models were loaded by wind from each side of rectangular floor plan under 90 ° angle. The wind load was computed by wind 3D generator, a part of Scia Engineer program. The model structure has to be covered by surfaces that have been loaded by wind. As a first, a clear 3D model of the high-rise building was created, then the surfaces were generated, that in our case represented the skin envelope. After dividing surfaces to the panels it was possible to implement the 3D wind generator, which calculated pressure coefficients of the skin envelope. Pressure coefficients were subsequently recalculated to areal loads.

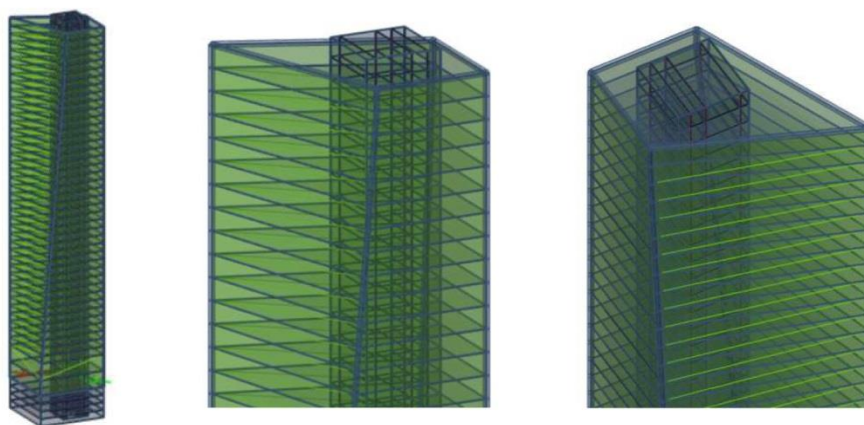


*Fig. 2: Model creating – reinforced concrete elements (core and slabs).*

### 4. Creating the Model

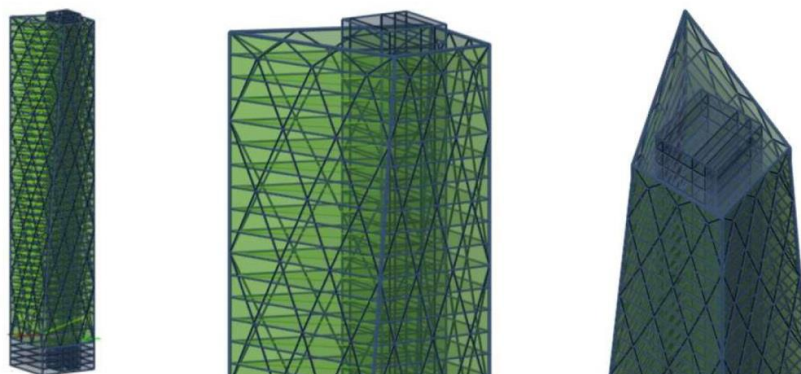
During creating the model, reinforced concrete elements of high-rise building were modeled at first. Reinforced concrete ductile core walls and flat plate slabs with changing shape for each floor were

modeled in dependence on building's tapering along the height. An addition of main ductile elements of tube exoskeleton situated in edges of the high-rise building was the second step. Steel tubes with diameter dimension about 914 mm and steel walls with thickness of 14.2 mm were used.



*Fig. 3: Model creating – addition of main ductile elements of tube exoskeleton in edges.*

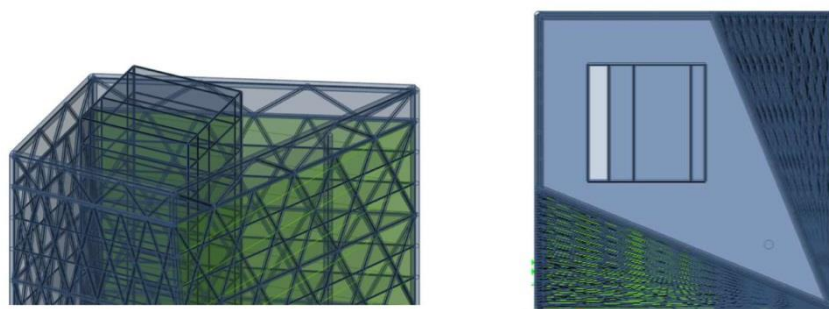
According to the architectural design, main diagonal elements of exoskeleton were added in next step. On this level of creating the model, three variants with various dimensions of exoskeleton steel tubes were made. In variant 3 we used steel tubes in edges with diameter 508/10 mm and steel tubes with diameter 244.5/10 mm for exoskeleton diagonals. Variant 4 was modeled with use of steel tubes 762/12.5 mm in edges and steel tubes 355.6/12.5 mm for exoskeleton diagonals. Variant 5 was modeled in edges with the same dimension of steel tubes as first three variants, but the diagonal steel tubes were used with dimensions 457 mm in diameter and steel wall with thickness of 12.5 mm.



*Fig. 4: Model creating – addition of main diagonal elements of exoskeleton.*

Created models still had not been reaching required stiffness to resist to the lateral wind loads. The rate of limit deformations was still exceeded. That was a reason for addition more diagonals according to the architectural design. For further research we chose variant 5, where added diagonals have the same dimensions, that means 457/12.5 mm. Resulted horizontal deformation was still over limit.

In the last variant one huge coupled reinforced concrete column was added to the structure in the middle of the span between the reinforced concrete core and the most distant edge of the floor plan. The column serves for elimination of excessive settlement of ceiling slab.



*Fig. 5: Model creating – addition of reinforced concrete column.*



## 5. Static Analysis of Wind Excitation

For static analysis, the design and characteristic loads were stated (Bilcik et al., 2008). The loads can be divided to own weight of structure, other constant loads and lateral wind load (STN EN 1991-1-4, 2009). We achieved design situations for Limit Serviceability State by combination of all these loads. We used program Scia Engineer including 3D wind generator for wind load computing.

## 6. Evaluation of Horizontal Displacement

The results of wind static analysis are maximal horizontal displacements of buildings. Results are documented in following tables according to the wind direction and particular displacements and rotations by X, Y and Z axis. Limit value of deformations must not exceed value 1/2000 of building's height that means in our case 82.7 mm (Harvan, 2011). The building was analyzed to Ultimate Limit State and Limit Serviceability State. We considered the combinations of wind load and own weight of the structure. These combinations were investigated for four wind directions.

*Tab. 1: Maximal and minimal displacement and rotation of the highest floor slab for all variants.*

Variant	$u_{x, \max}$ (mm)	$u_{x, \min}$ (mm)	$u_{y, \max}$ (mm)	$u_{y, \min}$ (mm)	$u_{z, \max}$ (mm)	$u_{z, \min}$ (mm)	$\varphi_{x, \max}$ (mrad)	$\varphi_{x, \min}$ (mrad)	$\varphi_{y, \max}$ (mrad)	$\varphi_{y, \min}$ (mrad)	$\varphi_{z, \max}$ (mrad)	$\varphi_{z, \min}$ (mrad)
1	253.1	-72.1	84.5	-237.7	0.5	-70.8	7.0	-8.0	7.1	-8.0	1.4	-1.3
2	199.7	-69.7	79.6	-187.4	0.6	-58.2	7.0	-8.0	7.0	-8.0	1.4	-1.4
3	113.6	-10.0	17.9	-103.7	0.6	-50.2	5.7	-5.8	5.8	-5.7	0.8	-0.8
4	80.3	-14.7	21.3	-73.0	0.6	-40.2	5.1	-5.0	5.2	-5.0	1.1	-1.1
5	75.6	-19.2	25.9	-68.3	0.6	-37.2	4.0	-4.1	4.0	-4.1	0.9	-0.9

We obtained the proper design of building by gradual sequential modeling. This design is proper from the viewpoint of maximal deformations. The improper design can produce excessive displacements of higher storeys, which could originate problems in skin envelope: glass cracking and water flowing. The amount of designed steel tube profiles is minimal for resistance to lateral wind load. Used reinforcement is sufficient.

## Acknowledgement

Authors express their sincere thanks to financial support of Grant Agency of Slovak Ministry of Education, registration numbers of projects are VEGA 1/0544/15 and 1/0266/16.

## References

- Bilcik, J. et al. (2008) Concrete structures. Design according to STN EN 1992-1-1, STU, (in Slovak).  
Eisele, J. and Kloft, E. (2002) Hochhaus Atlas, Callwey, Munchen, ISBN 3-7667-1524-0, (in German).  
Harvan, I. (2011), Reinforced Concrete Structures. High rise buildings. Design according European united standards, STU Press Bratislava, (in Slovak).  
Zhou, Y., Kijewski, T. and Kareem, A. (2002) Along-Wind Load Effects on Tall Buildings: Comparative Study of Major International Codes and Standards, Journal of Structural Engineering, June.  
STN EN 1991-1-4: (2009) Eurocode 1: Loading of structures; Part 1-4: Universal loads, wind load, Bratislava, STU Press.

## A HIGH-RISE BUILDING - INFLUENCE OF CHANGE OF SOIL STIFFNESS ON HORIZONTAL AND VERTICAL DEFLECTIONS

O. Ivankova<sup>\*</sup>, A. Valasik<sup>\*\*</sup>, L. Konecna<sup>\*\*\*</sup>

**Abstract:** This paper deals with static analysis of 17-storey high-rise building with complicated design of slabs above the 1<sup>st</sup> and the 2<sup>nd</sup> overground levels. An influence of settlement of the structure in time was taken into account with various values of the subsoil stiffness coefficients. For their calculations, two-parametric model of subsoil was used for modeling of soil-structure interaction. Short description of analyzed structure, applied loads and other input parameters are mentioned. At the end of the paper, obtained results for static analysis (deflections of the structure due to combinations of the permanent, variable and wind loads) are presented.

**Keywords:** Soil stiffness, Static analysis, High-rise building, Reinforced concrete structure, Deflections.

### 1. Description of the structure

Analyzed 17-storey high-rise building (Fig. 1a) was designed as an office building. In bottom part, there were 3 storeys designed as parking spots. Structural height was 3700 mm and total height of the building from the foundation to the top was 72.5 m.

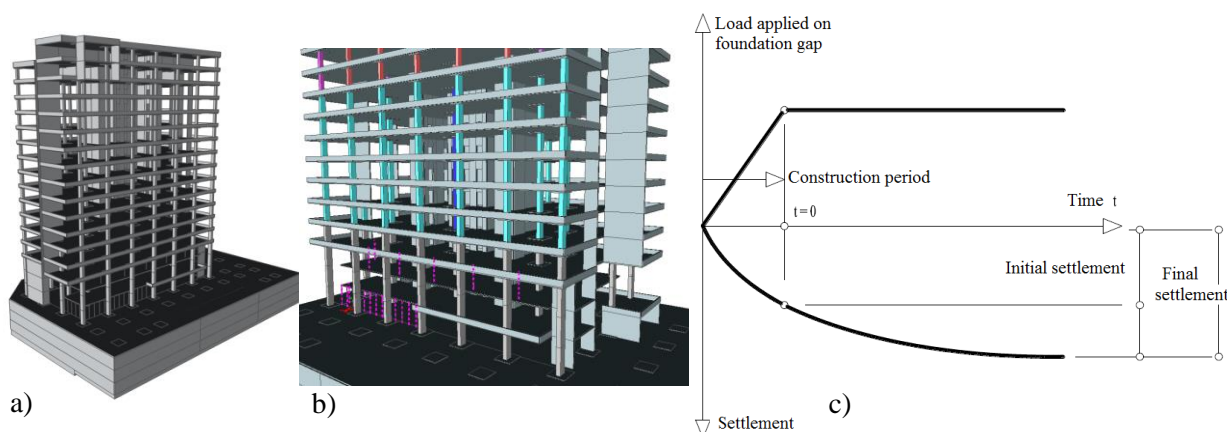


Fig. 1: a) Analyzed high-rise building, b) view of the 1<sup>st</sup> and 2<sup>nd</sup> overground levels, c) time dependence of settlement of structure (Simek, 1990).

Cast in-situ reinforced concrete superstructure was designed as a combination of columns with beamless slabs and central stiffening core located in the center of gravity of ground plan of a typical floor. The grid of load-bearing walls and columns had the dimensions of (7.8 × 8.1) m. The foundation slab was designed as a one dilatation block with the dimensions of (75.175 × 52.200) m and various thickness, because applied load (axial force) on columns in underground part under the high-rise building was larger than it was in the case of the columns placed in other places of underground part. Therefore, the thickness of foundation slab under the high-rise building was 1000 mm added by column capital with the thickness of

<sup>\*</sup> Assoc. Prof. Ing. Olga Ivankova, PhD.: Faculty of Civil Engineering, Slovak University of Technology in Bratislava; Radlinskeho 11; 810 05 Bratislava; SK, olga.ivankova@stuba.sk

<sup>\*\*</sup> Ing. Adrian Valasik: Faculty of Civil Engineering, Slovak University of Technology in Bratislava; Radlinskeho 11; 810 05 Bratislava; SK, adrian.valasik@stuba.sk

<sup>\*\*\*</sup> Ing. Lenka Konecna, PhD.: Faculty of Civil Engineering, Slovak University of Technology in Bratislava; Radlinskeho 11; 810 05 Bratislava; SK, lenka.konecna@stuba.sk

1600 mm. In other places of the underground part, the thickness of foundation slab was 400 mm added by column capital with the thickness of 1000 mm. The walls of stiffening core had various thicknesses with respect to the change of the height (200 - 400 mm) and they were made of the concrete C30/37. The columns in the high-rise building were made of concrete C40/50. The columns in underground part were made of concrete C30/37. The slab of typical floor (4<sup>th</sup>-17<sup>th</sup> overground levels) was designed as beamless slab with the thickness of 200 mm added by visible planked capitals with the thickness of 350 mm (together with slab). The same design was used for the slabs above the 1<sup>st</sup> and 2<sup>nd</sup> underground floors.

Atypical design of superstructure was in the part between the underground levels and overground levels. With the respect to the requirement of an architect to highlight the entrance space, the slabs above the 1<sup>st</sup> and 2<sup>nd</sup> floor had atypical shapes and they were not supported by all columns placed on the boundaries of ground plan (Fig. 1b).

The slab above the 1<sup>st</sup> floor was supported by steel sections on its boundaries. They were a part of glass façade and they were anchored to the slab above 3<sup>rd</sup> underground level. The slab above 2<sup>nd</sup> floor was suspended by draw rods on its boundaries. These draw rods were anchored to the slab above 3<sup>rd</sup> floor. Then, the lengths of columns located on the boundaries of slabs on 1<sup>st</sup>, 2<sup>nd</sup> and 3<sup>rd</sup> floor, were two times or three times of the structural height (Fig. 1b).

For the solution of 3D computing model, the Spatial Deformation Variant of Finite Element Method using 1D and 2D elements, introduced in Scia Engineer Software, was used.

## 2. Applied loads and considered input parameters

Permanent and variable loads were considered according to (STN EN 1991, Bilcik 2008). For the snow load, the height above the sea level of building site 139.4 m was taken into account (STN EN 1991-1-3). For the wind load, terrain category IV (big cities) and 2<sup>nd</sup> wind area with the basic wind velocity 26 m/s were considered (STN EN 1991-1-4). For the analysis, the following geological profile was considered: 0.0 - 4.0 m made-up ground, 4.0 - 14.90 m gravel poorly grained (classified as G2 (Turcek, 2004)), 14.90 - 20.00 m clay with middle plasticity (classified as F6). The level of underground water was 6.60 m.

Soil-structure interaction was considered by the calculated value of subsoil stiffness coefficient. It defines compliance of soil during insertion of structure (or its parts) to the soil. According to Winkler's hypothesis, there is direct proportional dependency between the load applied on foundation gap and its deflection. Then, the subsoil stiffness coefficient  $k$  [kN/m<sup>3</sup>] can be calculated as:

$$k = \frac{p(x, y)}{w(x, y)} \quad (1)$$

where  $p(x, y)$  is contact stress [kN/m<sup>2</sup>] and  $w(x, y)$  is deflection [m] (Jendzelovsky, 2009). Resultant value of subsoil stiffness coefficient was 7150 kN/m<sup>3</sup>. This value represents the material properties of soil before the loading of foundation gap. Therefore, other two values of subsoil stiffness coefficient were calculated (Frankovska, 2011 and Simek, 2009).

The value of subsoil stiffness coefficient after the primary soil consolidation  $k_{z,red,I}$  can be calculated using Eq. 2. The total time of primary soil consolidation was estimated as 1 year (it is time needed for building such structure).

$$k_{z,red,I} = k_{z,eff} e^{(\varphi_0 - \varphi_{0z})} \quad (2)$$

where  $k_{z,eff}$  is subsoil stiffness coefficient calculated by Winkler's hypothesis (Eq. 1) [kN/m<sup>3</sup>]. In our case it was  $k_{z,eff} = 7150$  kN/m<sup>3</sup>.  $\varphi_0$  is final creep coefficient of concrete (Harvan, 2006).  $\varphi_{0z}$  is final creep coefficient of soil (for normally consolidated clay can be considered by  $\varphi_{0z} = 1.0$  (Frankovska, 2011)). Resultant value of subsoil stiffness after the primary soil consolidation was 19500 kN/m<sup>3</sup>.

Compliance of the soil in the time when the settlement of structure will be finished, can be expressed by Eq. 3.

$$k_{z,red,II} = k_{z,eff} (1 + \varphi_{0z}) e^{(\varphi_0 - \varphi_{0z})} \quad (3)$$

Where  $k_{z,red,II}$  is subsoil stiffness coefficient [kN/m<sup>3</sup>] after final settlement of structure,  $k_{z,eff}$  is subsoil stiffness coefficient calculated by Winkler's hypothesis (Eq. 1) [kN/m<sup>3</sup>] (considered by 7150 kN/m<sup>3</sup>).  $\varphi_0$  (they were described thereinbefore). Then, calculated value of  $k_{z,red,II}$  was 38900 kN/m<sup>3</sup>. Time dependence of settlement of the structure from applied load is shown in Fig. 1c, (Frankovska, 2011), (Simek, 1990).

### 3. Results – comparison of deflections and its assessment

Obtained results for different directions of applied loads are compared in Figs. 2 - 6. Maximum value of deflection in  $z$ -direction was considered as 50 mm (STN 73 1001). Maximum value of deflection in  $x$  and  $y$ -direction was considered as  $H/2000$  (Harvan, 2006), where  $H$  is the total height of the structure above the foundation (in this case  $H = 72.5$  m and  $H/2000 = 36.25$  mm). For this assessment, characteristic values of load were used. Contact pressure in subsoil area is 353.83 kPa.

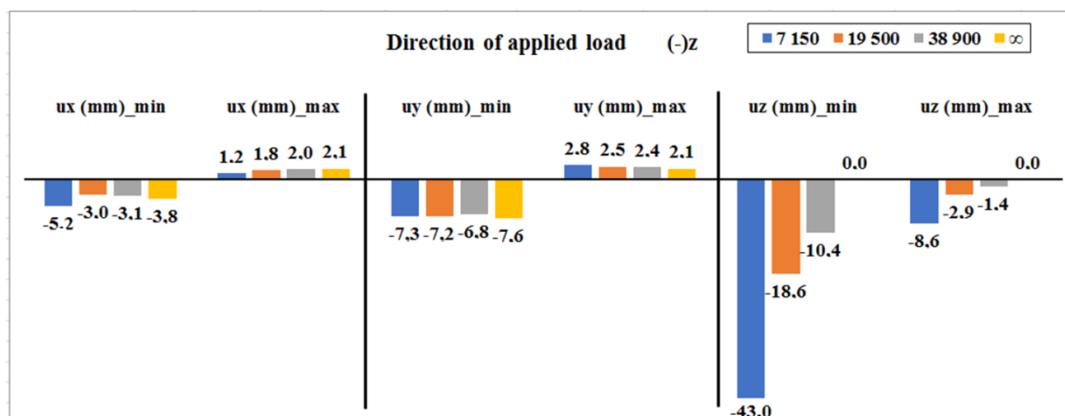


Fig. 2: Maximum and minimum values of deflections due to load applied in  $-z$ -direction.

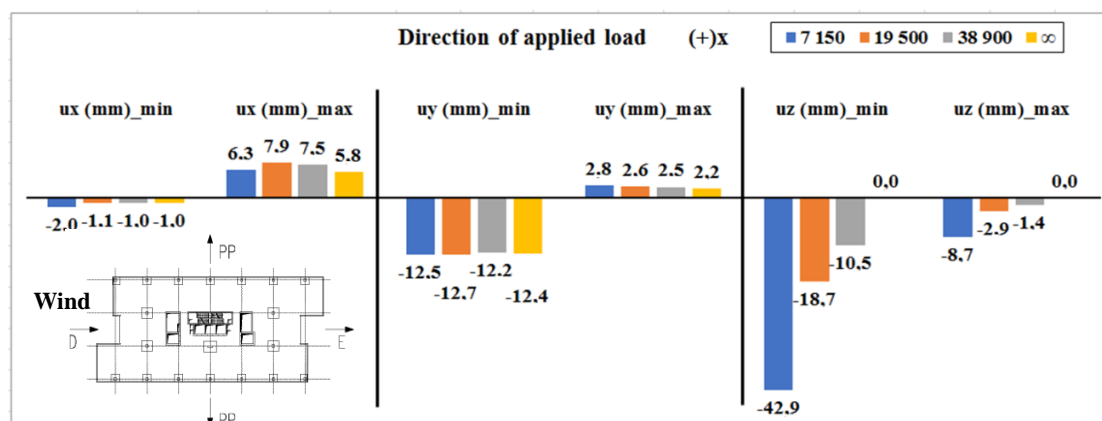


Fig. 3: Maximum and minimum values of deflections due to wind load applied in  $+x$ -direction.

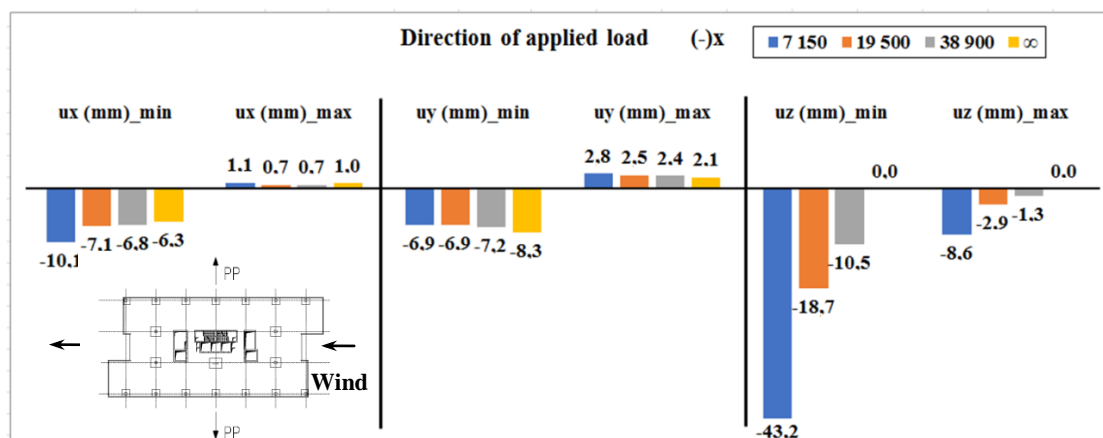


Fig. 4: Maximum and minimum values of deflections due to wind load applied in  $-x$ -direction.

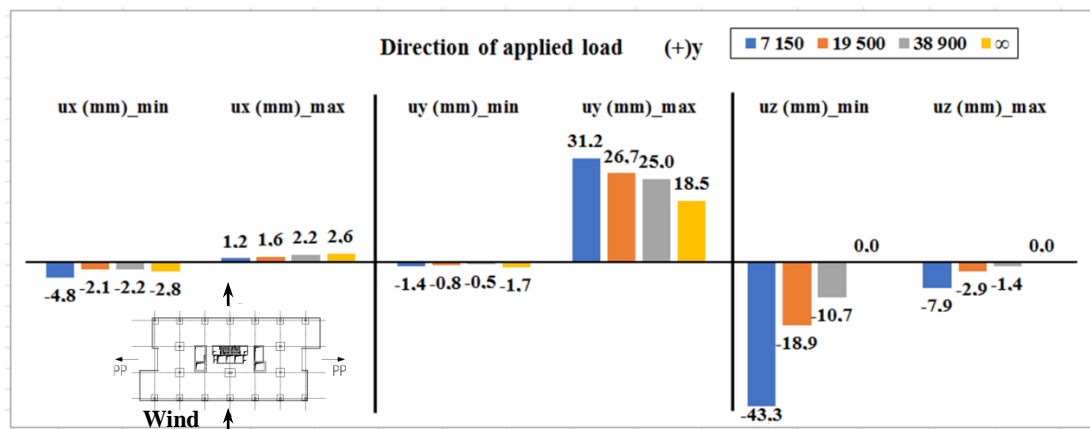


Fig. 5: Maximum and minimum values of deflections due to wind load applied in +y-direction.

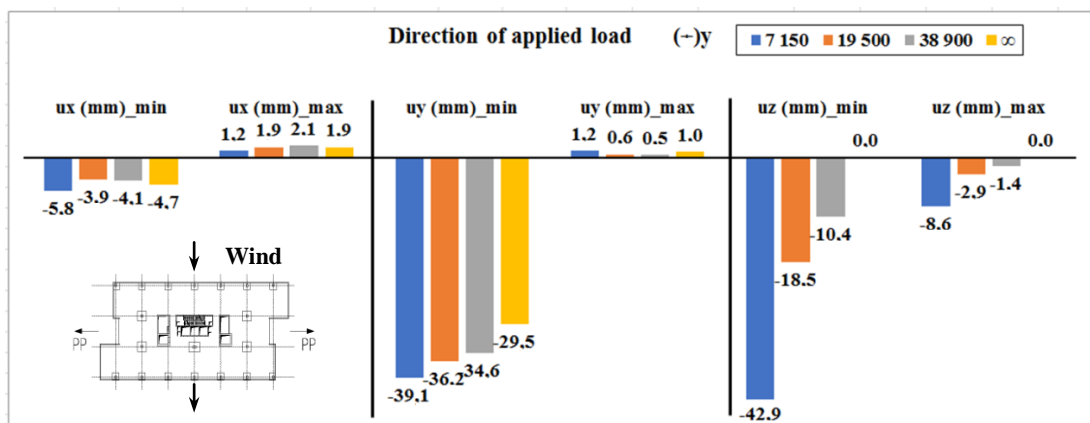


Fig. 6: Maximum and minimum values of deflections due to wind load applied in -y-direction.

#### 4. Conclusions

The building met the requirement for limit value of deflection in z-direction. The problem was in the case of the wind applied in -y-direction, when calculated maximum value for subsoil stiffness coefficient equalled to 7150 kN/m<sup>3</sup> was larger than limit value. Assessment of the structure for this value of subsoil stiffness coefficient is not correct, because the construction of structure is not completed. Furthermore, the structure is not loaded by full value of considered load in this time. For the assessment, it is better to take into account the primary soil consolidation, because it helps to increase the stiffness of soil. For the reduction of calculated deflections, it should be necessary to design additional stiffening walls in the ground plan of structure. Then, the structure should satisfy the limit values given by standards.

#### Acknowledgement

The paper was created with the support of the Scientific Grant Agency – VEGA grants No. 1/0265/16 and No. 01/0544/15. Authors thank to the STU in Bratislava for the support (grants No. 1619 and No. 1651).

#### References

- Bilcik, J. et al. (2008) Concrete structures. Design according to STN EN 1992-1-1, STU, 2<sup>nd</sup> ed., (in Slovak).
- Frankovska, J. et al. (2011) Foundation of structures. Design fundamentals, shallow foundation and deep foundation. Publishing house of STU in Bratislava, 1<sup>st</sup> ed., (in Slovak).
- Harvan, I. (2006) Reinforced concrete structures. STU in Bratislava, 1<sup>st</sup> ed., (in Slovak).
- Jendzelovsky, N. (2009) Modeling of foundations by FEM, STU in Bratislava, 1<sup>st</sup> ed., (in Slovak).
- STN 73 1001: Geotechnical structures. Foundation, Bratislava, SUTN.
- STN EN 1990: Eurocode: Basis of structural design, Bratislava, SUTN.
- STN EN 1991-1-3: Eurocode 1: Actions on structures, Part 1-3: General actions – snow load, Bratislava, SUTN.
- STN EN 1991-1-4: Eurocode 1: Actions on structures, Part 1-3: General actions – wind load, Bratislava, SUTN.
- Simek, J. et al. (1990) Soil mechanics, 1<sup>st</sup> ed., STNL, Prague, (in Czech).
- Turcek, P. and Hulla, J. (2004) Foundation of structures, Jaga group, Bratislava, 2<sup>nd</sup> ed., (in Slovak).

## SYSTEMS CONCEPTION OF PROBLEM-SOLVING

P. Janíček<sup>\*</sup>

**Abstract:** *The present paper deals with the causes that gave rise to Bertalanffy's General Systems Theory and Brno philosophy of systems methodology. It analyses what is a systems conception of the selection of method for solving a specific problem that is completely ignored by the current university teaching practice.*

**Keywords:** Problems, General Systems Theory, Systems methodology, Systems approach, Systems thinking, System of essential variables.

### 1. Introduction

Life in the sense of a whole formed by all living organisms in specific conditions of life within the Earth history puts different tasks on individuals. A term of a task is understood in the sense of responsibility delegated to humans (from their environment or by themselves, which is the case of the so-called self-motivation) to execute something on a certain entity (object, subject, process, etc.). If an individual knows the algorithm of how to accomplish a specific task, and if he/she has all that is essentially needed to implement the algorithm, it is the task of the type of labour. In the opposite case, it is the task of the type of problem. To solve this, it is necessary for the person to implement the following types of activities: informational, creative, evaluative, decision-making and executive.

The level of problem-solving depends on the level of knowledge of investigator (both in general and subjective meaning) about the characteristics of the entity. An important milestone at the general level was the period after 1926 in the field of philosophy (Jan Christiaan Smuts was the first who used the word holism in his book *Holism and Evolution*), and the period around 1950 when the Austrian biologist and philosopher Ludwig von Bertalanffy published his article "General Systems Theory - A New Approach to Unity of Science".

Let us ask a question: "What was this milestone like?" A holism predecessor was called reductionism. It is a school of thought that tries to explain the facts on complex entities so that these are converted into simple parts through which the problems can be solved

Unsustainability of reductionism can be traced as early as at the beginning of the thirties of the last century when, with such objects, the "problems" with determination of their global characteristics and behaviour began to appear as they were considered only on the basis of the characteristics and behaviour of their isolated elements. Experiments showed that the resulting behaviour of objects did not reflect reality. In 1940, when searching for a solution to a military problem of Bell Telephone Laboratories for NASA, the analyses of the results showed the identical solution to the problem. The behaviour of the object as a whole was different from the behaviour that the object showed when considering only the characteristics of individual isolated elements of the object. It was verified that this discrepancy was not a random phenomenon, but it is one of the fundamental laws of our world. It is related to holism (Gr. "holon" = whole), which is also a philosophy assigning objects with those characteristics which are not derivable only from their isolated elements.

The importance of the above-mentioned milestone in the transition period from reductionism to holism is that the analyses showed that in problem-solving, the entities have to be understood not only as a set of their elements but equally important are also the bonds between these elements. A set of entity elements and the bonds between them was termed a structure of the entity and the corresponding characteristic of

---

<sup>\*</sup> Prof. Přemysl Janíček, DSc.: Institute of Solid Mechanics, Mechatronics and Biomechanics, Faculty of Mechanical Engineering, Brno University of Technology, Technická 2, 616 69, Brno, CZ, janicek@fme.vutbr.cz

the entity is its structuring. In England, for the entity with these characteristics, the term "real system" was used. Issues that were addressed to the systems (problems of systems) were also marked as system problems.

## 2. Methods

All the above-mentioned findings represented a new paradigm in solving the problems in real systems. This was well reflected in the emergence of **General Systems Theory**, which was endeavoured by Austrian biologist and philosopher **Ludwig von Bertalanffy** around 1950, when he was looking for common patterns of both living and social real systems. He reasoned that these include openness (there exist energy, mass and information interactions between the elements of real system and their environments), complexity (in terms of internal interactions among elements of the real system and external interactions between the real system and its environment), feedback between the internal and external bonds, dynamic equilibrium, transformational relationships between the inputs into the real system and outputs, dedicated target behaviour of the real system and self-organizing processes in the real system. All this was considered to be characteristics of real systems, in other words, **systems characteristics**.

A systems theory needed for its existence an appropriate **theoretical and methodological discipline**. This should become: a discipline marked as **Systems analysis and synthesis** and **Systems engineering**. However, this was, in its infancy, drowning in "poverty of funds" needed for holistic solutions to problems. It was because appropriate theories, approaches and methods were not known, but mostly there was a lack of powerful computational tools. Although everything changed after the discovery and development of computers, because this allowed for the emergence of new methods and approaches to solving of holistic problems, the systems engineering was still getting into internal problems. It has been suffering from these problems up to now; among others, due to the changes in the entire "engineering". New engineering disciplines are being formed, e.g. information, knowledge, software, safety, risk, quality engineering, etc., which absorb many aspects of systems engineering so that the systems engineering suffers from "commutation". Both of these disciplines, while offering methods to solve systems problems, did not indicate how the specific system problem should be selected using a particular method for its solution, or on what basis the new theories should be created, failing to choose from.

At present, the following fact is also characteristic: the existence of computers enabled the development of numerical methods to solve professionally-varied problems by computational modelling. One of the best known, most versatile, and widely used methods is the finite element method. It is used in continuum mechanics, magnetism, electromagnetism, etc. Currently, it is a methodical top. If you are asked to solve the problem, solvable by FEM, you would select this method without being interested in any philosophising about a systems selection of method.

It can be stated that the publication "General Systems Theory-A New Approach to Unity of Science" was not followed by any other publication on a systems methodology. This is probably one of the reasons why there is currently such a poor situation in the systems approach to solving the problems that the individual meets in his/her environment or through his/her self - motivation.

A publication gap in the methodology of real systems was filled with a book written by Janicek (2014). It defines this methodology as an abstract entity with the following elements:

- **Systems approach** – is a generalized and sophisticated creative methodology of thinking and acting, applicable to any system entities. It consists of a sequence of conscious, describable, performable, or even formalized activities respecting **the attributes of the systems approach** that include all relevant facts in relation to the entity.
- **Systems disciplines**-are multifield disciplines that are applicable to the analyses and problem-solving in a specific group of scientific and practical fields (technical, medical, veterinary, agricultural, nature, philosophical, etc.). E.g. in technical sciences, these disciplines include: logic, mathematics, physics, systems engineering, cybernetics, systems dynamics, mechanics (solids, thermal, aero, hydro), statistics, logistics, deterministic chaos, self-organization, experiment, expert engineering, risks engineering, limit states.
- **Systems algorithms** are generalized algorithms for solving the problems in real systems of different disciplines (technical, social, socio-technical, technical and organizational), in their Hard systems, Soft



Systems, and Hard-Soft Systems.

- **Systems thinking** – is thinking in terms of generalized theory of systems and systems methodology, and at the same time it is an intersection of progressive structural and mental types of thinking (analytical, synthetic, creative, divergent, productive and comprehensive).

The use of **systems terminology** is a must.

Up to now, it has been not possible to define the term of systems conception, which is contained in the title of the paper. It is an approach to any activity undertaken on the entity when a systematically thinking individual uses a systems methodology.

## 2.1. Structure of systems approach

**First subgroup:** premises (assumptions) for application of systems approach

Attribute A0 – definition of "entity of interest" for subject;

Attribute A1 – requirement of term purity;

Attribute A2 – correct identification and formulation of problem.

**Second subgroup:** approaches to analysed entities

Attribute A3 – structured (to consider elements of entity and bonds between them);

Attribute A4 – purposeful (to assess the essentiality of characteristics, properties, behaviour);

Attribute A5 – comprehensive (in all internal and external relations);

Attribute A6 – hierarchical (bonds, interactions, activations, processes, states, manifestations, consequences);

Attribute A7 – oriented (orientation - temporal, causal, hierarchical).

**Third subgroup:** assess the characteristics of entities from these perspectives;

Attribute A8 – assess the entities in terms of openness (isolated entity, closed, open);

Attribute A9 – assess the entities in terms of level balance (in relation to the structure and activities of subjects);

Attribute A10 – assess the entities in terms of dynamics (i.e. changes over time);

Attribute A11 – assess the entities stochastically (stochasticity and determinism of variables and processes);

Attribute A12 – assess the states and target behaviour of entities;

Attribute A13 – assess the entities in terms of occurrence of deterministic chaos and self-organization.

**Fourth subgroup:** all human activities have to be at contemporary level;

Attribute A14 – use the latest knowledge of science and technology;

Attribute A16 – create "algorithms of activities";

Attribute A17 – analysis, verification and synthesis of results concerning the problem-solving process (in general, the activities).

**Fifth subgroup:** deal with ethical aspects

Attribute A18 – responsibility for the credibility of the results of problem-solving process;

Attribute A19 – maintain all ethical standards (general, personal, social, geo-environmental);

Attribute A20 – monitor the methods of results implementation.

## 3. System of essential variables

In the sense of the attribute A7, a causal problem is considered in relation to a certain entity  $\Omega$ . This problem is characterized by the fact that the input in the algorithm of its solution is represented by the causes (activations), which evoke the internal processes, while outputs are manifestations induced by these processes. In everyday life, when solving a practical problem, we always consciously or unconsciously analyse what its solution essentially depends on. The same is true for professional and scientific problems. The systems methodology for the "identification" of all the important components of the system produces a system of essential variables  $\Sigma(\Omega)$  which is a set with the following subsets. This

system is the basis for finding a credible and effective methods to solve the problem. The following is a list of subsets:

- **Subset S0** – environmental variables  $v_0$  describe the **elements in the environment** of entities.
- **Subset S1** – object variables  $v_1$  describe **the topology and structure of the entity**.
- **Subset S2** – bond variables  $v_2$  describe **essential bonds and interactions** between the entity and its environment.
- **Subset S3** – activation variables  $v_3$  representing such **activation of the entity  $\Omega$**  from its environment that evokes processes on this entity.
- **Subset S4** – affecting variables  $v_4$  from the environment **affect the processes on the entity**.
- **Subset S5** – structural and characteristics variables  $v_5$  expressing the **characteristics of elements of entity structure** on which the problem is solved (characteristics: geometric, structural, physical, mechanical and technological).
- **Subset S6** – process variables  $v_6$  describing the **processes** on the entity transforming the entity into different **states**.
- **Subset S7** – manifestation variables  $v_7$  expressing **the entity manifestations** in relation to its environment.
- **Subset S8** – consequential variables  $v_8$  describing **the consequences of entity manifestations** on the environment or on the entity itself.

For all of these variables, their characteristics must be listed in accordance with the attributes of the systems approach, i.e. whether they are open variables (closed, isolated), dynamic (static), stochastic (deterministic), whether the occurrence of deterministic chaos and self-organization can be expected.

#### 4. Selection of method for problem-solving

We have arrived at this situation. On the one hand, we have a system of variables  $\Sigma(\Omega)$  to solve a specific problem; on the other hand, there is a set of potentially applicable (potential) methods to solve it. This set is part of the knowledge database of the individual. Its scope and depth are individual. The investigator, when selecting a method to solve the problems, faces the following decision-making activity: "Is there, among potential methods of problem-solving, such a method that it is able to comply with all the variables of the system  $\Sigma(\Omega)$  with the respective characteristics?" Answers may include the following:

- 1) Yes. Then the respective method is accepted to solve the problem.
- 2) Partly. Then the following problem has to be solved: How is the solution to the problem affected, if certain variables of the system  $\Sigma(\Omega)$  are neglected? Is this the issue of the consequences of using simplifying assumptions?
- 3) No. Investigation must continue to find a new method of problem-solving. It may not be easy, if at all possible.

#### 5. Conclusions

We believe that the present text is understandable. Those who are familiar with the above-mentioned topic so that the text appears to them as useless, sorry. For those, who wish to extend their knowledge in this subject-field, the said publication on systems methodology is recommended. It is used to solve various scientific and professional problems as (Fuis et al., 2008, Fuis, 2004).

#### Acknowledgement

This work was supported by grant FSI-S-17-4004.

#### Reference

- Fuis, V. (2004) Stress and reliability analyses of ceramic femoral heads with 3D manufacturing inaccuracies, In: Proc. 11th World Congress in Mechanism and Machine Science, Tianjin, China pp. 2197-2201.
- Fuis, V. and Varga, J. (2008) Stress Analyses of the Hip Joint Endoprosthesis Ceramic Head with Different Shapes of the Cone Opening. In. IFMBE Proceedings Vol. 23, Iss. 1-3, pp. 2012-2015, Singapore.
- Janiček, P. (2014) Systems methodology – Gate to problem-solving, CERM, (in Czech).

## MODELLING – A TOOL FOR PROBLEM-SOLVING

P. Janíček\*, V. Fuis\*\*

**Abstract:** *The title and content of the present article seem to be thematically archaic, but the present knowledge about modelling as a tool for problem-solving is incredibly miserable; therefore, actually, the article is up to date. There are many individuals who are caught off by the question what exactly is, in that sense, the real essence of modelling, even though some of them write about it, and even teach it. In fact, the answer can be found in already the 27-year-old publication "Computational models in engineering practice" by the two authors from Brno. Three years ago, another publication "Systems Methodology" appeared in Brno (Janíček, 2014); it discusses modelling in terms of systems approach. These authors from Brno also published the book "Expert Engineering in systems approach", which is also dedicated to solving the problems by modelling. Literature sources thus exist; however, reading is not very popular, especially as for Czech subject-field books. Nevertheless, publications from the West do not always guarantee the quality of information and knowledge. Therefore, this article recapitulates the essence of modelling, its graphic display, types of modelling and terminology of modelling in Czech and English equivalents.*

**Keywords:** Model, Essence of modelling, Structure of model, Types of modelling, Computational modelling.

### 1. Essence of modelling

Problems  $P_R(\Omega)$  on entities  $\Omega$  can be solved by two basic approaches, direct and indirect.

A **direct approach** means to solve the problem without any auxiliary objects. Is it necessary to build a dam? So it is built without prior work with any of its models. Is it charlatanism? Of course, it is. But it is quick.

**Indirect approach** (Fig. 1a) – The essence is that to solve the problem of  $P_R(\Omega_1)$  on the primary object  $\Omega_1$ , the subject  $S$  uses an appropriate purpose-built secondary object  $\Omega_2$  (also called the auxiliary object, the model object), which should facilitate a solution on the primary object  $\Omega_1$  for the subject  $S$ . The findings in relation to the solved problem, obtained on the object  $\Omega_2$ , are transferred to the primary object  $\Omega_1$  by image  $Z$ . In the early days of modelling, the model object  $\Omega_2$  used to be a real physical object on which the observations and experiments were implemented and findings had a verbal form. Image  $Z$  may have in this case a **natural** level (based on the natural abilities of humans to consciously create the image of the object  $\Omega_2$ , and based on the acquired findings to create an image of the object  $\Omega_1$  on  $\Omega_2$ ), or a **scientific and technological** level (utilizes the natural abilities + scientific and technological knowledge). This type of modelling was identified as prehistoric experimental modelling.

For further development of modelling, it was characteristic that the auxiliary physical object (experimental object) served for measurements which were processed mathematically. This means that on the object  $\Omega_2$ , the investigator generated a system of numerical variables  $\Sigma(\Omega_2)$ , which were then transmitted via image  $Z$  to the system of numerical variables  $\Sigma(\Omega_1)$ . This was the basis for solving the problem  $P_R(\Omega_1)$  on the object  $\Omega_1$  (Fig. 1b). It is logical that in this case it is possible to use for  $Z$  the term of **systems image**.

The model object may have a **real** essence (physical object) or **abstract** (system of information, knowledge, numerical variables, fuzzy variables). If the model object  $\Omega_2$  is formed by two or more sub-

---

\* Prof. Přemysl Janíček, DSc.: Institute of Solid Mechanics, Mechatronics and Biomechanics, Faculty of Mechanical Engineering, Brno University of Technology, Technická 2, 616 69, Brno, CZ, janicek@fme.vutbr.cz

\*\* Assoc. Prof. Vladimír Fuis, PhD.: Centre of Mechantronics – Institute of Thermomechanics of AS CR and Faculty of Mechanical Engineering, Brno University of Technology, Technická 2, 616 69, Brno, CZ, fuis@fme.vutbr.cz

models, it is **hybrid modelling**.

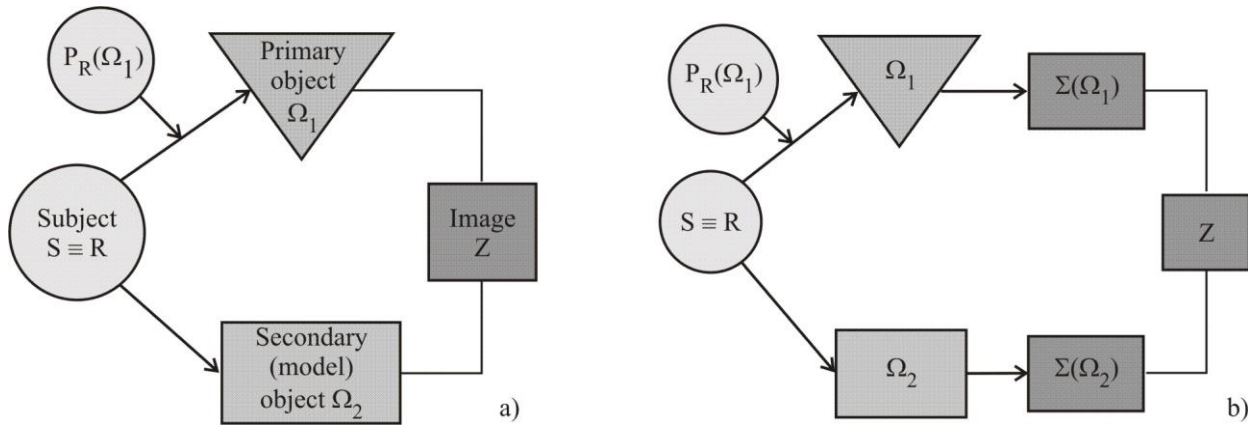


Fig. 1: Elements of essential structure of modelling.

## 2. Generalized structure of model

The previous text introduces the term of a model object in the sense that it is an auxiliary object that allows for solving the problem on a specific primary object  $\Omega_1$ . A systems theory of modelling uses also the term of **model** in the following two meanings. The first meaning is understood as a system of real and abstract elements, which is needed for modelling. It has the following elements: object model  $\Omega_2 \equiv O_M$ , system of variables  $\Sigma(\Omega_1)$  on the primary object  $\Omega_1$ , system of variables  $\Sigma(\Omega_2)$  on the model object  $\Omega_2$ , image  $Z$  between the respective systems of variables, method of MR solving of problem  $P_R(\Omega_1)$ , appropriate hardware mHW and software mSW. Elements of model are drawn into the basic structure of modelling in Fig. 2 in light grey colour.

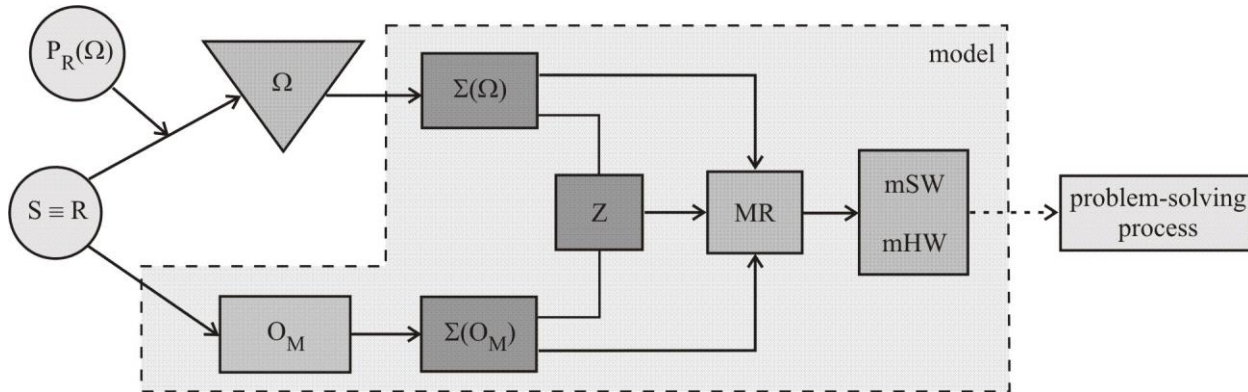


Fig. 2: Generalized structure of model (light grey).

In the other meaning, the term of model is used **as a result of simplification process** of characteristics, properties and behaviour of real entities to such a level so that the "simplified" entity could "work" in the problem-solving process using modelling (see the issues of computational sub-models).

### 2.1. Types of modelling

The above-mentioned philosophy of modelling leading to its simple basic structure also allowed for a simple **definition of each type of modelling** on the basis of this consideration. The model object  $\Omega_2$  can be anything that allows for problem-solving on the object  $\Omega_1$ . Depending on the nature of the object  $\Omega_2$  and the type of image  $Z$ , the existing modelling can be divided into the following types:

- **Mental modelling** –  $\Omega_2$  is the human brain and thought processes going there.
- **Prehistoric material modelling** –  $\Omega_2$  is a material object, image  $Z$  is natural.
- **Similarity modelling** – it is a hybrid modelling because the model object  $\Omega_2$  has a real part and an abstract one (see below). Objects  $\Omega_1$  and  $\Omega_2$  are structurally identical (e.g. turbines) with identical processes (running of turbines). However, they differ in size (e.g. a small model turbine  $\Omega_2$  and a large real turbine  $\Omega_1$ ). On the real part of  $\Omega_2$ , experiments are carried out while the abstract part of  $\Omega_2$

represents knowledge from experiments which are used to create a system of essential variables / lit / on the primary object  $\Omega_1$ . Image Z is of systems nature. Specifically, it is a computational image of equality between the similarity numbers on the objects  $\Omega_1$  and  $\Omega_2$ .

- **Analogue modelling** - it is a hybrid modelling because the model object  $\Omega_2$  has also a real and abstract part. This type of modelling uses the analogy of physical processes (processes that are formally described by the same differential equation (DR) and the same boundary conditions OP), regardless of the type of real object). On the real part of  $\Omega_2$ , experiments are carried out. The abstract part of  $\Omega_2$  represents the knowledge from the experiments, which are used to create a system of essential variables  $\Sigma(\Omega_1)$  on the primary object  $\Omega_1$  and to create essential variables  $\Sigma(\Omega_2)$  on the model object. Image Z expresses conformity of DR and of OP to  $\Omega_1$  and  $\Omega_2$ .
- **Knowledge-based modelling** – is an empty expert system for processing of knowledge from a set of experts from a particular field. System  $\Sigma(\Omega_2)$  is a subject-field expert system filled with a set of knowledge.
- **Theoretic modelling** –  $\Omega_2$  is an appropriate theory (descriptive, mathematical, graphic)
- **Computational modelling** –  $\Omega_2$  is a set of mathematical theories. System  $\Sigma(\Omega_2)$  is a suitable mathematical theory that is acceptable in accordance with the system of essential variables  $\Sigma(\Omega_1)$ , i.e. formed on  $\Omega_1$ .
- **Data-based modelling** –  $\Omega_2$  is a set of statistical methods. System  $\Sigma(\Omega_2)$  is a suitable statistical method for processing the data of a particular type: quantitative (regression analysis method), qualitative (analysis of variance), quantitative + qualitative (covariance analysis), fuzzy (fuzzy statistics).
- **Formal modelling** –  $\Omega_2$  are formal structures that:
  - a) are **analogies to living nature**. These include expert systems (simulating human thinking), genetic algorithm (simulating the evolution of biological species on earth), artificial network (simulating the processes of biological neural networks).
  - b) **purely formal structures** (meta algorithms, rule-based systems, syntactic recurrent trees).

### 3. Computational modelling

The previous section stated that the model object for computational modelling is a **mathematical theory** MT. To be usable, it must be mathematically solvable, there must be a computing device allowing for problem solving process, algorithm development for the problem - solving process, there must exist the input data related to the problem to be solved. Logically thought out: the term of **mathematical modelling** is not appropriate because, though the existence of mathematical theory is a necessary pre - condition to solve the problem, it is not sufficient in order to implement the computation.

Engineering Mechanics is mainly engaged in the so-called **causal problems concerning technical entities**. They are distinguished by the inputs to the algorithm that are formed by causes (entity environment, geometry and topology of entity, bonds between the entity and the environment, entity activation, influence on the entity, particular characteristics of entity); outputs are formed by the consequences induced by causes (processes on the entity, entity states, entity manifestations, consequences of manifestations).

All these causes and also the consequences have certain real properties and behaviour. For computational modelling, it is necessary to describe the properties and behaviour of entities by certain characteristics, and they should be expressed by quantitative variables (if possible). Given to the limited abilities of humans to transform the elements of objective reality to the elements with which it is necessary to perform some operations (e.g. computational), it is not possible to avoid certain simplifications of reality. What we receive after the transformation of objective reality to "usable reality" can be denoted as a model of the respective cause or consequence, particularly as its **computational sub-model**. One of the steps of the algorithm in computational modelling is the creation of these sub-models:

Model of entity environment, model of entity geometry, model of entity topology, model of bonds between the entity and the environment, model of entity activation, model of influences on the entity, model of particular properties of the entity, model of processes on the entity, model of entity state, model

of entity behaviour, model of entity manifestations, model of entity consequences, model of entity limit states. Computational modelling (CM) can be classified as follows:

- Classical CM;
- Identification of systems;
- Simulation CM;
- Soft modelling;
- Computational optimization;
- Sensitivity analysis.

#### 4. Creating the terms in modelling

A spontaneous process of terms creation, without any rules how to create them, often leads to vagueness of created terms. This applies in general, i.e. also for the sphere of modelling. To modify the terms of "modelling" and "model" that stand in sentences as subjects, a part of the sentence, termed an attribute, should be used. It may be congruent (before the subject, taking the form of an adjective) or incongruent (after the subject and it is one or more nouns). A congruent attribute can be converted to incongruent (reverse is true, which leads to a change in meaning of the term).

- **Congruent attribute** (adjectives) before the words "model" and "modelling" are used to express:
  - a) **Essence of model and modelling.** Then, **what** is the essence of model and modelling? Answers: material, experimental, theoretical, computational, data-based, hybrid, knowledge-based, etc. Therefore, defining a type of modelling by the adjective before the word modelling is used if the modification of the term "modelling" refers to:
  - b) **Characteristics of variables describing the model and modelling.** Then, **what** characteristics have the model and modelling? Answers: static, dynamic, deterministic, stochastic, fuzzy, isolated, closed, chaotic)
  - c) **Approach to the subject of modelling.** Then, what approach has the individual to models and modelling? Answers: intuitive, conscious, non-systems, systems.
- **Incongruent attribute.** It is one or more nouns placed after the words "model" or "modelling". It is used if we ask the question: the model or modelling of what? Answers: geometry, material, properties, activation, interactions, constitutive relations, states and manifestations of entities, consequences of manifestations, etc.

Therefore, the correct term is "model of entity geometry" (i.e. the geometry of what? - entity). The term "geometrical model" means that the model has a graphic layout (sketch, drawing), which is something else. Another example: "model of material constitutive relations", which means that the constitutive relations of a particular material are mathematically modelled. The term "constitutive model" would mean that modelling is of constitutive essence, constitutive property, or uses a constitutive approach – but this all is nonsense.

On the basis of what terms of modelling are employed by the authors in their articles, an idea is given of whether or not they conceived the essence of modelling. The contributions of our authors to English periodicals should be written considering the systems conception in terms of content and terminology, regardless of how they are written in abroad. Even there the authors "may be mistaken".

#### 5. Conclusions

Who wants to, he/she will understand. Who does not, there is a plenteous literature. It is just about your willingness. It is not easy, but worth doing it. Open the gate to a systems approach to problem-solving and you will find yourself in another world. System methodology is used to solve various scientific and technical problems, e.g in the construction industry (Kala et al., 2017).

#### Acknowledgement

This work was supported by grant FSI-S-17-4004.

#### References

- Janicek, P. (2014) Systems methodology – Gate to problem-solving, Brno, CERM.
- Kala, Z., Valeš, J. (2017) Global sensitivity analysis of lateral-torsional buckling resistance based on finite element simulations. Engineering Structures 134, pp. 37-47.

## ROLE OF RANDOM FACTORS IN NONLINEAR REGRESSION: A CASE STUDY FOR ESTIMATION OF THERMOPHYSICAL PARAMETERS

E. Janouchová<sup>\*</sup>, A. Kučerová<sup>\*\*</sup>, J. Sýkora<sup>\*\*\*</sup>

**Abstract:** *In order to design an optimal experimental setup the designers have to take into account uncertainties connected to the investigated system. The input random factors associated with for example values of loading, specimen dimensions or measurement errors influence behaviour of the system, which thus becomes also uncertain. From this point of view, the experiment design is a very important because it effects amount of information which can be obtained from the experiment. More specifically, accuracy of the identified parameters from indirect experimental measurements depends on experimental settings. In this contribution we demonstrate a role of random factors in a nonlinear model calibration on an illustrative example of one dimensional heat conduction. The thermophysical parameters such as thermal capacity and thermal conductivity are identified on a basis of noisy measurements from experiments with different setup. The experiments vary in a number of sensors and number of observed time steps. The presented statistical analysis shows dependence of the parameter estimation on the choice of measured quantities involving different uncertainties.*

**Keywords:** Random factors, Uncertainty quantification, Inverse problems, Nonlinear regression, Heat conduction.

### 1. Introduction

Thanks to extensive developments in the field of uncertainty quantification in the last decades we are enabled to simulate the nonlinear systems with uncertain input parameters. It brings advantages as for example opportunity to design optimized and robust experiments for calibrating the models of such systems (Jarušková et al., 2016).

Involving random factors into the analysis of the system requires an appropriate formulation of the problem with respect to the considered source of uncertainty. Uncertainties can be separated into two principal categories according to whether a source of nondeterminism is irreducible or reducible (Oberkampf et al., 2002; Der Kiureghian et al., 2009). This contribution focuses on epistemic (reducible, subjective, cognitive) uncertainties arising from our lack of knowledge which is supposed to be reduced by any new measurement according to the coherence of learning (Mantovan et al., 2006; Beven et al., 2007). While aleatory uncertainty expresses the inherent randomness which cannot be reduced.

An efficient experiment design provides enough amount of suitable information which allows successful estimation of the model parameters with maximal reduction of the epistemic uncertainties. The corresponding inverse problems can be solved in deterministic or stochastic way (Tarantola, 2005) but in the both cases the identification approach has to be chosen appropriately considering the involved uncertainties.

---

<sup>\*</sup> Ing. Eliška Janouchová: Faculty of Civil Engineering, Czech Technical University in Prague; Thákurova 7/2077; 166 29, Prague; CZ, eliska.janouchova@fsv.cvut.cz

<sup>\*\*</sup> Ing. Anna Kučerová, PhD: Faculty of Civil Engineering, Czech Technical University in Prague; Thákurova 7/2077; 166 29, Prague; CZ, anicka@cml.fsv.cvut.cz

<sup>\*\*\*</sup> Ing. Jan Sýkora, PhD: Faculty of Civil Engineering, Czech Technical University in Prague; Thákurova 7/2077; 166 29, Prague; CZ, jan.sykora.1@fsv.cvut.cz



This contribution concentrates on comparison of random factor influence on parameter estimation based on nonlinear regression (Seber et al., 1989). Distinct sources of uncertainty are included as well as different experimental conditions.

## 2. Numerical study

The role of uncertain parameters in estimation of the system parameters is demonstrated on an illustrative example of one dimensional heat conduction, where observable is temperature in the location  $x$  and time step  $t$ . The thermal diffusion equation

$$\rho c_p \frac{\partial T}{\partial t} = \lambda \frac{\partial^2 T}{\partial x^2} + \dot{q}, \quad (1)$$

where  $\lambda$  is thermal conductivity,  $\rho$  is density and  $c_p$  is thermal capacity, can be solved with using thermal diffusivity defined as  $\alpha = \frac{\lambda}{\rho c_p}$  for initial condition  $T = T_\infty = 10^\circ\text{C}$  and constant flux boundary condition at  $x = 0$   $q_x = -\lambda \frac{dT}{dx} = q_0 = 100 \text{ W/m}^2$  as

$$T = T_\infty + \frac{q_0}{\lambda} \left[ 2 \sqrt{\frac{\alpha t}{\pi}} \exp\left(-\frac{x^2}{4\alpha t}\right) - x \left(1 - \operatorname{erf}\frac{x}{2\sqrt{\alpha t}}\right) \right]. \quad (2)$$

The parameters to be identified are the thermal conductivity and the thermal capacity. Their true values are  $\lambda = 2 \text{ W.m}^{-1}\text{K}^{-1}$  and  $c_p = 1000 \text{ J.m}^{-3}\text{K}^{-1}$ . The considered domains of the parameters in the identification procedure are intervals  $[1.6, 2.4] \text{ W.m}^{-1}\text{K}^{-1}$  for  $\lambda$  and  $[750, 1700] \text{ J.m}^{-3}\text{K}^{-1}$  for  $c_p$ .

### 2.1. Uncertainties

In our particular example, there are three types of uncertain inputs. The first one is connected to loading, when the heat flux is burdened by an error  $\varepsilon_1$  which is a normal random variable with zero mean value and standard deviation  $1 \text{ W/m}^2$ . This uncertain input is a constant for the whole experiment regardless of the number of sensors and time steps. The second uncertainty is a systematic error  $\varepsilon_2$  of sensors, which is an additive error modeled as a normal random variable with zero mean value and standard deviation  $0.005^\circ\text{C}$ . This uncertain input is a constant for every sensor in the experiment regardless of the number of time steps. The last source of uncertainty is a measurement random error, which is also an additive error modeled as a normal random variable with zero mean value and standard deviation  $0.1^\circ\text{C}$ , but its value differs for each measured temperature.

### 2.2. Estimation of thermophysical parameters

Uncertainty quantification is based on statistical analysis of  $10^4$  repetitions of the experiments simulated numerically. The synthetic experimental data are generated according to the following equation of the model modified by involving the uncertainties:

$$T_{Exp}(x, t) = T_\infty + \frac{q_0 + \varepsilon_1}{k} \left[ 2 \sqrt{\frac{\alpha t}{\pi}} \exp\left(-\frac{x^2}{4\alpha t}\right) - x \left(1 - \operatorname{erf}\frac{x}{2\sqrt{\alpha t}}\right) \right] + \varepsilon_2(x) + \varepsilon_3(x, t). \quad (3)$$

The parameters are estimated from each experiment separately by using the method of nonlinear least squares regression. The identification is based on fitting the response of the numerical model to the experimental data. This deterministic approach leads to optimising parameters so as to minimise the objective function

$$f(\lambda, c_p) = \sum_{i=1}^{nx} \sum_{j=1}^{nt} \left( T_{Exp,i,j} - T_{i,j}(\lambda, c_p) \right)^2. \quad (4)$$

The parameter estimation is provided for different numbers of sensors  $nx$  from one to 40 sensors uniformly distributed on the interval  $x \in [0.02, 0.2] \text{ m}$  (and different numbers of observed time steps  $nt$  from 5 to 160 steps uniformly distributed on the interval  $t \in [10, 240] \text{ min}$ ).

Comparison of standard deviations of the parameters obtained for different combinations of  $nx$  and  $nt$  is shown in Tab. 1. As expected the standard deviations decrease for the specific  $nx$  with increasing  $nt$  as well as for the specific  $nt$  with increasing  $nx$ . The efficiency of the estimation does not depend only on the total number of measurements  $nt \cdot nx$ , but the specific experiment setup plays an important role.

Tab. 1: Identified standard deviation of the parameters depending on  $n_x$  and  $n_t$ .

$n_t \backslash n_x$	STD $\lambda$ [W.m <sup>-1</sup> K <sup>-1</sup> ]					STD $c_p$ [J.m <sup>-3</sup> K <sup>-1</sup> ]				
	1	5	10	20	40	1	5	10	20	40
5	0.3106	0.0634	0.0515	0.0409	0.0325	144.63	30.22	26.92	20.09	16.24
10	0.2793	0.0477	0.0396	0.0321	0.0276	126.12	24.64	19.92	16.19	13.89
20	0.2362	0.0369	0.0318	0.0274	0.0241	135.59	18.39	15.50	13.85	11.96
40	0.1864	0.0302	0.0265	0.0241	0.0220	94.69	14.84	13.33	12.11	10.99
80	0.1377	0.0258	0.0236	0.0223	0.0214	71.64	13.08	11.67	11.26	10.67
160	0.0997	0.0234	0.0224	0.0214	0.0207	51.73	11.60	11.14	10.73	10.30

For the case of measuring by only one sensor but in different numbers of time steps the obtained marginal distributions of the parameters are depicted in Fig. 1. For  $n_t \leq 40$  the influence of uncertain inputs is so significant that the optimisation algorithm pulls the optimum to the bounds of the domain. In the case of the higher numbers of time steps the mean value of the thermal conductivity  $\lambda$  is identified well whereas the mean value of the thermal capacity  $c_p$  is not a good match. This phenomenon can be explained by the fact that the influence of the random measurement error is reduced by increasing  $n_t$  but the systematic sensor error and random loading factor have the undiminished impact on the parameter estimation.

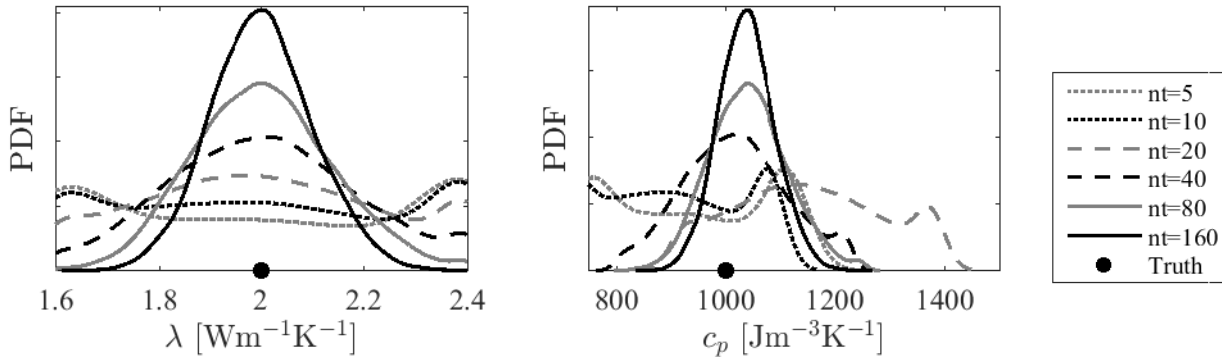


Fig. 1: Marginal distributions of  $\lambda$  and  $c_p$  identified from measurements obtained by only one sensor in different numbers of time steps  $n_t$ .

Fig. 2 shows the marginal distributions of the parameters identified from measurements obtained by different numbers of sensors  $n_x$  in 40 time steps. In this case the mean value of the thermal capacity obviously converges. Usage of several sensors enables to reduce the influence of the experimental random as well as systematic error.

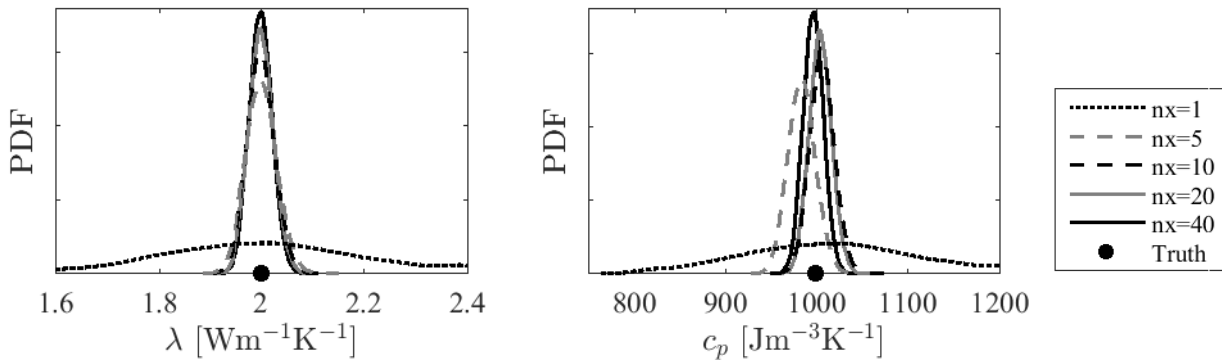


Fig. 2: Marginal distributions of  $\lambda$  and  $c_p$  identified from measurements obtained by different numbers of sensors  $n_x$  in 40 time steps.

The error associated with loading is not reduced at all because it has one constant value for the whole experiment regardless of the number of sensors and time steps. This fact causes that the variance of the parameters asymptotically converges with an increasing number of measurements to a non zero value.

### 3. Conclusions

The presented analysis of random factor impact on the parameter estimation compares different sources of epistemic uncertainties and corresponding possibilities to reduce them. The uncertain system under the study is one dimensional heat conduction with random heat flux and two types of experimental errors. The study shows efficiency of the identification of thermal conductivity and thermal capacity on a basis of the different experimental setups. The temperature measured by only one sensor does not provide enough information to allow reduction of the systematic experimental error but the random experimental error is reduced increasingly with a higher number of observed values of temperature in different time steps. In order to diminish the systematic error more sensors have to be employed. The uncertainty caused by randomness of loading cannot be reduced in any considered settings. The mentioned conclusions have to be taken into account in designing an optimal experiment whose purpose is to get sufficient information for parameter identification from noisy indirect experimental data.

### Acknowledgement

The financial support of the Czech Science Foundation (Projects No. 16-11473Y and 15-07299S) and the Grant Agency of the Czech Technical University in Prague (Project No. SGS17/042/OHK1/1T/11) is gratefully acknowledged.

### References

- Beven, K., Smith, P. and Freer, J. (2007) Comment on "Hydrological forecasting uncertainty assessment: Incoherence of the GLUE methodology" by Pietro Mantovan and Ezio Todini. *Journal of Hydrology*, 338, pp. 315-318.
- Der Kiureghian, A. and Ditlevsen, O. (2009) Aleatory or epistemic? Does it matter? *Structural Safety*, 31(2), pp. 105-112.
- Jarušková, D. and Kučerová, A. (2016) Estimation of thermophysical parameters revisited from the point of view of nonlinear regression with random parameters. *International Journal of Heat and Mass Transfer*, 106, pp. 135-141.
- Mantovan, P. and Todini, E. (2006) Hydrological forecasting uncertainty assessment: Incoherence of the GLUE methodology. *Journal of Hydrology*, 330, pp. 368-381.
- Oberkampf, W.L., DeLand, S.M., Rutherford, B.M., Diegert, K.V. and Alvin, K.F. (2002) Error and uncertainty in modeling and simulation. *Reliability Engineering and System Safety*, 75, pp. 333-357.
- Seber, G.A.F. and Wild, C.J. (1989) *Nonlinear regression*. John Wiley and Sons.
- Tarantola, A. (2005) *Inverse problem theory and methods for model parameter estimation*. Philadelphia, PA: Society for Industrial and Applied Mathematics, 348 p.

## DETERMINATION OF RIGIDITY AND DAMPING PARAMETERS OF HYDRODYNAMIC BEARINGS

T. Jarzyna\*

**Abstract:** *The article deals with the problems of identify of rigidity parameters  $k$  and damping parameters  $c$  of bearings of hydrodynamic two-stage mixed flow pumps. Bearings with diameters smaller than those used in reality were tested with the use of the principle of geometric and hydrodynamic similarity. The tests were conducted on a specially constructed test station. Parameters of bearings were identified by the method of amplitude-frequency characteristics.*

**Keywords:** Mixed flow pumps, Hydrodynamic bearings, Identification of bearing parameters.

### 1. Introduction

Tests of a dynamic system are carried out in a few steps. A physical model (commonly referred to as a structural model) is developed on the basis of a real object which, simply speaking, reflects a real system and preserves its significant characteristics. It provides the basis for development of a mathematical model describing analytically the phenomena that occur in the tested dynamic system (motion similar to a real system). Solution of motion equations enables exploring free motion, forced motion or stability (Holka, 2011 and Giergiel et al., 1990). It is possible on condition that all parameters of the analyzed physical model are known. Otherwise, it is necessary to carry out tests to identify the object parameters.

One of ten pump aggregates operating in a serial system was tested (Fig. 2) its capacity was  $Q = 5000 \text{ m}^3/\text{h}$  and it consisted of a two-stage mixed flow pump (Fig. 3), electric motor with power  $N = 1250 \text{ kW}$  (Fig. 1) and an discharge system. While performing tests it was necessary to identify rigidity parameter  $k$  and damping parameter  $c$  of a pump hydrodynamic bearings.



Fig. 1: Electric motor of a pump aggregate.

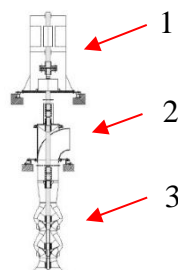


Fig. 2: Scheme of a pump aggregate:  
1 – electric motor, 2 – discharge system, 3 – pump.

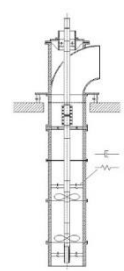


Fig. 3: Structural model of a pump.

There is abundant literature available on the subject of identification. Apart from the above listed publications (Holka, 2011 and Giergiel et al., 1990), works (Nizioł, 2005 and Skalmierski, 2001) are worth attention, as well. Due to the fact that a linear system of equations with constant coefficients was used for the description of the rotor motion, a method based on amplitude-frequency characteristics was used for identification of the model. Acceptance of a linear system with constant coefficients  $k$  and  $c$  makes calculations less complicated. Bearings are a frequent subject of study. Scientific papers cover different areas of this issue. In this field, positions (Avramov, 2009, Jiang et al., 1999, Laktyushin et al., 2003, Papadopoulos, 2008 and Temis et al., 2007) are considered to be interesting.

---

\* Tomasz Jarzyna, PhD.: Institute of Mechanics and Machine Design, University of Science and Technology; Al. prof. S. Kaliskiego 7; 85 796, Bydgoszcz; PL, tomasz.jarzyna@utp.edu.pl

The main goal of this work is to provide methodology and tests results in order to determine parameters of rigidity  $k$  and damping  $c$  for hydrodynamic bearings of pumps.

## 2. The research object

Hydrodynamic bearings with internal diameters equal to  $\phi 150$  mm were used in the pump. Carrying out experimental tests of such big bearings would be very difficult, so it was decided to test bearings with three different, smaller diameters (Fig. 4), with application of the principle of geometric and hydrodynamic similarity. Toughness of the tested bearings was consistent with toughness of the real bearing and it was 65 ShA. Dimensions of the tested bearings are presented in Tab. 1.

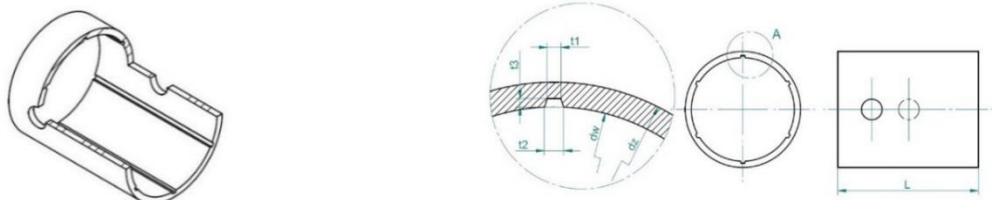


Fig. 4: Tested hydrodynamic bearings.

Apart of bearings with dimensions specified in Tab. 1, also bearings with analogical dimensions, though different toughness, were tested: 52 ShA, 78 ShA. The research was supposed to evaluate the influence of toughness of rubber on the tests results, however this was not included in the presented materials.

Tab. 1: Dimensions of the tested bearings.

Number of bearing	Dimensions in [mm]						Toughness [ShA]
	$d_w$	$d_z$	$t_1$	$t_2$	$t_3$	L	
1	30	33.6	1	1.4	0.6	41	65
2	50	56	1.65	2.3	1	683	
3	70	78.4	2.3	3.2	1.4	95.62	

A test station was constructed for the tests (Fig. 5). Its construction was inspired by work (Jiang et al., 2000). The major element of the station was rotor 1 with disc 2. The rotor was fixed in two bearings: self-aligning rolling bearing 3 and the tested hydrodynamic bearing set in a mounting (Fig. 6). Electric motor 5 was used to drive the rotor, whereas water to be used in bearings was pumped by means of a multi-stage mixed flow pump 6. Constructional elements, which are loaded by variable force, were checked for fatigue life by using the method presented in (Strzelecki et al., 2016).

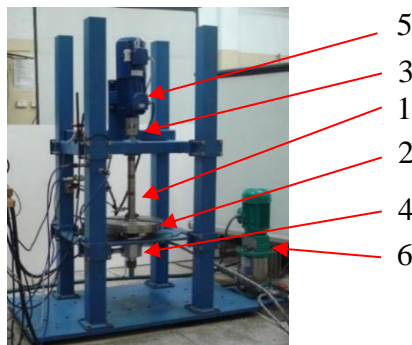


Fig. 5: A test station.



Fig. 6: Tested hydrodynamic bearings with different diameters in mountings.

## 3. Experimental tests

Bearings with smaller diameters, as compared to real bearings, were tested. It was possible thanks to preservation of constructional similarity, that is, ratio  $L/d_w$ , of the journal wrapping angle by a bearing and

the Sommerfeld number. At this stage two first conditions were taken into account, whereas the Sommerfeld number is a criterion of hydrodynamic similarity:

$$S = \frac{\eta \cdot n}{p_{sr} \cdot \psi^2} \quad (1)$$

where:  $\eta$  – dynamic viscosity of water [Pa·s],  $n$  – the shaft rotational speed [rev/s],  $p_{sr}$  – average surface pressure [Pa],  $\psi$  – relative clearance in the bearing.

The tests were performed with the use of the most loaded bearing in the pump (value of reaction on the bearing  $R = 8158.27$  N) with dimensions:  $d_w = 150$  mm,  $L = 220$  mm. Substituting data:  $\eta = 0.001030499$  Pa·s (for 19 °C),  $n = 740$  rev/min = 12.33 rev/s,  $\psi = 0.00266$ ,  $p_{sr} = 265309.5$  calculated from the dependence:

$$p_{sr} = \frac{R}{L \cdot d_w} \quad (2)$$

The Sommerfeld number was calculated  $S = 0.006737$ . To preserve similarity, model bearings should have the same value  $S$ .

It was decided that bearings with diameters  $\phi 30$ ,  $\phi 50$ ,  $\phi 70$  mm. would be tested. The lengths of bearings were determined maintaining ratio  $L/d_w$ . Average surface pressures (1)  $p_{sr}$  were calculated from formula (1) after transformation. Having data of  $p_{sr}$  and  $S$ ,  $p_{max}$  was provided from literature. On this basis it was possible to define pressure at which water should be fed to the bearing:

$$p = p_{max} + \rho_w \frac{v^2}{2} \quad (3)$$

where:  $v$  – circumferential speed of the shaft [m/s],  $\rho_w$  – density of water [kg/m<sup>3</sup>].

Whereas, centrifugal force loadning the bearing was calculated from dependence:

$$R = p_{sr} \cdot L \cdot d_w \quad (4)$$

Selected parameters according to which tests were conducted are presented in Tab. 2.

Tab. 2: Presentation of test parameters  $S = 0.006737$ .

$n$ rev/ min]	bearing $\phi 30$ mm			bearing $\phi 50$ mm			bearing $\phi 70$ mm		
	$p_{sr}$ [Pa]	$p$ [Pa]	$R$ [N]	$p_{sr}$ [Pa]	$p$ [Pa]	$R$ [N]	$p_{sr}$ [Pa]	$p$ [Pa]	$R$ [N]
200	2868	16862	3,53	7967	46838	27,208	15616	91803	104.52
350	5019	29573	6.17	13943	82147	47.614	27328	161008	182.91

Amplitudes of the shaft relative motion were measured during tests. The results are presented in Fig. 7. Due to high vibrations, higher than rotational speed equal to 950 rev/min, accompanying tests of a bearing with diameter  $\phi 70$  mm, at this speed the measurements were finished.

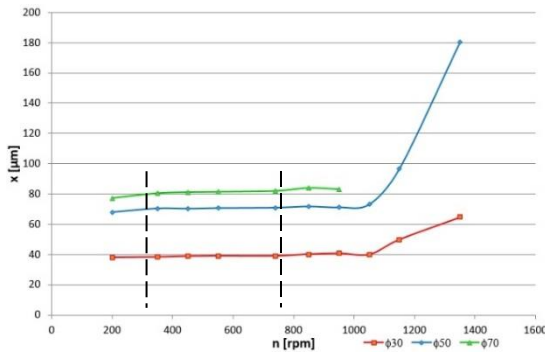


Fig. 7: Measurement of a shaft vibration amplitude for bearings with diameters  $\phi 30$ ,  $\phi 50$ ,  $\phi 70$  mm.

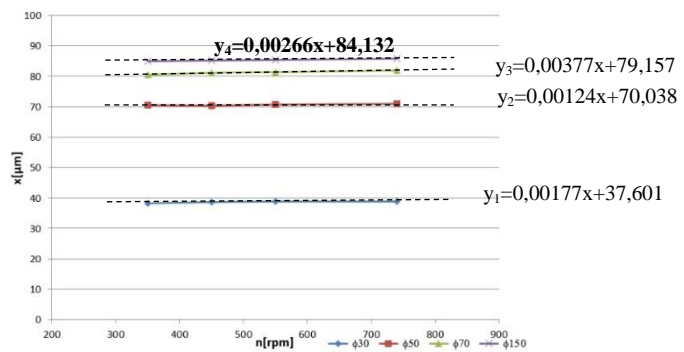


Fig. 8: Equations of straight lines running through two points of the diagrams.

While studying characteristics of the test station (results have not been presented in this work) it was found that the period of its stable operation was within the range of 350 – 740 rev/min, (Fig. 7). Above these speeds resonance states were observed in two orthogonal directions. For the speeds below

350 rev/min vibrations were also increased. For rotational speeds 350 – 740 rev/min, the diagrams are similar to linear ones. Therefore, this feature was used and straight lines were run through the first and the last points of the diagrams (Fig. 8). An equation of straight line was determined for a bearing with diameter  $\phi 150$  mm (Fig. 8). Coefficients  $k$  and  $c$  of bearings were determined on the basis of an equation of dynamic susceptibility:

$$\left| \frac{x}{P} \right| = \frac{1}{\sqrt{(k - m\omega^2)^2 + (\omega c)^2}} \quad (5)$$

where:  $m$  – mass of shaft [kg],  $P$  – force of unbalance [N],  $x$  – radial displacement of shaft in the bearing [m]. Diagram of dynamic susceptibility for bearing  $\phi 150$  mm is presented in Fig. 9.

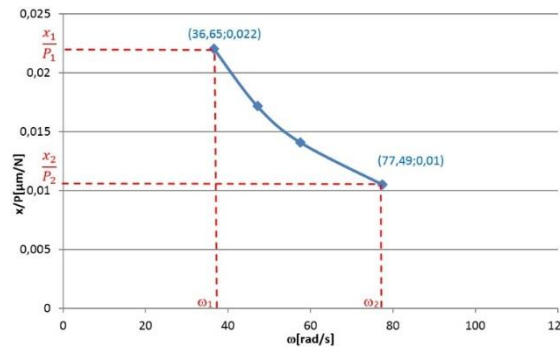


Fig. 9: Diagram of dynamic susceptibility of bearing  $\phi 150$  mm.

By using a linear simplification of the diagram and substituting coordinates of two points a system of equations with unknowns  $k$  and  $c$  is provided. By substituting data:  $m = 26.517$  kg,  $x_1 = 0.0000849224$  m,  $P_1 = 3858.64$  N,  $\omega_1 = 36.65$  rad/s,  $x_2 = 0.0000858032$  m,  $P_2 = 8158.27$  N,  $\omega_2 = 77.49$  rad/s, the values of coefficients:  $k = 7370746.313$  N/m,  $c = 1223436.493$  Ns/m were determined.

#### 4. Conclusions

1. In order to identify parameters of bearings  $k$  and  $c$  a method that involves using amplitude-frequency characteristics was used.
2. Vibrations of bearings are linear for the range of rotational speeds used in the pump.
3. It is planned that further studies of dynamics will take into account the pump mounting, as shown in Fig. 3.

#### References

- Holka, H. (2011) Vibrations and dynamics of machines. Wydawnictwa Uczelniane UTP, Bydgoszcz, Poland, (in Polish).
- Giergiel, J. and Uhl, T. (1990) Identification of mechanical systems, PWN, Warszawa, Poland, (in Polish).
- Nizioł, J. (2005) Dynamics of mechanical systems, Komitet Mechaniki PAN, Warszawa, Poland, (in Polish).
- Skalmierski, B. (2001) Analytical mechanics and vibration theory. T.3, Politechnika Częstochowska, Poland, (in Polish).
- Avramov, K.V. (2009) Vibrations of a single-disk rotor on nonlinear supports. International Applied Mechanics, vol. 45, no. 10, pp. 1112-1119.
- Jiang, P. L. and Yu, L. (1999) Dynamics of a rotor-bearing system equipped with a hydrodynamic thrust bearing. Journal of Sound and Vibration, vol. 227, no. 4, pp. 833-872.
- Laktyushin, A.N., Smilovenko, O.O. and Laktyushina, T.V. (2003) Dynamics of a rotor in film lubrication bearings. Journal of Engineering Physics and Thermophysics, vol. 76, no. 5, pp. 1131-1138.
- Papadopoulos, C.A., Nikolakopoulos, P.G. and Gounaris G.D. (2008) Identification of clearances and stability analysis for a rotor-journal bearing system, Mechanism and Machine Theory, vol. 43, pp. 411-426.
- Temis, Yu.M., Temis and M.Yu. (2007) Rigidity and damping characteristics of hydrodynamic sliding bearing with deformable working surfaces. Journal of Friction and Wear, vol. 28, no. 2, pp. 128-138.
- Jiang, P.L. and Yu, L. (2000) Identification of the oil-film dynamic coefficients in a rotor-bearing system with a hydrodynamic thrust bearing, Journal of Sound and Vibration, vol. 236, no. 4, pp. 733-740.
- Strzelecki, P. and Tomaszewski T. (2016) Application of Weibull distribution to describe S-N curve with using small number specimens, AIP Conference Proceedings 1780, vol. 020007, pp. 1-8.



## VERIFICATION OF A NEW THERMAL CALCULATION METHOD BY INDUSTRIAL RADIANT CHAMBER MEASUREMENTS

Z. Jegla<sup>\*</sup>, M. Reppich<sup>\*\*</sup>

**Abstract:** *The paper presents heat flux measurements performed on industrial radiant chamber of operated fired heater. Obtained measured results are used for verification of a new thermal calculation method for proper design and evaluation of combustion and radiant chambers containing inbuilt tubular heat transfer system. The very good agreement of results achieved using the proposed thermal calculation method with measured industrial data confirms its excellent ability to predict the real thermal behavior of combustion or radiant chambers employing up-to-date industrial complex systems of low emission burners.*

**Keywords:** Industrial Measurement, Combustion and Radiant Chambers, Heat Flux Density, Thermal Calculation Methods, Low Emission Burners.

### 1. Introduction

In response to rapidly increasing energy consumption and increasing emissions of pollutants is a major goal in the field of industrial combustion in the coming years, improving the efficiency of the combustion process to reduce emissions, especially nitrogen oxide emissions (NO<sub>x</sub>). Industrial companies operating power and process plants containing combustion equipment with inbuilt tubular heat transfer surfaces (such as fired heaters utilized in refineries or petrochemical industry, power boilers, waste incinerator furnaces, etc.) most often typically solves this environmental problem by replacing operated conventional burners with new low emission burners (so called low-NO<sub>x</sub> burners). This easiest and cheapest approach seems to be very effective and attractive because it enables to industrial companies meet environmental rules and regulations quickly and relatively cheaply.

However, there is one hidden problem which is very often ignored by the plant operators (especially if the combustion equipment operation had been trouble-free up until the point when the burners were replaced) - after replacing the conventional burners with a low-NO<sub>x</sub> types immediately changes occur not only in the amount of produced emissions, but also in thermal and aerodynamic conditions in the whole combustion chamber and significantly and negatively affects the thermal stress and lifetime of inbuilt tubular heat transfer system and also inside flowing heated fluid conditions. Moreover, the change in the thermal conditions inside the combustion (or radiant) chamber will usually take effect after a certain period of operation. Typically, deformations or failures of heat transfer tubes are found or undesired thermal degradation (such as cracking, coking or fouling) of heated fluid flowing inside heat transfer tubes is appeared.

### 2. Main features of the new thermal calculation method

A new thermal calculation method considering real thermal behavior of recent low-NO<sub>x</sub> burners placed in existing or new combustion or radiant chambers was developed. This new thermal calculation method for proper design and evaluation of combustion and radiant chambers with inbuilt tubular heat transfer system was formulated by Jegla et al. (2016). The aim of formulation is to provide a practical and accurate method considering (during evaluation of heat transfer to inbuilt tubular heat transfer system) the true thermal behavior of installed burners as dominant factor influencing accuracy of thermal-hydraulic

---

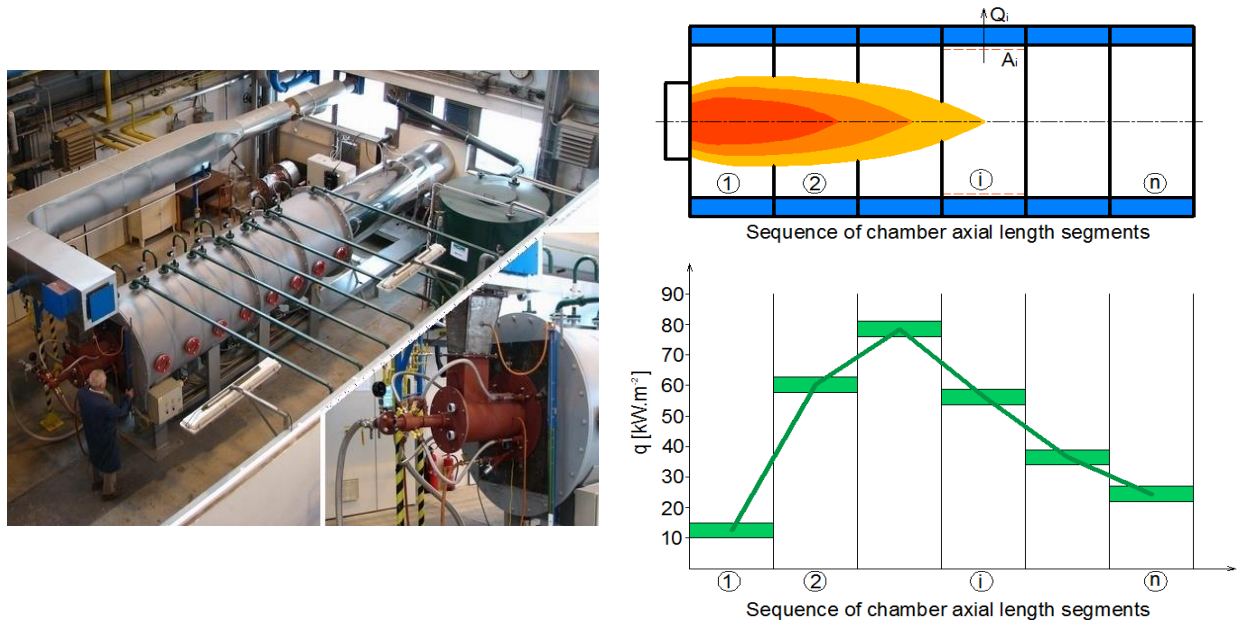
<sup>\*</sup> Assoc. Prof. Zdeněk Jegla, PhD.: Institute of Process Engineering, Faculty of Mechanical Engineering, Brno University of Technology; Technická 2896/2; 616 69 Brno; CZ, jegla@fme.vutbr.cz

<sup>\*\*</sup> Prof. Dr.-Ing. Marcus Reppich: Faculty of Mechanical and Process Engineering, Augsburg University of Applied Sciences; An der Hochschule 1; 86161 Augsburg; DE, marcus.reppich@hs-augsburg.de

prediction of state of heated fluid flowing inside tubes of tubular system, and stress and lifetime of tubular system material.

Based on an excellent experience with modified plug-flow (MPF) model developed and validated for providing real thermal behavior of individual burner from its testing on burner testing facility (for details see Jegla et al. (2016)) a new thermal method is formulated as a sequence of three steps: (i) Experimental determination (using a burner testing facility) of the heat flux profile of the burner (or burners) which will be installed in the proposed industrial combustion or radiant chamber with inbuilt tubular heat transfer system; (ii) Using MPF model for finding the corresponding fuel burnout profile of burner (allowing to estimate other effective thermal characteristics of the burner(s) – e.g. the flame length and width, heat release rate along the chamber, etc.); (iii) Design and evaluation of industrial combustion (or radiant) chamber with inbuilt tubular heat transfer system using any zonal or plug-flow method suitable adapted for considering a fuel burnout profile of burner (recognized by MPF model in previous step) and also for true considering inbuilt tubular heat transfer system placed in the chamber.

In addition, the Institute of Process Engineering has the tools and facilities that allow routine practice of the above mentioned individual steps of the developed thermal method. For example, the first step (i) and second step (ii) can be realized with the help of our burner testing facility (see Fig. 1a) and with developed MPF model (see principle of MPF model in Fig. 1b). For their detail description see Jegla et al. (2016).



a) Burner testing facility with detail of burner.

b) Schematic principle of MPF model.

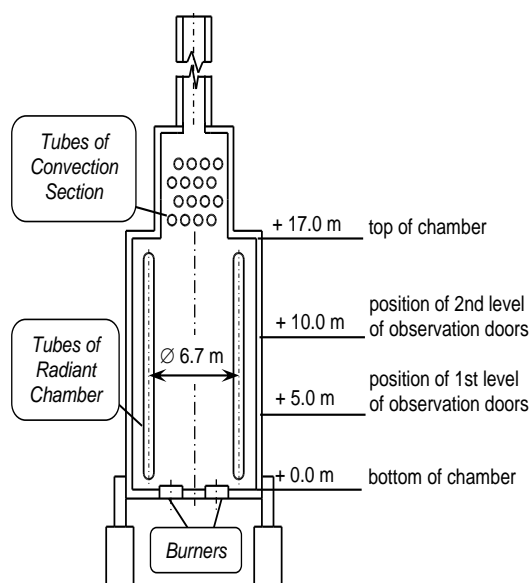
Fig. 1: Burner testing facility and principle of its calculation tool - MPF model.

Third step (iii) focused on design and evaluation of industrial combustion (or radiant) chamber with inbuilt tubular heat transfer system can be then covered by implementation of appropriate adapted MPF model. Such adaptation must allow considering: (i) type the inbuilt tubular heat transfer system (i.e. tube coil or membrane-wall type); (ii) the design shape of the combustion or radiation chamber (i.e. cylindrical or box type); (iii) efficient computing by using an optimum number of segments. Details of such adaptation of MPF model covering mentioned main considerations can be found in Jegla (2016).

### 3. Industrial radiant chamber measurements

For verification of accuracy of the new thermal calculation method employing the adapted modified plug-flow (AMPF) model for routine design and evaluation of combustion or radiant chambers with inbuilt tubular heat transfer area and containing system of several low-NO<sub>x</sub> burners an industrial radiant chamber of operated fired heater is measured from heat flux density point of view to be results of measurement confronted with calculation results of the new thermal calculation method.

The measured fired heater is a typical vertical cylindrical fired heater (see Fig. 2a), containing a standard radiant chamber and convection section, operated in a crude oil atmospheric distillation unit. The burner system contains a total of six staged-gas low- $\text{NO}_x$  burners vertically oriented and mounted on bottom of the radiant chamber, each of nominal firing duty 4 MW. Thus, the nominal firing capacity (heat released) of fired heater is 24 MW. Radiant chamber of the heater and its inbuilt tube coil type system has been designed in accordance with the relevant design standards. The tubular system of radiant chamber is arranged as two-passed tube coil created totally by 60 tubes placed in one row around circular lining wall with the constant tube outer diameter of 194 mm and with tube spacing of 350 mm. Each tube is approx. 17 m length and the tubular system is placed on tube coil circle diameter (D) of approx. 6.7 m (see Fig. 2a), so the shape of radiant chamber is characterized by ratio of tubular system height (or length L) to tube circle diameter which is  $L/D = 17/6.7 = 2.5$ . The radiant chamber is equipped by two levels of observation doors for viewing all radiant tubes and all burner flames for proper operation and light off. These observation doors are located at the level of 5.0 m and 10.0 m above the bottom of radiant chamber (see Fig. 2a). Each level contains 12 observations doors placed uniformly over the radiant chamber circumference.



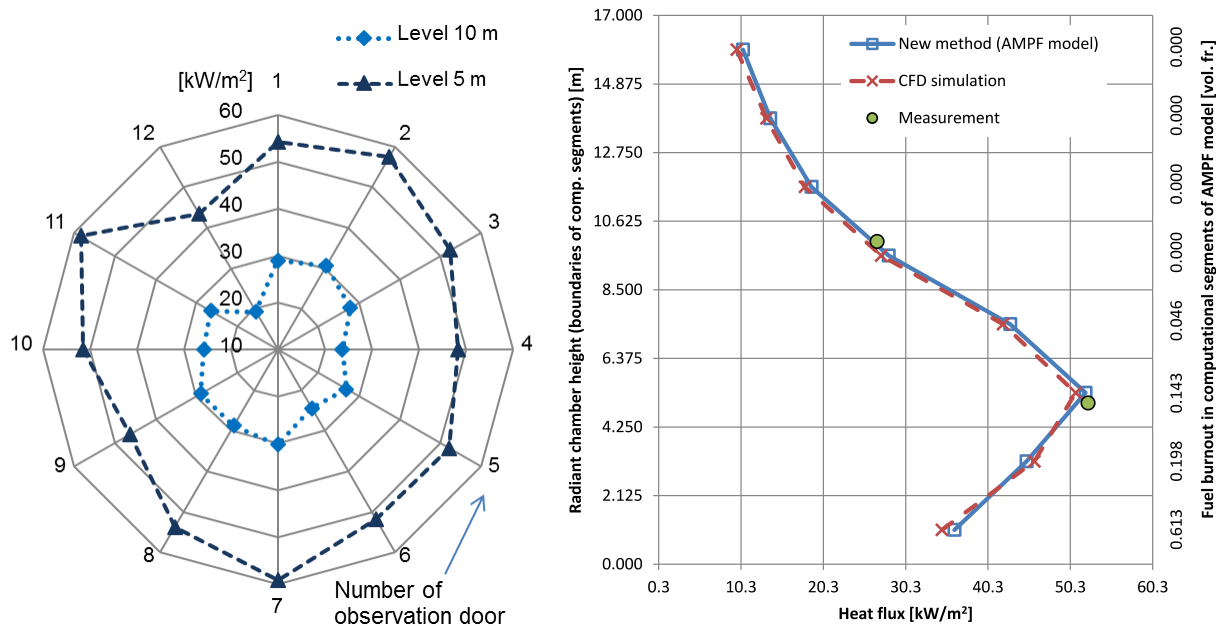
a) Fired heater scheme and observation doors levels.      b) Heat flux meter in one observation door.

Fig. 2: Arrangement of fired heater and principle photo of heat flux measurement via observation doors.

Measurements on fired heater during its operation usually allow to identify the real local heat flux at certain locations of radiation chamber only. So, it does not provide an overall picture of the distribution of heat flux along the chamber height (length). In the presented fired heater case, observation doors of radiant chamber were used as suitable places and positions to measurement of true local heat flux through installed commercial measuring equipment - heat flux meter (see Fig. 2b) to perform a scheduled independent two half-days' measurements of local heat flux inside radiant chamber.

Obtained results of measurements were statistically evaluated, and profiles of local maximums, minimums and average values of local heat fluxes located at the level of 5.0 m and 10.0 m above the bottom of radiant chamber (each completing measurements results from 12 observation doors circumferentially radiant chamber) were obtained. Mean values of the local heat flux provided by these operating measurements are presented for both measured radiant chamber levels in Fig. 3a.

Employing these measured results a mean average heat flux of  $52.42 \text{ kW/m}^2$  is evaluated from average measured values at level of 5.0 m above the bottom of radiant chamber, and a mean average heat flux of  $26.81 \text{ kW/m}^2$  is evaluated from average measured values at level of 10.0 m above the bottom of radiant chamber. These two measurement-based values are then used for characterization of longitudinal local heat flux profile (i.e. profile along height of radiant chamber) and together with calculated results of longitudinal local heat flux profile obtained from new thermal method (based on AMPF model) and from independent CFD simulation presented for mutual comparison purpose in Fig. 3b). Note that details of CFD simulation of heat transfer inside radiant chamber of the fired heater (i.e. input data, setting of CFD model, detailed results) have been published previously by Jegla et al. (2015).



a) Circumference local mean heat flux profiles. b) Longitudinal local mean heat flux profile.

Fig. 3: Results of heat flux measurement of radiant chamber and comparison with calculated results.

#### 4. Conclusions

Comparison of results of heat flux measurements with calculated results performed in Fig. 3 shows very good agreement. Results presented in Fig. 3 clearly confirm that the proposed thermal calculation method (based on AMPF model) developed for proper design and evaluation of combustion and radiant chambers containing inbuilt tubular heat transfer system provides a high accuracy comparable to much more sophisticated (and demanding) CFD simulations. Very good agreement of results of the new thermal calculation method with measured industrial data confirms its excellent ability to predict real thermal behavior of combustion or radiant chambers employing complex industrial systems of low- $\text{NO}_x$  burners.

Specifically, in this case, results of the developed method (obtained for optimum number only eight longitudinal computational segments) inform that the system of low- $\text{NO}_x$  burners installed in operated fired heater completely burn of fuel in first fourth length calculation segments, see Fig. 3b. Concretely 61.3 % of fuel is burnt in the first segment, 19.8 % in the second segment, 14.3 % in the third segment and 4.6 % in the fourth segment. Among other, these results indicate that flames reach a length of 6.5 m.

Finally, good agreement of calculation and measurement results confirms also warning (based on detail computational modeling) presented in Jegla et al. (2015) that the real thermal behavior of up-to-date types of low emission burners are significantly different from traditional thermal behavior considerations for low emission burners still recommended for design of combustion and radiant chambers with inbuilt tubular heat transfer system by world-wide recognized design standards.

#### Acknowledgement

The authors gratefully acknowledge financial support provided by Technology Agency of the Czech Republic within the research project No. TE02000236 “Waste-to-Energy (WtE) Competence Centre”.

#### References

- Jegla, Z., Vondál, J. and Hájek, J. (2015) Standards for fired heater design: An assessment based on computational modelling, *Applied Thermal Engineering*, 89, 1068-1078.
- Jegla, Z. (2016) Innovative Adaptation of MPF Model to Recognition of Thermal Behaviour of Operated Industrial Low Emission Burner System, *Chemical Engineering Transactions*, 52, pp. 667-672.
- Jegla, Z., Kilkovský, B. and Turek, V. (2016) Novel approach to proper design of combustion and radiant chambers, *Applied Thermal Engineering*, 105, pp. 876-886.

## STATIC NUMERICAL ANALYSIS OF A HYDRAULIC CURING PRESS

J. Jirásko<sup>\*</sup>, A. Max<sup>\*\*</sup>, J. Bezdekova<sup>\*\*\*</sup>

**Abstract:** *This paper introduces static numerical analysis of a whole hydraulic curing press. The analysis is done using finite element method in Marc Mentat software. Individual parts of the curing press are identified in the paper and the setting of the computational model is described. There are suggestions for design optimization with respect to the material savings and lowering of stress peaks. This computational model can be used as a guide for analysis of curing presses with similar designs.*

**Keywords:** Curing press, Finite element method, Mechanical engineering.

### 1. Introduction

The tire curing press is a machine which is used for the final stage of tire production. Semi-finished tires are inserted into the mould of the curing press and by treatment with a defined pressure and temperature they obtain their final shape and final mechanical properties. (The chemical reaction that occurs in the curing press is called vulcanization.) FEM analyses are used for this type of machine to achieve the required parameters, for the tire to be made to required quality. These computations can find significant material savings for the producer of the press and efficiently raise the machine's parameters. Static analyses of strength are usually done for these presses. Further analyses include the computation of the temperature field of the vulcanization chamber's outer surface which is crucial to the heat loss (Hynek, 2013) and thermal influences of the press frame (Jirasko, 2016). The distribution of the temperature inside the mould is also considered for the right technology of tire vulcanization (Hynek, 2011).

The static analyses of the whole press is summarized in this article for the purpose of identifying critical points of the design and finding possibilities of material savings while maintaining the machine's required parameters. The calculation is done using finite element method (FEM) in Marc Mentat.

Discovering oversized parts which are not justified with respect to the strength can lead to significant weight savings and lowering of the design demands of certain parts without decreasing the press functionality. These aspects are considered in this curing press design variant which is often used by Asian press producers. It is a design in which the crossbeam moves upwards (vertically) when the press opens and the slide table with the lower part of the mould moves horizontally to the position where the tire is removed by the crane. Hydraulic cylinders (positioned under the lower chamber) are used to impart the closing force. The crossbeam is fixed by four pins to the rods in its working and idle position. The press parts are shown in Fig. 1.

Lightening of the design also brings other economic benefits for the machine's producer besides lowering the price of the production. These benefits include: faster opening, lower operating energy requirements, lower price of the drives, etc.

The tire mould tightness is required for the sake of the tire's final quality. Peripheral clearance in the mould's dividing plane should be minimal, ideally none at all. If the pressure chamber is in use the

---

<sup>\*</sup> Ing. Jakub Jirásko: Department of Machine Design, Faculty of Mechanical Engineering, University of West Bohemia; Univerzitni 22; 306 14, Pilsen; CZ, jirasko3@kks.zcu.cz

<sup>\*\*</sup> Ing. Antonín Max: Department of Machine Design, Faculty of Mechanical Engineering, University of West Bohemia; Univerzitni 22; 306 14, Pilsen; CZ, antoon@kks.zcu.cz

<sup>\*\*\*</sup> Ing. Jitka Bezděková: Department of Machine Design, Faculty of Mechanical Engineering, University of West Bohemia; Univerzitni 22; 306 14, Pilsen; CZ, bezdekov@kks.zcu.cz



heating medium should not be able to leave the chamber and thus put the press staff in danger. Considering the not negligible displacements of the pressure chamber and subsequent parts of the press, it is necessary to use adequate sealing for the chamber in its peripheral groove. (Therefore we included pictures of the contact status in the area of the seal groove in the results of the analyses of individual variants of the press.) An analysis of the overlaps (or clearance) of the mould and the chamber is usually required for the ideal setting of every new machine design. This topic is more thoroughly described in the article (Keckstein, 2016), where the analyses algorithm for ideal setting is presented. In this press analysis only the optimal setting variant results are presented. Compression of the sealing as a consequence of the press closing must be sufficient to cover the size of the cover displacements.

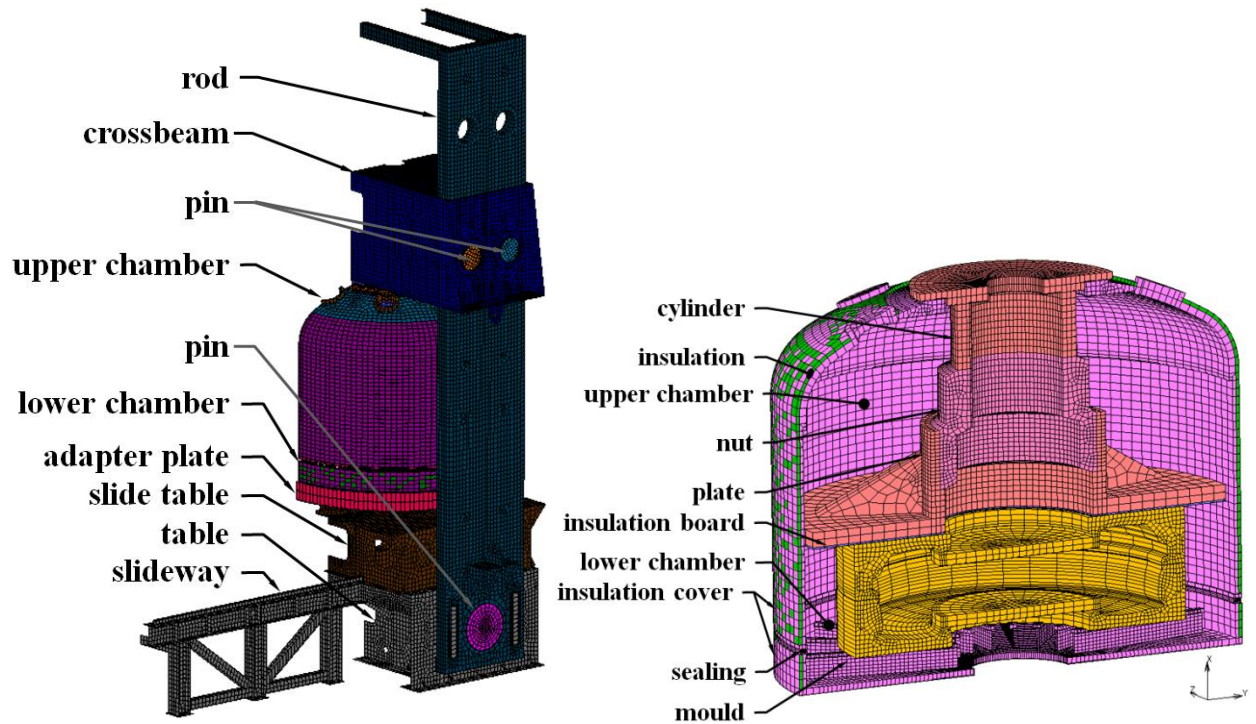


Fig. 1: Whole computational model of the press and the detail of the chamber.

## 2. Computational model

The curing press has one plane of symmetry so the model is only one half of the press. Individual parts of the press are meshed according to the following geometry: 3D elements (hex8), shell elements (quad4). The main examined machine components are connected by touching contacts. The material properties of the metal parts are listed in Tab. 1, rubber sealing properties (Mooney) are listed in Tab. 2.

Tab. 1: Mechanical properties of metal parts.

Part	Material	Density $\rho$ [kg·m <sup>-3</sup> ]	Young's modulus E [GPa]	Poisson's ratio $\nu$ [-]	Yield strength $R_e/R_{p0.2}$ [MPa]	Tensile strength $R_m$ [MPa]
stand, crossbeam, rod	S355	7800	210	0.27	300	500
pressure chamber	P265GH	7800	210	0.27	255	410
mould	GE 200	7850	170	0.30	200	450
plate, hang cylinder	GX7CrNiMo12-1	7850	210	0.30	440	590
nut	CuAl9Ni5Fe1Mn1	7800	110	0.34	295	590
cover insulation	foam glass	140	0.1	0.2	-	-

Tab. 2: Mechanical properties of the rubber sealing.

	Density [kg·m <sup>-3</sup> ]	C <sub>10</sub> [Pa]	C <sub>01</sub> [Pa]
sealing - 95 shore	1070	3000000	1400000

### 3. Boundary conditions

All degrees of freedom were removed from the press table base and an appropriate boundary condition was applied in the press symmetry plane. The analysis was divided into 3 steps. Every step was divided into 10 increments due to the higher number of contacts in the computational model:

Step 1: During this phase the lower part of the chamber with the mould is moved by 0.6 mm towards the upper part and thus both mould halves tightly press against each other while the peripheral chamber sealing is simultaneously deformed in the seal groove.

Step 2: Press closing force 4500 kN is imparted by the hydraulic cylinders. The boundary condition from the first step is deactivated in this step.

Step 3: A pressure of 2.4 MPa is applied to the inner surfaces of the mould and a pressure of 0.8 MPa is applied to all the inner surfaces in the chamber.

### 4. Results

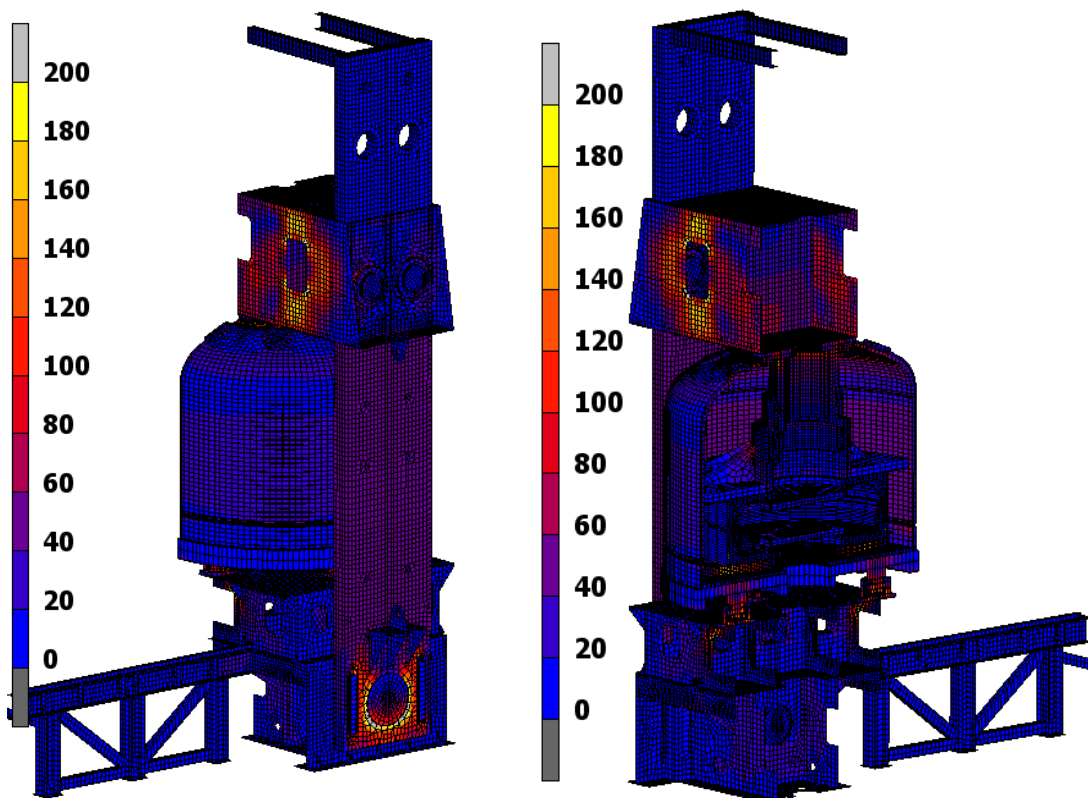


Fig. 2: Von Mises stress [MPa] in the press assembly (Step 3).

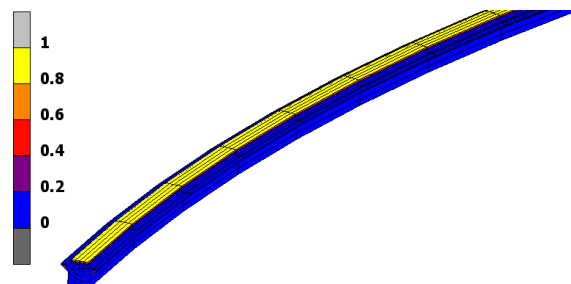
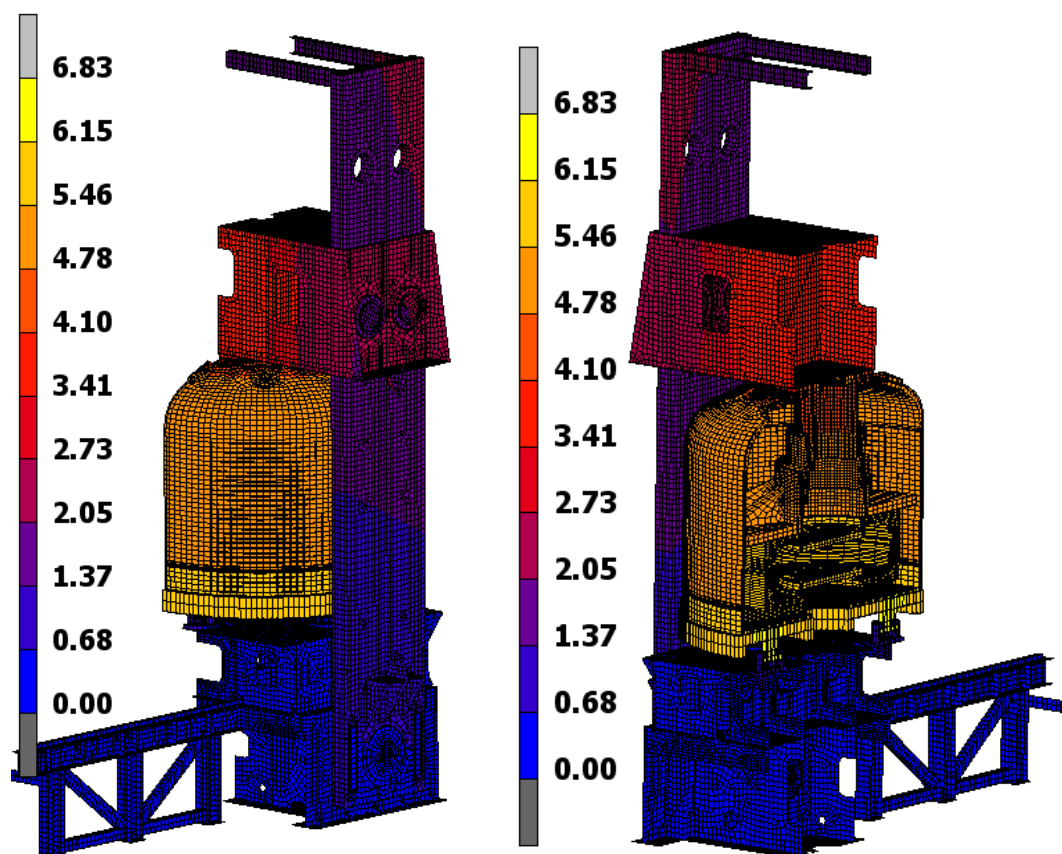


Fig. 3: Rubber sealing contact status- uninterrupted contact area.





*Fig. 4: Displacements [mm] in the press assembly (Step 3).*

## 5. Conclusions

This paper describes a method for carrying out the static analysis of a curing press using Marc Mentat. A similar computational model can be used when analysing curing presses with a different type of design. The computational model and its settings and parameters are described here. The analysed design of the press is oversized in all weldments with the exception of the crossbeam and the area of the pin connection of the stand and the rod. Another area with a higher value of stress is the area of the lower chamber which is supported by the hydraulic cylinders. The chamber is deformed in a similar manner as in other press designs. This meets the demand for uninterrupted contact between the upper and the lower half of the chamber. In the area of the mould sealing edge (in the dividing plane) the contact is also uninterrupted. With respect to the quality of the final product and safety of operation safety the design of the press is sufficient.

## Acknowledgement

This paper was supported by the project SGS-2016-012 of the University of West Bohemia.

## References

- Hynek, M. and Votapek, P. (2013) Numerical analysis of thermal fields in the insulated cover of tire curing presses. 18th International Conference Engineering mechanics 2012.
- Hynek, M. and Votapek, P. (2011) Thermal analysis of tyre curing process. In IM 2011. Praha: AVČR. pp. 223-226.
- Jirasko, J. and Kottner, R. (2016) Computational model for heat transfer in a tyre curing press. 22nd International Conference Engineering mechanics 2016. pp. 262-265.
- Keckstein, T., Jirasko, J. and Kottner, R. (2016) Finite Element Analysis of a Curing Press with Focus on Tightness of the Vulcanizing Chamber, Proceedings of the ASME 2016 International Mechanical Engineering Congress and Exposition.

## ANALYSIS OF RELATIONSHIP BETWEEN POSTURAL STABILITY AND DEGREE OF VISUAL IMPAIRMENT

M. Jureczko<sup>\*</sup>, P. Jureczko<sup>\*\*</sup>

**Abstract:** *The aim of study was to evaluate the postural stability in patients with various degree of visual impairment. Statistical analysis of influence of degree of visual impairment on postural stability opposed to people perfectly sighted also was conducted. The studies was conducted on 30 patients with various degree of visual impairment and 10 patients perfectly sighted. Postural stability was tested using two diagnostic machines. The patient stood in its habitual position with its arms lowered along its body and its feet spacing on hip width. In this position were done some tests, where patients were obligated to adopt two positions their bodies in variants with opened and closed eyes. Next, the stabilographic parameters were measured. Conducted statistical analysis of results from research allows to propose a conclusion that there is significant statistical dependence between degree of eyesight dysfunction and ability to maintain stable posture. The conducted researches revealed the influence of lack of visual control on increase of most of stabilographic parameters values.*

**Keywords:** Postural stability, People with various degree of visual impairment, One – way ANOVA test.

### 1. Introduction

Proper human posture is the necessary condition to realize of most his movement and physical activity. This is the reason why most of clinical test includes stability study. Stabilography is non-invasive diagnostic method that allows to estimate humans' stability system. In case of proper and stable position the projection of center of mass (CoM) which is simultaneously center of gravity (CoG) on the support base (BoS) is vertical (Mitchell, 2007 and Sturnieks, 2004). Studies based on ground reaction forces measurement in order to diagnose balance maintenance system are made by stabilographic platforms.

Humans eyesight is one of three basic input channels, other are aurical and somatosensoric control subsystem that is used to control position and its regulations (Abdelhafiz et al., 2003 and Schwartz et al., 2005). The complexity of the problems of the people with various degree of visual impairment in the context of normal gait and stable position are very big. Humans' visual system delivers 80 % information for perception which is essential to maintain structural stability. According to these data people with eyesight dysfunction has worse stability self-control (Friedrich et al., 2008). According to Schwesig (2011), the visual system of patients with birth defects in contrast to people with acquired disability is based on other incentives from the birth, and this leads to better posture control in situations where eyesight is ineffective. The results of studies provided by article of de Araújo et al. (2014) confirms that blind children has postural stability disorders. Tomomitsu (2013) research results suggest that feedback from visual system is necessary to maintain the body balance. Mentioned researchers found that visually impaired people has worse postural stability than people without eyesight dysfunctions. Conclusions were drawn both on dynamic tests and balance tests on the edge of the foam. Ray et al. (2008) reports that adults that have lost their sight uses more hip-joint moves than people well seeing to maintain balance.

Presented studies were designed to find and describe relationship between degree of visual impairment and problems with balance of the body in patients.

---

<sup>\*</sup> Mariola Jureczko, PhD. Eng.: Institute of Theoretical and Applied Mechanics, Silesian University of Technology, Konarskiego 18 A; 44-100 Gliwice; PL, Mariola.Jureczko@polsl.pl

<sup>\*\*</sup> Pawel Jureczko, PhD. Eng.: Institute of Theoretical and Applied Mechanics, Silesian University of Technology, Konarskiego 18 A; 44-100 Gliwice; PL, Pawel.Jureczko@polsl.pl

## 2. Materials and Methods

Researches were conducted on groups of patients with the following of degrees of visual impairment (there were no other dysfunctions legally or biological):

group 1: low vision;

group 2: partially sighted;

group 3: totally congenitally blind.

The results of these researches were compared with results of researches in patients perfectly sighted - control group. In every group studies were conducted for 10 patients. The all patients gave their informed consent prior to their participate in the study.

It is known that accuracy of stability measurements is dependent on conditions during tests. Because of that presented results of research in this article are based on recommendations Kapteyn'a, (1983).

Postural stability was tested using stabilographic platform AMT1, including software that allows measurements of ground reaction forces, foot point of contact with the ground, centre of pressure (CoP) in real time.

The patient stood in its habitual position with its arms lowered along its body and its feet spacing on hip width. In this position were done some tests, where patients were obligated to adopt two positions their bodies in variants with open (variant is marked as OE) and closed eyes – this one wasn't applied to 3'rd group (this variant is marked as CE): standing on left leg (position marked as LL); standing on right leg (position marked as RL).

Comparison of stabilographic parameters received from test with eyes opened and closed, allows to assess the role of the visual senses involved in postural control. By measuring pressure force on ground and moment of force location of CoP has been found. Six different motion parameters of CoP have been evaluated: SP – total path length, on both axes, in millimeters; SPAP – statokinesiogram path length on the OY axis (the sagittal plane), in millimeters; SPML – statokinesiogram path length on the OX axis (the coronal plane), millimeters; MA – the mean amplitude (radius) of CoP, on both axes, in millimeters; MV – mean velocity of the CoP movement, on both axes, in millimeters per second; SA- sway area of the CoP point, in square millimeters.

## 3. Results

Based on the data obtained from stabilograms analyzed the balance parameters of the patients in the test with open and closed eyes. Values of parameters determined from stabilograms for both variants are shown in Tabs. 1 – 4. Researches results were developed statistically. Results were subjected to one - way ANOVA variance analysis (Bartolucci, 2016, Boddy, 2009 and Tamhane, 2009). In situation where developed results allowed to reject null hypothesis, the Tukey-Kramer test was executed. Next step after developing HSD values was comparison of mean values of researched group with each other. This allows to verify, if both groups are statistically significant.

Tabs. 1 and 2 contains results of one – way ANOVA and Tukey-Kramer tests for CE and OE variants for the LL test.

*Tab. 1: Results of ANOVA and HSD tests of motion parameters of CoP for LLCE.*

	Anova		Tukey's test	group 1 and group 2	group 1 and control group	group 2 and control group
	F	$f_{\alpha-1, v, \alpha}$	HSD			
SP	5019.18	3.354	149.4	2004.49	5960.56	3956.07
SPAP	598.32	3.354	3.10	44.03	69.51	22.92
SPML	392.45	3.354	0.228	2.15	0.286	2.33
MA	83.09	3.354	1.94	1.703	9.49	7.78
MV	404.87	3.354	205.74	166.05	402.1	536.4
SA	2312.58	3.4668	199.33	104.6	70.5	4006.9

Tab. 2: Results of ANOVA and HSD tests of motion parameters of CoP for LLOE.

	Anova		Tukey's test	group 1 and group 3	group 1 and group 2	group 1 and control group	group 3 and group 2	group 3 and control group	group 2 and control group
	F	$f_{a-1,v,\alpha}$	HSD						
SP	5219.7	2.86	374.9	938.4	12.1	49.4	12126.3	16389	62.7
SPAP	916.5	2.86	4.187	25.59	41.62	32.98	16.46	7.78	9.35
SPML	1783.7	2.86	1.811	21.18	46.176	23.98	24.98	2.79	22.19
MA	596.64	2.86	0.79	5.14	12.26	0.695	7.16	4.446	11.606
MV	5652.5	2.86	70.08	562.19	3213.18	20.28	2650.9	541.9	192.9
SA	4096.1	2.86	150.12	1152.5	3856.2	48.6	3098.1	1034.3	4096.3

Tabs. 3 and 4 contains results of one – way ANOVA and Tukey-Kramer tests for CE and OE variants for the RL test.

Tab. 3: Results of ANOVA and HSD tests of motion parameters of CoP for RLCE.

	Anova		Tukey's test	group 1 and group 2	group 1 and control group	group 2 and control group
	F	$f_{a-1,v,\alpha}$	HSD			
SP	843.8	3.354	24.26	28.15	85.48	71.32
SPAP	958.23	3.354	19.16	98.12	21.12	174.68
SPML	6819.3	3.354	8.432	156.13	98.11	9.143
MA	74.72	3.354	0.154	0.103	1.89	1.97
MV	407.3	3.354	14.36	7.86	32.03	31.47
SA	4660.8	3.354	1.501	2.011	174.3	202.3

Tab. 4: Results of ANOVA and HSD tests of motion parameters of CoP for RLOE.

	Anova		Tukey's test	group 1 and group 3	group 1 and group 2	group 1 and control group	group 3 and group 2	group 3 and control group	group 2 and control group
	F	$f_{a-1,v,\alpha}$	HSD						
SP	589.16	2.86	100.1	228.79	178.3	187.3	267.4	228.6	198.3
SPAP	1034.67	2.86	3.98	129.7	129.45	21.13	9.12	125.13	174.26
SPML	3126.6	2.86	1.467	58.56	14.78	51.35	59.89	87.98	41.65
MA	47.97	2.86	0.283	0.321	0.998	0.154	0.876	0.678	1.178
MV	324.56	2.86	2.11	12.27	2.87	1.67	15.89	12.03	4.967
SA	4509.67	2.86	2.69	27.14	62.34	20.34	78.9	23.67	68.13

Tabs. 1 – 4 contain results achieved with one-way ANOVA method. In all cases the F results were greater than which was calculated according to Bartolucci, (2016), Boddy, (2009) and Tamhane (2009). Therefore hypothesis about equality of mean values of motion parameters of CoP was rejected. It was found statistically significant influence of degree of visual impairment on stable position of patient. Mentioned tables includes also results of Tukey-Kramer tests. Absolute values of difference of mean values between groups larger than calculated HSD value according to Boddy, (2009) and Tamhane (2009) are marked with boldface font in grey cells.

#### 4. Conclusions

Results of research are proof that different eyesight dysfunction causes different problems for control body balance. Comparative analysis of CoP parameters from stabilograms for LL-body position shows that most of these parameters (SP, SPAP, MA, MV and SA) were increased in experiments with exclusion visual control (CE) in contrast to a situation where eyesight body control was enabled (OE). This applied to all research groups. Simultaneously exclusion visual control for this position led to shortening of path length in the coronal plane (SPML). Reverse situation occurred in cause of RL-position. In this situation exclusion visual control causes decrease of the parameter for all 4 research groups. Research did not give a clear result. For control group the parameters SP, SPAP, MV hasn't changed in OE and CE variant, values MS and SPA parameters increased when eyesight control was disabled. Reverse situation appears in case of 1'st and 2'nd group (3'rd group hasn't taken part in CE variant research). For these groups MA and SA parameters haven't changed, and SP, SPAP and MV decreased its value.

Conducted experiments shows that exclusion visual control disabling causes increase of most stabilograms parameters. Obtained results suggest that next research should take into account possibility that left-handiness may affect body-balance control skill.

Statistical analysis shows that exclusion visual control (CE) in both positions, exclusion visual control for patients with 1st and 2nd group significantly worsens body balance control. Only comparison of MA and MV parameters for patients with some degree of visual impairment appears statistically irrelevant. Mentioned patients weren't able to maintain balance in both situations with or without visual control. Statistics analysis from research carried in both positions with open eyes (OE) shows that degree of visual impairment is statistical significance important for balance control skill. Only small defects appears to be no statistical significance.

#### References

- Abdelhafiz, A.H. and Austin, C.A. (2003) Vision factors should be assessed in older people presenting with falls or hip fracture. *Age Ageing*, 32, pp. 26-30
- Bartolucci, A.A., Singh, K.P. and Bae, S. (2016) Introduction to statistical analysis of laboratory data. John Wiley & Sons, 2016.
- Boddy, R. and Smith, G. (2009) Statistical Methods in Practice. John Wiley & Sons, 2009.
- De Araújo, P.P., De Moura Filho, O.F., Valenti, V.E. et al. (2014) Stabilometric parameters analysis in children with visual disorder. *International Archives of Medicine*, 7:1.
- Friedrich, M., Grein, H.J., Wicher, C., Schuetze, J., Mueller, A. et al. (2008) Influence of pathologic and simulated visual dysfunctions on the postural system. *Experimental Brain Research*, 186, 2, pp. 305-314.
- Kapteyn, T.S., Bles, W., Njiokiktjien, C.J., Kodde, L., Massen. C.H. and Mol, J.M. (1983) Standardization in platform stabilometry being a part of posturography. *Agressologie: Revue Internationale de Physio-biologie et de Pharmacologie Appliquees aux Effets de L'agression*, 24, 7, pp. 321-326.
- Mitchell, S., McCaskie, A., Francis, R., Peaston, R., Birrell, F. and Lingard, E. (2007) The need for a falls prevention programme for patients undergoing hip and knee replacement surgery. *Journal of Orthopaedic Nursing*, 11, 2, pp. 98-103.
- Ray, C.T., Horvat, M., Croce, R., Mason, R.C. and Wolf, S.L. (2008) The impact of vision loss on postural stability and balance strategies in individuals with profound vision loss. *Gait Posture*, 28, 1, pp. 58-61.
- Schwartz, S., Segal, O., Barkana, Y., Schwesig, R., Avni, I. and Morad, Y. (2005) The effect of cataract surgery on postural control. *Investigative ophthalmology & visual science*, 46, pp. 920-924.
- Sturnieks, D.L., Tiedemann, A., Chapman, K., Munro, B., Murray, S.M. and Lord, S.R. (2004) Physiological risk factors for falls in older people with lower limb arthritis. *The Journal of Rheumatology*, 31, 11, pp. 2272-2279.
- Schwesig, R., Goldich, Y., Hahn, A., Müller A., Kohen-Raz, R., Kluttig, A., et al. (2011) Postural control in subjects with visual impairment. *European Journal Ophthalmology*, 21, 3, pp. 303-309.
- Tamhane, A.C. (2009) Statistical Analysis of Designed Experiments: Theory and Applications. John Wiley & Sons.
- Tomomitsu, M.S., Alonso, A.C., Morimoto, E., Bobbio, T.G. and Greve, J.M. (2013) Static and dynamic postural control in low-vision and normal-vision adults. *Clinics*, 68, 4, pp. 517-521.

## THE CALIBRATION PROGRAM FOR THE HYPOPLASTIC SAND MODEL

T. Kadlíček<sup>\*</sup>, T. Janda<sup>\*\*</sup>, M. Šejnoha<sup>\*\*\*</sup>

**Abstract:** *The present paper is concerned with the development of calibration program for the Von Wolffersdorff hypoplastic model, often referred to as the hypoplastic model for sand, and as such to bring this model to the point of practical applications. The proposed methodology combines standard laboratory measurements with their numerical simulations at a material point to address, apart from experimentally derived data, those model parameters which can be inferred from these laboratory tests only indirectly. As an example, the entire calibration process is presented for a sand sample collected from a construction pit of the Komořany tunnel.*

**Keywords:** Coarse sand, Hypoplasticity, Model calibration, Von Wolffersdorff model.

### 1. Introduction

Although the well-known elastoplastic Mohr-Coulomb (MC) model offers a good estimation of failure criterion, it still suffers from several shortcomings. Not only that the strength parameters  $c$  and  $\varphi$  and Young's modulus  $E$  of this model are valid only for a certain range of stress, but the response below the yield stress is linear elastic both in loading and unloading. To overcome these shortcomings the MC model can be enhanced to include the dependence of strength parameters on the deviatoric plastic strain and thus to simulate hardening and softening or to include the evolution of Young's modulus with depth.

Another option is to adopt advanced soil models such as the elastoplastic CamClay model or a relatively new theory of hypoplasticity. Even in their basic form, the hypoplastic soil models well simulate the fundamental characteristics of soils such as the stiffness dependency on soil density and the nonlinear response in both the primary loading and unloading. When enhanced with the concept of so called small strain stiffness they allow for reflecting a relatively high stiffness at very small strains. Although these models have proved useful in many practical applications, see e.g. (Mašín, 2009), (Kadlíček, et al., 2016) and their reliability has been repeatedly verified, they are still mostly employed for the academic purposes only. This is perhaps attributed not as much as to the lack of theoretical knowledge but more to the exhausting process of their calibration.

Thus, to stimulate interest of practical engineers in advanced constitutive models, we have been recently focusing our attention on developing a suitable methodology and tools for their calibration. As for the calibration procedure of the Mašín hypoplastic model for clays (Mašín, 2013) we refer the interested reader to (Kadlíček, et al., 2015). In the present contribution, we concentrate instead on the essential steps associated with the calibration of the Von Wolffersdorff hypoplastic model, which is also referred as the hypoplastic model for sand (HS), (Wolffersdorff, 1996).

### 2. Hypoplastic model for sand

The advanced soil models define in the void ratio and stress  $e \times q \times p$  space the so called State Boundary Surface (SBS), see Fig. 1. This surface surrounds all admissible states. A significant advantage

---

<sup>\*</sup> Ing. Tomáš Kadlíček: CTU, Faculty of Civil Engineering, Thákurova 7/2077, Prague; CZ, tomas.kadlicek@fsv.cvut.cz

<sup>\*\*</sup> Ing. Tomáš Janda, PhD.: CTU, Faculty of Civil Engineering, Thákurova 7/2077, Prague; CZ, tomas.janda@fsv.cvut.cz

<sup>\*\*\*</sup> Prof. Ing. Michal Šejnoha, DSc.: CTU, Faculty of Civil Engineering, Thákurova 7/2077, Prague; CZ, sejnomo@fsv.cvut.cz

of the HS model can be found in the fact that its parameters can be determined on the basis of standard laboratory tests, i.e. the oedometric and triaxial tests.

The HS model is defined by eight parameters, namely  $\varphi_c$ ,  $h_s$ ,  $n$ ,  $e_{d0}$ ,  $e_{c0}$ ,  $e_{i0}$ ,  $\alpha$  and  $\beta$  (Herle, et al., 1999). These parameters can be divided into two groups according to the procedure needed for their determination. The first group consists of parameters that can be determined directly from the available experimental measurements. The second group represent parameters that have to be determined by means of a parametric study, thus by matching numerical simulations with experiments. Individual parameters are described in the following sections.

### Initial void ratios $e_{d0}$ , $e_{c0}$ and $e_{i0}$

These parameters control the positions of the limiting void ratio curves as seen in Fig. 2. The void ratio  $e_{d0}$  represents the void ratio in the densest possible state,  $e_{c0}$  represents the void ratio of the soil at the critical state and  $e_{i0}$  is introduced as a theoretical value of the initial void ratio for the state that occurs in the loosest possible state. This value can be represented by the spheres formed in a rectangular grid. The value of  $e_{c0}$  can be determined directly from the oedometric. The triaxial test is also an option. The recommended mutual relations between all three parameters is given by Eqs. (1) and (2). (Herle, et al., 1999)

$$e_{d0} = 0.5 e_{c0} \quad (1)$$

$$e_{i0} = 1.2 e_{c0} \quad (2)$$

### The critical friction angle $\varphi_c$

The critical friction angle  $\varphi_c$  represents the value of a friction angle at the moment when the soil specimen exposed to the shearing maintains a constant rate of volumetric deformation. This parameter can be evaluated based on the triaxial tests. However, in case of coarse grained soils it is advantageous to associate the value of with the so-called angle of repose. It has been shown that the angle of repose and the critical state friction angle are nearly identical. (Herle, et al., 1999)

### Parameters $h_s$ and $n$

These parameters control the slope ( $h_s$ ) and curvature ( $n$ ) of the normal compression line (NCL) in the  $\ln p \times e$  plane. Fig. 3 compares the simulations of the oedometric tests provided by the calibrated hypolastic model (full line) with experimental measurements (dotted line). For the sake of clarity the simulations associated with a higher value of the parameter  $n$  (dashed) and a higher value of the parameter  $h_s$  (dash-dotted) in comparison to their optimal (calibrated) values are also presented. The evaluation of these parameters can be performed based on the results of the isotropic compression test. However, the oedometric test is recommended as it is easier to execute, but more importantly it allows for achieving higher pressures. (Herle, et al., 1999)

### Parameters $\alpha$ and $\beta$

Calibration of these parameters requires conducting a triaxial test as they influence the peak friction angle. The parameter  $\alpha$  influences the dependency of the model on the soil density and consequently the overconsolidation ration and the value of the peak friction angle. Parameter  $\beta$  influences the overall stiffness depending on the density and the relative position of the overconsolidation peak in the  $\varepsilon \times q$  plane. The influence of these parameters is evident from Fig. 4 showing a nearly perfect match between simulation (bold solid line) and the triaxial test (narrow solid line). The two other lines shows HS model performance when setting the parameters  $\alpha$  and  $\beta$  to differ from the original calibrated values. (Herle, et al., 1999)

Further details can also be found in (Kadlíček, et al., 2015)



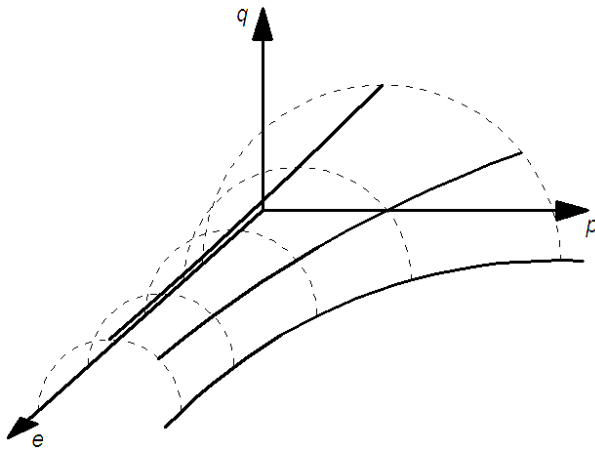


Fig. 1: State boundary surface.

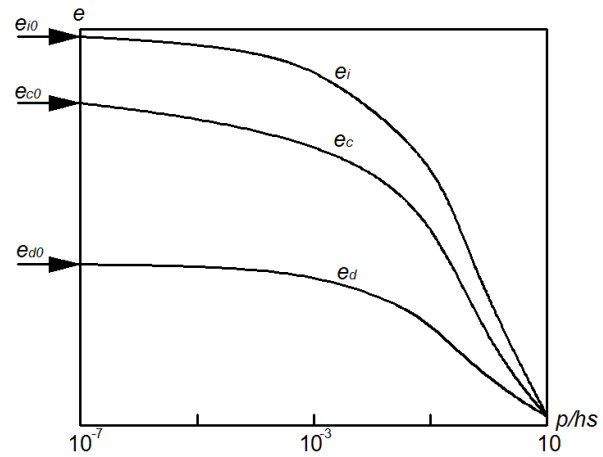


Fig. 2: The limiting void ratio curves in  $\ln p \times e$  plane.

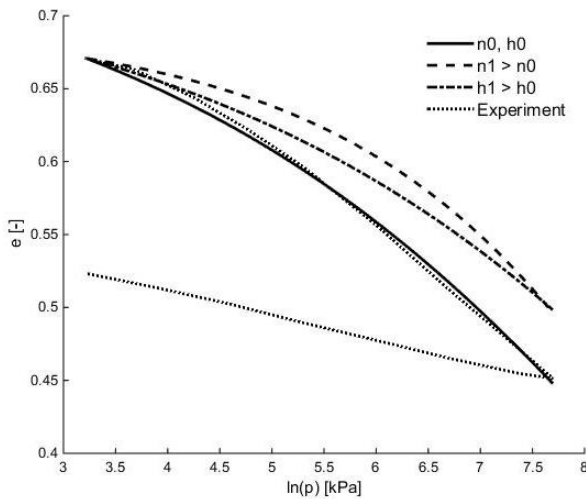


Fig. 3: Oedometric test in  $\ln p \times e$  plane.

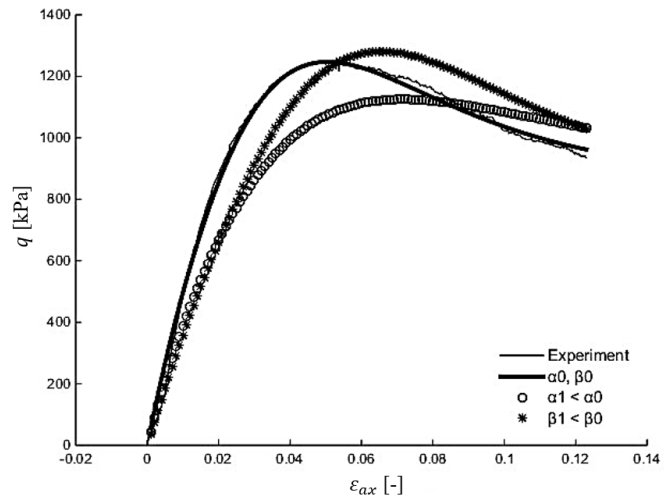


Fig. 4: Triaxial test in  $\varepsilon_{ax} \times q$ .

### 3. Calibration software

The calibration softwares have already been developed for two advanced soil models for fine grained soils, namely the elastoplastic CamClay model and the Masin hypoplastic model. This third calibration program thus completes the set of the calibration programs for advanced soil models.

To run program successfully, the laboratory test data has to be ordered in a predefined form consisting of oedometric and triaxial tests. While parameters  $h_s$ ,  $n$ ,  $e_{d0}$ ,  $e_{c0}$  and  $e_{i0}$  are calibrated for every oedmetric test included in the input file, parameters  $\varphi_c$ ,  $\alpha$  and  $\beta$  are determined for the whole set of triaxial tests. Once the calibration is finished, results of the calibration are saved to the well-arranged MS Excel file. This file includes comparison of the conducted laboratory tests with the HS model and a table of values of all parameters. The comparison charts are shown in Figs. 5 and 6, which represent a drained triaxial test and an oedometric test, respectively. Tab. 1 stores the values of calibrated parameters. The laboratory tests used for the calibration were performed on the sand specimen which was acquired from a construction pit of the Komořany tunnel. (Tichovká, 2012) An example of the input file with further instructions on how to successfully run the beta version of the calibration program is available on <https://mech.fsv.cvut.cz/TA04031603>.

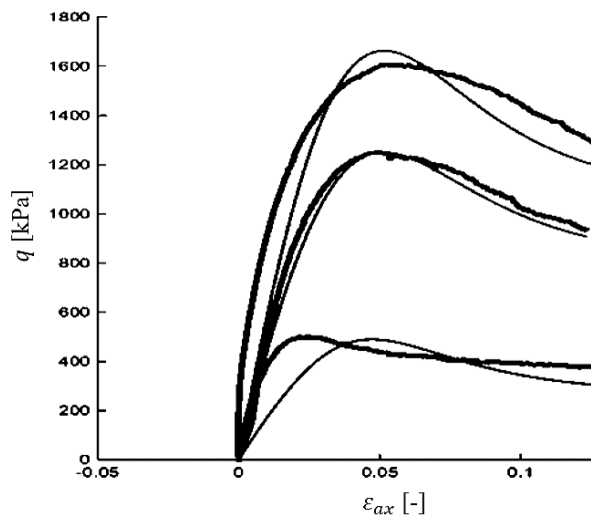


Fig. 5: Triaxial test with HS model.

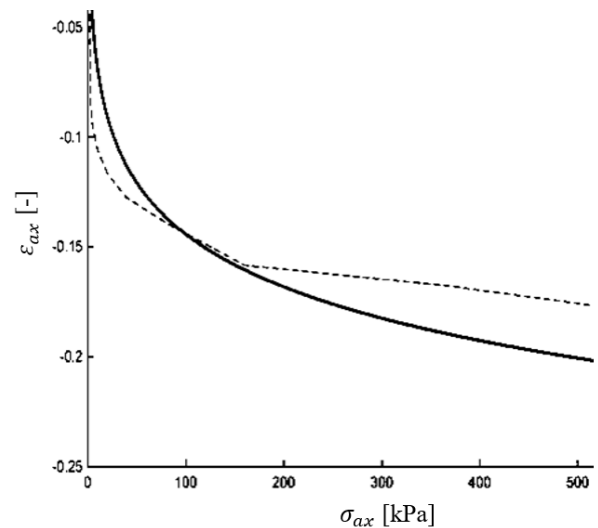


Fig. 6: Oedometric test with HS model.

Tab. 1: The calibrated parameters of the HS model for the Komořany specimen.

Parameters	$n$	$h_s$	$e_{c0}$	$e_{i0}$	$e_{d0}$	$\varphi_c$	$\alpha$	$\beta$
Values	0.112	15092	0.919	1.102	0.459	35.1	1.022	1.571

#### 4. Conclusion

This calibration software enables a prompt evaluation of the HS model's parameters and together with calibration programs for the CamClay model and the hypoplastic model for clay represents an effective tool when employing the advanced soil models for large scale engineering analyses. Apart from the calibration programs our effort is also directed to the search for suitable correlations between the advanced soil model parameters and standard index characteristics of soils. This should allow us to create calibration tables that would provide estimates of parameters of the selected model based on standard soil classification. This should make the advanced soil models even more accessible to practical engineers. Some preliminary results on this study can be found in (Kadlíček, et al., 2016).

#### Acknowledgement

The financial support provided by the project TA04031603 and the SGS project with application registered under the number OHK1-014/17 is gratefully acknowledged.

#### References

- Kadlíček, T., Janda, T. and Šejnoha, M. (2016) Correlation relations for the hypoplastic model for fine grained soils. Brno, Česká geotechnická společnost ČSSI, Zakládání staveb 2016 Brno, pp. 39-44, (in Czech).
- Herle, I and Gudehus, G. (1999) Determination of parameters of a hypoplastic constitutive model from properties of grain assemblies. Mechanics of cohesive-frictional materials. 4, pp. 461-486.
- Kadlíček, T., Janda, T. and Šejnoha, M. (2016) Applying hypoplastic model for soft soils to the analysis of anchored sheeting wall. Acta Geodynamica et Geomaterialia. 13, 2, pp. 125-136.
- Kadlíček, T., Janda, T. and Šejnoha, M. (2015) Calibration of Hypoplastic Models for Soils. Engineering Mechanics, Vol. 821, pp. 503-511.
- Mašín, D. (2009) 3D modeling of an NATM tunnel in high K0 clay using two different constitutive models. Journal of geotechnical and geoenvironmental engineering, pp. 1326-1335.
- Mašín, D. (2013) Clay hypoplasticity with explicitly defined asymptotic states. Acta geotechnica, Vol. 8, 5, pp. 481-496.
- Tichovská, M. (2012) Modelling of a deep excavation in sand. Diploma project, Charles University, Faculty of Science. Prague (in Czech).
- Wolffersdorff, P.A. (1996) A hypoplastic relation for granular materials with a predefined limit state surface. Mechanics of cohesive-frictional materials, Vol. 1, pp. 251-271.

## FATIGUE CRACK INITIATION AND GROWTH IN 316L STEEL IN TORSIONAL CYCLIC LOADING

M. Karol<sup>\*</sup>, A. Chlupová<sup>\*\*</sup>, V. Mazánová<sup>\*\*\*</sup>, T. Kruml<sup>\*\*\*\*</sup>

**Abstract:** *Fatigue crack initiation and growth study in 316L austenitic stainless steel was made in cyclic torsion. The experiments on hollow cylindrical specimens were performed at room temperature using fully reversed shear strain controlled cycles. The specimens used were polished mechanically and electrolytically to enable surface damage and crack propagation observation using optical light microscope, SEM. It was found that high density of extrusions and intrusions are formed on the specimen surface due to cyclic loading. TEM observations revealed that dislocation arrangement in well-known ladder-like structure is responsible for the localization of cyclic plastic deformation and for the origin of surface roughness in which the fatigue crack nucleate. The path of fatigue cracks leading to failure was observed, too. The crack path was found to be dependent upon the applied shear strain amplitude.*

**Keywords:** 316L austenitic steel, Fatigue crack initiation, Crack growth, Torsional loading, Crack path.

### 1. Introduction

The 316L austenitic stainless steel is a material widely used in the chemical and oil industries, medicine as well as food industry. In many industrial applications, the construction parts inherently contain stress concentrators as functional design features, Fatemi et al. (2014). Hence it is important to know its response to cyclic deformation including quantitative data of fatigue crack growth kinetics. The understanding of fatigue crack nucleation and propagation leads to better prediction of the fatigue lifetime of the material as well as adjustment of maintenance intervals, Suresh (1998).

Most of the studies until now have been made in strain controlled tension-compression setup. It is therefore important to study the crack initiation and growth in cyclic torsion, too. Mazánová et al. (2016) studied the fatigue crack initiation and the early stages of crack growth in cyclic torsion and multiaxial loading. Studies of Zhang et al. (1997) and Fatemi et al. (2011) had shown an evolution of crack path with the amplitude of the cyclic shear strain in cyclic torsion. They report propagation of a longitudinal crack along the specimen axis in the case of high shear strains and cracks in the form of letter X for low shear strains. In this work we have found a very similar crack path with addition of bifurcation of the ends of the longitudinal crack. Moreover, it was found that fatigue cracks growing from artificial transverse circular hole grow at 45 ° to the direction of the sample axis, which was also reported by Gladskyi (2013) on low carbon steel and by Fatemi et al. (2014) on aluminium.

### 2. Materials and Methods

The stainless steel 316L was manufactured by Acerinox Europa in form of 20 mm hot rolled plates. This treatment caused the internal structure to be equiaxed with an average grain diameter of 40 µm. The chemical composition is as given in the table pod. The manufacturer claims the following tensile properties of the material:  $R_{p0.2} = 336$  MPa,  $R_m = 586$  MPa, fracture elongation 57 %.

---

\* BSc. Michal Karol: Institute of Physics of Materials; Žitkova 22; 616 62, Brno; CZ, michal.karol.91@gmail.com

\*\* Ing. Alice Chlupová PhD.: Institute of Physics of Materials; Žitkova 22; 616 62, Brno; CZ, chlupova@ipm.cz

\*\*\* Ing. Veronika Mazánová: Institute of Physics of Materials; Žitkova 22; 616 62, Brno; CZ, mazanova@ipm.cz

\*\*\*\* prof. Mgr. Tomáš Kruml, CSc.: Institute of Physics of Materials; Žitkova 22; 616 62, Brno; CZ, kruml@ipm.cz

Tab. 1: Chemical composition of 316 L steel in wt. %.

C	Cr	Mn	Mo	N	Ni	P	S	Si	Fe
0.018	16.631	1.261	2.044	0.042	10.000	0.032	0.001	0.380	bal.

Hollow cylindrical specimen (Fig. 1) for cyclic fully reversed torsion were used. Some of the specimens had a transverse circular hole through one of its walls. Those were used for fatigue crack growth measurement.

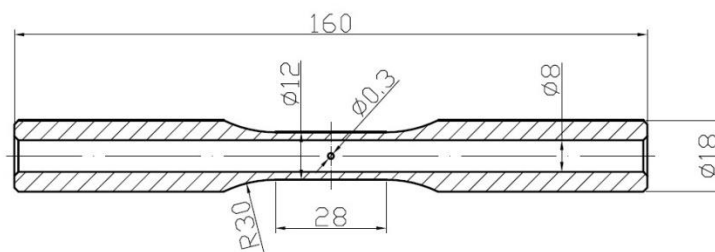


Fig. 1: Hollow specimen with a small hole drilled into the gauge length wall.

The tests were performed using computer controlled MTS servohydraulic machines at room temperature. A symmetrical strain controlled cycling was used and the total strain amplitude was kept constant during cycling ( $R_\epsilon = -1$ ) with the help of an extensometer attached to the specimen gauge length. Plastic strain amplitude was determined in the middle of fatigue life as a half-width of the stress-strain hysteresis loop.

The tests for measurements of crack growth rate were interrupted regularly and micrographs of growing fatigue cracks were taken using a light microscope Navitar. Micrographs were analyzed, fatigue crack nucleation mechanisms were determined and the crack growth rate was measured. The crack length was defined as half of the surface crack length. The crack growth was followed up to approx. 2 cm of surface length. The specimens were also dismantled and observed in SEM Tescan Lyra regularly. The initiation mechanism was investigated at the end of fatigue life, using nanofabricated craters perpendicular to the specimen surface, made by focused ion beam (FIB) technique.

Dislocation microstructure of the specimens after fracture was investigated by transmission electron microscopy (TEM). The foils were prepared by means of the traditional technique consisting of mechanical grinding and electrolytic polishing. They were observed on TEM Philips CM12 at 120 kV.

### 3. Results and Discussion

Cyclic torsional loading is known to induce surface roughness significantly, creating intrusions and extrusions on the strained sample. These act as stress concentrators for nucleation of fatigue cracks on the surface of the sample.

The internal structure of the specimens cycled to fracture was analyzed using TEM imaging. The  $\alpha'$  martensite islands, ladder-like persistent slip bands (PSBs) as well as thin deformation induced twins were found (Fig. 2). These microscopic features are formed due to the cyclic deformation of the material. Ladder-like dislocation arrangement was frequently observed. It is known to form bands in which cyclic plastic deformation localizes and surface persistent slip markings (PSM) made of intrusions and extrusions are formed, Mughrabi (1983). Fig. 2 was taken on specimen cycled in combined axial/torsional mode, however, the microstructural features are the same as observed in pure torsional cycling.

The orientation of small surface cracks and crack density were analyzed in order to understand the initiation mechanism. It was found that high concentration of PSMs is induced on the specimen surface (Fig. 3). These are the initiation sites for the fatigue cracks. This can be seen in the Fig. 4 showing a surface PSM with a small fatigue crack growing from it.

The direction of the normal tensile stress in a cyclic shear loading changes each half cycle and the fatigue cracks grow typically perpendicularly to this stress. This results in a zig-zag shape of the fatigue cracks on the microscopic level. This was reported in the work of Branco et al. (2014) as well.

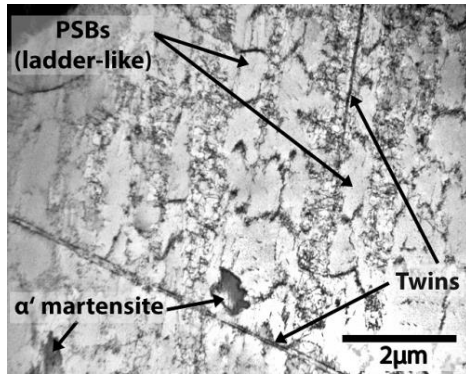


Fig. 2: TEM image of internal structure of the specimen after multiaxial in-phase cyclic loading.

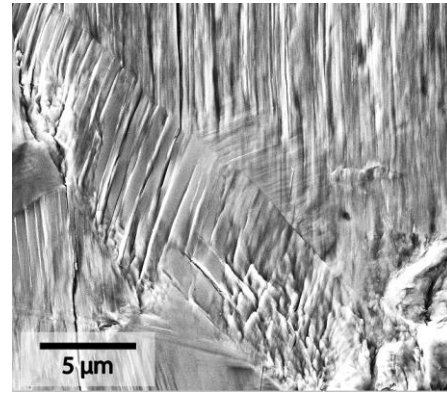


Fig. 3: Fatigue crack initiation at persistent slip markings of the surface.

It was found that the macroscopic crack path is strongly dependent on the imposed cyclic shear strain amplitude  $\gamma_a$ . We have found that in case of low  $\gamma_a$  the magistral cracks grow in a shapes resembling a letter X with the crack branches at  $45^\circ$  to the axis of the specimen (Fig. 5). On the other hand, high  $\gamma_a$  leads to a very long fatigue crack which grows parallel to the specimen axis and bifurcates at the last stages of the specimen fatigue life (Fig. 6). The observed crack paths are in agreement with observations of Zhang et al. (1997) and Fatemi et al. (2011) which show influence of the used cyclic torsional amplitude on the final crack path.

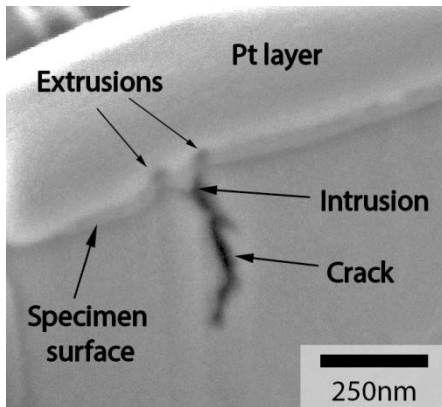


Fig. 4: Surface PSM with an initiated fatigue crack, FIB cross-section cut.

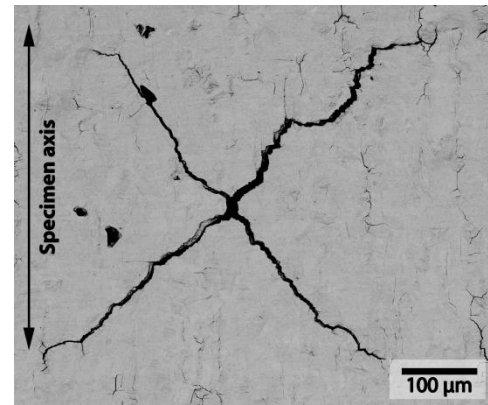


Fig. 5: SEM-BSE image of a fatigue crack, torsional cyclic loading,  $\gamma_a = 0.41\%$ .

Finally it was found that if an artificial crack starter is used, in our case transverse circular hole, the fatigue cracks grow outwards of the drilled hole under  $45^\circ$  to the specimen axis, Fig. 7. This was reported in works of Gladskyi (2013) and Fatemi et al. (2014) on different materials, too.

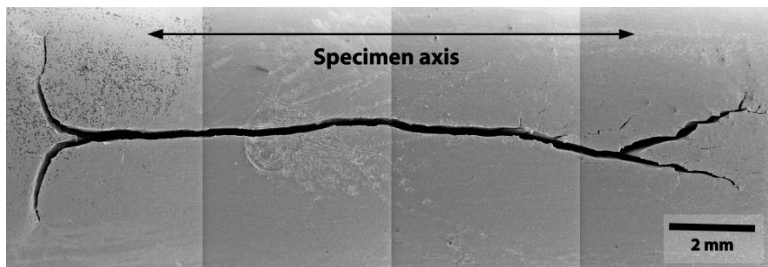


Fig. 6: Long fatigue crack along the specimen axis bifurcated on the ends  $\gamma_a = 1.73\%$ .

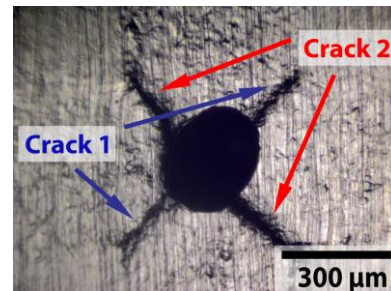


Fig. 7: Fatigue cracks growing from an artificial transverse circular hole  $\gamma_a = 0.45\%$ .

#### 4. Conclusions

The fatigue crack initiation and crack path was studied in cyclic torsional loading on 316L austenitic stainless steel and the following was concluded:

- The cyclic torsion changes the surface relief of the sample creating PSMs made of intrusions and extrusions.
- The fatigue cracks nucleate at the sites of stress concentration within the PSMs.
- The fatigue cracks in shapes of letter X are results of low shear strain amplitudes. The longitudinal cracks along the specimen axis with bifurcation on the ends are found on samples cycled at high shear strains.
- In the case of a transverse circular hole acting as an artificial crack starter, the cracks grew out of the hole in direction of 45 ° to the specimen axis irrespective of the loading amplitude.

#### Acknowledgements

The research was conducted in the frame of IPMinfra supported through project No. LM2015069 of MEYS. Financial support of the Grant Agency of CR, no. 15-08826S is acknowledged.

#### References

- Fatemi, A., Gates, N., Socie, D.F. and Phan, N. (2014) Fatigue crack growth behavior of tubular aluminium specimens with a circular hole under axial and torsional loadings, *Engineering Fracture Mechanics* 123, pp. 137-147.
- Suresh, S. (1998) *Fatigue of Materials*, Cambridge University press.
- Mazánová, V., Škorík, V., Kruml, T. and Polák, J. (2016) Cyclic response and early damage evolution in multiaxial cyclic loading of 316L austenitic steel, *International Journal of Fatigue*, *in press*.
- Zhang, W., Akid, R. (1997) Mechanism and fatigue performance of two steels in cyclic torsion with axial static tension/compression. *Fatigue Fract. Engng. Mater. Struct.* 20, 4, pp. 547-557.
- Zhang, W. and Akid, R. (1997) Effect of biaxial mean stress on cyclic stress-strain response and behavior of short fatigue cracks in a high strength spring steel. *Fatigue Fract. Engng. Mater. Struct.* 20, 2, pp. 167-177.
- Fatemi, A. and Shamsaei, N. (2011) Multiaxial fatigue: An overview and some approximation models for life estimation. *International Journal of Fatigue* 33, pp. 948-958.
- Gladskyi, M. and Fatemi, A. (2013) Notched fatigue behavior including load sequence effects under axial and torsional loadings, *International Journal of Fatigue* 55, pp. 43-53.
- Mughrabi, H. (1983) Dislocation wall and cell structures and long-range internal-stresses in deformed metal crystals. *Acta Metallurgica* 31, pp. 1367-1379.
- Branco, R., Costa, J.D. and Antunes, F.V. (2014) Fatigue behaviour and life prediction of lateral notched round bars under bending-torsion loading, *Engineering Fracture Mechanics* 119, pp. 68-84.



## IMPACT OF SUPERCHARGING ON THE NOISE LEVEL IN BIOGAS ENGINES

J. Kaszkowiak<sup>\*</sup>, M. Markiewicz-Patalon<sup>\*\*</sup>, S. Borowski<sup>\*\*\*</sup>, P. Dorszewski<sup>\*\*\*\*</sup>

**Abstract:** *In the study, there are compared the results of noise level measurements for the spark-ignition unsupercharged engine and a supercharged biogas engine. The examination was conducted for three values of rotational speed for unloaded and loaded engines. It has been determined, that as far as engines operating without loading, the noise level does not depend on an engine furnishing with a supercharging system. For loaded engines, a higher level of noise was found as compared to an engine not equipped with a turbo-compressor.*

**Keywords:** Biogas, Combustion engine, Noise, Additional charging.

### 1. Introduction

Emission of sound is an inseparable effect of combustion engines' operation. A continuous development of these units and improvement of their performance, apart from the improvement of functional characteristics, influences the environment among the others by the generated noise. Sounds emitted by combustion engines, may also be used to diagnose their technical condition. The noise transmitted within the selected range of frequencies, may be helpful at the time of establishing of the technical state of selected engine's elements (Komorowska et al., 2011). Noise also accompanies work processes in machines driven by combustion engines – as an example shredding and cutting – at the time of which, energy generated by a machine's engine is converted into resistances of a machine's working elements movement (Bochat et al., 2013). The most commonly occurring source of noise are the transportation and production works. The excessive noise is the cause of health problems of people and animals, and may result in disturbances in the natural habitat's flora (Bukovjanová et al., 2008). Lowering of combustion engines' noxiousness for the natural environment may be obtained on different planes, such as constructional changes limiting the fuel consumption, and adjust the exhaust gases' composition (Kaszkowiak et al., 2016). The use of engine oils on the basis of bioadditives may also be used for piston combustion engines to lower the level of noise (Tulik et al., 2013). Gas fuels used for feeding engines of spark ignition result in the decrease of emission of harmful pollutants and lowering of the costs of an unit's exploitation. Gas fuels, just like ethanol, may be considered substitute substances for combustion engines' supplying. They are characterised by high parameters, that is high octane number, high spontaneous ignition temperature, wide flammability limits of their mixtures with air and high calorific value (Lejda et al., 2003). Production of ethanol (Gumienna et al., 2016) and biogas, which may be produced both from specially cultivated plants as well as from ensilage (Kaszkowiak, 2014) is the alternative for fuels obtained from natural ground resources.

Reaching by the year 2020 in the final energy's consumption of 20 % share of the energy from renewable sources and 10 % share of biofuels in the overall consumption of transport fuels (COM (2006) 848 final), is one of the objectives in the policy of the European Union. The biofuels are, among the others,

---

<sup>\*</sup> Jerzy Kaszkowiak, PhD.: Faculty of Mechanical Engineering, UTP University of Science and Technology, Poland. Al. Prof. Kaliskiego 7, 85-796 Bydgoszcz, e-mail: kaszk@utp.edu.pl

<sup>\*\*</sup> Marietta Markiewicz-Patalon, PhD.: Faculty of Mechanical Engineering, UTP University of Science and Technology, Poland. Al. Prof. Kaliskiego 7, 85-796 Bydgoszcz, e-mail: marietta.markiewicz@utp.edu.pl

<sup>\*\*\*</sup> Sylwester Borowski, PhD.: Faculty of Mechanical Engineering, UTP University of Science and Technology, Poland. Al. Prof. Kaliskiego 7, 85-796 Bydgoszcz, e-mail: sylwester.borowski@utp.edu.pl

<sup>\*\*\*\*</sup> Piotr Dorszewski, DSc.: Faculty of Animal Breeding and Biology, UTP University of Science and Technology, Poland. Al. Prof. Kaliskiego 7, 85-796 Bydgoszcz, e-mail: piotr.dorszewski@utp.edu.pl



bioethanol and biogas. In the future,  $\frac{1}{4}$  of bioenergy may originate from biogas produced from organic matter, for ex. from ensilages, from whole plantsmanure and dunghill, wet food and fodder wastes, and other ones. Biogas is the product of bacterial anaerobic fermentation – methanogenesis, in which a mixture of gases is generated, among which there dominate methane, carbon dioxide and hydrated sulfides (Mrůzek et al., 2011). Methane present in biogas may be subject to conversion into heat, be an engine fuel and later on be used for electric power generation (Kalač, 2011). From 1 ha of herbs, there may be generated enough biogas, to make it possible to drive a passenger car the distance of 40 thou. km. The volume of 25 kg of biogas allows to cover a distance of 500 km (Vagonyte). From 1 ha of corn there may be generated enough bioethanole to drive a passenger car for the distance of 30 thou. km. Biogas is more productive, as there may be covered the distance more than twice as long – 70 thou. km (Michalski, 2007).

Generation of biogas is the form of energy's acquisition from the biomass's renewable energy for the purposes of effective and productive feeding of combustion engines (Stanek, 2009). Engines fed with gas (biogas including), are most often the engines constructed as high-pressure and adjusted for work with gas fuel. Adaptation consists in: lowering of the compression rate by modernization of a piston or head's construction to increase the combustion chamber's capacity, change of the system of the mixture's ignition from self-ignition into spark ignition and modernization of the feeding with gas system. Modification of the engine cooling's system shall be necessary in many cases.

Making use of the renewable energy sources in power engineering is the constantly developing field and may, to a considerable degree, contribute to making use of natural resources' limitation (Ziółkowski et al., 2009).

## 2. Materials and methods

There have been tested two combustion engines with spark ignition designed for biogas feeding. Both the engines had the identical construction. Constructed as 12- cylinder, vee-type engines of cubic capacity amounting to 12000 cm<sup>3</sup>. The engine's power rating without charging amounted to 330 kW, while the charged engine equipped with a turbo-compressor of constant geometry had the power of 380 kW. The rated speed of both the engines amounted to 157 rad s<sup>-1</sup> (1500 rpm). Both the engines powered the same power-generators. Supply of both the engines was conducted from the same biogas tank. Parameters of biogas are presented in Tab. 1.

*Tab. 1: Parameters of biogas supplying engines at the time of tests.*

Biogas components	Average content
Methane	65.25 %
Hydrogen sulfide	12 ppm
Carbon dioxide	35 %
Ammonia	0 ppm

That experiment was planned as a two-factor one of 3 levels of the first factor (engine's loading) and on 2 levels of the second factor [supercharging (1) and its absence (2)]. The experiment's factors and their values are presented in Tab. 2.

*Tab. 2: The experiment's factors and their values.*

Loading of the engine (factor A)	Supercharging (factor B)	
	Yes	No
	0 kW	0 kW
	180kW	180 kW
	280 kW	280 kW

The engines, together with aggregates, are in identical, closed rooms. The engines are fully efficient, have the run (about 1000 hours of operation), similar period from the last replacement of the engine oil (about 120 hours), are lubricated with the same engine oil. Prior to the measurements' commencement, each engine was heated up till it reached the ordinary operation's temperature (cooling liquid's temperature about 85 °C). The examinations were conducted for both the engines at the rotational speed of 157 rad s<sup>-1</sup> (1500 rpm), for each engine working without loading and with a loading respectively 180 kW and 280kW. The noise level was measured with the integrating sound meter HD 2010 UC, in the distance of 1m from the side engine's surface. The time of the test's performing amounted to 5 minutes for an engine operating without loading and next loadings. The reading was repeated 5 times after each 60 seconds of operation. The rotational speed was measured with a laser revolution counter Voltcraft DT-10L with measurement precision ±0.5 %, according to the manufacturer's data, comparing it with the speed displayed by the factory engine's revolution counter. The power absorbed from the engine was established on the basis of the generator's electric power.

The obtained results of measurements were subject to the statistical analysis for a two-factor experiment, with testing of significance of the differences with the Tukey test on the level of 0.05. The FR-ANALWAR programme on the basis of Excel was used for the analysis.

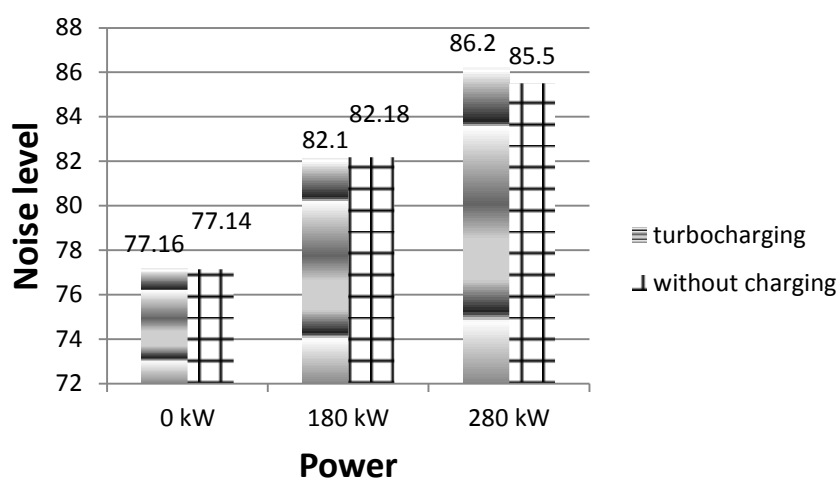


Fig. 1: Mean values of the level of noise.

On the basis of the conducted analyses it was established, that statistically significant differences in the noise level occur between the levels of the factor A (loading) in both the tested engines for all the loading values. No significant statistical differences in the noise level between the tested engines in case of no loading and at the loading of 180 kW were found. Significance of differences in the noise level was found only for the biggest loading of engines, that is 280 kW and amounted to 0.7 dB, a higher noise level was recorded for the supercharged engine.

### 3. Conclusions

On the basis of the conducted tests, the noise level in biogas powered engines, in the examined case it was found that the decisive factor was the value of an engine's loading. The applied supercharging inadvertently influenced the noise level only at the highest loading. Many factors may have an impact on the noise level. Most of all, application of supercharging influences the course of the fuel combustion's process. Suction murmurs in engines with supercharging (operation of a turbo-compressor, flow of air through the intercooler, higher volume and speed of air flowing through the wiring of the supply system, result in the increase of the noise level. For a man, the sounds of frequency higher than 20 kHz are not heard and it seems, that the sounds of a turbo-compressor most probably influence the level of nose only to a slight degree, especially in case of higher engine's power. However, one should not forget on undoubtful advantages of supercharging, just like for example higher engine's efficiency. Determination of the source of the increased level of noise is the subject matter of further (conducted at present) surveys. There are conducted studies on the level of noise of other engine models, for the purposes of receiving information to what extend the specific technical solutions (construction of an inlet system, construction of a turbo-compressor, the exhaust system) have an impact on the noise level. However, in the conditions

of an engine's operation for which the noise level is of high importance, special attention should be paid to the correct dampening.

## References

- Bochat, A. and Zastempowski, M. (2013) Modeling the dynamics of the vegetable material detachment process from undisturbed areas to improve the design of selected agricultural machines, Transactions of the ASABE, Vol. 56(4).
- Bukovjanová, E. and Slavík, R. (2008) Effect of noise on the environment, Tomas Bata University in Zlín. Faculty of Technology.
- Gumienna, M., Szwingiel, A., Lasik, M., Szambelan, K., Majchrzycki, D., Adamczyk, J., Nowak, J. and Czarnecki, Z. (2016) Effect of corn grain variety on the bioethanol production efficiency Fuel 164, pp. 386-392.
- Kalač, P. (2011) The required characteristics of ensiled crops used as a feedstock for biogas production: a review. J. Agrobiol. 28, pp. 85-96.
- Kaszkowiak, J., Kaszkowiak, E. and Markiewicz-Patalon, M. (2016) Analysis of the selected parameters of standard and premium type diesel oils, Trends in agricultural engineering, International Conference, Prague.
- Kaszkowiak, J. (2014) Technique of application of additives facilitating silaging of plant materials used for production of biogas, „Journal of Research and Applications in Agricultural Engineering”, Vol. 59(1).
- Komorowska, I. and Górnicka, D. (2011) Adaptation of engine vibration characteristics for diagnostics of mechanical defects, Silniki Spalinowe, 50(3).
- Lajda, K., Jaworski, A. (2003) Problems of gas supply to agricultural engines, Motrol. Automotive and Agricultural Power.
- Michalski, T. (2007) Corn - an excellent raw material for the production of biofuels. Maize - new possibilities. Handbook for producers, IV, Biznes Press Sp. z o. o. Warszawa.
- Mrůzek, M. and Groda, B. (2011) An analysis of biogas production from grass silage as dependent upon feed quality. Agric. Eng. 7(132), 107-114.
- Stanek, J. (2009) Biogas - an alternative gaseous fuels for spark ignition engines, The University of Pardubice Transport Faculty Jana Pernera, Department of Transport Means and Diagnostics.
- Tulík, J., Hujo, L., Stančík, B. and Ševčík, P. (2013) Research of new ecological synthetic oil-based fluid, Journal of Central European Agriculture, 14(4), pp. 1384-1393.
- Vagonyte, E., Agri-For-Energy 2, Work Package 4: Biogas & Biomethane, European Biomass Association, <http://www.biogaspartner.de/index.php?id=11510&L+1&fs=0\\%27%3Fiframe%3Dtrue>.
- Ziółkowski, M. and Balcerski, A. (2009) Internal combustion engines powered by biogas as a prospect of Polish power generation, Scientific Journals, Szczecin.

## DESIGN OF NEW PARAMETERS FOR EVALUATION OF LOAD CAPACITY OF SEMI-SHELL STRUCTURES

T. Katrňák\*

**Abstract:** *This paper presents the design and research of new specific parameters for faster determination of the load capacity of metal thin-walled semi-shell structures. The graphic visualization and evaluation of the avalanche propagation start is an additional method of load capacity determination based on results of analytical methods. New parameters were tested on evaluation of typical fuselage and stabilizer sections of a small transport aircraft in CS-23 regulation category.*

**Keywords:** Load capacity, Semi-shell, Stress analysis, Failure, Fuselage.

### 1. Introduction

Typical aircraft thin-walled metal structures are stiffened semi-shells, which are widely employed in aeronautical industry. These characteristic structures are composed of number of longitudinal stringers stiffening the outer thin shell skin. The example of semi-shell fuselage structure is presented in Fig. 1. A critical stage of the structural integrity is the global load capacity. After this stage the structure is not more able to support the outer load and the total collapse of structure will occur. Determination of the global load capacity is a complex analysis where particular element failures are investigated according to the detailed stress analysis. The critical point of the evaluation is the decision, when the limiting stage is reached and which element failure will start the avalanche propagation of following failures. Standard geometric parameters are utilized in graphic evaluation of changes in structural integrity per load increment. This article describes the design of new specific parameters for more efficient and faster determination of the structural load capacity.

The comprehensive reviews on stability failures of loaded shells in aerospace structures are presented in Niu (1999) and Kollár et al. (1984). This topic was extended in the interesting paper Hoff (1967) and Horák et al. (2016). Analytical solutions of skin buckling and effects of stringer torsional and warping failures and the verification by finite element methods are presented in Soares et al. (2013). The paper by Symonov et al. (2013) contributed with a comparison of utilized analytical gradually increased load method with nonlinear FEM approach of stiffened fuselage structure.

### 2. Methods

The stress analysis in selected sections of the structural part and the determination of skin and stringer failures was done using the Gradually increased load method GILM. This analytical method is based on the procedure described in Pištěk et al. (1987). Input allowable element stresses were derived separately according to Niu (1999). The applied load is gradually increased in each step and the following weakest structural element and its properties are investigated. This order of the development of element failures represents the history of load and changes of structural rigidity. The global load capacity of the structural section can be evaluated according to these results. The determination of the load capacity of semi-shell structure with significant elements is simple. The failure of significant structural element can be the stability damage of lower compressed flange or the rupture of upper tensioned flange of spars. The critical failure which starts the avalanche propagation of following failures and causes the total collapse is very difficult to derive for the semi-shell structure without significant elements. Typical example is fuselage structure, which is stiffened with longitudinal stringers with similar shape and cross-sectional area.

---

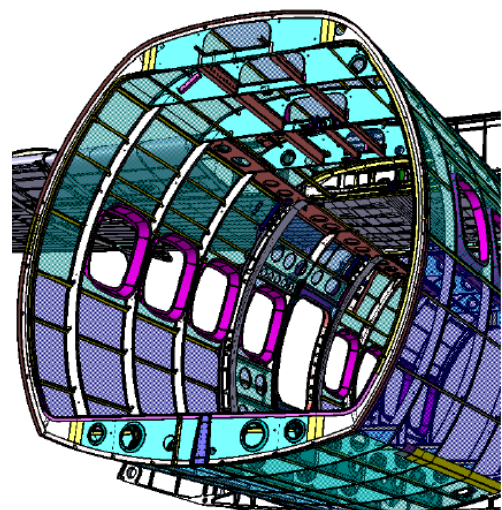
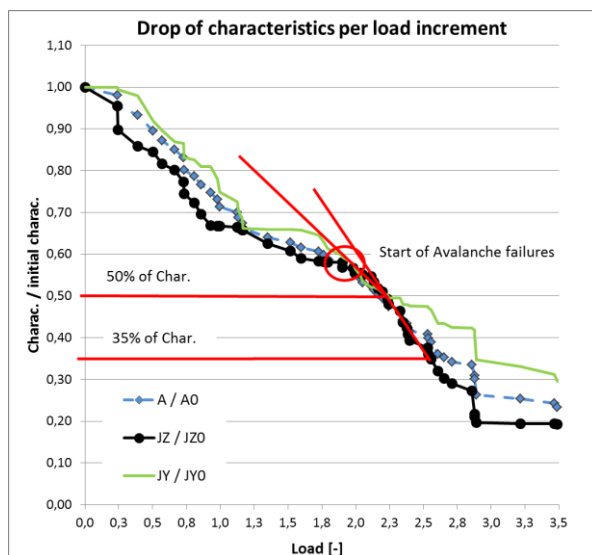
\* Ing. Tomáš Katrňák: Institute of Aerospace Engineering, Faculty of Mechanical Engineering Brno University of Technology, Technická 2896/2; 616 69, Brno; CZ, katrnak@fme.vutbr.cz

History of failures of structural elements obtained from analytical method can be ordered in table. The percentage of load of the particular element failure as well as its geometrical properties and remaining element stress are presented in Tab. 1. It is difficult to determine critical failure of total collapse or start of avalanche failures only from numbers in the table. The buckling failure of the first stringer S52 can be conservatively assumed as the critical failure. Experimental tests proved that the semi-shell stiffened structure can be still sufficiently rigid to support the load after few stringer failures. Therefore the graphic evaluation was employed as the post-processing visualization of analytical method.

*Tab. 1: Order of particular failures and element properties in results of load capacity analysis.*

Order of failure	Load coefficient [-]	Percentage of load [%]	Name of element	Element area $A_i$ [mm <sup>2</sup> ]	Second mom. $J_{zi}$ [mm <sup>4</sup> ]	Element stress [MPa]
1	0.241	24.1	<b>P24-27</b>	105.7	95846620	-7.4
2	0.242	24.2	<b>P27-30</b>	138.4	117679387	-7.4
3	0.390	39.0	<b>P30-33</b>	121.2	83021059	-21.0
4	0.502	50.2	<b>P49-52</b>	206.5	30858354	-13.5
...						
20	1.595	159.5	<b>P66-68</b>	69.4	39485107	-20.4
21	1.726	172.6	<b>S52</b>	48.6	26138856	-68.5
22	1.763	176.3	<b>S49</b>	48.6	3109175	-68.5
...						
28	2.036	203.6	<b>S55</b>	56.9	27671443	-86.3

The simulation of particular drop of certain parameter per load increment due to damage is presented in Fig. 1. The order of failures, location on load axis and change of characteristics on vertical axis was determined from analytical gradually increased load method. The level 100 % at the load axis represents ultimate level of applied outer load. The unit formulation, where the drop of parameter is related to the initial sectional characteristic, is utilized in graphic evaluation. The start of avalanche propagation of failures can be determined as the failure, which causes the drop of parameter under the level 50 % or 35 % of initial characteristics. Total initial characteristics are marked with the index 0. The gentle slope of drops of characteristics in Fig. 1 is caused by visualization of standard geometrical parameters.



*Fig. 1: Drop of geometric characteristics per load increment and typical fuselage structure.*

### 3. Standard parameters

The typical skin and stringer elements were selected for further evaluation from Tab. 1. The shell skin region P49-52 has a large cross-sectional area due to distance between stringers S49 and S52. Element

properties are presented in Fig. 2. Also the skin location on outer circumference creates significant second moment of area  $J_z$  along the  $z$  axis. The longitudinal stringer segments S52 and S49 have identical cross-sectional area, but the increased distance of S52 from  $z$  axis results in higher second moment of area  $J_z$  than stringer S49. These standard geometric parameters can be used in evaluation of global load capacity but it is not complete information about importance and utilization without element stress.

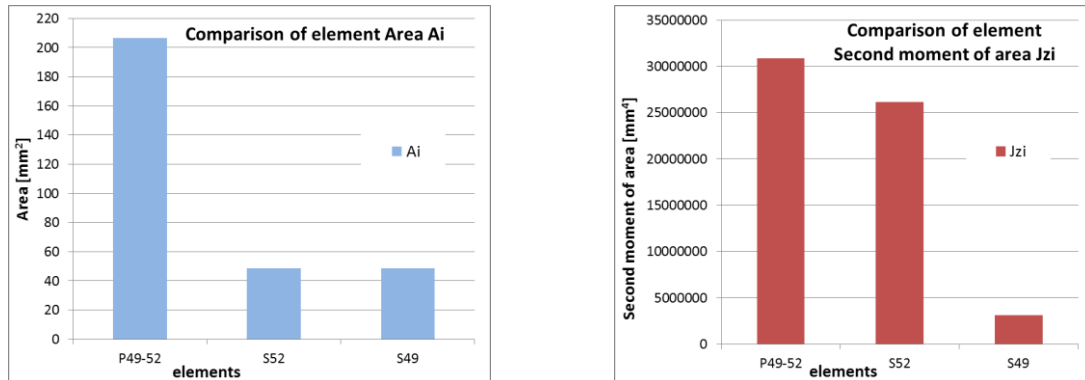


Fig. 2: Comparison of standard parameters of selected elements.

#### 4. Design of new parameters

Although the skin segment P49-52 has the highest area  $A$  and second moment of area  $J_z$  in comparison with stringers the induced critical stress in this skin element is minor. Therefore this skin region is not utilized as significantly as stringer segments. Stringer segments with minor area are more utilized in structural rigidity due to significant critical stresses. They are subjected to carry higher stresses and support the structure in higher levels of applied load, when skin regions are deformed and buckled. Standard geometric parameters are not able to provide sufficient information about importance and utilization of each element. Therefore additional parameters were designed. The combination of cross-sectional element area and conjugated element stress is represented by  $\text{Sigma} \cdot A$  parameter. Following combinations of second moment of area and allowable stress of single element created  $\text{Sigma} \cdot J_z$  and  $\text{Sigma} \cdot J_y$  parameters. A comparison of element  $\text{Sigma} \cdot J_z$  parameter is in Fig. 3, where stringer segment S52 demonstrates major effect in the structural integrity in bending along  $z$  axis. The failure of this S52 segment will cause the major drop of rigidity per load increment.

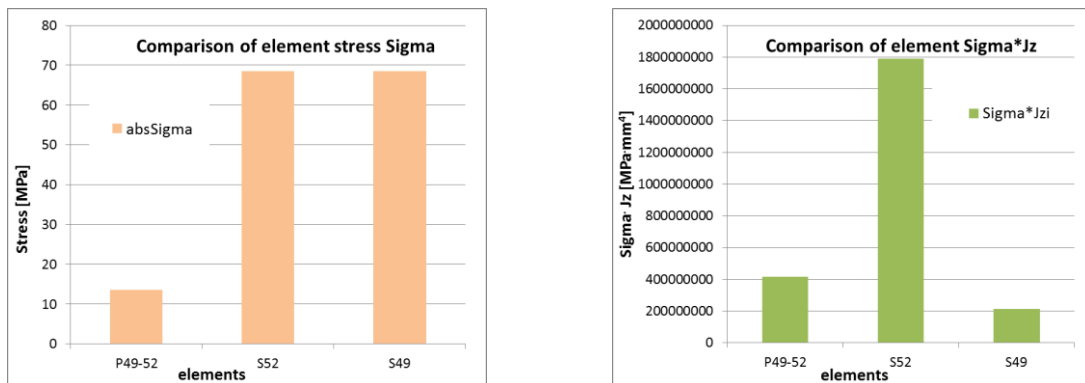


Fig. 3: Comparison of additional parameters of selected elements.

#### 5. Evaluation of results

Suitability and importance of new parameters in graphic evaluation of load capacity is validated in this chapter. Typical fuselage and stabilizer sections of small transport aircraft in CS-23 regulation category were tested as appropriate representatives of metal thin-walled semi-shell structures. The particular drops of  $\text{Sigma} \cdot A$ ,  $\text{Sigma} \cdot J_z$  and  $\text{Sigma} \cdot J_y$  parameters per load increment were simulated for a typical semi-shell fuselage section without cut-outs. It is beneficial that graphic visualizations are more sensitive to significant stringer failures than to minor skin failures. The comparison of effects of standard and new parameters for identical load case is presented in Fig. 4. Stability damages of skin regions in initial increments of the load and following compression failures are characteristic also in behavior observed

from experimental tests. The stability failure of the first stringer segment S52 was determined by analytical method at the level 172.6 % of the ultimate load. A steep slope of drops of characteristics facilitates to determine the significant element which starts the avalanche propagation of following failures and causes the total collapse of the structure. A detailed investigation with new parameters determined critical failure of stringer S43 at the level 190.2 % of the ultimate load. This superior predicting method increased the global load capacity of about 17.6 %.

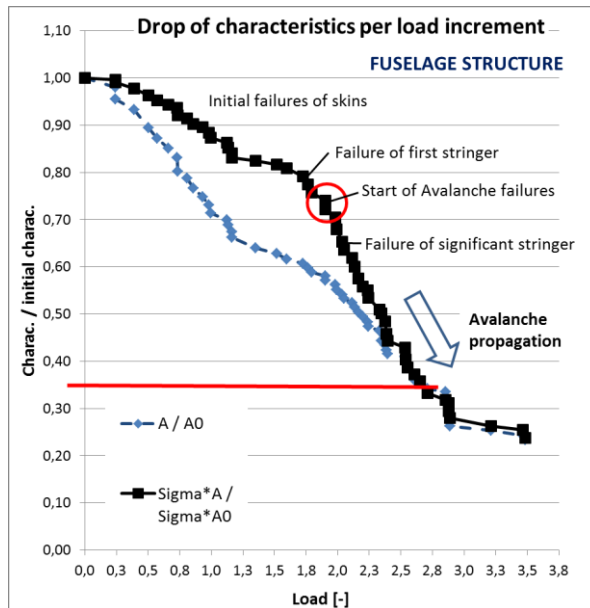


Fig. 4: Drop of parameters per load increment in fuselage section.

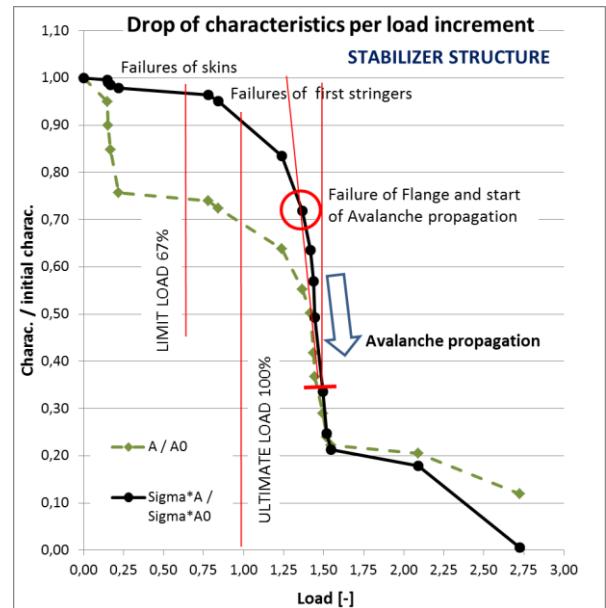


Fig. 5: Drop in stabilizer section.

Benefits of graphic evaluations with new parameters were confirmed also for stabilizer section in Fig. 5. The critical failure of flange was evaluated at the level 137 % of ultimate load.

## 6. Conclusions

The detailed research of new specific parameters confirmed more effective evaluation of the start of avalanche propagation of element failures. This additional method of determination of the critical element failure can improve the evaluation of the global load capacity for thin-walled metal semi-shell structures.

## Acknowledgement

These outcomes were supported by the project TE02000032 – Advanced Aerostructures Research Centre. This project was realized with financial support from national budget of the Technology Agency of the Czech Republic. The research leading to these results has received funding from the MEYS under the National Sustainability Programme I (Project LO1202).

## References

- Hoff, N.J. (1967) Thin shells in aerospace structures. Journal of Astronautics and Aeronautics, 5, 2, pp. 26-45.
- Horák, M. and Pištěk, A. (2016) Shear strength of thin web – influence of lighting openings and diagonal tension. Aviation journal, 20, 1, pp. 8-13.
- Kollár, L., Dulácska, E. (1984) Buckling of shells for engineers. John Wiley, Chichester.
- Niu, M.C.Y. (1999) Airframe stress analysis and sizing: Practical design information and data on aircraft, second edition. Hong Kong Conmilit Press Ltd.
- Pištěk, A., Grégr, O., Kahánek, V., Böhm, R. (1987) Strength and fatigue life of aircraft I. VUT v Brně, Brno (in Czech).
- Soares, P.T M.L., Monteiro, F.A.C., Neto, E.L., Bussamra, F.L.S. (2013) Skin buckling of fuselages under compression. in: Proc. 22nd International Congress of Mechanical Engineering COBEM 2013, Brazil, pp. 8976-8985.
- Symonov, V., Katrňák, T. (2013) FEM approach to estimate large deformations of stiffened fuselage structure. in: Proc. New Trends in Civil Aviation 2013. 1. Brno, pp. 90-92.



## PREOPERATIVE PLANNING OF CORRECTION OF CRANIAL DEFORMATIONS USING DISTRACTORS

E. Kawlewska<sup>\*</sup>, M. Zarwańska<sup>\*\*</sup>, D. Larysz<sup>\*\*\*</sup>, W. Wolański<sup>\*\*\*\*</sup>, M. Gzik<sup>\*\*\*\*\*</sup>

**Abstract:** *This paper presents a procedure of computer aided engineer's support of the treatment of craniosynostosis using distractors. The research encompassed morphological measurements of the skull before and after the surgical procedure, the FEM analysis and the assessment of effects of the correction of cranial deformations caused by the premature fusion of the lambdoid suture. The results of simulations enabled a 3D visualization of the surgical procedure using a distractor as well as the determination of optimum parameters of the operation and guidelines for medical doctors.*

**Keywords:** Craniosynostosis, Distraction osteogenesis, Preoperative planning.

### 1. Introduction

Developmental defects of the skull are one of the most serious and common issues in both maxillofacial surgery as well as plastic and reconstructive surgery (Cohen et al., 2000, Wolański et al. 2013). Congenital defects related to the structure of the skull include different types of craniosynostosis which consists in the premature fusion of one or more cranial sutures. Taking into account the statistics, this condition occurs in an isolated or complex form in one infant per two thousand infants (Hayward et al., 2004). The process of craniosynostosis treatment begins as early as in the first months of life of the patient and it requires a risky surgical procedure lasting for many hours (Cohen et al., 2000, Hayward et al., 2004, Wolański et al. 2013). Nowadays, the craniosynostosis treatment takes advantage of the state-of-the-art methods of virtual planning of surgical procedures based on computer tomography (CT) images (Wolański et al., 2015, Kawlewska et al., 2017). This research aimed to perform a preoperative planning of the surgical procedure of the correction of the cranial shape defect using distractors.

### 2. Methods

This work presents a computer aided engineer's support for the surgical procedure including the process of preoperative planning of the cranial shape correction using distractors in a 4-month female infant with diagnosed craniosynostosis. Apart from the segmentation of the head structure and virtual planning of the operation, a numerical model of the skull and distractor was developed within the framework of the computer aided planning of the neurosurgical procedure (Fig. 1).

#### 2.1. Virtual planning of neurosurgical procedure

In the first place on the basis of the patient's CT images, a 3D skull model was generated in Mimics v16.0 software programme and the brain's body was segmented. A geometrical model of the examined person's skull enabled the performance of basic morphological measurements of the skull, such as the length and

---

<sup>\*</sup> Edyta Kawlewska, PhD. Eng.: Department of Biomechanics, Silesian University of Technology, Zabrze, Poland, ekawlewska@polsl.pl

<sup>\*\*</sup> Magda Zarwańska, MSc. Eng.: Faculty of Biomedical Engineering, Silesian University of Technology. Foundation of Cardiac Surgery Development, Zabrze, Poland, zarwanskam@wp.pl

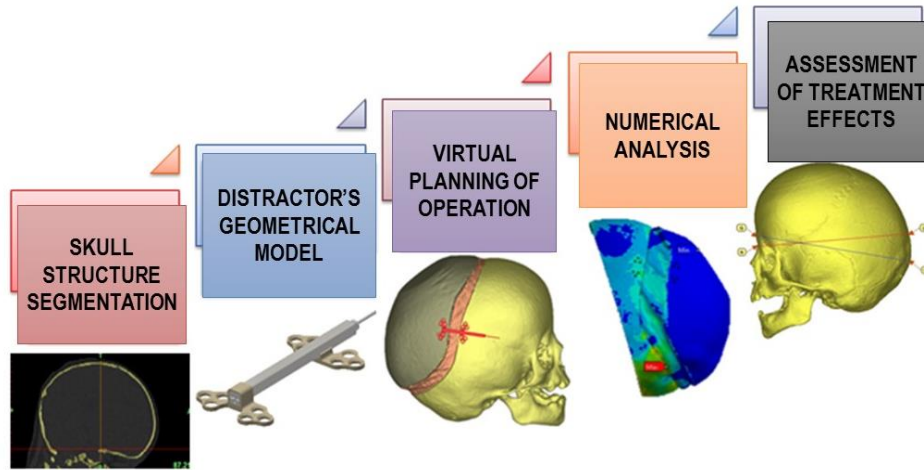
<sup>\*\*\*</sup> Prof. Dawid Larysz, DSc MD: Department of Radiotherapy, Maria Skłodowska-Curie Memorial Cancer Center and Institute of Oncology, Gliwice, Poland, dawilar@gmail.com

<sup>\*\*\*\*</sup> Assoc. prof. Wojciech Wolański DSc. Eng.: Department of Biomechanics, Silesian University of Technology, Zabrze, Poland, wwolański@polsl.pl

<sup>\*\*\*\*\*</sup> Prof. Marek Gzik: Department of Biomechanics, Silesian University of Technology, Zabrze, Poland, mgzik@polsl.pl

width as well as the volume of the brain before and after the surgical procedure.

In order to carry out the simulation of a virtual correction, it was also necessary to develop a distractor's geometrical model. On the basis of a real-life object, the geometry of the distractor was recreated in a software programme called Autodesk Inventor 2015. The structure of the distractor consisted of two mounting plates, which included holes for self-tapping bone screws and an adjusting screw in a special protective casing as well as an activator.

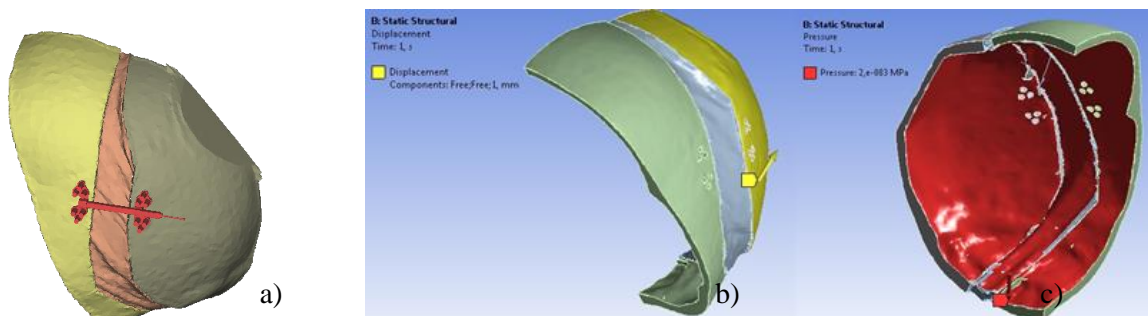


*Fig. 1: The course of computer aided surgical procedure of the skull shape correction using distractors.*

According to a medical doctor's instructions, the points of mounting the distractor's screws were determined on the segmented model of the skull. Also, the sites of incision were determined on the patient's skull in order to perform virtual osteotomy. Next, the distractor was correctly placed and implemented. Having done the osteotomy, the tissue connecting the separated bones was made, which simulated the development of the bone union. The final stage of the preparation of the skull model consisted in the isolation of the created callus as an individual structure. It enabled the introduction of the developed bone union as well as the anterior and posterior parts of the cranium as separate elements into the Ansys environment in order to conduct a strength analysis. Subsequently, the researchers carried out the simulation of a distraction process lasting 20 days, being developed at a velocity of 1 mm/day. The assessment of the correction was made on the basis of morphological measurements of the skull (anterior and posterior length and skull volume) before the operation and the comparison with the values obtained after the performance of the surgical procedure.

## 2.2. Preparation of models for numerical analysis

Within the framework of the computer aided engineer's support for the surgical procedure, numerical simulations were conducted to analyze the degree of loads occurring in the bone and callus during the distraction process. Due to the complexity of the model, it was necessary to introduce some simplifications in geometry, namely the facial skeleton as well as a half of the cranial vault were removed. The analyses were performed only for the side where the distractor was located.



*Fig. 2: A simplified model a) view of cranial bones, bone union and distractor, b) boundary conditions – vector displacement in the direction of axis Z, c) boundary conditions – intracranial pressure 15 mmHg on the internal surfaces.*

Tab. 1: Material properties of individual elements of the model.

Element	Young's modulus [MPa]	Poisson's ratio	Authors
Frontal bone	1265	0.22	(Wang et al. 2014)
Parietal and occipital bone	1103	0.22	(Wang et al., 2014)
Callus	130	0.30	(Zreiqat et al., 2015)
Distractor	108000	0.30	(Kromka-Szydek et.al, 2016)

The prepared model was discretized in a software programme called 3-matic using the Remesh module. Then, it was imported to the Ansys Workbench software programme. The whole model consisted of 77679 finite elements of a solid type including 34829 nodes. Individual parts of the model were joined by a bonded contact, making it impossible for the elements to move in relation to one another.

Next, the boundary conditions corresponding to the surgical procedure parameters were set in the model. The created model was fixed onto the anterior surface of the frontal lobe which was deprived of all degrees of freedom. The load consisted in the vector displacement operating in the direction of axis Z of the whole parietal-occipital lobe as well as the intracranial pressure exerting force in the normal perpendicular direction onto the internal surface of the cranial bones (Fig. 2). The simulations were conducted for a displacement of 1 mm and a pressure of 15 mmHg. Individual elements were attributed with proper material properties on the basis of literature (Tab. 1).

### 3. Results

As a result of the conducted simulation, the researchers obtained the distribution of stresses and strains reduced according to von Mises' hypothesis as well as the resultant displacement vectors occurring in the callus, frontal bone and parietal-occipital bone during the virtual surgical procedure of the correction of the skull deformation using a distractor.

The values of stress in the cranial bones at a forced displacement of 1mm did not exceed 100 MPa, and for the callus it amounted to approximately 30 MPa (Fig. 3). Simultaneously to the analysis of the stress-strain field, the analysis of the distribution of deformations was conducted. The highest value of a deformation amounting to 0.4 mm/mm was observed in the lower part of a newly-formed bone tissue.

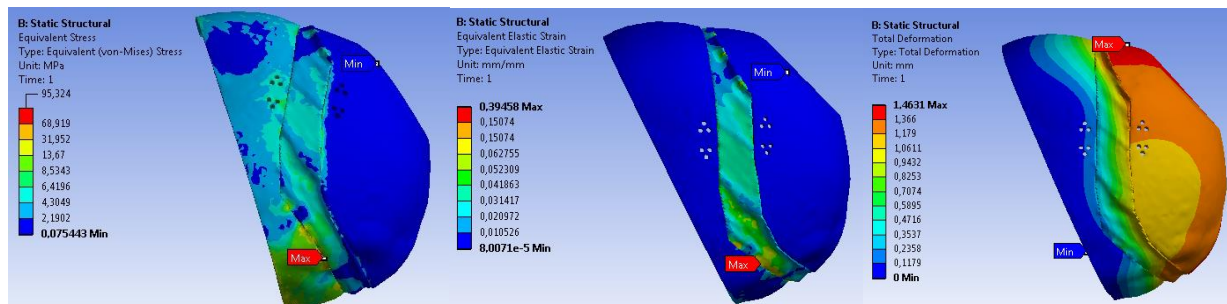


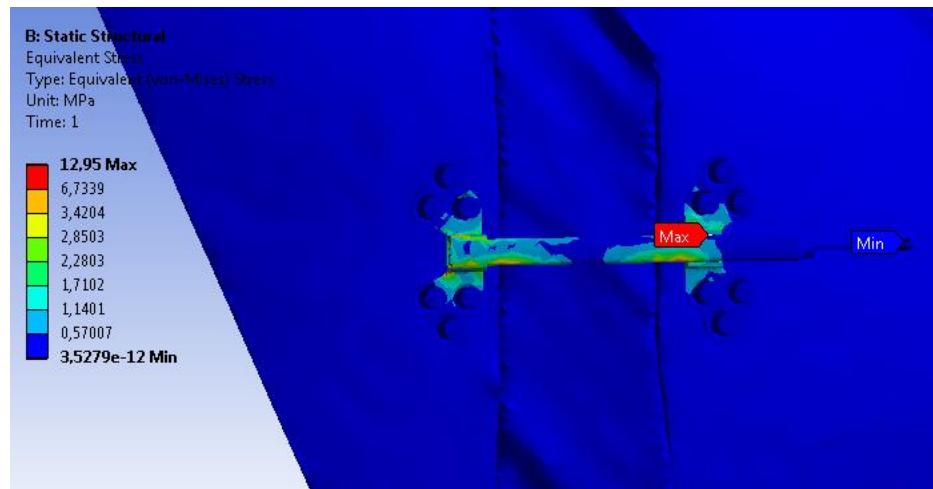
Fig. 3: Distribution of reduced stresses and strains as well as complete deformation.

The analysis of a complete deformation of the system revealed that a maximum displacement of approximately 1.5 mm was obtained on the parietal-occipital bone in the field which was located the furthest from the applied fixation. The obtained distribution of displacements results from the fact that bone elements were provided with directional displacement operating in the axis of the distractor.

In addition to that, the assessment included also the values of stresses in the distractor, which were obtained in the simulation of the surgical procedure of distraction osteogenesis. A maximum stress value amounting to approximately 13 MPa was observed on the junction of the mounting plate and the adjusting screw (Fig. 4). The distractor itself showed no high values of stress which could cause damage to the device made of material Ti-6Al-4V having high strength properties.

The evaluation of the effects of the computer aided preoperative planning of the correction of craniosynostosis was made on the basis of the comparison of the measurements of the patient's skull (anterior and posterior length as well as brain volume) before and after the surgical procedure. An

objective assessment was carried out on the grounds of a quantitative analysis of morphometric measurements, which showed the convergence of their values both after the surgical procedure and the virtual procedure of distraction (differences in the results of virtual simulation and real values of the parameters measured after the surgical operation do not exceed 10 %).



*Fig. 4: Distribution of stresses reduced in distractor.*

#### 4. Conclusions

Within the framework of the research, a virtual planning of the process of craniosynostosis treatment by means of distraction osteogenesis was performed. The conducted simulations enable the recreation of the applied surgical procedure making it possible for the surgeon to evaluate individual stages of the planned medical operation. A computer aided correction of the defects of the skull shape enables the selection of optimum parameters of the surgical procedure, which shortens the duration of such procedure, increases its efficiency and improves the treatment quality and patients' safety. The application of computer aided engineer's methods supporting the pre-operative planning also opens up possibilities of virtual training in the scope of complex surgical procedures, visualization of the distraction effects as well as the assessment of the tissue damage during distraction osteogenesis.

#### References

- Cohen, Jr., M.M. and MacLean, R.E. (eds.) (2000) Craniosynostosis: diagnosis, evaluation and management, Vol. 2, Oxford University Press, USA.
- Hayward, R., Jones, B., Dunaway, D. and Evans, R. (eds.) (2004) The clinical management of craniosynostosis, Mac Keith Press, London.
- Kawlewska, E., Wolański, W., Larysz, D., Gzik-Zroska, B., Jozsko, K., Gzik, M. and Gruszczyńska, K. (2017) Statistical analysis of cranial measurements - determination of indices for assessing skull shape in patients with isolated craniosynostosis. In: Vol. 526 of the series Advances in Intelligent Systems and Computing, Springer International Publishing, pp. 132-144.
- Kromka-Szydek, M. and Miodowska, J. (2016) FEM analysis of bone union process of the mandibulargraft system using dental implants for the dental reconstruction. Current Problems of Biomechanics, Vol. 10, pp. 25-30.
- Wang, J., Zou, D., Li, Z., Huang, P. and Li, D. (eds.) (2014) Mechanical properties of cranial bones and sutures in 1-2-year-old infants. Medical Science Monitor, Vol. 3(20), pp. 1808-1813.
- Wolański, W., Gzik-Zroska, G., Kawlewska, E., Gzik, M., Larysz, D., Dzielicki, J. and Rudnik, A. (2015) Preoperative planning of surgical treatment with the use of 3D visualization and finite element method. In: Lecture Notes in Computational Vision and Biomechanics, Vol. 19: "Developments in Medical Image Processing and Computational Vision", J.M.R.S. Tavares, R. Natal (eds.), Springer International Publishing, Switzerland.
- Wolański, W., Larysz, D., Gzik, M. and Kawlewska, E. (2013) Modeling and biomechanical analysis of craniosynostosis correction with the use of finite element method. International Journal for Numerical Methods in Biomedical Engineering, Vol. 29(9), pp. 916-925.
- Zreiqat, H., Dunstan, C. and Rosen, V. (eds.) (2015) A tissue regeneration approach to bone and cartilage repair. Mechanical Engineering Series, Springer International Publishing, Switzerland.



## AXISYMMETRIC DEFORMATION OF AN ELASTIC MEDIUM WEAKENED BY AN ANNULAR CRACK

B. Kebli\*, Z. Baka\*\*

**Abstract:** *The present work deals with the study of an axisymmetric flat annular crack problem in a semi-infinite elastic medium. The external surface is supposed without mechanical loads while the crack surface is subjected to a uniform internal pressure. The mixed boundary value problem is solved by the Hankel integral transforms method using the Boussinesq's stress functions. Then the three-part mixed boundary value problem is converted to a system of coupled triple integral equations of Bessel functions. Furthermore, by applying some integral relations and involving the addition Gegenbauer formula, the system is reduced to a solution of an infinite algebraic system equations for determining the unknown coefficients development. The explicit formula for the stress intensity factors near the crack fronts are derived, by means of those coefficients.*

**Keywords:** Axisymmetric deformation, Mixed boundary value problem, Annular crack, Triple integral equations, Stress intensity factors.

### 1. Introduction

The stress analysis of crack problems is of fundamental interest for the study of initiation and propagation of fracture and failure in brittle material. The annular crack form is one of the defect can be met. To examine such a problem diverse analytical and approximate methods were proposed by the researcher. The earlier studies were presented by Moss et al. (1971), who develop an iterative approximate solution for the stress intensity factors near the crack fronts. The analysis presented by Shibuya et al. (1975), (1976), and Koizumi et al. (1977) employ an analytical method to reduce the governing triple integral equations to a solution of an infinite algebraic system. Mastrojannis et al. (1981) present an approximate solution of the axisymmetric problem of an annular crack embedded in an infinite elastic solid. By using the Betti's reciprocal theorem, Choi et al. (1982) derive the integral equations for a problem involving flat toroidal crack subjected to axial or torsional load. Selvadurai et al. (1985) reduce the annular three-part mixed boundary value problem to the solution of a system Fredholm integral equations which they solve by the parameter method.

The purpose of this paper is to examine an annular crack in a semi-infinite elastic medium, opened up by an internal pressure. The used method is inspired from the works of Shibuya et al. (1976) and Koizumi et al. (1977), which deal with a crack problem in an elastic solid. The analysis transforms the three-part mixed boundary value problem to a resolution of system the two triples integral equations, which is reduced directly to a solution of an infinite algebraic system equations, for determining the unknown coefficients development. The stress intensity factors are expressed in term of the series involving those coefficients.

### 2. Problem formulation

The annular crack is located on the  $z = 0$  plane, with the inner and outer radii  $a$  and  $b$ , respectively, as shown in Fig. 1. The external surface of the infinite half-space medium  $z = -h$  is supposed without mechanical load, while the crack is assumed under a uniform internal pressure  $p_0$ . Since the crack

---

\* Prof. Belkacem Kebli, PhD.: Department of Engineering Mechanics, National Polytechnic School, El-Harrach; 16200, Alger; Algeria, belkacem.kebli@g.enp.edu.dz

\*\* Eng. Zakaria Baka, PhD. Student: Department of Engineering Mechanics, National Polytechnic School, El-Harrach; 16200, Alger; Algeria, zakaria.baka@g.enp.edu.dz

The displacement and stress components should be reduced to zero as  $r^2+z^2 \rightarrow \infty$  for  $z \geq 0$ . Furthermore, the appropriate boundary and continuity conditions can be formulated as follows

$$u_r^{(1)}(r, 0^+) = u_r^{(2)}(r, 0^-), \quad u_z^{(1)}(r, 0^+) = u_z^{(2)}(r, 0^-), \quad 0 \leq r \leq a \text{ or } r \geq b \quad (4)$$

451

$$\begin{aligned} \int_0^\infty [Ee^{2\lambda h} - (2\lambda h + 1)F] J_1(\lambda r) d\lambda &= 0, \quad r \leq a, r \geq b \\ \int_0^\infty \lambda [ (e^{2\lambda h} + 2\lambda h - 1)E + (e^{-2\lambda h} - 2\lambda h - 1)F ] J_1(\lambda r) d\lambda &= 0, \quad a < r < b \end{aligned} \quad (9)$$

Following Shibuya et al. (1976) and Koizumi et al. (1977) works, for solving the above system we use the integrals

$$\int_0^\infty G_n(\lambda) J_0(\lambda r) d\lambda \quad \text{and} \quad \int_0^\infty Z_n(\lambda) J_1(\lambda r) d\lambda \quad (10)$$

The first integral equations of (8) and (9) are then satisfied by taking

$$Ee^{2\lambda h} - (2\lambda h - 1)F = \sum_{n=1}^\infty a_n G_n(\lambda) \quad \text{and} \quad Ee^{2\lambda h} - (2\lambda h + 1)F = \sum_{n=1}^\infty b_n Z_n(\lambda) \quad (11)$$

where  $a_n$  and  $b_n$  are unknown coefficients. Next, from the equations (11), by expressing  $E$  and  $F$  in term of the two unknown coefficients, and substituting in the second equations of (8) and (9), and using the addition Gegenbauer formula, after some algebra, one gets an algebraic system stated in a closed matrix form as

$$\begin{aligned} \sum_{n=1}^\infty \int_0^\infty (A_{mn} a_n + B_{mn} b_n) d\lambda &= 2p_0 \delta_{1,m} \\ \sum_{n=1}^\infty \int_0^\infty (C_{mn} a_n + D_{mn} b_n) d\lambda &= 0 \end{aligned} \quad m=1, 2, \dots \quad (12)$$

where  $\delta_{1,m}$  denotes the Kronecker delta, and

$$\begin{aligned} A_{mn} &= \int_0^\infty [ - (2\lambda^2 h^2 + 2\lambda h + 1) e^{-2\lambda h} + 1 ] G_m(\lambda) G_n(\lambda) d\lambda \\ B_{mn} &= \int_0^\infty 2\lambda^2 h^2 e^{-2\lambda h} G_m(\lambda) Z_n(\lambda) d\lambda \\ C_{mn} &= \int_0^\infty 2\lambda^2 h^2 e^{-2\lambda h} G_n(\lambda) Z_m(\lambda) d\lambda \\ D_{mn} &= \int_0^\infty [ - (2\lambda^2 h^2 - 2\lambda h + 1) e^{-2\lambda h} + 1 ] Z_m(\lambda) Z_n(\lambda) d\lambda \end{aligned} \quad (13)$$

Consequently, the governing integral equations were reduced to the solution of algebraic system equations (12). On the basis of these results, the displacements and stresses components as well as the stress intensity factors given by the following formulas

$$\begin{aligned} \begin{bmatrix} K_{Ia} \\ K_{IIa} \end{bmatrix} &= \lim_{r \rightarrow a^-} \sqrt{a-r} \begin{bmatrix} \sigma_z(r, 0) \\ \tau_{rz}(r, 0) \end{bmatrix} \\ \begin{bmatrix} K_{Ib} \\ K_{IIb} \end{bmatrix} &= \lim_{r \rightarrow b^+} \sqrt{r-b} \begin{bmatrix} \sigma_z(r, 0) \\ \tau_{rz}(r, 0) \end{bmatrix} \end{aligned} \quad (14)$$

can be derived.

#### 4. Results and discussion

The unknown coefficients  $a_n$  and  $b_n$  discussed in previous section are determined by solving the system (12), whereas the infinite integrals in (13) can be evaluated numerically. Here, it had been tested that fifteen terms of coefficients are sufficient to get numerically good results of stress intensity factors.

Fig. 2 shows the variations of normalized stress intensity factors corresponding of mode I and II near the crack fronts in function of  $a/b$  for different values of  $h/b$ . It is noted that the stress intensity factors are giving their large values when  $a/b \rightarrow 0$  with a thinner thickness  $h/b \rightarrow 0$ , decrease with increasing one of the preceding parameters. Additionally, it is clear that the SIFs corresponding of mode I is always greater than the SIFs of mode II. The SIFs corresponding of mode I in the inner crack is greater than the other,



however, the opposite behavior occurs for the SIFs corresponding of mode II. Moreover, with increasing the layer thickness  $h/b \rightarrow \infty$ , the obtained results are in good agreement with those reported in the current literatures, such as the works of Shibuya et al. (1975), Koizumi et al. (1975), Mastrojannis et al. (1981), Choi et al. (1982) and Selvadurai et al. (1983).

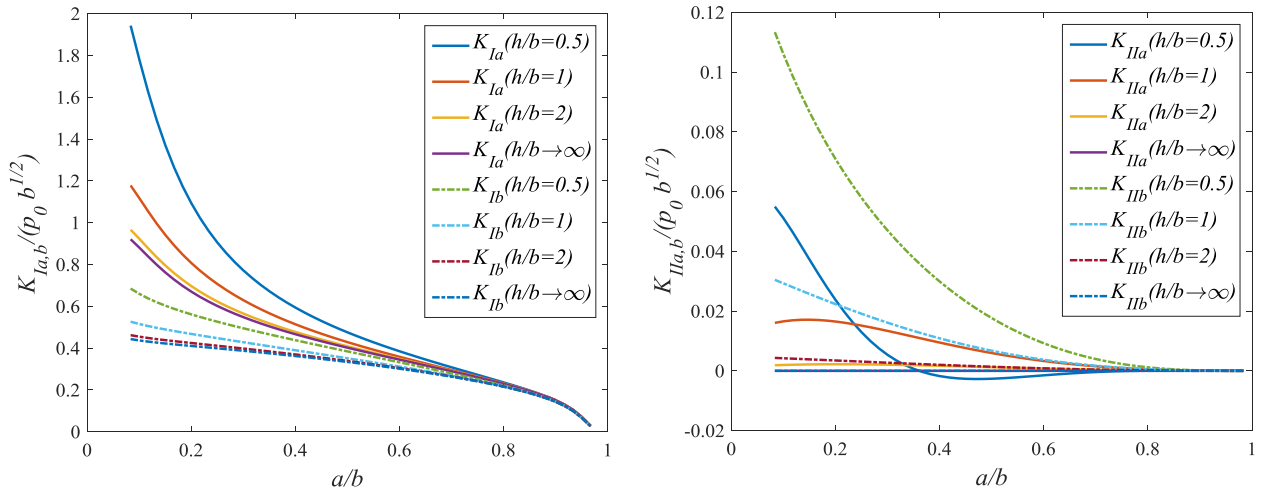


Fig. 2: Variations of stress intensity factors corresponding of mode I and II at the inner and the outer radii of the crack against  $a/b$  for various values of  $h/b$ .

## 5. Conclusions

This work studies the axisymmetric problem related to the internal loading of an annular crack located in a semi-infinite elastic medium. The mixed boundary value problem was reduced to the solution of an infinite algebraic system equations. A closed form solution of stress intensity factors were obtained. As a result, we can analyze their variations, to figure out the depth effect of the thickness and the radii on the crack propagation.

## Acknowledgement

This work was supported by the Laboratoire de Génie Mécanique et développement (LGMD), ENP.

## References

- Choi, I. and Shield, R.T. (1982) A note on a flat toroidal crack in an elastic isotropic body. *International Journal of Solids and Structures*, 18, 6, pp. 479-486.
- Koizumi, T., Shibuya, T. and Nakahara, I. (1977) A crack problem on a slab with an annular crack subjected to pressure. *Bulletin of JSME*, 20, 139, pp. 17-23.
- Mastrojannis, E.N. and Kermanidis, T.B. (1981) An Approximate solution of the annular crack problem. *International Journal for Numerical Methods in Engineering*, 17, pp. 1605-1611.
- Moss, L.W. and Kobayashi, A.S. (1971) Approximate analysis of axisymmetric problems in fracture mechanics with application to a flat toroidal crack. *International Journal of Fracture Mechanics*, 7, 1, pp. 89-99.
- Selvadurai, A.P.S. and Singh, B.M. (1985) The annular crack problem for an isotropic elastic solid. *Quarterly Journal of Mechanics and Applied Mathematics*, 38, 2, pp. 233-243.
- Shibuya, T., Koizumi, T. and Nakahara, I. (1976) The axisymmetric stress distribution in an infinite elastic solid containing a flat annular crack under torsion. *Bulletin of JSME*, 19, 134, pp. 857-862.
- Shibuya, T., Nakahara, I. and Koizumi, T. (1975) The axisymmetric distribution of stresses in an infinite elastic solid containing a flat annular crack under internal pressure. *ZAMM*, 55, pp. 395-402.

## STATIC CHECKING COMPUTATION OF A LATHE TAILSTOCK

T. Keckstein<sup>\*</sup>, J. Bezděková<sup>\*\*</sup>, P. Votápek<sup>\*\*\*</sup>

**Abstract:** Working accuracy is one of the crucial parameters of every machine and especially of machine tools. This is the reason why checking and computation of the primary parts of all new designed lathes has to be performed to ensure the optimal rigidity, dimensions and weight. This paper describes the computation and results of the strength evaluation, static stiffness assessment and checking of contact normal stress in the guideways of a tailstock of a universal centre lathe. To acquire all of these values, a computation was performed using the finite element method (FEM) in MSC Marc 2011. The computational model was loaded by the maximum forces that were obtained via analytic calculations from the load spectrum of a lathe. The strength evaluations of all individual parts of the lathe were investigated according to two different criteria. Computed values of contact normal stress were compared with maximum pressure loads. Displacements of the centre of the tailstock were found by using this FEM computation. The stiffness was calculated in three mutually orthogonal directions from these displacements and loading forces.

**Keywords:** Tailstock, Lathe, Stiffness, Machine tool, Finite element method.

### 1. Introduction

The demand for higher accuracy NC lathes has increased dramatically with respect to machining accuracy requirements (Mori et al., 2009). The bodies of contemporary machine tools are required to be rigid and to efficiently damp vibration (Staniek et al., 2012). The goal of this computation was to investigate the contact normal stress, evaluate the strength and calculate the static stiffness of the tailstock assembly (Fig. 1a) by using finite element method (FEM). If the tailstock is used for turning operations, its stiffness has a significant influence on machining accuracy. Checking the contact normal stress in the guideways and strength evaluation is important for every designed machine and this complex task can be solved only by using computational software. Modern computational software and sufficient computer power mean that a computational model can be created that approaches reality (Max et al., 2016).

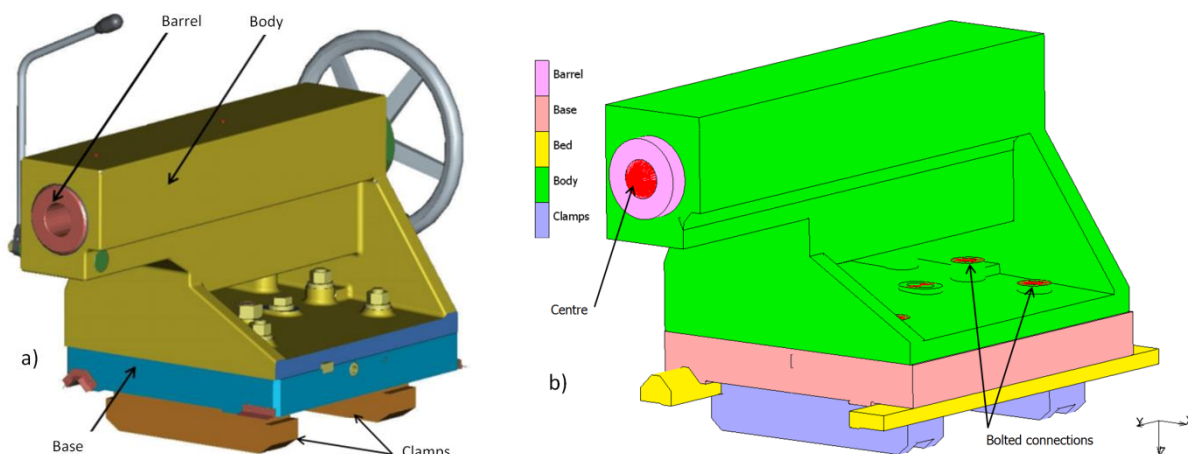


Fig. 1: a) CAD model of a tailstock assembly of a universal centre lathe; b) Computational model.

<sup>\*</sup> Ing. Tomáš Keckstein: Department of Machine Design, Faculty of Mechanical Engineering, University of West Bohemia, Univerzitní 8; 306 14, Pilsen; CZ, tomkec@kks.zcu.cz

<sup>\*\*</sup> Ing. Jitka Bezděková: Department of Machine Design, Faculty of Mechanical Engineering, University of West Bohemia, Univerzitní 8; 306 14, Pilsen; CZ, bezdekova@kks.zcu.cz

<sup>\*\*\*</sup> Ing. Petr Votápek PhD.: Department of Machine Design, Faculty of Mechanical Engineering, University of West Bohemia, Univerzitní 8; 306 14, Pilsen; CZ, pvotapek@kks.zcu.cz

Body, base, barrel, clamps of the tailstock and the lathe bed were modelled volumetrically. The lathe bed was simplified and only part of guideways was modelled. The rest of the lathe bed was considered to be absolutely rigid. The centre, bolts connections and moving mechanism of the barrel were simplified for this computation (Fig. 1b). Stiffness was examined in three mutually orthogonal directions by loading the tip of the centre. The calculations were made in the FEM system MSC Marc 2011. Only small deformations were considered in this calculation.

## 2. Calculation settings

Body, base, barrel, clamps of the tailstock and the lathe bed were considered to be pliable in the computational model and were discretized using linear volume elements with 8 (hex8) and 6 (penta6) nodes. Bolt connections were simplified in the computational model using two types of ties. The contact surface between the bolts and body of the tailstock were linked by an imaginary point in the centre of the hole by using absolutely rigid links (Rigid Link in MSC Marc). Also the contact surface between the nuts and clamps were simplified in the same manner. These two imaginary points were connected by links with a possibility of preload (Overclosure link in MSC Marc). These overclosure links were loaded with the preloading force recommended by the bolt producer. Lašová et al., (2006) described other methods for simplifying preloaded bolted joints. The centre of the tailstock was considered to be absolutely rigid and was simplified using rigid links. The tip of this simplified centre was loaded by force. Also the mechanism that ensures the movement of the barrel was considered to be absolutely rigid.

Hook's law was considered to be valid for all the materials used. Material parameters are stated in Tab. 1. Cast iron (EN-GJL-300) was used for the body of the tailstock, the base of the tailstock and the lathe bed. The barrel and clamps were made of steel (S235JRG2).

*Tab. 1: Mechanical properties of used materials.*

Material	Density [kg·m <sup>-3</sup> ]	Young's modulus [GPa]	Poisson's ratio [-]	Compressive strength [MPa]	Tensile strength [MPa]	Yield strength [MPa]
EN-GJL-300	7350	130	0.25	860	300	-
C45	7800	210	0.3	540		325

For the evaluation of the contact normal stress the values of maximum pressure load was considered to be loaded without simultaneous movement. The value of 40 MPa is valid for contact surfaces without heat treatment and the value of 70 MPa is valid for hardened contact surfaces.

The friction contact (contact touching in MSC Marc) was defined between parts of the model: barrel and body, body and base, base and bed, bed and clamps. This contact allows the transfer of all forces except for tensile normal forces. The values of tangential forces that are transmitted via this contact are derived from the coefficient of friction that was specified as 0.15 for all contacts. Only for the contact between the base of the tailstock and lathe bed the coefficient of friction was specified as 0.01 because in the real machine there is a bearing material with low friction.

Specific geometric and static boundary conditions were set for the investigation of all outlined goals. All displacement in the lower and side surfaces of the simplified bed were prohibited in the model - Fig. 2b. For this computation, the computational model was loaded with static forces applied on the tip of the centre - Fig. 2a. The value of the loading forces was calculated via analytical calculations from the load spectrum of the lathe and these forces are stated in Tab. 2 in column 1. Forces in column 1 were used to investigate the contact normal stress and for strength evaluation. Forces stated in columns 2, 3 and 4 were rounded and used for simple investigation of the stiffness in three mutually orthogonal directions.

*Tab. 2: Loading forces.*

Calculation - $n$	1	2	3	4
Force in the X direction [N]- $F_{X,n}$	-21 000	-20 000	0	0
Force in the Y direction [N]- $F_{Y,n}$	-41 500	0	-40 000	0
Force in the Z direction [N]- $F_{Z,n}$	-20 000	0	0	-20 000

Also the bolted connections in the model were loaded with static preloading force - Fig 2b. The preloading force of the bolt joints was always exerted on the node in the centre of the screw contact

surface, while this central node was rigidly tied to nodes that correspond with their position to the contact surface between the tailstock body and the bolt head. The computational model was loaded in three steps. In the first step the geometric boundaries were activated (prohibition of displacement of the lathe bed). In the next step the bolted joints were preloaded and in the last step the force was applied.

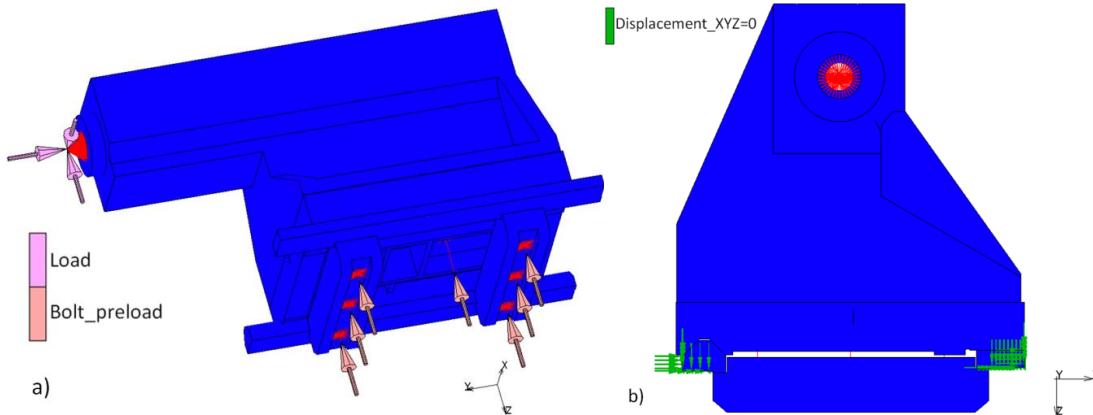


Fig. 2: a) Static boundary conditions; b) Geometric boundary conditions.

### 3. Evaluation of contact pressure

Values of resultant contact normal stress in all surfaces were lower than values of maximum pressure load except the values of the contact normal stress between the bed and the clamps. Values of stress in this contact surface reached 185 MPa while the permissible load is 70 MPa, but this permissible value was defined for analytical calculation when considering absolutely rigid contact surfaces with uniform distribution of stress. Also in this case the peak value of the stress was present only in one node and if the values of the contact normal stress were averaged the permissible load would not be exceeded.

### 4. Strength evaluation

Strength evaluation was based on the values of the stress that were linearly extrapolated to the nodes from the values of the integration points. The Von Mises criterion was used to evaluate the strength of the barrel and clamps. For strength evaluation of the body, base and bed, all individual components of the stress tensor were investigated according to the maximum stress criterion. The distribution of the major principal values of the stress on the tailstock is shown in Fig. 3a). The maximum value of the tensile stress was 101 MPa and the compressive stress 100 MPa. It is possible to calculate the safety factor from these values and from strengths of the material (Tab. 1)  $S_{\text{tensile}} = 860/101 = 8.5$  and  $S_{\text{compressive}} = 300/100 = 3$ . The worst safety factor of the assembly was calculated for the clamps. The distribution of the equivalent tensile stress of the clamps is shown in Fig. 3b) when  $S_{\text{clamps}} = 325/200 = 1.6$ .

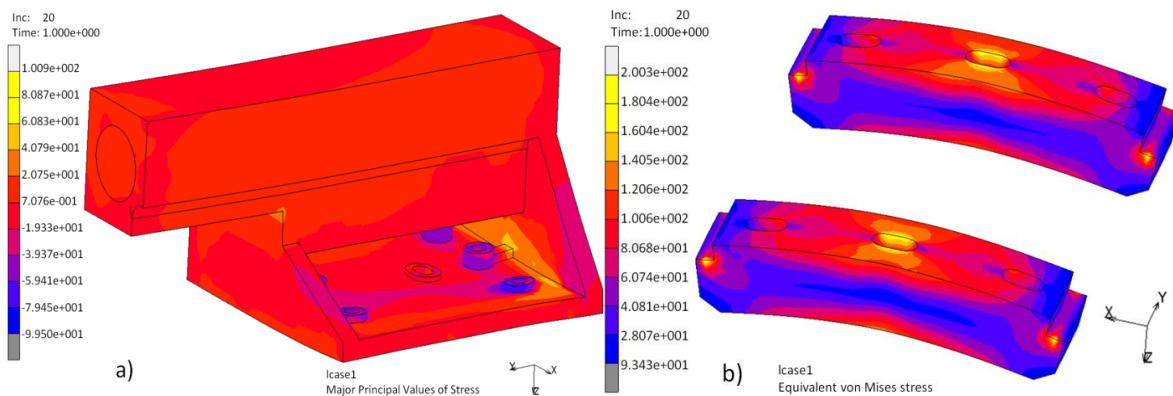


Fig. 3: a) Stress distribution of the tailstock body [MPa]; b) Stress distribution of the clamps [MPa].

### 5. Stiffness evaluation

The stiffness was investigated in the directions of three coordinate axes based on the loading forces and the resulting displacements of the tip of the centre, according to the equation:

$$k_{i,n} = \frac{F_i}{u_{i,n}} \quad (1)$$

while  $F_i$  is loading force from Tab. 2, where the index  $i$  is coordinate X, Y or Z and the index  $n$  is the number of calculation (2-4) from the same table.

Ascertained displacement of the tip of the centre  $u_{i,n}$  and calculated values of stiffness according to equation (1) are given in Tab. 3. In Fig. 4a you can see an example of the discovered displacement of all nodes in the direction X for calculation 2 (load only in X direction). In Fig. 4b you can see an example of the discovered displacement of all nodes in the direction Z for calculation 4 (load only in Z direction).

Tab. 3: Displacement of the tip of the centre and stiffness of the tailstock.

Calculation	2		3		4	
Quantity	Displacement	Stiffness	Displacement	Stiffness	Displacement	Stiffness
Unit	mm	kN/mm	mm	kN/mm	mm	kN/mm
X direction	-0.195	<b>103.6</b>	0.133	-	0.099	-
Y direction	0.021	-	-0.128	<b>312.5</b>	-0.016	-
Z direction	0.067	-	0.063	-	-0.085	<b>235.3</b>

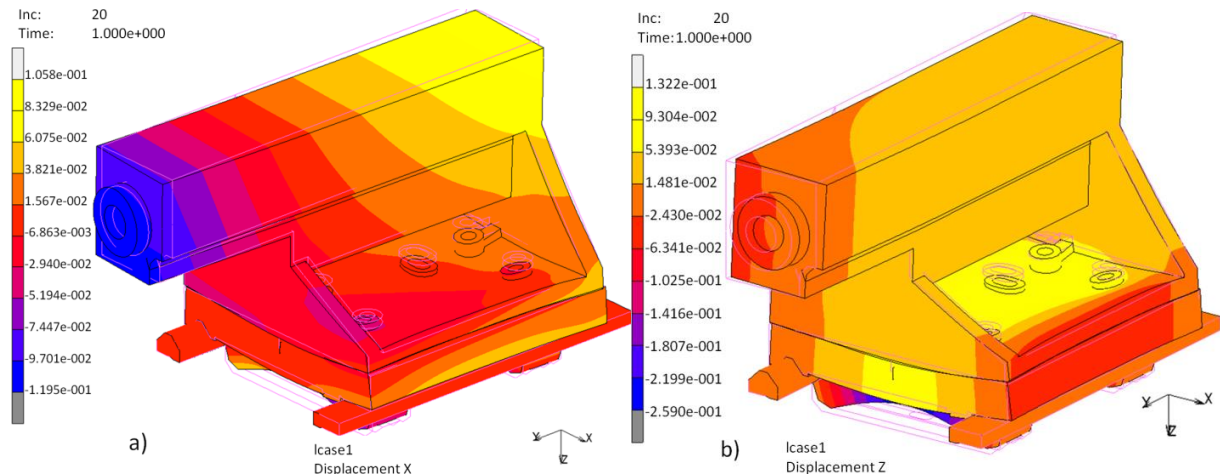


Fig. 4: a) Displacement X, calculation 2 [mm]; b) Displacement Z, calculation 4 [mm].

## 6. Conclusion

The aim of this computation was to investigate the strength of the entire design, evaluate the static stiffness of the tailstock assembly and check the contact normal stress in the guideways of a tailstock. All values were gained via a FEM computational model that is described in this article. The results of all three tasks are briefly described. The discovered values of stiffness show that the tailstock has the lowest stiffness in the X axis. Computation also showed that the clamps are the most stressed part of the assembly and also have the highest value of contact normal stress.

## References

- Lašová, V. and Kosnar, M. (2006) Numerical modelling of preloaded bolted joints of machine tool. CADAM 2006. Rijeka: Zigo, 2006. pp. 57-58. ISBN: 953-7142-19-1.
- Max, A., Hynek, M. and Řehounek, L. (2016) Dynamic analysis of CNC milling machine frame. in: Proc. Int. Conf. on Engineering Mechanics 2016 (eds. Zolotarev, I and Radolf, V.), Svratka, Czech Republic, pp. 352-355.
- Mori, M., Mizuguchi, H., Fujishima, M., Ido, Y., Mingkai, N. and Konishi, K. (2009) Design optimization and development of CNC lathe headstock to minimize thermal deformation. CIRP Annals-Manufacturing Technology, 58(1), 331-334.
- Staniek, R., Gessner, A., Zielnica, J., Ptaszynski, W., Myszkowski, A., Ciszak, O. and Stoic, A. (2012) Stress and displacement analysis of a modern design lathe body by the finite element method (FEM). Metalurgija/Metallurgy, 51(1), 51-54.



## WAYSIDE DIAGNOSIS OF METRO WHEELSETS USING ACOUSTIC SENSOR DATA AND ONE-PERIOD ANALYSIS

O. Kilinc<sup>\*</sup>, J. Vágner<sup>\*\*</sup>

**Abstract:** *This research promises a wheelset fault diagnosis methodology for metro train sets using wayside acoustic sensor information. Throughout the research, two different feature extraction techniques; Wavelet Packet Energy (WPE) and Time-domain Features (TDF) are employed in association with two state-of-art classifiers Fisher Linear Discriminant Analysis (FLDA) and Support Vector Machines (SVMs). The database is prepared by the acquisition of wayside acoustic sensor data accompanied by optical gates that detect wheelset center position while multiple passing of a single metro train set of type 81-71M is in daily operation with the contribution of a novel approach; one-period analysis. Acquired database is then divided into two classes which represent the healthy and faulty states of the wheelsets referring to the ground truth information of a faulty wheelset. Since the faulty states are insufficient to demonstrate the real classification performance, an adaptive synthetic sampling technique (ADASYN) is utilized to increase the number of faulty states. Promising results are observed up to 93 % in classification of faulty wheelsets of the metro with the proposed techniques on acoustic sensor data. This study may aid to maintenance specialists by providing a cost effective monitoring of faulty condition of metro wheelsets.*

**Keywords:** Wheelset fault diagnosis, Wavelet packet energy, Time-domain features, One-period analysis, Condition monitoring.

### 1. Introduction

Condition monitoring of a railway vehicle, which is cost effective in comparison to on-condition repairs, is a tough job due to varying environmental conditions and different operational parameters related to the vehicle. Stationary diagnostics approaches are costly and complex because of high number of sensors (Ward et al., 2010) and calibration difficulties. Thus, a wayside monitoring approach is sufficient to detect abnormal condition of a railway vehicle. Several approaches are already proposed in the literature for wayside; acoustic bearing fault diagnosis (Liu et al., 2014), wheel profile and wheel impact detection using ultrasound and laser systems (Ngigi et al., 2012) and wheel defect detection (Jakimovska et al., 2015).

This paper is focused on some efficient methods that provide condition monitoring of metro wheelsets by using acoustic sensors on wayside due to the existence of cost friendly techniques is limited in the literature.

The organization of the paper is as follows: Proposed methods are given in Section 2. Data recording and measurement system is told in Section 3. Analysis results and discussion are given in Section 4. Finally, conclusion part is presented in Section 5.

### 2. Proposed Methods

In fault diagnosis, it is vital to form signal samples into representative way of related class as well as maintaining the dimensions in acceptable range due to possible complexity in classification. Several approaches are presented in the following sections.

---

<sup>\*</sup> Onur Kilinc, MSc.: Department of Transport Means and Diagnostics, Jan Perner Transport Faculty, University of Pardubice, Czech Republic, Studentska 95; 530 09, Pardubice; CZ, onur\_kilinc@anadolu.edu.tr

<sup>\*\*</sup> Ing. Jakub Vágner, PhD.: Department of Transport Means and Diagnostics, Jan Perner Transport Faculty, University of Pardubice, Czech Republic, Studentska 95; 530 09, Pardubice; CZ, jakub.vagner@upce.cz



## 2.1. One-period Analysis

In wayside diagnostics, signal characterization is affected significantly due to speed variations of different vehicle passes. In this research, to overcome this issue, a novel one-period analysis (Kilinc et al., in press) is presented. In this method, sample interval for each individual wheelset is calculated according average of wheel perimeters referring to the latest revision parameters and signals are recorded so that they cover one rotational period of each bogie wheelset. Thus, the effect of wear which may significantly change the wheel radius on each wheelset is diminished.

## 2.2. Time-domain Features

Time-domain statistics is a common approach in fault diagnosis especially for one-dimensional signals which also exists in contemporary literature (Poulimenos et al., 2006). In the proposed framework, eight Time-domain Features (TDF) are selected as in Eq.(1) as proposed in the research (Yu et al., 2015) which investigates characteristics of machinery faults. For each sample that is retrieved by one-period analysis, those features are calculated and 8x1 size feature vectors are created.

$$TDF = [\text{energy}, \text{mean}, \text{std\_deviation}, \text{max}, \text{min}, \text{kurtosis}, \text{skewness}, \text{crest factor}] \quad (1)$$

## 2.3. Wavelet Packet Energy Features

In railway vehicle diagnostics, most signal characteristics behave in a non-stationary manner (Mao et al., 2015). Calculating Wavelet Packet Energy (WPE) is a simple and efficient way of dealing non-stationary behavior. Firstly, Wavelet Packet Transform (WPT) for each sample is calculated. Since WPT is not time-invariant (Yen et al., 2000), energy components of WPT is calculated for each level and WPE features are achieved. In this research, for both classes, five-level WPE features are calculated which result feature vector size is  $2^5 \times 1$ .

## 3. Signal Acquisition and Database

In this study, a wayside measurement system is installed into a metro tunnel near Dejvická Metro Station which is located on Prague Metro Line-A due to the opportunity of small variations in operational speed of train sets. In order to obtain acoustic characteristics of each train passing, a pre-polarized free-field microphone ( $M_1$ ) is mounted between sleepers and signal recording is performed at 51.2 kHz with the instrumentation device NI-cDAQ-9234 during all day long. Thanks to an optical gate ( $G_A$ ) that is placed exactly in the same cross section with the microphone that detects each wheelset centers at 500 Hz rate. Measurements are carried out in the project Competence Centre of Railway Vehicles, No. TAČR TE01020038. All metro train sets that travel on Line-A have five 4-axes passenger cars (total number of wheelsets are 20, all wheelsets are powered). One-day duration of measurements make it able to investigate 226 passes of 40 unique metro train sets type 81-71M. The wayside measurement system and arrangement of sensors allocation is shown in Fig. 1.

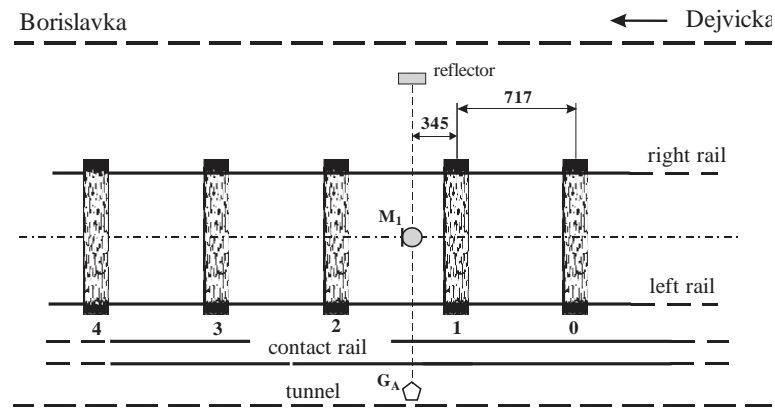


Fig. 1: Measurement system nearby Dejvická metro station.

Since multiple passing's of each vehicle are existed, the database includes 8 signal samples of a known faulty wheelset that has wheel flats on both wheels. Two datasets, A1-A2 and B1-B2 are prepared to detect faulty wheelsets; the former is consistent of randomly chosen 8 normal wheelset samples against 8

faulty samples of the train set that has faulty wheelsets while the latter includes 64 normal against 64 faulty samples. Since the number of faulty samples are limited, B2 (faulty) samples are generated from A2 by a contemporary adaptive synthesizing method (ADASYN) (He et al., 2008) to achieve more accurate model evaluation.

#### 4. Results and Discussion

In the analyzes, two feature extraction techniques TDF and WPE are applied on the signal samples after one-period analysis and sufficient number of cross validation is performed to obtain classification results. The complexity of the problem may be seen in Fig. 2 which shows the classes in datasets A1-A2 in two-dimensional form by using the common dimension reduction technique; Principal Component Analysis (PCA) (Ferraz et al., 1998).

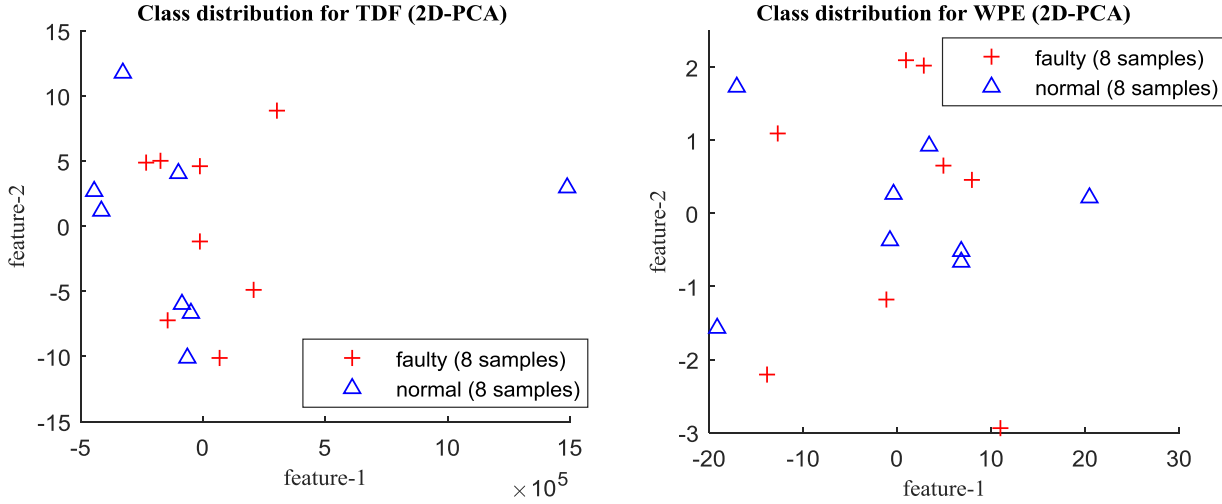


Fig. 2: Class distribution of feature vectors of dataset A1-A2 after 2D-PCA; TDF (left), WPE (right).

Tab. 1: Classification accuracies of proposed methods of raw (A1-A2) and synthesized (B1-B2) datasets.

Classifier	% Classification Accuracy		Training	Testing	Total Samples	Class Label	
	WPE	TDF				Normal	Faulty
SVM (4-fold)	WPE	TDF	[2x2]	[6x2]	16	A1	A2
Average Std. Dev.	68.80 12.5	62.50 14.4					
FLDA (4-fold)	WPE	TDF	[2x2]	[6x2]	16	A1	A2
Average Std. Dev.	62.50 32.3	56.25 23.9					
SVM (8-fold)	WPE	TDF	[8x2]	[56x2]	128	B1	B2
Average Std. Dev.	82.80 14.5	85.90 5.5					
FLDA (8-fold)	WPE	TDF	[8x2]	[56x2]	128	B1	B2
Average Std. Dev.	82.00 10.3	93.00 7.0					

After utilizing training process on the classifiers; linear Support Vector Machine (SVM) and Fisher Linear Discriminant Analysis (FLDA) the average classification rates and their standard deviation are acquired. Referring to Tab. 1:, highest classification rate of A1-A2 datasets, which has short number of

normal and faulty samples, is observed as 68.80 % with linear SVM kernel while on adaptively generated samples according to ADASYN; datasets B1-B2 shows promising results with TDF feature extraction technique as much as 93 %.

## 5. Conclusions

In this research, two different feature extraction techniques are applied on acoustic signals that are retrieved from real world conditions of a metro after the novel one-period analysis. Since the dataset is limited to only eight number of known faulty wheelsets, an adaptive upsampling technique; ADASYN is applied on faulty conditions in order to see classification performance when enough measurements are acquired.

According to the results, accuracy of classification of short datasets A1-A2 with acoustic sensor data is considered to be insufficient. However, after equalizing the faulty minority class from the samples of real world conditions, more plausible results are obtained up to 93 % by the utilization of TDF feature extraction after one period analysis on datasets B1-B2.

Further effort on pre-processing may improve classification accuracy by discarding the effects of unwanted environmental behavior in metro tunnels which badly affects acoustic sensor activity. This research may be a contribution for maintenance specialists and others who are interested in cost-efficient condition monitoring systems of railway vehicles.

## Acknowledgement

This paper was supported by SG570001/20/51030 grant.

## References

- Ferraz, A., Esposito, E., Bruns, R.E., and Durán, N. (1998) The use of principal component analysis (PCA) for pattern recognition in *Eucalyptus grandis* wood biodegradation experiments. *World Journal of Microbiology and Biotechnology*, 14, 487-490.
- He, H., Bai, Y., Garcia, E.A., and Li, S. (2008) ADASYN: Adaptive synthetic sampling approach for imbalanced learning. *IEEE International Joint Conference on Neural Networks*, pp. 1322-1328.
- Jakimovska, K., Vasilev, V., Stoimenov, N., Gyoshev, S., and Karastoyanov, D. (2015) Train control system for railway vehicles running at operational speed. *Manufacturing Engineering*, 69, 86-92.
- Liu, F., Shen, C., He, Q., Zhang, A., Liu, Y., and Kong, F. (2014) Wayside Bearing Fault Diagnosis Based on a Data-Driven Doppler Effect Eliminator and Transient Model Analysis. *Sensors*, 14, 8096-8125.
- Mao, C., Jiang, Y., Wang, D., Chen, X., and Tao, J. (2015) Modeling and simulation of non-stationary vehicle vibration signals based on Hilbert spectrum. *Mechanical Systems and Signal Processing*, 50-51, 56-69.
- Ngigi, R.W., Pislariu, C., Ball, A., and Gu, F. (2012) Modern techniques for condition monitoring of railway vehicle dynamics. *Journal of Physics*, 364, 012016.
- Kilinc, O. and Vágner, J. (In press) Sensing anomalous sensor data in wayside diagnostic using enhanced LBP-Kurtograms. *Scientific Papers of the University of Pardubice. Series B, The Jan Perner Transport Faculty*, 21.
- Poulimenos, A.G., and Fassois, S.D. (2006) Parametric time-domain methods for non-stationary random vibration modelling and analysis — A critical survey and comparison. *Mechanical Systems and Signal Processing*, 20, 763-816.
- Ward, C.P., Goodall, R.M., Dixon, R., and Charles, G. (2010) Condition monitoring of rail vehicle bogies. *UKACC International Conference*, pp. 1-6.
- Yen, G.G., and Lin, K.-C. (2000) Wavelet packet feature extraction for vibration monitoring. *IEEE Transactions on Industrial Electronics*, 47, 650-667.
- Yu, X., Ding, E., Chen, C., Liu, X., and Li, L. (2015) A novel characteristic frequency bands extraction method for automatic bearing fault diagnosis based on Hilbert Huang transform. *Sensors*, 15, 27869-27893.

## NUMERICAL SIMULATION OF STEAM FLOW AROUND VIBRATING TURBINE BLADES

J. Klečková<sup>\*</sup>, J. Hamza<sup>\*\*</sup>

**Abstract:** This paper is devoted to the numerical simulations of a two-dimensional turbulent steam flow around vibrating turbine blades in a software ANSYS Fluent. Computational domain contains a passage of three blade profiles which were cut near the tip of long curved turbine blade. The movement of each blade was based on the results of a modal analysis which was accomplished by a software ANSYS Mechanical. The mode shape of the blade was described by User – defined function (UDF) which defines the displacement of a two-dimensional rigid body and the rotation of this body around an axis placed in the center of gravity. Numerical simulations of the steam flow through the passage were carried out for a range of nodal diameters defining a phase lag between each pair of blades on a turbine disk and the results of CFD analysis were used for the computation of aerodynamic work of the steam on the blade surface to assess the blade stability.

**Keywords:** Turbine blade, ANSYS Fluent, Steam flow, Mode shape, Stability.

### 1. Introduction

Unsteady pressure distribution along the turbine blade surface which occurs during a steam turbine operation can cause unstable behavior of the blade. One of the tools which can help by assessing the stability of the blade is numerical simulation of the steam flow around the vibrating blades and evaluation of loading that provides work on the blade surface. CFD analysis of the flow around moving bodies is a complex problem which comprises the preparation of a geometry model, generation of a high - quality computational mesh, definition of the blade motion and of the movement of deforming mesh and the correct setting of transient solver.

### 2. Computational domain and description of blade motion

First of all, the modal analysis in ANSYS Mechanical was provided for three-dimensional low-pressure turbine blades. Natural frequencies for free-standing blade, presented in this paper, were the same for all nodal diameters. However in cases with shrouded blades, natural frequencies differ for different nodal diameters, because blades are bonded at shroud and in the middle.

On the basis of modal analysis the two – dimensional profile was cut near the blade tip which is obviously the place of maximum deformation as seen in Fig. 1 (left). The mode shape of blade profile consists of the displacement in direction of Cartesian coordinates  $x$ ,  $y$  (bending in 3D) and the rotation around the axis placed in the center of gravity (torsion in 3D). Directional vector of displacement and maximal rotational angle were gotten from the results of modal analysis. The amplitude of bending vibrations was obtained from Blade tip timing measurement. Vibrating motion was considered as a sinusoidal time-dependent function

$$\begin{aligned}x(t) &= x_0 \sin(\omega t) \\y(t) &= y_0 \sin(\omega t) , \\ \alpha(t) &= \alpha_0 \sin(\omega t)\end{aligned}\tag{1}$$

---

<sup>\*</sup> Ing. Jitka Klečková: Department of Mechanics, Faculty of Applied Sciences, University of West Bohemia, Technická 8, 306 14, Pilsen; CZ, jkleckov@ntis.zcu.cz

<sup>\*\*</sup> Ing. Jan Hamza: Research and Testing Institute Pilsen, Tylova 1581/46, 301 00, Pilsen; CZ, hamza@vzuplzen.cz

where  $t$  is time,  $\omega = 2\pi f$  is angular frequency, where  $f$  is natural frequency,  $x_0$ ,  $y_0$  are the amplitudes of bending vibrations and  $\alpha_0$  is the amplitude of torsional vibrations.

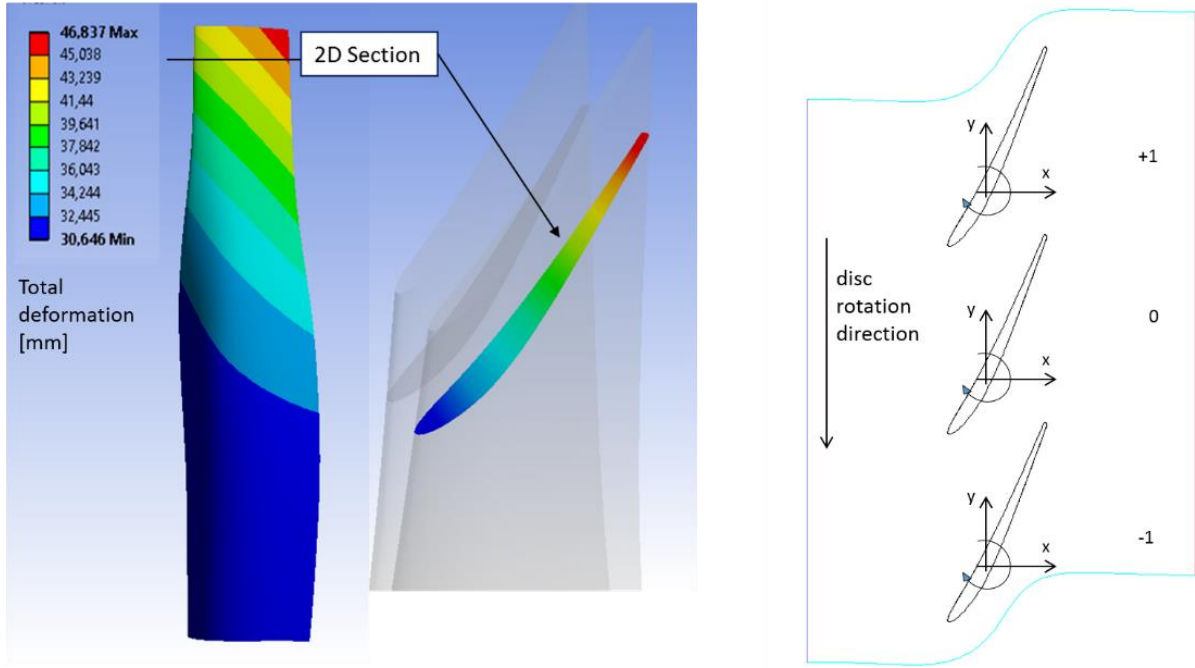


Fig. 1: Total deformation of 3D blade (left). Computational domain (right).

Fig. 1 (right) shows computational domain which contains three two – dimensional blade profiles. The blade numbered zero is referential and this blade is the main subject of this research. The neighboring blades are numbered  $\pm 1$ . These two blades are included in computational domain because they have the greatest influence on origin of unsteady pressures at the surface of referential blade in comparison to other blades of the bladed disk which was proved in paper (Panovsky et al., 2000).

The blades were considered to vibrate according to harmonic function (1), where each pair of blades vibrate with particular constant phase angle  $\pm \varphi$  - so called inter-blade phase angle (IBPA). The blade number +1 moves with phase angle  $+\varphi$  with respect to referential blade and similarly the blade -1 vibrate with phase angle  $-\varphi$  according to equations

$$\begin{aligned} x(t) &= x_0 \sin(\omega t) & x(t) &= x_0 \sin(\omega t + \varphi) & x(t) &= x_0 \sin(\omega t - \varphi) \\ y(t) &= y_0 \sin(\omega t) & y(t) &= y_0 \sin(\omega t + \varphi) & y(t) &= y_0 \sin(\omega t - \varphi) \\ \alpha(t) &= \alpha_0 \sin(\omega t) & \alpha(t) &= \alpha_0 \sin(\omega t + \varphi) & \alpha(t) &= \alpha_0 \sin(\omega t - \varphi) \end{aligned} \quad (2)$$

Numerical simulations were accomplished for IBPAs from interval  $(-180^\circ, 180^\circ)$ . The so called traveling wave propagates along bladed disk for each phase angle. The number of these waves is denoted as a nodal diameter  $nd$  which could be computed from IBPA as

$$nd = \frac{IPBA \cdot N}{360} \quad (3)$$

where  $N$  is the number of blades at the disk.

### 3. Mesh motion method

Quadrilateral computational mesh with boundary layer at the blade surface was created using software GridPro, see Fig. 2. The mesh quality was checked by the value of parameter  $y^+$  in the first cell of boundary layer. In this case lies the value of  $y^+$  in interval  $(0.1; 4)$  and average value is around 1.

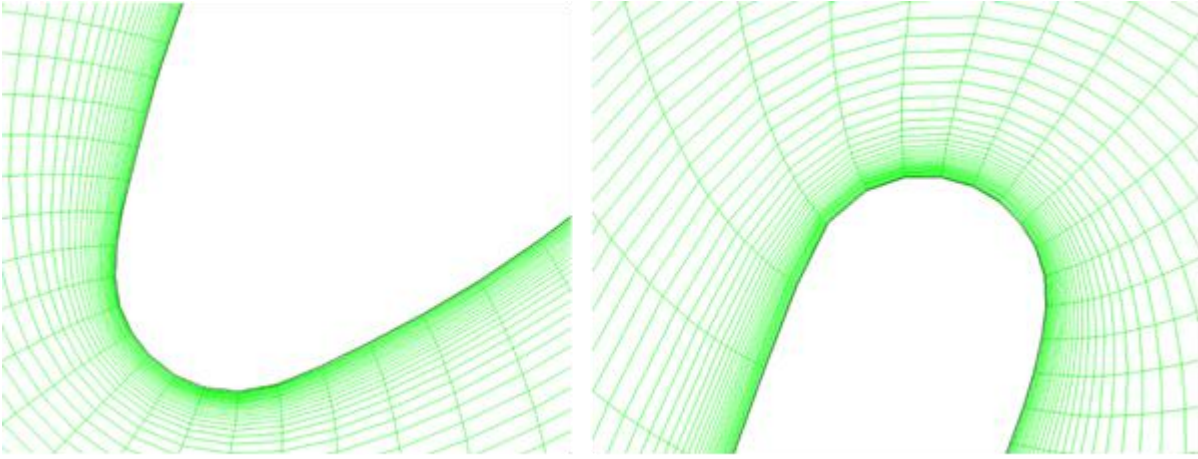


Fig. 2: Details of computational mesh – leading edge (left), trailing edge (right).

Smoothing method was used for defining of mesh motion. This algorithm is convenient for cases with body motion which has a small amplitude of vibrations because it doesn't change whole mesh structure, just repositions each mesh node according to movement of the body. This method, which is described for example in contribution (Řídký et al., 2015), moves mesh nodes in response to displacement of boundaries by calculating a mesh velocity by an equation

$$\nabla \cdot (\gamma \nabla \vec{u}) = 0 \quad (4)$$

where the velocity  $\vec{u}$  at the moving boundary is used as a Dirichlet boundary condition. The diffusion coefficient  $\gamma$  is computed from boundary distance  $d$  by formula

$$\gamma = \frac{1}{d^\beta}, \quad (5)$$

where parameter  $\beta$  could be from interval  $(0, 2)$  and controls how far from moving boundary the diffusion affects the mesh. The diffusion parameter in our simulations was 2. Higher values of  $\beta$  preserve the shape of mesh cells near the moving boundary and spread the movement further from body. In opposite for  $\beta = 0$  the equation (5) gives the diffusion coefficient  $\gamma = 1$ , which means a uniform diffusion of the mesh motion.

#### 4. Numerical simulation and results

Numerical simulations of a two-dimensional steam flow through the computational domain were accomplished by software ANSYS Fluent for eighteen different nodal diameters covering a whole range of bladed disk mode shapes.

Transient computation was initialized by steady simulation. Density based solver was chosen which is more convenient for compressible fluid flow. The steam was substituted by a compressible ideal gas with particular material properties which correctly describe the steam behavior. Two – equation SST k-omega turbulence model was used to set the turbulent viscosity. The disk rotation was included using a single moving reference frame approach which assigns constant velocity to whole domain. Vibrating motion of blades was defined by UDF *Define-cg-motion* which assigns the blade the translational and rotational velocity in form of a time derivative of equations (2).

Numerical results of CFD analysis were used to assess the option of unstable behavior of the referential blade. Aerodynamic work of fluid on the blade was computed from pressure distribution along the blade surface. Negative value of aerodynamic work means that the fluid absorbs blade energy and the blade motion would be damped. On the other hand positive value of aerodynamic work could lead to unstable blade behavior. Aerodynamic work of fluid on the referential blade is computed as the time integral of power as described in thesis (Panovsky, 1997)

$$W = \int_t^{t+T} \int_A p \vec{u} \cdot \vec{n} dA dt, \quad (6)$$



where  $p$  is unsteady pressure on the surface of the referential blade,  $\vec{u}$  is the local velocity vector,  $\vec{n}$  is the outer unit normal vector,  $A$  is blade surface area and  $T$  is the time period of oscillation. Dependence of aerodynamic work on nodal diameter is shown in Fig. 3.

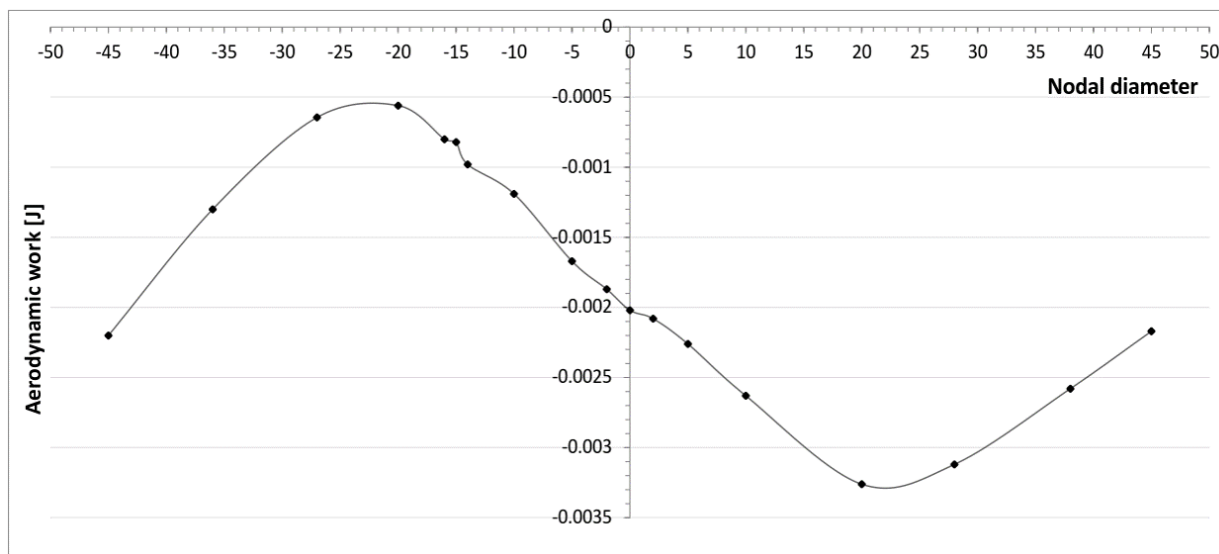


Fig. 3: Aerodynamic work for nodal diameters from interval  $(-45, 45)$ .

## 5. Conclusions

This contribution describes the numerical simulation of steam flow around vibrating 2D – blade profiles and stability analysis for the turbine blade. Aerodynamic work of fluid at the blade surface was evaluated. Positive value of aerodynamic work would mean that the blade absorbs energy from the flow which would lead to unstable blade behavior. The tested blade would be stable according to the results depicted in graph in Fig. 3 because of the negative value of aerodynamic work which results in the damped motion of referential blade.

## Acknowledgement

The work has been supported by the internal student grant project SGS-2016-038 of the University of West Bohemia and by the research project TA ČR n. TE01020068 “Center of research and experimental development of reliable energy production”.

## References

- Panovsky, J. (1997) Flutter of Aircraft Engine Turbine Blades. Ph.D. thesis, University of Cincinnati, Cincinnati, OH.
- Panovsky, J., Kielb, R.E. (2000) A Design Method to Prevent Low Pressure Turbine Blade Flutter. ASME Paper No. 98-GT-575, Vol. 122, pp. 89-98.
- Řídký, V., Šidlov, P. (2015) Numerical simulation of deformation of dynamic mesh in the human vocal tract model. EPJ Web of conferences, Vol. 92.

## ENERGY TRANSFORMATION IN TURBULENT FLOW INSIDE REVERSING CHAMBER

R. Kłosowiak<sup>\*</sup>, J. Bartoszewicz<sup>\*\*</sup>, R. Urbaniak<sup>\*\*\*</sup>

**Abstract:** *This paper presents results of measurements of static pressure distribution and pressure fluctuation on inner surfaces of the reverse chamber. Analyzed geometry is a geometrical model of the combustion chamber occurring, inter alia, in solid fuel boilers. An important aspect of the analysis is identification of reversing phenomena occurring inside the chamber. Due to the analyzed geometry shape, the flowing jet flow changes twice the direction of the jet impingement on the wall. As a result, on the walls of the chamber there is a transformation of medium kinetic energy into potential energy pressure. The test results describing the distribution of pressure on the impinged wall of the reverse chamber and pressure changes and fluctuations for various inflow velocities and various distances between the pipe outlet and the impinged surface have been presented. Characteristics of turbulent flow in chamber were measured with the use of constant temperature anemometer. The purpose of the paper is to indicate differences between different flows: an axisymmetrical free jet outflowing to the stationary surroundings, a jet impinging a stationary flat surface, and a jet flow impinging flat surface in close round chamber, which generates axisymmetrical return flow. Efficiency being a part of the conducted analysis of the flow in the combustion chamber, was also used to prepare a mathematical model for numerical analysis. This analysis shows also that there is a need to validate CFD calculations due to limited possibilities of turbulence models to visualize the transformation of energy at the stagnation points.*

**Keywords:** Impinging jet, Reverse chamber, Combustion chamber, Energy transformation, Turbulent flow.

### 1. Introduction

Different kinds of free and impinging jets analyses have been described in world literature over years. That is because many authors try to find solutions for problems with flows of this type. One of main problems with these flows occurs when any author tries to use the results obtained for free unstimulated jets to describe other flows of similar type. This kind flow geometry influences on momentum, mass and energy transport inside thermal flow machines. In such situations, despite of the frequently apparent likeness to free jets, we deal with different class of flows, the restricted flows. One of the purposes of this paper is to indicate the differences between the above mentioned flow geometries.

With comparison to the free jet flowing into stationary surroundings, in case of the impinging jet only part of the area should be deemed free. The appearance of the wall changes the flow structure, i.e. restricts the propagation of the free jet. Fig. 1 presents the schematic areas of the impinging jet. The impinging jet's case, however, is considered to be the boundary case of free jets, because it only requires the change of the boundary conditions in the axial direction related to the axial velocity component and the parameter describing the turbulence model, e.g. kinetic energy of turbulence. This opinion shared in particular by researchers involved in the numerical description. Fig. 2 and 3 show profiles of normalized velocity and kinetic energy in impinging jet flow (Bartoszewicz 2009, 2012). The presented results shall be used for comparisons with the results obtained in the reverse chamber.

---

<sup>\*</sup> Dr inż Robert Kłosowiak, Poznań University of Technology, Faculty of Machines and Transport, Chair of Thermal Engineering, Piotrowo 3, 60965 Poznań, Poland; robert.klosowiak@put.poznan.pl

<sup>\*\*</sup> Dr hab. inż. Jarosław Bartoszewicz, Poznań University of Technology, Faculty of Machines and Transport, Chair of Thermal Engineering, Piotrowo 3, 60965 Poznań, Poland

<sup>\*\*\*</sup> Dr inż. Rafał Urbaniak, Poznań University of Technology, Faculty of Machines and Transport, Chair of Thermal Engineering, Piotrowo 3, 60965 Poznań, Poland

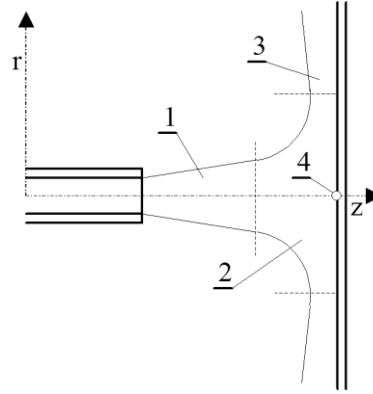


Fig. 1: Schema of impinging jet flow 1 – region of free jet, 2 – region of stagnation, 3 – region of wall jet, 4 – stagnation point.

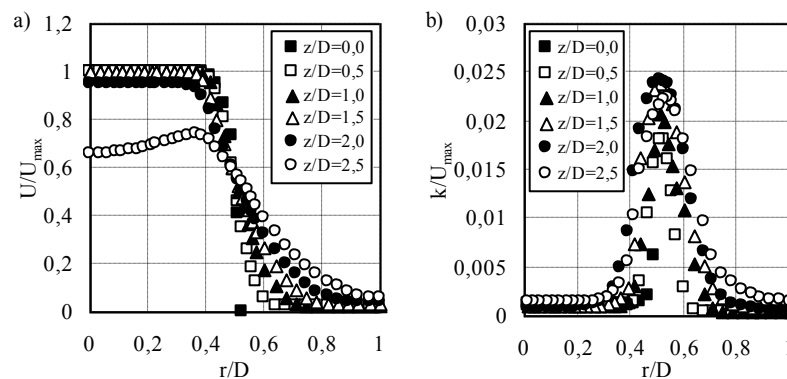


Fig. 2: Radial profiles of normalized velocity (a) and kinetic energy of turbulence in impinging jet (b) (Bartoszewicz 2012) at the distance between pipe outlet and impinging wall  $3D$ .

## 2. Geometric model and test methods

An object of tests is the axisymmetrical reverse chamber shown in Fig. 3. The main flow direction changes twice in reverse chambers. The jets flowing out of the internal pipe, in its initial run, is of free jet nature, then it impinges the flat surface of the chamber bottom, where the flow direction changes by  $90^\circ$  for the first time. Within the inflowing jet's axis, at the so-called stagnation point, the maximum pressure occurs. Such flow can be given as a simplified definition of the impinging jet. Upon change of direction, the wall jet heads towards the radial direction. Before it reaches the flow wall, however, it separates from the impinged wall and thus the second stagnation point is located on the side wall near the reverse chamber corner. The jet again changes its flow direction by  $90^\circ$  angle. From this point, as the counter-flow jet in relation to the basic one, flowing out of the internal pipe, it heads towards the reverse chamber outlet. As the distance from the outlet wall increases, the wall jet may tear apart from the flow wall in the point depending on the jet's kinetic energy. The test chamber reflecting the nature of such flow is built of a steel sharp-edged pipe of the internal diameter  $D = 0.04$  m and of thickness of 0.005 m. The chamber casing was made of plexiglas of the internal diameter  $R = 0.475$  m and length of 0.7 m. The test chamber was mounted on an open aerodynamic tunnel shown in Fig. 4. The air in the tunnel is forced through a fan connected to the tunnel by means of two elastic couplers. A filter reducing particles contaminating the air was installed in the initial section, while the straightening vanes unify the velocity and turbulence fields in the channel. The whole reverse chamber with the internal pipe is positioned with the use of a laser situated behind the impinging surface.

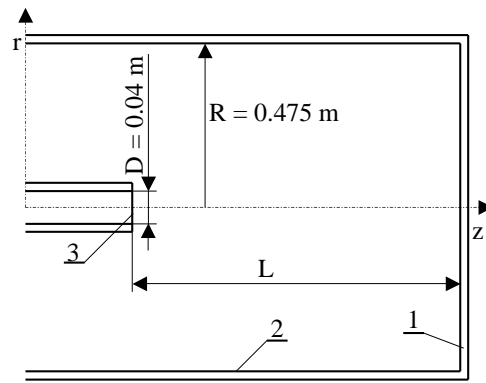


Fig. 3: Schema of reverse chamber: 1 – impinging wall, 2 – side wall, 3 – outlet of pipe.

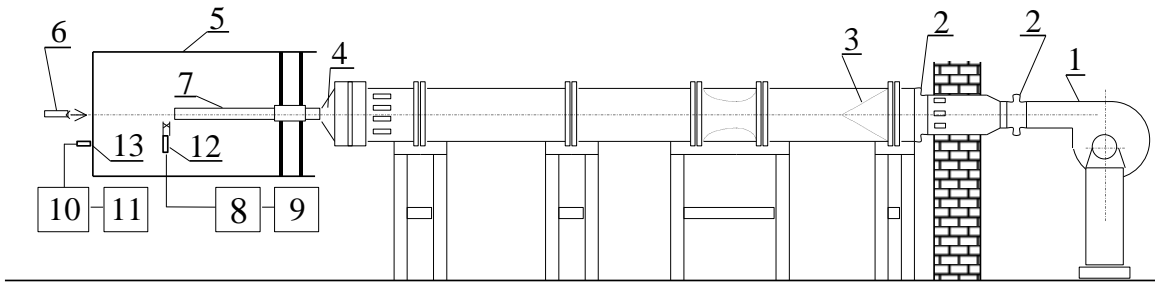


Fig. 4: Schema of measurements: 1 – fan, 2 – elastic coupler, 3 – filter, 4 – nozzle, 5 – reverse chamber, 6 – calibration laser, 7 – steel pipe, 8 – CTA module, 9 – computer, 10 – digitizer of pressure and its fluctuation, 11 – millimeter, 12 – CTA probes, 13 – phone.

Measurement of velocity and its fluctuation was carried out by the CTA anemometer. Standard X probe TSI-1241 was used to measure two components of velocity. Position of the jet axis was indicated by the laser beam. Probes were connected to the TSI-1050 constant temperature anemometer bridge. CTA signal was recorded by Iotech ADC488/8SA A/D converter which was controlled by TurboLab 4.0. Auto trigger option was selected. Subsequently, the recorded signal was processed and analyzed by means of the same program.

### 3. Numerical analysis

SST turbulence model combines the advantages of both, the standard model of the  $k-\epsilon$  and  $k-\omega$  model. As compared to the equations in the  $k-\omega$  model, SST turbulence model changes the concept of production of turbulence in the equation for kinetic energy turbulence.

### 4. Boundary condition

Measurements were made on an axisymmetrical jet, not swirled and unstimulated, flowing out from the sharp-edged round channel of diameter of 0.04 m to the reverse chamber of 0.39 m diameter. The geometrical conditions corresponded to the pipe outlet position in relation to the impinging surface, varying from  $z/D = 10$  to  $z/D = 0.2$ . Measurements were made for three velocities at pipe outlet: 10, 30 and 50 m/s, which corresponds to Reynolds numbers: 26000, 78000 and 130000, respectively. Air temperature was maintained at the level of 20 °C. Measurements of mean values in time: pressure, axial component and their fluctuations were carried out.

### 5. Results and conclusion

Results of modeling the flow in the reverse chamber were very promising. Possibility to simulate flow brought new information on the turbulence and energy transformation inside the chamber. During simulations, one can presume the established formation of turbulence by velocity fields observation. However, in case of the wall impingement, velocity gradient does not suggest the formation of such a

thick layer of vortices. Flow modeling shows the mechanism of vortices formation. Moreover, it enables determining the vortex metrology and analysis construction. Such data are essential to determine the Strouhal number describing the simultaneity of the flow. The simulation results are consistent with transient flow in steady-flow simulations and experiments.

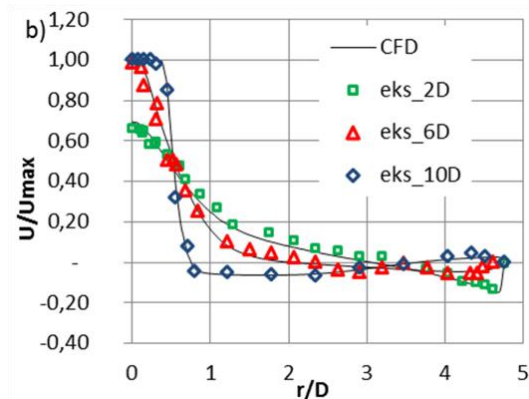


Fig. 5: Comparison of experimental measurements.

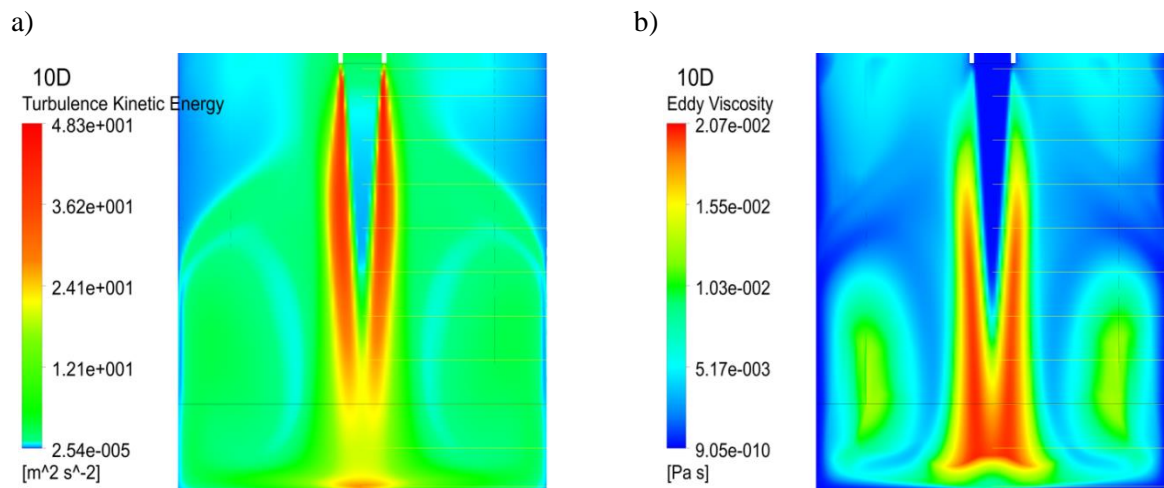


Fig. 6: Results of numerical analysis, a) distribution of turbulence kinetic energy; b) distribution of eddy viscosity.

## References

- Bartoszewicz, J. and Bogusławski, L. (2009) The effectivity of two-equation turbulence model in an impinging jet in a short nozzle to surface distance, *Journal of Theoretical and Applied Mechanics*.
- Bartoszewicz, J., Kłosowiak, R. and Bogusławski, L. (2012) The analysis of the flow structure in a jet at variable geometry of the reverse chamber, *International Journal of Heat and Mass Transfer*, 55, 3239-3245.
- Deo, R.C. et al. (2007) Comparison of turbulent jets issuing from rectangular nozzles with and without sidewalls, *Experimental Thermal and Fluid Science*, 32, 596-606.
- Gutmark, E. and Wygnanski, I. (1976) The planar turbulent jet, *Journal of Fluid Mechanics*, 73, 465-495.
- Kłosowiak, R. and Bogusławski, L. (2014) Shear stress distribution on flat surface impinged by jets, in: *21st International Congress of Chemical and Process Engineering CHISA 23-27 Prague*.
- Koseoglu, M.F. and Baskaya, S. (2009) Experimental and numerical investigation of natural convection effects on confined impinging jet heat transfer, *International Journal of Heat and Mass Transfer*, 52, 1326-1336.
- Launder, B.E. and Spalding, D.B. (1972) *Mathematical models of turbulence*, Academic Press.
- Launder, B.E. and Spalding, D.B. (1974) The numerical computation of turbulent flows, *Comp. Meth. in Appl. Mech. & Eng.*, Vol. 3, pp. 269.
- Wygnanski, I. and Peterson, R.A. (1974) Coherent motion in excited free shear flows, *AIAA Journal*, 25, 201-213.

## SOME REMARKS ON PREVENTIVE REPLACEMENT MODEL

L. Knopik<sup>\*</sup>, K. Migawa<sup>\*\*</sup>, K. Peszyński<sup>\*\*\*</sup>, S. Wawrzyniak<sup>\*\*\*\*</sup>

**Abstract:** *This paper presents a policy of preventive replacement that consists of the burn-in procedure and age-replacement. Criteria function in the derived maintenance model is a cost per unit time. Properties of criteria function are obtained. Illustrative example based on the derived maintenance model is given in this paper.*

**Keywords:** Lifetime distribution function, Reliability function, Failure rate function, Early failure, IFR-class, Burn-in procedure, Age-replacement, Criteria function.

### 1. Introduction

With development of the contemporary manufacturing technology, products have become more technologically advanced and more reliable. Burn-in is the procedure used to eliminate early failures in maintenance process. Preventive maintenance policy such as age-replacement is often used in maintenance. Age-replacement plays a key role in organization of the maintenance because it can significantly contribute to reducing cost of maintenance. As it is well known, in age-replacement model, if the technical object does not fail before a perspective time  $x$ , then it is replaced by a new one preventively; otherwise object is replaced at the failure time. Burn-in procedure consists of testing a new technical object for a given period before its active life in order to predict early failures. Burn-in procedure has been studied by several authors, including (Kuo and Kuo, 1983) who presented a main aspect of this procedure. In paper (Block and Savits, 1997), the burn-in optimization examples are derived. Many research studies combined policies of burn-in with age-replacement, for example (Jiang and Jardine, 2007; Canfield, 1975; Mi, 1994 and Drapella and Kosznik, 2002). The use of this combined policy is sometimes more effective than use of burn-in procedure without age-replacement. An example of combined policy is presented in (Mi, 1994). In this paper the period of inspection method and the replacement method are determined. Often the situation is that a population time to failure is heterogeneous and consists of two sub-populations, which represent early failures and wear-out failures. For the early failures the mean time to failure (MTTF) is "short", while for the wear-out failures the MTTF is "long". The sets times to failures is a mixture of two set early failures and wear-out failures. Mixture distributions model often arises for a reasons in statistical data of times to failures. Reduction of early failures is done in the burn-in process and failures in wear-out are removed by age-replacement. In this paper the sufficient conditions for the existence of the minimum per unit time for age-replacement are investigated. In this paper the sufficient condition of existence of minimum cost per unit time for age-replacements investigation. This is investigated assuming that the burn procedure was previously used to point time  $b$ . Distribution of lifetime  $T$  has non-decreasing failure rate function  $\lambda(t)$ . Criteria function considered in this paper was introduced in paper (Jiang and Jardine, 2007). A numerical example is analyzed to illustrate investigation of this paper.

---

<sup>\*</sup> Assoc. Prof. Leszek Knopik, PhD.: Faculty of Management, UTP University of Science and Technology, Fordońska Street 430, 85-790 Bydgoszcz, Poland, knopikl@utp.edu.pl

<sup>\*\*</sup> Assoc. Prof. Klaudiusz Migawa, PhD.: Faculty of Mechanical Engineering, UTP University of Science and Technology, Prof. S. Kaliskiego Street 7, 85-789 Bydgoszcz, Poland, klaudiusz.migawa@utp.edu.pl

<sup>\*\*\*</sup> Assoc. Prof. Kazimierz Peszyński, PhD.: Faculty of Mechanical Engineering, UTP University of Science and Technology, Prof. S. Kaliskiego Street 7, 85-789 Bydgoszcz, Poland, kazimierz.peszynski@utp.edu.pl

<sup>\*\*\*\*</sup> Assist. Prof. Sylwester Wawrzyniak, PhD.: Faculty of Mechanical Engineering, UTP University of Science and Technology, Prof. S. Kaliskiego Street 7, 85-789 Bydgoszcz, Poland, sylwester.wawrzyniak@utp.edu.pl



## 2. Model

Suppose that the population times consist of two sub-populations, one is weak with early failures and the other has with has a longer lifetime. To reduce the early failures, all technical objects experience a burn-in process with burn-in time  $b$ . In this article the following notation is used:  $T$  – time to failure,  $F(t)$  – distribution function of  $T$ ,  $F(t) = P(T < t)$ ,  $R(t)$  – reliability function of  $T$ ,  $R(t) = 1 - F(t)$ ,  $f(t)$  – density function of  $T$ ,  $f(t) = F'(t)$ ,  $\lambda(t)$  – failure rate function  $\lambda(t) = f(t) / R(t)$ ,  $IFR$  – class of lifetime with non-decreasing failure rate function  $\lambda(t)$ ,  $ET(x)$  – mean time to failure or preventive replacement at moment  $x$  is  $ET(x) = \int_0^x R(t) dt$ ,  $b$  – long of period burn-in,  $x$  – moment of preventive replacement,  $C_r$  – unit cost of repair in burn-in process,  $C_f$  – unit cost of repair after burn-in process,  $C_p$  – unit cost of preventive replacement,  $C_0$  – unit cost of burn-in procedure.

In this paper we assume that:

Assumption 1:  $C_f - C_p > 0$ ,

Assumption 2:  $C_r - C_p > 0$ .

The expected burn-in and replacement cost per unit time is considered by (Jang and Jardine, 2007) given by

$$C(x, b) = \frac{C_B(b) + C_r C(x, b)}{w(x, b)} \quad (1)$$

where  $C_B(b)$  is the expected burn-in cost and

$$\begin{aligned} C_B(b) &= \frac{C_r F(b)}{R(b)} + C_0 T_b \\ T_b &= \frac{1}{R(b)} \int_0^b R(t) dt \\ C_r(x, b) &= C_p + (C_f - C_p) + \frac{F(x+b) - F(b)}{R(b)} \end{aligned}$$

After a simple transformation of  $C(x, b)$  given by (1) is now

$$C(x, b) = \frac{(C_f - C_p)F(x+b) + (C_r - C_f)F(b) + C_0 ET(b) + C_p}{ET(x+b) - ET(b)} \quad (2)$$

The first partial derivative respect to  $b$  of criteria function  $C(x, b)$  is given by

$$\begin{aligned} \frac{\partial C}{\partial b}(x, b) &= \frac{(C_f - C_p)[H(x+b, x+b) - H(x+b, b)] + (C_r - C_p)[H(b, x+b) - H(b, b)]}{[ET(x+b) - ET(b)]^2} + \\ &\quad \frac{C_0 [R(b)ET(x+b) - ET(b)R(x+b)] - C_p [R(x+b) - R(b)]}{[ET(x+b) - ET(b)]^2} \end{aligned} \quad (3)$$

where  $H(x, y) = f(x)ET(y) - F(x)R(y)$ .

The first partial derivative respect to  $y$  of the function  $H(x, y)$  is given by

$$\frac{\partial H}{\partial y}(x, y) = f(x)ET(y) + F(x)R(y)$$

Function  $H(x, y)$  is increasing under  $y$ . Now, we conclude that

$$H(x+b, x+b) - H(x+b, b) \geq 0, \quad (4)$$

$$H(b, x+b) - H(b, b) \geq 0. \quad (5)$$

For last but one term of nominator of (2), we obtain

$$C_0 [R(b)ET(x+b) - ET(b)R(x+b)] = C_0 ET(x+b)ET(b) \left[ \frac{R(b)}{ET(b)} - \frac{R(x+b)}{ET(x+b)} \right]$$

The function  $v(x) = \frac{R(x)}{ET(x)}$  is decreasing, and

$$C_0 [R(b)ET(x+b) - ET(b)R(x+b)] \geq 0 \quad (6)$$

For last term of nominator of (2), we obtain

$$C_p [R(x+b) - R(b)] \leq 0 \quad (7)$$

By assumptions A1, A2, and (4 – 7), we obtain

$$\frac{\partial C}{\partial b}(x, b) \geq 0$$

**Corollary 1.** The criteria function  $C(x, b)$  is non-decreasing with respect to  $b$ .

We will analyze of the first derivative of criteria function  $C(x, b)$  with respect to  $x$ .

$$\begin{aligned} \frac{\partial C}{\partial x}(x, b) = \frac{1}{R^2(x+b)} \{ & [(C_f - C_p) [H(x+b, x+b) - f(x+b)ET(b)] - (C_r - C_p) F(b)R(x+b)] \\ & - C_p R(x+b) - C_0 ET(b)R(x+b) \} \end{aligned}$$

Let  $H_1(x, b) = H(x+b, x+b) - f(x+b)ET(b)$ .

We can see  $H_1(0, b) = R(x+b)F(x+b) < 0$  and  $H_1(\infty, b) = 0$ .

$$\frac{\partial C}{\partial x}(x, b) = \frac{1}{R(x, b)} [(C_f - C_p)h(x, b) - A(b)] \quad (8)$$

where  $h(x, b) = \lambda(x+b) [ET(x+b) - ET(b)]$  and  $A(b) = (C_r - C_p)F(b) + C_p + C_0 ET(b)$ .

We can see that  $h(0, b) = -F(b) \leq 0$  and by assumption A1 is  $A(b) > 0$ .

The first derivative with respect to  $x$  of  $h(x, b)$  is given by

$$\frac{\partial h}{\partial x}(x, b) = \lambda'(x+b) [ET(x+b) - ET(b)]$$

If  $T \in IFR$  then

$$\frac{\partial h}{\partial x}(x, b) \geq 0$$

**Theorem.** If  $C_f - C_p > 0$ ,  $C_r - C_p > 0$ ,  $T \in IFR$  and

$$\lambda(\infty) > \frac{\left[ \frac{A(b)}{C_f - C_p} + 1 \right]}{(ET - ET(b))} \quad (9)$$

then exactly one minimum of criteria function  $C(x, b)$  exists.

Proof. Let  $u(x, b) = (C_f - C_p)h(x, b) - A(b)$ . By  $C_f - C_p > 0$ , we conclude that  $u(0, b) < 0$  and  $u(x, b)$  increasing under  $x$ . If  $u(\infty, b) > 0$  then the first derivative (8) exactly one change of sign for  $-$  to  $+$ .

The condition  $u(\infty, b) > 0$  is equivalent to inequality (9).

**Corollary 2.** If  $\lambda(\infty) = \infty$  then, the assumption (4) is true and criteria function  $C(x, b)$  approaches one minimum.

### 3. Numerical example

This section presents a numerical example to illustrate our results obtained in Section 2. The time to failure of a unit is assumed to follow a Weibull distribution and have the reliability function:

$$R(t) = \exp\left(-\left(\frac{t}{a}\right)^c\right) \text{ for } a, c > 0, t \geq 0, \text{ the failure rate function } \lambda(t) = \left(\frac{c}{a}\right)\left(\frac{t}{a}\right)^{c-1}, t \geq 0.$$

Also, we assume that  $b = 1.25$ ,  $C_r = 8$ ,  $C_f = 10$ ,  $C_p = 1$ ,  $C_0 = 0.2$

Limit value of criteria function is

$$C(\infty, b) = \frac{((C_r - C_f + C_p) + C_p ET(b) + C_f - C_p)}{(ET - ET(b))}$$

In this example for every Weibull distributions parameter  $c \in \{2.5, 3, 3.5, 4\}$  we compute a value of parameter  $a$  such that  $C(\infty, b) = 2.4$ . Fig. 1 shows the graphs that describe the cost per unit time. We observe that for every  $c \in \{2.5, 3, 3.5, 4\}$  function  $C(x, b)$  approaches the minimum cost per unit time.

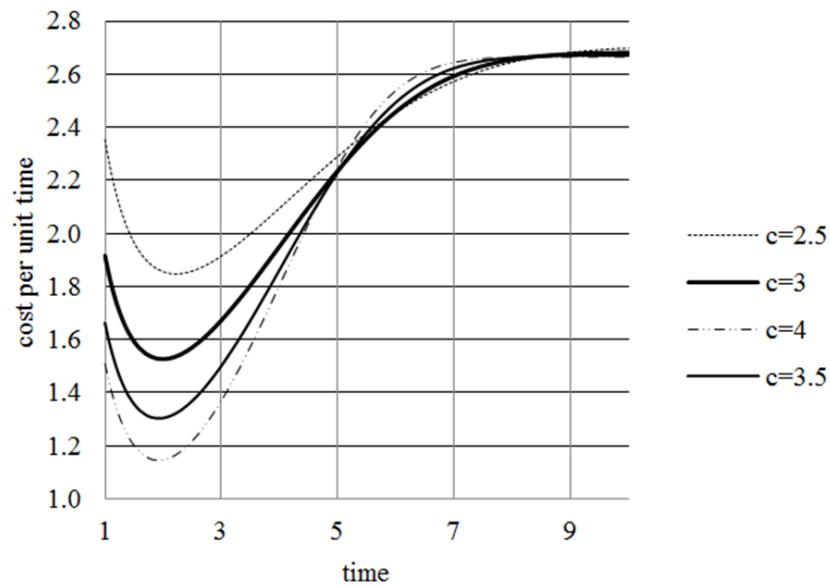


Fig. 1: Cost  $C(x, b)$  as function of time  $x$  of preventive replacement.

### 4. Conclusions

Cost function  $C(x, b)$  proposed by (Jiang and Jardine, 2007) approaches a minimum respect to time of age-replacement. In this paper the sufficient conditions for the existence of the minimum per unit time for age-replacement are formulated.

### References

- Block, H.W. and Savits, T.H. (1997) Burn-In. Statistical Science, 12, pp. 1-19.
- Canfield, R.V. (1975) Cost Effective Burn-In and Replacement Times. IEEE Transactions on Reliability, 24, pp. 154-156.
- Drapella, A and Kosznik, S. (2002) Short Communications Combining preventive replacement and burn-in procedures. Quality Reliability Engineering International, 18, pp. 423-427.
- Jiang, R. and Jardine, A.K.S. (2007) An Optimal Burn-In Preventive-replacement Model Associated with a mixture distribution. Quality Reliability Engineering International, 23, pp. 83-93.
- Kuo, W, and Kuo, Y. (1983) Facing the Headaches of Early Failures: A State-of-the-Art Review of Burn-In Decisions. Proceedings of the IEEE, 71, pp. 1257-1266.
- Mi, J. (1994) Burn-in and maintenance policies. Advanced in Applied Probability, 246(1), pp. 207-221.

## AN EXPLICIT TIME SCHEME WITH LOCAL TIME STEPPING FOR ONE-DIMENSIONAL WAVE PROPAGATION IN A BIMATERIAL BAR

R. Kolman<sup>\*</sup>, S.S. Cho<sup>\*\*</sup>, J.G. Gonzalez<sup>\*\*\*</sup>, K.C. Park<sup>\*\*\*\*</sup>, A. Berezovski<sup>\*\*\*\*\*</sup>

**Abstract:** *In this paper, we test a two-time step explicit scheme with local time stepping. The standard explicit time scheme in finite element analysis is not able to keep accuracy of stress distribution through meshes with different local Courant numbers for each finite element. The used two-time step scheme with the diagonal mass matrix is based on the modification of the central difference method with pullback interpolation. We present a numerical example of one-dimensional wave propagation in a bimaterial elastic bar. Based on numerical tests, the employed time scheme with pullback interpolation and local stepping technique is able to eliminate spurious oscillations in stress distribution in numerical modelling of shock wave propagation in heterogeneous materials.*

**Keywords:** Wave propagation in heterogeneous materials, Explicit time integration, Finite element method, Local stepping, Spurious oscillations.

### 1. Introduction

Currently, application potential for heterogeneous and, mainly, functionally graded materials (FGM) in industrial and engineering problems grows up. The reason is that 3D printing manufacturing processes and tools are available and financially attractive for a wider range of users. Further, functionally graded materials offer many advantages in real problems in comparison with conventional materials (Ebrahimi, 2016).

We focus on numerical solution of wave propagation in an elastic bar consisting of two different materials as the simplest problems of heterogeneous media. Wave propagation in functionally graded materials has been analyzed in (Chiu et al., 1999). More complex modelling of such heterogeneous materials has been done in (Berezovski et al., 2008).

In this paper, we use the finite element method (FEM) with explicit direct time integration based on the central difference method (Hughes, 2000). As it is known, the finite element method produces dispersion behaviour and spurious oscillations of stress components in numerical modelling of wave propagation in solids (Kolman et al., 2016b). Moreover, elastic waves run through bodies with different wave speeds. Further, elastic wave speed in heterogeneous media influences on local material parameters, therefore wave speed is different for each material position. This phenomenon means a big trouble for numerical methods, because wave speed affects stability limit for explicit schemes. Several numerical approaches for elimination of spurious oscillations in heterogeneous media have been developed, as the Park method (Park et al., 2012, Cho et al., 2013) based on pullback interpolation or the Idesman method based on post-processing filtering (Idesman 2014).

---

<sup>\*</sup> Dr. Radek Kolman: Institute of Thermomechanics, The Czech Academy of Sciences, Dolejškova 5, 182 00 Prague; CZ, kolman@it.cas.cz

<sup>\*\*</sup> Dr. Sang Soon Cho: Reactor Mechanical Engineering Division, Korea Atomic Energy Research Institute, 999-111 Daedeok-Daero, Yuseong-gu, Daejeon 305-353; Korea, sscho96@kaist.ac.kr

<sup>\*\*\*</sup> Assoc. Prof. Jose G. Gonzalez: Escuela Técnica Superior de Ingeniería, Universidad de Sevilla, Camino de los Descubrimientos s/n, Sevilla 41092; Spain, japerez@us.es

<sup>\*\*\*\*</sup> Prof. K.C. Park: Department of Aerospace Engineering Sciences, University of Colorado at Boulder, CO 80309-429; USA, kcpark@colorado.edu

<sup>\*\*\*\*\*</sup> Dr. Arkadi Berezovski: School of Science, Tallinn University of Technology, Akadeemia tee 21, 12618 Tallinn; Estonia, Arkadi.Berezovski@cs.ioc.ee

## 2. Problem definition and explicit time scheme with local stepping

We consider the initial stage of wave propagation in an one-dimensional “thin” bimaterial bar in the framework of the classical small strain elasticity theory, see Fig.1. The linear constitutive equation in the form of Hooke’s law is assumed, but material parameters are different for each part of a bar.

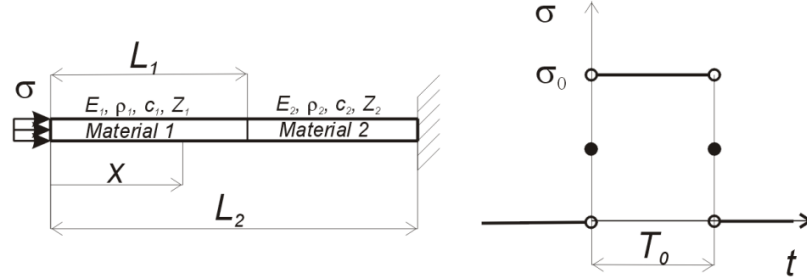


Fig. 1: Scheme of a free-fixed bimaterial elastic bar under shock loading.

One-dimensional wave motion in a bimaterial elastic bar (Fig. 1) is governed by the equations of motion for each part, see (Graff 1975), as

$$\rho_1 \frac{\partial^2 u_1}{\partial t^2} = E_1 \frac{\partial^2 u_1}{\partial x^2} \quad \text{on } [0, L_1] \times [0, T] \quad \text{and} \quad \rho_2 \frac{\partial^2 u_2}{\partial t^2} = E_2 \frac{\partial^2 u_2}{\partial x^2} \quad \text{on } [L_1, L_2] \times [0, T] \quad (1)$$

with boundary conditions on interface for displacement field  $u_1(x = L_1, t) = u_2(x = L_1, t)$  and stress field  $\sigma_1(x = L_1, t) = \sigma_2(x = L_1, t)$ . Further,  $t \geq 0$  denotes the time,  $\rho_1, \rho_2$  are the mass densities, and  $E_1, E_2$  denote the Young moduli. Wave speeds in each bar domain are given by relationships  $c_{01} = \sqrt{E_1 / \rho_1}$ ,  $c_{02} = \sqrt{E_2 / \rho_2}$ . Based on analytical solution (Graff 1975), the transmitted and reflected amplitudes of

the waves are prescribed as  $T = \frac{2Z_2}{Z_1 + Z_2}$  and  $R = \frac{Z_1 - Z_2}{Z_1 + Z_2}$ , where  $Z_1 = \sqrt{E_1 \rho_1}$ ,  $Z_2 = \sqrt{E_2 \rho_2}$  are the

acoustic impedance for each material, respectively. This theoretical stress distribution along an elastic bimaterial free-fix bar under shock loading is used for the comparison with numerical solutions.

## 3. Numerical method for wave propagation in a heterogeneous bar

The used numerical method for wave propagation in heterogeneous materials is based on the algorithm presented in the Park’s papers (Park et al., 2012) and (Cho et al., 2013). This scheme has been reformulated into the two-time step scheme in work (Kolman et al., 2016a). The used time stepping process is consisted of following two computational steps for predictor-corrector form:

### Step 1: Pull-back integration with local stepping

- Integration by the central difference scheme with the local (elemental) critical time step size for each finite element (i.e.  $\Delta t_{c1}$  or  $\Delta t_{c2}$ ).
- Pull-back interpolation of local nodal displacement vector at the time  $t_{n+1} = t_n + \Delta t$ .
- Assembling of local contributions of displacement vector from Step 1b.

### Step 2: Push-forward integration with averaging

- Push-forward integration by the central difference scheme with the time step size  $\Delta t$ .
- Averaging of the total displacement vectors at the time  $t_{n+1}$  from Steps 1c and 2a.
- Evaluation of acceleration and velocity nodal vectors at the time  $t_{n+1}$ .

Implementation details and formulae for this two-time step scheme, one can see in (Park et al., 2016; Cho et al., 2013; Kolman et al., 2016a). A scheme of pullback interpolation for two different local critical time step sizes is depicted in Fig. 2.

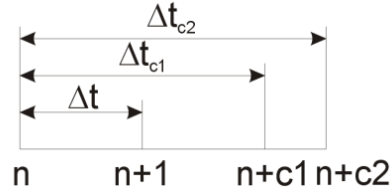


Fig. 2: Extrapolation of the displacement  $u(x, t)$  at steps  $(n + c1)$  and  $(n + c2)$  followed by interpolation at the next step  $(n + 1)$ .

#### 4. Formulation of bimaterial test and results

In this Section, we present results of numerical solution of wave propagation problem in a bimaterial elastic bar defined in the previous Section. Geometrical and material parameters of the task are set as: the domain lengths  $L_1 = 1 \text{ m}$ ,  $L_2 = 2 \text{ m}$ , the cross-section  $A = 1 \text{ m}^2$ , Young's modulus  $E_1 = 16 \text{ Pa}$ ,  $E_2 = 1 \text{ Pa}$ , the mass density  $\rho_1 = \rho_2 = 1 \text{ kg/m}^3$  and the amplitude of impact pressure  $\sigma_0 = 1 \text{ Pa}$ , thus the applied force is  $F_0 = A\sigma_0 = 1 \text{ N}$ . We use computational mesh with 240 uniform finite elements, the FE length is taken as  $H = L_2 / NE = 0.0083 \text{ m}$ . Time duration of the loading is takes as  $T_0 = 0.5L_1 / c_1$ , final time of computations is set as  $t_{end} = 1.8L_1 / c_1$ . The critical time step sizes for finite elements of material 1 and material 2 are given as  $\Delta t_{c1} = H / c_{01}$  and  $\Delta t_{c2} = H / c_{02}$ . In the case,  $c_{01} > c_{02}$ , the value  $\Delta t_{c1}$  dictates the global stability limit so  $\Delta t_c = \Delta t_{c1}$ . For computations by the Park method with and without local stepping, we use the time step size as  $\Delta t = 0.5\Delta t_{c1}$ . For analysis of accuracy of the central difference method, results are computed for time step sizes  $\Delta t = 0.5\Delta t_{c1}$  and  $\Delta t = 0.9\Delta t_{c1}$ . It means by the Courant numbers:  $Co = 0.5$  and  $Co = 0.9$ . The transmitted and reflected amplitudes for the test are given as  $T = 2/5$  and  $R = 3/5$ .

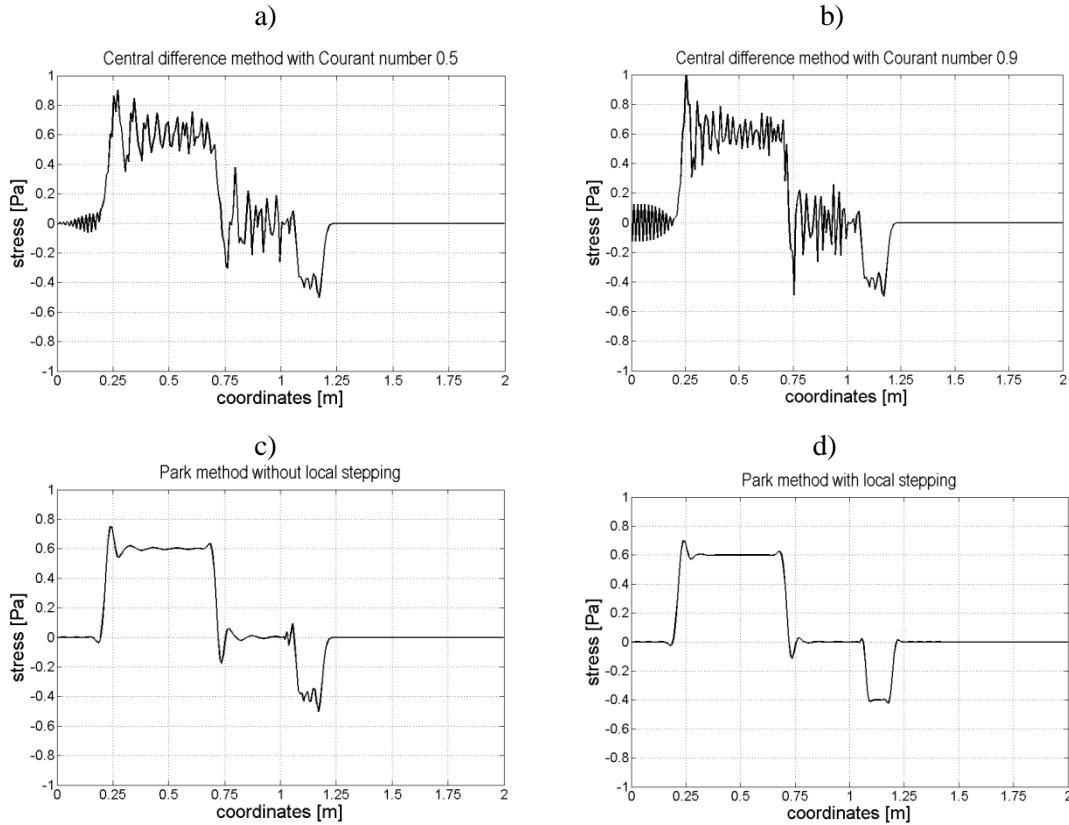


Fig. 3: Stress distributions at a bimaterial elastic bar under shock loading obtained by a) the central difference method with Courant number 0.5; b) the central difference method with Courant number 0.9; c) the Park method without local stepping; d) the Park method with local stepping.



In Fig. 3, one can see results of stress distributions in a bimaterial elastic bar defined above. We employ the central difference method with Courant numbers 0.5 and 0.9, the Park method without and with local stepping technique. Based on comparison, we can say that the Park method with local stepping technique cardinally improves the stress distribution and, in principle, spurious oscillations are eliminated, but only small cusps on the corners of stress discontinuities can be observed.

## 5. Conclusions

In this paper, we have tested the two-time step explicit scheme based on pullback interpolation with local stepping for accurate tracking of elastic wave in heterogeneous media. The bimaterial bar test has showed accuracy of the presented scheme. Further, the scheme is able to eliminate spurious oscillations in numerical modelling against the central difference method. In the future, we will focus on using the presented scheme for wave modelling in layered and functionally graded materials.

## Acknowledgement

The work R. R. and A. B. was supported by the Centre of Excellence for Nonlinear Dynamic Behaviour of Advanced Materials in Engineering CZ.02.1.01/0.0/0.0/15\_003/0000493 (Excellent Research Teams) in the framework of Operational Programme Research, Development and Education, and also by the bilateral project No. ETA-15-03. The work of R. R. was supported by the grant project Nos. 16-03823S and 17-22615S of the Czech Science Foundation within institutional support RVO:61388998.

## References

- Berezovski, A., Engelbrecht, J. and Maugin, G.A. (2008) Numerical Simulation of Waves and Fronts in Inhomogeneous Solids, World Scientific Pub Co Inc.
- Ebrahimi, F. (2016) Advances in Functionally Graded Materials and Structures. InTech.
- Graff, K.F. (1975) Wave motion in elastic solids, first ed., Oxford University Press.
- Hughes, T.J.R. (2000) The Finite Element Method: Linear and Dynamic Finite Element Analysis. Dover Publications: New York.
- Chiu, T.-C. and Erdogan, F. (1999) One-dimensional wave propagation in a functionally graded elastic medium. *Journal of Sound and Vibration*, 222, pp. 453-487.
- Cho, S.S., Park, K.C. and Huh, H. (2013) A method for multi-dimensional wave propagation analysis via component-wise partition of longitudinal and shear waves. *International Journal for Numerical Methods in Engineering* 95, 3, pp. 212-237.
- Idesman A. (2014) Accurate finite-element modeling of wave propagation in composite and functionally graded materials. *Composite Structures* 117, pp. 298-308.
- Kolman, R., Cho, S.S. and Park, K.C. (2016a) Efficient implementation of an explicit partitioned shear and longitudinal wave propagation algorithm. *Inter. Journal for Numerical Methods in Eng.* 107, 7, pp. 543-579.
- Kolman, R., Plešek, J., Červ, J., Okrouhlik, M. and Pařík, P. (2016b) Temporal-spatial dispersion and stability analysis of finite element method in explicit elastodynamics. *International Journal for Numerical Methods in Engineering*, 106, 2, pp. 113-128.
- Park, K.C., Lim, S.J. and Huh, H. (2012) A method for computation of discontinuous wave propagation in heterogeneous solids: basic algorithm description and application to one-dimensional problems. *International Journal of Numerical Methods and Engineering*, 91, 6, pp. 622-643.

## **EVALUATION OF KNEE JOINT STIFFNESS IN CHILDREN WITH CEREBRAL PALSY**

**A. Konopelska<sup>\*</sup>, M. Jureczko<sup>\*\*</sup>**

**Abstract:** *The knee joint stiffness is a very complex issue, which occurs in many children with cerebral palsy (CP). Therefore, in children with CP are carried out studies both clinical and biomechanical. They are carried out to evaluate the locomotors system and to choose the most appropriate treatment. Biomechanical evaluation of the musculoskeletal system focused on the analysis of gait. The aim of the research presented in this paper was to evaluate of the knee joint stiffness in children with CP based on the designated during gait studies of kinematic magnitudes.*

**Keywords:** Knee joint, Stiffness, Stiff-knee gait, Cerebral palsy (CP), Range of motion (ROM).

### **1. Introduction**

For many years, children with impaired muscle tone were subject to many clinical studies. In recent years, into these studies were included biomechanical test. Selection of the best method of treatment for a given patient depends on a correct diagnosis of his health. In order to select an appropriate method of treatment it should be known precisely the mechanisms of muscle tone regulation, as well as diseases causing the occurrence impairment of muscle tone (Olchowik, 2009). Stiffness beside spasticity and dystonia is one of the form of increased muscle tone. Analysis of the knee joint stiffness is very important in studies of gait of children with impaired muscle tone, especially for children with CP. The knee joint stiffness is an impairment of muscle tone, and in particular malfunction of rectus femoris. This appear especially during gait, e.g. during initial swing of the rectus femoris what limits the rate of knee flexion. Rectus femoris transfer surgery is often performed to treat stiff-knee gait (Gage, 1993 and Reinbolt, 2008). The knee joint stiffness influences on all phases of child's gait, and first of all, makes it difficult to bend and unbend. The knee joint stiffness causes excessive flexion, limited extension and a smaller range of motion of the knee joint (Goldberg, 2003 and Van der Krogt, 2010 and Thawrani, 2012). During flexing or extension stiff of lower limb it appears continuous resistance. Sometimes while moving the lower limb may occur jumping symptom of reduction of muscle tone, so-called "cogwheel rigidity". It is a characteristic symptom of tension and relaxation of antagonist muscles that occurs in people with intensified muscle tone that primarily can be observed when straightening the knee. Since patients with stiff-knee gait have limited knee flexion ability, they might use for example pelvic hike during swing phase of gait to assist their toe clearance (Böhm, 2014 and Campenhouta, 2014). These plantigrade gait determinants, such as knee flexion during stance phase, pelvic movements, and joint coordination, cause displacement of the body's centre of mass in the direction shifted in the side axis of the limb (Massaad, 2004).

For doctors involved in the treatment of disorders of muscle tone in patients with CP the selection of the most appropriate method of treatment is a major challenge. In recent years, a biomechanical methods, in particular gait analysis, make it easier to evaluate of the musculoskeletal system. Analysis of gait parameters obtained during the study delivers various information concerning a given pathology. Commonly during the studies are evaluated: spatio-temporal parameters, kinematic and kinetic quantities and ground reaction forces. The kinematic parameters usually are read ranges of movements in individual joints. In clinical practice it is rare to evaluate the stiffness of knee joint basing on only one measured kinematic parameter such as the knee angle in the sagittal plane.

---

\* Agnieszka Konopelska, Phd. Eng.: Institute of Theoretical and Applied Mechanics, Silesian University of Technology, Street Konarskiego 18a, 44-100 Gliwice, PL; Agnieszka.Konopelska@polsl.pl

\*\* Mariola Jureczko, Phd. Eng.: Institute of Theoretical and Applied Mechanics, Silesian University of Technology, Street Konarskiego 18a, 44-100 Gliwice, PL; Mariola.Jureczko@polsl.pl

## 2. Materials and methods

Twelve patients with bilateral cerebral palsy, (8 boys and 4 girls) with mean age 10.6 (SD = 3.7) years with mean weight 32 (SD = 15.1) kg and with mean height 136 (SD = 22.6) cm were compared to fifteen typical developing children (TP) (7 boys and 8 girls) with mean age 10 (SD = 2.8) years, with mean weight 34 (SD = 13.4) kg and with mean height 138 (SD = 18.2) cm (these data were taken from the publications Goldberg et al., 2006). All children's parents signed an informed consent form.

Studies have been conducted in John Paul II Upper Silesian Child Health Centre. The subject of this study was analysis of gait in children with cerebral palsy. Anthropometric data of individual children with CP are given in Tab. 1.

Tab. 1: Anthropometric data of individual children with CP.

patient	sex	age [years]	weight [kg]	height [cm]
No 1	boy	13	40	153
No 2	girl	6	16	110
No 3	boy	7	19	113
No 4	boy	7	16	110
No 5	boy	15	45	150
No 6	boy	12	30	146
No 7	boy	12	50	150
No 8	girl	6	23	120
No 9	boy	15	60	170
No 10	girl	6	15.5	113
No 11	girl	13	25	135
No 12	boy	15	42	168

The study of gait analysis was conducted in order to evaluate the stiffness of knee joint. System for three dimensional motion analysis BTS Smart was used. This system contained eight optoelectronic camera operating in the infrared range. The registered measurements allowed the determination of the kinematic parameters based on the modified Davis' model. The following parameters were read from the obtained plots:

- parameter T [% gait cycle] – time at which followed detachment toes from the ground (toe-off),
- parameter 1 [°] – peak knee flexion angle,
- parameter 2 [°] – range (ROM) of knee flexion in early swing measured from toe-off to peak flexion,
- parameter 3 [°] – total range of knee motion (knee ROM total),
- parameter 4 [% gait cycle] – timing of peak knee flexion in swing.

The standard diagram dependence the angle of the knee joint in the sagittal plane on the phase of gait, along with the selected parameters, is shown in Fig. 1. Stiffness in the knee joint occurs when three or more of the parameters deviate from normal values. The stiffness of the knee occurs when at least two parameters shown in Fig. 1 are abnormal. However, when the two parameters are abnormal it cannot be concluded clearly whether stiffness of the knee joint occurs or not. Parameters from 1 to 3 are considered abnormal when their value are at least twice smaller than the standard deviation value of the parameter 4 considered normative. However, if the parameter value is at least equal to twice the standard deviation of the normative value is considered to be abnormal (Goldberg et al., 2006).

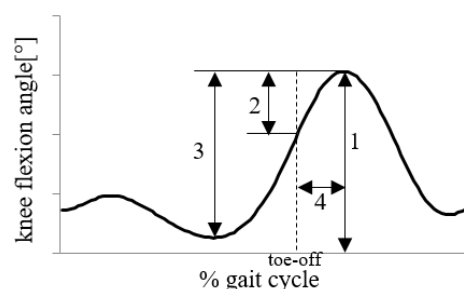


Fig. 1: The knee angle in the sagittal plane with marked parameters.

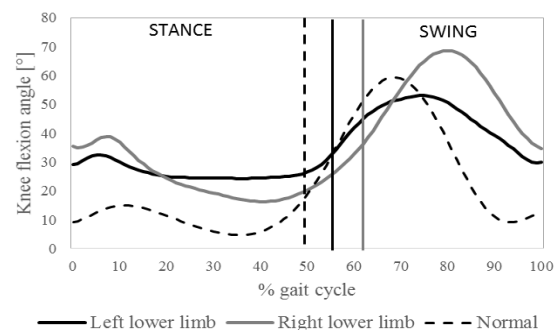
## 3. Results

In the case of people with cerebral palsy should be also checked if they have a gait excessively bent knees (a condition called crouch gait). In such case these persons may have stiffness in the knee during the whole gait cycle, and the value of angle of flexion of the knee joint considerably differs from normal

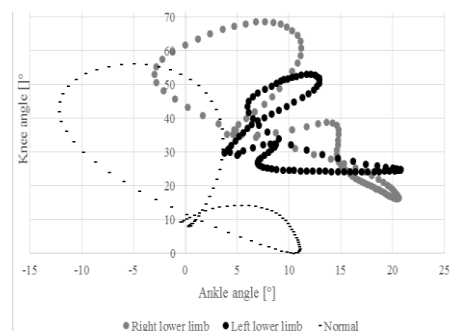
values. This phenomenon also affects the value of the parameter 1, i.e. peak knee flexion angle. For people with crouch gait should be taken into account the value of angle of flexion of the knee joint during initial contact. Fig. 2 shows a graph of the abnormal knee angle of the phase gait cycle for one of the patients with respect to healthy children. All results of study were summarized in Tab. 2 and referred to the standard literature after analyzing the research group in the author's program (Goldberg S. et al., 2006).

*Tab. 2: Measures of stiff-knee gait (where L-left lower limb, R-right lower limb).*

	Parameter T [%]		Parameter 1 [°]		Parameter 2 [°]		Parameter 3 [°]		Parameter 4 [%]		Stiff -knee
Lower limb	L	R	L	R	L	R	L	R	L	R	
T P	62 ± 1		66 ± 5.3		31 ± 4.3		60 ± 6.8		13 ± 1.2		
Patient 1	61.0	58.0	49.8	67.1	17.1	11.6	34.7	38.9	14.0	10.5	L
Patient 2	55.0	66.0	53.0	49.0	20.8	23.6	28.8	24.5	20.0	24.0	L, R
Patient 3	60.0	54.0	70.1	78.6	24.6	12.6	42.5	60.1	21.0	15.0	
Patient 4	65.0	64.0	59.4	62.8	23.4	11.9	57.4	55.8	19.0	21.0	
Patient 5	80.0	74.0	53.6	61.3	6.4	5.4	9.9	8.4	21.0	15.0	L
Patient 6	66.0	84.0	33.8	54.6	1.3	5.2	7.4	10.0	23.0	16.0	L, R
Patient 7	77.0	74.0	72.1	75.8	7.6	9.4	10.6	8.3	18.0	26.0	L, R
Patient 8	64.0	65.0	70.8	76.4	14.5	13.4	20.6	17.6	20.0	15.5	L, R
Patient 9	61.0	69.0	72.9	63.8	24.1	25.9	61.4	70.7	23.0	17.0	
Patient 10	78.0	81.0	77.2	76.5	11.9	16.3	37.0	38.6	9.0	9.0	
Patient 11	81.0	76.0	66.7	63.5	9.8	9.2	20.3	14.5	12.0	15.0	
Patient 12	76.0	71.0	100.8	97.5	1.9	2.6	8.8	10.2	7.0	9.0	



*Fig. 2: The knee angle in the sagittal plane (left and right lower limb) for one of the children with CP in relation to control group (TP).*



*Fig. 3: Intra – limb coordination of knee and ankle for gait cycles for one child with CP in relation to control group (TP).*

Fig. 3. describes differences in joints coordination (knee and ankle) for children with CP and healthy ones. Pattern of coordination of knee-joint and ankle for child with stiffness in left knee joint is deeply

impaired both for left and right side. Healthy children has initial contact coordinates at (-1; 10), but for CP-children values are deeply different - (4; 35.4) for right and (5; 29) for left limb. When picking up fingers from base/ground coordinates for healthy children are (-12; 40), and for CP-children respectively for right limb (-1; 45.7), and left (10.2; 32.2).

#### 4. Conclusions

The results of the study gait, that were presented in Tab. 2, allow us to conclude that among twelve investigated children, two children has a stiff-knee joint of left lower limb and four children has a stiff-knee joint of both lower limbs. Only one patient acknowledged a lack of stiffness of knee joints of both lower limbs. However, for a few patients it cannot be clearly determined presence of stiffness of knee joint of any of the lower limbs. One patient had abnormal values for all four parameters for both lower limbs. Analysis of results for majority of patients shows that most deviations from normal values are related to the parameter 2 and 3. On the other hand first parameter is incorrect in comparison to the standard value for the four patients. For two of patients its value is invalid for the both lower limbs and for other two patients only for one lower limb. In this article been made to evaluation of intra-limb coordination of angles of knee and ankle during gait because of the fact that the stiffness of the knee changes the pattern of motion in all joints of the lower limb.

One of the universal conclusions from the study is the necessity to join a routinely generated research reports with gait analysis evaluation stiffness of the knee joint in children with impaired muscle tone with cerebral palsy.

Patients with crouch gait may suffer or not stiffness in the knee joint. Numeric data of research that characterize the stiffness in the knee joint in patients with crouch gait are generally missing (in particular the data for parameter peak knee flexion angle and its dependence on initial contact). Lack of such data indicates the possibility of further development and research in this direction.

#### References

- Böhm, H., Hösl, M., Schwameder, H. and Döderlein L. (2014) Stiff-knee gait in cerebral palsy: How do patients adapt to uneven ground? *Gait & Posture*, 39, pp. 1028-1033.
- Campenhouta, A.V., Bar-Onb, L., Aertbeliënc, E., Huenaertsb, C., Molenaersa, G. and Desloovere K. (2014) Can we unmask features of spasticity during gait in children with cerebral palsy by increasing their walking velocity? *Gait & Posture*, 39, 3, pp. 953-957.
- Gage, J.R. (1993) Gait analysis. An essential tool in the treatment of cerebral palsy. *Clinical Orthopaedics and Related Research*, 288, pp. 126-134.
- Goldberg, S.R., Öunpuu, S. and Delp, S.L. (2003) The importance of swing-phase initial conditions in stiff-knee gait. *Journal of Biomechanics*, 36, pp. 1111-1116.
- Goldberg, S.R., Öunpuu, S., Arnold, A.S., Gage, J.R., and Delp, S.L. (2006) Kinematic and kinetic factors that correlate with improved knee flexion following treatment for stiff-knee gait, *Journal of Biomechanics*, 39, 4, pp. 689-698.
- Massaad, F., Dierick, F., Van den Hecke, A. and Detrembleur, Ch. (2004) Influence of gait pattern on the body's centre of mass displacement in children with cerebral palsy, *Developmental Medicine & Child Neurology*, 46, pp. 674-680.
- Olchowik B., Sobaniec, W., Sołowiej, E. and Sobaniec P. (2009) Clinical aspects of spasticity treatment, *Neurologia Dziecięca*, 18, 36, pp. 47-57.
- Reinbolt, J.A., Fox, M.D., Arnold, A.S., Öunpuu, S. and Delp, S.L. (2008) Importance of preswing rectus femoris activity in stiff-knee gait, *Journal of Biomechanics*, 41, pp. 2362-2369.
- Thawrani, D., Haumont, T., Church, Ch., Holmes, L., Dabney, K.W. and Miller, F. (2012) Rectus femoris transfer improves stiff knee gait in children with spastic cerebral palsy. *Clinical Orthopaedics and Related Research*, 470, pp. 1303-1311.
- Van der Krogt, M.M., Bregman, D.J., Wisse, M., Doorenbosch, C.A.M., Harlaar, J. and Collins, S.H. (2010) How crouch gait can dynamically induce stiff-knee gait. *Annals of Biomedical Engineering*, 38, 4, pp. 1593-1606.

## AN INVESTIGATION OF MASS TRANSFER IN A VORTEX SHEDDING PAST SQUARE CYLINDER

T. Kořínek\*, M. Petříková\*\*

**Abstract:** *This work investigates mass transfer in a vortex shedding past a square cylinder. The investigation is done by numerical simulations and an experiment on a hydrodynamic table. Turbulence is modeled by Large Eddy Simulation method. Investigated range of Reynolds numbers ( $Re$ ) is  $Re = 6\,600 - 20\,000$  for numerical simulations and  $Re = 1\,000 - 2\,000$  for the experiment. Obtained results indicate influence of  $Re$  on a distribution of an additional fluid in flow, where the leading edge of the square cylinder had a significant effect to the mass transfer in the spanwise direction.*

**Keywords:** CFD, Turbulent flow, Large Eddy Simulation, Mass transfer.

### 1. Introduction

There are a lot of engineering applications, where flow is influenced by surrounding bodies. Flow over a square cylinder was many times numerically and experimentally studied (Bouris et al., 1999, Davidson et al., 2000; Lyn, 1995). It is well known, that vortex shedding has a significant effect on heat and mass transfer past bluff body (Abbasi, 2003). Investigations of flow past cylinder were due to various Reynolds number, different attack angle etc. In case of heat transfer, there were done a lot of works. But in case of mass transfer, it was significantly smaller (Bošković-Vragolović et al., 2013). A typical investigated case in mass transfer is flow over obstacles, which represent air pollutions dispersion in an urban area (Rigas et al., 2004).

Main aim of this work was on spreading of additional fluid past square cylinder. The vortex shedding served to achieve uniform concentration profile in shorter distance comparing with a simple channel. This phenomenon was primary investigated using numerical simulations. There were used experimental data from the ERCOFTAC database (Lyn, 1995) to validate numerical simulations. The validation consisted from comparing mean streamwise velocities obtained by numerical simulations and by measurements.

### 2. Methods

An investigated domain was a simple channel with one vertically placed square cylinder. The domain with dimensions is shown in Fig. 1. The characteristic length  $D$  was 10 mm. The Reynolds number was calculated using the formula:

$$Re = \frac{u_{\infty} D}{\nu} \quad (1)$$

Where  $u_{\infty}$  is mean velocity on inlet and  $\nu$  is kinematic viscosity. Three moderate Reynolds numbers were investigated only numerically  $Re_1 = 6\,600$ ,  $Re_2 = 13\,300$ ,  $Re_3 = 20\,000$ . Lower Reynolds numbers were investigated experimentally. The variation of Reynolds numbers was achieved by changing initial velocity.

---

\* Ing. Tomas Korinek: Department of Power Engineering Equipment, Faculty of Mechanical Engineering, Technical University of Liberec, Studentska 2; 461 17, Liberec; CZ, tomas.korinek@tul.cz

\*\* Ing. Marketa Petrikova, PhD.: Department of Power Engineering Equipment, Faculty of Mechanical Engineering, Technical University of Liberec, Studentska 2; 461 17, Liberec; CZ, marketa.petrikova@tul.cz



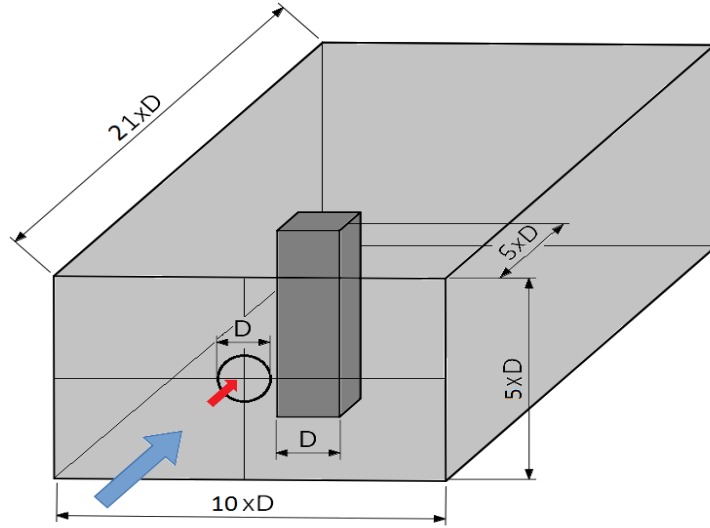


Fig. 1: Domain.

## 2.1. Numerical setup

The mathematical model was simplified for incompressible, isothermal flow of two fluid mixture and contained continuity equation, momentum equation and species transport equation.

$$\frac{\partial \rho}{\partial t} + \nabla \cdot (\rho u) = 0 \quad (2)$$

$$\frac{\partial}{\partial t} (\rho u) + \nabla \cdot (\rho u u) = -\nabla p + \nabla \tau \quad (3)$$

$$\frac{\partial}{\partial t} (\rho Y) + \nabla \cdot (\rho u Y) = -\nabla J \quad (4)$$

Where  $J$  is diffusion mass flux,  $p$  is pressure,  $u$  is velocity,  $\rho$  is density of mixture.

The computational grid was created with 3.6 million of cells for 3D and 52 400 cells for 2D. The number of elements on square cylinder in streamwise and crosswise direction was 45. There were created two additional grids for a test of mesh resolution. The first contained 2.5 million of cells and the second 1.8 million of cells. Special attention was given on a creating fine boundary layer with  $y^+$  value below 1. This was due to use the Large Eddy Simulation (LES) method to solve turbulence. Numerical simulations were carried out by open source software OpenFOAM 4.1.

## 2.2. Experimental setup

In spite of the fact, that experiment is primary used for the validation of mathematical models, in this case served as an alternative method to the observation of mass transfer past bluff bodies. The experiment was simplified to 2D solution and was done on a hydrodynamic table shown in Fig. 2 left. Flow was visualized by aluminum particles with size  $35 \mu\text{m}$ . A capture from the experiment with inverted colors is shown in Fig. 2 right.

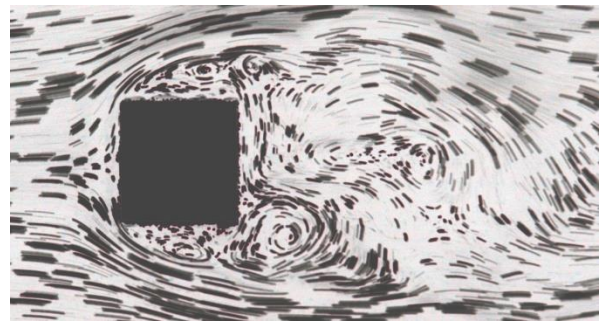
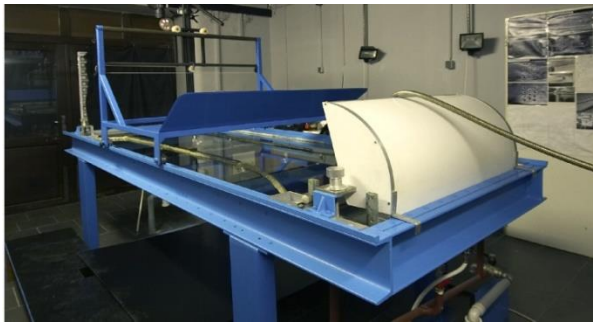


Fig. 2: Hydrodynamic table (left), a capture from experiment (right).

### 3. Results

The influence of Reynolds number to the mean concentration past square cylinder is shown in Fig. 3 for crosswise direction and in Fig. 4 for spanwise direction. There are shown four downstream transverse cross sections. The spreading of the additional gas is decreasing with increase of the Reynolds number. As it is shown in Fig. 3, there was a significant mass transfer in the crosswise direction. However the mass transfer in spanwise direction was also considerable, which is shown on chart in Fig. 4.

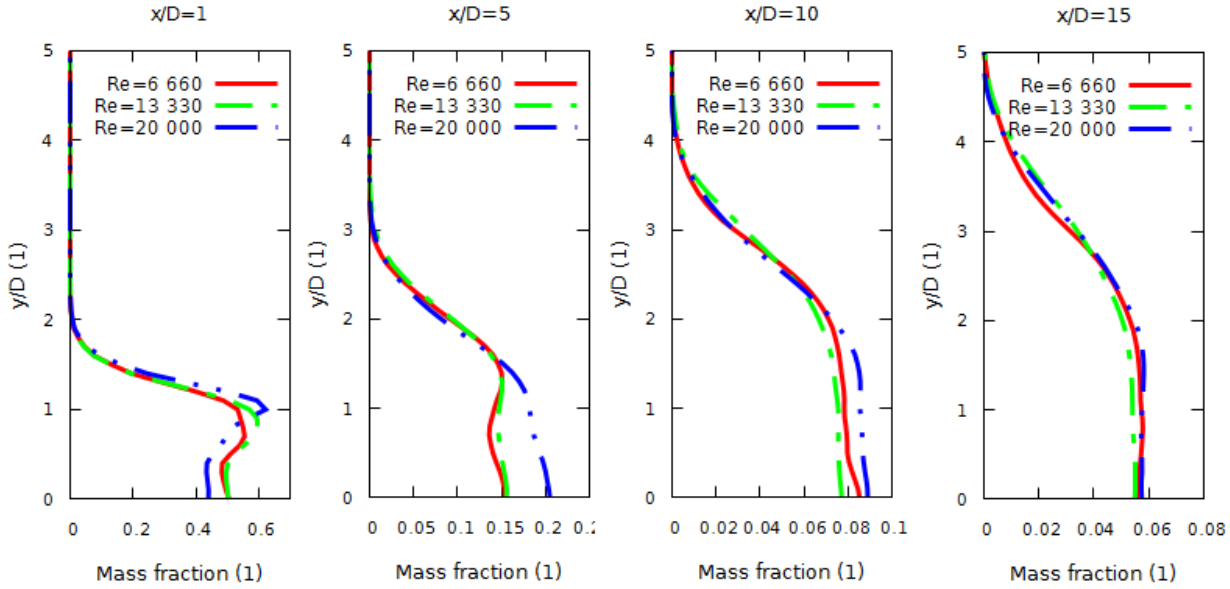


Fig. 3: Mean mass fraction profile in crosswise direction.

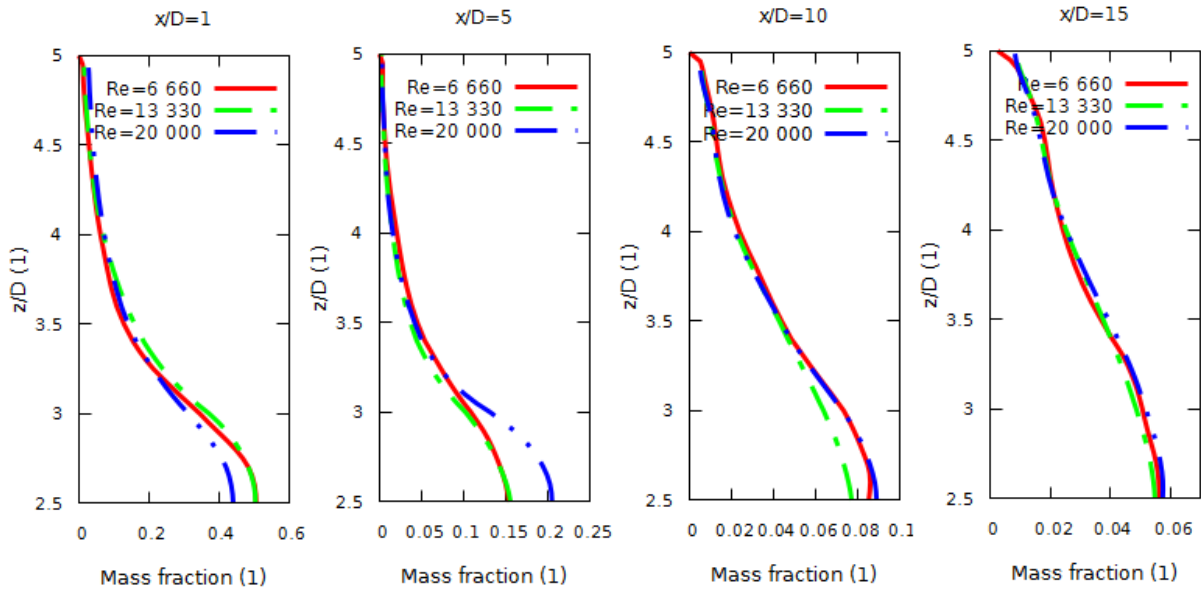


Fig. 4: Mean mass fraction profile in spanwise direction.

One of the methods for observation of mass transfer is using isosurfaces of mass fraction. The isosurface of mass fraction  $Y = 0.05$  is shown in Fig. 5. There was a significant accumulation of mass behind the leading edge of the square cylinder. This occurred below and above the mainstream of the additional gas on both side of the cylinder. This accumulation was due to vortices formed behind the leading edge. The accumulated mass was periodically released and it led to more intense spreading of the additional gas in the spanwise direction.

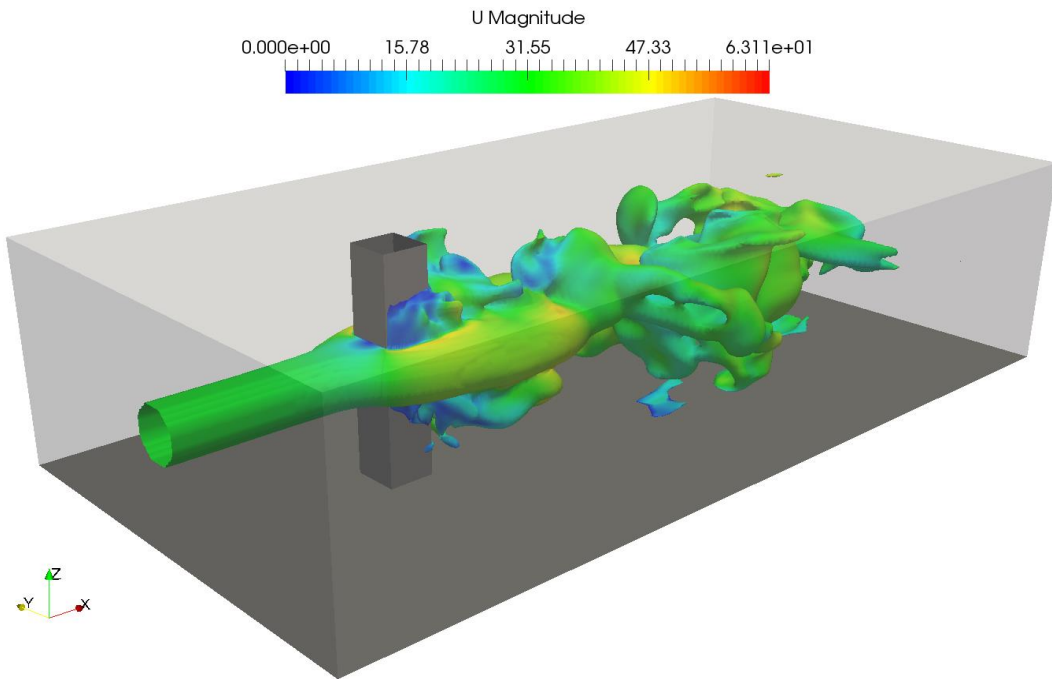


Fig. 5: Isosurface of instantaneous mass fraction  $Y = 0.05$  colored by velocity magnitude.

#### 4. Conclusions

There were done a few calculations of mass transfer past a square cylinder for moderate Reynolds numbers ( $Re = 6\,600 - 20\,000$ ). The lower Reynolds numbers were investigated experimentally.

The study provides results of influence of  $Re$  on the concentration profile past the square cylinder. There was a significant effect of the blockage in the channel to the mass transfer in the crosswise direction of flow and also in the spanwise direction. The accumulation of mass behind the leading edge of the square cylinder led to the intense mass transfer in the spanwise direction.

#### Acknowledgement

This publication was written at the Technical University of Liberec as part of the project "Experimental and numerical investigation in applied fluid mechanics and energy devices" with the support of the Specific University Research Grant No. 21124, as provided by the Ministry of Education, Youth and Sports of the Czech Republic in the year 2017.

Computational resources were provided by the CESNET LM2015042 and the CERIT Scientific Cloud LM2015085, provided under the programme "Projects of Large Research, Development, and Innovations Infrastructures"

#### References

- Abbassi, H., Nasrallah, S.B. and Turki, S. (2003) Two-dimensional laminar fluid flow and heat transfer in a channel with a built-in heated square cylinder. *Int. J. of Thermal Sciences*, 42, pp. 1105-1113.
- Bošković-Vragolović, N., Garić-Grulović, R., Grbavčić, Ž. and Pjanović, R. (2013) Mass transfer and fluid flow visualization for single cylinder by the adsorption method. *Int. J. Heat Mass Transfer*, 59, pp. 155-160.
- Bouris, D. and Bergeles, G. (1999) 2D LES of vortex shedding from a square cylinder. *J. of Wind Engineering and Industrial Aerodynamics*, 80, pp. 31-46.
- Davidson, L., Norberg, C. and Sohankar, A. (1998) Low-Reynolds Flow around a Square Cylinder at Incidence: Study of Blockage, Onset of Vortex Shedding and Open Boundary Condition. *Int. J. of Numerical Methods in Fluids*, 26, pp. 39-56.
- Lyn, D.A. (1995) A laser-Doppler velocimetry study of ensemble-averaged characteristics of the turbulent near wake of a square cylinder. *J. of Fluid Mechanics*, 304, pp. 285-319.
- Rigas, F. and Sklavounos, S. (2004) Validation of turbulence models in heavy gas dispersion over obstacles. *J. Hazard. Mater.*, A108, pp. 9-20.

## A CONTROL WITH THE USE OF LQR MODIFIED METHOD IN THE GYROSCOPE SYSTEM OF TARGET TRACKING

Z. Koruba<sup>\*</sup>, I. Krzysztofik<sup>\*\*</sup>

**Abstract:** An algorithm of the gyroscope system control in the seeker with the use of LQR (linear quadratic regulator) modified method was presented in this paper. The modification of the method consists in applying Jacobian  $J$  derived from the equations of the non-linear motion of the gyroscope system in the place of state matrix  $A$  with constant values. It makes it possible to determine the motion equations of the matrix system of  $K$  reinforcements of the closed control system with a square quality indicator in every step of integration. The research results showed that this type of control provides greater precision and effectiveness of control of the gyroscope system of tracking a moveable target in space. Some research results were presented graphically.

**Keywords:** LQR control, Jacobian, Target tracking, Gyroscope system.

### 1. Introduction

Gyroscope systems (GS) are widely applied in systems of observation and target tracking situated on the board of moveable objects (Koruba, 2010 and Dziopa et al., 2010). Due to the fact that high precision is required from them, stabilizing and tracking control should be carefully selected (Gapiński et al., 2014 and Gapiński, 2014). The classic method of optimal control of the gyroscope axis motion with a square quality indicator seems to be unsatisfactory as far as the influence of external disturbances in the form of kinematic base influence as well as the parameters of the gyroscope itself changeable over time (friction in frame bearings, rotor imbalance, a situation when the mass centre does not overlap with frame rotation centre, etc.) are concerned. LQR method assumes that the linear system and state matrix  $A$  with constant parameters are in question (Grzyb, 2016, Krzysztofik, 2014 and Koruba, 2013). Such simplification results in the fact that after relatively short time, tracking is not precise enough. In order to prevent this, Jacobian should be determined on the basis of the nonlinear equations describing the gyroscope system motion (Kim, 2010) in the following way:

$$J = \begin{bmatrix} \frac{\partial f_1}{\partial \mathcal{G}_g} & \frac{\partial f_1}{\partial \dot{\mathcal{G}}_g} & \frac{\partial f_1}{\partial \psi_g} & \frac{\partial f_1}{\partial \dot{\psi}_g} \\ \frac{\partial f_2}{\partial \mathcal{G}_g} & \frac{\partial f_2}{\partial \dot{\mathcal{G}}_g} & \frac{\partial f_2}{\partial \psi_g} & \frac{\partial f_2}{\partial \dot{\psi}_g} \\ \frac{\partial f_3}{\partial \mathcal{G}_g} & \frac{\partial f_3}{\partial \dot{\mathcal{G}}_g} & \frac{\partial f_3}{\partial \psi_g} & \frac{\partial f_3}{\partial \dot{\psi}_g} \\ \frac{\partial f_4}{\partial \mathcal{G}_g} & \frac{\partial f_4}{\partial \dot{\mathcal{G}}_g} & \frac{\partial f_4}{\partial \psi_g} & \frac{\partial f_4}{\partial \dot{\psi}_g} \end{bmatrix} \quad (1)$$

where:  $f_1, f_2, f_3, f_4$  – non-linear functions of right sides of the motion equations of the gyroscope system;  $\mathcal{G}_g, \psi_g$  – deviation angles of the internal and external frames of the gyroscope (angles defining

<sup>\*</sup> Prof. dr. habil. Zbigniew Koruba, Eng.: Department of Applied Computer Science and Armament Engineering, Faculty of Mechatronic and Mechanical Engineering, Kielce University of Technology, Aleja Tysiąclecia Państwa Polskiego 7; 25-314, Kielce; PL, ksmzko@tu.kielce.pl

<sup>\*\*</sup> Eng. Izabela Krzysztofik, PhD.: Department of Applied Computer Science and Armament Engineering, Faculty of Mechatronic and Mechanical Engineering, Kielce University of Technology, Aleja Tysiąclecia Państwa Polskiego 7; 25-314, Kielce; PL, pssik@tu.kielce.pl

the position of the gyroscope axis in space);  $\dot{\mathcal{G}}_g, \dot{\psi}_g$  – angular velocity of the deviation of the internal and external gyroscope frames.

Controlling the gyroscope system consists in tracking the set direction in space by its axis, e.g. the line of sight (LOS) connecting the centre mass of the optical system of the gyroscope system with the moveable point in space being tracked. The angular position of the line of sight in comparison with the axis of the non-moveable reference system will be marked with angles:  $\varepsilon$  i  $\sigma$ , which specify the so called desired motion of the gyroscope axis. During the operation of the gyroscope, the rotor axis adopts the positions determined with angles:  $\mathcal{G}_g$  i  $\psi_g$ , which define the so called performed motion of the gyroscope axis. The line of sight might be then determined incorrectly, on the basis of which the missile is guided towards the target in homing systems. With too excessive deviations of the line of sight from the set position, the sight of the target image might be lost.

Deviation of the performed motion from the desired one is determined in the following way:

$$\Delta = \sqrt{(\mathcal{G}_g - \varepsilon)^2 + (\psi_g - \sigma)^2} \quad (2)$$

Quantity  $\Delta$  is called an actual control deviation. Apart from that, the notion of partial control deviations as the differences of angles is used:

$$e_g = \mathcal{G}_g - \varepsilon, \quad e_\psi = \psi_g - \sigma \quad (3)$$

The task of the tracking system is to minimize those deviations to zero. In order to perform the control in question, control with the use of LQR modified method might be applied.

## 2. An algorithm of optimal control of the gyroscope system

In order to determine the optimal control, the following quality criterion (target function) is formulated (Lewis et al., 2012 and Takosoglu, 2016):

$$I(u) = \frac{1}{2} \int_0^{t_f} (e^T Q e + u^T R u) dt \quad (4)$$

where  $e$  is a vector, whose components are the deviations described with an eq. (3) together with their derivatives in relation to time;  $u$  is a vector of the controlling moments put against the gyroscope frames;  $Q$  is a positive semi-definite square, symmetric matrix called the state weighting matrix;  $R$  is a positive definite square, symmetric matrix called the control cost matrix.

The optimal control problem consists in solving the feedback gain matrix,  $K$ , so that the scalar objective function,  $I(u)$ , is minimized if all state variables can be measured.

One of the important properties of LQR is that provided certain conditions are met, they guarantee nominally stable closed-loop system. The conditions for achieving a stable linear quadratic system are as follows (Tewari, 2002):

$$R > 0, \quad Q \geq 0, \quad (A, B) \text{ – controllable} \quad (5)$$

where  $A, B$  – matrices of state and control of the gyroscope system, respectively (as described in Koruba et al., 2010).

The reinforcement matrix might be determined with the use of Matlab function:

$$K = \text{lqr}(J, B, Q, R) \quad (6)$$

It should be highlighted that in LQR function described with eq. (6), the state matrix  $A$  state of the gyroscope system was replaced with Jacobian  $J$  which was presented with eq. (1). It constitutes an essence of the modified control of the gyroscope system. Matrix of reinforcements  $K$  becomes non-stationary and is calculated at each stage of determining the control signals  $u = -Kx$  ( $x$  – state vector with components:  $\mathcal{G}_g, \dot{\mathcal{G}}_g, \psi_g, \dot{\psi}_g$ ). Choosing the weight matrices  $Q$  and  $R$  usually involves some kind of trial and error.

### 3. Numerical example and the results

Let us consider the following issue. A moveable point in space is observed from the Earth by the seeker. The control task consists in the fact that the gyroscope axis is to overlap with the line of sight. Thus, the moveable target is being tracked. In the example, the results of which were presented in Figs. 1 – 4, the moveable point (target) determines the angles which are the desired signals, on the basis of the following equations:

$$\varepsilon(\tau) = a + 0.2 \cdot v \cdot \tau^2, \quad \sigma(\tau) = b + v \cdot \tau \quad (7)$$

where:

$a = 0.1; b = -0.2; v = 1.5$  – motion parameters of the point in space (set motion).

The research was conducted with an integration step amounting to  $dt = 0.00001$  (Baranowski, 2013).

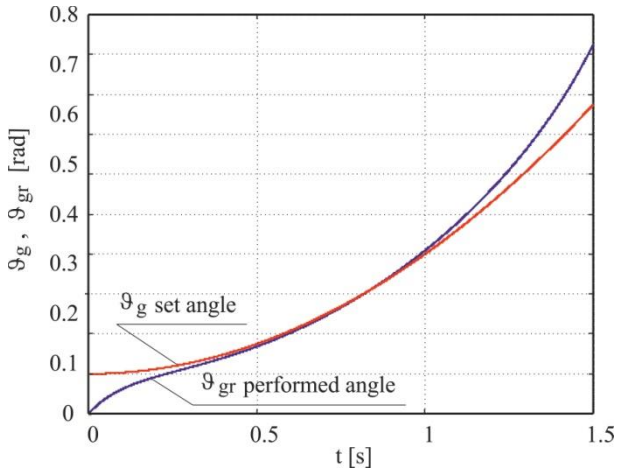


Fig. 1: Changes of performed and set angles in the time function with the use of matrix  $A$  with constant parameters.

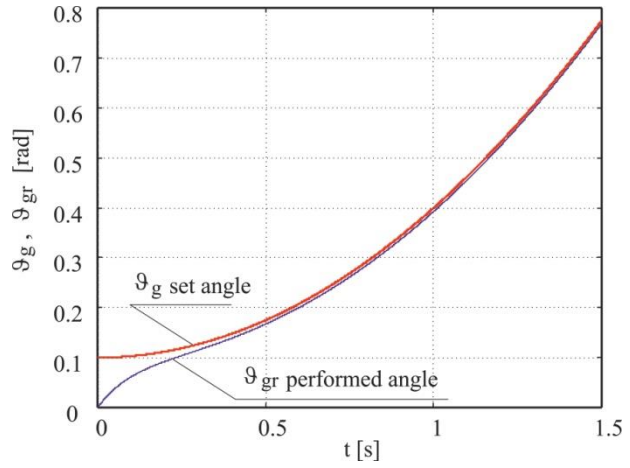


Fig. 2: Changes of performed and set angles in the time function with the use of Jacobian  $J$ .

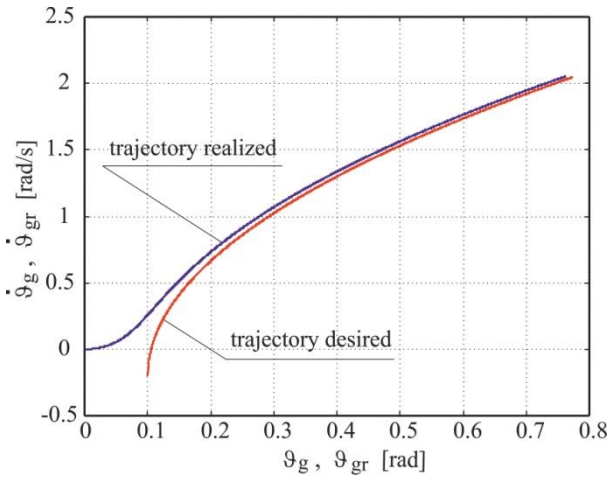


Fig. 3: Trajectories of the performed and desired motion with the use of matrix  $A$  with constant parameters.

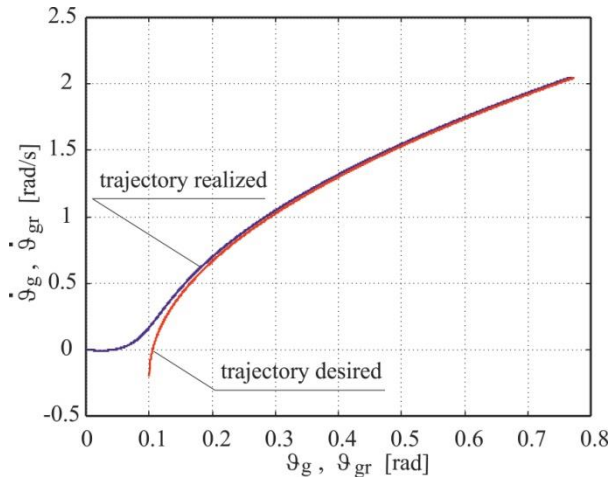


Fig. 4: Trajectories of the performed and desired motion with the use of Jacobian  $J$ .

The following matrix values were adopted:

$$A = [0 \ 1 \ 0 \ 0; 0 \ -200 \ 0 \ -1200; 0 \ 0 \ 0 \ 1; 0 \ 1200 \ 0 \ -200];$$

$$B = [0 \ 0; 4000 \ 0; 0 \ 0; 0 \ 4000];$$

$$Q = [1000 \ 0 \ 0 \ 0; 0 \ 10 \ 0 \ 0; 0 \ 0 \ 1000 \ 0; 0 \ 0 \ 0 \ 10];$$

$$R = [0.25 \ 0; 0 \ 0.25].$$



Taking the above charts showed in Figs. 1 – 4 into consideration, it is clear that control with the use of LQR modified method using Jacobian J operates in a better way – the gyroscope system axis reflects more faithfully the set motion along the observation line of the moveable point in space described with eq. (7).

#### 4. Conclusions

The control algorithm presented in this paper makes it possible to control the gyroscope system more precisely also in the case of changing its parameters over time. The example analyzed in the article shows that tracking the moveable material point in space by the gyroscope system with the use of Jacobian in a closed control loop is more effective than with the use classical LQR control method. As the research results showed, the improvement of control precision of the gyroscope system of 10 % might be of crucial importance as far as the target achievement in system of missile homing using the gyroscope system of this type is concerned. Further studies will refer to the influence of random disturbances in conditions with no measurement data of some state variables of the gyroscope system in homing systems.

#### References

- Baranowski, L. (2013) Effect of the mathematical model and integration step on the accuracy of the results of computation of artillery projectile flight parameters. *Bulletin of the Polish Academy of Sciences: Technical Sciences*, 61, 2, pp. 475-484.
- Dziopa, Z., Krzysztofik, I. and Koruba, Z. (2010) An analysis of the dynamics of a launcher-missile system on a moveable base. *Bulletin of the Polish Academy of Sciences: Technical Sciences*, 58, 4, pp. 645-650.
- Gapiński, D., Krzysztofik, I. and Koruba Z. (2014) Analysis of the dynamics and control of the modified optical target seeker used in anti-aircraft rocket missiles. *Journal of Theoretical and Applied Mechanics*, 52, 3, pp. 629-639.
- Gapiński, D. and Stefański, K. (2014) A control of modified optical scanning and tracking head to detection and tracking air targets. *Solid State Phenomena*, 210, pp. 145-155.
- Grzyb, M. and Stefański, K. (2016) The use of special algorithm to control the flight of anti-aircraft missile, in: *Proc. 22th Int. Conf. Eng. Mech. 2016* (eds. Zolotarev, I. and Radolf, V.), Inst. Thermomechanics, Acad. Sci. Czech Republic, Prague, pp. 174-177.
- Kim, P. (2010) Kalman filter for beginners with Matlab Examples. A-JIN Republic of Korea.
- Koruba, Z. and Krzysztofik, I. (2013) An algorithm for selecting optimal controls to determine the estimators of the coefficients of a mathematical model for the dynamics of a self-propelled anti-aircraft missile system. *Proceedings of the Institution of Mechanical Engineers, Part K: Journal of Multi-Body Dynamics*, 227, 1, pp. 12-16.
- Koruba, Z., Krzysztofik, I. and Dziopa, Z. (2010) An analysis of the gyroscope dynamics of an anti-aircraft missile launched from a mobile platform. *Bulletin of the Polish Academy of Sciences: Technical Sciences*, 58, 4, pp. 651-656.
- Koruba, Z. and Ładyżyńska-Kozdraś, E. (2010) The dynamic model of a combat target homing system of an unmanned aerial vehicle. *Journal of Theoretical and Applied Mechanics*, 48, 3, pp. 551-566.
- Krzysztofik, I. and Koruba, Z. (2014) Mathematical Model of Movement of the Observation and Tracking Head of an Unmanned Aerial Vehicle Performing Ground Target Search and Tracking. *Journal of Applied Mathematics*, 2014, Article ID 934250, 11 p.
- Lewis, F.L., Vrabie, D.L. and Syrmos, V.L. (2012) *Optimal Control*. John Wiley & Sons, Hoboken.
- Takosoglu, J.E. (2016) Control system of delta manipulator with pneumatic artificial muscles, in: *Proc. 22th Int. Conf. Eng. Mech. 2016* (eds. Zolotarev, I. and Radolf, V.), Svratka, Czech Republic, pp. 546-549.
- Tewari, A. (2002) *Modern Control Design with Matlab and Simulink*. John Wiley & Sons, Chichester.



## EFFECT OF CONTACT PARAMETERS ON THE PATTERN OF VEHICLE COLLISIONS WITH A ROUND PILLAR

R. Kostek<sup>\*</sup>, P. Aleksandrowicz<sup>\*\*</sup>

**Abstract:** *This article presents the effect of contact parameters on the pattern of a passenger car crash with a round pillar. First the default parameters and then the parameters identified from a crash test were applied to the simulation. Finally, the obtained results were studied. The differences observed between the results of these two simulations are considerable, which show the sensitivity of the obtained results to the input data. Usually expert witnesses do not have other data at their disposal, except for the default data offered by the program, which can lead to inadequate accident pattern evaluation, and an approximate incident reconstruction. This shows the difficulty of accident reconstruction.*

**Keywords:** Contact parameters, Crash simulation, Collision.

### 1. Introduction

For research purposes, collisions are simulated with the Finite Element Method. This allows for precise computations of crashes for various scenarios, vehicles and barriers (Dias de Meira et. al., 2016, Qi et al., 2006, Zhang, et al., 2015) whereas expert witnesses apply simpler IT tools offering computations in the MBS (Multi Body System) convention (<http://www.cyborgidea.com.pl>, <http://www.pc-crash.com>, <http://www.vcrashusa.com>). These programs use simplified models: linear relationships between the body crush and the force, as well as constant mass parameters during the crash (McHenry, 1997 and Rose et al., 2006). These programs are applied to the analysis of accidents, braking process and accident visualisation (Aleksandrowicz, 2016, Bułka et al., 2006 and Wolak, 2011). Certified property valuers usually assume default parameters offered by the program, without matching them to the studied incident, which is due to a lack of additional data. This article presents the problems faced in practice, of a change in the results of the simulation depending on the input data. The crashes investigated with computer programs are coupled with modelling of the contact between the vehicle, barrier and the road surface. Various contact models are applied, depending on the purpose, from linear to non-linear with memory (Kostek, 2012). It is also known that the systems with contact are sensitive to initial conditions, which are a result of non-linearity (Kostek, 2014). The model with the parameters identified from the crash test is studied in this article.

### 2. Collision simulations

The applied program (V-SIM) uses a few co-ordinate systems. The first one is a global system of co-ordinates  $x, y, z$ , which describes a positions of the barriers and displacement of vehicles. The second one is vehicle-related:  $x', y', z'$  (Fig. 1a). Axis  $x'$  is parallel to the ground and it passes through the mass centre of the vehicle  $C$  and is directed to the front; axis  $z'$  is directed vertically upwards and it passes through the mass centre of the vehicle  $C$  (Fig. 1a). Simulations were started from modelling a pillar (barrier) made from a material with the coefficient of friction equal to 1 and the coefficient of stiffness of  $100 \text{ MN/m}^2$  –both for the phase of compression and restitution. The object of this study is a passenger car – a Renault Twingo I. The vehicle's initial velocity was 50 km/h. However its mass equaled 981 kg and it did not change during the accident, which is typical for the MBS convention. The wheelbase was 2.247 m, while the tire contact with the road was described using the TM-Easy model. Mass and geometrical parameters as well as the model of the tire contact with the road were taken from V-SIM, and

<sup>\*</sup> Robert Kostek, PhD.: UTP University of Science and Technology in Bydgoszcz, Al. prof. S. Kaliskiego 7; 85 796, Bydgoszcz; PL, robertkostek@o2.pl

<sup>\*\*</sup> Piotr Aleksandrowicz, PhD.: UTP University of Science and Technology in Bydgoszcz, Al. prof. S. Kaliskiego 7; 85 796, Bydgoszcz; PL, almot@op.pl

the input data describing contact between the car and the pillar were identified from a crash test. The coefficients of stiffness of the car body were  $378 \text{ kN/m}^3$  for the phase of compression, and  $300 \text{ kN/m}^3$  for the phase of restitution; whereas the value of the coefficient of restitution was 0.08, and the grip index was 0.5. There was also introduced blocking of the left front wheel for  $t \geq 32 \text{ ms}$ . The program does not introduce that action automatically, even though the area of deformation covers the wheel. The vehicle was positioned in a way as to receive the overlap 40 % (0.65 m). The time being  $t = 0 \text{ ms}$  was assumed for the moment of the contact initiation between the vehicle and the pillar (Fig. 1b). Firstly, for the default parameters (body stiffness during compression and restitution  $414 \text{ kN/m}^3$ , the coefficient of restitution 0.19, the grip index 0.9 the changes of linear velocity, angular velocity and the position for time being  $t = 100 \text{ ms}$  and  $t = 1000 \text{ ms}$  were (Figs. 1c and 1e). At the next stage of the study, results were obtained for experimentally identified data (Figs. 1d and 1f). It was found that at the beginning the differences were not clear. However, with time, for  $t = 100 \text{ ms}$  there were observed various values of linear and angular velocities, the differences being  $2.4 \text{ km/h}$  and  $0.18 \text{ rad/s}$ . There were also noted different directions of linear velocity vectors. Larger differences were observed for  $t = 1000 \text{ ms}$ . The difference of linear velocity was  $7.2 \text{ km/h}$ , which is a result of wheel blocking and a lower value of the coefficient of restitution. The vehicle positions for that time were also different. Nevertheless, both vehicles stopped rotating for this time. The results obtained for experimentally identified data seem to be more reliable, which should be considered by software producers and certified property values in order to enhance the precision of accident reconstruction (<https://www.youtube.com/watch?v=d3tcoG8ynqI>, V-SIM4.0 – User manual, 2016).

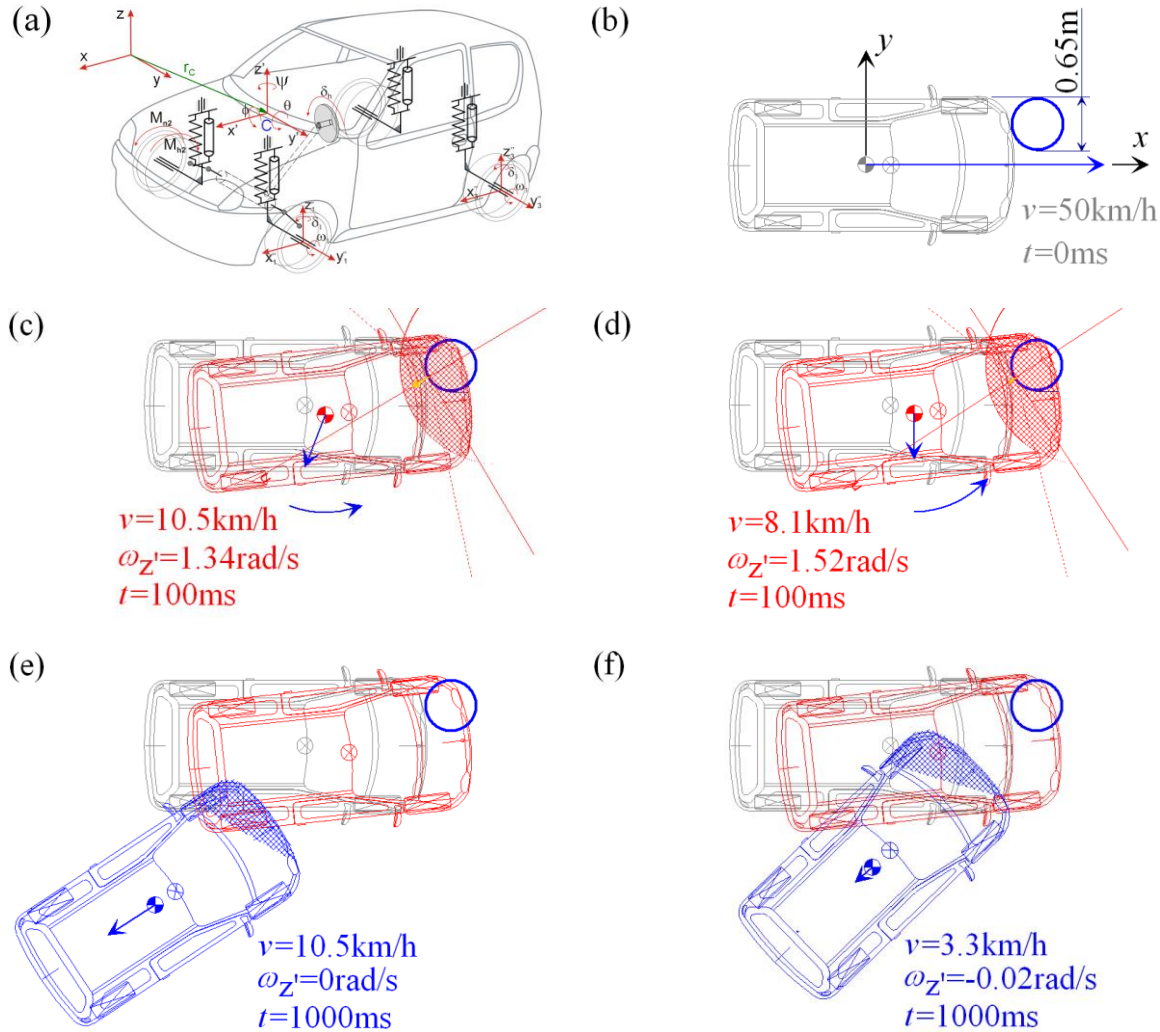
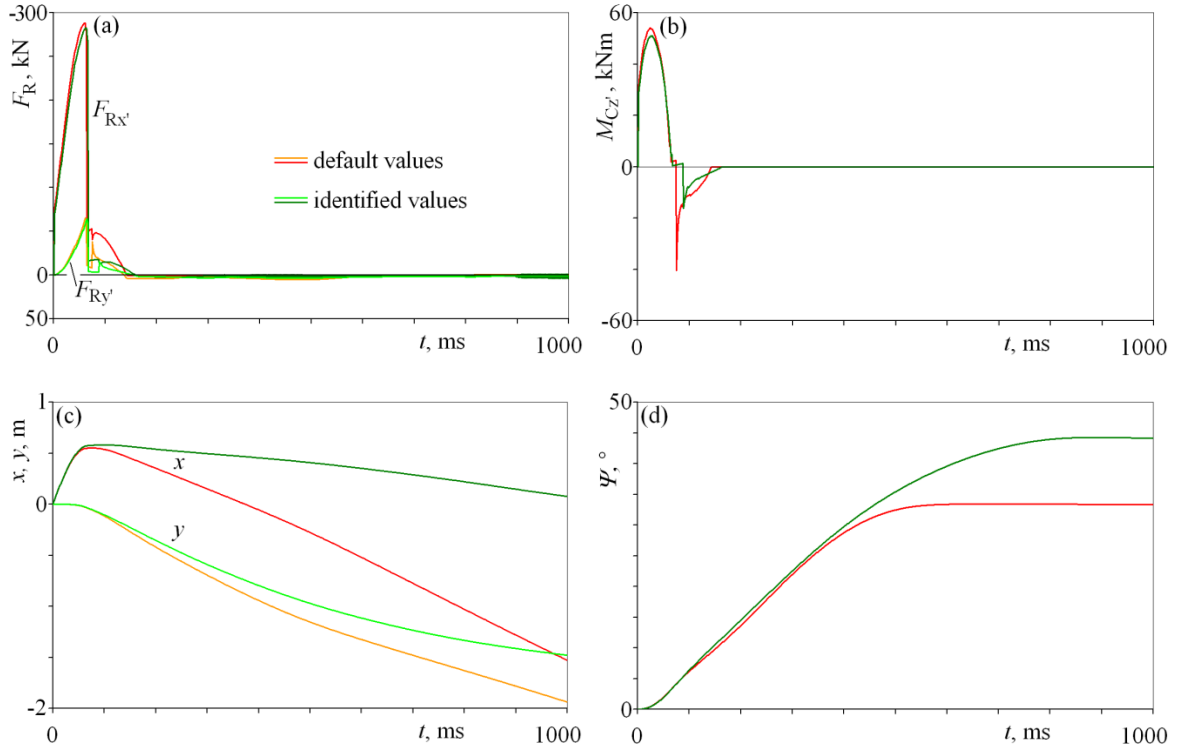


Fig. 1: Vehicle model with co-ordinate systems (a) and a comparison of the simulation results obtained for default program parameters (b, c, e) and the identified ones (b, d, f).

Next, the time histories of forces, moment, linear and angular displacement were presented. The analyses lead to a few conclusions. Large forces and moments act on the vehicle's users over a very short period of

time. It was found that the period is about 84 ms, it determines the effects of the crash, especially the users' injuries, the probability of their survival, as well as financial losses (Aleksandrowicz, 2014). Clear differences between acting forces and moments occurred from  $t = 84$  ms to  $t = 160$  ms, at the phase of restitution (Figs. 2a and 2b). It was also observed that the differences between the vehicle positions were increasing with the lapse of time after the phase of restitution (Figs. 2c and 2d). Initially for  $t = 100$  ms, the vehicle displacements for the default parameters were greater than for identified data  $\Delta x = 0.043$  m and  $\Delta y = 0.012$  m, whereas the difference between the angles of rotation  $\psi$  was  $\Delta \psi = 0.2^\circ$ . Then, for the time being  $t = 300$  ms, the differences were  $\Delta x = 0.16$  m,  $\Delta y = 0.016$  m and  $\Delta \psi = 1.7^\circ$ . This time corresponds to the end of contact between the vehicle and pillar for the default parameters; whereas for identified parameters the vehicle was in contact. Next, for the time  $t = 600$  ms, the differences increased further and they were  $\Delta x = 0.516$  m,  $\Delta y = 0.045$  m and  $\Delta \psi = 4.9^\circ$ , respectively. After that, differences  $\Delta x$ ,  $\Delta y$  were observed for  $t = 1000$  ms, and were considerable and they were still increasing; whereas the difference in the angles of rotation became stabilised  $\Delta \psi = 10.2^\circ$ . Finally, positions  $x$ ,  $y$  and  $\psi$  were presented for  $t = 1738$  ms. It was the time in which the vehicle, from the identified data, stopped  $v = 0$  km/h ( $x = 1.942$  m,  $y = 2.533$  m,  $\psi = 43.5^\circ$ ); whereas for the default data it was still moving backwards with the velocity of  $v = 10.1$  km/h ( $x = 5.053$  m,  $y = 3.931$  m,  $\psi = 33.4^\circ$ ). To illustrate these two cases, a film was presented (<https://www.youtube.com/watch?v=d3tcoG8ynqI>). It clearly shows the different scenarios of the incidents and a different post-impact movement and sensitivity to the adopted parameters.



*Fig. 2: Time histories of: projection on axis  $x'$ ,  $y'$  of resultant force  $F_R$  acting on the vehicle (a), a component of resultant moment acting on vehicle  $M_{Cz'}$  (b) displacement of vehicle (c) and angle of rotation  $\psi$  (d) obtained for default values (red and orange) and identified values (brightly green and dark green).*

### 3. Conclusions

The presented results of simulations show large differences after introducing changes to the input data. There was found a clear change in the post-accident position of the vehicle. The simulation of the crash for the default parameters leads to a smaller rotation of the vehicle around axis  $z'$  and unnatural movement backwards. It should be noted that for the time being at  $t = 1738$  ms for identified parameters, the vehicle stops; whereas for default parameters it goes back with velocity  $v = 10.1$  km/h. It confirms the sensitivity of the results of simulations to input data, which leads to a practical conclusion: the application

of default parameters offered by IT tools can lead to incorrect results. To make good accident reconstruction, the expert should not only be highly qualified but also perform many calculations to receive the best solution or a group of solutions, which would be closest to a/the real accident. He or she should also use the possibility of changes in input parameters in the program based on the data received from crash tests and literature, and not to accept the default data offered by the program uncritically. Simulation programs, on the other hand, should use experimentally verified data to enhance the reliability of any results. The deformation models should be non-linear. To recapitulate, the sensitivity of simulation results to the input data makes the accident reconstruction very difficult, and it should be noted that computation errors can affect the responsibility of the parties to the court proceedings.

## References

- Aleksandrowicz, P. (2016) Analysis of the process of vehicle stopping with the use of emergency braking system. 42nd International Scientific Congress on Powertrain and Transport Means. Journal of KONES, 11-14.09.2016 Jastrzębia Góra, Vol. 23, No. 1, pp. 9-15.
- Aleksandrowicz, P. (2014) Biomechanics in road accident analysis. The Press of the University of Science and Technology in Bydgoszcz, Bydgoszcz, (in Polish).
- Bulka, D., Walczak, S. and Wolak, S. (2006) Braking process – legal and technical aspect in simulation and analytical approach. The 3rd Scientific and training conference, Car technology development and traffic insurance 7-8.06.2006 Radom, pp. 19-52, (in Polish).
- Dias de Meira, A., Iturrioz, I., Walber, M. and Goede, F. (2016) Numerical Analysis of an intercity bus structure: A simple unifilar model proposal to assess frontal and semifrontal crash scenarios. Latin American Journal of Solids and Structures, Vol. 13, No. 9, pp. 1616-1640.
- Kostek, R. (2014) Simulation and analysis of vibration of rolling bearing. Key Engineering Materials, Vol. 588, pp. 257-265.
- Kostek, R. (2012) The modelling of loading, unloading and reloading of the elastic-plastic contact of rough surfaces. Journal of Theoretical and Applied Mechanics, Vol. 50, Issue: 2, pp. 509-530.
- McHenry, R. and McHenry, B. (1997) Effects of Restitution in the Application of Crush Coefficients. SAE Paper no 970960.
- Qi, W., Jin, X.L. and Zhang, X.Y. (2006) Improvement of energy-absorbing structures of a commercial vehicle for crashworthiness using finite element method. The International Journal of Advanced Manufacturing Technology, Vol. 30, Issue 11, pp. 1001-1009.
- Rose, N., Fenton, S. and Beauchamp, G. (2006) Restitution modeling for crush analysis: Theory and validation. SAE Paper no 2006-01 – 0908.
- VSIM4.0 – User manual. (2016), CIBID, Cracow, (in Polish).
- Wolak, S. (2011) Vehicle trajectory – practical use of driver model in the VSIM program. Paragraph on the road, Vol. 7, pp. 55-65, (in Polish).
- Zhang, X.Y., Jin, X.L., Qi, W. and Guo, Y.Z. (2008) Vehicle crash accident reconstruction based on the analysis 3D deformation of the auto-body. Advances in Engineering Software, Vol. 39, Issue 6, pp. 459-465.

## IDENTIFICATION OF THE PARAMETERS OF VEHICLE CONTACT WITH A RIGID BARRIER FROM A CRASH TEST

R. Kostek<sup>\*</sup>, P. Aleksandrowicz<sup>\*\*</sup>

**Abstract:** *This article presents both the results of computer simulations of vehicle crashes with a rigid barrier, simulated with the V-SIM simulation software, as well as the experimental results published by ADAC (Allgemeiner Deutscher Automobil-Club). The results were obtained for the same initial conditions, which provide an opportunity to evaluate the computer simulation's credibility and the identification of selected parameters; wheel blocking time, car body stiffness and the coefficients of friction and restitution. Once those parameters have been changed, a good agreement with experimental results was reported. The remaining difference is a result of a simplified modelling of forces which act during a vehicle collision. All that shows that expert witnesses should provide, in their expertise, a range of parameters for which they receive a similar accident reconstruction and not to base it on a single simulation only. They should do it due to input data uncertainty, and the sensitivity of the accident reconstruction to input data.*

**Keywords:** V-SIM, Crash model, Parameter identification, Sensitivity, Contact.

### 1. Introduction

Today's road accidents are reconstructed by expert witnesses, being commissioned by the bodies involved in a court case with the use of computer software, which generates specific consequences for the parties to the court proceedings. The models applied in such programs are simplified, which introduces errors into the results of the calculations. Similarly, the default values of the parameters do not always correspond to the real values of parameters which occurred during the crash. It refers to e.g. the body stiffness and friction coefficients (McHenry et al., 1997, Rose et al., 2006). All that does is to introduce some uncertainty of the calculations, which is additionally increased by the sensitivity of the accident reconstruction to the input values of the given parameters, which is typical for the systems with body contact (Kostek, 2014, Kostek, 2012). Expert witnesses are not, unfortunately, aware of those phenomena and so they approach the results without any reservations. Accident simulation and reconstruction are thus an important issue, with both cognitive and practical qualities (Aleksandrowicz, 2016, Bułka et al., 2006 and Wolak, 2011). This article focuses on the identification of said parameters, e.g. wheel blocking time, parameters of the contact of the car body with the barrier and the coefficient of friction between the tire and the "road surface", as well as the effect of those parameters on the accident pattern. Expert witnesses use the software which performs calculations in MBS (Multi Body System) convention on a PC (<http://www.cyborgidea.com.pl>, <http://www.pc-crash.com>, <http://www.vcrashusa.com>). Such calculations are burdened with some errors due to constant mass parameters of the vehicle during a crash; a linear dependence between the vehicle deformation and the contact force, as well as uncertain input data affecting the result of the accident reconstruction (Wach et al., 2007a and Wach et al., 2007b). In Poland, expert witnesses commonly use V-SIM software which models crashes in the MBS convention (<http://www.cyborgidea.com.pl>). In literature known to the authors, the errors of simulation obtained with V-SIM for head-on collisions were not investigated, hence the study of this issue in this article.

---

<sup>\*</sup> Robert Kostek, PhD.: University of Science and Technology in Bydgoszcz, Al. prof. S. Kaliskiego 7; 85-796, Bydgoszcz; PL, robertkostek@o2.pl

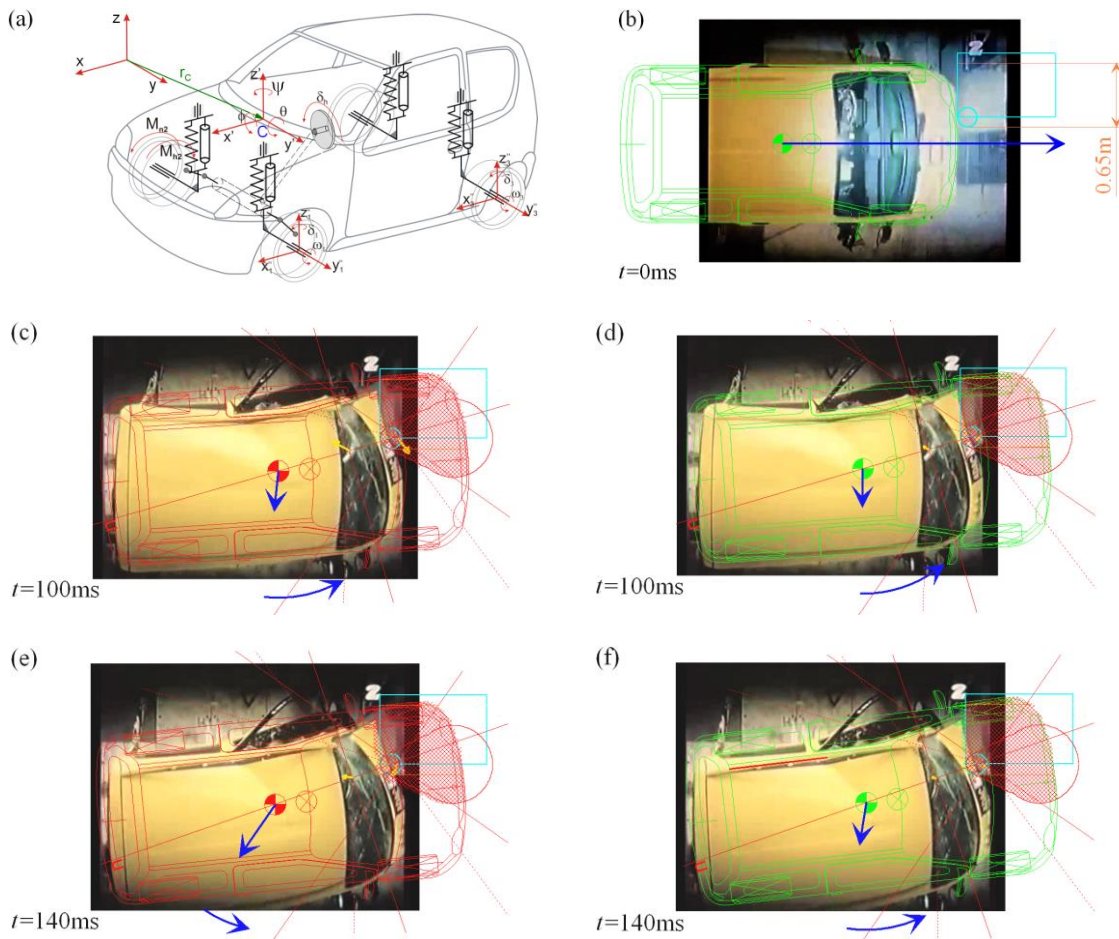
<sup>\*\*</sup> Piotr Aleksandrowicz, PhD.: University of Science and Technology in Bydgoszcz, Al. prof. S. Kaliskiego 7; 85-796, Bydgoszcz; PL, almot@op.pl



## 2. Crash investigation

The V-SIM software applies two co-ordinate systems, the global one related to ground  $xyz$  and the local one  $x', y', z'$  related to the car body (Figs. 1a, 2e). Crash test involved a Renault Twingo manufactured before July 1993. For the purpose of the calculations, the following data were applied: a vehicle from V-SIM database (VSIM4.0 – User manual, 2016) and 845 kg as vehicle's curb weight, the driver and passenger weights – 68 kg, 155/65 R14 tires and tire model TM – Easy, 2.247 m wheelbase, and wheel tracks – 1.416 m for the front axle and 1.374 m for the rear axle, respectively. The vehicle's initial velocity was 50 km/h.

The experiment was started from the modelling of a barrier which consists of a cuboidal block and a round pillar. Then the vehicle was positioned in a way so as to receive a 40 % (0.65 m) overlap, as declared by ADAC (Brieter, 1993, <https://www.youtube.com/watch?v=UoaI-NuGBN4>). In the next step, there were matched to the images recorded by a camera which filmed the collision from the top. Time  $t = 0$  ms was assumed for the moment of the initiation of the contact between the vehicle and the barrier (Fig. 1b). For that film frame the vehicle scale was adjusted. Then the vehicle was slowed down and for  $t = 100$  ms there was observed large body deformation and a decrease in the vehicle's speed. The images received for  $t = 100$  ms look similar (Fig. 1c, 1d).



*Fig. 1: a) Vehicle model and co-ordinate systems; as well as a comparison of the experimental results with the simulation results – default (b, c, e) and changed (b, d, f) input data.*

Then the vehicle bounces and turns ( $t = 140$  ms). In this case the speeds and positions received for the two simulations differ clearly. For the modified parameters, the rotation of the vehicle is larger, which reflects better post-impact movement. The red line marks the left edge of the roof to demonstrate a good agreement between the angles of rotation (Fig. 1f).

The next stage involved a comparison of the time histories obtained for the default model, the model with modified parameters and a presentation of experimental results measured from the images recorded. The measurements were made by reading the position of selected points on a bitmap. In this case the base was provided by the back and white scale for  $t = 0$  ms and non-deformed part of the vehicle right behind the

vehicle door. And then a correction was introduced for the rotation of the vehicle based on simulation results. Performing the series of iterations, a satisfactory agreement between the results was received (Fig. 1f, 2e).

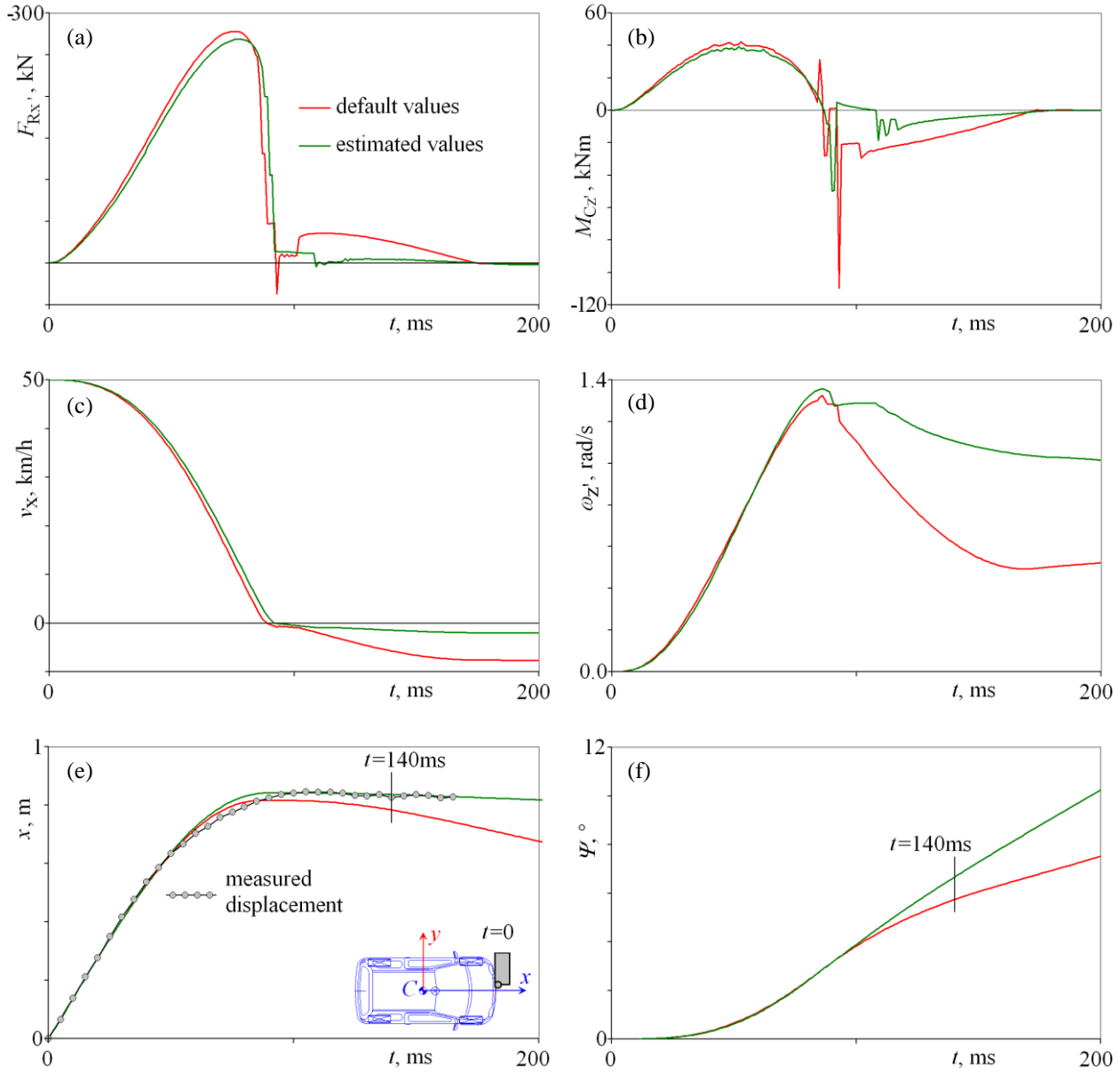


Fig. 2: Time histories of: a) projection on axis  $x'$  of resultant force  $F$  acting on the vehicle; b) component of resultant moment acting on vehicle  $M_{Cz'}$ ; c) linear velocity  $v_x$ ; d) angular velocity  $\omega_z$ ; e) displacement of the center of mass of the vehicle in the global system  $x_c$ ; f) angle of rotation  $\psi$ .

The identification resulted in the following changes of parameters: the coefficient of body stiffness for the compression phase was decreased from 414 kN/m<sup>3</sup> to 378 kN/m<sup>3</sup>, and for the restitution phase – it was decreased from 414 kN/m<sup>3</sup> to 300 kN/m<sup>3</sup>, the coefficient of restitution was decreased from about 0.25 to 0.08. Additionally, the left front wheel was blocked for  $t = 32$  ms. The coefficient of friction between the tyre and the ground was decreased to 0.5 due to a loss of contact between the back wheels and the “road surface”, both for static and kinetic friction. A decrease in the coefficient of stiffness at the compression phase allowed for matching the body deformation, whereas the other parameters helped to match the rotation of the body. As a result, the greatest differences between the results are visible for the restitution phase.



### 3. Conclusions

The study shows a satisfactory agreement between the experimental results and the results of the simulation only after introducing changes in the value of the parameters and wheel blocking. There was received a similar accident reconstruction, a similar body deformation and a similar angle of rotation for  $t = 140$  ms. A growing difference between the results at a later simulation phase comes from sensitivity to input parameters; stiffness and coefficient of restitution, friction coefficient. Another pattern is found for the forces and, as a result the vehicle bounces off the barrier differently and velocity vectors have a different direction and module. As a result, another post-accident position is obtained. Such effect is typical for non-linear systems and it is referred to as a butterfly effect. Simulation in the mode of default parameters offered by the program generated worse results, which confirms an essential role of experts and their experience. Additionally, instead of the application of simple contact models, one should use the characteristics received in FEM (Finite Element Method) or experimentally. Such a solution would not cause any doubt, and, at the same time, the computational costs would be low. Another solution would involve a simplified or partial vehicle modelling in FEM. For example a deformed part of the vehicle could be modelled in FEM and the rest – in MBS convention. The study demonstrates a sensitivity of the results to selected parameters, which is typical for non-linear systems. Bearing that in mind, a practical conclusion can be developed: each accident reconstruction simulation software should also include an optimizing module facilitating the identification of initial conditions and the accident reconstruction.

### References

- Aleksandrowicz, P. (2016) Safety of armed forces vehicles driving in a motorcade. Part II – Verifying a safe distance and driving speed in motorcade, effects of vehicles crash – injuries and material loss. Military Institute of Armoured and Vehicle Technology, BelStudio, Warszawa, pp. 137-147 (in Polish).
- Bułka, D., Walczak, S. and Wolak, S. (2006) Braking process – legal and technical aspect in simulation and analytical approach. The 3rd Scientific and training conference, Car technology development and traffic insurance 7-8.06.2006, Radom, pp. 19-52 (in Polish).
- Brieter, K. (1993) Crash of 5 small cars in ADAC – test, ADAC Motorwelt 9/93 pp. 10-17 (in Germany).
- Kostek, R. (2014) Simulation and analysis of vibration of rolling bearing. Key Engineering Materials, Vol. 588, pp. 257-265.
- Kostek, R. (2012) The modelling of loading, unloading and reloading of the elastic-plastic contact of rough surfaces. Journal of Theoretical and Applied Mechanics, Vol. 50, Issue: 2, pp. 509-530.
- McHenry, R. and McHenry, B. (1997) Effects of Restitution in the Application of Crush Coefficients. SAE Paper no. 970960.
- Rose, N., Fenton, S. and Beauchamp, G. (2006) Restitution modeling for crush analysis: Theory and validation. SAE Paper no 2006-01-0908.
- VSIM4.0 – User manual. (2016), CIBID, Cracow (in Polish).
- Wach, W. and Unarski, J. (2007) Determination of collision location – uncertainty analysis by means of Monte Carlo simulation, 16th EVU Annual Meeting Proceedings, 8-10. 11.2007 Cracow, pp. 73-93.
- Wach, W. and Unarski, J. (2007) Uncertainty of calculation results in vehicle collision analysis. Forensic Science International, Vol. 167, Issue 2-3, pp. 181-188.
- Wolak, S. (2011) Vehicle trajectory – practical use of driver model in the VSIM program. Paragraph on the road, Vol. 7, pp. 55-65 (in Polish).

## INTELLIGENT SCHEDULED MAINTENANCE METHODOLOGY FOR GENERAL AVIATION STRUCTURES BASED ON MSG-3 AND MULTIPLE- CRITERIA DECISION MAKING ANALYSIS

R. Košťál\*, L. Janhuba \*\*, J. Hlinka \*\*\*

**Abstract:** Aircraft scheduled maintenance requirements are rapidly extending and developing. Scheduled maintenance has to be effective, reliable and economically reasonable. In the field of general aviation and FAR 23/ EASA CS-23 especially, preventive maintenance based on part replacing or repairing is still dominant. DAMAGE TOLERANCE philosophy implementation into an aircraft design influences maintenance procedures, which are adjusted to older SAFE LIFE philosophy. Aircraft manufactures are developing new ways, how to integrate requirements of damage tolerance application into scheduled maintenance procedures. Huge airliners manufactures (FAR 25/ CS-25) are using the ATA MSG-3 intelligent maintenance approach based on inspection. This paper describes development of intelligent scheduled maintenance methodology, utilizing ATA MSG-3 procedures, expert knowledge and multiple criteria decision making.

**Keywords:** MSG-3, Maintenance, Aircraft, Structures, Multiple-Criteria Decision Analysis.

### 1. Introduction

In nowadays FAR 23/ CS-23 aircraft structures design is still usually applied SAFE LIFE philosophy. It means, that structure is designed to survive specific design life with an appropriate reserve. Failure of this structure is than highly improbable. Main disadvantage of this philosophy is that each structure has specified life-time and due to safety reserves higher weight compared to the structure designed according to the DAMAGE TOLERANCE philosophy. Scheduled maintenance of these structures is based on their replacement after specific time interval. Therefore, specific structure life-time could be lower than aircraft life-time. It is not an exception, that structure is replaced, when it is still functional and reliable.

However, structures designed according to the DAMAGE TOLERANCE has ability to sustain occurring defect. It is possible to manage extension of defect due to maintenance based on inspection. Grow of defect (more precisely crack) must be slow, which makes possible to detect these defects. In the case of low severity defects, scheduled maintenance is created to monitor its spreading. Structures with high severity defects are restored or replaced. Therefore, the amount of replaced items is significantly reduced, for the price of increased maintenance requirements.

Application of MSG-3 is one of the solutions, how make maintenance more effective and adequate to the elevated complexity. It has been successfully used for decades in airliner aviation (FAR 25/ CS-25).

MSG-3 (ATA, 2011) is task oriented process of scheduled maintenance based on Reliability-Centered Maintenance (RCM) management adjusted for aviation industry application. Process of scheduled maintenance creation is designed to establish most effective method how to maintain particular items and systems. MSG-3 utilizes logic decision tress to determine relevant requirements for preventive maintenance according to identified item failure modes, degradation process and resulting consequences.

---

\* Ing. Rostislav Košťál: Institute of Aerospace Engineering, Brno University of Technology, Technická 2896/2 616 69 Brno; CZ, kostial@fme.vutbr.cz

\*\* Ing. Luboš Janhuba: Institute of Aerospace Engineering, Brno University of Technology, Technická 2896/2 616 69 Brno; CZ, janhuba@fme.vutbr.cz

\*\*\* Assoc. Prof. Jiří Hlinka, PhD.: Institute of Aerospace Engineering, Brno University of Technology, Technická 2896/2 616 69 Brno; CZ, hlinka@fme.vutbr.cz

MSG-3 consists of four categories: Aircraft Systems and Powerplant; Aircraft Structures; Zonal Inspections; Lightning/High Intensity Radio Frequency (L/HIRF).

For simplification, this paper illustrates purposed intelligent scheduled maintenance methodology only on Aircraft Structures.

In the case of aircraft structures, there are three basic failure causes: Fatigue Damage (FD); Accidental Damage; Environmental Damage (ED). For aircraft structures the most relevant type of failure cause is fatigue damage (FD) especially in the case of DAMAGE TOLERANCE philosophy application. MSG-3 contains Fatigue Damage Analysis Diagram as mean of maintenance task definition for structures with fatigue failures possibility. There are three resulting tasks: General Visual Inspection (GVI); Detailed Visual Inspection (DET); Special Detailed Inspection (SDI) including Nondestructive Testing (NDT). However, MSG-3 does not offer way, how to choose a proper task for particular item. Purposed methodology uses multiple-criteria decision analysis as a part of multiple criteria decision making to establish most effective tasks set based on various requirements.

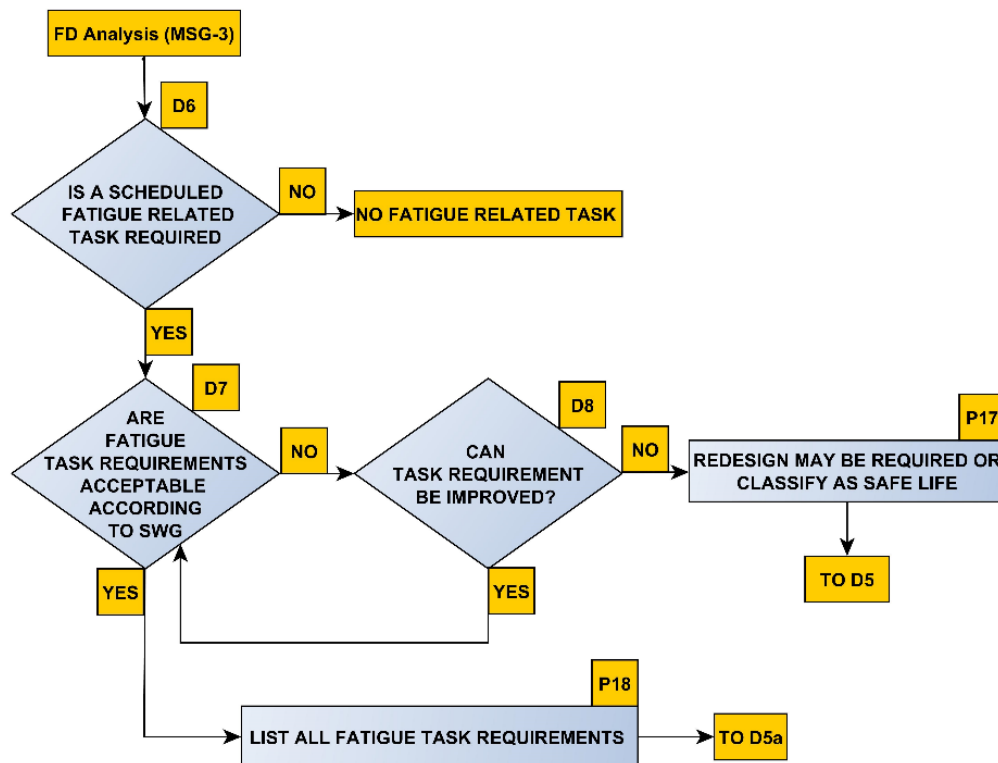


Fig. 1: MSG-3 Fatigue Damage Analysis Logic Diagram (FDALD).

## 2. Multiple-Criteria Decision Analysis

Multiple-criteria decision analysis (MCDA) described in textbook (Fiala et al., 1997) is the process of multiple variant evaluation using several criteria. As a variant is taken type of inspection. The main goal of this process is to sort multiple variants by their suitability, eliminate non-effective variants and find the best ranked variant.

Proposed method is using selected MSG-3 tasks- **GVI**, **DET** and **SDI** inspection. **SDI** inspection is further divided into particular methods applicable on metal or non-metal (composite) aircraft structures, for example penetration tests, eddy currents methods, ultrasonic testing, radiographic method and magnetic defectoscopy.

MCDA uses qualitative and quantitative criteria to represent various attributes and characteristics of a structure. Through these criteria particular variants are compared. As basic criteria are selected- Intervals between inspections, Inspection cost, Inspection time and Inspection complexity.

Particular criteria are not equal. There are preferences among the criteria to represent its importance in relation to other rules. There are used three types of criteria preference- **NO PREFERENCE**, **ASPIRATION LEVEL**, **ORDINAL** (see Tab. 1.

Tab. 1: Criteria preference definition.

CRITERIA PREFERENCE	DEFINITION	APPLICABLE METHODS
NO PREFERENCE	No criteria preferences. <i>Example: preliminary methods selection at the start of the aircraft development.</i>	Scoring method
ASPIRATION LEVEL	Threshold values are given to the criteria, which has to be fulfilled and then taken as usable variants (compromise). <i>Example: Final stage of maintenance creation when inspection interval is established to 4000 hours and inspection time has to be up to 30 minutes on the particular item.</i>	PRIAM Conjunctive Disjunctive
ORDINAL	Analyst has to know sequence of preference from the most preferred to the lowest. It is favorable for the aircraft operators, who are able adjust maintenance accreting to their requirements. <i>Example: Inspection cost =&gt; inspection complexity (required equipment) =&gt; Inspections intervals =&gt; Inspection time.</i>	ORESTE Lexicographic method

In this case, MCDA is implemented into MSG-3 Fatigue Damage Logic Diagram (Fig. 1), the analysis itself is performed between D6 and D7 points of FDLD in Fig. 1. At first, a set of possible methods is established. For each of these methods, detectable crack size is calculated (based on methodology by Bent (2010)) and time intervals are determined according to the equation (1).

$$T_I = \frac{T_{Crit} - T_{Det}}{RF} \quad (1)$$

$T_I$  is the interval between inspections.  $T_{Crit}$  is time of unstable crack, which is established by the calculation or fatigue tests.  $T_{Det}$  is time until the detectable size of crack occurs.  $RF$  is scattering factor. Further, the cost, time, inspection complexity, etc., factors are taken into a process.

### 3. A Case Study

As a case study was chosen a small area (ca. 240 cm<sup>2</sup>) on root part of flange on wing main spar of EASA CS-23 Commuter aircraft. The aim was maintenance interval extension from 2400 flight hours to the 3200 flight hours. Selected structure was designed according to the DAMAGE TOLERANCE philosophy with 50 000 hours' calculated lifetime.

**Possible maintenance variants:** GVI, DET, Eddy current, Penetration tests. **Considered variants:** Inspection cost, Inspection time, Interval between inspections, Inspection complexity.

Tab. 2: Definition of basic values for flange inspection.

VARIANT	CRITERIA			
	Price [USD]	Time interval between inspections [hour]*	Inspection Time [min]	Inspection complexity [-]**
GVI	5	733	35	Very low
DET	6	2400	40	Low
Eddy current	10	10667	45	High
Penetrating methods	12	3900	100	Low

\* Conversion to the minimization volumes  $y_{2jmin} = y_{23} - y_{2j}$

\*\* Quantification by using the score tables: 1 (Very low) – 3 (High)

**Resulting decision matrix, A (Minimized criteria values => lower is better):**

$$A = \begin{pmatrix} 5 & 9934 & 35 & 1 \\ 6 & 8267 & 40 & 2 \\ 10 & 0 & 45 & 3 \\ 12 & 6767 & 100 & 2 \end{pmatrix} \quad (2)$$

Flange maintenance requirements: Price 8 USD (changeable aspiration level), Interval between inspection 3200 hours (fixed), Inspection time 60 minutes (changeable aspiration level), Inspection complexity High (fixed).

Among all possible variants  $A_i$ , acceptable variants  $M_i$  will be variant with volume (according to the all considered aspects) equal to the preselected aspiration level volume  $y_j^*$ . See (4).

$$M = \{A_i | y_{ij} \leq y_j^*, \forall j = 1, 2, \dots, n\} \quad (3)$$

While aspiration levels reach  $y^{(1)} = (8, 7467, 60, 3)$ , it occurs, that  $M = \emptyset$ . In this case, it is necessary to lower the aspiration levels. The aspirations levels were changed to  $y^{(2)} = (12, 7467, 120, 3)$ . After aspiration levels change, the result was, that two options (Eddy current, Penetration test) reached given requirements. Through to aspiration levels change, it is possible to select one variant among all available variants.

In this case, the compromise variant is inspection by using eddy currents. **It results in maintenance interval extension from 2400 hours to the 3200 hours.** Alternative variant is usage of penetration methods (lower score volume compared to the eddy currents).

#### 4. Conclusions

Intelligent scheduled maintenance methodology based on ATA MSG-3 and multiple- criteria decision analysis is discussed in this paper. ATA MSG-3 maintenance methodology is nowadays commonly used in airliner FAR 25/ CS-25 category. Further latest development of certification procedures described in FAA Advisory Circular documentation (FAA AC-121-22C, 2012) aims to mandatory application of MSG-3 procedures for civil airplanes with more than 10 passengers or maximal takeoff weight higher than 33000 pounds.

Proposed intelligent maintenance methodology extends MSG-3 procedures by multiple-criteria decision making analysis. Paper presents results of prepared case study, which is a part of dissertation thesis **“Modern maintenance procedures for airframe inspections for general aviation category aircraft”**. The dissertation thesis contains methodology, how to use multiple criteria decision making based usage of the ordinal criteria, aspiration levels criteria and without preferred criteria.

This paper presents example of multiple criteria decision making application, more precisely aspiration levels usage. Example goal was to extend interval between inspections of particular aircraft structure using proposed intelligent maintenance methodology. Results show, that it is possible to extend this interval from 2400 hour to the 3200 hours using the eddy currents inspection method.

In future, presented methodology could be used for aircraft structure critical parts (from the inspection point of view) and Structure Health Monitoring application.

#### References

- ATA (2011) MSG-3 Operator/Manufacturer Scheduled Maintenance Development, rev. 2011.1, Washington.
- Fiala, P. Jablonksy, J. and Manas, M. (1997) Multiple criteria decision, University of Economics, Prague, (in Czech).
- Bent, L.J. (2010) Practical airframe fatigue and damage tolerance, 1<sup>st</sup> ed: Sigma K Ltd.
- AC-121-22C (2012) Maintenance Review Boards, Maintenance Type Boards, and OEM/TCH Recommended Maintenance Procedures, FAA, Washington.

## NUMERICAL MODELLING OF EXPANSIVE CLAYS

T. Koudelka<sup>\*</sup>, T. Krejčí<sup>\*\*</sup>, J. Kruis<sup>\*\*\*</sup>

**Abstract:** *The paper deals with the hypoplastic model for expansive clays which takes into account the double structure of clays. The model is formulated in the rate form which requires integration in time. Several integration schemes based on the Runge-Kutta-Fehlberg (RKF) methods of different order have been investigated. The RKF methods have been implemented in the FE code SIFEL and there is a comparison of their performance on a benchmark example of triaxial test. The mechanical model is accompanied with the model of one-phase water flow in the porous medium.*

**Keywords:** Expansive clays, Hypoplasticity, Runge-Kutta-Fehlberg method, Water flow in porous medium, Coupled problem.

### 1. Introduction

Expansive clays are known for their large swelling/shrinkage capacity which is influenced by the water content namely. Bentonites are also known for their very low permeability coefficient whose typical magnitude ranges from  $10^{-14}$  to  $10^{-12}$  m.s<sup>-1</sup> according to void ratio. Swelling accompanied with low permeability comprises self-sealing properties of bentonites that have been exploited in the sealing of dams for example. The bentonites are also assumed to be a part of engineering barrier at deep geological repositories in high level radioactive waste disposals. The engineering barrier is composed from the special containers for spent nuclear fuel sealed by the bentonite layer which should be able to stop the radionuclides migration in the case of container failure. Obviously, it is crucial for the design of engineering barrier to use the proper model of bentonite behaviour.

In the soil modelling, two major groups of models are exploited. One large (older) group of models is based on theory of elasto-plasticity (Hughes 1987) where the model assumes plastic strains in the form

$$\dot{\boldsymbol{\varepsilon}} = \dot{\lambda} \frac{\partial f(\boldsymbol{\sigma}, \mathbf{h})}{\partial \boldsymbol{\sigma}}, \quad (1)$$

$$\boldsymbol{\sigma} = \mathbf{D}_e : (\boldsymbol{\varepsilon} - \boldsymbol{\varepsilon}_p), \quad (2)$$

where  $f(\boldsymbol{\sigma}, \mathbf{h})$  represents selected yield function. In the above equations,  $\boldsymbol{\sigma}$  stands for the stress tensor,  $\mathbf{h}$  is the vector of hardening parameters,  $\dot{\lambda}$  is the consistency parameter,  $\mathbf{D}_e$  is the fourth-order elastic stiffness tensor,  $\boldsymbol{\varepsilon}$  is the total strain tensor and  $\boldsymbol{\varepsilon}_p$  is the tensor of plastic strains. Several models for the partially saturated soils have been proposed (e.g. Alonso, 2011). Advantages of the mentioned elasto-plastic models is the pressure dependent loading, direct incorporation of the state boundary surface and, in the case of extended model, the taking into account the influence of suction pressure. But they have also important shortcoming related to the elastic unloading which is not in agreement with the observed soil behaviour.

To avoid of these shortcomings, a relatively new group of hypoplastic models has been developed by Gudehus, 2004 and Herle, 20011. They have involved different loading/unloading moduli directly in the rate form of stress-strain relation:

$$\dot{\boldsymbol{\sigma}} = \mathcal{M}(\boldsymbol{\sigma}, \Delta \boldsymbol{\varepsilon}, \mathbf{v}) : \dot{\boldsymbol{\varepsilon}}, \quad (3)$$

---

<sup>\*</sup> Ing. Tomáš Koudelka, PhD.: Faculty of Civil Engineering of Czech Technical University in Prague, Thákurova 7; 166 29, Prague; CZ, koudelka@cml.fsv.cvut.cz

<sup>\*\*</sup> Ing. Tomáš Krejčí, PhD.: Faculty of Civil Engineering of Czech Technical University in Prague, Thákurova 7; 166 29, Prague; CZ, koudelka@cml.fsv.cvut.cz

<sup>\*\*\*</sup> Prof. Jaroslav Kruis, PhD.: Faculty of Civil Engineering of Czech Technical University in Prague, Thákurova 7; 166 29, Prague; CZ, koudelka@cml.fsv.cvut.cz



where  $\mathcal{M}$  is the fourth-order generalized stiffness tensor which depends on the actual stresses  $\boldsymbol{\sigma}$ , increment of strains  $\Delta\boldsymbol{\varepsilon}$  and other state variables denoted by vector  $\mathbf{v}$ . The rate from of stress-strain relation of the hypoplastic models thus constitutes the system of ordinary differential equations. The total stress needed at the equilibrium conditions have to be obtained by the integration of Eq. (3) in time. Additionally, the state variables are also given in the rate from and therefor they have to be integrated too.

## 2. Hypoplastic model for expansive clays

The advanced hydro-mechanical model based on hypoplasticity has been proposed in Mašin, 2013. The model takes into account the double structure of the aggregated clayey soils and it exploits separated formulation of macro and micro behaviour according to well established models (Alonso, 2011 and Romero, 2011) but there is added dependence of water retention on volumetric deformation. Coupling between macro and microstructure levels depends on size of macropores (interaggregate pores) and there is assumed that the shear strength of soil is attributed to the macrostructure and it is given by effective stress measure independent on microstructural quantities. Hydraulic equilibrium is assumed between both structure levels.

The model assumes additive decomposition of the total strain rate  $\dot{\boldsymbol{\varepsilon}}$  in the form

$$\dot{\boldsymbol{\varepsilon}} = \dot{\boldsymbol{\varepsilon}}^M + f_m \dot{\boldsymbol{\varepsilon}}^m, \quad 0 \leq f_m \leq 1 \quad (4)$$

where  $f_m$  stands for the factor that quantifies the level of occlusion of macro-porosity by aggregates ranging from 0 to 1. Similarly, the total void ratio  $e$  together with the consistent definition of the porosity measures for particular structural levels are defined in the model. Two different mechanical models for macro and microstructure level are defined in the model. Assuming local hydraulic equilibrium and the Bishop's effective stresses concept, the following terms for the rates of effective stresses at macro and micro levels are given

$$\dot{\boldsymbol{\sigma}}^M = f_s - (\mathcal{L} : \boldsymbol{\varepsilon}^M + f_d \mathbf{N} \|\boldsymbol{\varepsilon}^M\|) + f_u \mathbf{H}, \quad (5)$$

$$\dot{\boldsymbol{\sigma}}^m = \mathbf{I} \frac{p^m}{\kappa_m} \varepsilon_V^m \quad (6)$$

where  $f_s$  is the barotropy factor,  $\mathcal{L}$  is the hypoelastic fourth-order tensor,  $f_d$  is the pyknotropy factor,  $\mathbf{N}$  is the second order tensor defined according to the failure condition, the factor  $f_u$  and the second order tensor  $\mathbf{H}$  control wet induced collapse. In the microlevel stress term,  $\mathbf{I}$  is the second order identity tensor,  $p^m$  is the mean stress at the microlevel,  $\kappa_m$  is the model parameter and  $\varepsilon_V^m$  is the volumetric strain at microlevel. It should be noted, that the reversible behaviour linear in  $\ln p^m$  vs.  $\ln(1 + e^m)$  plot is adopted at the microstructure level. The more details about the model can be found in Mašin, 2013.

## 3. Model of water flow in deforming porous medium

In this case, the assumption of isothermal one-phase flow is adopted for the model based on Lewis and Schrefler (Lewis, 1971). Neglecting the water vapour exchange and assuming the dependency of the degree of saturation on the pore water pressure results in continuity equation for one-phase (liquid water) flow in deforming medium

$$\begin{aligned} & \left( \frac{\alpha - n}{K_g} S_r^2 + \frac{n S_r}{K_w} \right) \frac{\partial u_w}{\partial t} + \left( \frac{\alpha - n}{K_g} S_r u_w + n \right) \frac{\partial S_r}{\partial u_w} \frac{u_w}{t} + \alpha S_r \operatorname{div} \mathbf{u} + \\ & + \frac{1}{\rho^w} \operatorname{div} \left[ \rho^w \frac{k^{rw} \mathbf{k}_{sat}}{\mu^w} (-\operatorname{grad} u_w + \rho^w \mathbf{g}) \right] = 0, \end{aligned} \quad (7)$$

where  $\alpha$  is the Biot's constant,  $n$  is the porosity,  $S_r$  is the degree of saturation,  $K_g$  and  $K_w$  are bulk moduli of water and grains respectively,  $u_w$  is the pore water pressure,  $\rho^w$  is the density of water,  $k^{rw}$  stands for the relative permeability which depends on the degree of saturation,  $\mathbf{k}_{sat}$  is the matrix of intrinsic permeability of the fully saturated medium,  $\mu_w$  is the coefficient of dynamic viscosity and  $\mathbf{g}$  is the gravity acceleration vector.

#### 4. Time integration of hypoplastic model

Recall that in hypoplasticity model described in Section 2, the total stress rate  $\dot{\boldsymbol{\sigma}}$  is defined. Additionally, the hypoplastic model involves state variables given by vector  $\mathbf{v}$  that can be also formulated in the rate form and thus generally, the stress rate can be defined by

$$\dot{\boldsymbol{\tau}} = \mathcal{M}\dot{\boldsymbol{\epsilon}} = \boldsymbol{\Psi}(\boldsymbol{\tau}(t), \Delta\boldsymbol{\epsilon}(t)), \quad (8)$$

where  $\boldsymbol{\tau}$  is the generalized stress vector  $\boldsymbol{\tau} = \{\boldsymbol{\sigma}, \mathbf{v}\}^T$ ,  $\mathcal{M}$  represents the generalized stiffness matrix and  $\boldsymbol{\epsilon}$  is the generalized strain vector  $\boldsymbol{\epsilon} = \{\boldsymbol{\epsilon}, s\}^T$  where  $s$  is the suction and  $\boldsymbol{\Psi}$  represents the model response function on the given input of strain increment  $\Delta\boldsymbol{\epsilon}$  of the actual time step and attained stress level  $\boldsymbol{\tau}$ . With respect to experiences and conclusions in Sloan, 2014, the explicit integration Runge-Kutta-Fehlberg algorithm with substepping has been selected and implemented in SIFEL. Eq. (8) represents initial value problem given by the set of ordinary differential equations. These equations can be written in generic substep  $k$  at time interval  $[t_n; t_{n+1}]$  formally as follows

$$\boldsymbol{\tau}_{k+1} = \boldsymbol{\tau}_k + \Delta t_k \sum_{i=1}^s b_i \mathbf{k}_i(\boldsymbol{\tau}_k, \Delta\boldsymbol{\epsilon}(t_{n+1}), \Delta t_k), \quad (9)$$

where  $\mathbf{k}_i(\boldsymbol{\tau}_k, \Delta\boldsymbol{\epsilon}(t_{n+1}), \Delta t_k)$  represents the function  $\boldsymbol{\Psi}$  evaluated for the given strain increment of the actual time step  $\Delta\boldsymbol{\epsilon}(t_{n+1}) = \boldsymbol{\epsilon}(t_{n+1}) - \boldsymbol{\epsilon}(t_n)$  and attained stress levels at the prescribed points of time interval. In Eq. (9), dimensionless step length  $\Delta t_k \in (0; 1]$  has been introduced with the following definition

$$\Delta t_k = \frac{t_{k+1} - t_k}{t_{n+1} - t_n}. \quad (10)$$

In RKF method, the step length  $\Delta t_k$  is constructed according the difference between solution of two embedded Runge-Kutta algorithms of different order of accuracy obtained by the set of coefficients  $\tilde{b}_i$  and  $\tilde{b}_i$ . These coefficients may be summarized in the form of Butcher table whose generalized example is given in Tab. 1. According to this table, coefficients  $\mathbf{k}_i$  can be evaluated in selected times and corresponding stress values

$$\mathbf{k}_i(\boldsymbol{\tau}_k, \Delta\boldsymbol{\epsilon}(t_{n+1}), \Delta t_k) = \boldsymbol{\Psi}(\boldsymbol{\tau}_k + \Delta t_k \sum_{j=1}^{i-1} \tilde{a}_{i,j} \mathbf{k}_j, \Delta\boldsymbol{\epsilon}(t_{n+1})). \quad (11)$$

Coefficients  $\tilde{a}_{i,j}$ ,  $\tilde{b}_j$ ,  $\tilde{b}_j$ ,  $\tilde{c}_i$  are selected so that the method provides the numerical approximation of the solution of order  $s$  and  $s+1$ .

Tab. 1: Generalized example of the Butcher table.

0	0	0	...	0	0
$\tilde{c}_2$	$\tilde{a}_{2,1}$	0	...	0	0
$\vdots$	$\vdots$	$\ddots$	$\ddots$	$\vdots$	$\vdots$
$\tilde{c}_{s-1}$	$\tilde{a}_{s-1,1}$	$\tilde{a}_{s-1,2}$	...	0	0
$\tilde{c}_s$	$\tilde{a}_{s,1}$	$\tilde{a}_{s,2}$	...	$\tilde{a}_{s,s-1}$	0
<hr/>					
	$\tilde{b}_1$	$\tilde{b}_2$	...	$\tilde{b}_{s-1}$	$\tilde{b}_s$
	$\bar{b}_1$	$\bar{b}_2$	...	$\bar{b}_{s-1}$	$\bar{b}_s$

Several time integration RKF schemes have been implemented and their description in the form of Butcher's tables is given in Tabs. 2, 3 and 4. Should be noted that the algorithm RKF-23bs is the Bogacki-Shampine coefficient pairs proposed in Shampine, 1987 and the advantage of the method is that it provides the better estimate of error with the minimum cost because the  $\mathbf{k}_4$  can be used as  $\mathbf{k}_1$  in the next step - First Same As Last (FSAL) concept.

Tab. 2: Butcher table for RKF-23 (left) and RKF-23bs Bogacki-Shampine (right).

0				0			
1/2	1/2			1/2			
1	-1	2		3/4	0	3/4	
<hr/>				<hr/>			
	1/6	2/3	1/6		2/9	1/3	4/9
	0	1	0		7/24	1/4	1/3
							1/8

Tab. 3: Butcher table for RKF-45.

0						
1/4	1/4					
3/8	3/32	9/32				
12/13	1932/2197	-7200/2197	7296/2197			
1	439/216	-8	3680/513	-845/4104		
1/2	-8/27	2	-3544/2565	1859/4104	-11/40	
	16/135	0	6656/12825	28561/56430	-9/50	2/55
	25/216	0	1408/2565	2197/4101	-1/5	

## 5. Performance comparison of various integration schemes

The implemented hypoplasticity model was tested on a benchmark example with axisymmetrical specimen 1x1 m subjected by triaxial drained test with constant confining pressure and gradually increasing axial load, initial stress -200 kPa, constant suction -1.9 MPa. Comparison of integration schemes for various tolerances on benchmark example is given in Tab. 4.

Tab. 4: RKF schemes comparison.

$\vartheta$		RKF-23	RKF-23bs	RKF-45
$10^{-7}$	$\sigma_{err}$	1.57e-2	2.08e-3	0
	$t$ [s]	34.6	21.1	84.7
$10^{-6}$	$\sigma_{err}$	1.85e-2	2.37e-3	1.89e-3
	$t$ [s]	19.3	13.2	10.7
$10^{-5}$	$\sigma_{err}$	2.23e-2	5.78e-3	2.97e-3
	$t$ [s]	11.95	8.81	8.41
$10^{-4}$	$\sigma_{err}$	3.67e-2	9.45e-3	6.07e-3
	$t$ [s]	7.70	6.44	8.11
$10^{-3}$	$\sigma_{err}$	—	1.34e-2	8.92e-3
	$t$ [s]	—	6.43	8.07

In Tab. 4, the relative error between two solutions of RKF is denoted by  $\vartheta$ ,  $\sigma_{err}$  stands for relative error of stress vector compared to RKF-45 with the minimum  $\vartheta$  value and there are also elapsed times of particular benchmarks denoted by  $t$ .

The constitutive fourth-order tensor exhibited high nonlinearity and high computational demands in the selected benchmark example and therefore selection of suitable integration scheme plays important role. Comparison revealed that RKF-23bs can be regarded as be optimum choice for this benchmark.

## Acknowledgement

Financial support for this work was provided by project number 15-05935S of Czech Science Foundation. The financial support is gratefully acknowledged.

## References

- Alonso, E.E., Romero, E. and Hoffman, C. (2011) Hydromechanical behavior of compacted granular expansive mixtures: experimental and constitutive study, *Géotechnique*, 61, 4, pp. 329-344.
- Ding, Y., Huang, W., Sheng, D. and Sloan, S.W. (2015) Numerical study on finite element implementation of hypoplastic models, *Computers and Geotechnics*, 68, pp. 78-90.
- Gudehus, G. (2011) *Physical Soil Mechanics*, Springer-Verlag, Berlin, Heidelberg.
- Herle, I. and Kolymbas, D. (2004) Hypoplasticity for soils with low friction angles, *Computer and Geotechnics*, 31, pp. 365-373.
- Hughes, T.J. (1987) *The Finite Element Method. Linear Static and Dynamic Finite Element Analysis*, Prentice-Hall, inc. Englewood Cliffs, New Jersey, USA.
- Lewis, R.W. and Schrefler, B.A. (1998) *The finite element method in static and dynamic deformation and consolidation of porous media*, John Wiley & Sons, Chichester-Toronto.
- Mašín, D. (2013) Double structure hydromechanical coupling formalism and a model for unsaturated expansive clays, *Engineering Geology*, 165, 73-88.
- Romero, E., Della Vecchia, G. and Jomi, C. (2011) An insight into water retention properties of compacted clayey soils, *Géotechnique*, 61, 4, 313-328.
- Shampine, L. (1987) Some Practical Runge-Kutta Formulas. *Mathematics Computation*, 46, 173, pp. 135-150.

## ANALYSIS OF THE MANUFACTURE PERTURBATIONS OF THE TOTAL HIP REPLACEMENT

M. Koukal\*

**Abstract:** *One type of total hip replacement function loss is acetabular cup loosening from the pelvic bone. This article examines manufacture deviations as one of the possible reasons for this kind of failure. Both dimensions and geometry manufacturing deviations of ceramic head and polyethylene cup were analyzed. We find that deviations in the variables analysed here affect considered values of contact pressure and frictional moment. Furthermore, contact pressure and frictional moment are quantities affecting replacement success and durability.*

**Keywords:** Total hip replacement, FEM, Roundness, Contact pressure, Frictional moment.

### 1. Introduction

This article examines a number of the biomechanical problems associated with total hip replacements (THR). The manufacture perturbations (fabrication tolerances) and impacts of femoral head and acetabular cup upon the failure of function of THR. THR failure is typically accompanied with severe pain and necessitates reoperation and prolonged convalescence (Fuis et al., 2001 – 2010).

THR function loss is associated with a combination of several risk factors – use of inappropriate prosthesis materials, geometry, surface finish treatment, ... A recent clinical study of 600 THR's with ceramic-ceramic contact between femoral head and acetabular cups showed there was 20 % failure in period 1977 – 1989 (Gualtieri et al., 2001). One type of THR functionality loss is loosening of the acetabular cup from pelvic bone (Fig. 1).



*Fig. 1: Continuity of acetabular cup loosening from pelvic bone (Krbec et al., 2001).*

The Faculty Hospital Brno (FHB) has an ongoing project examining the clinical impact of manufacture perturbations in hip prostheses (Krbec et al., 2001). During a five year period, a failure rate of 26 % (Walter Motorlet Co. – Fig. 2) in THR due to loosening was at the FBH.

Loosening of the cups is thought to be caused by the deterioration of the polyethylene, worn particles dislodged from the prosthesis then damage the tissue around the cup (Charnley et al., 1969). Amount of polyethylene wear is influenced by contact pressure and frictional moment between head and cup (Mak et al., 2002) and (Saiko and Calonijs, 2003). Maximal value of the contact pressure is thought to be influenced by contact surfaces inaccuracies created during the fabrication process.

---

\* Ing. Milan Koukal, PhD.: Institute of Solid Mechanics, Mechatronics and Biomechanics, Faculty of Mechanical Engineering, Brno University of Technology, Brno, CZ

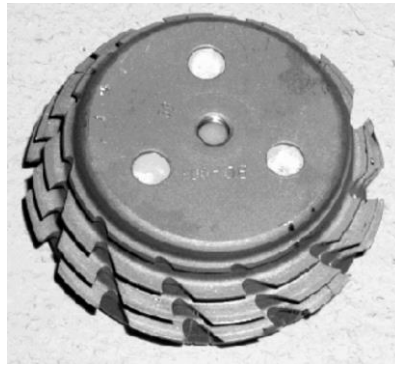


Fig. 2: Acetabular cup made by Walter-Motorlet Co. (Krbec, et al., 2001).

## 2. Computational modelling

The parametric geometry model of the system was created due to the possibility to study influences of perturbations of the shape deviations. Model consists of the following parts: 1 – pelvis bone with cortical and cancellous part, 2 – acetabular shell (titanium), 3 – acetabular cup (UHMW polyethylene) and 4 – femoral head (ceramic) (Fig. 3).

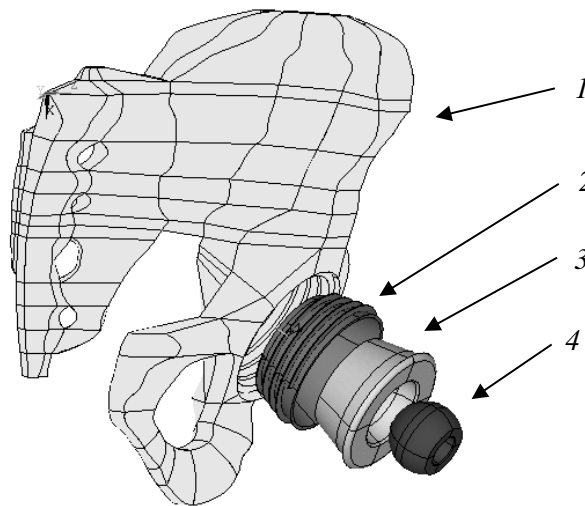


Fig. 3: Components of the analysed system.

The variable geometry parameter was inner cup's diameter – from 31.7 mm to 32.4 mm (from interference fit (overlap) 0.3 mm to clearance fit (gap) 0.4 mm - nominal diameter is 32 mm). The variable material parameter was modulus of elasticity of the acetabular cup – Tab. 1. Linear isotropic material models were used for all components with characteristics summarized in Tab. 1.

Tab. 1: Material characteristics.

Model part - material	Modulus of elasticity E [MPa]	Poisson's ratio $\mu$ [-]
Femoral head - ceramics $\text{Al}_2\text{O}_3$ (Fuis et al., 2009, 2011)	$3.9 \times 10^5$	0.23
Acetabular cup - UHMWPE	600 – 1200 (analysed interval)	0.40
Acetabular shell - titanium	$1.0 \times 10^5$	0.30
Pelvis - cancellous / cortical bone (Dunham et al., 2005; Boyce et al. 1996; Jiahau, 2006; Rho et al., 1998)	$2.0 \times 10^3 - 1.4 \times 10^4$	0.25 – 0.30

The first contact pair was modelled by creating contact elements between femoral head and acetabular cup, with coefficient of friction  $f = 0.1$ . The second contact pair was created between acetabular cup and shell. The loading and boundary condition of the analysed system is shown in Fig. 5 and is realized by the

force  $F = 2500$  N which is applied in the centre of femoral ball head ( $\alpha = 13.5^\circ$ ). This loading corresponds to the physiological loading of the pelvis (weight of a human is 80 kg).

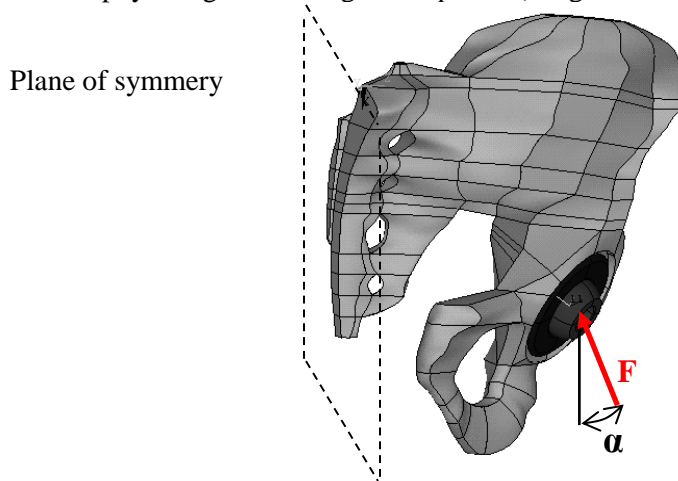


Fig. 5: Loading of the head.

### 3. Results

In order to model the dimension perturbations the inner diameter of the acetabular cup was varied. This resulted in change of the fit between the femoral head and the acetabular cup (from interference fit to clearance fit). We found that by increasing the clearance starting from 0.0 mm (fine fit) the value of contact pressure raised linearly within the investigated interval (Fig. 6 for  $E = 1000$  MPa). Increasing the clearance between the head and the cup by 0.1 mm the contact pressure raised by  $\sim 10\%$ . Reducing the clearance below 0.0 mm (fine fit), we found that the value of contact pressure raised with approximately double speed than for the positive clearance values.

To study the influence of the elasticity modulus of the polyethylene cup the modulus of elasticity value varied from 600 MPa to 1200 MPa. Results shows that if the value of elasticity modulus of cup decrease, than the values of contact pressure decrease due to increase of contact area for all types of fit.

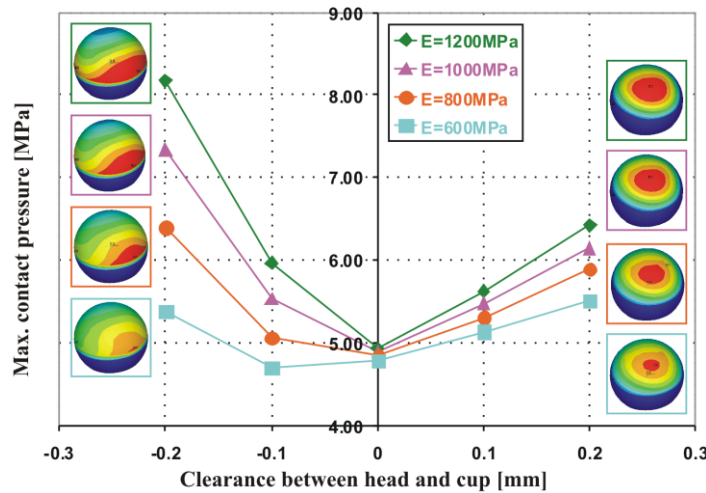


Fig. 6: Acetabular cup modulus of elasticity vs. contact pressure and different clearance.

### 4. Conclusion

We discovered, that if the value of deviations increase, the contact conditions deteriorate. We also found, that the best type of fit was fine fit, it means without clearance and interference. As this type of fit is hard to fabricate we recommend to fit head and cup together with clearance value ranging 0 mm to 0.05 mm. In this clearance interval the values of considered quantities varied in less than ten percents. We do not recommend using interference type of fit because of strong deterioration of the contact conditions.



Value of the contact pressure affects the success and durability of the replacement, therefore it is recommended to minimize their values. The relationship between contact pressure and wear is analyzed at (Teoh et al., 2001; Ipavec et al., 1999 and Genda et al., 2001).

## Acknowledgment

This work was supported by grant FSI-S-17-4004.

## References

- Boyce T.M., Fyhrie D.P., Brodie F.R. and Schaffler M.B. (1996) Residual Mechanical Properties of Human Cortical Bone Following Fatigue Loading, in: 20<sup>th</sup> Annual Meeting of the American Society of Biomechanics, Atlanta, Georgia.
- Charnley, J., Kamangar, A. and Longfield, M. (1969) The Optimum Size of Prosthetic Heads in Relation to the Wear of Plastic Socket in Total Replacement of the Hip, *Medical & Biological Engineering*, Vol. 7, pp. 31-39.
- Dunham, Ch. E., Takaki, S.E., Johnson, J.A. and Dunning, C.E. (2005) Mechanical Properties of Cancellous bone of the Distal Humerus; in: ISB XXth Congress - ASB 29<sup>th</sup> Annual Meeting, 564, Cleveland, Ohio.
- Fuis, V. and Janicek, P. (2001) Stress and reliability analyses of ceramic femoral heads with axisymmetric production inaccuracies. in: Proc. 9<sup>th</sup> Mediterranean Conference on Medical and Biological Engineering and Computing, Pula, Croatia, IFMBE Proceedings Pts. 1 and 2, pp. 632-635.
- Fuis, V. (2004) Stress and reliability analyses of ceramic femoral heads with 3D manufacturing inaccuracies, in: Proc. 11<sup>th</sup> World Congress in Mechanism and Machine Science, Tianjin, China pp. 2197-2201.
- Fuis, V. et al. (2006) Reliability of the Ceramic Head of the Total Hip Joint Endoprosthesis Using Weibull's Weakest-link Theory. in: World Congress on Medical Physics and Biomedical Engineering, IFMBE Proc. Vol. 14, pp. 2941-2944.
- Fuis, V., Janicek, P. and Houfek, L. (2008) Stress and Reliability Analyses of the Hip Joint Endoprosthesis Ceramic Head with Macro and Micro Shape Deviations, in: 13<sup>th</sup> Conf. ICBME, IFMBE Proc. Vol. 23, Iss. 1-3, pp: 1580-1583.
- Fuis, V. and Varga, J. (2009) Stress Analyses of the Hip Joint Endoprosthesis Ceramic Head with Different Shapes of the Cone Opening. in: Proc. 13<sup>th</sup> International Conference on Biomedical Engineering, IFMBE Proceedings Vol. 23, Iss. 1-3, pp. 2012-2015.
- Fuis, V., Navrat, T. and Vosynek, P. (2010) Analyses of the Shape Deviations of the Contact Cones of the Total Hip Joint Endoprostheses. in: Proc. 6<sup>th</sup> World Congress of Biomechanics (WCB 2010) Singapore, Series: IFMBE Proc. Vol. 31, pp. 1451-1454.
- Fuis, V., Malek, M. and Janicek, P. (2011) Probability of destruction of Ceramics using Weibull's Theory, in: Proc. 17<sup>th</sup> International Conference on Engineering Mechanics, Svratka, Czech Republic, pp. 155-158.
- Genda, E., Iwasaki, N., Li, G., MacWilliams, B.A., Barrance, P.J. and Chao, E.Y.S. (2001) Normal Hip Joint Contact Pressure Distribution in Single-Leg Standing – Effect of Gender and Anatomic Parameters; *J. of Biomechanics* 34, pp. 895-905.
- Gualtieri, G., Calderoni, P., Ferruzzi, A., Frontali, P., Calista, F. and Gualtieri, I. (2001) Twenty Years Follow-up in Ceramic-Ceramic THR at Rizzoli Orthopaedic Institute, in: 6<sup>th</sup> Int. BIOLOX Symposium, pp. 13-17.
- Jiahau, B.Y. (2006) Mechanical Properties and Testing of Bone, Postdoctoral Research Associate, Dental Biomaterials, Indiana.
- Krbec, M. et al., (2001) Loosening of the uncemented cups of total hip replacement from pelvic bone, V. National congress ČSOT, p. 108, Prague.
- Mak, M.M. and Jin, Z.M. (2002) Analysis of Contact Mechanics in Ceramic-on-Ceramic Hip Joint Replacement; *Journal of Engineering in Medicine*, Vol. 216. No. 4.
- Ipavec, M., Brand, R.A., Pedersen, D.R., Mavcic, B., Kralj-Iglic, V. and Iglic, A. (1999) Mathematical Modelling of Stress in the Hip During Gait; *Journal of Biomechanics* 32, pp. 1229-1233.
- Rho, J.Y., Kuhn-Spearing, L. and Zioupos, P. (1998) Mechanical properties and the hierarchical structure of bone, *Medical engineering & physics*, Vol. 20, No. 2, pp. 92-102.
- Saikko, V. and Calonius, O. (2003) An Improved Method of Computing the Wear Factor for Total Hip Prostheses Involving the Variation of Relative Motion and Contact Pressure with Location on the Bearing Surface; *Journal of Biomechanics*, Vol. 36, pp. 1819-1827.
- Teoh, S.H., Chan, W.H. and Thampuran, R. (2001) An Elasto-plastic Finite Element Model for Polyethylene Wear in Total Hip Arthroplasty, *J. Biomech* 2002, 35: 323-330.

## THE INFLUENCE OF CONTACT REGION ON PROBABILITY OF CERAMICS FRACTURE

J. Kovář\*

**Abstract:** This paper focuses on assessment of probability of ceramic component fracture. The component is loaded by four point bending with different boundary conditions. The Weibull's weakest link theory, which includes the effect of first principal stress only, was chosen for calculation of probability of fracture. The stresses for calculations were evaluated numerically by finite element method. The component was discretized by plane elements and constraints were considered in two variants. In the first variant, the constraints and loads are considered at the centerline of the rod (in accordance with rod theory). The second variant considers constraints and loads on the outer surface of the body. The contact between body and constraint (support) is considered in this variant. The influence of the radius of support on the value of probability of body fracture and the width of contact region is analyzed.

**Keywords:** Weibull's weakest link theory, Contact, Probability of fracture, Hertz's theory, Ceramic.

### 1. Introduction

In the process of loading, ceramic materials have very small plastic deformation (Menčík, 1990). The fracture of this material is caused by initiation and growth of the crack, which was made in manufacturing process. The crack starts growing, when the stress intensity factor reaches its critical value. The value of stress intensity factor depends on the stress at the crack tip, length of the crack, the shape of the crack and the orientation in space. Therefore, the fracture mechanics is not used in this case. The statistic methods based on evaluating the probability of fracture are used, for example Weibull's weakest link theory (Weibull, 1939). The probability of fracture can be evaluated considering one or all of the three principal stresses. The following results were found with only the first principal stress considered. The probability of fracture of component, which has Weibull's distribution can be evaluated as:

$$P_f(V) = 1 - e^{-\frac{1}{V_0} \int_V \left( \frac{\sigma - \sigma_u}{\sigma_0} \right)^m dV} \quad (1)$$

where:  $V_0$  is the volume of tested specimen, when the stress is lower than  $\sigma_u$  the component cannot crack,  $m$  is Weibull's modulus, which determines the width of probability density function of Weibull's distribution, and  $\sigma_0$  is scale parameter, it is stress which makes 63 % specimens fractured.

The volume of specimen can be included in parameter  $\sigma_0$ , which will have the unit  $[MPa \cdot mm^{3/m}]$ , because the volume of specimen and  $\sigma_0$  are constants. If the stress  $\sigma_u = 0$ , then we have the two-parameter Weibull's distribution and all tensile first principal stresses cause the process of body fracture. When the FEM is used to determine the stress in the component, the summation instead of integral can be used.

$$P_f(V) = 1 - e^{-\int_V \left( \frac{\sigma}{\sigma_0} \right)^m dV} = 1 - e^{-\sum_{i=1}^N \left( \left( \frac{\sigma_i}{\sigma_0} \right)^m \Delta V_i \right)} \quad (2)$$

### 2. Computational model

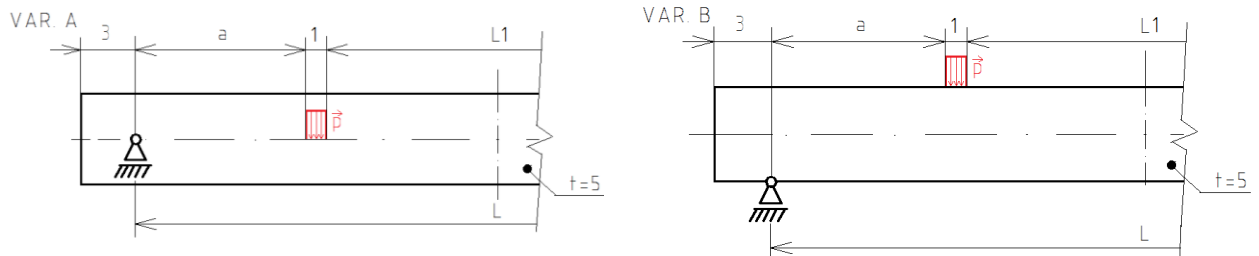
The body, which is loaded by four point bending, is symmetrically supported by two supports, with distance  $L = 40$  mm, forces (500 N) were replaced by pressure ( $p = 100$  MPa, which acts at length 1 mm) at the distance  $L_1 = 19$  mm (Fig. 1). The body is discretized by plane elements PLANE 182. Two variants of boundary conditions are considered. In the first variant, the constraints are considered at the centerline

---

\* Bc. Jaroslav Kovář.: Institute of Solid Mechanics, Mechatronics and Biomechanics, Faculty of Mechanical Engineering, Brno University of Technology; Technická 2896/2; 616 69, Brno; CZ, 160811@vutbr.cz

of the rod (in accordance with rod theory) and this variant is identified as VAR A. The second variant considers the constraints and the loads realistically, on the outer surface of body. This variant is identified as VAR B. At this variant the contact between the body and the constraint (support) is considered. Material of the body is bioceramics  $\text{Al}_2\text{O}_3$ , which is considered as linear isotropic continuum with elastic material parameters  $E = 390 \text{ GPa}$ ,  $\mu = 0.24$  (Fuis, 2004 and Fuis et al., 2001, 2009, 2010 and 2011) and parameters of Weibull's distribution  $\sigma_0 = 473.8 \text{ MPa}\cdot\text{mm}^{3/7.19}$  and  $m = 7.19$  (Málek, 2011; Fuis et al., 2006 and 2008).

Fig. 1: Geometry and the



constraints on the body: a) Constraints and the loads at the centerline of the rod (VAR. A); b) Constraints and the loads on the outer surface (VAR. B).

### 3. Results of computational modelling

#### 3.1. Sensitivity analysis

The uniaxial stress is almost in the entire volume of the body, when the rod is loaded by four point bending. Exceptions are the positions of constraints (there is concentration of stress - in VAR. A. concentration is biggest, because the constraint is realized only in one node), loads (there is plane stress) and the area of overhanging end (there is zero stress). The first principal stress is illustrated in Fig. 2 and the values of probability of failure are in Tab. 1 ( $a = 9.5 \text{ mm}$ ). For small density of discretization of body (460 elements), the same value of probability of fracture was calculated, if the entire body is considered ( $P_{f \text{ with constraint}}$ ) or if the region near the constraints is not considered ( $P_{f \text{ without constraint}}$ ). With the increasing density of discretization, the difference between these probabilities is bigger.

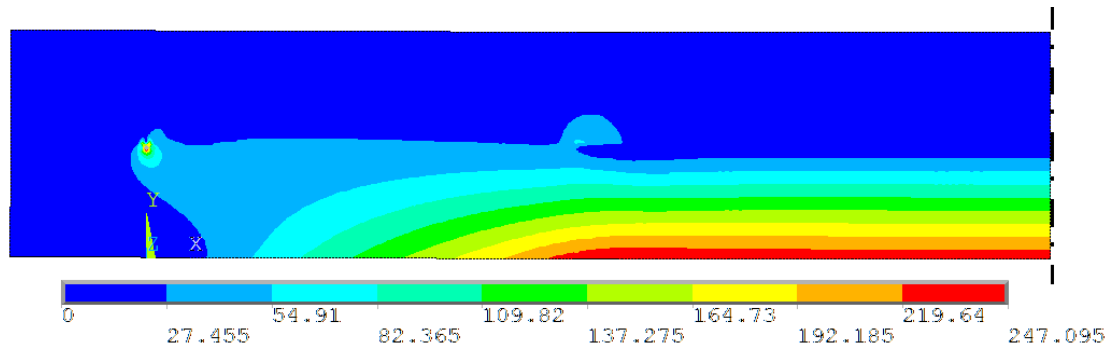


Fig. 2: First principal stress [MPa] in the body (max. stress in the constraint is 446 MPa).

Tab. 1: The influence of density of discretization at probability of fracture.

Size of element [mm]	0.5	0.25	0.125	0.076
Number of elements	460	1 840	7 360	20 064
$P_{f \text{ with constraint}}$ [%]	27.5	24.7	34.6	90.7
$P_{f \text{ without constraint}}$ [%]	27.5	24.4	23.6	23.4

The next analysis compares extreme values of stress in the areas of the loads for both variants, which have different positions of supports and loads (VAR. A and VAR. B.). The distances  $a$ ,  $L$  and force  $F$  were changed, to cause constant bending moment between the loads at the length  $L1$ , which was constant (i.e. analytical calculated values of extreme stress were identical). The height of the body was constant. Fig. 3 shows extreme stresses at the body with different conditions. With the increasing slenderness of the

rod, the numerically determined values approach analytical values. If we consider constraints at the centerline (VAR. A), the curve approaches from above and if we consider constraints on the outer surfaces (VAR. B), the curve approaches from the bottom.

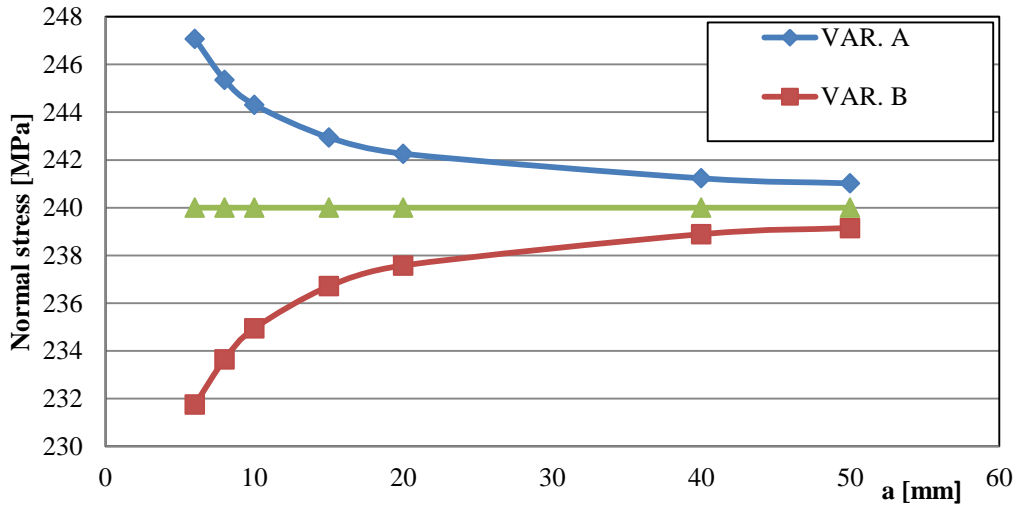


Fig. 3: Stress in depend on the distance between constraint and load (bending moment is constant).

### 3.2. Contact analysis

As it was said in the previous paragraph, the existence of constraint has an influence on probability of fracture. The task was modelled as contact, with considering real supports. At the place of the constraint, the ceramic component was supported by steel cylinder, which acts as the support. The component was loaded by moving steel cylinder, but loads in volume of body remained the same. The different radii of the supports were modelled ( $R = 0.5$  mm, 1 mm, 2 mm and 4 mm). The contact stresses were compared with Hertz's theory for assessing the correctness. The mesh for this model was taken from the previous model (VAR. B size of element 0.076 mm), but the contact regions were refined. The results of modelling are in Tab. 2, where the results from numerical calculations are compared with the values evaluated by Hertz's theory ( $b$  is half width of contact region). The Hertz's theory shows that the stresses at  $x$  and  $y$  axis at contact region should be identical (Budynas et al., 2011). The stress at  $x$  axis is more different from theoretical results than stress at  $y$  axis, because its gradient at contact region is steeper. For more accurate results of this stress, the mesh would have to be more refined. The stresses in  $x$  and  $y$  axes are shown in Fig. 4. This error has no influence on probability of fracture, because the first principal stress in this region is compressive.

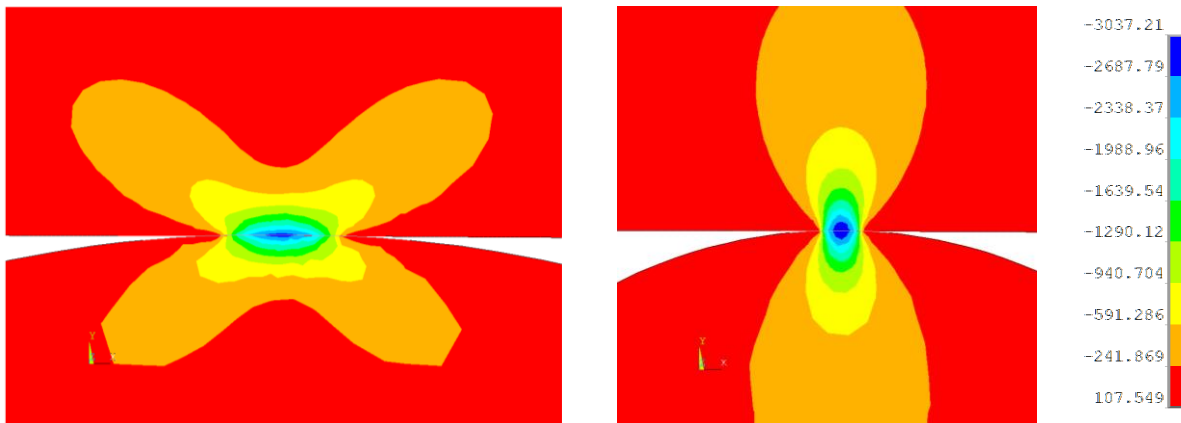


Fig. 4: Stress at  $x$  and  $y$  axis [MPa] for contact with  $R=0.5$  mm.

In the terms of probability of fracture only the tensile first principal stresses  $\sigma_1$  are significant. Near contact region, according to Hertz's theory  $\sigma_1$  is compressive, which causes that this stress does not influence the probability of fracture. The results of probability confirmed this fact and Tab. 3 shows the values of probability of fracture for different radii of supports.

Tab. 2: Comparison of theoretical and calculated values.

Radius of support [mm]	0.5	1	2	4
$p_{maxHERTZ}$ [MPa]	-3092	-2186	-1546	-1094
$\sigma_{xmax}$ [MPa]	-2888	-2044	-1438	-1027
$\sigma_{ymax}$ [MPa]	-3037	-2128	-1498	-1069
$b_{theor}$ [mm]	0.026	0.029	0.041	0.058
$b_{FEM}$ [mm]	0.023	0.026	0.038	0.061

Tab. 3: Comparison of probabilities of failure.

	VAR. A	VAR. B			
Radius of support [mm]	-	0.5	1	2	4
$\sigma_{1max}$ [MPa]		243.8	243.7	243.6	243.3
$P_{fFEM}$ [%]	23.39	22.85	22.79	22.70	22.53

#### 4. Conclusion

At the body loaded by four point bending, the extreme tension stresses approach analytical values with increasing slimness of the rod. In VAR. A (loads and constraints are at the centerline) values approach from above, in VAR. B (loads and constraints are on the outer surfaces of body) values approach from bottom. With the use of Weibull's theory, the probability of ceramic component fracture can be determined by FEM. The probability of fracture does not depend only on the stresses, but on the volume too, which causes that the probability of fracture is influenced by discretization. The probability of fracture of the model with loads and constraints at node is bigger than probability of fracture of the model with contact pair. The bigger radius of supports reduces the probability of fracture.

#### Acknowledgment

This work was supported by grant FSI-S-17-4004.

#### References

- Budynas, R.G. et al. (2011) Shigley's mechanical engineering design McGraw-Hill Science.
- Fuis, V. and Janicek, P. (2001) Stress and reliability analyses of ceramic femoral heads with axisymmetric production inaccuracies. in: Proc. 9<sup>th</sup> Mediterranean Conference on Medical and Biological Engineering and Computing, Pula, Croatia, IFMBE Proceedings Pts. 1 and 2, pp. 632-635.
- Fuis, V. (2004) Stress and reliability analyses of ceramic femoral heads with 3D manufacturing inaccuracies, in: Proc. 11<sup>th</sup> World Congress in Mechanism and Machine Science, Tianjin, China pp. 2197-2201.
- Fuis, V. et al. (2006) Reliability of the Ceramic Head of the Total Hip Joint Endoprosthesis Using Weibull's Weakest-link Theory. in: World Congress on Medical Physics and Biomedical Engineering, IFMBE Proc. Vol. 14, pp. 2941-2944.
- Fuis, V., Janicek, P. and Houfek, L. (2008) Stress and Reliability Analyses of the Hip Joint Endoprosthesis Ceramic Head with Macro and Micro Shape Deviations, in: 13<sup>th</sup> Conf. ICBME, IFMBE Proc. Vol. 23, Iss. 1-3, pp: 1580-1583.
- Fuis, V. and Varga, J. (2009) Stress Analyses of the Hip Joint Endoprosthesis Ceramic Head with Different Shapes of the Cone Opening. in: Proc. 13<sup>th</sup> International Conference on Biomedical Engineering, IFMBE Proceedings Vol. 23, Iss. 1-3, pp. 2012-2015.
- Fuis, V., Navrat, T. and Vosynek, P. (2010) Analyses of the Shape Deviations of the Contact Cones of the Total Hip Joint Endoprostheses. in: Proc. 6<sup>th</sup> World Congress of Biomechanics (WCB 2010) Singapore, Series: IFMBE Proc. Vol. 31, pp. 1451-1454.
- Fuis, V., Malek, M. and Janicek, P. (2011) Probability of destruction of Ceramics using Weibull's Theory, in: Proc. 17<sup>th</sup> International Conference on Engineering Mechanics, Svratka, Czech Republic, pp. 155-158.
- Menčík, J. (1990) Strength and fracture glass and ceramic, SNTL Praha (in Czech).
- Weibull, W. (1939) A statistical theory of the strength of materials, Generalstabens litografiska anstalts förlag, Stockholm.

## PROBABILITY NONLINEAR ANALYSIS OF THE FAILURE OF THE NPP HERMETIC STEEL DOOR DUE TO ACCIDENTAL EXTREME OVERPRESSURE

J. Králík\*

**Abstract:** *This paper describes the probabilistic nonlinear analysis of the hermetic steel door of the reactor shaft failure due to extreme pressure and temperature. The scenario of the hard accident in nuclear power plant (NPP) and the methodology of the calculation of the fragility curve of the failure overpressure using the probabilistic safety assessment PSA 2 level is presented. The model and resistance uncertainties were taken into account in the response surface method (RSM).*

**Keywords:** Nuclear power plant, Hermetic door, Nonlinearity, Fragility curve, PSA, RSM, ANSYS.

### 1. Introduction

After the accident of nuclear power plant (NPP) in Fukushima the IAEA in Vienna adopted a large-scale project "Stress Tests of NPP", which defines new requirements for the verification of the safety and reliability of NPP under extreme effects of the internal and external environments and the technology accidents (ENSREG, 2012). The experience from these activities will be used to develop a methodology in the frame of the project ALLEGRO, which is focused to the experimental research reactor of 4th generation with a fast neutron core. The new IAEA safety documents (IAEA, 2010) initiate the requirements to verify the hermetic structures of NPP loaded by two combinations of the extreme actions.

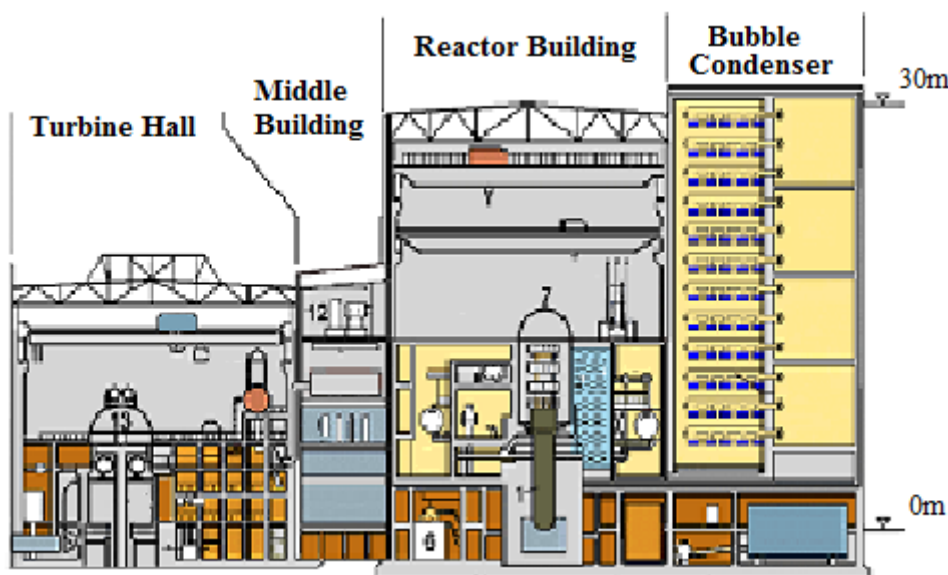


Fig. 1: Section plane of the NPP with reactor VVER440/213.

In the case of the loss-of-coolant accident (LOCA) the steam pressure expand from the reactor hall to the bubble condenser (IAEA, 2010). The reactor and the bubble condenser reinforced structures with steel liner are the critical structures of the NPP hermetic zone (Králík, 2009, 2015). The critical technology steel segments are covers and hermetic doors on the border of containment. The safety and reliability of

\* Prof. Ing. Juraj Králík, CSc.: Faculty of Civil Engineering, Slovak University of Technology Bratislava Radlinského 11; 810 05 Bratislava; SK, juraj.kralik@stuba.sk

these segments were tested considering the scenario of the hard accidents. The previous analysis was achieved for the overpressure value of 100 kPa due to design basic accident (DBA), which corresponds of the loss of coolant accident due to guillotine cutting of the coolant pipe (Králík, 2009). When the bobble tower operates in the partial or zero performance the overpressure is equal to the 150 - 300 kPa

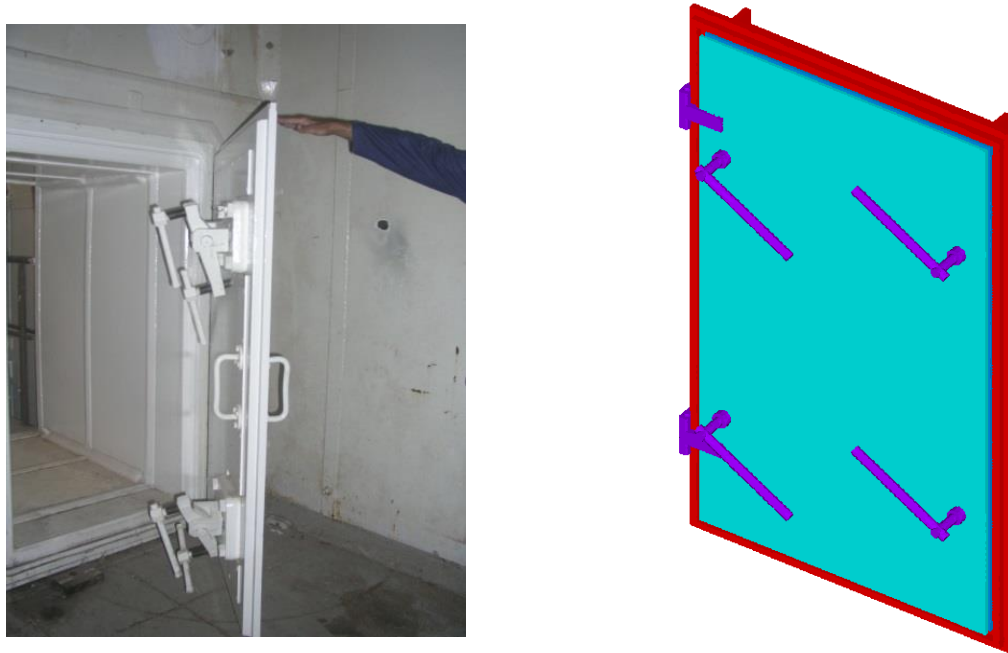
*Tab. 1: The assumed scenarios of the accidents in the hermetic zone.*

Type	Duration	Overpressure in HZ [kPa]	Internal temperature [°C]
I.	1 hour – 1 day	150	127
II.	2 hours – 7 days	250	150
III.	1 year	-	80 - 120

The SE-ENEL proposes the maximum temperature in the reactor shaft is equal about to 1 800 °C and in the containment around the reactor shaft is equal about to 350 °C (Králík, 2015). The possibility of the temperature increasing to the containment failure state is considered in the scenario too. In the case of the hard accident the overpressure can be increased linearly and the internal and external temperature are constant. Three types of the scenarios were considered (Tab. 1). The critical was the accident during 7 days with the overpressure 250 kPa, internal temperature 150 °C and external temperature -28 °C.

## 2. Calculation model of hermetic steel door

The hermetic steel doors type A251 (with dimension 1600 / 900 / 50 mm) are located at safety room in the box of the steam generators. The steel doors fulfils both the sealing and shielding functions. The technology segments of the NPP hermetic zone are made from the steel (S235). The steel door is fitted in the frame cast in concrete and sealed to the frame with double rubber packing of 15 mm in width.



*Fig. 2: Hermetic door of the reactor shaft and its FEM model.*

The FEM model of the steel door is shown in Fig. 2. Two calculation FEM models of the steel door structures with the steel frame and the mechanical closure were considered. The detailed FEM model has 535 290 SOLID186 and SURFACE154 elements with 140 452 nodes. The simplified FEM model has 86 581 SOLID185 and SURFACE154 elements with 18 393 nodes.

## 3. Probability and sensitivity nonlinear analysis

Huber-Mises-Hencky model (HMH) of the elastic - plastic steel material properties for MCP steel covering was used. The "Central Composite Design Sampling" (CCD) method of the "Response Surface Method" (RSM) is based on 45 nonlinear simulations depending on the 6 variable input data. The nonlinear solution for the one simulation consists about the 50 to 150 iteration depending on the scope of



the plastic deformations in the calculated structures. The uncertainties are coming from the standard requirements and the other publications (Handbook 5, 2005, JCSS, 2011, Krejsa et al., 2015, Sýkora et al., 2013). The mean values and standard deviations were defined in accordance of the experimental test and design values of the material properties and the action effects (see Tab. 2). Based on the results from the simulated nonlinear analysis of the technology segments and the variability of the input parameters  $10^6$  Monte Carlo simulations were performed in the software ANSYS.

The sensitivity analyses give us the informations about the influences of the variable properties of the input data to the output data (Fig. 3). These analyses are based on the correlations matrixes.

Tab. 2: Variability of input parameters.

Quantity	Charact. value	Variable	Histog. type	Mean $\mu$	Deviat. $\sigma$ [%]	Minim. value	Maxim. value
Material							
Strength	$F_k$	$f_{var}$	N	1.1	6.6	0.774	1.346
Action effects							
Dead load	$G_k$	$g_{var}$	N	1	5	0.808	1.195
Live load	$Q_k$	$q_{var}$	GU	0.643	22.6	0.232	1.358
Pressure LOCA	$p_k$	$p_{var}$	N	1	8	0.698	1.333
Temperature	$T_k$	$t_{var}$	GU	0.667	14.2	0.402	1.147
Model uncertainties							
Action	$E_k$	$e_{var}$	N	1	5	0.813	1.190
Resistance	$R_k$	$r_{var}$	N	1	5	0.812	1.201

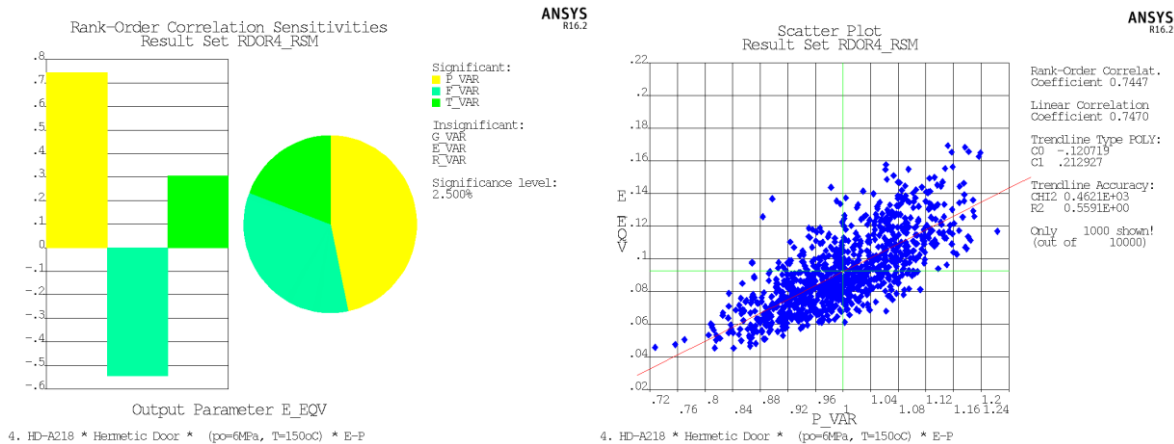


Fig. 3: Sensitivity and trend analysis of the safety function of the steel door of type A251 for the overpressure 6 MPa and temperature 150 °C.

#### 4. Fragility curves of failure pressure

The PSA approach to the evaluation of probabilistic pressure capacity involves limit state analyses (Králík, 2009). The limit states should represent possible failure modes of the confinement functions. The failure of the steel structure is limited with the max. strain values or with the stability of the nonlinear solution (Abraham, 1998). The standard STN EN 1993 1-2 (Handbook 5, 2005) define following characteristic values of the strain for the structural steel – the yield strain  $\varepsilon_{ay,\theta} = 0.02$ , the ultimate strain

$\varepsilon_{au,\theta} = 0.15$ , the max. limite strain  $\varepsilon_{ae,\theta} = 0.20$ . The fragility curve of the failure pressure was determined using 45 probabilistic simulations using the RSM approximation method with the experimental design CCD for  $10^6$  Monte Carlo simulations for each model and 5 level of the overpressure (Fig. 4). The various probabilistic calculations for 5 constant level of overpressure next for the variable overpressure for gauss and uniform distribution were taken out. The failure criterion of the steel structures using HMM plastic criterion with the multilinear kinematic hardening stress-strain relations for the various level of the temperatures and the degradation of the strength were considered.

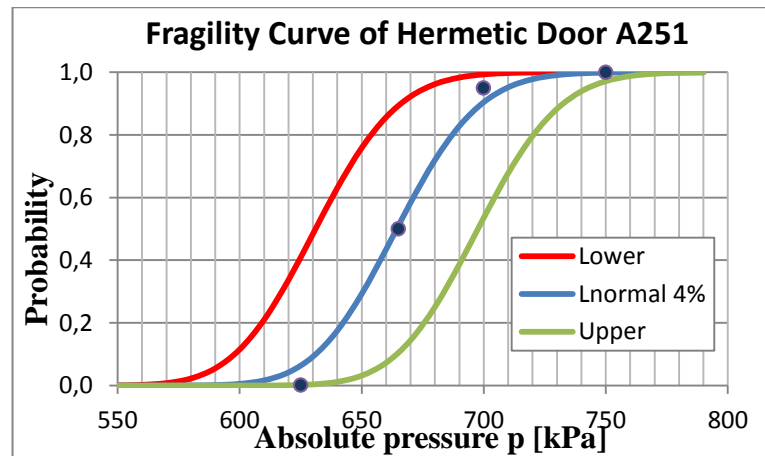


Fig. 4: Fragility curves of hermetic steel door determined for lognormal distribution with 5 % envelope.

## 5. Conclusions

This report is based on the methodology of the probabilistic analysis of structures of the hermetic zone of NPP with reactor VVER44/213 detailed described in the work (Králík, 2009, 2015). The uncertainties of the loads level, the material model of the steel structures as well as the inaccuracy of the calculation model and the numerical methods were taken into account in the approximation RSM method for CCD experimental design and  $10^6$  Monte Carlo simulations (Králík, 2009).

One from the critical technology segments of the containment is the hermetic steel door type A251 with the failure pressure  $p_{u,0.05} = 625$  kPa. The mean value of pressure capacity of the steel door type A251 is  $p_{u,0.50} = 665$  kPa, the upper bound of 95 % is  $p_{u,0.95} = 710$  kPa. These fragility curves (Fig. 4) are the input data for the following risk analysis of the NPP safety.

## Acknowledgements

The project was performed with the financial support of the Grant Agency of the Slovak Republic (VEGA 1/0265/16).

## References

- Abraham (1998) ASME Boiler and Pressure Vessel Code, Section III, Div. 1, Appendix F, "Rules for Evaluation of Service Loadings with Level D Service Limits," American Society of Mechanical Engineers.
- ENSREG (2012) Post-Fukushima accident. Action Plan. Follow-up of the peer review of the stress tests performed on European nuclear power plants.
- HANBOOK 5. (2005) Implementation of Eurocodes Reliability Backgrounds. Design of Buildings for the Fire Situation. Development of Skills Facilitating Implementation of Eurocodes. Leonardo Da Vinci Pilot Project CZ/02/B/F/PP-134007. Prague, CR.
- IAEA (2010) Safety Series No. SSG-4, Development and Application of Level 2 Probabilistic Safety Assessment for Nuclear Power Plants, Vienna.
- JCSS 2011. JCSS Probabilistic Model Code. Zurich: Joint Committee on Structural Safety. <www.jcss.byg.dtu.dk>.
- Králík, J. (2009) Safety and Reliability of Nuclear Power Buildings in Slovakia. Earthquake-Impact-Explosion. Ed. STU Bratislava, 307 p. ISBN 978-80-227-3112-6.
- Králík, J. et al. (2015) Structural Reliability for Containment of VVER 440/213 Type, In Safety and Reliability: Methodology and Applications - Nowakowski et al. (Eds) © Taylor & Francis Group, London, pp. 2279-2286.
- Krejsa, M. and Králík, J. (2015) Probabilistic Computational Methods in Structural Failure Analysis, Journal of Multiscale Modelling, Vol. 6, No. 2 (5 p.), Imperial College Press, DOI: 10.1142/S1756973715500067.
- Králík, J. (2015) Safety and Reliability of NPP in Slovakia Within IAEA Project "Stress Tests", In: Monograph Selected Practical and Theoretical Aspects of Contemporary Mechanics, (eds. Major, I. and Major, M.), Wydawnictwo Wydziału Zarządzania, Politechniki Częstochowskiej, Częstochowa, pp. 21-36.
- Sýkora, M. and Holický, M. (2013) Assessment of Uncertainties in Mechanical Models, Applied Mechanics and Materials, Vol. 378 pp. 13-18, © Trans Tech Publications, Switzerland, doi:10.4028/www.scientific.net/AMM.378.13.

## PROBABILISTIC ESTIMATION OF A BRIDGE FATIGUE LIFE IN ACCORDANCE TO *fib* MODEL CODE 2010

J. Krejsa<sup>\*</sup>, M. Sýkora<sup>\*\*</sup>

**Abstract:** *The service life of bridges is significantly affected by fatigue induced by crossings of heavy vehicles. Therefore, information of traffic flow, covering frequencies and vehicle weights, is of crucial importance for the calculation of fatigue damage and the prediction of the bridge lifetime. This paper investigates accuracy of fatigue life estimates depending on a length of traffic flow records. The presented data were obtained from the measurements carried out on a bridge of the Prague Highway Ring. The analysis reveals that the optimal length of records for fatigue life assessment is about 30 days.*

**Keywords:** Length of records, Fatigue, Heavy traffic, Traffic flow, Palmgren-Miner rule.

### 1. Introduction

The service life of a bridge depends on the effects of loadings imposed to a bridge. The *fib* Model Code 2010 introduces a fatigue limit state, which may be a critical criterion for road and railway bridges. Generally, the fatigue damage is caused by cyclic loading and depends on frequency and stress magnitude of loading cycles. Fatigue damage relates to the structures exposed to considerable dynamic stresses. The paper is focused on the effect of the length of traffic flow records on the accuracy of estimating road bridge fatigue life.

### 2. Fatigue

#### 2.1. Material properties – Wöhler curve

Augustin Wöhler proposed in 1850 a theory of the fatigue failure of a material, describing the relationship between stress amplitudes and a number of loading cycles. This dependence is called the Wöhler fatigue curve (*S-N* curve) (*fib*, 2013), which is the most widely used tool for the assessment of fatigue life of concrete structures.

#### 2.2. Palmgren-Miner rule of the cumulative damage

The Palmgren-Miner rule of the cumulative damage can be applied to account for different weights of heavy vehicles (*fib*, 2013):

$$D_{\text{fat}} = \sum (n_i/N_i) \quad (1)$$

where  $D_{\text{fat}}$  is the fatigue damage,  $n_i$  the number of recorded cycles and  $N_i$  the number of cycles from the Wöhler curve. Variables  $n_i$  and  $N_i$  depend on the response of the structure induced primarily by weights of vehicles passing the bridge.

### 3. Data

The database contains measurements recorded in the period from January 2008 to January 2010 with the total number of 628 days. A number of recorded vehicles is over 1.8 million. The traffic flow data were

---

<sup>\*</sup> Ing. Jan Krejsa: Klokner Institute: Department of Structural reliability, CTU in Prague, Solinova 7, 166 08, Prague; CZ, jan.krejsa@cvut.cz

<sup>\*\*</sup> Assoc. Prof. Ing. Miroslav Sykora, PhD.: Klokner Institute: Department of Structural reliability, CTU in Prague, Solinova 7, 166 08, Prague; CZ, miroslav.sykora@cvut.cz

obtained on a bridge that is a part of the Prague Highway Ring (Polak et al., 2009, Polak et al., 2011 and Morales et al., 2014). The data contain real vehicle weights. Numbers of vehicles per day are divided into 32 categories:

- Light vehicles with weights from 0 to 10 tons,
- 30 categories in the range from 10 to 85 tons, with the difference of 2.5 ton between categories,
- One category for the range from 85 to 200 tons.

#### 4. Procedure for data analysis

The main goal of this study is optimisation of the length of traffic flow records for a general design situation. The assessment is thus based on the Wöhler curve given by the *fib* Model Code 2010 (fib, 2013) for C35/45 concrete class and stress amplitudes caused by the real traffic spectrum. To provide a representative case study, the magnitude of stress amplitudes is chosen so that the partial factor method according to *fib* Model Code 2010 (fib, 2013) leads to cumulative damage obtained by the Palmgren-Miner rule slightly lower than unity for a reference period of 100 years. The calculation procedure can be summarised in the following steps:

- Development of sub-databases for different record lengths (1, 7, 30 and 120 days); the following steps are conducted for each of the sub-databases.
- Prediction of numbers of vehicles  $n_i$  for each weight category, considering a reference period  $t_{\text{ref}}$  as a study parameter, i.e. by extrapolating the average number of vehicles given a particular length of record.
- Estimation of the stress amplitudes for vehicles  $\sigma_{\text{veh},i}$  in each weight category.
- Determination of the Wöhler curve according to *fib* Model Code 2010 (fib, 2013) considering the coefficient related to a concrete strength class as  $s = 0.38$ , the concrete age during the first loading  $t = 90$  days, minimum compressive stress  $\sigma_{\text{c,min}} = 5$  MPa and maximum compressive stress  $\sigma_{\text{c,max},i} = \sigma_{\text{c,min}} + \sigma_{\text{veh},i}$ .
- Assessment of the cumulative damage by Palmgren-Miner rule (1).
- Statistical evaluation of  $D_{\text{fat}}$ -characteristics.
- Probabilistic modelling of basic variables and reliability analysis.
- Estimation of fatigue life for a given target reliability level.

#### 5. Statistical evaluation of $D_{\text{fat}}$

The results of the statistical evaluation (the mean value  $m_{D_{\text{fat}}}$ , of the coefficient of variation  $v_{D_{\text{fat}}}$  and the skewness  $w_{D_{\text{fat}}}$ ) of fatigue damage for different lengths of record are reported in Tab. 1. Only the mean value  $m_{D_{\text{fat}}}$  depends on  $t_{\text{ref}}$ , other parameters are dependent only on database.

Tab. 1: Statistical evaluation of fatigue damage for different lengths of record for  $t_{\text{ref}} = 100$  years.

Length of record	Number of lengths of records	Total number of days under consideration	Total number of vehicles	$D_{\text{fat}}$		
				$m_{D_{\text{fat}}}$	$V_{D_{\text{fat}}}$	$w_{D_{\text{fat}}}$
Extrapolation from all data	1	628	1864886	0.186	-	-
1 day	628	628	1864886	0.186	2.17	3.19
7 days	89	623	1852822	0.188	1.06	2.15
30 days	20	600	1818270	0.194	0.69	0.69
120 days	5	600	1818270	0.194	0.62	1.14

Tab. 1 shows the effect of different lengths of record on  $D_{\text{fat}}$  during the reference period  $t_{\text{ref}} = 100$  years. Only complete measurements for a particular length of record are involved in the analysis, which causes

minor differences in the total numbers of days and vehicles. Coefficient of variation significantly decreases with an increasing length of record while the mean value is nearly independent. When the length of record is 120 days, the coefficient of variation is 3.5 times lower than for daily records. The verification by the partial factor method according to the *fib* Model Code 2010 (fib, 2013) indicates that a fatigue life is longer than 100 year since the fatigue damage is less than unity,  $D_{\text{fat}} = 0.85$ .

## 6. Probabilistic modelling and estimation of fatigue life

Reliability indicators - failure probability  $p_f(t_{\text{ref}})$  and reliability index  $\beta(t_{\text{ref}})$  – are obtained by a probabilistic reliability analysis as follows:

$$p_f(t_{\text{ref}}) = P[\theta_D \theta_E D_{\text{fat}}(t_{\text{ref}}) > 1]; \beta(t_{\text{ref}}) = -\Phi^{-1}[p_f(t_{\text{ref}})] \quad (2)$$

where  $-\Phi^{-1}$  is the negative value of inverse function of general normal distribution; see EN 1990,  $\theta_D$  the model uncertainties associated with Palmgren-Miner rule and  $\theta_E$  the model uncertainty associated with load effects. The notation and probabilistic models for the basic variables are provided in Tab. 2.

Tab. 2: Statistical parameters for uncertainties.

Uncertainty	$m$	$V$	$w$
$\theta_D$	1	0.5	1.63
$\theta_E$	1	0.1	0.30

It is assumed that uncertainty related to material resistance (the application of Wöhler curves) is covered by  $\theta_D$ . The Wöhler curve applied strictly according to the *fib* Model Code and using a mean concrete compressive strength instead of its characteristic values leads to mean numbers of cycles to failure (fib, 2013).

Three-parametric lognormal distribution is chosen for  $D_{\text{fat}}$ ,  $\theta_D$  and  $\theta_E$ . The probabilistic lognormal model for  $D_{\text{fat}}$  is based on the database and previous experience. Models for the uncertainty in load effect  $\theta_E$  and the uncertainty related to the Palmgren-Miner rule  $\theta_D$  are based on the information provided in the Probabilistic Model Code of the Joint Committee on Structural Safety (JCSS, 2006) (Tab. 2). Uncertainties in the load effect model take into account inaccuracies in determining the load effect, such as internal forces and stresses resulting from model simplifications in geometry, supporting and boundary conditions, redistribution of forces amongst structural members, uncertainties in specifying model parameters that are unknown, etc. Coefficient of variation of  $\theta_D$  for structural steel is 0.3 (JCSS, 2006). It is estimated that uncertainty associated with the Palmgren-Miner rule for concrete is larger and coefficient of variation of 0.5 is thus taken into account.

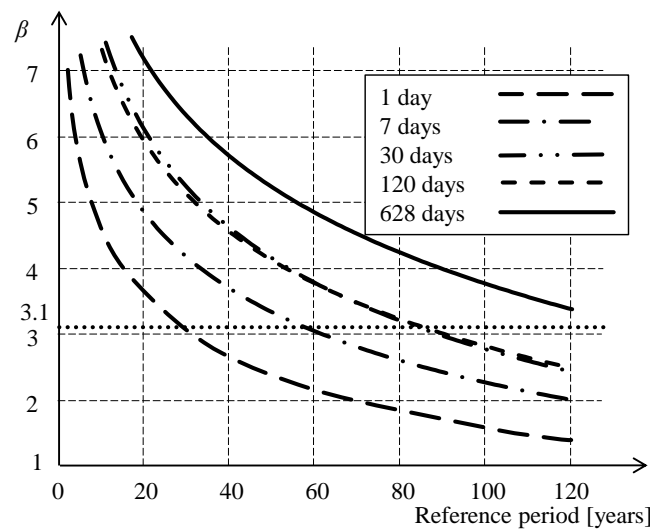


Fig. 1: Reliability index as a function of reference period for different lengths of record.

Fig. 1 shows the variability of reliability index with a reference period for different lengths of record and a target reliability level of 3.1 (fib, 2013). It appears that the optimal length of record is 30 days as a

fatigue life for this length of record – 85 years – is more than three-times longer than daily records. Increasing a length of record above 30 days seems to improve fatigue life estimates insignificantly. For shorter lengths the effect of statistical uncertainty increases and the accuracy of the estimate of fatigue life decrease.

It is emphasised that changes in the traffic flow intensity are not considered; i.e. stationary conditions and ergodicity (Melchers, 2002) are assumed. Dynamic effects are to be considered in a fatigue analysis unless they are included in measurements (as is the case of this study). In further investigations sensitivity analysis will be conducted to identify basic variables, probabilistic models of which should be improved.

## 7. Conclusions

The paper investigates the effect of a length of traffic flow records on fatigue life estimates for road bridges. It appears that:

- With an increasing length of record, coefficient of variation of fatigue damage significantly decreases while the mean value changes insignificantly.
- Optimal length of record is 30 days; longer lengths of record improve fatigue life estimates insignificantly.
- The verification by the partial factor method indicates that a fatigue life is longer than 100 year while a fatigue life estimated by the probabilistic analysis is about 85 years for the optimum length of record; this is indicative of the need for updating the partial factor method procedure for fatigue verifications.

Within further studies, a more detailed analysis of traffic flow and an assessment of uncertainties will be conducted.

## Acknowledgement

The study is a part of the research projects SGS16/195/OHK1/2T/31 supported by the SGS of CTU in Prague and P105/12/G059 supported by the Czech Science Foundation. Support of Prof. Michal Polak who kindly provided the data is appreciated.

## References

- EN 1990-1 (2006) Basis of structural design, Prague: ÚNMZ.
- JCSS. JCSS Probabilistic Model Code (2001). Zurich: Joint Committee on Structural Safety. ISBN 978-3-909386-79-6.
- fib* (2013) *fib* Model Code for concrete structures 2010: final draft. Lausanne, Switzerland: International Federation for Structural Concrete (*fib*), *fib*. 653 pp. ISBN 978-3-433-03061-5.
- Melchers, R.E. (2002) Structural Reliability, Analysis and Prediction. John Wiley & Sons.
- Morales-Nápoles, O., Steenbergen, R.D.J.M. (2014) Analysis of axle and vehicle load properties through Bayesian Networks based on Weigh-in-Motion data, Reliability Engineering & System Safety, Volume 125, pp. 153-164, ISSN 0951-8320, <http://dx.doi.org/10.1016/j.ress.2014.01.018>.
- Polak, M., Plachy, T. and Rotter, T. (2009) Vibration Monitoring of the Bridge Loaded by Heavy Vehicle Traffic. In: Proceedings of the 5th WSEAS International Conference on Applied and Theoretical Mechanics (Mechanics '09). Mathematics and Computers in Science and Engineering. Puerto de la Cruz, SPAIN, pp. 120-123, ISBN 978-960-474-140-3.
- Polak, M., Plachy, T. and Rotter, T. (2011) Long-time monitoring of the bridge response caused by heavy traffic and temperature changes. In: Proceedings of the 49th International Scientific Conference on Experimental Stress Analysis. Brno, pp. 341-348, ISBN 978-802144275-7.

## THE EVALUATION OF HOKUYO URG-04LX-UG01 LASER RANGE FINDER DATA

J. Krejsa<sup>\*</sup>, S Vechet<sup>\*</sup>

**Abstract:** *Laser range finders are essential sensors in mobile robot navigation tasks, such as robot localization, or simultaneous localization and mapping. As the probabilistic approach is commonly used to fuse the robot motion model with sensor data, the knowledge of the sensor parameters, such as linearity, variance, etc. is essential for fusing algorithms to perform correctly. This paper presents the results of extensive tests on performance of Hokuyo URG-04LX-UG01 range finder, that becomes nowadays popular among robot designers due to its reasonable cost, compact dimensions and low weight. The influence of obstacle color, error distribution and offset drift are examined.*

**Keywords:** Laser range finder, Mobile robot, Localization.

### 1. Introduction

There are several essential issues in mobile robot navigation task, such as localization and simultaneous localization and mapping (SLAM). While sensors based on various physical principles can be used as environment description measurement component for fusion of robot dynamic model with such data (Krejsa, 2010), the direct determination of the distances from surrounding obstacles is necessary to handle the obstacle detection and avoidance issue. Moreover, the scan matching based techniques (Vechet, 2007) and most of SLAM algorithms are solely based on laser range finder observations. To correctly utilize measured distances in fusion algorithms, it is necessary to know the properties of the sensor in order to identify its probability model.

There are two major types of laser range finders (LRF) differing in measurement principle. The first one, represented by SICK LMS200 sensor (Ye, 2002), is based on time-of-flight principle. This type of LRF intended for larger outdoor robots is hard to beat in terms of precision and reliability. However, the second group, based on phase shift measurement principle, is much more suitable for most indoor robots, as compact dimensions, low weight and low power consumption can be reached. Hokuyo URG-04LX-UG01 sensor by Hokuyo, Japan (see Fig. 1-left), is currently the most wide spread representative of such a sensor mainly due to its low cost.

### 2. Sensor evaluation

Hokuyo URG-04LX-UG01 sensor (Hokuyo Automatic) specifications are given in Tab. 1. The sensor has combined power source and communication interface through USB. It is intended for indoor use, due to its compact dimensions it is ideal for smaller autonomous robots navigating in office spaces, hospitals, etc. The example of LRF sensor mounted on mobile robot Breach by Bender Robotics is given in Fig. 1. The evaluation of the sensor was therefore performed on surfaces that are typical for environments the robots equipped with the sensor are likely to be used, in particular the painted walls and highly reflective metal and plastic panels.

The sensor was mounted on a linear drive enabling to change the distance between the sensor and obstacle in the range of 250 – 4000 mm. Scan frequency used was 10 Hz, the maximum the sensor allows. Only a single beam measurement located in the axis of the sensor and thus perpendicular to the

---

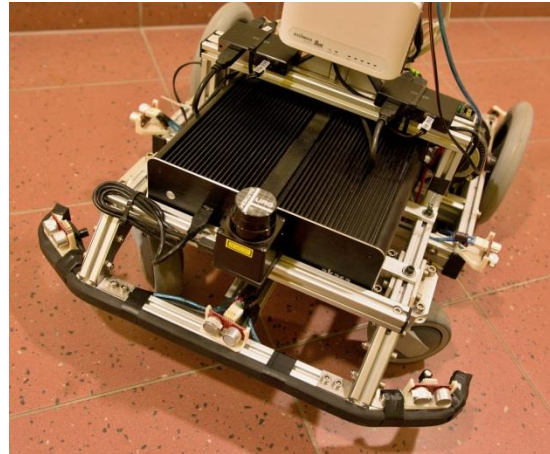
<sup>\*</sup> Assoc. Prof. Jiri Krejsa, PhD., Assoc. Prof. Stanislav Vechet, PhD.: Institute of Thermomechanics AS CR, v.v.i., Technicka 2, 616 69, Brno, Czech Republic, krejsa@fme.vutbr.cz, vechet.s@fme.vutb.cz



obstacle was taken into account and analyzed. First the stability of the measurement was evaluated (see below), followed by the influence of measured distance and materials the obstacles are made of.

*Tab. 1: Sensor data sheet specifications.*

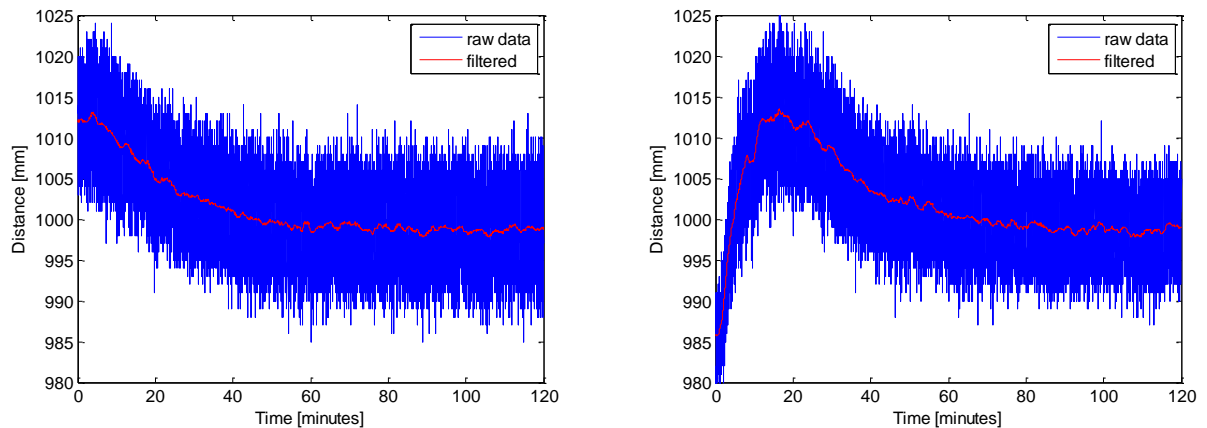
Variable	Value (range), unit
Measuring distance	20 – 5600 mm
Angular range	240 degrees
Distance resolution	1 mm
Angular resolution	0.36 degree
Scan frequency	10 Hz
Dimensions	50 x 50 x 70 mm
Weight	160 g



*Fig. 1: Hokuyo URG-04LX-UG01 scanner (left), scanner mounted on Breach mobile robot (right).*

## 2.1. “Warm-up” mean drift

Time stability of the measurement is the key factor. The scanner of ambient room temperature was positioned into the distance of 1000 mm from the white painted wall and measurement was performed for 2 hours. The results are shown in Fig. 2, the raw measurement values together with the filtered data calculated by floating average filter with the length of 1000 samples, that corresponds to 100 seconds. One can see obvious drift of the mean, it takes about 50 minutes for the readings to become stable. As the only factor that changes during the test is the temperature, another experiment was evaluated, with the scanner precooled to 0 °C prior to the measurement. The results are shown in Fig. 2-right. One can see, that the dependency on sensor internal temperature is a complex process, as the measured distance for the cooled sensor starts as far as 20 mm below the nominal value, rises and then follows the previous experiment course.



*Fig. 2: Mean “warm up” drift. Room temperature scanner (left), scanner cooled to 0 °C (right).*

## 2.2. Measured distance related errors and variations

The consistency of measurement along measured distance was tested with following setup. The sensor was positioned against the white wall in defined set of distances in the range of 250 – 4000 mm and data was collected for 30 seconds (300 samples). The mean error and standard deviations are shown in Fig. 3. One can see that standard deviations are about the same in the whole range of measurement, the error of the mean does not exhibit relation to the distance measured. All the measurements were obtained using sensor that was warmed up for 60 minutes prior to the test. The same holds for all further measurements.

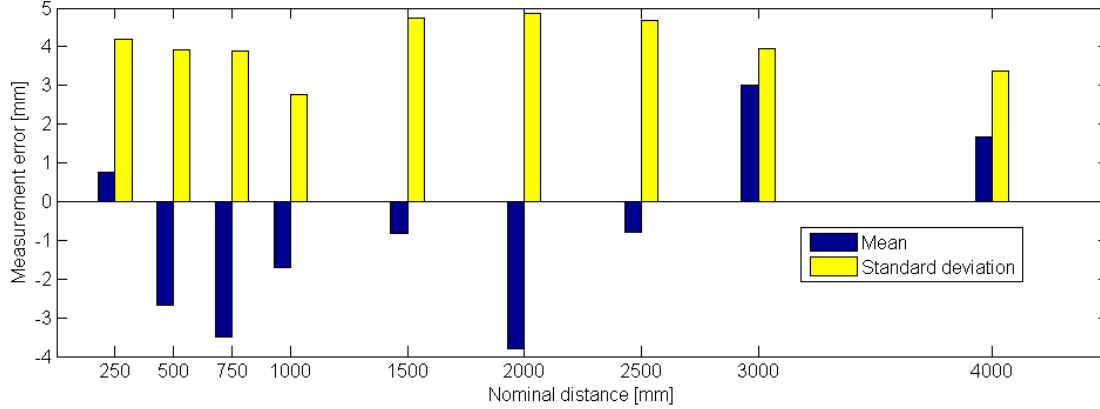


Fig. 3: Linearity test results, mean error and standard deviation of measured data.

## 2.2. Sensor manufacturing differences

The repeatability of the measurement when using different sensor units of the same type was tested. Three units were available with different manufacturing date (sensor A - 2013, sensor B - 2015 and sensor C - 2016). The tests were performed in following manner. Value of 1000 mm was selected as nominal distance. The sensor was positioned against the white painted wall and data were measured for 500 seconds (5000 samples). The experiment was repeated under the same conditions for all three sensor units. The results are shown in Fig. 4. The normal distribution of the measurement noise is apparent from the measurements, however, one can see that there are significant differences in mean, with older sensors giving smaller values. Whether it is caused by sensor degradation in time is yet unknown, larger set of sensors is currently being collected.

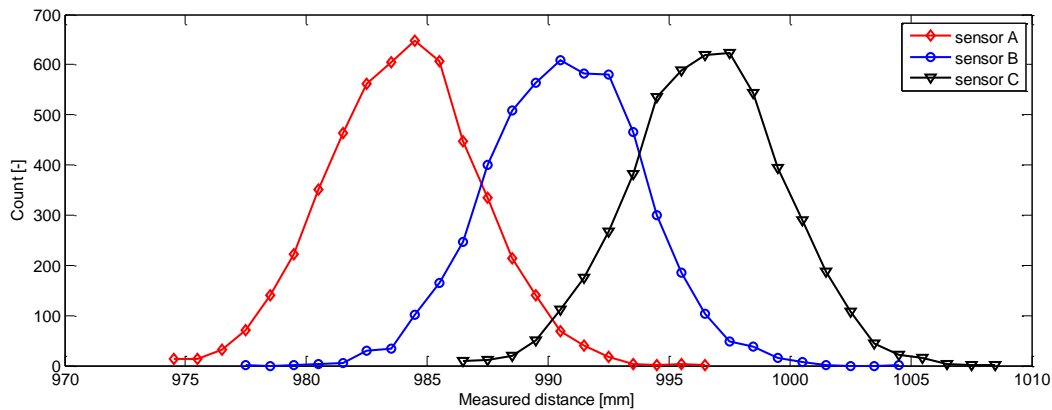


Fig. 4: Measurement of different sensor units.

## 2.3. Obstacle color and material

The influence of obstacle color and material was tested in following manner. Value of 1000 mm was selected as nominal distance. The sensor was positioned against the wall and data were measured for 50 seconds (500 samples). The experiment was repeated for several wall colors and materials, with the emphasis on reflexive materials commonly available in office spaces where the robot equipped with the sensor is intended to be used. The results are shown in Fig. 5. One can see that the variance of measurements is substantial. The difference in mean between the green and red painted walls is 11.5 mm.

The influence of material gives interesting results, note in Fig. 5 that the measurements for aluminum and reflexive foil are almost identical, while the stainless steel measurement is not too different from the white painted wall. The reason is yet to be found.

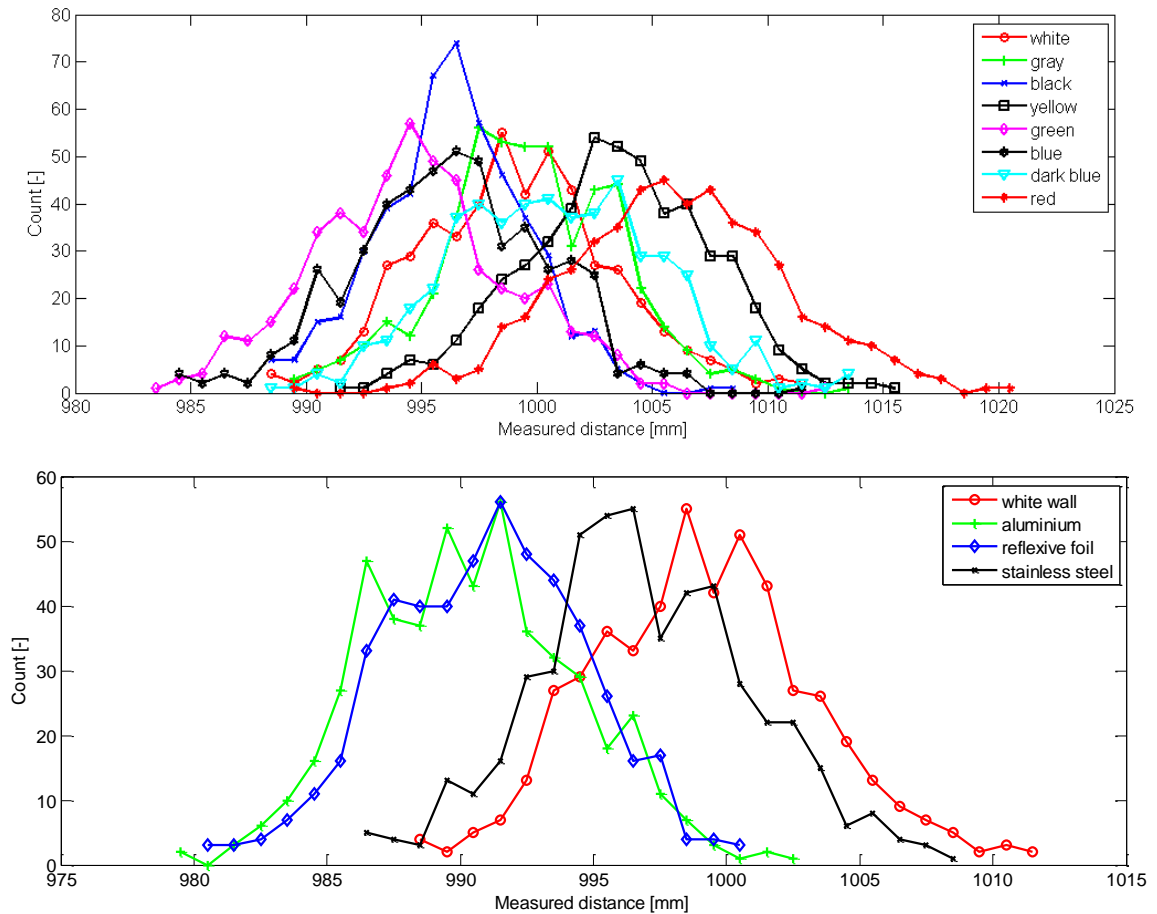


Fig. 5: Influence of obstacle color (top) and material (bottom).

### 3. Conclusions

Number of experiments was performed with the Hokuyo URG scanner. Mean drift was observed that is dependent on the initial sensor temperature. Measured distances errors are not influenced by the actual distance of the obstacle both in terms of mean and variance. Repeated measurements proved the normal distribution of the measured distance. The influence of obstacle color and material is significant.

### Acknowledgement

The results were obtained with institutional support RVO 61388998 of the Institute of Thermomechanics AS CR v.v.i.

### References

- Vechet, S., Krejsa, J. and Houska, P. (2007) The enhancement of PCSM method by motion history analysis. Recent Advances in Mechatronics, 107-110. Doi 10.1007/978-3-540-73956-2\_22.
- Krejsa, J. and Vechet, S. (2010) Odometry-free mobile robot localization using bearing only beacons. Proceedings of 14th International Power Electronics and Motion Control Conference (Epe-Pemc 2010). Doi 10.1109/Epepmc.2010.5606893.
- Ye, C. and Borenstein, J. (2002) Characterization of a 2D laser scanner for mobile robot obstacle negotiation, in Proc. of the IEEE Intrl. Conf. on Robotics and Automation, vol. 3, pp. 2512-2518.
- Vechet, S., Chen, K.S. and Krejsa, J. (2014) Hybrid Navigation Method for Dynamic Indoor Environment Based on Mixed Potential Fields, Mechatronics 2013: Recent Technological and Scientific Advances, Springer, pp. 575-582, DOI: 10.1007/978-3-319-02294-9\_73.
- Hokuyo Automatic Co Ltd. [online] <http://www.hokuyo-aut.jp>.

## ON THE CHOICE OF GEOMETRICAL IMPERFECTIONS IN GMNIA STRENGTH CALCULATIONS OF THIN-WALLED STRUCTURES

J. Kriváček\*, Z. Sadovský\*\*

**Abstract:** *In the light of the recently developed method for implementation of initial geometrical imperfections in the ultimate buckling strength calculations of thin-walled structural elements by the materially and geometrically nonlinear FEM analysis (GMNIA), special choices of the imperfections are discussed.*

**Keywords:** Thin-walled structures, Geometrical imperfections, Strain energy, Ultimate strength, Non-linear finite-element simulations.

### 1. Introduction

A method for implementation of initial geometrical imperfections in the ultimate buckling strength calculations of thin-walled structural components has been developed in (Sadovský et al., 2012, Sadovský and Kriváček, 2017). The method takes into account imperfections in the shapes of eigenmodes of the corresponding linearized problem and their combinations. Essentially, any other imperfection shape, e.g. the measured shapes, can be used. Substantial feature of the method is that in the search for the most unfavourable shape the geometrical imperfections are normalized by the energy measure, i.e. imperfections are compared at an energy measure level. The energy measure EM of imperfections is defined by the square root of elastic strain energy of a structure hypothetically accumulated when the structure transfers from its presumed perfect state into the considered imperfect state. The energy measure is derived from the total strain energy (TSE) of the linear statics or linearized buckling FEM calculations. The applied commercial code MSC.Nastran (version 2013 and 2014) provides TSE as a by-product of the linearized buckling.

Some authors suggest that considering initial imperfections in the shapes of failure modes may lead to the most unfavourable ultimate strength values. In the present paper this conjecture is checked for the case of a cold formed lipped channel column in axial compression studied in (Sadovský and Kriváček, 2017).

The ultimate strengths are calculated using the load incremental arc-length approach of MSC.Nastran. Obtained results are compared with those of the MSC.Marc code (version 2016). Marc is executed from inside Nastran as MSC.Nastran Implicit Nonlinear solution (SOL 600, 106). For this solution a displacement incremental approach is applied.

### 2. Numerical study

Centreline cross-section dimensions, length and material properties of the channel are shown in Tab. 1. The cross-sectional dimensions and material properties correspond to the test specimen ST15A90 (Young and Hancock, 2003). The roundness of corners is not considered, thereby residual stresses are neglected and universal material model for cold-formed steel (von Mises yield criteria with isotropic hardening) is adopted. The task was carried out by the MSC.Nastran code applying the quadrilateral four-noded linear QUAD4 element. Three element sizes of approximately 7.5, 5 and 3.3 mm have been used to produce meshes denoted as coarse, medium and fine, respectively. The multipoint constraint equations for element nodes located at the bottom end of the column ( $x = 0$ ) provided uniform translation in axial direction. The

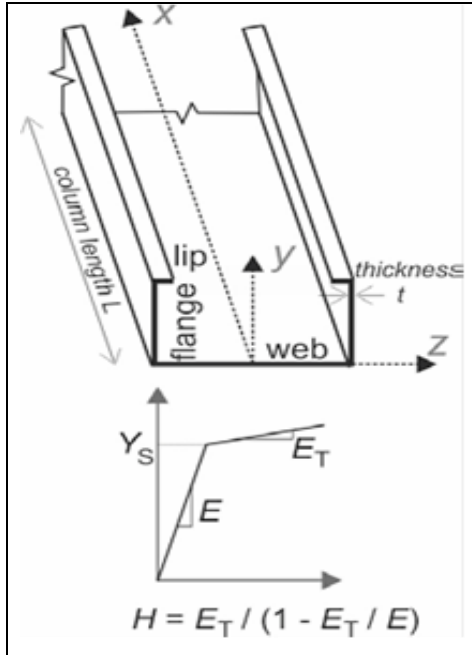
---

\* Ing. Jozef Kriváček, CSc.: Institute of Construction and Architecture, Slovak Academy of Sciences, Dúbravská cesta 9; 845 03 Bratislava; SK, [usarjkri@savba.sk](mailto:usarjkri@savba.sk)

\*\* Ing. Zoltán Sadovský, DrSc.: 831 03 Bratislava; SK, [zoltan@sadovsky.info](mailto:zoltan@sadovsky.info)

translations in other directions and all translations of nodes at the column top end were fixed. These boundary conditions were chosen to match the attachment into the test rigs of the specimen ST15A90 (Young and Hancock, 2003) (see Sadovský et al., 2017).

Tab. 1: Dimensions and material characteristics of the studied channel.

	web [mm]	97.4
	flange [mm]	48
	lip [mm]	9.95
	thickness $t$ [mm]	1.5
	length $L$ [mm]	2000
	Young modulus $E$ [GPa]	210
	Poisson's ratio	0.3
	yield stress $Y_s$ [MPa]	515
	plasticity modulus $H$ [MPa]	21.002

The presented results were obtained using the FEM model with medium mesh discretization (17 600 QUAD4 elements with 108 276 DOF).

The eigenmode imperfections — Modes 27, 28, 44 and the reversed Mode R27 (multiplying Mode 27 by -1) provided the least collapse loads among the first 60 eigenmodes normalized by the energy measure. (Sadovský et al., 2017). They are shown in Fig. 1 along with the chosen (moderate) energy measure level, the corresponding amplitudes and resulting failure loads. The term amplitude should be understood as the maximum of cross-sectional co-ordinate displacements.

Fig. 2 shows the corresponding failure shapes. For their use as initial imperfections the shapes are adjusted to the same energy measure level as given in Fig. 1. The corresponding amplitudes and failure loads obtained in subsequent calculations are presented in Fig. 2. Because the failure shapes are highly distorted, their normalisation by the energy measure resulted in significantly lower amplitudes than obtained for the eigenmodes. Note that only the cross-sectional displacements of the failure shapes are normalized and applied as initial imperfections. This corresponds to the measurements of initial out of nominal geometry of a member. Including the axial displacements would lead to even smaller amplitudes of the normalized shapes yielding higher values of failure loads.

The failure loads are defined as the peak of load-shortening response function of the channels. The function is obtained by load arc-length incremental solution. The channel is subject to axial load of 120 kN divided into ten uniform load steps. The magnitudes of individual load step increments were estimated by Crisfield type of arc-length method, so the increments could be less than zero. Stiffness update was performed at each iteration (full Newton-Raphson method) with error tolerance criteria of Load & Work ( $10^{-3}$ ,  $10^{-7}$ ). The number of iterations for each increment was limited to 25. No convergence led to bisection of the increment and the solution was repeated. The number of controlled step increments was limited to 15. The problems with solution such as described in (Sadovský et al., 2017) did not occur in presented cases.

The MSC.Marc code with bilinear thin shell Element 139 is used to verify the failure loads given in Fig. 2. A displacement (shortening) incremental solution with Marc input data file generated by MSC.Nastran Implicit Nonlinear module (SOL 600, 106) (for details see Sadovský et al., 2017) is applied. Two uniform shortening steps (at  $x = 0$ ) are adopted: 0.01 and 0.002 mm.

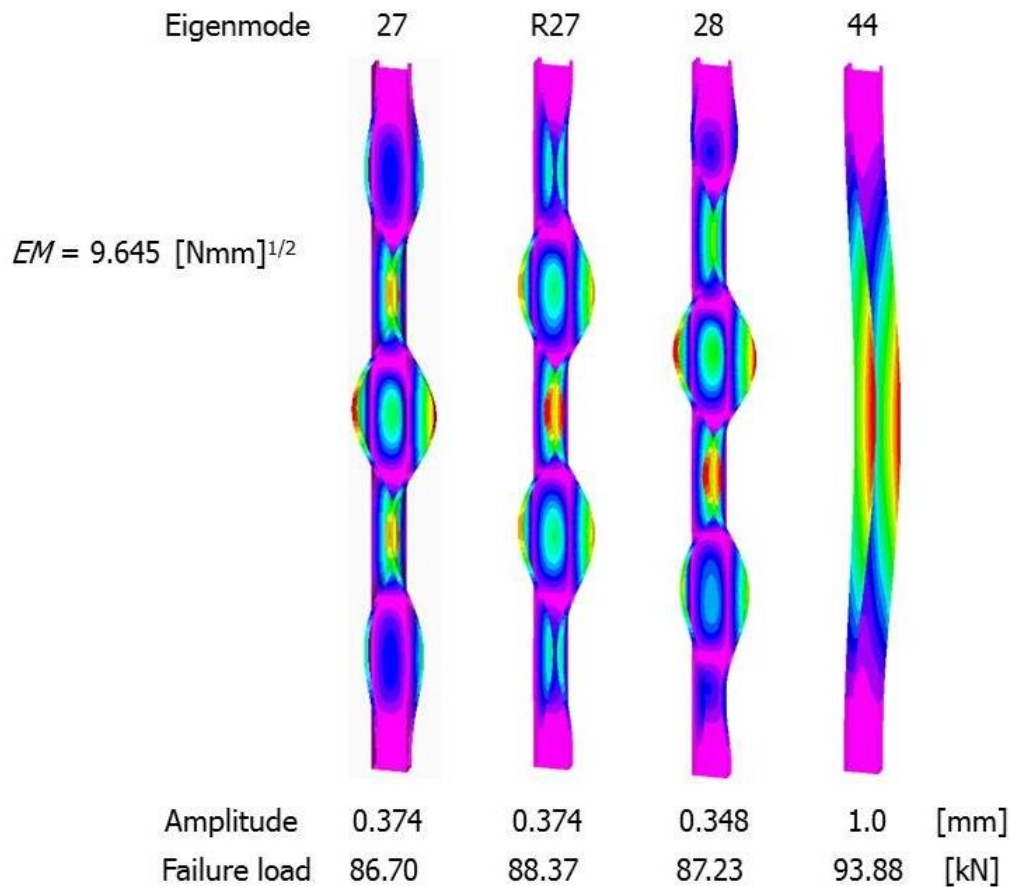


Fig. 1: The most influential eigenmode imperfections normalized to  $EM = 9.645 [N.mm]^{1/2}$  with corresponding amplitudes and failure loads.

The Marc failure loads are given in Tab. 2. The largest difference occurred for R27 case. Solution of this case was recalculated using two ways: a) for load incremental arc-length solution smaller 5 kN load steps were applied and b) the shortening incremental solution by MSC.Nastran was adopted. The failure loads of 93.60 and 94.13 kN were obtained.

Tab. 2: Failure loads by MSC.Marc code.

Failure shape	27	R27	28	44
Failure load [kN]	100.82	97.12	100.26	103.89

Comparing the failure loads in Figs. 1 and 2 it is seen that in each individual eigenmode — failure shape succession of imperfections the latter provides markedly higher failure loads.

The CPU time consumption of load incremental solution ranged between 15 and 18 minutes. The displacement incremental solutions consumed larger amount of time – approximately 60 and 70 minutes for Marc and Nastran codes, respectively. Using ten times larger shortening increments decreased the time consumption to one sixth, however the value of failure load for Marc solution increased by 2.5 %. The change of Nastran strength value due to increase of shortening increments was negligible. Note that the calculations were performed on a work station with two eight-core Xeon processors (13 089 of cpu benchmark) and four SAS disks operating under Windows 7 ultimate.

The imperfections depicted in Fig. 2 were obtained as the sum of eigenmode imperfections given in Fig. 1 and the additional displacements at failure loads calculated for those imperfections (however without axial displacements as mentioned above). If applying only the additional displacements at failure loads as imperfections and normalizing them to  $EM = 9.645 [N.mm]^{1/2}$ , new amplitudes of 0.109, 0.163, 0.111 and 0.119 [mm] are obtained. Corresponding failure loads by MSC.Nastran arc-length approach are



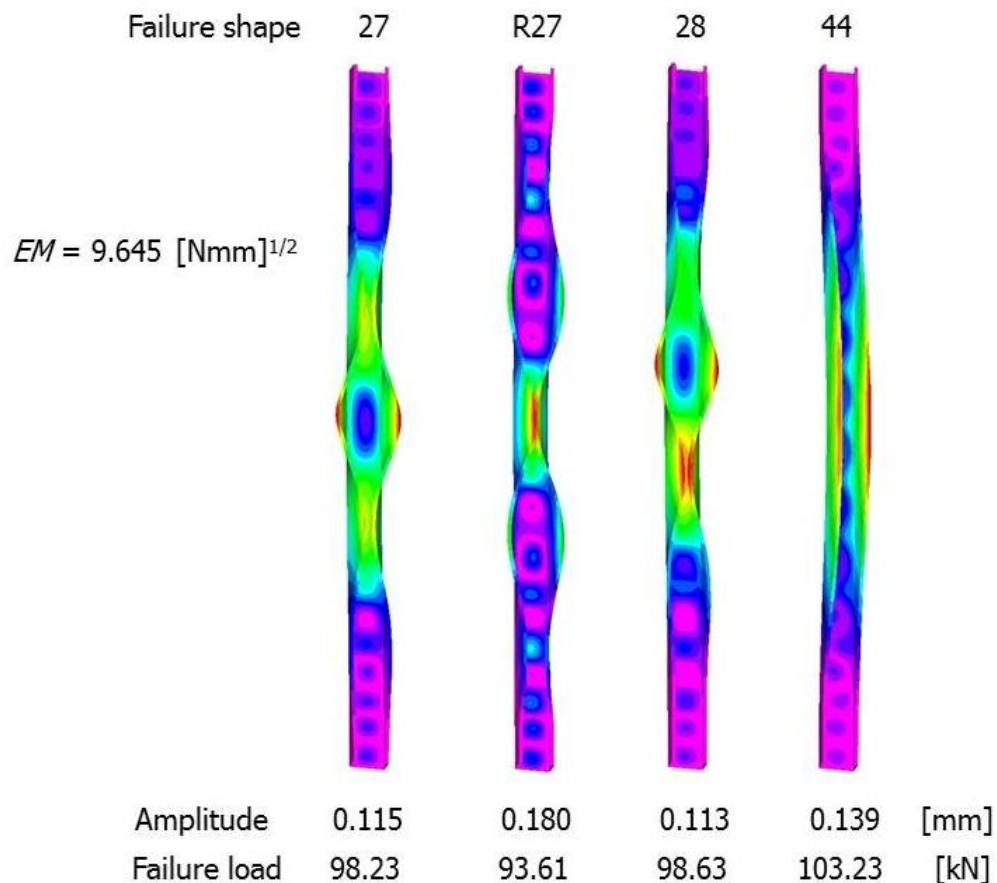


Fig. 2: The imperfections in failure shapes normalized to  $EM = 9.645 \text{ [N.mm]}^{1/2}$  with corresponding amplitudes and failure loads.

98.48 kN, 95.07 kN, 98.86 kN and 103.15 kN. These failure loads are also considerably higher than those in Fig. 1. Note that using only additional displacements at some load level as imperfections simplifies processing of input data for subsequent non-linear solution of this type of tasks.

### 3. Conclusions

Comparison of the most important eigenmode imperfections with the corresponding failure mode shapes revealed that under the energy measure normalization the latter possess significantly smaller amplitudes. This is a consequence of their high distortion, which suggests their classification as unrealistic imperfections. The corresponding failure loads are higher than those obtained for the eigenmode shapes normalized to the same energy measure level. For the eigenmode imperfection – Mode 27, providing the lowest failure load, the axial shortening at failure is about 7 % lower, while the maxima of lateral coordinate displacements at failure are 4.6 (z axis) and 2.7 (y axis) multiples of those obtained for the corresponding failure shape imperfection.

### Acknowledgement

The authors acknowledge a partial support of their work by grant agency VEGA under grant 2/0154/15 Modelling of post-buckling behaviour and strength of thin-walled cold formed columns.

### References

- Sadovský, Z., Kriváček, J., Ivančo, V. and Ďuricová, A. (2012) Computational modelling of geometric imperfections and buckling strength of cold-formed steel. *Journal of Constructional Steel Research*, 78, pp. 1-7.
- Sadovský, Z. and Kriváček, J. (2017) Tolerances of imperfections and strength of cold-formed lipped channel column. *Journal of Constructional Steel Research*, 128, pp. 762-771.
- Young, B. and Hancock, G.J. (2003) Compression tests of channels with inclined simple edge stiffeners. *Journal of Structural Engineering ASCE*, 129, 10, pp. 1403-11.



## APPLICATION OF THE SLIDING CONTROLLER FOR THE GYROSCOPE SYSTEM OF THE ANTI-AIRCRAFT MISSILE

I. Krzysztofik<sup>\*</sup>, Z. Koruba<sup>\*\*</sup>

**Abstract:** Precision of anti-aircraft missile homing depends mainly on correct determination of the current angle between the axis of the gyroscope system and the line of sight. The system of automatic gyroscope control should ensure automatic minimization of that angle, and thus, constant directing of the gyroscope system axis towards the line of sight, i.e. tracking the target by the homing head. This paper presents a sliding controller applied to control the gyroscope system. Subsequently, the dynamics of that system during the process of anti-aircraft missile homing onto a moveable target was studied. Some chosen results of the simulation research were presented graphically.

**Keywords:** Gyroscope system, Sliding controller, Missile.

### 1. Introduction

The process of homing a surface-to-air missile consists mainly in determining the line of sight (LOS) – a straight line positioned from the homing head to the target (Dziopa et al., 2015 and Grzyb, 2016). The gyroscope system (GS), i.e. a controlled gyroscope on the Cardan joint, is a drive element of the head. In the moment when the gyroscope system axis overlaps with the line of sight, it is assumed that the missile tracks and follows the target. The sensors measure the angle between the line of sight and the missile axis and transfer it to the autopilot. Regardless of the above, the autopilot measures with its own devices the angular position of the missile axis in relation to the Earth, and subsequently, determines control signals and transfers them to the executive control system. Precision of missile homing depends mainly on correct determination of the current angle between the gyroscope axis and the line of sight. The system of automatic gyroscope control should ensure automatic minimization of that angle, and thus, constant directing of the gyroscope system axis towards the line of sight, i.e. tracking the target by the head (Krzysztofik, 2014).

The errors of the gyroscope system are caused mainly by the friction to be found in the bearings and the fact that the rotor mass centre does not overlap with the intersection point of the suspension frame axis. That is why, the gyroscope system reacts to angular motions and changes of the linear velocity of the missile. Especially great changes of parameters are to be found at the initial stage of homing. The line of sight might be then determined incorrectly, on the basis of which the missile is directed to the target. With too excessive deviations of the line of sight from the set position, the sight of the target image might be lost (Gapinski, 2014a).

Therefore, in order to minimize the influence of all disruptions coming from the missile (basis of the gyroscope system) on the accuracy of the motion of the gyroscope system axis, the parameters of the control system should be selected carefully (Gapiński, 2014b and Koruba, 2013). The scope of research conducted should entail formulation of a proper physical and mathematical model as it was presented in (Blasiak et al., 2014; Koruba, 2010; Laski et al., 2015 and Takosoglu, 2016).

---

<sup>\*</sup> Eng. Izabela Krzysztofik, PhD.: Department of Applied Computer Science and Armament Engineering, Faculty of Mechatronic and Mechanical Engineering, Kielce University of Technology, Aleja Tysiąclecia Państwa Polskiego 7; 25-314, Kielce; PL, pssik@tu.kielce.pl

<sup>\*\*</sup> Prof. dr. habil. Zbigniew Koruba, Eng.: Department of Applied Computer Science and Armament Engineering, Faculty of Mechatronic and Mechanical Engineering, Kielce University of Technology, Aleja Tysiąclecia Państwa Polskiego 7; 25-314, Kielce; PL, ksmzko@tu.kielce.pl

This paper includes an analysis of the dynamics of the gyroscope system with the use of a sliding controller. A mathematical model of motion of non-linear gyroscope system described in a detailed way in (Koruba et al., 2010) was adopted for considerations. A PD controller with optimal parameters chosen with the use of a modified method of optimization by Gołubienecw was applied to control the gyroscope system in this paper.

## 2. Sliding control for the gyroscope system during missile homing onto a moveable target

For the gyroscope system in question, two sliding surfaces are defined (Utkin, 2008 and Wang, 2011):

$$s_{g1} = \dot{e}_g + \lambda_1 e_g \quad (1a)$$

$$s_{g2} = \dot{e}_\psi + \lambda_2 e_\psi \quad (1b)$$

where:

$e_g = \vartheta_g - \varepsilon$ ;  $e_\psi = \psi_g - \sigma$  – control errors;

$\dot{e}_g = \dot{\vartheta}_g - \dot{\varepsilon}$ ;  $\dot{e}_\psi = \dot{\psi}_g - \dot{\sigma}$  – change of errors;

$\lambda_1, \lambda_2$  – positive constant;

$\vartheta_g, \psi_g$  – angles determining the position of the gyroscope system axis in space;

$\varepsilon, \sigma$  – angles determining the position of the line of sight in space.

Sliding controls are derived from the following equations:

$$M_b = -K_1 \operatorname{sgn}(s_{g1}) + M_{beq} \quad (2a)$$

$$M_c = -K_2 \operatorname{sgn}(s_{g2}) + M_{ceq} \quad (2b)$$

where:

$M_{beq}, M_{ceq}$  – equivalent controls;

$K_1, K_2$  – sliding reinforcements.

Equivalent controls are determined by comparing the derivative of the control surface to zero, i.e.  $\dot{s}_{g1} = 0$  and  $\dot{s}_{g2} = 0$ .

*Signum* function is defined in the following way:

$$\operatorname{sgn}(s_{g1,2}) = \begin{cases} -1 & \text{for } s_{g1,2} < 0 \\ 0 & \text{for } s_{g1,2} = 0 \\ +1 & \text{for } s_{g1,2} > 0 \end{cases} \quad (3)$$

In order to reduce the phenomenon of the so called *chattering*, instead of *signum* function, *saturation* is applied (Lee, 2007 and Shtessel et al., 2013):

$$M_b = -K_1 \operatorname{sat}(s_{g1} / \phi) + M_{beq} \quad (4a)$$

$$M_c = -K_2 \operatorname{sat}(s_{g2} / \phi) + M_{ceq} \quad (4b)$$

where :

$\phi$  – thickness of the border layer.

## 3. Simulation research

Simulation research of the dynamics of the gyroscope system during missile homing onto a moveable target was conducted in Matlab/Simulink environment.

The real and set flight path of the missile and the target was shown in Fig. 1. Figs. 2 - 6 present the results of the simulation of the missile and GS dynamics during homing onto a moveable target.

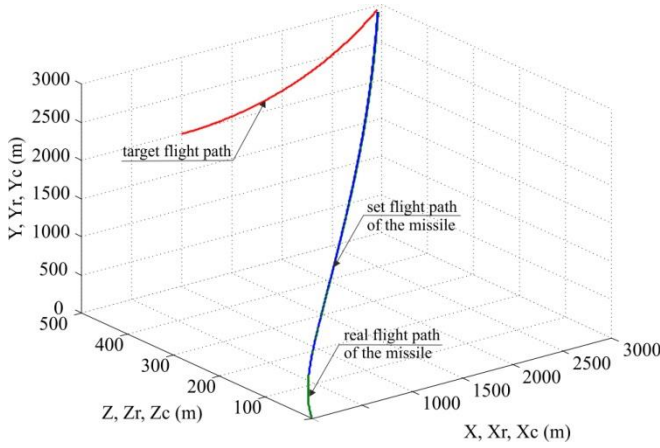


Fig. 1: The real and set flight path of the missile and the target.

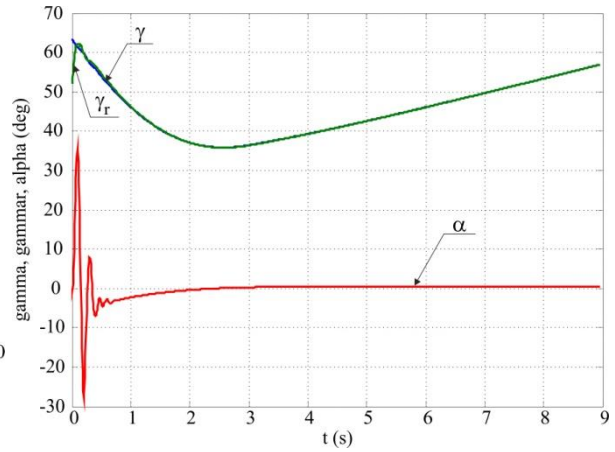


Fig. 2: The real  $\gamma_r$  and set  $\gamma$  flight angles of missile and angle of attack  $\alpha$ .

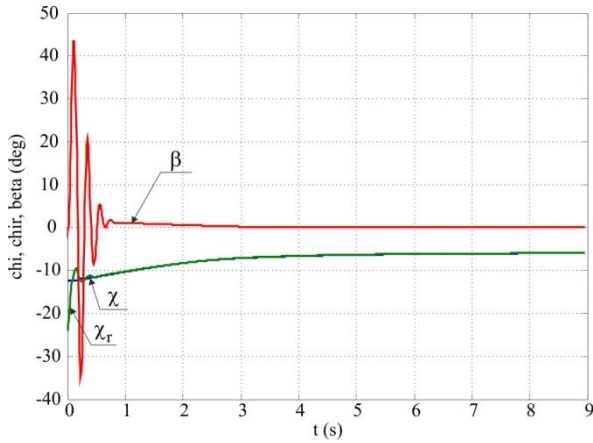


Fig. 3: The real  $\chi_r$  and set  $\chi$  flight angles of missile and sideslip angle  $\beta$ .

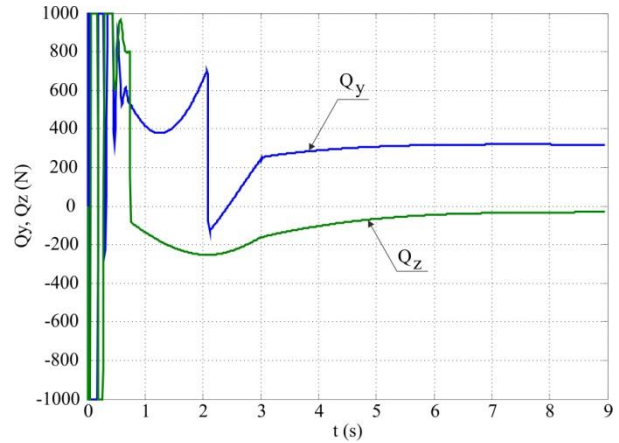


Fig. 4: Forces controlling the missile flight.

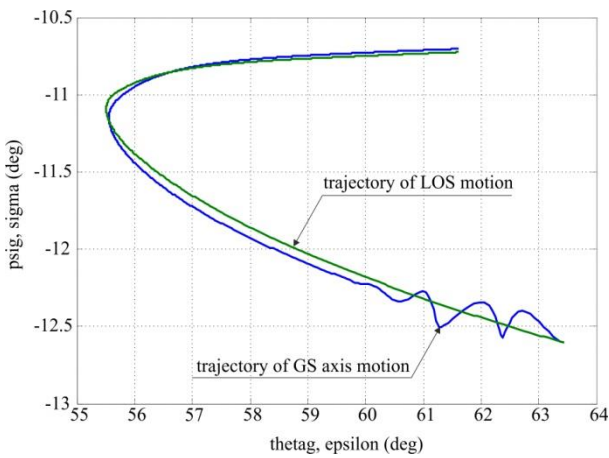


Fig. 5: The trajectories of motion of GS axis and LOS with the use of a PD controller.

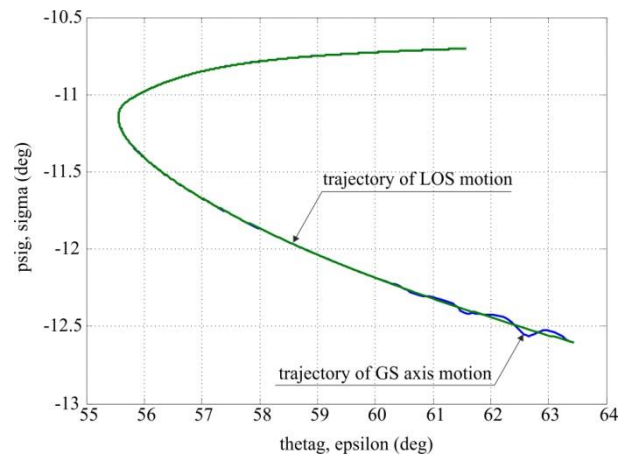


Fig. 6: The trajectories of motion of GS axis and LOS with the use of a sliding controller.

The missile flight was controlled with the use of a PID controller, however, to control the gyroscope system – a PD controller described in a detailed way in (Koruba et al., 2010) and a designed sliding

controller were applied. The parameters of the motion of the missile, target and gyroscope system were the same as in the case of papers. As a result of simulation research conducted, the following parameters of a sliding controller were selected:  $\lambda_1 = 75$ ,  $K_1 = 15$ ,  $\lambda_2 = 150$ ,  $K_2 = 15$ ,  $\phi = 1$ . The studies were conducted with an integration step amounting to  $dt = 0.00001$  (Baranowski, 2013).

#### 4. Conclusions

The results of the numerical studies showed great efficiency of the sliding control for the gyroscope system of the anti-aircraft missile. A significant improvement of the operation accuracy of the gyroscope system operation might be easily noticed in the case of application of the sliding controller (Figs. 5 and 6).

The selected sliding controller allows stable and continuous maintenance of the target in the field of sight vision of the homing head. It minimizes the deviation of the gyroscope system axis as a result of the kinematic influence of the missile onto the suspension of the gyroscope system.

#### References

- Baranowski, L. (2013) Effect of the mathematical model and integration step on the accuracy of the results of computation of artillery projectile flight parameters. *Bulletin of the Polish Academy of Sciences: Technical Sciences*, 61, 2, pp. 475-484.
- Blasiak, S., Takosoglu, J.E. and Laski, P.A. (2014) Heat transfer and thermal deformations in non-contacting face seals. *Journal of Thermal Science and Technology*, 9, 2, pp. JTST0011-JTST0011.
- Dziopa, Z., Buda, P., Nyckowski, M. and Pawlikowski, R. (2015) Dynamics of an unguided missiles launcher. *Journal of Theoretical and Applied Mechanics*, 53, 1, pp. 69-80.
- Gapinski, D. and Krzysztofik, I. (2014a) The process of tracking an air target by the designed scanning and tracking seeker, in: *Proc. 15th Int. Carpathian Control Conf.* (eds. Petras, I., Podlubny, I., Kacur, J., and Farana, R.), IEEE, pp. 129-134.
- Gapiński, D. and Stefański, K. (2014b) A control of modified optical scanning and tracking head to detection and tracking air targets. *Solid State Phenomena*, 210, pp. 145-155.
- Grzyb, M. and Stefański, K. (2016) The use of special algorithm to control the flight of anti-aircraft missile, in: *Proc. 22th Int. Conf. Eng. Mech. 2016* (eds. Zolotarev, I. and Radolf, V.), Svratka, Czech Republic, pp. 174-177.
- Koruba, Z. and Krzysztofik, I. (2013) An algorithm for selecting optimal controls to determine the estimators of the coefficients of a mathematical model for the dynamics of a self-propelled anti-aircraft missile system. *Proceedings of the Institution of Mechanical Engineers, Part K: Journal of Multi-Body Dynamics*, 227, 1, pp. 12-16.
- Koruba, Z., Krzysztofik, I. and Dziopa, Z. (2010) An analysis of the gyroscope dynamics of an anti-aircraft missile launched from a mobile platform. *Bulletin of the Polish Academy of Sciences: Technical Sciences*, 58, 4, pp. 651-656.
- Koruba, Z. and Ładyżyńska-Kozdraś, E. (2010) The dynamic model of a combat target homing system of an unmanned aerial vehicle. *Journal of Theoretical and Applied Mechanics*, 48, 3, pp. 551-566.
- Krzysztofik, I. and Koruba, Z. (2014) Mathematical Model of Movement of the Observation and Tracking Head of an Unmanned Aerial Vehicle Performing Ground Target Search and Tracking. *Journal of Applied Mathematics*, Article ID 934250, 11 p.
- Laski, P.A., Takosoglu, J.E. and Blasiak, S. (2015) Design of a 3-DOF tripod electro-pneumatic parallel manipulator. *Robotics and Autonomous Systems*, 72, pp. 59-70.
- Lee, H. and Utkin, V.I. (2007) Chattering suppression methods in sliding mode control systems. *Annual Reviews in Control*, 31, pp. 179-188.
- Shtessel, Y., Edwards, C., Fridman, L. and Levant, A. (2014) Introduction: Intuitive Theory of Sliding Mode Control, in: *Sliding Mode Control and Observation*. Springer New York, pp. 1-42.
- Takosoglu, J.E. (2016) Control system of delta manipulator with pneumatic artificial muscles, in: *Proc. 22th Int. Conf. Eng. Mech. 2016* (eds. Zolotarev, I. and Radolf, V.), Svratka, Czech Republic, pp. 546-549.
- Utkin, V.I. (2008) Sliding mode control: mathematical tools, design and applications, in: *Nonlinear and Optimal Control Theory*. Springer-Verlag Berlin Heidelberg, pp. 289-347.
- Wang, C.-C. and Yau, H.-T. (2011) Nonlinear dynamic analysis and sliding mode control for a gyroscope system. *Nonlinear Dynamics*, 66, 1, pp. 53-65.

## METHODOLOGY FOR PREDICTING DYNAMIC BEHAVIOUR OF MACHINE TOOLS BASED ON A VIRTUAL MODEL

F. Kšica<sup>\*</sup>, J. Vetiška<sup>\*\*</sup>, Z. Hadaš<sup>\*\*\*</sup>

**Abstract:** *This paper focuses on methodology for predicting dynamic behaviour of a machine tool based on a virtual model. The conventional approach based on a Finite Element Method is improved by including advanced modelling techniques, such as component mode synthesis, dynamic system identification and state-space transformation. Up to date, one of the available approaches to suppress the unstable behaviour during an operation is based on compensation of insufficient characteristics of the existing machine, however the goal is to optimize crucial parameters before the machine is manufactured. Presented method enable an effective prediction of unstable behaviour due to insufficient dynamic stiffness during an early stage of the product pre-production phase. In this paper, the theoretical foundation of virtual modelling of machine tools is set and a basic principle of the implemented techniques is discussed. Their application is a subject of an ongoing research.*

**Keywords:** Machine Tool, Dynamics, Virtual Model, Simulation, FEM.

### 1. Introduction

The aim of the present manufacturing industry is to produce parts in the most cost-effective way, matching required standards, and in the shortest time possible. The increasing product complexity makes testing and optimization of physical prototypes rather difficult. Therefore, the design process slowly shifts away from using economically ineffective physical prototypes and employs virtual prototyping to reduce the cost and time necessary for testing and optimization of the final product during the pre-production phase.

To increase the precision and effectivity of machine tools, various steps are being made to compensate geometric errors of the machine tool (Holub et al., 2015; Holub et al., 2016). However, it is also important to focus on describing dynamic behaviour during the operation, which might involve unstable phenomena, such as chatter vibrations. Up to date, description of the unstable behaviour has been mostly based on operational measurements of cutting forces and simplified analytical models (Siddhpura & Paurobally 2012). However, the goal is to predict it in the pre-production phase, where time-effective optimization of the machine tool takes place. For that reason, a complex virtual model of the machine tool is assembled (Altintas et al., 2005), that should substitute the real machine in the fields of interest (e.g. statics, dynamics etc.). The accuracy of predicting unstable operational behaviour is directly conditioned on the precision of the virtual model. Although the whole structure of the machine tool should be considered, current analytical models used for predicting chatter vibrations are usually concentrated into a 2D system of a workpiece and a tool (Yue et al., 2016). The dynamic stiffness is usually modelled as a spring-damper element, whose parameters are identified by impact hammer measurements with a relatively high estimation error. Due to the stochastic character of chatter, the inaccurate dynamic stiffness estimation may lead to incorrect results, which might distinctly differ from reality. The Moreover, the dynamic stiffness also changes as the tool moves along the path during operation, resulting

---

<sup>\*</sup> Filip Kšica: Faculty of Mechanical Engineering, Brno University of Technology; Technická 2896/2, 616 69 Brno; CZ, Filip.Ksica@vutbr.cz

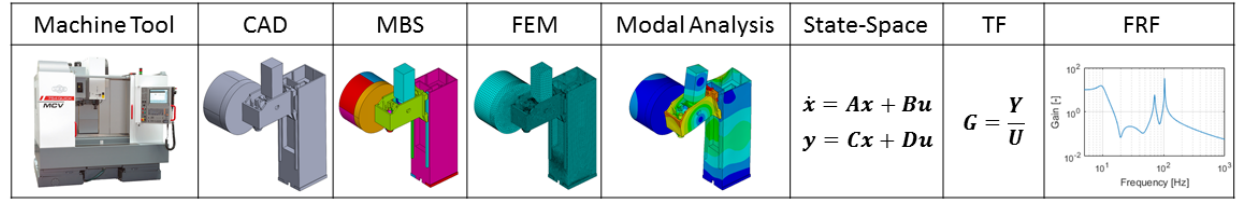
<sup>\*\*</sup> Jan Vetiška, PhD.: Faculty of Mechanical Engineering, Brno University of Technology; Technická 2896/2; 616 69 Brno; CZ, vetiska@fme.vutbr.cz

<sup>\*\*\*</sup> Assoc. Prof. Zdeněk Hadaš, PhD.: Faculty of Mechanical Engineering, Brno University of Technology; Technická 2896/2; 616 69 Brno; CZ, hadas@fme.vutbr.cz

in position-dependent stability of the cutting process (Law et al., 2013; Luo et al., 2014). Facts such as these should be considered when creating a virtual model of a machine tool.

## 2. Methods

The proposed methodology for creating a functional virtual model of a machine tool for predicting dynamic behaviour combines multiple modelling techniques. Firstly, Computer Aided Design (CAD) of the machine tool geometry is used, followed by flexible Multi-Body System (MBS) and Finite Element Method (FEM) modelling is used. The large order FEM model should be reduced using sub-structuring by component mode synthesis (CMS) (Craig et al., 2011). Secondly, transformation into state-space is made and transfer function (TF) is obtained (Fig. 1). Meanwhile, experimental data are subjected to dynamic system identification (Ljung 2007), resulting in estimated TF of the real system (Brezina et al., 2012). Finally, time and frequency domain responses are simulated and the virtual model is validated.



*Fig. 1: Procedure of creating virtual model of a machine tool.*

In the following part, highlighted steps in the modelling process as well as the thorough principle of the individual methods are described.

### Finite Element Method (FEM)

In this step, CAD models are imported into ANSYS where the Finite Element Analysis (FEA) takes place. The quality of the mesh directly affects the accuracy of the results. The meshing process differs substantially for static and dynamic analyses; there are different rules for suitable types, shapes and dimensions of the elements. Based on these rules, the mesh should be kept as uniform as possible and emphasis should be put on creating regular mesh (i.e. mapped or swept) in locations where either joints or external loads are present. In contrast, the refinement around stress concentrators usual for static analyses should be avoided.

The individual flexible components of the MBS are connected by flexible connectors. In the concept of machine tools, three general types of flexible connectors are to be considered: bearings, linear guides and ball screws. Different modelling techniques are used for each of these connector types.

In FEM environment, they can be modelled with massless spring-damper elements. Before the elements can be added, coupling of the joint areas should be done. Coupling means that the areas that are functional for the contact are concentrated into one single point, which represents the displacement of the contact area in the characteristic direction. In other words, the contact area (i.e. all elements and their nodes) behaves in that particular direction as a single entity.

### FE Model Order Reduction

Large-scale machine tools consisting of several parts result in large order FEM models. The computational time needed for dynamic analyses, such as modal, harmonic, and transient, depends exponentially on the amount of degrees of freedom (DOF). Therefore, it is necessary to reduce the amount of DOF to an acceptable amount by sub-structuring via a component mode synthesis (CMS) technique, which is frequently used in the field of dynamic analyses. An example of CMS may be the Craig-Bampton method, which considers the interface as fixed (Bampton et al., 1968).

### State-Space Transformation

In this step, a FE model is transformed into state-space using modal transformation. It is used for time-effective simulations of behaviour of the structure in time or frequency domain using software like Matlab/Simulink and implement other systems that contribute to the behaviour during operation (e.g.



control systems). Depending on the number of input and output variables, we can represent the system either a Single-Input-Single-Output (SISO) or Multiple-Input-Multiple-Output (MIMO).

As a part of this step, state-space matrices are assembled with the use of a reduction method based on a modal transformation. The input and output vectors of the system have to be defined. In case of ANSYS, these are DOF in which either input or output variable (i.e. displacement, velocity, acceleration, and/or force) is required. Mathematical description in a state-space represents a Linear Time-Invariant (LTI) model of a machine tool (Hadas et al., 2012).

The transformation of state-space system into transfer function matrix is given by the equation (1), where  $A, B, C, D$  are state-space matrices and  $I$  is an identity matrix.

$$G(s) = \frac{Y(s)}{U(s)} = C(sI - A)^{-1}B + D \quad (1)$$

The transfer function directly represents the dynamic stiffness of the system, the main benefit is an easy implementation into a multi-domain co-simulation and its suitability for time and frequency domain response simulations.

### Measurements of Static and Dynamic Parameters

Experiments and measurements have an important role in the virtual model creation. As mentioned above, many of the input parameters for the virtual model of machine tool are based on experiments. Furthermore, it is necessary to verify the validity of the virtual model by measuring key static and dynamic parameters and comparing them with simulated results. The sequence of necessary measurements follows the previous steps in virtual model assembly.

For static stiffness measurements, chosen location is subjected to a static force, generated by accurate hydraulic actuator. The applied force is measured with a force transducer with an implemented strain gauge. Deflection of the part can be measured with different sensors such as laser interferometer, capacitive displacement sensor, inductive displacement sensor, mechanical displacement gauge or contact linear gauge. This type of measurement might be also used for simulation of a cutting process to empirically determine conditions for stable operation (Knobloch et al., 2015).

For dynamic response measurement, a combination of an impact hammer and piezoelectric accelerometers are used. The accelerometer is mounted in the location that corresponds with the output of the virtual model. The impact hammer is used as a source of impact force in a location, which corresponds with the input of the virtual model. When dynamic behaviour during operation is measured, usually a set of accelerometers is used and based on their position on the structure, they are considered either as input or output. Due to complexity of the structure, it is crucial to avoid placing sensors into nodes of individual mode shapes (i.e. places, where the displacement is nearly zero). Proper sensor placement based on simulated modal analysis is recommended.

### Dynamic System Identification

The response function of the real system is obtained via dynamic system identification (Ljung, 2007). This technique is a mathematical operation that for the given set of input and output data and a chosen mathematical model (e.g. transfer function, state-space system) quantifies the parameters of the model in such way that the response of the mathematical model corresponds with the response determined by the measurement. However, the order of the mathematical model should be set with care, as higher order does not guarantee better accuracy and may lead to controversial results. Various least-squares methods for minimizing the difference between the two responses can be used.

### Virtual Model Validation

Although several theoretical approaches are available for the verification of the dynamic response of the virtual model, their suitability is based on the type of measured data. If the input data have a stochastic character (e.g. vibrations of a base during operation), the corresponding response of the virtual model would be obtained only if it is excited by the same signal. That would lead to a transient analysis of a structural FEM model, which is very time-consuming and may lead to problems with a convergence.



The proposed approach is based on an impulse response of two transfer function matrices, where the first one represents the virtual model and the second one represents the real system. They are compared based on an impulse response in frequency domain, also called Frequency Response Function (FRF). Furthermore, the FRF may be used for adjustments of some fuzzy parameters (e.g. damping) of the virtual model.

### 3. Conclusions

As the complexity of the products and the demands for machine tool precision are increasing, constant improvement of machining process is required. The structure of a machine tool is being subjected to various types of optimization and steps to compensate certain undesired deviations are being made. The aim of this study is to propose an approach based on a virtual model of the machine tool that would be used for predicting its dynamic properties in the pre-production phase. Presented methods utilize the benefits of a state-space system, such as direct transformation into a transfer function and its use for time-effective response simulations. Implementation of experimental data is done via dynamic system identification technique, which enables accurate validation of the virtual model and adjustments of its fuzzy parameters. However, some of these methods have not been originally used for virtual modelling of machine tools and further development is necessary. The application of proposed techniques for a real machine tool is a subject of an ongoing research.

### Acknowledgement

This work is an output of research and scientific activities of NETME Centre, supported through project NETME CENTRE PLUS (LO1202) by financial means from the Ministry of Education, Youth and Sports „National Sustainability Programme I“.

### References

- Altintas, Y. et al. (2005) Virtual Machine Tool. *CIRP Annals - Manufacturing Technology*, 54, 2, pp. 115-138.
- Bampton, M.C.C. and Craig, Jr., R.R. (1968) Coupling of substructures for dynamic analyses. *AIAA Journal*, 6, 7, pp. 1313-1319.
- Brezina, T., Hadas, Z. and Vetiska, J. (2012) Simulation behavior of machine tool on the base of structural analysis in multi-body system. *Mechatronika, 2012 15th International Symposium*, pp.1-4.
- Craig, R.R. and Kurdila, A.J. (2011) *Fundamentals of Structural Dynamics* 2nd ed., Wiley.
- Hadas, Z. et al. (2012) Simulation modelling of mechatronic system with flexible parts. In *2012 15th International Power Electronics and Motion Control Conference (EPE/PEMC)*. IEEE, p. LS2e.1-1-LS2e.1-7.
- Holub, M. et al. (2016) Geometric errors compensation of CNC machine tool. *MM Science Journal*, 6, pp. 1602-1607.
- Holub, M. et al. (2015) Volumetric compensation of three-axis vertical machining centre. *MM Science Journal*, 3, pp. 677-681.
- Knobloch, J., Marek, T. and Kolibal, Z. (2015) Error motion analysis of machine spindle under load. *MM Science Journal*, 2015(4), pp. 744-747.
- Law, M., Altintas, Y. and Srikantha Phani, A. (2013) Rapid evaluation and optimization of machine tools with position-dependent stability. *International Journal of Machine Tools and Manufacture*, 68, pp. 81-90.
- Ljung, L. (2004) State of the art in linear system identification: Time and frequency domain methods. *American Control Conference*, pp. 1-14.
- Luo, H. et al. (2014) Rapid Evaluation for Position-Dependent Dynamics of a 3-DOF PKM Module. *Advances in Mechanical Engineering*, 2014, pp. 1-17.
- Siddhpura, M. and Paurobally, R. (2012) A review of chatter vibration research in turning. *International Journal of Machine Tools and Manufacture*, 61, pp.27-47.
- Yue, C., Liu, X. and Liang, S.Y. (2016) A model for predicting chatter stability considering contact characteristic between milling cutter and workpiece. *International Journal of Advanced Manufacturing Technology*, pp.1-10.

## DYNAMIC VISCOSITY OF COMMERCIALY AVAILABLE MAGNETORHEOLOGICAL FLUIDS

M. Kubík\*, O. Macháček, Z. Strecker, J. Roupec, I. Mazůrek

**Abstract:** *The paper presents measurement and comparison of the dynamic viscosity of commercially available magnetorheological fluids and their temperature dependency of the dynamic viscosity. The appropriate choose of the MR fluid has positively effect to efficiency of the magnetorheological damper. The lower value of the dynamic viscosity (magnetic field independent) increases the dynamic force range. Eight samples of MR fluids from three manufactures were measured. MR fluids were tested on the Haake Rotovisco 1 in the temperature range -5 °C to 100 °C. The lowest dynamic viscosity with the similar solid content by weight is exhibited by MR fluids manufactured by Lord company.*

**Keywords:** Magnetorheological fluid, MR fluid, Dynamic viscosity of MR fluid, Magnetorheological damper, MR damper.

### 1. Introduction

The magnetorheological (MR) fluid is a smart material which is composed of micro-scale ferromagnetic particles, the carrier fluid and additives. This material exhibits rapid and strong change of rheological behavior under an external magnetic field. Ferromagnetic particles in the MR fluid form a chain-like structure in the direction of a magnetic field which causes change of the yield stress. The chain forms cause the yield stress of MR fluid depending on type of the MR fluid and level of a magnetic field. This effect is known as the magnetorheological effect.

The magnetorheological (MR) damper is a device that can benefit from interaction of the MR fluid and the magnetic field. The chain-like structures in the magnetic field restrict the flow of the fluid in an active zone, thereby increasing the damping force of the MR damper. The MR damper is using in the automotive industry (Nguyen, 2009), in the railway industry (Sun, 2013) or for the control of seismic vibrations in buildings (Yang, 2002). The common design of the MR damper is composed of an electromagnetic coil, a magnetic circuit and the MR fluid. One of the most important relations describing the behaviour of the MR damper is damping force- piston velocity- electric current (F-v-I) course. The efficiency of the MR damper depends on dynamic force range and response time (Strecker, 2015).

The dynamic force range  $D(v, H)$  of the MR damper is the damping force in on-state  $F(v, H)$  divided by uncontrollable damping force in off-state  $F_{uc}(v)$  for given piston velocity  $v$  and given electric current which causes magnetic flux intensity  $H$  in MR damper (Yang, 2002).

$$D(v, H) = \frac{F(v, H)}{F_{uc}(v)} = \frac{F_t(H) + F_{uc}(v)}{F_{uc}(v)} = 1 + \frac{F_t(H)}{F_{\eta}(v) + F_f}$$

The damping force in on-state  $F(v, H)$  is composed of the controllable force  $F_t(H)$  and the uncontrollable force in off-state  $F_{uc}(v)$ . The force in off-state is consisted of the friction force  $F_f$  and the viscous force  $F_{\eta}(v)$ . The value of the viscous force  $F_{\eta}(v)$  is depends on flow velocity in active zone, the geometry and the dynamic viscosity (field-independent) of the MR fluid in off-state (Sapiński, 2013). The higher value of the viscous force  $F_{\eta}(v)$ , the lower the dynamic force range  $D(v, H)$ . The dynamic force range of the MR damper is also influenced by in-use-thickening of the MR fluid (Roupec, 2013). Nevertheless, the dynamic viscosity of MR fluid is the most critical off-state property of MR fluid

---

\* All authors: Institute of Machine and Industrial Design, Brno University of Technology, Technická 2896/2; 616 69, Brno; CZ, michal.kubik@vutbr.cz

(Kumbhar, 2015). The MR fluid dynamic viscosity is most influenced by three factors: the intrinsic viscosity of the carrier fluid, the particle volume fraction and additives (Kumbhar, 2015).

The main goal of this paper is comparison of the dynamic viscosity at 40 °C and the temperature dependency of the dynamic viscosity of commercially available MR fluids with similar solid content by weight.

## 2. Methods

MR fluids were measured by rotational rheometer Haake RotoVisco 1 (Fig. 1). The sensor system ISO 3219 Z20 DIN was used (Fig. 1-right). The experiment was controlled by software RheoWin. In every single test was used 8.2 ml of a MR fluid. MR fluids were homogenized 30 min before experiment.

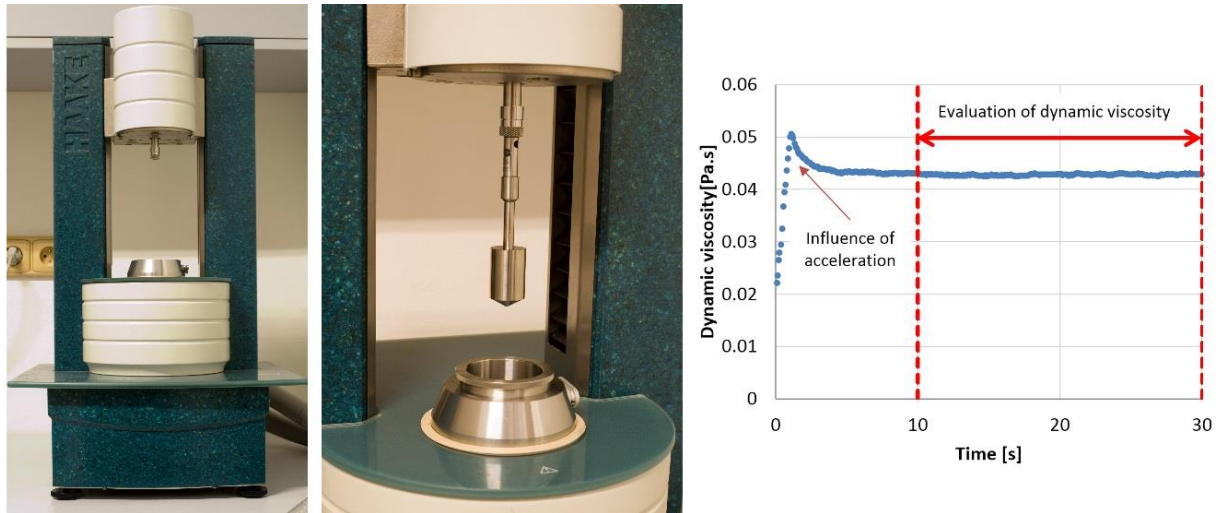


Fig. 1: Haake RotoVisco 1 and sensor Z20 DIN (left, middle); the evaluation of dynamic viscosity (right).

The dynamic viscosity of MR fluid was measured with the constant shear rate  $800 \text{ s}^{-1}$  in 30 s. The temperatures of measured MR fluids were in range from  $-5 \text{ }^{\circ}\text{C}$  to  $100 \text{ }^{\circ}\text{C}$ . The MR fluid was mixed with shear rate  $50 \text{ s}^{-1}$  when the MR fluid was tempering. Eight samples of MR fluids with the different solid content by weight and made by different producers were tested, see Tab. 1.

Tab. 1: List of tested MR fluids.

Category	Name of the MR fluid	Solid content by weight [%]	Density [kg/m <sup>3</sup> ]	Producer
A	MRF-122EG	72	2280 - 2480	Lord
B	MRF-132DG	80.98	2950 - 3150	Lord
C	MRF-140CG	85.44	3540 - 3740	Lord
A	MRHCCS4-A	70	2490	Liquid Research
B	MRHCCS4-B	80	3080	Liquid Research
A	2.55	75.5	2550	Haohua
B	3.05	80.5	3050	Haohua
C	3.55	85.5	3550	Haohua

The presented value of dynamic viscosity of the MR fluid was evaluated from last 20 s of the experiment as arithmetic average, see Fig.1 right. The last 20 s was chosen due to acceleration of measuring rotor. The acceleration has significant effect to measured data. The viscosity index was determined by ISO 2909. The viscosity index (VI) is shown near the name of the MR fluid in each graph.

### 3. Results

The measured data are presented in Figs. 2 – 4 with logarithmic scale in Y axis. In Fig. 2 were compared three MR fluids with the similar solid content by weight 72 % (category A). The MR fluid MRHCCS4-A achieved the dynamic viscosity 0.17 Pa.s at 40 °C and Haohua 2.55 the dynamic viscosity 0.23 Pa.s at 40 °C. The dynamic viscosity of MR fluid Lord MRF-122EG at 40 °C has 4.4 times lower than MRHCCS4-A and 5.6 times lower than Haohua 2.55.

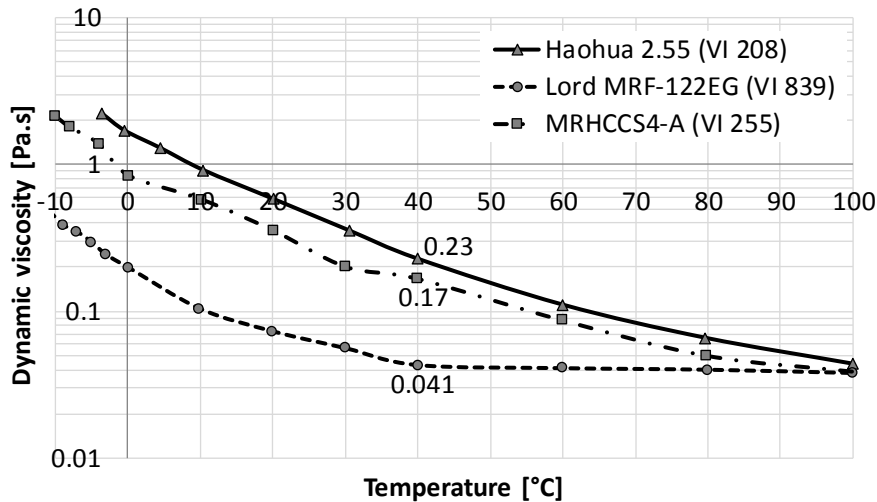


Fig. 2: Comparison of MR fluids in category A (approximately 72 % solid content by weight).

Three MR fluids with the similar solid content by weight 80 % (category B) were compared, see Fig. 3. In this category, the MR fluid Haohua 3.05 has the highest viscosity 0.35 Pa.s at 40 °C. The Lord MRF-132DG has 2.1 times lower viscosity than MRHCCS4-B and 3 times lower viscosity than Haohua 3.05 at 40 °C.

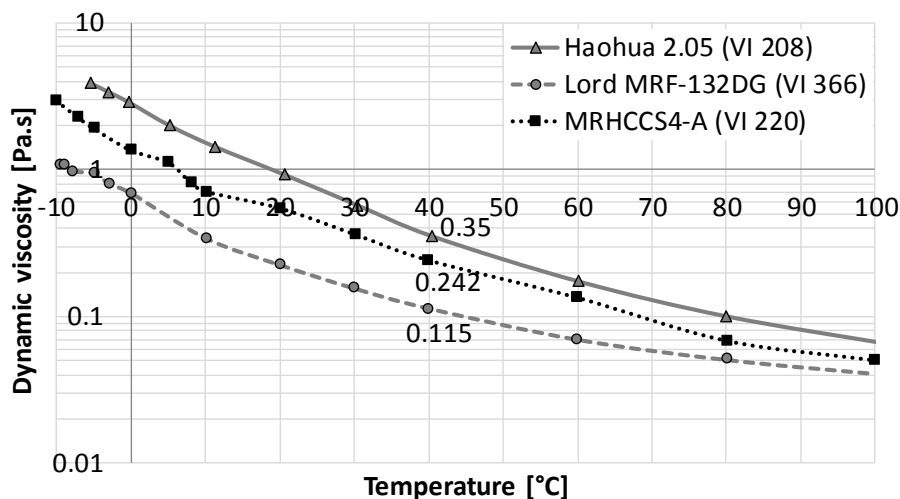


Fig. 3: Comparison of MR fluids in category B (approximately 80 % solid content by weight).

In Fig. 4 were compared MR fluids with the similar solid content by weight 85 % (category C). In this category were measured two MR fluids because the company Liquid Research hasn't manufacture the MR fluid with 85 % solid content by weight in their product list. The Lord MRF-140CG has 1.64 times lower viscosity than Haohua 3.55 at 40 °C.

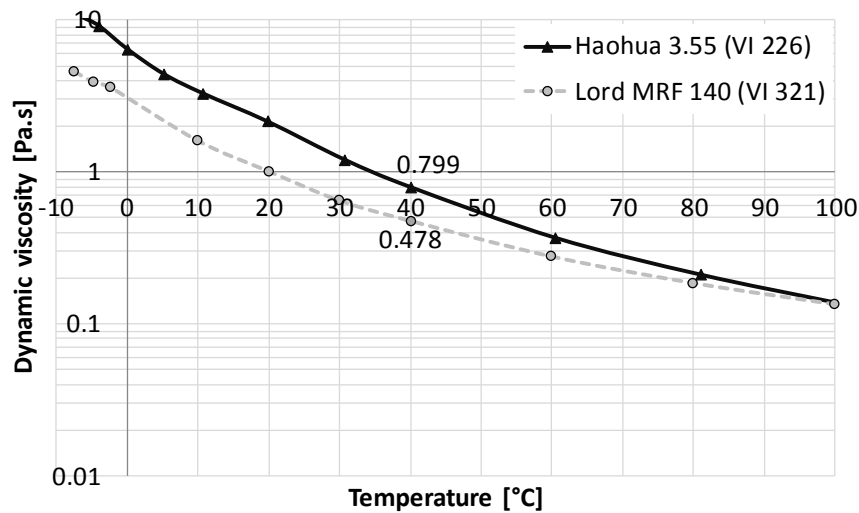


Fig. 4: Comparison of MR fluids in category C (approximately 85 % solid content by weight).

#### 4. Conclusions

The paper presents a comparison of the dynamic viscosity and their temperature dependency of commercial available MR fluids with similar solid content by weight. The lowest viscosity in every group achieved MR fluid made by Lord. The low dynamic viscosity of MR fluid suggests the low dynamic viscosity of the carried fluid or suitably chosen additives. The highest viscosity index (VI 839) achieved MRF-122EG. MR fluids made by Liquid Research and Haohua achieved viscosity index between 200 and 300.

However, it is necessary to compare MR fluids also in others aspects: yield stress, sedimentation stability, fluid life, lubricity or wear aspects. The subsequent research will be focused on measurement and comparison of MR fluids in these aspects.

#### Acknowledgement

This experiment could be provided thanks to the kind sponsorship of various grants and numerous agencies. We would like to thank explicitly to the GAČR 17-10660J, GAČR 17-26162S, FEKT/FSI-J-17-4483, FCH/FSI-J-17-4534 and FSI-S-17-4428.

#### References

- Kumbhar, B.K., Satyajit, R.P. and Suresh, M.S. (2015) Synthesis and Characterization of Magneto-Rheological (MR) Fluids for MR Brake Application. *Engineering Science and Technology, an International Journal*, 18, 3.
- Nguyen, Q.-H. and Choi, S.-B. (2009) Optimal Design of MR Shock Absorber and Application to Vehicle Suspension. *Smart Materials and Structures*, 18, 3.
- Roupec, J., Mazurek, I., Strecker, Z. and Klapka, M. (2013) The Behavior of the MR Fluid during Durability Test. *Journal of Physics: Conference Series*, 412, 1.
- Sapiński, B. and Horak, W. (2013) Rheological Properties of MR Fluids Recommended for Use in Shock Absorbers. *Acta Mechanica et Automatica*, 7, 2.
- Strecker, Z., Roupec, J., Mazurek, I., Machacek, O., Kubik, M. and Klapka, M. (2015) Design of Magnetorheological Damper with Short Time Response. *Journal of Intelligent Material Systems and Structures*, 26, 14.
- Sun, S., Deng, H., Li, W., Du, H., Ni, Y.Q., Zhang, J. and Yang, J. (2013) Improving the Critical Speeds of High-Speed Trains Using Magnetorheological Technology. *Smart Materials and Structures*, 22, 11.
- Yang, G., Spencer, Jr., Carlson, D. and Sain, K. (2002) Large-Scale MR Uid Dampers: Modeling and Dynamic Performance Considerations. *Engineering Structures*, 24.

## SIMULATION OF THE SMALL PUNCH TEST OF AISI 316L AUSTENITIC STEEL

P. Kubík<sup>\*</sup>, J. Petruška<sup>\*\*</sup>, J. Hůlka<sup>\*\*\*</sup>, F. Šebek<sup>\*\*\*\*</sup>

**Abstract:** *Present paper deals with numerical simulation of the small punch test of austenitic stainless steel, AISI 316L, which is often used in the nuclear industry. In order to model the plastic material behavior, the well-known von Mises yield criterion with isotropic hardening and associated flow rule was adopted. The ductile fracture was modeled using two widespread ductile fracture criteria which were calibrated using various fracture tests. The whole material model was implemented into the explicit finite element code using the user subroutine of Abaqus/Explicit commercial software. The results were compared to those obtained experimentally.*

**Keywords:** Small punch test, AISI 316L, Multi-linear material model, Ductile fracture, Element deletion technique.

### 1. Introduction

The Small Punch Test (SPT) was developed by Manahan et al. (1981) for assessment of actual mechanical properties of irradiated materials in the beginning of the nineties. Its great advantage is a very small dimension of the testing specimen which allows to extract a small amount of material from the structure. Most of the properties such as yield stress, ultimate tensile strength, creep behavior or ductility are obtained on the basis of empirical correlation or numerical simulation (Abendroth and Kuna, 2003).

The disk-shaped specimen is mounted between the upper and lower dies and then it is punched using the piston with hemispherical end or using a ball which is placed between the piston and specimen (Rouse et al., 2013). The illustration of SPT apparatus is in Fig. 1 together with important dimensions and description of particular components.

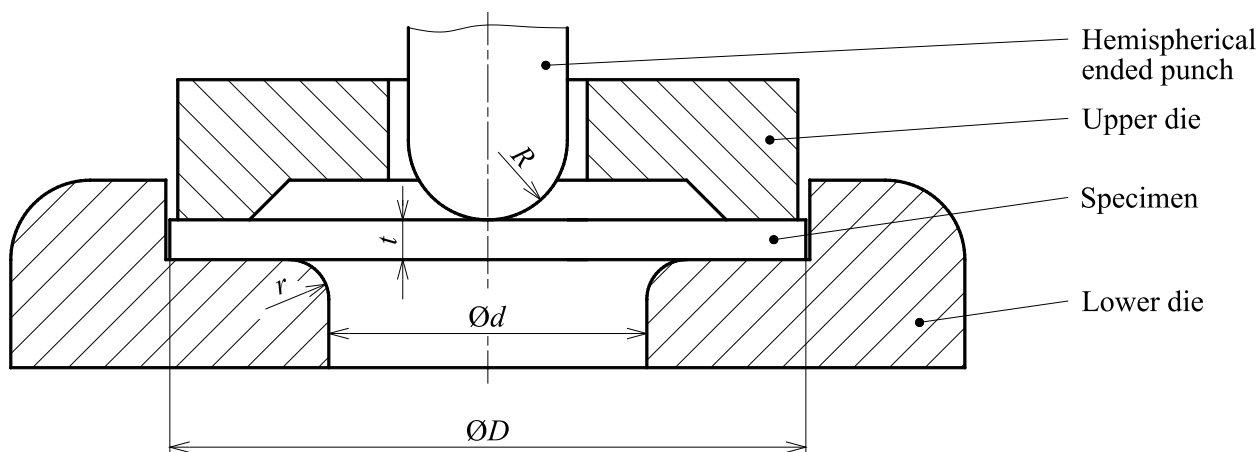


Fig. 1: Schematic drawing of SPT apparatus.

<sup>\*</sup> Ing. Petr Kubík, PhD.: Institute of Solid Mechanics, Mechatronics and Biomechanics, Faculty of Mechanical Engineering, Brno University of Technology; Technická 2896/2; 616 69, Brno; CZ, kubik.p@fme.vutbr.cz

<sup>\*\*</sup> Prof. Ing. Jindřich Petruška, Ph.D.: Institute of Solid Mechanics, Mechatronics and Biomechanics, Faculty of Mechanical Engineering, Brno University of Technology; Technická 2896/2; 616 69, Brno; CZ, petruska@fme.vutbr.cz

<sup>\*\*\*</sup> Ing. Jiří Hůlka, PhD.: Institute of Applied Mechanics; Resslova 972/3; 602 00 Brno; CZ, hulkaj@uam.cz

<sup>\*\*\*\*</sup> Ing. František Šebek, PhD.: Institute of Solid Mechanics, Mechatronics and Biomechanics, Faculty of Mechanical Engineering, Brno University of Technology; Technická 2896/2; 616 69, Brno; CZ, sebek@fme.vutbr.cz

## 2. Experimental program

All tested specimens were manufactured from the cold-rolled plate with  $400 \times 300 \times 20$  mm. The specimens' axes were coincident with the rolling direction.

Tensile tests of smooth cylindrical specimen with 8 mm diameter and 40 mm gauge length and notched cylindrical specimens with 1.2, 2.5 and 5 mm notch radii were performed. The smallest diameter of the notched cylindrical specimens was 6 mm and the gauge length was 30 mm. All mentioned tests were repeated twice.

Another specimen geometry was a notched tube with 7 mm inner diameter and 14 mm outer diameter. The notch with 3 mm radius was on the diameter of 9 mm. These specimens were loaded by a combination of a tension and torsion. The ratios of axial displacement and twist angle were 0, 1 and  $\infty$  mm/rad. There were done always two tests for each of three ratios.

The upsetting tests of six cylinders with a spherical recess of 5 mm radius were carried out (Kubík et al., 2016). The height and diameter of the cylinders were both 10 mm.

The disk with  $D = 8$  mm diameter and  $t = 0.5 \pm 0.005$  mm thickness was used for SPT. It was punched using a piston with hemispherical end of  $R = 1$  mm radius. The fillet radius of lower die was  $r = 0.5$  mm. Four tests were executed without using any lubrication between the contact pairs. The crack was initiated on the radius of 1.05 mm. Then, it propagated tangentially along the circumference until the spherical cap was folded out (Fig. 4).

## 3. Calibration of material models

The classical von Mises plasticity with isotopic hardening and associated flow rule, used in various applications (Petruška et al., 2012, 2016), were chosen for the description of material behavior. The flow curve was identified using a tensile test of smooth cylindrical specimen in multi-linear form (Kubík et al., 2011). Then, the curve was approximated using Hollomon hardening law in the following form

$$\bar{\sigma} = K \bar{\varepsilon}^n \quad (1)$$

where  $\bar{\sigma}$  is the equivalent stress,  $K = 1529.7$  MPa is the strength coefficient,  $\bar{\varepsilon}$  is the total strain and  $n = 0.4858$  is the strain hardening exponent.

The ductile fracture was simulated using two chosen phenomenological criteria. The first one was the four-parametric,  $F_1, \dots, F_4$ , Xue–Wierzbicki model (Wierzbicki et al., 2005). The fracture strain is dependent on the stress triaxiality  $\eta$  and normalized third invariant of deviatoric stress tensor  $\xi$  as

$$\bar{\varepsilon}_{XW}^f = F_1 e^{-F_2 \eta} - (F_1 e^{-F_2 \eta} - F_3 e^{-F_4 \eta} - \left(1 - |\xi|^{\frac{1}{n}}\right)^n) \quad (2)$$

The second was the modified Bai–Wierzbicki model (Španiel et al., 2014). Here, the fracture strain is not symmetric with respect to the normalized Lode angle

$$\bar{\varepsilon}_{MBW}^f = \left( \frac{1}{2} (N_1 e^{-N_2 \eta} + N_5 e^{-N_6 \eta}) - N_3 e^{-N_4 \eta} \right) \bar{\theta}^4 + \frac{1}{2} (N_1 e^{-N_2 \eta} - N_5 e^{-N_6 \eta}) \bar{\theta} + N_3 e^{-N_4 \eta} \quad (3)$$

where  $\bar{\theta}$  is the normalized Lode angle and  $N_1, \dots, N_6$  are the material constants.

Numerical simulations of experiments were conducted in order to obtain the state variables  $\xi$ ,  $\bar{\theta}$  and  $\eta$  which enter the calibration and are not directly measurable. The geometry in Abaqus/Standard was discretized using 4-node CAX4R elements with reduced integration. Elements with the size of 0.075 mm were applied within the gauge lengths in order to eliminate the size effect. The state variables evolutions were obtained from the crack initiation loci (Abbassi et al., 2013).

All experiments mentioned in Chapter 2 except of the small punch tests were used for ductile fracture criteria calibration. The identification was carried out in the MATLAB R2015a software. Fracture envelopes of respective criteria are in Fig. 2 where the red circles correspond to the tensile tests of smooth and notched cylindrical specimens, black squares represent the biaxial tests of notched tubes and the blue diamond shows the position of the upsetting test of a cylinder with a specific recess.



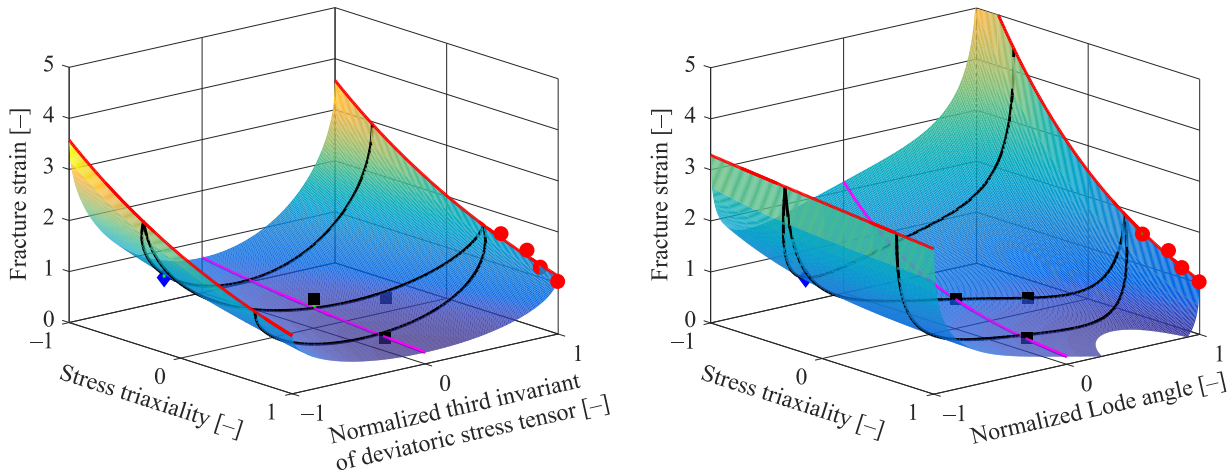


Fig. 2: Fracture envelope of Xue–Wierzbicki (left) and modified Bai–Wierzbicki (right) model.

#### 4. Simulations of SPT

The spatial model of SPT was realized. The specimen was discretized by 8-node C3D8R elements with reduced integration. Central part of the specimen was discretized using the fine mesh with elements of 0.075 mm. Tools were modeled as analytical rigid surfaces and discretized by special ARSR elements. The friction coefficient was taken 0.1 as it is usual for the steel-to-steel contacts with no lubrication.

Both ductile fracture criteria were implemented using Vectorized User MATERIAL (VUMAT) within the Abaqus finite element software. VUMAT and explicit finite element method are suitable for dynamic processes (Peč et al., 2016), non-linear problems or ductile fracture simulations (Šebek et al., 2014). The ductile fracture initiation and propagation were realized through the element deletion technique.

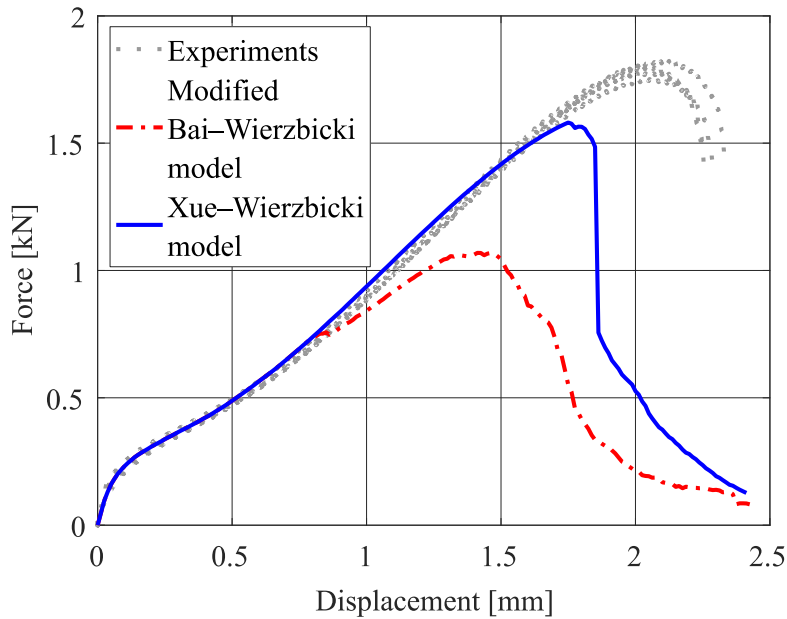
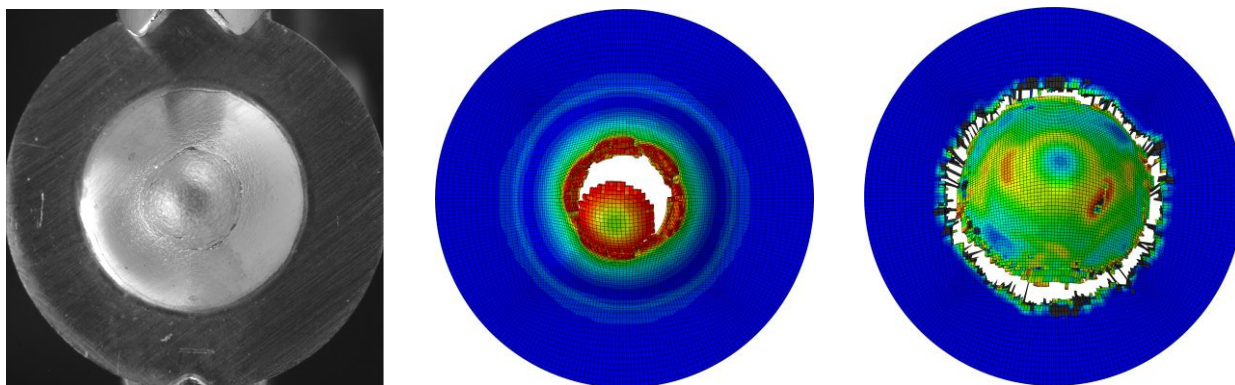


Fig. 3: Force–displacement responses from experiments and numerical simulations of SPT.

Force–displacement responses from the experiment together with those obtained computationally using particular criteria are in Fig. 3. Good result was achieved with Xue–Wierzbicki model which predicted the rupture slightly earlier than in experiment. The crack initiation was on the diameter of 0.55 mm, which increased during loading (it is 1.08 mm in Fig. 4). Modified Bai–Wierzbicki model predicted the ductile fracture wrongly. The initiation was too early and on the diameter where the fillet radius of lower die was situated. This situation was more close to blanking of circular holes, which is in contradiction with current experiment. The comparison between experimental observation and predictions of crack propagation is in Fig. 4, where there are damage contours represented by a rainbow colors. The blue color corresponds to a virgin material without any damage and the red color to exhaustion of load-carrying capacity. The grey color represents a negative value which is physically unrealistic (Kubík et al., 2014).



*Fig. 4: Cracked small punch test specimen in a top view from the experiment (left) and numerical simulations depicting the damage predicted by Xue–Wierzbicki (center) and modified Bai–Wierzbicki (right) models.*

## 5. Conclusions

The prediction ability of ductile fracture at a small punch testing of AISI 316L steel was presented using Xue–Wierzbicki and modified Bai–Wierzbicki models. Xue–Wierzbicki model predicted the crack initiation prematurely. It was due to the position of the initiation which was different from the one in the experiment. Bai–Wierzbicki predicted wrongly both the timing and the position of the ductile crack initiation.

## Acknowledgement

This work is an output of project NETME CENTRE PLUS (LO1202) created with financial support from the Ministry of Education, Youth and Sports under the „National Sustainability Programme I“.

## References

- Abbassi, F., Belhadj, T., Mistou, S. and Zghal, A. (2013) Parameter identification of a mechanical ductile damage using Artificial Neural Networks in sheet metal forming. *Materials and Design*, 45, 605-615.
- Abendroth, M. and Kuna, M. (2003) Determination of deformation and failure properties of ductile materials by means of the small punch test and neural networks. *Computational Materials Science*, 28, pp. 633-644.
- Kubík, P., Hůlka, J. and Petruška, J. (2011) Ductile fracture criteria in prediction of chevron cracks, in: *Proc. Of Int. Conf. on Engineering mechanics 2011* (ed. Fuis, V.), Svratka, Czech Republic, pp. 339-342.
- Kubík, P., Šebek, F., Hůlka, J. and Petruška, J. (2016) Calibration of ductile fracture criteria at negative stress triaxiality. *International Journal of Mechanical Sciences*, 108-109, pp. 90-103.
- Kubík, P., Šebek, F., Petruška, J., Hůlka, J., Růžička, J., Španiel, M., Džugan, J. and Prantl, A. (2014) Calibration of selected ductile fracture criteria using two types of specimens. *Key Engineering Materials*, 592-593, pp. 258-261.
- Manahan, M.P., Argon, A.S. and Harling, O.K. (1981) The development of a miniaturized disk bend test for the determination of postirradiation mechanical properties. *Journal of Nuclear Materials*, 104, pp. 1545-1550.
- Peč, M., Kubík, P., Šebek, F., Návrát, T. and Petruška, J. (2016) Modeling of the blast load effects in explicit dynamics, in: *Engineering mechanics 2016*, Svratka, pp. 442-445.
- Petruška, J., Návrát, T. and Šebek, F. (2012) A new model for fast analysis of leveling process. *Advanced Materials Research*, 586, pp. 389-393.
- Petruška, J., Návrát, T., Šebek, F. and Benešovsky, M. (2016) Optimal intermeshing of multi roller cross roll straightening machine, in: *AIP Conference Proceedings*, 1769, pp. 120002-1-4.
- Rouse, J.P., Cortellino, F., Sun, W., Hyde, T.H. and Shingledecker, J. (2013) Small punch creep testing: review on modelling and data interpretation. *Materials Science and Technology*, 29, pp. 1328-1345.
- Šebek, F., Kubík, P. and Petruška, J. (2014) Localization problem of coupled ductile failure models compared to uncoupled ones, in: *Engineering mechanics 2014*, Svratka, pp. 632-635.
- Španiel, M., Prantl, A., Džugan, J., Růžička, J., Moravec, M. and Kuželka, J. (2014) Calibration of fracture locus in scope of uncoupled elastic–plastic–ductile fracture material models. *Advances in Engineering Software*, 72, pp. 95-108.
- Wierzbicki, T., Bao, Y., Lee, Y.-W. and Bai, Y. (2005) Calibration and evaluation of seven fracture models. *International Journal of Mechanical Sciences*, 47, 4-5, pp. 719-743.

## SHAFT VIBRATION OF THE TRUCK

P. Kučera\*, V. Pištěk\*\*

**Abstract:** *This article describes analysis of vibrations in a powertrain of a truck with 8 x 8 drive. It may be caused by a deflection of the rotating drive shaft. The aim was to reduce the vibrations, therefore, a transient computational model I for analysis of shaft deflection was created in Matlab software. Analytical and differential equations are used. This model I was compared to the simulation of the transient behaviour of model II with the use of FEM. To verify the computational models, measurements of the shaft deflection and directional vibrations were carried out. The conclusion presents the interpretation of the results of old and new modification of the powertrain and the cause of vibration is also demonstrated.*

**Keywords:** Truck, Drive shaft, Vibration, Powertrain, Matlab, Deflection, FEM.

### 1. Introduction

The vibrations affect the drive comfort and may also affect the health of the driver. Therefore, an analysis of the vibrations has become important not only with the passenger cars but also with trucks. The vibrations in trucks may be more intensive and may generate noise. This article deals with the truck vibration. It is a complex dynamic system where the vibrations may occur in any of powertrain parts. These vibrations may be caused by a deflection of the powertrain rotating shaft. The analysed truck showed problems with vibrations and noise after reaching a certain speed. It was documented abroad, where the limits of the European legislations are irrelevant. Therefore, a dependence on the shaft speed and deflection was assumed. To analyse the longest shaft deflection, the transient computational model I was created using analytical and differential equations. Model II uses Finite Element Method (FEM) and this model II works as a check for model I. The validation of the computational models was carried out by several measurements on the truck with 8x8 and 8x4 drive. The directional vibrations and shaft deflection were measured. The conclusion presents results from both the computational models and measured data. This article is based on the literature by Kučera (2015), Waller (1989) and Tůma (2014).

### 2. Computational models

Two computational models of the shaft deflection were prepared. Fig. 1 shows the 3D model of the drive shaft used for the computational model analysis and measuring position.

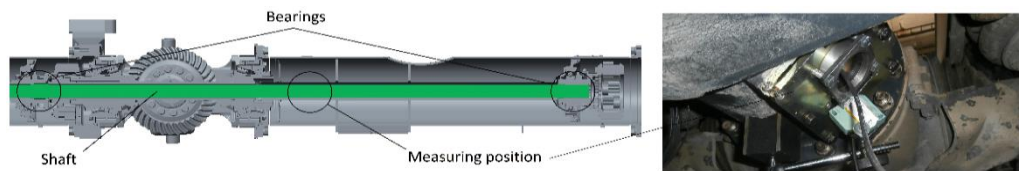


Fig. 1: 3D model of the drive shaft and the measuring position on the right.

First computational model of a rotating shaft with equations based on Budynas (2015) was created. The computational model I of the drive shaft includes the part of the shaft between the two bearings in Fig. 1. This part of the shaft is divided into  $n$  mass points. Number of  $n$  is depended on converge of the task. In this example, there is  $n$  equal to 100. Boundary conditions of the shaft deflection were carried out by the

\* Ing. Pavel Kučera, PhD.: Institute of Automotive Engineering, University of Technology, Technická 2896/2; 616 69, Brno; CZ, kucera@fme.vutbr.cz

\*\* Prof. Ing. Václav Pištěk, DrSc.: Institute of Automotive Engineering, University of Technology, Technická 2896/2; 616 69, Brno; CZ, pistek.v@fme.vutbr.cz

measurement on the truck. This initial deflection was set in the models. The shaft deflection is based on these equations

$$A = A_s / (\sin(L_m \pi / L)), \quad (1)$$

$$r_s = A \sin(x_i \pi / L), \quad (2)$$

where  $A$  is deflection in the middle of the analysed shaft length,  $A_s$  – deflection in the measured position,  $L_m$  – location of measurement,  $L$  – shaft length,  $r_s$  – initial shaft deflection in the individual points dependent on shaft segments and  $x_i$  – coordinates of the shaft section.

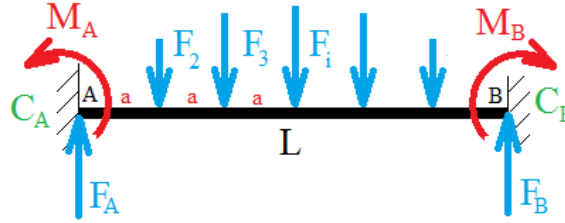


Fig. 2: Forces and torques impacting on the drive shaft model I.

Centrifugal forces act on the individual mass points of the shaft. Their values were determined in each step of the simulation. The following equation was used

$$F_i = m_i r_i \omega_j^2 - F_{i-1}, \quad (3)$$

where  $F_i$  is the centrifugal force in the location of the individual mass points,  $m_i$  – mass of the mass point,  $r_i$  – shaft deflection in the location of the given mass point and  $\omega_j$  – shaft angular speed. It may be assumed that the shaft boundary conditions will be between the hinged and fixed. The most important boundary condition is presented in Fig. 2. It describes the shaft with rotational stiffness in the support.  $M_A$ ,  $M_B$  are the moment reactions and  $F_A$ ,  $F_B$  the force reactions. For the beam with the defined stiffness in the support the force equation, moment equation and two equations (4 – 5) for rotation in points A and B will be used. It is calculated using the Maxwell-Mohr variant of the Castigliano's theorem.

$$\varphi_A = \int_0^L \frac{M_o(x)}{EJ(x)} \frac{\partial M_o(x)}{\partial M_A} dx = -\frac{M_A}{C_A}, \quad (4)$$

$$\varphi_B = \int_0^L \frac{M_o(x)}{EJ(x)} \frac{\partial M_o(x)}{\partial M_B} dx = -\frac{M_B}{C_B}, \quad (5)$$

where  $\varphi_A$ ,  $\varphi_B$  are rotations in points A and B,  $C_A$ ,  $C_B$  – rotational stiffness in the support,  $M_o$  – bending moment,  $E$  – modulus of elasticity, and  $J$  – quadratic moment of the shaft cross-section. To gain values of the deflections in the individual steps, the equation of the deflection line is used. The distance between the mass points is the same as the distance between the forces. The equations of the deflection line are defined as follows

$$EJ\ddot{w} = -F_A x_i + \sum_{i=1}^{n+2} F_i (x_i - (i-1)a), \quad (6)$$

$$EJ\dot{w} = -\frac{F_A x_i^2}{2} + \sum_{i=1}^{n+2} F_i \left( \frac{x_i^2}{2} - (i-1)a x_i \right) + C_q, \quad (7)$$

$$EJw = -\frac{F_A x_i^3}{6} + \sum_{i=1}^{n+2} F_i \left( \frac{x_i^3}{6} - (i-1)a \frac{x_i^2}{2} \right) + C_q x_i + C_{q+1}, \quad (8)$$

where  $i$  is 1, 2, 3,  $n+2$ ,  $q$  is 1, 3, 5,  $n+2$ ,  $w$  is displacement and  $C$  integration constants. These constants have to be determined from the boundary conditions, i.e. the zero displacements in the support. Furthermore, the rotation and deflection values have to be equal between the individual segments. The computational model I is formed in Matlab software. Subsequently, analyses of the 3D parts of the shaft, differential to name but a few were performed using FEM. This computational model II works as a check for model I, therefore, there is no need for detailed description.

### 3. Measurement and evaluation of the directional vibration and computational models

The measurement of the rotating shaft deflections and directional vibrations was carried out with the use of a modular switchboard IMC CRFX 400, card ICPU2-8 and the card CRFX/ISO2-8. Two three-axial



accelerometers, a deflection sensor and a photoelectric reflex switch were used. During the measurement the speed was increased to gain data from the whole span of the truck speed. Subsequently, FFT spectrums, Tuma (2014), of measured vibrations and shaft deflections were interpreted depending on the shaft speed. Scripts to process the data in Matlab software were created. The signal of the shaft rotations is averaged. The measuring position is illustrated in Fig. 1. The speed signal was recorded as a mark per rotation from the photoelectric reflex switch. The measurement of the shaft deflections was carried out by a BAW M30ME-UAC10B-S04G sensor. To measure the drivetrain vibration, two three-axial piezoelectric accelerometers Brüel & Kjær 4524 were used. To interpret the vibration, the FFT analysis from the segment representing the given speed was used. The sample frequency was 20 kHz. From these analyses FFT spectrums were calculated (see in Figs. 3 – 6). The figures show the peak which stands for the 1st shaft speed harmonic order.

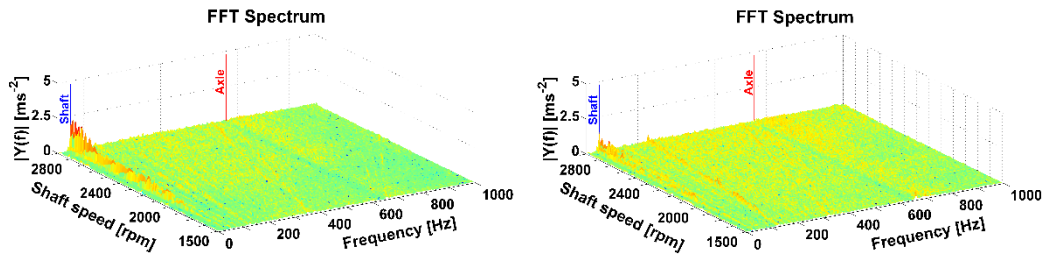


Fig. 3: Analysis of directional vibration – 8 x 4 drive, old and new powertrain (accelerometer 1).

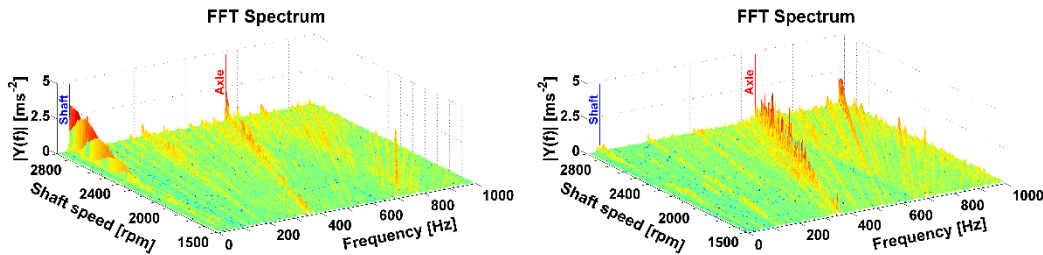


Fig. 4: Analysis of directional vibration – 8 x 8 drive, old and new powertrain (accelerometer 1).

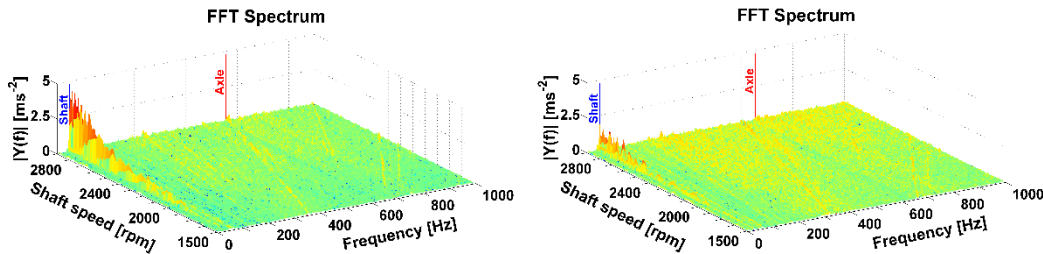


Fig. 5: Analysis of directional vibration – 8 x 4, old and new powertrain (accelerometer 2).

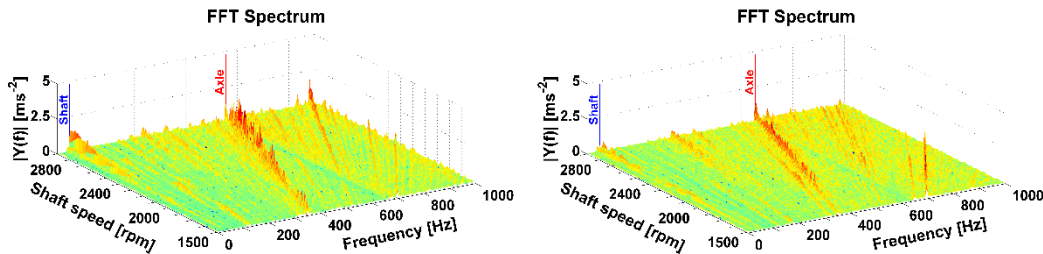


Fig. 6: Analysis of directional vibration – 8 x 8 drive, old and new powertrain (accelerometer 2).

This is the most important factor of the vibration affecting the driver. More peaks occur mainly with the all-wheel drive. But these frequencies are higher than 100 Hz, therefore, it is not important for drive comfort ISO 2631-1 (1997). The comparison of measurements before and after the powertrain modification is also shown. A reduction of vibrations was reached and it is illustrated in Figs. 3 – 6 on the right.

The results of shaft deflection of computational models and measurement are shown in Fig. 7. Other submodels of the model I and II are also compared.

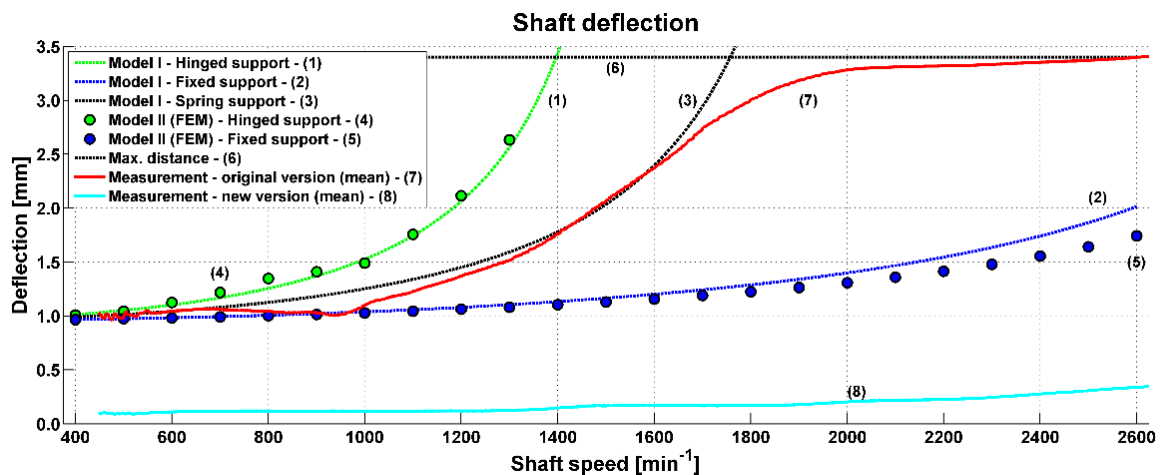


Fig. 7: Comparison of the measured values and computational models.

The measured data were for the span of the shaft rotations in the area of 400 – 2600 min<sup>-1</sup>. These values were averaged and compare with computational models. There is a correspondence of measurement and computational models in the range to 1700 min<sup>-1</sup>. Another section of the graph is different because the deflection is limited in the real shaft (measurement). The shaft deflection limit is 3.4 mm by the dimensions around the shaft. The results of the deflection measurement, vibration analysis and model simulation show that the deflection of this shaft is the main cause of the vibration. To decrease the truck vibration, it was necessary to minimize this shaft deflection. Therefore, a powertrain modification was designed. Two new shafts had been designed and they replaced the original one. These shafts are connected by a special hub with a bearing. The following measurement proved that the shaft deflection was decreased (see curve 8 in Fig. 7 or in Figs. 3 – 6 on the right).

#### 4. Conclusions

There were some problems with vibrations and noise after reaching a certain speed. Therefore, the measurements were carried out. Then their values were compared with the transient computational models and FFT analyses were performed. Based on the results, the computational model I is suitable for another analysis of the shaft deflection. The shaft deflection was reduced by the constructional design. The support of the analysed shaft led to the decrease of vibrations and a near loss of the 1<sup>st</sup> shaft speed harmonic order. This corresponds to the analysis of the directional vibration and 1<sup>st</sup> shaft speed harmonic order is the main cause of the vibrations on the truck. The first computational model may be easily used for the development of the powertrain with long shafts where some deformation or unbalance may occur.

#### Acknowledgement

This work is an output of the internal BUT research project Reg. No. FSI-S-14-2334 and was also supported through NETME CENTRE PLUS (LO1202) by financial means from the Ministry of Education, Youth and Sports under the „National Sustainability Programme I“.

#### References

- Kučera, P. (2015) Mechatronic approach to vehicle dynamics. Doctoral thesis, BUT Brno.
- Budynas, R.G. and Nisbett, J.K. (2015) Shigley's mechanical engineering design. McGraw-Hill Education, New York.
- Waller, H. and Schmidt, R. (1989) Schwingungslehre für Ingenieure: Theorie, Simulation, Anwendungen. BI Wissenschaftsverlag, Zürich.
- Tůma, J. (2014) Vehicle gearbox noise and vibration: measurement, signal analysis, signal processing and noise reduction measures. Wiley, Chichester.
- ISO 2631-1. (1997) Mechanical vibration and shock - Evaluation of human exposure to whole-body vibration - Part 1. Second edition. International Organization for Standardization, Switzerland.

## EFFECTIVE HEAT AND MOISTURE TRANSPORT PROPERTIES OF SPRUCE

L. Kucíková<sup>\*</sup>, J. Vorel<sup>\*\*</sup>, J. Sýkora<sup>\*\*\*</sup>, M. Šejnoha<sup>\*\*\*\*</sup>

**Abstract:** *The present paper is devoted to the determination of effective properties of wood needed in the macroscopic description of heat and moisture transport in the framework of multi-scale computational scheme. Although computationally feasible, we do not attempt to account for all microstructural details and instead adopt a simplified analytical micromechanical model based on the Mori-Tanaka homogenization scheme to derive effective thermal conductivities of wood and effective diffusivities for the bound water present in the cell wall of wood and water vapor transported through lumens. As one particular example we consider a spruce wood as representative of softwood and most common in the production of glued laminated timber beams.*

**Keywords:** Spruce, Thermal conductivity, Moisture diffusivity, Homogenization, Mori-Tanaka method.

### 1. Introduction

An important issue in the safety and reliability design of timber structures is the prediction of the transport of heat and moisture in various structural elements and their impact on both material and structural durability, strength and stiffness. In this regard, the moisture induced stresses in particular belong to principal contributors triggering the evolution of failure. Owing to a considerable complexity in both the material and geometrical description the computational modeling typically relies on hierarchical or staggered solution where the mechanical and transport analyses are decoupled. This approach is also exploited in our current research effort.

The present contribution addresses the mass transport description with emphases on the evolution of moisture content being the stepping stone for the mechanical analysis. It has been suggested, see e.g. (Krabbenhopft et al., 2004 and Frandsen et al., 2007), to abandon a traditional description of one-phase flow in the modeling of transient moisture transport in wood and consider a two-phase flow of bound water in cell walls and water vapor in lumens in the framework of so called non-Fickian moisture transfer. This approach has also been examined in a series of papers by (Eitelberger et al., 2011c, 2011d). Therein, a special procedure for the evaluation of the coupling term, the sorption rate, based on homogenization has been introduced. As also indicated in (Eitelberger et al., 2011c) the two moisture diffusion equations have to be supplemented by the energy conservation equation to account for the changes in energy caused by adsorption and desorption between the water vapor and the bound water and the energy transport owing to the diffusion of both water phases. The complete set of equations to be solved on macroscale is presented in Fig. 1.

Clearly, the solution of macroscopic problem 1 requires the knowledge of effective transport properties such as the macroscopic diffusivities of bound water ( $D_b$ ) and water vapor ( $D_v$ ), and the effective thermal conductivity  $\lambda$ . Since these depend on the current value of moisture content and temperature, the solution of the two problems has to be carried out adopting a coupled multiscale computational strategy. The need

---

<sup>\*</sup> Bc. Lucie Kucíková: Czech Technical University in Prague, Thákurova 7; 166 29, Prague; CZ, lucie.kucikova@fsv.cvut.cz

<sup>\*\*</sup> Ing. Jan Vorel, PhD.: Czech Technical University in Prague, Thákurova 7; 166 29, Prague; CZ, jan.vorel@fsv.cvut.cz

<sup>\*\*\*</sup> Ing. Jan Sýkora, PhD.: Czech Technical University in Prague, Thákurova 7; 166 29, Prague; CZ, jan.sykora.1@fsv.cvut.cz

<sup>\*\*\*\*</sup> Prof. Ing. Michal Šejnoha, DSc.: Czech Technical University in Prague, Thákurova 7; 166 29, Prague; CZ, sejnom@fsv.cvut.cz



for efficiency usually calls for the application of analytical homogenization schemes such the Mori-Tanaka method discussed next, see e.g. Benveniste (1987) and (Šejnoha et al., 2013).

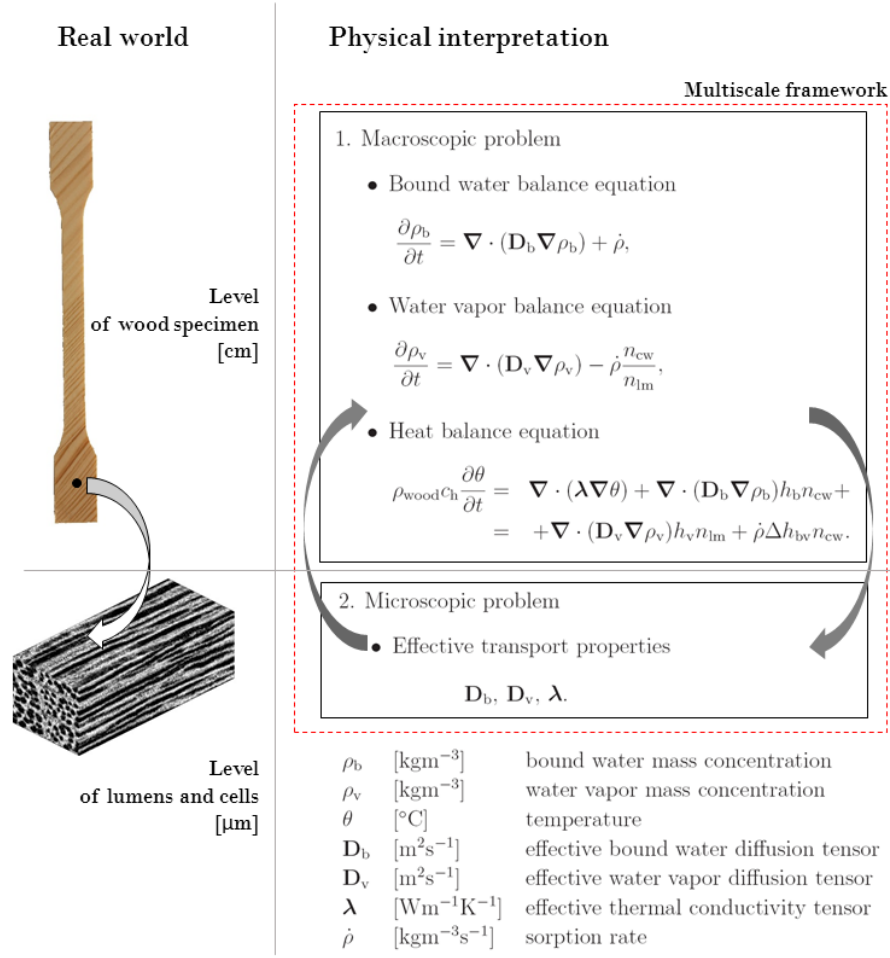


Fig. 1: Summary of material parameters and governing equations to describe the coupled heat and moisture transport in wood.

## 2. Determination of effective properties

The theoretical background for the derivation of effective transport properties of wood is well described in (Eitelberger et al., 2011a, 2011b). Henceforth, we summarize only the most essential steps with particular application to spruce wood used in the study of glued laminated timber beams.

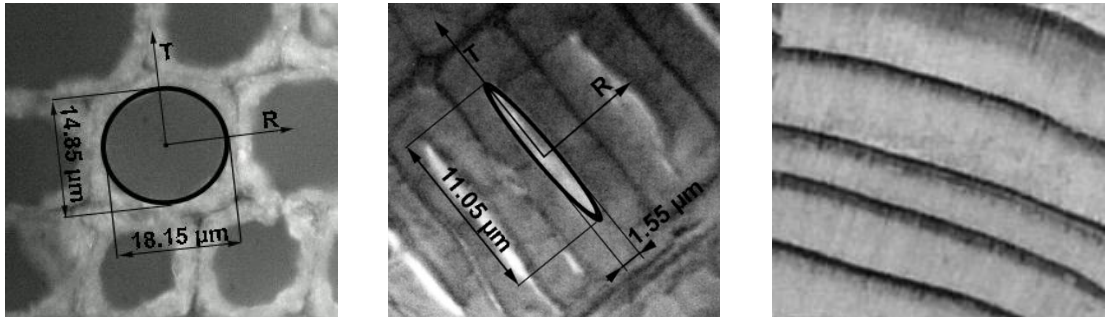


Fig. 2: Microstructure of wood: earlywood, latewood, early and late-wood transition.

### 2.1. Evaluation of effective properties

Limiting our attention to moisture transport we start with local constitutive equations in the form

$$\mathbf{J}_{cwm}^{\rho} = -D_{cwm} \nabla \rho_{cwm} = -\hat{D}_{cwm} \nabla \rho \quad (1)$$

$$\mathbf{J}_{air}^{\rho} = -D_{air} \nabla \rho_{air} = -\hat{D}_{air} \nabla \rho \quad (2)$$

where  $\mathbf{D}_{cwm}$  and  $\mathbf{D}_{air}$  are the diffusivity tensors of cell wall and air, respectively. In (Eitelberger et al., 2011a) these tensors were reformulated ( $\hat{\mathbf{D}}_{cwm}$ ,  $\hat{\mathbf{D}}_{air}$ ) to relate the local phase fluxes and the gradient of macroscopic concentration. The simple volume averaging then reads

$$\mathbf{D}_{AV}^{hom} = c_{cwm} \hat{\mathbf{D}}_{cwm} + c_{air} \hat{\mathbf{D}}_{air} \quad (3)$$

In the spirit of the Mori-Tanaka method the effective diffusivity tensor is provided by

$$\mathbf{D}_{MT}^{hom} = c_{cwm} \mathbf{D}_{cwm} \mathbf{A}_{cwm} + c_{air} \mathbf{D}_{air} \mathbf{A}_{air} \quad (4)$$

where  $\mathbf{A}_{cwm}$  and  $\mathbf{A}_{air}$  are the Mori-Tanaka localization tensors relating the macroscopic and phase concentration gradients as

$$\nabla \rho_{cwm} = \mathbf{A}_{cwm} \nabla \rho, \quad \nabla \rho_{air} = \mathbf{A}_{air} \nabla \rho \quad (5)$$

These tensors, see e.g. (Šejnoha et al., 2013), depend on the properties of cell walls and lumens and the shape and orientation of lumens. The latter differs for the early and latewood as evident from Fig. 2. The volume fractions  $c_{cwm}$ ,  $c_{air}$  were found from image analysis of actual microstructures also depicted in Fig. 2. The last homogenization step to get the properties of wood at the level of annual rings reduces to the application of simple Voight and Reuss bounds as

$$\mathbf{D}_{AR} = c_{EW} \mathbf{D}_{EW} + c_{LW} \mathbf{D}_{LW}, \quad \mathbf{D}_{AR}^{-1} = c_{EW} \mathbf{D}_{EW}^{-1} + c_{LW} \mathbf{D}_{LW}^{-1} \quad (6)$$

where  $c_{EW}$ ,  $c_{LW}$  are the volume fractions of earlywood and latewood, respectively, found again from images such as the one in Fig. 2c. Similar procedure leads to the effective thermal conductivity.

## 2.2. Results

As an example, we provide in Tabs. 1 and 2 the results derived for spruce wood used already in the stochastic analysis of glued laminated timber beams where similar type of homogenization was used to get the effective elastic properties, see (Šejnoha et al., 2017). The values correspond to the selected moisture content 10 % and temperature  $\theta = 20^\circ \text{C}$ .

Tab. 1: Effective thermal conductivities.

Homogenization step	Phase	$c_r$ [-]	$\lambda_{11}$ [W/mK]	$\lambda_{22}$ [W/mK]	$\lambda_{33}$ [W/mK]
Step 1	Lignin	0.39	0.39	0.39	0.39
3 phases	Hemicellulose	0.37	0.34	0.34	0.34
	Water+ext	0.24	0.60	0.60	0.60
Step 2	Polymer network	0.65	0.42	0.42	0.42
2 phases	Cellulose	0.35	0.26	0.26	1.04
Step 3	Cell wall	0.58/0.82	0.36	0.36	0.64
2 phases	Lumen	0.42/0.18	0.03	0.03	0.03
Step 4	Earlywood	0.67	0.17	0.16	0.38
2 phases	Latewood	0.33	0.18	0.29	0.53
	Annual ring	-	0.17	0.20	0.43

Tab. 2: Effective diffusivities.

Homogenization step	Phase	$c_r$ [-]	$\mathbf{D}_{11}$ [ $10^{-12} \text{ m}^2/\text{s}$ ]		$\mathbf{D}_{22}$ [ $10^{-12} \text{ m}^2/\text{s}$ ]		$\mathbf{D}_{33}$ [ $10^{-12} \text{ m}^2/\text{s}$ ]	
			AV	M-T	AV	M-T	AV	M-T
Step 1	Cell wall	0.58/0.82	2.26		2.26		5.65	
2 phases	Lumen	0.42/0.18	26x10 <sup>-6</sup>		26x10 <sup>-6</sup>		26x10 <sup>-6</sup>	
Step 2	Earlywood	0.67	6.72	5.90	6.72	5.24	1486.78	2962.00
2 phases	Latewood	0.33	3.36	2.83	3.36	6.30	454.65	11080.00
	Annual ring	-	5.00	4.34	5.01	5.59	960.77	5640.94

While only two step-homogenization scheme is needed when deriving the effective diffusivities, additional two homogenization steps are required on the level of cell walls to get the effective thermal

conductivities, see (Eitelberger et al., 2011a, 2011b) from where the phase properties were adopted. The volume fractions of phases below the cell wall level were taken from (Hofstetter et al., 2005). As already mentioned, the volume fractions at the level of lumens and the level of wood rings were derived for the analyzed wood from actual images. Note that at the level of wood the classical Voigt and Reuss bounds were exploited, see e.g. (Šejnoha et al., 2013).

### 3. Conclusions

The present paper reviewed a classical steady state homogenization method based on both the Mori-Tanaka method and simple averaging. The homogenized properties listed in Tabs. 1 and 2 were found for one specific value of the moisture content and temperature. When introduced into the macroscopic transient analysis, recall the macroscopic model 1 in Fig. 1, these have to be calculated at each time integration step.

While the effective thermal conductivities are obtained from the actual step 4 of the homogenization scheme, recall Tab. 1, the diffusivity tensor  $\mathbf{D}_b$  follows from Eqs. (3) and (4) when setting the air diffusivities equal to 0. On the contrary, the tensor  $\mathbf{D}_v$  is identical to  $\mathbf{D}_{air}$ , see (Eitelberger et al., 2011c).

Similar types of experiments as presented in (Eitelberger et al., 2012) are currently under way to provide data for the validation of implementation of macroscopic model 1. The realistic prediction of mechanical behavior is highly dependent on the moisture gradients. Therefore, the physically-based model for transport processes in wood presented here profiting from the multi-scale analysis is a crucial step in the safety and reliability design of timber structures.

### Acknowledgement

The financial support provided by the GAČR grant No.15-10354S and the SGS project with the application registered under the No. OHK1-038/17 is gratefully acknowledged.

### References

- Benveniste, Y. (1987) A new approach to the application of Mori-Tanaka theory in composite materials. *Mechanics of Materials*, 6, pp. 147-157.
- Eitelberger, J. and Hofstetter, K. (2011a) Prediction of transport properties of wood below the fiber saturation point – A multiscale homogenization approach and its experimental validation. Part I: Thermal conductivity. *Composites Science and Technology*, 71, pp. 134-144.
- Eitelberger, J. and Hofstetter, K. (2011b) Prediction of transport properties of wood below the fiber saturation point – A multiscale homogenization approach and its experimental validation. Part II: Steady state moisture diffusion coefficient. *Composites Science and Technology*, 71, pp. 145-151.
- Eitelberger, J., Hofstetter, K. and Dvinskikh, S.V. (2011c) A multi-scale approach for simulation of transient moisture transport processes in wood below the fiber saturation point. *Composites Science and Technology*, 71, pp. 1727-1738.
- Eitelberger, J., Svensson, S. and Hofstetter, K. (2011d) Theory of transport processes in wood below the fiber saturation point. Physical background on the microscale and its macroscopic description. *Holzforschung*, 65, pp. 337-342.
- Eitelberger, J. and Svensson, S. (2012) The Sorption Behavior of Wood Studied by Means of an Improved Cup Method. 92, pp. 321-335.
- Frandsen, H.L., Damkilde, L. and Svensson, S. (2007) A revised multi-Fickian moisture transport model to describe non-Fickian effects in wood. *Holzforschung*, 61, pp. 563-572.
- Krabbenhopft, K. and Damkilde, L. (2004) A model for non-Fickian moisture transfer in wood. *Materials and Structures*, 37, pp. 615-622.
- Hofstetter, K., Hellmich, Ch. and Eberhardsteiner, J. (2005) Development and experimental validation of a continuum micromechanics model for the elasticity of wood. *European Journal of Mechanics - A/Solids*, 24:6, pp. 1030-1053.
- Šejnoha, M. and Zeman, J. (2013) *Micromechanics in practice*, WIT Press, Boston.
- Šejnoha, M., Janda, T., Melzerová, L., Nežerka, V. and Šejnoha, J. (2017) Modeling glulams in linear range with parameters updated using Bayesian inference, *Engineering Structures*. Under review.

## **THERMOMECHANICAL MODELING AND ANALYSIS OF THE THREAD ROLLING PROCESS WITH ELECTROCONTACT HEATING**

**K. Kukielka<sup>\*</sup>, L. Kukielka<sup>\*\*</sup>**

**Abstract:** *The work presents application of the variational and finite element methods for the modelling and analysis of the physical phenomena in the thread rolling operation with electric current. This process is considered as geometrical, physical and thermal nonlinear boundary–initial problem with surface (as a result of friction and the flow of electrical current by contact zone) and volume heat source (as a result of visco-plastic deformation and the flow of electrical current), which move with the tool. But the boundary conditions for displacement and temperature are not known in the contact zone. Physical and mathematical model of the process of thread rolling and an thermo-elastic (for reversible zone) and thermo-visco-plastic (for non reversible zone) material model have been elaborated. The model takes into account the strain, strain rate, temperature histories of the material and the impact of visco-plastic deformation of the body on temperature rise.*

**Keywords:** Thread rolling process, Constitutive laws, Modelling, Variation formulation, FEM, DEM.

### **1. Introduction**

This article is about a new method of modelling and analysis of the thread rolling processes, including thermodynamics of physical phenomena. The methodology was developed in team of prof. L. Kukielka with the author (Kukielka L., 1994; Kukielka L., 1999; Kukielka L. et al., 2012; Kukielka L. et al., 2014).

Whereas, very often are made the assumption that the processes are isothermal treatment and are realized on cold (Kukielka K. et al., 2014; Kukielka K., 2016) do not take into account the variability of thermo-physical constant with temperature. This results in significant errors in both qualitative and quantitative.

In applications using a theoretical calculations and modelling processes precision machining of modern parts (Kukielka L., 1999; Kukielka L., 2001; Kukielka L. et al., 2015; Kukielka L. et al., 2016; Myśliński et al., 2004) are geometrical, physical and thermal nonlinear boundary–initial problem, where there are nonlinear, movable and variable in time and in time and state of: stress, strain and space heat sources and boundary conditions were described by using the incremental models. Wherein, the boundary conditions are unknown in the contact zones between the tool and workpieces. The application of the developed general methodology to solve complex problems of modelling specific problems seen in several examples of technology. In particular, it shows examples of modelling of thread rolling process.

Proposed in this paper a new way through the centerless rolling doesn't have the above drawbacks (Kukielka K. et al., 2014; Kukielka K., 2016; Kukielka K. et al., 2013; Kukielka L. et al., 2006). The analysis of the literature and own experimental studies and computer simulations shown (Kukielka K. et al., 2014; Kukielka K., 2016; Kukielka L. et al., 2006; Kukielka L. et al., 2007; Patyk et al., 2014), that the thread forming with desirable technological quality in the rolling process is very complex problem, because it depends significantly on many factors, which can be divided into four groups: factors and material, geometric factors and tools thread, technological parameters, force pressure, torque and friction force (type of lubricant) (Kukielka K., 2016; Kukielka K., 2017). Therefore, for a comprehensive analysis process it is necessary to develop adequate mathematical model and numerical methods of solving them.

---

<sup>\*</sup> Krzysztof Kukielka, PhD.: Mechanical Engineering Department, Koszalin University of Technology, Raclawicka Street 75-, 620 Koszalin; PL, krzysztof.kukielka@tu.koszalin.pl

<sup>\*\*</sup> Prof. Leon Kukielka, PhD.: Mechanical Engineering Department, Koszalin University of Technology, Raclawicka Street 75-, 620 Koszalin; PL, leon.kukielka@tu.koszalin.pl

## 2. MODELLING OF HEAT TRANSFER

For the design and control of TRWC process, knowledge of the course of thermal distribution and temperature fields in the system (object-tool) is needed. The paper presents a physical model of thermal phenomena in thread rolling process and description of the heat sources in an incremental differential equation with appropriate initial and boundary conditions for temperature. It uses the application of the variational methods to modelling the temperature field during the thread rolling operation with electric current.

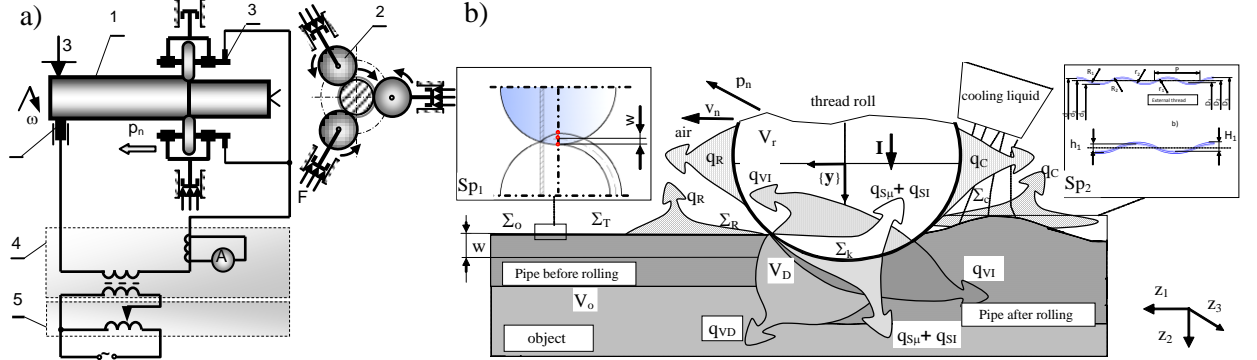


Fig. 1: a) Scheme thread rolling: 1 – workpiece, 2 – roller, 3 – brush plate, 4 – transformer, 5 – autotransformer; b) Diagram of the system of heat fluxes arising in characteristic volumes  $V$  and areas  $\Sigma$  during thread rolling: pipe before rolling and pipe after - surface of the object and outer layer after previous treatment and after rolling, respectively.

### 2.1. Heat sources in the thread rolling with electric current

The TRWC process is performed with high speed heat sources which move with tool. Depending on where they occur, it is divided into (Fig. 1b):

- **plane** with capacities  $q_{F\mu}$  (by friction tool-object) and  $q_{FI}$  (as a result of flow electrical current through the contact zone with electrical contact resistance  $R_s$ ), they are in the contact area  $\Sigma_k$  tools with object,
- **spacious** with capacities  $q_{VO}$  in the zone of plastic deformation of the material, while the sources with capacities  $q_{VI}$  are in volumes tools and the object through which an electric current flows.

### 2.2. Mathematical incremental model of heat transfer

Uses an updated Lagrange description, assuming knowledge of the temperature field in the initial moments  $t_0$  and present time  $t$ , while looking for a solution to the next time  $\tau = t + \Delta t$ , where  $\Delta t$  is a very small incremental of time (Kukielka L., 1999; Kukielka L. et al., 2012; Kukielka L., et al., 2014). Then the equation for a typical incremental step  $t \rightarrow \tau$ , in the global coordinate  $\{z\}$  is assumed:

$$\text{div}\{\lambda(T) \cdot \text{grad}[\Delta T(z, \Delta t)]\} + \Delta q_{VI}[\cdot] + \Delta q_{VD}[\cdot] = C(T) \cdot \rho(T) \cdot \Delta \dot{T}(z, \Delta t), \quad (1)$$

where  $\Delta \dot{T}(z, \Delta t) = \partial[\Delta T(z, \Delta t)] / \partial t$ , is the speed of the temperature increment,  $\lambda(T)$ ,  $C(T)$ ,  $\rho(T)$  are depended on the temperature in the initial step: heat conductivity, heat capacity and mass density, however:

$$\Delta q_{VI}[\cdot] = k_e \cdot \left[ \frac{\tau I^2 \cdot \tau R(\tau T)}{\tau V} - \frac{t I^2 \cdot t R(t T)}{t V} \right] = k_e \cdot \left[ \left( \frac{\tau I}{\tau S_\Sigma} \right)^2 \cdot \tau \rho_1(\tau T) - \left( \frac{t I}{t S_\Sigma} \right)^2 \cdot t \rho_1(t T) \right] \quad (2)$$

$$\Delta q_{VD}[\cdot] = \frac{(1-\xi) \cdot \tau V}{t + \Delta t} \int_{t \cdot \epsilon_i^{(VP)}}^{\tau \cdot \epsilon_i^{(VP)}} \sigma_Y(\tau \epsilon_i^{(VP)}, \tau \dot{\epsilon}_i^{(VP)}, \tau T) - \frac{(1-\xi) \cdot t V}{t} \int_{t \cdot \epsilon_i^{(VP)}}^{t \cdot \epsilon_i^{(VP)}} \sigma_Y(t \epsilon_i^{(VP)}, t \dot{\epsilon}_i^{(VP)}, t T), \quad (3)$$

are the rate of incremental spatial heat sources generated by electrical current (2) and by visco-plastic deformation (3), where  $\sigma_Y(\epsilon_i^{(VP)}, \dot{\epsilon}_i^{(VP)}, T)$  is accumulated yield stress, depending on the history of visco-plastic strain  $\epsilon_i^{(VP)}$  and strain rate  $\dot{\epsilon}_i^{(VP)}$  and temperature  $T$ ,  $R(T)$  is temperature-dependent electrical resistance of material,  $\rho_1(T)$  is temperature-dependent resistivity of material,  $S_\Sigma$  is the field of the areas

contact  $\Sigma_k$ ,  $\xi = 0.05 \div 0.1$  is the coefficient energy absorption,  $k_e$  is the coefficient (for constant current  $k_e = 1$  and  $k_e = 0.7 \div 0.97$  for alternating current).

### **Initial and boundary conditions for temperature**

The equation of heat transfer (1) is completed with the initial condition and the four boundary conditions.

#### **Initial condition**

*Initial condition* describes the temperature field at time which is the initial moment:  $T(\mathbf{z}, t = t_0) = T_0(\mathbf{z})$ ,  $\mathbf{z} \in V$ . In typical processing conditions TRWC, the temperature of the object at time  $t = t_0$  is constant then:  $T(\mathbf{z}, t = t_0) = T_0 = \text{const}$ , where  $T_0$  is ambient temperature.

#### **Boundary conditions**

*conditions of I gender* - the temperature may be prescribed at specific points in the surfaces, denoted by  $\Sigma_T$ , and/or at the specific points in the volume of the body.

*conditions of II gender* – in the contact area tool and object  $\Sigma_k$ , (heat flows).

*conditions of III gender* (continuity of the heat flows):

$$\begin{aligned} -\lambda_o(T) \mathbf{n} \circ \text{grad}[\Delta T_o(\mathbf{z}, \Delta t)] &= [\Delta T_o(\mathbf{z}, \Delta t) - \Delta T_b(\mathbf{z}, \Delta t)] / R_s(\mathbf{z}, \Delta t) = \\ &= -\lambda_b(T) \mathbf{n} \circ \text{grad}[\Delta T_b(\mathbf{z}, \Delta t)], \end{aligned} \quad \mathbf{z} \in \Sigma_k, \quad (4)$$

where  $R_s$  is the heat resistance in the surface contact (for ideal contact  $R_s = 0$ ),  $b_o$  and  $b_b$  is the heat division coefficients for rolling element ( $b$ ) and object ( $o$ ),  $\mathbf{n} \circ \text{grad}[\Delta T(\cdot)]$  is the scalar product,  $\Delta q_{SI}[\cdot]$  and  $\Delta q_{Su}[\cdot]$  are the rate of incremental surface heat sources generated by electrical current (heat of Joule's) and fretting per unit surface,

*conditions of IV gender* – they are in areas  $\Sigma_c$  i  $\Sigma_R$ , in which exchange heat is on road convection and radiation, then the boundary conditions.

Equation (1) with initial condition (4) and boundary conditions are a full mathematical description of heat transfer during the TRWC, at the typical incremental time step. The analytical solution is impossible, therefore we are introduced variational formulation.

### **Variational formulation equations of heat transfer**

For the variational formulation of the equations of heat transfer in the TRWC, at the typical time step, introduced an incremental functional  $\Delta F(\Delta \dot{T}, \Delta T', \Delta T, \dots)$ , in which is one independent field – it is temperature field, and its derivatives:  $\Delta \dot{T} = d(\Delta T)/dt$ ,  $\Delta T' = d(\Delta T)/dy_3$ . This functional has differential equation (1) in the global Cartesians coordinate  $\{\mathbf{z}\}$  and boundary conditions. When using the conditions of stationarity of functional:

$$\delta[\Delta F(\Delta \dot{T}, \Delta T', \Delta T)] = \{\partial[\Delta F(\cdot)]/\partial(\Delta T)\} \delta(\Delta T) = 0, \quad (5)$$

and using the approximations adequate to the finite element method we obtain the discretized equation of heat transfer equilibrium in the global coordinate  $\{\mathbf{z}\}$  (the non stabilized heat transfer):

$$[C]\{\Delta \dot{\Theta}\} + ([K^K] + [K^C] + [K^R] + [K^{IV}])\{\Delta \Theta\} = \{\Delta Q\} + \{\Delta Q^I\} \quad (6)$$

where  $[C]$  and  $[K^K]$ ,  $[K^C]$ ,  $[K^R]$ ,  $[K^{IV}]$  are the heat capacities, conductivity, convection and radiation matrices and total nodal point conditions of IV gender,  $\{\Delta Q\}$  is the nodal point increment heat flow input vector,  $\{\Delta Q^I\}$  is the vector of nodal point of the boundary conditions of I gender.

## **3. Conclusions**

The paper presents a possibility of applying the variational and finite element methods for the analysis of heat transfer in thread rolling with electric current operation. The developed methodology step by step solutions allows for: effective scheme solutions, various constitutive models; the ability to analyze a variety of physical problems: displacement, strain, stress and temperature; the opportunity to load



a variety of boundary conditions and kinematic and thermal constraints; the opportunity to load a variety of initial conditions (and history); efficient algorithm for analysis of the contact issue.

For the most important possibilities of the numerical analysis in application for the thread rolling is determination of: dimensions of the pipe before rolling (mainly nominal and outline diameter), local strain, stress and temperature states in the thread, geometry and thread outline during thread rolling and after elastic relieving, maximum strain – where crack of the thread is possible, expected rolling force, influence of the friction coefficient on the process flow and quality of the thread, number and geometry of the rolls, in that active rolls surface in the introducing, shaping, calibrating and outing zone, state of loads, stresses and strains of the tools and areas of contact, slip and stick.

## References

- Kukielka, K. and Kukielka, L. (2013) External thread rolling head. The polish patent No PL402652–A1, PL220175–B1, 4.02.2013. (in Polish).
- Kukielka, K., Kukielka, L., Bohdal, L., Kulakowska, A., Malag, L. and Patyk, R. (2014) 3D Numerical Analysis the State of Elastic/Visco–Plastic Strain in the External Round Thread Rolled on Cold. *Applied Mechanics and Materials*, Vol. 474, pp. 436-441.
- Kukielka, K. (2016) Ecological Aspects of the Implementation of New Technologies Processing for Machinery Parts. *Annual Set of Environment Protection*, vol. 18, pp. 137-157.
- Kukielka, K. (2017) Numerical simulations of the thread rolling process as ecological and economical research tool in the implementation of modern technologies. *Annual Set of Environment Protection*, vol. 19.
- Kukielka, L. (1994) Theoretical and experimental foundations of surface roller burnishing with the electrocontact heating. Book WM nr 47. WSI Koszalin, (in Polish).
- Kukielka, L. (1999) Application of the variational and finite element methods to dynamic incremental nonlinear analysis in the burnishing rolling operation. *ESM'99 - Modelling And Simulation A Tool For The Next Millennium*, Vol. II, pp. 221-225.
- Kukielka, L. (2001) Mathematical modelling and numerical simulation of non-linear deformation of the asperity in the burnishing cold rolling operation. *Computational Methods in Contact Mechanics V*, Book Series: *Computational and Experimental Methods*, Vol. 5, pp. 317-326.
- Kukielka, L. and Kukielka, K. (2006) Numerical analysis of the process of trapezoidal thread rolling. *High Performance Structures and Materials III*, Southampton–Boston, WITPRESS, pp. 663-672.
- Kukielka, L. and Kukielka, K. (2007) Numerical analysis of the physical phenomena in the working zone in the rolling process of the round thread. *Computer Methods and Experimental Measurements for Surface Effects and Contact Mechanics VIII*, Southampton–Boston, WITPRESS, pp. 125-124.
- Kukielka, L., Geleta, K. and Kukielka, K. (2012) Modelling and Analysis of Nonlinear Physical Phenomena in the Burnishing Rolling Operation with Electrical Current. *Steel Research International, Special Edition: 14th International Conference Metal Forming*, Kraków, pp. 1379-1382.
- Kukielka, L., Geleta, K. and Kukielka, K. (2012) Modelling of Initial and Boundary Problems with Geometrical and Physical Nonlinearity and its Application in Burnishing Processes. *Steel Research International, Special Edition: 14th International Conference Metal Forming*, Krakow, pp. 1375-1378.
- Kukielka, L. and Kukielka, K. (2012) The modern method of modeling and analysis precision machining processes auto parts. *Environmental aspects of the use of new technologies in transport*, Book of Mechanical Engineering, No 235 of Mechanical Faculty, Koszalin University of Technology. Koszalin, pp. 109-128, (in Polish).
- Kukielka, L., Bohdal, L., Chodór, J., Forsiewicz, M., Geleta, K., Kałduński P., Kukielka, K., Patyk, R. and Szyk, M. (2012) Numerical analysis of selected processes precision machining of automotive parts. *Environmental aspects of the use of new technologies in transport*, Book of Mechanical Engineering No 235 of Mechanical Faculty, Koszalin University of Technology, Koszalin, pp. 129-194.
- Kukielka, L., Kukielka, K., Kulakowska, A., Patyk, R., Malag, L. and Bohdal, L. (2014) Incremental Modelling and Numerical Solution of the Contact Problem between Movable Elastic and Elastic/Visco–Plastic Bodies and Application in the Technological Processes. *Applied Mechanics and Materials*, Vol. 474, pp. 159-165.
- Kukielka L. and Kukielka K. (2015) Modelling and analysis of the technological processes using finite element method. *Mechanik*, Vol. 88, pp. 317-340.
- Kukielka, L. et al. (2016) Analysis of the states of deformation and stress in the surface layer of the product after the burnishing cold rolling operation. *Novel Trends in Production Devices and Systems "Materials Science Forum"*. pp. 278-287.
- Patyk, R., Kukielka, L., Kukielka, K., Kulakowska, A., Malag, L. and Bohdal, L. (2014) Numerical Study of the Influence of Surface Regular Asperities Prepared in Previous Treatment by Embossing Process on the Object Surface Layer State after Burnishing. *Applied Mechanics and Materials "Novel Trends in Production Devices and Systems"*, Vol. 474, pp. 448-453.

## DYNAMICS OF MULTIBODY SURGICAL ROBOTIC SINGLE INCISION LAPAROSCOPIC SURGERY TOOL

Z. Kulesza<sup>\*</sup>, R. Trochimczuk<sup>\*\*</sup>

**Abstract:** *The current paper introduces a method for modeling the dynamics of highly specialized robotic tools, used in the Minimally Invasive Surgery (MIS) or Single Incision Laparoscopic Surgery (SILS) operations. The method is based on an original approach presented in detail in (Wittbrodt et al, 2016). The kinematic model of the analyzed laparoscopic tool was presented earlier in (Leniowski et al., 2010). In the current paper the model is extended by including the dynamics of the tool and the flexibility of its links. Numerical results demonstrate the influence of loading conditions on accuracy of movements of the end effector.*

**Keywords:** Dynamics modelling, Flexible links modelling, Multibody system, SILS, MIS.

### 1. Introduction

Modern medicine is growing rapidly due to the use of modern mechatronic devices supporting surgeons in standard surgical interventions. Among different solutions, special attention is paid to technologically advanced surgical robots, dedicated to minimally invasive surgery (MIS) – laparoscopic surgery. Such treatments are performed with the introduction of tools (endoscopic cameras and other laparoscopic tools) through small incisions in the patient's abdominal wall. This method is used successfully since the early 90s of the twentieth century. An extension of the classical technique MIS operations is single incision laparoscopic surgery (SILS). This method is also referenced in the literature as single-port access (SPA) surgery or minimal access surgery through a single incision (MASTSI). With the SILS procedure, the cosmetic effect is even better than with the MIS technique. However, the SILS is much more difficult to implement than the MIS.

Usually, the dynamics of surgical tools is not analyzed. This is perhaps due to the prevailing popular opinion that surgical robots move so slowly that their dynamics may be neglected. However, the engineering practice indicates that there is a need to include the dynamics of flexible, multibody laparoscopic tools in order to improve the accuracy of their movements. The current paper introduces a method for modeling the dynamics of highly specialized surgical robotic SILS tool – multibody open kinematic chain with flexible beam-like links, dedicated to different robotic surgical procedures.

### 2. Materials and Methods

Modern surgical tools used in MIS techniques usually take form of a pipe with diameter of 5 or 10 mm and length of approximately 500 mm. The tool is equipped with a system of tendons routed inside the pipe for opening or closing the end effector (e.g. a gripper). The tendons are pulled by a system of levers driven by the operator's hand. The tool is also equipped with a locking clamp and a rotating head at the main arm. The tool has the interface to connect the apparatus to the pneumoperitoneum and to plug-in the electric system necessary to operate the coagulant. Surgical tools for SILS techniques are more complicated because they are equipped with multiple arms with different end effectors. In this case the tool diameter is usually greater due the fact that it may consist of two (or more) active arms in the operating field and an additional arm with an integrated endoscopic camera. Operating the part of the tool above the integument is very complicated and exhaustive for the surgeon. On the other hand, mounting

---

<sup>\*</sup> D.Sc., Eng. Zbigniew Kulesza, Prof.: Faculty of Mechanical Engineering, Department of Automatic Control and Robotics, Białystok University of Technology, Wiejska 45C; 15-351, Białystok; PL, z.kulesza@pb.edu.pl

<sup>\*\*</sup> Ph.D., Eng. Roman Trochimczuk: Faculty of Mechanical Engineering, Department of Automatic Control and Robotics, Białystok University of Technology, Wiejska 45C; 15-351, Białystok; PL, r.trochimczuk@pb.edu.pl

the tool on an arm of a surgical robot is troublesome, as the robots are not usually equipped with multiple end effectors to operate several arms of the SILS tools.

Therefore, for the purposes of robotic minimally invasive surgery, a novel concept of a tool having the structure of an open kinematic chain with six degrees of freedom has been proposed. The kinematic chain is made of six links connected with rotary joints. The links are driven with integrated gears and micromotors installed at the joints of the mechanism. The tool is designed so that it can be attached not only to a specialized surgical robot, but also to an arm of a typical industrial robot adapted for an operating theater. This way the implementation costs of the robotic surgery system may be considerably reduced. The kinematic structure of the novel robotic tool has been adopted from the structure of a similar tool proposed by (Leniowski et al., 2010). The CAD model of the SILS robotic tool has been designed in SolidWorks (Fig. 1a) with all components of the system made of the targeted material. The kinematic chain is shown in Fig. 1b. The model has been used to test the possible mobility of the tool and decide how to manufacture its prototype. The model has been also used to evaluate inertia properties of the links: masses, mass moments of inertia, locations of centers of masses. These parameters have been included in the dynamical model of the tool developed with the rigid finite element method and implemented in Matlab.

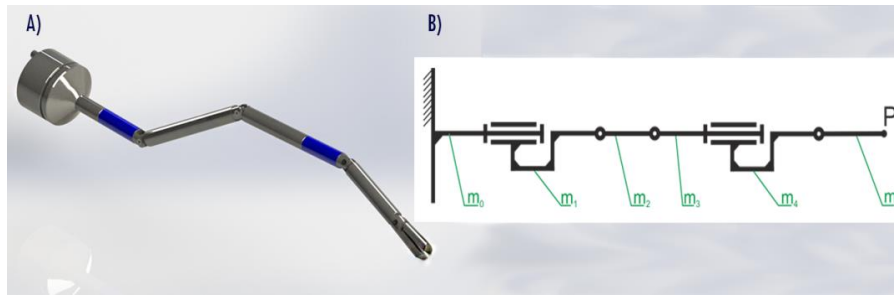


Fig. 1: Surgical robotic tool for SILS procedures (A) and its kinematic structure (B).

The original method of modeling the dynamics of open kinematic chains of multibody systems presented in this section is described in detail in works. The origins of this method go back to the scientific school created by Kruszewski (Kruszewski et al., 1999) and continued by Wittbrodt. The method was further improved and extended by Adamiec-Wojcik and Wojciech (Wittbrodt et al., 2006). The idea of this method consists in replacing a flexible link of a kinematic chain with a series of rigid finite elements, connected by spring-damping elements. In the so called primary division a single link of a multibody system modeled as a beam of length  $L_p$  and constant profile is divided into  $m_n$  sections of the same lengths. These sections are called *rigid finite elements (rfes)*. In the secondary division the flexibility properties of the link are substituted in *spring-damping elements (sdes)* located at the middles of lengths of the *rfes*. This way the flexible link is divided into  $m_p + 1$  rigid finite elements connected by  $m_p$  massless and dimensionless spring-damping elements. Coordinate systems are assigned to the *rfes* as follows:  $\{0\}$  - inertial coordinate system,  $\{p,0\}$  - coordinate system assigned to *rfe* 0,  $\{p,i'\}$  - coordinate system assigned to *rfe*  $i$  in the undeformed state (the axes of this system are parallel to the principal, central inertial axes of *rfe*  $i$ ),  $\{p,i\}$  - local system assigned to *rfe*  $i$ ,  $\varphi_1^{(p,i)}, \varphi_2^{(p,i)}, \varphi_3^{(p,i)}$  - Euler angles ZYX. Index  $p$  denotes the considered flexible link of the kinematic chain. A detailed description of the discretization method is presented in (Kruszewski et al., 1999). Equations of motion of an open kinematic chain including the energy of spring deformation of flexible links can be presented as

$$\mathbf{A}\ddot{\mathbf{q}} + \mathbf{K}_R\dot{\mathbf{q}} = \mathbf{Q} - \mathbf{G} - \mathbf{h} - \mathbf{S} \quad (1)$$

where:  $\mathbf{A}$ ,  $\mathbf{h}$  are matrix and vector components of Lagrange's operator derived from the kinetic energy of the system,  $\mathbf{G}$  is the vector of gravitational forces,  $\mathbf{Q}$  is the vector of generalized external forces,  $\mathbf{K}_R$  is the stiffness matrix,  $\mathbf{S}$  is the vector of translational forces due to elastic deformation of the flexible link,  $\mathbf{q}$  is the vector of generalized coordinates. The details on calculating the components of Eq. (1) using the rigid finite element method, generalized coordinates and Euler angles are described in (Wittbrodt et al., 2006).

For simulation purposes it has been assumed that the last link of the proposed tool is flexible. Therefore,

it is presented as a system of three *rfe*s of equal lengths connected with two *sdes*, following the discretization procedure described above (Fig. 2).

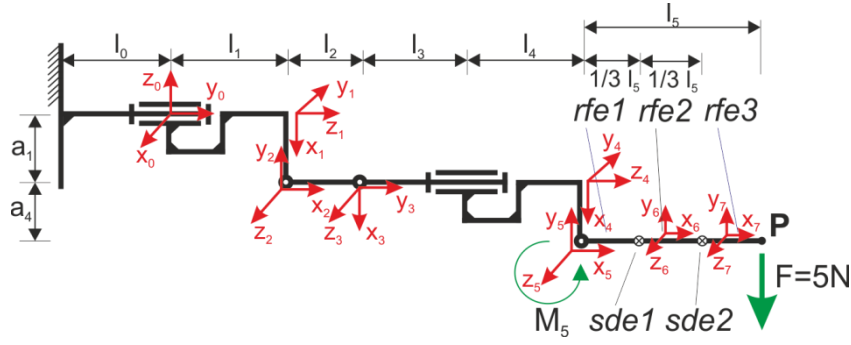


Fig. 2: Kinematic structure of the SILS tool after discretization of the last link.

Coordinate systems  $x_1y_1z_1$ , ...,  $x_5y_5z_5$  of the first five links are assumed in accordance to Denavit-Hartenberg notation used in the *rfe* method. Centers of the coordinate systems  $x_6y_6z_6$ ,  $x_7y_7z_7$  of the *rfe*s are at their mass centers, and axes are at their principal, central inertial axes. Lengths of the links are as follows:  $l_0 = 56 \text{ mm}$ ,  $l_1 = 51.09 \text{ mm}$ ,  $l_2 = 92 \text{ mm}$ ,  $l_3 = 56 \text{ mm}$ ,  $l_4 = 36 \text{ mm}$ ,  $l_5 = 150 \text{ mm}$ . The links are of equal diameter  $D = 5 \text{ mm}$ . To reduce the total mass of the tool the links are made of the special, biomedical material called PEEK polymer (polyether ether ketone) of Young's modulus  $E = 4 \text{ GPa}$  and density  $\rho = 1320 \text{ kg/m}^3$ .

### 3. Results

Based on the mathematical model presented in the previous section, the simulation model of the SILS tool has been prepared in Matlab. The model contains of a set of seventeen nonlinear, time-variant equations of motion in the form given by Eq. (1). The vector of generalized coordinates  $q$  contains of five joint angles  $\theta_1, \dots, \theta_5$  about  $z_1, \dots, z_5$  axes, three linear and three angular deformations along/about  $x_6, y_6, z_6$  axes of the first *sde*, and three linear/angular deformations along/about  $x_7, y_7, z_7$  axes of the second *sde*. The equations are solved numerically using the implicit Newmark's integration scheme (Newmark, 1959). Rotations  $\theta_1, \dots, \theta_5$  at the joints are controlled with five proportional controllers in angular position closed-loop systems. During simulations the following test scenario has been assumed:

- 1) initial joint angles  $\theta_{p|0}$  is defined in such a way that the axes of the first four links are aligned horizontally and the fifth link is directed vertically downwards;
- 2) proportional controllers maintain initial four angular positions  $\theta_1, \dots, \theta_4$  unchanged from their initial values by applying external force moments  $M_1, \dots, M_4$  to the links at the joints;
- 3) the 5th link changes its angular position from  $\theta_{5|0} = 0^\circ$  to  $\theta_{5|f} = 90^\circ$  by applying the external force moment  $M_5$  (see: Fig. 3) generated at the 5th joint by the proportional controller;
- 4) the fifth link is loaded by an additional force  $F = 5 \text{ N}$  applied at the end of the 5th link (at the tool center point, TCP) perpendicularly to  $x_7$  axis (Fig. 3); the force simulates external loadings impacting the SILS tool due to the resisting action of tissues inside human's body;
- 5) the calculations are conducted twice: for the 5th link assumed as non-flexible (stiff), and for the 5th link assumed as flexible (non-stiff); for the stiff link, the 5th link is not divided into *rfe*s and *sdes*.

Time histories of local joint angles  $\theta_1, \dots, \theta_5$  and vertical positions  $y_5, y_7$  of the TCP in the global coordinate system are presented in Fig. 3. As can be seen, if the 5th link is assumed as stiff, the vertical position of the TCP changes smoothly from the initial  $y_{5|0} = -0.15 \text{ m}$  to the final  $y_{5|0} = 0 \text{ m}$  (Fig. 3b). If the 5th link is assumed as flexible, the vertical position of the TCP at the beginning changes in a similar manner (Fig. 3d). However, when the final position  $y_{7|f} = 0 \text{ m}$  is attained, the oscillations of the tool tip appear. The amplitude of the oscillations is about 20 mm. Certainly, the oscillations would have a

detrimental effect for the results of patient's operation. Therefore, some technical measures should be undertaken to avoid them. The diameter of the tool links can be increased or the material of the links can be changed to be more stiff. However, not all of these solutions may be acceptable in a given design of the tool due to biomedical requirements of the SILS technique. It should be noted that these oscillations are not present in the time history of the  $\theta_5$  joint angle (Fig. 3c), which means that only the end part of the last link oscillates. Therefore, if only the angular position of the 5th link was measured, the position controller would not react to these oscillations.

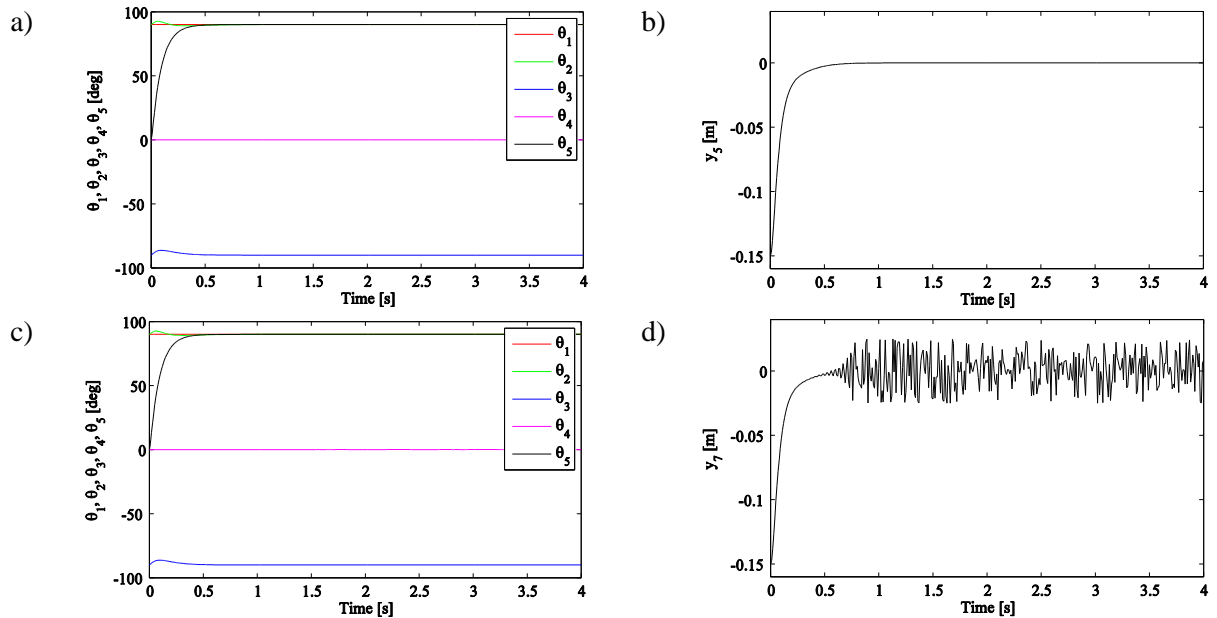


Fig. 3: Time histories of the manipulator: a) joint angles  $\theta_1, \dots, \theta_5$  (rigid 5th link), b) vertical position  $y_5$  of the TCP in the global coordinate system (rigid 5th link), c) joint angles  $\theta_1, \dots, \theta_5$  (flexible 5th link), d) vertical position  $y_7$  of the TCP' in the global coordinate system (flexible 5th link).

#### 4. Conclusions

The application of the presented rigid finite element method of modeling multibody systems can significantly accelerate the design process of novel laparoscopic tools for medical robotics. It has been demonstrated numerically that by using the method for the dynamics analysis of robotic SILS tools it is possible to evaluate their dynamic properties if the flexibility of links is assumed. This way the trajectory of the end effector can be tested in different loading conditions, for different geometric and material properties, etc. Control strategies for position controllers of the links can be also verified. The design process of the proposed SILS tool is underway and more accurate results will be presented soon.

#### Acknowledgement

This work was performed within the framework of statutory research of the Department of Automatic Control and Robotics at Bialystok University of Technology no. S/WM/1/2016 and financed with funds for science from the Ministry of Science and Higher Education, Poland.

#### References

- Wittbrodt, E., Adamiec-Wójcik, I. and Wojciech, S. (2006) Dynamics of flexible multibody systems. Rigid finite element method. Springer.
- Leniowski, R., Pajda, R., Leniowska, L. and Cieřlik, J. (2010) Design of a next generation multibody surgical manipulator. Scientific Papers of the Warsaw University of Technology, Electrotechnics, Robotics Problems 175 (1), pp. 63-78, (in Polish).
- Kruszewski, J., Sawiak, S. and Wittbrodt, E. (1999) Method of rigid finite elements in dynamics of construction. WNT, Warsaw, Poland (in Polish).
- Newmark, N.M. (1959) A method of computation for structural dynamics. ASCE Journal of Engineering Mechanics Division 85, pp. 67-94.

## ALTERNATIVE POSSIBILITIES OF BIAXIAL TESTING OF FIBER AND FABRIC MATERIALS IN NONSTANDARD CONDITIONS

P. Kulhavý\*, M. Syrovátková\*\*, M. Petru\*\*\*

**Abstract:** *The commonly used static uniaxial tensile tests don't describe the properties of materials based on fibers sufficiently therefore a biaxial test has been utilized. An important requirement is to conduct the test also at significantly higher speeds and under various climatic conditions; due to sensitivity of fibrous materials to climatic influences, in particular temperature and humidity. This is for existing testing devices point where we encounter two significant insufficiencies. Firstly they have limited speed and maximal loading force. Secondly, their use for testing under extreme climatic conditions is almost impossible due to their usually electronic control. The aim of this work was to propose appropriate experimental facilities using only two engines instead of the usually required four that would be able to work at higher speed, under climatic loading and in limited space. Based on these findings a testing mechanism that can be placed in an external box of climate chambers connected to a laboratory hydrodynamic-circuit has been created. This method utilizes a sliding displacement of the jaws controlled with inner forces in a tested sample and four springs. Increased sensitivity of fibrous materials to the speed of strain and climatic conditions were detected during following experiments. Compared with other used tests, the concept seems to be sufficiently precise.*

**Keywords:** Fibers, Biaxial loading, Multiaxial stress, Ortotropic materials, Climatic loading.

### 1. Introduction

The basic requirement for a successful design of a final product is the perfect knowledge of mechanical properties of used materials with under real conditions. For textile materials which show considerable anisotropy or orthotropy it is generally not sufficient to perform tests in one axis, it is necessary to load in two axes simultaneously. Because of the small thickness of fabrics the component of the stress in thickness direction of the material could be usually neglected, see Quaglini (2008), Seibert (2014). Technical textiles are typically subjected to plane stress conditions. For industrial materials containing fibres it is especially important to take into account the real ambient conditions occurring in real operations. In an effort be as close as possible to real condition in vehicle, with a significant climatic influence, it was necessary to do test in a climatic chamber with variable temperature and humidity. The climate changes in the textile material with significant sorption process, affecting their properties. For testing textiles the conditions are given in the standard. For orthotropic materials, which are loaded plane state of stress, it's possible to use following relationship:

$$\begin{bmatrix} \varepsilon_{11} \\ \varepsilon_{22} \\ 2\varepsilon_{12} \end{bmatrix} = \begin{bmatrix} \frac{1}{E_{11}} & -\frac{\mu_{21}}{E_{22}} & 0 \\ -\frac{\mu_{12}}{E_{11}} & \frac{1}{E_{22}} & 0 \\ 0 & 0 & \frac{1}{G_{12}} \end{bmatrix} \begin{bmatrix} \sigma_{11} \\ \sigma_{22} \\ \sigma_{12} \end{bmatrix} \quad (1)$$

Where  $E_{ij}$  are moduli of elasticity in the main directions of the material,  $G_{ij}$  are moduli of elasticity in shear and  $\mu$  is Poisson's ratio taking into account transverse contraction.

\* Ing. Petr Kulhavý: Institute for Nanomaterials, Advanced Technology and Innovation, Technical University of Liberec, Bendlova 1409, Liberec, Czech, petr.kulhavy@tul.cz

\*\* Ing. Martina Syrovátková: Institute for Nanomaterials, Advanced Technology and Innovation, Technical University of Liberec, Bendlova 1409, Liberec, Czech, martina.syrovatkova@tul.cz

\*\*\* Assoc. Prof. Ing. Michal Petru, PhD.: Institute for Nanomaterials, Advanced Technology and Innovation, Technical University of Liberec, Bendlova 1409, Liberec, Czech, michal.petru@tul.cz



The conditions for testing textile materials are given in the standard. The air temperature must be  $20\text{ }^{\circ}\text{C}$  and humidity of  $65 \pm 2\%$ . The fabric should be dried before the test and then placed in a precisely air conditioned environment for 12 – 24 hours.

## 2. Biaxial testing

As Reinhardt (1976) and Kawabata (1984) historically pointed at their works aimed to testing methods, textile materials are almost always burdened biaxially. In one axis tensile test in a longitudinal direction, there are typically main stress concentrators with a subsequent rupture formed at the site near the clamping jaws. In contrast, in transverse direction the stress is concentrated more equally in the centre of the sample. According to Escárpita (2012), for testing of biaxially loaded samples it is necessary to ensure that the test device meets the basic requirements. There must be strictly a tension or compression, avoiding spurious shear or bending loads. The orthogonality between the loading axis must be guaranteed throughout the entire test. Generally it is recommended to use hydraulic devices or mechanical system with linear motors, system of cables, pulleys and bearings.

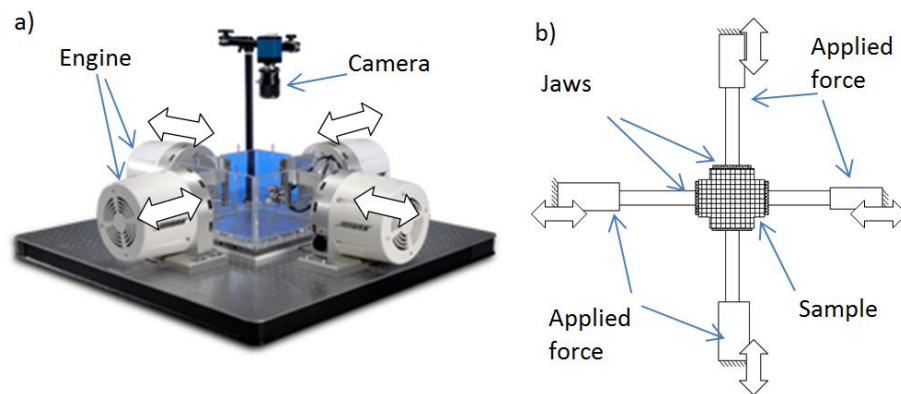


Fig. 1: Ideal and common case of static - biaxial testing device.

Fig. 1. shows the ideal and desired state simultaneous tension in all directions. To perform multiaxial tests in a climatic chamber, with significantly limited space, it is not possible to use any electric propulsion. With electric linear motors it is not possible to achieve the required strength and speed for dynamic testing. Use of the hydrodynamic circuit is a solution to the problem. Hydrodynamic parts are not so sensitive to ambient conditions and compared to pneumatic parts we obtain a more fluent running without steps, caused by compressibility of inner medium. When studying the literature, it is possible to find concepts that are incorrect as pointed e.g. Quagliny (2008), Kulhavy (2014) and Srb (2014) see (Fig. 2). In these cases the arising stress in the sample depends on increasing displacement and significantly changes the nature and distribution of forces.

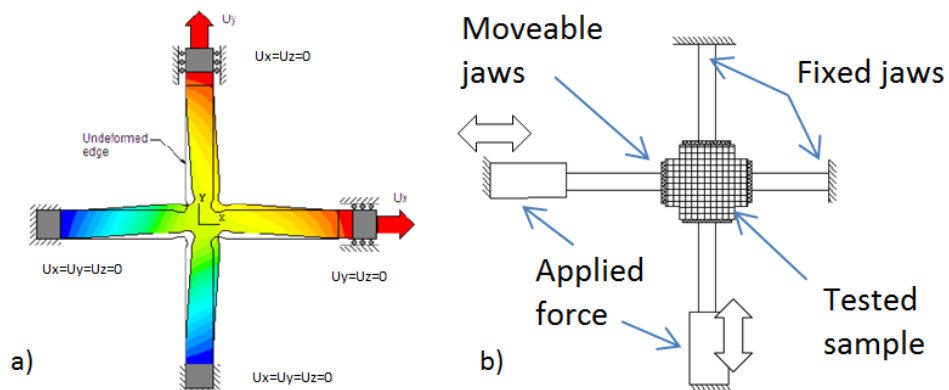


Fig. 2: Wrong simplified version of the test - an uneven loading.

## 3. Clamping device

A problem with using hydrodynamic devices in the climate box is the necessity to use simultaneously 4 horizontal engines. For this reason a concept that could have only two engines, but able to fulfill all the

prerequisites of biaxial testing, where the centre point of jaws connecting lines is still coincident, was sought.

A suitable variant may use sliding jaws with movement normal to the direction of the applied loading force (Fig. 3a), so that the required position is still adjusted. The results of this process are considerably better than in the variant of Fig. 2. Due to friction in the sliding bearing arising in the sample some shearing forces and as could be seen from the simulation, the stress distribution is not entirely appropriate. Design modification that can eliminate all these problems seems to be a mutual connection of the sliding jaws with springs (Fig. 3b). Due to constant rigidity of used springs, the forces ensure an almost ideal position during the entire course of the test. The Fig. 4a shows simulation for a case when the shear stress is transmitted through the textile sample. The situation when the "unwanted" force is transmitted by springs could be seen in the Fig. 4b. It is possible to see (Fig. 4) that the stress distribution is for the second concept better.

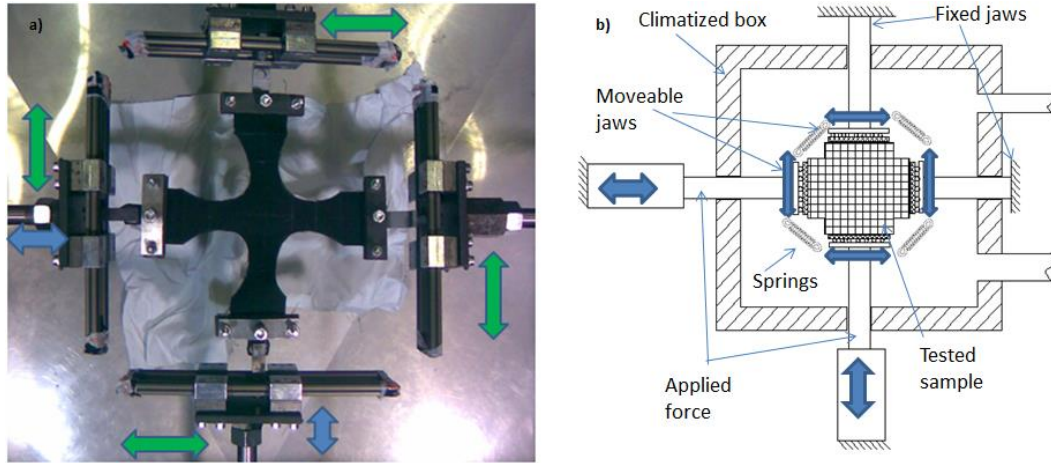


Fig. 3: Sliding jaws concepts: a) First - force transmission via textiles; b) Second –springs.

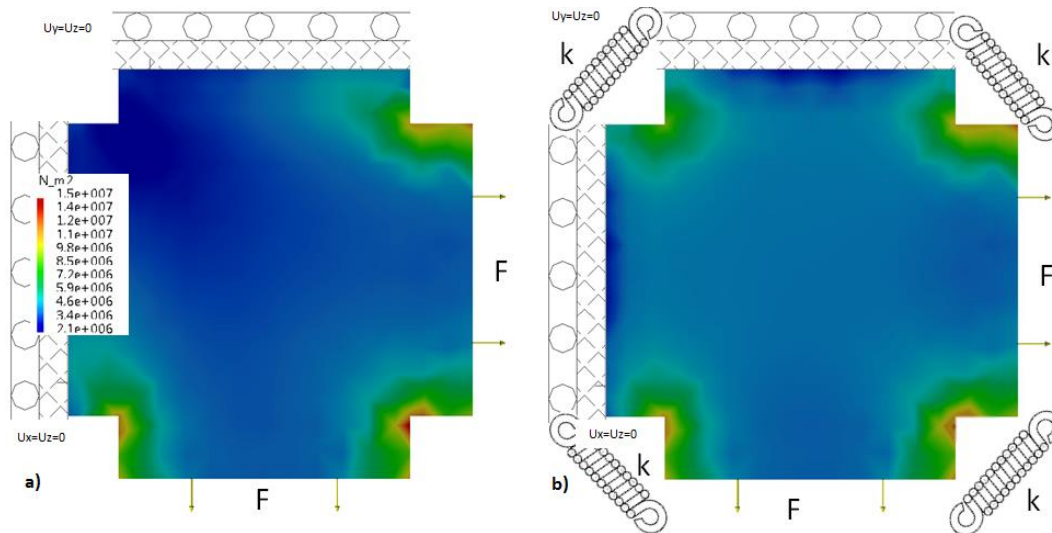


Fig. 4: Equivalent stress in the simulated models: a) Frictional variant; b) Variant with springs (displayed with a common scale).

#### 4. Experimental comparison

The graphs in Fig. 5 show the arithmetic average (5 pieces of samples for each of the three devices - ideal, shear sliding and springs) of individual measurements for the warp and weft directions. As can be seen, the "ideal" variant and concept with springs has a quite similar course. In the variant 2 where the symmetrical loading could not be guaranteed, the maximal force values are slightly lower. This is caused probably due to stress unilateral concentrations in the edges of fabric.

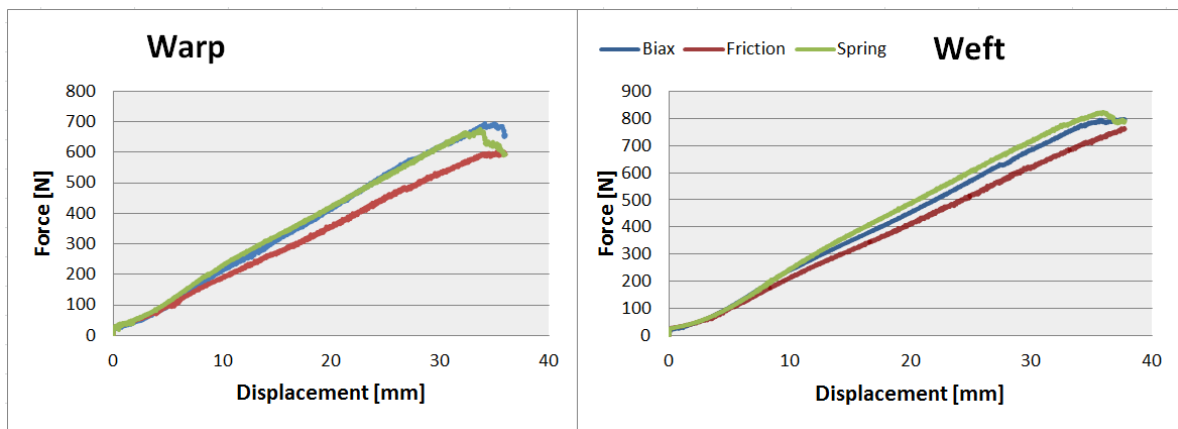


Fig. 5: Biaxial tension diagram of a tested fabric for the three tested concepts.

## 5. Conclusions

The presented work aimed to an alternative biaxial testing method, used primarily for fabrics and textile reinforcement materials such as composites and rubber. As has been mentioned in the introduction, are the common testing devices suitable mainly for static loads. For possibilities of dynamic testing also in a climatic chamber it was necessary to find a new design solution. It is suitable to use hydraulic motors, but an installation of four engines in a climatic chamber is technically very complicated. Some authors therefore solved this problem incorrectly by simultaneous two axial tension, when however as could be seen above, results may significantly vary. Therefore the mechanism with movable jaws, whose mutually position is adjusted by springs has been designed. This concept has been verified on some testing fabrics and compared with the other devices.

The tensile curve of the fabric has an almost linear character. The difference in the shape of the curves is because of different yarn density. The density of warp is usually higher and that is why the fabric in weft direction shows less tensile strength compared to warp direction. Strength of the fabric generally decreases, when humidity increases. This is because of the moisture absorption by the fibres and also by changing the value of friction between the fibres.

## Acknowledgement

The results of this project LO1201 were obtained with co-funding from the Ministry of Education, Youth and Sports as part of targeted support from the "Národní program udržitelnosti I" program.

## References

- Quaglioni, V., Corazza, C. and Poggi, C. (2008) Experimental characterization of orthotropic technical textiles under uniaxial and biaxial loading. *Composites Part A: Applied Science and Manufacturing*, Vol. 39, Iss. 8, pp. 1331-1342. DOI: 10.1016/j.compositesa.2007.07.008.
- Seibert, H., Scheffer, T. and Diebels, S. (2014) Biaxial Testing of Elastomers – Experimental Setup, Measurement and Experimental Optimisation of Specimen's Shape, *Technische Mechanik*, Vol. 34, Iss. 2, pp. 72-89.
- Reinhardt, H.W., Corazza, C. and Poggi, C. (1976) On the biaxial testing and strength of coated fabrics. *Experimental Mechanics*, Vol. 16, Iss. 2, pp. 71-74. DOI: 10.1007/BF02328607.
- Kawabata, S. and Niwa, M. (1984) Validity of the Linearizing Method for Describing the Biaxial stress-strain relationship of textile. The University of Shiga Prefecture.
- Escarrita, D., Koenders, E.A.B. and Carvalhod, B.F. (2012) Biaxial Tensile Strength Characterization of Textile Composite Materials. *Composites and Their Properties*. InTech, DOI: 10.5772/48705.
- Kulhavý, P., Kovalova, N., Martonka, R. and Petrik, J. (2014) Biaxial Stress of the Textile Car Seat Cover Tested in a Climatic Chamber. In: *ICMD 2014: Czech Republic Prague*: ISBN 978-80-01-05542-7.
- Srb, P. and Martonka, R. (2014) Mechanical Properties of Polyurethane Foam in Different Climate Conditions. In: *Modern methods of construction design: Proceedings of ICMD 2013*. ISBN 9783319052021.

## SEGMENTATION OF HUMAN MOTION ACCELERATION WITH PROBABILISTIC CLASSIFIER

P. Kumpán\*

**Abstract:** *This paper describes a method for signal segmentation in human motion analysis. Proposed method uses a probabilistic change point estimator combined with a Trigg's tracking signal for detection of changes in a signal variation and segmentation to the subsections by these change points. Main usage of this method is in fields of sport training or health condition monitoring but it can be also used in technical monitoring.*

**Keywords:** Signal segmentation, Change point detection, Motion analysis, Trigg's tracking signal.

### 1. Introduction

Detection of changes in time-series data is frequently solved task in the quality control, statistics and data mining for decades. Besides of alarm triggering, change points can be used for segmentation of acquired data into parts with similar properties.

If the nature of the signal changes significantly at some point in time, this point can be marked as the change point which separates two subsections of the signal, so called signal segments. These segments usually differ in some parameter of their probability distribution. Identifying changes in parameters of the probability distributions of points preceding and following the actual sample is usually called distributional change detection.

In motion analysis, various movement types like walking, running or jumping usually differs in the signal properties. With the use of a segmentation algorithm, data of these individual motions can be selected from the acquired dataset and processed separately.

### 2. Method

#### 2.1. Probabilistic change point estimator

Let's consider digital signal as the set of realizations of random variable which has a probability density function with the vector of parameters  $\theta$ . In most technical cases, probability density function follows a normal distribution  $N(\mu, \sigma^2)$  (Vechet et al., 2010). The vector of parameters consists of two elements – mean and variation –  $\theta = (\mu, \sigma^2)$ .

Finite set of samples  $X = \{x_1, x_2, \dots\}$  can be separated into  $K$  subsets. In the case of change point detection in acceleration, the subsets mainly differ in a variation  $\sigma_k^2$ . Mean value  $\mu_k$  of each segment is very close to zero, so its changes are not tracked and probability density function is considered symmetric around zero.

The elements of the  $k$ th segment can be expressed as the realization of the random variable with normal distribution  $N(0, \sigma_k^2)$ . The task is to find the  $n$ th sample, which separates segments  $k$  and  $k+1$ . The change occurs, when the preceding points have different probability density function then the followings.

The probability, that point  $x$  follows the probability density function with zero mean and variance  $\sigma^2$  is expressed with a function  $p(x, \sigma)$  according to equation (1).

---

\* Ing. Pavel Kumpán: Institute of Solid Mechanics, Mechatronics and Biomechanics, Faculty of Mechanical Engineering, Brno University of Technology, Technická 2896/2; 602 00 Brno; CZ, Pavel.Kumpán@vutbr.cz

$$p(x, \sigma) = e^{-\frac{x^2}{\sigma^2}} \quad (1)$$

The probability of change  $L_k$  for  $k$ th sample of the signal  $X$  can be expressed with the change estimator  $\hat{w}(x)$ . A logarithmic density ratio is a good estimate of change (Sugiyama, 2015). This estimator is described with equation (2) as a log-ratio of two probabilities – whether sample  $X_k$  follows probability density function of the following or preceding samples. Due to the shape of the logarithmic function around zero, this estimator provides sensible detection of small changes but is also prone to be sensitive to outliers.

$$L_k = \ln \frac{p(X_k, \sigma_1)}{p(X_k, \sigma_0)} \quad (2)$$

In this equation,  $\sigma_0$  represents standard deviation of the preceding points and  $\sigma_1$  is the standard deviation of the following points. Standard deviations are computed from the finite windows of length  $H = 50$ .

The value of  $L_k$  is close to zero for similar p-values – this refers to the fact, that the preceding and following points have similar statistical parameters.  $L_k$  is positive for a higher likelihood of increasing the variation and negative for decreasing. Due to the large variations in scale of  $L$  caused by the logarithmic function, simple thresholding cannot be used.

## 2.2. Change point evaluation with use of the tracking signal

Many statistical quality control techniques are used in a field of economics, technical monitoring, medical applications (Blackwell et al., 1992) and others for decades. One of them is the Trigg's tracking signal, which is widely used especially in forecasting and change detection in processes monitoring. Trigg defined the tracking signal TTS as (Trigg et al., 1967)

$$TTS_n = \frac{SFE_n}{MAD_n} \quad (3)$$

where  $SFE$  represents exponentially smoothed forecast error. This one is recursively defined with adjustable smoothing parameter  $\alpha$  according to equation (4). A decent value of  $\alpha$  in this study is 0.2, which provides an acceptable compromise between detection delay and smoothing.

$$SFE_n = \alpha \cdot FE_n + (1 - \alpha) \cdot SFE_{n-1} \quad (4)$$

The probability of change  $L_k$  is used as the forecasting error  $FE_k$ . Mean absolute deviation ( $MAD$ ) represents the exponentially smoothed absolute forecast error according to equation (5).

$$MAD_n = \alpha \cdot |FE_n| + (1 - \alpha) \cdot MAD_{n-1} \quad (5)$$

Because of its definition as ration,  $TTS$  takes the values of interval  $[-1, 1]$ .  $TTS$  zero-crossing is the sign of change in the input signal. For consecutive segments, which parameters are changing monotonously, the tracking signal will approach the theoretical minimum or maximum. This is the main disadvantage, which makes monotonous changes detection very difficult, even impossible.

## 2.3. Change point detection in acceleration

The proposed method was used for a segmentation of a human motion acceleration measured with the inertial MEMS sensor. Because of the character of human motion, the signal segments differ mainly in variance and changes in mean value of acceleration are insignificant. This property can be even amplified with the use of acceleration derivation – the jerk  $j(t)$  – instead of acceleration. Because of discrete nature of the signal, jerk is obtained with numerical derivation according to equation (6).

$$j_n = \frac{a_n - a_{n-1}}{\Delta t} \quad (6)$$

## 3. Results

Fig. 1 displays a forward acceleration of front crawl swimmer. Data were acquired during one swimming pool length using MEMS accelerometer with 100 Hz sample rate. Data were pre-processed and the influence of gravity field was removed.

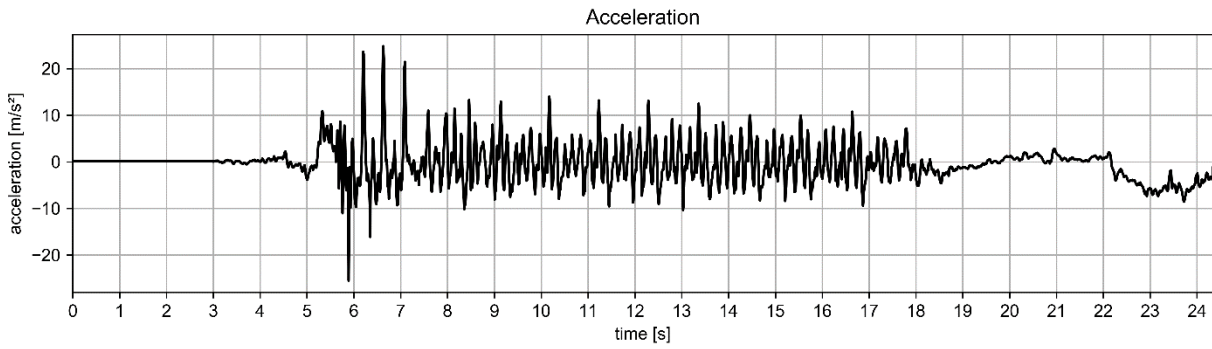


Fig. 1: Forward acceleration of the front crawl swimmer.

The first graph of Fig. 2 shows a jerk obtained as numerical differentiation of the forward acceleration. Jerk was processed by running average filter with a length of 3 samples for outliers removal. The second graph displays the value of change estimation expressed log-ratio  $L$ . The third graph shows the Trigg's tracking signal with change points marked with blue points.

The criterion of minimal distance between two changes was used for suppressing of false-positive detection. Change point is accepted only if the criterion of minimal distance  $t = 0.25$  s from the preceding point is met.

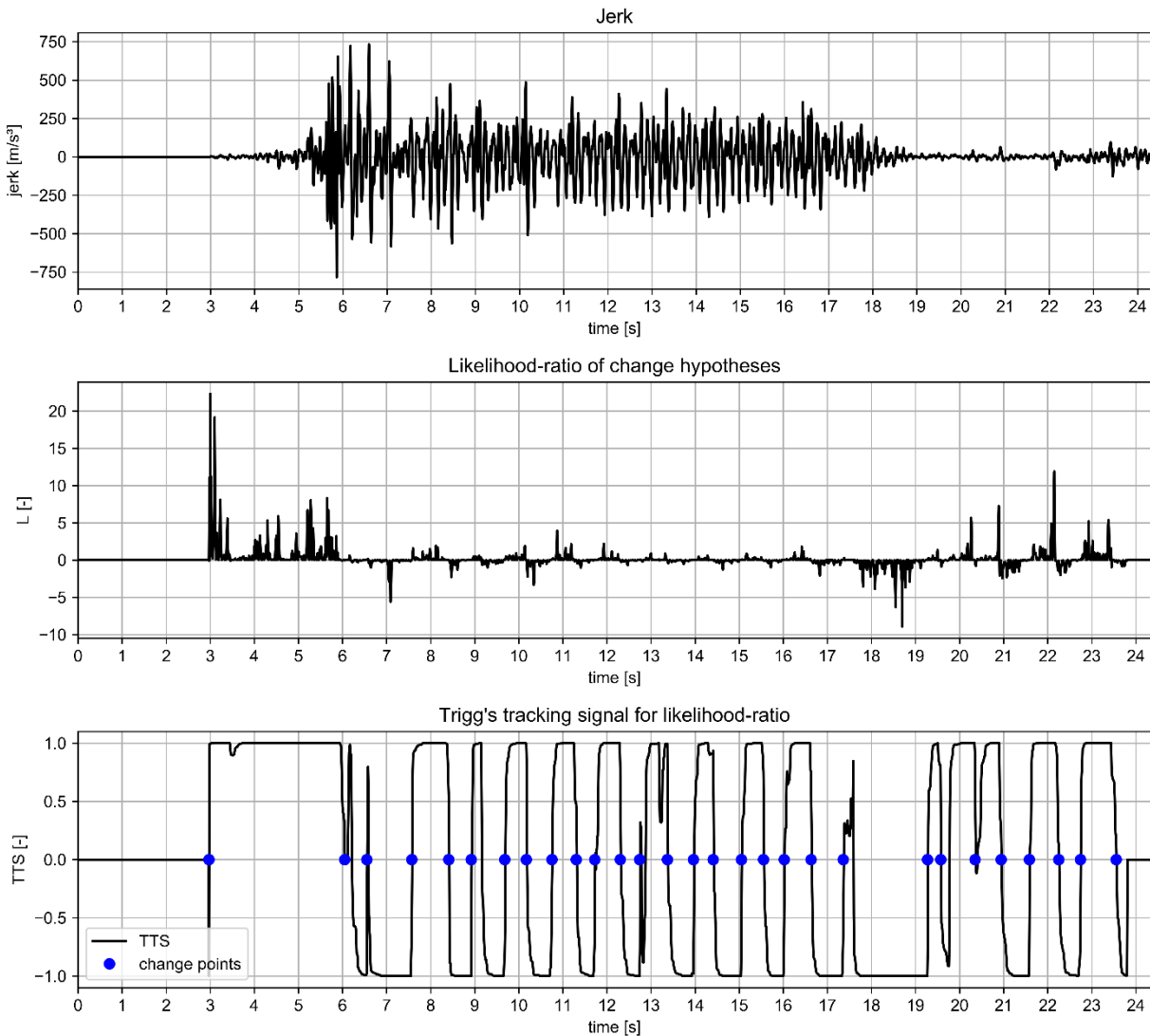


Fig. 2: Jerk obtained as derivation of swimmer's forward acceleration, it's log-likelihood of change and Trigg's tracking signal of the log-likelihood. Blue points mark detected change points.

In Fig. 3, the output set of change point is showed. Blue vertical lines separate detected segments, which differs in jerk variation. It can be seen, that signal segments between time 7 – 18 s are in a good match



with swimmer's arm strokes. The second graph of the Fig. 3 provides a comparison with an angular velocity measured with gyroscope in perpendicular axis. Change point at time 6.5 s is a typical example of false-positive change detection error. It can be seen, that change in TTS is for this change point very narrow. From the previously described reasons, the algorithm cannot detect consecutive segments with monotonously increasing or decreasing variation.

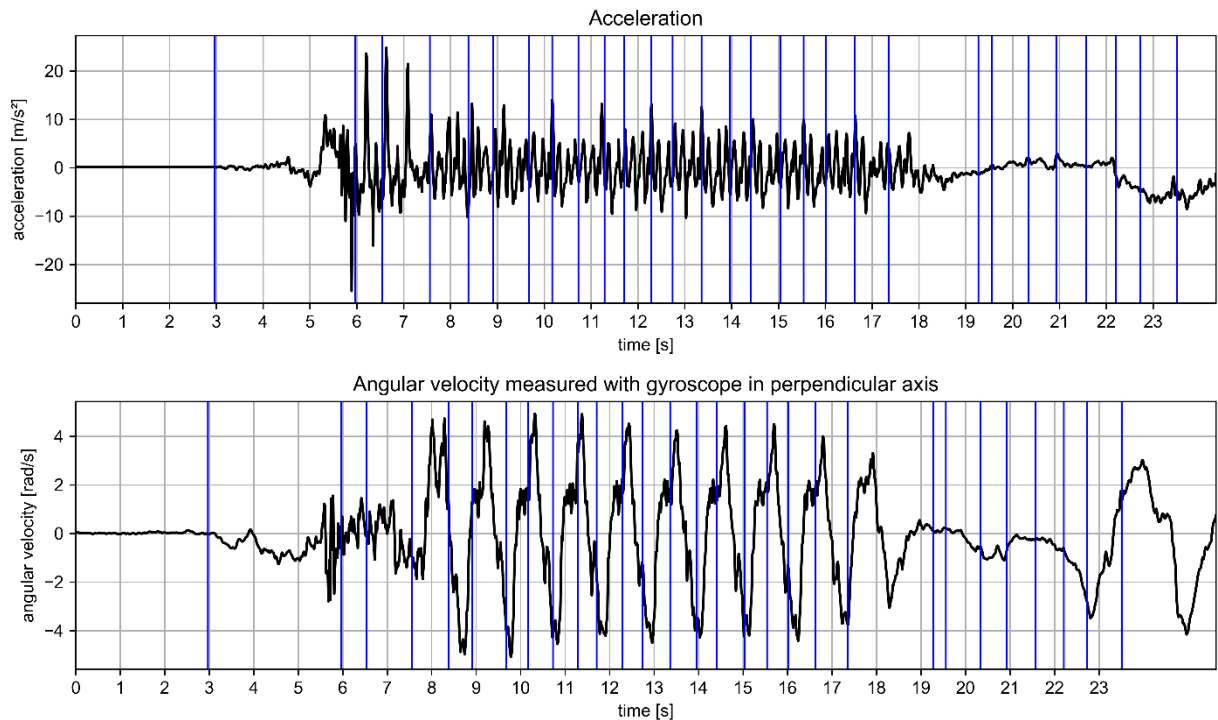


Fig. 3: Acceleration data with marked segments. The lower graph displays the angular velocity measured in perpendicular axis for evaluation of the arm-stroke detection.

#### 4. Conclusions

This paper presented the method for segmentation of human motion acceleration. This method combines probabilistic change estimator with a Trigg's tracking signal for change detection in obtained motion data variation. The method was demonstrated on the segmentation of swimmer's acceleration into individual arm strokes. The results show sensitivity of proposed method. For further development, it would be appropriate to eliminate false-positive detections with an use of advanced probabilistic change estimator.

#### Acknowledgement

Published results were acquired with the support of the project FSI-S-14-2204 Research and development of mechatronics system with the application of "Model Based Design".

#### References

- Blackwell, L.F. and Brown, J.B. (1992) Application of time-series analysis for the recognition of increases in urinary estrogens as markers for the beginning of the potentially fertile period. *Steroids*, 57(11), pp. 554-562. DOI: 10.1016/0039-128X(92)90025-5.
- Granjon, P. (2013) The CuSum algorithm: a small review. <https://hal.archives-ouvertes.fr/hal-00914697>
- Sugiyama, M. (2015) *Introduction to Statistical Machine Learning*. Elsevier. ISBN 9780128021217.
- Trigg, D.W. and Leach, A.G. (1967) Exponential Smoothing with an Adaptive Response Rate. *Journal Of The Operational Research Society*, 18(1), pp. 53-59. DOI: 10.1057/jors.1967.5.
- Vechet, S., Krejsa, J. and Ondrousek, V. (2010) Sensors Data Fusion via Bayesian Filter. *Proceedings of 14th International Power Electronics and Motion Control Conference (Epe-Pemc 2010)*. DOI: 10.1109/Epepemc.2010.5606874. WOS:000319521600289.

## EFFECT OF LOOP DIAMETER ON TWO-PHASE NATURAL CIRCULATION LOOP PERFORMANCE

K. K. Kupireddi<sup>\*</sup>, S. V. Sai Sudheer<sup>\*\*</sup>, K. Balasubramanian<sup>\*\*\*</sup>

**Abstract:** *This paper aims to present the effect of loop diameter on steady state performance of the two-phase rectangular natural circulation loop (NCL). A one dimensional homogeneous equilibrium model is developed to estimate the two-phase pressure drop across each section of the loop. Thermophysical properties and state properties are considered at local pressure. Uniform heat flux is applied at both evaporator and condenser sections. Mass flux is obtained by solving loop momentum equation using iterative procedure. Results are presented for different loop diameters under same heat load, gravitational head and fluid quantity. The effect of the loop diameter on the mass flow rate is also analysed.*

**Keywords:** Two phase, Natural Circulation Loop (NCL), Mass flow rate, Homogeneous equilibrium model, Quality.

### 1. Introduction

In the present scenario, effective utilization of energy plays prominent/important role in day to day life. versatile needs of energy, demands various transporting mechanisms. Among many methods adopted for different industrial and commercial applications, Forced Circulation Loops (FCLs) and NCLs play key role in the vicinity of energy transport. The fluid circulation can be attained either by external power sources like pumps or by the natural circulation due to buoyancy. In natural circulation, thermally developed density gradients are the driving force. One cannot rely on the external source to run the loop for longer period. Therefore, NCL is a lucrative choice. In NCL, riser and down comer connects the source and sink for energy transfer. Simplicity in configuration and reliability in performance grabs the attention of researchers to make it useful for diversified applications like cooling of nuclear reactor, gas turbine blades, solar heaters, and waste heat recovery boilers so on (Close 1962; Hagen et al., 1997; Heisler 1982; Shitzer et al. 1979).

Based on the state of working fluid NCLs can be either single phase or two phase. Two-phase NCLs have advantages over single phase NCLs due to large density gradients across the loop.

From the past few decades, different analytical approaches are reported in the literature to study the performance of two phase NCL. Thermally equilibrium based homogeneous model (Chen et al., 1988; Rao et al., 2006) and drift flux models (Rao et al., 2006; Jeng et al., 1999) and one dimensional two fluid model with thermodynamic non equilibrium Basu et al. (2009) are developed to analyze the loop. The present work, aims to develop a model to study the performance of two phase NCL with one-dimensional approach. Pressure drop in two phase regions is estimated by using homogeneous equilibrium model. Viscosity of two phase mixture is estimated based on correlation developed by McAdams et al. (1942). The effect of diameter on loop performance is also analyzed.

### 2. Mathematical Modeling

Fig. 1 shows the schematic representation of two phase NCL considered for the analysis. A uniform cross sectional rectangular loop is considered. Evaporator and condenser sections are positioned on horizontal arms at an elevation difference to add the favorable gravity gradients to the loop fluid. Constant heat flux

---

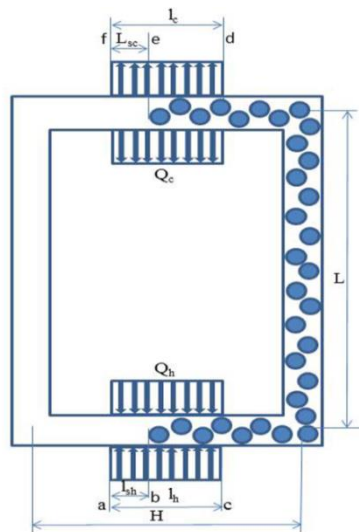
<sup>\*</sup> Dr. Kiran Kumar K, PhD.: National Institute of Technology Warangal- 506004, India, kiran@nitw.ac.in

<sup>\*\*</sup> S. Venkata Sai Sudheer: National Institute of Technology Warangal- 506004, India, svssnitw@gmail.

<sup>\*\*\*</sup> Dr. Karthik Balasubramanian, PhD.: National Institute of Technology Warangal- 506004, India, karthik@nitw.ac.in

boundary condition is considered at evaporator and condenser sections. Based on the loop fluid state the loop is categorized into six regions which are represented in Fig. 1 and Tab. 1.

Nomenclature			
A	Flow cross sectional area, m <sup>2</sup>	D	Diameter, m
G	Mass flux, kg/m <sup>2</sup> s	g	Acceleration due to gravity, m <sup>2</sup> /s
h	Enthalpy, kJ/kg	H	Length of horizontal arm, m
$\Delta h$	Change in enthalpy at evaporator, kJ/kg	L	Loop height, m
$l_{sh}$	Sub cooled length in evaporator, m	$l_h = l_{evap}$	Heater length, m
$l_{sc}$	Sub cooled length in condenser, m	$l_c = l_{cond}$	Cooler length, m
$\dot{m}$	Mass flow rate, kg/s	p	Pressure, bar
P	Heat load, kW	$dp/ds$	Pressure gradient, N/m <sup>2</sup>
$Q_h$	Heat input per length, kW/m <sup>2</sup>	$Q_c$	Heat flux at condenser, kW/m <sup>2</sup>
s	Space coordinate, m	$v$	Specific volume, m <sup>3</sup> /kg
$x$	Dryness fraction	$v_{bar}$	Mixture specific volume, m <sup>3</sup> /kg
Subscripts			
a	Acceleration	avg	Average
f	Saturated liquid/frictional	g	Saturated gas (vapour)
fg	Difference between gas (vapour) and liquid properties at saturated state	tp	Two phase
i	Inlet		
$\mu$	Viscosity, kg/m.s		



Tab. 1: Loop regions.

S.No	Regions	Zone description
1	a-b	sub-cooled heating region
2	b-c	vaporization region
3	c-d	adiabatic two-phase region
4	d-e	condensation region
5	e-f	sub-cooled cooling region
6	f-a	adiabatic single phase region

Fig. 1: Schematic diagram of a two phase NCL.

The following assumptions are made to simplify the solution.

1. Bulk temperature of the loop fluid reaches saturation temperature in the evaporator section.
2. Thermo physical properties are considered at local pressure only instead of system pressure.
3. Loop is perfectly insulated.
4. Minor losses in the loop neglected.
5. Quality in the loop linearly varies.
6. Flow is in counter clockwise direction.

The mass flow rate, heat transfer rate and pressure drop in the loop are inter related. Loop mass flow rate is evaluated by iterative procedure. Since the total pressure drop in NCL is zero, the one dimensional momentum equation of loop by considering frictional, gravitational and acceleration pressure drop is as follows

$$\oint \left( \frac{dp}{ds} \right)_f ds + \oint \left( \frac{dp}{ds} \right)_g ds + \oint \left( \frac{dp}{ds} \right)_a ds = 0 \quad (1)$$

The pressure drop in each section of the loop is tabulated in Tab. 2.

Tab. 2: Pressure drop at various sections of loop.

Regions	Friction pressure drop	Gravitational pressure drop	Acceleration pressure drop
ab	$\frac{2C_{foavg}G^2v_{avg}l_{sc}}{D}$	0	$G^2(v_f - v_{fi})$
bc	$\frac{2C_{f\overline{tp}}G^2v_{\overline{avg}}(l_{evap}-l_{sc})}{D}\left(1 + \frac{x}{2}\frac{v_{fg}}{v_f}\right)$	0	$G^2v_{fg}x$
cd	$\frac{2C_{f\overline{tp}}G^2v_{bar}(H - l_{evap} + L)}{D}\left(1 + x\frac{v_{fg}}{v_f}\right)$	$\frac{gL}{v_{bar}}$	0
ef	$\frac{2C_{f\overline{tp}}G^2v_{\overline{avg}}(L_{cond}-l_{sc})}{D}\left(1 + \frac{x}{2}\frac{v_{fg}}{v_f}\right)$	0	$-G^2(v_f - v_{fi})$
fa	$\frac{2C_{foavg}G^2v_{avg}(H - l_{cond} + L)}{D}$	$\frac{gL}{v_{fi}}$	0

Where  $C_{favg}$ ,  $v_{avg}$  are the average of the properties at inlet and saturation state of the liquid.

$C_{f\overline{tp}}$  &  $v_{\overline{avg}}$  are average of the properties at quality 0 and x

Appropriate energy balance equations are applied at every section to find the lengths.

### 3. Result and discussion

By keeping the mass of the loop and height of the loop constant, the required diameter, horizontal section length and heat section length are derived. These values are shown in Tab. 3. Fig. 2 shows the effect of diameter on loop mass flow rate for different heat inputs. As the heat flux increases mass flow rate increases up to certain limit and then after decreases. As diameter increases mass flow rate increases and the peak value is shifted to right. This happens because of the quality and pressure drop in the riser section.

Tab. 3: Two phase NCL configuration.

Diameter [m]	Horizontal section length [m]	Height of the loop [m]	Heating section length [m]
0.01225	1.5098	2	0.5408
0.01325	1	2	0.5
0.01425	0.5937	2	0.4649

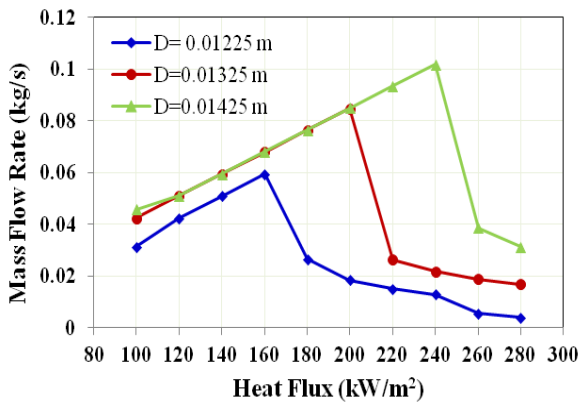


Fig. 2: a) Effect of diameter on loop mass flow rate.

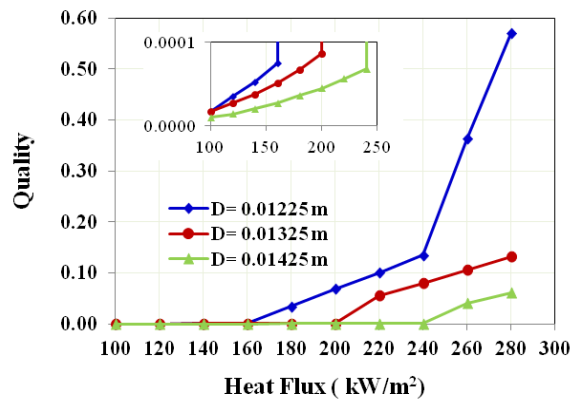


Fig. 2: b) Effect of diameter on loop quality.

Fig. 2b shows the variation of quality in the loop. In homogeneous 1D modeling, quality is estimated as the area averaged value. As diameter increases the evaporator length decreases, even though the fluid quantity in the evaporator increases. Thus, for the same amount of heat flux supplied at evaporator, exit quality of loop fluid decreases and higher quality can be obtained at higher heat fluxes. Fig. 3 shows the two phase pressure drop in the loop for different diameters. As loop diameter increases the friction loss and quality reduces. The decrease in quality provokes gravitational head in the riser. Hence the overall two phase pressure drop increases.

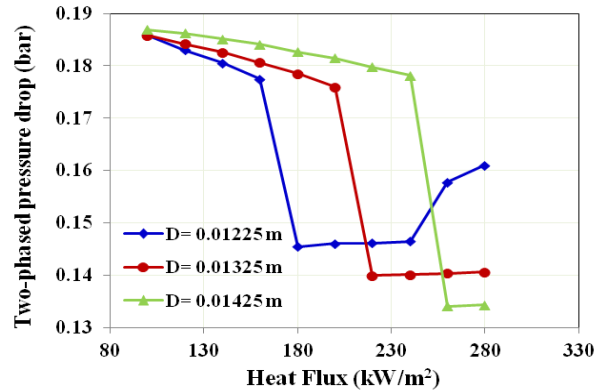


Fig. 3: Two phase pressure drop in the loop at different heat flux.

#### 4. Conclusions

The steady state performance of a two phase natural circulation loop by varying loop diameter is analysed. One dimensional homogeneous model is used. Loop steady state solution is obtained in terms of mass flux by solving the momentum equation. The following important findings are noted during the analysis

- NCLs performance is strongly affected by loop diameter.
- For a particular loop height and quantity of loop fluid, loop diameter has significant influence on quality.

#### Acknowledgement

The present work is carried out under a project sponsored by Department of Atomic Energy, Board of Research in Nuclear sciences (BRNS), Government of India. The financial support offered by BRNS is gratefully acknowledged.

#### References

- Basu, D.N., Bhattacharyya, S. and Das, P.K. (2009) Steady-State Behavior of a Two-Phase Natural Circulation Loop With Thermodynamic Nonequilibrium. *Journal of Heat Transfer*, 131(2), p. 22901.
- Chen, K.S. and Chang, Y.R. (1988) Steady-state analysis of two-phase natural circulation loop. *International Journal of Heat and Mass Transfer*, 31(5), pp. 931-940.
- Close, D.J. (1962) The performance of solar water heaters with natural circulation. *Solar Energy*, 6(1), pp. 33-40. Available at: <http://www.sciencedirect.com/science/article/pii/0038092X62900968>.
- van der Hagen, T.H.J.J., van Bragt, D.D.B., van der Kaa, F.J., Killian, D., Wouters, J.A.A., Karuza, J., Nissen, W.H.M., Stekelenburg, A.J.C. (1997) Exploring the Dodewaard Type-I and Type-II stability: from start-up to shut-down, from stable to unstable. *Annals of Nuclear Energy*, 28(12), pp. 659-669.
- Heisler, M.P. (1982) Development of scaling requirements for natural convection liquid-metal fast breeder reactor shutdown heat removal test facilities. *Nuclear Science and Engineering*, 80, pp. 347-359.
- Jeng, H.R. and Pan, C. (1999) Analysis of two-phase flow characteristics in a natural circulation loop using the drift-flux model taking flow pattern change and subcooled boiling into consideration, *Annals of Nuclear Energy*, 26.
- McAdams, W.H., Woods, W.K. and Heroman, L.C.J. (1942) Vaporization inside horizontal tubes -- II, benzene oil mixtures. *American Society of Mechanical Engineers -- Transactions*, 64(3), pp. 193-200. Available at: [papers3://publication/uuid/452AB06E-0E4D-44DF-A9CB-AE059AE75774](https://papers3://publication/uuid/452AB06E-0E4D-44DF-A9CB-AE059AE75774).
- Rao, N.M. et al. (2006) Steady-state performance of a two-phase natural circulation loop. *International Communications in Heat and Mass Transfer*, 33(8), pp. 1042-1052.
- Shitzer, A. et al. (1979) Experiments with a flat plate solar water heating system in thermosyphonic flow. *Solar Energy*, 22(1), pp. 27-35.

## **ANALYSIS OF CERAMIC-METALLIC COMPOSITES OF BALLISTIC RESISTANCE ON SHOTS BY 5.56 MM AMMUNITION**

**A. Kurzawa<sup>\*</sup>, M. Bocian<sup>\*\*</sup>, K. Jamroziak<sup>\*\*</sup>, D. Pyka<sup>\*\*\*</sup>**

**Abstract:** *This paper presents a portion of the work focused on the development of innovative, lightweight composite materials with the prospect of constructing modern ballistic shields. The aim of the study was to determine the reinforcement of the ballistic resistant materials by the introduction of  $Al_2O_3$  particles in the aluminum alloy matrix. Tests were performed on composites prepared by compression in a liquid-state based on an alloy of AC-44200 with the addition of  $Al_2O_3$  particles. Produced materials were tested on the ballistic test field, subjecting them to shots of 5.56 mm by a Beryl rifle, Polish production. Damaged materials were subjected to metallographic analysis and identification of the destruction process. From the presented analysis and test results, we can conclude that tested materials with the participation of interpenetrating phases: plastic (matrix) and fragile (reinforcement) can be an attractive alternative to currently used materials.*

**Keywords:** Composites, Fracture Mechanics, Mechanical Properties, Cermets, Ballistic Impact.

### **1. Introduction**

The progress of materials science is focused on the search for new material solutions. In this context the energy-intensive materials play a significant role, their objective is primarily to disperse as much impact energy as possible. In this regard, military technologies take an important part. Based on analysis (Hazell, 2006) it is shown that in the second half of the twentieth century, there was a significant increase in the participation of innovative composite material sets in the production of ballistic protection systems. In this way, mobility of military vehicles and the passive safety of the crews were highly increased (Hogg, 2003). Constant competition between the development of projectiles and armor drives the progress in search of different solutions. Understanding the mechanisms of the destruction of ballistic structures or their weight reduction (Abrate, 2009 and Demir et al., 2008) allows the development of better and more efficient ballistic shields. In earlier work authors (Bocian et al., 2015) sought optimal solutions of material composition while describing the mechanism of destruction of composite structures considering mathematical models.

In this study, the main focused is on materials which parameters are characterized as ballistic ceramic but with improved mechanical properties. In this way, the process of searching for effective ballistic shielding, which are resistant to penetration by rifle bullets containing hard cores, as a replaced for steel armor can be performed.

### **2. Recognition of the problem**

The process of fracture in the ceramic material is related to fracture propagation. Scheme of the destruction for critical conditions at released energy are presented in the form:

---

<sup>\*</sup> Asst. Prof. Adam Kurzawa, DSc., Ing.: Department of Foundry, Plastics and Automation, Wrocław University of Science and Technology, Smoluchowskiego 25; 50-370, Wrocław; PL, adam.kurzawa@pwr.edu.pl

<sup>\*\*</sup> Asst. Prof. Mirosław Bocian, DSc., Ing.: Department of Mechanics, Materials Science and Engineering, Wrocław University of Science and Technology, Smoluchowskiego 25; 50-370, Wrocław; PL, miroslaw.bocian@pwr.edu.pl

<sup>\*\*</sup> Assoc. Prof. Krzysztof Jamroziak, DSc., Ing.: Department of Mechanics, Materials Science and Engineering, Wrocław University of Science and Technology, Smoluchowskiego 25; 50-370, Wrocław; PL, krzysztof.jamroziak@pwr.edu.pl

<sup>\*\*\*</sup> Eng. Dariusz Pyka, PhD Student: Department of Plastic and Metrology, Wrocław University of Science and Technology, Lukasiewicza 5; 50-371, Wrocław; PL, pykadariusz@gmail.com



$$G_{IC} = \frac{(1-\nu^2)K_{IC}}{E} = 2\gamma_F \quad (1)$$

where:  $\gamma_F$  – surface fracture energy,  $E$  – Young's modulus,  $\nu$  – Poisson's ratio,  $K_{IC}$  – brittle fracture toughness.

Microcracks in the ceramic structures are accompanied by absorption of part of the energy by fracture propagation, identified in the equation:

$$\gamma_F = \gamma_0 \left( 1 - \frac{d}{d_s} \right) + \gamma_p \quad (2)$$

where:  $\gamma_0$  – surface fracture energy of polycrystalline in the absence of microcracks for  $d \leq 1 \mu\text{m}$ ,  $d_s$  – grain size at which there is a spontaneous development of a fracture.

The energy absorbed by the microcracks ( $\gamma_p$ ) identified in the equation:

$$\gamma_p = qW_p \quad (3)$$

where:  $q$  – number of microcracks per unit of area,  $W_p$  – average energy absorbed by one microcrack.

In this case, the process of destruction of the material is related to the kinetic energy of the projectile. It was assumed that the overall energy of the projectile is converted into plastic deformation of the projectile and into the process of material fracture. If the projectile is fragmented it must be taken into consideration in the equation as fragments velocity.

Thus, the deformation energy can be written as the product of force and displacement:

$$U = \int_{L_0}^L F dl \quad (4)$$

where:  $L_0$  – length/initial diameter,  $L$  – length/final diameter,  $F$  – force used for deformation,  $U$  – work done per unit of material volume to achieve strain, it is equal to the area under the strain curve – on the assumption that  $v_{mat} = \text{const}$ .

### 3. Objective and scope of the study

Tests were done on newly developed material based on aluminum AC-44200 containing ceramic particles of  $\text{Al}_2\text{O}_3$  (Kurzawa et al., 2015). Materials prepared for the study contain 20 % and 40 % of reinforcing particles in their volume. Samples prepared for firing had a cylindrical shape of a diameter of 120 mm and a height of 14 mm (Fig. 1). Due to the different reinforcing particle content materials had a hardness of 70 HB to 150 HB. Samples were shot with 5.56 mm SS109 ammunition according to the methodology specified by the standard (CEN EN 1522). Destroyed samples (Fig. 2) were subjected to metallographic examination and the analysis of impact energy absorption. This paper attempts to describe the process of damage development and attempts to determine the work necessary to destroy the sample



Fig. 1: A general view of a cermet sample.



Fig. 2: Sample after firing.

### 4. Results and analysis

The results of ballistic tests were registered as the records of the sample destruction process. Based on the analysis of the destruction process and the models described in the literature (Feli et al., 2010 and Nayak et al., 2013) with the focus of comparing effective work of destroying the material to such an extent as to

maximize dispersion of the impact energy in a layer at the cermet front, provided for a multi-layered ballistic shield (projectile blunting, its fragmentation) and increase the local absorption-area of this energy in the composite layer based on fibrous materials (Kevlar, Twaron, etc.). Based on the research and the observation of measured velocity of the projectile by the means of the Doppler Weibel SL-525PE radar, parameters at the time of the collision were estimated, change in the speed after hitting the target and its change in volume (Fig. 3).

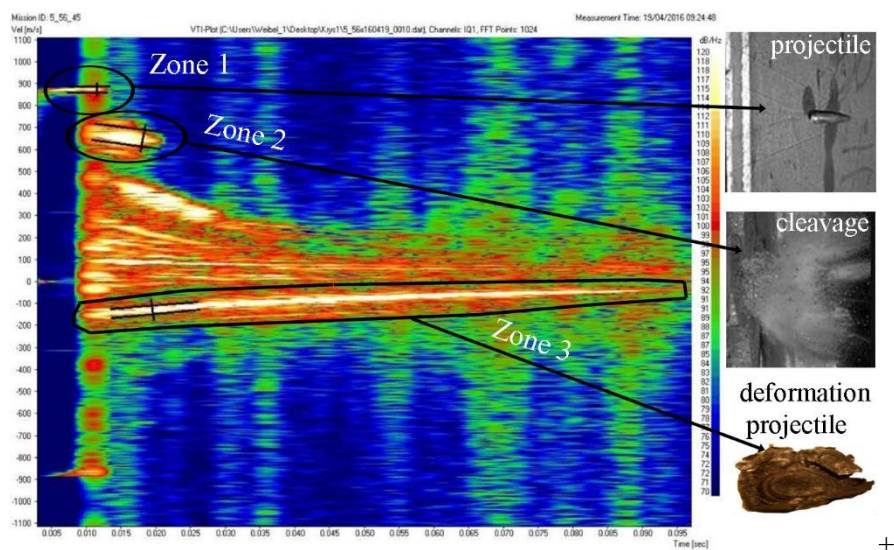


Fig. 3: Image of the projectile velocity obtained in the WinDopp software with projectile fragments for a sample of AC-44200 with 30 % of  $Al_2O_3$ .

From charts obtained by the radar field range, the size of the deformed projectile can be specified. For the sample containing 30 % of alumina, a projectile of a diameter of 5.56 mm defines a trace of 1.5 mm width (Zone 1), and measuring traces for the fragments on the graph (9.5 mm) an outlet diameter of 35 mm is obtained (Zone 2), as confirmed by visual inspection of the sample (e.g. see Fig. 2). The bandwidth for the deformed projectile is 3.5 mm (Zone 3), which gives a distorted field of 12.5 mm. By estimating the size of the projectile deformation it is possible to estimate the amount of dispersed energy in the process of energy absorption by the tested sample. The sample surface in the vicinity of major fractures that occur as a result of firing as well as breakthrough fracture are subjected to metallographic examination. SEM images were used for the description of the mechanics of the samples destruction after projectile impact. As shown in Fig. 4 as a result of acting forces the sample will fracture in a perpendicular direction to the projectile path. Fracture is a type of a mixed breakthrough with a predominance of a brittle fracture. Observations indicate that the destruction of the material follows the outline of  $Al_2O_3$  particles and it was less likely to follow the reinforced particle. Within damaged area a slight plastic flow of the material also occurs, as indicated by the distribution of the reinforced strip regions of the sample in a direction parallel to the trajectory of the projectile (Fig. 5). Such a deformation occurs mainly in composites of 20 % by volume, of  $Al_2O_3$  particles. The advantage of brittle fracture is observed in samples of 40 % by volume of reinforcing particle.

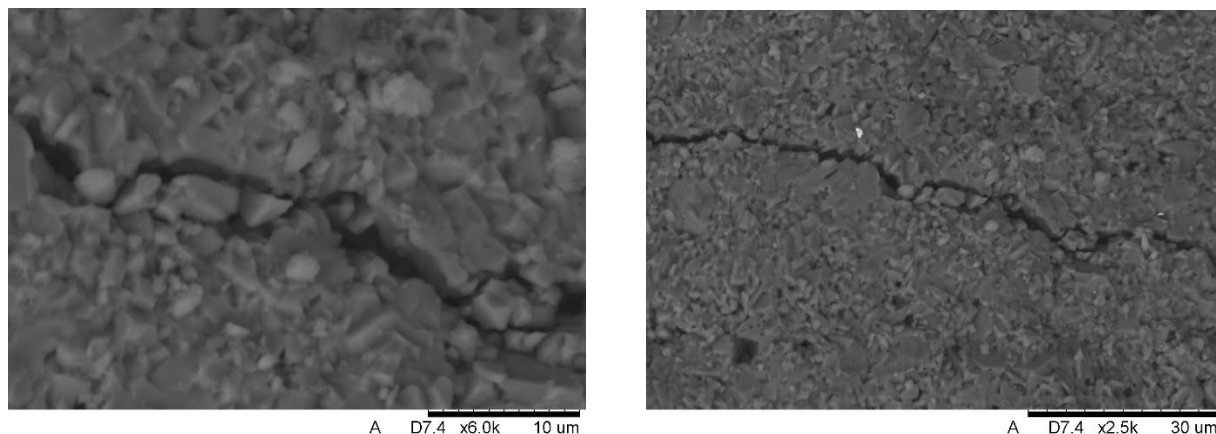
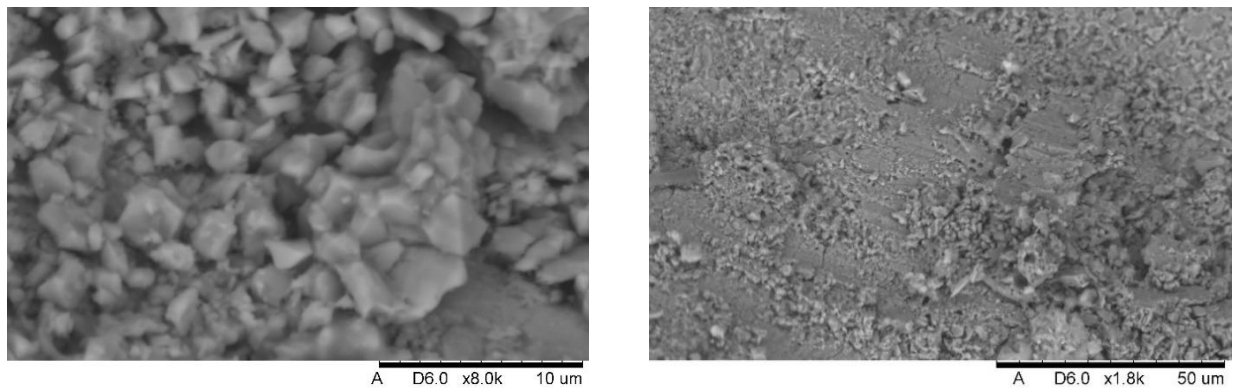


Fig. 4: The process of fracture propagation in AC-44200 with 40 % of  $Al_2O_3$ .



*Fig. 5: Fracture of a sample after firing containing AC-44200 with 40 % of  $\text{Al}_2\text{O}_3$ .*

## 5. Conclusions

The study attempted to determine the energy-intensity of a metal-ceramic material composite produced by a compression of the liquid, subjected to fire with an ammunition of 5.56 mm diameter. As it is shown, the introduction of 20 % reinforcing particles by volume to the AC-44200 alloy causes approx. 28 – 31 % impact energy dispersion. Increasing the volume of  $\text{Al}_2\text{O}_3$  particles to 40 % alters the impact energy dispersion to the range of 47 – 50 %. This represents an approx. fivefold increase in impact energy dispersion capacity when compared with the pure non-altered AC-44200 alloy, which decelerates the impact energy only by approx. 8 – 10 %. After examination, such a large reduction of kinetic energy is associated with 2.5 fold increase in hardness of the composite material (40 % of  $\text{Al}_2\text{O}_3$  by vol.) with respect to the base material.

Resulting materials reveal a reduction in mass in comparison to the conventional alumina ceramics by approx. 10 – 14 %. However, in comparison to a popular ballistic material of a boron carbide the mass is still higher by approx. 20 – 21 %. Therefore, application of the proposed materials for ballistic shields brings the desired shields weight reduction and reasonable economic factors.

Mechanical aspects of fracture creation during the firing based on the brittle fracture has a significant effect on the scattering of high energy concentration points at the contact of shield-projectile. At the time of impact occurs a fragmentation of the samples, which may preferably influence the further process of dispersion of kinetic energy, e.g. in combination with layers of ballistic laminates imposed on the test sample. Therefore, in the further work the authors will present studies of applying the composite metal material in combination with ballistic laminates. The authors are also predicting conducting a research on bullets containing armor piercing cores.

## References

- Abrate, S. (2009) Ballistic Impact on Composite and Sandwich Structure, in: Major Accomplishments in Composite Materials and Sandwich Structures (eds. Daniel I.M. et al.), Springer Science+Business Media B.V., pp. 461-501.
- Bocian, M., Jamroziak, K. and Kosobudzki, M. (2015) Analysis of material punching including a rotational speed of the projectile. Solid State Phenomena, 220-221, pp. 571-576.
- Demir, T., Übeyli, M., Yildirim, R.O. and Karakas M.S. (2011) Investigation on the Ballistic Performance of Alumina/4340 Steel Laminated Composite Armor Against 7.62 mm Armor Piercing Projectiles. Science and Engineering of Composite Materials, 16, 2, pp. 89-98.
- Feli, S., Alami Aaleagha, M.E. and Ahmadi, Z. (2010) A new analytical model of normal penetration of projectiles into the light-weight ceramic-metal targets. International Journal of Impact Engineering, 37, 5, pp. 561-567.
- Hazell, P.J. (2006) Ceramic Armour: Design, and Defeat Mechanisms. Argos Press, Canberra.
- Hogg, P.J. (2003) Composites for ballistic applications. Journal of Composites Processing, CPA, Bromsgrove U.K., March, 2003.
- Kurzawa, A., Kaczmar J.W. (2015) Bending strength of composite materials with EN AC-44200 matrix reinforced with  $\text{Al}_2\text{O}_3$  particles. Archives of Foundry Engineering, 15, pp. 61-64.
- Nayak, N., Banerjee, A. and Sivaraman P. (2013) Ballistic Impact Response of Ceramic-faced Aramid Laminated Composites Against 7.62 mm Armour Piercing Projectiles. Defence Science Journal, 63, 4, pp. 369-37.

## ATMOSPHERIC GAS FLOW AROUND AND INSIDE HIGH HALLS SUPPORTED WITH THE SIMULATION OF THE FANS

M. Kyncl<sup>\*</sup>, J. Pelant<sup>\*\*</sup>

**Abstract:** Here we work with the system of equations describing the non-stationary compressible turbulent multi-component flow in the gravitational field, and we focus on the numerical solution of these equations. The RANS equations are discretized with the use of the finite volume method. The exact solution of the modified Riemann problem (original results) is used at the boundary faces. The presented computational results are computed with the own-developed code (C, FORTRAN, multiprocessor, unstructured meshes in general).

**Keywords:** Atmospheric Gas Flow, RANS, Riemann Problem, Software, Fan Simulation, 3D.

### 1. Introduction

The physical theory of the compressible fluid motion is based on the principles of conservation laws of mass, momentum, and energy. The mathematical equations describing these fundamental conservation laws form a system of partial differential equations. In this contribution we consider the Reynolds-Averaged Navier-Stokes equations with the k- $\omega$  model of turbulence, shown in Wilcox (1998), Kok (2000). We focus on the real gas flow in the gravitational field. Further we suggest a method for the simulation of the simple fan, using two compatible boundary conditions, used previously in Kyncl et al. (2013). We focus on the numerical solution of these equations, using own-developed software.

### 2. Methods

For the discretization of the system we use either explicit or implicit finite volume method in order to discretize the analytical problem, represented by the system of equations in generalized (integral) form. In order to apply this method we split the area of the interest into the elements, and we construct a piecewise constant solution in time, as described in Feistauer et al. (2003). The crucial problem of this method lies in the evaluation of the so-called fluxes (and its Jacobians) through the edges/faces of the particular elements. We use the exact Riemann solver for the solution of the local problem at each face, with the theory shown in Toro (1997). At the boundary faces it is necessary to solve the incomplete Riemann problem, where the right-hand side initial condition is not known. It can be shown, that this right-hand side initial condition for the local problem can be partially replaced by the suitable complementary condition. Various original modifications of the Riemann problem (and exact solutions of these modifications) were shown and analyzed in Pelant (1996-2000), Kyncl (2011).

In this paper we simulate the fan using two connected boundaries. At these boundaries we solve the conservation laws, using the modification of the Riemann problem by the preference of the total quantities at the inlet, and the modification by the preference of the mass flow at the outlet. Using such boundary conditions it is necessary to compute the solution of the resulting non-linear problems. The combination of these two boundary conditions was used previously for the simulation of the propeller disk in Kyncl and Pelant (2013). The partial boundary condition with the preference of mass flow is sometimes being implemented with the use of some iterative process, guessing the correct values (for the pressure, density, velocity) in order to match the given mass flow through the boundary. In our approach we try to be as exact as possible, using our own original procedures. We follow the exact solution of the

---

<sup>\*</sup> RNDr. Martin Kyncl, PhD.: Výzkumný a zkušební letecký ústav, a. s., Beranových 130, 199 05 Prague; CZ, kyncl@vzlu.cz

<sup>\*\*</sup> RNDr. Jaroslav Pelant, CSc.: Výzkumný a zkušební letecký ústav, a. s., Beranových 130, 199 05 Prague; CZ, pelant@vzlu.cz



initial-value problem for the system of hyperbolic partial differential equations, the original analysis was shown in Kyncl et al. (2016).

The own-developed software (C, FORTRAN) is based on the finite volume method with the implicit or explicit time discretization, solution is computed on unstructured 3D meshes in general, MPI parallelizations (OpenMPI, MPICH, CUDA) are used, see also Kyncl et al. (2012). The large linear systems within the implicit method are solved with the implemented preconditioned GMRES matrix solver.

### 3. Examples

Here we show the computational results for the flow around and inside the high hall in the isothermal atmosphere. The initial condition was constant in the whole domain with the total temperature  $T_0 = 293.15\text{K}$ , zero velocity, and the total pressure distribution modified in the gravity field as  $p_0 = p_{00}e^{9.81y/(RT_0)}$ , where  $p_{00} = 101325\text{Pa}$ ,  $y$  denotes the vertical coordinate, and  $R$  is the gas constant  $R = 287.04\text{Jkg}^{-1}\text{K}^{-1}$ . The horizontal fan simulation consisted of two connected boundary conditions: the inlet with the total temperature  $T_{0X}$  and the total pressure  $p_{0X}$ , which are the local values of the total temperature  $T_0$  and the total pressure  $p_0$ , augmented by the influence of the fan

$$T_{0X} = T_0 \left( 1 + \frac{\gamma-1}{(2\gamma RT_0)} v_{FAN}^2 \right), \quad p_{0X} = p_0 \left( 1 + \frac{\gamma-1}{(2\gamma RT_0)} v_{FAN}^2 \right)^{\frac{\gamma}{\gamma-1}}, \quad (1)$$

with  $\gamma = 1.4$ , and  $v_{FAN} = 5\text{ms}^{-1}$  is the fan parameter. Then the computed massflow was used to complement the incomplete the Riemann problem at the outlet boundary condition. Both direction of the flow through the fan were simulated. The geometry, the computational mesh (anisotropically refined), and the resulting isolines of velocity magnitude, density are shown in the Figs. 1 – 5.

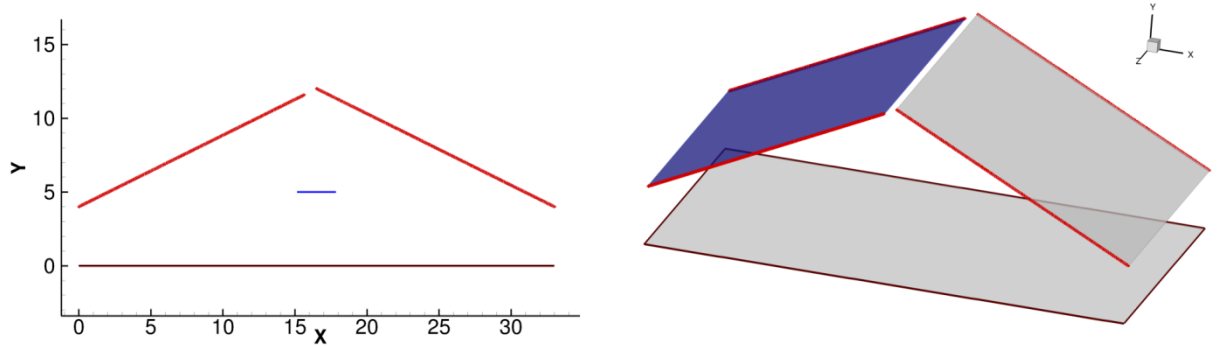


Fig. 1: Geometry used for the simulation. The fan is placed inside the high hall.

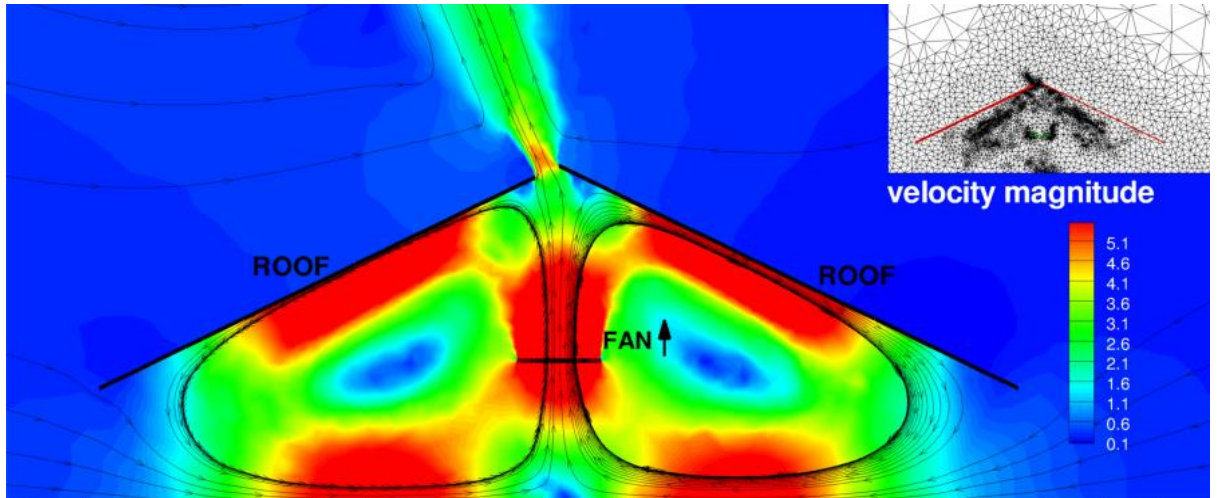


Fig. 2: The fan inside hall simulation, velocity magnitude isolines. The direction of the flow is demonstrated by the streamtraces.

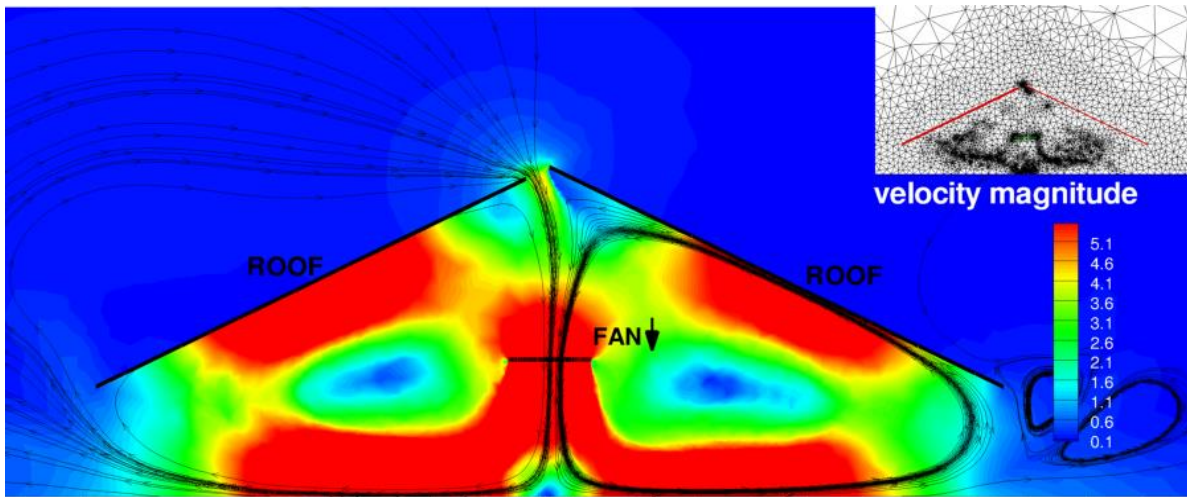


Fig. 3: The fan inside hall simulation, velocity magnitude isolines. The direction of the flow is demonstrated by the streamtraces.

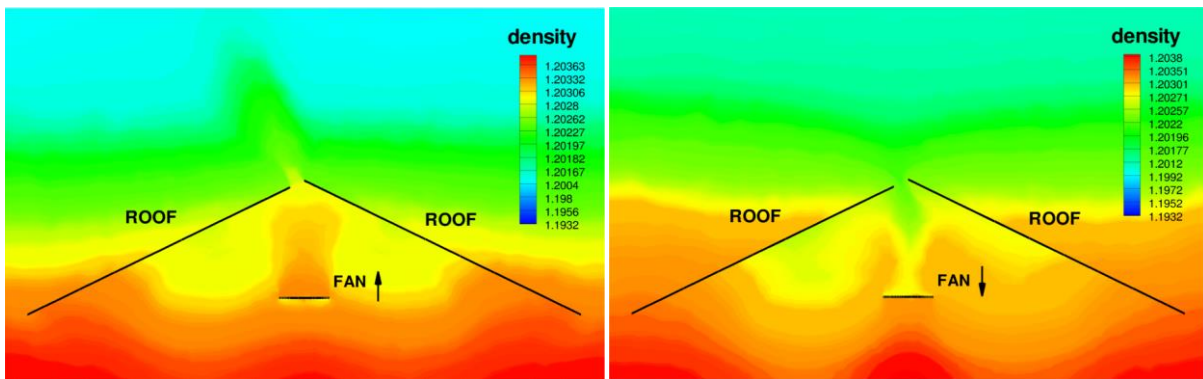


Fig. 4: The fan inside hall simulation, density isolines, comparison of two possible fan orientations. There is a visible effect of the gravitational force.

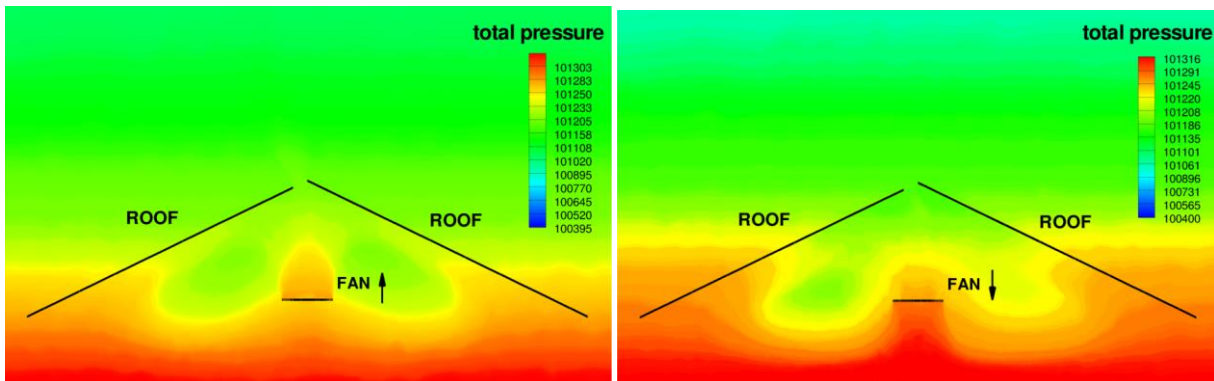


Fig. 5: The fan inside hall simulation, total pressure isolines, comparison of two possible fan orientations.

#### 4. Conclusions

This paper shows the numerical simulation of the fan situated inside the high hall. The partial differential equations describing the conservation laws are solved numerically with the finite volume method. Own software was programmed. The modification of the Riemann problem and its solution was used at the boundaries. The combination of these boundary conditions was used for the simulation of the fan, which is the original result of this work.



## Acknowledgement

The results originated with the support of Ministry of the Interior of the Czech Republic, project SCENT, Grant MSM 0001066902 of the Ministry of Education of the Czech Republic, and Ministry of Industry and Trade of the Czech Republic for the long-term strategic development of the research organization. The authors acknowledge this support.

## References

- Feistauer, M., Felcman, J., and Straškraba, I. (2003) Mathematical and Computational Methods for Compressible Flow, Oxford, England.
- Kok, C.J. (2000) Resolving the dependence on free-stream values for k-omega turbulence model, in: AIAA Journal, Vol. 38, No. 7.
- Kyncl, M. and Pelant, J. (2012) Implicit method for the 3d RANS equations with the k-w (Kok) Turbulent Model, Technical report R-5453, VZLU, Beranovych 130, Prague.
- Kyncl, M. (2011) Numerical solution of the three-dimensional compressible flow, Doctoral Thesis, Prague.
- Kyncl, M. and Pelant, J. (2013) Simulation of the Propeller Disk Inside the Symmetrical Channel, EPJ Web of Conferences, Volume 67, 2014, EFM13.
- Kyncl, M. and Pelant, J. (2016) The Inlet and Outlet Boundary Problem with the Preference of Mass Flow, ECCOMAS Congress 2016.
- Pelant, J. (1996-2000) Arti reports VZLÚ, z-65, z-67 to z-73. Prague.
- Toro, E.F. (1997) Riemann Solvers and Numerical Methods for Fluid Dynamics, Berlin, Germany.
- Wilcox, D.C. (1998) Turbulence Modeling for CFD, California, USA.

## SHEAR FORCES OF THE APPROACH SLABS OF THE ROAD BRIDGES

K. Laco\*, V. Borzovič\*\*

**Abstract:** The transition zone of the road bridges is located right behind the abutment. Function of this structure is to ease the vehicle transition from the bridge on the rigid support to the embankment with much smaller subsoil stiffness. Very important element of the transition zone structure is the approach slab. It is the reinforced concrete slab, which by its longitudinal span overcomes the uneven settlement of the bridge abutment and the embankment. This paper is focused on the shear forces caused by traffic loads represented by uniform distributed load (UDL) and tandem systems (TS) according to European standards. The results from the model with spring area support are also compared with conservative model.

**Keywords:** Approach slab, Transition zone, Shear forces, Springs with gap.

### 1. Introduction

The approach slab is designed to compensate the different settlement of the bridge abutment and a road embankment. In Fig. 1 the typical cross section of the transition zone can be seen.

Driving comfort can be interrupted by the so called “bump” on both ends of the bridge. These disorders caused by the exceeded size of the different settlements should be eliminated by the approach slabs. When the settlement difference is increasing, the structural scheme of the slab is also changing and shear forces and bending moments are higher.

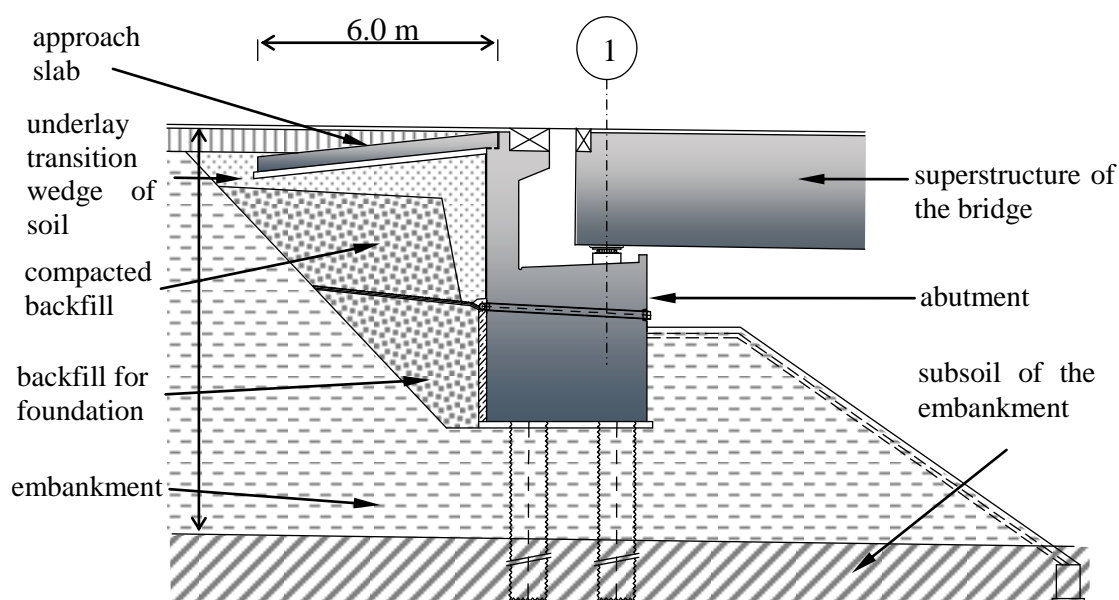


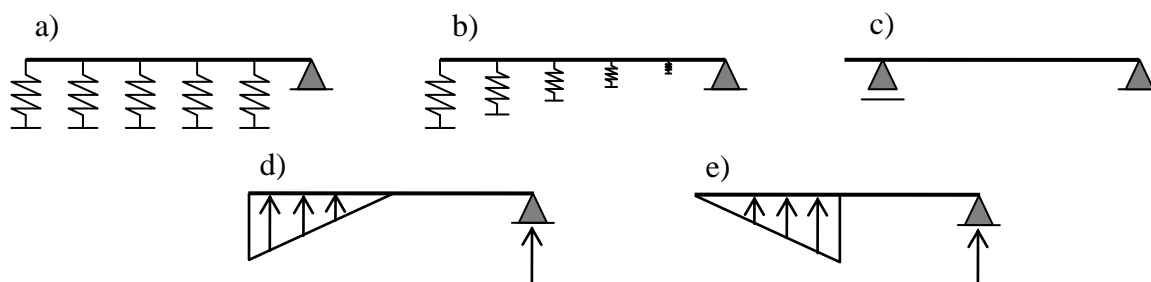
Fig. 1: Typical cross-section of the transition zone.

\* MSc. Kamil Laco: Slovak University of Technology, Faculty of Civil Engineering, Radlinského 11, 810 05 Bratislava, Slovak republic, kamil.laco@stuba.sk

\*\* Assoc.Prof. Viktor Borzovič, PhD.: Slovak University of Technology, Faculty of Civil Engineering, Radlinského 11, 810 05 Bratislava, Slovak republic, viktor.borzovic@stuba.sk

## 2. Structural Model of the Approach Slab

Simplified structural model can be represented by the slab with hinged line support in the place of the connection to the abutment and another line support at the free end of the approach slab. Description of the structural scheme of the approach slab is difficult, because it is changing during its life span. Right after the completion of the bridge and transition zone construction the scheme can be described with hinged line support representing the joint with the abutment and the bottom area is supported by subsoil (which can be modelled as springs with constant stiffness). After the bridge opens to traffic the slab and its subsoil have to resist the cyclic action caused by trespassing vehicles. The uneven settlement is increasing, what can cause the gap creation under the slab. There are also another reasons such as consolidation of the subsoil, or accidental situation (e.g. washout of the fine particles). Possible structural schemes are shown as sections in Fig. 2. Fig. 2a is scheme with constant area stiffness, Fig. 2b with linear changing stiffness, Fig. 2c simplified, Figs. 2d and 2e based on support reaction forces.

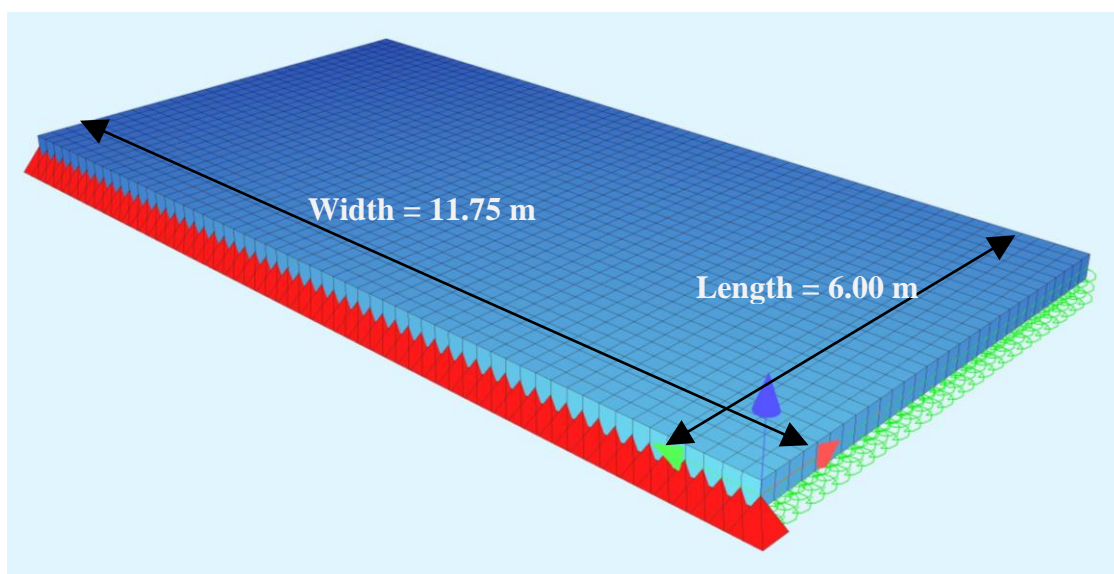


*Fig. 2: Alternative structural schemes and models of the approach slab (right end – connection with abutment, left end – free end of approach slab).*

## 3. Numerical Model of the Approach Slab

Fig. 3 represents the numerical model in FEM software SOFiSTiK. The approach slab is modelled by 2D elements with defined concrete and reinforcement properties. The main bottom reinforcement along the span of the slab is  $\Phi 16$  with 125 mm spacing. The other layers of the reinforcement are  $\Phi 10$  with 200 mm spacing. The length of the slab is 6.0 m, width 11.75 m and thickness 0.3 m. Thickness and the bars of the main reinforcement were chosen according to previous study (Laco, Borzovič 2016) performed on conservative scheme.

By current Slovak technical specifications for the design of the transition zones (OTN 73 6244, 1981) the gaps of the springs were chosen. Allowable change of the slope of the approach slab is 0.4 % for the highways and motorways with the speed limit above 80 km/h. For the other roads it is 0.8 %.



*Fig. 3: Numerical model of the approach slab.*

Properties of the springs were set for well graded gravel with modulus of subgrade reaction of  $22 \text{ MN/m}^3$ . Transverse spring stiffness value is multiplication of the factor 0.4 and axial stiffness. Values of the gaps of the springs have linear function from maximum in the line hinged support to 0 at the free end of the slab. Two cases were analysed, with maximum gap 24 mm for 0.4 % change of the slope and 48 mm for 0.8 % change.

The load for the analysis was represented by TS and UDL with two alternatives of the notional lane system distribution. The first, with the most loaded lane at the edge of the slab. The second, placing the heaviest traffic load in the middle. Each of the alternatives has 20 load cases for different position of the TS along the slab.

#### 4. Analysis of the Shear Forces of the Approach Slab

The main goal of the analysis was to verify whether the values of the shear forces on the conservative structural scheme has unfavourable results as the slab supported by springs with gap.

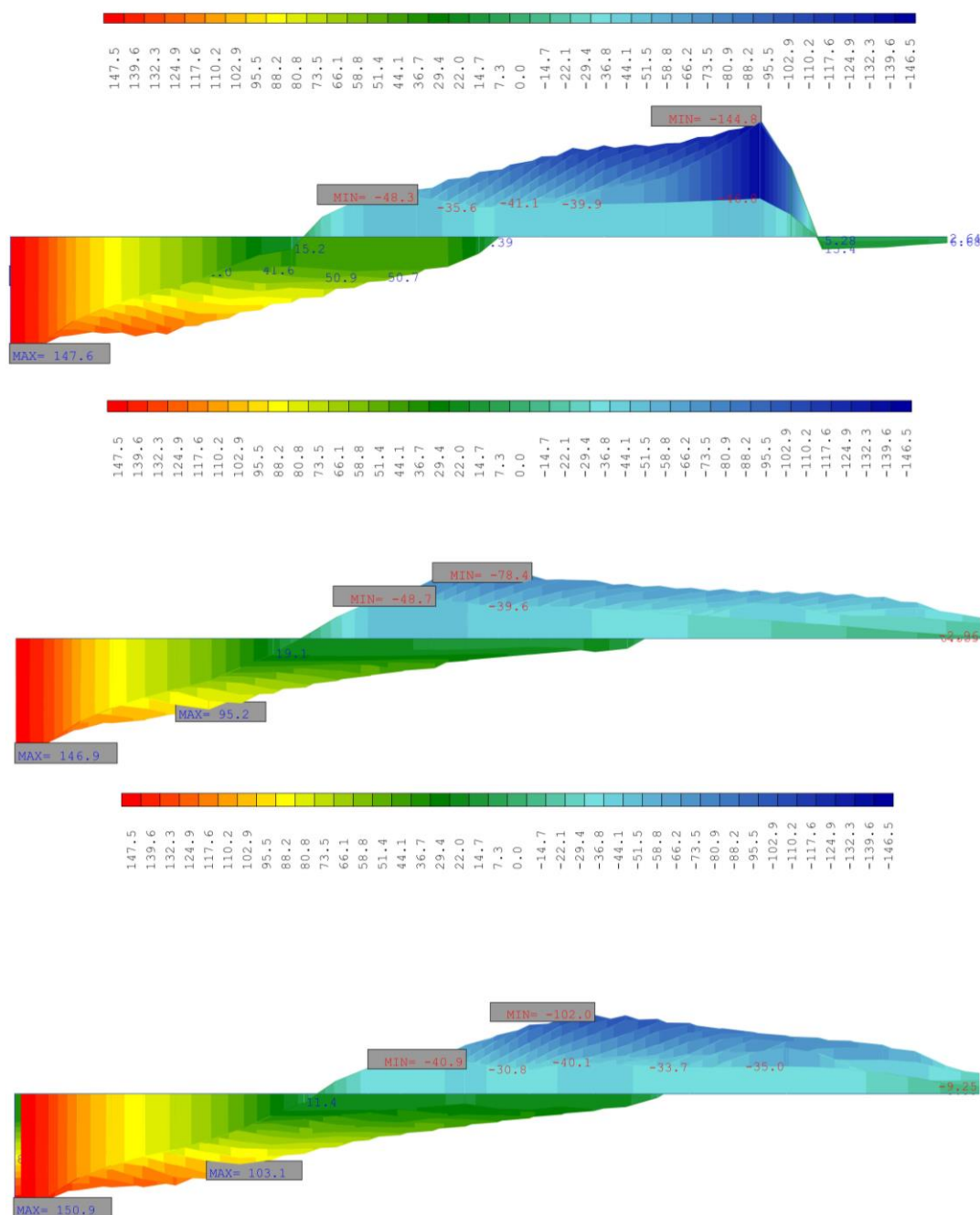


Fig. 4: Envelope of the shear forces  $v-x$  [kN/m] in the axis of wheel of the TS (from above: 1 - on simplified scheme, 2 – 0.4 % change of slope, 3 - 0.8 % change of slope).

In Fig. 4 envelopes of the shear forces along the slab are presented. The cut is placed in the axis of most loaded wheel of TS. Three cuts are from alternative, where the most loaded lane is in the middle of the slab. Similar results are also in the second alternative.

The main difference of the gap model and simplified one are the concentration of the shear forces near the free end. The gap model has more realistic distribution of the forces near the free end. Minimum values for the model with 0.4 % change of slope are all below values of the simplified model. In model with 0.8 % change of slope the values of the shear forces are much closer to simplified, especially near the middle of the slab. The peak is distributed because of area spring support at the free end. The gap model is also showing the behaviour of the supporting springs. In Fig. 5 can be seen, that with TS located in the middle of the slab, spring forces below the slab are creating similar pattern as structural scheme in Fig. 2e.

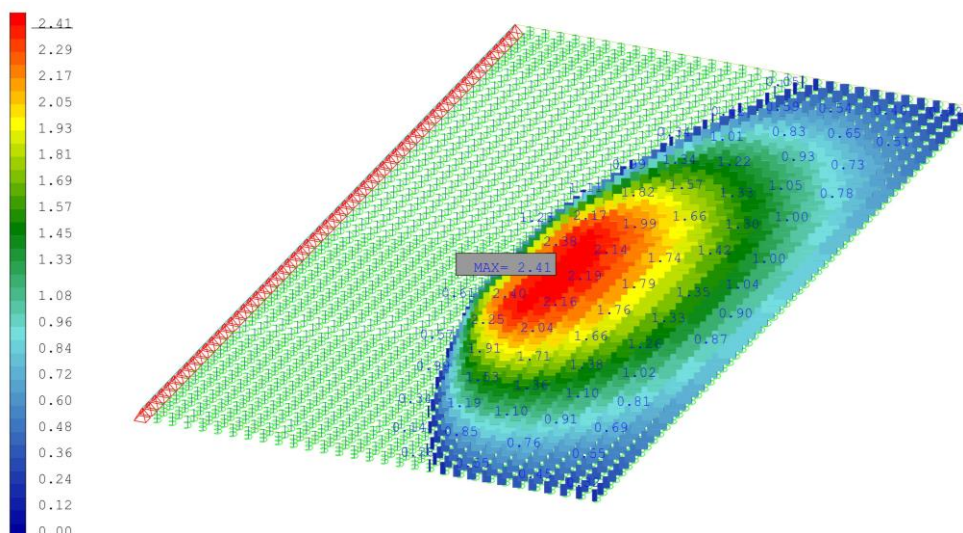


Fig. 5: Supporting forces of the activated springs [kN].

## 5. Conclusion

Using the simplified scheme for the shear reinforcement design is time-effective and apart from the concentration of the shear forces at the free end of the slab not so exaggerated. For the approach slabs used on roads with speed limit of 80 km/h values for conservative and gap model are very similar.

Chosen conservative scheme with linear support with the distance Length/6 from the free end chosen in previous work (Laco et al, 2016) seems to be suitable also for the shear reinforcement design. Although for the parametrical study and calculations for the possible change of the current Slovak technical specification for the transition zone design (OTN 73 6244, 1981) the gap model will be used.

Extensive parametrical study, where various lengths, subsoils and widths will be used, will serve as the background for the preparing tool for the structural engineers. The tool will help designers to choose suitable structural scheme, but also for quick design graphs, schemes and tables for geometry, bending and shear reinforcement design will be available.

## Acknowledgement

This work was supported by the Slovak Research and Development Agency under the contract No APVV-15-0658 and by the University Science Park (USP) of the Slovak University of Technology in Bratislava (ITMS: 26240220084).

Authors gratefully acknowledge technical support provided by companies YIT Reding and Geoexperts.

## References

- Laco, K. and Borzovič, V. (2016) Design of Approach Slab of Road bridges, in: Solid State Phenomena : selected, peer reviewed papers from the 22nd International Conference Concrete Days 2015, Litomyšl, Czech Republic. Vol. 249, (2016), ISSN 1012-0394, pp. 215-220.
- OTN 73 6244 (1981) Transition zones of the roadway and highway bridges. Praha, (in Slovak).



## **KINEMATICS AND WORKSPACE ANALYSIS FOR A 6-DOF PARALLEL MANIPULATOR WITH COAXIAL CTUATED ARMS**

**P. A. Laski\***

**Abstract:** *The article presents a kinematic model of a manipulator with a closed kinematic change, with coaxial actuated arms, Hexarot type. The structure references widely used SCARA type industrial robots. The discussed coaxial manipulator structure posses six coaxial rotation drives with active arms, to which passive drive arms are mounted via spherical joints. The work platform, to which the effector is mounted, has been designed on a regular triangle base, and connects passive arms via spherical joints. The workspace shape has been designed on the basis of sample geometric dimension.*

**Keywords:** Parallel manipulator, 6-DOF, Hexarot, Kinematics, Workspace.

### **1. Introduction**

Regular SCARA (Selectively Compliant Assembly Robot Arm) robots possess a kinematic chain which includes two rotation drives and one progression drive (Zwierzchowski, 2016a, Takosoglu, 2016a). The SCARA family of robots was designed for a variety of general-purpose applications requiring fast, repeatable and articulate point-to-point movements such as palletizing, depalletizing, machine loading/unloading and assembly (Blasiak, M., 2016). Now, the main areas of use for SCARA robots are: welding, handling, assembly, painting and finishing, picking, packing, palletizing and machine tending (Blasiak et al., 2016, Koruba et al., 2013). Key markets include automotive, plastics, metal fabrication, foundry, electronics, machine tools, pharmaceutical and food and beverage (Zwierzchowski, 2016b, Takosoglu, 2016b).

There is research being conducted into finding machines which could replace SCARA robots, while retaining similar functionality, while displaying better dynamics and positional accuracy. One such machine could be a structure with a closed kinematic chain with coaxially actuated Hexarot type arms. A prototype of such machine has been built by ABB, but their robot possess a smaller number of degrees of freedom, being a 3-DOF type machine. The kinematic structure of the device has been described in an article (Brogårdh, 2007). The rotary actuators have equipped on the prototype coaxially on a cylindrical column, and the drive is transferred onto the platform using passive drive units and the joints between them. Robots with rotary drives mounted on a common cylindrical column have been analyzed in scientific works (Marlow et al., 2014) (Isaksson et al., 2012; Isaksson et al., 2013; Pedrammehr et al., 2016 and Qazani et al., 2015). An article (Isaksson et al., 2012) analyses the kinematic structure and the shape of the workspace of a 5-DOF manipulator, which possess a closed kinematic chain with coaxially actuated drive arms. Similarly to other solutions, this type of structure is based on a truss, whose columns do not transfer shear and torsion load, which means they can be produced from light, high rigidity material (Isaksson et al., 2012, Pietrala, 2016). The link structure of the octahedral Hexarot robot was inspired by the original platform designed by E. Gough. In robots of this type, cross and spherical joints have been used.

### **2. Kinematic analysis of a 6-DOF spatial manipulator with a rotary drive**

For the analyzed 6-DOF manipulator a basic set of Cartesian coordinates has been assumed. The axes of this set have been marked with color:  $x$  axis – red,  $y$  axis – green,  $z$  axis – blue. Moreover, all sets used in

---

\* Pawel Anrzej Laski, PhD.: Department of Automation and Robotics, Faculty of Mechatronics and Machine Design, Aleja Tysiaclecia Panstwa Polskiego 7; 25-314 Kielce; PL, pawell@tu.kielce.pl



kinematic analysis have been assumed as having a positive orientation. Also defined are homogenous transformation matrixes, which have been presented as matrixes (1) and (2):

$$RotX(\alpha) = \begin{pmatrix} 1 & 0 & 0 & 0 \\ 0 & c\alpha & -s\alpha & 0 \\ 0 & s\alpha & c\alpha & 0 \\ 0 & 0 & 0 & 1 \end{pmatrix}; \quad RotY(\alpha) = \begin{pmatrix} c\alpha & 0 & s\alpha & 0 \\ 0 & 1 & 0 & 0 \\ -s\alpha & 0 & c\alpha & 0 \\ 0 & 0 & 0 & 1 \end{pmatrix}; \quad RotZ(\alpha) = \begin{pmatrix} c\alpha & -s\alpha & 0 & 0 \\ s\alpha & c\alpha & 0 & 0 \\ 0 & 0 & 1 & 0 \\ 0 & 0 & 0 & 1 \end{pmatrix}; \quad (1)$$

$$TransX(d) = \begin{pmatrix} 1 & 0 & 0 & d \\ 0 & 1 & 0 & 0 \\ 0 & 0 & 1 & 0 \\ 0 & 0 & 0 & 1 \end{pmatrix}; \quad TransY(d) = \begin{pmatrix} 1 & 0 & 0 & 0 \\ 0 & 1 & 0 & d \\ 0 & 0 & 1 & 0 \\ 0 & 0 & 0 & 1 \end{pmatrix}; \quad TransZ(d) = \begin{pmatrix} 1 & 0 & 0 & 0 \\ 0 & 1 & 0 & 0 \\ 0 & 0 & 1 & d \\ 0 & 0 & 0 & 1 \end{pmatrix}; \quad (2)$$

The analyzed structure is one of the more interesting spatial solutions using six degrees of freedom along with a rotary drive. Analogous to using delta type manipulator is utilizing rotary drives and passive arms. The structure being discussed possess six drives mounted one on top of another, creating a column with a common axis. Similarly to devices described previously, every individual kinematic chain contains a rotary drive link and passive arms with spherical joints. A single kinematic chain can be written down a 6-RSS where: (R) symbolizes a rotary joint, and (S) symbolizes a spherical joint. The device possesses a work platform based on the shape of a regular triangle with cut vertices, on which the passive arms' spherical joints are mounted. Fig. 1 presents a simplified solid model of the manipulator with six rotary drive, in which the passive arms do not receive one degree of freedom. This DOF is the rotation around the longitudinal axis of the rod, which does not influence the position nor the orientation the work platform. Figs. 1 and 2 present characteristic dimension of the device, as well as views of the local coordinate systems  $R_{i,1}$ ,  $R_{i,2}$ ,  $R_{i,3}$ ,  $R_{i,4}$  for individual arms.

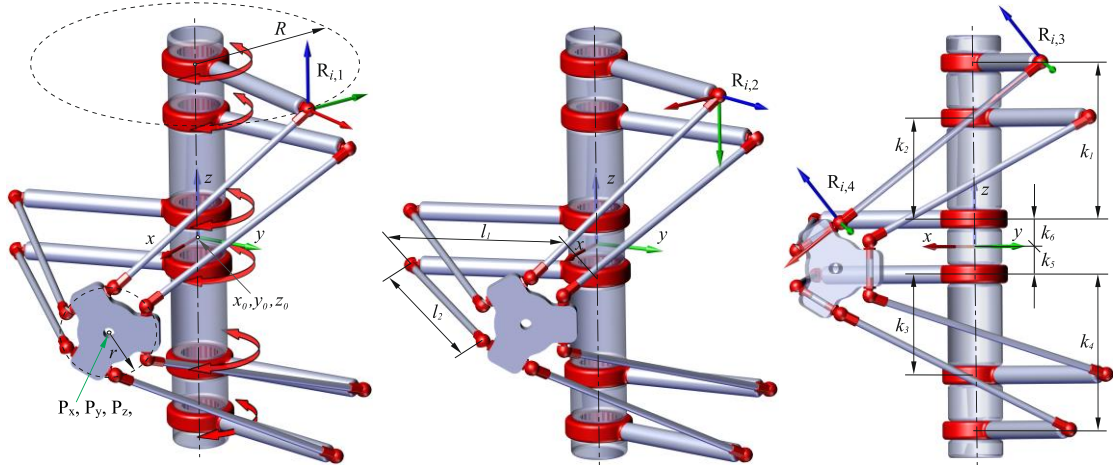


Fig. 1: . Spatial mechanism with 6 DOF – view of local coordinate systems  $R_{i,1}$ ,  $R_{i,2}$ ,  $R_{i,3}$ ,  $R_{i,4}$ .

Kinematic equations have been determined for the structure being analyzed (3). This equations take into account the relationship tying the arms to the work platform. The analyzed kinematic structure is characterized by being symmetrical to the  $xy$  plane. Additionally, the distances  $k_1 = 500$  mm,  $k_2 = 350$  mm,  $k_3 = -350$  mm,  $k_4 = -500$  mm,  $k_5 = -75$  mm,  $k_6 = 75$  mm on the  $z$  axis have been determined and represent the height at which each (arm number symbolized by  $i$ ) is mounted. In other words – the distances at which all of the rotary drives are place along the  $z$  axis. Kinematic equations have been determined for the arms, with  $i$  marking the arm number, and their corresponding work platform point, placed in a circle with a radius of  $r = 125$  mm and spaced at the following angles:  $\zeta_1 = \zeta_0$ ,  $\zeta_2 = 120^\circ - \zeta_0$ ,  $\zeta_3 = 120^\circ + \zeta_0$ ,  $\zeta_4 = 240^\circ - \zeta_0$ ,  $\zeta_5 = 240^\circ + \zeta_0$ ,  $\zeta_6 = -\zeta_0$ . An additional base angle for the platform has been introduced at  $\zeta_0 = 36.8699^\circ$ . It determines the placement of joint in the circle, and is equal to half of the angle between two platform joints in one coupling.

$$f(\theta_{i,1}, \theta_{i,2}, \theta_{i,3}) = \begin{pmatrix} -P_{i,x} + \cos \theta_{i,1}(l_1 + l_2 \sin \theta_{i,3}) + l_2 \sin \theta_{i,1} \cos \theta_{i,2} \cos \theta_{i,3} \\ -P_{i,y} + \sin \theta_{i,1}(l_1 + l_2 \sin \theta_{i,3}) - l_2 \cos \theta_{i,1} \cos \theta_{i,2} \cos \theta_{i,3} \\ -P_{i,z} + k_i - l_2 \sin \theta_{i,2} \cos \theta_{i,3} \end{pmatrix} = 0 \quad (3)$$

### 3. Workspace of the 6-DOF manipulator

The workspace has been determined for the mechanism being analyzed, assuming geometrical constraints and physical constraints for the range of movement of the joints. The working range for the rotary drives has been assumed at  $-2\pi/3 \div 2\pi/3$  while the working range of the joints has been assumed at  $-\pi/2 \div \pi/2$  for ball joints on the first axis, indexes  $i = 1, 2, 3, 4$  and  $\pi/2 \div 3\pi/2$  for arms with indexes  $i = 5, 6$ , as well as  $-\pi/6 \div \pi/6$  as the working range for ball joints on the second axis. Figs. 2 and 3 present the shapes of the workspaces for zero orientations of the work platform.

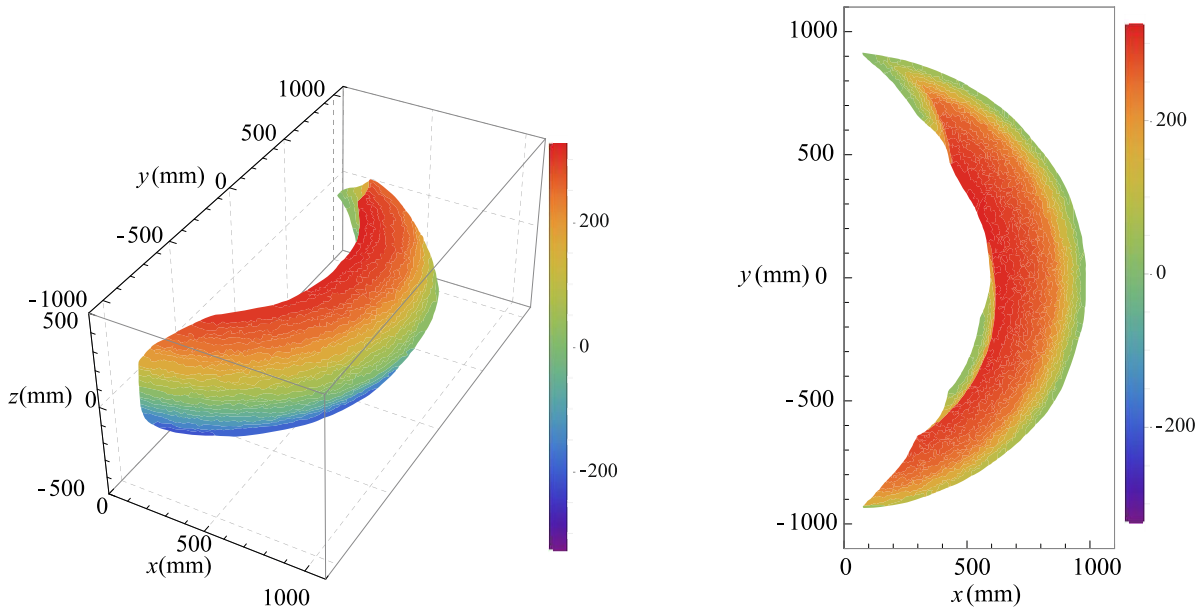


Fig. 2: Workspace: a) axonometric view; b) x, y plane view.

Fig. 3 shows the view of the workspace of the mechanism with rotary drives, in view for  $x, z$  and  $y, z$  planes for the zero orientation of the work platform.

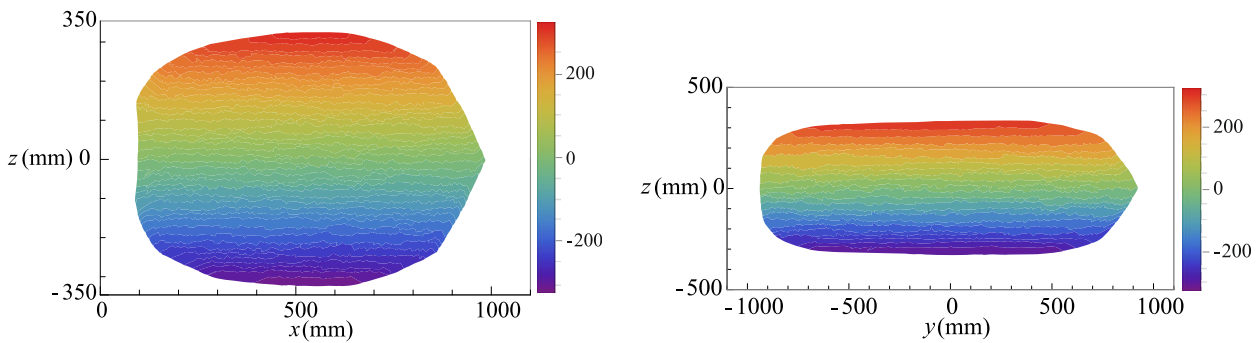


Fig. 3: Workspace – view of  $x,z$  and  $y,z$  planes for the zero orientation of the work platform.

### 4. Conclusion and future work

Fully parallel manipulators with a large range of platform rotations are unusual, even more so if combined with a large positional workspace. This article describes a new type parallel Hexarot manipulator. The analyzed structure possess significant potential, in relation to the shape and (large) volume of the workspace. The Hexarot type structure possess six active drive arms, which can be rotated around the column, which at the same time is a cylindrical base. All of the drives rotate on a common axis. The

passive arm system transmits the drive from active units to the work platform via spherical joints, while the platform is the mounting point of the effector. The complicated system of passive arms presents a significant risk of collisions occurring between the element of the manipulator and other objects. The characteristic of the 6-DOF Hexarot manipulator, including the size of the workspace and working ranges, are highly reliant on the parameters of the kinematic structure. The lengths of the arms and axis ranges achievable by the spherical joints have the most impact on the shape of the workspace. Simulations indicated, that no inconsistencies have appeared in the volume of the workspace. However, a factor exists, which limits the possibility of achieving full rotation of the work platform, which is the collisions between the parts of the manipulator. However, such a limitation does not impact on the already wide functionality of the manipulator. In the future, optimizing the length of the passive and active arms as well as other geometric dimensions of the manipulator will be necessary, to achieve a possibly large (in terms of volume) workspace. Moreover, the shape of the workspace is significantly changed along with the orientation of the work platform changing. The achieved workspace shape shows significant potential in industrial applications of such a manipulator, similar to that of SCARA robots.

## References

- Blasiak, M. (2016) Parametric analysis of piezoelectric transducer used for signal processing, in: Proc. Int. Conf. on Engineering Mechanics 2016 (eds. Zolotarev, I and Radolf, V.), Svratka, Czech Republic, pp. 66-69.
- Blasiak, S. and Zahorulko, A.V (2016) A parametric and dynamic analysis of non-contacting gas face seals with modified surfaces, *Tribology International*, 94, , pp. 126-137, doi:10.1016/j.triboint.2015.08.014.
- Brogårdh, T. (2007) Present and future robot control development—an industrial perspective, *Annual Reviews in Control*, 31, 1, pp. 69-79, doi:10.1016/j.arcontrol.2007.01.002.
- Isaksson, M., Brogårdh, T. and Nahavandi, S. (2012) A 5-dof rotation-symmetric parallel manipulator with one unconstrained tool rotation, in: 2012 12th International Conference on Control Automation Robotics & Vision (ICARCV) IEEE, pp. 1095-1100, doi:10.1109/ICARCV.2012.6485310.
- Isaksson, M., Brogårdh, T. and Nahavandi, S. (2012) Parallel manipulators with a rotation-symmetric arm system, *Journal of Mechanical Design*, 134, 11, pp. 114503-114506, <http://dx.doi.org/10.1115/1.4007305>.
- Isaksson, M., Brogårdh, T., Watson, M., Nahavandi, S. and Crothers, P. (2012) The octahedral hexarot — a novel 6-dof parallel manipulator, *Mechanism and Machine Theory*, 55, pp. 91-102.
- Isaksson, M. and Watson, M. (2013) Workspace analysis of a novel six-degrees-of-freedom parallel manipulator with coaxial actuated arms, *Journal of Mechanical Design*, 135, 10, pp. 104501-104509, Retrieved from <http://dx.doi.org/10.1115/1.4024723>.
- Koruba, Z. and Krzysztofik, I. (2013) An algorithm for selecting optimal controls to determine the estimators of the coefficients of a mathematical model for the dynamics of a self-propelled anti-aircraft missile system, *Proceedings of The Institution of Mechanical Engineers Part K-Journal of Multi-Body Dynamics*, 227, K1, pp. 12-16, doi:10.1177/1464419312455967.
- Marlow, K., Isaksson, M., Abdi, H. and Nahavandi, S. (2014) Workspace analysis of two similar 3-dof axis-symmetric parallel manipulators. *bt - 2014 ieee/rsj international conference on intelligent robots and systems*, chicago, il, usa, september 14-18, 2014, doi:10.1109/IROS.2014.6942782.
- Pedrammehr, S., Chalak Qazani, M.R., Abdi, H. and Nahavandi, S. (2016) Mathematical modelling of linear motion error for hexarot parallel manipulators, *Applied Mathematical Modelling*, 40, 2, pp. 942-954, doi:10.1016/j.apm.2015.07.004.
- Pietrala, D.S. (2016) Parallel manipulator with pneumatic muscle drive, in: Proc. Int. Conf. on Engineering Mechanics 2016 (eds. Zolotarev, I and Radolf, V.), Svratka, Czech Republic, pp. 458-461.
- Qazani, M.R.C., Pedrammehr, S., Rahmani, A., Danaei, B., Ettefagh, M.M., Rajab, A.K.S. and Abdi, H. (2015) Kinematic analysis and workspace determination of hexarot-a novel 6-dof parallel manipulator with a rotation-symmetric arm system, *Robotica*, 33, 8, pp. 1686-1703, doi:10.1017/S0263574714000988.
- Takosoglu, J.E. (2016a) Control system of delta manipulator with pneumatic artificial muscles, in: Proc. Int. Conf. on Engineering Mechanics 2016 (eds. Zolotarev, I and Radolf, V.), Svratka, Czech Republic, pp. 546-549.
- Takosoglu, J.E. (2016b) Experimental research of flow servo-valve, in: *Proceedings of the International Conference Experimental Fluid Mechanics 2016* (ed. Dancova, P.), Techn. Univ. Liberec, pp. 819-823.
- Zwierzchowski, J. (2016a) Design type air engine di pietro, in: *Proceedings of the International Conference Experimental Fluid Mechanics 2016* (ed. Dancova, P.), Techn. Univ. Liberec, pp. 983-988.
- Zwierzchowski, J. (2016b) Industrial robot vision system for moving spherical elements, in: Proc. Int. Conf. on Engineering Mechanics 2016 (eds. Zolotarev, I and Radolf, V.), Svratka, Czech Republic, pp. 626-629.

## FAILURE INDEX BASED TOPOLOGY OPTIMIZATION FOR MULTIPLE PROPERTIES

F. Löffelmann\*

**Abstract:** Aim of the presented work is to introduce a method which is being coded. It works in conjunction with an open-source finite element solver CalculiX. One of the topology optimization methods - The Bi-directional Evolutionary Structural Optimization method (BESO) was chosen due to its simplicity, which is used in the way of python code standing above FE solver. Two test examples are presented. First demonstrates ability to achieve results similar to compliance based topology optimization on short beam leading to solid-void structure. Second example shows possibility to switch among different materials with regard to their allowable stresses.

**Keywords:** Structural optimization, Heuristic, BESO, Solid-void, Multiple material.

### 1. Introduction

Topology optimization searches for convenient material distribution of product in the design space. In recent years it is increasingly used thanks to increase in computational power and increasing number of software integrating FEM and topology optimization. Out of complex optimization packages there are several optimizers freely available (non-trial versions), but only a few with open-source codes, mostly scientific explanatory papers, e.g. Sigmund (2001), Zuo et al. (2015), or a master thesis Denk (2016). A presented python code is available on <https://github.com/fandaL/beso> and it works as an optimizer which currently uses the open-source FE solver CalculiX and a user defined input file for a common FE analysis. The BESO method was initially taken from Huang (2010), but in the current state it is significantly modified. Contrary to most of topology optimizers, which are compliance based or stress based (e.g. Querin, 1997) and modifies element stiffness matrices, this code is close to stress based methods since it is based directly on failure indices and modifies element materials which both are listed by a user. Similar tasks were solved also by Ramani (2011).

### 2. Methods

Description follows schema in Fig. 1. At the beginning a user defines common FE analysis and sets optimization parameters, from which most important are domain parameters (lists of switching materials, effective densities, thicknesses, failure criteria; lists must be ordered from weakest to strongest material), type of filter and filter radius, and mass goal ratio.

Several operations can be done only ones before iterating. It is importing a mesh for user defined domains to be optimized or only included in monitoring and filter range. Another operation is computing volumes (resp. areas of shells) to evaluate mass during iteration. Volumes together with centers of gravity and finding near elements are used for filtering.

Basic measure of efficiency of each element is in an actual state defined as its sensitivity number

$$\alpha = \frac{FI_e}{\rho_e}, \quad FI_e = \frac{\sigma_{e,evaluated}}{\sigma_{e,allowable}} \quad (1)$$

Higher element failure index  $FI_e$  means that element is used closer to its failure capacity and division by effective element density  $\rho_e$  is used to prefer lighter (cheaper) material.  $\sigma_e$  is element stress.

---

\* Ing. František Löffelmann: Institute of Aerospace Engineering, Brno University of Technology, Technická 2896/2, 616 69 Brno, CZ, Frantisek.Loffelmann@vutbr.cz

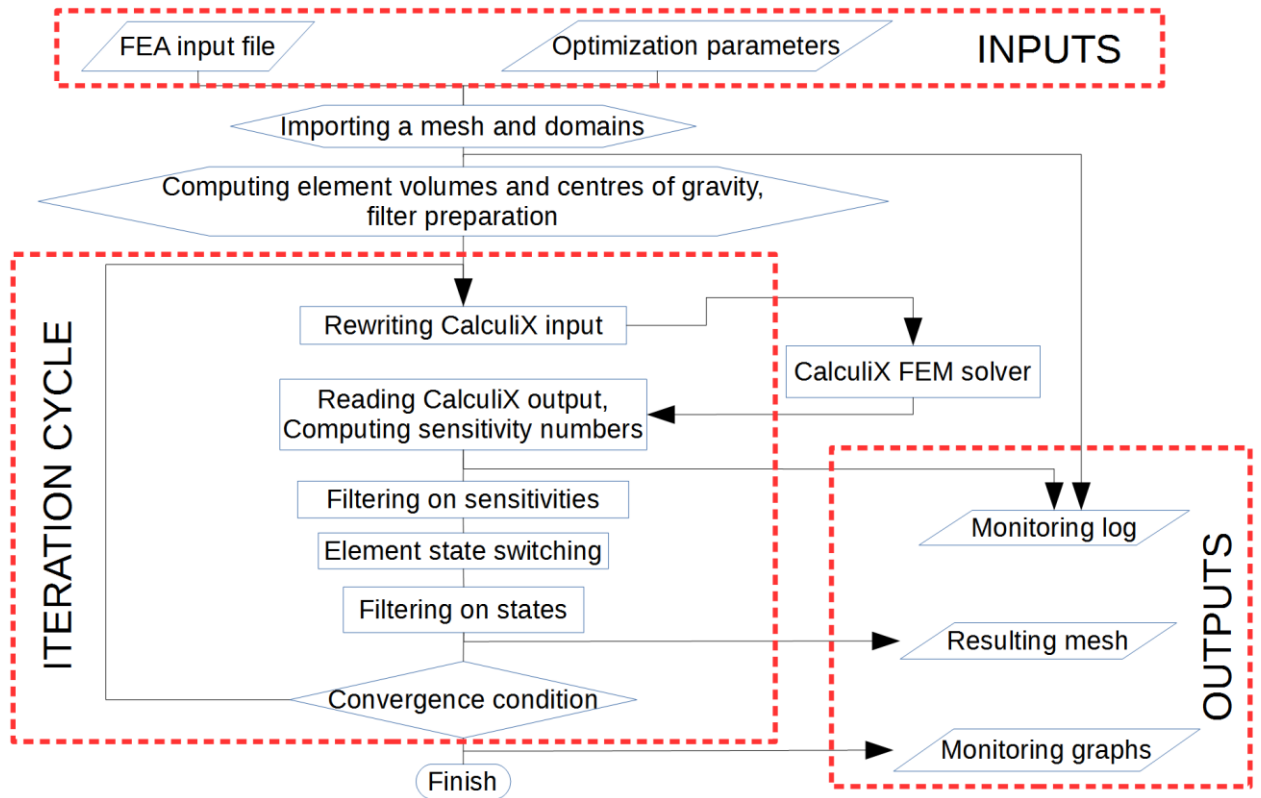


Fig. 1: Simplified flowchart of the program.

Very important section is for element switching. In each iteration prescribed mass is switched up (to stronger state) defined by Mass Addition Ratio  $AR$ , and in the same iteration mass defined by Mass Removal Ratio  $RR$  is switched down (to weaker state). Difference between them yields goal decrease in total mass from the previous iteration. Removing is limited by achieving the mass goal, or by exceeding allowable number of violated elements which have failure ( $FI_e \geq 1$ ). Violated elements are forced to switch up and their mass difference is added to the goal mass of the current iteration. The rest of elements is ordered according to their sensitivity numbers (eq. 1). Switching up is done from elements with highest sensitivity number, then switching down from the lowest (least effective elements).

When failure occurs on more than allowable number of elements, decaying is activated which means that Mass Addition Ratio  $AR$  exponentially decreases between iterations. Speed of decaying is driven by exponent  $k$  in the equation

$$AR_i = AR_0 \cdot e^{k \cdot (i - i_v)}, \quad k < 0 \quad (2)$$

Where  $AR_0$  is the Mass Addition Ratio used at the beginning,  $i$  is the actual iteration number, and  $i_v$  is number of the iteration in which tolerance in failed elements was exceeded. Until more failing elements are present, Mass Removing Ratio equals actual  $AR_i$  which assures that mass is not removed. Using this approach is an artificial way how to stabilize results from continuing switching some elements up and others down.

Criterion for terminating iterations is given by mean  $FI$  weighted by element mass which should remain in prescribed tolerance for the last 5 iterations. Iterating can be also terminated by the maximum number of iterations.

### 3. Examples

#### Solid-void properties

A short cantilevered beam modeled in 2D was picked since it can be compared with typical results of usually used compliance based methods. The initial model is shown in Fig. 2. Material was isotropic linear elastic with a modulus  $E = 70$  GPa, Poisson ration  $\mu = 0.3$  and chosen effective density 1, allowable von Mises stress 320 MPa. Void material properties were set to low modulus  $E = 70$  Pa,  $\mu = 0.3$ , low effective density  $10^{-6}$ , but high stress limit  $320 \times 10^6$  MPa setting void material far from failure.

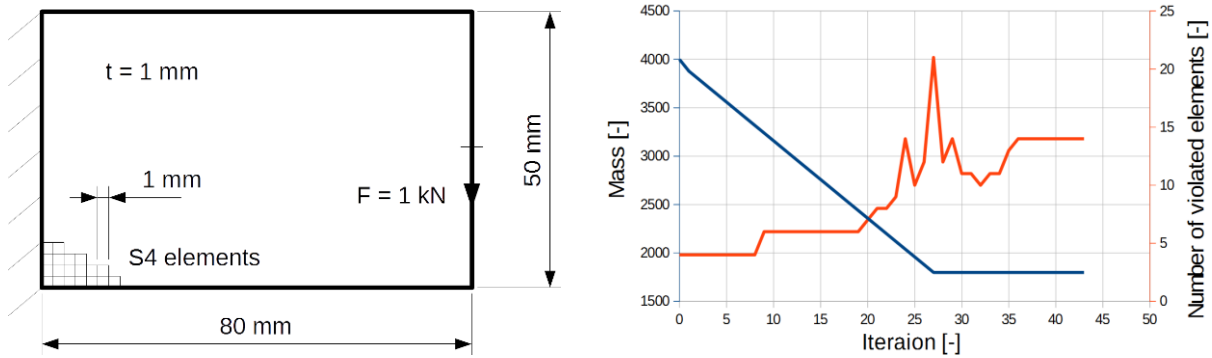
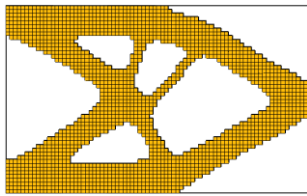
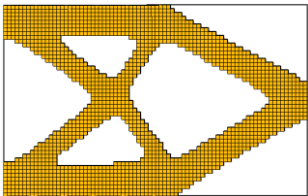
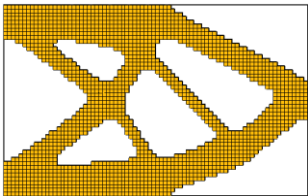


Fig. 2: Short beam schema (left), Mass and number of failed elements (right) for  $AR = 0.01$  and  $RR = 0.03$ .

Results for 3 different settings are in Tab. 1. Mass Addition Ratio  $AR = 0.01$  and Mass Removal Ratio  $RR = 0.03$  means that in each iteration 2 % of initial mass was removed. Resulting mesh for these settings corresponds well with a comparison of this task between BESO and SIMP method described by Huang (2007). In this case exactly the same filter scheme as in the literature for BESO method was used with same filter range 3 mm, which is described there and also in the book Huang (2010). Tolerance of failed elements was 10 over initial failed elements, i.e. 14 elements.

Tab. 1: Results for different Mass Addition Ratio and Mass Removal Ratio.

AR	0.005	0.01	0.015
RR	0.015	0.03	0.045
Iterations	63	43	31
Failing elements	15	14	12
Resulting mass	1899	1799	1899
Resulting mesh			

### Multiple properties

In the next example same geometry as in Fig. 2-left was used. A difference was in using multiple materials. First material was the same (Al alloy in Tab. 2). Second material had lower properties (with effective density as a ratio of magnesium and aluminum density  $1.7 / 2.8 = 0.607$ , void material was set in the similar way as previously. Mass Addition Ratio  $AR = 0.01$  and Mass Removal Ratio  $RR = 0.03$  were taken as relative values to actual mass (not related to initial mass as in the first example). In case of multiple properties (states) it is not possible to use simple filtering of sensitivities as previously. Instead open-close filter working on element states was used with radius 1.5 mm. This morphology based filter works on principles used in topology optimization by Sigmund (2007).

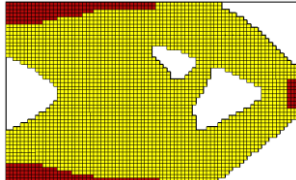
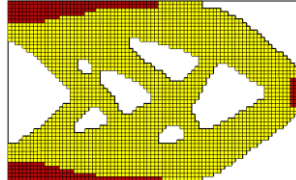
Tab. 2: Used material properties.

		Al alloy	Mg alloy	Void material
E	[GPa]	70	45	$45 \times 10^{-6}$
$\mu$	[-]	0.3	0.3	0.3
Effective density	[-]	1	0.607	$0.607 \times 10^{-6}$
Allowable von Mises stress	[MPa]	320	150	$150 \times 10^6$



In the first run model finished on higher mass then in case of 1 material (stronger one) in the previous example because of violated elements. Higher mass was caused by removing least effectively used material which was also stronger one (farther from allowable stress) so that softer material stayed also less effectively used. Second run was a continuation of the first one where elements, which ended previously in the stronger state, were frozen by excluding from optimization domain. This process led to significantly lower mass but also more elements with exceeded allowable stress (Tab. 3).

*Tab. 3: Results for the model with 2 solid materials and void material.*

	First run	Continuation	<div style="display: flex; align-items: center; justify-content: center;"> <div style="width: 20px; height: 10px; background-color: red; margin-right: 5px;"></div> Al alloy  <div style="width: 20px; height: 10px; background-color: yellow; margin-right: 5px; margin-top: 5px;"></div> Mg alloy </div>
Iterations	40	19	
Failing elements	7	17	
Resulting mass	2042	1433	
Resulting mesh			

#### 4. Conclusions

The method, which was described, was tested on simple examples. Short beam example lead to the result corresponding with BESO and SIMP method for a “solid” or “void” material, although some level of result dependency on input parameters is obvious from Tab. 2. Second example tested switching among different properties from a prescribed list given by 2 solid materials and void material. Manual freezing of elements in stronger state was needed to achieve lower mass which was expected by adding softer material in compare to the first example. Programmed optimization method can be used on more complex problems but with aware that it may automatically finish too early and results can be dependent on parameter settings.

#### Acknowledgement

The research leading to these results has received funding from the MEYS under the National Sustainability Programme I (Project LO1202).

#### References

- Denk, M. (2016) Entwicklung einer Applikation für eine automatisierte multiphysikalische Topologieoptimierung und Geometrierückführung. Hochschule für angewandte Wissenschaften München.
- Huang, X. and Xie, Y.M. (2007) Convergent and mesh-independent solutions for the bi-directional evolutionary structural optimization method, *Finite Elements in Analysis and Design*, 43, 14, pp. 1039-1049.
- Huang, X. and Xie, Y.M. (2010) *Evolutionary Topology Optimization of Continuum Structures: Methods and Applications*. John Wiley & Sons. Hoboken, NJ, USA.
- Ramani, A. (2011) Multi-material topology optimization with strength constraints. *Struct Multidisc Optim* 43, pp. 597-615. DOI 10.1007/s00158-010-0581-z.
- Sigmund, O. (2001) A 99 line topology optimization code written in Matlab. *Structural and Multidisciplinary Optimization*, 21, pp. 120–127. DOI: 10.1007/s001580050176.
- Sigmund, O. (2007) Morphology-based black and white filters for topology optimization. *Struct Multidisc Optim* 33, pp. 401-424. DOI: 10.1007/s00158-006-0087-x.
- Querín, O.M. (1997) *Evolutionary Structural Optimisation: Stress Based Formulation and Implementation*. PhD. Dissertation, Department of Aeronautical Engineering, University of Sydney.
- Zuo, H.Z. and Xie, Y.M. (2015) A simple and compact Python code for complex 3D topology optimization. *Advances in Engineering Software* 85, pp. 1-11.

## **A NEW METHOD OF MAGNETORHEOLOGICAL DAMPER QUALITY EVALUATION**

**O. Macháček<sup>\*</sup>, M. Kubík, P. Novák**

**Abstract:** *The paper describes the comparison of magnetorheological dampers controlled by semi-active algorithm with different parameters in one suspension system. Response time, dynamic range and damping in activated state are the most important parameters of MR damper. Without any analysis it is extremely difficult to determine the best setting of these parameters. The analysis mentioned in this study compares acceleration transmissibility of system with different damper parameters. This comparison is based on conversion of transfer function into the newly defined single value - transfer coefficient. The more suitable parameters of MR damper, the lower transfer coefficient is exhibited by the suspension system. The analysis also shows that the high-efficient MR damper should have response time as short as possible. Furthermore, it could be inefficient or even counterproductive to achieve the highest dynamic range for each value of damping in activated state. The method of MR damper quality evaluation helps to define the best parameters of MR damper for the specific suspension system where the damper is going to apply.*

**Keywords:** MR damper, Semi-active, Adaptive, Acceleration transmissibility, Transfer coefficient.

### **1. Introduction**

Magnetorheological (MR) dampers can change damping due to magnetorheological effect described by Winslow (1949). In adaptive mode, the most important parameters are damping forces in activated and inactivated state, Yang (2002) referred the ratio between them as dynamic range. There are several ways how to improve the dynamic range, for example by friction elimination mentioned in our previous study, Macháček (2016).

Besides, the damping in activated state and dynamic range, in semi-active mode there is another essential parameter – response time. This fact was confirmed by Eslaminasab (2008) for semi-active suspension performance on 1 DOF system, or by Strecker (2015) for the quarter model of car suspension.

The response time of MR damper is an interval necessary to change the damping force. The measurement published by Strecker (2015) confirm, that the damping force increase or decreases exponentially, when the control signal is much faster than the response time of MR damper. Therefore, it is hard to detect exactly finish of force increase or decrease. For that reason the response time of MR damper is defined as a period necessary for change from 0 % to 63.2 % or from 100 % to 36.8 % of damping force, see Goncalves (2002).

There are many algorithms of semi-active control which improve efficiency of MR damper compared with the adaptive mode, see Liu (2005). Liu compared several algorithms by acceleration transmissibility. This curve can be also called transfer function but only for linear systems. The lower the transfer the more suitable algorithm for vibration elimination of sprung mass.

The aim of this work is to evaluate the impact of different adjustment of MR damper to the specific semi-active suspension system behaviour. And define a combination of the parameters (time response, dynamic range and damping in activated state) which exhibits the lowest transfer of vibration.

---

<sup>\*</sup> All authors: Institute of Machine and Industrial Design, Brno University of Technology, Technická 2896/2, 616 69 Brno; CZ, Ing. Ondřej Macháček: Ondrej.Machacek@vutbr.cz

## 2. Methods

A chosen suspension system was created in multi-body software ADAMS view 2012, the system is described in chapter 2.1. Moreover, a new method of MR damper quality evaluation in respect of sprung mass vibration elimination. The method is described in chapter 2.2. It is based on the acceleration transmissibility comparison using a newly defined single value - transfer coefficient.

### 2.1. Model of suspension system

A simple suspension system with one degree of freedom has been chosen, see Fig. 1. It consists of two rigid bodies, the first one - base is cinematically excited by acceleration  $a_0$  in vertical direction. The excitation respects sweep sine function in frequency range  $0 - 100 \text{ Hz}$  and amplitude  $a_{0max} = 9.81 \text{ m/s}^2$ . The second one: sprung mass, has mass  $m = 100 \text{ kg}$ , it is linked in vertical direction and the response of acceleration  $a_1$  can be observed there. There is spring and damper between the sprung mass and the base. The stiffness of the spring is  $k = 395\,000 \text{ N/m}$ , so the natural frequency of the suspension system is  $f_n = 10 \text{ Hz}$  and critical damping  $C_c = 12\,570 \text{ Ns/m}$ . The sampling frequency used for the simulations was  $f_s = 4 \text{ kHz}$ .

The damper in model is considered as a magnetorheological, therefore the damping  $C$  is adjustable. The ON/OFF skyhook algorithm was used for semi-active mode in this study. The algorithm control the damping according to equations (1 – 2), shown in described by Liu (2005):

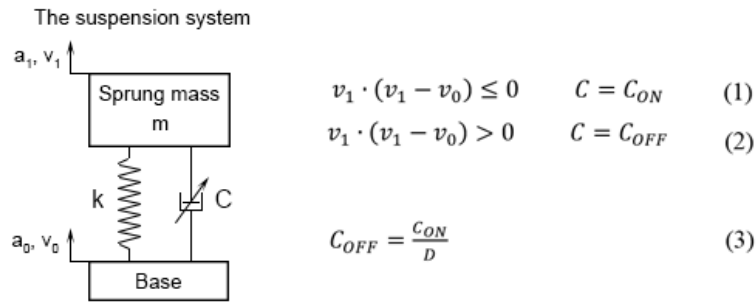


Fig. 1: The suspension system and equations of control algorithm ON/OFF Skyhook.

Where  $v_1$  is velocity of the sprung mass and  $v_0$  is velocity of the base. Both variables are monitored in the direction of excitation (vertical).

The damping of the MR damper in activated state  $C_{ON}$  was set between  $0.2 C_c$  and  $1 C_c$  in this article. The damping is considered linear, therefore the damping in inactivated state  $C_{OFF}$  can be defined by dynamic range using equation (3).

Ideally, the skyhook algorithm uses zero as  $C_{OFF}$ , thus the dynamic rang has to be infinitely high  $D = \text{inf}$ . This impossible scope was taken into account only for comparison with other feasible dynamic ranges  $D = 2; 5; 7; 10$ .

Infinitely short response time  $t_{re} = 0 \text{ ms}$  is another idealization which is often used in simulations of MR. However, it was also used in this study for comparison with other response times  $t_{re} = 1 \text{ ms}; 2 \text{ ms}; 5 \text{ ms}; 10 \text{ ms}$ .

### 2.2. Transfer coefficient

Frequency response of sprung mass acceleration  $a_1$  and frequency response of excitation (base acceleration)  $a_0$  were used for the acceleration transmissibility  $T$  calculation. Both frequency responses were converted into frequency domain using FFT with the same parameters. The fraction was counted separately for each the frequency component:

$$T(f) = \frac{a_1(f)}{a_0(f)} \quad (4)$$

A newly defined variable for the MR damper quality evaluation, transfer coefficient  $T_c$ , is defined as a sum of power spectral density of the suspension system acceleration transmissibility.

$$T_c = \int_{f_{min}}^{f_{max}} T(f)^2 \cdot df \quad (5)$$

Frequency range of the sum was chosen with respect to the excitation from  $f_{min} = 0 \text{ Hz}$  to  $f_{max} = 100 \text{ Hz}$ .

### 3. Results and discussion

Many simulations with parameters described previously were provided. The results of these simulations help to answer the questions. The first one about response time was tested for several different damping. The results showed, as expected, that the shorter response time the lower transfer coefficient was in all configurations. However, only one damping in activated state ( $C_{on} = 1 \cdot C_c$ ) is presented in Fig. 2. There is the transfer coefficient – dynamic range dependency on the left of the figure. The acceleration transmissibility curves which was used for transfer coefficient calculation for the dynamic range  $D = 10$  (marked by triangles) are shown on the right of the Fig. 2.

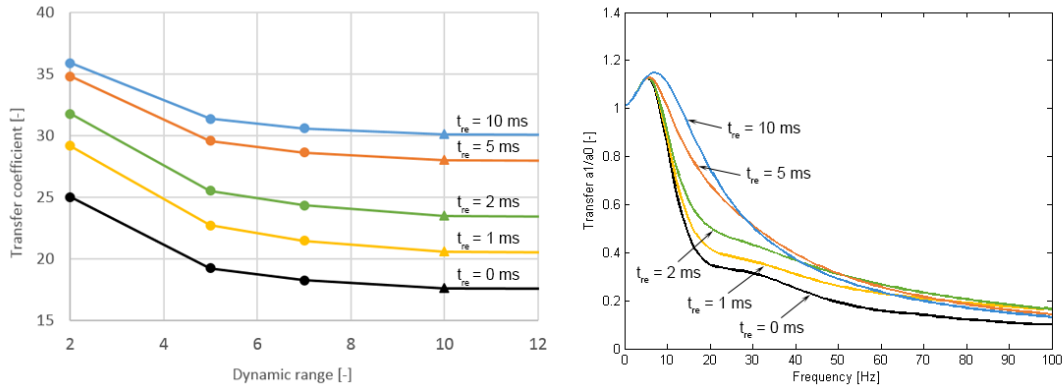


Fig. 2: The MR damper response time influence to the transfer coefficient for  $C_{on} = 1 \cdot C_c$  and different dynamic range (left) for  $C_{on} = 1 \cdot C_c$  and  $D = 10$  (right).

The most appropriate adjusting of MR damper depends on the dynamic range. When the dynamic range is  $D = 1$ , the MR damper works with constant damping. The system with low damping exhibits higher transfer near natural frequency than highly damped system. However the lower damping of the system cases lower transfer for higher frequencies than highly damped system, see Fig. 3-left.

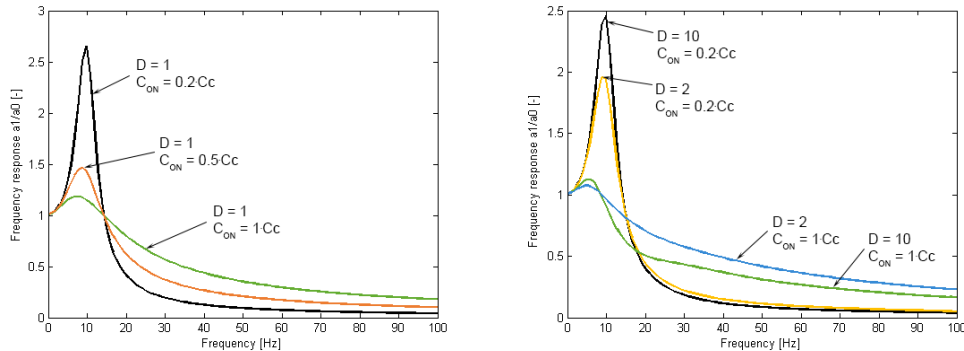


Fig. 3: The acceleration transmissibility curves for different adjusting of MR damper with constant damping (left) and for semi-active damper (right).

The same phenomenon can be observed in semi-active mode (when the dynamic range  $D > 1$ ), but effect of the phenomenon is not the same for all configurations of the system. Dynamic range increasing for  $C_{ON} = 0.2 \cdot C_c$  significantly increases the transfer near natural frequency while, decreasing of transfer for high frequencies is marginally. Otherwise, dynamic range increasing for  $C_{ON} = 1 \cdot C_c$  insignificantly increase the transfer near natural frequency while, decreasing of transfer for high frequencies is significant. Thus, increasing of dynamic range can be considered as positive for high damped system, and negative for low damped system with semi-active damper.

This feature affects the results of transfer coefficient calculation. Therefore, it is possible to find minimum of transfer coefficient for each dynamic range of MR damper, which is marked by square in Fig. 4. This minimum can be considered as the best adjustment of  $C_{ON}$ .

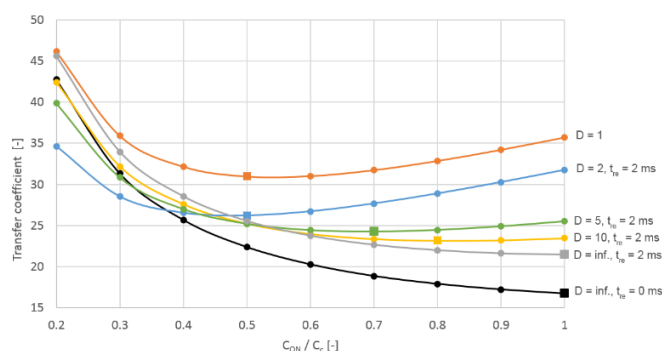


Fig. 4: The transfer coefficients for different adjusting of MR damper parameters.

#### 4. Conclusions

This paper presents a new method of efficiency evaluation of MR damper in a suspension system using comparison of acceleration transmissibility curves, due to conversion the curve into single value – transfer coefficient. Calculation of the transfer coefficient is based on sum of power spectral density of suspension system acceleration transmissibility. The results showed that for MR damper with short time response and high dynamic range, it is beneficial to increase the damping in activated state.

Application of described methodology shows that the shorter response time of MR damper the better. Moreover, when the response time of semi-active damper is higher than  $10\text{ ms}$ , the transfer coefficient is higher than the lowest transfer coefficient achieved by MR damper with constant damping. Significant decrease of transfer coefficient was achieved with response time  $2\text{ ms}$  or lower.

The higher dynamic range the lower transfer coefficient is valid only for  $C_{ON} > 0.5 C_c$ . MR damper with very high dynamic can be advantageously used in the suspension system with damping in activated state near to critical. But, the differences between the transfer coefficient for  $D = \text{inf}$  and  $D = 10$  are minimal. Therefore, the dynamic range  $D = 10$  can be considered as suitable for the suspension system described in this study. The optimal damping of the MR damper in activated state for this dynamic range is  $C_{ON} = 0.8 C_c$ . When the ON/OFF skyhook was used for control of MR damper with these parameters, the transfer coefficient is reduced by 25 %, compared with the best adjustment of damper with constant damping.

#### Acknowledgement

This study could be provided thanks to the kind sponsorship of various grants and numerous agencies. We would like to thank explicitly to the GAČR 17-10660J, GAČR 17-26162S, FCH/FSI-J-17-4534 and FSI-S-17-4428.

#### References

- Eslaminasab, N. and Golnaraghi, M.F. (2008) The effect of time delay of the semi-active dampers on the performance of on-off control schemes, in: Proc. of the Congress and Exposition 2007, ASME, pp. 1911-1918.
- Goncalves, F.D., Koo, J.H. and Ahmadian M. (2003) Experimental Approach for Finding the Response Time of MR Dampers for Vehicle Applications, in: Proc. 19th Biennial Conference on Mechanical Vibration and Noise, ASME, pp. 425-430.
- Liu, Y., Waters, T.P. and Brennan, M.J. (2005) A comparison of semi-active damping control strategies for vibration isolation of harmonic disturbances. Journal of Sound and Vibration [online]. 280, 1-2, pp. 21-39.
- Macháček, O., Kubík, M., Mazůrek, I., Strecker, Z. and Roupec, J. (2016) Frictionless bellows unit connected with the magnetorheological valve, in: Proc. Engineering mechanics 2016, Svratka, pp. 354-357.
- Strecker, Z., Roupec, J., Mazůrek, I. and Klapka, M. (2015) Limiting factors of the response time of the magnetorheological damper. International Journal of Applied Electromagnetics and Mechanics, 47, 2, pp. 541-550.
- Strecker, Z., Mazůrek, I., Roupec, J. and Klapka, M. (2015) Influence of MR damper response time on semiactive suspension control efficiency. Meccanica, 50, 8, pp. 1949-1959.
- Winslow, W.M. (1949) Induced Vibration of Suspensions. Journal of Applied Physics, 20, 12, pp. 1137-1140.
- Yang, G.B.F., Carlson, J.D. and Sain, M.K. (2002) Large-scale MR fluid dampers: modelling and dynamic performance considerations. Engineering Structures, 24, 3, pp. 309-323.

## DAMAGE TO ADHESIVE SINGLE LAP JOINT MADE OF MATERIALS WITH DIFFERENT PROPERTIES UNDER STATIC LOADING CONDITIONS

P. Maćkowiak\*, B. Ligaj\*\*

**Abstract:** *Adhesive joints are increasingly used in construction of machines. Calculation models for determination of strains in adhesive joints used by engineers are burdened with simplification errors. Tests of joints of homogenous materials, especially metals have already been widely discussed in literature. The goal of this study is to define actual strength of a single lap joint made of homogenous and non-homogenous materials. The tests results have confirmed that a decrease in Young modulus of bonded materials is accompanied by reduction of the joint temporary strength. It was observed that the amount of work needed for a specimen to be destroyed is similar for joints characterized by cohesion fracture through the glue layer. For specimens with adhesive or cohesive fracture running through the bonded material, the work assumes lower values.*

**Keywords:** Adhesive joint, Single lap joint, Stress distribution, Hybrid joints.

### 1. Introduction

An adhesive joint involves bonding surfaces of two elements by means of a glue layer. Strength of the joint depends on adhesion forces (ability of the glue to adhere to a material surface) and cohesion forces (internal cohesion) hardened glue and the bonded material (Godzimiski, 2002 and Skorupa et al., 2013).

There are a few different calculation models of single lap joints which allow to determine the distribution of stress in the bonded joint. The most commonly used calculation model assumes a uniform distribution of tangent stresses throughout the joint. Volkersen model (Volkersen, 1938), closer to reality, includes strain of the connected elements. Goland Reisner (Goland et al., 1940) model neglects the impact of bending moment. Benson and Kesley model (Benson, 1970) additionally includes the theory of material strength which assumes that tangent stresses cannot occur on free surfaces. Subsequently, the maximum stresses do not occur on the edges of the joint but in their proximity (Hart-Smith, 1973 and Lucas et al., 2009 and Silva et al., 2012).

Connection of elements with different stiffness makes the distribution of stresses unsymmetrical in relation to the joint center and the maximum occurs at the end of the stiffest part.

An increase in differences of the bonded elements stiffness is accompanied with a drop in the joint stability expressed by the ratio of average stresses to maximum stresses (Hart-Smith, 1973 and Silva et al., 2011)

The goal of this study is to compare temporary strength of single lap joint specimens of material with different mechanical properties. Additional aim of the study is to compare work  $L$  involved in fracture of the specimens. The scope of work included an analysis of tests results for five types of joints made from materials: steel 1.0503, aluminum D16CzATW and epoxide- glass laminate.

---

\* mgr inż. Paweł Maćkowiak: Wydział Inżynierii Mechanicznej, Uniwersytet Technologiczno-Przyrodniczy w Bydgoszczy, al. Prof. S. Kaliskiego 7, 85-796 Bydgoszcz, PL, pawel.mackowiak@utp.edu.pl

\*\* dr hab. inż. Bogdan Ligaj: Wydział Inżynierii Mechanicznej, Uniwersytet Technologiczno-Przyrodniczy w Bydgoszczy, al. Prof. S. Kaliskiego 7, 85-796 Bydgoszcz, PL, bogdan.ligaj@utp.edu.pl



## 2. Methods

### 2.1. Test specimens

The specimens were prepared according to norm PN-EN 1465:2009. Dimensions of the specimens are given in Fig. 2. The surfaces to be bonded underwent grinding with abrasive paper with grain of P240, and then were cleaned with acetone .

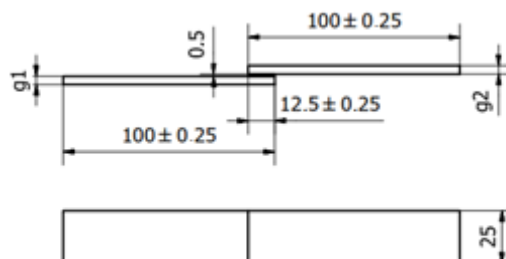


Fig. 1: Dimensions of specimens used for the tests.

Some parts of specimens were glued by methacrylic M20 in a device providing them with an axial position. Equal thickness of the joint was provided through placing in it a copper wire with diameter 0.5 mm. A clamp equal to 300n was used. The average thickness of the connected elements for given materials was respectively: steel 1.0503 –  $g = 3.89$  mm (standard deviation 0.03 mm), aluminum D16CzATW –  $g = 3.87$  mm (standard deviation 0.04 mm), polyester-glass laminate  $g = 3.61$  mm (standard deviation 0.06 mm). Mechanical properties are presented in Tab. 1. Five specimens of each joint type were prepared and tested. The results are presented in Tab. 2.

Tab. 1: Properties of Construction Materials (Ligaj, 2015 and Ligaj, 2015).

Material		Steel 1.0503 (C45)	Aluminum alloy D16CzATW	Polyester-glass laminate
Tensile strength	MPa	682.0	460.0	213.4
Yield limit	MPa	458.0	336.0	-
Prolongation	%	24.3	25.2	2.4
Modulus of elasticity	GPa	215.00	68.40	11.56

Tab. 2: Types of joints

Lp.	Bonded material		Denotation
	Element 1	Element 2	
1	Steel 1.0503	Steel 1.0503	S-S
2	Steel 1.0503	Aluminum alloy D16CzATW	S-A
3	Aluminum alloy D16CzATW	Aluminum alloy D16CzATW	A-A
4	Steel 1.0503	Polyester – glass laminate	S-L
5	Polyester-glass laminate	Polyester -glass laminate	L-L

### 2.2. Test stand

Tests were performed on a strength testing machine Instron. During the tests the displacement parameter was controlled for which a constant value was accepted to be equal to 1 mm/min. The force was measured by means of a dynamometer with 10 kN range. Displacement was assumed to be consistent with the machine traverse. Force was applied to axes of the specimens, in the middle of the joint thickness through application of pads in the strength testing machine gripe. Thickness of the pad was the thickness of the opposite element and of the joint.

### 2.3. Tests results

Exemplary dependencies of force in the function of displacement  $F = f(s)$  for each type of the joint are presented in Fig. 2a. Mean values of forces destroying a given type of joint are presented in Fig. 2b.

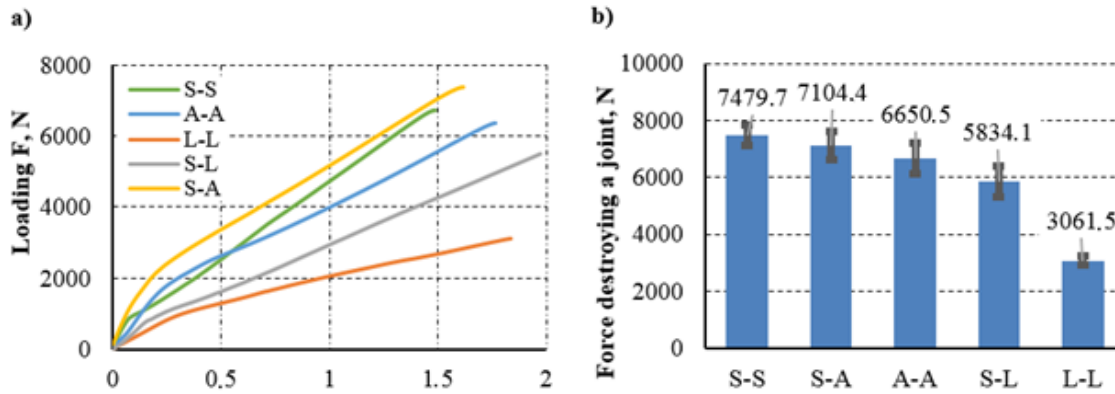


Fig. 2: a) Dependence of force in the function of displacement  $F = f(s)$  for tested adhesive joints; b) Presentation of maximum destruction forces  $F$ .

### 3. Conclusions

It was observed that the lower the stiffness of bonded elements the lower the temporary strength of adhesive joints. Damage to an adhesive joint involving bonding materials with different Young modulus occurred at a force whose value was a medium value of forces which destroy homogenous joints of these materials. This means that an increase in a joint strength is more affected by total stiffness of bonded elements. Results of tests were not consistent with the analysis of stress distribution according to Volkersen method. This analysis reveals higher maximum stresses for tested joints S-L or S-A than for homogenous joints with lower added stiffness, respectively L-L and A-A, which is inconsistent with experimental tests. Joints with higher total stiffness of bonded elements can be more resistant to bending moment. It is included in Golan-Reissner analysis, however it does not find application in joints made of non-homogenous elements. Stress at break that occurs in result of bending can have a significant influence on strength of the glue layer. Acceptance of linear properties of glue can also be the cause of error in majority of calculation models.

Analysis of diagrams  $F = f(s)$  (Fig. 2a) enabled calculation of the value of amount of work needed for each specimen to be destroyed. The method for determination of this work is presented in Fig. 3a. The determined values were averaged for a given type of joint and standard deviation was calculated. The results are presented in Fig. 3b.

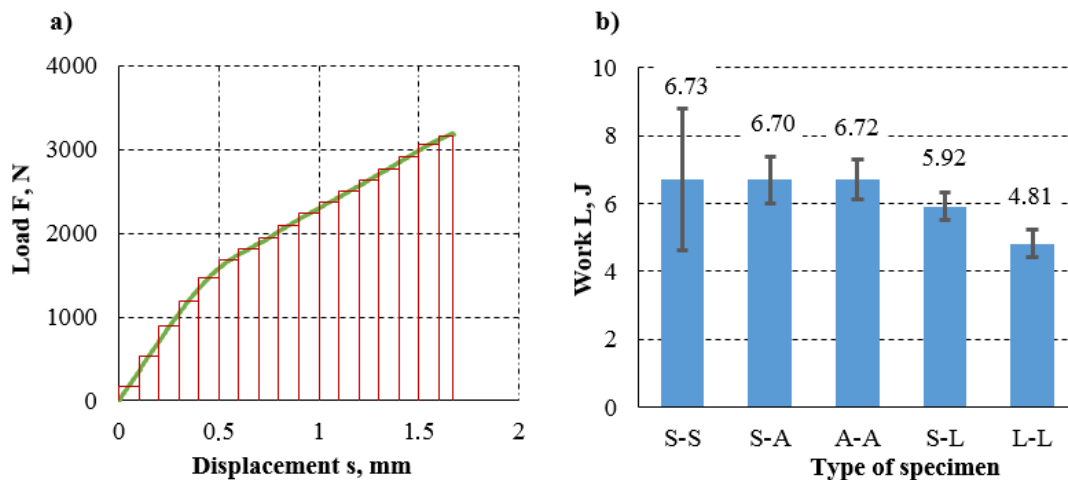


Fig. 3: a) Method for determination of work needed for a given specimen to be destroyed; b) Mean values of work performed until destruction of the specimens of a given joint with standard deviation.

The calculation results of the amount of work needed for joints of the type S-S, S-A, A-A to be destroyed, revealed similar values. The character of damage to specimens of these joints was found to be of adhesive. Joints, whose one part was made of laminate showed local separation of the laminate in the

closest to the joint layer (Fig. 4a). Full one sided separation of laminate was found for specimens in Fig. 4b.

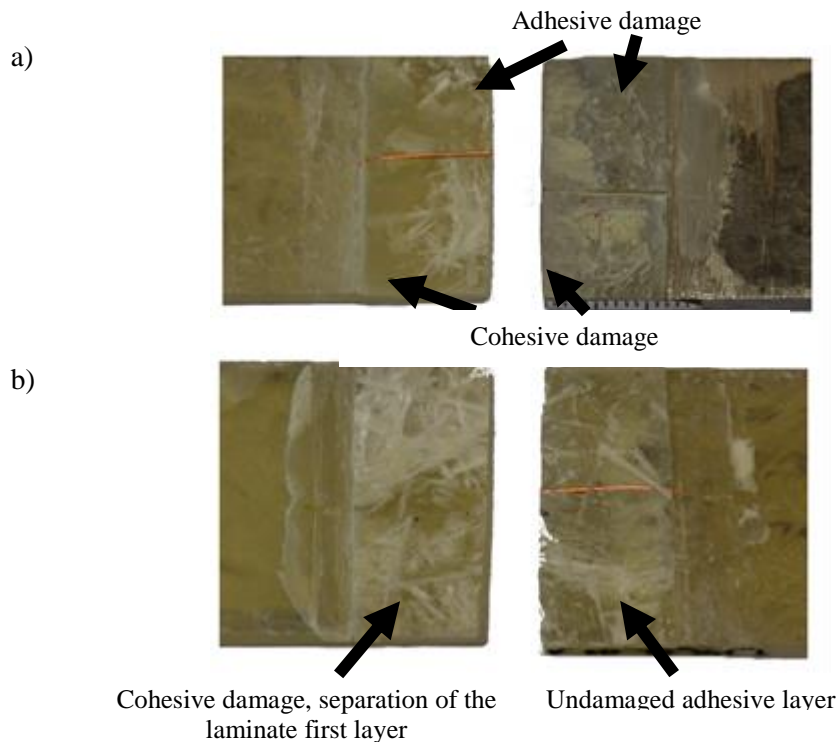


Fig. 4: Fractures of bonded joints: a) laminate – steel 1.0503; b) laminate – laminate.

## References

- Benson, N.K. (1970) Influence of stress distribution on the strength of bonded joints, Adhesion. Fundamentals and Practice, Elsevier.
- Godzimirski, J. (2002) Ad-hoc strength of structural adhesive joints, Wydawnictwo Naukowo-Techniczne, (in Polish).
- Goland, M. and Reissner, E. (1940) The stresses in cemented joints, J Appl Mech, 66, A17-A27.
- Hart-Smith, L.J. (1973) NASA Contract Report, NASA CR-112235.
- Ligaj, B. (2015) Cumulative Energy of Fatigue Cracking under Variable Amplitude Loading on the Example of C45 Steel, Solid State Phenomena, 224, 51-56.
- Ligaj, B. (2015) Programmable Tests of Fatigue Life for D16CzATW Aluminum Alloy, Machine Dynamics Research, vol. 39, No. 2, s. 61-70.
- Lucas, F.M., Paulo, J.C., Adams, R.D. and Spelt, J.K. (2009) Analytical models of adhesively bonded joints – Part I: Literature survey, International Journal of Adhesion & Adhesives, 29, 319-330.
- Norma PN-EN 1465:2009, Glues - Determination of shear strength when stretching to joints, (in Polish).
- Silva, L.F.M, Dillard, D.A, Blackman, B. and Adams R.D. (2012) Testing Adhesive Joints, Weinheim: John Wiley & Sons.
- Silva, L.F.M, Öchsner, A. and Adams R.D. (2011) Handbook of Adhesion Technology, Berlin, Heidelberg: Springer Berlin Heidelberg.
- Skorupa, A. and Porębska, M. (2013) Cohesive connections, Wydawnictwo PWN, Warszawa (in Polish).
- Volkersen, O. (1938) Rivet strength distribution in tensile-stressed rivet joints with constant cross-section, Luftfahrtforschung, 15, 41-47.

## INNOVATIVE CONCRETE-POLYURETHANE COMPOSITE BLOCKS LOCATED IN THREE-LAYER WALL – THERMAL NUMERICAL ANALYSIS

M. Major<sup>\*</sup>, K. Kuliński<sup>\*\*</sup>, I. Major<sup>\*\*\*</sup>

**Abstract:** *In this paper thermal conductivity numerical analysis of an innovative blocks made of concrete with polyurethane inserts/injects, located in a three-layer wall was performed. Mentioned polyurethane cross pads were assumed to be inserted or injected in specially formed holes in the process of production. Moreover, it was assumed that the wall should meet the conditions of building intended for continuous human presence. In order to estimate the percentage warmth comfort improvement and thermal conductivity the same wall with the use of solid concrete blocks was investigated. On the basis of obtained results one can state that the heat resistance was only slightly improved via the polyurethane cross pads inserts/injects in comparison with solid concrete blocks, whereas measurable benefits could only be observed in the wall without separate insulation layer. Presented numerical analyses were performed with the use of finite element method based software – ADINA program.*

**Keywords:** ADINA, Thermal analysis, Heat flow, Concrete-polyurethane, Composite.

### 1. Introduction

Nowadays a wide access to computers and the finite element method based software allow to perform experimental tests of almost any model without the necessity of purchasing expensive research equipment and materials. Utilization of such software not only allows to solve simply stated boundary problems, but also allows to identify other various types of phenomena. According to that due to the simple thermal load acting in construction, results not only concerning thermal conductivity, heat flow/flux can be obtained, but also results concerning stresses, displacements etc. can be investigated. As an example wave propagation phenomenon in simple elastic structures was discussed in (Major and Major 2014). It is worth to notice that finite element method solutions may be utilized in almost any area of life sciences – statics, dynamics, fluid flows, electromagnetics etc.

Today composite materials are frequently used in civil engineering due to their special mechanical properties. The most common composites in civil engineering are concrete with steel and also steel with rubber. Such utilization of two different materials allow to combine advantages of separate materials into an individual composite. In the first mentioned case i.e. concrete with steel, the compressive load bearing capacity of concrete with the high tensile load bearing capacity of steel provide composite material with relatively high resistance to the both types of loading. In the second case i.e. utilization of steel and rubber allow to obtain composite with high vibrations damping factor at relatively high bearing capacity. Appropriate composite materials arise mainly due to a special market demands for materials with determined properties.

In this paper composite block made of concrete with polyurethane inserted/injected pads located in a three-layer wall in terms of thermal conductivity was investigated. Such wall comprised of bricks with mortars as an exterior layer, wool insulation in the middle of the wall and mentioned composite blocks as an interior layer, respectively. In considered composite, concrete blocks in the production process might

---

<sup>\*</sup> Assoc. Prof. Eng. Maciej Major, PhD.: Department of Steel Structures and Building materials, Częstochowa University of Technology, Akademicka 3 street; 42-200 Częstochowa; PL, mmajor@bud.pcz.czest.pl

<sup>\*\*</sup> Eng. Krzysztof Kuliński, M.Sc.: Department of Concrete Structures and Geotechnics, Częstochowa University of Technology, Akademicka 3 street, 42-200 Częstochowa; PL, kkulinski@bud.pcz.czest.pl

<sup>\*\*\*</sup> Assoc. Prof. Eng. Izabela Major, PhD.: Department of Technological Mechanics and Engineering Graphics, Częstochowa University of Technology, Akademicka 3 street; 42-200 Częstochowa; PL, imajor@bud.pcz.czest.pl

have embedded special forms and after it removal, polyurethane cross pads could be inserted or injected. For the analysis purposes it was assumed that the wall had to meet the conditions of building intended for continuous human presence. In order to estimate the improvement of heat conditions in the composite wall and on the inner building surface, additionally a reference model made of exactly the same wall with solid concrete block was investigated. It is worth to notice that discussed composite block allowed transferring significant compressive forces – load bearing capacity of such block in comparison with solid concrete block was only slightly reduced via specially prepared holes. Due to the lack number of research concerning utilization of concrete with polyurethane inserts/injects, presented in this paper material may be treated as innovative. In order to solve stated heat transfer problem, finite element method approach with the use of ADINA program was chosen.

## 2. Numerical model

In order to perform numerical analysis of thermal conductivity and temperature redistribution, section of a wall made of bricks with mortars as an exterior layer, wool insulation in the middle and composite blocks as an interior layer was adopted. Separate bricks had following dimensions: length equal 0.25 m, width 0.12 m and height of 0.065 m, where mortars were assumed to be 1 cm thick. Thickness of wool insulation was assumed as 0.10 m. Separate composite block had: length equal 0.47 m, width 0.25 m and height equal 0.22 m. Mentioned dimensions were presented with respect to the Cartesian coordinate system, where length was measured along Y-axis, width along X-axis and height along Z-axis, respectively. The polyurethane cross pad inserts dimensions and their arrangement was presented in Fig. 1a, whereas whole numerical model was presented in Fig. 1b. Four different temperature measurement points were adopted on the top surface of composite block, which was presented in Fig. 2. Due to the boundary condition i.e. infinite length of model in both Z-axis directions, the precise location of measurement points on Z-axis had no meaning. Values of temperature from specified measurement points were read-out at four different time steps of the analysis i.e.  $t = 6, 12, 18$  and  $24$  hours.

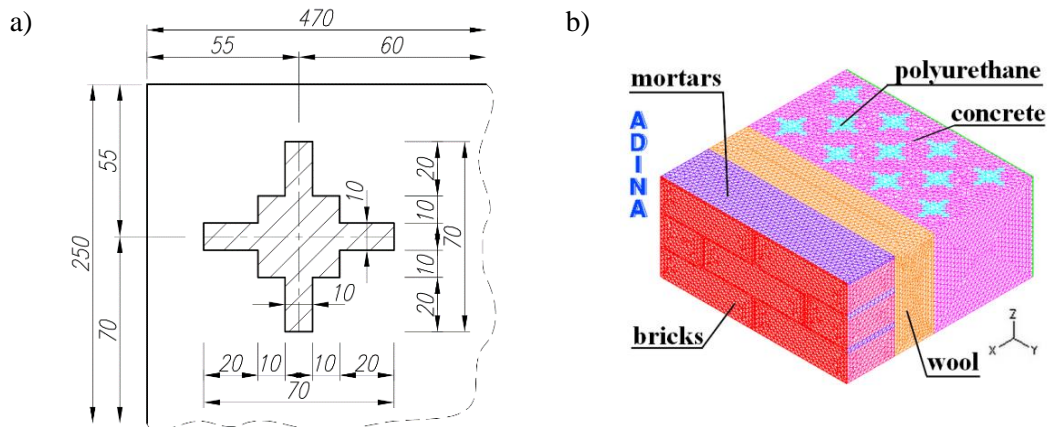


Fig. 1: Three-layer wall: a) arrangement and dimensions of polyurethane cross inserts/injects; b) discretized numerical model of the wall with composite block.

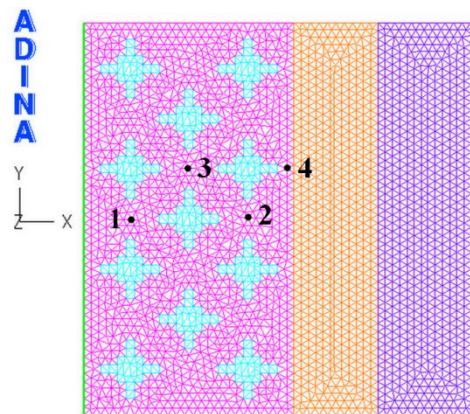


Fig. 2: Localization of temperature measurement points 1-4 on the top surface of the wall section.

Due to the fact that the wall had to meet conditions of a building intended for continuous human presence, on the basis of the polish standard of heat flow analysis PN-EN ISO 12831:2006, on the exterior wall surface temperature equal 20 °C was adopted, whereas on the exterior surface of the wall temperature of -20°C, respectively. Moreover, it was assumed according to the polish standard PN-EN ISO 6946:2008 that the convection on boundary surfaces (interior and exterior surface of the wall - “YZ” plane) acts horizontally. The heat resistance for the inner wall surface was adopted as  $R_{si} = 0.13$  and for the exterior wall surface as  $R_{se} = 0.04$ . Thermal properties for each utilized in the wall material were adopted in accordance with PN-EN ISO 6946:2008.

### 3. Results and discussion

According to the Polish standard PN-EN ISO 12831:2006 the coefficient of heat transfer for any partition is given via the following formula:

$$U = \frac{1}{R_{si} + \sum_{i=1}^n R_i + R_{se}} \quad (1)$$

where:  $R_{si}$  – denotes the thermal resistance of inner convection,  $R_i$  – denotes the thermal resistance of i-th material and  $R_{se}$  – thermal resistance of exterior convection, respectively. Knowing that  $R_i = d_i / \lambda_i$ , where  $d_i$  - denotes the i-th material thickness and  $\lambda_i$  is the i-th material thermal conductivity coefficient, it was possible to determine the composite heat transfer coefficient. For the solid concrete block mentioned  $\lambda$  coefficient was equal 2.00 W/m·K, whereas for the composite block 1.686 W/m·K, respectively. The percentage decrease of thermal coefficient was equal 15.7%, which in fact should significantly affect the temperature redistribution. The heat transfer coefficient for the whole wall section where composite was used stood at 0.341 W/m<sup>2</sup>K, whereas for the section of the wall with solid sandstone 0.344 W/m<sup>2</sup>K was obtained, respectively. It is worth to notice that for the separate concrete block heat transfer coefficient was equal 3.390 W/m<sup>2</sup>K, whereas for composite 3.142 W/m<sup>2</sup>K was obtained. The difference between mentioned values of heat transfer in the three-layered wall was minimal i.e. 0.003 W/m<sup>2</sup>K, while more significant difference of 0.248 W/m<sup>2</sup>K was obtained in case of single-layered wall made of only composites or solid concrete blocks. The other main advantage of composite blocks was good noise damping factor and relatively high compressive load bearing capacity in comparison to the solid concrete blocks. Obtained temperature values for four different time steps of the analysis and at four specified measurement points were presented in Tab. 1.

*Tab. 1: Temperature values obtained at specified measurement points and time steps on the composite and solid concrete block located in the three layer wall partition.*

		Temperature [ °C ]			
Model	Point	t = 6 h	t = 12 h	t = 18 h	t = 24 h
Composite	1	6.587	9.263	11.086	12.480
Solid	1	5.553	8.152	10.092	11.624
Composite	2	1.566	4.260	6.620	8.519
Solid	2	1.983	4.769	7.096	8.971
Composite	3	3.705	6.614	8.801	10.507
Solid	3	3.546	6.357	8.549	10.293
Composite	4	1.469	4.137	6.495	8.395
Solid	4	1.948	4.722	7.047	8.921

According to the presented values in Tab. 1 one can state that the composite block accumulates more heat near the interior side (compare point 1 for solid concrete block and composite at any time step) in comparison to the solid concrete block. That phenomenon was connected with the volume of concrete material. Knowing that the initial condition for all the layers of the wall was temperature equal 0 °C,



concrete material with lesser volume absorbed more heat from the interior, according to the rule that smaller area/volume is easier to heat in relation to the object with higher area/volume.

Moreover, the longer the way from the interior side the temperature started to change between two considered numerical models i.e. temperature near the wool insulation (compare point 2 and 4 at any time step) in the composite block was lower than for the solid concrete. That was connected with the conductivity of material used and lack of different material with lower conductivity embedded inside the solid concrete block. Comparing temperatures obtained in point 3 and 4 for both considered blocks at  $t = 24$  h, one can state that the difference in temperature for the composite block stood at  $2.112$  °C, whereas in the solid concrete  $1.372$  °C, which means that the temperature in the building interior would be easier to retain in case of composite blocks utilization.

The heat flux in the whole wall partition for both composite and solid concrete blocks at  $t = 24$  h was presented in Fig. 3.

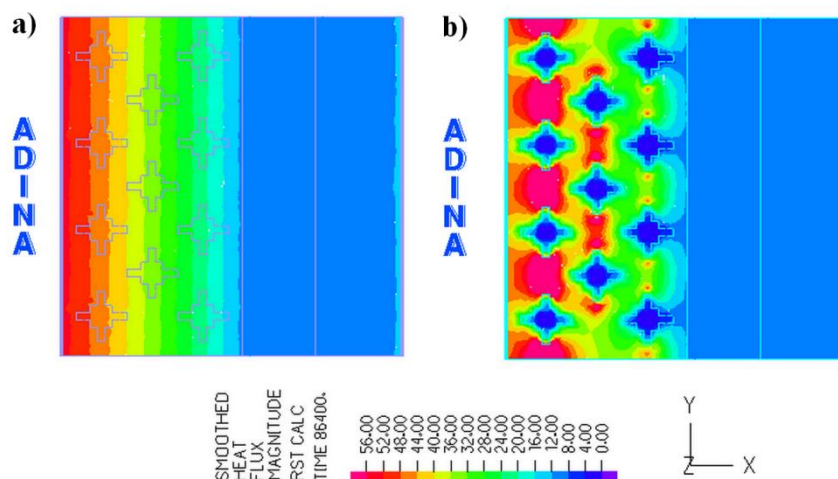


Fig. 3: Heat flux: a) three layer wall with solid concrete blocks;  
b) three layer wall with composite blocks.

#### 4. Conclusion

The finite element method approach today is very often utilized as an introduction to the expensive experimental tests. Via this method it is not only possible to analyse mechanical stresses and displacements but also other types of phenomena such as heat/fluid flow, effects of electromagnetics etc. Mentioned finite element method is not only used for small scaled problems but also in engineering problems such as validation of adopted solutions in building constructions (Cajka and Krejsa 2014; Melcer and Lajčáková 2014), bridges constructions (Vican and Sykora 2013) etc.

In this paper proposition of composite made of concrete with polyurethane foam cross inserts/injects was investigated in terms of thermal conductivity in three-layer wall. Due to the lack number of research concerning such connection of materials, presented composite may be treated as an innovative solution. It was shown that the composite in the three layer wall slightly changed the isotherms redistribution and there is slightly lesser heat loss. Moreover, it should be noted that presented solution have significantly better noise damping factor and comparable compressive load bearing capacity in relation to the solid concrete block.

#### References

- Cajka, R. and Krejsa, M. (2014) Validating a computational model of a rooflight steel structure by means of a load test, *Applied Mechanics and Materials*, 501, pp. 592-598.
- Major, I. and Major, M. (2014) Modeling of wave propagation in the ADINA software for simple elastic structures, *Advanced Materials Research*, 1020, pp. 171-176.
- Melcer, J. and Lajčáková, G. (2014) Comparison of finite element and classical computing models of reinforcement pavement, *Advanced Material Research*, 969, pp. 85-88.
- Vican, J. and Sykora, M. (2013) Numerical analysis of the bridge orthotropic deck time dependent resistance, *Komunikacie*, 15, pp. 112-117.

## STABILITY MARGINS EXPERIMENTAL SEARCH OF AN AEROELASTIC SYSTEM

P. Malínek\*

**Abstract:** Aircraft developers and builders commonly design and produce potentially unstable aeroelastic systems. Detailed and reliable knowledge of real dynamic properties of the system has a crucial importance to safety requirements compliance. Dynamic stability margins of an aeroelastic system are identified analytically in the first step and finally verified experimentally. Dynamic response analysis of a real aeroelastic system under operational conditions represents key approach to the experimental study of the systems stability margins in a complex experimental verification process. Operational modal parameters in the form of modal frequencies, modal damping and mode shapes are identified on each stage of operational parameters combination series. Modal damping parameter evolution is of special interest during the testing. The paper presents a technique of combined approaches to the dynamic response analysis during wind tunnel dynamic stability margins testing of an aeroelastic demonstrator.

**Keywords:** Aeroelastic system, Modal parameters, Dynamic response, Damping identification.

### 1. Introduction

Measured vibration response of an aeroelastic system contains valuable information on the dynamic stability of the system at actual operational conditions. Starting by linearity assumption of the mechanical system, it is reasonable to treat with a series of modal models of the system, related to a series of operational conditions states. Basic modal model describes specific aircraft type structure dynamic properties at laboratory conditions. Classical experimental technique Ground vibration test is a standard milestone of a prototype testing and provides the basic modal model suitable to enter in to the fine tuning process of a numerical model. Tuned numerical model then serves as a base for flutter clearance and other simulation of aircraft structural dynamics related phenomena: gust response, excitation due to failure of a rotating part. Operational modal analysis and other experimental dynamics techniques are at disposal to extract modal parameters of aeroelastic system under operational conditions. Parameters of operation are gradually varied according to a carefully designed experimental procedure. Vibration amplitude limit criterion is closely checked in real time to prevent catastrophic destruction of a tested system. Vibration responses are measured and recorded at defined operational parameters levels. Modal parameters, specially, modal damping of potentially unstable modes are then evaluated, to locate operational state of the system between stable – unstable. The paper presents a technique of combined approaches to dynamic response analysis, during wind tunnel stability margins testing of a whirl flutter aeroelastic demonstrator. Theoretical background sketch describes concepts of modal model, dynamic response and stability criteria. Concepts of interpretation set  $\Sigma$  and parameter space  $\Pi$  are explained. Potentially unstable mode detection and tracking in the process of variation of operational parameters are demonstrated on real vibration data measured during whirl flutter aeroelastic demonstrator wind tunnel testing campaign.

### 2. Mathematical model

We begin a brief theoretical review with standard mathematical model of linear structure in physical space or in the state space (Bold symbols denote matrices or vectors):

$$\mathbf{M}\ddot{\mathbf{q}}(t) + \mathbf{B}\dot{\mathbf{q}}(t) + \mathbf{K}\mathbf{q}(t) = \mathbf{F}(t), \quad \begin{bmatrix} \mathbf{0} & \mathbf{M} \\ \mathbf{M} & \mathbf{B} \end{bmatrix} \begin{bmatrix} \ddot{\mathbf{q}} \\ \dot{\mathbf{q}} \end{bmatrix} + \begin{bmatrix} -\mathbf{M} & \mathbf{0} \\ \mathbf{0} & \mathbf{K} \end{bmatrix} \begin{bmatrix} \dot{\mathbf{q}} \\ \mathbf{q} \end{bmatrix} = \begin{bmatrix} \mathbf{0} \\ \mathbf{F} \end{bmatrix} \quad (1)$$

---

\* Ing. Petr Malínek: Aeronautical research and test establishment, Beranových 130, 19905 Prague, Czech Republic, malínek@vzlu.cz

Corresponding modal model consists of right side and left side modal matrices  $\mathbf{U}_{(m \times n)}$  and  $\mathbf{W}_{(n \times m)}$  and of spectral matrix  $\Lambda_{n \times n}$ , usually  $n \neq m$  in the case of an experimentally identified model.

$$\mathbf{U} = \begin{bmatrix} \mathbf{u}\lambda & \mathbf{u}^*\lambda^* \\ \mathbf{u} & \mathbf{u}^* \end{bmatrix}, \quad \mathbf{W} = \begin{bmatrix} \mathbf{w}\lambda & \mathbf{w}^*\lambda^* \\ \mathbf{w} & \mathbf{w}^* \end{bmatrix}, \quad \Lambda = \text{diag} \begin{bmatrix} \lambda \\ \lambda^* \end{bmatrix}, \quad \mathbf{f} = \begin{bmatrix} \mathbf{0} \\ \mathbf{F} \end{bmatrix} \quad (2)$$

This description of linear structure can handle non conservative and gyroscopic systems, (Byrtus et al., 2010). Using modal decoupling we obtain response function in the frequency domain

$$\mathbf{u}(\omega) = \mathbf{U}(i\omega\mathbf{I} - \Lambda)^{-1}\mathbf{W}^T\mathbf{f}(\omega) \quad (3)$$

Application of Laplace transforms on the decoupled system of differential equations finally provides time domain general solution of original state space model. For  $t=0$ ,  $\mathbf{u}_0=\mathbf{0}^T$ .

$$\mathbf{u}(t) = \mathbf{U} \int_0^t \mathbf{W}^T\mathbf{f}(\tau)e^{\Lambda(t-\tau)}d\tau, \quad (4)$$

where  $\mathbf{u}(t) = [\dot{\mathbf{q}}(t)^T, \mathbf{q}(t)^T]^T$  is the vector of state space coordinates.

For eigenvalues holds:  $\lambda_i = \delta_i \pm j\omega_{di}$ , where  $\delta_i = -\zeta_i\omega_{0i}$ , and  $\omega_{0i} = \sqrt{\omega_{di}^2 + \delta_i^2}$ , whereas  $\omega_{di} = 2\pi f_i$ .

Relation (4) formulates general solution of (1) in time domain in the case of arbitrary waveform of input excitation forces. The structure of (4) gives insight into any response of linearized aeroelastic system. Forced response reflects frequency content of all acting excitation sources. Periodic or quasi-periodic, random and transient forces are acting on the aircraft structure in flight and by acceleration, braking and taxi movements on the ground. These forces are summed in to resultant generalized force vector  $\mathbf{F}$ . Real amplitudes of exciting forces are limited. Thus the exponential term with spectral matrix  $\Lambda$  has fundamental role in vibration response amplitude evolution. Resonance and instability phenomena can arise depending on the properties of system related eigenvalues  $\lambda_i$ . Resonance problem occurrence becomes in the case of coincidence of excitation force frequency components with imaginary parts of eigenvalues. Instability problem is associated with real parts of eigenvalues. It is necessary take in to account both phenomena during aeroelastic system testing, to carefully distinguish instability and other frequency components of the vibration response.

Simplified dynamic stability criteria for the system with no repetitive roots are: The equilibrium of the system is stable, if all  $\delta_i < 0$ . If at least one  $\delta_i > 0$ , the systems equilibrium is unstable, (Muller, 1977). Experimental operational modal analysis is working commonly with damping factor,  $\zeta_i$ . Thus we consider in the stable operational region,  $\zeta_i > 0$  for all modes, on the instability margin  $\zeta_i = 0$  for at least one mode and in the unstable operational region,  $\zeta_i < 0$  for at least one mode.

### 3. Vibration response analysis

It seems reasonable to introduce interpretation set  $\Sigma$ , in which all relevant data on the tested system are collected, as basic modal model parameters, results of numerical simulations, geometric position and directions of all transducers definition, configuration of the tested system, number of engines, propeller blades and characteristics of all other sources of internal and external excitation. The set  $\Sigma$  serves as correct interpretation base by frequency analysis of system vibration response.

Moreover a set of parameters  $P$  is defined, for a potentially unstable system. The set  $P$  contains all parameters relevant to influence the systems stability characteristics. Generally operational modal parameters are functions of  $P$ , we can write  $\Lambda = \Lambda(P)$ ,  $\mathbf{U} = \mathbf{U}(P)$ ,  $\mathbf{W} = \mathbf{W}(P)$ . An aircraft aeroelastic system contains as parameters in the  $P$  wind speed  $v$ , air density  $\rho$ , fuel distribution and mass  $m$  and occasionally propeller rotational speed  $n$ , which is relevant to the special whirl flutter phenomenon. Parameters of  $P$  define  $r$ -dimensional space  $\Pi$ . Stability characteristics of a tested system are systematically evaluated and stable subspace  $\Pi+$ , stability margin  $O$  and unstable subspace  $\Pi-$  are identified inside  $\Pi$ , in the course of experimental campaign, (Malinek, 2016).

Vibration responses of the aeroelastic demonstrator presented in the article were measured at six points and recorded on the PC disc during experimental wind tunnel runs. In the same time the vibration responses were analyzed on-line to detect vibration amplitude immediately and compare them with a predefined limit to prevent demonstrator catastrophic failure in the case of a fast unstable vibrations ramp-up due to instability. Moreover two parameters of  $P$  were continually measured and recorded: wind speed  $v$  and propeller rotational speed  $n$ . Series of operational conditions points in the  $v - n$  space was

sequentially set up with increasing  $v$  and  $n$  during wind tunnel testing for a given demonstrator variant. Vibration response of the demonstrator at the wind speed level was recorded and vibration amplitude evaluated. If the vibration amplitude was lower than a preset limit, wind speed  $v$  was increased by a small step and propeller speed accommodated to wind speed, as the propeller was working in wind-milling mode. Vibration response was then measured and evaluated for a new wind speed point. The sequence continued until maximal wind speed 45 m/s was reached, or vibration limit was exceeded. The process is demonstrated on the next example of aeroelastic demonstrator V2L+2.5 and V2T0 variants results.

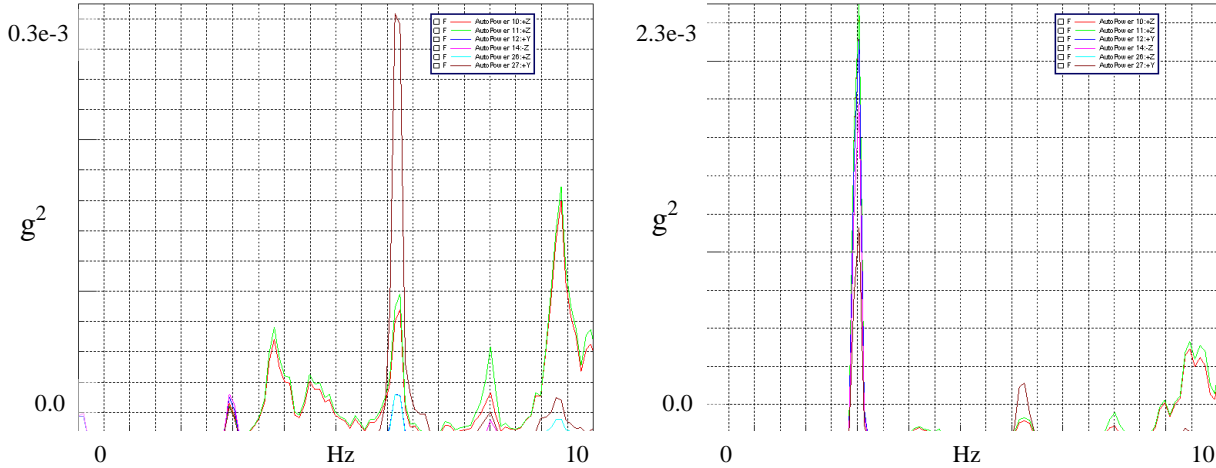


Fig. 1: Variant V2L+2.5, Frequency spectra of vibration response:  $v = 20$  m/s,  $n = 1511$  RPM Left, no instability;  $v = 30$  m/s,  $n = 2391$  RPM Right, unstable vibrations starts on frequency 2.8 Hz.

Frequency spectra interpretation is based on the  $\Sigma$  set of information relevant to the aeroelastic demonstrator. Laboratory modal test results: Frequency of engine vibration modes 2.8 Hz, 1st vertical wing bending mode 3.5 Hz, 2nd vertical wing bending mode 9.9 Hz and 1st horizontal wing bending mode 9.4 Hz. The frequency 6.2 Hz is 1st bending of test stand. Point 12-Y and 14-Z are on the engine nacelle front, point 26-Z and 27-Y are on the nacelle aft, points 10-Z and 11-Z are on the wing tip, Z –vertical, Y – perpendicular to the wind flow horizontal. The demonstrator models one half of wing with one engine.

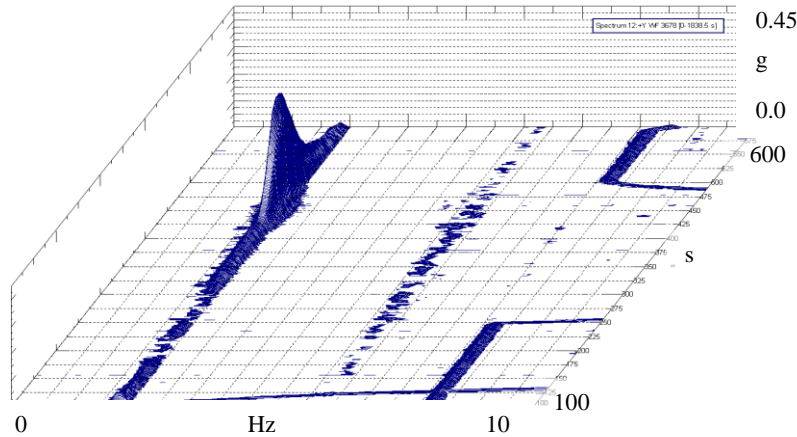


Fig. 2: Variant V2L+2.5, Frequency spectra time evolution. Unstable vibrations ramp-up of the 2.8 Hz mode. Wind speed was quickly returned to stable region after vibration amplitude limit overrun.

Stability margin was reached during the run according to amplitude criterion. Vibration data were analyzed on the constant levels of parameters  $v$  and  $n$  off-line. Modal parameters of potentially unstable modes were extracted from vibration responses. Operational modal analysis (OMA) software package from LMS TestLab system was applied. Nevertheless OMA fails by identification of negative damping factor in the unstable region. Logarithmic decrement concept was then used instead of OMA to determine negative damping factor by procedure modified to frequency-time-amplitude domain.

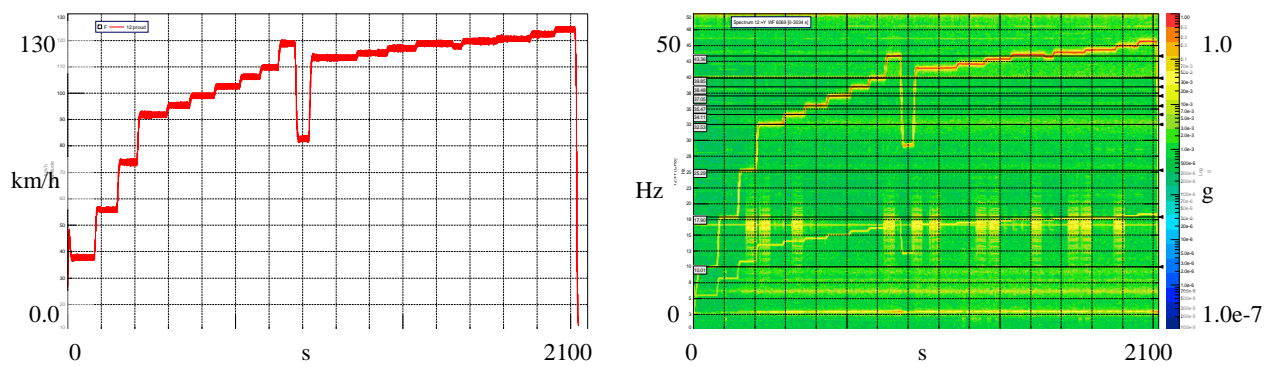


Fig. 3: Variant V2L+2.5, Wind speed  $v$  was carefully varied, until stability margin was (two times) reached. Propeller speed was derived from unbalance vibration response.

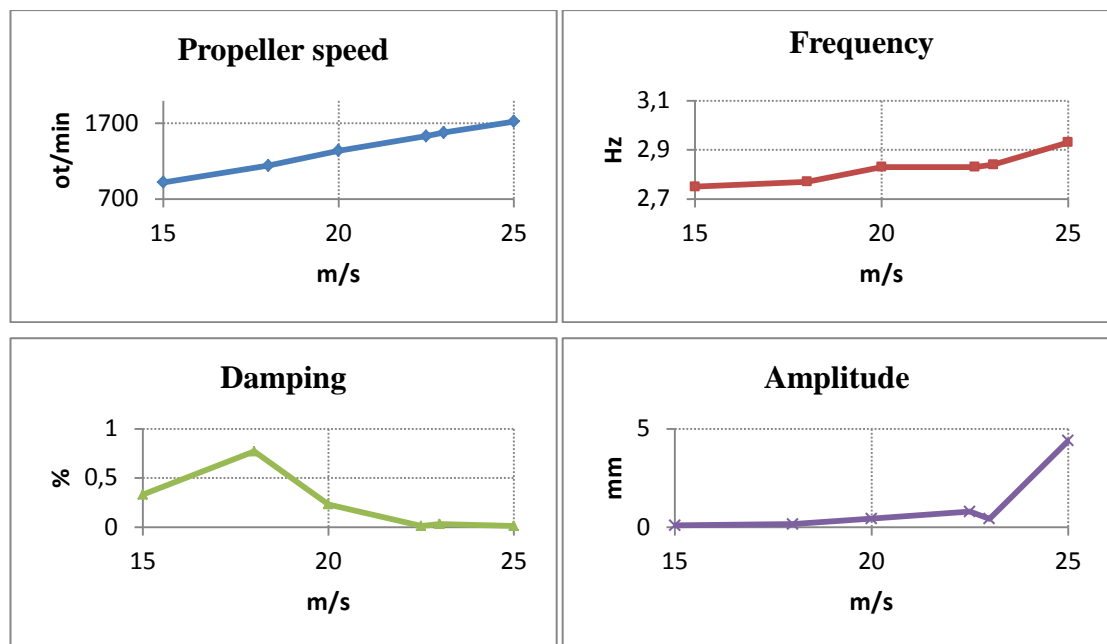


Fig. 4: Variant V2T0, Modal parameters and amplitude of whirl flutter mode as a function of wind speed.

As an example of experimental procedure output the composed results of operational modal parameters of the demonstrator variant V2T0 are presented in the Fig. 4.

#### 4. Conclusions

The article presents briefly a procedure of experimental investigation of operational modal parameters of an aeroelastic demonstrator during wind tunnel testing. The method is suitable for stability margins research of real aeroelastic systems as well as other potentially unstable mechanical systems.

#### Acknowledgement

The work has been supported by the research project COSTRES granted by The Ministry of Industry and Trade of Czech Republic.

#### References

- Muller, P.C. (1977) Stability and Matrices, Springer Verlag Berlin, 1977.
- Byrtus, M., Hajžman, M. and Zeman, V. (2010) Dynamics of rotating systems, West Bohemia University Plzeň.
- Malínek, P. (2016) Methodology of dynamic response analysis of unstable systems, Report VZLÚ R-6611, Prague.

## **SIMULATION OF PILOT LOAD DURING EMERGENCY LANDING CONDITIONS**

**M. Mališ<sup>\*</sup>, J. Šplíchal<sup>\*\*</sup>**

**Abstract:** *Models of dummy embedded in numerical commercial software packages are calibrated using Anthropometric Testing Dummies (ATD). The dummies vary according to the loading character different for aeronautic or automotive industries. The aim of the article is to find a solution of analysis of loads in lumbar column, based on aeronautical regulation requirements using available dummies in commercial software systems MSC.Nastran and MSC.Dytran. Simulation results were compared with experimental test data obtained from dynamic sled test with implemented ATD.*

**Keywords:** Aircraft passive safety, Finite element method, Dummy, Dynamic test.

### **1. Introduction**

Present article was initiated within the frame of project “Increased passive safety of TL-ultralight aircraft, deals with passive safety of very small aircrafts. The passive safety is not included into regulation requirements for this aircraft category. The complex solution of the passive safety leads to assessment of a crash landing condition effect on aircraft crew members. This approach is ambitious especially on execution of complex crash tests. Commercial software packages based on finite element method (FEM) might reduce range of the tests.

Assessment of a passive safety in aerospace industry using injury criteria leads to evaluations of a head injury, thorax injury, represented by maximal force in safety belts, and estimation of a lumbar spine injury. An assessment of head and thorax injuries is not a problem from FEM simulation point of view and correlation with experiments. However Tabei (2009) revealed considerable inaccuracies in correlation with experiments for lumbar spine injury assessment. The paper investigates methods, how to evaluate spinal forces obtained from ATB (articulated total body) dummies implemented in commercial FEM software packages.

### **2. Dynamic test**

The dynamic test was executed at Dekra a.s. company on testing facility for automotive industry (Fig. 1). The seat was fixed on a steel frame and mounted on a dynamic sledge. A FAA 50th percentile Hybrid II testing dummy was belted using four point safety belts.

The testing facilities have been primarily developed for testing of automotive safety belts, where testing conditions are different than in aircraft seats testing. In order to comply maximum deceleration defined in aircraft Certification Specifications for Normal Utility and Commuter Category Airplanes CS23, specified in AC 23.562 (1989), the loading pulse had to be changed. An initial velocity has to be increased and time duration on high deceleration level was enlarged. It can be remarked, that seat and dummy during the test absorbed higher energy than would be necessary according to requirements in CS23. After the frame with seats stopped, a slight rebound backward occurred. The Fig. 2 shows comparison between applied deceleration pulse during the dynamic test and pulse defined in CS23.562(b)(1).

---

<sup>\*</sup> Ing. Michal Mališ, PhD.: Institute of Aerospace Engineering, Brno University of Technology, Technická 2896/2; 616 69 Brno; CZ, malis@fme.vutbr.cz

<sup>\*\*</sup> Ing. Jan Šplíchal, PhD.: Institute of Aerospace Engineering, Brno University of Technology, Technická 2896/2; 616 69 Brno; CZ, splichal@fme.vutbr.cz



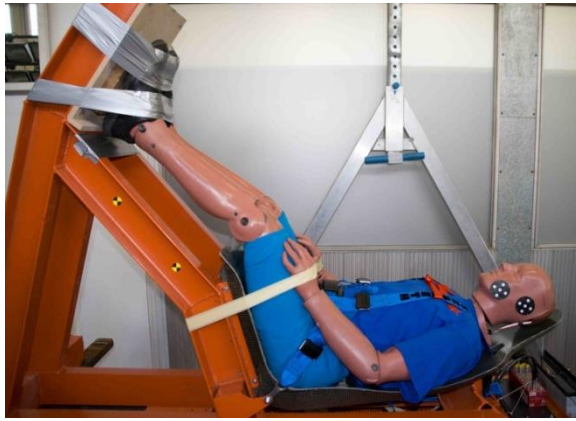


Fig. 1: Dynamic sled test with 50 % HybridII.

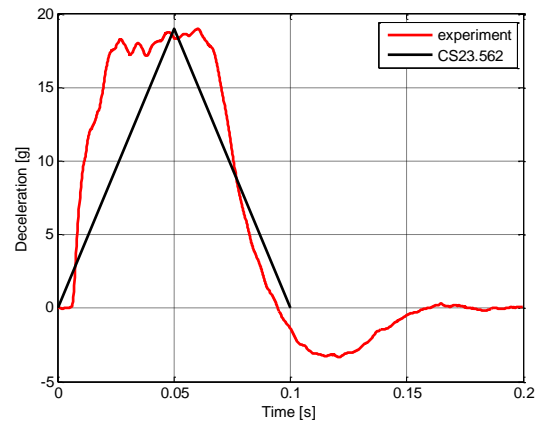


Fig. 2: Test pulse used in experiment and pulse defined in CS23.

### 3. FEM models

Two types of ATB models available in MSC.Software products had been used for experimental evaluation. MSC.Software portfolio uses two explicit codes: MSC.Dytran and MSC.Nastran 700. The MSC.Dytran is an original explicit solver among the MSC. Software products and MSC.Nastran has core taken from LS-Dyna software package with all enhancements including ATB dummy models.

The dummy model implemented in MSC.Dytran is assembled from two parts. The first one is system of rigid ellipsoids (Fig. 3a) with defined mass and inertial properties representing parts of the body. Those ellipsoids are connected by analytical joints to ensure realistic flexibility of the dummy. The second part is skin of the dummy (Fig. 3b) analytically linked with ellipsoids which enables contacts of the dummy with the surrounding. The kinematical properties of the dummy are based on anthropometric fidelity with ATD testing dummy (Cheng, 1989).

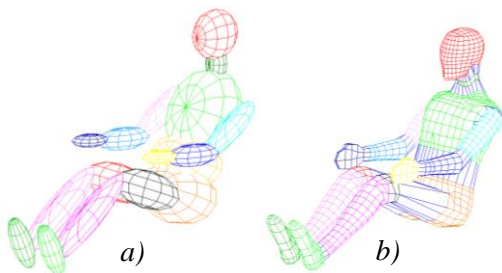


Fig. 3: The dummy in MSC. Dytran.

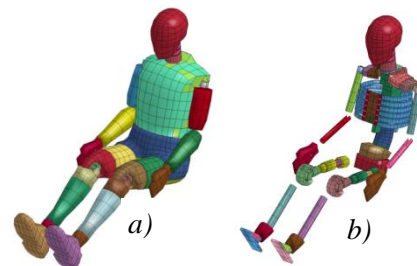


Fig. 4: The dummy in MSC.Nastran 700.

The model of the 50<sup>th</sup> percentile Std. Hybrid III dummy available in LS-Dyna was developed in Livermore Software Technology Corporation as a full FEM model of the Std. HIII ATD (Fig. 4). Oliva-Perez (2010) mentions that model of the dummy has been primarily designed for frontal crash in the automotive industry and its lumbar spine column does not correspond with the ATD testing dummy accepted by Federal Aviation Administration (FAA) for measurement of spine load. The internal structure of the dummy (Fig. 4b) has been created from rigid objects which are connected by analytical joints and contacts. The model of the external parts of the dummy is assembled partly from objects with rigid material properties (head, legs), and with objects from a low density foam material (pelvis and thorax). The models are available on the internet , with announcement that, FAA HIII is not available yet and the dummy is in a planning stage.

### 4. Modeling of the experiment

Numerical simulations of the dynamic test have been performed using MSC.Dytran and MSC.Nastran 700 explicit codes. Global properties of the seat models were equivalent with the real tested seat. The models of the seats are stiff without any devices for energy absorbing. The safety belts can be modeled using 2d shell elements in MSC.Nastran 700, because of available material model for orthotropic fabric. The MSC.Dytran allows modeled safety belts using 1d elements (Fig. 5).

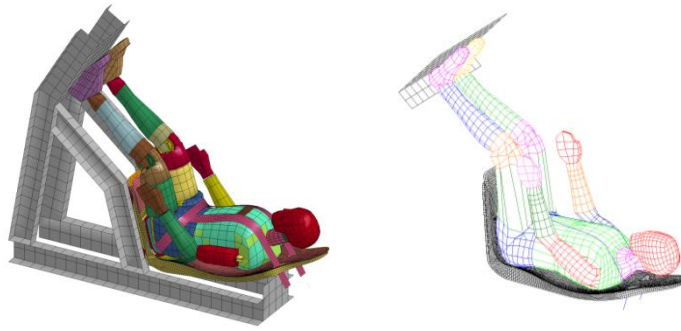


Fig. 5: Model of the test in MSC.Nastran700 (left) and in MSC.Dytran (right).

## 5. Results

Results of the compressive loading in the lumbar spine simulations were executed in MSC.Nastran 700 and MSC.Dytran and compared with the experiment. The forces in lumbar spine were evaluated using two approaches for both solvers. The first approach uses resulting force directly from ATB dummies; the second one evaluates contact forces between seats and dummy. It was assumed, that the force acting to the seat produced by dummy equals the force acting to the lumbar spine. The Results pulses were filtered with SAE J211 CFC digital filter described by Alem (1995). The main evaluated parameters were correlation of maximal forces in the lumbar spine with the experiment related on the CFC filter used.

### 5.1. Simulation in MSC.Nastran 700

The dummy implemented in MSC.Nastran enables to obtain the force in lumbar spine directly from the spine column. Force in „z” direction is acting in the spine direction. A force tangential to surface of lumbar load cell is acting in „x” direction. Raw results obtained from simulation are considerably noisy and therefore the results were filtered by CFC filters. The filtering causes distortion of signals.

Selection of the filter has to be done to avoid of “over-filtering”. Forces in lumbar spine were filtered with CFC30 and the results are presented in the Fig. 6 for X and Z direction. Total force was calculated using vector sum of the X and Z components. It could be emphasized, that the Std. HIII dummy used in model is primarily designed for frontal impact test in automotive industry, where realistic response of dummy especially in bending is required for contact analysis with an airbag or steering wheel. Compressive loading in lumbar spine for that type of analysis are not demanded. The Fig. 6 revealed the load pulses divided into two peaks. The first one corresponds with initial contact of the body with the seat. The second one arises at the time of maximal tangential forces in lumbar load cell. This pulse can be caused by bending of the lumbar spine. Fig. 7 displays contact force between dummy and seat pan. The resulting pulse is not filtered and it is raw signal obtained from the simulation.

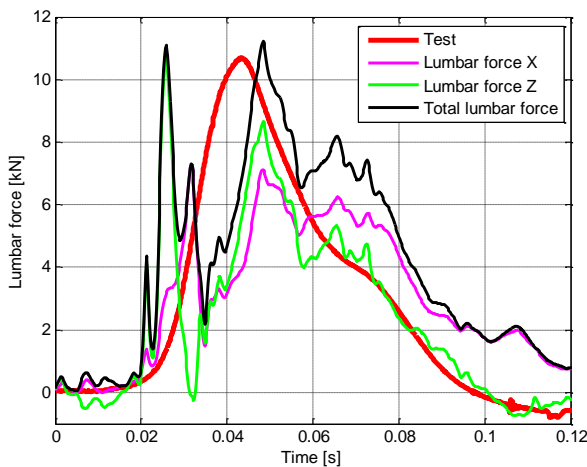


Fig. 6: Force obtained from directly from lumbar spine in MSC.Nastran.

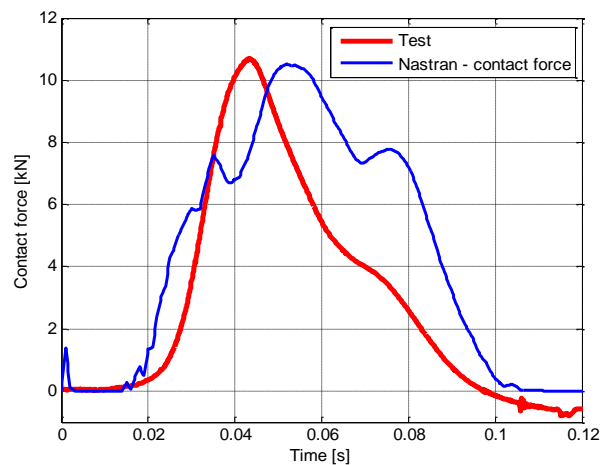


Fig. 7: Force in contact between seat pan and the dummy in MSC.Nastran.

## 5.2. Simulation in MSC.Dytran

The dummy used in MSC.Dytran does not allow obtaining load in lumbar spine directly. The force has to be calculated for acceleration in centers of gravity of selected rigid. The ellipsoids representing the head, neck, abdomen, thorax and both hands were considered to the calculation of the spinal load.

The results of the simulation (Fig. 8) analyzed in MSC.Dytran suffer distinct oscillation of the signal. This may be due to the contact between rigid ellipsoids and rigid seat. Therefore filtering using CFC filters with different cut - off frequency were performed.

Fig. 9 presents the results of contact forces between seat pan and the dummy. The result demonstrates that the cut -off frequency of the filter considerably affects the results. The Fig. 9 shows comparison of the results filtered by the CFC 15 and the CFC 30 with the experimental data. The reason of the signal oscillation from simulation is probably the same as reason for the force analyzed directly from ellipsoids of the dummy. The frequency of oscillation in both evaluation methods is identical, only the maximum forces differ.

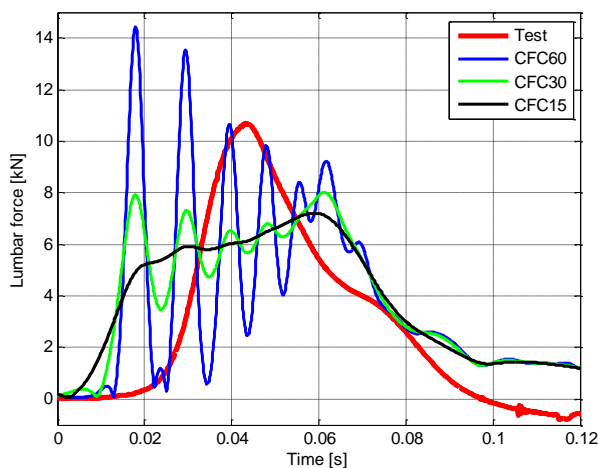


Fig. 8: Comparison of the spinal load calculated from ellipsoids with the test.

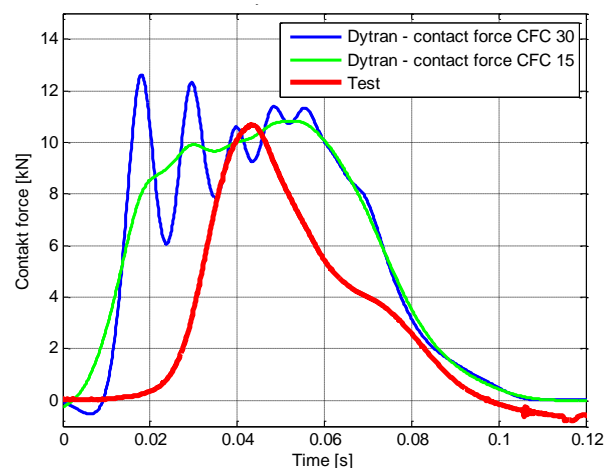


Fig. 9: Comparison of contact force between the dummy and the seat pan from MSC. Dytran with the test.

## 6. Conclusion

In frame of presented work the dynamic laboratory sledge test according to CS23.561(b)(1) was executed with the rigid seat. The 50 percentile FAA Hybrid II testing dummy was used for measuring the force in the lumbar spine. Afterwards numerical simulations have been performed using commercial explicit codes produced by MSC.Software (MSC.Nastran 700 and MSC.Dytran) and the results were compared with experiment. An approach for lumbar spine evaluation was selected according to correlation with the experiment. The most promising result of force of the lumbar spine was obtained from analysis of the contact force between seat and the model of the ATB Std. Hybrid III testing dummy analyzed in explicit code MSC.Nastran 700.

## References

- AC 23.562 (1989) Dynamic Testing of Part 23 Airplane Seat /Restraint Systems and Occupant Protection, Federal Aviation Administration, Washington, D.C. 6/1989.
- Alem, N.M. and Perry, M. (1995) Design of Digital Low-pass Filters for Time Domain Recursive Filtering of Impact Acceleration Signals, United States Army Aeromedical Research Laboratory, Report No 95-13.
- Cheng, H., Rizer, A. and Obergefell, L. (1989) Articulated Total Body Model Version V User's Manual, United States Air Force Research Laboratory, AFRL-HE-WP-TR-1998 – 0015.
- Oliva-Perez, O. (2010) Evaluation of the FAA HybridIII 50th percentile anthropometric test dummy under the FAR 23.562 and 25.562 emergency landing conditions for the combine horizontal and vertical dynamic loading, Bachelors of Science thesis , Polytechnic University of California.
- Tabei, A., Lawrence, Ch. and Fasanella, E. (2009) Validation of Finite Element Crash Test Dummy Models for Predicting “Orion” Crew Member Injuries during a Simulated Vehicle Landing, NASA Technical Report, NASA/TM-2009-215476.

## THERMO-MECHANICAL ANALYSIS OF A FUNCTIONALLY GRADED ANNULAR FIN

A. Mallick<sup>\*</sup>, R. Ranjan<sup>\*\*</sup>

**Abstract:** Temperature distribution and thermal stress analyses are presented for an annular fin of functionally graded material (FGM). The closed form solution of stress field is obtained by solving the steady-state nonlinear differential equation of heat transfer using homotopy perturbation method (HPM) coupled with elasticity theory. The properties of the fin material are expressed as linear and power law distribution with temperature and radius. The effect of various thermal parameters on the temperature field, and subsequently stress field are discussed.

**Keywords:** Functionally graded fin, Homotopy perturbation method, Inverse analysis, Thermal stresses.

### 1. Introduction

It is common observation and experience that the stresses are induced in the fin material due to nonuniform temperature distribution. Thus, a significant concentration on thermal stress analysis is required for fin designing. Nonlinear heat transfer analyses for isotropic annular fins have been well studied (Kraus et al., 2001 and Ganji et al., 2011), but there are few works on thermal stress analysis. The thermal stress analysis for a perfect elastic isotropic circular fin was presented by Chiu et al. (2002) using Adomian's double decomposition method. Lee et al. (2002) employed Laplace transformation coupled with finite difference method for thermo-elastic analysis of an annular fin. Mallick et al. (2015) recently presented closed form solution for thermal stresses of an isotropic annular fin using HPM coupled with classical thermo-elasticity equation. An open literature search reveals that no one attempt to study the fin of functionally graded material (FGM) subjected to thermal loading.

This work presents thermal stress analysis for FGM annular fin. The nonlinear heat transfer equation has been solved using HPM. The stress fields are obtained from temperature field, coupled with the elasticity equation. The HPM solution are compared with the results obtained using finite difference method.

### 2. Governing equations

#### 2.1. Temperature distribution

Let us consider an annular fin made of functionally graded material as shown in Fig. 1. The base temperature of the fin is assumed to be a constant temperature,  $T_b$  and its tip is considered to be adiabatic.

The energy balance equation for heat transfer together with boundary conditions can be expressed as (Kraus et al., 2001):

$$t \frac{d}{dr} \left[ \{k(T) + k(r)\} r \cdot \frac{dT}{dr} \right] - 2h(T)r(T - T_a) - 2\varepsilon\sigma r(T^4 - T_s^4) + q(T)tr = 0 \quad (1)$$

$$T = T_b \text{ at } r = r_i \text{ and } \frac{dT}{dr} = 0 \text{ at } r = r_o \quad (2)$$

where  $k(T) = k_o \{1 + \kappa(T - T_a)\}$ ,  $k(r) = k_o \{1 + \gamma(r - r_i)/(r_o - r_i)\}$ ,  $q(T) = q_o \{1 + e(T - T_a)\}$ , and

---

<sup>\*</sup> Assoc. Prof. Ashis Mallick, PhD.: Indian Institute of Technology (ISM), Dhanbad 826 004; India, al123\_us@yahoo.com

<sup>\*\*</sup> Rajiv Ranjan, PhD. Student: Indian Institute of Technology (ISM), Dhanbad 826 004; India, rajivranjan050@gmail.com

$$h(T) = h_b \left\{ (T - T_a) / (T_b - T_a) \right\}^n.$$

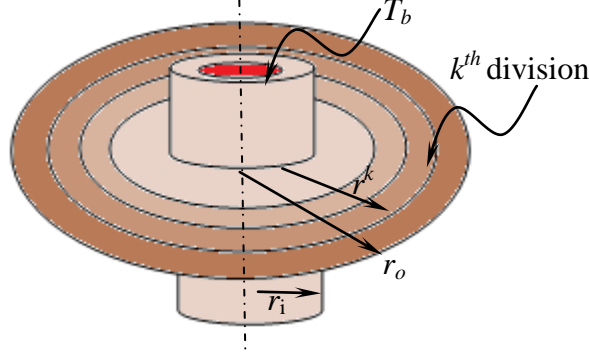


Fig. 1: Fin geometry of FGM.

Introducing the non-dimensional parameters, the energy balance equation and the boundary conditions are reduced to:

$$\begin{aligned} \theta'' + \frac{\beta}{2}(\theta - \theta_a)\theta'' + \frac{\gamma\xi}{2(R-1)}\theta'' + \frac{\beta}{2}(\theta')^2 + \frac{\gamma}{2(R-1)}\theta' + \frac{1}{2(1+\xi)}\theta' + \frac{\beta(\theta - \theta_a)}{2(1+\xi)}\theta' \\ + \frac{\gamma}{2(R-1)}\frac{\xi}{1+\xi}\theta' - N_c \frac{(\theta - \theta_a)^{(m+1)}}{(1 - \theta_a)^m} - N_r(\theta^4 - \theta_s^4) + \frac{G}{2}\{1 + E_G(\theta - \theta_a)\} = 0 \end{aligned} \quad (3)$$

$$\theta = 1 \text{ at } \xi = 0 \text{ and } \theta' = 0 \text{ at } \xi = R - 1 \quad (4)$$

All the above terms are described separately in the nomenclature. Constructing the HPM formulation, Eq. 3 can be rewritten as,

$$\begin{aligned} (1-p)L(\theta - \theta_0) + p \left( \theta'' + \frac{\beta}{2}(\theta - \theta_a)\theta'' + \frac{\gamma\xi}{2(R-1)}\theta'' + \frac{\beta}{2}(\theta')^2 + \frac{\gamma}{2(R-1)}\theta' + \frac{1}{2(1+\xi)}\theta' \right. \\ \left. + \frac{\beta(\theta - \theta_a)}{2(1+\xi)}\theta' + \frac{\gamma\xi}{2(R-1)(1+\xi)}\theta' - N_c \frac{(\theta - \theta_a)^{(m+1)}}{(1 - \theta_a)^m} - N_r(\theta^4 - \theta_s^4) + \frac{G}{2}\{1 + E_G(\theta - \theta_a)\} \right) = 0 \end{aligned} \quad (5)$$

where  $p \in [0, 1]$  is an imbedding parameter and  $L$  denotes the linear operator as  $d^2/d\xi^2$ . The HPM solution converges for  $p = 1$ , and the final solution for temperature field can be expressed as:

$$\theta = \theta_0 + \theta_1 + \theta_2 + \dots \quad (6)$$

The details pertaining to the solution procedure have been presented in ref. (Mallick et al., 2015).

## 2.2. Thermo-elastic solution

For functionally graded material, the elastic constant and the co-efficient of thermal expansion are assumed to be a function of fin radius:

$$E(r) = E_0 (r/r_i)^{n_1} \text{ and } \alpha(r) = \alpha_0 (r/r_i)^{n_2} \quad (7)$$

Introducing a stress function,  $\psi(r)$ , such that  $\sigma_r = \psi/r$  and  $\sigma_\phi = d\psi/dr$  which satisfy the stress equation of equilibrium. Applying Hooke's law for plane stress condition and employing the strain compatibility condition, the differential equation in terms of stress function in the non-dimensional form yields,

$$\xi_1^2 \frac{d^2\psi}{d\xi_1^2} + (1 - n_1)\xi_1 \frac{d\psi}{d\xi_1} + (vn_1 - 1)\psi = -Er_i\chi\xi_1^{(n_1+n_2+2)} \frac{d\theta}{d\xi_1} - n_2Er_i\chi\xi_1^{(n_1+n_2+1)}\theta \quad (8)$$

where  $\xi_1 (= r/r_i)$  is the non-dimensional radius. The general solution for  $\psi(\xi_1)$  is given as,

$$\psi = D_1\xi_1^{\eta_1} + D_2\xi_1^{\eta_2} + A_0\xi_1^{(\eta_3+1)} + A_1\xi_1^{(\eta_3+2)} + A_2\xi_1^{(\eta_3+3)} + A_3\xi_1^{(\eta_3+4)} + A_4\xi_1^{(\eta_3+5)} + B\xi_1^{(\eta_3+2)} \log \xi_1 \quad (9)$$

The constants  $D_1$  and  $D_2$  are obtained from the boundary conditions,  $\sigma_r = 0$  at bore and tip of the fin.



The terms  $\eta_{1,2} = n_1 / 2 \mp \sqrt{(1 - \nu n_1 + n_1^2 / 4)}$ ,

$$A_1 = \frac{4\chi \{(1+n_2)L_1 + L_5\}}{\{(n_1^2 - 4n_1\nu + 4) - (n_1 + 2n_2 + 4)^2\}},$$

$$B = \frac{16\chi(1+n_2)L_5}{\{(n_1^2 - 4n_1\nu + 4) - (n_1 + 2n_2 + 4)^2\}^2}.$$

$$A_0 = \frac{4n_2\chi L_0}{\{(n_1^2 - 4n_1\nu + 4) - (n_1 + 2n_2 + 2)^2\}},$$

$$A_4 = \frac{4\chi(4+n_2)L_4}{\{(n_1^2 - 4n_1\nu + 4) - (n_1 + 2n_2 + 10)^2\}} \text{ and}$$

### 3. Results and discussion

The closed form solution and inverse study of an axisymmetric annular fin of functionally graded material is presented. Unless mentioned otherwise, the values of non-dimensional parameters  $N_c = 0.5$ ,  $N_r = 0.2$ ,  $\beta = 0.2$ ,  $m = 0.25$ ,  $\gamma = 0.2$ ,  $G = 0.2$ ,  $n_1 = 0.5$ ,  $n_2 = 0.5$  and  $R = 2$  are to be taken in the analysis. Fig. 2 shows the HPM results for the temperature field. For the correctness of the solution, the temperature field has been compared with finite difference solution. The result shows only 2.7 % variation in the temperature at the tip. The effect of various thermal parameters,  $N_c$ ,  $N_r$ ,  $\beta$  and  $\gamma$ , on the temperature field are presented in Fig. 3. It can be seen that the local temperature along the fin radius gradually decreases for all the cases. With the increase of the parameters  $\beta$  and  $\gamma$ , responsible for the variation of thermal

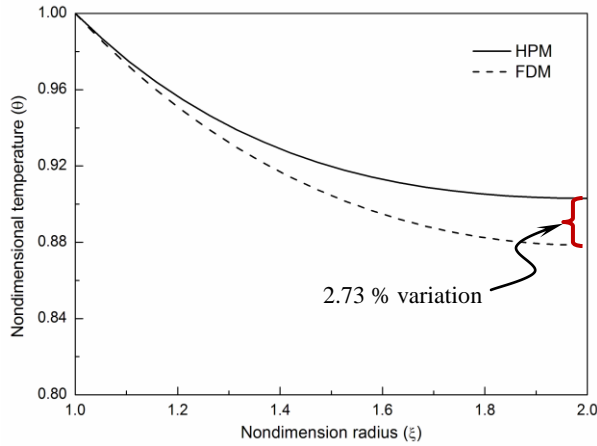


Fig. 2: Validation of HPM solution for temperature distribution in a fin.

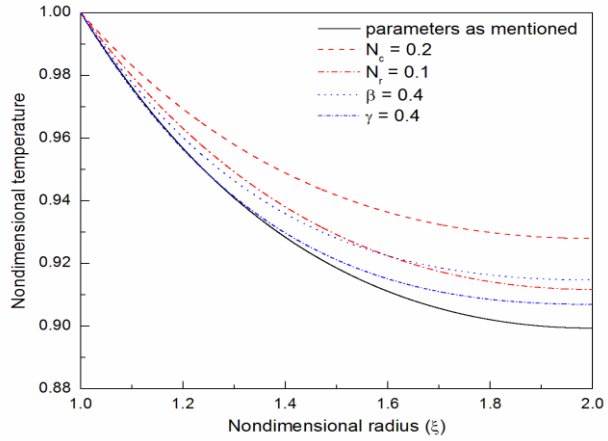


Fig. 3: Effect of various thermal parameters on the variation of temperature distribution.

conductivity, the local temperature field increases. This result suggests that the heat transfer through the fin material enhances with the increasing of variable thermal conductivity parameters. On the other side, it can be noticed that the heat transfer process expedites with decrease in parameters,  $N_c$  and  $N_r$ . The variation of radial and tangential stresses developed due to the variation of temperature gradient along the fin radius. The effect of the parameters describing the variation of Young's modulus ( $n_1$ ) and coefficient of thermal expansion ( $n_2$ ) on the thermal stresses are presented in Fig. 4 and Fig. 5. It can be seen, the magnitude of radial and tangential stresses increase with the increase of parameter,  $n_1$ , as the elastic modulus increases with  $n_1$ . The tangential stress near to the bore is found to be compressive and tensile is near to the tip. On the other hand, for the positive value of  $n_2$ , the co-efficient of thermal expansion exponentially increases from the base to tip of the fin. As a result, the tendency of tensile behaviour in radial stress is predominant when the value of  $n_2$  is positive. Just opposite behaviour is observed when  $n_2$  is negative.

### 4. Conclusions

An approximate closed form solution for temperature and stress field in a fin of FGM has been derived successfully. The present work gives an open choice to the designer for selecting and adjusting the fin parameters for a desired temperature and stress fields. The stress field mainly depends on the temperature gradient, as well as, the parameters responsible for the variation of Young's modulus and the coefficient



of thermal expansion. Mainly, the tangential stress dominates in the fin material and may be responsible for the mechanical failures due to thermal loading.

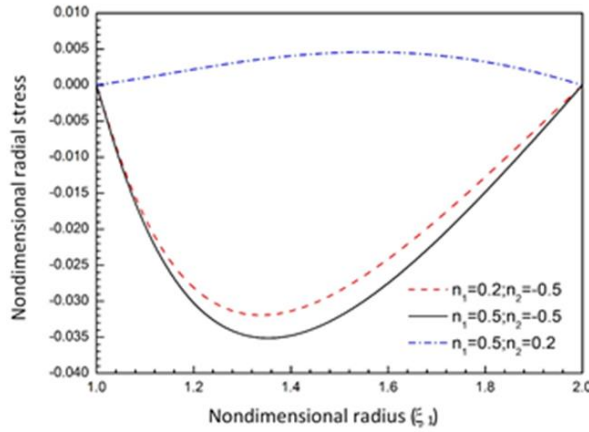


Fig. 4: Effect of the parameters  $n_1$  and  $n_2$  on radial stresses.

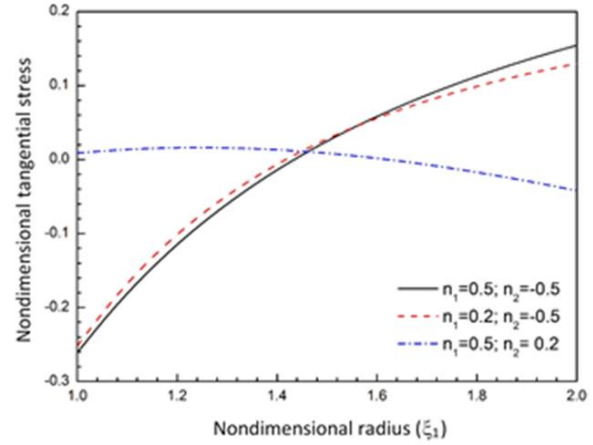


Fig. 5: Effect of the parameters  $n_1$  and  $n_2$  on tangential stresses.

## Nomenclature

$r_i, r_o, t$	inner radius, outer radius and thickness of the fin,
$h(T), k(T), k(r)$	variable heat transfer coefficient and thermal conductivity parameter,
$h_b, q_o, \varepsilon$	heat transfer coefficient, heat generation and emissivity parameters,
$k_0$	thermal conductivity at convection sink temperature or at the bore of the fin,
$\kappa, \gamma, \lambda, e$	parameters describing the linear variation of thermal conductivity, surface emissivity and internal heat generation,
$\beta$	non-dimensional parameter describing the variation of thermal conductivity with respect to temperature, $\beta = \kappa T_b$ ,
$m$	exponent of variable convective heat transfer coefficient,
$N_c$	non-dimensional thermo-geometric parameter, $(2hr_i^2/k_o t)^{0.5}$ ,
$N_r$	non-dimensional conduction-radiation parameter, $(2r_i^2 \sigma \varepsilon T_b^3 / k_o t)$ ,
$G$	non-dimensional heat generation parameter, $G = q_o r_i^2 / k_o T_b$ ,
$E_G$	non-dimensional parameter describing the variation of heat generation, $E_G = e T_b$ ,
$T_b, T_a, T_s$	base temperature of fin, ambient temperature and radiation sink temperature,
$\theta$	dimensionless temperature, and dimensionless radiation sink temperature, $\theta = T/T_b$ ,
$\theta_a, \theta_s$	dimensionless convection and radiation sink temperature, $\theta_a = T_a/T_b$ and $\theta_s = T_s/T_b$ ,
$\xi, \xi_1$	dimensionless radius of fin, $\xi = (r - r_i)/r_i$ and $\xi_1 = r/r_i$ ,
$R$	annular ratio, $R = r_o/r_i$ ,
$\bar{\sigma}_r, \bar{\sigma}_\theta$	non-dimensional radial stress ( $\bar{\sigma}_r = \sigma_r/E_0$ ) and tangential stress ( $\bar{\sigma}_\theta = \sigma_\theta/E_0$ ),
$E(r), \alpha(r)$	variation of elastic modulus and co-efficient of thermal expansion,
$n_1, n_2$	power index of elastic modulus and co-efficient of thermal expansion variation,
$E_0, \alpha_0$	modulus of elasticity and co-efficient of thermal expansion at the base of the fin,
$\chi$	non-dimensional coefficient of thermal expansion, $\chi = \alpha_0 T_b$ .

## References

- Chiu, C.H. and Chen, C.K. (2002) Thermal stresses in annular fins with temperature-dependent conductivity under periodic boundary condition, *J. Thermal Stresses*, 25, pp. 475-492.
- Ganji, D.D., Ganji, Z.Z. and Ganji, H.D. (2011) Determination of temperature distribution for annular fins with temperature dependent thermal conductivity by HPM, *Thermal Science*, 15, pp. 111-115.
- Kraus, A.D., Aziz, A. and Welty, J.R. (2001) *Extended Surface Heat Transfer*. John Wiley and Sons, NY (USA).
- Lee, H.L., Yang, Y.C. and Chu, S.S. (2002) Transient thermoelastic analysis of an annular fin with coupling effect and variable heat transfer coefficient, *J. Thermal Stresses*, 25, 1105-1120.
- Mallick, A., Ghosal, S., Sarkar, P. K. and Ranjan, R. (2015) Homotopy perturbation method for thermal stresses in an annular fin with variable thermal conductivity, *J. Thermal Stresses*, 38, pp. 110-132.

## **ANALYSIS OF BOUNDARY CONDITIONS IN FINITE ELEMENT SUB-MODELS OF INTERACTION OF HUMAN MANDIBLE WITH DENTAL IMPLANT**

**P. Marcián<sup>\*</sup>, Z. Florian<sup>\*\*</sup>, L. Horáčková<sup>\*\*\*</sup>, L. Borák<sup>\*\*\*\*</sup>**

**Abstract:** *This paper deals with the computational modelling of dental implant interacting with bone tissue. For the purposes of the study, one human mandible and a segment of a different human mandible were examined. In total, five variants of geometry models with dental implant were investigated: One full mandible and four segments. For the latter, two different boundary conditions were used (first based on the sub-modeling approach and second assuming fixed support). If the coarse model for the particular bone segment model is not available, it is possible to use a generic boundary condition for a typical mandible subjected to a typical loading.*

**Keywords:** Biomechanics, FEM, Dental Implant, Sub-modeling.

### **1. Introduction**

Constantly developing computer technology entails increasing demands for quality of computational models in many fields of engineering practice as well as of research. Biomechanics is not an exception. On the contrary, despite the fact that biomechanical systems have some specific traits including complex (and often uncertain) material properties of living tissues or boundary conditions that are difficult to grasp, it is a common request from scientific community members (such as journal reviewers etc.) to provide a model that would include high-level features that are often needless or unnecessary for the solution of the problem. Such requests often expose one's misunderstanding of what the modeling is about than his expertise or experience.

Typical challenge in biomechanics is a computational modeling of complex systems consisting of small artificial elements such as dental implants or micro screws (Ridwan-Pramana et al., 2016). In such cases, it appeared to be useful and appropriate to use the sub-modeling method which allowed computational solution of a given problem at a sufficient level. One of the most significant features of the bone in which the implant or screw is embedded is the trabecular architecture of its cancellous part. Nowadays, it is possible to create a detailed model of such architecture using micro-FE methods. However, creating a computational model including the trabecular architecture in the entire bone is impractical. The most common procedure is to create only a segment of bone with appropriate boundary conditions. The boundary conditions might be derived from a coarse model which consists of a larger part of (or whole) bone with coarser FE mesh and with other simplifications such as screws/implants modeled without a thread. After the coarse model solution is carried out, the boundary condition might be applied to the sub-model with much finer FE mesh and more detailed representation of the implant/screw. However, the coarse model might not be always available and the question is whether a typical boundary condition for a sub-model might be found.

---

<sup>\*</sup> Ing. Petr Marcián, PhD.: Institute of Solid Mechanics, Mechatronics and Biomechanics, Faculty of Mechanical Engineering, Brno University of Technology, Technická 2896/2, 616 69 Brno, Czech Republic; CZ, marcian@fme.vutbr.cz

<sup>\*\*</sup> Assoc. Prof. Ing. Zdeněk Florian, PhD.: Institute of Solid Mechanics, Mechatronics and Biomechanics, Faculty of Mechanical Engineering, Brno University of Technology, Technická 2896/2, 616 69 Brno, Czech Republic; CZ, florian@fme.vutbr.cz

<sup>\*\*\*</sup> Assoc. Prof. RNDr. Ladislava Horáčková, PhD.: Department of Anatomy, Faculty of Medicine, Masaryk University, Kamenice 126/3, 625 00 Brno, Czech Republic; CZ, lhorac@med.muni.cz

<sup>\*\*\*\*</sup> Ing. Libor Borák, PhD.: Institute of Solid Mechanics, Mechatronics and Biomechanics, Faculty of Mechanical Engineering, Brno University of Technology, Technická 2896/2, 616 69 Brno, Czech Republic; CZ, liborborak@seznam.cz

The aim of this study is to analyze different levels of boundary conditions for a sub-model of a human mandible with a dental implant.

## 2. Methods

### 2.1. Geometry model

For the purpose of this study, one human mandible and a segment of a different human mandible were scanned on CT (voxel size 0.5 x 0.5 x 1.0 mm). CT images were further processed in STL Model Creator (Matlab, 2012) to obtain 3D models of the mandible (Fig. 1), (Marcían et al., 2011). In this software, surfaces of cortical and cancellous bones were created using the automatic segmentation (Huotilainen et al., 2014). Finally, volume models of both bone tissues were created in ANSYS 17.2. Branemark dental implant (Brånemark® System Mk III Groovy, NP Ø 3.3 mm, 11.5 mm) with abutment was chosen as typical implant for this study (Fig. 1).

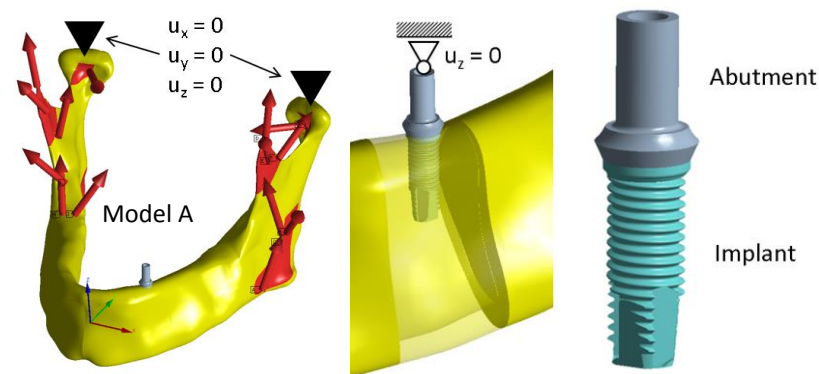


Fig. 1: Human mandible and detail of dental implant. Model A – loading and boundary conditions.

In total, five variants of geometry model of mandible with dental implant were investigated: Model A – The entire mandible (Fig. 1); Model B – A larger segment of mandible from Model A (length of 60 mm, Fig. 2a); Model C – A shorter segment of mandible from Model A (length of 15 mm, Fig. 2b); Model D – The segment from different mandible (length of 15 mm, Fig. 2c); Model E – Model D with modified cortical bone thickness (Fig. 2d).

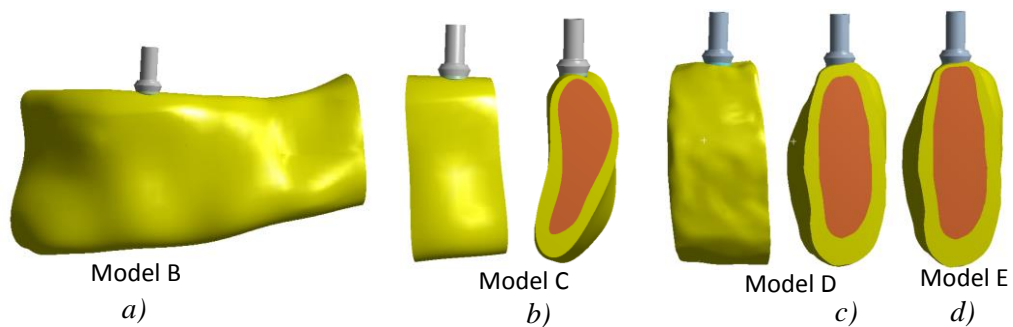


Fig. 2: Mandibular segments. a) Model B; b) Model C; c) Model D; d) Model E.

### 2.2. Loads and boundary conditions

Model A was loaded by forces applied in locations of muscle inserts and in directions of that muscles. The force magnitudes were taken from literature (Narra et al., 2014). The implant was constrained in axial direction of the implant as shown in Fig. 1. These loads and constraint represent an occlusion of the first premolar.

Models B through E were treated in two ways:

1. As sub-models using displacements from Model A (regardless that Models D and E have slightly different geometry). The implant was constrained in axial direction of the implant. Sub-models with this treatment were denoted with number 1 (B1, C1, D1, E1).
2. As fixed segments, i.e. the segments were fixed by both faces. This approach is very popular and often used in many studies dealing with bone-implant interactions (Marcían et al., 2014; Mellal et

al., 2004). The implant was loaded by an axial force obtained from Model A (i.e. the reaction force in the implant constraint). Models with this treatment were denoted with number 2 (B2, C2, D2, E2).

### 2.3. FE Mesh

The models were meshed by quadratic tetrahedral elements SOLID187 (Fig. 3). In case of Model A, the general element size was 3 mm and element size in the implant region was 1 mm. In total, Model A consisted of 184 409 nodes. In case of Models B through E, the general element size was 1 mm and element size in the implant region was 0.05 mm. The segment models consisted of 4.5 – 5 million nodes. The dental implant was assumed to be fully osseointegrated; therefore, the bonded contact algorithm was employed and contact elements CONTA160 and TARGE174 were used to model the interaction between the implant and the bone (Marcian et al., 2014).

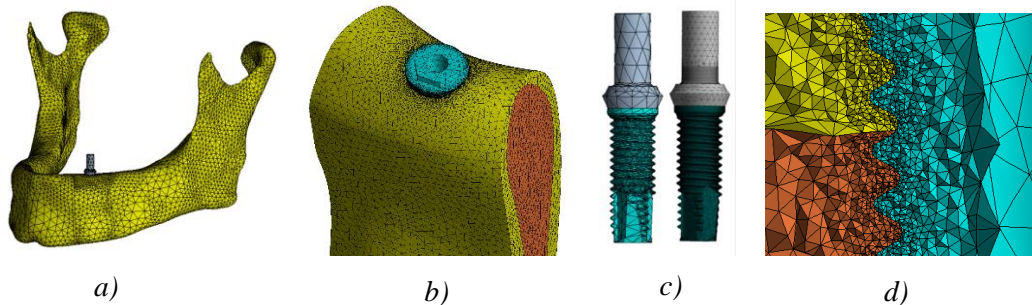


Fig. 3: Finite element (FE) mesh. a) Model A; b) Typical mesh of segment (Model B); c) Dental implant; d) bone-implant interface.

### 2.4. Material Properties

Cortical as well as cancellous bones were assumed to be linear, isotropic, elastic and homogeneous material. This simplification was considered to be sufficient for the purpose of this study. Specifically, both bone tissues were modeled by following Young's modulus and Poisson's ratio values:  $E_c = 13\,700\text{ MPa}$ ,  $\mu_c = 0.3$ ;  $E_s = 700\text{ MPa}$ ,  $\mu_s = 0.3$  (Natali et al., 2003)). The dental implants are usually manufactured from a titanium alloy. For the purpose of this study, the implant was modeled using Young's modulus and Poisson's ratio of  $E_i = 110\,000\text{ MPa}$  and  $\mu_i = 0.3$  respectively (Mellal et al., 2004).

## 3. Results

Bones were evaluated for von Mises strains and dental implant was evaluated for von Mises stresses. Both stress as well as strain distributions in the region of interest in all models are presented in Fig. 4. For clarity, only maximum stresses (typically in the second thread from the top) and maximum strains (in first thread from the bottom) were compared in the graph in Fig. 4.

## 4. Discussion

The results of Model A indicate (especially in comparison with those of Models B1 and C1) that Model A is inappropriate for detailed analysis of bone-implant interaction. The results from this model are not satisfactory as the FE mesh in the region of interest is not fine enough. Such the mesh was employed on purpose to show the differences between this coarse model and the sub-models. If a sensitivity study was carried out and if Model A was run with a sufficient mesh, the calculation would be at least as time-consuming as Models B1 and C1, but more likely much more. It is evident from the graph in Fig. 4 that Model C is sufficient for the investigation of bone-implant interaction, i.e. the segment length of 15 mm is good enough to provide accurate results in a reasonable time.

It is evident, that Models B2 and C2 provide stresses that are significantly lower than those of B1 and C1 because the implant is not subjected to a significant bending that occurs in reality (and in Models B1 and C1). The results of Models D1 and E1 show that it is possible to use boundary condition from coarse model of different mandible (under the condition that a typical geometry and loading are assumed). Maximum von Mises stresses in Model D1 are approx. 7 and 12 MPa lower than in Models B1 and C1.



The maximum difference of 18 MPa can be observed in Model E1; in this case, the difference is caused primarily by different cortical bone thickness as the cortical bone thickness is a significant factor affecting the implant performance (its success or failure). The maximum strain results in all models have similar trends as the stresses in the implants (Fig. 4).

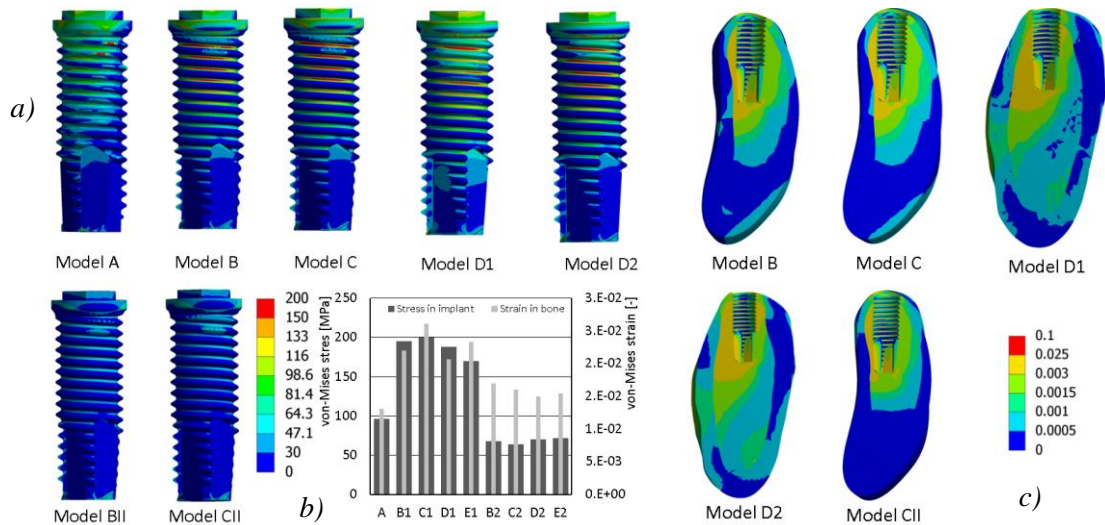


Fig. 4: Results: a) von Mises stress distribution in dental implant; b) maximum von Mises stress in dental implant and von Mises strain in bone; c) von Mises strain in bone-implant.

## 5. Conclusion

If the coarse model for the particular bone segment model is not available, it is possible to use a generic boundary condition for a typical mandible subjected to a typical loading. In such a case, using a generic boundary condition would be a better option than using a fixed constraint as the results tend to be biased with such an oversimplification. This observation can be helpful in models with a detailed trabecular architecture of cancellous bone. In such a case, it is highly impractical to model the entire mandible as the solution would be extremely time-consuming with no benefit.

## Acknowledgement

The research was supported by the Czech Science Foundation by grant No. 16-08944S.

## References

- Ridwan-Pramana, A., Marcián, P., Borák, L., Narra, N., Forouzanfar, T. and Wolff, J. (2016) Structural and mechanical implications of PMMA implant shape and interface geometry in cranioplasty – a finite element study. *Journal of Cranio-Maxillofacial Surgery*, 44, 1, pp. 34-44.
- Marcián, P., Konečný, O., Borák, L., Valášek, J., Řehák, K., Krpalek, D. and Florian, Z. (2011) On the Level of Computational Models in Biomechanics Depending on Gained Data from Ct/Mri and Micro- Ct, in: MENDEL 2011 - 17th International Conference on Soft Computing. 1. Brno: Brno University of Technology, pp. 255-267.
- Huottilainen, E., Jaanimets, R., Valášek, J., Marcián, P., Salmi, M., Tuomi, J., Mäkitie, A. and Wolff, J. (2014) Inaccuracies in Additive Manufactured Medical Skull Models Caused by the DICOM to STL Conversion Process. *Journal of Cranio-Maxillofacial Surgery*, 42, 5, pp. e259 (e265 s.).
- Narra, N., Valášek, J., Hannula, M., Marcián, P., Sándor, G., Hyttinen, J. and Wolff, J. (2014) Finite element analysis of customized reconstruction plates for mandibular continuity defect therapy. *Journal of Biomechanics*, 47, 1, pp. 264-268.
- Marcián, P., Borák, L., Valášek, J., Kaiser, J., Florian, Z. and Wolff, J. (2014) Finite element analysis of dental implant loading on atrophic and non-atrophic cancellous and cortical mandibular bone – a feasibility study. *Journal of Biomechanics*, 47, 16, pp. 3830-3836.
- Natali, A.N., Hart, R.T., Pavan, P.G. and Knets, I. (2003) Mechanics of bone tissue, in: A.N. Natali (Ed.), *Dental Biomechanics*, Taylor & Francis, London, 2003, pp. 1-19.
- Mellal, A., Wiskott, H.W., Botsis, J., Scherrer, S.S. and Belser, U.C. (2004) Stimulating effect of implant loading on surrounding bone. Comparison of three numerical models and validation by in vivo data. *Clinical Oral Implants Research* 15, 2, pp. 239-248.

## THERMO-VACUUM TEST CHAMBER DEVELOPMENT FOR HEAT SWITCH TESTING IN SIMULATED MARTIAN CONDITIONS

J. Mašek\*, P. Brožek\*\*, M. Horák\*\*\*

**Abstract:** *In the fall of 2014 the Institute of Aerospace Engineering had been awarded by contract to perform Miniaturized Heat Switch testing. The Miniaturized Heat Switch was the unique technology developed by Italian company Aero Sekur for European Space Agency's missions to Mars. The aim of the project was to develop an innovative but simple experimental thermo-vacuum test chamber to simulate Martian atmospheric conditions. Conditions such as vacuum of 50 Pa absolute, temperatures in the range from  $-125\text{ }^{\circ}\text{C}$  to  $+60\text{ }^{\circ}\text{C}$  and pure  $\text{CO}_2$  environment of 1000 Pa absolute. The vacuum tightness of the chamber, deep cooling of the specimen under vacuum environment, thermal insulations or heat transfer paths had to be precisely considered. Important decision was to use the liquid nitrogen as the most appropriate cooling medium and copper rods for heat transfer outside the chamber. Later, elementary calibration vacuum-tightness test of the facility showed that the pressure increased from initial value of 220 Pa absolute to 450 Pa absolute within 16.5 hours and thus proved excellent chamber design. Therefore in the future, the test chamber modular design can be easily modified to allow testing of other space equipment in different simulated conditions.*

**Keywords:** Space technology, Thermo-vacuum test chamber, Martian conditions, Miniaturized Heat Switch, Vacuum-cryogenic insulation.

### 1. Introduction

Italian company Aero Sekur, on behalf of European Space Agency (ESA), had developed a unique Miniaturized Heat Switch for space applications. The Miniaturized Heat Switch, a key technology for rover mission to Mars, had to keep a temperature of any scientific instrument carried on-board in predefined range.

Our research at the Institute of Aerospace Engineering aimed to develop an innovative but simple experimental thermo-vacuum facility for Miniaturized Heat Switch testing under various simulated operational conditions. Challenging conditions such as vacuum of 50 Pa absolute, temperatures in the range from  $-125\text{ }^{\circ}\text{C}$  to  $+60\text{ }^{\circ}\text{C}$  and pure  $\text{CO}_2$  atmosphere of 1000 Pa absolute.

The test facility development was the first essential step to perform final Qualification tests of the Miniaturized Heat Switch technology to prove its design and performance in simulated Martian conditions.

### 2. Miniaturized Heat Switch and test requirements

Miniaturized Heat Switch (MHS), the unique key technology for rover mission to Mars scheduled beyond the 2020 horizon and possibly for further deep space applications, was developed by Italian company Aero Sekur. The Miniaturized Heat Switch was designed to be lightweight (less than 90 g), small in size (diameter less than 50 mm), of simple construction and self-sufficient in energy. It is worth to mention that similar technology had been developed decades ago in the form of mechanical switches which were complex mechanisms big in size as presented in the paper of significant importance (Batteux et al., 2003).

---

\* Ing. Jakub Mašek: Institute of Aerospace Engineering, Brno University of Technology, Technická 2896/2; 616 69, Brno; CZ, Jakub.Masek@vutbr.cz

\*\* Ing. Petr Brožek: S.A.B. Aerospace s.r.o., Purkyňova 649/127; 612 00, Brno; CZ, pbrozek@sabaerospace.com

\*\*\* Ing. Marek Horák, PhD.: Institute of Aerospace Engineering, Brno University of Technology, Technická 2896/2; 616 69, Brno; CZ, horak@fme.vutbr.cz



The significant drawbacks were the bigger weight and the dependence on power supply. The Miniaturized Heat Switch thus represented a true revolution.

The Fig. 1 shows the Miniaturized Heat Switch (MHS). Switch had two interfaces. The cold interface mounted to the heat sink that radiated the excessive heat to outer environment and the hot interface mounted to the scientific instrument. If the Heat Switch hot interface temperature increased above the limit, the actuator closed a contact. And vice versa if the hot interface temperature decreased below the limit, the heat path was closed and the MHS created a thermal insulation to the equipment.

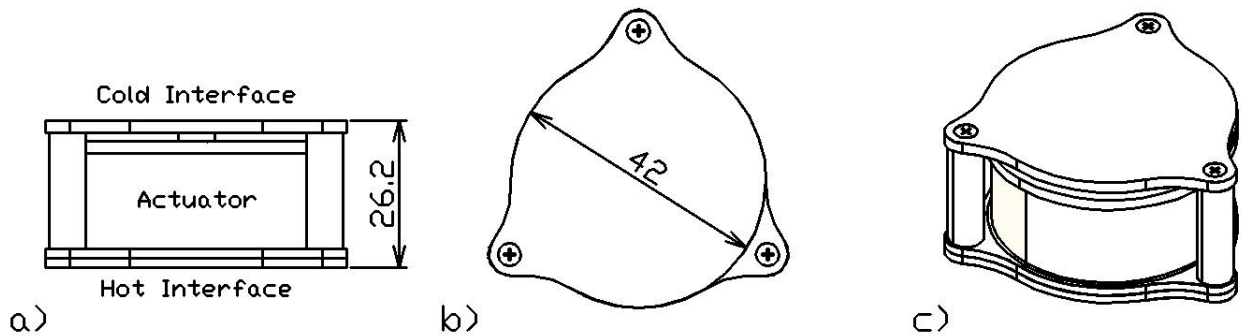


Fig. 1: Miniaturized Heat Switch (a) front b) top c) isometric view; dimensions are in millimeters).

The MHS was designed to keep temperature of any scientific instrument mounted to its hot interface in the range from 15 °C to 25 °C. The temperature range was maintained due to a change of MHS thermal conductivity by two positions of an actuator; position ON – the heat passed away through a radiator and position OFF – the heat generated by any scientific instrument was kept inside. The actuator motion was automatically controlled without any external power supply thanks to thermo-physical properties of paraffin.

According to the Miniaturized Heat Switch predefined performance, Aero Sekur in cooperation with ESA prescribed basic test campaign requirements. The test campaign had to determine whether or not the MHS switched within the specified temperature range as well as its thermal conductivity under different anticipated operating conditions. The first set of conditions was to keep several different constant temperatures on the cold interface and simultaneously to apply predefined heat loads up to 10 W on the hot interface. The second set of conditions was to apply temperature cycles from –125 °C to + 50 °C on the cold interface and –55 °C to + 60 °C on the hot interface to simulate a day/night cycle on Mars.

The test campaign defined strict requirements for the test chamber development. Except achieving the most extreme temperatures there were other requirements: to measure and control temperatures independently on both the MHS interfaces, heat transfers through the MHS and pressure inside of the test chamber.

### 3. Thermo-vacuum test chamber development:

To fulfill the test campaign requirements we faced the first important question: Would it be cheaper to modify a commercial thermo-vacuum chamber or would it be better to develop a new one?

There had been identified facilities which were suitable for modification to perform desired tests. However these facilities were built for other purposes and therefore were much bigger than needed. The extent of changes to meet the special requirements for the MHS testing would be significant. Even if there was a modified device, the calibration tests would have to be performed anyway. At the end all these aspects meant large expenses.

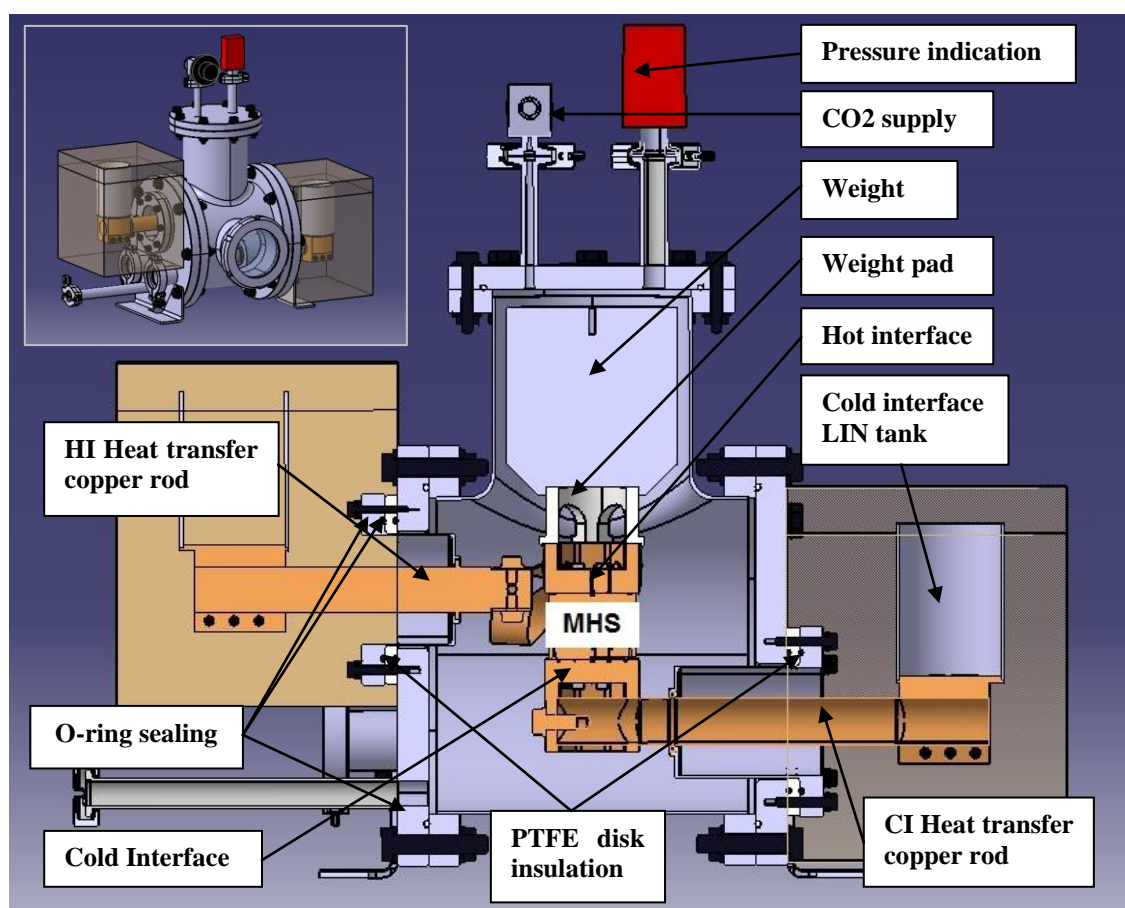
These facts lead us to idea of designing a new test facility based on the simplest technologies possible to reduce initial and operating costs while the test requirements would be met. Since the Miniaturized Heat Switch was the unique and new technology, the development resulted into an original and tailor-made test facility design consisting of special thermo-vacuum chamber and external supply systems for cooling, heating, vacuum and CO<sub>2</sub> environmental control and data acquisition system for measuring of the temperature and pressure.

However, how to design the thermo-vacuum chamber without prior knowledge of such extreme conditions? We decided to adopt the method of gradual development based on several anticipated hypotheses:

- 1) Soldered joint between the stainless steel used for chamber walls and copper rods will be vacuum-tight and withstand a load of 10 kg weight at  $-125\text{ }^{\circ}\text{C}$  on the cold interface.
- 2) Special stainless steel cylinders and PTFE disks will isolate efficiently the extremely cold copper rods from O-ring sealing used in the grooves of all flanges.

The principle was to define predictions on the basis of which the facility was developed. After the chamber assembly, several initial tests to confirm or reject the hypotheses had been performed and the facility had to be modified accordingly. Therefore a decision that the chamber had to be of modular design was essential.

At that point, the development turned into answering simple question: How to deal with cooling of the cold interface down to  $-125\text{ }^{\circ}\text{C}$  in the vacuum environment? Liquid nitrogen (LIN) was chosen as the best option. It satisfied both the extreme low temperature limit and easy operation in comparison to the other cryogenic liquids. It became shortly obvious that the initial concepts using labyrinth of pipes to deliver LIN directly into the chamber, LIN regulators and other high-tech pieces of hardware did not represent a cheap and easy way. Moreover there were operational restrictions with the LIN flowing through the capillaries, such as a quick medium evaporation or frozen moisture. Better idea that fitted to the safe low-cost solution was to cool down both interfaces through thermal conductivity rods as shown in Fig. 2.



*Fig. 2: Thermo-vacuum test chamber cross section.*

The development now got to the selection of materials. Inspired by fundamental papers (Lee, 1989 and Jelínek, 1982), three materials were chosen with respect to the market commonality and intended application in the chamber construction: Stainless steel was used for chamber walls predominantly loaded by external pressure; Copper was used for components acting as a heat path and Teflon (PTFE) as a

thermal contact insulator in the vacuum environment. Additionally Polystyrene was used outside of the chamber as LIN tanks thermal insulation.

One of the biggest challenges was to ensure a vacuum tightness in cryogenic environment, especially next to the deep cold elements going through the chamber walls. Cheap common O-ring sealing used in the grooves of all flanges did not sustain such a low temperatures and caused malfunction. Therefore special stainless steel cylinders with a wall thickness of 1 mm acting as heat resistors were developed. These cylinders held the pure copper rods by solder joint and were isolated by PTFE disks from the chamber walls. Additionally in this case, the common O-rings were replaced by the PTFE ones.

The solder joints were critical to the chamber design. Mainly because of the stresses that result from the tight connection of two materials with different thermal expansion coefficients, but also because of the mechanical stresses caused by the weight of the whole heat transfer assembly and additional weight above the MHS. Small modifications to improve the joints from both perspectives of soldering technology and joint properties were applied in cooperation with the Institute of Scientific Instruments of the CAS, Brno.

#### **4. Results**

Initial chamber tests proved that all Hypotheses were correct. Elementary calibration tests of the chamber showed the pressure increase from initial value of 220 Pa absolute to 450 Pa absolute within 16.5 hours and thus proved the vacuum tightness of the chamber design and particularly the tightness of the soldered joints. This result confirmed the Hypothesis 1). Soldered joint between the special stainless steel cylinder and copper rod close to the cold interface endured the load of 10 kg weight and cooling down to  $-140^{\circ}\text{C}$ .

Wall temperature of the chamber and used O-ring sealing never dropped below  $0^{\circ}\text{C}$  in any case due to the proper insulation made by special stainless steel cylinders and PTFE disks, this result confirmed the Hypothesis 2).

#### **5. Conclusions**

Our concept was intended to be as simple as possible but still able to meet all the challenging requirements. We ultimately considered the use of more automatic control, for example a control of the cooling medium amount or the implementation of long-term computer simulations in the design process, but all of that would increase the expenses significantly. The test facility and especially the chamber modular design could be easily modified in the future to allow testing of other space equipment even in different simulated environments. Internal modification of the interfaces would have to be done.

The presented thermo-vacuum test chamber design proved after the initial load tests exceptional viability and endurance for further improvement. That resulted in one year lasting successful facility calibration tests which have been confirmed by ESA. The first tests of the Miniaturized Heat Switch samples followed in short time after.

#### **Acknowledgement**

The research leading to these results has received funding from the MEYS under the National Sustainability Programme I (Project LO1202).

On this place above all I would like to thank Ing. Robert Popela, PhD., the project leader at Institute of Aerospace Engineering, BUT Brno, my colleagues Ing. Petr Brožek and Ing. Marek Horák, PhD. for cooperation. Many thanks also to Ing. Aleš Srnka, CSc. and Ing. Pavel Hanzelka (group of Cryogenics and Superconductivity) and Ing. Ivan Vlček, PhD. (Soldering operator, group of New Technologies) from the Institute of Scientific Instruments of the CAS, Brno for their willingness to help in any situation. My acknowledgement further belongs to Stéphane Lapensée, the ESA project representative (ESA-ESTEC, Noordwijk, The Netherlands) and Giuseppe Bonzano, project leader at Aero Sekur, Italy.

#### **References**

- Batteux, J.D., Labov, S.E. and van den Berg, M.L. (2003) Electro-mechanical heat switch for cryogenic applications. Google Patents, US Patent 6, 532, 759.
- Lee, G. (1989) Materials for Ultra-High Vacuum. Fermi National Accelerator Laboratory, Illinois.
- Jelínek, J. and Málek, Z. (1982) Cryogenic technology. Student text, SNTL, Prague (in Czech).

## RELIABILITY ASSESSMENT OF THE PRETENSIONED BOLTS BASED ON PROBABILITY

M. Maťas<sup>\*</sup>, K. Frydryšek<sup>\*\*</sup>

**Abstract:** *The experience indicates that the most common reason of the construction or assembly incoherency are not really irregular outside loads or influences but unpredictable standard behaviour of the bolted joints. Incorrect application or design of the bolted joints can lead to catastrophic accidents. The most common mistakes are under-sizing or inappropriate over-sizing, ignoring the fatigue, creep or anticorrosion protection. Bolted joints are in their working conditions exposed to action of internal or external forces with a different magnitudes and orientations. Presented article should provide a basic guide how to set certain loads acting on the bolted joint and calculate the reliability of the bolted joint considering the probabilistic approaches. In order to capture random variables in design and validation stage of the bolted joints, Simulation Based Reliability Assessment (SBRA) using Monte Carlo method is presented.*

**Keywords:** Pretensioned bolted joint, Probability, Reliability, AntHill, Monte Carlo.

### 1. Introduction

Presented paper is further development in the problems of the pretensioned sealing joints presented in articles Maťas et al. (2014) and Frydryšek et al. (2014). Author's attention in the previous articles was focused on the specific problem solved by deterministic and semi-probabilistic approaches. Nowadays, relatively big number of researches deals with the problems of the bolted joints using deterministic methods. However, many factors such as type of loading, operational loads, desired pretension in the bolts, cyclic loading or the presence of the heat loads need to be taken into account. Unfortunately, all this factors are hand in hand with tolerances which make the design and reliability assessment of the bolted joints even more difficult. This paper should demonstrate completely new and modern approach in this area, developed towards the Simulation Based Reliability Assessment (SBRA), i.e. probabilistic direct Monte Carlo approach. Hence, all inputs are given by truncated histograms. For more information about SBRA method see Frydryšek (2010), Frydryšek (2008), Frydryšek (2012), Marek et al. (2003).

### 2. Reliability assessment of the bolt based on probability

The following text outlines an example how to carry out a reliability assessment analysis of the bolt, considering not only pretension force but also additional loading such as bending and temperature. This procedure will be demonstrated on the M8 bolt with the material grade 10.9.

*Tab. 1: Independent random variables for the pretension force of the M8 screw.*

Input variable	Description	Distribution function	Nominal	Minimum	Maximum
$M_{ut}$ [N.mm]	Wrench torque	Normal distr. $\pm 6$ %	32 000	30 080	33 920
$f$ [1]	Friction coefficient	Uniform distr.	0.12	0.11	0.13
$d_2$ [mm]	Middle diam. of the thread	User defined distr.	7.10	7.04	7.16
$P$ [mm]	Pitch of the thread	Normal distr. $\pm 1$ %	1.250	1.237	1.262
$s$ [mm]	Screw head diam.	Normal distr. $\pm 1$ %	13.00	12.87	13.13
$\delta$ [mm]	The screw hole diameter	Normal distr. $\pm 1$ %	9.00	8.91	9.09

<sup>\*</sup> M.Sc. Martin Maťas: Department of Applied Mechanics, Faculty of Mechanical Engineering, VŠB – Technical University of Ostrava, 17. listopadu 15, 708 33 Ostrava - Poruba, CZ, martin.matas.st@vsb.cz

<sup>\*\*</sup> Assoc. Prof. M.Sc. Karel Frydryšek, PhD., ING-PAED IGIP: Department of Applied Mechanics, Faculty of Mechanical Engineering, VŠB – Technical University of Ostrava, 17. listopadu 15, 708 33 Ostrava - Poruba, CZ, karel.frydrysek@vsb.cz

## 2.1. Pretension force of the bolt

First of all will be generated pretension force based on the six independent variables (see Tab. 1) defined by the bounded histograms. The theoretical bolt pretension force is given by the following equation:

$$F_Q = M_{ut} / \left( \frac{d_2}{2} \cdot \tan(\gamma + \varphi') + f \cdot r_s \right) \text{ [N]}. \quad (1)$$

The necessary subequations are as follows:

$$\gamma = \arctan(P/\pi \cdot d_2) \text{ [}^\circ\text{]}, \quad \tan \varphi' = f[1], \quad r_s = (s + \delta)/4 \text{ [mm]}, \quad (2)$$

where  $\gamma$  - angle of the thread pitching,  $\varphi'$  - friction angle and  $r_s$  - friction radius.

AntHill software allows defining any type of bounded histograms. It's possible to use a library with the distribution functions or to use user defined distribution. You can see the example in following Fig. 1.

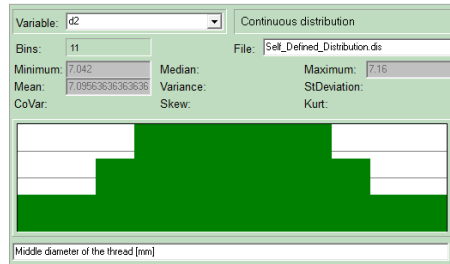


Fig. 1: User defined distribution function for  $d_2$  (ANTHILL).

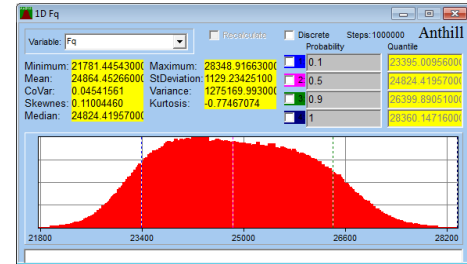


Fig. 2: Output histogram of the pretension force  $F_Q$  (ANTHILL).

Outputted bounded histogram of the bolt pretension force is shown in Fig. 2. Demonstrated variables are pure examples; the more accurate the bounded histograms are defined the closer are the results to the reality. The next step is to take into account operation loads.

## 2.2. Bending and temperature loading

Bending loading can easily occur when the flanges of the bolted joint are deformed due to operational loads such as for instance pressure. Another case could be inclined surface under the bolt head or nut. Bending stress can be a couple of times higher than the tensile stress of the screw. This inappropriate loading reduces the screw capacity significantly and mostly results in the screw breakage at the thread run-out. The formula to calculate the bending stress  $\sigma_0$  of the bolt is following

$$\sigma_0 = \varphi \cdot E \cdot d_3 / l \text{ [MPa]} \quad (3)$$

In following Tab. 2 can be found the variables used in eq. (3). These variables were again defined by the bounded histograms; similarly to histograms in Fig. 1.

Tab. 2: Independent random variables for the bending loading of the screw

Input variable	Description	Distribution function	Nominal	Minimum	Maximum
$\varphi$ [rad]	Bolt deformation angel	Uniform distr.	0.001	0.000	0.002
$E$ [MPa]	Young modulus	Normal distr. $\pm 3$ %	210 000	203 700	216 300
$d_3$ [mm]	Minor diam. of the thread	User defined distr.	6.466	6.272	6.619
$l$ [mm]	Clamped length	Normal distr. $\pm 5$ %	22.0	20.9	23.1

The Fig. 3 shows that the bending stress can cause really high additional loading. In this case it's almost 135 MPa. The way to reduce the bending stress is to extend the length of the clamped flanges or to reduce the screw diameter. It is necessary to mention that the input values of the loading angle  $\varphi$  were defined again just as an example. The temperature influence depends on the thermal expansion coefficient of the bolted flanges and of the screw as well. If this thermal expansion coefficient is the same for both, warming up the bolted joint to the same temperature of all parts will not cause significant influence to the joint.

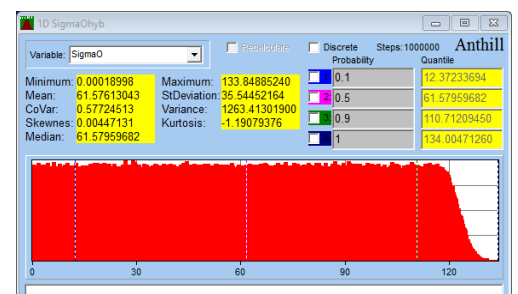


Fig. 3: Output histogram of the bending stress  $\sigma_0$  (ANTHILL).



In the bolted joints with a bigger gap between the bolt and flanges is the thermal transfer to the bolt much more difficult. That means the temperature of the bolt will be lower than the temperature of the flanges. This phenomena will cause additional loading of the bolt due to the thermal expansion of the flanges, especially at the beginning of the heating. Considering a different thermal expansion coefficient for a bolt and for flanges, while the temperature of the bolt is lower by  $\Delta t$ , then the formula to calculate the extension of the bolted flanges is following

$$\Delta l_1 = l \cdot [(\alpha_2 - \alpha_1)(t - t_0) + \alpha_1 \cdot \Delta t] \text{ [mm]}. \quad (4)$$

Corresponding force to this extension is calculated by the equation

$$\Delta F_V = \Delta l_1 (C_1 \cdot C_2) / (C_1 + C_2) \text{ [N]}, \quad (5)$$

where  $C_1$  is the stiffness constant of the bolt and  $C_2$  is the stiffness constant of the clamped flanges.

$$C_1 = E_1 \cdot S_1 / l \text{ [N} \cdot \text{mm}^{-1}], \quad C_2 = E_2 \cdot S_2 / l \text{ [N} \cdot \text{mm}^{-1}] \quad (6)$$

In order to calculate the resultant force  $\Delta F_V$  based on probability, the following variables shown in Tab. 3 were defined. Variable  $E_1$  and  $E_2$  are equal to variable  $E$  defined in Tab. 2.

Tab. 3: Independent random variables for the force  $\Delta F_V$ .

Input variable	Description	Distribution function	Nominal	Minimum	Maximum
$\alpha_1 \text{ [K}^{-1}]$	Thermal expansion coeff.	Normal distr. $\pm 3 \%$	0.000011	0.00001067	0.00001133
$\alpha_2 \text{ [K}^{-1}]$	Thermal expansion coeff.	Normal distr. $\pm 3 \%$	0.000017	0.00001649	0.00001751
$t \text{ [K]}$	Operation temperature	Normal distr. $\pm 10 \%$	373.15	298.52	447.78
$t_0 \text{ [K]}$	Base temperature	Normal distr. $\pm 20 \%$	293.15	263.84	322.47
$\Delta t \text{ [K]}$	Temp. difference bolt-flanges	Normal distr. $\pm 25 \%$	293.15	219.86	366.43
$S_1 \text{ [mm}^2]$	Bolt section area	Dependent variable	32.82	30.90	34.41
$S_2 \text{ [mm}^2]$	Flanges section area	$5 \times S_1$	164.10	154.48	172.05

Fig. 4 shows output histogram of the force resulting from the different thermal expansion of the bolt and the flanges. It's very important to notice that not the whole component of the force will be transmitted to the bolt. Most of the force will actually flow through the flanges. More information about the force distribution in the pretensioned bolts is excellently explained in reference Málík et al. (2009). The formula to calculate the force component in the bolt  $\Delta F_{V1}$  and the force loading the flanges  $\Delta F_{V2}$  is:

$$\Delta F_{V1} = \Delta F_V \cdot [C_1 / (C_1 + C_2)] \text{ [N]}, \quad \Delta F_{V2} = \Delta F_V \cdot [C_2 / (C_1 + C_2)] \text{ [N]} \quad (7)$$

Presented paper shows the results only of the force acting in the bolt -  $\Delta F_{V1}$  (see Fig. 4).

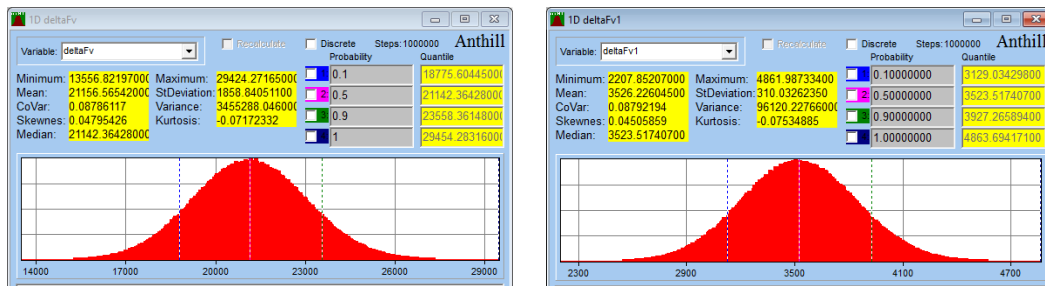


Fig. 4: Output histogram of the force  $\Delta F_V$  and  $\Delta F_{V1}$  (ANTHILL).

While designing the bolted joint loaded by heat, it is necessary to consider following rules: to secure a good heat transfer to the bolt so the temperature of the flanges and of the bolt will equalize and stabilize as quick as possible, by screwing the bolt to the bottom flange or by filling the gap between the bolt and the flanges by conductive material such as metal or graphite powder; to secure higher elasticity of the bolt by local diameter reduction at the bolt non-threaded area; to use metal with high Yield strength and low ultimate tensile strength; define adequately reduced pretension force  $F_Q$ , for instance  $F_Q < 3\Delta F_{V1}$ .

### 2.3. Resultant loading of the bolt

The resultant stress  $\sigma$  acting in the analyzed bolt is calculated simply as a sum of stresses.

$$\sigma = \sigma_{F_Q} + \sigma_o + \sigma_{\Delta F_{V1}} \quad (8)$$



Outputted bounded histogram of the resultant stress  $\sigma$  is shown in Fig. 5. The stress range is from 740 MPa to 1142.5 MPa. Using SBRA method, the probability of failure is obtained by analyzing the reliability function  $RF$ :

$$RF = Re - \sigma \quad (9)$$

The probability of failure is the probability that  $\sigma$  exceeds  $Re$  (material Yield strength), i.e.  $P(RF \leq 0)$ . For the studied bolt M8, the probability of failure  $P(RF \leq 0) = 0.0007$  (app. 0.1 %).

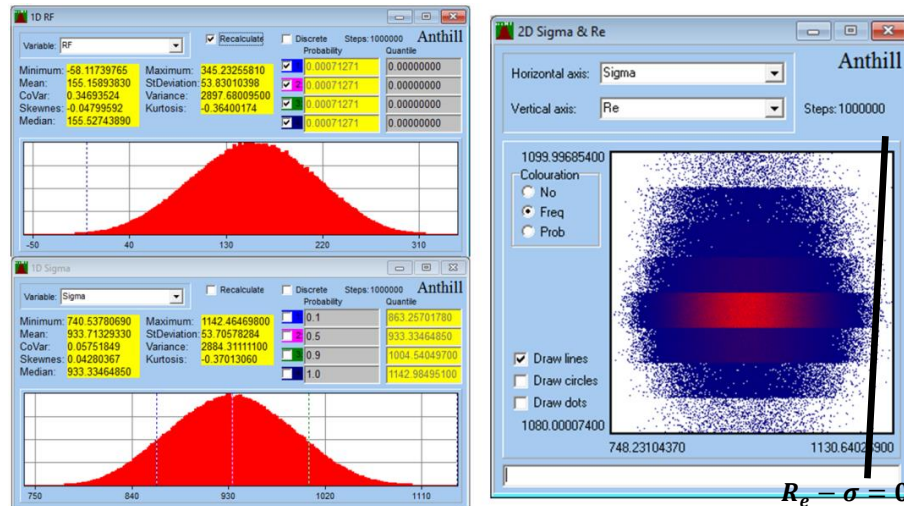


Fig. 5: Output histogram of the total stress  $\sigma$  and 2D diagram of the reliability function  $RF$  (ANTHILL).

### 3. Conclusions

Using bolts to join parts together introduces lots of problems which is necessary to understand in order to design reliable connection. Using presented SBRA method allows to do a reliable construction design, while variables used in this method include realistic safety coefficients. As already mentioned in the text above, the more precisely bounded histograms are defined, the more accurate and more realistic results are. This means that by using SBRA method engineers are not forced to blindly define safety coefficients which usually leads to inappropriate over-sizing of the construction but on the contrary, they have a full control over the whole design or validation of the construction. Presented article shows only operational loads of the bolts such as bending and temperature loading due to article size constraints. However, one of the most common fastener failure modes is fatigue crack initiation and growth. Therefore, as a future enhancement, fatigue of the bolts will be analyzed by using probabilistic SBRA method.

### Acknowledgement

This work was supported by Czech projects SP2017/136.

### References

- Frydrýšek, K. (2010) Probabilistic Calculations in Mechanics 1, VŠB - Technical University of Ostrava, pp. 1-149.
- Frydrýšek, K. (2008) Simulation-Based Reliability Assessment and Performance-Based Design Applied for Beams, In: Book and CD-ROM of 3rd International Conference "From Scientific Computing to Computational Engineering" (3rd IC-SCCE), Athens, Greece, pp. 1-8.
- Frydrýšek, K. (2012) Monte Carlo approach Applied in the Design of Machine Parts and Structures, International Journal of Mechanics, vol. 6, Issue 4, pp. 222-229.
- Frydrýšek, K., Mařas, M. and Novák, P. (2014) Analysis of Sealing Properties on a Bolted Joint Based on Probability. Trans Tech Publications, Applied Mechanics and Materials, Vol. 684, Switzerland, pp. 279-285.
- Málik, L., Chrzová, J., Medvecký, Š. and Lukáč, M. (2009) Designing II. University of Zilina, Zilina, pp. 1-510.
- Marek, P., Brozzetti, J., Gruštar, M. and Tikalsky, P. (2003) Probabilistic Assessment of Structures Using Monte Carlo Simulation Background, Exercises and Software, (2nd extended edition), ITAM CAS, Prague (in Czech).
- Mařas, M., Novák, P. and Balco, P. (2014) Analysing of Sealing Properties on a Bolted Joints with a Steel Gasket by Using Finite Element Method, Transactions of the VŠB – Technical University of Ostrava, Mechanical Series No. 1, vol. LX, article No. 1981.
- Sága, M., Vaško, M. and Kopas, P. (2011) Stress and strength - Chosen methods and applications, Žilina: VTS. pp. 400.

## RANS CALCULATIONS ON SUBMERGED BODIES

F. Mauro<sup>\*</sup>, P. Cerni<sup>\*\*</sup>, R. Nabergoj<sup>\*\*\*</sup>

**Abstract:** *The study of the total resistance of a submerged body is a matter of interest not only for the development of submerged vehicles like submarines or ROV, but also for the study of particular appendages that are fitted on a vessel, like a sonar dome or the under-keel of a sailing yacht. For this purpose RANS calculations can give an accurate estimate of the resistance without too much calculation effort. To perform an accurate estimate, a validation study, using STARCCM+ solver, has been carried out on a standard geometry of the 58 Series. The validated mesh has been used for the resistance evaluation of a new body.*

**Keywords:** CFD calculations, Validation study, 58 Series, Submerged body.

### 1. Introduction

The determination of the resistance of a fully submerged body can be determined by means of different kind of approaches. Once it will be not possible to perform dedicated model tests on the selected geometry, use can be made of systematic series. For the particular case of a submerged body, the only available material covering a wide range of geometries is the 58 Series (Gertler, 1950). Once the selected geometry is not falling inside the definition range of the series, dedicated calculation should be performed. Calculations can be made by means of codes based on non-lifting potential theory (Hess and Smith, 1964), where viscous effects are not directly considered, or an approach based on RANS equation can be used. For this purpose STARCCM+ solver has been used to determine the total resistance of a submerged body. Prior to the effective calculation, a validation study has been carried out to determine calculation uncertainty and mesh independence on geometry of the 58 Series, where model test data were available. Thereafter the same settings of the validated mesh have been used to determine the resistance of a new submerged body having geometrical parameters different from the 58 Series ones.

### 2. Geometry of the submerged bodies

The geometries selected for this study are the 4164 hull of the 58 Series and a generic body (named SB01) designed to be used as sub-keel appendage on a sailing yacht for ORC competitions. The main dimensions of the two geometries are reported in Tab. 1 and an overview is given in Fig. 1.

*Tab. 1: Main dimensions of 4164 and SB01.*

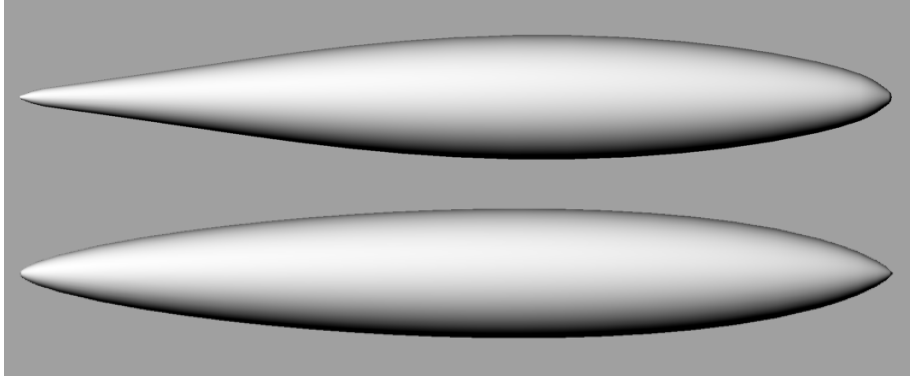
	Symbol	4164	SB01	unit
Length overall	$L$	2.7432	2.7432	m
Maximum Diameter	$D$	0.3919	0.4040	m
Wetted Surface	$S$	2.726	2.611	m <sup>2</sup>
Volume	$\nabla$	0.231	0.216	m <sup>3</sup>
Length diameter ratio	$L/D$	7.000	6.790	-

---

<sup>\*</sup> Ir. Francesco Mauro: Department of Engineering and Architecture, University of Trieste, Via Valerio 10; 34100, Trieste; IT, fmauro@units.it

<sup>\*\*</sup> Ing. Pietro Cerni: Department of engineering and Architecture, University of Trieste, Via Valerio 10; 34100, Trieste, IT.

<sup>\*\*\*</sup> Prof. Radoslav Nabergoj: NASDIS PDS d.o.o.; Indusrijska Cesta 2E, 6310 Izola, SI, radoslav.nabergoj@nasdispds.com



*Fig. 1: 4164 (top) and SB01 (bottom) geometries.*

The geometries are streamlined bodies of revolutions; all the hulls of the 58 Series got this peculiarity and the designers of SB01 decided to maintain this configuration to reduce construction costs. For the calculations this will be also an advantage because in such a case just a quarter of domain can be modeled, reducing consequently the calculation time.

### 3. Physical assumptions and Numerical setup

The total resistance  $R_T$  of a deeply submerged body can be split in a contribution given by shear stress  $R_S$  and a second one given by normal stress (pressure)  $R_P$ . In absence of a free surface, gravitational effects (waves generation) can be neglected and both two components can be considered function of the Reynolds Number  $Rn$  without other dependency. Due to the streamlined shape of the geometry, a steady flow assumption has been adopted for the calculation, selecting a segregated approach for the RANS equations solution, using Rhie-Chaw interpolation for pressure-velocity coupling. The effect of turbulent fluctuations on the mean flow has been approximated by realizable  $k-\varepsilon$  turbulence model. A three-dimensional rectangular domain has been used to represent the calculation environment. Because of the geometry symmetry and the deeply-submerged condition of the body, the domain takes in consideration the symmetry on vertical and horizontal plane, means that only a quarter of body and total domain are modeled. The finite volume domain is than meshed with a trimmed cell method, where a block refinement was inserted to capture with more detail the geometry wake and the flow around the body. A prism layer mesh has been adopted in the near-wall region, to generate orthogonal prismatic cells close to the body surface. The total prism layer thickness is obtained from geometrical progression of step  $Pls$  starting from the first cell thickness, calculated in such a way to reach a target  $y^+$  of about 55 at all the  $Rn$  of the simulations. In order to obtain a mesh usable for different kind of geometries all the mesh parameters have been parameterized on the length  $L$  of the body to analyze, these parameters are reported in Tab. 2. As mentioned the right and the top side of the domain have been set as symmetry plane while the other faces are considered as velocity inlet, despite the pressure outlet on the backside. All the calculations have been carried out considering fresh water as reference fluid with a density  $\rho$  of  $997.561 \text{ kg/m}^3$  and a dynamic viscosity  $\mu$  of  $8.887 \text{ Pa s}$ .

*Tab. 2: Main mesh parameterization details.*

	Symbol	value
Domain length	$L_n$	5 L
Domain breadth	$B_n$	1 L
Domain height	$H_n$	1 L
Number of prism layers	$Npl$	8
Prism layer stretching	$Pls$	1.3

### 4. Validation study on 4164 geometry form and SB01 resistance calculation

As first step of the validation study on 4164 geometry, a mesh sensitivity study has been carried out. The aim of this first investigation is to find a mesh where the discretisation error can be considered negligible.

In fact the numerical error consists of three parts (Roache, 1998): the iterative error, the round-off error and the discretisation one. The iterative error is related to equations resolution and can be discarded once solution convergence reaches machine accuracy (possible to obtain in steady state calculations). To estimate the discretisation error use has been made of the Grid Convergence Index (GCI) and Richardson Extrapolation of the real value (Eça et al., 2004). The selected speed for the sensitivity study is corresponding to  $Rn$  1.2 E7, and a total of 6 meshes have been studied considering a base size refinement ratio of 1.25 per each mesh, resulting in a total number of cells going from 181380 up to 3870976. As it can be seen in Tab. 3, the results of the grid convergence study show that grid 2 is sufficient to ensure the grid independency for the total resistance  $R_T$  estimation on the tested velocity.

Tab. 3: Mesh sensitivity study results.

Grid	N°cells	$B_s$	Ref ratio	$R_T$ (N)	GCI
1	3870976	0.168 $L$	-	53.39	-
2	2076984	0.210 $L$	1.25	53.40	0.043
3	1118676	0.263 $L$	1.25	53.44	0.085
4	581647	0.328 $L$	1.25	53.57	0.266
5	328805	0.410 $L$	1.25	53.84	0.654
6	181380	0.513 $L$	1.25	53.94	0.837

Then, considering  $E$  the difference between the experimental data and the simulation, and  $U_{TOT}$  the total uncertainty of the process (evaluated as the norm within numerical and experimental uncertainties), the simulation can be considered validated when the condition  $|E| < U_{TOT}$  is satisfied. Assuming an experimental uncertainty of 2.5 % on the measured data (ITTC, 2011), the validation process has been carried out on a speed range from  $Rn$  6.0 E6 to 2.4 E7 and is reported in Tab. 4.

Tab. 4: Validation study on 4164 geometry ( $E$  and  $U_{TOT}$  expressed as % $R_T$ ).

$Rn$ (-)	$V$ (m/s)	$R_T$ (N)	$R_{T_{58}}$ (N)	$ E $	$U_{TOT}$	Validated
6.0 E6	1.910	14.37	13.91	3.307	3.380	YES
8.0 E6	2.546	25.05	24.80	1.008	3.420	YES
1.0 E7	3.183	38.02	38.04	0.001	3.439	YES
1.2 E7	3.819	53.40	54.27	1.603	3.468	YES
1.4 E7	4.456	71.25	72.24	1.370	3.463	YES
1.6 E7	5.093	91.47	92.83	1.465	3.465	YES
1.8 E7	5.729	114.01	115.57	1.350	3.463	YES
2.0 E7	6.366	138.87	140.78	1.357	3.463	YES
2.2 E7	7.002	165.99	168.63	1.566	3.467	YES
2.4 E7	7.639	195.35	198.63	1.651	3.469	YES

For the analyzed geometry the resistance curve is validated through all the selected speed range of interest. Adopting a mesh as the one validated for 4164 geometry, simulations were carried out on the SB01 through the validated speed range. Because the length  $L$  of the second geometry is equal to 4164 (see Tab. 1), the meshes result with the same dimensional parameter of the validated ones through all the speed range. In Fig. 3 the obtained resistance curve is presented and compared with the 4164 experimental and numerical results. As it can be seen the resistance level of the new geometry is higher than the 4164 hull. 4164 is the Series 58 geometry closer to SB01. By simply adopt the series as a reference the non dimensional coefficient  $C_T$  of the 4164 can be scaled on the new geometry considering the new wetted surface of SB01. The change of volume can be also considered by scaling the speed according to the volumetric Reynolds number. By means of this process the total resistance  $R_T$  would have been underestimated for the new geometry because both volume and wetted surface are lower than 4164 ones. A comparison between the pressure patterns along the two hulls is presented in Fig. 2, showing the differences in the pressure distribution at the same  $Rn$  for the two geometries.

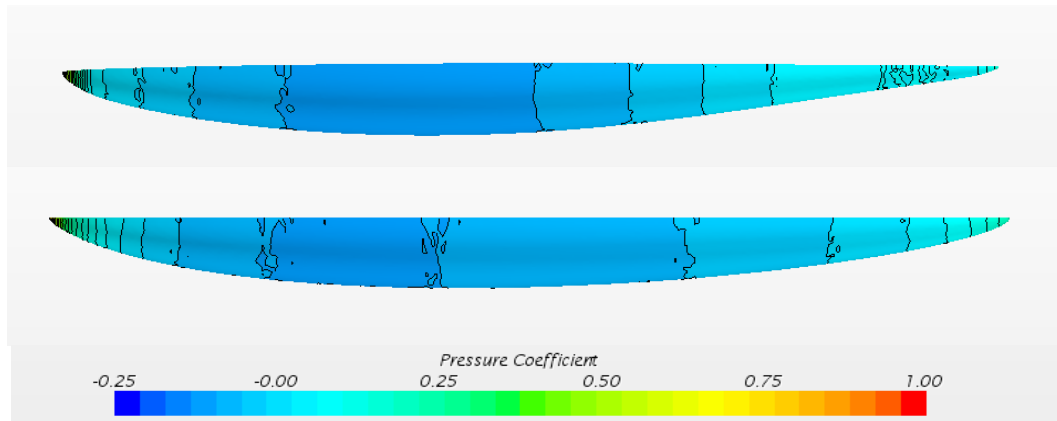


Fig. 2: Pressure distribution on 4164 (top) and SB01 geometries at  $Re$  1.2 E7.

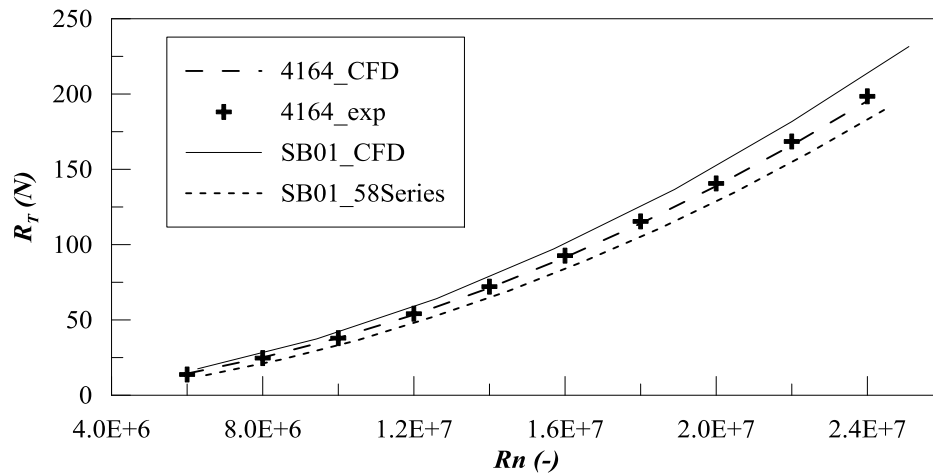


Fig. 3: Comparison between the calculated resistance curves.

## 5. Conclusions

The current work highlights that RANSE based method are for sure reliable for the total resistance prediction of a submerged body. However the reliability of the equation solver on the discrete domain should be validated with a correct methodology on standard test cases. Just a comparison between a measured and a calculated quantity is not sufficient to ensure the validation of a resistance curve. The present work is a starting point to perform different kind of analysis also on other aspects of the simulations, like the adoption of other turbulence models or the consideration of an unsteady flow condition. The obtained results for these particular bodies have to be intended as a good starting point to develop a more complex simulation on vessels with appendages, where, adopting a mesh like the validated one, the solution around the submerged appendage will give a reliable result.

## References

- Eça, L. and Hoekstra, M. (2004), Workshop on CFD Uncertainty Analysis. Instituto Superior Tecnico, Lisbon.
- Ferziger, J.H. and Perić, M. (2002), Computational Methods for Fluid Dynamics. 3<sup>rd</sup> rev. Ed., Springer Verlag, Berlin.
- Gertler, M. (1950) Resistance Experiments on a Systematic Series of Streamlined Bodies of Revolution for Application to the Design of High-speed Submarines. David Taylor Model Basin internal report, Washington D.C.
- Hess, J. and Smith, A. (1964) Calculation of Nonlifting Potential Flow About Arbitrary Three-Dimensional Bodies. Journal of Ship Research, pp. 22-44.
- ITTC (2011) Practical Guidelines for Ship CFD Applications. ITTC Recommended Procedures and Guidelines 7.5-03-02-03.
- Roache, P.J. (1998) Verification and Validation in Computational Science and Engineering. Hermosa Publisher, Albuquerque.

## DETERMINATION OF NON-LINEAR ROLL DAMPING COEFFICIENTS FROM MODEL DECAYTEST

F. Mauro<sup>\*</sup>, R. Nabergoj<sup>\*\*</sup>

**Abstract:** A conventional method to estimate the damping of an oscillatory system is the execution of amplitude extinction tests. In the specific case of the roll motion of a vessel, the so-called roll decay tests are performed in a model basin. During these tests, the system is posed in an imbalance condition by an external moment. For systems where the damping is far below critical value, the transient decay to equilibrium condition is oscillatory. There are several methodologies to analyze the decay test time-series, all based on the assumption that a pure roll motion has been reproduced. Through this paper an overview of the most commonly used methods is given and a comparison of the results is shown for a single ship model decay test.

**Keywords:** Roll motion, Damping coefficient, Decay test.

### 1. Introduction

To estimate the damping coefficient of the roll motion for a surface vessel, dedicated model tests are carried out in specialized hydrodynamic laboratories. The specific test to be performed is the so-called rolldecay test. When performed according to the ITTC (International Towing Tank Conference) standard, it consists in measuring the amplitude of the roll motion of the ship model as function of time. To do that, a predetermined transversal inclination must be given to the model and then let it to oscillate up to reaching the equilibrium. The procedure should be performed for all the vessel speeds of interest. From the obtained time-series record there are several methods to analyze the data in order to estimate the damping coefficients, based on non-linear dynamic equation of roll motion. In the theory of Ship motions, it is common practice to linearize the dynamic system by decoupling all the motion equations (Blagoveshchensky, 1964). In such a way only the roll equation is considered by neglecting couplings with other motion as sway and yaw. In such a way the mathematical treatment of the problem results simplified especially when non-linear damping has to be analyzed. Introduction of linear sway or yaw coupling, only slightly complicates the problem. The most commonly used methods to evaluate the coefficients are here described and applied to a roll decay record.

### 2. Roll motion equation

To describe the pure roll behavior of a vessel subjected to external active forces, the following single degree of freedom equation can be written:

$$I_{\phi} \ddot{\phi} + B_{\phi}(\dot{\phi}) + C_{\phi}(\phi) = M_{\phi} \quad (1)$$

where  $I_{\phi}$  represents the virtual mass moment of inertia along the longitudinal roll axis,  $B_{\phi}$  is the damping moment,  $C_{\phi}$  is the restoring moment and  $M_{\phi}$  represents the external moment due to waves or other external forces. In the specific case of a standard decay test, the external moment  $M_{\phi}$  is not considered, leading to:

$$I_{\phi} \ddot{\phi} + B_{\phi}(\dot{\phi}) + C_{\phi}(\phi) = 0 \quad (2)$$

---

<sup>\*</sup> Ir. Francesco Mauro: Department of Engineering and Architecture, University of Trieste, Via Valerio 10; 34100, Trieste; IT, fmauro@units.it

<sup>\*\*</sup> Prof. Radoslav Nabergoj: NASDIS PDS d.o.o.; Industrijska Cesta 2E, 6310 Izola, SI, radoslav.nabergoj@nasdispds.com



Equation (2) can be expressed with several orders of non-linearity, depending on the modeling of the damping moment  $B_\phi$  and of the restoring moment  $C_\phi$ .

The damping moment  $B_\phi$  of a vessel can be expressed as a power series of  $\dot{\phi}$  and  $|\dot{\phi}|$  usually up to the third order but, in case of small oscillations, a second order approximation is sufficient; resulting in:

$$B_\phi(\dot{\phi}) = B_{\phi 1}\dot{\phi} + B_{\phi 2}\dot{\phi}|\dot{\phi}| \quad (3)$$

The restoring moment  $C_\phi$  of a vessel is expressed in the following form:

$$C_\phi(\phi) = \Delta \overline{GZ}(\phi) \quad (4)$$

where  $\Delta$  is the vessel displacement and  $\overline{GZ}(\phi)$  is the righting arm of the vessel. In this case the righting arm can be expressed in terms of odd-order polynomials. In case of small amplitude oscillations, a linear righting arm can be considered with the following form:

$$C_\phi(\phi) = \Delta \overline{GM}\phi \quad (5)$$

where  $\overline{GM}$  is the so-called metacentric height, function of the center of gravity height, of the ship volume and of the transversal inertia of the waterplane area. So, by considering formulation (3) for the damping moment and (5) for the restoring moment, equation (2) can be rewritten as:

$$I_\phi \ddot{\phi} + B_{\phi 1}\dot{\phi} + B_{\phi 2}\dot{\phi}|\dot{\phi}| + \Delta \overline{GM}\phi = 0 \quad (6)$$

Dividing (6) by  $I_\phi$  the motion equation takes the following non-dimensional form:

$$\ddot{\phi} + 2\nu\dot{\phi} + w\dot{\phi}|\dot{\phi}| + n^2\phi = 0 \quad (7)$$

where  $2\nu$  is the linear damping coefficient and  $w$  is the quadratic damping coefficient.

### 3. Logarithmic decrement

The most common way to analyse a decay test is to find the logarithmic decrement of the consecutive oscillation in order to figure out the behaviour of the decay process. Once the oscillation peaks have been extracted from the time series, the analysis will proceed with the determination of the successive oscillations decrements. In case that equation (7) is used for the roll modelling, a particular solution can be found for the first swing, supposing that the first peak is positive. In such a case the term  $\dot{\phi}|\dot{\phi}|$  can be defined as  $\dot{\phi}^2$  and the solution becomes:

$$\phi = \left( \phi_0 - \frac{2}{3}w\phi_0^2 \right) e^{-\nu t} \cos \omega t + \phi_0^2 w e^{-2\nu t} \left( \frac{1}{2} + \frac{1}{6} \cos 2\omega t \right) \quad (8)$$

where the frequency of oscillation  $\omega$  is defined as  $\sqrt{n^2 - \nu^2}$ . The decrease in amplitude of the first swing and generally of the  $i+1^{th}$  swing can be determined in the following form:

$$\Delta\phi_{i+1} = \phi_i \left( 1 - e^{-\nu T_c/2} \right) + \frac{2}{3}w\phi_i^2 e^{-\nu T_c/2} \left( 1 + e^{-\nu T_c/2} \right) \quad (9)$$

where  $T_c$  is the period of the oscillation and, in case of a vessel, can be approximated by the rolling period without damping  $T = 2\pi/n$  (Vlasov, 1930). It must be noted that, by using this kind of notation, all the peaks should be considered. When the procedure is applied only to maxima or minima, then the period to be considered in (9) is  $T_c$  instead of  $T_c/2$ . The quantity of the decrement of the single swings can also be directly determined from the decay record, making the difference between the consecutive peaks.

### 4. Equivalent linear damping

Another way to evaluate the damping coefficients from the decay test is to use the so-called equivalent linear damping representation. This way to represent the data is coming from a theoretical assumption based on the Newton statement, establishing that, for small damped oscillations with a resistance law in quadratic polynomial form, the decay law for amplitudes can be expressed in approximated form as:

$$\Delta\phi = a_1\phi_m + a_2\phi_m^2 \quad (10)$$

where  $\phi_m$  is the average value of the amplitude of the examined swing. Considering that the restoring moment in equation (7) is linear with respect to  $\phi$ , in the instants where the vessel passes through the equilibrium position the  $\phi$ -dependent part of the equation goes to zero. Means that, for these time instants, the roll equation can be represented as:

$$\phi = f(t)\cos\omega t \quad (11)$$

where  $f(t)$  is a function slowly decaying with time. If  $f(t)$  is considered as the envelope curve of the decay oscillation (Pavlenko, 1947), then a relation can be found between linear and quadratic damping, equating the integral of the resistance laws between 0 and  $\phi_m$ . Resulting in:

$$2N = \frac{8}{3\pi} W\omega\phi_m \quad (12)$$

where  $2N$  and  $W$  are the damping coefficients in dimensional form. The dimensional linear damping coefficient can be obtained directly from the decay record at each  $\phi_m$  with the following formulation:

$$2N = \frac{2T}{\pi} k\phi_m \frac{1}{\phi_i - \phi_m} \quad (13)$$

where  $k$  is a constant function of the ship righting arm. Other approximate formulations can be also derived as given by several authors (Meskell, 2011, Rawson et al., 2001) but are not applied here.

## 5. Test case

The procedures explained in the previous sections are here applied on a decay test performed in a model basin of a hydrodynamic institute. The time series of the recorded data is represented in Fig. 1 where, as usual, the first peak of the record is discarded from the analysis and only the first 6/8 oscillations are considered. In fact the last swings, where the amplitude is significantly small (below 1.5 degrees of amplitude), can affect the quality of the data analysis. For this reason, just the part indicated in the box of Fig. 1 was selected for the analysis.

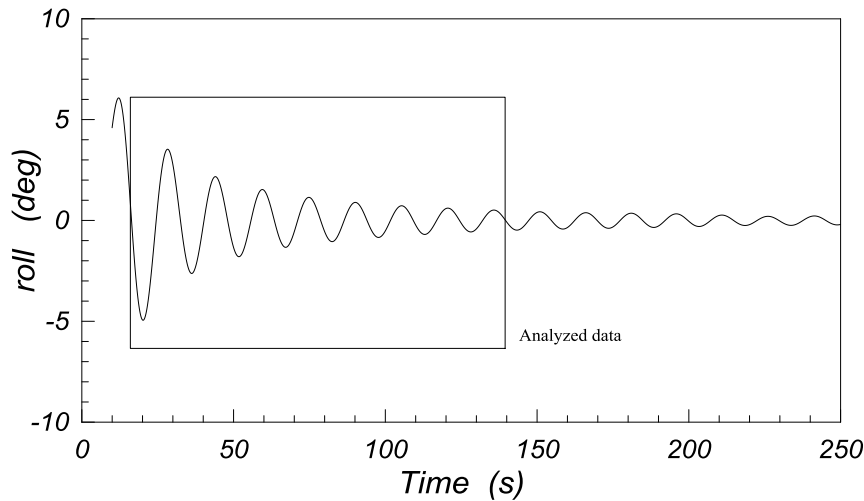


Fig. 1: Time series of the analyzed roll decay test.

As common practice, the analyzed data are presented in graphical form (Fig. 2) in such a way that the linear damping coefficient is represented as function of the swing amplitude or mean amplitude as per the selected method of analysis. In addition, also the quadratic damping coefficient can be determined from the linear regression of the plotted data. In Tab. 1 the damping coefficients according to the different methods are reported.

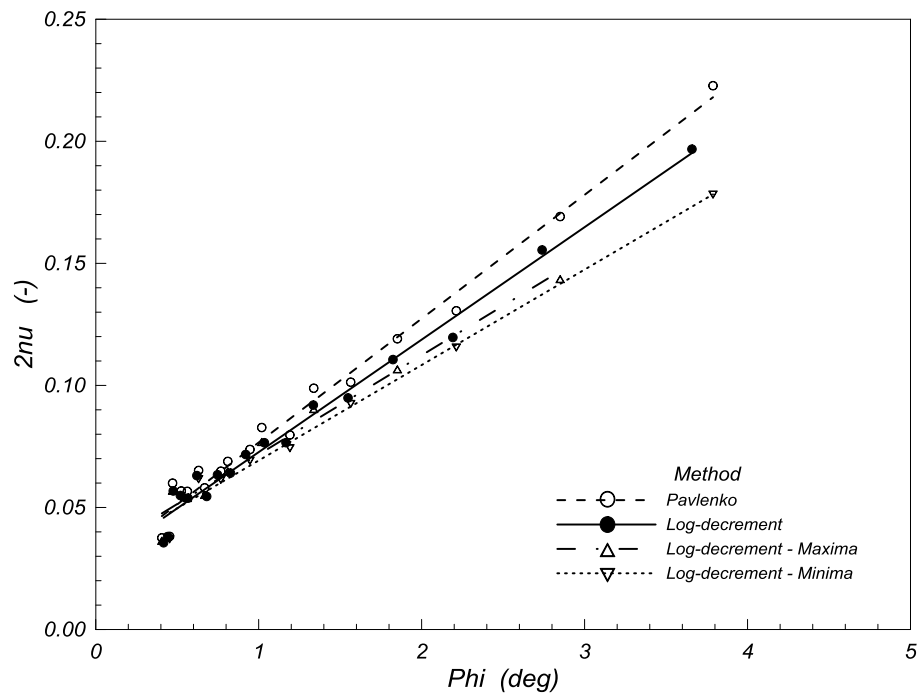


Fig. 2: Graphical comparison of the different analysis methods.

The results in Tab. 1 show that the considered methods are giving comparable results regarding the linear damping coefficient  $2\nu$ . However, due to the different kind of approximations adopted to extract the roll decrements, the quadratic damping part is presenting quite some spread in the obtained data. This can be also seen in Fig. 1, observing the different slopes of the regression curves

Tab. 1: Damping values according to different analysis methods.

Method	$2\nu$	$w$
Logarithmic decrement	0.027	3.110
Logarithmic decrement (maxima)	0.031	2.742
Logarithmic decrement (minima)	0.030	2.640
Pavlenko	0.026	3.424

## 6. Conclusions

The classical methods presented in this paper and the derived formulations for the determination of non-linear damping coefficients for the roll motion of a vessel are giving comparable results in the determination of the linear damping coefficient. The quadratic coefficient is suffering a higher spread in the predictions. Once small amplitude motions are analyzed the current methods can be considered satisfactory for the determination of the roll damping coefficients. When non-linearities become of higher order, not only in the damping but also in the righting arm, then it will be necessary to study new methods to overcome to this issue.

## References

- Blagoveshchensky, S.N. (1964) Theory of ship motions, volume I. Dover Publications Inc., New York.
- Blagoveshchensky, S.N. (1964) Theory of ship motions, volume II. Dover Publications Inc., New York.
- Meskel, C. (2011) A decrement method for qualifying nonlinear and linear damping in multi-degree of freedom systems. ISRN Mechanical Engineering 2011.
- Rawson, K.J. and Tupper, E.C. (2001) Basic ship theory. Butterworth-Heinemann.
- Vlasov, V.G. (1930) On the period of free oscillation in rolling. NTK UVMS, Bjul.

## ANALYSIS OF A BOOM CONVEYOR

A. Max<sup>\*</sup>, M. Hynek<sup>\*\*</sup>, L. Řehounek<sup>\*\*\*</sup>

**Abstract:** *The aim of this paper is to analyse the reaction forces between the chassis of a boom conveyor and a rail-track. The study includes the determination of the stability of the machine. Increased attention was paid to recommendations for modification of the construction for better stability and wider usage.*

**Keywords:** Boom conveyor, Chassis, FEM analysis.

### 1. Introduction

Every machine always has some design problems. A boom conveyor is no different. For example, Velmurugan et al. (2014) described some of them. Without hesitation, it can be said that they covered only a small number of them. This paper focuses on issues with the stability of a conveyor on a rail and recommendations for eliminating these problems.

### 2. Analysis of the boom conveyor

Finite element method (FEM) analyses of the construction were performed using MSC.Marc software with approximately 778000 elements.

#### 2.1. FEM model

A CAD model of the boom conveyor was prepared from technical documentation and drawings that were provided by the contracting authority. It is necessary to realize that the CAD model is too complicated to be converted to a FE model. Therefore, the FE model was simplified and the computational model only includes parts relevant for the calculation. Fig. 1 shows the final FE model.

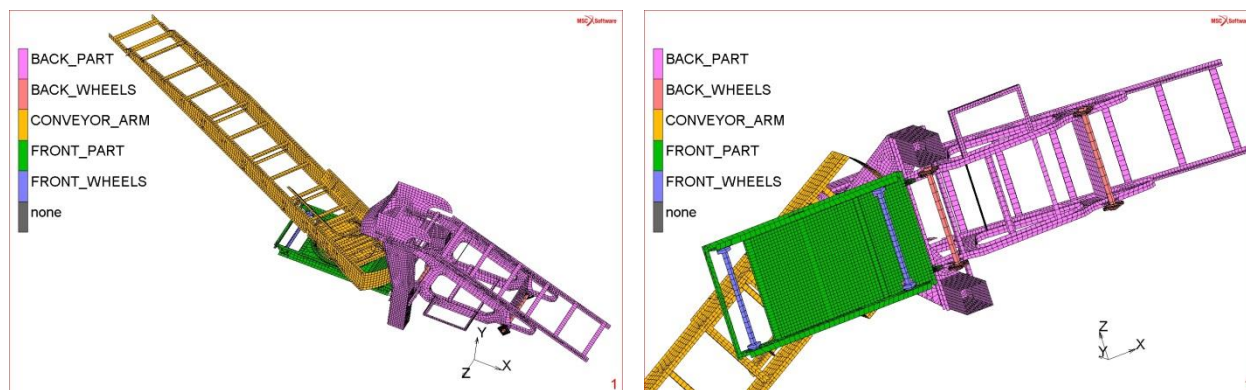


Fig. 1: FE model for numerical calculation.

<sup>\*</sup> Ing. Antonín Max.: Department of Machine Design, Faculty of Mechanical Engineering, University of West Bohemia, Univerzitní 22; 306 14, Pilsen; CZ, antoon@kks.zcu.cz

<sup>\*\*</sup> Assoc.Prof. Ing. Martin Hynek, PhD.: Department of Machine Design, Faculty of Mechanical Engineering, University of West Bohemia, Univerzitní 22; 306 14, Pilsen; CZ, kynek@kks.zcu.cz

<sup>\*\*\*</sup> Ing. Luboš Řehounek, PhD.: Department of Physics, Faculty of Science, University of Hradec Králové, Rokitsanského 62; 500 03, Hradec Králové; CZ, lubos.rehounek@uhk.cz

The FE model was created by combining structured and unstructured meshes. The main parts of the machine are welded from thick plates or profiles. Therefore, to reduce the computational time, these parts were meshed with bilinear thin-triangular shell elements (tria3 - element 138) and bilinear thin-shell elements (quad4 - element 139), with global displacements and rotations as degrees of freedom. Rotational parts (wheel axles, wheels) were meshed with three-dimensional, arbitrarily distorted bricks (hex8 - element 7). This classification of the element types is shown in Fig. 2.

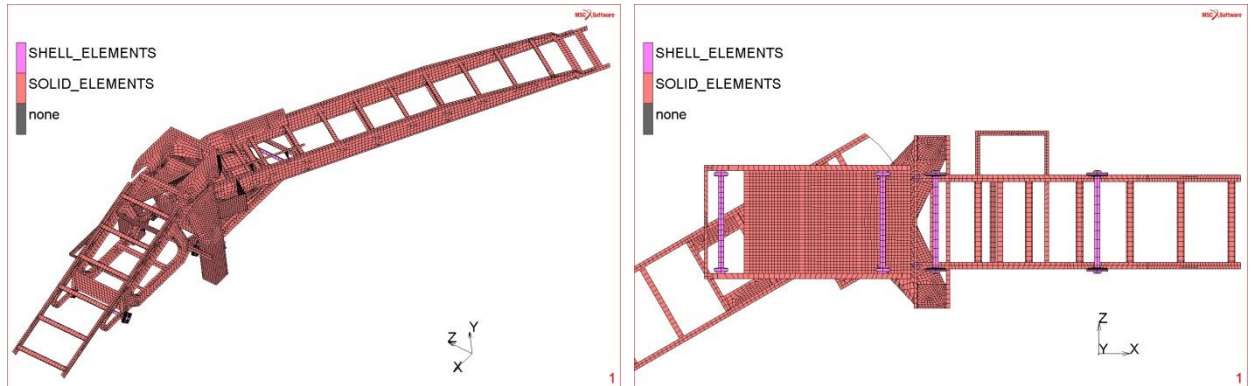


Fig. 2: Classification of the element types.

The individual parts were interconnected by aligning appropriately selected nodes for all parts except the arm of the conveyor. A rigid link (type 80) was applied between the front part and the arm (the stiffest part of the machine), that allows tilting according to the deformation of the frame (see Fig. 3).

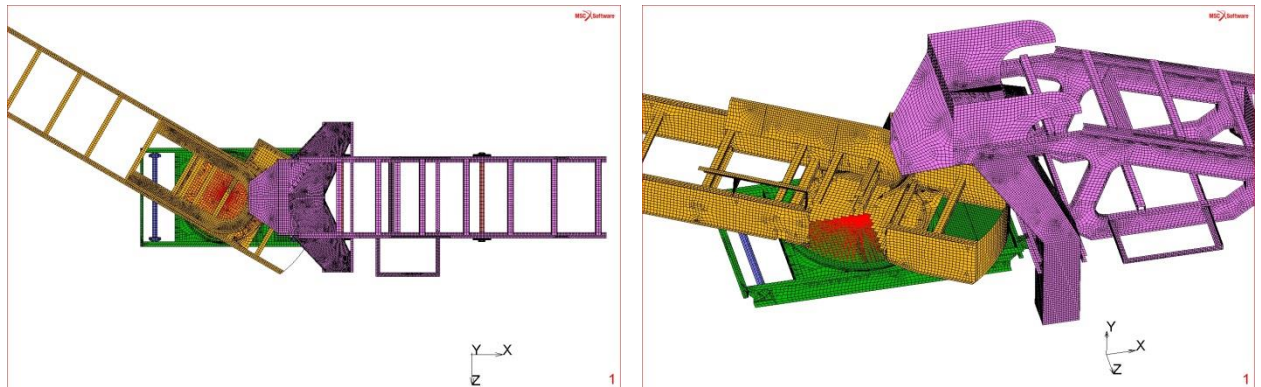


Fig. 3: Interconnection of parts.

## 2.2. Boundary condition

Fig. 4 (left) shows the approximate weight distribution of the main components of the machine which was replaced by specifying the appropriate boundary conditions applied to the computational model. Fig. 4 (right) shows the boundary conditions (FIX\_XYZ; FIX\_Y) for the chassis and also the labelling of the wheels which are referred to in Tab. 1.

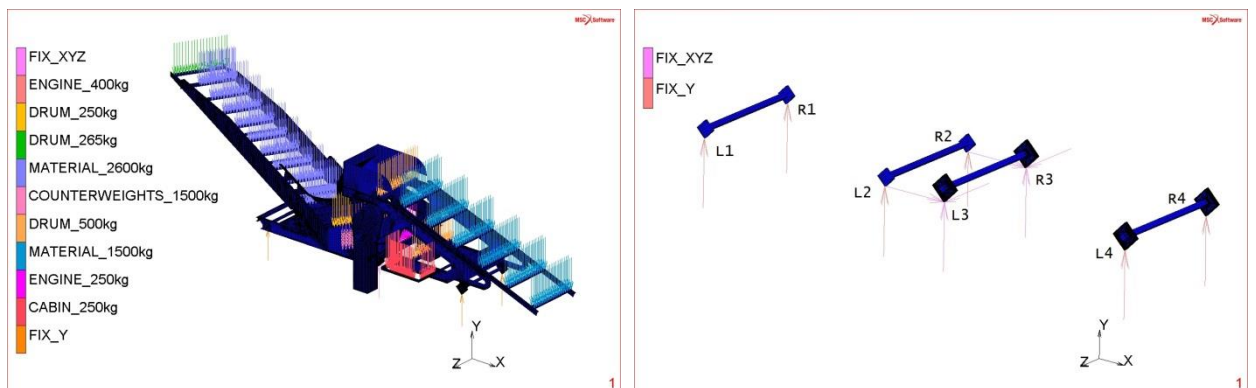


Fig. 4: Boundary condition: all (left), axles (right).

Boundary conditions FIX\_XYZ and FIX\_Y were modified during the calculation. If the results of the calculation showed a negative reaction force at one of the wheels (when the wheel moved away from the rail), the boundary condition FIX for the Y-axis was disabled and the task was solved again. This procedure was repeated until all of the reaction forces acquired positive values.

### 3. Results

Since the computational model and loads are almost symmetrical, the task was solved only for tilting of the arm to the left side. The initial angle was 0 degrees and the increment for the other variants was 5(10) degrees. The reaction forces are shown in Tab. 1. Loss of contact between the wheel and the rail is marked by the symbol "-". Figs. 5 – 7 show the displacement in the Y-axis and Fig. 8 shows the values of the equivalent static stress.

Tab. 1: Reaction forces for the wheels.

	REACTION FORCES [kN]										
WHEEL	60 °	50 °	40 °	35 °	30 °	25 °	20 °	15 °	10 °	5 °	0 °
L1	69.4	79.4	80.6	82.1	78.9	75.2	71.0	66.4	61.3	55.6	48.5
L2	70.2	52.5	38.0	27.0	21.8	16.8	11.9	7.3	3.0	-	-
L3	-	8.4	15.2	16.1	17.2	18.2	19.3	20.3	21.4	21.6	20.0
L4	31.3	21.1	15.3	16.8	16.7	16.6	16.5	16.4	16.3	16.2	16.4
R1	-	-	7.3	10.2	16.5	22.9	29.5	36.0	42.6	49.3	56.4
R2	-	-	-	-	-	-	-	-	-	-	-
R3	-	-	-	6.3	7.5	9.0	10.7	12.6	14.6	16.6	18.3
R4	2.7	12.1	17.4	15.2	15.1	14.9	14.8	14.6	14.4	14.2	14.1

#### 3.1. Displacement

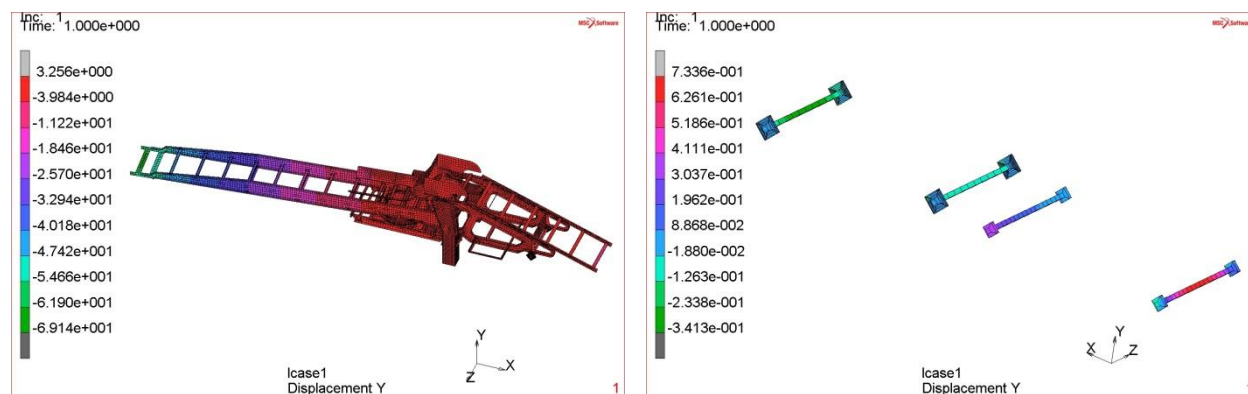


Fig. 5: Displacement [mm] of the frame for 5 °: whole construction (left) and wheels (right).

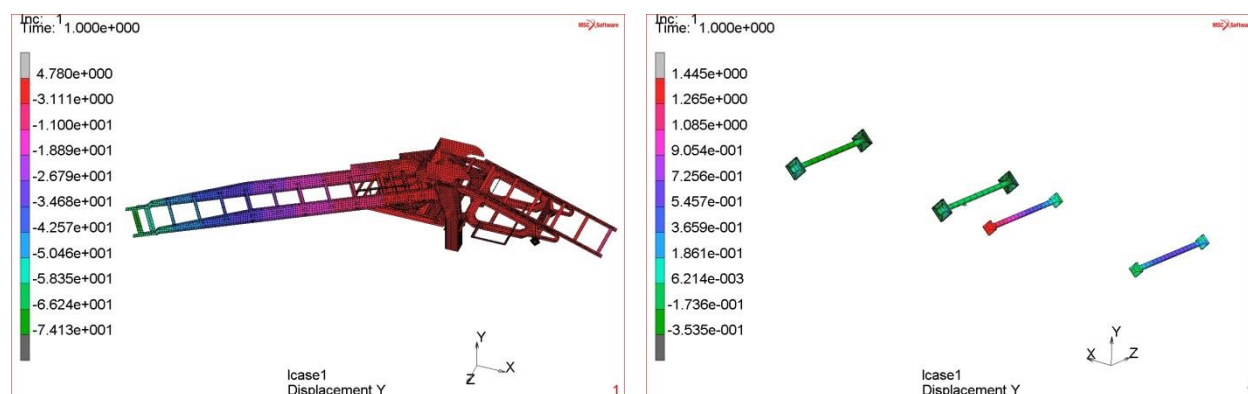


Fig. 6: Displacement [mm] of the frame for 30 °: whole construction (left) and wheels (right).



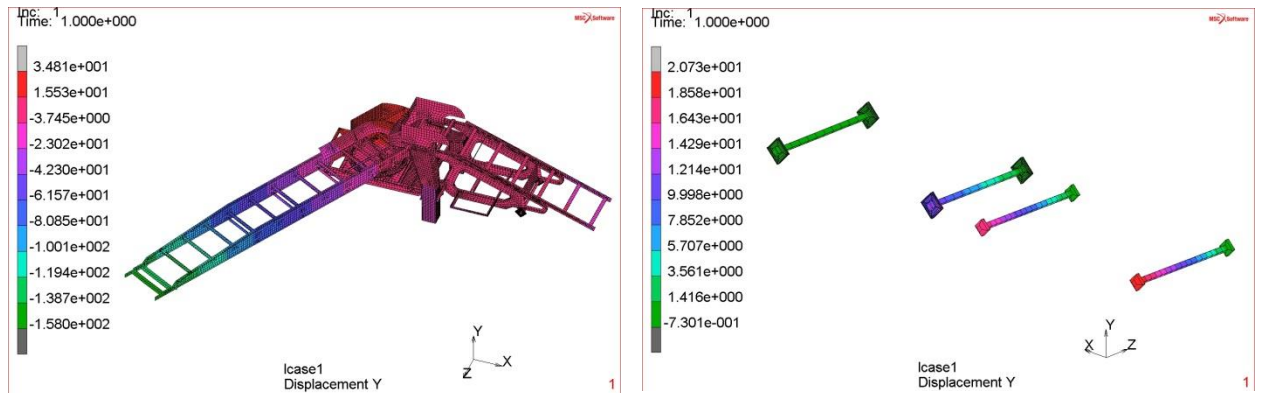


Fig. 7: Displacement [mm] of the frame for 60 °: whole construction (left) and wheels (right).

### 3.2. Equivalent von Mises Stress results

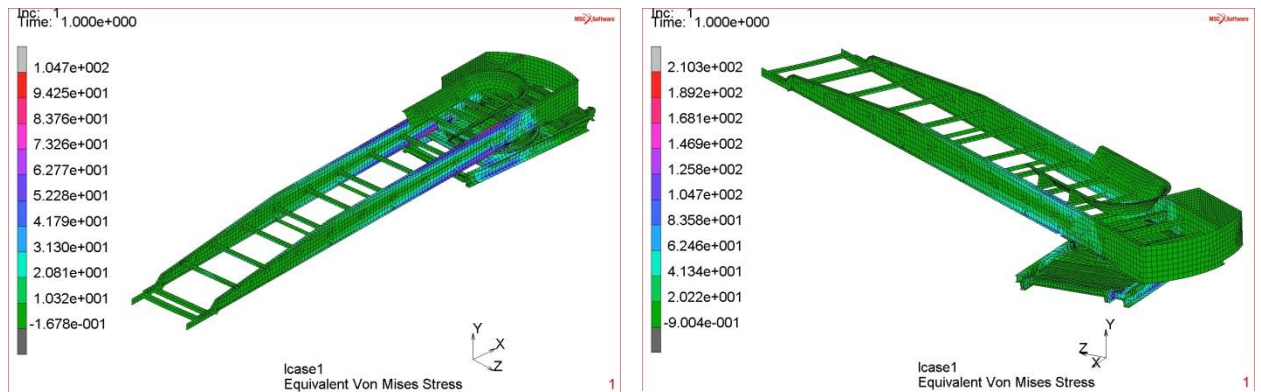


Fig. 8: Equivalent von Mises stress [MPa]: 5 ° (left) 60 ° (right).

### 3.3. Evaluation of results

With the arm at 0 ° and 5 ° the rear axle of the front part of the machine is significantly lightened and wheels L2 and R2 are not in contact with the rail. By increasing the angle of rotation of the arm between 5 ° to 35 ° (resp. -5 ° to -35 °) the machine is stabilized and the reaction is not only between wheel R2 (resp. L2). A further increase of the angle leads to enlargement of the gap between the other wheels and the rail, and operation begins to be dangerous. The machine is unstable and flips after exceeding 60 ° rotation of the arm.

### Conclusion

The results indicate that the machine (for the existing design) is safely operable only for relatively small angles of rotation of the arm (about 30 °). Therefore, the machine cannot be used to its full potential. This problem could be solved by, for example, changing the design of the arm, because from the perspective of stiffness and stress the construction is significantly oversized, see Fig. 5 – 8. It is clear that displacement of the arm in the Y axis is heavily influenced by tilting the front part of the vehicle. The aim should be to move the centre of gravity closer to the axis of rotation of the arm, perhaps by placing more counterweights on the frame.

### Acknowledgement

This work was supported by the project SGS-2016-012 of the University of West Bohemia.

### References

- Velmurugan, G., Palaniswamy, E., Sambathkumar, M., Vijayakumar, R., and Sakthimuruga, T. M. (2014) Conveyor Belt Troubles (Bulk Material Handling). International Journal of Emerging Engineering Research and Technology, 2(3), 21-30.

## IMPACT OF MINERAL CONTENT IN HUMAN TRABECULAR BONE ON ITS ELASTIC PROPERTIES

A. Mazurkiewicz<sup>\*</sup>

**Abstract:** *The paper discusses the results of measurement of elastic modulus and the mineral content for 42 samples of trabecular bone, collected from femoral heads after alloplastic implantation of hip joint. The samples were collected from femoral heads with coxarthrosis and osteoporosis. Measurement of elastic modulus in compression test, and with the use of ultrasonograph technique with 0.5, 1 and 2 MHz frequency of transducers was performed for the samples. Also, evaluation of mineral density of the bone - BMD, and ash density - Ash.D was performed. The results obtained suggested usability of BMD and Ash.D indicators for assessment of elastic properties of trabecular bone. The relations with elastic modulus evaluated using R correlation coefficient were similar for BMD and Ash.D, and contained within the range  $R = 0.57 - 0.68$ .*

**Keywords:** Trabecular bone, Elastic modulus, Compression test, Ash density, BMD.

### 1. Introduction

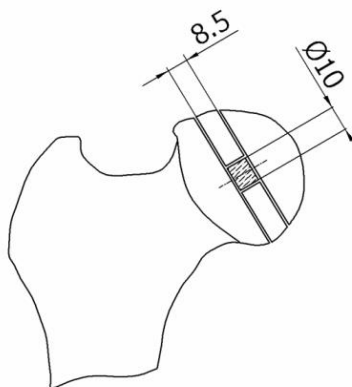
Trabecular bone is a part of the bone, the quality of which has high significance for its strength. It is a spacial structure of trabeculae built of collagen fibres and mineral crystals seated on them, mainly hydroxyapatite. The amount of minerals contained in the structure is important for its mechanical properties (Mosekilde et al., 1987 and Yuehuei and Draugh, 1999). Reduction in the amount of mineral components with age or during bone diseases leads to loss of bone mass, and, consequently, to loss of strength properties of the whole bones (Covin, 1999). "In vivo" bone quality assessment is performed mostly through densitometric examination. By comparing the result obtained with values adopted as standard for the given gender and age in the given population, it can be evaluated whether the bones have sufficient strength. One of the indicators obtained from the test is bone mass density – BMD. The measurement is performed through the skin and soft tissues, and so it contains certain inaccuracies resulting from the individual characteristics of patients. The actual number of mineral components contained in the bone can be evaluated "in vitro" based on ash density measurement – Ash.D. To do so, the sample must be incinerated in order to burn out the organic part of the bone, i.e. collagen fibres. After this, only the mineral components of the bone will remain. Comparison of mass before and after incineration will allow for quantitative evaluation of the mineral phase content in the sample. This type of examination may only be performed "in vitro". It is difficult to definitely determine the relationship between these indicators and the mechanical properties of bones, since the former is measured "in vivo", while the latter - "in vitro". Thus, the aim of this paper was to determine the usability of both these indicators for evaluating elastic properties of trabecular bone. The value of elastic modulus of trabecular bone was assumed to be the measure of elastic properties. The modulus was evaluated using two methods: in a compression test, and through the ultrasonographic method, with the use of transducers of three different frequencies. Ash density and BMD evaluations were performed on samples collected from human femoral heads. The BMD measurement was performed on a clinical densitometer, as "in vitro" examination of the samples. A protocol allowing for simulation of such examination performed "in vivo" was used for the measurement.

---

<sup>\*</sup> Assoc. Prof. Adam Mazurkiewicz, PhD.: Department of Mechanical Engineering, University of Sciences and Technology, Kaliskiego 7 Street; 85-789 Bydgoszcz; PL, e-mail: adam.mazurkiewicz@utp.edu.pl

## 2. Methods

42 samples were collected from osteoporotic and coxarthritic femoral bones obtained as a result of hip joint implanting. The age of the patients ranged from 51 to 82 years with an average of 70 years. The samples used for the tests were not divided according to the type of disease or the age of patients. The samples were stored in 10 % formalin solution at the room temperature (Edmondston et al., 1994). Samples collecting scheme is shown in Fig. 1.



*Fig. 1: Samples collecting scheme.*

BMD measurement was performed using Lunar Expert (General Electric) clinic-grade densitometer, according to the procedure specified by the manufacturer in the technical documentation of the device for bone mass density measurements on bone samples, performed "in vitro". The procedure includes simulating the presence of soft tissues surrounding the bone, same as in "in vivo" evaluation. BMD values were obtained in  $\text{g/cm}^2$ .

Elastic modulus measurement on the sample was performed with the use of ultrasonographic method, and through a non-destructive compression test. To perform the USG measurement was used Panametric 5058RP generator. The samples were placed in a vacuum pump for 30 minutes in order to remove air from pores lying near the sample surface. Then, the samples were put under water. Longitudinal waves transducers of 0.5, 1 and 2 MHz frequency were used for the measurements. The sending and receiving transducers were placed near head surfaces of the sample. Wave passage time through the sample was measured, and - based on this - the value of elastic modulus of the trabecular bone was calculated. During the measurement, the transducers and the sample were kept in a water tank in order to prevent penetration of air to pores of the sample.

The compression test was performed using testing device Instron E3000 as follows: the sample was placed in a testing machine. Initial load was 3 N. Next five preliminary cycles were performed until reaching deformation value  $\varepsilon = 0.3 \%$  of sample height, in order to stabilize the surface of contact between head surfaces of the sample and working surfaces of the machine. The next cycle was performed until obtaining deformation equal  $\varepsilon = 0.8 \%$ , i.e. the limit of elastic deformation for trabecular bone (Yuehuei et al., 1999). After this, value of secant elastic modulus was calculated from deformation range  $\varepsilon = 0.2 - 0.8 \%$ .

In order to perform the ash density measurement, the samples were dried in a temperature of  $120^\circ\text{C}$  for 24 hours, and were weighted afterwards. Then, they were incinerated in a furnace, in a temperature of  $800^\circ\text{C}$  for 18 hours, according to the procedure described by Yuehuei et al. (1999). After this, the samples were weighted again. The mass of each sample after incinerating was divided by its initial volume - before incinerating. This way, Ash.D value in  $\text{g/cm}^3$  was obtained.

Additionally, mass content of mineral components in the dry sample, marked as %Min, was measured. The value was calculated as a quotient of sample mass before and after incineration (but after drying in  $120^\circ\text{C}$ ), and expressed in percents.

### 3. Results

Tab. 1 presents the results of measurements performed. The range of values obtained, mean result, standard and relative standard deviation is presented. Tab. 2 presents values of coefficients of correlation between BMD values, Ash.D, % Min, and the modulus values from compression tests – marked as  $M_{Mt}$  and measurements with USG method at transducers frequency: 0.5 MHz -  $M_{0.5}$ , 1 MHz -  $M_1$  and 2 MHz -  $M_2$ .

Tab. 1: Values of density and elastic moduli obtained from the measurements.

	Age [year]	BMD [g/cm <sup>2</sup> ]	Ash.D [g/cm <sup>3</sup> ]	%Min [%]	$M_{Mt}$ [MPa]	$M_{0.5}$ [MPa]	$M_1$ [MPa]	$M_2$ [MPa]
<b>Min</b>	51	0.136	0.114	15.95	41.3	1612.3	1646.7	1706.4
<b>Max</b>	82	0.432	0.592	65.54	1306.4	7093.4	8601.4	11029.7
<b>Av</b>	70.0	0.264	0.302	33.22	391.7	4594.1	5150.2	5960.6
<b>SD</b>	10.4	0.078	0.087	7.93	263.3	1432.8	1551.3	1912.1
<b>RSD [%]</b>	15.0	29.7	28.8	23.9	67.2	31.2	30.1	32.1
where: <b>Min</b> – minimum, <b>Max</b> – maximum, <b>Av</b> – average, <b>SD</b> – standard deviation, <b>RSD</b> – relative standard deviation.								

Tab. 2: Values of the obtained coefficients of correlation  $R$  between different densities and elastic moduli.

	$M_{Mt}$ [MPa]	$M_{0.5}$ [MPa]	$M_1$ [MPa]	$M_2$ [MPa]
<b>BMD</b> [g/cm <sup>2</sup> ]	0.57	0.64	0.62	0.64
<b>Ash.D</b> [g/cm <sup>3</sup> ]	0.66	0.68	0.61	0.63
<b>%Min</b> [%]	0.47	0.32	0.30	0.31

Fig. 2 present example of relationship between ash density and  $M_{0.5}$  modulus measured through USG method at 0.5 MHz frequency.

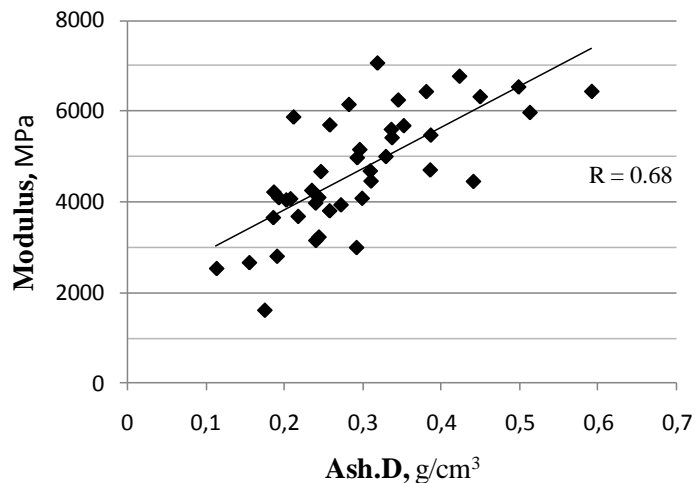


Fig. 2: Relation between ash density and  $M_{0.5}$  module measured by USG method.

#### 4. Conclusions

The values of compression moduli from the compression test and USG method correlate with the values obtained by other authors for the given test method (Goldstein, 1987, Ashmann et al., 1988, Rho et al., 1993 and Nikodem, 2012).

The mean values of elastic moduli obtained from the compression test and USG measurement differ by an order of magnitude. However, the values of coefficients of correlation for BMD and Ash.D with elastic moduli fall within the range of 0.57 – 0.68. This points to the fact that, despite such large differences, the results obtained from compression test and USG are well correlated qualitatively, in spite of such large quantitative differences. The above allows to conclude that the methodics of both measurements was accepted and performed correctly. Correlation between percentage content of minerals in dry mass of the sample, and the modulus from the compression test is weaker. Correlation between percentage mineral content in dry mass of the sample, and the moduli measured with an ultrasonographic method is not existent ( $R = 0.30 - 0.32$ ). This likely results from the fact that this indicator refers to dry mass, and the moduli measurements were performed on wet samples. Loss of humidity after drying could have impact on the weakening of relations between the values evaluated. This impact is, however, higher for elastic moduli measured with USG method than with the compression test. The author did not find in scientific literature the descriptions of using this parameter for evaluating elastic properties of trabecular bone - perhaps due to its poor usability for that purpose.

Ash. D values obtained are at a level obtained in examinations of other authors (Mosekilde et al., 1987 and Keyak et al., 1996). Value of BMD correlation with elastic modules values were similar as the value of Ash. D. correlations with these modules. This proves the qualitative similarity of BMD and Ash.D. results obtained. BMD measurement was performed on a clinical device, according to the procedure foreseen for bone samples. With those samples, the outer layer of soft tissues surrounding the bone does not occur, as is the case with "in vivo" examinations. This procedure takes these differences into account. The samples were immersed in water of adequate depth simulating the presence of soft tissues surrounding the bone. The test parameters were also set for this type of evaluation, according to the device manufacturer's guidelines. This allows to assume that the results of actual BMD evaluations on "in vivo" patients before alloplastic implantation could give similar results. However, the author could not perform a similar verification, since the consent of the local ethics committee for the performance of tests did not permit the author of the work to access medical documentation of the persons subjected to the alloplastics treatment. It will be subject for further examination.

#### Acknowledgement

The author of the paper had the consent of the local ethics committee for performing the tests described in text.

#### References

- Ashmann, R.B. and Rho, J.Y. (1988) Elastic modulus of trabecular bone material. *Journal of Biomechanics*, 21, 3, pp. 177-181.
- Covin, S. (1999) Bone mechanics handbook – second edition. CRC Press, New York.
- Edmondston, S.J., Singer, K.P., Day, R.E., Breidahl, P. D. and Price, R.I. (1994) Formalin fixation effects on vertebral bone density and failure mechanics: an in-vitro study of human and sheep vertebrae. *Clinical Biomechanics*, 9, 3, pp. 175-179.
- Goldstein, S.A. (1987) The mechanical properties of trabecular bone: dependence on anatomic location and function. *Journal of Biomechanics*, 20, 11-12, pp. 1055-1061.
- Keyak, J.H., Lee I.Y., Nath, D.S. and Skinner, H.B. (1996) Postfailure compressive behavior of tibial trabecular bone in three anatomic directions. *Journal Biomedical Material Research*, 31, 3, pp. 373-378.
- Mosekilde, T. and Danielsen, C.C. (1987) Biomechanical competence of vertebral trabecular bone in relation to ash density and age in normal individuals. *Bone*, 8, 2, pp. 79-85.
- Nikodem, A. Correlations between structural and mechanical properties of human trabecular femur bone. *Acta of Bioengineering and Biomechanics*, 14, 2, pp. 37-46.
- Rho, J.Y., Ashmann, R.B. and Turner, C.H. (1993) Young's modulus trabecular and cortical bone material: ultrasonic and microtensile measurements. *Journal of Biomechanics*, 26, 2, pp. 111-119.
- Yuehuei, H. and Draugh, R. (1999) Mechanical testing of bone and the bone-implant interface. CRC Press, New York.

## IMPACT OF MINERAL CONTENT IN HUMAN TRABECULAR BONE ON ITS STATIC AND FATIGUE PROPERTIES

A. Mazurkiewicz\*

**Abstract:** *The paper presents results of static and fatigue strength, and mineral content for 60 trabecular bone samples. The samples were collected from human femoral heads after alloplastic treatment of femoral head, of patients suffering from coxarthrosis and osteoporosis. Evaluation of mineral density of the bone - BMD, and ash density - Ash.D were performed. Static and fatigue strength of the bones was determined through compression test. Fatigue compression test was performed with stepwise increasing amplitude. The results obtained suggested correlation between BMD, Ash. D and the results of static and fatigue test. The relations obtained, evaluated using R correlation coefficient, fell within the range  $R = 0.70 - 0.75$ . The results confirmed the usability of BMD and Ash.D indicators for evaluating static and fatigue strength of trabecular bone.*

**Keywords:** Trabecular bone, Static compression test, Fatigue compression test, Ash density, BMD.

### 1. Introduction

Bones form the human skeleton, serving supporting functions for the body. Together with the muscles and ligament system, they form the motor system of human. Due to its structure, and the specifics of daily activity of man, the majority of bones is subjected to compression loads. Human bones are a composite material built of organic and mineral materials of different properties, and of different physical state. The components include compact bone, trabecular bone, articular cartilage, bone marrow, blood, nerve fibres, blood vessels, bone cells and periosteum. One of the components, the trabecular bone, is one of the factors mostly decisive for its strength. Its quality and quantity changes quicker than with the remaining components, which causes the strength of bones to also change. One of the factors determining bone strength is mineral content (Mosekilde et al., 1987 and Kang et al., 1998). The assessment of mineral content allows to prognose bone strength. Therefore, the aim of this paper was to assess the impact of mineral content in the trabecular bone on its static (marked as US) and fatigue (marked as Ns) strength. The strengths were determined through compression test. Due to the fact that the variable stresses to which the bone is subjected are of low-cycle nature - below 1 Hz (Yuehuei et al., 1999 and Covin, 1999), the fatigue test was performed in the examination with stepwise increasing amplitude. This allowed to reduce the time necessary to perform the examinations.

Mineral content in the bone is difficult to determine "in vivo". The basic examination used for this type of assessment is densitometric examination. One of the indicators used in evaluations is bone mass density – BMD. During "in vitro" examinations, such indicator is ash density - Ash.D. Both of these indicators were used to assess mineral content in trabecular bone, and the results obtained were correlated with results obtained from static and cyclic strength tests.

### 2. Methods

60 samples of human femoral head of 10 mm diameter and 10 mm height were used. The samples were cut from femoral heads obtained as a result of implanting hip joint of patients with osteoporosis and coxarthrosis. The age of the patients ranged from 49 to 84 years with an average of 71 years. The samples were split into two groups, 30 pieces each. The number of samples originating from osteoporotic and coxarthrotic bones was not the same, therefore the authors assigned to each test group an equal number of

---

\* Assoc. Prof. Adam Mazurkiewicz, PhD.: Department of Mechanical Engineering, University of Sciences and Technology, Kaliskiego 7 Street; 85-789 Bydgoszcz; PL, e-mail: adam.mazurkiewicz@utp.edu.pl



samples of the same type. One group was used to test static strength, while the other was used for cyclic tests. The samples were not divided according to the type of disease or the age of patients. The samples were stored in 10 % formalin solution at the room temperature. Fig. 1 presents the method of cutting samples from the femoral head (Topolinski et al., 2011).

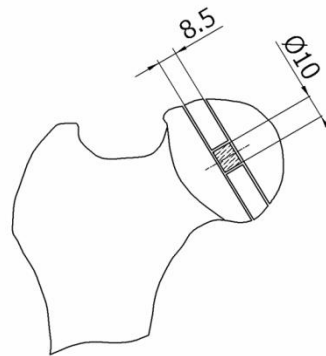


Fig. 1: Samples collecting scheme.

BMD measurement was performed using a clinic-grade densitometer type Lunar Expert (General Electric), according to the procedure specified by the manufacturer in the technical documentation of the device for bone mass density measurements on bone samples performed "in vitro".

Instron 8874 (Instron Company) machine was used to perform compression and fatigue tests. During measurement of static strength, the sample was placed in a strength testing machine between working surfaces of the machine. Then, five initial cycles were performed in order to obtain deformation value  $\varepsilon = 0.5\%$  of sample height, to stabilize the contact surface between head surfaces of the sample and working surfaces of the machine. The duration of one loading-unloading cycle was 30 seconds. The interval between the cycles was 5 seconds. Then, the test was performed at fixed deformation speed equal to 0.1 mm/min. The value of compression strength corresponded to the moment of occurrence of the first maximum on the compression curve, i.e. when strength is starting to visibly lower for the first time, at fixed rate of increase of deformation (Gibson, 1985). The test was performed in room temperature.

The fatigue tests were carried out under load with stepwise increasing loading. The frequency of sinusoidal loading was 1 Hz. The minimum loading for all the loading levels was 5 – 7 N, maximum loading started from 20 N at first step with a gain every 10 N at successive steps. Each level of load maintained 500 cycles realized under constant amplitude loadings. The test was conducted in constant temperature  $37 \pm 2^\circ\text{C}$  in 0.7 % NaCl water solution (Winwood et al., 2006 and Brouwers et al., 2009). Program of the test is presented in Fig. 2. Fatigue life (Ns) was estimated using modification method described by Bowman et al. (1998). In this purpose determined the median values of deformation increment of sample. Assumed that fatigue life is defined as: number of the first loop for which value the deformation gain exceeded the value of the median by 10 % (Topolinski et al., 2011). Fig. 2 presents the test program.

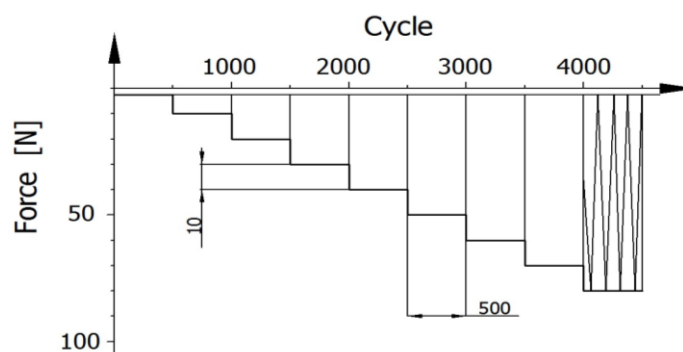


Fig. 2: Cyclic test program.

Before the ash density measurement, the samples were dried for 24 hours in  $120^\circ\text{C}$ , and then weighted. After this, they were placed in a furnace for 18 hours in  $800^\circ\text{C}$  temperature (Yuehuei et al., 1999). Then,

they were weighted again. After dividing the mass of each sample after burning by its volume before burning, Ash density in  $\text{g/cm}^3$  was obtained.

Also, mineral content of dry sample, marked as % Min, and defined as the quotient of sample mass after drying and burning was measured and expressed in percentage.

### 3. Results

Tab. 1 presents the results of measurements performed in the form of a range of obtained values, average value and the value of standard deviation, relative standard deviation and distribution. BMD, Ash.D and % Min values were specified separately for both groups of the samples tested. Normality of distribution of results was checked by Shapiro-Wilk tests, with  $p = 0.05$  value. Tab. 2 presents the values of correlation coefficient R between BMD, Ash.D, % Min and static and cyclical strength.

*Tab. 1: Values of density and static and cyclic strength.*

	<b>BMD</b> [ $\text{g/cm}^2$ ]	<b>Ash.D</b> [ $\text{g/cm}^3$ ]	<b>% Min</b> [%]	<b>US</b> [MPa]	<b>BMD,</b> [ $\text{g/cm}^2$ ]	<b>Ash.D,</b> [ $\text{g/cm}^3$ ]	<b>% Min,</b> [%]	<b>Ns</b> [n]
<b>Test</b>	<b>Static</b>				<b>Fatigue</b>			
<b>Min</b>	0.135	0.173	20.7	1.68	0.094	0.174	37.7	1185
<b>Max</b>	0.436	0.514	47.3	36.14	0.522	0.617	101.3	50535
<b>Av</b>	0.295	0.322	35.8	12.46	0.275	0.326	57.3	20649
<b>SD</b>	0.085	0.088	6.4	7.96	0.091	0.095	8.1	11671
<b>RSD [%]</b>	28.8	27.3	17.9	63.9	33.1	29.1	14.1	56.5
<b>Dis</b>	N	N	N	logN	N	logN	logN	N
where: <b>Min</b> – minimum. <b>Max</b> – maximum. <b>Av</b> – average. <b>SD</b> – standard deviation. <b>RSD</b> – relative standard deviation. <b>Dis</b> – distribution: N –Normal, LogN – logNormal (verified by Shapiro-Wilk tests, $p = 0.05$ )								

*Tab. 2: Values of the correlation coefficients obtained between static - US, fatigue - Ns strength and different indicators of density.*

	<b>BMD</b> [ $\text{g/cm}^2$ ]	<b>Ash.D</b> [ $\text{g/cm}^3$ ]	<b>% Min</b> [%]
<b>US [MPa]</b>	0.70	0.71	0.57
<b>Ns [n]</b>	0.74	0.75	0.22

### 4. Conclusions

The results of measurements of indicators describing bone density, i.e. BMD and Ash.D are similar, taking into account the average value in tested groups, and the value of standard deviation. This suggests that the groups tested were selected properly. The results obtained both for static and fatigue strength exhibited a larger dispersion, which is suggested by the values of relative standard deviation.

While the defining of strength in the static compression test is clear and unequivocal, it is not so simple in case of fatigue test with gradually increasing amplitude. An appropriate sample destruction criterion must be adopted here. This criterion was created and adopted based on paper Bowman et al. (1998). For

constant-amplitude fatigue tests, fatigue strength, i.e. the sample destruction moment is assumed to be the number of cycles after which the loss of elastic modulus by 30 % compared to the first cycles occurs (Covin, 1999). In tests with gradually increasing amplitude the issue is not so simple, and it is very important to correctly choose this criterion, not to make mistakes in assessing fatigue strength.

The values of correlation coefficients presented in Tab. 2 are insignificantly higher for fatigue strength than static strength. The reason for this may be that the static test was performed in room temperature, while the fatigue strength was performed at human body temperature. Nevertheless, this approach is conformant with literature, since the difference in results of static strength for bone tests performed in room temperature and human body temperature does not exceed 5 % (Carter et al., 1976). Despite the fact that the described results should not differ significantly, this could have had an insignificant impact on the obtained results static test, and on the value of correlation between them.

Correlation between the percentage content of minerals in dry mass of the sample, and the strength is much smaller, and non-existent in case of fatigue strength. This probably results from the fact that this indicator refers to mineral content in dry mass, and the measurement static and fatigue strength were performed on wet samples. Removal of humidity from the samples prior to measuring % Min indicator could change the strength of correlation between its value, and the values of static and fatigue strength.

### **Acknowledgement**

The author of the paper had the consent of the local ethics committee for performing the tests described in text.

### **References**

- Bowman, S.M., Guo, X.E., Cheng, D.W., Keaveny, T.M., Gibson, L.J., Hayes, W.C. and McMahon, T.A. (1998) Creep contributes to the fatigue behavior of bovine trabecular bone. *Journal of Biomechanical Engineering*, 120, 5, pp. 647-654.
- Brouwers, J.E.M., Ruchelsman, M., Rietbergen, B. and Boussein, M.L. (2009) Determination of rat vertebral bone compressive fatigue properties in untreated intact rats and zoledronic-acid-treated, ovariectomized rats. *Osteoporosis International*, 20, 8, pp. 1377-1384.
- Carter, D.R., Hayes W.C. and Schurman, D.J. (1976) Fatigue life of compact bone. Effects of microstructure and density. *Journal of Biomechanics*, 9, 4, pp. 211-18.
- Covin, S. (1999) *Bone mechanics handbook – second edition*. CRC Press, New York.
- Gibson, L.J. (1985) The mechanical behaviour of cancellous bone. *Journal of Biomechanics*, 5, 18, pp. 317-328.
- Kang, Q., An, Y.H. and Friedman, R.F. (1998) Mechanical properties and bone densities of canine trabecular bone. *J Mater Sci Mater Med*, 9, 5, pp. 263-7.
- Mosekilde, T. and Danielsen, C.C. (1987) Biomechanical competence of vertebral trabecular bone in relation to ash density and age in normal individuals. *Bone*, 8, 2, pp. 79-85.
- Topolinski, T., Cichanski, A., Mazurkiewicz, A. and Nowicki, K. (2011) Study of the behavior of the trabecular bone under cyclic compression with stepwise increasing amplitude. *Journal of the Mechanical Behavior of Biomedical Materials*, 4, 8, pp. 1755-1763.
- Winwood, K., Zioupos, P., Currey, J.D., Cotton, J.R. and Taylor, M. (2006) Strain patterns during tensile, compressive, and shear fatigue of human cortical bone and implications for bone biomechanics. *Journal of Biomedical Materials Research Part A*, 79, 2, pp. 289-297.
- Yuehuei, H. and Draugh, R. (1999) *Mechanical testing of bone and the bone-implant interface*. CRC Press, New York.

## THICK-WALLED COMPOSITE PIPES UNDER BENDING

O. Menshykov\*, M. Menshykova\*, I. A. Guz\*

**Abstract:** *The current study is focused on stress-strain analysis of multi-layered thick-walled fibre reinforced composite pipes (manufactured by filament winding) subjected to bending loading. The problem is solved numerically using the equilibrium equations with the appropriate boundary and interface conditions. Comparative analysis of stresses distribution in the pipes with inner homogeneous layer and inner unidirectional reinforced composite layer is presented.*

**Keywords:** Fibre-reinforced composite, Thick-walled pipes, Bending load, Stress distribution.

### 1. Introduction

The formulation of the problem of anisotropic single-layer pipe subjected to bending load was initially given by Lekhnitskii (1981). Later the bending behaviour of thick-walled filament-wound sandwich pipes made of a non-reinforced core layer and alternate-ply skin layers was studied by Xia et al. (2002). Laminated plate theory and Lekhnitskii's stress function approach was used for obtaining the analytical solution for multi-layered filament-wound composite pipes under bending loading. Furthermore the analytical solution for the design of spoolable composite tubes was presented by Starbuck et al. (2000) and the prediction of bending strength and failure modes for filament-wound composite pipes was given by Natsuki et al. (2003). The multi-parametric investigation of stress distribution as a function of the inner layer material properties, its thickness, the number of layers, lay-up and the magnitude of bending load was carried out by Menshykova et al. (2014).

The current study is focused on stress analysis of multi-layered thick-walled fibre reinforced composite pipes subjected to bending loading. The research focuses on the pipes with multi-layered outer part and thin homogeneous inner layer. It provides analytical solution (within the framework developed Natsuki et al. (2003)) and comparative study of stresses distribution in the pipes with inner homogeneous layer and inner composite layer of 0° fibre orientation. The investigation of stress distribution as a function of the inner layer material properties was carried out.

### 2. Stress analysis

Let us consider a multi-layered fibre reinforced filament-wound composite pipe with  $r_0$  inner radius and  $r_a$  outer radius subjected to bending load. Each layer of the pipe consists of two laminae with principal material directions symmetrical to the axial direction. Consequently, each layer (two adjacent lay-ups) is assumed to behave as an orthotropic unit. Then for each orthotropic layer we have the constitutive equation for strains in terms of stresses (see Natsuki et al. (2003)):

$$\begin{bmatrix} \varepsilon_r \\ \varepsilon_\theta \\ \varepsilon_z \\ \gamma_{r\theta} \end{bmatrix} = \begin{bmatrix} S_{11} & S_{12} & S_{13} & 0 \\ S_{12} & S_{22} & S_{23} & 0 \\ S_{13} & S_{23} & S_{33} & 0 \\ 0 & 0 & 0 & S_{44} \end{bmatrix} \begin{bmatrix} \sigma_r \\ \sigma_\theta \\ \sigma_z \\ \tau_{r\theta} \end{bmatrix} \quad (1)$$

where  $S_{ij}$  are compliance constants and  $r$ ,  $\theta$  and  $z$  denoted as radial, hoop and axial coordinates. The compliance constants can be obtained from:

---

\* School of Engineering, University of Aberdeen, Aberdeen AB24 3UE, UK

$$(S_{ij}) = (Q_{ij})^{-1}(a_{ij})(P_{ij}), \quad (2)$$

where matrix  $(a_{ij})$  can be obtained from engineering constants; matrices  $(P_{ij})$  and  $(Q_{ij})$  are the coordinate transformation matrices between the on-axis and the cylindrical axis.

The components of the stress field (Natsuki et al., 2003)) could be presented in the form:

$$\begin{aligned} \sigma_r &= (Br^{-1+\beta} - Cr^{-1-\beta} + A\eta r) \sin \theta, \quad \sigma_\theta = [B(1+\beta)r^{-1+\beta} - C(1-\beta)r^{-1-\beta} + 3A\eta r] \sin \theta, \quad (3) \\ \tau_{r\theta} &= -(Br^{-1+\beta} - Cr^{-1-\beta} + A\eta r) \cos \theta, \quad \sigma_z = (s_1 Br^{-1+\beta} + s_2 Cr^{-1-\beta} + s_3 Ar) \sin \theta, \quad (4) \end{aligned}$$

where  $A, B, C$  are the unknown constants and

$$\begin{aligned} s_{1,2} &= \mp \frac{S_{13} + S_{23}(1 \pm \beta)}{S_{33}}, \quad s_3 = 1 - \frac{(S_{13} + 3S_{23})\eta}{S_{33}}, \\ \beta &= \sqrt{1 + \frac{R_{11} + 2R_{12} + R_{44}}{R_{22}}}, \quad \eta = \frac{S_{23} - S_{13}}{R_{11} + 2R_{12} + R_{44} - 3R_{22}}, \quad R_{ij} = S_{ij} - \frac{S_{i3}S_{j3}}{S_{33}} \quad (i, j = 1, 2, 4). \end{aligned}$$

Radial and hoop displacements have the following form:

$$\begin{aligned} u_r &= (p_1 Br^\beta + p_2 Cr^{-\beta} + p_3 Ar^2) \sin \theta, \\ u_\theta &= (q_1 Br^\beta + q_2 Cr^{-\beta} + q_3 Ar^2) \cos \theta, \end{aligned} \quad (5)$$

and

$$\begin{aligned} p_{1,2} &= \frac{R_{11} + R_{12}(1 \pm \beta)}{\beta}, \quad p_3 = \frac{(R_{11} + 3R_{12})\eta + S_{13}}{2}, \\ q_{1,2} &= \frac{R_{11} + R_{12} \mp R_{22}\beta(1 \pm \beta)}{\beta}, \quad q_3 = \frac{(R_{11} + R_{12} - 6R_{22})\eta + S_{13} - 2S_{23}}{2}. \end{aligned}$$

Material properties in laminated multi-layered tube vary from layer to layer, however it is required that the stress and displacement continuity conditions be satisfied at the layer interfaces (Herakovich, 1998). As the tube is subjected to no inner or outer pressure, the boundary conditions have the following form:

$$\sigma_r^{(1)}(r_0) = 0, \quad \sigma_r^{(N)}(r_a) = 0. \quad (6)$$

For perfectly bonded layers all displacements must be continuous from layer to layer. For the displacements and stresses on the layer interfaces the continuity conditions are (Xia et al., 2002):

$$\begin{aligned} u_r^{(k)}(r_k) &= u_r^{(k+1)}(r_k), \quad u_\theta^{(k)}(r_k) = u_\theta^{(k+1)}(r_k), \\ \sigma_r^{(k)}(r_k) &= \sigma_r^{(k+1)}(r_k) \quad k = \overline{1, N-1}, \end{aligned} \quad (7)$$

where  $N$  is the number of layers.

As a result one can derive the system of equations (including the equilibrium equations for bending moment, boundary conditions and continuity conditions for the interfaces, e.g. see Menshykova et al. (2014)) solving which the stress in the tube can be obtained.

### 3. Numerical results and discussion

To get the numerical results the software for bending stiffness and bending stress calculation was developed. As a numerical example we will consider the filament wound pipes of different designs made of carbon/epoxy composite (T300/LY5052) under bending load. The inner diameter of the pipes is 0.5cm and the outer diameter is 1.5 cm. The investigation of the pipes stiffness change and the comparative study of the stress distribution in the pipes with inner layer of homogeneous material (steel) and unidirectional inner layer of  $0^\circ$  fibre orientation was carried out in Menshykova et al. (2014). The properties of steel and composite are given in Tab. 1.

Tab. 1: Properties of materials.

	Carbon/Epoxy unidirectional fibre composite (T300/LY5052) (Bakaiyan et al., 2009)	Steel
$E_1$ (GPa)	135	205
$E_2$ (GPa)	8	205
$G_{12}$ (GPa)	3.8	77
$\nu_{12}$	0.27	0.33
$\nu_{23}$	0.49	0.33

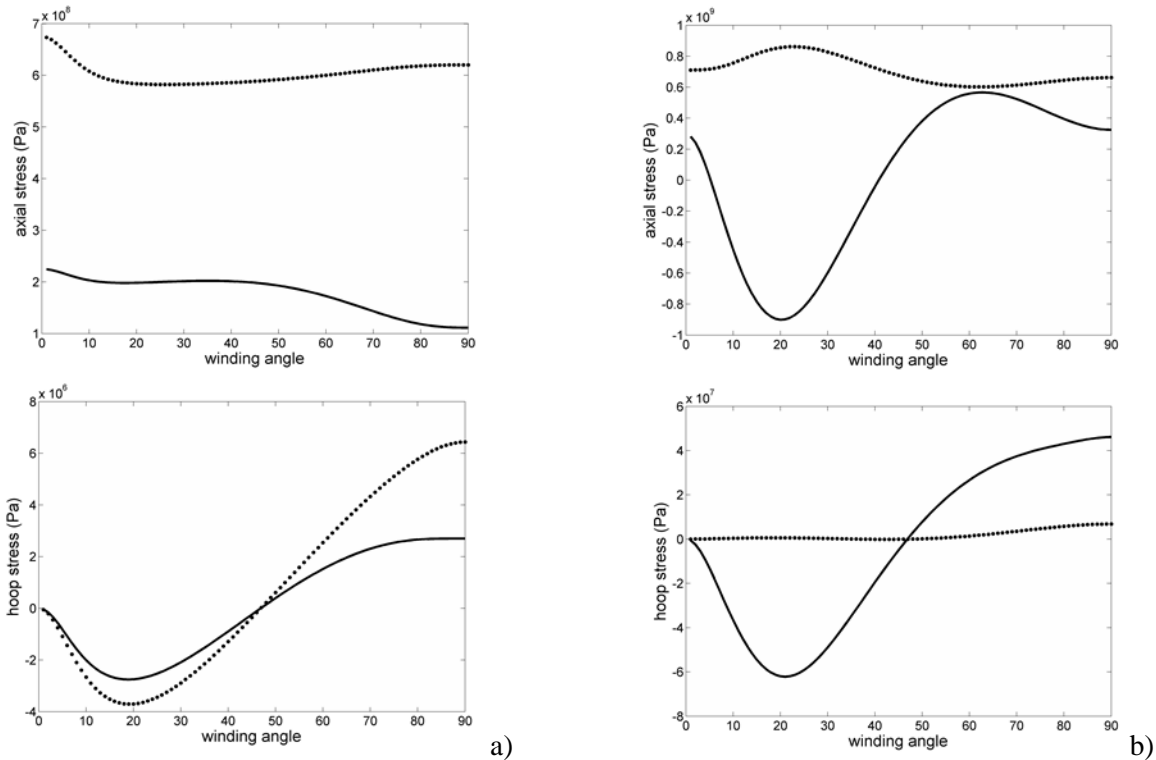


Fig. 1: Effect of the winding angle on the axial and hoop stresses for the pipe with a)  $[0, a, -a, 0]$ ; b)  $[\text{steel}, a, -a, 0]$  lay-up and layer thicknesses  $[1 \text{ mm}, 1.5 \text{ mm}, 1.5 \text{ mm}, 1 \text{ mm}]$  (solid line – inner radius; dotted line – outer radius) (Menshykova et al., 2014).

The effect of winding angle on axial and hoop stresses on inner and outer pipe surfaces is presented in Figs. 1a and 1b. Axial stresses on inner surface are lower than on outer for pipes with inner steel and inner  $0^\circ$  fibre layer. The hoop stress in pipe with inner steel layer is higher on inner surface than on outer for winding angles from  $40^\circ$  till  $90^\circ$  and lower on inner surface than on outer for winding angles from  $0^\circ$  till  $40^\circ$ . But for the pipe with inner  $0^\circ$  fibre layer the situation is vice versa. The hoop stress in pipe with inner  $0^\circ$  fibre layer is lower on inner surface than on outer for winding angles from  $40^\circ$  till  $90^\circ$  and higher on inner surface than on outer for winding angles from  $0^\circ$  till  $40^\circ$ .

Figs. 2a and 2b (Menshykova et al., 2014) provide trough the thickness distribution of axial and hoop stresses for a range of winding angles for the pipes with inner steel and  $0^\circ$  fibre layers.

Multi-parametric analysis of the results obtained for various properties of the pipe (thickness, lay-out, reinforcement orientation, etc.) was also carried out.



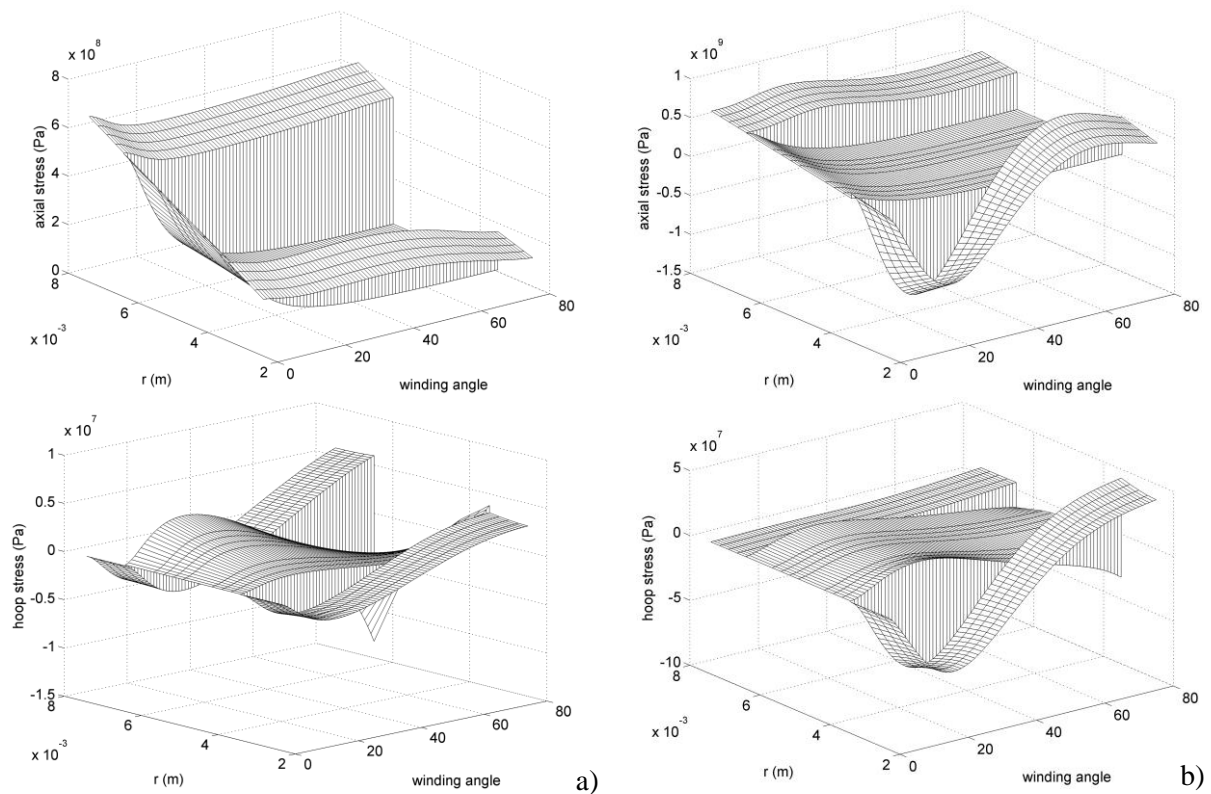


Fig. 2: Effect of the winding angle on the axial, hoop and radial stress distribution through the wall thickness for the pipe with a)  $[0, a, -a, 0]$ ; b)  $[\text{steel}, a, -a, 0]$  lay-up, layer thicknesses  $[1 \text{ mm}, 1.5 \text{ mm}, 1.5 \text{ mm}, 1 \text{ mm}]$ .

#### 4. Conclusions

Due to the advantages over conventional materials in strength, stiffness, corrosion resistance and the ability to be tailored for the purpose the composite coiled tubing has a potential to replace the conventional steel coiled tubing. Coiled tube is thick walled tube which must withstand various loading conditions one of which is obviously bending loading. Due to the manufacturing issues the inner pipe is used for multi-layered pull winding fibre reinforced tube production. The comparative study of stress distribution in multi-layered fibre reinforced pipes with inner steel layer and inner  $0^\circ$  fibre layer is presented. The analysis shows how the stresses depend on the material of inner layer. Multi-parametric analysis of the results obtained for various properties of the pipe (thickness, lay-out, reinforcement orientation, etc.) was also carried out.

#### References

- Bakaiyan, H., Hosseini, H. and Ameri, E. (2009) Analysis of multi-layered filament-wound composite pipes under combined internal pressure and thermomechanical loading with thermal variations, *Composite Structures*, 88, pp. 532-541.
- Herakovich, C. (1998) *Mechanics of fibrous composites*, John Wiley and Sons, Inc.
- Lekhnitskii, S.G. (1981) *Theory of elasticity of an anisotropic body*, MIR Publishers 1981, Moscow.
- Menshykova, M.V. and Guz I.A. (2014) Stress analysis of layered thick walled composite pipes subjected to bending loading, *International Journal of Mechanical Sciences*, 88, pp. 289-299.
- Natsuki, T., Takayanagi, H. and Tsuda, H. (2003) Prediction of bending strength for filament-wound composite pipes, *Journal of Reinforced Plastics and Composites*, 22, 8, pp. 695-710.
- Starbuck, J.M. and Eberle, C. (2000) Analytical solution for the design of spoolable composite tubing, *Third International Conference on Composite Materials for Offshore Operations*, Houston, TX, October 31 – November 2.
- Xia, M., Takayanagi, H. and Kemmochi, K. (2002) Bending behaviour of filament-wound fiber-reinforced sandwich pipes, *Composite Structures*, 56, pp. 201-210.

## SIMULATION OF THE MODEL OF TECHNICAL OBJECT AVAILABILITY CONTROL

K. Migawa<sup>\*</sup>, L. Knopik<sup>\*\*</sup>, A. Neubauer<sup>\*\*\*</sup>, D. Perczyński<sup>\*\*\*\*</sup>

**Abstract:** *The paper presents the description of algorithm for calculation characteristics of simulation model for the operation process realized at the transport system. The model presented in the paper constitutes an integral element of the developed complex method of quality control in elaborate technical object performance systems. In this method stochastic models were implemented, including Markov and semi-Markov decisive processes as well as genetic and evolutionary algorithms. Due to the adopted assumptions, it will be possible to use the constructed models for evaluation and control of operation process because of various criteria such as availability and reliability of technical objects, efficiency as well as safety of complex performance systems. In the example presented in the paper, the evaluation criteria consist of the availability of technical object as well as unit income generated in the states of the modeled operation process. On the basis of the results of research carried out at an existing means of transport operation system, entry data for the model were obtained and simulation experiments were carried out. As a result, typical values for the analyzed characteristics of the performance of technical system were designated.*

**Keywords:** Technical object, Availability, Simulation model.

### 1. Introduction

The problem of controlling operation process carried out at complex technical systems on the basis of a selected criterion of evaluation is presented in many papers (eg.: Kulkarni, 1995, Lee, 2000, Marbach et al., 2001 and Woropay et al., 2007). In the paper (Grabski, 2010), the analyzed model is the safety control of marine ships developed with the use of precise semi-Markov decisive processes and Howard algorithm. Also in the paper (Migawa et al., 2016) for the evaluation of availability of technical objects the semi-Markov decisive model was used, in which the selection of control strategy was realized via genetic algorithm. However, in the paper (Knopik et al., 2016) the authors delineated optimal solution of criterion function defining income generated in operation system in the case of decreasing number of secondary failures of vehicle electrical system.

Significant complexity of the modeled operation processes carried out in real systems of technical objects operation and maintenance involves the need to use appropriate methods and tools including computer simulation programs providing the possibility of effective studies of models representing the operation processes and an analysis of the obtained results (Marbach et al., 2001 and Muślewski et al., 2016). Depending on the kind of analyzed research problems, appropriate mathematical models as well as methods of delineating optimal and quasi-optimal solutions were implemented (Grabski, 2010, Knopik et al., 2016, Migawa et al., 2016 and Zastempowski et al., 2014).

### 2. Simulation model of availability control

The program developed for simulation of the operation process makes it possible to perform simulation

---

<sup>\*</sup> Assoc. Prof. Klaudiusz Migawa, PhD.: Faculty of Mechanical Engineering, UTP University of Science and Technology, Al. prof. S. Kaliskiego 7, 85-789 Bydgoszcz, Poland, klaudiusz.migawa@utp.edu.pl

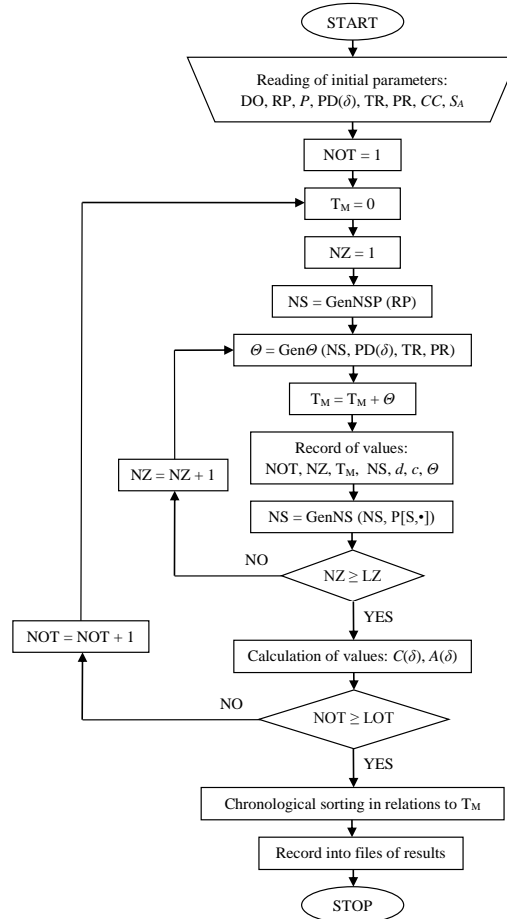
<sup>\*\*</sup> Assoc. Prof. Leszek Knopik, PhD.: Faculty of Management, UTP University of Science and Technology, Fordońska Street 430, 85-790 Bydgoszcz, Poland, knopikl@utp.edu.pl

<sup>\*\*\*</sup> RNDr. Andrzej Neubauer, DSc.: Nicolaus Copernicus University, Gagarina Street 11, 87-100 Toruń, Poland, aneub@umk.pl

<sup>\*\*\*\*</sup> Assist. Prof. Daniel Perczyński, PhD.: Faculty of Mechanical Engineering, UTP University of Science and Technology in Bydgoszcz (Poland), Al. Prof. S. Kaliskiego 7, Bydgoszcz; PL, daniel.perczynski@utp.edu.pl

experiments for different numbers of operational events (changes in the process states), intervals of simulation time both for an individual technical object and a group of technical objects. In the simulation program, successive duration times of the operation process states are determined by generating pseudorandom numbers yielding values from exponential, gamma, normal, logarithmic-normal and Weibull distributions. The structure of the simulation program was created so that the simulation experiment will be able to reflect a set of the analyzed technical objects and the sequence of events happening to each technical object in the analyzed real system.

In Fig. 1 there is a block scheme depicting operation of the program for the model of technical objects operation process.



*Fig. 1: Block scheme depicting operation of the program for technical objects operation process simulation model.*

In order to carry out a simulation experiment it is necessary to prepare a set of defined input data:

- a) DO (general data characterizing the simulation experiment):
  - LOT – number of technical objects used in the simulation experiment,
  - LZ – number of a technical object events in the simulation experiment,
  - $m$  – number of the process states, defined on the basis of a set of the modeled operation process states,
  - LD – number of decisions possible to be made in particular states of the modeled operation process,
  - $L\delta$  – number of strategies  $\delta$  possible to be used in the simulation experiment;
- b) RP (the process initial distribution);
- c)  $P$  (matrix of probabilities of the process states changes);
- d) PD (matrix of probability of decision choice in the process states);
- e) TR, PR (types and parameters of time distributions of being in particular states of the process);
- f) CC (matrix of unit profit in the process states);
- g)  $S_A$  (set of the process availability states).

In each moment of the simulation experiment in which the modeled operation process undergoes change (for the analyzed technical object) the following data is being entered into the file of results: number of the technical object NOT, number of the current event NZ, time of the current event (current time of model  $T_M$ ), number of the model current state NS, current decision  $d$ , value of unit profit  $c$  related to the object's being in the process current state, generated value of the object's being in a current state  $\Theta$ .

Next, values of functions applied in the simulation program are determined for the set of data generated during the simulation experiment (for the used strategy  $\delta$ ):

- value of the mean unit profit  $C(\delta)$ :

$$C(\delta) = \frac{\sum_{i=1}^Z c_i \cdot \Theta_i}{\sum_{i=1}^Z \Theta_i} \quad (1)$$

where:

$c_i$  –  $i$ -th performance of a unit profit connected with being in the states of the modeled operation process  $S = \{1, 2, \dots, m\}$ ,

$\Theta_i$  –  $i$ -th time of the object's being in the states of the modeled operation process  $S = \{1, 2, \dots, m\}$ ,

$Z = LOT \cdot LZ$  – number of events (changes of the model states) for a specified number of technical objects;

- value of the technical object availability function  $A(\delta)$ :

$$A(\delta) = \frac{\sum_{i=1}^Z \Theta_i(S_A)}{\sum_{i=1}^Z \Theta_i} \quad (2)$$

where:

$\Theta_i(S_A)$  –  $i$ -th time of the object's being in the modeled operation process states belonging to availability states  $S_A \in S = \{1, 2, \dots, m\}$ .

Fig. 1 has been completed with the following symbols: GenNSP – generation of the model initial state number, GenNS – generation of the model current state, Gen $\Theta$  – generation of the time value of being in the model state.

For 9<sup>th</sup> state semi-Markov model of the means of transport operation process presented in the paper (Migawa et al., 2016) as well as data obtained from tests of the existing operation system, simulation experiments were carried out.

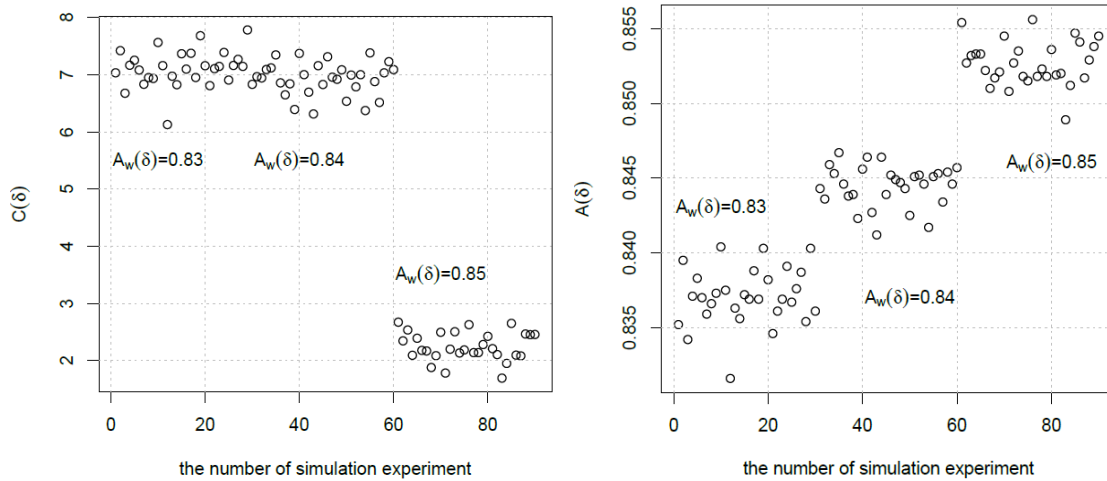


Fig. 2: Values of mean unit income as well as availability of technical object on the basis of simulation experiments for individual control strategies.

In Fig. 2 typical results of simulation experiments were presented for three selected strategies of technical object operation control process  $\delta$ , so that the designated availability of technical objects  $A(\delta)$  was at least equal to expected availability  $A_w(\delta)$  for appropriate realization of transport tasks (for  $A_w(\delta) = 0.83; 0.84, 0.85$ ). Experiments carried out consisted of 30 rounds of operation simulation process for each analyzed strategy  $\delta$ . As a result of the realization of simulation experiments, sets of 30 values of mean unit income  $C(\delta)$  as well as 30 values of technical object availability  $A(\delta)$  were obtained.

Mean values were designated for the results of carried out simulation experiments: unit income as well as availability of technical object (means of transport), presented in Tab. 1.

*Tab. 1: Values of mean unit income as well as availability of technical object obtained on the basis of simulation program.*

$A_w(\delta)$	$C(\delta)$ [PLN/h]	$A(\delta)$
0.83	7.1066	0.8371
0.84	6.9229	0.8445
0.85	2.2451	0.8527

### 3. Conclusions

One of the ways to facilitate effective evaluation and control of the quality of performance of complex technical object operation systems is implementing mathematical and simulation models for description and analysis of processes of operation carried out in these systems. Models of this type may be utilized for quality evaluation and control of complex technical systems performance from the point of view of various evaluation criteria such as: costs, income, reliability, availability, safety, efficiency, etc.

The simulation model of the operation process presented in the paper facilitates evaluation of the quality of the performance of analyzed technical system from the point of view of selected evaluation, i.e. mean income per time unit as well as technical object availability. On the basis of the obtained typical results it may be concluded that ensuring a higher level of availability of technical objects results in the necessity for additional expenses, at the same time resulting in decrease of unit income generated in operation system.

### References

- Grabski, F. (2014) Semi-Markov processes: Applications in system reliability and maintenance. Elsevier, Amsterdam.
- Grabski, F. (2010) Analiza ryzyka w decyzyjnych semi-markowskich modelach procesu eksploatacji. XXXVIII Zimowa Szkoła Niezawodności, Szczyrk, pp. 43-52.
- Knopik, L., Migawa, K. and Wdzięczny, A. (2016) Profit optimalization in operation systems. Polish Maritime Research, vol. 23, no. 1(89), pp. 93-98.
- Kulkarni, V.G. (1995) Modeling and analysis of stochastic systems. Chapman & Hall, New York.
- Lee, K.W. (2000) Stochastic models for random-request availability. IEEE Trans. Reliability 49, pp. 80-84.
- Marbach, P. and Tsitsiklis, T.N. (2001) Simulation based optimization of Markov reward process. IEEE Trans. Automat. Contr. 46, pp. 191-209.
- Migawa, K., Knopik, L. and Wawrzyniak, S. (2016) Application of genetic algorithm to control the availability of technical systems. Engineering Mechanics, Institute of Thermomechanics Academy of Sciences of the Czech Republic, pp. 386-389.
- Muślewski, Ł., Migawa, K. and Knopik, L. (2016) Control of technical objects operation quality with the use of simulation modeling PE. Risk, Reliability and Safety: Innovating Theory and Practice: Proceedings of ESREL, pp. 1388-1395.
- Woropay, M. and Migawa, K. (2007) Markov model of the operational use process in an autonomous system. Polish J. Environmental Studies, vol. 16, no. 4B, pp. 192-195.
- Zastempowski, M. and Bochat, A. (2014) Modeling of cutting process by the shear-finger cutting block. ASABE Applied Engineering in Agriculture, vol. 30, no. 3, pp. 347-353.

## THE METHOD OF RISK ASSESSMENT IN TRANSPORT SYSTEMS

**K. Migawa<sup>\*</sup>, L. Knopik<sup>\*\*</sup>, A. Sołtysiak<sup>\*\*\*</sup>, P. Kolber<sup>\*\*\*\*</sup>**

**Abstract:** *One of the methods for an assessment of the system ability to perform its task properly is to establish the risk connected with the transport means functioning. The presented approach involves determination of the risk connected with functioning of one technical object in transport system. The risk associated with functioning of a single technical object has been determined on the basis of a mathematical model of the operation and maintenance process, in the studied transportation system. A mathematical model of the operation and maintenance process has been developed with acceptance of an assumption that the process model is to be represented by a homogeneous semi-Markov model  $X(t)$ .*

**Keywords:** Risk assessment, Operation and maintenance process, Transport system.

### 1. Introduction

In the case of analysis of risk connected to the operation of technical systems, the probability of an unwelcome or dangerous event is determined on the basis of data obtained from functioning research of authentic process of functioning technical objects, e.g. means of transport. The results of an unwelcome or dangerous event may be connected to both the technical object (mean of transport), the worker (i.e. an operator carrying out the assigned transport task) and the environment. The effect of an unwelcome or dangerous event can lead to financial losses, health deterioration or loss of life, most often expressed as the cost, range of influence and duration of inconvenience (Szpytko, 2009).

The following is an examples of definition of the risk contained in acts on standardization:

Risk – the product of frequency or probability of the occurring of a specific dangerous event and economic and social implications of such an event (PN-IEC 60300-3-9),

Risk – the product of probability of the occurring of an unwelcome event and the extent of its results (PN-EN 1050),

Risk – combination of the probability of an event and its consequence (ISO Guide 73:2009 Ed.2.0).

Due to the complexity of the modeled processes and technical systems, there is a need for use of appropriate methods and tools, including stochastic models (Grabski, 2010 and Kulkarni, 1995), matrix calculus (Woropay et al., 2007 and Landowski et al., 2016 and Zastempowski et al., 2015) as well as models and simulation programs (Marbach et al., 2001 and Muślewski et al., 2016) ensuring effective realization of research and analysis of results obtained.

### 2. Mathematical model of the operation and maintenance process of transport means

The model of the operation and maintenance process was created on the basis of the analysis of the space of operation and maintenance states and events connected with technical objects (transport means) operating in the analyzed authentic transport system. Due to the criterion of risk in the observed system functioning, based on the identification of the multi-state operation and maintenance process of technical

---

<sup>\*</sup> Assoc. Prof. Klaudiusz Migawa, PhD.: Faculty of Mechanical Engineering, UTP University of Science and Technology, Al. prof. S. Kaliskiego 7, 85-789 Bydgoszcz, Poland, klaudiusz.migawa@utp.edu.pl

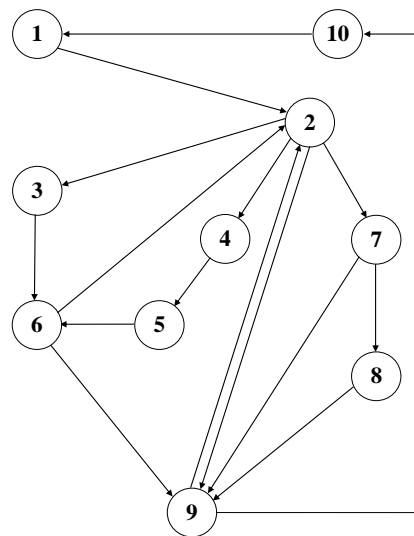
<sup>\*\*</sup> Assoc. Prof. Leszek Knopik, PhD.: Faculty of Management, UTP University of Science and Technology, Fordońska Street 430, 85-790 Bydgoszcz, Poland, knopikl@utp.edu.pl

<sup>\*\*\*</sup> Agnieszka Sołtysiak, MSc.: Faculty of Mechanical Engineering, UTP University of Science and Technology, Al. prof. S. Kaliskiego 7, 85-789 Bydgoszcz, Poland, aga.soltysiak87@gmail.com

<sup>\*\*\*\*</sup> RNDr. Piotr Kolber, DSc.: Faculty of Mechanical Engineering, UTP University of Science and Technology, Al. prof. S. Kaliskiego 7, 85-789 Bydgoszcz, Poland, piotr.kolber@utp.edu.pl



object, crucial states as well as possible passages between selected states were identified. On such basis a graph of changes of the states of operation and maintenance process was prepared, presented in Fig. 1.



*Fig. 1: A directed graph depicting operation and maintenance process of transport means  
1 – stopover at depot parking space, 2 – carrying out of transport task, 3 – downtime caused by damage (unwelcome event), 4 – downtime caused by an accident or collision (unwelcome event), 5 – intervention and rescue action after accident or collision (unwelcome event), 6 – repair after an unwelcome event, 7 – preventive diagnosis, 8 – preventive repair, 9 – supply, 10 – servicing (operation day, periodical, seasonal).*

Applying semi-Markov processes in the mathematical operation and maintenance process, the following assumptions were made:

- the modelled process has a finite number of states  $i = 1, 2, \dots, 10$ ,
- if the technological object at moment  $t$  is in state  $i$ , then  $X(t) = i$ ,
- random process  $X(t)$  being a mathematical model of the operation and maintenance process is homogenous,
- at moment  $t = 0$  the process is in state 1, i.e.  $P\{X(0) = 1\} = 1$ .

Limit probabilities  $p_i^*$  of remaining in states of the analyzed process  $X(t)$  were determined based on limit theorem for semi-Markov processes (Grabski, 2014):

If complex Markov chain in a semi-Markov process of finite state set  $S$  and kernel of continuous type contains one class of positive recurring states for each state  $i \in S$  and the expected positive average values  $\overline{\Theta}_i$ ,  $i \in S$  are finite, there exist limit probabilities:

$$p_i^* = \lim_{t \rightarrow \infty} p_i(t) = \frac{\pi_i \cdot \overline{\Theta}_i}{\sum_{i \in S} \pi_i \cdot \overline{\Theta}_i} \quad (1)$$

where:

the probabilities  $\pi_i$  comprise stationary distribution of the complex Markov chain fulfilling the system of linear equations:

$$\sum_{i \in S} \pi_i \cdot p_{ij} = \pi_j, \quad j \in S, \quad \sum_{i \in S} \pi_i = 1 \quad (2)$$

$p_{ij}$  signifies conditional probability of passing from state  $i$  to state  $j$ :

$$p_{ij} = \lim_{t \rightarrow \infty} p_{ij}(t) \quad (3)$$

$$p_{ij}(t) = P\{X(t) = j | X(0) = i\} \quad (4)$$

$\bar{\theta}_i$  signifies average values of unconditional duration of the states of process.

In order to delineate the values of limit probabilities  $p_i^*$  of remaining in states of semi-Markov model of the operation and maintenance process of transport means, based on the directed graph presented in Fig. 1 the following were created: matrix  $P$  of the probabilities of changes of states and matrix  $\theta$  of conditional duration of the states of process  $X(t)$ . Then, with the use of MATHEMATICA software, stationary distribution was delineated for complex Markov chain in the process as well as the limit distribution of semi-Markov process.

### 3. The unit risk of functioning disruption of the transport system

In this paper the unit risk of disruption of correctly functioning means of transport is defined as a sum of products of limit probabilities of remaining in unwelcome states of semi-Markov model of the operation and maintenance process and values of losses resulting from remaining in those states. The unwelcome states of the modeled operation and maintenance process of transport means are such which cause disruption of correctly functioning means of transport as well as states with generated losses due to such disruption. The correlation defining the unit risk of functioning disruption of transport means while carrying out the operation and maintenance process is described with the formula:

$$r_U = \sum_{i \in W} p_i^* \cdot c_i \quad (5)$$

where:

$c_i$  - unit cost incurred in connection with remaining in the  $i$ -th unwelcome state of the model of process  $X(t)$ ,

$W \subset S$  - subset of the states of the model of process  $X(t)$  being unwelcome states.

In order to define the unit risk of functioning disruption of the analyzed means of transport on the basis of semi-Markov model of the operation and maintenance process, one should distinguish the subset of unwelcome states  $W \subset S$ , in which additional costs are incurred due to damage, destruction, collision or an accident of the discussed technical objects (costs of intervention and rescue missions, costs of emergency pull offs, costs of repairs, costs of diagnostics, costs of stopover, costs of replacing the technical object with a substitution object, etc.). In the presented model the following unwelcome states of technical object have been distinguished: state 3 – downtime caused by damage (unwelcome event), state 4 – downtime caused by an accident or collision (unwelcome event), state 5 – intervention and rescue action after accident or collision (unwelcome event), state 6 – repair after an unwelcome event.

Then the unit risk of unwelcome event connected with disruption of correctly functioning means of transport:

$$r_U = p_3^* \cdot c_3 + p_4^* \cdot c_4 + p_5^* \cdot c_5 + p_6^* \cdot c_6 \quad (6)$$

$$r_U = \frac{\left\{ \left[ (p_{2,3} + p_{2,4}) \cdot p_{6,9} + p_{2,7} \cdot (p_{7,8} + p_{7,9}) + p_{2,9} \right] \cdot p_{9,10} + p_{2,3} \right\} \cdot \bar{\theta}_3 \cdot c_3 + p_{2,4} \cdot \left( \bar{\theta}_4 \cdot c_4 + p_{4,5} \cdot \bar{\theta}_5 \cdot c_5 \right) + (p_{2,3} + p_{2,4}) \cdot \bar{\theta}_6 \cdot c_6}{\left[ (p_{2,3} + p_{2,4}) \cdot p_{6,9} + p_{2,7} \cdot (p_{7,8} + p_{7,9}) + p_{2,9} \right] \cdot \left[ p_{9,10} \cdot (\bar{\theta}_1 + \bar{\theta}_3 + \bar{\theta}_{10}) + \bar{\theta}_9 \right] + \bar{\theta}_2 + p_{2,3} \cdot (\bar{\theta}_3 + \bar{\theta}_6) + p_{2,4} \cdot (\bar{\theta}_4 + p_{4,5} \cdot \bar{\theta}_5 + \bar{\theta}_6) + p_{2,7} \cdot (\bar{\theta}_7 + p_{7,8} \cdot \bar{\theta}_8)}$$

For the analyzed model of the operation and maintenance process of transport means, basing on the functioning data, values were estimated for the elements of matrix  $P$  of passage probabilities as well as unconditional times and unit profit generated in the states of process  $X(t)$  were determined (Tab. 1).

*Tab. 1: Average unconditional duration times for states of process in [h] as well as unit costs in [PLN/h] generated in states of process  $X(t)$ .*

Process state	$\bar{\theta}_i$	$c_i$	Process state	$\bar{\theta}_i$	$c_i$
1	5.659	6.77	6	2.333	98.21
2	8.852	-32.74	7	0.414	54.98
3	0.514	69.08	8	2.140	86.89
4	0.873	162.80	9	0.152	23.09
5	1.712	304.63	10	0.582	164.72

$$P = \begin{pmatrix} 0 & 1 & 0 & 0 & 0 & 0 & 0 & 0 & 0 & 0 \\ 0 & 0 & 0.2320 & 0.0030 & 0 & 0 & 0.4988 & 0 & 0.2661 & 0 \\ 0 & 0 & 0 & 0 & 0 & 1 & 0 & 0 & 0 & 0 \\ 0 & 0 & 0 & 0 & 1 & 0 & 0 & 0 & 0 & 0 \\ 0 & 0 & 0 & 0 & 0 & 1 & 0 & 0 & 0 & 0 \\ 0 & 0.4702 & 0 & 0 & 0 & 0 & 0 & 0 & 0.5298 & 0 \\ 0 & 0 & 0 & 0 & 0 & 0 & 0 & 0.0799 & 0.9201 & 0 \\ 0 & 0 & 0 & 0 & 0 & 0 & 0 & 0 & 1 & 0 \\ 0 & 0.2242 & 0 & 0 & 0 & 0 & 0 & 0 & 0 & 0.7758 \\ 1 & 0 & 0 & 0 & 0 & 0 & 0 & 0 & 0 & 0 \end{pmatrix} \quad (7)$$

As a result of the calculations unit risk of functioning disruption of transport means was developed:

$$r_U = 6.06 \text{ [PLN/h]}.$$

#### 4. Conclusions

The method presented in the article is the partial result of research to develop a comprehensive method of the control process for using the means of transport where decisive semi-Markov processes are used for control. The assessment of the risk connected with technical objects is an issue of complex character and involves determining numerical value of risk and criteria values (e.g. values of unit profit), to be used for deciding whether so determined risk is possible or impossible to be accepted. In further research a method for determination of criteria risk assessment values will be developed. Assessment of risk connected with technical objects operation and maintenance can be the point of reference to formulate design requirements concerning of the operated objects (transport means) as well as assumptions concerning design or modernization of the technical means necessary for assurance of the vehicle availability in a given transport system.

#### References

- Grabski, F. (2010) Risk analysis in decisive semi-Markov models of operation process. The 38<sup>th</sup> Winter Reliability School, Szczyrk, pp. 43-52 (in Polish).
- Grabski, F. (2014) Semi-Markov processes: Applications in system reliability and maintenance. Elsevier, Amsterdam.
- ISO Guide 73:2009 Ed.2.0 – Risk management – Vocabulary – Guidelines for use in standards.
- Kulkarni, V. G. (1995) Modeling and analysis of stochastic systems. Chapman & Hall, New York.
- Landowski, B., Perczyński, D., Kolber, K. and Muślewski, Ł. (2016) An example of Markov model of technical objects maintenance process. Engineering Mechanics, Svratka, pp. 346-350.
- Marbach, P. and Tsitsiklis, T.N. (2001) Simulation based optimization of Markov reward process. IEEE Trans. Automat. Contr. 46, pp. 191-209.
- Muślewski, Ł., Migawa, K. and Knopik, L. (2016) Control of technical objects operation quality with the use of simulation modeling PE. Risk, Reliability and Safety: Innovating Theory and Practice: Proceedings of ESREL, pp. 1388-1395.
- PN-IEC 60300-3-9: Analiza ryzyka w systemach technicznych. Risk analysis of technological systems.
- PN-EN 1050: Maszyny. Bezpieczeństwo. Zasady oceny ryzyka. Safety of machinery. Principles for risk assessment.
- Szpytko, J. (2009) Risk shaping in transport processes. Logitrans Conference Materials, Radom (in Polish).
- Woropay, M. and Migawa, K. (2007) Markov model of the operational use process in an autonomous system. Polish J. Environmental Studies, vol. 16, no. 4B, pp. 192-195.
- Zastempowski, M. and Bochat, A. (2015) Mathematical modelling of elastic deflection of a tubular cross-section. Polish Maritime Research, vol. 22, no. 2(86), pp. 93-100.

## ON EFFICIENCY OF QUASICONTINUUM SIMULATION OF CRACK PROPAGATION IN ELASTIC-BRITTLE DISORDERED LATTICES

K. Mikeš\*, M. Jirásek\*\*

**Abstract:** A quasicontinuum (QC) method can effectively reduce the computational demand of atomistic simulations by combining continuum and atomistic approaches. In this paper, the QC method is applied to simulations of crack propagation in materials represented by three-dimensional disordered particle systems with elastic-brittle links. The accuracy and efficiency of different QC approaches are evaluated by comparison with the fully resolved particle model.

**Keywords:** Quasicontinuum, Multiscale modeling, Lattice model, Finite elements, Elastic-brittle material.

### 1. Introduction

Discrete particle models can effectively capture complex material responses, especially localized phenomena such as damage or plastic softening. Such models use a network of particles interacting via discrete links or connections to represent a discrete microstructure of the modeled material. They can reproduce fine details of the microstructure and the resulting material properties if the resolution of particles is sufficiently high. On the other side, particle models have two main disadvantages: Firstly, a huge number of particles needed to describe the response of large-scale physically relevant models results in an extensive system of equations, which is expensive to solve. Secondly, the process of assembling of this system is also computationally expensive because all discrete connections must be individually taken into account.

A quasicontinuum (QC) based method can remove both of these disadvantages of high-resolution particle models. The QC method can efficiently handle regular atomistic lattices by combining continuum and atomistic approaches. Two types of subdomains are considered in a QC simulation. In the area of low interest, only a small subset of particles is selected to characterize the behavior of the entire system. These so-called *representative nodes* (in short *repnodes*) are used as nodes of an overlaid triangular finite element mesh, and the displacements of other particles (so-called *hanging nodes*) in the region of low interest are interpolated. In the regions of high interest, all particles are selected as repnodes, in order to provide the exact resolution of the particle model. Furthermore, a summation or homogenization rule can be applied in order to eliminate the requirement of visiting all particles during assembly of the global equilibrium equations.

The QC method was originally proposed in (Tadmor et al., 1996). Since that time, the QC method has been widely used and extended to applications for a variety of materials represented by regular lattices. Five QC-based approaches for simplification of irregular lattices have recently been developed by the authors (Mikeš, 2017). These approaches are based on interpolation (A2), global isotropic homogenization (A3i), global anisotropic homogenization (A3a), local isotropic homogenization (A4i) and local anisotropic homogenization (A4a).

All approaches mentioned above have been implemented into OOFEM (Patzák, 2012), an open-source object-oriented simulation platform. The accuracy and efficiency of simplified approaches is evaluated by comparison with an exact non-simplified lattice model (A1).

---

\* Ing. Karel Mikeš: Department of Mechanics, Faculty of Civil Engineering, Czech Technical University, Thákurova 7, 166 29, Prague; CZ, karel.mikes.1@fsv.cvut.cz

\*\* Prof. Ing. Milan Jirásek, DSc.: Department of Mechanics, Faculty of Civil Engineering, Czech Technical University, Thákurova 7, 166 29, Prague; CZ, milan.jirasek@fsv.cvut.cz

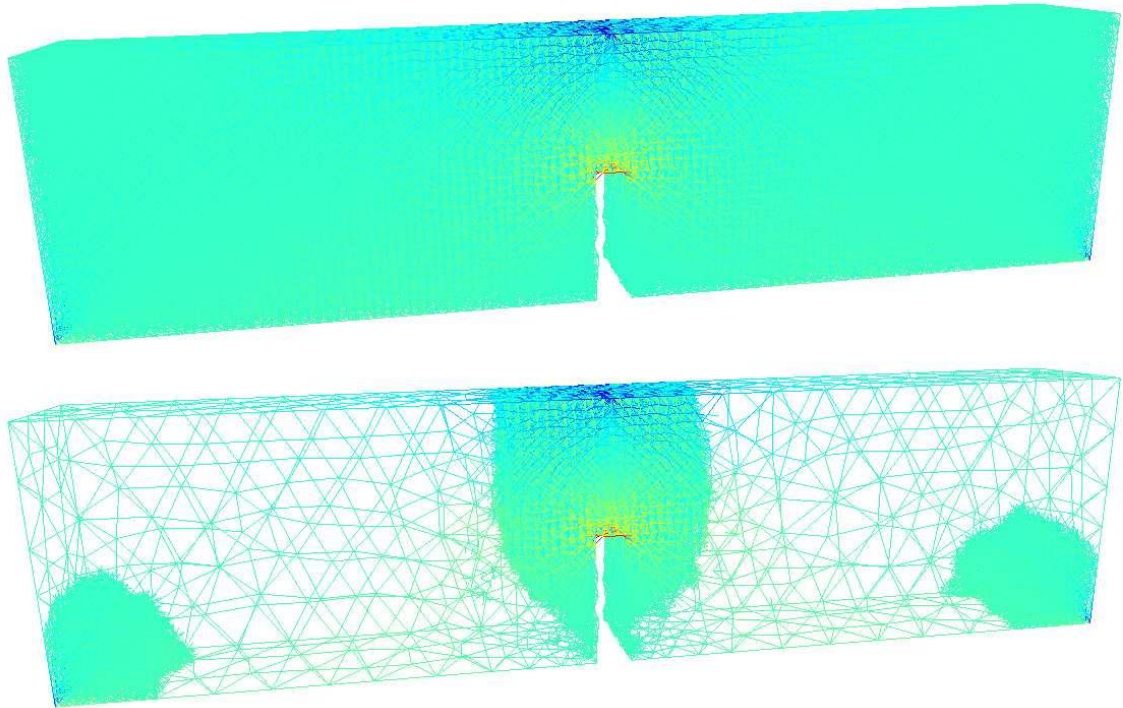
## 2. Failure simulation

In the failure simulation of a lattice network with elastic-perfectly brittle links, the prescribed displacement is increased until the critical value of tensile strain is reached in the most stretched link. Subsequently, the link is removed and the loading is imposed again. Repeating this process results in a series of link breakages that define the macroscopic crack trajectory.

As an example, the failure of a notched beam in a three-point bending test is simulated in three dimensions. The microstructure of the beam is represented by  $30 \times 60 \times 120$  randomized lattice cells, which results in 59 296 particles (with 177 823 unknown DOFs) connected by 502 172 links. The area of high interest is placed around the notch and around points with prescribed boundary conditions, see Fig. 1. Parameters of full and simplified models are listed in Tab. 1.

*Tab. 1: Numbers of particles, links, elements, renodes, hanging nodes and DOFs for various QC approaches.*

	A1	A2	A3, A4
NoP	59 296	59 296	13 812
NoL	502 172	50 2172	92 138
NoE	0	4 169	4 169
NoRN	59 296	59 296	11 413
NoHN	0	47 883	2 399
NoDOFs	177 823	34 174	34 174



*Fig. 1: Strain computed in all links for fully resolved particle model (top). Strain computed in links in area of high interest and surface edges of interpolation elements in area of low interest for simplified model (bottom).*

### 2.1. Accuracy

For simplified approaches, the prediction of cracked links is not completely exact. The sequence of cracked links is not completely the same and some links are predicted incorrectly. However, the agreement is reasonable: Just 6 – 8 % of links cracked in the first 1500 steps computed by one of the simplified approaches are not predicted to crack in one of 2000 steps computed by exact approach, and the macroscopic shape of the crack is very similar for all approaches, see Fig. 2.

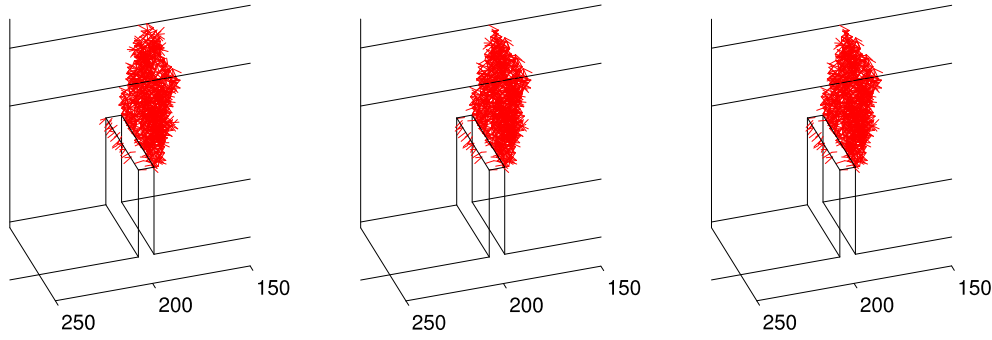


Fig. 2: Middle area of notched beam: edges of the beam (black) and cracked links (red) computed by the exact particle approach A1 (left), interpolation approach A2 (middle) and local anisotropic homogenization approach A4a (right).

The initial elastic response obtained by the simplified approaches is stiffer than the exact solution. However, the shape of the softening branch is captured by all approaches very well, see Fig. 3.

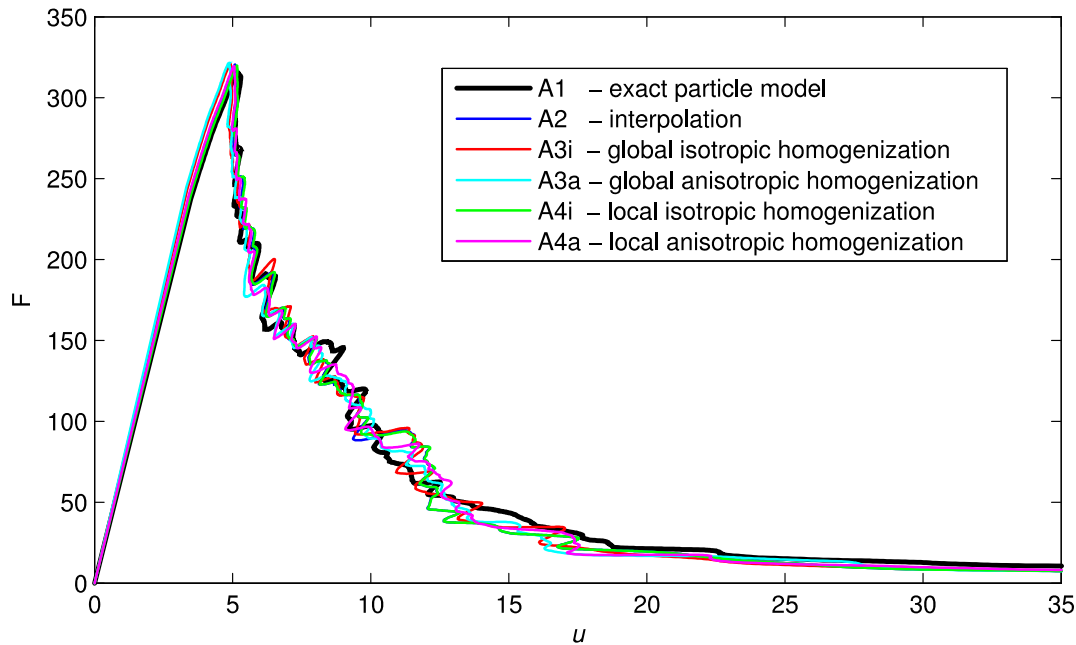


Fig. 3: Force-displacement diagrams for a microstructure with 2000 cracked links computed according to different approaches and smoothed by averaging  $\pm 25$  neighboring values.

## 2.2. Efficiency

The QC simplification is a preparatory stage which is realized once before the actual simulation. Time consumptions of individual procedures used by a QC simplification are listed in Tab 2. A conjugate gradient solver with incomplete Cholesky preconditioning and a symmetric compressed column matrix storage scheme have been found to be the most effective combination to solve the numerical problem. The simulation times are summarized in Tab. 3. One can expect that the assembling times for systems with a huge number of hanging nodes (A2) will be significantly higher in comparison with full models (A1). An unpleasant fact is that the assembling times of A2 are even higher than the solution time of A1. The assembly of matrices with symmetric skyline storage formats is faster than the assembly in a symmetric compressed column storage format. But skyline matrices consumed more memory and, for large systems, this difference is critical. It is questionable whether the hanging nodes assembly procedure for compressed column matrix scheme can be implemented more effectively. But a more important fact is that the full assembly of the stiffness matrix or load vector needs to be done only once before the first step of simulation. Before each next step, just the influence of a cracked link connection needs to be taken into account in updating of the stiffness matrix.



Tab. 2: Time consumption of QC simplifications for various QC approaches.

Computational time [s]	A1	A2	A3i/a	A4i/a
Generate interpolation mesh	-	0.20	0.20	0.20
Transform mesh to particles	-	0.34	0.34	0.34
Find element for all particles	-	1.97	1.97	1.97
Global stiffness tensor	-	-	0.23	-
Connectivity table	-	-	-	0.13
Individual stiffness tensors	-	-	-	21.61
<b>Total simplification time</b>	<b>0 s</b>	<b>2.51 s</b>	<b>2.74 s</b>	<b>24.25 s</b>

In the simulation of the crack propagation process, only the time consumed by solving and updating in one step is multiplied by the number of steps. For long simulations with thousands of steps, the time of QC simplification and assembly becomes negligible and the total relative acceleration is approaching the ratio between the times needed for the solution and update by the simplified and full models. The A2 approach with interpolation without homogenization is four time faster than a full particle simulation. The approaches with homogenization (A3 and A4) achieve speed-ups by a factor of 8 – 9, see Tab. 3.

Tab. 3: Time consumption of simulation for various QC approaches.

Computational time [s]	A1	A2	A3i/a	A4i/a
QC simplification	-	2.51	2.74	24.25
Assemble stiffness matrix	2.14	12.81	0.64	0.62
Assemble load vector	1.34	5.89	0.34	0.32
Solve one step	16.06	1.85	1.77	1.73
Update one step	0.80	2.36	0.18	0.19
Simulation of 2000 steps	9 h 22 m 3 s (1.00)	2 h 20 m 41 s (0.25)	1 h 5 m 4 s (0.12)	1 h 4 m 25 s (0.11)

### 3. Conclusion and future work

All proposed QC approaches have been shown to be very accurate and effective in simulations of crack propagation in lattices with elastic-brittle links. Future work will deal with implementation of an adaptive algorithm which allows for changes of the area of high interest as well as of the interpolation mesh in the area of low interest.

### Acknowledgement

Financial support of this research received from the Grant Agency of the Czech Technical University in Prague (SGS16/038/OHK1/1T/11) and from the Czech Science Foundation (GAČR projects 14-00420S and 17-04150J) is gratefully acknowledged.

### References

- Mikeš, K. and Jirásek, M. (2017) Quasicontinuum method extended to irregular lattices. Submitted for review, arXiv preprint 1701.07651.
- Patzák, B. (2012) OOFEM – an object-oriented simulation tool for advanced modeling of materials and structures. Acta Polytechnica, 52, pp. 59-66.
- Tadmor, E.B., Ortiz, M. and Phillips R. (1996) Quasicontinuum analysis of defects in solids, Philosophical Magazine A, 73, pp. 1529-1563.

## EXPLICIT DYNAMIC FINITE ELEMENT ANALYSIS OF A FIRING PIN ASSEMBLY

D. Mochar<sup>\*</sup>, D. Gabriel<sup>\*</sup>, J. Masák<sup>\*</sup>, J. Kopačka<sup>\*</sup>, R. Kolman<sup>\*</sup>, J. Plešek<sup>\*</sup>

P. Hynek<sup>\*</sup>, J. Vtípil<sup>\*\*</sup>

**Abstract:** *In this paper, explicit dynamic finite element analysis of a firing pin assembly was performed. Two different geometries of the firing pin were considered using the finite element software PMD and Abaqus. For both variants there was evaluated a stress distribution at the critical point of a tested component, that is going to be later used for a fatigue analysis of the firing pin.*

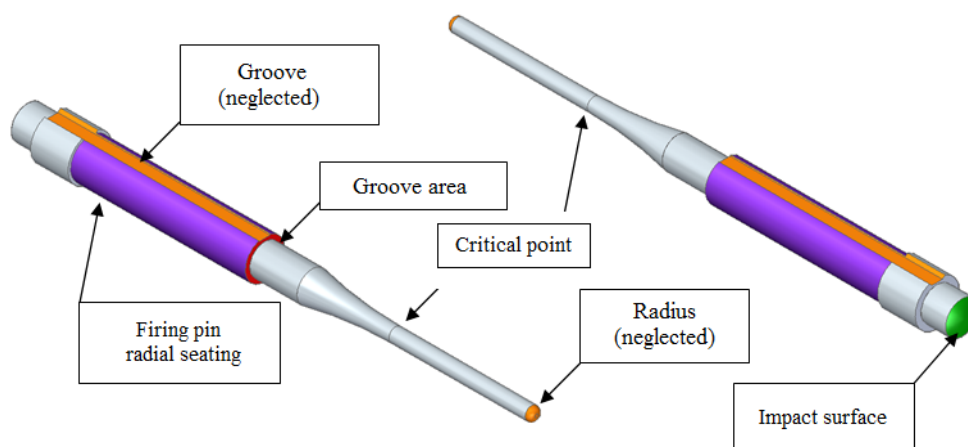
**Keywords:** Firing pin, Explicit dynamic analysis, FEM, Fatigue.

### 1. Introduction

A firing pin is a central structural element of any firearm. Therefore, it is crucial to secure its correct operation, which is necessary for functionality of a complete firearm. In some cases during real construction process the stress damage is cumulated in the critical point and can lead to a fatigue fracture. Due to the nature of the firing pin, especially its low weight and high impact forces, it is necessary to take into account the stress wave propagation in the structure (Mochar, 2016). In this paper, time distributions of kinematic and stress quantities in the critical point of firing pin was calculated in the dynamic finite element analysis (FEA). Two different geometries of the firing pin were considered using the finite element software PMD (VAMET LLC. 2013) and Abaqus. Finally, the rough estimation of lifetime of both variants was determined.

### 2. Finite element analysis

CAD model of a firing pin is plotted in Fig. 1. Two geometries of firing pin were considered varying in the length between the impact surface and critical point of the firing pin (tip of the radius R50) denoted as R50 – 42.0 mm (var. A) and R50 – 44.7 mm (var. B).



*Fig. 1: CAD model of a firing pin.*

<sup>\*</sup> Institute of Thermomechanics of the CAS, v. v. i., Dolejškova 5, 182 00 Prague, Czech Republic

<sup>\*\*</sup> Česká zbrojovka, a.s., Svatopluka Čecha 1283, 688 27 Uherský Brod, Czech Republic

The firing pin is radially imposed on the surface denoted as „Firing pin radial seating“. The axial movement of the firing pin with prescribed initial velocity  $v = 9 \text{ m/s}$  is excited by hit a hammer on the impacted surface. After travelling a distance of 2 mm the firing pin hits the backstop.

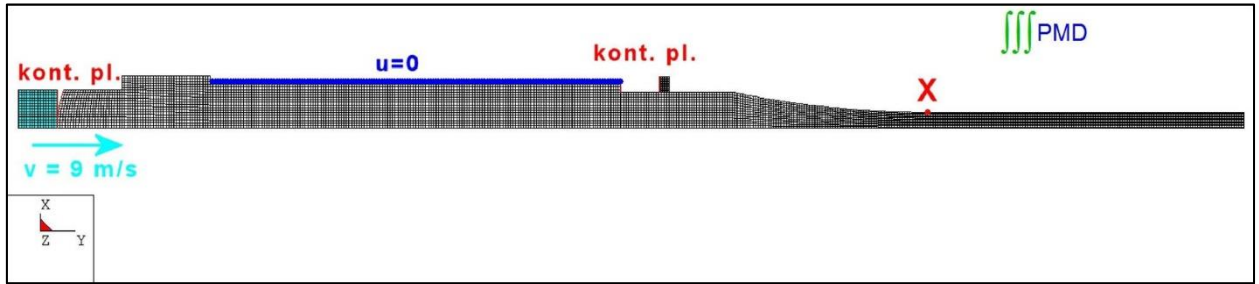


Fig. 2: Finite element model of the firing pin including hammer and backstop.

For both variants of the firing ring the material properties were considered linear elastic with Young's modulus  $E = 1.98 \cdot 10^5 \text{ MPa}$ , Poisson's ratio  $\nu = 0.28$  and density  $\rho = 7850 \text{ kg} \cdot \text{m}^{-3}$ . It corresponds to the speed of longitudinal waves  $c_L = 5653.3 \text{ m/s}$ . Young's modulus of rigid hammer and rigid backstop were chosen two orders of magnitude greater than modulus of the firing pin, i.e.  $E = 1.98 \cdot 10^7 \text{ MPa}$ ; Poisson's ratio was the same value as for the firing pin. Since correct transmission of prescribed initial velocity of firing pin  $v = 9 \text{ m/s}$  the fictitious density of hammer was calculated so its weight was the same as the firing pin:

- var. A - volume of firing pin  $677.262 \text{ mm}^3$ , volume of hammer  $25.133 \text{ mm}^3$ , density of hammer  $211537.121 \text{ kg} \cdot \text{m}^{-3}$ ,
- var. B – volume of firing pin  $701.131 \text{ mm}^3$ , volume of hammer  $25.133 \text{ mm}^3$ , density of hammer  $218992.462 \text{ kg} \cdot \text{m}^{-3}$ .

The problem was treated as axisymmetric one discretized by four-node quadrilateral elements with  $2 \times 2$  integration. Based on the recommendation of a choice of permissible dimensionless wavelength for linear and quadratic serendipity finite element meshes to suppress dispersion error (Kolman et al., 2013), the length of elements was set  $H = 1.2 \cdot 10^{-4} \text{ m}$  at the most. The hammer and backstop were modelled as a rigid body. The finite element model of the firing pin including hammer and backstop is shown in Fig. 2, where the location of the critical point of the firing pin is marked by X. Note that axial groove and radius on the tip of the firing pin are neglected in the finite element model. Furthermore, 3D model was also considered in the Abaqus containing eight-node linear elements with reduced integration (C3D8R elements). The number of nodes and elements of 2D and 3D models including hammer and backstop for both geometric variants are shown in Tab. 1.

Tab. 1: Number of nodes and elements of 2D and 3D models including hammer and backstop for geometric variants A and B.

	Var. A – 42.0 mm		Var. B – 44.7	
	nodes	elements	nodes	elements
Firing pin 2D model	7 885	7 396	7 810	7 326
Hammer 2D model	225	196	225	169
Backstop 2D model	117	96	117	96
Firing pin 3D model	58 240	62 982	58 432	63 191
Hammer 3D model	2 016	2 410	2 016	2 410
Backstop 3D model	1 280	1 728	1 280	1 728

The explicit contact-impact analysis of the firing pin was performed for variants A and B. For direct integration of the equations of motion the central difference method with the diagonal mass matrix was used. In PMD and Abaqus calculation the time step was set carefully to  $\Delta t = 10^{-9} \text{ s}$  and the stability of

the integration process was ensured by energy balance monitoring (Kolman et al., 2016). The impact response was calculated for  $t = 4.0 \cdot 10^{-4}$ s.

The influence of the penalty parameter  $\xi$  on the accuracy of the numerical solution was studied in PMD calculation for penalty-based contact algorithm (Gabriel et al., 2004). The results were compared with the Abaqus software, where the penalty was set automatically. Quite a good agreement between PMD and Abaqus was achieved for the penalty parameter  $\xi = 10^{15} \text{ N} \cdot \text{m}^{-3}$ .

### 3. Results

The results of explicit contact-impact analysis of the firing pin for variant A and variant B are summarized in Tab. 2 and Tab. 3, respectively for PMD and Abaqus calculations. The maximum and minimum values of axial stress in the tip of radius R50 of firing pin are presented including the instant of time when those extremes were occurring. For illustration time distribution of the axial stress in the tip of radius R50 of firing pin is plotted in Fig. 3 for variant A.

Tab. 2: Extremes of axial stresses in the critical point–variant A.

	Abaqus 2D	Abaqus 3D	PMD 2D
$S_{yy} \text{ max [MPa]}$	818	810	729
time of occurrence [s]	$3.42 \cdot 10^{-4}$	$3.32 \cdot 10^{-4}$	$3.54 \cdot 10^{-4}$
$S_{yy} \text{ min [MPa]}$	-853	-838	-916
time of occurrence [s]	$2.77 \cdot 10^{-4}$	$2.67 \cdot 10^{-4}$	$2.66 \cdot 10^{-4}$

Tab. 3: Extremes of axial stresses in the critical point–variant B

	Abaqus 2D	Abaqus 3D	PMD 2D
$S_{yy} \text{ max [MPa]}$	1 119	1 132	1 128
time of occurrence [s]	$2.98 \cdot 10^{-4}$	$2.99 \cdot 10^{-4}$	$2.98 \cdot 10^{-4}$
$S_{yy} \text{ min [MPa]}$	-1 190	-1 109	-1 156
time of occurrence [s]	$3.64 \cdot 10^{-4}$	$3.65 \cdot 10^{-4}$	$3.64 \cdot 10^{-4}$

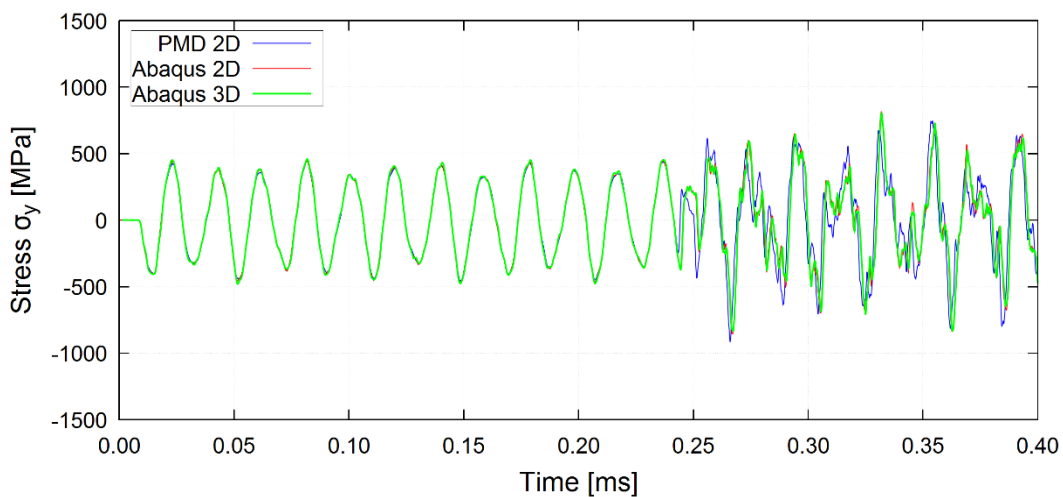


Fig. 3: Time distribution of axial stresses in the critical point–variant A.

After the evaluation of time distribution of axial stresses had been determined, the lifetime of those variants was roughly estimated using Wöhler's curve approximation power relation. The parameters  $w$  and  $C$  of power form ( $\sigma_a^w \cdot N = C$ ) were chosen for high-strength steel. Since the progress of this tension is almost symmetrically changing the amplitude tension  $\sigma_a$  is being determined as difference between

maximum and minimum value of axis tension. One cycle of burden N is simple taken as an idle shot. The comparisons of lifetime of both variants is plotted in Fig. 4.

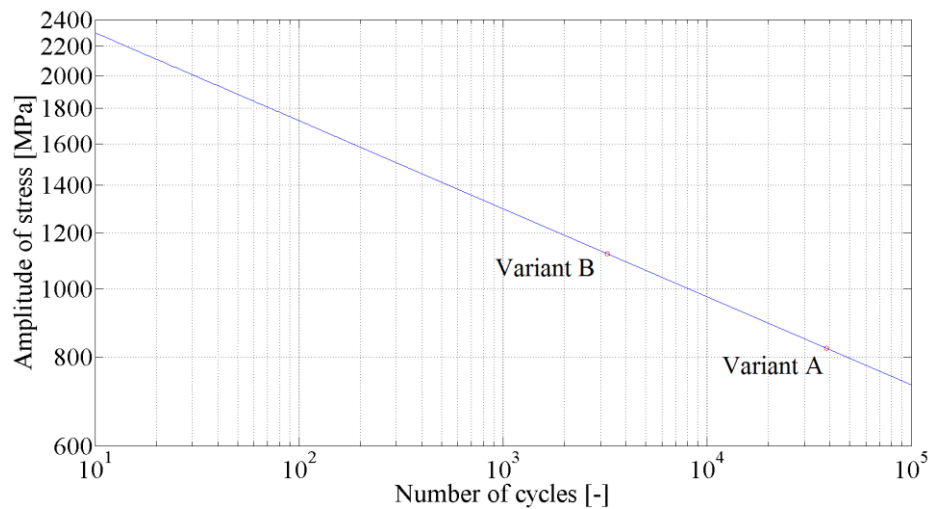


Fig. 4: Wohler's curve for comparison of lifetime of variants A and B.

#### 4. Conclusion

After the impact of the hammer the stress waves of the sinusoidal character propagates throw the firing pin. This phenomenon stands during travelling distance of 2 mm until the firing pin hits backstop in time  $t = 2.54 \cdot 10^{-4}$  s. At this moment stress waves propagation rapidly changes due to contact condition, which significantly influences resulting stresses in the firing pin. Based on the comparison of both variants it can be concluded that variant A is more favourable where maximum reduced stress value was 917 MPa. For variant B this value was five times exceeded and the maximum reduced stress reached the maximum value 1192 MPa. Thus, the maximum difference of reduced stress between variant A and B was 275 MPa. Finally, rough lifetime estimation was done for both variants. It was demonstrated that variant A of the firing pin should be more resistant to fatigue fracture. This conclusion will be validated by experimental measurements during shooting tests with the real firearms in the future.

#### Acknowledgements

This work was supported by the Technology Agency of the Czech Republic under grant No TH01010772 within institutional support RVO:61388998 and the Centre of Excellence for Nonlinear Dynamic Behaviour of Advanced Materials in Engineering CZ.02.1.01/0.0/0.0/15 003/0000493 (Excellent Research Teams) in the framework of Operational Programme Research, Development and Education.

#### References

- Gabriel, D., Plešek, J. and Ulbin, M. (2004) Symmetry preserving algorithm for large displacement frictionless contact by the pre-discretization penalty method. *International Journal for Numerical Methods in Engineering* 61(15): 2615-2638.
- Kolman, R., Plešek, J., Červ, J., Okrouhlík, M. and Pařík, P. (2016) Temporal-spatial dispersion and stability analysis of finite element method in explicit elastodynamics. *International Journal for Numerical Methods in Engineering* 106(2), 113-128.
- Kolman, R., Plešek J., Okrouhlík, M. and Gabriel, D. (2013) Grid dispersion analysis of plane square biquadratic serendipity finite elements in transient elastodynamics. *International Journal for Numerical Methods in Engineering* 96(1), 1-28.
- Mochar, D. (2016) Explicit dynamic FE analysis of a firing pin assembly. Diploma thesis. CTU in Prague (in Czech).
- VAMET LLC. (2013) PMD version f77.11; <http://www.pmd-fem.com/>.

## BEAM RESTED ON UNILATERAL ELASTIC FOUNDATION – (THEORY, EXPERIMENTS AND FINITE ELEMENT APPROACH)

Z. Morávková\*, I. Tomečková\*\*, K. Frydryšek\*\*\*

**Abstract:** This work presents theory and numerical approach suitable for the solution of straight plane beams rested on an elastic unilateral (i.e. nonlinear modified Winkler's) foundation. The nonlinear reaction of the foundation can be described via nonlinear expression, in our particular case it is the positive part of the deflection function. The nonlinear differential equation of 4th-order is solved via standard Finite Element Method, which discretize the weak formulation of the problem. The Semi-smooth Newton's method is used to solve discrete problem.

**Keywords:** Unilateral elastic foundation, Beam, Nonlinearity, Finite Element Method, Semi-smooth Newton's method.

### 1. Introduction

There are beams on elastic foundations which are frequently used in the technical practice; see Fig. 1a. In mechanics, the deflection  $v = v(x)$  [m] of the beam without any volume loads is described by differential equation  $EJ_{ZT} \frac{d^4 v}{dx^4} + q_R = 0$ , where  $E$  [Pa] is the modulus of elasticity of the beam,  $J_{ZT}$  [m<sup>4</sup>] is the major principal second moment of the beam cross-section and  $q_R = q_R(x, v, \dots)$  [N.m<sup>-1</sup>] corresponds to the reaction of the foundation (Frydryšek et al., 2013; Frydryšek et al., 2014); see Fig. 1b. Our work focuses on the solution of straight 2D beams of length  $2L$  on an elastic foundation with nonlinear unilateral behaviour (linear Bernoulli's beam, small deformations in the beam, Finite element Method); see Fig. 1. The methodology of the elastic foundation measuring applied in this paper is based on the pressing of a beam into the foundation (Klučka et al., 2014; Frydryšek et al., 2014). on the displacement in the foundation can be approximated by nonlinear expression  $q_R(v) = \frac{k}{2}(|v| + v)$ , see Fig. 1b.

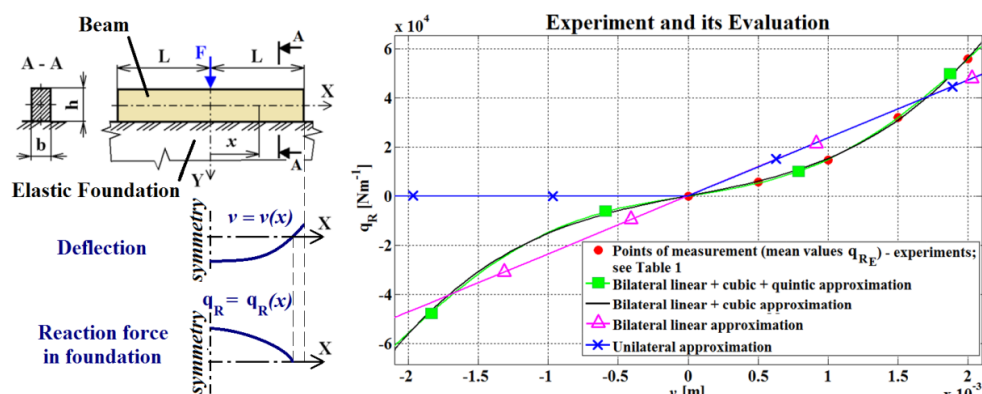


Fig. 1: a) Beam with cross-section  $b \times h$  and length  $2L$  is resting on elastic unilateral foundation; b) Dependence of reaction force on deflection (i.e. foundation load-settlement behavior for a sand, experiment and suitable linear and nonlinear approximations) (Frydryšek et al., 2014).

\* Mgr. Zuzana Morávková PhD.: Department of Mathematics and Descriptive Geometry, VSB-Technical University of Ostrava; 17. listopadu 15/2172; 708 33, Ostrava; Czech Republic, zuzana.moravkova@vsb.cz

\*\* Mgr. Ivona Tomečková PhD.: Department of Mathematics and Descriptive Geometry, VSB-Technical University of Ostrava; 17. listopadu 15/2172; 708 33, Ostrava; Czech Republic, ivona.tomeckova@vsb.cz

\*\*\* Assoc. Prof. M.Sc. Karel Frydryšek, PhD.: Department of Applied Mechanics, Faculty of Mechanical Engineering, VSB-Technical University of Ostrava; 17. listopadu 15/2172; 708 33, Ostrava; Czech Republic, karel.frydrysek@vsb.cz



For the sake of simplicity, the symbol  $v^+$  is used instead of the expression  $\frac{1}{2}(|v| + v)$  in this paper, i.e.  $q_R(v) = k \frac{|v|+v}{2} = kv^+$ , where the  $v^+$  is known as the positive part of  $v$ .

## 2. Solved Example and its Boundary Conditions

Let us suppose that the solved beam has symmetry (i.e. the beam geometry, beam material, the volume and surface loads and the foundation are symmetrical). Therefore it is sufficient to solve the differential equation for a half of the beam, i.e.  $x \in \langle 0; L \rangle$ , see Fig. 1a. Hence, the deflection of the beam is described by the equation  $EJ_{ZT} \frac{d^4 v}{dx^4} + kv^+ = 0$  for  $x \in (0, L)$  with the following boundary conditions (prescribed in points  $x = 0$  and  $x = L$ )

$$\frac{dv(x=0)}{dx} = 0, \quad (x = L) = 0, \quad T(x = 0) = -\frac{F}{2}, \quad T(x = L) = 0, \quad (1)$$

where  $T(x) = -EJ_{ZT} \frac{d^3 v(x)}{dx^3}$  [N] is shearing force and  $M_o(x) = -EJ_{ZT} \frac{d^2 v(x)}{dx^2}$  [N.m] is bending moment.

## 3. Weak formulation of beam on unilateral foundation

Let's denote  $V$  as a space of virtual displacements and then  $V = \left\{ w \in H^2((0, L)) : \frac{dw(x=0)}{dx} = 0 \right\}$ , where  $H^2((0, L))$  is Sobolev function space (i.e. Hilbert space with inner product  $(v, w) = \int_0^L \frac{d^2 v}{dx^2} \frac{d^2 w}{dx^2} + \frac{dv}{dx} \frac{dw}{dx} + v w dx$ ), see (Kufner et al., 1977). We multiply differential equation by virtual displacement  $w \in V$  and integrate over the half length of the beam.

Then we obtain equation  $EJ_{ZT} \int_0^L \frac{d^4 v}{dx^4} w dx + k \int_0^L v^+ w dx = 0$ , which is fulfilled for arbitrary  $w \in V$ . If we apply the integration by parts formula to the first integral and once more and subtract the boundary expressions from the left side to the right side we get

$$EJ_{ZT} \int_0^L \frac{d^2 v}{dx^2} \frac{d^2 w}{dx^2} dx + k \int_0^L v^+ w dx = - \left[ EJ_{ZT} \frac{d^3 v}{dx^3} w \right]_0^L + \left[ EJ_{ZT} \frac{d^2 v}{dx^2} \frac{dw}{dx} \right]_0^L. \quad (2)$$

From the boundary conditions (1) and from the property of  $w \in V$  we obtain

$$- \left[ EJ_{ZT} \frac{d^3 v}{dx^3} w \right]_0^L = -EJ_{ZT} \frac{d^3 v(L)}{dx^3} w(L) + EJ_{ZT} \frac{d^3 v(0)}{dx^3} w(0) = \frac{F}{2} w(0)$$

and  $\left[ EJ_{ZT} \frac{d^2 v}{dx^2} \frac{dw}{dx} \right]_0^L = EJ_{ZT} \frac{d^2 v(L)}{dx^2} \frac{dw(L)}{dx} - EJ_{ZT} \frac{d^2 v(0)}{dx^2} \frac{dw(0)}{dx} = 0$ , and then the weak formulation of the beam deflection on the unilateral foundation is following

$$\text{find } v \in V \text{ such that } EJ_{ZT} \int_0^L \frac{d^2 v}{dx^2} \frac{d^2 w}{dx^2} dx + k \int_0^L v^+ w dx = \frac{F}{2} w(0) \text{ is fulfilled for all } w \in V. \quad (3)$$

The solvability (the existence of any solution) of (3) depends on the beam loads in general. In our particular case the necessary condition is inequality  $\frac{F}{2} p(x=0) > 0$ , which is supposed to be fulfilled for arbitrary linear polynomial  $p$  positive on  $(0, L)$ . It means that the prescribed external force  $F$  must be positive. See (Sysala, 2008) for details.

## 4. Discretization by FEM

Let's divide the interval  $(0, L)$  into  $n$  parts of the same length. This equidistant discretization with nodes  $x_1 = 0, x_{i+1} = x_i + h$  has the constant step  $h = L/n$ . The discrete approximation of the space  $V$  denoted by the symbol  $V_h$  is a subspace of the set of all smooth piecewise-cubic functions. Moreover, the first derivative of the every element of  $V_h$  is zero for  $x = 0$ . The choice of the space  $V_h$  stems from the convergence requirements of FEM theory, see (Haslinger, 1980) and from the mathematical embedding theory, see (Kufner et al., 1977). Follows that  $V_h \subset V$ . It is a finite dimensional space and therefore it has a basis, which is formed by piecewise-cubic functions

$$\varphi_{2i-1}(x) = \begin{cases} 1 - \frac{2(x-x_i)^3}{h^3} - \frac{3(x-x_i)^2}{h^2} & \text{for } x \in \langle x_{i-1}, x_i \rangle, \\ 1 + \frac{2(x-x_i)^3}{h^3} - \frac{3(x-x_i)^2}{h^2} & \text{for } x \in \langle x_i, x_{i+1} \rangle, \\ 0 & \text{otherwise,} \end{cases} \quad \varphi_{2i}(x) = \begin{cases} \frac{(x-x_i)^3}{h^2} + \frac{2(x-x_i)^2}{h} + (x-x_i) & \text{for } x \in \langle x_{i-1}, x_i \rangle, \\ \frac{(x-x_i)^3}{h^2} - \frac{2(x-x_i)^2}{h} + (x-x_i) & \text{for } x \in \langle x_i, x_{i+1} \rangle, \\ 0 & \text{otherwise.} \end{cases}$$

It is obvious that the base functions are nonzero only on two subintervals of the beam discretization. The discrete form of (3) is following

$$\text{find } v_h \in V_h \text{ such that } EJ_{ZT} \int_0^L \frac{d^2 v_h}{dx^2} \frac{d^2 \varphi_i}{dx^2} dx + k \int_0^L v_h^+ \varphi_i dx = \frac{F}{2} \varphi_i(0) \text{ for all } i = 1, \dots, 2n+2. \quad (4)$$

Because the solution  $v_h$  of (4) is element of the space  $V_h$ , we can write  $v_h = \sum_{i=1}^{2n+2} u_i \varphi_i(x)$ . The values  $u_i$  for odd indexes are the deflections of  $v_h$  in the nodes of the discretization and values  $u_i$  for the even indexes are the slopes in nodes  $x_i$  and therefore  $\mathbf{u} = (v_h(x_1), \frac{dv_h(x_1)}{dx}, v_h(x_2), \frac{dv_h(x_2)}{dx}, \dots, v_h(x_{n+1}), \frac{dv_h(x_{n+1})}{dx})^T$ . The algebraic FEM representation of the first integral in (4) and the right side of (4) can be set by a standart way and the local stiffness matrix on one subinterval of discretization can be derived

$$\mathbf{K}_e = \begin{pmatrix} 12 & 6h & -12 & 6h \\ 6h & 4h^2 & -6h & 2h^2 \\ -12 & -6h & 12 & -6h \\ 6h & 2h^2 & -6h & 4h^2 \end{pmatrix}, \text{ see (Kolář et al., 1979).}$$

The global stiffness matrix  $\mathbf{K}$  and the global load vector  $\mathbf{f}$  corresponding to (4) are shown (example for  $n = 4$ ,  $h = L/n$  constant).

$$\mathbf{K} = \frac{1}{h^3} \begin{pmatrix} 12 & 0 & -12 & 6h & 0 & 0 & 0 & 0 & 0 & 0 \\ 0 & h^3 & 0 & 0 & 0 & 0 & 0 & 0 & 0 & 0 \\ -12 & 0 & 24 & 0 & -12 & 6h & 0 & 0 & 0 & 0 \\ 6h & 0 & 0 & 8h^2 & -6h & 2h^2 & 0 & 0 & 0 & 0 \\ 0 & 0 & -12 & -6h & 24 & 0 & -12 & 6h & 0 & 0 \\ 0 & 0 & 6h & 2h^2 & 0 & 8h^2 & -6h & 2h^2 & 0 & 0 \\ 0 & 0 & 0 & 0 & -12 & -6h & 24 & 0 & -12 & 6h \\ 0 & 0 & 0 & 0 & 6h & 2h^2 & 0 & 8h^2 & -6h & 2h^2 \\ 0 & 0 & 0 & 0 & 0 & 0 & 12 & -6h & 12 & -6h \\ 0 & 0 & 0 & 0 & 0 & 0 & 6h & 2h^2 & -6h & 4h^2 \end{pmatrix}, \quad \mathbf{f} = \begin{pmatrix} \frac{F}{2} \\ 0 \\ 0 \\ 0 \\ 0 \\ 0 \\ 0 \\ 0 \\ 0 \\ 0 \end{pmatrix} \quad (5)$$

## 5. The nonlinear mapping

We will present a way how to find an algebraic representation of the second integral in (4), which contains the nonlinear expression  $v_h^+ = (|v_h| + v_h)/2 = (|\sum v_i \varphi_i| + \sum v_i \varphi_i)/2$ . We first use the trapezoidal rule for approximating the integral  $\int_0^L v_h^+ w_h dx$ . The main goal of this is that we get approximation  $|\sum_i v_i \varphi_i| \approx \sum_k |v_k| \varphi_k$ , where the index  $i$  is form the set  $\{1, 2, 3, \dots, 2n+2\}$  and  $k$  is form  $\{1, 3, 5, \dots, 2n+1\}$ . Now we get the homogenous equation  $G(u) = 0$  for  $G(u) = EJ_{ZT} \mathbf{K} u + k \mathbf{B} u^+ - \mathbf{f}$  instead of (4), where matrix  $\mathbf{K}$  and vector  $\mathbf{f}$  are from (5) and where the matrix  $\mathbf{B}$  is diagonal,  $\mathbf{B} = \text{diag}(h/2, 0, h, 0, h, 0, h, 0, h/2, 0)$ .

Because we do not have available any derivation due to the absolute value in  $u^+$ , we cannot use the well-known Newton-Raphson's method. For this reason, we use semi-smooth Newton's method, see (Chen et al., 2001). This method introduces so called slanting function  $G^o$  and use it instead of Jacobian in the iterations. We define  $G^o(u) = EJ_{ZT} \mathbf{K} + k \mathbf{B} \text{diag}(A(u^+))$  in our case, where the symbol  $A(u^+)$  stands for the active set of indexes of nodes, in which subsoil is active. The resulting iterative equation in the  $(n+1)$ -th step is  $u^{(n+1)} = u^{(n)} - G^o(u^{(n)})^{-1} G(u^{(n)})$  for known solution  $u^{(n)}$  from the previous step. This iteration process converges for sufficiently small distance between the initial vector  $u^{(0)}$  and the exact solution of the equation  $G(u) = 0$ .

## 6. Results

The acquired FE results, see Fig. 2, were compared with the Central Difference Method too (Frydryšek et al., 2014) with good agreement. There is a comparison of unilateral and bilateral approaches of elastic foundation in Fig. 2. For example:

$$v_{MAX,bilateral} = 9.0607 \times 10^{-4} \text{ m}, \quad v_{MAX,unilateral} = 9.4242 \times 10^{-4} \text{ m},$$

$$M_{o MAX,bilateral} = 6.2070 \times 10^4 \text{ N.m and } M_{o MAX,unilateral} = 6.6701 \times 10^4 \text{ N.m.}$$

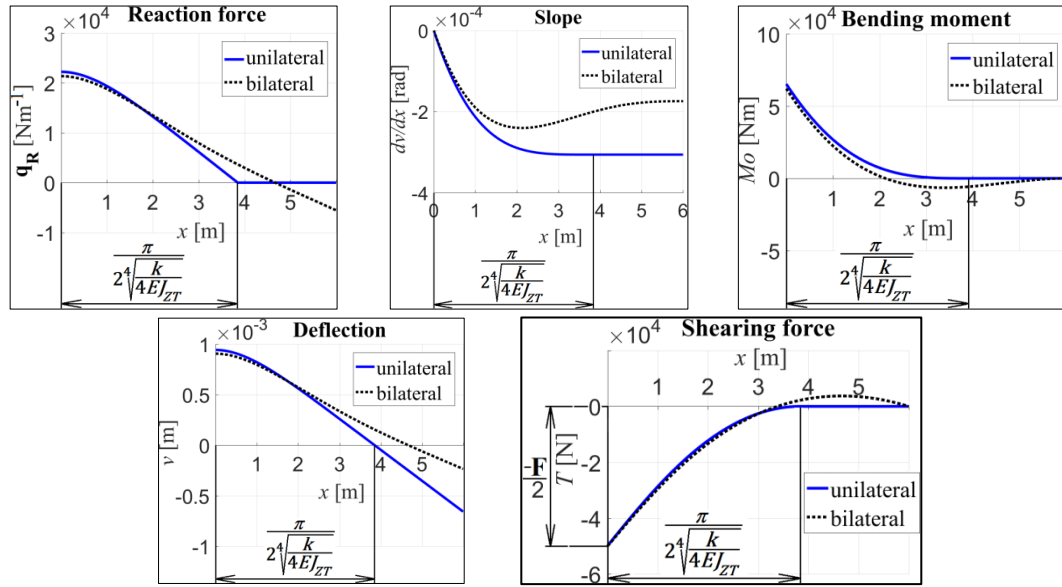


Fig. 2: Beam on unilateral and bilateral elastic foundation ( $L = 6 \text{ m}$ ,  $b = 0.2 \text{ m}$ ,  $h = 0.4 \text{ m}$ ,  $F = 10^5 \text{ N}$ ,  $E = 2 \times 10^{11} \text{ Pa}$ ,  $k = 2.3587 \times 10^7 \text{ Pa}$ ).

## 7. Conclusions

Straight beams on elastic foundations which nonlinear unilateral foundation were exposed and solved (i.e. theory, weak formulation, finite elements, semi-smooth Newton's method and results). The differences between unilateral and simple bilateral foundation are shown. Note, the beams on unilateral foundation cannot be solved via Newton's method but via semi-smooth Newton's method as shown in our article.

## Acknowledgement

This work was supported by Czech projects SP2017/136.

## References

- Frydrýšek, K., Michenková, Š. and Nikodým, M. (2014) Straight Beams Rested on Nonlinear Elastic Foundations – Part 1 (Theory, Experiments, Numerical Approach). In: Applied Mechanics and Materials. Volume 684, Trans Tech Publications, Switzerland, pp. 11-20.
- Frydrýšek, K. and Michenková, Š. (2016) Theory, Experiment and Numerical Approach for the Beam Rested on Nonlinear Elastic Foundation, in: Proc. of 22<sup>nd</sup> Int. Conf. on Engineering Mechanics 2016, Svratka, Czech Republic, ISSN: 1805-8248, ISBN:978-80-87012-59-8, pp. 162-165.
- Frydrýšek, K., Tvrda, K., Jančo, R. et al. (2013) Handbook of Structures on Elastic Foundation. VŠB - Technical University of Ostrava, Ostrava, Czech Republic, pp. 1-1691.
- Klučka, R., Frydrýšek, K. and Mahdal, M. (2014) Measuring the Deflection of a Circular Plate on an Elastic Foundation and Comparison with Analytical and FE Approaches. In: Applied Mechanics and Materials, Trans Tech Publications, Switzerland, Vol. 684, pp. 407-412.
- Kolář, V., Kratochvíl, J., Leitner, F. and Ženíšek, A. (1979) Calculation of surface and spatial structures by finite element method, SNTL, Praha (in Czech).
- Sysala, S. (2008) Unilateral elastic subsoil of Winkler's type: Semi-coercive beam problem, AppMath 53 (2008), No. 4, pp. 347-379.
- Haslinger, J. (1980) Finite element method for solving elliptical equations and inequalities, SPN, Praha (in Czech).
- Kufner, A., John, O. and Fučík, S. (1977) Function Spaces. Monographs and Textbooks on Mechanics of Solids and Fluids; Noordhoff International Publishing, Leyden; Academia, Praha.
- Chen, X., Nashed, Z. and Qi, L. (2001) Smoothing Methods a Semismooth Methods pro Nondifferentiable Operator Equations, SIAM Journal Numerical Analysis, Vol. 38, No. 4, pp. 1200-1216.

## SHAPING THE STRUCTURE OF LOW WATER-BINDER RATIO CEMENT PASTES

**Ł. Mrozik\***

**Abstract:** *Cement and aggregate composites constitute one of the basic structural and material solutions applied in civil engineering. A wide application range results mainly from the possibility of relatively flexible adjustment of required parameters, including the leading mechanical property which is the compression strength. As is known from the basic source literature, there exists an approximate proportional relation between the strength of a hardened paste and analogous characteristics of a cement paste and concrete, while the differences result from aggregate feeding. Considering the above, this paper describes selected issues and problems related to the design of cement composites of the assumed strength. Particular attention is paid to the problem of shaping low water-binder ratio cement dispersion.*

**Keywords:** Concrete, Cement paste, Water demand, Superplasticizer.

### 1. Introduction

Concrete is a composite which obtains its technical properties as a result of cement paste bonding and hardening. It is well known that the strength of concrete depends on the water-binder ratio ( $\omega$ ), thus on the rated content of a liquid phase in a fresh paste. Moreover, according to Neville (Neville, 2010), there exists an approximate proportional relation between the strength of a hardened paste and analogous characteristics of a cement paste and concrete, while the differences result from the feeding of fine aggregate and coarse aggregate, respectively. Therefore, a cement paste plays a particular role in shaping properties of modern cement composites. It follows that a paste of proper parameters is necessary to receive concrete of assumed properties. The problem of shaping the paste and cement stone structure has been widely studied, and the large number of research approaches resulting from actual needs and scientific objectives indicates the complexity of the analyzed problem.

### 2. Parameters of the fresh paste structure

One of the most popular methods of shaping the structure is an approach involving particle packing method (Chan, 2014, Dewar, 1999, Fennis, 2012, Jones, 2002, Li, 2014). It is a commonly used method, e.g. in material engineering, powder technology and processing industry. It can be applied to describe relations between particles of bulk solid. There is a range of interactions (Fig. 1) to include: filling effect, occupying effect, loosening effect, wall effect or wedging effect (Chan, 2014). These refer to a dry grain arrangement. A cement paste, however, is a suspension, the packing tightness of which depends on the relative water content (Li, 2014). It is important that the minimum water quantity is obtained at an aggregate composition provided for a mixture of dry grains of the highest tightness (Fennis, 2012, Li, 2014). This determines the suitability of the particle packing method for a selection of aggregate grading. Generally, it refers to a centre consisting of aggregate, binder and additives. However, there are significant limits when shaping the structure of pastes alone, resulting from the insufficient adequacy for centres of such a high degree of fineness (Chan, 2014).

---

\* Łukasz Mrozik, PhD. Eng.: Faculty of Civil and Environmental Engineering and Architecture, University of Science and Technology, Al. prof. S. Kaliskiego 7; 85-796, Bydgoszcz; PL, lukasz.mrozik@utp.edu.pl

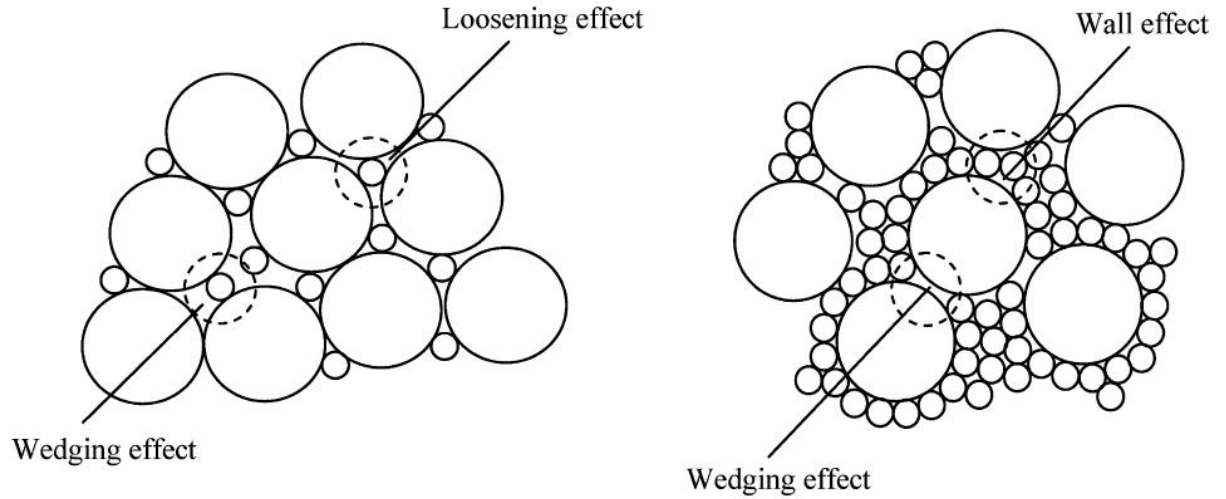


Fig. 1: Interactions in particle packing method (Chan, 2014).

Another approach methods are applying analytical and empirical relations between structure parameters and properties of the centre, e.g. a model presented in the study (Bleszczik, 1977) and its application for description of rheological properties of the paste (Świtoński, 2004).

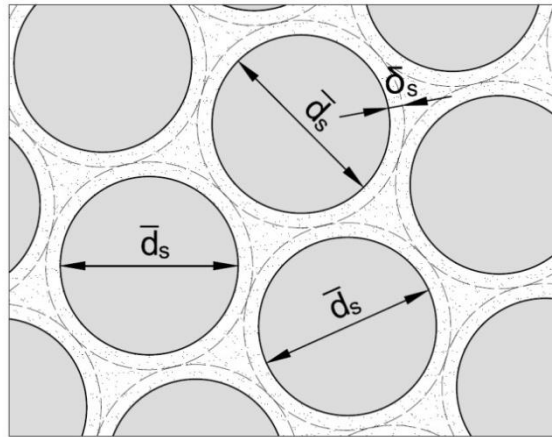


Fig. 2: Model of structure of fresh cement paste based on (Świtoński, 2004).

Similar assumptions were made in the paper (Świtoński, 2004) to design a three-level model of the structure of a concrete mixture, a cement paste (Fig. 2) and a micro-filler suspension. A geometrical model of a suspension of grains of an average size of  $\bar{d}_s$  has been applied. The distance between them is equal to the double thickness of the layer of its surrounding liquid  $\delta_s$ , whereas tightness of the binder grain arrangement  $s_{sz}$  is expressed as a ratio of the volume of grains with a water film to the total volume. A mathematic description was defined in the monograph (Świtoński, 2004) which can be used to develop a relation connecting structure parameters with the quantitative composition. Furthermore, it was proved that the highest tightness of the binder grain arrangement is at a quantity of the liquid phase corresponding to the normative water demand of cement  $\omega_n$  (i.e. a standard paste). It was established in the paper (Sebok, 1986) that there is a minimum quantity of the liquid phase resulting from the surface forces, constituting 45 % of the total volume of liquid in the paste. According to (Świtoński, 2004), an assumption can be made that such liquid phase fractions will be maintained in a paste of  $\omega \geq \omega_n$ .

### 3. Influence of a superplasticizer

A standard paste consists of binder grains surrounded by a liquid layer and liquid in intergranular spaces. Extreme reduction of the water-binder ratio (below  $\omega_n$ ) is effective only when a superplasticizer is applied. If there is no admixture, it will not be possible to discharge air from the intergranular spaces or to condense the material.

Due to the complexity of this problem, experimental tests should be relied upon. Considerations in respect of the above were taken in the paper (Mrozik, 2012) where results of paste bulk density tests were included. The selected results concerning vibrating pastes with CEM II/A-M (S-LL) 52.5 cement are shown in Tab. 1 and Fig. 3.

Tab. 1: Comparison of structure parameters (Mrozik, 2012).

Item	Water-binder ratio $\omega$ [-]	Bulk density [kg/dm <sup>3</sup> ]		Air content $p$ [%]	Binder volume fraction $V_c/V_z$ [-]
		Actual ( $\rho_{act.}$ )	Theoretical ( $\rho_{theor.}$ )		
1	0.200	1.480	2.296	35.55	0.398
2	0.250	1.805	2.183	17.32	0.466
3	0.280 = $\omega_n$	2.120	2.124	0.20	0.534
4	0.310	2.060	2.071	0.53	0.507
5	0.350	1.992	2.007	0.76	0.476
6	0.400	1.932	1.938	0.28	0.445
7	0.500	1.820	1.824	0.19	0.391
8	0.600	1.731	1.734	0.19	0.349
9	0.700	1.661	1.662	0.09	0.315
10	0.800	1.598	1.603	0.34	0.286

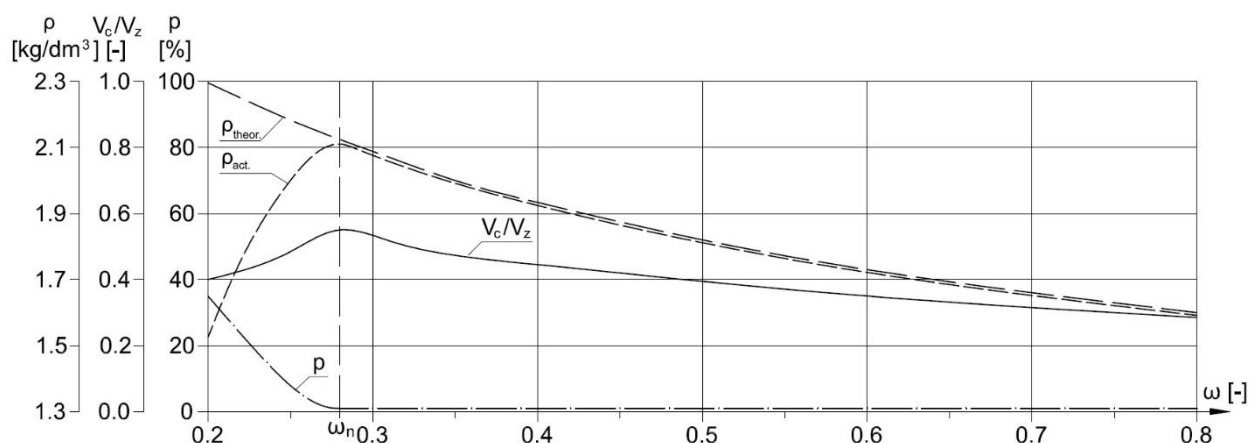


Fig. 3: Bulk density, air content and particle volume (Mrozik, 2012).

Presented results confirm that there is a specific liquid phase fraction at which the maximum bulk density is acquired. For pastes without admixtures, this fraction is determined by the standard water demand of the binder (Świtoński, 2004). It was also proved that at  $\omega = \omega_n$  the volume fraction of binder grains is also the highest, and this is a limit level below which the air content is  $p > 0$ . Superplasticizers can be used to significantly reduce this level, as this was the author's subject of research. Below (Fig. 4), there is a sample set of so-called efficiency curves for a selected binder-admixture set (CEM II/A-M (S-LL) 52.5 + an admixture based on polycarboxylate ether in limit quantities recommended by the manufacturer).

The research shows that the similar density line is obtained after adding a superplasticizer. However, the  $\omega$  level corresponding to the maximum value is reduced. Therefore, for each binder-additive set, the superplasticizer efficiency can be characterized by stating a minimum value of the water-binder ratio at which the density is equal to the value of  $\rho_{theor.}$ . Considering the widely known relation between the  $\omega$  indicator and the strength, the determined limit level corresponds to the maximum strength value. Efficiency curves may then become a useful tool, e.g. when selecting a binder-additive set for high performance concrete of the assumed strength.



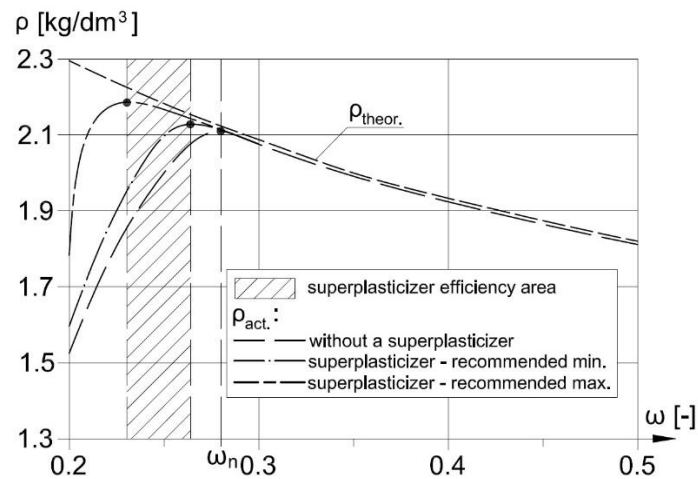


Fig. 4: Bulk density of cement pastes with superplasticizer.

#### 4. Conclusions

- Selection of cement paste parameters is required to obtain concrete of specified properties.
- In order to design a paste composition of specified parameters, its structure has to be properly shaped.
- Plasticizers and superplasticizers have a significant influence on the binder grain arrangement, in particular at low water-binder ratios.
- Analytical and empirical efficiency curves for binder-additive sets can be used as a tool for designing modern cement composites.

#### References

- Bleszczik, N.P. (1977) Structure and mechanics of the hereditary and rheumatoid arthritis and presswakumbietona. Minsk, Science and Technology (in Polish).
- Chan, K.W. and Kwan, A.K.H. (2014) Evaluation of particle packing models by comparing with published test results. Particuology no. 16, pp. 108-115.
- Dewar, J.D. (1999) Computer modelling of concrete mixtures. London, E & FN Spon.
- Fennis, S.A.A.M. and Walraven, J.C. (2012) Using particle packing technology for sustainable concrete mixture design. HERON vol. 57, no. 2, pp. 73-101.
- Jones, M.R., Zheng, L. and Newlands, M.D. (2002) Comparison of particle packing models for proportioning concrete constituents for minimum voids ratio. Materials and Structures no. 35, pp. 301-309.
- Li, L.G. and Kwan, A.K.H. (2014) Packing density of concrete mix under dry and wet conditions. Powder Technology no. 253, pp. 514-521.
- Mrozik, Ł. (2012) Structure model and strength of high-quality concrete. Bydgoszcz, University of Science and Technology (in Polish).
- Neville, A.M. (2010) Concrete properties. Kraków, Wyd. Polish Cement.
- Sebok, T. (1986) A study of sorption of water on the surface of grains of cement in the first phase of hydration. Cement and Concrete Research no. 4, pp. 461-471 (in Polish).
- Szerafin, J. (2011) Cement dispersions in the process of injection repair of defects in concrete. Lublin, Wyd. Universities. Lublin University of Technology (in Polish).
- Świtoński, A. (2004) Structure and strength of high-quality concrete. Koszalin, Wyd. Universities. Koszalin University of Technology (in Polish).

## **THE CONCEPT OF MOBILE SYSTEM OF ANALYSIS AND VISUALIZATION OF HUMAN GAIT PARAMETERS**

**A. Muraszkowski<sup>\*</sup>, J. Szrek<sup>\*\*</sup>**

**Abstract:** *The article presents briefly the current state of knowledge concerning methods of rehabilitation using Nordic Walking poles. The concept of mechatronic poles that allow to measure the human gait parameters is presented. They will be used to determine the correctness of exercise performance, progress in rehabilitation and planning further methods to restore the patient health, as well as gait techniques improvement in sports. Mechatronic poles enclose inertial sensors, which generate measurement data, so that it will be possible to exercise in any area, indoors and outdoors. Examples of data obtained from the inertial sensor are also presented. The possible use of mechatronic Nordic Walking poles are described.*

**Keywords:** Human gait kinematic, Gait parameters registration, Nordic Walking poles.

### **1. Introduction**

Analysis of human movement has had its place among the issues that are the interest of researchers for a long time. Especially nowadays, when the quality of life value is increasing.

For a thorough analysis of human movement, computer musculo-skeletal models are created, in order to perform kinematic and dynamic simulations (Pandy, 2001). They contain a number of parameters, which are determined on the basis of statistical data. Some are easy to determine, such as the length of individual body segments, or their mass. Others are more complex to define the values, such as the length of the muscle, contraction range, the exact position of the points of attachment of the muscle to the skeletal system. Torques loading joints or forces in muscle can be concluded on the basis of such created models. The models created on the basis of statistical data are often used in medicine to define disease, their classification and to develop general methods for the rehabilitation (Perry, 2010). There is a tendency to create individual models in order to obtain results which are closer to the actual for individual person. This method is used especially in sport disciplines where gait technique are optimized for each athlete taking into account his differences in physique (Nakashima, 2014). The method is being increasingly used in rehabilitation noting, that each patient suffers from a given physical dysfunction in varying degrees.

When the dynamic model of the human is already given, there is need for data on the kinematics. To determine the trajectory of human move, there are various methods used. Currently, the most commonly used method for measuring kinematic parameters is optical method. The person wear many markers, the movement of which is recorded by a camera system (infrared or visible light range). This calls for the deployment of cameras with high accuracy in a specific area and can be used in principle only indoors. In addition, the deployment of markers on human body is difficult. Placement of markers results from the protocol. In medicine, the most commonly used is Davis protocol (Davis, 1991).

Today, there are other methods to obtain information on the location and orientation of objects in space, including those that do not require the use of external stationery devices in the form of transmitter or receiver stations. One of them involves the use of inertial sensors to measure linear accelerations and

---

<sup>\*</sup> MSc. Artur Muraszkowski: Faculty of Mechanical Engineering, Department of Biomedical Engineering, Mechatronics and Theory of Mechanisms, Wrocław University of Science and Technology, ul. Ignacego Łukasiewicza 7/9, 50-371 Wrocław; PL, artur.muraszkowski@pwr.edu.pl

<sup>\*\*</sup> PhD. Jarosław Szrek: Faculty of Mechanical Engineering, Department of Biomedical Engineering, Mechatronics and Theory of Mechanisms, Wrocław University of Science and Technology, ul. Ignacego Łukasiewicza 7/9, 50-371 Wrocław; PL, jaroslaw.szrek@pwr.edu.pl

angular velocity. Currently, there is a whole range of measuring systems integrating various inertial sensors. They are called inertial measurement unit (IMU). They include accelerometers, gyroscopes, magnetometers and sometimes barometers. The use of inertial sensors has the advantage over the above described optical method. They do not need fixed installations for movement recording so there is no need of predefined workspaces, limited by number of cameras. Moreover, they are not sensitive to variable, changing lighting. This makes it well suited for applications involving the study of human movement during the course of everyday tasks or exercises performed in the field, both by athletes and patients during rehabilitation.

Another phenomenon contributing to the development of computer technology in the field of physiotherapy is the effect of significantly increase in the rehabilitation progress through the use of methods of biological feedback (biofeedback). It consists in the fact that the patient gets information about the parameters of their body, for example the angle of knee joint, gait length, data from devices such as ECG (electrocardiography), EEG (electroencephalography), EMG (electromyography). It turns out that the person who receives such information can better control the behavior of his body, and even learn to control the reactions of the body, even those which normally are not controlled consciously, such as breathing, heartbeat, brain waves. As a result, properly selected, to match the rehabilitation method, biofeedback signal significantly accelerates recovery and increases the effects of performed exercise (Tate, 2010). Successfully it is used for people with impaired posture caused by diseases of the musculoskeletal system, nervous system, or as a result of internal diseases (Allum, 2005).

One of the newer methods of rehabilitation is the commissioning exercises with the use of Nordic Walking (NW) poles with appropriately technique. This technique increases the activity of the muscles of the upper body, increasing oxygen consumption by 20 %, energy expenditure and at the same time reduces the load on individual muscles and joints (Skena, 2009) (Hagen, 2011). It is used with the rehabilitation of patients after heart attacks and other diseases of the cardio-respiratory system (Morgulec-Adamowicz, 2011). It increases the mobility of people with Parkinson's disease (Van Eikeren, 2008), It is also used to improve the physical condition and overall development and strengthening of muscles (Kocur, 2009).

Currently, diagnosis of this kind of rehabilitation methods is performed in appropriately equipped rooms with an optical measurement system that uses a set of cameras installed permanently, and strain mats to determine forces on feet. This test method is good for determining disease conditions and periodic improvement during rehabilitation. But it is not suitable for everyday use because of the sophisticated equipment usage under specific conditions. It has little in common with the actual conditions in which a major part of rehabilitation is performed - walking in the open field without the direct supervision of a physiotherapist. As a result, the patient for the better part of rehabilitation is left alone without feedback about how well does exercise and what is the effectiveness of health improvement. Physiotherapist after a longer time can identify these factors but only during short, relatively to period of rehabilitation, meetings with the patient, during which conditions are far different from the natural.

## **2. The Concept**

Taking into account the information presented in the previous section, a device were developed that can be used to analyze human gait during exercise in the field with NW poles. There is proposed mechatronisation of typical poles, which can be purchased at sport stores. It involves equipment of the poles with multi-axis inertial sensors - for example nine-axis unit consisting of a three-axis gyroscope, accelerometer and magnetometer. In addition, the force sensor is mounted for measuring the force along the axis of the pole and a contact sensor in the handle (Fig. 1, left).

Considering the expansion of the device with additional force sensors placed in such points that the bending torque of pole can be determined. The occurrence of torque would mean an incorrect method of gait, requiring correction, and the read value would serve to identify and parameterization of algorithms for improve gait technique. Signals from the sensors are read, stored and processed by a control unit placed on a pole. Processed data will be transmitted to the device, which acts as the user interface (ex. Tablet, smartphone, SmartWatch) to visualize them and to inform the person exercising about the

progress, mistakes and methods for improving technique. The data will also be stored on the device for

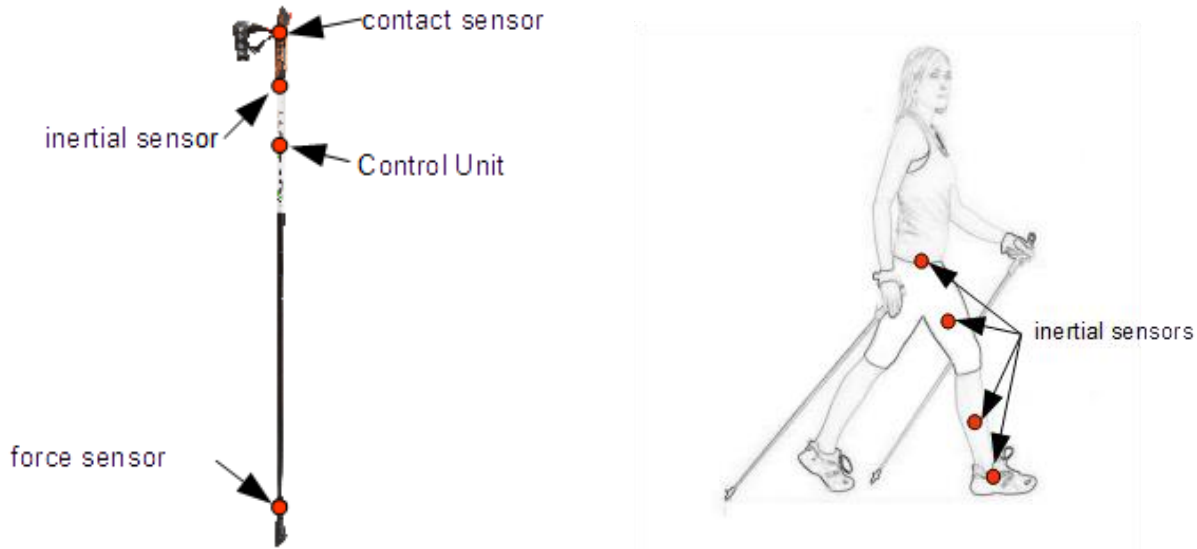


Fig. 1: Concept of mechatronic Nordic Walking pole – left.  
Sensors locations on human body for kinematic data acquisition – right.

later analysis by specialists, physiotherapists, doctors, or sent in real time to an immediate confrontation with the recommendations of the person that leads rehabilitation process.

In order to obtain the additional data needed to determine the gait technique, together with an indication of disability and motor dysfunction of a subject, proposed a set of sensors mounted on the human body. This would be the inertial sensors, such as those mounted on NW poles. They would be placed on the individual segments of the body (Fig. 1, right) to determine their position and orientation in space. For each lower limb 3 sensors are mounted, one sensor would provide further information on the movement of the pelvis. These sensors would be connected to an additional control unit placed on the person or could be connected to the unit placed on the NW pole.

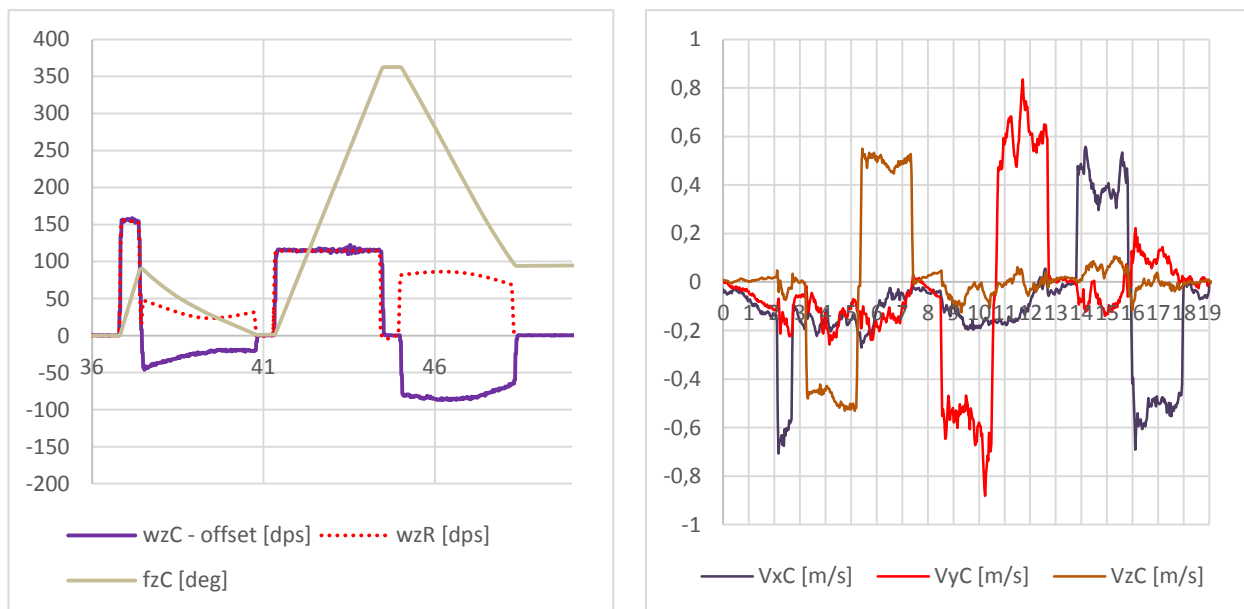


Fig. 2: Characteristic of IMU.  $wzC$  – angular velocity along Z axis of sensor,  $wzR$  – theoretical angular velocity along sensor Z axis,  $fzC$  – angular displacement along Z axis (integrated  $wzC$  signal),  $VxC, VyC, VzC$  – linear velocity along sensor axis respectively X, Y, Z.

In order to implement the concept, in the first place, tests of signals from the inertial sensors were performed. There was selected relatively cheap sensor, which was dictated by economic considerations of endpoint device, which is expected to have the widest possible audience. The data shown in Fig. 2 were obtained from the inertial sensor. The results and analysis (Kiwala, 2016) have been presented here in

order to show that an inexpensive IMU gives very good results with gyroscopic data and worse for the accelerometer. However, appropriate processing such as filtering, averaging can reduce the size of the error acceleration. In addition to these applications, the key element is the orientation of the various parts of the body and NW poles obtained mainly from gyroscopes.

### 3. Conclusions

Computer technology, including dynamic modeling is increasingly used both in sports and in medicine. They are used to improve performance of athletes but also for the analysis of locomotor system diseases and development of new techniques of rehabilitation. The paper presents a new concept of mechatronic Nordic Walking poles, which will help collect data in both laboratory and real conditions during daily exercise. At the beginning, Mechatronic Nordic Walking poles (MNW) will be used for the rehabilitation of people with various disabilities. Patients will use it in the initial phase under the control of physiotherapists. Then patients will rent equipment for home and practice on their own, coming to periodic checks, where a specialist will be able to assess the progress of rehabilitation on the basis of the data contained in the poles and suggest the next set of exercises. Different area of application is the use of MNW to sports training, for the purpose of improving health, techniques, and creation of new habits through biofeedback. Commercialization of MNW will require such configuration of the device to make it user friendly, characterizing by ease of calibration, operation, had a simply interface, generating messages understandable for people who does not have knowledge of biology, mechanics and computer science and the price range must be appropriate for the target audience.

### References

- Allum, J.H. and Carpenter, M.G. (2005) A speedy solution for balance and gait analysis: angular velocity measured at the centre of body mass. *Current Opinion in Neurology*, 18(1), pp. 15-21.
- Davis, R. (1991) A gait analysis data collection and reduction technique. *Hum Movement Sci*, 10, pp. 575-587.
- Hagen, M., Ewald, H.E. and Stieldorf, P. (2011) Lower and upper extremity loading in nordic walking in comparison with walking and running. *J Appl Biomech*, 27(1), pp. 22-31.
- Kiwała, S.K. (2016). Fast trajectory planning and programming of a robotic manipulator using RobotStudio software for inertial sensor testing. *Interdisciplinary Journal of Engineering Sciences*, 4(1), pp. 56-64.
- Kocur, P.D.-Ś. (2009) Effects of Nordic Walking training on exercise capacity and fitness in men participating in early, short-term inpatient cardiac rehabilitation after an acute coronary syndrome – a controlled trial. *Clinical Rehabilitation*, 23(11), pp. 995-1004.
- Morgulec-Adamowicz, N.M. (2011) Nordic Walking - A New Form of Adapted Physical Activity (A Literature Review). *Human Movement*, 12(2), pp. 124-132.
- Nakashima, M. (2014) Maximum joint torque dependency of the crawl swimming with optimized arm stroke. *Journal of Biomechanical Science and Engineering*, 9(1), pp. 1-9.
- Pandy, M. (2001) Computer modeling and simulation of human movement. *Annu Rev Biomed Eng.*, 3, pp. 245-273.
- Pandy, M.Z. (1991) Optimal muscular coordination strategies for jumping. *Journal of Biomechanics*, 24(1), pp. 1-10.
- Perry, J. (2010) *Gait Analysis: Normal and Pathological Function*. New Jersey: SLACK Incorporated.
- Schena, F. et al. (2009) Kinematic and force comparison between Walking and Nordic Walking. A pilot study. *Proceedings of 14th Annual Congress of the ECSS – European College of Sport Science*. Oslo.
- Tate, J.J. (2010, August) Real-time kinematic, temporospatial, and kinetic biofeedback during gait retraining in patients: a systematic review. *Physical Therapy*, 90(8), pp. 1123-1134.
- Van Eikeren, F.R. (2008) Nordic walking improves mobility in Parkinson's disease. *Movement Disorders*, 23(15), pp. 2239-2243.

## MODELLING AND MEASUREMENT OF NON-UNIFORM ELASTOSTATIC TORSION OF HOLLOW CROSS-SECTION BEAMS

J. Murín<sup>\*</sup>, V. Goga<sup>\*\*</sup>, V. Kutíš<sup>\*\*\*</sup>, J. Hrabovský<sup>\*\*\*\*</sup>, T. Sedlár<sup>\*\*\*\*\*</sup>, J. Paulech<sup>\*\*\*\*\*</sup>

**Abstract:** *This paper presents results from measurements of hollow thin-walled cross-section beam under the non-uniform torsion conditions where the warping effect is evaluated and compared with the numerical analysis results using new finite element (Murín et al., 2014) and with results from finite element analysis by program ANSYS.*

**Keywords:** Non-uniform torsion, Modeling and simulation, Experimental verification.

### 1. Introduction

In stress and deformation analyses of thin-walled structures subjected to torsion, the effect of warping must be considered. Extreme values of axial stress, caused by the bimoment, mainly occurs at the points of action of concentrated torsion moments (except for free ends) and at sections with warping restraints.

Special theories of torsion with warping, usually referred to as non-uniform torsion or warping torsion were used to solve such problems analytically (e.g. Vlasov, 1961). The analogy between the 2nd order beam theory with axial tension and torsion including warping has also often been exploited (e.g. Roik et al., 1966 and Rubin, 2005). However, it is worth of note that in the literature and in engineering practice, as well as in the guidelines provided by Eurocode 3 (EN 1993 – Eurocode 3, 2004), the significance of the effect of warping is assumed to be restricted to open cross-sections.

Warping based stresses and deformations in hollow cross-section (HCS) are assumed to be insignificant and have, therefore, generally been neglected. According to the aforementioned theory of torsion of open cross-sections including warping and according to the mentioned analogy, special finite beam elements were designed and implemented into finite element codes (e.g. ANSYS and RSTAB, 2006). Important progress in the solution of torsion with warping is documented in (Sapountzakis et al., 2007), where a combination of the boundary element method (BEM) and the finite element method (FEM) was used, allowing warping analysis of composite beams with a longitudinally varying cross-section. There are several other papers, e.g. (Mokos et al., 2004, Kim et al., 2005, Genoese et al., 2013 and Minghini et al., 2007), which deal with the problem of non-uniform torsion. However, recent theoretical results have shown that the effect of warping must also be considered for the case of HCS beams (Rubin, 2006). Based on recent research concerning the aforementioned analogy, reported in (Rubin, 2006, Rubin, 2007, Rubin et al., 2007 and Aminbaghai et al., 2012), the local stiffness relation of a new two-node finite element for torsion including warping of cross-sections of straight beams was derived (Murín et al., 2014). This new finite element can be used for non-uniform torsion analysis of straight beams with open

---

<sup>\*</sup> Prof. Ing. Justín Murín, DrSc.: Institute of Automotive Mechatronics, Faculty of Electrical Engineering and Information Technology, STU in Bratislava, Ilkovičova 3; 812 19, Bratislava; Slovakia, justin.murin@stuba.sk

<sup>\*\*</sup> Assoc. Prof. Ing. Vladimír Goga, PhD.: Institute of Automotive Mechatronics, Faculty of Electrical Engineering and Information Technology, STU in Bratislava, Ilkovičova 3; 812 19, Bratislava; Slovakia, vladimir.goga@stuba.sk

<sup>\*\*\*</sup> Assoc. Prof. Ing. Vladimír Kutíš, PhD.: Institute of Automotive Mechatronics, Faculty of Electrical Engineering and Information Technology, STU in Bratislava, Ilkovičova 3; 812 19, Bratislava; Slovakia, vladimir.kutis@stuba.sk

<sup>\*\*\*\*</sup> Ing. Juraj Hrabovský, PhD.: Institute of Automotive Mechatronics, Faculty of Electrical Engineering and Information Technology, STU in Bratislava, Ilkovičova 3; 812 19, Bratislava; Slovakia, juraj.hrabovsky@stuba.sk

<sup>\*\*\*\*\*</sup> Ing. Tibor Sedlár: Institute of Automotive Mechatronics, Faculty of Electrical Engineering and Information Technology, STU in Bratislava, Ilkovičova 3; 812 19, Bratislava; Slovakia, tibor.sedlar@stuba.sk

<sup>\*\*\*\*\*</sup> Ing. Juraj Paulech, PhD.: Institute of Automotive Mechatronics, Faculty of Electrical Engineering and Information Technology, STU in Bratislava, Ilkovičova 3; 812 19, Bratislava; Slovakia, juraj.paulech@stuba.sk



as well as hollow cross-sections. This paper presents results from measurements of hollow thin-walled cross-section beam under the non-uniform torsion conditions where the warping effect is evaluated and compared with the numerical analysis results using new finite element (Murín et al., 2014) and with results from finite element analysis by program ANSYS.

## 2. Experimental measurements

The original experimental device (Sedlár et al., 2013) for the measurement of warping effects in thin-walled beams were designed, see Fig. 1. Device allows an arbitrary torque position plus a variety of boundary conditions at various beam positions (e.g. at beam's ends). The twist angle, the free-end cross-section warping and the normal stress caused by bimoment can be measured.

Measuring device characteristics: beam sample positioning: horizontal; boundary conditions - supports: free, fixed, and forked; advantages: variable beam length, variable beam supports, torque application at various positions; disadvantage: complicated equipment for ideal torque application.

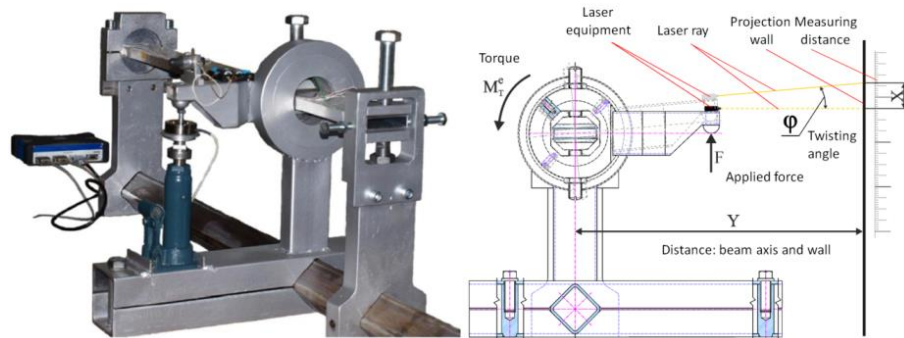


Fig. 1: Measuring device.

The aluminium beam with hollow rectangular cross-section were loaded with a torque of  $M_T = 100 \text{ Nm}$ . Material properties of the beam are: the Young modulus  $E = 68 \text{ GPa}$ , the shear modulus  $G = 26 \text{ GPa}$ , the Poisson's ratio  $\nu = 0.33$ . The beam length  $L = 980 \text{ mm}$ . Dimensions of the rectangular hollow cross-section are: the height  $H = 40 \text{ mm}$ , the width  $B = 20 \text{ mm}$ , the wall thickness  $t = 2 \text{ mm}$ . Both ends of the beams are clamped and the torque was applied in the middle of the beam span.

Expected normal stress distribution along the beam axis is based on the theory of non-uniform torsion (Vlasov, 1961, Roik et al., 1966 and Rubin, 2005), see Fig. 2 (left). This normal stresses were measured using six strain gauges. Positions of the strain gauges (signed  $T_1$ - $T_6$ ) are shown in Fig. 2 (right).

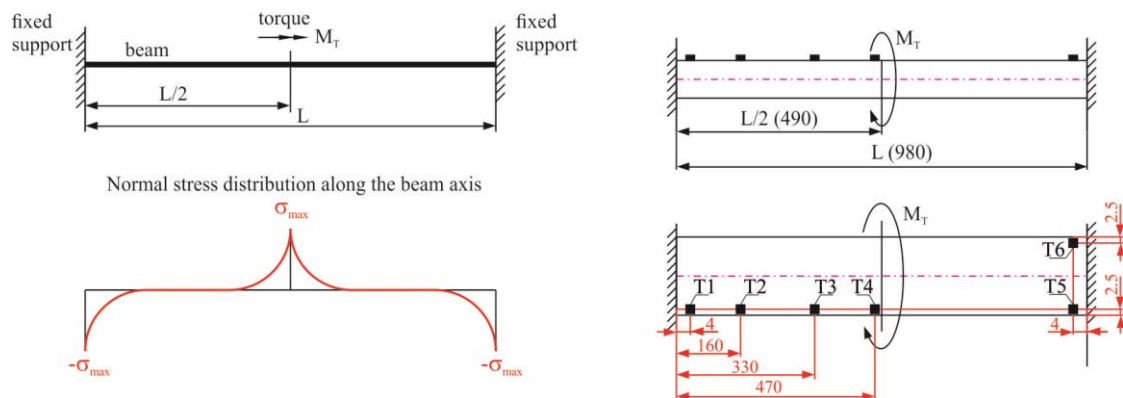


Fig. 2: Theoretically expected bimoment normal stress distribution along the beam edge (left), the strain gauges positioning (right).

## 3. Finite element calculation

The non-uniform torsion of the measured beam was also solved using the SOLID186 finite element of the program ANSYS and by new warping beam finite element (WB) (Murín et al., 2014). In the case of the SOLID186 model, the beam was modeled in the half length. The left beam's end is clamped and the symmetrical boundary conditions are applied at the right beam's end. At the right beam's end the half

torque was applied through the rigid steel flanges with frictionless contact. By this way, the accordance of the measured and the calculated model is relatively well obtained. The finite element model was created using very fine mesh of 50000 SOLID186 elements, see Fig. 3. Only 2 WB finite elements are used in the calculation of whole beam by our approach (Murín et al., 2014). The SOLID186 finite element result for normal stress distribution along the beam edge is shown in Fig. 4. As shown in Fig. 4, a difference occurs between the expected theoretical and the calculated distribution.

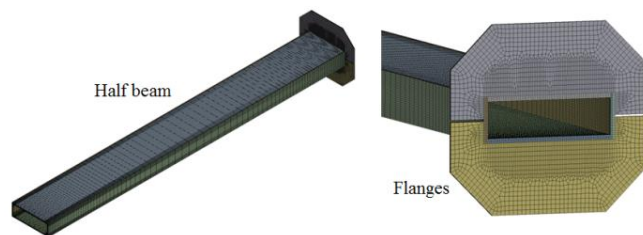


Fig. 3: The finite element model (SOLID186).

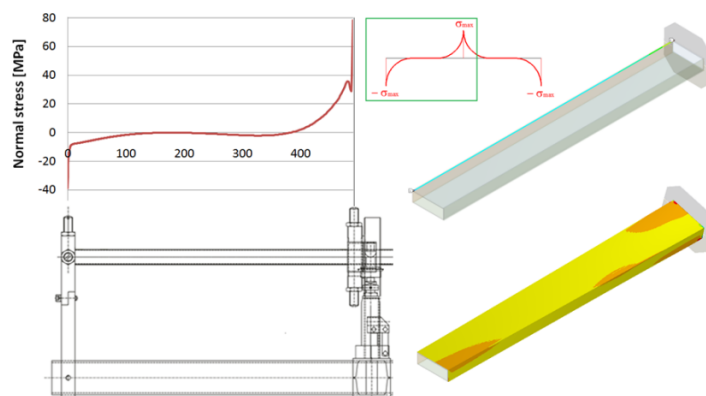


Fig. 4: The calculated (by SOLID186) and the theoretical (red line) normal stress distribution.

Tab. 1 present results for the maximal normal stress on the beam edge at the positions where the strain gauges were placed (Fig. 2). The differences between the measurement and numerical calculations are denoted as  $\Delta_{\text{Me-WB}}$  – for WB, and  $\Delta_{\text{Me-An}}$  for ANSYS.

Tab. 1: Measured and calculated results.

Torque = 100 Nm					
Position	Normal stress				
	Measurement	WB (Murín et al., 2014)	ANSYS	$\Delta_{\text{Me-WB}}$	$\Delta_{\text{Me-An}}$
	[MPa]	[MPa]	[MPa]	[%]	[%]
T <sub>1</sub>	-12.04	-12.49	-11.56	-3.7	4.0
T <sub>2</sub>	-1.97	-0.54	-1.75	72.6	11.2
T <sub>3</sub>	-1.69	0.21	-1.85	112.4	-9.5
T <sub>4</sub>	25.86	5.86	25.47	77.3	1.5
T <sub>5</sub>	-12.47	-12.49	-11.56	-0.2	7.3
T <sub>6</sub>	12.54	12.49	11.56	0.4	7.8

Outputs of the measurements and numerical analysis show significant effect of the warping on the normal bimoment stress by non-uniform torsion of beam with closed thin walled cross-section. This finding is in contrary to the statement in EN 1993 – Eurocode 3 that influence of the non-uniform torsion can be neglected by twisted beams with closed cross-sections. The measured and SOLID186 results are in good agreement each to other. But the WB results differ significantly at the acting point of the torque from the other ones. This difference is caused by the way, how the torque is applied in the real model and in the 3D-solid finite element model. In the WB finite element model, the torque acts on the longitudinal beam axis but in reality as well in the SOLID186 model the torque is realized by contact between the rigid flanges and the beam cross-section surfaces. This contact produces local stress concentration due to contact pressure. If the task is solved with the BEAM188 (warping restraint or unrestrained, ANSYS), the results are not relevant.

## 4. Conclusions

Numerical analyses of the rectangular hollow cross-section beams loaded by non-uniform torsion are performed. The SOLID186 (ANSYS) and warping beam (WB) (Murín et al., 2014) finite elements are used for evaluation of the normal bimoment stress and the twist angle. Experimental verification of the numerical results is done. From the results comparison, following conclusions can be drawn:

- normal stress caused by non-uniform torsion of the rectangular hollow cross-section beams are not neglectable as stated in EN 1993 - Eurocode 3;
- in opposite to standard warping beam finite elements, the results obtained by our new warping beam finite element (WB) (Murín et al., 2014) agree well with the measured results except the case when the boundary conditions and load action do not fulfil the appropriated beam theory;
- realisation of the boundary conditions and the load action affect the stress state significantly what leads to differences in calculated and measured results.

## Acknowledgement

This work was supported by Grant Agency VEGA, grant No. 1/0453/15.

## References

- Aminbaghai, M. and Mang, H.A. (2012) Characteristics of the solution of the consistently linearized eigenproblem for lateral torsional buckling. *Bulletin of the Georgian National Academy of Science*, 6, pp. 47-58.
- ANSYS Swanson Analysis System Inc. 201 Johnson Road, Houston, PA 15342/1300, USA.
- EN 1993- Eurocode 3 (2004). Design of steel structures. European Committee for Standardization (CEN).
- Genoese, A., Genoese, A., Bilotta, A. and Garcea, G. (2013) A mixed beam model with nonuniform warping derived from the Saint Venant rod. *Computer Structures*, 121, pp. 87-98.
- Kim, N.-I. and Kim M.-Y (2005) Exact dynamic/static stiffness matrices of non-symmetric thin-walled beams considering coupled shear deformation effects. *Thin-Wall Structures*, 43, 5, pp. 701-734.
- Minghini, F., Tullini, N. and Laudiero, F. (2007) Locking-free finite elements for shear deformable orthotropic thin-walled beams. *International Journal for Numerical Methods in Engineering*, 72, pp. 808-834.
- Mokos, V.G. and Sapountzakis, E.J. (2004) 3-D beam element of variable composite cross-section including warping effect. *Acta Mechanica*, 171, 3-4, pp. 703.
- Murín, J., Aminbaghai, M., Kutiš, V., Kráľovič, V., Sedlár, T., Goga, V. and Mang, H. (2014) A new 3D Timoschenko finite beam element including non-uniform torsion of open and closed cross section, effective finite element for torsion of constant cross sections including warping with secondary torsion moment deformation effect. *Engineering Structures*, 59, pp. 153-160.
- Roik, K., Sedlacek, G. (1966) Theory of the warping torsion with regard to the secondary shear deformations - Analogue view for the calculation of the transverse loaded tensile rod. *Steel construction*, 35, pp. 43.
- Rubin, H. (2005) Warping torsion of trough beam with constant cross-section taking into account secondary shear deformation. *Steel Construction*, 74, Issue 11: p. 826.
- Rubin, H. (2006) Torsional cross-sections for rectangular hollow profiles according to EN 10210-2, *Steel Construction*, 76, Issue 1: 2007.
- Rubin, H. (2007) On the warping torsion of closed cross - sections and their error - basics, 'Steel construction seminar, volume 29: 5 p.
- Rubin, H. and Aminbaghai, M. (2007) Warping torsion with a variable, open cross-section - does the bending tensile analysis still have validity? *Steel construction*, 76, pp. 747.
- Rubin, H., Aminbaghai, M. and Weier, H. (2006) IQ-100. The civil engineering structures program. TU Vienna, Building tables for engineers, Werner Verlag, 17th edition.
- Rubin, H. (2007) Construction 2, Manuscript of the lecture. Institute of Structural Analysis, Vienna University of Technology.
- RSTAB (2006), Ingenieur - Software Dlubal GmbH, Tiefenbach.
- Sapountzakis, E.J. and Mokos, V.G. (2007) 3-D beam element of composite cross-section including warping and shear deformation effect. *Computer Structure*, 85, pp. 102-116.
- Sedlár, T., Murín, J., Kráľovič, V., Kalaš, A. (2013) Universal device for the measurement of the beams loaded in torsion: Number of utility model: 6389, Date of: 22.1.2013. Banská Bystrica: Industrial Property Office SR.
- Vlasov, V.Z. (1961) Thin-walled elastic beams. Washington: National Science Foundation.

## PARAMETRIC INSTABILITY OF THE PLANE FREE SURFACE OF THE LIQUID IN CYLINDRICAL STORAGE TANKS

M. Musil<sup>\*</sup>, M. Sívý<sup>\*\*</sup>

**Abstract:** *The paper deals with the dynamic analysis of the ground-supported cylindrical vertical liquid storage tanks with the aim to determine the response of the upper liquid portion during vertical excitation. Tanks are used as storage for liquids in various sectors of industry. Hence, it is a request for satisfactory performance during dynamic loadings (e.g. earthquakes). The paper is dedicated to the phenomenon associated with the vertical oscillations of the liquid which results in the standing waves at the free surface known as Faraday waves. The analysis of a linear mathematical model for ideal liquid subjected to the vertical excitation with the constant amplitude and frequency is presented. It takes into account the theory introduced by Benjamin and Ursell which leads to the Mathieu equation for parametric vibration. Using Mathieu formulation, the  $m$ th mode of oscillation is excited when the combination of parameters corresponding to the amplitude and frequency lies in an unstable region of the stability chart. The free surface remains plane when assuming a pair of parameters in a stable region.*

**Keywords:** Faraday waves, Parametric instability, Mathieu equation, Free surface, Liquid storage tank.

### 1. Introduction

Tanks containing liquid are used as storage in various industry sectors. Their ordinary operation can be threatened by loading of various nature which may result in negative consequences. Dynamically loaded tank-liquid systems can take a variety of damages to which are exposed and which are caused by the oscillation of the liquid. There are procedures applied for evaluating dynamic effects in liquid storage tanks. The most widely used is the one based on a spring-mass model (Housner, 1954) in which the total liquid mass is divided into two zones – impulsive and convective. The impulsive zone is a part representing the effects of the portion of liquid which moves in unison with the tank. The convective part represents the free surface which moves against the walls. Using Housner's theory, this zone of liquid can be substituted for an infinite number of convective masses connected to the tank with springs of appropriate stiffness. Each of the masses represents another mode of oscillation of the convective liquid. In addition to the spring-mass model, the convective liquid can be replaced by another equivalent – system of simple pendulums (Ibrahim, 2005). For a formulation of specific equations describing a behavior of the convective liquid, classical Euler hydrodynamics theory is used instead of simplified models (scientific works of Faraday, Rayleigh, Matthiessen, etc.).

One of the phenomena observed at the free surface is a sloshing of the liquid which can be caused by parametric excitation. These standing sloshing waves are known as Faraday waves named after Michael Faraday who first observed and described them. Parametric oscillations are the results of having time-varying (periodic) parameters in the system. When the system experiences parametric resonance, the amplitude of the oscillations of the system will be increased exponentially. For parametrically excited sloshing, the effective gravitational field becomes time dependent. Sloshing waves can be generated when the liquid in the vessel is vertically excited at the frequency close to the twice the natural frequency of the convective liquid. Oscillation of the convective liquid in the containers may lead to negative effects such

---

<sup>\*</sup> Prof. Ing. Miloš Musil, CSc.: Institute of Applied Mechanics and Mechatronics, Faculty of Mechanical Engineering, Slovak University of Technology, Námetie slobody 17; 812 31, Bratislava; SK, milos.musil@stuba.sk

<sup>\*\*</sup> Ing. Martin Sívý: Institute of Applied Mechanics and Mechatronics, Faculty of Mechanical Engineering, Slovak University of Technology, Námetie slobody 17; 812 31, Bratislava; SK, martin.sivy@stuba.sk

as deformations of the tank walls (closed tanks) or liquid spilling (tanks without roofs). Therefore, the sufficient freeboard between the free surface and the top of the tank must be designed.

## 2. Basic concept of the parametric oscillation of the contained liquid

This section shortly describes the procedure for the parametric oscillation of the free surface subjected to the vertical periodic motion. It is based on the work published by T. B. Benjamin and F. Ursell (1954) which uses the Euler equations of hydrodynamics and the equation of continuity for the formulation of the Mathieu equation of the free surface of liquid. It is assumed a vertical cylindrical model of a vessel of an arbitrary cross-section with horizontal free surface and bottom at depth  $H_L$  (Fig. 1).

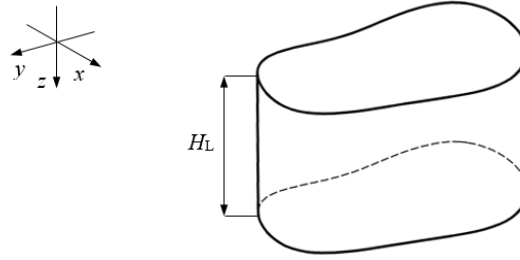


Fig. 1: Model of the tank containing liquid.

The liquid in the vessel is assumed as ideal (i.e. incompressible and non-viscous) due to small viscosity effects which may be neglected. The vessel-liquid system is moving periodically in the vertical  $z$ -direction with imparted acceleration of  $a \cos \omega t$  in which  $a$  represents a maximum acceleration and  $\omega$  is an angular frequency. The vertical oscillation can be represented by the effective gravitational acceleration  $(g - a \cos \omega t)$  while the vessel walls remain at rest. This effective gravitational acceleration is time-varying parameter whose consequence results in a parametric resonance of Faraday waves.

After introducing the Euler equations of hydrodynamics, the equation of continuity and basic assumptions for velocity potential  $(u, v, w) = \left( \frac{\partial}{\partial x}, \frac{\partial}{\partial y}, \frac{\partial}{\partial z} \right) \phi$ , pressure at free surface  $p = \gamma \left( \frac{\partial^2 \zeta}{\partial x^2} + \frac{\partial^2 \zeta}{\partial y^2} \right)$  and the equation of the free surface  $z = \zeta(x, y, t)$ , the equation of motion at  $z = 0$  can be defined as

$$\frac{\gamma}{\rho} \left( \frac{\partial^2 \zeta}{\partial x^2} + \frac{\partial^2 \zeta}{\partial y^2} \right) + \left( \frac{\partial \phi}{\partial t} \right)_{z=0} + \frac{1}{2} (u^2 + v^2 + w^2) - (g - a \cos \omega t) \zeta = 0 \quad (1)$$

where  $\rho$  represents the constant density during the motion and  $\gamma$  represents the surface tension. For the further formulation of Mathieu equation, the procedure is simplified by assuming that the liquid velocity and displacement of the free surface are sufficiently small. Therefore, (1) is linearized by omitting squares of velocities.

Assuming boundary conditions (Benjamin, 1954), the solution of wave equation  $\zeta(x, y, t)$  may be presented as a superposition of particular solutions and they are expressed as the product of two functions, first of which depends only on time and second one depends only on space coordinates.

$$\zeta(x, y, t) = \sum_0^\infty a_m(t) S_m(x, y) \quad (2)$$

Applying the substitution of (2) into wave equation, Helmholtz equation can be obtained

$$\left( \frac{\partial^2}{\partial x^2} + \frac{\partial^2}{\partial y^2} + k_m^2 \right) S_m(x, y) = 0 \quad (3)$$

where  $k_m$  represents the wave number. The pressure at the free surface and the potential can be developed using particular solutions respectively

$$\frac{\partial^2 \zeta}{\partial x^2} + \frac{\partial^2 \zeta}{\partial y^2} = - \sum_0^\infty k_m^2 a_m(t) S_m(x, y) \quad (4)$$

$$\phi(x, y, z, t) = - \sum_1^\infty \frac{da_m(t)}{dt} \frac{\cosh k_m(H_L - z)}{k_m \sinh k_m H_L} S_m(x, y) \quad (5)$$

Substitution of (2), (4) and (5) into (1) shows that

$$\sum_1^\infty \frac{S_m(x, y)}{k_m \tanh k_m H_L} \left[ \frac{d^2 a_m}{dt^2} + k_m \tanh k_m H_L \left( \frac{k_m^2 \gamma}{\rho} + g - a \cos \omega t \right) a_m \right] = 0 \quad (6)$$

which must satisfy

$$\frac{d^2 a_m}{dt^2} + k_m \tanh k_m H_L \left( \frac{k_m^2 \gamma}{\rho} + g - a \cos \omega t \right) a_m = 0 \quad (7)$$

The parameters  $P_m$  and  $Q_m$  are introduced using (7)

$$P_m = \frac{4 k_m \tanh k_m H_L}{\omega^2} \left( g + \frac{k_m^2 \gamma}{\rho} \right) \quad Q_m = \frac{2 k_m a \tanh k_m H_L}{\omega^2} \quad (8)$$

and after substitution  $\tau = \frac{1}{2} \omega t$  and assuming parameters defined in (8), the equation (9) represents the standard form of the Mathieu equation

$$\frac{d^2 a_m}{d\tau^2} + (P_m - 2Q_m \cos 2\tau) a_m = 0 \quad (9)$$

Mathieu equation can have solutions depending on the values of the parameter  $P_m$  and  $Q_m$ . The stability chart (Fig. 2a) reflects regions in which for the point  $(P_m, Q_m)$  the solution is stable, i.e. bounded (white regions) or unstable, i.e. unbounded with the time (shaded regions).

### 3. Mode of oscillation of the liquid

The following section is focused on the analysis of the parametric oscillation of the liquid in the circular vertical tank of the radius  $R$  (0.2 m), the height  $H$  (0.32 m) and the wall thickness  $t$  (5e-4 m). The vessel is filled with liquid (water) to the depth  $H_L$  (0.24 m).

The aim is to determine the mode of oscillation (1, 2) and respective regions of instability in dependence on the frequency and the amplitude of the acceleration. From the formulation of the Mathieu equation, it was shown, values  $P_m$  and  $Q_m$  depend on the wave number. Since modes have different wave numbers, it follows each of them has different stability chart of excitation frequency vs. amplitude of acceleration.

Using (8), frequency and amplitude of acceleration are expressed as

$$f = \frac{1}{\pi} \sqrt{\frac{k_m \tanh k_m H_L}{P_m} \left( g + \frac{k_m^2 \gamma}{\rho} \right)} \quad a = \frac{2 Q_m \left( g + \frac{k_m^2 \gamma}{\rho} \right)}{P_m} \quad (10)$$

Applying the values from the boundaries of stability chart (Fig. 2a) into (10), assuming the (1, 2) mode of oscillation and its wave number equal to  $5.33 / R$ , the stability chart is defined and presented in Fig. 2b.

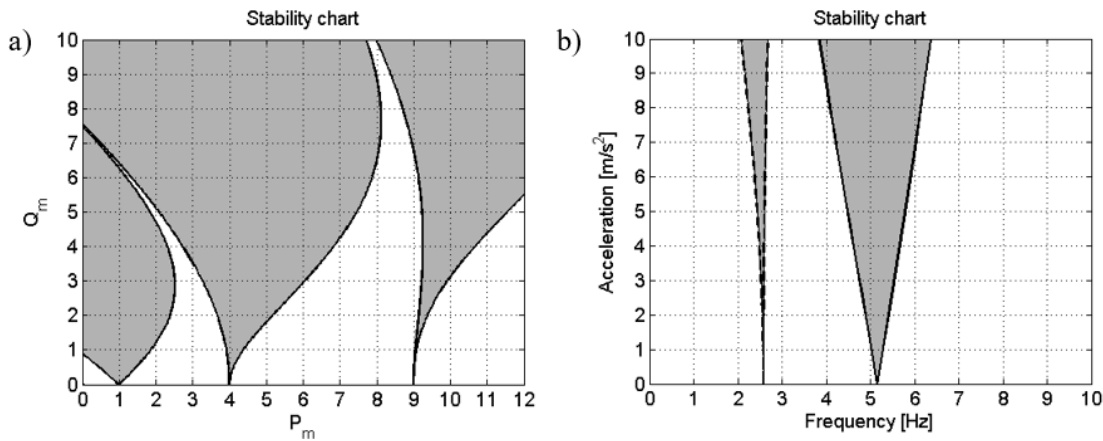


Fig. 2: Stability chart for the (1, 2) mode of oscillation.

If the combination of the excitation frequency and the amplitude of acceleration lies in any of the white regions (Fig. 2b), the solutions of the Mathieu equation can be stable with an oscillatory periodic solution. For other combinations lying in any of the shaded regions, the solutions are unstable with oscillatory exponentially increasing amplitude. In the Fig. 2b, a dashed and solid instability boundaries are depicted. The former represents the region of the (isochronous) mode with the frequency equal to the excitation frequency; the latter reflects the region for the mode with half frequency of the excitation.

Using the analytical procedure for definition of the (1, 2) mode shape (Fig. 3a) considering the investigated circular tank of radius  $R$  and using polar coordinates in terms of which  $S_m$  must satisfy



$$\left(\frac{\partial^2}{\partial r^2} + \frac{1}{r}\frac{\partial}{\partial r} + \frac{1}{r^2}\frac{\partial^2}{\partial \theta^2} + k_m^2\right)S_m = 0 \quad (11)$$

$$S_{l,m} = J_l(k_{l,m}r) \cos l\theta \quad (12)$$

where  $J_l$  represents the Bessel function and  $k_{l,m}$  is the  $m$ th zero of  $J_l'(k_{l,m}R)$ .

The natural frequency of the mode shape with respective wave number may be calculated using following equation

$$f_{l,m} = \frac{1}{2\pi} \sqrt{\tanh k_{l,m} H_L \left( \frac{k_{l,m}^3 \gamma}{\rho} + k_{l,m} g \right)} \quad (13)$$

From the analysis, it can be observed the (1, 2) mode occurs at excitation principal frequency 5.16 Hz. Applying (13), the natural frequency of the respective mode of oscillation is at 2.58 Hz. Using finite element analysis in ANSYS Multiphysics this phenomenon occurs at 2.61 Hz and the mode is presented in Fig. 3b. Results between each solution represent good conformity.

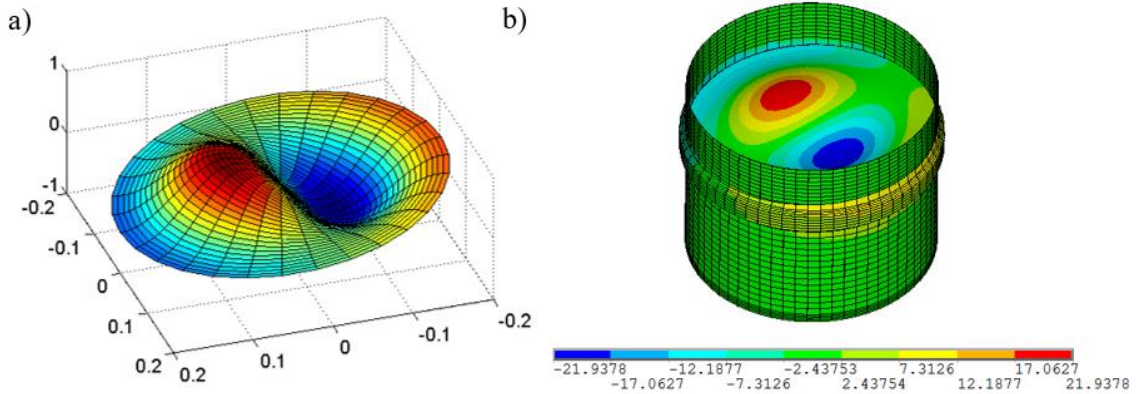


Fig. 3: (1, 2) mode of oscillation using analytical and numerical computation.

#### 4. Conclusions

The aim of this paper was focused on the parametrically excited sloshing waves at the free surface due to the time-varying effective gravitational acceleration. Mathieu equation of the free surface was formulated using an ideal liquid theory. Stable or unstable solutions of the equation depend on the combinations of  $P_m$  and  $Q_m$  values representing the location in the stability chart. At the parametric resonance, the amplitude of liquid oscillation is exponentially increasing. However, for real liquids, the amplitudes have limited values due to damping and nonlinear effects (not included in the ideal liquid theory). Since modes have different wave numbers, each of them has different stability chart of excitation frequency vs. amplitude of acceleration. Following results, it can be said that isochronous modes have narrower unstable regions than modes with half excitation frequency. Therefore, modes at this frequency are more difficult to excite and observe experimentally. To sum up, when investigating unstable solutions of the individual modes, each of them has the respective frequency at which a non-viscous liquid can be excited by an arbitrarily small amplitude of acceleration. But in a real liquid, a limit amplitude must be exceeded. It is affected by various factors such as viscosity, tank geometry and liquid depth.

#### Acknowledgement

This work was supported by the grant from the Grant Agency of VEGA no. 1/0742/15 and by the Slovak Research and Development Agency under the contract no. APVV-15-0630.

#### References

- Benjamin, T.B. and Ursell, F. (1954) The Stability of the Plane Free Surface of a Liquid in Vertical Periodic Motion. Proceedings of the Royal Society a Mathematical, Physical and Engineering Sciences, 225, 1163.
- Cartmell, M.C. (1990) Introduction to Linear, Parametric and Nonlinear Vibrations. New York: Chapman and Hall.
- Housner, G.W. (1954) Earthquake Pressures on Fluid Containers. California Institute of Technology, California.
- Ibrahim, R.A. (2005) Liquid Sloshing Dynamics Theory and Applications. Cambridge: Cambridge University Press.

## SHIFTING OF LHS DESIGN FOR SURROGATE MODELING

E. Myšáková\*, M. Lepš\*\*

**Abstract:** *Surrogate modeling (Meta-modeling) is a commonly used approach for analysis of complex systems' behavior. Time and computing demands of analytical models describing such systems are usually very high and in cases of need of multiple evaluations (for example in Monte Carlo based reliability analysis) they cannot be used. Instead, a model of the original model called surrogate model can be used. The purpose of the surrogate model is to approximate an original model's response in an arbitrary point of the design domain while constructed on a very limited and thus computationally cheap training data. The training data consist of the Design of Experiments (DoE) and corresponding responses of the original model. The choice of the DoE is crucial for the quality of the surrogate's approximation and therefore the LHS design is often used for its convenient properties. The contribution proposes a procedure of shifting of a part of the design of experiments in cases where the area of interest is located after some original model's evaluations were performed. The goal is clear: to use the already computed training data while not deteriorate the quality of the DoE.*

**Keywords:** Surrogate modeling, Design of Experiments, Latin Hypercube Sampling, Space-filling.

### 1. Introduction

Analyses of complex systems constitute a common daily content of scientists and engineers worldwide. Systems' behavior is usually described by time-consuming and computationally demanding models, often Finite Element based. If the actual analysis is based on multiple evaluations of the model with different combinations of input parameters' values the original demanding model cannot be used. Such case is for example the Monte Carlo based reliability assessment (Metropolis, 1949), where hundreds of thousands evaluations can be needed, especially in cases of low failure probabilities (Bucher, 1988).

Possible solution is a utilization of the Surrogate model (or Meta-model) which can be described as a model of the original model (Forrester, 2008). Constructed on the computationally manageable training data it is able to provide an approximation of the original model's response anywhere within the design domain. The training data consist of **i)** the Design of Experiments (DoE) which gives positions of the support points and **ii)** responses of the original model in these support points. Note that the individual coordinates of the support points correspond to the values of individual input parameters (with some transformation and scaling).

The quality of the Design of Experiments is crucial for the meta-model's ability of good approximation. Therefore it should be chosen with consideration. An often used approach is to use an LHS design whose properties are discussed later in Chapter 2.

In our recent problem the area of interest (the failure region) is not known in advance. Therefore at first the initial surrogate model is constructed covering the area of  $\mu \pm 3\sigma$ , where  $\mu$  is mean and  $\sigma$  is standard deviation of the original distribution. The optimized LHS design is used providing the positions of training points. Then the surrogate is used for search of the probable position of the Design Point (DP). Shortly, the Design Point marks the area of interest - the failure region. It is convenient to sample from this area where much more samples hit the failure region and then using Importance Sampling (IS)

---

\* Ing. Eva Myšáková: Faculty of Civil Engineering, Czech Technical University in Prague, Thákurova 7, 166 29, Prague, CZ, [eva.mysakova@fsv.cvut.cz](mailto:eva.mysakova@fsv.cvut.cz)

\*\* Assoc. Prof. Ing. Matěj Lepš, PhD.: Faculty of Civil Engineering, Czech Technical University in Prague, Thákurova 7, 166 29, Prague, CZ, [leps@cml.fsv.cvut.cz](mailto:leps@cml.fsv.cvut.cz)

compute the probability of failure (Chapter 3). For new sampling the second surrogate model is needed constructed on the training points lying in the identified region as shown in Fig. 1.

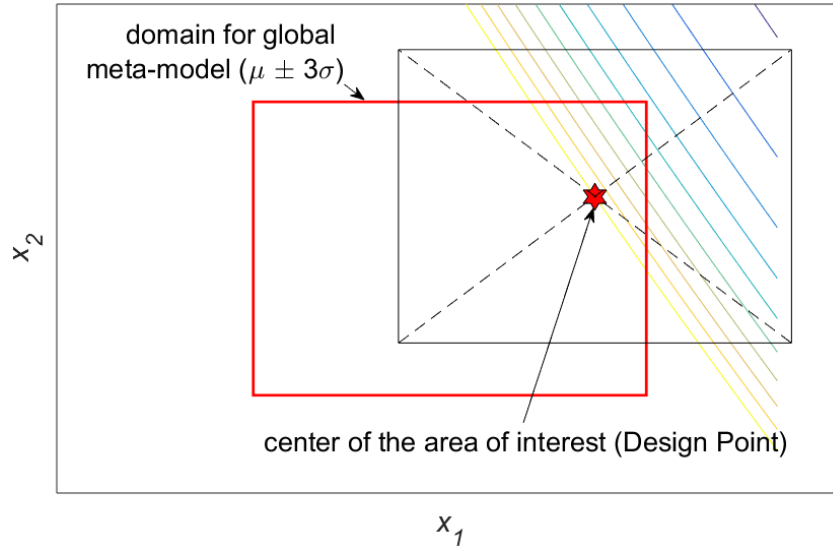


Fig. 1: Two domains for surrogates' construction.

The procedure proposed in this contribution focuses on the LHS design used for the construction of the surrogate models. Once the original model's responses are computed it is not efficient to throw them away if the possibility of its utilization still exists which is our case as described in more detail in Chapter 4.

## 2. LHS design

Latin Hypercube Sampling (LHS) is a method for generation of samples using stratification of individual variables (McKay, 1979). Needed  $np$  sample points, in LHS each variable is divided into  $np$  intervals; the LHS rule then requires that in each interval of each variable lies exactly one point.

Two variants of the method are used differing in the position of the points within the interval. MATLAB uses marking **smooth off** (the points lie in the middle of interval) and **smooth on** (the points lie randomly within the interval).

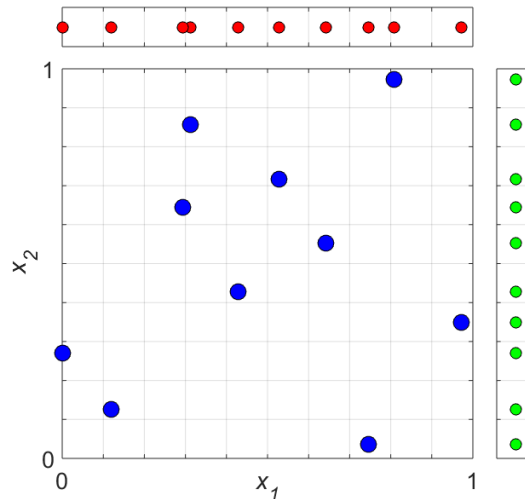


Fig. 2: LHS design in 2D with its reduction to individual axes.

The convenient and often desired attribute of the LHS design are the perfect projection properties. It is guaranteed by the LHS restriction. In case of dimension reduction induced by sensitivity analysis there is no problem to cut off the insignificant variables without getting duplicities, see Fig. 2.

### 3. Importance Sampling

Importance Sampling (IS) is a method for sampling in cases where the standard Monte Carlo integration cannot be used because it is not possible to sample from the target distribution of the variables (Rubinstein, 1981). It can be case of reliability assessment with very small expected probability of failure where the failure region is located in tail of variables' distribution. With standard Monte Carlo an enormous number of samples would be needed to at least hit the failure region. In IS the proposal distribution better covering the area of interest is used and the targeted integral is re-weighted using importance weights.

### 4. Design shifting

Because the surrogate model is constructed twice two sets of training data are demanded. But if the domains are overlapping, there is no need to construct two individual Design of Experiments. In fact it is desired to use as many of already evaluated training points as possible. But at the same time also the DoE for the second surrogate model should be as good as possible. Therefore the following procedure is proposed which ensures the utilization of the part of already evaluated training points while the properties of the LHS design remain preserved.

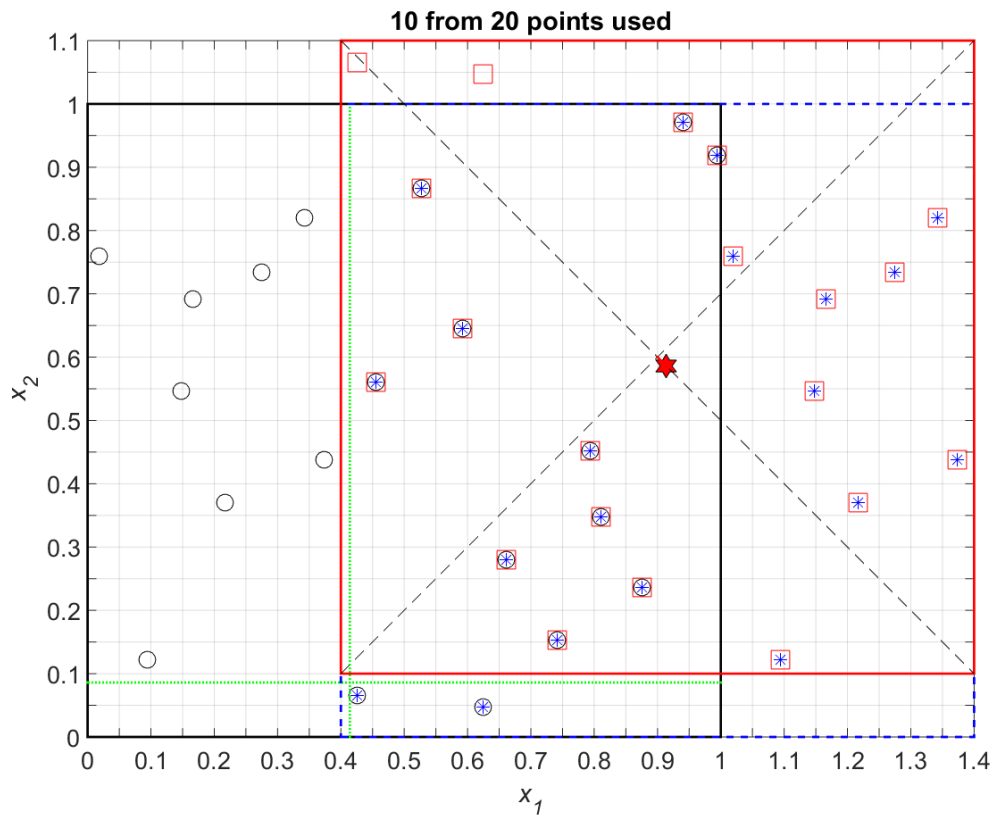


Fig. 3: Illustration of the proposed method.

An illustration of the proposed procedure is brought in Fig. 3. A legend for the figure is shown below:

○	<b>original LHS design</b>
★	Design Point (DP)
.....	limits based on DP's position
*	LHS design shifted according to x1
□	LHS design shifted according to x2 → <b>new LHS design</b>
- - -	new LHS design's diagonal
—	difference between DP's position and new LHS design's center

During the initial sampling position of the Design Point (DP) is found. It is the center of the identified area of interest. Then the lower limit for each axis is computed. Because it is intended to preserve the LHS properties of the design the closest interval bounds are found. The procedure then loops over each dimension and finds points lying outside the new bounds. These points are shifted which means that one is added or subtracted from its coordinate in actual dimension. Note that the procedure is run in normalized  $[0, 1]^{dim}$ -space, where *dim* is a number of problem's dimension, which is appropriate for the surrogates' construction.

## 5. Conclusions

The proposed procedure enables the utilization of already computed training data which is convenient because of the computational demands of every single evaluation. At the same time the properties of the design given by LHS restrictions remains in effect which ensures perfect projective properties and space-filling even for the second set of training data.

Of course the number of training points which can be used also for the second surrogate model is given by **i)** the position of the Design Point and **ii)** the actual LHS design to be shifted. If the Design Point lies the bounds of original training data none of them can be used again and the DoE for the second surrogate model has to be generated and evaluated by the original model. Also the actual appearance of the LHS design is important for the possibility of usage of the already evaluated points. In an extreme case none of the original training points can lie in the overlapping area of the domains.

## Acknowledgement

Financial support from the Czech Science Foundation, Project No. 16-11473Y, and the Grant Agency of the Czech Technical University in Prague, Project No. SGS17/042/OHK1/1T/11, is gratefully acknowledged.

## References

- Bucher, C.G. (1988) Adaptive sampling - an iterative fast Monte Carlo procedure. *Structural Safety*, 5, 2, pp. 119-126, ISSN 0167-4730.
- Forrester, A., Sóbester, A. and Keane, A. (2008) *Engineering Design via Surrogate Modelling: A Practical Guide*. John Wiley & Sons Ltd, ISBN 978-0-470-06068-1.
- McKay, M.D., Beckman, R.J. and Conover, W.J. (1979) A Comparison of Three Methods for Selecting Values of Input Variables in the Analysis of Output from a Computer Code. *Technometrics*, 21, 2, pp. 239-245.
- Metropolis, N. and Ulam, S. (1949) The Monte Carlo Method. *Journal of the American Statistical Association*, 44, 247, pp. 335-341.
- Rubinstein, B.Y. (1981) *Simulation and the Monte Carlo Method*. New York: Wiley & Sons.

## EXPERIMENTAL STUDIES ON $\text{Fe}_3\text{O}_4$ NANOFLUID FLOWING THROUGH A CIRCULAR TUBE

P. D. Nagireddy\*, Ch. Srinivasa Rao\*\*

**Abstract:** This study deals with an experimental investigation of  $\text{Fe}_3\text{O}_4$ -water nanofluid flowing through a circular tube. Flow is maintained in the turbulent region and tube is exposed to constant heat flux along the length. Experiments are conducted to study the entropy generation of nanofluid for different particle volume concentrations varying from 1 % to 6 % and also for the different Reynolds numbers. Measured data from the experimentation is taken as input to calculate the thermal entropy and frictional entropy generation. Finally total entropy generation and Bejan number are calculated and analyzed. Experimentally it is proved that the changes in the thermal and frictional entropy generations are opposite, such a way that, as particle concentration increases thermal entropy generation decreases whereas frictional entropy generation increases. Finally experimental results reveal that there exists an optimum particle volume concentration where the total entropy generation is minimal. The same result has also appended by calculating the Bejan number.

**Keywords:** Nanofluid, Experimental, Entropy generation, Bejan number, Heat transfer.

### 1. Introduction

Exponential growth in the electronics industry leads to the higher heat generation rates from different electronic devices and demands for safer and more efficient cooling systems. Due to the limitations over heat transfer characteristics, air-cooling and liquid-cooling with conventional fluid as working fluid reaches the saturation limit. Because of favorable thermal characteristics, nanofluids are proven as alternative coolant in various thermal management systems (Godson et al. 2009, Ahammed et al. 2016). However, nanofluids possess high viscosity compared to that of the base fluid. This higher viscosity leads to the more pressure drop there by increases the pumping power requirement. So, always there exists a trade-off between higher heat transfer characteristics and higher pumping power. Thermodynamic second law analysis is an effective tool to find the suitability of the nanofluid in any thermal management system. It is to be noted that, with nanofluids, entropy generation due to the heat transfer decreases where as entropy generation due to the friction increases.

In this study, a customized test rig is developed to represent different flow conditions (different Reynolds numbers) and different heat fluxes. Due to its vast usage in electronic cooling systems,  $\text{Fe}_3\text{O}_4$ -water nanofluid is chosen for the study. Particle volume concentrations are varied from 1 % to 6 % V/V. Circular tube section is considered for the study. Experiments are conducted by varying Reynolds number and volume fraction. Experimental data is used to calculate entropy generation and Bejan number.

### 2. Methodology

#### 2.1. Nanofluid thermo physical properties

In order to determine the entropy generation, precise information on the thermophysical properties of the working fluid is necessary. The thermophysical properties of nanofluid strongly depends on the quantity of nanoparticles added to the base fluid.

Density of nanofluid is estimated based on the principle of the mixture rule and can be calculated by using following equation proposed by Pak et al. (1999).

---

\* Praveena Devi N, M.Tech., Asst. Prof., S R Engineering College, Warangal-506004, TS, India, praveenadevi@gmail.com

\*\* Prof. Ch Srinivasa Rao, PhD, Andhra University, Visakhapatnam, AP, India, csr\_auce@yahoo.co.in



$$\rho_{nf} = \Phi \rho_{np} + (1 - \Phi) \rho_{bf} \quad (1)$$

Thermal conductivity is one of the vital property, which governs the heat transfer characteristics of the nanofluid, and it can be estimated by using Maxwell correlation (1883).

$$k_{nf} = k_{bf} \left\{ \frac{[k_{np} + 2k_{bf} - 2\Phi(k_{bf} - k_{np})]}{[k_{np} + 2k_{bf} + \Phi(k_{bf} - k_{np})]} \right\} \quad (2)$$

Heat Capacity can be calculated by the correlation proposed by Pak et al. (1999).

$$C_{p,nf} = (\Phi \rho_{np} C_{p,np} + (1 - \Phi) \rho_{bf} C_{p,bf}) / \rho_{nf} \quad (3)$$

Viscosity can be calculated by the correlation proposed by Batchelor (1977)

$$\mu_{nf} = (1 + 2.5\Phi + 6.2\Phi^2) \mu_{bf} \quad (4)$$

Nomenclature		Greek Letters	
k	Thermal conductivity [W/mK]	$\rho$	Density [kg/m <sup>3</sup> ]
C <sub>p</sub>	Specific heat [kJ/kg K]	$\Phi$	Particle concentration
E <sub>g,f</sub>	Frictional entropy generation [W/K]	$\mu$	Viscosity [kg/m s]
E <sub>g,T</sub>	Thermal entropy generation [W/K]	Subscripts	
E <sub>g</sub>	Total entropy generation	np	Nano particle
d	Diameter of the tube [m]	bf	Base fluid
m	Mass flow rate [kg/s]	av	Average
q	Heat flux [W/m <sup>2</sup> ]	nf	Nanofluid
Dimensionless numbers		i	Inlet
Re	Reynolds number	o	Outlet
Nu	Nusselt number		
Pr	Prandtl number		
Be	Bejan number		

## 2.2. Experimental set up

A detailed schematic of the experimental facility used in this investigation is shown in Fig. 1. Photograph of the test rig is shown in Fig. 2. All the thermocouples, mass flow meters and differential pressure gauges are well calibrated and calibration errors are taken into account while doing the data reduction.

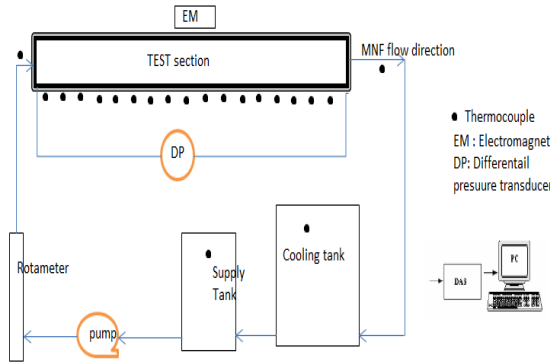


Fig. 1: Schematic of the test facility.



Fig. 2: Photograph of test facility.

## 2.3. Data Reduction

K-type thermo-couples are used to log the temperature data. Average temperature of the fluid is calculated by using Equation given as  $T_{av} = T_i - T_o / \ln \left( \frac{T_i}{T_o} \right)$ .

Mass flow rate and surface temperature are taken from the experimental data. Whereas, other thermo-physical properties are calculated from the correlations given in the previous section. Based on these experimental and calculated values dimensionless parameters such as Nu and Pr are calculated.

The entropy generation due to friction can be expressed as (Bejan, 1982)  $E_{g,f} = \frac{32m^3 fL}{\rho_{nf}^2 \pi^2 d^2 T_{av}}$ .

The entropy generation due to heat transfer can be expressed as (Bejan, 1982)  $E_{g,T} = \frac{\pi d^2 L q^2}{k_{nf} Nu T_{av}}$ .

The total entropy generation can be given by  $E_g = E_{g,T} + E_{g,f}$ .

To find the relative influence of thermal and frictional entropy generations on the total entropy generation, a non-dimensional number, i.e. Bejan number can be used  $Be = \frac{E_{g,T}}{E_g}$ .

### 3. Results and Discussion

It is well known that, heat transfer characteristics are favorable with nanofluid as working fluid when compared with that of the base fluid. This is due to the enhancement of some thermo-physical properties such as thermal conductivity. However, due to the increased viscosity, frictional resistance also increases. In order to find the optimum particle concentration for the given Reynolds (Re) number, experiments are conducted and results are presented in the present section. Bejan (1982) derived closed form solutions to calculate the entropy generation per unit length of the circular tube section and the corresponding formulae are presented in the preceding section. Data collected from the experimentation is used to calculate the entropy generation.

#### 3.1. Effect of nano particle concentration

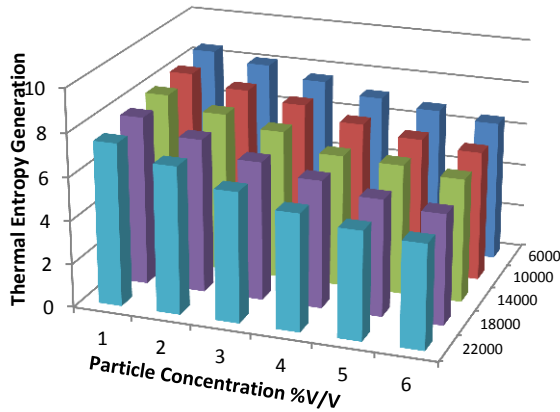


Fig. 3: Variation of thermal entropy generation.

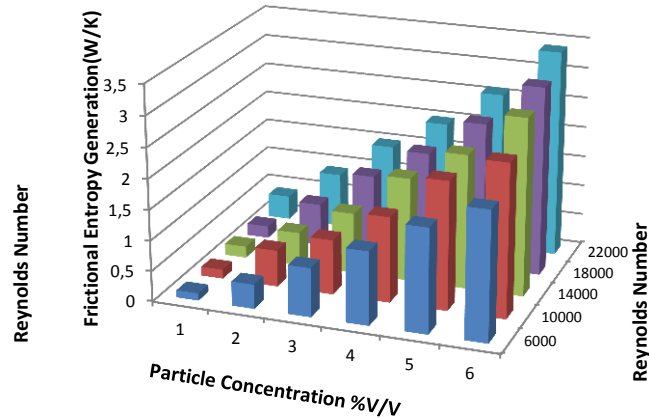


Fig. 4: Variation of frictional entropy generation.

Fig. 3 and Fig. 4, respectively, show the affect of particle concentration on the thermal and frictional entropy generations. It is to be noted that, Reynolds number is varied from 6000 to 22000 for all the particle concentrations. Heat flux is kept constant for all the cases. It is evident from Figs. 3 and 4 that the thermal entropy generation is dominant compared with the frictional entropy generation in all the cases within the range of study. Furthermore, with the increase in concentration of nanoparticles, the thermal and frictional entropy generations have opposing trends of variation. From equations it is clearly evident that the effective thermal conductivity and Nusselt number increases with increase of particle concentration which is responsible for the decreasing trend of entropy generation. However, the frictional entropy generation, increases with particle concentration since the effective viscosity increases. Although with the increase of nanoparticle concentration both the viscosity and density of nanofluid increases, the increase of viscosity dominates the increase of density which leads to an increase of the shear stress.

#### 3.2. Effect of Reynolds Number

From Figs. 3 and 4, it can be witnessed that thermal entropy generation decreases with the increase of the Reynolds number, where as the frictional entropy generation increases. This may be attributed to the increase in Nusselt number with Reynolds number. It is further noticed that the variation in frictional entropy generation is low at lower concentrations (up to 3 %) and there after it is predominant.

Because of the decreasing and increasing trends of thermal and frictional entropy generations, the total entropy generation exhibits an optimum condition with minimum entropy generation. Fig. 5 shows the variation of total entropy generation with concentration and Reynolds number. The same result may be detected by examining the trend of Bejan number, in Fig. 6, which shows that at the higher Reynolds number and particles concentration, frictional entropy generation dominates. So from these results it can be concluded that there exists an optimum particle concentration for the given Reynolds number. Depending on the flow, irreversibilities due to heat transfer and irreversibilities due to frictional resistance may dominate each other.

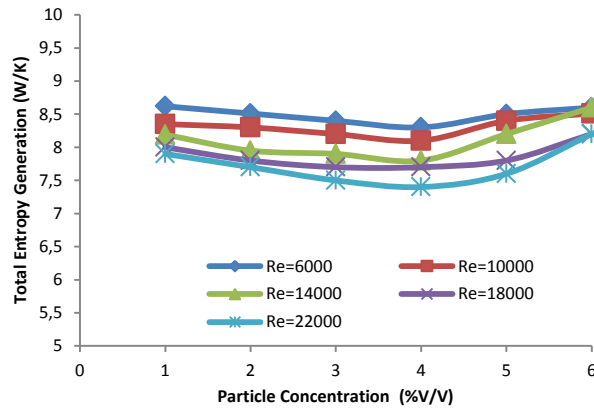


Fig. 5: Variation of total entropy generation.

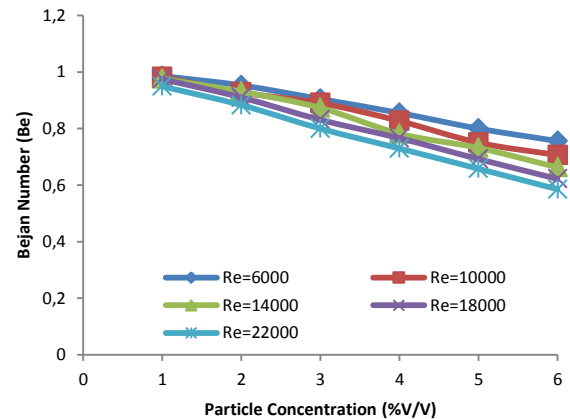


Fig. 6: Variation of Bejan number.

### 3. Conclusions

In this paper, analysis of entropy generation is presented in order to investigate the optimum value of particle concentration for the given Reynolds number in the turbulent region. Experiments are conducted and results are analyzed. The following conclusions are drawn from the present study:

1. With increase in nanoparticle volume concentration the entropy generation due to heat transfer decrease, whereas entropy generation due to fluid friction increases.
2. The reverse trend is observed with increase in Reynolds number.
3. There exists an optimum value of concentration for the given Reynolds number where the total entropy generation is found minimum.

### Acknowledgement

The present work is carried out under a project sponsored by UGC, GoI(MRP-6230/15(SERO/UGC)). The financial support offered by UGC is gratefully acknowledged.

### References

- Ahammed, N., Asirvatham, L.G., Wongwises, S. (2016) Thermoelectric cooling of electronic devices with nanofluid in a multiport minichannel heat exchanger, *Exp. Therm. Fluid Sci.*, 74, pp. 81-90.
- Batchelor, G.K. (1977) The effect of Brownian motion on the bulk stress in a suspension of spherical particles, *J. Fluid Mech.*, 83(01), pp. 97-117.
- Bejan (1982) *Entropy Generation Through Heat and Fluid Flow*, Wiley, New York.
- Godson, L. (2009) Enhancement to heat transfer using nanofluids-an overview. *Renewable and Sustainable Energy Reviews*, 2 (14), pp. 629-641.
- Maxwell, C. (1873) *Electricity and Magnetism*, Clarendon Press, Oxford, UK.
- Pak, B.C. and Cho, Y.I. (1999) Hydrodynamic and heat transfer study of dispersed fluids with sub micron metallic oxide particles, *Exp. Heat Transfer*, 11, pp. 151-170.
- Wen, D., Lin, G., Vafaei, S. and Zhang, K. (2008) Review of nanofluids for heat transfer applications, *Particulatorgy*, 7 pp. 141-50.

## NON-HOLONOMIC PLANAR AND SPATIAL MODEL OF A BALL-TYPE TUNED MASS DAMPING DEVICE

J. Náprstek<sup>\*</sup>, C. Fischer<sup>\*\*</sup>

**Abstract:** *The area of tuned mass dampers is a wide field of inspiration for theoretical studies in non-linear dynamics and dynamic stability. The studies attempt to estimate behaviour of diverse damping devices and their reliability. The current paper deals with the response of a heavy ball rolling inside a spherical cavity under horizontal kinematic excitation. The non-linear system consists of six degrees of freedom with three non-holonomic constraints. The contact between the ball and the cavity surface is supposed to be perfect without any sliding. The mathematical model using the Appell-Gibbs function of acceleration energy is developed and discussed. Comparison with previous planar (SDOF) model which is based on the Lagrangian procedure is given. The system has an auto-parametric character and therefore semi-trivial solutions and their dynamic stability can be analysed. The most important post-critical regimes are outlined and qualitatively evaluated in resonance domain. Numerical experiments were performed when excitation frequency is slowly swept up and down to identify different modes of response. Some applications in civil engineering as a tuned mass damper, which can be used on slender structures, are mentioned. The proposed device is compared with a conventional pendulum damper. Strengths and weaknesses of both absorbers types are discussed.*

**Keywords:** Tuned mass damper, Moving ball, Appell-Gibbs formulation.

### 1. Introduction

Various types of passive vibration absorbers are regularly used in civil engineering for suppression of wind induced vibration. Transmission towers, TV masts and other slender structures exposed to wind excitation are usually equipped by such devices. Usual pendulum-style passive absorbers, see, e.g., (Haxton, 1974), utilize the auto-parametric resonance for their damping effect. Although they are very effective and reliable their application can be limited by several disadvantages. Dimensions of the pendulum and namely its suspension length cannot be neglected or minimized and it could easily happen that the structure cannot accommodate this device. This is particularly true for existing structures, where an absorber should be installed as a supplementary equipment. Also horizontal constructions, like foot bridges, usually cannot include a pendulum-style absorber. Moreover, the complete installation has to remain accessible to allow a regular maintenance.

The ball-type absorber represents an alternative solution, which is less spatially-demanding and practically maintenance-free. The basic principle comes out of a rolling movement of a metallic ball of a radius  $r$  inside of a metallic rubber coated spherical cavity of a radius  $R > r$ , Fig. 1a. The system can be closed in an airtight case. Its vertical dimension depends only on the dimension of the rolling ball and thus the assembly can be relatively very small. Such device can be used in cases where a pendulum absorber is inapplicable due to lack of vertical space or difficult maintenance.

First papers dealing with the theoretical and practical aspects of ball absorbers have been published by Pirner and Fischer (1994, 2000). The first analysis of the problem on the basis of the rational dynamics has been published by the authors in (Náprstek and Pirner, 2002) and later extended in (Náprstek et al., 2011). The approach in the referenced papers was based on planar model, constructed using the Hamiltonian functional with non-holonomic constraints and the respective Lagrangian governing system

---

<sup>\*</sup> Ing. Jiří Náprstek, DSc.: Institute of Theoretical and Applied Mechanics AS CR, v.v.i., Prosecká 76, 190 00 Praha 9, naprstek@itam.cas.cz

<sup>\*\*</sup> RNDr. Cyril Fischer, PhD.: Institute of Theoretical and Applied Mechanics AS CR, v.v.i., Prosecká 76, 190 00 Praha 9, fischer@itam.cas.cz

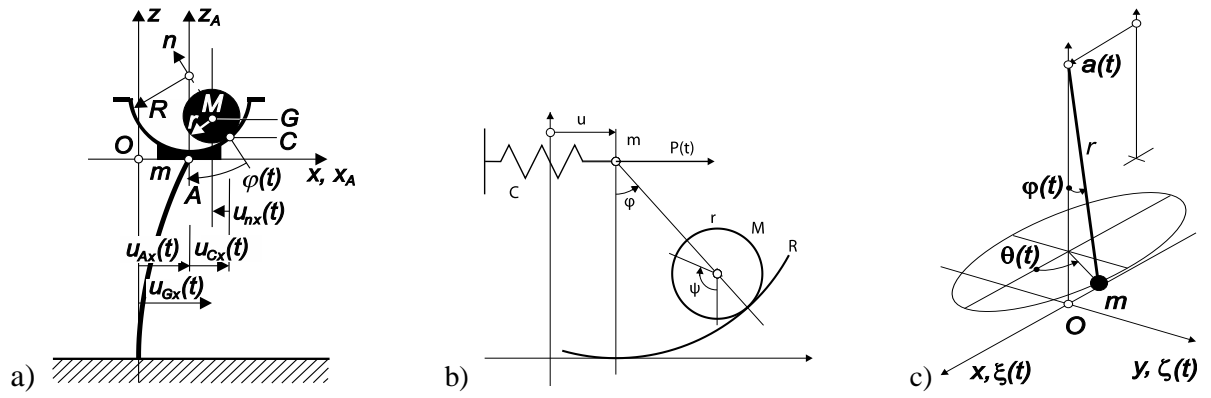


Fig. 1: a) Outline of the ball absorber; b) Scheme of the simplified 2D model; c) The spherical pendulum.

in 2D, cf. Fig. 1b. The theoretical derivation together with its numerical evaluation was compared to practical application up to the state of the realization including some results of long-term measurements.

Dynamics of the real ball absorber is significantly more complicated in comparison to the pendulum one, Fig. 1c. Movement of the ball cannot be described in a linear state although for the first view its behaviour is similar to the pendulum absorber type. A number of problems that are related with movement stability, auto-parametric resonances, etc., originate from the spherical cavity and ball surface imperfections. The ball moving inside the spherical cavity is very sensitive to the stability loss of its movement in forcing direction. However, this type of motion is requested, as it determines efficiency of the damper. Due to probability of the stability loss, which is much higher than of the spherical pendulum, semi-trivial states should be carefully analysed including a large variety of post-critical processes.

The fully spatial model, unlike the 2D approximation, does not allow the usual approximations of the exact formulations. The deflection  $\varphi$  of the pendulum, cf. Fig. 1c, can be assumed relatively small, it is usually lower than  $20 - 30^\circ$ , and the approximations in form of a short Taylor series are acceptable:  $\sin \varphi \approx \varphi - 1/6\varphi^3$ ,  $\cos \varphi \approx 1 - 1/2\varphi^2$ . On the other hand, movement of the ball within the cavity should respect the full expressions due to the fact that the ball deflection can reach nearly the “equator” of the cavity. This fact prevents to get through the matter by an analytical way, but suitable combination of both numerical/analytical procedures is still possible and, moreover, the model presented in this contribution does not include any limits of the response amplitudes.

Authors tried to formulate this problem in the past by a classical way constructing the Hamiltonian functional with non-holonomic constraints. However, the resulting Lagrangian governing system provides the differential system which is too complicated and its physical interpretation can be multivalent. For easier analysis is the problem formulated using Appell-Gibbs function. Its main advantage consists in easier problem definition and more transparent introduction of non-holonomic constraints.

## 2. Mathematical models

### 2.1. Simple planar model

The dynamic character of the complete structure is modelled by a linear SDOF system represented by a total mass  $m$  (which includes the structure, cavity and the ball) and stiffness  $C$ . The ball with mass  $M$  is moving freely in a vertical plane in a cavity directly attached to the structure, i.e., 2DOF system should be investigated as it is outlined in Fig. 1b. For full derivation see (Náprstek et al., 2011).

$$\ddot{\varphi} + \kappa b_{\varphi} \dot{\varphi} + \kappa \omega_M^2 \sin \varphi + \kappa \ddot{\zeta} \cdot \cos \varphi = 0 \quad \omega_M^2 = \frac{g}{\rho}, \quad \kappa = \frac{Mr^2}{J + Mr^2}, \quad (1a)$$

$$\mu \ddot{\varphi} \cos \varphi - \mu \dot{\varphi}^2 \sin \varphi + (1 + \mu) \ddot{\zeta} + b_u \dot{\zeta} + \omega_m^2 \zeta = p(t) \quad \mu = \frac{M}{m}, \quad \omega_m^2 = \frac{M}{m}. \quad (1b)$$

Here  $g$  is the gravitational acceleration and  $J = 2/5 \cdot Mr^2$  is the central inertia moment of the ball.

The theoretical efficiency of the absorber can be assessed using its frequency characteristics for excitation by harmonic force  $p(t)$ . However, to relate the planar model to the fully spatial one, only the first equation (1a) regarding the ball rolling in the cavity will be used here. The action of the elastic structure is replaced by the kinematic excitation  $\ddot{\zeta} = \ddot{\zeta}_0 \cdot \sin \omega t$ .

## 2.2. Appell-Gibbs approach to the full spatial model

In the spatial model of the ball absorber (Fig. 1a) is the Appell-Gibbs approach used to formulate the governing non-linear differential system. The basis is the Appell function (often referred to as an energy acceleration function), which is defined as a function of six components characterizing motion of the stiff body in 3D:

$$S = \frac{1}{2}M(\ddot{u}_{Gx}^2 + \ddot{u}_{Gy}^2 + \ddot{u}_{Gz}^2) + \frac{1}{2}J(\dot{\omega}_x^2 + \dot{\omega}_y^2 + \dot{\omega}_z^2), \quad (2)$$

where  $M$  is the mass of the ball,  $J = 2/5 \cdot Mr^2$  central inertia moment of the ball with respect to its centre,  $\omega$  angular velocities of the ball with respect to its centre,  $u_{G\cdot}$  displacements of the ball centre with respect to absolute origin  $O$ ,  $u_{C\cdot}$  displacements of the contact point with respect to origin  $O$ , and  $u_A$  prescribed movement of the cavity with respect to origin  $O$ .

Following the detailed derivation of the equations of motion the governing system reads (Náprstek and Fischer, 2016)

$$\dot{u}_{Cx} = \omega_y(u_{Cz} - R) - \omega_z u_{Cy} \quad (3a)$$

$$\dot{u}_{Cy} = \omega_z u_{Cx} - \omega_x(u_{Cz} - R) \quad (3b)$$

$$\dot{u}_{Cz} = \omega_x u_{Cy} - \omega_y u_{Cx} \quad (3c)$$

$$J_s \rho \dot{\omega}_x = -(\ddot{u}_{Ay} + \rho(\omega_z \dot{u}_{Cx} - \omega_x \dot{u}_{Cz}))(u_{Cz} - R) - u_{Cy} \left( g + \rho(\omega_x \dot{u}_{Cy} - \omega_y \dot{u}_{Cx}) \right) - \rho D_{Gx}/M \quad (4a)$$

$$J_s \rho \dot{\omega}_y = -(\ddot{u}_{Ax} + \rho(\omega_y \dot{u}_{Cz} - \omega_z \dot{u}_{Cy}))(u_{Cz} - R) + u_{Cx} \left( g + \rho(\omega_x \dot{u}_{Cy} - \omega_y \dot{u}_{Cx}) \right) - \rho D_{y}/M \quad (4b)$$

$$J_s \rho \dot{\omega}_z = -(\ddot{u}_{Ax} + \rho(\omega_y \dot{u}_{Cz} - \omega_z \dot{u}_{Cy}))u_{Cy} - (\ddot{u}_{Ay} + \rho(\omega_z \dot{u}_{Cx} - \omega_x \dot{u}_{Cz}))u_{Cx} - \rho D_y/M \quad (4c)$$

where:  $J_s = (J + M\rho^2 R^2)/(M\rho^2)$ ,  $\rho = 1 - r/R$  and terms  $D_{G\cdot}$  cover influence of damping.

Damping in the contact point has to be treated separately for rolling and spinning component. Supposing that no slipping arises in the contact, the dissipation process can be approximated as proportional to the relevant components of the angular velocity. Thus, the damping terms in Eqs. (4) include coordinate transformation from local coordinates of the ball distinguishing rolling and spinning movement.

## 2.4. Comparison of the models

Although the models aim to describe a single real system, their difference is more than dimensional settings. The simplified model was set up to describe interaction of the ball absorber and the structure, its auto-parametric character originates from coupling between the ball, cavity and elastic structure. The spatial model in the current state describes only the movement of the ball in the cavity and assumes only the kinematic excitation of the cavity. The auto-parametric character follows from interaction of the individual  $x$  and  $y$  components. Hence only the equation (1a) from the planar model can be directly related to the 3D model.

In order to show correspondence of the full model (3, 4) and Eq. (1a) the following conditions will be assumed, which assure the planar movement of the ball in the cavity:

$$u_{Cy} = 0, \omega_x = 0, \omega_z = 0 \quad (5)$$

Introducing conditions (5) into Eqs (3,4) (without damping), three equations are fulfilled trivially and only Eqs (3a,3c,4b) remain active. Elimination of  $\dot{\omega}_y$  from Eq. (4b) using the derived Eq. (3a) and substitution of the geometric relation  $u_{Cz} = R - \sqrt{(R^2 - u_{Cx}^2)}$  gives the single equation which involves only  $u_{Cx}$ :

$$\ddot{u}_{Cx} = \frac{M\rho}{J+M\rho^2 R^2} \left( (u_{Cx}^2 - R^2)\ddot{u}_{Ax} - g u_{Cx} \sqrt{R^2 - u_{Cx}^2} \right) - \frac{u_{Cx} \dot{u}_{Cx}^2}{R^2 - u_{Cx}^2} \quad (6)$$

Transformation of the translational motion to rotation  $u_{Cx} = R \sin \varphi$  restores the equation (1a).

Performance of both models is compared in Fig. 2. The system parameters used:  $M = 1, R = 1, r = 1/2$ , the excitation amplitude  $\zeta_0 = 0.1$  and damping:  $b_\varphi = \alpha = 0.1, \beta = 0.01$ . Symbols  $\alpha, \beta$  are the damping coefficients in the spatial model for rolling and spinning, respectively. The left plot shows the positions of the turning points in lateral direction depending on the excitation frequency  $\omega$ . Because the ball in the maximal motion crosses the equator of the cavity, the actual extremal value of the coordinate can become



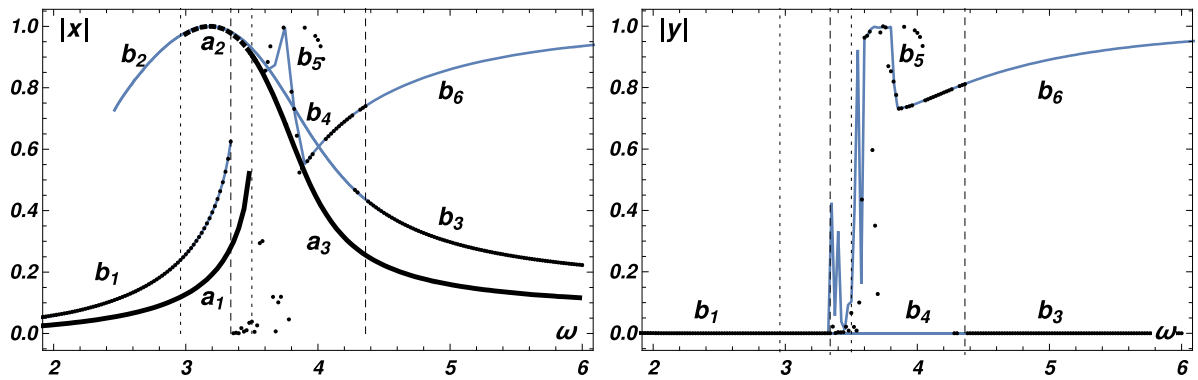


Fig. 2: Resonance behaviour of planar and spatial models. Maximal responses in lateral (left) and transversal (right) direction. Planar model – thick lines, spatial model – thin lines and dots.

smaller for increasing amplitudes (cf. concave part of the curve in the left plot). The resonance curve corresponding to the planar model is shown in the left plot as the thick solid line  $a_1 - a_3$  with thick dotted overhanging part  $a_2$ . The thin dotted vertical lines delimit area where the resonance curve shows two stable solutions, lines  $a_1$ ,  $a_2$ . The curves  $b_1 - b_6$  in the both plots correspond to the spatial model. The parts  $b_1 - b_4$  show planar (semi-trivial) solution which can be directly related to the result of the planar model. The branches  $b_5$  and  $b_6$  correspond to spatial periodic ( $b_6$ ) or chaotic ( $b_5$ ) movement of the ball, as can be seen comparing both plots. It is worth to note that the periodic branch  $b_6$  continues over right border of the plot. It represents stable cycling which approaches equator of the cavity for increasing excitation frequency. From the left part of Fig. 2 can be seen that the planar model underestimates response and width of the resonance area. Moreover, it cannot encompass the upper spatial branch of the response ( $b_6$ ), which can have devastating effect on the structure.

### 3. Conclusions

Two approaches to modelling of behaviour of the ball-style tuned mass damper were presented and compared. Whereas the non-linear planar approach models the ball in the cavity using a single DOF, the spatial one comprises six degrees of freedom with three non-holonomic constraints. The equations of the motion in the spatial model of the ball are derived using the Appell-Gibbs function of acceleration energy. The Appell-Gibbs formulation of a non-holonomic system dynamics approved excellent efficiency in comparison with a conventional way being based on Lagrangian differential system and non-holonomic constraints adjoined via indefinite Lagrange multipliers. The resulting system has an auto-parametric character, it permits to formulate the semi-trivial (planar) solution. The models were numerically analysed with respect to harmonic horizontal excitation. The interval of frequencies leading to instability of the semi-trivial solution was shown and studied and its dangerous character was pointed out.

### Acknowledgement

The kind support of the Czech Science Foundation project No. 15-01035S and the institutional support RVO 68378297 are gratefully acknowledged.

### References

- Haxton, R., Barr, A. (1972) The autoparametric vibration absorber, ASME J Manuf Sci Eng, 94, pp. 119-125.
- Náprstek, J. and Pirner, M. (2002) Non-linear behaviour and dynamic stability of a vibration spherical absorber, in: Proc. 15<sup>th</sup> ASCE Eng. Mech. Div. Conf. (ed. Smyth, A.), Columbia Univ., New York, 2002, paper 150, 10 p.
- Náprstek, J., Fischer, C., Pirner, M. and Fischer, O. (2011) Non-linear dynamic behaviour of a ball vibration absorber, in: Proc. COMPDYN 2011 (eds. Papadrakakis, M., Fragiadakis, M., Plevris, V.), ECCOMAS - NTU Athens, Kerkyra, Corfu, 2011, paper 180, 14 p.
- Náprstek, J. and Fischer, C. (2016) Dynamic behavior and stability of a ball rolling inside a spherical surface under external excitation, in: Insights and innovations in structural engineering, mechanics and computation (ed. Zingoni, A.), Taylor & Francis, London, pp. 214-219.
- Pirner, M. (1994) Dissipation of kinetic energy of large-span bridges, Acta Technica, CSAV, 39, pp. 407-418.
- Pirner, M. and Fischer, O. (2000) The development of a ball vibration absorber for the use on towers, J Int Assoc Shell Spatial Struct, 41, pp. 91-99.

## TESTING OF FULL STAGE MIXED-FLOW TURBINE FOR AUTOMOTIVE APPLICATIONS

M. Němec<sup>\*</sup>, T. Jelínek<sup>\*\*</sup>, J. Klíma<sup>\*\*\*</sup>

**Abstract:** This paper summarizes experimental results of an aerodynamic performance study carried out on mixed-flow full turbine stage of a exhaust gas turbocharger TCR12 produced by PBS Turbo. The investigation was carried out alternatively on two nozzle geometries. The stage was adapted for a VZLU test rig which is integrated into a cool flow closed-loop wind tunnel. The aim of the experiments was to acquire the stage overall performance in wide range of pressure ratio and rotational speed. The turbine stage outlet conical diffuser efficiency was also studied.

**Keywords:** Mixed-flow turbine, Full stage, Stage efficiency, Diffuser efficiency, Test rig.

### 1. Introduction

TCR12 exhaust gas turbocharger produced by PBS Turbo is used in a very wide range for the charging of diesel and gas engines. It can be used for engines with constant and pulse pressure turbocharging with power output up to 760 kW. The main goal of the work was to verify data used for complete engine cycles design. An overall performance was measured in a wide range of design and off-design regimes with constant pressure operation. Another objective was a study of the flow field at the outlet of the rotor and in a conical diffuser downstream. Two nozzle rings geometries characterized by two vane stagger angles and the throat area difference of approximately 15 % were compared.

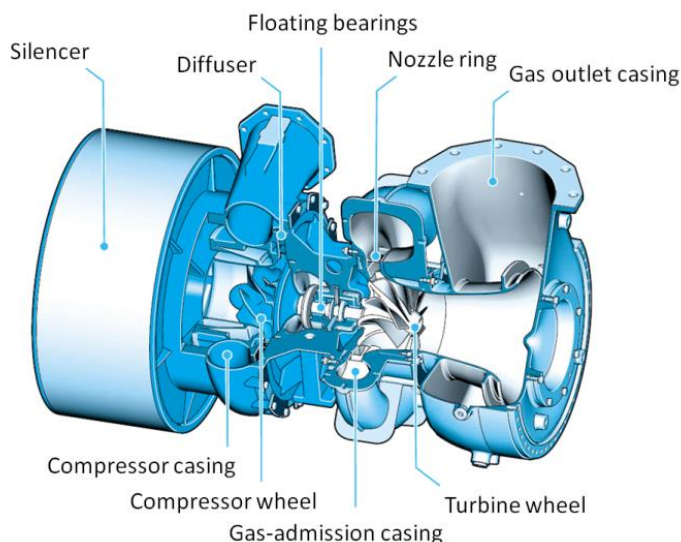


Fig. 1: PBS Turbo TCR turbo-charger.

### 2. Test rig configuration

A modular conception of the turbocharger enabled using original turbocharger parts for the test rig configuration. A compressor section was replaced by a dynamometer which loaded the turbine and the

<sup>\*</sup> Martin Němec: Aerospace Research and Test Establishment, Beranových 130; 199 05, Prague; CZ, nemec@vzlu.cz

<sup>\*\*</sup> Tomáš Jelínek: Aerospace Research and Test Establishment, Beranových 130; 199 05, Prague; CZ, jelinek@vzlu.cz

<sup>\*\*\*</sup> Jiří Klíma: PBS Turbo; Vlkovská 279; 595 01, Velká Bíteš; CZ, Jiri.Klima@pbsturbo.eu

turbine was driven by VZLU closed-loop wind tunnel. This configuration allowed to set up independently pressure ratio and turbine rotational speed. The work medium was a dry air with inlet total pressure  $p_{cin}$  up to 130 kPa and inlet total temperature  $T_{cin}$  up to 60 °C.

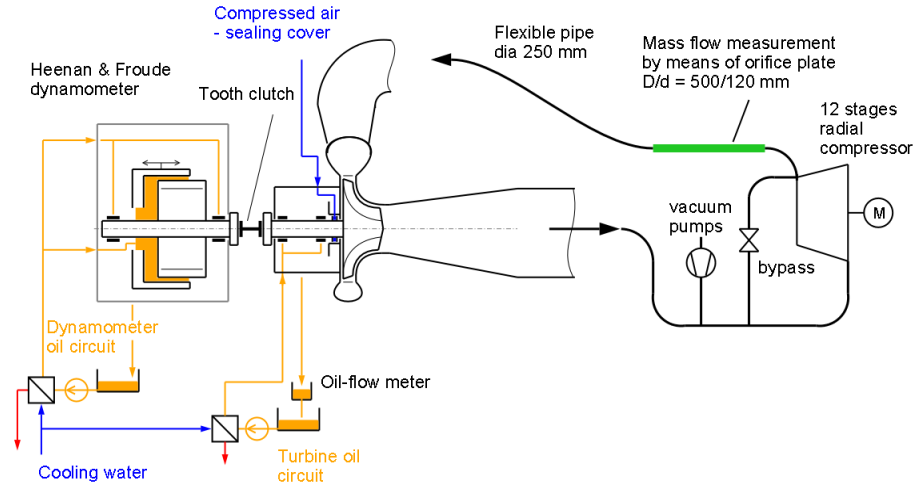


Fig. 2: The test rig and the wind tunnel scheme.

A mass flow through the turbine was measured by means of an orifice plate placed far before the turbine inlet. The torque was determined by a force transducer HBM C9B placed on the arm of the high-speed dynamometer Heenan & Froude V-375 – oil as a working fluid. The turbine inlet volute, nozzle and diffuser were fitted with static pressure taps (100 measured positions) and thermocouples (24 positions). Radial distribution of the flow field was measured by a five-hole pneumatic probe at the inlet of the turbine, at the outlet of the rotor and at the outlet of the diffuser.

A bearing oil flow rate, required for bearing losses estimation, was obtained by measurement of the oil level in the tank with a sharp-edged hole in the bottom of the tank.

### 3. Turbine overall performance

The overall performance measurement matrix was defined by hot pressure ratios and hot reduced speeds. It covered range of pressure ratio  $\pi$  up to 4.6 and range of speed ratio  $u/c_{is}$  from 0.35 to 0.9. Regimes adjustment was done as accurately as possible, thus it wasn't necessary to use data interpolation in a post processing procedures. The accuracy was kept under 0.05 in the case of the pressure ratio and around 50  $\text{min}^{-1} \text{K}^{-0.5}$  for reduced speed. A comparison of the two nozzle rings geometries results is shown in graphs (Figs. 3 and 4) with mass flow capacity and efficiency characteristics.

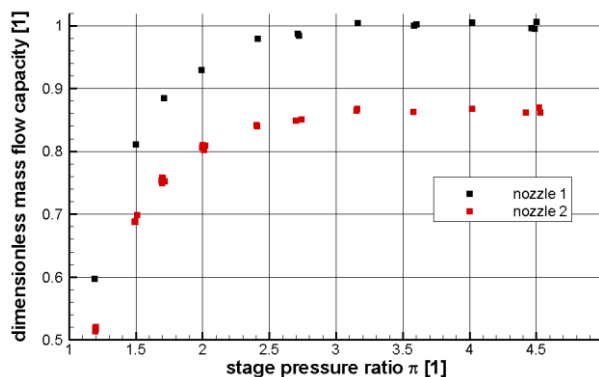


Fig. 3: Turbine mass flow capacity.

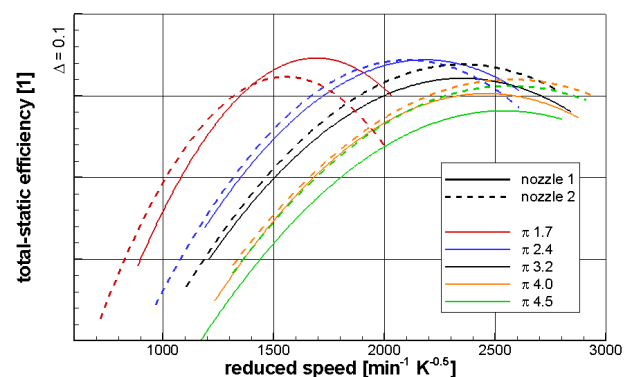


Fig. 4: Turbine efficiency changes.

### 4. Hot parameters equation

The measurement was performed under a cool flow conditions with the air, but hot parameters (H subscript) performances with exhaust gas were required. Therefore, correction to hot conditions had to

be applied. Following equations were found for the hot parameters calculation. These equations were obtained with a presumption of the equalities of Mach numbers and speed ratios of the cool and hot flow.

$$Q_{tH} = Q_t \cdot \sqrt{\frac{\kappa_H \cdot r \cdot \left(1 + \frac{\kappa_H - 1}{2} \cdot M_{isS}^2\right)^{\frac{\kappa_H + 1}{1 - \kappa_H}}}{\kappa \cdot r_H \cdot \left(1 + \frac{\kappa - 1}{2} \cdot M_{isS}^2\right)^{\frac{\kappa + 1}{1 - \kappa}}}} \quad (1)$$

$$n_{redH} = n_{red} \cdot \sqrt{\frac{\frac{\kappa_H}{\kappa_H - 1} \cdot r_H \cdot \left(1 - \pi_H^{\frac{1 - \kappa_H}{\kappa_H}}\right)}{\frac{\kappa}{\kappa - 1} \cdot r \cdot \left(1 - \pi^{\frac{1 - \kappa}{\kappa}}\right)}} \quad (2)$$

$$\pi_H = \left(1 + \frac{\kappa_H - 1}{\kappa - 1} \cdot \left(\pi^{\frac{\kappa - 1}{\kappa}} - 1\right)\right)^{\frac{\kappa_H}{\kappa_H - 1}} \quad (3)$$

Nomenclature in equations:  $c_{is}$  – stage outlet isentropic velocity,  $M_{isS}$  – nozzle outlet isentropic Mach number,  $n_{red}$  – reduced rotational speed,  $Q_t$  – mass flow capacity,  $r$  – specific gas constant,  $u$  – rotor tip velocity,  $\kappa$  – specific heats ratio,  $\pi$  – stage pressure ratio

## 5. Diffuser performance

It is a simple conical diffuser which geometry is specified by non-dimensional length  $L/d_{in} \sim 3.1$  and by area ratio  $A_{out}/A_{in} \sim 2.9$ . A pressure recovery efficiency  $\sim 0.63$  for such diffuser with uniform inlet flow can be expected.

The diffuser performance is noticeably affected by non-uniform swirling inlet flow. It is demonstrated by measured diffuser efficiency (Fig. 5). The efficiency is much higher than expected in wide range of velocity ratio  $u/c$ . It is caused by a positive effect of swirling inlet flow kinetic energy. On the other hand, the strong negative effect of diffuser inlet conditions occurs for extremely overloaded and unloaded turbine. The centrifugal force of the swirling flow causes a huge backflow region in the center of the diffuser in these regimes (see radial distribution of reduced mass flow in Fig. 7).

An increase of the turbine pressure ratio leads to a better diffuser performance, namely in optimal turbine regimes ( $u/c \sim 0.7$ ). It is shown in Fig. 6 with pressure recovery coefficient distribution along the diffuser length.

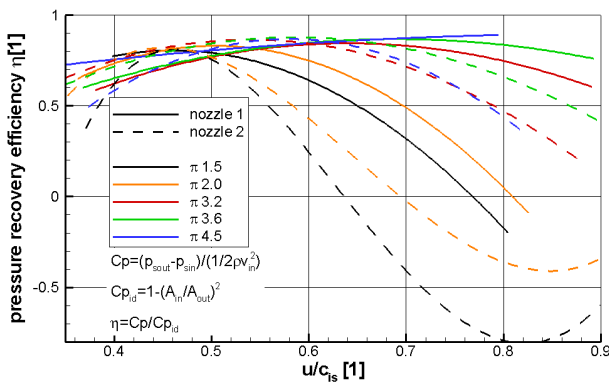


Fig. 5: The diffuser efficiency characteristic.

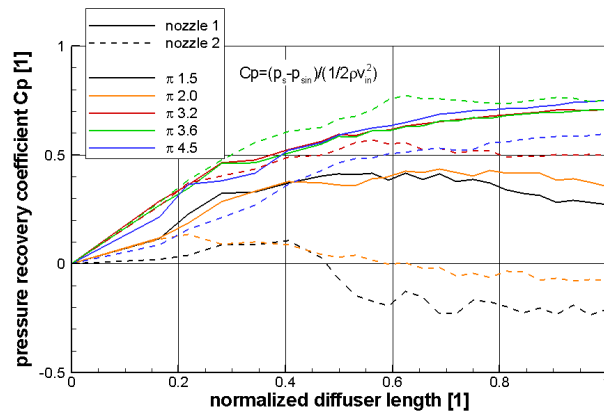


Fig. 6: Diffuser pressure recovery coefficient distribution – pressure ratio influence.

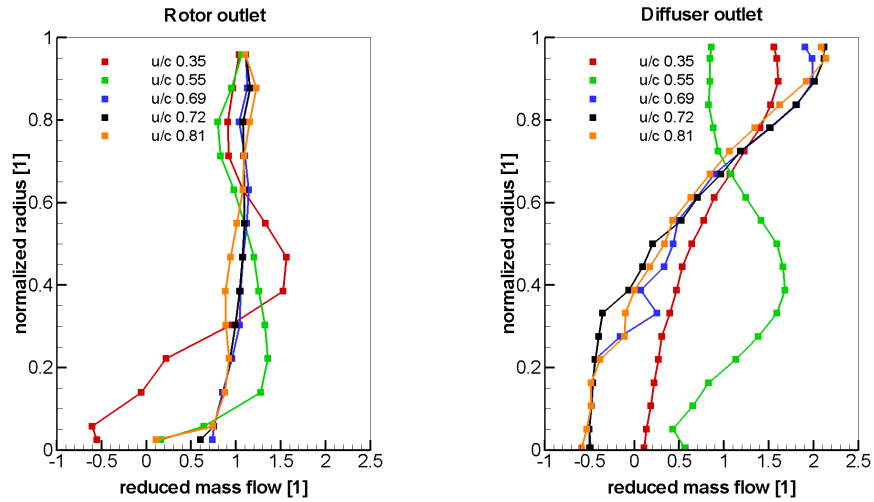


Fig. 7: Radial distribution of mass flow at the rotor outlet and the diffuser outlet (turbine pressure ratio 2.0).

## 6. Uncertainties

Uncertainty estimation was done with assumption of Gaussian distribution and confidence interval 95 %.

The most important parameters of the overall performance is the stage efficiency and the turbine mass flow capacity. These parameters are computed from conditions measured - pressure ( $\pm 0.1$  % of reading), temperature ( $\pm 1$  K), torque ( $\pm 0.13$  Nm). As a result, uncertainty of the mass flow capacity is  $\pm 0.7$  % of reading in complete range of the measurement. An estimation of total-static efficiency uncertainty is shown in graph in Fig. 8. The efficiency uncertainty shown contains also turbine bearing losses determination uncertainty, which strongly affect the uncertainty level.

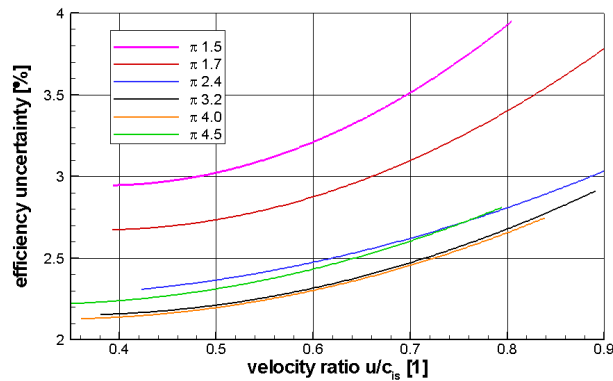


Fig. 8: Estimated turbine efficiency uncertainty (% of reading).

## 7. Conclusions

This paper has shown experimental results of the mixed-flow full stage turbine overall performance measurement. The measurement was performed in cool flow turbine test rig. The advantage of such experiment is, that the turbine stage can be equipped with standard instrumentation. Another advantage is independent flow source which ensures capturing of the turbine stage characteristics in wide range of operational conditions including off-design regimes.

The conical diffuser measurement results confirmed that efficiency of the diffuser preceded by turbine stage is completely different in comparison with a diffuser with uniform flow field at the inlet. An effect of the swirling flow on a stability of the diffuser flow field can be positive, but also strongly negative. The diffuser characteristic is strongly affected also by the absolute value of the mass flow (comparison of the nozzle 1 and 2 in Fig. 5 and 6).

## MODELING OF ROAD ROLLER DRIVE EQUIPPED WITH HYDROSTATIC RECOVERY OF KINETIC ENERGY

Z. Němec\*, J. Nevrlý\*\*

**Abstract:** The present article substantiates and describes the creation of drive model of a road roller equipped with hydraulic recovery of kinetic energy. The article introduces technical parameters of the roller, a scheme of the recovery system, a scheme of the closed hydraulic circuit of the roller, a simulation model of the pump driven by diesel engine, an example of simulation results – time courses of model quantities - and evaluation of model results.

**Keywords:** Modeling, Roller, Drive, Hydrostatic, Recovery.

### 1. Introduction

The international project “Recovery hydrostatic module for commercial vehicles”, EUREKA CZ LF12029, was solved by Brno University of Technology in cooperation with the German company Bosch Rexroth and the Swiss company AMMANN. Mathematical modeling and computer simulation were chosen to deal with the task. For this purpose, the road roller AMMANN AP 240 H (Nevrlý, 2015), a product of the Swiss company AMMANN, was selected as an experimental vehicle.

### 2. Basic parameters of road roller AMMANN AP 240 H

The road roller AMMANN AP 240 H (Nemec, 2014), a product of the Swiss company AMMANN, is a pneumatic roller for finishing of road surfaces. A structure of the roller has a basic frame of modular type on which the driver’s cabin is situated, space for a ballast reservoir and an ICE.

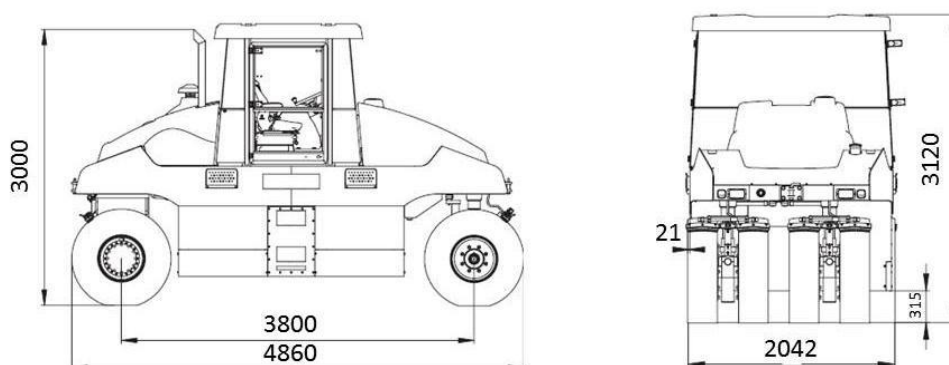


Fig. 1: Road roller AMMANN AP 240 H, basic dimensions of the roller.

### 3. Scheme of recovery system, scheme of hydraulic circuit of roller

A high-pressure accumulator (Fig. 2) accumulates the kinetic energy of the road roller during braking and delivers this energy back to the hydraulic motor during acceleration of the roller.

\* Assoc. Prof. Ing. Zdeněk Němec, CSc.: Faculty of Mechanical Engineering, Brno University of Technology, Technická 2, 616 69 Brno, CZ nemec@fme.vutbr.cz

\*\* Prof. RNDr. Ing. Josef Nevrlý, CSc.: Faculty of Mechanical Engineering, Brno University of Technology, Technická 2, 616 69 Brno, CZ, nevrlý@fme.vutbr.cz



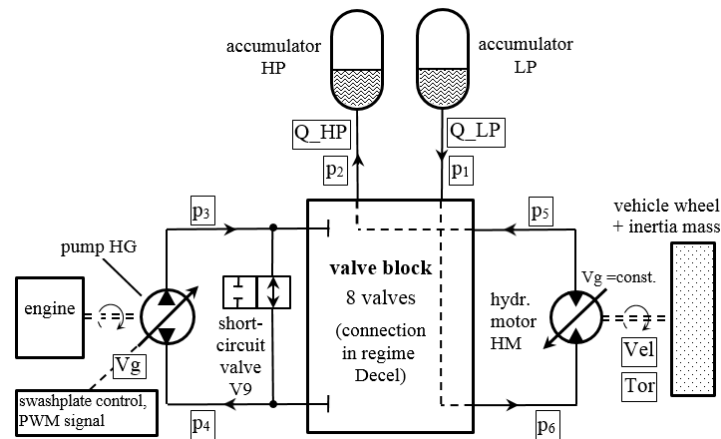


Fig. 2: The basic scheme of the recovery system.

The scheme of hydraulic circuit of the roller with the hydrostatic recovery module can be seen in Fig. 3 (regime ACCEL – acceleration). The internal combustion engine (ICE) driving the pump which delivers pressurized oil to the hydraulic circuit can be seen in the figure on the left. This oil then drove two hydraulic motors of the drive (in the figure on the left). The hydrostatic recovery module was connected to the existing hydraulic circuit of the roller as auxiliary equipment. The valve control block can be seen in the figure inside of the dashed rectangle.

Further operation regimes DECEL (braking) and FREE RUN (idle run, see as well in Fig. 5) are described in (Nevrly, 2015).

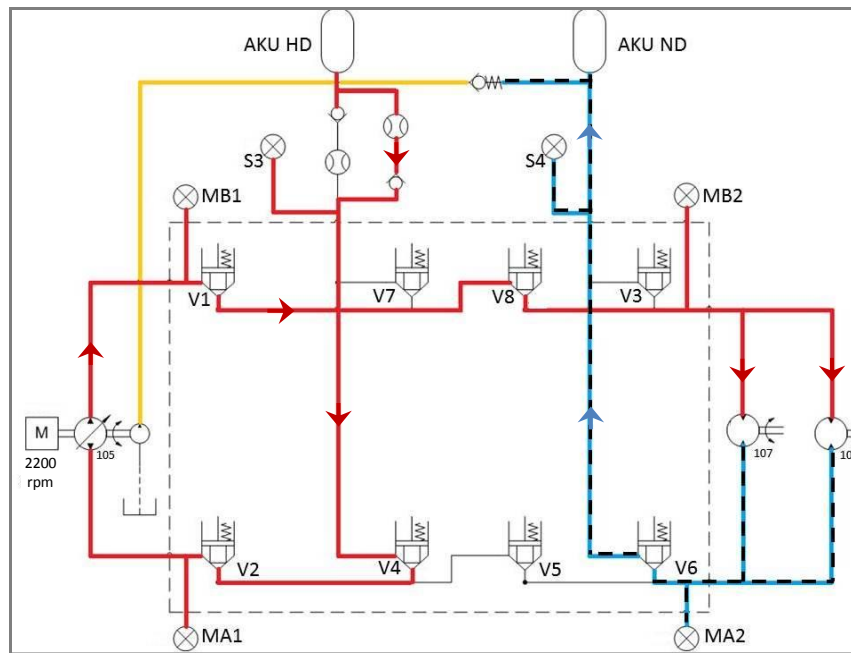
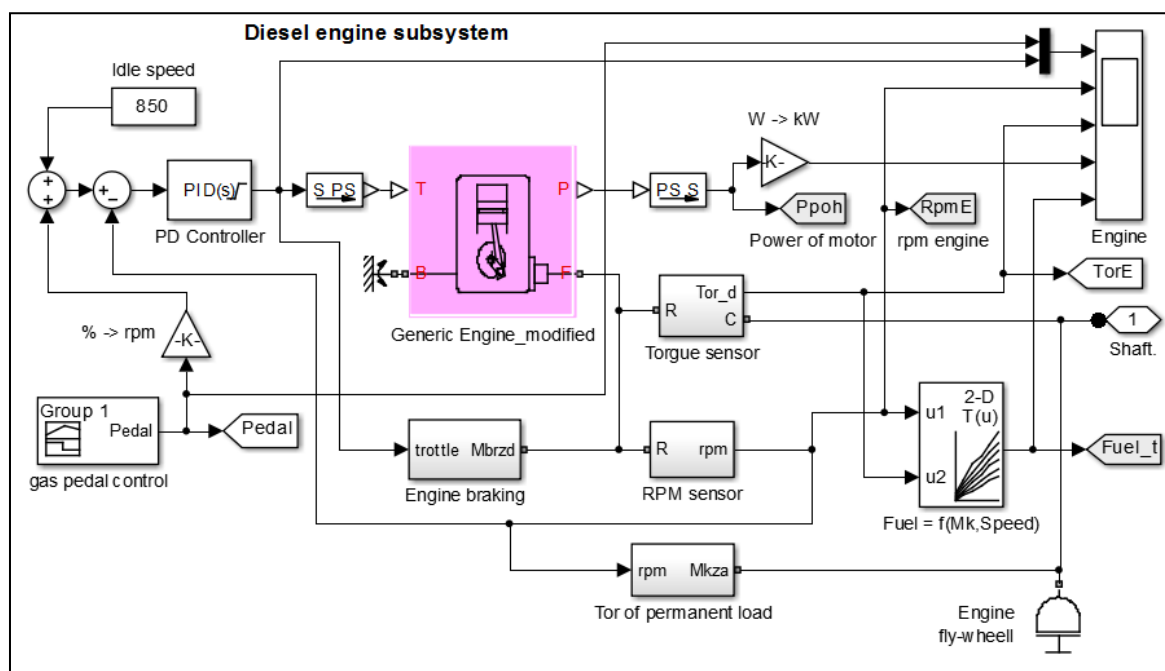


Fig. 3: The scheme of the circuit of the roller with hydrostatic recovery module (regime ACCEL).

#### 4. Mathematical model of drive

Computer simulation (Nemec, 2016; Filipi, 2010; Stecki, 2002 and Nevrlly, 2014) by software Matlab/Simulink was used to model a diesel engine pump drive. The required simulation model of diesel engine drive of the pump can be seen in Fig. 4. This model was created to analyze a fuel consumption in greater detail as well.

The main part of the roller drive model is a model of diesel engine pump drive (Fig. 4). In this case, the central member is a model of diesel engine (Generic Engine modified) which is controlled by a PD controller and connected to a torque sensor.



## 5. Computer simulation of drive

Fig. 5 illustrates the courses of valve control, pump activation, speed of hydraulic motor, speed of diesel engine, values of pressure (1 bar = 0.1 MPa) in front of hydraulic accumulators of the recovery system (see in Fig. 2).

The left part of the figure shows the acceleration of the road roller which is apparent from speed growth (the third course from above). Valves activation of the regime Accel (use of accumulated energy) can be seen in the first row from above. Growth of diesel speed is apparent in the fourth course from above. This growth is initiated by moving the pedal. Delivery of energy from high pressure accumulator is apparent from the drop of pressure  $p_2$ .

The right part of the figure also contains speed; a steeper course of diesel engine speed and hydraulic motor speed is connected with active braking due to energy recovery. Growth of pressure  $p_2$  illustrates charging of the high-pressure accumulator. The simulated courses are in reasonable agreement with the measured ones.

Measurement of fuel consumption was carried out by means of repeated tests (Nevrly, 2015) during drive on a defined test route, practical tests of the roller equipped with energy recovery were carried out during field tests.

Operating travel speed of the road roller is very low compared with some other commercial vehicles working in start-stop regime, e. g. with garbage vans, city buses, etc. Kinetic energy of vehicle translation movement, as is well known, decreases with the square of the vehicle speed. In spite of this, due to energy recovery, more than 25 % of fuel was saved at vehicle speed of mere 8.6 km/h.

## 6. Conclusion

Modeling of road roller drive equipped with hydrostatic recovery of kinetic energy was an essential part of the model of the entire road roller. This model and its parts served as a tool for design optimization. The result – fuel savings of up to 25 % at vehicle speed of only 8.6 km/h - is considered as unique. It proves that modeling is a way of how to increase effectiveness of hydrostatic recovery of kinetic energy and decrease fuel consumption.

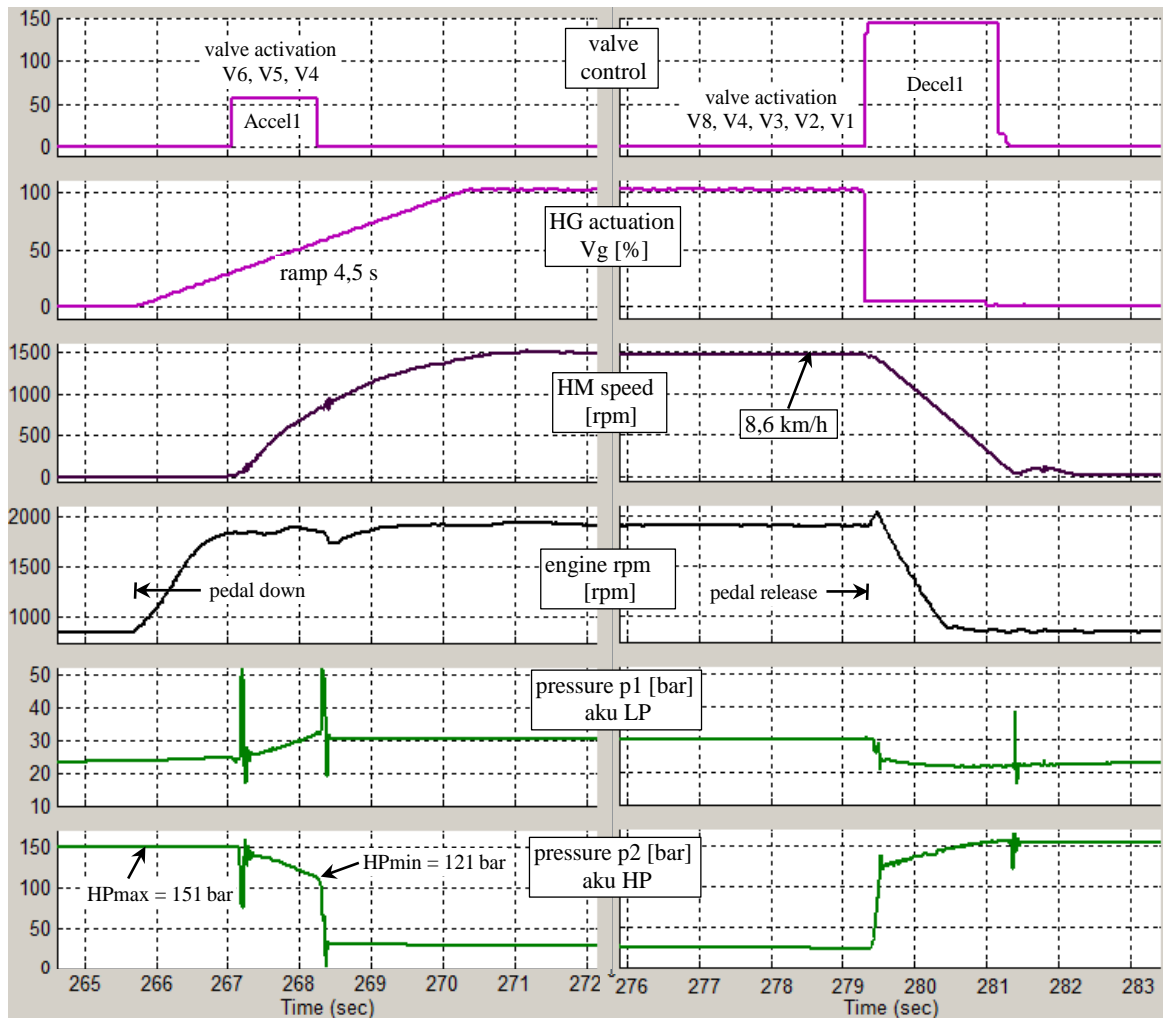


Fig. 5: Example of start and stop with weight load using energy recovery.

## Acknowledgement

This work is an output of research and scientific activities of NETME Centre, regional R&D centre built with the financial support from the Operational Programme Research and Development for Innovations within the project NETME Centre, Reg. No. CZ.1.05/2.1.00/01.0002 and, in the follow-up sustainability stage, supported through NETME CENTRE PLUS (LO1202) by financial means from the Ministry of Education, Youth and Sports under the „National Sustainability Programme I“.

## References

- Filipi, Z. and Kim, Y.J. (2010) Hydraulic Hybrid Propulsion for Heavy Vehicles: Combining of Simulation and Engine-in-the-Loop Techniques to Maximize the Fuel Economy. Oil & Gas Science and Technology - Rev. IFP. Vol. 65, No. 1, pp. 155-178.
- Nemec, Z. (2014) Models and simulation of road roller equipped with recovery hydrostatic drive. Partial research report. Faculty of Mechanical Engineering, Brno University of Technology, (in Czech).
- Nemec, Z. and Nevrlý, J. (2016) Influence of short-circuit valve on hydraulic recovery of vehicle kinetic energy. In: Dynybyl, V., Berka, O., Petr, K., Lopot, F., Dub, M. The Latest Methods of Construction Design. Switzerland, Springer International Publishing, Copyright 2016, ISBN 978-3-319-22761-0.
- Nevrlý, J. and Nemec, Z. (2014) Valve timing of recovery module of road roller. Hydraulika a pneumatika, No. 1, pp. 8-12, Hydronetech, Žilina, ISSN 1335-5171.
- Nevrlý, J. et al. (2015) Recovery hydrostatic module for commercial vehicles (in Czech). Periodic research report, project LF12029 concerning year 2014. Faculty of Mechanical Engineering BUT, Brno, (in Czech).
- Nevrlý, J. and Nemec, Z. (2015) Pump part of the hydrostatic system for kinetic energy recovery of vehicle. Inženýrská mechanika, No. 1, pp. 43-49, ISSN 1802-1484.
- Stecki, J.S. et al. (2002) Development of Hydraulic Drive for a Novel Hybrid Diesel-Hydraulic System for Large Commercial Vehicles. Fifth JFPS International Symposium on Fluid Power. Nara, Japan.

## MODELING OF CHLORIDE MIGRATION IN CONCRETE

J. Němeček<sup>\*</sup>, J. Kruis<sup>\*\*</sup>, T. Koudelka<sup>\*\*\*</sup>

**Abstract:** *In many cases, reinforced concrete structures are influenced by penetration of deteriorating salts that cause corrosion of the steel reinforcement. From a micro-structural point of view, concrete is a heterogeneous composite with tortuous pore microstructure with partially or fully saturated pores. Water in pores allows salt ions to be dissolved and transported towards reinforcement. Different mechanisms such as diffusion or convection take place. The ion convection can be caused by electromotive force acting on charged particles and is caused by an electrical potential gradient. This contribution is devoted to modeling of the diffusion-convection problem applied to chloride migration in concrete. The influence of an external electric field is studied and problems of chloride penetration and extraction are solved. It is shown in the paper that the electric field accelerates the chloride migration by multiple times compared to natural diffusion and can be used as an efficient treatment for rehabilitation of reinforced concrete structures affected by chloride attack.*

**Keywords:** Reinforced concrete, Chlorides, Electromigration, Diffusion, Convection.

### 1. Introduction

Durability issues of reinforced concrete structures are widely connected with the transport of deteriorating salts within the porous system of concrete. Serious problems of steel corrosion that can be encountered at many engineering structures such as bridge decks and columns lead to the reduction of loading capacity and ultimately to the their failure. As an indicator, critical chloride concentration at the reinforcement is used as a measure to find the onset of steel corrosion. The critical chloride level is in the order of 0.2 – 0.4 % of Cl<sup>-</sup> per cement weight and can be found in the literature (e.g. Angst, 2009; Ann, 2007). Once the corrosion starts it leads to concrete cracking and spalling of the concrete cover. The transport of salts in concrete obeys different mechanisms including diffusion and convection as the most prominent.

Repair technologies of affected structures are mostly destructive but a few non-destructive techniques like electrochemical chloride extraction (ECE) exist. The technique utilizes accelerated motion of chloride ions in electric field which is superior to diffusion. The extraction of the chlorides only takes days on a regular structure compared to diffusion of that usually takes years in which ions slowly travel to the reinforcement. The ECE method is successfully used for mitigation of chloride attack on various structures including concrete bridges.

### 2. Transport to ions in concrete

In this paper, transport of ions in saturated environment is assumed to be governed by three main driving forces. First, the concentration gradient governs the ion flux density (Fick's law) as

$$\mathbf{j}_d = -D\rho\nabla c \quad (1)$$

where  $D$  is the diffusion coefficient (m<sup>2</sup>/s),  $\rho$  is the total density of concrete (kg/m<sup>3</sup>) and  $c$  is the concentration, i.e. ratio of the weight of chlorides in an unit volume and total weight of the unit volume.

---

<sup>\*</sup> Assoc. Prof. Jiří Němeček, PhD.: Czech Technical University, Faculty of Civil. Eng., Thákurova 7, Praha 6, 16629; CZ, jiri.nemeczek@fsv.cvut.cz

<sup>\*\*</sup> Prof. Jaroslav Kruis, PhD.: Czech Technical University, Faculty of Civil. Eng., Thákurova 7, Praha 6, 16629; CZ, jk@cml.fsv.cvut.cz

<sup>\*\*\*</sup> Assist. Prof. Tomáš Koudelka, PhD.: Czech Technical University, Faculty of Civil. Eng., Thákurova 7, Praha 6, 16629; CZ, koudelka@cml.fsv.cvut.cz

In reality, the  $D$  is a function of different variables such as concrete age, porosity, degree of hydration, aggregate size, temperature, humidity and local chloride concentration (Oh, 2007; Xi, 2007). The second part of the ion flux density is driven by the intensity of applied electric field. The flux density is expressed by the Nernst-Planck equation as

$$\mathbf{j}_e = \frac{DFzc\rho}{RT} \mathbf{E} = -\frac{DFzc\rho}{RT} \nabla\Phi \quad (2)$$

where  $D$  is the diffusion (migration) coefficient ( $\text{m}^2/\text{s}$ ),  $F=96.487$  C/mol is the Faraday constant,  $z$  is the valence of ions,  $R = 8.314$  J/K/mol is the molar gas constant,  $T$  is the temperature (K),  $\mathbf{E}$  is the intensity of electric field (V/m),  $\Phi$  is the electric potential (V). More details can be found in (Černý, 2002). Finally, ion transport can be driven by water convection in which case the ion flux density is

$$\mathbf{j}_c = \rho c \mathbf{v}. \quad (3)$$

Overall, the total flux density of ions has the form

$$\mathbf{j}_c + \mathbf{j}_d + \mathbf{j}_e = \rho \left( -D\nabla c - \frac{DFzc}{RT} \nabla\Phi + c\mathbf{v} \right). \quad (4)$$

The mass balance equation for ions has the form

$$\frac{\partial c}{\partial t} = \text{div} \rho \left( D\nabla c + \frac{DFzc}{RT} \nabla\Phi - c\mathbf{v} \right). \quad (5)$$

An electric field can be applied to accelerate the extraction of ions from concrete in repair applications because pure diffusion would be very slow. In these applications, the electric field is given and it can be assumed to be constant in time. Therefore, the last two terms in the balance equation could be aggregated into a single term as

$$c\hat{\mathbf{v}} = \frac{DFzc}{RT} \nabla\Phi - c\mathbf{v}. \quad (6)$$

Special attention must be devoted to the gradient of the electric potential, In many papers on the ion penetration or extraction, the gradient of the electric potential is assumed to be constant which is generally not true, especially in the case of reinforced structures with sparse reinforcing bars that serve as counter electrodes. In contrary, the electric potential has to satisfy the Gauss law of electrostatics in the form

$$\varepsilon_r \varepsilon_o \text{div} \mathbf{E} = \varepsilon_r \varepsilon_o \Delta\Phi = \varphi \quad (7)$$

where  $\varphi$  is the density of charge ( $\text{C}/\text{m}^3$ ),  $\varepsilon_r$  is the relative permittivity (-) and  $\varepsilon_o = 8.854 \cdot 10^{-12}$  F/m is the permittivity of the vacuum. Equation (7) has to be solved for an appropriate domain and boundary conditions first. The electric potential obtained is then used in calculation of the flux density (6). With the help of (6) one can rewrite the mass balance equation (5) as

$$\frac{\partial c}{\partial t} = \text{div} D\nabla c + \text{div}(c\hat{\mathbf{v}}). \quad (8)$$

The term  $\text{div} D\nabla c$  represents the diffusion and the term  $\text{div}(c\hat{\mathbf{v}})$  represents the convection. The convection term can be further modified into the form

$$\frac{\partial c}{\partial t} = \text{div} D\nabla c + \hat{\mathbf{v}}^T \nabla c \quad (9)$$

because the mass balance equation for water is described by  $\text{div} \mathbf{v} = 0$  and the charge density is zero. The mass balance equation (9) is defined on a domain  $\Omega$  with boundary  $\Gamma$  which is split into two disjoint parts  $\Gamma_D$  and  $\Gamma_N$ . The concentration is prescribed on  $\Gamma_D$  (Dirichlet boundary condition) while ion flux density is prescribed on the part  $\Gamma_N$  (Neumann boundary condition). The problem is solved in time interval  $(0, t_{\max})$ . Because of the time dependent problem, initial condition has to be defined. The boundary and initial conditions can be written in the form

$$\forall \mathbf{x} \in \Gamma_D, t \in (0, t_{\max}): c(\mathbf{x}, t) = c_D(\mathbf{x}, t) \quad (10)$$

$$\forall \mathbf{x} \in \Gamma_N, t \in (0, t_{\max}) : \mathbf{n}^T \mathbf{j}(\mathbf{x}, t) = j_N(\mathbf{x}, t) \quad (11)$$

$$\forall \mathbf{x} \in \Omega : c(\mathbf{x}, 0) = c_0(\mathbf{x}) \quad (12)$$

where  $c_D$  is the prescribed concentration,  $\mathbf{n}$  is the unit normal vector to  $\Gamma_N$ ,  $j_N$  is the prescribed ion flux density in the normal direction to the boundary  $\Gamma_N$  and  $c_0$  is the initial concentration. The problem (9-12) was solved by the finite element method based on the Galerkin-Petrov approach.

### 3. Numerical example

As an example, chloride extraction process accelerated by an electric field from a cantilever bridge deck with a barrier was modeled with the help of numerical approach described above. Scheme of the bridge deck part with the vertical barrier is shown as a blue domain in Fig. 1a. Prior to extraction part of the domain (white line in Fig. 1a) was exposed to 10 years of chloride diffusion. The chloride concentration distribution after this exposure on the deck and barrier is shown in Fig. 1b. For this simulation, the diffusion coefficient of concrete was assumed as  $7.4 \cdot 10^{-12} \text{ m}^2/\text{s}$ . For the extraction process, the electric field was created by the application of voltage of 20 V to the reinforcement while 0 V was assumed on the top deck and the top and left cornice surface. Distribution of the electric potential was obtained from equation (7) where the permittivity of concrete is  $39.843 \cdot 10^{-12} \text{ F/m}$  and the permittivity of the air is  $8.854 \cdot 10^{-12} \text{ F/m}$ . It should be emphasized that the mesh is larger than the deck with cornice itself because the electric potential is distributed also in their vicinity (green domain in Fig. 1a). The distribution of the electric potential is depicted in Fig. 2.

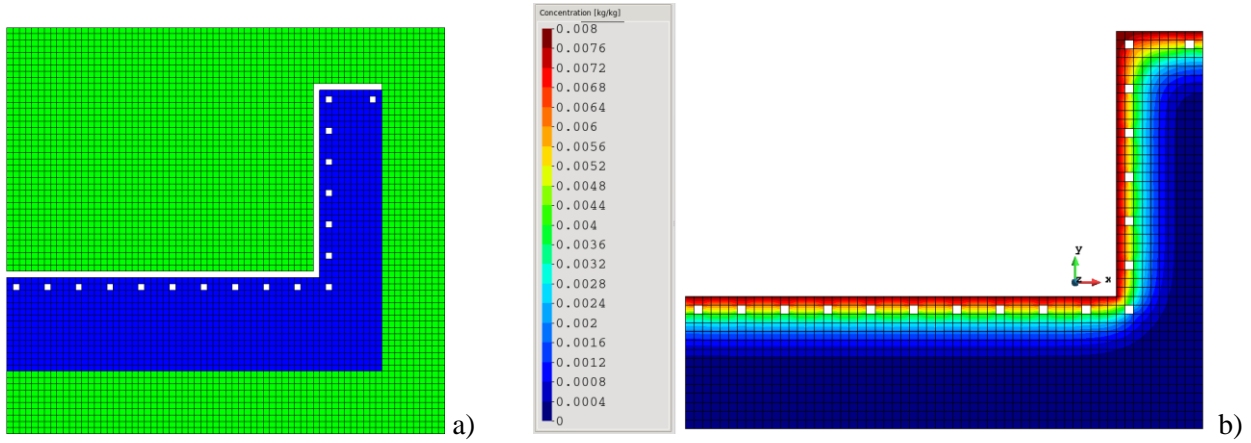


Fig. 1: a) FE mesh; b) Distribution of the chloride concentration after 10 years of exposure.

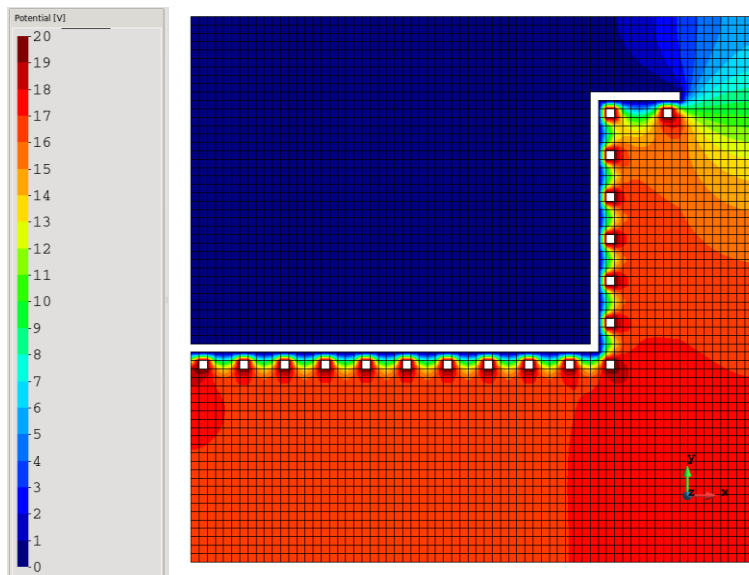


Fig. 2: Distribution of the electric potential.



The extraction process was prescribed by imposing Dirichlet boundary condition (zero Cl concentration to the deck and barrier top surface) lasting for 48 hours. Concentration from Fig. 1a was assumed as an initial condition. Fig. 3 shows distribution of the chloride concentration in two times 8.2 and 48 hours after the start of extraction. It can be seen in Fig. 3 that the process is highly efficient and after 48 hours leads to zero surface concentration and 80 % reduction of original concentration at the reinforcement layer. It can also be seen that still high chloride concentrations remain behind the reinforcement and are not extracted. The reason lies in the distribution of the electric field (Fig. 3) that does not allow the development of a higher potential gradient in this region. Thus, the extraction is only effective for the chlorides located in front and partially between the reinforcement bars. Chlorides located behind the reinforcement either stay there or need to be extracted later after their diffusion to upper concrete layers.

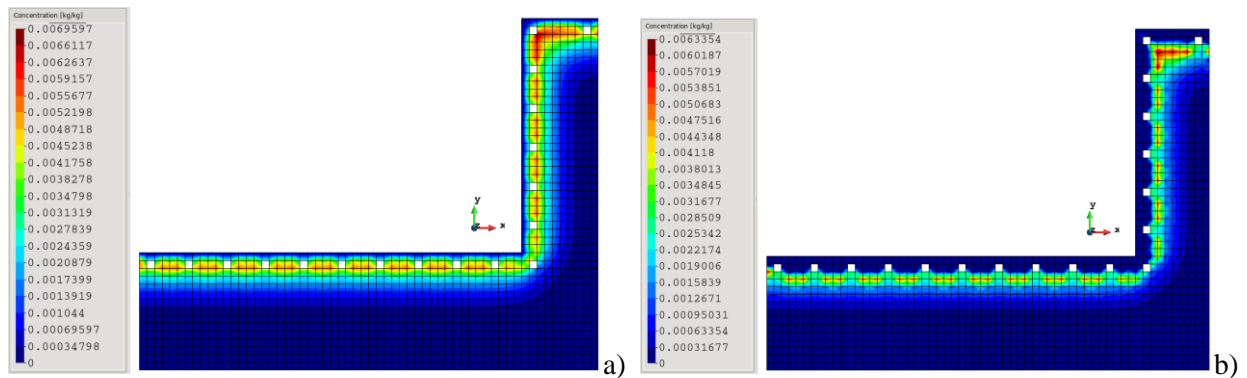


Fig. 3: Chloride concentration after extraction in time of: a) 8.2 hours; b) 48 hours).

#### 4. Conclusions

The paper shows a numerical framework for the solution of convection-diffusion process applied to a practical example of chloride penetration and extraction on a bridge deck with vertical barrier. The framework is based on the finite element solution of the extended Nernst-Planck equation. The electric potential is described by the Gauss law of electrostatics and gives uneven distribution within the reinforced concrete structure. Electrochemical chloride extraction process is solved in the example to show the efficiency of the repair technology applied to a real structure and to show the effect of uneven potential gradient distribution. Although, the extraction was found to be very efficient between the deck surface and the reinforcement, caution must be paid to the regions between and behind the reinforcement where the potential gradient is small leading to decreased efficiency of the method.

#### Acknowledgement

Financial support of the Czech Science Foundation (project 16-11879S) is gratefully acknowledged.

#### References

- Angst, U., Elsener, B. and Larsen, C.K. (2009) Vennesland, Critical chloride content in reinforced concrete a review, *Cement and Concrete Research* 39 (12), 1122-1138.
- Ann, K.Y. and Song, H.-W. (2007) Chloride threshold level for corrosion of steel in concrete, *Corrosion Science* 49 (11), 4113-4133.
- Oh, B.H. and Jang, S.Y. (2007) Effects of material and environmental parameters on chloride penetration profiles in concrete structures, *Cement and Concrete Research* 37 (1), 47-53.
- Xi, Y. and Bazant, Z. (1999) Modeling chloride penetration in saturated concrete, *J. Mater. Civ. Eng.* 11 (1), 51-57.
- Černý, R. and Rovnaníková, P. (2002) *Transport Processes in Concrete*, Spon Press, London, New York, ISBN 0-415-24264-9.

## MODIFICATIONS OF CONTROL ACTUATION SYSTEMS OF ATGM

L. Nocoń<sup>\*</sup>, Z. Koruba<sup>\*\*</sup>

**Abstract:** *The paper presents the modifications of missile control actuation systems. The control actuation system was modified by adding a swiveling nozzle of the rocket engine. In that way, a hybrid control system consisting of aerodynamic rudders and gasodynamic rudders (i.e. change of the direction of the rocket engine thrust). The control effectiveness with the use of aerodynamic rudders alone was compared with ATGM control effectiveness with the use of the hybrid control actuation system. The results of the research are shown in a graphical form.*

**Keywords:** Anti-tank guided missile, Engine thrust vectorization, Control actuation systems, Homing.

### 1. Introduction

An anti-tank guided missile (ATGM) should consist of components cooperating well with each other and be characterized with great maneuverability which guarantees hitting the target effectively. The control actuation system, whose task is to respond to control signals effectively and quickly, is responsible for the maneuverability of the anti-tank guided missile. These signals are transmitted from the autopilot as a result of the homing algorithm, as e.g. in the article (Grzyb, 2016; Stefański et al., 2014 and Koruba, 2013). The autopilot is the brain of the whole missile. It is responsible for a rapid processing of information about the missile and target position in space. The scanning and tracking seeker (Gapinski, 2014a; Gapinski, 2014b; Koruba, 2010 and Koruba, 2013) is one of the main components transferring the data to the autopilot. It provides information about the angular position of the line of sight.

In urban areas and areas with a different topography, a missile capable of omitting the obstacles is required. Therefore, the control actuation system of the anti-tank guided missile needs to be facilitated and its maneuverability needs to be increased. A hybrid control actuation system consisting of aerodynamic rudders and a swiveling nozzle of the rocket engine was applied. Popular aerodynamic rudders are ineffective at the stage of starting and accelerating. Their effectiveness increases with the increase of the flight velocity (the control force is proportional to the square of the flight velocity). In the case of anti-tank guided missiles, the cruise velocity of which does not exceed 250 m/sec., providing the control with the thrust vector of the rocket engine can improve the maneuverability of the anti-tank guided missile. Thus, the anti-tank guided missile will be controlled effectively from the start, when the missile is at the stage of increasing its velocity. A booster engine of much greater thrust than during the stage of a marching flight operates in this phase. A marching flight is performed at a constant velocity, with the aerodynamic rudders and the swiveling engine nozzle cooperating well and stably with each other. The essence of this paper is to check, whether the maneuverability of the anti-tank guided missile will be improved if a hybrid executive system is applied.

### 2. The object of control

A mid-range anti-tank guided missile, type: fire & forget, is the object of control (Fig. 1). The missile is stabilized along longitudinal axis  $S\xi$  and does not perform any rotations on it. It is controlled by two

---

<sup>\*</sup> Research Assistant Łukasz Nocoń, M.Sc.Eng.: Department of Applied Computer Science and Armament Engineering, Faculty of Mechatronic and Mechanical Engineering, Kielce University of Technology, Aleja Tysiąclecia Państwa Polskiego 7; 25-314, Kielce; PL, lnocon@tu.kielce.pl

<sup>\*\*</sup> Prof. dr. habil. Zbigniew Koruba, Eng.: Department of Applied Computer Science and Armament Engineering, Faculty of Mechatronic and Mechanical Engineering, Kielce University of Technology, Aleja Tysiąclecia Państwa Polskiego 7; 25-314, Kielce; PL, ksmzko@tu.kielce.pl

channels: separately for the channel controlling the height, and separately for the channel controlling the flight direction. The aim of the dual control actuation system is to minimize the control angles and maximize the reproduction of the set flight trajectory. It is assumed that the missile moves in dense air streams.

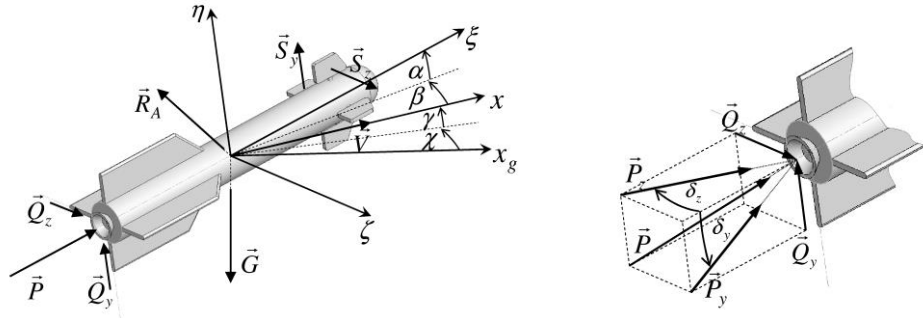


Fig. 1: The system of forces affecting the anti-tank guided missile with the accepted system of axes. The pattern of arising the control forces out of deviations of the nozzle of the rocket engine.

In Fig. 1 the following quantities and marking were introduced:  $\vec{R}_A$  – vector of net aerodynamic forces;  $\vec{P}$  – missile engine thrust;  $\vec{G}$  – gravity;  $\vec{Q}_Y, \vec{Q}_Z, \vec{S}_Y, \vec{S}_Z$  – controlling forces;  $\vec{V}$  – missile velocity vector;  $Sx_g y_g z_g$  – ground-fixed system;  $Sxyz$  – system of coordinates connected with the flow;  $S\xi\eta\zeta$  – system of coordinates connected with the missile (body-fixed system);  $\alpha = \vartheta - \gamma$  – missile angle-of-attack;  $\beta = \psi - \chi$  – missile sideslip angle;  $\gamma, \chi$  – flight-path angles;  $\delta_z$  – horizontal control angle of nozzle,  $\delta_y$  – vertical control angle of nozzle.

The equations of dynamics (1a – 2c) of the missile flight are consistent with the accepted coordinate systems and the forces affecting the missile (Fig. 1) (Koruba, 2016 and Harris, 2009).

$$m\dot{V} = P \cos \alpha \cos \beta - G \sin \gamma - m\lambda_x V^2 \quad (1a)$$

$$mV\dot{\gamma} = P \sin \alpha - G \cos \gamma + m\lambda_y \alpha V^2 + Q_Y + S_Y \quad (1b)$$

$$mV\dot{\chi} \cos \gamma = P \cos \alpha \sin \beta - m\lambda_z \beta V^2 - Q_Z - S_Z \quad (1c)$$

$$\omega_\xi = \dot{\psi} \sin \vartheta, \quad \omega_\eta = \dot{\psi} \cos \vartheta, \quad \omega_\zeta = \dot{\vartheta} \quad (2a)$$

$$\dot{\omega}_\eta + \left( \frac{J_{ok}}{J_k} - 1 \right) \omega_\xi \omega_\zeta = -D_1 \frac{\beta}{L} V^2 - D_2 V \dot{\beta} - D_3 V \dot{\psi} - e \frac{Q_Z}{J_k} + f \frac{S_Z}{J_k} \quad (2b)$$

$$\dot{\omega}_\zeta + \left( \frac{J_{ok}}{J_k} - 1 \right) \omega_\xi \omega_\eta = -D_1 \frac{\alpha}{L} V^2 - D_2 V \dot{\alpha} - D_3 V \dot{\vartheta} - e \frac{Q_Y}{J_k} + f \frac{S_Y}{J_k} \quad (2c)$$

where:  $m$  – mass of the missile;  $\lambda_x, \lambda_y, \lambda_z$  – coefficients of aerodynamic forces;  $D_i = (C_i L) / J_k$ ;  $C_1, C_2, C_3$  – coefficients of aerodynamic moments (constans values were adopted);  $J_{ok}, J_k$  – main central moments of inertia of the missile in relation to vertical and horizontal axes of the missile;  $L$  – length of the missile;  $e, f$  – the distance of the missile centre of mass from the controlling force;  $\vartheta$  i  $\psi$  – pitch and yaw angle of the missile body.

Deviations of the thrust vector of the rocket engine from the longitudinal missile result from the control forces in both surfaces (Fig. 1). In the vertical plane the force controlling the height of the flight is arising  $\vec{Q}_Y$ , and in the horizontal plane - the force controlling the direction of the flight  $\vec{Q}_Z$  (Nocoń, 2016).

$$Q_Y = \sqrt{\frac{P^2 \cos^2 \delta_z \cdot \sin^2 \delta_y}{1 - \sin^2 \delta_z \cdot \sin^2 \delta_y}} \approx P \cdot \delta_y, \quad Q_Z = \sqrt{\frac{P^2 \cos^2 \delta_y \cdot \sin^2 \delta_z}{1 - \sin^2 \delta_z \cdot \sin^2 \delta_y}} \approx P \cdot \delta_z \quad (3)$$

The aerodynamic rudders are located in the front part of the missile. A lightweight layered composite construction of the rudders (Chatys, 2013) guarantees a quick reaction to the control signals. For low angles of deviation of the aerodynamic rudders  $\alpha_Y, \alpha_Z$  it is true that lift and lateral (controlling) forces  $S_Y, S_Z$  which were formed on the rudder surface, take a simplified form of the equation:

$$S_Y = 2\alpha_Y S \rho \frac{V^2}{2}, \quad S_Z = 2\alpha_Z S \rho \frac{V^2}{2} \quad (4)$$

where:  $S$  - surface of the rudders;  $\rho$  - air density.

The signals controlling the missile are calculated with the use of an implemented control algorithm developed in the articles (Koruba, 2016). A dual PID controller is applied. It was assumed that the control angles for both executive systems are the same but have opposite signs:  $\delta_y = -\alpha_Y, \delta_z = -\alpha_Z$ .

$$\alpha_Y = k_{y1}e_y + k_{y2}\frac{de_y}{dt} + k_{y3}\int_{t_0}^{t_k} e_y dt + h_{y1}f_y + h_{y2}\frac{df_y}{dt} + h_{y3}\int_{t_0}^{t_k} f_y dt \quad (5a)$$

$$\alpha_Z = k_{z1}e_z + k_{z2}\frac{de_z}{dt} + k_{z3}\int_{t_0}^{t_k} e_z dt + h_{z1}f_z + h_{z2}\frac{df_z}{dt} + h_{z3}\int_{t_0}^{t_k} f_z dt \quad (5b)$$

where:  $e_y = \gamma^\circ - \gamma$ ;  $e_z = \chi^\circ - \chi$ ;  $f_y = y - y_p$ ;  $f_z = z - z_p$ ;  $\gamma, \chi, y_p, z_p$  – real coordinates of the ATGM;  $\gamma^\circ, \chi^\circ, y, z$  – coordinates of the planned trajectory result of the homing algorithm.

### 3. The simulation results

The following figures present the results of the numerical simulation of the anti-tank guided missile passing through two points  $P_1(100; 4; 0)$  and  $P_2(300; 2; -8)$ . The target starts from point  $P_C(500; 1; 0)$  and moves at a velocity of 30 m/sec., and deviates by  $\chi_C = 30^\circ$  in the horizontal plane. The simulation presents the results obtained for the hybrid control actuation system as well as for the single system consisting only of aerodynamic rudders.

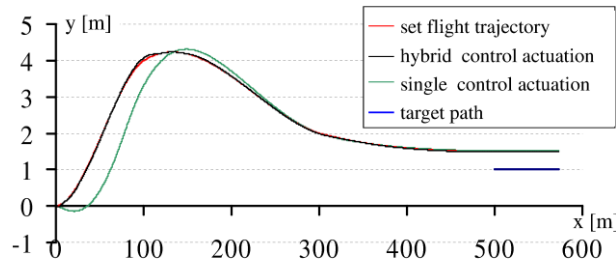


Fig. 2: The realized and set flight trajectory in the vertical plane detailing the hybrid and single control.

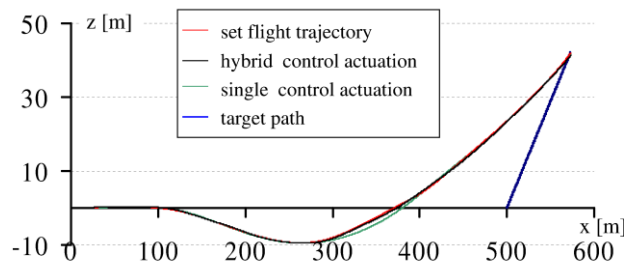


Fig. 3: The realized and set flight trajectory in the horizontal plane detailing the hybrid and single control.

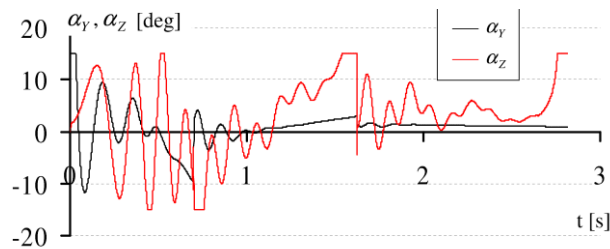


Fig. 4: The realized angles of the flight control in the channel of height and direction for the hybrid executive system.



Fig. 5: The realized angles of the flight control in the channel of height and direction for the single executive system.

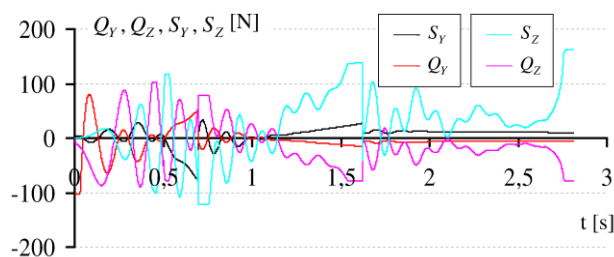


Fig. 6: The realized control forces of the anti-tank guided missile with the hybrid executive system.

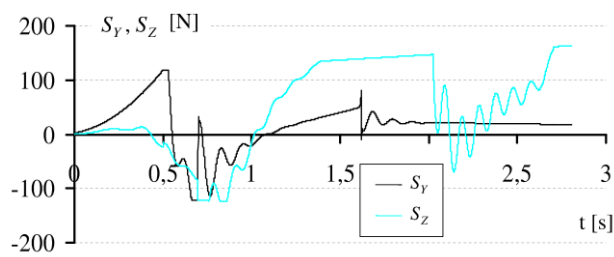


Fig. 7: The realized control forces of the anti-tank guided missile with the aerodynamic rudders alone.

#### 4. Conclusions

Taking the above presented comparison of two control actuation systems into consideration, it might be concluded that a hybrid executive system consisting of aerodynamic rudders and a swiveling nozzle of the rocket engine performs the set trajectory in a better way than a single executive system consisting only of aerodynamic rudders. A hybrid control is effective right from the start of the anti-tank guided missile when its velocity is low (Fig. 2). The effectiveness of control only with the aerodynamic rudders is greater with the velocity increase of the anti-tank guided missile and thus, the first 0.5 sec. of control are ineffective. Control only with the aerodynamic rudders is effective after during the first 0.5 sec. Adding vectorization of the rocket engine thrust improves the maneuverability of the anti-tank guided missile significantly. Instead of two controlling forces – there are four. Two forces control the height, whereas the remaining two control the direction of the flight (Fig. 6). The rocket engine thrust is responsible for controlling the flight at its initial stage, even though the deviation angles of the rudders and the rocket engine nozzle are equal. Additionally, for the period of the booster operation, the deviation angles of the nozzle are limited to 10 % of the deviation possibilities.

#### References

- Chatys, R. (2013) Investigation of the Effect of Distribution of the Static Strength on the Fatigue Failure of a Layered Composite by Using the Markov Chains Theory. *Mechanics of Composite Materials*, vol. 48, No. 6, pp. 629-638
- Gapinski, D. and Krzysztofik, I. (2014a) The process of tracking an air target by the designed scanning and tracking seeker, in: *Proc. 2014 15th Int. Carpathian Control Conf.* (eds. Petras, I., Podlubny, I., Kacur, J. and Farana, R.), IEEE, pp. 129-134.
- Gapinski, D., Koruba, Z. and Krzysztofik, I. (2014b) The model of dynamics and control of modified optical scanning seeker in anti-aircraft rocket missile. *Mechanical Systems and Signal Processing*, 45, 2, pp. 433-447.
- Grzyb, M., and Stefanski, K. (2016) The use of special algorithm to control the flight of anti-aircraft missile, in: *Proc. 22th Int. Conf. Eng. Mech. 2016* (eds. Zolotarev, I. and Radolf, V.), Svratka, Czech Republic, pp. 174-177.
- Harris, J., and Slegers, N. (2009) Performance of a fire-and-forget anti-tank missile with a damaged wing. *Mathematical and Computer Modelling*, Vol. 50, 1-2, pp. 292-305.
- Koruba, Z., Dziopa, Z. and Krzysztofik, I. (2010) Dynamics of a controlled anti-aircraft missile launcher mounted on a moveable base, *Journal of Theoretical and Applied Mechanics*, 48, 2, pp. 279-295.
- Koruba, Z. and Krzysztofik, I. (2013) An algorithm for selecting optimal controls to determine the estimators of the coefficients of a mathematical model for the dynamics of a self-propelled anti-aircraft missile system, in: *Proc. of the Institution of Mechanical Engineers, Part K: Journal of Multi-Body Dynamics*, 227, 1, pp. 12-16.
- Koruba, Z. and Ładyżyńska-Kozdraś, E. (2010) The dynamic model of a combat target homing system of an unmanned aerial vehicle. *Journal of Theoretical and Applied Mechanics*, 48, 3, pp. 551-566.
- Koruba, Z. and Nocoń, Ł. (2016) Numerical analysis of the dynamics of automatically tracked anti-tank guided missile using polynomial functions, *Journal of Theoretical and Applied Mechanics*, 54, 1, pp. 13-25.
- Nocoń, Ł. and Koruba, Z. (2016) Optimal compensator for anti-ship missile with vectorization of engine thrust. *Applied Mechanics and Materials*, Vol. 817, pp. 279-288.
- Stefański, K., Grzyb, M. and Nocoń, Ł. (2014) The Analysis of Homing of Aerial Guided Bomb On the Ground Target By Means of Special Method of Control, in: *Proc. 2014 15th Int. Carpathian Control Conf.* (eds. Petras, I., Podlubny, I., Kacur, J., and Farana, R.), IEEE, pp. 551-556.

## IMPACT OF STRENGTHENING OF THE ERECTOR SPINAE MUSCLE ON THE VALUES OF LOADS OF THE MUSKULOSKELETAL SYSTEM IN THE LUMBAR SPINE SECTION

K. Nowakowska<sup>\*</sup>, R. Michnik<sup>\*\*</sup>, A. Myśliwiec<sup>\*\*\*</sup>, M. Chrzan<sup>\*\*\*\*</sup>

**Abstract:** *This work aimed to determine resultant changes of reactions in the lumbar spine section (L5-Sacrum) influenced by strengthening of the erector spinae (spinal erectors) muscle. Identification of the loads of the musculoskeletal system was conducted by means of a mathematical model of the human body created in the Anybody Modeling System environment. The results of the measurements of kinematics were used as input data. Strengthening of the muscle was simulated by increasing a maximum isometric force which could be generated by a single muscle by means of increasing its physiological cross section. On the basis of the performed calculations, it was observed that the increase in the cross section of the transverse erector spinae muscle causes the increase of reactions in the L5-Sacrum joint, simultaneously lowering the strength of the transverse abdominal muscle and the value of the intra-abdominal pressure. Conclusions resulting from this research may be used in physiotherapeutic practice for the selection of exercises which aim to reduce pain ailments in the lumbar spine section.*

**Keywords:** Anybody Modeling System, Erector spinae muscles, Mathematical modeling, Lumbar spine.

### 1. Introduction

Pains occurring in the lower part of the back are one of the most common chronic ailments. They cause considerable limitations to movement and make it impossible to maintain a correct body posture. Pain in the lower section of the spine is commonly caused by weak paraspinal muscles, i.e. the muscles stabilizing the spine. The stabilization of the spine in its lumbar section is influenced by: paraspinal muscles and abdominal muscles. In most cases, pain in the lower part of the spine results from overload caused by a sedentary lifestyle. In physiotherapeutic practice the decrease of suffering due to pain in the lumbar section is carried out by means of exercises strengthening selected groups of muscles. A therapeutic programme usually consists of two main parts aiming to strengthen deep abdominal muscles and to increase the strength of dorsal muscles. In order to effectively run physiotherapeutic workout, it is necessary to determine the impact of exercises strengthening certain muscle groups on the load values in the lumbar spine section. Nowadays, mathematical modelling and optimization methods constitute the only non-invasive methods which enable the determination of the values of loads in the skeletal system and evaluation of the force value generated by the muscles during a certain movement (Nowakowska, 2017).

This work aimed to define a change of the values of the loads exerted on the musculoskeletal system in the area of the lumbar spine due to strengthening of the erector spinae muscle.

---

<sup>\*</sup> Katarzyna Nowakowska, MSc. Eng.: Department of Biomechanics, Faculty of Biomedical Engineering, Silesian University of Technology; Poland, Katarzyna.Nowakowska@polsl.pl

<sup>\*\*</sup> Robert Michnik, PhD. DSc. Eng: Department of Biomechanics, Faculty of Biomedical Engineering, Silesian University of Technology; Poland, Robert.Michnik@polsl.pl

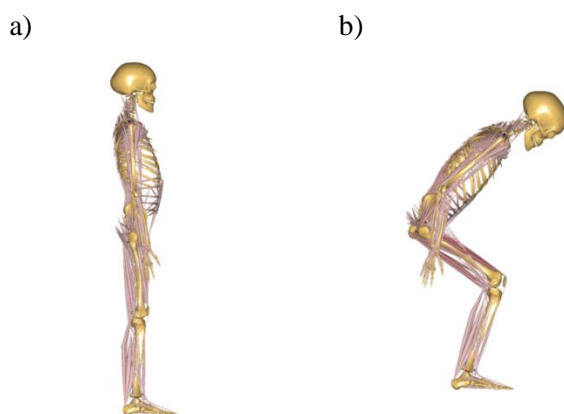
<sup>\*\*\*</sup> Andrzej Myśliwiec, PhD. DSc. Eng: Department of Kinesiotherapy and Special Methods of Physiotherapy, Academy of Physical Education in Katowice; Poland, a.mysliwiec@awf.katowice.pl

<sup>\*\*\*\*</sup> Miłosz Chrzan, MSc. Eng.: Department of Biomechanics, Faculty of Biomedical Engineering, Silesian University of Technology; Poland, Milosz.Chrzan@polsl.pl



## 2. Methods

In order to determine loads exerted on the human body, the Anybody Modeling System environment was used. This software programme provided a modified model of the whole body ('Standing Model'), in which feet have a constant contact with the ground. The model consisted of 69 bones, which were modelled as rigid bodies connected by means of various kinematic pairs as well as over 1000 muscle actons. Forces generated by particular muscles were modelled by means of a Hill-type dependency. Over 180 actons of dorsal muscles and abdominal muscles as well as the impact of intra-abdominal pressure were taken into consideration in the model of the lumbar spine section (Zee, 2007). The values of muscular forces were determined on the basis of a static optimization procedure. A set of equations of balance of individual parts of the model creates boundaries of an optimization task and the objective function describes controlling of the work of muscles by the nervous system. The so-called energy criterion consisting in the energy expenditure minimization was applied in the performed calculations. According to this criterion, the objective function was adopted in a form of a sum of the cubes of muscle forces. The static optimization procedure requires the input of kinematic data into the model. The first stage of the work encompassed experimental tests of motion kinematics of sitting down on a chair and standing up using an optic system called APAS. The determined angles in the joints were entered into the model enabling thus the performance of simulations of loads of the musculoskeletal system. The simulations were carried out for a model of a 50-centile woman of a weight of 65 kg and a body height of 1.65 m. The applied model was calibrated according to the ScalingLengthMassFat procedure. At the beginning of this procedure the body height and weight are entered into the system enabling thus the calculation of the Body Mass Index (BMI). This index is next used to evaluate fat tissue. Lengths of particular elements of body segments are evenly calibrated according to the defined body height of a given person, whereas the percentage of fat tissue is used for the assessment of muscular forces. The applied model of the whole body was subjected to verification consisting in the comparison of the results obtained on the basis of simulations of the activation of the erector spinae muscle with the EMG signal recorded during experimental tests. Moreover, the values of reactions obtained in intervertebral joint Th12-L1 coincide with the results of in vivo measurements conducted by Rohlman et al. (2014). The application of the methods of mathematical modelling and static optimization (enabling the solution of the reverse dynamic task) made it possible to determine the values of loads of the musculoskeletal system in the lumbar spine section, i.e. the reaction components in individual intervertebral joints and the values of muscular forces. This work encompassed the research on the impact of the strengthening of the erector spinae muscle on the obtained values of loads exerting forces in the area of the lumbar spine. The effect of the strengthening of the muscle was achieved by introducing various values of physiological cross section (PCSA) into the model of muscular forces. The force generated by a muscle depends on the above-mentioned PCSA values. Simulations were performed by means of increasing the PCSA values of the erector spinae muscle by 25 %, 50 %, 75 % and 100 %. The model of the erector spinae muscle consisted of four groups of muscles, which were divided into the total number of 29 bundles – muscle fibres on each side, according to the description by Bagduk et al. (1992). Simulations were performed for two selected positions of the recorded activity, i.e. for the upright standing position and sitting down (just until the moment of touching the surface of the chair). The applied model and analyzed positions have been presented in Figs. 1 and 2.



*Fig. 1: Analyzed positions: a) standing position;  
b) sitting down.*



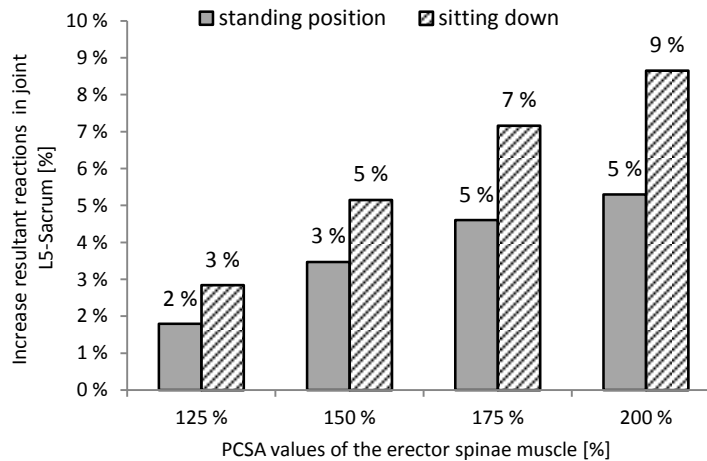
*Fig. 2: Erector spinae muscle ' in the applied model.*

### 3. Results and discussion

The values of resultant reactions in joint L5-Sacrum which were obtained in subsequent simulations of the strengthening of the erector spinae muscle for the upright standing position and sitting down have been presented in Tab. 1. Fig. 3 presents percentage changes of the load values resulting from the increase of the cross section of all muscle fibres of the erector spinae muscle.

*Tab. 1: Values of resultant reaction in joint L5-Sacrum for the strengthening of erector spinae muscle.*

PCSA values of the erector spinae muscle [%]	Resultant reactions in joint L5-Sacrum [N]	
	Standing position	Sitting down
100	432.77	1159.62
125	440.53	1192.58
150	447.80	1219.39
175	452.69	1242.66
200	455.68	1259.95



*Fig. 3: A change of reaction value in joint L5-Sacrum in upright standing position and during sitting down due to the increase of cross section of erector spinae muscle.*

It was observed that the double increase of the cross section of the erector spinae muscle in a position of a forward bend may cause the increase in the reaction in joint L5-Sacrum by almost 10 %. Considerably lower differences in percentages were noted for the upright standing position due to the fact that the muscles building the erector spinae muscle constitute a set straightening the spinal column. They contribute to maintaining an upright posture of the body. Due to the points of attachment of individual muscle actons, the increase of their PCSA and the force generated by them cause the compression of subsequent vertebrae. The simulation results enabled also the determination of forces generated by the muscles acting in the lumbar spine section. One of the most active muscles during the analyzed movements was the transverse abdominal muscle. It was observed that the strengthening of the erector spinae muscle resulted in the decrease of the force value generated by the transverse abdominal muscle. The double increase of the cross section of the erector spinae muscle causes more than double decrease of the force value generated by the transverse abdominal muscle during a forward bend (Fig. 4). The transverse abdominal muscle is one of the muscles taking part in the creation of the abdominal prelum, that is why the strengthening of the erector spinae muscle also causes a considerable reduction of the intra-abdominal pressure (Fig. 5).

### 4. Conclusion

The performed mathematical simulations along with optimization techniques made it possible to determine the values of loads of the musculoskeletal system in the lumbar spine section (Tab. 1). It was noted that the increase of the PCSA of the erector spinae muscle causes the increase of reactions in the

lumbar spine. Moreover, it was observed that the strengthening of the sole erector spinae muscle may cause the reduction of the force value generated by the transverse abdominal muscle and the intra-abdominal pressure. The above-mentioned conclusions partly confirm hypotheses proposed by physiotherapists. They suggest that better effects, namely greater reduction of pain ailments, are achieved by applying exercises which strengthen both dorsal and abdominal muscles or those which strengthen only abdominal muscles. In addition, the results of this work provide to some extent the explanation why stressed people very often complain of backbone pain. The reason for that could be an excessive tension of the dorsal muscles, which results in the increase of loads in spinal bone structures and intensifies pain. As follow-up of this work it is planned to examine the impact of the strengthening of transverse abdominal muscles on the values of loads in the lumbar spine section. The results obtained from the simulations may be useful in a daily physiotherapeutic practice to increase the efficiency of a therapeutic training programme. The analysis of the research results will make it possible to indicate to what extent the strengthening of particular paraspinal muscles will influence the values of loads in the lumbar spine section.

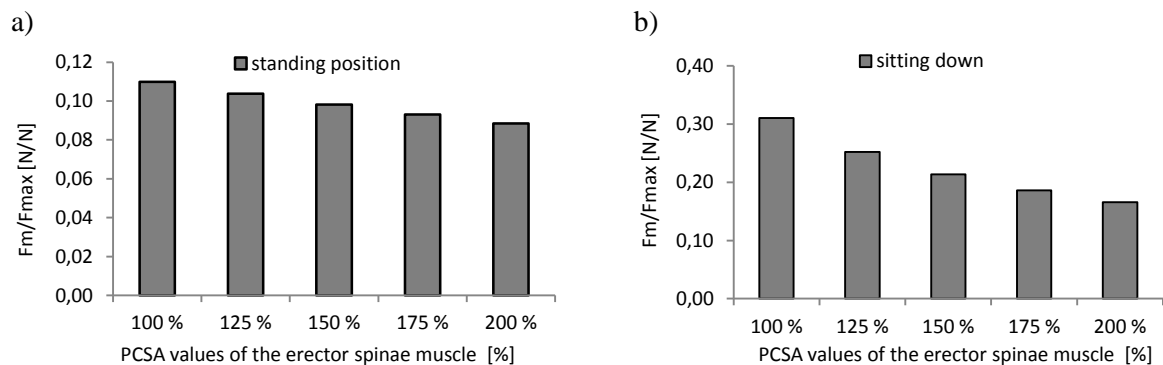


Fig. 4: Force value of transverse abdominal muscle standardized in relation to maximum force which can be generated by this muscle for subsequent values of cross section of erector spinae muscle during: a) upright standing position, b) sitting down.

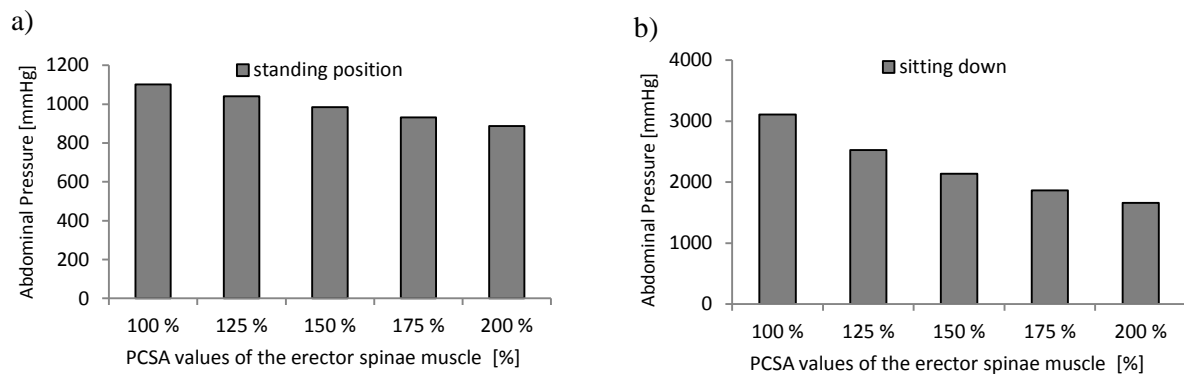


Fig. 5: Value of intra-abdominal pressure for subsequent values of cross section of erector spinae muscle during: a) upright standing position, b) sitting down.

## References

- Bogduk, N., Macintosh, J.E. and Percy, M.J. (1992) A universal model of the lumbar back muscles in the upright position. *Spine* 17, pp. 897-913.
- Nowakowska, K., Gzik, M., Michnik, R., Myśliwiec, A., Jurkojć, J., Suchoń, S and, Burkacki, M. (2017) The loads acting on lumbar spine during sitting down and standing up. *Innovations in biomedical engineering*, Gzik M., Tkacz, E., Paszenda, Z., Piętko, E. (eds.), in: *Advances in Intelligent Systems and Computing*, 526, pp. 169-176.
- Rohmann, A., Pohl, D., Bender A., Graichen, F. and Dymke, J. (2014) Activities of Everyday Life with High Spinal Loads. *PloS ONE*, 9, 5, e98510.
- Zee de, M., Hansen, L., Wong, Ch., Rasmussen, J. and Simonsen, E.B. (2007) A generic detailed rigid-body lumbar spine model. *Journal of Biomechanics*, 40, pp. 1219-1227.

## DESIGNATION OF THE MINIMUM THICKNESS OF MACHINED LAYER FOR THE MILLING PROCESS OF DURALUMIN PA6

Ł. Nowakowski<sup>\*</sup>, E. Miko<sup>\*\*</sup>, M. Skrzyniarz<sup>\*\*\*</sup>

**Abstract:** This article is to present the result of experimental research concerning measurements of the minimum thickness of machined layer to initiate the end milling process of duralumin PA6. The research was conducted in two stages at the laboratories of the Kielce University of Technology. The research required performance of machining tests that involved initiation of the milling process. The gradual initiation of the milling process was achieved thanks to a flowing change of machining depth by tilting the working surface of samples at a slight angle (Fig. 1). The designation of the minimum thickness of machined layer was implemented with the use of a 2D profile that represented the initiation zone of the machining process, which was achieved by measuring the working surface of samples with a skidless contact profilometer TOPO 01P. The results of experiments concerning the impact of feed and cutting speed on the value of the minimum thickness of machined layer have been presented in form of charts. Machining tests were conducted at a numerically controlled machining center AVIA VMC 800 with a milling head CoroMill 490 manufactured by Sandvik Coromant.

**Keywords:** End milling, Minimum thickness of machined layer, Feed, Cutting speed.

### 1. Introduction

The parameter determining the beginning of the material separation process is the minimum thickness of the machined layer ( $h_{min}$ ), which is the smallest possible layer of material that can be removed under particular conditions. Depending on the thickness of machined layer within the machining zone, one may distinguish three stages of impact of the cutting edge on the machined material (Nowakowski et al., 2016):

- I – when  $a_p < h_{min}$ : there are elastic deflections and malleable pressure of the treated material,
- II – when  $a_p \approx h_{min}$ : there are elastic and malleable deflections with partial cutting of the treated material,
- III – when  $a_p > h_{min}$ : beginning of removing the material in form of shavings.

When the minimum thickness of the machined layer is known, it is possible to achieve additional optimization and low vibrations (Błasiak, 2016) of the end milling process conducted with a very high feed on the cutting blade and little depth of cut, resulting in the effect of thinning of chips. The milling process with high cutting speeds would allow more efficient and accurate machining of precision machine parts (Adamczak et al., 2016), i.e. engine parts (Ambrozik et al., 2014), precision valves (Takosoglu, 2016), (Chatys and Polyakov, 2013), non-contact face seals (Błasiak and Zahorulko, 2016), (Błasiak et al., 2014) and water jet machines (Krajcarz, 2014), (Krajcarz and Spadło, 2016). A large impact on the value of the minimum thickness will be caused by the actual geometry of the cutting edge, which is not perfect under realistic conditions (Grzesik et al., 2005), (Depezyński et al., 2016), (Bochnia, 2012) it has some losses and has a rounding with a radius  $r_n$  resulting from the method of performance (Miko, 2005), (Nowakowski and Wijas, 2016). The aim of the scientific research was to determine the value of the minimum thickness of the machined layer for the process of end milling of duralumin PA6.

<sup>\*</sup> Łukasz Nowakowski, M.Sc., PhD.: Chair of Mechanical Engineering and Metrology, Kielce University of Technology; Aleja Tysiąclecia Państwa Polskiego 7; 25-314 Kielce; PL, lukasn@tu.kielce.pl

<sup>\*\*</sup> Edward Miko, M.Sc., PhD.hab.: Chair of Mechanical Engineering and Metrology, Kielce University of Technology; Aleja Tysiąclecia Państwa Polskiego 7; 25-314 Kielce; PL, emiko@tu.kielce.pl

<sup>\*\*\*</sup> Michał Skrzyniarz, MSc.: Chair of Mechanical Engineering and Metrology, Kielce University of Technology; Aleja Tysiąclecia Państwa Polskiego 7; 25-314 Kielce; PL, skrzyniarzmichal@gmail.com

## 2. Methods

The subject of the research was to designate the minimum thickness of the machined layer for the milling process of duralumin PA6 in the function of variable feed and cutting speed. On the basis of the literature and the current own research, it was decided that the most relevant programme of experimental research would be the statistical determined and selective univariate programme PS/DS-U. The variable factors were feed per tooth and cutting speed  $v_c$ . Parameters of processing were selected according to instructions of the manufacturer, bearing in mind the machined material. The machining parameters have been presented on the Fig. 3.

The material selected for the tests of machining was a material that is frequently used in industry, duralumin PA6. A cuboid sample was placed on the track at a known angle and it was fixed in a vise Bison Bial 6620 (Fig. 1b). The face surface of the sample, on which the milling process was planned, was grinded on a surface grinder JOTES SPC 20b, with a disc 250 x 25 x 76 mm 99A 60K7 VE01-35 and with a cutting speed of  $v_c = 30$  m/s. Due to the accuracy of the image of the phenomenon, it is advantageous when the face surface of the sample is made with roughness that is smaller by an order of magnitude from the smallest roughness possible to be obtained by machining with the analyzed tool. Before starting the machining test with the subject probe and measurement cycle, the angle of the sample was determined according to Fig. 1a.

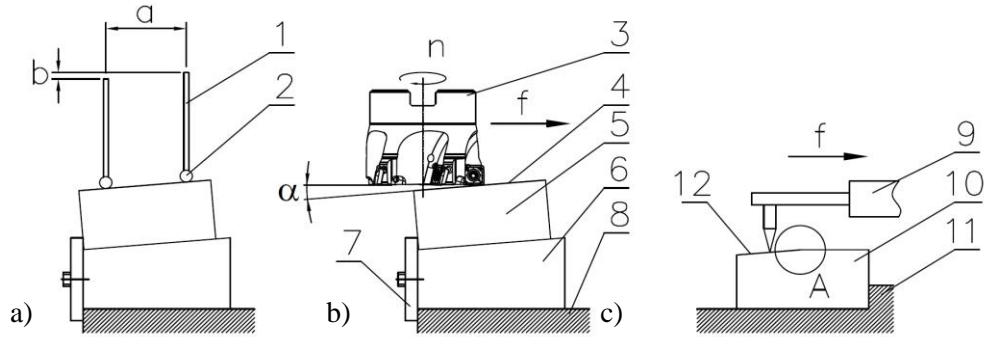


Fig. 1: a) Designation of the angle of sample  $\alpha$ ; b) Machining test; c) Measurement of the sample with a profilometer. 1 – stylus of the subject probe TS640, 2 – ruby ball with a radius of 5 mm, 3 – tool, 4 – grinded surface of the sample, 5 – sample, 6 – tilted track, 7 – bumper, 8 – vise, 9 – head of the profilometer, 10 – measured sample, 11 – grip of the profilometer, 12 – machined surface, A – initiation zone for the milling process  $f$  – feed,  $n$  – rotations of the tool,  $a$  – distance of measurement points,  $b$  – difference in height.

Machining tests were conducted at a CNC machine AVIA VMC800 with end mill CoroMill 490–050Q22–08M with one plate 490–08T308M–PL –1030. Directly after the machining test, the sample was placed at the bench of the profilometer and the head surface was subjected to an analysis within the initiation area of the machining process, as a result of which the profile of the surface, presented in Fig. 2, was obtained.

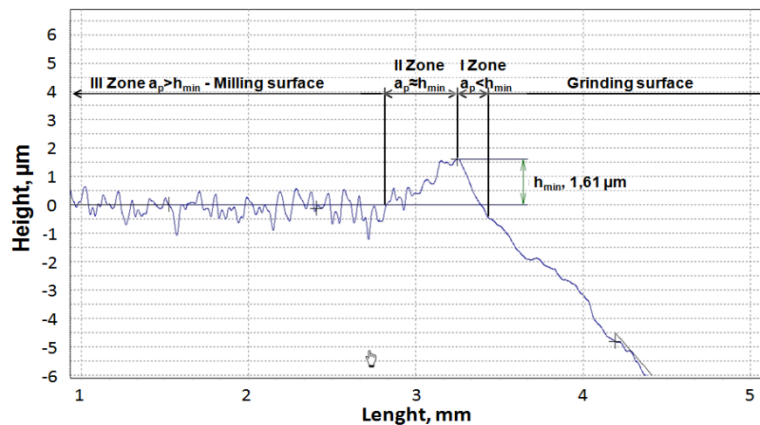


Fig. 2: View of the measured 2D profile of the working surface of the milled sample:  $v_c = 280$  m/min,  $f_z = 0.1$  mm/tooth.

### 3. Results

As a result of conducted research, the impact of the cutting speed  $v_c$  and the feed on the cutting edge  $f_z$  on the minimum value of the machined layer  $h_{min}$  of duralumin PA6. The results of research have been presented in form of a chart representing the course of changes in  $h_{min}$  depending on the feed on the cutting edge and the cutting speed.

Fig. 3 has presented the results of measurements of  $h_{min}$  for duralumin PA6. When considering the impact of the feed on the cutting edge  $f_z$  on the minimum thickness of the machined layer, it was observed that in the initial stage, along with the increase of the feed (0.02 ÷ 0.08 mm/tooth), the minimum thickness of the machined layer increased gradually. Within the range 0.08 ÷ 0.16 mm/tooth, the parameter  $h_{min}$  oscillated around the value of 2  $\mu\text{m}$  and after further increase of cutting speed there was only a gradual decrease of the minimum value of thickness of the machined layer. In order to determine the course of changes of the parameter  $h_{min}$ , the chart includes a line of the tendency which shows that along with the increase of the feed on the cutting edge, the value of the parameter  $h_{min}$  reflects an increasing tendency.

Fig. 3 has also presented the influence of the cutting speed on the minimum value of thickness of the machined layer  $h_{min}$ . When analyzing the chart presented in Fig. 3, it has been determined that in the initial stage, the increase of cutting speed  $v_c$  caused a rapid decrease of the value of the parameter  $h_{min}$ . Another increase of the parameter  $h_{min}$  was observed after exceeding the cutting speed of 220 m/min. The increasing tendency maintained up to the cutting speed of 260 m/min. The further increase of the cutting speed caused, alternately, an increase and decrease of  $h_{min}$ , until  $v_c = 380$  m/min, in case of which there was a decrease of  $h_{min}$ .

The general impact of cutting speed  $v_c$  on the value of the minimum thickness of machined layer  $h_{min}$  has been represented by the trend line introduced in the chart. It might be noticed that there has been a slight decreasing tendency.

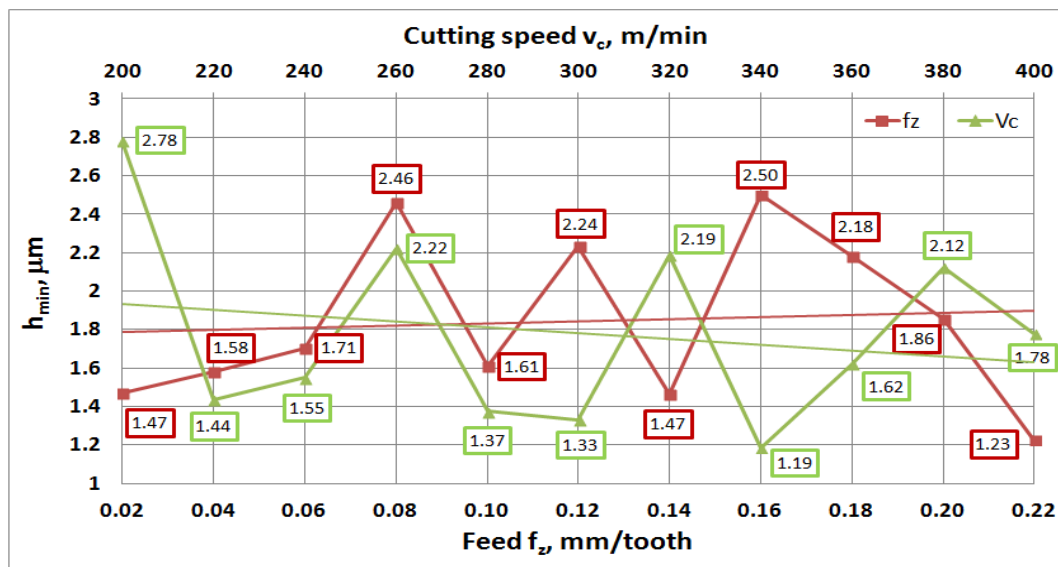


Fig. 3: Results of measurements of the parameter  $h_{min}$  for duralumin PA6.

### 4. Conclusions

The conducted research concerning initiation of the end milling process of duralumin PA6 allowed designation of the impact of feed of the cutting edge and the cutting speed on the minimum value of thickness of the machined layer, as well as allowed formulation of the following conclusions:

1. The use of a skidless profilometer enables a direct and indirect designation of the minimum thickness of the machined layer; it allows measuring of the angle of the working surface of the sample. The high resolution of the measurement system facilitates interpretation and identification of areas where the tool had impact on the surface of the machined sample, which enables an easy measurement of their length.



2. The minimum value of thickness of the machined surface during the milling process of duralumin depends on the value of feed and cutting speed.
3. In the case of small feed values, the increase of the feed value on the cutting edge from 0.02 to 0.08 mm/cutting edge caused an increase of the parameter of the minimum thickness of machined layer from  $h_{\min}=1.147 \mu\text{m}$  to  $2.46 \mu\text{m}$ . Within the range of feeding rate of 0.08 to 0.16 mm/cutting edge, the increase of the feeding rate caused an oscillation  $h_{\min}$  within the range  $1.47 \div 2.5 \mu\text{m}$ . In the case of feed per tooht above 0.16 mm/cutting edge, the value  $h_{\min}$  decreased along with the increase of the feed, reaching the lowest value of  $1.23 \mu\text{m}$  for  $f_z = 0.22 \text{ mm/tooth}$ .
4. When taking into consideration the overall impact of feed on the cutting edge on the minimum thickness of the machined layer, a growing tendency has been observed.
5. Cutting speed has an advantageous impact on the parameter  $h_{\min}$ . Along with the increase of the cutting speed value, it has been observed that there is a decreasing tendency of the minimum thickness parameter of the machined layer. The lowest value of the parameter  $h_{\min}$  has been noted for the cutting speed equal to 380 m/min, that is the value of  $1.19 \mu\text{m}$ .
6. Equipping the milling head with a cutting plate allowed elimination of axial and radial run-out of the cutting edges, which could have affected the results of measurements. There is a necessity of conducting further research that would include the influence of errors concerning setting of edges in the milling head on the parameter  $h_{\min}$ .
7. The results obtained and presented in the article might be used in models to predict the roughness of milled surfaces.

## References

- Adamczak, S., Zmarzły, P. and Stępień, K. (2016) Identification and analysis of optimal method parameters of the v-block waviness measurements, *Bulletin of the Polish Academy of Sciences Technical Sciences*, 64, 2, pp. 325-332.
- Ambrozik, A., Ambrozik, T., Łagowski, P. and Kurczyński, D. (2014) The influence of injection advance angle on fuel spray parameters and nitrogen oxide emissions for a self-ignition engine fed with diesel oil and fame, *Polish Journal of Environmental Studies*, 23, pp. 1917-1923.
- Błasiak, S., Takosoglu, J.E. and Laski, P.A. (2014) Heat transfer and thermal deformations in non-contacting face seals, *J of Thermal Science and Technology*, 9, 2, pp. JTST0011-JTST0011. doi:10.1299/jtst.2014jtst0011.
- Błasiak, S. and Zahorulko, A.V (2016) A parametric and dynamic analysis of non-contacting gas face seals with modified surfaces, *Tribology International*, 94, pp. 126-137. doi:10.1016/j.triboint.2015.08.014.
- Błasiak, M. (2016) Parametric analysis of piezoelectric transducer used for signal processing, in: *Eng. Mech.* 2016 pp. 66-69.
- Bochnia, J. (2012) Ideal material models for engineering calculations, *Procedia Engineering*, 39, 0, pp. 98-110. doi:http://dx.doi.org/10.1016/j.proeng.2012.07.013.
- Chatys, R. and Polyakov, V. (2013) Acoustic conductance of an anisotropic spherical shell submerged in a liquid, *Mechanics of Composite Materials*, 49, pp. 401-410.
- Depczyński, W., Kazała, R., Ludwinek, K. and Jedynak, K. (2016) Modelling and microstructural characterization of sintered metallic porous materials, *Materials*, 9(7), 567, pp. 1-12.
- Grzesik, W., Bartoszek, M. and Nieslony, P. (2005) Finite difference method-based simulation of temperature fields for application to orthogonal cutting with coated tools, *Machining Science and Technology*, 9, 4, pp. 529-546.
- Krajcarz, D. (2014) Comparison metal water jet cutting with laser and plasma cutting, 24th DAAAM Inter. Symp.on Intelligent Manufacturing and Automation, 2013, *Procedia Engineering*, 69, pp. 838-843.
- Krajcarz, D. and Spadło, S. (2016) Influence of the process conditions on the diameter of cylindrical holes produced by abrasive water jet cutting, in: *Proc. 25th Int. Conf. Metall. Mater. Met.* 2016 pp. 1462-1467.
- Miko, E. (2005) Micro-irregularities of metal surfaces, *Strojnicki Vestnik-Journal of Mechanical Engineering*, 51, 10, pp. 634-645.
- Nowakowski, L. and Wijas, M. (2016) The evaluation of the process of surface regeneration after laser cladding and face milling, in: *Eng. Mech.* 2016 pp. 430-433.
- Nowakowski, L., Miko, E. and Skrzyniarz, M. (2016) The analysis of the zone for initiating the cutting process of x37crmov51 steel, in: *Eng. Mech.* 2016 pp. 426-429.
- Takosoglu, J.E. (2016) Experimental research of flow servo-valve, in: *Proc. Int. Conf. Exp. Fluid Mech.* 2016 (ed. Dancova, P.), Techn. Univ. Liberec, pp. 819-823.

## MILLING WITH A TOOL WITH UNEVENLY DISTRIBUTED CUTTING PLATES

Ł. Nowakowski<sup>\*</sup>, E. Miko<sup>\*\*</sup>, M. Skrzyniarz<sup>\*\*\*</sup>

**Abstract:** *This article is to present the results of experimental research and the analysis of recorded signals of relative displacements in the tool-workpiece system during face milling with an endmill with 3 unevenly distributed cutting plates and 6 evenly distributed cutting plates. The measurement stand was prepared on a numerically controlled vertical milling center VMC 800 manufactured by AVIA, with the use of a laser interferometer system manufactured by Renishaw and a measurement track. The processing involved machining of samples made of C45 steel with the use of a CoroMill R245-080Q27-12M cutter with the diameter of Ø80 mm, manufactured by Sandvik Coromant. This article has presented the results of experimental research concerning the influence of asymmetrical and symmetrical distribution of plates in the tool body and the feed velocity on the value of relative displacements in the tool-workpiece system. The results have been presented in form of charts reflecting the relative displacements in the tool-workpiece system, depending on the time, FFT analysis charts (Błasiak, 2016), standard deviation of relative displacements, and feed on the cutting edge.*

**Keywords:** Vibrations, Shifts, End milling, Tools with uneven tooth pitch, Feed, FFT analysis.

### 1. Introduction

The process of end milling involves a machining tool, grip, tool, and the machined object, which together form a structural layout with dynamic characteristics. The process of milling is a machining process that results in formation of unwanted relative displacements (vibrations) of the component elements of the layout machining tool - grip - machined object - tool in that layout. Those vibrations are caused by forcible and kinetic interaction. Such displacements have a significant impact on the accuracy and the quality during the milling process of precision machine parts, i.e. seals (Błasiak and Zahorulko, 2016), pistons (Adamczak et al., 2015), (Ambrozik et al., 2014), pneumatic parts e.g. valves, muscles (Takosoglu, 2016), (Takosoglu et al., 2016). Displacements in the layout machining tool - grip - machined object - tool cause tool wear, release of heat (Bartoszek and Grzesik, 2011), (Pastuszko, 2014), and noise emission during the process of machining (Nowakowski, Łukasz Mięsikowska and Błasiak, 2016), (Mięsikowska, 2016). A dynamic layout is formed by: a mass-dissipative-elastic system and working processes that are affected by forcing, controlling, and distorting signals. During the operation of the machining tool, there is the possibility of occurrence of three types of displacements (vibrations): free (own) movements, movements forced kinetically, and self-oscillations.

The displacements generated during the machining process in the tool-workpiece system constitute a great limitation in the suspension of performance of the milling process and they have a significant impact on the obtained geometrical structure of the machined surface (Miko, 2005), (Nowakowski and Wijas, 2016).

There are four basic factors that influence the formation of relative displacements in the tool-workpiece system during the milling process: the setting angle and the cutting force, the tool diameter and the radial depth of cut, geometry of the plate, the tooth pitch of the tool. This article has described the research

---

<sup>\*</sup> Łukasz Nowakowski, MSc. PhD.: Chair of Mechanical Engineering and Metrology, Kielce University of Technology; Aleja Tysiąclecia Państwa Polskiego 7; 25-314 Kielce; PL, lukasn@tu.kielce.pl

<sup>\*\*</sup> Edward Miko, MSc. PhD. hab.: Chair of Mechanical Engineering and Metrology, Kielce University of Technology; Aleja Tysiąclecia Państwa Polskiego 7; 25-314 Kielce; PL, emiko@tu.kielce.pl

<sup>\*\*\*</sup> Michał Skrzyniarz, MSc.: Chair of Mechanical Engineering and Metrology, Kielce University of Technology; Aleja Tysiąclecia Państwa Polskiego 7; 25-314 Kielce; PL, skrzyniarzmichal@gmail.com

concerning the influence of the tooth pitch of the cutter on the relative displacements in the tool-workpiece system. One of the reasons for changing the tooth pitch of the tool during this research might have been caused by damage of the plates in the body of the tool.

## 2. Methods

The subject of the research was to record and analyze the signal of relative displacements in the tool-workpiece system during an end milling process with a simulated damage of 3 plates in the body of the tool, as well as without such damage.

Machining attempts were conducted at a vertical milling center AVIA VMC 800, where rectangular samples (dimensions of 30 x 70 x 50 mm) made of C45 steel were milled with a CoroMill R245-080Q27-12M tool; the length of the length of the tool movement was 70 mm. The cutter CoroMill R245-080Q27-12M has, as a standard, 6 symmetrically distributed plates every 60 ° sockets for cutting plates. During the attempts, an uneven distribution of R245-12T3M-PL4230 plates was achieved with enforcing the 1st, 3rd, and 6th socket. The uneven distribution of the cutting plates in the cutter disturbed the symmetry of the milling process by changing the feed on the tooth for sockets 3 and 6. For comparison purposes, machining attempts were also conducted with a tool facilitated with all 6 plates. The view of the cutter plate and the parameters of work of each plate have been presented in Tab. 1.

Tab. 1: View of the cutter plate and the parameters of work of each plate.

$v_c = 205 \text{ m/min}, a_p = 1 \text{ mm}, z = 3$								
$f_z, \text{ mm/tooth}$								
0.1			0.15			0.2		
Slot 1	Slot 3	Slot 6	Slot 1	Slot 3	Slot 6	Slot 1	Slot 3	Slot 6
$f_{z1}$	$f_{z3}$	$f_{z6}$	$f_{z1}$	$f_{z3}$	$f_{z6}$	$f_{z1}$	$f_{z3}$	$f_{z6}$
0.1	0.2	0.3	0.15	0.3	0.45	0.2	0.4	0.6

The measurement of relative displacements during the machining attempts with various feed values were implemented on a patented working stand (Miko and Nowakowski, 2013) with a laser interferometer system manufactured by Renishaw and an accurate measurement track; the working stand was mounted on the machining tool VMC 800 manufactured by AVIA (Fig. 1).

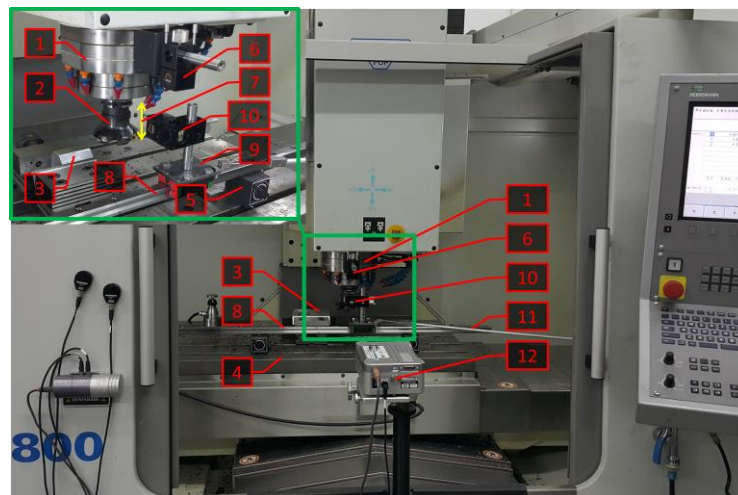


Fig. 1: Schematic of device for measuring displacements in the tool-workpiece system: 1- spindle, 2 - milling head, 3 - workpiece, 4 - table, 5 - magnetic base, 6 - linear reflector, 7 - vibrations in the tool-workpiece system, 8 - rail, 9 - block, 10 - linear interferometer, 11 - link, 12- XL 80 laser.

### 3. Results and conclusion

As a result of the conducted research, it was possible to determine the influence of velocity of feed on the tooth  $f_z$  and the uneven distribution of cutting plates in the body of the cutter on the peak-to-peak value and the standard deviation of the signal of relative displacements in the tool-workpiece system during the process of face milling. Fig. 2 has presented an example of a part of the signal reflecting the displacements in the tool-workpiece during the process of milling (Tab. 1, no. 1), for the measurement time of 1 s. Fig. 3 has presented the FFT analysis of the recorded signal of relative displacements for the feed of  $f_z = 0.1$  mm/tooth.

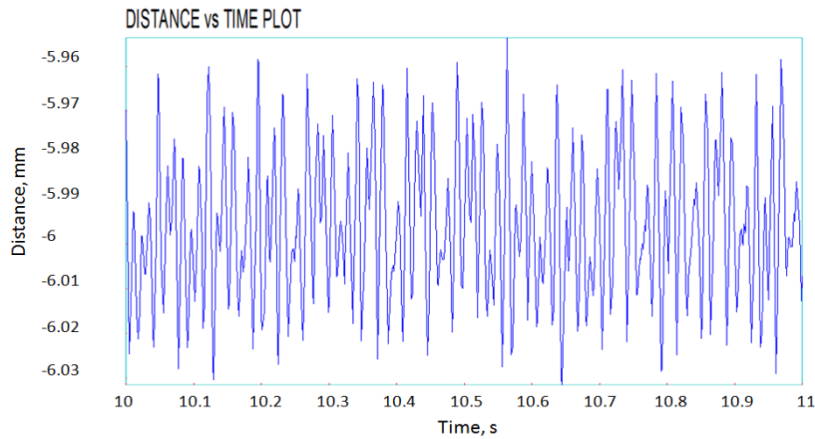


Fig. 2: Fragment of an unfiltered signal of relative displacements in the tool-workpiece for the milling process ( $v_c = 205$  m/min,  $f_z = 0.1$  mm/tooth,  $a_p = 1$  mm,  $z = 3$ ).

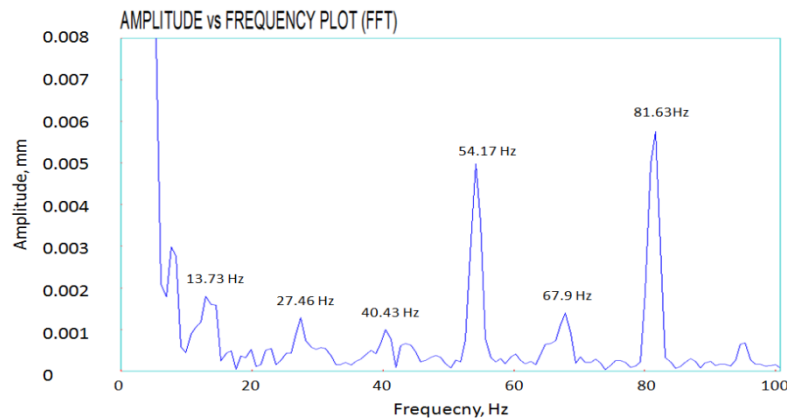


Fig. 3: The amplitude-frequency chart for the signal of relative relative displacements in the tool-workpiece for the milling process ( $v_c = 205$  m/min,  $f_z = 0.1$  mm/tooth,  $a_p = 1$  mm,  $z = 3$ ).

Tab. 2: The analysis of recorded signals of relative displacements in the tool-workpiece system.

Lp.	Cutting parameters				The results of signal analysis, $\mu\text{m}$			
	$v_c$ , m/min	$f_z$ , mm/tooth	$a_p$ , mm	$z$ , szt	Max	Min	Peak to peak	Standard deviation
1.	205	0.1	1	3	50.32	-44.17	94.49	16.38
2.		0.15			70	-56.89	126.89	22.98
3.		0.2			69.12	-56.84	125.89	24.72
4.		0.1		6	21.75	-14.61	36.36	7.41
5.		0.15			23.68	-16.55	40.23	8.2
6.		0.20			25.56	-17.65	43.21	8.83

During the analysis of the results presented in Tab. 2, it has been concluded that in both cases, when the cutter was facilitated with all plates and when only the 1st, 3rd, and the 6th socket were used, the increase of the feed caused an increase of the peak-to-peak value of the displacements signal and its standard deviation. Introduction of asymmetry in the distribution of cutting plates in the sockets of the cutter

resulted in an increase of the value of relative displacements in the tool-workpiece system in relation to the cutter facilitated with all 6 plates. In the case of small values of feed 0.1/tooth, the standard deviation of the signal of displacements for the simulated damage of 3 plates increased by 120 %, while the peak-to-peak parameter – 120 % in comparison to the work with 6 undamaged plates. Along with the increasing feed on the tooth, those differences increased and amounted, respectively, for feed of 0.15 mm/tooth – 180 % for the standard deviation of the signal and 215 % for the peak-to-peak parameter. In the case of the highest tested value of feed on the tooth of 0.2 mm/tooth, there were lower increases than in the case of the feed of 0.15 mm/tooth since the value of the standard deviation increased by 179 % and the peak-to-peak value by 191 %.

#### 4. Conclusions

The conducted research allowed tests concerning the impact of changes in the tooth pitch of the cutter on relative displacements in the layout tool - machined objects and allowed formulation of the following conclusions:

1. The increase of feed on the tooth, from 0.1 to 0.2 mm/cutting edge, for a tool with 6 cutting plates, results in an increased standard deviation of the signal within the range of 7.41 – 8.83  $\mu\text{m}$ .
2. In the case of a tool with 3 unevenly distributed cutting plates, the increase of the feed on the cutting edge from 0.1 to 0.2 mm/cutting edge caused a change in the standard deviation within the range of 16.38 ÷ 24.72  $\mu\text{m}$ .
3. In the amplitude-frequency characteristics, it is possible to distinguish characteristic components related to the process of machining and originating from the rotations:  $f_0$  – basic frequency originating from rotations (13.73 Hz),  $2 \cdot f_0$  – the first harmonics (27.46 Hz),  $3 \cdot f_0$  – the second harmonics (40.43 Hz),  $4 \cdot f_0$  – the third harmonics (54.17 Hz), and  $5 \cdot f_0$  – the fourth harmonics (67.9 Hz),  $6 \cdot f_0$  – basic frequency increased by the number of cutting edges (81.63 Hz).
4. The amplitude-frequency analysis has also presented which sockets had cutting plates and which were empty. On that basis, it is also possible to monitor the wear of individual cutting plates during the machining process.

#### References

- Adamczak, S., Zmarzły, P. and Janecki, D. (2015) Theoretical and practical investigations of v-block waviness measurement of cylindrical parts, *Metrology and Measurement Systems*, 22, 2, pp. 181-192.
- Ambrozik, A., Ambrozik, T., Łagowski, P. and Kurczyński, D. (2014) The influence of injection advance angle on fuel spray parameters and nitrogen oxide emissions for a self-ignition engine fed with diesel oil and fame, *Polish Journal of Environmental Studies*, 23, pp. 1917-1923.
- Bartoszek, M. and Grzesik, W. (2011) Numerical prediction of the interface temperature using updated finite difference approach, *MODELLING OF MACHINING OPERATIONS Book Series: Advanced Materials*, 223, pp. 231-239.
- Blasiak, S. and Zahorulko, A.V (2016) A parametric and dynamic analysis of non-contacting gas face seals with modified surfaces, *Tribology International*, 94, , pp. 126-137. doi:10.1016/j.triboint.2015.08.014.
- Blasiak, M. (2016) Parametric analysis of piezoelectric transducer used for signal processing, in: *Eng. Mech.*, pp. 66-69.
- Mięsikowska, M. (2016) Analysis of polish vowels of tracheoesophageal speakers, *Journal of Voice*, 30.
- Miko, E. (2005) Micro-irregularities of metal surfaces, *Strojnicki Vestnik-Journal of Mechanical Engineering*, 51, 10, pp. 634-645.
- Miko, E. and Nowakowski, Ł. (2013) A set of machine tools and laser system to measure the relative displacements (zestaw obrabiarki i systemu laserowego do pomiaru przemieszczeń względnych), PL 217 590 B1.
- Nowakowski, Łukasz Mięsikowska, M. and Blasiak, M. (2016) Speech intelligibility in the position of cnc machine operator, in: *Eng. Mech.*, pp. 422-425.
- Nowakowski, L. and Wijas, M. (2016) The evaluation of the process of surface regeneration after laser cladding and face milling, in: *Eng. Mech.*, pp. 430-433.
- Pastuszko, R. (2014) Pool boiling on rectangular fins with tunnel-pore structure, in: *EPJ Web Conf. Vol. 45*, p. 1020.
- Takosoglu, J.E. (2016) Experimental research of flow servo-valve, in: *Proc. Int. Conf. Exp. Fluid Mech. 2016* (ed. Dancova, P.), Techn. Univ. Liberec, pp. 819-823.
- Takosoglu, J.E., Laski, P.A., Blasiak, S., Bracha, G. and Pietrala, D. (2016) Determining the static characteristics of pneumatic muscles, *Measurement and Control*, 49, 2, pp. 62-71. doi:10.1177/0020294016629176.

## THE ANALYSIS OF RELATIVE OSCILLATION DURING FACE MILLING

L. Nowakowski<sup>\*</sup>, M. Skrzyniarz<sup>\*\*</sup>, E. Miko<sup>\*\*\*</sup>

**Abstract:** *This article is to present the results of research concerning oscillation generated by end milling of steel C45. Measurement of rooms in the layout tool-machined object was conducted at a vertical milling center AVIA VMC 800 with the use of a laser interferometer Renishaw XL-80. The process of machining was performed with a milling cutter R245-80Q27-12M manufactured by Sandvik Coromant, equipped with 6 cutting plates. The analysis concerned the impact of technological parameters, such as: cutting speed, feed on the cutting edge, and the depth of cut on the value of relative oscillation in the layout tool - machined object generated during the machining. Additionally, an amplitude-frequency analysis of selected machining tests was also performed.*

**Keywords:** Oscillation, End milling, Shifts in layout tool - machined object, Amplitude-frequency analysis, Vertical milling.

### 1. Introduction

The process of forming the surface of manufactured machine parts (Takosoglu et al., 2016a, 2016b) depends on many factors that accompany the process of machining. The greatest influence on the quality of formed surface (Nowakowski et al., 2016) is caused by technological parameters of the conducted machining process and the physical phenomena (Blasiak et al., 2014; Blasiak et al., 2016) accompanying those processes (Bartoszek et al., 2011; Miko, 2005; Nowakowski et al., 2016). One of the physical phenomena that accompany the process of end milling are shifts generated within the layout machine tool-grip-tool-machined object (Nowakowski, Lukasz Miecesikowska et al., 2016). Oscillation occurring during the process of machining has a direct impact on the condition of formed surface and the speed of wear of cutting edge (Grzesik et al., 2005). What is more, oscillation has an impact on the value of forces that occur during the process. Oscillation is also the reason for the noise generated during the machining process. Oscillation during machining result in an increase of production costs and constitutes a significant limitation for the technological parameters available for the process of machining (Adamczak et al., 2016; Bochnia, 2012).

### 2. Methods

The process of machining involved end milling of rectangular samples made of C45 steel with dimensions of 30 x 70 x 50 mm. All machining tests were conducted at a vertical machining center AVIA VMC 800. The machining process was executed with a milling cutter CoroMill R245-080Q27-12M manufactured by Sandvik Coromant with the diameter of Ø80 mm, equipped with 6 cutting plates R245-12 T3 M-PM 4030. The process involved a single movement of the tool within a section with length of 70 mm and width of 30 mm. All the parameters of the machining process have been presented in Tab. 1. The measurement of oscillation within the layout tool-machined object was executed with a laser interferometer. One of the mirrors was fixed directly to the spindle of the machining tool (10), while

---

<sup>\*</sup> Lukasz Nowakowski, M.Sc., PhD.: Chair of Mechanical Engineering and Metrology, Kielce University of Technology; Aleja Tysiąclecia Państwa Polskiego 7; 25-314 Kielce; PL, lukasn@tu.kielce.pl

<sup>\*\*</sup> Michał Skrzyniarz, MSc.: Chair of Mechanical Engineering and Metrology, Kielce University of Technology; Aleja Tysiąclecia Państwa Polskiego 7; 25-314 Kielce; PL, skrzyniarzmichal@gmail.com

<sup>\*\*\*</sup> Edward Miko, M.Sc., PhD. hab.: Chair of Mechanical Engineering and Metrology, Kielce University of Technology; Aleja Tysiąclecia Państwa Polskiego 7; 25-314 Kielce; PL, e.miko@tu.kielce.pl



another was fixed to the bench of the machining tool on which the machined object was mounted (14). Fig. 1 presents the drawing of the working stand for the measurement of relative shifts.

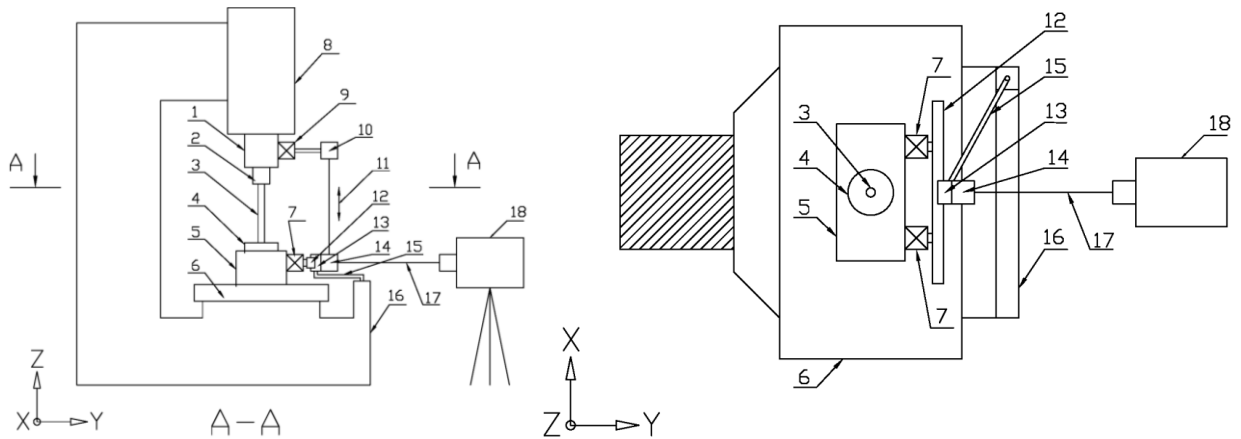


Fig. 1: Schematic of device for measuring vibrations in the tool-workpiece system: 1- spindle body, 2 - spindle, 3 - tool holder, 4 - milling head, 5 - workpiece, 6 - table, 7 - magnetic base, 8 - headstock, 9 - magnetic base, 10 - linear reflector, 11 - vibrations in the tool-workpiece system, 12 - rail, 13 - block, 14 - linear interferometer, 15 - link, 16 - machine body, 17 - laser beam, 18 - XL 80 laser (Miko and Nowakowski, 2012).

### 3. Results

The results of conducted research, along with their technological parameters, have been collected and presented in Tab. 1. In the table, the respective designations are  $f_z$  – feed on the cutting edge,  $h_{ex}$  – theoretical thickness of chip,  $v_c$  – cutting speed,  $a_p$  – depth of cut,  $A$  – peak to peak value of relative oscillation,  $D_\xi$  – standard deviation of relative oscillation.

Tab. 1: Measurement of relative shifts within the layout tool-machined object.

	1	2	3	4	5	6	7	8	9	10	11	12
$f_z$ [mm/edge]	0.1	0.15	0.2	0.25	0.2	0.2	0.2	0.2	0.2	0.2	0.2	0.2
$h_{ex}$ [mm]	0.07	0.11	0.14	0.18	0.14	0.14	0.14	0.14	0.14	0.14	0.14	0.14
$v_c$ [m/min]	205	205	205	205	205	220	235	250	205	205	205	205
$a_p$ [mm]	1	1	1	1	1	1	1	1	0.5	1	1.5	2
$A$ [ $\mu$ m]	36.4	40.2	43.2	51.5	43.2	70.2	116.6	57.5	30.4	43.2	54.5	66.1
$D(\xi)$ [ $\mu$ m]	7.4	8.2	8.8	10.6	8.8	16.5	21.4	11.1	6.0	8.8	11.4	13.6

The obtained results show that the value of oscillation amplitude and its standard deviation increases along with the increase of the feed on the cutting edge. That results from the increasing cross section of the chip, which is reflected by the greater cutting resistance. The peak to peak value, in comparison to the machined object, increases in that case from 36.4  $\mu$ m to 51.5  $\mu$ m, while the standard deviation of oscillation changes within the range of 7.4 – 10.6  $\mu$ m. The increase of oscillation parameters occurs when there is an increase of the depth of cut resulting from the increased volume of material removed by each plate of the cutting head. In that case, the peak to peak is within the range from 30.4 – 66.1  $\mu$ m, while the standard deviation of that oscillation covers the range from 6  $\mu$ m to 13.6  $\mu$ m. In the case of the influence of cutting speed on the size of generated oscillation in the layout, it has been noticed that the increase of the cutting speed does not directly affect the increase of oscillation. The oscillation for the speed of 205 m/min is 43.2  $\mu$ m and increases up to 116.6  $\mu$ m at the speed of 235 m/min. Another increase of cutting speed up to 250 m/min results in a decrease of oscillation by over a half and amounts to 57.5  $\mu$ m. Such a result means that in the case of cutting speed of 235 m/min, additional self-oscillation is generated for that tool, resulting in disruption of the conducted machining process. The process of machining is, then, conducted under unstable conditions.

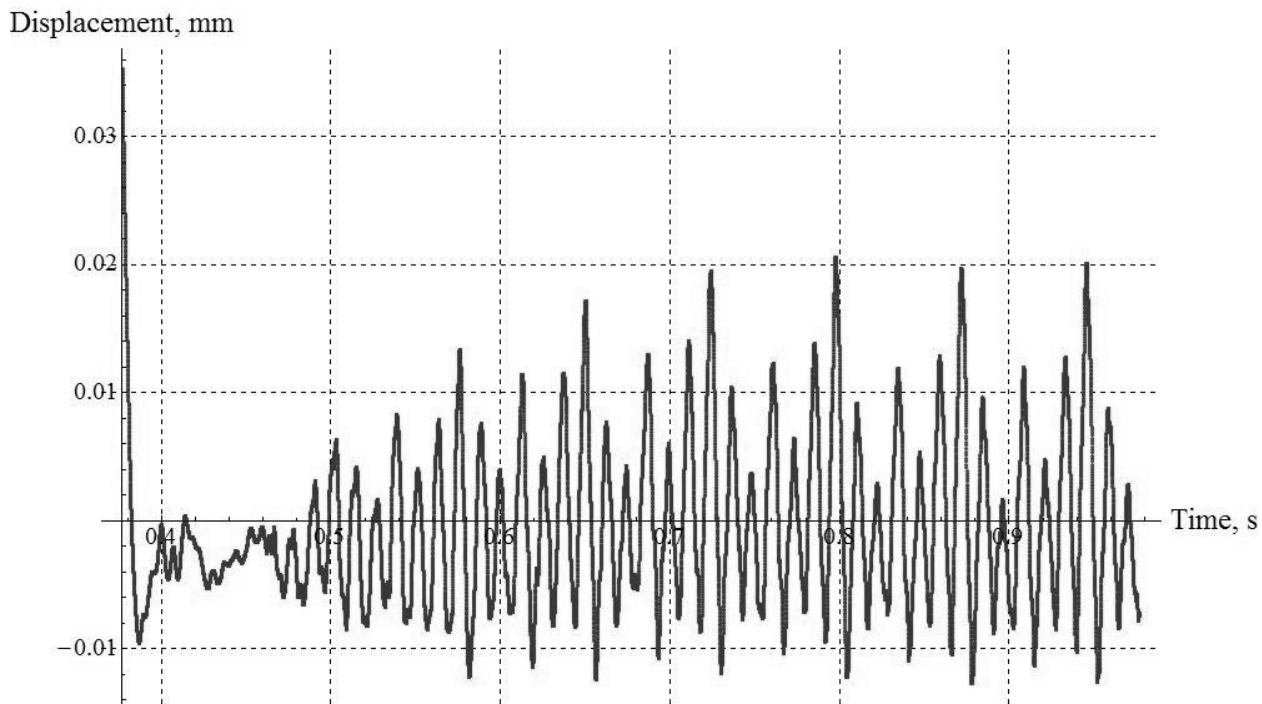


Fig. 2: Chart of the filtered signal of relative shifts within the layout tool-machined object machined under the following conditions:  $V_c = 205 \text{ m/min}$ ,  $f_z = 0.1 \text{ mm/tooth}$ ,  $a_p = 1 \text{ mm}$ .

Fig. 2 has presented the chart of shifts in the tool against the machined objects for sample no. 1. The chart has been divided into 3 characteristic areas. The first area is the characteristic movement of the tool to the material, the moment of cut of the tool into the machined material. The second area is the one with visible shifts caused during the machining. The last area is the one with the tool leaving the machined object and moving away. On the basis of those charts, an analysis of the value of shifts generated during the machining has been conducted.

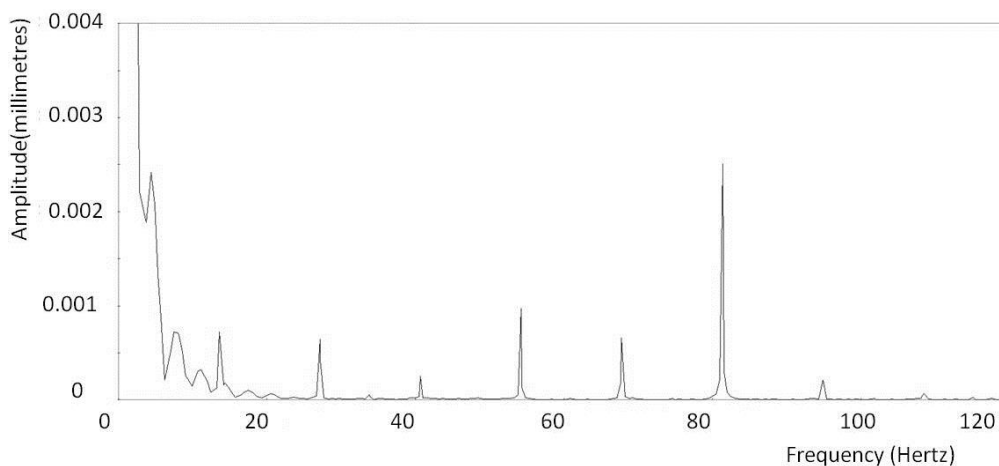


Fig. 3: Amplitude-frequency chart for the sample for  $V_c = 205 \text{ m/min}$ ,  $f_z = 0.1 \text{ mm/tooth}$ ,  $a_p = 1 \text{ mm}$ .

Fig. 3 has presented the amplitude-frequency analysis for sample no. 1. The chart has included 6 component frequency characteristics that are responsible for each cutting place mounted in the end milling head, respectively: 13.6, 27.1, 40.7, 54.2, 67.8, 81.3 Hz. The last component characteristic is 81.3 Hz and it results from the rotations of the spindle of the machining tool, which were, in that case, 813 rpm. The component amplitude values for individual harmonics are responsible for the load of individual sockets of the head. The chart suggests that the socket with the highest load is the last socket with a honing plate. The lowest load is on the plate no. 3 that removes the smallest layer of material. That is why it is the one with the lowest load. The load of cutting plates resulting from the amplitude-frequency analysis overlaps with the radial and length error of their placement in the body of the tool head, measured with a tool setter.

#### 4. Conclusions

The conducted research on oscillation in the layout tool-machined object allowed the analysis of the impact of technological parameters on the size of occurring oscillation, which enabled drawing the following conclusions:

1. An increase of feed on the cutting edge causes an increase of peak to peak value and standard deviation of oscillation within the range 7.4 – 10.6  $\mu\text{m}$ , which is reflected in an increased cutting resistance. It is the result from the increased cross section of generated chip.
2. The increase of depth of cut causes an increase of the size of peak to peak of relative displacement and its standard deviation, which results from a greater load of the cutting head during the process of machining.
3. The amplitude and standard deviation of oscillation increases and for the speed of 235 m/min, it reaches the maximum value. Then, for the speed of 250 m/min, it decreases twofold. With the cutting speed at 235 m/min, the layout loses its stability and self-oscillation occurs.
4. Thanks to the amplitude-frequency spectrum, the load of individual cutting plates mounted in the body of the head has been determined. After measurements conducted with a tool setter and the analysis of the spectrum, it has been determined that the highest load was in socket no. 6 with a honing plate, while the lowest load was in socket no. 3.

#### References

- Adamczak, S. and Bochnia, J. (2016) Estimating the approximation uncertainty for digital materials subjected to stress relaxation tests, *Metrology and Measurement Systems*, 23, 4, SI, pp. 545-553. doi:10.1515/mms-2016-0048.
- Bartoszuk, M. and Grzesik, W. (2011) Numerical prediction of the interface temperature using updated Finite Difference Approach, *Modelling of Machining Operations Book Series: Advanced Materials*, 223, pp. 231-239.
- Blasiak, S., Takosoglu, J.E. and Laski, P.A. (2014) Heat transfer and thermal deformations in non-contacting face seals, *Journal of Thermal Science and Technology*, 9, 2, pp. JTST0011-JTST0011. doi:10.1299/jtst.2014.jtst0011.
- Blasiak, S. and Zahorulko, A.V. (2016) A parametric and dynamic analysis of non-contacting gas face seals with modified surfaces, *Tribology International*, 94, , pp. 126-137. doi:10.1016/j.triboint.2015.08.014.
- Bochnia, J. (2012) Ideal Material Models for Engineering Calculations, *Procedia Engineering*, 39, 0, pp. 98-110. doi:http://dx.doi.org/10.1016/j.proeng.2012.07.013.
- Grzesik, W., Bartoszek, M. and Nieslony, P. (2005) Finite difference method-based simulation of temperature fields for application to orthogonal cutting with coated tools, *Machining Science and Technology*, 9, 4, pp. 529-546.
- Miko, E. (2005) Micro-irregularities of metal surfaces, *Strojnicki Vestnik-Journal of Mechanical Engineering*, 51, 10, pp. 634-645.
- Miko, E. and Nowakowski, L. (2012) Vibrations in the Machining System of the Vertical Machining Center, *Procedia Engineering*, 39, pp. 405-413. doi:10.1016/j.proeng.2012.07.044.
- Nowakowski, L., Miko, E. and Skrzyniarz, M. (2016) The analysis of the zone for initiating the cutting process of X37CrMoV51 steel, In *Engineering Mechanics 2016*, pp. 426-429.
- Nowakowski, L. and Wijas, M. (2016) The evaluation of the process of surface regeneration after laser cladding and face milling, In *Engineering Mechanics 2016*, pp. 430-433.
- Nowakowski, L., Miecsikowska, M. and Blasiak, M. (2016) Speech intelligibility in the position of cnc machine operator, In *Engineering Mechanics 2016*, pp. 422-425.
- Takosoglu, J.E., Laski, P.A., Blasiak, S., Bracha, G. and Pietrala, D. (2016a) Determination of flow-rate characteristics and parameters of piezo valves, In P. Dancova (Ed.), *Proceedings of the International Conference Experimental Fluid Mechanics 2016*, pp. 814-818, Techn. Univ. Liberec.
- Takosoglu, J.E., Laski, P.A., Blasiak, S., Bracha, G. and Pietrala, D. (2016b) Determining the Static Characteristics of Pneumatic Muscles, *Measurement and Control*, 49, 2, pp. 62-71, doi:10.1177/0020294016629176.

## THE ASSESSMENT OF THE IMPACT OF THE INSTALLATION OF CUTTING PLATES IN THE BODY OF THE CUTTER ON THE SIZE OF GENERATED VIBRATIONS AND THE GEOMETRICAL STRUCTURE OF THE SURFACE

L. Nowakowski<sup>\*</sup>, M. Skrzyniarz<sup>\*\*</sup>, E. Miko<sup>\*\*\*</sup>

**Abstract:** *This article is to present the assessment of the impact of the installation of cutting plates in the body of the cutter on the vibration amplitude generated during machining and the 3D parameters of the geometrical structure of the surface. The research was conducted, respectively, for one, two, three, and six cutting plates mounted in the body of the endmill head CoroMill 245. The experiment was conducted at a vertical machining center AVIA VMC 800. The machined material was C45 steel. The measurements of displacements in the layout tool-workpiece were conducted with the use of a laser interferometer Renishaw XL-80, while the measurements of the geometrical structure of the surface were conducted with the use of an optical profilometer TalySurf CCI.*

**Keywords:** Vibration, End milling, Displacement in layout tool - workpiece, Geometrical structure of the surface.

### 1. Introduction

The formation of the geometrical structure of the surface is determined by the interaction of individual elements of the machined layout (Miko, 2005; Miko and Nowakowski, 2012). The impact of individual factors that significantly affect the quality of created surfaces (Adamczak and Bochnia, 2016) might be classified in four main groups: factors related to the machining tool (Nowakowski, Lukasz et al., 2016), the cutting tool, the properties of the machined material (Blasiak et al., 2014), and the phenomena accompanying the process of machining (Nowakowski, L et al., 2016). Among the factors related to the tool used in the shaping of the surface (Adamczak et al., 2015), we might include: its shape, radius of curvature of the cutting edge, material and its coating (Grzesik et al., 2005, 2001), the radius of curvature of the corner of the cutting edge, wear of the cutting edge, firmness, number of cutting edges, as well as errors concerning their setting. Errors in the setting of cutting plates, both radial and axial, have a significant meaning for machining with tool heads. It is possible to solve that problem by applying one, so-called, honing plate, meaning a plate the position of which is lower than in the case of other plates, so that the shaping process of the surface in the case of such cutter is performed only by one plate. Such an assumption is correct and enables limiting the roughness parameter of produced parts (Krajcarz, 2014; Krajcarz and Spadło, 2015). In fact, the process of surface shaping in the case of such cutters is also affected by the plates set above the honing plate. That phenomenon is caused by vibrations occurring in the layout tool - workpiece (Miko and Nowakowski, 2012; Nowakowski et al., 2016). In the case of occurrence of vibrations with higher amplitude components, the outline of individual plates shaping the surface is distinguishable in the 3D image presenting the roughness of the surface (Nowakowski, L and Wijas, 2016). Those issues are of significant importance in the case of forming precision machine parts (Takosoglu et al., 2016a, 2016b). In order to limit costs of production, there are attempts to achieve that directly by the use of tool heads or preparation of the most precise surfaces for next operations, e.g.

---

<sup>\*</sup> Lukasz Nowakowski, M.Sc., PhD.: Chair of Mechanical Engineering and Metrology, Kielce University of Technology; Aleja Tysiąclecia Państwa Polskiego 7; 25-314 Kielce; PL, lukasn@tu.kielce.pl

<sup>\*\*</sup> Michał Skrzyniarz, MSc.: Chair of Mechanical Engineering and Metrology, Kielce University of Technology; Aleja Tysiąclecia Państwa Polskiego 7; 25-314 Kielce; PL, skrzyniarzmichal@gmail.com

<sup>\*\*\*</sup> Edward Miko, M.Sc., PhD. hab.: Chair of Mechanical Engineering and Metrology, Kielce University of Technology; Aleja Tysiąclecia Państwa Polskiego 7; 25-314 Kielce; PL, e.miko@tu.kielce.pl

grinding of surfaces. In many articles concerning prediction of roughness of the surface, one of the factors acknowledged in prediction of Ra parameter of surface roughness is axial displacement of blades of the cutter.

## 2. Methods

The process of machining involved end milling with identical technological parameters ( $V_c = 250$  m/min,  $a_p = 0.5$  mm,  $f_z = 0.2$  mm/tooth) of rectangular samples made of C45 steel with dimensions of 30 x 70 x 50 mm. Individual machining attempts differed from one another by the number of plates used in the formation of the surface. Respectively, the performed attempts involved one, two, three, and six mounted cutting plates. The machining attempts with the use of four and five cutting plates were skipped due to the lack of possibility of their symmetrical distribution in the body of the tool, i.e. the even load of the sockets of the tool head (thus, the same cross section of the formed chip). Before starting the machining attempts after fixing the plates in the sockets of the tool head, the measurement of the maximum length of individual plates was performed with the use of the external tool setter Kalimat-C manufactured by KELCH. Such an operation was to clearly determine that, theoretically, the process of formation of the surface should involve only one plate placed as low as possible in the body of the cutter. Then, machining attempts were performed at the vertical machining center AVIA VMC 800. What is more, during the experiment, relative displacements in the layout tool-workpiece were measured with the use of a laser interferometer. Then, the measurement of the 3D geometrical structure was performed with the optical profilometer TalySurf CCI for the obtained surface.

## 3. Results

Results of the obtained results for relative displacements in the layout tool - workpiece for individual attempts of the experiment, as well as the protrusion distance of the honing plate, have been presented in Tab. 1.

*Tab. 1: Measurement of relative displacements in the layout tool - workpiece, where (z - number of cutting edges placed in the tool head,  $f_z$  - feed on the cutting edge,  $a_p$  - depth of cut,  $v_c$  - cutting speed, A - the maximum peak-to-peak amplitude of the vibrations of the tool in relation to the machined object,  $D_\xi$  - standard deviation of relative vibrations,  $\Delta L$  - the minimum difference of the axial placement of the honing plate).*

No.	z	$f_z$ [mm/tooth]	$a_p$ [mm]	$v_c$ [m/min]	A [ $\mu$ m]	D ( $\xi$ ) [ $\mu$ m]	$\Delta L$ [ $\mu$ m]
1	1	0.2	0.5	250	25.38	4.8	-
2	2	0.2	0.5	250	31.82	6.3	10
3	3	0.2	0.5	250	42.87	8.25	22
4	6	0.2	0.5	250	94.44	16.29	16

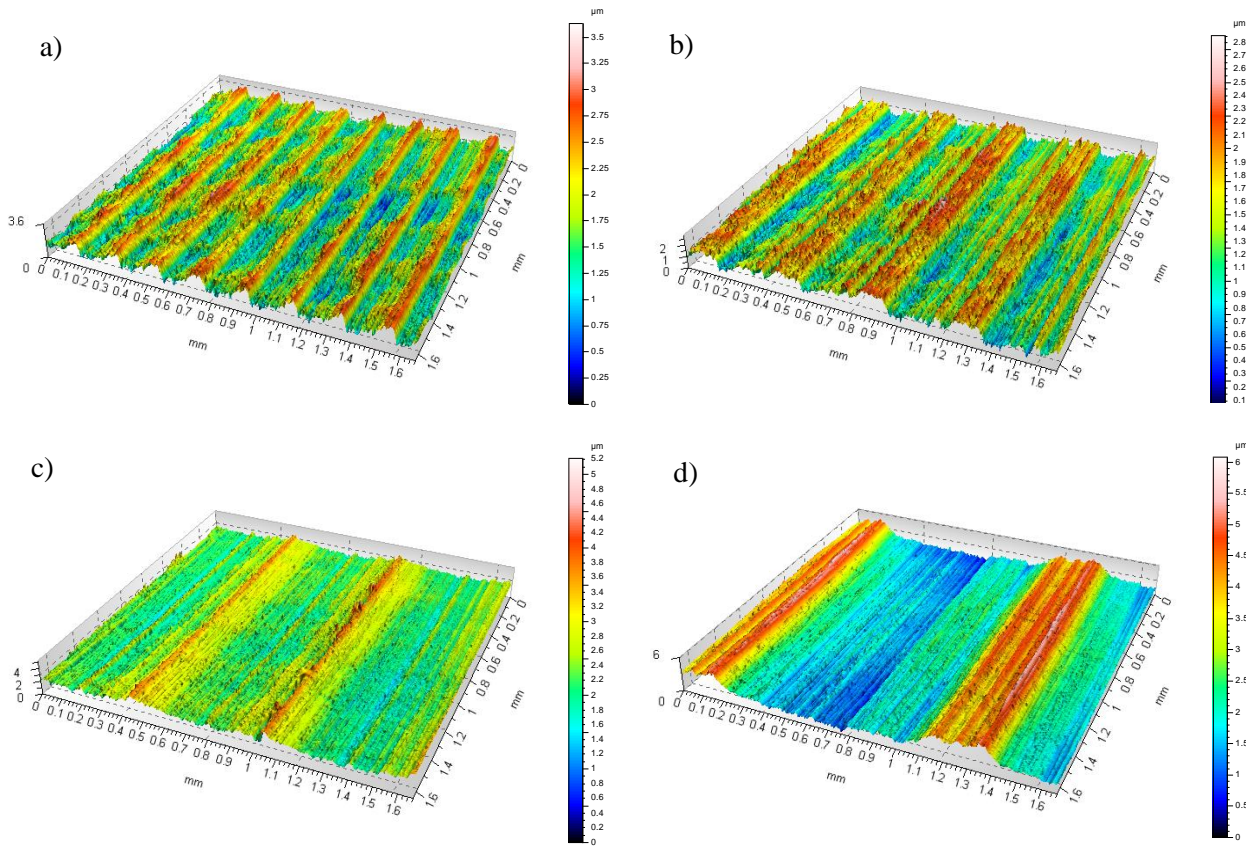
The analysis of the obtained results helped in the conclusion that the maximum peak-to-peak amplitude of the vibrations and their standard deviation increase along with the increasing number of cutting placed used in the process of machining. In the case of machining attempts with one plate, the standard deviation is 4.8  $\mu$ m and increases up to 16.29  $\mu$ m for machining with six plates for identical machining conditions. In the case of sample no. 4, those values might be higher than in the case of newly mounted plates due to the increased radius of curvature of the machined edge  $-r_n$  resulting from the wear of the cutting edge from previous operations. What is more, it was noticed that the peak-to-peak amplitude of vibrations occurring during the machining process was significantly higher than the minimum difference of the axial setting of cutting plates in the body of the cutter. That suggests that vibrations generated in the machining layout should have an impact on the created surface by involving the remaining plates fixed in the tool head in the process of the final shaping of the surface. Additionally, in the case of Sample no. 4 with six cutting plates, the value of standard deviation of relative vibrations is higher than the difference of axial shift of the cutting plate. In order to verify those assumptions, a 2D and 3D analysis of roughness and surface waviness were conducted in the performed experiment. The results of the obtained parameters of

the surface have been presented in Tab. 2. The comparison of isothermal images of the measured surface has been presented in Fig. 1.

*Tab. 2: The comparison of average parameters of roughness for the obtained surfaces.*

No.	tooth	Sq [ $\mu\text{m}$ ]	Sp [ $\mu\text{m}$ ]	Sv [ $\mu\text{m}$ ]	Sz [ $\mu\text{m}$ ]	Sa [ $\mu\text{m}$ ]	Ra [ $\mu\text{m}$ ]	Rt [ $\mu\text{m}$ ]	RSm [mm]	Wa [ $\mu\text{m}$ ]	WSm [mm]
1	1	0.24	0.96	1.13	2.09	0.19	0.16	1.25	0.026	0.31	0.21
2	2	0.43	1.46	1.39	2.85	0.36	0.20	1.40	0.041	0.18	0.39
3	3	0.28	2.23	2.69	4.94	0.20	0.19	2.28	0.036	0.12	0.61
4	6	0.59	2.48	1.44	3.92	0.47	0.31	2.19	0.034	0.50	1.21

Thanks to Tab. 2, it might be concluded that along with the increased number of involved plates used in the process of final shaping of the surface, the roughness parameters also increase. The Ra parameter for the involvement of one plate in the machining process is  $0.16 \mu\text{m}$  and increases along with the number of plates involved in the machining process. In the case of six plates, that parameter is  $0.31 \mu\text{m}$ . Similar behavior has been noted for other parameters depicting the roughness of the surface. The parameter Wsm, which changes within the range from 0.21 to 1.21 mm, has had a significant importance for the performance parameters of created surfaces.



*Fig. 1: Comparison of isometric images for the conducted machining attempt: a) the number of cutting places  $z = 1$ ; b) the number of cutting places  $z = 2$ ; c) the number of cutting places  $z = 3$ ; d) the number of cutting places  $z = 6$ .*

By analyzing the isometric images and results of the measurements presented in Tab. 2 and Fig. 1, it is possible to notice that in the case of machining with only 1 cutting plate placed in the head of the cutter, the results indicate the highest bearing capacity of the created surface. The most visible difference in the performance parameters of the surface may be noticed in Fig. 1d. The unevenness of the formed irregularities of the surface results not only from the axial, but also from the radial error of placement of the cutting plates in the head of the cutter. The difference in the radial error of the placement of cutting



plates results in an uneven load on the sockets of the head due to different actual feed per respective sockets of the head.

#### 4. Conclusions

The conducted research on vibrations in the layout tool - workpiece, with the simultaneous measurement of errors of the placement of cutting plates in the endmilling head, as well as measurement of roughness of the surface, has enabled formulation of the following conclusions:

1. The increase of the use of cutting plates influences the maximum peak-to-peak amplitude and the standard deviation of vibrations occurring in the layout tool - workpiece.
2. The increase of the number of cutting plates in the tool head facilitated with a honing plate results in an increase of the roughness parameters of the created surfaces.
3. The shaping of the surface performed by the remaining plates is caused by the presence of higher vibrations in the layout tool - machined object with regard to the axial difference of the shift of the honing plate.
4. The axial shift of the honing plate for the machining conducted under conditions recommended by the manufacturer is insufficient. In order to perform the final formation of the surface only by the honing plate, it was necessary to move it axially by a value higher than the maximum amplitude of vibrations occurring in the layout.

#### References

- Adamczak, S. and Bochnia, J. (2016) Estimating the approximation uncertainty for digital materials subjected to stress relaxation tests, *metrology and measurement systems*, 23, 4, SI, pp. 545-553.
- Adamczak, S., Zmarzly, P. and Janecki, D. (2015) Theoretical And Practical Investigations Of V-Block Waviness Measurement Of Cylindrical Parts, *Metrology and Measurement Systems*, 22, 2, pp. 181-192.
- Blasiak, S., Takosoglu, J.E. and Laski, P.A. (2014) Heat transfer and thermal deformations in non-contacting face seals, *Journal of Thermal Science and Technology*, 9, 2, pp. JTST0011----JTST0011. doi:10.1299/jtst.2014.jtst0011.
- Grzesik, W., Bartoszek, M. and Nieslony, P. (2005) Finite difference method-based simulation of temperature fields for application to orthogonal cutting with coated tools, *Machining Science and Technology*, 9, 4, pp. 529-546.
- Grzesik, W., Nieslony, P. and Bartoszek, M. (2001) Thermophysical-property-based selection of coatings for dry machining of carbon and stainless steels, *Transactions of the North American Manufacturing Research Institution of Sme*, 29, pp. 343-350.
- Krajcarz, D. (2014) Comparison Metal Water Jet Cutting with Laser and Plasma Cutting, In *Procedia Engineering*, pp. 838-843.
- Krajcarz, D. and Spadło, S. (2015) Influence of the Process Conditions on the Diameter of Cylindrical Holes produced by Abrasive Water Jet Cutting, In *Proceedings of 25th International Conference on Metallurgy and Materials Metal 2016*, pp. 1462-1467.
- Miko, E. (2005) Micro-irregularities of metal surfaces, *Strojnicki Vestnik-Journal of Mechanical Engineering*, 51, 10, pp. 634-645.
- Miko, E. and Nowakowski, L. (2012) Vibrations in the Machining System of the Vertical Machining Center, *Procedia Engineering*, 39, pp. 405-413, doi:10.1016/j.proeng.2012.07.044.
- Nowakowski, L., Miecesikowska, M. and Blasiak, M. (2016) Speech intelligibility in the position of cnc machine operator, in *engineering mechanics 2016*, pp. 422-425.
- Nowakowski, L., Miko, E. and Skrzyniarz, M. (2016) The analysis of the zone for initiating the cutting process of X37CrMoV51 steel, In *Engineering Mechanics 2016*, pp. 426-429.
- Nowakowski, L., Skrzyniarz, M. and Miko, E. (2016) Proceedings of the International Conference on Experimental Fluid Mechanics 2016, In *The impact of cooling methods on the maximum temperature of the processed object during side milling*, pp. 528-531.
- Nowakowski, L. and Wijas, M. (2016) The evaluation of the process of surface regeneration after laser cladding and face milling, In *Engineering Mechanics 2016*, pp. 430-433.
- Takosoglu, J.E., Laski, P.A., Blasiak, S., Bracha, G. and Pietrala, D. (2016a) Determination of flow-rate characteristics and parameters of piezo valves, In P. Dancova (Ed.), *Proceedings of the International Conference Experimental Fluid Mechanics 2016*, pp. 814-818, Techn. Univ. Liberec.
- Takosoglu, J.E., Laski, P.A., Blasiak, S., Bracha, G. and Pietrala, D. (2016b) Determining the Static Characteristics of Pneumatic Muscles, *Measurement and Control*, 49, 2, pp. 62-71, doi:10.1177/0020294016629176.

## SHAPING THE STARTING OF A HYDROSTATIC TRANSMISSION WITH PROPORTIONALLY CONTROLLED ELEMENTS

P. Osiński\*, M. Stosiak\*\*

**Abstract:** *This paper focuses on selected adverse phenomena accompanying the starting of a hydrostatic transmission with a linear motor. Some practical ways of attenuating the process of starting the hydrostatic transmission are presented. A hydraulic system, being in a transient process state and incorporating a proportional control valve, was analysed. The aim of the investigations was to reduce dynamic pressure excesses and to determine the effect of this factor on the noisiness of the hydrostatic system in the transient state.*

**Keywords:** Hydrostatic transmission, Starting, Pressure excess, Noise.

### 1. Introduction

The current trends in the development of hydrostatic drives consist in, among other things, minimizing energy losses and weight and increasing the transmitted power, and so increasing the power/weight ratio. One of the limitations on improving this ratio is the fact that the noisiness of hydrostatic systems and elements increases as the generated or transmitted power is increased. It emerges from the available literature and the authors' own experiments that one of the principal causes of the excessive noisiness of hydraulic systems are pressure fluctuations due to flow rate oscillations and pressure excesses during hydraulic system starting or braking.

The starting process (pressure buildup) can be attenuated by introducing additional leakages through the use a starting valve (e.g. an adjustable throttle valve or a specially designed starting valve). But the incorporation of a throttle valve between the hydraulic motor's feed conduit and its drain conduit to increase leakages results in lower efficiency, whereby it is necessary to install greater power for the performance of the drive function.

The starting process can also be attenuated by introducing proportional control valves.

### 2. Tested system

The initial system shown in Fig. 1a was adopted to examine the possibilities of the effective attenuation of hydraulic transmission starting. During the experiments special attention was given to the process of starting the hydraulic system. In order to attenuate this process the structure of the system was modified by introducing a proportional distributor into the pump shunt conduit, Fig. 1b.

### 3. Measuring apparatus and methodology

The measured quantities were:

- 1) pressure (points 6 and 7 (Figs 1a and 1b)), using SPAIS PT5101 extensometric pressure transducers with a measuring range of 0-6 MPa with an SPAIS AT-5210N instrumentation amplifier and an SPAIS BZ5202 power supply unit;

---

\* Piotr Osiński, Hab. PhD.: Hydraulic Drives and Machine Vibroacoustics Laboratory, Wrocław University of Science and Technology, Faculty of Mechanical Engineering, Department of Maintenance and Operation of Logistics, Transportation and Hydraulic Systems; PL, piotr.osinski@pwr.edu.pl

\*\* Michał Stosiak, Hab. PhD.: Wrocław University of Science and Technology, Faculty of Mechanical Engineering, Department of Maintenance and Operation of Logistics, Transportation and Hydraulic Systems; PL  
michal.stosiak@pwr.edu.pl

- 2) the equivalent level ( $L_{Aeq}$  [dB]), the maximum level ( $L_{Amax}$  [dB]) and the minimum level ( $L_{Amin}$  [dB]) of sound A, using a sonometer and a type 2250, series 2519832 modular B&K sound level meter with a type ZC 0032 preamplifier (serial number 4112), a type 4189, series 2519832 microphone and BZ 5503 software;
- 3) the displacement of the proportional distributor, using an induction displacement sensor integrated with the proportional distributor.

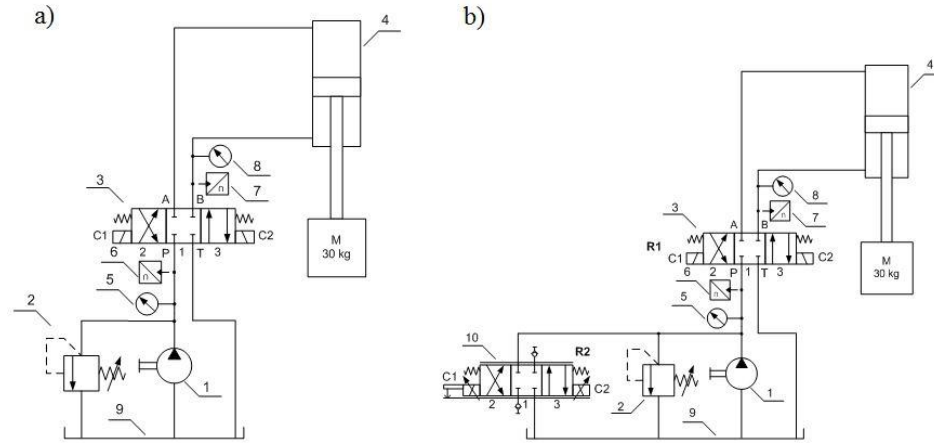


Fig. 1: a) diagram of hydraulic system of hydrostatic transmission with linear motor: 1 – displacement pump ( $Q_{pt} = 6.5 \text{ dm}^3/\text{min}$  at 1450 rpm); 2 – pressure relief valve; 3 – conventionally electrically controlled 4/3 distributor; 4 – linear hydraulic motor (piston diameter 25 mm, piston rod diameter 16 mm, stroke 200 mm); 5, 8 – manometer; 6, 7 – pressure transducer; 9 – hydraulic oil tank; b) diagram of modified hydraulic system of hydrostatic transmission with linear motor: 1 – displacement pump ( $Q_{pt} = 6.5 \text{ dm}^3/\text{min}$  at 1450 rpm); 2 – relief valve; 3 – conventionally electrically controlled 4/3 distributor; 4 – linear hydraulic system (piston diameter 25 mm, piston rod diameter 16 mm, stroke 200 mm); 5, 8 – manometer; 6, 7 – pressure transducer; 9 – hydraulic oil tank; 10 – 4/3 proportional distributor.

The signal from the pressure measuring circuit was fed into a four-channel digital oscilloscope with an FFT analysis module (Tektronix TDS 224) and then into a measuring computer. The signal from the sonometer was transmitted directly to the measuring computer. The sound level meter can simultaneously record the time history and perform a frequency analysis. During the experiments the sonometer was situated at a distance of 1 m from the source. The whole measuring circuit was calibrated before and after the measurements.

The hydraulic system schematically shown in Fig. 1a and b was subjected to tests. As the system shown in Fig. 1a was being tested, coil C1 of the 4/3 distributor was surgeswised (in accordance with the step function) energized at instant  $t_0$ . This resulted in the abrupt connection of the actuator's piston rod chamber with the operating hydraulic feeder, forced by an abrupt change in the rate of flow. The pressure (in points 6 and 7 acc. to Fig. 1a) and the accompanying acoustic signal were recorded. As the system shown in Fig. 1b was being tested, distributor 10 was overdriven. Distributor 2 was constantly in position 2, while distributor 10 was in initial position 2. In this case, the feature of proportional control valves, enabling one to gradually increase or decrease the electrical signal fed into the coil of the proportional electromagnet, was exploited. This feature is referred to as “*Rampenzeit*” in the German-language literature and as “*time of delay*” in the English-language literature on the subject. As a result, the proportional distributor could be gradually moved from position 2 towards neutral position 1.

#### 4. Test results

Traces of: the pressure at the pump, the proportional distributor slide displacement and the sound level during the starting of the investigated hydraulic systems were obtained from the tests.

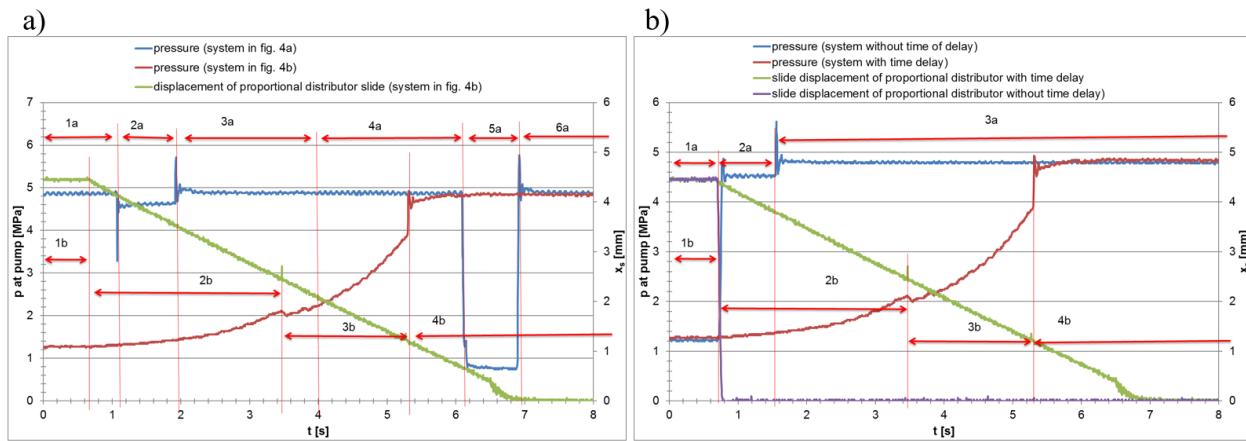


Fig. 2: Pressure at pump and slide displacement traces for tested hydraulic systems.

The time intervals corresponding to the working phases of the systems are marked in Figs. 2a and 2b. In Fig. 2 one can distinguish the following time intervals: interval 1a – the coils of distributor 3 (Fig. 1a) are not powered and the liquid fed by the pump returns via pressure relief valve 2 to the tank. At the end of this interval coil C1 of distributor 3 (Fig. 1a) was surgeswively energized (24 V), whereby the latter was abruptly overdriven, the actuator (the piston rod chamber) was connected to the supply and actuator 4 was started. Interval 2a corresponds to the movement of actuator 4, which subsequently reaches its upper extreme position and stops abruptly (the piston strikes against the bottom). Interval 3a corresponds to the situation when the actuator remains in the upper extreme position and is connected with the feed pump; this is also the working phase of the relief valve. At the end of this interval the electric circuit of coil C1 of distributor 3 was opened and the distributor slide returned to the neutral position, while the pump continued pumping the whole liquid via over overflow valve 2 to the tank. This state lasted over interval 4a. Then by surgeswively energizing coil C2 distributor 3 was overdriven into the other extreme position. Interval 5a corresponds to the return motion (downwards) of the actuator, which performing its full stroke, reaches the extreme position and stops abruptly. The pressure increases and the pump again begins to return the liquid to the tank via relief valve 2 – interval 6a. A similar analysis of time intervals can be carried out for the modified system shown in Fig. 1b. Interval 1b corresponds to the situation when proportional distributor 10 is overdriven into extreme position 2 and the whole pumped liquid finds its way, via this distributor, to the tank (relief valve 2 remains closed). Interval 2b corresponds to the movement (using the time of delay) of the slide of distributor 10 from position 2 to (neutral) position 1. As a result, the throttle gap of distributor 10 diminishes and pressure slowly builds up, while the actuator remains motionless (occupying the lower extreme position). It starts to move at the beginning of interval 3b. The gentle movement of the actuator continues to the end of this interval. Subsequently, the actuator stops abruptly as it reaches its upper extreme position. Then pressure in the system rises to the relief valve opening value. This corresponds to interval 4b in Fig. 2a. In a similar way one can describe Fig. 2b, where the systems from Fig. 2b, in which the slide was overdriven with and without the time-of-delay function turned on. Interval 1a corresponds to the situation when proportional distributor 10 is overdriven to extreme position 2 and the whole pumped liquid passes through it to the tank (relief valve 2 remains closed). Interval 2a corresponds to the movement of actuator 4. Then the actuator reaches its upper extreme position and stops abruptly (the piston strikes against the bottom). Interval 3a corresponds to the situation in which the actuator remains in the upper extreme position and is connected with the feed pump. This is also the working phase of the relief valve. Time intervals 1b – 4b in Fig. 2b are analogous to the ones in Fig. 2a.

In order to determine the effect of the particular starting methods on the acoustic climate the measured acoustic quantities were compared for the actuator's two working phases: standstill and stopping (Tab. 1). In the case of phase 1, i.e. cutting off hydraulic supply to the actuator and directing the working medium from the pump via the relief valve or the proportional distributor to the tank, the acoustic parameter values measured for the considered systems are comparable, amounting to 62 dB. In both cases, the character of the spectra is similar in most of the thirds, with characteristic broadband noise in the range of average and high frequencies and with a tonal component at 500 Hz. Larger differences are observed in the third with the midband frequency of 250 Hz and 1 kHz, which in the case of proportional control have a tonal character. The tones are present also in the other working cycles of the system with proportional control. This means that they appear when the proportional distributor is incorporated into the system. As

the impedance of the system changes, pressure and dynamic pump shaft torque fluctuations increase to 250 Hz. The next displacement pump pressure fluctuation harmonics are 500 Hz and 1 kHz. No dominant components were observed in the range of harmful infrasounds.

Tab. 1: Comparison of measured acoustic quantities.

	Type of control					
	conventional		proportional without time of delay		proportional with time of delay	
Cycle	denotation	$L_{AFmax}$ [dB]	denotation	$L_{AFmax}$ [dB]	denotation	$L_{AFmax}$ [dB]
Standstill	1a	61.8	1b	62.2	1b	62.2
Stopping	3a	82.4	3a	83.5	4b	80.6

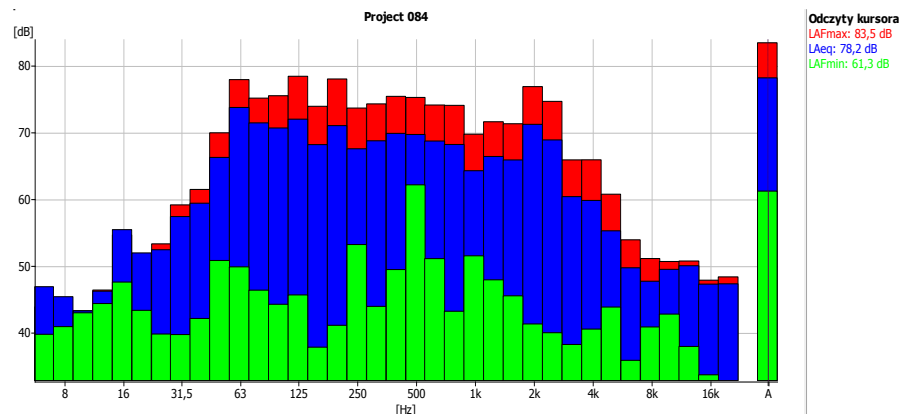


Fig. 3: One-third octave spectrum of average  $L_{Aeq}$ , maximum  $L_{AFmax}$  and minimum  $L_{AFmin}$  level of sound A during actuator stopping for proportional-control system without time of delay (stage 4b in Fig. 2b and stage 3a in Fig. 2b).

In the case of both conventional control and proportional control, the acoustic signal recorded for the actuator stopping cycle, without piston final run braking, has a nonstationary character. Considerable differences between the maximum level and the minimum level are observed in a broad band in the 1/3 octave spectrum (Fig. 3). This indicates the occurrence of pulse-like noise produced as the piston strikes against the cylinder bottom. The lower values (2 – 3 dB) of the level of sound A measured for proportional control with time of delay are due to the incomplete overdrive of the slide in the proportional distributor.

## 5. Conclusion

Dynamic changes in pressure, especially dynamic pressure excesses arising during transient states (e.g. during starting or braking), are to a large extent responsible for the noisy operation of hydraulic systems. Dynamic pressure excesses also result in instantaneous impact or pulse loads acting on hydraulic system elements, contributing to the excitation of vibrations in the elements and to the degradation of their durability.

The adverse effects of dynamic pressure changes (pressure fluctuations, dynamic pressure excesses during the starting or braking of the hydraulic system) can be most effectively reduced through the simultaneous use of several methods, which often have a selective character, i.e. are effective in selected frequency ranges. The results of the experiments show that the dynamic pressure excess during the starting of the investigated transmission was reduced thanks to the use a proportional distributor with the time-of-delay function (Figs. 2a and 2b). However, this is achieved at the cost of longer starting process time. The results for the extreme cases – without time of delay and with the maximum time of delay (amounting to about 6 s) – are reported intentionally, however, the control card of the proportional distributor is equipped with a potentiometer enabling the infinitely variable setting of this time up to  $t_{max} = 6$  s.

## VERIFICATION OF VELOCITY MEASUREMENT METHODS BY HIGH SPEED CAMERA AND ACCELEROMETER ON EXAMPLE OF IMPACT TESTER

P. Osowski<sup>\*</sup>, M. Wolski<sup>\*\*</sup>, T. Piatkowski<sup>\*\*\*</sup>

**Abstract:** In the paper the velocity measurement accuracy analysis of impact testers dropping platen is shown. The measurement is carried out by two devices: accelerometer and high speed camera. During research it was assumed that dropping platen is moving in uniformly accelerated motion. The uncertainty of velocity measurement for each method was determined depending on the sampling frequency of measuring devices and the free fall height of dropping platen.

**Keywords:** Linear velocity measurement, Uncertainty measurement, Impact tester.

### 1. Introduction

The key role in packaging construction are cushioning materials. The main tasks of this materials is absorption and dissipation of kinetic energy from sudden stop of object caused by collision. In order to predict the behavior of packages during collision the characteristic of cushioning materials (cushioning curve) (Young, 2009) is used. It is determined experimentally by means of so-called impact testers. In order to obtain reliable research results, the knowledge of linear velocity of dropping platen of the tester during collision with the sample is required.

Methods for the linear velocity determination are indirect methods. They use devices, which record the position or acceleration time history, then differentiate (position) or integrating (acceleration) (Webster et al., 2014).

Dropping platen position registration (marker placed on the platen, Fig. 1) is performed using a high speed camera (AOS Q-PRI). To read the position from a recorded video the method proposed in paper (Das et al., 2014) is used. Registration of acceleration is performed using the triaxle acceleration recorder (SAVER 3X90) attached to platen.

The purpose of this article is verification, which examined methods of velocity measurement is more accurate. Obtained research results allow to choose a more effective method to measure the velocity of the platen at the impact moment with the sample.

### 2. Object of research

The object of research is impact tester, which is used to test of the protective properties of cushioning materials. The device consists of dropping platen (3) with acceleration recorder (7), free falling from specified height on tested sample, placed on reaction mass (5). The free fall of the platen is initiated by disconnection of the electromagnet (6). The dropping platen is attached to guideway (4), on which it moves by a linear bearing (2). To the need of the presented paper all kinds of resistance omitted – it was assumed that dropping platen falls in accordance with gravity acceleration.

---

<sup>\*</sup> M. Eng. Przemyslaw Osowski: Faculty of Mechanical Engineering, UTP University of Science and Technology, Al. Prof. S. Kaliskiego 7, 85-796, Bydgoszcz; Poland, przoso000@utp.edu.pl

<sup>\*\*</sup> M. Eng. Mirosław Wolski: Faculty of Mechanical Engineering, UTP University of Science and Technology, Al. Prof. S. Kaliskiego 7, 85-796, Bydgoszcz; Poland, Mirosław.Wolski@utp.edu.pl

<sup>\*\*\*</sup> Assoc. Prof. Tomasz Piatkowski, PhD.: Faculty of Mechanical Engineering, UTP University of Science and Technology, Al. Prof. S. Kaliskiego 7, 85-796, Bydgoszcz; Poland, topiat@utp.edu.pl



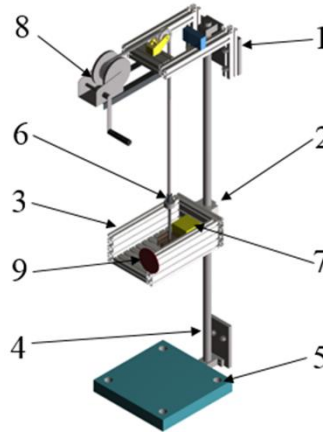


Fig. 1: Impact tester: 1 – crown, 2 – linear bearing, 3- dropping platen, 4 – guideway, 5 – reaction mass, 6 – electromagnet, 7 – triaxle acceleration recorder, 8 – rope winch, 9 – marker.

### 3. Uncertainty determination of velocity measurement

#### 3.1. High speed camera

The method of the velocity determination from recorded video consists of two stages. The first stage involves marker extraction from recording. It is done by binarization of the extracted data stream from established color model. Through this process cluster of pixels is singled representing the marker, which we call BLOB (Binary Large Object) (Jia et al., 2008). In order to determine the position of BLOB centroid the individual pixels are considered as the squares of edge 1 pixel

$$Lp_i = \frac{\sum_{j=1}^N x_j p^2}{\sum_{j=1}^N p^2} \quad (1)$$

where  $x_j$  is the  $j$ -th pixel position in the rectangular coordinate system OXY of the frame,  $p$  is the length of the edge of the pixel ( $p=1$  px) and  $N$  is the number of detected pixels in BLOB which is determined by equation:

$$N = \frac{\pi}{4} \left( \frac{Lp_u \cdot d_B}{p_u} \right)^2 = \frac{\pi}{4} (w \cdot d_B)^2 \quad (2)$$

where  $p_u$  is the length of the square-shaped frame ( $p_u = 0.957$  m),  $Lp_u$  is the number of pixels attributable to length  $p_u$  (value depends on the applied frame resolution),  $d_B$  is marker diameter ( $d_B = 0.1$  m) and  $w$  is a constant calculated during  $p_u$  determination.

Uncertainty of object centroid position depends on the pixels number contained in the BLOB:

$$u(Lp_i) = \sqrt{\sum_{j=1}^N \left[ \left( \frac{p^2}{N \cdot p^2} \right)^2 u(x_j)^2 \right]} = \sqrt{N \frac{p^4}{N^2 p^4} u(x_j)^2} = \sqrt{\frac{u(x_j)^2}{N}} \quad (3)$$

where  $u(x_j)$  is  $j$ -th pixel position uncertainty ( $u(x_j) = 1$  px).

After the marker centroid position determination in each frame, the second stage is carried out: the platen displacement calculation:

$$\Delta s_i = w(Lp_i - Lp_{i-1}), \text{ when } i=2, \dots, k \quad (4)$$

where  $k$  is the number of captured frames.

Uncertainty of the displacement determination is calculated by following equation:

$$u(\Delta s_i) = \sqrt{2(w)^2 u(Lp_i)^2}, \text{ when } i=2, \dots, k \quad (5)$$

Knowing displacement  $\Delta s$ , we can determine the dropping platen velocity at the impact moment:

$$V_i = \frac{\Delta s_i}{\Delta t_u}, \text{ when } i=2, \dots, k \quad (6)$$

where  $\Delta t_u$  is set up sampling time.

Using the Eq. (4) and (6) and knowing that the uncertainty of sampling time  $u(\Delta t_u)$  is so small that it can be neglected, the uncertainty of the velocity determination is defined by equation:

$$u(V_i) = \sqrt{\left(\frac{1}{\Delta t_u}\right)^2 u(\Delta s_i)^2}, \text{ when } i=2, \dots, k \quad (7)$$

Uncertainty of velocity is also caused by the error of numerical differentiation method. We can determine this value by Taylor series (Bjorck et al., 1987):

$$u(Vf_i) = \frac{1}{2} s_i^{(2)} \Delta t_u = \frac{s_{i-2} - 2s_{i-1} + s_i}{2\Delta t_u}, \text{ when } i=3, \dots, k \quad (8)$$

where  $s_i$  is a position of dropping platen in  $i$ -th frame.

Due to the two velocity uncertainties existence, the resultant value  $u(Vres_i)$  is determined by equation:

$$u(Vres_i) = \sqrt{u(V_i)^2 + u(Vf_i)^2}, \text{ when } i=3, \dots, k \quad (9)$$

### 3.2. Acceleration recorder

The measuring velocity method which uses acceleration recorder relies on numerical integration by trapezoidal rule of the acceleration time history:

$$V_n = \sum_{i=2}^m \frac{a_i + a_{i-1}}{2} \Delta t_u = \frac{a_1 + a_m}{2} \Delta t_u + \sum_{i=2}^{m-1} a_i \Delta t_u \quad (10)$$

where  $V_m$  is the velocity determined at the  $m$  point,  $a_i$  is  $i$ -th measure of acceleration and  $\Delta t_u$  is set up sampling time.

The uncertainty of the velocity at the point  $k$  is determined, knowing that the uncertainty of sampling time  $u(\Delta t_u)$  is so small that it can be neglected and the error of numerical integration method is presented by

$\sum_{i=1}^n \frac{1}{12} a_i^{(2)} (\Delta t_u)^3$  (Bjorck et al., 1987):

$$u(V_k) = \sqrt{(k-2)(\Delta t_u)^2 (u(a))^2 + 2\left(\frac{\Delta t_u}{2}\right)^2 (u(a))^2 + \left(\sum_{i=2}^{m-1} \frac{a_i^{(2)} (\Delta t_u)^3}{12}\right)^2} \quad (11)$$

where  $a_i^{(2)}$  is a second order derivative of acceleration (in uniformly accelerated motion  $a_i^{(2)} = 0$ ) and  $u(a)$  is uncertainty of the measured acceleration which is determined by equation:

$$u(a) = \frac{2a_r}{2^{(A/D-1)}} \quad (12)$$

where  $a_r = 981 \text{ m/s}^2$  is acceleration range and  $A/D = 16$  bit is analogue/digital conversion.

#### 4. Presentation and discussion of results

In order to evaluate the accuracy of methods to measure the impact velocity of dropping platen it was assumed that platen falls in accordance with acceleration of gravity. For this assumption the maximum uncertainty of velocity for each method was determined according to free fall height  $h$  and sampling frequency  $f$  (Fig. 2a). In the case of camera the relations between resolution and frame frequency was also taken into account (Fig. 2b). As can be seen, the acceleration recorder determines the velocity with lower uncertainty than camera for each height  $h$  and sampling frequency  $f$ . This is due to the fact that the camera resolution depends on the sampling frequency (Fig. 2b) affecting the BLOB uncertainty position and that the accuracy of numerical differentiation method depends strongly on the sampling time.

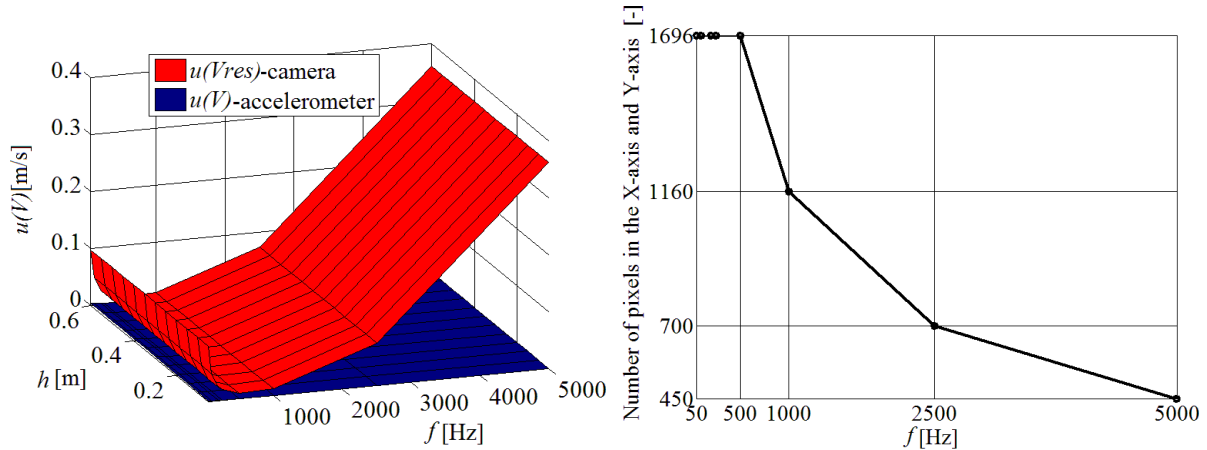


Fig. 2: a) Chart of linear velocity uncertainty as a function of free fall height and sampling frequency, b) chart of camera resolution in X-axis as a function of sampling frequency from which we acquired  $Lp_u$  value.

#### 5. Conclusion

Uncertainty of measured dropping platen velocity was estimated for two motion registration methods (high speed camera and acceleration recorder) in a wide range of sampling frequency  $f$  and free fall height  $h$ . It turned out that in examined range of values  $h$  and  $f$ , the uncertainty of velocity determined by the acceleration recorder is lower than by the camera. This is due to fact, that intended use of acceleration recorder is to measure the kinematics parameters of one point, i.e.: displacement, velocity or acceleration. In case of deformation measure of flexible body (where the relative position of body points also change) the only way to measure such a complex motion is to use the multi-point measure method, which allows e.g. camera.

#### References

- Bjorck, A. and Dahlquist G. (1987) Numerical methods, PWN, Warsaw (in Polish).
- Das, P., Ghoshal, R., Kole, D.K. and Ghosh, R. (2014) Measurement of Displacement and Velocity of Moving Object from Real Time Video. International Journal of Computer Applications, 49, 13, pp. 12-16.
- Fiedler, R.M. (2009) Shock, w: Yam K.L., Encyclopedia of packaging technology. A John Wiley & Sons, pp. 1107-1111.
- Jia, T., Sun, N. and Cao, M. (2008) Moving object detection based on blob analysis, in: International Conference on Automation and Logistic, Qingdao, China, pp. 322-325, doi: 10.1109/ICAL.2008.4636168.
- Webster, J.G. and Eren H. (2014) Velocity Measurement. Measurement, Instrumentation, and Sensors Handbook, Second Edition. Spatial, Mechanical, Thermal, and Radiation Measurement. CRC Press.

## EXPERIMENTAL STUDIES OF VIBRATION OF THE TECHNOLOGICAL DEVICE FOR ELECTROCHEMICAL MACHINING OF CURVILINEAR SURFACES

T. Paczkowski\*, J. Sawicki\*\*

**Abstract:** *The paper provides the results of dynamic experiments of the technological device facilitating electrochemical machining of any shaped curvilinear surfaces and rotary shaping surfaces with curvilinear profile. With the experimental analysis of vibration, in selected points of the technological device the vibration was identified.*

**Keywords:** Technological device, ECM, Vibration analysis.

### 1. Introduction

Designing the technological device (research stand) providing the function of the machine tool or mini machine tool, one shall note the necessity of solving the problems immediately connected with the dynamics of the phenomena accompanying the operation of the device (Marchelek, 1991). The key job is to ensure a stable motion of the tool and the object being machined. The deviations from the assumed motion of the tool and the machined object are usually a result of external effects on mass-spring system, OUPN (machine tool-holder-object machined-tool), as well as mass-spring properties of the OUPN system. The mass-spring properties of the OUPN system have a crucial effect on the nature of oscillating motions (Cannon, 1973 and Gutowski et al., 1986). The real dynamic OUPN system is a nonlinear continuous system. Very often, investigating dynamic phenomena in machine tools, due to poor mass-spring nonlinearity of the OUPN system and vibration for analysis, one uses the linear approximation. The technological device will, in fact, meet the input functions if the OUPN system is stable and, on top of that, it will demonstrate specific dynamic properties. Most frequently, to evaluate those properties, the so-called dynamic quality indices are applied (Cannon, 1973 and Piszczek et al., 1982).

This paper has been an attempt at evaluating the technological device meeting the function of the research stand (machine tool) for ECM for selected excitations generating vibration, based on the analysis of time and amplitude-frequency characteristics.

### 2. Technological device

#### 2.1. Characteristics of the technological device

Designing the technological device for examining the ECM with shaping electrodes, it was assumed that the size of the surface machined will not exceed 40 cm<sup>2</sup>. The values of the machined surface assumed provide mostly the parameters of DC power supply, the mass of the electrodes and the forces acting on them, which determines the mechanical load of the stand. It has an essential effect mostly on the stiffness of the elements of the body, their shape and the size (Paczkowski, 2010, Osiński, 2013). The technological device facilitates performing ECM with a fixed shaping electrode, vibrating across the gap (Fig. 1).

---

\* Assoc. Prof. Tomasz Paczkowski: University of Technology and Life Sciences in Bydgoszcz, Faculty of Mechanical Engineering, tomasz.paczkowski@utp.edu.pl

\*\* Assoc. Prof. Jerzy Sawicki: University of Technology and Life Sciences in Bydgoszcz, Faculty of Mechanical Engineering, jerzy.sawicki@utp.edu.pl.

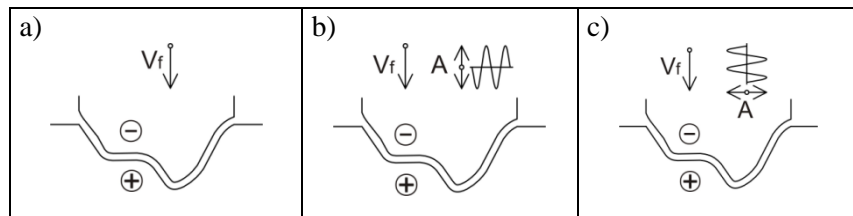


Fig. 1: Kinematics of the working electrode motion.

## 2.2. Components of the technological device

The basic component of the stand is its body. It is made up of two basic plates 1 and 2, as well as two mobile plates 4 and 5 (Fig. 2a) connected with each other with four guide-posts 3 together with closed linear bearings type LM20UU. Electrodes are connected with mobile plates.

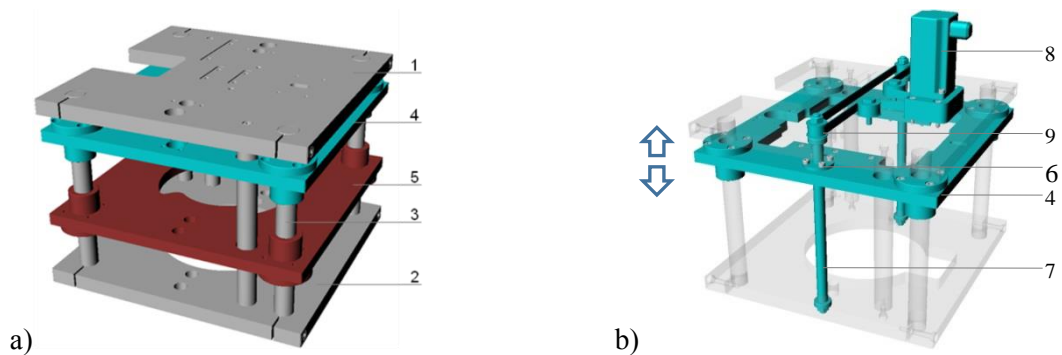


Fig. 2: a) Research stand body; b) Main feed of the working electrode.

The stand body, depending on the type of machining, is mounted with adequate drive systems of electrodes producing motions: feed motion and velocity  $V_f$  and circular motion with velocity and drive systems causing vibration of electrodes in directions normal and perpendicular to in-feeding motion.

The drive system of the main feed Fig. 2b of the working electrode consists of mobile plate 4 mounted on guide-posts with rolling sleeves and connected with nuts 6 with guide screws 7. Guide screws are driven with servomotor 8 with the toothed belt drive 9.

The drive system of transverse vibration of the working electrode Fig. 3a consists of the support 10 embedded through sliding elements 11 and guides 12 on plate 4. Support 10 is driven with servomotor 13 through toothed belt drive 14 and eccentric cam 15. A constant pressure of the support to cam is ensured by a spring 16.

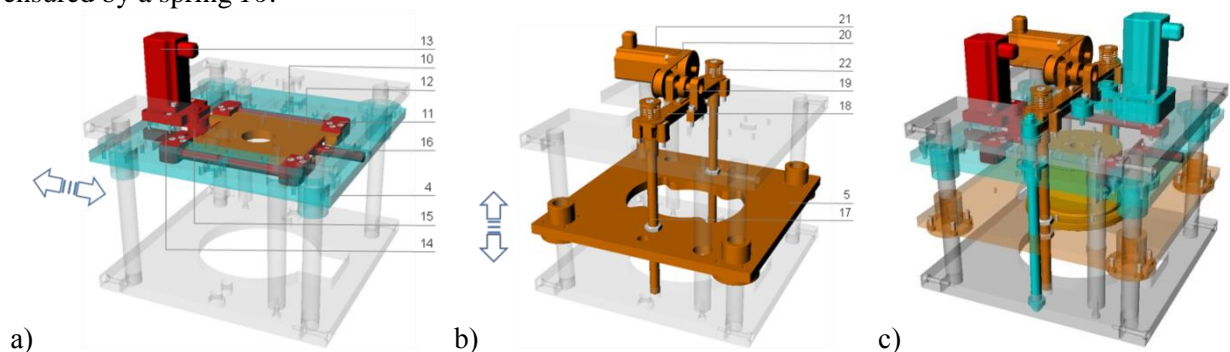


Fig. 3: a) Drive of transverse vibration of the working electrode; b) Drive of longitudinal vibration of the electrode; c) Technological device – configuration with shaping electrode.

The drive system of longitudinal vibration of the electrode Fig. 3b consists of the mobile plate 5, mounted on guide-posts with rolling sleeves and connected through tappets 17 with beam 18. The beam 18 cooperates with eccentric cam 19 driven with the toothed belt drive 20 with servomotor 21. The constant pressure of beam 18 with cam is ensured by springs 22. Fig. 3c demonstrates the configuration of the research stand for drilling with shaping.

For the right operation, the technological device is supplemented with the following components: DC power supply, the system of feeding with electrolyte, process parameters control system.

### 2.3. Machining cells

The key component of the stand is the machining cell. Depending on the ECM type, two different design forms of the machining cell were considered for drilling with curvilinear shaping electrode (Fig. 4).

Irrespective of the type of machining, in the machining cell one will find the object machined 1 and working electrode 2 (Fig. 4). Depending on the type of erosion machining, the electrodes are mounted adequately to mobile plates 10 and 11 (Fig. 2).

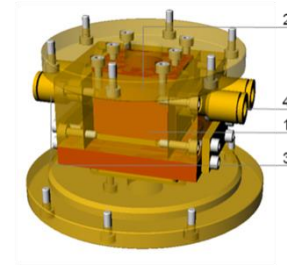


Fig. 4: Machining cells with shaping curvilinear electrode.

### 3. Technological device experiments

The experiments of the technological device included the measurement of vibration:

- the component performing horizontal translational motion,
- the component performing vertical translational motion,
- a rigid plate merging the structure of the research stand (namely the entire research stand).

The experiments were performed under working conditions (regular operation) of the research stand, namely for the assumed conditions of ECM shaping machining of shaping surfaces with curvilinear profile. Tab. 1 presents possible configurations of excitations of translational vibration, horizontal and vertical, the measurements were taken for.

Tab. 1: Possible configurations of excitations of horizontal and vertical vibration.

Measurement No.	1	2	Flow rate electrolyte  Q = 2 l/min
Horizontal forced vibration (sensor 1 - Hz)	0	50	
Vertical forced vibration (sensor 2 - Hz)	75	0	

The distribution of measurement points and privileged directions of measurements are shown in photograph (Fig. 5). Sensor 1 is mounted to the working component, performing horizontal translational motions produced by the circular motion of the eccentric mechanism the drive of which was executed using the toothed belt drive and the stepper motor. The theoretical amplitude of vibration comes from the eccentric mechanism applied and it is  $\pm 0.05$  mm. Sensor 2 is mounted on a mobile plate the vertical translational motion of which is also produced by the eccentric mechanism. Similarly, the eccentric mechanism is driven by the toothed belt drive and the stepper motor. The theoretical amplitude of vibration is  $\pm 0.1$  mm.

Sensor 3 has been mounted on a fixed plate of the research stand. The results of the measurements have been presented graphically in a form of time characteristics and frequencies characteristics for respective sequences of measurements have been plotted (Fig. 6). The dynamic identification of the kinematic system of the technological device, equipped with machining cell to ECM digestion of axisymmetric surfaces, similarly as in point 4.2, was performed to identify the nature of real vibration of the working electrode forced with cams driven with belt drives with an additional source of vibration generated by servomotor, producing the circular motion of the object machined.

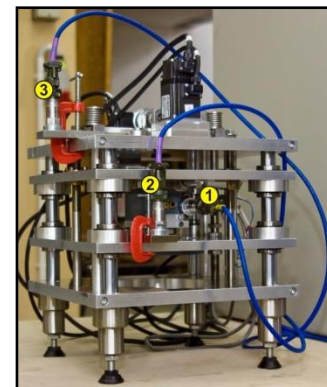


Fig. 5: Vibration sensors distribution.

### 4. Conclusions

The results of the experiments in terms of the research stand vibration as well as the presented plots of time characteristics and amplitude-frequency characteristics facilitate drawing the following conclusions:

- the FTT analysis shows that the dominant ones are the components with frequencies equal to the frequency of the input excitation (e.g. 37.5 Hz, 75 Hz),



- components of vibration with frequencies lower than the frequency of excitation come from self-vibration of the system resulting from the hydrodynamics of electrolyte flow (pressure of feeding, volumetric flow rate of electrolyte) in the interelectrode gap of the machining cell,
- components of vibration with frequencies higher than the frequency of excitation of the motion system of the stand are caused by the effect of rotating elements of the stand (belt drives, toothed wheels, stepper motors),
- the velocities of vibration of the component forcing vertical vibration are similar to the theoretical values specified for harmonic signal with known frequency and amplitude (Fig. 7a),
- velocities of vibration of the component forcing horizontal vibration differ from the theoretical values specified for harmonic signal with known frequency and amplitude (Fig. 7b).

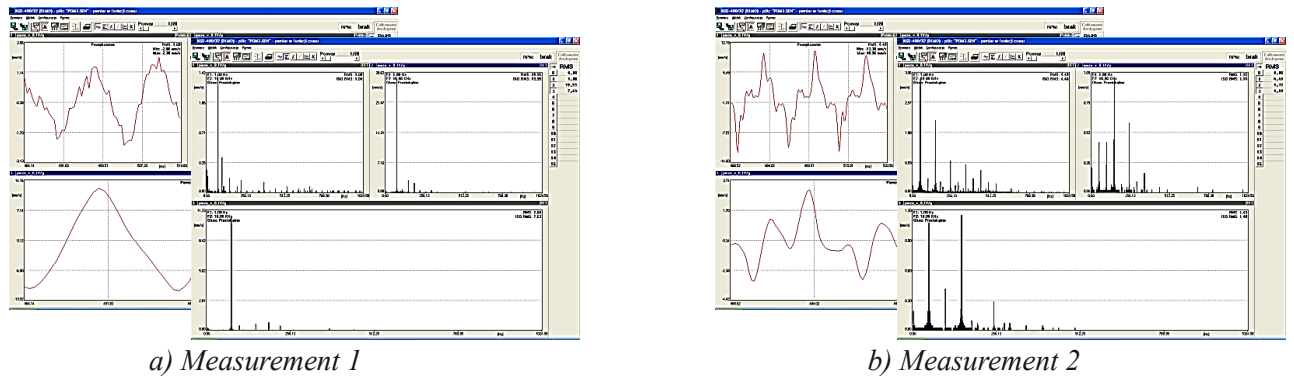


Fig. 6: Time patterns for the velocity of vibration for selected measurement points FFT analysis for selected measurement points for: a) vertical vibration  $f = 75$  Hz and horizontal vibration  $f = 0$  Hz; b) vertical vibration  $f = 0$  Hz, horizontal vibration  $f = 50$  Hz.

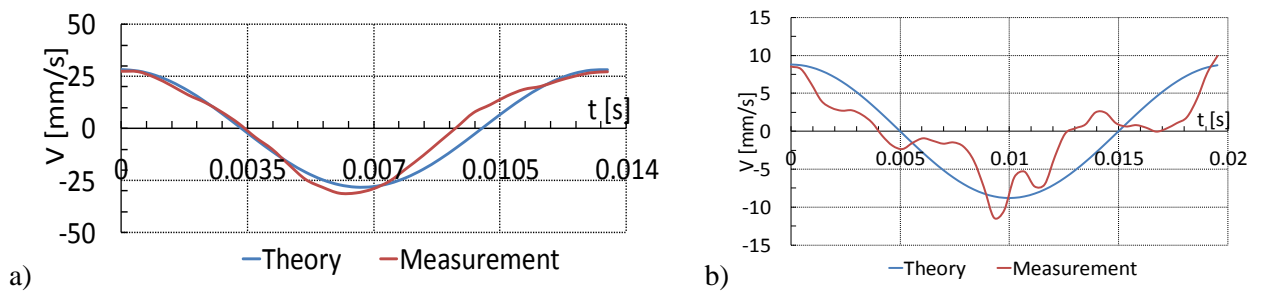


Fig. 7: Time patterns for the velocity of vibration: a) vertical vibration  $f = 75$  Hz, horizontal vibration  $f = 0$  Hz; b) vertical vibration  $f = 0$  Hz, horizontal vibration  $f = 50$  Hz.

## References

- Cannon, R.H. (1973) Dynamics of physical systems. WNT, Warszawa (in Polish).
- Gutowski, R. and Swetlicki, W.A. (1986) Dynamics and vibration of mechanical systems. PWN, Warszawa (in Polish).
- Marchelek, K. (1991) Dynamics of machine tools. WNT, Warszawa (in Polish).
- Paczkowski, T. (2010) Technological equipment for ECM surface curvilinear processing, World machine tools (in Polish).
- Piszczyk, K. and Walczak, J. (1982) Vibration in machine construction. PWN, Warszawa (in Polish).
- Osiński, Z. (2013) Machine construction basics, PWN, Warszawa (in Polish).

## A MODIFIED MATHEMATICAL MODEL OF HUMAN VENTRICULAR CARDIOMYOCYTE INCORPORATING SEPARATE T-TUBULAR AND SURFACE DYADS AND SUBMEMBRANE SPACES

M. Pásek<sup>\*</sup>, M. Bébarová<sup>\*\*</sup>, G. Christé<sup>\*\*\*</sup>

**Abstract:** Intracellular  $\text{Ca}^{2+}$  load and  $\text{Ca}^{2+}$  transient are considerably dependent on distribution of sarcolemmal  $\text{Ca}^{2+}$  pump and  $\text{Na}^+$ - $\text{Ca}^{2+}$  exchanger between the t-tubular and surface membranes in the presence of separate dyadic and subsarcolemmal spaces in rat ventricular cell model. To explore analogical phenomenon in human, we modified our previously published model of human ventricular myocyte. When the t-tubular fractions of  $\text{Na}^+$ - $\text{Ca}^{2+}$  exchanger and of sarcolemmal  $\text{Ca}^{2+}$  pump were increased to the newly proposed value of 0.95 in the modified model, the following changes were observed at 1 Hz steady-state stimulation: a shortening of the action potential duration at 90 % repolarisation by 6 % and an increase of the cytosolic  $\text{Ca}^{2+}$  transient by 22 %. Further analysis revealed a critical role of  $\text{Ca}^{2+}$  concentration changes in the subsarcolemmal spaces and consequent change in cellular  $\text{Ca}^{2+}$  cycling in this effect.

**Keywords:** Human ventricular cell model, T-tubules, Dyads, Subsarcolemmal spaces, Calcium cycling.

### 1. Introduction

In 2003, we first revealed that activity-induced ion concentration changes in t-tubules of cardiac ventricular cells may be large enough to significantly modulate membrane currents and cellular electrical activity (Pásek et al., 2003). Later, works on species-specific models for rat (Pásek et al., 2006) and guinea-pig (Pásek et al., 2008) were published. They demonstrated that, during a single beat at steady-state stimulation, the activation of L-type  $\text{Ca}^{2+}$  channels that are predominantly localized in the t-tubular membrane caused a transient  $\text{Ca}^{2+}$  depletion in the t-tubular lumen. This depletion reduced  $\text{Ca}^{2+}$  entry into the cell, intracellular  $\text{Ca}^{2+}$  load and, hence, the magnitude of the intracellular  $\text{Ca}^{2+}$  transient.

Recently, a modified model of rat ventricular cell incorporating separate dyadic and subsarcolemmal spaces at the t-tubular and surface membranes (Pásek et al., 2012) clearly showed that the intracellular  $\text{Ca}^{2+}$  load and  $\text{Ca}^{2+}$  transient are also considerably dependent on distribution of sarcolemmal  $\text{Ca}^{2+}$  pump and  $\text{Na}^+$ - $\text{Ca}^{2+}$  exchanger between these two membrane pools (Pásek et al., 2012, 2017). On the contrary, dependency of the intracellular  $\text{Ca}^{2+}$  transient on membrane distribution of these two transporters was rather small in our model of human ventricular cardiomyocyte (Hrabcová et al., 2013) that did not include the formulation of peripheral dyads and restricted submembrane spaces. To find out whether this simplification in the formulation of the human model was responsible for the difference and to explore the importance of ion concentration changes in subsarcolemmal spaces for activity of human ventricular cardiomyocytes, we modified the model description by incorporating the function of dyads and submembrane spaces at both the t-tubular and surface membranes.

### 2. Modification of the model

The schematic diagram of the modified model is illustrated in Fig. 1. The presence of peripheral dyads and ion gradients under the membrane is taken into account by incorporation of the following new

---

<sup>\*</sup> Assoc. Prof. Ing. Michal Pásek, PhD.: Institute of Thermomechanics, Czech Academy of Science - branch Brno; Technická 2; 616 69 Brno; Czech Republic; e-mail: pasek.avcr@centrum.cz

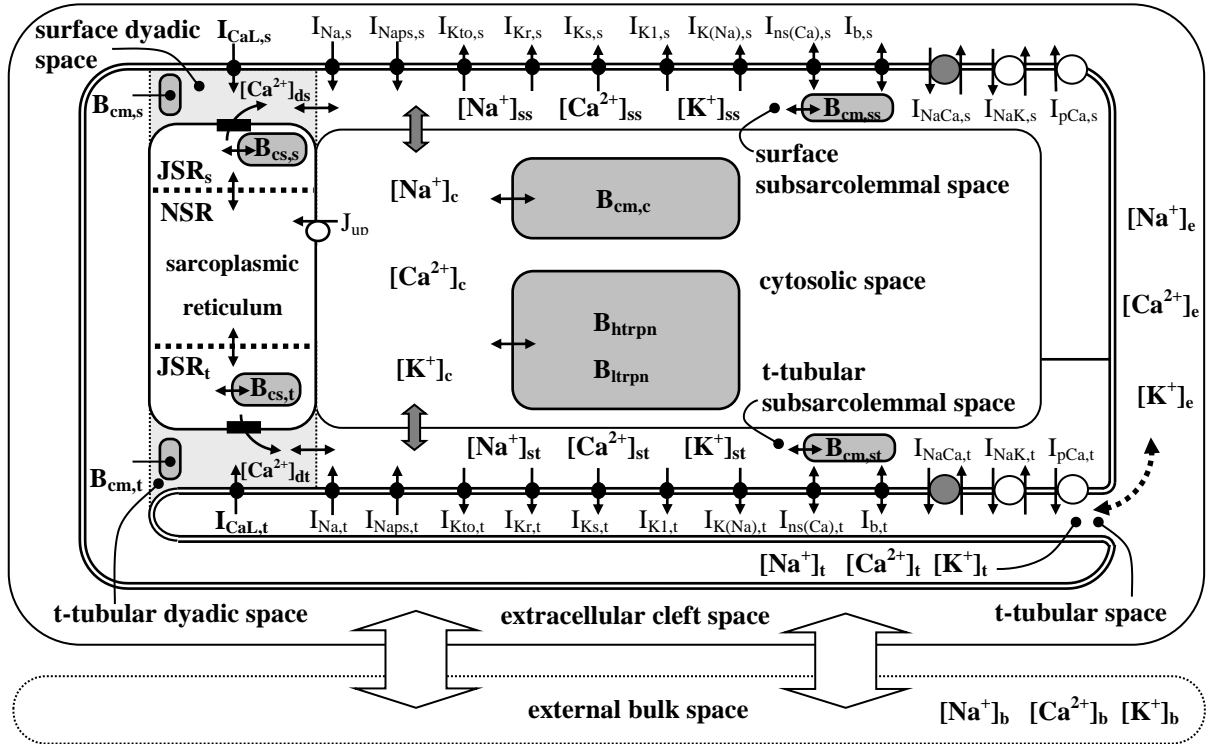
<sup>\*\*</sup> Assoc. Prof. MUDr. Markéta Bébarová, PhD.: Department of Physiology, Faculty of Medicine, Masaryk University, Kamenice 5; 625 00; Brno; Czech Republic; e-mail: bebarova.lfmu@centrum.cz

<sup>\*\*\*</sup> Dr. Georges Christé.: Laboratoire de Neurocardiologie, EA4612, Université Lyon 1, F-69003 Lyon; France; e-mail: christe.georges@laposte.net

compartments: dyadic space adjacent to the surface membrane (i.e. the surface dyadic space), junctional sarcoplasmic reticulum (JSR) adjacent to the surface dyadic space ( $JSR_s$ ), and subsarcolemmal spaces adjacent to the surface and t-tubular membranes (i.e. the surface and t-tubular subsarcolemmal space, respectively).

The total volume of the model cell ( $V_{tot}$ ) was set to 20.9 pL. The total volumes of myoplasm, network sarcoplasmic reticulum (NSR), JSR and dyadic space (14.2 pL, 1.15 pL, 0.088 pL and 0.00066 pL, respectively) were left the same as in our previous model (Hrabcová et al., 2013). The total volume of subsarcolemmal space (0.412 pL) was set to represent 2 % of  $V_{tot}$  (Shannon et al., 2004). The fractional volumes of t-tubular JSR ( $JSR_t$ ) and t-tubular dyadic space were set to conform with the fraction of L-type  $Ca^{2+}$  channels in the t-tubular membrane ( $f_{Ca,t} = 0.64$ ). The fractional volumes of surface and t-tubular subsarcolemmal spaces ( $f_{V,s,s} = 0.59$  and  $f_{V,s,t} = 0.41$ , respectively) were set to be proportional to the non-junctional area of each membrane (92.3 % of surface membrane and 52 % of t-tubular membrane; Brette et al., 2006).

The time constants controlling the rate of ion diffusion from the dyadic spaces to the subsarcolemmal spaces ( $\tau_{dss} = 0.547$  ms,  $\tau_{dst} = 0.214$  ms) and from the subsarcolemmal spaces to the cytosol ( $\tau_{ssc} = 2.3$  ms,  $\tau_{stc} = 3.4$  ms) were set to be consistent with the rate of ion diffusion from dyads in our previous model (Hrabcová et al., 2013) and to ensure that during action potential (AP) the physiological magnitude of  $Ca^{2+}$  transients under the sarcolemma is higher than in the bulk cytosol (Shannon et al., 2004).



*Fig. 1: Schematic diagram of the modified model of human ventricular cell. Description of electrical activity of the surface (s) and t-tubular (t) membranes comprises formulations of the following ion currents: fast sodium current ( $I_{Na}$ ), persistent sodium current ( $I_{Naps}$ ), L-type calcium current ( $I_{CaL}$ ), transient outward potassium current ( $I_{Kto}$ ), rapid and slow components of delayed rectifier potassium current ( $I_{Kr}$  and  $I_{Ks}$ ), inward rectifying potassium current ( $I_{K1}$ ), background currents ( $I_b$ ), sodium-activated potassium current ( $I_{K(Na)}$ ), calcium-activated non-specific current ( $I_{ns(Ca)}$ ), sodium-calcium exchange current ( $I_{NaCa}$ ), sodium-potassium pump current ( $I_{NaK}$ ), and calcium pump current ( $I_{pCa}$ ). The intracellular space contains the cytosolic space (c), surface and t-tubular subsarcolemmal subspaces (ss, st), surface and t-tubular dyadic spaces (dt, ds), and network and junctional compartments of sarcoplasmic reticulum (NSR,  $JSR_s$ ,  $JSR_t$ ).  $J_{up}$  represents  $Ca^{2+}$  flow via SR  $Ca^{2+}$  pump and the small filled rectangles in JSR membrane ryanodine receptors. The small black and grey bi-directional arrows denote intracellular ion diffusion. Ion diffusion between the t-tubular and cleft spaces is represented by the dashed arrow, and between the cleft and external bulk spaces by the thick white arrows.*

To reliably simulate changes of the human action potential induced by inhibition of membrane ionic currents, a partial modification of membrane transport system description was also necessary. A block of  $I_{K1}$  was shown to induce only small prolongation of action potential duration (APD) in human ventricular myocytes (Fink et al., 2008). However, our previous human model showed a substantially larger effect (Pásek et al., 2014). To resolve this inconsistency, we have adopted the formulation of  $I_{K1}$  from the work published by Fink et al. (2008) in the modified model. This change, however, resulted in unphysiological prolongation of control APD due to smaller  $I_{K1}$ . To compensate for this effect, the conductivities related to  $I_{Ks}$  ( $g_{Ks}$ ) and  $I_{Kr}$  ( $g_{Kr}$ ) had to be increased. Their new values were found to simulate the experimentally proved human epicardial APD<sub>90</sub> (action potential duration at 90 % repolarisation) and 3 % prolongation of APD<sub>90</sub> when  $I_{Ks}$  was blocked by 90 % (Li et al., 1998 and Jost et al., 2013, respectively). The conductivities, permeabilities or maximum current densities of all ion transporters related to total membrane area and their t-tubular fractions ( $f_{x,t}$ ) are specified in Tab. 1.

Tab. 1: Electrical properties of ion transporters in the modified model of human cardiomyocyte. The t-tubular fractions of ion transporters ( $f_{x,t}$ ) were adopted from Hrabcová et al. (2013). \*Modified values.

$g_{Na}$	25 mS cm <sup>-2</sup>	$f_{Na,t}$	0.57	$g_{K(Na)}$	0.129 mS cm <sup>-2</sup>	$f_{K(Na),t}$	0.56
$g_{Naps}$	0.01 mS cm <sup>-2</sup>	$f_{Naps,t}$	0.56	$g_{Nab}$	0.141 μS cm <sup>-2</sup>	$f_{Nab,t}$	0.56
$P_{CaL}$	0.00185 cm s <sup>-1</sup>	$f_{CaL,t}$	0.64	$g_{Cab}$	2.413 μS cm <sup>-2</sup>	$f_{Cab,t}$	0.56
$P_{KL}$	0.0000032 cm s <sup>-1</sup>	$f_{KL,t}$	0.64	$P_{ns(Ca)}$	1.75 nm s <sup>-1</sup>	$f_{ns(Ca),t}$	0.56
$g_{Kto}$	0.132 mS cm <sup>-2</sup>	$f_{Kto,t}$	0.56	$k_{NaCa}$	0.15 nA cm <sup>-2</sup> mM <sup>-4</sup>	$f_{NaCa,t}$	0.56
$g_{Kr}$	0.216 mS cm <sup>-2</sup> *	$f_{Kr,t}$	0.56	$I_{NaK}$	0.975 μA cm <sup>-2</sup>	$f_{NaK,t}$	0.56
$g_{Ks}$	0.074 mS cm <sup>-2</sup> *	$f_{Ks,t}$	0.56	$I_{pCa}$	1.725 μA cm <sup>-2</sup>	$f_{pCa,t}$	0.20
$g_{K1}$	0.682 mS cm <sup>-2</sup> *	$f_{K1,t}$	0.80				

### 3. Sensitivity of the model to changes in membrane distribution of $I_{NaCa}$ and $I_{pCa}$

The t-tubular fractions of Na<sup>+</sup>-Ca<sup>2+</sup> exchanger and of sarcolemmal Ca<sup>2+</sup> pump ( $f_{NaCa,t}$  and  $f_{pCa,t}$ , respectively) in the basic model are 0.56 and 0.2 (Tab. 1). The recently published studies (Pásek et al., 2017 and Chase and Orchard, 2011) however indicated that the t-tubular fractions of both transporters might be even higher than 0.9 in ventricular cardiomyocytes. To explore whether such redistribution of these transporters affects the behavior of the model, we compared the simulated AP and Ca<sup>2+</sup> transients in control with those when both  $f_{NaCa,t}$  and  $f_{pCa,t}$  were increased to 0.95. The results illustrated in Fig. 2 show that this change would lead to a shortening of APD<sub>90</sub> by 6 % and to an increase of cytosolic Ca<sup>2+</sup> transient by 22 % at steady state under 1 Hz stimulation. This change of Ca<sup>2+</sup> transient is about tenfold higher than in our previous human model (Hrabcová et al., 2013). However, it is comparable with our recent simulations on the model of rat ventricular cardiomyocyte showing a rise of the steady state Ca<sup>2+</sup> transient by 19 % when  $f_{NaCa,t}$  was increased from 0.48 to 0.93 at 1 Hz stimulation (Pásek et al., 2017). Deeper analysis of the simulations revealed a critical role of Ca<sup>2+</sup> concentration changes in the subsarcolemmal spaces (see  $[Ca^{2+}]_{st}$  and  $[Ca^{2+}]_{ss}$  in Fig. 2) and consequent change in cellular Ca<sup>2+</sup> cycling in this effect (see Pásek et al., 2017 for detailed explanation). Repeating the same simulations under conditions of high

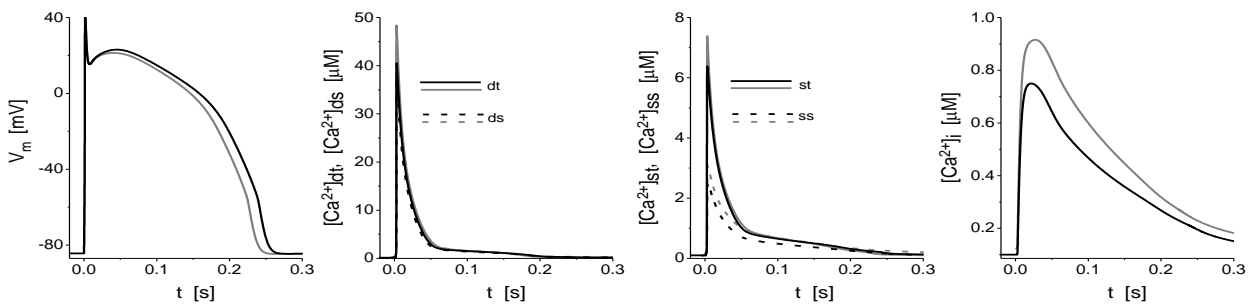


Fig. 2: Action potential and Ca<sup>2+</sup> transients in t-tubular and surface dyadic spaces ( $[Ca^{2+}]_{dt}$ ,  $[Ca^{2+}]_{ds}$ ), subsarcolemmal spaces ( $[Ca^{2+}]_{st}$ ,  $[Ca^{2+}]_{ss}$ ) and cytosol ( $[Ca^{2+}]_i$ ) at 1 Hz steady state stimulation (after 600 s) in the basic model (black lines) and after an increase of  $f_{NaCa,t}$  and  $f_{pCa,t}$  to 95 % (gray lines).

rate of ion exchange between the subsarcolemmal spaces and cytosol (to eliminate the ion concentration differences between these spaces), the steady state change of cytosolic  $\text{Ca}^{2+}$  transient in response to the increase of  $f_{\text{NaCa,t}}$  and  $f_{\text{pCa,t}}$  was substantially lower (relative increase of peak  $[\text{Ca}^{2+}]_i$  was  $\sim 2\%$ ). This explains the small sensitivity of our previous human model to membrane redistribution of  $\text{Na}^+$ - $\text{Ca}^{2+}$  exchanger and sarcolemmal  $\text{Ca}^{2+}$  pump. Notably, it highlights the importance of restricted  $\text{Ca}^{2+}$  diffusion and formation of  $\text{Ca}^{2+}$  concentration gradients under sarcolemma in the control of intracellular  $\text{Ca}^{2+}$  load and  $\text{Ca}^{2+}$  transient. The present model also showed that the role of activity-induced variations of  $[\text{K}^+]_{\text{ss}}$ ,  $[\text{K}^+]_{\text{st}}$ ,  $[\text{Na}^+]_{\text{ss}}$  and  $[\text{Na}^+]_{\text{st}}$  in this effect is minor (not shown).

#### 4. Conclusion

The presented modification of the model of human ventricular cell represents a further step to reliably simulate the electrophysiological activity of human cardiomyocytes in different conditions. Our simulations revealed that distribution of  $\text{Na}^+$ - $\text{Ca}^{2+}$  exchanger and sarcolemmal  $\text{Ca}^{2+}$  pump between the t-tubular and surface membranes governs restricted  $\text{Ca}^{2+}$  diffusion and formation of  $\text{Ca}^{2+}$  concentration gradients between the corresponding submembrane spaces and cytosol. These are of key importance in the control of intracellular  $\text{Ca}^{2+}$  load and  $\text{Ca}^{2+}$  transient and, hence, of excitation-contraction coupling features in human ventricular cells.

#### Acknowledgement

This study was realized with the institutional support RVO: 61388998 and with the support of the grant project 16-30571A from the Ministry of Health of the Czech Republic.

#### References

- Brette, F., Sallé, L. and Orchard, C.H. (2006) Quantification of calcium entry at the t-tubules and surface membrane in rat ventricular myocytes, *Biophysical Journal*, 90, pp. 381-389.
- Chase A. and Orchard C.H. (2011) Ca efflux via the sarcolemmal Ca ATPase occurs only in the t-tubules of rat ventricular myocytes. *Journal of Molecular and Cellular Cardiology*, 50, pp. 187-193.
- Fink, M., Noble, D., Virag, L., Varro, A. and Giles, W.R. (2008) Contributions of HERG  $\text{K}^+$  current to repolarisation of the human ventricular action potential. *Progress in Biophysics and Molecular Biology*, 96, pp. 357-376.
- Hrabcová, D., Pásek, M., Šimurda, J. and Christé, G. (2013) Effect of ion concentration changes in the limited extracellular spaces on sarcolemmal ion transport and  $\text{Ca}^{2+}$  turnover in a model of human ventricular cardiomyocyte. *International Journal of Molecular Sciences*, 14, pp. 24271-24292.
- Jost, N., Virág, L., Comtois, P., Ordög, B., Szuts, V., Seprényi, G., Bitay, M., Kohajda, Z., Koncz, I., Nagy, N., Szél, T., Magyar, J., Kovács, M., Puskás, L.G., Lengyel, C., Wettwer, E., Ravens, U., Nánási, P.P., Papp, J. G., Varro, A. and Nattel, S. (2013) Ionic mechanisms limiting cardiac repolarization reserve in humans compared to dogs. *Journal of Physiology*, 591, pp. 4189-4206.
- Li, G.R, Feng, J., Yue, L. and Carrier, M. (1998) Transmural heterogeneity of action potentials and  $\text{I}_{\text{to1}}$  in myocytes isolated from the human right ventricle. *American Journal of Physiology*, 275, pp. 369-377.
- Pásek, M., Christé, G. and Šimurda, J. (2003) A quantitative model of the cardiac ventricular cell incorporating the transverse-axial tubular system. *General Physiology and Biophysics*, 22, pp. 355-356.
- Pásek, M., Šimurda, J. and Christé, G. (2006) The functional role of cardiac T-tubules explored in a model of rat ventricular myocytes. *Philosophical Transactions of The Royal Society A*, 364, pp. 1187-206.
- Pásek, M., Šimurda, J., Orchard, C.H. and Christé, G. (2008) A model of the guinea-pig ventricular cardiac myocyte incorporating a transverse-axial tubular system. *Progress in Biophysics and Molecular Biology*, 96, pp. 258-280.
- Pásek, M., Šimurda, J. and Orchard, C.H. (2012) Role of t-tubules in the control of trans-sarcolemmal ion flux and intracellular  $\text{Ca}^{2+}$  in a model of the rat cardiac ventricular myocyte. *European Biophysics Journal*, 41, pp. 491-503.
- Pásek, M., Šimurda, J. and Christé, G. (2014) Sensitivity of action potential to changes of inward rectifier potassium current  $\text{I}_{\text{K1}}$  is different in recent models of human ventricular cardiomyocytes. In: *Proc. 20<sup>th</sup> Int. Conf. Engineering Mechanics*, Svratka, Czech Republic, pp. 476-479.
- Pásek, M., Šimurda, J. and Christé, G. (2017) Different densities of Na-Ca exchange current in t-tubular and surface membranes and their impact on cellular activity in a model of rat ventricular cardiomyocyte. *Biomedical Research International*, vol. 2017, ID 6343821, 9 p.
- Shannon, T.R, Wang, F., Puglisi, J., Weber, C. and Bers, D.M. (2004) A mathematical treatment of integrated Ca dynamics within the ventricular myocyte. *Biophysical Journal*, 87, pp. 3351-3371.



## NUMERICAL METHOD FOR DETERMINING THE MAIN FORCE OF BURNISHING ROLLING OF ROUGH CYLINDRICAL SURFACE WITH REGULAR PERIODICAL OUTLINES ASPERITIES

S. Patyk<sup>\*</sup>, R. Patyk<sup>\*\*</sup>, L. Kukielka<sup>\*\*\*</sup>, P. Kaldunski<sup>\*\*\*\*</sup>, J. Chojnacki<sup>\*\*\*\*\*</sup>

**Abstract:** *The article presents a numerical method for determining the main force of burnishing rolling of rough surface with periodic regular outline asperities. This is a basic problem, the solution of which is integral to the design of a technological process using surface forming. As part of the work to solve the problem the physical, mathematical and computer modelling methods were used. An algorithm for specifying the main force burnishing has been developed, assuming that the burnishing of the surface is determined with regular and periodic roughness profile. The solution of developed equations of the object motion was performed using the finite element method.*

**Keywords:** Burnishing rolling, Surface layer, Technological quality, DEM, Numerical analysis.

### 1. Introduction

The main problem in the design process of burnishing is the selection of the optimal values of technological parameters (Bohdal et al., 2016). The most important of these parameters is the main burnishing force  $F_3$ , which is a normal component of the resultant burnishing force  $F$  (Kulakowska et al., 2008, Kulakowska et al., 2014). Improper selection of this parameter causes unintended dimensional changes and the formation of the surface layer properties which do not comply with requirements. In extreme cases, it would cause damage to the surface layer of the object. Hitherto, the use of burnishing as very accurate finishing operation was associated with carrying out experimental research for each process. On the basis of these studies the technological parameters were determined (Kulakowska et al., 2016). Therefore, formulas reported in the literature for the burnishing forces calculation are an empirical formulas. A multitude of solutions proposed by different authors leads to compare the results of the forces calculated by various empirical formulas (Kukielka et al., 2008, Kukielka et al., 2010). The example of burnishing of spigot shaft surface was analysed. The most famous solutions for calculating the main burnishing force  $F_3$  are formulas, given by Hegenscheidt, Kudryavtsev, Chejfic, Kudryavtsev - Chejfic, Drozd, Ivanov, which are cited i.a. in the works (Kukielka, 1994, Przybylski, 1987, Patyk, 2010). The values of the forces  $F_3$ , necessary to strengthen the surface layer to a depth of  $\delta = 3$  [mm], which are calculated on the basis of these correlations, for the case of the burnishing shaft having a diameter of part  $d = 500$  [mm], the hardness of the materials  $HB = 250$ , yield stress  $Re = 400$  [MPa], tensile strength  $Rm = 600 \div 710$  [MPa], with burnishing element as a form of two-toroidal disk with diameter  $D = 100$  [mm] are respectively:  $F_3 = 417.2$  [kN];  $7.2$  [kN];  $9.5$  [kN];  $93.8$  [kN];  $53$  [kN] and  $430$  [kN]. When independent technological parameters of burnishing process are: velocity ( $v$ ) feed rate ( $f$ ) and the burnishing depth ( $g$ ), the output parameter is the main normal force ( $F_3$ ), which also depends on the

---

<sup>\*</sup> PhD.:Faculty of Mechanical Engineering, Koszalin University of Technology, Raclawicka Street 15-17; 75-620 Koszalin; PL, sylwia.patyk@interia.pl

<sup>\*\*</sup> PhD.:Faculty of Mechanical Engineering, Koszalin University of Technology, Raclawicka Street 15-17; 75-620 Koszalin; PL, radoslaw.patyk@tu.koszalin.pl,

<sup>\*\*\*</sup> Prof.:Faculty of Mechanical Engineering, Koszalin University of Technology, Raclawicka Street 15-17; 75-620 Koszalin; PL, leon.kukielka@tu.koszalin.pl, jerzy.chojnacki@tu.koszalin.pl

<sup>\*\*\*\*</sup> PhD.:Faculty of Mechanical Engineering, Koszalin University of Technology, Raclawicka Street 15-17; 75-620 Koszalin; PL, kaldunski.pawel@tu.koszalin.pl,

<sup>\*\*\*\*\*</sup> Prof.:Faculty of Mechanical Engineering, Koszalin University of Technology, Raclawicka Street 15-17; 75-620 Koszalin; PL, jerzy.chojnacki@tu.koszalin.pl,



previous operation before the treatment and on the conditions of the process. In case of burnishing with elastic-loaded force, operation does not depend on the size of the final machining allowance for burnishing, but depends on the elastic-loaded element settings such as springs tools, pneumatic and hydraulic. Then the resultant force  $F_3$  assumes a constant value during processing. Technological parameters of such process are: the main burnishing force ( $F_3$ ), velocity ( $v$ ), feed rate ( $f$ ). The output parameter is the value of depth ( $g$ ). Inappropriate selection of process parameters, primarily burnishing force, can cause damage the surface layer of the workpiece by its peeling, surface cracks, etc. This issue appears because at the absence of guidance it is easy to exceed the force required for a particular type of material and material properties, and treatment conditions prior to burnishing (Patyk, 2015). Influence of main burnishing force on deformation of surface layer of burnishing product is shown in Fig. 1.

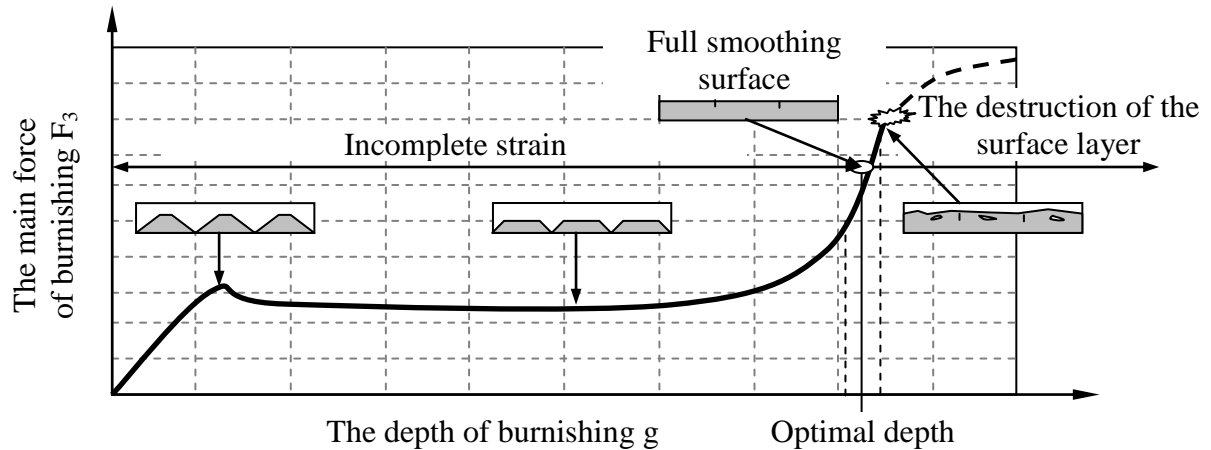


Fig. 1: The impact of the main force of burnishing  $F_3$  on the properties of the surface layer of the burnish product.

The aim of the research was developing an application for the determination of the main force of burnishing. The authors of this publication, in the previous studies and analyzes, have shown that modelling with using finite element method is an effective method of obtaining the large convergence to results from experimental research, therefore, to determine the forces in the rough rolling burnishing with rollers this method was used (Kukielka et al., 2016, Patyk et al., 2008, Patyk, 2010).

## 2. Numerical model of burnishing rolling of cylindrical rough surface

The authorial software BURNISHING FORCE has been elaborated in the ANSYS APDL language (Patyk et al., 2014). It has been developed as a three-dimensional model of the process. The object and a tool was discretized as elements of the type of solid.

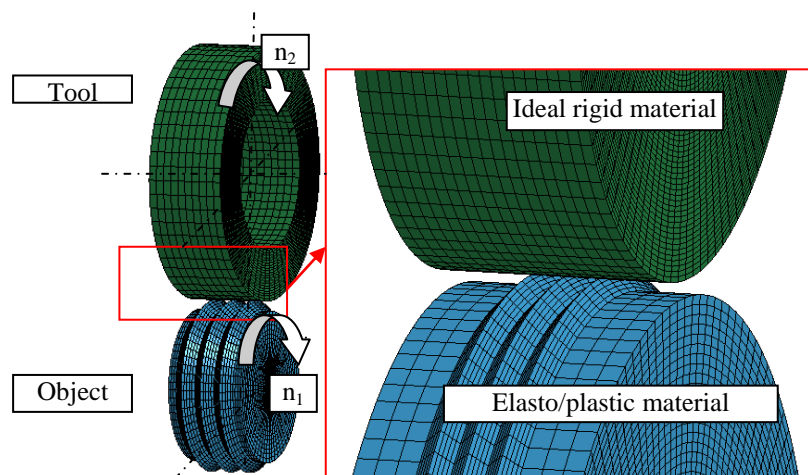


Fig. 2: Discrete model of the burnishing rolling process of shafts with regular periodical outlines asperities.

The tool was discretized by 10 000 finite elements, but the object is discretized by 550 000 finite elements. The tool was pressed into a rotating object to the second limit depth (Fig. 2). A discrete system of equations of motion are solved using the DEM (dynamic explicit method of integration - central differences) method (Patyk et al., 2009, Patyk et al., 2014, Patyk et al., 2016). Examples of the simulation results of the burnishing rolling process of shafts with roughness surface is shown in Fig. 3 (state of plastic deformation for different degrees of advancement of the process). The developed numerical model was used to determine changes of the main burnishing force (maximum value) from: yield stress of the material  $R_e$ , module of material hardening  $E_T$ , the apex angle of the regular triangular asperity  $2\theta$ , spacing of individual asperities from each other  $f$ . Analyses were performed for typical ranges of material parameters and technological processes (Figs. 4 and 5).

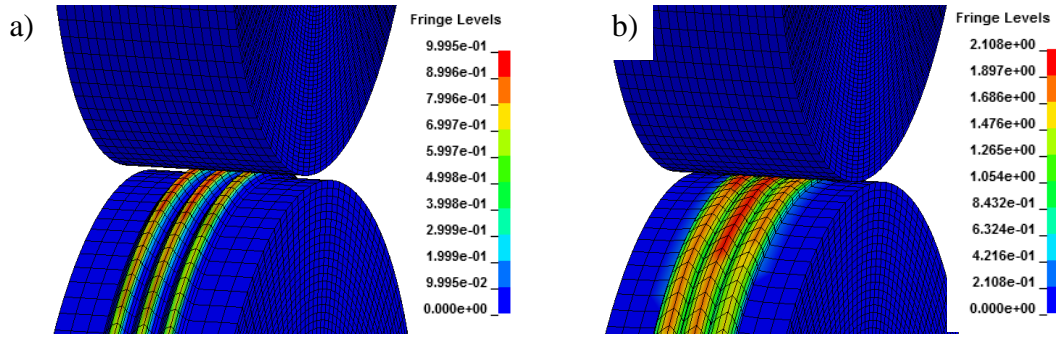


Fig. 3: State of reduced plastic strain for the case of a rolling burnishing shafts rough with apex angles of inequalities  $2\theta = 90^\circ$ ,  $f = 1.5$  mm, for the material S235JR, for: a) 30 % and b) 60 % of advancement of the process.

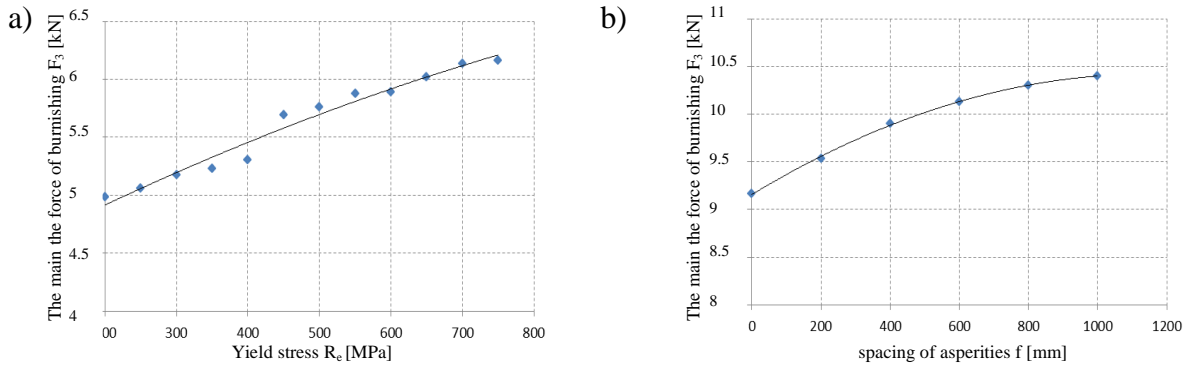


Fig. 4: Graph of the main burnishing force depending on the: a) yield stress  $R_e$  for: apex angle  $2\theta = 90^\circ$ , feed  $f = 1$  mm, hardening modulus  $E_T = 500$  MPa and static friction coefficient  $\mu = 0.2$ , b) hardening modulus  $E_T$  for: apex angle  $2\theta = 90^\circ$ , feed  $f = 1.5$  mm, yield stress  $R_e = 420$  MPa and static friction coefficient  $\mu = 0.2$ .

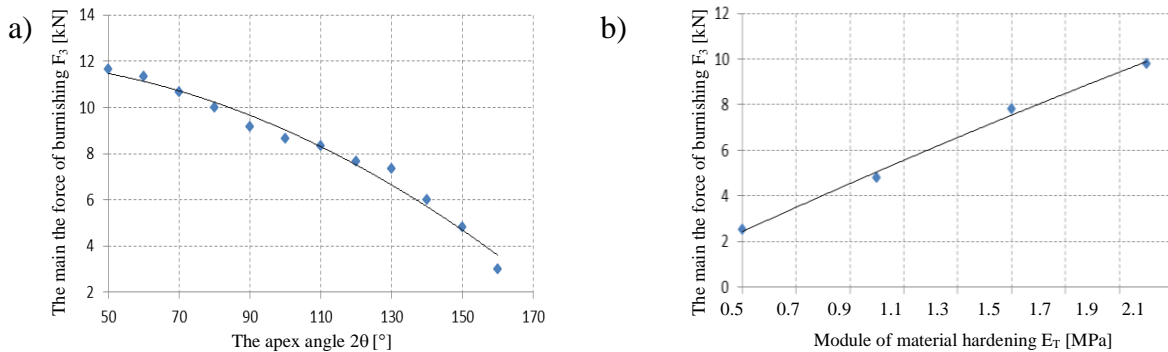


Fig. 5: Graph of the main burnishing force depending on the: a) apex angle for: feed  $f = 1.5$  mm, yield stress  $R_e = 420$  MPa and static friction coefficient  $\mu = 0.2$  and hardening modulus  $E_T = 500$  MPa and b) asperities of the distance from each: for yield stress  $R_e = 420$  MPa, static friction coefficient  $\mu = 0.2$ , hardening modulus  $E_T = 500$  MPa, apex angle  $2\theta = 120^\circ$ .

### 3. Conclusions

The developed application BURNISHING FORCE with using the finite element method, in order to determine the main force burnishing, has proven to be the most effective method from among previously used (analytical methods and experimental studies) because: allows to create adequate numerical models of the process of burnishing rolling of cylindrical rough surface (cheaper and faster) and obtained results of numerical simulations are consistent with experimental results. There is possible quickly modification of the model and adaptation it to the other cases. This will significantly shorten the time and reduces costs for selection of optimal technological parameters of the process (particularly the main burnishing force).

### References

- Bohdal, L., Kulakowska, A., Patyk, R. and Kulakowski M. (2016) Numerical investigations of the effect of process parameters on residual stresses, strains and quality of final product in blanking using SPH method, *Materials Science Forum*, Vol. 862, pp. 238-245.
- Kulakowska, A. and Kukielka, L. (2008) Problems of surface preparation in turning process in aspect of technological quality of burnished product, *Pomiary Automatyka Kontrola* Vol. 54, No. 7, pp. 421-424, (in Polish).
- Kulakowska, A., Patyk, R. and Bohdal, L. (2014) Application of burnishing process in creating environmental product, *Annual Set The Environment Protection*, 16, pp. 323-335.
- Kulakowska, A., Kulakowski, M., Bohdal, L. and Patyk, R. (2016) Aspects of burnishing rolling process of the surface prepared in different previous treatments, *Materials Science Forum*, Vol. 862, pp. 78-85.
- Kukielka, L., Kulakowska, A. and Patyk, R. (2008) Problematics of parts technological quality forming in burnishing rolling process, *Pomiary Automatyka Kontrola*, R. 54, No 4, pp. 196-199, (in Polish).
- Kukielka, L., Kulakowska, A. and Patyk, R. (2010) Numerical analysis of embossing process of regular inequalities with triangular outline on cylindrical semi product, *Journal of Systemics, Cybernetics and Informatics*. Vol. 8, No. 3, pp. 36-41.
- Kukielka, L. (1994) Theoretical and experimental base surface burnishing rolling contact with electrical heating, *Monography no 47*, Koszalin (in Polish).
- Kukielka, L., Szczesniak, M., Patyk, R., Kulakowska, A., Kukielka, K., Patyk, S., Gotowala, K. and Kozak, D. (2016) Analysis of the States of Deformation and Stress in the Surface Layer of the Product after the Burnishing Cold Rolling Operation, *Materials Science Forum*, Vol. 862, pp. 278-287.
- Patyk, R., Patyk, S. and Kukielka L. (2015) Determination of the principal burnishing force roller roughnes surface with regular periodical outlines asperities using numerical methods, *Mechanik* 2015, 3, pp. 270-280 (in Polish).
- Patyk, R., Patyk, S. and Kukielka L. (2009) The numerical determination of contact zone tool and work-pieces in burnishing rolling process, *Computer Methods in Materials Science* 2009, Vol. 9, No. 1, pp. 61-65.
- Patyk, R., Kukielka, L., Kukielka, K., Kulakowska, A., Malag, L. and Bohdal, Ł. (2014) Numerical Study of the Influence of Surface Regular Asperities Prepared in Previous Treatment by Embossing Process on the Object Surface Layer State after Burnishing, *Applied Mechanics and Materials*, Vol. 474, pp. 448-453.
- Patyk, R., Kulakowska, A. and Bohdal, Ł. (2014) Environmental, economic and exploitation aspects of the use of burnishing rolling treatments, *Annual Set The Environment Protection* 2014, Vol. 16 part. 1, pp. 351-362.
- Patyk, R. (2010) Theoretical and experimental basis of regular asperities about triangular outline embossing technology. *Steel Research International*, vol.81/9, pp. 190-193.
- Patyk, R. and Kukielka, L. (2008) Optimization of geometrical parameters of regular triangular asperities of surface put to smooth burnishing. *Steel Research International*, 2, pp. 642-647.
- Patyk, R., Bohdal, Ł. and Kulakowska, A. (2016) Study the possibility of controlling the magnitude and distribution of residual stress in the surface layer of the product after the process double duplex burnishing, *Materials Science Forum*, Vol. 862, pp. 262-269.
- Patyk, S. and Patyk, R. (2010) The methodologies of force parameters determination in burnishing rolling process of rough surface, *Logistyka* 2010, 2, pp. 2087-2096 (in Polish).
- Przybylski, W. (1987) *Processing technology burnishing*, WNT, Warsaw (in Polish).

## THE FORMATION OF ZONES OF THE COAL ARRAY VOLUMETRIC IMPREGNATION AS A RESULT OF THE VIBRATION IMPACT

M. V. Pavlenko<sup>\*</sup>

**Abstract:** *This article deals with the application of vibrations and hydraulic impacts exposing the low-permeability coal seams with the aim to increase the capillary impregnation and the volumetric saturation of the micropores. This technological procedure contributes to increasing the gas recovery from a coal array. The method of vibration exposure utilizing the boreholes leading from the surface is new. Its applicability was tested at a mine site. The results confirm its efficiency in creating new systems of gas-conducting cracks. The results of empirical calculations and industrial experiments confirm the possibility of its application for increasing the permeability of the deep coal layers and their saturation with liquid. The obtained results are described and commented. The development of an appropriate physical model of the studied phenomenon, its refinement, and development of the adequate mathematical tools are in progress at present time.*

**Keywords:** Vibration, Capillary, Crack, Gas drainage, Installation, Impregnation, Methane, Liquid movement.

### 1. Introduction

The aim of this article is to study the influence of the vibration exposure on deep coal layers concentrating on the increase of their volume saturation. The idea of using the vibration effect comes from the low permeability of coal and low gas recovery of the coal seams. The paper is focused on working out the principal rules and recommendations for timely preparation of the coal seams originating from the practical experiments, which were carried out in the coal seam field of the mine of "Komsomolskaya" belonging to JSC "Vorkutaugol" (hole no. 4447).

### 2. Analytical solution

The hydraulic pressing of fluid in the coal seam through the bore from the surface is an important stage of timely preparation of the field for the safe and effective excavation. Enlarging the width of the cracks is achieved by changing the fluid flow regimes in the open fractures and in the pore space. Comparing with other ones, the method of vibro excitation increases the saturation of the coal seam several times, which is enabled by utilization of the capillary effects.

The purpose of the vibration exposure through the bore from the surface is to increase the flow rate of the fluid in the capillaries due to the alternating forcing effects and to rise the volumetric saturation of the coal array, in general.

An important step of the research is the determination of the saturation velocity of the liquid permeating in capillaries. The calculation of the steady state volumetric flow rate  $V$  is given by the Poiseuille's equation, which reads

$$V = \frac{\pi r_k^4 \Delta P}{8 \mu l} \quad (1)$$

$r_k$  is the radius of the capillary,  $l$  is its effective length,  $\mu$  is the viscosity of the fluid flowing through the capillary, and  $\Delta P$  is the pressure gradient.

---

<sup>\*</sup> Prof. Mikhail Pavlenko, Mining Institute NUST "MISiS", National research technological University "Moscow Institute of steel and alloys" Institute of mines. Street Leninski. 6. room. 431. 119991 Moscow Russia, mihail\_mggy@mail.ru

Fig. 1 shows the vibration impact on the changes of the fluid flow rate in the borehole drilled in a reservoir.  $\Delta H$  denotes the relative decrease of the water level, OA is the decrease of the hydrostatic pressure, AO\* is the refilling water height in the well, O\*B is the period of the vibration ( $\lambda = 3 - 6$  cm,  $\omega = 4 - 6$  Hz), C is the demotion of the oscillations, and CD is the stabilization level.

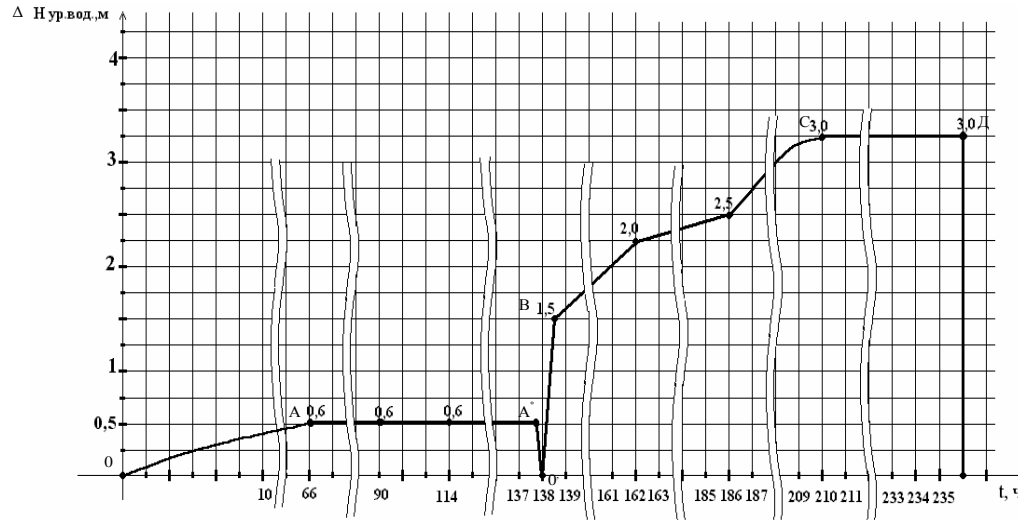


Fig. 1: The hydrodynamics phenomena in the period of the vibration exposure of field mine.

The analysis of the obtained experimental results enabled to identify the main ways leading to increasing the coal array capillary impregnation. To induce the oscillations of the liquid, the machine producing alternating excitation was applied. Its principle is shown in Fig. 2.

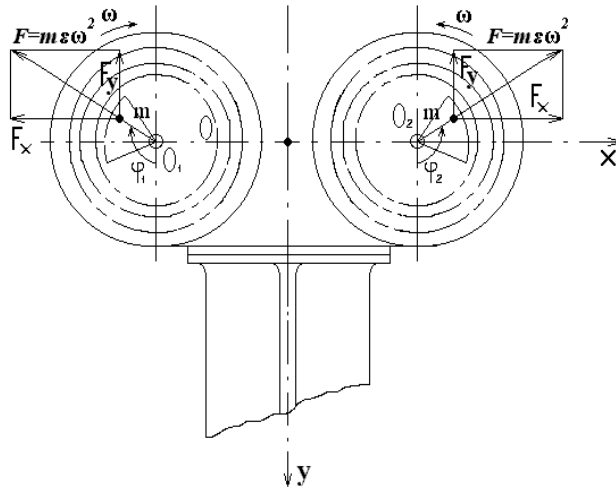


Fig. 2: Self-balancing vibration exciter of directed oscillations.

The oscillation amplitude as given

$$x(p) = \frac{m_0 e p^2}{c - (M + m_0) p^2}. \quad (2)$$

To find the optimum amplitude and frequency of the excitation, the data recorded in well No. 4447 drilled in a low-permeability and high gas-bearing formation were utilized.

The alternating dynamic effects, which drive the fluid in the bore, were induced by rotation of the eccentrically situated weights mounted on a platform. Therefore, the excitation pressure amplitude  $F$  is a harmonic function of time

$$F = m l \omega^2 \sin(\omega t). \quad (3)$$

$\omega$  is the angular speed of the rotation,  $m$  is the mass of the eccentric weights and  $l$  is the weights eccentricity.

The vibration tests made in the well enable to predict the absorption characteristics of the fluid.

### 3. Results and discussion

The liquid flow through the capillaries depends on the capillary pressure  $P_k$ , which is a function of the contact angle  $\alpha$  between the liquid surface and the capillary wall, the liquid surface tension  $\sigma$ , and the capillary radius  $r$

$$P_k = \frac{2\sigma \cos \alpha}{r}. \quad (4)$$

If the capillary is situated in the horizontal direction, the influence of the liquid hydrostatic pressure is insignificant on its flow. For other cases as shown in Fig. 3, the hydrostatic pressure must be taken into account. Its magnitude is given by relation (5)

$$P_h = \rho g l \sin \alpha \quad (5)$$

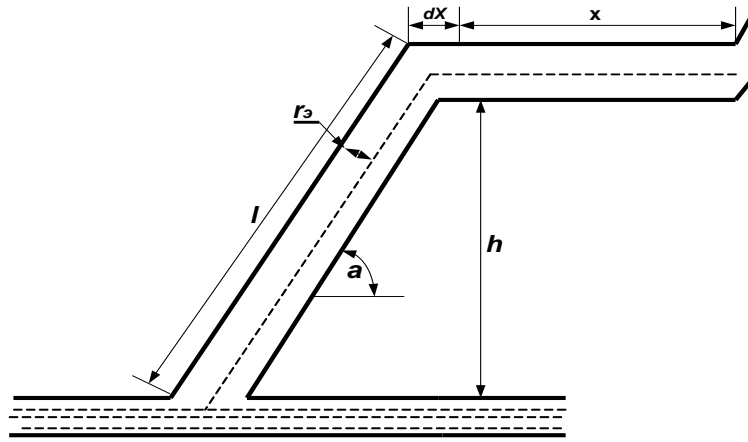


Fig. 3: The layout of the arbitrarily oriented capillary in the coal array.

The volumetric flow rate of the liquid through the capillaries the shape of which is uneven is governed by relations (6) and (7)

$$V = \frac{\pi r_k^4 (\rho_F - \rho_G)}{8\mu}, \quad (6)$$

$$V = \frac{\pi r_k^4}{8\mu} \left( \frac{2\sigma \cos \alpha}{r_k} - \rho_F g l \sin \alpha \right). \quad (7)$$

$r_k$  is the effective capillary radius.

It is difficult to find out the capillaries effective radius and the contact angle  $\alpha$  because their values cannot be determined by direct measurements. Therefore, to simplify the problem one of the quantities should be excluded utilizing that the liquid in the capillary rises to the height of  $H = l \sin \alpha$  during the coal wetting.

In the case when the capillaries are located horizontally in the coal array, then the hydrostatic pressure has no effect on the fluid flow velocity. Then it holds

$$\frac{dl}{dt} = \frac{r_k \sigma \cos \alpha}{4\eta l} \quad (8)$$

The same consideration is used to describe the flow rate in the capillaries driven by the methane

$$V = \frac{r_k \sigma \cos \alpha}{4(\eta_1 l_1 + \eta_2 l_2)} \quad (9)$$



where  $l_1$ ,  $l_2$  are the lengths of the capillary filled with the liquid and the methane, respectively,  $\eta_1$  and  $\eta_2$  are the liquid and methane viscosities,  $\sigma$  is the surface tension at their boundary, and  $\alpha$  is the contact angle at the border between the liquid and the gas.

#### **4. Conclusion**

The carried out research on the vibration exposure to the low-permeability coal massif presented in this article has not been terminated yet. The achieved results can be considered as one of the stages dealing with this important problem in the mining industry. The author expresses his gratitude to all persons who took part in accomplishing the industrial experiment.

#### **References**

- Blekhman, I.I. and Vaisberg, L.A. (2000) The use of self-synchronizing of vibromassazhery in mining vibrating machines. Mining journal, No. 11-12. pp. 81-82.
- Kolmakov, V.A. (1976) On the calculation of the velocity of fluid at variable pressure, the resistance of the medium and mode, Proc. Article, Kuz. PL. Kemerovo. pp. 203-209.
- Nikolaev, V.N. (1989) The mechanism of vibroseis stimulation on oil recovery from fields and the dominant frequency, Proc. USSR Academy of Sciences, T. 307, No. 3, pp. 570-575.
- Pavlenko, M.V. et al. (2001) Vibrating effect through the well from the surface with in order to increase the permeability of the coal, GORN. -M.: Moscow state mining University. No. 1. pp. 40-43.
- Pavlenko, M.V. (2002) Vibrational effects on low-permeability gas-bearing coal seams, Moscow state mining University, p. 15.

## DETERMINATION OF THE NUMBER OF CYCLES FOR ASYNCHRONOUS PERIODIC MULTIAXIAL LOADINGS USING ENERGY BASED CUMULATIVE DAMAGE THEORY

Ł. Pejkowski\*

**Abstract:** *The problem of definition of loading's cycle and fatigue life in case of asynchronous loadings is not fully solved in the literature. A few different approaches can be found, but none of them is widely accepted. In this work, an energy based definition of loading's cycle for asynchronous loadings is proposed. The method uses plastic strain energy density of complex loading's components as a weighting factors to calculate weighted arithmetic mean of loading's components lives.*

**Keywords:** Multiaxial fatigue, Asynchronous loadings, Cumulative damage, Fatigue life prediction.

### 1. Introduction

In multiaxial fatigue testing of materials, the experimental fatigue lives are usually used to analyse achieved results using two methods:

- the experimental fatigue life is compared for different types of loadings, which result in the same value of selected fatigue damage parameter; usually, damage parameter–fatigue life curves are used (Mei and Dong, 2017, 2016, Pejkowski et al., 2014a, 2014b; Skibicki et al., 2014) (Fig. 1a),
- a damage parameter is calculated for different types of loading, and on its basis the fatigue life is predicted by inversion of damage parameter–fatigue life equation for uniaxial loading (Carpinteri et al., 2016); next, calculated–experimental fatigue life diagrams ( $N_{f,cal} - N_{f,exp}$ ) are usually generated (Böhm and Niesłony, 2015; Karolczuk, 2016; Pejkowski, 2016; Pejkowski et al., 2012) (Fig. 1b).

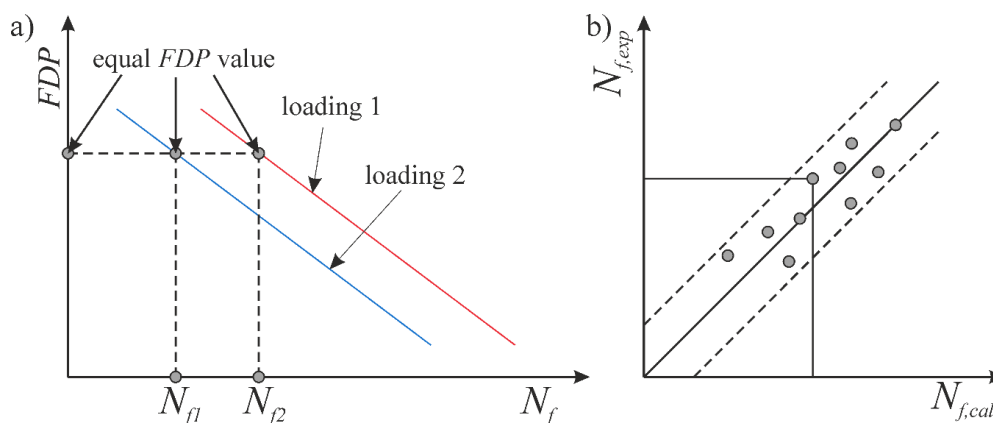


Fig. 1: a) Comparison of experimental fatigue lives for two loadings of the same FDP value;  
b) Comparison of experimental and calculated fatigue lives.

Comparison of calculated fatigue lives with experimental ones is unequivocal in case of any uniaxial, complex proportional or out-of-phase non-proportional loadings, since their components have the same frequencies, and thus their numbers of cycles to failure are equal.

\* Łukasz Pejkowski, PhD.: Faculty of Mechanical Engineering, University of Science and Technology, Kaliskiego 7, 85-796 Bydgoszcz, PL, lukasz.pejkowski@utp.edu.pl

Another case of non-proportional loadings, that is also being often analysed, are asynchronous loadings for which a difference in frequencies of components is present. An example of asynchronous loading with strain frequency ratio  $f_\gamma/f_\epsilon = 0.5$  is shown in Fig. 2.

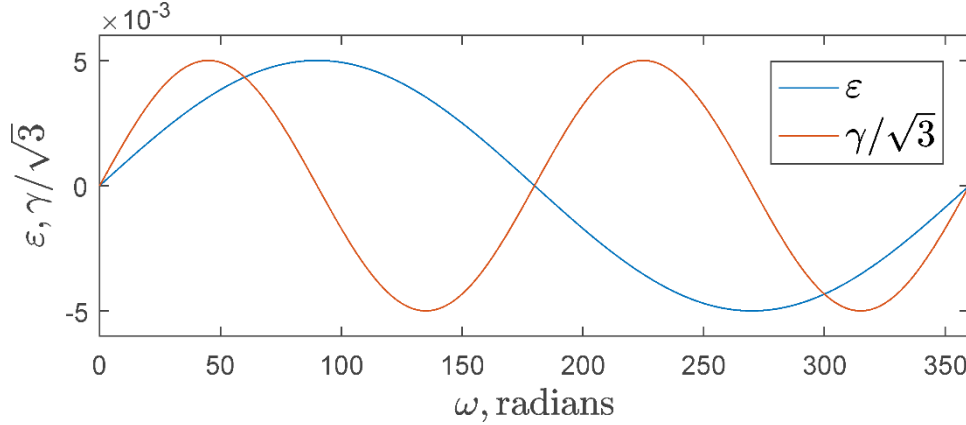


Fig. 2: An example of asynchronous loading.

A term “experimental fatigue life” becomes ambiguous, since each loading’s component reaches different number of cycles at failure. The number of cycles cannot also be counted using simple damage parameter such as Huber-von Mises equivalent stress or strain. And here comes the question: what is the fatigue life in case of this case of loadings? To compare fatigue lives in case of asynchronous loadings with fatigue life for axial loading, which is usually used as basic, it is fundamental problem to answer this question.

In (Anes et al., 2014), Anes et al. showed that cycle counting of SWT or Fatemi-Socie damage parameter on critical plane using popular Bannantine and Socie method or Wang and Brown damage parameter and cycle counting method, which are dedicated to multiaxial loadings, would result in errors in case of asynchronous loadings. An observation of the problem with loading’s cycle definition in case of loadings being discussed, has been also done by Dong et al. in (Dong et al., 2010; Mei and Dong, 2017, 2016). They aptly pointed that many authors ignore this problem and proposed path-dependent cycle counting method, which seems to be more reasonable.

## 2. Energy based cycle definition

Jahed, Noban et al. (Jahed et al., 2007; Noban et al., 2011), proposed a simple linear rule to calculate the fatigue life of complex loadings. Fatigue lives are first calculated on the basis of total energy value by introduction into equations for axial and torsional loadings separately. Then, following formula is used to estimate final fatigue life:

$$N_f = \frac{\Delta W_A}{\Delta W_T} N_A + \frac{\Delta W_S}{\Delta W_T} N_S, \quad (1)$$

where  $N_f$  is calculated fatigue life,  $N_A$  and  $N_S$  are the numbers of cycles calculated using equations for axial and torsional loadings, respectively and  $\Delta W_T$ ,  $\Delta W_A$  and  $\Delta W_S$  are total, axial and shear elastic-plastic strain energies.

Based on this approach, the generalized, “equivalent fatigue life” term can be introduced. It is defined as a weighted arithmetic mean:

$$N_f = \frac{\sum_{i=1}^n W_i N_i}{\sum_{i=1}^n W_i}, \quad (2)$$

where  $W_i$  is the plastic strain energy density and  $N_i$  is a number of cycles of complex loadings component.

In (Pejkowski et al., 2016) part of series of multiaxial fatigue test conducted on CuZn37 brass was presented. Among the others, two cases of asynchronous loadings were utilized. For the first one  $f_\gamma/f_\epsilon = 0.5$  and for the second one  $f_\gamma/f_\epsilon = 2$ . Numbers of cycles for one common period of loading’s components (for complete loading path in other words) are equal to  $N_A = 2$  and  $N_S = 1$  for  $f_\gamma/f_\epsilon = 0.5$  and  $N_A = 1$  and  $N_S = 2$  for  $f_\gamma/f_\epsilon = 2$ . To estimate the equivalent fatigue life for these loadings, two axial and one shear hysteresis loops energy have to be introduced to eq. (2) in the first case and conversely. For

both loading cases this approach results in number of cycles for one common period equal approximately to 1.6. It is worth to notice that this number is close to values obtained by Anes et al. (Anes et al., 2014) by their own proposal, used for high cycle, stress controlled tests. For  $f_\gamma/f_\varepsilon = 0.5$  these author determined 1.8 cycles and for  $f_\gamma/f_\varepsilon = 2$  respectively 1.4 cycles.

The results of presented approach for fatigue life estimation, for the two cases of loadings being discussed are presented in Fig. 3. Results for tension-compression (TC) are introduced for comparison. Power function was used to fit the results for TC.

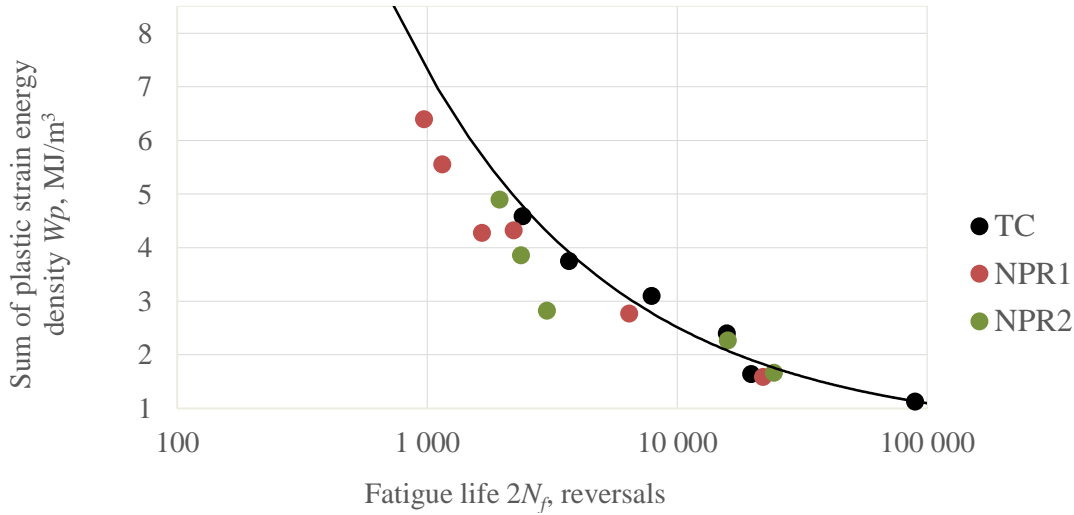


Fig. 3: Correlation of total plastic strain energy density with fatigue life; NPR1: loading with  $f_\gamma/f_\varepsilon = 0.5$  and NPR2: loading with  $f_\gamma/f_\varepsilon = 2$ .

A very good correlation with fatigue life, determined using the above described method, can also be observed for cumulated total plastic strain energy density to fracture (Fig. 4). The loading's sequence effect is not present in case of asynchronous loadings, thus the “equivalent fatigue life” coupled with energy based cumulative damage theory can be used for fatigue life prediction.

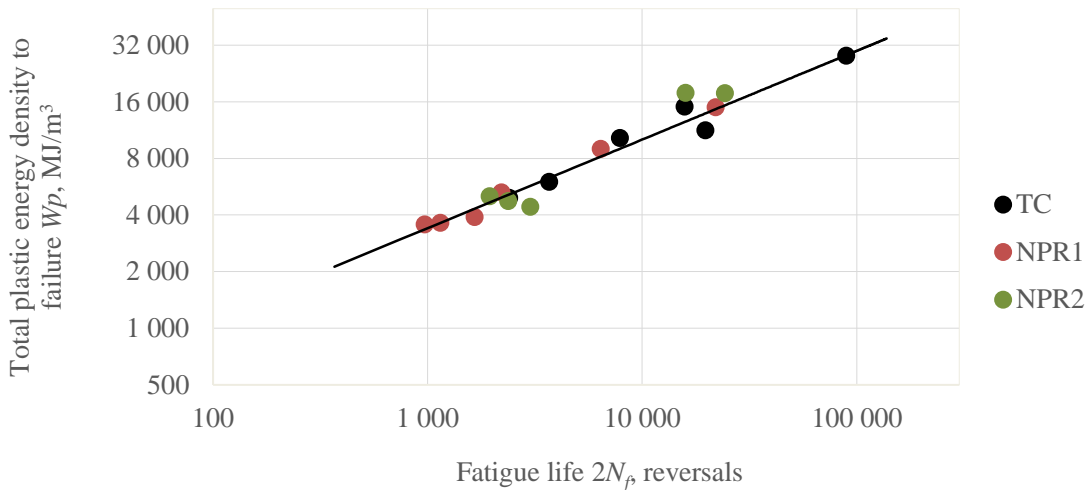


Fig. 4: Correlation of cumulated total plastic strain energy density to fracture with fatigue life; NPR1: loading with  $f_\gamma/f_\varepsilon = 0.5$  and NPR2: loading with  $f_\gamma/f_\varepsilon = 2$ .

### 3. Conclusions

The “equivalent fatigue life” method based on Jahed, Noban et al. approach was used for asynchronous loadings to define and determine the experimental fatigue life for one loading path. It seems to be a very good way of comparison of fatigue lives for asynchronous and synchronous harmonic loadings. It is also very promising as a method of fatigue life prediction for asynchronous loadings.

## References

- Anes, V., Reis, L., Li, B. and de Freitas, M. (2014) New cycle counting method for multiaxial fatigue. *International Journal of Fatigue*, 67, pp. 78-94.
- Böhm, M. and Niesłony, A. (2015) Strain-based multiaxial fatigue life evaluation using spectral method. *Procedia Engineering*, 101, pp. 52-60.
- Carpinteri, A., Kurek, M., Łagoda, T. and Vantadori, S. (2016) Estimation of fatigue life under multiaxial loading by varying the critical plane orientation. *International Journal of Fatigue* (in press).
- Dong, P., Wei, Z. and Hong, J.K. (2010) A path-dependent cycle counting method for variable-amplitude multi-axial loading. *International Journal of Fatigue*, 32, pp. 720-734.
- Jahed, H., Varvani-Farahani, A., Noban, M. and Khalaji, I. (2007) An energy-based fatigue life assessment model for various metallic materials under proportional and non-proportional loading conditions. *International Journal of Fatigue*, 29, pp. 647-655.
- Karolczuk, A., Kluger K. and Łagoda T. (2016) A correction in the algorithm of fatigue life calculation based on the critical plane approach. *International Journal of Fatigue*, 83, pp. 174-183.
- Mei, J. and Dong, P. (2017) Modeling of path-dependent multi-axial fatigue damage in aluminum alloys. *International Journal of Fatigue*, 95, pp. 252-263.
- Mei, J. and Dong, P. (2016) A new path-dependent fatigue damage model for non-proportional multi-axial loading. *International Journal of Fatigue*, 90, pp. 210-221.
- Noban, M., Jahed, H., Winkler, S. and Ince, A. (2011) Fatigue characterization and modeling of 30CrNiMo8HH under multiaxial loading. *Materials Science and Engineering A*, 528, pp. 2484-2494.
- Pejkowski, Ł. (2016) On the material's sensitivity to non-proportionality of fatigue loading. *Archives of Civil and Mechanical Engineering* (in press).
- Pejkowski, Ł., Skibicki, D. and Lipski, A. (2016) Plastic strain energy of CuZn37 brass in low-cycle multiaxial fatigue loading regime, *AIP Conference Proceedings*, 1780, pp. 30004-1-30004-8.
- Pejkowski, Ł. and Skibicki, D. (2014) Modification of Zenner and Liu Criterion due to Non-Proportionality of Fatigue Load by Means of MCE Approach, *Key Engineering Materials* 598, pp. 201-206.
- Pejkowski, Ł., Skibicki, D. and Sempruch, J. (2014) High cycle fatigue behavior of austenitic steel and pure copper under uniaxial, proportional and non-proportional loading, *Strojniski Vestnik - Journal of Mechanical Engineering*, 60, 9, pp. 549-560.
- Pejkowski, Ł., Skibicki, D. and Sempruch, J. (2012) Steel X2CrNiMo17-12-2 Testing for Uniaxial, Proportional and Non-Proportional Loads as Delivered and in the Annealed Condition. *Materials Science Forum*, 726, pp. 171-180.
- Skibicki, D., Sempruch, J. and Pejkowski, Ł. (2014) Model of non-proportional fatigue load in the form of block load spectrum. *Materialwissenschaft und Werkstofftechnik*, 45, pp. 68-78.

## IMPACT OF FILTER CONTAMINATION ON EFFICIENCY AND EFFECTIVENESS OF AIR FILTER

K. Perz<sup>\*</sup>, A. Rewolińska<sup>\*\*</sup>

**Abstract:** *Compressed air is one of the main sources of energy used in manufacturing processes in various industries. Its production requires considerable financial outlays incurred on the supply of compression equipment and transmitting this medium to reception facilities. At the time of generation and transmission of compressed air there occur drops of air pressure due, among others, to: flow resistance and resistance caused by the air treatment facilities, etc. The work shows the influence of contamination of compressed air filters, after a certain time of operation, on the pressure drop in the installation. Conducted preliminary tests that measure the impact of air velocity on pressure drop. In this part of the experiment, determined the linear dependence of the pressure drop to fluid flow rate. Basic research consisted in determining the pressure drop arising on the filter correctly in the installation depending on the degree of contamination of the filter. These contaminants cause a drop in air pressure downstream of the filter, which can affect the proper operation of the equipment supplied by it.*

**Keywords:** Compressed air, Pressure drop, Loss, Installation, Energy savings.

### 1. Introduction

Compressed air is a very widely used energy medium used in various industries (e.g. in the chemical, food, pharmaceutical, electronics, or lacquering industry). The basic parameter of compressed air, in addition to pressure, is its purity (Duszyński et al., 2006, Grzeskowiak et al., 2014). The most common contaminants, which may affect the quality of the final product, are solid particles, oil and water particles (both in the form of vapor and aerosol). An end user of the medium is therefore responsible for determining the air quality required in the technological process. The elements responsible for the cleanliness of compressed air in the installation are filters and dryers (Perz, 2009, 2011, 2013). Selection of appropriate treatment products is dependent on the desired class of air quality.

The basic criterion for assessing the filtration materials are: filtration efficiency and flow resistance (Semkło et al., 2015). Factors, that affect these parameters, are related to the structure of the filtering septum (geometric dimensions of fibers, shape, density and surface of the filtering septum), to the parameters of the compressed air (flow rate, temperature, density, viscosity and pressure), and to the contamination (size, density, shape, type, chemical composition). Assuming constant parameters of the outside air and a steady set of contamination parameters, it can be said that the filtration efficiency and air flow resistance is a function of parameters associated with the construction of the filter. Due to the fact that the air compressor is operating in the "on - off" cycle, in the system are present variable values of the air flow, and hence the air flow rate is also variable. Thus, the filtration efficiency and air flow resistance will depend on parameters such as:

$$\varphi, \Delta P = f(d_{wt}, b, \beta, v_F)$$

where:

$d_{wt}$  - the diameter of the filter fiber,

$\beta$  - the packing density of the filter layer,

$b$  - the thickness of the filter layer,

$v_F$  - air flow velocity.

---

<sup>\*</sup> Karolina Perz, PhD.: Institutes of Machines and Motor Vehicles, Poznań University of Technology, ul. Piotrowo 3, 60 – 965 Poznań, Poland, karolina.perz@put.poznan.pl

<sup>\*\*</sup> Aleksandra Rewolińska, PhD.: Institutes of Machines and Motor Vehicles, Poznań University of Technology, ul. Piotrowo 3, 60 – 965 Poznań, Poland, aleksandra.rewolinska@put.poznan.pl



For these considerations, it was assumed that the fiber thickness and the initial thickness of the filter layer is constant due to the use of a particular type of filter. Also, the density of non-woven filter is assumed as a constant value. In the case of using in the installation a new filter, flow resistance slightly varies taking a specified initial value. This generates a pre-established minimum pressure drop without significantly affecting the energy consumed by the compressor. However, during operation of the network, the contamination emerging in the filter cause the formation on its surface a layer which alters the filtration efficiency and increasing the resistance of the filter. To ensure proper performance of the installation, the compressor must therefore overcome air resistance, which will result in increased energy consumption of the network (Dittmer et al., 2016).

The work shows the influence of contamination of compressed air filters, after a certain time of operation, on the pressure drop in the installation.

## **2. Experimental part**

### **2.1. Research subject**

In all filter applications, the contamination of the air supply can cause performance degradation of the installation, which in turn will translate into higher costs associated with increased pressure of the compressor. The magnitude of this decrease depends on the kind of the filter, and, above all, on the filter layers constituting the replaceable cartridge. A proper selection of materials forming the filter layer should provide an adequate air quality, with a minimum pressure drop, and hence with minimal performance degradation. The filter material in the tested filter is a filter system consisting of four layers reinforced by a layer of perforated steel. The outer portion of the filter is formed by a double layer of polyurethane foam and a layer of paper of cellulose fibers. Another part of the filter is reinforced glass fiber. The inner part consists of a paper layer, which prevents direct contact of the filter material and the steel core of the filter. The whole is protected by a metal, sealed housing (Fig. 1).



*Fig. 1: Object of research 1 - tested filter, 2 - differential pressure gauge.*

### **2.2. Measuring station**

Filters were exploited in the actual compressed air installation. The screw compressor was a drive, and before the compressor installed dust pre-filters (Fig. 2).

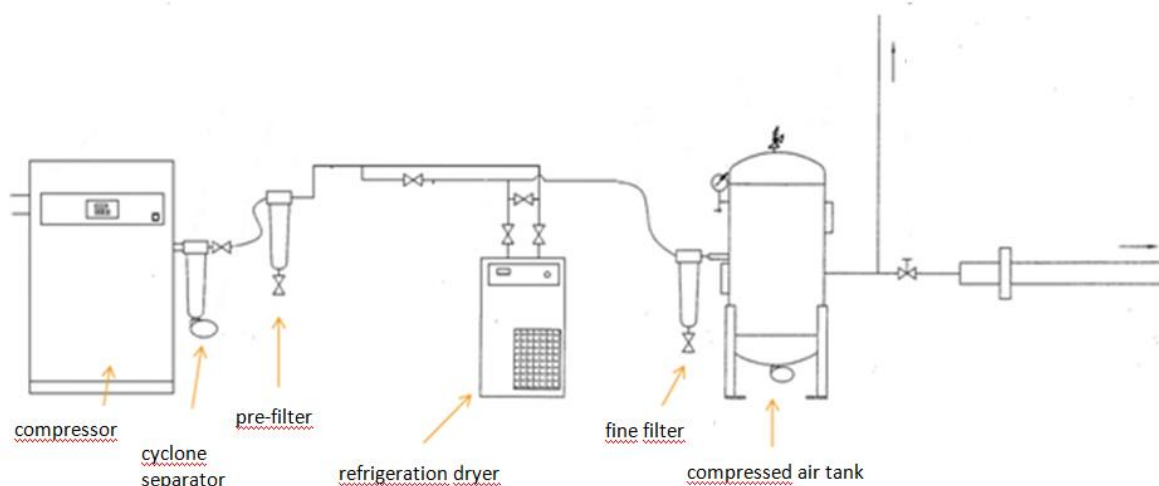


Fig. 2: Real installation of compressed air (Perz, 2013).

The rest of the installation is used for air treatment and behind the compressor installed cyclone separator, the task of which is to separate the mixture of water and oil from air. Another element is a pre-filter, which roughly separates larger particles of solids, oil and water. In a further step of treatment a refrigeration dryer was used. Further the tested fine filter is used, whose task is to clear the air from debris particle (maximum particle size is equal to 1  $\mu\text{m}$ ). In the case where there is a need for sterile air, upstream of the device installed a filter with active carbon.

### 2.3. Methodology of research

The study was based on measuring the pressure drop behind the tested air filter. For this purpose, a differential pressure gauge, with a measuring range 0 - 160 bar, was used. The variable for the study was the air flow rate, which was measured by the orifice plate. Contamination of the filter was simulated by the reduction in the flow field of the air stream. The operating pressure, during the experiment, was set at 10 bar. The object being tested was fine filter - it allows to capture particles of solids with dimensions less than 1  $\mu\text{m}$ .

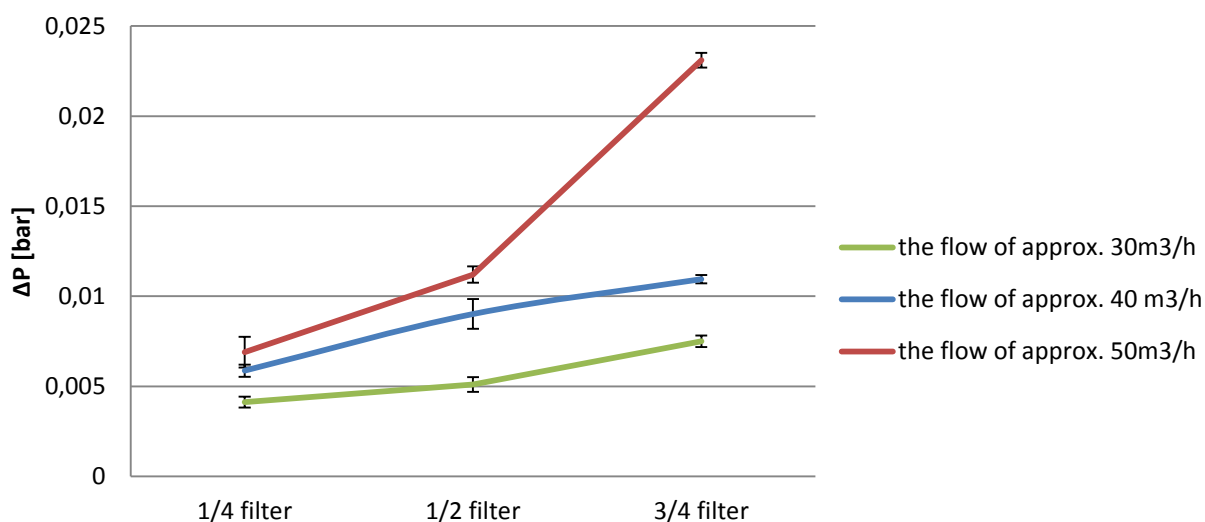


Fig. 3: The dependence of the pressure drop across the filter from the air filter contamination.

The pressure drop across the filter was tested according to the simulated contamination of the filter, and also depending on the speed of the air flow. At a given pressure (10 bar), the flow rate will depend on the diameter of the pipe used in the installation. In preliminary studies carried out in this experiment (due to the reduced volume of the work, it is not presented herein), we investigated the effect of different speeds

of the compressed air at a pressure drop of clean filters. We have found that the pressure drop is linearly dependent on the fluid velocity and with increase of this velocity the pressure drop also increases. During the execution of fundamental research, as can be seen from the graph, pressure drop depends on both, the filter contamination and flow velocity of air in the system, wherein the drop is greater the more contaminated filter has been used. To prevent the growth of flow resistance, it is worth to consider reducing the speed of air flow by increasing the diameter of the flow. Increasing the flow resistance in the installation resulting in increased work of the air compressor, which significantly affects the costs of the production process. In the compressed air installation, depending on the expected class of air cleanliness, a multistage filtration system is used. It results in a larger number of filters with different parameters, but the pressure drop always occurs on them. Therefore, the final value of air resistance is the sum of all the pressure drops on individual filters and reuse devices. It should therefore ensure the proper use of filters (correct time of the filters replace, the use of pre-filters, etc.), since this has a direct impact on energy consumption in the manufacturing process of compressed air.

### 3. Conclusions

Impurities in compressed air are particulate matters (dust, dirt, wear particles, rust particles, etc.), particles of moisture and oil particles. Absorption of filtering septum and the grain composition of dust, which flows to it, determines the working time of the air filter. The appearance of contamination on the filter leads to an additional layer, affecting significantly the resistance of air flow through the filter. Increasing this parameter lowering the air pressure behind the filter, which in turn increases the power demand of the compressor. Therefore, it is important to monitor air pressure drops in the filter during operation. Equally important is the recognition of contamination emerging in the installation - in the case of the food and pharmaceutical industry, in situations where the air is in direct contact with the product, the appearance of oil in the compressed air is not permitted.

### References

- Dittmer, Bradlle (2016) Saving Energy in Compressed-Air Systems. *Hydraulics & Pneumatics*. 2016, 11, pp. 32-37.
- Duszyński, J., Olborska, K. and Lewicki, P. (2006) Compressed Air in Foodstuffs - Treatment Food Industry 2006 No. 9 pp. 33-35, (in Polish).
- Grześkowiak, K., Perz, K. and Rewolińska, A. (2014) Determination of pressure losses in the compressed air system *Inż. Ap. Chem.* 2014, 53, 2, 101-102, (in Polish).
- Perz, K. (2009) Possibilities of using waste heat in the food industry *Inż. Ap. Chem.* 2009, 2, 110-111, (in Polish).
- Perz, K. (2011) Contamination of compressed air used in the food industry *Inż. Ap. Chem.* 2011, 2, 44-45, (in Polish).
- Perz, K. (2013) Concept of construction of a station for testing of compressed air parameters, *Agricultural Engineering*, 2013 R.17, pp. 149-159, (in Polish).
- Semkło, Ł., Urbaniak, R. and Nygard, A. (2015) Comparative analysis of models for linear loss coefficient in pipeline transport, *Rail Transport Technology* 2015, 12, pp. 1366-1396, (in Polish).

## EXPERIMENTAL VERIFICATION OF VELOCITY DISTRIBUTION IN DIFFERENT CROSS-SECTIONAL VENTILATION DUCTS

K. Peszyński<sup>\*</sup>, D. Perczyński<sup>\*\*</sup>, E. Smyk<sup>\*\*\*</sup>, P. Kolber<sup>\*\*\*\*</sup>

**Abstract:** The paper presents experimental verification of theoretical models for the velocity distribution in circular, rectangular, and rounded rectangular cross-sectional ventilation ducts. This verification is based on the knowledge of circular and rectangular cross-section ducts' properties and the new cross-section contains both aforementioned. These studies are aimed at finding ways of reducing the necessary measurements to determine the average flow rate in ventilation air ducts. Due to the size of the ducts it was decided to determine the flow rate based on the integration of flow velocity over the considered cross-section. This method requires knowledge of velocity distribution in the cross section. The approximation of measured actual profile by the basic and modified Prandtl power-law velocity profile was verified.

**Keywords:** Ventilation duct, Power-law velocity profile, Rounded rectangular cross-section duct.

### 1. Introduction

Testing the ventilation system components and their design can be greatly simplified by finding analytical solutions which determine the velocity distribution of air flow in a duct. Mechatronics Group of Mechanical Engineering Faculty UTP in Bydgoszcz in cooperation with Nuair Technologies Sp. z o.o., Solec Kujawski, Poland, conducted research of new type ventilation ducts of rounded rectangular cross-section. This duct type has significant operational advantages, but the aerodynamic phenomena occurring in these ducts have not been studied yet.

### 2. Analysis of circular ducts

Before an experimental research and theoretical analysis of rounded rectangular ventilation ducts, circular  $D = 0.4 \text{ m}$  and rectangular  $W = 0.5 \text{ m}$ ,  $H = 0.25 \text{ m}$  ventilation ducts were examined. Flow velocity in particular measurement points was measured using HWA anemometer, while in central point was verified using Prandtl tube (also called Pitot static tube). Measurements were performed along symmetry axes with step of 4 mm. Obtained experimental curves were approximated by theoretical curve known as power-law velocity profile expressed as Basic power-law velocity profile

$$V(r) = V_c \left(1 - \frac{r}{R}\right)^{\frac{1}{n}} \quad (\text{m/s}) \quad (1)$$

where  $V_c = V_{\max}$  (m/s) velocity at the centerline where  $r = 0$ ,  $r$  (m) radius from  $r \in [0; R]$ ,  $R$  (m) inner radius of circular duct.

The method of least squares is used to estimate parameters of theoretical model  $V_c$  and  $n$ . Estimation for the parameters was obtained by minimizing the sum of squared differences between the measured values

---

<sup>\*</sup> Assoc. Professor Kazimierz Peszyński, PhD., Faculty of Mechanical Engineering, UTP University of Science and Technology in Bydgoszcz, Al. Prof. S. Kaliskiego 7, Bydgoszcz; PL, kazimierz.peszynski@utp.edu.pl.

<sup>\*\*</sup> Assist. Prof. Daniel Perczyński, PhD.: Faculty of Mechanical Engineering, UTP University of Science and Technology in Bydgoszcz, Al. Prof. S. Kaliskiego 7, Bydgoszcz; PL, daniel.perczynski@utp.edu.pl.

<sup>\*\*\*</sup> Assist. Prof. Emil Smyk, MSc.: Faculty of Mechanical Engineering, UTP University of Science and Technology in Bydgoszcz, Al. Prof. S. Kaliskiego 7, Bydgoszcz; PL, emil.smyk@utp.edu.pl.

<sup>\*\*\*\*</sup> Assist. Prof. Piotr Kolber, PhD.: Faculty of Mechanical Engineering, UTP University of Science and Technology in Bydgoszcz, Al. Prof. S. Kaliskiego 7, Bydgoszcz; PL, piotr.kolber@utp.edu.pl.

and the predicted values under the model. Because, first of all, for a rectangular cross-section, obtained solutions were not very good, an attempt to approximate using the modified power-law velocity profile was taken under consideration. Modified power-law velocity profile is expressed as (Peszyński et al., 2016) Modified power-law velocity profile

$$V(r) = V_C \left( 1 - \left( \frac{r}{R} \right)^2 \right)^{\frac{1}{n}} \quad (2)$$

There are two parameters in two equations (1) and (2): velocity in central point  $V_C$  and exponent  $1/n$ . Fig. 1 presents approximation results of measurement using both equations (1) and (2) for circular duct (pipe) of  $R = 0.2 \text{ m}$ .

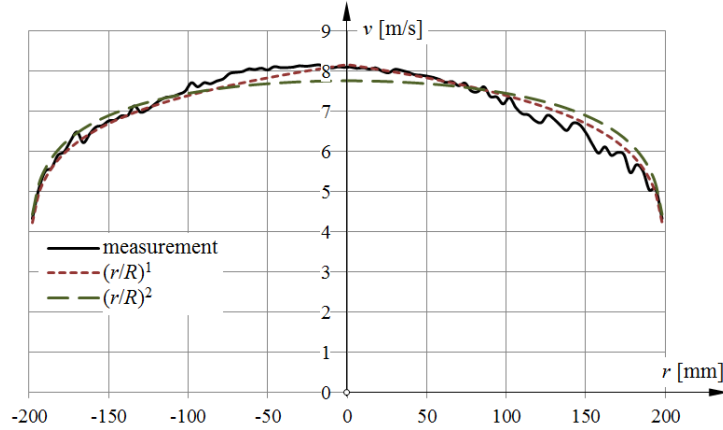


Fig. 1: Measurement results approximated by Prandtl classical and modified power law for  $n = 7$ .

Notice that approximation by basic Prandtl power-law velocity profile is good. However, this result is not important for practical use. We want to limit the number of measurements. In this case, we should rather seek the optimal exponent  $1/n$  for velocity  $V_C$  treated as measured parameter.  $n$  is integer number in all text books (Cengel et al., 2006; Orzechowski et al., 1997). We must remember that Prandtl power-law velocity profile was invented almost a hundred years ago. In those days, when there was no electronic computer technology, calculations using  $n$  as decimal number were almost impossible. Nowadays, it is not a problem. Therefore, velocity  $V_C$  is treated as measured constant parameter, and we are looking for decimal number  $n$  as approximation parameter. This method has proved itself mainly in the analysis of rectangular ducts.

### 3. Analysis of rectangular ducts

Application of the Prandtl power law formula is recommended by the literature (Cengel et al., 2006) for analysis of rectangular cross-section ducts. The longer side of the rectangle should be substituted instead of radius, and the degree of its flattening is taken into account by the correction factor.

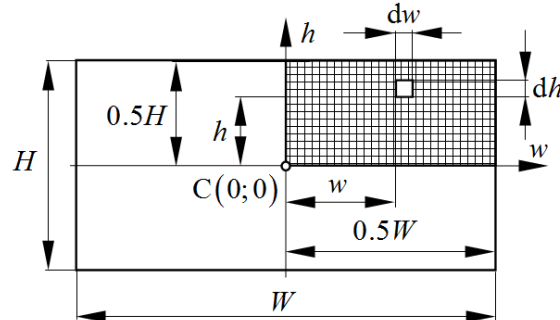


Fig. 2: Basic dimensions for rectangular duct.

Another procedure was chosen during presented tests. The velocity distribution along two axes  $w$  and  $h$  (Fig. 2) was measured. Formulas similar to basic and modified power law were used for approximations,

when  $r \rightarrow w$ , and  $r \rightarrow h$ . Then,  $dQ(w, h) = V(w, h)dA$ ,  $dA = dw \cdot dh$ ,  $Q = \int_A V(w, h)dA$ , and  $V_{avg} = Q/A_{rec}$ :

Basic power law 
$$V(w) = V_c \left(1 - \frac{2w}{W}\right)^{\frac{1}{n}} \quad \text{and} \quad V(h) = V_c \left(1 - \left(\frac{2w}{W}\right)^2\right)^{\frac{1}{n}} \quad (3)$$

Modified power law 
$$V(h) = V_c \left(1 - \frac{2h}{H}\right)^{\frac{1}{n}} \quad \text{and} \quad V(h) = V_c \left(1 - \left(\frac{2h}{H}\right)^2\right)^{\frac{1}{n}} \quad (4)$$

Fig. 3 shows measurement results and approximation curves for rectangular duct of width  $W = 0.5 \text{ m}$  and height  $H = 0.25 \text{ m}$ ,  $V_c = V_{w=0} = V_{h=0} = 7.067 \text{ m/s}$  when. Approximating curves were plotted for  $n_1 = 8.45$  in case of basic power law and for  $n_1 = 5.67$  in case modified one.

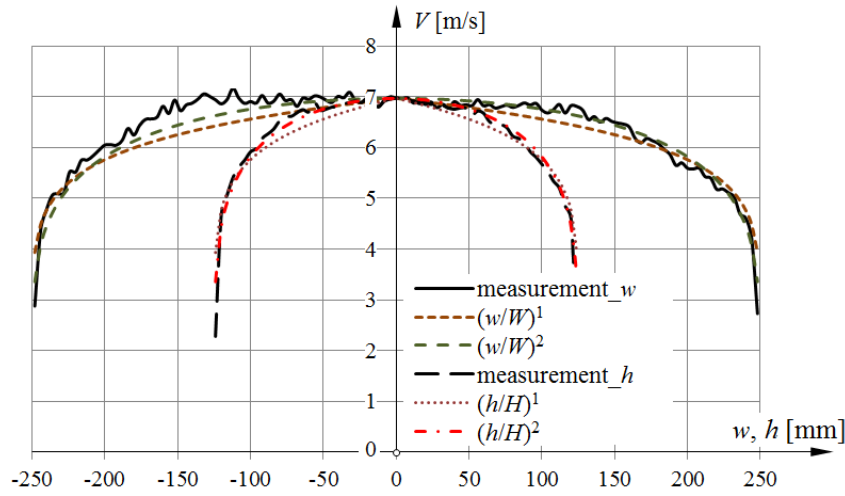


Fig. 3: Measurement results of rectangular duct approximated curves for measured  $V_c = 7.067 \text{ m/s}$ .

These formulas were verified by numerical verification (Peszyński et al., 2016), the same formulas were used for rounded rectangular ducts.

#### 4. Analysis of rounded rectangular ducts

Rounded rectangular duct is defined by three basic dimensions  $W, H, R$ , see Fig. 4.

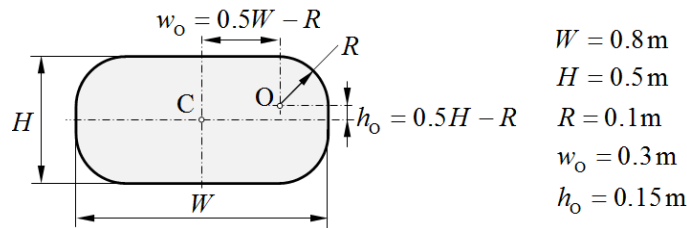


Fig. 4: Tested rounded rectangular duct dimensions.

Fig. 5 shows measurement results for the rounded rectangular duct of width  $W = 8.5 \text{ m}$ , height  $H = 0.5 \text{ m}$  and  $R = 0.1 \text{ m}$ . These dimensions (Fig. 4) and results (Fig. 5) are one of 77 possibilities. Area, perimeter, and hydraulic diameter are  $A = 0.391 \text{ m}$ ,  $U = 2.428 \text{ m}$ , and  $D_h = 0.654 \text{ m}$  respectively for this cross-section dimensions. All measurements were provided for  $Re = 100000$ . This Reynolds number implicates that average velocity is  $V_{avg} = 2.055 \text{ m/s}$ . Then, by using coefficient of profile fill  $\varpi = 0.86$ , we can obtain velocity  $V_c = V_{avg} / \varpi = 2.389 \text{ m/s}$  in central point C.

The profiles were measured on symmetry axes,  $w$  and  $h$ . Only  $V(w)$  is presented in Fig. 5. Note that  $V$  starts from  $V = 1.6 \text{ m/s}$  and big fluctuation of  $V(w)$  can be observed.



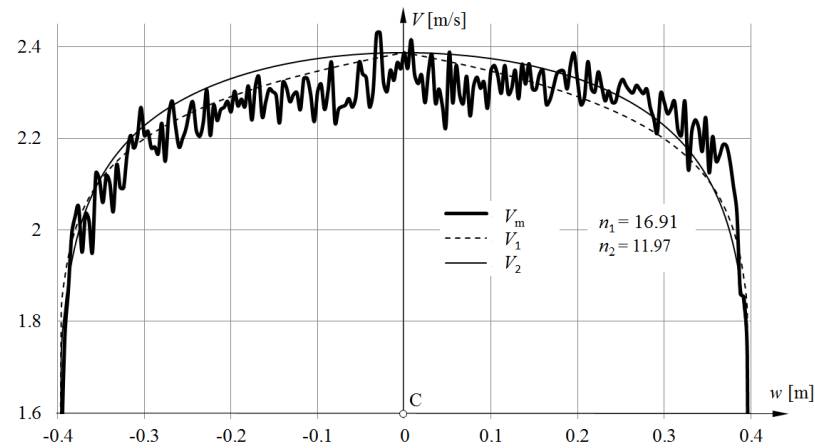


Fig. 5: Measurement results for above mentioned rounded rectangular duct.

The traversing step of the HWA anemometer probe (Fig. 6) was  $\Delta w = \Delta h = 4 \text{ mm}$ . During the measurements, the same velocity  $V_c$  of the air flow at the point of intersection of the two axes should be provided and proved.



Fig. 6: Hot wire anemometer Dantec was used for velocity profile distribution measurement.

## 5. Conclusions

Both, the basic Prandtl power law for velocity distribution in circular ducts and its modified version presented in this paper, can be used for modelling of velocity distribution in ventilation rounded rectangular ducts. Basic Prandtl power law gives better results for circular cross-sections, whereas modified Prandtl power law gives better results for rectangular and rounded rectangular cross-sections.

At the present state of knowledge, determination of Prandtl power law exponent  $n$  requires measuring the velocity of flowing air in at least several points of the cross-section axis.

## Acknowledgement

The authors would like to kindly thank the company for the performance of tested ducts and the delivery of air supply system. Authors also received institutional support BS 16/2013 granted by Faculty of Mechanical Engineering of UTP University.

## References

- Cengel Y.A. and Cimbala J.M. (2006) Fluid Mechanics. Fundamentals and Applications, McGraw-Hill.
- Orzechowski, Z., Prywer J. and Zarzycki R. (1997) Fluid Mechanics in Environmental Engineering (Polish: Mechanika płynów w inżynierii środowiska), WNT, Warszawa.
- Peszyński K., Olszewski L., Smyk E. and Perczyński D. (2016) Analysis of the Velocity Distribution in Different Types of Ventilation System Ducts, International Conference Experimental Fluid Mechanics 2016, Nov. 15th – 18th, 2016, Mariánské Lázně, Czech Republic, pp. 577-580.

## EXPERIMENTAL AND NUMERICAL STUDY OF STAYED STEEL COLUMNS

**R. Pichal<sup>\*</sup>, J. Machacek<sup>\*\*</sup>**

**Abstract:** *The numerical model of stainless steel stayed columns validated by tests is presented. 3D geometrical and material analysis including initial imperfections (GMNIA) is used for the study of nonlinear buckling and post-buckling behavior of 3 tested columns. Following study compares common 2D modelling with 3D results, elastic-plastic common steel with nonlinear stainless steel behavior and influence of the value of initial deflections. Finally significance of interconnection type between stays and central crossarm is studied with respect to possible assembly procedure. Recommendation for practical design are presented.*

**Keywords:** Stayed column, Experimental analysis, Nonlinear buckling, 3D analysis, Sliding stays.

### 1. Introduction

Stayed columns are used for decades as slender prestressed compression elements, with slenderness and strength depending on the overall geometry, number of crossarms along its length, number of stays and their prestressing (Fig. 1).



*Fig. 1: Stayed column with 3 spaced crossarms (with 3 stays) supporting roof of Estádio Algarve Faro (left), planar stayed column (with 2 stays) supporting facade of a building in London (right).*

Principal analytical analysis and explanation of behavior of the column with one central crossarm and stays fixed to the crossarm were presented by Smith et al. (1975) and Hafez et al. (1979). They distinguished 3 zones according to the value of the stay prestressing and derived respective formulas for critical loads (summarized by Pichal and Machacek, 2017). The formulas enable to establish minimal ( $T_{min}$ ) and optimal ( $T_{opt}$ ) prestressing in each of the stays and maximal external critical load for the column (Fig. 2). Recent research (Saito and Wadee, 2008, 2009, Osofero et al., 2012 and Wadee et al., 2013) introduced initial deflections to study post-buckling behavior using numerical nonlinear analysis. Based on a range of initial deflections they proposed approximate formulas for maximum capacity of the stayed columns  $N_{max}$ , depending on the element geometry and prestressing level (Fig. 2).

---

<sup>\*</sup> Ing. Radek Pichal: Czech Technical University in Prague, Faculty of Civil Engineering, Thakurova 7; 166 29, Prague; CZ, radek.pichal@fsv.cvut.cz

<sup>\*\*</sup> Prof. Ing. Josef Macháček, DSc.: Czech Technical University in Prague, Faculty of Civil Engineering, Thakurova 7; 166 29, Prague; CZ, machacek@fsv.cvut.cz

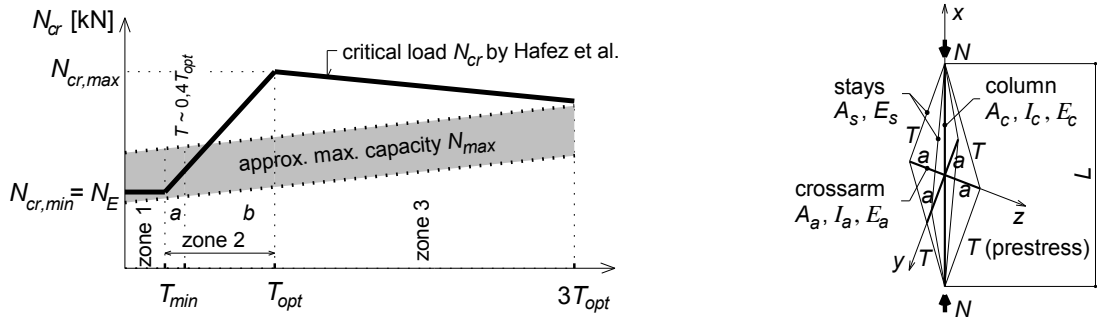


Fig. 2: Critical and maximal external load (left), geometry and terminology of the stayed column (right).

In this paper the numerical model of the column with one central crossarm in ANSYS software is proposed and validated using tests results by Servitova and Machacek (2011). The following studies concern influence of the mode and amplitude values of initial deflections on maximal strength of the column and significance of connection type between the stays and the central crossarm.

## 2. Tests, numerical modelling and validation of results

Three tests of stainless steel stayed columns with one central crossarm and the same geometry were performed at the CTU of Prague. For the central column was used tube  $\varnothing 50 \times 2$  [mm] ( $L = 5000$  mm,  $A_c = 302$  mm<sup>2</sup>,  $I_c = 87009$  mm<sup>4</sup>,  $E_{c,ini} = 184$  GPa), for the crossarm tube  $\varnothing 25 \times 1.5$  [mm] ( $a = 250$  mm,  $A_a = 111$  mm<sup>2</sup>,  $I_a = 7676$  mm<sup>4</sup>,  $E_{a,ini} = 184$  GPa) and for the stays Macalloy cable 1 x 19 stainless steel  $\varnothing 4$  mm ( $L_s = 2513$  mm,  $A_s = 12.6$  mm<sup>2</sup>,  $E_{s,ini} = 200$  GPa). The stress-strain relationship of the stainless steel tubes was derived as an average from the three full cross-section measurements and is presented in Fig. 3. The stays run continuously over crossarm at saddles, while the Column 3 was tested also without any stays.

Initial deflections of the columns and deflection under loading were monitored by total station (3D scanning) and local potentiometers together with strain measurements in stays by strain gauges located in turnbuckles. The prestressing of the stays needed to be uneven in the 4 stays to receive initial deflection in accord with EN 10219-2 (i.e. amplitude  $< L/500 = 10$  mm). This requirement was fulfilled in the Column 1 under total prestressing  $4T = 5.44$  kN ( $w_{0y} = 1.9$  mm,  $w_{0z} = 8.3$  mm) and Column 3 ( $w_{0y} = 0.5$  mm,  $w_{0z} = 2.2$  mm), but not in Column 2 with  $4T = 4.54$  kN ( $w_{0y} = 3.8$  mm,  $w_{0z} = 19.9$  mm). Loads were applied in steps of 2.5 kN followed by unloading up to termination of tests, usually due to large central deflection.

Numerical model in ANSYS was arranged in 3D with BEAM188 elements used for the central column and all crossarms, LINK180 for cable stays and SHELL281 for saddles (all covering large deflection and material nonlinearity), after assessing suitable meshing (finally  $L/250$ ,  $a/25$ , for shell elements 23.0 mm<sup>2</sup>). Loading was applied by axial displacement  $\Delta x$ , and the stay's prestressing by a thermal change.

Comparison of test and numerical results for Column 1 is shown in Fig. 3-right. The test was terminated under loading of 17.7 kN and the agreement of numerical results with test is very good. Test of the Column 2 (with rather large initial deflection) terminated under loading of 14.9 kN. Numerical analysis gives maximal loading 16.2 kN (exceeding test value by 8.7 %), see Fig. 4-left.

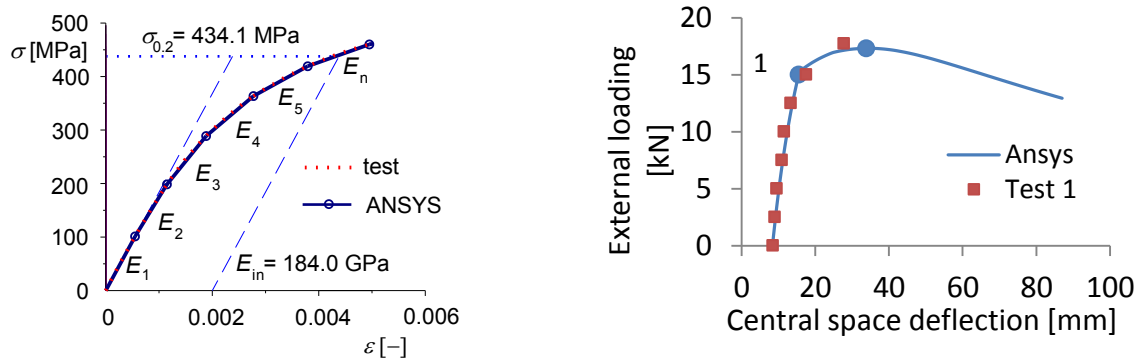


Fig. 3: Stainless steel stress-strain relationship (left), Column 1 comparison (right).

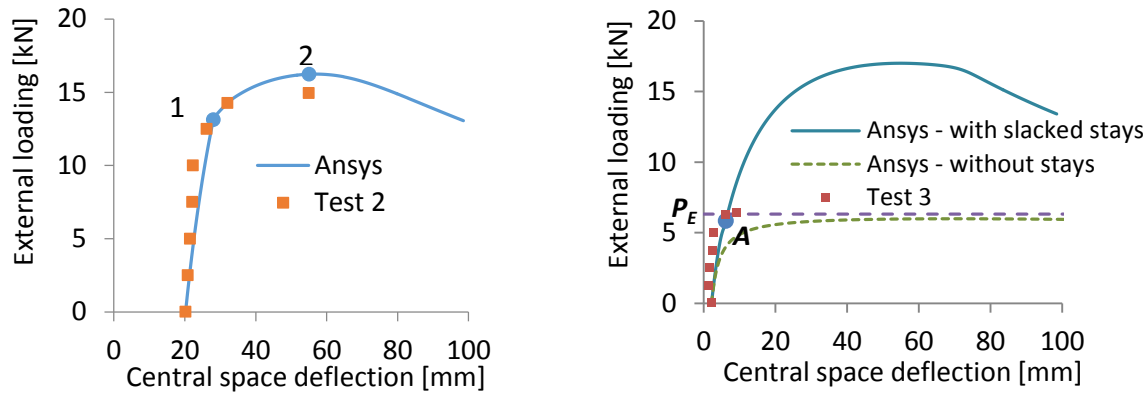


Fig. 4: Column 2 comparison (left), Column 3 comparison (right).

Column 3 was tested without any stays (as a comparative sample) and later the same one with very slightly prestressed stays. Euler's critical load is  $P_E = 6.3$  kN while the test value of imperfect column was detected surprisingly somewhat higher as  $N_{test} = 6.5$  kN, when the column started to deflect rapidly, see Fig. 4-right. This difference (2.8 %) is however negligible and may be assigned to rather questionable determination of the cross-section average modulus of elasticity. The numerical analysis in this case was performed for both arrangements. The first one for simple initially deflected column without any stays, giving maximal load  $N_{max} = 6.0$  kN, the second one with unprestressed stays and giving  $N_{max} = 17.0$  kN (see Fig. 4-right). The latter value is approaching the maximal test loading of the column with initially slacked stays of  $N_{test} = 16.2$  kN. The mechanism of this behavior was revealed from the numerical analysis, when the stays on concave side after buckling were activating (approx. at loading of 12.2 kN) to change the simple column into stayed column. Such behavior was discovered also by Wadee et al. (2013), see Fig. 2.

The described numerical modelling in ANSYS software can therefore be considered as successfully validated.

### 3. Parametrical studies

Former studies concerning differences between in-plane and space buckling (2D and 3D analysis) by Pichal and Machacek (2017) resulted into conclusion that the stayed columns buckle into space (in between the arms of the crossarm) but the critical and maximal loading for both analyses are nearly identical. Results of preliminary studies in 3D concerning influence of the initial deflection amplitude values  $w_0$  with shapes acc. to Fig. 5 for the stayed column analyzed in Chapter 2 is given in Tab. 1. It should be noted, that obtaining optimal prestressing  $T_{opt}$  requires a number of solutions with different prestressing of stays. The decisive mode of buckling for the shallow amplitudes is antisymmetrical (while for reasonable amplitudes  $> L / 1000$  and ratio  $2a / L < 0.175$  in acc. with Wadee et al. 2013 is expected to be symmetrical). The enormous influence of the deflection amplitude value is obvious.

Tab. 1: Optimal prestressing and corresponding maximal loading.

$w_0$ [mm]	Symmetrical initial deflections		Antisymmetrical initial deflections		$N_{cr,max}$ [kN]
	$T_{opt}$ [kN]	$N_{max,sym}$ [kN]	$T_{opt}$ [kN]	$N_{max,anti}$ [kN]	
0.01 (L/500000)	1.51	39.73	1.35	36.18	36.18
0.05 (L/100000)	1.58	39.25	1.43	35.77	35.77
0.10 (L/50000)	1.61	38.62	1.52	35.43	35.43

Another study concerned comparison of GNIA (geometrically nonlinear analysis with imperfections) and GMNIA (incl. material nonlinearity of stainless steel in acc. with Fig. 3). For the above geometry the tangent modules  $E_1$  and  $E_2$  up to the maximal loading values needed to be used only and the differences of both analyses were therefore negligible. The prestressing of cable stays is usually very low with respect to 0.2 % proof yield and initial elastic modulus (such as nominal one) is a reasonable choice.

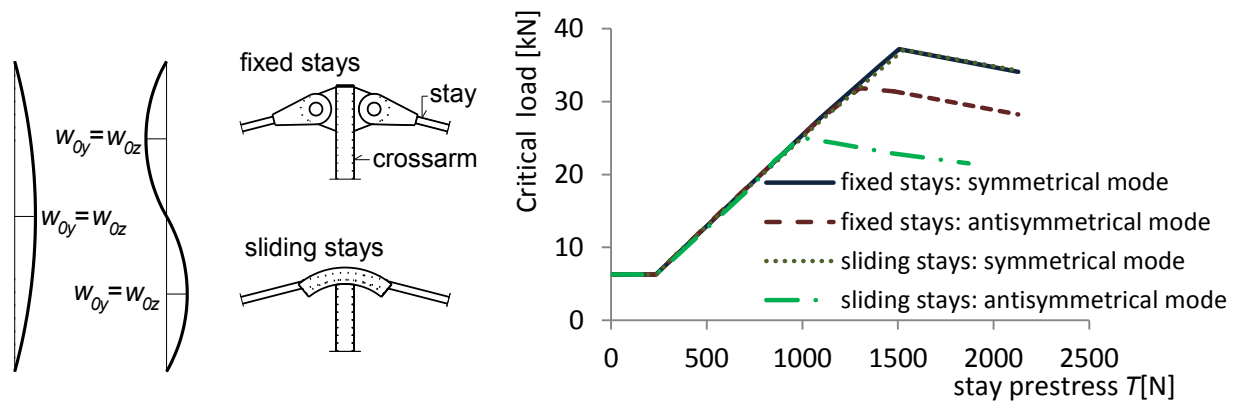


Fig. 5: Amplitudes of initial deflections (left), influence of conditions at crossarm (right).

Finally the boundary conditions at the crossarms were studied. In the tests the saddles and sliding stays were applied (Fig. 5), considering a very low friction coefficient 0.01 (whilst common friction between steel-steel is expected to be 0.1). Frequent arrangement represents hinged (fixed) connection of the stays, analyzed by other authors in the References. Nevertheless, from assembly view the sliding stays are more advantageous and were used in our tests. As obvious from a comparison between the two (Fig. 5-right, with initial deflection of the central column  $w_0 = L / 500000$ ) the different behavior arises at antisymmetrical mode of buckling only, where reduction of maximal critical load is substantial.

#### 4. Conclusions

Tests and validated numerical modelling of the three stayed prestressed columns made of stainless steel is presented. The numerical analysis of critical load and optimal prestressing in zone 2 according to Fig. 2 requires GMNIA with an arbitrary infinitesimal initial deflection, as LBA (linear buckling analysis) can't be used due to sudden change of the column axial energy at the instant of buckling.

The following numerical studies with the given geometry proved a little impact of a nonlinear column/stay material properties such as has stainless steel. On the contrary the influence of initial deflection value and mode is substantial as expected. Also boundary conditions at crossarm concerning possible slip of stays may lead to strong reduction of the final strength of the column. This will, however, happen for antisymmetric modes of buckling only, which are expected at large aspect ratios  $2a / L$ .

#### Acknowledgement

Support of the Czech Grant Agency grant GACR No. 17-24769S is gratefully acknowledged.

#### References

- Hafez, H.H., Temple, M.C. and Ellis, J.S. (1979) Pretensioning of single-crossarm stayed columns. J. Struct. Div. ASCE, 14362 ST2, pp. 359-375.
- Pichal, R. and Machacek, J. (2017) Buckling and post-buckling of prestressed stainless steel stayed columns. J. Engineering Structures and Technologies, Taylor & Francis, 9, 1, online.
- Osofero, A.I., Wadee, M.A. and Gardner, L. (2012) Experimental study of critical and post-buckling behaviour of prestressed stayed steel columns. J. Construct. Steel Research, 79, pp. 226-241.
- Servitova, K. and Machacek, J. (2011) Analysis of stainless steel stayed columns, in: Proc. 6<sup>th</sup> Int. Symp. Steel Structures (eds. Kim, W. B., Kim, K. D. and Sung-Won, Y.), Korean Society of Steel Construction, Seoul, pp. 874-881.
- Saito, D. and Wadee, M.A. (2008) Post-buckling behaviour of prestressed steel stayed columns. Eng. Struct., 30, pp. 1224-1239.
- Saito, D. and Wadee, M.A. (2009) Numerical studies of interactive buckling in prestressed steel stayed columns. Eng. Struct., 31, 2, pp. 432-443.
- Smith, R.J., McCaffrey, G.T. and Ellis, J.S. (1975) Buckling of a single-crossarm stayed column. J. Struct. Div. ASCE, 11071 ST1, pp. 249-268.
- Wadee, M.A., Gardner L. and Osofero, A.I. (2013) Design of prestressed stayed columns. J. Construct. Steel Research, 80, pp. 287-298.



## APPLICATION OF WOLFRAM MATHEMATICA PACKAGE TO CONTROL THE 6-DOF PARALLEL ROBOT

D. S. Pietrala<sup>\*</sup>, P. A. Laski<sup>\*\*</sup>, G. F. Bracha<sup>\*\*\*</sup>, K. Dzierżek<sup>\*\*\*\*</sup>

**Abstract:** *The article presents the application of Wolfram Mathematica software for solving kinematic equations in the process of rapid control prototyping for controlling the parallel manipulator 6-DOF with six degrees of freedom, delta type, with an electric drive. The process of manipulator control required the preparation of simple and inverse kinematic algorithms of the manipulator. The algorithms were implemented in the control system.*

**Keywords:** Parallel manipulator, 6-DOF, Delta, Kinematics.

### 1. Introduction

At present, the development of robotics forces the search for new kinematic structures as well as simple and reliable control systems. Already at the stage of designing, methods Rapid Control Prototyping and Hardware-in-the-loop are used (Takosoglu, 2016). In the newly designed robots, especially in structures with parallel kinematics, it is required to solve nonlinear equations with many unknown (Zwierzchowski, 2016a). Examples are known of using the Rapid Control Prototyping technology in the process of controlling and solving kinematic equations for parallel robots 3-DOF and 6-DOF (Laski et al., 2014). At present, there are many cheap development platforms on the market, such as single-circuit microprocessor based platforms like ARM and Atmega, which can be successfully applied in uncomplicated control systems (Blasiak, M., 2016). In the case of controlling a parallel robot delta 6-DOF type it is required to solve kinematic equations in real time. With view to the above, an intermediate solution was proposed: in Wolfram Mathematica software kinematic equations are solved with the use of the function FindRoot based on the Newton – Raphson method, while the development platform with the STM32F4 microcontroller is responsible for the physical process of control (Janecki et al., 2015; Blasiak, S. et al., 2014). Such a solution allows for quick prototyping the control system with a parallel robot with significantly lower financial resources involved (Nowakowski et al., 2016). The present manipulator has six degrees of freedom. It consists of a fixed base connected with a moving platform with six arms (Laski et al., 2014). Delta type manipulators are characterized by high load carrying capacity, but small working space when compared to serial structures (Pietrala, 2016). The precursors of papers on devices with closed kinematic circuits include Gough, V. E. and Stewart, D., hence parallel manipulators are commonly referred to as Gough's – Stewart's platforms.

### 2. Manipulator structure and principle of operation

Manipulator role consists in performing the movement of the working platform in relation to its fixed base. Output elements performing the movement are modelling servo-drives performing rotary movement and directly driving the arms. The arms are connected with the moving platform with ball-and-socket

---

<sup>\*</sup> Dawid Sebastian Pietrala, MSc.: Department of Automation and Robotics, Kielce University of Technology, Aleja Tysiąclecia Państwa Polskiego 7; 25-314 Kielce; PL, dpietrala@tu.kielce.pl

<sup>\*\*</sup> Paweł Anrzej Laski, PhD.: Department of Automation and Robotics, Kielce University of Technology, Aleja Tysiąclecia Państwa Polskiego 7; 25-314 Kielce; PL, pawell@tu.kielce.pl

<sup>\*\*\*</sup> Gabriel Franciszek Bracha, MSc.: Department of Applied Computer Science and Armament Engineering, Kielce University of Technology, Aleja Tysiąclecia Państwa Polskiego 7; 25-314 Kielce; PL, gbracha@tu.kielce.pl

<sup>\*\*\*\*</sup> Kazimierz Dzierżek, DSc, PhD, Eng.: Faculty of Mechanical Engineering, Białystok University of Technology, str. Wiejska 45c; 15-351, Białystok; PL, k.dzierzek@pb.edu.pl



joints. The movement of the platform is the resultant displacement of all six drives of the manipulator. Due to the problem of controlling the working platform, manual control of the manipulator, consisting in the change of angular location of each drive independently of the others, known from open kinematic chain manipulators, is in this structure very difficult or even impossible. Each of manipulator arms has six degrees of freedom: one class 5 kinematic pair and two class 3 kinematic pairs (joint rotation in longitudinal axis of the upper part of the arm in both ball-and-socket joints). The solid model of the manipulator created with the use of the 3D CAD software and the general view of the manipulator were shown in Fig. 1.

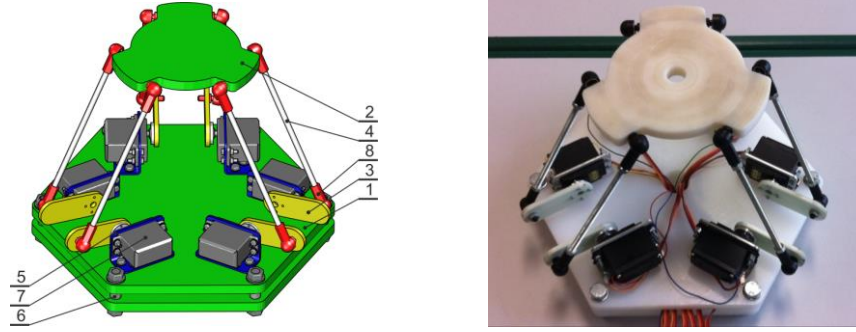


Fig. 1: Mechanism . Solid model: 1 – base plate, 2 – moving platform, 3 – lower part of the arm, 4 – upper part of the arm, 5 – drive fixing, 6 – spacing sleeve, 7 – servo-drive, 8 – ball-and-socket joint.

Due to the complicated manipulator structure, in the control process it is necessary to solve a simple and inverse kinematic equation. The simple kinematic equation consists in finding the coordinates of location and orientation of the platform knowing joint coordinates of individual arms. The inverse kinematic equation consists in finding joint coordinates of individual arms knowing the coordinates of location and orientation of the working platform. Joint coordinates have been designated as:  $\theta_{1,1}, \theta_{1,2}, \dots, \theta_{6,3}$ , where  $\theta_{1,1}, \theta_{2,1}, \theta_{3,1}, \theta_{4,1}, \theta_{5,1}, \theta_{6,1}$  are angles of rotation of drives axes. Cartesian coordinates of the location and orientation of the platform were marked as:  $P_x, P_y, P_z, M$ , where  $P_x, P_y, P_z$  are the coordinates of the centre of the working platform in the base system of coordinates  $U_0$ , and  $M$  is the matrix of nine cosines defining the orientation of the system  $UP_{i,1}$  in the base system of coordinates  $U_0$ . In order to solve the inverse kinematic equation of the manipulator, the following assumptions were adopted: the symbols used in introduced dependences shall mean –  $P_x, P_y, P_z$  – Cartesian coordinates of the set location of the manipulator,  $\alpha_{xx}, \alpha_{xy}, \alpha_{zx}, \alpha_{zy}, \alpha_{zz}$  – direction cosines defining the set orientation of the working platforms,  $U_0$  – the base system of coordinates connected with the plate,  $Wsp_{i,x}, Wsp_{i,y}, Wsp_{i,z}$  – coordinates  $x, y, z$  of  $i$  ball-and-socket joint in the base system of coordinates  $U_0$ ,  $UP_{i,x}$  – the system of coordinates with number  $x$  connected with  $i$  ball-and-socket joint of the platform,  $UR_{i,x}$  – the system of coordinates with number  $x$  connected with  $i$  arm,  $\zeta_i, \xi_i, R, r, h, l_1, l_2$  – geometrical dimensions of individual manipulator elements

- the basic Cartesian coordinate system  $U_0$ , was connected with manipulator base. Plane  $X_0Y_0$  of that system overlaps with the surface of upper plate of the base. The beginning of the system lies in the points of crossing of base diagonals. Axis  $Z_0$  points towards the platform, and axis  $X_0$  lies on the plane which is symmetrical for one arm pair and it points towards the arms,
- the manipulator moving platform was connected with the Cartesian coordinate system  $UP_{i,1}$ , identical for all joints. That system is orientated according to the following assumptions: plane  $X_{i,1}Y_{i,1}$  lies on the plane passing through centres of platform joints, the beginning of the system of coordinates lies in the point of crossing of the platform diagonals, axis  $Z_{i,1}$  points in the opposite direction than the direction of the base, axis  $X_{i,1}$  lies on the plane symmetrical for one arm pair and it points towards the arms,
- the coordinates of platform position are the coordinates of the beginning of system  $UP_{i,1}$  in system  $U_0$ , hence platform shifts are done in relation to axis  $X_0, Y_0, Z_0$ . Coordinate  $P_x$  corresponds to the shift

along axis  $X_0$ , coordinate  $P_y$  corresponds to the shift along axis  $Y_0$ , and the coordinate  $P_z$  corresponds to the shift along axis  $Z_0$ ,

- orientation of the working platform is the orientation of system  $UP_{i,1}$  in the base system  $U_0$ . That orientation is defined by the matrix of nine direction cosines defining the position of axes of the system of coordinates  $UP_{i,1}$  in relation to the axes of the system  $U_0$ . Because both systems are dextral systems of Cartesian coordinates, five out of nine direction cosines fully define the orientation of the platform.

Solving the inverse kinematic equation of the manipulator was done in two stages:

- the first stage consists in finding the coordinates of points lying in centres of ball-and-socket joints of the platform, in relation to system  $U_0$ , knowing the set position and orientation of the platform,
- the second stage consists in finding joint variables of each manipulator arm, knowing the coordinates of ball-and-socket joints connecting an arm with the platform enumerated in the first stage.

In the first stage the manipulator base, together with the platform, should be treated as the manipulator with an open kinematic chain with six degrees of freedom. In such a structure, the platform is connected with six class 5 kinematic pairs, three of which are progress pairs and another three are rotation pairs. In such a manipulator, the simple kinematic equation should be solved for each platform joint separately, with the consideration that the positions of platform joints in relation to the platform centre may differ from one another. They are however fixed and they appear from geometrical conditions of the platform, that is why the introduced dependencies are universal and true for all joints. The problem posed in such a way was solved by using the Denavit – Hartenberg parameters (Zwierzchowski, 2016b). Kinematic equations have been determined for the structure being analyzed (1). This equations take into account the relationship tying the arms to the work platform.

$$\begin{aligned} f_{i,x}(\theta_{i,1}, \theta_{i,2}, \theta_{i,3}) &= -Wsp_{i,x} + R \cos \xi_i + \cos(\xi_i \pm \xi_0)(l_1 \cos \theta_{i,1} + l_2 \cos(\theta_{i,1} + \theta_{i,2}) \cos \theta_{i,3}) + \\ &\quad - l_2 \sin(\xi_i \pm \xi_0) \sin \theta_{i,3} = 0 \\ f_{i,y}(\theta_{i,1}, \theta_{i,2}, \theta_{i,3}) &= -Wsp_{i,y} + R \sin \xi_i + \sin(\xi_i \pm \xi_0)(l_1 \cos \theta_{i,1} + l_2 \cos(\theta_{i,1} + \theta_{i,2}) \cos \theta_{i,3}) + \\ &\quad + l_2 \cos(\xi_i \pm \xi_0) \sin \theta_{i,3} = 0 \\ f_{i,z}(\theta_{i,1}, \theta_{i,2}, \theta_{i,3}) &= -Wsp_{i,z} + h + l_1 \sin \theta_{i,1} + l_2 \sin(\theta_{i,1} + \theta_{i,2}) \cos \theta_{i,3} = 0 \end{aligned} \quad (1)$$

Variables  $\theta_{i,1}, \theta_{i,2}, \theta_{i,3}$  are joint variables of individual arms, where variable  $\theta_{i,1}$  is the angle of rotation of the drive shaft of  $i$  arm. For solving the systems of equations, the function *FindRoot* of the Mathematica software was used which is based on the Newton – Raphson method which is described by the formula:

$$x_{k+1} = x_k - \left( F'(x_k) \right)^{-1} \cdot F(x_k) \quad (2)$$

where:  $k$  – iteration number,  $x_k$  – approximation of the sought value calculated for a given iteration,  $F(x_k)$  – value of the function for a given approximation,  $F'(x_k)$  – value of matrices derived from partial functions  $F$  for a given approximation.

### 3. Manipulator control system

For constructing the manipulator control system a PC was used with the installed Wolfram Mathematica software, and the development platform with the built-in microcontroller STM32F103ZET6. The control system has 12-bit A/C transmitters and USART interface enabling communication in standard RS232. Communication interface USB-RS232 was used for sending information between the computer and the microcontroller. DC servo drives were used in the manipulator. These servos are equipped with potentiometric position sensors modified to access signals with the current angular position of the drive. Fig. 2 shows the general view of the manipulator connected to the control system. Then, also from the level of Mathematica software, the inverse kinematic equation was solved for the set trajectory. For that, for each manipulator arm the system of three nonlinear equations with three unknown was solved. For solving the function *fline[]* was made which uses the built-in function *FindRoot[]* based on the Newton-Raphson method. The function requires providing the initial values vector. Because the system of three equations with three unknown has more than one solution, the initial values vector must be close to the sought solution. Via the interface USB-RS232 the calculated joint variables were sent to the

microcontroller. In order to control the serial port from the level of Mathematica software, an additional library was downloaded from the website of the Wolfram company. The library contains two files: SerialIO.exe and init.m. Next, the downloaded package was started, the serial port opened and data transfer speed set. In the next step, the joint variables were calculated, converted to text and sent to the microcontroller. Suitable control signals for the drives were generated. Then, with the use of A/C transmitters, measurements of signals from angular location sensors were made. Measurement data was sent to the Mathematica software with the use of USB-RS232 interface.

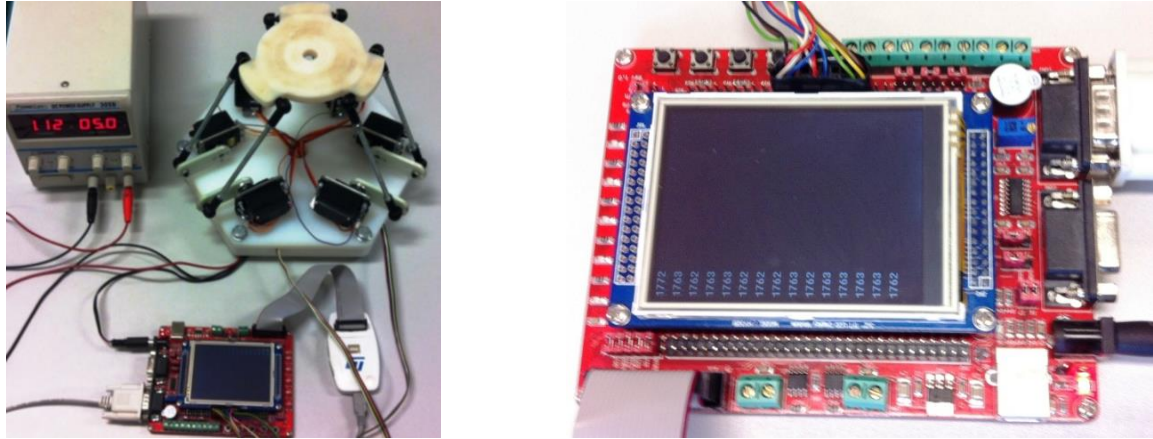


Fig. 2: General view of the manipulator with the control system microcontroller STM32F103ZET6.

#### 4. Concluding remarks

The process of controlling parallel manipulators requires solving simple and inverse kinematic equations. The use of the Mathematica software allows to simplify solving the simple and inverse kinematic equations to a great degree. Performing matrix operations enables a quick construction of the kinematic model of the manipulator with the use of in-built functions solving nonlinear systems of equations, what in turn enables determining joint variables of the manipulator. Moreover, the Mathematica software includes functions controlling the serial port of a PC or its virtual equivalent. Thanks to that, communication with most microcontrollers available on the market is possible. Such type of manipulator may be applied for instance in the process of positioning cameras, palletisation. It may be used as a machining device controlled numerically. Solving a simple kinematic equation allows to use the manipulator as a device setting the position and orientation (a haptic device).

#### References

- Blasiak, M. (2016) Parametric analysis of piezoelectric transducer used for signal processing, in: Proc. of Int. Conf. Engineering Mechanics 2016 (eds. Zolotarev, I. and Radolf, V.), Svratka, Czech Republic, pp. 66-69.
- Blasiak, S., Takosoglu, J.E. and Laski, P.A. (2014) Heat transfer and thermal deformations in non-contacting face seals, Journal of Thermal Science and Technology, 9, 2, pp. 1-8. doi:10.1299/jtst.2014jtst0011.
- Janecki, D., Zwierzchowski, J. and Cedro, L. (2015) A problem of optimal cylindricity profile matching, Bulletin If The Polish Academy of Sciences-Technical Sciences, 63, 3, pp. 771-779.
- Laski, P.A., Takosoglu, J.E. and Blasiak, S. (2014) A delta type closed kinematics chain with pneumatic muscle actuator manipulator, in: Proc. of Int. Conf. Engineering Mechanics 2014 (ed. Fuis, V.), Svratka, Czech Republic, pp. 360-363.
- Nowakowski, L., Miesikowska, M. and Blasiak, M. (2016) Speech intelligibility in the position of cnc machine operator, in: Proc. of Int. Conf. Engineering Mechanics 2016 (eds. Zolotarev, I. and Radolf, V.), Svratka, Czech Republic, pp. 422-425.
- Pietrala, D.S. (2016) Parallel manipulator with pneumatic muscle drive, in: Proc. of Int. Conf. Engineering Mechanics 2016 (eds. Zolotarev, I. and Radolf, V.), Svratka, Czech Republic, pp. 458-461.
- Takosoglu, J.E. (2016) Experimental research of flow servo-valve, in: Proceedings of the International Conference Experimental Fluid Mechanics 2016 (ed. Dancova, P.), Techn. Univ. Liberec, pp. 819-823.
- Zwierzchowski, J. (2016a) Design type air engine di pietro, in: Proceedings of the International Conference Experimental Fluid Mechanics 2016 (ed. Dancova, P.), Techn. Univ. Liberec, pp. 983-988.
- Zwierzchowski, J. (2016b) Industrial robot vision system for moving spherical elements, in: Proc. of Int. Conf. Engineering Mechanics 2016 (eds. Zolotarev, I. and Radolf, V.), Svratka, Czech Republic, pp. 626-629.

## UNMANNED AIRCRAFT VEHICLE DESIGN FOR TEMPERATURE FIELD ANALYSIS

D. Piwowarski<sup>\*</sup>, S. Anweiler<sup>\*\*</sup>, R. Ulbrich<sup>\*\*\*</sup>, M. Tańczuk<sup>\*\*\*\*</sup>

**Abstract:** *This paper presents the design and implementation of device for remote and automatic monitoring of temperature field of large objects like pipes, PV fields and building complexes. With the help of originally designed system based on commercial low cost unmanned aircraft vehicle equipped with an open source software and commercially available infrared camera, thermal imaging was performed. Research was made on the temperature field of working district heating system during winter in Poland. The system is based on open source PixHawk automatic pilot device and implementation of FLIR-One thermal micro camera under the Android environment.*

**Keywords:** UAV, Aerial Robotics, Remote Sensing, Infrared Camera, Thermal Imaging, District Heating.

### 1. Introduction

Unmanned Aerial Vehicles (UAVs) or more extensively Unmanned Aerial Systems (UAS) are platforms considered under the Remotely Piloted Aircraft (RPAs) paradigm. All of them are presently in continuous development at a rapid rate. Altogether, the development of sensors and instruments to be installed onboard UAV platforms is growing exponentially. These factors together have led to the increasing use of these platforms and sensors for remote sensing applications with new potential (Pajares, 2015). Recent advances in UAVs for civilian use make it possible to regularly monitor environments from the thermophysical point of view, at spatial and temporal scales that would be difficult to achieve using conventional methods. Previous aerial monitoring of thermophysical environments has been expensive and time consuming (Nishar et al., 2016). Thermal and visual image registration consist of different methods to improve the quality of interspectral registration for the purpose of real-time monitoring and mobile mapping. Images captured by low-altitude UAVs represent a very challenging scenario for interspectral registration due to the strong variations in overlap, scale, rotation, point of view and structure of such scenes (Yahyanejad and Rinner 2015). Drones are now routinely used for collecting aerial imagery and creating digital elevation models (DEM). Lightweight thermal sensors provide another payload option for generation of very high-resolution aerial thermal orthophotos. This technology allows for the rapid and safe survey of thermal areas (Harvey et al., 2016). For example, as reported by (Tsanakas et al., 2016) standard Electro-Luminescence imaging method for large Photo-Voltaic fields gives no information on the thermal impact of a potential fault and, thus, no estimation on the result and power output loss can be done for the impacted PV module. It is purely qualitative rather than quantitative diagnosis. This approach is suitable not only for PV fields but also for solar thermal fields (Carlson et al., 2014).

This paper validates the use of cost effective and small (< 2 kg) quadcopter UAV to safely and precisely map the physical characteristics of industrial and urban thermal locations. Thermal infrared imaging and photogrammetry are used to capture complete information of thermal exterior features. The general objective of this paper is to deliver device for distant recognizing applications based on unmanned aerial platforms, equipped with a set of specific sensors and onboard instruments specifically intended to easily

---

<sup>\*</sup> Dawid Piwowarski, MSc.: Environmental Engineering Department (EED), Faculty of Mechanical Engineering (FMechEng), Opole University of Technology (OUTech), Mikołajczyka 5; 45-271, Opole; PL, piwowarskidawid@o2.pl

<sup>\*\*</sup> Stanisław Anweiler, PhD.: EED, FMechEng, OUTech, Mikołajczyka 5; 45-271, Opole; PL, s.anweiler@po.opole.pl

<sup>\*\*\*</sup> Prof. Roman Ulbrich.: EED, FMechEng, OUTech, Mikołajczyka 5; 45-271, Opole; PL, r.ulbrich@po.opole.pl

<sup>\*\*\*\*</sup> Mariusz Tańczuk, PhD.: EED, FMechEng, OUTech, Mikołajczyka 5; 45-271, Opole; PL, m.tanczuk@po.opole.pl

capture thermal data. Applications in several areas are proposed, where the combination of unmanned platforms and sensors, together with methods, algorithms, and procedures provide complex thermal imaging.

In the era of reducing energy consumption in the industrial processes, an important issue is good thermal insulation of devices. This problem applies to pipelines from industrial heat networks as well as district heating (DH) networks and finally in the whole area of municipal structure. The effect of thermal bridge previously well recognized in the range of building insulation aims the fact that even a small point leakage or line leakage can cause significant heat loss. With regard to industrial facilities thermal bridges resulting from the structural design are difficult to avoid and much more difficult to locate. Usually, when the object is not big hand infrared camera is enough. Considering the long pipes or heating networks, or clusters of residential houses one should have an automated device that will allow to complete the imaging task in reasonable time. Assembling such a device for solving the interdisciplinary problem – from knowledge of the mechanisms of heat transport through the construction or adaptation of flying device with supply of infrared camera and appropriate software is essential and specific to mechanical engineering, energy, mechatronics, automation and control and finally sustainable development of urban and suburban areas.

## 2. Methods

Rising fuel prices are forcing to look for savings. One way to search for such savings is constant or cyclical verifying the thermal insulation of industrial pipelines, heat distribution networks from internal and hot water pipes: both of low and high temperature. These issues are problematic for the large areas and the use of manned survey cost will certainly exceed the benefits of the potential savings as manual network monitoring by trained staff can be very tedious and take a lot of time. The use of unmanned aircraft instead of traditional heat loss surveillance methods reduces network maintenance costs by precise indication of the problematic spots. The tests may be carried out in an fully automatic way.

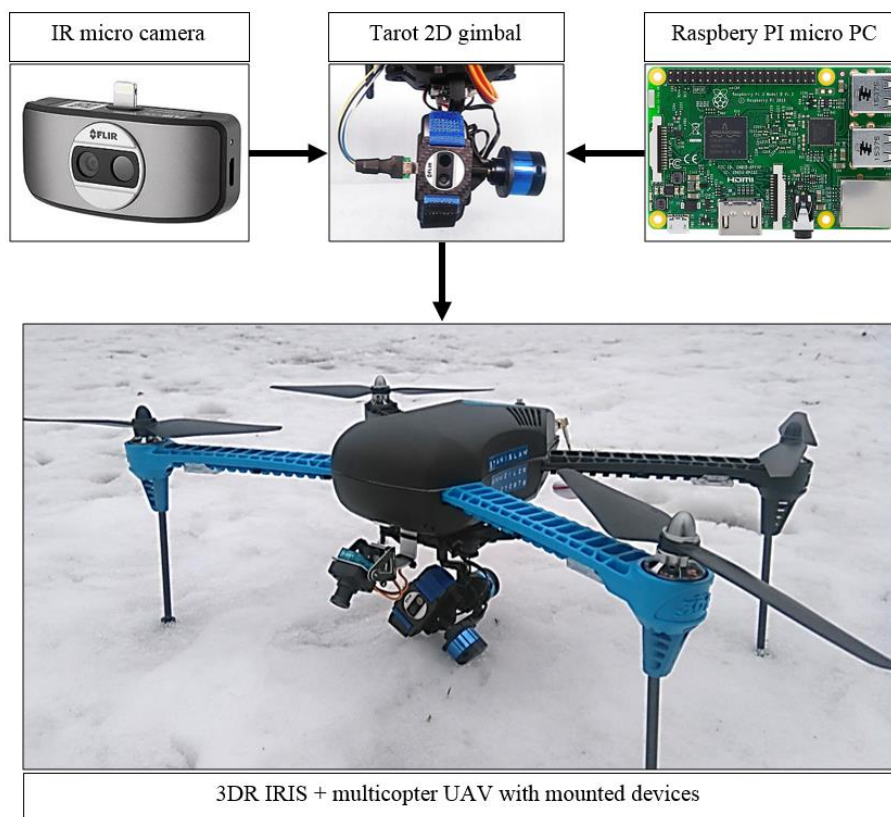
The project aimed to create a quadcopter flying platform equipped with a thermal imaging camera. For this commercially available UAV model was used – 3DR-Iris+ (Fig. 1). The model is capable of 20 minutes flight on a single battery and perform autonomous flight along the pre-programmed route. The platform is equipped with advanced flight control – Pixhawk which allows for further. Successful use of this model in the research, was possible thanks to custom equipment with a set of devices such as – Raspberry-Pi-3 microcomputer, infrared micro camera FlirOne and AV transmitter that transmits real-time image to the ground. Image stabilization during the flight is provided by gimbal device – Tarot-2D (Fig. 1).

The Pixhawk flight controller contains sensors like accelerometer, gyroscope and barometer. Barometer allows to fly at a constant height and hovering. Taking pictures at a constant height is a prerequisite for the subsequent processing of visual data. The sensor also allows the imposition of the platform of the upper limit of the amount to which the model can soar. This is a very important aspect in the conduct of research in the active area of flight. The presence of GPS module allows to fly the programmed route, the ability to lock the area over which the platform cannot find and track the position of the model in real time. (Anweiler and Piwowarski, 2016). Iris+ platform is not waterproof, but it is designed to allow the usage in areas with high humidity, during fog, low temperature (below 0 °C) and during fine rain. The maximum wind speed in the course of research is approx. 20 km/h. Iris+ power source is a lithium-polymer 3S 5000 mAh, 11.1 V battery. Reserve power model allowed to mount on the camera Flir-One along with the necessary equipment without affecting the stability of the flight. In summary, the UAV platform 3DR-Iris+ looks very promising as a carrier of measuring devices. It meets all the requirements while offering additional options and possibilities. This is an easy development platform that allows further modifications and improvements to provide valuable information about the test object or area.

Thermal images are made using the Infrared camera FlirOne (Fig. 1). The camera is characterized by the possibility of carrying out the measurement temperature in the range of from -20 °C to 120 °C, with the resolution of 160 x 120 pix and a low weight of 30 grams. This camera works in the Android software environment. To equip the camera to the UAV platform the use of microcomputer Raspberry Pi 3 is recommended (Fig. 1). This micro device includes Broadcom 1.2 GHz quad-core processor, 1 GB of RAM and HDMI connector. These features enabled the installation and commissioning of required



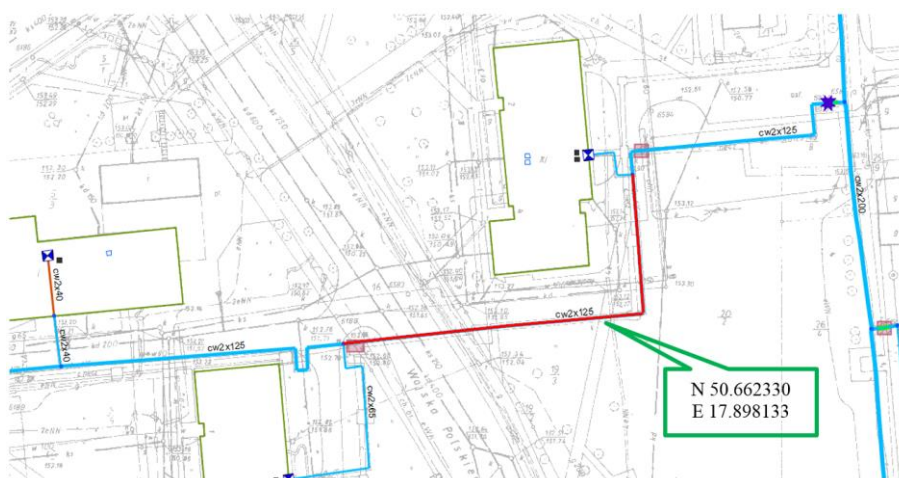
applications and proved to be sufficient. Android environment is installed on a micro SD card affixed later in the Raspberry Pi.



*Fig. 1: Multicopter UAV – imaging aerial platform 3DR Iris+ and mounted devices: IR FLIR micro camera, Tarot 2D gimbal, Raspberry Pi 3 microcomputer and visual recording camera.*

### 3. Results

A fragment of Opole municipal district heating network with the part of a high temperature pipeline (design values 126/68°C) under study is presented in Fig. 2. Thermally imaged heat pipe line lays underground and is constructed as twin preinsulated system that consists of two pipes with a diameter equal to 125 mm. During the thermal imaging the temperature of water in a supply pipe was equal to 91 °C, while the temperature of water in a return pipe was equal to 50 °C.

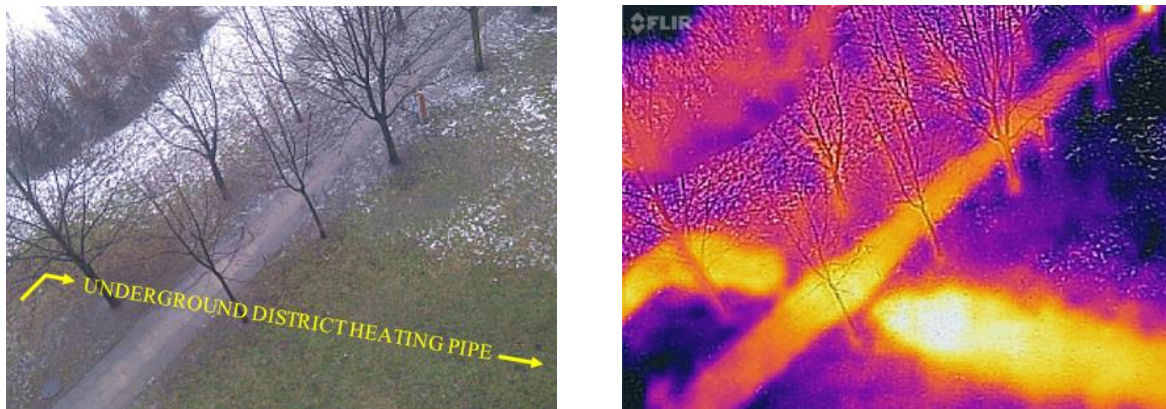


*Fig. 2: GIS map of district heating system network. Analyzed section of the heat pipeline is marked with red color. Corresponding geographical coordinates marked in green. (1:1000 scale).*

Fig. 3 presents the images that have been made with visual and IR FlirONE camera. It was made on 5/2/2017 at 12:30 hours. Outside temperature was –1 °C and atmospheric pressure 1020 hPa. The



geographical coordinates of the photographed location: N50.662330, E17.898133. Despite the low resolution of the camera underground pipeline is clearly visible.



*Fig. 3: Visual and infrared capture of the location with underground district heating pipe.*

#### 4. Conclusions

The development of the energy and heating industry, requires the use of new technologies for energy production, as well as the monitoring of industrial processes. This reveals a whole new area where the unmanned aircrafts can be used successfully. This article describes how to visualize the temperature field using the multicopter platform Iris + equipped with a thermal imaging camera FlirONE. It proved to be an excellent tool for locating underground heating lines. This is a very good alternative to currently used methods. It allows quick and precise determination the course of the pipeline and an indication of a possible leaks in case of failure. The used method also enables visualization and determination the size of the heat loss in the individual sections of the heating network. Presented example, studies thermal imaging has proven effective in the location of the preinsulated pipeline with reduced heat losses. It must therefore be assumed that the proposed method can be a good tool to diagnose the traditional networks, with a much larger heat losses, commonly used in Poland. Low assembly cost of the platform (below 1000 \$) and low maintenance cost allows frequent measurements. By comparing the data collected in time the wear of pipeline can be detected in advance, and plan their earlier exchange or establish the maintenance schedule to the network. All these aspects lead to a reduction in the risk of failure, reduce network maintenance costs of transmission and thus, by reducing the loss of heating medium and heat loss, reducing the impact on the environment. UAVs used in monitoring temperature field reveal only a portion of their capabilities. Fast growing market of the multicopter platforms still provides new solutions and improvements.

#### References

- Anweiler, S. and Piwowarski, D. (2016) Multicopter platform prototype for environmental monitoring, *Journal of Cleaner Production*, <http://dx.doi.org/10.1016/j.jclepro.2016.10.132>
- Carlson, J., Menicucci, D., Vorobieff, P., Mammoli, A. and He, H. (2014) Infrared imaging method for flyby assessment of solar thermal panel operation in field settings. *Applied Thermal Engineering*, 70(1), 163-171.
- Harvey, M.C., Rowland, J.V. and Luketina, K.M. (2016) Drone with thermal infrared camera provides high resolution georeferenced imagery of the Waikite geothermal area, New Zealand. *Journal of Volcanology and Geothermal Research*, 325, 61-69.
- Nishar, A., Richards, S., Breen, D., Robertson, J. and Breen, B. (2016) Thermal infrared imaging of geothermal environments and by an unmanned aerial vehicle (UAV): A case study of the Wairakei–Tauhara geothermal field, Taupo, New Zealand. *Renewable Energy*, 86, pp. 1256-1264.
- Pajares, G. (2015) Overview and current status of remote sensing applications based on unmanned aerial vehicles (UAVs). *Photogrammetric Engineering and Remote Sensing*, 81(4), pp. 281-329.
- Tsanakas, J.A., Ha, L. and Buerhop, C. (2016) Faults and infrared thermographic diagnosis in operating c-Si photovoltaic modules: A review of research and future challenges. *Renewable and Sustainable Energy Reviews*, 62, 695-709.
- Yahyanejad, S. and Rinner, B. (2015) A fast and mobile system for registration of low-altitude visual and thermal aerial images using multiple small-scale UAVs. *ISPRS Journal of Photogrammetry and Remote Sensing*, 104, 189-202.

## NUMERICAL SIMULATIONS OF FREE SURFACE FLOWS USING A THREE-EQUATION MODEL

S. Plánička<sup>\*</sup>, J. Vimmr<sup>\*\*</sup>

**Abstract:** Numerical results obtained from the application of a three-equation model for free surface flows are presented in the paper. The compressible two-phase flow model is suitable for complex free surface flow simulations that can, for example, include breaking waves. Compared to commonly used shallow water models, the model described in the paper offers certain advantages and wider applicability as it can deal with problems associated with complex interfaces. On the other hand, it should be noted that the model describes only flow field of one phase and the solution of pressure field is significantly simplified. Derived from the seven-equation Baer-Nunziato model and completed with the Tait equation of state, it consists of mass and momentum evolution equations in conservative form and of an advection equation for volume fraction in non-conservative form. A numerical code based on the finite volume method was developed, in which the inviscid numerical flux is approximated by an AUSM scheme. For spatial discretization of the non-conservative term contained in the model, an AUSM-based scheme is applied. The developed algorithm was successfully verified by a well-known dambreak test and further a bubble ascension problem was solved.

**Keywords:** Free surface flow, Three-equation model, AUSM scheme, Finite volume method.

### 1. Introduction

Multi-phase flow phenomena occur frequently in nature as well as in human-impacted activities such as industry. Considering their global significance, it is, therefore, useful to pursue their computer modeling. Especially free surface flows need to be solved, which often include flows in open channels and ducts and propagation of waves on liquid surface. Currently there are many significantly different techniques, which were developed to solve free surface flow problems. The choice of an appropriate model depends on the degree of problem simplification. Two classes of models based on the finite volume method are usually distinguished: the interface tracking methods, which use boundary-fitted grids to precisely capture the free surface, and the interface capturing methods, which use a stationary grid, and as such are unable to describe the interface as sharp boundary (e.g. the MAC and VOF methods). Additionally, other efficient methods are developed such as the smoothed particle hydrodynamics or the multiphase lattice Boltzmann methods.

The main objective of this paper is to demonstrate the applicability of a simple three-equation model for the solution of complex free surface flow problems. For this purpose, a two-phase model proposed in the paper Dumbser (2011) is introduced and derived from a seven-equation model, which was designed by Baer-Nunziato (1986) for the modeling of compressible detonation two-phase waves. The numerical solution of the aforementioned flow problems is carried out by in-house computational software based on the finite volume method. The developed code was tested for the dambreak and bubble ascension problems. A comparison between the obtained numerical results and the sample results are presented.

### 2. Mathematical model

The three-equation model employed in this paper belongs to a class of Eulerian interface capturing methods, in which an amount of tracked fluid per volume is defined by the volume fraction  $\alpha$  determined

---

<sup>\*</sup> Ing. Stanislav Plánička: Department of Mechanics, Faculty of Applied Sciences, University of West Bohemia, Technická 8; 306 14, Plzeň; CZ, staplan@ntis.zcu.cz

<sup>\*\*</sup> Assoc. Prof. Ing. Jan Vimmr, PhD.: European Centre of Excellence NTIS – New Technologies for the Information Society, Faculty of Applied Sciences, University of West Bohemia, Technická 8; 306 14, Plzeň; CZ, jvimmr@ntis.zcu.cz

from advection equation. The described model is applicable for the description of fluid flow with free surface, wherein the second phase is negligible (vacuum or fluid with a significantly lower density). By contrast, the approach is not suitable for solving dispersed flows, sedimentation and thermodynamics problems because of its characteristics and due to performed simplifications.

The original Baer-Nunziato model contains conservation equations of mass, momentum and energy for both phases and an advection equation of volume fraction. In this paper, the model is reduced following various simplifications proposed by Dumbser (2011). As mentioned above, the three-equation model completely neglects the secondary phase, making it possible to omit all the evolution equations belonging to the secondary phase as well as the corresponding variables from the set of equations. Additionally, it is necessary to determine appropriate values of unknown parameters at the interface, i.e., the interface pressure  $p_I$  and the interface velocity vector  $\mathbf{v}_I$ . The interface pressure is always kept on atmospheric pressure ( $p_I = p_2 = p_{ATM} = 0 \text{ Pa}$ ), when choosing that all pressures value are relative to the atmospheric one. The interface velocity, which corresponds to the rate of advection of the volume fraction, is set to be equal to the velocity of the primary phase ( $\mathbf{v}_I = \mathbf{v}_1$ ). In other words the interface propagates along with the primary fluid. This option is well-suited for free surface flow problems. The system was closed with the simple Tait equation of state for the primary phase

$$p = K ((\rho / \rho_0)^\gamma - 1), \quad (1)$$

which directly relates the pressure  $p$  and the density  $\rho$ . For more information, see, for example, the work MacDonald (1966).  $K, \gamma$  are constants affecting the compressibility of the fluid and  $\rho_0$  is the density at the reference pressure. The determination of speed of sound uses a common formula, which is valid for general equation of state during isentropic process. A major advantage of this formulation is that the density is calculated directly from the corresponding evolution equations and afterwards the pressure is determined using the equation of state in the simple algebraic form. This approach makes the energy equation unnecessary and enables us to omit it from the final set of equations. The resulting mathematical model in two dimensions can be written as

$$\frac{\partial}{\partial t}(\alpha \rho) + \frac{\partial}{\partial x}(\alpha \rho u) + \frac{\partial}{\partial y}(\alpha \rho v) = 0, \quad (2)$$

$$\frac{\partial}{\partial t}(\alpha \rho u) + \frac{\partial}{\partial x}(\alpha (\rho u^2 + p)) + \frac{\partial}{\partial y}(\alpha \rho v u) = 0, \quad (3)$$

$$\frac{\partial}{\partial t}(\alpha \rho v) + \frac{\partial}{\partial x}(\alpha \rho u v) + \frac{\partial}{\partial y}(\alpha (\rho v^2 + p)) = \alpha \rho g, \quad (4)$$

$$\frac{\partial}{\partial t}\alpha + u \frac{\partial}{\partial x}\alpha + v \frac{\partial}{\partial y}\alpha = 0, \quad (5)$$

where  $u, v$  denote the velocity components and the independent variables of space and time are labelled as  $x, y$  and  $t$ , respectively. The source term on the right hand side of Eq. (4) represents the gravitational force per unit volume with the acceleration of gravity  $g$ . The nonlinear system of Eqs. (2) – (5) is hyperbolic when the fluid density is positive ( $\rho > 0$ ) and the volume fraction is  $0 < \alpha < 1$ . This means that the primary phase or even more the neglected secondary phase cannot vanish within whole domain. Under these conditions, eigenvalues  $\{u - a, u, u, u + a\}$  and  $\{v - a, v, v, v + a\}$  are real.

### 3. Numerical method

With the goal to examine the suitability of the presented model for free surface flow simulations, a numerical code written in Matlab was developed. The finite volume method was used for spatial discretization of the system of equations. The inviscid numerical flux was approximated by the first order scheme in order to damp instabilities of the two-phase flow model. Specifically, an AUSM scheme was used due to its simplicity, efficiency, stability and accuracy, for more information see for example papers Evje (2003) or Paill  re (2003). The numerical flux vector through the  $k$ -th edge belonging to the cell  $L$  with the adjacent cell  $R$  with the unit vector of the outward normal  $[n_x^e, n_y^e]^T$  is then defined as

$$\mathbf{F}_k^{AUSM} = \frac{M_{LR}}{2} (\mathbf{w}_L a_L + \mathbf{w}_R a_R) - \frac{|M_{LR}|}{2} (\mathbf{w}_R a_R - \mathbf{w}_L a_L) + P_{LR} [0, n_x^e, n_y^e, 0]^T, \quad (6)$$

where  $M_{LR}(M_L^n, M_R^n)$  and  $P_{LR}(M_L^n, M_R^n, p_L, p_R, \alpha_L, \alpha_R)$  represent the splitting functions. Unlike the approximate Riemann solvers or the characteristic flux schemes, the AUSM scheme does not require any

characteristic analysis. This is a significant advantage for two-phase flow simulations, which enables us to use the AUSM scheme in a whole range of different two-phase models.

For numerical solution, the advection equation for volume fraction (5) in the non-conservative form presents a certain complication. For this reason, it was rewritten into a new form

$$\frac{\partial}{\partial t} \alpha + \frac{\partial}{\partial x} (\alpha u) + \frac{\partial}{\partial y} (\alpha v) - \alpha \left( \frac{\partial u}{\partial x} + \frac{\partial v}{\partial y} \right) = 0, \quad (7)$$

where the second and the third additional terms form basically a conservative convective flux of volume fraction and the fourth term is a non-conservative source term. Note that Eq. (7) was utilized in the numerical code instead of Eq. (5). The AUSM scheme was used for the inviscid flux discretization of the entire set of Eqs. (2) – (4), (7). The non-conservative term in Eq. (7) was discretized in the sense of the AUSM scheme due to consistency. The entire coupled system of Eqs. (2) – (4), (7) was time-iterated by an explicit two stage Runge-Kutta scheme.

#### 4. Test cases

The developed numerical code was verified by the two-dimensional test case – the dambreak with bottom step into a wet bed area. The computational domain  $\Omega = ([-5; 5] \times [0; 3]) \setminus ([0; 5] \times [0; 0.2])$  m is divided with an unstructured triangular mesh. The domain initially containing the fluid ( $\alpha = 0.95$ ) is  $\Omega_L^{IC} = ([-5; 0] \times [0; 1.46]) \cup ([0; 5] \times [0.2; 0.51])$  m. The gravity acceleration in the  $y$ -direction is  $g = -9.81 \text{ m/s}^2$  and the parameters of the Tait equation (1) are artificially set as  $\gamma = 1$ ,  $\rho_0 = 1000 \text{ kg/m}^3$ ,  $K = 0.637 \text{ MPa}$  to improve the solution convergence. The initial velocities are  $u = v = 0 \text{ m/s}$  and the pressure is set to be equal to the hydrostatic one with zero pressure level at height  $h = 1.46 \text{ m}$ . A wall boundary condition is applied to all boundaries of the computational domain. The parameters of the performed numerical simulation are the same as the parameters in the original work Dumbser (2011). In doing so, the purpose is to compare the results obtained using our developed solver with the published results, which were achieved with discontinuous Galerkin schemes. Both simulations used unstructured grids of comparable quality. The comparison of volume fraction results is shown in Fig. 1: developed numerical code – isolines, Dumbser (2011) – blue/red field (trimming used as  $\alpha < 0.5 \rightarrow \text{blue}$ ,  $\alpha > 0.5 \rightarrow \text{red}$ ), shallow water equations – thick black line.

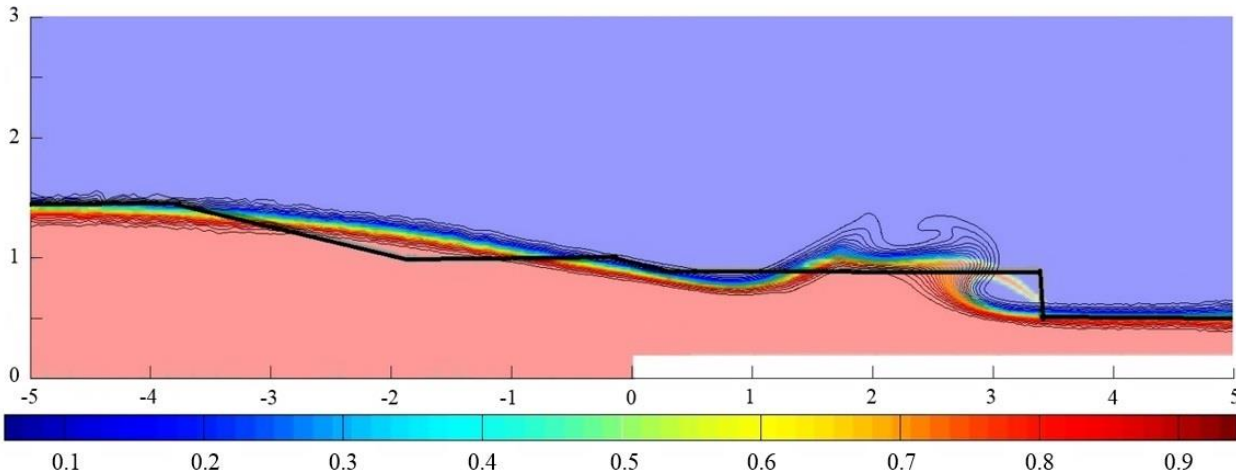


Fig. 1: Dambreak with wet step: volume fraction at the time  $t = 1 \text{ s}$ .

Further, the suitability of the three-equation model for the description of the bubble ascension problem was analyzed. This task is very different from the problem of breaking waves, for which the model was primarily designed. In this case, the bubble rises under the influence of gravity acting on the surrounding fluid, making the phase interface very complex. Initially, the circular bubble  $\Omega_{Bub}^{IC} = \text{circ}([1; 0.3], 0.2)$  m is at rest in a closed box  $\Omega = ([0; 2] \times [0; 2])$  m filled with fluid. The gravity acceleration in the  $y$ -direction is  $g = -9.81 \text{ m/s}^2$  and the parameters of the Tait equation are the same as in the previous case. The initial pressure field has a hydrostatic profile with zero pressure level at height  $h = 1 \text{ m}$ . The results of numerical simulations carried out by the developed software are shown in the Fig. 2 (left) at time  $t = 1 \text{ s}$ . For illustration, Fig. 2 (right) shows the results from the paper Murrone (2005). Note that Murrone and Guillard used a more sophisticated five-equation model, different

parameters of the Tait equation of state and a finer mesh. In our case, the simulation was performed on a computational grid with square cells. The results are entirely symmetrical until approximately the time  $t = 0.5$  s, when the symmetry is broken probably due to accumulation of numerical errors.

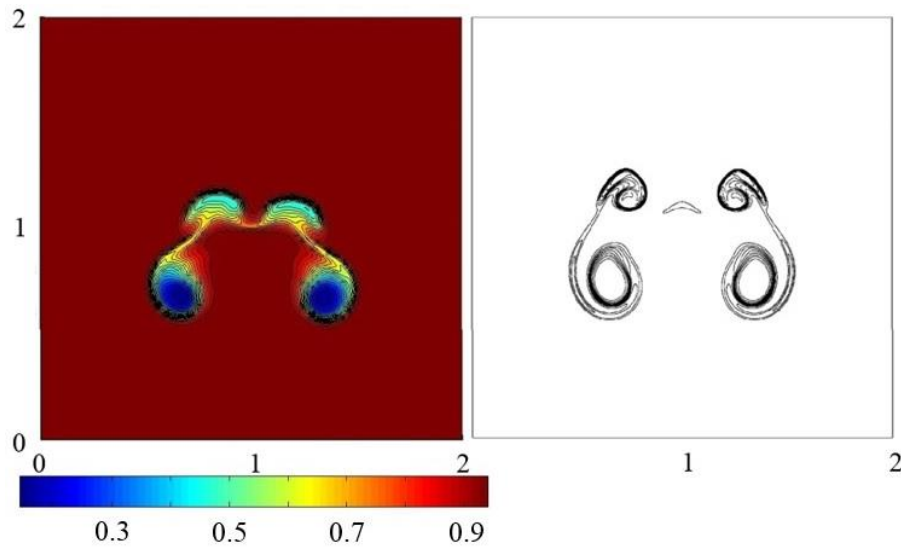


Fig. 2: Bubble ascension problem: volume fraction at the time  $t = 1$ s.

## 5. Conclusions

The results presented in this paper demonstrated the applicability of the three-equation model for the solution of free surface flow problems using FVM and AUSM scheme. Compared to other high-order solvers (e.g., DGFEM), our algorithm exhibits higher artificial viscosity, but is able to capture the initial breaking wave better than the shallow water equations model, see Fig. 1. Good results were also achieved for the bubble ascension problem, which demonstrated the ability of the model to handle complex free surface interfaces.

## Acknowledgement

This study was partly supported by the internal student grant project SGS-2016-38 of the University of West Bohemia and partly by the project LO1506 of the Ministry of Education, Youth and Sports of the Czech Republic.

## References

- Baer, M.R. and Nunziato, J.W. (1986) A two-phase mixture theory for the deflagration-to-detonation transition (DDT) in reactive granular materials. *International Journal of Multiphase Flow*, 12, 6, pp. 861-889.
- Dumbser, M. (2011) A simple two-phase method for the simulation of complex free surface flows. *Computer methods in applied mechanics and engineering*, 200, pp. 1204-1219.
- Evje, S. and Fjelde, K.K. (2003) On a rough AUSM scheme for a one-dimensional two-phase model. *Computers and fluids*, 32, pp. 1497-1530.
- MacDonald, R. (1966) Some simple isothermal equations of state. *Reviews of modern physics*, 38, 4, pp. 669-679.
- Murrone, A. and Guillard, H. (2005) A five equation reduced model for compressible two phase flow problems. *Journal of Computational Physics*, 202, pp. 664-698.
- Paillère, H., Corre, C. and García Cascales, J.R. (2003) On the extension of the AUSM+ scheme to compressible two- fluid models. *Computers and fluids*, 32, pp. 891-916.



## THE EFFECT OF VELOCITY PROFILE DEFORMATION OF AN AVERAGING PITOT TUBE

S. Pochwała<sup>\*</sup>, J. Wydrych<sup>\*\*</sup>, G. Borsuk<sup>\*\*\*</sup>

**Abstract:** Many industrial facilities, such as modern boiler equipment, demonstrate a high level of complexity. The management of the space around them forms the reason why it is impossible to install a flow meter in an appropriate location in accordance with the manufacturer's recommendations. An adequate location of a flowmeter forms a key aspect in securing correct measurements. Usually, a sufficiently long run of straight section of a pipeline upstream and downstream of the flowmeter is a part of such recommendations. The failure to meet such a condition can lead to the increase of the measurement uncertainty above the value that recommended by the flowmeter producer. The rationale for a study into applicability of averaging Pitot tubes in the area of flow disturbance is associated with operating problems with such equipment.

**Keywords:** Averaging Pitot tubes, Flowmeter, Measurement uncertainty.

### 1. Introduction

A number of methods are currently used to determine fluid velocity, mass and volume flow. Such studies play an important role in the development of control and measuring systems. The measurement of these quantities is important in the context of apparatus and systems operation (Spitzer, 1996; Miller, 1983). The classification of the methods and equipment applied for measurements of mass or volume flow rate was based on multiple criteria (Chmielniak, 2008). The measured value forms the most important criterion of the classification applied with regard to the existing flowmeters (Turkowski, 2013; Vinod, 2012). As a principle, the criterion adopted for this distribution is based on the physical principle of their operation.

On the basis of the above criteria, the following classification of flowmeters was developed (Pospolita, 2004):

- an averaging flowmeter (orifice, averaging Pitot tubes),
- rotameter,
- turbine flowmeter, electromagnetic flowmeter, ultrasonic flowmeter,
- positive displacement flowmeters,
- Coriolis flowmeter,
- thermal flowmeter,
- vortex flowmeter,
- other (optical flowmeter, correlation flowmeter).

The range of the application of flowmeters applied in the metering and billing is very extensive. This area primarily includes various types of liquid and gas fuels, as well as heat and water supply to municipal and industrial customers, as well as the metering and billing based on the amount of wastewater discharge. Repeatedly the flow rates are counted in the hundreds of thousands m<sup>3</sup> of a medium per hour and pipe diameters are in the range of one or two and even more meters. This leads to considerable problems

---

<sup>\*</sup> Adjunct prof. Sławomir Pochwała, PhD.: Department of Thermal Engineering and Industrial Facilities, Opole University of Technology, 76 Prószkowska str.; 45-758, Opole; Poland, s.pochwała@po.opole.pl

<sup>\*\*</sup> Adjunct prof. Jacek Wydrych, PhD.: Department of Thermal Engineering and Industrial Facilities, Opole University of Technology, 76 Prószkowska str.; 45-758, Opole; Poland, j.wydrych@po.opole.pl

<sup>\*\*\*</sup> Adjunct prof. Grzegorz Borsuk, PhD.: Department of Thermal Engineering and Industrial Facilities, Opole University of Technology, 76 Prószkowska str.; 45-758, Opole; Poland, g.borsuk@po.opole.pl



associated with the selection of flowmeters and their installation. In spite of a wide range of flow conditioners available, all of them generate an additional value of local pressure drop. This, in turn, exclude their use in certain applications (Frattolillo et al., 2002). An incorrect selection can have a significant impact on the results of the measurement.

## 2. Methods

The metering and billing based on actual measurements are associated with a need to maintain the smallest possible measurement uncertainty. This condition often limits the selection of an appropriate flowmeter. For this reason, there is a need to develop and apply a variety of normative documents in the industrial installation. (Dobrowolski et al., 1992). Flowmeters with averaging Pitot tubes are being increasingly used because of significantly smaller pressure drops resulting from their installation, which is additionally coupled with simple system design and low operating cost. Pitot tubes are often used for fluid velocity and velocity profile measurements, along with Pitot tubes and other types of micro-orifices (molders). A pipe with an adequate design of the pressure tapping points for the reception of pressure forms the most important part of this type of a flowmeter. A moldor is located in the measurement section of a pipeline. During the flow around the pressure sensor, the pressure in the front part of the sensor is higher than the static pressure in the pipeline because of the dynamic effect of the fluid flow. On the sides and the rear side of the sensor, the pressure is lower from the static pressure in the pipeline. Sensor shapes applied in the industry and the location of impulse tapping points can lead to a relatively constant value of flow coefficient  $K$  in a relatively wide range of flow parameters. This value is usually in the range from 0.6 to 0.8. The velocity determined for the averaging Pitot tubes was obtained on the basis of the formula:

$$w = K \sqrt{\frac{2\Delta p}{\rho}} \quad (1)$$

where:  $K$  – flow coefficient,  
 $\Delta p$  – pressure drop,  
 $\rho$  – fluid density.

## 3. Results

The research was carried out on a measuring system built with the purpose of experimental determination of the impact of flow obstacles on the results registered by a sensor during the measurement of averaging dynamic pressure. In the study, a centrifugal fan with a maximum flow rate of 12000 m<sup>3</sup>/h was responsible for driving flow in the pipe, and it was powered by 37 kW three-phase motor (Kabaciński et al., 2010; Kabaciński et al., 2011 and Pochwała et al., 2016).



*Fig. 1: General view of the measuring system.*

Fig. 1 shows a general view of the measuring system. The research reported in this paper was carried out in a  $3 \times 30^\circ$  segmented elbow. In the analyzed design of the averaging tube, six pressure tapping points were used upstream of the flowmeter, and they were arranged according to the principle of circle division into concentric rings with an equal area. Pressure tapping points applied for the measurements of the negative pressure were located downstream of the tube. The operating principle of a averaging tube is based on an adequate location of pressure tapping points. The research was carried out within the frequency range of the electric motor of 8.0 – 29.0 Hz with a step of 0.5 Hz, corresponding to the measured velocity with a reference flowmeter in the range 8.0 – 30 m/s.

Reference measurements were carried out in a straight tube section at a distance of 35 diameters from the flowmeter. Measurements were carried out by setting the averaging tube in two characteristic positions with respect to the obstacle in the horizontal and vertical axes with a vertical air inflow to the fully open throttle valve. As a result of the calculations, it was possible to make a comparison between the flow rates and values of the flow coefficient in the sections where the measured velocity profile was fully developed. For fully open throttle valve the distance was 35 diameters – as it is shown in the diagrams  $K/K_{35}$ . Figs. 2 and 3 show the results of the experimental research for the Introbar flowmeter.

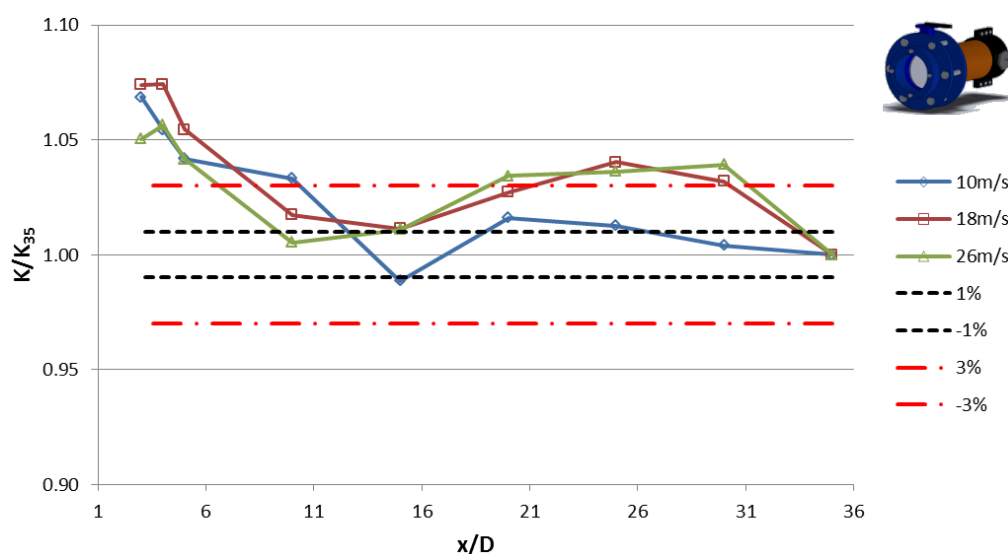


Fig. 2: Flow coefficient  $K/K_{35}$  Introbar flowmeter related to the distance from the obstacle for vertical tube orientation.

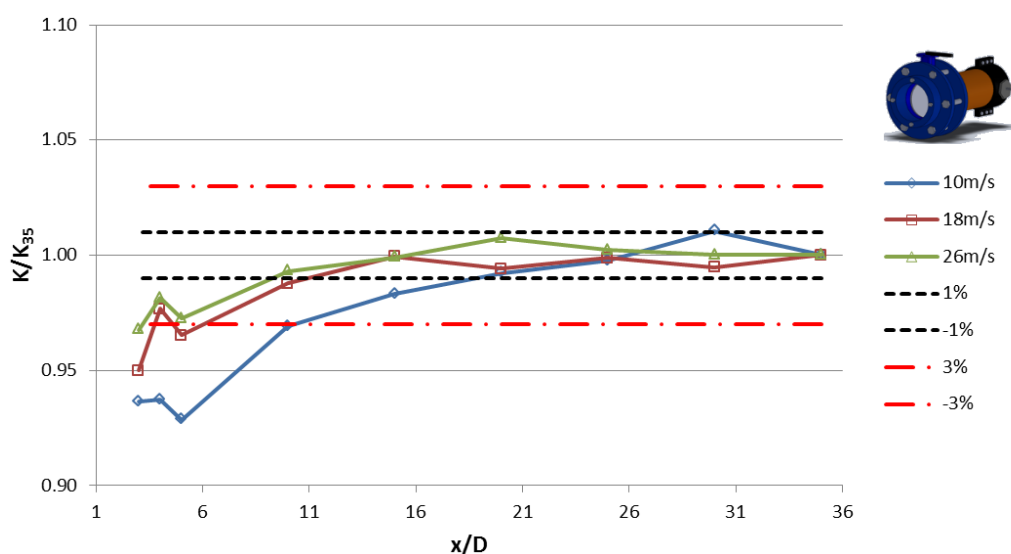


Fig. 3: Flow coefficient  $K/K_{35}$  Introbar flowmeter related to the distance from the obstacle for horizontal tube orientation.

Tab. 1 shows the variations of flow coefficient  $K_{av}/D$  with respect to  $K_{av35}$  of the tested flowmeter. The values of  $K_{av}/D$  were averaged for the entire range of the analyzed velocity (10 ÷ 30 m/s at 93 measuring

points) and subsequently compared with the value of the flow coefficient determined for the position where the velocity profile is fully developed. The summary of deviations  $K_{av}/D$  with respect to  $K_{av20}$  was based on the formula:

$$\delta K_{lok} = \frac{K_{av/D} - K_{av35}}{K_{av35}} * 100\% \quad (2)$$

The disadvantageous places from the metrological point of view, i.e. ones for which the additional uncertainty associated with the location of the sensor is greater than  $\pm 3\%$  in the table are marked in red.

*Tab. 1: List of additional uncertainty depending on the location of the sensor  $\delta K_{lok}$ .*

INTROBAR									
$\delta K_{lok}$	3D	4D	5D	10D	15D	20D	25D	30D	35D
Vertical	6.4 %	6.2 %	4.9 %	1.2 %	0.7 %	3.0 %	3.1 %	3.0 %	0.0 %
Horizontal	4.9 %	3.1 %	4.3 %	1.8 %	0.8 %	0.3 %	0.2 %	0.0 %	0.0 %

#### 4. Conclusions

The research reported in this paper focused on the influence of the installation comprising a fully open throttle valve on the results registered by the averaging Pitot tubes. The research was carried out for three gas velocities equal to 10, 18, and 26 m/s. The reference velocity was determined using a turbine flow meter with a total uncertainty of  $\pm 0.5\%$  over the entire range of the analyzed velocities. The research was conducted in several tube sections located at various distances from a flow obstacle. The research and analysis led to the formulation of a few statements for application in metrology. For the distance equal to 3, 4, 5 and 25 equivalent diameters, a significant increase in additional uncertainty was noted for all analyzed velocities for the vertical tube orientation. This is attributable to the formation of a vortex downstream from the fully open throttle valve. The analysis of the results demonstrated that it is possible to use averaging Pitot tubes at much smaller distances than the ones recommended by the manufacturers. A total uncertainty of  $\pm 4\%$  can offer the applicability of the analyzed flowmeters in a series of control systems in technological processes, e.g. for the control of the combustion process.

#### References

- Chmielniak, T., Kotowicz, J. and Węcel, D. (2008) Experimental and numerical investigations of the averaging Pitot tube and analysis of installation effects on the flow coefficient. *Flow Measurement and Instrumentation*, No. 19, pp. 301-306.
- Dobrowolski, B. and Kabza, Z. (1992) Theoretical analysis of the influence of axisymmetric deformation of the velocity profile and stream swirling on metrological characteristics of pressure differential devices. *Opole University of Technology, Opole* (in Polish).
- Frattolillo, A and Massarotti, N. (2002) Flow conditioners efficiency a comparison based on numerical approach. *Flow Measurement and Instrumentation*, No. 13, pp. 1-11.
- Kabaciński, M. and Pospolita, J. (2011) Experimental research into a new design of flow-averaging tube. *Flow Measurement and Instrumentation*. Vol. 22, Iss. 5, pp. 421-427.
- Kabaciński, M., Kabza, Z. and Pospolita, J. (2010) Laboratory set for flowmeters testing, *Measurements Automation Robotics*, No. 10, pp. 53-57.
- Miller, R.W. (1983) *Flow measurement engineering handbook*, Mc Graw Hill Book Company.
- Pochwała, S. and Pospolita, J. (2016) Analysis of applicability of flow averaging pitot tubes in the areas of flow disturbance. *Metrology and Measurements Systems*, Vol. XXIII, No. 1, pp. 71-84.
- Pospolita, J. (2004) *Measurements of fluid streams*. Opole University of Technology, Opole (in Polish).
- Spitzer, D.W. (1996) *Flow Measurement. Practical Guides for Measurement and Control*, Instrument Society of America, United States of America.
- Turkowski, M. and Szufleński, P. (2013) New criteria for the experimental validation of CFD simulations. *Flow Measurement and Instrumentation*, No. 34, pp. 1-10.
- Vinod, V., Chandran, T., Padmakumar, G. and Rajan, K.K. (2012) Calibration of an averaging Pitot tube by numerical simulations. *Flow Measurement and Instrumentation*, No. 24, pp. 26-28.

## MATHEMATICAL MODELLING OF ROTOR SYSTEMS WITH JOURNAL BEARINGS IN LIMIT CASES

P. Polach<sup>\*</sup>, M. Hajžman<sup>\*\*</sup>, M. Byrtus<sup>\*\*\*</sup>, Š. Dyk<sup>\*\*\*\*</sup>, L. Smolík<sup>\*\*\*\*\*</sup>

**Abstract:** Dynamics of rotating systems involves behaviour and diagnostics of rotating structures. When hydrodynamic journal bearings are used to support a rotor the rotor-bearing system becomes a complex dynamic system that may exhibit serious fluid film instabilities. The understanding of the behaviour of a fluid film bearing closely before, during and after the rotor instability origin and growth is the main motivation for the complex research of local and global dynamics of a rotor-bearing system. Deep knowledge of the relations between local fluid film dynamics and dynamic response of rotating systems during instabilities can help to improve design of many modern rotating machines.

**Keywords:** Rotor dynamics, Reynolds equation, Fluid film bearings.

### 1. Introduction

Dynamics of rotating systems supported by journal bearings is an interesting topic of computational mechanics. When hydrodynamic journal bearings are used to support a rotor the rotor-bearing system becomes a complex dynamic system that may exhibit serious fluid film instabilities related to various limit cases, which are the main subject of this paper. The understanding of the fluid film bearing behaviour closely before, during and after the rotor instability origin and growth is the main motivation for the complex research of local and global dynamics of a rotor-bearing system.

In 1925 Newkirk and Taylor discovered that a journal bearing can induce unstable vibrations of a supported rotor. This instability – commonly called oil whirl (Hori, 1959) – remains troublesome and of great concern. Lund (1962) investigated bifurcations analytically within the scope of the Hopf bifurcation theory and introduced the method of multiple scales. Later Meyers (1986) applied the bifurcation theory to oil whirl employing numerical methods. Recent development in numerical methods for nonlinear models and numerical continuation methods allowed studying the oil-induced instabilities and resulting bifurcations even deeper. Castro et al. (2008) implemented successfully nonlinear hydrodynamic forces and predicted oil whirl/whip for a real vertical power plant and a horizontal test rig. Boyaci et al. (2010) used a numerical continuation method to detect bifurcations of stationary and periodic solutions for a flexible rotor supported by two identical journal bearings. Adiletta et al. (2011) and Laha and Kakoty (2011) published the work similar to Boyaci's. Adiletta et al. (2011) studied a rigid rotor supported by two-lobe journal bearings, whereas Laha and Kakoty (2011) studied a flexible rotor supported by porous hydrodynamic journal bearings. Mishra (2012) investigated whirl ratio for an adiabatic solution of a bearing with non-Newtonian fluid. Amamou and Chouchane (2014) discussed the stability issues including hysteresis and jump phenomena of long journal bearings utilizing nonlinear model and continuation methods. Yang et al. (2014) proposed second-order nonlinear stiffness and damping

---

<sup>\*</sup> Dr. Ing. Pavel Polach: New Technologies for the Information Society, European Centre of Excellence, University of West Bohemia, Univerzitní 8; 306 14, Pilsen; CZ, ppolach@ntis.zcu.cz

<sup>\*\*</sup> Ing. Michal Hajžman, PhD.: New Technologies for the Information Society, European Centre of Excellence, University of West Bohemia, Univerzitní 8; 306 14, Pilsen; CZ, mhajzman@kme.zcu.cz

<sup>\*\*\*</sup> Ing. Miroslav Byrtus, PhD.: New Technologies for the Information Society, European Centre of Excellence, University of West Bohemia, Univerzitní 8; 306 14, Pilsen; CZ, mbyrtus@rice.zcu.cz

<sup>\*\*\*\*</sup> Ing. Štěpán Dyk: New Technologies for the Information Society, European Centre of Excellence, University of West Bohemia, Univerzitní 8; 306 14, Pilsen; CZ, sdyk@ntis.zcu.cz

<sup>\*\*\*\*\*</sup> Ing. Luboš Smolík: New Technologies for the Information Society, European Centre of Excellence, University of West Bohemia, Univerzitní 8; 306 14, Pilsen; CZ, carlist@ntis.zcu.cz

coefficients. The proposed method can be used for studying the nonlinear behaviour of the oil film instead of the continuation methods.

This paper deals with the summary of computational modelling methods related to the rotor dynamics with fluid film bearings. Basic steps of the methodology are explained and the consideration of various effects close to the limit behaviour is introduced.

## 2. Equations of motion of rotating systems

There are several common methods for the modelling and dynamical analysis of rotating systems. Two of them are mentioned in this paper.

### 2.1. Finite element modelling

A standard possibility of the dynamical modelling of rotating bodies is based on the finite element method considering one-dimensional Euler-Bernoulli or Timoshenko beams. The models respect continuous mass of rotating shafts and possible effects of lumped masses such as disks, gear wheels, etc. The mathematical model is derived in the form of the second order ordinary differential equation

$$\mathbf{M}_S \cdot \ddot{\mathbf{q}}_S(t) + (\mathbf{B}_S + \omega_0 \cdot \mathbf{G}_S) \cdot \dot{\mathbf{q}}_S(t) + \mathbf{K}_S \cdot \mathbf{q}_S(t) = \mathbf{f}_E + \mathbf{f}_B, \quad (1)$$

where  $\mathbf{M}_S$  is the shaft mass matrix,  $\mathbf{B}_S$  is the damping matrix,  $\omega_0 \cdot \mathbf{G}_S$  represents gyroscopic effects,  $\mathbf{K}_S$  is the shaft stiffness matrix,  $\mathbf{f}_E$  is the general vector of external forces and  $\mathbf{f}_B$  is the vector representing bearing forces, which will be described in next chapter. The whole mathematical model is derived in the configuration space defined by the vector of generalized coordinates of the shaft denoted as  $\mathbf{q}_S(t)$ .

### 2.2. Approaches based on multibody dynamics

Another possibility is the utilization of approaches based on the multibody dynamics. Vibrations and global motion of each flexible body are described by a system of differential algebraic equations (DAE) defined by Offner (2011) in the form

$$\begin{aligned} \mathbf{M} \cdot \dot{\mathbf{v}} + \mathbf{f}^{rbAcc}(\mathbf{s}, \dot{\mathbf{s}}) &= \mathbf{f}^{gyros}(\mathbf{s}) + \mathbf{f}^j(\mathbf{s}, \mathbf{w}) + \mathbf{f}^e(\mathbf{s}) - (\alpha_1 \cdot \mathbf{M} + \alpha_2 \cdot \mathbf{K}) \cdot \mathbf{v} - \mathbf{K} \cdot \mathbf{q}, \\ \dot{\mathbf{q}} &= \mathbf{v}, \\ \dot{\mathbf{x}}_B &= \mathbf{v}_B, \\ \mathbf{S}(\boldsymbol{\theta}_B) \cdot \dot{\boldsymbol{\theta}}_B &= \boldsymbol{\omega}, \\ \boldsymbol{\theta}_B^T \cdot \boldsymbol{\theta}_B &= 1, \\ r(\mathbf{q}) &= 0, \end{aligned} \quad (2)$$

where  $\mathbf{s} = [\mathbf{x}_B^T, \boldsymbol{\theta}_B^T, \dot{\mathbf{x}}_B^T, \boldsymbol{\Omega}_B^T, \mathbf{q}^T, \dot{\mathbf{q}}^T]^T$  is the state vector, which includes vector  $\mathbf{x}_B \in \mathcal{R}^3$  and quaternion  $\boldsymbol{\theta}_B \in \mathcal{R}^4$  defining the position and the orientation of the body's relative coordinate system. Vectors  $\dot{\mathbf{x}}_B \in \mathcal{R}^3$  and  $\boldsymbol{\Omega}_B \in \mathcal{R}^3$  hold translational and rotational velocities of the body's relative system, and  $\mathbf{q} \in \mathcal{R}^N$  is the generalized displacement vector, which covers elastic deformations. Diagonal mass matrix  $\mathbf{M}$ , symmetric stiffness matrix  $\mathbf{K}$  and symmetric damping matrix  $\mathbf{D} = \alpha_1 \cdot \mathbf{M} + \alpha_2 \cdot \mathbf{K}$  are constant in time due to the formulation with respect to the body's relative system.  $\alpha_1$  and  $\alpha_2$  are the coefficients of proportional (Rayleigh) damping.

Vectors  $\mathbf{f}^{gyros}(\mathbf{s}) \in \mathcal{R}^{6 \cdot N}$  and  $\mathbf{f}^{rbAcc}(\mathbf{s}, \dot{\mathbf{s}}) \in \mathcal{R}^{6 \cdot N}$  are forces resulting from gyroscopic effects and rigid body accelerations,  $\mathbf{f}^j(\mathbf{s}, \mathbf{w}) \in \mathcal{R}^{6 \cdot N}$  is the vector of joint and contact forces dependant on state vector  $\mathbf{s}$  of the modelled body and state vectors of all coupled bodies combined in  $\mathbf{w}$ , and  $\mathbf{f}^e(\mathbf{s}) \in \mathcal{R}^{6 \cdot N}$  is the vector of external loads. Further details are discussed by Offner (2011).

### 3. Modelling of journal bearings

The supports of rotating systems can be realized using journal bearings. Elasto-hydrodynamic forces acting in radial journal bearings are computed from bearing loads  $W$ , which can be expressed as an integral of oil pressure  $p = p(x, z, t)$  over bearing surface  $A$  showed by Stachowiak and Batchelor (2014) in the form

$$W = - \iint_{(A)} \cos x \cdot p(x, z) dx dz, \quad (3)$$

where  $x$  and  $z$  are circumferential and axial coordinates in a coordinate frame fixed to a bearing shell, where the origin of circumferential coordinate  $x$  is located on the upper point of the shell. Hydrodynamic oil pressure  $p$  is computed employing modified averaged Reynolds equation defined by Offner (2013) in the form

$$\frac{\partial}{\partial x} \left( \frac{\phi_x \cdot \theta \cdot h^3}{12 \cdot \eta} \cdot \frac{\partial p}{\partial x} \right) + \frac{\partial}{\partial z} \left( \frac{\phi_z \cdot \theta \cdot h^3}{12 \cdot \eta} \cdot \frac{\partial p}{\partial z} \right) = \frac{u_j - u_s}{2} \cdot \frac{\partial [\theta \cdot (h_T + \sigma_c \cdot \phi_s)]}{\partial x} + \frac{\partial (\theta \cdot h_T)}{\partial t}, \quad (4)$$

where  $h = h(x, z, t)$  represents a nominal clearance gap between the shell and the journal,  $h_T = h_T(x, z, t)$  is the total clearance gap including surface roughness,  $\theta = \theta(x, z, t)$  is the fill ratio, i.e. percentage of gap  $h$  filled with oil, and  $\eta$  is the dynamic viscosity of oil. Stoke's sticking condition in  $x$  direction are considered in equation (4) with boundary conditions  $u_j$  and  $u_s$  being circumferential velocities of the journal and the shell. Couette flow factors  $\phi_x$ ,  $\phi_z$  and shear flow factor  $\phi_s$  (Prat et al., 2002) and composite roughness  $\sigma_c$  (Greenwood and Tripp, 1970) are also considered. Equation (4) should be solved for pressure  $p$  in lubrication regions and for  $\theta$  in cavitation regions. Once the film pressure distribution is obtained, the elasto-hydrodynamic forces acting on the system components can be expressed by integrating hydrodynamic pressure  $p$  over the bearing inner surface.

### 4. Consideration of limit interaction

There are certain limit cases that could be considered in the rotor-bearing interaction. Majority of such effects is related to the variations of the clearance gap and consequent changes of force effects during a bearing operation. It comprises modifications or alternative solutions of the Reynolds equation or additional contact and friction influences.

Surface roughness starts to play an important role in the system response (Lin, 2012; Bhaskar et al., 2013; Li et al., 2015). Wear occurs when contact of surfaces is direct. Wear and thus change of geometry further influence behavior of the system (Papadopoulos et al., 2008; Machado and Cavalca, 2015). Direct contact may also trigger another instability called dry whip that may lead to a machine catastrophic failure. Moreover, a rotor-to-stator rubbing changes significantly the dynamic characteristics of the system (Ma et al., 2015; Xiang et al., 2015).

### 5. Conclusions

Mathematical modelling of rotating systems supported by journal bearings is still a big issue and dynamical analysis of these systems brings interesting findings. Approaches to the modelling of rotating shafts based on the finite element method and on the multibody system dynamics are summarized in this paper. Fluid film bearing models are mainly related to the Reynolds equation of various modifications. The models considering the limit behaviour operate with surface roughness, contact interaction, friction effects, etc.

### Acknowledgement

The paper has originated in the framework of solving the project of the Czech Science Foundation No. 17-15915S entitled "Nonlinear dynamics of rotating systems considering fluid film instabilities with the emphasis on local effects".



## References

- Adiletta, G., Mancusi, E. and Strano, S. (2011) Nonlinear behaviour analysis of a rotor on two-lobe wave journal bearings. *Tribology International*, 44, 2, pp. 42-54.
- Amamou, A. and Chouchane, M. (2014) Nonlinear stability analysis of long hydrodynamic journal bearings using numerical continuation. *Mechanism and Machine Theory*, 72, pp. 17-24.
- Bhaskar, S.U., Hussain, M.M. and Ali, M.Y. (2013) Stability analysis on plain journal bearing with effect of surface roughness. *International Journal of Scientific & Engineering Research*, 4, 3, pp. 1-8.
- Boyaci, A., Seeman, W. and Proppe, C. (2010) Stability and bifurcations of rotors in fluid film bearings. *Proceedings in Applied Mathematics and Mechanics*, 10, 1, pp. 235-236.
- Cole, J.A. and Hughes, C.J. (1956) Oil flow and film extent in complete journal bearings. *Proceedings of the Institution of Mechanical Engineers*, 170, 1, pp. 499-510.
- De Castro, H.F., Cavalca, K.L. and Nordmann, R. (2008) Whirl and whip instabilities in rotor-bearing system considering a nonlinear force model. *Journal of Sound and Vibration*, 317, 1-2, pp. 273-293.
- Greenwood, J.A. and Tripp, J.H. (1970) The contact of two nominally flat rough surfaces. *Proceedings of the Institution of Mechanical Engineers*, 185, pp. 625-633.
- Hori, Y. (1959) A Theory of oil whip. *ASME Journal of Applied Mechanics*, 26, 2, pp. 189-198.
- Laha, S.K. and Kakoty, S.K. (2011) Nonlinear dynamic analysis of a flexible rotor supported on porous oil journal bearings. *Communications in Nonlinear Science and Numerical Simulation*, 16, 3, pp. 1617-1631.
- Li, Y.-H., Yu, X.-D., Li, C. and Meng, X.-L. (2011) Study of Monitoring for Oil Film Thickness of Elastic Metallic Plastic Pad Thrust Bearing. *Advanced Design and Manufacture III*, 450, pp. 239-242.
- Lin, J.-R. (2012) The surface roughness effects of transverse patterns on the Hopf bifurcation behaviors of short journal bearings. *Industrial Lubrication and Tribology*, 64, 5, pp. 265-270.
- Lund, J.W. (1967) Oil whip whirl orbit of a rotor in sleeve bearings. *ASME Journal of Engineering for Industry*, 89, 4, pp. 813-823.
- Ma, H., Zhao, Q., Zhao, X., Han, Q. and Wen, B. (2015) Dynamic characteristics analysis of a rotor-stator system under different rubbing forms. *Applied Mathematical Modelling*, 39, 8, pp. 2392-2408.
- Machado, T.H. and Cavalca, K.L. (2015) Modeling of hydrodynamic bearing wear in rotor-bearing systems. *Mechanics Research Communications*, 69, pp. 15-23.
- Meyers, C.J. (1986) Bifurcation theory applied to oil whirl in plain cylindrical journal bearings. *ASME Journal of Applied Mechanics*, 51, 2, pp. 244-250.
- Newkirk, B.L. and Taylor, H. (1925) Shaft whipping due to ill action in journal bearings. *General Electric Review*, 28, 8, pp. 559-568.
- Offner, G. (2011) Modelling of condensed flexible bodies considering non-linear inertia effects resulting from gross motions. *Proceedings of the Institution of Mechanical Engineers, Part K: Journal of Multi-body Dynamics*, 225, 3, pp. 204-219.
- Offner, G. (2013) Friction power loss simulation of internal combustion engines considering mixed lubricated radial slider, axial slider and piston to liner contacts. *Tribology Transactions*, 56, 3, pp. 505-515.
- Papadopoulos, Ch.A., Nikolakopoulos, P.G. and Gounaris, G.D. (2008) Identification of clearances and stability analysis for a rotor-journal bearing system. *Mechanism and Machine Theory*, 43, 4, pp. 411-426.
- Prat, M., Plouraboué, F. and Letalleur, N. (2002) Averaged Reynolds equation for flows between rough surfaces in sliding motion. *Transport in Porous Media*, 48, 3, pp. 291-313.
- Stachowiak, G.W. and Batchelor, A.W. (2014) *Engineering Tribology*. 4th ed. Butterworth-Heinemann, St. Louis.
- Xiang, L., Hu, A., Hou, L., Xiong, Y. and Xing, J. (2016) Nonlinear coupled dynamics of an asymmetric double-disc rotor-bearing system under rub-impact and oil-film forces. *Applied Mathematical Modelling*, 40, 7-8, pp. 4505-4523.

## GUST ALLEVIATION OF NASA COMMON RESEARCH MODEL USING CFD

A. Prachař\*, P. Hospodář\*\*, P. Vrchota\*\*\*

**Abstract:** This paper presents a CFD study of a typical commercial aircraft entering the gust. The NASA Common Research model of an airliner is used as the baseline configuration. The gust model is based on adding artificial gust velocities into the governing equations, this method is usually referred to as Disturbance Velocity Approach. A series of gusts is used to measure response of the aircraft and to establish dynamic gust model. The movable control surfaces are defined and their efficiency is assessed by the CFD using the mesh deformation technique in the unsteady simulation. Finally, the dynamic model based on both the gust data on one hand and on the control surfaces action on the other hand is used to prescribe movement of the control surfaces with the aim to alleviate the gust interaction. The required time response of the control surfaces is studied to clarify limits of this alleviation technique.

**Keywords:** CFD, Gust response, Active control surfaces, NASA Common Research Model.

### 1. Introduction

The gust, as a sudden and unpredictable disturbance of the airflow relative to the flight path, is source of potential troubles. Besides compromising passenger comfort, the gusts also cause severe problems for aircraft stability, control, and introduce additional force exerted on the airframe. Therefore, gust alleviation methods come to play. The idea behind this paper is to use aircraft's control surfaces to counteract the gust input and to develop rules for the controls action based on the gust evaluation and identification.

The requirement for the aircraft to handle gusts is part of the certification process and is covered in detail in relevant regulations, as EASA (2007). Both vertical (positive and negative) and lateral gusts have to be considered. The gust profile is given by the '1-cosine' shape with gradient distance between 9 to 107 meters and amplitude (maximum perpendicular velocity deviation) depending on the aircraft weight parameters and flight altitude.

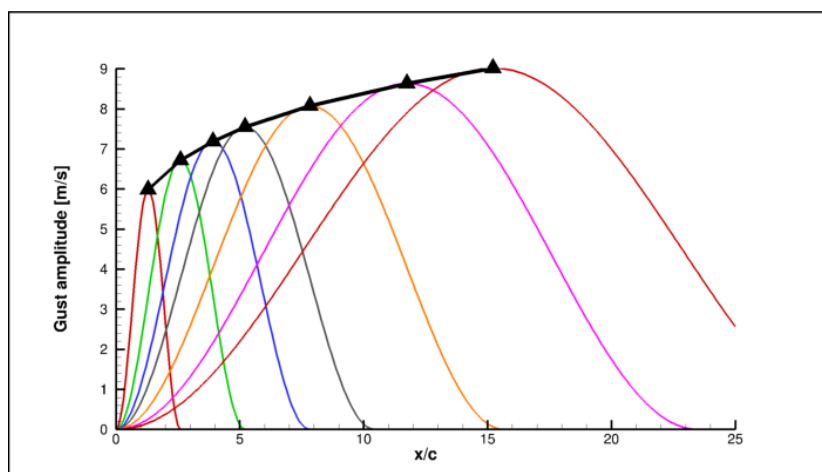


Fig. 1: Gust shapes in the required range.

\* RNDr. Aleš Prachař, PhD.: Výzkumný a zkušební letecký ústav, Beranových 130, 199 05, Prague; CZ, prachar@vzlu.cz

\*\* Ing. Pavel Hospodář: Výzkumný a zkušební letecký ústav, Beranových 130, 199 05, Prague; CZ, hospodar@vzlu.cz

\*\*\* Ing. Petr Vrchota, PhD.: Výzkumný a zkušební letecký ústav, Beranových 130, 199 05, Prague; CZ, vrchota@vzlu.cz

Fig. 1 shows example of gust shapes and amplitude envelope required by the regulations, relative to the scale of the aircraft wing chord. We are focusing on upward vertical gusts, because they introduce additional stresses to the already loaded structure of the aircraft's main wing. On the other hand, the wing is equipped with number of control surfaces that can be used to act against the gust input.

The computational geometry used throughout this paper is the NASA Common Research Model (CRM) described by Vassberg et al. (2008), which consists of a contemporary supercritical transonic wing and a fuselage that is representative of a widebody commercial transport aircraft. The CRM is designed for a cruise Mach number  $M = 0.85$  and a corresponding design lift coefficient  $C_L = 0.5$ . These conditions were used in our calculations. The CRM is widely used for various Computational Fluid Dynamics (CFD) studies, and it is also used for code evaluation during the Drag Prediction Workshops (Eliasson et al., 2013).

The Edge (Eliasson, 2002) is the CFD code used for the presented simulations. All the simulations are carried out as unsteady RANS with EARSM turbulence model. The gust model implemented in the solver is based on the Disturbance Velocity Approach validated among others by Heinrich (2014). For example, the continuity equation includes the contribution from the gust velocity,

$$\frac{d}{dt} \int_V \rho dV - \oint_S \rho (\mathbf{v} - \mathbf{v}_b - \mathbf{v}_g) \cdot \mathbf{n} ds = 0, \quad (1)$$

where  $\mathbf{v}_b$  is the velocity of boundary of the control volume and  $\mathbf{v}_g$  is the gust velocity. The advantage of this approach is that it can be used on standard CFD grids with no special requirements on the resolution in the far field. The mesh deformation technique was used to simulate movement of the control surfaces which are used to alleviate the gust. The obtained data from gust response and control surfaces effect are processed in MATLAB. The dynamic systems are identified and feed-forward law is designed to prescribe control surfaces movement to counteract the gust effect.

## 2. Gust response identification

To create dynamic model of the gust a series of CFD calculations was carried out for the selected gusts within the required range (Fig. 1). The response of the aircraft was evaluated and decomposed to individual parts; main wing, horizontal tail plane (HTP) and fuselage. It was observed that this decomposition plays important role in gust identification. The transport delay between gust acting on the main wing and on the HTP is clearly visible for shortest gust, as Fig. 2 shows. While HTP contribution to  $C_L$  is minor, the pitching moment  $C_M$  augmentation is more significant due to long moment arm. As we can see, while gust amplitude varies by at most 30 %, the  $C_L$  increments by a factor of 4 in the prescribed gust length range. There is an interesting  $C_M$  dependence with maximum deviation at medium-length gusts which is due to the gust interaction with the fuselage.

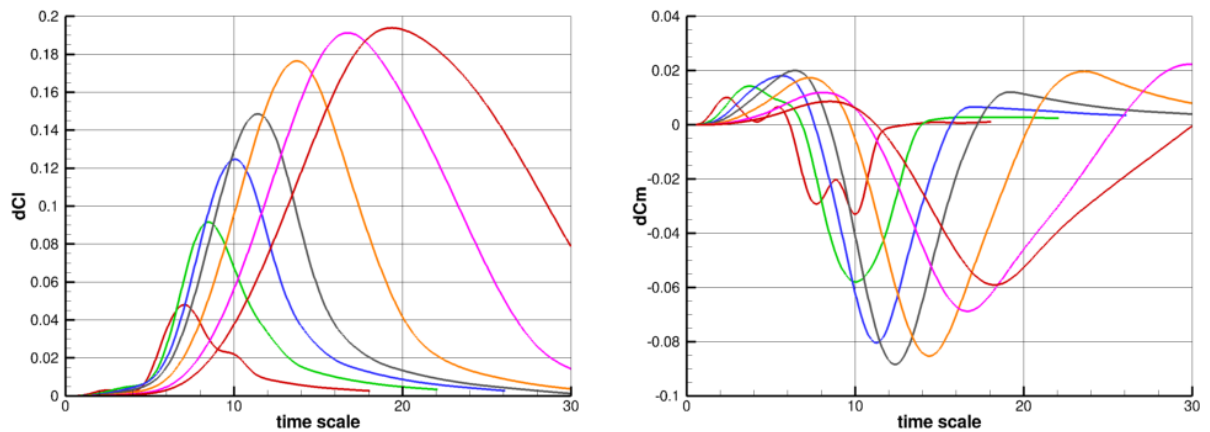


Fig. 2: Dynamic response of the gust. Deviation of  $C_L$  and  $C_M$ .

## 3. Control surfaces and gust alleviation

A set of control surfaces was defined on the airplane model, see Fig. 3. In the real-world application we anticipate that flaperon, aileron and spoilers should be used. However, in CFD calculation the spoiler

deployment is very demanding and, hence, this contribution is modeled by additional trailing edge devices similar to ailerons. The '1-cosine' input to the control surfaces was prescribed and the response was evaluated.

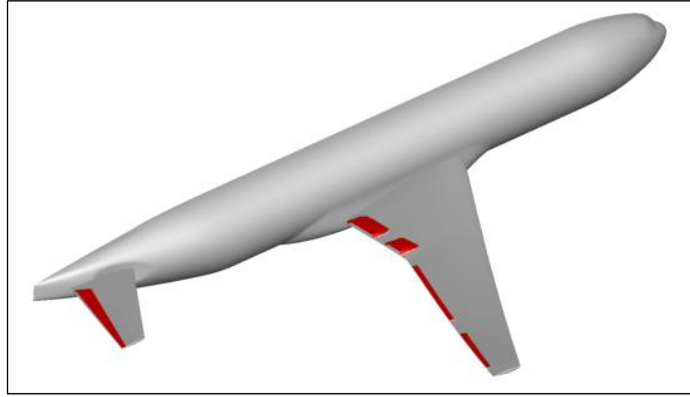


Fig. 3: NASA Common Research model with defined control surfaces (red). Control surfaces on the inboard and middle section simulate the effect of spoilers.

The obtained data served as a basis to set up control laws to prescribe control surfaces movement based on measured gust, identified as the change in the angle of attack. Both systems, gust response and controls deflection, are identified using System Identification Toolbox in Matlab. Time delay in gust dynamics plays significant role in feed-forward control. It provides time slot to compute controls deflection. Dynamics of controls deflection (aileron, flaperon, spoilers) are identified together.

It was decided that that control surfaces of the main wing will be responsible for the alleviation of the  $C_L$  increment measured on the main wing and the role of HTP will be to reduce pitching moment  $C_M$  deviation. Several calculations were carried out to understand how the control surfaces on the wing influence flowfield near the HTP. It was observed that the movement of the control surfaces on the main wing in order to reduce  $C_L$  causes increased contribution to the  $C_L$  and  $C_M$  by the HTP. On the other hand, the elevator movement contributes to the total values only through the alteration of the flowfield on the HTP and on the rear section of the fuselage.

As mentioned above, control law is designed as feed-forward (Stevens, 1992). Gust alleviation has two targets in this case. The first one is to reduce gust effect on the wing ( $C_L$ ), second one to reduce total pitching moment ( $C_M$ ). Scheme of the control law is depicted in Fig. 4. Five dynamic systems are identified using Laplace transform. Wing controls and elevator deflections are described based on the control law scheme.

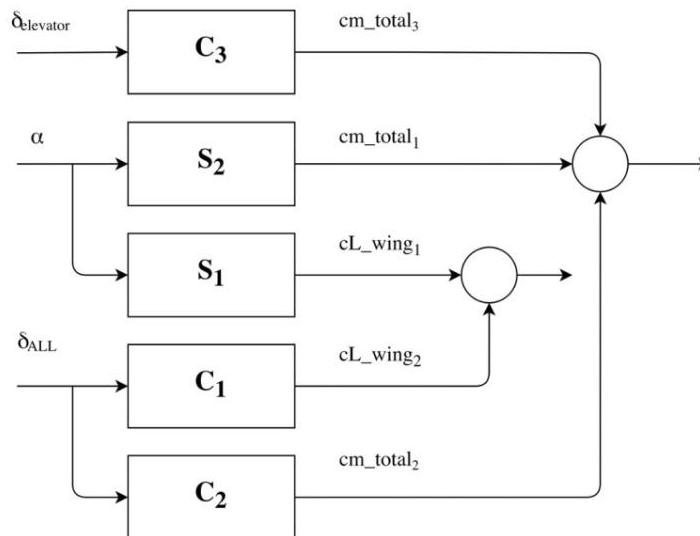


Fig. 4: Control laws diagram.

The described method was applied to the gust with medium length. Fig. 5 shows encouraging results as the maximum increment of  $C_L$  was reduced by approximately 85 % and the pitching moment by almost

90 %. It is worth to note that the control system used only a-priori information and no feedback from the course of the CFD computation with gust and active control surfaces was used. Such a feedback loop could further improve the results.

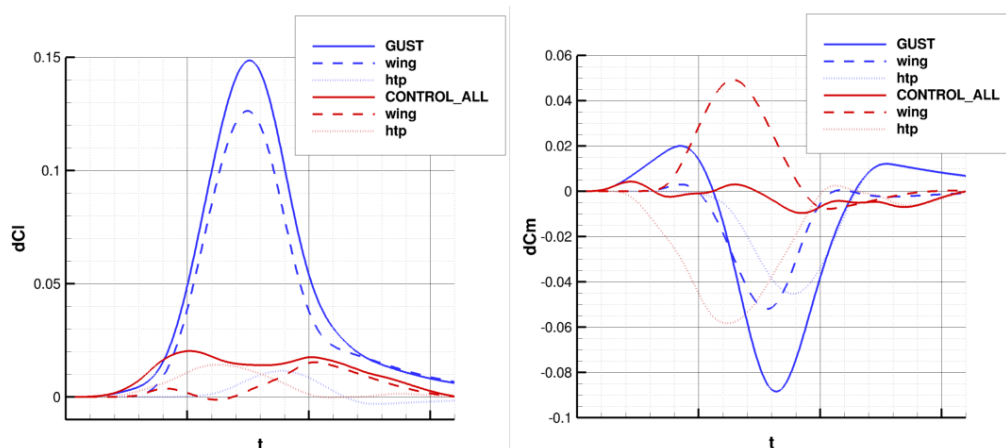


Fig. 5: Comparison of plain (blue) and controlled gust (red). Contributions from the main wing (dashed) and HTP (dotted) is displayed.

#### 4. Conclusions

Computation study of the gust alleviation using active control surfaces was presented. Although only forward control system was used, the maximum increment of the lift and pitching moment was reduced by the order of magnitude.

In the next step we plan to focus on the gust interaction with the flexible aircraft using decomposition to the normal modes, which was studied in our previous work (Vrchota et al., 2017). This aeroelastic coupling would provide additional information about, e.g., wing bend and twist caused by the gust. The combination of feed-forward and feedback control law could be used to minimize loading of the wing locally through the use of various control surfaces independently.

These results could be further generalized to produce Reduced-Order Model for the gust response, which was investigated by, e.g., Zaide et al. (2006).

#### Acknowledgement

This research was supported by The Ministry Industry and Trade of the Czech Republic for long term strategic development. Access to computing and storage facilities owned by parties and projects contributing to the National Grid Infrastructure MetaCentrum, provided under the programme "Projects of Large Infrastructure for Research, Development, and Innovations" (LM2010005), is greatly appreciated.

#### References

- EASA (2007) Certification Specifications for Large Aeroplanes (CS-25). Amendment 3, European Aviation Safety Agency, September 2007.
- Eliasson, P. (2002) Edge, a Navier-Stokes solver for unstructured grids, in Proceedings to Finite Volumes for Complex Applications III., pp. 527-534. ISTE Ltd., London.
- Eliasson, P., Peng, S.-H. and Tysell, L. (2013) Computations from the fourth drag prediction workshop using the Edge solver. Journal of Aircraft, 50, 5, pp. 1646-1655.
- Heinrich, R. and Reimer, L. (2014) Simulation of Interaction of Aircraft and Gust Using the TAU-Code, in: New Results in Numerical and Experimental Fluid Mechanics IX, Springer.
- Stevens, B.I. and Lewis, F.L. (1992) Aircraft Control and Simulation. John Wiley and Sons, ISBN 0471613975.
- Vassberg, J.C., DeHaan, M.A., Rivers, M.B. and Wahls, M.S. (2008) Development of a Common Research Model for Applied CFD Validation Studies, AIAA Paper 2008-6919.
- Vrchota, P., Prachar, A. and Šmíd, M. (2017) Improvement of Computational Results of NASA Common Research Model by Modal Analysis, Journal of Aircraft (accepted).
- Zaide, A. and Raveh, D.E. (2006) Numerical Simulation and Reduced-Order Modeling of Airfoil Gust Response, AIAA Journal, 44, 8, pp. 1826-1834.

## INFLUENCE OF AN INITIAL IMPERFECTION ON THE LATERAL AND TORSIONAL BUCKLING OF A HYBRID BEAM

I. Pravdová\*, M. Eliášová\*\*

**Abstract:** Glass has grown in importance in modern architecture because of its transparency. Various types of hybrid structures, consisting of glass and another material (e.g. timber, concrete, steel), are analyzed to ensure optimal structural interaction between the two materials. Hybrid steel–glass beams can also be used as vertical elements – as supporting fins for glass facades. Wind suction then becomes a source of instability of the beams because the compressed side is unsupported. Initial geometric imperfections can significantly influence the stability response of hybrid beams. This paper deals with measurements of the imperfections of hybrid steel–glass beams, and reports on a numerical investigation into the effect of imperfections on the behavior of simply supported hybrid beams subjected to four-point bending.

**Keywords:** Imperfection, Hybrid beam, Glass, Lateral and torsional buckling, Critical moment.

### 1. Introduction

In practice, real beams are not perfectly straight. Geometric imperfections have a significant effect on their behavior and strength. Lateral and torsional buckling is a crucial problem of glass beams, particularly in the case of vertical glass structural elements that support facades, (Luible, 2005), (Belis, 2007), (Kasper, 2007). Geometric imperfections can be divided into two categories: global imperfections and local imperfections.

Global geometric imperfections vary according to the type of glass. It is known that annealed glass has very low initial deformation ( $< L / 2500$ , where  $L$  is the length of the beam). However, tempered glass has higher initial deformation up to  $L / 300$ . This is caused by the production process for tempered glass, which is warmed up  $650\text{ }^{\circ}\text{C}$  and then rapidly cooled. During this process the glass panes are placed on rollers, which cause a sinusoidal initial deformation.

Local imperfections occur when the cross-section deviates from its ideal shape.

This paper describes measurements of the initial imperfections of a steel–glass beam, and shows the effect of a geometric imperfection on the behavior of the beam in a numerical model.

### 2. Hybrid steel–glass beams

Research in progress at the Faculty of Civil Engineering, CTU in Prague, is focused on an experimental investigation of lateral and torsional buckling of hybrid steel–glass beams. The beams were 4.75 m in length and consisted of a 10 mm thick glass web and steel grade S235 flanges with dimensions of  $40 \times 8$  mm. Direct connections between steel and glass were realized by a 3 mm thick layer of 2-component SikaFast-5215 NT acrylate adhesive (Pravdová, 2016).

Three hybrid beam experiments were performed in 2016. The beams were simply supported with a 4500 mm span, and were subjected to a four-point bending test. The load introducing points were 2900 mm apart. Lateral supports were arranged at the load introducing points. The beams were loaded by controlling the force value until total collapse. Horizontal displacements were measured in the mid-span

---

\* Ing. Iva Pravdová: Czech Technical University in Prague, Faculty of Civil Engineering, Thákurova 2077/7; 160 00, Prague; CZ, iva.pravdova@fsv.cvut.cz

\*\* Assoc. Prof. Ing. Martina Eliášová, CSc.: Czech Technical University in Prague, Faculty of Civil Engineering, Thákurova 2077/7; 160 00, Prague; CZ, eliasova@fsv.cvut.cz



and close to the supports. Buckling of the hybrid beam before collapse is shown in Fig. 1. The image was taken by a high-frequency camera that recorded the experiments.



*Fig. 1: Buckling of the hybrid steel-glass beam.*

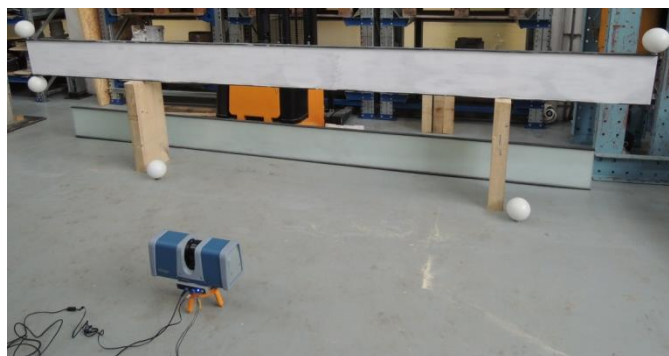
### **3. Measurements of initial imperfections**

Geometrical imperfections (both local and global) of the steel-glass beams were measured using a laser scanning method. To enable the laser scanning method to be used on a hybrid steel-glass beam, it was first necessary to apply white paint to the glass web.

The Surphaser 25HSX accurate laser scanning system was used on two standpoints in order to scan both the upper flange and the lower flange of the beams, see Fig. 2 and Fig. 3. Subsequently, the scans were transformed to the unique coordinate system using identical points, which were formed by white spheres 145 mm in diameter. The spheres were fixed on the steel flanges by a magnetic pad.

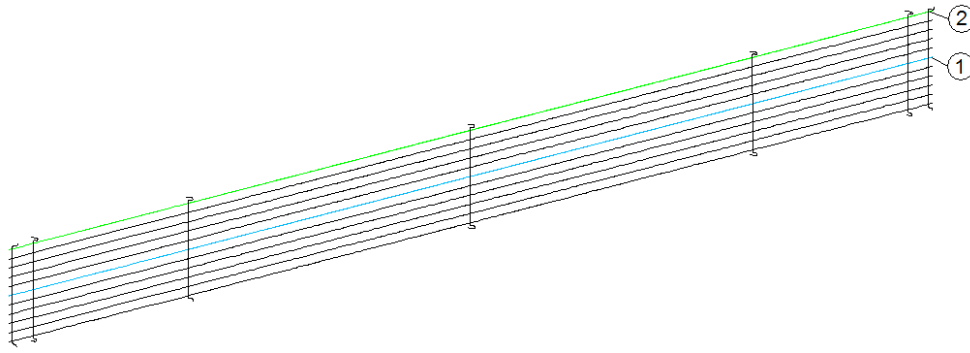


*Fig. 2: Laser scanning, first standpoint.*



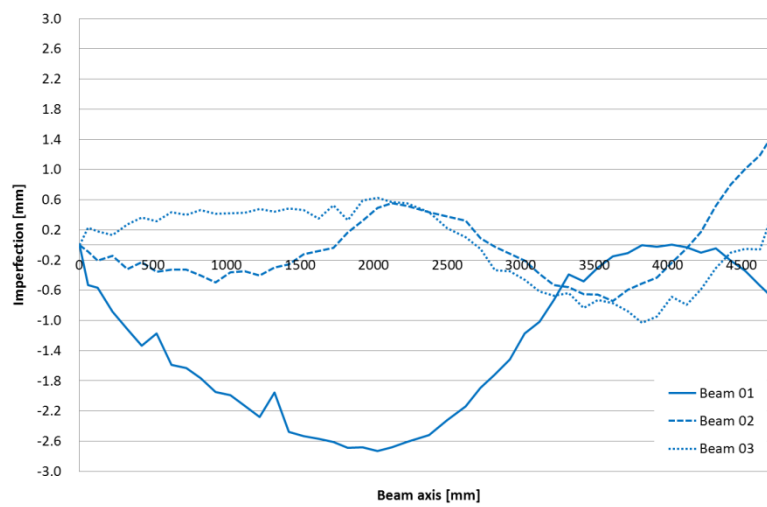
*Fig. 3: Laser scanning, second standpoint.*

The laser scanning system creates a model of the point cloud, and finally the horizontal and vertical sections are obtained. Fig. 4 shows the horizontal and vertical sections of the beams. The first horizontal line is placed in the middle of the cross-section, while the second horizontal line is from the top part of the glass web.

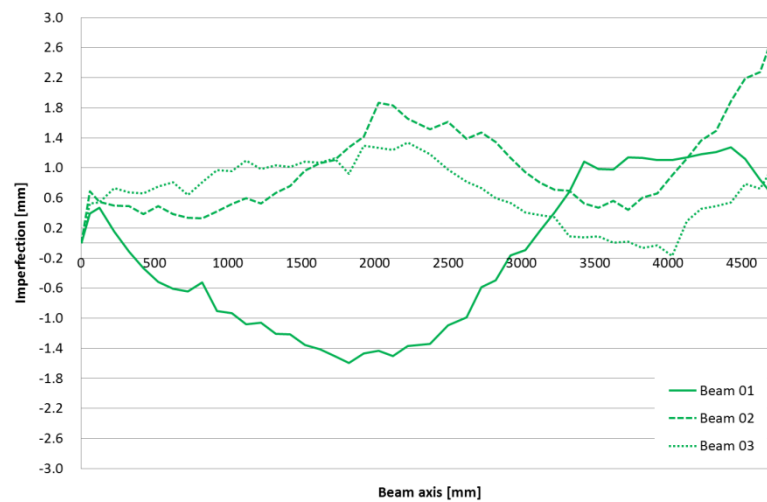


*Fig. 4: Horizontal and vertical sections of the hybrid beam.*

Fig. 5 and Fig. 6 illustrate the first and second horizontal sections of three beams. It is worth mentioning that the maximum imperfection of the glass web was very small ( $< L / 1500$ ), although thermally toughened glass was used.



*Fig. 5: Imperfections from the first horizontal section.*



*Fig. 6: Imperfections from the second horizontal section.*

#### 4. Numerical models of a hybrid steel-glass beam

Numerical models were created in RFEM 5.05 software using surface elements. Material models of glass, steel and adhesive were defined as isotropic linear elastic. Large deformation analysis was applied.

The initial imperfection has a significant influence on the lateral and torsional stability of hybrid beams. This imperfection was taken into account to obtain conformity between the numerical model and the experimental results. A geometrical imperfection was introduced into the model in a sinusoidal waveform of the beam with different amplitudes.

A comparison of the FE calculation with experimental results is shown in Fig. 7. Both numerical models, without imperfections and with imperfections with an amplitude of geometrical imperfections  $L / 3600$  ( $a = 1.25$  mm),  $L / 1800$  ( $a = 2.5$  mm),  $L / 400$  ( $a = 11.25$  mm), were analyzed by FEM. It can be observed that the numerical model with amplitude of geometrical imperfection  $L / 1800$  corresponds to hybrid beam 03.

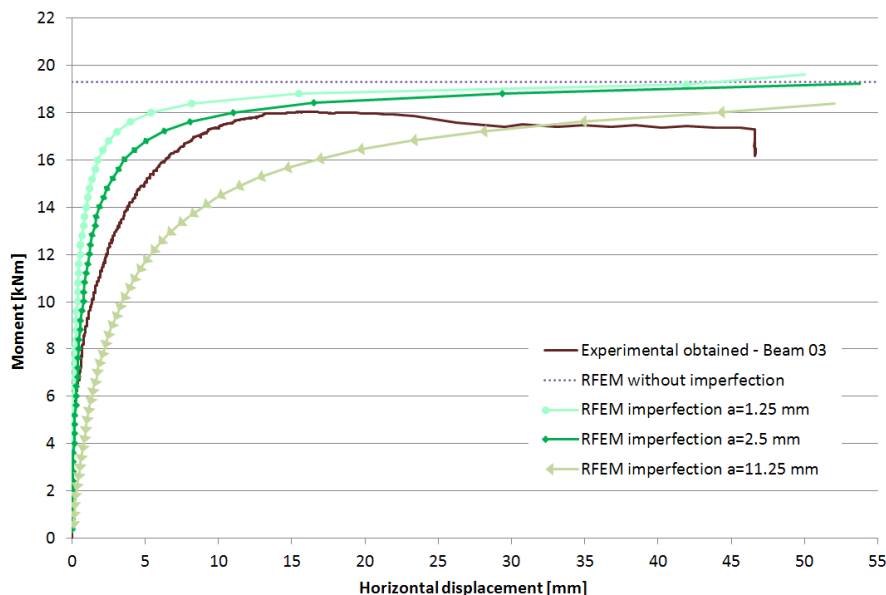


Fig. 7: Dependence of moment and horizontal displacement in the middle of the beam.

## 5. Conclusions

The lateral and torsional stability of steel-glass beams were investigated by a set of experiments. Beams were simply supported and subjected to a four-point bending test. Before the experiments, geometrical imperfections were measured by the Surphaser 25HSX laser scanning system on two standpoints. Horizontal and vertical sections of the beams were created, and the imperfections of all beams were read.

A numerical model of the beam was verified by the experimental results. Significant influence of the initial imperfection on the buckling of the beam was demonstrated by the numerical model. The results of a numerical analysis that fails to introduce the initial imperfection could be on the unsafe side.

## Acknowledgement

This paper was written with support from GAČR project No. 16-17461S. We gratefully acknowledge Dlubal Software, which provided the RFEM 5.05 software that was used for the calculations.

## References

- Luible, A. and Crisinel, M. (2005) Stability of Load Carrying Elements of Glass. Proceedings of the Conference Eurosteel 2005, Maastricht.
- Belis, J. and Van Impe, R. (2007) Buckling-related Problems of Glass Beams. Glass & Interactive Building Envelopes, Final Report EU COST C13, IOS Press, pp. 169-176.
- Kasper, R. and Sedlacek, G. (2007) Stability of Laminated Glass Beams. Glass & Interactive Building Envelopes, Final Report EU COST C13, IOS Press, pp. 177-187.
- Pravdová, I. and Eliášová, M. (2016) Lateral and torsional stability of hybrid steel-glass beams. Proceedings of the 3rd International Conference on Structures and Architecture (ICSA2016), CRC Press/Balkema., pp. 1029-1035. ISBN 978-1-138-02651-3.

## ON THE ENERGY RELEASE RATE OF THE CRACK EMANATING FROM THE INCLUSION INTERPHASE

T. Profant<sup>\*</sup>, M. Hrstka<sup>\*\*</sup>, J. Klusák<sup>\*\*\*</sup>, Z. Keršner<sup>\*\*\*\*</sup>

**Abstract:** *The problem of the crack emanating from the interphase region of the circular inclusion is investigated. The problem combines an application of dislocation distribution technique for a crack modelling and the method of boundary integral equations to approximate the loading along the boundary of the domain containing an inclusion. The topological derivative method provides the combination of both approaches and results to the evaluation of the energy release rate of the arbitrary oriented microcrack emanating from the inclusion and matrix interphase. The fundamental solution intended to the boundary integral method such as the continuously distributed dislocation technique is based on the application of Muschelishvili complex potentials in the form of the Laurent series. The coefficients of the series are evaluated from the compatibility conditions along the interfaces of inclusion, interface and matrix.*

**Keywords:** Microcrack, Inclusion, Interphase, Singular integral equation, Dislocation distribution technique, Complex potentials.

### 1. Introduction

The paper takes on the scheme of the energy release rate  $G$  associated with a finite small crack initiation at any boundary location based on the topological derivative method, Silva et al. (2011). It is supposed that the crack is initiated and emanating from the interface region between the inclusion and arbitrarily loaded finite matrix in the studied problem. The crack initiation from some tip of the sharp shaped inclusion can be appeared in the silicate-based composites. The applied simplified mathematical model can be used to study the influence of the material mismatch of the inclusion/matrix interphase to the fracture toughness of this composite even that the mathematical simplification suppresses the sharpness of the inclusion. The topological derivative field indicates the variation of a response functional when an infinitesimal hole is introduced in the body. The response functional is the total potential energy in the discussed problem. The kernel of the mathematical scheme is the fundamental solution of the unit point force or edge dislocation interacting with an inclusion and an interphase, Cheeseman et al. (2001). This fundamental solution is applied to the approximation of the loaded boundary of the finite uncracked matrix containing an inclusion such as to model the crack. There is many ways to model the uncracked matrix with the inclusion and its interphase. The most common tool is the finite element method, but due to the modesty of the external domain shape and the emphasis on the influence of the inclusion interphase on the near stress distribution along the inclusion in the matrix, the boundary integral method was used. The boundary integral method allows one to rather precise evaluate the stress and strain distribution in the matrix near the inclusion interphase independently of the quality of the domain and especially thin interphase mesh. The second application of the bellow mentioned fundamental solution is the crack model via the continuously distributed dislocation technique, Hills et al. (1996). The condition that the crack faces have to be stress free, the continuously distributed dislocations technique leads to the solution of the integral equation with the Cauchy type singular kernel. The advantage of this method is the simply evaluation of the stress intensity factor of the crack as the limiting value of Jacobi polynomials which are

---

<sup>\*</sup> Assoc. Prof. Tomáš Profant, PhD.: Institute of Solid Mechanics, Mechatronics and Biomechanics, Brno University of Technology; Technická 2896/2, 616 69, Brno; CZ, profant@fme.vutbr.cz

<sup>\*\*</sup> Ing. Miroslav Hrstka: Institute of Solid Mechanics, Mechatronics and Biomechanics, Brno University of Technology; Technická 2896/2, 616 69, Brno; CZ, hrstka@fme.vutbr.cz

<sup>\*\*\*</sup> Assoc. Prof. Jan Klusák, PhD.: Institute of Physics of Materials; Žitkova 22, 616 62, Brno; CZ, klusak@ipm.cz

<sup>\*\*\*\*</sup> Prof. Zbyněk Keršner, PhD.: Institute of Structural Mechanics, Brno University of Technology; Veveří 95, 66237, Brno; CZ, kersner.z@fce.vutbr.cz

used to interpolate the continuous array of dislocations along the crack. The asymptotic analysis combines both solutions, i.e. the non-cracked finite domain and cracked infinite domain. It is based on the stress composite expansion, evaluating of the energy momentum tensor and approximation of the energy release rate for any crack size by means of topological derivative, Silva et al. (2011).

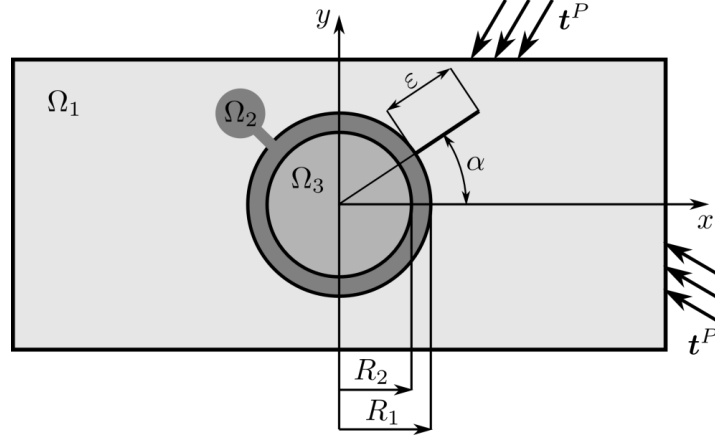


Fig. 1: The geometry of the studied problem.

## 2. Topological derivative for cracked body

It is known that the shape sensitivity of the total potential energy  $\psi$  with respect to crack length  $\varepsilon$  is given by the energy release rate, Silva et al. (2011),

$$G(\Omega_\varepsilon) = \frac{d}{d\varepsilon} \psi(\Omega_\varepsilon), \quad (1)$$

where the derivative is meant in the shape sense and  $\Omega_\varepsilon$  is the domain with a small crack in the matrix with boundary  $\partial\Omega_\varepsilon = \partial\Omega \cup \gamma_\varepsilon$  with  $\gamma_\varepsilon$  being the crack boundary and  $\partial\Omega = \bigcup_{i=1,2,3} \partial\Omega_i$ , where  $\partial\Omega_i$  are matrix and interface boundary between matrix or inclusion and their interphase, Fig. 1. Then the total potential energy is given by

$$\begin{aligned} \psi(\Omega_\varepsilon) = & \frac{1}{2} \int_{\Omega_\varepsilon} \nabla^s \mathbf{u}_\varepsilon : \mathbf{T}_\varepsilon dV - \int_{\partial\Omega_1} \mathbf{t}^P \cdot \mathbf{u}_{1\varepsilon} dS - \\ & - \int_{\partial\Omega_2} (\mathbf{T}_{1\varepsilon} \mathbf{n}_2 \cdot \mathbf{u}_{1\varepsilon} + \mathbf{T}_2 \mathbf{n}_2 \cdot \mathbf{u}_2) dS - \int_{\partial\Omega_3} (\mathbf{T}_2 \mathbf{n}_3 \cdot \mathbf{u}_2 + \mathbf{T}_3 \mathbf{n}_3 \cdot \mathbf{u}_3) dS. \end{aligned} \quad (2)$$

In the above the index  $\varepsilon$  denotes the response quantities evaluated on the crack domain,  $\mathbf{u}$  is the displacement vector,  $\nabla^s \mathbf{u} = \frac{1}{2} (\nabla \mathbf{u} + \nabla \mathbf{u}^T)$ ,  $\mathbf{T}$  is the symmetric Cauchy stress tensor and tractions  $\mathbf{t}^P$  are applied to the boundary  $\partial\Omega_1$ . The displacements and stress tensor satisfying the governing equations of the linear elasticity on the domain  $\Omega_\varepsilon$ ,

$$\text{div} \mathbf{T}_\varepsilon = 0 \text{ in } \Omega_\varepsilon, \mathbf{T}_{1\varepsilon} \mathbf{m} = 0 \text{ on } \gamma_\varepsilon, \mathbf{T}_{1\varepsilon} \mathbf{n}_1 = \mathbf{t}^P \text{ on } \partial\Omega_1, \quad (3)$$

$$\mathbf{T}_{1\varepsilon} \mathbf{n}_2 = -\mathbf{T}_2 \mathbf{n}_2 \wedge \mathbf{u}_{1\varepsilon} = \mathbf{u}_2 \text{ on } \partial\Omega_2, \mathbf{T}_2 \mathbf{n}_3 = -\mathbf{T}_3 \mathbf{n}_3 \wedge \mathbf{u}_2 = \mathbf{u}_3 \text{ on } \partial\Omega_3, \quad (4)$$

where  $\mathbf{m}$  and  $\mathbf{n}$  are the outward normal to  $\gamma_\varepsilon$  and  $\partial\Omega$ , respectively. The body forces are neglected and the crack faces are assumed to be traction free. The evaluation of the topological derivation (1) leads to the relation, e.g. Silva (2011),

$$J(\Sigma_\varepsilon) = -\frac{d}{d\varepsilon} \psi(\Omega_\varepsilon) = \lim_{r \rightarrow 0} \int_{B_r} \Sigma_\varepsilon \mathbf{n} \cdot \mathbf{e}_r dS, \quad (5)$$

where  $B_r$  is a ball of radius  $r$  centered at the crack tip,  $\mathbf{e}_r$  is a unit vector aligned with the crack and oriented in the crack growth direction and  $J(\Sigma_\varepsilon)$  is the  $J$ -integral joined with the energy momentum tensor  $\Sigma_\varepsilon$ .

## 3. Fundamental solution

The evaluation of the displacement and stress field at the crack tip depends on the knowledge of the fundamental solution, i.e. solution describing the interaction between the unit point force or dislocation

and the circular inclusion with thin interphase, see Cheeseman et al. (2001). The problem is formulated using Muskhelishvili complex potentials in the form of Laurent series,

$$\varphi_1(z) = \sum_{k=1}^{\infty} A_k z^k + \sum_{k=1}^{\infty} h_{-k} z^{-k}, \psi_1(z) = \sum_{k=1}^{\infty} B_k z^k + \sum_{k=1}^{\infty} p_{-k} z^{-k}, \quad (6)$$

$$\varphi_2(z) = \sum_{k=-\infty}^{\infty} q_k z^k, \psi_2(z) = \sum_{k=-\infty}^{\infty} r_k z^k, \quad (7)$$

$$\varphi_3(z) = \sum_{k=1}^{\infty} s_k z^k, \psi_3(z) = \sum_{k=1}^{\infty} t_k z^k, \quad (8)$$

where the coefficients  $A_k$  and  $B_k$  are known and account for the point force or dislocation singularity. The coefficients  $h_{-k}$ ,  $p_{-k}$ ,  $q_k$ ,  $r_k$ ,  $s_k$ ,  $t_k$  are evaluated from the compatibility conditions (4).

#### 4. Asymptotic analysis

Assuming the crack length  $\varepsilon$  is sufficiently small with respect to the inclusion size  $R_2$  the evaluation of the stress tensor  $\mathbf{T}_\varepsilon(\mathbf{x})$  at the crack tip and after that the energy momentum tensor  $\mathbf{\Sigma}_\varepsilon$  in (5) can be provided using the following stress composite expansion, Silva et al. (2011),

$$\mathbf{T}_\varepsilon(\mathbf{x}) = \mathbf{T}(\hat{\mathbf{x}}) + \tilde{\mathbf{T}}(\mathbf{y}) + O(\varepsilon), \quad (9)$$

where  $\hat{\mathbf{x}} \in \partial\Omega_2$  is reference point of matrix/interphase boundary from which the crack emanates and  $\mathbf{y} = \mathbf{x}/\varepsilon$  is the scaled position vector. The outer stress  $\mathbf{T}(\hat{\mathbf{x}})$  is evaluated along the crack position in the matrix without the crack and under the external load  $\mathbf{t}^P$ . The stress  $\mathbf{T}(\hat{\mathbf{x}})$  is observed from the Hooke's law and the displacement solution of the well-known boundary integral equations appearing in the boundary value problem, Brebbia et al. (1984),

$$c(\hat{\mathbf{x}})\mathbf{u}(\hat{\mathbf{x}}) + \int_{\partial\Omega_1} \mathbf{t}^*(\hat{\mathbf{x}}, \boldsymbol{\xi}) \cdot \mathbf{u}(\boldsymbol{\xi}) dS(\boldsymbol{\xi}) = \int_{\partial\Omega_1} \mathbf{u}^*(\hat{\mathbf{x}}, \boldsymbol{\xi}) \cdot \mathbf{t}^P(\boldsymbol{\xi}) dS(\boldsymbol{\xi}) \quad (10)$$

where the displacements  $\mathbf{u}^*(\hat{\mathbf{x}}, \mathbf{x})$  and tractions  $\mathbf{t}^*(\hat{\mathbf{x}}, \mathbf{x})$  follow from the Muskhelishvili complex potentials (6), (7) and (8). They are the response at the point  $\boldsymbol{\xi}$  correspond to a unit point force acting at the point  $\hat{\mathbf{x}}$ . The inner stress  $\tilde{\mathbf{T}}(\mathbf{y})$  annihilates the leading order term of the tractions  $\mathbf{T}(\hat{\mathbf{x}})$  on the crack faces. Because the inner stress is expressed in terms of the stretched position vector  $\mathbf{y}$ , points  $\mathbf{y}$  far away from the crack correspond to points  $\mathbf{x}$  only in a small distance from  $\hat{\mathbf{x}}$ . Hence the inner boundary value problem is that of the infinite domain with inclusion and interphase of radius  $R_2/\varepsilon$  and  $R_1/\varepsilon$ , respectively, from which emanates the crack of unit length to the matrix. Using the distributed dislocation technique, Hills et al. (1996), the inner stress components  $\tilde{T}_{ij}$  are given by,

$$\tilde{T}_{ij}(\mathbf{y}) = \int_0^1 [b_\theta(t)K_{ij\theta}(\alpha, \mathbf{y}, t) + b_r(t)K_{ijr}(\alpha, \mathbf{y}, t)] dt, \quad (11)$$

where  $\alpha$  is crack orientation, see Fig. 1, and kernels  $K_{ij\theta}$  and  $K_{ijr}$  are developed from complex potentials (6), (7) and (8). The unknown dislocation densities  $b_\theta$  and  $b_r$  are obtained in such a way, that the negative value of  $\mathbf{T}(\hat{\mathbf{x}})$  is substituted to the left hand side of (11) for  $\mathbf{y} \in \gamma_1$ . Using the polar coordinate system, the inner stress field near the crack tip can be expressed in terms of the Williams asymptotic series,

$$\tilde{\mathbf{T}}(r/\varepsilon, \theta) = \sqrt{\frac{\varepsilon}{r}} A_1 \mathbf{F}_1(\theta) + A_2 \mathbf{F}_2(\theta) + \sqrt{\frac{r}{\varepsilon}} A_3 \mathbf{F}_3(\theta) + O(r). \quad (12)$$

Only the leading term of the expression above contributes to  $J(\mathbf{\Sigma}_\varepsilon)$ . This term is proportional to the squared values of stress intensity factors. Hence, one can get from (1) and (5),

$$G(\varepsilon, \hat{\mathbf{x}}, \alpha) = \frac{\varepsilon}{E} [K_I^2(\hat{\mathbf{x}}, \alpha) + K_{II}^2(\hat{\mathbf{x}}, \alpha)]. \quad (13)$$

#### 5. Numerical example

The numerical examples show the intermediate results of the character of the convergence of the series appearing in the fundamental solution (6), (7) and (8) and its application to the boundary integral method (10) with respect to its dependency on the material properties of the inclusion interphase. Fig. 2a shows the convergence of the displacement  $u_y$  of the fundamental solution along the  $x$ -axis for various degree  $n$  of the Laurent series. The unit force is oriented in the direction of  $x$ -axis and it is situated at the point [30, 30] mm. The radius of the inclusion and its interphase are 10 and 11 mm, respectively. The Young



modulus of the matrix, interphase and inclusion are  $0.8\text{E}+11$ ,  $0.2\text{E}+11$  and  $0.2\text{E}+12$  MPa and Poisson's ratios are 0.15, 0.2 and 0.3, respectively. It can be seen that for this randomly chosen values, except the  $n = 2$  degree of the Laurent series, the curves cannot be distinguished especially with respect to the FEM solution. Fig. 2b shows the influence of the interphase material on the  $\sigma_x$  stress field in the finite domain under the tension  $\sigma_x^P = 100$  MPa. The domain contains an inclusion with the radius 4 mm with 1mm interphase. The width of the domain is 20 mm. The values inside the inclusion are not calculated, but can be evaluated from the received values along the boundary  $\partial\Omega_2$ . However these values are not necessary for the future analysis. It is interesting to point out the inappropriate values near the outer boundary  $\partial\Omega_1$ . It is a typical behavior of the boundary integral method near the discretized boundary.

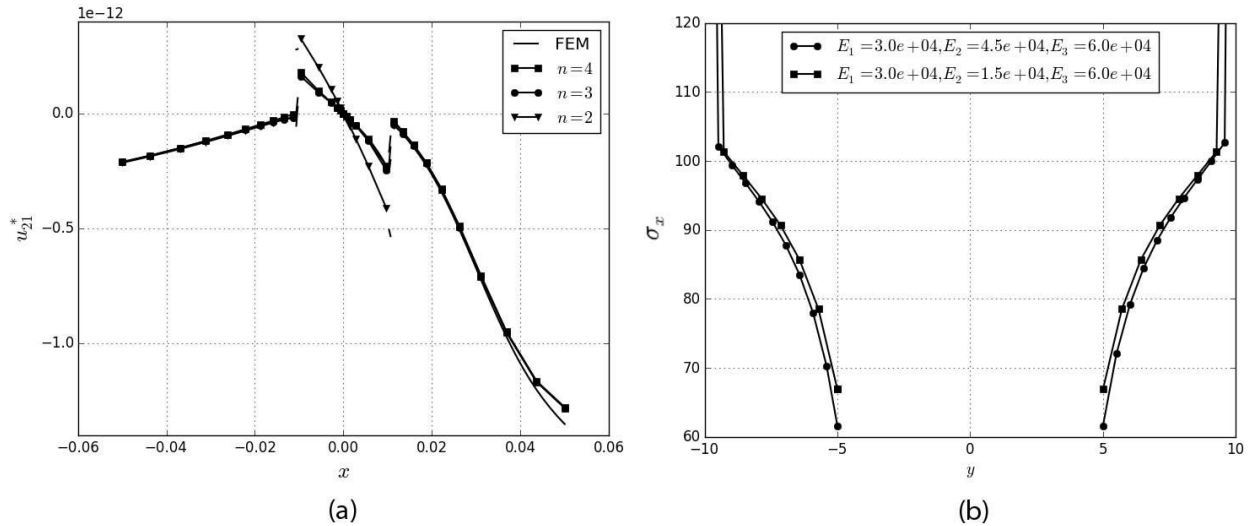


Fig. 2: a) The displacement of the fundamental solution; b) The stress  $\sigma_x$  along the  $y$ -axis of the finite domain under the tension  $\sigma_x^P = 100$  MPa.

## Acknowledgement

This research has been financially supported by the Czech Science Foundation through the Grant 16/18702S.

## References

- Silva, M., Geubelle, P.H. and Tortorelli, D.A. (2011) Energy release rate approximation for small surface-breaking cracks using the topological derivative. *Journal of the Mechanics and Physics of Solids*, 59, pp. 925-939.
- Cheeseman, B.A. and Santare, M.H. (2001) The effect of the interphase on crack-inclusion interactions. *International journal of Fracture*, 109, pp. 303-323.
- Hills, D., Kelly, P., Dai, D. and Korsunsky, A. (1999) *Solution of crack problems: The distributed dislocation technique*. Kluwer Academic Publishers, Amsterdam.
- Brebbia, C.A., Telles, J.C.F. and Wrobel, L.C. (1984) *Boundary element techniques*. Springer-Verlag, New York.

## **VIRTUAL PROTOTYPE APPLICATION TO HEAVY-DUTY VEHICLE GEARBOX CONCEPT**

**A. Prokop<sup>\*</sup>, K. Řehák<sup>\*\*</sup>**

**Abstract:** *This paper deals with application of virtual prototype to the heavy-duty vehicle gearbox concept. First the methodology is developed and tested on the single-stage gearbox concept, where the sensitivity of input parameters is investigated and validated by the experiment. The methodology is applied to the heavy-duty vehicle gearbox concept, where all inputs parameters are calculated similarly as in case of single-stage gearbox. The virtual prototypes enable to investigate influence of different input parameters on the design parameters, which are necessary at design phase. The surface normal velocity, which is related to noise prediction, can be evaluated. An experimental approach to validate the application on such high level of gearbox has not been performed yet.*

**Keywords:** Surface normal velocity, Noise, Vibration, Harshness.

### **1. Introduction**

The powertrain unit is continuously being developed to satisfy limits and requirements. The customer demands are related to the increase of power at continual stroke volume decreasing and fuel consumption decreasing. The harmful gas production is limited by legislation, which is getting stricter. At last but not at least, the legislation determines the noise limits for passenger and also for people around and also cities and locations where the traffic density is higher. The vibrations and related noise play an important role from the comfort point of view, thus they belong to one key factor of competitiveness between products in automotive industry. To decrease the overall noise level of the car, the dominant sources of noise have to be investigated.

Because of customer demands on low fuel consumption and also low price of the product acquisition, producers have to decrease both the development phase costs and material consumption. If the modification is performed, for example wall thickness is decreased in wrong area, the noise and related vibration could increase significantly. For that reason, these tasks cannot be performed without verification. This leads to a high number of prototype testing at the developing phase. Many manufacturers created their own methodology to predict behaviour of product without the necessity of creating numerous prototypes. On the other hand, all procedures should be validated by technical experiment. The noise, vibration and harshness (NVH) is very actual topic, because the new limits need to be met. Therefore, it is necessary to decrease the noise of the whole product by detecting potentially critical sub-products and decrease the noise of the most significant source. The gearbox belongs to the key components of almost every transport means, thus impacts on material saving and NVH parameters are taken into account. Moreover, when the other parts, as for example combustion engine, are not connected to the transmission, the dominant excitation is due to gear meshing phenomena (Tuma, 2014). In the end, vibrations of the external surface of the transmission due to inner processes are also accompanied by the noise emitting to the surroundings.

### **2. Methods**

The numerical simulation is a frequently used approach in research and at developing phase of

---

<sup>\*</sup> Ing. Aleš Prokop, PhD.: Institute of Automotive Engineering, Brno University of Technology, Technická 2896/2; 61669, Brno; CZ, prokop.a@fme.vutbr.cz

<sup>\*\*</sup> Ing. Kamil Řehák: Institute of Automotive Engineering, Brno University of Technology; Technická 2896/2; 61669, Brno; CZ, rehak@fme.vutbr.cz

transmission (Kumar, 2014). In the presented paper the combination of multibody software ADAMS and finite element method (FEM) software ANSYS is used. Each part of the methodology is verified separately by an experimental approach on the single stage gearbox which was designed and manufactured for that purpose (Loutas, 2009). The parameters of the gearbox and validation with experiment measurement are thoroughly described in (Prokop, 2015). The software ADAMS is used to create parametrical open code to be used at different transmissions. It enables to include flexible bodies, bearings stiffness, gear mesh stiffness, backlash, variable input speed, and torque.

The FEM is used for Craig Bampton reduction which replaces real modal properties with the simplified approximation established from the two variants of degrees of freedom, multiplied by the special Craig-Bampton transform matrix, see Eq. (1):

$$\begin{Bmatrix} \mathbf{u}_A \end{Bmatrix} = \begin{Bmatrix} \mathbf{u}_b \\ \mathbf{u}_L \end{Bmatrix} = \begin{bmatrix} \mathbf{I} & \mathbf{0} \\ \boldsymbol{\Phi}_R & \boldsymbol{\Phi}_L \end{bmatrix} \begin{Bmatrix} \mathbf{u}_b \\ \mathbf{q} \end{Bmatrix} = \boldsymbol{\Phi}_{CB} \begin{Bmatrix} \mathbf{u}_b \\ \mathbf{q} \end{Bmatrix}, \quad (1)$$

where  $\mathbf{u}_A$  is the original vector of deformation,  $\mathbf{u}_b$  are the boundary degrees of freedom (DOFs),  $\mathbf{u}_L$  stands for interior DOFs,  $\mathbf{q}$  represents modal DOFs,  $\mathbf{I}$  is the identity matrix element,  $\boldsymbol{\Phi}_R$  is rigid body matrix element and in the analogical way  $\boldsymbol{\Phi}_L$  are the fixed base mode shapes matrix element.

The stiffness of bearings is calculated on one rolling segment and afterwards converted to the whole bearing. The gear mesh stiffness is calculated for one tooth, which repeats periodically. The stiffness corresponds to the results, which are mentioned in (Kiekbush, 2011).

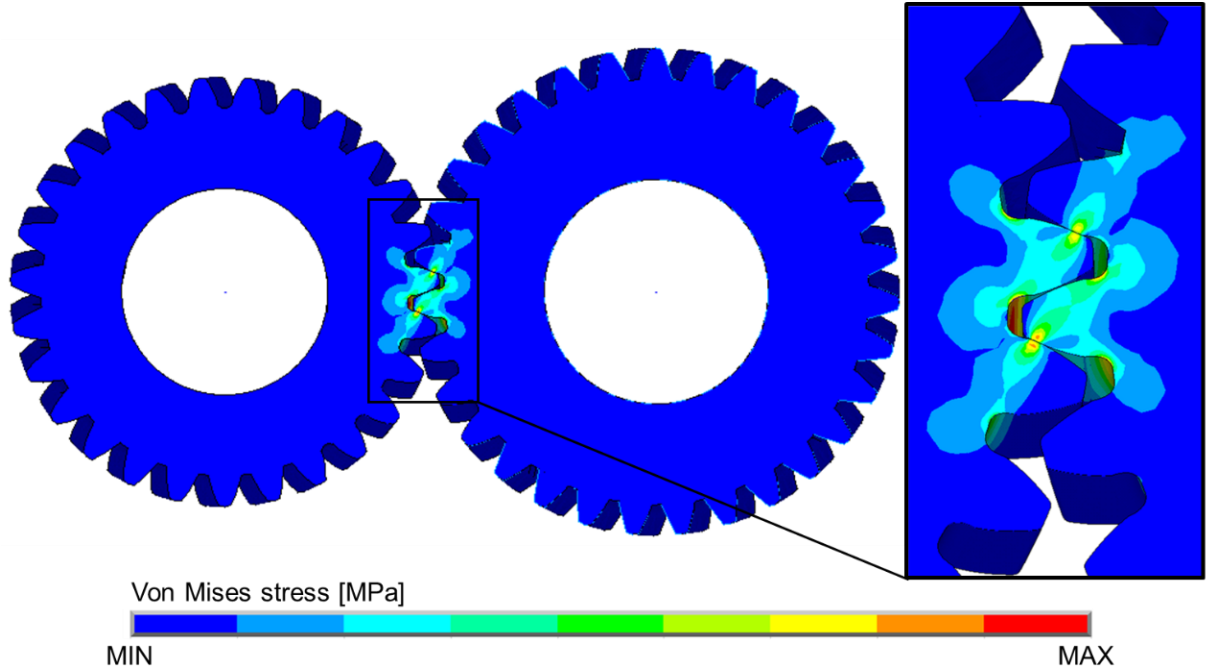


Fig. 1: Gear mesh Von Mises stress distribution.

### 2.1. Application to the heavy-duty vehicle gearbox concept

The heavy-duty gearbox concept is shown in Fig. 2. This virtual prototype enables to simulate dynamic properties of the transmission. On the input shaft variable speed is applied. Based on the functional principle of the combustion engine, output shaft is loaded by torque evaluated from traction forces. The gear mesh stiffness is calculated for each couple of gears at different torque up to designed maximal value. The bearing stiffness is calculated for proposed type and enables to confirm the lifetime of bearings. The backlash is taken from similar gearboxes.

## 3. Results

The virtual prototype enables to simulate steady state, as well as run up and run down for different selected gear. The surface normal velocity distribution is the most important result from the acoustic point of view, which is shown for run up simulation in Fig. 3. This velocity can be used as the input for another

simulation to get sound pressure level acoustic map, which is important at the final phase of some product. Another possible virtual prototype outputs, which are important at design phase or when investigating some issue, are progress of axial distance between gears, deformation in bearings, reaction forces in bearings or reaction forces at the transmission housing handles, see Fig. 4.

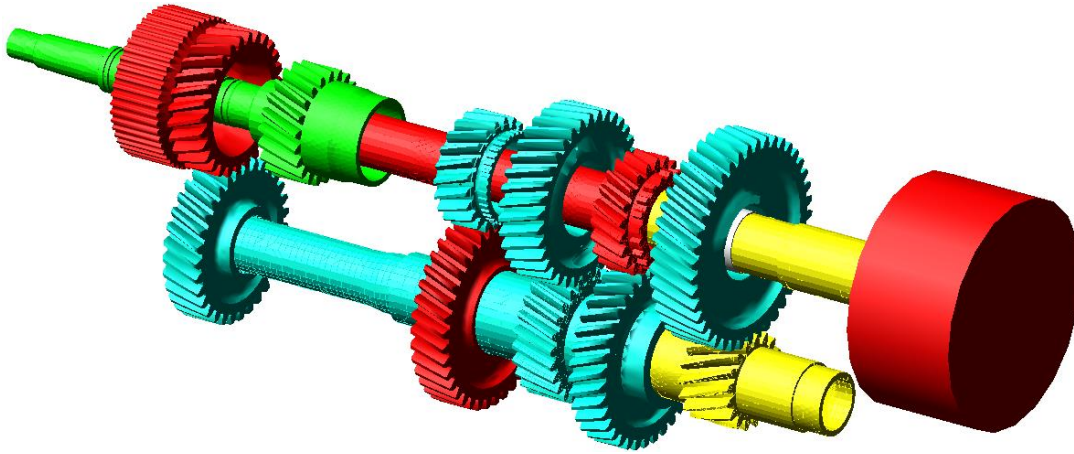


Fig. 2: Heavy-duty gearbox concept.

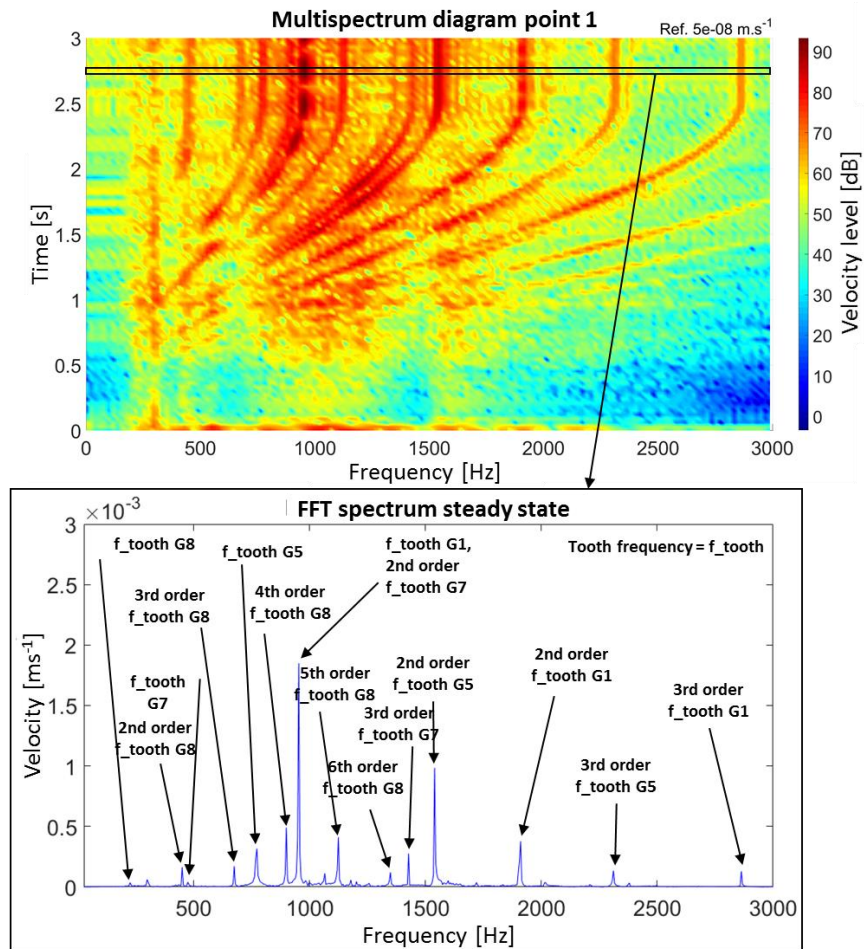
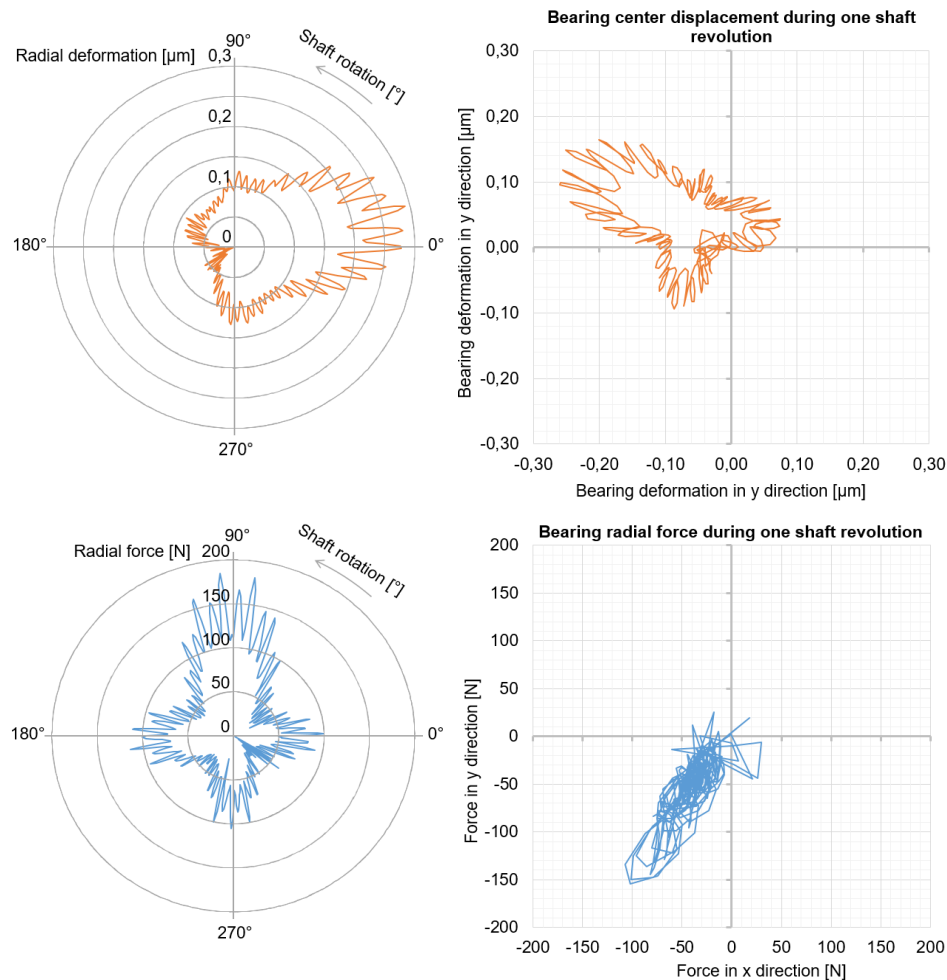


Fig. 3: Run up simulation for maximum rotational input speed 2160 rpm.

#### 4. Conclusions

The methodology, which is based on the combination of FEM and MBS, is developed on the single stage gearbox. One of the most important advantages of this methodology is the open code and an easy way of modification with aim to use it for wide range of transmissions. Also very useful is the possibility to use

results as input from FEM, thus include own geometry modification. This article presents results and possibilities of using this methodology on the more complex transmission concepts. Nonetheless, this concept of gearbox is developed and the methodology is applied as another option to gain important information without the need to create high number of prototypes.



*Fig. 4: Bearing radial displacement and force during one shaft rotation.*

## Acknowledgement

The research leading to these results has received funding from the Ministry of Education, Youth and Sports under the National Sustainability Programme I. (Project LO1202) and with help of the project FSI-S-17-4104 granted by specific university research of Brno University of Technology. The authors gratefully acknowledge this support.

## References

- Kiekbush, T., Sppok, D., Bernd, S. and Ian, H. (2011) Calculation of the Combined Torsional Stiffness of Spur Gears with Two- and Three-Dimensional Parametrical FE Models, *Journal of Mechanical Engineering*, 57, 2011, pp. 810-818.
- Kumar, A., Jaiswal, H., Jain, R. and Pati, P.P. (2014) Free Vibration and Material Mechanical Properties Influence Based Frequency and Mode Shape Analysis of Transmission Gearbox, *Procedia Engineering*, 2014, 97, pp. 1097-1106.
- Loutas, T.H., Sotiriades, G., Kalaitzoglou, I. and Kostopoulos, V. (2009) Condition monitoring of a single-stage gearbox with artificially induced gear cracks utilizing on-line vibration and acoustic emission measurements, *Applied Acoustics*, 2009, 70, pp.1148-1159.
- Prokop, A., Rehak, K., Zubik, M. and Novotny, P. (2015) Experimental Validation of the Gearbox NVH Parameters, *Journal of Middle European Construction and Design of Cars*, 13(2), 2015, pp. 16-21.
- Tuma, J. (2014) *Vehicle gearbox noise and vibration: measurement, signal analysis, signal processing and noise reduction measures*, Chichester: John Wiley, 2014, 243 p.



## RUNNING FLUTTER WAVES IN BLADES CASCADE

L. Půst\*, L. Pešek\*\*

**Abstract:** The simplified mathematical model of dynamic properties of bladed cascade excited by wakes of flowing steam from the stationary cascade is derived. Interaction of this kind of forced excitation with aero-elastic self-excitation described by Van der Pol formula causes origin of flutter and its running waves. It is shown that the velocity, direction of flutter running waves and mode of vibration depend on the blades' number ratio and on kind of self-excitation forces on individual blade or on inter-blade distance.

**Keywords:** Running waves, Flutter, Self-excitation, Wakes, Ratio of blade numbers.

### 1. Introduction

Dynamic properties of blades cascades in turbines excited by the aero-elastic effects of flowing gas – flutter – have been intensively investigated and published during the several last decades up to the present time (Rao, 1991; Rządowski, 2007 and Pust, 2011). During experimental investigation of blades flutter properties, the existence of running waves was observed and mentioned (Yan, 1990 and Kielb, 2004). Comparatively small attention has been given to the explanation what is the cause of origin and properties of flutter running waves. Presented paper contains an attempt to reveal the possible impulses, which can excite and synchronize the flutter phenomenon. Flutter phenomenon is an intensive self-excited vibration of blade cascade structure. There are many types of description of flutter phenomena, however for simplicity an expression based on well-known Van der Pol model (Pust, 2016) is used in this study. Two modifications of this model are applied. The first one is oriented on self-excited vibration of each individual blade, the second one acts on relative motion between two neighboring blades. Different blades' number of rotating and of stator wheels causes the phase delays of excitation forces produced by the wakes of gas flow from the stator blades cascade. Consequently, the running waves of forced vibration exist, which initiate also the flutter running waves.

### 2. Methods

The dynamic properties of a model of turbine wheel with ten blades and excited by phase delayed harmonic forces caused by distorted stream of flowing gas from the stator blades cascade were studied in the paper (Pust, 2016) shown in Fig. 1. Another type of graphical presentation computational model of turbine blades row is shown in Fig. 2, where the tenth blade is connected with the first blade again by the same elastic element. The spring with stiffness  $k_1$  [kg.s<sup>-2</sup>] represents elastic properties of disc or of shroud.

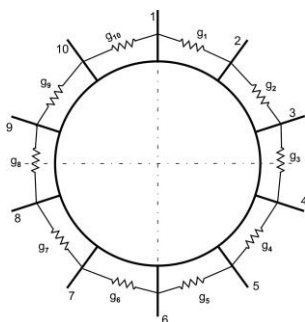


Fig. 1: Model of blade wheel.

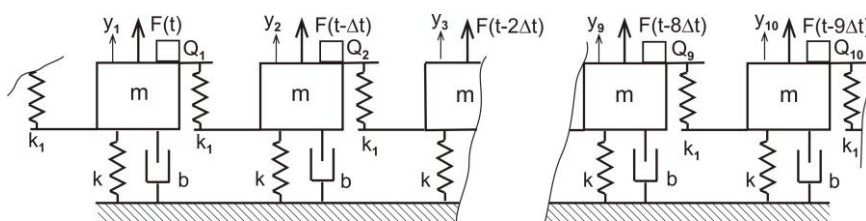


Fig. 2: Model of blade cascade.

\* Ing. Ladislav Půst, DrSc, Institute of Thermomechanics AS CR, v.v.i., Dolejšková 5, 18200 Praha 8, pust@it.cas.cz

\*\* Ing. Ludek Pešek, CSc, Institute of Thermomechanics AS CR, v.v.i., Dolejšková 5, 18200 Praha 8, pesek@it.cas.cz



Dynamic properties of blades are investigated in the narrow frequency range near the selected blade's eigen-frequency and modeled as a 1DOF system with parameters  $m, k, b$ . The wakes of steam flow from stator blades excite the blades on the rotating wheel by external periodic forces. Running periodic forces arise if the number  $l_r$  of blades on rotating wheel differs from the number  $l_s$  of blades on stator cascade  $l_r \neq l_s$ . These periodic forces can be simplified to one harmonic component  $F_0 \cos(\omega t - (i-1)\Delta\varphi)$ , where the phase delay  $\Delta\varphi$  between the neighboring excitation forces depends on ratio  $l_s/l_r$  according the following relations:  $\Delta\varphi = 2\pi * (1 - \frac{l_s}{l_r})$ . As example for  $l_s/l_r = 9/10$  is  $\Delta\varphi = \pi/5$ .

### 3. Self-excited oscillation

Steam flowing through the blade-cascade can cause decrease of damping and rise of flutter. Exact mathematical model of this aero-elastic phenomenon is very complicated, therefore we will use in this study the Van der Pol model, (Pust and Pesek, 2016) described by equation

$$G = -\mu(1 - (x/r)^2)\dot{x}, \quad (1)$$

where  $G$  is the aerodynamic force,  $x, \dot{x}$  are general displacement and velocity,  $r$  is displacement of blade at which the aerodynamic force changes its sign,  $\mu$  gives intensity of this non-linear damping.

### 4. Position of flutter activity

The flowing steam from the stationary blade cascade influence both individual blades and also the interaction forces between neighboring blades. These situations can be graphically modelled by different positions of points of action. The position of direct self-excitation  $G$  on individual blade is depicted in Fig. 3. The inter-blades self-excitation  $G$  is shown in Fig. 4.

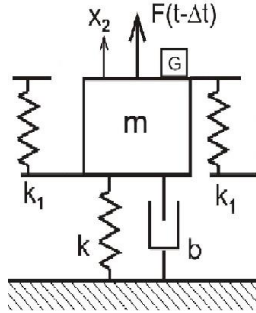


Fig. 3: Blade's self-excitation.

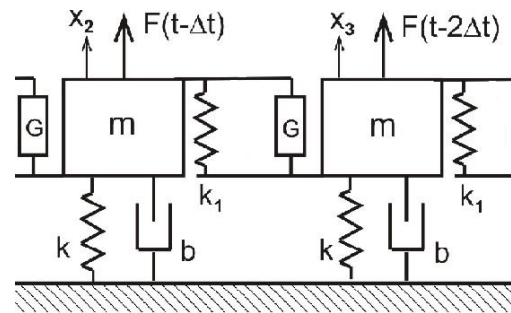


Fig. 4: Inter-blades self-excitation.

$$\text{In the first case it is: } G_i = -\mu_1(1 - (x_i / r_1)^2)\dot{x}_i, \quad (2a)$$

where index  $i$  denotes the number of blade. The self-exciting force in the second case is

$$G_{i,i+1} = -\mu_2(1 - ((x_i - x_{i+1}) / r_2)^2)(\dot{x}_i - \dot{x}_{i+1}) \quad (2b)$$

### 5. Vibrations of forced and aero-elastic excitation

Ten differential equations describe motion of blade cascade

$$m\ddot{x}_i + b\dot{x}_i + kx_i + g_i - g_{i-1} + G_i + G_{i,i-1} + G_{i,i+1} = F_0 \cos(\omega t + (i-1)\Delta\varphi), \quad (3)$$

where  $g_i$  describes connections between  $g$  blades  $g_i = k_1(y_i - y_{i+1}) \quad i=1, \dots, 10, \quad y_{11} = y_1$ .

Response curves are computed in the following examples for one blade's mass, stiffness and damping coefficient:  $m = 0.182 \text{ kg}$ ,  $k = 105000 \text{ kg.s}^{-2}$ ,  $b = 2 \text{ kg.s}^{-1}$ . The blades' interconnections stiffness is  $k_1 = 1000 \text{ kg.s}^{-2}$  and amplitude of external wakes force is  $F_0 = 1 \text{ N}$  with frequency  $\omega = 762 \text{ rad/s}$ .

## 6. Individual blade self-excitation

The graphical presentation of influence of forced wake vibration interaction with direct self-excitation  $G_i$  of individual blades is shown in Fig. 3. There are two damping forces acting on each blade: positive structural damping with coefficient  $b = 2 \text{ kg.s}^{-1}$  and negative aero-elastic damping with coefficient  $\mu_1$ . Self-excited oscillations can arise if  $\mu_1 > b = 2$ , but it needs an initial impulse for its expansion. If external wake force does not exist ( $F_0 = 0$ ), no self-excited oscillation arises, in spite of high negative aerodynamic coefficient  $b - \mu_1 = 2 - 2.5 = -0.5$  as shown in Fig. 5. However, the wakes of steam flowing from the stator blade cascade at amplitude  $F_0 = 1 \text{ N}$  initiate increase of self-excited vibrations as it is shown in Fig. 6 for the same numbers of stator and rotor blades  $l_s / l_r = 1$  and so for  $\Delta\varphi = 0$ . Registered time courses of all blades are shown in these figures. The lowest and upper bold line belong to the first blade, upper dashed line belongs to the 10<sup>th</sup> blade.

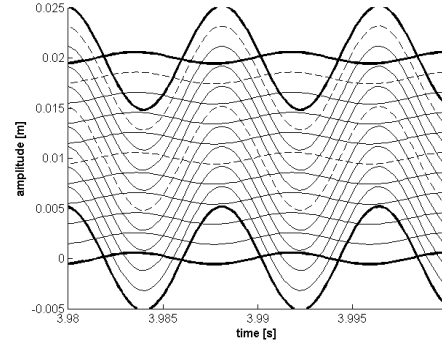
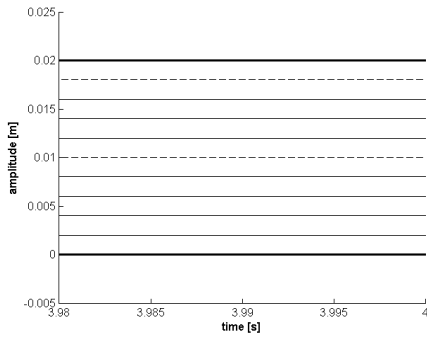


Fig. 5: Self-excitation without initial impulses.

Fig. 6: Self-excitation with initiation by wakes.

If the ratio of stator and rotor blades is  $l_s / l_r = 9/10$  then  $\Delta\varphi = \pi/5$  and backward running wave occurs as it is seen in Fig. 7. The change of blade's numbers to  $l_s / l_r = 8/10$  causes increase of phase shift to  $\Delta\varphi = 2\pi/5$  and the backward running wave velocity is half, the period of one wave's revolution is double, as shown in Fig. 8. The corresponding wave mode contains two cosines forms, as distinct from the case in Fig 8, where the form is described by one cosine form.

If the ratio of stator and rotor blades numbers is greater than 1 e.g.  $l_s / l_r = 11/10$  then  $\Delta\varphi = -\pi/5$  and running waves have forward direction as it is seen in Fig. 9.

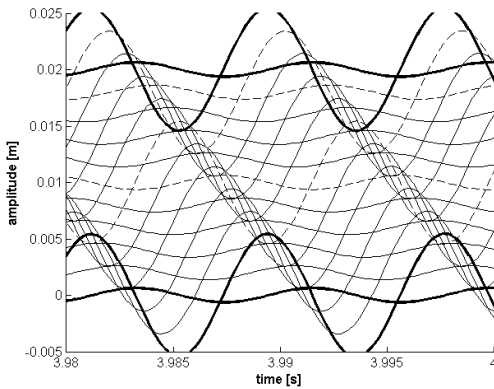


Fig. 7: Backward waves at  $\Delta\varphi = \pi/5$ .

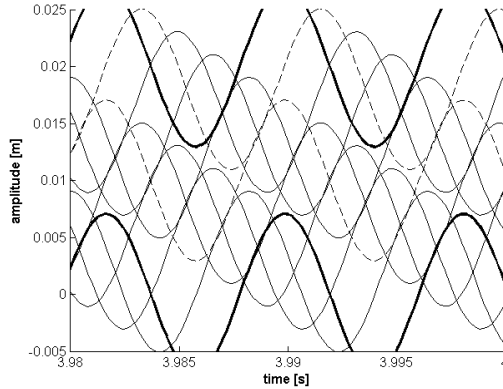


Fig. 8: Backward waves at  $\Delta\varphi = 2\pi/5$ .

## 7. Inter-blades excitation

The behavior of running waves in the case that the flowing steam from the stationary blade cascade influences the interaction between neighboring blades (see Fig. 4) distinguishes from the properties of blades' cascade with the individual blade self-excitations.

The dynamic properties of rotor blade cascade with  $l_s / l_r = 9/10$  ( $\Delta\varphi = \pi/5$ ) are shown in Fig. 10. The mode of vibration has five cosine forms on the periphery and there exist two running waves forward and

backward – designated by arrows in figure. The velocities of these running waves are five times lower than running waves depicted in Fig. 7 or 9.

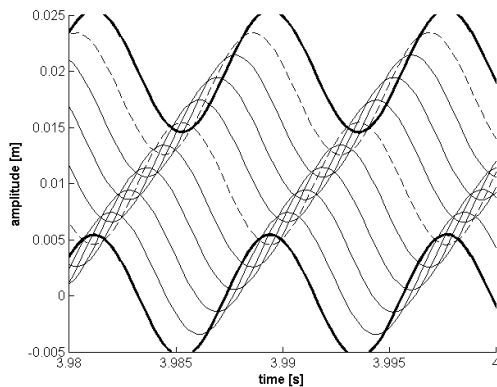


Fig. 9: Forward waves at  $\Delta\varphi = -\pi/5$ .

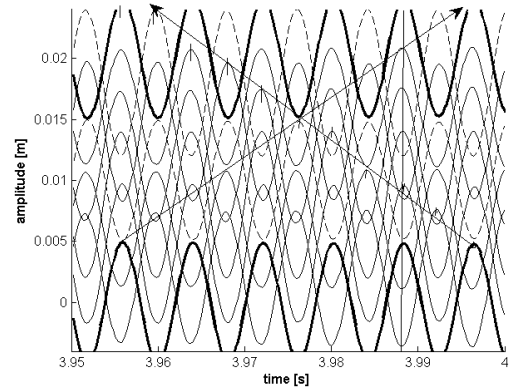


Fig. 10: Waves at inter-blades self-excitation.

## 8. Conclusions

The presented paper deals with investigation and ascertaining of conditions for origin of flutter in turbine including its running waves.

It is shown that the ratio of blades' numbers of stationary and of rotating disk influences due to the wakes of gas flow the phase shift between neighboring blades and consequentially also direction and velocity of forced or flutter running waves. The flutter self-excitation is realized by Van der Pol model.

There are different blade-cascade responses in the cases when the self-exciting effect of flowing steam acts direct on individual blades or by interaction forces between neighboring blades. The running velocities as well as modes of vibration in both cases are different.

Presented study is the first stage of deeper analysis. In the future the bladed cascade will be improved by addition of torsion DOF and the self-excitation elements will be modified according to the results of prepared experiments.

## Acknowledgement

This work has been supported by the grant project of the Czech Science Foundation No. 16-04546S "Aero-elastic couplings and dynamic behavior of rotational periodic bodies".

## References

- Kielb, R.E., et al. (2004) Flutter of low pressure turbine blades with cyclic symmetric modes: A preliminary design method, *Journal of Turbomachinery- transactions of the ASME* 126, pp. 306-309.
- Pust, L. and Pesek L. (2016) Interaction of self-excited and delayed forced excitation on blade bunch, *Proc VETOMAC XII, Warsaw, 2016*, pp. 139-148.
- Rao, J.S. (1991) *Turbomachine Blade Vibration*, Wiley Eastern Limited, New Delhi.
- Rzadkowski, R. and Gnesin, V. (2007) A3D Inviscid self-excited vibration of the last stage turbine blade row, *Journal of Fluids and Structure* 23, pp. 858-873.
- Yan, L.-T. and Li, Q.-H. (1990) Investigation of Travelling Wave Vibration for Bladed Disk in Turbomachinery, in: *Proc. 3rd Int. Conf. on Rotordynamics-IFTOMM*, (Lalanne, M., ed.), Lyon, pp. 133-135.
- Pust, L. and Pesek, L. (2011) Vibration Of Circular Bladed Disk With Imperfections, *International Journal of Bifurcation And Chaos*, Vo. 21, No. 10, pp. 2893-2904.

## MECHANICAL BEHAVIOR OF A TITANIUM ALLOY TRABECULAR STRUCTURE

L. Řehounek<sup>\*</sup>, A. Jíra<sup>\*\*</sup>, F. Denk<sup>\*\*\*</sup>

**Abstract:** *The advancement of technology in the field of 3D printing of metal alloys allows for creating very complex structures. Newfound technologies of manufacturing, however, require testing of basic mechanical properties of the new structures. This paper is dedicated to the analysis of mechanical properties of a trabecular Ti-6Al-4V titanium alloy. Due to its complex morphology, the trabecular structure could not be created by traditional manufacturing process and was made by 3D printing. It was found that by creating this structure, the Young's modulus of the whole body of the specimen was significantly reduced. The methods used for the determination of the mechanical properties are nanoindentation, tensile and compression tests.*

**Keywords:** Trabecular, Nanoindentation, Modulus of elasticity, Titanium, 3D printing.

### 1. Introduction

A trustworthy representation of the behavior of the trabecular implant demands a detailed mathematical model representing the true stress-strain relation of the structure. Because of the nonlinear behavior and a yet unknown nature of deformation characteristics, it is imperative to provide a series of test data to serve as a guideline for the development of the model. The stress-strain relations have been provided by means of uniaxial tensile and compression tests. These tests have been carried out on specifically designed specimens shown in Fig. 1. The trabecular structure brings with itself many benefits, such as reduced risk of implant loosening (Dabrowski et al, 2010), osseointegration, complex implant integration and more acceptable (lower) values of Young's modulus, compared to other homogeneous implants (Niinomi, 1998 and Niinomi 1998). This reduction is a significant benefit because it provides a smoother transition region in between the faces of the dental materials. The trabecular structure also provides an environment into which bone cells are able to grow into, thus further improving the transition region and contact properties. The body of the implant has been 3D-printed using the M2 Cusing Concept Laser machine using a specialized Rematitan Cl metal powder in cooperation with ProSpon spol. s. r. o.

### 2. 3D printing technology

The first step in the process of creation of a 3D-printed product is creating a 3D-model. This part is usually done using a computer-aided design (CAD) environment. Upon its completion, an STL model file is divided into thin cross sections (Wiria et al., 2010 and Aouni et al., 2014) and sent to the 3D printer to be processed. Up to this point, the process is similar to the common layer-by-layer 3D-printing of plastic.

What differentiates the process of printing metals from the standard technology is using a laser beam to melt down a layer of metal powder, such as Rematitan Cl. During each cycle, the coater applies a thin layer of powder, which is processed by a laser at a pre-set melting point in a pre-determined order (Hartmann-H'Lawatscheck, 2015).

---

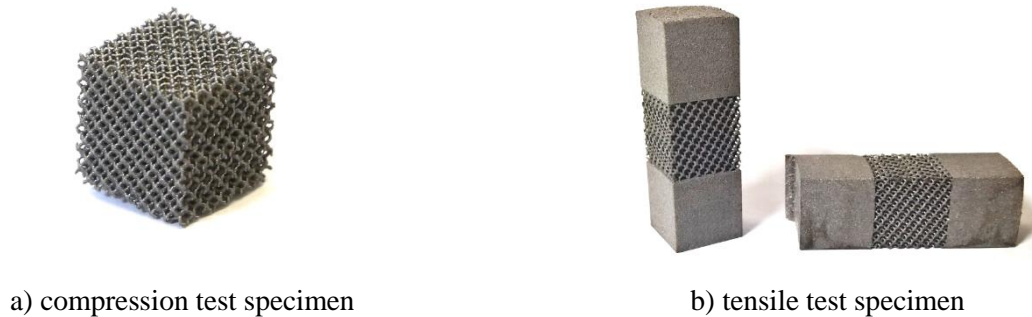
<sup>\*</sup> Bc. Luboš Řehounek: Department of Mechanics, Czech Technical University in Prague, Thákurova 7; 166 29, Prague; CZ, lubos.rehounek@fsv.cvut.cz

<sup>\*\*</sup> Ing. Aleš Jíra, PhD.: Department of Mechanics, Czech Technical University in Prague, Thákurova 7; 166 29, Prague; CZ, jira@fsv.cvut.cz

<sup>\*\*\*</sup> Ing. arch. et Ing. František Denk, PhD.: Department of Mechanics, Czech Technical University in Prague, Thákurova 7; 166 29, Prague; CZ, frantisek.denk@fsv.cvut.cz

This process solidifies the loose powder into a 3D-layered object. 3D printing is a very modern and perspective method in manufacturing the bodies of the implants. It allows for very complex structures, which would not have been conceivable with traditional metalworking.

It also proves to be beneficial in terms of manufacturing speed and storage, because there is no need to produce large batches of specific implants at once due to the long process associated with the calibration of the assembly line.



*Fig. 1: Trabecular structure specimens for global mechanical tests.*

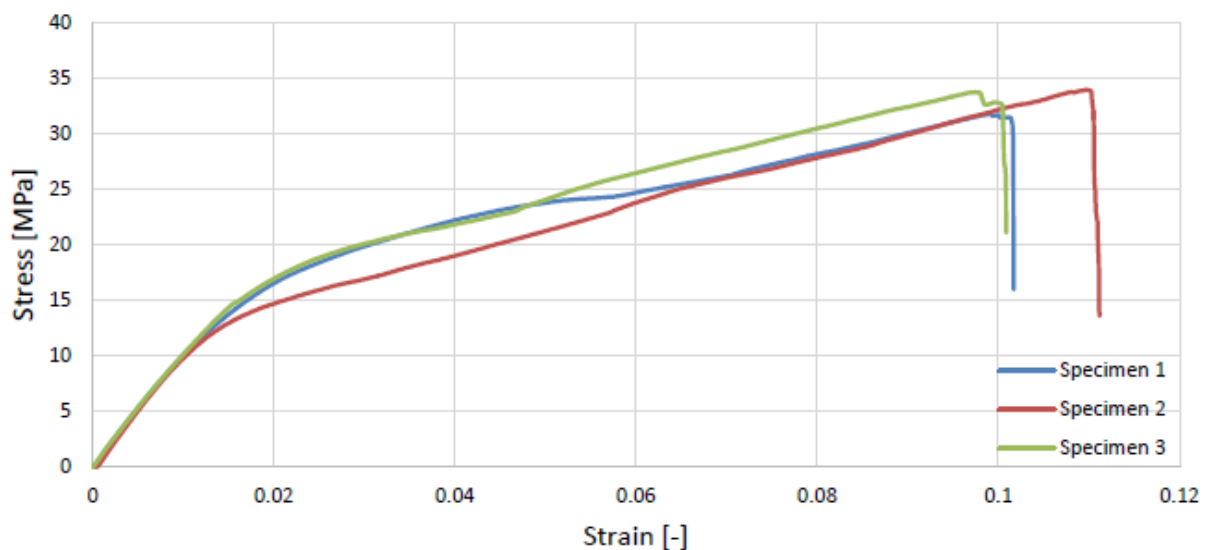
### 3. Methodology

#### 3.1. Nanoindentation

To investigate the micromechanical properties of the alloy, nanoindentation tests were made considering reduced modulus of elasticity, hardness and contact depth. The micromechanical analysis was performed using the CSM Instruments nanoindenter in the mode of directed force and repeated loading. The load program was set with consideration of eliminating surface tension and shear stiffness in the atomic material structure. The values of reduced modulus  $E_r$  were in the range of 118 – 131 GPa. For further information about nanoindentation, please refer to the paper Řehounek et al. (2016).

#### 3.2. Global mechanical tests

To investigate the global mechanical properties, we conducted compression and tensile tests. For this purpose, we used the 3D Dode-Thick [MSG] structures with dimensions of  $14 \times 14 \times 14$  mm (a cube for the compression test) and a  $14 \times 14 \times 42$  mm (a block for the tensile test). The tensile test specimen had a 14 mm trabecular middle section and end portions of homogeneous volume for ensuring a better anchor in the MTS Alliance RT-30 machine. The results show an ultimate compressive strength of 31.30 MPa and an ultimate tensile strength of 32.80 MPa. Diagram showing the stress-strain relations of the specimens obtained by tensile tests is shown in Fig. 2.



*Fig. 2: Stress-strain relation diagram of the tensile test specimens.*





The diagram shown in Fig. 4 represents the stress-strain relation of the curve-fitted FEM model. The main task was to manipulate its mechanical properties in order to curve-fit the tensile test experiment data of specimen n.3. This has been done by importing the strain data from the MTS Alliance RT-30 test machine as a displacement load into the computation software, thus fully simulating the tensile test experiment. Please note that the model does not provide failure of the structure (Fig. 4). This is a fully acknowledged fact, as the model will need to incorporate additional algorithms to provide an accurate solution in the area of failure. This approach is the subject of our further efforts and the presented model is in the middle stage of its development.

## 5. Conclusions

The macromechanical tests have been conducted as a pilot experiment and cannot be therefore compared with other authors. The compression tests have proven to be more diverse due to the yet unclear nature of the deformation of the trabecular structure. The mean Young's modulus  $E$  of the trabecular specimens calculated from the linear part of the loading curves of the stress-strain diagrams is  $E_{ten} = 974.26$  MPa for the tensile test and  $E_{comp} = 960.68$  MPa for the compression test.

As predicted, the analysis showed that incorporating the trabecular structure has great effect on lowering the Young's modulus  $E$  of the whole structure. As opposed to regularly produced Ti-6Al-4V implants, where values of  $E$  are approximately 110 GPa, the values of  $E$  of the trabecular implant are below 1 GPa. This is a very significant reduction and the results are still to be compared with other experiments.

Further effort has been made to develop a material model which describes the trabecular structure. This model has been tuned to accurately represent the stress-strain diagram of the tensile test specimens. The geometry of the numerical model corresponds with dimensions of the real specimens. With this model developed, the next goal will be to incorporate failure of the structure and introduce a FEM model of a whole implant, which contains both trabecular and homogeneous cross-sections (Fig. 5) and will ultimately describe the nature of the mechanical behavior of the whole implant.



*Fig. 5: Specimens (left) and structure composition (right) of the final implant for future analyses.*

## Acknowledgment

The financial support provided by SGS project application registered as OHK1-031/17 is gratefully acknowledged.

## References

- Aouni, E. et al. (2014) Physical and mechanical characterisation of 3D-printed porous titanium for biomedical applications, *J Mater Sci.*, 25, pp. 2471-2480.
- Dabrowski, B. et al. (2010) Highly porous titanium scaffolds for orthopaedic applications, *J Biomed Mater Res*, 95B, pp. 53-61.
- Hartmann-H'Lawatscheck, T. (2015) Metal Laser Melting, *Laser Technik Journal*, 12, pp. 41-43.
- Jíra, A. and Denk, F. (2016) Micromechanical analysis of dental implants and their surface modification, *App. mech and mat.*, 827, pp. 367-370.
- Niinomi, M. (1998) Design and mechanical properties of new b type titanium alloys for implant materials, *Materials Science and Engineering*, A243, pp. 244-249.
- Niinomi, M. (1998) Mechanical properties of biomedical titanium alloys, *Materials and Science Engineering*, A243, pp. 231-236.
- Řehounek, L., Denk, F. and Jíra, A. (2016) Trabecular structures of dental implants formed by 3D printing and their mechanical properties, 54<sup>th</sup> International Conference on Experimental Stress Analysis, EAN 2016; Hotel Srní, Srní; Czech Republic; 30 May 2016 through 2 June 2016; Code 123122.
- Wiria, F.E. et al. (2010) Printing of Titanium implant prototype, *Materials & Design*, 31, pp. 101-105.

## THE ANTIPLANE PROBLEM FOR A STRIP WEAKENED BY A CRACK

O. V. Reut<sup>\*</sup>

**Abstract:** *The problem on an arbitrary oriented crack in a strip is solved. The new approach for the elasticity problems with the curvilinear defects is proposed. With the help of the generalized scheme of the integral transformation method the problem is reduced to the singular integral equation, which effective approximate solution can be constructed.*

**Keywords:** Arbitrary oriented crack, Singular integral equation.

### 1. Introduction

The problems on the stress concentration near the defects (the cuts, the cracks, the inclusions) play an important role in the modern fracture mechanics. The scheme of the reduction of the elasticity boundary valued problems with a defect to the integral equations, based on the integrals transformation, is well known. In this scheme the defects are inscribed in a certain coordinate system, apparatus of integral transformation is used or perpendicular or parallel to the defect. In proposed paper this methodic is generalized on a case of a curvilinear defect on the example of the antiplane problem for a strip, weakened by an arbitrary oriented crack. It is shown that the problem is reduced to the known singular equation allowing the effective approximate solving.

### 2. The problem's statement

Let's consider the antiplane problem for a strip  $\{|x| < \infty, |y| < l\}$ , the edges of it are fixed. The crack  $\{y = \varphi(x), |x| < 1\}$  is situated inside the strip. The load of intensity  $T(x)$  is applied to the branches of the crack along axis  $OZ$ . It is supposed that parameters of crack are such that it is situated inside the strip and don't go to the bound. Without loss of generality (it is required only that function  $\varphi(x)$  should be continuous and differentiating on the segment  $[-1, 1]$ ) the final formulas we give for the case of straight crack  $\varphi(x) = kx + c$ . It is necessary to estimate the stress intensity factor near the crack's ends. The mathematics statement of the formulated problem is following one:

$$\left\{ \begin{array}{l} \frac{\partial^2 W}{\partial x^2} + \frac{\partial^2 W}{\partial y^2} = 0, |x| < \infty, y \in (-l, \varphi(x) - 0) \cup (\varphi(x) + 0, l) \\ W, \frac{\partial W}{\partial x} \Big|_{x \rightarrow \infty} \rightarrow 0 \\ W \Big|_{y=-l} = W \Big|_{y=l} = 0 \\ \sqrt{1 + (\varphi'(x))^2} \frac{\partial W}{\partial \nu} \Big|_{y=\varphi(x)-0} = T(x), \quad |x| < 1 \end{array} \right. \quad (1)$$

Here  $W(x, y)$  is displacement of point with the coordinates  $(x, y)$  along axis  $OZ$ . The displacements is continuously different table till the bound of given area, except the angle points – ends of the crack, where  $W(x, y)$  should be continuous.

---

<sup>\*</sup> Odessa I.I. Mechnikov National University, Dvoryanska, 1; 65082, Odessa; UA reut@onu.edu.ua

Let's designate  $\nu$  as the normal direction to the curve  $y = \varphi(x)$  and  $s$  as the tangent direction to this curve  $\nu$ ,  $\alpha$  is an angle between lines  $OX$  and  $OS$ . One can get that  $tg(\alpha) = \varphi'(x)$  and

$$\begin{cases} \frac{\partial W}{\partial s} = [1 + (\varphi'(x))^2]^{-1} [\frac{\partial W}{\partial x} + \varphi'(x) \frac{\partial W}{\partial y}] \\ \frac{\partial W}{\partial \nu} = [1 + (\varphi'(x))^2]^{-1} [-\varphi'(x) \frac{\partial W}{\partial y} + \frac{\partial W}{\partial x}] \end{cases} \quad (2)$$

Let's note, that if a crack is the straight one and is parallel to one of the coordinate axis, then with the generalized scheme of the integral transformation method the problem will be reduced to a singular integral equation. This equation can be solved and one can get the effective numerical solution. At the case of the arbitrary oriented curvilinear crack the additional difficulties are appeared. They are connected with the changing of the differentiation and integration operations' order at the integral

$$\int_{-l}^l \frac{\partial W}{\partial x} \sin \lambda y dy$$

when function  $W(x, y)$  is the discontinuous one. This work is dedicated to the overcoming of these difficulties.

### 3. Reduction to the one dimensional problem

Let's apply to the boundary problem (1) the finite *sin*-Fourier transformation with regard to variable  $y$

$$\begin{aligned} W_\lambda(x) &= \int_{-l}^l w(x, y) \sin \lambda(y + l) dy; \\ W(x, y) &= \frac{1}{l} \sum_{k=1}^{\infty} W_{\lambda_k}(x) \sin \lambda_k(y + l) \\ \lambda_k &= \frac{k\pi}{2l} \end{aligned}$$

Previously one should change the last condition in (1) on the next one

$$\begin{aligned} \left. \frac{\partial W}{\partial \nu} \right|_{y=\varphi(x)} &= \frac{\partial W}{\partial \nu}(x, \varphi(x)-0) - \frac{\partial W}{\partial \nu}(x, \varphi(x)+0) = 0 \\ \langle W \rangle|_{y=\varphi(x)} &= W(x, \varphi(x)-0) - W(x, \varphi(x)+0) = \chi(x) \end{aligned} \quad (3)$$

where  $\chi(x)$  is the unknown function, describing the jump of the function  $W(x, y)$  during the transition across the crack. Than  $\chi(x) \equiv 0$  when  $|x| > 1$ . Let's use the integrals:

$$\begin{aligned} \int_{-l}^l \frac{\partial^2 W}{\partial y^2} \sin \lambda y dy &= \left. \frac{\partial W}{\partial y} \right|_{y=\varphi(x)} \sin(\lambda \varphi) - \chi(x) \lambda \cos(\lambda \varphi) - \lambda^2 W_\lambda(x) \\ \int_{-l}^l \frac{\partial^2 W}{\partial x^2} \sin \lambda y dy &= -\varphi(x) \left. \frac{\partial W}{\partial x} \right|_{y=\varphi(x)} \sin(\lambda \varphi) - \frac{d}{dx} [\varphi'(x) \chi(x) \lambda \sin(\lambda x)] + W_\lambda''(x) \end{aligned}$$

With regard to the condition (3) one get the one-dimensional boundary problem

$$\begin{cases} \left( \frac{d^2}{dx^2} - \lambda^2 \right) W_\lambda(x) = \mathcal{F}_\lambda(x), |x| < \infty \\ W_\lambda, W_\lambda'|_{x \rightarrow \mp \infty} \rightarrow 0, \mathcal{F}_\lambda(x) = \chi(x) \lambda \cos(\lambda \varphi) + \frac{d}{dx} [\varphi'(x) \chi(x) \lambda \sin(\lambda x)] \end{cases}$$

Its solution can be written in the form:

$$W_\lambda(x) = \int_{-\infty}^{+\infty} \mathcal{F}_\lambda(\xi) G_\lambda(x, \xi) d\xi, \quad G_\lambda(x, \xi) = -\frac{1}{2\lambda} e^{-\lambda|x-\xi|}$$

$$W_\lambda(x) = \int_{-1}^1 \chi(\xi) [\lambda \cos(\lambda \varphi(\xi)) G_\lambda(x, \xi) d\xi - \varphi'(\xi) \sin(\varphi(\xi)) \frac{\partial G_\lambda}{\partial \xi}(x, \xi)] d\xi$$

After application of the inverse integral Fourier's transformation one derives

$$W(x, y) = \int_{-1}^1 \chi(\xi) \frac{\partial G_\lambda}{\partial v_\xi}(x, y, \xi, \varphi(\xi)) \sqrt{1 + [\varphi'(\xi)]^2} d\xi \quad (4)$$

where derivative  $\frac{\partial}{\partial v_\xi}$  is defined by the second formula in (2) after variable changing of the variables  $(x, y)$  on the variables  $(\xi, \eta)$ .

#### 4. The weak convergent part extraction

The function  $G(x, y, \xi, \eta)$  has form

$$\left\{ \begin{aligned} G(x, y, \xi, \eta) &= \frac{1}{l} \sum_{m=1}^{\infty} \left( -\frac{1}{2\lambda_m} e^{-\lambda_m|x-\xi|} \right) \sin \lambda_m(y+l) \sin \lambda_m(\eta+l) \\ \lambda_m &= \frac{m\pi}{2l} \end{aligned} \right.$$

Function  $G(x, y, \xi, \eta)$  can be expressed through the elementary functions with the help of formula (Dwight, 1961)

$$\sum_{m=1}^{\infty} \frac{1}{m} e^{-mA} \sin(mB) \sin(mC) = \frac{1}{4} \ln \frac{sh^2\left(\frac{A}{2}\right) + \sin^2 \frac{B-C}{2}}{sh^2\left(\frac{A}{2}\right) + \sin^2 \frac{B+C}{2}}$$

$$G(x, y, \xi, \eta) = \Phi(x - \xi, y - \eta) + G^*(x, y, \xi, \eta)$$

$$G^*(x, y, \xi, \eta) = \psi(x - \xi, y - \eta) + \Omega(x - \xi, y + \eta + 2l) \quad (5)$$

$$\Psi(x, y) = \frac{1}{4\pi} \ln[ch(\beta x) - \cos(\beta y)]; \quad \Phi(x, y) = \frac{1}{2\pi} \ln \sqrt{x^2 + y^2}$$

$$\Omega(x, y) = -\Psi(x, y) - \Phi(x, y)$$

Let's note that the formula (4) satisfies all conditions of the boundary value problem (1) except last one for any values of the function  $\chi(\xi)$ . After it one will derive the integral equation on the finite interval  $(-1, 1)$  with regard to the unknown function  $\chi(x)$

$$\lim_{y \rightarrow \varphi(x) \neq 0} \int_{-1}^1 \chi(\xi) \frac{\partial^2 G}{\partial v_x \partial v_\xi}(x, y, \xi, \eta) \sqrt{1 + [\varphi'(\xi)]^2} d\xi = \sqrt{1 + [\varphi'(x)]^2} T(x), |x| < 1 \quad (6)$$

All transformations were done for the curvilinear crack  $y = \varphi(x)$ . To simplify the calculations let's take  $y = kx + b$ . As a result, after extraction of the singular kernel, one will derive the equation

$$\frac{d^2}{dx^2} \int_{-1}^1 \chi(\xi) \ln|x - \xi| d\xi + \int_{-1}^1 \chi(\xi) R(x, \xi) d\xi = \sqrt{1 + k^2} T(x), |x| < 1$$

$$R(x, \xi) = (1 + k^2) \Omega_{22}(x - \xi, k(x + \xi) + 4\xi) + R^*(x - \xi)$$

$$R^*(x - \xi) = \left[ (1 - k^2) \Omega_{22}(x - \xi, k(x - \xi)) - 2k \Omega_{12}(x - \xi) - \frac{1}{2\pi} (x - \xi)^2 \right] \quad (7)$$

$$\Omega_{12}(z) = \frac{1}{4\pi} \frac{\beta^2 sh(\beta z) \sin(\beta z)}{(ch(\beta z) - \cos(\beta k z))^2}, \quad \beta = \frac{\pi}{2l}$$

$$\Omega_{22}(z, y) = -\frac{1}{2\pi} \beta^2 \frac{(ch(\beta z) \cos(\beta y) - 1)}{(ch(\beta z) - \cos(\beta y))^2}$$

It is possible to show that

$$\lim_{z \rightarrow 0} R^*(z) = \frac{1}{2} (a + k^2)$$

If to use the expansion of the function  $R^*(x, \xi)$  in the series, it is possible to show that the function is continuous one, and moreover, it is infinitely differentiable at point  $z = 0$ . Hence,  $R(x, \xi)$  is infinitely differentiable too. It allows to use the orthogonal polynomials methods (Popov, 2007) for the equation (7) solving and to find the stress intensity of factor near crack's ends.

## 5. Conclusions

Thus, the stated problem is reduced to the singular integral equation, allowing the construction of the effective approximate solution (Popov, 1982).

## References

- Popov, G.Y. (1982) The elastic stress' concentration around dies, cuts, thin inclusions and reinforcements. Nauka, Moskow (in Russian).
- Dwight, G. (1961) Tables of integrals and other mathematical DATA. N.Y.
- Popov, G.Y., Reut, V.V., Moiseev, M.G. and Vaysfeld, N.D. (2007) Equation of Mathematical Physics. Methods of orthogonal polynomials (in Ukrainian).

## NUMERICAL ANALYSIS FOR OPTIMAL LOCALIZATION OF GAS INLET IN A VENTURI MIXER

M. Romańczyk<sup>\*</sup>, W. Elsner<sup>\*\*</sup>

**Abstract:** *The research is devoted to numerical analysis for the optimal localization of gas inlet in a Venturi mixer. Performance of the gas engine depends heavily on the quality of mixing of air and fuel, and therefore homogeneity of the mixture. In addition, there must be a suitable, adapted to the current load of fuel, air ratio  $\lambda$ . Responsible for the fact, among others is the mixer located before entering the combustion chamber of the engine. Incorrect parameter value  $\lambda$  can lead to unstable operation of the engine as well as higher emissions going beyond current environmental standards. The Air-Fuel Ratio (AFR) was calculated for an air-fuel mixture of lean combustion gas engine for  $\lambda = 1.6$  where the stoichiometric AFR for methane  $\text{CH}_4$  equals  $\rightarrow 9.52 \frac{\text{m}^3 \text{air}}{\text{m}^3 \text{CH}_4}$ . In this study, three-dimensional computational fluid dynamics (CFD) modelling has been used to investigate and analyze the influence of different positions of the gas inlet on mixer characteristics and performances. Attention was focused on the air-fuel ratio changes, pressure loss and improvement of the mixing quality in the Venturi mixer.*

**Keywords:** Venturi mixer, Air-fuel ratio, Pressure loss, Turbulence, CFD.

### 1. Introduction

Performances of industrial gas engines depend heavily on the quality of mixing of air and fuel, and therefore homogeneity of the mixture. Air-fuel ratio characteristic has a large influence on the exhaust emissions and fuel economy in industrial gas engines. With increasing demand for high fuel efficiency and low emissions, the need to supply the engine with a well-defined, homogeneous mixture under all circumstances has become more and more essential for better engine performance (Gorjibandpy et al., 2010). An ideal Venturi mixer provides a mixture of appropriate Air-fuel ratio (AFR) to the engine over its entire range of operation, from no load to full load conditions (Devarajan, 2008). To ensure correct performance of the engine, the Venturi mixer should be equipped with a gas inlet in optimal position, which causes a better mixing and a smaller pressure loss. Additionally an incorrect parameter value of  $\lambda$  can lead to unstable operation of the engine as well as higher emissions going beyond current environmental standards. For industrial gas engines the combustion anomalies differ highly from conventional combustion processes and can lead to strong impairments of the engine operation as well as to several engine failures (Han, 2010). On how the combustion process develops, has a huge impact the proper mix of fuel and air. If the mixture is optimal prepared appears an optimal combustion and an environmental friendly power generation. If the mixture is too lean (more air than necessary), it can lead to misfire. Misfire results with unburned gas-fuel in the exhaust. Another problem what can occur is the slow combustion. In effect there would be high CO-Emissions, high instability of the whole combustion process. On the other side, if the mixture is too rich (more gas than necessary) there may occur undesired processes such as pre-ignition and glow-ignition. They occur often during high load operations. Glow Ignition causes a very high instability of the combustion process, and is very dangerous for the engine. Different reasons for pre-ignition have been suggested previously, especially the mixture composition of the gas-air phase itself and also the particle-droplet-induced ignition (Günther et al., 2013). In addition can occur abnormal combustion knock which has a strong impact of the deterioration of engine durability and a negative environmental impact by exhaust emissions.

---

<sup>\*</sup> MSc. Mathias Romańczyk: Institute of Thermal Machinery, Czestochowa University of Technology, Armii Krajowej 21; 42-201, Czestochowa; Poland, mathias@imc.pcz.czyst.pl

<sup>\*\*</sup> Prof. Witold Elsner: Institute of Thermal Machinery, Czestochowa University of Technology, Armii Krajowej 21; 42-201, Czestochowa; Poland, welsner@imc.pcz.czyst.pl



As seen, a very important “component” in the combustion process is an optimal preparation of good quality air-fuel mixture. Therefore in this paper the numerical investigations were performed on a basic Venturi mixer, to compare different positions of gas inlet and determine the optimal localization of it.

## 2. Mixer design and modeling software OpenFOAM

In modern gas engines more often the manufacturers trying to design gas mixers based on the Venturi effect. The Venturi effect is caused by the drop in fluid pressure that results when a fluid flows through a constricted section of a pipe. In fluid dynamics, a fluid's velocity increases, as it passes through a constriction in according with the principle of the mass continuity, while its static pressure decreases in according with the principle of conservation of the mechanical energy. In place of the constriction, due to the decrease of static pressure (negative pressure), is sucked in gas, and in this way the gas is mixed with air. The flow through a Venturi mixer is a turbulent flow, so there was used a turbulence model in the numerical calculations. Therefore a  $k-\varepsilon$  transport equation turbulence model was used to study the turbulence kinetic energy (TKE). The different Venturi mixer geometries of models used in these CFD simulations were designed in Autodesk Inventor, while the numerical calculations have been performed using the software OpenFOAM. This software is an open source CFD tool which gives very good results in validation with experimental data. This program is a package for solving a wide range of engineering problems, from complex CFD among other things, including chemical reactions, turbulence flows etc. In these CFD analyzes the *reactingFoam* was used. *ReactingFoam* is one of the standard OpenFOAM Solvers, which using a VOF (Volume of Fluid) method to capture the mixing interface between analyzed gases. In this paper were analyzed the mixing between methane  $\text{CH}_4$  and air. The composition of air was set in the CFD simulations by 21 % of oxygen, and 79 % of nitrogen. In Fig. 1 were shown on the left hand side the Venturi mixer and on the right hand side the analyzed cases 1 – 6 with the dimensions of the Venturi mixer.

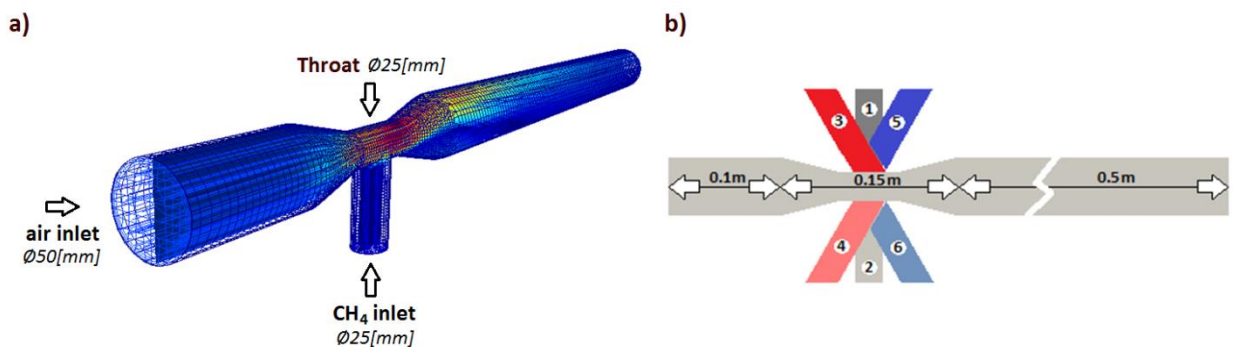


Fig. 1: a) Venturi mixer; b) Analyzed cases 1–6 with the dimensions.

The Venturi mixer constructed in Autodesk Inventor was equipped with the following dimensions. The air inlet diameter was set on 50 mm, while the gas inlet diameter on 25 mm. At the constriction point of the Venturi mixer (Throat) the diameter equals 25 mm. The length of the analyzed Venturi mixer types in all cases was set on 750 mm.

The analyzed cases in this paper were presented below:

- Case 1) **normal**↓ – normal location of the gas inlet from the top,
- Case 2) **normal**↑ – normal location of the gas inlet from the bottom,
- Case 3) **30°**↙ – location of the gas inlet from top on left side at an angle of 30°,
- Case 4) **30°**↗ – location of the gas inlet from bottom on left side at an angle of 30°,
- Case 5) **30°**↘ – location of the gas inlet from top on right side at an angle of 30°,
- Case 6) **30°**↖ – location of the gas inlet from bottom on right side at an angle of 30°.

## 3. Results and discussion

The results presented in this paper show the comparison between six analyzed cases of the gas inlet localization in the Venturi mixer. The Air-Fuel Ratio (AFR) was calculated for an air-fuel mixture for

lean combustion gas engine with  $\lambda = 1.6$  where the stoichiometric AFR for  $CH_4$  equals  $\rightarrow 9.52 \frac{m^3 air}{m^3 CH_4}$  (Rażniewicz, 1966). The calculation has been presented below:

$$AFR = \frac{m_{air}}{m_{fuel}}$$

$$AFR_{stoich} = 9.52 \frac{m^3 air}{m^3 CH_4}$$

$$\lambda = \frac{AFR}{AFR_{stoich}}$$

$$1.6 = \frac{AFR}{9.52} \Rightarrow AFR = 15.232 \frac{m^3 air}{m^3 CH_4}$$

$$for AFR = 15.232 \frac{m^3 air}{m^3 CH_4} \Rightarrow \frac{0.9384 m_{air}}{0.0616 m_{CH_4}}$$

Therefore the concentration of methane mass fraction  $CH_4$  equals  $\Rightarrow 0.0616 m_{CH_4}$  while the concentration of air mass fraction equals  $\Rightarrow 0.9384 m_{air}$ . The concentrations of methane mass fraction  $CH_4$  and air through the Venturi mixer were shown in Fig. 2.

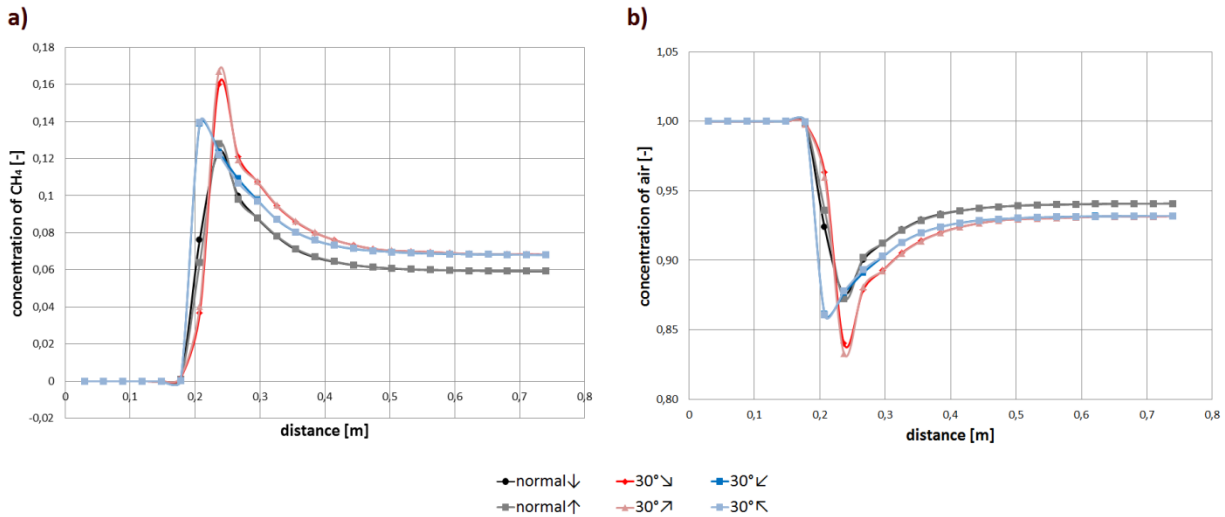


Fig. 2: Concentration of methane mass fraction  $CH_4$  - a) and air - b) through the Venturi mixer.

Analyzing Fig. 2 it is seen, that the suction of methane appears earlier and faster in the gas inlet located indirectly to the flow stream (blue colored lines). The gas inlet located directly to the flow stream (red colored lines) show that the suction of methane appears a little bit later and initially slower, but in the end more methane  $CH_4$  is sucked in, which results in a better mixing process of the two components – air and gas. These drops are also seen on the concentration of air through the Venturi mixer. The normal position of the location of gas inlet has been optimally simulated for  $\rightarrow \lambda = 1.6$ . It is seen in both cases (left and right side of the location of gas inlet) – that the mixture preparation is richer in the end (more gas) what causes a smaller value of  $\lambda < 1.6$ . Here we could observe the air-fuel ratio changes, which could be explained with the angle of the gas inlet flow which causes more suction of gas into the flow stream of the Venturi mixer, at identical inlet conditions for all analyzed cases.

In Fig.3 were presented the distributions of turbulence kinetic energy (TKE) and pressure loss [Pa] through the Venturi mixer. In fluid dynamics the turbulence kinetic energy (TKE) is defined as the mean kinetic energy per unit mass, related with eddies in a turbulent flow. Physically, TKE is characterized by measured root-mean square (RMS), therefore velocity fluctuations. In Reynolds-averaged Navier Stokes equations (RANS), the turbulence kinetic energy (TKE) can be calculated based on the closure method, i.e. a turbulence model. As it was mentioned before, in the numerical simulations the turbulence model k- $\epsilon$  was applied. Turbulence kinetic energy (TKE) can be generated by fluid shear, friction or buoyancy, or through an external force at low-frequency eddy scales (Absi, 2008).

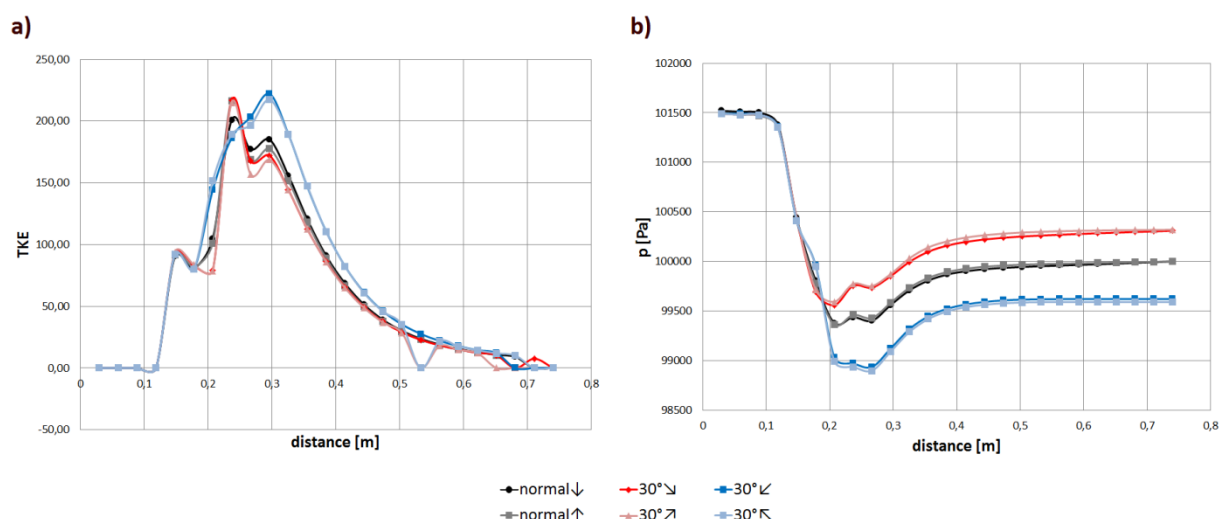


Fig. 3: Distribution of turbulent kinetic energy - a) and pressure loss [Pa] - b) through the Venturi mixer.

Analyzing the distributions of pressure loss [Pa] through the Venturi mixer it is clearly seen that the smallest drop in pressure appears for red colored lines – in the location of the gas inlet on the left side at an angle of 30 °. The reason for this is, that the gas entering the Venturi mixer flows directly into the flow stream and is mixed with air without much resistance from the air itself, due to the fact that the analyzed flow through the Venturi mixer is from left to right. The biggest pressure loss is seen for the blue colored lines, where the gas enters the Venturi mixer in the opposite direction to the flow.

#### 4. Conclusions

The research shows that the best localization for the gas inlet in the Venturi mixer is case 3 and 4 (red colored lines), where the gas inlet is located on the left side at an angle of 30 °, where the gas CH<sub>4</sub> is supplied directly into the flow stream of air.

#### Acknowledgement

This research is part of a project that has received funding from the European Union's Horizon 2020 research and innovation programme under grant agreement No 691232-Knocky-H2020-MSCA-RISE-2015/H2020-MSCARISE-2015.

#### References

- Absi, R. (2008) Analytical solutions for the modeled k-equation. ASME J. Appl. Mech. 75 (044501): 1-4.
- Devarajan, R. (2008) Comparative Evaluation of a Two Stroke Compressed Natural Gas Mixer Design using Simulation and Experimental Techniques", International Conference on Association of Science and Technology for Development, Power and Energy Systems, Langkawi, 359-362.
- Günther, M., Uygun, Y., Kremer, F. and Pischinger, S. (2013) Pre-ignition and glow-ignition of gasoline biofuels, Research Fuels, pp. 46-53, MTZ 1212013 Vol. 74.
- Gorjibandpy, M. and Sangsereki, M.K. (2010) Computational Investigation of Air-Gas Venturi Mixer for Powered Bi-Fuel Diesel Engine, World Academy of Science, Engineering and Technology International Journal of Mechanical, Aerospace, Industrial, Mechatronic and Manufacturing Engineering Vol. 4, No. 11.
- Han, K-M. (2010) Fiber-based methods for the optical analysis of spatial combustion processes and combustion anomalies in Ottomotors, Karlsruhe Institute of Technology, Dissertation.
- Raźniewi , K. (1966) Tablice cieplne z wykresami, eng. Heat tables with charts, Warsaw, WNT.

## TENSILE STRENGTH OF PURE IRON SAMPLES MANUFACTURED BY SELECTIVE LASER MELTING METHOD

J. Roupec, I. Mazůrek, Z. Strecker, M. Kubík, O. Macháček\*

**Abstract:** This paper deals with the tensile strength measurement of samples produced by additive manufacturing. Tested samples were made of pure iron on machine SLM280HL based on Selective Laser Melting method (SLM). The pure iron was selected as a semi-finished product for future manufacturing of a magnetic circuit in magnetorheological damper. The magnetic circuit is an inseparable part of damper piston, which is high mechanically loaded during the operation. Therefore, it is highly important to have suitable mechanical properties. The free-cutting steel 11SMn30 was used as a reference sample. Five different settings of laser power, scanning speed and hatch distance were used for preparation of five sets of samples. The highest tensile strength was achieved at samples produced with the highest energy density and the lowest volume speed of building. These conditions were achieved by laser power 300 W, scanning speed 750 mm/s and hatch distance 84  $\mu\text{m}$ . The tensile strength of these samples was 461 MPa, which is higher than at reference steel (452 MPa). From the point of view of economic aspects, the second most strength steel is better choice, because its tensile strength is 456 MPa but the building speed is about 50 % higher.

**Keywords:** Selective Laser Melting, Pure iron, Tensile strength, Magnetorheological valve.

### 1. Introduction

The Selective Laser Melting (SLM) is one of the most progressive techniques in the field of Additive Layer Manufacturing (ALM). This technique uses laser beam to melt the metal powder and builds the final product layer by layer. Ilčík (2014) tested material AlSi12 on SLM 280HL and achieved guaranteed roughness Ra10  $\mu\text{m}$  for surfaces inclined at an angle 0 to 140 ° from the building platform. The surface roughness for stepper angle was significantly higher, around Ra50  $\mu\text{m}$ . The best geometrical accuracy was measured around 0.02 mm. The common accuracy was around 0.05 mm. These very good results were achieved in the second production batch after the subsequent calibration and show, that SLM is suitable method for magnetic circuit manufacturing. Koukal (2015) described processes and method leading to manufacture of samples from high strength aluminum alloy EN AW 2618 with relative density 99.66 %. This high relative density promises good mechanical properties. Vrána (2016) published paper describing special lattice structure with high impact resistance. Especially gyroid structure can be advantageously used for lightweight parts with high strength in all directions of loading.

This paper focuses on the manufacture of samples from pure iron powder and measurement of their tensile strength. If the material strength is suitable, this material can be used in future for building ultra-fast magnetic valves by SLM technology – magnetorheological or electromechanical valves, which are nowadays limited by occurring eddy currents (Strecker et al., 2014).

### 2. Methods

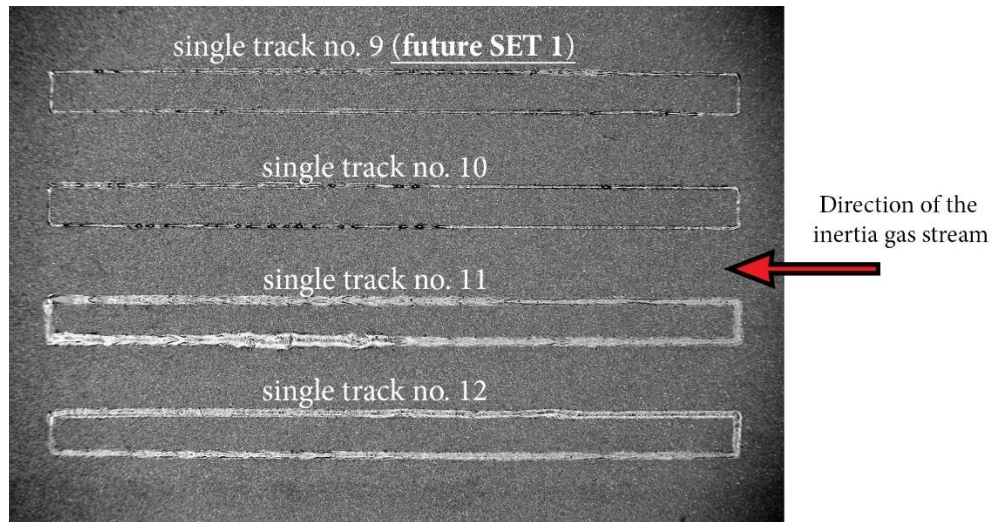
The material of samples was high purity iron ATOMET Fe AM (Rio Tinto, QMP) (Palousek et al., 2017) with high permeability, high magnetic saturation and low remanence. The machine SLM 280HL (SLM Solution GmbH) was used for manufacturing of all samples. The machine uses one 400 W ytterbium laser and argon atmosphere.

---

\* All authors: Institute of Machine and Industrial Design, Brno University of Technology; Technická 2896/2; 616 69, Brno; CZ, roupec.j@fme.vutbr.cz

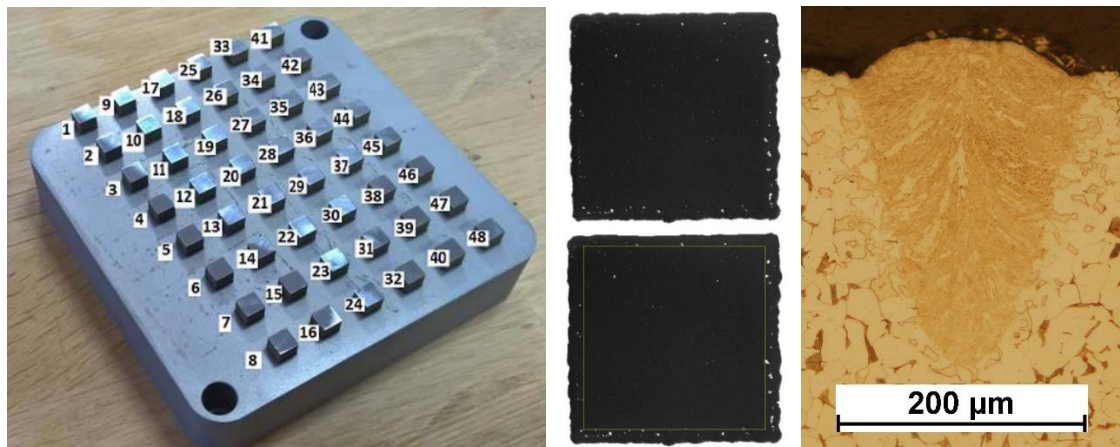


The choice of perspective parameters was carried out in two steps. Firstly the 1-D tracks (single tracks) were produced by melting of one 50  $\mu\text{m}$  layer of powder on building platform. All combinations of laser power (300, 350 and 400 W) and scanning speed (200, 300, 400, 500, 550, 600, 650, 700, 750 and 800 mm/s) were tested. Each single track was built in two directions – after and against the direction of gas stream because of build influence by gas stream (see Fig. 1). The metallographic microscope OLYMPUS GX 51 with 200x magnification was used for polished samples evaluation. The ideal weld should be 50  $\mu\text{m}$  high and the weld root should reach from 30 to 50  $\mu\text{m}$  under the surface.



*Fig. 1: Example of single tracks no. 9 to no. 12.*

Secondly, three the best selected sets of parameters from single track test were used in cube test for porosity analysis. The print of cubes with dimensions 5 x 5 x 5 mm used a chessboard scanning strategy. Hatch distance (distance between two laser tracks) was set according to weld width obtained from single track test and according to overlap ratio. Interval of overlap ratio was chosen from 5 to 50 %. For example, hatch distance for 120  $\mu\text{m}$  weld was changing from 60 to 116  $\mu\text{m}$ , where 60  $\mu\text{m}$  means 50 % overlap. One hatch distance set corresponds to one cube. The 24 combinations were created with one repeating. It gives 48 cubes (see Fig. 2a). The identical cube variants were placed on the platform at opposite sides from the inert gas inlet. The printed cubes were polished and analyzed by the software ImageJ. This SW can recognizes the porosity as white places. Compact material is presented by black color. Ratio between white and black determines a cube porosity. The analysis was carried out within the inscribed square to the cube outline that the uneven outline does not enter to the analysis (see Fig. 2b). The three best results were selected for printing of samples for tensile strength test. Other two sets of parameters were selected because of observation of high porosity and high scanning speed influence on tensile strength.



*Fig. 2: a) Built cubes on platform; b) Polished cube with square area used for porosity analysis; c) Polished single track.*

Two samples from each set of parameters were manufactured, i.e. together 10 samples. The samples were cut from building platform by electro-spark machining. The samples were manufactured with square cross-section, which was subsequently machined on circular (circular cross-section need support structures during the print and has imperfect contact with heated building platform). The sample cross-section was changed in the second print batch on semi-circular for ensuring of faster print. The sample dimensions were obtained from standard DIN 50125 – diameter of tested section was 6 mm.

The tensile strength test was carried out on hydraulic linear actuator Inova. Firstly, the stiffness of fixing frame had to be obtained for result correction. Measured frame stiffness was 44000 N/mm. The free-cutting steel 11SMn30 was used as a reference. Two tests of reference samples were performed on testing machine Zwick Z250 because of results verification of measurement on Inova. The difference between Inova and Zwick measurement was 20 MPa – Inova 452 MPa, Zwick 471 MPa. This difference is considered sufficient for comparative measurement (see Fig. 4b).

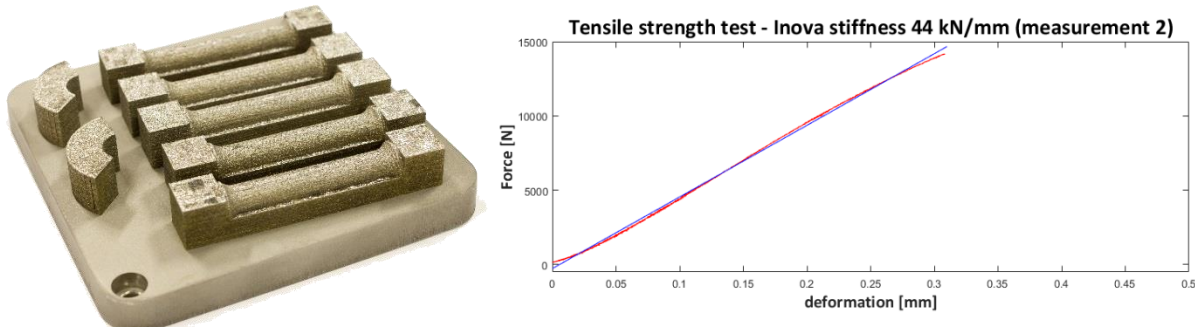


Fig. 3: a) Semi-circular cross section of samples; b) Frame stiffness of Inova machine.

### 3. Results

Tab. 1 shows parameters of printing selected on the base of tests with single tracks and cubes (No. 1, 2 and 3). Parameters set No. 4 presents high relative porosity and No. 5 maximal scanning speed in combination with maximal laser power. In fact, parameters No. 5 do not provide the fastest building due to small hatch distance (see last column in the table). Fig. 4a shows measurement on Inova machine.

Tab. 1: Overview of selected sets of parameters for 3D printing of samples for tensile strength test.

Set No. [-]	Laser Power [W]	Scanning Speed [mm/s]	Hatch Distance [ $\mu\text{m}$ ]	Energy [ $\text{J}/\text{mm}^3$ ]	Building Speed [ $\text{mm}^3/\text{s}$ ]
1	300	750	84	95	3.15
2	400	700	138	83	4.83
3	300	750	108	74	4.05
4	350	700	186	54	6.51
5	400	1400	84	64	5.88

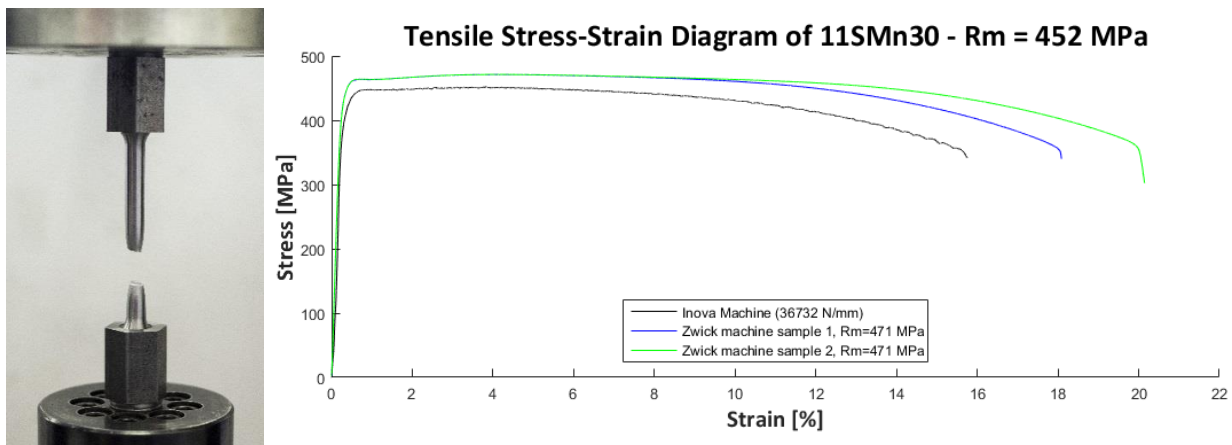


Fig. 4: Tensile strength test of free-cutting steel 11SMn30: a) Inova; b) Difference (Inova versus Zwick).



Fig. 5 shows results of tensile strength tests of samples made by parameters No. 1 and No. 2, which have the highest strength. Both samples have almost similar tensile strength which is simultaneously little higher than reference steel. Contrary to reference steel, the region of yielding is significantly developed and characterized by lower and upper yield strength. Both samples show very good elongation at fraction. On the other hand, the time for printing of the second sample is about 50 % shorter than for the parameters No. 1.

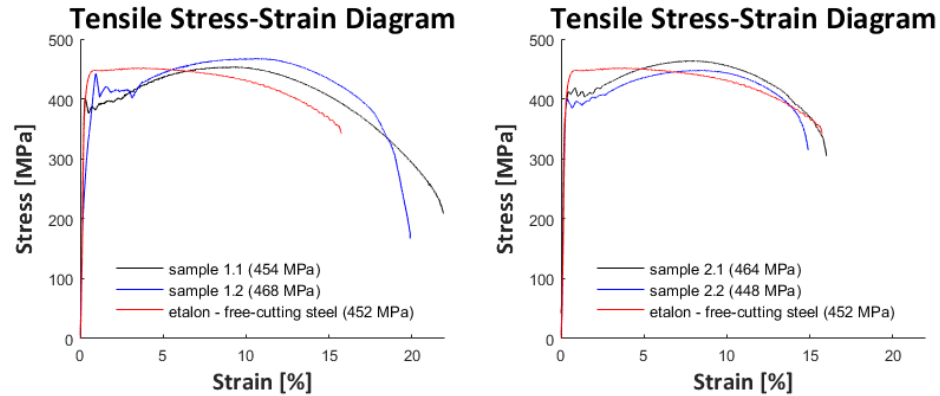


Fig. 5: Tensile Stress-Strain diagram of a) set No. 1; b) set No. 2.



Fig. 6: Fractured samples produced wit parameters a) No. 1; b) No. 2.

#### 4. Conclusion

The published work provides a method for determination of suitable parameters for 3D printer. The tensile strength is around 460 MPa which is in accordance with result published by Palousek (449 MPa) (Palousek et al., 2017).

#### Acknowledgement

There is very appreciated a kind sponsorship of many grants of numerous agencies, which granted as much as they could. The research leading to these results has received funding from GAČR 17-10660J, GAČR 17-26162S and FSI-S-17-4428.

#### References

- Ilčík, J., Koutný, D. and Paloušek, D. (2014) Geometrical Accuracy of the Metal Parts Produced by Selective Laser Melting: Initial Tests. In Lecture Notes in Mechanical Engineering, pp. 573-582.
- Koukal, O. et al. (2015) Research about the Influence of Process Parameters of Selective Laser Melting on Material EN AW 2618. Proceedings of Euro PM 2015: pp. 1-6.
- Palousek, D. et al. (2017) Processing of nearly pure iron using 400W selective laser melting – initial study. MM Science Journal 2017, 1, pp. 1738-1743.
- Strecker, Z., Roupec, J. and Mazurek, I. (2014) Limiting factors of the response time of the magnetorheological damper. International Journal of Applied Electromagnetics and Mechanics 47, 2, pp. 541-550.
- Vrana, R., Koutny, D. and Palousek, D. (2016) Impact resistance of different types of lattice structures manufactured by SLM. MM Science Journal 2016(6): 1579-1585.

## SPECIAL ELEMENT FOR NUMERICAL MODELLING OF THE ROCK BOLT REINFORCEMENT

D. Runt<sup>\*</sup>, J. Novotný<sup>\*\*</sup>, J. Pruška<sup>\*\*\*</sup>

**Abstract:** Rock bolts as construction elements are often used in underground civil engineering projects. This work deals with their mathematical modelling. Finite elements of Aydan type were used for the description of rock bolts and hexahedral quadratic finite elements were used for the description of rock massif. A new code for the computation of stiffness matrices and right hand sides of these elements was developed by us. Stresses in a rock massif around an excavation reinforced by rock bolts were computed using the mentioned code and the solver PMD (noncommercial code developed at the Institute of Thermomechanics AS CR). The results show that the use of rock bolts can reduce the area of the maximal mechanical stress in the vicinity of excavations.

**Keywords:** Rock bolt, Finite element method (FEM), Element of Aydan type, Tunnels, Stiffness matrix.

### 1. Introduction

Rock bolts as reinforcing construction elements are often used in underground civil engineering projects, especially tunnels. A typical rock bolt is created by a steel bar fastened by a cement grout in a borehole (Fig. 1). The reduction of the area of maximal mechanical stress in the vicinity of excavation is a main function of rock bolts. They can also stabilize separated blocks of rock.

Nowadays it is common to use numerical modelling for designing of various types of constructions, and rock bolts are no exception. Several special finite elements for rock bolt modelling were developed. The most widely used element was presented in the paper of Aydan (1989). The so-called Aydan element consists of two groups of nodes. The first group represents a rod sub-element, which is a simple model of the steel bar. The remaining nodes are located on the interface of the cement grout and the rock massif. The connection of the bar with the surrounding rock by the cement grout is represented by the joint action of both groups of nodes. This paper is focused on a six-node type of the Aydan element with quadratic shape functions, which is used in the 3D model and which has not been presented in literature until these days. The description of this element and its application in the 3D model of an excavation reinforced by rock bolts are presented below.

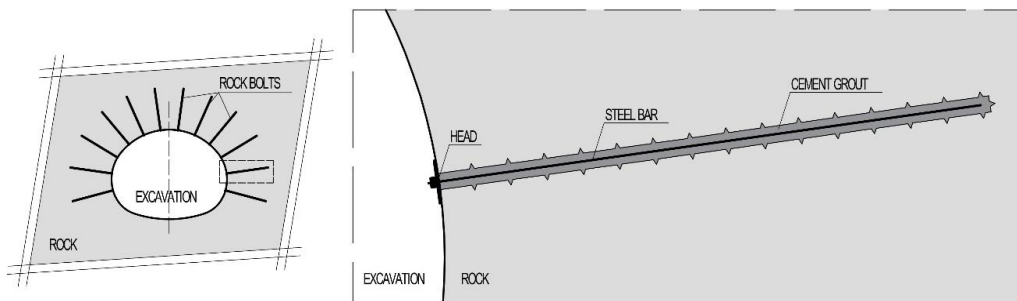


Fig. 1: Rock bolt as reinforcing construction.

<sup>\*</sup> Ing. David Runt: Department of Mathematics, Czech Technical University in Prague; Thákurova 7; 166 29, Prague; CZ, david.runt@fsv.cvut.cz

<sup>\*\*</sup> RNDr. Jaroslav Novotný, PhD.: Department of Mathematics, Czech Technical University in Prague; Thákurova 7; 166 29, Prague; CZ, jaroslav.novotny@cvut.cz

<sup>\*\*\*</sup> Assoc. Prof. Dr. Ing. Jan Pruška: Department of Geotechnics, Czech Technical University in Prague; Thákurova 7; 166 29, Prague; CZ, pruska@fsv.cvut.cz

## 2. Classical formulation of a linear elasticity problem

Differential equations describe real physical processes inside the material. Therefore the classical formulation of the linear elasticity problem, described for instance in Brdička (1959), is mentioned first.

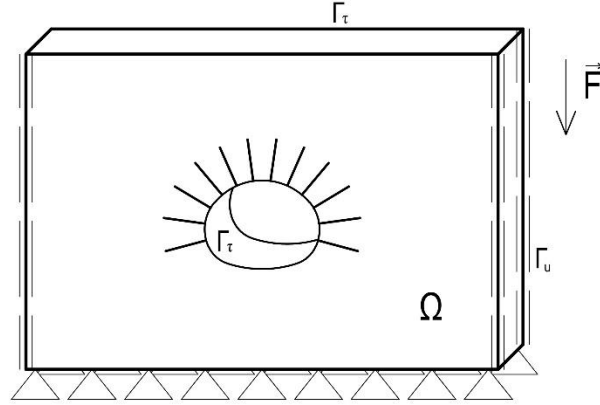


Fig. 2: Classical formulation of the linear elasticity problem.

Linear elastic body, that occupies the domain  $\Omega$  (Fig. 2), is considered. We look for the vector of displacement  $\mathbf{u} = (u_1, u_2, u_3)$  satisfying Lamé equations in the domain  $\Omega$ , see Eq. (1).

$$(\lambda + \mu) \sum_{j=1}^3 \left( \frac{\partial^2 u_j}{\partial x_i \partial x_j} \right) + \mu \Delta u_i + F_i = 0 \quad (i = 1, 2, 3), \quad (1)$$

where  $\lambda, \mu$  are Lamé coefficients,  $u_i$  is a component of the displacement vector,  $x$  is a coordinate,  $F_i$  is a component of density of volumetric load. Two types of boundary conditions are considered,

$$u_i = u_i^0, \quad (i = 1, 2, 3) \rightarrow \text{on } \Gamma_u, \quad (2)$$

$$\tau_{ij} v_j = T_i^0, \quad (i = 1, 2, 3) \rightarrow \text{on } \Gamma_\tau, \quad (3)$$

where  $u_i$  is a component of the displacement vector,  $u^0$  is a prescribed displacement,  $\tau_{ij}$  is a component of the stress tensor,  $v_i$  is an outward unit normal to the boundary of  $\Omega$ ,  $T^0$  is a prescribed stress vector.

We prescribed zero displacements on the bottom, on sides and on the front and back faces of the domain  $\Omega$ , see Eq. (2). The zero stress vector is prescribed on the surface inside the excavation and on the top surface, see Eq. (3).

## 3. The finite element method

### 3.1. Rock bolt element of the Aydan type

The rock bolt element with quadratic shape functions has six nodes (Fig. 3). Three of them represent the steel rod (nodes 1, 2 and 3). The others are located on the interface between the cement grout and the surrounding rock. The rock bolt element is connected to elements which represent the rock massif by nodes 4, 5 and 6 (Fig. 3). The connection of the bar with the surrounding rock by the cement grout is represented by the joint action of both groups of nodes.

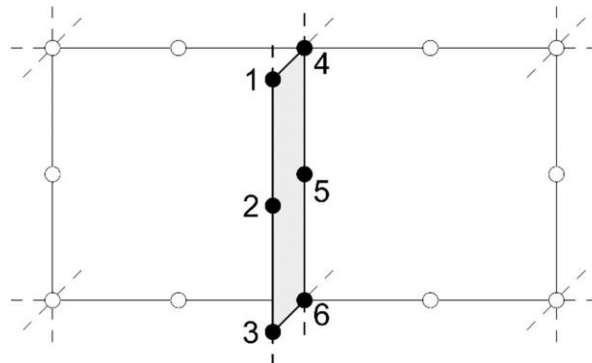


Fig. 3: Six-node rock bolt element and its connection to the finite element mesh.

Several simplifications were considered during the derivation of the stiffness matrix of the Aydan element. The steel rod and body formed by the fastening material are assumed axially symmetric and coaxial bodies. Both mentioned materials are considered homogenous, isotropic and linear elastic. Because of this assumption, dependence between stresses and deformations is described by linear Hook's law. The radius of the rock bolt is negligible with respect to nodal coordinates. Therefore, nodes 1 and 4 have identical coordinates. The same is valid for nodes 2 and 5 or 3 and 6. However, the assumption of the negligible radius cannot be applied to the process of the derivation of the stiffness matrix.

Only four types of deformations of the Aydan element are included in the computation:

- relative longitudinal deformation of the steel bar caused by different axial displacements of nodes 1, 2 and 3,
- relative cross shear deformation of the steel bar caused by different radial displacements of nodes 1, 2 and 3,
- relative longitudinal shear deformation of fastening material caused by different axial displacements of nodes 1, 2 and 3 with respect to nodes 4, 5 and 6,
- relative cross deformation of fastening material caused by different radial displacements of nodes 1, 2 and 3 with respect to nodes 4, 5 and 6.

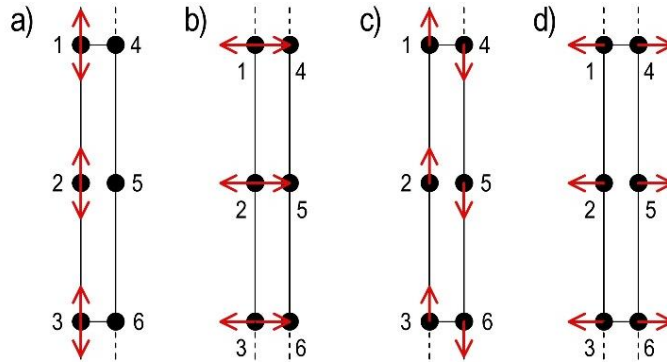


Fig. 4: Types of deformations of the Aydan element.

The stiffness matrix of the Aydan element is expressed as a volume integral. We consider constant values of displacement across the cross section of the rock bolt. Therefore, we are able to reduce the volume integral to the one-dimensional integral with an integration area of the length of the rock bolt element. Three-point Gaussian numerical integration was used for calculation of this integral.

### 3.2. Hexahedron – rock element for 3D model

In the 3D model the rock mass is represented by hexahedral elements with 20 nodes and quadratic shape functions, which are described, for instance, in Babuška and Szabo (1976). Eight nodes are located in vertices, remaining twelve are located in the centers of edges (Fig. 5).

The stiffness matrix and the right hand side of the hexahedral element is expressed as volume integrals. Gaussian numerical integration was used for calculating of these integrals. 27 Gauss points are needed for each element. Weights of these points were defined by the modification of the method in a one dimension by Fubini's theorem. This method is described in the work of Babuška and Szabo (1976).

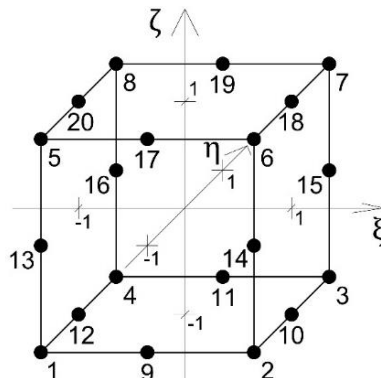


Fig. 5: Nodes of hexahedral element.

#### 4. Model of excavation reinforced by rock bolts

Geometry of the model corresponds to the characteristic cross section of the Brusnice tunnel, which is a part of the Blanka tunnel complex. All data necessary for the creation of the model were taken from the dissertation of Nosek (2015). The excavation height is about 12.8 m and the width is about 16.6 m. The rock massif is formed by mildly eroded slates which are very common in the surrounding of the tunnel.

Two studies were considered. In the first one we assumed the excavation without any rock bolts. They were added only to the second calculation. We are able to evaluate the influence of rock bolts by a comparison of results of both studies.

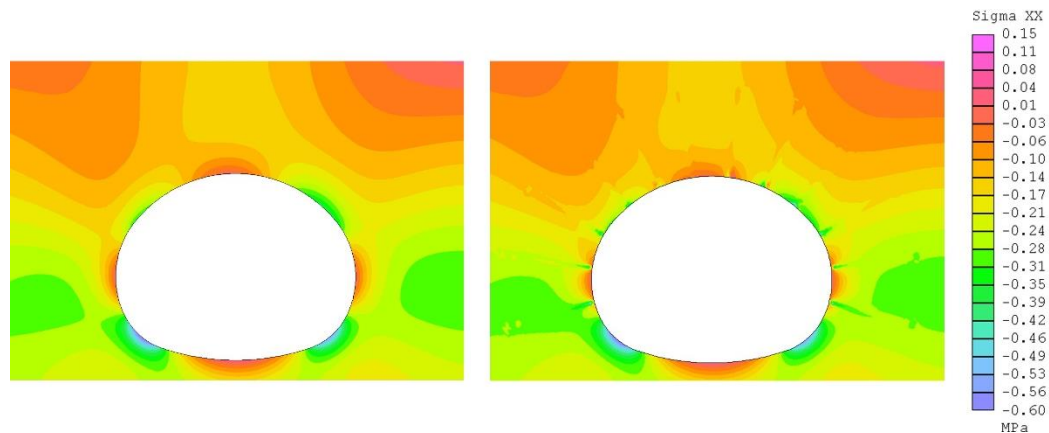


Fig. 6: Stress  $\sigma_{xx}$  in the surrounding of the excavation without rock bolts (left) and with rock bolts (right).

#### 5. Conclusions

The results show that use of rockbolts can reduce areas of the maximal mechanical stress in the vicinity of excavations. In general, rock bolts help to create a rock arch by increasing normal stress in the radial direction. Described influence corresponds to theoretical knowledge of the function of rock bolts.

It is possible to combine special rock bolt elements with other types of elements with appropriate shape functions. This is the way how to create complex numerical models of reinforced excavations. Due to the relative simplicity of the described rock bolt element it is quite easy to create its various modifications with various shape functions. These modifications could be used in both 2D and 3D models. These modifications were described by Aydan (1989), Chao (1998) or Runt (2014, 2016).

#### Acknowledgement

This work was supported by the grant project SGS CVUT Numerical computation of tunnels and membrane constructions using FEM provided by Czech Technical University in Prague, Faculty of Civil Engineering.

#### References

- Aydan, O. (1989) The stabilization of rock engineering structures by rockbolts. Nagoya University, Nagoya.
- Babuška, I. and Szabo, B. (1976) Finite element analysis. John Wiley & Sons, New York.
- Brdička, M. (1959) Continuum mechanics. Czechoslovak Academy of Science, Prague (in Czech).
- Chao, T. (1998) The numerical modelling of rockbolts in geomechanics by finite element methods. Brunel University, Department of Mathematics and Statistics, London.
- Nosek, J. (2015) Evaluation of reliability of structural analyses of tunnels in the Czech Republic on the bases of analyses of the monitoring results. Doctoral thesis, Czech Technical University in Prague, Faculty of Civil Engineering, Prague (in Czech).
- Runt, D. (2014) Numerical modelling of rock bolts by finite element method. Bachelor thesis, Czech Technical University in Prague, Faculty of Civil Engineering, Prague (in Czech).
- Runt, D. (2016) Rock bolt element in finite element method, Diploma thesis. Czech Technical University in Prague, Faculty of Civil Engineering, Prague (in Czech).

## POLYURETHANE COMPOSITES WITH IMPROVED MECHANICAL PROPERTIES

M. Sadej<sup>\*</sup>, Ł. Gierz<sup>\*\*</sup>

**Abstract:** *This work presents results of investigation of composite materials based on polyurethane (PUR) and hydrophilic fillers: A200 (nanosilica). The effect of the filler content on the mechanical properties of the final composite material are determined. The introduction of nanosilica (5 wt.-%) to foams gives the best mechanical properties (highest compressive strength). The obtained results are discussed in terms of effects of content of filler particles on density and thermal properties of the polymer composites. These results correlate well with the results of microscope analysis. Increasing filler percentage reduced the PUR foam density and size of pores.*

**Keywords:** Polymer Composite, Silica, Mechanical Properties, Polyurethane, Foams.

### 1. Introduction

In recent years much attention has been focused on development of new inorganic-organic composite materials of prospective use in many areas (Hajji et al., 1999). Polymers have been modified by incorporating various inorganic fillers to achieve special (exciting bulk, mechanical, functional, electrical, surface etc.) properties (Sadej et al., 2016, 2014, M. Sadej-Bajerlain et al., 2011, Ziobrowski et al., 2014). From among the inorganic substances, silicon dioxide has become of greatest importance as an active filler of polymers because of its good resistance to heat and electricity, mechanical stability, relatively low costs, hardness, high specific surface area (Rotzoll et al., 2008, Kuo et al., 2000). Silica has been widely applied in various industries, besides common plastics and rubber reinforcement, many other potential and practical applications of polymer/silica nanocomposites have been reported: coatings, flame-retardant materials, optical devices, electronics photoluminescent conducting film, ultrapermeable reverse-selective membranes, proton exchange membranes, grouting materials, sensors, etc. (Zou et al., 2004).

Many investigations have been made by the researchers on the potential of the nanosilica as reinforcements for polymers composites. Yern Chee Ching et al. (Ching et al. 2013) studied effect of nanosilica filled polyurethane composite coating on polypropylene substrate. The macroscopic properties of composites are affected by the polymer-nanofiller molecular architecture. Fan et al. (Fan et al. 2012) studied the physical properties of soybean oil-based rigid PU foams modified with glass microspheres and nanoclay. Foams with fillers displayed roughly the same thermal conductivity as soy-polyol based foams without fillers. Banik and Sain (Banik et al. 2009) enhanced the foam loading property by incorporating cellulosic materials such as fibers, but the effect was limited due to the tendency to aggregate for cellulosic materials. The presence of cellulosic materials was observed to have a notable influence on the density of the foams.

Polyurethane foams are a special type of engineering plastic with excellent physical properties (including toughness, and resistance to abrasion and temperature), used in the automotive industry, thermal insulation, packaging material and in commercial applications. However, little is known, about the influence of unmodified silica on the pores network, and the resulting material-specific properties. The main objective of the study was to obtain a polyurethane composites containing filler (unmodified silica A200) and to determine its effect on the physical properties of polymer composites.

---

<sup>\*</sup> Assist. Prof. Mariola Sadej, PhD.: Poznań University of Technology, ul. Berdychowo 4, 60-965 Poznan, Poland, Institute of Technology and Chemical Engineering, mariola.sadej@put.poznan.pl

<sup>\*\*</sup> Assist. Prof. Łukasz Gierz, PhD.: Poznań University of Technology, ul. Piotrowo 3, 60-965 Poznan, Poland, Institute of Machines and Motor Vehicles lukasz.gierz@put.poznan.pl



## 2. Methods

Polyurethane (PU) foam with various amounts of nanosilica contents were prepared. The isocyanate, used in this study was a polymeric diphenylmethane diisocyanate (MDI), with functionality 2.7 and isocyanate equivalent weight 134. Dimethylcyclohexylamine and pentamethyldiethylenetriamine were used as catalysts. The average primary particle size of Aerosil A 200 was 7 nm in average diameter with the specific surface area of 200 m<sup>2</sup>/g. The fillers were dried at 110 °C for 2 h before use. For preparation of the PUR foam with silica, the necessary silica content (0-5 wt.-%) was added to the siloxane polyol (Sigma Aldrich) and mixed with the other ingredients according to the standard procedure. The expansion time was 600s (the form prior to pouring of the foam was heated in an oven to a temperature of 40 °C).

### Compressive strength

Compression tests were performed on prismatic bar specimens with dimension of 50 x 50 x 50 mm using a testing machine, Zwick Material Testing ZW TN1P 2.5. Tests were performed according to the ASTM C365-00 at a speed of 10 mm/min.

### Thermal conductivity

Thermal conductivity measures the ability of a material to transfer heat. The Heat Flow meter method, designed specifically for insulating materials, is defined by international standards ASTM C518, ISO 8301, and DIN EN 12667. The coefficient of thermal conductivity was measured (at 20 °C) using a Laser Comp Fox Heat Flow instrument 200. To perform the test, polymer composites were prepared with dimensions of 200 x 200 x 30 mm.

### Density foams

The density of the foam material (50 x 50 x 50 mm) was determined from specific gravity measurements in accordance with ASTM D792. The specific gravity measurements were found by conducting buoyancy tests with water as the medium for immersion. The equipment consisted of analytical balance (accuracy 0.0001 g). Density was calculated from the formula:

$$\rho = m/V \text{ [kg / m}^3\text{]} \quad (1)$$

$\rho$  - density [kg / m<sup>3</sup>]

m - mass of the sample [kg]

V -volume [m<sup>3</sup>]

### Examination of the structure porous polymer composites

Examination of the porous structure of the polymer composites were made using a microscope Xi CAM BVMS 109C-28. During the study we used an approximation x300. Selected for the unfilled matrix polymer and polymer composites containing 5 % wt.-% (by weight silica relative to the weight of the polyol).

## 3. Results

Mechanical properties of the investigated polymer composites are shown in Fig. 1a. The compressive strength increases almost linearly with the filler content (to 3 wt.-%). This indicates that the addition of nanosilica has helped in improving mechanical properties in the polyurethane foam. Addition of only 3 wt. -% of silica into the PUR foam increases its compressive strength about 30 %.

Fig. 1b illustrates the thermal properties of PUR filled silica at different applied loads. Since 5 wt.-% of nano-SiO<sub>2</sub> filled PUR composite shows the lowest thermal conductivity. The results obtained indicate that the filler addition affect the thermal properties of the polymer matrix.

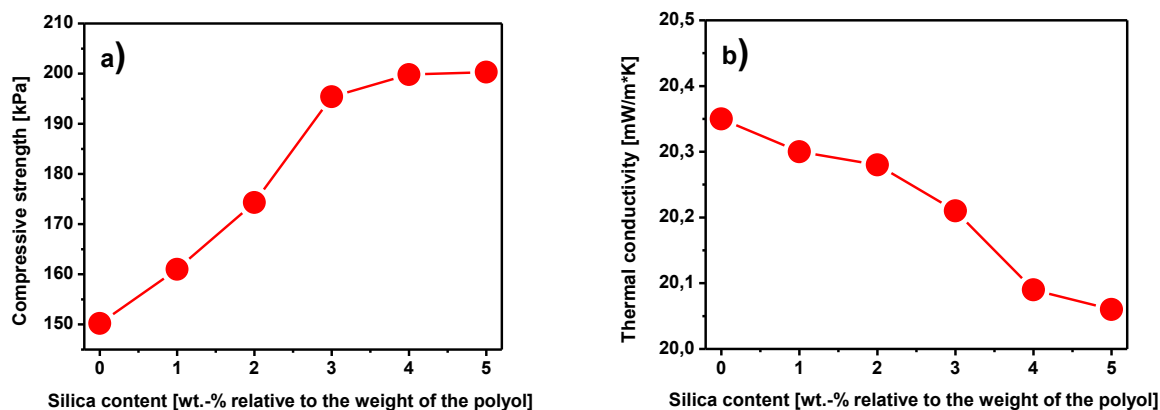


Fig. 1: The dependence of the: a) compressive strength; b) thermal conductivity on silica content in the system.

The compressive strength of foams increases with silica content and with foam density, this is shown in Fig. 2, which illustrates a decrease in compressive strength value with decreasing foam density.

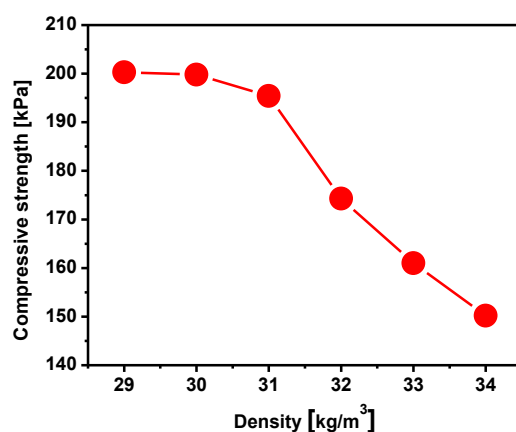


Fig. 2: The dependence of density foam on silica content in the system.

Microscope Xi CAM was used to investigate the dispersion of nano-SiO<sub>2</sub> particle and porous surface changes of the nano-SiO<sub>2</sub> filled PUR. The image in Fig. 3 reveals the dispersion condition of 0 wt.-% and 5 wt.-% of nano-SiO<sub>2</sub> contents in polyurethane foams. As can we see, introduction of the fillers causes changes in structure of foam. Foams reinforced with fillers had more cells and smaller cell size than foams without fillers.

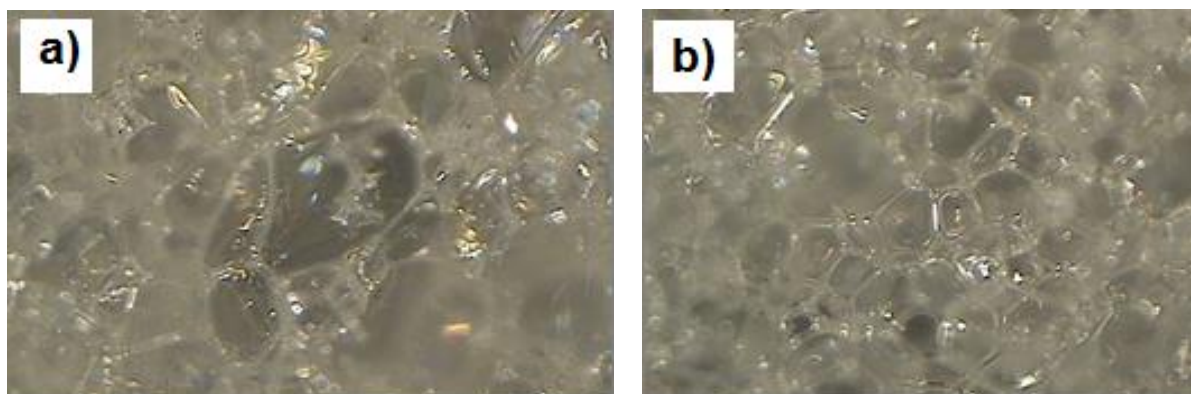


Fig. 3: Porous structure of the polymer composites: a) 0 wt.-% and b) 5 wt.-% of silica content in the system.

#### 4. Conclusions

The effect of the PU/nano-SiO<sub>2</sub> composite on compressive strength and thermal behavior of polymer composite was investigated and compared. It can be concluded that the addition of small amounts of nano-SiO<sub>2</sub> (5 wt.-%) content can exhibit the improvement of compressive strength of the polyurethane matrix. Foams reinforced with fillers had more cells and smaller cell size than foams without fillers. These materials are interest because of their wide applications.

#### Acknowledgement

This work was supported by the Research Projects of Poznan University of Technology 03/32/DSPB/0604.

#### References

- Ching, Y.C. and Syamimie, N. (2013) Effect of nanosilica filled polyurethane composite coating on polypropylene substrate, *J. Nanomat.* 8 pp.
- Banik, I. and Sain, M.M. (2009) Water-blown soy polyol based polyurethane foams modified by cellulosic materials obtained from different sources, *J. Appl. Polym. Sci.* 112: 1974–1987.
- Hajji, P., David, L., Gerard, J.F., Pascault, J.P. and Vigier, G. (1999) Synthesis, structure, and morphology of polymer–silica hybrid nanocomposites based on hydroxyethyl methacrylate, *J. Polym. Sci. Part B: Polym. Phys.* 37: 3172-3187.
- Fan, H., Tekeei, A., Suppes, G.J. and Hsieh, F.H. (2012) Properties of biobased rigid polyurethane foams reinforced with fillers: microspheres and nanoclay, *Intern. J. Polym. Sci.* Article ID 474803, pp. 8.
- Kuo, P.L., Chen, Ch.L. and Hou, S.S. (2000) Function and performance of silicone copolymers, 5. Syntheses and surface characterization of an acrylized silica monomer, *Macromol. Chem. Phys.* 201:1451-1457.
- Sadej, M., Andrzejewska, E., Kurc, B., Gojzewski, H. and Jesionowski T. (2014) Surface-dependent effect of functional silica fillers on photocuring kinetics of hydrogel materials, *J. Polym. Sci. Part A: Polym. Chem.* 52: 3472-3487.
- Sadej, M. and Andrzejewska, E. (2016) Silica/aluminum oxide hybrid as a filler for photocurable composites, *Prog. Org. Coat.* 94:1-8.
- Sadej, M., Gojzewski, H. and Andrzejewska E. (2016) Photocurable polymethacrylate-silica nanocomposites: correlation between dispersion stability, curing kinetics, morphology and properties, *J. Polym. Res.* 23: 116.
- Rotzoll, R. and Vana, P. (2008) Synthesis of poly(methyl acrylate) loops grafted onto silica nanoparticles via reversible addition-fragmentation chain transfer polymerization, *J. Appl. Polym. Sci.: Part A: Polym. Chem.* 45:7656-7666.
- Ziobrowski, P., Andrzejewska, E., Szybowicz, M., Nowicka, A., Sadej-Bajerlein, M., Gojzewski, H. and Drozdowski, M. (2014) Particle clustering in photocurable nanocomposites: dependence of curing kinetics and viscoelastic properties *J. Appl. Polym. Sci.*, 131:1-9.
- Zou, H., Wu, S. and Shen J. (2008) Polymer/silica nanocomposites: preparation, characterization, properties, and applications, *Chem. Rev.* 108:3893-3957.

## SIMULATION OF DAILY LIFE ACTIVITIES IN BIOMECHANICS

**Z. Sant<sup>\*</sup>, L. Mifsud<sup>\*\*</sup>, C. Muscat<sup>\*\*\*</sup>**

**Abstract:** *Finite Element Analysis (FEA), the widely accepted virtual testing process, involves creation of a virtual geometry model that is converted into a Finite Element Model (FEM) and complemented by material and load models. The creation of geometry model is presently supported by various NURB packages while the material model can be translated from CT scan via techniques of power law or micro-mechanics. The load model remains at discretion of the researcher and his resources. This leads to a situation when the load model is limited to simulate over simplified daily life activity (DLA) such as standing position and any other activity where the forces can be computed from static equations without consideration of the muscular activity. This creates a drawback for correct simulation of the test ‘in silico’ that should be carried under the maximum load condition thus considering inertial forces and additional muscular load. This paper will provide brief overview of the present way to evaluate the load for required DLA and the final results obtained when modelling an ordinary walk. The results (Sant et al., 2012), based on validated model (Arjmand et al., 2006), will be compared with results of AnyBody load model applied to the lumbar spine.*

**Keywords:** Finite elements, Lumbar spine, Inverse dynamics, Muscular activity.

### 1. Introduction

The analysis of DLA effect on the bone cannot be measured directly thus ‘in silico’ testing is widely accepted. The results of these tests provide a valuable feedback, which can offer a better view on the outcome of the planned surgery or in case of a designer it provides a response, which initiates corrections of the design if necessary. The walk is a natural movement for people of all generations therefore it was selected as a DLA. Another reason why walk should be selected is the fact of that more than 33 % of population suffers at least once in their life a low back pain associated with this activity. It is the lumbar spine that undergoes around 3 millions of cycles per year for an average person and even more for active people or sportsmen. To model the load, which the lumbar spine must support during walking is a very complex task since the lumbar spine undergoes during each step a combined motion consisting of simultaneous flexion, and rotation of the spine accompanied by shear load between two adjacent vertebrae in anterior-posterior direction. Why is it so difficult to evaluate the load that our body must support? There are various reasons that can be summarized into a short answer: The musculo-skeletal system is an open system due to muscle physiology. There is no valid computational model that describes the behaviour of the muscle in agreement with thermodynamics laws. One of the first muscle force models is based on the proportionality between the force generated at the muscle and its geometry, mainly the length and cross-section. This model provides only maximum force that can be generated at the muscle. Better understanding of muscular physiology is necessary to understand the activation of the muscle and the force generation.

#### 1.1. Muscle behaviour

We are able to move thanks to the voluntary muscular system, which is activated by the Central Nervous System (CNS) by the process that is still not fully understood. The brain receives a ‘request’ to move upon which it creates an electric signal that is transferred through the nerve system to the location of the

---

<sup>\*</sup> Dr. Ing. Zdenka Sant: Mechanical Engineering Dept., University of Malta, Tal Qroqq; MSD2080, Msida; MT, zdenka.sant@um.edu.mt

<sup>\*\*</sup> Louise Mifsud, B. Eng.(Hons.): Department of Mechanical Engineering, University College London, Torrington Place, London WC1E 7JE, UK, loumif@gmail.com

<sup>\*\*\*</sup> Carl Muscat, B. Eng. (Hons.): Department of Biomedical Engineering, University of Strathclyde, 16 Richmond Street, Glasgow G1 1XQ, Scotland, UK, carl.muscat.10@um.edu.mt

muscle to be activated. Once signal reaches the muscle membrane it evokes a biochemical reaction that allows the depolarization of the membrane thus the action potential can travel along the stimulated muscle fibre. Activated muscle then forms a biomechanical bridge between two types of filaments that produces the muscle contraction as shown in Fig. 1. That explains why it is easier to measure the electric potential during the muscular activity than calculate the force magnitude at the instant when the muscle starts ‘firing’ or reaches its peak force. The measurement of el. potential is possible via use of electromyography (EMG). The necessity to convert el. volts into forces remains one of disadvantages of this method. This paper will deal with present study based on the evaluation of muscular activity by means of kinematics and dynamics applied to a recorded data to compute a specific muscular forces during normal walk of a subject.

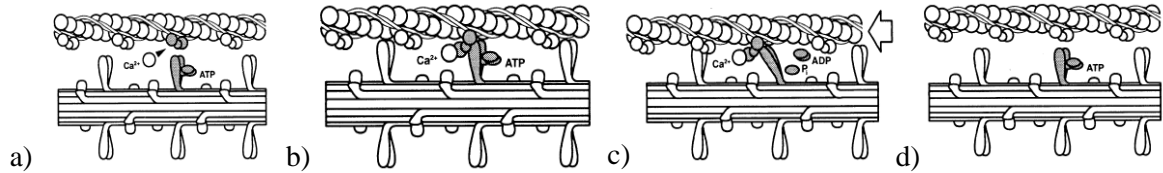


Fig. 1: Cross-bridge connection a) activation, b) connection, c) contraction, d) detachment.

## 2. Methods

The geometry model of the lumbar spine as one of the most affected musculo-skeletal structures was segmented from CT scans obtained from Mater Dei hospital, Malta by means of Simpleware software. Through segmentation of geometry a FE model was created, and simplified material models, characterizing tissue property as a part of the segmentation process from CT scans as listed in Tab. 1. Then the three load models were created - the one of 2 kN compressive normal force, the second model is based on the published data (Arjmand et al., 2006) consisting of normal, and shear force together with flexion moment. The third model is a subject specific load model based on the processed data measured in the newly established Motion laboratory at University of Malta. The motion is captured by means of VICON system consisting of an eight high speed infra red cameras of 4 MP with frequency of 1000 Hz that are able to capture the light reflected from the markers attached to a moving object; in our case to the bare skin of the subject. The force plate installed within the system measures the subject’s response in static and dynamical activity during the walk. In the first step the gait cycle was recorded while in the second step the recorded data was processed by an open software AnyBody to obtain the muscular forces acting on the spine mainly on the selected vertebra.

Tab. 1: List of material properties as assigned to components of the FE segment.

Component	Young’s Modulus E[MPa]	Poisson’s Ratio $\nu$ [–]
Cortical Bone	12000	0.3
Cancellous Bone	150	0.3
Endplate	500	0.3
IVD	550	0.3
Cartilage	24	0.4

### 2.1. Gait cycle

When we walk, we provide support and propulsion to our body. The term gait refers to the manner of walking, rather than the actual walking process. The analysis of a gait cycle provides important information either in case of pain reported by the patient or an evaluation of the surgery outcome to compare the subject's gait with a ‘normal’ gait. For this purpose the time between two consecutive identical events of walk is considered as a one gait cycle. It is a common practice to start the cycle with first contact of the foot with the ground called ‘heel strike’. The subject was asked to move on the platform with a normal walking speed for minimum of three successful trials. The recorded positions of all reflective markers were saved, visually inspected mainly the correct record of two specific events in

the gait cycle called ‘heel strike’ and ‘toe off’, which must happened within the capture area of the force plate, and for any ‘drop off’ markers causing then discontinued trajectories. The data was cleaned and released in C3D format for further investigation by means of use AnyBody open software.

## 2.2. Evaluation of muscular force using AnyBody

The AnyBody is an open simulation software with aim to analyze the musculoskeletal system, mainly humans, as a rigid-body system. In engineering tasks the application of kinematics and dynamics has a direct approach to compute a position, acceleration, and velocity based on the known applied loads. This is not the case for analysis of musculoskeletal systems where goal is to compute the muscular forces. The fundamental problem lays in the amount of muscles that is higher than it's necessary to drive the system with finite degrees of freedom. This means that there are infinitely many muscle recruitment patterns that are acceptable from a dynamical point of view (Damsgaard et al., 2006), often referred to as the redundancy problem of the muscle recruitment. There are two types of dynamical tasks – forward approach is very common in engineering to compute the motion that is driven by a defined force, and inverse dynamics where the computation of forces is derived from the known trajectory. This is a case of musculoskeletal systems. Thus solving statics and dynamics Eq. (1) can provide computation of forces and moments developed at the joints.

$$\mathbf{C} \mathbf{f} = \mathbf{d} \quad (1)$$

Where  $\mathbf{C}$  represents the matrix of coefficients within the static equations that are dependent on the position,  $\mathbf{f}$  is a matrix of muscular and reaction forces, and  $\mathbf{d}$  is a matrix of external and inertia forces. Use of inverse dynamics analysis for a system of equations that include the effect of muscles resolves indeterminacy but the system of muscle recruitment has to be optimized by introduction of an objective function  $G(f^{(M)})$  to minimize the muscular forces, subject to a system of static Eq. (1) with the prescribed condition

$$0 \leq f_i^{(M)} \leq N_i, \quad i \in \{1, \dots, n^{(M)}\} \quad (2)$$

Defining  $f_i^{(M)}$  as the force of  $n$ -th muscle in the system while  $N_i$  represents the normalizing factor defining typical muscle strength. There are presently available three objective functions – polynomial criterion (3)

$$G(f^{(M)}) = \sum_{i=1}^n \left( \frac{f_i^{(M)}}{N_i} \right)^p \quad (3)$$

soft saturation criterion, and the Min/Max criterion (4), which represents the solution of a polynomial criterion while the polynomial degree  $p \rightarrow \infty$  is considered

$$G(f^{(M)}) = \max \left( \frac{f_i^{(M)}}{N_i} \right) \quad (4)$$

which leads to a distribution of muscular forces that keeps maximum relative load to minimum.

## 2.3. Results simulation of AnyBody and FEA

AnyBody software provides the user of AnyScrip module with possibility to control any variables and parameters associated with the model. The user has possibility to create his own model or select suitable model from AnyBody Managed Model Repository (AMMR). We adopted a generic model AnyBody with markers, which was optimized to fit the segment lengths and all other parameters recorded in our C3D database and the model can follow the marker trajectories, which was done by calling different subroutines and their adjustment. Once the model was optimized the subject specific features had to be taken into account via morphing the shape of the generic L4 vertebra of AnyBody model into the shape of a L4 model created from CT scans as shown in Fig. 2. The morphed L4 vertebra was imported back to AnyBody model via specific subroutine performing 'custom scaling'. Then the inverse dynamics was performed on the system to obtain the muscular forces that were exported in XML format to be readable by AnyFE subroutine that converts the XML data into a format suitable for FEA in ANSYS. The spinal segment as described earlier was loaded into ANSYS 15 and the coordinate system

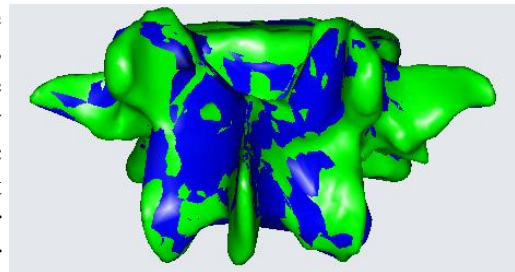


Fig. 2: The result of morphing -Green target L4 CT based with the blue transformed generic STL L4 vertebra.



was aligned to correspond the one in AnyBody prior to running a code of instruction that translates the XML data through ANSYS Parametric Design Language. Within this code a local coordinate system for each muscle insertion is created, the computed force is applied to this point, and connection between the point and the bone surface is set. Then boundary conditions were set to constrain the inferior endplate of L5 vertebra while the nodes between IVD and adjacent vertebrae were coupled by constrain equations.

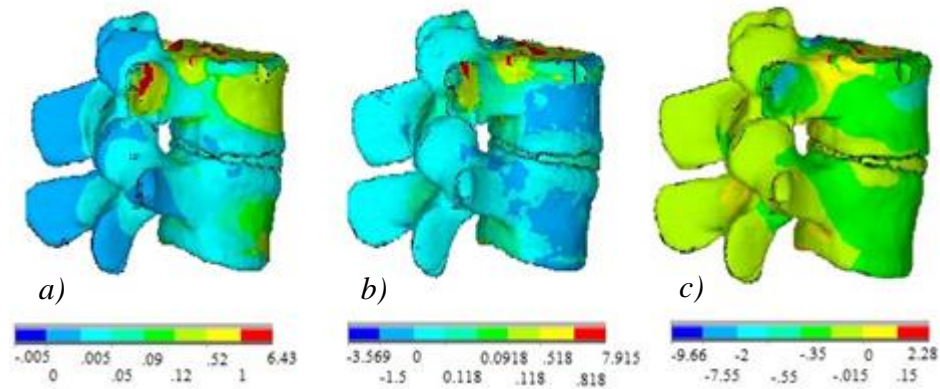


Fig. 3: Stress contour plot [MPa] at 0 % gait cycle (heel strike) – a) Von-Mises stress, b)  $\sigma_1$  principal stress, c)  $\sigma_3$  principal stress.

### 3. Conclusion

The results shown in Fig. 3 demonstrate a significant difference compared to response to two forces and moment as shown in Fig. 4 (Sant et al., 2012). The major disparity originates from the load distribution; where 64 points at ‘physiologically correct positions’ originated from the scaled generic AnyBody model opposed to a single point of load application at the centre of IVD. The AnyBody load forces vary in directions and magnitudes between 0 – 800 N maximum while the other model provides normal force of 688 N, shear force of 90 N and sagittal moment of 3.1 Nm. This comparison shows the necessity of better load models to simulate more specific loads corresponding closer to reality. As the von Mises,  $\sigma_1$ , and  $\sigma_3$  stress shows in Fig. 3 in case of AnyBody load model generated maximum of 6.43 MPa, 7.92 MPa, and -9.66 MPa respectively, while the load by normal, and shear force accompanied by moment presented in Fig. 4 the stresses reached 18.47 MPa, 116.16 MPa, and -21.37 MPa respectively. The drawback of the improved loads models lays in the computational power and need for long CPU time.

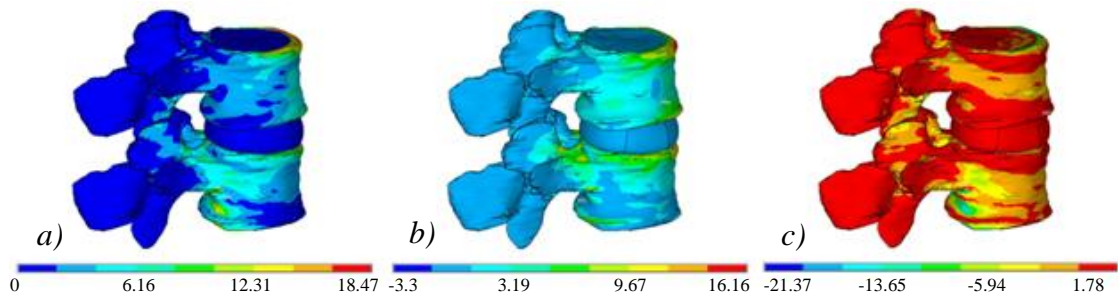


Fig. 4: Stress contour plot [MPa] – a) Von-Mises stress; b)  $\sigma_1$  principal stress; c)  $\sigma_3$  principal stress.

### Acknowledgement

This work was possible with kind support of BioPark Lab, and OTH Regensburg, Germany providing access to Simpleware, and Mater Dei hospital to access CT scans based on permission ENG02/2014.

### References

- Arjmand, N. and Shirazi-Adl, A. (2006) Model and in vivo studies on human trunk load partitioning and stability in isometric forward flexions. *Journal of Biomechanics*, 39, pp. 510-521.
- Damsgaard, M., Rasmussen, J., Christensen, S.T., Surma, E. and de Zee, M. (2006) Analysis of musculoskeletal systems in the AnyBody Modeling System. *Simulation Modelling Practice and Theory*, 14, pp. 1100-1111.
- Sant, Z., Cauchi, M. and Spiteri, M. (2012) Analysis of stress-strain distribution within a spinal segment. *Journal of Mechanics of Materials and Structures*, 7, 3, pp. 255-263.

## VERIFICATION OF MECHANISM'S FUNCTIONALITY FOR POSITIONING THE CAR SEAT USING MSC.ADAMS

A. Sapietová<sup>\*</sup>, P. Šulka<sup>\*\*</sup>, M. Sapieta<sup>\*\*\*</sup>, T. Domański<sup>\*\*\*\*</sup>

**Abstract:** *This paper presents dynamic of a virtual prototype (VP) of a lock mechanism, which would lead to verify its functionality in terms of kinematic and dynamic parameters. The proposed modifications of input parameters of the technical equipment addressed were verified using the software environment of MSC.ADAMS.*

**Keywords:** Simulation, Sensitivity analysis, Dynamic, Kinematic, Virtual prototype, MSC.ADAMS.

### 1. Introduction

The possibilities of new products design process implementation are changing with the rapid development of computer technology. It is the process of software environment simulation of the equipment being developed that has become an essential and very powerful tool needed to handle even the most complex problems of engineering practice. The initial proposal and more accurate design of new equipment made in the simulation process bring savings of time as well as financial gain. Savings are also shown in the performance of the experiment itself, because the very experiment can be prepared with minimum weaknesses thanks to the simulation. A structure created using the synthesis method enjoys a great advantage in the opportunity to assess the shape, form, appropriateness and functionality of the technical equipment design. In this paper, we present a simulation of a new design of technical equipment, which would lead to verify its functionality in terms of kinematic and dynamic.

### 2. Dynamic analysis of a locking mechanism virtual prototype

A car seat positions, supports and protects the passenger. In order for the ride to be comfortable, ergonomic and safe at the same time, the car interior elements must be modified or adjusted so to suit the widest possible range of passengers. One of the most important modifications of the car interior is the distance of the seat from the steering wheel. Based on these facts it is necessary to adapt the seat individually and enable its adjustment according to the size and needs of the passenger. Quick and safe securing of the distance of the seat from the steering wheel is provided by a locking mechanism that attaches the seat to the car floor. Ideally, the car seat position adjustment can be changed within the shortest time possible. At the same time, this process should take place as smoothly as possible, and with maximum safety for the passenger. The locking mechanism portfolio comprises a number of design types, for example, vertical or horizontal ratchet or permanent engaged locking. This paper presents analysis of a virtual prototype (VP) mechanism of a modular lock that is used to lock, or prevent the movement of, the car seat sliding rails in the direction of the vehicle travel (Arnold, 2008).

---

<sup>\*</sup> Assoc. Prof. Ing. Alžbeta Sapietová, PhD.: Department of Applied Mechanics, Žilina University, Univerzitná 8215/1, 010 26 Žilina, SK, alzbeta.sapietova@fstroj.uniza.sk

<sup>\*\*</sup> Ing. Peter Šulka: Department of Applied Mechanics, Žilina University, Univerzitná 8215/1, 010 26 Žilina, SK, peter.sulka@fstroj.uniza.sk

<sup>\*\*\*</sup> Ing. Milan Sapieta, PhD.: Department of Applied Mechanics, Žilina University, Univerzitná 8215/1, 010 26, Žilina, SK, milan.sapieta@fstroj.uniza.sk

<sup>\*\*\*\*</sup> Dr inż. Tomasz Domański: Department of Applied Mechanics, Czestochowa University of Technology, Czestochowa, PL, domanski@imipkm.pcz.pl

### 3. Mobility of the lock mechanical system

Fig. 1 displays a kinematic diagram of the locking mechanism. This scheme includes only those structural elements which have a decisive influence on the results of dynamic analysis. The elements are: frame (1), housing that includes the upper rail (UR) (2), locking element (LP1/LP2) (3). Scheme A shows the state when turning the locking rod unlocks the seat and the locking elements lean upon the side of the lower (blue) rail. The seat travels along the lower rail at the velocity  $v_z$  from position A to the position where there is an opening. Subsequently, a pre-stressed leaf spring enables insertion of the locking element into the opening at the velocity  $v_x$  (Dekýš, 2015).

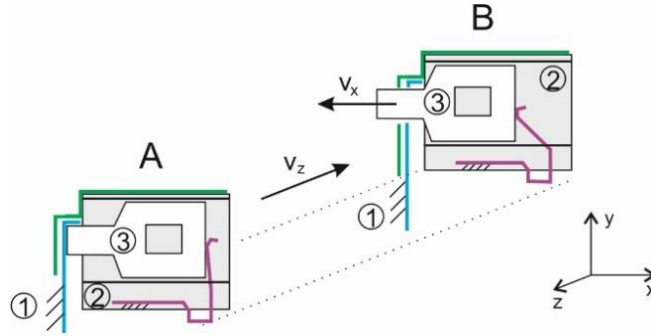


Fig. 1: Kinematic scheme of the mechanism: A – initial position, B – final position.

This kinematic has two degrees of freedom  $n$ . The upper rail moving on the lower rail defines the first degree of freedom, and the second degree of freedom is the movement of the locking element to be inserted into the opening using the pre-stressed spring. During the dynamic analysis in the MSC.ADAMS environment we consider two moving bodies in a three dimensional space. Then, the equation for calculating the constrained mechanical system degrees takes the following form:

$u$  – the total number of members in the constrained mechanical system, including the frame,

$n_v(u-1)$  – mobility of a group of free bodies,

$\sum_{t=1}^{n_v-1} ts_t$  – removed degrees of freedom due to constraints between pairs of members of the constrained mechanical system.

That between pairs of members of the constrained mechanical system is provided by the equation:

$$s_t = \sum_{v=2}^{v_m} s_{tv} (v-1), \quad (1)$$

$s_t$  – the number of links of class  $t$  of all pairs of constrained bodies in the constrained mechanical system,

$s_{tv}$  – the number of links of class  $t$  linking the number  $v$  of members,

$v$  – the number of bodies in the link  $s_t$  of bodies,

$v_m$  – the maximum number of bodies links of class  $t$  in constrained mechanical system.

Two situations may occur during locking: a partial lockdown, i.e. the locking element passes through only one opening in the upper rail, and a complete lockdown of the mechanism when the locking element passes through both openings in the upper rail (Fig. 1) (Vavro, 2015).

### 4. Input parameters

It should be noted that if the modular lock is unlocked even during a ride a sudden deceleration / acceleration occurs, then the locking elements might not bog down into either of the openings in the lower rail (LR). This would prevent locking the car seat and it would move all the way to the improper extreme position, i.e. to the dash board. The task of dynamic analysis in MSC.ADAMS software is to verify whether the modular lock is able to provide and ensure sufficiently safe locking of the moving car seat even at maximum deceleration / acceleration values. The acceleration parameter was obtained from the data measured in a crash test. A 3D model of the locking lock mechanism was created in Catia

software. Individual VP files were imported in .stl format to the MSC.ADAMS/View environment. The bodies were considered as rigid (Rigid Bodies) (Fig. 2). The VP model used shifting geometric constraints and contact function. The total VP mechanism weight was calculated as the sum of the child dummy weight (22 kg), child safety seat weight (8 kg) and the car seat itself (20 kg). Since the car seat is screwed to the two rails and each rail has its own modular lock, the calculated total weight was divided equally between the two rails. To carry out VP simulation, we recommended acceleration 25.25 g [m.s<sup>-2</sup>]. This parameter was obtained during a real crash test (Močilan, 2016).

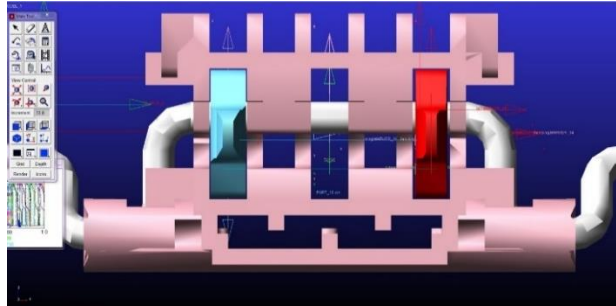


Fig. 2: Virtual prototype of locking mechanism.

A real spring is represented in the VP by a geometric constraint (SPRING). The spring is connected to the housing in the marker located at the height of the centre of gravity LP1/LP2, and to the marker of the locking element's centre of gravity LP1/LP2. Monitoring the current position of LP1 and LP2 in the rail opening uses meter for detection of distance markers. One meter is on the LP1 and LP2 edge and the other, reference meter, is situated on the edge of the upper rail outer opening (Fig. 3). In geometric constraints, we considered passive resistances in order to achieve simulations displaying more accurately the real mechanism behaviour (Jakubovičová, 2015).

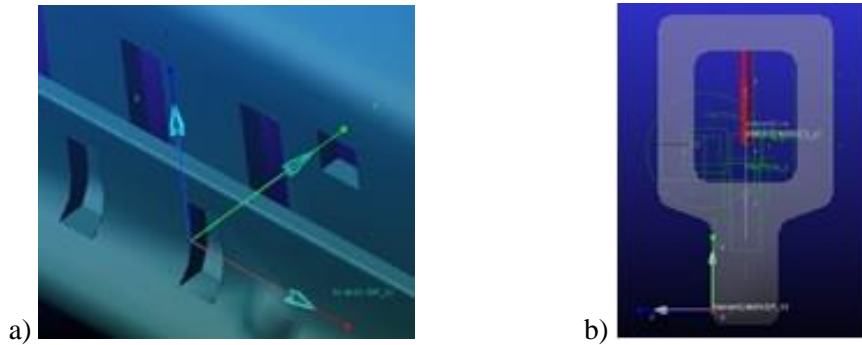


Fig. 3: Position of markers: a) on upper rail; b) on LP.

## 5. Simulation considering the system's concurrent motions

When solving the proper functioning of the locking mechanism in the MSC.ADAMS software environment we carried out several sensitivity analyses, the outcome of which were specification of the force effect range in the mechanism's spring, structural modification of LP1/LP2, and passive resistances in geometric constraints. Then we followed with considering only those parameters that have the greatest influence on the equipment proper functioning, and carried out simulation with consideration of the system's concurrent motions. In the following, we will present simulation in which the lower rail carries the upper rail at a constant velocity. The lower rail then abruptly stops and upper rail moves further due to inertial effects. During this event, it is necessary that LP1 and LP2 fit into the lower rail openings, which would confirm proper functioning of the locking mechanism.

$$t = \frac{v}{a} = \frac{11.19}{25.25g} = 0.0451s \quad (2)$$

Thus, the rails moved relative to each other by, more than 6 mm, hence these two events could occur insertion of LP1/LP2 into the rail openings, and the subsequent locking of mechanism. Simulation in MSC.ADAMS was controlled by STEP function: STEP (time, 0, 0, 30, 11 190) + STEP (time, 31, 0, 31.0451, -11 190). We carried out a significant number of simulations with varying loads applied by the

springs onto LP1/LP2. The best results in terms of the equipment functionality were achieved with the load from the spring forces 20 N and 25 N.

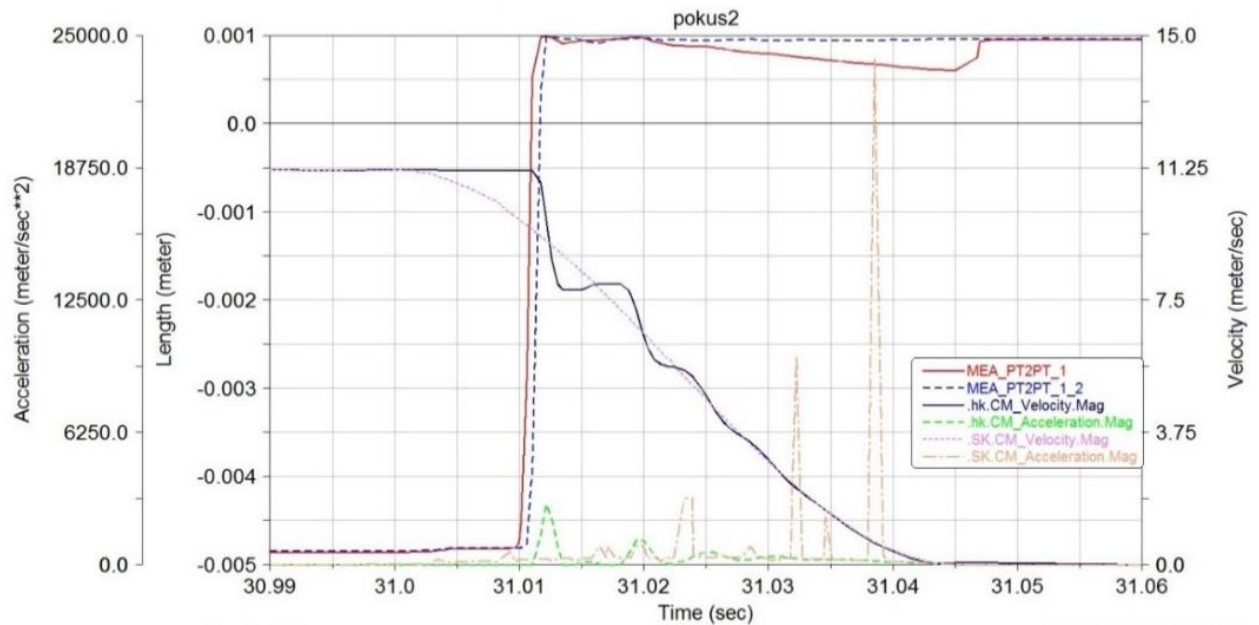


Fig. 4: Upper rail acceleration and velocity relative to the lower rail (25 N-mod. geom.).

The curve (blue and red) in (Fig. 4) shows the relative position of the locking elements marker and the reference marker on the rail at the spring force of 25 N. The (Fig. 4) clearly displays that the two locking elements engaged in full lockdown, where LP2 remained in the full lockdown and LP1 slid by 0.5 mm, while it remained in the fully locked position. This phenomenon is caused by an abrupt impact of the lower rail onto LP1. The (Fig. 4) shows further velocities and accelerations of the upper and lower rails according to time. Here it should be noted that the peaks seen in acceleration in all scenarios are caused by impact forces in contacts after LP clicking, and their value is affected by the fact it is a contact of rigid bodies.

## 6. Conclusion

Dynamic simulations in MSC.ADAMS confirmed that the locking mechanism fulfils its function in terms of full lockdown, when a boundary condition of acceleration is defined. It is necessary to consider the load from leaf spring force value of 10 N as proposed by the manufacturer is insufficient for safe lockdown of the mechanism. This topic represents, that the construction of mechanism complies with the dynamic load.

## Acknowledgement

This work was supported by the Slovak Grant agency VEGA 1/0795/16 and VEGA 1/0983/15.

## References

- Arnold, M. and Schiehlen, W. (2009) Simulation Techniques for Applied Dynamics, CISM Courses and Lectures, Springer Wien: New York, Vol. 507, 313 p.
- Dekýš, V., Novák, P. and Dvouletý, O. (2015) The contribution to the analysis of the run up test, 20th International Slovak-Polish conference on Machine Modeling and Simulations (MMS), 2015, Terchová.
- Jakubovičová, L., Gašparec, A., Kopas, P. and Sága, M. (2015) Optimization of the induction heating process in order to achieve uniform surface temperature, 20th International Slovak-Polish conference on Machine Modeling and Simulations (MMS), 2015, Terchová.
- Močilan, M., Žmindák, M. and Pastorek, P. (2016) Dynamics analysis of fuel tank, Proceedia Engineering, 20th International Slovak-Polish conference on Machine Modeling and Simulations (MMS), 2016, Terchová.
- Vavro, J., Ondrušová, D. and Pajtašová, M. (2015) Kinematic and Dynamic analysis of the manipulator for removal of rough tyres, 20th International Slovak-Polish conference on Machine Modeling and Simulations (MMS), 2015, Terchová.



## EXPERIMENTAL DETERMINATION OF VISCO-ELASTIC PROPERTIES OF LAMINATED GLASS INTERLAYER

J. Schmidt<sup>\*</sup>, T. Janda<sup>\*\*</sup>, M. Šejnoha<sup>\*\*\*</sup>, J. Valentin<sup>\*\*\*\*</sup>

**Abstract:** A specific experimental procedure employing the dynamic shear rheometer for the determination of dynamic properties of laminated glass interlayer is examined. An ethylene-vinyl-acetate (EVA) polymer interlayer experiencing strong rate and temperature depended behavior is considered as one particular example. This has been confirmed by performing cyclic measurements at various frequencies and temperatures to get corresponding variations of storage, loss, and complex dynamic shear moduli. One particular master curve for the reference temperature  $T_R = 20\text{ }^{\circ}\text{C}$  was constructed for both the storage and loss modulus. Such master curves serve as a stepping stone for the calibration of the Maxwell-chain viscoelastic model needed in the actual analysis of the laminated class.

**Keywords:** Laminated glass, Viscoelasticity, Complex shear moduli, Rheometer, Generalized Maxwell-chain model.

### 1. Introduction

Apart from classical application to windows the use of glass as structural elements with particular requirements for strength and safety has been on continuous rise over the last few decades. In this regard, attention has been accorded to the development of laminated glass. Multilayered glass units composed typically of two glass sheets bonded to a polymer interlayer have expanded into the building constructions, such as roof and floor systems, columns, staircases, hurricane-resistant windows, or pedestrian bridges. Such applications inevitably call for a proper characterization of the behavior of such structures often subjected to complex mechanical and atmospheric loading conditions adopting reliable and accurate computational methods.

While glass units can be considered as perfectly homogeneous, isotropic material experiencing more or less brittle response, the behavior of polymer interlayer is more complex manifesting itself by rate and temperature dependency. The most common interlayers are made of a polyvinyl butyral (PVB), ethylene-vinyl acetate (EVA) or ionoplast polymer. At minimum the viscoelastic constitutive models should therefore be adopted. This essentially precludes the use of analytical methods and suggest the application of various numerical methods such as the finite element method (FEM). The literature offers a number of methodologies allowing for the implementation of composite laminated glass into FEM computations. The most simple but the least accurate concept of effective thickness was introduced by (Galuppi et al., 2012) where the laminated glass element is converted to a solid one with an equivalent stiffness. Much more accurate approach, particularly when studying the geometrically nonlinear effects, has been presented in Zemanová (2014). Therein, the refined laminated plate theory by Mau (1973) was adopted to account for the viscoelastic behavior of the polymer interlayer. In particular, the viscoelastic properties of the polymer interlayer are described by the generalized Maxwell chain model, which describes the material response at a material point through a parallel connection of purely elastic spring and several

---

<sup>\*</sup> Bc. Jaroslav Schmidt: Faculty of Civil Engineering, Czech Technical University in Prague, Thákurova 7, 166 29, Prague, CZ, jaroslav.schmidt@fsv.cvut.cz

<sup>\*\*</sup> Ing. Tomáš Janda, PhD.: Faculty of Civil Engineering, Czech Technical University in Prague, Thákurova 7, 166 29, Prague, CZ, tomas.janda@fsv.cvut.cz

<sup>\*\*\*</sup> Prof. Ing. Michal Šejnoha, PhD., DSc.: Faculty of Civil Engineering, Czech Technical University in Prague, Thákurova 7, 166 29, Prague, CZ, sejnom@fsv.cvut.cz

<sup>\*\*\*\*</sup> Ing. Jan Valentin, PhD.: Faculty of Civil Engineering, Czech Technical University in Prague, Thákurova 7, 166 29, Prague, CZ, jan.valentin@fsv.cvut.cz



Maxwell cells, see Fig. 1. Since the behavior of the interlayer is driven by shear, see Fig. 2, we consider the formulation in terms of the viscoelastic shear modulus  $G$  and constant Poisson's ratio.

The dependent response of the shear modulus is then written in terms constants  $G_\infty; G_1 \dots G_n$  and selected relaxation times  $\tau_i$  as

$$G(t) = G_\infty + \sum G_i e^{-\frac{t}{\tau_i}} = f(G_\infty, G_1, \dots, G_n). \quad (1)$$

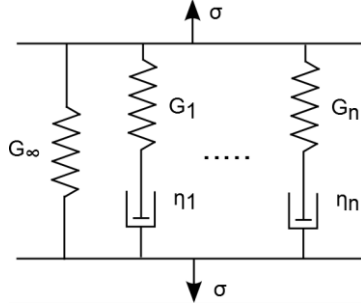


Fig. 1: Generalized Maxwell chain model.

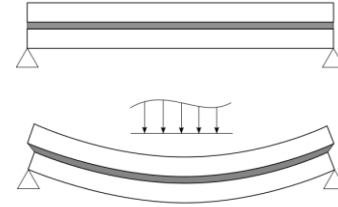


Fig. 2: Shear strain in interlayer.

The same material constants can be used for the description of the response to loading caused by harmonic excitation

$$G^*(\omega) = G'(\omega) + iG''(\omega) = f(G_\infty, G_1, \dots, G_n). \quad (2)$$

The ability of the generalized Maxwell chain model to represent both the static shear modulus given by Eq. (1) and the dynamic shear modulus given by Eq. (2) thus allows us to investigate the viscoelasticity and temperature dependency of the polymer interlayer with the help of dynamic mechanical analysis. Typically, the tests are conducted in tension mode, see e.g. (Mohagheghian et al., 2017), resulting into the complex Young modulus. To avoid a subsequent transformation into the shear modulus we proceed in the footsteps of (Andreozzi et al., 2014) and perform the dynamic measurements directly in the shear mode using rheometer testing device as described in detail in Section 2.

It has been already mentioned that the mechanical properties of the polymer layer depend strongly on temperature. Increasing temperature significantly reduces the interlayer stiffness. The temperature dependency is conveniently expressed in terms of the temperature shift factor  $a(T)$ , recall Eq. (1), fitted to the William, Landel and Ferry (WLF) equation

$$a(T) = \exp\left(\frac{-C_1(T-T_R)}{C_2+T-T_R}\right). \quad (3)$$

where  $C_1, C_2$ , are the model parameters,  $T_R$  is the reference temperature and  $T$  is the actual temperature. The model parameters are found by constructing a master curve from measurements carried out at various temperatures but at the same frequency sweep. The individual curves are then horizontally shifted to match the results corresponding to the reference temperature that would be obtained at either much smaller or much higher frequencies such that  $G^*(\omega, T) = G^*(a(T)\omega, T_R)$ .

## 2. Measurement setup

The dynamic shear rheometer HAAKE MARS, typically used for asphalts, was employed to derive the frequency characteristics of the polymer interlayer with attention limited to EVA material. This device operates on the plate-plate shear principle and allows for stress as well as strain loading conditions applied either in a static (simple rotation) or dynamic (oscillatory) mode under the prescribed temperature. Unlike asphalts, which do not require any special treatment, testing the glass composite sample requires more elaborate approach as described in detail in (Andreozzi et al., 2014 and Zulli et al., 2016).

The measurements were performed on layered cylindrical samples having diameter 20 mm and thickness of  $5 + 0.76 + 5$  mm. To ensure that the oscillatory loading is taken by the interlayer only a relatively stiff epoxy glue had to be applied when mounting the specimen on the two plates (one fixed and one rotating). Figs. 3 and 4 show a sample of the laminated glass fixed between the two plates.

Note that testing the actual composite is particularly advantageous as the polymer properties may change during the composite production and thus may differ from the properties of the original material. Clearly, this cannot be accounted for when testing the polymer interlayer only, e.g. in tension.

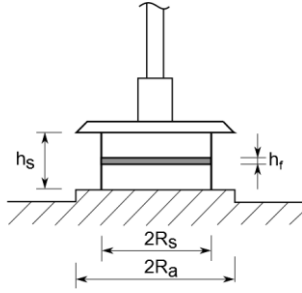


Fig. 3: Rheometer setup.



Fig. 4: Specimen glued to rheometer plates.

In the rheometer oscillatory tests the cyclic loading undergoing a certain frequency and temperature sweep is prescribed. The rheometer provides directly the frequency dependent variation of the storage and loss moduli for a given temperature. However, such results apply to the geometry of the entire composite. Since it is expected that the entire torsion is concentrated in the EVA sample, the results provided directly by the rheometer have to be adjusted to reflect properly the thickness  $h_f$  and the radius  $R_s = 10$  mm of the interlayer with reference to the actual sample thickness  $h_s$  and the plate radius  $R_a = 12.5$  mm in our particular case, see Fig. 3. As suggested in (Andreozzi et al., 2014) the complex modulus  $G_f^*$  of the interlayer relates to the rheometer modulus  $G_s^*$  as

$$G_f^* = \frac{R_a^4}{R_s^4} \cdot \frac{h_f}{h_s} G_s^*. \quad (4)$$

### 3. Measured results

The tested specimens were drilled from laminated glass with two-ply EVA (Ethylene-vinyl acetate) polymer interlayer. Each of six tested samples experienced a slightly different total height. On average the interlayer thickness  $h_f$  amounted to 0.81 mm with standard deviation of 0.028 mm. The measurements were performed for the following set of temperatures: 10 °C, 20 °C, 30 °C, 40 °C, 50 °C, 60 °C. The following range of frequencies was considered: 0.001 Hz, 0.01 Hz, 0.05 Hz, 0.1 Hz, 0.5 Hz, 1 Hz, 5 Hz, 10 Hz, 20 Hz, 30 Hz, 40 Hz, 50 Hz. The range of frequencies 50 Hz – 100 Hz was also examined. However, for the present testing device, as seen from the available results, the predicted response is highly unreliable suggesting a rapid decrease in the storage modulus for frequencies beyond 50 Hz, see Fig. 5. The results in Fig. 6, pertinent to the loss modulus, show even larger discrepancies.

As already mentioned the proposed experimental program was applied of the six specimens one day after being fixed to the testing device to allow for sufficient curing of the epoxy glue. Performing the entire temperature and frequency sweep required about 9 hours. The resulting variations of the storage and loss moduli are plotted for one particular specimen in Figs. 5 and 6. For each specimen such measurements were repeated three times one day apart (runs 1 – 3) to examine the influence of both loading and heating/cooling sequence. The results for the reference temperature  $T_R = 20$  °C are shown in Fig. 7. This trend, manifested itself by the stiffness reduction with repeating tests, has been observed for all samples. Such a dependency on the history of loading is, however, difficult to reflect through a simple Maxwell chain model.

The final step needed for the calibration of the Maxwell chain model is to construct a master for the selected reference temperature set equal to  $T_R = 20$  °C in our present study. The master curve is created by horizontal shifting (in a logarithmic scale) original curves in Fig. 5. This automatically prolongs the frequency range. The result appears in Fig. 8. Such a master curve then allows us to determine the parameters  $C_1$  and  $C_2$  in Eq. (3), being equal to 300 and 350, respectively.

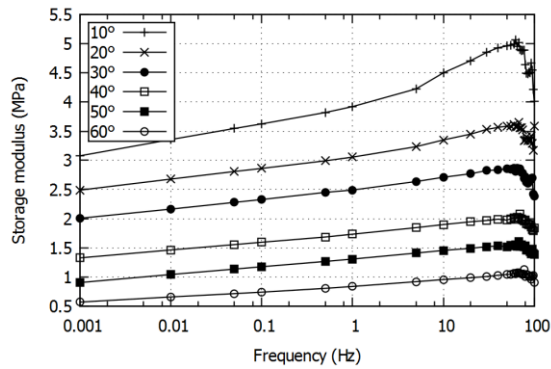


Fig. 5: Storage modulus.

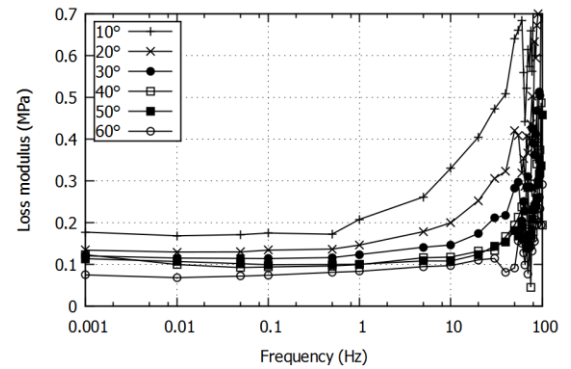


Fig. 6: Loss modulus.

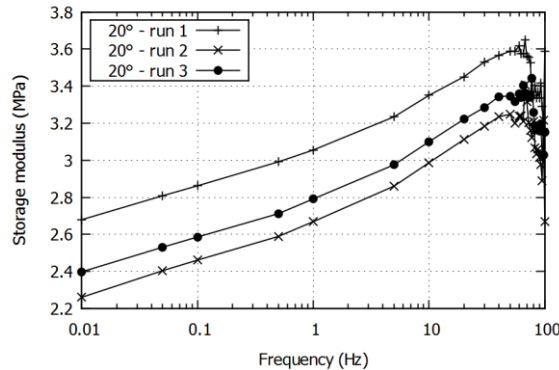


Fig. 7: Storage modulus for three consecutive runs.

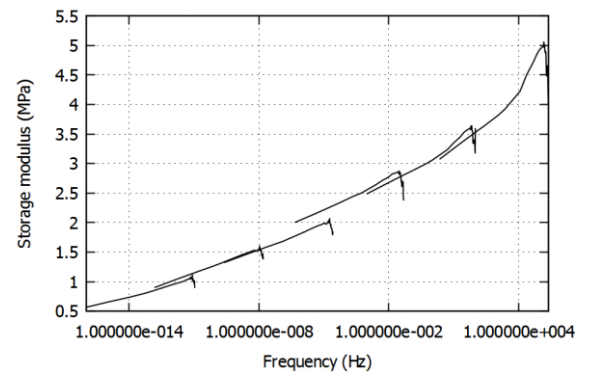


Fig. 8: Master curve for storage modulus.

#### 4. Conclusions

This paper summarizes the results of the dynamic oscillatory measurements using the dynamic shear rheometer to address the viscoelastic behavior and temperature dependency of the EVA interlayer in a three-layer laminated glass composite. The applicability of the selected testing device was demonstrated through the construction of one particular master curve, which in turns is to be used in the calibration of the generalized Maxwell chain model needed in complex FEM simulations of a low velocity impact. Similar experimental program is currently under way to acquire the viscoelastic properties of PVB interlayer. In this regard, special attention will be devoted to the influence of loading history in order to reconcile the results plotted in Fig. 7.

#### Acknowledgement

The financial support provided by the GAČR grant No.16-14770S and the SGS project with the application registered under the No. OHK1-014/17 is gratefully acknowledged.

#### References

- Andreozzi, L., Batti, S.B., Fagone, M., Ranocchiaci, G. and Zulli, F. (2014) Dynamic torsion tests to characterize the thermo-viscoelastic properties of polymeric interlayers for laminated glass. *Construction and Building Materials*, 65, pp. 1-13.
- Galuppi, L., Royer-Carfagni, G. (2012) The effective thickness of laminated glass plates. *Journal of Mechanics of Materials and Structures*, 7, pp. 375-400.
- Mau, S.T. (1973) A refined laminated plate theory. *Journal of Applied Mechanics*, pp. 606-607.
- Mohagheghian, I., Wang, Y., Jiang, L., Zhang, X., Guo, X., Yan, Y. and Kinloch, A.J. (2017) Quasi-static and low velocity impact performance of monolithic and laminated glass windows employing chemically strengthened glass. *European Journal of Mechanics A/Solids*, 63, pp. 165-186.
- Zemanová, A. (2014) Numerical modeling of laminated glass structures. PhD. Thesis, Czech Technical University in Prague.
- Zulli, F., Andreozzi, L., Giovanna, R. and Fagone, M. (2016) Test Methods for the Determination of Interlayer Properties in Laminated Glass. *Journal of Materials in Civil Engineering*.

## DUCTILE FRACTURE CRITERIA IMPLEMENTATION AND CALIBRATION USING THE TENSION–TORSION TESTS

F. Šebek<sup>\*</sup>, J. Petruška<sup>\*\*</sup>, P. Kubík<sup>\*\*\*</sup>

**Abstract:** Ductile fracture calibration needs to be done on the basis of reliable experimental testing. Reliable from the proportional loading path point of view, and the knowledge of crack initiation location too. Tubular specimen was designed and biaxially tested to be used for calibration of phenomenological criterion as well as for the comparison to other tubular biaxially tested specimens from recent literature. Calibrated phenomenological criterion was implemented by developed algorithm to Abaqus using the user subroutine in order to predict the cracking onset. The proportionality of loading path was tracked together with the evolution of state variables through the wall thickness to conclude the applicability of each specimen for a specific loading.

**Keywords:** Damage indication, Tubular specimen, Failure initiation, Ductile crack, Plastic deformation.

### 1. Introduction

Ductile fracture is typical separation mechanism of polycrystalline materials. The loading yields in deformation of the solid which gives rise to stress. The stress rises with elastic deformation until the yield point, after which the inelastic deformation develops (Petruška et al., 2012, 2016). Continuing straining leads to development of plastic deformation (Peč et al., 2016) which is accompanied by the degradation of material physical properties. The process is known as a damage accumulation. The material is not capable to bear any further load in the final stage of damage accumulation, the ductility limit is exhausted, and the material ruptures (Šebek et al., 2014). The ductile fracture is driven by the cumulative intensity of plastic strain

$$\bar{\varepsilon}^p = \int_0^t \sqrt{\frac{2}{3} \dot{\varepsilon}^p : \dot{\varepsilon}^p} dt \quad (1)$$

where  $\dot{\varepsilon}^p$  is the tensor of plastic strain rate and  $t$  is the time. One of the most influencing quantities is the stress triaxiality (Španiel et al., 2014)

$$\eta = \frac{I_1}{3\bar{\sigma}} \quad (2)$$

where  $I_1$  is the first invariant of the Cauchy stress tensor and  $\bar{\sigma}$  is the equivalent von Mises stress. Apart from the stress triaxiality, recent criteria include also Lode angle, or another deviatoric stress parameter, as independent state variable (Kubík et al., 2014; Park and Huh, 2014). The normalized Lode angle is

$$\bar{\theta} = \frac{2}{\pi} \arcsin\left(\frac{27}{2} \frac{J_3}{\bar{\sigma}^3}\right) \quad (3)$$

where  $J_3$  is the third invariant of the deviatoric stress tensor.

---

<sup>\*</sup> Ing. František Šebek, PhD.: Institute of Solid Mechanics, Mechatronics and Biomechanics, Faculty of Mechanical Engineering, Brno University of Technology; Technická 2896/2; 616 69, Brno; CZ, sebek@fme.vutbr.cz

<sup>\*\*</sup> Prof. Ing. Jindřich Petruška, PhD.: Institute of Solid Mechanics, Mechatronics and Biomechanics, Faculty of Mechanical Engineering, Brno University of Technology; Technická 2896/2; 616 69, Brno; CZ, petruska@fme.vutbr.cz

<sup>\*\*\*</sup> Ing. Petr Kubík, PhD.: Institute of Solid Mechanics, Mechatronics and Biomechanics, Faculty of Mechanical Engineering, Brno University of Technology; Technická 2896/2; 616 69, Brno; CZ, kubik.p@fme.vutbr.cz

## 2. Experimenting and modelling

Fracture tests must be realized in order to calibrate a fracture model. Very important is the crack initiation location as well. Specimens used in calibration of fracture models may have different geometries and may be loaded uniaxially or biaxially to achieve one specific or variety of stress states. The basic experiments were the tensile tests of smooth (6 mm diameter) and notched (R5, R2.5 and R1.2) cylindrical specimens of AISI 1045 carbon steel. Zwick Z050 testing machine with the test speed of 2 mm/min was used. Biaxial tests of Notched Tube (NT) specimens were realized too. The circumferential notch with notch radius R3 was situated on the outer surface. The outer radius in the notch was 4.5 mm and the inner radius of straight hole was 3.5 mm, so the wall thickness was 1 mm in the notch. A pin was put into the shoulder with hole to prevent unwanted deformation during mounting into grips. MTS Bionix 370.02 testing machine was used for biaxial loading. The loading combination may be described by the ratio of axial to torsional movements of testing machine. Loading combinations  $L = 0, 0.5, 1$  and  $\infty$  mm/rad were chosen.

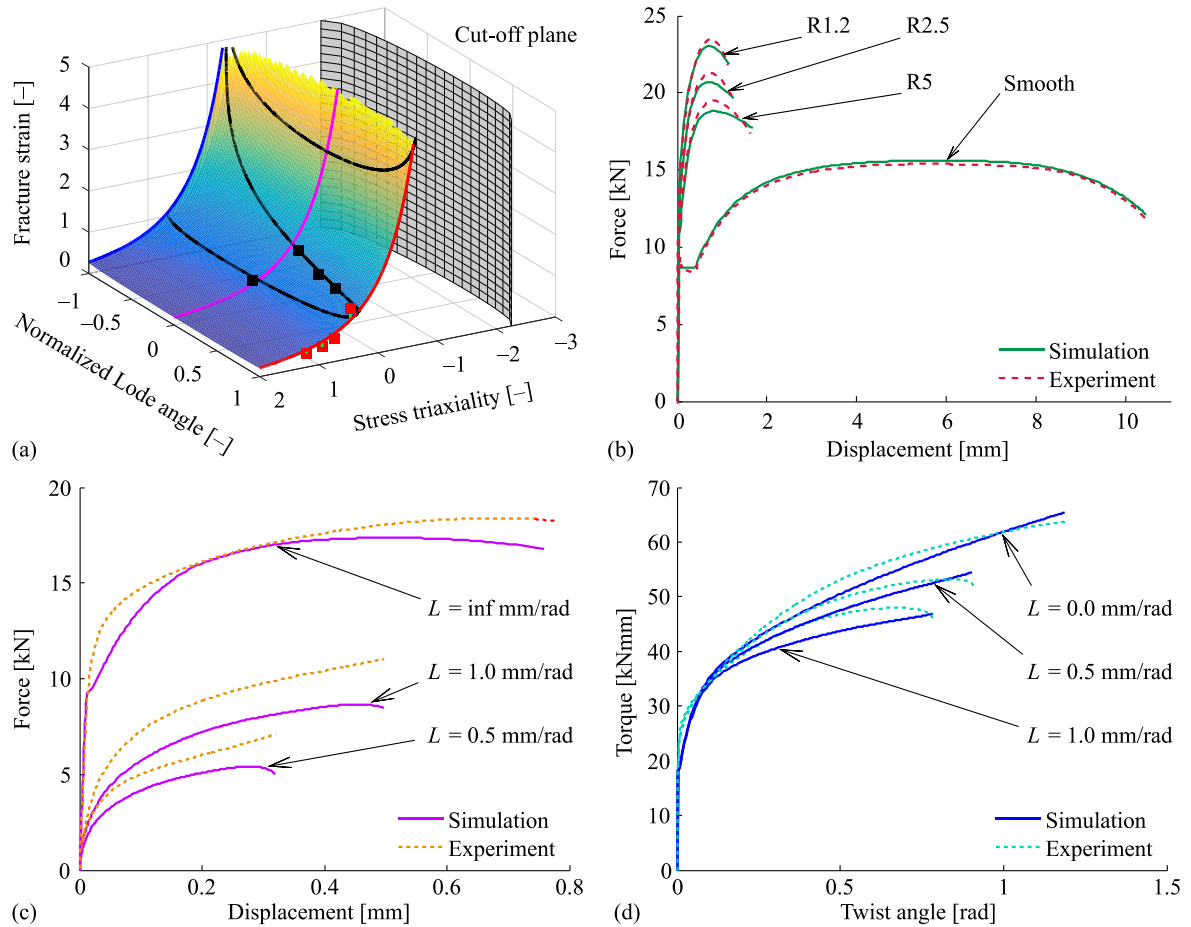


Fig. 1: a) Calibrated Extended Mohr–Coulomb criterion; b) force–displacement responses of round bars; c) force–displacement responses of tubes; d) torque–twist angle responses of tubes.

The von Mises plasticity with isotropic hardening and associated flow rule was adopted. The multi-linear flow curve was calibrated using the tensile smooth round bar (Fig. 1b). Simulations of other tests were carried out (Fig. 1b, c, d) in order to calibrate the Extended Mohr–Coulomb criterion (Bai and Wierzbicki, 2010). It was chosen for the prediction of initiation locations, as described further. The criterion was calibrated with constants 0.2464 and 753.708 MPa and it is depicted in Fig. 1a.

## 3. Simulations of tension–torsion tests

Tension–torsion specimens create a group of universal specimens because of varying the stress state by changing the loading combination. This chapter deals with comparison of selected four specimens. Those were Double Notched Tube (DNT) (Barsoum and Faleskog, 2007), Modified Lindholm (ML) (Gao et al., 2011), NT (used for calibration) and Tubular Tension–Torsion (TTT) specimen (Papasidero et al., 2014).

First, the torsion was examined. The initiation locations were in the notch roots of all specimens on the outer surfaces (Fig. 2). There were two initiation locations in case of ML and TTT specimens which is not desired (Fig. 2b, d). Note that there is no scale between the geometrical models, therefore the size should be derived from real dimensions.

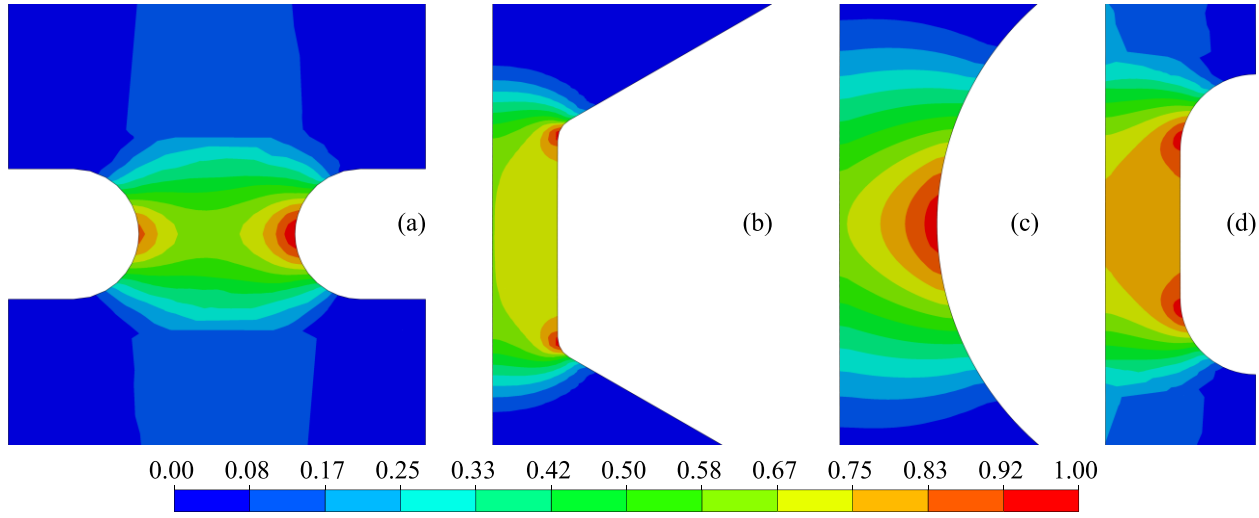


Fig. 2: Damage contours for torsion and (a) DNT; (b) ML; (c) NT; (d) TTT.

The initiation locations for loading combination with prevailing torsion were similar to those obtained for torsion. The worst distribution of state variables through the normalized thickness was in the case of DNT specimen (Fig. 3). It might be caused by very sharp notches and a thin wall.

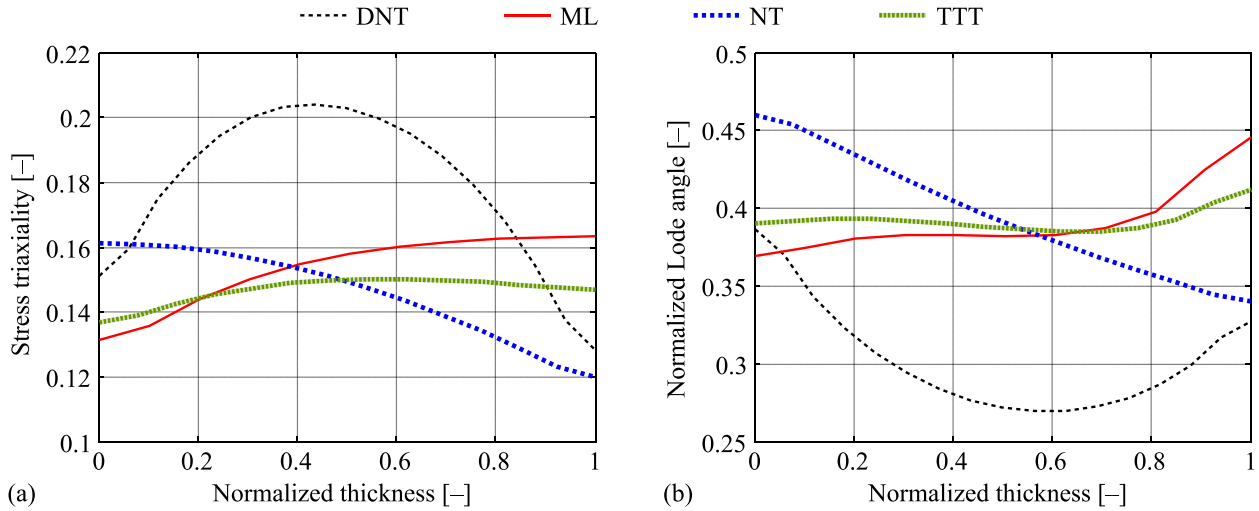


Fig. 3: Distribution of state variables for prevailing torsion along the normalized thickness: a) stress triaxiality; b) normalized Lode angle.

The crack initiated nearby the center of the wall thickness in case of DNT specimen for prevailing tension. The locations of ML and TTT specimens were just beneath the inner surfaces at the central prismatic parts. The initiation location was in the center of the wall at NT specimen for the prevailing tension loading combination. Generally, the initiation was located to one specific site for each specimen. Moreover, it was concentrated to the prismatic part, which is desirable. The stress state reached by DNT specimen was distinctly different than those obtained by the others (Fig. 4). Moreover, the others were closer to the proportional loading that DNT. Therefore, the fracture strain was also noticeably smaller because of much higher stress triaxiality due to the sharp notch radii. The situation was basically similar for tension compared to the prevailing tension.

Generally, the initiation locations of DNT and NT specimens were moving from the outer surface to the center of the wall thickness with increasing tension component of tension–torsion loading. The locations in case of ML and TTT moved from the outer surface to the inner at first, and then to the wall center. The proportionality of loading paths was globally comparable and satisfactory for ductile fracture calibration.



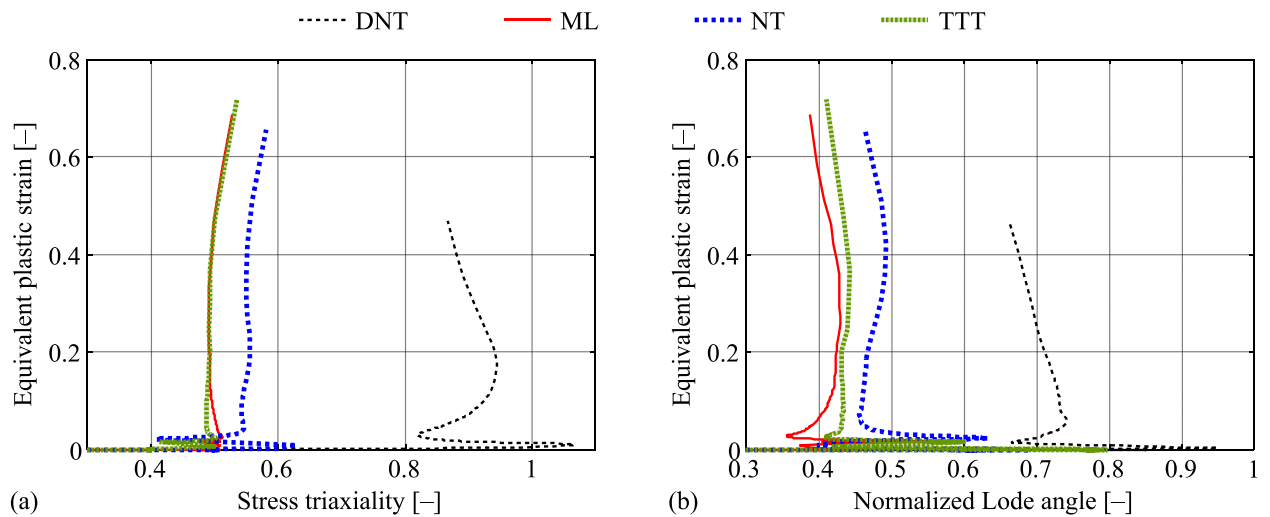


Fig. 4: Equivalent plastic strain for prevailing tension: a) stress triaxiality; b) normalized Lode angle.

#### 4. Conclusions

The experimental testing on designed tension–torsion specimen was conducted and the fracture criterion was calibrated. The criterion was implemented into the commercial software using user subroutine, and it was applied to other tubular specimens from literature, which could be also used for ductile fracture calibration. Generally, ML and TTT behaved similarly as NT, while DNT specimen was noticeably different. The difference was primarily caused by the geometry with double notches of sharp radii. DNT and NT specimens had naturally the fracture initiation locations in one specific cross-section in axial plane of symmetry independently on the loading, which is very good.

#### Acknowledgement

This work is an output of project NETME CENTRE PLUS (LO1202) created with financial support from the Ministry of Education, Youth and Sports under the „National Sustainability Programme I“.

#### References

- Bai, Y. and Wierzbicki, T. (2010) Application of extended Mohr–Coulomb criterion to ductile fracture. *International Journal of Fracture*, 161, pp. 1-20.
- Barsoum, I. and Faleskog, J. (2007) Rupture mechanisms in combined tension and shear—Experiments. *International Journal of Solids and Structures*, 44, pp. 1768-1786.
- Gao, X., Zhang, T., Zhou, J., Graham, S.M., Hayden, M. and Roe, C. (2011) On stress-state dependent plasticity modeling: Significance of the hydrostatic stress, the third invariant of stress deviator and the non-associated flow rule. *International Journal of Plasticity*, 27, pp. 217-231.
- Kubík, P., Šebek, F., Petruška, J., Hůlka, J., Růžička, J., Španiel, M., Džugan, J. and Prantl, A. (2014) Calibration of selected ductile fracture criteria using two types of specimens. *Key Engineering Materials*, 592-593, pp. 258-261.
- Papasidero, J., Doquet, V. and Mohr, D. (2014) Determination of the effect of stress state on the onset of ductile fracture through tension-torsion experiments. *Experimental Mechanics*, 54, pp. 137-151.
- Park, N. and Huh, H. (2014) Prediction of fracture strains for DP980 steel sheets using a modified Lou–Huh ductile fracture criterion. *Key Engineering Materials*, 626, pp. 347-352.
- Peč, M., Kubík, P., Šebek, F., Návrat, T. and Petruška, J. (2016) Modeling of the blast load effects in explicit dynamics, in: *Engineering mechanics 2016*, Svratka, pp. 442-445.
- Petruška, J., Návrat, T. and Šebek, F. (2012) A new model for fast analysis of leveling process. *Advanced Materials Research*, 586, pp. 389-393.
- Petruška, J., Návrat, T., Šebek, F. and Benešovský, M. (2016) Optimal intermeshing of multi roller cross roll straightening machine, in: *AIP Conference Proceedings*, 1769, pp. 120002-1-120002-4.
- Šebek, F., Kubík, P. and Petruška, J. (2014) Localization problem of coupled ductile failure models compared to uncoupled ones, in: *Engineering mechanics 2014*, Svratka, pp. 632-635.
- Španiel, M., Prantl, A., Džugan, J., Růžička, J., Moravec, M. and Kuželka, J. (2014) Calibration of fracture locus in scope of uncoupled elastic–plastic–ductile fracture material models. *Advances in Engineering Software*, 72, pp. 95-108.

## LOCATION OF LEAKS IN THE WATER SUPPLY NETWORK

L. Semkło<sup>\*</sup>, A. Frąckowiak<sup>\*\*</sup>, M. Ciałkowski<sup>\*\*\*</sup>

**Abstract:** *The presented algorithm is used to locate the leak of water from the network. The operation of this algorithm is divided into two stages. In the first stage we search the entire water supply network and is selected a pipeline, in which the damage occurs. In a second step it is determined the exact location of the leak. The article presents numerical calculations based on the algorithm developed for the calculation of water supply network. The pipeline, in which the location of the damage has been selected so that finding of the pipeline network was the most difficult. Fault location in the pipeline has been chosen at random. The study shows that in all variants of the measurement nodes and selected locations of damage, the program correctly locates the leak.*

**Keywords:** Pressure drop, Leak, Water supply network, Pipeline, Node.

### 1. Introduction

Water supply system is a complex system of piping in which water flows. It can be considered as the electricity network, to which the Kirchhoff law applies (Semkło et al., 2013). Using this analogy, it can be assumed that the current strength in the electricity network corresponds to the mass flow rate (heat flow) in the mains supply (Semkło et al., 2014), and the voltage drop on the section of the power supply - pressure drop (Semkło et al., 2014a) You can therefore save the balance equation for water flow in the nodes of the water supply system and the balance of energy (pressure drop) in the sections of the water supply network (Semkło et al., 2013a).

In this paper will be presented method for detecting leaks of water supply network based on the analysis of the pressure in the selected nodes. This issue is important because the network failure can cause considerable damage not only in its functioning, but in the whole infrastructure of the city.

### 2. Methodology

The methodology is based on repeated determination of parameters of a damaged water supply system with changing the location of a failure node, symbolizing the network. In this way it is need to solve  $n$  (the number of network elements) variants of the water supply system with a damage of known value of leakage (flowing out of the network node by an additional water volume flow) arranged one after the other in each element of the water supply system. Solved equations are increased by one additional mass balance equation. Determining the value of the functional for all variants of the damaged networks, variant of the actual satisfies the minimum of the functional (1).

$$J = \sum_{k=1}^{n_p} (p_{kj} - p_{ref\_k})^2 \quad (1)$$

Denoting by  $p_{ref\_k}$  pressure measured in the  $k$  node measuring network damaged, and the pressure  $p_{kj}$  calculated in  $k$  node measuring networks damaged with damage located in the  $j$  node of this element. As you can see, the method described is based on the search for a minimum of functional (1) has faults that

---

<sup>\*</sup> Łukasz Semkło, PhD.: Chair of Thermal Engineering, Poznań University of Technology, Street Piotrowo 3, 60-965, Poznań; PL, lukasz.semκλο@put.poznan.pl

<sup>\*\*</sup> Prof. Andrzej Frąckowiak, DSc.: Chair of Thermal Engineering, Poznań University of Technology, Street Piotrowo 3, 60-965, Poznań; PL, andrzej.frackowiak@put.poznan.pl

<sup>\*\*\*</sup> Prof. Michał Ciałkowski, DSc.: Chair of Thermal Engineering, Poznań University of Technology, Street Piotrowo 3, 60-965, Poznań; PL, michal.cialkowski@put.poznan.pl

cause a variety of complications during solving nonlinear algebraic equations (Semklo et al., 2013b). However, the most serious of them, especially for large networks is a long calculation time.

The algorithm for determining network leakage consists of two steps. In the first step for each line in the network is determined minimum value of the functional (1) based on a bisection method. This process ends for each pipeline when the condition is satisfied:

$$|J_{u2} - J_{u1}| < \varepsilon_r \quad (2)$$

where  $\varepsilon_r$  is treated as a fraction of the length of the pipeline. The value of this parameter affects the length of the calculation. A low value increases computing time and too much will cause the selection of the pipeline, where the damage occur is incorrect. Distribution of minimum values for functional damage to the network in the next pipeline shows an example of Fig. 1. You can see that the risk of error choice of the pipeline, in which the damage appear, because the distribution of minima of the functional (1) allows for assessment of the risk of error. At high uncertainty can be reduced  $\varepsilon_r$  value, which increases the computation time or the second step may search for the minimum of the functional in more than one pipeline.

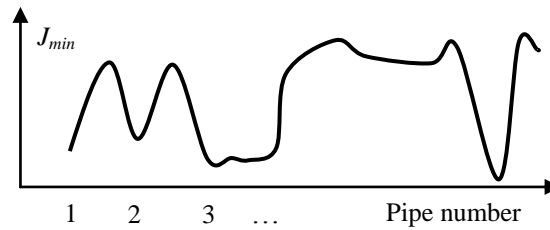


Fig. 1: Dependence of minimum of the functional (1) on the location of damage on the network, example.

In the second step the search for the leak from the network in the selected pipe, the location is searched as in the first step with the difference that the value  $\varepsilon_r$  is reduced by several orders.

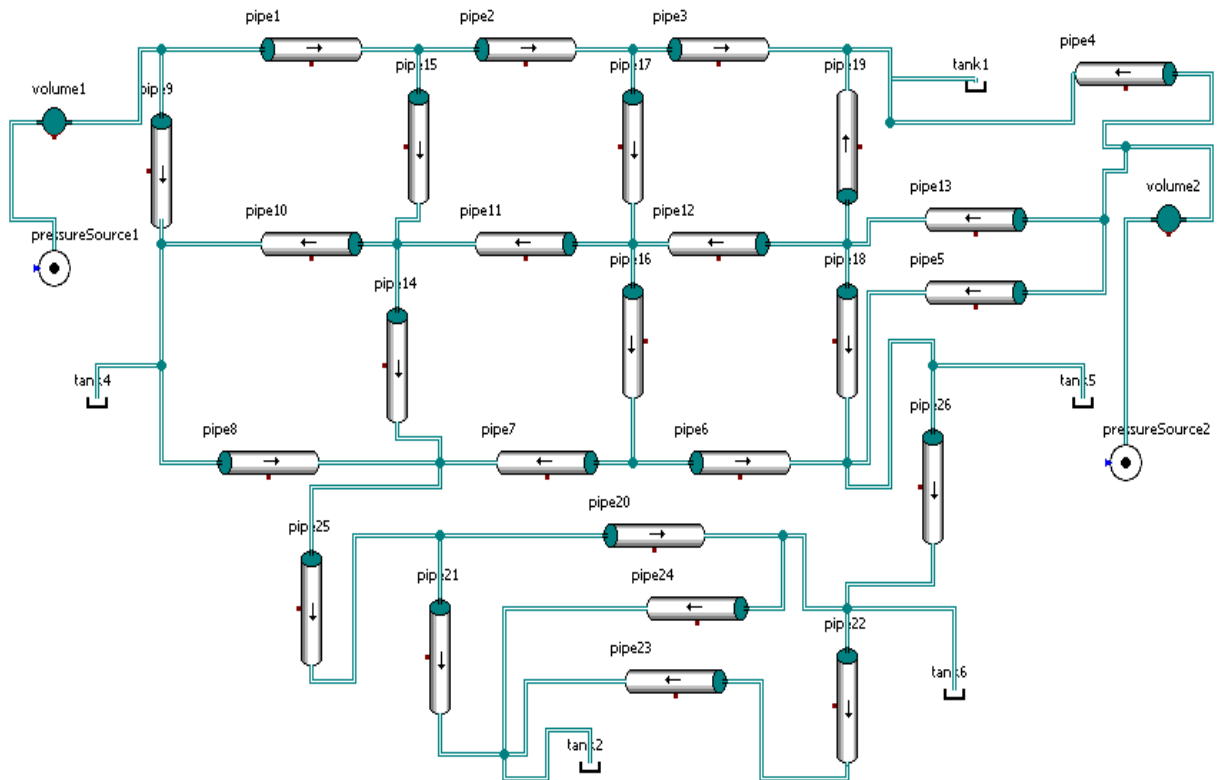


Fig. 2: Sample water supply network with 26 pipes and 18 nodes.

### 3. Calculation

In order to determine the location of a leak, the algorithm recalculates the network on the basis of the measurement node. Measurement nodes are used only in the first step. The number of measuring nodes varies from 1 to 6. It should be remembered that for more complex examples of the network 1 measurement node may not be sufficient and may adversely indicate the location of the leak.

For simple, less complex networks from a single measurement node is sufficient to properly identify the location of pipeline damage. The value of the functional (1) (determined in step 1) marked in green is several orders less than in other pipelines.

For networks with complex structure (Fig. 2) and a large number of data correlation minimum of the functional (1) the location of the damage in the next pipe network is shown in Figs. 3 and 4. Properly found the pipe in which there is physical damage is identified in these drawings, circled in green. Wrong identification is red. There is a possibility of a situation for which the value of the functional (1) is similar to the value of this functional for the pipeline, in which the actual damage occur. In this case, the location of leaks may be incorrectly interpreted.

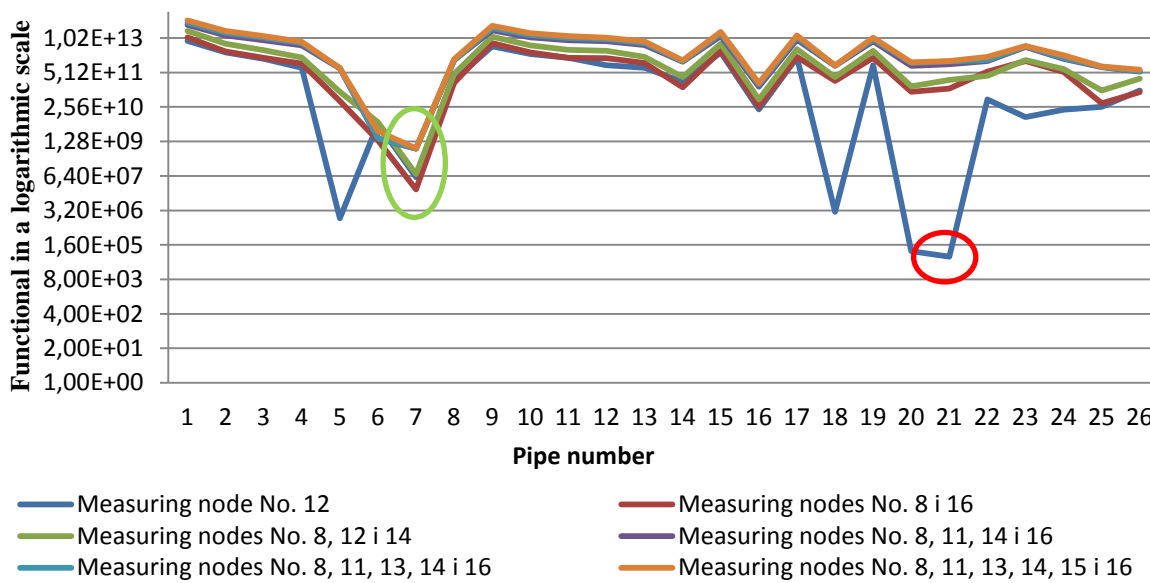


Fig. 3: The minimum of the functional dependence (1) of the leak location in the next pipes of the network; leak in pipe 7.

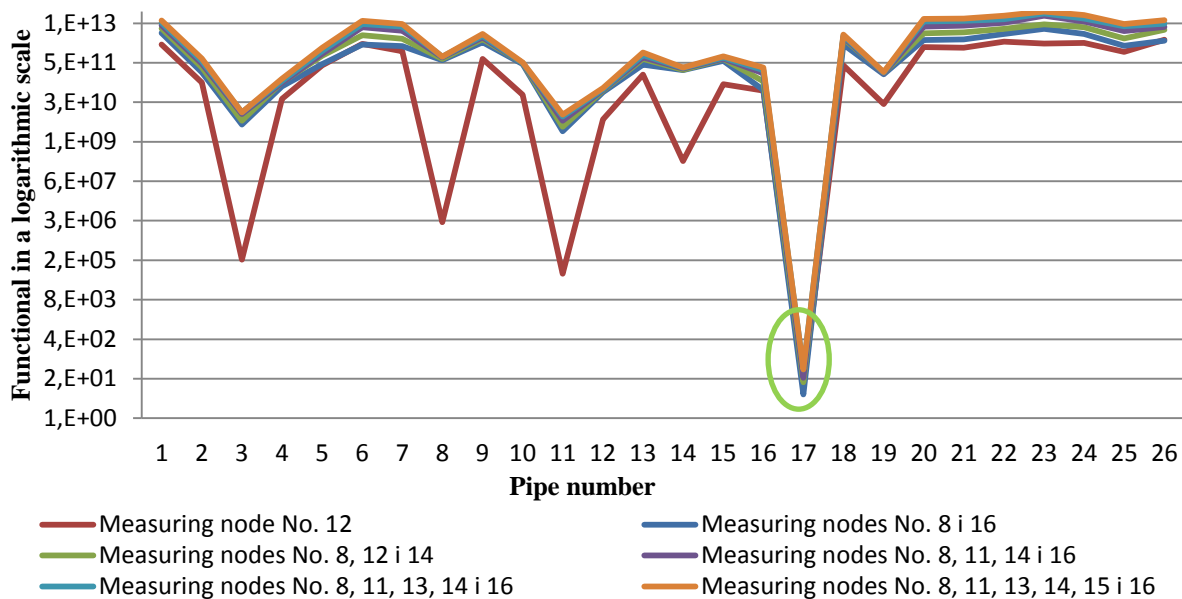


Fig. 4: The minimum of the functional dependence (1) of the leak location in the next pipes of the network; leak in pipe 17.

Fig. 2 shows an example where the damage is generated in the two pipelines numbers 7 and 17. In these pipes damage location was chosen random. Identification of this place was settled by comparing in the functional (1) the reference pressure in measuring nodes with the pressure values calculated during the search algorithm leaks network. Figs. 3 and 4 is shown to correctly identify the faulty pipeline for variants of calculations of the measurement nodes from 2 up to 6. For one node measuring algorithm identified the wrong place damage.

In Fig. 3 we can observe the occurrence of misidentification leak caused by the use of only one measurement node. This place is marked with a red circle. Green circle defines the leak correctly determined both shown in Figs. 3 and 4.

*Tab. 1: Values of the functional established for leaks in pipes; the location of the leak is calculated from the starting node.*

Number of damaged pipe	Number of measuring nodes					
	1	2	3	4	5	6
7	196.983 (21)	22.86	22.84	22.86	22.86	22.86
17	320.03	320.04	320.04	320.04	320.04	320.04

Tab. 1 presents a summary leaks locations. It can be seen that the leakage predicting on the pipe 17 is almost identical for any number of measurement nodes. There are no derogation. In the case of a leak on a pipe 7 there is a false reading. In case of using from 2 to 6 measurement nodes there was successful leak detection. If you use only one measuring node the result will be incorrect.

#### 4. Conclusions

The algorithm for finding leaks in the water supply system comprised of two stages: in the first step there is identification number of the pipes in the network in which the damage occur and the second one step the exact location of the leak. On the basis of this algorithm has been developed own program used to locate leaks in water supply network. On the basis of the testing program examples, they were made numerical simulations location of the leak. The results of calculations indicate a faultless location of the leak in all variants calculations.

#### References

- Semkło, Ł., Ciałkowski, M. and Krzyślak, P. (2013) Analysis of distribution of velocity and pressure in the water supply network. *Ciepłownictwo, ogrzewnictwo, odnawialne źródła energii*, (eds. Zima, W and Taler, D.), Publishing Home of Cracow University of Technology, Cracow. ISBN 978-83-7242-721-2, (in Polish).
- Semkło, Ł., Ciałkowski, M. and Krzyślak, P. (2014) The theory of graphs as a potential tool for modeling of combined heat and power plant network elements, *Journal of Mechanic and Transport Engineering*, Publishing Home of Poznan University of Technology, Vol. 66, No. 4, pp. 57-70.
- Semkło, Ł. and Nowak, A. (2014a) Analysis of the pressure drop caused by leaks on the hydraulic system, *Zastosowanie analizy termodynamicznej do opisu zjawisk fizycznych i urządzeń energetycznych*, (ed. Szewczyka, M.), Publishing Home of Rzeszow University of Technology, Rzeszow, ISBN 978-83-7199-951-8, (in Polish).
- Semkło, Ł., Krzyślak, P. and Ciałkowski, M. (2013a) Analysis of pressure distribution and velocity of the water supply network, *III Konferencja Naukowo-Techniczna Współczesne Technologie i Urządzenia Energetyczne (Modern Energy Technologies, Systems, and Units)*, Cracow, (in Polish).
- Semkło, Ł., Ciałkowski, M. and Krzyślak, P. (2013b) Analysis of distribution of velocity and pressure in the water supply, *27<sup>th</sup> Turbomachinery Workshop*, Szczyrk.

## INFLUENCE OF CERAMIC FOAM PARAMETERS ON THE FRACTURE BEHAVIOUR UPON THE TENSILE TEST

O. Ševeček\*, Z. Majer\*\*, M. Kotoul\*\*\*

**Abstract:** *The contribution deals with numerical simulation of response of the open cell ceramic foam to tensile loading and attempts to predict experimental fracture-mechanics behaviour of the foams using numerical FE model composed of beam elements. Models of different structure irregularity (including regular one) are considered and generated using 3D Voronoi tessellation technique. Complete fracture of the model is simulated by iterative FE simulations where in each step, one strut with maximal tensile stress (higher than the material tensile strength) is removed – until complete separation of the model in two parts. Critical forces, leading to complete breakage of the foam structure, together with final fracture “surfaces”, are investigated and compared for both regular and irregular structures. It is shown that the regular foam structure, composed of Kelvin cells, exhibit generally 10 – 20 % higher fracture resistance than the irregular foam structures and also that structures with smaller cells should be more fracture resistant than the structures with bigger cells.*

**Keywords:** Ceramic foam, Fracture, FEM, Voronoi tessellation, Tensile test.

### 1. Introduction

The growing exploitation of ceramic foams with open cell porosity in a great number of industrial branches and/or as bone replacement materials, has instigated experimental and theoretical studies of their mechanical behaviour. The main drawback still impairing the use of ceramic open foams in load-bearing applications is their intrinsic brittleness. Understanding and prediction of the fracture of such foams under various loading conditions is thus essential for employment of them in the mechanically loaded applications. Most authors employed perfectly periodic tetrakaidecahedron cells corresponding to the open-cell Kelvin foam, e.g. (Warren and Kraynik, 1997), (Zhu et al., 1997) or (Li et al., 2005). Real irregular foams were modelled by a random dispersion of the joint positions from that of the perfect lattice, see e.g. (Tekoglu et al., 2011), (Roberts and Garboczi, 2002). With regard to the overall elastic properties it was shown that the Kelvin foam based models very often provide a reasonably good approximation. However, with regard to strength prediction, irregular foam structure exhibit different behaviour comparing to regular one (usually lower resistance to fracture). Another parameters influencing the fracture resistance could be the cell and structure size and the foam porosity. Effect of these parameters is thus going to be investigated within this contribution using the simplified beam element based model, enabling modelling of larger foam structure volumes even with relatively low demands on the computation time. The main aim of the work is to understand how the tensile strength of the given ceramic foam depends on the foam (primarily geometrical) characteristics. The work will also extend recent pieces of knowledge of a previous work of authors, where a study of the influence of the structure irregularity on the apparent Young's modulus of the foam structure has been carried out - see (Ševeček et al., 2017).

---

\* Ing. Oldřich Ševeček, PhD.: Institute of Solid Mechanics, Mechatronics and Biomechanics, Faculty of Mechanical Engineering, Brno University of Technology, Technická 2896/2; 616 69 Brno; CZ, seveczek@fme.vutbr.cz.

\*\* Ing. Zdeněk Majer, PhD.: Institute of Solid Mechanics, Mechatronics and Biomechanics, Faculty of Mechanical Engineering, Brno University of Technology, Technická 2896/2; 616 69 Brno; CZ, majer@fme.vutbr.cz.

\*\*\* Prof. RNDr. Michal Kotoul, DSc.: Institute of Solid Mechanics, Mechatronics and Biomechanics, Faculty of Mechanical Engineering, Brno University of Technology, Technická 2896/2; 616 69 Brno; CZ, kotoul@fme.vutbr.cz.



## 2. Computational model

To investigate an influence of the ceramic foam parameters (such as foam porosity, cell irregularity or cell size) on the response of the foam to a tensile loading, a 3D-beam element based FE model was developed (with both regular and irregular structure – see Fig. 1a). First, as the reference case, the FE model of the foam composed of regular Kelvin cells was prepared using the 3D Voronoi tessellation in mathematical software Matlab, where the cores of the future cell were regularly distributed within the volume of a block. To create the irregular structure, each of these cores, were moved in the random direction (within a spherical volume) by random distance  $d$  (lying within interval  $0-d_{\max}$ ) before running of the tessellation process. Value  $d_{\max}$  is related to the size of the cell  $D_C$  using parameter  $\delta$  - as shown in Fig. 1b). After modification of all cores positions within the whole model volume (for specific  $\delta$ ), the irregular structure of cells was created again using the Voronoi tessellation routine and subsequently exported using APDL (Ansys Parametric Design Language) text commands into FE system ANSYS 16.2 where simulations and post-processing were executed. Particular struts of the foam structure were meshed using quadratic 3D beam elements BEAM189. Each strut has been meshed using a single element to reduce number of elements in the model. Since the used element type is a quadratic one, even this simplification provides a sufficiently accurate solution to stresses within the struts, in comparison with a finer discretization. The struts were considered to be of circular cross-section and of the same thickness all along their length. This simplification does not correspond with a real state, but it is sufficient for qualitative comparison of various geometrical configurations of the foam structure. The dimensions of the model were designed to meet dimensions of a typical tensile test specimen – in our case 10 x 10 x 30 mm. The applied boundary conditions (simulating tensile test) are depicted in Fig.1a).

A pure stress criterion was employed to define failure of the particular struts. The model was subjected to stepwise displacement load (in z-direction) and in each loading sub-step the stress conditions in all struts were monitored. In case, when the tensile stress in the strut exceeded its critical value (in our case corresponding to the strength of the bulk ceramic  $\sigma_c = 60$  MPa) the corresponding element of the strut was removed and a new FE solution step was performed. Such a simulation process was iterated until the whole cross-section of the foam structure was broken or at least until that moment when the reaction force at top fixture of the model started to drop (which indicates the achievement of the tensile strength of the foam structure). Young's modulus of the considered ceramic material was considered to be  $E_{\text{bulk}} = 90$  GPa and Poisson ratio  $\nu_{\text{bulk}} = 0.25$  (corresponding to source material of “VUCOPOR®A” -  $\text{Al}_2\text{O}_3$  based ceramic foam).

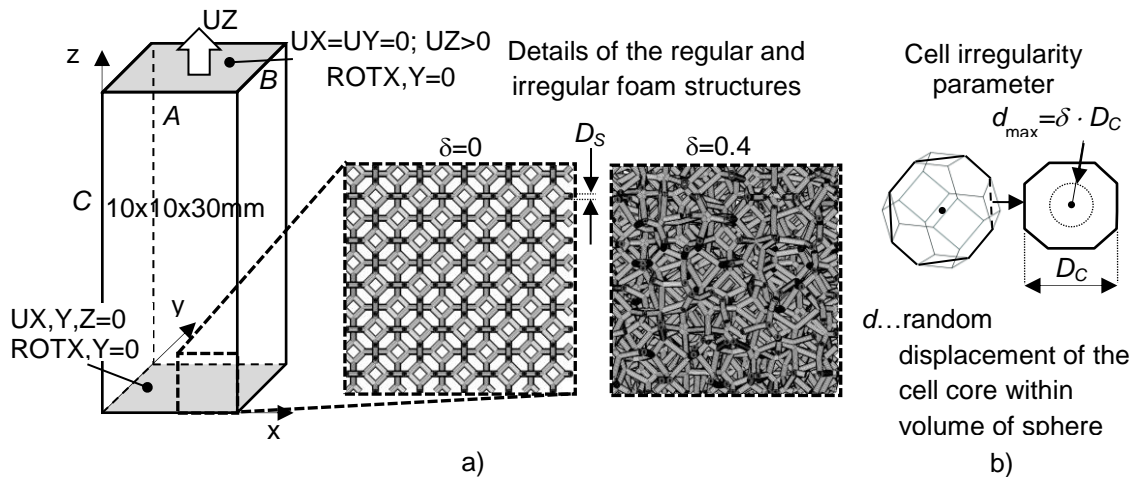


Fig. 1: a) Scheme of the boundary conditions applied to the FE model;  
b) Definition of the cell irregularity parameter  $\delta$ .

## 3. Results

Using the above described FE model a parametric study, investigating an influence of the cell size and foam porosity on the tensile strength of the foam (critical fracture force), has been performed. For three different cell dimensions  $D_C$  a set of foam structures with various strut diameter was generated – for more details about the geometrical combinations used within the study see Tab. 1. With these parameters both

regular and irregular foam structure models were subjected to tensile test simulation. In case of the irregular structure, several different meshes with same parameters were always simulated (to involve into the study also a statistical factor of the mesh irregularity).

Tab. 1: Varied geometrical characteristics of the investigated foam structures.

Porosity [%]	$D_C=800\mu\text{m}$	$D_C=1200\mu\text{m}$	$D_C=1600\mu\text{m}$
	$D_S [\mu\text{m}]$	$D_S [\mu\text{m}]$	$D_S [\mu\text{m}]$
99	30	45	60
95	70	105	140
90	110	165	220
80	160	240	320
70	200	300	400

The results of the failure stresses and displacements for various geometrical configuration of the foam structure model of dimensions 10 x 10 x 30 mm are summarized in the plots of Fig. 2a and 2b.

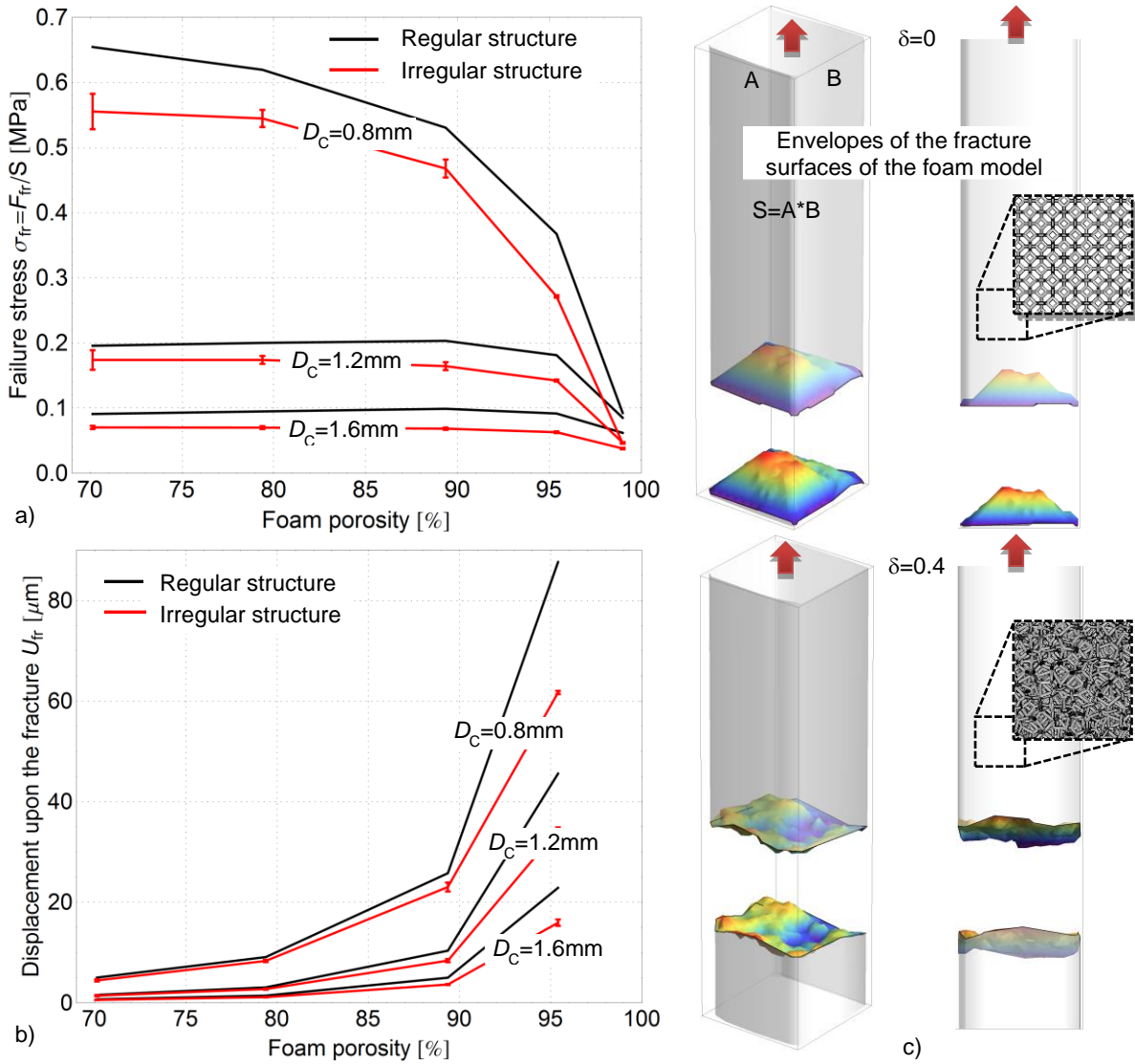


Fig. 2: Dependence of: a) Fracture stress, b) Displacement of top of the specimen upon the fracture, on the foam porosity and cell size  $D_C$  for a specimen of dimensions 10 x 10 x 30 mm; c) Demonstration of the simulated fracture surfaces in case of the regular ( $\delta = 0$ ) and irregular mesh ( $\delta = 0.4$ ).

Based upon the performed simulations the tensile strength of the regular structure is about 10 – 20 % higher than of the irregular one. This fact can be explained by different orientation of the struts to loading direction in both models. While in case of the regular structure, most (2/3) of the struts are oriented under 45 ° to loading direction, in case of the irregular structure, most of the struts are oriented with angle higher than 50 ° to loading direction so these struts have higher bending stress components resulting in increase of tensile stresses on the strut surface. Since the bending of struts leads to higher stresses in comparison with a pure tension (upon same external loading conditions), the struts are broken under lower applied loads and the structure thus globally exhibit lower resistance to fracture. The plots also shows that the tensile strength of the foams is higher for structures composed of smaller cells than of the bigger ones. This can be explained by the bending theory of beams. The bending moment at the end of the strut depends on the length of the strut, so the longer the strut is, the higher bending moment is achieved and the higher stress is induced at the strut end. The longer strut will thus fail earlier than the shorter one.

To demonstrate how the final fracture of the foam structure model can look like, envelopes of the separated model surfaces were created, see Fig. 2c). In case of the regular structure, the fracture usually starts at the site of the supports and extends under the angle of 45 ° towards the centre of the specimen. On the other hand in case of the irregular structure, the fracture can occur at arbitrary place along the specimen length and the fracture “surface” is of irregular shape.

#### 4. Conclusions

Fracture mechanics response of the ceramic foam structure of various porosity and cell size on the applied mechanical load was studied using the FE analysis and beam element based models. Based upon the performed simulations it can be concluded that the tensile strength of the regular structure is about 10 – 20 % higher than the strength of the irregular structure. The results also show that foam structures with smaller cells should exhibit higher resistance to fracture than structures with bigger cells (under consideration of the same porosity of both structures). The smaller the cell (and correspondingly strut length) is, the lower stresses are generated on them and the foam structure thus sustain higher applied loads before reaching the critical failure stress on particular struts. It must be pointed out yet, that the beam element based model of the foam structure, used in this work, is a strong simplification of the real state of the foam structure which should be primarily used for qualitative comparison of various geometrical configurations, but quantitatively can produce different results in comparison with the realistic 3D (solid element based) models. On the other hand, with realistic 3D models it would be very difficult to study failure of bigger foam structure volumes, because of necessity of the very fine discretization of particular struts which in combination with iterative simulation process (described above) would lead to very long computation times. A solution of this problem could be a utilization of the sub-modelling technique, where just critical part of the foam structure is modelled using the realistic 3D mesh. This is planned to be done in the future studies.

#### Acknowledgement

A financial support of the Czech Science foundation under the project no. 17-08447Y is gratefully acknowledged. Computational resources were provided by the CESNET LM2015042 and the CERIT Scientific Cloud LM2015085, provided under the programme "Projects of Large Research, Development, and Innovations Infrastructures".

#### References

- Li, K., Gao, X. and Roy, A.K. (2005) Micromechanical modeling of three-dimensional open-cell foams using the matrix method for spatial frames. *Composites Part B: Engineering* 36, pp. 249-262.
- Roberts, A.P. and Garboczi, E.J. (2002) Elastic properties of model random three-dimensional open-cell solids. *J. Mech. Phys. Solids* 50, pp. 33-55.
- Ševeček, O., Navrátil, P., Papšík, R., Skalka, P. and Kotoul, M. (2017) Influence of the Ceramic Foam Structure Irregularity on the Tensile Response. *Solid State Phenomena* 258, pp. 161-164.
- Tekoglu, C., Gibson, L.J., Pardoen, T. and Onck, P.R. (2011) Size effects in foams: Experiments and modeling. *Progress in Materials Science* 56, pp. 109-138.
- Warren, W.E. and Kraynik, A.M. (1997) Linear Elastic Behavior of a Low-Density Kelvin Foam With Open Cells *Journal of Applied Mechanics* 64, pp. 787-794.
- Zhu, H.X., Knott, J.F. and Mills, N.J. (1997) Analysis of the elastic properties of open-cell foams with tetrakaidecahedral cells. *J. Mech. Phys. Solids* 45, pp. 319-343.

## EFFECT OF CRACKS CLOSURE IN PLATES AND SHELLS UNDER COMBINED TENSION AND BENDING

I. Shatskyi<sup>\*</sup>, M. Makoviichuk<sup>\*\*</sup>, V. Perepichka<sup>\*\*\*</sup>, T. Dalyak<sup>\*\*\*\*</sup>

**Abstract:** *The stress-strain state and limiting equilibrium of cracked plates and shells in combined tension and bending have been studied. The effect of crack closure caused by bending strains is taken into account according to the model of contact of crack lips along a line. The diagrams of ultimate loads for any ratio of tensile and bending loads using the energy fracture criterion have been built.*

**Keywords:** Plate, Shell, Crack closure, Tension, Bending, Strength.

### 1. Introduction

The prediction of failure of thin-walled constructional elements with damages is incorrect without the analysis of contact interaction of crack faces in bending of plates and shells. In the present work we describe the methods and summarize the author's results of investigations of the stress-strain state and limiting equilibrium of cracked plates and shells loaded by simultaneous bending and tension (Shatskyi, 1989, 1995, 2015; Shatskyi et al., 2004; Shatskyi et al., 2005). The crack closure caused by bending strains is taken into account according to the model of contact of crack lips (Shatskyi, 1988, 1998, 2001; Zozulya, 1991; Young et al., 1992; Khludnev et al., 2000; Shatskyi et al., 2002; Liu et al., 2004; Dovbnya et al., 2014). This approach enables one to avoid contradictions caused by the mutual penetration of the opposite edges of cracks in the zone of compression stresses even within the framework of the classical theory of bending of shells.

### 2. Formulation of problem

We consider an isotropic plate  $(x, y, z) \in \mathbf{R}^2 \times [-h, h]$  weakened by a through rectilinear crack of length  $2l$  located along the line  $L$  and oriented along  $x$ -axis. The crack edges are subjected to the action of bending moments  $m$  and membrane forces  $n$  with equal values and opposite directions. The remaining surfaces of the plate, including points at infinity, are free of load. We study the influence of crack closure on the stressed state and limiting equilibrium of the plate.

We describe the edges contact within the framework of the classical Kirchhoff theory by using the model of contact along a line that is proposed in (Shatskyi, 1988, 2001). The mixed boundary problem for pair of biharmonic equations for the generalized plane strain state and the bending of plate has the form:

$$\Delta \Delta \varphi = 0, \quad \Delta \Delta w = 0, \quad (x, y) \in \mathbf{R}^2 \setminus L, \quad (1)$$

---

<sup>\*</sup> Prof. Ivan Shatskyi, DSc.: Department of modelling of damping systems, Ivano-Frankivsk Branch of Pidstryhach Institute for Applied Problems of Mechanics and Mathematics, NAS of Ukraine, Mykytynetska str., 3; 76002, Ivano-Frankivsk; UA, ipshatsky@gmail.com

<sup>\*\*</sup> Assoc. Prof. Mykola Makoviichuk, PhD.: Department of modelling of damping systems, Ivano-Frankivsk Branch of Pidstryhach Institute for Applied Problems of Mechanics and Mathematics, NAS of Ukraine, Mykytynetska str., 3; 76002, Ivano-Frankivsk; UA, makoviy@ua.fm

<sup>\*\*\*</sup> Assoc. Prof. Vasyl Perepichka, PhD.: Department of modelling of damping systems, Ivano-Frankivsk Branch of Pidstryhach Institute for Applied Problems of Mechanics and Mathematics, NAS of Ukraine, Mykytynetska str., 3; 76002, Ivano-Frankivsk; UA, an\_w@i.ua

<sup>\*\*\*\*</sup> Assoc. Prof. Taras Dalyak, PhD.: Department of modelling of damping systems, Ivano-Frankivsk Branch of Pidstryhach Institute for Applied Problems of Mechanics and Mathematics, NAS of Ukraine, Mykytynetska str., 3; 76002, Ivano-Frankivsk; UA, tdalyak@ukr.net

$$N_y = -n, \quad M_y = -m, \quad [u_y] - h|[\theta_y]| > 0, \quad x \in L_1, \quad (2)$$

$$[u_y] = h|[\theta_y]| > 0, \quad M_y + m = h(N_y + n) \operatorname{sgn}[\theta_y], \quad N_y + n \leq 0, \quad x \in L_2, \quad (3)$$

$$[u_y] = 0, \quad [\theta_y] = 0, \quad N_y + n \pm (M_y + m)/h \leq 0, \quad x \in L_3, \quad (4)$$

$$N_{xy} = 0, \quad Q_y^* = 0, \quad x \in L = L_1 \cup L_2 \cup L_3, \quad (5)$$

$$[N_y] = 0, \quad [M_y] = 0, \quad [N_{xy}] = 0, \quad [Q_y^*] = 0, \quad (6)$$

$$N_x = N_{xy} = N_y = 0, \quad M_x = M_{xy} = M_y = 0, \quad (x, y) \rightarrow \infty. \quad (7)$$

Here  $\varphi$  is the function of stresses,  $w$  is the deflection of the plate,  $\Delta = \partial^2/\partial x^2 + \partial^2/\partial y^2$ ,  $[u_y]$  is a crack opening displacement in the base surface of the shell,  $[\theta_y]$  is the jump of the angle of rotation of the normal,  $N_x$ ,  $N_{xy}$  and  $N_y$  are membrane forces,  $M_x$ ,  $M_{xy}$  and  $M_y$  are moments,  $Q_y^*$  are generalized transverse forces,  $L = (-l, l) = L_1 \cup L_2 \cup L_3$  is the crack contour,  $L_1$  is the line of contact of the crack lips, and  $L_2$  is an open section,  $L_3$  is the section where the crack is completely closed. The points separating the domains  $L_1$ ,  $L_2$  and  $L_3$  are a priori unknown and should be found in the course of solution of the problem.

The theoretical questions of existence, uniqueness and smoothness of solutions of such problems in Sobolev spaces have been investigated by means of the theory of variational inequalities (Khludnev and Kovtunenکو, 2000).

### 3. Integral equations

We use the forces and moments integral expressions via the derivatives of the jump functions:

$$N_y(x, 0) = \frac{B}{4\pi} \int_L K_{11}(\xi, x) [u_y]'(\xi) d\xi, \quad M_y(x, 0) = -\frac{D}{4\pi} \int_L K_{33}(\xi, x) [\theta_y]'(\xi) d\xi. \quad (8)$$

Here  $B = 2Eh$ ,  $D = 2Eh^3/(3(1-\nu^2))$ ,  $E$  and  $\nu$  are, respectively, the Young modulus and Poisson's ratio of the material of the plate. The kernels in integrals (8) are expressed via the fundamental solutions for the biharmonic equations.

As a result, problem (1) – (7) is reduced to a system of singular integral equations with constraints in the form of inequalities:

$$\begin{aligned} \frac{B}{4\pi} \int_L K_{11}(\xi, x) [u_y]'(\xi) d\xi &= -n, \quad \frac{D}{4\pi} \int_L K_{33}(\xi, x) [\theta_y]'(\xi) d\xi = m, \\ [u_y](x) - h[\theta_y](x) \operatorname{sgn}[\theta_y](x) &> 0, \quad x \in L_1; \\ -\frac{D}{4\pi} \int_L K_{33}(\xi, x) [\theta_y]'(\xi) d\xi - \frac{Bh}{4\pi} \operatorname{sgn}[\theta_y](x) \int_L K_{11}(\xi, x) [u_y]'(\xi) d\xi &= hn \operatorname{sgn}[\theta_y](x) - m, \end{aligned}$$

$$n + \frac{B}{4\pi} \int_L K_{11}(\xi, x) [u_y]'(\xi) d\xi \leq 0, \quad x \in L_2;$$

$$[u_y] = 0, \quad [\theta_y] = 0,$$

$$n + \int_L K_{11}(\xi, x) [u_y]'(\xi) d\xi \pm \left( m - \int_L K_{33}(\xi, x) [\theta_y]'(\xi) d\xi \right) / h \leq 0, \quad x \in L_3. \quad (9)$$

If we consider the problem for cracked shell, then relations (1) should be replaced by shallow shells theory equations. In this case the kernels of the integral equations are determining by the shape and curvature of shell and by the crack orientation.

#### 4. Fracture criterion and analysis of results

The state of limiting equilibrium of plates and shells with defects under combined tension and bending is specified by the condition of equality of the flow of energy into the crack tip to its ultimate value:

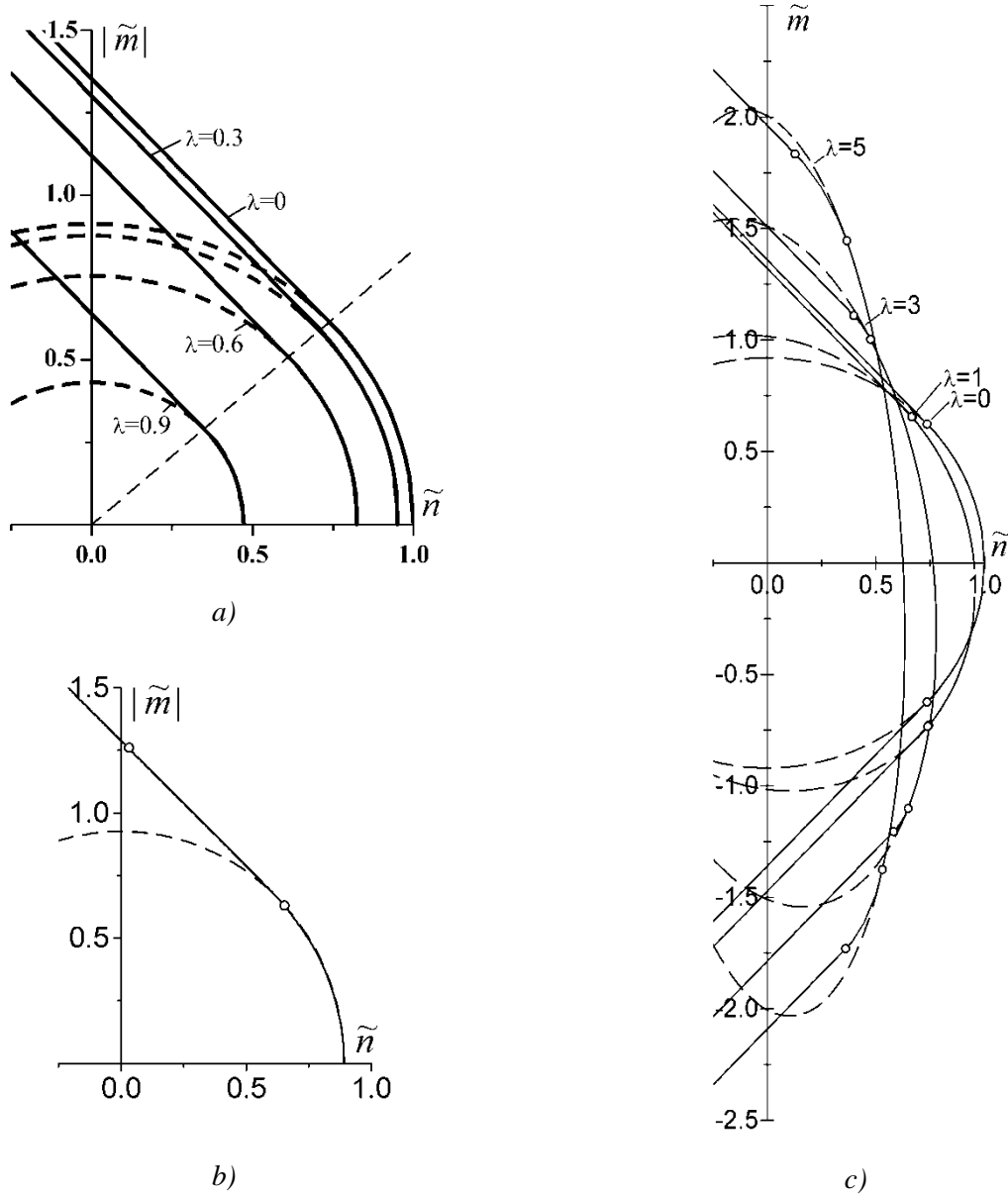


Fig. 1: Diagrams of ultimate loads: a) for plate with periodic system of collinear cracks ( $\lambda = 2l/d$ ,  $d$  is distance between defects); b) for semi-infinite plate with edge crack of length  $l$ ; c) for cylindrical shells with circumferential crack ( $\lambda = \sqrt[4]{3(1-\nu^2)} l / \sqrt{Rh}$ ,  $R$  is shell radius); the solid and dashed lines correspond to crack closure and no closure respectively;  $\tilde{n} = n/n^0$ ,  $\tilde{m} = m/(hn^0)$  and  $n^0 = 2h\sqrt{2E\gamma_*/(\pi l)}$  is the Griffith force for an infinite cracked plate.

$$\frac{\pi}{4h^2E} \left\{ K_N^2 + \frac{3(1+\nu)}{3+\nu} (K_M/h)^2 \right\} = 2\gamma_*,$$

where  $K_N$  and  $K_M$  are the intensity factors of forces and moments:



$$K_N = \mp \frac{B}{4\sqrt{l}} \lim_{x \rightarrow \pm l} \sqrt{l^2 - x^2} [u_y]'(x), \quad K_M = \pm \frac{D(3-2\nu-\nu^2)}{4\sqrt{l}} \lim_{x \rightarrow \pm l} \sqrt{l^2 - x^2} [\theta_y]'(x)$$

and  $\gamma_*$  is the effective surface energy of the material.

The numerical solution of system of equations (9) for uniform load ( $m(x) = m = \text{const}$ ,  $n(x) = n = \text{const}$ ) has been built using parametric and iterative versions of quadrature method. Some examples of simulations are presented in Fig. 1.

## 5. Conclusions

A model of contact of crack edges along a line is developed. The model enables us to obtain in two-dimensional statement the solutions of the problems of combined tension and bending of cracked plates and shells in the absence of kinematic contradictions.

The diagrams of limiting equilibrium of plates and shells are constructed for any ratio of the parameters of loading by tension and bending. It is shown that, in general, the contact of crack lips in bending increases the level of ultimate loads, but for the shells the ranges of the parameters of combined loading in which the effect of crack closure decreases the load-carrying capacity are established.

Despite the limited capacity of the classical plates and shells bending theory, the proposed approach allowed to avoid kinematic contradictions associated with mutual penetration of opposite surfaces of cracks in compression zones.

## References

- Dovbnya, K.M. and Shevtsova, N.A. (2014) Studies on the stress state of an orthotropic shell of arbitrary curvature with the through crack under bending loading. *Strength of Materials*, 46, 3, pp. 345-349.
- Khludnev, A.M. and Kovtunenkov, V.A. (2000) *Analysis of Cracks in Solids*. WIT-Press, Boston.
- Liu, R., Zhang, T., Wu, X.J. and Wang, C.H. (2004) Crack closure effect on stress intensity factors of an axially and a circumferentially cracked cylindrical shell. *Int. J. Fracture*, 125, 3-4, pp. 227-248.
- Shatskii, I.P. (1989) Contact of the edges of the slit in the plate in combined tension and bending. *Materials Science*, 25, 2, pp. 160-165.
- Shatskyi, I.P. (1995) Limit equilibrium of plate with collinear cracks under combined tension and bending. *Proc. Nat. Acad. Sciences of Ukraine*, 10, pp. 62-64, (in Ukrainian).
- Shats'kyi, I.P. and Perepichka, V.V. (2004) Limiting state of a semiinfinite plate with edge crack in bending with tension. *Materials Science*, 40, 2, pp. 240-246.
- Shats'kyi, I.P. and Makoviichuk, M.V. (2005) Contact interaction of crack lips in shallow shells in bending with tension. *Materials Science*, 41, 4, 486-494.
- Shatskyi, I.P. (2015) Closure of crack connected with a slot in a plate under bending and tension-compression. *Odessa Nat. Univ. Gerald. Math. Mech.*, 4, pp. 103-107, (in Ukrainian).
- Shatskyi, I.P. (1988) Bending of plate weakened a cut with contacting edges. *Proc. Acad. Sciences UkrRSR. Ser. A*, 7, pp. 49-51, (in Ukrainian).
- Shatskii, I.P. (1998) Problem on cut with contacting edges in bending shallow shell. *Mechanics of Solids*, 5, pp. 164-173, (in Russian).
- Shatskii, I.P. (2001) Model for contact of crack boundaries in a bending plate. *J. Math. Sci.*, 103, 3, pp. 357-362.
- Shatskii, I.P. and Dalyak, T.M. (2002) Closure of cracks merged with slots in bent plates. *Materials Science*, 38, 1, pp. 24-33.
- Young, M.J. and Sun, C.T. (1992) Influence of crack closure on the stress intensity factor in bending plates. A classical plate solution. *Int. J. Fracture*, 55, pp. 81-93.
- Zozulya, V.V. (1991) Bending of plate weakened a crack with contacting edges under dynamic loading. *Proc. Acad. Sciences UkrRSR. Ser. A*, 4, pp. 55-60, (in Ukrainian).

## MODELLING OF ENERGY DISSIPATION IN SHELL DAMPERS

I. Shatskyi<sup>\*</sup>, I. Popadyuk<sup>\*\*</sup>, A. Velychkovych<sup>\*\*\*</sup>

**Abstract:** *The achievements of the authors in the analytical modeling of hysteretic energy dissipation in the shells with a filler at the expense of dry friction are presented. The last result describes the effect of maximum energy absorption by a shell damper. Importance of tribology settings of contact system, for which the dissipated energy of the external load reaches the maximum, is revealed.*

**Keywords:** Vibration protection, Shell, Filler, Dry friction, Structural hysteresis.

### 1. Introduction

Vibration processes that occur in the operation of almost all, without exception, modern machines and mechanisms, typically lead to undesirable consequences. In the vast majority of cases, vibration decreases the strength, reliability and durability of industrial machines, mechanisms and structures, as well as affects health of personnel. Thus, the problem of vibration insulation proves to be quite urgent both in technical and social terms. One of the ways used to solve the formulated problem is connected with the application of vibration protecting devices, such as shock absorbers, dampers, dynamic vibration absorbers, etc. This is why the research and design works and theoretical investigations in the field of development of new means of vibration protection and methods for their numerical analyses are of crucial importance.

The authors have developed advanced design of vibration insulators (Shopa et al., 2002), among which the leading place belongs to shell elastic elements with deformable filler (Fig. 1). In the mechanical and mathematical modeling of the behavior of elastic elements under (generally speaking, non-monotonic) loading, we get a class of nonlinear non-conservative mixed contact problems of the frictional interaction of thin shells with deformable fillers (Popadyuk et al., 2003 and Shopa et al., 2015).



*Fig. 1: Laboratory samples of shell dampers.*

---

<sup>\*</sup> Prof. Ivan Shatskyi, DSc.: Department of modelling of damping systems, Ivano-Frankivsk Branch of Pidstryhach-Institute for Applied Problems in Mechanics and Mathematics, NAS of Ukraine; Mykitynetska Str., 3; 76002, Ivano-Frankivsk; UA, ipshatsky@gmail.com

<sup>\*\*</sup> Assoc. Prof. Ihor Popadyuk, PhD.: Department of modelling of damping systems, Ivano-Frankivsk Branch of Pidstryhach-Institute for Applied Problems in Mechanics and Mathematics, NAS of Ukraine; Mykitynetska Str., 3; 76002, Ivano-Frankivsk; UA, igorpopadyuk60@gmail.com

<sup>\*\*\*</sup> Assoc. Prof. Andrii Velychkovych, PhD.: Department of structural mechanics, Ivano-Frankivsk National Technical University of Oil and Gas; Karpatska Str., 15; 76019, Ivano-Frankivsk; UA, velja2@mail.ru

The aim of the report is to acquaint the scientific audience with the results obtained due to the analytical modeling of hysteretic energy dissipation in the shells with a filler at the expense of dry friction. Thus, the latest achievement, i.e. the effect of maximum energy absorption by shell damper, is described.

## 2. Formulation of the problem

Consider an elastic deformable cylinder (filler) of radius  $R$  and length  $2a$  placed into a cylindrical shell with thickness  $h_0$  (Fig. 2a). The filler is compressed on the end faces by perfectly rigid pistons subjected to the action of an external load  $Q$  non-monotonic as a function of time. Dry position friction occurs on contact surface of the shell with a filler. We need to study the phenomenon of structural damping in the given non-conservative system.

The shell, depending on the conditions of use of the structure, can be of closed (solid – Fig. 2b) or open (cut along a generating line – Fig. 2c) profiles. In the first case (Fig. 2b), the shell works on the tangential stress, and in the second case (Fig. 2c) – on the bending.

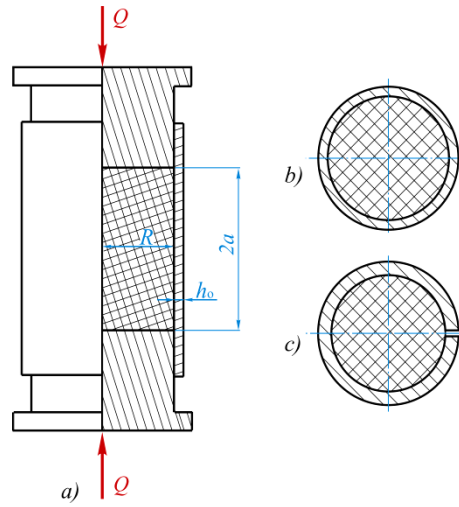


Fig. 2: Scheme of a shell damper.

## 3. Analysis of the results

Using applied shell and filler models the analytic algorithm of solving nonlinear mixed problem on frictional interaction of elastic filler with a shell at non-monotonic quasi-static loading has been developed. The solution of the problem at the stages of active loading, unloading and repeated loading has been proposed, characteristics of stress-strain state, stiffness and damping ability of the system have been obtained.

An approximate analytical description of the structural hysteresis loop obtained for shells with shear-unresisting slight-compressible filler is provided in the works (Popadyuk et al., 2003 and Shopa et al., 2015). Thus, we describe the dependences without displacements of the piston and loading with arbitrary asymmetry cycle coefficient  $s = Q_{\min} / Q_{\max} \in [0, 1]$  by the following relations.

For active loading

$$\delta^I = \frac{Q}{c} \frac{1 - e^{-\lambda}}{\lambda}, \quad 0 \leq Q \leq Q_{\max};$$

for unloading

$$\delta^{II} = \begin{cases} \delta_{\max}^I - \frac{1}{c} \left[ b(Q_{\max} - Q) + \left( \sqrt{Q_{\max}} - \sqrt{Q} \right)^2 / \lambda \right], & Q_{\max} \geq Q \geq s_* Q_{\max}; \\ \frac{Q}{c} \left( b - \frac{e^{\lambda} - 1}{\lambda} \right), & s_* Q_{\max} \geq Q \geq 0; \end{cases}$$

for repeated loading

$$\delta^{III} = \begin{cases} \delta_{\min}'' + \frac{1}{c} \left[ b(Q - Q_{\min}) + (\sqrt{Q} - \sqrt{Q_{\min}})^2 / \lambda \right], & Q_{\min} \leq Q \leq \min\{Q_{\min} / s_*, Q_{\max}\}; \\ \delta^I, & \min\{Q_{\min} / s_*, Q_{\max}\} \leq Q \leq Q_{\max}. \end{cases}$$

Here,  $\lambda = 2f a/R$ ,  $f$  is the coefficient of dry friction in the shell–filler pair;  $s_* = e^{-2\lambda}$ ;  $c$  is the linear stiffness of the conservative system, which depends on type, size and physical and mechanical characteristics of the shell and filler.

$$c = \frac{\pi R^2 E}{a} \frac{1}{3(1-2\nu) + (2-\nu_o)\varepsilon}, \quad b = \frac{\nu_o \varepsilon}{3(1-2\nu) + (2-\nu_o)\varepsilon} \quad \text{and} \quad c = \frac{\pi R^2 E}{a} \frac{1 + 36 \frac{R^2}{h_o^2} \varepsilon}{36 \frac{R^2}{h_o^2} \varepsilon}, \quad b = 0$$

for a solid shell, for a shell cut along a generating line respectively;  $\varepsilon = ER/(E_o h_o)$ ;  $E$ ,  $\nu$ ,  $E_o$ ,  $\nu_o$  are Young's modulus and Poisson's ratio of the materials of the filler and shell respectively.

System “shell–deformable filler” with parameters  $h_o/R = 0.1$ ,  $E/E_o = 0.001$ ,  $\nu = 0.499$ ,  $\nu_o = 0.3$ ,  $a/R = 2$  was chosen as an example. A diagram of cyclic deformation of damper is provided in Fig. 3.

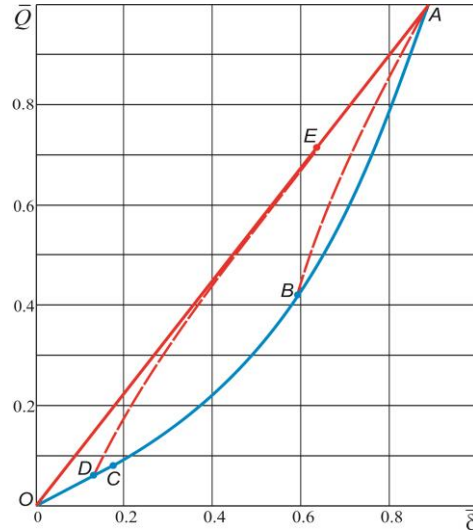


Fig. 3: The loop of constructive hysteresis: active loading (line OA), unloading (line AO), repeated loading (lines BA and DEA).

The value of dissipated energy was defined as the area of the hysteresis loop.

$$\psi = \begin{cases} \frac{Q_{\max}^2}{3c\lambda} (1-s)(1-\sqrt{s})^2, & s_* \leq s \leq 1; \\ \frac{Q_{\max}^2}{6c\lambda} \left[ (2 + e^{-\lambda})(1 - e^{-\lambda})^2 - s^2(e^{\lambda} - 1)^2(2 + e^{\lambda}) \right], & 0 \leq s \leq s_*. \end{cases}$$

Fig. 4 features a typical dependence of the normalized value of the dissipated energy  $\tilde{\psi} = \psi/A$  on the coefficients of dry friction  $f$  and asymmetry of the load cycle  $s$ . Energy of the elastic deformation of a conservative system was taken as a normalizing factor  $A = Q_{\max}^2/(2c)$ .

For each value of stress ratio there is a value  $\lambda_*(s)$ , at which function  $\psi(\lambda, s)$  reaches the extreme  $\max_{\lambda} \psi(\lambda, s) = \psi(\lambda_*(s), s) = \psi^*(s)$ . Fig. 5 features results of such analysis. The global maximum is attained for pulsating cycle at  $f \approx 0.253$ . Then  $\lambda_*(0) = 4f = 1.012$ , and  $\max_{\lambda, s} \tilde{\psi}(\lambda, s) = \tilde{\psi}(1.012, 0) \approx 0.304$ .

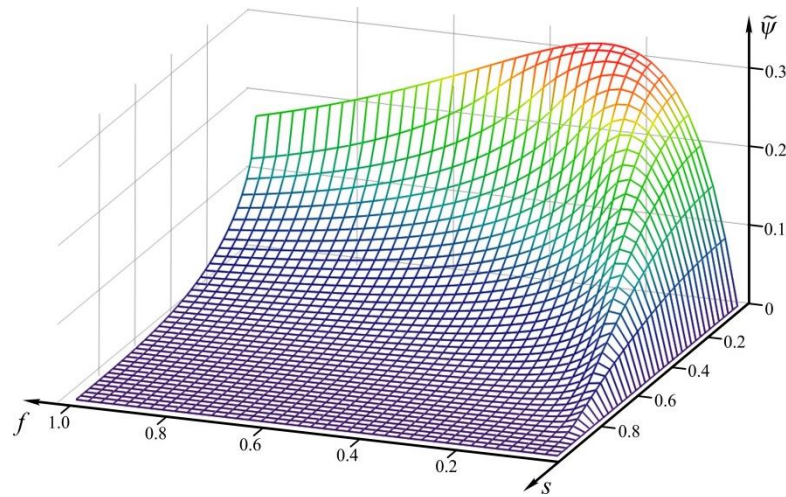


Fig. 4: The value of dissipated energy.

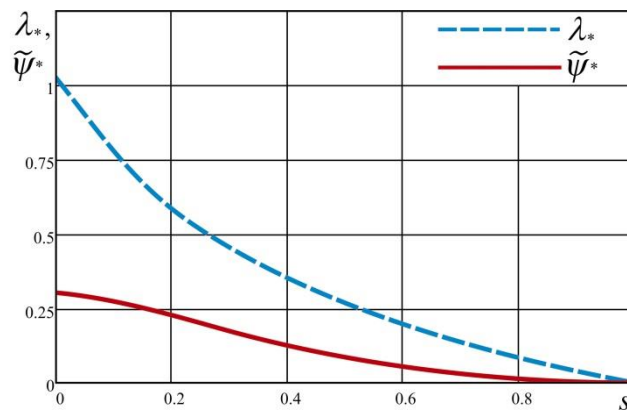


Fig. 5: Stationary value  $\lambda$  and the highest values of dissipation, which are achieved for them.

Existence of the extreme value is explained by the fact that in systems with dry positional friction distribution of the friction forces depends on the deformations of the contact pair (the filler and shell), and deformations, in turn, depend on the friction forces. Such a close relationship identifies specific, often intuitively unpredictable behaviors of such structures. In this situation, the increase in the coefficient of dry friction  $f$  leads to a reduction in the area of mutual slippage of the shell and filler, and, consequently, reduction of structural energy dissipation, which occurs only in this area.

#### 4. Conclusions

The article presents the main analytical results of the modeling of structural hysteresis at frictional interaction of solid and cut shells with a filler. It has been first established that for a fixed ratio of cycle asymmetry with increasing coefficient of friction between the shell and filler, the amount of energy dissipated per cycle grows, reaches an extremum, and then gradually decreases. The maximum capabilities of the shell damper as for the energy absorption have been determined, and the optimal coefficients of friction in the contact pair have been calculated. Therefore, the idea of optimization of shell vibration protecting devices according to the criterion of maximum energy absorption of external influences by providing the desired tribologic properties of the contacting pairs is declared.

#### References

- Shopa, V.M., Velychkovych, A.S., Velychkovych, S.V. et al. (2002) Shell Springs, Fakel, Ivano-Frankivsk, (in Ukrainian).
- Popadyuk, I.Y., Shatskyi, I.P. and Shopa, V.M. (2003) Mechanics of Frictional Contact of Shells with Deformable Filler, Fakel, Ivano-Frankivsk, (in Ukrainian).
- Shopa, V.M., Shatskyi, I.P., Bedzir, O.O. and Velychkovych, A.S. (2015) Interaction of Cut Shells with Deformable Bodies, IFNTUOG, Ivano-Frankivsk, (in Ukrainian).

## THE ADVANTAGES OF A NEW HYDRAULIC CYLINDER DESIGN WITH A CONTROL SYSTEM

T. Siwulski<sup>\*</sup>, U. Warzyńska<sup>\*\*</sup>

**Abstract:** *In the paper, a new design of a hydraulic cylinder is presented and some of its advantages in comparison to a standard hydraulic cylinder design are discussed. The mathematical comparative analysis of standard and a new cylinder design, including analytical and numerical approach is shown. A new cylinder design is characterized by a better heat dissipation, improved fluid circulation in cylinder chambers and higher stiffness of a system.*

**Keywords:** Hydraulic cylinder, Heat dissipation, Bulk modulus.

### 1. Introduction

An extensive use of hydraulic systems in drives of machines and devices results directly from the advantages of this type of drive, such as high power to weight ratio and modular design. However, the disadvantages of hydraulic systems, such as changing fluid properties with temperature and high demands on its purity make the operation of hydraulic systems hindered because of increased degradation of system components in harsh environmental conditions, occurring eg. in mines, steel mills and processing plants. The research on the causes of hydraulic machines failures operated in underground copper ore mines, made by the authors and other research teams (Król et al., 2009) indicate that the most common elements prone to wear are hydraulic cylinders. Described in this article a new design of hydraulic cylinder has some certain advantages, including among others, better exchange of heat and increased stiffness of a system.

### 2. Theoretical analysis

#### Thermal energy

Classic hydraulic cylinders with power supply lines form a system wherein fluid cannot exchange completely in the cylinder chambers, and thus the ability to dissipate thermal energy stored in the actuator and to remove contaminants out of the system is significantly limited (Fig. 1). Research carried out by the authors (Siwulski and Warzyńska, 2017) indicate that temperature of fluid in classic hydraulic cylinders operating with great intensity in the environment characterized by high temperature and dust, greatly exceeds the permissible value of operation. The relationship describing the hydro-mechanical efficiency of a cylinder  $\eta_{hmc}$ , which for hydraulic cylinders is taken as the total efficiency  $\eta_c$ , takes into account the power losses occurring in the piston sealing  $\Delta N_{f1}$ , the gland sealing  $\Delta N_{f2}$  and hydraulic losses associated with flow resistance  $\Delta N_h$  and for the extension stroke of a piston takes the form:

$$\eta_c = \frac{F \cdot v - \Delta N_{f1} - \Delta N_{f2} - \Delta N_h}{Q \cdot p} \quad (1)$$

---

<sup>\*</sup> Tomasz Siwulski, PhD. Eng.: Wrocław University of Science and Technology, Faculty of Mechanical Engineering, Department of Maintenance and Operation of Logistics, Transportation and Hydraulic Systems, PL, tomasz.siwulski@pwr.edu.pl

<sup>\*\*</sup> Urszula Warzyńska, MSc. Eng.: Wrocław University of Science and Technology, Faculty of Mechanical Engineering, Department of Maintenance and Operation of Logistics, Transportation and Hydraulic Systems, PL, urszula.warzyńska@pwr.edu.pl



The above analysis indicates that the efficiency of hydraulic cylinders mainly depends on the amount of energy dissipated in the piston and gland sealing. Therefore, maintenance of a high sealing efficiency during the whole operation time is essential to its proper operation.

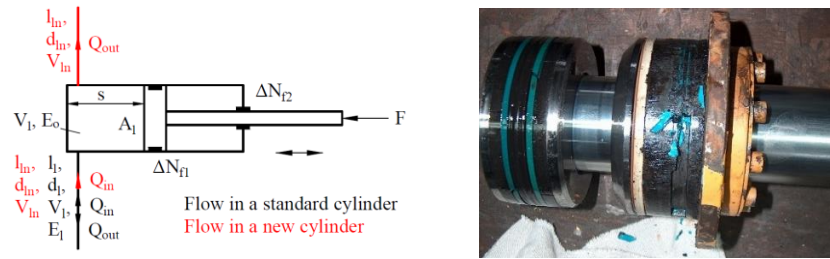


Fig. 1: Scheme of double-acting cylinder and an example of a degraded sealing.

The power loss in sealing is a function of the technical parameters of sealing and guide elements (related to the type of material) and also surface which cooperate with the sealing elements or any impurities. As a source of thermal energy can be regarded mechanical losses at sealing nodes, hydraulic losses, and in some cases external influence, eg. heat source (diesel engine). The possibility to remove heat from a cylinder is enabled only through returning of fluid to a tank or a cooler and through the radiating to the environment. However, in the case of machines operating in high ambient temperature, the possibility of emitting heat to the environment is limited. The construction of a hydraulic cylinder itself also prevents the complete replacement of the fluid contained in the chambers. The volume  $V_c$  of fluid to be discharged into the supply line during the movement is proportional to stroke  $s$  and piston area  $A_1$  (or piston minus rod area,  $A_2$ ). Thus, the volume  $V_o$  of fluid discharged from the cylinder ( $V_c$ ) and then from a supply line ( $V_l$ ) is:

$$V_o = \begin{cases} 0 & \text{for } V_l \geq V_c \\ V_c - V_l & \text{for } V_l < V_c \end{cases} \quad (2)$$

It is reasonable, therefore, to formulate a claim that during operation of a cylinder, a certain volume of the fluid never will be released to the tank, and upon using long and relatively large diameter supply lines in combination with a relatively small cylinder diameter and small stroke, the effect of no circulation of fluid outside the region of cylinder and a supply line will take place.

### Stiffness of the system

Another important aspect is the stiffness of a system: cylinder – power supply line. This issue is particularly important in hydraulic drives of booms and operating arms, from which is required to achieve significant accuracy and position constancy of a tool over operating time (e.g. drilling machines, cranes, etc.). The most used applications cylinders are permanently connected to the hydraulic supply lines, creating a system whose rigidity is significantly affected by hydraulic lines stiffness (Hružík et al., 2013; Burrows and Edge, 2002). The displacement of cylinder piston with rigid non-deformable walls and excluding friction in the seals may be described by the equation:

$$\Delta s_c = \frac{s \cdot \Delta p}{E_o} \quad (3)$$

where:  $\Delta s_c$  – change of cylinder stroke as a result of fluid compressibility,  $s$  – fluid column height in a cylinder chamber,  $\Delta p$  – pressure difference between pressure in a cylinder chamber and pressure outside the system,  $E_o$  – fluid bulk modulus (oil).

While the displacement of a piston including power supply line takes the form of:

$$\Delta s_{cl} = \frac{\Delta V_o + \Delta V_l}{\frac{\pi \cdot D^2}{4}} = \frac{\frac{\pi \cdot (s \cdot D^2 + l \cdot d^2) \cdot \Delta p}{4 \cdot E_o} + \frac{\pi \cdot l \cdot d^2 \cdot \Delta p}{4 \cdot E_l}}{\frac{\pi \cdot D^2}{4}} = \frac{\Delta p}{D^2} \cdot \left( \frac{s \cdot D^2 + l \cdot d^2}{E_o} + \frac{l \cdot d^2}{E_l} \right) \quad (4)$$

where:  $\Delta s_{cl}$  – change of cylinder stroke as a result of fluid compressibility and hydraulic line (hose) elasticity,  $l$  – length of a supply line,  $d$  – internal diameter of a supply line,  $E_l$  – bulk modulus of a supply line.

Effective bulk modulus of a system including compressibility of fluid and elasticity of a hose is equal to:

$$E_{ol} = \frac{s \cdot D^2 + l \cdot d^2}{\frac{s \cdot D^2 + l \cdot d^2}{E_o} + \frac{l \cdot d^2}{E_l}} \quad (5)$$

### 3. A new design of a hydraulic cylinder

The results of fluid flow analysis and the theoretical system stiffness analysis, which were briefly presented above, clearly indicated that it is reasonable to provide a solution which allows the improved circulation of fluid in the system, while limiting the impact of the supply line on system stiffness. Based on these assumptions an innovative hydraulic system was developed that allows exchange of fluid in the cylinder chambers, part of which is specially made hydraulic cylinder (Fig. 2). A description of the invention may be found in (Siwulski and Radziwanowska, 2016).

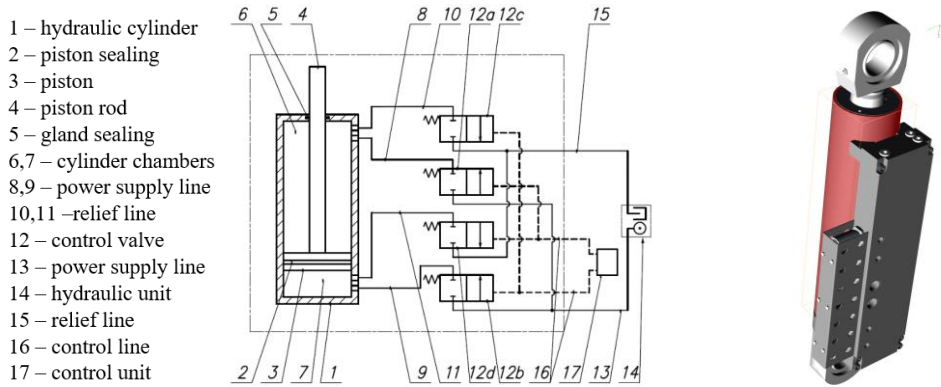


Fig. 2: A schematic diagram of a new design of hydraulic cylinder with a control system and a model of prototype hydraulic cylinder.

A comparative mathematical analysis was performed for the standard design of a cylinder with two different power supply line lengths ( $l = 2000$  mm and  $l = 500$  mm) supplying fluid power to a bottom chamber and the new design of a cylinder (supply line length  $l_n = 100$  mm). According to the new idea, the control valves are mounted on a cylinder in order to limit the impact of effective bulk modulus in cylinder supply lines when the cylinder is blocked. Assuming for the standard cylinder bulk modulus for oil equal to  $E_o = 1500$  MPa (Yang et al., 2016), and bulk modulus for hydraulic line (hose)  $E_l = 400$  MPa (Burrows and Edge, 2002) the effective bulk modulus (Eq. (5)) for the standard cylinder  $l = 2000$  mm is equal to  $E_{ol} = 1009$  MPa while for a standard cylinder  $l = 500$  mm,  $E_{ol} = 1322$  MPa. In a new cylinder design, the infinite stiffness of supply lines walls was assumed (because they are made in a block of steel) and therefore the effective bulk modulus is equal to oil bulk modulus  $E_o = 1500$  MPa.

### 4. Numerical simulations results

Numerical simulations in the field of computational fluid dynamics (CFD) were done in Ansys CFX using immersed solid algorithm. The boundary condition at the inlet was mass flow rate  $Q = 1.5$  kg/s, while at the outlet a free outflow at atmospheric pressure. The difference in temperature between the fluid in a chamber and fluid in a supply line was set at  $\Delta t_p = 40$  °C. Pre-start temperature in the entire fluid domain was set at  $t_2 = 80$  °C while the temperature of the fluid at inlet equal to  $t_1 = 40$  °C. Piston movement function was set in the range of 50 % of the full stroke. As a result of numerical analyses, temperature distributions in the domain of fluid in the individual time steps in transient simulation were obtained. Total analysis time was equal to two cycles of the cylinder. The amount of heat discharged from the system  $\Delta E_c$  during one cycle describes the relationship:

$$\Delta E_c = E_{c2} - E_{c1} = c_w \cdot t_{sr} \cdot m_2 - c_w \cdot t_1 \cdot m_1 = C \cdot (t_{sr} - t_1) \quad (6)$$

where  $C$  is a constant:

$$C = c_w \cdot m_2 = c_w \cdot m_1 \quad (7)$$

and  $c_w$  – specific heat of oil (constant value, independent of temperature),  $c_w = 1880$  kJ / kg.K,  $m_1$ ,  $m_2$  – fluid mass supplied to and discharged from a system respectively,  $t_{sr}$  – average temperature of fluid flowing out of the system measured at the outlet during one cycle of cylinder operation.

To enable the comparison of results, the average temperature of fluid flowing out of the system versus time of simulation was depicted in Fig. 3 and the parameter SPOC was introduced, defined as:

$$SPOC = \frac{(t_{sr2} - t_1) - (t_{sr1} - t_1)}{\Delta t_p} \cdot 100 \% \quad (8)$$

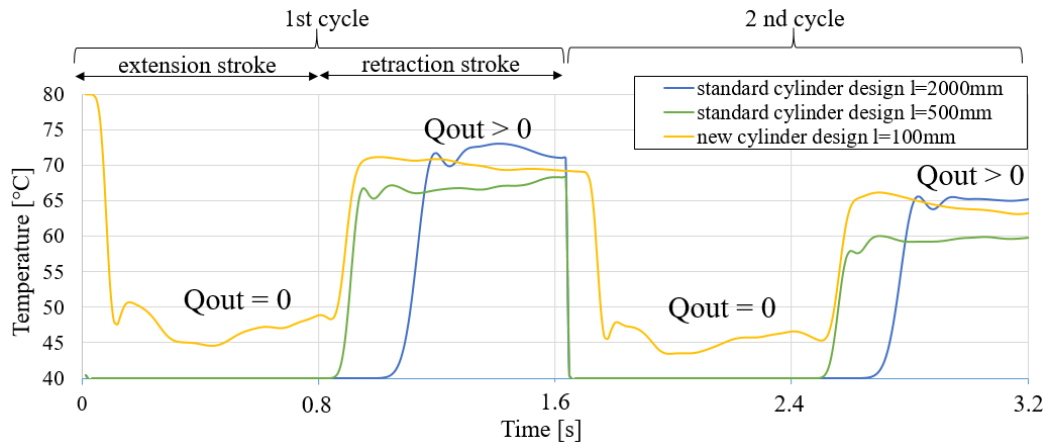


Fig. 3: The results of temperature at the outlet during the double cycle of the hydraulic cylinders.

In Tab. 1 the comparison of thermal energy dissipation (SPOC parameter) for the analyzed cylinders is shown calculated in reference to a standard cylinder design  $l = 2000$  mm.

Tab. 1: A comparison of the cylinder designs on the basis of thermal energy dissipation.

Hydraulic cylinder type	1st cycle			2nd cycle		
	standard		new	standard		new
<b><math>l</math> or <math>l_n</math> [mm]</b>	2000	500	100	2000	500	100
<b>Improvement of heat dissipation (SPOC) [%]</b>	-	10.15	20.52	-	3.39	15.55

## 5. Conclusions

The carried out research, undertaken development project and presented results of numerical simulations clearly indicate a significant potential of the presented solution in many areas. Its advantages, including, inter alia, indicated in this publication the possibility of significant improvement of fluid exchange in the cylinder chambers, which increases a possibility of heat energy and contamination discharge from the cylinder, and a positive effect on the rigidity of the system. Other than those mentioned positive features of the presented solution is increased safety by preventing free movement of the cylinder under load in case of supply line damage, but this aspect is the subject of a separate publication.

## References

- Burrows, C.R. and Edge, K.A. (2002) Power Transmission and Motion Control: PTMC 2002. Professional Engineering Publishing Ltd.
- Hružík, L., Vašina, M. and Bureček A. (2013) Evaluation of bulk modulus of oil system with hydraulic line. EPJ Web of Conferences 45, 01041.
- Król, R., Zimroz, R. and Stolarczyk, Ł. (2009) Failure analysis of hydraulic systems used in mining machines operating in copper ore mine KGHM POLSKA MIEDZ S.A. Scientific Papers of the Institute of Mining of the Wrocław University of Technology, 128, pp. 127-139 (in Polish).
- Siwulski, T. and Radziwanowska, U. (2016) A new design of the controlled hydraulic cylinder piston with a total fluid exchange, Patent Application No. P415174 (in Polish).
- Siwulski, T. and Warzyńska, U. (2017) Hydraulic cylinder with the system supporting the exchange of fluid in the chambers. Proceedings of 30th PRMR Conference, Zakopane (in Polish).
- Yang, S., Tao, A., Luo, Y., Zhang J., Zhou, P. and Zhou, L. (2016) Experimental measurements of bulk modulus for two types of hydraulic oil at pressures to 140MPa and temperatures to 180°C. 10th International Fluid Power Conference, Dresden, pp. 193-204.

## THIN WALLED PIPE CRUSHED IN JAWS

S. Ślawski\*, S. Duda\*\*, T. Machoczek\*\*\*

**Abstract:** In the paper the authors present the process of creating physical model. The experiment consisted in crushing the sample in the jaws of a testing machine. The values of force were selected to enable verification of the physical model. During the experiment the strain in the areas under strain gauges and displacements of selected points were observed. The material properties of the tested element were determined by performing static tensile test.

**Keywords:** Finite element method, True stress – strain curve, Strain gauge, Static tensile test.

### 1. Introduction

Conducting reliable numerical simulation requires a well-validated physical model. In the paper the authors present process of creating physical model. In order to validate it an experiment has been performed where displacement and strain were recorded. The authors compared results from the experiment and numerical simulation developed in LS Dyna.

### 2. Experiment

The experiment which relays on crushing a sample in testing machine MTS 858 Table Top System was performed. The dimensions of steel sample which have been used in experiment were 52 mm of diameter and 2.5 mm wall thickness. The sample was 50 mm long. On front surface of the sample markers were applied. Their positions and numeration were shown in Fig. 1. Those markers were used to determine displacement of these points based on video which was recorded during the experiment. On the inside and outside surface of sample three strain gauges were glued. Glued strain gauges were product of Vishay, type EA-13-120LZ-120/E. Numeration and position of those strain gauges were shown in Fig. 2.

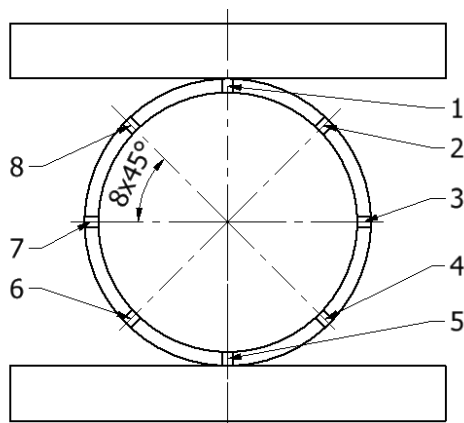


Fig. 1: Numeration and positions of markers.

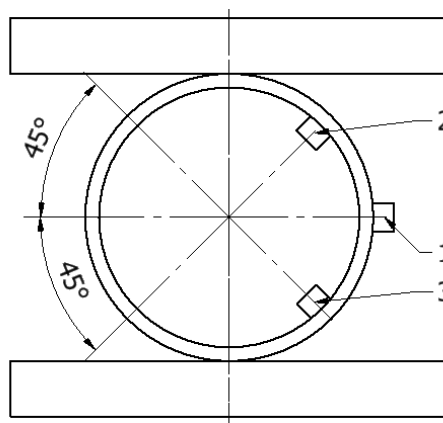


Fig. 2: Numeration and positions of strain gauges.

\* M.Sc. Eng. Sebastian Ślawski: Institute of Theoretical and Applied Mechanics, Silesian University of Technology, Konarskiego 18a; 44 100, Gliwice; PL, sebastian.slawski@polsl.pl

\*\* Assoc. Prof. Sławomir Duda, PhD.: Institute of Theoretical and Applied Mechanics, Silesian University of Technology, Konarskiego 18a; 44 100, Gliwice; PL, slawomir.duda@polsl.pl

\*\*\* PhD. Eng. Tomasz Machoczek: Institute of Theoretical and Applied Mechanics, Silesian University of Technology, Konarskiego 18a; 44 100, Gliwice; PL, tomasz.machoczek@polsl.pl

The strain values of strain gauges during the experiment were shown in Fig. 4.

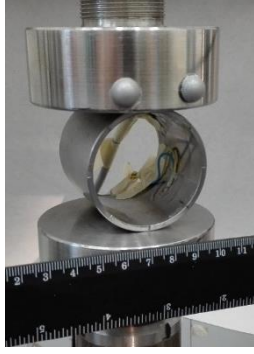


Fig. 3: Experiment – sample between testing machine jaws.

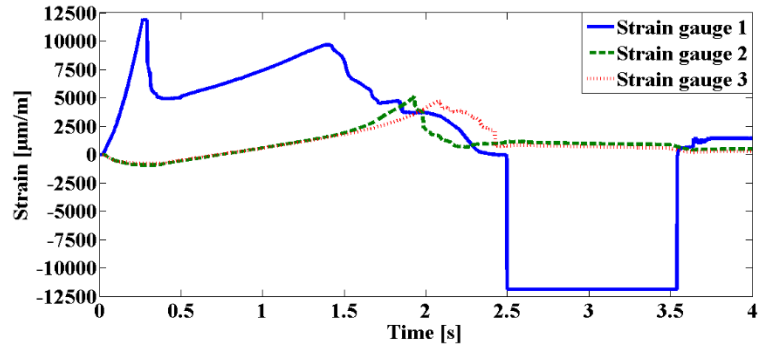


Fig. 4: Values of strain gauges strain.

In order to recognize parameters of sample material a static tensile test has been performed. Dimension of the sample were in accordance with the applicable standard. The static tensile test was performed on MTS 858 Table Top System testing machine. Basing on the sample dimensions and registered data from testing machine engineering stress – strain curve was determined (Jakubowicz et al., 1984). The next step was to transform engineering stress – strain curve to true stress – strain curve using equations 1 and 2.

$$\sigma_T = \sigma \cdot (1 + e), \quad (1)$$

$$e_T = \ln(1 + e), \quad (2)$$

where:  $\sigma$  – engineering stress [MPa],

$\sigma_T$  – true stress [MPa],

$e$  – engineering strain,

$e_T$  – true strain.

The determined true stress – strain curve has been shown in Fig. 6.



Fig. 5: Static tensile test.

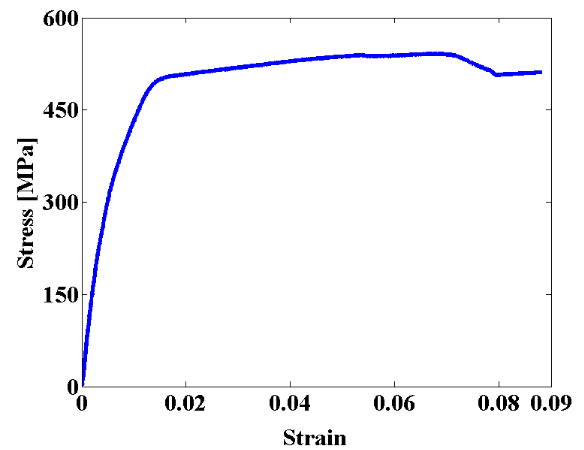


Fig. 6: True stress – strain curve.

Based on true stress – strain curve value of Young's ratio was determined using Eq. (3).

$$E = (\Delta F \cdot L_0) / (S_0 \cdot \Delta L), \quad (3)$$

where:  $\Delta F$  – force increase [N],

$S_0$  – cross sectional area of sample [mm<sup>2</sup>],

$L_0$  – measuring length [mm],

$\Delta L$  – measuring length increase.

Young's ratio value has been determined as 234 GPa.



### 3. Numerical simulation

A numerical model was created using LS PrePost. The model consists of three parts: thin walled pipe and two circular surfaces. Circular surfaces are simplification of testing machine jaws. Maximum finite element size for circular surfaces is 2 mm. Maximum finite elements size for pipe is 1 mm. During discretization process 11538 nodes and 11284 shell finite elements were created. Contact between created parts was defined as *AUTOMATIC\_SURFACE\_TO\_SURFACE* with 0.15 static coefficient of friction and 0.1 dynamic coefficient of friction (Zienkiewicz, 1972). Jaws material was defined as *RIGID* with standard steel properties. Pipe material was defined as *PICewise\_LINEAR\_PLASTICITY*. Curve defining stress versus plastic strain was defined (Fig. 9). Boundary conditions which were applied received all degrees of freedom for one node of the motionless jaw and received degrees of freedom without movement in Z axis for one node of movable jaw. Load was defined based on data from testing machine which was recorded during the experiment. Curve defining force values were defined and shown in Fig. 8. Load was applied to movable jaw by *RIGID\_BODY*.

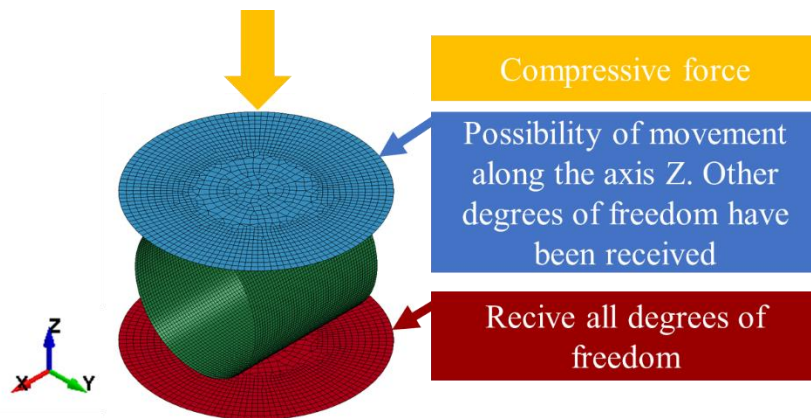


Fig. 7: Finite elements grid and boundary conditions.

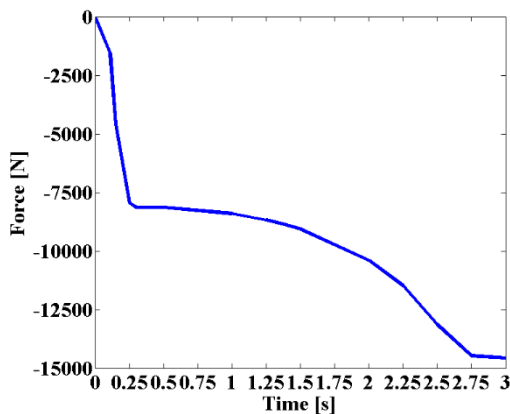


Fig. 8: Values of compressive force.

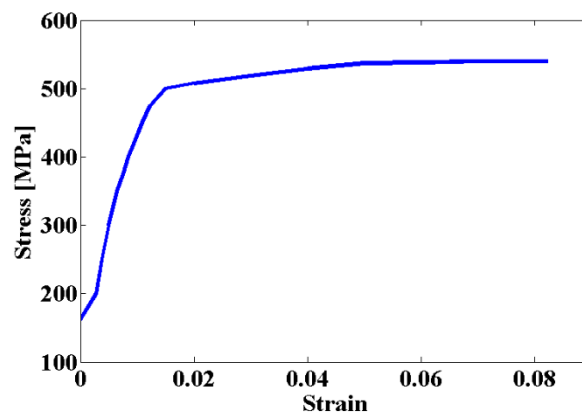


Fig. 9: True stress – plastic strain curve.

### 4. Results and conclusions

Displacement values for selected points have been compared. Fig. 10 shows compared values of displacement of selected points in a few moments of time while crushing the sample. Behavior of pipe from numerical simulation is a little bit different as compared to its real counterpart. Displacement of marker 1 in vertical axis is different. It results from type and size of finite elements which have been used. The size of shell finite element should be greater than its thickness. In this case the size of shell finite elements was lower than its thickness because the authors try to have most precise results which they could get using those types of finite element. The authors use shell finite elements also because of time which is needed to receive the solution. Receiving the solution using solid finite elements with the same size is few times longer. Average value of relative error calculated in relation to values of displacement from experiment is 72 % for horizontal axis and 11 % for vertical axis. In this case value



of displacement error in vertical axis is more important because this is main direction of deformation. Such high error value of horizontal axis is caused due to finite element size. Only 12.5 % differences in horizontal axis between displacement value from experiment and numerical simulation are higher than finite element size. Most of differences are few times smaller than finite element size. 50 % of differences of displacement in vertical axis are smaller than finite element size. Biggest displacement errors were for nodes corresponding to markers 2 and 8 because of the wrong shape of deformation of the sample in numerical simulation. Strain and displacement between nodes are calculated using shape functions which based on result in nodes. That fact suggests that finite elements grid should be denser. Behavior of nodes corresponding to markers 1 and 5 showed restrictions of using shell finite elements and the reason why their size should be greater than theirs thickness. Deformation of the sample could not be as big as in the experiment because of the size of used finite elements. Summary of results from experiment, numerical simulation with shell type of finite element and numerical simulation with solid type of finite elements were shown in Fig. 11 (Sławski et al., 2017). In the case of solid finite elements deformation of the top of the sample looks like in the experiment.

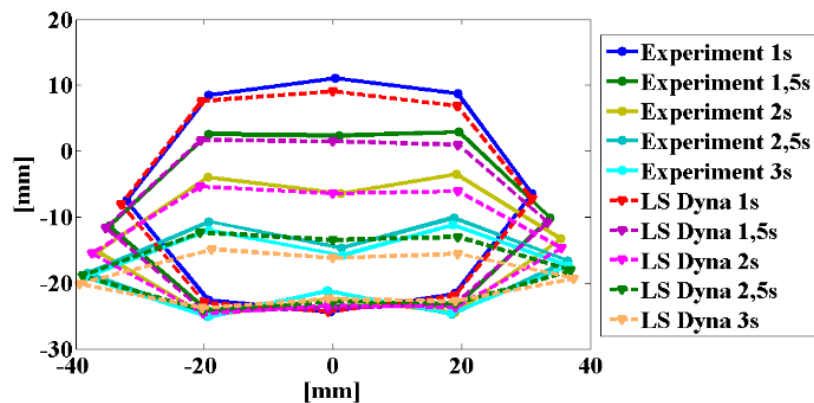


Fig. 10: Deformation of sample based on displacement of the markers in selected moment of time.

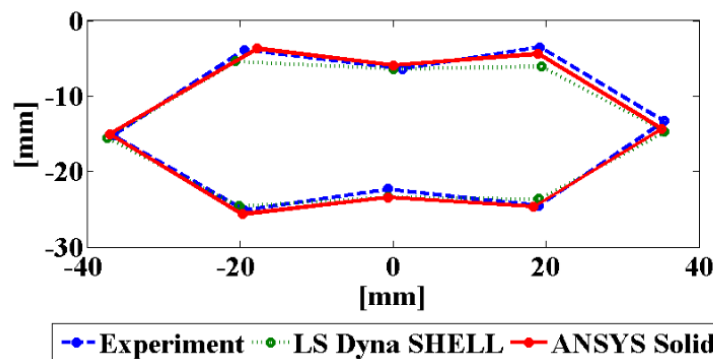


Fig. 11: Compare deformation of the sample in 2s time of the experiment.

The developed physical model could be considered as responding to its real counterpart. The model can be used to test behavior of pipe for different boundary conditions. Using shell finite elements in numerical simulations gives good results relative to time which is needed to solve a problem. Simulation engineer must be aware of restrictions which are associated with using this type of finite elements.

## References

- Sławski, S., Duda, S. and Machoczek, T. (2017) Determination of the state of effort in crushed thin walled pipes. *Modelowanie Inżynierskie*, Vol. 30, No. 61 (in Polish).
- Jakubowicz, A. and Orłoś, Z. (1984) *Strength of materials*, Wydawnictwa Naukowo – Techniczne, Warszawa (in Polish).
- Zienkiewicz, O. (1972) *The finite element method*, Wydawnictwo Arkady, Warszawa (in Polish).

## TUBULAR AIR DEFLECTOR IN VENTILATION DUCTS

E. Smyk<sup>\*</sup>, D. Mrozik<sup>\*</sup>, S. Wawrzyniak<sup>\*</sup>, K. Peszyński<sup>\*</sup>

**Abstract:** Flow stabilization in ventilations ducts is very important issue. This can affect the separation of the stream in the different type of fittings (e.g. T-shaped connectors). The use of perforated sheet or tubular deflector (thin-walled tubes arranged side by side in the duct) for faster flow stability is common practice in the industry. This elements are mounted especially near fan with ducts connection, although lack of studies proving the effectiveness of this methods. In this paper has been investigated the effect of tabular air deflector on flow stabilization with numerical simulation used.

**Keywords:** Ventilations, Deflector, Air flow, Numerical simulation.

### 1. Introduction

One of the most important problem in investigation of different type of flows is its stabilization, in case of continuous flows. Usually it is recommended to use a straight section after a disturbance. This section should be 10 – 20 hydraulic diameters length. This solution is very problematic in case of ducts with a large diameter investigation, e.g. ventilation ducts (hydraulic diameter even up to 2 m or more). For these reason to investigation of different type of duct system are used analytical methods (Gan et al., 1996; Oliveira et al., 2006) and more often numerical methods (Maharudrayya et al., 2004; Parra et al., 2006). Experimental methods are used mainly in case of relatively small systems (Sippola et al., 2003) or existing and operated systems (Parra et al., 2006). However in case of determination of some non-linear phenomenon using of analytical methods is impossible and numerical methods aren't enough accurate. Then experimental method is necessary. In case of large duct system investigation them size is a big problem. For example the T-shaped connector investigation by hydraulic diameter equal 400 mm requires the use of duct 4 m length before each measure point. It reduces the effect of disturbances caused by the change in shape on measurements. Therefore we are looking for ways to faster flow stabilization.

The use of perforated sheet or tubular deflector (thin-walled tubes arranged side by side in the duct) for faster flow stabilization is common practice in the industry. However, the authors of this papers found any data to support the validity of this method. The aim of this work is to verify whether the tubular deflectors have an influence on the flow stabilization.

At this point it should also emphasize what is understood as stable flow. Stable flow is situation when velocity profile of stream is constant or varies slightly. As flow stabilization is the process when after a disturbance the velocity profile of this flow is changing and strives for some constant shape, which is dependent on kind and cross-area of the ducts, velocity etc.

---

<sup>\*</sup> Assist. Prof. Emil Smyk, MSc.: Faculty of Mechanical Engineering, UTP University of Science and Technology in Bydgoszcz (Poland), Al. Prof. S. Kaliskiego 7, Bydgoszcz; PL, emil.smyk@utp.edu.pl.

<sup>\*\*</sup> Dariusz Mrozik, BSc.: Faculty of Mechanical Engineering, UTP University of Science and Technology in Bydgoszcz (Poland), Al. Prof. S. Kaliskiego 7, Bydgoszcz; dariuszmrozik1@gmail.com.

<sup>\*\*\*</sup> Assist. Prof. Sylwester Wawrzyniak, PhD.: Faculty of Mechanical Engineering, UTP University of Science and Technology in Bydgoszcz (Poland), Al. Prof. S. Kaliskiego 7, Bydgoszcz; PL, sylwester.wawrzyniak@utp.edu.pl.

<sup>\*\*\*\*</sup> Assoc. Professor Kazimierz Peszyński, PhD., Faculty of Mechanical Engineering, UTP University of Science and Technology in Bydgoszcz (Poland), Al. Prof. S. Kaliskiego 7, Bydgoszcz; PL, kazimierz.peszynski@utp.edu.pl.

## 2. Methods

In order to verify the influence of tubular deflectors on the flow stabilization was used simulation method. To this aim a two channel models was modelled. One with deflector presented in the Fig. 1 and a second having the same dimensions but without deflectors. It is model of real part of ventilation system (connection of the fan with ducts). This connections causes severe flow disturbance due to the sudden change in cross- section. Ten meter long duct is installed after the deflector in order to stabilize the flow. Example real velocity profile measured on the exit of this system is showed in Fig. 2a (measured by hot- wire anemometer). As you can see after ten meter from deflector flow is stable but you should consider whether a ten meter length is necessary to flow satiation if the deflector is used.

For that purpose the velocity changes on the measurement axis was investigate with different Reynolds number. Arrangement of measurement axis is presented in the Fig. 2b. During the investigation, it was assumed that the flow is stable if the different between the final velocity (velocity on the end of ducts) and velocity at the some point is equal or less than 10 %, 5 % or 1 %. Distance between the first point that meets the above condition and beginning of duct is the length needed to stabilize the flow in specific axis. The maximum distance of flow stabilization from 13 axis with specific Reynolds number is the sought distance about which we can say that the flow is stable.

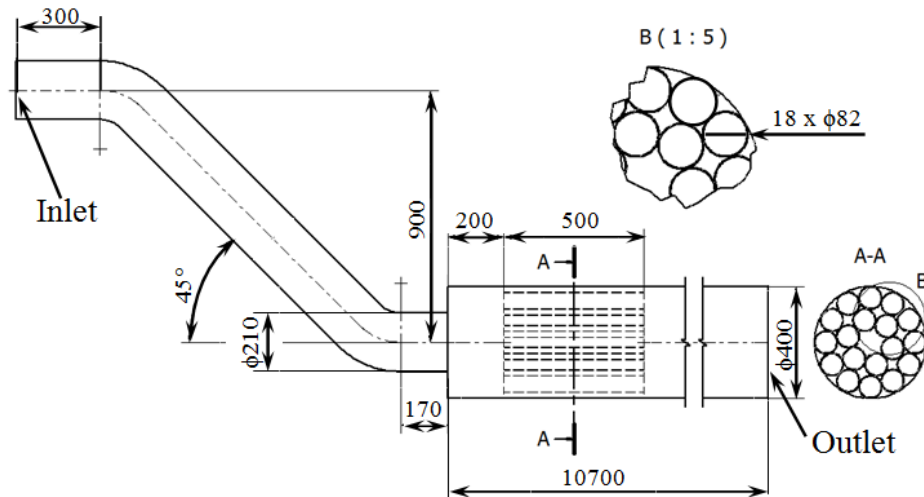


Fig. 1: Drawing of model with tubular deflector.

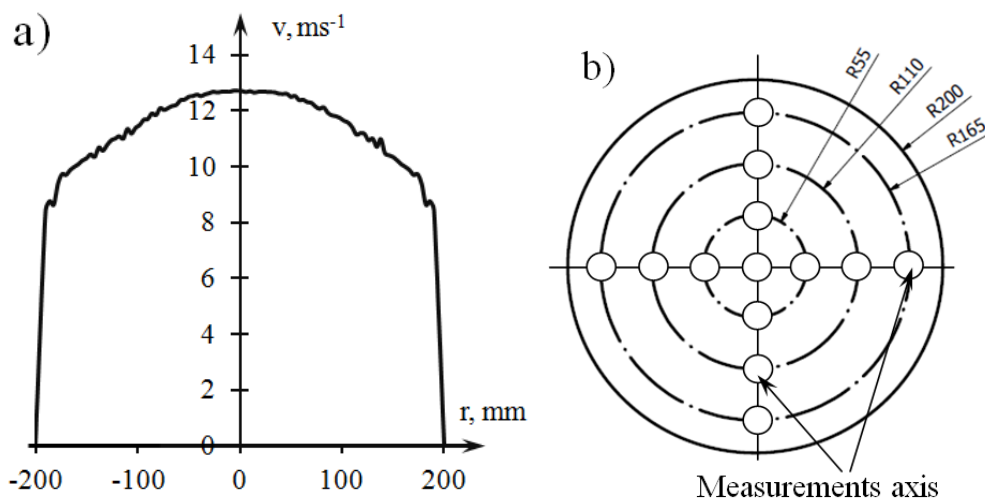


Fig. 2: a) velocity profile in real ducts system for  $Re = 130\,000$ ; b) arrangement of measurement axis.

Simulation was executed in ANSYS Fluent with used Spalart– Allmaras simulation model. The operating fluid was air. In the Fig. 1 are indicated boundary conditions – inlet and outlet, walls indescribable surfaces were wall boundary conditions type. Outlet was pressure–outlet boundary conditions type and inlet was velocity–inlet boundary conditions type. Velocity on inlet was defined so as to obtain a specified Reynolds number in investigated duct ( $\phi$  400 mm).

### 3. Results

The result of simulation – distances of flow stabilization– are showed in the Fig. 3. In the Fig. 3a are showed results for model with tubular air deflector and in the Fig. 3b without. On charts are showed distances after with the flow was stable – from this distance the velocity hasn't changed, taking into account 10 %, 5 % or 1 % error. Distances was calculated by different Reynolds numbers and additionally on chart are indicated average values by lines for different errors.

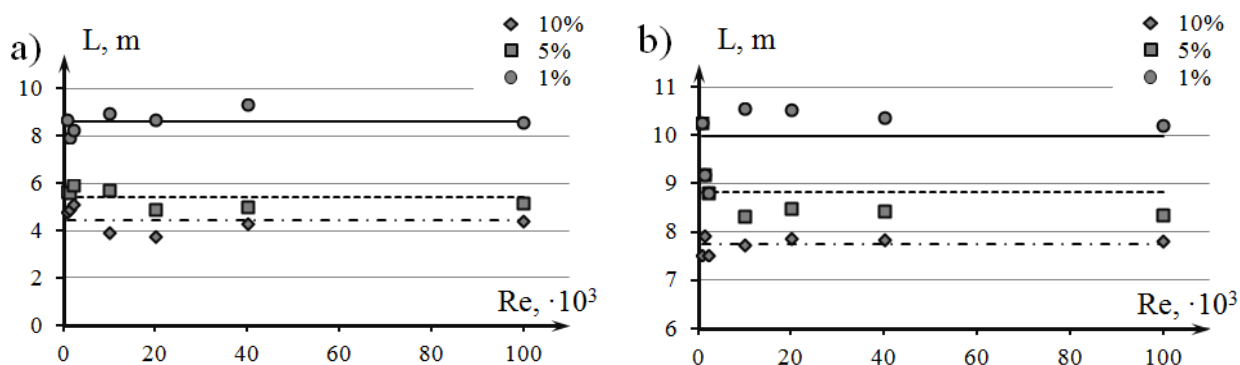


Fig. 3: Distances on which followed flow stabilization for different Reynolds number, error of stabilization for ducts model a) with tubular air deflector; b) without deflector with additionally average value of stabilization distance.

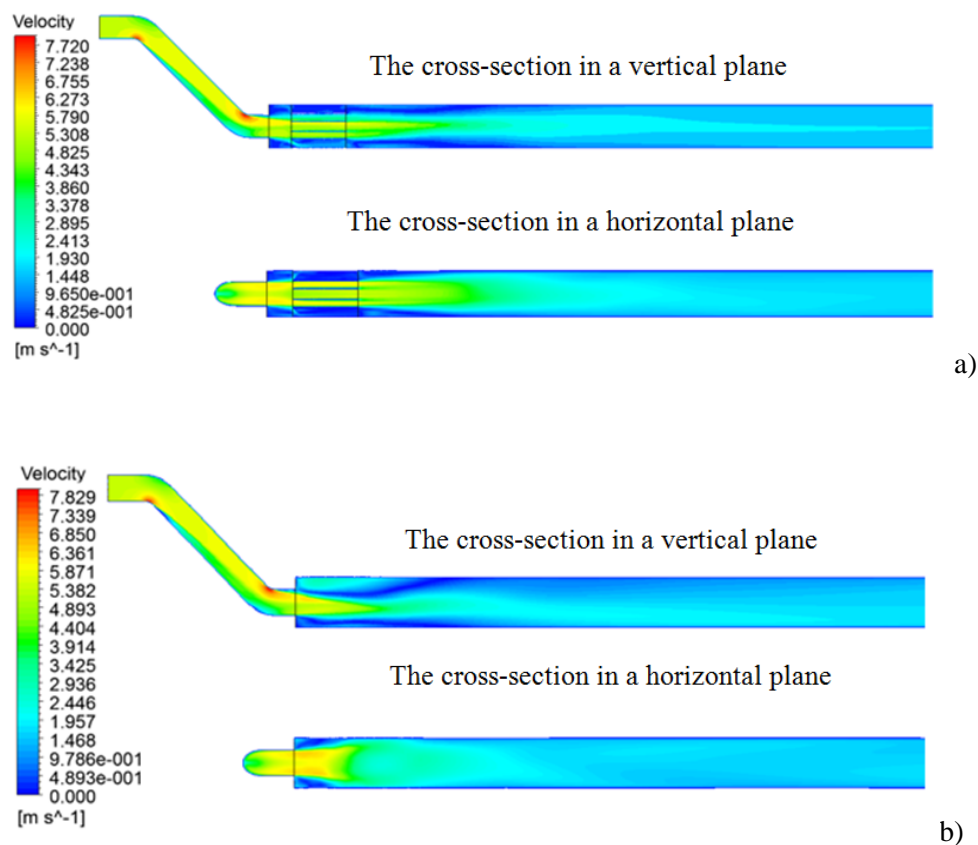


Fig. 4: Example contours of velocity on vertical and horizontal cross-section, first 4 m of ducts ducts a) with, and b) without tubular air deflector.

Results for model with air deflector are lower than for model without deflector. However the differences between them are different depending on error. By 10 % error the distances of flow stabilisation by case with deflector is almost twice lower then by case without deflector. If the accuracy is increasing, the difference diminishes but doesn't disappear.

Surprising is the fact that the distance of flow stabilization is not dependent on Reynolds number. The simulation was made by different Reynolds number from 1 000 to 100 000. We expected that the stream stabilization distance is dependant from Reynolds number what is exhibited in some article (Maharudrayya et al., 2004), but in our case this relationship doesn't exist. The stabilization distance is almost constant.

In the Fig. 4 is showed velocity count contours on vertical and horizontal cross-section. The used of deflector increase influence of disturbances caused by channels located before main duct. Additionally after changing the cross-sectional area occurred expansion of stream (Fig. 4b, horizontal plan). In case with tubular air deflector this expansion isn't so sudden and violent. It means that used of deflector can reduce disturbances caused by preceding its elements.

Modelled deflector are real and operates in ventilation system. In this point we should consider what is its coefficient drag and how influence on flow stabilisation its dimensions (length, diameters an number of pipes). Additionally conducted numerical analysis should be confirmed by experimental methods.

#### **4. Conclusions**

Analysis of stabilisation flow distances and velocity contour in ducts with and without tubular deflector revealed that deflectors have influence on flow stabilization, and they can reduce disturbances caused by elements located near before them.

Additionally next research objectives have been designated.

#### **Acknowledgement**

Scientific work financed from the budget for science in the years 2015/2018 as a research project within the program under the name "Diamond Grant".

Authors thank the company Nucair Technologies Sp. z o.o., Solec Kujawski, Poland, for the opportunity to carry out the measurements and access to the test bench.

#### **References**

- Gan, G. and Riffat, S.B. (1996) Measurement and computational fluid dynamics prediction of diffuser pressure-loss coefficient. *Applied Energy*, 54(2), pp. 181-195.
- Maharudrayya, S., Jayanti, S. and Deshpande, A.P. (2004) Pressure losses in laminar flow through serpentine channels in fuel cell stacks. *Journal of Power Sources*, 138(1-2), pp. 1-13.
- Oliveira, P.J. and Pinho, F.T. (2006) Pressure drop coefficient of laminar Newtonian flow in axisymmetric diffusers. *International Journal of Heat and Fluid Flow*, 27(2), pp. 319-328.
- Parra, M.T., Villafruela, J.M., Castro, F. and Mendez, C. (2006) Numerical and experimental analysis of different ventilation systems in deep mines. *Building and Environment*, 41(2), pp. 87-93.
- Sippola, M.R. and Nazaroff, W.W. (2003) Modeling particle loss in ventilation ducts. In *Atmospheric Environment*. pp. 5597-5609.

## AXISYMMETRIC VALVE WITH SYNTHETIC JET ACTUATOR

E. Smyk\*, S. Wawrzyniak\*, D. Perczyński\*, P. Kolber\*

**Abstract:** *The paper presents the principle of axisymmetric valve operation. The investigated valve used synthetic jets as control jet and it is the fluidic valve without moving or deforming elements. The investigation has focused on the influence of actuator supply power on the main stream velocity profile, including stream switching. Additionally resonant frequency of actuator and operation characteristic of actuator was designated.*

**Keywords:** Fluidic valve, Synthetic jet, Coanda effect.

### 1. Introduction

One of the most commonly used devices, in fluidic systems, are different types of valves. One of the special type of valve is axisymmetric valve patented by Tesař and Trávníček, 2010. Example application of axisymmetric valve is showed in Fig. 1, and its operation is described in (Tesař et al., 2014; Tesař et al., 2012).

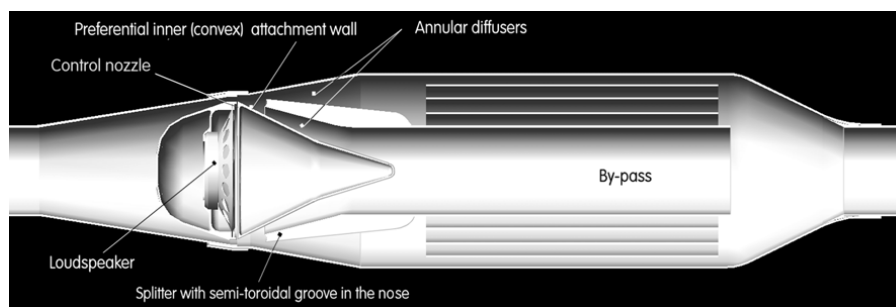


Fig. 1: Example of axisymmetric valve application from Patent document (Tesař and Trávníček, 2010).

Axisymmetric valve use two phenomena: synthetic jets and Coanda effect. Normally the main stream flows around the core of the valve and adheres to the inner cone. As a result, most volume of main stream flows through inner pipe (in Fig. 1 named by-pass). If the synthetic jet actuator (mounted in the core) will start operating then the main stream is repelled from inner cone by synthetic jet flowing from the control nozzle and stream adheres to the outer cone. As a result, most of the main stream volume flows through annular pipe (outer pipe). After deactivation of synthetic jet actuator main stream go back to the first state.

Described valve belongs to fluidic valve. Fluidic valves are distinguished by the lack of moving or deforming elements. Therefore they are reliable, robust and fast acting. The way of fluidic valve operation makes that they can be used with small and weak input. Due to restrictions as to the size of the input and a relatively complex operating rules the fluidic valves aren't widely used. Example application and type of fluidic valve are described in Tesař, 2004, Tesař 2005, Trávníček et al., 2014.

As mentioned described fluidic valve use two phenomena: synthetic jets and Coanda effect. Coanda effect is a phenomenon of jets adhesion and flow nearby solid boundaries. This effect is used in every fluidic valve and in other applications (Singh and Ramamurthi, 2009; Lalli et al., 2010). Synthetic jets are responsible for the main stream switching and serve as a control jets. They are generated

---

\* Sylwester Wawrzyniak, PhD., Daniel Perczyński, PhD., Piotr Kolber, PhD., Emil Smyk, MSc: Faculty of Mechanical Engineering, UTP University of Science and Technology, Al. prof. S. Kaliskiego; 85-796 Bydgoszcz; PL, sylwester.wawrzyniak@utp.edu.pl, daniel.perczynski@utp.edu.pl, piotr.kolber@utp.edu.pl, emil.smyk@utp.edu.pl.



by periodically ingestion and expulsion of fluid at the exit of a nozzle or across orifice (Tanh and Zhong, 2006). The expulsion volume of fluid moves away from orifice and on its edges are formed edge vortices. Although the time-averaged mass flow rate through the nozzle during one full cycle of operation is zero, the edge vortices generates nonzero mass flow rate at some distance from the orifice. Periodically suction and blowing of fluid to some chamber is possible by replacement one of actuator's wall by movable element. Depending on the method of accomplishing the movement of wall, can distinguish piezoelectric, electromagnetic, acoustic and mechanical synthetic jet actuators. Most commonly used for this purpose are speakers (Trávníček et al., 2014; Tesař and Trávníček, 2010; Gil and Strzelczyk, 2016). They are available, cheap and produced on a mass-scale. However they are now better actuator solution (Saha et al., 2012).

The aim of this work is to investigate the influence of synthetic jet actuator supply power to change the main stream velocity profile, including the stream switching. In the investigation will be carried out with different value of main stream volume flow rate.

## 2. Experimental setup

The laboratory model of valve is showed in the Fig. 2. The model is composed of the main nozzle with core and outer cone mounted on the nozzle outlet. In core is build-in the synthetic jet actuator and at the circuit of the core is made a control nozzle through which synthetic jet flows. The control nozzle width is  $b_x = 0.5$  mm. The valve operates as described previously.

As mentioned above the synthetic jet actuator is built in the core. It consist, of two opposite loudspeakers Monacor SP-6/8SQ (the input impedance is  $R = 8 \Omega$  and nominal electric input power is  $P = 20$  W) mounted on a metal ring. On the circuit therefore (ring) was done 24 holes in diameter  $\phi 3$  mm, through which flow synthetic jet. The ring is mounted in a core and synthetic jet outflow is confined by control nozzle (Fig. 2).

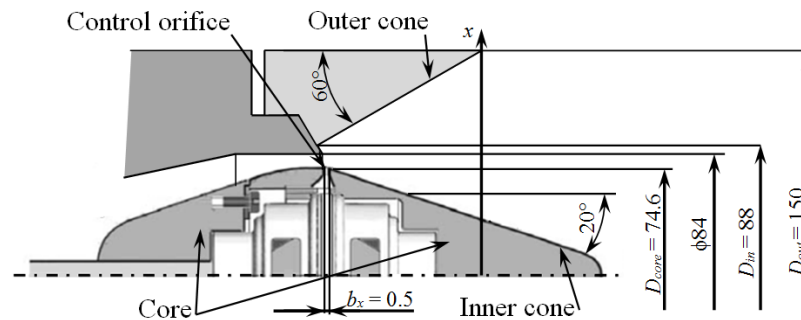


Fig. 2: Detail drawing of the laboratory model of the fluidic valve used in the experiments.

During the experiment it was necessary to measure the volume flow rate through the valve. For this purpose was used an orifice-type flowmeter. Whereas to measuring of the local velocity was used hot-wire anemometer. In tests was used probe model 55P16 (wire length 1.25 mm and diameter 5  $\mu$ m) connected to MiniCTA 54T42. The temperature correction has been included.

## 3. Results

### 3.1. Measurements of synthetic jet

First step of investigation was to find characteristic frequency of synthetic jet actuator and designation of dependence between the supply power of the actuator and synthetic jet velocity. During the measurements the hot-wire probe was placed 1mm from the control nozzle and volume flow rate in a valve was  $Q = 0$  m<sup>3</sup>s<sup>-1</sup>.

To find the characteristic frequency was used two methods (Fig. 3a and 3b) with constant value of actuator supply power  $P = 3$  W. It was designated dependence between frequency of power supply and impedance of loudspeakers (Fig. 3a) or synthetic jet velocity ( $v_{sj}$  Fig. 3b). The maximum value of measured parameters (impedance or velocity) reveals the characteristic resonant frequency for actuator. In bout case the resonant frequency was  $f = 147$  Hz. Next step of the measurements was designated

the main operation characteristic of synthetic jet actuator (dependence between supply power and synthetic jet velocity) (Fig. 3c). The measurements were carried out for frequency  $f = 147$  Hz. As shown in Fig. 3c, this dependence is logarithmic.

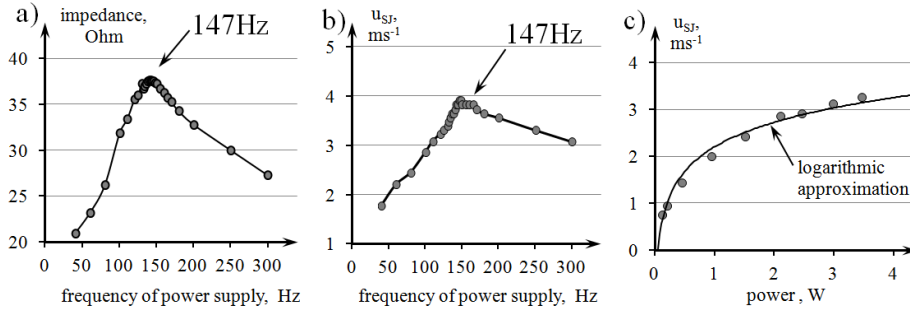


Fig. 3: Operation characteristic of annular synthetic jet actuator: dependence between frequency of supply power and a) speakers impedance or b) synthetic jet velocity for  $P = 3$  W, c) dependence between actuator supply power and synthetic jet velocity for  $f = 147$  Hz.

### 3.2. Main tests

As described above, the main stream flows along inner or outer cone depending on whether the synthetic jet actuator is active or not. In this part of an experiment it was measured how the main stream velocity profile changes depending on the synthetic jet velocity. For this purpose it was measure velocity profile on the  $x$  axis shown in the Fig. 2. The  $x$  axis overlaps with end of outer cone. It must be noted that value 0 on the  $x$  axis means intersection of the  $x$  axis and symmetry axis of the valve.

The measurements have been carried out with three different volume flow rate –  $Q_1 = 0.004 \text{ m}^3\text{s}^{-1}$ ,  $Q_2 = 0.0025 \text{ m}^3\text{s}^{-1}$ ,  $Q_3 = 0.0018 \text{ m}^3\text{s}^{-1}$  – and with five different synthetic jet actuator supply power –  $P_1 = 0 \text{ W}$  ( $v_{SJ1} = 0 \text{ m.s}^{-1}$ ),  $P_2 = 0.5 \text{ W}$  ( $v_{SJ2} = 1.43 \text{ m.s}^{-1}$ ),  $P_3 = 1 \text{ W}$  ( $v_{SJ3} = 2 \text{ m.s}^{-1}$ ),  $P_4 = 2 \text{ W}$  ( $v_{SJ4} = 2.86 \text{ m.s}^{-1}$ ),  $P_5 = 3 \text{ W}$  ( $v_{SJ5} = 3.12 \text{ m.s}^{-1}$ ), where  $P_1 = 0 \text{ W}$  means that actuator was turned off.

The velocity profiles on the  $x$  axis are presented in the Fig. 4. Fig. 4a shows the velocity profile by main stream volume flow rate  $Q_1 = 0.004 \text{ m}^3\text{s}^{-1}$  with different synthetic jet supply power. As expected the stream is concentrated near the inner cone if the actuator is turn off. After turning actuator the velocity profile of main stream is changing. However, in the Fig. 4a the stream is switched over and adheres to the outer cone only for actuator supply power  $P_5 = 3 \text{ W}$ . Evidence of this is high velocity near the outer cone and low near the inner cone (core). It must be noted that in case of stream flows near inner cone the velocity for  $x \geq 45 \text{ mm}$  is close to zero and it means that practically all volume of stream flows near the inner cone, but for  $P_5 = 3 \text{ W}$  the velocity near inner cone is still relatively high and it means that only some part of main stream adheres to outer cone.

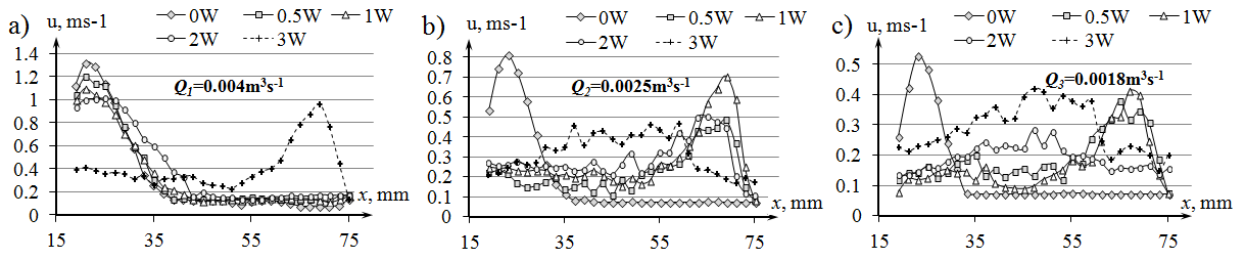


Fig. 4: Velocity profile of main stream for different actuator supply power and volume flow rate of main stream, a)  $Q_1 = 0.004 \text{ m}^3\text{s}^{-1}$ , b)  $Q_2 = 0.0025 \text{ m}^3\text{s}^{-1}$ , c)  $Q_3 = 0.0018 \text{ m}^3\text{s}^{-1}$ .

Fig. 4b shows velocity profile of main stream by volume flow rate  $Q_2 = 0.0025 \text{ m}^3\text{s}^{-1}$ . As can be seen, the switching over of the main stream occurs when  $P_2 = 0.5 \text{ W}$ ,  $P_3 = 1 \text{ W}$  and  $P_4 = 2 \text{ W}$ . The best results are obtained for  $P_3 = 1 \text{ W}$ , the stream adhered to the outer cone most preferably. It means that the velocity of control jet shouldn't be too high or too low. If control jet velocity is too low the main stream won't be detached from inner cone or only some little part of stream adheres to outer cone. If control jet velocity is too high in main stream will be created vortices, which disturb the flow. This phenomenon is shown in the Fig. 6b at  $P_5 = 3 \text{ W}$ . Very close results were obtained by volume flow rate  $Q_3 = 0.0018 \text{ m}^3\text{s}^{-1}$  (Fig. 4c).

As shown in the above analysis, selection of appropriate supply power of actuator isn't a simple issue. For more accurate analysis in tab. 1 are noted the conditions of the experiments, at which the main stream adheres to the outer cone most preferably (in opinion of authors). Additionally Tab. 1 contain average velocity of main stream in a interaction region (the cross-section where the synthetic jet affect to main stream), synthetic jet velocity at specific supply power of actuator and the velocity ratio (the ratio of synthetic jet velocity and main stream average velocity). The best results were obtained when the control jet velocity and main stream velocity was similar, the velocity ratio is similar to one.

*Tab. 1: Summary of the experiment for the most favorable power of supply value.*

Volume flow rate $Q$ [ $\text{m}^3 \cdot \text{s}^{-1}$ ]	Average velocity $u_{ave}$ [ $\text{m} \cdot \text{s}^{-1}$ ]	Actuator supply power $P$ [W]	Velocity of synthetic jet $v_{SJ}$ [ $\text{m} \cdot \text{s}^{-1}$ ]	Velocity ratio $C_u = v_{SJ} / [u_{ave}]$
0.004	3.42	3	3.12	0.91
0.0025	2.14	1	2.00	0.94
0.0018	1.54	0.5 / 1	1.43 / 2.00	0.93 / 1.30

#### 4. Conclusions

The investigation demonstrates influence of the supply power of actuator on the main stream velocity profile, including stream switching. This relationship has been widely discussed in the paper and it was indicated the most favorable supply power for three different volume flow rate of main stream. As shown above, inadequate (too high or too low) value of synthetic jet velocity influences negatively on the valve operation.

Additionally the velocity ratio was calculated. It was similar to one for the most favorable supply power. It means that average velocity of main stream and synthetic jet velocity should be of similar value so that occurs stream switching.

#### Acknowledgement

Scientific work financed from the budget for science in the years 2015/2018 as a research project within the program under the name "Diamond Grant".

#### References

- Gil, P. and Strzelczyk, P. (2016) Performance and efficiency of loudspeaker driven synthetic jet actuator. *Experimental Thermal and Fluid Science*, 76, pp. 163-174.
- Lalli, F., Bruschi, A., Lama, R., Liberti, L., Mandrone, S. and Pesarino, V. (2010) Coanda effect in coastal flows. *Coastal Engineering*, 57(3), pp. 278-289.
- Saha, C.R., Riley, P.H., Paul, J., Yu, Z., Jaworski, A.J. and Johnson, C.M. (2012) Halbach array linear alternator for thermo-acoustic engine. *Sensors and Actuators A: Physical*, 178, pp. 179-187.
- Singh, N.K. and Ramamurthi, K. (2009) Formation of Coanda jet from sharp-edged swirl nozzle with base plate. *Experimental Thermal and Fluid Science*, 33(4), pp. 675-682.
- Tanh, H. and Zhong, S. (2006) Incompressible Flow Model of Synthetic Jet Actuator. *AIAA Journal*, 44(4), pp. 908-912.
- Tesař, V., Pavelka, M., Smyk, E. and Peszynski, K. (2014) Control of flow separation by vestigial "synthetic jet". In *Fluidic Dynamics*.
- Tesař, V. (2004) Fluidic Valve for Reactor Regeneration Flow Switching. *Chemical Engineering Research and Design*, 82(3), pp. 398-408.
- Tesař, V. (2005) Fluidic Valves for Variable-ConFiguration Gas Treatment. *Chemical Engineering Research and Design*, 83(9), pp. 1111-1121.
- Tesař, V., Broučková, Z., Kordík, J., Trávníček, Z. and Peszyński, K. (2012) Valves with flow control by synthetic jets. *EPJ Web of Conferences*, 25, pp. 1092.
- Tesař, V. and Trávníček, Z. (2010) Ways and means for two-regime control of fluid flow, Patent document, (in Czech).
- Trávníček, Z., Tesař, V., Broučková, Z. and Peszyński, K. (2014) Annular Impinging Jet Controlled by Radial Synthetic Jets. *Heat Transfer Engineering*, 35(16), pp. 1-12.

## FORCED VIBRATION ANALYSIS OF PRESTRESSED EULER-BERNOULLI BEAM WITH DISCONTINUITIES BY MEANS OF DISTRIBUTIONS WITHOUT USING MODAL ANALYSIS

J. Sobotka<sup>\*</sup>

**Abstract:** *This paper is a continuation of the previous paper in which the author published the generalized mathematical model for forced vibration of Euler-Bernoulli beam covering discontinuities caused by concentrated loading, concentrated support, concentrated inertia forces or internal hinges. In this new paper, the generalized mathematical model is augmented to cover geometric nonlinearity of stress stiffening or weakening of the beam with the same type of discontinuities. This new analytic approach can offer three advantages. Firstly, steady-state responses of the beam can be found directly without doing modal analysis. Secondly, these responses of the beam are expressed in closed form. Thirdly, remaining continuity conditions at points of the discontinuities are fulfilled automatically. To give an example of using this new approach based on distributions, new closed-form expressions for forced steady-state response of pre-stressed simply supported beam with concentrated harmonic loading are presented.*

**Keywords:** Vibration, Beam, Discontinuities, Distributions, Dirac, Heaviside.

### 1. Introduction

Classical analytical method of calculating harmonic steady-state response of the beam is based on the following main steps (Rao, 2007 and Weaver et al., 1990). Firstly, we obtain a frequency equation for specific support conditions of the beam. Secondly, we solve the frequency equation for natural frequencies. Thirdly, we find orthogonal mode shapes corresponding to the natural frequencies of the beam. Finally, we express a forced response of the beam as a linear combination of the mode shapes by finding corresponding modal participation coefficients.

Applying distributional derivative for discontinuous shear force, discontinuous bending moment, and discontinuous rotation of cross section of a beam, we can derive a mathematical model for forced transverse vibration of a beam with discontinuities caused by concentrated supports or concentrated masses or concentrated mass moments of inertia or concentrated transverse forces or concentrated moments situated between ends of the beam, or hinges connecting beam segments. This mathematical model can be solved like only one differential task without dividing the beam into segments where all the continuity conditions among adjoining segments are fulfilled automatically. Using this approach, we have only four integration constants irrespective of the number of the discontinuities. Applying distributions, we do not have to compute natural frequencies, mode shapes or modal participation coefficients in analyzing forced harmonic response of beams.

Various ways of applying distributions can be found in papers by Kozien (2013), Wang (2007), Yesilce (2012), Zhao et al. (2016).

### 2. The classical equation of motion for forced vibration of pre-stressed Euler-Bernoulli beam

Equation of motion of a beam under distributed transverse force without discontinuities in shear force, in bending moment or in rotation of cross section of the beam is given by (Rao, 2007)

$$\left( \frac{\partial^2}{\partial x^2} \left( E J(x) \left( \frac{\partial^2}{\partial x^2} w(x, t) \right) \right) \right) - \left( \frac{\partial}{\partial x} \left( N \left( \frac{\partial}{\partial x} w(x, t) \right) \right) \right) + \rho A(x) \left( \frac{\partial^2}{\partial t^2} w(x, t) \right) = f(x, t), \quad (1)$$

---

<sup>\*</sup> Ing. Jiří Sobotka, PhD., ČEZ, a.s., 67550 Dukovany; CZ, jiri.sobotka@cez.cz

where  $w(x, t)$  is transverse displacement of the beam centerline,  $A(x)$  is cross-sectional area,  $J(x)$  is area moment of inertia,  $E$  is modulus of elasticity (Young's modulus),  $\rho$  is density,  $f(x, t)$  is the distributed transverse force and  $N$  is an axial load.

### 3. A mathematical model for forced transverse vibration of pre-stressed Euler-Bernoulli beam with discontinuities

In order to be able to express possible discontinuities in shear force, bending moment or in rotation of cross section along a centerline of a beam mathematically without cutting the beam into segments which would be without discontinuities, distributional derivative (Schwartz, 1972 and Štěpánek, 2001 and Kanwal, 2004) can be used.

The generalized mathematical model for forced vibration of Euler-Bernoulli beam with various discontinuities without axial loading was published in (Sobotka, 2016) containing distributional derivatives of shear force, bending moment and cross section rotation.

By augmenting the classical part of distributional derivative of shear force in accordance with Eq. (1), new generalized mathematical model for forced vibration of Euler-Bernoulli beam with discontinuities allowing for stress stiffening (in case of tensile axial load) or stress weakening (in case of compressive axial load) can be obtained as follows:

$$\begin{aligned} \frac{\partial}{\partial x} Q(x, t) = & \rho A(x) \left( \frac{\partial^2}{\partial t^2} w(x, t) \right) - \left( \frac{\partial}{\partial x} (N \phi(x, t)) \right) + \left( \sum_{i=1}^{n_1} r_i(t) \delta(x - a_i) \right) \\ & + \left( \sum_{i=1}^{n_2} m_i \left( \frac{\partial^2}{\partial t^2} w(x, t) \right) \Big|_{x=b_i} \delta(x - b_i) \right) - \left( \sum_{i=1}^{n_3} f_i(t) \delta(x - c_i) \right), \end{aligned} \quad (2)$$

$$\frac{\partial}{\partial x} M(x, t) = Q(x, t) - \left( \sum_{i=1}^{n_2} J_i \left( \frac{\partial^2}{\partial t^2} \phi(x, t) \right) \Big|_{x=b_i} \delta(x - b_i) \right) + \left( \sum_{i=1}^{n_4} s_i(t) \delta(x - d_i) \right), \quad (3)$$

$$\frac{\partial}{\partial x} \phi(x, t) = -\frac{M(x, t)}{E J(x)} + \left( \sum_{i=1}^{n_5} \psi_i(t) \delta(x - e_i) \right), \quad (4)$$

$$\frac{\partial}{\partial x} w(x, t) = \phi(x, t). \quad (5)$$

The right-hand side of Eq. (2) is the distributional derivative of shear force with respect to  $x$  where  $N$  is axial load (positive if tensile, negative if compressive),  $r_i(t)$  is a reaction force at  $i$ th concentrated support at  $x = a_i$  ( $0 < a_i < L$ ),  $L$  is total length of the beam,  $m_i$  is a concentrated inertia mass at  $x = b_i$  ( $0 < b_i < L$ ),  $f_i(t)$  is a concentrated transverse load at  $x = c_i$  ( $0 < c_i < L$ ),  $\delta(x - a_i)$  denotes Dirac's singular distribution moved to a point of the specific discontinuity,  $n_1$  is a number of point supports (without end supports), if any,  $n_2$  is a number of concentrated inertia masses (without end masses), if any, and  $n_3$  is a number of concentrated transverse loads (without end loads), if any.

The right-hand side of Eq. (3) is the distributional derivative of bending moment with respect to  $x$  where  $J_i$  is a concentrated mass moment of inertia at  $x = b_i$ , if any,  $s_i(t)$  is a concentrated moment load at  $x = d_i$  ( $0 < d_i < L$ ), and  $n_4$  is a number of concentrated moment loads (without end moment loads), if any.

The right-hand side of Eq. (4) is the distributional derivative of cross section rotation with respect to  $x$  where  $\psi_i(t)$  is a magnitude of jump discontinuity in rotation of the cross sections at a hinge connecting segments of the beam at  $x = e_i$  ( $0 < e_i < L$ ), and  $n_5$  is a number of internal hinges, if any.

### 4. Forced vibration solution

Supposing harmonic time variation of loading as

$$f_i(t) = F_i e^{(j\omega t)}, \quad s_i(t) = S_i e^{(j\omega t)},$$

and solution to Eqs. (2) to (5) as

$$Q(x, t) = Q_a(x) e^{(j\omega t)}, \quad M(x, t) = M_a(x) e^{(j\omega t)}, \quad \phi(x, t) = \phi_a(x) e^{(j\omega t)}, \quad w(x, t) = w_a(x) e^{(j\omega t)}$$

$$r_i(t) = R_i e^{(j\omega t)}, \quad \psi_i(t) = \Psi_i e^{(j\omega t)}, \quad j^2 = -1$$

where  $\omega$  is circular frequency of vibration, and denoting amplitudes of vibration at points with concentrated inertia masses and moments of inertia as

$$W_i = \lim_{x \rightarrow b_i} w_a(x), \quad \Phi_i = \lim_{x \rightarrow b_i} \phi_a(x), \quad (6)$$

Eqs. (7) to (10) can be derived for unknown general amplitudes of deflection,  $w_a$ , rotation of cross section,  $\phi_a$ , bending moment,  $M_a$ , and shear force,  $Q_a$ , for a uniform beam as:

$$\frac{d}{dx} Q_a(x) = -\rho A w_a(x) \omega^2 - N \left( \frac{d}{dx} \phi_a(x) \right) + \left( \sum_{i=1}^{n_1} R_i \delta(x - a_i) \right) - \left( \sum_{i=1}^{n_2} m_i W_i \omega^2 \delta(x - b_i) \right) - \left( \sum_{i=1}^{n_3} F_i \delta(x - c_i) \right), \quad (7)$$

$$\frac{d}{dx} M_a(x) = Q_a(x) + \left( \sum_{i=1}^{n_2} J_i \Phi_i \omega^2 \delta(x - b_i) \right) + \left( \sum_{i=1}^{n_4} S_i \delta(x - d_i) \right), \quad (8)$$

$$\frac{d}{dx} \phi_a(x) = -\frac{M_a(x)}{EJ} + \left( \sum_{i=1}^{n_5} \Psi_i \delta(x - e_i) \right), \quad (9)$$

$$\frac{d}{dx} w_a(x) = \phi_a(x). \quad (10)$$

By using Laplace transform method, general solution to Eqs. (7) to (10) can be computed, in which integration constants are in the form of initial parameters.

As an example of using the proposed method, new closed-form expressions for the amplitude of the deflection, Eq. (11), and for the amplitude of the bending moment, Eq. (12), of forced steady-state response of simply supported (pinned-pinned) uniform beam subjected to a concentrated transverse harmonic force,  $F \sin(\omega t)$ , at  $x=a$ , and to a constant axial force,  $N$ , have been obtained as follows:

$$w_a(x) = \left( \frac{\lambda_1^2 \lambda_2 \sin(\lambda_2(-x+a))}{(\lambda_1^2 + \lambda_2^2) m \omega^2} - \frac{\lambda_2^2 \sinh(\lambda_1(-x+a)) \lambda_1}{(\lambda_1^2 + \lambda_2^2) m \omega^2} \right) F H(x-a)$$

$$+ \left( -\frac{\lambda_1^2 \sin(\lambda_2(-l+a)) \lambda_2 \sin(\lambda_2 x)}{\sin(\lambda_2 l) (\lambda_1^2 + \lambda_2^2) m \omega^2} + \frac{\lambda_2^2 \sinh(\lambda_1 x) \sinh(\lambda_1(-l+a)) \lambda_1}{\sinh(\lambda_1 l) (\lambda_1^2 + \lambda_2^2) m \omega^2} \right) F, \quad (11)$$

$$M_a(x) = \left( \frac{\lambda_2 \sin(\lambda_2(-x+a))}{\lambda_1^2 + \lambda_2^2} + \frac{\lambda_1 \sinh(\lambda_1(-x+a))}{\lambda_1^2 + \lambda_2^2} \right) F H(x-a)$$

$$+ \left( -\frac{\lambda_2 \sin(\lambda_2(-l+a)) \sin(\lambda_2 x)}{(\lambda_1^2 + \lambda_2^2) \sin(\lambda_2 l)} - \frac{\lambda_1 \sinh(\lambda_1 x) \sinh(\lambda_1(-l+a))}{(\lambda_1^2 + \lambda_2^2) \sinh(\lambda_1 l)} \right) F, \quad (12)$$

where

$$m = \rho A, \quad \omega = 2\pi f, \quad (13)$$

$$\lambda_1 = \frac{\sqrt{2} \sqrt{\frac{N + \sqrt{N^2 + 4EJm\omega^2}}{EJ}}}{2}, \quad \lambda_2 = \frac{\sqrt{2} \sqrt{\frac{-N + \sqrt{N^2 + 4EJm\omega^2}}{EJ}}}{2}. \quad (14)$$

Notation  $H(x-a)$  in Eq. (11), (12) is used for Heaviside's unit step function. When finding a value of the deflection at the point of the concentrated load, it is important for a limit of the right hand side of Eq. (11) to be evaluated as follows:



$$\lim_{x \rightarrow a} w_a(x) = \frac{1}{2} \frac{\lambda_2^2 \lambda_1 \sinh(-\lambda_1 l + \lambda_1 a) F e^{(\lambda_1 a)}}{\sinh(\lambda_1 l) (\lambda_1^2 + \lambda_2^2) \omega^2 m} + \frac{1}{2} \frac{\lambda_2 \lambda_1^2 (-\cos(\lambda_2 l) + \cos(2 \lambda_2 a - \lambda_2 l)) F}{\sin(\lambda_2 l) (\lambda_1^2 + \lambda_2^2) m \omega^2} - \frac{1}{2} \frac{\lambda_2^2 \lambda_1 \sinh(-\lambda_1 l + \lambda_1 a) F e^{(-\lambda_1 a)}}{\sinh(\lambda_1 l) (\lambda_1^2 + \lambda_2^2) \omega^2 m}. \quad (15)$$

Correctness of Eq. (11), (12), (15) has been verified by using FEM.

## 5. Conclusions

Equations (2) to (5) making the generalized mathematical model for forced response of pre-stressed Euler-Bernoulli beam with different discontinuities are the first contribution of this paper to vibration analysis of beams.

In this model, each unknown dependently variable quantity has got its own distributional derivative covering specific jump discontinuities where Dirac's singular distribution, denoted here as  $\delta(x)$ , is always moved to the point with a specific jump discontinuity, and multiplied by a magnitude of the discontinuity. Discontinuities in shear force are supposed to be owing to idealized concentrated supports or inertia masses or concentrated transverse forces situated between ends of the beam. Likewise, discontinuities in bending moment are assumed to be due to idealized concentrated moments of inertia or concentrated moment loads situated between ends of the beam. Discontinuities in cross section rotation may be caused by real hinges connecting beam segments.

To be able to find forced steady-state response of Euler-Bernoulli beams analytically with discontinuities mentioned allowing for stress stiffening or weakening of the beam, equations (7) to (10) have been derived as the second contribution of this paper for unknown amplitudes of shear force, bending moment, cross section rotation and deflection of the beam. When using these equations, boundary conditions are given directly, which means that internal forces are not expressed through the deflection and its derivatives.

By using this proposed approach, new equations (11), (12), (15) for forced steady-state response of pre-stressed simply supported beam subjected to concentrated transverse harmonic loading have been obtained as the third contribution. These new expressions have got the closed form, which would not be possible if modal analysis were used. The right hand side of Eq. (11), (12), (15) is exact in the sense of Euler-Bernoulli theory. The effect of stress stiffening in Eq. (11), (12), (15) is covered by choosing a positive value for axial force. The effect of stress weakening in Eq. (11), (12), (15) is covered by choosing a negative value for axial force not allowing buckling of the beam.

## References

- Kanwal, R.P. (2004) Generalized Functions. Birkhäuser, Boston.
- Kozien, M.S. (2013) Analytical Solutions of Excited Vibrations of a Beam with Application of Distribution. ACTA PHYSICA POLONICA A, Vol. 123, No. 6, pp. 1029-1033.
- Rao, S.S. (2007) Vibration of Continuous Systems. Wiley, New Jersey.
- Schwartz, L. and Brabec, J. (1972) Mathematical methods in physics. SNTL, Prague (in Czech).
- Sobotka, J. (2016) Forced vibration analysis of Euler-Bernoulli beam with discontinuities by means of distributions without doing modal analysis, in: Proc. 22nd Int. Conf. on Engineering Mechanics (eds. Zolotarev, I. and Radolf, V.), Svratka, Czech Republic, pp. 510-513.
- Štěpánek, J. (2001) Distributions and differential equations. Karolinum, Prague (in Czech).
- Wang, J. and Qiao, P. (2007) Vibration of beams with arbitrary discontinuities and boundary conditions. Journal of Sound and Vibration, Vol. 308, Is. 1, pp. 12-27.
- Weaver, W., Timoshenko, S.P. and Young, D.H. (1990) Vibration Problems in Engineering, 5th ed., John Wiley & Sons, Inc.
- Yesilce, Y. (2012) Free and forced vibrations of an axially-loaded Timoshenko multi-span beam carrying a number of various concentrated elements. Shock and Vibration, Vol. 19, No. 4, pp. 735-752.
- Zhao, X., Zhao, Y. R., Gao, X. Z., Li, X. Y. and Li, Y. H. (2016) Green's functions for the forced vibrations of cracked Euler-Bernoulli beams. Mechanical Systems and Signal Processing, Vol. 68, pp. 155-175.

## **INSTABILITY OF A STEPPED COLUMN LOADED BY THE EXTERNAL FOLLOWER FORCE**

**K. Sokół\***

**Abstract:** *In this paper the instability problem of a stepped column loaded by the follower force is discussed. The column is composed of three sections with different cross-sectional areas. The connection of the each section is realized by means of the pins strengthened by the rotational springs. This type of connection allows one to simulate the different method of assembly of sections or even the defect (attenuation) in the connection. The boundary problem of the instability of the presented slender system has been formulated on the basis of the Hamilton's principle and solved with small parameter method. The results of the numerical simulations are concern on the shape of the characteristic curves under an influence of the different cross sectional areas of the segments.*

**Keywords:** Column, Flutter, Instability, Boundary Problem, Follower Force.

### **1. Introduction**

In this paper the instability of the slender system in the form of the column loaded by the follower force is presented. The introduced load causes that the column loses stability via divergence or flutter, depending on the follower factor. According to the nomenclature proposed by Kordas and Życzkowski (1963) the discussed type of external load can be classified as:  $\eta < 0$  – anti-follower force,  $0 < \eta < 1$  – sub-follower force,  $\eta = 1$  – follower force,  $\eta > 1$  – super-follower force.

The studies on slender structures loaded by the follower force have been done by Przybylski and Sokół (2012). Authors have investigated the multimember column integrated with piezoceramic element. The piezo-rod induced the additional compressive or tensional forces, what lead to pre-stressing of the column and finally the shift of divergence/flutter instability regions has been obtained. Kukla (2009) have investigated the stepped cracked column. The size of the crack has been calculated on the basis of presentation written by Ostachowicz and Krawczuk (1991). Kukla has proposed the solution of the boundary problem by means of Green's functions and obtained the characteristic curves of the cracked structure. Zamorska et.al (2015) have presented the analytical simulation done with Green's function of the cracked beam with variable cross-sectional area and the numerical ones from FEM module of CATIA software. In the same time Cekus and Waryś (2015) have studied an identification of parameters of discrete-continuous models in the form of stepped columns. The chosen parameters of the systems have been found on the basis of free vibration frequency magnitude obtained from experimental studies. The proposed mathematical model has been solved according to the Lagrange multiplier formalism, while an optimization based on the genetic algorithm. The studies on the divergence/flutter instability regions have been also done by Towski and Uzny (2011). Authors have studied a column with constant cross sectional area strengthened by the spring at the fixed end and loaded by the generalized Beck's load and obtained the regions of divergence/flutter instability. Continuation of the studies has been presented in 2013.

In this paper the stepped column loaded by follower force is investigated. The proposed structure is composed of three sections connected by the pins strengthened by the rotational springs. This type of connection allows one to simulate the different methods of assembly of sections. The presented results are concern on the shape of characteristic curves (external load – vibration frequency) and divergence/flutter instability regions in relation to the different cross-sectional areas of sections.

---

\* Krzysztof Sokół, PhD.: Institute of Mechanics and Machine Design Foundation, Częstochowa University of Technology  
Dąbrowskiego 73, 42-200 Częstochowa, Poland, sokol@imipkm.pcz.pl

## 2. Boundary problem formulation

The investigated system is presented in the Fig. 1. As shown, the structure is loaded by external force  $P$  localized on the top end of the cantilever column. Sections have lengths  $l_1, l_2, l_3$ . Even and odd sections are connected by rotational springs.

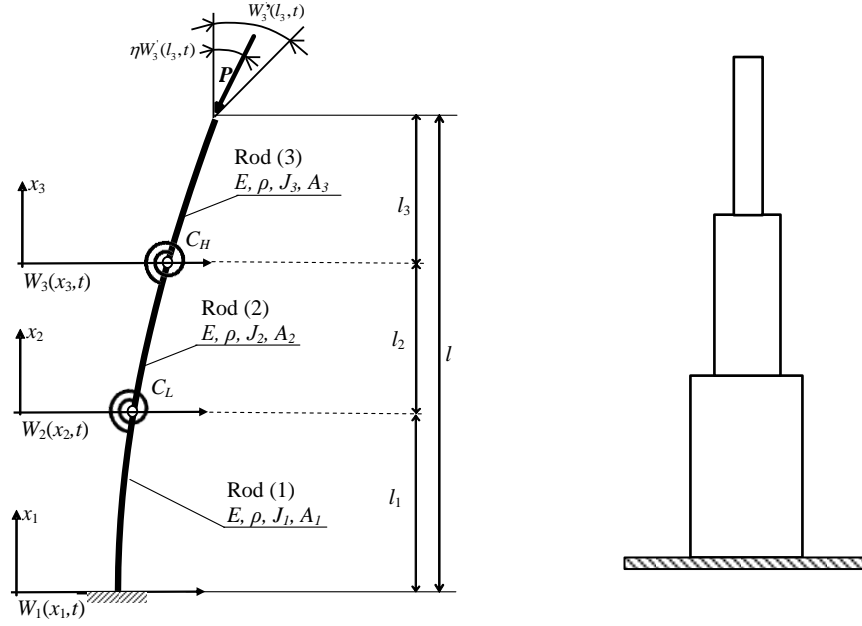


Fig. 1: Investigated system.

The boundary problem has been formulated on the basis of the Hamilton's principle:

$$\delta \int_{t_1}^{t_2} (T - V + L_c) dt + \int_{t_1}^{t_2} \delta L_n dt = 0 \quad (1)$$

The kinetic and potential energies and components of work of conservative and non-conservative forces are as follows:

$$\begin{aligned} V = & \frac{1}{2} \left\{ \sum_{i=1}^3 \int_0^{l_i} EJ_i \left[ \frac{\partial^2 W_i(x_i, t)}{\partial x_i^2} \right]^2 dx + \int_0^{l_i} EA_i \left[ \frac{\partial U_i(x_i, t)}{\partial x_i} + \frac{1}{2} \left( \frac{\partial W_i(x_i, t)}{\partial x_i} \right)^2 \right]^2 dx \right\} + \\ & + \frac{1}{2} C_H \left( \frac{\partial W_3(x_3, t)}{\partial x_3} \Big|_{x_3=0} - \frac{\partial W_2(x_2, t)}{\partial x_2} \Big|_{x_2=l_2} \right)^2 + \frac{1}{2} C_L \left( \frac{\partial W_2(x_2, t)}{\partial x_2} \Big|_{x_2=0} - \frac{\partial W_1(x_1, t)}{\partial x_1} \Big|_{x_1=l_1} \right)^2 \\ T = & \frac{1}{2} \sum_{i=1}^3 \int_0^{l_i} \rho A_i \left( \frac{\partial W_i(x_i, t)}{\partial t} \right)^2 dx \quad L_c = -PU_3(l_3, t), \quad L_n = \eta P \frac{\partial W_3(x_3, t)}{\partial x_3} \Big|_{x_3=l_3} W_3(l_3, t) \end{aligned} \quad (2a, d)$$

On the basis of the Hamilton's principle and integration and variation operations inter alia the equations of motion in transversal direction are found:

$$EJ_i W_i^{IV}(x_i, t) + P W_i^{II}(x_i, t) + \rho A_i \ddot{W}_i(x_i, t) = 0 \quad i = 1, 2, 3 \quad (3)$$

The natural and geometrical boundary conditions are as follows:

$$\begin{aligned} W_1(0, t) = W_1^I(0, t) = EJ_3 W_3^{II}(l_3, t) = 0, \quad W_j(l_j, t) = W_{j+1}(0) \quad j = 1, 2 \\ EJ_j W_j^{III}(l_j, t) + S_j W_j^I(l_j, t) - EJ_{j+1} W_{j+1}^{III}(l_{j+1}, t) - S_{j+1} W_{j+1}^I(l_{j+1}, t) = 0 \quad j = 1, 2 \\ -EJ_j W_j^{II}(0, t) + C_{L/H} (W_j^I(0, t) + W_{j-1}^I(l_{j-1}, t)) \quad j = 2, 3 \quad EJ_j W_j^{II}(l_j, t) - C_{L/H} (W_{j+1}^I(0, t) + W_j^I(l_j, t)) \quad j = 1, 2 \\ EJ_3 W_3^{III}(l_3, t) + P(1 - \eta) W_3^I(l_3, t) \end{aligned} \quad (4a - 1)$$

The presented problem can be solved numerically by introduction of Eq. (3) into boundary conditions (4a – l). The obtained matrix determinant equated to zero leads to the transcendental equation on the basis of which the external load – natural vibration frequency relationship is computed.

### 3. Results of numerical simulations

The discussion of the results of numerical simulations is done by means of the non-dimensional parameters:

$$p = \frac{Pl^2}{EJ_1}, c_H = \frac{C_H l}{EJ_1}, c_L = \frac{C_L l}{EJ_1}, d_i = \frac{l_i}{l}, \mu_{21} = \frac{EJ_2}{EJ_1}, \mu_{32} = \frac{EJ_3}{EJ_2}, \omega = \sqrt{\Omega^2 \frac{\rho A_1 l^4}{EJ_1}}, \quad (5a - f)$$

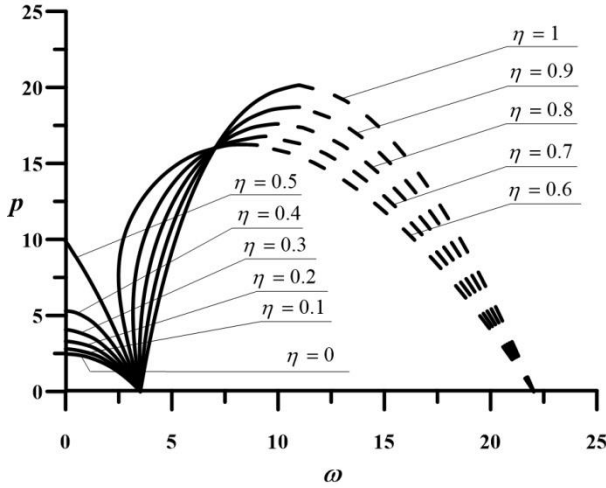


Fig. 2: Influence of cross sectional area on the shape of characteristic curves ( $c_H = c_L = 10^3$ ,  $d_1 = d_2 = d_3 = 0.33$ ,  $\mu_{21} = \mu_{32} = 1$ ).

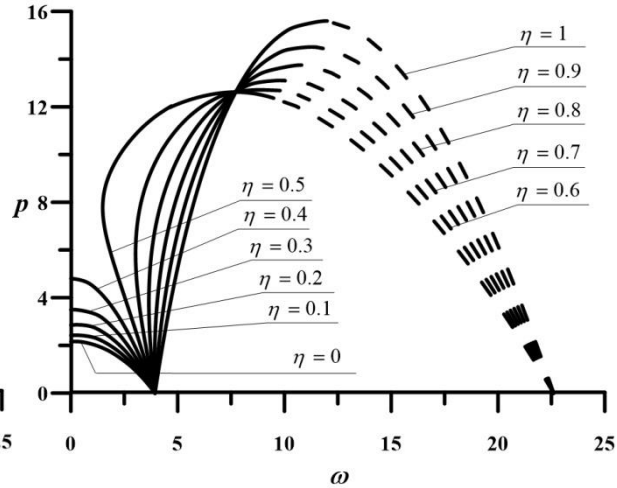


Fig. 3: Influence of cross sectional area on the shape of characteristic curves ( $c_H = c_L = 10^3$ ,  $d_1 = d_2 = d_3 = 0.33$ ,  $\mu_{21} = 0.75$ ,  $\mu_{32} = 1$ ).

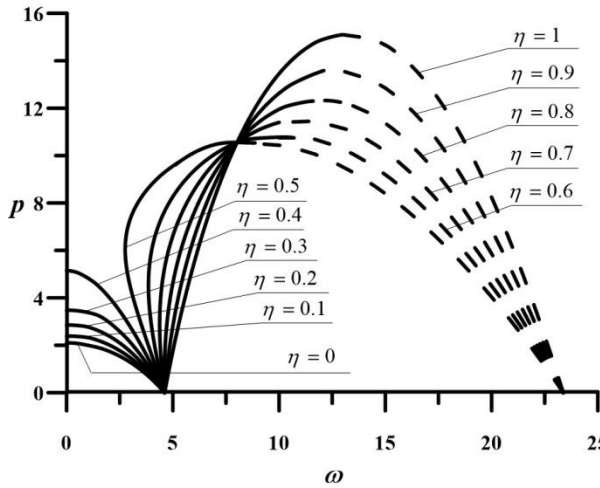


Fig. 4: Influence of cross sectional area on the shape of characteristic curves ( $c_H = c_L = 10^3$ ,  $d_1 = d_2 = d_3 = 0.33$ ,  $\mu_{21} = 0.75$ ,  $\mu_{32} = 0.5$ ).

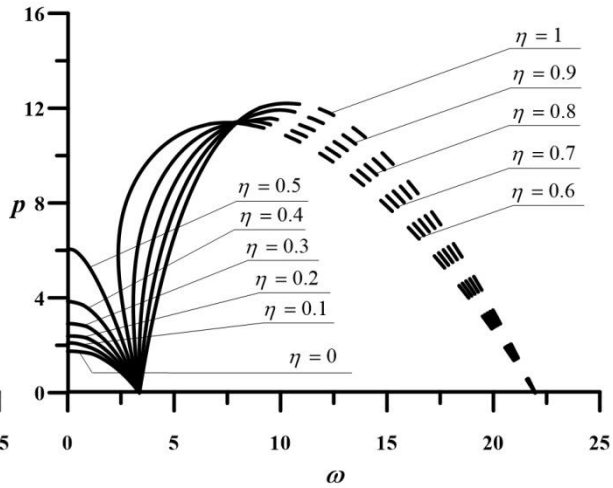


Fig. 5: Influence of cross sectional area on the shape of characteristic curves ( $c_H = c_L = 10^3$ ,  $d_1 = d_2 = d_3 = 0.33$ ,  $\mu_{21} = 0.5$ ,  $\mu_{32} = 2$ ).

The presentation of the results has been started from the case when all the segments have equal cross-sectional area (Fig. 2). That allows on to check the validity of the proposed mathematical model. The column loses stability by divergence up to  $\eta = 0.5$ . Above that magnitude the flutter instability occurs. The highest flutter external load magnitude is 20.05; divergence 9.86. The reduction of cross sectional area of segments 2 and 3 (Fig. 3) results in an increase of first as well as second vibration frequency magnitude. At this configuration the reduction of divergence instability region has been noticed – the column changes divergence instability to flutter one at  $\eta > 0.4$  in relation to the Fig. 1 configuration. The

change of cross-sectional area causes also the reduction of divergence and flutter maximum loading. The location of common point (point in which the characteristic curves at flutter instability are crossing) is shifted to the higher vibration frequency and is present at lower external load magnitude. The further reduction of the cross-sectional area of the top segment (Fig. 4) results in further maximum loading capacity drop, increase of free vibration frequency and shift of the common point (present at higher vibration frequency and at lower external load). The change of instability type occurs at  $\eta > 0.4$ . In the last case (Fig. 5) when the first and top segments have equal cross-sectional areas and the middle one is thinner than the others the lowest loading capacity has been observed. The free vibration frequency has lowered in relation to the Figs. 3 and 4. The instability change has now shifted to  $\eta > 0.5$ . At flutter instability the difference in maximum loading is the smallest from the all presented cases.

#### 4. Conclusions

The following conclusions have been made on the basis of the results of the numerical simulations:

- the control of divergence/flutter instability regions can be done by means of follower factor or by change of cross-sectional area of chosen segments,
- the maximum loading as well as vibration frequency can be controlled both by the follower factor and cross-sectional area,
- the location of common point at flutter instability changes in relation to the cross-sectional area of segments,

In the future studies the different length of the elements as well as the connection stiffness between sections should be considered. Furthermore the higher components of natural vibration frequency can be solved by means of small parameter method. The verification of the proposed mathematical model can be done during the experimental studies, where the follower load is realized by the small scale jet engine.

#### Acknowledgement

The study has been carried out within the statutory funds of the Czestochowa University of Technology (BS/MN -1-101-304/16/P).

#### References

- Cekus, D. and Waryś, P. (2015) Identification of parameters of discrete-continuous models, AIP Conf. Proc. 1648 , 850055, <http://dx.doi.org/10.1063/1.4913110> .
- Kordas, Z. and Życzkowski, M. (1963) On the loss of stability of a rod under-super tangential force, *Archiwum Mechaniki Stosowanej*, 21 (1), pp. 7-31.
- Kukla, S. (2009) Free vibrations and stability of stepped columns with cracks, *Journal of Sound and Vibration*, 319 (3-5), pp. 1301-1311.
- Ostachowicz, W.M. and Krawczuk, M. (1991) Analysis of the effect of cracks on the natural frequencies of a cantilever beam, *Journal of Sound and Vibration*, 150, pp. 191-201.
- Przybylski, J. and Sokół, K. (2012) The control of divergence and flutter instability of the geometrically non-linear system by means of the piezoelectric force, chapter 10, *Free vibrations and stability of slender systems subjected to conservative or non-conservative load*, WNT 2012, (in Polish).
- Tomski, L. and Uzny, S. (2011) The regions of flutter and divergence instability of a column subjected to Beck's generalized load, taking into account the torsional flexibility of the loaded end of the column, *Research Mechanics Communications*, 38, pp. 95-100.
- Tomski, L. and Uzny, S. (2013) Free vibrations and stability of a new slender system subjected to a conservative or nonconservative load, *Journal of Engineering Mechanics*, 139 (8), pp. 1133-1148.
- Zamorska, I., Cekus, D. and Miara, M. (2015) Effect of crack parameters on free vibrations of the Bernoulli-Euler beam, *Journal of Applied Mathematics and Computational Mechanics*, 14 (4), pp. 167-174.

## OPTIMUM DESIGN OF TUNED LIQUID COLUMN DAMPER FOR HIGH-RISE BUILDING

M. Sokol<sup>\*</sup>, K. Lamperová<sup>\*\*</sup>, M. Venglár<sup>\*\*\*</sup>, L. H. Hernández Carrasco<sup>\*\*\*\*</sup>

**Abstract:** Tuned mass damper for high-rise building has been designed. Two numerical models with different detail have been used. The influence and performance of tuned mass damper has been analyzed. Its effects have been checked for both models – simplified and full 3D Finite Element Method model. Alternatively tuned liquid damper has been assumed and its basic characteristics, like eigenfrequencies and mode shapes, have been calculated.

**Keywords:** Tuned mass damper, Tuned liquid column damper, Dynamic response, High-rise building.

### 1. Introduction

A tuned mass damper (TMD) for high-rise building with total height of 280 m (Fig. 1) has been assumed for decreasing of dynamic effects. The modification of TMD via using the water tank effect so-called Liquid Column Damper (TLCD) and its modifications have been investigated many times as in Yalla and Kareem (2003) or Soto and Adeli (2013). The primary aim is to reduce dynamic vibrations caused by different sources like wind effects, earthquake etc. The structure has been modeled by FEM (Fig. 1a) and for checking purposes modeled also as 7 degree of freedom (7 DOF) system (Fig. 1b), where the influence of damping could be checked easier, but without the lack of significant accuracy. Second model has been tuned such a way, that it finally had the same basic dynamic response in one plane (eigenfrequencies and eigen modes) as the original 3D model.

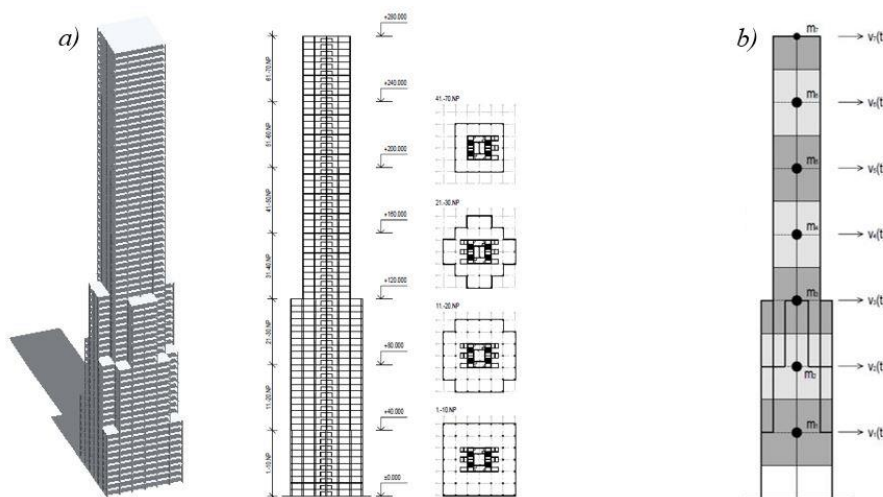


Fig. 1: The high-rise building a) original 3D model with thousands DOF  
b) simplified model with 7 DOF.

<sup>\*</sup> Prof. Milan Sokol, PhD.: Department of Structural Mechanics, Slovak University of Technology, Faculty of Civil Engineering, Radlinského 11; 810 05, Bratislava; SK, milan.sokol@stuba.sk

<sup>\*\*</sup> Ing. Katarína Lamperová: Department of Structural Mechanics, Slovak University of Technology, Faculty of Civil Engineering, Radlinského 11; 810 05, Bratislava; SK, katarina.lamperova@stuba.sk

<sup>\*\*\*</sup> Ing. Michal Venglár: Department of Structural Mechanics, Slovak University of Technology, Faculty of Civil Engineering, Radlinského 11; 810 05, Bratislava; SK, michal.venglar@stuba.sk

<sup>\*\*\*\*</sup> Luis.Horacio Hernández Carrasco: Escuela de Diseño, Ingeniería y Arquitectura, Tecnológico de Monterrey, Puebla, MX, lhernandez@itesm.mx



Eigenfrequencies and eigen modes (Fig. 2) have been calculated for both models and they are very close each to other.

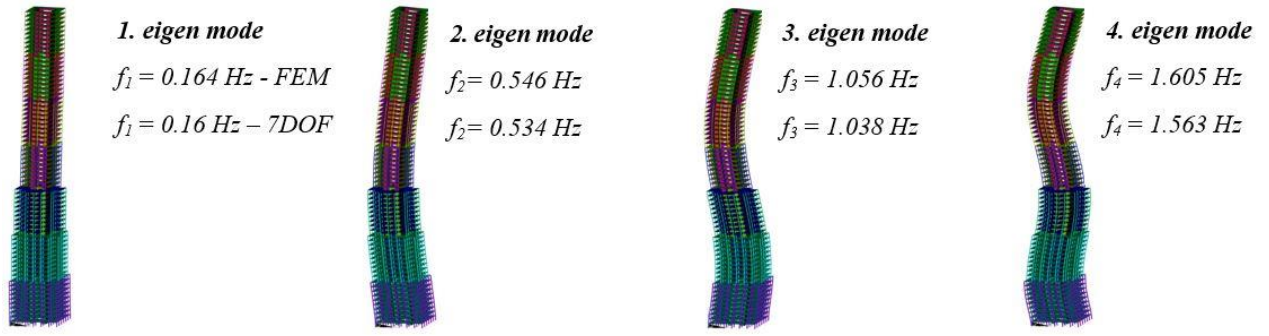


Fig. 2: Eigenfrequencies and eigen modes.

## 2. Methods

Theory of optimal design of TMD is derived for SDOF in e.g. Flesch (1993) because of complexity of general solution, but some authors used also much complicated assumptions (McNamara, 1977 and Kareem, Kijewski, Tamura, 1999). Then this results can be used for MDOF system too, with only small compromise in accuracy. The simplified model with 7 DOFs (Fig. 1 b) is then used for checking the real behavior of damper working on MDOF system.

### 2.1. Single degree of freedom system with damper

For the effectiveness of TMD, some parameters must be optimally selected (Penzien, Clough, 2003 and Sokol, Tvrda, 2016). These parameters are given by the equations:

$$\mu = \frac{m_2}{m_1} \quad (1)$$

$$\alpha = \frac{1}{1+\mu} = \frac{\omega_2}{\omega_1} \quad (2)$$

$$\xi_{opt} = \sqrt{\frac{3 \cdot \mu}{8(1+\mu)^3}} \quad (4)$$

$$\omega_2 = \omega_1 \cdot \alpha = \sqrt{\frac{k_2}{m_2}} \quad (3)$$

$$c_2 = 2 \cdot m_2 \cdot \omega_2 \cdot \xi_{opt} \quad (4)$$

$$k_2 = m_2 \cdot \omega_2^2 \quad (5)$$

In practice, stiffness effect in equation (5) is usually assumed as pendulum effect calculating for its length

$$L = \left(\frac{1}{\omega_2}\right)^2 \cdot g \quad (6)$$

### 2.2. Effective mass of system

Due to the fact that all characteristics from (1) to (6) are derived for SDOF there is necessary to calculate the effective mass of MDOF system

$$M_{eff} = \frac{2E_k}{\dot{v}_d^2} \quad (7)$$

where  $E_k$  is kinetic energy of the whole system,  $\dot{v}_d$  is velocity at the place where TMD is located.

### 2.3. Design of TLCD

There is proposed a variant of TMD system using liquid column damper, where the effect of pendulum is represented by column of water moving in the vessel. The location inside of the building is clear in Fig. 3 and it takes the top 4 stories of the building. There is used only the one direction TLCD because of lack of

time and only for checking purposes, but still without the lack of the accuracy, because an alternative TLCD can be assumed in perpendicular direction. In next paragraphs the performance of this system is checked.

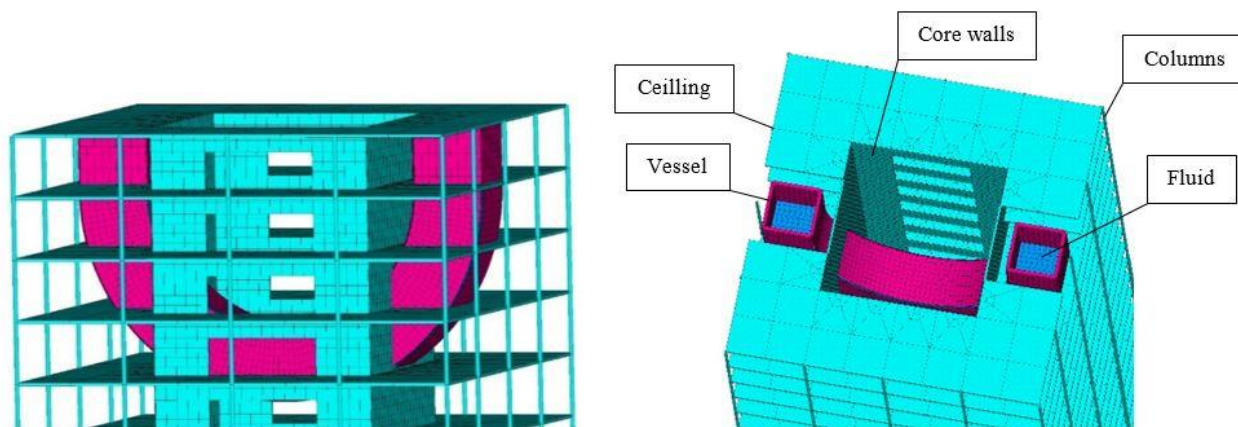


Fig. 3: Location of TLCD.

For calculating of eigenfrequencies of the water inside the vessel FEM has been used. 3D FEM model was created from shell and fluid elements. A vessel of half cylindrical shape with upper additional parts has been considered. Contact between vessel and water elements has been assumed only in perpendicular direction to the common surface, representing the effects of hydraulic pressure.

Tab. 1: Eigenfrequencies of the pendulum and the water inside of vessel.

	Calculation	Weight [t]	1. eigenfrequency [Hz]
Pendulum $L = 9.6$ m	Analytical	392.890	0.161
Water $r = 9.6$ m	ANSYS	412.881	0.162

In Tab. 1 it is possible to compare eigenfrequencies between simple pendulum and water moving inside of the vessel (Fig. 4a). Splashing effects of water are also included as you can see in higher eigen modes (Fig. 4b).

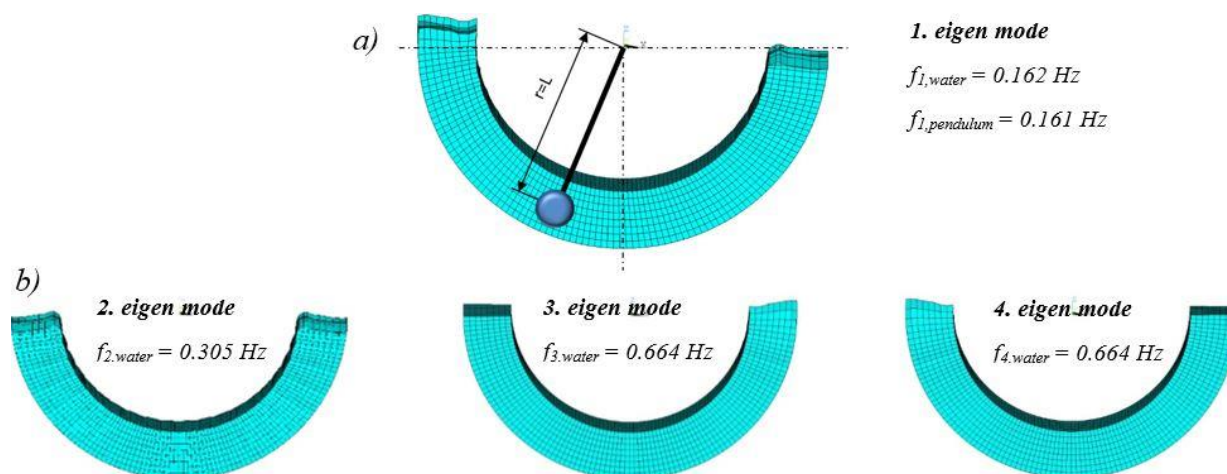


Fig. 4: Eigen modes of water inside of half cylindrical vessel a) the first eigen mode; b) more eigen modes.

## 2.4. Assessment of dynamic effects

Real dynamic response has been checked on 7 DOF system using time history analysis. The building was subjected to harmonic load representing e.g. wind effects. By activation of TMD (TLCD), maximum displacement on the top of building was reduced more by 40 % (Fig. 5).

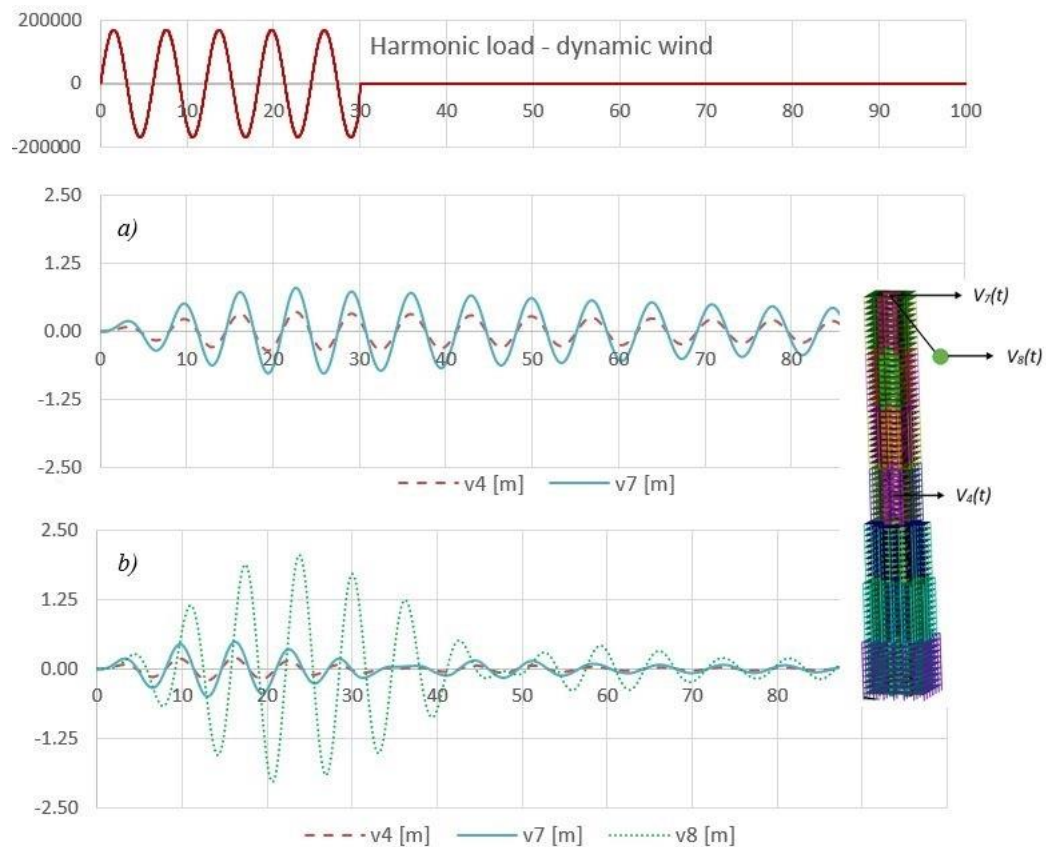


Fig. 5: Dynamic response of structure on harmonic load a) without damper; b) with damper.

### 3. Conclusions

The structure has been modeled by FEM and for checking purposes modeled as simplified 7 DOF system, with the same basic dynamic response in one plane as the original 3D model. TMD has been designed for elimination of vibrations of dynamic load. Assuming that the length of pendulum equals to the radius of water inside of half cylindrical vessel an alternative TLCD has been designed and its performance has been checked. TLCD has been modeled by FEM and placed into FEM model of high-rise building. Dynamic response has been assessed on MDOF system. The structure without and with damper has been subjected to harmonic load to assess of dynamic effects. Maximum displacement on the top was decreased by 40 %.

### Acknowledgement

This paper has been supported by the Slovak Research and Development Agency (SRDA) – grant from research program No. APVV-0236-12.

### References

- Flesch, R. (1993) Dynamics of structures in practice. Bauverlag, Berlin (in German).
- Soto, M.G. and Adeli, H. (2013) Tuned Mass Dampers. Archives of Computational Methods in Engineering, 20, 4, pp. 419-431.
- Kareem, A., Kijewski, T. and Tamura, Y. (1999) Mitigation of Motions of Tall Buildings with Specific Examples of Recent Applications. Wind and Structures 2, 3, pp. 201-251.
- McNamara, R.J. (1977) Tuned Mass Dampers for Buildings. Journal of Structural Division, 103, 9, pp. 1785-1798.
- Penzien, J. and Clough, R. (2003) Dynamics of Structures. McGraw-Hill, Inc., Singapore.
- Sokol, M. and Tvrdá, K. (2016) Dynamics of structures. STU Press, Bratislava (in Slovak).
- Yalla, S.K. and Kareem, A. (2003) Semiactive Tuned Liquid Column Dampers: Experimental Study. Journal of Structural Engineering, 129, 7, pp. 960-971.

## LOAD BEARING TEST OF WALL FROM HOLLOW GLASS BLOCKS USING VITRALOCK INSTALLATION SYSTEM

Z. Sokol<sup>\*</sup>, J. Fíla<sup>\*\*</sup>, M. Eliášová<sup>\*\*\*</sup>

**Abstract:** *Hollow glass blocks are used in building for more than century. Originally, they were used in industrial buildings but soon new applications quickly followed. They gained popularity in modern architecture of 1920 – 1930 and again in 1960s. The hollow glass blocks were always combined with reinforced concrete leading to traditional installation method. Ever growing popularity leads to demand of new, easier and faster installation methods. The performance of these new systems needs to be verified to develop reliable design models and application rules.*

**Keywords:** Hollow glass blocks, Dry installation system, Experimental verification.

### 1. Introduction

Traditional installation of glass blocks is carried out using cement mortar in similar way the walls from ceramic bricks are made. The installation can be facilitated by using plastic spacers, however, it still requires experience of the workers and precise planning. For this reason, alternative methods are developed which allow installation without mortar or adhesives. Vitralock by Seves is the promising method as it allows fast assembling without special tools and skills.

Vitralock is dry installation system consisting of two plastic pieces, the spacer and the connector (Fig. 1), which make the assembling of the walls very easy. The connector is locked into the spacers forming a rectangular grid, see Fig. 2. The glass blocks are simply placed into openings of the grid. When necessary, the wall can be reinforced by steel bars placed in the spacers.



*Fig. 1: The elements of the Vitralock system.*

---

<sup>\*</sup> Ing. Zdeněk Sokol, PhD.: Czech Technical University in Prague, Faculty of Civil Engineering, Thákurova 2077/7; 160 00, Prague; CZ, sokol@fsv.cvut.cz

<sup>\*\*</sup> Ing. Jiří Fíla: Czech Technical University in Prague, Faculty of Civil Engineering, Thákurova 2077/7; 160 00, Prague; CZ, jiri.fila@fsv.cvut.cz

<sup>\*\*\*</sup> Assoc. Prof. Ing. Martina Eliášová, PhD.: Czech Technical University in Prague, Faculty of Civil Engineering, Thákurova 2077/7; 160 00, Prague; CZ, eliasova@fsv.cvut.cz



## 2. Preparation of the test

Purpose of the test was to obtain the response of interior partition wall exposed to horizontal load. The wall was assembled in the laboratory using 12 rows, each containing 14 glass block. The dimensions of the wall were 2.81 m (width) a 2.42 m (height), see Fig. 3 and Fig. 4. The wall was fixed to a timber frame made from  $50 \times 80$  mm sections, each plastic spacer on the perimeter was connected by 4 screws  $4 \times 35$  mm, see Fig. 2.



*Fig. 2: The Vitralock system during the wall assembly.*

The wall was reinforced by steel bars diameter 5 mm located on both surfaces. The system allows arranging the bars in either vertical or horizontal directions, therefore the loaded side was reinforced by bars in vertical direction and the non-loaded side by bars in horizontal direction. The bars were anchored to the timber frame by the plastic spacers.

The wall was firmly connected to the ceiling by three sets of wooden wedges, see Fig. 3. The joints were filled by grout for ceramic tiles. The wall was assembled in the same way it would be used in real building.



*Fig. 3: The completed wall prior to filling of the joints (left) and during the test (right).*

## 3. Execution of the test

The wall was loaded by horizontal load at height 900 mm above the floor, see Fig. 3. The load was created by hydraulic jack and distributed by steel beams to 4 points in the middle of the glass blocks (marked as 5, 6, 8 and 9 in Fig. 4).

Horizontal deformations at 10 locations were measured during the test, see Fig. 4 for the location of the transducers.

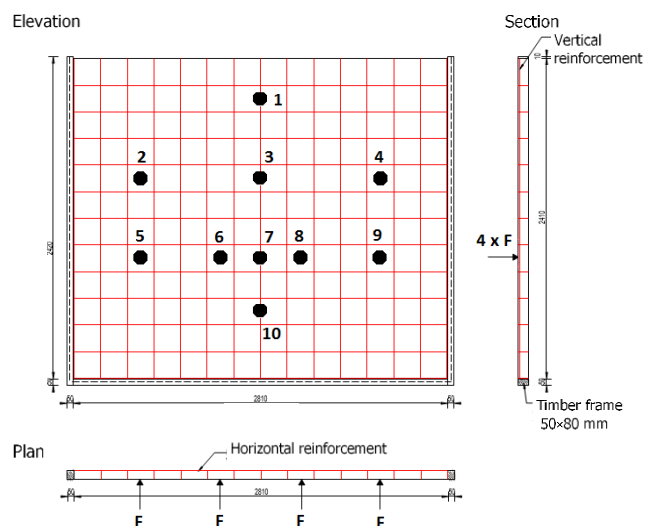


Fig. 4: Dimensions of the wall and location of the transducers.

The load was applied manually in 22 cycles. The loading was controlled by horizontal deformation at the point number 7. As soon as the required deformation was reached, the wall was left for 1 minute and then unloaded. The magnitude of the deformation increased over the load cycles, see Fig. 5.

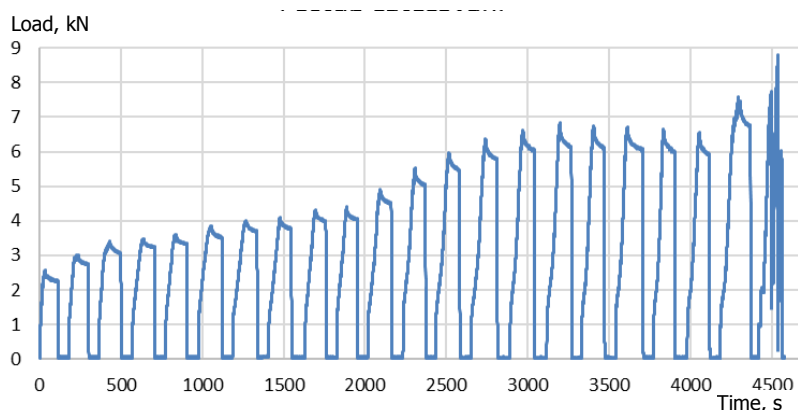


Fig. 5: Load procedure.

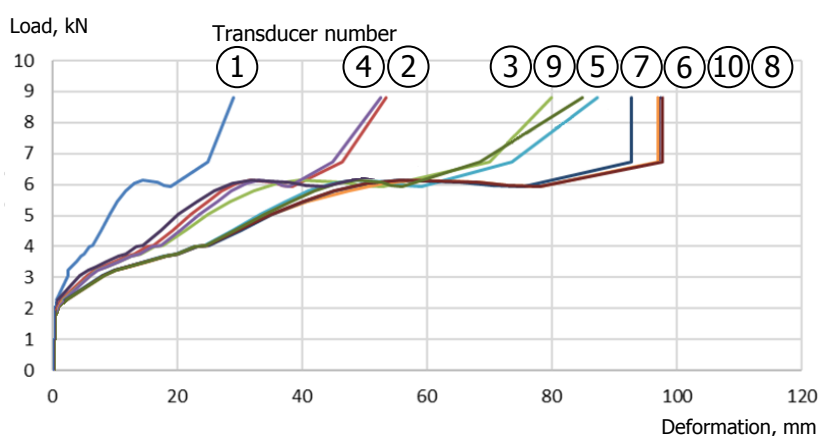


Fig. 6: Load - deformation diagram for the measured points.

The behaviour of the wall is linear for small deformations. Assuming the limit for horizontal deformation is

$$\delta_{lim} = L / 200 = 2410 / 200 = 12.0 \text{ mm}, \quad (1)$$

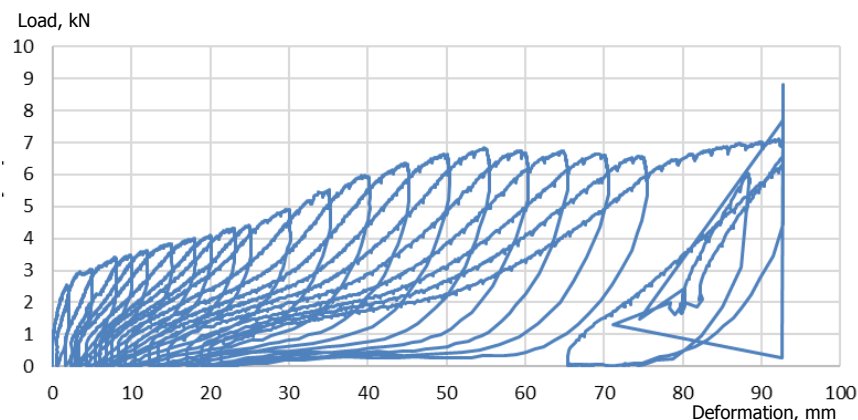
the load to reach the limiting deformation is 3.58 kN.





*Fig. 7: Cracks in the joint.*

At the deformation approx. 10 mm first crack in the joint appeared which grew in the following load cycles, see Fig. 7. As the load increase, highly non-linear behaviour and significant permanent deformation was measured after unloading of each cycle, see Fig. 8. This is caused by plastic deformation of the spacers and slip of the reinforcement at the anchoring. However, the wall was able to resist the maximum load 8.8 kN which resulted in horizontal deformation of 93 mm when the hollow block was pushed out of the Vitralock grid.



*Fig. 8: Load - deformation diagram for the point 7.*

#### 4. Conclusions

Load-bearing test of wall made from hollow glass bricks using Vitralock system was tested to horizontal load. The experiment shows linear behaviour at loads which are expected in "everyday situation". Cracks in the joints appear with increasing load but they have no influence on the performance of the wall and represent only an aesthetic problem. When cracks should be avoided (in bathrooms, etc.) elastic sealing material should be used for joints.

Highly non-linear behaviour was observed at later stages when also permanent deformations were encountered. However, the wall was able to resist the applied load. Failure of the wall was observed at horizontal deformation 93 mm (i.e.  $L / 26$ ) when the hollow brick was pushed out of the Vitralock grid.

#### Acknowledgement

The paper has been written with support by grant No. 16-14770S of the Czech Science Foundation (GAČR). The authors would like to thank Vitrablok s.r.o for supplying the components used for the test.

#### References

- ČSN EN 13116 Curtain walling - Resistance to wind load - Performance requirements, CNI Prague (in Czech).
- Eliášová, M., Sokol, Z. and Fíla, J. (2016) Load Test of Wall Made From Hollow Glass Bricks, Research report, CTU Prague (in Czech).
- Installation guide for Vitralock system, <http://www.sevesglassblock.com/install-vitralock.html>.
- Zeitoun, X.G.M. (1995) Glass Block Handbook, Builder's Book, Canoga Park.

## **ACOUSTIC CLIMATE IN THE CABINS AS A FACTOR OF REBUILDING EFFECTIVENESS OF LONG TERM OPERATED BUCKET WHEEL EXCAVATORS – A CASE STUDY**

**M. Sokolski<sup>\*</sup>, P. Sokolski<sup>\*\*</sup>**

**Abstract:** *The unprecedented case of two old bucket wheel excavators type SRs–1800 which were relocated from Spain to Poland is treated. Both machines were submitted to total reconstruction in Poland and then they were put into operation. Then, the complex investigations during continuous removal process of overburden was carried out. One of the goals was to evaluate the acoustic climate in the cabins - as a factor which determines the comfort and safety of the operators of these machines. In the paper the research results of one of this excavators are presented. It has been shown that the acoustic climate in the cabin after modernization of this excavator meets the relevant requirements.*

**Keywords:** Bucket Wheel Excavator, Operators' Cabin, Noise Hazards, Acoustic Climate.

### **1. Introduction**

More than 35 % of the total electric energy production in Poland is based on brown coal. This is largely due to considerable domestic resources and lower costs of this kind of energy by about 20 % then that from black coal. To maintain this cost advantage many mining companies tend to extend the useful service life of their most expensive basic machinery beyond that specified in the original design.

The basic machines for open pit lignite mines are very expensive. For example a new bucket wheel excavator with annual capacity of 7 million bank cubic meters may cost up to 4.5 million US dollars. For this reason its purchase is in generally justified if the expected pit life is over of 10 - 15 years (Dudek and Sokolski, 2000; Sokolski, 2007).

However, during long time of operation these machines are subjected to several degradation processes which are in detail analyzed in the works (Dudek and Nowakowski, 1995; Nowakowski, 1999; Smolnicki et al., 2010). These degradation processes contribute to the reduction of safety level and can cause dangerous events: serious damages or even catastrophes (Mlynczak, 2014). One of their symptoms are increased noise and vibrations level which, beside thermal and weather conditions, are the most important factors creating a microclimate of work environment for operators (Sokolski, 2007).

That is why since the 1990s the complex program of modernization of all the old basic machines has been consistently put into practice in Polish brown coal companies. This revitalization strategy is of particularly importance for improving the energy security of Poland.

### **2. Problem formulation**

An alternative solution to buying new basic machines for open pit mining is acquiring used objects. Spectacular results were achieved when two old bucket wheel excavators SRs 1800 (years of construction 1985 and 1986) have been purchased and transported to Poland from a lignite mine which was decided to be closed (As Pontes de Garcia Rodrigues in Spain).

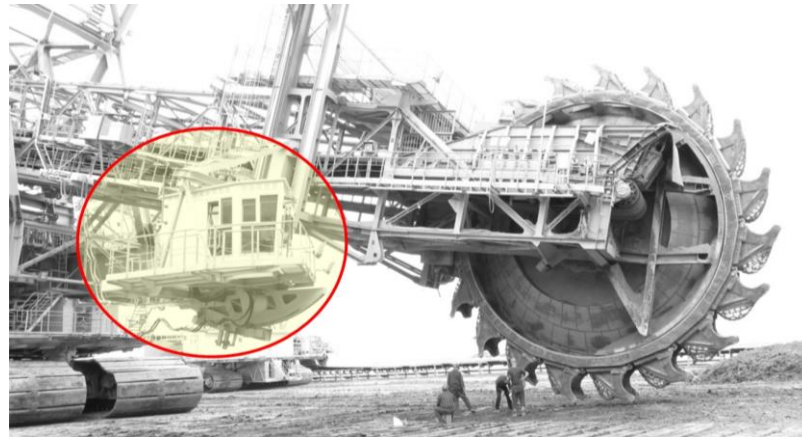
---

<sup>\*</sup> Marek Sokolski, PhD. Assistant Professor: Faculty of Mechanical Engineering, Wroclaw University of Science and Technology, Lukasiewiczza Street 4; 50-371 Wroclaw; PL, marek.sokolski@pwr.edu.pl

<sup>\*\*</sup> Piotr Sokolski, PhD.: Faculty of Mechanical Engineering, Wroclaw University of Science and Technology, Lukasiewiczza Street 4; 50-371 Wroclaw; PL, piotr.sokolski@pwr.edu.pl

Both excavators were upgraded in Poland. In particular, the electrical equipment of driving units was rebuilt, moreover many elements of the steel structures were replaced or regenerated. The first of these excavators was put into operation in 2010 and the second one (Fig. 1) started working in 2011. Then both bucket wheel excavators were subjected to attestation tests carried out by the team from the Faculty of Mechanical Engineering of Wroclaw University of Science and Technology.

One of the main targets of these approval tests was to assess the comfort and safety of the operators. The research program included, among other things measurement and analysis of noise level and noise spectrum in the operators' cabins of each of these excavators. The research was carried out in summer time during the continuous removal process of overburden. Due to the limited length of this paper, the research results of one of these bucket wheel excavators (shown in Fig. 1) are presented.



*Fig. 1: Research object - bucket wheel excavator. Operator's cabin is marked (authors' own archive).*

### 3. Method of assessment of acoustic climate in cabin

Evaluation of acoustic climate is nowadays an important issue. It can be done for both a small area like an operator's cabin and surrounding of an open pit mine. In the second case it can be performed through different techniques. An example of such a procedure is presented in (Pinzari et al., 2015). Assessment of the noise hazards and acoustic microclimate in the workplace is generally performed under the assumption that the noise level is deterministic.

In this approach, the acoustic microclimate in the cabin of bucket wheel excavator is evaluated by the A-weighted equivalent sound pressure level  $L_{Aeq}$  (determined for a nominal eight hour exposure period). The recommended occupational exposure limits of noise level are defined in proper international standards (e.g. ISO R 1996) and in the Ordinance of the Polish Minister of Labor and Social Policy ("Ordinance on maximum permissible concentration and intensity of harmful factors in the work environment in accordance with national limit values"). In accordance with these guidelines, the noise level should not exceed the following values:

- in the cabins and control rooms without telephone communications  $L_{Aeq(perm)} = 75 \text{ dB(A)}$ ,
- in the cabins and control rooms with telephone communications  $L_{Aeq(perm)} = 65 \text{ dB(A)}$ .

In the more detailed assessment of acoustic microclimate, according to the recommendation of ISO R 1996, the sound spectrum and so-called Noise Rating curves NR are used. According to this idea, the octave noise spectrum is compared with the values of the relevant curve  $NR_x$ , recommended for places where the assessment of noise hazard is made (e.g. in cabs, engine rooms, etc.). Index  $x$  of noise curve  $NR_x$  is assumed from the formula:

$$x \cong L_{Aeq(perm)} - 5; \text{ dB(A)} \quad (1)$$

However in real conditions, especially in cases of basic machines for open pit mining which are continuously operated in varying weather conditions, the noise level is a random variable. The main causes of noise in these machines are changeable in time force excitations generated particularly in driving units of bucket wheels, belt conveyors, slewing units and crawler movement units.

For these reasons, the noise in these machines should be treated in a probabilistic approach, wherein the  $p$ -Quantile  $Q_p$  of noise level (where  $p$  – confidence level) is a measure of acoustic microclimate.

According to this idea, if the Quantile  $Q_p$  is not greater than the permissible value of noise  $L_{Aeq(perm)}$  i.e. when:

$$Q_p \leq L_{Aeq(perm)} \quad (2)$$

then the acoustic microclimate in the cabin meets the requirements determined in relevant standards.

#### 4. Results

In accordance with the deterministic approach, the acoustic microclimate in the cabin should be analyzed on the basis of the octave noise spectrum and the relevant curves *NR60* (for cabins with telephone communication) and *NR70* (for cabins without telephone communication).

However the noise spectrum is by nature a temporary image (specific “screen-shot”) of acoustic climate and therefore is not representative for several hours working cycle of excavators. This was confirmed by results of the research. Exemplary results are shown in Fig. 2. In some points the noise spectrum in the cabin exceeded the permissible values in the bands  $f \geq 1$  kHz.

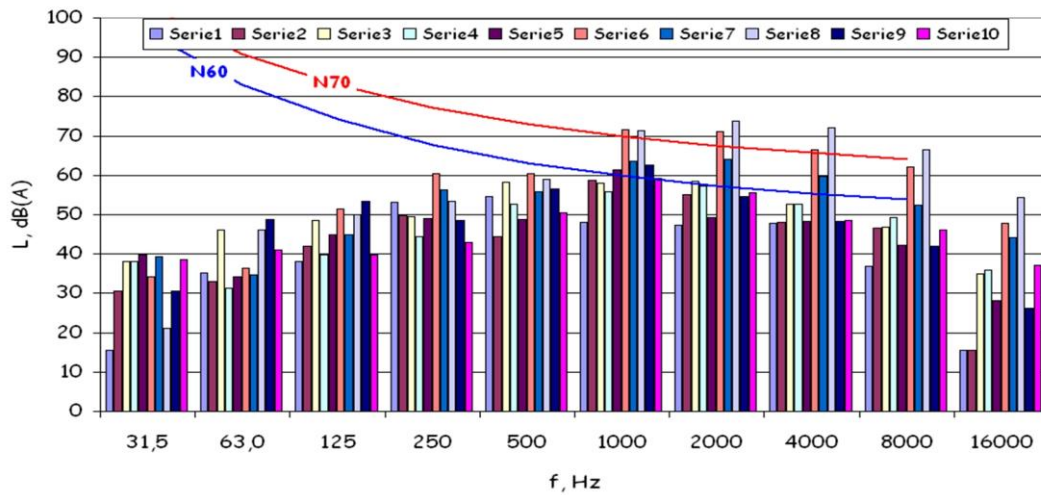


Fig. 2: Noise spectrum in the closed cabin.

In accordance with the probabilistic approach, the noise level in the cabin was analyzed in order to estimate its statistical distribution. The relevant histograms are shown in Fig. 3.

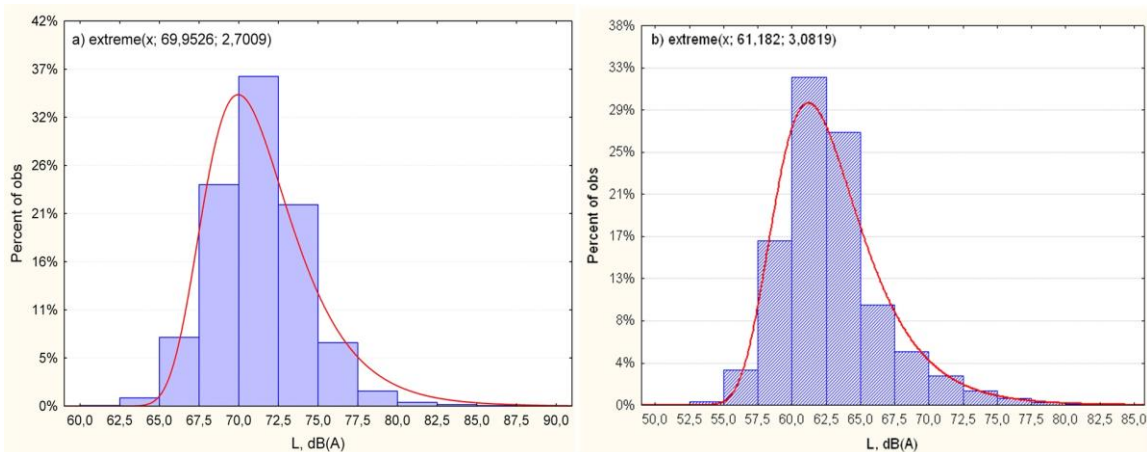


Fig. 3: Histograms of noise level: a) in the open cabin, b) in the closed cabin.

Then the Kolmogorov–Smirnov test was applied and the parameters of statistical distributions of noise level were estimated by using the method of maximum likelihood (with Statistica package).

The best accordance with experimental data was obtained for the Gumbel Extreme Value Distribution (Type I) which can be expressed as:

$$f_G(L_{Aeq}) = \frac{1}{b} \exp \left\{ -\frac{L_{Aeq} - a}{b} - \exp \left( -\frac{L_{Aeq} - a}{b} \right) \right\} \quad (3)$$

where:  $b$  – the scale parameter,  $a$  – the threshold (location) parameter.

On this basis the following values of Quantiles  $Q_{0.95}$  were estimated:

- in the open cabin  $Q_{0.95(open)} = 78.0$  dB(A).

- in the closed cabin  $Q_{0.95(closed)} = 70.3$  dB(A).

Therefore the results show that the closed cabin of the tested bucket wheel excavators meets the requirements for cabins and control rooms without telephone communication.

This is quite a significant achievement, when considering that the cabin is located near the bucket wheel, which is a source of noise level of the order of  $L_{Aeq} = 90 - 95$  dB(A).

## 5. Conclusions

Significant increase in noise hazards and deterioration of acoustic climate is an attribute of degradation processes of long time operated basic machines for open pit mining. This effect is especially important in the areas of continuous human presence, in particular in operators' cabins as long exposure to excessive noise can have a critical influence on human health. Virtually all of systems can be damaged, including respiratory, digestive, visual, cardiovascular and nervous ones (Cannistraro et al., 2016).

One way to solve these problems is to rebuild driving units of these machines in the context of reducing their acoustic activity. Such a procedure has been applied to two old bucket wheel excavators (built in 1980s) which were brought from Spain and subjected to a thorough reconstruction in Poland.

Total approval investigations have shown that the renewed excavators meet the stringent requirements for acoustic microclimate. Some relevant results of research of microclimate in the operator's cabin are presented in this paper.

However because the noise level in the basic machines for open pit mining is a random variable, the assessment of noise hazards should be done in a probabilistic approach. As a measure of the microclimate the  $p$ -Quantile of noise level (where  $p$  – assumed confidence level) determined on the basis of relevant model of statistical distribution can be assumed. This model should be estimated on the basis of consecutive long time research of basic machines for open pit mining.

## References

- Cannistraro, G., Cannistraro, A., Cannistraro, M. and Engineer, F. (2016) Evaluation of the sound emissions and climate acoustic in proximity of one railway station. *International Journal of Heat and Technology*, Vol. 34/2, pp. 589-596.
- Dudek, D. and Nowakowski, T. (1995) Problems of degradation and maintenance of surface mine engineering machines. In: *Proc. of Int. Symposium on Materials Ageing and Component Life Extension*, Milan, Italy, Vol. 2. Eds. V. Bicego, A. Nitta, R. Viswanathan Warley: Engineering Materials Advisory Services, pp. 1285-1294.
- Dudek, K. and Sokolski, M. (2000) Improved vibroacoustic characteristics - A goal to be pursued in the open pit mining machinery of the XXI century, in *Proc. of Mining Symp. Mining in the new millennium. Challenges and opportunities*, Las Vegas, Nevada, USA, (ed. Golosinski). Rotterdam; Brookfield, A. A. Balkema, pp. 193-199.
- Mlynczak, M. (2014) Bucket wheel excavators : past to present experiences in safety operation, in: *Probabilistic Safety Assessment and Management, PSAM 12*, Honolulu, Hawaii, USA, International Association for Probabilistic Safety Assessment and Management (IAPSAM), pp. 1-8.
- Nowakowski, T. (1999) Comparative analysis of degradation degree of bucket wheel excavators. *Proceedings of ESREL '99 - The Tenth European Conference on Safety and Reliability*, Munich-Garching, Germany, Vol. 1, Eds. G. I. Schueller, P. Kafka Rotterdam: A. A. Balkema, 1999, pp. 223-227.
- Pinzari, M., Alfaro Degan, G. and Lippiello, D. (2015) Environmental noise impact from opencast quarries: A comparison between stochastic and deterministic approaches. In *15th International Multidisciplinary Scientific Geoconference and EXPO, SGEM 2015*, Vol. 3, No. 1, pp. 263-270.
- Smolnicki, T., Harnatkiewicz, P. and Stanco, M. (2010) Degradation of a geared bearing of a stacker. *Archives of Civil and Mechanical Engineering*, vol. 10, No. 2, pp. 131-139.
- Sokolski, M. (2007) High vibroacoustic hazards level – attribute of the degradation of the open pit mining machinery. *Surface Mining*, R. 49, nr 3/4, pp. 148-152 (in Polish).



## ON WEAR PROCESSES IN PIN JOINTS IN CATERPILLARS OF LARGE-SIZE WORKING MACHINES

P. Sokolski\*

**Abstract:** *The paper is focused on wear processes which occur in undercarriage units during operation of large-size working machines. Special attention is paid to pin joint pairs which have the biggest influence on durability of driving units and for this reason the mobility of the entire large-size working machine as well. Two main negative processes which can take place in elements of those joints while such a machine is moving are distinguished: a gradual degradation and sudden damages. Those phenomena are discussed and illustrated.*

**Keywords:** Mining machinery, Wear, Friction, Failures, Pin joints.

### 1. Introduction

In most of large-size working machines which are operated in open-pit mines, caterpillar driving units are used. Those units are extremely endangered to failures as a result of adverse working conditions. For this reason it is essential to understand all phenomena and processes which run within large-size undercarriages. This knowledge plays a key role in safe and reliable operation of the machinery where those subassemblies are applied. Among factors which influence such an operation one can list most of all loading acting on parts of undercarriages and wear processes which take place there.

### 2. Problem identification

A verified method of identification of both loads within those undercarriages and areas which are endangered to occurrence of the highest stresses is presented in (Maslak et al., 2013). Also in that article attention is paid to a significant problem that even during normal and stable movement of a large-size machine, forces acting inside caterpillar units are of a stochastic character. Variations of values of those loads are considerable.

To ensure reliable work of friction joints one should most of all properly match mating materials and correctly shape geometrical features of joint members. Because of that, knowledge about tribological parameters is a key requirement for both the designer and the operator of a machine in which a given tribological node is applied (Capanidis, 2007). Both friction and wear are very complex processes and for this reason a comprehensive approach must be applied to study them properly. Such a research is even more difficult when corrosion is included as well (Dobrowolska et al., 2015). A comprehensive study on wear processes in mining conditions is presented among others in (Petrica et al., 2013; Petrica et al., 2014). Abrasive wear is the most common type of wear which is observed during operation of large-size caterpillars. One of the most important conclusions from those works is that rocks' influence strictly depends on character of work of a machine. What is more, mechanical properties of rocks, e.g. uniaxial compressive strength primarily influence wear rate: the highest wear rate of undercarriages parts is when those elements are in contact with rocks with the highest values of uniaxial compressive strength. On the other hand, influence of rocks with low uniaxial compressive strength results in abrasive embedment most of all. Another important factors on which wear rate depends are hardness and grain size of a material subjected to wear (Petrica, 2014).

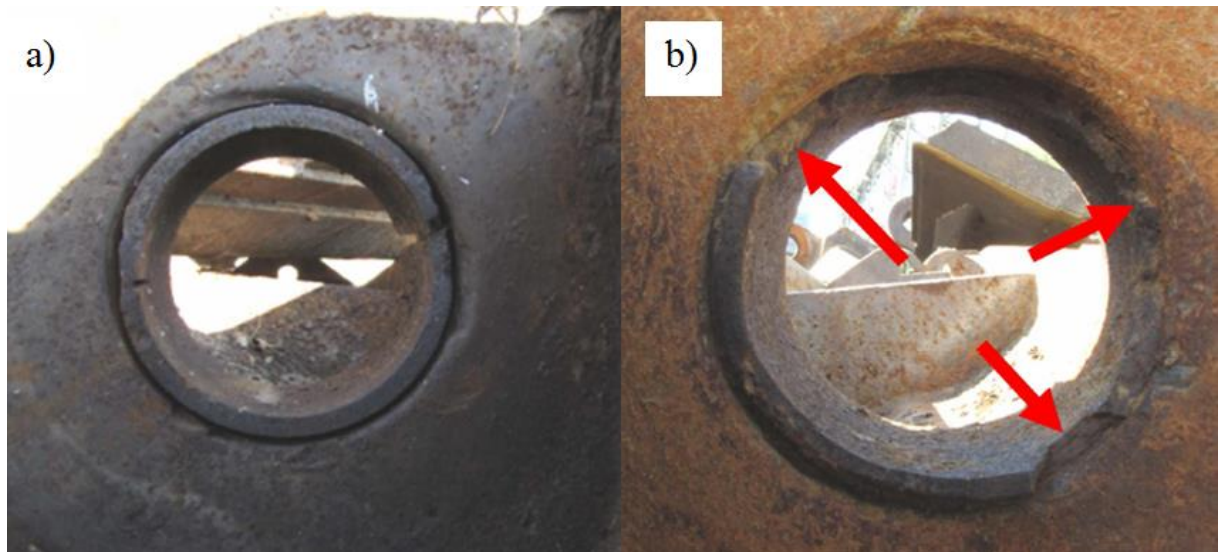
---

\* Piotr Sokolski, PhD.: Faculty of Mechanical Engineering, Wroclaw University of Science and Technology, Lukasiewicza Street 4; 50-371 Wroclaw; PL, piotr.sokolski@pwr.edu.pl



The most significant failures of undercarriages are those which influence movement and for this reason operation of the entire machine. Among such failures those located in caterpillar chain are the most critical (Wocka, 2011). Durability of the chain depends most of all on technical condition of elements of pin joints kinematic pairs. A typical pin joint node consists of a links' lug, a pin and a bushing which separates them.

Degradation of pins, regardless of the nature of its course, is relatively easy to remove by exchanging pins with new or remanufactured ones (Onichimiuk, 2004). In case of a bushing defect, if the damage is not too large an effective solution may be a replacement of the bushing with a new one. Much more difficult is to remove the effects of degradation of pin joint holes. It is unacceptable to operate a basic machine if at least 1 member of its caterpillar chain is damaged (for example there is a degradation of a pin joint, cracks in welds, large deformation or rupture of lugs or rupture of a plate). Pictures of pin joint nodes without pins are shown in Fig. 1.



*Fig. 1: Examples of a pin joint pair in large size caterpillar undercarriage: a) new bushing, b) bushing with its edges chipped off, highlighted with arrows (author's archive).*

Nowadays in most cases in holes of pin joints of large-size undercarriages, one applies interchangeable bushings made of manganese steel. Based on years of operational experience it is assumed that limiting level of diametric wear in holes/bushings in undercarriages of basic open-pit mining machines should not exceed the value of 1.5 mm (measured in the diameter). If the degradation is greater, it is necessary to replace a worn element with a new chain link what is difficult, time consuming and most of all requires the machine to be out of service for some period of time.

The process of replacement of a part of a chain link includes the following steps (Onichimiuk, 2004): to set a damaged item in the position under the driving wheel, to unscrew the chain by shifting the idler wheel, to disassembly the link-plate pair by removing pins connecting the link with adjacent elements. After replacing a given element with a new one tension of the chain is set so that the value of overhang between the roller bearings is kept within a required range (typically a range of 80 to 120 mm).

Replacement of bushings or regeneration of holes in lugs of links is carried out in workshops on special stands which are partially or completely robotic. Nowadays virtually all working surfaces of links are regenerated by welding operations, and the regenerated links are connected with plates using semiautomatic technique (Onichimiuk, 2004; Wocka and Warcholak, 2011).

### **3. Processes of degradation of pin joints in large-size undercarriages**

Wear processes which occur in pin joints in large-size caterpillars can be divided depending on how long do they evolve. If it takes time to progress a failure one can classify it as a gradual one while if it occurs instantly, i.e. with no earlier symptoms, it can be named as a sudden damage.

### 3.1. Gradual failures

The gradual degradation takes place in chain links in large-size undercarriages under the influence of tribological processes, most of all because of abrasive wear. Such a wear is caused by soil particles which get into rotating joints. Additionally electrochemical (oxidizing) influence results in corrosion which occurs in these kinematic pairs.

As a result of mud particles getting into the friction nodes at contact surfaces between the cooperating parts a peculiar kind of lubricant is obtained. Under conditions of considerable surface pressure (several dozens of MPa or more), this substance is squeezed between the surfaces of a bushing and a pin. Under the influence of these processes on the working surfaces of nodes micro-cracks can be formed. These defects gradually enlarge and the final result is chipping of portions of the surface layer in pin joint holes or bushings.

If wear of a node is small, further usage of the caterpillar chain is allowed conditionally and for a limited period of time. It can proceed without further increase of degradation of neither pin nor hole.

However due to wear exceeding the limit value, increased clearances are formed, causing a further deterioration in terms of cooperation between the pin and its hole and as a result additional dynamic loads occur and intensification of the processes of abrasive wear can be observed. Through increased clearances larger quantities of subsoil, sand and hard rock particles can penetrate inside the node and act as abrasives.

In order to prevent these negative phenomena in pin joint holes in large-size caterpillar undercarriages tight fitting bushings are mounted. These bushings are made of a material of lower hardness comparing to the material of the pins, so that the bushing wears quicker than pin and surfaces of holes in link's lugs. After crossing the limiting values of wear (described as a specified loss of volume) in a given bushing, it is removed and replaced with a new one. That significantly reduces wear process of pins and holes in the caterpillar links and contributes to lower operating costs of these assemblies (a set of bushings is in fact much cheaper and its replacement is faster than regeneration of the hole in the links' lugs or production of new links which also must be attached to plates).

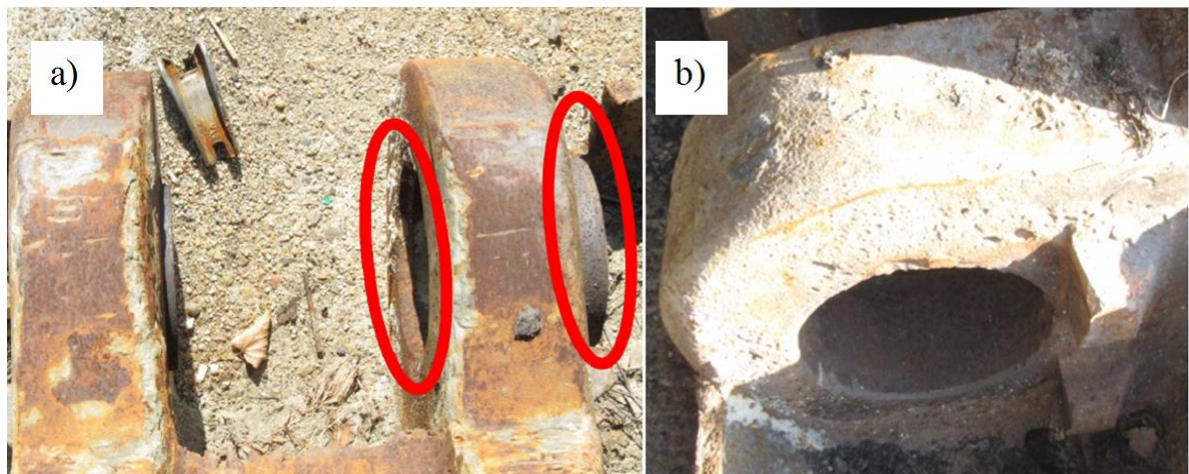
In the initial stage of wear processes of a bushing fragments of its subsurface are chipped off (Fig. 1b). In the next step, as a result of further degradation the holes are exposed. Continuation of operation of the links under these conditions results in direct wear of the links.

In extreme cases of degradation of the pin joint nodes, bushings can fall out of the hole under excessive lateral forces that arise during driving a curvilinear trajectory. Another factors favoring the tendency to fall out of the bushings from the holes in links can be manufacturing or mounting errors (e.g. improper fit of a bushing). Therefore mounting of a bushing should be performed with a particular care.

### 3.2. Sudden damage

Sudden damages of pin joints most commonly occur as a result of an excessive burden of additional loading (unexpected by the designer). It can occur for example when a machine is moving on a straight line on the ground with large bumps. In such a case additional forces occur causing movements of the plates in the vertical plane. These extra loads may result for example in movement of a bushing (Fig. 2a), its fall out of the hole (Fig. 2b), plastic deformations of pins and links' lugs or even rupture of links' lugs.

Formation of brittle cracks in lugs is often a result of a combination of several destructive factors. One of the factors of a structural nature is weakening of a cross-section in the area of a lug whereas among technological factors one can distinguish imperfections in material or inadequate thermochemical treatment (obtaining an incorrect structure of the links' material). Destructive operational factors are: gradual degradation like wear of a hole or corrosion and errors committed by the operator (e.g. to perform unauthorized maneuvers such as turning with too small turning radius, driving on highly uneven ground). Sudden damages of elements of caterpillar chain are essentially unrecoverable. Exceptions are damages of pin joint bushings which can be exchanged with new ones.



*Fig. 2: Examples of sudden damages: a) translated bushing, b) links' lug with its bushing fallen out of the hole (author's archive).*

#### 4. Conclusions

Issues of wear are of a special importance in such compound mechanisms as caterpillar chains. Basing on experience of previous researches pin joint nodes can be considered as key elements in terms of proper work of those assemblies. Study presented in this paper contributes to understanding those phenomena what is indispensable to use large-size undercarriages effectively. What is more, for safe and failure-free operation of large-size caterpillar undercarriages their reliability should be taken into account. A method of evaluation of this parameter is presented in (Sokolski, 2017).

#### References

- Capanidis, D. (2007) Selected aspects of the methodology of tribological investigations of polymer materials. Archives of civil and mechanical engineering, 7(4), pp. 39-55.
- Dobrowolska, A., Kowalewski, P. and Ptak, A. (2015) Influence of the lubricating fluid on the changes on rubbing metallic biomaterials surface. Colloids and Surfaces A-Physicochemical and Engineering Aspects, Vol. 480, pp. 419-425.
- Maslak, P., Smolnicki, T. and Pietrusiak, D. (2013) Strain gauges measurements and FEM analysis of elements of chassis of open cast mining machines. Technicki vjesnik—Technical Gazette, 20(4), pp. 655-658.
- Onichimiuk, M. (2004) Regeneration of caterpillar links in SRs-1200 excavators and A2RsB-8800 stackers. Surface Mining, 46(1), pp. 33-36 (in Polish).
- Petrica, M., Badisch, E. and Peinsitt, T. (2013) Abrasive wear mechanisms and their relation to rock properties. Wear, 308(1), pp. 86-94.
- Petrica, M., Painsi, M., Badisch, E. and Peinsitt, T. (2014) Wear mechanisms on martensitic steels generated by different rock types in two-body conditions. Tribology Letters, 53(3), pp. 607-616.
- Sokolski, P. (2017) Method of reliability assessment of pin joints in undercarriages of open-pit mining machinery - a case study, in: Risk, reliability and safety: innovating theory and practice: proceedings of the 26th European Safety and Reliability Conference, ESREL 2016, Glasgow, Scotland, CRC Press/Balkema, pp. 2472-2477.
- Wocka, N. and Warcholak, A. (2011) Innovative activities to increase exploitative durability and reliability of crawler mechanism for driving excavators and spreaders in Polish coal mines Mining and Geoengineering, 35(3/1), pp. 291-307, (in Polish).

## COMPUTER AIDED OPTIMIZATION OF A NOZZLE IN AROUND-THE-PUMP FIRE SUPPRESSION FOAM PROPORTIONING SYSTEM

M. Sosnowski\*

**Abstract:** *The paper presents the results of numerical analysis oriented at the optimum design of the Venturi nozzle applied in the around-the-pump proportioning systems of fire suppression foam. The dimensions of the system are limited by the available space in the fire engine on one hand and the effective operation on the other hand. The computational fluid dynamics research tool was used within the confines of carried out analysis. Numerous designs were investigated in term of mass flow rate of the foam compound. The obtained results allowed to improve the efficiency of the system by 9.5 % in comparison to the baseline design.*

**Keywords:** Computational fluid dynamic, Nozzle, Fire suppression, Foam proportioning.

### 1. Introduction

The around-the-pump proportioning systems of fire suppression foam provide a simple and effective means to introduce a foam concentrate at the desired percentage to the water being discharged in a fire pump system (Conroy et al., 2015; Zhao et al., 2016). They are widely applied due to numerous reasons. First of all, they are very robust and cost-effective because no additional foam compound pump is required. Moreover they are suitable for very large foam compound outputs and are easy to operate. Therefore they are commonly installed as an auxiliary device in modern fire engines. The principle of its operation is based on a well-known and widely applied Venturi nozzle (Gupta et al., 2016; Long et al., 2016; Mi et al., 2012), which is located in the drive water line which creates suction for the foam compound as depicted in Fig. 1. In this way, very high foam compound outputs can be generated. A fire truck may have a dual proportioning system with one tank having a Class B foam concentrate for flammable liquid fires and a second tank having Class A foam concentrate for structural fire attack or other ordinary combustible fire materials.

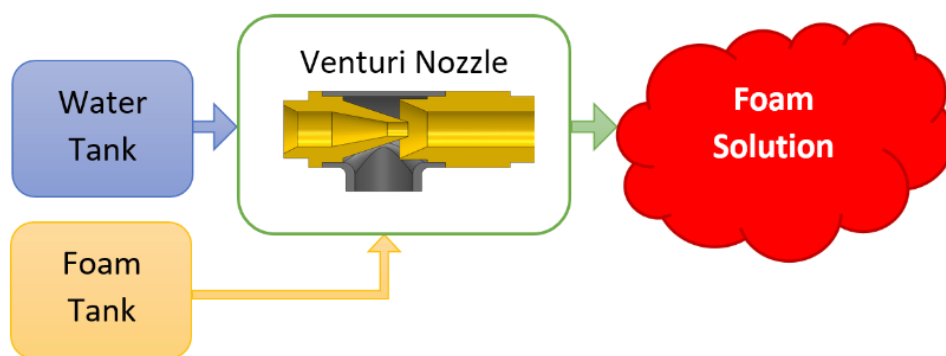


Fig. 1: Schematic diagram of around-the-pump fire suppression foam proportioning systems.

In practical applications the dimensions of the system are limited by the available space in the fire engine on one hand and the effective operation on the other hand. Therefore the optimum design of the Venturi nozzle is crucial in terms of proper operation of the system quantified by the ratio of mass flow rate of the foam compound to the mass flow rate of foam solution.

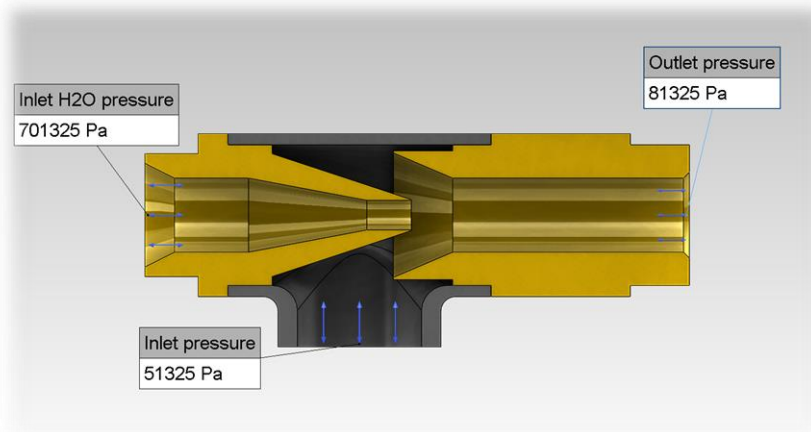
---

\* Marcin Sosnowski, PhD.: Institute of Technology and Safety Systems, Faculty of Mathematics and Natural Sciences, Jan Długosz University in Częstochowa, 13/15 Armii Krajowej Avenue; PL42-200, Częstochowa; PL, m.sosnowski@ajd.czest.pl



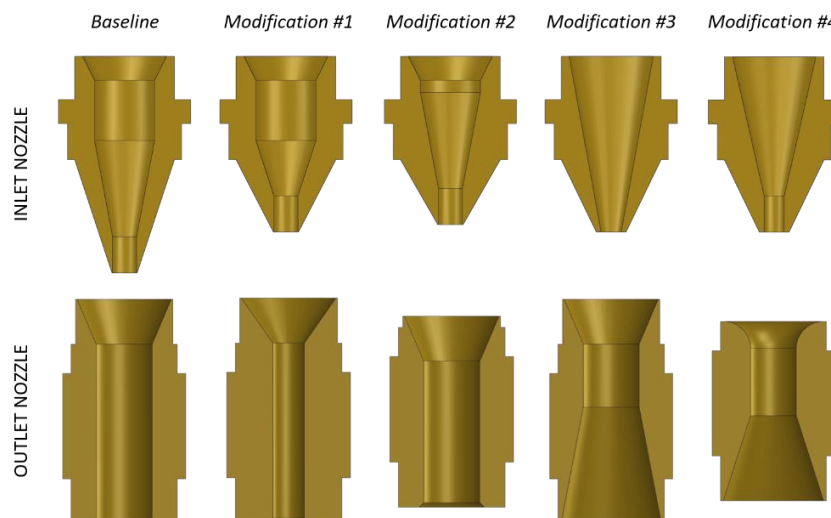
## 2. Methods

Computational Fluid Dynamics (CFD) has been selected as a research tool in order to specify the design of the nozzle because it is commonly and successfully applied in numerous branches of industry such as aerospace, automotive (Jamrozik et al., 2013), civil engineering (Gnatowska, 2015; Gnatowska, Sosnowski et al., 2017), power engineering (Krzywanski et al., 2014; Sosnowski et al., 2017), medicine and others. CFD has also been applied in the analysis of Venturi nozzles (Kuldeep et al., 2016; Manzano et al., 2016; Tukimin et al., 2016). This technique allows to perform very robust analysis of various configurations in a time-effective manner.



*Fig. 2: The boundary conditions of the analyzed computational domain.*

SolidWorks Flow Simulation was used as a CFD tool that solves the Navier-Stokes equations, which are formulations of mass, momentum and energy conservation laws. In addition it employs transport equations for the turbulent kinetic energy and its dissipation rate, using the k- $\epsilon$  model. The adaptive Cartesian mesh was applied in order to capture gradients in the flow field. Pressure boundary conditions were selected with turbulence intensity equal 2 % and turbulence length equal  $0.55e^{-3}$  m. The analysis assume the inlet pressure of water (Inlet H<sub>2</sub>O) at the level of 701 325 Pa (ambient pressure + 600 kPa), the inlet pressure of foam compound (Inlet) equal 51 325 Pa (ambient pressure – 50 kPa) and outlet pressure (Outlet) equal 81 325 Pa (ambient pressure – 20 kPa) – Fig. 2. Such values were measured by the manufacturer of the system used during research as a baseline design. The outside dimensions of the nozzle must not be changed in relevance to the baseline design in order to fit the optimized nozzle into the installation without modifying the existing systems already installed in the fire engines. Some simplifications have been introduced to the inner part of the baseline geometry in order to eliminate the low quality elements of computational mesh and in consequence improve the convergence of the numerical model.



*Fig. 3: Analyzed modifications of inlet and outlet nozzles.*

Four modifications of inlet nozzle and four modifications of outlet nozzle (Fig. 3) were analyzed in eleven different configurations shown in Tab. 1. The results were compared to the baseline model.

Tab. 1: Analyzed configurations.

CONFIGURATION NUMBER	INLET NOZZLE	OUTLET NOZZLE
Baseline Configuration	Baseline	Baseline
Configuration #1	Modification #1	Baseline
Configuration #2	Modification #2	Baseline
Configuration #3	Modification #3	Baseline
Configuration #4	Modification #4	Baseline
Configuration #5	Baseline	Modification #1
Configuration #6	Baseline	Modification #2
Configuration #7	Baseline	Modification #3
Configuration #8	Baseline	Modification #4
Configuration #9	Modification #1	Modification #2
Configuration #10	Modification #1	Modification #4
Configuration #11	Modification #2	Modification #4

### 3. Results

Mass Flow Rate (MFR) was selected as a key indicator of the nozzle effectiveness in firefighting applications therefore maximizing the MFR was the main goal of the design modifications. The MFR provides information on the ratio of foam compound to the inlet water and simultaneously indicates the pressure drop in the whole system (lower overall MFR). As can be seen in Fig. 4, six investigated configurations are characterized by higher overall mass flow rate in comparison to the baseline configuration. It is worth mentioning that the water content in all but one (#3) configurations does not differ significantly. Therefore the main contribution to the increased MFR results from higher foam compound content in the foam solution at the outlet of the system.

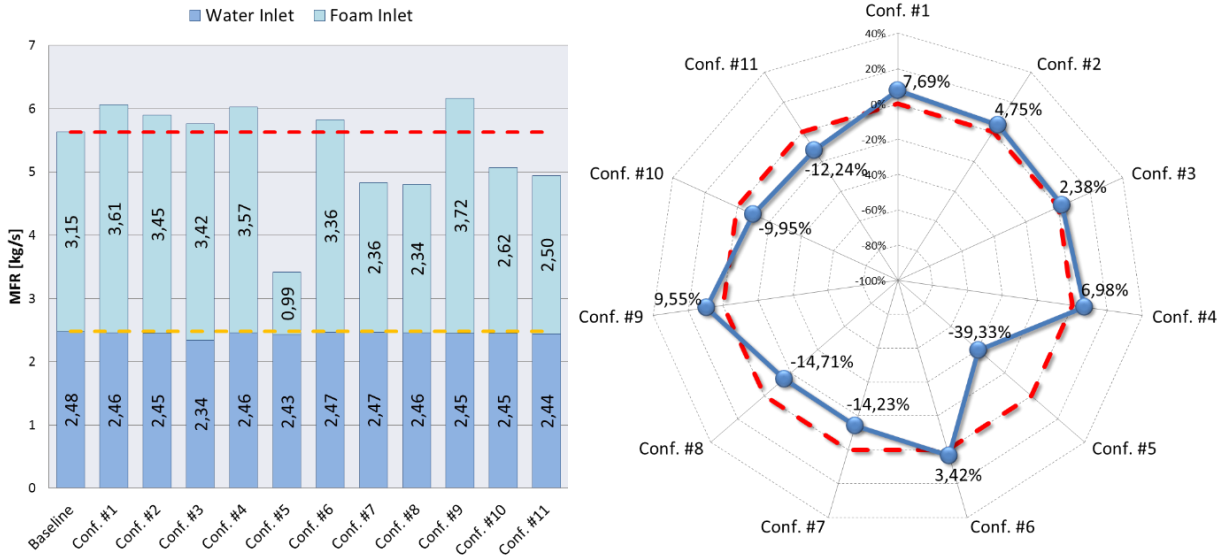


Fig. 4: The mass flow rate of the investigated configurations (left) and the relative difference of mass flow rate on the outlet in relation to the baseline configuration marked with the red line (right).

Configuration #9 was selected for further investigations as it is characterized by the highest MFR and highest foam compound content in the foam solution. Pressure and velocity distribution for both above mentioned configurations are depicted in Fig. 5.

### 4. Discussion

The original baseline as well as eleven modified configurations of the nozzle shape were analyzed using computational fluid dynamics in order to improve the efficiency of the around-the-pump proportioning



systems of fire suppression foam. The research allowed to improve the efficiency of the original design by 9.5 % due to changing the inner shape of the inlet and outlet nozzle of the proportioning system without modifying the outer dimensions of the assembly. The obtained results were confirmed by the field tests performed by the manufacturer of the system. Therefore the applicability of CFD as a research tool was confirmed and allowed to optimize the baseline design in a very robust and effective way.

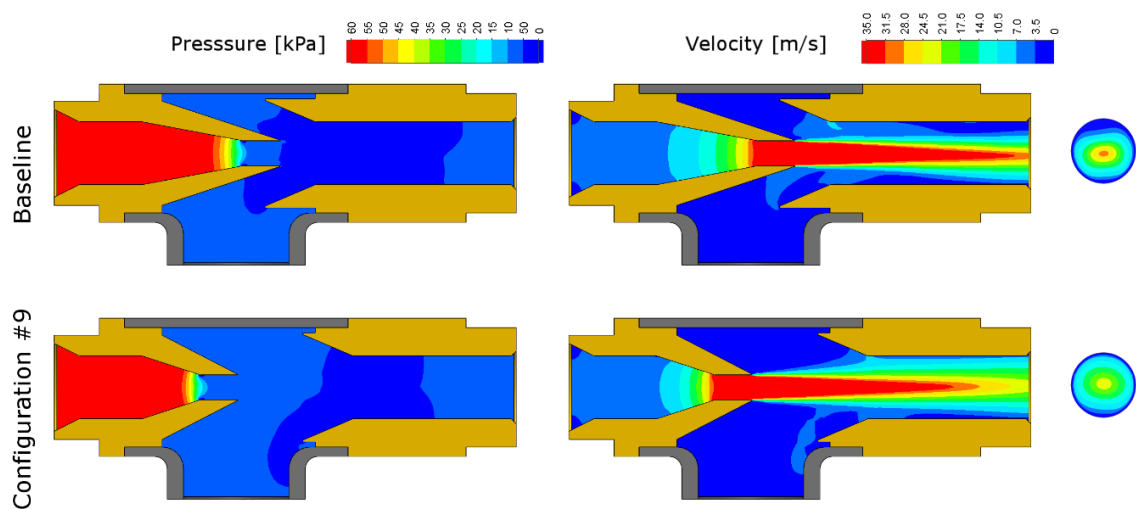


Fig. 5: Pressure and velocity distribution for the baseline and #9 configuration.

## 5. References

- Conroy, M.W. and Ananth, R. (2015) Fuel Surface Cooling by Aqueous Foam: A Pool Fire Suppression Mechanism. *Fire Technology*, 51(3), 667-689.
- Gnatowska, R. (2015) A Study of Downwash Effects on Flow and Dispersion Processes around Buildings in Tandem Arrangement. *Polish Journal of Environmental Studies*, 24(4), 1571-1577.
- Gnatowska, R., Sosnowski, M. and Uruba, V. (2017) CFD modelling and PIV experimental validation of flow fields in urban environments. *E3S Web of Conferences*, 14.
- Gupta, B., Nayak, A.K., Kandar, T.K. and Nair, S. (2016) Investigation of air-water two phase flow through a venturi. *Experimental Thermal and Fluid Science*, 70, 148-154.
- Jamrozik, A., Tutak, W., Kociszewski, A. and Sosnowski, M. (2013) Numerical simulation of two-stage combustion in SI engine with prechamber. *Applied Mathematical Modelling*, 37(5), 2961-2982.
- Krzywanski, J., Rajczyk, R. and Nowak, W. (2014) Model research of gas emissions from lignite and biomass co-combustion in a large scale CFB boiler. *Chemical and Process Engineering-Inzynieria Chemiczna i Procesowa*, 35(2), 217-231.
- Kuldeep, and Saharan, V.K. (2016) Computational study of different venturi and orifice type hydrodynamic cavitating devices. *Journal of Hydrodynamics*, 28(2), 293-305.
- Long, X.P., Zhang, J.Q., Wang, Q.Q., Xiao, L.Z., Xu, M.S., Lyu, Q. et al. (2016) Experimental investigation on the performance of jet pump cavitation reactor at different area ratios. *Experimental Thermal and Fluid Science*, 78, 309-321.
- Manzano, J., Palau, C.V., De Azevedo, B.M., Do Bomfim, G.V. and Vasconcelos, D.V. (2016) Geometry and head loss in venturi injectors through computational fluid dynamics. *Engenharia Agricola*, 36(3), 482-491.
- Mi, T. and Yu, X.M. (2012) Dust removal and desulphurization in a novel venturi scrubber. *Chemical Engineering and Processing*, 62, 159-167.
- Sosnowski, M., Krzywanski, J. and Gnatowska, R. (2017) Polyhedral meshing as an innovative approach to computational domain discretization of a cyclone in a fluidized bed CLC unit. *E3S Web of Conferences*, 14.
- Tukimin, A., Zuber, M., Ahmad, K.A. and Iop (2016) CFD analysis of flow through Venturi tube and its discharge coefficient *Aerotech Vi - Innovation in Aerospace Engineering and Technology*, Vol. 152.
- Zhao, H. and Liu, J.S. (2016) The feasibility study of extinguishing oil tank fire by using compressed air foam system. *2015 International Conference on Performance-Based Fire and Fire Protection Engineering (Icnpffe 2015)*, 135, 61-66.

## THE USE OF GYROSCOPIC EXECUTIVE SYSTEM FOR HOMING OF THE MISSILE ON THE AERIAL TARGET

K. Stefański<sup>\*</sup>, R. Chatys<sup>\*\*</sup>, A. Stefańska<sup>\*\*\*</sup>

**Abstract:** *The paper considers the possibility of use of the executive system for missile flight control in the form of fast rotating rotor, versatile suspended in the rocket body. The constrained deviations of the rotor axis (gyroscope) relative to the body axis generate the moments of force which change the missile flight direction and cause its homing on the moving target. Some of the numerical simulation results were presented in the graphic form.*

**Keywords:** Homing, Missile, Control, Rotor, Gyroscope, Target.

### 1. Introduction

One of the most important problems in the analysis of the anti-aircraft missile homing systems is the choice of the method for homing the missile to the meeting point with the target. It is equivalent to the choice of the missile flight path determined by so-called homing algorithm, namely the equation describing constraints folded on the rocket motion. In theory there is an infinite number of possibilities for formulating such algorithms. However, only the algorithms, which completed lots of additional and necessary conditions should be chosen (like for example minimal overload, minimal power demand, ease of homing algorithm realization, etc.). In general the homing algorithm formulating is very complex task, which in the most cases can only be solved with use of digital methods. It is caused by the complex rocket dynamics equations, control circuit dynamics, homing executive element and other. In the paper the attempt was made to analyze one of the possibilities for anti-aircraft missile flight control by means of the method similar to proposed in the patent Epperson (1984) and in the paper Osiecki (2001).

### 2. The description of the executive anti-aircraft missile control element

Inside the missile the bulky rotor (Fig. 1) suspended on the Cardan's joint is placed. Before the shot the rotor is put into rotating motion in relation to the missile body by means of externally charged electric motor. The control of missile flight happens by acting on the rotor suspension with four pneumatic actuators, activated from gas generators by autopilot. The pneumatic actuators are pairwise placed in two planes perpendicular to each other. The actuators deviate the rotor axis in relation to missile body, what causes that the rotor takes features of gyroscope. In the same time when the gyroscope axis direction changes, the moments of gyroscopic forces appear, which act on the missile body and proper change of its attack angles and sideslip angles, and thereby on change of missile flight direction. The missile realizes homing on the target, by use of the optical homing head (Gapiński et al., 2014) with autopilot (Koruba, 2015). The difference in relations to well-known solutions applied in anti-aircraft rockets is the executive system, which does not realizes homing by means of aerodynamic forces, but of inertia force. Before the shot of the missile the rotor is brought up to specific speed with electric motor, and then the motor is disconnected, but the rotor is still rotating with free motion (it is enough for several seconds missile flight).

---

<sup>\*</sup> Assistant Prof. Konrad Stefański, Ph.D. Eng.: Faculty of Mechatronics and Mechanical Engineering, Kielce University of Technology, al. 1000-lecia P.P. 7; 25-345, Kielce; PL, kstefanski@tu.kielce.pl

<sup>\*\*</sup> Assistant Prof. Rafał Chatys, Post-doctoral degree Eng.: Faculty of Mechatronics and Mechanical Engineering, Kielce University of Technology, al. 1000-lecia P.P. 7; 25-345, Kielce; PL, chatys@tu.kielce.pl

<sup>\*\*\*</sup> Anna Stefańska, MSc Eng.: non affiliation, stefanska.anna@poczta.fm

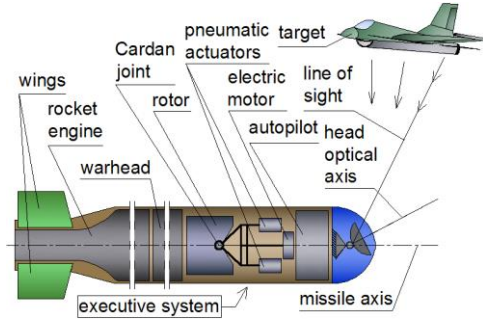


Fig. 1: General diagram of elements of the proposed guided missile.

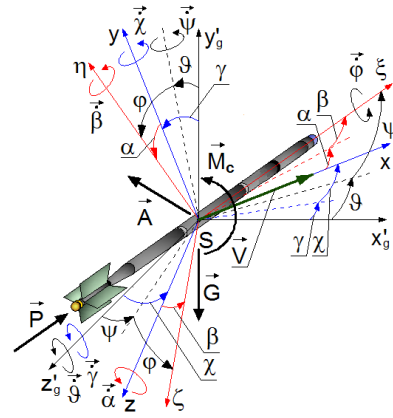


Fig. 2: Coordinate system with angles of rotation.

### 3. The missile flight equations

Fig. 2 summarizes the coordinate systems in which the missile flight equations were introduced and the forces that act on the moving missile. The following symbols are used (Koruba, 2015):  $\alpha, \beta$  – attack angle and sideslip angle [rad];  $\psi, \theta, \varphi$  – pitch angle, yaw angle and roll angle of the missile [rad];  $\gamma, \chi$  – flight-path angle in vertical plane and horizontal plane – pitch angle and yaw angle of missile velocity vector [rad],  $S\xi\eta\zeta$  – coordinate system for the missile;  $Sxyz$  – velocity coordinate system;  $Sx'_gy'_gz'_g$  – coordinate system with the missile as an origin, parallel with the starting system  $\vec{V}$  – missile velocity vector;  $\vec{P}$  – thrust;  $\vec{A}$  – resultant of aerodynamic forces;  $\vec{G}$  – gravitational force;  $\vec{M}_c$  – control moment;  $\varepsilon, \sigma$  – pitch and yaw angles of the line-of-sight (LOS) [rad].

For the purposes of these calculations, the missile is assumed to be a rigid body which does not rotate around its longitudinal axis. With these assumptions applied, the missile dynamic equations are as follows (Krzysztofik, 2014 and Grzyb, 2012):

$$\begin{aligned} \dot{V} &= \frac{P}{m} \cos \alpha \cos \beta - g \sin \gamma \cos \chi - \lambda_x V^2, & V\dot{\gamma} \cos \chi &= \frac{P}{m} \sin \alpha \cos \beta - g \cos \gamma + \lambda_y V^2 \alpha \\ & & -V\dot{\chi} &= -\frac{P}{m} \sin \beta - g \sin \gamma \sin \chi + \lambda_z V^2 \beta \\ \dot{\omega}_\zeta + \left( \frac{J_{ok}}{J_k} - 1 \right) \omega_\eta \omega_\xi &= -D_1 \frac{V^2}{L} \alpha - D_2 V \dot{\alpha} - D_3 V \dot{\theta} + \frac{M_{c\zeta}}{J_k} \\ \dot{\omega}_\eta - \left( \frac{J_{ok}}{J_k} - 1 \right) \omega_\xi \omega_\zeta &= -D_1 \frac{V^2}{L} \beta - D_2 V \dot{\beta} - D_3 V \dot{\psi} + \frac{M_{c\eta}}{J_k} \\ \omega_\xi &= -\dot{\theta} \sin \psi, & \omega_\eta &= \dot{\psi}, & \omega_\zeta &= \dot{\theta} \cos \psi, & \lambda_y &= \lambda_z \end{aligned} \quad (1)$$

where:  $L$  – length of the missile body [m];  $m$  – mass of the missile [kg];  $J_{ok}, J_k$  – moments of inertia of the missile in relation to its transverse axis and longitudinal axis [kg.m<sup>2</sup>];  $M_{c\eta}, M_{c\zeta}$  – missile flight control moments [N.m];  $g$  – acceleration of gravity [m/s<sup>2</sup>];  $\lambda_x, \lambda_y, D_{1,2,3}$  – relative aerodynamic coefficients of aerodynamic forces and moments [1/m].

Kinematic relationships between the missile and target have the form (Koruba et al., 2010):

$$\begin{aligned} \dot{r} &= V_t [\cos \chi_t \cos \sigma \cos(\varepsilon - \gamma_t) + \sin \chi_t \sin \sigma] - V [\cos \chi \cos \sigma \cos(\varepsilon - \gamma) + \sin \chi \sin \sigma] \\ r\dot{\varepsilon} \cos \sigma &= -V_t \cos \chi_t \sin(\varepsilon - \gamma_t) + V \cos \chi \sin(\varepsilon - \gamma) \\ -r\dot{\sigma} &= V_t [\cos \chi_t \sin \sigma \cos(\varepsilon - \gamma_t) - \sin \chi_t \cos \sigma] - V [\cos \chi \sin \sigma \cos(\varepsilon - \gamma) - \sin \chi \cos \sigma] \end{aligned} \quad (2)$$

where:  $V_t$  – target velocity [m/s];  $\gamma_t, \chi_t$  – angles of the target flight-path [rad];  $r$  – distance between the missile and the target [m].

The equations of the rotor axis according to the technical gyroscope theory (Gapiński, 2014) are as follows:

$$J_B(\ddot{\vartheta}_g + \ddot{\vartheta}) + c_B\dot{\vartheta}_g - J_0 n(\dot{\psi}_g - \dot{\psi}) = M_{c\eta}, \quad J_B(\ddot{\psi}_g + \ddot{\psi}) + c_C\dot{\psi}_g + J_0 n(\dot{\vartheta}_g - \dot{\vartheta}) = M_{c\zeta} \quad (3)$$

where:  $\vartheta_g, \psi_g$  – pitch and yaw angles of rotor axis [rad];  $c_B, c_C$  – coefficient of viscous friction in the gimbal bearings [N.m.s];  $n$  – rotational speed of the rotor [1/s];  $J_0$  – moment of inertia of the rotor in relation to its rotation axis [kg.m<sup>2</sup>];  $J_B$  – moment of inertia of the rotor in relation of the lateral axis running through the centre mass [kg.m<sup>2</sup>].

The control moments were formulated according to the algorithm of proportional navigation (Yanushevsky, 2011 and Takosoglu, 2016b).

#### 4. Digital simulation results

Numerical simulations were conducted for a hypothetical missile attacking an aerial target from the front hemisphere. The following numerical values were used: starting missile position:  $x_{m0} = 0$  [m],  $y_{m0} = 0$  [m],  $z_{m0} = 0$  [m]; starting target position:  $x_{t0} = 4000$  [m],  $y_{t0} = 3000$  [m],  $z_{t0} = 0$  [m]; angle of a missile launch:  $\gamma_{m0} = 25.41$  [deg];  $\chi_{m0} = 0$  [rad]; starting angle of pitch and yaw of a target velocity vector:  $\gamma_{t0} = 180$  [deg],  $\chi_{t0} = 1.15$  [deg]; starting missile velocity:  $V_0 = 20$  [m/s]; target velocity:  $V_t = \text{const} = 300$  [m/s];  $L = 1.6$  [m];  $m = 10.8$  [kg];  $J_{ok} = 0.018$  [kg.m<sup>2</sup>],  $J_k = 2.4$  [kg.m<sup>2</sup>];  $\lambda_x = 0.000171$ ,  $\lambda_y = 0.0051$  [1/m];  $D_1 = 0.081$ ,  $D_2 = 0.0821$ ,  $D_3 = 0.00041$  [1/m];  $J_B = 0.0132$  [kg.m<sup>2</sup>];  $J_0 = 0.00754$  [kg.m<sup>2</sup>];  $c_B = c_C = 0.05$  [N.m.s];  $P = 3150$  [N] for  $t \leq 1$  [s] and  $P = 700$  [N] for  $t > 1$  [s];  $t$  – time. The flight path of the target was described as follows:  $\gamma_t(t) = \gamma_{t0} - 0.0001 \cdot t$ ;  $\chi_t(t) = -\chi_{t0} \cdot 0.6 \cdot t^2$ .

Graphical presentation of the results is shown in Figs. 3 - 8.

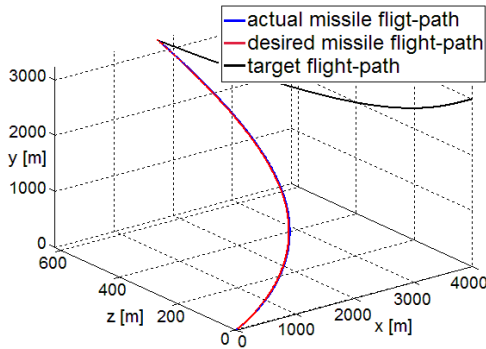


Fig. 3: The missile and target flight-paths.

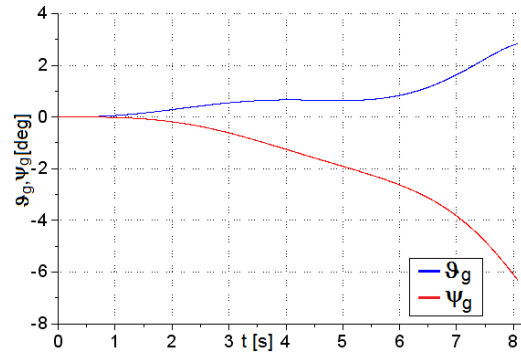


Fig. 4: Pitch and yaw angles of rotor axis.

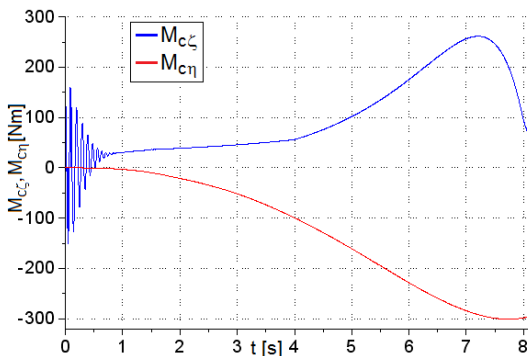


Fig. 5: Values of control moments required for homing the missile on the target.

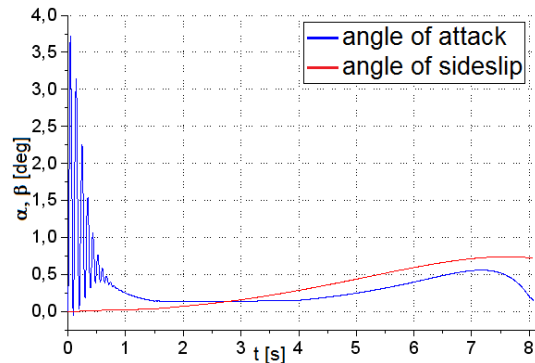


Fig. 6: The angles of attack and angles of sideslip.

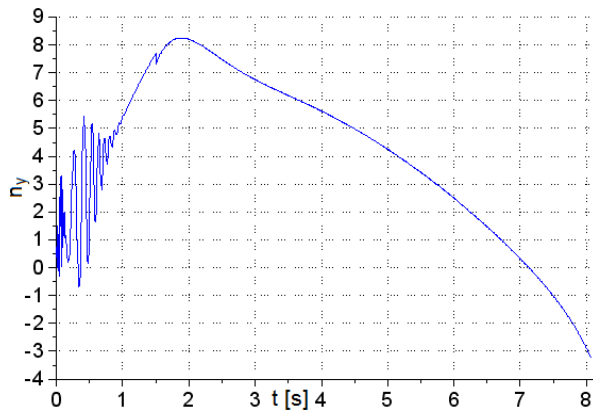


Fig. 7: Lateral overload acting on the missile during the flight.

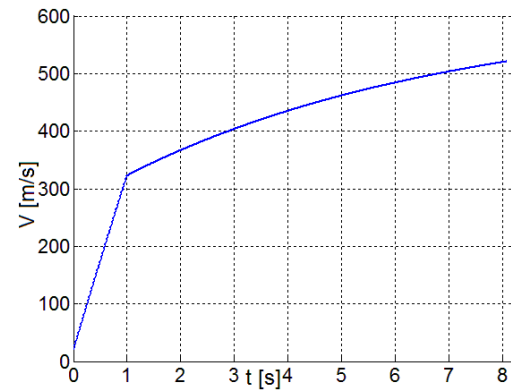


Fig. 8: Flight velocity of the missile.

Numerical simulation results presented above indicate that use of proposed executive system for homing of missile is practicable. Pitch and yaw angles of the rotor axis amount ca. a few degrees and are attainable. Similarly, the values of control moments are moderate.

## 5. Conclusions

The proposed executive system for control of missile flight is original, but its efficacy is needed to be tested thoroughly. This solution lacks the control forces. Homing is carried out only by the moment of forces. However it also has advantages. The rotor can be placed in any place of the missile body (the action of the couple of forces does not depend on the position). The disadvantage of this solution is the dimension of the rotor, which are limited in relation to its mass. This rotor should have relatively big mass to enable the generating bigger control moments by little pitch angles and yaw angles of its axis. Therefore I suggest the rotor to be made of high density material, e.g. tungsten or depleted uranium.

## References

- Epperson, E.H.Jr. (1984) Gyroscopically Steerable Bullet. Patent USA, No. 4,431,150 appropriate by General Dynamic, Pamona, California, 14.02.1984.
- Gapinski, D. and Krzysztofik, I. (2014) The process of tracking an air target by the designed scanning and tracking seeker, in: Proc. 2014 15th Int. Carpathian Control Conf. (eds. Petras, I., Podlubny, I., Kacur, J., and Farana, R.), IEEE, pp. 129-134.
- Gapiński, D., Krzysztofik, I. and Koruba, Z. (2014) Analysis of the dynamics and control of the modified optical target seeker used in anti-aircraft rocket missiles. *Journal of Theoretical and Applied Mechanics*, 52, 3, pp. 629-639.
- Grzyb, M. and Stefański, K. (2012) Numerical simulation of attack on the non-maneuvering target of guided bomb with implemented homing algorithms. *Computer Technologies in Science, Technology and Education – Computer Science in the Age of 21<sup>st</sup> Century* (eds. Jastriebow, A., Kuzminska-Solsnia, B., Raczynska, R.), Radom. pp. 97-107.
- Koruba, Z., Dziopa, Z. and Krzysztofik, I. (2010) An analysis of the gyroscope dynamics of an anti-aircraft missile launched from a mobile platform. *Bulletin of the Polish Academy of Sciences – Technical Sciences*, 58, 4, pp. 651-656.
- Koruba, Z. and Nocoń, Ł. (2015) Automatic control of an anti-tank guided missile based on polinomial functions. *Journal of Theoretical and Applied Mechanics*, 53, 1, pp. 139-150.
- Krzysztofik, I. and Koruba, Z. (2014) Mathematical model of movement of the observation and tracking head of an unmanned aerial vehicle performing ground target search and tracking. *Journal of Applied Mathematics*, Article ID 934250, 11 p.
- Osiecki, J.W. (2001) The anti-aircraft artillery bullets controlled with rotor suspended on the Cardan's joint. Proc. of 4<sup>th</sup> International Scientific and Technical Conference "Development and Modernization of Battle Means", Skarżysko-Kamienna/Ameliwka, pp. 119-129, (in Polish).
- Takosoglu, J.E., Laski, P.A., Blasiak, S., Bracha, G. and Pietrala, D. (2016b) Determining the static characteristics of pneumatic muscles, *Measurement and Control*, 49, 2, pp. 62-71. doi:10.1177/0020294016629176.
- Yanushevsky, R. (2011) *Guidance of Unmanned Aerial Vehicles*. Taylor & Francis Group, New York.

## MODELING OF PRESTRESSED BOLT CONNECTION IN LS-DYNA CRASH TEST ANALYSIS OF ROAD INFRASTRUCTURE

M. Stopel<sup>\*</sup>, A. Cichański<sup>\*\*</sup>, D. Skibicki<sup>\*\*\*</sup>

**Abstract:** Bolted connections are the most frequently used type of separable connections in the construction of machines and devices. In this study possibilities of modelling of this type of connections in the LS-Dyna environment with reference to designing a supporting construction of road infrastructure have been presented. Modelling a safety connector with the use of BEAM elements brings satisfactory results mainly when object of interest is a whole structure not a bolt only. In the case when mainly mechanisms of damage of a bolted connection are analysed it is justifiable to model a safety connector with the use of SOLID elements.

**Keywords:** LS-Dyna, Road infrastructure, Bolt connection, Preload.

### 1. Introduction

With reference to a new safety standard PN-EN 12767 newly designed structures located in the road verge must meet the passive safety requirements. In the supporting construction of road infrastructure, proposed by the authors (Cichański, 2015), a safety connector has been used, which is subject to damage as a result of a crash of a moving vehicle into the construction. The main element determining the effectiveness of a safety connector is a bolted connection. However, it should also transfer loads resulting from the conditions of exploitation. Because of this it is very important to precisely specify, during a construction process, geometric and material properties of a connection, which would have an impact on the operation of a safety connector. Analytical calculations often occur to be insufficient. In such cases numerical simulations are successfully applied based on the finite element method. Then there is a series of issues to be solved and one of the basic ones is a manner of modelling a connection (Hadjoannou, 2016).

In the study the issue of modelling pre-load in safety connectors has been raised. Selected methods of modelling have been discussed. For consideration issue presented in the work the subarea of the road mast was chosen. Numerical analyses for a chosen subarea of a road infrastructure mast have been conducted. As a results of analysis normal and shear forces appearing in a bolt connector and reduced stresses were presented.

### 2. Object and conditions of tests

The foot of the mast being analysed has been presented in Fig. 1a. From the presented structure a subarea has been cut out, which is, namely, a safety connector being designed. It has been subject to further analysis in this study Fig. 1b. The lower plate of the thickness of 25 mm has been fixed by taking away degrees of freedom in all the directions. Constant translation has been applied to the bottom plate of the thickness of 10mm. Two analyses have been made. One with the pre-load of the 100 MPa introduced to the bolt shank and the other without pre-load.

---

<sup>\*</sup> Ing. Michał Stopel.: University of Science and Technology, Mechanical Engineering Faculty, Kaliskiego 7; 85-796, Bydgoszcz; PL, [michal.stopel@utp.edu.pl](mailto:michal.stopel@utp.edu.pl)

<sup>\*\*</sup> Ing. Artur Cichański, PhD.: University of Science and Technology, Mechanical Engineering Faculty, Kaliskiego 7; 85-796, Bydgoszcz; PL, [artur.cichanski@utp.edu.pl](mailto:artur.cichanski@utp.edu.pl)

<sup>\*\*\*</sup> Prof. Dariusz Skibicki.: University of Science and Technology, Mechanical Engineering Faculty, Kaliskiego 7; 85-796, Bydgoszcz; PL, [dariusz.skibicki@utp.edu.pl](mailto:dariusz.skibicki@utp.edu.pl)



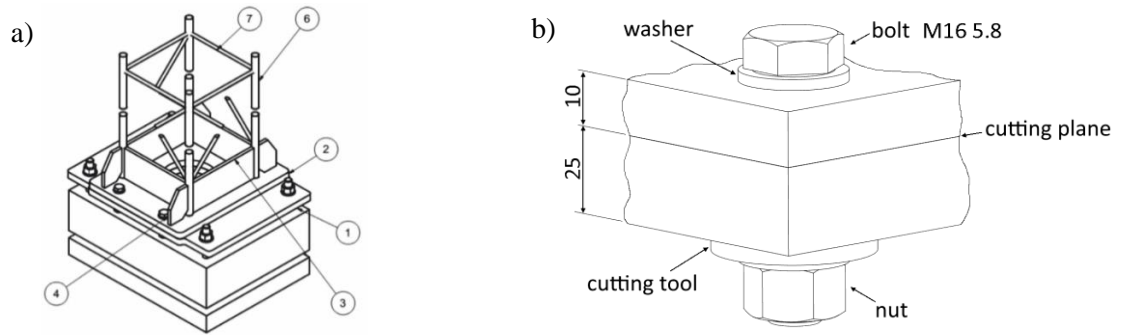


Fig. 1: a) Foot of the supporting construction equipped with a safety connector (1-foundation, 2-anchor bolt, 3-frame, 4-safety connector, 6, 7- rods of girder); b) safety connector.

### 3. Numerical modelling of a bolted connection

In order to verify the accepted assumptions and in order to analyse behaviour of the whole safety connector a numerical analysis has been conducted with the finite element method in the LS-Dyna environment. One of the basic issues during preparation of a numerical model has been the choice of a proper methodology of a bolted connection representation. Three manners of approach have been considered to model this type of connection in a wide range of possibilities available in the LS-Dyna environment. The main differences between them consisted in the application of SOLID and BEAM elements to model a coupler. The choice of a particular type of structural elements for a coupler has determined the application of other types of contact elements between a coupler and a hole.

#### Beam model

The most frequently used technique of a bolted connection representation is the application of a beam element Fig. 2 (Shailesh, 2010). The bolt shank in this case is a beam with the defined cross-section, however, a connection of the shank with the holes in the plates can be made in two ways: with the application of SPOTWELD type contacts or with the use of NODAL\_RIGID\_BODY type constraints. These elements are strain resistant and if they are applied there is no need to define additional contacts between particular parts of a connector.

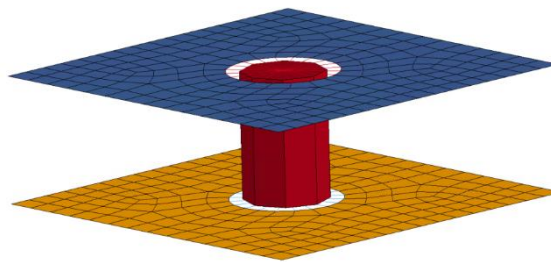


Fig. 2: BEAM type elements and NODAL\_RIGID\_BODY constraint.

In order to introduce pre-load into bolted connection, the \*INITIAL\_AXIAL\_FORCE\_BEAM card should be used by providing the value of force resulting from a bolt tension. Values of normal and cutting forces in the bolt shank can be read directly from a BEAM element, however, there is no possibility of analysing shear stress in the contact point of the bolt and the hole.

#### Beam model with the application of contact beams

Another method used to model bolted connections is the application beam elements (Fig. 3), both to model a shank and to model the contact of a bolt with plates. For this purpose on the edge of the holes additional beam elements of a very small diameter (which allows for the use of \*MAT\_NULL) are created, and then between them and a beam, constituting the bolt shank, a separate contact is defined (Sonnenschein, 2008). In this case the application of an AUTOMATIC\_GENERAL contact is recommended. Between the bolt head, a cap and plates an \*AUTOMATIC\_SINGLE\_SURFACE contact should be introduced.

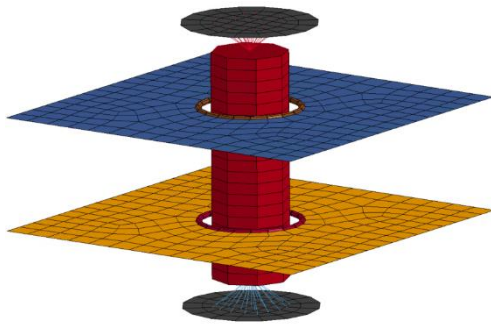


Fig. 3: BEAM type elements and CONTACT\_BEAM elements.

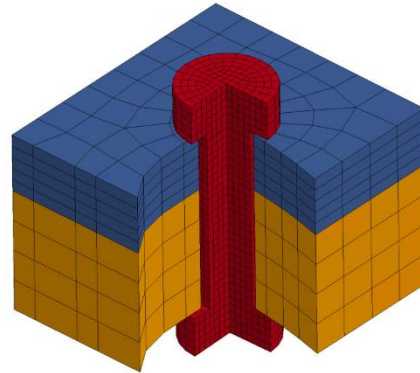


Fig. 4: SOLID type elements.

Similarly as in the previous approach, in order to introduce pre-load the \*INITIAL\_AXIAL\_FORCE\_BEAM card can be used. Apart from a possibility of reading the values of normal and cutting forces, this method allows for reading shear stresses. One needs to remember that if we use shell type elements they should have the second order shape function (Cichański, 2011).

#### Solid model

The fullest representation of a bolted connection is provided by modeling a connection with the application of solid elements (Fig. 4). A mutual interaction between bolt elements and plates is realized with the application of an AUTOMATIC\_SURFACE\_TO\_SURFACE contact. In the case of applying this method pre-load of a bolt is possible through the introduction of stress in the initial phase of analysis. Then a STRESS\_SECTION surface perpendicular to the bolt axis should be introduced. The introduced surface will also allow to read from the model of normal and cutting values and shear stresses for the elements. A connection between a bolt and a cap can be made in this case in two ways: through a connection of the shared nodes of the mesh or also through a TIED type contact. Thanks to the application of solid elements one can use advanced material models, and in this group also models providing for speed of strains and its impact on the character of strengthening and damage (Stopel, 2016).

#### 4. Results

Form the point of view of the operation of a safety connector, crucial information, for the analysis of which the simulations conducted have allowed, is the value of forces operating inside the bolt shank and strains and stresses resulting from them. In Fig. 5 normal and cutting forces for particular cases have been presented.

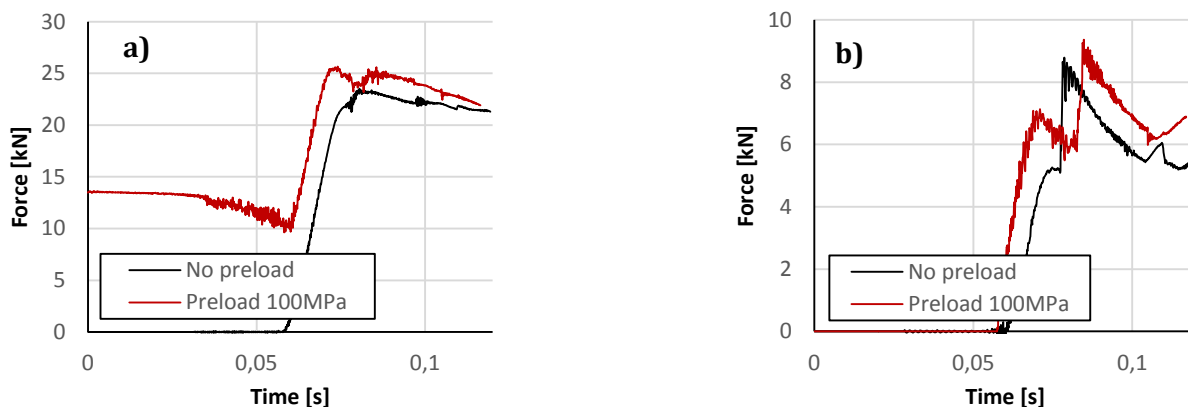
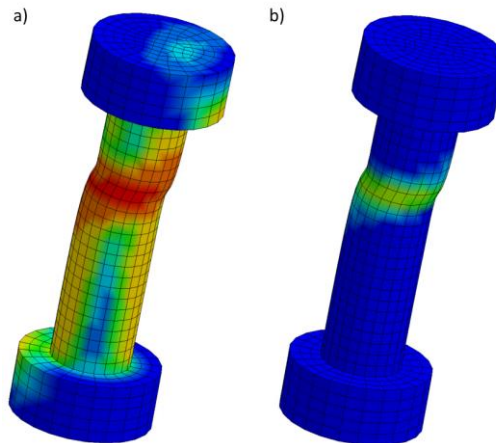


Fig. 5: Forces acting in a bolt connector a) normal forces; b) cutting forces.

Introduction of pre-load causes big differences of loading a shank in the initial phase of plate shift. At the moment of destruction differences between forces are small.

Modelling a safety connector with the use of SOLID elements has allowed for analysis of stress and strains in the bolt shanks. In Fig. 6 below a map of stresses and plastic strains in the shank for the analysed case of the node load along with the pre-load have been presented.



*Fig. 6: Map of distribution of a) reduced stresses; b) plastic strains.*

## 5. Conclusions

Designing a supporting construction that meets the requirements of the standard in the scope of passive safety the bolt used in the safety connector should be regarded as the most essential element of the construction. Because of the dynamics and complexity of the phenomena a proper tool to make calculations of such structures is the LS-Dyna software environment as there is a possibility of making explicit analyses.

Modelling a safety connector with the use of BEAM elements in the specified cases brings satisfactory results, mainly if a researcher is less interested in behaviour of a bolt only. In the case where mainly mechanisms of damage of a bolted connection are analysed, and the analysis of a safety connector is just such a case, in the authors' opinion it is justifiable to model a safety connector with the use of SOLID elements.

One needs to assume the application of the method based on solid elements where a bolted connection plays a vital role from the point of the operation of safety mechanisms. First of all from the point of view of assessment of the condition and behaviour of a bolted connection, a possibility to analyse the distribution of stresses and strains is extremely significant.

## References

- Cichański, A. (2011) Influence of finite element order on SCF precision for U-shaped notches in flat bars under tension", Proceedings of XVII 17th International Conference Engineering Mechanics 2011, Svratka, Czech Republic, pp. 79-82.
- Cichański, A. and Stopel, M. (2015) Experimental validation of the numerical model of a testing platform impact on a road mast, Solid State Phenomena, 224, pp. 222-225.
- Hadjioannou, M., Stevens, D. and Barsotti, M. (2016) Development and validation of bolted connection modeling in LS-DYNA for large vehicle models, 14<sup>th</sup> Int. LS-Dyna User Conf. pp. 1-12.
- Shailesh, N. Lokhande, N., Gangani, B. und Gadekar, G. (2010) Boltet joint representation in LS-DYNA to model bolt pre-stress and bolt failure characteristics in crash simulation, 11<sup>th</sup> Int. LS-Dyna User Conf, pp. 11-19.
- Sonnenscheing, U. (2008) Modelling of bolts under dynamic loads, LS-DYNA Anwenderforum, Bamberg, pp. 13-24.
- Stopel, M. and Skibicki, D. (2016) Determination of Johnson-Cook model constants by measurement of strain rate by optical method, AIP Conference Proceedings, 1780, pp. 060003-1-06003-9.

## COMPUTATIONALLY EFFICIENT MODEL OF THE HUMAN VOCAL FOLD

J. Štorkán<sup>\*</sup>, T. Vampola<sup>\*\*</sup>, J. Horáček<sup>\*\*\*</sup>

**Abstract:** *One mass model of the vocal folds with three degrees of freedom in 2D space was created and used to simulate the movement of the vocal folds. Vocal folds are modeled as a solid mass stored flexibly in 2D. The model is excited by aerodynamic forces. The flow is solved by analytical model incompressible and non-viscous fluid with constant flow. In case of close of the glottis are aerodynamic forces replaced by Hertz model of the contact forces. Movement equations are solved by numerical method. The model allows to solve the movement of the vocal folds in the time domain, pressure field acting on the vocal folds or contact pressures.*

**Keywords:** Simulation of vocal folds, Ideal fluid flow, Nonlinear vibration, Self-exciting vibration, Bio-acoustic, Hertz contact, Aerodynamics forces.

### 1. Introduction

Vocal folds (VF) are a fundamental part of the human vocal tract. They create a source voice that is modulated in the vocal tract. This creates a human voice. That's one theory of phonation (Fant, 1970). VF are also one of the main source of voice failures. They are mechanically strong and cyclically loaded. VF are sensitive to wear and pathological changes. That is one reason why they are intensively investigated. Research of VF may in the future allow the production and implementation of synthetic VF to human larynx. This will improve the lives of people with voice disorders.

VF research began in middle of the last century the first successful mathematical models are dual mass models. Dual mass models are simple they have 2 DOF and are used today. Team of authors (Horáček et al., 2002) created the single body model with 2 DOF (transverse displacement and rotation) his advantage is a fully parametric geometry of VF profile. Allows to study the influence of geometry on mechanical properties. This mechanical model is linear and does not allow to study the self-excited oscillations. In 2005 was model generalized to enable simulation of nonlinear self-excited oscillation. This work is based on the work (Horáček et al., 2005) in order to generalize the mechanical model by adding a longitudinal movement (3 DOF).

### 2. Model of VF

Single body model is composed of a body in 2D space (Fig. 1). The shape of the body is defined by independent function  $a(x)$  that defines the profile. The body is flexibly attached to the frame by springs and dampers. The springs and dampers are placed in the center of mass of the profile. This makes the stiffness and damping matrix diagonal. Mass characteristic are determined by direct integration profile. The values of stiffness and damping may be prescribed directly or prescribe natural frequency and the width of the resonance peaks and that define the stiffness and damping.

$$M\ddot{V} + B\dot{V} + KV = F, \quad (1)$$

---

<sup>\*</sup> Ing. Jaroslav Štorkán, Department of Mechanics, Biomechanics and Mechatronics, Faculty of Mechanical Engineering, Czech Technical University in Prague. Technická 4, Praha 6, Czech Republic, jaroslav.storkan@fs.cvut.cz

<sup>\*\*</sup> Prof. Dr. Ing. Tomáš Vampola, Department of Mechanics, Biomechanics and Mechatronics, Faculty of Mechanical Engineering, Czech Technical University in Prague. Technická 4, Praha 6, Czech Republic, tomas.vampola@fs.cvut.cz

<sup>\*\*\*</sup> Ing. Jaromír Horáček, Drc, Institute of Thermodynamics, Academy of Sciences of the Czech Republic. Dolejšova 1402/5 Praha 8 Czech Republic, jaromirh@it.cas.cz

where

$$\mathbf{M} = \begin{bmatrix} m & 0 & 0 \\ 0 & m & 0 \\ 0 & 0 & I \end{bmatrix}, \mathbf{B} = \begin{bmatrix} b_x & 0 & 0 \\ 0 & b_y & 0 \\ 0 & 0 & b_t \end{bmatrix}, \mathbf{K} = \begin{bmatrix} k_x & 0 & 0 \\ 0 & k_y & 0 \\ 0 & 0 & k_t \end{bmatrix}, \mathbf{V} = \begin{bmatrix} x_T \\ y_T \\ \varphi \end{bmatrix}, \mathbf{F} = \begin{bmatrix} F_x \\ F_y \\ M \end{bmatrix}.$$

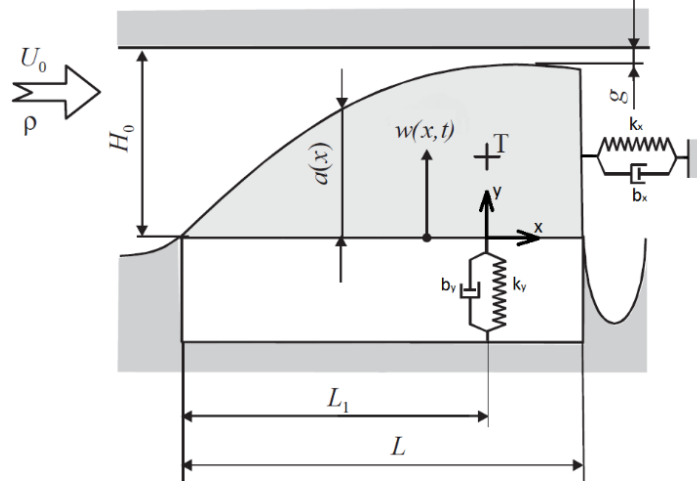


Fig. 1: Solved mechanical model of VF with 3 DOF.

## 2.1. Excitation of model

The main source of excitation VF are aerodynamics forces of the air flow. Aerodynamics forces are determined by integration of pressure field. The air is replaced by an ideal fluid. To obtain the pressure field is needed to get the velocity field. The pressure and velocity fields are divided into time-constant and fluctuation component. Time-constant component can be chosen freely by using relations (3, 5).

$$U(x, t) = \bar{U}(x) + \tilde{u}(x, t) \quad (2)$$

$$\bar{U}(x) = \frac{H_0 U_0}{H_0 - a(x)} \quad (3)$$

$$P(x, t) = \bar{P}(x) + \tilde{p}(x, t) \quad (4)$$

$$\frac{1}{2} \rho \bar{U}^2(x) + \bar{P}(x) = \text{const} \quad (5)$$

The basic equation of fluid mechanics is the continuity equation. For used fluid model and nonstationary channel cross has the form (6). Where  $U(x, t)$  is the speed and  $H(x, t)$  is the channel height. The height of the channel (7) is derived from the basic height  $H_0$ , VF profile  $a(x)$  and the position of the VF  $w(x, t)$ . Parameters  $V_1, V_2, V_3$  are the elements of the vector  $\mathbf{V}$ .

$$\frac{\partial H(x, t)}{\partial t} + \frac{\partial (H(x, t) U(x, t))}{\partial x} = 0 \quad (6)$$

$$H(x, t) = H_0 - a(x) - w(x, t) \quad (7)$$

$$w(x, t) = V_2(t) + V_3(t)(x - V_1(t)) \quad (8)$$

The solution of velocity in the glottis (9) was founded by modifying equations. Elements  $i_1$ - $i_7$  are function of position. Was used boundary condition at the inlet to the larynx  $\tilde{u}$  is zero.

$$\tilde{u}(x, t) = i_1 V_2 + i_2 V_3 + i_3 V_1 V_3 + i_4 \dot{V}_2 + i_5 \dot{V}_3 + i_6 V_1 \dot{V}_3 + i_7 V_3 \dot{V}_1 \quad (9)$$

The equation of motion for used fluid model is 1D Euler equation (10) is solved after substitution decomposition of pressure and velocity fields. To the solution was used boundary condition  $\tilde{p}$  at the output of the larynx is zero. The shape of the solution (11) is formally identical to (9). The solution is the sum of multiply time functions ( $\mathbf{V}_p(t)$ ) with space functions ( $\mathbf{J}(x)$ ). Both vectors have 39 elements. Column vector  $\mathbf{V}_p(t)$  containing different combinations of the elements of  $\mathbf{V}, \dot{\mathbf{V}}, \ddot{\mathbf{V}}$ . Using a pressure field (11) we can determine the forces and moment acting on the VF.

$$\rho \frac{\partial U(x,t)}{\partial t} + \rho U(x,t) \frac{\partial U(x,t)}{\partial x} + \frac{\partial P(x,t)}{\partial x} = 0 \quad (10)$$

$$\tilde{p}(x,t) = J(x)V_p(t) \quad (11)$$

$$F_x = h \int_{-L_1}^{L-L_1} \tilde{p}(x,t) \frac{da(x)}{dx} dx \quad (12)$$

$$F_y = h \int_{-L_1}^{L-L_1} -\tilde{p}(x,t) dx \quad (13)$$

$$M = h \int_{-L_1}^{L-L_1} \tilde{p}(x,t) \left( \frac{da(x)}{dx} (y_T - a(x)) - x \right) dx \quad (14)$$

The forces and moment can be formally expressed as (12) only the vector  $J(x)$  is changed to constant vectors. If contact occurs between the VF is not used model the aerodynamics forces. When collision is used sub-glottis pressure and hertz (contact) force (16). Where  $r$  is radius of curvature,  $E, \mu$  are elastic constants of the VF and  $\delta$  is size of penetration.

$$F_{hertz} = \frac{4\sqrt{r}E}{3(1-\mu^2)} \delta^{3/2} \quad (15)$$

## 2.2. Simulation results

Self-excited vibration was simulated for time interval of one second. The model is fully parametric. VF profile is formed of a part of parabola taken from (Horáček et al., 2005). The flow rate was set  $Q = 0.11$  l/s and gap = 0.2 mm. Natural frequencies was taken from the results (Vampola et al., 2016). Stabilization of the model takes about 0.1 s. Model after stabilization periodically vibrates with the collisions (Fig. 2). Thick marked parts of the graph show the collision. The first harmonic vibration frequency is 105 Hz. Closure of the glottis takes about 30 % of the oscillation period. Frequency spectrum of displacement VF is In Fig. 3. Fig. 4 shows the pressure field acting on the VF in the simulation during the last three periods of movement. Discontinuities in the pressure field are generated by switch aerodynamics forces to the subglottic pressure during VF collision. This pressure field was used for excitation FEM model of the VF. Results of dynamic FEM analysis (Figs. 5 and 6) confirmed the applicability of the model to generate the correct pressure fields. This can save a lot of time in comparison with co-simulation because it is not necessary solve CFD part.

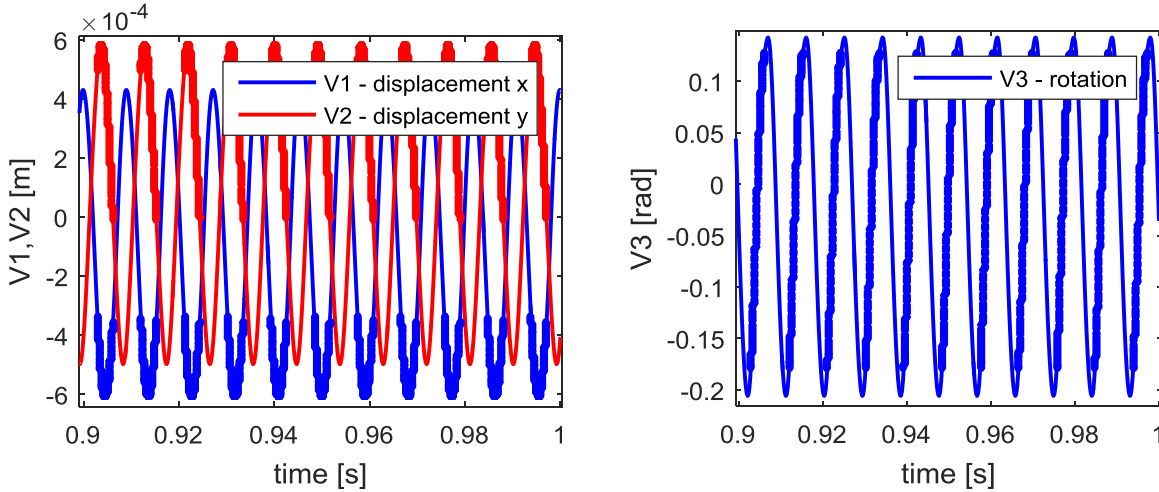


Fig. 2: Displacement and rotation vocal fold after stabilization vibration.

## 3. Conclusion

Single body parametric simulation model of self-excited vibration of the VF with 3 DOF was created by generalization of model (Horáček et al., 2005). VF is attached to be able to move in the longitudinal direction. Excitation consist of aerodynamics forces and hertz forces during the collision. The model shows a similar behavior as model (Horáček et al., 2005) which has good agreement with the generally acknowledged behavior of the VF. The model is not numerically consuming. Simulation takes about two



times of simulation time interval on the standard office PC. The model was used for generating pressure fields for excitation more sophisticated FEM model of VF.

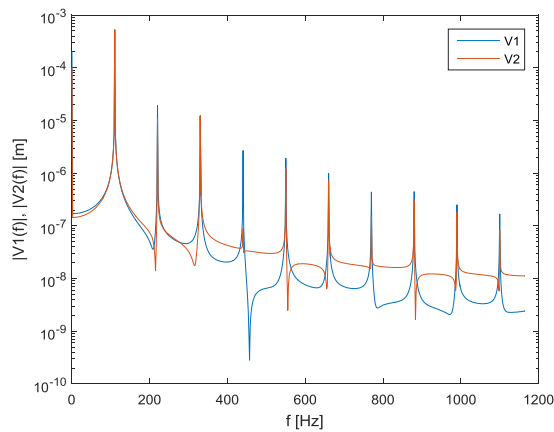


Fig. 3: Amplitude spectrum of V1 and V2.

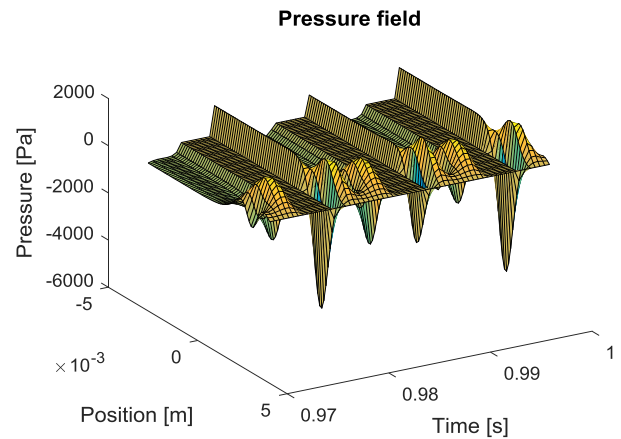


Fig. 4: Pressure field in the last three periods of vibration.

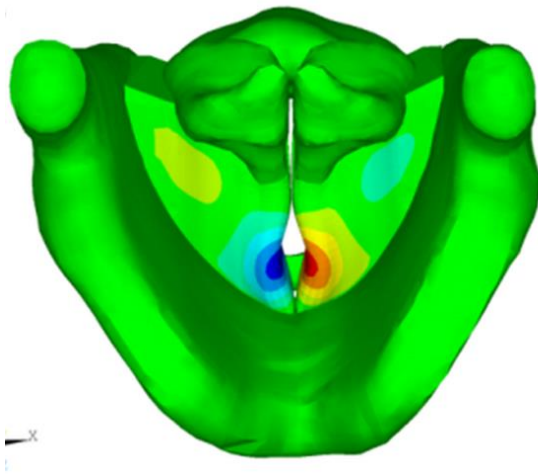


Fig. 5: Displacement field of FEM simulation.

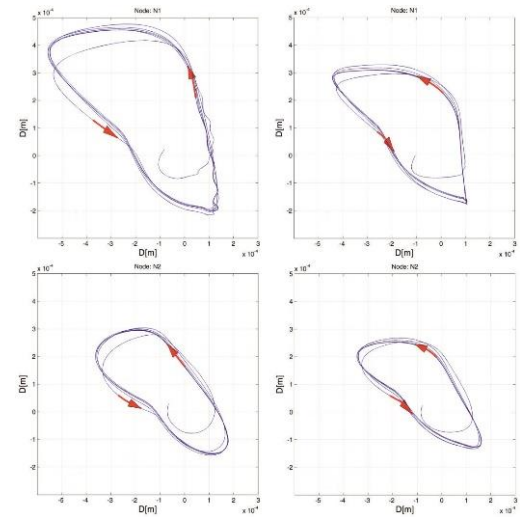


Fig. 6: Trajectories of four point from the FEM simulation.

## Acknowledgement

The research is supported by the Grant Agency of the Czech Republic by project No 16-01246S “Computational and experimental modelling of self-induced vibrations of vocal folds and influence of their impairments on human voice”.

## References

- Fant, G. (1970) Acoustic Theory of Speech Production. 2<sup>nd</sup> edition, The Hague, Netherlands: Mouton.
- Horáček, J. and Švec, J.G. (2002) Aeroelastic model of vocal-fold-shaped vibrating element for studying the phonation threshold. Journal of Fluid and Structures, Vol. 16, pp. 931-955.
- Horáček, J., Šidlof, P. and Švec, J.G. (2005) Numerical simulation of self-oscillations of human vocal folds with Hertz model of impact forces. Journal of Fluids and Structures, Vol. 20, pp. 853-869.
- Vampola, T., Horáček, J. and Klepáček, I. (2016) Computer simulation of muscoal waves on vibrating human vocal folds. Biocybernetic and Biomedical Engineering, Vol. 36, Iss. 3, pp. 451-465.

## MODELLING OF FLOW IN LINEAR BLADE CASCADE WITH THICK TRAILING EDGE AT A LOWER REYNOLDS NUMBER

P. Straka<sup>\*</sup>, J. Přihoda<sup>\*\*</sup>

**Abstract:** *In this paper there are compared results of numerical simulation of compressible turbulent flow through low-pressure turbine blade cascade with relatively thick trailing edges for various physical models. Steady, unsteady, fully turbulent, transitional, two-dimensional and three-dimensional models are compared. Results show that: a) steady simulation gives an incorrect prediction of the boundary layer development, b) two-dimensional unsteady simulation leads to inaccurate prediction of the far wake development and c) only three-dimensional unsteady transitional simulation gives sufficiently accurate prediction. Results of numerical simulations are compared with the experimental data.*

**Keywords:** Linear blade cascade, Boundary layer transition, Vortex series.

### 1. Introduction

The contribution deals with modelling of unsteady compressible flow through linear blade cascade with a relatively thick trailing edge. The linear blade cascade presented in this work represents an unrolled section of low-pressure turbine wheel of jet engine. The operating chord-based Reynolds number of used blade cascade is in order of magnitude from  $10^4$  to  $10^5$ . These relatively low values indicate that the laminar/turbulent boundary layer transition plays an important role in forming of flow field.

Modelling of flow through the linear blade cascade belongs today to routine calculations in industrial practice. Commonly used approach is that the flow field is supposed as periodic and two-dimensional. It allows dramatically decrease the computational cost.

In cases, where the laminar/turbulent boundary layer transition plays an important role (such as presented case), appropriate turbulence models should be used (Langtry and Menter, 2009, Walters and Cokljat, 2008, Kubacki and Dick, 2016, Straka and Přihoda, 2010).

In case of the relatively thick trailing edge there is another important phenomenon which has an impact on forming of the flow field: the vortex series. In transonic and high subsonic regimes the vortex series generated in near wake causes pressure waves (weak acoustic waves), which influence development of the boundary layer on the suction side of the neighboring blade. It means that not only transition modelling is necessary, but also time accurate simulation for resolving the vortex series is needed.

One of the main outputs of flow simulation in linear blade cascade is prediction of the kinetic energy losses across the wake behind the blade cascade. In case of relatively thick trailing edge it means to simulate the development of the vortex series in the far wake. This is not possible correctly perform under the supposition of two-dimensional flow because of the three-dimensional principle of the phenomenon.

In this work there are compared following results: a) two-dimensional steady simulation of fully turbulent flow without the effects of the boundary layer transition and the vortex series, b) two-dimensional steady simulation of transitional flow without the effect of the vortex series, c) two-dimensional unsteady simulation of transitional flow including the effect of the vortex series but without three-dimensional development in the far wake, d) three-dimensional unsteady simulation of transitional flow.

---

<sup>\*</sup> Ing. Petr Straka, PhD.: Aerospace Research and Test Establishment, Plc.; Beranových 130; 199 05, Prague; CZ, straka@vzlu.cz

<sup>\*\*</sup> Prof. Ing. Jaromír Přihoda, PhD.: Institute of Thermomechanics AS CR, v.v.i.; Dolejškova 140/5; 182 00, Prague; CZ, prihoda@it.cas.cz

## 2. Turbulence model

The compressible turbulent flow is described by the system of the Favre-averaged Navier–Stokes equations. The system of governing equations is closed by two-equation  $k$ - $\omega$  nonlinear (quadratic) turbulence model (Rumsey and Gatski, 2001):

$$\frac{D(\rho k)}{Dt} = \gamma P_k - \gamma D_k + \frac{\partial}{\partial x_j} \left[ \left( \mu + \sigma_k \frac{\rho k}{\omega} \right) \frac{\partial k}{\partial x_j} \right], \quad (1)$$

$$\frac{D(\rho \omega)}{Dt} = P_\omega - D_\omega + \frac{\partial}{\partial x_j} \left[ \left( \mu + \sigma_\omega \frac{\rho k}{\omega} \right) \frac{\partial \omega}{\partial x_j} \right] + C_D, \quad (2)$$

where  $\rho$  is the density,  $k$  is the turbulent energy,  $\omega$  is the specific dissipation rate of the turbulent energy,  $P_k$  and  $P_\omega$  are the production terms,  $D_k$  and  $D_\omega$  are the destruction terms,  $C_D$  is the cross-diffusion term,  $\mu$  is the molecular viscosity and  $\sigma_k$  and  $\sigma_\omega$  are the model constants. The Reynolds stress tensor  $\tau_{ij}^t$  is given as a quadratic function of the strain rate tensor  $S_{ij}$ :

$$\tau_{ij}^t = \gamma \left\{ 2\mu_t \left( S_{ij} - \frac{1}{3} \frac{\partial u_k}{\partial x_k} \delta_{ij} \right) - \frac{2}{3} \rho k \delta_{ij} + 2\mu_t \left[ b_1 (S_{ik} \Omega_{kj} - \Omega_{ik} S_{kj}) - 2b_2 \left( S_{ik} S_{kj} - \frac{1}{3} S_{kl} S_{lk} \delta_{ij} \right) \right] \right\}, \quad (3)$$

where  $\mu_t$  is the turbulent viscosity,  $\Omega_{ij}$  is the vorticity tensor and  $b_1$ ,  $b_2$  are the model constants (for more details see Rumsey and Gatski, 2001). In equations (1) and (3)  $\gamma$  is the intermittency coefficient. The role of the intermittency coefficient  $\gamma$  is to control the laminar/turbulent transition:  $\gamma = 0$  in the laminar part,  $\gamma = 1$  in the turbulent part and  $0 < \gamma < 1$  in transitional part of the boundary layer. In this work there is used the algebraic bypass and separation-induced transition model of Straka and Příhoda (2010), where the transition onset and the length of the transition region depend on the free-stream turbulence intensity, the longitudinal pressure gradient and on the wall-roughness (more details can be found in Straka and Příhoda, 2010).

## 3. Computational setup

In Fig. 1 there is shown a scheme of the linear blade cascade with definition of geometrical parameters and the flow regime (chord  $c$ , pitch  $t$ , trailing edge thickness  $d_{te}$ , stagger angle  $\gamma_{st}$ , inlet angle  $\alpha_1$ , outlet angle  $\alpha_2$ , outlet isentropic Mach number  $M_{2is}$ , outlet isentropic Reynolds number  $Re_{2is}$ , inlet turbulence intensity  $Tu_1$  and the turbulent to molecular viscosity ratio  $\mu_t / \mu$ ). More description can be found in (Straka and Příhoda, 2014 and Michálek and Straka, 2013).

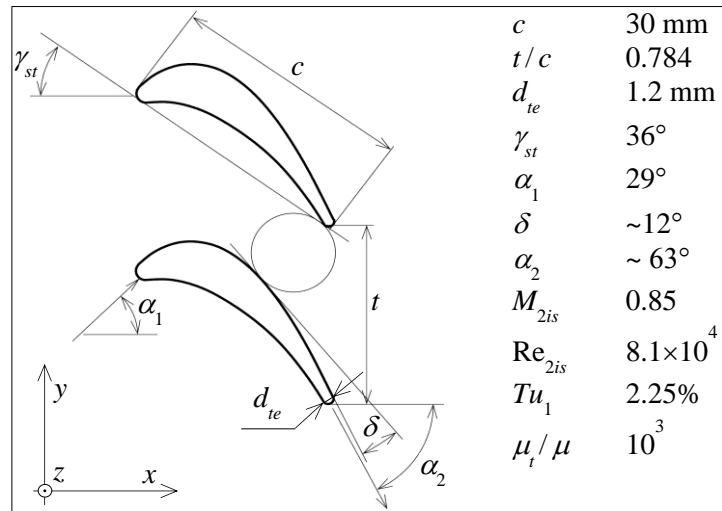


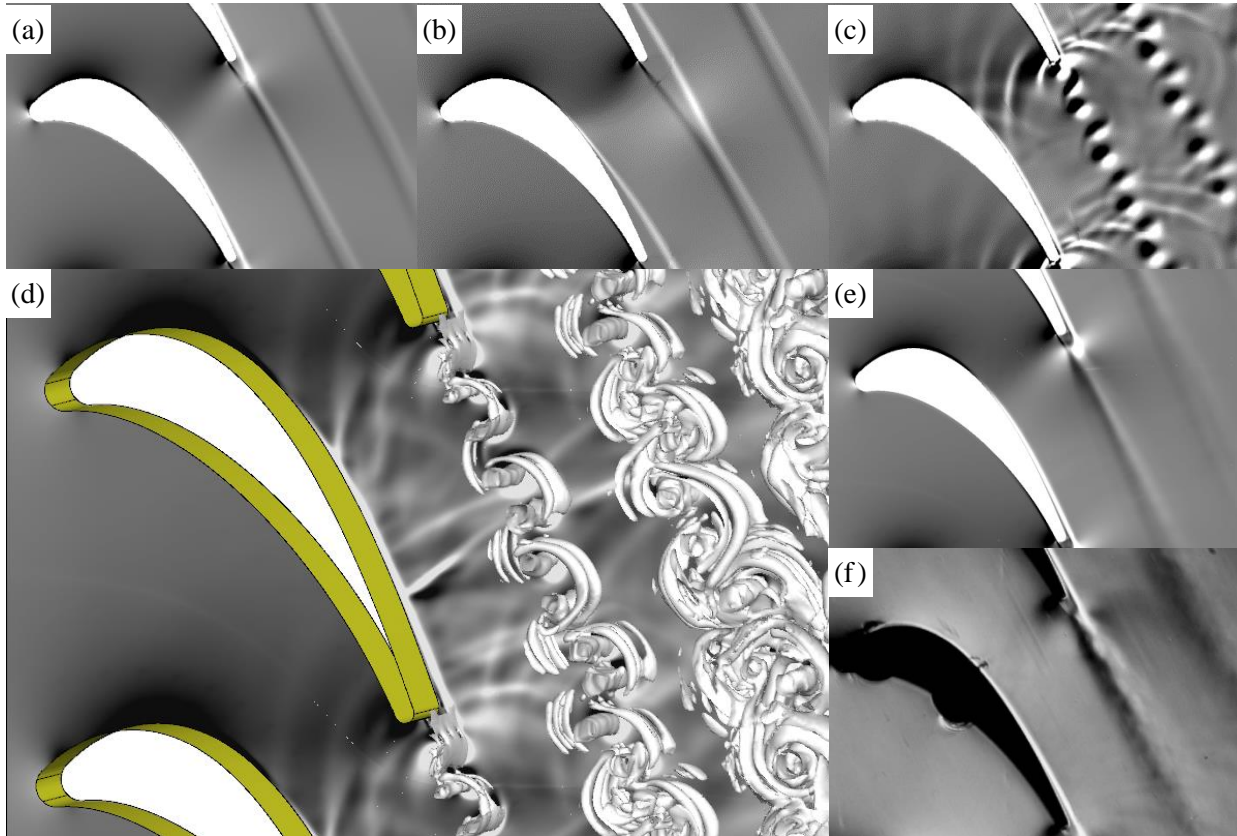
Fig. 1: Scheme of the linear blade cascade.

The computational mesh for two-dimensional simulation contains 51,000 quadrilateral cells, mesh for three-dimensional simulation contains 1,750,000 hexahedral cells. In both cases the mesh is refined near

the blade profile to ensure that there are at least five cells in the viscous sub-layer. The blade profile is discretized by 300 points. For three-dimensional simulation the geometry of the blade is pulled in “z” direction up to thickness of  $2\pi d_{te}$  with 35 cells across “z” direction.

#### 4. Results

In Fig. 2 there is a comparison of the schlieren images (directional derivative of density) of fully turbulent, transitional, steady, unsteady, two-dimensional and three-dimensional models and experiment (Michálek and Straka, 2013). Note that in part (d) of Fig. 2 there are also shown an instantaneous iso-surfaces of  $(|\Omega|^2 - |S|^2)$  for highlighting of the three-dimensionality of the far wake. The experimental schlieren photography in part (f) of Fig. 2 was taken with exposure time of approx. 20 to 30  $\mu$ s, while the frequency of the vortex series is around 45 kHz. Fig. 3 shows the distribution of the kinetic energy losses across the wake in the distance of 18 mm behind the trailing edges.



*Fig. 2: Numerical schlieren; 2D steady fully turbulent (a), 2D steady transitional (b), 2D unsteady transitional (c), 3D unsteady transitional (d), 3D unsteady transitional – time averaged (e), experiment (f).*

From comparison of the schlieren images and the kinetic energy losses distributions follows that the two-dimensional steady fully turbulent model predicts too narrow wake with high level of the kinetic energy losses, whilst the two-dimensional steady transitional model predicts massive separation of the boundary layer at the middle of the suction side, which leads to increase of the kinetic energy losses. The unsteady transitional model predicts generating of the vortex series in the near wake which causes the pressure waves (weak acoustic waves). These pressure waves prevent formation of the massive separation of the boundary layer on the suction side of the neighboring blade. The two-dimensional unsteady transitional model does not allow the decay of the vortex series, which leads to overestimation of the kinetic energy losses. Only the three-dimensional unsteady transitional model predicts correctly the development of the boundary layer on the suction side and the development of the far wake in a good agreement with the experimental data, as is shown in Fig. 3.

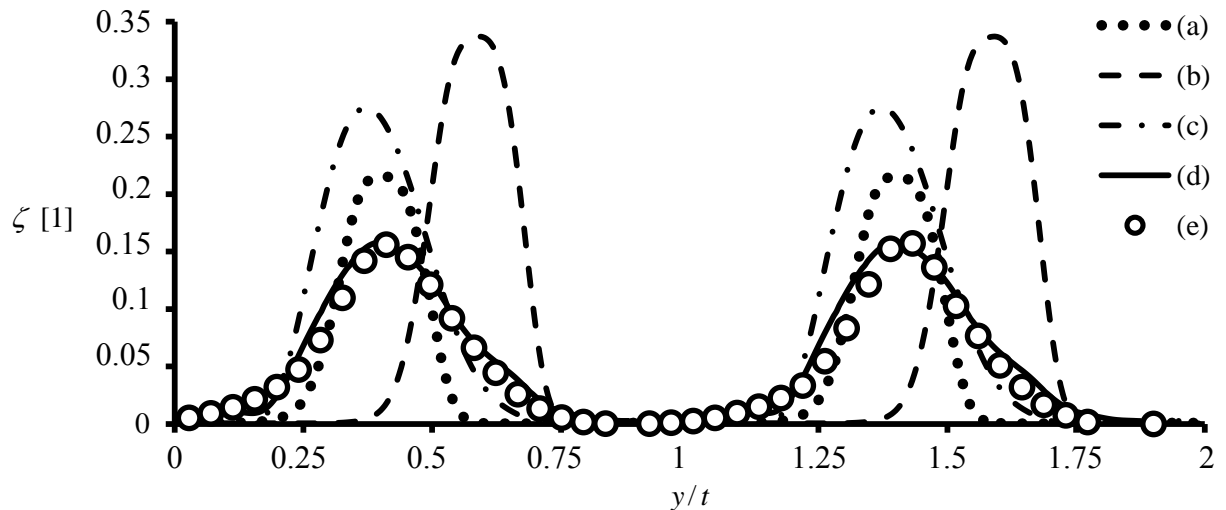


Fig. 3: Kinetic energy losses distribution across the wake; 2D steady fully turbulent (a), 2D steady transitional (b), 2D unsteady transitional (c), 3D unsteady transitional (d), experiment (e).

## 5. Conclusions

This work shows that although the simulation of flow in the linear blade cascade is really routine task nowadays, there are still cases with high demands on the physical model and on the computational costs. If we compare the computational time of used models with the computational time needed for the two-dimensional steady fully-turbulent simulation, we find that the computational time of the two-dimensional steady transitional simulation is comparable, the computational time of the two-dimensional unsteady transitional simulation is approx. twenty times higher and the computational time of the three-dimensional unsteady transitional simulation is more than seven hundred times higher. Therefore, the problem of sufficiently accurate and sufficiently efficient simulation of flow in the linear blade cascades with relatively thick trailing edges at lower level of the Reynolds number is still open.

## Acknowledgement

This work was supported by the Long-term Framework Advancement Plan provided by the Ministry of Industry and Trade of the Czech Republic, by the project TA04020129 of the Technology Agency of the Czech Republic and by the institutional support RVO 61388998.

## References

- Langtry, R.B. and Menter, F.R. (2009) Correlation-based transition modeling for unstructured parallelized computational fluid dynamics codes. *AIAA Journal*, 47, 12, pp. 2894-2906.
- Walters, D.K. and Cokljat, D. (2008) A three-equation eddy-viscosity model for Reynolds-averaged Navier-Stokes simulations of transitional flow. *Jour. Fluid Engineering*, 130, pp. 121401/1-121401/14.
- Kubaci, S. and Dick, E. (2016) An algebraic intermittency model for bypass, separation-induced and wake-induced transition, *International Journal of Heat and Fluid Flow*, 62, pp. 344-361.
- Straka, P. and Přihoda, J. (2010) Application of the algebraic bypass-transition model for internal and external flows, *Proc. Conf. Experimental Fluid Mechanics 2010, Liberec*, pp. 636-641.
- Rumsey, C.L. and Gatski, T.B. (2001) Recent turbulence model advances applied to multi-element airfoil computations. *Jour. of Aircraft*, 38, 5, pp. 904-910.
- Straka, P. and Přihoda, J. (2014) Numerical simulation of compressible transitional flow through high-loaded turbine blade cascade. *Proc. Conf. Topical Problems of Fluid Mechanics 2014, Prague*, pp. 131-134.
- Michálek, J. and Straka, P. (2013) A comparison of experimental and numerical studies performed on a low-pressure turbine blade cascade at high-speed conditions, low Reynolds numbers and various turbulence intensities. *Jour. of Thermal Science*, 22, 5, pp. 413-423.

## DESIGN OF FAST MAGNETORHEOLOGICAL DAMPER USING SOFT MAGNETIC COMPOSITES

Z. Strecker<sup>\*</sup>, T. Strmiska, J. Roupec, M. Kubík, O. Macháček

**Abstract:** *The article investigates the suitability of soft magnetic composite (SMC) material for construction of magnetorheological damper piston. The SMC materials have, in comparison with steel, high electric resistance, which secures very short response time of magnetic induction in the magnetic circuit. In comparison with ferrite materials, the SMC materials have better mechanical properties and high magnetic saturation level, which secures high dynamic range. The disadvantage of SMC material is low permeability. The measurements and simulations showed that MR damper piston made of SINTEX STX SMC prototyping material achieves high magnetic flux density in the MR damper piston gap (only 20 % lower than piston made of steel) and very short response time of magnetic flux density in the gap (more than 20 times shorter than in case of steel piston).*

**Keywords:** MR damper, Fast response, Soft magnetic composite, SMC.

### 1. Introduction

The response time and the dynamic range of Magnetorheological (MR) damper is one of the key factors influencing performance of semiactive suspension. Strecker (2015) described the dependence of MR damper response time on the passenger car semiactive suspension controlled by Modified groundhook algorithm. The simulations and measurements showed that the response time 8 ms (usual for commercial MR dampers) is too long for efficient semiactive control. Therefore it is necessary to develop MR dampers with short response time. Reasons of long response time of MR devices were described in Maas (2011). One of the most important sources of long response time of MR dampers are eddy-currents. They can be eliminated using material with high electrical resistivity. Strecker (2015) designed a fast MR damper, with response time of damper force on control signal up to 1.5 ms. The magnetic circuit of the MR damper was made of ferrite material Epcos N87. Ferrites have good permeability ( $\mu_r = 2200$ ) and very high electrical resistivity 10  $\Omega \cdot m$ . This material, however, has bad mechanical properties, very poor machinability and low magnetic saturation (490 mT). Therefore, the dynamic range of MR damper made of ferrite material is much smaller in comparison with the piston made of steel. Another way of reducing the eddy currents while keeping high dynamic range seem to be the use of structured cores made of steel. The steel cores with a structure preventing eddy currents can be printed from pure iron by 3D SLM print (Palousek, 2017). It is, however, very difficult to design the appropriate structure. Soft magnetic composites (SMC) seem to be suitable material for construction of MR damper piston. The electrical resistivity of SMC materials can be more than thousand times higher than the resistivity of steel, which practically eliminates eddy-currents (Shokrollahi, 2007). The magnetic saturation level of SMC materials is much higher than in case of ferrites, which allows designing of MR dampers with higher dynamic range. Some SMC materials are easily machinable. However, SMC materials have very small relative permeability. Therefore it is necessary to evaluate the suitability of this material for the design of MR damper.

### 2. Methods

The objective was to design a new MR damper piston which eliminates eddy currents induced in the magnetic circuit of the MR damper and which enables large control range of achievable magnetic flux

---

<sup>\*</sup> All authors: Institute of Machine and Industrial Design, Brno University of Technology, Technická 2896/2; 616 69, Brno; CZ, strecker@fme.vutbr.cz



density in the gap of MR piston. The performance of the new piston made of soft magnetic composite material was compared to the piston made of 11SMn30 steel.

The geometry of the MR damper piston used for measurements is in Fig. 1. The new piston was made of SMC material SINTEX STX prototyping material with relative permeability  $\mu_r = 430$ , electrical resistivity  $280 \mu\Omega.m$  and magnetic saturation  $B_s = 1.46$  T. In order to verify magnetic FEM model, transient and static magnetic flux density dependencies in the gap filled by air were measured. The model is necessary for estimating the dependency of magnetic flux density on the current in the gap filled by MR fluid, because this dependency can not be measured directly by Hall probe.

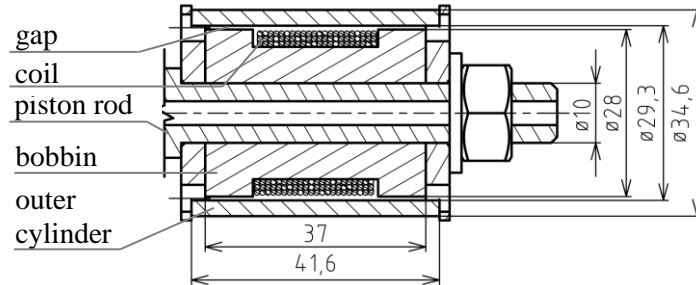


Fig. 1: Dimensions of MR piston.

### 2.1. Magnetic model

Magnetic model was done in Ansys electronics desktop 17.1. The magnetic circuit was modeled in 3D. Because of magnetic circuit symmetry, it was enough to simulate only 1/8 of the magnetic circuit. The time step of transient analysis was 0.0125 ms, the length based mesh consisted of 53779 elements.

### 2.2. Measurement of response time of B

The response time of the magnetic flux density on electric current step was considered as the time needed for reaching 63.2 % of the steady state magnetic flux density at 2 A. The current was generated by fast current controller of our construction. Magnetic flux density in the gap was measured by Tesla meter FW Bell 5180. All the signals were collected by DEWE 50 data acquisition station (Fig. 2).

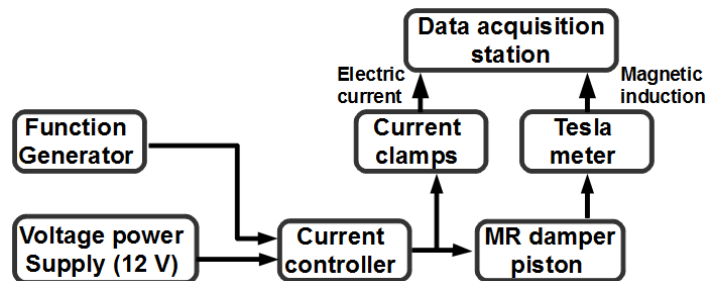


Fig. 2: Block scheme of measurement.

## 3. Results

### 3.1. Static analysis

Fig. 3 compares the dependencies of magnetic flux density in the gap filled by air on the electric current in the coil. The differences between measured and simulated values are up to 15 %. It can be seen that magnetic flux density in the piston made of SMC material is lower than in the piston made of steel. The magnetic circuits with air in the gap are not saturated even at 5 A.

Fig. 4 shows the simulated values of magnetic flux density in the gap filled with MR fluid. The magnetic flux density in the gap of the piston made of SMC is about 15 % lower than for steel variant.

### 3.2. Transient analysis

Fig. 5 compares measured and simulated responses of magnetic flux density on the electric current for the piston made of steel and with air in the gap. The measured response time of the magnetic flux density on current step is 1.7 ms. The response time of the current is 0.12 ms.

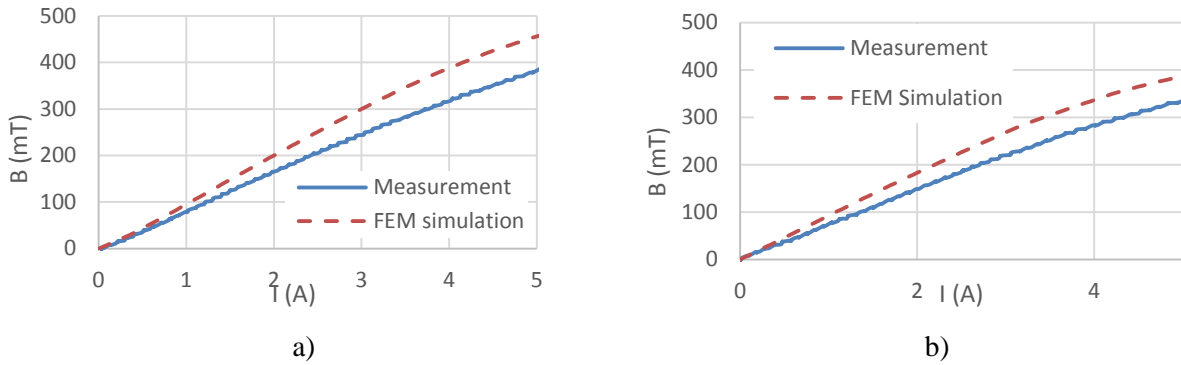


Fig. 3: Magnetic flux density in the gap with air for piston made of: a) steel, b) SMC Sintex.

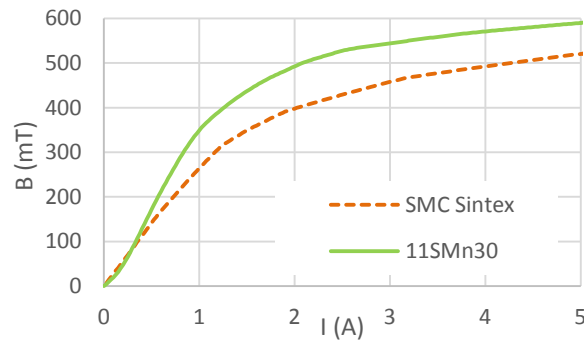


Fig. 4: FEM simulation of magnetic flux density in the gap filled by MR fluid.

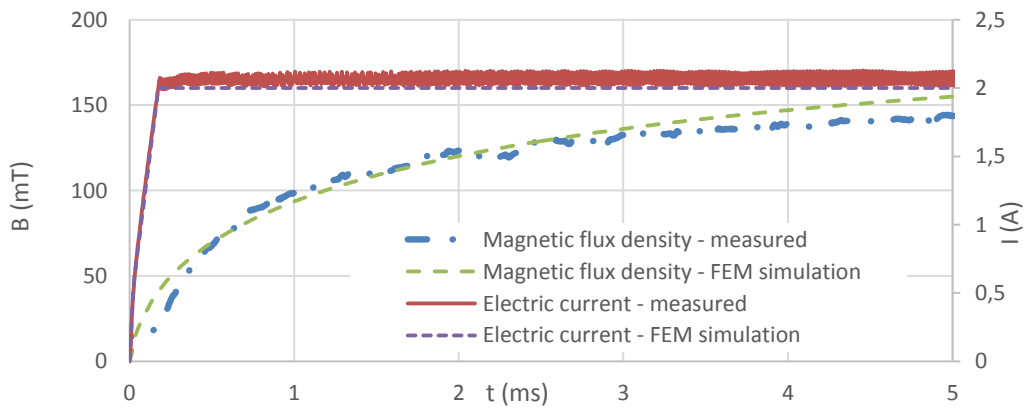


Fig. 5: Transient response of magnetic flux density in the gap with air on electric current – piston made of 11SMn30.

Fig. 6 compares measured and simulated responses of magnetic flux density on the electric current for the piston made of SMC Sintex material and with air in the gap. The response time of the magnetic flux density on current step is 0.56 ms. The measured response time of the current in this case is 0.37 ms.

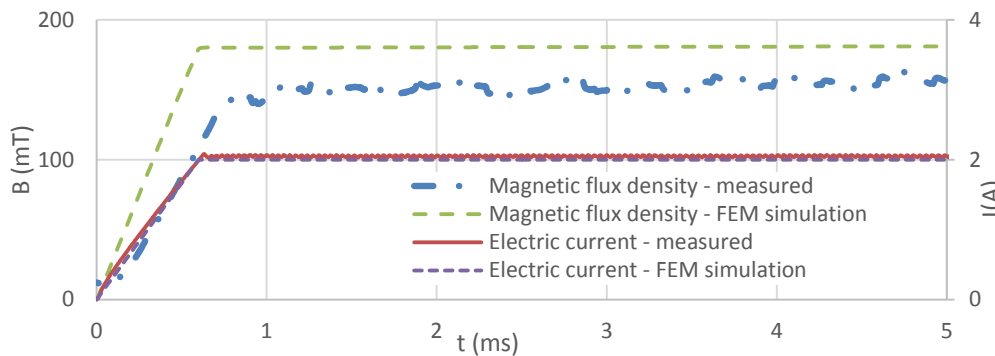


Fig. 6: Transient response of magnetic flux density in the gap with air on electric current – piston made of SMC Sintex material.

Fig. 7 shows the simulation of magnetic flux density in the piston gap filled by MR fluid for piston made of SMC Sintex and piston made of steel. The simulation shows that the predicted response time of magnetic flux density in the gap of steel piston is 8.1 ms. The course of magnetic flux density for piston made of SMC is similar with electric current. The predicted response time is 0.3 ms. The overall response time of MR damper force on control signal can be expected longer because of response time of MR fluid (time needed for forming MR particles chains). The response time of MR fluid was measured between 0.45 – 0.6 ms (Goncalves et al., 2005). The overall response time of the MR damper with piston made of SMC material can be therefore expected shorter than 1 ms.

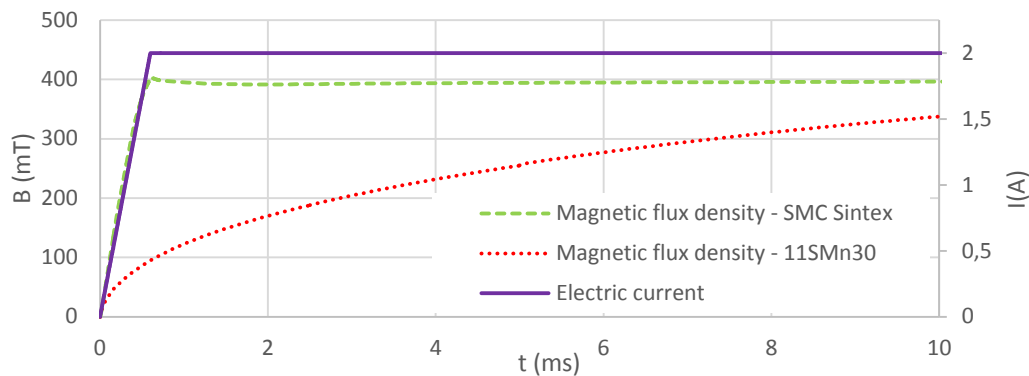


Fig. 7: Transient response of magnetic flux density in the gap with air on electric current – piston made of SMC Sintex.

#### 4. Conclusions

Measurements and simulations clearly showed that the use of SMC material can significantly improve the performance of MR damper. The FEM model was verified by measurements of the magnetic flux density in the piston gap filled by air. The measurements proved very good agreement of simulations and measurements. Despite much smaller relative permeability of SMC Sintex material, the FEM simulation showed that magnetic flux density in the gap of piston made of SMC material filled with MR fluid is only 20 % lower than in case of piston made of steel. The response time of the magnetic flux density in the piston made of steel is 8.1 ms. Such value corresponds to the force response time measured by Strecker (2015). The use of SMC Sintex material reduces the response time of magnetic flux density in the gap filled by MR fluid to 0.3 ms, which is more than 20 times shorter than in case of steel piston.

#### Acknowledgement

This experiment could be provided thanks to the kind sponsorship of various grants and numerous agencies. We would like to explicitly thank to the GAČR 17-10660J, GAČR 17-26162S, FSI-S-17-4428 and FCH/FSI-J-17-4534.

#### References

- Goncalves, F.D., Ahmadian, M. and Carlson, J.D. (2005) Investigating the magnetorheological effect at high flow velocities. *Smart Materials and Structures*, 15, 1, pp. 75-85.
- Maas, J. and Güth, D. (2011) Experimental investigation of the transient behavior of MR fluids. in: *ASME 2011 Conference on Smart Materials, Adaptive Structures and Intelligent Systems, SMASIS 2011*, pp. 229-238.
- Palousek, D. et al. (2017) Processing of nearly pure iron using 400W selective laser melting - initial study. *MM Science Journal*: 1738-1743.
- Shokrollahi, H. and Janghorban, K. (2007) Soft magnetic composite materials (SMCs). *Journal of Materials Processing Technology*, 189, 1-3, pp. 1-12.
- Strecker, Z. et al. (2015) Design of magnetorheological damper with short time response, *Journal of Intelligent Material Systems and Structures*, 26, 14, pp. 1951-1958.
- Strecker, Z. et al. (2015) Influence of MR damper response time on semiactive suspension control efficiency, *Meccanica*, 50, 8, pp. 1949-1959.

## RETESTED RUNOUT SPECIMENS IN FATIGUE RESEARCH

P. Strzelecki\*

**Abstract:** *The problem of samples that did not break is quite often seen in fatigue tests. This situation particularly frequently occurs in the staircase method. With this in mind a question occurs whether these samples may be loaded again. This paper includes tests on steel S355J2+C for finite fatigue life, as well as for infinite fatigue life. The samples that did not break in the staircase method were repeatedly tested at higher load. The results obtained were compared with the results obtained on samples that had not been previously loaded. An impact of the previous tests was identified. With the use of statistic calculations, it is possible for adjust for the obtained values of cycle numbers, so that they correspond to the values of samples not previously loaded. The results obtained may be accepted as satisfactory.*

**Keywords:** Fatigue tests, S-N curve, Steel, Statistical analysis, Runout.

### 1. Introduction

The occurrence of samples that did not break at the assumed level of stress is an issue that frequently comes up during the performance of fatigue limit tests with the purpose of determining S-N characteristics. It is related with the fact that the research, performed according to ISO-12107 (2003) standard, are performed at two areas. The first is a finite life range, where the relation between fatigue life and stress is described by linear regression according to the following formula:

$$\log(N) = m \cdot \log(S) + c \quad (1)$$

where:  $N$  – number of cycles,  
 $S$  – stress amplitude [MPa],  
 $m$  – slope coefficient,  
 $c$  – intercept term.

The other range is the infinite life area, where tests are performed until reaching the basic number of cycles, e.g.  $5 \cdot 10^6$  cycles. This value is adopted depending on the material. Suggested values may be found in papers Sonsino (2007), Dyląg and Orłoś (1962). Infinite life fatigue strength is evaluated using the staircase method. The application of this method effects in that about 50 % of the samples do not break (see Tab. 1, Fig. 1a).

In the case when the number of samples for performing the examinations is limited, like in case of biological material, research on which may be found in paper Topoliński et al. (2012). Another example is collection of samples from a real object, as presented in paper Tomaszewski et al. (2017). Sampling method for such samples is presented in paper Zastempowski et al. (2015). In such case, each sample is important from the point of view of statistical calculations. The use of not broken samples that reached the basic number of cycles is recommended.

This paper presents a statistical method for adjusting the number of cycles obtained for samples not broken in previous tests, which the method is described in paper Gänser et al. (2015). This method assumes that neither strengthening nor weakening occurs in the material during the previous loading. In the case of occurrence of the above effects, research papers for the given material must be referred to. Examples of papers in this regard include AKITA et al. (2012), Sinclair (1952) or Kheder et al. (2011).

---

\* Ing. Przemysław Strzelecki, PhD.: Institute of Mechanical Engineering, University of Sciences and Technology, 85 789 Bydgoszcz, Poland; PL, p.strzelecki@utp.edu.pl

## 2. Statistical model

This method assumes that the distribution of fatigue life logarithm is normal. Moreover, it is assumed that the not broken samples, for infinite life, have reached the following probability of failure for the given population:

$$P_j = \begin{cases} f_j / n_j & \text{for } f_j > 0 \\ 1 / 2n_j & \text{for } f_j = 0, \end{cases} \quad (2)$$

where:  $f_j$  – samples failure at stress  $S_j$ ,  
 $n_j$  – number of samples tested at stress  $S_j$ .

The following formula must be used for determining the adjusted number of cycles:

$$N_i = N_i^* \cdot 10^{-\frac{\sigma_N}{1-P_j} \cdot \frac{1}{\sqrt{2\pi}} \exp\left(-\left(\Phi^{-1}(P_j)\right)^2 / 2\right)}, \quad (3)$$

where:  $N_i$  – number of cycles to failure after correction,  
 $N_i^*$  – number of cycles to failure of the runout at stress  $S_i$ ,  
 $\Phi^{-1}$  – the inverse of the cumulative distribution function (the quantile),  
 $\sigma_N$  – standard deviation of  $N = \log(N)$ .

## Test results

S355J2+C material was used for the tests. Examinations for evaluating the S-N characteristics are presented in paper Strzelecki et al. (2016). The S-N curve for this steel is presented in Fig. 1.

Tab. 1 presents the cycle number values obtained for not broken and repeatedly tested samples. Additionally, the last column contains values calculated according to formula (3). Graphical representation of these results is presented in Fig. 2.

Tab. 1: Coefficients of regression for standard test results and with retested runouts.

Stress level $j$	$S_j$	$N_j$	$P_j$	$S_i$	$N_i^*$	$N_i$
1	350	5 000 000	0.125	415	191 486	222 912
	350	5 000 000	0.125	460	60 628	70 578
	350	5 000 000	0.125	415	239 337	278 616
	350	5 000 000	0.125	460	57 711	67 182
2	357	5 000 000	0.4	415	97 648	150 823
	357	5 000 000	0.4	460	57 973	89 542
3	363	5 000 000	0.5	415	145 527	321 141
	363	5 000 000	0.5	460	74 845	165 163

Calculations were performed for the results obtained from Tab. 1 for the purpose of evaluating the S-N characteristics. Coefficients from formula (1) for 5 data cases were determined. In the first case only the results obtained without repeatedly tested samples were taken into account. In the subsequent case, the results for the repeatedly tested samples were added to the set, without any cycle number adjustment. In the third case, the characteristics for the repeatedly tested samples was determined, again without any cycle number adjustment. The fourth characteristics refers to the set from the standard tests, and to fatigue life from the repeatedly tested samples, with cycle number adjustment. The last case refers to a set only for repeatedly tested samples, with cycle number correction. The calculation results are presented in Tab. 2. Fig. 2 presents the obtained characteristics.

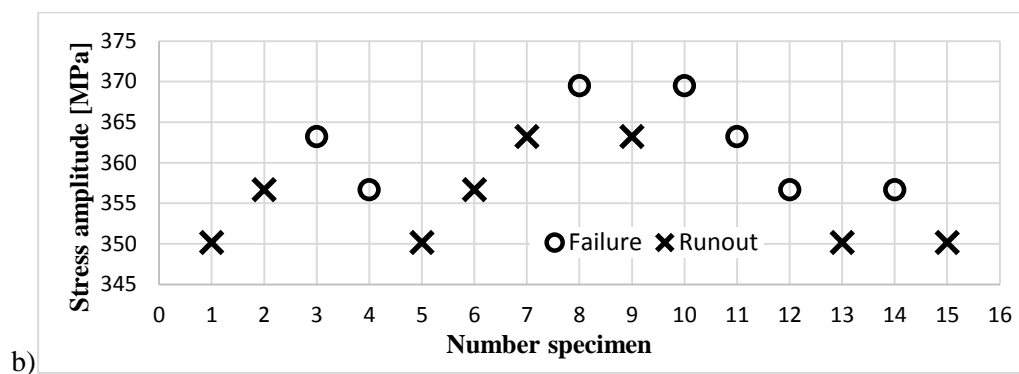
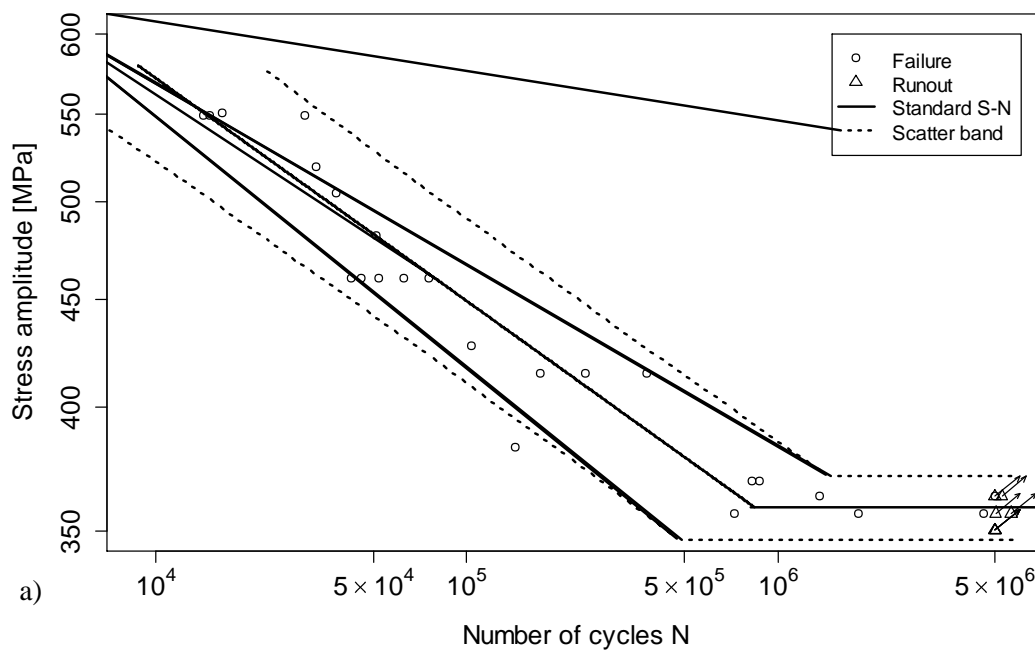


Fig. 1: S-N curves for S355J2+C a) and staircase method b).

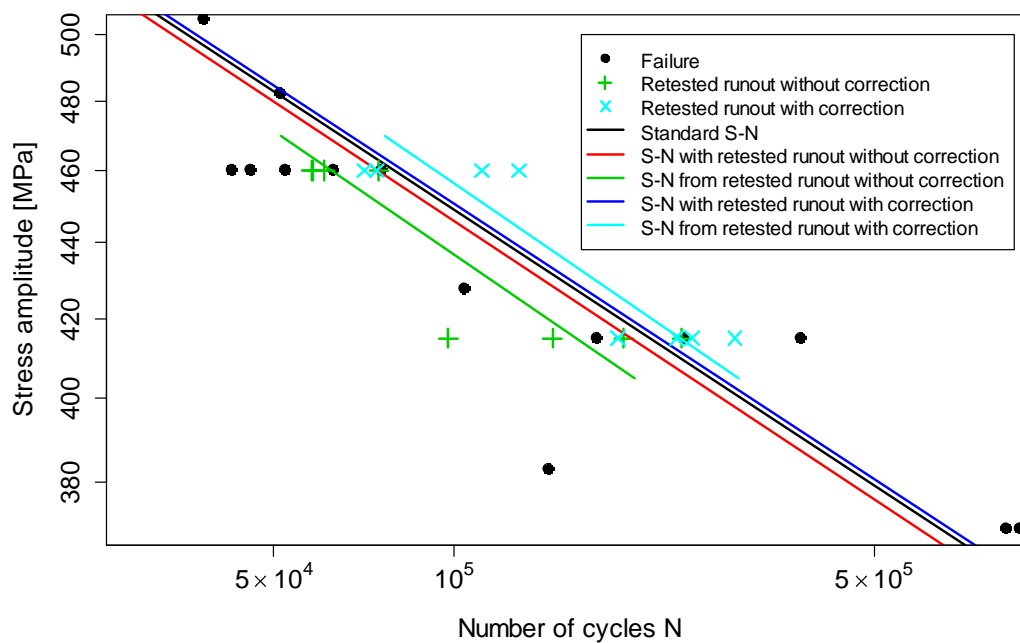


Fig. 2: S-N curves for S355J2+C steel with retested runouts.



Tab. 2: Coefficients of regression for standard test results and with retested runouts.

Type of data	Coefficient of regression	
	<i>m</i>	<i>c</i>
Standard tests	9.523	30.25
Standard tests + retested runout without correction	9.455	30.04
retested runout without correction	9.128	29.10
Standard tests + retested runout with correction	9.533	30.30
retested runout with correction	9.128	29.27

### 3. Conclusions

Cycle number adjustment according to formula (3) for the not broken and repeatedly tested samples gave a satisfactory result. Fig. 2, shows that the obtained characteristics for the repeatedly tested samples with adjustment, and those tested in the standard way are close to each other, compared to the other ones. The fact that the characteristics obtained for samples repeatedly tested without cycle number adjustment is shifted to the left (which effects in lowered number of cycles) results in that is located on the safe side. Such characteristics is useful for applying for calculations of structural element fatigue life. It must be remembered, however, that different construction materials may hardening or weakening, causing this statistical method not to apply.

### References

- Akita, M., Nakajima, M., Uematsu, Y., Tokaji, K. and Jung, J.-W. (2012) Some factors exerting an influence on the coxing effect of austenitic stainless steels. *Fatigue Fract. Eng. Mater. Struct.* 35, 12, pp. 1095-1104. doi:10.1111/j.1460-2695.2012.01697.x
- Dyla, Z. and Orłoś, Z. (1962) *Fatigue strength of materials*. Wydawnictwo Naukowe-Techniczne, (in Polish).
- Gänsler, H.-P., Maierhofer, J. and Christiner, T. (2015) Statistical correction for reinserted runouts in fatigue testing. *Int. J. Fatigue* 80, pp. 76-80. doi:10.1016/j.ijfatigue.2015.05.015.
- ISO-12107 (2003) *Metallic materials - fatigue testing - statistical planning and analysis of data*. Geneva.
- Kheder, A.R.I., Jubeh, N.M. and Tahah, E.M. (2011) *Fatigue Properties under Constant Stress / Variable Stress Amplitude* 5, 4, pp. 301-306.
- Sinclair, G.M. (1952) An investigation of the coxing effect in fatigue of metals. *ASTM Proc.* pp. 743-758.
- Sonsino, C.M. (2007) Course of SN-curves especially in the high-cycle fatigue regime with regard to component design and safety. *Int. J. Fatigue* 29, pp. 2246-2258, doi:10.1016/j.ijfatigue.2006.11.015
- Strzelecki, P., Tomaszewski, T. and Sempruch, J. (2016) A method for determining a complete S-N curve using maximum likelihood, in: Zolotarev, I., Radolf, V. (Eds.), *22nd International Conference on Engineering Mechanics*. Acad. Sci. Czech Republic, Inst Thermomechanics, Dolejšková 5, Prague 8, 182 00, Czech Republic. Svratka, Czech Republic, pp. 530-533.
- Tomaszewski, T. and Sempruch, J. (2017) Fatigue life prediction of aluminium profiles for mechanical engineering. *J. Theor. Appl. Mech.* 55, 2.
- Topoliński, T., Cichański, A., Mazurkiewicz, A. and Nowicki, K. (2012) Applying a Stepwise Load for Calculation of the S-N Curve for Trabecular Bone Based on the Linear Hypothesis for Fatigue Damage Accumulation. *Mater. Sci. Forum* 726, pp. 39-42, doi:10.4028/www.scientific.net/MSF.726.39.
- Zastempowski, M. and Bochat, A. (2015) Mathematical Modelling Of Elastic Deflection Of A Tubular Cross-Section. *Polish Marit. Res.* 22, 2, pp. 93-100, doi:10.1515/pomr-2015-0022.

## PROPOSAL OF HYPERELASTIC PROPORTIONAL DAMPING AS DISSIPATED ENERGY MODEL OF HARD RUBBERS

P. Šulc, L. Pešek, V. Bula, J. Košina, J. Cibulka \*

**Abstract:** *The paper deals with a stress analysis of hard rubber under large torsion deformations. This study was motivated by effort to find the dependency the dissipated energy on the deformation energy. Based on the results of an experiment, a function of dissipation energy of hard rubbers for finite strains using the theory hyperelasticity was proposed herein analogically as a proportional damping for elastic theory. Samples of hard rubber of different hardness (EPDM, Silicone) were dynamically tested on the developed torsional test-rig at different frequencies, amplitudes. First the Mooney Rivlin model (MRM) for a shear case of loading was analytically developed and then MRM constants were attained by fitting of the MRM to the experimental torsion-deformation curve. These constants were used to obtain the deformation energy of the MRM models. The coefficients of hyperelastic proportional damping relating a dissipated energy to a strain energy were evaluated for tested rubbers on the basis of experimental results.*

**Keywords:** Torsion vibration, Large deformation, Hyperelasticity, Dissipated energy, Deformation energy.

### 1. Introduction

For rubber materials unlike conventional structural materials under dynamic loading, a nonlinear time-varying behavior occurs due to the size of straining, creep, temperature and aging (Pešek, 2008 and Pešek, 2015). Tests of rubbers with higher hardness Sh 50 – 80 (Nashif, 1985) were performed in the laboratories of IT AS CR in recent years (Šulc, 2017). The dynamic tests of hard rubbers require usually a costly long-term operation of heavy hydraulic machines. Therefore we have started to look for realization of the tests in laboratory conditions with the lighter laboratory technique. Currently we have been developing a torsional dynamic test rig for torsional straining of hard rubber samples with a circular cross-section (Šulc, 2016). The reason for torsion straining was that hard rubber materials are softer in torsion than in pressure and therefore it is easier to achieve larger strains. Furthermore at this straining the shape changes are smaller in comparison with pressure loading when so-called barreling effect arises due to incompressibility of the material.

The torsional test rig should serve to dynamic material tests of hard synthetic rubbers for determination of the thermo-viscous-elastic material characteristics under small as well as finite strains, different amplitudes, frequencies and temperatures.

This paper deals with the deformation analysis of cylindrical samples at larger shear strains (about 30 %) which led to finding the relationship between dissipated energy and strain energy at larger torsion deformations. Function of dissipation energy of hard rubbers under finite strains was proposed as a hyperelastic proportional damping similar to modeling of damping in elastic theory. So, the dissipated energy is expressed as product of a function of deformation energy, excitation frequency and coefficient of hyperelastic proportional damping. The coefficients of hyperelastic proportional damping relating a dissipated energy to a strain energy were then evaluated for tested rubbers on the basis of experimental results. Mooney\_Rivlin hyperelastic model (MRM) considered as an isotropic incompressible material is used for description of the deformation energy.

As to the temperature of the material testing we choose temperature -20 °C where the effect of excitation amplitudes of the torque to the value of the loss factor is most evident. We tested two samples of EPDM rubber of different hardness (Sh 70 and Sh 85) with excitation amplitudes of torque moment in a range

---

\* Institute of Thermomechanics of the Czech Academy of Sciences, v. v. i., Dolejškova 1402/5, 182 00 Prague

from 0.2 N.m to 9.2 N.m. Excitation frequencies were 2 Hz and 5 Hz. Stress-strain curves and deformation and dissipated energies were evaluated for different excitation torque moment amplitudes.

## 2. Experimental observations

The shear modulus and loss factor for each of torque harmonic excitation amplitudes were evaluated from experimental hysteresis of deformation loops. The methodology of the evaluation is in (Šulc, 2016). The loss factors for two excitation torque frequency (2 Hz, 5 Hz) in dependence on strain [%] are plotted in Fig. 1. From dependences of the loss factor on strain, it is seen that the ratio between deformation and dissipation energy for higher values of strains is almost constant, which is typical for the proportional damping model ( $B = \beta \cdot K$ ) for linear elasticity. Furthermore the dependences of loss factor on the shear modulus (Fig. 2) show that the loss factor and therefore the dissipated energy decrease with increasing modulus for larger deformations. It means that dissipated energy is also related to the deformation energy. Based on these observations we proposed (see below) a function of dissipation energy of hard rubbers for finite strains analogically as a proportional damping for elastic theory and extended for hyperelasticity.

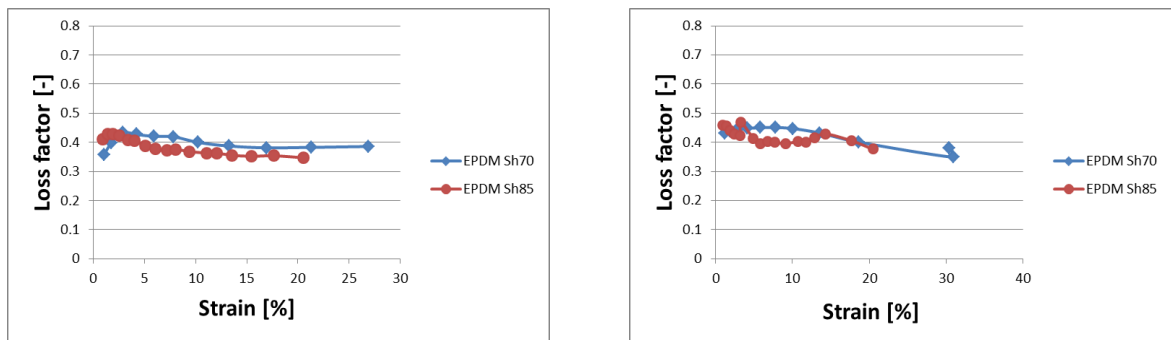


Fig. 1: The loss factor versus strain for two excitation frequencies 2 Hz (left) and 5 Hz (right) - temperature -20 °C.

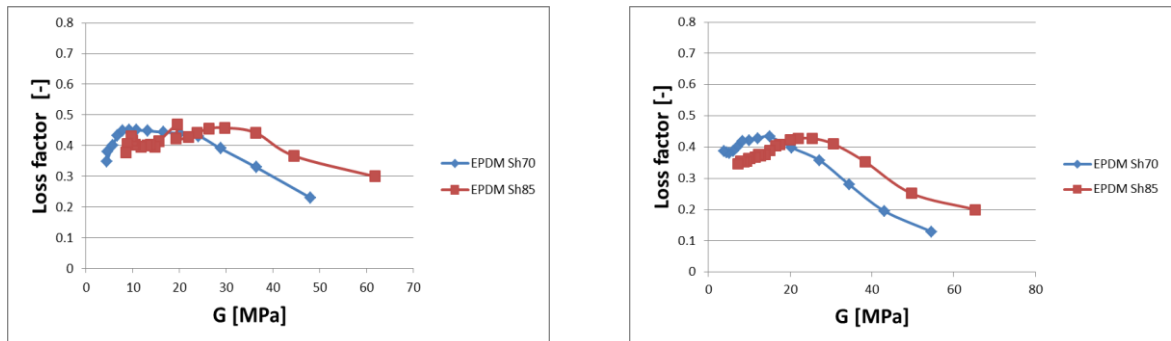


Fig. 2: The dependence the loss factor on the shear modulus at the temperature -20 °C for two excitation frequencies 2 Hz on the left and 5 Hz on the right.

## 3. Constants of hyperelatic model and proposal of hyperelastic proportional damping

To evaluated deformation energy analytically we needed first tune the MRM constant to experimental shear stress-strain curve. The constants of the MRM are evaluated from the experimental shear stress-strain curve using the least square method (LSM) (Šulc, 2016).

Experimental shear stress-strain curves of selected hard rubbers were obtained by our torque test rig for a temperature -20 °C. The test specimen was of cylindrical shape glued at both heads to steel consoles pins mounting in the collets. By usage of the consoles the test sample is not deformed in the vicinity of the heads due to clamping. The dimensions of the test sample of rubber were: diameter  $D = 0.03$  m, length  $L = 0.095$  m.

The material was isoprene butadiene rubber (EPDM) of hardness Sh 70 and Sh 85, temperature -20 °C and frequency 2 Hz of torsional loading. Experimental curves of shear stress  $\tau$  verse. Strain (skew)  $\gamma$ , where skews maximum of about 30 % (sample Sh 70) and 20 % (sample Sh 85) are shown in Fig. 3.

Tuned constants of the three and five-parametric MRM models based on LSM method result in:

Rubber EPDM Sh 70

- a)  $C_{10} = -0.2172e^8, C_{11} = 0.3663e^8, C_{01} = 0.0728e^8, C_{20} = -3.4316e^8, C_{02} = 0.7382e^8$   
b)  $C_{10} = -1.0760e^7, C_{11} = -0.1203e^7, C_{01} = 0.3649e^7$

Rubber EPDM Sh 85

- a)  $C_{10} = -0.3067e^8, C_{11} = -0.1021e^8, C_{01} = 0.1025e^8, C_{20} = -6.2160e^8, C_{02} = 1.9206e^8$   
b)  $C_{10} = -1.988e^7, C_{11} = -0.4016e^7, C_{01} = 0.6676e^7$

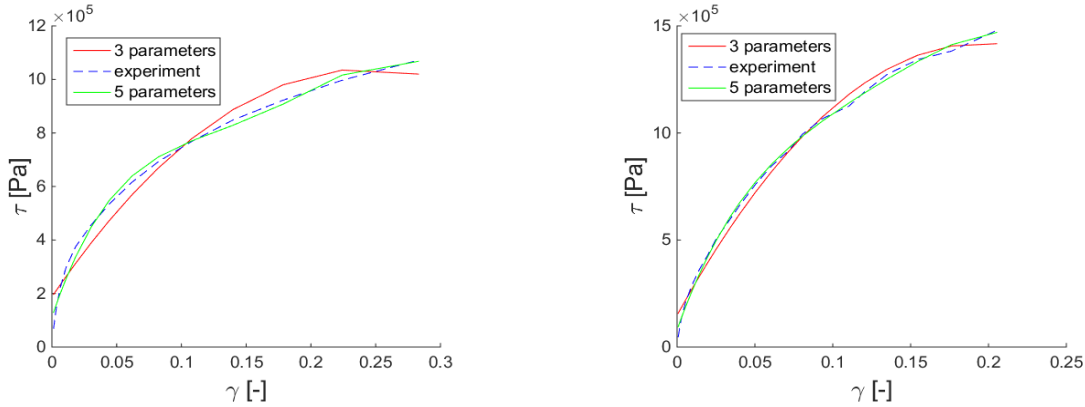


Fig. 3: Deformation curves of experiment and Mooney Rivlin models for 3 and 5 parameters EPDM Sh 70 on the left and EPDM Sh 85 on the right.

As mentioned previously based on experimental observations, dissipation energy was proposed as a hyperelastic proportional damping similar to modeling of damping in elastic theory. The dissipated energy  $U_{Dis}$  is expressed as product of the coefficient of hyperelastic proportional damping  $\beta$ , excitation frequency  $\omega$  and deformation energy  $U_{Def}$  coming from a hyperelastic Money Rivlin model with five parameters:

$$U_{Dis} = \beta \cdot \omega \cdot U_{Def}, \quad (1)$$

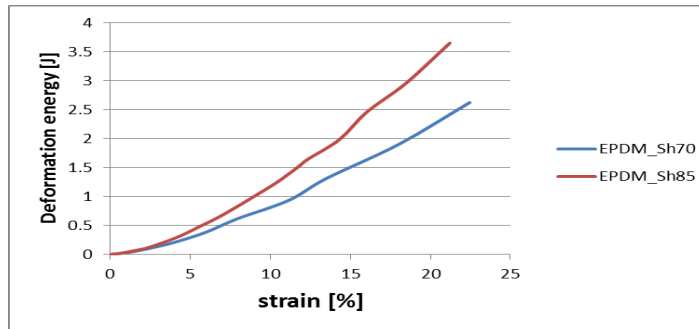


Fig. 4: The deformation energy of Money Rivlin models versus strain for EPDM Sh 70 and EPDM Sh 85 rubbers - temperature -20 °C, excitation frequency 2 Hz.

The experimental dissipation energy was obtained from the area of the hysteresis deformation loops for each case of testing torque moment. Total deformation energy was analytically evaluated from a deformation energy density  $u_{Def}$  multiplied by specific torque volume  $V_{red}$ . Deformation energy density is evaluated as integral in time over a quarter of excitation period  $T$

$$u_{Def} = \int_0^{T/4} \tau_{\max Mooney} \cdot \dot{\gamma}_{\max} dt, \quad (2)$$

where  $\tau_{\max Mooney}$  is a shear stress on surface of the cylindrical sample and  $\dot{\gamma}_{\max}$  is its associated shear

strain rate. Then total deformation energy is calculated from this relationship

$$u_{Def} = \int_0^{T/4} \tau_{\max Mooney} \cdot \dot{\gamma}_{\max} dt, \quad (3)$$

The calculated total deformation energies (EPDM Sh 70 and EPDM Sh 85 rubbers) of Mooney Rivlin (5 parametric) models are in Fig. 4. It shows that the higher hardness of rubber the higher deformation energy. The hyperelastic proportional damping coefficients evaluated from expression (1) in dependence on a strain are presented for both rubbers in Fig. 5. It shows that the coefficient is almost the same for both hardness of rubbers and it remains almost constant with a size of strain.

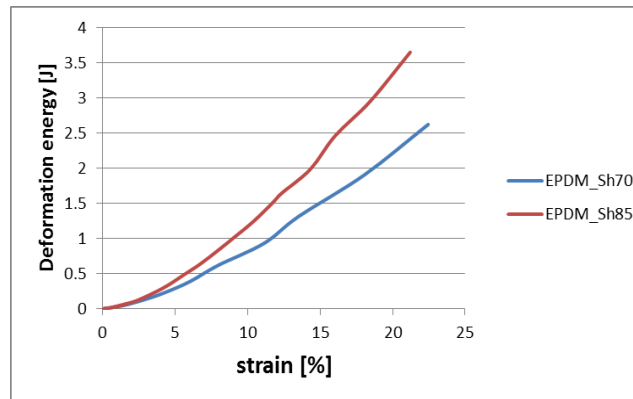


Fig. 5: The hyperelastic proportional damping coefficient versus strain for EPDM Sh 70 and EPDM Sh 85 rubbers - temperature -20 °C, excitation frequency 2 Hz.

#### 4. Conclusions

Two EPDM hard rubbers were tested on our torque test rig for study of their material constants and damping behavior under different amplitudes and frequencies of the harmonic excitations and under finite shear deformations. The shear modulus and loss factor were first evaluated for each of the excitation settings. Based on the experimental observations, the model of hyperelastic proportional damping was proposed here and the unknown coefficients of hyperelastic proportional damping were identified for both rubbers. The results of the coefficient values show that the coefficient is almost same for both hardness of rubbers and it remains almost constant with a size of strain. Since the higher hardness of rubber the higher deformation energy the dissipation energy grows up, too, as it is related to deformation energy by the proportional damping expression. The model of dissipation will be a subject of the next research and its validation. The model will be implemented into our in-house finite element code. It enables to simulate the thermo-dynamic behavior of the rubber dampers of more complicated shapes, states of stress and finite deformations.

#### Acknowledgement

This work was supported by the research project of the Czech Science Foundation No. 16-04546S “Aero-elastic couplings and dynamic behaviour of rotational periodic bodies”.

#### References

- Holzappel, A.G. (2000) Nonlinear Solid Mechanics, John Wiley & Sons.
- Nashif, A.D., Johnes D.I.G. and Henderson J.P. (1985) Vibration Damping, John Wiley & Sons.
- Pešek, L., Půst, L., Balda, M., Vaněk, F., Svoboda, J., Procházka, P. and Marvalová, B. (2008) Investigation of dynamics and reliability of rubber segments for resilient wheel, Procs. of ISMA, KU Leuven, pp. 2887-2902.
- Šulc, P., Pešek, L., Bula, V., Cibulka, J. and Košina, J (2016) Amplitude-temperature analysis of hard rubber by torsional vibration. Journal of Applied Mechanics and Materials. Vol. 821, No. 2016, pp. 295-302.
- Pesek, L., Pust, L., Bula, V. and Cibulka, J. (2015) Imposed Rubber Elements for Bladed Wheel Vibration Suppression, Journal of Vibration Engineering & Technologies, Vol. 3, No. 6, pp. 733-741.
- Šulc, P., Pešek, L., Bula, V., Cibulka, J., Boháč, T. and Tašek, H. (2017) Pre-stressed rubber material constant estimation for resilient wheel application. Journal of Advances in Engineering Software. DOI:10.1016/j.advengsoft.2016.07.009.

## COUPLED SIMULATION FOR FIRE-EXPOSED STRUCTURE USING CFD AND THERMO-MECHANICAL MODELS

S. Šulc<sup>\*</sup>, V. Šmilauer<sup>\*\*</sup>, F. Wald<sup>\*\*\*</sup>

**Abstract:** Fire resistance of buildings belong to fire safety assessment for centuries. It is based on fire element tests in horizontal and vertical furnaces, which are exposed to a rapid increase of temperature by gas burners. However, the tests are very expensive and time consuming. This article presents a coupled simulation of an element loaded by force and fire loading. The simulation solves a weakly-coupled problem, consisting of fluid dynamics, heat transfer and mechanical model. The temperature field from the CFD simulation creates Cauchy boundary condition for the thermal model. Then, the temperature field from element is passed to the mechanical model, which induces thermal strain and modifies material parameters. The fluid dynamics is computed with Fire Dynamics Simulator and the thermo-mechanical task is solved in OOFEM. Both softwares are interconnected with MuPIF python library, which allows smooth data transfer across the different meshes, orchestrating simulations in particular codes, exporting results to the VTK formats and distributed computing.

**Keywords:** Thermo-mechanical model, Virtual furnace, Computational fluid dynamics, Multiphysics, Fire resistance.

### 1. Introduction

Several single physical models exist for description of particular physical phenomena. Multi-physical coupled problems extend applications to more complicated tasks. In order to alleviate coupling among models, we created a python library which integrates solutions for computing simulations of structures exposed to fire. This paper presents approach how to interconnect single physical models.

### 1.2. Fire dynamics analysis

The issue of predicting fire process in defined space domain is solved with the Fire Dynamics Simulator software (FDS), developed at NIST (NIST, 2017). We had to modify the structure of the code to be able to call each computational time-step individually and we had to add several interface functions to get the dimensions of the meshes, the temperatures in the nodes, etc.

### 1.3. Thermo-mechanical analysis

The thermo-mechanical analysis of the element takes place in OOFEM (Patzák, 2000 and Patzák, 2012) software. The thermal analysis uses a temperature field from FDS, which defines Cauchy boundary conditions on the element. Then, the solution of thermal analysis passes temperature to the mechanical analysis, which induces the thermal strain and modifies the material parameters as yield strength and elastic modulus. Temperature will also be used for timber structures where it controls carbonization process and changes the thermal conductivity.

---

<sup>\*</sup> Ing. Stanislav Šulc: Department of Mechanics, Faculty of Civil Engineering, CTU in Prague; Thákurova 7/2077, 166 29, Prague; CZ, sulcstanda@seznam.cz

<sup>\*\*</sup> Assoc. Prof. Ing. Vít Šmilauer, PhD.: Department of Mechanics, Faculty of Civil Engineering, CTU in Prague; Thákurova 7/2077, 166 29, Prague; CZ, vit.smilauer@fsv.cvut.cz

<sup>\*\*\*</sup> Prof. Ing. František Wald, PhD.: Department of Steel and Timber Structures, Faculty of Civil Engineering, CTU in Prague; Thákurova 7/2077, 166 29, Prague; CZ, wald@fsv.cvut.cz



## 2. Interfacing FDS and OOFEM using MuPIF

Interfacing FDS and OOFEM using MuPIF (Patzák, 2010 and Patzák et al., 2015) library, which provides several useful tools such as exporting data to VTU format, parallel computations and advanced handling with data fields and meshes. Both the FDS Fortran and OOFEM C++ codes provide API for communication and they are compiled as shared libraries. Top-level steering script controls execution of both codes, data synchronization etc. The flowchart of the codes is given in Fig. 1.

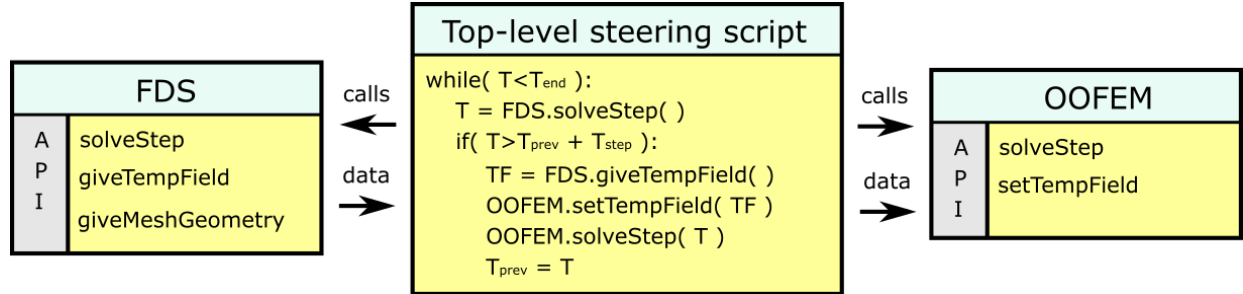


Fig. 1: Flowchart of the codes.

The FDS task consists of one or several uniform hexahedral meshes. In the beginning of the computation the geometries of all meshes are mapped from FDS to MuPIF. The meshes contain discretized temperature field.

Here we describe the loop over one OOFEM time-step, see the data workflow in Fig. 2. First, FDS is called to process several computational steps until we reach the length of our defined time-step of the thermo-mechanical task. The FDS application determines its time-step itself and it is usually much shorter than the OOFEM time-step. Then, we load the temperature fields from FDS and copy them into the MuPIF fields and into the OOFEM boundary-condition field. Then, OOFEM is asked to solve computational step of the thermal task and passes the computed temperatures of the construction to the mechanical task. The material parameters are updated due to the change of the temperature and the temperature strain is added. The mechanical response of the construction is obtained, which is the end of the computational loop.

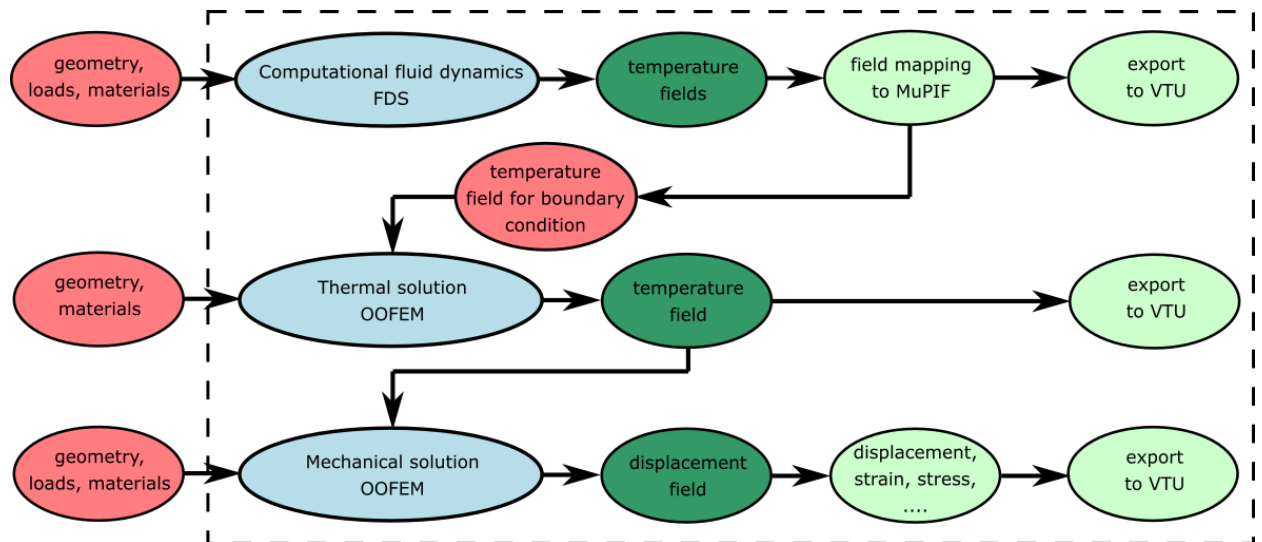


Fig. 2: Data workflow.

As the FDS analysis is very time-consuming process and the computations can last couple of days, we use another MuPIF functionality to store the meshes with all the temperatures in all defined time-steps in files. In this regard, it is possible to precompute FDS simulation and compute multiple thermo-mechanical analyses separately and much faster.

Coarse FDS mesh can be refined in areas where structure elements occur. This improves precision in temperature predictions and gives more realistic results of the thermo-mechanical task.

The MuPIF library has a tool to export the loaded FDS meshes to VTU, so that the FDS temperature fields can be exported into this useful format. OOFEM exports its results to VTU format as well.

### 3. Example

We demonstrate functionality of coupled CFD-thermo-mechanical task, consisting of a steel beam placed into a furnace with gas burners, see the geometry in Fig. 3. A horizontal furnace of fire laboratory PAVUS a.s. is of dimensions 3.0 m x 4.0 m and 2.2 m height. The furnace is heated by 8 natural gas burners. The simply-supported beam is made from steel I profile, placed just under the furnace ceiling. The steel parameters are  $E = 200 \text{ GPa}$ ,  $\nu = 0.3$ ,  $\rho = 7850 \text{ kg/m}^3$  and  $\alpha = 12 \times 10^{-6}$ . The length of the beam is 3.8 m. Geometry of the cross-section of the beam is in Fig. 4a. It is loaded only by its weight and the temperature.

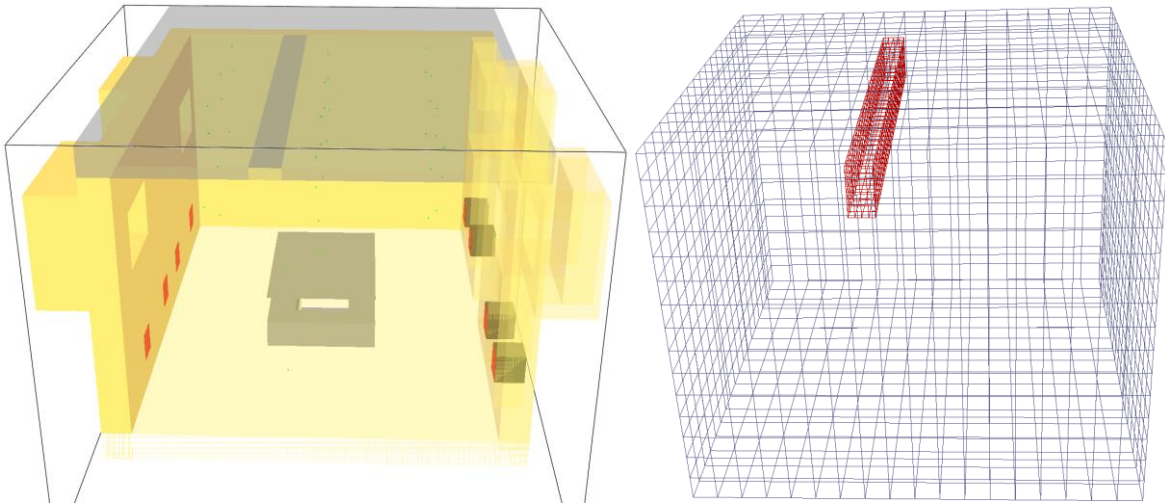


Fig. 3: a) FDS model (Smokeview), b) FDS meshes from MuPIF (Paraview).

The results were computed and exported to VTU files. Fig. 4b shows a cross-section through the middle of the furnace. We can see the two FDS meshes, one coarse on the whole furnace and one finer around the beam, which is necessary for the interpolation close to the ceiling. Detailed temperatures of the beam are displayed in Fig. 5a, the normal stress  $\sigma_x$  is in Fig. 5b.

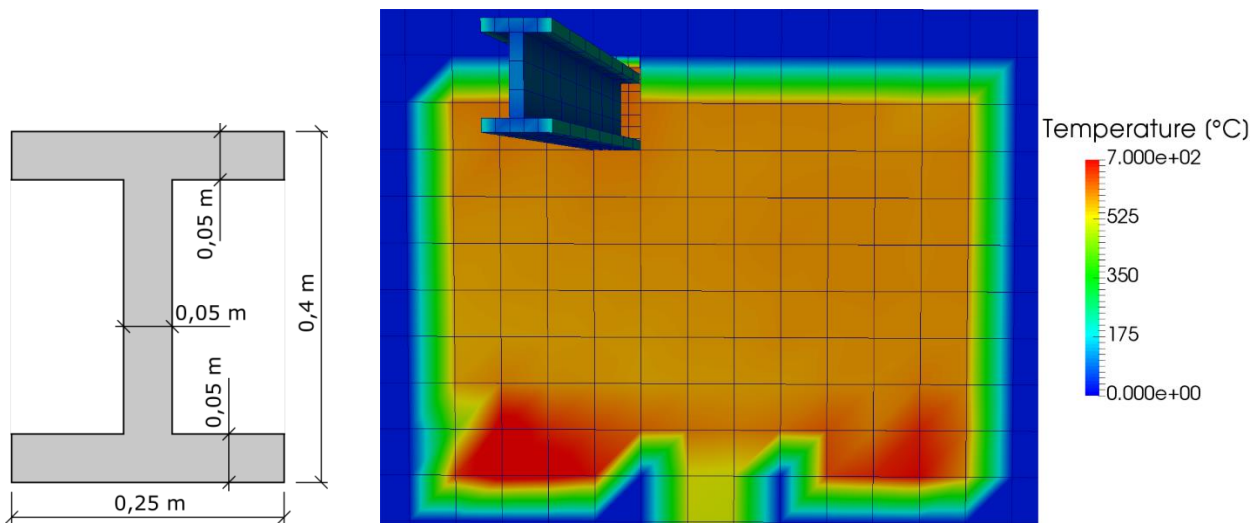


Fig. 4: a) Cross-section of the beam, b) Results at  $t = 576 \text{ s}$ , section in the middle of the furnace.

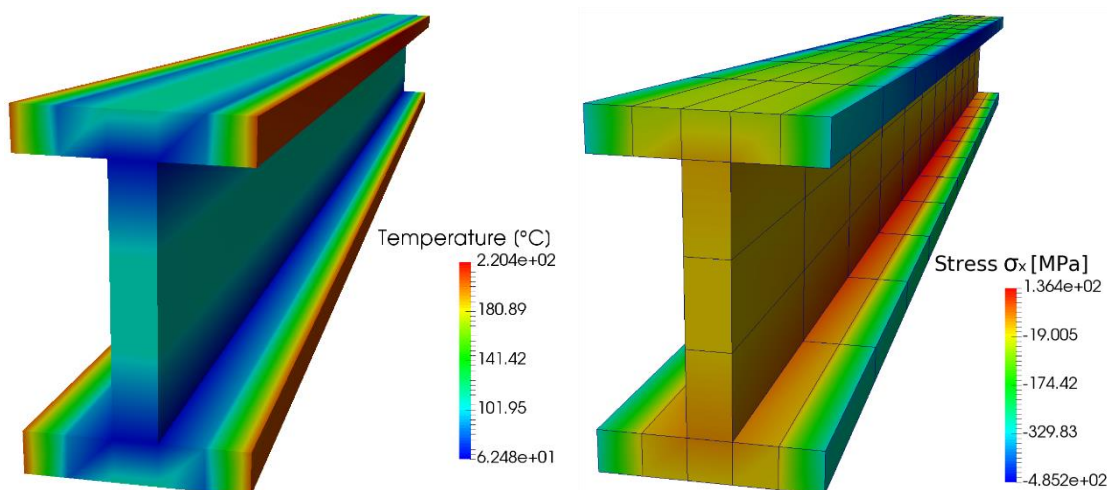


Fig. 5: Results at  $t = 576$  s, a) temperature, b) stress  $\sigma_x$ .

#### 4. Conclusions

This paper presents an approach for computing weakly-coupled problems, focusing on computational fluid dynamics coupled with thermo-mechanical analysis. Temperature field from FDS was validated previously (Cábová et al., 2017), Performance of structure elements presents a consecutive step. Validation of this multi-physical approach happens during 2017 on steel and timber structural elements.

#### Acknowledgement

We gratefully acknowledge the financial support from the Czech Technical University in Prague, the grant SGS17/042/OHK1/1T/11.

We also gratefully acknowledge the financial support from the Czech Science Foundation, the grant GACR 16-18448S.

#### References

- Cábová, K. et al. (2017) Modelling of Standard Fire Test, in: Proc. Int. Conf. on Engineering Mechanics 2017, (ed. Fuis, V.), Svratka, Czech Republic, pp. 226-229.
- Patzák, B. (2012) OOFEM – an object-oriented simulation tool for advanced modeling of materials and structures. Acta Polytechnica, 52(6):59-66.
- Patzák, B., Šmilauer, V. and Pacquaut, G. (2015) Design of a Multiscale Modelling Platform, in: Proc. Int. Conf. on Civil, Structural, and Environmental Engineering Computing, Prague, Czech Republic.
- Patzák, B. (2000) OOFEM project home page. <http://www.oofem.org/>.
- Patzák, B. (2010) MuPIF project home page. <http://mech.fsv.cvut.cz/mupif/>.
- NIST (2017) FDS, Fire Dynamics Simulator, home page. <https://pages.nist.gov/fds-smv/>.

## ANALYSIS OF NON-STATIONARY VIBRATION MODE MECHANICAL DEVICE

P. Šulka<sup>\*</sup>, A. Sapietová<sup>\*\*</sup>, V. Dekýš<sup>\*\*\*</sup>, M. Sapieta<sup>\*\*\*\*</sup>

**Abstract:** Presented article relates to principal mathematical methods in field of vibration research using computational software. Analysis of vibration and processing vibration signals by start-up (non-stationary mode) of mechanical device with purpose to detect vibration amplitude, effect of resonance and excitation of self-excited oscillations was performed. In this topic, there are listed a description and relevant approach serving for processing vibration signals. Core of this article is formed by make-ready data gained from real measurement, processing data through the calculation software, assembling computational algorithms for acquirement of results for next analysis and equation.

**Keywords:** Vibration signal, Non-stationary mode, Mathematical algorithms, Analysis, Vibration amplitude and oscillation.

### 1. Introduction

Measurement, processing and analysis of the mechanical vibrations are principal part of the diagnostic system to monitor operating conditions of machinery in all industrial sectors. The aim of machinery diagnostics includes the detection of occurrence and causes of vibrations and subsequent elimination of the possibility of their occurrence with an effort to ensure life prediction and maximize the reliability of the machinery in operation (Sága, 2009).

Vibrations measurement is very important, as evidenced by the still more emphasis put on the analysis of vibrations and noise, as well as advancing the development of diagnostic machinery. Increased vibration affects the life cycle of machines and causes material stress leading to direct failure, but also has a detrimental effect on humans, whether in the form of noise or vibrations that are closely related. This means that the diagnostic of the vibration is important assessment methodology in all industrial sectors (Handřík, 2016).

In this paper, there is a procedure for investigation of the vibration behavior of specific mechanical device presented. Firstly, mathematical methods, which were used for solving and evaluating of measured data, were defined. Secondly, analysis of vibration signal with computational software through the algorithms on basis of specific mathematical methods was conducted and finally, obtained results and graphical contour with purpose to detect amplitudes, natural frequency, and effect of resonance were investigated.

### 2. The investigated mechanical device

The investigated machinery is rolling mill, which consists of reinforced ground, supporting steel structure, electric motor, gearbox and rolling cartridge. Power transmission between (gearbox and axle is secured by coupling shafts, which are connected to both end of the claw couplings. Drive the rolling

---

<sup>\*</sup> Ing. Peter Šulka.: Department of Applied Mechanics, Žilina University, Univerzitná 8215/1, 010 26 Žilina, SK, peter.sulka@fstroj.uniza.sk

<sup>\*\*</sup> Assoc. Prof. Ing. Alžbeta Sapietová, PhD.: Department of Applied Mechanics, Žilina University, Univerzitná 8215/1, 010 26 Žilina, SK, alzbeta.sapietova@fstroj.uniza.sk

<sup>\*\*\*</sup> Assoc. Prof. Ing. Vladimír Dekýš, PhD.: Department of Applied Mechanics, Žilina University, Univerzitná 8215/1, 010 26 Žilina, SK, vladimir.dekys@fstroj.uniza.sk

<sup>\*\*\*\*</sup> Ing. Milan Sapieta, PhD.: Department of Applied Mechanics, Žilina University, Univerzitná 8215/1, 010 26, Žilina, SK, milan.sapieta@fstroj.uniza.sk

cartridges is ensured by cardan shafts. The measurement was taken at the measuring point No. 1 in the axial direction.

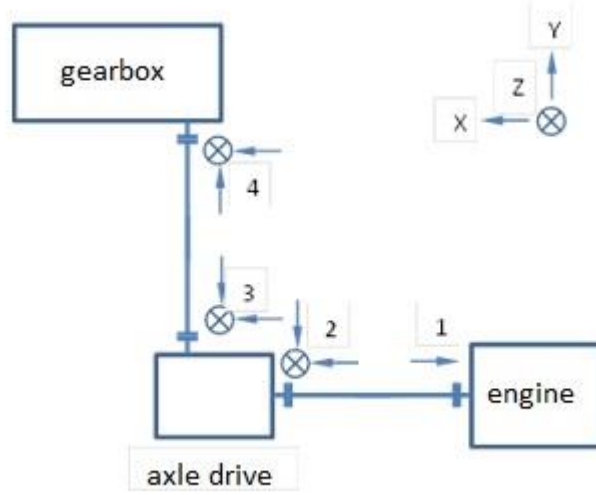


Fig. 1: The investigated rolling mill.

### 3. Mathematical methods

Fourier transform and its applications along with relying on wavelet transformations of various types are effective methods for processing various signals. Methods provide relevant information and results of the measurement data by applying appropriate mathematical algorithms of these methods using computer software. The results are graphic representations of the vibration signals in the time or frequency domain values with a possible detection of vibrations. The following paragraphs are different mathematical methods thoroughly described.

Short-time Fourier transform (STFT) is a tool for time-frequency analysis of non-stationary signals. The transformation provides information of the signal  $f(t)$  and its spectrum  $F(\omega)$  in the time-frequency window. The principle of this method is that, by multiplying the signal  $f(t)$  to be analyzed with a certain type of symmetry of a window function (i.e. Window  $\omega * (t - \tau)$  of constant length, and the computation of the Fourier transform of the sections to the signal  $f(t)$  (Grigorian, 2009 and Samajova, 2015) is as follows:

$$STFT\{x(t)\}(\tau, \omega) \equiv X(\tau, \omega) = \int_{-\infty}^{\infty} f(t) \omega * (t - \tau) e^{-j\omega t} dt = \langle f(t), \omega * (t - \tau) e^{-j\omega t} \rangle, (1)$$

where the symbol (\*) indicates complex conjugation and  $\tau$  represents time offset of window.

Wavelet transformation consists of unfolding and folding the input signals via the function called wavelet. Wavelet is time-localized wave i.e. wave packet. Wavelet transform has all the features created from a single parent prototype basic wavelet  $\psi(t)$  by means of two basic operations scaling and offset in time contour (Qian, 2011).

$$SWT_f(a, b) = \int_{-\infty}^{\infty} f(t) \psi_{[a,b]}^*(t) dt = \langle f(t), \psi_{[a,b]}(t) \rangle \quad a \in R^+, b \in R, (2)$$

Wavelet transform of function  $f(t) \in L^2(r), R = (-\infty, \infty)$  is defined as representation  $L^2(R) \rightarrow L^2(R^2)$ .

$L^2(a, b)$  is space, where squares of functions exist, are integral and finite.

### 4. Solution and evaluating the results

By the measurement process of rolling mill 6,228,215 data representing acceleration values was acquired. Sensor sampling rate was set to 25,600 kHz, corresponding to a time step  $t = 1 / f = 3.90625e-005$  s. Start-up, constant speed and run-out of the machinery (rolling mill) is shown in Fig. 2. Time dependent values of acceleration and the corresponding values of rotation speed (RPM) for about 243 s are displayed are in Fig. 2. From Fig. 2 it is clear that the start-up (non-stationary mode) of the machinery is performed

at a time interval  $< 0.75 \text{ s} >$ , increasing the speed from 100 to approximately 1,500 revolutions per minute and having the current acceleration of  $40 \text{ m/s}^2$ .

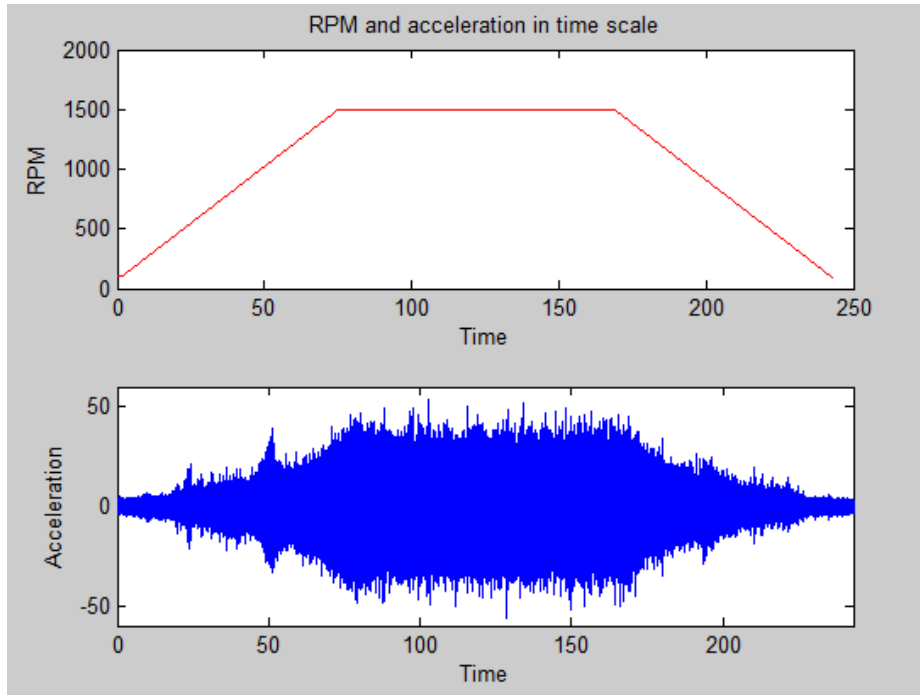


Fig. 2: Graphical contour of RPM and acceleration.

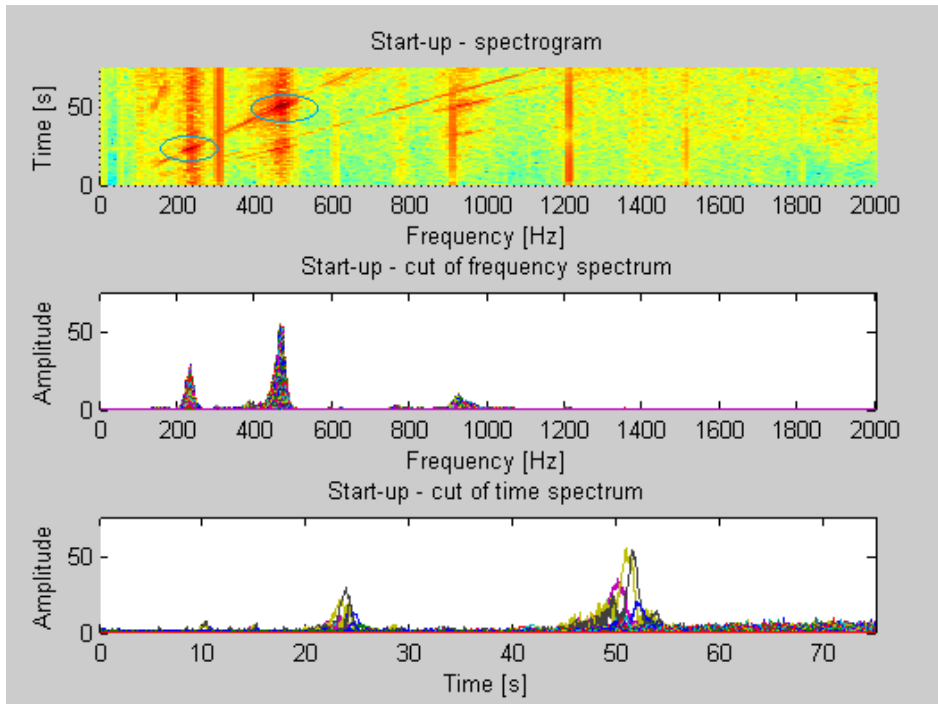


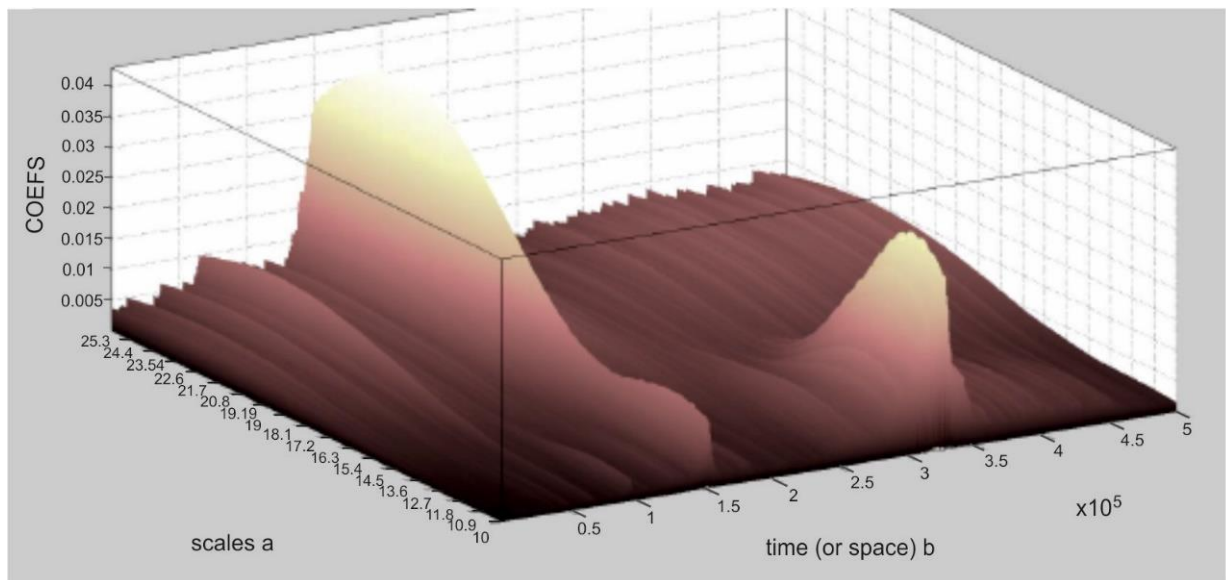
Fig. 3: Detection of resonance and natural frequency by means of STFT.

Displayed graphical contours investigated natural frequency and frequency aggregation that show appearance of resonance effect. From Figs. 3 and 4, we are able to investigate following parameters and their occurrence at specific frequency, time and RPM.

$$t = 23 \text{ s} \rightarrow 230 \text{ Hz} \rightarrow 517.8 \text{ RPM} \rightarrow 9.22 \text{ order}$$

$$t = 51 \text{ s} \rightarrow 470 \text{ Hz} \rightarrow 1031 \text{ Hz} \rightarrow 18.43 \text{ order}$$





*Fig. 4: Detection of resonance and natural frequency by means of Wavelet transformation.*

## 5. Conclusion

STFT Method and Wavelet transform provide more extensive analysis options that are relevant to the processing the data of non-stationary modes (start-up). The most important advantage of the application of these mathematical methods is the detection of effects arising in complex installations oscillations in the time domain as well as in frequency domain. Algorithms for signal analysis method STFT, Wavelet transform (CWT) and graphical outputs were created in MATLAB R2014 user environment. The environment provides fairly wide range of graphic processing (color maps, 3D charts, graphical contours to coordinate frequency-amplitude and time-amplitude spectrum) (Sága, 2011). The purpose of the analysis was to find out events of oscillation (resonance identification, natural frequency) during ongoing measurements, i.e. during operation of mechanical object. We can assume that the results obtained by these methods will be in scale of necessary resolution, comparable and virtually the same.

## Acknowledgement

This work was supported by the Slovak Grant agency VEGA 1/0787/15.

## References

- Grigorian, M.A. and Grigorian M.M. (2009) Brief Notes in Advanced DSP. Fourier analysis with Matlab, ISBN 9781439801376, CRC Press, Boca Raton.
- Handrik, M., Vaško, M., Kopas, P. and Mozer, V. (2016) The linear and nonlinear stability loss of structures due to thermal load, in": 20<sup>th</sup> International Conference Machine and Simulations, MMS 2015, Terchová.
- Qian, S.C. (2011) Joint Time-Frequency Analysis. Methods and Applications, ISBN 0-13-254384-2, Prentice Hall, New Jersey.
- Samajova, H., Ftorek, B. and Spanikova, E. (2015) Asymptotic character of non-oscillatory of functional differential systems, Electronic Journal of Qualitative Theory of Differential Equations, Szeged.
- Sága, M., Bednár, R. and Vaško, M. (2011) Contribution to Modal and Spectral Interval Finite Element Analysis, in: 10<sup>th</sup> Biennial International Conference on Vibration Problems (ICOVP), Praha.
- Sága, M., Žmindák, M., Dekýš, V. and Sapietová, A. (2009) Selected methods of analysis and synthesis of mechanical systems, UNIZA – Žilina University, (in Slovak).

## STRESS ANALYSIS OF THE TOTAL REPLACEMENT OF THE TRAPEZIOMETACARPAL JOINT

T. Svojanovský\*, L. Trtík\*\*

**Abstract:** The article devotes to finite element analysis of the total replacement of the trapeziometacarpal (TMC) joint. Various types of analyzes were carried out dealing with influence of different geometry of the replacement. Apart from detailed models, more complex one including bones and ligaments was created to achieve more realistic conditions and thus, more trustworthy results. The goal of this study is to bring awareness about stress states depending on geometry of the replacement as well as provide an image of contact pressure distribution when loading the replacement.

**Keywords:** Stress analysis, Finite element method, Trapeziometacarpal joint, Total replacement.

### 1. Introduction

Biomechanics is a scientific-medical branch that has been developing for decades, however, still offering many challenges regarding new inventions and innovations (Fuis et al., 2001, 2004, 2009, 2010, 2011 and 2011a) which help people avoid pain, make their physical activities easier and their lives satisfied. As a follow-up to (Svojanovský et al., 2014 and 2015), this article aims mainly at advanced comparison of contact pressure distribution between parts of the TMC replacement. Such a replacement serves as a surgical solution of a joint disease called rhizarthrosis which reduces mobility of a thumb or totally prevents from any motion.

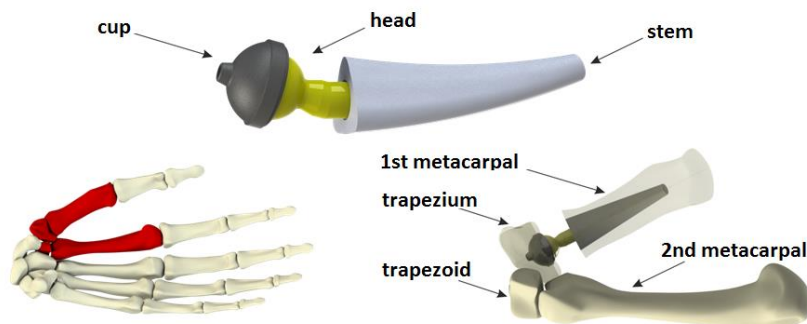


Fig. 1: Trapeziometacarpal replacement, its placement in thumb bones.

One of several types of TMC replacements, which are currently available, was chosen for this analysis. The replacement consists of three parts – a head interconnecting a cup and stem. These parts of the TMC replacement are inserted surgically to thumb bones – trapezium on one side and metacarpal on the other side (Fig. 1). Complex geometrical model of the TMC replacement inserted in thumb bones was performed on the basis of X-ray images of a real surgical intervention (Trtík, 2011).

### 2. Overview of analyzed models

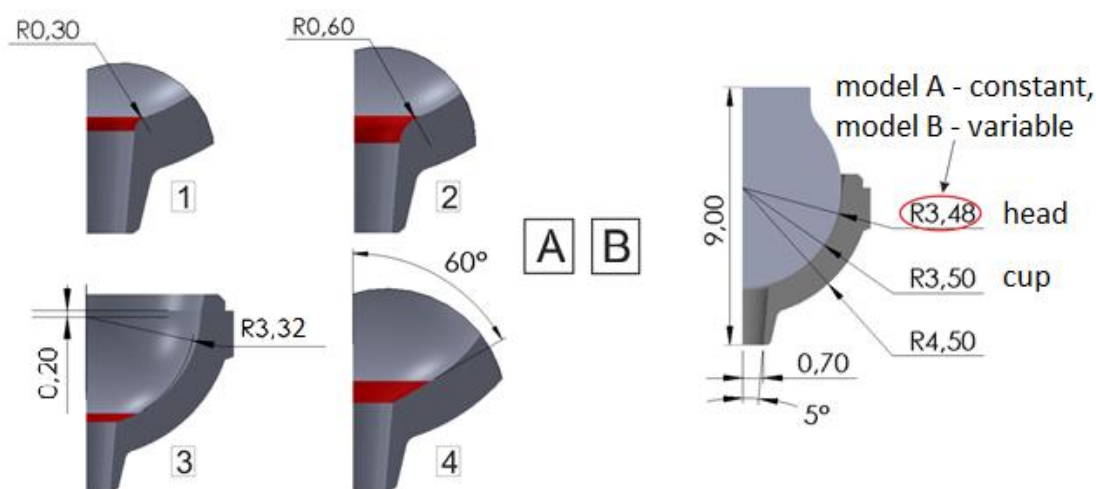
Various models of the TMC replacement are to be analyzed using finite element method. As introduced

\* Ing. Tomáš Svojanovský: Institute of Solid Mechanics, Mechatronics and Biomechanics, Brno University of Technology, Technická 2896/2; 616 69, Brno; CZ, svojanovsky.t@seznam.cz

\*\* MUDr. Lubomír Trtík: Department of Orthopedic Surgery, Husova 2624; 580 01 Havlíčkův Brod; CZ, lubomir.trtik@klikni.cz

below, there are three model sets (A, B, C), each of them dealing with specific conditions (Fig. 2). Material properties of the models A, B, C of the cup and head correspond with CoCrMo alloy.

*Fig. 2: Loading of models A and B.*



*Fig. 3: Description of models A and B.*

All the four variants of the model A are loaded by maximum force of 1000 N which is approximately the highest force achievable in normal life. In addition, the loading is carried out symmetrically with regards to the axis of rotation symmetry.

To analyze influence of the head size, nine variants were created while preserving shape and size of the cup (Tab. 1). Material properties and loading conditions are the same as for the model A.

Variant number	1	2	3	4	5	6	7	8	9
Spherical radius of the head [mm]	3.42	3.43	3.44	3.45	3.46	3.47	3.48	3.49	3.50

**MODEL C** – complex model of the cup, head and stem including relevant bones and ligaments (Fig. 4).

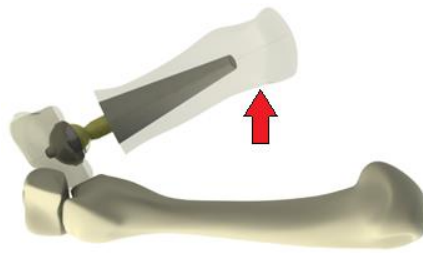


Fig. 4: Loading of the model C.

### 3. Results

In terms of results of the model A, variant number 4 (conical transition) evinces lowest equivalent stress as well as contact pressure (Tab. 2).

Tab. 2: Results for four variants of the model A.

Variant number	Description	Maximum equivalent stress [MPa]	Maximum contact pressure [MPa]
1	Rounded transition 0.3 mm	618	845
2	Rounded transition 0.6 mm	589	839
3	Nested spherical surface	518	834
4	Conical transition	376	584

Comparing profiles of contact pressure distribution along a path on the cup surface, Fig. 5 shows dependence of contact pressure distribution on the head size (spherical radius). Number 0 on the horizontal axis of the graph means connection line connecting conical and spherical surface.

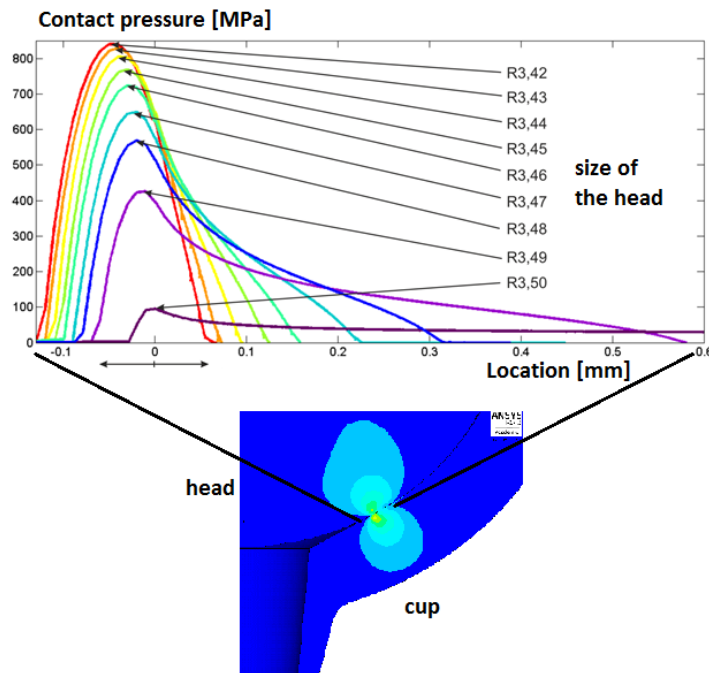


Fig. 5: Contact pressure distribution depending on the head size (spherical radius).

As emerged from the analysis of the complex model C including bones and ligaments, maximum contact pressure may achieve approximately 380 MPa when loading the thumb by force of 100 N as depicted in Fig. 6.

### 4. Conclusions

Finite element method was used to analyze stress states in contact between parts of the TMC replacement. Two detailed models and a complex one were created to investigate desired conditions.

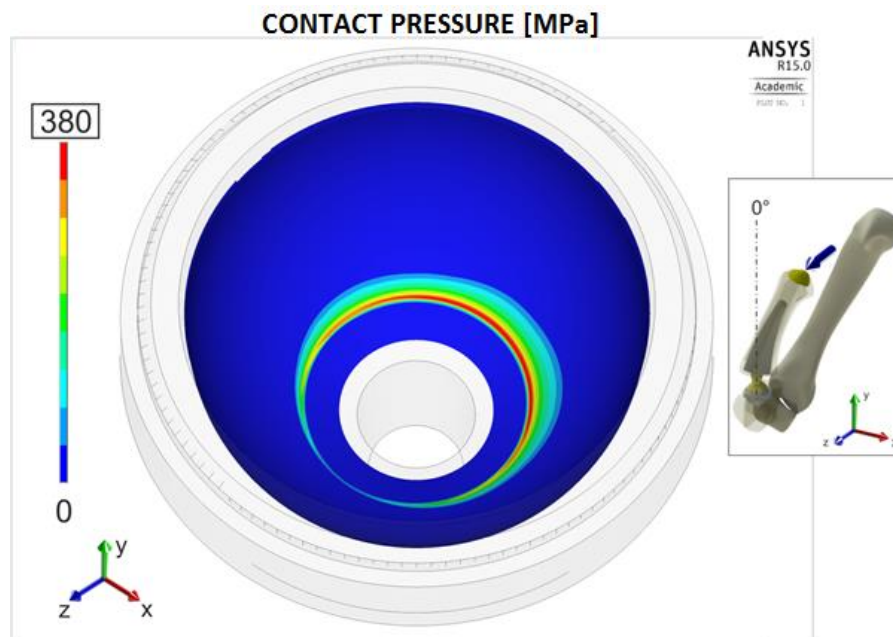


Fig. 6: Contact pressure distribution on the cup surface of the model C.

The detailed model A dealing with different types of a cup proved that the cup with conical-spherical shape evinces lowest maximum contact pressure as well as lowest maximum equivalent stress. The detailed model B compares stress states depending on size of the spherical part of the head. It came out that lowest contact pressure occurs when sizes of the head and cup are the same, alternatively head size is slightly smaller than cup size. There is a distinctively higher maximum contact pressure when the head reaches smaller sizes. However, going further to smaller head sizes, maximum contact pressure changes only slightly. Analysis of the model C proves that contact is mostly occurred in a narrow zone following spherical-conical surface transition. This is chiefly caused by ligaments which ensure static equilibrium among individual parts.

### Acknowledgement

This work was supported by grant FSI-S-17-4004.

### References

- Fuis, V. and Janicek, P. (2001) Stress and reliability analyses of ceramic femoral heads with axisymmetric production inaccuracies. in: Proc. 9<sup>th</sup> Mediterranean Conference on Medical and Biological Engineering and Computing, Pula, Croatia, IFMBE Proceedings Pts. 1 and 2, pp. 632-635.
- Fuis, V. (2004) Stress and reliability analyses of ceramic femoral heads with 3D manufacturing inaccuracies, in: Proc. 11<sup>th</sup> World Congress in Mechanism and Machine Science, Tianjin, China pp. 2197-2201.
- Fuis, V. and Varga, J. (2009) Stress Analyses of the Hip Joint Endoprosthesis Ceramic Head with Different Shapes of the Cone Opening. in: Proc. 13<sup>th</sup> International Conference on Biomedical Engineering, IFMBE Proceedings Vol. 23, Iss. 1-3, pp. 2012-2015.
- Fuis, V., Navrat, T. and Vosynek, P. (2010) Analyses of the Shape Deviations of the Contact Cones of the Total Hip Joint Endoprostheses. in: Proc. 6<sup>th</sup> World Congress of Biomechanics (WCB 2010) Singapore, Series: IFMBE Proc. Vol. 31, pp. 1451-1454.
- Fuis, V., Koukal, M. and Florian, Z. (2011) Shape Deviations of the Contact Areas of the Total Hip Replacement, in: 9<sup>th</sup> International Conference on Mechatronics, Warsaw, Poland pp. 203-212.
- Fuis, V., Malek, M. and Janicek, P. (2011a) Probability of destruction of Ceramics using Weibull's Theory, in: Proc. 17<sup>th</sup> International Conference on Engineering Mechanics, Svratka, Czech Republic, pp. 155-158.
- Svojanovský, T. and Trtík, L. (2014) Rhizarthrosis and Its Treatment, Stress and Deformation Analysis of the Total Joint Replacement. in: Proc. 20<sup>th</sup> International Conference on Engineering Mechanics, Svratka, Czech Republic, pp. 616-619.
- Svojanovský, T. (2015) Deformation and Stress Analysis of the Parts of the Total Replacement of the Trapeziometacarpal Joint. Thesis Brno University of Technology, Brno, 88 p. (in Czech).
- Trtík, L. (2011) Rhizarthrosis, Current Possibilities of Treatment. Ortopedie 1: 30-35, 2011 Available on: [http://fvconsult.krivanekludek.cz/prednasky/Trtik\\_Rizartroza.pdf](http://fvconsult.krivanekludek.cz/prednasky/Trtik_Rizartroza.pdf), pp. 28-33.



## CONSTRUCTION OF RANDOM FIELD BASED ON IMAGE ANALYSIS

J. Sýkora<sup>\*</sup>, A. Kučerová<sup>\*\*</sup>, J. Zeman<sup>\*\*\*</sup>

**Abstract:** *The principal challenge in implementation of random fields arises from the need for determination of their correlation/characteristic lengths in the simplest case or more generally their covariance functions. The present contribution is devoted to the construction of random fields based on image analysis utilising statistical descriptors, which were developed to describe the different morphology of random material. A numerical study of one-dimensional images is performed in order to investigate the quality of obtained random fields.*

**Keywords:** Random fields, Two-point probability function, Covariance function, Karhunen-Loève expansion, Principal component analysis.

### 1. Introduction

When dealing with a heterogeneous material, some material parameters can vary spatially in an uncertain fashion and therefore random fields are suitable for their description. In a computational setting, the random field and the numerical model must be discretized. Therefore, the most common approach for achieving this is the Karhunen-Loève expansion (KLE), see (Kučerová et al., 2012). The KLE allows for representation of random fields utilising surprisingly few orthogonal terms from spectral decomposition of covariance function, see (Adler and Taylor, 2007). Several analytical covariance functions were developed to describe the spatial variability, but their relevance in describing real material properties remains questionable and poorly identified. Recently, relatively new techniques of extracting the spatial randomness from images were developed, see (Soize, 2006; Jürgens et al., 2012).

Here, we introduce a novel construction of covariance function based on the two-point probability density function (see Torquato, 2002), which is calculated from the given discretised image. Due to the limited space it is impossible to present the mathematical formulation of entire methodology. Therefore, we refer only basic features of each procedure used for the different constructions of random fields.

- Karhunen-Loève expansion. It is an extremely useful tool for the concise representation of the stochastic processes. Based on the spectral decomposition of covariance function, the KLE decomposes the process into a series of orthogonal functions with the random coefficients, see (Adler and Taylor, 2007). For practical implementation, the KLE is truncated after  $M$  terms, yielding the suitable approximation. Based on the spectral decomposition of covariance function  $C(\mathbf{x}, \mathbf{x}')$  and the orthogonality of eigenfunctions  $\phi_i$ , the real-valued random field  $\lambda(\mathbf{x}, \omega)$  can be written as

$$\lambda(\mathbf{x}, \omega) \approx \mu_\lambda(\mathbf{x}) + \sum_{i=1}^M \sqrt{\zeta_i} \xi_i(\omega) \phi_i(\mathbf{x}), \quad (1)$$

where  $\mu_\lambda(\mathbf{x})$  is the mean value,  $\zeta_i$  are the positive eigenvalues and  $\xi(\omega)$  is a set of uncorrelated random variables of zero mean and unit variance.

- Two-point probability function ( $S_2$ ). It is a statistical descriptor developed for the morphology description of multi-phase random heterogeneous material, see (Havelka et al., 2016). Here, the

---

<sup>\*</sup> Ing. Jan Sýkora, PhD.: Czech Technical University in Prague, Faculty of Civil Engineering, Thákurova 7, 166 29, Prague, CZ, jan.sykora.1@fsv.cvut.cz

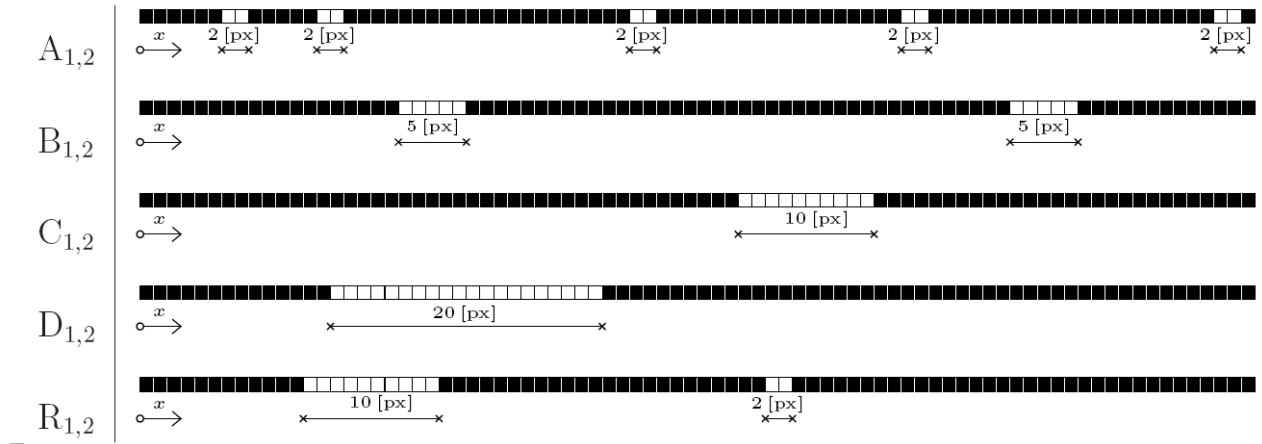
<sup>\*\*</sup> Ing. Anna Kučerová, PhD.: Czech Technical University in Prague, Faculty of Civil Engineering, Thákurova 7, 166 29, Prague, CZ, anicka@cml.fsv.cvut.cz

<sup>\*\*\*</sup> Assoc. Prof. Ing. Jan Zeman, PhD.: Czech Technical University in Prague, Faculty of Civil Engineering, Thákurova 7, 166 29, Prague, CZ, zemanj@cml.fsv.cvut.cz



two-point probability function is utilised for the computation of covariance function.

- Covariance function (CF). It is a spatial measure of how much two variables change together and plays a key role in the construction of random field. There are several well-known analytical functions (e.g. Exponential, Gaussian, see (Kučerová and Sýkora, 2013)), and/or it can be directly calculated from the images employing the statistical descriptor, see (Lombardo et al., 2009) for transformation formula.
- Principal component analysis (PCA). It is an orthogonal linear transformation that transforms a set of correlated variables into a set of linearly uncorrelated variables called principal components, see (Jolliffe, 2002).



*Fig. 1: Reference media, size 1 x 100000 px:  $A_1$  – particles 1 x 2 px filling 10 % of volume;  $A_2$  – particles 1 x 2 px filling 50 % of volume;  $B_1$  – particles 1 x 5 px filling 10 % of volume;  $B_2$  – particles 1 x 5 px filling 50 % of volume;  $C_1$  – particles 1 x 10 px filling 10 % of volume;  $C_2$  – particles 1 x 10 px filling 50 % of volume;  $D_1$  – particles 1 x 20 px filling 10 % of volume;  $D_2$  – particles 1 x 20 px filling 50 % of volume;  $R_1$  – particles ranging from 1 x 2 px to 1 x 20 px filling 10 % of volume;  $R_2$  – particles ranging from 1 x 2 px to 1 x 20 px filling 50 % of volume.*

## 2. Numerical examples

The first part of numerical analysis is devoted to the identification of the correlation lengths used in the analytical relations of covariance functions. As an illustration, we utilised a set of digitised images representing artificially created particulate suspensions consisting of rectangular white particles randomly distributed within a black matrix. The initial binary structures 1 x 100000 px and their basic statistical properties are shown in Fig. 1 and in Tab. 1, respectively.

*Tab. 1: Basic statistical properties.*

		$A_1$	$A_2$	$B_1$	$B_2$	$C_1$	$C_2$	$D_1$	$D_2$	$R_1$	$R_2$
Vol. '0'	[%]	90.0	50.0	90.0	50.0	90.0	50.0	90.0	50.0	90.0	50.0
$\mu$	[-]	0.10	0.50	0.10	0.50	0.10	0.50	0.10	0.50	0.10	0.50
$\sigma$	[-]	0.30	0.50	0.30	0.50	0.30	0.50	0.30	0.50	0.30	0.50

The calibration procedure of the covariance lengths is relatively simple and intuitive process. The proper optimization algorithm is used to minimise the difference between the original covariance function calculated from two-point probability function of reference medium (see (Lombardo et al., 2009)) and the computed one. In our study, we utilised the in-house GRADE algorithm, which is a real-coded stochastic optimization algorithm combining the principles of genetic algorithms and differential evolution, see (Ibrahimbegović et al., 2004). The results obtained for two covariance kernels, i.e. Gaussian and Exponential, are summarised in Tab. 2.

In the next example, several numerical constructions of random fields from input digitised images are examined to achieve a real description of spatial variability. To keep this study clear, let us consider the

same set of one-dimensional binary images as in the previous example, see Fig. 1. The results in Tab. 2 show that the computed correlation lengths are approximately ten thousand times smaller than the original dimensions of the investigated structure. Thanks to this fact we can reduce the dimensions of our problem to 1 x 100 px, and thus decrease the computational demands to a reasonable level. Besides that, it is necessary to objectively assess the construction techniques of random field in terms of their accuracy. For this purpose we prepare a verification set for each reference medium consisting of 10000 images with dimensions 1 x 100 px randomly cut from the original image.

Tab. 2: Optimised covariance lengths calibrated for Gaussian (GK) and Exponential kernel (EK).

	$A_1$	$A_2$	$B_1$	$B_2$	$C_1$	$C_2$	$D_1$	$D_2$	$R_1$	$R_2$
GK - $l_x$ [px]	0.75	0.50	1.91	1.10	3.78	2.33	7.66	4.77	4.91	2.48
EK - $l_x$ [px]	0.87	0.50	2.39	1.20	4.68	2.59	9.64	5.40	6.37	3.10

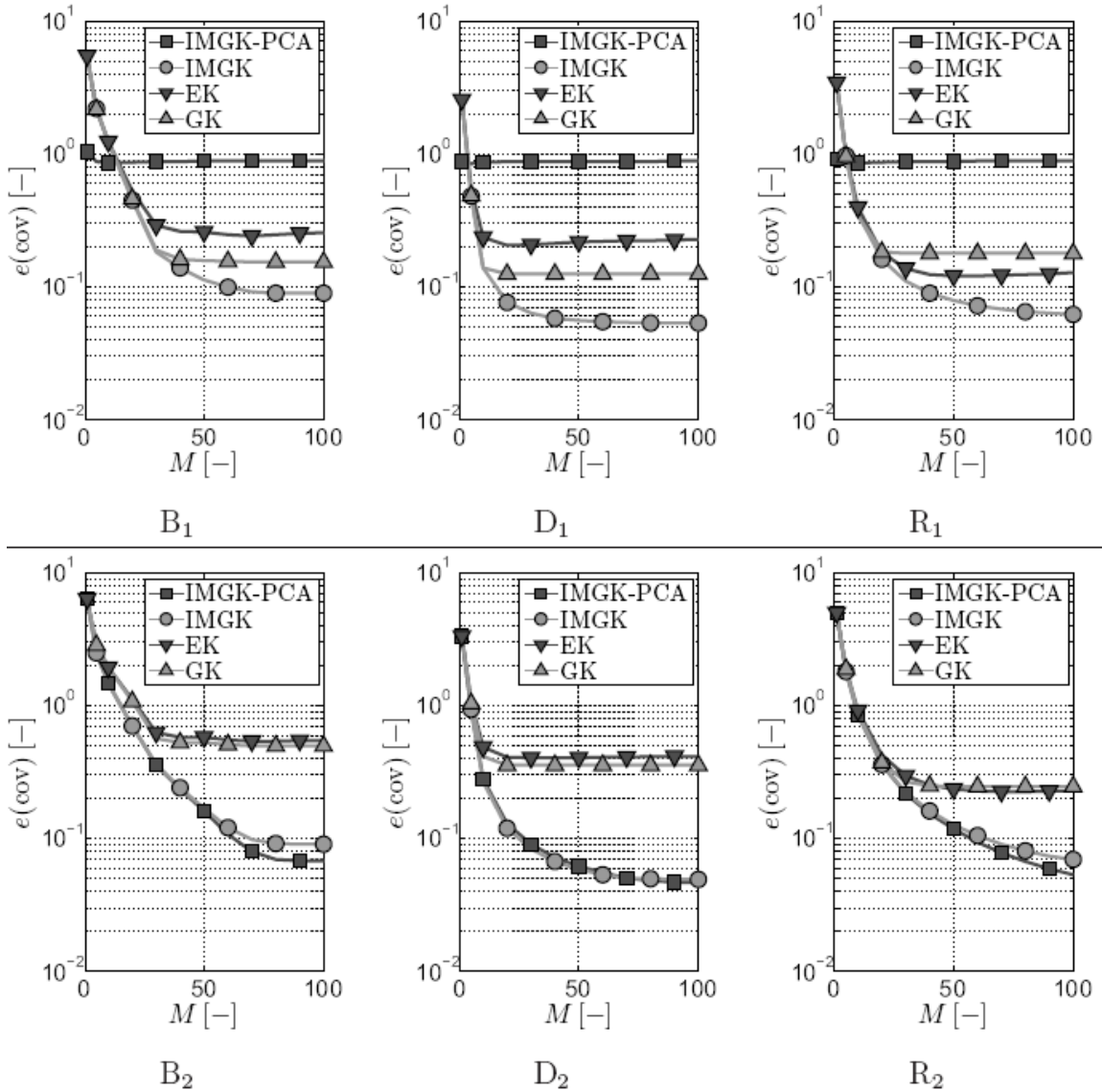


Fig. 2: Relative error of covariance matrix as a function of KLE terms  $M$  [-] calculated for reference media -  $B_1$ ,  $B_2$ ,  $D_1$ ,  $D_2$ ,  $R_1$ ,  $R_2$ .

Overall, four methods for a construction of random fields: (i) Gaussian-based (GK), (ii) Exponential-based (EK), (iii) Image-based (IMGK), and (iv) Image-PCA-based (IMGK-PCA) were examined for 10000 realisations. The errors  $e(\text{cov})$  on the prediction of covariance computed relatively to the verification sets are plotted as a function of the number of KLE terms in Fig. 2. It can be seen the gain of

image-based random fields' construction and strong dependencies of relative errors for a small number of KLE modes.

### 3. Conclusions

In this contribution, we present different strategies for construction of random fields. A comparison of classical approach based on the analytical covariance functions, namely Exponential and Gaussian, and a novel methodology based on image analysis was shown to assess the quality and accuracy of obtained random fields. The whole concept was demonstrated on a digitised binary image of two phase medium.

The most interesting finding is that the image-based random fields' construction provides more precise description of spatial variability than constructions based on the analytical covariance functions with optimised correlation lengths. It is a probably logical conclusion, but the use of analytical covariance functions, especially without calibrated correlation lengths, in random fields' construction is very widespread technique in numerical modelling of heterogeneous material and leads evidently to inaccurate results.

Another important result is related to the truncation of the Karhunen-Loève expansion. It is evident from the presented figures that the proposed methodology is very sensitive to small number of Karhunen-Loève terms. In this region, the relative error of random fields compared to verification set decreases very sharply.

### Acknowledgement

We are thankful for financial support from the Czech Science Foundation, projects No. 15-07299S and No. 16-11473Y.

### References

- Adler, R.J. and Taylor, J.E. (2007) Random Fields and Geometry. Springer.
- Havelka, J., Kučerová, A. and Sýkora, J. (2016) Compression and reconstruction of random microstructures using accelerated lineal path function. *Computational Materials Science*, 122, pp. 102-117.
- Ibrahimbegović, A., Knopf-Lenoir, C., Kučerová, A. and Villon, P. (2004) Optimal design and optimal control of structures undergoing finite rotations and elastic deformations. *International Journal for Numerical Methods in Engineering*, 61, 14, pp. 2428-2460.
- Jolliffe, I. (2002) Principal component analysis. Wiley Online Library.
- Jürgens, D., Krosche, M. and Niekamp, R. (2012) A Process for Stochastic Material Analysis based on Empirical Data. *Technische Mechanik*, 32, 2-5, pp. 303-306.
- Kučerová, A., Sýkora, J., Rosić, B. and Matthies, H.G. (2012) Acceleration of uncertainty updating in the description of transport processes in heterogeneous materials. *Journal of Computational and Applied Mathematics*, 236, 18, pp. 4862-4872.
- Kučerová, A. and Sýkora, J. (2013) Uncertainty updating in the description of coupled heat and moisture transport in heterogeneous materials. *Applied Mathematics and Computation*, 219, 13, pp. 7252-7261.
- Lombardo, M., Zeman, J., Šejnoha, M. and Falsone, G. (2009) Stochastic modeling of chaotic masonry via mesostructural characterization. *Int. Journal for Multiscale Computational Engineering*, 7, 2, pp. 171-185.
- Soize, C. (2006) Non-Gaussian positive-definite matrix-valued random fields for elliptic stochastic partial differential operators. *Computer Methods in Applied Mechanics and Engineering*, 195, pp. 26-64.
- Torquato, S. (2002) Random heterogeneous materials: Microstructure and macroscopic properties. Springer-Verlag.

## TEMPERATURE ANALYSIS DEPENDENCE IN THE VICINITY OF THE BRAKE DISK

M. Szews<sup>\*</sup>, D. Perczyński<sup>\*\*</sup>, L. Knopik<sup>\*\*\*</sup>, S. Wawrzyniak<sup>\*\*\*\*</sup>

**Abstract:** The paper demonstrates the friction nodes statistical analysis of road tractor brakes as well as the temperatures analysis of selected wheel braking systems. The measurement system consists of six temperature sensors mounted in the vicinity of the friction nodes and seventh to measure the ambient temperature. The output signals of the sensors are transmitted to a digital temperature meter based on ATmega 64 microcontroller. The measurement results were recorded on the SD memory card. The digital temperature sensors of the 1-wire interface manual DS18B20 of Dallas Semiconductor were used to measure the temperature. Moreover, the paper presents the research regarding the wheel temperature dependency of the outside temperature. Based on the multiple regression coefficients of approximations made equation describing the temperature increase as a function of the braking force and the distance from the blade point.

**Keywords:** Statistical analysis, Road tractor brakes, Brake temperature, Multiple regression.

### 1. Introduction

The braking system of a truck is an especially important system for road safety and operation of a vehicle. The intensive experiments and theoretical analysis of the system have been conducted in the Control Division of the Faculty of Mechanical Engineering at UTP University of Science and Technology in Bydgoszcz (Perczyński et al., 2016). It has been assumed that the temperature at the selected point of a wheel brake is a measure of correct operation of the system under operational conditions.

Operation of braking systems in motor vehicles shows occurrence of abnormal operating conditions. The abnormality is defined as e.g. wheel blocking, braking force difference on the axis over 30 %, inadequate braking force of the wheel in relation to mass of examined system and, in extreme cases, lack of braking force. Higher speed of vehicles as well as reducing the size of braking friction pair (disc-brake pad) require the use of higher pressure of friction parts on the disc and affect the growth of thermal load of the braking system. Increased requirements for braking systems force not only the periodic monitoring of the state of the friction, but also constant monitoring of the condition of the braking system, together with the control system and actuators.

To diagnose the friction pair of the braking system, various measurements are carried out which provide information about its condition in direct or indirect way. The direct methods refer mainly to wear and tear of the friction pair by using micrometric tests and devices. The other group of direct methods consists of these applied in non-destructive examination (penetration and magnetic particle testing), which are used to control and measure the length of thermal cracking on the braking disc.

The indirect methods, used to estimate the technical condition of the braking system, consist of measurements of braking distance, tightness or pressure of the braking system. These methods provide information about condition of the system without its disassembly. Unfortunately, the measurements of

---

<sup>\*</sup> Maciej Szews: MAKTRONIK, Autoryzowany Servis IVECO, Bydgoszcz, PL, [szewsmaciej@wp.pl](mailto:szewsmaciej@wp.pl)

<sup>\*\*</sup> Assist. Prof. Daniel Perczyński, PhD.: UTP University of Science and Technology, Faculty of Mechanical Engineering, Al. prof. S. Kaliskiego 7, 85-796 Bydgoszcz; PL, [daniel.perczynski@utp.edu.pl](mailto:daniel.perczynski@utp.edu.pl)

<sup>\*\*\*</sup> Assoc. Prof. Leszek Knopik, PhD.: UTP University of Science and Technology, Faculty of Management, Fordońska 430, 85-790 Bydgoszcz, PL, [leszek.knopik@utp.edu.pl](mailto:leszek.knopik@utp.edu.pl)

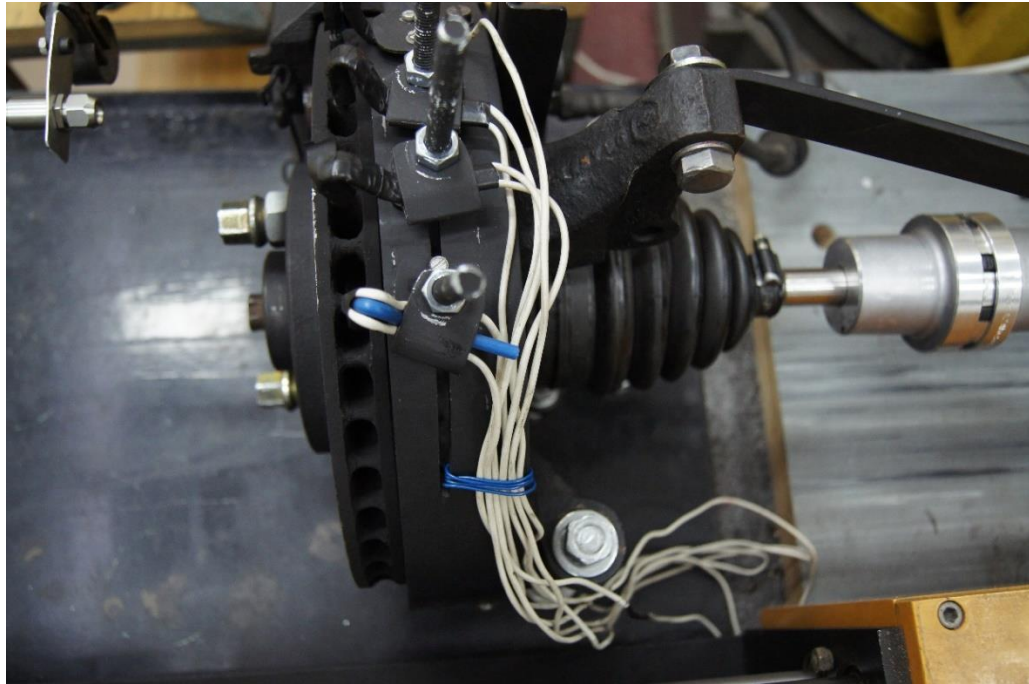
<sup>\*\*\*\*</sup> Assist. Prof. Sylwester Wawrzyniak, PhD.: UTP University of Science and Technology, Faculty of Mechanical Engineering, Al. prof. S. Kaliskiego 7, 85-796 Bydgoszcz; PL, [sylwester.wawrzyniak@utp.edu.pl](mailto:sylwester.wawrzyniak@utp.edu.pl)

braking distance cannot provide full information about the condition of a specific wheel friction system, but only total score of braking system operation.

During the braking process, kinetic energy of the motor vehicle is converted into heat in the braking system (braking disc – brake pad or brake drum and friction lining). It seems that this diagnostic signal can give useful information about the state of the analysed system. Establishment of optimal place and way how to measure temperature of the friction pair can be a method which allows determination of the emergency status of the braking system.

## 2. Measuring position

The realization of the target temperature measurement and its surroundings were made to built test bench shown in Fig. 1.



*Fig. 1: Measuring position.*

In order to record temperature measurement system was built based on a microcontroller ATmega 64 and the digital temperature sensors of the 1-wire interface manual DS18B20 of Dallas Semiconductor. Temperature measurements were made in four points disposed on the circumference of the disk using DS18B20 sensors. The temperature of the disk was measured using a pyrometer OPTCT3MLSF. Furthermore, in order to determine the braking force, the measurements of the fluid pressure in the brake system.

## 3. Mathematical model

The dependence of temperature changes in the disk and four points distant from the disk 5 mm, 10 mm, 15 mm, and 20 mm described by means of the function  $F(t)$  of the form:

$$F(t) = \begin{cases} A(1 - \exp(-\lambda_1 t)) & \text{for } t \in [0, t_1], \\ B \exp(-\lambda_2 t) & \text{for } t \in (t_1, t_2), \end{cases} \quad (1)$$

where:

$A, B, \lambda_1, \lambda_2$  are fixed coefficients,  $t_1$  – the time braking the end,  $t_2$  – the moment of completion of temperature measurement.

Sample values of the parameters  $A, B, \lambda_1, \lambda_2$  with the selected pressure values given in Tab. 1. In addition, in the last row of the table contains the standard error for the approximation of the empirical data by using the tool according to Eq. (1).

*Tab. 1: The values of parameters  $A, B, \lambda_1, \lambda_2$  and standard error approximations.*

0.25 MPa	Disk	5 mm	10 mm	15 mm	20 mm
$A$	412.10	61.28	53.91	50.33	40.23
$\lambda_1$	0.00242	0.00429	0.00400	0.00344	0.00363
$B$	3051.00	314.33	251.32	193.80	163.43
$\lambda_2$	0.01499	0.01053	0.01022	0.00975	0.00985
Std	4.30	0.36	0.29	0.27	0.20
0.23 MPa	Disk	5 mm	10 mm	15 mm	20 mm
$A$	750.65	132.41	82.56	78.24	72.30
$\lambda_1$	0.0014	0.0019	0.0031	0.0027	0.0024
$B$	1545.99	242.74	231.92	186.31	152.36
$\lambda_2$	0.0143	0.0113	0.0112	0.0108	0.0105
Std	5.19	0.79	0.83	0.78	0.66
0.21 MPa	Disk	5 mm	10 mm	15 mm	20 mm
$A$	468.83	628.45	628.63	628.63	204.38
$\lambda_1$	0.00313	0.00047	0.00046	0.00039	0.00079
$B$	927.12	146.41	146.41	127.74	113.27
$\lambda_2$	0.01894	0.01420	0.01420	0.01463	0.01169
Std	4.60	0.80	0.81	0.62	0.54
0.19 MPa	Disk	5 mm	10 mm	15 mm	20 mm
$A$	887.70	628.96	34.60	628.72	25.50
$\lambda_1$	0.00091	0.00029	0.00704	0.00025	0.00653
$B$	540.67	78.47	84.00	73.39	62.51
$\lambda_2$	0.01639	0.01138	0.01206	0.01216	0.01238
Std	3.19	0.58	0.41	0.53	0.36

Graphs of the function  $F(t)$  for the case where measurements are performed directly on the face and at a distance  $d = 10 \text{ mm}$  of the disc and the pressure of the brake fluid 0.21 MPa shown in Fig. 2. On the presented figure  $\tau$  is a constant delay of transport between the disk and the heated temperature sensor.

The dependence of the maximum temperature increase  $\Delta T_{\max}(x, y)$  with distance measuring the temperature of the disc and the brake pressure is described by the equation (Draper et al., 1998 and Morrisom, 1990):

$$\Delta T_{\max}(x, y) = ax + by + cx^2 + dy^2 + exy + f \quad (2)$$

where:  $x$  – pressure [MPa],  $y$  – the distance between the sensor and disk face [mm].



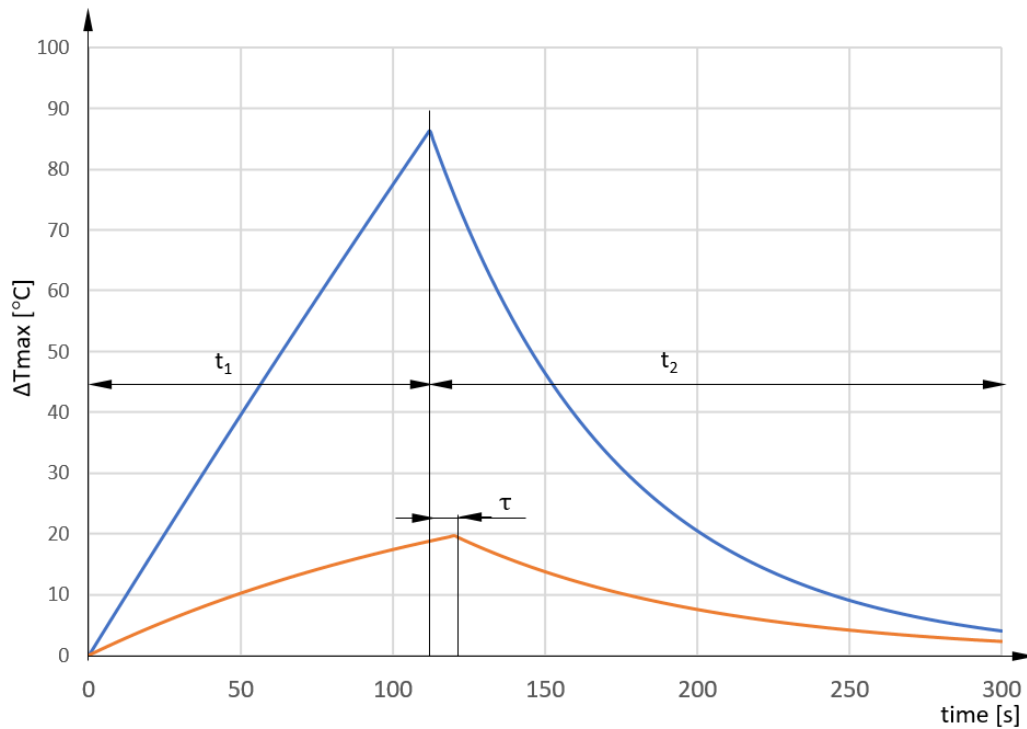


Fig. 1: Relationship between the growth temperature of the target and at a distance  $d = 10$  mm as a function of time of measurement. The pressure of the brake fluid 0.21 MPa.

For the measurement point on the disk takes up a distance equal to 0.

Using the methods of multivariate approximation made the parameters of the Eq. (2). The values of the coefficients of Eq. (2) are as follows:

$$\begin{aligned} a &= 133.186, & b &= -9.68766, \\ c &= -2.96375, & d &= 0.609143, \\ e &= -0.3466, & f &= -1328.98. \end{aligned} \quad (3)$$

The calculated value of the coefficient of multiple correlation to empirical data and the adopted model is  $R = 0.93$ . The study analyzed the level of significance of the equation gives the value  $p - \text{value} < 0.00001$ .

#### 4. Conclusions

Eq. (2) gives the possibility of the temperature increase maximum calculating for different values of pressure and distance than used to determine Eq. (2) parameters. Based on the value of the temperature increase recorded, Eq. (2) makes possible to calculate of the braking force values on the wheels of the same axle. This information is essential for analysing the efficiency state of the braking system. The last possibility is important in practice, so further research is presented in this work will be continued in the direction of seeking "good" according to the binding temperature increase of the target, the distance measuring point and the value of the braking force.

#### References

- Draper, N R. and Smith, H. (1998) Applied Regression Analysis, JOHN WILEY & SONS, INC. New York.
- Morrisom, D.F. (1990) Wielowymiarowa analiza statystyczna (Eng. Multivariate statistical methods, New York: McGraw-Hill), PWE, Warszawa.
- Perczyński, D., Peszyński, K., Knopik, L. and Wawrzyniak, S. (2016) Temperature analysis in the vicinity of triaxial trailer disc brake, in: Proc. of Int. Conf. on Engineering Mechanics 2016, Svratka, Czech Republic, pp. 450-453.

## BIOMECHANICAL STUDY OF THE CERVICAL SPINE WITH DISC IMPLANTS: A FINITE ELEMENT ANALYSIS

K. Szkoda<sup>\*</sup>, P. Gałąska<sup>\*\*</sup>, M. Żak<sup>\*\*\*</sup>, C. Pezowicz<sup>\*\*\*\*</sup>

**Abstract:** *Overloads of the spine often lead to the formation of degenerative changes. Additionally, the progression of these changes is led to instability and destruction of intervertebral disc structures. Therefore, the cervical disc implants are usually used as technical aids to improve the stability. The aim of the study was to assess changes occurring in the cervical spine, as a result of application of the cervical disc implants.*

**Keywords:** Cervical spine, Finite element modeling, Disc implants, Mechanical properties.

### 1. Introduction

Variable loads and overloads of the spine can often lead to injuries and mechanical damage, as well as the formation of degenerative changes. Degenerative intervertebral disc disease of the cervical spine is a prevalent condition in our population, because the studies have shown that 95 % of men and 70 % of women after age 65 will have some sort of degenerative change (Phillips et al., 2005). Treatment of the damaged cervical spine segment is a very complicated process, resulting mainly from a complex construction of spine structure. It is usually based on the use of technical aids in the form of intervertebral disc implants, which must fulfill the basic aspects in term of the biomechanical as well as the clinical ones. The main aim of this study was to assess the impact introduction of the cervical disc implants to changes occurring in the cervical spine under the load transmission (axial compression, flexion and extension). By using finite element model of the cervical spine, the study was conducted to compare the intact segments versus the segments with the DCI implant and the segments with the ProDisc-C implant. This study evaluated the distribution of displacements, stress and strain of considered models.

### 2. Materials and methods

The numerical model of four-level cervical spine (C3 – C7) was built on the basis of diagnostic computed tomography (CT). The values of each parametric dimensions of the vertebrae included in the numerical model were verified with the dimensions of the vertebrae available in the literature (Panjabi et al., 1990). The final files of the vertebrae models were created in ANSYS. The segments of cervical spine were divided into several structures with different tissues material properties, which are shown in Tab. 1. The vertebrae were modeled of a solid volume (cancellous bone) and a layer of vertebral cortical walls. The models of intervertebral disc were contained 3 layers of annulus fibrosus and the height of the intervertebral discs were between 4.5 mm and 5 mm. The geometry of the implants was constructed with primary dimension available in the literature, which are shown in Fig. 2. Bone and soft tissue and the implants were described by the isotropic, linear elastic material properties using tetrahedral 10-node elements type Solid187. Additionally, three different ligaments were modelled as 4-node shell elements

---

<sup>\*</sup> M.Sc. Eng. Klaudia Szkoda: Department of Biomedical Engineering, Mechatronics and Theory of Mechanisms, Wrocław University of Science and Technology, ul. Łukasiewicza 7/9, 50-371 Wrocław, Poland, klaudia.szkoda@pwr.edu.pl

<sup>\*\*</sup> Eng. Paulina Gałąska: Interdepartmental Scientific Circle of Biomechanics, Wrocław University of Science and Technology, ul. Łukasiewicza 7/9, 50-371 Wrocław, Poland

<sup>\*\*\*</sup> Ph.D. Eng. Małgorzata Żak: Department of Biomedical Engineering, Mechatronics and Theory of Mechanisms, Wrocław University of Science and Technology, ul. Łukasiewicza 7/9, 50-371 Wrocław, Poland, malgorzata.a.zak@pwr.edu.pl

<sup>\*\*\*\*</sup> Prof. Celina Pezowicz: Department of Biomedical Engineering, Mechatronics and Theory of Mechanisms, Wrocław University of Science and Technology, ul. Łukasiewicza 7/9, 50-371 Wrocław, Poland, celina.pezowicz@pwr.edu.pl

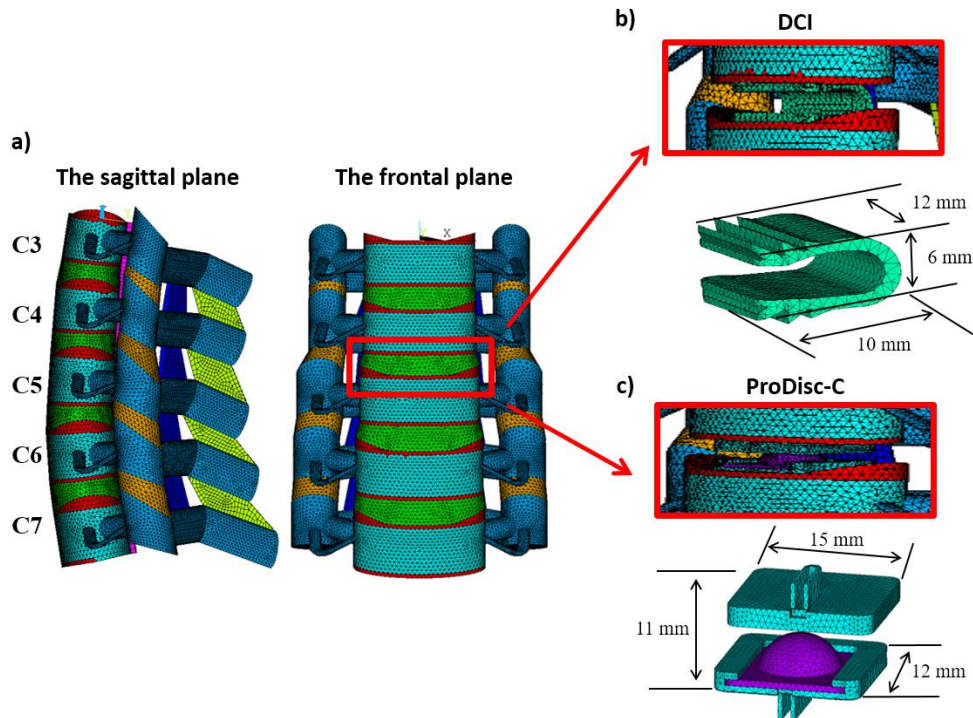
type Shell181. Numerical simulations have been performed for three cases: intact segments, segments with the DCI implant and segments with the ProDisc-C implant (Fig. 1).

*Tab. 1: Material properties of the cervical spine components.*

	Young's modulus [MPa]	Poisson's ratio [-]
<b>SOLID component name</b>		
Cortical bone	12 000	0.30
Cancellous bone	100	0.20
Posterior bone	3500	0.25
Cartilaginous endplate	25	0.10
Nucleus pulposus	1	0.49
Annulus fibrosus	8.4	0.45
Articular cartilage	33	0.30
CoCrMo (Prodisc-C)	210 000	0.29
UHMWPE (Prodisc-C)	800	0.40
Ti-6Al-4V (DCI)	110 000	0.36
<b>SHELL component name</b>		
Posterior longitudinal ligaments (PLL)	50	0.30
Interspinous ligaments (ISL)	12	0.30
Ligamentum flavum (LF)	19	0.30

\* Shirazi-Adl et al., 1986; Sharma et al., 1995; Smit et al., 1997; Kumaresan et al., 1999

In first stage, the analysis has been carried out under the influence of an axial compression force equal to 200 N. In each of the considered cases, the axial compression force was applied to the superior endplate of the upper vertebral body (C3), as recommended in the literature (Wilke et al., 1998). In next stage, a pure unconstrained bending moment in flexion and extension (equal to 1.2 N.m) was applied the same as the axial compression. This force is responsible for loading transmission by the cervical spine of an average adult human, resulting from the weight of the head. All configurations of the model were fixed by deducting all the degrees of freedom on the inferior endplate of the lower vertebral body (C7).



*Fig. 1: Finite element model of cervical segment spine (C3 – C7): a) an intact model in the sagittal and the frontal plane, b) model with the DCI implant, c) model with the Prodisc-C implant.*

### 3. Results

The numerical simulations allowed the analysis of the distribution of displacements, stress and strain of considered models, in particular, changes occurring in the intervertebral disc implants. The results of the distribution of global displacement of considered models under axial compression are presented in Fig. 2.

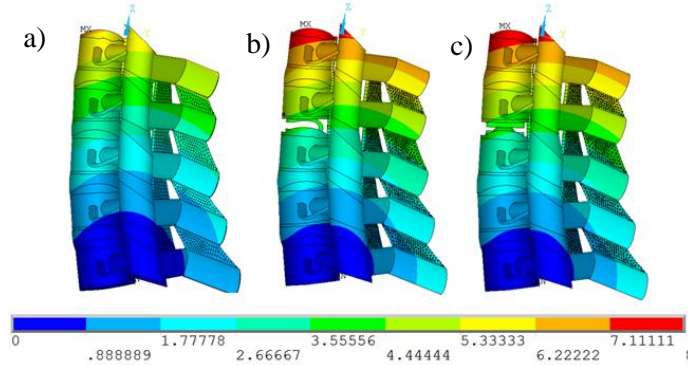


Fig. 2: Distribution of global displacement of three configurations of the model under axial compression: a) an intact model, b) with the DCI implant, c) with the ProDisc-C implant.

It can be concluded that maximum displacement in an intact segments amounts to 6.4 mm. The resulting value is smaller than the maximum displacement of the segments with the DCI and ProDisc-C implants, where the value is equal to 7.8 mm for both of considered models. The maximum global displacement and von Mises total mechanical strain of considered models during axial compression, flexion and extension are presented in Fig. 3.

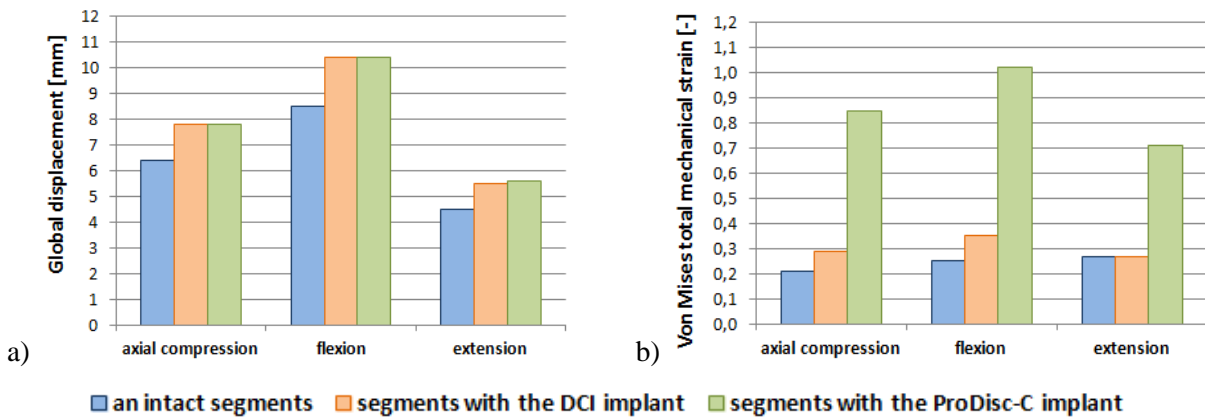


Fig. 3: The mechanical properties of the considered models during compression, flexion and extension: a) the maximum global displacement, b) the maximum von Mises total mechanical strain.

The analysis of the distribution of von Mises stress under axial compression (Fig. 4) showed that the largest value of stress was obtained for the segments with these implants. The maximum values of stress for the segment with the DCI implant amounted to 60 MPa and it is the same as for the segment with the ProDisc-C implant.

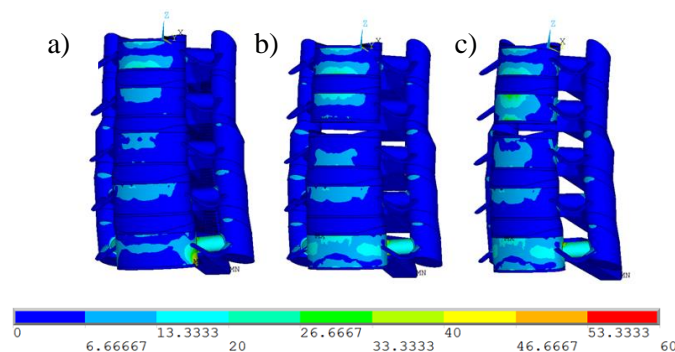


Fig. 4: Distribution of von Mises stress of three configurations of the model under axial compression: a) an intact model, b) with the DCI implant, c) with the Prodisc-C implant.

Considering distribution of the von Mises stress (Fig. 5) for the intervertebral discs implants it can be seen that the maximum values was higher for the DCI implant than the values obtained for the ProDisc-C. In the case of the DCI implant under axial compression, the maximum value was 375 MPa and 337 MPa for ProDisc-C implant. The maximum von Mises stress of considered models during axial compression, flexion and extension are presented in Fig. 6.

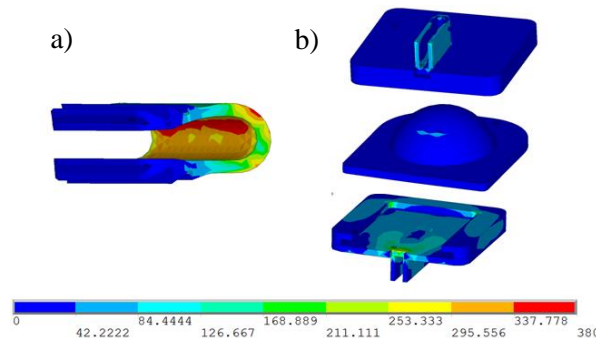


Fig. 5: Von Mises stress distribution in the considered implants under axial compression: a) the DCI implant, b) the Prodisc-C implant.

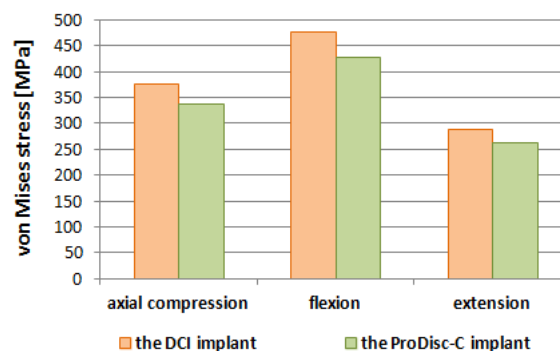


Fig. 6: The maximum von Mises stress in the considered implants under the load transmission.

#### 4. Conclusions

The biomechanical aspect of application the intervertebral disc implants is fundamental to maintain appropriate stiffness and continuity of strain of the injured segments of spine. The analysis showed that the application of the Prodisc-C implant does not given the opportunity to provide to the displacement as in a healthy spine and also does not reduce the mobility. The DCI implant could better maintain the spinal kinematic motion, because after the introduction in the cervical spine there are smaller strain.

#### Acknowledgement

Calculations have been carried out using resources provided by Wroclaw Centre for Networking and Supercomputing (<http://wcss.pl>), grant No. 423.

#### References

- Phillips, F.M. and Garfin, S.R. (2005) Cervical disc replacement. *Spine*, 30, 17S, S27.
- Panjabi, M.M. and White, A.A. (1990) *Clinical biomechanics of the spine*, LWW, Philadelphia.
- Shirazi-Adl, A., Ahmed, A.M. and Shrivastava, S.C. (1986) A finite element study of a lumbar motion segment subjected to pure sagittal plane moments. *Journal of Biomechanics* 19, 4, pp. 331-350.
- Sharma, M., Langrana, N.A. and Rodriguez, J. (1995) Role of ligaments and facets in lumbar spinal stability. *Spine*, 20, pp. 887-900.
- Smit, T.H., Odgaard, A. and Schneider, E. (1997) Structure and function of vertebral trabecular bone. *Spine*, 22, pp. 2823-2833.
- Kumaresan, S., Yoganandan, N. and Pintar, F.A. (1999) Finite element analysis of the cervical spine: a material property sensitivity study. *Clin. Biomech.*, 14, pp. 41-53.
- Wilke, H.J., Wenger, K. and Claes, L. (1998) Testing criteria for spinal implants: recommendations for the standardization of in vitro stability testing of spinal implants. *Eur. Spine J.*, 7, 2, pp. 148-154.



## THE ANALYSIS OF SELECTION OPTIMAL PARAMETERS OF PID CONTROLLERS FOR A MODIFIED ARTILLERY-MISSILE SYSTEM

P. Szmidt \*, D. Gapiński \*\*, Z. Koruba \*\*\*

**Abstract:** The paper presents a numerical selection method for PID controller gains used for controlling cannons azimuth and elevation angles in the modified artillery and missile system named “Wróbel II”. The selection of parameters was carried out with a method of numerical optimisation and some of the research results were presented graphically.

**Keywords:** Controlling, PID controller, Optimisation.

### 1. Introduction

Manual tracking of a manoeuvring air target may be inaccurate in some cases. Inaccuracy may be caused by many factors including, among others, a complicated trajectory and high speeds of a target, stress caused by the aggressor's attack and bad weather conditions during military operations. Considering that fact, it is very favourable to replace human work with automatic control systems which, on the basis of signals from a head or seeker heads (Gapiński et al., 2016), render programmed angular positions over time. In these systems, control algorithms are very important – they are responsible for efficient use of electromechanical drive units (Koruba et al., 2013 and Grzyb et al., 2016).

### 2. The system model

3D system model designed in SolidWorks is presented in Fig. 1. Basing of used construction materials it is possible to calculate masses and inertia moments of specified elements. The scheme of the system model is presented in Fig. 2.

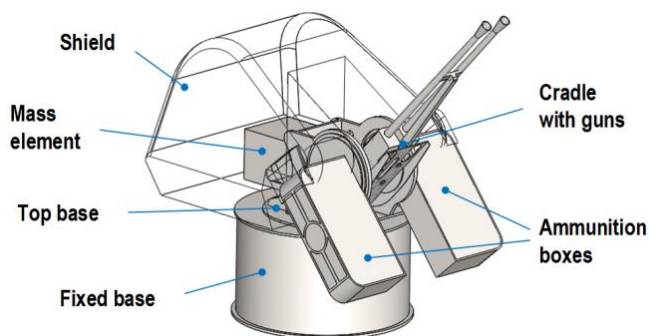


Fig. 1: 3D model of the presented artillery and missile system.

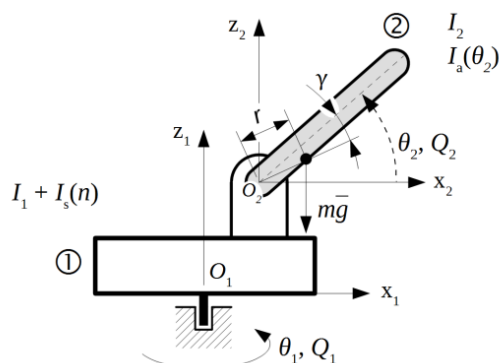


Fig. 2: The scheme of the system physical model.

\* Ph.D. student Piotr Szmidt, M.Sc. Eng.: Faculty of Mechatronics and Mechanical Engineering, Kielce University of Technology, al. 1000-lecia P.P. 7; 25-345, Kielce; PL, petersz@wp.pl

\*\* Research Assistant Daniel Gapiński, Ph.D. Eng.: Faculty of Mechatronics and Mechanical Engineering, Kielce University of Technology, al. 1000-lecia P.P. 7; 25-345, Kielce; PL, dgapinski@tu.kielce.pl

\*\*\* Vice Rector Zbigniew Koruba, Prof. Ph.D. Eng.: Faculty of Mechatronics and Mechanical Engineering, Kielce University of Technology, al. 1000-lecia P.P. 7; 25-345, Kielce; PL, dgapinski@tu.kielce.pl



Designations presented in Fig. 2:

$\theta_1$  – azimuth angle (angle of system rotation),

$\theta_2$  – elevation angle (lifting),

$Q_i = M_i - T_i$  – generalised torque impacting on  $i$ -th element,

$M_i$  – control torque (drive) impacting on  $i$ -th element,

$T_i$  – friction torque impacting on  $i$ -th element,

$I_1$  – constant mass inertia moment of 1 element in relation to  $z_1$  axis,

$I_s(n)$  – variable mass inertia moment of 1 element in relation to  $z_1$  axis depending on a number of cartridges in  $n$  boxes,

$I_2$  – constant mass inertia moment of 2<sup>nd</sup> element in relation to  $y_2$  axis,

$I_a(\theta_2)$  – variable mass inertia moment of 2<sup>nd</sup> element in relation to  $z_1$  axis depending on elevation angle,

$m$  – mass of 2<sup>nd</sup> element,

$g$  – gravitational acceleration,

$r$  – distance from the centre of gravity of 2<sup>nd</sup> element in relation to  $y_2$  rotation axis,

$\gamma$  – angular displacement of the centre of gravity of 2<sup>nd</sup> element in relation to an axis of a gun barrel.

The Lagrange II equations were used to generate equations of the system motion. After calculating the Lagrangean and derivatives, (1) and (2) equations of generalised torques –  $Q_1$  and  $Q_2$  – were created.

$$(3a\theta_2^2 + 2b\theta_2 + c)\dot{\theta}_1\dot{\theta}_2 + (I_1 + pn + q + a\theta_2^3 + b\theta_2^2 + c\theta_2 + d)\ddot{\theta}_1 = Q_1 \quad (1)$$

$$I_2\ddot{\theta}_2 - \frac{1}{2}(3a\theta_2^2 + 2b\theta_2 + c)\dot{\theta}_1^2 + mgr \cos(\theta_2 + \gamma) = Q_2, \quad (2)$$

where:  $a, b, c, d$  – coefficients of polynomial describing the change of the inertia moment  $I_a$  in an angle function of  $\theta_2$ ;  $p$  – number of cartridges in boxes;  $n$  – coefficient depending on a cartridge mass.

Generalised torque  $Q_i$  impacting on  $i$ -th element consists of the driving torque  $M_i$  reduced by the friction torque  $T_i$  generated by movements in the element.

$$Q_i = M_i - T_i \quad (3)$$

The friction torque includes  $T_{i0}$  component which depends on velocity and  $T_{i1}$  component depending on load and impacting only during element movements (Ioannides and Guillermo, 2012).

$$T_i = T_{i0} + T_{i1} \quad (4)$$

$$T_{i0} = f_0 \cdot 10^{-7} \cdot (v \cdot n)^{2/3} d_i^3 \quad (5)$$

$$T_{i1} = u_1 \cdot f_1 \cdot P_{i0} \cdot \frac{d_i}{2}, \quad (6)$$

where:  $f_0, f_1, u_1$  – coefficients depending on bearings types;  $v$  – lubricant viscosity, mm<sup>2</sup>/s;  $n$  – rotational speed, rot/min;  $d_i$  – bearing pitch diameter, mm;  $P_{i0}$  – loading force, N

### 3. The control system structure

The adopted control system structure of angular positions of the system elements is presented in Fig. 3. The structures of the azimuth control system and the elevation control system are identical, so, as the example, the azimuth control system will be explained. The central element of the system is PID controller in a parallel, so-called, independent form.

$$u(t) = K_p e(t) + K_I \int e(t) dt + K_D \frac{de(t)}{dt}, \quad (7)$$

where:  $K_p, K_I, K_D$  – continuous gain coefficients of proportional, integral and derivative terms,  $e(t)$  – position error;  $u(t)$  – control signal (an output of a controller) (Dębowski, 2008).

The control error  $e(t)$  is the difference between the desired signal of an angular position –  $\theta_{1zad}$  and position  $\theta_1$  detected by a displacement sensor (Stefański et al., 2014). On the basis of the error, the controller creates the control signal  $u(t)$  which is sent to the driver of the azimuth control system. The model of the drive system consists of *Rate limiter* block that is responsible for limiting torque acceleration to real values (100 N.m/s were considered), then the saturation block (maximal torque  $\pm 20$  N.m for the considered motors) and a mechanical transmission designed for increasing torque on the

motor shaft. Then signal gets into *Backlash* block causing the non-linearity in a form of backlash (0.05 °). The driving torque  $M_1$  drives the first element of the system responsible for azimuth rotation (Dziopa et al., 2012). In *The system model* block the previously presented system model was implemented. The output of the model is an angular position  $\theta_1$ . Next, the measurement is distorted with a white noise with an amplitude of  $\pm 0.01^\circ$  (i.e. quantisation noise from sensor).

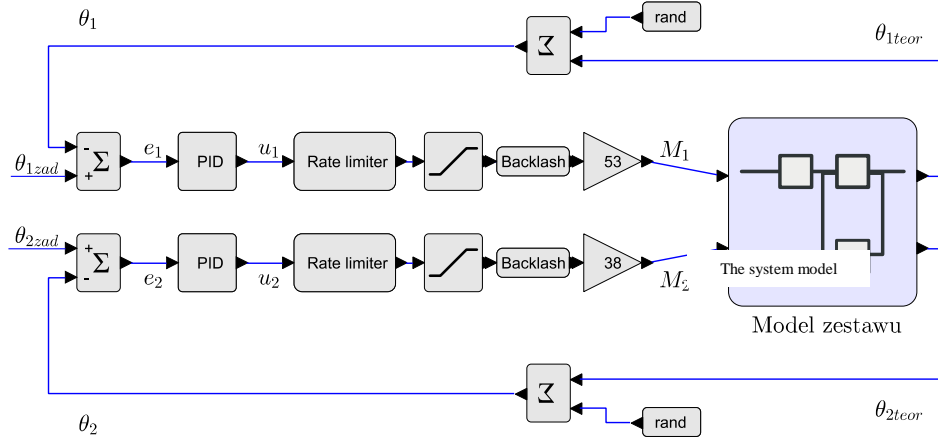


Fig. 3: General structure of the control system.

#### 4. Controller optimal parameters selection

Considering optimal adjustment some criterion was adopted. The integral of absolute error (IAE) was chosen because this index does not decrease small errors like, e.g. the integral of the squared error (ISE), which would not be favourable in accurately controlling. The procedure of optimal parameters selection used Nelder-Mead algorithm (Stachurski, 2009) in iterative simulation of the controlling system impacted by forces by using. The minimised objective function was a performance index and decision variables were PID controller gains (parameters):  $K_P$ ,  $K_I$ ,  $K_D$  (Takovoglu, 2016). Optimisation was performed subsequently for the controller of element 1 and next, for the controller of element 2. Values of the performance indexes in subsequent iterations of optimisation are presented in Fig. 4.

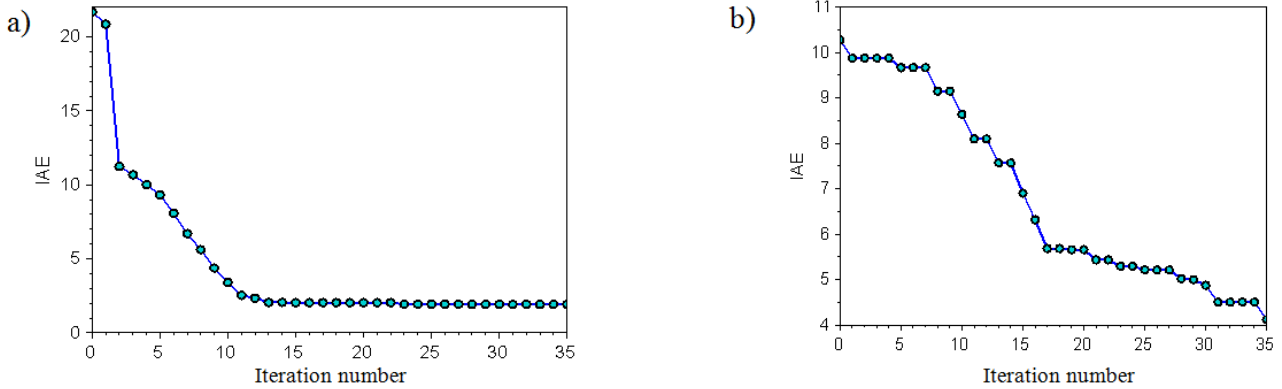


Fig. 4: Values changes of a quality index during optimisation process a) for the controller of 1 element position (azimuth), b) for the controller of 2 element position (elevation).

#### 5. The simulation of the system movement by using optimal parameters

The obtained gain coefficients for the controller of element 1 were:  $K_{P1} = 9.81$ ;  $K_{I1} = 0$ ;  $K_{D1} = 3.31$  and for the controller of element 2 were:  $K_{P2} = 9.23$ ;  $K_{I2} = 4.16$ ;  $K_{D2} = 1.31$ . Simulations of the system movements were compared to the desired signals in Fig. 5. The desired signals kept limits provided for the real system, i.e. for both elements the maximal angular acceleration did not exceed  $1.05 \text{ rad/s}^2$  ( $60 \text{ deg/s}^2$ ) and maximal speed was not higher than  $1.31 \text{ rad/s}$  ( $75 \text{ deg/s}$ ) for azimuth rotation and  $1.05 \text{ rad/s}$  ( $60 \text{ deg/s}$ ) for an elevation movement. Driving torques for specified elements are presented in Fig. 6.

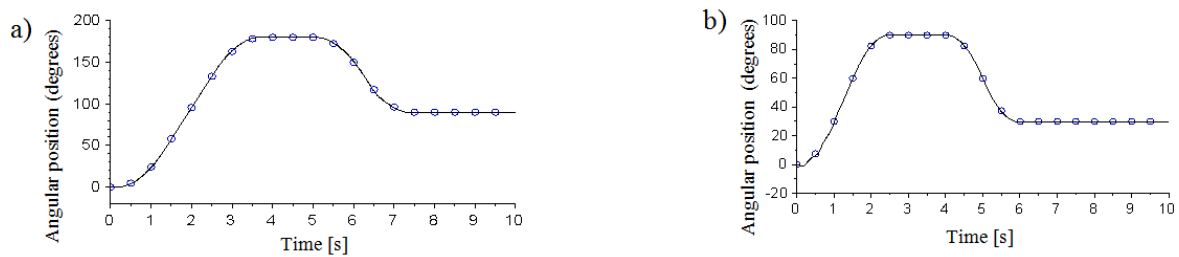


Fig. 5: Comparison of changes in desired processes  $\circ$  and processes performed  $\text{—}$  by  
a) element 1 (azimuth), b) element 2 (elevation).

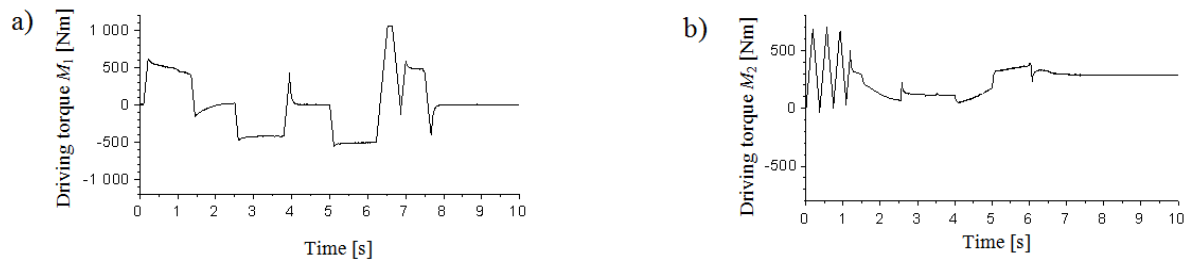


Fig. 6: Changes of driving torques of programmed movements for a) element 1, b) element 2.

## 6. Conclusions

It was ascertained that after adopting the quality and optimization criterion for controllers gain coefficients, the determined numerical parameters of controllers will allow for correct and efficient controlling both azimuth and elevation positions. The steady-state error for azimuth did not exceed  $0.02^\circ$ . For elevation the steady-state error was  $0.07^\circ$ . At the same time, it should be considered that there were backlash and noise modelled in the system. It can be stated, that tracking for desired angles is satisfactory. A further step in the work will be examination of the stability of the system for a variety of desired signals and control system robustness to change system parameters, including the variable weight of the ammunition boxes or growth moments of friction.

## References

- Dębowski, A. (2008) Automation: the basic theory. WNT, Warsaw (in Polish).
- Dziopa, Z. and Koruba, Z. (2012) Modelling and the Elements of Controlled Dynamics of the Anti-Aircraft Missile Launcher Based Onboard the Warship. Mechatronics System, Mechanics and Materials. Vol. 180, pp. 269-280.
- Gapiński, D. and Koruba, Z. (2016) Analysis of reachability areas of a manoeuvring air target by a modified maritime missile-artillery system ZU-23-2MRE. Dynamical Systems: Theoretical and Experimental Analysis, Springer Proceedings in Mathematics & Statistics, Vol. 182, pp. 125-144.
- Grzyb, M. and Stefanski, K. (2016) The use of special algorithm to control the flight of anti-aircraft missile, in: Proc. 22th Int. Conf. Eng. Mech. 2016 (eds. Zolotarev, I. and Radolf, V.), Svatka, Czech Republic, pp. 174-177.
- Ioannides, E. and Guillermo, M. (2012) Handbook of Lubrication and Tribology: Theory and Design, Second Edition, Vol. II, pp. 49-1:49-38, CRC Press Taylor & Francis Group, Boca Raton.
- Koruba, Z. and Krzysztofik, I. (2013) An algorithm for selecting optimal controls to determine the estimators of the coefficients of a mathematical model for the dynamics of a self-propelled anti-aircraft missile system. Proceedings of the Institution of Mechanical Engineers, Part K: Journal of Multi-body Dynamics, 227, 1, pp. 12-16.
- Stachurski, A. (2009) An introduction to optimization. Publishing House of Warsaw University of Technology, Warsaw (in Polish).
- Stefanski, K., Grzyb, M. and Nocon, L. (2014) The analysis of homing of aerial guided bomb on the ground target by means of special method of control, in: Proc. 2014 15th Int. Carpathian Control Conf. (eds. Petras, I., Podlubny, I., Kacur, J., and Farana, R.), IEEE, pp. 551-556.
- Takosoglu, J.E. (2016) Control system of delta manipulator with pneumatic artificial muscles, in: Proc. 22th Int. Conf. Eng. Mech. 2016 (eds. Zolotarev, I. and Radolf, V.), Svatka, Czech Republic, pp. 546-549.

## MODELLING AND SIMULATION RESEARCHES OF DYNAMICS OF TRANSLATIONAL PARALLEL MECHANISM

J. Szrek<sup>\*</sup>, J. Bałchanowski<sup>\*\*</sup>

**Abstract:** *The paper presents a method of modeling and simulation research of translational parallel mechanisms with three degrees of freedom and linear actuators. The analyzed mechanisms are characterized by their platform, which can move translationally with respect to the base keeping a constant orientation. Simulation researches were carried out in a computer multibody dynamic analysis system. The simulation model for the given system was built. The control system was chosen, parameters of controllers were matched. Simulation researches of the dynamics (the simple and inverse issues) were made in order to determine the basic characteristics of the system (driving forces, forces in joints, the accuracy of the actuators excitations and execution of trajectory).*

**Keywords:** Translational parallel mechanism, Dynamics, Simulation researches, Control system.

### 1. Introduction

Parallel mechanisms are systems with a closed kinematic chain structure, in which the driven link is connected with the base through several independent chains. Due to their many advantages, such mechanism find progressively wider application in industry as machine tools, positioners or manipulators (Merlet, 2000 and Tsai, 1999). Translational parallel mechanisms are peculiar systems in which the platform can move only translationally relative to the base (Bałchanowski, 2016a and Tsai, 2000).

In this paper, the subject of study is a translational parallel mechanism mt-utu (Tsai, 2000 and Bałchanowski, 2016a, 2016b). The topology and geometry of that system were determined in the Mechanical Engineering Faculty at Wrocław University of Science and Technology (Bałchanowski, 2016a), where the researches on parallel mechanisms were conducted (Fig. 1).

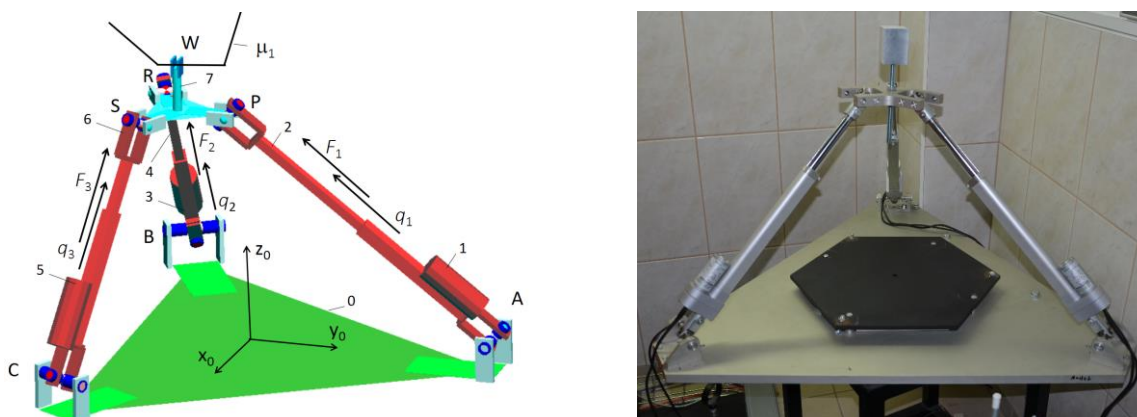


Fig. 1: The mt-utu translational parallel mechanism: numerical model and view of real system.

In the system mt-utu motion of the links is enforced by three linear actuators. The proper control of actuator excitations in order to carry out the given trajectory requires the development of a dedicated control system (Tsai, 1999; Bałchanowski et al., 2008, 2010, Bałchanowski, 2016a). Thus one of the main

<sup>\*</sup> Jarosław Szrek, PhD.: Faculty of Mechanical Engineering, Wrocław University of Science and Technology, ul. Łukasiewicza 7/9, 50-371 Wrocław, PL, jaroslaw.szrek@pwr.edu.pl

<sup>\*\*</sup> Jacek Bałchanowski, PhD., DSc.: Faculty of Mechanical Engineering, Wrocław University of Science and Technology, ul. Łukasiewicza 7/9, 50-371 Wrocław, PL, jacek.balchanowski@pwr.edu.pl

objectives of research carried out in this work was to develop computational models of the mechanism and the model of control system for realization of simulation researches. The results of simulation were the basis for the development of a mechanism with the control system (Fig. 1).

## 2. Methods of modelling and simulations

It was assumed, that analyses of the mt-utu mechanism carried out in this paper, were made using the computer simulation (Bałchanowski et al., 2008, 2010, Bałchanowski, 2016a). For this purpose computational models of the mechanism and the control system were built. Studies of the dynamics relied on performed numerical simulations of typical working movements of the mechanism. LMS DADS system was chosen to be used for carried simulation. It is a computer program for dynamic analysis of multibody system.

### 2.1. The development of a computational model of mt-utu mechanism

For this purpose of parametric calculation computational model of the mechanism was built. The model included all the basic geometric parameters of the links and the ranges of the kinematic and dynamic excitations of the actuators (Fig. 1). The assumed basic parameters of the systems were:

$$AB = BC = CA = 0.96 \text{ m}; PS = PR = RS = 0.2 \text{ m}; m_1 = m_3 = m_5 = 1.52 \text{ kg}; m_2 = m_4 = m_6 = 0.85 \text{ kg}; m_7 = 6.3 \text{ kg}, 0.45 \text{ m} < q_i < 0.85 \text{ m}; F_i < F_{max} = 250 \text{ N}, \text{ for } i = 1, 2, 3.$$

The study of the point  $W$  motion, associated with the platform, relative to the global coordinate system  $x_0y_0z_0$  enforced by  $F_1, F_2$  and  $F_3$  forces in linear actuators  $q_1, q_2$  and  $q_3$  was considered in the paper.

### 2.2. Design of control system

Motion of mechanism is realized by the control system, which for the setpoint (excitations of linear actuator)  $q_{iz}$  generates the active forces  $F_i$  necessary to enforce the displacement along of the preset trajectory. General conceptual scheme of the mechanism control system is shown in Fig. 2. The forces  $F_i$

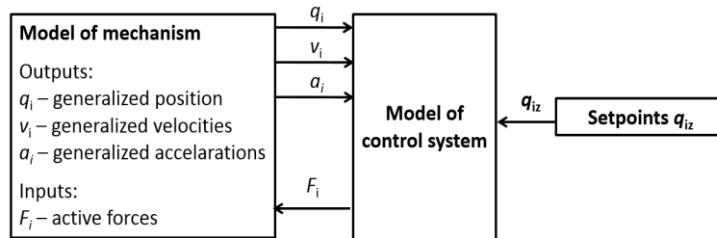


Fig. 2: Conceptual scheme of model of mechanism with control system.

are output parameters from the control system and input to the model of dynamic of the mechanism. The kinematic parameters  $q_i, v_i, a_i$  of the motion of mechanism's parts are output parameters from the model of the dynamics and input to the control system. The mt-utu mechanism have three DOFs, therefore in order to unequivocally determine the position of the system's links one should calculate independent variables  $q_1, q_2, q_3$

describing the kinematic excitations of linear actuators 1, 2 and 3. It was assumed that the classic PID controllers will be used in the control system of the mechanism (Szrek, 2016). The control process of one linear actuator in the mechanism is based on the determination of the control signal, which is the active force  $F_i(t)$  ( $i = 1, 2, 3$  – number of actuator), determined according to the formula (Gessing, 2001):

$$F_i(t) = K_P e_i(t) + K_I \int_0^t e_i(t) dt + K_D \frac{de_i(t)}{dt} \quad (1)$$

where:  $e_i = q_i(t) - q_{iz}(t)$  – the error value, the process variable, the setpoint,  
 $K_P, K_I, K_D$  – the proportional, integral, derivative gains.

Considering the character of the object, the complete control system of mechanism was divided into three separate blocks with PID controllers, one for each actuator (Fig. 3). Computer models were built in LMS DADS and combined with the models of the mechanism in order to investigate the system dynamics.

For the purpose of this research, the parameter values were matched using a numerical procedure based on the modified Ziegler-Nichols method (Ziegler et al., 1942). The procedure consisted of an assumption of parameter values  $K_P$  subjected with the object to unit excitations and observing the responses. Parameter  $K_P$  in this simulation (for  $K_D, K_I = 0$ ) was being increased until critical values  $K_{Pcr}$

( $K_{Pcr} = 1.9 \times 10^4$ ), was reached. The system response  $q_1$  in the form of cyclic oscillations with period  $T_{cr} = 0.61$  s (Fig. 4a) was the criterion for reaching the critical values. The initial values of the parameters for PID controller were calculated with the formula (Gessing, 2001 and Ziegler et al., 1942):

$$K_P = 0.6 K_{cr} = 1.14 \times 10^4; \quad K_I = 2 K_P / T_{cr} = 3.8 \times 10^6; \quad K_D = K_P T_{cr} / 8 = 8690 \quad (2)$$

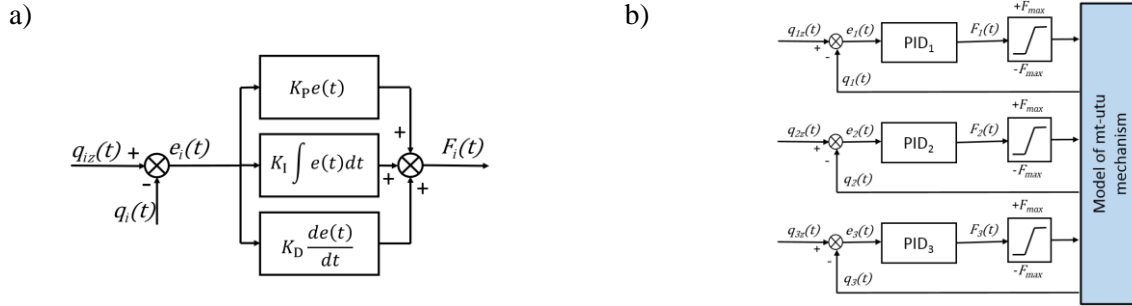


Fig. 3: a) The scheme of PID controller; b) The scheme of control system of the mt-utu mechanism.

The verifying simulation was performed for parameters from Eq. (2). The obtained response signal  $q_1$  have small over-regulations with long time of stabilization  $t_s < 0.4$  s (Fig. 4b - curve a). The next step of the matching parameters procedure was to adjust the values of parameters  $K_I$ ,  $K_D$ . Those values were iteratively changed until the system responded without over-regulations and time  $t_s < 0.1$  s was obtained (Fig. 4b - curve b, c). Finally the received parameter values of PID as a result of the simulations were the following (Fig. 4b - curve c):

$$K_P = 1.14 \times 10^4, \quad K_I = 8.1 \times 10^3, \quad K_D = 3200 \quad (3)$$

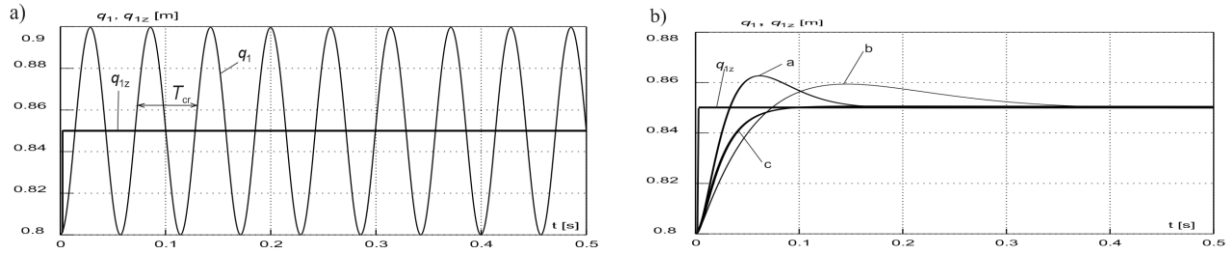


Fig. 4: a) Response  $q_1$  for unit excitations  $q_{1z}$  for critical gain  $K_{Pcr}$ ; b) Response  $q_1$  for parameters from Eq. (2) - curve a; for parameters from Eq. (1) - curve c.

### 3. Results of simulation researches

In order to determine the basic dynamic properties of the mechanism and to verify the control parameter matching, simulations of the motion were carried out. The simulation consisted of the enforcement of point W motion on the platform along the selected trajectory  $\mu_1$ . The general view of analyzed trajectory is presented in the Fig. 1 and the change of coordinates  $x_W$ ,  $y_W$ ,  $z_W$  of point W in Fig. 5a. The setpoint values for control system were the actuators settings  $q_{1z}$ ,  $q_{2z}$ ,  $q_{3z}$  which were calculated for the assumed trajectory  $\mu_1$  by solving the inverse problem of kinematics for the mt-utu mechanisms (Bałchanowski, 2014) (Fig. 5b).

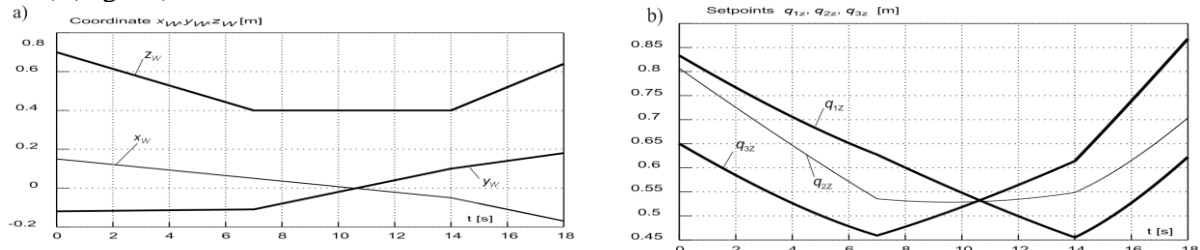


Fig. 5: Runs of  $x_W$ ,  $y_W$ ,  $z_W$  coordinates of analysed trajectory  $\mu_1$  of point W and runs of setpoints  $q_{1z}$ ,  $q_{2z}$ ,  $q_{3z}$  of actuators forcing motion along trajectory  $\mu_1$ .

Simulations were made for the mechanism loaded by mass forces of the links. The results of the simulations researches of the mechanism are presented below. Errors  $\Delta q_1$ ,  $\Delta q_2$ ,  $\Delta q_3$  in the execution of



the actuators settings  $q_{1z}$ ,  $q_{2z}$ ,  $q_{3z}$  are presented in the Fig. 6. The actuators execution settings accuracy of below 0.35 mm for mechanisms was achieved. The errors  $\Delta x_w$ ,  $\Delta z_w$  in the execution of the assigned trajectory  $\mu_1$  by the mechanism are presented in Fig. 7a. The achieved trajectory of the execution accuracy is below 0.33 mm. The control systems swiftly respond to interference (Figs. 6a and 6b – the points for  $t = 7$  s and 14 s) and short stabilization time. The runs of actual active forces  $F_1$ ,  $F_2$ ,  $F_3$  in actuators for mechanism mt-tuu are presented in Fig. 7a and runs of resultant forces  $F_A$ ,  $F_P$  in joints A, P in Fig 7b. The active force margin in the actuators ( $F_{\max}=150$  N) relative to the required forces ( $F_i < 85$  N - Fig. 7a) contributes to the quick stabilization.

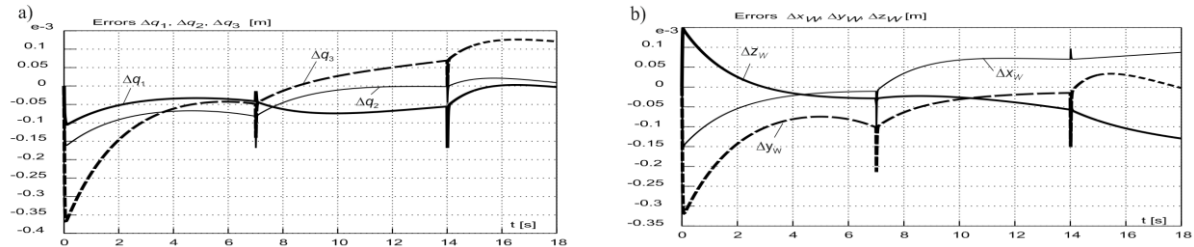


Fig. 6: Runs errors  $\Delta q_1$ ,  $\Delta q_2$ ,  $\Delta q_3$  of drives forcing motion along trajectory  $\mu_1$  and runs of errors  $\Delta x_w$ ,  $\Delta y_w$ ,  $\Delta z_w$  of point W on the platform.

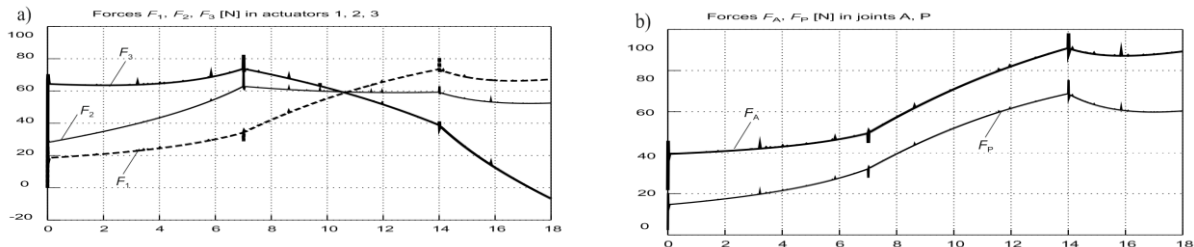


Fig. 7: Runs of actual forces  $F_1$ ,  $F_2$ ,  $F_3$  in actuators and runs of resultant forces  $F_A$ ,  $F_P$  in joints A, P for mechanism mt-tuu.

#### 4. Conclusion

The basic dynamic and kinematic properties of the translational parallel mechanisms mt-utu were determined through simulation studies. The simulations confirmed that the control system structure was correct and the controller parameters were adjusted properly. The obtained numerical results can be used to design and develop real mechanisms (Bałchanowski, 2016a, Bałchanowski et al., 2010).

#### References

- Bałchanowski, J. (2016a) Spatial parallel mechanisms. Synthesis and Analysis. Oficyna Wydawnicza Politechniki Wrocławskiej, Wrocław (in Polish).
- Bałchanowski, J. (2016b) General method of structural synthesis of parallel mechanisms. Archives of Civil and Mechanical Engineering., vol. 16, no. 1, pp. 256-268.
- Bałchanowski, J. (2014) Some aspects of topology and kinematics of a 3DoF translational parallel mechanism. International Journal of Applied Mechanics and Engineering. vol. 19, no 1, pp. 5-15.
- Bałchanowski, J., Szrek, J. and Wudarczyk, S. (2010) Design of control system of translational parallel manipulator. Pneumatyka, Wrocław. no. 4, pp. 9-15 (in Polish).
- Bałchanowski, J. and Wudarczyk, S. (2008) Simulation researches of translational parallel mechanisms, in: X. International Conf. on the Theory of Machines and Mechanisms, Liberec, Czech Republic, pp. 35-40.
- Merlet, J-P. (2000) Parallel Robots, Kluwer Academic Publishers, London.
- Szrek, J., Muraszkowski, A. and Sperzyński, P. (2016): Type synthesis, modelling and analysis of the manipulator for wheel-legged robot. Acta Mechanica et Automatica. 2016, vol. 10, nr 2, s. 87-91.
- Tsai, L-W. (1999) Robot analysis. The Mechanics and Parallel Manipulators. John Wiley & Sons, New York.
- Tsai, L-W. and Joshi, S. (2000) Kinematics and optimization of a spatial 3-UPU parallel manipulator. ASME Journal of Mechanical Design 122(4), pp. 439-446.
- Ziegler, J. and Nichols, N. (1942) Optimum Settings for Automatic Controllers, Trans. ASME, Vol. 64, pp. 759-768.

## DYNAMIC CHARACTERISTICS OF PNEUMATIC ARTIFICIAL MUSCLES

J. E. Takosoglu<sup>\*</sup>

**Abstract:** *The article presents the test stand to determine the dynamic characteristics of pneumatic artificial muscles (PAM). Trigonometric dependencies occurring during the muscle operation were formulated. On the basis of the derived equations, a degree of the relative muscle contraction was calculated. The experimental research was conducted for two different masses affecting the pneumatic artificial muscles. The hysteresis of the muscle as well as dynamic characteristics for three different input signals were presented.*

**Keywords:** Pneumatic artificial muscle, Dynamic characteristics, Proportional pressure valve, Pneumatronics.

### 1. Introduction

Pneumatic artificial muscles are used mainly in drive systems of humanoid and anthropomorphic robots, bio-robots, exoskeletons and are more and more frequently applied in automation of production processes (Nowakowski et al., 2016a and Nowakowski et al., 2016b). Their application results from the advantages of pneumatic artificial muscles. The muscles are characterised by low mass, they generate greater forces in comparison with typical pneumatic cylinders with the same diameter, work smoothly even at a low speed, start and stop gently, a detrimental phenomenon of stick slip as well as the process of dry friction (Blasiak, 2016 and Blasiak et al., 2014) do not occur, they are completely hermetic and might operate in harsh and harmful environments (Laski et al., 2015 and Pietrala, 2016). Pneumatic artificial muscles are controlled by pressure changes in the muscle (Takosoglu, 2016). Proportional pressure valves or proportional flow valves are applied thereto the most frequently. An increase in the inner part of the muscle results in an increase of the muscle diameter (the muscle swells) and thus, the muscle is contracted and the pulling force is formed. The pulling force decreases from its max value (the muscle rests) to zero (the muscle is completely contracted). Fig. 1a shows an example of applying pneumatic artificial muscles in a bionic robot arm, whereas Fig. 1b presents an example of the application thereof in the vibrator of powdered materials.



Fig. 1: A bionic robot arm a), a vibrator of powdered materials b).

### 2. Test stand

The test stand is built of stainless steel and its construction resembles scales (Bochnia, 2012). A centrally rotating arm was attached to an inverted T-shaped frame. At one end of the frame there is a pneumatic artificial muscle, whereas at the second one – load mass. Under the influence of the muscle contraction,

---

<sup>\*</sup> BSc Jakub Emanuel Takosoglu, PhD.: Faculty of Mechatronics and Mechanical Engineering, Kielce University of Technology, Aleja Tysiąclecia Państwa Polskiego 7, 25-314, Kielce; PL, qba@tu.kielce.pl

the arm rotates on two needle bearings, and the change of the rotational angle is registered by the angular position sensor. Fig. 2a presents a general diagram of the test stand, while Fig. 2b a general view of the test stand to determine the dynamic characteristics.

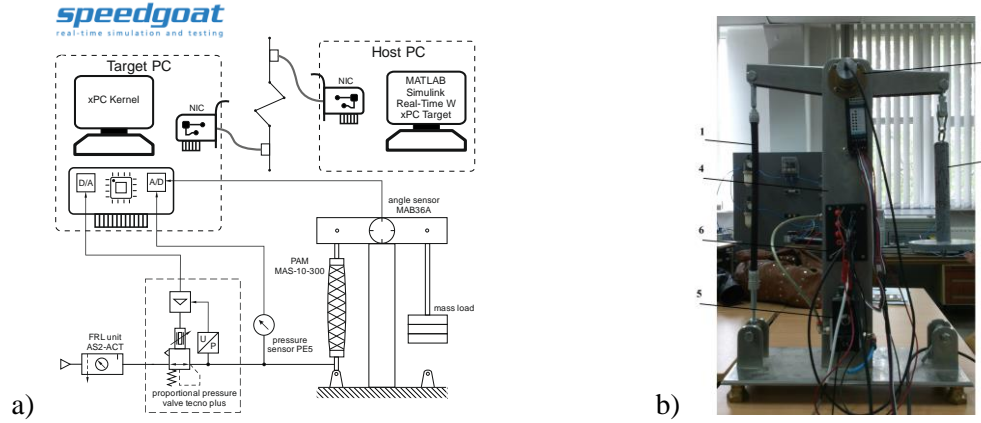


Fig. 2: Test stand diagram a), general view of the test stand b).

Piezoelectric proportional pressure value Hoerbiger Tecno Plus was applied to control the pneumatic muscle. The valve has a very short response time and low power consumption (Blasiak, 2016) (due to the piezoelectric transducer in the valve). An angular position sensor with an analog output, and a pressure sensor with an analog output were used in the measurement system (Adamczak et al., 2016 and Adamczak et al., 2015). The angular position sensor measures the rotational angle of the arm resulting from the muscle contraction. In order to collect the measurement and the valve control data, real time system Matlab and SpeedGoat hardware was applied (Dindorf, 2014 and Wos, 2015). The system consists of Intel Core 2 Duo 2.23 GHz CPU computer, 2048MB RAM, 1024MB industrial-grade CompactFlash device, 32 single-ended or 16 differential analog input (software selectable), 4 analog output (single-ended), and 8 digital TTL input and 8 digital TTL output channels (16-bit), I/O cable, terminal board. In order to determine the dynamic characteristics (Koruba, 2013 and Krzysztofik, 2014 and Grzyb, 2016 and Gapinski, 2014), the familiarity with the degree of the relative muscle contraction (contraction ratio) is crucial. In the measurement system, there is no direct measurement (Janecki, 2015) of the muscle contraction, that is why, trigonometric dependencies occurring during the muscle operation were formulated. Fig. 3a shows a diagram of trigonometric dependencies of the pneumatic muscle in the initial position, whereas Fig. 3b – during the muscle contraction.

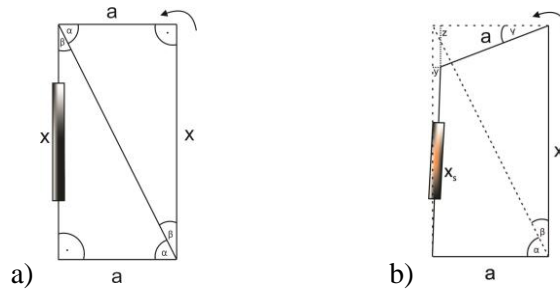


Fig. 3: Diagram of trigonometric dependencies: a) at rest, b) during working.

During the muscle contraction by  $z$  value,  $a$  arm rotates counter-clockwise, and in that way, acute angle  $\gamma$  is formed (Fig. 5b). The following dependencies might be formulated on the basis of the diagram:

$$\alpha + \beta + (90^\circ - \gamma) = 180^\circ \quad (1)$$

$$\sin \gamma = \frac{z}{a} \quad (2)$$

$$\cos \gamma = \frac{a-y}{a} \quad (3)$$

$$x_s^2 = y^2 + (x-z)^2 \quad (4)$$

By substituting (1), (2) and (3) to equation (4), the length of the contracted pneumatic muscle was obtained:

$$x_s = \sqrt{(x - a \cdot \sin \gamma)^2 + (a - a \cdot \cos \gamma)^2} \quad (5)$$

It is important that static and dynamic characteristics be calculated using relative contraction of the muscle, also known as the contraction ratio (Takosoglu et al., 2016):

$$\varepsilon = \frac{L_n - x_s}{L_n} \cdot 100 \% \quad (6)$$

where:  $L_n$  – nominal length of the muscle,  
 $x_s$  – actual length of the muscle.

### 3. Experimental research

The pneumatic artificial muscle manufactured by Festo and marked as MAS-10-300 was applied in the experimental studies. The muscle parameters were included in Tab. 1.

Tab. 1: Parameters of artificial pneumatic muscle MAS-10-300.

Parameter	Value
Symbol	MAS-10-300
Mode of operation	<i>single-acting, pulling</i>
Internal diameter $D_n$	<i>10 mm</i>
Nominal length $L_n$	<i>300 mm</i>
Max. operating pressure $p$	<i>0.8 MPa</i>
Max. permissible pre-tensioning $\varepsilon_{min}$	<i>-2 % of <math>L_n</math></i>
Max. permissible contraction $\varepsilon_{max}$	<i>16 % of <math>L_n</math></i>
Lifting force at max. permissible operating pressure $F_{max}$	<i>630 N</i>
Max. additional load, freely suspended	<i>30 kg</i>
Operating frequency $f$	<i>35 Hz</i>
Max. hysteresis	<i>3 % of nominal length</i>
Max. relaxation	<i>4 % of nominal length</i>
Repetition accuracy	<i>1 % of nominal length</i>
Ambient temperature	<i>-5 °C+60 °C</i>

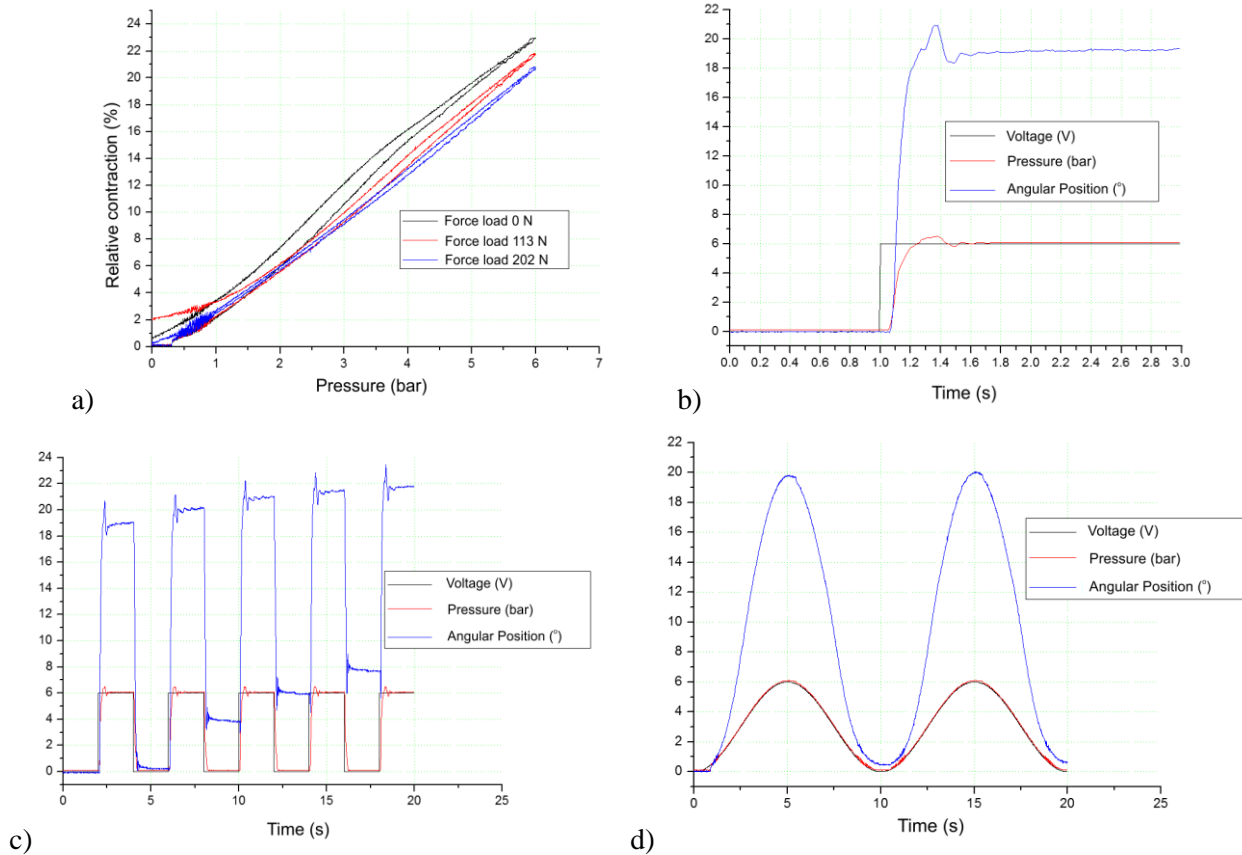


Fig. 4: Relative muscle contraction in the pressure function a) dynamic characteristics of the muscle for three different control signals: b) step signal, c) rectangular signal, d) sinusoidal signal.

Fig. 4a shows the obtained characteristics of the relative muscle contraction in the pressure function together with the hysteresis of the pneumatic muscle. Fig. 4b – 4d shows the dynamic characteristics of the pneumatic artificial muscle for three different control signals: step, rectangular and sinusoidal.

#### 4. Conclusions

Taking the above research into consideration, it might be concluded that the hysteresis of MAS-10-300 pneumatic muscle is consistent with catalogue data and does not exceed 3 %. The repetition accuracy was verified for the rectangular control signal. The muscle performs 5 cycles (contraction – extension) within 20 sec. As it might be seen in the chart (Fig. 5b), the repetition does not exceed 1 %. The research was conducted with the max. pressure value of 0.6 MPa and for this pressure value, the degree of relative contraction reaches the max. value of 14 %. The designed test stand makes it possible to perform experimental studies of various types of pneumatic muscles.

#### References

- Adamczak, S., Zmarzly, P. and Janecki, D. (2015) Theoretical and practical investigations of v-block waviness measurement of cylindrical parts, *Metrology and Measurement Systems*, 22, 2, doi:10.1515/mms-2015-0023.
- Adamczak, S., Zmarzly, P. and Stepień, K. (2016) Identification and analysis of optimal method parameters of the v-block waviness measurements, *Bulletin of the Polish Academy of Sciences Technical Sciences*, 64, 2.
- Blasiak, M. (2016) Parametric analysis of piezoelectric transducer used for signal processing, in: *Proc. 22th Int. Conf. Eng. Mech. 2016* (eds. Zolotarev, I. and Radolf, V.), Svratka, Czech Republic, pp. 66-69.
- Blasiak, S., Takosoglu, J.E. and Laski, P.A. (2014) Heat transfer and thermal deformations in non-contacting face seals, *Journal of Thermal Science and Technology*, 9, 2, pp. 1-8, doi:10.1299/jtst.2014jtst0011.
- Blasiak, S. and Zahorulko, A.V. (2016) A parametric and dynamic analysis of non-contacting gas face seals with modified surfaces, *Tribology International*, 94, , pp. 126-137, doi:10.1016/j.triboint.2015.08.014.
- Bochnia, J. (2012) Ideal material models for engineering calculations, *Procedia Engineering*, 39, 0, pp. 98-110, doi:http://dx.doi.org/10.1016/j.proeng.2012.07.013.
- Dindorf, R. and Wos, P. (2014) Contour error of the 3-dof hydraulic translational parallel manipulator, *Advanced Materials Research*, 874, pp. 57-62, doi:10.4028/www.scientific.net/AMR.874.57.
- Gapinski, D. and Krzysztofik, I. (2014) The process of tracking an air target by the designed scanning and tracking seeker, in: *Proc. 2014 15th Int. Carpathian Control Conf. IEEE*, pp. 129-134.
- Grzyb, M. and Stefanski, K. (2016) The use of special algorithm to control the flight of anti-aircraft missile, in: *Proc. 22th Int. Conf. Eng. Mech. 2016* (eds. Zolotarev, I. and Radolf, V.), Svratka, Czech Republic, pp. 174-177.
- Janecki, D. and Zwierzchowski, J. (2015) A method for determining the median line of measured cylindrical and conical surfaces, *Measurement Science And Technology*, 26, 8, doi:10.1088/0957-0233/26/8/085001.
- Koruba, Z. and Krzysztofik, I. (2013) An algorithm for selecting optimal controls to determine the estimators of the coefficients of a mathematical model for the dynamics of a self-propelled anti-aircraft missile system, in: *Proc. Institution of Mechanical Engineers, Part K: Journal of Multi-Body Dynamics*, 227, 1, pp. 12-16.
- Krzysztofik, I. and Koruba, Z. (2014) Mathematical model of movement of the observation and tracking head of an unmanned aerial vehicle performing ground target search and tracking, *J. of Appl. Mathematics*, 2014, pp. 1-11.
- Laski, P.A., Takosoglu, J.E. and Blasiak, S. (2015) Design of a 3-dof tripod electro-pneumatic parallel manipulator, *Robotics And Autonomous Systems*, 72, pp. 59-70, doi:10.1016/j.robot.2015.04.009.
- Nowakowski, L., Miesikowska, M. and Blasiak, M. (2016) Speech intelligibility in the position of cnc machine operator, in: *Proc. 22th Int. Conf. Eng. Mech. 2016* (eds. Zolotarev, I. and Radolf, V.), Svratka, Czech Republic, pp. 422-425.
- Nowakowski, L., Miko, E. and Skrzyniarz, M. (2016) The analysis of the zone for initiating the cutting process of x37crmov51 steel, in: *Proc. 22th Int. Conf. Eng. Mech. 2016* (eds. Zolotarev, I. and Radolf, V.), Svratka, Czech Republic, pp. 426-429.
- Pietrala, D.S. (2016) Parallel manipulator with pneumatic muscle drive, in: *Proc. 22th Int. Conf. Eng. Mech. 2016* (eds. Zolotarev, I. and Radolf, V.), Svratka, Czech Republic, pp. 458-461.
- Takosoglu, J.E. (2016) Control system of delta manipulator with pneumatic artificial muscles, in: *Proc. 22th Int. Conf. Eng. Mech. 2016* (eds. Zolotarev, I. and Radolf, V.), Svratka, Czech Republic, pp. 546-549.
- Takosoglu, J.E., Laski, P.A., Blasiak, S., Bracha, G. and Pietrala, D. (2016) Determining the static characteristics of pneumatic muscles, *Measurement and Control*, 49, 2, pp. 62-71, doi:10.1177/0020294016629176.
- Wos, P. and Dindorf, R. (2015) Synchronized trajectory tracking control of 3-dof hydraulic translational parallel manipulator, in: *Mechatronics - Ideas Ind. Appl.* (eds. Awrejcewicz, J., Szewczyk, R., Trojnecki, M. and Kaliczynska, M.), Springer International Publishing, pp. 269-277, doi:10.1007/978-3-319-10990-9\_24.

## ANALYSIS OF SIZE EFFECT FOR NOTCHED MINI SPECIMENS MADE OF STAINLESS STEEL

T. Tomaszewski\*

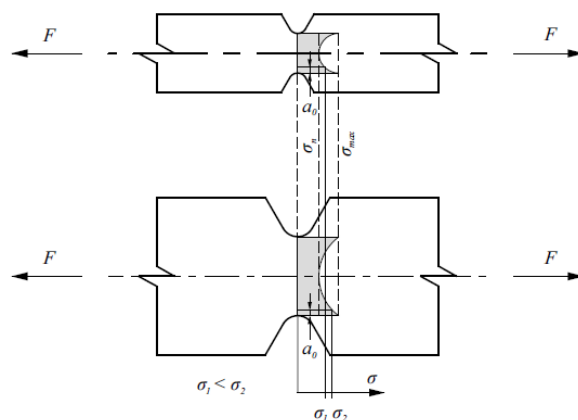
**Abstract:** *The use of test results obtained on mini specimens requires that the size effect is taken into consideration. The impact of object size on strength properties is interpreted depending on the test conditions. In this paper, a geometrical size effect resulting from the non-linear distribution of stress occurring in the notched specimen was analysed. Two specimens of different sizes were prepared of 1.4301 stainless steel. The finite elements method was used for calculating theoretical stress concentration factor. The impact of size effect was evaluated based on the test results obtained for high-cycle fatigue strength.*

**Keywords:** High-cycle Fatigue, Steel, Notch, Size effect, Mini specimen.

### 1. Introduction

There is an existing need for identifying strength properties based on mini specimens (Sokolov et al., 2009). This applies to situations where it is impossible to collect a standard specimen (Tomaszewski et al., 2017), as well as situations of limited test material (Zastempowski et al., 2015) or higher speed of performing fatigue examinations required (Strzelecki et al., 2016). Due to the impact of the tested object size on strength properties (size effect), it is necessary that such results are referred to tests performed on standard specimens. Such tests were performed on smooth specimens made of several construction materials (Tomaszewski et al., 2016). The obtained divergences of results resulted from the statistical or technological size effect (Kloos et al., 1981). Moreover, the analysis of the size effect is relevant in the case of a large-size object (Richard et al., 2013 and Holka et al., 2016). In this situation, the strength decrease significantly affect the fatigue life of element.

In the tests reported an attempt was made to verify the size effect in reference to notched specimens, in which non-linear distribution at high value of stress concentration (Fig. 1) (geometrical size effect) occurs. At specified length ( $a_0$ ), stress concentration in the mini specimen ( $\sigma_1$ ) is smaller compared to the standard specimen ( $\sigma_2$ ). The relation is true provided that identical distribution of stress is assumed, i.e. fixed value of nominal stress ( $\sigma_n$ ), shape coefficient ( $\alpha_k = \sigma_{max} / \sigma_n$ ) (Makkonen et al., 2003 and Schumacher et al., 2009).



*Fig. 1: Stress distribution in the notch tip for various specimen size.*

\* Dr. Ing. Tomasz Tomaszewski, Institute of Mechanical Engineering, University of Technology and Life Sciences, 85-789 Bydgoszcz, Poland; PL, tomaszewski@utp.edu.pl



The purpose of the paper is to determine fatigue properties for material sensitive to the size effect. 1.4301 stainless steel was used for the tests, featuring relatively high sensitivity to minor changes to the smooth specimen cross-sectional area (Tomaszewski et al., 2016). The test conditions proposed (tension, compression; notched specimens) allow to verify this material in terms of the occurrence of geometrical size effect.

## 2. Experimental tests

The test specimens were collected from 1.4301 steel in the form of cold-rolled steel sheet of 4 mm thickness ( $R_m = 710$  MPa,  $R_e = 319$  MPa). This stainless steel is commonly applied in some of the machinery used in the food industry. The tests were performed for two different specimen shapes and sizes (Fig. 2, Tab. 1).

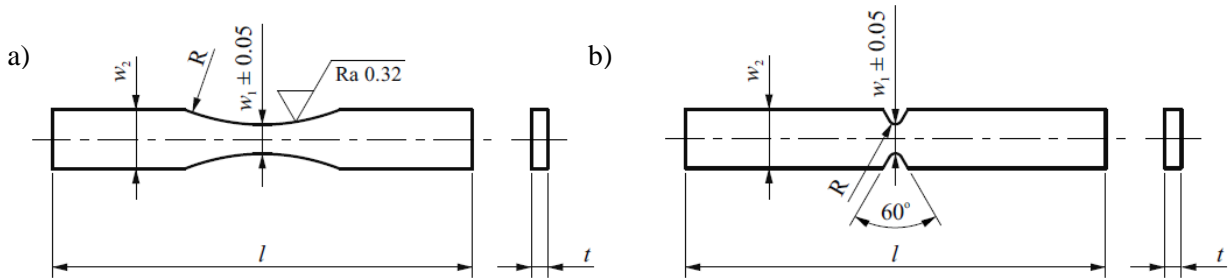


Fig. 2: Geometry of the flat specimen for fatigue testing made of 1.4301 steel: a) smooth, b) notched.

Tab. 1: Specimen dimensions.

Type of geometry		$t$ [mm]	$w_1$ [mm]	$R$ [mm]	$l$ [mm]	$S_o$ [mm <sup>2</sup> ]
Smooth	Standard specimen	4	7	25	100	28
	Mini specimen	1.4	2.5	18	35	3.5
Notched	Standard specimen	4	7	1.5	100	28
	Mini specimen	1.4	2.5	0.5	35	3.5

Theoretical stress concentration factor ( $\alpha_k$ ) was evaluated with the use of software basing on the finite elements method (Zienkiewicz et al., 1972) and on the diagrams presented in (Peterson et al., 1953). Calculations were performed based on a two-dimension numerical analysis for isotropic elastic modulus of steel ( $E = 210000$  MPa,  $\nu = 0.33$ ). Due to the symmetry of specimens in x and y axes, a simplified flat model was employed, as shown in Fig. 3. A grid was built of four-node quadrangular elements, the dimensions of which were chosen experimentally (depending on the accuracy of result). The adopted geometric values corresponded to actual dimensions of the test specimens (Tab. 1). Even stress was applied on the extreme nodes in the form of a force applied along the x axis. Ansys software environment (Ansys) was used for modelling the finite elements grid and for numerical calculations. The results of analyses are presented in Tab. 2.  $\alpha_k$  factor values were the same for the standard specimen and the mini specimen.



Fig. 3: Stress distribution map for the notched specimen.

Tab. 2: Theoretical stress concentration factor.

Type of geometry	$\alpha_k$	
	numerical	according to (Peterson et al., 1953)
Notched specimen	2.28	2.1
Smooth specimen	1.05	-

### 3. Test result review

The stressing procedure included stress-controlled fatigue tests for high-cycle fatigue life (PN-74/H-04327). Micro-cracks were assumed as the end of test criterion. The tests were performed for symmetrical load ( $R = -1$ ) at frequency 7 Hz. The results of fatigue tests were described through linear regression and Basquin's equation (Tab. 3). Fig. 4 presents graphically the obtained  $\sigma - N$  fatigue characteristics for smooth specimen and notched specimen.

Tab. 3:  $\sigma$ - $N$  characteristic parameters for various specimen size and shape.

Type of geometry		Linear regression line $\log \sigma_a = a \log N + b$		Basquin relation $C = N(\sigma_a)^\beta$		Correlation coefficient, $R^2$
		$a$	$b$	$C$	$\beta$	
Smooth	Standard specimen	-0.0399	2.578	$2.78 \cdot 10^{64}$	25.00	0.983
	Mini specimen	-0.0558	2.695	$1.87 \cdot 10^{48}$	17.91	0.933
Notched	Standard specimen	-0.0706	2.719	$3.15 \cdot 10^{38}$	14.16	0.966
	Mini specimen	-0.0794	2.756	$5.35 \cdot 10^{34}$	12.60	0.898

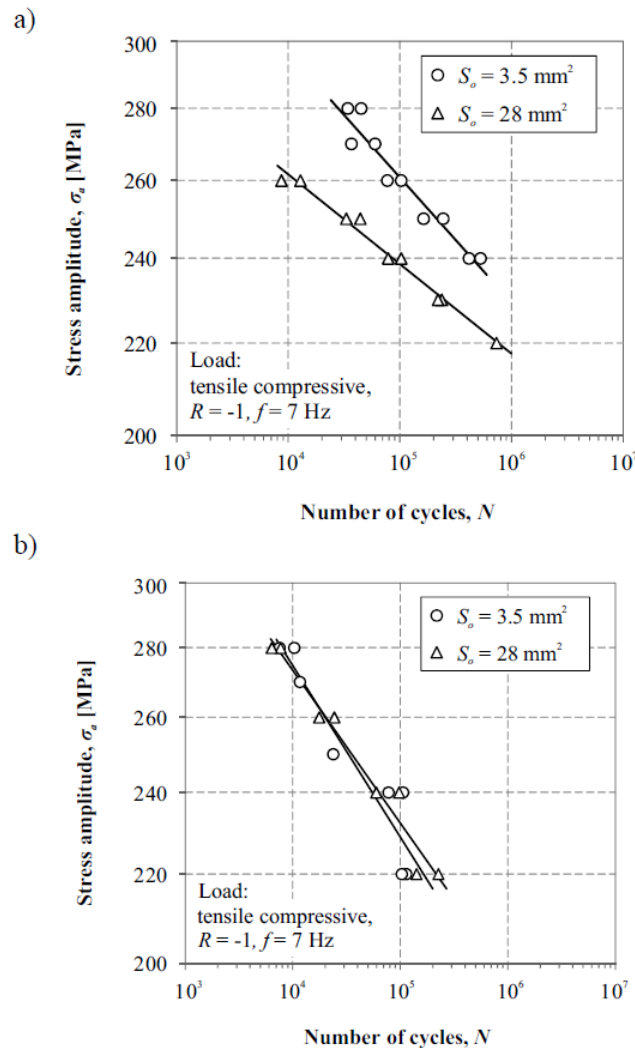


Fig. 4:  $\sigma$ - $N$  characteristics compared for the different sizes of: a) smooth specimen, b) notched specimen.

Cross-sectional area coefficient ( $K_{HC}$ ) (Tomaszewski et al., 2016) was assumed as the measure of material sensitivity to changes in cross-sectional area. Diversification in the fatigue test results was noted for smooth specimens ( $K_{HC} = 1.089$ ). No differences in test results were observed for the notched specimens ( $K_{HC} = 1$ ).

#### 4. Summary

A relationship between fatigue strength and cross-sectional area value was demonstrated in the smooth specimens tests. An increase in fatigue strength compared to the standard specimen can be noted. No size effect was observed for the notched specimen shape tested.

The data obtained deviate from the assumed geometrical size effect theory. This may result from an inappropriate approach to analysing the size effect, or different interpretation of the size effect in terms of crack development mechanism for small specimen geometries. This would result in application of the geometrical size effect assumptions, as presented in the introduction, to a different range of variability of the object's cross-sectional area. Proper explanation of this phenomenon will require further research.

#### References

- Ansys. Release 16.0. Help System.
- Holka, H. and Jarzyna, T. (2016) Rectilinearity of large sized shafts. in: Proc. Int. Conf. on Engineering Mechanics 2016 (eds. Zolotarev, I and Radolf, V.), Svratka, Czech, pp. 202-205.
- Kloos, K.H., Buch, A. and Zankov, D. (1981) Pure geometrical size effect in fatigue tests with constant stress amplitude and in programme tests. *Materialwissenschaft und Werkstofftechnik*, 12, pp. 40-50.
- Makkonen, M. (2003) Notch size effects in the fatigue limit of steel. *International Journal of Fatigue*, 25, pp. 17-26.
- Peterson, R.E. (1953) Stress concentration design factors. John Wiley & Sons, New York.
- PN-74/H-04327 The study of metal fatigue. The test of axial tension - compression at constant cycle of external loads (in Polish).
- Richard, H.A., Sander, M., Schramm, B., Kullmer, G. and Wirxel, M. (2013) Fatigue crack growth in real structures. *International Journal of Fatigue*, 50, pp. 83-88.
- Schumacher, A., Borges, L.C. and Nussbaumer, A. (2009) A critical examination of the size effect correction for welded steel tubular joints. *International Journal of Fatigue*, 31, pp. 1422-1433.
- Sokolov, M.A. (2009) Small Specimen Test Techniques, 5th Volume, Journal of ASTM International.
- Strzelecki, P. and Sempruch, J. (2016) Experimental method to plot S-N curve with a small number of specimens. *Polish Maritime Research*, 23(4), pp. 129-137.
- Tomaszewski, T., Strzelecki, P. (2016) Study of the size effect for non-alloy steels S235JR, S355J2+C and acid-resistant steel 1.4301. *AIP Conference Proceedings*, 1780, pp. 020008-1-020008-8.
- Tomaszewski T. and Sempruch, J. (2017) Fatigue life prediction of aluminium profiles for mechanical engineering. *Journal of Theoretical and Applied Mechanics*, 55(2).
- Zastempowski, M. and Bochat, A. (2015) Mathematical model ling of elastic deflection of a tubular cross-section. *Polish Maritime Research*, 2(86), 22, pp. 93-100.
- Zienkiewicz, O.C. (1972) The Finite Elements Method (in Polish). Arkady, Warsaw.

## **EVALUATION OF DEFORMATIONS OF THICK-LAYER GLUED JOINTS APPLIED IN CONSTRUCTION OF RAIL VEHICLES**

**T. Topolinski<sup>\*</sup>, B. Ligaj<sup>\*\*</sup>, A. Mazurkiewicz<sup>\*\*\*</sup>, S. Miterka<sup>\*\*\*\*</sup>**

**Abstract:** *This paper presents the measurement results of deformations of glued joints applied in construction of rail vehicles. The joint materials and technology of making used were the same as in the technological process used in the manufacturing of such vehicles. The specimens prepared were divided into eight groups and subjected to different types of aging according to guidelines specified in regulations for examinations obligatorily performed by rail vehicle manufacturers. Measurements of deformations during shearing test of glued joint were performed. The results obtained exhibited the existence of impact of the way the glued joint ages on its properties. Different types of aging of specimens effect in the loss of joint strength and its deformability.*

**Keywords:** Glued joint, Rail vehicle, Aging of glued joints, Deformation of glued joints.

### **1. Introduction**

Glued and welded joints are currently commonly applied in the construction of rail vehicles. The gluing technology has a number of benefits compared to welding or riveting. It allows to join elements made of different materials, of entirely different physical properties, shape, as well as of large differences in size. Gluing permits obtaining joints in which no installation stresses occur, which lowers internal tensions in large-size rail structures, including, among others, rail car bodies. One of the more frequent application of gluing technology in presently manufactured rail vehicles is fixture of external plastic or metallic plating to metal frame, and installation of internal equipment of cars. When fixing skin plates to the car framing, the glued joint must perform several functions. The primary function is stable and reliable joining of the elements. Another function is eliminating inaccuracies in making of the car framing, and adequate mutual amortization of the glued elements, so that any tensions from the framing occurring while driving are not transferred onto the car plating. For this reason, thick-layer glued joints are applied in framing-plating type connections. The joint obtained must feature adequate elasticity in order to correctly perform its functions. During operation of the vehicle, these types of joints are exposed to variable load, and to the effect of variable atmospheric conditions, including temperature, humidity, saltiness, sunlight. Therefore, the glues applied for these types of joints must feature resistance to the factors mentioned. Thus, the aim of this paper is to evaluate the elasticity of think-layer glued joints subjected to aging in conditions simulating real-world conditions to which these types of joints are exposed in rail vehicles. The paper presents the results of examinations of joints made of materials applied in constructing rail vehicles according to the technology used by their manufacturer.

---

<sup>\*</sup> Prof. Tomasz Topoliński, PhD.: Department of Mechanical Engineering, University of Sciences and Technology, Kaliskiego 7 Street; 85-796, Bydgoszcz; PL, e-mail: topol@utp.edu.pl

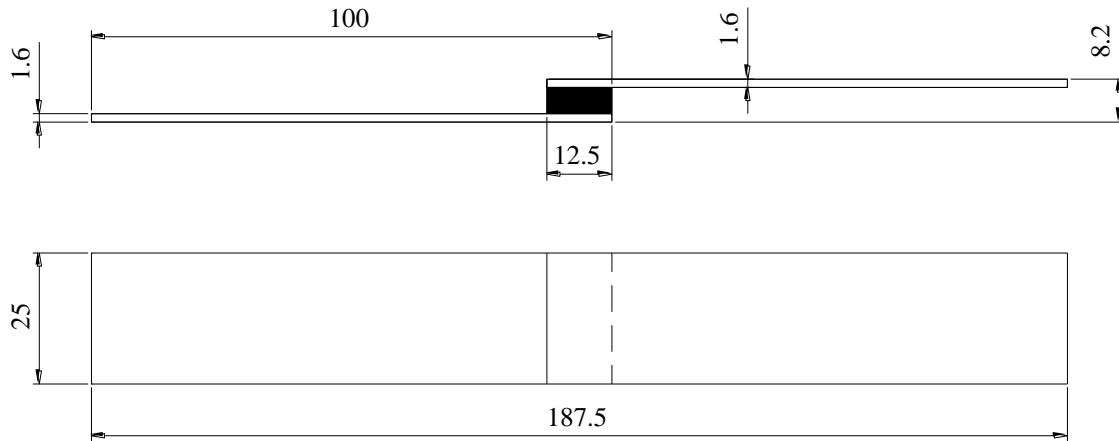
<sup>\*\*</sup> Prof. Bogdan Ligaj, PhD.: Department of Mechanical Engineering, University of Sciences and Technology, Kaliskiego 7 Street; 85-796, Bydgoszcz; PL, e-mail: bogdan.ligaj@utp.edu.pl

<sup>\*\*\*</sup> Assoc. Prof. Adam Mazurkiewicz, PhD.: Department of Mechanical Engineering, University of Sciences and Technology, Kaliskiego 7 Street; 85-796, Bydgoszcz; PL, e-mail: adam.mazurkiewicz@utp.edu.pl

<sup>\*\*\*\*</sup> Eng. Sebastian Miterka: Student Scientific Group BioMed, University of Sciences and Technology, Kaliskiego 7 Street; 85-796, Bydgoszcz; PL, e-mail: sebamiteras92@wp.pl

## 2. Methods

The material glued was a sheet of 1.6 mm thickness made of X2CrNi12 steel (PN-EN 10027-1:2007). The shape of the specimen resulted from the guidelines of Standard PN-EN 1465:2009. Strips of length 100 and width 20 mm were cut from the sheet. The strips were ground with fine-grained sand paper (granulation 180), and then degreased (BETACLEAN 3350 degreaser) at the area to which the joint will be applied. Subsequently elements were cap by the primer BETAPRIME 1707B. Then, they were degreased BETACLEAN 3350 again. For gluing, the strips were placed in a special shape that ensures proper positioning of the plates relative to each other, and thus the required shape and dimensions of the joint (according guidelines of DVS 1618:2002). BETAMATE 7120 glue was used for gluing. Gluing was performed in strictly controlled conditions, i.e. 20 °C temperature and 23 % humidity. Then, the specimens were left to dry for 7 days in the same conditions. The shape of a ready specimen is presented in Fig. 1. After aging, the specimens were kept for 2 hours in ambient temperature (DIN 54457), after which the tests were performed.



*Fig. 1: Shape and dimensions of the specimen.*

The specimen were aged according to the guidelines specified in DIN 54457 and DIN EN ISO 9142. Specimens aging methods are specified in Tab. 1. The specimens made were divided into eight groups. Five specimens were tested in each group.

*Tab. 1: Specimens aging method.*

Group number	Aging method	Number of specimens
G1	Specimens not aged	5
G2	Specimens stored for 1 week in water in 20° C temperature	5
G3	Specimens stored for 2 weeks in water in 20 °C temperature	5
G4	Specimens stored for 3 weeks in water in 20 °C temperature	5
G5	Specimens stored for 4 weeks in water in 20 °C temperature	5
G6	Specimens stored for 1 week in water, and then for 1 day in 80 °C temperature	5
G7	Specimens stored for 1 week in water in 20 °C temperature, then tightly closed (using foil not permitting air and humidity) in 70 °C temperature (so-called cataplasma test)	5
G8	Specimens stored for 1 week in water in 20 °C temperature, and then for 1 day in -30 °C temperature	5

Shearing test was performed on the joint using Instron E3000 testing device. Temperature during the test was 20 °C, humidity 23 %. Test performance speed was set at 10 mm/min, based on the

results of preliminary test on specimens of the same properties. Washers of adequate depth were used when fixing the specimens to the machine holders, to ensure action of the force along the joint. Force increases and elongation were registered at 10 Hz frequency.

### 3. Results

Fig. 2 presents average diagrams of the tested specimen groups (average diagram for the given group was equivalent to the averaged diagram for all specimens in the group). Tab. 2 presents average results for  $F_{\max}(\text{Av})$  force and elongation obtained for tensioning the specimens  $\Delta L(\text{Av})$  in individual groups, and values of standard deviation and relative standard deviation.

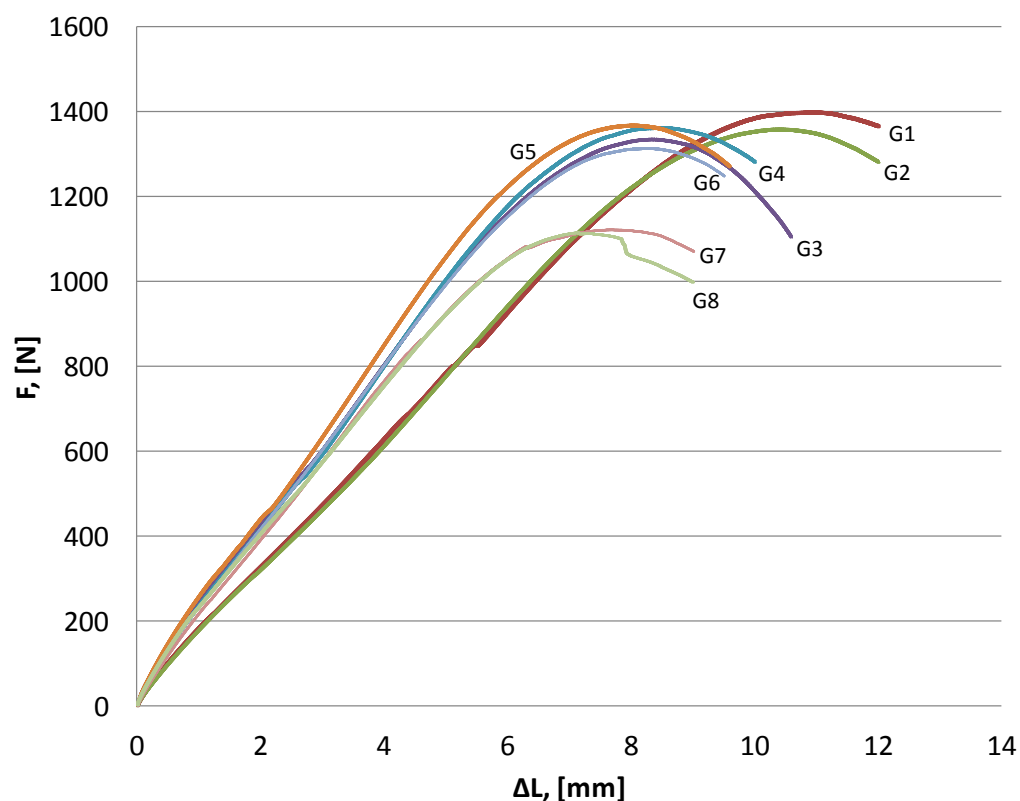


Fig. 2: Groups of specimens average diagrams.

Tab. 2: Average values of force and elongation obtained from tension test.

	G1	G2	G3	G4	G5	G6	G7	G8
$F_{\max}(\text{Av})$	1401.6	1361.5	1337.9	1365.1	1370.6	1316.5	1125.4	1118.7
SD	156.3	126.3	106.3	145.2	158.9	126.7	138.2	119.2
RSD	11.1	9.3	7.9	10.6	11.6	9.6	12.3	10.7
$\Delta L(\text{Av})$	10.968	10.395	8.332	8.518	7.989	8.289	7.604	7.129
SD	0.892	1.123	0.865	0.623	0.834	0.916	0.876	0.8125
RSD	8.1	10.8	10.4	7.3	10.4	11.0	11.5	11.4
SD – standard deviation, RSD – relative standard deviation								

### 4. Conclusions

The experimental tests performed on joints glued with BETAMATE 7120 glue in monotonic-variable stress conditions indicate that the aging process has an impact on the change of  $F_{\max}$



maximum force value and  $\Delta L$  elongation. The highest value of forces occurs for those joint specimens that were not subjected to aging. The value of forces decreased in response to increasing the aging process time and changing its conditions. The lowest stress force value amounts to 79.8 % of the force value obtained for specimens not subjected to aging. For  $\Delta L$  elongation, the highest value was obtained for groups 1 and 2 (the test results were similar). For the remaining specimen groups,  $\Delta L$  values amounted to 65.0 % to 77.6 % of the deformation value for the glued joint specimens not subjected to aging.

It must also be noted that  $F = f(\Delta L)$  correlation graphs for the specimens from group 1 and 2 exhibit different tension curve slope. The value of longitudinal elasticity modulus (Young's modulus) is lower than for the other specimens. The result obtained may be caused by absence of the aging effect on the glued joint. The changes identified may be important for performing numerical calculations for the strength of these types of joints.

The lowest values of breaking forces and elongation were obtained for specimens from groups 7 and 8. These results effect from the aging process leading to degradation of the glued joint in the area where the highest destructive stress occurs. Lap joints feature a complex stress condition resulting from shearing and tensioning loads.

The results obtained confirm the existence of an impact of ambient conditions on the elasticity of the glued joint examined. It is therefore necessary to limit the effect of those conditions on the glue joint. This is partly practicable. The joint may be covered with a layer of glue or paint, which protects it from the effect of humidity and sunlight. Also, adequate design of the glued joint may significantly limit the effect of those factors on the joint. It is more difficult to ensure proper temperature protection, however. The temperature difference outside and inside the vehicle, especially in winter conditions, may amount to tens of degrees, and lead to additional thermal stress on the joint. The joint will thus be exposed to overall stress resulting from movement of the vehicle, temperature differences, and - to a lesser degree - other factors.

The measurement results obtained will constitute basis for evaluating cyclic resistance of the joints tested. Based on the diagrams obtained, stress levels at which cyclic tests are to be performed will be determined in the next examination stage. The purpose of this examination will be to determine fatigue life of a joint subjected to different aging methods at different stress levels. Further examinations will be conducted according to the requirements of PN\_EN\_15190-2009 standard: „Glues for structural joints. test methods for evaluating long-term fatigue life of glued structural joints of metals“.

## References

- PN-EN 10027-1:2007: Designation systems for steels. Steel names (in Polish: Systemy oznaczania stali. Część 1: Znaki stali).
- PN-EN 1465:2009: Adhesives. Determination of tensile lap-shear strength of bonded assemblies (in Polish: Kleje. Oznaczanie wytrzymałości na ścinanie przy rozciąganiu połączeń na zakładkę).
- DVS 1618:2002: Elastic thick film bonding in rail vehicle construction, (in German).
- DIN 54457: Structural adhesives - Testing of adhesively bonded joints - Bead peel test.
- DIN EN ISO 9142: Adhesives. Guide to the selection of standard laboratory ageing conditions for testing bonded joint (in Polish: Kleje. Wytyczne wyboru znormalizowanych warunków laboratoryjnego starzenia do badania połączeń klejowych).
- PN-EN 15190-2009: Structural adhesives. Test methods for assessing long term durability of bonded metallic structures (in Polish: Kleje do połączeń konstrukcyjnych. Metody badań do oceny długookresowej trwałości klejowych połączeń konstrukcyjnych metali).

## ALL-PASS FILTERS AS A TOOL FOR CONVERTING A POSITIVE FEEDBACK TO A NEGATIVE FEEDBACK WHEN CONTROLLING WEAKLY DAMPED SYSTEMS

J. Tůma<sup>\*</sup>, P. Šuránek<sup>\*\*</sup>, M. Mahdal<sup>\*\*\*</sup>

**Abstract:** *The problem of active vibration control of weakly damped mechanical structures is potentially unstable modes of vibrations due to the positive feedback for some vibration modes. The paper will discuss the change of positive feedback on the negative one using all-pass discrete-time filters which are arranged in a cascade. The piezoelectric actuator as a source of force is used to damp vibration. It is well known that this actuator type has hysteresis.*

**Keywords:** Active vibration control, All-pass filter, Cantilever beam.

### 1. Introduction

The problem of the active vibration control of weakly damped mechanical structures consists in potentially unstable modes of vibrations. If the gain feedback is increased, then some of the poles of the transfer function recedes the stability boundary which is the imaginary axis, while the other poles approach it, even the boundary is crossed for a large feedback gain, and the system becomes unstable due to the positive feedback for these vibration modes. The paper will discuss the change of positive feedback to the negative one using all-pass discrete-time filters which are arranged in a cascade. Theory will be illustrated by an example of the active vibration control of the cantilever beam.

### 2. Model of a mechanical structure

As assumed the paper deal with the mechanical systems of  $N$  degrees of freedom. The properties of these mechanical systems describe the equation of motion. In addition to this equation, the system can be described by a modal or experimental model. The modal model represents the modal matrix  $\mathbf{U}$ , which is a matrix of eigenvectors, and spectral matrix  $\mathbf{\Lambda}$ , which is a diagonal matrix with the eigenvalues on the main diagonal. The experimental model is represented by measured frequency response functions (matrix  $\mathbf{H}$ ). The frequency transfer functions may be formed from all types of models as follows

$$H_{r,q}(\omega) = \sum_{n=1}^N \frac{v_{n,r}v_{n,q}}{\Omega_n^2 - \omega^2 + j2\xi_n\Omega_n\omega}, \quad r, q = 1, 2, \dots, N \quad (1)$$

where  $v_{n,r}, v_{n,q}, n, r, q = 1, \dots, N$  are the elements of the  $N$ -dimensional normalized eigenvector  $\mathbf{v}_n = [v_{n,1}, \dots, v_{n,N}]^T$  which is associated with the natural frequency  $\Omega_n$  and relative damping  $\xi_n$ . The coordinates  $v_{n,1}, v_{n,2}, \dots, v_{n,N}$  determine a vibration or mode shape. The transfer function (1) is a sum of the transfer functions of the second order systems which correspond to the mode indexed by  $n$ . The product  $k_n = v_{n,r}v_{n,q}$  for given value of indexes  $r$  and  $q$  is called a modal constant and depends on the modal shapes for the natural frequency  $\Omega_n$ . The modal constant plays a critical role for the type of feedback.

---

<sup>\*</sup> Prof. Ing. Jiří Tůma, PhD.: VSB – Technical University of Ostrava, Faculty of Mechanical Engineering, Ostrava, Czech Republic, 17. listopadu 15; 708 33, Ostrava; CZ, jiri.tuma@vsb.cz

<sup>\*\*</sup> Ing. Pavel Šuránek, PhD.: VSB – Technical University of Ostrava, Faculty of Mechanical Engineering, Ostrava, Czech Republic, 17. listopadu 15; 708 33, Ostrava; CZ, pavel.surane@vsb.cz

<sup>\*\*\*</sup> Ing. Miroslav Mahdal, PhD.: VSB – Technical University of Ostrava, Faculty of Mechanical Engineering, Ostrava, Czech Republic, 17. listopadu 15; 708 33, Ostrava; CZ, miroslav.mahdal@vsb.cz

### 3. Active vibration control

The purpose of the system for the active vibration control (AVC) is to compensate the effect of a disturbing external force on a vibration of the mechanical structure. The dampening effect of AVC can be assessed by changes in displacement, velocity or acceleration of the selected point of the structure. It can be the free end of the cantilever beam. The result of the active damping is the minimum motion around the steady-state position and the minimum velocity or acceleration of vibrations. Mechanical structures are usually weakly damped. The analysis shows that for undamped systems there are absent terms of the odd powers of the complex variables  $s$  in the Laplace transfer function. The undamped system is at the margin of stability. It has been shown that the most appropriate controller for such systems uses a proportional feedback based on the velocity of the controlled displacement (Tüma et al., 2014, 2016). The set point (SP) for such closed-loop system is equal to zero. The gain of the velocity feedback is designated by  $T$ .

There are two possible solutions, the collocated and non-collocated active vibration control. For the collocated system, the correcting force acts and the response is measured at the same point. For the non-collocated system, it the correcting force acts at the point indexed by  $q$  and the vibrations are sensed at the point indexed by  $r$  ( $q \neq r$ ). An example of the non-collocated system is shown on the right of Fig. 1. The vibration of the free end element of this cantilever beam is sensed at the point  $r = 5$ , and the correcting force acts at the element just next to the clamped end, therefore  $q = 1$ .

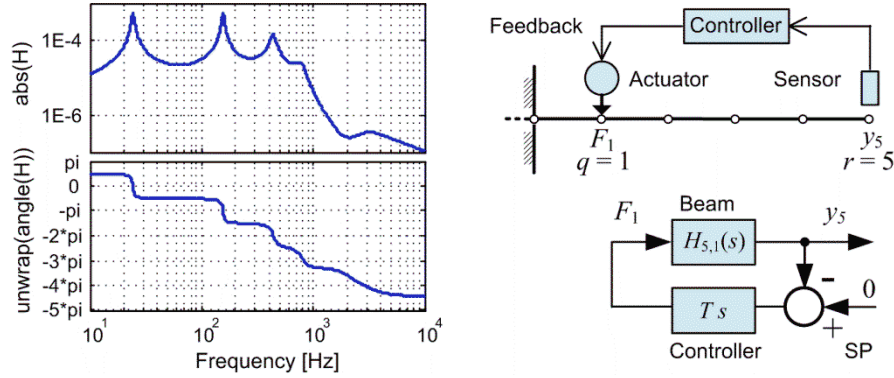


Fig. 1: Frequency response function  $j\omega H_{5,1}(\omega)$  and AVC system.

The stability of the feedback system determines the position of the pole of the closed-loop transfer function. The beam is a stable system without control due to the natural damping; it does not start to vibrate by itself. The increase of the feedback gain causes one of the poles that are associated with the two lowest resonant frequencies moves away from the instability margin while the other pole is approaching or exceeding the stability margin.

For the given beam, which is divided into 5 elements, and the assumption of the Rayleigh's damping, the locus of the closed-loop poles are shown in Fig. 2 (Tüma et al., 2014). The root locus demonstrates the effect of the controller time constant  $T$  change on the system stability. The time constant varies from 0 to 1E6. The poles are calculated as the roots of the polynomial  $1 + TsH_{5,1}(s)$ .

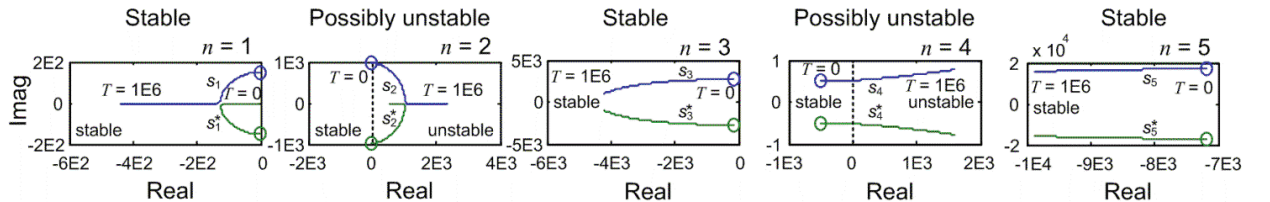


Fig. 2: Root locus to demonstrate the effect of the time constant  $T$  change.

Because the degree of polynomial equals to ten in the variable  $s$ , the number of roots, i.e. the number of poles is ten as well. Five pairs of poles are complex conjugate. The stability margin crosses the pole for the mode  $n = 2$  and the pole for the mode  $n = 4$  approaches this margin.

The analysis shows that the opposite sign of the modal constants reduces the damping effect of velocity feedback. There are two possible ways how to improve the efficiency of the active vibration control of weakly damped systems

- either control each vibration mode separately
- or change positive feedback to the negative one.

Both the methods indicate the transition of the controller design from the frequency range from zero to infinity to the control in a narrow frequency band (Šuránek et al., 2013, 2014).

The first possible solution with the filter of the band-pass type is shown in Fig. 3. This arrangement of the active vibration control is called a Positive Position Feedback (PPF) controller, see Premont. In the mentioned figure, PPF is intended for two resonant frequencies with the negative and positive feedbacks. The input signal of the filter is a signal of the velocity type because a controller of the proportionality type is used. The velocity signal is obtained by integrating the acceleration signal with respect to time. The acceleration is measured on the free end of the beam as the controlled variable. The integration and band-pass filtering together form a band-pass filter, whose transfer function has been designed previously by many authors (Premont, 1997). The filter is of the second order and therefore causes the least possible delay in the control loop. The output of this band-pass filter is amplified as necessary. The frequency range of the controller is restricted to a narrow band around the resonant frequency.

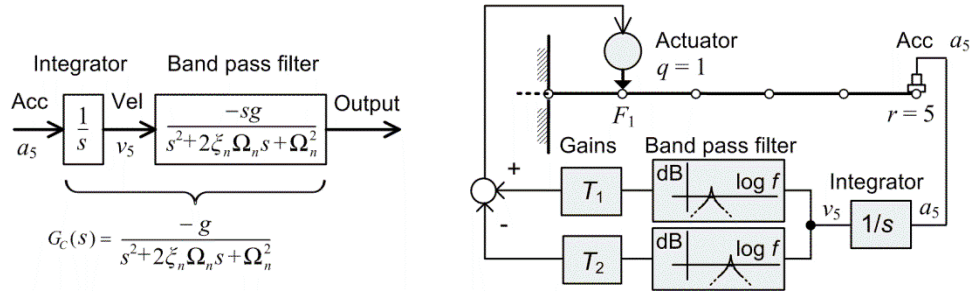


Fig. 3: Principle of Positive Position Feedback (PPF).

The second method for controlling the weakly damped systems is converting the positive feedback to the negative one with the use of an all-pass filter. This type of the frequency filter modifies the phase of the harmonic signal at the output compared to the input without changing the amplitude of the signal frequency components. The filter of this type of the first-order type changes the phase from 0 to  $\pi$  radians in the frequency range from 0 to infinity. The all-pass filter of the second order which transfer function is defined by the formula (2) doubles the phase change. For the possibly unstable modes, it is necessary to change the phase by  $\pi$  at the resonant frequency  $\omega_n$  of this vibration mode whose modal constant is to be changed from the negative to positive value. The advantage of this filter is the controllable rate of change of phase in comparison to the change of the frequency by setting the value of the relative damping parameter  $\xi_{APF}$ .

$$G_{APF,n}(s) = \frac{s^2 - 2\xi_{APF}\omega_n s + \omega_n^2}{s^2 + 2\xi_{APF}\omega_n s + \omega_n^2} \quad (2)$$

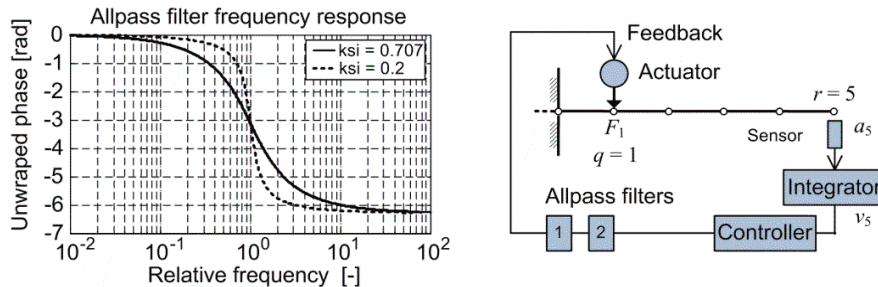


Fig. 4: All-pass filter frequency response ( $ksi = \xi_{APF}$ ).

Since  $|G_{APF,n}(j\omega)| = 1$  only a phase frequency response for two values of the damping parameter  $\xi_{APF}$  is shown on the left of Fig. 4. The all-pass filters are connected in series (cascade) with the controller as is shown on the right of Fig. 4. The count of these filters is as many as the count of the negative modal constants. The feedback is of the velocity type and needs an integrator for a sensor of the acceleration type to obtain the velocity signal.

#### 4. Simulation results

The effect of the all-pass filter on the damping of the cantilever beam vibration demonstrates the comparison of the control system response based on the use of two all-pass filters in the closed loop and without them as is shown in Fig. 5. One of the all-pass filters is tuned to the frequency of the second vibration mode and the second one to the frequency of the fourth vibration mode. The beam is excited by a short pulse after 1 second from the beginning of the simulation. During the time delay, the piezo actuator is gradually prestressed. The decaying vibration response without any active vibration control (AVC OFF) is shown on the left of Fig. 5. The effect of ACV without using the all-pass filter (ALL-PASS FILTER OFF) is shown in the middle of Fig. 5. Due to the stability, the open-loop gain can be selected less or equal to 4. The serial connection of two mentioned all-pass filters in the cascade allows increasing the gain of the open-loop in such a way that the time constant  $T$  may be increased up to the value of 25 but less than 30 with correspondingly increasing the damping effect as is shown on the right of Fig. 5.

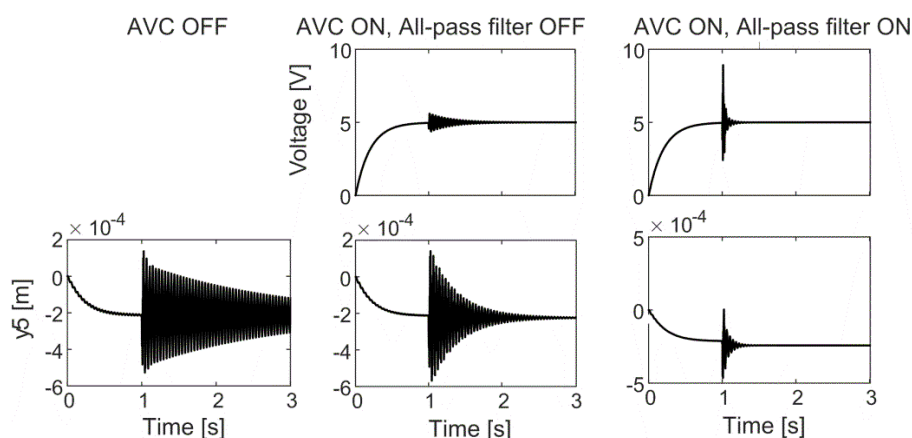


Fig. 5: Decaying vibration without any AVC and two ways of the AVC.

#### 5. Conclusions

The Matlab-Simulink model of the cantilever beam was designed using the method based on the modal analysis. Mechanical systems are generally weakly damped. Stable active damping cannot be designed by classical methods, which were developed for the synthesis of controllers. Some modes for these systems become potentially unstable. The paper describes the method that converts the positive feedback to the negative feedback using the all-pass filter. The effect of the all-pass filter on increasing the damping by shortening the impulse response has been verified by simulation approach.

#### Acknowledgement

This research has been done in the framework of the project No: SP2017/106 „Advanced Methods for Machine and Process Control“ supported by the Ministry of Education, Youth and Sports.

#### References

- Preumont, A. (1997) Active Vibration Control of Active Structures. An Introduction. Kluwer Academic Publishers.
- Šuránek, P., Mahdal, M., Tůma, J. and Zavadil, J. (2013) Modal analysis of the cantilever beam. Proceedings of the 14th International Carpathian Control Conference (ICCC 2013), Rytro, Poland, pp. 367-372. ISBN: 978-1-4673-4490-6.
- Šuránek, P., Mahdal, M. and Tůma, J. (2014) Modeling and Simulation of an Active Damped Structure, In: 15th International Carpathian Control Conference (ICCC 2014), Velké Karlovice, Czech Republic, IEEE Catalog Number: CFP1442L-CDR ISBN: 978-1-4799-3527-7.
- Tůma, J., Šuránek, P. and Mahdal, M. (2014) Vibration damping of the cantilever beam with the use of the parametric excitation, In: Proceedings of the 21st International Congress on Sound and Vibration (ICSV 21), Beijing, China, Paper 905.
- Tůma, J., Šuránek, P., Mahdal, M. and Wagnerová, R. (2016) Linear piezoactuators in systems of the active vibration control, In: Proceedings of the 23rd International Congress on Sound and Vibration (ICSV 23), Athens, Greece.



## BIOMECHANICS – VERIFICATION OF FORCE CHARACTERISTICS OF A DEVICE FOR REDUCTION OF BONE FRAGMENTS IN PATIENTS WITH FINGER FRACTURES

O. Učeň<sup>\*</sup>, K. Frydryšek<sup>\*\*</sup>, F. Fojtík<sup>\*\*\*</sup>, L. Bialý<sup>\*\*\*\*</sup>, L. Pleva<sup>\*\*\*\*\*</sup>

**Abstract:** *Finger fractures present a common type of fracture of the upper limb; they are most frequently caused with a direct mechanism of injury. These fractures are mostly unstable, indicated for surgical treatment (osteosynthesis of the fracture). The principle of osteosynthesis includes appropriate reduction (realignment) of the fracture, and its stabilization with an osteosynthetic material, most commonly using screws or plates. However, reduction of dislocated fractures is very difficult, that is why a new apparatus for repositioning of bone fragments has been developed, which may be simply used to reduce the fracture and maintain its appropriate position for subsequent osteosynthesis. The multifunctional apparatus makes repositioning of fragments in patients with finger fractures more easier, improves the quality of the final result and reduces the duration of surgery. In order to improve the quality of care provided for patients with finger fractures, it is possible to recommend introduction of this newly designed device into clinical practice (shortening of the operating time and the operating cycle). Laboratory experiments performed at the VŠB – Technical University of Ostrava provide a basic overview of force characteristics of fracture fragments compression induced by screwing the apparatus together in the course of surgery. The obtained results serve as a basis for introduction of the device into everyday clinical practice.*

**Keywords:** Biomechanics, Finger fractures, Device for reduction of bone fragments, Experiments, Compression force.

### 1. Introduction

In human hand, there are five bones in the palm of the hand (metacarpals), and 14 bones in the fingers (phalanges).

When a finger bone is broken, it can cause misalignment of the whole hand; see Fig. 1. Diagnosis of a finger fracture is based on physical examination and X-ray imaging. Without treatment, the broken finger may remain stiff and painful. People with weak bones (such as the elderly or patients with a calcium deficiency) but also manual labourers, athletes etc. have an increased risk of breaking their fingers. Therefore, it is important to perform and develop good methods for fracture treatment, see Karthikeyan (2013).

This article is focused on the evaluation of a new device intended for reduction of finger fractures; see Fig. 2. The obtained results (measured force characteristics, based also upon our earlier work, see Frydryšek et al. (2015)) serve as a basis for introducing the developed product into clinical practice.

---

<sup>\*</sup> M.Sc. Oldřich Učeň, Ph.D.: Department of Production Machines and Design, Faculty of Mechanical Engineering, VŠB-Technical University of Ostrava; 17. listopadu 15/2172; 708 33, Ostrava; Czech Republic, oldrich.ucen@vsb.cz

<sup>\*\*</sup> Assoc. Prof. M.Sc. Karel Frydryšek, Ph.D., ING-PAED IGIP: Department of Applied Mechanics, Faculty of Mechanical Engineering, VŠB-Technical University of Ostrava; 17. listopadu 15/2172; 708 33, Ostrava; Czech Republic, karel.frydrysek@vsb.cz

<sup>\*\*\*</sup> M.Sc. František Fojtík, Ph.D.: Department of Applied Mechanics, Faculty of Mechanical Engineering, VŠB-Technical University of Ostrava; 17. listopadu 15/2172; 708 33, Ostrava; Czech Republic, frantisek.fojtik@vsb.cz

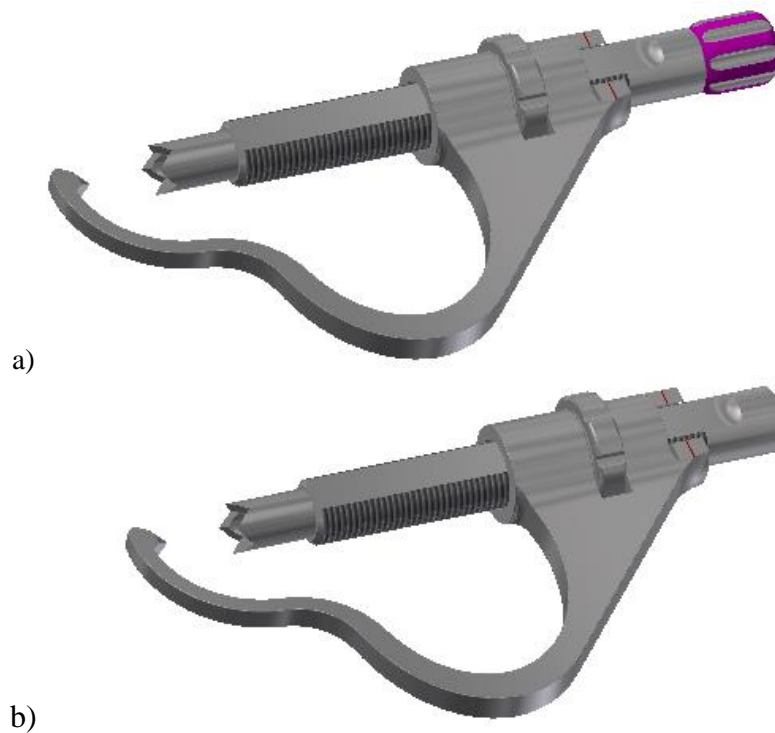
<sup>\*\*\*\*</sup> Bialý Lubor, MD: Traumatology Centre University Hospital Ostrava, 17. listopadu 1790, 708 52 Ostrava, Czech Republic, vatavah@centrum.cz

<sup>\*\*\*\*\*</sup> Assoc. Prof. Pleva Leopold, MD, CSc. Traumatology Centre University Hospital Ostrava and Institute of Emergency Medicine Faculty of Medicine, 17. listopadu 1790, 708 52 Ostrava, Czech Republic, leopold.pleva@fno.cz





*Fig. 1: Phalangeal fracture and its treatment (i.e. repair with small screws).*



*Fig. 2: Device for reduction of finger fractures: a) with the drill guide; b) without the drill guide for insertion of screws.*

## **2. Device for reduction of finger fractures**

The designed device (see Fig. 2) should provide the physicians with an instrument for reduction of finger fractures. It is ergonomically shaped and adjusted for insertion of mini-screws with the diameter of 1 to 2 mm into bone fractures, in the course of surgical procedures performed on small bones of the hand. The size of the screw head varies, depending on the screw used, from 2 to 4 mm (according to the anatomy of individual patients). The direction of drilling is perpendicular. One part of the device contains a curvilinear arc with a fixed tip. The other part consists of a targeting case and a nut, enabling compression of bone fragments. Exchangeable cases enable drilling with a K-wire, or a drill, or insertion of screws during osteosynthesis, see Fig. 1b.

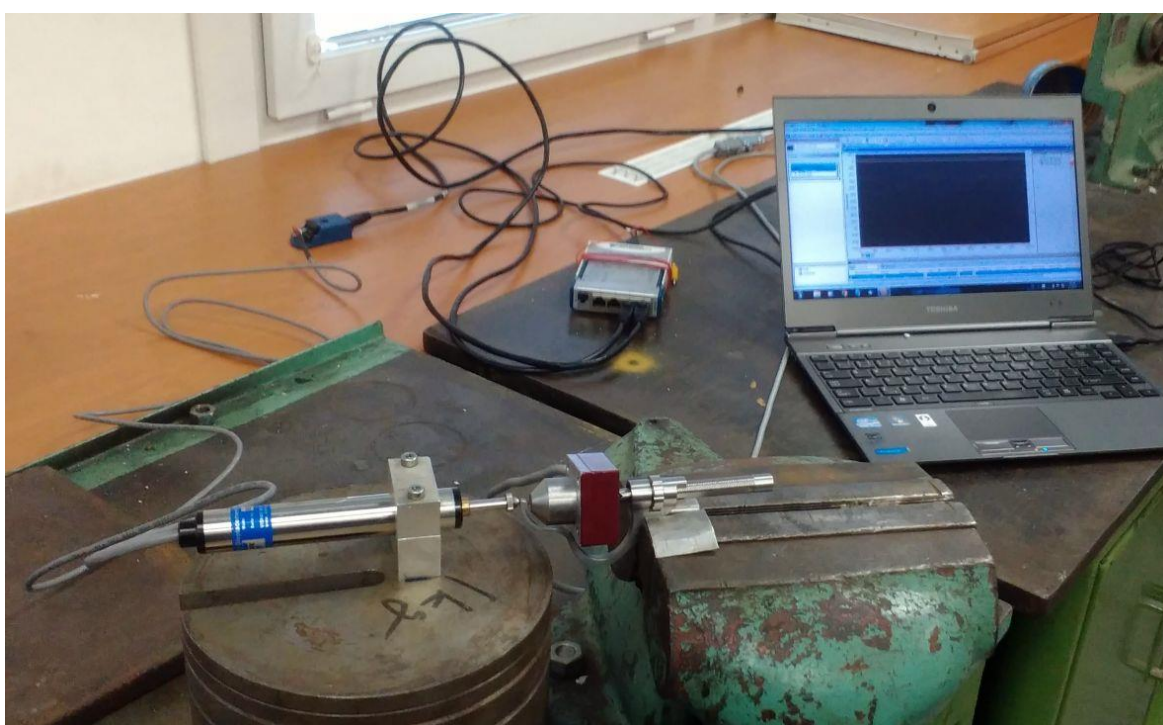
## **3. Measurement of force characteristics of the device for reduction of finger fractures**

Due to the need to introduce the device for reduction of finger fractures into clinical practice, it is necessary to evaluate it also from the biomechanical point of view. The selected method of testing was to

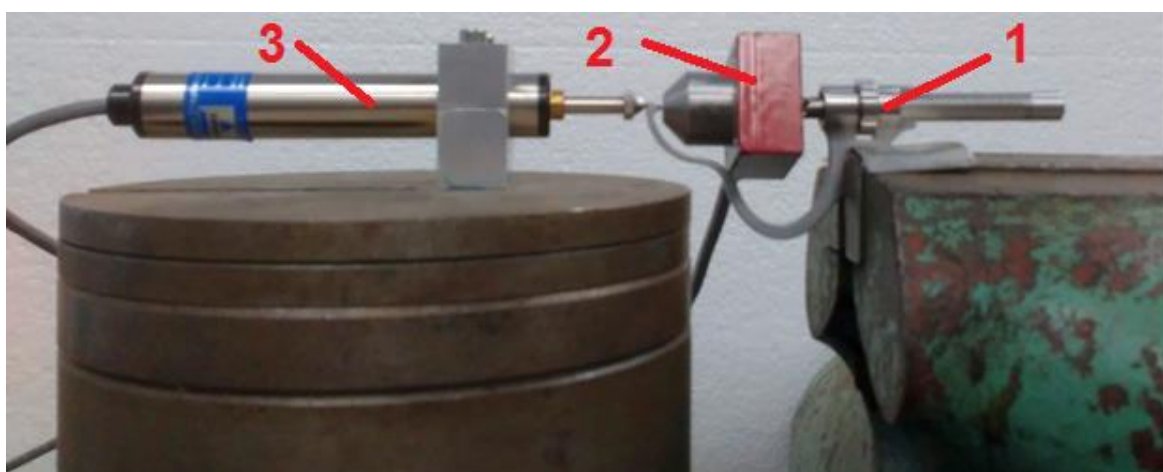
perform measurements at laboratories of the VŠB – Technical University of Ostrava (Ostrava, Czech Republic, see Macura (2001)).

It is very important for the physicians to know precisely the capabilities of the device. From the point of view of biomechanics/mechanics, this represents namely its sufficient stiffness, reliability and exertion of sufficient compression forces  $F_c$  [N], depending on the displacement  $u$  [mm/ of the free end of the arc (the tip – left side of the device, see Fig. 2), in the axis of the clamping screw. This displacement occurs during compression of finger fractures and depends on the stiffness of the device.

According to the description above, we performed an experiment, which is documented in Figs. 3 and 4. In order to perform the measurements, the device was fastened into a clamp in the place of presumed zero deformation. In order to measure the  $F_c$  force, we used an adjusted strain gauge, with a membrane structure and nominal range of 300 N. For measurement of displacement of the end of the arc on the device we used a linear displacement sensor type HS25 (Vishay Precision Group, Malvern, Pennsylvania, USA). Both sensors were connected to a measuring apparatus, strain card and accessories (National Instruments, Austin, Texas, USA). The forces and displacements were recorded with software created in the LabVIEW interface.



*Fig. 3: Laboratory measurement.*



*Fig. 4: Laboratory measurement: 1 device for reduction of finger fractures, 2 force sensor, 3 linear displacement sensor HS25.*

#### 4. Results of measurements

The results of measurements of compression forces in the device for reduction of finger fractures are presented in Fig. 5.

For practical reasons, the acquired dependence  $F_c = f(u)$  can be linearized via equation

$$F_c = 44.857u, \quad (1)$$

see Fig. 5.

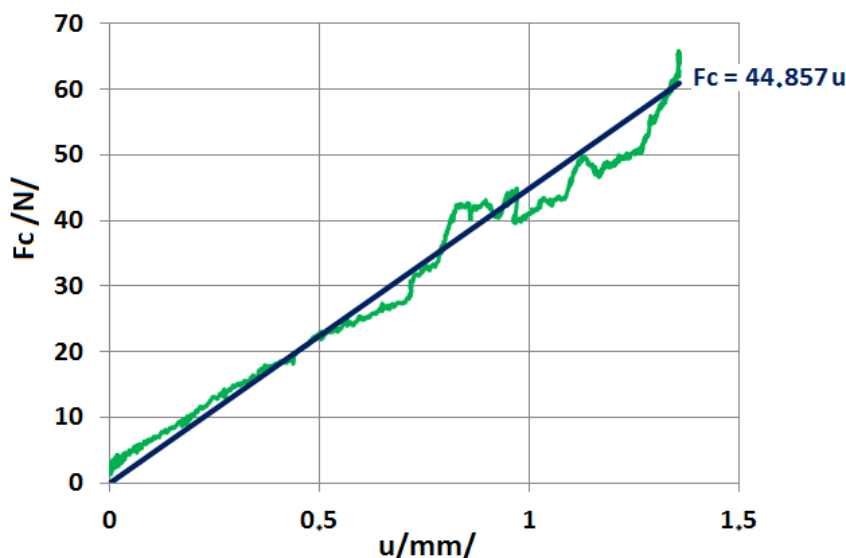


Fig. 5: Dependence of compression force on displacement (measurement and its linearization).

#### 5. Conclusions

The results of measurements proved sufficient magnitudes of compression forces required for osteosynthesis performed with the newly designed device for reduction of finger fractures. Measurement of dependency of these compression forces is what makes this article truly original. The maximum magnitudes of compression forces (i.e. an additive loading during the operation) reaching up to 70 N are sufficient for surgical procedures in traumatology/orthopaedics.

Based upon the experiments, it is possible to conclude that the device for reduction of finger fractures may be safely introduced into clinical practice, which will result in improvement of medical care provided for patients.

#### Acknowledgement

This work was supported by Czech projects TA03010804, SP2017/136, SP2017/23 and IT4Innovations excellence in science - LQ1602.

#### References

- Frydrýšek, K., Theisz, G., Bialy, L., Pliska, L. and Pleva, L. (2015) Finite element modelling of T-plate for treatment of distal radius, *Advances in Intelligent Systems and Computing*. Vol. 423, Springer, pp. 1-10.
- Karthikeyan, G. (2013) *Manual of Reconstructive Hand Surgery*, ISBN 978-9350905128, Jaypee Brothers Medical Publishers Ltd., New Delhi, India.
- Macura, P. (2001) *Experimental Methods in Elasticity and Plasticity*, Ostrava, VŠB-TUO, (in Czech).

## THREE-POINT BENDING FATIGUE DAMAGE MECHANISMS ASSOCIATED WITH THE DIFFERENT STRUCTURE OF AL-MG CAST ALLOYS

M. Uhříčik\*, M. Oravcová\*, P. Palček\*, M. Chalupová\*, L. Kuchariková\*

**Abstract:** *The article is monitoring the influence of the structure on the fatigue properties of aluminium alloys for the casting of type Al-Mg. As an experimental material were used aluminium alloys EN AC 51200 and EN AC 51500, supplied in a cast state without a heat treatment. These alloys were selected on the basis of the chemical composition, where the content of most alloying elements is comparable, only in the case of the concentration of magnesium are these alloys significantly different. Fatigue properties of aluminium alloys were tested by three-point bending cyclic loading. The fracture surface of the testing sample was examined using scanning electron microscopy (SEM), where samples were observed on various stages of the fatigue process, their characteristics and differences of fracture surfaces.*

**Keywords:** Fatigue, Fracture, Aluminium alloy, Three-point bending loading, Structure.

### 1. Introduction

Fatigue failures in metallic structures are a well-known technical problem. In a specimen subjected to a cyclic load, a fatigue crack nucleus can be initiated on a microscopically small scale, followed by crack grows to a macroscopic size, and finally to specimen failure in the last cycle of the fatigue life. Understanding of the fatigue mechanism is essential for considering various technical conditions which affect fatigue life and fatigue crack growth, such as the material surface quality, residual stress, and environmental influence. This knowledge is essential for the analysis of fatigue properties of an engineering structure (Belan et al., 2014 and Hurtalová et al., 2014).

### 2. Material characteristics

As an experimental material were used aluminium cast alloys of type Al-Mg (EN AC-51200 and EN AC-51500), supplied in a cast state without a heat treatment in the form of plates. They were produced by the continuous casting method. Test samples for determining the fatigue properties were made by the cutting operation from these plates, which were cut from casts. The chemical composition of both alloys was examined by spark emission spectrometer SPECTROMAXx and results are shown in Tab. 1. These alloys were selected based on this chemical composition, where the content of most of alloying elements is comparable, only a concentration of magnesium is considerably different.

### 3. Results and discussion

#### 3.1. Microstructural analysis and phase analysis

Considering that alloys were casted under the same technological conditions, it can be said that the structure affects only the chemical composition of alloys. Microstructure of materials is expressively dendritic (Fig. 1 and Fig. 2). The highest percentage representation of dendrites has  $\alpha$ -phase (matrix) that is a solid solution of aluminium together with other additive elements. In the structure, there is also an

---

\* Ing. Milan Uhříčik, PhD., Ing. Monika Oravcová, Prof. Ing. Peter Palček, PhD., Ing. Mária Chalupová, Ing. Lenka Kuchariková, PhD. : Department of Materials Engineering, University of Žilina, Univerzitná 8215/1; 010 26, Žilina; SK, milan.uhricik@fstroj.uniza.sk, monika.oravcova@fstroj.uniza.sk, peter.palcek@fstroj.uniza.sk, maria.chalupova@fstroj.uniza.sk, lenka.kucharikova@fstroj.uniza.sk



intermetallic phase  $Mg_2Si$ . This phase has a different morphology in alloys. In the case of EN AC 51200 alloy, it has a shape of skeleton formation and is distributed in interdendritic areas. There is also  $\beta$ -phase, which is formed in interdendritic areas and has a stoichiometric basis  $Al_3Mg_2$ . In alloy EN AC 51500, intermetallic phase  $Mg_2Si$  has a finer morphology and does not have a typical shape of skeleton formation. Because elements such as iron and manganese are also in alloys, can be observed a small amount of Fe-rich phase in structure of both materials, probably  $Al_6(FeMn)$ .  $\beta$ -phase is not present in this alloy, because of the smaller content of magnesium.

Tab. 1: The chemical composition of alloys, in wt. %.

	Si	Fe	Cu	Mn	Mg	Cr	Pb	Al
<b>EN AC 51200</b>	1.3	0.102	0.003	0.416	10.32	0.006	0.027	balance
<b>EN AC 51500</b>	1.53	0.11	0.004	0.529	6.28	0.008	0.031	balance

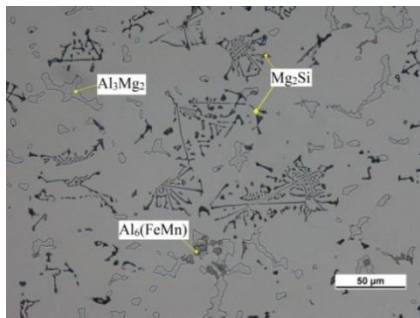


Fig. 1: Microstructures of alloys EN AC 51200.

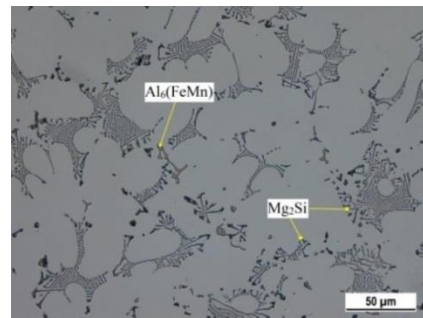
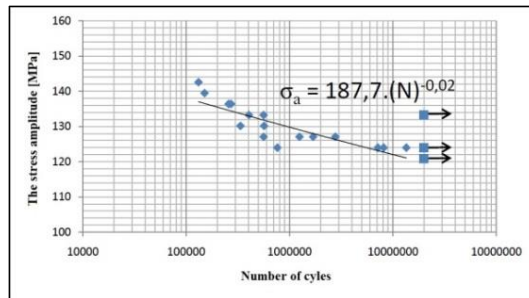


Fig. 2: Microstructures of alloy EN AC 51500.

### 3.2. Fatigue lifetime

Fatigue tests were carried out on the test equipment ZWICK/ROELL AMSLER 150 HFP 5100 according to norm STN 42 0363. This equipment is using the resonance principle with constant or variable amplitude and mean load. Smooth rectangular specimens without notches (10 x 18 x 40 mm) were loaded by cyclic three-point bending loading with mean stress  $\sigma_m = -144$  MPa and frequency 120 Hz, only stress amplitude was changing. From results of fatigue tests were constructed graphs  $\sigma_a \cdot N$  in semi-logarithmic coordinates, for every alloy (Fig. 3 and Fig. 4). By comparing of graphs can be stated that alloy EN AC 51500 has better fatigue properties than alloy EN AC 51200 in analyzed area of the number of cycles.

Fig. 3: Results of fatigue tests for alloy EN



AC 51200.

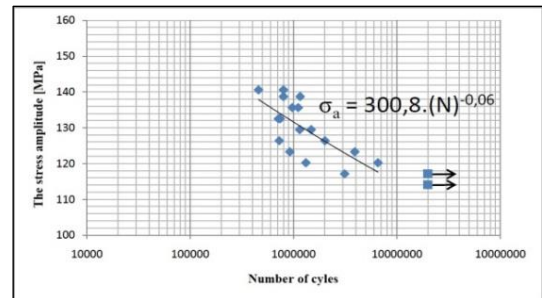


Fig. 4 Results of fatigue tests for alloy EN AC 51500.

### 3.3. Fractographic analysis

Fractographical assessment of fracture surfaces was realized on samples from each material after the fatigue test. On samples were observed various stages of fatigue process, their characteristics and differences of fracture surfaces between samples loading in high and low amplitude of stress. It has also been observed an area of final fracture. Fracture surfaces were evaluated by scanning electron microscopy TESCAN VEGA LMU II. From analysis it is possible to determine initiation (nucleation) of fatigue crack, surfaces of individual areas of fracture, namely the fatigue fracture area and the area of static final failure.

A general view of the fracture area for the alloy EN AC 51500 after 1314148 cycles at a stress of 120 MPa is documented in Fig. 5a, where can be seen various stages of fatigue process. Detail of initiation site is shown in Fig. 5b. Transgranular fatigue failure of  $\alpha$ -phase (matrix) and there were observed typical signs of fatigue – striations and also an interfacial and a fission failure of  $Mg_2Si$  phase, this all is shown in Fig. 5c. Fig. 5d displays the area of static final failure, where can be seen plastic's transformed ridges of  $\alpha$ -phase, together with a transgranular ductile fracture of  $\alpha$ -phase with dimple morphology and also is visible an interfacial failure of  $Mg_2Si$  phase.

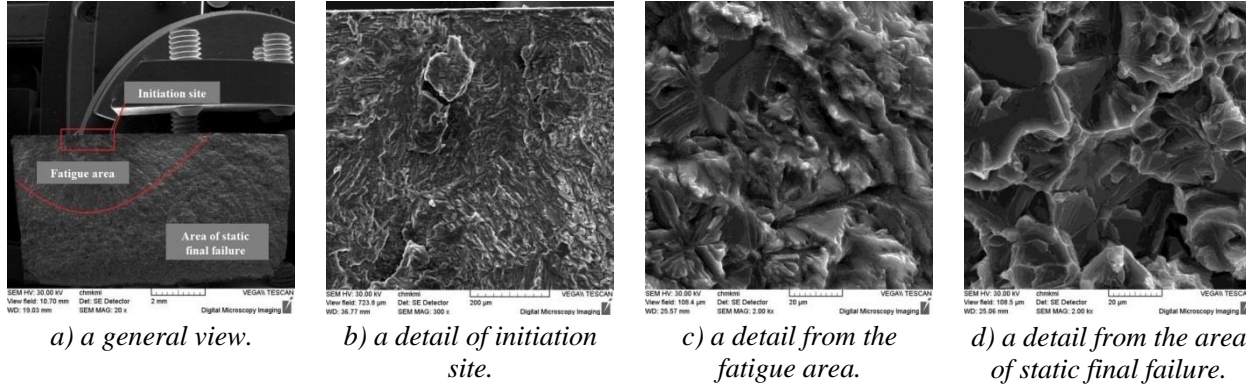


Fig. 5: Fracture surface of aluminium alloy 51500,  $\sigma_a = 120$  MPa,  $N_f = 1314148$  cycles.

A general view of the fracture area for the alloy EN AC 51500 after 799229 cycles at a stress of 138 MPa is shown in Fig. 6a. Here can be seen that when higher amplitude of stress was applicate, the fatigue crack was spread from several initiation sites on the specimen surface and there was also a reduction of the fatigue area. Detail of one initiation site is shown in Fig. 6b. Transgranular fatigue failure of  $\alpha$ -phase (matrix) and there were observed typical signs of fatigue – striations as it is shown in Fig 6c. Fig. 6d displays the area of static final failure, where can be also seen plastic's transformed ridges of  $\alpha$ -phase, together with transgranular ductile fracture of  $\alpha$ -phase with dimple morphology and also is visible an interfacial failure of  $Mg_2Si$  phase.

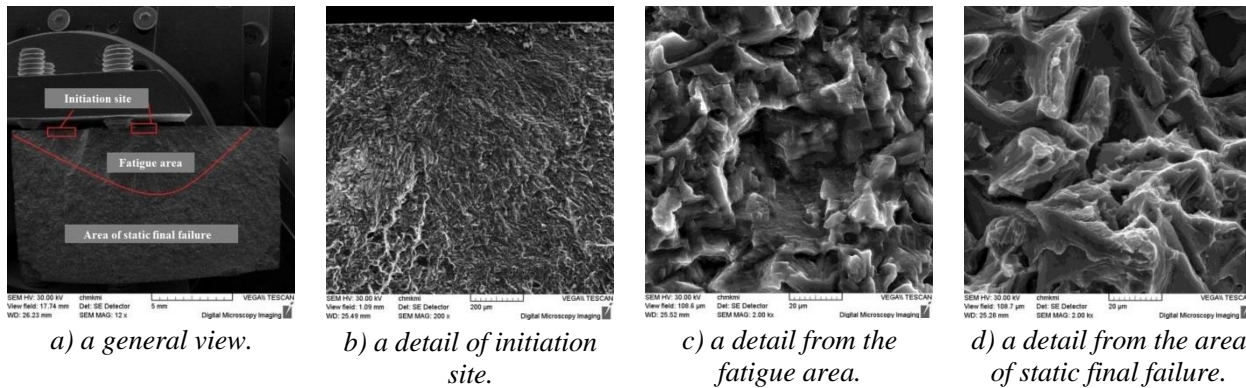


Fig. 6: Fracture surface of aluminium alloy 51500,  $\sigma_a = 138$  MPa,  $N_f = 799229$  cycles.

A general view of the fracture area for the alloy EN AC 51200 after 761899 cycles at a stress of 124 MPa is documented in Fig. 7a, where can be seen various stages of fatigue process. Detail of initiation site is shown in Fig. 7b. In Fig 7c can be seen an interfacial failure of intermetallic phases ( $Al_3Mg_2$ ,  $Al_6(FeMn)$  and  $Mg_2Si$ ) and also a transgranular fatigue failure of  $\alpha$ -phase (matrix). Fig. 7d displays the area of static final failure, where can be seen interfacially broken intermetallic phases and plastic's transformed ridges of  $\alpha$ -phase, together with transgranular ductile fracture of  $\alpha$ -phase with dimple morphology.

A general view of the fracture area for the alloy EN AC 51200 after 150530 cycles at a stress of 139 MPa is shown in Fig. 8a. Here can be seen that when higher amplitude of stress was applicate, the fatigue crack was spread from several initiation sites on the specimen surface and there was also a reduction of the fatigue area and a smaller number of cycles to fracture. Detail of one initiation site is shown in Fig. 8b. In Fig 8c can be seen a transgranular fatigue failure of  $\alpha$ -phase (matrix) and also an interfacial failure of intermetallic phases ( $Al_3Mg_2$  and  $Al_6(FeMn)$ ). Fig. 8d displays the area of static final failure, where can be seen plastic's transformed ridges of  $\alpha$ -phase, together with a transgranular ductile fracture of  $\alpha$ -phase with dimple morphology and also is visible an interfacial failure of  $Mg_2Si$  and  $Al_3Mg_2$  phases.



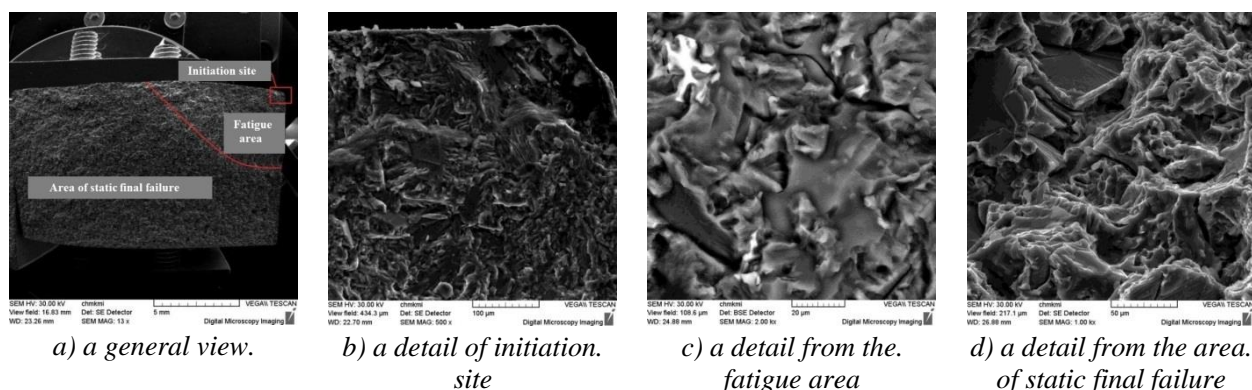


Fig. 7: Fracture surface of aluminium alloy 51200,  $\sigma_a = 124$  MPa,  $N_f = 761899$  cycles.

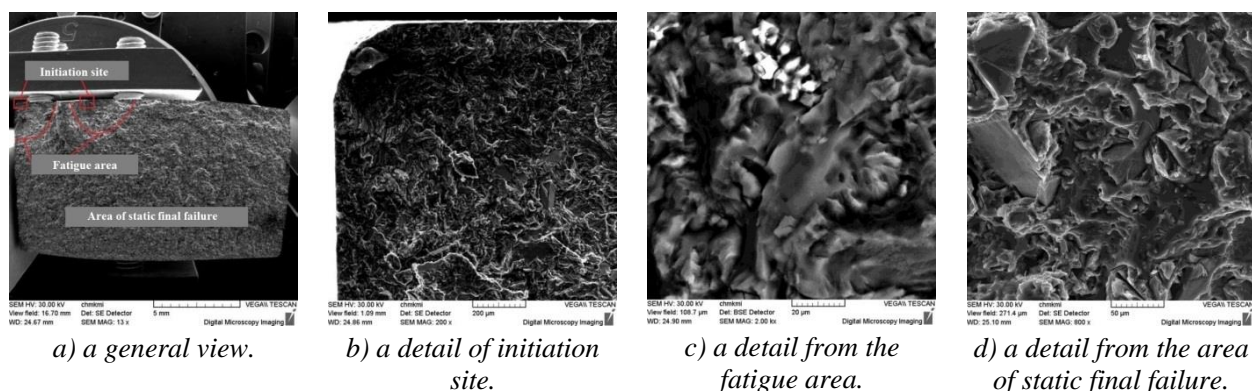


Fig. 8: Fracture surface of aluminium alloy 51200,  $\sigma_a = 139$  MPa,  $N_f = 150530$  cycles.

#### 4. Conclusions

Alloys have a clearly dendritic structure consisting mainly  $\alpha$ -phase. In the structure of both alloys are intermetallic  $\text{Al}_6(\text{FeMn})$  and  $\text{Mg}_2\text{Si}$  phases. In alloy EN AC 51200, there is also an intermetallic  $\text{Al}_3\text{Mg}_2$  phase. Alloys are comparable in terms of morphology and the amount of  $\text{Al}_6(\text{FeMn})$  phase. From fatigue tests, it can conclude that alloy EN AC 51500 has better fatigue properties than alloy EN AC 51200, in the analyzed areas of number of cycles under the same conditions of loading. Fractographic analysis did not reveal significant changes of micromechanisms of fracture surfaces after fatigue tests. Fatigue area is characterized by transgranular fatigue failure of  $\alpha$ -phase (matrix). Intermetallic phases in this area were violated interfacially, only  $\text{Mg}_2\text{Si}$  phase had also a fission failure somewhere. The area of static final failure is typical of a transgranular ductile fracture of  $\alpha$ -phase with dimple morphology with plastic's transformed ridges. When comparing both of alloys, it can be stated that the only difference is that on the fracture surface of alloy EN AC 51500 is not an interfacially broken  $\text{Al}_3\text{Mg}_2$  phase, because this alloy does not contain it. In terms of stress amplitude can be said that in case of a higher amplitude of cyclic loading there was a multiple initiation of fatigue crack.

#### Acknowledgement

This work has been supported by Scientific Grant Agency of Ministry of Education of Slovak republic, N°1/0683/15 and N°1/0533/15.

#### References

- Belan, J., Hurtalová, L., Vaško, A. and Tillová, E. (2014) Metallography evaluation of IN 718 after applied heat treatment. *Manufacturing Technology*, 14, 3, pp. 262-267.
- Hurtalová, L., Tillová, E., Chalupová, M., Belan, J. and Vaško, A. (2014) Microstructure control of secondary A 231 cast alloy used in automotive industry. *Manufacturing Technology*, 14, 3, pp. 326-333.

## MODELING OF FRICTIONAL STICK SLIP EFFECT LEADING TO DISC BRAKE NOISE VIBRATION AND HARSHNESS

J. Úradníček<sup>\*</sup>, P. Kraus<sup>\*\*</sup>, M. Musil<sup>\*\*\*</sup>, M. Bachratý<sup>\*\*\*\*</sup>

**Abstract:** Paper describes mechanism of vibration of disc brake components which can lead into noise effects known as brake Noise Vibrations and Harshness (NVH). Self-excited vibrations due to stick-slip effect and stability conditions are defined using 1 degree of freedom mechanical system. Nonlinear behavior of friction force with negative slope is considered. Response is obtained by numerical solution of ordinary differential equation. Conditions for self-exciting vibrations exhibition has been defined and discussed.

**Keywords:** Stick-slip, NVH, Self-excited vibrations, Brake squeal, Dynamical instability.

### 1. Introduction

The unwanted side effect of the braking operation is its occasional squeal and other unwanted harshness effects. In the literature and in many studies we can find different classifications of brake noise, such as judder, hum, groan, squeal, squeak, wire-brush, chatter and moan, among others (Suchal, 2013). NVH is a problem that has been challenging engineers in industry for decades. It is commonly agreed that it occurs due to a friction induced oscillation. There are several mechanisms which can lead into NVH. Most discussed are stick and slip, sprag and slip effects (Guran, 2001), non-conservative follower force (Krillov, 2013) and mode coupling (Úradníček et al., 2016). Numerous works have analyzed the phenomenon of brake squeal, ranging from basic studies on mechanisms up to the development of suitable measurement techniques (Kinkaid et al., 2003). Nowadays, there is a strong research focus on numerical simulation (Dihua et al., 1998). Some years ago stability studies in the form of eigenvalue analysis of the linearized system became the state of the art. This kind of linear stability analysis is now used broadly in industry to analyze stability borders and to suggest measures against squeal. Nowadays, producers of braking components especially braking pads are strongly bounded by legislation to follow trends of sustainable reduction of environmental burdening and recyclability of materials (Peciar et al., 2016) which makes the process of developing the silent brake system even more challenging.

### 2. Modeling of Stick-slip effect

Stick-slip can be described as surfaces alternating between sticking to each other and sliding over each other, with a corresponding change in the force of friction. Typically, the static friction coefficient between two surfaces is larger than the kinetic friction coefficient. If an applied force is large enough to overcome the static friction, then the reduction of the friction to the kinetic friction can cause a sudden jump in the velocity of the movement. This effect can be demonstrated on simplified representation of the brake pad/disc frictional pair represented by 1 degree of freedom (DOF) mechanical model (Fig. 1a), where only pad elasticity in one direction is considered.

---

<sup>\*</sup> Ing. Juraj Úradníček, PhD.: Faculty of Mechanical Engineering, Slovak University of Technology in Bratislava, Námestie slobody 17, 812 31 Bratislava, Slovakia, Tel. number: +421 57296587, e-mail: juraj.uradnicek@stuba.sk.

<sup>\*\*</sup> Ing. Pavel Kraus: Faculty of Mechanical Engineering, Slovak University of Technology in Bratislava, Námestie slobody 17, 812 31 Bratislava, Slovakia, Tel. number: +421 5729 315, e-mail: pavel.kraus@stuba.sk.

<sup>\*\*\*</sup> prof. Ing. Miloš Musil, PhD.: Faculty of Mechanical Engineering, Slovak University of Technology in Bratislava, Námestie slobody 17, 812 31 Bratislava, Slovakia, Tel. number: +421 5729 389, e-mail: milos.musil@stuba.sk.

<sup>\*\*\*\*</sup> Ing. Michal Bachratý, PhD.: Faculty of Mechanical Engineering, Slovak University of Technology in Bratislava, Námestie slobody 17, 812 31 Bratislava, Slovakia, Tel. number: +421 57296585, e-mail: michal.bachraty@stuba.sk

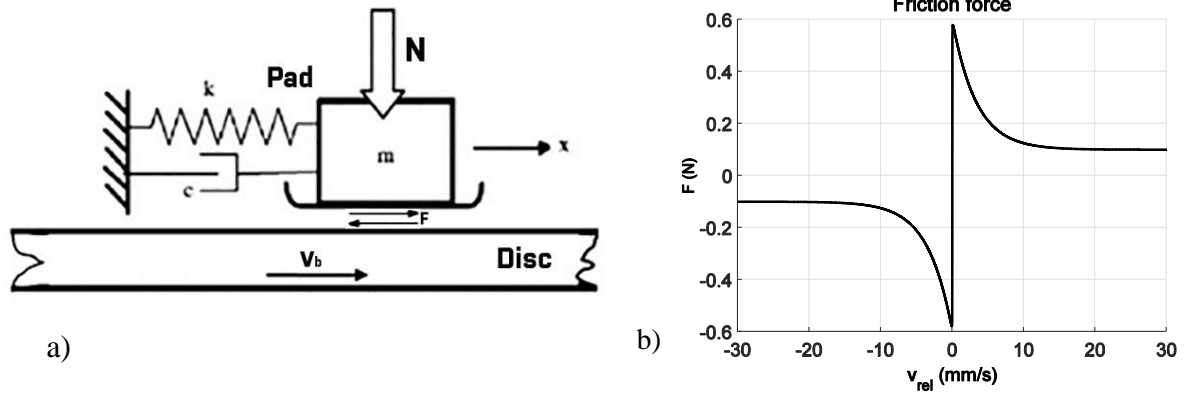


Fig. 1: a) Single DOF mechanical model of disc brake; b) Friction force function.

Governing differential equation for the model is

$$m\ddot{x}(t) + c\dot{x}(t) + kx(t) = F(t, v_{rel}), \quad (1)$$

and negative slope friction force is derived from Armstrong (1995).

$$F(t, v_{rel}) = N \left[ \mu_c + (\mu_{brk} - \mu_c) e^{-c_v |v_{rel}|} \frac{2}{\pi} \text{atan}(s v_{rel}) \right]. \quad (2)$$

Where  $m$  – friction material mass,  $x$  – displacement,  $c$  – damping coefficient,  $k$  – stiffness, relative velocity  $v_{rel} = (v_b - \dot{x})$ ,  $v_b$  – disc velocity,  $N$  – normal force,  $\mu_s$  – Coulomb friction coefficient,  $\mu_{brk}$  – breakaway friction coefficient (static friction coefficient),  $\mu_c$  – kinetic friction coefficient,  $s$  – sharpness coefficient, time derivatives  $\dot{x}$  and  $\ddot{x}$  represents velocity and acceleration of friction material in  $x$  direction. Function  $2/\pi \text{atan}(-)$  in (2) is used to represent friction force transition along zero relative velocity. The frictional force function is shown in Fig. 1b.

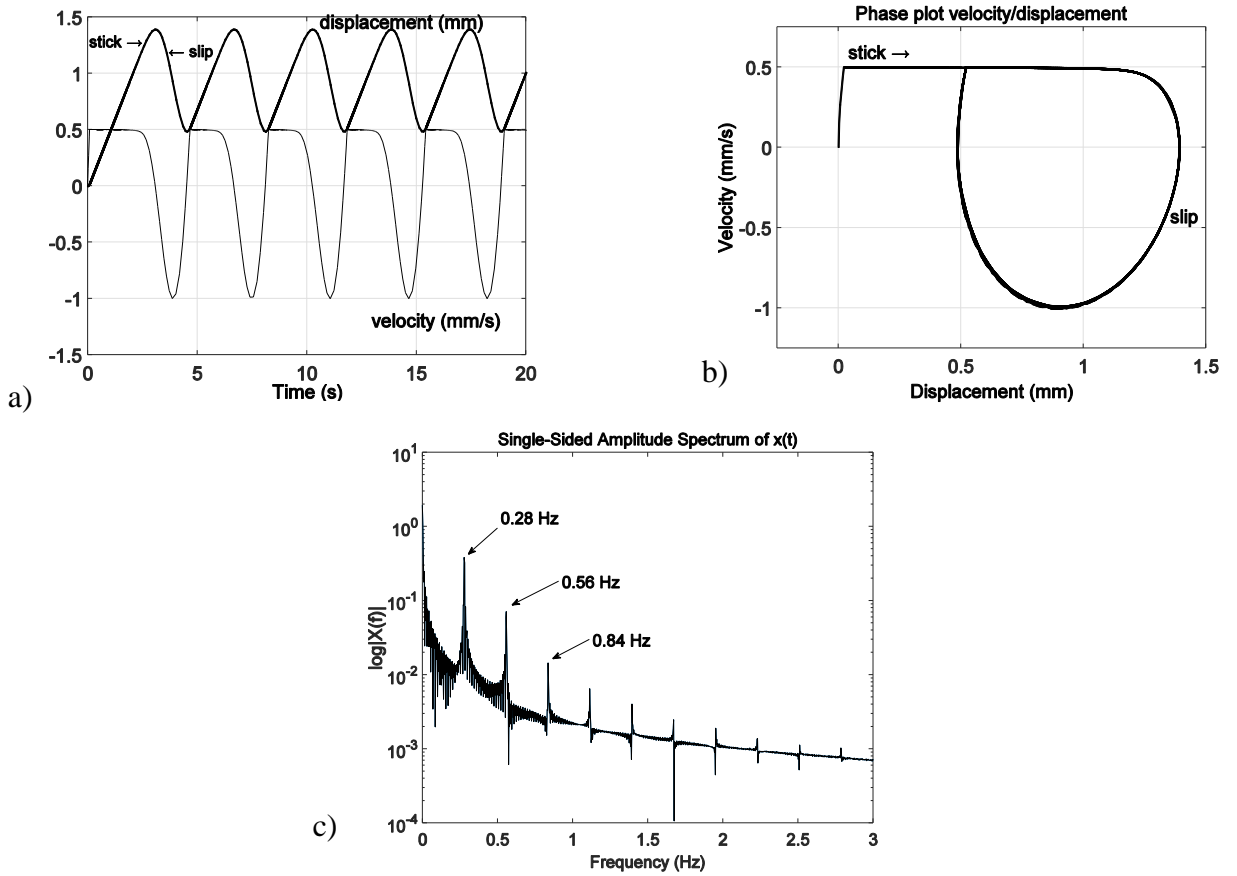


Fig. 2: a) displacement, velocity of mass; b) phase plot of displacement/velocity of mass; c) amplitude spectrum of displacement, for parameters:  $m = 1$  kg;  $v_b = 0.5$  mm/s;  $k = 5$  N/mm;  $\mu_{brk} = 0.6$ ;  $\mu_c = 0.1$ ;  $c = 0.2$  N/mm.s;  $N = 10$  N;  $s = 500$  and initial conditions  $x = 0$ ,  $dx/dt = 0$ .

Substituting (2), into (1)

$$m\ddot{x}(t) + c\dot{x}(t) + kx(t) = N \left[ \mu_c + (\mu_{brk} - \mu_c) e^{-c_v|(v_b - \dot{x})|} \frac{2}{\pi} \text{atan}(s(v_b - \dot{x})) \right]. \quad (3)$$

The equation (3) is nonlinear differential equation due to the nonlinear friction force changing its orientation and value with respect to relative velocity. Negative gradient of friction force is in contradiction with damping of the system which, under specific conditions, can destabilize system in the meaning that response amplitude is increasing with the time (Úradníček et al., 2017).

The response of the nonlinear dynamical system corresponding to the initial condition was calculated numerically using Runge-Kutta integration method included in MATLAB software through ODE45 function. For all following calculations, constant disc speed  $v_b(t)$  and zero initial conditions  $x(0) = \dot{x}(0) = 0$  have been considered.

In the first calculation, the negative slope friction force (2) and low disc velocity  $v_b = 0.5$  mm/s has been considered. Under these conditions system generates self-excited vibrations with polyharmonic response (Fig. 2a) due to strong nonlinearity of the friction force. System is dynamically stable with stick-slip limit cycles (Fig. 2b). Response is the combination of two motions. The first is stick motion in which the mass has the same velocity as the disc and second is the slip motion which occurs when the forces acting on the mass are greater than the friction force, which results in mass sliding over the disc. Amplitude spectrum of the displacement response is depicted in Fig. 2c. Response consists of fundamental frequency 0.28 Hz and higher harmonics which are integer multiples of fundamental frequency. Fundamental frequency value is given by friction force. In general, it depends on the difference between the static and the kinetic friction force (the bigger is the friction force around zero relative velocity the longest stick mode is lasting). System under given conditions produces stable self-excited polyharmonic vibrations.

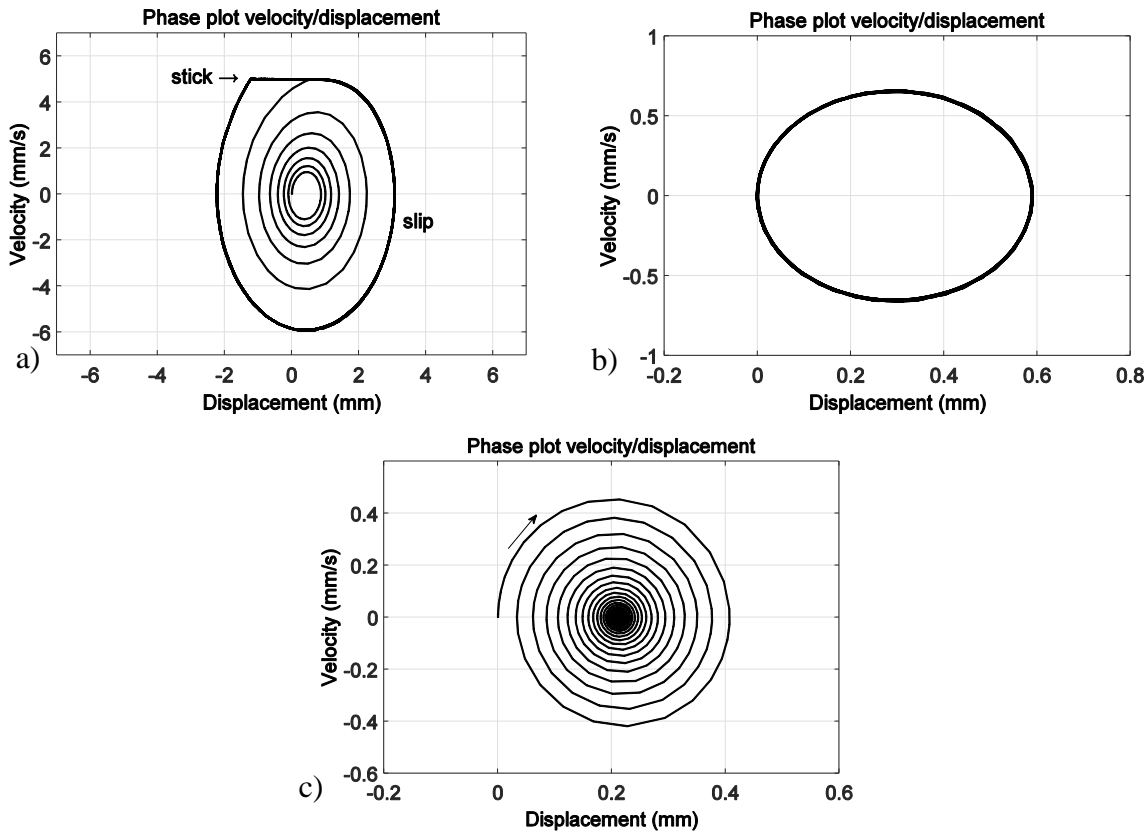


Fig. 3: Phase plot of displacement/velocity of the mass for: a)  $v_b = 5$  mm/s; b)  $v_b = 6.99$  mm/s; c)  $v_b = 10$  mm/s.

Increasing the disc velocity  $v_b$ , the sticking phase is shortening (Fig. 3a). At the critical disc speed value, the stick phase do not occur anymore and system is stable oscillating along equilibrium position (Fig. 3b). When the critical base speed is exceeded, system doesn't produce self-excited vibrations anymore and is oscillating about equilibrium position with decreasing amplitude Fig. 3c.

### 3. Conclusions

Stick-slip frictional effect have been described through single degree of freedom mechanical system. Frictional force has been modeled as the function with negative slope with respect to relative velocity. Nonlinear behavior has been demonstrated using numerical time integration of ordinary differential equation.

From the numerical analyses of simplified mechanical brake model, it can be seen, that stick-slip effect is source of stable self-excited vibrations. When stick-slip effect disappears due to critical velocity of the disc system is in purely sliding vibrations state. When critical velocity of the disc is exceeded, system stable oscillates about equilibrium position with decreasing amplitude.

### Acknowledgement

This work was supported by the Slovak Research and Development Agency under the contract No. APVV-15-0630.

### References

- Armstrong, B., De Wit, C.C. (1995) Friction Modeling and Compensation, The Control Handbook, CRC Press.
- Dihua, G., Dongying, J. (1998) A study on disc brake squeal using finite element methods, In Proceedings of International SAE Congress and Exposition.
- Guran, A. et al. (2001) Dynamics with friction: modelling, analysis and experiment, part II., World scientific publishing Co. Pte. Ltd., ISBN 98-128112-73.
- Kinkaid, N.M., O'reilly O.M. and Papadopoulos, P. (2003) Automotive disc brake squeal, In Journal of Sound and Vibration 267, 105-166.
- Krillov, O.N. (2013) Nonconservative Stability Problems of Modern Physics., De Gruyter Studies in Mathematical Physics 14, ISBN 97-831102703-41.
- Peciar, M., Fekete, R. and Peciar, P. (2016) Agglomeration Technologies of Processing Powder Wastes, Solid State Phenomena, Vol. 244, pp. 121-129.
- Suchal, A. (2013) Influence of Thermal Effect on Dynamics of Disc Brakes and Brake Squeal Propensity, PhD. Thesis, Slovak University of Technology in Bratislava, Slovakia.
- Úradníček, J., Musil, M. and Kraus, P. (2016) Predicting the self-excited vibrations in automotive brake systems. In Noise and vibration in practice: peer-reviewed scientific proceedings. 1. vyd. Bratislava: Nakladateľstvo STU, pp. 129-134. ISBN 978-80-227-4563-5.
- Úradníček, J., Kraus, P. and Musil, M. (2017) Investigation o the frictional stick slip and sprag slip mechanisms leading to disc brake noise vibration and harshness effects, In Aplimat 2017: proceedings of the 16th conference on applied mathematics 2017. Bratislava, 31.1.-2. 2. 2017. 1st. ed. Bratislav: Vydavateľstvo STU, ISBN 978-80-227-4649-6.

## INFLUENCE OF LONGITUDINAL ELASTIC SUPPORT ON STABILITY OF A PARTIALLY TENSIONED COLUMN

S. Uzny\*, M. Osadnik\*\*

**Abstract:** *The paper presents the results of theoretical and numerical research on the stability of a partially tensioned column subjected to the Euler's load which is an external force applied between the ends of the slender system. Discrete element in a form of a translational spring which controls the longitudinal displacement was used on upper end of the system. The differential equations of motion and boundary conditions of considered column have been obtained on the basis of Hamilton's principle and Bernoulli – Euler's theory. In frame of this study the relationships between critical load and parameters such as translational spring stiffness or location of the external load were investigated.*

**Keywords:** Slender systems, Stability, Spring elements, Euler's load, Hamilton's principle.

### 1. Introduction

The aim of the stability investigations is to determine the maximum loading force (in this case the longitudinal force) at which the system will not be destroyed due to the loss of stability. In the scientific literature stability of slender flexible systems is described for both conservative and non-conservative loads. Euler's load applied to the considered system is belongs to the conservative group. Uzny et.al. (2016) first began the research on the partially tensioned slender systems subjected to Euler's load. The load was placed between the ends of the fixed-fixed column and point of force location has changed along the length of the structure. The numerical calculations have shown that the first natural vibration frequency of the studied system depends both on the point of location and magnitude of the external force. Such systems are geometrically non-linear, in which the nonlinear component of the natural frequency depends on an amplitude of the vibration. In the papers (Tomski 1985, Uzny 2011) due to the geometric non-linearity of the considered systems the solution of the boundary problem was done with small parameter method. On the basis of mathematical model authors determined the bifurcation load where the investigated systems change the rectilinear form of equilibrium into the curvilinear one. Tomski and Kukla (1989) studied slender supporting systems subjected to eccentrically applied Euler's load on both ends of the system. Additional discrete elements have great influence on critical or bifurcation load magnitude and natural vibration frequency of the systems. In the considered system the translational spring limits the axial displacement and can be adapted to the real structure to control the vibration frequency and the critical load. Discrete elements are widely used because of easy modelling of real objects. Spring elements are important for the study of vibration and stability of flexible systems. Properly chosen can affect the way of loss of stability if the slender system is subjected to compressive non-conservative load (Sundararajan 1976, Ryu et al. 2000, Kounadis 1981, 1983). Discrete components in the form of rotational springs are often used for crack modeling of flexible systems (Sokół 2014, Sokół and Uzny 2016). In the point of crack presence the reduction of local stiffness takes place thereby the discontinuity of the structure occurs, that has great influence on vibration frequency magnitude. These studies are important for the detection of cracks that may contribute to the destruction of the object.

In this work the spring can be used to model vibration isolator placed at the upper fixing of the mechanical screw mounted in the vertical lift platform. The main scope of the studies presented in this paper is to determine the critical load of partially tensioned column in relation to the point of application

---

\* Sebastian Uzny, Prof.: Institute of Mechanics and Machine Design Foundation, Częstochowa University of Technology Dąbrowskiego 73, 42-200 Częstochowa, Poland, uzny@imipkm.pcz.pl

\*\* Michał Osadnik, MSc.: Institute of Mechanics and Machine Design Foundation, Częstochowa University of Technology Dąbrowskiego 73, 42-200 Częstochowa, Poland, m.osadnik@imipkm.pcz.pl



of the external force for different stiffness of translational spring which is used to optimize the considered system by means of longitudinal displacement control.

## 2. Boundary problem

The system presented in this paper models a screw along which moves a nut loaded by external force. The considered system (column) is shown in Fig. 1. The column is subjected to Euler's load. The direction of a force is always accordant to the undeformed axis of the column. External loading force  $P$  was applied at the point marked with the letter  $O$ . Applied load causes that the lower part of the column is compressed while the upper one is tensioned. In addition, longitudinal displacement of the tensioned part of the column is limited by the translational spring of stiffness  $C$ . In order to formulate the boundary problem, the overall length of the system is divided into two parts of length  $l_1$  and  $l_2$  respectively ( $l_1 + l_2 = l$ ). The compressed part is indicated by the index 1 and tensioned one is designated by the index 2. The ends of the system (both on the compressed and tensioned section) are fitted in such a manner that their transversal displacements and the deflection angles are null.

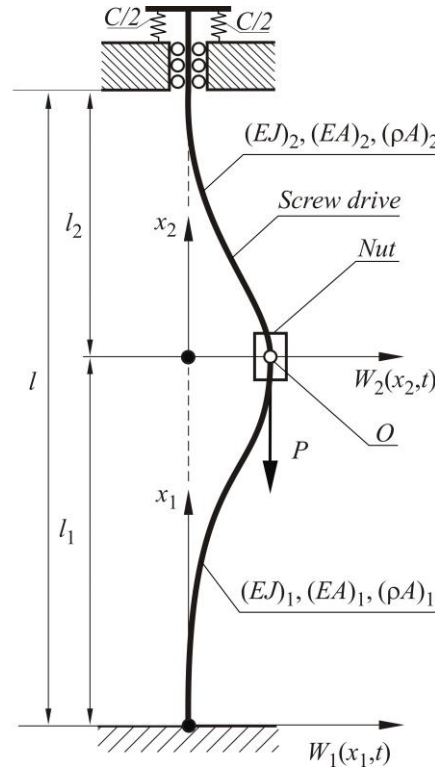


Fig. 1: Physical model of investigated system.

In this study the problem of stability is considered in order to determine the critical force.

Differential equations of transversal displacements and boundary conditions in the static case are as follows:

- differential equations of transversal and longitudinal displacements

$$W_{i0}^{IV}(x_i) + \frac{S_{i0}}{(EJ)_i} W_{i0}''(x_i) = 0; \quad U_{i0}(x_i) - U_{i0}(0) = -\frac{S_{i0}}{(EA)_i} x_i - \frac{1}{2} \int_0^{x_i} (W_{i0}^I(x_i))^2 dx_i \quad (1a-b)$$

- geometrical and natural boundary conditions

$$U_{10}(0) = W_{10}(0) = W_{10}^I(0) = W_{20}(l_2) = W_{20}^I(l_2) = 0; \quad U_{10}(l_1) = U_{20}(0); \quad W_{10}(l_1) = W_{20}(0); \quad W_{10}^I(l_1) = W_{20}^I(0)$$

$$-(EJ)_1 W_{10}''(l_1) + (EJ)_2 W_{20}''(0) = 0; \quad (EJ)_1 W_{10}'''(l_1) - (EJ)_2 W_{20}'''(0) + S_{10} W_{10}^I(l_1) - S_{20} W_{20}^I(0) = 0$$

$$S_{10} - S_{20} - P = 0; \quad S_{20} - C U_{20}(l_2) = 0 \quad (2a-h)$$

where:  $W_{i0}(x_i)$ ,  $U_{i0}(x_i)$  – transversal and longitudinal static displacements,  $A_i$  – cross-sectional area,  $J_i$  – 2nd moment of area,  $S_{i0}$  – internal force in individual rods of column in the static case,  $(EJ)_i$  – bending stiffness,  $(EA)_i$  – compression stiffness;  $(EJ)_1 = (EJ)_2$ ;  $(EA)_1 = (EA)_2$ . The index  $i$  refers to the  $i$ -th element of the column.

Solutions of differential equations can be written as:

$$W_{10}(x_1) = A_1 \sin\left(\frac{S_{10}}{(EJ)_1} x_1\right) + B_1 \cos\left(\frac{S_{10}}{(EJ)_1} x_1\right) + C_1 x_1 + D_1 \quad (3a)$$

$$W_{20}(x_2) = A_2 \sinh\left(\left|\frac{S_{20}}{(EJ)_2}\right| x_2\right) + B_2 \cosh\left(\left|\frac{S_{20}}{(EJ)_2}\right| x_2\right) + C_2 x_2 + D_2 \quad (3b)$$

Internal forces in compressed part and tensioned one are determined with the following formulas:

$$S_{10} = P \frac{\frac{1}{Cl_2} + \frac{1}{(EA)_2}}{\frac{1}{Cl_2} + \frac{1}{(EA)_1} \frac{l_1}{l_2} + \frac{1}{(EA)_2}}; \quad S_{20} = S_{10} - P \quad (4a-b)$$

Substitution of the solutions (3a, 3b) into boundary conditions of transversal displacements leads to the set of equations. Determinant of the matrix of coefficients equated to zero is an equation that is used to determine the critical forces.

### 3. Results of numerical simulations

The results of numerical calculations are presented in the non-dimensional form by means of the following parameters:

$$\lambda_{cr} = \frac{P_{cr} l^2}{(EJ)_1}; \quad c = \frac{Cl}{(EA)_1}; \quad \zeta = \frac{l_1}{l} \quad (4a-c)$$

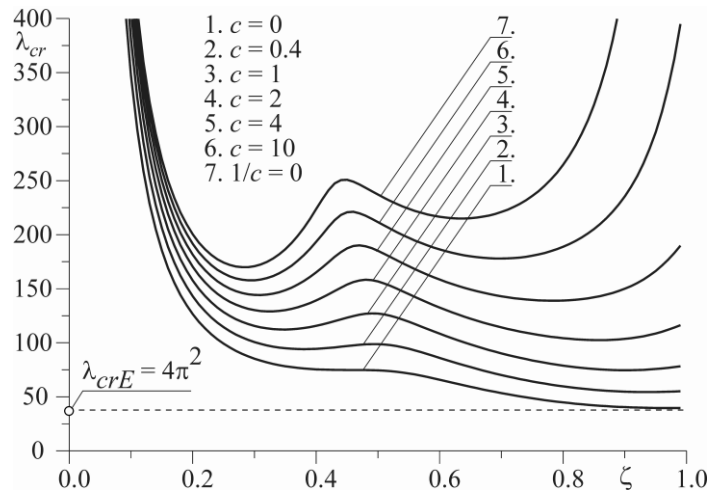


Fig. 2: The critical load  $\lambda_{cr}$  - point of external load application  $\zeta$  relationship at different translational spring stiffness  $c$ .

Change of critical load parameter  $\lambda_{cr}$  depends on the  $\zeta$  coefficient what is shown in Fig. 2. The numerical calculations were performed at seven different magnitudes of the stiffness of the translational spring that affects the longitudinal displacements of the upper end of the column. The influence of the translational spring stiffness parameter on critical load parameter  $\lambda_{cr}$  is greater at greater magnitudes of  $\zeta$  coefficient. The reduction of the spring stiffness decreases the critical load, especially when external load is placed in the upper part of a considered column. At lower localized points of an application of an external load ( $\zeta = 0.1 - 0.2$ ) the critical load decreases very rapidly. Fig. 2 shows very clearly that when the point of application of the external load is closer to the end of the column at which the spring is installed (oriented along the undeformed axis of the column) the greater control of critical load and transversal

displacements can be obtained. Interesting results were obtained when the point of the force application (nut position) is close to the half of the total length of the system  $\zeta \approx 0.5$ . Close to the half of total length of the system when the spring stiffness is greater than zero  $c > 0$  the presented curves on a plane  $\lambda_{cr} - \zeta$  reach the local extreme - maximum. The maximum magnitude depends on spring stiffness. The maximum which is present at different stiffness of translational spring does not occur at the same value of the  $\zeta$  parameter. When an increase of spring stiffness takes place the maximum point which corresponds to the critical force occurs at lower  $\zeta$ .

#### 4. Conclusions

In this study the system composed of a nut which moves along threaded rod was modeled. This system was modeled as a column subjected to Euler's load applied between the ends. The mathematical model takes into account the longitudinal elasticity of the support at one end. The study was carried out with numerical simulations with regard to the critical load of a column. On the basis of numerical simulations it was shown that the critical load of the considered system strongly depends on the stiffness of the applied longitudinal elastic support. An increase of the stiffness of the elastic element causes an increase of the loading capacity of the system. Between the ends of the column such a position of the point of force application (nut position) can be observed at which the extremum - maximum is present. The extreme point location depends on the spring stiffness which affects the longitudinal displacement of the column. During the design of threaded rod – moveable nut systems it must be taken into account that the change of critical load affects the critical rotational velocity which is not constant along the rod.

#### Acknowledgement

The study has been carried out within the statutory funds of the Czestochowa University of Technology (BS/PB-1-101-3020/11/P).

#### References

- Kounadis, A.N. (1981) Divergence and flutter instability of elastically restrained structures under follower forces, *Int. J. Engng. Sci.* 19(4), 1981, 553-562.
- Kounadis, A.N. (1983) The existence of regions of divergence instability for nonconservative systems under follower forces, *Int. Journal Solids Structures* 19(8), 1983, 725-733.
- Ryu, J.B., Sugiyama, Y., Yim, K.B. and Lee, G.S. (2000) Dynamic stability of an elastically restrained column subjected to triangularly distributed subtangential forces, *Computers & Structures* 76, 2000, 611-619.
- Sokół, K. (2014) Linear and Nonlinear Vibrations of a Column with an Internal Crack, *Journal of Engineering Mechanics* 140(5), [http://dx.doi.org/10.1061/\(ASCE\)EM.1943-7889](http://dx.doi.org/10.1061/(ASCE)EM.1943-7889).
- Sokół, K. and Uzny, S. (2016) Instability and vibration of multi-member columns subjected to Euler's load, *Archive of Applied Mechanics*, 86 (5), 883–905, DOI: 10.1007/s00419-015-1068-6.
- Sundararajan, C. (1976) Influence of an elastic end support on the vibration and stability of Beck's column, *Int. J. Mech. Sci.* 18, 1976, 239-241.
- Tomski, L. (1985) Prebuckling Behaviour of Compound Column – Direct Nonlinear Analysis, *Z. Angew. Math. U. Mech.*, 65(1), 59-61.
- Tomski, L. and Kukla, S. (1989) Free Vibrations of a Certain Geometrically Nonlinear System with Initial Imperfection, *AIAA Journal* 28(7) 1240-1245.
- Uzny, S., Sokół, K. and Osadnik, M. (2016) Free vibrations of the partially tensioned geometrically non-linear system subjected to Euler's load, *Vibrations in Physical Systems* 27, 399-406.
- Uzny, S. (2011) Local and global instability and vibrations of a slender system consisting of two coaxial elements, *Thin-Walled Structures*, 49, 618-626.

## EFFECTIVE ELASTIC AND STRENGTH PROPERTIES OF UNIDIRECTIONAL FIBROUS CERAMIC COMPOSITES

S. Valentová<sup>\*</sup>, J. Vorel<sup>\*\*</sup>, M. Šejnoha<sup>\*\*\*</sup>

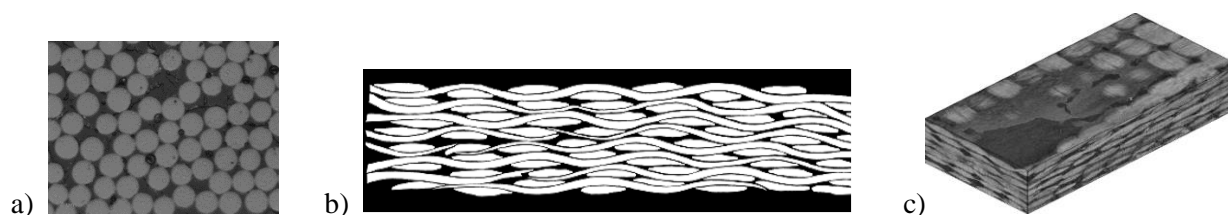
**Abstract:** *The present paper is concerned with the evaluation of effective properties and macroscopic tensile strengths of unidirectional fibrous composites made of basal fibers bonded to a ceramic matrix. The actual random distribution of fibers in transverse plane is taken into through the application of statistically equivalent periodic unit cell. A simple maximum stress failure criterion, combined with a linear format of traction separation law, is used to track the onset and subsequent gradual evolution of damage in the composite. The resulting macroscopic stress-strain curves are finally examined to define the searched macroscopic strength of the composite needed, e.g. in the meso-scale analysis of plain weave textile composites.*

**Keywords:** Spruce, Thermal conductivity, Moisture diffusivity, Homogenization, Mori-Tanaka method.

### 1. Introduction

Owing to a relatively low cost at one hand and good mechanical properties comparable to glass fibers (Černý et al., 2007), the basalt fiber based composites have received considerable attention in recent years. Due to their good thermal stability the basalt fibers can serve as reinforcement of ceramic matrices manufactured by means of heat treatment such as pyrolysis of, e.g. polysiloxane resins (Glogar et al., 2007a, Černý et al., 2009). When referring to this type of composite, a number of studies addressing fracture properties is also available (Glogar et al., 2007b).

Apart from elastic behavior, see e.g. (Vorel et al., 2015), little attention, however, has been accorded to composite system reinforced by textiles. This might be attributed to the complexity of the microstructure at various scales as see in Fig. 1. To reflect a random nature of fiber distribution in individual yarns as well as various imperfection at the level of plies developed during fabrication, the concept of statistically equivalent periodic unit cell (SEPUC) is usually adopted to define a suitable representative volume element at a respective scale (Šejnoha et al., 2013).



*Fig. 1: Micro and meso-structure of basal fiber/ceramic matrix plain weave textile composites: a) level of yarns, b) binary image of the 8-layer laminate cross-section, c) reconstructed CT-scan.*

Because of considerable brittleness of the matrix and fibers, the analysis beyond elasticity often draws on the concept of damage mechanics, see e.g. (Šmilauer et al., 2011, Zhou et al., 2013) with particular application to textiles. This approach is also adopted in the present study. Due to space limitation we

<sup>\*</sup> Ing. Soňa Valentová: Czech Technical University in Prague, Thákurova 7; 166 29, Prague; CZ, sona.urbanova@fsv.cvut.cz

<sup>\*\*</sup> Assoc. Prof. Ing. Jan Vorel, PhD.: Czech Technical University in Prague, Thákurova 7; 166 29, Prague; jan.vorel@fsv.cvut.cz

<sup>\*\*\*</sup> Prof. Ing. Michal Šejnoha, PhD., DSc.: Czech Technical University in Prague, Thákurova 7; 166 29, Prague; CZ, sejnomo@fsv.cvut.cz

address the level of yarns only by examining the nonlinear response of the unidirectional fibrous composite, see Fig. 1a.

## 2. Theoretical formulation

The influence of random distribution fibers in the cross-sectional plane on the macroscopic response is investigated by considering two different SEPUC plotted in Fig. 2. Their construction is described in detail in (Šejnoha et al., 2013).

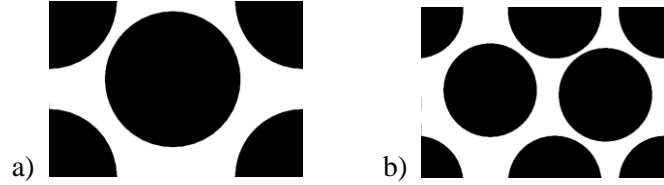


Fig. 2: Examples of SEPUC at the level of yarns: a) two-fiber SEPUC-1, b) five-fiber SEPUC-2.

The elastic material properties partially taken from (Černý et al., 2009) and partially derived from nanoindentation are listed in Tab. 1.

Tab. 1: Material parameters of individual phases.

Material	$E$ [GPa]	$G$ [GPa]	$\nu$ [-]	$G_f$ [N/mm]	$S_T$ [GPa]
Fiber - longitudinal direction	100	25	0.24	-	2.0
Fiber – transverse direction	18	6.4	0.4	-	0.5
Matrix	80	32.3	0.24	0.001	0.08

### 2.1. Evaluation of effective properties

To verify the computational implementation we begin by deriving the effective elastic properties using both the 1<sup>st</sup> order homogenization approach and the Mori-Tanaka method (Vorel et al., 2015), where the latter one is also discussed in details in (Šejnoha et al., 2013). In the framework of 1<sup>st</sup> order homogenization we begin by writing the local displacements and local strains in terms of macroscopically constant strain  $\mathbf{E}$  and fluctuation displacement  $u^*$  and strain  $\varepsilon^*$  fields, which are periodic, as

$$u_i(x) = E_{ij}x_j + u_i^*(x), \quad \varepsilon(x) = \mathbf{E} + \varepsilon^*(x). \quad (1)$$

Applying the Hill's lemma yields the system of equations to be solved for unknown displacements and macroscopic strains

$$\begin{aligned} \delta \mathbf{E}^T \mathbf{\Sigma} &= \delta \mathbf{E}^T (\langle \mathbf{L}(x) \rangle \mathbf{E} + \langle \mathbf{L}(x) \varepsilon^*(x) \rangle), \\ 0 &= \langle \delta \varepsilon^{*T}(x) \mathbf{L}(x) \rangle \mathbf{E} + \langle \delta \varepsilon^{*T}(x) \mathbf{L}(x) \varepsilon^*(x) \rangle, \end{aligned} \quad (2)$$

where  $\mathbf{\Sigma}$  represents the prescribed macroscopic stress. Note that under strain loading ( $\mathbf{E}$  is prescribed) conditions the first equation disappears since  $\delta \mathbf{E}^T = 0$ . Solving Eq. (2) for six unit load vectors then yields the macroscopic compliance matrix. The extracted effective moduli, together with the Mori-Tanaka results, are listed in Tab. 1. Evidently, in case of elasticity, the response provided by the two SEPUC agrees well with the Mori-Tanaka predictions.

Tab. 2: Effective elastic moduli.

	$E_{11}$ [GPa]	$E_{22}$ [GPa]	$E_{33}$ [GPa]	$G_{23}$ [GPa]	$G_{31}$ [GPa]	$G_{12}$ [GPa]	$c_f$ [-]
SEPUC-1 – FEM	30.9	29.8	92.4	27.5	27.6	12.4	0.62
SEPUC-2 – FEM	29.9	30.7	92.4	27.6	27.5	12.6	0.62
Mori-Tanaka method	32.6	32.6	92.4	27.6	27.6	12.1	0.62

## 2.2. Progressive damage formulation

The present analysis builds upon classical continuum damage mechanics with the crack band model to yield objective results. To proceed with the formulation, we begin by writing the constitutive equation for 1D model in the form

$$\varepsilon = \frac{\sigma}{E} + \varepsilon_c, \quad \varepsilon_c = \frac{w_c}{L_s} = (1 - D)E\varepsilon, \quad (3)$$

where  $\varepsilon_c, w_c$  are the crack strain and the crack opening displacement, respectively,  $L_s = \sqrt[3]{V_e}$  represents the size of the band to which the cracks are localized (here related to the finite element volume  $V_e$ ), and  $D$  is the damage parameter to reflect a material degradation with the evolution of cracks. In the context of damage mechanics, this is associated with a suitable traction-separation law, which is assumed linear in the present analysis, see Fig. 3.

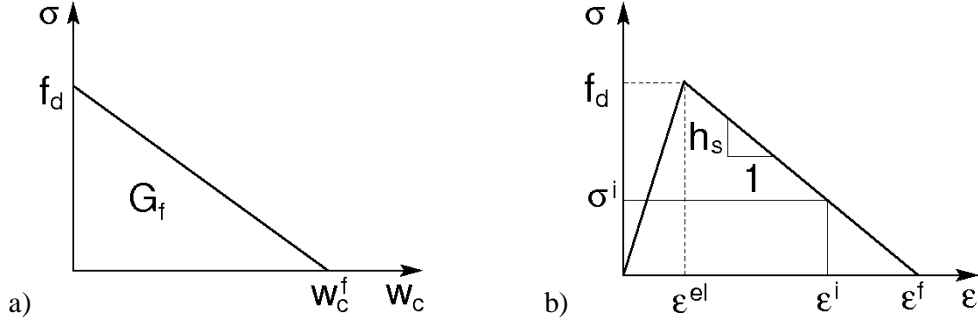


Fig. 3: Linear softening law: a) stress-crack opening displacement diagram, b) stress-strain diagram with linear softening.

The principal material parameter, entering the nonlinear constitutive model, is the fracture energy  $G_f$  [N/mm], which corresponds to the area under the stress-crack displacement opening diagram in Fig. 3a

$$G_f = \int_0^{w_c^f} \sigma dw_c = L_s \int_0^{\varepsilon^f} (\varepsilon - \varepsilon^{el}) d\sigma = L_s \int_0^{\varepsilon^f} \sigma d\varepsilon. \quad (4)$$

It follows from Eq. (4) and Fig. 3(b) that

$$G_f = L_s \left( \frac{1}{2} f_d \varepsilon^f \right) > G_f^{min} = \frac{f_d^2 L_s}{2E}, \quad (5)$$

$$\varepsilon^f = \frac{2G_f}{L_s f_d}, \quad w_c^f = \varepsilon^f L_s = \frac{2G_f}{f_d}. \quad (6)$$

Clearly, while the fracture energy is a material property independent of mesh, the failure strain depends on the smearing distance and thus the mesh characteristics. A simple maximum stress criterion is adopted in the present study

$$F_{1T} = \left( \frac{\sigma_{11}}{S_{1T}} \right)^2, \quad F_{2T} = \left( \frac{\sigma_{22}}{S_{2T}} \right)^2, \quad F_{3T} = \left( \frac{\sigma_{33}}{S_{3T}} \right)^2. \quad (7)$$

where  $S_{JT}$  is the tensile strength in the direction  $J$ . Assuming linear softening the damage parameter  $D$  evolves as

$$D_J = \frac{\varepsilon_{eq}^{Ji} (\varepsilon_{eq}^{Jf} - \varepsilon_{eq}^J)}{\varepsilon_{eq}^{Jf} (\varepsilon_{eq}^{Jf} - \varepsilon_{eq}^{Ji})}, \quad J = 1T, 2T, 3T, \quad (8)$$

where in case of 3D analysis the uniaxial tensile strain  $\varepsilon$  is replaced by an equivalent strain  $\varepsilon_{eq} = \sqrt{\varepsilon_{ii}^2}$ . In Eq. (8),  $\varepsilon_{eq}^{Ji}$  represents the equivalent strain at the onset of failure whereas  $\varepsilon_{eq}^{Jf}$  is the strain at complete separation, recall Fig. 3b.

## 3. Numerical experiments

As an example, we consider the two periodic unit cells in Fig. 2 loaded in the transverse direction by the prescribed increments of the macroscopic tensile stress  $\Sigma_{JJ} = \Sigma_{11}$  ( $J=3$  is the fiber direction). The necessary material parameters are available in Tab. 2. The resulting macroscopic stress-strain curves are



plotted in Fig. 4a. The points associated with the assumed tensile macroscopic strength are marked. In cases, where no visible deviation from the linearity is detected, as is the case of SEPUC1, the tensile strength is defined at intersection of the stress-strain diagram with the line of the same elastic stiffness with  $5 \times 10^{-5}$  strain offset. The distributions of damage patterns for SEPUC1 associated with the assumed tensile strength and the maximum stress reached are drawn for illustration in Fig. 4b.

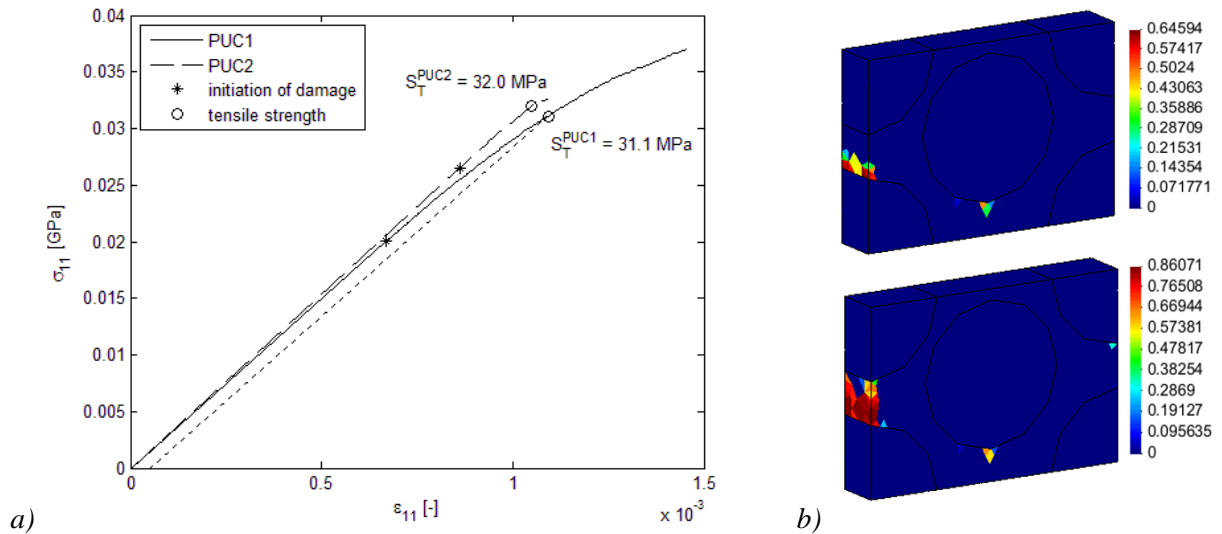


Fig. 4: a) Macroscopic stress-strain curves, b) Damage patterns at  $\Sigma_{11} = \Sigma_{1T}$  and  $\Sigma_{11} = \Sigma_{11}^{max}$ .

#### 4. Conclusions

The presented contribution was concerned with the derivation of effective elastic properties and macroscopic tensile strength of unidirectional basalt fiber reinforced ceramic matrix composite through virtual numerical experiment. These parameters will be subsequently used in an independent meso-scale analysis of the textile laminate where yarns will be considered as homogeneous. Such an analysis will also call for the effective yarn fracture energy. This quantity can be derived from similar experiments but under strain control conditions to allow for softening evolution on macroscale. This study will be presented elsewhere.

#### Acknowledgement

The financial support provided by the SGS project with the application registered under the No. OHK1-014/17 is gratefully acknowledged.

#### References

- Černý, M., Glogar, P., Giliáš, V., Hruška, J., Jakeš, P., Sucharda, Z. and Vávrová, I. (2007) Comparison of mechanical properties and structural changes of continuous basalt and glass fibres at elevated temperatures, *Ceramics – Silikáty*, 51(2), pp. 82-88.
- Černý, M., Glogar, P. and Sucharda, Z. (2009) Mechanical Properties of Basalt Fiber Reinforced Composites Prepared by Partial Pyrolysis of a Polymer Precursor. *Journal of Composite Materials*, 43(9), pp. 1109-1120.
- Glogar, P., Sucharda, Z., Černý, M., Puchegger, S. and Peterlik, H. (2007a) Microstructure and mechanical properties of heat resistant composites reinforced with basalt fibers. *Ceramics – Silikáty*, 51(4), pp. 190-197.
- Glogar, P., Černý, M. and Tolde, Z. (2007b) Fracture behaviour of the basalt fibre reinforced composites with polysiloxane-derived matrix. *Acta Geodynamica et Geomaterialia*, 4(2), pp. 27-37.
- Šejnoha, M. and Zeman, J. (2013) *Micromechanics in practice*, WIT Press, Boston.
- Šmilauer, V., Hoover, Ch.G., Bažant, Z.P., Caner, F.C., Waas, A.M. and Shahwan, K.L. (2011) Multiscale simulation of fracture of braided composites via repetitive unit cells. *Engineering Fracture Mechanics*, 78, pp. 901-918.
- Vorel, J., Grippon, E. and Šejnoha, M. (2015) Effective thermoelastic properties of polysiloxane matrix based plain weave textile composites. *International Journal for Multiscale Computational Engineering*, 13, 181-200.
- Zhou, Y., Lu, X. and Yang, Z. (2013) Progressive damage analysis and strength prediction of 2D plain weave composites. *Composites: Part B*, 47, pp. 220-229.

## WEAK AXIS BUCKLING - ELASTIC RESISTANCE OF A COLUMN

J. Valeš\*, Z. Kala\*\*

**Abstract:** A solid finite element model for lateral buckling of column was developed in Ansys software. It was tested for calculation of elastic resistance. Series of random realizations for a long range of non-dimensional slenderness were created for this. As average relative differences as correlation between analytical results and results from Ansys software is presented.

**Keywords:** Lateral buckling, Column, Imperfection, Elastic resistance, Steel.

### 1. Introduction

It is common to model lateral buckling and lateral-torsional buckling problems using shell elements instead of solid elements. However, there are some undesirable effects associated with shell elements, which may have an influence on the final resistance e.g. the material overlap at the web-flange junction (Jönsson and Stan, 2017). Another disadvantage of using shell elements can be a problematic modelling of varying thickness of a cross-section. Therefore, a solid model in Ansys software was developed.

### 2. Finite element model

The finite element research was performed on a model of a simply supported column subjected to a centric load on one end. European hot-rolled steel I200 cross-section was used for the column. Generally, the I200 is defined by seven dimensions  $h$ ,  $b$ ,  $t_1$ ,  $t_2$ ,  $R_1$ ,  $R_2$  and  $\alpha$ , see Fig. 1a. However, its geometry was simplified to ensure the finite element mesh would be regular. Thus all fillets were removed. Their influence on load-carrying capacity was found neglectable (Kaim, 2004). The simplified cross-section is depicted in Fig. 1b.

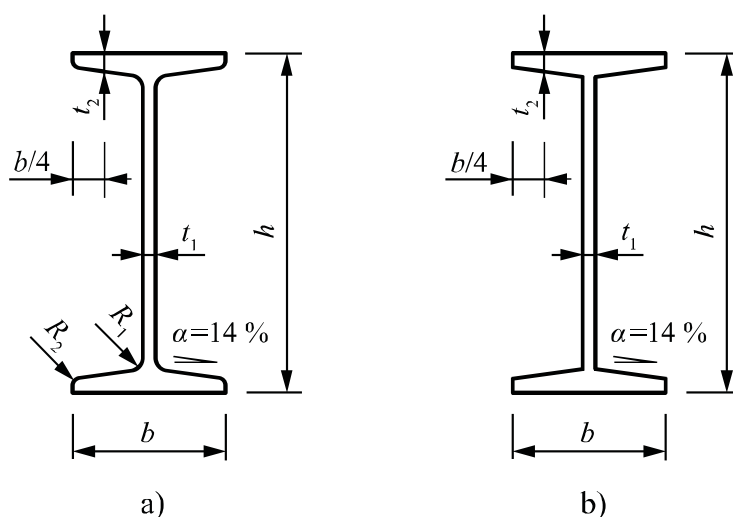


Fig. 1: Cross-section: a) real, b) idealized.

\* Ing. Jan Valeš: Brno University of Technology, Faculty of Civil Engineering, Department of Structural Mechanics; Veveří 331/95; 602 00, Brno; CZ, vales.j@fce.vutbr.cz

\*\* Prof. Ing. Zdeněk Kala, PhD.: Brno University of Technology, Faculty of Civil Engineering, Department of Structural Mechanics; Veveří 331/95; 602 00, Brno; CZ, kala.z@fce.vutbr.cz

The computational model was created in Ansys APDL software. Homogeneous structural solid element SOLID185 was used for the model. It is an 8-node solid element that is suitable for 3D modelling of solid structures having three degrees of freedom at each node: translations in the nodal  $x$ ,  $y$ , and  $z$  directions. The enhanced strain formulation was considered. This formulation prevents shear locking in bending-dominated problems and volumetric locking in nearly incompressible cases. The element introduces nine internal degrees of freedom to handle shear locking, and four internal degrees of freedom to handle volumetric locking. All internal degrees of freedom are introduced automatically at the element level and condensed out during the solution phase of the analysis (Ansys, 2014).

The meshing was performed similarly to the lateral-torsional buckling analysis (Kala and Valeš, 2017). The boundary conditions of the member end are generally taken from (Kala and Kala, 2011), however, a number of specific problems relating to elements SOLID185 is modelled more detailed and sophisticated.

## 2.1. Geometrical imperfection and elastic resistance

Initial deflection of the column was assumed to be a half sine wave with the amplitude  $e_0$ , as shown in Fig. 2.

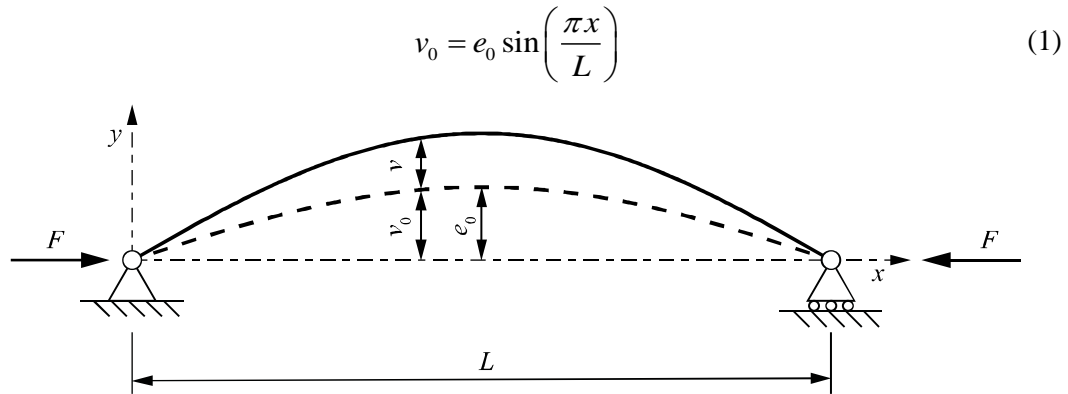


Fig. 2: Simply supported column with initial imperfection.

It is a common choice for the representation of imperfections (Boissonade et al., 2006). An additional deflection  $v(x)$  appears on the column, when the axial force  $F$  is applied on it. Since the boundary conditions are considered as  $x = 0: v + v_0 = 0$  and  $x = L: v + v_0 = 0$ , the additional deflection can be written as

$$v(x) = K \sin\left(\frac{\pi x}{L}\right) \quad (2)$$

where  $K$  is the maximum value of the additional deflection at mid-span. The classical elastic flexural equilibrium equation, accounting for the initial imperfection, becomes:

$$v'' + \frac{F(v_0 + v)}{EI_z} = 0 \quad (3)$$

where  $I_z$  is the second moment of area to axis  $z$ . Replacing Eq. (1) and Eq. (2) in Eq. (3) leads to the expression of  $K$  as follows:

$$K = \frac{F}{F_{cr} - F} e_0 \quad (4)$$

where  $N_{cr}$  is the critical flexural buckling load

$$N_{cr} = \frac{\pi^2 EI}{L^2} \quad (5)$$

The total column deflection at mid-span is

$$v_{\max} = \frac{e_0}{1 - \frac{F}{F_{cr}}} \quad (6)$$

The maximum stress  $\sigma_{\max}$  due to compression and bending is

$$\sigma_{\max} = \frac{R}{A} + \frac{R|\nu_{\max}|}{W_z} = f_y \quad (7)$$

$R$  represents the load-carrying capacity. It is the maximum load action  $F$  of elastic member, which is obtained when  $\sigma_{\max}$  is equal to yield strength  $f_y$ .  $A$  is the area of the cross-section and  $W_z$  is the sectional module to axis  $z$ . Replacing Eq. (6) in Eq. (7) and isolating expression for  $R$ , we get the formula for elastic resistance published in (Kala, 2009) as

$$R = \frac{AD + F_{cr}W_z - \sqrt{A^2D^2 + 2AF_{cr}W_z(|e_0|F_{cr} - f_yW_z) + F_{cr}^2W_z^2}}{2W_z} \quad (8)$$

where  $D$  is a substitution

$$D = |e_0|F_{cr} + f_yW_z \quad (9)$$

### 3. Random input quantities

In general, the resistance  $R$  is a random quantity. It is a function of random geometrical and material characteristics (Melcher et al., 2004) and it can be studied using simulation methods, e.g. Latin Hypercube Sampling method (LHS) (McKey et al., 1979). A comparative analysis was performed for 13 selected non-dimensional slendernesses  $\bar{\lambda}_z \in (0.4; 0.5; 0.6; 0.7; 0.8; 0.9; 1.0; 1.1; 1.2; 1.3; 1.4; 1.5; 1.6)$ . 400 simulation runs were generated. Material characteristics of steel grade S235 and geometrical characteristics of the cross-section I200 based on (Melcher et al., 2004, Kala et al., 2009) were the random input quantities, see Tab. 1. All input random quantities were mutually statistically independent. The Gaussian probability distribution was considered for all of them. All other geometric and material characteristics were considered by their nominal values ( $h = 200$  mm,  $b = 90$  mm,  $t_1 = 7.5$  mm, Poisson's ratio  $\nu = 0.3$ ). Residual stress was not considered in this analysis.

Tab. 1: Random quantities.

Quantity	Symbol	Mean value	Std. deviation
Flange thickness	$t_2$	11.3 mm	0.518 mm
Yield strength	$f_y$	297.3 MPa	16.8 MPa
Modulus of elasticity	$E$	210 GPa	10 GPa
Initial imperfection	$e_0$	0	1.5L/1960

### 4. Conclusions

A stochastic analysis of elastic resistance of compressed steel columns was carried out. The analysis was performed without the effect of residual stress. A linear stress-strain relationship of steel was used. Tab. 2 shows the correlation and average relative difference between elastic resistances from the analytical solution and the results calculated by Ansys.

Except of the slenderness  $\bar{\lambda}_z = 1.6$  all the average relative differences are positive which means that the analytical resistances are in average higher than those calculated by Ansys. Correlation between results is almost 1.0 for each slenderness. Such a good match confirms the accuracy of the finite element model.

This advanced solid model is suitable for subsequent analysis where residual stress and material nonlinearity will be considered. A specific instance where solid elements are more appropriate is the modelling of members in which the variation of residual stresses through plate thickness is non-negligible, while shell elements should be used for slenderer sections for which local imperfections affect the load carrying capacity.

Tab. 2: Correlation and average relative difference between elastic resistances.

Nondim. Slenderness $\bar{\lambda}_z$ [-]	Correlation	Average relative difference [%]
0.4	0.999 98	1.23
0.5	0.999 99	1.14
0.6	0.999 99	1.01
0.7	0.999 99	0.87
0.8	0.999 98	0.68
0.9	0.999 96	0.49
1.0	0.999 91	0.32
1.1	0.999 95	0.23
1.2	0.999 89	0.14
1.3	0.999 86	0.07
1.4	0.999 84	0.04
1.5	0.999 89	0.02
1.6	0.999 76	-0.03

## Acknowledgement

The paper was elaborated within a framework of project GAČR 17-01589S.

## References

- ANSYS (2014) Theory Release 15.1, ANSYS Inc.
- Boissonade, N., Grenier, R., Jaspart, J.P. and Lindner, P. (2006) Rules for member stability in EN1993-1-1. Background documentation and design guidelines. (ECCS publication no. 119). European Convention for Constructional Steelwork.
- Jönsson, J. and Stan, T-C. (2017) European column buckling curves and finite element modelling. *Journal of Constructional Steel Research*, 128, pp. 136-151.
- Kaim, P. (2004) Spatial buckling behaviour of steel members under bending and axial compression. Ph.D. thesis, Technischen Universität Graz, pp. 1-257.
- Kala, Z. (2009) Sensitivity assessment of steel members under compression. *Engineering Structures*, 31, pp. 1344-1348.
- Kala, Z., Melcher, J. and Puklický, L. (2009) Material and geometrical characteristics of structural steels based on statistical analysis of metallurgical products. *Journal of Civil Engineering and Management*, 15, 3, pp. 299-307.
- Kala, Z. and Valeš, J. (2017) Global sensitivity analysis of lateral-torsional buckling resistance based on finite element simulations. *Engineering Structures*, 134, pp. 37-47.
- Kala, Z. and Kala, J. (2011) Sensitivity analysis of stability problems of steel structures using shell finite elements and nonlinear computation methods, in: *Proc. 1st Int. Conf. on Numerical Analysis and Applied Mathematics (ICNAAM)*. AIP Conference Proceedings, 1389, 1. <http://dx.doi.org/10.1063/1.3636974>.
- Melcher, J., Kala, Z., Holický, M., Fajkus, M. and Rozlívka, L. (2004) Design characteristics of structural steels based on statistical analysis of metallurgical products. *Journal of Construction Research*, 60, 3-5, pp. 795-808.
- McKey, M.D., Conover, W.J. and Beckman, R.J. (1979) A comparison of three methods for selecting values of input variables in the analysis of output from a computer code. *Technometrics*, 21, 2, pp. 239-245.

## INFLUENCE OF THE NASAL CAVITIES TO HUMAN VOICE QUALITY

T. Vampola<sup>\*</sup>, J. Horáček<sup>\*\*</sup>

**Abstract:** Nasal cavities (NC) form the side branches of the human vocal tract and exhibit antiresonance and resonance properties which influence the produced voice quality. This study investigates the possibility of these resonances to contribute to the speaker's or singer's formant cluster around 3 – 5 kHz. A reduced finite element (FE) model was created which allows numerical simulation of the effects of changing the volumes of NC on the acoustic resonance and antiresonance characteristics of the vocal tract. This model, created from an accurate three-dimensional (3D) FE model of the human vocal tract for vowel [a:] and [i:] is computationally-effective and allows parametric changes of the volume connecting the nasal tract with the human vocal tract. Developed FE models of acoustic spaces of nasal and vocal tract for vowels /a:/ and /i:/ are used to study the influence of (NC) on phonation of these vowels. Acoustics frequency-modal characteristics are studied by modal analysis and numerical simulation of acoustic signals in time domain is performed by transient analysis of the FE models.

**Keywords:** Human vocal tract, Nasal cavities, Human voice quality, Self-exciting vibration, Bio-acoustic, FE parametric model, Velopharyngeal insufficiency.

### 1. Introduction

Velopharyngeal insufficiency (VPI) is an insufficient closing of nasal cavity (nasopharynx) and its airproof separation from the oral cavity (oropharynx). VPI leads to open nasality (rhinolalia aperta) affecting all oral speech sounds that should not be nasal. Small defects of the velopharyngeal closure become evident first by a different timber of the voice, bigger defects influence formant structure of vowels. According to the literature (Carney et al., 1971) the VPI influence in particular the production of vowels /i:/ and on the other hand its influence on the production of vowel /a:/ is smaller. Several types of nasal speech are not easily diagnosed even specialized physicians are often not fully aware of the differences. Acoustic analysis of VPI are oriented mainly on differences in voice timbre because the resonant changes are the most essential. While the influence of the vocal tract on vocal out-put has been studied rather extensively, the influence of side cavities of human vocal tract, such as the nasal cavities (NC) has received less attention. Generally, these cavities have been re-ported to cause antiresonances in the resulting vocal spectrum, i.e., largely decreasing radiation of some of the spectral frequencies out of the mouth, particularly those around 4 – 5 kHz (Dang et al., 1997). As such, their role for the resulting vocal intensity may be considered undesirable, since it contradicts the general goal of enhancing vocal output with the smallest vocal effort. However, newest studies with perceptual evaluations of sounds produced using 3D mathematical and physical models of the singers' vocal tracts revealed that the voice quality is perceived as being better when side branches are present (Mokhtari et al., 2008). Furthermore, spectral analysis of singers indicates that the formant structure around 3 – 5 kHz is more complex than usually expected. A more detailed analysis shows that besides the antiresonances there are also new resonances which occur due to these side cavities. In technical terms, the side cavities create zero-pole, i.e. antiresonance-resonance pairs in the overall transfer function of the vocal tract.

---

<sup>\*</sup> Prof. Dr. Ing. Tomáš Vampola: Department of Mechanics, Biomechanics and Mechatronics, Faculty of Mechanical Engineering, Czech Technical University in Prague. Technická 4, Praha 6, Czech Republic, tomas.vampola@fs.cvut.cz

<sup>\*\*</sup> Ing. Jaromír Horáček, DSc.: Institute of Thermodynamics, Academy of Sciences of the Czech Republic, Dolejšova 1402/5 Praha 8 Czech Republic, jaromirh@it.cas.cz



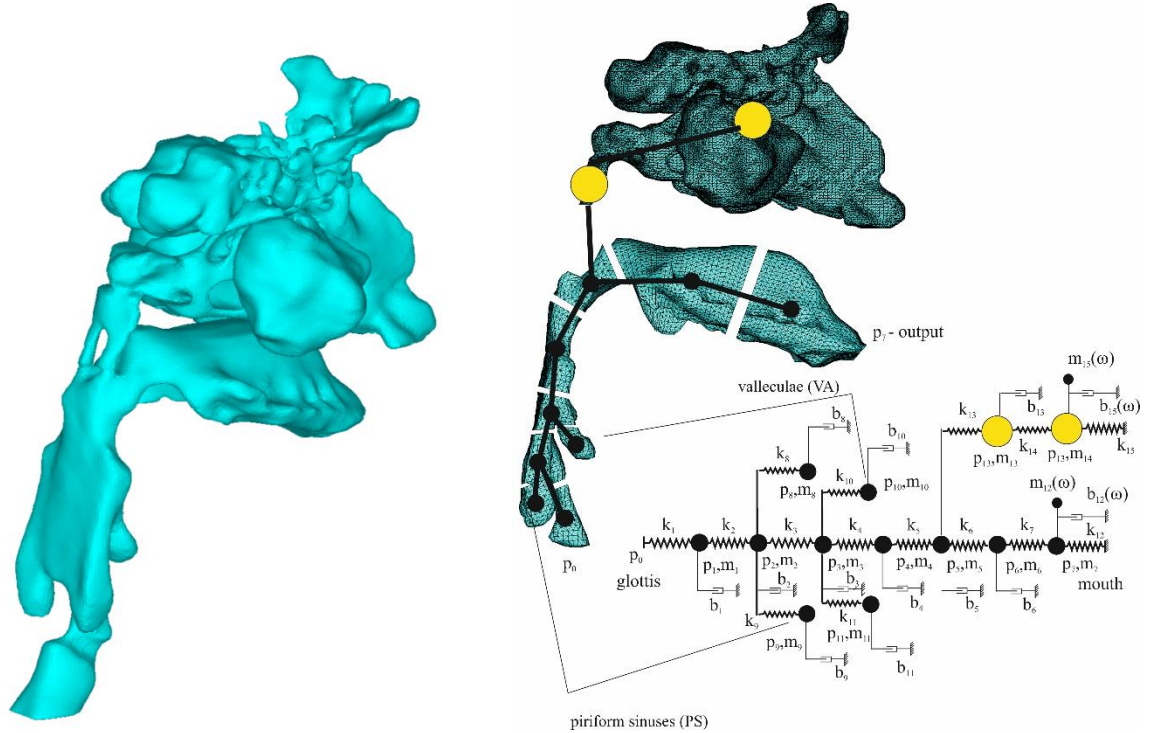
## 2. Computational model

The construction of the FE model of the female vocal tract from the CT images was described in the previous papers of the authors and the mathematical background for finite element analysis of the acoustic eigenfrequencies and eigenmodes of the human supraglottal acoustic spaces of the human vocal tract can be found in (Vampola et al., 2008). The sophisticated accurate 3D FE models of the vocal tract are, however, problematic to use for investigating the effect of vocal tract shape modifications on the changes in acoustic resonance properties since the calculations of each single configuration takes many hours of time. Simple 1D models based on the knowledge of the cross-sectional area of the vocal tract are more advantageous for this purpose since they allow a fast online computer simulation of phonation. The analysis of the resonance and antiresonance characteristics and of the acoustic mode shapes is based on a three-dimensional (3D) finite element (FE) model of the human vocal tract constructed from the CT measurements of a subject phonating on [a:] and /i:/ vowel. Then, a reduced FE model is created which includes the side cavities and its resonance and antiresonance frequencies are tuned to correspond to those of the full FE model. This reduced model is then used for analyzing the antiresonances, resonances and the pressure transfer function of the vocal tract. The accuracy of the results obtained using the reduced model is examined by comparing these to the results obtained with the full 3D FE model. Then the effect of the volume changes of the nasal cavities on the acoustic pressure transfer function is studied.

The basic mathematical description governing equations for acoustic pressure in an acoustic cavity can be written in the FE formulation as

$$\mathbf{M}\ddot{\mathbf{p}} + \mathbf{B}\dot{\mathbf{p}} + \mathbf{K}\mathbf{p} = \mathbf{0} \quad (1)$$

where  $\mathbf{M}$ ,  $\mathbf{B}$  and  $\mathbf{K}$  represent global ( $N \times N$ ) mass, damping and stiffness matrices,  $\mathbf{p}$  is vector of nodal pressures in  $N$  nodes inside the vocal tract, and the dot and double dots above the pressure denote the first and second time derivatives, respectively.



*Fig. 1: Volume model of the human vocal tract for vowel/a:/ (left); Simplified computational model of the human vocal tract for vowel/a:/ (right).*

### 2.1. Acoustic modal analysis

The acoustic frequency - modal characteristics of the FE models were studied by the modal analysis considering air density  $\rho_0 = 1.2 \text{ kg.m}^{-3}$ , sound speed  $c_0 = 350 \text{ m.s}^{-1}$ , co-efficient of the boundary admittance  $\mu = r/\rho_0.c_0 = 0.005$ , where  $r$  is the real component of the specific acoustic impedance (Vampola et al., 2015) and the pressure  $p = 0 \text{ Pa}$  at the lips and nose.

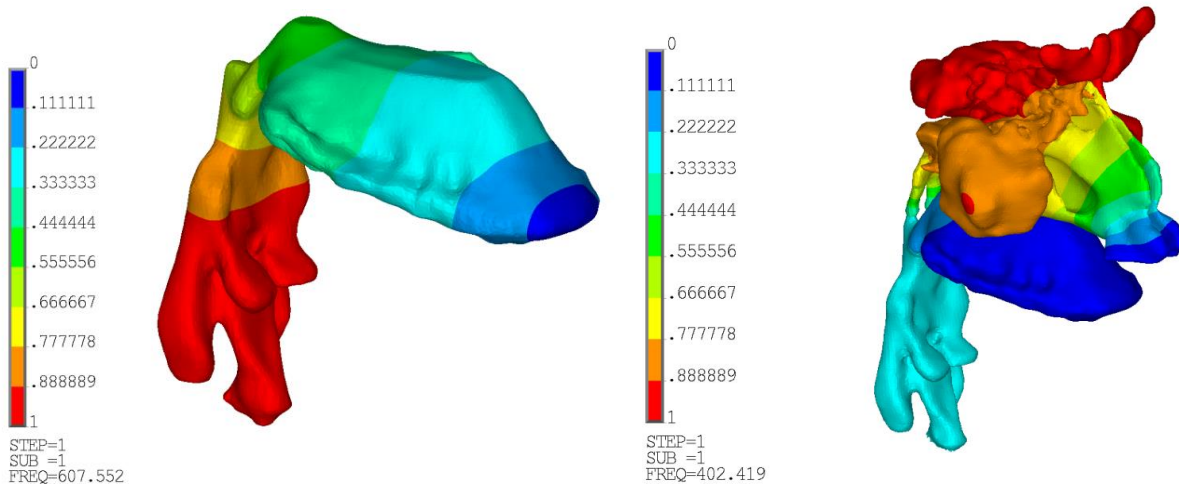


Fig. 2: The first oral mode of the human vocal fold – vowel /a:/ without nasal cavities (left, 607 [Hz]) and with nasal cavities (right, 402 [Hz]).

Tab. 1: Vowel /a:/ (ON-oral-nasal frequency, O-oral frequency, N-nasal frequency).

	F <sub>1</sub> [Hz]		F <sub>2</sub> [Hz]	
Without nasal cavities	607		1233	
With nasal cavities	ON	O	N	ON
	402	708	1096 1240	1440

Due to the velopharyngeal insufficiency the oro-nasal frequencies  $f_{nas}$  for vowels /a:/ appear below the first formant ( $f_{nas} < F_1$ ) and between the first and second formants ( $F_1 < f_{nas} < F_2$ ). The first pure oral frequency is shifted to second formant. For the vowel /i:/, the oro-nasal frequencies appear between the first and second formants ( $F_1 < f_{nas} < F_2$ ) of the normal voice and between the second and third formants ( $F_2 < f_{nas} < F_3$ ). The first pure oral frequency disappeared.

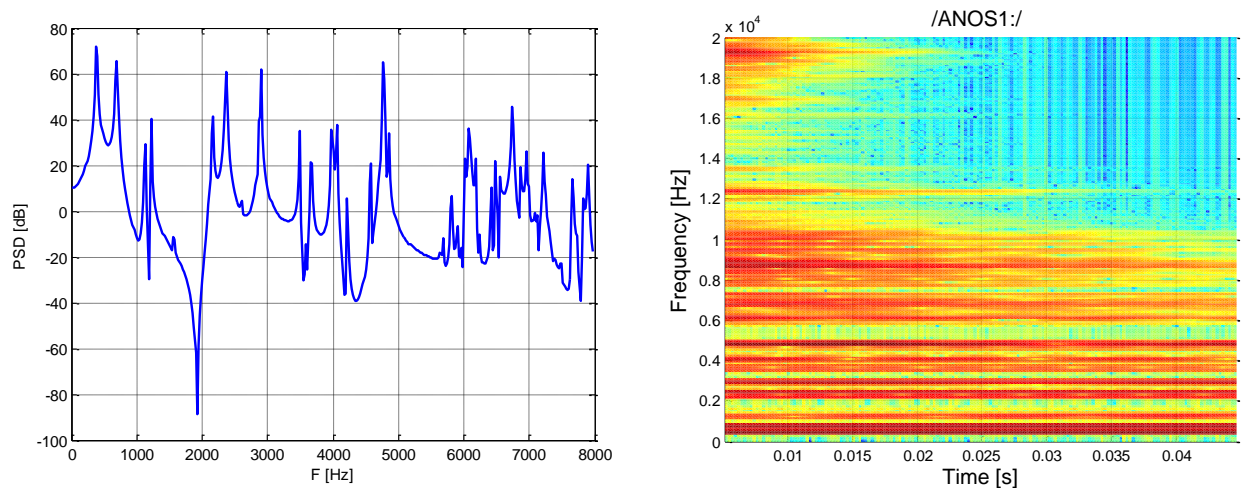
## 2.2. Acoustic transient analysis

The FE models of the supraglottal spaces were excited in time domain at the position of the vocal folds and the sound radiation losses were modeled at the lips and nose. The broad band frequency pulse was used for excitation of the resonant frequencies of the acoustic spaces for simulation of phonation in time domain. The Newmark method for integration of the governing equations for the pressure in FE formulation was used. The interconnection of the acoustic spaces diminishes the pressure level at the lips. This pressure decrease is more considerable for vowels and /i:/ than for the vowel /a:/. The decrease of the pressure level at the lips due to the VPI for the vowel /a:/ is much smaller value than the decrease of for the vowels /i:/. The results support the clinical observations (Carney et al., 1971), the VPI influence more substantially the phonation of vowels /i:/ than the vowel /a:/. However, the increasing size of the interconnecting area has only small influence on the level of the pressure at the lips and thus a quantification of a degree of connecting the vocal and nasal tract on such basis is difficult.

## 3. Conclusion

The results show that the human vocal tract is a very complex resonator. Side branches are generally known to cause antiresonances, i.e., sharp local minima in the resulting transfer function. In speech research the antiresonance phenomenon is well known from the studies of nasalized vowels where the nose acts as the side branch of the vocal tract (Hattori et al., 1958). The NS cavities act as antiresonators which severely decrease the sound level radiating out of the mouth around the antiresonance frequency. Simultaneously, however, they act also as resonators which amplify the acoustic output at different frequencies. The larger the volume of the NS cavities, the lower their antiresonance and resonance frequencies are. There has been good evidence that humans can willingly change the size of these

cavities. These findings suggest that the NS cavities may play a beneficial role in producing the "resonant voice".



*Fig. 3: Acoustic pressure response computed at the lips (left), spectrogram of the computed acoustic pressure of the lips using the simplified model with VPI harmonically excited (right).*

### Acknowledgement

The research is supported by the Grant Agency of the Czech Republic by project No 16-01246S "Computational and experimental modelling of self-induced vibrations of vocal folds and influence of their impairments on human voice".

### References

- Carney, P.J. and Sherman, D. (1971) Severity of nasality in three se-lected speech tasks. *Journal of Speech and Hearing Re-search* 14, 396-407.
- Dang, P. and Honda, K. (1997) Acoustic characteristics of the piriform fossa in models and humans. *Journal of the Acoustical Society of America* 101, 456465.
- Mokhtari, P., Takemoto, H. and Kitamura, T. (2008) Single-matrix formulation of a time domain acoustic model of the vocal tract with side branches. *Speech Com-munication* 50, 179190.
- Vampola, T., Horáček, J. and Švec, J.G. (2008) Fe modeling of human vocal tract acoustics: Part I - Models for normal phonation of czech vowels. *Acta Acustica united with Acustica* 94.
- Vampola, T., Horáček, J. and Švec, J.G. (2015) Modeling the Influence of Piriform Sinuses and Valleculae on the Vocal Tract Resonances and Antiresonances In: *Acta Acustica United with Acustica*.
- Hattori, S., Yamamoto, K. and Fujimura, O. (1958) Nasalization of vowels in relation to nasals. *Journal of the Acous-tical Society of America* 30, 267274.

## EXPERT SYSTEM SHELL ARCHITECTURE BASED ON DECISION NETWORK

S. Vechet<sup>\*</sup>, J. Krejsa<sup>\*\*</sup>, K.-S. Chen<sup>\*\*\*</sup>

**Abstract:** Presented paper deals with preliminary design of an empty expert system suitable for system monitoring in various engineering applications. Discussed expert system is rule-based with the possibility of importance factor definition within each rule. The deduced result can be composited from more than one possible hypothesis based on different confidence level. The core of the system is based on Bayesian decision network and simple autonomous mobile robot use-case is used for results presentation.

**Keywords:** Expert System, Decision Network, Knowledge Engineering.

### 1. Introduction

Development of reliable mobile robot system highly depends on capabilities of used onboard diagnostics. There are various robotic systems which have lack of any onboard diagnostic (Masek, 2015). These robots count on usage reliable components itself and in case of mechanical, electrical or other failure this system crashes. Such system are used as a toys or experimental devices (Gibbons, 2009 and Krejsa, 2010) with no impact on user/operators health. Other kinds of robotics machines have off-line diagnostics, which can be used while searching for failure causes. The most advanced diagnostic subsystems are used for on-line full system diagnostic with possible failure prediction (Buchanan, 1984).

This paper describes the diagnostic expert system, which is running independently on other onboard systems on mobile robots. This diagnostic tool is designed as an empty expert system and can be used in different fields e.g. smart homes (Vechet, 2016). The main idea behind the expert system is that the expert system is probabilistic and has the ability of simultaneously deduce various hypothesis with different likelihood. The user can support the decision process with answering given questions or the expert system can get adequate answers directly from the system in question itself.

### 2. Expert system architecture

The architecture for the expert system is based on traditional expert system shell described by Merritt (1989). The traditional concept was also used in MYCIN or EMYCIN (Melle, 1984) and consists from:

- knowledge base which holds the information of an expert about selected domain,
- inference engine which derives possible solutions for given inputs,
- user interface which interacts with the user,
- working storage of domain specific data structures for temporal/long term usage.

Further described expert system uses this traditional paradigm, however the implementation of selected parts differs in order to enable following behavior:

- it starts as an empty expert system which can be used as a state-of-the-art system regardless the type of the problem to be solved,

---

<sup>\*</sup> Assoc. Prof. Stanislav Vechet, PhD.: Institute of Thermomechanics AS CR, v.v.i., Technicka 2, 616 69. Brno, Czech Republic, vechet.s@fme.vutb.cz

<sup>\*\*</sup> Assoc. Prof. Jiri Krejsa, PhD.: Institute of Thermomechanics AS CR, v.v.i., Technicka 2, 616 69. Brno, Czech Republic, krejsa@fme.vutbr.cz

<sup>\*\*\*</sup> Prof. Kuo-Shen Chen, Ph.D. National Cheng Kung University, Department of Mechanical Engineering, No. 1, Ta-Hsueh Road, Tainan 701, Taiwan, kschen@mail.ncku.edu.tw

- multiple hypothesis can be deduced simultaneously with various level of confidence,
- each hypothesis can be supported or negated with additional information gathered from user/system under observation,
- information presented to the expert systems are ternary (e.g. {Yes, No, Unknown}, {True, False, None}, ...),
- the expert system can adapt in time to new conditions using user interaction.

To provide such behavior we implemented the knowledge base as a set of independent naive Bayesian networks with decision node. The decision node takes into account the reward for doing or not doing deduced action and it is used for changing the internal believe in the hypothesis and thus it evolves in time. The decision network is implemented on paradigm described by Korb (2010).

### 2.1. Decision network structure

The decision network can be described as direct acyclic graph. The core concept is shown in Fig. 1. Even that the decision network is defined as a naive Bayesian network, the resulting decision process can be chaining using recursion where a selected hypothesis can be used as an input for next decision to be made.

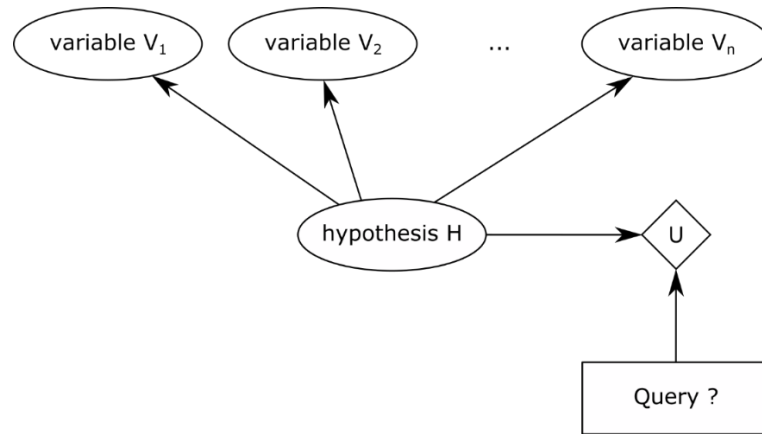


Fig. 1: Single decision network structure as a core of the expert system.

Tab. 1: Utility node reward definition. *H*-hypothesis, *Q*-query, *U*-utility.

H	Q	U(H,Q)	Notes	Outcome
True	Yes	100	System state changend and ES prove it.	Excelent
True	No	50	System state changed, however ES didn't prove it.	Poor
False	Yes	-100	Nothing to prove and ES proved wrong hypothesis.	Terible
False	No	100	Nothing to prove, no hypothesis in scope.	Excelent

### 3. Architecture evaluation

The evaluation of designed expert system was performed using a concept of question/answering system meant to help a customer with online assistance when solving malfunctioning autonomous mobile service robot originally developed via Bender Robotics company (Hrbacek, 2010, Masek, 2013 and Krejsa, 2014).

The expert system should help to identify the problem while asking the user questions based on system state. Typical use case is demonstrated on basic situation: considering the robot OS is running and GUI interface successfully shows the map and a position of the robot inside the map, however the robot is not moving. The user is asked if the data from laser range finder (LIDAR) are present, which implicates the hypothesis that the LIDAR is not connected properly. The second thought (hypothesis) of the expert system is that in case the LIDAR is working, the reason for not moving robot is motor driver (which is

unreliable component). The partial (removed all occurrences where *RobotNotLocalized* is False) decision process for hypothesis *LidarNotConnected* is shown in Tab. 2 where the expected utilities are calculated.

The probabilities used in this sample case are defined as:

$$P(\text{RobotNotLocalized}=T | \text{LIDARNotConnected}=T) = 0.9 \quad (1)$$

$$P(\text{WrongMap}=T | \text{LIDARNotConnected}=T) = 0.6 \quad (2)$$

$$P(\text{DataNotShown}=T | \text{LIDARNotConnected}=T) = 0.95 \quad (3)$$

The definition for expected utility is based on Korb (2010) and is given as:

$$EU(Q|E) = \sum_i P(O_i|E, Q)U(O_i|Q) \quad (4)$$

where  $E$  is available evidence,  $Q$  is action/query with possible outcome  $O_i$ ,  $U(O_i|E)$  is the utility of each outcome or reward (see Tab. 1),  $P(O_i|E, Q)$  is the probability over possible outcomes given evidence  $E$  and query action  $Q$  performed.

The results shown in Tab. 2. were calculated using equations (5 – 8) which are based on Bayesian conditional probability theory.

Tab. 2: Expected utility calculated as a reaction to given evidences presented to the ES.

Evidences	EU (Query=Yes)	EU (Query=No)	Decision
True True True	<b>51.1</b>	25.85	Do
True True False	-1.1	5.15	
True True None	<b>50</b>	31	Ask
True False True	<b>33.9</b>	17.4	Ask
True False False	-3.9	6.6	
True False None	<b>30</b>	24	Ask
True None True	<b>85</b>	43.25	Ask
True None False	-5	11.75	
True None None	<b>80</b>	55	Ask
False - -	...	...	...
None True True	<b>55</b>	30.5	Ask
None True False	-35	39.5	
None True None	20	70	
None False True	<b>35</b>	22	Ask
None False False	-55	58	
None False None	-20	80	
None None True	<b>90</b>	52.5	Ask
None None False	-90	97.5	
None None None	0	150	

Presented decision network results in three possible outcomes  $\{do, ask, none\}$ . Where *do* means, that the result cannot be more supported with any other evidence or additional information from system (all supporting evidences are known and *True*).

The decision *ask* means, that this hypothesis is likely, however more information from the user or the system is needed. The decision *none* handle hypothesis that are unlikely to appear or there is not enough information available.



In case we have measured all needed evidences the joint probability is calculated as a product of equations (1 – 3) using (4) where:

$$P(LIDARNotConnected=T|RobotNotLocalized,WrongMap,DataNotShown) = 0.513 \quad (5)$$

$$P(LIDARNotConnected=F|RobotNotLocalized,WrongMap,DataNotShown) = 0.002 \quad (6)$$

Expected utility calculated using all above defined equations:

$$EU(Q=Yes)=P(LIDARNotConnected=T)*U(H=T,Q=Yes)+P(LIDARNotConnected=F)*U(H=F,Q=Yes)=0.513*100 + 0.002*(-100) = 51.1 \quad (7)$$

$$EU(Q=No)=P(LIDARNotConnected=T)*U(H=T,Q=No)+P(LIDARNotConnected=F)*U(H=F,Q=No) = 0.513*50 + 0.002*(100) = 25.85 \quad (8)$$

#### 4. Conclusions

We present a preliminary design of an expert system which is able to generate multiple hypothesis with different probabilities and via query/answer interface is able to deduce most likely hypothesis which is presented to the user.

Since the query/answer mechanism is not limited to interaction with the user, the additional information can be obtained directly from monitored system itself. Thus the expert system can be used for online diagnostic of various mechatronic systems from autonomous mobile robots to smart houses.

The actual and future work on presented expert system is focused on advanced human-machine interaction to ensure it can be naturally used in various engineering applications.

#### Acknowledgement

The results were obtained with institutional support RVO 61388998 of the Institute of Thermomechanics AS CR v.v.i.

#### References

- Buchanan, B.G. and Shortliffe, E.H. (1984) Rule-Based Expert Systems: The MYCIN Experiments of the Stanford Heuristic Programming Project, Addison-Wesley, Reading, Mass.
- Gibbons, P., Mason, M., Vicente, A., Bugmann, G. and Culverhouse, P. (2009) Optimisation of dynamic gait for small bipedal robots. In: Proc. 4th Workshop on Humanoid Soccer Robots (Humanoids 2009), pp. 9-14.
- Hrbacek, J., Ripel, T. and Krejsa, J. (2010) Ackermann mobile robot chassis with independent rear wheel drives. Proceedings of 14th International Power Electronics and Motion Control Conference (Epe-Pemc 2010). Doi 10.1109/Epepemc.2010.5606853.
- Korb, K.B. and Nicholson, A.E. (2010) Bayesian Artificial Intelligence, Second Edition, CRC Press, Inc., Boca Raton, FL, USA, 2010, ISBN 1-58488-387-1.
- Krejsa J., Vechet S. and Chen K. (2014), Multiple Indoor Robot Localization using Infrared Beacons, Engineering Mechanics 2014, pp. 336-339.
- Krejsa, J. and Vechet, S. (2010) Odometry-free mobile robot localization using bearing only beacons. In Proc. of 14th International Power Electronics and Motion Control Conference (Epe-Pemc 2010). Doi 10.1109/Epepemc.2010.5606893.
- Mašek, P. and Růžička, M. (2015) A Task Planner for Autonomous Mobile Robot Based on Semantic Network. In Advanced Mechatronics Solutions. Advances in Intelligent Systems and Computing. Switzerland: Springer International Publishing, pp. 637-642. ISBN: 978-3-319-23921- 7. ISSN: 2194-5357.
- Mašek, P. and Růžička, M. (2013) Human-Machine Interface for Mobile Robot Based on Natural Language Processing. In Mechatronics 2013, Recent Technological and Scientific Advances. Switzerland: Springer International Publishing, 2013. p. 583-590. ISBN: 978-3-319-02293- 2.
- Melle, W., Shortliffe, E.H. and Buchanan, B.G. (1984) EMYCIN: A Knowledge Engineer's Tool for Constructing Rule-Based Expert Systems. In Buchanan and Shortliffe (Eds.), Rule-Based Expert Systems: The Mycin Experiments of the Stanford Heuristic Programming Project, Addison-Wesley, pp. 302-313.
- Merritt, D. (1989) Building experts systems in Prolog. Springer-Verlag, New York, ISBN:978-1-4613-8913-2.
- Věchet, S., Hrbáček, J. and Krejsa, J. (2016) Environmental Data Analysis for Learning Behavioral Patterns in Smart Homes. In: Proc. of 17th Int. Conf. on Mechatronics – Mechatronika (ME) 2016. 1. Prague: Czech Technical University in Prague, 2016. pp. 386-391. ISBN: 978-80-01-05882- 4.

## INFLUENCE OF COMPRESSIVE STRESS ON SHEAR FORCE DISTRIBUTION IN BRIDGE DECK SLABS

R. Vida<sup>\*</sup>, J. Halvonik<sup>\*\*</sup>

**Abstract:** *Shear resistance is a long-term problem of reinforced concrete structures. It is also one of the decisive checks for bridge deck slabs assessment. In contrast with bending failure (which is ductile), the shear failure is brittle, which makes it even more dangerous and therefore undesirable. This paper deals with concentrated loads acting on a bridge deck slab and their transverse distribution to the support. The main focus is laid on the question whether compression force (either caused by prestressing or by the compression in the top parts of the cross section under bending moment) has any influence on the distribution of shear forces in a bridge deck slab.*

**Keywords:** Shear force, Distribution, Compression, Bridge slab.

### 1. Introduction

Bridge deck slabs are subjected to different types of loading, compared to common slabs in buildings. This fact results in a different behavior of the structure. The loads acting on a bridge deck slab are a combination of distributed loads on a large area and concentrated loads on a small part of the structure.

According to Lantsoght et al.(2012), the behavior of slab under uniformly distributed load is very similar to a beam loaded by continuous load and the common methods for calculating the shear resistance of beams lead to satisfactory results. On the other hand, slabs under concentrated loads act different and the internal forces caused by this load tend to spread over certain width (Rombach et al., 2008, Lantsoght et al., 2012.).

One of the parameters that influences the ability of the slab to transfer the local load in transverse direction is the cracking pattern of the slab (Lantsoght et al., 2010). This leads to a question, whether the prevention of cracks due to compressive stress in the slab can lead to a change in the internal forces distribution.

### 2. Bridge Loads and Internal Forces

A common highway bridge shall be designed in such a way that it is able to withstand all actions introduced in relevant standards, e.g.in EN 1991-1-1 or EN 1991-2. Some of these loads are similar to the ones in buildings, such as the self- weight, the weight of carriageway surfacing, kerbs, parapets, crash barriers, noise barriers and other bridge furnishing. These loads are usually uniformly distributed and cause a steady flow of internal forces in the bridge slab.

An important part of load acting on a bridge is produced by vehicles. According to EN 1991-2, these effects are substituted by load models, e.g. LM1, which represents effects of trucks and cars in real traffic on European roads in the year 2000. The model LM1 (shown in Fig. 1) consists of two parts:

- Uniformly Distributed Load (UDL) ( $q_{ik}$ )
- Tandem System (TS), consisting of two axles with axle load  $Q_{ik}$  and the wheel size 0.4 x 0.4 m.

---

<sup>\*</sup> MSc. Radoslav Vida: Department of Concrete Structures and Bridges, Slovak University of Technology, Radlinskeho 11, 810 05 Bratislava; SR, radoslav.vida@stuba.sk

<sup>\*\*</sup> Prof. MSc. Jaroslav Halvonik: Department of Concrete Structures and Bridges, Slovak University of Technology, Radlinskeho 11, 810 05 Bratislava; SR, jaroslav.halvonik@stuba.sk

The TS causes a variable flow of internal forces in plane members (such as slabs). The difference in the flow of internal forces can be seen in Fig. 2.

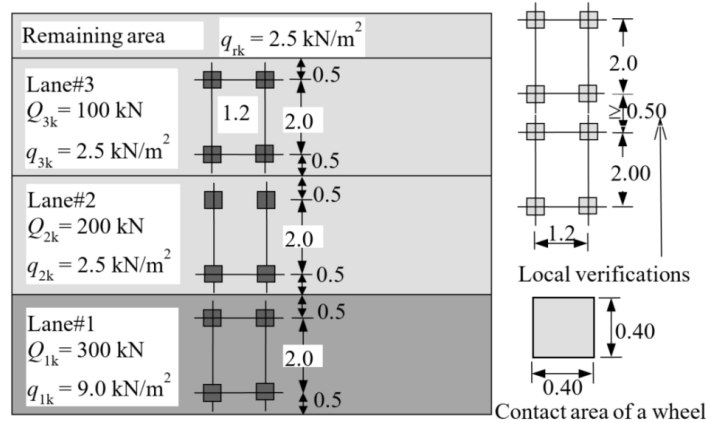


Fig. 1: Load Model LM1, according to EN 1991-2.

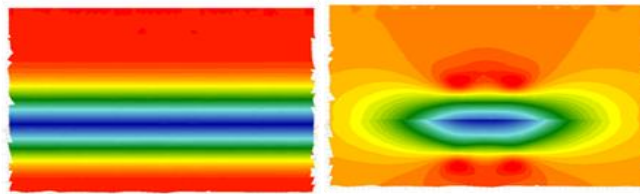


Fig. 2: a) steady flow of internal forces caused by UDL; b) variable flow of internal forces caused by TS.

### 3. Description of the Analyzed Structure

For the analysis, a typical highway bridge cross-section from the mid of 80s in Bratislava was chosen (Fig. 3). Only the left side cantilever has been analyzed. The length of the cantilever is 2.7 m, with variable thickness from 240 to 500 mm. The web of the box section supporting the cantilever is 460 mm thick. The depth of the inner slab changes from 500 mm near the web to 200 mm in the middle part of the slab.

The reinforcement of the cantilever slab is provided by  $4 \phi 22 + 4 \phi 16$  per meter, which means  $25.3 \text{ cm}^2$  per meter. Considering the concrete cover of 30 mm, the effective depth of the slab is 459 mm and the reinforcement ratio 0.0055 at the web-slab connection. The concrete C 35/45 and steel B 420B were used.

The loads caused by traffic are considered according to EN 1991-2, as described in chapter 2. Other (permanent) loads consist of self-weight, kerbs and parapets –  $10.4 \text{ kN/m}$  and carriageway surfacing  $100 \text{ mm} - 2.4 \text{ kN/m}^2$ .

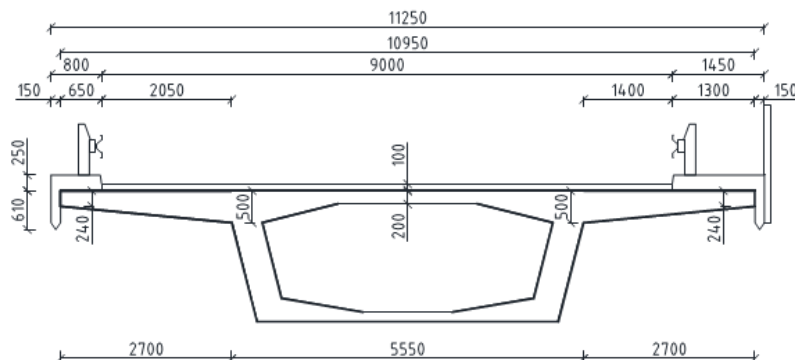


Fig. 3: Cross-section of the analyzed bridge deck.

All internal forces have been calculated on a 3D finite element model using quadrilateral area elements. This model was subjected to both linear (marked LA) and nonlinear (marked NA) analysis (taking into account the cracked concrete and the provided reinforcement) with the partial safety factors equal to 1.35 for both permanent and variable loads.

The compressive stresses in the slab which prevent the development of cracks in concrete can be obtained in two ways. The first is longitudinal prestressing, which should lead to compressive stress in all parts of the cross section. As for the second way, the longitudinal bending moment caused by the loads on the bridge also creates compressive stress in the top parts of the cross section. For this to happen, the cross-section must of course be located between the supports, in the area with a positive bending moment.

Different levels of compressive stresses have been introduced into the analysis. The first level was without additional compressive force. For the second and third level, compressive stress of 1 MPa and 4 MPa respectively, were introduced.

Two locations of the TS were selected for the analysis. The first (marked as 1. position) is in the distance  $d$  from the face of the web, for the maximum shear force and the second (marked as 2. position) creates the maximum bending moment in the control section.

#### 4. Results of the analysis and summary

Figs. 4 – 7 show the shear force along the section at the face of the web caused by a design combination of loads acting on the cantilever slab. Each figure shows shear forces with compressive stress of three levels (0, 1 and 4 MPa). Since the LA does not cover the stress conditions of the member, there is no difference in shear forces for various levels of compressive stress.

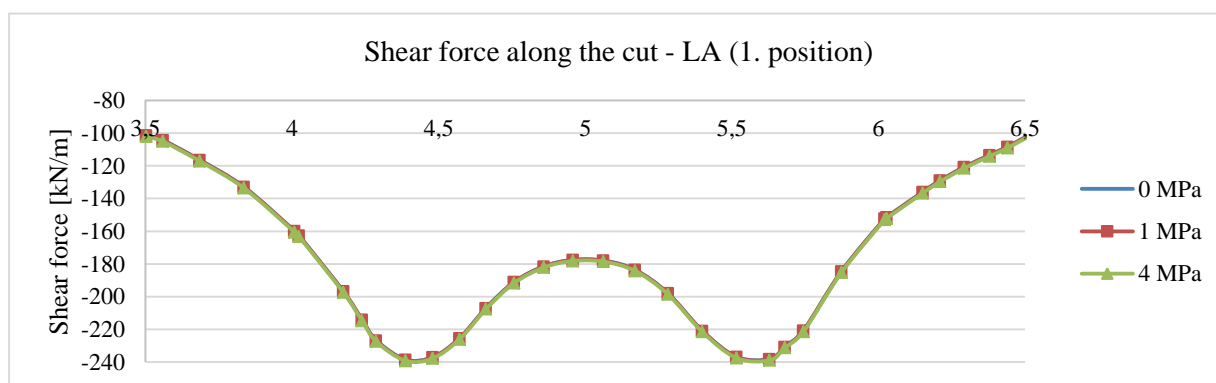


Fig. 4: Shear force along the control section (linear analysis, 1. position).

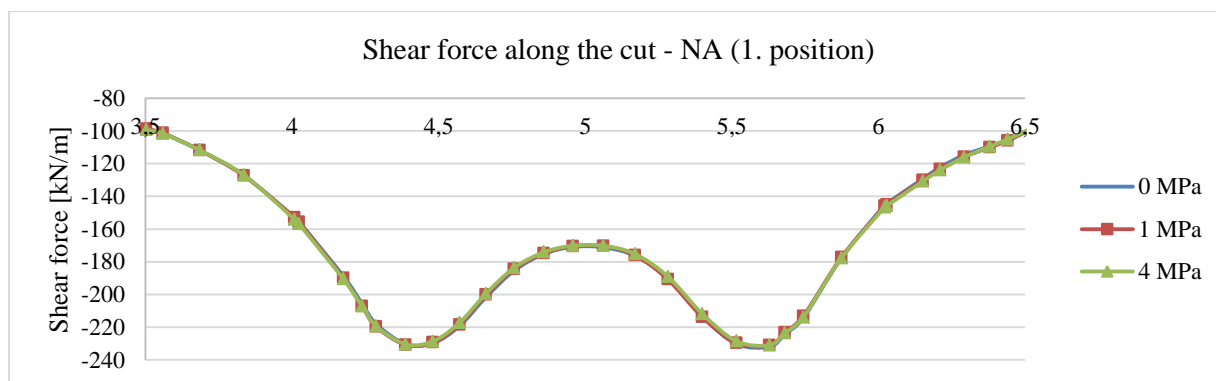


Fig. 5: Shear force along the control section (non-linear analysis, 1. position).

As could be expected, the different positions of the TS load lead to different distribution of shear forces. For the position near the web of the cross-section, two peaks are clearly visible, caused by the two wheels of the load model. For the second position, there is only one maximum value, because the shear force can distribute more evenly to a wider effective width.

In Figs. 4 and 5 a difference between LA and NA can be seen, mainly in the maximum shear force. The shear force obtained from NA is 4 % lower than from LA. For this position of the load, the compression stress does not have any influence on the shear force distribution.

For the second position of the load, only slight difference between LA and NA for no compression stress state is visible. The distribution of the shear force is a little bit different, but the maximum shear force is equal. On the other hand, the addition of compressive force into the analysis helps, as the distribution of

the shear force is smoother, more evenly distributed along the effective width of the slab. The peak shear force is also slightly lower, with the difference of around 4 %.

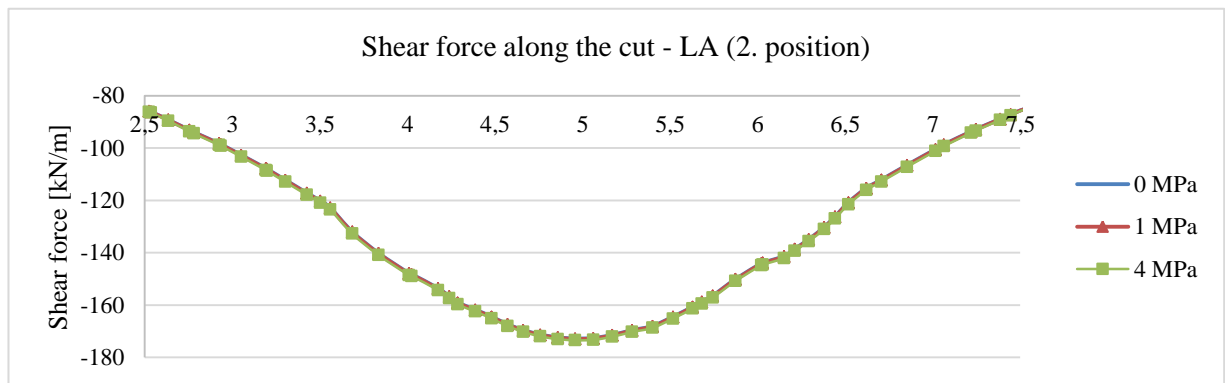


Fig. 6: Shear force along the control section (linear analysis, 2. position).

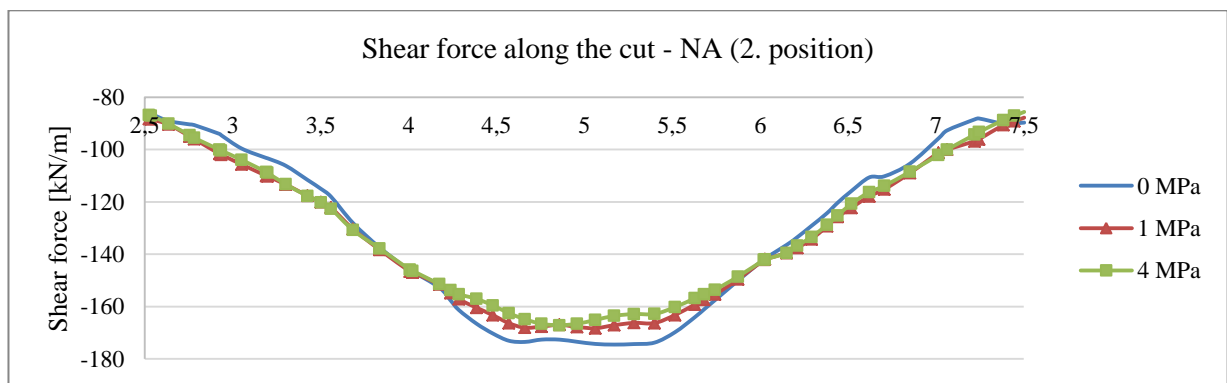


Fig. 7: Shear force along the control section (non-linear analysis, 2. position).

## 5. Conclusions

The differences between LA and NA are rather small, within 4 % for all positions of concentrated load, with LA resulting in slightly higher values of shear force.

The longitudinal compressive stress in real cantilever slab which leads to limitation of the cracks can in turn have a positive influence on the shear force distribution and consequently on the shear resistance in the critical section. This case also shows, that the differences between the LA and NA are not really significant and are on the safe side when using the LA.

These results show that the linear analysis, which is simpler and less time consuming, offers acceptable and safe results, compared to non-linear analysis. On the other hand, if more accurate results are necessary, the non-linear analysis with compressive stresses can show certain reserves in the verification of shear resistance of the structure.

## Acknowledgement

This work was supported by the Scientific Grant Agency of the Ministry of Education, science, research and sport of the Slovak Republic and the Slovak Academy of Sciences no. 1/0810/16.

## References

- Lantsoght, E. and van der Veen, C. (2010) Experimental study of reinforced concrete bridge decks under concentrated loads near to supports, 13th International Conference and Exhibition - Structural Faults and Repair.
- Lantsoght, E., van der Veen, C. and Walraven, J. (2012) Shear capacity of slabs and slab strips loaded close to the support, ACI SP-287, Recent Development in Reinforced Concrete Slab Analysis, Design and Serviceability, 01/2012.
- Rombach, G.A. and Latte, S. (2008) Shear resistance of bridge decks without shear reinforcement, Tailor Made Concrete Structures, pp. 519-525, 2008.

## ESTIMATION OF MINOR LOSSES IN A NATURAL CIRCULATION HELIUM LOOP

F. Világi<sup>\*</sup>, B. Knížat<sup>\*\*</sup>, F. Urban<sup>\*\*\*</sup>, R. Olšiak<sup>\*\*\*\*</sup>, M. Mlkvik<sup>\*\*\*\*\*</sup>, F. Ridzoň<sup>\*\*\*\*\*</sup>,  
P. Mlynár<sup>\*\*\*\*\*</sup>

**Abstract:** *The article deals with steady flow of highly compressed helium in a natural circulation loop. To describe the mechanism of circulation, it is necessary to properly determine the losses which the functionality of the entire facility depends on. The biggest losses in the system are minor losses for the cooler and the heater. This article describes the way of defining minor losses in the elements at non-isothermal flow. The derived equations are used for evaluation of measurement of the cooler's minor loss (DHR), with installed input power of 500 kW, which is a crucial part of the experimental helium loop. The results are compared with calculations published in referenced literature. The process described leads to a derivation of minor loss coefficient of the DHR (i.e. the element with non-isothermal flow). The results obtained are necessary to develop an 1D model of flow in the loop.*

**Keywords:** Natural circulation, Helium loop, Minor losses, State equation.

### 1. Introduction

The helium natural circulation loop is a prospective facility for decay heat removal from a fast nuclear reactor. There is very intensive ongoing research in this field.

Helium, if used as a coolant, has several advantages over other methods of nuclear reactor cooling such as sodium or liquid metals. Helium has suitable chemical and physical properties because it is non-toxic and has high values of thermal conductivity and specific heat. This concept represents a safe method of emergency cooling of nuclear reactors. The faculty of mechanical engineering in Bratislava has built an experimental loop, under the Allegro project, for testing the behavior of naturally circulating helium. The facility has undergone a trial period and several experiments are ongoing. Some of the results are presented in this article.

### 2. Experimental facility

The diagram of the experimental facility is shown in Fig. 1. The facility is used for a research of heat transfer from the GFR device (substitute for a nuclear reactor). The piping circuit provides an opportunity for research and verification of thermodynamic and hydraulic properties of highly compressed naturally circulating helium. The facility consists of hot and cold piping branches, the heat source (the "GFR"

---

<sup>\*</sup> Ing. František Világi.: Slovak University of Technology in Bratislava, Nám. slobody 17, 812 31 Bratislava 1, SR, frantisek.vilagi@stuba.sk

<sup>\*\*</sup> Assoc. Prof. Ing. Branislav Knížat, PhD.: Slovak University of Technology in Bratislava, Nám. slobody 17, 812 31 Bratislava 1, SR, branislav.knizat@stuba.sk

<sup>\*\*\*</sup> Prof. Ing. František Urban, PhD.: Slovak University of Technology in Bratislava, Nám. slobody 17, 812 31 Bratislava 1, SR, frantisek.urban@stuba.sk

<sup>\*\*\*\*</sup> Assoc. Prof. Ing. Róbert Olšiak, PhD.: Slovak University of Technology in Bratislava, Nám. slobody 17, 812 31 Bratislava 1, SR, robert.olsiak@stuba.sk

<sup>\*\*\*\*\*</sup> Ing. Marek Mlkvik, PhD.: Slovak University of Technology in Bratislava, Nám. slobody 17, 812 31 Bratislava 1, SR, marek.mlkvik@stuba.sk

<sup>\*\*\*\*\*</sup> Assoc. Prof. Ing. František Ridzoň, CSc.: Slovak University of Technology in Bratislava, Nám. slobody 17, 812 31 Bratislava 1, SR, frantisek.ridzon@stuba.sk

<sup>\*\*\*\*\*</sup> Ing. Peter Mlynár, PhD.: Slovak University of Technology in Bratislava, Nám. slobody 17, 812 31 Bratislava 1, SR, peter.mlynar@stuba.sk



device) and the cooler (the “DHR” device). The experimental facility enables adjustment of input and output power, temperatures and pressures of circulating helium. The steady and unsteady flow for a given range of operating conditions is also the subject of this research.

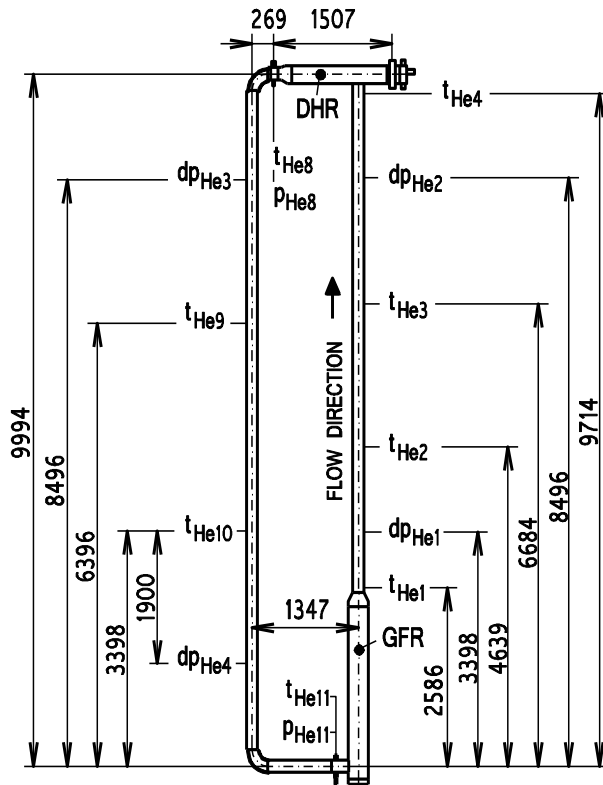


Fig. 1: Diagram of experimental facility.

### 3. Flow conditions

The flow in the pipes can be considered as isothermal because of very effective thermal insulation. However, the flow in the GFR and DHR devices is non-isothermal (Urban et al., 2016). Also, the helium compressibility along the loop can be neglected, because of relatively small pressure changes (maximum hundreds of pascals). According to the output power set-up of the devices and the operating pressure, helium can reach the following values:

- Temperature of He on the outlet: GFR: 400 °C - 520 °C
- Temperature of He on the inlet: GFR: 150 °C - 250 °C
- Operating pressure of He: 3 MPa - 7 MPa

To create a numerical model and to determine the resistance characteristics of devices it is very important to know the density of helium at critical points of the process. Thanks to continuous measurements, the temperature and pressure is a known value at any moment, so the density of helium can be calculated from the equation of state.

#### 3.1. State properties

In order to make the most accurate determination of state properties, three methods of calculation were considered, which are commonly used to model the behavior of real gases. When comparing the results of our calculations, the data from (McCarty et al, 1998) were taken as reference values. Helium densities were calculated using three different methods for temperature range 300 – 800 K and pressure range 1.0 – 7.0 MPa. The first compared method was the Redlich-Kwong cubic equation of state, which has showed a maximum deviation of 5.8 %, the second method was the Benedict-Webb-Rubin equation, which showed a maximum deviation of 3.78 %. The third used method was the Soave-Redlich-Kwong, which exhibited a maximum deviation of only 0.47 %. This accuracy is sufficient for the calculation of

In addition to the geometric information, the locations of sensors are also described in the diagram. The GFR device has a maximum installed input power of 500 kW. The facility encompasses an advanced system of automated collection and evaluation of measured data. Pressures, temperatures and pressure differences of devices are continuously measured at various locations of the piping circuit. The measurements of flow velocities are conducted by Pitot tubes (Urban et al., 2016). Since the radiation of the heat to the surroundings is generally neglected in pipe lines and will not be evaluated in this paper, the most crucial values for our calculations are the temperatures from the following sensors:  $t_{He1}$ ,  $t_{He4}$ ,  $t_{He8}$ ,  $t_{He11}$  and the velocity values. For sufficiently accurate description of flow in a helium loop, it is necessary to know the resistance characteristics of the system. Therefore the purpose of the measurement was to determine the resistance characteristics of the GFR and the DHR devices.

thermal and hydraulic parameters. Therefore the calculation of density was carried out iteratively using the Soave-Redlich-Kwong state equation shown below (Novák, 2007):

$$p = \frac{RT}{V_m - b} - \frac{a}{V_m(V_m + b)} = \frac{\rho RT}{1 - b\rho} - \frac{a\rho^2}{1 + b\rho} \quad (1)$$

$$a = 0.427482 \frac{R^2 T_c^2}{p_c} \alpha; \quad b = 0.008664 \frac{R T_c}{p_c} \quad (2)$$

$$\alpha = \left[ 1 + m \left( 1 - \sqrt{T_r} \right) \right]^2 = \left[ 1 + \left( 1 - \sqrt{T_r} \right) (0.480 + 1.574\omega - 0.176\omega^2) \right]^2 \quad (3)$$

In Eqs. (1 – 3), the critical temperature and pressure of the gas are identified as  $T_c$ ,  $p_c$ , respectively. The acentric factor is  $\omega$  and the reduced temperature is  $T_r$  calculated as:  $T_r = T / T_c$ . By further analytical integrations of general equations other thermodynamic properties such as enthalpy and heat capacity can be calculated. The deviation from the reference value for enthalpy was a maximum of 0.11 % and for heat capacity 0.16 %.

### 3.2 Transport properties

For calculation of the helium viscosity at various temperatures and pressures, the Sutherland law was used. As the accuracy of this law largely depends on the fluid used and can be inaccurate at higher pressures, the results had to be compared with reference values in (McCarty et al., 1998). The maximum deviation was 3.2 %. During flow calculations, viscosity is relevant only for the friction losses, which are extremely small because of low velocity, compared to the losses in the GFR and the DHR. Therefore the Sutherland formula provided sufficient accuracy.

## 4. Minor losses in the loop

The largest pressure loss occurs in the heater (GFR) and in the cooler (DHR). Therefore their estimation is the goal of this work. These losses are so-called “minor losses” in terms of fluid flow and a generally known formula applies to them:

$$\frac{\Delta p_m}{\rho} = \xi \frac{v^2}{2} \quad (4)$$

The equation (4) makes it possible to calculate the coefficient of minor loss  $\xi$ , if the values of mean velocity  $v$ , density  $\rho$  and the pressure difference  $\Delta p_m$  are known. Since the flow in GFR and DHR is non-isothermal, the mean velocity and the pressure changes from inlet to outlet in both elements. Thus the coefficient of minor loss was calculated in relation to averaged values of the above parameters. Averaged mean velocity and averaged density for non-isothermal elements were introduced as:

$$v_{ie} = \frac{v_i + v_e}{2} \quad (5)$$

$$\rho_{ie} = \frac{\rho_i + \rho_e}{2} \quad (6)$$

where  $\rho_i$ ,  $v_i$  are the density and mean velocity on the inlet, respectively.  $\rho_e$ ,  $v_e$  are the density and mean velocity on the outlet, respectively. The equation for minor pressure loss was defined as:

$$\frac{\Delta p_m}{\rho_{ie}} = \xi \frac{v_{ie}^2}{2} \quad (7)$$

Equation (7) was edited into:

$$\sqrt{\Delta p_m} = \sqrt{\xi} \left( \sqrt{\frac{\rho_{ie}}{2}} v_{ie} \right) \quad (8)$$

Equation (8) is a straight line with the slope  $\sqrt{\xi}$ . This assumption was experimentally verified on the described facility. The velocities  $v_i$ ,  $v_e$ , and the temperatures and pressures were measured on the inlet and

outlet of the element. The densities on the inlet and outlet  $\rho_i$ ,  $\rho_e$  were calculated using the state equation. The measured pressure difference of the element was also evaluated. The measured values for equation (8) are plotted for the cooler DHR in Fig. 2. Fig. 2 represents a summary of more than 6000 data points at different operating temperatures and pressures. The regression curve fitting shows that the calculated linear relationship given in (Urban et al., 2016) was confirmed. The minor loss coefficient  $\zeta_{DHR}$  (the slope of the line is  $\sqrt{\zeta_{DHR}}$ ) was determined from the regression equation.

The resulting value of minor loss coefficient was determined as  $\zeta_{DHR} = 48.634$ . A theoretical value of this coefficient was previously estimated as  $\zeta_{DHR} = 55.307$  in the work (Urban et al., 2016).

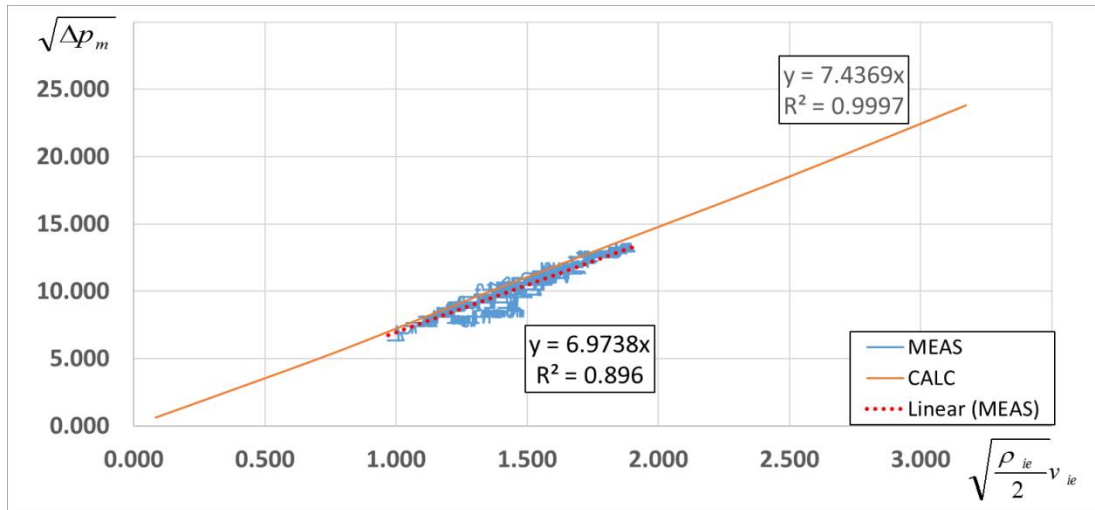


Fig. 2: Determination of minor losses in the DHR device.

## 5. Conclusions

The article presents a suggested expression of minor loss in the DHR cooler in the helium loop, intended for heat removal from the nuclear reactor substitute. General equation was modified and expressed in relation to averaged values of densities and mean velocities of the DHR element. This approach to local loss determination has proved very suitable. The expected linear relationship was proved by measurements on the helium loop at a wide range of operating conditions (more than 6000 measured points). It was possible to determine the coefficient of minor loss for the cooler from the regression curve. The measured relationship is in conformity with calculated values stated in (Urban et al., 2016). The results obtained are necessary to develop one-dimensional model of flow in the loop. Similar measurements will be conducted on the GFR device.

## Acknowledgement

This contribution was created on the basis of the project "Research centre ALLEGRO" (ITMS project code: 26220220198), supported by Operational Programme Research and Development funded by the European Regional Development Fund.



## References

- Knížat, B., Urban, F., Mlkvik, M., Ridzoň, F. and Olšiak, R. (2016) Numerical simulation of losses along a natural circulation helium loop. AIP Conference Proceedings 1745, 020023 (2016); doi: 10.1063/1.4953717.
- Knížat, B., Hlbočan, P. and Mlkvik, M. (2014) CFD simulation of a natural circulation helium loop. Scientific proceedings 2014, Faculty of Mechanical Engineering, STU in Bratislava.
- Novák, P.J. (2007) Thermodynamic properties of gases. Technical University in Prague, ISBN 978-80-7080-003-4.
- McCarty, D.R., Arp, D.V. and Friend, G.D. (1998) Thermophysical properties of Helium-4 from 0.8 to 1500 K with pressures to 2000 MPa. NIST Technical note 1334 (revised).
- Urban, F., Élesztös, P., Palenčár, R., Emmer, Š., Jelemenský, K., Knížat, B. and Kolláth, L. (2016) Modeling of natural circulation flow of helium in the experimental helium loop. Research report for research center Allegro.

## CONCENTRATION DISTRIBUTION AND SLIP VELOCITY OF COARSE-PARTICLE-WATER MIXTURE IN HORIZONTAL AND INCLINED PIPE SECTIONS

P. Vlasák<sup>\*</sup>, Z. Chára<sup>\*\*</sup>, J. Konfršt<sup>\*\*\*</sup>

**Abstract:** *Narrow particle size distribution basalt pebbles of mean particle size 11.5 mm conveyed by water in the pipe sections of different inclination were investigated on an experimental pipe loop of inner diameter  $D = 100$  mm. Mixture flow-behaviour and the concentration distribution were studied in a pipe viewing section and with the application of a gamma-ray densitometer. The study refers to the effect of mixture velocity, overall concentration, and angle of pipe inclination on chord-averaged concentration profiles and local concentration maps. The study revealed that the coarse particle-water mixtures in the inclined pipe sections were significantly stratified, the solid particles moved principally close to the pipe invert, and for higher and moderate flow velocities particle saltation becomes the dominant mode of particle conveying.*

**Keywords:** Hydraulic Conveying,, Concentration Distribution, Pipe Inclination, Gamma-Ray Radiometry, Mixture Flow Behaviour.

### 1. Introduction

Pipeline conveying of bulk materials in the form of heterogeneous mixtures is of special interest in, e.g. mining, dredging, building or land reclamation (Vlasak et al., 2012). The particles in the turbulent flow are supported by turbulent diffusion, and near the pipe wall a lift force, associated with slip velocity and concentration profile, contributed to particle lift-off. For the particles with size larger than the thickness of viscous sub-layer, Saffman force, induced due to the shear of the fluid, supports particle movement and together with Magnus force (due to the particle rotation) could reach a significant fraction of the total weight of particles (Wilson et al., 2010). A lot of theoretical or experimental studies have been carried out on transport of sand or fine particles in horizontal pipes. However, a relatively little research has been done on hydraulic conveying of gravel or bigger particles, especially in vertical and inclined pipes.

The flow of heterogeneous solid-liquid mixtures in a horizontal pipe may be defined as the flow with an asymmetrical concentration and velocity distribution. Based on macroscopic modelling, where the conservation equations are formulated using averaged quantities over the control volume, Wilson proposed a two-layer model for settling slurries with fully stratified flow pattern (Wilson, 1976, Wilson et al., 2006). Because the layers differ in the local solids concentration and velocity, there is a difference in the mean velocities of the particles and the liquid, which results in a continuous transfer of energy from the fluid to the particle and from the particle to the pipe wall (Vlasak et al., 2017).

Slip velocity in two-phase flow is defined as the velocity difference between the solid and liquid phase, it is one of mechanism of particle movement in two-phase flow. In the homogeneous model of two-phase flow the slip velocity  $V_s$  is by definition assumed to be close to zero. For heterogeneous slurry flow it was experimentally observed that the slip velocity depends on the flow pattern (e.g. stratified flow, slug flow). Due to slip velocity, there is difference between delivery (transport  $c_d$ ) and spatial (in situ  $c_v$ ) concentrations, and the slip ratio ( $c_d/c_v = V_s/V_a$ ) is the parameter describing flow stratification in a pipe.

---

<sup>\*</sup> Prof. Ing. Pavel Vlasák, DSc., FEng.: Institute of Hydrodynamics CAS, v. v. i., Pod Patankou 30/5; 160 00, Prague 6; CZ, vlasak@ih.cas.cz

<sup>\*\*</sup> Prof. Ing. Zdeněk Chára, PhD.: Institute of Hydrodynamics CAS, v. v. i., Pod Patankou 30/5; 160 00, Prague 6; CZ, chara@ih.cas.cz

<sup>\*\*\*</sup> Ing. Jiří Konfršt, PhD.: Institute of Hydrodynamics CAS, v. v. i., Pod Patankou 30/5; 160 00, Prague 6; CZ, konfrst@ih.cas.cz

## 2. Experimental Equipment and Material

The experimental investigation was carried out on the pipe loop of inner diameter  $D = 100$  mm with horizontal and inclinable pipe sections. Glass viewing sections were used to study the slurry flow behaviour. The mixture flow was recorded using a high speed digital camera NanoSence MK III+ with a frequency up to 2 000 frames per second, image resolution  $1280 \times 1024$ . Slurry velocity was measured by a Krohne OPTIFLUX 5000 magnetic flow meter, the flow divider and the sampling tank allow measuring of the flow rate and delivered concentration. The loop is equipped with gamma-ray density meters placed on a special support controlled by the computer. The studied mixtures consist of basalt pebbles (particle diameter,  $d$ , ranging from 8 to 16 mm, the mean diameter  $d_{50} \approx 11.5$  mm, particle density  $\rho_p = 2\,895$  kg.m<sup>-3</sup>) and water, the overall volumetric concentration,  $c_v$ , ranged from 3 to 15 %.

## 3. Local Concentration

Distribution of the local concentration in the pipe cross-section is important for understanding the mechanism of the heterogeneous mixture flow; it has a great effect on both the mixture's flow behaviour and pressure drop. The local concentration distribution was measured using a  $\gamma$ -ray densitometer (Krupicka and Matousek, 2014; Matousek et al., 2015). The effect of mean concentration, mixture velocity and angle of pipe inclination on chord-averaged vertical profiles of local concentration was studied. The measured chord-average concentration profiles for different transport concentration  $c_d$  confirmed the stratified flow pattern of the coarse particle-water mixture in inclined pipe sections. The chord-average concentration profiles can be divided into three parts similarly as in horizontal pipe sections (Vlasak et al., 2014a; 2016). The local concentration  $c_v$  approaches practically zero in the upper portion of the pipe, this region increases for the descending flow with decreasing mixture velocity and mean transport concentration. A nearly linear concentration distribution was observed in the central portion of the pipe cross-section. Local concentration reached maximum near the pipe invert, however, in inclined pipe sections never reached value close to the loose-packed value for studied conditions.

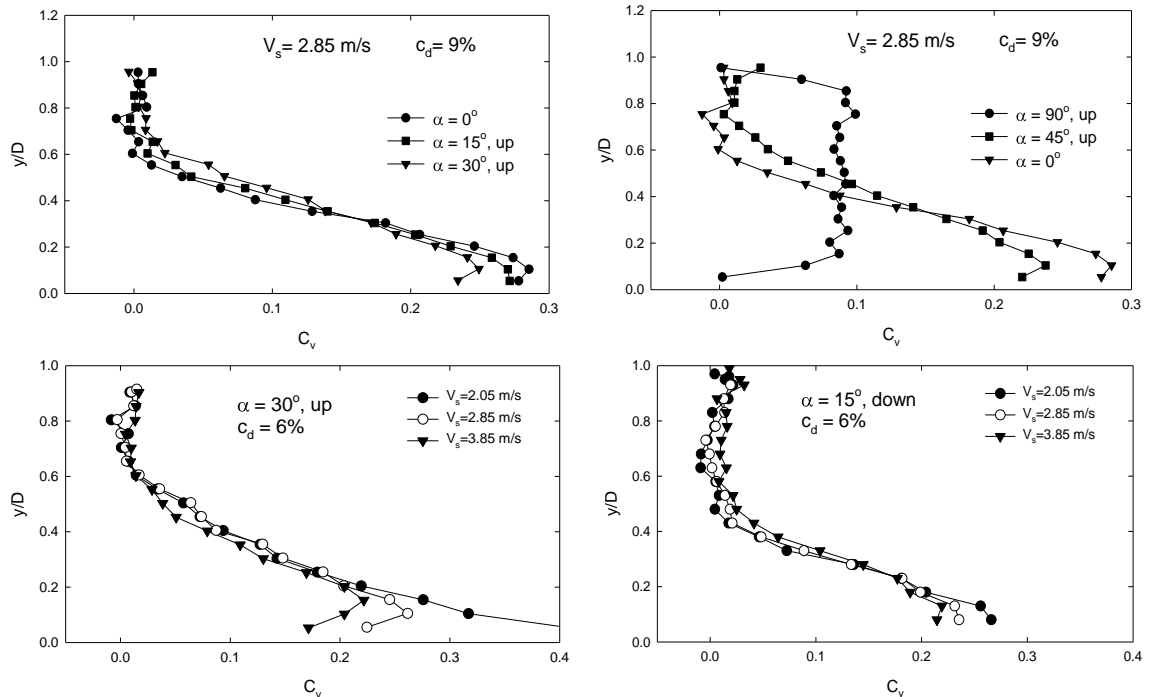


Fig. 1: Effect of inclination angle  $\alpha$  and mean mixture velocity  $V_s$  on profiles of local concentration  $c_v$ .

Similarly as it was confirmed for pressure drop, the effect of pipe inclination for low values of inclination angle  $\alpha$  (up to about  $30^\circ$ ) is not significant (Vlasak et al., 2014b). Local in situ concentration  $c_v$  at the pipe invert slightly decreased with increasing pipe inclination. For higher inclination angle  $\alpha$ , a decrease in concentration close to the pipe invert was observed. For the vertical pipe a nearly constant concentration distribution was observed, see Fig. 1. Bed layer with thickness of about 20 % of the pipe diameter were formed for moderate and higher mixture velocities. Local concentration in the bed layer decreased with increasing velocity; this effect increased with increasing inclination angle  $\alpha$ . Fig. 2 (upper

panels) illustrates the effect of the transport concentration  $c_d$  for inclination angle  $\alpha = 30^\circ$  and the mixture velocity  $V_s = 2.85 \text{ m s}^{-1}$ , both for ascending and descending flow directions. No maximum of local concentration was observed for descending flow direction, concentration profiles were nearly linear in the lower portion of the pipe, and the zero concentration part of the chord-averaged concentration profile was significantly more extended than that for the ascending flow direction due to the braking effect of gravity force on ascending flow and accelerating effect of gravity force on descending flow. The positive effect of gravity decreases and the negative effect of gravity increase the particle–liquid slip velocity.

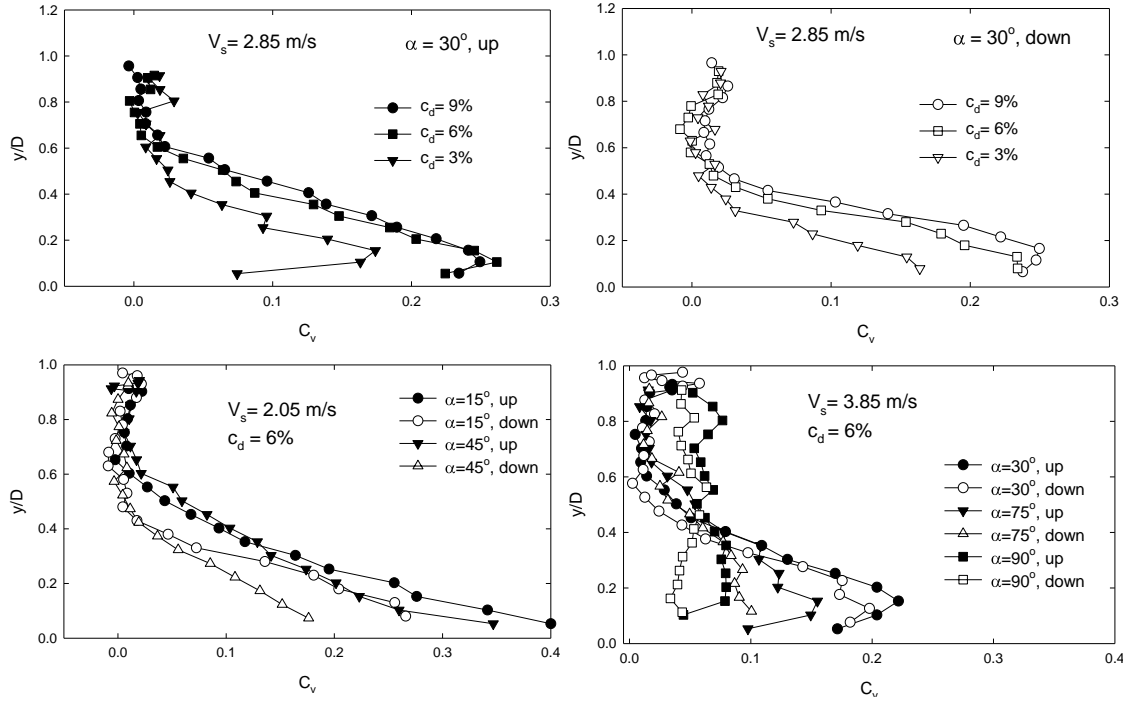


Fig. 2: Effect of the transport concentration  $c_d$  and flow direction on profiles of local concentration  $c_v$ .

The effect of up and down flow is illustrated in Fig. 2 (lower panels) for inclination angle  $\alpha$  in range from  $15^\circ$  to  $90^\circ$ . The local concentration in ascending pipe section is always higher than that in descending pipe section. It is valid also for vertical up-ward and down-ward flow, where difference between the concentration values corresponds to particle–liquid slip velocity, which can be approximated by hindered settling velocity.

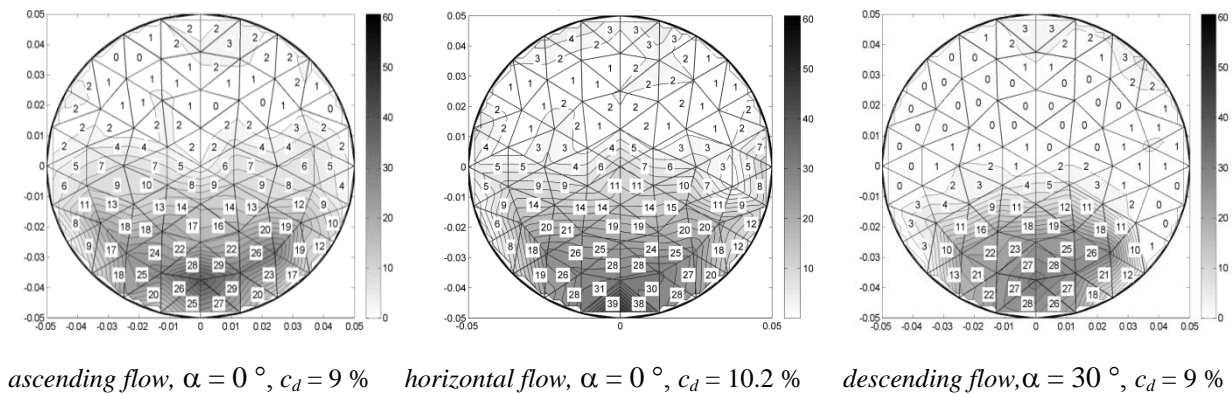


Fig. 3: Maps of local concentration  $c_v$  in inclined and horizontal pipe sections ( $V_s = 2.8 \text{ m.s}^{-1}$ ).

The concentration maps measured in inclined pipe sections (see Fig. 3) confirmed that coarse particles tended to occupy the bottom part of the pipe. However, with increasing mixture velocity and concentration, even the coarse particles lifted off the pipe bottom and moved up to the central area of the pipe, similarly as it was found in the horizontal pipe section (Vlasak et al., 2014b). Some differences were found for ascending and descending flow direction due to the effect of gravity force on particle movement and slip velocity. In descending pipe sections the observed local concentration near lateral walls of the



pipe was slightly less than that in the ascending pipe sections, where especially for higher mean concentration significantly higher local concentration values were reached close to the pipe invert, probably due to the higher slip velocity and breaking effect of the gravity force acting on the particles.

Effect of mean mixture velocity and concentration on values of slip ratio in horizontal ( $V_s/V_a$ ) and vertical ascending ( $V_{s,a}/V_a$ ) and descending ( $V_{sd}/V_a$ ) pipe sections, determined from measured basalt pebbles-water mixture concentration are indicated in Tab. 1.

*Tab. 1: Slip ratio in horizontal and vertical ascending and descending pipe sections.*

$V_a$ [m/s]	$c_v$	$c_d$	$V_s / V_a$	$V_a$ [m/s]	$c_{v,a}$	$c_{v,d}$	$c_d$	$V_{s,a}/V_a$	$V_{sd}/V_a$
2.0	0.136	0.105	0.77	2.05	0.063	0.037	0.049	0.78	1.32
2.8	0.102	0.075	0.74	2.85	0.071	0.048	0.059	0.83	1.23
3.8	0.121	0.105	0.87	3.85	0.067	0.053	0.061	0.91	1.15

#### 4. Conclusions

The effect of slurry velocity and mean concentration on a basalt pebbles – water mixtures' flow behaviour in the turbulent regime was studied in inclined smooth pipe sections of inner diameter  $D = 100$  mm.

The stratified flow pattern of the coarse particle-water mixture in inclined pipe sections was revealed. The particles moved mostly near to the pipe invert, where dune formations and for velocities higher than deposition limit a sliding bed layer were formed. For moderate and higher mixture velocities, particle saltation became the dominant mode of sediment transport.

Concentration distribution in ascending and descending vertical pipe section confirmed effect of fall velocity on particle-carrier liquid slip velocity and higher in situ concentration in ascending pipe section.

For inclination angle  $\alpha$  (lower than about  $30^\circ$ ), the effect of pipe inclination on local concentration distribution is not significant. The zero concentration region increases for descending flow direction with decreasing mixture velocity and mean transport concentration and it is bigger than that for the ascending flow direction. With increasing mean mixture velocity the local concentration in the bed layer slightly decreased; this effect increased with increasing inclination angle.

#### Acknowledgement

Supports under the project 17-14271S of the Grant Agency of the Czech Republic, and RVO: 67985874 of the Czech Academy of Sciences are gratefully acknowledged.

#### References

- Krupicka, J. and Matousek, V. (2014) Gamma-ray-based measurement of concentration distribution in pipe flow of settling slurry: vertical profiles and tomographic maps. *J. Hydrology and Hydromechanics*, 62, 2, pp. 126-132.
- Matousek, V., Vlasak, P., Chara, Z. and Konfrst, J. (2015) Experimental study of hydraulic transport of coarse-basalt. *Maritime Engineering*, 168, pp. 93-100.
- Vlasak, P., Chara, Z. and Konfrst, J. (2017) Flow behaviour and local concentration of coarse particles-water mixture in inclined pipes. *Journal of Hydrology and Hydromechanics*, 65, DOI: 10.1515/johh-2017-0001.
- Vlasak, P., Kysela, B. and Chara, Z. (2012) Flow Structure of coarse-grained slurry in horizontal pipe. *Journal of Hydrology and Hydromechanics*, 60, 2, pp. 115-124.
- Vlasak, P., Chara, Z., Konfrst, J. and Krupicka, J. (2014a) Experimental investigation of coarse particle conveying in pipes. *EPJ Web of Conferences, Proc. EFM 2014*, (eds. Dancova P. and Vit T.), TUL Liberec, pp. 712-719.
- Vlasak, P., Chara, Z., Krupicka, J. and Konfrst, J. (2014b) Experimental investigation of coarse particles-water mixture flow in horizontal and inclined pipes. *Journal of Hydrology and Hydromechanics*, 62, 3, pp. 241-247.
- Vlasak, P., Chara, Z., Konfrst, J. and Krupicka, J. (2016) Distribution of concentration of coarse particle-water mixture in horizontal smooth pipe. *Canadian Journal of Chemical Engineering*, 94, pp. 1040-1047.
- Wilson, K.C. (1976) A unified physically based analysis of solid-liquid pipeline flow, in: *Proc. of Hydrotransport 4* (eds. Stephens, H.S., Streat, M. Clark, J. and Coles, N.G.), B.H.R.A., Cranfield, UK, Pap. A1.
- Wilson, K.C., Addie, G.R., Sellgren, A. and Clift, R. (2006) *Slurry Transport Using Centrifugal Pumps*. Springer.
- Wilson, K.C., Sanders, R.S., Gillies, R.G. and Shook, C.A. (2010) Verification of the near-wall model for slurry flow. *Powder Technology*, 197, pp. 247-253.

## SOME ENERGY RELATIONS OF THE SELF-EXCITED PROFILE VIBRATION IN FLOWING FLUID

V. Vlček<sup>\*</sup>, I. Zolotarev<sup>\*</sup>, J. Kozánek<sup>\*</sup>, P. Šidlof<sup>\*,\*\*</sup>, M. Štěpán<sup>\*</sup>

**Abstract:** *The aeroelastic measurements on the oscillating NACA0015 profile vibrating as the dynamic system with two degrees of freedom (pitch and plunge) were realized within the interval of Mach numbers  $M = 0.08$  to  $0.45$  and Reynolds numbers  $Re = (1 - 5) \cdot 10^5$  in the wind tunnel of the Institute of Thermomechanics of the CAS. Frequency and amplitude characteristics of the vibrating profile and values of elastic strain energy corresponding maximum pitch and plunge displacements of the studied profile were detected.*

**Keywords:** Airfoil NACA 0015, Aeroelasticity, Stall flutter, Dynamic stall, Limit cycle oscillation.

### Introduction

The effort to reduce energy losses and to increase the reliability of technologies, where aeroelastic phenomena occur, requires obtaining accurate additional supporting data (Dowell, 2015; Fung, 1993). Their completion is one of the goals of this study, which summarizes some experimental results published by the authors earlier (Šidlof, 2016, Vlček, 2016).

### 1. Experimental equipment

The schema of the experiment is in Fig. 1. Measurements were realized in the vacuum wind tunnel of the laboratory of the Institute of Thermomechanics CAS in N. Knín. Test section has a cross section 210x80 mm and the profile NACA0015 had a chord with a length of 59.5 mm. The effect of seven different values of pitch support stiffness was studied. Modification of the stiffness was realized by using a set of interchangeable springs.

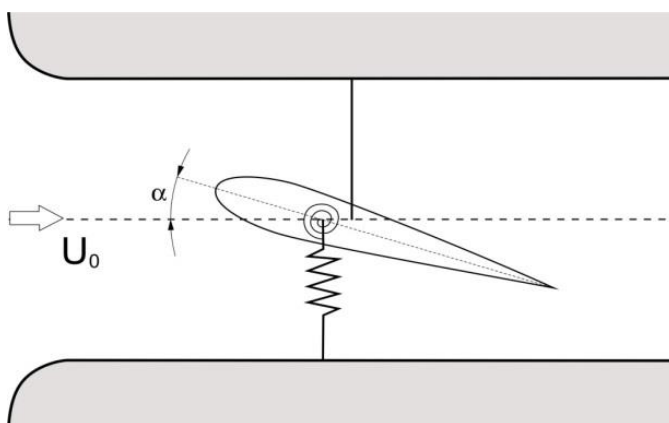


Fig. 1: General schema of the experiment.

<sup>\*</sup> Institute of Thermomechanics CAS, v. v. i., Dolejšková 5, 18200 Prague 8; CZ, vlcek@it.cas.cz.

<sup>\*\*</sup> Technical University of Liberec, Studentská 1402, 640 01 Liberec 1, Czech Republic, petr.sidlof@tul.cz.

## 2. Frequency of the self-excited oscillation

The dependence of the frequency of self-excited oscillation to the flow velocity is indicated in Fig. 2 in the form of dimensionless Strouhal number  $Sh = f \cdot l / v$ , where  $f$  is the frequency [Hz],  $l$  is the chord of the profile [m] and  $v$  is the flow velocity [m / s].

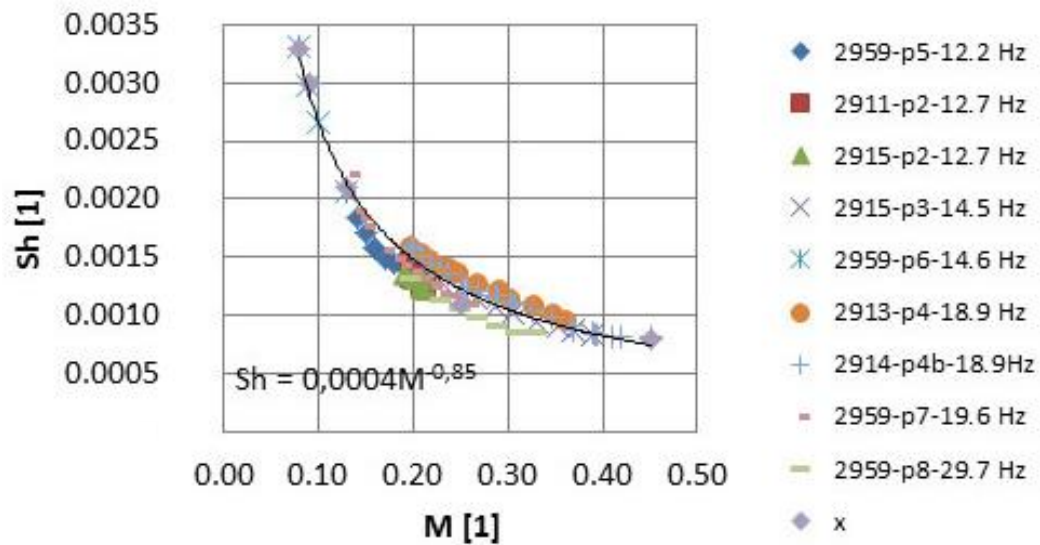


Fig. 2: Dimensionless frequency of the profile oscillation.

A more detailed analysis of this course, including the relationship between the frequency of self-excited profile oscillation and the eigenfrequencies of both degrees of freedom for zero fluid velocity is shown in (Vlček, 2017).

## 3. Energetic relation between plunge and pitch harmonic vibrations during the self-excited profile

Real waveform of plunge and pitch was not precisely harmonic, therefore the calculation of energy was performed for the case of the maximum amplitude.

### Energy of the plunge for one value of the plunge stiffness

First plunge eigenfrequency was found as  $f_{0\text{plunge}} = 16.4$  Hz. Corresponding angular velocity will be

$$\omega_{\text{plunge}} = 2\pi f_{0\text{plunge}} = (k_{\text{plunge}}/m)^{1/2},$$

where  $m$  is the body mass, approximately 1 kg. Then the total plunge stiffness is  $k_{\text{plunge}} = 10\,609$  N/m.

Tab. 1: Calculation of the plunge energy.

$N_0$	$M$	$y_{\text{max}}$ [mm]	$f$ [Hz]	$E_{\text{plunge}}$ [J]
2959-46	0.14	0.9	14.90	0.0043
2959-47	0.15	0.6	14.90	0.0019
2959-48	0.16	1.7	14.60	0.0153
2959-49	0.16	2.6	14.60	0.0359
2959-50	0.17	3.6	14.60	0.0687
2959-52	0.19	6.3	15.10	0.2105
2959-42	0.20	7.7	15.40	0.3145

Potential energy  $E_{\text{plunge}}$  [J] of the plunge at the maximum deflection is

$$E_{\text{plunge}} = \frac{1}{2} k_{\text{plunge}} \cdot (y_{\text{max}})^2,$$

where  $y_{\max}$  is maximum plunge amplitude determined from measurements. Data № 2959-46 up to 52 has values denoted in Tab. 1,  $M$  is the Mach number of the fluid flow,  $f$  is the self-excited frequency.

### Energy of the pitch for different pitch stiffness corresponding of variable elasticity support

Potential pitch energy  $E_{\text{pitch}}$  [J] for one vibration period is defined by relation

$$E_{\text{pitch}} = \frac{1}{2} k_{\text{pitch}} \cdot (\varphi_{\text{pitch}})^2,$$

where  $k_{\text{pitch}}$  [N·m/rad] is the pitch stiffness and  $\varphi_{\text{pitch}}$  [rad] is maximum pitch angle amplitude, both determined from experiments.

Numerical values of the pitch energy are calculated in Tab. 2.

Tab. 2: Calculation of the pitch energy.

№	M	$\varphi_{\text{pitch}}$ [rad]	$k_{\text{pitch}}$ [N.m/rad]	$E_{\text{pitch}}$ [J]
2959-46	0.14	0.03	0.305	0.000137
2959-47	0.15	0.02	0.431	0.000086
2959-48	0.16	0.06	0.400	0.00072
2959-49	0.16	0.09	0.622	0.0025
2959-50	0.17	0.43	0.7905	0.0731
2959-52	0.19	0.88	1.991	0.7709
2959-42	0.20	0.91	0.030	0.1242

The pitch eigenfrequency for the case 2959-47:  $f_{0 \text{ pitch}} = 14.9$  Hz.

The calculation of the moment of inertia  $I$  from the equation

$$\omega_{\text{pitch}} = 2 \pi f_{\text{pitch}} = (k_{\text{pitch}} / I)^{1/2}.$$

For pitch stiffness  $k_{\text{pitch}} = 0.431$  [N·m/rad], determined from measurement, the profile moment of inertia is

$$I = k_{\text{pitch}} / (2 \pi f_{\text{pitch}})^2 = 5.2 \cdot 10^{-5} \text{ kg} \cdot \text{m}^2.$$

We note, that the above energy calculations concern the individual plunge and pitch maximum energy which are not realized at the same time.

The illustration of the ratio of the maximum plunge and pitch potential energy  $E_{\text{plunge}} / E_{\text{pitch}}$  is given in Fig. 3.

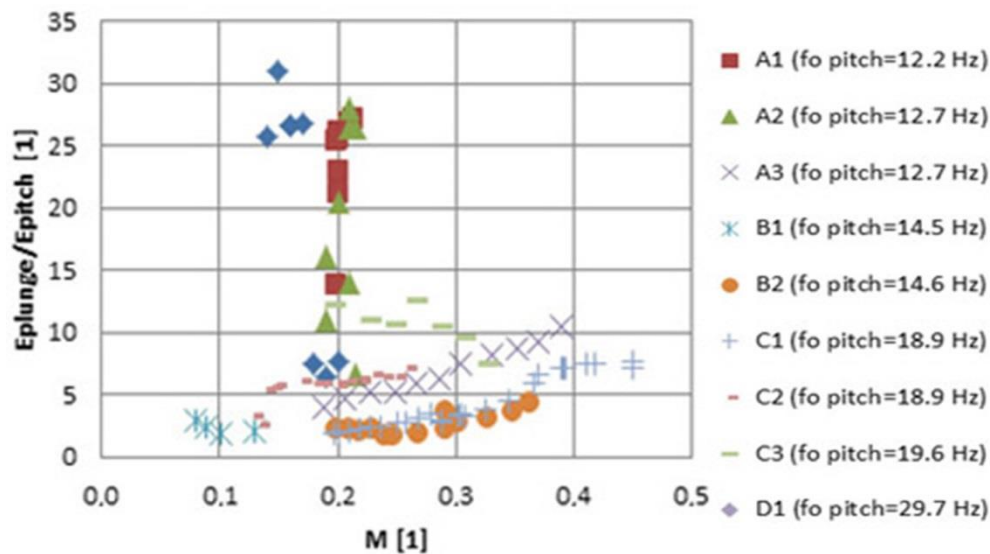


Fig. 3: The energy ratio of the plunge and pitch elastic support deformation for different flow velocity.

#### 4. Conclusions

The paper is concerned with the aeroelastic energy in the self-excited vibration of the profile in fluid flow and follows the results published in (Vlček, 2017) devoted to the frequency of this vibration.

The relationship between the plunge and pitch support elasticity deformation energy changes with a specific form with the pitch stiffness or with the flow velocity (see Fig.4). We can expect connection of this character with attributes of the origin and attributes of the periods of the self-excited oscillations of the profile. The potential energy was evaluated in the plunge and pitch mode separately.

The calculation of the total plunge and pitch deformation for one case was shown. For future calculation of the total energy deformation their phase shift must be considered.

#### Acknowledgement

The authors have been sponsored by the Pilot project of the Institute of Thermomechanics AS CR, v. v. i. № 903101 and Strategy AV21 № 3 "Effective transformation and storage of the energy" of the Academy of Sciences of the Czech Republic. The paper was created in cooperation with J. Horáček, M. Luxa and D. Šimurda.

#### References

- Dowell, E. (2015) A Modern Course in Aeroelasticity, Springer, Switzerland.
- Fung, Y.C. (1993) An Introduction to the Theory of Aeroelasticity, Dover Publications, Inc, Mineola, New York.
- Šidlof, P., Vlček, V. and Štěpán, M. (2016) Experimental investigation of flow-induced vibration of a pitch-plunge NACA 0015 airfoil under deep dynamic stall. *Journal of Fluids and Structures*. Vol. 67, № 2016, pp. 48-59.
- Vlček, V., Štěpán, M., Zolotarev, I. and Kozánek, J. (2016) Innovation of the experimental facility for the study of flutter in the Institute of Thermomechanics AS CR and some results obtained from initial experiments. *Applied Mechanics and Materials*, Vol. 821 (2016), pp. 141-151.
- Vlček, V., Zolotarev, I., Kozánek, J., Šidlof, P. and Štěpán, M. (2017) Some experimentally determined properties of a profile in case of self-excited oscillations in subsonic flow. *Proc. of the conference Dymamesi 2017, Krakow*.

## BACK ANALYSIS FOR DETERMINATION OF TENSION-SOFTENING DIAGRAM

J. Vorel<sup>\*</sup>, P. Kabele<sup>\*\*</sup>

**Abstract:** Concrete and other cementitious materials are undoubtedly the most important and widely used construction material nowadays. However, there exist other building materials, such as wood or composites, which are on high demand as well. Different mathematical models describing the complex material behaviour of these mostly quasi-brittle materials are used. Their application often requires the knowledge of experimentally determined fracture properties of studied material. The total fracture energy can be often determined directly from experimental measurements as the total work divided by the ligament area. However, the determination of true tensile strength and the traction-separation diagram is usually problematic. The primary objective of this paper is to present a numerical scheme, that can be used to determine the traction-separation diagram in the framework of sequentially linear analysis (SLA).

**Keywords:** Back analysis, Damage, Traction-separation diagram, Wood, Concrete.

### 1. Introduction

Concrete and other cementitious materials are undoubtedly the most important and widely used construction material nowadays. However, there exist other building materials, such as wood or composites, which are on high demand as well. Different mathematical models describing the complex material behaviour of these mostly quasi-brittle materials are used. Their application often requires the knowledge of experimentally determined fracture properties of studied material, e.g., the tensile strength, the fracture energy and the traction-separation (TS) diagram (strain-softening curve). The experimental setups used to determine the fracture properties are, e.g., uniaxial tension test, three- or four-point bending test, Brazilian splitting test, etc. While the fracture energy may be directly obtained from experiments by measuring the total work done by the test loads and dividing it by the ligament area, the determination of tensile strength and TS diagram appears to be technically difficult.

Several scholars have developed numerical procedures, different in complexity and experimental data requirements, to obtain the tension-softening curve. Li and Ward (1989) introduced a technique based on the J-integral to determine the tension-opening relation in cementitious composites. Cohesive force model analysis with poly-linear softening diagram was presented in (Kitsutaka et al., 1993), where the system of simultaneous equations, called crack equations, is solved by performing several iterations to obtain the parameters of poly-linear tension-softening curve. An indirect method utilising the bending test of a notched beam was proposed in (Nanakorn and Horii, 1996). In the approach, the slope of TS diagram is directly obtained for a given slope of the input load-deflection curve. Therefore, there is no iteration required for each incremental step. The interested reader can find another techniques, e.g., in (Skočec and Stang, 2008) or (Slowik et al, 2006).

The primary objective of this paper is to present a numerical scheme, that is used to determine the traction-separation diagram by means of the sequentially linear analysis (SLA). This scheme is particularly well suited to large-scale structural analyses (Rots and Invernizzi, 2004; Vorel and Boshoff, 2014; Vorel and Boshoff, 2015).

---

<sup>\*</sup> Assoc. Prof. Ing. Jan Vorel, PhD.: Department of Mechanics, Faculty of Civil Engineering, Czech Technical University in Prague; Thákurova 7; 166 29, Prague; CZ, jan.vorel@fsv.cvut.cz

<sup>\*\*</sup> Prof. Ing. Petr Kabele, PhD.: Department of Mechanics, Faculty of Civil Engineering, Czech Technical University in Prague; Thákurova 7; 166 29, Prague; CZ, petr.kabele@fsv.cvut.cz



## 2. Back analysis

Sequentially linear analysis was designed to overcome the difficulty of snap-back behaviour (Rots and Invernizzi, 2004), which typically occurs when full-scale structures are modelled. The procedure is based on the solution of physically nonlinear tasks by a sequence of linear (secant) steps. Relations between stresses and strains have to be defined as a collection of elasto-brittle teeth, called a "saw-tooth" law. This approach is generally applicable for materials with nonlinear softening, jumps in constitutive law, or hardening (Billington, 2009) for which the failure process is stably controlled.

In the present study, a back analysis method to obtain the TS diagram is presented. More specifically, the cohesive interface elements are introduced in the position of the crack for the finite element analysis and the corresponding crack-opening diagram for these elements is determined during the SLA. As an input for the proposed procedure, any measured loading curve can be used, e.g., force load versus displacement, force load versus crack mouth opening, etc. However, the measure used to control the loading process must have strictly increasing order to determine the unique critical multiplier ( $\lambda$ ).

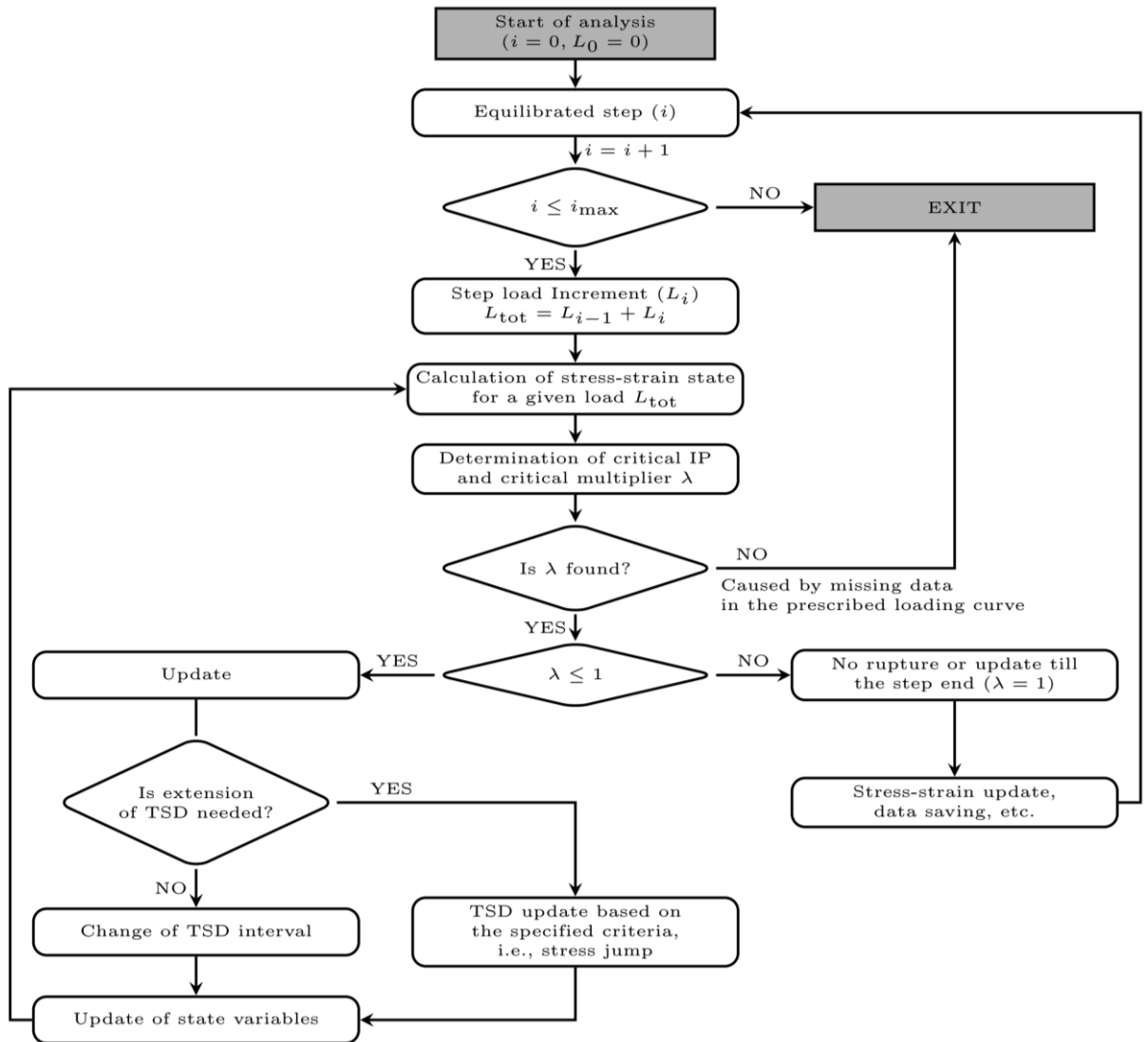


Fig. 1: Flowchart of proposed back analysis.

In the initial state, no tensile strength and no parameters of TS diagram have to be defined. The only parameters needed to be setup by the user are: 1) allowable overshooting of the prescribed diagram ( $F_{err}$ ); 2) reduction of the damage parameter ( $\Delta\omega$ ); 3) initial normal and shear stiffness of the interface element ( $k_n, k_s$ ). In this paper the  $F_{err}$  value is set as the percentage of the maximum load determined from the experimental data and can be seen as the error in the experimental measurement, and

$$\Delta\omega = \frac{k_n^{(i+1)} - k_n^{(i)}}{k_n} = \frac{\Delta\sigma_{cr}}{w_{cr}^{(i)} k_n}, \quad (1)$$

where index  $i = 1, 2, \dots$  refers to point number of the searched TS diagram,  $k_n^{(i)}$  denotes current and new normal stiffness of the element, and  $w_{cr}^{(i)}$  is the opening for the current critical multiplier.  $\Delta\sigma$  stands for the maximum allowable stress jump which characterises the damage change and is prescribed as the percentage of the determined tensile strength, i.e., the first stress value of searched TS diagram.

The flow chart of the proposed procedure is shown in Fig. 1. This procedure allows combination of elements used to determine the search TS diagram together with the standard elements for the SLA where the “saw-tooth” approximation is prescribed in advance. The critical multiplier  $\lambda$  is determined as the minimum load needed to exceed a given failure criterion or to exceed the prescribed loading curve. The determined TS diagram is subsequently utilised in the remaining elements involved in the back analysis. In most cases, e.g., three-point bending test, Brazilian splitting test, etc. only one element governs the shape of softening (hardening).

### 3. Numerical simulation

This section deals with the presentation of the obtained results for wood compact tension specimen shown in Fig. 2. Two different experimental data, presented in (Blass, 2011) are utilized in this study. The wood is modelled as the orthotropic material and is characterised by the user-defined properties (Kasal and Blass, 2013; Kasal and Heiduschke, 2004)

- Experiment No. 1:  $E_{xx} = 18.9$  GPa,  $E_{yy} = E_{zz} = 0.8$  GPa,  $G_{xy} = G_{xz} = 0.62$  GPa,  $G_{yz} = 0.19$  GPa,  $\nu_{yz} = \nu_{xz} = \nu_{xy} = 0.3$ ,  $k_n = 18.9$  MN/m,  $k_s = 18.9 \cdot 10^4$  MN/m.
- Experiment No. 2:  $E_{xx} = 18.9$  GPa,  $E_{yy} = E_{zz} = 0.74$  GPa,  $G_{xy} = G_{xz} = 0.57$  GPa,  $G_{yz} = 0.19$  GPa,  $\nu_{yz} = \nu_{xz} = \nu_{xy} = 0.3$ ,  $k_n = 18.9$  MN/m,  $k_s = 18.9 \cdot 10^4$  MN/m.

The presented back analysis is implemented for plane stress problems in the open source object oriented finite element program OOFEM (Patzák and Bittnar, 2001). The isoparametric four-node quadrilateral plane-stress finite elements and the interface cohesive elements with linear approximation of displacement field are used for the finite element calculations. The element size in the region of interest is equal to 1 mm. The comparison between the experimental data and the calculated load-CMOD diagrams is shown in Fig. 3a. The calculated traction-separation diagrams is depicted in Fig. 3b.

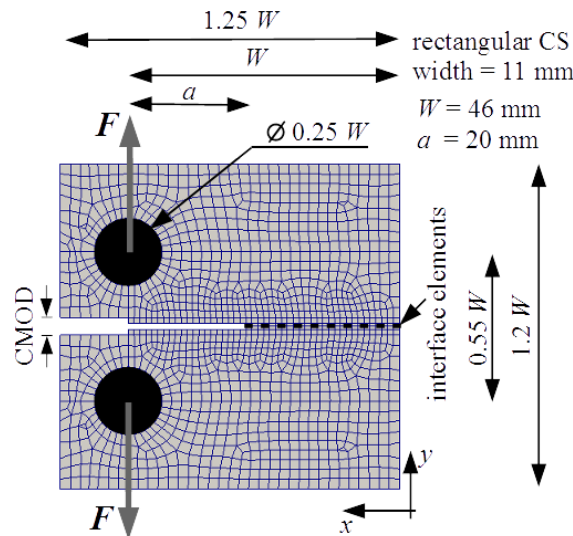


Fig. 2: Compact tension test setup.

### 4. Conclusions

The new procedure for the determination of traction-separation diagrams was introduced in the paper. The method is utilised to obtain the fracture properties of wood samples. More specifically, the traction-

separation diagrams are presented in Fig. 3b. As can be seen from the presented results, the agreement between the experimental data and numerical analysis is sufficient. However, it has to be stressed out that the back analysis depends on the quality of experimental data, especially the part used for the determination of the traction-separation diagram. In Fig. 3a, this part of diagram lies between the origin and the cross mark.

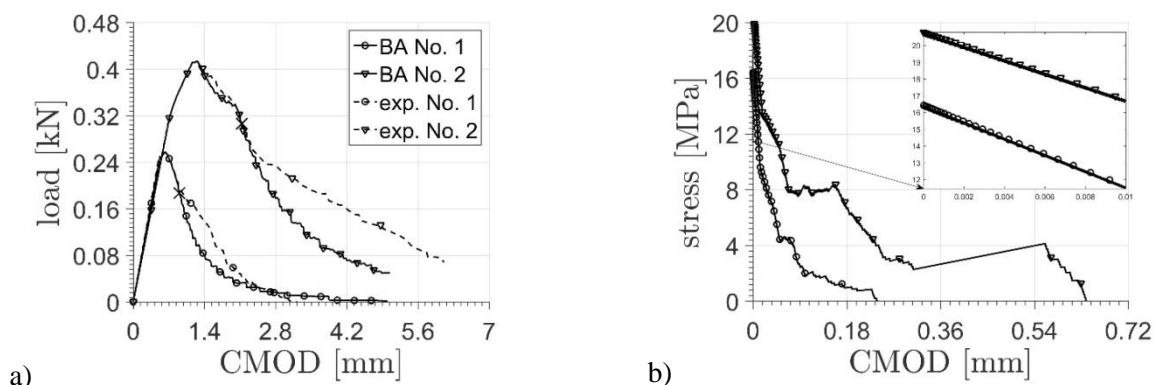


Fig. 3: Compact tension test: a) load-CMOD diagram; b) TS diagram.

### Acknowledgement

The first author would like to gratefully acknowledge the financial support provided by the GAČR grant No. 15-10354S. The second author would like to acknowledge the support by the GAČR grant No. 13-15175S.

### References

- Billington, S. (2009) Nonlinear and sequentially linear analysis of tensile strain hardening cement-based composite beams in flexure. Computational modeling workshop on concrete, masonry and on fiber-reinforced composites, pp. 7-10.
- Blass, R. (2011) Laminated wooden arches reinforced with glass fiber rods. Ph.D. thesis, The Pennsylvania State University.
- Kasal, B. and Blass, R. Experimental and analytical investigation of crack development in composite reinforced laminated arch. Materials and structures, 46, 1-2, pp. 173-180.
- Kasal, B. and Heiduschke, A. (2004) Radial reinforcement of curved glue laminated wood beams with composite materials. Forest products journal, 54, 1, 74-7.
- Kitsutaka, Y., Kamimura, K. and Nakamura, S. (1993) Poly-linear approximation analysis of tension softening diagram for concrete. Journal of Structural and Construction Engineering, 453, pp. 15-25.
- Li, V. and Ward, R. (1989) A novel testing technique for post-peak tensile behaviour of cementitious materials. Fracture toughness and fracture energy, pp. 183-195.
- Nanakorn, P. and Horii, H. (1996) Back analysis of tension-softening relationship of concrete. Journal of materials, concrete structures and pavement, 32, 544, pp. 265-275.
- Patzák, B. and Bittnar, Z. (2001) Design of object oriented finite element code. Advances in Engineering Software, 32, 10-11, pp. 759-767.
- Rots, J. and Invernizzi, S. (2004) Regularized sequentially linear saw-tooth softening model. International Journal for Numerical and Analytical Methods in Geomechanics, 28, 7-8, pp. 821-856.
- Skoček, J. and Stang, H. (2008) Inverse analysis of the wedge-splitting test. Engineering Fracture Mechanics, 75, 10, pp. 3173-3188.
- Slowik, V., Villmann, B., Bretschneider, N. and Villmann, T. (2006) Computational aspects of inverse analyses for determining softening curves of concrete. Computer Methods in Applied Mechanics and Engineering, 195, 52, pp. 7223-7236.
- Vorel, J. and Boshoff, W. (2014) Numerical simulation of ductile fiber-reinforced cement-based composite. Journal of Computational and Applied Mathematics, 270, 433-442.
- Vorel, J. and Boshoff, W. (2015) Computational modelling of real structures made of strain-hardening cement-based composites. Applied Mathematics and Computation 267, 562-570.

## PLATFORM STABILIZED BY MEANS OF TWO GYROSCOPES AND DAMPED WITH MAGNETORHEOLOGICAL DAMPER

R. Votrubec\*

**Abstract:** The paper deals with stabilization of platform by means of gyroscopes. Whole platform consists of parallelogram, cardan frame and two contra rotating gyroscopes. Whole system is described with five generalized coordinates and with two cyclic coordinates. Pneumatic motors and pneumatic springs are used to actuating gyroscopes and cardan frame. Magnetorheological controlled damper was used to damping rotary frame. Control algorithm is based on frequency analysis.

**Keywords:** Gyroscope, Active damping, LabView, Vibroisolation, Magnetogheological damper.

### 1. Introduction

In the past, our team dealt with the development of active ambulance stretcher (Votrubec, 2011 and Votrubec, 2009). This platform is similar and it consists of parallelogram and two rotating frames, Fig. 1. First prototype of stabilized platform is simplified and it consists of frame rotating around one axis only, Fig. 2. Upper frame is propelled by pneumatic springs. Pressures in both springs are controlled by electrical proportional valves. Two gyroscopes with vertical rotation axis are mounted to upper inner frame. Gyroscopes have the air bearing support in precession frames. Gyroscopic stabilizer mechanical system was described in (Skliba, 2007 and Sivcak, 2010). Gyroscopes are driven by air turbine. Its nominal speed is 30.000 rpm. Manufacturing of gyroscopes with aerostatic bearings is described in (Simek at al., 2011 and Simek, 2011). Speed of gyroscopes is measured with magnetic sensor which generates pulses. The torque motor of radial correction is mounted on precession frame axis between upper inner stabilizer and precession frame. This pneumatic torque motor is actuating device of correction and compensation system. It was described in (Votrubec, 2010). Pneumatic springs and motors are controlled using pneumatic valves.

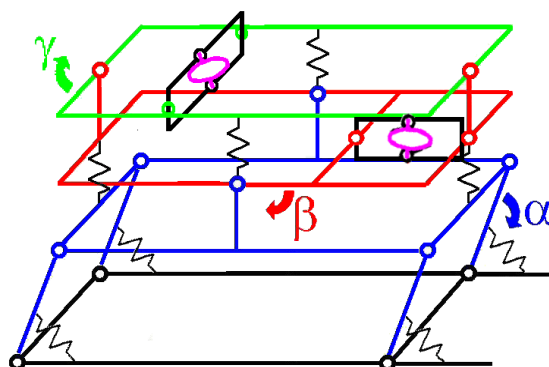


Fig. 1: Scheme of stabilized platform.

### 2. Description of Stabilized Plate

A photograph of prototype is in Fig. 3. The scheme of stabilized plate is in Fig. 2. Auxiliary ground frame is red. Base frame is green. Upper inner stabilized frame is blue. This frame is propelled by pneumatic springs. Precession frames of gyroscopes are mounted on blue frame. They are driven by pneumatic

---

\* Ing. Radek Votrubec, PhD.: Technical University of Liberec, Studentska 2; 461 17, Liberec; CZ, radek.votrubec@seznam.cz

motors. Problems of using tandem of gyroscopes are solved in (Skliba, 2008). Blue frame is controlled to horizontal position.

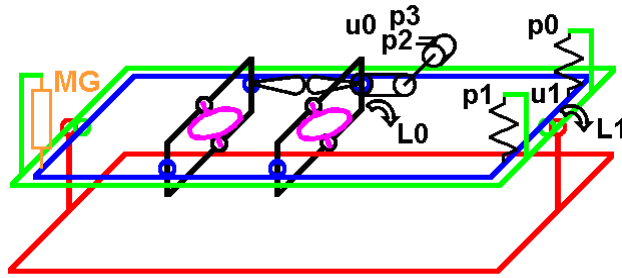


Fig. 2: Scheme of one-axis prototype.

Correction and compensation systems consist of two proportional feedbacks with PID controllers. Correction torque motor on precession frame axis is controlled by feedback from sensor of stabilized frame position. It indicates direction of an apparent vertical. Compensation system has feedback, which applies the torque on stabilized frame. It is driven with respect to magnitude of precession frame angular displacement.

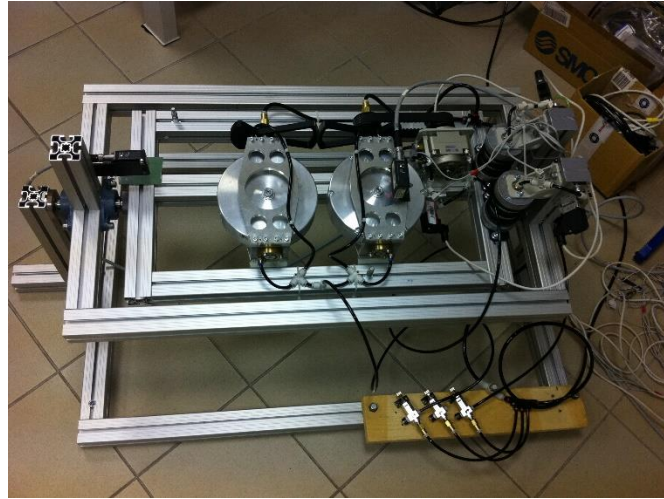


Fig. 3: Prototype of stabilized platform.

The model consists of motion equations, which are derived from Lagrange equations. External torques are on right side.

$$\frac{d}{dt} \frac{\partial T}{\partial \dot{q}_i} - \frac{\partial T}{\partial q_i} + \frac{\partial U}{\partial q_i} = M_{s_i} + M_{d_i} + M_{pas_i} + M_{cor_i} \quad i = 1..3 \quad (1)$$

Stabilized frame has index  $i = 1$  with angle displacement  $q_1$ . Precession frame has index  $i = 2$  with angle displacement  $q_2$ . Sensor of apparent vertical has index  $i = 3$ .  $q_3$  is angle between apparent vertical and z-axis of stabilized frame.  $M_{s_i}$  are torques of air springs.  $M_{d_i}$  are torques of dampers,  $M_{pas_i}$  are torques of passive resistances and  $M_{cor_2}$  is torque of correction motor. It is only on the precession frame axis. The whole model contains air spring models and models of electric valves.

### 3. Magnetorheological Damper

Magnetorheological damper is a controlled damper, which characteristic is changed by the modification of the properties of the working liquid using controlled magnetic field. Mathematical model of the damper was created. Damper was described multidimensional static characteristic. It is two dimensional function of damping force that depends on velocity and actuating current. This function is nonlinear. Entire range is divided into several sections. Identification consists in finding polynomial functions at borders of each interval

$$A(\dot{x}) = a_r \dot{x}^r + \dots + a_2 \dot{x}^2 + a_1 \dot{x} + a_0 \quad (2)$$

where  $\dot{x}$  means velocity and  $a_i$  mean found coefficients.

Next translation of coordinates was used

$$b_n = \sum_{i=0}^{N-n} a_{n+i} \binom{n+i}{i} (-1)^i x_0^i \quad (3)$$

where  $b_i$  mean new coefficients and  $a_i$  mean original coefficients in Eq. (2).

Next it is necessary to find two-dimensional function passing through these border conditions.

$$F = c_{2n+1} \dot{x}^n I + c_{2n} \dot{x}^n + \dots + c_5 \dot{x}^2 I + c_4 \dot{x}^2 + c_3 \dot{x} I + c_2 \dot{x} + c_1 I + c_0 \quad (4)$$

where  $\dot{x}$  is velocity and  $I$  is actuating current.

Identified function is in Fig. 4.

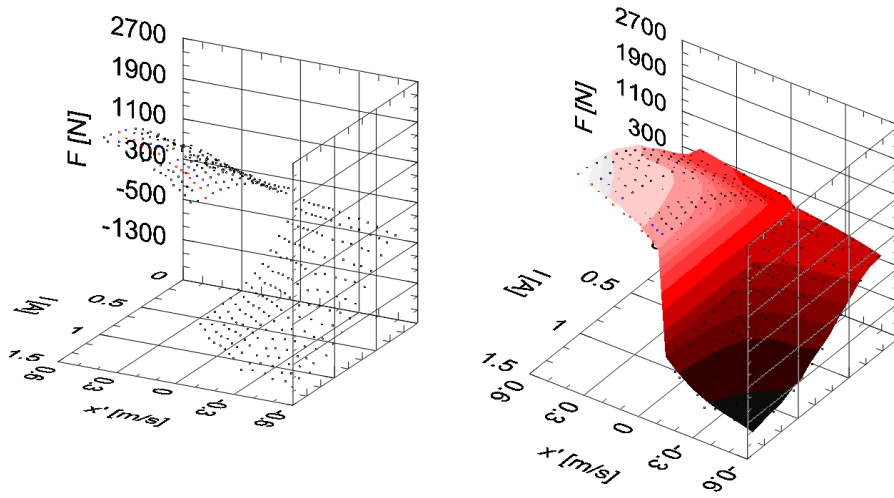


Fig. 4: Static characteristic of magnetorheological damper.

Next it was necessary to identify dynamical properties of damper. That means its transfer function of velocity and transfer function of actuating current. Complex model of damper is in Fig. 5.

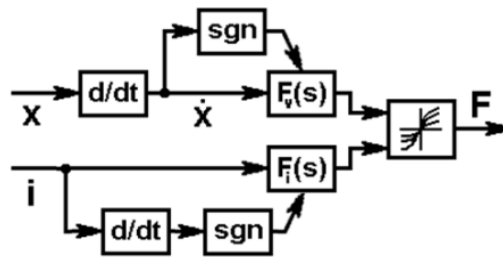


Fig. 5: Model of magnetorheological damper.

Control circuit of magnetorheological damper is in Fig. 6. It is a quasistationary control of actuating current. Frequency analysis of the excitation signal is performed every 5 s, Fig. 7.

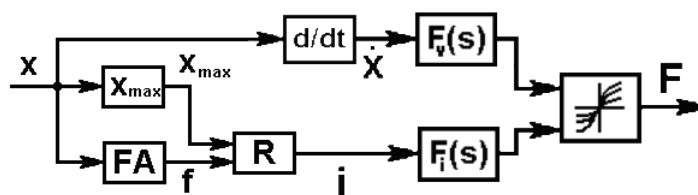


Fig. 6: Model of magnetorheological damper.



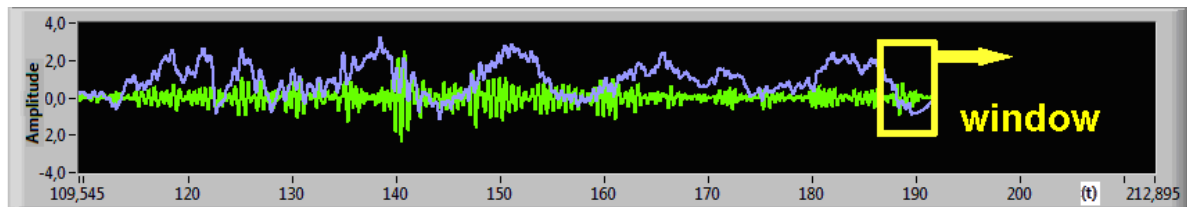


Fig. 7: Frequency analysis of excitation signal using Hanning window.

Controller R sets actuating current of magnetorheological damper every 5 s according to maximum amplitude and dominant frequency of excitation signal.

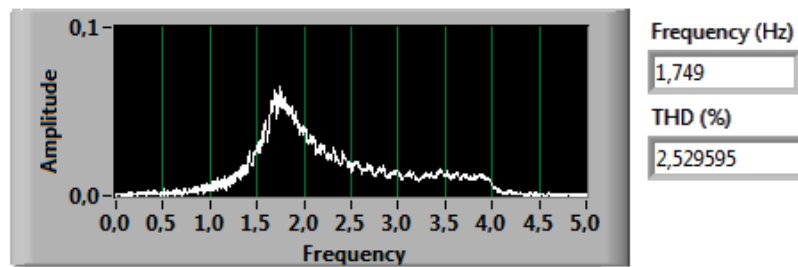


Fig. 8: Frequency analysis.

#### 4. Conclusions

The prototype with control system of stabilized platform with gyroscopes was designed and realized. Its mathematical model was created and used for optimization of controller parameters. Simulation results were verified on real prototype. For technical reasons it was not possible to achieve the required speed gyroscopes 30000 rpm, but only 12000 rpm. Increasing speed of gyroscopes will cause their stabilizing effect even higher. System was improved with active damping system with magnetorheological damper. Damping force was controlled with frequency analysis algorithm.

#### Acknowledgement

The research has been supported by project SGS 21130 "Research and development in the field of 3D technology, manufacturing systems and automation".

#### References

- Votrubec, R. (2011) Control of Active Sanitary Coach, Annals of DAAAM for 2011 & Proc. of the 22nd Int. DAAAM Symposium, Vienna, Austria, Vol. 22, No. 1, ISBN 978-3-901509-83-4, ISSN 1726-9679, (ed. Katalinic, B.), pp. 617-618, Published by DAAAM International Vienna.
- Votrubec, R. (2009) Identification of Magnetorheological Damper, Annals of DAAAM for 2009 & Proc. of the 20th International DAAAM Symposium, Vienna, Austria, ISBN 978-3-901509-70-4, ISSN 1726-9679, (ed. Katalinic, B.), pp. 1791-1792, Published by DAAAM International Vienna.
- Skliba, J. (2007) About a possibility of a gyroscopic stabilisation of the vibroisolation system. National Conference with International Participation Engineering Mechanics 2007, in Proc. of Int. Conf. Engineering Mechanics 2007. Svatka, pp.275-276.
- Sivcák, M. and Skoda, J. (2010) Radial correction controllers of gyroscopic stabilizer. Journal of Vibroengineering Vol. 12, Iss. 3, pp. 300-304.
- Simek, J., Skliba, J., Sivcak, M. and Skoda, J. (2011) Power gyroscopes of stabilizing system. Engineering Mechanics, Vol. 18, No. 3/4, pp. 259-267.
- Simek, J. (2011) Application of a new type of aerodynamic tilting pad journal bearing in power gyroscope, Colloquium Dynamics of Machines 2012, Prague, pp. 130-136.
- Votrubec, R. and Sivcak, M. (2010) The Correction and Compensation Motors for the Gyroscopic Stabilizer, Mechatronic Systems and Materials, Diffusion and Defect Data - Solid State Phenomena, Vol. 164.
- Skliba, J. and Sivcak, M. (2008) Some Problems of the Application of Tandem of Opposite Running Gyroscopes. X. International Conference on the Theory of Machines and Mechanisms Proceedings, pp. 601-606.

## SIMPLIFIED OSCILLATORY BOUNDARY CONDITION FOR EFFICIENT CFD SIMULATION OF AFC EFFECT

P. Vrchota\*, A. Prachař\*\*, P. Hospodář\*\*\*, D. Dolgopyat\*\*\*\*, A. Seifert\*\*\*\*\*

**Abstract:** CFD simulations of the Active Flow Control (AFC) effect are usually highly time consuming and require extensive computational resources and effort. These aspects almost exclude the simulation of actuator arrays and disables AFC in the design process. This study is focused on the development of the simplified surface boundary condition of the actuator's effect on the flow field and to enable to significant reduction of the computational resources. The simplified boundary condition is based on the high-fidelity unsteady CFD simulations of the Suction and Oscillatory Blowing (SaOB) actuator in still air and takes into account the flow field variables at the actuator's exit.

**Keywords:** Active Flow Control, CFD, Suction and Oscillatory Blowing actuator, boundary condition.

### 1. Introduction

The Active Flow Control (AFC) techniques are still regarded as a key evolution, offering new solutions for the performance maximization of existing designs. In the last decades it becomes very popular to control the flow in many aeronautical, transport and industrial applications. CFD simulations of AFC is still very challenging mainly due to the high complexity of the actuators themselves requiring very complex computational grids and also from the aerodynamic and turbulence modeling point of views. Some efforts have been done by Chow (1993), Galbraith (2006) and Vrchota (2012) to simulate the effect of AFC by surface boundary condition applying uniform flow field on it. Throshin (2014) used a Proper Orthogonal Decomposition to create reduced order model of the actuator's effect on the flow field. Lakebrink (2017) in his paper has found that it is necessary to model also the actuators' geometry or part of it at least, to enable the development of the velocity profile inside these cavities to obtain more realistic flow field at the actuator's exit. But on the other hand the embedded actuators or cavities increase the workload during the grid creation process and also make the CFD simulations more time consuming from higher number of cells point of view, especially if arrays of actuators are used. Shatzman et.al. (2015) in their paper defined the functional representation for the nozzles' oscillatory velocity profiles, which can be used as boundary conditions for a complex AFC simulation by CFD. It matched the measured velocity profile at the nozzle's exit quite well, on the other hand this representation is only 2D.

The developed boundary condition described in this paper is based on the high-fidelity CFD simulations of the internal flow field of the Suction and Oscillatory Blowing actuator developed by Arwatz (2008).

### 2. SaOB actuator

Oscillatory blowing is an effective tool to delay boundary-layer separation. The general idea of oscillatory blowing actuators is the use of periodic blowing through a narrow spanwise slot or array of holes to enhance shear-layer mixing and transfer high momentum fluid from outside the shear layer to the wall region and thus prevent boundary-layer separation. The SaOB actuator combines steady suction and

---

\* Ing. Petr Vrchota, PhD.: Vyzkumný a zkušební letecký ústav, a.s., Beranových 130; 199 05, Prague; CZ, vrchota@vzlu.cz

\*\* RNDr. Aleš Prachař, PhD.: Vyzkumný a zkušební letecký ústav, a.s., Beranových 130; 199 05, Prague; CZ, prachar@vzlu.cz

\*\*\* Ing. Pavel Hospodář.: Vyzkumný a zkušební letecký ústav, a.s., Beranových 130; 199 05, Prague; CZ, hospodar@vzlu.cz

\*\*\*\* Danny Dolgopyat, MSc.: Tel Aviv University, 69978 Tel Aviv, Israel, dannydol@gmail.com

\*\*\*\*\* Prof. Avraham Seifert, PhD.: Tel Aviv University, 69978 Tel Aviv, Israel, seifert@eng.tau.ac.il

oscillatory blowing, both proven to be very effective AFC tools. The actuator is a combination of an ejector and a bistable fluidic amplifier (see Fig. 1). The ejector (Fig. 1a) is a simple fluidic device based on Bernoulli's law. When a jet stream is ejected into a bigger conduit, it creates a low-pressure region around it due to entrainment. The cavity behind the jet is open to the free atmosphere or to a lower-pressure environment (such as the upper surface of an airfoil). As a result, the pressure gradient around the internal jet will cause the external air to be sucked into the cavity. More detail description of SaOB actuator and its principle can be found in Arwatz's paper (2008).

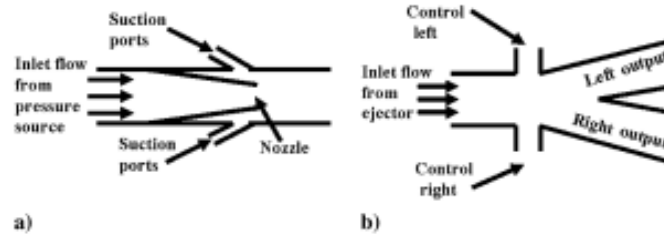


Fig. 1: Schematic rendering of the SaOB actuator: a) ejector; b) switching valve (Dolgopyat, 2014).

### 3. CFD simulations of SaOB actuator

The CFD simulations of the SaOB focusing on the internal flow field and on the flow at the nozzle exit have been done on isolated single SaOB actuator. These simulations corresponded to the bench top test of the SaOB in laboratory conditions without any cross flow done by Dolgopyat (2014). The main aim of this study was to obtain the time dependent flow field variables at the nozzle exit for different supply pressures.

#### 3.1. Model's geometry

A single SaOB actuator has been used to obtain the all needed information for development of the simplified boundary condition. It is depicted in Fig. 2. The effect of the neighbouring actuators was simulated by periodic boundary conditions. These conditions were connected to the sides of the box where the suction holes are located. The boundary, where the different supply pressures were adjusted, was weak characteristic type with defined values of the pressure and temperature. The same boundary condition was used to define the suction rate through holes with prescribed ambient pressure corresponded to the pressure in the laboratory.

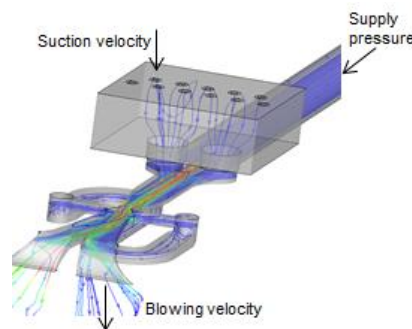


Fig. 2: Geometry of SaOB actuator used for CFD simulations.

#### 3.2. Grid generation and flow solver

The internal grid of the SaOB actuator and the computation domain was created in Pointwise grid generation software. The grid was hybrid unstructured with a first cell height at  $y^+ 0.7$ . The grid inside the actuator has approximately 5.5 million grid points.

All simulations were carried out by means of URANS approach by an in-house CFD solver. It uses the finite volume technique to solve the governing flow equations with the EARSM  $k-\omega$  turbulence model.

#### 3.3. Verification by experimental data

The data obtained from the bench top test in the Meadow Aerodynamics Laboratory at Tel Aviv University have been used to verify the CFD results. The peak blowing velocity along the streamwise and

spanwise direction at the actuator's nozzle exit has been extracted from the simulations in order to compare its value with the experimental data (see Fig. 3). The Fast Fourier Transformation (FFT) technique was used to obtain the oscillation frequency of the flow. The comparisons of the peak blowing velocity and oscillation frequency depending on the supply pressure from the simulations and experiments are depicted in Fig. 4. Very good match of the CFD results with experimental data have been reached.

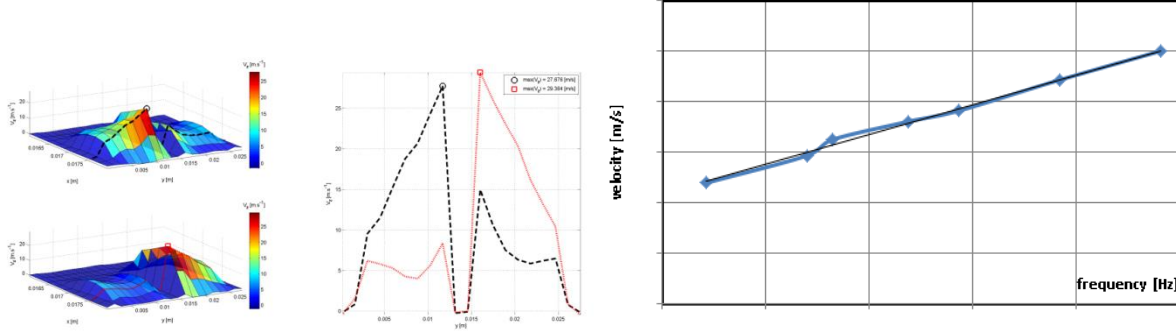


Fig. 3: Determination of the peak velocity from the surface interpolation of the velocity vector at the nozzle's exits.

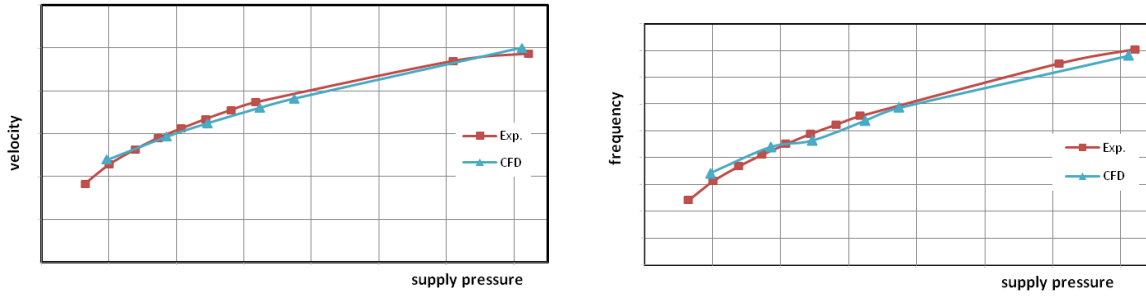


Fig. 4: Dependence of the blowing velocity and oscillation frequency on supply pressure compared with experimental data.

#### 4. Simplified oscillatory boundary condition

The time dependent flow field variables at the actuator's exit including the frequency of the flow oscillation corresponding to the different supply pressure into the SaOB actuator have been extracted from the CFD simulations and they have been approximated by the sum of the two-dimensional Gaussian function. Example of the Gaussian function for the vertical velocity component is described by Eq. (1).

$$V_{z(x,y,z)}^* = \sum_{i=1}^N A_i \cdot e^{-\left( \frac{(x-x_i)^2}{2\sigma_{xi}^2} + \frac{(y-y_i)^2}{2\sigma_{yi}^2} \right)} \cdot (\sin(2\pi f t + \varphi_i) + c_i) \quad (1)$$

Gaussian itself is defined by the five parameters ( $A_i$ ,  $x_i$ ,  $y_i$ ,  $\sigma_{xi}^2$ ,  $\sigma_{yi}^2$ ) and the character of the oscillations is described by the sine function specified by additional three parameters (oscillation frequency, phase shift and mean value). The comparison between the calculated and approximate velocity at the nozzle's exit together with the estimated error is depicted in Fig. 5. The difference between the CFD and approximated data is very small and can be neglected at this stage of the development process.

#### 5. Conclusion

The time-dependent simplified boundary condition of the SaOB actuator in still air condition has been developed and verified for different supply pressures at the inlet of the actuator. A linear dependency of the oscillation frequency on blowing velocity has been achieved. Applying this simplified boundary condition will reduce complexity of the problem by omitting the meshing of the actuator's geometry to simulate the internal flow field and hence to save the computational resources and time. The level of complexity reduction is possible to see in Fig. 6. The whole internal geometry is omitted and replaced by

the boundary condition with defined time dependent variables on it. This simplified boundary condition will enable the efficient simulations of the actuator arrays used in low-speed and high-speed engineering applications and also include the AFC technique directly into the design process.

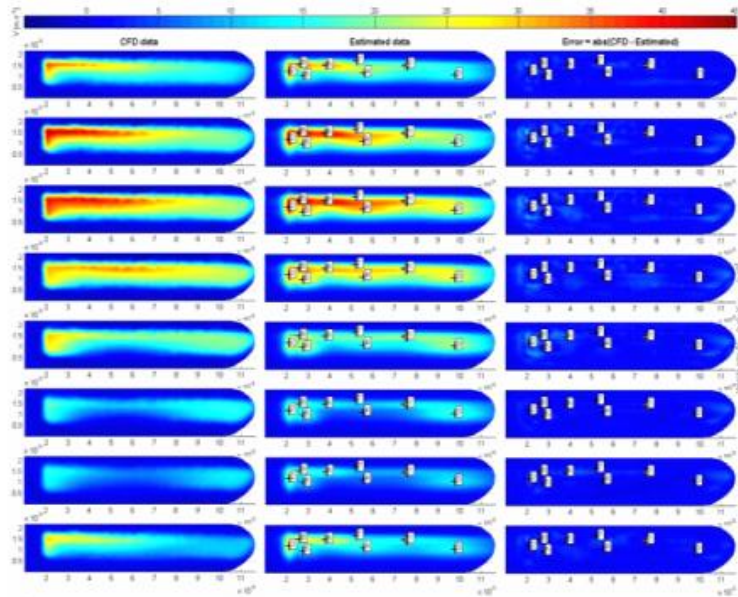


Fig. 5: Comparison of calculated and approximated vertical velocity component.

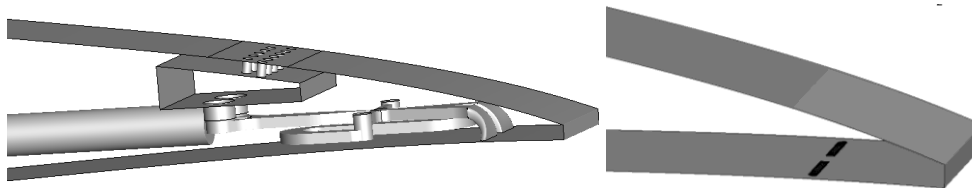


Fig. 6: Level of complexity reduction by applying boundary condition.

## Acknowledgements

Access to computing and storage facilities owned by parties and projects contributing to the National Grid Infrastructure MetaCentrum, provided under the program "Projects of Large Infrastructure for Research, Development, and Innovations" (LM2010005), is greatly appreciated.

This work was supported by The Ministry of Education, Youth and Sports from the Large Infrastructures for Research, Experimental Development and Innovations project IT4Innovations National Supercomputing Center LM2015070.

## References

- Chow, R., Chu, K. and Carpenter, G. (1993) Navier-Stokes Simulation of the Flow Field Around a Blown-Flap High-Lift System, AGARD-CP-515, September 1993, Paper 15.
- Galbraith, M.C. (2006) Numerical Simulation of a High-Lift Airfoil Employing Active Flow Control, AIAA 2006-147.
- Vrchota, P. and Hospodář, P. (2012) Response Surface Method Application to High-Lift Configuration with Active Flow Control," Journal of Aircraft, Vol. 49, No. 6, 2012, pp. 1796-1802.
- Lakebrink, M.T., Mani, M., and Winkler, Ch. (2017) Numerical Investigation of Fluidic Oscillator Flow Control in an S-Duct Diffuser, 55th AIAA Aerospace Sciences Meeting, Grapevine, Texas, (AIAA 2017-1455).
- Schatzman, D.M., Wilson, J., Maron, L., Palei, V., Seifert, A. and Arad, E. (2015) Suction and Oscillatory Blowing Interaction with Boundary Layers, 53rd AIAA Aerospace Sciences Meeting, AIAA SciTech Forum, (AIAA 2015-0808).
- Arwatz, G., Fono, I. and Seifert, A. (2008) Suction and Oscillatory Blowing Actuator Modeling and Validation, AIAA Journal, Vol. 46, No. 5 (2008), pp. 1107-1117.
- Dolgopyat, D. (2014) On the Feasibility of Hinge-less Flow Control Manoeuvring System, Master thesis, Tel Aviv University, Israel.



## TESTING THE STRENGTH OF THE ADHESIVE CONNECTION IN SPECIMEN - MONOTONIC TENSILE AND SHEAR WITH UNDER VARIABLE LOAD

M. Wirwicki<sup>\*</sup>, M. Andryszczyk<sup>\*\*</sup>, A. Andrzejewska<sup>\*\*\*</sup>, T. Topoliński<sup>\*\*\*\*</sup>

**Abstract:** Ceramic implants can create original terms of occlusion in mouth. The results obtained for zirconium dioxide as the ceramic material used in implantology. Describes the technology of the blank (trabecular) and research glued connection of two trabecular zirconia 3M ESPE LAVA with batch number:508150. Performed with the help of two different dental adhesive properties glue named: 3M ESPE RelyX and Kerr Maxcem Elite. Monotonic tensile tests were carried out for two groups of 15 samples and the shear tests were adopted one group of 11 samples. The results obtained are characterized by high reproducibility in the sample geometry made of zirconia, as confirmed by the p Shapiro-Wilk test ( $p = 0.06$ ). It showed no statistical differences in an attempt to monotonic tensile Student's t test ( $p = 0.608$ ).

**Keywords:** Zirconium dioxide, Static stretching tests, Adhesive, Dentistry.

### 1. Introduction

Zirconium dioxide has versatile applications. It is used as a heavy-duty material in engineering but also in dentistry: for production of implants designed to restore the original occlusion of teeth after a major damage to, or loss of, the tooth crown. Featuring very good mechanical strength and hardness, this zirconium dioxide continues to replace conventional materials providing similar performance, such as gold alloys (Rizkalla, 2004; Guazzato, 2004; Yilmaz, 2007 and Manicone, 2007). Both these materials have good biocompatibility but the advantage of zirconium dioxide over other materials is its natural bony colour. The present production of very sophisticated dentures, such as 6-point full-ceramic bridges, is possible only due to excellent strength of the materials involved: up to 1200 MPa. (Raigrodski, 2006; Edelhoff, 2008). Today, suppliers of dental materials offer hybrid (multi-component) self-adhesive cements featuring better strength than unary adhesives (Watanabe, 1994).

The purpose of the work was to compare two types of adhesives featuring the same adhesive properties, one much more expensive than the other. An additional aim was to show differences between bonds and between denture materials in terms of their mechanical properties.

### 2. Methods

#### 2.1. Zirconium dioxide

The ceramic material we tested was 3M Zirconium Lava commonly used for production of crowns and bridges (designed using CAD/CAM software). The advantages of the material include good strength, very natural appearance, translucency, biocompatibility and absence of metals in its structure.

---

<sup>\*</sup> PhD. (Eng.) Mateusz Wirwicki: Faculty of Mechanical Engineering, UTP University of Sciences and Technology in Bydgoszcz, Al. Prof. S. Kaliskiego 7; 85- 796, Bydgoszcz; PL, Mateusz.Wirwicki@utp.edu.pl

<sup>\*\*</sup> M.Sc. (Eng.) Marek Andryszczyk: Faculty of Mechanical Engineering, UTP University of Sciences and Technology in Bydgoszcz, Al. Prof. S. Kaliskiego 7; 85- 796, Bydgoszcz; PL, Marek.Andryszczyk@utp.edu.pl

<sup>\*\*\*</sup> M.Sc. (Eng.) Angela Andrzejewska: Faculty of Mechanical Engineering, UTP University of Sciences and Technology in Bydgoszcz, Al. Prof. S. Kaliskiego 7; 85- 796, Bydgoszcz; PL, Angela.Andrzejewska@utp.edu.pl

<sup>\*\*\*\*</sup> Prof. Tomasz Topoliński: Faculty of Mechanical Engineering, UTP University of Sciences and Technology in Bydgoszcz, Al. Prof. S. Kaliskiego 7; 85- 796, Bydgoszcz; PL, Tomasz.Topolinski@utp.edu.pl



We cut the material supplied by the manufacturer nominal dimensions 25 mm x 16 mm x 90 mm and batch number: 508150. He was cutted with a circular saw (Isomet 5000 from Buehler, Poland) into 25 x 16 x 1.87 mm blocks. Cutting material was cooled with distilled water. Then, we cut each block into 9 blanks sized 1.87 x 1.87 x 15 mm with a laser cutter (Alfalas WS, Poland). The beam power settings protected the material against overheating. See Fig. 1 for the blank cutting design before sintering.

Next step was sending the blanks (trabeculae) to a manufacturer-certified laboratory for sintering. This process was performed on a device called The Lava Furnace 200 [POLAND]. The samples were sintered at 1400 °C for 8 hours, which caused material volume shrinkage by 20 %, on average (according to the material manufacturer). After sintering, the material is snow-white, much harder and more resistant to 3-point bending. See Fig. 1b for the geometry of the blanks after sintering, now measuring 1.5 x 1.5 x 12 mm.

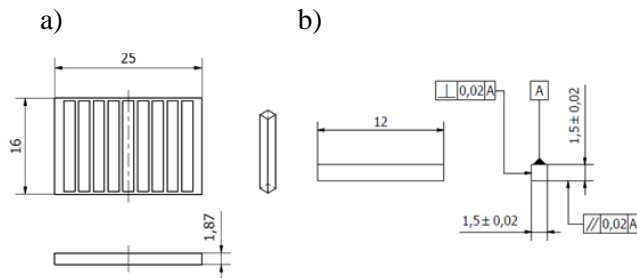


Fig. 1: a) Blank cutting; b) Blank geometry and dimensions.

## 2.2. Tested adhesives

We tested the strength of bond provided by two adhesives: 3M ESPE RelyX U200 Automix with batch number: 56895 and Kerr Maxcem Elite with batch number: 34055. Adhesives used were characterized by similar: consistency of the product and similar aesthetic properties of adhesive connection, which formed. These adhesives are used in partner dental clinics. The former is a latest generation self-adhesive cement. The adhesives are hardened after application between two surfaces with 420 – 480 nm UV light. We used the Satelec Mini Led Black UV light with 1.250 mW/cm<sup>2</sup> power. The exposure time was 10 seconds in each instance.

In Tab. 1 shown summary of the study provided the monotonic tensile strength, shear fatigue test and the shear strength.

Tab. 1: Summary of the research strength of the joint adhesive.

Tests name	Number of specimen	Group name	Dental adhesive	Glue data
Monotonic tensile strength testing	15	A1	3M ESPE RelyX	Made in Germany by 3M ESPE AG Seefeld
	15	A2	Kerr MaxCem Elite	Made in Italy by Kerr Italia S.r.l. Scafati

## 2.3. Strength of bond

We tested the tensile strength of the bond on the blanks prepared beforehand (zirconium dioxide trabeculae). Each blank was bonded to two custom-made stainless steel plates using a pre-made special device for axially bonding the zirconia samples.

First, the samples were subjected to a degreasing formulation Emulsol RN-1. Then glued 15 samples adhesive 3M ESPE RelyX U200 Automix (A1) and 15 samples of adhesive Kerr ^ maxc Elite (A2). Using a previously described UV lamp company Satelec Mini LED Black. The exposure process lasted 10 seconds. The last step was the mechanical removal of excess adhesive dental device Dremel 200 of the grinding wheel spindle alumina.

Before each test, we checked each sample for bond quality under a stereoscopic microscope (OPTA-Tech MN-800). The thickness of the bond was  $0.05 \pm 0.002$  mm. See Fig. 3 for the design of the bonded sample.

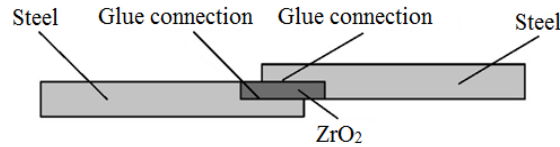


Fig. 2: Test sample cross-section.

### 3. Results and analysis

Compared their pattern to the normal distribution with the Shapiro-Wilk test, compared the bond strengths using the t Student test for independent variables. The statistical comparisons relied on the critical value of  $p < 0.05$  for checking whether the variation of the results was statistically significant. We measured the samples to ensure that they were uniform, i.e., to exclude bonding area variability as a possible influence on the bond strength. The distribution of the dimension values was statistically significantly similar to the normal distribution, which we verified using the Shapiro-Wilk test (Tab. 2).

Tab. 2: Descriptive statistics of sample dimensions and Shapiro-Wilk test results.

	Mean	SD	Relative SD [%]	Value p
Mean x [mm]	1.47	0.02	1.51	0.819
Mean y [mm]	1.47	0.02	1.54	0.304
Cross-section area $A_0$ [mm <sup>2</sup> ]	2.16	0.06	2.58	0.06

In Tab. 3 the tensile strengths of the bonds formed by the two adhesives. The mean destructive forces were 63.5 N for RelyX and 66.8 N for Maxcem, with the mean stress of approx. 7 MPa for the two adhesives. The results were widely scattered for the both adhesives: up to 15.9 % and 27.9 %, respectively. Results distribution destructive force as the minimum and maximum waveforms and standard deviation values obtained from the samples tested. Fig. 3 presented Values course force in three point bending test.

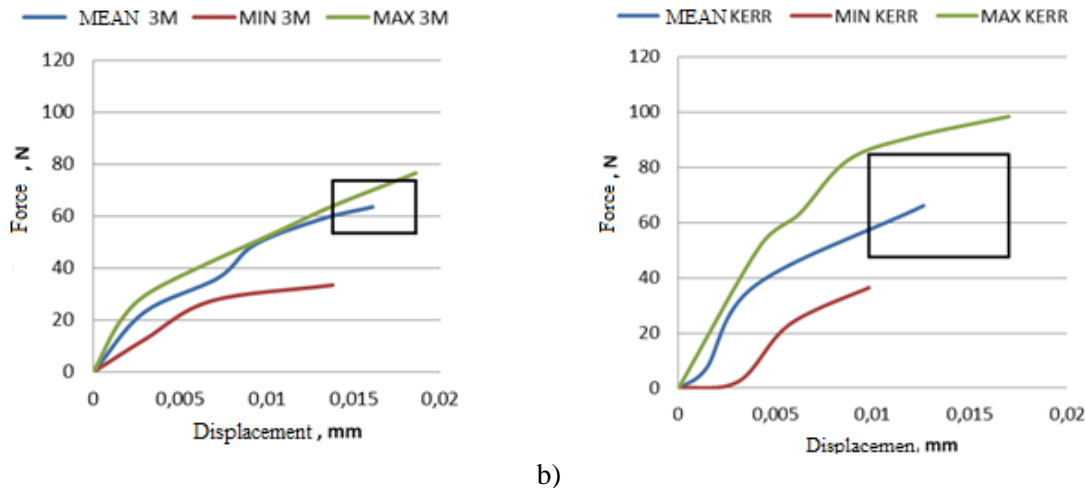


Fig. 3: Values course force max, min, average, along with a distribution that for:  
a) 3M ESPE, b) Kerr Maxcem Elite.

Tab. 3: Test results for bonds formed by 3M ESPE RelyX U200 and Kerr Maxcem Elite.

Adhesive	Bonded area [mm <sup>2</sup> ]	Mean force [N]	Mean stress [MPa]	SD [N]	Relative SD [%]
3M ESPE RelyX U200	9	63.5	7.05	10.1	15.9
Kerr Maxcem Elite	9	66.8	7.42	18.6	27.9

We checked the results statistically, with the Shapiro-Wilk test, for similarity to the standard distribution, and the results indicated that the distribution was indeed standard (see Tab. 4). The t Student test of the mean results achieved during the test did not reveal any statistically significant differences between the

tensile strengths of, or stresses in, the bond between the blanks. Statistics for bonds formed by 3M ESPE RelyX U200 and Kerr Maxcem Elite

*Tab. 1: Results statistically, with the Shapiro-Wilk and t-Student tests.*

Adhesive	Shapiro-Wilk test critical value	Shapiro-Wilk test p value	t Student test critical value	t Student test p Value
3M ESPE RelyX U200	0.910	0.248	-0.520	0.608
Kerr Maxcem Elite	0.939	0.518		

#### 4. Discussion

Authors managed to obtain repeatable geometry of the blanks with the coefficient of variability of approx. 1.5 % for dimensions “x” and “y” (see Tab. 1). Next, our material processing method provided low variability of the bonding result and consistent bonding area. The typical methods of blank processing by researchers included cutting with diamond saw blade disks or machining. The mean monotonic tensile strengths of the two self-adhesive cements of the same generation that we tested were  $63.5 \pm 10.1$  N for 3M ESPE RelyX U200 and  $66.8 \pm 18.6$  N for Kerr Maxcem Elite. Our statistical review of the strengths did not reveal any significant differences between the adhesives ( $p = 0.608$  for the t Student test). The strengths of the bonds had a 15.9 % scatter for the former adhesive and 27.9 % scatter for the latter one. Static stretch tests of the adhesive bond similar to ours, are described in paper (Poitevin, 2010). Its authors cut out trabeculae with transverse section area of 1 x 1 mm from natural teeth topped with all-ceramic crowns bonded with three adhesives. The bond strengths of the three tested adhesives were as follows:  $51 \pm 17.6$  N for OptiBond FL,  $43.7 \pm 14.3$  N for Clearfil SE and  $28 \pm 15.3$  N for G-Bond. The coefficients of variability were 34.5 %, 32.7 % and 54.6 %, respectively. The scatter in these results is much wider than the scatter described in this paper.

#### 5. Conclusion

The methods described in the references were strongly varied in terms of sample preparation, which is problematic from the point of view of comparability of the results. Another important factors that can possibly bear on the results are the size of adhesive squeeze-out (extra bonding area) and preparation of surface (which should be clean, degreased and free from foreign matter or oxidation). Our monotonic tensile strength test method has no matching equivalent in the existing sources. We recommend undertaking further research into the monotonic stretch of the adhesive bond to identify other possible factors affecting the denture lifetime and to minimize implant visual flaws and rework rates.

#### References

- Edelhoff, D., Florian, B., Florian, W. and Johnen, C. (2008) HIP zirconia fixed partial dentures--clinical results after 3 years of clinical service., Vol. 39, No. 6, pp. 459-471.
- Guazzato, M., Albakry, M., Ringer, S.P. and Swain, M.V. (2004) Strength, fracture toughness and microstructure of a selection of all-ceramic materials. Part II. Zirconia-based dental ceramics, Dent. Mater. Vol. 20, No. 5, pp. 449-456.
- Manicone, P.F., Rossi Iommetti, P. and Raffaelli, L. (2007) An overview of zirconia ceramics: Basic properties and clinical applications, Journal of Dentistry, Vol. 35, No. 11. pp. 819-826.
- Poitevin, A., De Munck, J., Cardoso, M.V., Mine, A., Peumans, M., Lambrechts, P. and Van Meerbeek, B. (2010) Dynamic versus static bond-strength testing of adhesive interfaces, Dent. Mater., Vol. 26, No. 11, pp. 1068-1076.
- Rizkalla, A.S., and Jones, D.W. (2004) Mechanical properties of commercial high strength ceramic core materials, Dent. Mater., Vol. 20, No. 2, pp. 207-212.
- Raigrodski, A.J., Chiche, G.J., Potiket, N., Hochstedler, J.L., Mohamed, S.E., Billiot, S. and Mercante, D.E. (2006) The efficacy of posterior three-unit zirconium-oxide-based ceramic fixed partial dental prostheses: A prospective clinical pilot study, J. Prosthet. Dent., Vol. 96, No. 4, pp. 237-244.
- Yilmaz, H., Aydin, C. and Gul, B.E. (2007) Flexural strength and fracture toughness of dental core ceramics, J. Prosthet. Dent., Vol. 98, No. 2, pp. 120-128.
- Watanabe, I. and Nakabayashi, N. (1994) Measurement methods for adhesion to dentine: the current status in Japan, J. Dent., Vol. 22, No. 2, pp. 67-72.

## VARIANTS OF UPPER LIMB MOTION INDEX CALCULATIONS IN THE ASSESSMENT OF UPPER LIMB MOTION DYSFUNCTION

P. Wodarski<sup>\*</sup>, R. Michnik<sup>\*\*</sup>, M. Gzik<sup>\*\*\*</sup>, J. Jurkojc<sup>\*\*\*\*</sup>, A. Bieniek<sup>\*\*\*\*\*</sup>, K. Nowakowska<sup>\*\*\*\*\*</sup>

**Abstract:** *The use of objective human diagnostics methods when identifying motion dysfunctions often comes down to the use of various types of scales or indexes facilitating the analysis of large amounts of kinematic data recorded during the performance of movements. An example of an index dedicated for assessing upper limb motion dysfunction can be the ULMDI (Upper Limb Motion Deviation Index) referred to in this study. The research aimed to identify the effect of different UMLDI variants, allowing for various numbers of repeated upper limb movements as well as with and without consideration of mobility measurements related to the sternoclavicular joint, on the obtained index values. The research also involved the assessment of motion dysfunction (based on different ULMDI calculation variants) related to individual patients and comparing it with the assessment performed by the physiotherapist. The research-related tests involved 23 healthy subjects constituting the reference group and 3 patients for whom different ULMDI variants were calculated. The analyses resulted in the determination of the effect of various quantities taken into consideration when calculating the above-named index on the value of the ULMDI in relation to patients subjected to the tests.*

**Keywords:** ULMDI, Upper limb dysfunction, Indexes, Diagnosis.

### 1. Introduction

The use of objective human diagnostics methods when identifying motion dysfunctions often comes down to the use of various types of scales or indexes. The use of related scales makes it possible to classify patients of various disability levels in groups characterized by similar motor abilities (Gzik, 2016). As regards the assessment of upper limb motor dysfunction it is possible to distinguish indexes enabling the quantitative comparison of the shapes of anatomic angle courses in joints in relation to specific activities and in relation to patients with courses determined on the basis of the motoric model based on healthy individuals. An exemplary index could be the RMS (Root Mean Square distance) used in tests (Jaspers, 2011) and (Butler, 2012), which, in a quantitative manner, identifies the area between the patient-related course and the model course. It is also possible to use the PULMI (Paediatric Upper Limb Motion Index) (Butler, 2012) expressing, in a numerical manner, the mean “distance” between the course of angular quantities in joints in relation to patients and the identified motion model referred to the standard deviation of the entire study group. When applying the PULMI it seems justified to use the supplementary SDDI (Standard Deviation of Differential Index), the algorithm of which is based on the same measured quantities as the PULMI, yet it enables the identification of other features of angular

---

<sup>\*</sup> Piotr Wodarski PhD. Eng: Department of Biomechatronics, Faculty of Biomedical Engineering, Silesian University of Technology; Poland, piotr.wodarski@polsl.pl

<sup>\*\*</sup> Robert Michnik PhD. DSc. Eng: Department of Biomechatronics, Faculty of Biomedical Engineering, Silesian University of Technology; Poland, robert.michnik@polsl.pl

<sup>\*\*\*</sup> Prof. Marek Gzik, Professor PhD DSc. Eng.: Department of Biomechatronics, Faculty of Biomedical Engineering, Silesian University of Technology; Poland, marek.gzik@polsl.pl

<sup>\*\*\*\*</sup> Jacek Jurkojc PhD. Eng: Department of Biomechatronics, Faculty of Biomedical Engineering, Silesian University of Technology; Poland, jacek.jurkojc@polsl.pl

<sup>\*\*\*\*\*</sup> Andrzej Bieniek MSc. Eng: Department of Biomechatronics, Faculty of Biomedical Engineering, Silesian University of Technology; Poland, andrzej.bieniek@polsl.pl

<sup>\*\*\*\*\*</sup> Katarzyna Nowakowska MSc. Eng: Department of Biomechatronics, Faculty of Biomedical Engineering, Silesian University of Technology; Poland, katarzyna.nowakowska@polsl.pl

courses. The above-named index supplements the PULMI by assessing the manner of motion performance.

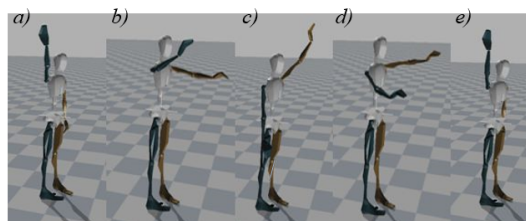
Measured kinematic quantities, i.e. the time values of anatomical angles in the upper limb joints, constitute the basis of the ULMDI (Upper Limb Motion Deviation Index) (Jurkojc, 2017) developed for the purposes of previously performed tests. The ULMDI algorithm comes from the algorithm of calculations enabling the biometric identification of faces on the basis of the SVD matrix distribution. The above-named algorithm is also used in gait analysis when calculating the GDI (Schwartz, 2008) using 9 courses of kinematic quantities in time to identify the patient's level of disability. On the basis of calculations of kinematic quantities used in the algorithm, including, the number of group members and the number of repetitions performed by individual persons, it is possible to take into consideration different ULMDI variants. The question which arises is whether, similar to the GDI, the algorithm of the ULMDI calculations should include 9 courses of kinematic quantities which, in relation to the upper limb, could constitute the time values of anatomic angles in the sternoclavicular, carpal, cubital and humeral joint, or whether, similar to the PULMI, should include fewer of the above-presented courses. In the case under consideration it is also worth considering how much the values of the ULMDI will change without taking into consideration the trunk mobility in the area of the sternoclavicular joint.

The research-related tests aimed to determine the effect of the different variants of the UMLDI taking into account the number of repetitions of movements performed by the upper limb as well as taking and not taking into account mobility measurements in the sternoclavicular joint area on the obtained index values. The subsequent stage also involved the assessment of motion dysfunction (based on different ULMDI calculation variants) related to individual patients and comparing it with the assessment performed by the physiotherapist.

## 2. Methods

**Participants:** The tests involved 23 healthy individuals (10 females and 13 males (aged 23.35 SD 1.37)) and 3 patients with motion dysfunctions in the area of upper limbs (aged p1:17, p2:15, p3:41). The motion dysfunction of patient p1 included damage to peripheral nerves in the left limb through mechanical trauma. The patient had difficulty performing movements in the area of the left cubital and carpal joint. The motion dysfunction of patient p2 included motion anomalies in the area of both limbs; the patient suffered from the spasticity of both limbs caused by infantile cerebral palsy. Patient p3 suffered from damage to the upper part of the brachial plexus responsible for difficulty in moving the left limb.

**Selected pattern motions:** The patients performed a motion sequence related to the tasks of gross graphomotor ability performed within daily clinical therapy. The motion sequence consisted in lifting the upper limbs and lowering them in the manner presented in Fig. 1. The sequence started with position a) followed by the movement to position c) followed by a short pause, after which the movement from position c) reached position e).



*Fig. 1. Motion sequence.*

**Data collection:** The collection of kinematic data included the recording of three repetitions of performed actions using the motion analysis systems provided with the MVNBioMech inert sensors manufactured by Xsens. The collected data included the course of anatomic angle values in the sternoclavicular, humeral, cubital and carpal joints.

**Calculations:** The quantities recorded during the tests were uploaded to the Matlab software programme for further analysis. The algorithm discussed in the publication by Jurkojc (2017) was used to calculate the values of the ULMDI in relation to the entire motion (from position a to position e). The primary version input data included the following 9 kinematic quantities recorded in the upper limb area:



- flexion/ extension of the upper section of the trunk around the sternoclavicular joint,
- the rotation of the upper section of the trunk around the sternoclavicular joint,
- abduction / adduction at the glenohumeral joint,
- rotation in the glenohumeral joint,
- flexion/ extension the glenohumeral joint,
- pronation / supination of the elbow joint,
- flexion/ extension of the elbow joint,
- elbow adduction / radial abduction of the wrist joint,
- palmar / dorsal flexion of the wrist joint.

W The first stage involved the collection of data concerning 23 healthy individuals and 3 patients in one matrix, which, at the subsequent stage, was subjected to the SVD decomposition with the retaining of the unitary lengths of single vectors and single values. The following step consisted in the calculations of appropriate data contiguity indexes and their mean values. The final stage included the calculation of the raw index value, which afterwards was normalised in relation to the mean value and the standard deviation calculated for the group of healthy individuals. The calculated UMDI value measured the “distance” between the tested upper limb movement of the person having motion difficulties and the pattern adopted for the healthy individuals. The above-named value should be calculated independently for each upper limb. This quantity can be interpreted by stating that when the UMDI is close to 100 or higher, the motion sequence of a given person is closer to the adopted pattern and motion pathology does not take place. A repetitive decrease in the UMDI by 10 below 100 depicts one standard deviation from the adopted TD pattern.

The test-related calculations took into consideration all recorded movements, i.e. three repetitions stand for so-called group 1, one repetition related to each person stands for so-called group 2. The test-related calculations also took into account 2 versions of the index calculations, i.e. ULMDI<sub>9</sub> including 9 courses of anatomic angles and calculated in accordance with the algorithm described by Jurkojc (2017) and ULMDI<sub>7</sub> not including movements in the sternoclavicular joint.

### 3. Results

The test results concerning different ULMDI variants are presented in Tab. 1. In Tab. 1 colours were used to designate threshold values including the linear change in the colour gradient between them.

*Tab. 1: Values of the ULMDI calculations, green colour designates values above 90, whereas red colour designates values below 70.*

			Group of healthy people		p1	p2	p3
			Mean	SD			
GROUP 1	Left limb	ULMDI <sub>7</sub>	100	10	75.57	77.77	77.29
		ULMDI <sub>9</sub>	100	10	74.53	76.31	76.53
	Right limb	ULMDI <sub>7</sub>	100	10	90.70	73.33	90.43
		ULMDI <sub>9</sub>	100	10	90.75	72.18	90.37
GROUP 2	Left limb	ULMDI <sub>7</sub>	100	10	81.63	75.96	79.55
		ULMDI <sub>9</sub>	100	10	80.52	74.29	78.65
	Right limb	ULMDI <sub>7</sub>	100	10	92.09	67.68	88.57
		ULMDI <sub>9</sub>	100	10	91.93	66.57	88.64

### 4. Discussion

The ULMDI coefficients in Tab. 1 correspond to the greater values for the healthy limbs than those concerning limbs with dysfunction in relation to each calculated index value. In terms of the healthy limbs, the value of calculated quantities exceeded 88 points, whereas in relation to the limbs with motion dysfunction, the related values were even below 70 points. The colours assigned to the individual values in Tab. 1 related to the ULMDI coefficients enable the identification of the limb with dysfunction and the



healthy limb. In terms of the first patient (p1) and their right (healthy) limb the value of the ULMDI coefficients were higher by approximately 10 points. In Tab. 1, the aforesaid values are marked green. The values related to the limb with motion dysfunction are marked red and orange. As regards the first patient (p1), the above-presented coloring enables an easy indication of the healthy limb and the limb having motion dysfunction. A slightly different situation is that concerning the second patient (p2), where low values of the ULMDI coefficients (in red) for the right limb and only slightly higher for the left limb were observed. In terms of the third patient (p3), the results explicitly indicate the presence of motion dysfunction in the left limb. In addition, the left limb of the third patient (p3) was clinically diagnosed as being disabled.

To identify the effect of the different variants of the calculated indexes (7 and 9) and to take into account the two groups of the tested courses it was necessary to perform the comparative analysis of the results obtained in the tests. The first stage involved the comparison of values obtained for variants 7 and 9 of the calculated indexes. The data contained in Tab. 1 justify the conclusion that the ULMDI7 and the ULMDI9 adopted, roughly, the same value in relation to the same group and limb, with differences usually not exceeding 2 points in the adopted scale. Taking into consideration the sternoclavicular joint increased the differences between the values concerning the healthy limb and that with the motion dysfunction.

Greater differences were obtained in relation to the comparative analysis of the index-related results with the division of the courses included in the calculations into groups (group 1 and group 2). The increase in the number of the courses when calculating the indexes also resulted in the increase in the difference between the values obtained for the healthy limbs and the limbs with the motion dysfunction. In some cases, the above-named differences changed from 10 points to even 14 points in the adopted scale. In addition, the above-presented manner of the calculation of the indexes led to the change in the background coloring determined on the basis of the value related to patient 1 and in the case of the left limb from orange to yellow, possibly implying the lower level of motion dysfunction.

## 5. Conclusions

The index-based analysis led to the obtainment of the objective method enabling the assessment of a disability degree based on the trajectory of angles in relation to the upper limb joints. The analysis, in the quantitative manner, identified the degree of disability by comparing the results obtained in the tests with those of the assumed model. Each value-based variant of the index properly indicated the limb with a greater motion dysfunction. Taking the sternoclavicular joint into consideration increased the difference between the healthy limb and the limb with the dysfunction by approximately 2 points in the adopted scale, which facilitated the detection of the limb with dysfunction. Similar conclusions were reached on the basis of the analysis of different variants of the index in relation to three repetitions performed by each of the persons. The difference between the indexes calculated for the various number of repetitions was greater and reached between 4 and 12 points in the adopted scale. When performing analyses enabling the assessment of motion dysfunction using the ULMDI, it is important to take into account a greater number of recorded courses and measurements in the sternoclavicular joint.

## References

- Butler, E.E. and Rose, J. (2012) The Pediatric Upper Limb Motion Index and atemporal-spatial logistic regression: Quantitative analysis of upper limb movement disorders during the Reach & Grasp Cycle, *Journal of Biomechanics*, No. 45, pp. 945-951.
- Gzik, M., Wodarski, P., Jurkoć, J., Michnik, R. and Bieniek, A. (2016) Interactive System of Engineering Support of Upper Limb Diagnosis, *Innovations in Biomedical Engineering, Advances in Intelligent Systems and Computing*, Springer, ISBN 978-3-319-47153-2, ISSN 2194-5357, Vol. 526, pp. 115-123.
- Jaspers, E., Desloovere, K., Bruyninckx, H., Klingels, K., Molenaers, G., Aertbelien, E., Gestel, L. and Feys, H. (2011) Three-dimensional upper limb movement characteristics in children with hemiplegic cerebral palsy and typically developing children, *Research in Developmental Disabilities*, No. 32, pp. 2283-2294.
- Jurkoć, J., Wodarski, P., Michnik, R., Nowakowska, K., Bieniek, A. and Gzik, M. (2017) The Upper Limb Motion Deviation Index: A new comprehensive index of upper limb motion pathology, *Acta of Bioengineering and Biomechanics*, ISSN: 1509-409X, article in press, DOI assigned: 10.5277/ABB-00784-2016-02.
- Schwartz, M. and Rozumalski, A. (2008) The gait deviation index: A new comprehensive index of gait pathology, *Gait & Posture* 28, pp. 351-357.

## ROTARY MOTION SELECTED CONTROL METHODS ANALYSIS FOR PADDLE SORTERS ARMS

M. Wolski<sup>\*</sup>, T. Piatkowski<sup>\*\*</sup>, P. Osowski<sup>\*\*\*</sup>

**Abstract:** *The paper presents the research results of two methods for the paddle sorter rotary motion control used in the sorting process of the objects transported on a conveyor belt. The paddle sorter arm is driven by a set of servo which consists of a servomotor and a servo drive where motion control is carried out using the voltage pulses generated by microcontroller board, designed by the author. In the control of the paddle sorter motion the smallest possible acceleration achievement is important while the assumed trajectory tracking error obtains permissible value. It turned out that open loop motion control method based on IIR filter (Infinite Impulse Response) is a better solution than PLL motion control (Phase Locked Loop) due to the lower extreme acceleration obtainment at the same assumed permissible trajectory error.*

**Keywords:** High speed paddle sorters, Servo, Motion control, PLL, IIR.

### 1. Introduction

Contemporary methods of parts separation for assembly lines or parcel deliveries in logistic centres implement entirely automatic stream sorting systems where control reliability subject to high regime.

Sorting process involves sorters as they have a direct impact on safety of units sorted in the context of dynamic overloads. Paddle sorters are well-known and appreciated devices due to their simple constructions and reliability (McGuire P. M., 2009). Paddle sorters can be driven by various types of mechanisms e.g. a four-bar linkage, although today servo drives and motors are more popular due to a possibility to choose from a variety of motion profiles such that mentioned overloads are minimized. Set of servo can include various servomotors such as PMSM (permanent magnet synchronous motors), BLDC motors (brushless direct current motor) or stepper motors. Different position control systems based on feedback loops (Linares-Flores et al., 2015) as well as digital filters damping overload can be implemented in order to control the servo drive (Besset et al., 2016, Chang, Tsu-Chin Tsao, 2014, Biagiotti et. al., 2012). The purpose of this paper is to compare two contemporary motion control solutions with implementation of the PLL (Phase Locked Loop) and the IIR filter (Infinite Impulse Response) for paddle sorter arm. The control method with IIR filter is the variant preferred as it allows smooth out the course of position such that the first derivatives of position – velocity is continuous and finally finite acceleration values.

### 2. Unit examined

The unit examined has been presented in Fig. 1. Paddle sorters driven by a stepper servomotor have been installed beside the conveyor belt. The unit has been equipped with a set of servo consisting of the (1) ES-DH2306 (servo drive) and (2) ES-MH342200 (servomotor) made by Leadshine with GL80 planetary gearbox. Information about angular position of the paddle sorters is passed to the servo drive with (3) STM32F429 microcontroller by means of (4) EL7202 (MOSFET driver) and two lines in a form of

---

<sup>\*</sup> M. Eng. Mirosław Wolski: Faculty of Mechanical Engineering, UTP University of Science and Technology, Al. Prof. S. Kaliskiego 7, 85-796, Bydgoszcz; Poland, Mirosław.Wolski@utp.edu.pl

<sup>\*\*</sup> Assoc. Prof. Tomasz Piątkowski, PhD.: Faculty of Mechanical Engineering, UTP University of Science and Technology, Al. Prof. S. Kaliskiego 7, 85-796, Bydgoszcz; Poland, topiat@utp.edu.pl

<sup>\*\*\*</sup> M. Eng. Przemysław Osowski: Faculty of Mechanical Engineering, UTP University of Science and Technology, Al. Prof. S. Kaliskiego 7, 85-796, Bydgoszcz; Poland, przoso000@utp.edu.pl

pulses, steps and direction with the implementation of timer module hardware and the microcontroller working in PWM mode (Pulse Width Modulation).

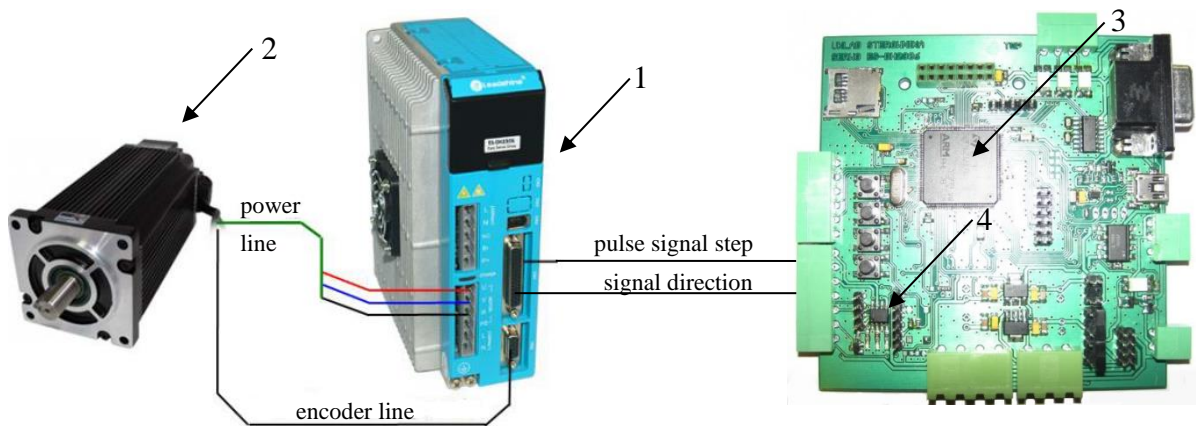


Fig. 1: Scheme of the unit examined: 1 – servo drive, 2 – servomotor, 3 – microcontroller board as a master control unit, 4 – MOSFET driver for step and direction pulses generation.

### 3. Hardware and software for microcontroller board

Microcontroller, SD card slot and MOSFET driver are the most important elements of the microcontroller board. Fig. 2 is divided into three blocks: microcontroller software (1), microcontroller hardware (2) and device board hardware (3).

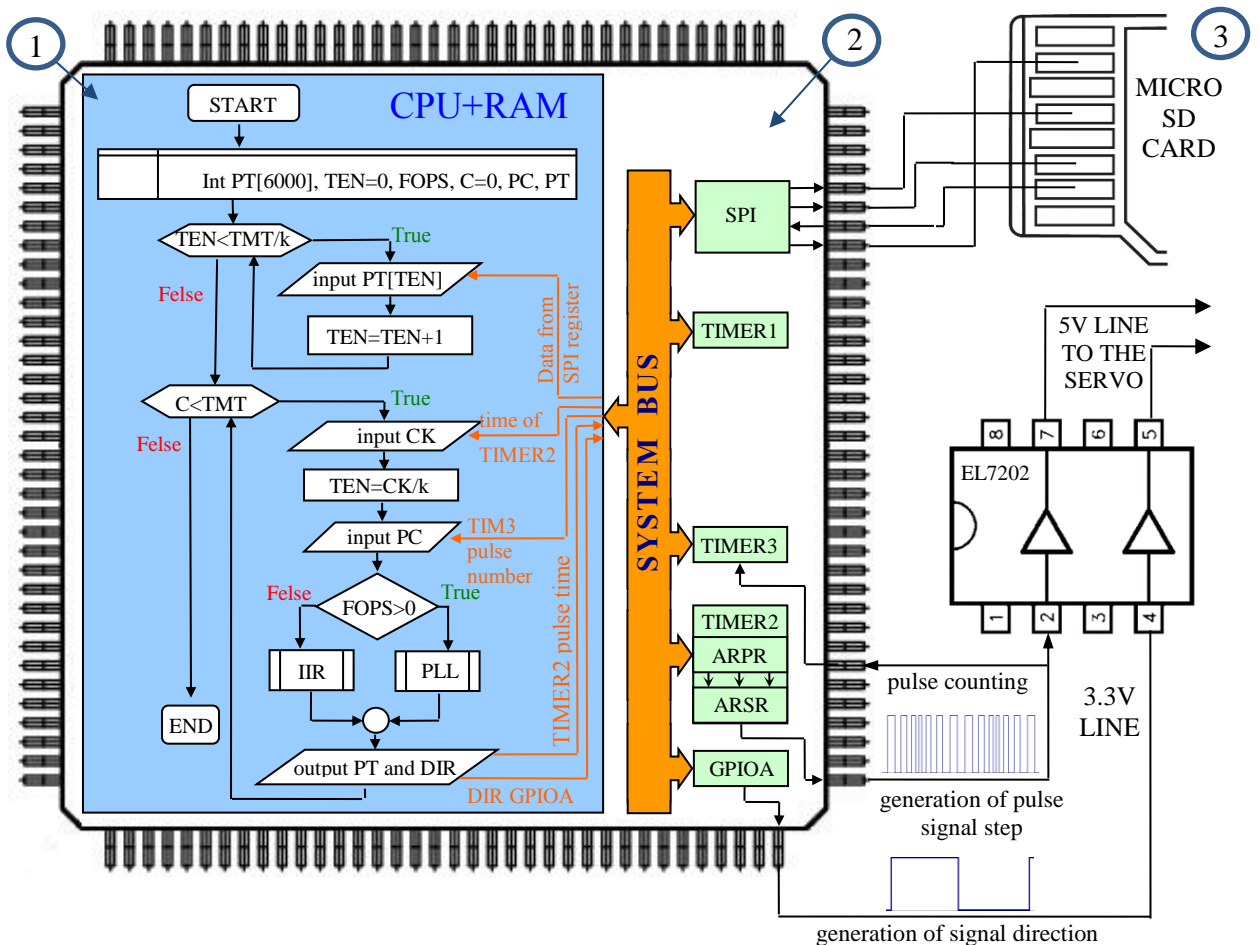


Fig. 2: Program block diagram of microcontroller (flowchart) and connection scheme of main devices of microcontroller board: TEN – table element number, PT – position table, FOPS-FIR or PLL select, CK– clock, TMT – total movement time, PT – pulse time, PC – pulse counter, k – the time interval between successive elements of the array.

Peripheral modules in a microcontroller such as timer modules or SPI (Serial Peripheral Interface) are available for CPU through the bus system. Blue field shows the flowchart of program executed by CPU microcontroller. At first the array of integers from the SD card is transferred to the RAM memory which represents course of reference position. As soon as this operation is completed the program moves to the execution of the main loop control.

The following parameters are provided: time counted from the start of motion with TIMER2, the number of pulses from TIMER3 and the value of the array element for the reference position which number is proportional to time. On the basis of the data collected calculations for control variable with PLL or FIR method due to selected control mode are implemented. The control value in a form of pulse period is transferred to the ARPR register (Auto Reload Preload Register) in TIMER2 which after the completion of the previous pulse is transferred to ARSR (Auto Reload Shadow Register).

#### 4. Control algorithm

Flowchart of the control program presented in Fig. 2 allows to select one of the two control variants using the buttons on the microcontroller board: in the closed loop with the implementation phase locked loop (PLL predefined process flowchart in Fig. 2) or the open loop with the implementation of infinite pulse response (IIR predefined process flowchart in Fig. 2).

By introducing marking specified in Fig. 2 for the PLL block:

$$T = \frac{KP}{PT[TEN] - PC} \quad (1)$$

where:

$T$  – pulse period (calculated as a integer),  $KP$  – proportional coefficient of the PID controller,  $PT[TEN]$  – element of the array of course of reference position requested with number  $TEN$  proportional to  $CK$  time in TIMER1,  $PC$  – number of pulses counted by TIMER3 (Fig. 2), which have been provided in  $CK$  time to the servo drive.

For IIR block:

$$PT_{\text{smoothed}}[TEN] = \sum_{i=0}^{i=TEN} \frac{PT[i] \cdot a^{-(TEN-i)}}{a^{-(TEN-i)}} \quad (2)$$

$$T = \frac{f_{\text{TIM2}} \cdot k}{PT_{\text{smoothed}}[TEN] - PT_{\text{smoothed}}[TEN - 1]} \quad (3)$$

where:

$a$  – coefficient for the filter taking values from 0 to 1,  $f_{\text{TIM2}}$  – TIMER2 clock speed [MHz],  $k$  – the time interval between successive elements of the array,  $TMT$  – total motion time for the arm [ $\mu$ s],  $PT_{\text{smoothed}}[TEN]$  – output value which is a floating point number,  $TEN$  – element of the array for the filtration element provided.

#### 5. Results and discussion

The key element during the paddle sorters motion time history is tracking the reference motion profile with small track errors for the angular position and small values of accelerations.

The reference course angular position is based on the sinusoid function presented in Figs. 3a and 4b. The time of working cycle of the paddle sorter arm amounts to 0.76 s., The time for single control iteration amounted to 350  $\mu$ s. The course of motion of the arm for both control modes has been carried out so that the maximum error of tracking the angular position amounted to 0.33 ° (angle in degrees).

IIR method regulation (Fig. 3b) allows to achieve over 20 times smaller extreme accelerations (revolution per second squared) in relation to PLL method regulation (Fig. 4b).

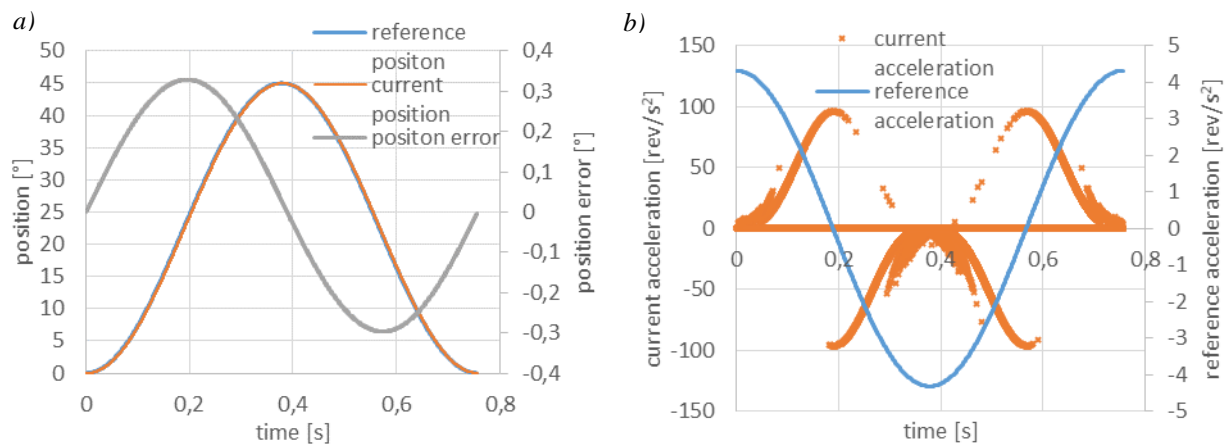


Fig. 3: Course of position and acceleration for motion control of paddle sorter arm with IIR filter.

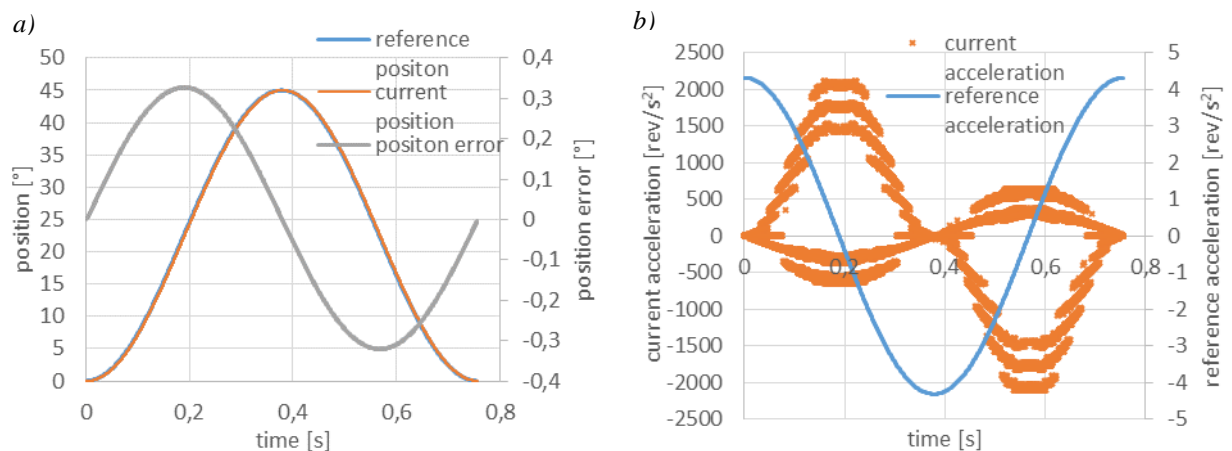


Fig. 4: Course of position and acceleration for PLL motion control of paddle sorter arm.

## 6. Conclusions

The use of the PLL method provides position error compensation, due to the presence of a closed loop system, so that a significant deviation between current course and reference course position is impossible. However, this method for rotational motion control causes large acceleration values in relation to the IIR control method. In case of rotational motion control of the paddle sorter arm, the reference position profile is well known while tuning. Therefore it is easy to verify if there is a small position error between current position course and assumed reference position before we start the sorting process. Due to this reason, the IIR method of the motion control of the paddle sorter arm should be used and resign from it, only when the arm does not follow the reference position profile during the preliminary tuning.

## References

- McGuire, P.M. (2009) Conveyors: Application, Selection, and Integration. Taylor and Francis Group.
- Linares-Flores, J., García-Rodríguez, C., Sira-Ramírez, H. and Ramírez-Cárdenas, O.D. (2015) Robust Backstepping Tracking Controller for Low-Speed PMSM Positioning System: Design, Analysis, and Implementation, IEEE Transactions on Industrial Informatics, Vol. 11, No. 5.
- Besset, P., Bearee.R., Gibaru O. (2016) FIR Filter-Based Online Jerk-Controlled Trajectory Generation, 2016 IEEE International Conference on Industrial Technology (ICIT).
- Chang, H.L. and Tsao, T.-Ch. (2014) High-Sampling Rate Dynamic Inversion-Filter Realization and Applications in Digital Control, IEEE/ASME Transactions on Mechatronics, Vol. 19, No. 1.
- Biagiotti, L. and Melchiorri, C. (2014) FIR filters for online trajectory planning with time- and frequency-domain specifications, Control Engineering Practice 20 (2012), 1385-1399.

## A SEMI-ACTIVE PNEUMATIC SUSPENSION OF THE WORKING MACHINE SEAT

P. Woś\*, R. Dindorf\*\*

**Abstract:** The paper presents issues related to improving the vibro-isolating properties of the semi-active electro-pneumatic suspension of the working machine seat. A practical implementation of the system controlling the force of the pneumatic spring mounted in the seat suspension mass-produced was presented herein. An output function controlling the pressure valve of the pneumatic system supplying the bellows actuator was suggested. The developed solution made it possible to conduct dynamic tests over the pneumatic spring applied in relation to the semi-active suspension system.

**Keywords:** Vibro- Isolation, Semi-Active Suspension Control, Bellows Actuator.

### 1. Introduction

Vibrations are transferred from the mechanical vibrating systems to humans and negatively affect the functioning of their various tissues, blood vessels and organs. A number of body disorders are found among humans exposed to continuous influence of mechanical vibrations, and as a consequence, persistent lesions in the form of vibration syndrome. It applies to many professional groups performing their work in a sitting position, i.e.: operators of construction machines, vehicle and tractor drivers (Guglielmino et al., 2008; Maciejewski and Krzyżyński, 2011; Mizuno, 2005).

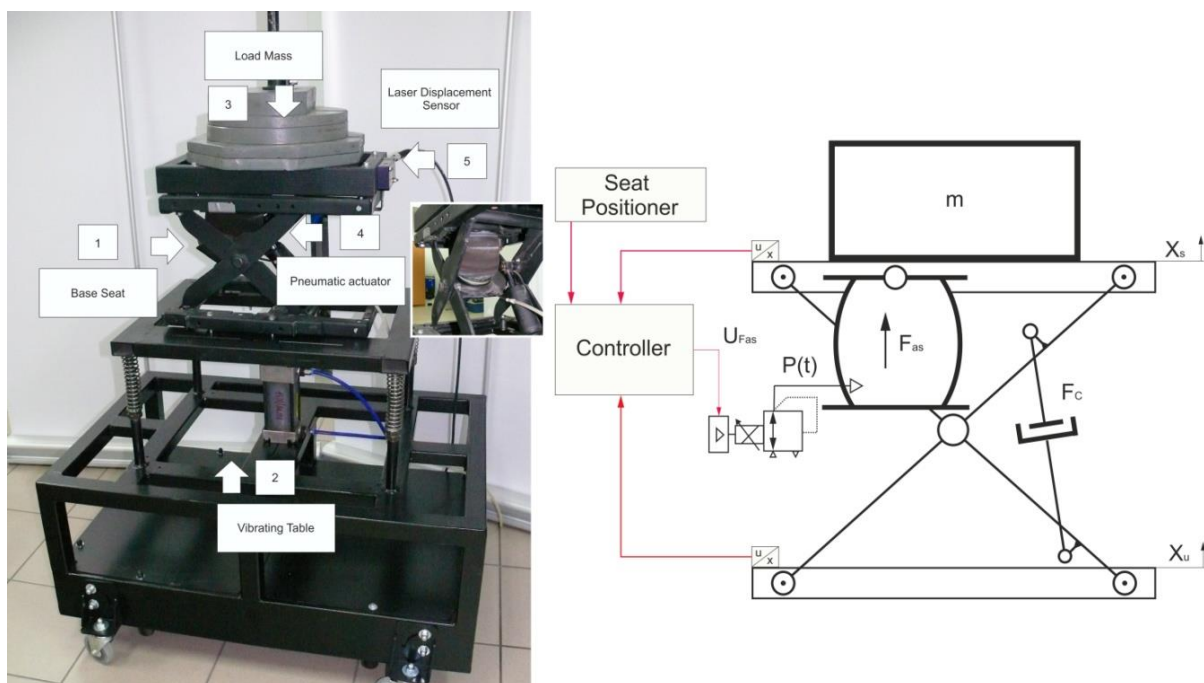


Fig. 1: General view of the experimental stand, a block diagram of the semi-active control system of the seat suspension.

\* PhD. Piotr Woś: Faculty of Mechatronics and Machine Design, Kielce University of Technology, Kielce, 25-314, Poland, wos@tu.kielce.pl

\*\* Prof. Ryszard Dindorf: Faculty of Mechatronics and Machine Design, Kielce University of Technology, Kielce, 25-314, Poland, dindorf@tu.kielce.pl



Many structures use solutions which make it possible to change the damping factor by the operator depending on the individual assessment of his weight and the working conditions. Effective damping can be obtained automatically or manually by setting the constant pressure value (pneumatic spring) or voltage (current) in the silencer with variable damping characteristics (magneto-rheological fluid). Semi-active systems with dampening or elasticity coefficients variable over time and determined by the control system constitute an extension of this method. The value of elasticity or damping coefficients changes continuously, and thus, it can be updated during the operation of the machine which is exposed to vibrations caused by the conditions of the road, or the vibrations themselves caused by the devices. The advantages of the semi-active systems include their low requirements as far as the power of an external energy source is concerned. That is why, such systems are often used in practice. They make it possible to reduce the seat vibrations with low frequency of excitation forces (up to 5 Hz), while maintaining good vibro-isolating properties at higher frequencies of excitation forces (Tora, 2013). The works in order to develop new constructions for seat suspensions with the use of active and semi-active and active vibration reduction systems are conducted in the Department of Manufacturing Engineering and Metrology at the Faculty of Mechatronics and Mechanical Engineering of the Kielce University of Technology. A design of a semi-active seat suspension with a controlled pneumatic bellow spring was developed. An experimental test stand to study the vibro-isolating properties of the working machine seat is shown in Fig. 1. The basic element thereof is a pneumatic-hydraulic vibro-isolator of the base of the working machine seat (1). The vibro-isolator is composed of a frame in the shape of a bi-link four-bar linkage which the seat of the machine operator is ultimately mounted to. A pneumatic bellow actuator and a hydraulic damper are connected with the rocking levers of the quadrangle (Woś et al., 2013).

## 2. Modelling the vibro-isolating properties of the test stand

A simplified model of the seat suspension includes system elastic force derived from pneumatic spring  $F_{as}$ , damping force  $F_c$  of the hydraulic damper and G-force of mass load  $F_g$ . A bellow actuator applied in the system has some specific physical properties. After filling it with compressed air, it may act as a pneumatic spring. If a charged bellow actuator is loaded with mass, the vibrating system will be received. Force  $F_{as}$  coming from the pneumatic spring and acting in the vertical direction on the object isolated from vibrations, was defined as the product of effective area  $A_{ef}$  and relative pressure  $p-p_0$ :

$$F_{as} = A_{ef} \cdot (p - p_0) \quad (1)$$

With an increase of pressure  $p$ , and thus, an increase of volume  $V$ , height  $h$  of the bellow increases and simultaneously its effective area  $A_{ef}$  is reduced.

Stiffness  $k$  of the pneumatic bellow is expressed with the ratio of load  $F_g$  compared to deflection  $h$  of bellow  $k = dF_g / dh$ , and the dependencies on deflection  $h$  and pressure  $p$  were specified in the following way (Dindorf, 2013):

$$k(h, p) = p \frac{dA_{ef}}{dh} + \frac{A_{ef}^2}{C_g(p)} \quad (2)$$

Where:  $C_g$  gas capacity of the bellow,  $C_g = V/K_g$ ,  $K_g$  modulus of air elasticity,  $K_g = \kappa p$ ,  $\kappa = 1.4$  – adiabatic exponent.

The bellow force acting on the suspension system was defined in the following way:

$$F_{as}(h) = k(h)(h_0 - h) = \kappa \cdot p_0 \cdot A_{ef} \frac{h_0 - h}{h_0} \left( \frac{h_0}{h_0 - h} \right)^{\kappa+1} \quad (3)$$

Frequency  $f_0$  of the bellow vibrations amounts to:

$$f_0 = \frac{1}{2\pi} \sqrt{\frac{\kappa \cdot p_0 \cdot g}{h_0 \cdot p}} \quad (4)$$

An appropriate degree of vibro-isolations of the bellow actuator (pneumatic spring) is found in for frequency  $f = 1.4 f_0$ . Fig. 2 shows the timeline of the vibro-isolating seat mass for rectangular extortion. The research was conducted with determined pressure values  $p$ . Fig. 3 shows the timelines of the vibro-

isolating mass (72 kg) with extortion frequency of 2 Hz and a pressure change in the bellow. The system achieved the best vibro-isolating properties for the pressure ranging from 3.44 to 4.25 bar.

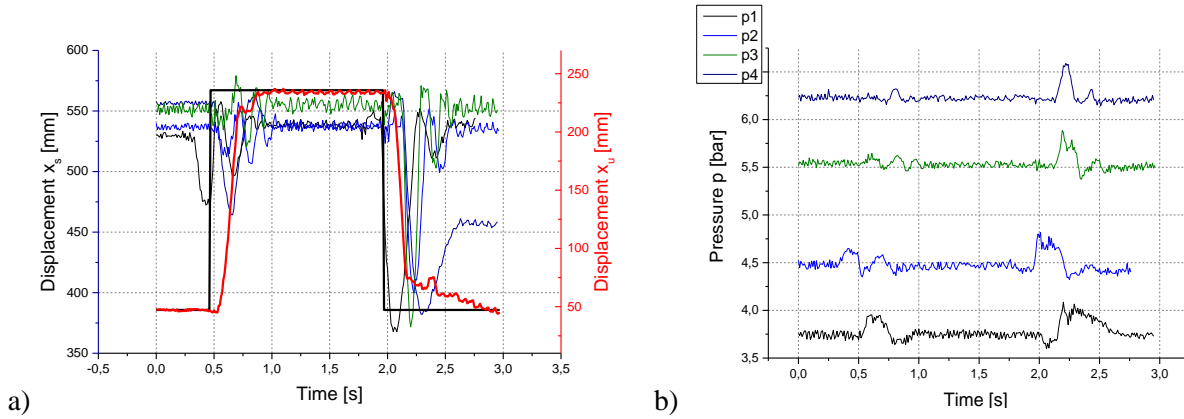


Fig. 2: Timelines of the displacements of vibro-isolating mass  $x_s$  and extortion  $x_u$  a) for various pressure values b).

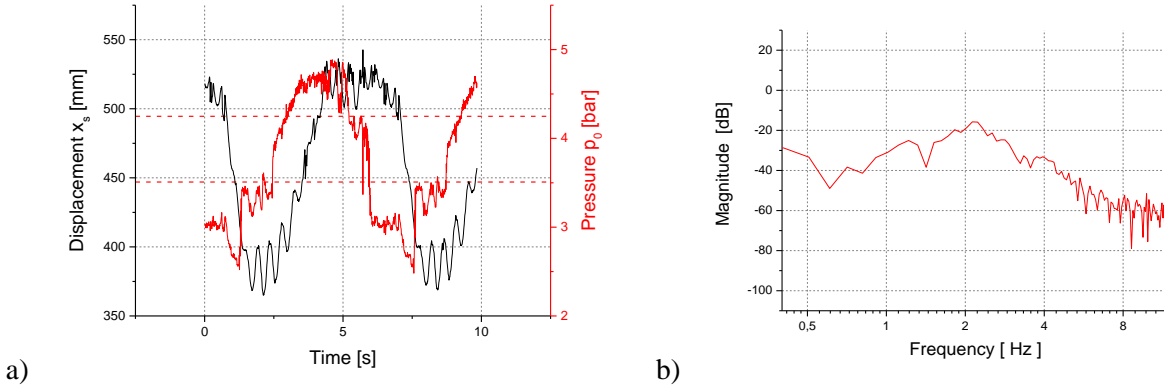


Fig. 3: Timelines of vibro-isolating mass displacements with pressure change  $p$  a) and frequency response of displacements of system vibrations b).

### 3. Control system

The primary objective of the seat control is to reduce the acceleration, which the driver is affected by. Controlling the suspension system (Fig. 1) is based on the measurements: the displacement of the working seat system with the mass, and the relative displacement of driver's seat ( $x_s$ ) and substrate ( $x_u$ ). The function of the controller is to tune the pre-determined pressure in the bellow actuator in such a way so that as the acceleration of the seat is minimized. The initial pressure determination in the bellow depends on the weight of the vibro-isolating mass. Force  $F_{as}$  generated in the semi-active system does not depend only on the control signal, but also on current seat deflection  $x_u$ ,  $x_s$ . The value of the voltage controlling the pressure valve is calculated on the basis of the mass function:

$$u_{F_{as}} = u_{ref} + w \cdot (k_1 \cdot u_2(\dot{x}_u - \dot{x}_s) + k_2 \cdot u_2(x_u - x_s)) \quad (5)$$

where:  $w = \frac{x_u - x_s}{(x_u - x_s)_n}$ ,  $(x_u - x_s)_n$  - nominal value of the relative displacement of the suspension system,

$k_1$ ,  $k_2$  - coefficients of the controller reinforcements.

Fig. 4 presents the timelines of the displacements of vibro-isolating mass  $x_s$  and substrate  $x_u$  for extortions with a sinusoidal signal with the amplitude of 80 mm and modulated frequency ranging from 0.1 Hz to 6 Hz. As a result of the controller's operation of the semi-active system with an adjustable stiffness of the pneumatic spring, the amplitude of the vibro-isolating mass response was decreased. For mass of 72 kg, bellow pressure of 4.6 bar and frequency of free vibrations of 2.2 Hz, the transmission of vibrations decreased by approximately 22 dB. At high frequencies (from 4 Hz), the change of dampening properties of the system with a pneumatic spring is almost unnoticeable.

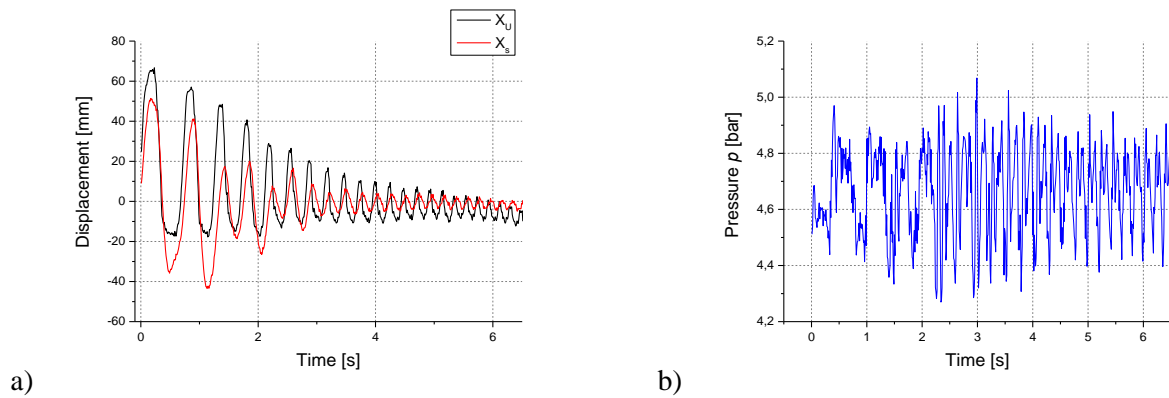


Fig. 4: Timelines of the displacements of the vibro-isolating mass a) and adjustable pressure value b).

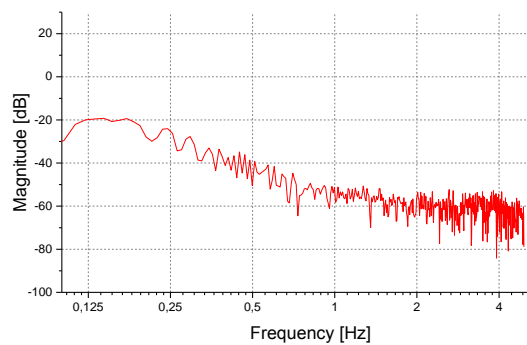


Fig. 5: Frequency response of semi-active vibro-isolation.

#### 4. Conclusions

The solution of the seat vibro-isolation suggested herein is based on the existing construction solution of the passive suspension system applied commonly in working machines. Such systems are characterized by low effectiveness of vibration reduction as far as low frequencies of extortions are concerned, as there is an amplification of vibrations in the case of frequencies of free vibrations (1 – 2 Hz). Due to the control system applied to adjust the stiffness of the pneumatic spring, the vibro-isolating properties of the seat for a given range of extortion frequencies were improved. A significant advantage of the developed system is its low demand for power of the external energy source. The suggested system effectively reduces the values of the relative seat displacements, and hence, the comfort and safety at work might be improved in the future.

#### References

- Dindorf, R. (2013) Flexible pneumatic actuators, Publisher Kielce University of Technology, M55.
- Guglielmino, E., Sireteanu, T., Stammers, C.W., Ghita, G. and Giuclea, M. (2008) Semi-active Suspension Control: Improved Vehicle Ride and Road Friendliness, Springer-Verlag, London.
- Maciejewski, I. and Krzyżyński, T. (2011) Control design of semi-active seat suspension systems, Journal of theoretical and applied mechanics 49, 4, pp. 1151-1168.
- Mizuno, T., Murashita, M., Takasaki, M. and Ishino, Y. (2005) Pneumatic Active Vibration Isolation Systems Using Negative Stiffness, Trans. SICE, Vol. 41, No.8, pp. 676-684.
- Tora, G. (2013) Synthesis of the active cab suspension mechanism, Advanced Materials in Machine Design., Trans Tech Publications Ltd, Vol. 542, pp. 219-231.
- Woś, P. and Dindorf, R. (2014) Active suspension seat of working machine, Logistyka, Vol. 6, pp. 11355-11360.

## LEAK MEASURING SYSTEM OF COMPRESSED AIR IN PIPELINE

P. Woś\*, R. Dindorf\*\*

**Abstract:** The new innovative measurement method of compressed air leakage flow rate in compressed air pipeline is proposed. The methods can be used to measure compressed air leakage in any place of compressed air pipeline: in main line, distribution line and connection line. The controlled air flow through the throttle valve is directly measured by flow meter. The proposed measurement methods of compressed air leakage in pipeline are independent of receiver and compressor parameters, which is not the case with traditional method measuring leaks by emptying the receiver. A device for the automatic measurement of leakage flow rate in compressed air pipeline.

**Keywords:** Compressed Air, Leakage Flow Rate Measurement, Energy Efficiency.

### 1. Introduction

Leakage is usually the largest source of energy waste associated with compressed air usage. Leakage can occur at a number of points in a compressed air pneumatic pipeline system. There are many various ways of determining or measuring the quantity of compressed air leaking out (Dudić et al., 2012; Huang Liang et al., 2010; Radgen and Blaustein, 2001; Shibata et al., 2009; Souza et al., 2000). For compressors that have on/off controls or load/unload controls, there is an easy way to estimate the amount of leakage in the system. This method involves starting the compressor when there are no demands on the system (when all the air-operated end-use equipment is turned off). Leakage can be estimated in compressed air pipelines by emptying the compressed air receiver. Compressed air leakage measurement method based on the controlled flow in branch line. The diagram of the air leakage measuring circuit in compressed air pipelines based on the controlled flow in branch line is shown in Fig. 1.

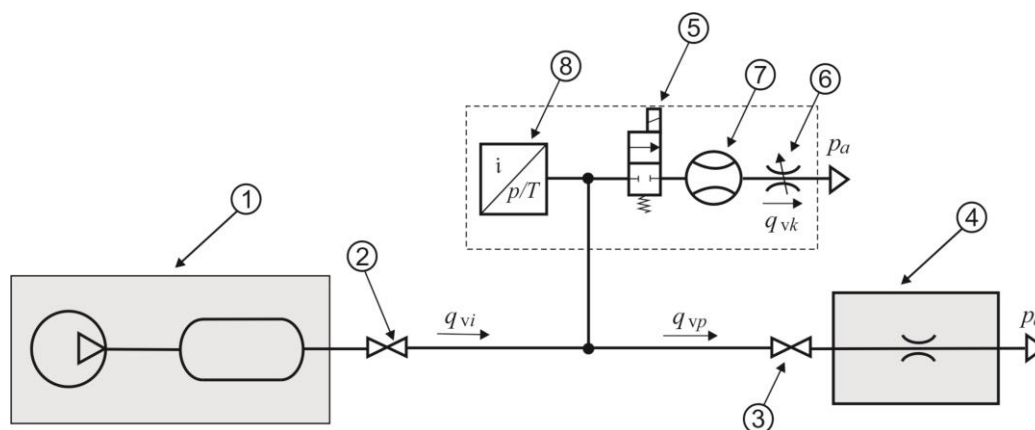


Fig. 1: Diagram of the air leakage measuring circuit based on the controlled flow in branch line:  
1 – compressor and receiver, 2, 3 – shut-off valve, 4 – leak point in pipeline, 5 – switching valve,  
6 – adjustable throttle valve, 7 – flow meter, 8 – dual pressure and temperature sensor.

The new measurement method of compressed air leakage in pipelines based on the controlled flow consists in determining the relation between air leakage flow rate  $q_L$  in leak point of pipeline (4) and the

\* PhD. Piotr Woś, Faculty of Mechatronics and Machine Design, Kielce University of Technology, Kielce, 25-314, Poland, wos@tu.kielce.pl

\*\* Prof. Ryszard Dindorf, Faculty of Mechatronics and Machine Design, Kielce University of Technology, Kielce, 25-314, Poland, dindorf@tu.kielce.pl

controlled air flow rate  $q_{vc}$  in adjustable throttle valve 6, directly measured by flow meter (7) in branch line. The formula used to calculate air leakage flow rate based on the controlled flow in branch line (Dindorf and Woś, 2014):

$$q_L = q_{vc} \frac{\ln\left(\frac{p_{Lu}}{p_{Ld}}\right) t_{Lc}}{\ln\left(\frac{p_{Lcu}}{p_{Lcd}}\right) t_L - \ln\left(\frac{p_{Lu}}{p_{Ld}}\right) t_{Lc}} \quad (1)$$

where:

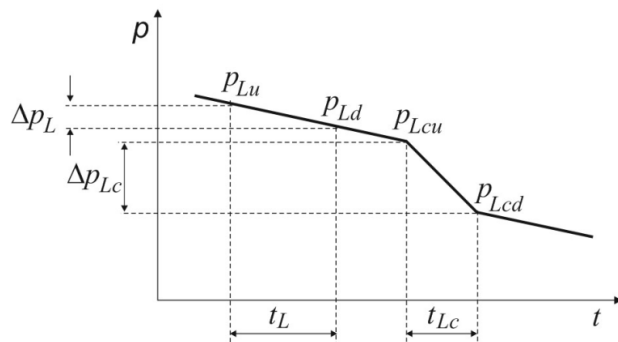
$p_{Lu}, p_{Ld}$  – upstream and downstream absolute pressure during leakage without the controlled flow,

$p_{Lcu}, p_{Lcd}$  – upstream and downstream absolute pressure during leakage with the controlled flow.

With a new indirect method compressed air leakage is estimated by measurement of pressure ratio in a two time intervals (Fig. 2a):

1. For the air leakage without the controlled flow the valve switching (5) (Fig. 1) is closed and the pressure ratio  $p_{Lu}/p_{Ld}$  in time intervals  $t_L$  is measured.
2. For the air leakage with the controlled flow the valve switching (5) (Fig. 1) is open and the pressure ratio  $p_{Lcu}/p_{Lcd}$  in time intervals  $t_{Lc}$  is measured.

a)



b)

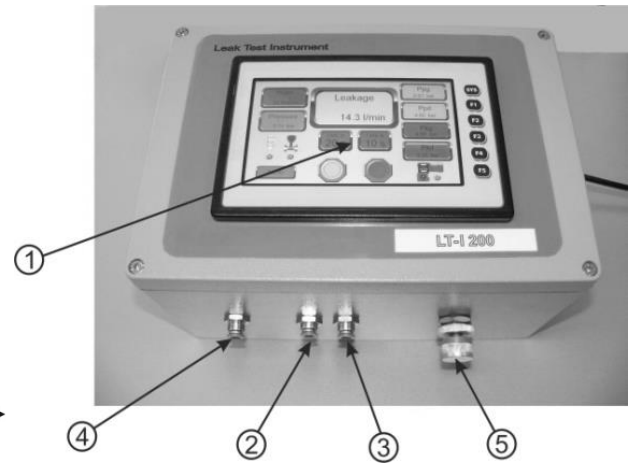


Fig. 2: Pressure change in two time intervals in compressed air pipelines during the air leakage measurement based on the controlled flow in branch line, b) View of the device type LT-I 200 for measuring of leakage flow rate in compressed air systems: 1 – touch panel, 2 – pneumatic connector for direct measurements of the air flow rate, 3 – pneumatic connector for indirect measurements of the leakage flow rate, 4 – output of pneumatic line, 5 – knob of the throttle valve.

## 2. Leak Test Instrument

The portable compact measurement device type LT-I 200 for automatic measurement of leakage flow rate in compressed air pipeline is shown in Fig. 2b. This measuring procedure makes it possible to measure the determination of leakage flow rate in the test installation in a fully automatic way. The device (Fig. 2b) is configured with membrane keyboard and touch screen (1) on the front panel. The touch screen device has the basic functions for measuring the leakage in compressed air systems: F1 - measuring the mass flow rate, F2 - measuring the pressure, F3 - measuring the leakage in the compressed air. Pneumatic connection (2) allows direct measurement of mass flow rate of compressed air. Connection (3) is used for automatic measurement of the indirect method of leakage. Pneumatic throttle valve (5) is used to determine the controlled leakage flow rate  $q_{vc}$ . This instrument after introducing the initial operating parameters such as: times  $t_L$ ,  $t_{Lc}$ , the intensity of the controlled leakage flow rate  $q_{vc}$  performs automatic procedure for measuring and computing. As a result, we obtain directly, the value leakage flow rate  $q_L$  of compressed air system. A block diagram of the measurement system shown in Fig. 3. The measurement

system MS is designed to work with a measuring device MD that reads the voltage input signals of the measuring transducer (1) ( $u_T$ ,  $u_p$ ), the thermal flowmeter (2) and generates a voltage signal that controls proportional throttle valve (3). The measuring system MS consists of a calculation block of leakage (4), a block forming the reference signal (5) a calculation block of flow rate (6), the feedback block (7), the controller block (8), and a block that limits the set signal (9). The way of measuring leakages that uses the measuring system MS includes: calibration, measurement without controlled flow and measurement of controlled flow (Takosoglu et al., 2014, 2016). During the calibration of the measurement path of constant time of  $t_L$  of polytropic pressure drop across the choke valve is defined (3). On the basis of the measurement the pressure  $p_i$  in the pneumatic system, the critical pressure to the limit range of critical flow is determined. It is reasonable to agree the critical flow in the throttle valve (3), because the air flows into the atmosphere. By measuring the time constant  $T_p$ , the pressure  $p_i$  in the pneumatic system and the critical pressure  $p_{cr}$  selected measurement time  $t_{Lc}$  controlled. Block (6) determines the flow rate through the valve  $q_{Lc}$  (3) on the base of  $p_i$  measurement. It is possible to determine the gas flow rate through the valve  $q_{Lc}$  (3) on the base of the measurement using the thermal flowmeter (2).

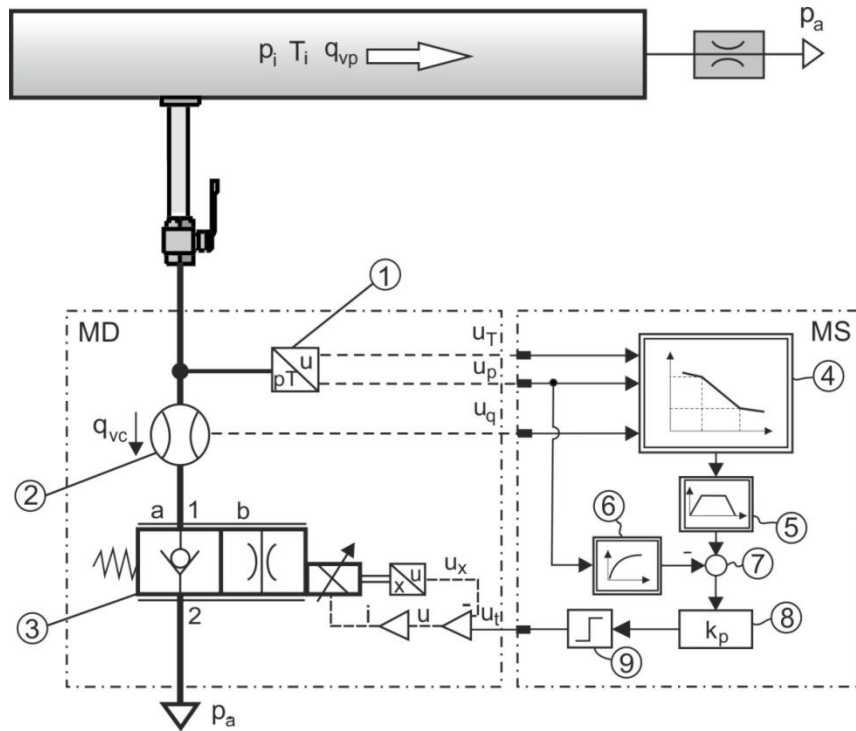


Fig. 3: The schematic diagram of a measurement system.

During measurements without leakage of controlled calculation block (4) during  $t_L$  measures the pressure  $p_{Lu}$  upper and lower pressure  $p_{Ld}$ , when the valve (3) is closed and on this basis, the pressure drop is determined  $\Delta p_L = p_{Lu} - p_{Ld}$  caused by the leakage of compressed air in the pneumatic system. When measuring controlled flow calculation block (4), during  $t_{Lc}$  measures the pressure  $p_{Lcu}$  upper and lower pressure  $p_{Lcd}$ , when the valve (3) is opened and on this basis the pressure drop is determined  $\Delta p_{LC} = p_{Lcu} - p_{Lcd}$  due to leakage of compressed air in the pneumatic system and the flow of compressed air to the atmosphere through an adjustable throttle valve (3). To carry out controlled flow, there was a block forming the reference signal (5) that generates a voltage of limited duration at the inlet valve (3). To keep the measuring time a constant flow rate  $q_{lc}$  by the throttle valve (3), feedback block (7) determines the adjustment error, the controller (8) generates a voltage signal limited to the value of by the block (9). Time pulse voltage determined for controlled measurement time  $t_c$  is determined in the range of  $T = t_c = 5 - 50$  s. The minimum measurable leakage depends on the measuring range of the flowmeter mounted in the device. The Fig. 4 shows an example of waveforms of pressure changes.

### 3. Conclusions

An indirect method of measuring the leakage of compressed air in the pneumatic system is a method which is independent from the parameters of the tank and the compressor, as in the case of standard



indirect methods of measuring the leakage. Including the elements of the measuring device to the pneumatic system does not require dismantling or modifying the installation. It is enough to connect the measuring devices to proper places where the compressed air is received. With the use of this method, the leakages might be measured at any time and in any place of the pneumatic installation: in the main pipeline, distribution cables or wires connecting the receivers (machines, equipment, tools).

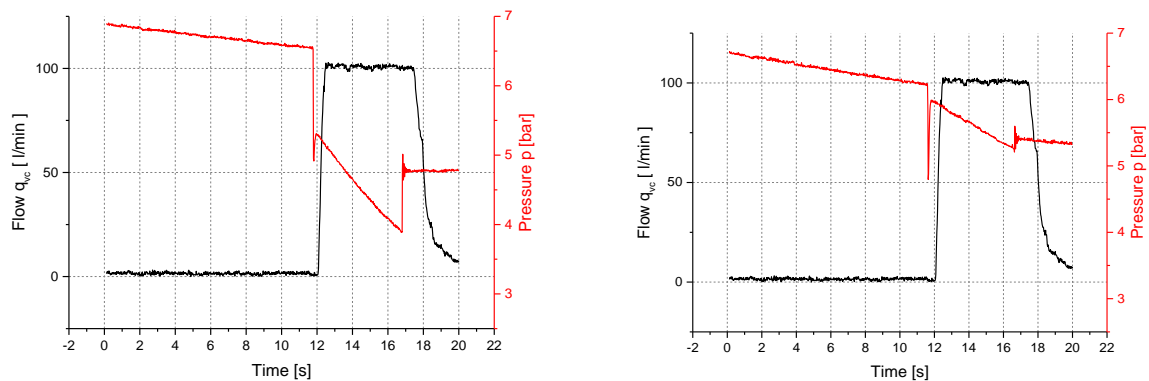


Fig. 4: Diagrams of flow rate measurement  $q_{VC}$  and pressure drop  $\Delta p$ .

### Acknowledgement

The demonstrative mobile measurement equipment type LT-I 200 was realized within the project „The perspective Swietokrzyskie RSI - IV the stage”, The task 5: „Creating the new forms of the co-operation of the science with the business”, The Operating programme Capital Human co-financed from The European Social Fund.

### References

- Dindorf, R. and Wos, P. (2014) Indirect method of leakage flow rate measurement in compressed air pipelines, *Applied Mechanics and Materials*, 630, pp. 288-293.
- Dudić, S.P., Ignjatović, I.M., Šešlija, D.D., Blagojević, V.A. and Stojiljković, M.M. (2012) Leakage quantification of compressed air on pipes using thermovision, 16, pp. 621-631.
- Liang, H., Maolin, C. and Jiawei, W (2010) Instantaneous leakage flow rate measurement of compressed air, in: 2010 Int. Conf. Mech. Autom. Control Eng. IEEE, pp. 2675-2679.
- Radgen, P. and Blaustein, E. (2001) Compressed air systems in the european union energy, emissions, savings potential and policy actions.
- Shibata, A., Konishi, M., Abe, Y., Hasegawa, R., Watanabe, M. and Kamijo, H. (2009) Neuro based classification of gas leakage sounds in pipeline, in: Int. Conf. Networking, Sens. Control IEEE,
- Souza, A.L., Cruz, S.L., and Pereira, J.F.R. (2000) Leak detection in pipelines through spectral analysis of pressure signals, *Brazilian Journal of Chemical Engineering*, 17, 4-7, pp. 557-564.
- Takosoglu, J.E., Laski, P.A. and Blasiak, S. (2014) Innovative modular pneumatic valve terminal with self-diagnosis, control and network communications, in: Proc. 20th Int. Conf. Eng. Mech. 2014 (ed. Fuis, V.), Svratka, Czech Republic, pp. 644-647.
- Takosoglu, J.E., Laski, P.A., Blasiak, S., Bracha, G. and Pietrala, D. (2016) Determination of flow-rate characteristics and parameters of piezo valves, in: Proc. Int. Conf. Exp. Fluid Mech. 2016 (ed. Dancova, P.), Techn. Univ. Liberec, pp. 814-818.

## ANALYSIS OF THE EROSIWE WEAR MODELING RESULTS OF THE PNEUMATIC CONVEYING SYSTEMS

J. Wydrych<sup>\*</sup>, G. Borsuk<sup>\*\*</sup>, S. Pochwała<sup>\*\*\*</sup>

**Abstract:** *This paper attempts a qualitative and quantitative comparison of the calculation results of multiphase flow gas - solid particles in a flow system with built-in bend. The movement of the gas phase and particle trajectories are described by Euler and Lagrange models respectively. Simulation tests were performed for several different inlet conditions, in order to determine their impact on results. The study allowed us to identify the model of Euler-Lagrange as useful for this type of flows, and the formulation of a number of important conclusions. The paper presents the possibility of applied mathematical models to predict the erosive wear of flow system with built-in elbow. The emphasis of the work was put on qualitative comparison the effect of inlet conditions on the change of the gas velocity field and the concentration of particulate matter. These elements made it possible to locate areas of increased wear as well as the degree of wear.*

**Keywords:** Erosive wear, CFD, Euler-Lagrange method.

### 1. Introduction

Operating of pneumatic conveying systems brings many problems. Uncontrolled particle segregation or local erosion of the system components are only some of them. Problems of pneumatic transport system designing are the subject of a many types of research (Borsuk et al., 2006; Liang et al., 2014; Olszowski et al., 2007; Taylor, 1998 and Wydrych, 2010). However, current methods for the design of pneumatic conveying systems did not allow for a proper assessment of the erosive wear. The paper presents a method that allows to evaluate the aerodynamics and erosion as a function of inlet conditions in the test flow system. The movement of the gas phase and particles was described by Euler and Lagrange models respectively, which was extended by the turbulence model equation. Numerical calculations were performed for the two particle diameters. The results of numerical calculations are compared with the results of experimental installation shown in Fig. 1a. It is a part of a pipeline of circular cross section with a built-in elbow. The system is made of pipes with the diameter  $\phi D = 76$  mm. In the measuring section was made research material loss due to wear erosion. During the numerical calculations length of the inlet section was changed and amounted to 100, 500 or 1000 mm. Outlet section has a length of 600 mm.

Bending angle measuring section in the shape of the elbow is  $90^\circ$ , while the bending radius  $R = 1.5 \cdot D = 114$  mm. In the illustrated arrangement gas - mixture flow was tested with the following molecular characteristics. The air density  $\rho = 1.2$  kg/m<sup>3</sup>, and a dynamic viscosity  $\mu = 1.8 \cdot 10^{-5}$  Pa·s provided a cross-sectional view of the inlet velocity of 23.0 m/s, which corresponds  $1.17 \cdot 10^5$  Reynolds number. At the same time, the inlet section supplied with particles of quartz sand from 6200 inlet points. Particles with diameters of 150 and 300  $\mu$ m have the same velocity as air at the inlet, and the density was 2650 kg/m<sup>3</sup>. Sand particles with a hardness of HV 9.8, were applied in an amount of 0.033 kg/kg of air. The flow system was stainless steel 316, wherein the density of 7990 kg/m<sup>3</sup>, the hardness HV is 1.83, and the BH is 178.9.

---

<sup>\*</sup> Adjunct prof. Jacek Wydrych, PhD.: Department of Thermal Engineering and Industrial Facilities, Opole University of Technology, 76 Prószkowska str.; 45-758, Opole; Poland, j.wydrych@po.opole.pl

<sup>\*\*</sup> Adjunct prof. Grzegorz Borsuk, PhD.: Department of Thermal Engineering and Industrial Facilities, Opole University of Technology, 76 Prószkowska str.; 45-758, Opole; Poland, g.borsuk@po.opole.pl

<sup>\*\*\*</sup> Adjunct prof. Sławomir Pochwała, PhD.: Department of Thermal Engineering and Industrial Facilities, Opole University of Technology, 76 Prószkowska str.; 45-758, Opole; Poland, s.pochwała@po.opole.pl

## 2. Methods

A mathematical model consisting equations of the gas phase and particles motion was formulated in order to realize numerical calculations. Motion of the gas is described by Euler method while the movement of particles by Lagrange. In order to correctly analyze motion poly-dispersed mixture gas - solid particles, in this paper, the method of PSI-Cell was used (Source Particle in Cell) (Wydrych, 2010), (Fidaros et al., 2007). Bitter model was selected for calculation of the erosive losses (Bitter, 1963), with attention to the smallest differences in the numerical calculations results of measurements. In the Bitter model, erosion was classified in two categories, i.e. shearing and deformation. Generally, shear and deformation are used simultaneously and they are independent, so the total amount of the wall material, which is removed, can be written as the sum of these two mechanisms. In this section, the equations were solved using a commercial package ANSYS Fluent (Fluent Inc., 2015).

## 3. Analysis of the results

The Fig. 1.a shows the flow system with built-in elbow, in which numerical calculations was realized. Detailed calculation carried out for the system in three different configurations at the inlet section, for three different lengths of inlet: 100, 500 and 1000 mm. Tests were conducted for two different diameters of the dust particles, i.e.: 150 and 300  $\mu\text{m}$ . In addition, the calculation of particle trajectories was made without turbulent fluctuations in the motion of particles and taking account of these fluctuations. The result is series of 12 data set, which take into account changes in the above factors and in the rest of the work will be determined in a symbolic way. For example, the inlet length of 100 mm, a particle diameter 150  $\mu\text{m}$  without taking into account the fluctuation is applied to symbol - 100\_d150, and for the inlet of length 500 mm, particle diameter, included fluctuations in the calculations 300 $\mu\text{m}$  - 500\_d300\_rnd.

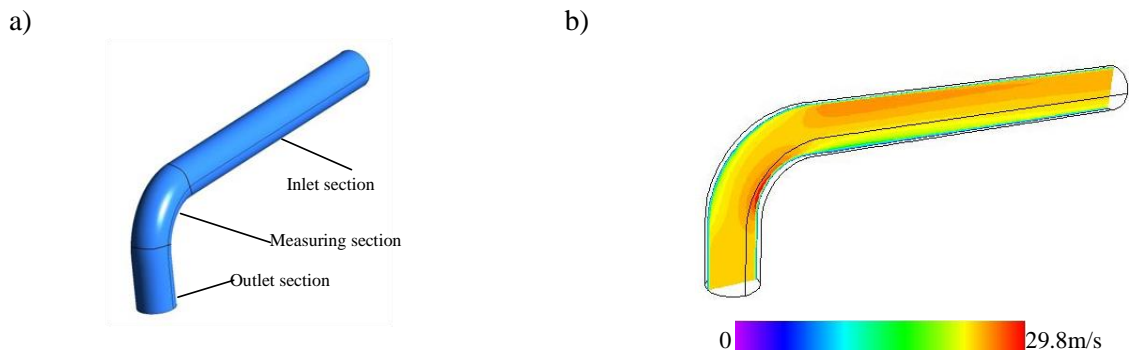


Fig. 1: Experimental set (a) and distribution of module gas velocity (b) for the set 100\_d150.

At the inlet to the system were set uniform velocity distributions and particle concentration. The calculations were made for the velocity of 23 m/s, and the concentration of particles 0.033 kg/kg gas. The results of calculation of the velocity field in the selected cross-section of the flow system are shown in Fig. 1b.

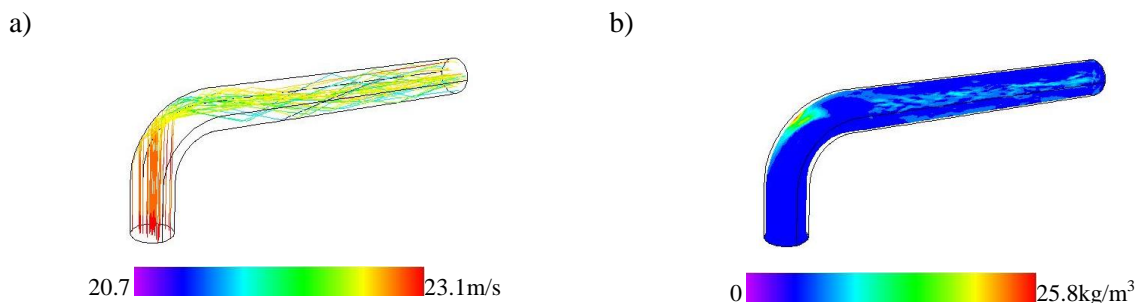


Fig. 2: Trajectories of particles (a) and distribution of the concentration of the solid phase (b) for the set 100\_d150.

Velocity distributions for all lengths of the inlet confirm that movement of the gas phase in the presence of particulate matter in the areas of the elbows occurs primarily close to internal arcs. Extending intake causes major gas recirculation zones downstream the elbow and reducing the effective cross-section of

the outlet. This may induce of increased resistance of the mixture motion. The Fig. 2a presents exemplary trajectories of the particles supplied to the inlet section arranged in one plane. Analysis of particle trajectories shows that particles at inlet section change their trajectories as a result of turbulent fluctuations only slightly, while the particles at the outlet section with turbulent fluctuations spread over a larger area and at shorter distance occupy the entire cross-section of the outlet. Concentration of the solid phase was calculated based on specific locations of the solid particles, as shown in Fig. 2b.

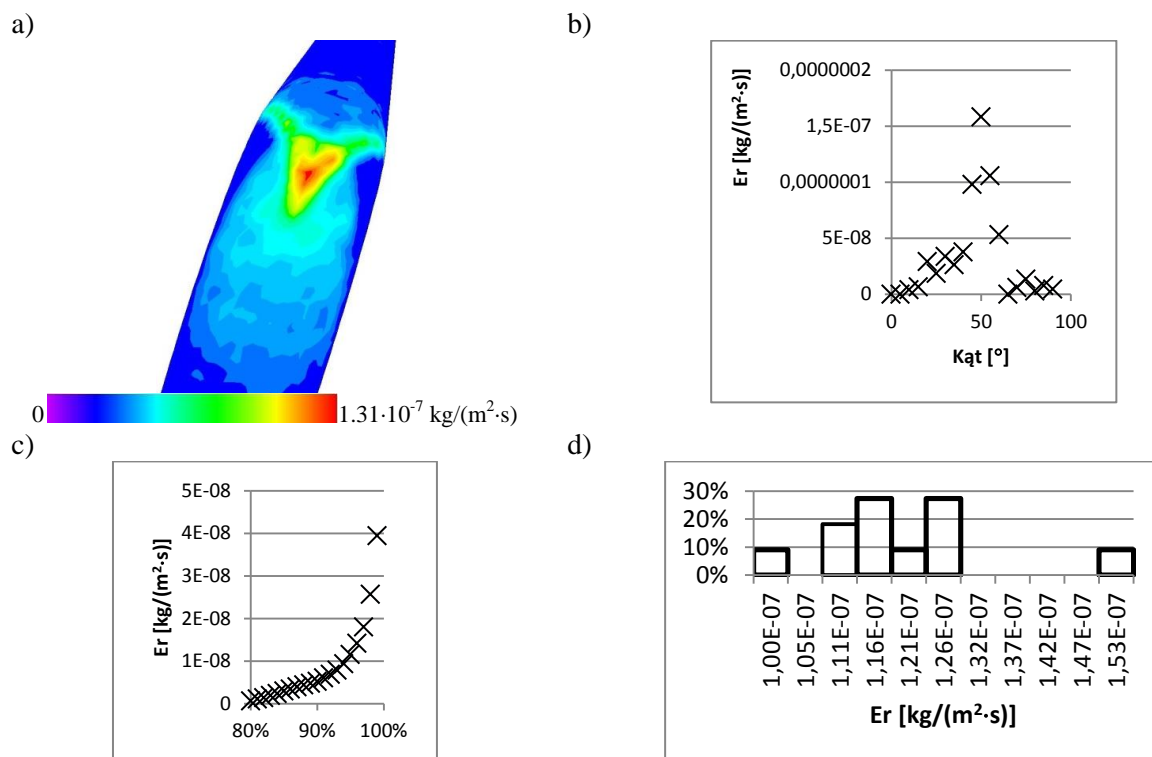


Fig. 3: A set of analytical data for the 1000\_d150 a) distribution of consumption erosion; b) dependence of the consumption of the angular position of the measuring point, c) graph percentile consumption, d) histogram of the percentage of consumption zones.

The presence of the elbow significantly distorts the distribution of concentration in the elbow and downstream the elbow. Clearly, the uniform concentration distribution in the inlet section is deformed by the centrifugal force as an effect of the elbow, to form the external increase of solid particles concentration. In contrast, there are no notable changes in the concentration distributions for tested systems. Because of the mixture movement which composition comprises solid particles of sand will gradually wear the wall. High wear zones are located in areas of the elbow which results from the rejection of the particles by centrifugal force. The Fig. 3 presents sets of results to analyze the wear-life of the erosion caused by the presence of particles in the conveying mixture. Data analysis leads to the conclusion that the area of the greatest erosion is located on a small area of the external elbow arch. Percentiles charts and histograms provide information, which shows that this area is less than 1 % of the entire surface of the tested element. Graphs b) and c) allow to conclude that the inclusion in the calculation of the random fluctuations of particles reduces the maximum consumption and at the same time increasing the area of the occurrence of erosion. Furthermore, the results shown in Fig. 3b were compared with the experimental results. Measurements were carried out for the erosive loss of elbow, for which detailed data were available regarding the time and operating conditions. Experimental data for the test system were taken from the literature (Vieira et al., 2016). The results of calculations apply only to the outer curve of the elbow in the measuring section. Elbow in this section has been divided into 18 parts angle  $\varphi$  per  $5^\circ$ . For each measuring point, losses of erosion were calculated using ANSYS FLUENT (Fluent, 2015). The Fig. 4 shows the comparison of the numerical calculations results with experimental. Analysis of erosive wear distribution on the surface of the elbow received by experiment and calculation shows that the developed method of modeling erosive wear gives qualitatively similar results for a given element. Areas of greatest wear were correctly predicted by model 100\_d150\_rnd for angle  $50^\circ$ . However, in the area of the whole range of computational model it was the most effective 1000\_d300.

This demonstrates the significant influence on the length of the inlet section calculation results erosive wear.

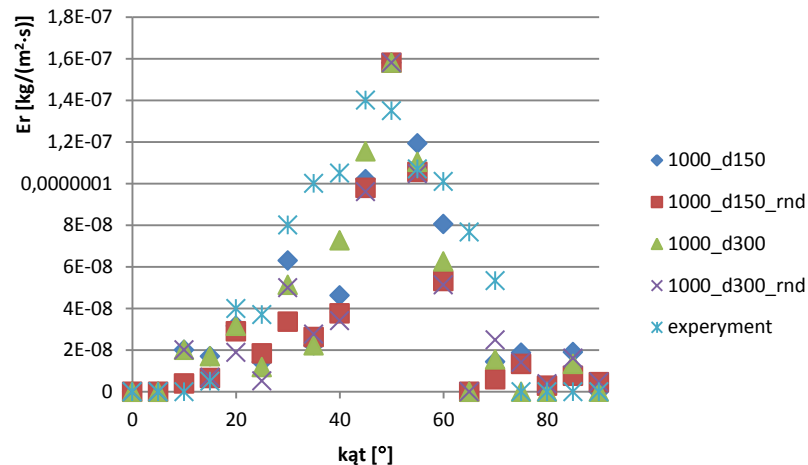


Fig. 4: Influence of the angular position of the measuring point on errors of erosive wear.

#### 4. Conclusions

The analysis leads to the conclusion that the method used for the prediction of erosive wear get correct results for considered installations. The observed discrepancies between the results of the calculations and the results of the measurements can be related to:

- lack of full information about the operating conditions of the analyzed system in the long term,
- simplifications accepted at the stage of formulating a mathematical model,
- assumption of sphericity of the particles.

Nevertheless, authors observed qualitative compliance the results of calculations with the measurements of erosion losses. Examination of the data leads to the conclusion that the area of greatest consumption is located on the side of the outer curve of the elbow in a small area occupying less than 1 % of the entire surface of the test element. Considering random fluctuations of the particle in calculations, results a reduction of maximum erosive wear, and simultaneously increasing the area of the erosion occurrence. A significant effect studies is that in complex systems flow erosion process was conditioned by the aerodynamics of movement mixture of gas - solids.

#### References

- Bitter, J.G.A. (1963) A study of erosion phenomena, *Wear*, 6, pp. 5-21.
- Borsuk, G., Dobrowolski, B. and Wydrych, J. (2006) Gas - solids mixture flow through a two-bend system, *Chemical and Process Engineering*, 27, no. 3/1, pp. 645-656.
- Fidaros, D.K., Baxevanou, C.A., Dritselis, C.D. and Vlachos, N.S. (2007) Numerical modelling of flow and transport processes in a calciner for cement production, *Powder Technology*, 171, pp. 81-95.
- FLUENT, INC. (2015) Fluid Dynamics Analysis Package. s. l.: Fluid Dynamic Internationale Inc.
- Liang, C. et al. (2014) Comparison of pressure drops through different bends in dense-phase pneumatic conveying system at high pressure. *Experimental Thermal and Fluid Science*, 57, pp. 11-19.
- Mujumdera, K.S., Ganesh, K.V., Kulkarnia, S.B. and Ranade V.V. (2007) Rotary Cement Kiln Simulator (RoCKS): Integrated modeling of pre-heater, calciner, kiln and clinker cooler, *Chemical Engineering Science*, 62, pp. 2590-2607.
- Olszowski, T. and Pospolita, J. (2007) Conditions of dust sampling in pneumatic conveying through the horizontal pipeline. *Powder Technology*, 171, Issue 1, pp. 1-6.
- Taylor, T. (1998) Specific energy consumption and particle attrition in pneumatic conveying. *Power Technology*, 95, pp. 1-6.
- Vieira, R.E., Mansouri, A., McLaury, B.S., and Shirazi, S.A. (2016) Experimental and computational study of erosion in elbows due to sand particles in air flow, *Powder Technology*, 288, pp. 339-353.
- Wydrych, J. (2010) Comparative analysis of the methods of simulation of flow in boiler dust systems. *Chemical and Process Engineering*, 31, 4, pp. 603-623.

## NUMERICAL THERMAL COMPARISON OF HEAT SINK MATERIALS FOR AUTOMOTIVE LED HEADLAMPS

M. Zachar<sup>\*</sup>, M. Guzej<sup>\*\*</sup>, J. Horský<sup>\*\*\*</sup>

**Abstract:** Currently, aluminium is the most widely used heat sink material for cooling LEDs in automotive headlamps because of its good thermophysical properties. But the headlamps manufacturers are still looking for other material solutions, which could be better than the aluminium one. One of the possibilities is using plastics with high thermal conductivity, because even if its conductivity is lower than aluminium's, it is much easier to shape to various forms, which could be better for heat transportation and the cost of this solution could be much lower. This paper deals with the comparison of a real heat sink geometry, used in the front headlamp of automobile, where it serves to cool LEDs. A numerical comparison between three materials was made: firstly the actually used aluminium alloy, secondly a imaginative material with isotropic thermal conductivity  $20 \text{ W}\cdot\text{m}^{-1}\cdot\text{K}^{-1}$  serving as a comparison between plastic material and thirdly a plastic material with anisotropic thermal conductivity which ranges from 5 to  $20 \text{ W}\cdot\text{m}^{-1}\cdot\text{K}^{-1}$ .

**Keywords:** Heat sink, Aluminium, Plastic, LED, Headlamp.

### 1. Introduction

Technology is constantly evolving and with this progress many electronic devices are becoming more compact. Not every component works with perfect efficiency and lots of its input power is transformed into heat, which needs to be transferred away from the device. This cooling can be achieved in three ways, by active cooling using a fan, passive cooling using a heat sink or a combination of the previous two.

The second form of cooling, even with lesser efficiency, has its advantages in not using any moving parts (it is needed to only put the component on the heat sink), no external energy for cooling, heat sink transfers heat away by thermal properties of its material. The most common heatsink materials are copper and aluminium for their high thermal conductivity ( $401 \text{ W}\cdot\text{m}^{-1}\cdot\text{K}^{-1}$ ,  $237 \text{ W}\cdot\text{m}^{-1}\cdot\text{K}^{-1}$  respectively). Aluminium is more widely used, because it is lighter than copper and therefore it puts less stress on the component it is placed on. Its density is  $2702 \text{ kg}\cdot\text{m}^{-3}$  while coppers's density is  $8933 \text{ kg}\cdot\text{m}^{-3}$  (Incropera, 2007).

Today, the world is looking for new materials with better overall properties than aluminium. One of these new materials could be plastics with high thermal conductivity. While their thermal conductivity is lower than aluminium's, they are much lighter, so they put even less stress on the components, easier to mould and could be much cheaper solution.

### 2. Plastics with high thermal conductivity

Metals have been highly used in the past for the purpose of heat transfer for its excellent thermal properties, but metal parts are costly to produce. Nowadays, these metal materials are being replaced by plastics with high thermal conductivity which provide less expensive solutions. Other advantages of

---

\* Ing. Martin Zachar: Heat Transfer and Fluid Flow Laboratory, Brno University of Technology, Technická 2; 616 69, Brno, CZ, martin.zachar@vut.cz

\*\* Ing. Michal Guzej: Heat Transfer and Fluid Flow Laboratory, Brno University of Technology, Technická 2; 616 69, Brno, CZ, michal.guzej@vut.cz

\*\*\* prof. Ing. Jaroslav Horský, PhD.: Heat Transfer and Fluid Flow Laboratory, Brno University of Technology, Technická 2; 616 69, Brno, CZ, jaroslav.horsky@vut.cz



replacing metals with plastics are design flexibility, corrosion and chemical resistance and reduction of secondary finishing operations (Stewart, 2004).

Thermally conductive plastics have thermal conductivity of 5 to 500 times higher than conventional plastics. Range of their conductivity is from 1 to 100  $\text{W}\cdot\text{m}^{-1}\cdot\text{K}^{-1}$  (<http://coolpolymers.com/eseries.asp>). This high thermal conductivity is achieved via thermally conductive fillers. These fillers can be for example aluminium, graphite or aluminium-boron nitride (Heinle, 2010). The main difference between graphite fillers and ceramic fillers is that in graphite, thermal conductivity rises in the direction of graphite flakes while using ceramic fillers makes the materials equally conductive in all directions (Stewart, 2004), (Grundler, 2015).

### 3. Numerical thermal simulation of a heat sink

A numerical thermal simulation of a heat sink was created, using the software ANSYS CFX 17.2. Heat sink from a real LED headlamp has was as a model. In Fig. 1, a comparison between the actual heat sink and a simplified model is shown.

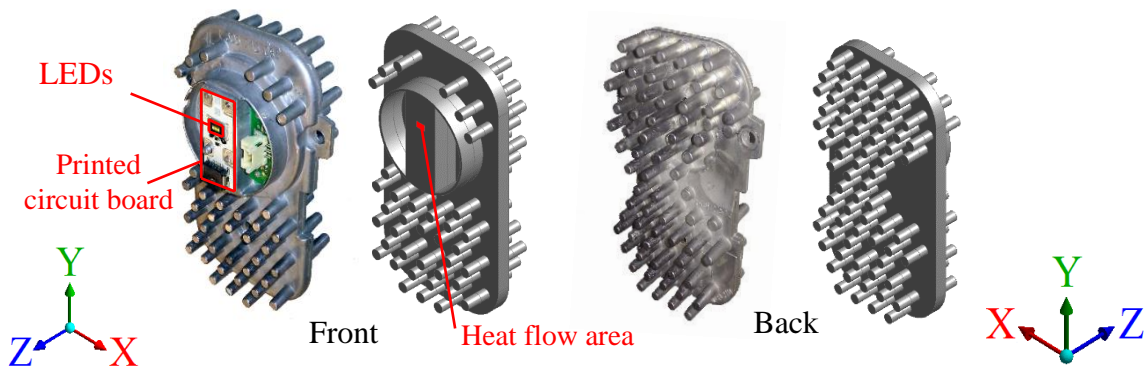


Fig. 1: Comparison between real heat sink (left) and a simplified model for the simulation (right).

In the simulation the LEDs were replaced by an area with the heat flow and natural convection with turbulent flow and non-constant air density have been considered. The thermal resistance between an aluminium plate with a printed circuit board with LEDs and the heat sink were neglected, the heat flow was placed as shown in Fig. 1. Furthermore, heat transfer by radiation was not considered, either.

A comparison between different materials was made. Firstly, aluminium alloy AlSi12(Cu) used in the real heat sink with a thermal conductivity between  $120 \text{ W}\cdot\text{m}^{-1}\cdot\text{K}^{-1}$  and  $150 \text{ W}\cdot\text{m}^{-1}\cdot\text{K}^{-1}$  (<https://www.matbase.com/material-categories/metals/non-ferrous-metals/cast-aluminium/material-properties-of-g-alsi12cu-231-cast-aluminium-grade.html#properties>). For the purpose of simulation, an average value was chosen to be  $135 \text{ W}\cdot\text{m}^{-1}\cdot\text{K}^{-1}$ . Secondly, an imaginative material with isotropic thermal conductivity  $20 \text{ W}\cdot\text{m}^{-1}\cdot\text{K}^{-1}$  was chosen. And thirdly, for the thermally conductive plastic material, a material marked as E5101 from company Cool Polymers was selected. It is a thermally conductive Polyphenylene Sulphide (PPS). Its in-plane thermal conductivity was  $20 \text{ W}\cdot\text{m}^{-1}\cdot\text{K}^{-1}$  ([http://coolpolymers.com/Files/DS/Datasheet\\_e5101.pdf](http://coolpolymers.com/Files/DS/Datasheet_e5101.pdf)). Thermal conductivity through-plane was measured in Heat Transfer and Fluid Flow Laboratory and it was equal to  $5 \text{ W}\cdot\text{m}^{-1}\cdot\text{K}^{-1}$ . This anisotropy is result of the orientation of filler particles by injection molding (Grundler, 2015).

Five different simulations were made. The first one was with the aluminium alloy, for the second one a material with  $20 \text{ W}\cdot\text{m}^{-1}\cdot\text{K}^{-1}$  isotropic thermal conductivity for the comparison with anisotropic plastic and three more simulations, where the plane with high thermal conductivity changed between XY, YZ and XZ planes. For the ambient air, the temperature of  $20^\circ\text{C}$  was chosen for all five cases.

### 4. Results

Average temperature of the heat flow area and distribution of temperature across the heat sink was monitored to show the difference between usage of different materials.

### Average temperature of the heat flow area

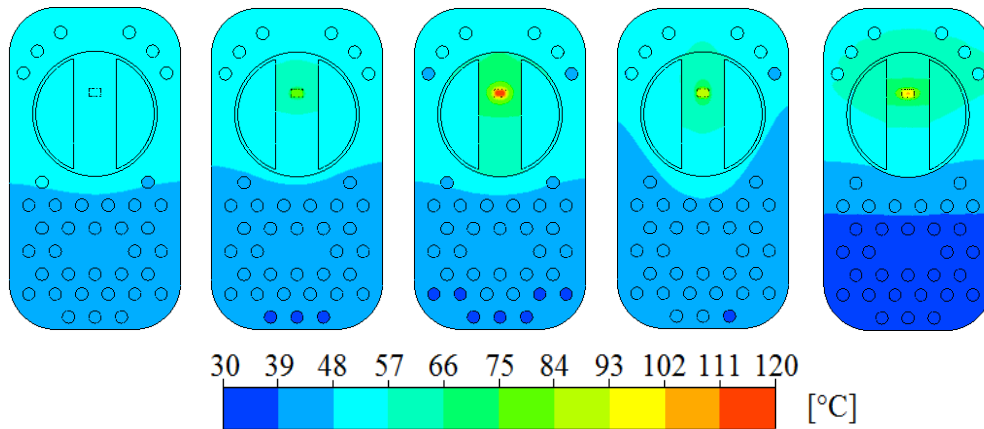
The most important part of the heat sink, as far as temperature is concerned, is the area of the heat flow, because it is the part where the heat source is placed and which needs to be cooled down. The comparison between different simulations is shown in Tab. 1. The aluminium alloy is used as a reference material.

*Tab. 1: Comparison of average heat flow area temperature between materials with different thermal conductivity.*

Material	AlSi12(Cu) ( $135 \text{ W}\cdot\text{m}^{-1}\cdot\text{K}^{-1}$ )	$20 \text{ W}\cdot\text{m}^{-1}\cdot\text{K}^{-1}$	E5101 (in-plane = XY)	E5101 (in-plane = YZ)	E5101 (in-plane = XZ)
Temperature [°C]	53	78	110	87	96
Percentage difference [%]	-	147	208	164	181

### Distribution of temperature across heat sink

A comparison of temperature distribution is showed in Fig. 2. A front view was used, to show the difference between temperature on the heat flow area and the rest of the heat sink. Temperature range is constant for all five cases and is from 30 to 120 °C.



*Fig. 2: Distribution of temperature across heat sink, from left to right: AlSi12(Cu), material with conductivity  $20 \text{ W}\cdot\text{m}^{-1}\cdot\text{K}^{-1}$ , E5101 (in-plane = XY), E5101 (in-plane = YZ), E5101 (in-plane = XZ).*

### Temperature on the farthest pin

Next, the temperature on the farthest pin from the heat source was compared. The place of this pin is showed in Fig. 3 and the temperatures with percentage differences are shown in Tab. 2. The aluminium alloy is used as a reference material.



*Fig. 3 The farthest pin from the heat source.*

*Tab. 2 Comparison between temperatures of the most distant pin from the heat source.*

Material	AlSi12(Cu) (135 W·m <sup>-1</sup> ·K <sup>-1</sup> )	20 W·m <sup>-1</sup> ·K <sup>-1</sup>	E5101 (in-plane = XY)	E5101 (in-plane = YZ)	E5101 (in-plane = XZ)
Temperature [°C]	47	39	39	40	31
Percentage difference [%]	-	83	83	85	64

## 5. Conclusion

A comparison of simulations of different heat sink materials was made. The first one was a material used for the heat sink in practice. It was an aluminium alloy with thermal conductivity 135 W·m<sup>-1</sup>·K<sup>-1</sup>. Second one was an imaginative material with conductivity 20 W·m<sup>-1</sup>·K<sup>-1</sup>, serving as a comparison for the anisotropic plastic material, used for the other three instances, where the plane with high conductivity varied.

The results show that for this exact geometry a replacement of aluminium alloy for plastic material with high thermal conductivity is not such a good option, because the LEDs would have a temperature 164 % higher in the best case (from 53 to 87 °C), where the plane with the high thermal conductivity is YZ plane. This solution was the closest one to using the isotropic material where the temperature on the heat flow area was 79 °C, so the difference between temperatures was only 8 °C. In the case of the XZ plane as the one with high conductivity, half of the heat sink had a temperature below 39 °C, which means, that this half has almost no usefulness. Still, the worst solution was the one with high conductivity in the XY plane, temperature on the heat flow area was 110 °C.

However, using plastics with high thermal conductivity as an aluminium replacement could be a solution for different geometries, where the heat source isn't placed on a ledge like in this case and the heat can be transferred through the entire base, not only in one direction to even reach the heat sink base.

## References

- Grundler, M., Dereith, T. and Heinzl, A. (2015) Polymer Compounds with High Thermal Conductivity. In: Proceedings of the Regional Conference Graz 2015 - Polymer Processing Society (PPS): Conferece Papers. 5 p.
- Heinle, C. and Drummer, D. (2010) Potential of thermally conductive polymers for the cooling of mechatronic parts. Physics Procedia. 3(5), pp. 735-744.
- Incropera, F. and DeWitt, D. (2007) Fundamentals of heat and mass transfer. 6th ed. /. Hoboken, NJ: John Wiley, xxv, 997 p.
- Stewart, R. (2004) Thermally Conductive Polymers. Plastics Engineering. Brookfield Center, (1), 20.

## DETERMINATION OF THE STRESS - STRAIN STATE FOR INDUSTRIAL PIPELINE BASED ON ITS VIBRATION

J. Zachwieja<sup>\*</sup>, K. Peszyński<sup>\*\*</sup>

**Abstract:** *The pipelines are subject to various constraints variable in time. Those vibrations, if not monitored for amplitude and frequency, may result in both the fatigue damage in the pipeline profile at high stress concentration and the damage to the pipeline supports. The industrial system pipelines, unlike the transfer pipelines, are straight sections at some points only, which makes it more difficult to formulate the equation of motion. In those cases, numerical methods can be used to determine stresses using the kinematic inputs at a known vibration velocity amplitude and frequency. The study presents the method to determine the stresses.*

**Keywords:** Pipeline vibrations, Natural vibrations, Transverse vibrations, Resonance frequencies, Allowable pipes vibration levels.

### 1. Introduction

The literature includes the criteria for the analysis of the vibration levels for pipelines, which define the permissible displacement amplitudes or the vibration velocities as a function of the frequency (von Nimmritz 1974). Lin (1996) has observed that the criterion can mainly be used for the oil pipelines, where slim pipes are usually supported by very flexible supports. For rigid supports, the relationship must be modified. Long (1955) has presented an alternative solution of the equation of motion for the pipe supported on both ends and has compared the results of the analysis with the experimental results to validate the mathematical model used. The results were ambiguous, since the maximum medium velocity used in the experiment was too low to result in a significant change in the frequency of the transverse vibrations of the pipe. This issue has also been studied by Benjamin (1961) and Niordson (1953), who showed that the conditions for the stability of pipe vibrations depend on the support used. The vibrations of straight supported pipes, excited by the medium flow are characterized by high amplitude, if the flow velocity exceeds the critical velocity.

A simple fatigue analysis based on the displacement criterion was suggested for the oil system pipelines vibrations by Wachel and Bates (1976). A similar approach has been positively verified by an extensive study of the pipeline vibrations in the power industry (Mortuik, 1994). The method can be used to determine the dynamic state of the pipelines in which the vibrations are excited at the lowest natural frequency, and the pipe is considered a vibrating beam. Its disadvantage is that it applies to the frequency range up to  $f = 300$  Hz, which is significantly below the frequencies excited by the pump vanes. A wide excitation band may also include the frequencies higher than occurring in the oil pipelines (Graham, 1997), (Motriuk and Harvey, 1998).

### 2. Industrial pipeline testing

The subject of the test was a pipeline in the liquor circulation line of the digester used in a paper mill. The pipeline length is  $l = 33$  m. A medium transported in the pipeline is a soda lye (i.e. white liquor) at a concentration of several percent. It is a liquid with the density similar to water. The pipeline pressure is  $p = 1.1$  MPa. A volume flow rate of the medium is  $Q = 0.07$  m<sup>3</sup>·s<sup>-1</sup>. The medium flow rate is 4.5 m s<sup>-1</sup>.

---

<sup>\*</sup> Assoc. Professor Janusz Zachwieja, PhD., Department of Applied Mechanics, University of Technology and Life Sciences in Bydgoszcz (Poland), Kaliskiego 7, Bydgoszcz; PL, janusz.zachwieja@utp.edu.pl,

<sup>\*\*</sup> Assoc. Professor Kazimierz Peszynski, PhD., Faculty of Mechanical Engineering, UTP University of Science and Technology in Bydgoszcz (Poland), Al. Prof. S. Kaliskiego 7, Bydgoszcz; PL, kazimierz.peszynski@utp.edu.pl.

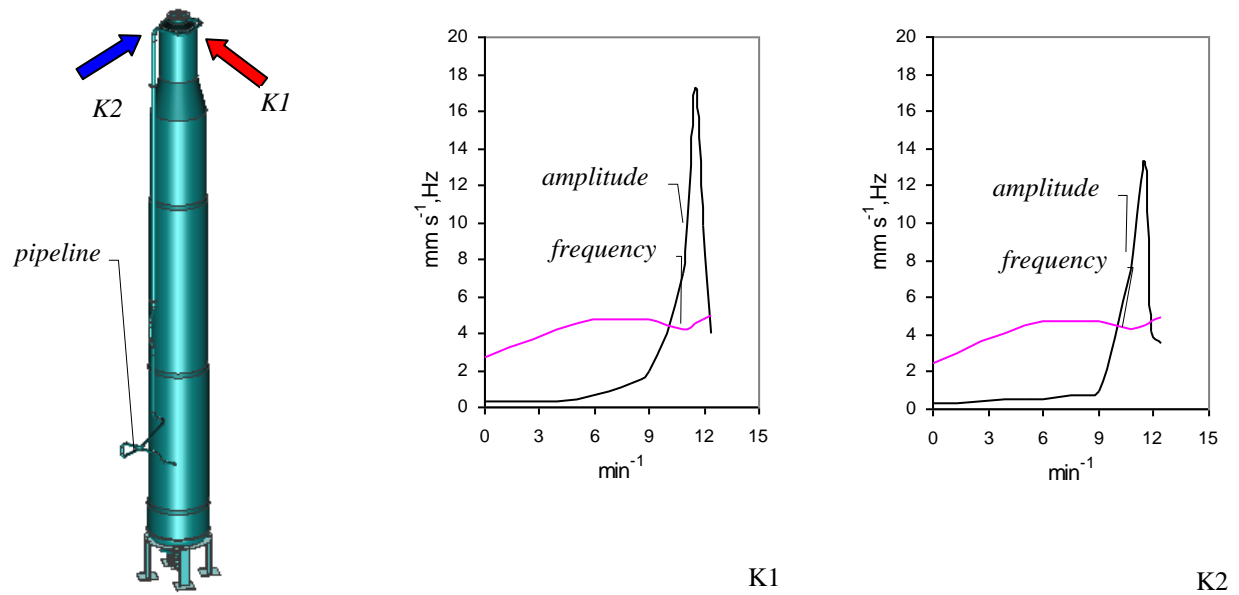


Fig. 1: Digester with a pipeline. Amplitude and frequency of the prevalent vibration velocity component in K1 and K2 direction as a function of the feeder speed.

The digester (Fig. 1) is a  $1.2 \cdot 10^5$  kg vessel mounted on four supports. The digester filled with medium weights twice as much, approx..  $2.4 \cdot 10^5$  kg. The wood chips are fed to the loading chamber via a screw conveyor. The wood chips are fed to the digester from the low pressure zone to the high pressure zone via a high-pressure feeder.

The resonance curve of the digester vibrations is very steep and the frequency range within which a sudden change in the vibration amplitude is observed is narrow (Fig. 1). It is a preferred response, since the transition through the resonance zone is very rapid. The position of the resonance zone shows that the excitation of the digester vibrations is due to the pressure pulsation in the pipeline as a result of opening and closing the feeder chambers. The modal analysis of the digester vibrations confirms the previous hypothesis that the frequency is in fact the resonant frequency.



Fig. 2: The upper pipe section mounted to the digester.

The article includes an excerpt from the stress strain state analysis of the pipeline in its upper section with the diameter of  $d = 273$  mm, i.e. by the digester and in its lower section including the section from level  $h = 0$  m (pump level) to level  $h = 9$  m. The pipeline section diameter is  $d = 219$  mm. Fig. 2 shows the upper section as an approach to the digester. Fig. 3 shows a resonant response of the pipe section.

Fig. 4 shows the frequencies and corresponding natural vibration forms determined for the model.

A comparison between the calculation results and the measured values shows that the rigidity, damping and weight of the pipe section with medium are correct. The resonant frequency of the pipe section without medium is lower (Fig. 5).

The vibration velocity of the pipeline was measured at the fixing points at the support and at the straight pipe section. Fig. 6 shows the vibration amplitudes at prevalent frequencies.

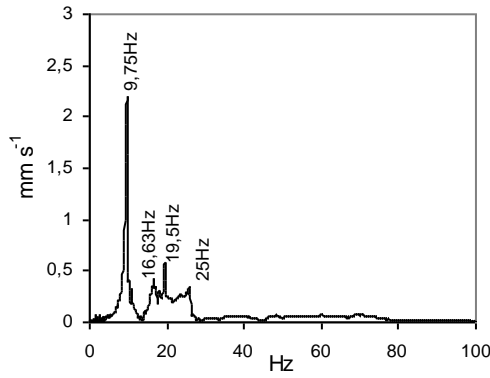


Fig. 3: The resonant response of the pipe section.

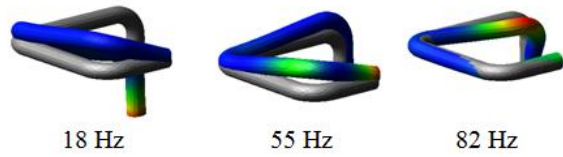


Fig. 4: The frequencies and corresponding natural vibration forms determined for the model.



Fig. 5: The method of excitation of the resonant vibrations in the pipeline.

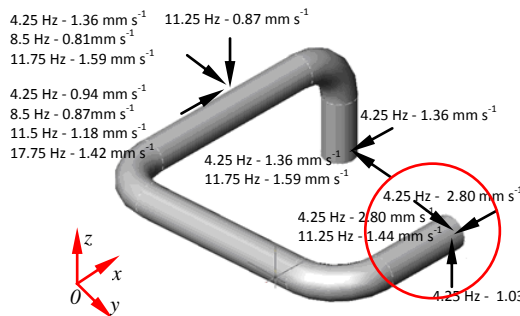


Fig. 6: The vibration amplitudes at prevalent frequencies.

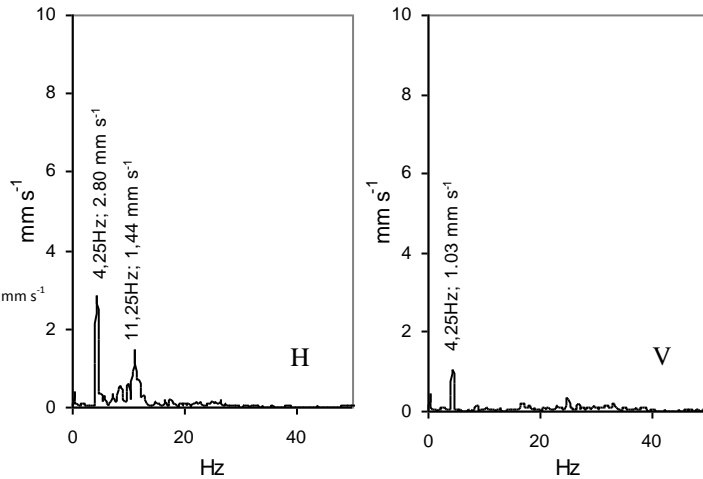


Fig. 7: The vibration spectra.

Fig. 7 shows the vibration spectra for the analysis of the characteristics of the pipe vibration in time in horizontal and vertical direction in point shown in Fig. 6.

The constraint used in the numerical analysis corresponds to the actual constraint due to the similarity between the measured and the calculated spectrum of the vibration velocity (Fig. 8).

Fig. 9 shows the stress pattern in the pipeline profile determined based on the measured vibration velocities. Maximum values of the stress reduced according to the Huber-von Mises-Hencky hypothesis in the analyses pipe section are between  $\sigma_{\text{red}} = 10 - 18 \text{ MPa}$ . The values reach  $\sigma_{\text{red}} = 30 \text{ MPa}$  at the joint between the pipeline and the digester only. The values are considered safe.



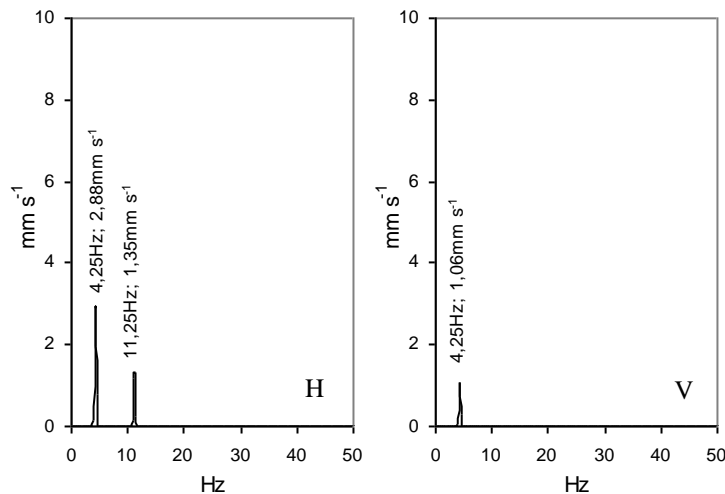


Fig. 8: The calculated spectrum of the vibration velocity.

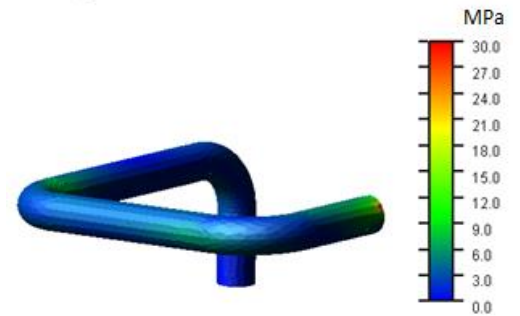


Fig. 9: The stress distribution in the pipe sections.

### 3. Summary

The presented method to determine the stresses in pipe structures based on their vibration velocities has a sound theoretical background. It is a tool, which is expected to be in common use due to the simplicity of both the measurement of the vibration parameters and the numerical analysis. It allows to determine the maximum strain and thus the stress strain state of the pipe. The main issue is, that the method requires to determine the parameters of the relative pipeline vibrations, when the pipeline is constrained by the structure characterized by vibrations at other frequencies. Use of the laser vibrometers to determine the time characteristics of the vibrations allows automatic measurements and stress strain state analysis of both short and very long as well as very complex pipelines.

### References

- Benjamin, T.B. (1961) Dynamics of a system of articulated pipes conveying fluid: I. Theory', Proc. R. Soc. (A), pp. 457.
- Graham, J.P. (1997) Assessment of design and operating experience of pipework fatigue in the offshore and petrochemical industries. Health and Safety Executive – Offshore technology report OTI 95, pp. 631.
- Lin, C.E. (1996) Design guide to reduce potential for vibration caused by fluid flow inside pipes – review and survey. WRC Bulletin 417. Welding Research Council.
- Long, R.H. (1955) Experimental and Theoretical Study of Transverse Vibration of a tube Containing Flowing Fluid. J.Appl.Mech, 22, pp. 65-68.
- Motriuk, R.W. (1994) Field measurement of piping vibration - the relationship of vibration velocity with dynamic strain and stress. Second international conference on motion and vibration control. Yokohama, pp. 783-786.
- Motriuk, R.W. and Harvey, D.P. (1998) Centrifugal compressor modifications and their effect on high frequency pipe wall vibration. Journal of Pressure Vessel Technology, 120, pp. 276-282.
- Niordson, F.I.N. (1953) Vibrations of a Cylindrical Tube Containing Flowing Fluid. Trans. Roy. Inst. Technol.Stockholm 73.
- Wachel, J.C. and Bates, C.L. (1976) Escape piping vibrations while designing. Hydrocarbon Processing.

## APPLICATION OF HAMILTONIAN MECHANICS IN EXPONENTIALLY STABLE CONTROL OF ROBOTS

V. Záda \*

**Abstract:** *The paper deals with tracking control for robots-manipulators, where the dynamics is described by means of Hamiltonian mechanics. This way leads to different physical descriptive quantities used in control design. In the paper, the model-oriented Lyapunov-based control is considered. It is introduced in novel formulation by means of Hamiltonian mechanics.*

**Keywords:** Robotic manipulators, Hamiltonian mechanics, Robot dynamics, Robot control.

### 1. Introduction

Engineers usually use classical vector oriented Newton's mechanics. Force interactions can be also described by scalar functions, recall Lagrangian or Hamiltonian formalism (Golstein, 1950), (Fasano, 2004). The majority of scientists use Lagrange's equations for expression of robot dynamics (Siciliano, 2008), and robot control too. Generally, there are some limits for positions, velocities etc. These limits are constant for all configurations of robot (Arimoto, 1996). The state space, for control, is represented by positions and velocities, therefore by kinematic quantities. Momentums are not respected here. But, momentums change very quickly. Hence, the study of control methods may be interesting from Hamiltonian point of view too. Hamiltonian formalism with using a modified Hamiltonian was used as new function (Wen, 1988). A novel constructive method presented with a new Hamiltonian formulation in (Wang, 2005). The paper Teo (2013) presents a method for design of a set-point controller. The robot is described as a port-Hamiltonian system. In this contribution, we do not want continue similar way. We shall present a new exponentially stable method which may be used for electromechanical systems, especially for robot-manipulators.

### 2. Hamiltonian formalism

The basic ideas of Hamiltonian formalism and its using in the robot dynamics can be founded in the paper Záda (2016), therefore we shall omit them. The robot dynamics can be described by

$$\dot{\mathbf{q}} = \mathbf{M}^{-1}\mathbf{p} \quad (1)$$

$$\dot{\mathbf{p}} = \mathbf{F} - \mathbf{g}(\mathbf{q}) - \left( \frac{\partial K(\mathbf{q}, \mathbf{p})}{\partial \mathbf{q}} \right)^T \quad (2)$$

The second form of these equations suitable for control of robot-manipulators can be represented by the set (Záda, 2016) of equations as follows

$$\dot{\mathbf{q}} = \mathbf{M}^{-1}\mathbf{p} \quad (3)$$

$$\dot{\mathbf{p}} = \left( \frac{1}{2} \dot{\mathbf{M}} - \mathbf{S} \right) \mathbf{M}^{-1}\mathbf{p} - \mathbf{g}(\mathbf{q}) + \mathbf{u} \quad (4)$$

Now we return our attention to the problem of robot control.

---

\* Assoc. Prof. Václav Záda, PhD.: Institute of Mechatronics and Engineering Informatics, Faculty of Mechatronics, Technical University of Liberec, Studentská 1402/2; 461 17, Liberec 1; CZ, vaclav.zada@tul.cz

### 3. Tracking control of robotic systems

The tracking control problem in the joint space consists of a given time-varying trajectory  $\mathbf{q}_d(t)$  and its derivatives. The robot must follow this trajectory with sufficiently precision. Let us define vectors

$$\mathbf{e} = \mathbf{q} - \mathbf{q}_d, \quad \mathbf{z} = \mathbf{M}(\dot{\mathbf{e}} - \mathbf{A}\mathbf{e}), \quad \mathbf{y} = \mathbf{p} - \mathbf{z} \quad (5)$$

Let the controlled system be controlled by the control law, which hides model of controlled system

$$\mathbf{u} = \dot{\mathbf{y}} - \left( \frac{1}{2} \dot{\mathbf{M}} - \mathbf{S} \right) \mathbf{M}^{-1} \mathbf{y} + \mathbf{g} - \mathbf{B} \mathbf{z} \quad (6)$$

So (5) and (6) represent our control system (model of controller). Matrices  $\mathbf{A}$  and  $\mathbf{B}$  are non-singular. They will be chosen lately. The vector  $\mathbf{y}$  represents an estimation of the momentum  $\mathbf{p}$ , and  $\mathbf{z}$  is a difference between actual momentum  $\mathbf{p}$  of the robot and  $\mathbf{z}$ . If we use the equations (4) and (6) then we can derive a feedback equation for control process

$$\dot{\mathbf{z}} = \left( \frac{1}{2} \dot{\mathbf{M}} - \mathbf{S} \right) \mathbf{M}^{-1} \mathbf{z} - \mathbf{B} \mathbf{z} \quad (7)$$

Let a positive definite quadratic form be defined in the form

$$W = \frac{1}{2} \mathbf{z}^T \mathbf{M}^{-1} \mathbf{z} \quad (8)$$

Then its time derivative along the trajectory given by (7) leads to the following inequality

$$\dot{W} = -\mathbf{z}^T \mathbf{M}^{-1} \mathbf{B} \mathbf{z} \leq 0 \quad (9)$$

Generally, the multiplication of matrices in a quadratic form is positive definite. Hence the function  $W$  sinks in time. From (9) follows the chain of inequalities

$$0 \leq \int_0^t \mathbf{z}^T \mathbf{M}^{-1} \mathbf{B} \mathbf{z} dt = -\int_0^t \dot{W} dt = W(0) - W(t) \leq W(0) \quad (10)$$

Let us define the smallest proper value of the matrix  $\mathbf{M}^{-1} \mathbf{B}$

$$\lambda_{\min} = \min \{ \lambda_q; \mathbf{M}^{-1}(\mathbf{q}) \mathbf{B} \mathbf{x}(\mathbf{q}) = \lambda_q \mathbf{x}(\mathbf{q}), \mathbf{q} \in Q \} \quad (11)$$

Where  $\mathbf{x}(\mathbf{q})$ , in (11), is a proper vector,  $Q$  is a working area of the controlled system. Then  $\lambda_{\min} > 0$  and for all  $\mathbf{z}$  it is valid

$$\lambda_{\min} \mathbf{z}^T \mathbf{z} \leq \mathbf{z}^T \mathbf{M}^{-1} \mathbf{B} \mathbf{z} \quad (12)$$

From these relations we derive the inequalities

$$\int_0^t \mathbf{z}^T \mathbf{z} dt = \frac{1}{\lambda_{\min}} \int_0^t \mathbf{z}^T \mathbf{M}^{-1} \mathbf{B} \mathbf{z} dt \leq \frac{W(0)}{\lambda_{\min}} < \infty \quad (13)$$

Since  $\|\mathbf{z}\|^2 = \mathbf{z}^T \mathbf{z}$  and  $0 \leq W(t) \leq W(0)$  we see that  $\mathbf{z} \in L_2 \cap L_\infty$ . Similarly let us define following values

$$\lambda_m = \min \{ \lambda_q; \mathbf{M}(\mathbf{q}) \mathbf{x}(\mathbf{q}) = \lambda_q \mathbf{x}(\mathbf{q}), \mathbf{q} \in Q \} \quad (14)$$

$$\lambda_M = \max \{ \lambda_q; \mathbf{M}(\mathbf{q}) \mathbf{x}(\mathbf{q}) = \lambda_q \mathbf{x}(\mathbf{q}), \mathbf{q} \in Q \} \quad (15)$$

The numbers (14) and (15) are positive and hence the following inequalities (16) are valid too

$$\lambda_m \mathbf{z}^T \mathbf{z} \leq \mathbf{z}^T \mathbf{M} \mathbf{z} \leq \lambda_M \mathbf{z}^T \mathbf{z} \quad (16)$$

Remember, these inequalities of these quadratic forms are valid for all  $\mathbf{z}$ , and, as usual, they can be simply written as

$$\lambda_m \mathbf{I} \leq \mathbf{M}(\mathbf{q}) \leq \lambda_M \mathbf{I} \quad (17)$$

The reader can prove that from (16) it can be derived the result

$$\lambda_M^{-1} \mathbf{I} \leq \mathbf{M}^{-1}(\mathbf{q}) \leq \lambda_m^{-1} \mathbf{I} \quad (18)$$

Then, we can obtain a new inequality

$$\frac{\dot{W}}{W} = -2 \frac{\mathbf{z}^T \mathbf{M}^{-1} \mathbf{B}(\mathbf{q}) \mathbf{z}}{\mathbf{z}^T \mathbf{M}^{-1}(\mathbf{q}) \mathbf{z}} \leq -2 \frac{\mathbf{z}^T \mathbf{z} \lambda_{\min}}{\mathbf{z}^T \mathbf{z} \lambda_m^{-1}} \quad (19)$$

and so we have obtained the result

$$\frac{\dot{W}}{W} \leq -2 \lambda_{\min} \lambda_m \quad (20)$$

Let the multiplication of the proper values be denoted as  $a = \lambda_{\min} \lambda_m$ . The (20) may be rewritten as

$$\frac{\dot{W}}{W} \leq -2a \quad (21)$$

Integration of (21) leads to the interesting estimation

$$W(t) \leq W(0) e^{-2at} \quad (22)$$

Now, from (8) and (18) we can derive the following chain of inequalities

$$\lambda_M^{-1} \mathbf{z}^T \mathbf{z} \leq \mathbf{z}^T \mathbf{M}^{-1} \mathbf{z} = 2W \leq 2W(0) e^{-2at} = \mathbf{z}^T(0) \mathbf{M}^{-1}(\mathbf{q}_0) \mathbf{z}(0) e^{-2at} \leq \|\mathbf{z}(0)\|^2 \lambda_m^{-1} e^{-2at} \quad (23)$$

Hence, the variable  $\mathbf{z}$  is exponentially bounded from above, how we see it from following inequality

$$\|\mathbf{z}(t)\| \leq c_1 e^{-at}, \text{ for } c_1 = (\lambda_M \lambda_m^{-1})^{0.5} \|\mathbf{z}(0)\| \quad (24)$$

The parameter  $c_1$  depends only on initial estimation of the vector  $\mathbf{z}(0)$ . Now it can be seen that for  $t \rightarrow \infty$  the variable  $\mathbf{z} \rightarrow 0$ . Let us study the differential equation (18) rewritten in the form

$$\dot{\mathbf{e}} - \mathbf{A} \mathbf{e} = \mathbf{M}^{-1} \mathbf{z} \quad (25)$$

This equation has a solution, for initial condition  $\mathbf{e}_0 = \mathbf{e}(0)$ ,

$$\mathbf{e}(t) = \exp(\mathbf{A}t) \mathbf{e}_0 + \int_0^t \exp(\mathbf{A}(t-\tau)) \mathbf{M}^{-1} \mathbf{z} d\tau \quad (26)$$

Using classical inequalities for norms of matrices and vectors we can derive the following estimation

$$\|\mathbf{e}(t)\| \leq c_2 e^{-bt} \quad (27)$$

where  $c_2$  and  $b$  are some positive constants. Hence, for  $t \rightarrow \infty$  the error vector  $\mathbf{e} \rightarrow 0$ , too.

Proof of (27): Let the solution (26) be considered. Then we obtain, with using norm for matrices,

$$\|\mathbf{e}(t)\| \leq \|\exp(\mathbf{A}t)\| \cdot \|\mathbf{e}_0\| + \int_0^t \|\exp(\mathbf{A}(t-\tau))\| \cdot \|\mathbf{M}^{-1}\| \cdot \|\mathbf{z}\| d\tau \quad (28)$$

Because  $\mathbf{A}$  is stable, there are positive constants  $k$  and  $c$ , such that for all  $s \geq 0$  (here  $e$  is the Euler number) it is valid

$$\|\exp(\mathbf{A}s)\| \leq k e^{-cs} \quad (29)$$

So we can write (e is the Euler number) the inequality

$$\|\mathbf{e}(t)\| \leq k \cdot \|\mathbf{e}_0\| \cdot e^{-ct} + k \int_0^t e^{c(\tau-t)} \cdot \|\mathbf{M}^{-1}\| \cdot \|\mathbf{z}\| d\tau \quad (30)$$

The working space  $Q$  of all admissible vectors  $\mathbf{q}$  is bounded, hence there are constant  $k_M$  such that

$$\|\mathbf{M}^{-1}(\mathbf{q})\| \leq k_M \quad (31)$$

Hence with using these facts and (26) we can write

$$\|\mathbf{e}(t)\| \leq k \|\mathbf{e}_0\| e^{-ct} + c_1 k k_M e^{-ct} \int_0^t e^{\tau(c-a)} d\tau \quad (32)$$

If  $c = a$  then the integral in (32) is  $t$ . Generally it is  $c \neq a$ . But the case  $c = a$  can be included in this general case, if we replace  $c$  by any smaller positive  $c$ . So we can rewrite (32)

$$\|\mathbf{e}(t)\| \leq k\|\mathbf{e}_0\|e^{-ct} + c_1 k k_M \frac{e^{-at} - e^{-ct}}{c - a} \quad (33)$$

Let  $b = \min\{a, c\}$ . Then

$$0 \leq \frac{e^{-at} - e^{-ct}}{c - a} = \frac{e^{-bt}}{|c - a|} \quad (34)$$

and so (33) can be expressed in the following form

$$\|\mathbf{e}(t)\| \leq e^{-bt} \left[ k\|\mathbf{e}_0\| + \frac{c_1 k k_M}{|c - a|} \right] \quad (35)$$

Hence (35) has really the form of (27) for suitable constant  $c_2$ . Let us rewrite the (25) in the form

$$\dot{\mathbf{e}} = \mathbf{M}^{-1} \mathbf{z} + \mathbf{A} \mathbf{e} \quad (36)$$

Then we obtain the following chain of inequalities

$$\|\dot{\mathbf{e}}\| \leq \|\mathbf{M}^{-1}\| \cdot \|\mathbf{z}\| + \|\mathbf{A}\| \cdot \|\mathbf{e}\| \quad (37)$$

Now with using (24), (27) and (31), respectively, we obtain the following inequality with suitably constant  $c_3$ .

$$\|\dot{\mathbf{e}}(t)\| \leq c_3 e^{-bt} \quad (38)$$

Here  $c_3$  is the positive constant, too. Hence, if  $t \rightarrow \infty$  then the signal,  $d\mathbf{e}/dt$ , converges to 0. Relations (27) and (38) show that the control algorithm is exponentially stable.

It is necessary to choose the matrix  $\mathbf{A}$  to be stable. That is, its proper values must be in the left side of the complex plane. The matrix  $\mathbf{M}^{-1}\mathbf{B}$  must be positive definite. Because  $\mathbf{M}$  and so  $\mathbf{M}^{-1}$  are positive definite matrices, it suffices to choose a matrix  $\mathbf{B}$  to be diagonal with positive coefficients on diagonal. Then the multiplication  $\mathbf{M}^{-1}\mathbf{B}$  is positive definite too. For simplicity, the matrix  $\mathbf{B}$  can be chosen as  $\mathbf{B} = b_0 \mathbf{I}$ , where  $b_0$  is any function or constant, respectively. An alternative choice is to define a matrix  $\mathbf{B}_0$  which is positive definite and then define matrix  $\mathbf{B}$  as  $\mathbf{B} = \mathbf{M}(\mathbf{q})\mathbf{B}_0$ . Then the matrix  $\mathbf{M}^{-1}\mathbf{B} = \mathbf{B}_0$  is automatically positive definite.

#### 4. Conclusions

In this article was developed the mathematically oriented text which describes the way how to control robots along a desired trajectory. The proved mathematical formulae show that the desired method is exponentially stable. This result is interesting for applications, because the exponential stability automatically leads to robustness of asked algorithm of control.

#### References

- Arimoto, S. (1996) Control Theory of Non-linear Mechanical Systems. Clarendorf Press, Oxford.
- Fasano, A. and Marmi, S. (2004) Analytical Mechanics. Oxford Press.
- Golstein, H. (1950) Classical Mechanics, Addison-Wesley, Camb.
- Samson, C. , Le Borgne, M. and Espiau, B. (1991) Robot Control, The task fun. approach. Clf. Press, Oxford.
- Siciliano, B. and Khatib, O. (Eds.) (2008) Handbook of Robotics. Springer.
- Teo, Y.R., Donair, A. and Perez, T. (2013) Regulation and Integral Control of an Underactuated Robotic systems Using IDA-PBC with Dynamic Extension", IEEE/ASME International Conference of Advanced Intelligent mechatronics (AIM) Wollongong, Australia, pp. 920-925.
- Wen, J.T. et al. (1988) New class of control laws for robotic manipulators. J. Control, Vol.47 (5), pp. 1361-1385.
- Záda, V. and Belda, K. (2016) Robot control in terms of Hamiltonian mechanics. in: Proc. Int. Conf. on Engineering Mechanics 2016 (eds. Zolotarev, I and Radolf, V.), Svratka, Czech Republic, pp. 627-630.

## COMPREHENSIVE SERVICE OF CONFERENCE PARTICIPANTS USING AUTOMATIC IDENTIFICATION

P. Zajac<sup>\*</sup>, L. Kowalczyk<sup>\*\*</sup>

**Abstract:** *This paper discusses the issue of logistic service of conference participants in terms of their automatic identification. A conference participant ID badge was de-signed for purposes of this paper. A participant information vector was developed and coded using different bar code symbologies. Subsequently, on the basis of the presented criteria, the best solution was chosen. On the basis of questionnaire surveys conducted in 2014 – 2015, feedback concerning service of conference participants was compiled for comparison purposes. Further, a comparative assessment of the labour intensity of registration of conference guests was carried out.*

**Keywords:** Reliability, Automatic identification systems, RFID.

### 1. Introduction

Security requirements in the organisation of events such as a scientific conference are being constantly raised. Currently, at the Wrocław University of Science and Technology, there is a requirement of identification of conference guests. “Logistics” Student Scientific Circle, which is active at the Faculty of Mechanical Engineering of the Wrocław University of Science and Technology, has been organising the Translogistics.pl, conference since 2005, (Kowalczyk, 2016). In 2014, at a member meeting summing up a conference, directions of improvements were brainstormed, one of them having been the introduction of a person automatic identification system. It applies to persons working in the registration section. One of the larger difficulties, in particular during the registration of students for workshops and trips, lies in the manual action. The basis for collecting and storing information are handwritten lists which introduce a great deal of difficulties. Not only are the data recorded on the forms only, meaning they can be easily damaged or lost, but also their updating or a change of mind of a participant lead to crossing-out and make the content less legible. Hastily carried out registrations may cause failure to observe registration limits/double registration of one of the students or result in unclear information which will prevent clear identification of a participant. Moreover, control over the number of participants, who have not chosen the form of their classes for the second conference day yet, gets more difficult. A boundary condition had been to develop a conference database which was carried out, the database having been optimised, (Kwasniowski et al., 2011). Next, the database was programmed in Microsoft Access, (Świeboda, 2016 and Świeboda, 2015).

### 2. Automation participant identification

GS-1-13 bar codes and tags were initially taken into account. Additionally, a prerequisite was adopted that the code had to fit onto the participant ID badge, in the paper (Zajac, 2015).

Bar codes reflect graphically various kinds of data. EAN-13 codes are commonly used in marking goods in retail. They consist of 12 coded digits and a control digit, in the paper (Kwasniowski, 2004). It is worth pointing out here that the GTIN (Global Trade Item Number) methodology is currently used in commerce, including GTIN-13 which identifies consumer units – a unique code of a retail item presented in the form of the EAN-13 bar code, in the paper (Bujak and Zajac, 2012). Nevertheless, one should

---

<sup>\*</sup> Paweł Zajac, PhD.: Wrocław University of Science and Technology, 27 Wybrzeże Wyspiańskiego st.; 50-370, Wrocław; RP, pawel.zajac@pwr.edu.pl

<sup>\*\*</sup> Lucyna Kowalczyk, Msc.: “Logistics” Student Scientific Circle, Wrocław University of Science and Technology; 27 Wybrzeże Wyspiańskiego st.; 50-370, Wrocław; RP, 210101@student.pwr.edu.pl



distinguish at this point between the use of a code for commerce purposes, which is supervised and subject to strict rules, and the use of a code symbology in a local project, as in the case discussed here. Since we do not deal with publication of codes and their common use, it is possible to use the EAN-13 symbology skipping part of the requirements established for the use of the GTIN. Further on in the paper, references to the EAN-13 code are to be understood as the use of the code symbology without taking into account the commercial context. The codes themselves allow clear identification of a participant on the basis of an individual identification number in the form of a code which was assigned to them. Additionally, they are cheap and simple to create and use. Since they are supposed to have meaning solely within a conference database, it is not necessary to preserve the conventional meanings of digits whereby the first two ones are the country code, the next five ones identify the manufacturer and the subsequent ones designate the product. It should be taken into account, however, that a scanner is still necessary to read such codes.

RFID tags give the ability to store a larger amount of data. Apart from the participant identification number, it would also be possible to record such data as first name and last name or scientific circle. The use does not require that the tag “establish a visual contact with a scanner”, which is one of the greatest advantages of this technology. In addition, here we can edit the data and therefore one could also save in a tag the information on selected activity on the second day or confirm the registration. Work with many tags at the same time would also be possible, (Bujak and Zajac, 2013). Obviously, a drawback is the cost of purchase of tags whereby it would not increase the expenses on participant ID badges when using codes.

Both technologies would constitute a good solution in the implemented system. However, it was necessary to make a decision and choose the technology. Since it is always the budget which is a limitation, additional costs connected with the purchase of the RFID tags may prove to be unnecessary if their application does not provide additional improvements. In the discussed case, it is most important to enhance the work with data and for this purpose the use of bar codes such as EAN-13 will suffice. The biggest advantage of RFID tags for the Scientific Circle is reading many participants at the same time. Nonetheless, in reality these deficiencies can be made up for with right software and code structure. Lack of additional costs and a far simpler placement on the ID badge make one choose the bar codes.

### 3. Impact of bar codes on the participant ID badge project

However, the choice in the context of development of a bar code system does not end the decision process. For comparative purposes, the EAN-13 code was used. Other bar codes also serve the same function while keeping the above-mentioned advantages. The choice of the right coding has to take into account the ability to code data in the context of a database as well as the minimum area taken up on a finished ID badge. As standard, participant ID badges have the A7 size:  $105\text{ mm} \times 74\text{ mm}$  and the minimum area occupied by a bar code will be assessed relative to this size. The following symbologies were taken for consideration: EAN-8, EAN-13, GS1-128, 39, RSS, 2z5, PDF-417, QR, AZTEC.

The EAN-13 code will be considered in the first place. 12 characters can be specified in coding which leaves one free relative to the required whole. It will be added to the participant ID which in result gives the following order: rrrr uu kk oooo c where: r – year, u – higher education institution code, k – scientific circle code, o – individual (participant ID), c – control digit. The code for sample data was shown in Fig. 1; “2” is the control digit calculated following the modulo39 rules. In accordance with the magnification factors and provided that the magnification is kept at 0.80, the code will take up  $29.83\text{ mm} \times 20.73\text{ mm}$ , i.e. it will occupy 7.96 % of an ID badge. Other codes, along with their factors and descriptions, were included in Tab. 1.








### 4. Comparative analyses of processes in 2014-2015

Further improvements came into view in the information processing phase. Thanks to better control when introducing the data, it is not necessary to re-check all e-mails and compare them with the data. Instead, relationships are verified concerning whether or not all users have a scientific circle and a higher education institution selected. Subsequently, simple generation of data can be performed which will be used to create ID badges or certificates using the mail merge function. In addition, there is a bar code generation step. However, it is worth reminding that it only requires to turn on the query before the export

of data and start up a script before using the mail merge function. New tasks are not only simple to accomplish, but they also bring about large benefits in the later part of work with the system.

The biggest changes occurred while working on the conference day. Thanks to the system, registration is carried out more efficiently and accurately. Participants spend less time in queues, in particular during the time of registration for activities of the second conference day. Moreover, the organisers have better control and can verify faster the registrations and the number of already registered students. For instance, if one scientific circle still has not registered after the end of registration period, this can be quickly verified by contacting the tutor of the scientific circle designated by the organisers or the participants directly.

*Tab. 1: Sample data coding in different coding methods with determined magnification factors, occupied areas on the ID badges, ranges and comments. Source: own work.*

<i>Code name</i>	<i>Code</i>	<i>Magnification factor</i>	<i>Occupied area [%]</i>
<i>GSI-128</i>	 (2015)1718001	0.5	23.19
<i>39</i>	 *20151718001*	0.8	13.41
<i>RSS</i>	 (01)00201517180012	1.0	3.65
<i>2z5</i>	 20151718001	1.0	6.09
<i>PDF-417</i>		1.0	15.87
<i>QR</i>		0.5	6.81
<i>AZTEC</i>		0.5	5.07

One of the main criteria of making a decision was simplicity and area occupied on a participant ID badge. Codes which took up over 10 % of the area were eliminated due to high importance of the sign in the project. Other codes were analysed in terms of their disadvantages and advantages. The focus here was to satisfy software needs while maintaining minimum impact on the project. Simplicity, legibility and commonness were also taken into account. Due to the specified parameters of the individual codes, a decision was made to use the EAN-13 coding, since it fully met system expectations, having occupied little space on the ID badge which made its placement easier. Furthermore, it was commonly recognised and that was why it did not require any additional explanation. The issue of colour selection was passed

over in the paper, which had been analysed. Having made those decisions, it was possible to design the ID badge. On the basis of the created maps of processes before and after system implementation, it is possible to assess the labour intensity of solutions which will additionally help to identify the disadvantages and advantages of the solution. As can be seen in Table 1, in the case of the implemented system, demand for persons and equipment gets reduced, except for the phase of service of participants on the conference day when it is necessary to use a computer and a bar code scanner. It is worth emphasising that work of one person at the stages of data preparation allows maintaining continuity of correspondence with participants and decreases time demand for information exchange. Maintaining the database in the cloud makes it possible for other members of a scientific circle to control or select the needed data at the same time. With the use of the system, the quality of service of participants increases. One of the main criteria concerning this point is time. Members of scientific circles come many a time from places far away. After a long journey, they unwillingly spend time waiting for registration, and it is impossible to get admitted without it. Waiting time reduction and division of the registration into two stages make the participants wait for a much shorter time, even when there is a lot of scientific circles. Firstly, they receive their ID badges. Next, the code gets read and their presence gets checked. However, the greatest amount of time is saved during registration for workshops and trips. The participants have time to talk to company representatives and members of befriended scientific circles. Once again, they do not intend to spend time in queues. Thanks to scanning of codes, registration of a single participant takes a dozen or so seconds. What is more, the ability to perform a context search additionally speeds up the process if participants from one scientific circle or higher education institution report for registration in groups. Quality of service is also the number of complaints and the ability to make corrections. During a conference, it may happen that an identification number/certificate printout is incorrect or that the data for the invoice are wrong. Since it is possible to fully eliminate human errors, every effort should be taken for the errors to be rectifiable as soon as possible. A change of data of a participant does not cause a change of bar codes which depend on the identification numbers of a higher education institution, a scientific circle or a participant. Thus, the impact on the rest of the data is not a concern. The last element of quality is reliability. Scanning a prepared code not only speeds up the work, but also reduces the number of errors compared to manual service.

## References

- Bujak, A. and Zajac, P. (2013) Monitoring of cargo in logistics of transport and storage, in: "Communications in Computer and Information Science", Vol. 395, pp. 361-369, <http://dx.doi.org/10.1007/978-3-642-41647-7>.
- Bujak, A. and Zajac, P. (2012) Can the increasing of energy consumption of information interchange be a factor that reduces total energy consumption of a logistic warehouse system?, in: "Communications in Computer and Information Science", Vol. 329, [http://dx.doi.org/10.1007/978-3-642-34050-5\\_23](http://dx.doi.org/10.1007/978-3-642-34050-5_23).
- Kowalczyk, L. (2016) Improving the process of handling conference participants using the GS-1 database and barcodes on the example of TransLogistics conference, unpublished work, Wroclaw University of Technology.
- Kwasniowski, S. (2004) The role of automatic identification systems (AUTO-ID) of goods, persons and documents in logistics, (eds. Kwasniowski S. and Zajac P.), Automatic identification in logistic systems, Publishing House of Wroclaw University of Technology, Wroclaw (in Poland), pp. 9-16, ISSN 1425-0993, 16.
- Kwasniowski, S., Zajac, M. and Zajac, P. (2011) Logistic management of commodity information in distribution, *Logistics*, 2011, 6, pp. 2141-2149.
- Kwasniowski, S., Zajac, M. and Zajac, P. (2011) Telematic problems of unmanned vehicles positioning at container terminals and warehouses, Berlin, Heidelberg, Springer, cop. 2011, (ed. Mikulski J.) *Communications in Computer and Information Science*, pp. 391-399, ISSN 1865-0929, Vol. 104, [http://dx.doi.org/10.1007/978-3-642-16472-9\\_43](http://dx.doi.org/10.1007/978-3-642-16472-9_43).
- Swieboda, J. (2016) Analysis and assessment of an information subsystem in an inland container terminal, *Journal of KONBiN*, 38(1), pp. 99-130.
- Swieboda, J. (2015) System resilience at an intermodal transshipment node, CLC 2015, Carpathian Logistics Congress-Conference Proceedings, pp. 502-511.
- Zajac, P. (2015) Evaluation of automatic identification systems according to ISO 50001. *Advances in Intelligent Systems and Computing*, Vol. 350, pp. 345-355, <http://dx.doi.org/10.1007/978-3-319-15796-2>

## **MODELLING FORKLIFT TRUCK MOVEMENT IN THE VDI CYCLE AND THE POSSIBILITY OF ENERGY RECOVERY**

**P. Zajac<sup>\*</sup>, S. Kwasniowski<sup>\*\*</sup>**

**Abstract:** *This paper puts forward a proposal of description of movement of a forklift truck in the form of a non-linear differential equation. In this model, resistance to motion while driving in a straight line and along curves is taken into account. The external traction characteristics of a drivetrain are calculated on the basis of power of traction motors and static forces acting on the driving axle of a forklift truck, for an empty and loaded forklift truck. A model designed in such a way is used to carry out a simulation of forklift truck operation in a specified cycle defined by the VDI 2198 standard. This standard makes it possible to compare operating parameters of various forklift trucks under identical operating conditions. In the paper's conclusions, the amounts of possibly recoverable energy, coming from braking and lowering loads collected from racks by means of fork of a forklift truck, are estimated.*

**Keywords:** Forklift trucks, Modelling, Logistics warehouse systems.

### **1. Introduction**

Similarly to other branches of industry and economy, modern logistics engineering searches for new technical solutions connected with moving goods in transport processes. In this search, we pay particular attention to ecological aspects and energy consumption. In modern drive system solutions, we strive to recuperate energy. These actions are part of global efforts to reduce energy consumption. Due to ecology and convenience, more and more internal combustion drives are replaced with electric drives. Such tendencies have been present in railway engineering and in the automotive industry for a long time, but also in industrial vehicles' drives paper Kwasniowski et al. (2008). Hybrid drives (internal combustion and electric with electric transmissions) have also become part of this trend. Research into energy consumption makes it possible to implement latest technologies and recuperate energy. Energy recovery is also employed in forklift trucks which are the subject of this paper. Energy recovery makes sense in machines in which the operating cycle involves frequent acceleration and braking of masses. Currently, we usually recover energy from the process of braking. Forklift truck's operation consists in constant accelerating and braking which provides a basis for closer investigation of those processes in terms of energy-efficiency. First energy recovery solutions have emerged in underground, light railway, trams, trolley buses, electric buses, diggers and forklift trucks. The key is to answer the question under what conditions one can recover energy using the results of a computer simulation of the operating cycle of a vehicle or a device and to what extent such a simulation corresponds to real operating conditions. In technical solutions, there has been a difficulty in accumulating recovered energy thus far. The answers to these questions can be obtained by way of modelling forklift truck's movement, taking into account the specifics of their motion. This paper Kwasniowski et al. (2011) presents a computational model of movement of a forklift truck in the form of a non-linear differential equation (taking resistance to motion and non-linear characteristics of a drive system under consideration). This tool allows calculating recoverable energy streams as a results of processes of braking and lowering loads from high racks using forklift trucks.

---

<sup>\*</sup> Pawel Zajac, PhD.: Wroclaw University of Science and Technology, 27 Wybrzeze Wyspianskiego st.; 50-370, Wroclaw; RP, pawel.zajac@pwr.edu.pl

<sup>\*\*</sup> Stanislaw Kwasniowski, PhD.: Wroclaw University of Science and Technology; 27 Wybrzeze Wyspianskiego st.; 50-370, Wroclaw; RP, stanislaw.kwasniowski@pwr.edu.pl

## 2. Model of movement of a forklift truck

The movement of a forklift truck as a concentrated mass in accordance with Newton's second law of motion is the paper Zajac (2015):

$$\xi * m \frac{dV}{dt} + W_t = F_N \quad (1)$$

where:  $\xi$  – rotating masses coefficient ( $\xi = 1.05$  – it takes into account the rotating parts of the forklift truck's drive system which affect its total kinetic energy. In forklift trucks, only wheels, traction motors and driveshafts are rotating parts. These parts accumulate a relatively small amount of energy in the rotational motion compared to the kinetic energy of translational masses. In this paper, a coefficient, which increases the substitute mass of a forklift truck by the effects of rotating masses, was set at 5 % of energy contained in the translational masses.)  $m$  – forklift truck's translational mass,  $W_t$  – rolling resistance (as a total value which varies as a function of the nature of linear or curvilinear motion),  $F_N$  – maximum driving force (resulting from the external characteristics of the drive system – it depends on the speed of motion),  $\Delta t$  – time increment,  $\Delta s$  – distance increment along the test section,  $V_{sr}$  – average speed. Rearranging the above equation, one can obtain the formula for forklift truck's distance increment:

$$\xi * \frac{G}{g} * \frac{dV}{dt} = F_N - W_t \quad (2)$$

$$\frac{\xi}{g} * \frac{dV}{dt} = \frac{F_N - W_t}{G} \quad (3)$$

$$\frac{\xi}{g} * \frac{dV}{dt} = p(v) \quad (4)$$

The following have to be substituted:  $dV = \Delta V$ ,  $dt = \Delta t$ ,  $dt = \frac{\Delta s}{V_{sr}}$

$$\frac{\xi}{g} * \frac{\Delta V}{\Delta t} * V_{sr} = p(v) \quad (5)$$

$$\Delta s = \frac{\xi}{g} * \frac{\Delta V}{p(V)} * V_{sr} \quad (6)$$

where:  $\Delta s$  – distance increment along a given section,  $\xi$  – rotating masses coefficient ( $\xi = 1.05$ ),  $g$  – gravitational acceleration ( $g = 9.81 \frac{m}{s^2}$ ),  $\Delta V$  – speed increment along a given section,  $p(V)$  – unitary accelerating ( $p_N(V)$ ) / decelerating ( $p_H(V)$ ) force per unit mass of the vehicle,  $V_{sr}$  – average speed. The work performed is defined by the following formula:

$$\Delta W = F_N * \Delta s \quad (7)$$

where:  $\Delta W$  – work increment,  $F_N$  – forklift truck's driving force,  $\Delta s$  – distance increment. The travel time can be determined using the following formula:

$$\Delta t = \frac{\Delta s}{V_{sr}} \quad (8)$$

$\Delta t$  – time increment along a given section,  $\Delta s$  – distance increment,  $V_{sr}$  – average speed.

## 3. Forklift truck's movement cycle according VDI2198

In order to compare the energy consumption of various designs of forklift trucks, forklift truck's movement cycle described in the VDI 2198 standard is used. The said cycle was shown in Fig. 1.

In the discussion, it was assumed that the forklifts truck's curvilinear motion was performed at a speed of 0.25 m/s, whereas its acceleration in each stage was achieved using its full power (external characteristics of the drive system). In practice, due to cost constraints and safety, full performance (acceleration) of a forklift truck is usually not used during its operation. It was assumed that the forklift truck carried a load of 1000 kg.

A forklift truck placed in the starting position accelerates and goes in a straight line over a distance of approx. 28 m and then limits its speed to 0.25 m/s in order to make a turn and pulls up to a rack. The next stage involves lifting empty fork to a height of 2 m, pulling up to a load, lifting it and backing up with the load.

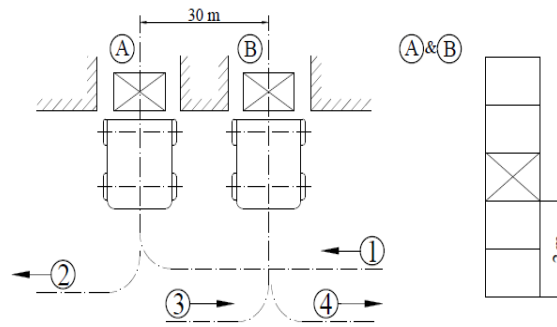


Fig. 1: VDI2198 cycle in the VDI2198.

Once the fork has been lowered, the next action involves backing up with the load and making a turn. Subsequently, after covering a straight stretch of road, the forklift truck makes a turn and then pulls up to rack B. The load is put back onto the rack at a height of 2 m and the empty forklift truck returns to its starting position in the papers Zajac (2011 and 2014 and 2015).

#### 4. Results of simulation of forklift truck's movement

A simulation of movement of two forklift trucks was carried out: HYUNDAI 10/13/15BTR and Jungheinrich EFG-220. The evolution of changes in motion as a function of distance and time of covering individual phases of motion for both forklift trucks was shown in Fig. 2.

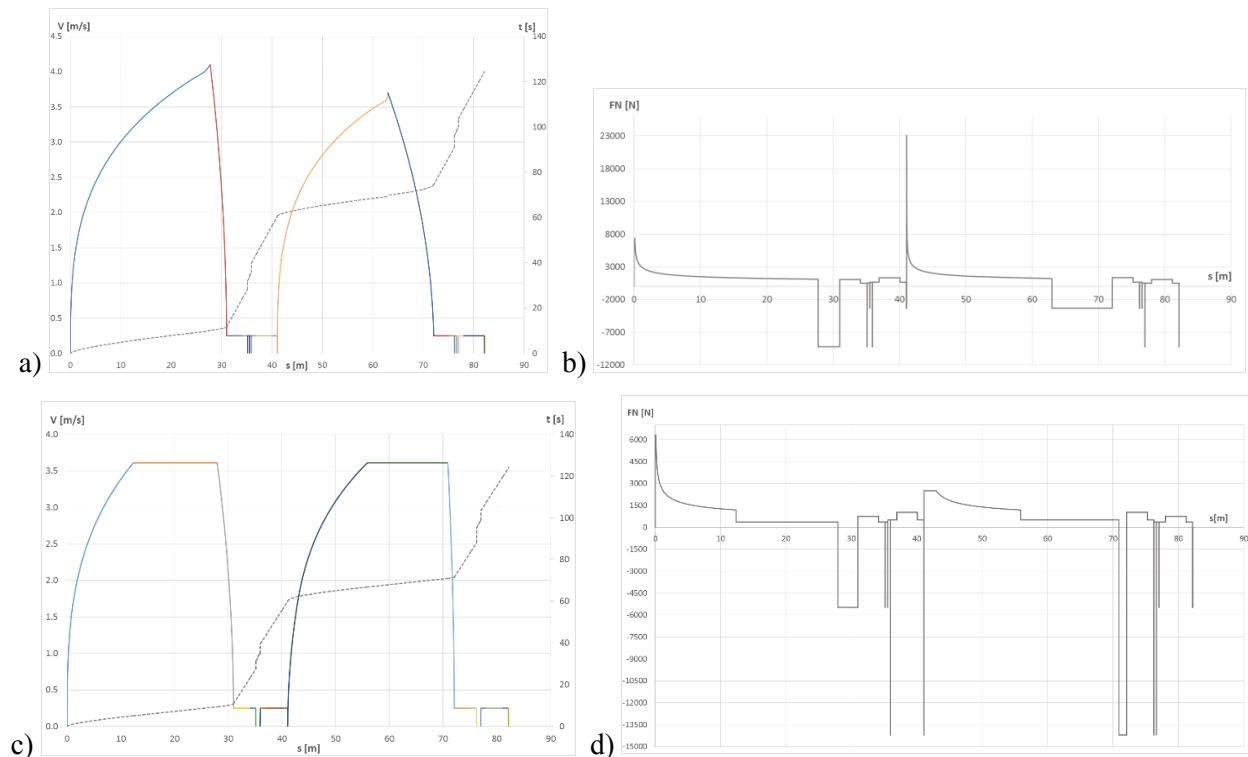


Fig. 2: Evolution of changes in motion as a function of distance and time of covering individual phases of motion: a), b) Run of Jungheinrich EFG 220 forklift truck; c), d) Hyundai 10/13/15BTR.

#### 5. Conclusions

The results of simulation calculations made it possible to determine the total streams of energy in the investigated VDI operating cycle for both forklift trucks. They enable us to get to know better the advantages and disadvantages of both designs of forklift trucks with rear wheel drive (Hyundai 10/13/15BTR and Jungheinrich EFG-220). Important parameters of calculations in an operating cycle according to the VDI were summarised in Tab. 1.



The conducted simulation calculations of operation of forklift trucks indicated what theoretical streams of energy were recoverable in the processes of braking and lowering load masses. The calculations were carried out with the assumption that a forklift truck moved in accordance with the characteristics of its external drive system. In practice, this style of driving a forklift is used rather rarely. The process of recovery of energy of lowering a load on fork is in this case justified to a lesser extent. However, it should be borne in mind that the height of lowering assumed in the paper was just 2 metres. Recovering energy from the process of lowering loads is justified in cases of high rack stacker forklift trucks.

*Tab. 1: Comparison of energy parameters of work of forklift trucks according to the VDI cycle (source: own work).*

Parameter	Unit	Hyundai 10/13/15BTR	Jungheinrich EFG-220
Energy used up for movement $E_i$	kJ	73.6	356.8
Energy used up for lifting a load $E_p$	kJ	30.2	30.2
Forklift truck's braking energy $E_h$	kJ	34.4	54.9
$E_p / E_i$	%	41	8.5
$E_p / E_i + E_p$	%	21.2	7.8
$E_i / E_i + E_p$	%	70.9	92.2
$E_h / E_i$	%	46.7	15.4
$E_h / E_i + E_p$	%	33.1	14.2

## References

- Kwasniowski, S., Nowakowski, T. and Zajac, M. (2008) Analysis of intermodal transport reliability in Poland, in: Research Bulletin – University of Gdansk, Land transport economics, 2008(36), pp. 187-197.
- Kwasniowski, S., Nowakowski, T. and Zajac, M. (2008) Intermodal Transport in Logistics Networks. Oficyna Wydawnicza Politechniki Wrocławskiej, Wrocław (in. Poland), Navigator, ISSN 1425-0993; 18.
- Kwasniowski, S. and Zajac, M. (2008) Parametrisation of transshipment capacity of container terminals. Transport Review, Ch. 47, No. 10, pp. 83-108, in: 18th Scientific Conference on Rail Vehicles, Katowice-Ustroń.
- Kwasniowski, S., Zajac, M. and Zajac, P. (2011) Telematic problems of unmanned vehicles positioning at container terminals and warehouses, in: Communications in Computer and Information Science (ed. Mikulski, J.), Berlin Heidelberg Springer, vol. 104, pp. 391-399, [http://dx.doi.org/10.1007/978-3-642-16472-9\\_43](http://dx.doi.org/10.1007/978-3-642-16472-9_43).
- Zajac, P. (2015) Evaluation method of energy consumption in logistic warehouse systems. EcoProduction, Environmental Issues in Logistics and Manufacturing, pp. 145-158, <http://dx.doi.org/10.1007/978-3-319-22044-4>.
- Zajac, P. (2015) Method of assessing energy consumption in the transport of pallets in logistics, A.Y.Oral, Z.B. Bahsi Oral, M. Ozer (eds.), Springer Proceedings in Energy, pp. 195-200, <http://dx.doi.org/10.1007/978-3-319-16901-9>.
- Zajac, P. (2014) Model of forklift truck work efficiency in logistic warehouse system. EcoProduction: Environmental Issues in Logistics and Manufacturing (ed. Golinska P.), pp. 467-479, [http://dx.doi.org/10.1007/978-3-319-07287-6\\_33](http://dx.doi.org/10.1007/978-3-319-07287-6_33).
- Zajac, P. (2011) The idea of the model of evaluation of logistics warehouse systems with taking their energy consumption under consideration. Archives of Civil and Mechanical Engineering, vol. 11, No. 2, pp. 479-492, <http://www.acme.pwr.wroc.pl/repository/329/online.pdf>.
- VDI2198 Standard.

## **RELIABILITY OF AUTOMATIC IDENTIFICATION SYSTEMS IN LOGISTICS SYSTEMS**

**P. Zajac<sup>\*</sup>, S. Kwasniowski<sup>\*\*</sup>**

**Abstract:** *This paper discusses basic issues affecting the reliability of automatic identification systems, which use 1D and 2D bar codes. The impact of significant factors on the reliability of reading information from bar codes was discussed. The impact of the spot size on the module and the background colour on the colour of bars were discussed as were the effects of the depth of field. The test station in the Laboratory of Automatic Identification in Logistics Systems at the Wrocław University of Science and Technology was presented where as yet unpublished research had been conducted on the reliability of reading 1D and 2D bar codes under static and dynamic reading conditions, with varying number of coded characters. Research results were compiled in a collective graph.*

**Keywords:** Reliability, Automatic identification, Bar codes.

### **1. Introduction**

A continuous strive in logistics systems is to increase the efficiency of automatic identification systems. Furthermore, yet another objective is to achieve the maximum possible reliability of reading scanned information in the paper Kwasniowski (2004). Self-adaptation to changing working conditions is not one of the characteristics of automatic identification systems, the effect of this being more and more errors connected with data transmission processes. In the Laboratory of Automatic Identification in Logistics Systems at the Wrocław University of Science and Technology, tests of reliability of reading different 1D and 2D codes were conducted in order to determine the reading reliability both under static and dynamic conditions. Results of the said tests may be useful in applications in various practical situations.

### **2. Reliability of reading bar codes – causes of errors**

There are several most common reasons why reading bar codes is reliable. A condition for correct reading is for a reader's beam to scan a code across its length. With each passing of the beam, an autocheck of the so-called control digit is carried out. The majority of codes have an autocontrol algorithm. Causes of errors may be as follows: laser spot diameter emitted by the reader, inconsistency of laser beam diameter relative to the size of code's module. Due to such reasons, it is necessary that the diameter of the beam does not exceed 0.8 of the size of code's module. Failure to meet this condition may cause signal interference in the electrical domain, which is emitted in the photoresistor's circuit. Possible situations were shown in Fig. 1.

The second cause in code reading is a ratio of the background grey to the grey of code's bar. This situation applies to colour codes on colour backgrounds. Contrasting codes are read most accurately (black code on white background). In the case of codes of various colours and background colours, the optical signal has a smaller value, is less contrasting and therefore generates electrical signals with smaller value differences which in turn may cause reading interference. This situation was shown in Fig. 2.

---

<sup>\*</sup> Pawel Zajac, PhD.: Wrocław University of Science and Technology, 27 Wybrzeże Wyspiańskiego st.; 50-370, Wrocław; RP, pawel.zajac@pwr.edu.pl

<sup>\*\*</sup> Stanisław Kwasniowski, PhD.: Wrocław University of Science and Technology; 27 Wybrzeże Wyspiańskiego st.; 50-370, Wrocław; RP, stanislav.kwasniowski@pwr.edu.pl

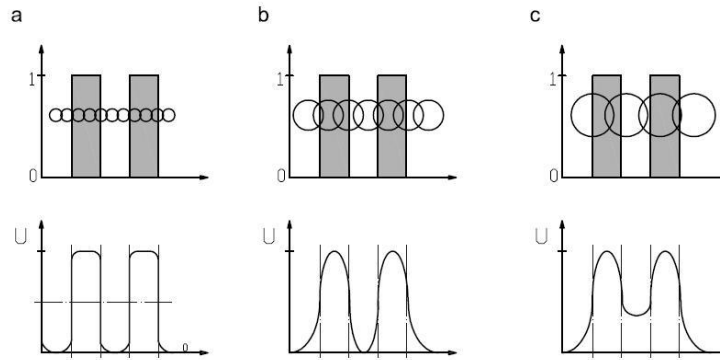


Fig. 1: Configuration of a beam with code's bars as the background vs. electrical signal value in the scanner's circuit. Cases a and b – correct relationship, c – incorrect relationship. Own work.

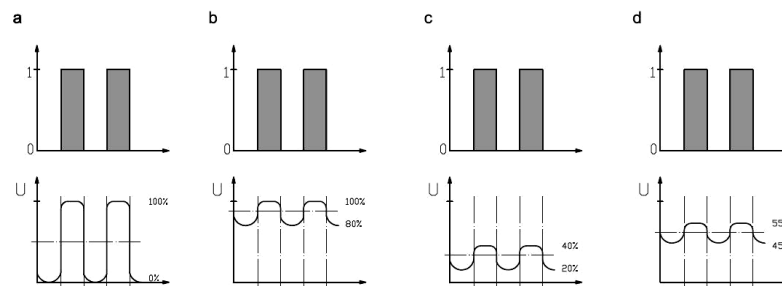


Fig. 2: Signal value at various code contrasts relative to the background: a) black code on white background, b) dark code on dark background, c) bright code on brighter background, d) approx. 50 % grey code on little contrasting background. Own work.

The third cause of difficulties in correct reading of a code may be incorrect distance of a scanner from the code's plane. Scanner, as an electro-optical device, is characterised by such parameters as focal length and depth of field (Fig. 3). Code image is only clear within a certain range of distance from the scanner.

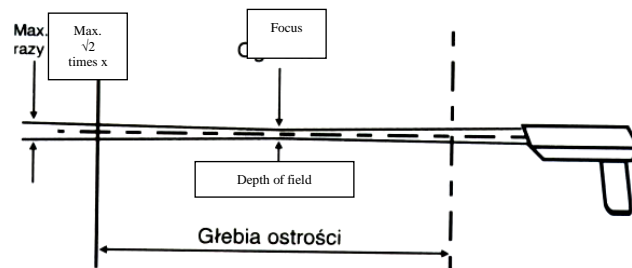


Fig. 3: Scanner and depth of field.

Yet another cause of difficulties in reading may be an illegible code overprint, e.g. highly hygroscopic background which smears the ink in the case of a wet overprint. Difficulties may also occur when the surface with overprinted code is not flat, e.g. it is highly curved (vial or small bottle) in the papers Bujak and Zajac (2012 and 2013). Then the code image will be distorted and the direction of code placement on packaging has to be changed, in the paper Kwasniowski (2011a).

### 3. Test of reliability of reading bar codes under static and dynamic conditions

In order to shorten the reading of codes and the transmission of information, readings are carried out while marked items are in motion. The aim is to achieve reading and transmission of information in real time, without the need to slow down the stream of scanned items. The test of reliability of reading bar codes also included the following bar codes: code 39, 128, PDF-417, AZTEC, DataMatrix, UPC in the paper Kwasniowski (2004). It was conducted at the measurement station in the Laboratory of Automatic Identification in Logistics Systems at the Wrocław University of Science and Technology. The test was carried out in accordance with ISO/IEC 15416. The schematic diagram was shown in Fig. 4.

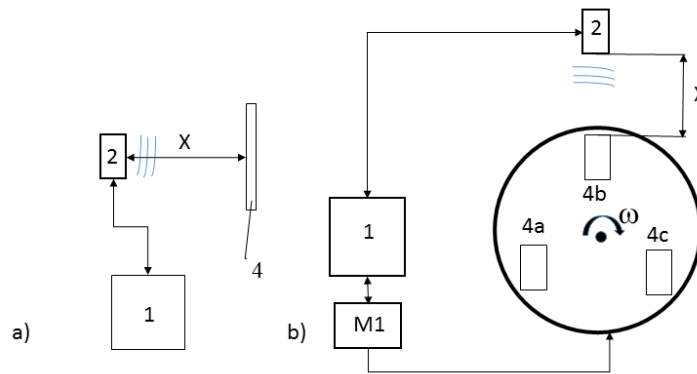


Fig. 4: Measurement station diagram: a) static tests station; b) dynamic tests station.

In the case of a static reading, the code reader (2) was connected with a computer (1) using a wired interface (3) with the RS 232 connector. The reader was powered by a power supply. In order to measure the maximum code reading distance, a card (4, a, b, c) with code symbology was being brought closer and closer to the reader. In the case of a dynamic test, a rotating disc was used which was powered by a motor (M1) with speed control. The motor drove the disc with bar codes stuck on top of it. The reader was placed perpendicularly to the surface of the disc with rotating bar codes. The distance between the reader and the disc was being changed during the test.

Initially, before reading a code, the quality of its symbology was measured: symbol's contrast is the relationship between the smallest factor of bar reflection and the largest factor of space reflection. The higher the contrast, the better the quality of a symbol. The minimum edge contrast is the smallest contrast value when passing from a space to a bar. The higher the value, the clearer the symbol. Modulation is a relationship between minimum edge contrast and symbol contrast, reflecting the constancy of contrast within a symbol. Defects of irregularity of light reflection from an element. Decodability describes print precision in relation to a comparative decoding algorithm. All those parameters are measured separately, the obtained mark of a bar code being the smallest result for any the parameters. Rules of assessment of overprint of codes were compiled in Tab. 1.

Tab. 1: Rules for assessing bar codes.

ISO/IEC 15416 mark	Minimum reflection	Symbol contrast	Minimum edge contrast	Modulation	Defects	Decodability
4	$\leq 0.5$	$\geq 70 \%$	$\geq 15 \%$	$\geq 0.70$	$\leq 0.15$	$\geq 0.62$
3		$\geq 55 \%$		$\geq 0.60$	$\leq 0.20$	$\geq 0.50$
2		$\geq 40 \%$		$\geq 0.50$	$\leq 0.25$	$\geq 0.37$
1		$\geq 20 \%$		$\geq 0.40$	$\leq 0.30$	$\geq 0.25$
0	$> 0.5$	$< 20 \%$	$< 15 \%$	$< 0.40$	$> 0.30$	$< 0.25$

Source: ISO/IEC 15416 standard.

The following explanations make it possible to choose the appropriate mark depending on the scanning environment: 3.5 – 4.0 is the highest mark, 2.5 – 3.4 is an acceptable mark (good), 1.5 – 2.4 is the minimum mark, 0.5 – 1.4 means that there is a very high probability that the symbol will not be read – it is doubtful whether such codes will be accepted in a supply chain and 0 is a mark given to symbols which are unusable.

#### 4. Conclusions

The test results were compiled in the form of a diagram illustrating areas of application of bar codes in technical systems.

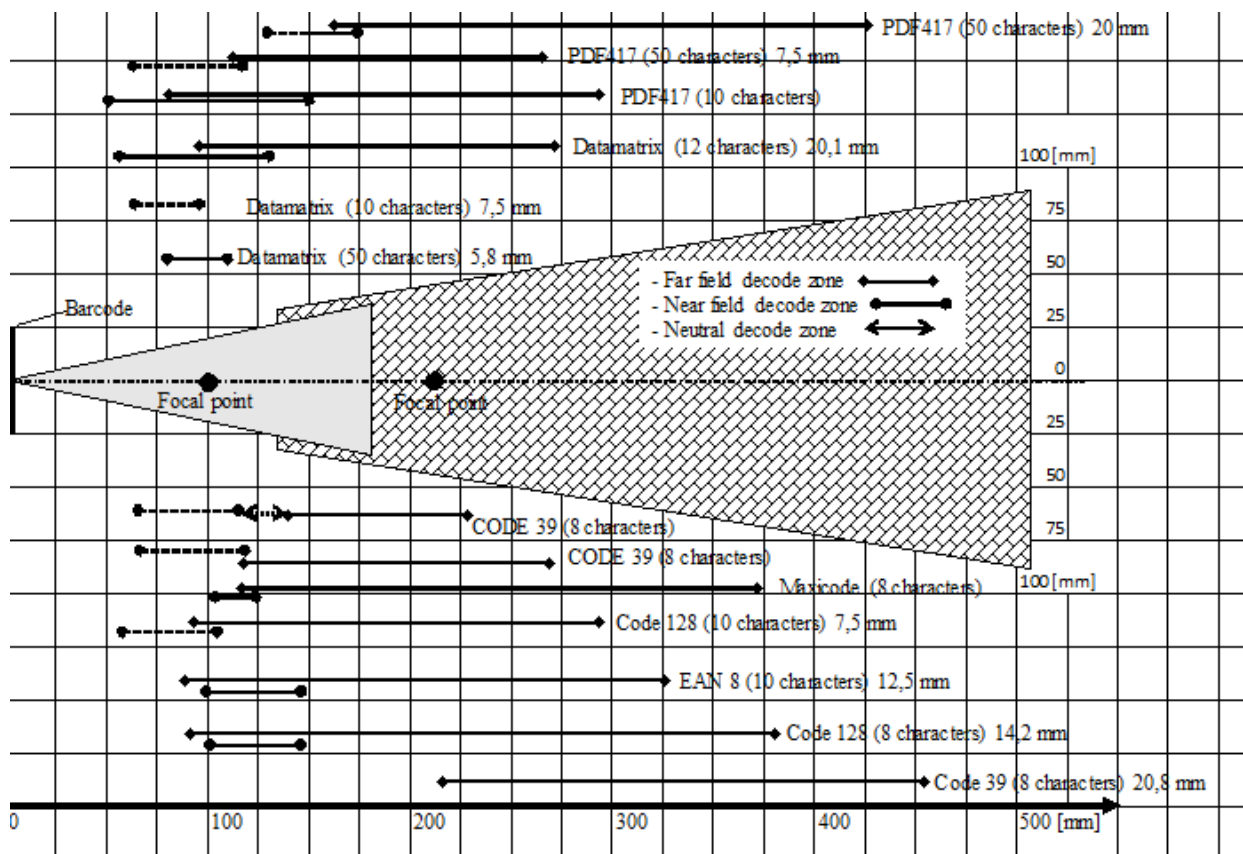


Fig. 5: Areas of application of bar codes.

## References

- Bujak, A. and Zajac, P. (2013) Monitoring of cargo in logistics of transport and storage, in: "Activities of Transport Telematics" (ed. Mikulski, J.), Springer Heidelberg New York Dordrecht London.
- Bujak, A. and Zajac, P. (2012) Can the increasing of energy consumption of information interchange be a factor that reduces total energy consumption of a logistic warehouse system?, in: Activities of Transport Telematics, Springer Heidelberg New York Dordrecht London, (ed. Mikulski, J.).
- Kwasniowski, S. (2004) The role of automatic identification systems (AUTO-ID) of goods, persons and documents in logistics, (eds. Kwasniowski S. and Zajac P), Automatic identification in logistics systems, Publishing House of Wroclaw University of Technology, Wroclaw (in Poland), pp. 9-16, ISSN 1425-0993, 16.
- Kwasniowski, S., Zajac, M. and Zajac, P. (2011) Logistic management of commodity information in distribution, Logistics, 2011, 6, pp. 2141-2149.
- Kwasniowski, S., Zajac, M. and Zajac, P. (2011a) Telematic problems of unmanned vehicles positioning at container terminals and warehouses, Berlin, Heidelberg, Springer, cop. 2011, (ed. Mikulski J.) Communications in Computer and Information Science, pp. 391-399, ISSN 1865-0929, vol. 104, [http://dx.doi.org/10.1007/978-3-642-16472-9\\_43](http://dx.doi.org/10.1007/978-3-642-16472-9_43)
- Zajac, P. (2015) Evaluation of automatic identification systems according to ISO 50001. Advances in Intelligent Systems and Computing, vol. 350, pp. 345-355, <http://dx.doi.org/10.1007/978-3-319-15796-2>

## FULL WIDTH WARP TENSION SENSOR

J. Žák\*

**Abstract:** *The manufacturing of a fabric, it is to say the process of weaving, is based on the creation of binding points between the yarns of weft and the yarns of warp. While the tension of weft is given principally by the type of weft picking and there are few means to control it, the tension of warp yarns is set by the weaver and depends on the textile technology parameters such as the fabric sett, the yarn strength, etc. Thus the control system must enable the operator to set it with a reasonable precision. With the use of servos on the modern looms the designers have all assets to reach a good level of control. In this paper we present a new approach to the problem of the warp tension monitoring which is important in the control loop. We use a statically indeterminate bar with a given number of load cells in the bearings. Based on the read values in the load cells we can estimate the distribution of the warp tension along the woven width.*

**Keywords:** Weaving, Process monitoring, Statically indeterminate structures.

### 1. Introduction

During the creation of a binding point in a fabric the yarns are subject to a number of forces of which the tension forces along the yarn axis are the most important. Their values determine the shape of the final product. While the weft tension is hard to control, especially on the air jet looms, the warp tension is controlled relatively easily. It is given principally by the difference of angular velocities of the warp beam let-off and the cloth roll take up. This tension changes within the weaving cycle due to the beat-up forces, movement of the compensating backrest, the shed creating harness action etc. These changes are cyclic and the tension forces in the warp yarns may change by several orders during the working cycle. Anyway the maximum given by the yarn strength must never be exceeded, such a failure leads to the yarn breakings and the machine stops. Nevertheless this phenomenon is well known and relatively easily predictable. Its effect on the tension monitoring may be well compensated using suitable technique of tension value reading.

To complicate the things, this warp tension is not constant along the woven width. This is caused partly by the warping process which is subject e.g. to some imperfections in the warping machine setting and partly by the weaving itself. Different tension in the weft yarn on the left and right edges respectively causes also differences in the fabric shape on the left and right hand side. In consequence this charges differently the warp yarns. Such an effect increases greatly with different types of weaves along the cloth width.

Actually the simple load cells are used to monitor the warp tension. This single cell can pick either a limited number of yarns either all the yarns along the whole woven width. The cell of the former concept is usually placed at about one third of the woven width according to some empirical data (e.g. CAM EL 220, 2014), the latter one measures the reaction forces in one of the backrest side bearings (VEGA). In the rare cases where two load cells are used, the second one is placed in an area of warp where problems are to be expected and usually does not intervene in the control loop. In any case the use of a single load cell does not allow the weaver to obtain more than one value characterizing the warp tension.

In order to overcome this shortcoming we opted for a multi cell solution. The number of cells determines the number of information we can obtain about the warp tension distribution. Due to the textile technology requirements we were obliged to use a one piece bar spanning over the whole woven width. This bar is supported by a certain number of bearings, of which some are fitted with load cells.

---

\* Ing. Josef Žák, PhD.: VÚTS, a. s., Svárovská 619; 460 01, Liberec; CZ, josef.zak@vuts.cz



## 2. Methods

The use of multi cell tension sensor means to find the relation between the reactions in the bearings and the parameters chosen to describe the tension distribution. The statically indeterminate bar does not facilitate the task, nevertheless it is not quite difficult.

### 2.1. Calculation of bearing reactions

Using the theory of thin beam and the Euler-Bernoulli's differential equation of beam we obtain the system of equations (Höschl, 1971):

$$u_i^{IV} = \frac{q(x)}{E \cdot J} \quad (1)$$

where index  $i$  denotes  $i$ -th section of the measuring bar and goes from 1 thru the number of sections  $n$ ,  $E \cdot J$  are cross sectional and mechanical properties of the bar, constant along the span of the sensor, and  $q$  is distribution of yarn loading. Its form may be chosen arbitrary but must be linear in coefficients  $Q_j$ . We opted for a polynomial shape of distribution, thus  $j$  is going from zero up to the degree of polynomial.

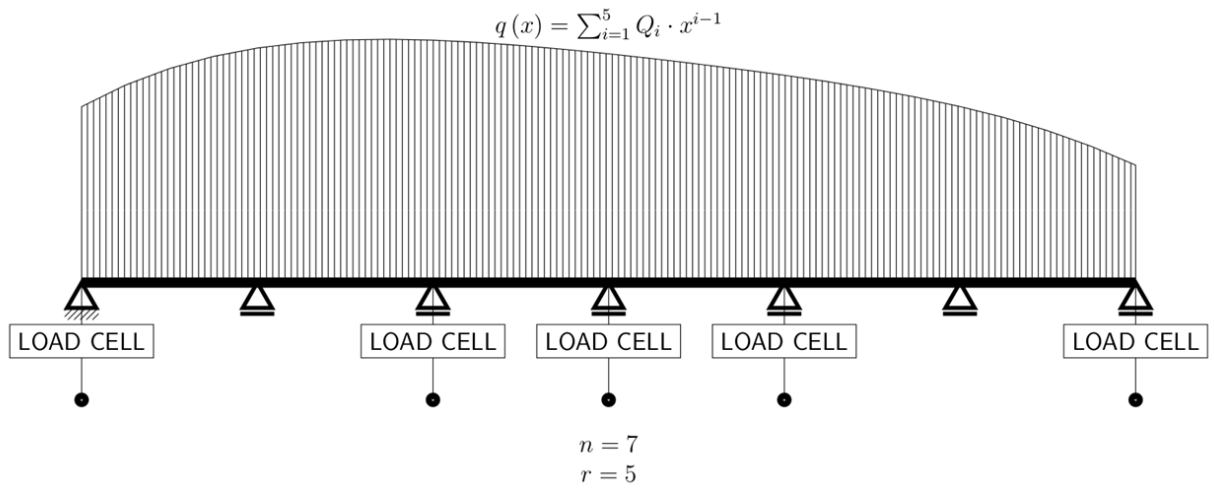


Fig. 1: Example of the multi load cell tension sensor with a typical warp load.

Integrating four times those  $n$  ordinary differential equations we get a system of  $n$  algebraic equations, each containing 4 constants of integration. Assuming continuity of slopes  $u^{(I)}$  and moments  $u^{(II)}$  above the bearings we get 2 additional equations for each section which, with the addition of known – e.g., vanishing - moments on the outer bearings and zero flexion in all bearings, closes the system of  $4 \cdot n$  algebraic equations for  $4 \cdot n$  unknowns.

N.B.: In reality the calculation was complicated by the flexibility of the bearings whose known stiffness is of the same order as the stiffness in flexure of the measuring bar. More complex procedure than presented in the previous paragraph must be actually used.

Once the system of algebraic equation is solved we can find the values of reactions in the bearings as:

$$R_i = E \cdot J \cdot (u_{i+1}^{III} - u_i^{III}) \quad (2)$$

with special respect to the outer bearings to which only one section adjoins.

Reactions as given by (2) are linear functions of coefficients  $Q_j$ , as far as the  $q$  is linear function of these coefficients (which is satisfied in the case of a polynomial distribution):

$$R_i = \sum_{j=1}^r K_{ij} \cdot Q_j$$

where  $r$  is degree of polynomial augmented by 1 (or generally number of coefficients  $Q_j$ ).

We can rewrite this relation in a matrix form:

$$|\mathbf{R}|_{((n+1) \times 1)} = [\mathbf{K}]_{((n+1) \times r)} \cdot |\mathbf{Q}|_{(r \times 1)} \quad (3)$$

where  $\mathbf{R}$  is matrix (or column vector) of dimension  $(n+1,1)$ ,  $\mathbf{Q}$  has dimension  $(r,1)$  and  $\mathbf{K}$  is matrix of coefficients of dimension  $(n+1,r)$ . Generally there is no restriction on the values of  $n$  and  $r$ , but as the number of load cells actually cannot be greater than the number of bearings we cannot get more than  $n+1$  information values on the load distribution, thus the number  $r$  of independent coefficients  $Q_i$  cannot be greater than  $n+1$ .

## 2.2. Relation between reactions and the load distribution

While we have determined the reactions in all bearings only a limited number of load cells is used. Then we have to choose those values of  $R_i$  which match the “measured” bearings. Of course their number must be equal identically to the number of coefficients  $Q$ .

We can reduce the relation (3) as follows:

$$|\mathbf{R}|_{(rx1)} = [\mathbf{K}_{red}]_{(rxr)} \cdot |\mathbf{Q}|_{(rx1)} \quad (4)$$

by using only appropriate lines of  $\mathbf{K}$  (i.e. appropriate values of  $K_{ij}$ ).

Then we get

$$|\mathbf{Q}|_{(rx1)} = [\mathbf{K}_{red}]_{(rxr)}^{-1} \cdot |\mathbf{R}|_{(rx1)} \quad (5)$$

Relation (5) express explicitly the values of  $\mathbf{Q}$  as function of measured values  $\mathbf{R}$ .

For a given geometry the  $\mathbf{K}_{red}$  is constant so a very simple linear relation can be coded into the control system in the form:

$$Q_i = \sum_{j=1}^r k_{ij} \cdot R_j \quad (6)$$

Actually, in order to keep the device simple (and cheap) the number of cells should not exceed 4 per one warp tension sensor. Thus even with a higher number of bearings we get only 4 values of  $Q_i$  and thus a parabolic distribution of no more than third degree can be modelled.

## 2.3. Result processing

The use of  $\mathbf{Q}$  in a control loop requires some more processing. Analogically to the use of one cell sensor we must find one constant of regulation. Unlike the simple case we can use a whole set of values. Using expression (6) for  $Q_i$  we can for example calculate a mean value of  $q$ :

$$\bar{q} = \frac{1}{L} \int_0^L q(x) \cdot dx = \sum_{i=1}^N \frac{Q_i \cdot L^{i-1}}{i} = \sum_{j=1}^r C_j \cdot R_j \quad (7)$$

where  $C_j$  are for the given configuration constants, in principle used as weights for the measured values of  $\mathbf{R}$ .

Yet again, by expanding the original expression and reordering the terms we get a simple linear combination of values  $R_j$ . Analogically we can calculate maximum or minimum of  $q$  on the given interval, it is to say, along the woven width.

Then any of these values can be used as constant of regulation to be put into the control loop. For example we can regulate the warp tension so that the minimum tension be equal to a required value, by checking in the same loop the maximum tension in the interval in order to not to exceed the strength of yarns. Another possible way to process the values of  $\mathbf{Q}$  is to use all values disposable with some user defined weights, for example.

In any case the processing of  $\mathbf{Q}$  offers a fair opportunity to the weaver to monitor the tension distribution in the warp.

## 2.4. Actual implementation in the control system

All the previous calculations were made by using a symbolic mathematic calculus software so that the coefficients  $k_{ij}$  in (6) were determined explicitly in function of  $E$ ,  $J$  and other geometric characteristics. Numerical values of  $C_j$  were then implemented in the evaluation of regulation constant in the control loop using relation (7). As the control system is still under development actually no other enumeration of e.g. local minima or maxima in the interval is implemented in the control loop. For now the values of  $Q_j$  serve as a monitoring parameters only.

## 3. Conclusions

Actually the warp tension sensor of presented pattern is installed on the prototype of the new generation loom. It is in the stage of vigorous testing using a rather complicated weave of a 3D fabric which - should a simple load cell sensor be used - could not even be produced.

Nevertheless, there are some issues in the sensor system that will require more attention. For example calibration of the gauges should be done using some regression technique, actually a simple loading with single weights at several levels is used. Although very simple yet the evaluation of the regulation constant could be further simplified by using a low level programming language in the control system.

The use of multi signal tension sensor represents a new approach to the monitoring of weaving process. It allows the loom control system to handle better the irregularities in the weaving and thus increase the final product quality.

## Acknowledgement

Work presented in this paper was granted by NPU - LO 12/13.

## References

- Höschl, C. (1971) Strength in engineering. SNTL, Prague, (in Czech).
- VEGA 220 - Air weaving machine, User's Guide, VÚTS Liberec, Liberec, (in Czech).
- CAM EL 220 - Air weaving machine (2014) User manual, VÚTS Liberec, Liberec, (in Czech).

## A FINITE ELEMENT STRESS ANALYSIS TO PREDICT THE RISK FACTORS OF AORTIC DISSECTION - PRELIMINARY STUDIES

M. Żak<sup>\*</sup>, J. Filipiak<sup>\*\*</sup>, T. Plonek<sup>\*\*\*</sup>

**Abstract:** *The risk of cardiovascular disorders, including aortic aneurysms and aortic dissection increases with age. So far, there has been no effective method of diagnosing and predicting the risk of dissection of the aorta. The aim of the study was to examine the potential role of the finite elements method to predict the risk of aortic dissection and the impact of the geometry of the aorta, aortic root motion and blood pressure on the wall stress in the aortic wall.*

**Keywords:** Aorta, Dissection, Aneurysm, Numerical simulations, Mechanical properties.

### 1. Introduction

Aortic dissection is a catastrophic complication which usually occurs in patients with a dilated aorta. The risk of cardiovascular disorders, including aortic dissection, increases with age (Rylski et al., 2014). The mechanism of aortic dissection has not yet been fully explained. It is believed that the gradual structural remodeling caused by the histological alterations and mechanical stimuli (blood pressure, aortic root movement) may be responsible for aortic wall degeneration and subsequent dissection (Beller et al., 2004; Plonek et al., 2015).

The aim of the study was to analyze the impact of mechanical factors on the dynamics of the process of dissection of the ascending aorta and its physical properties. In this study was to determine whether: (1) the geometry of the vessel and its curvature have a significant impact on the formation and propagation of aortic dissection, (2) blood pressure acting on the blood vessel and aortic root movement on the stress in the aortic wall.

### 2. Materials and methods

#### 2.1. Geometry and wall properties

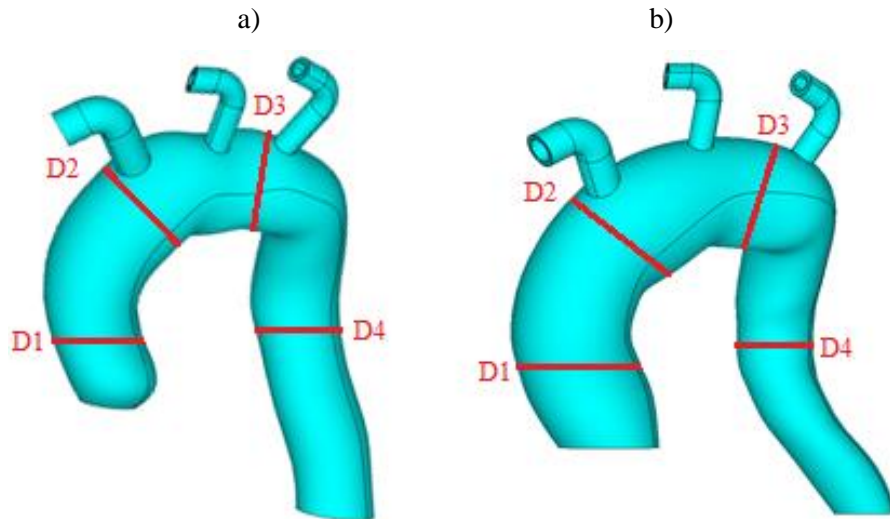
In this research, numerical models were obtained from computed tomography angiography (angio-CT) scans of two patients obtained before the occurrence of aortic dissection. External surface model of the aorta was performed on the 3D reconstruction of the thoracic aorta obtained from the angio-CT images (Fig. 1). The artifacts were to avoid discontinuity of the shape of the model of the aorta (Burzyńska et al., 2016). The blood vessel wall was modeled as a three-layer composite structure with a total thickness of 2 mm. It was assumed that the thickness of the individual layers of the vessel were as follows: intima  $t_i = 0.2$  mm, media  $t_m = 1.2$  mm, and adventitia  $t_a = 0.6$  mm. The simplified reconstruction of the aortic arch branches were also included in the final model.

---

<sup>\*</sup> PhD. Małgorzata Żak: Department of Biomedical Engineering, Mechatronics and Theory of Mechanisms, Wrocław University of Science and Technology, ul. Łukasiewicza 7/9, 50-371 Wrocław, Poland, malgorzata.a.zak@pwr.edu.pl

<sup>\*\*</sup> Prof. Jarosław Filipiak: Department of Biomedical Engineering, Mechatronics and Theory of Mechanisms, Wrocław University of Science and Technology, ul. Łukasiewicza 7/9, 50-371 Wrocław, Poland, jaroslaw.filipiak@pwr.edu.wroc.pl

<sup>\*\*\*</sup> MD PhD. Tomasz Plonek: Department of Cardiac Surgery, Wrocław Medical University, ul. Borowska 213, 50-556 Wrocław, Poland, tomaszplonek@gmail.com



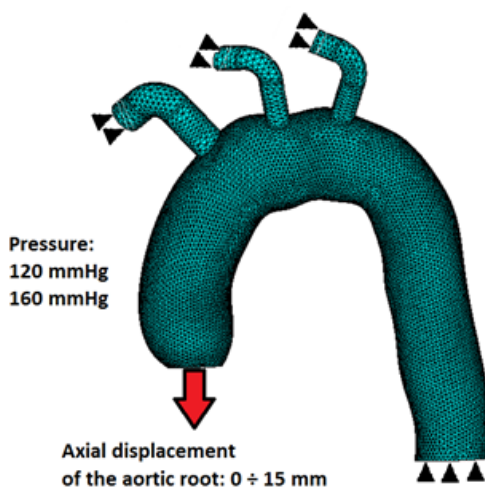
Model	Diameter of the aorta [mm]			
	D1	D2	D3	D4
Patient A	37.49	41.09	37.97	32.37
Patient B	45.23	48.75	32.37	28.06

Fig. 1: The three-dimensional models of the aortas reconstructed from the angio-CT images: (a) patient A, (b) patient B.

## 2.2. Finite element modeling

Numerical finite elements models of the human aorta were built for stress analyses using the ANSYS 17.2 software (ANSYS). The models were discretized into 632000 (in patient A) and 423000 (in patient B) tetrahedral structural solid elements (SOLID187). The material properties of the aortic wall were represented as linear elastic, and isotropic, with a Young's modulus of: intima  $E_i = 2.98$  MPa, media  $E_m = 8.95$  MPa, adventitia  $E_a = 2.98$  MPa and a Poisson's ratio of 0.49 for all layers (Gao et al., 2006).

Luminal pressures of 120 mmHg and 160 mmHg were used in both aortic models (Fig. 2). Additionally, aortic root base axial displacement (0mm - 15 mm) was applied in the models. The distal end of the aorta (descending aorta) and at the distal ends of the aortic arch branches were fixed in all directions to better represent the immobilization of the vessel in the chest.



Model	Number of elements		
	Intima	Media	Adventitia
Patient A	78500	208500	345000
Patient B	78100	141200	203700

Fig. 2: Exemplary front view of the finite element model of the aorta with number of elements throughout the individual layers in model: patient A and patient B.

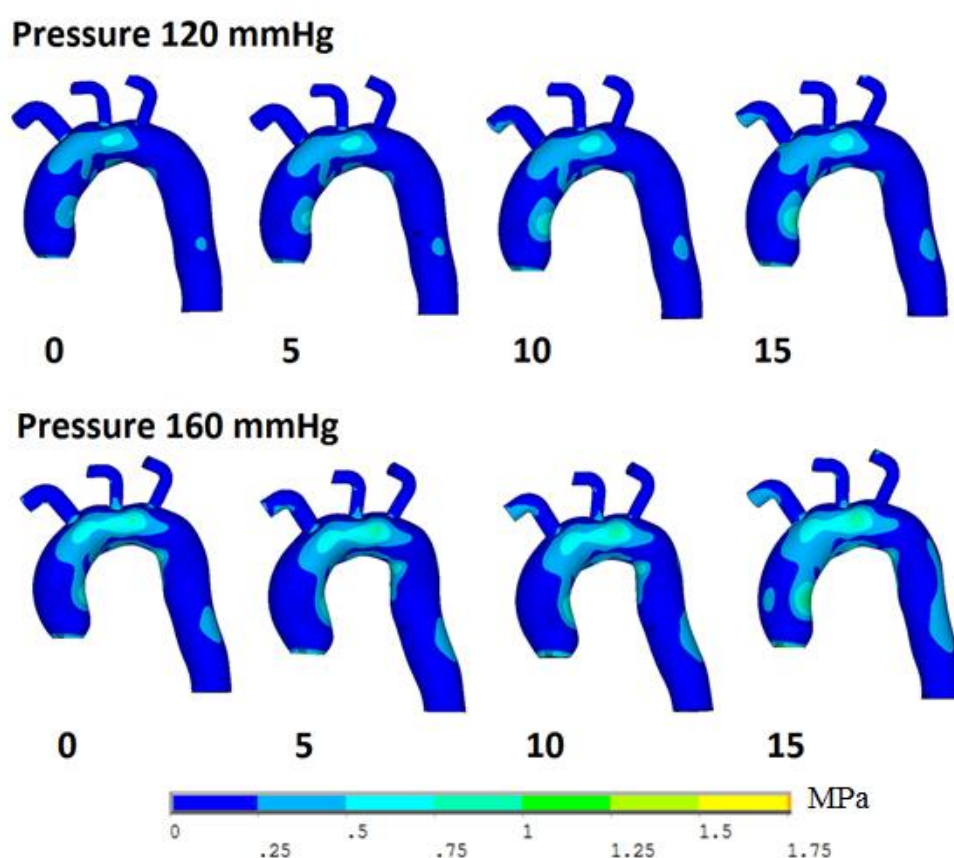
### 3. Results

The results of numerical simulations show how the geometry of the vessel, blood pressure and aortic root motion influenced the distribution of stress exerted on the aortic wall.

In patient A, the aorta had smaller diameter than in patient B (Fig. 1). In patient A, the area of the highest stress was located mainly in the aortic arch (Fig. 3). In the model of aorta of patient B, this area also included part of the ascending aorta (Fig. 4).

As expected, higher stress values were observed at blood pressure of 160 mmHg compared to 120 mmHg. In patient A the maximum stress was 0.6 MPa at 120 mmHg and 1.0 MPa at 160 mmHg. In patient B the maximum stress was 0.8 MPa at 120 mmHg and increased to 1.2 MPa at 160 mmHg.

The aortic root axial displacement has also an impact on the stress in the aortic wall. When the movement of the aortic root was changed from 0mm to 15mm the maximal stress in the aortic wall increased to 1.0 MPa at a pressure 120 mmHg and to 1.5 MPa at a pressure 160 mmHg (in patient A). In patient B the stress was changed from 1.1 MPa to 1.75 MPa at a pressure 160 mmHg and they were greater than at the pressure of 120 mmHg.



*Fig. 3: The map of the wall von Mises stress values distribution on its surface throughout the aorta wall patient A, after finite element analysis in pressure: 120 mmHg and 160 mmHg and displacement of the aortic root 0÷15 mm.*

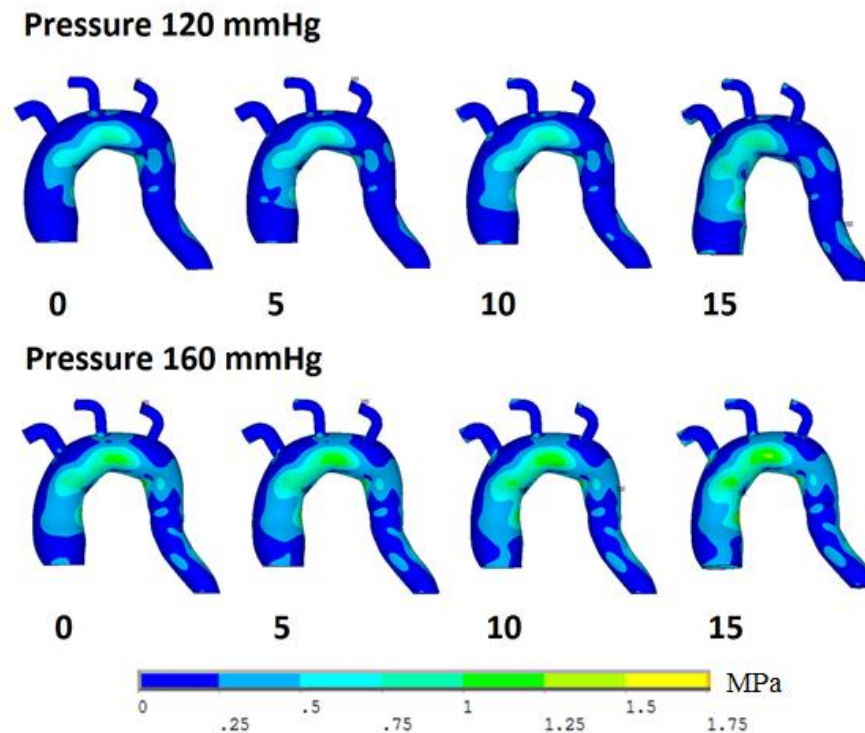
### 4. Conclusions

Our research results show that the physical properties of the aorta and mechanical factors (blood pressure and aortic root movement) influence significantly aortic wall stress and subsequently the risk of its dissection. Finite elements method has a potential to be a good tool to evaluate the risk of aortic dissection.

### Acknowledgement

Calculations have been carried out using resources provided by Wroclaw Centre for Networking and Supercomputing (<http://wcss.pl>), grant No. 423.





*Fig. 4: The map of the wall von Mises stress values on its surface throughout the aorta wall patient B, after Finite Element Analysis in pressure: 120 mmHg and 160 mmHg and displacement of the aortic root 0÷15 mm.*

## References

- Beller, C.J., Labrosse, M.R., Thubrikar, M.J. and Robicsek, F. (2004) Role of aortic root motion in the pathogenesis of aortic dissection, *Circulation*, 109, pp.763-769.
- Burzyńska, K., Morasiewicz, P. and Filipiak, J. (2016) The Use of 3D Printing Technology in the Ilizarov Method Treatment: Pilot Study, *Advances in Clinical and Experimental Medicine*, 25(6), pp.1157-1163.
- Gao, F., Watanabe, M. and Matsuzawa, T. (2006) Stress analysis in a layered aortic arch model under pulsatile blood flow. *Biomed. Eng. Online*. 5, p. 25.
- Plonek, T., Rylski, B., Dumanski, A., Siedlaczek, P. and Kustrzycki, W. (2015) Biomechanical analysis of wrapping of the moderately dilated ascending aorta, *Journal of cardiothoracic surgery*, 10 (1), pp.1-6.
- Rylski, B., Blanke, P., Beyersdorf, F., Desai, N.D., Milewski, R.K., Siepe, M., Kari, F.A., Czerny, M., Carrel, T., Schlensak, C. et al. (2014) How does the ascending aorta geometry change when it dissects?, *Journal of the American College of Cardiology*, 63, pp. 1311-1319.

## REDUCTION OF THE ENERGY LOSSES BY APPLICATION OF CONTROLLABLE SQUEEZE FILM DAMPERS

J. Zapoměl<sup>\*</sup>, P. Ferfecki<sup>\*\*</sup>, J. Kozánek<sup>\*\*\*</sup>

**Abstract:** *The unbalance induces lateral oscillations of rotors and forces transmitted to the rotor casing. The squeeze film dampers with integrated rolling element bearings represent a technological solution, which enables to reduce their magnitude, and consequently the resistance against the rotor rotation. To achieve optimum performance of the damping devices, their damping effect must be adaptable to the current rotor speed. This paper reports a proposal of a controllable squeeze film damper, the damping effect of which is controlled mechanically by shifting its outer ring in the axial direction. The developed mathematical model of the damper is based on assumptions of the classical theory of lubrication and is completed with implementation of a gas cavitation. The results of the computational simulations show that an appropriate control of the damping force enables to reduce the energy losses in a wide range of operating speeds.*

**Keywords:** Squeeze film damper, Controllable damping, Friction in bearings, Energy losses reduction.

### 1. Introduction

The imbalance induces lateral vibration of rotors and increases the forces transmitted to the rotor stationary part. Their magnitude can be reduced by application of squeeze film dampers with integrated rolling element bearings. The resistance against the rotor rotation due to loading the bearings arrives in the energy losses. A simple dynamical analysis shows that adapting the damping effect to the current operating speed (Zapoměl et al., 2013) enables to reduce their magnitude.

The mathematical models of squeeze film dampers based on application of the classical theory of lubrication and the Reynolds equation can be found in a number of publications. The implementation of a cavitation caused by sucking the air from the ambient space is presented in Olsson (2004). Some approaches to control the damping force can be found e.g. in (Mu et al., 1991) and (El-Shafei et al., 2000). In this paper, a concept of a squeeze film damper with a cylindrical gap and the axially movable outer ring is presented. Changing the axial position of the ring changes the damper land length and thus the damping force. A gas cavitation is implemented in the damper mathematical model. The efficiency of the damping element was proved by the computational simulations.

### 2. The design configuration of the proposed controllable squeeze film damper

The main parts of the proposed controllable squeeze film damper operating with conventional oil (Fig. 1) are two concentric rings, between which there is a thin layer of a lubricating film. The inner ring is coupled with the damper housing by a squirrel spring and with the rotor journal by a rolling element bearing. The oil is supplied to the damper gap by a central groove. The outer ring is mounted with the damper body movably (Fig. 1). Its shifting in the axial direction changes the damper land length, which results in changing the pressure distribution in the damper gap and thus in controlling the damping force.

---

<sup>\*</sup> Prof. Ing. Jaroslav Zapoměl, DSc.: Institute of Thermomechanics, Dolejškova 5; 182 00 Prague; CZ, and Department of Applied Mechanics, VSB-Technical University of Ostrava, 17. listopadu 15, 708 33 Ostrava-Poruba; CZ  
jaroslav.zapomel@vsb.cz

<sup>\*\*</sup> Ing. Petr Ferfecki, PhD.: IT4Innovations National Supercomputing Center and Department of Applied Mechanics VŠB - Technical University of Ostrava, 17. listopadu 15, 708 33 Ostrava-Poruba; CZ petr.ferfecki@vsb.cz

<sup>\*\*\*</sup> Ing. Jan Kozánek, CSc.: Institute of Thermomechanics, Dolejškova 5; 182 00 Prague; CZ, kozanek@it.cas.cz

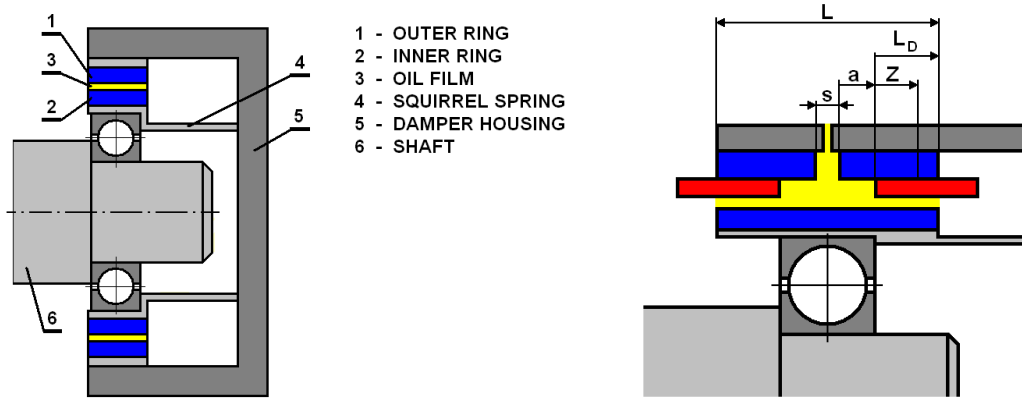


Fig. 1: The proposed controllable squeeze film damper.

### 3. Components of the controllable damping forces in cavitated squeeze film damper

The determination of the pressure distribution in the damper gap is based on application of the classical theory of lubrication, e.g. in Zapoměl (2007). In addition, it is assumed that both the geometric and design parametres enable to consider the damper as short, see e.g. in Zapoměl (2007).

The Reynolds equation governing the pressure profile reads

$$\frac{\partial^2 p}{\partial Z^2} = \frac{12\eta}{h^3} \frac{\partial h}{\partial t}. \quad (1)$$

$p$  is the pressure,  $Z$  is the axial coordinate,  $\eta$  is the oil dynamical viscosity,  $h$  is the oil film thickness, and  $t$  is the time.

Double integration of (1) arrives in the relation for the pressure distribution

$$p = \frac{6\eta}{h^3} \frac{\partial h}{\partial t} Z^2 + C_1 Z + C_2. \quad (2)$$

$C_1$  and  $C_2$  are the integration constants.

In the first step, the integration constants are determined for the boundary conditions

$$p = p_s \text{ for } Z = 0 \quad (3)$$

$$p = p_A \text{ for } Z = L_D \quad (4)$$

$p_s$  is the inlet oil pressure in the central groove,  $p_A$  is the atmospheric pressure and  $L_D$  is the land length of one half of the damper (Fig. 1).

If the pressure gradient at the end of the damper ( $Z = L_D$ ) is positive, a gas cavitation occurs. In cavitated area the Reynolds equation does not hold and it is assumed that the pressure remains constant there and equal to the pressure in the ambient space. In this case, the integration constants  $C_1$  and  $C_2$  are determined by application of the following conditions

$$p = p_s \text{ for } Z = 0 \quad (5)$$

$$p = p_A \text{ for } Z = Z_C \quad (6)$$

$$\left[ \frac{\partial p}{\partial Z} \right]_{Z=Z_C} = 0 \text{ for } Z = Z_C \quad (7)$$

$Z_C$  is the axial coordinate of the border between the non-cavitated and cavitated regions. Because the pressure of the medium in cavitated area is constant, the pressure gradient is zero. As a result, no flow occurs between the non-cavitated and cavitated regions. This is expressed by the boundary condition (7).

The hydraulic force components are obtained by integration of the pressure distribution around the circumference and along the length of the damper. The land length of the half of the damper  $L_D$  reads

$$L_D = \frac{L}{2} - \frac{s}{2} - a. \quad (8)$$

$L$  is the total length of the damper,  $s$  is the width of the central feeding groove and  $a$  is the axial shift of the outer ring. It is evident that the change of  $a$  changes  $L_D$  and thus it controls the damping force.

#### 4. Energy losses in the rolling element bearings

Several approaches have been developed to determine the friction moment in rolling element bearings. If the loading is not extreme, the friction moment can be expressed

$$M_{RB} = F_{BE} f_B \frac{d_H}{2} \quad (9)$$

where  $F_{BE}$  is the magnitude of the equivalent force transmitted through the bearing,  $f_B$  is the friction coefficient and  $d_H$  is the diameter of the bearing hole (diameter of the shaft journal).  $f_B$  depends on the type of the bearing and its value ranges approximately from 0.0010 to 0.0045.

The equivalent force for radial bearings is calculated as

$$F_{BE} = X F_R + Y F_A. \quad (10)$$

$F_R$ ,  $F_A$  are the radial and axial component of the force transmitted through the bearing and  $X$ ,  $Y$  are the radial and axial loading coefficients, the value of which depends on the bearing type (Bolek et al., 1989).

The radial bearing force  $F_R$  consists of three components, of the hydraulic damping force that is transmitted through the oil film, the elastic force produced by bending of the squirrel spring and of a prestress force that acts on the squirrel spring to centralize the equilibrium position of the rotor in the damper. The loss power  $P_{RB}$  in the rolling element bearing is given as the product of the friction moment  $M_{RB}$  and angular speed of the rotor rotation  $\omega$

$$P_{RB} = M_{RB} \omega. \quad (11)$$

#### 5. The investigated rotor system

The investigated rotor is rigid. It consists of a shaft and of one disc. With the stationary part it is coupled by squeeze film dampers with integrated rolling element bearings. The rotor turns at constant angular speed, is loaded by its weight and excited by the rotor unbalance. The whole system can be considered as symmetric relative to the disc middle plane. The squirrel springs are prestressed to eliminate their deflection caused by the rotor weight.

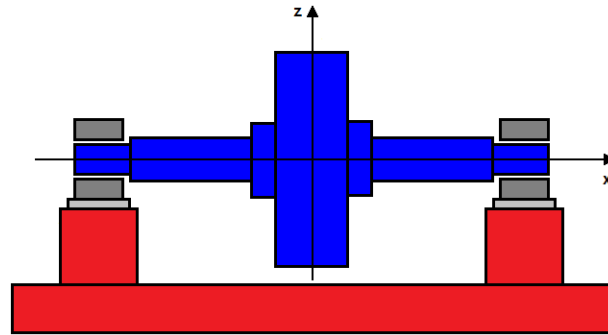


Fig. 2: The investigated rotor system.

The technological and operating parameters of the investigated rotor system are: the rotor mass 430 kg, the stiffness of one squirrel spring 2 MN/m, the rotor imbalance 21.3 kg.mm, the squeeze film damper length/diameter 50/150 mm, the width of the central feeding groove 5 mm, the width of the damper gap 0.2 mm, the oil dynamic viscosity 0.02 Pas, the inlet pressure 200 kPa, the diameter of the bearing hole 110 mm, the radial and axial loading coefficients  $X$  and  $Y$  are 1.0 and 0.0, respectively, and the bearing friction coefficient 0.0015 (one row ball bearing).

A simple dynamical analysis shows that the critical speed of the rotor rotation is approximately 96 rad/s.

Fig. 3 provides the time histories of the loss power related to one rolling element bearing for two angular speeds of the rotor rotation of 100 and 500 rad/s and two shifts of the outer damper ring of 0 and 10 mm. Larger shift means lower damping effect. It is evident that higher damping arrives at reduction of the loss power for the velocity close to the critical speed. When the rotor turns at a speed much higher than the critical one, lower damping reduces the loss power.

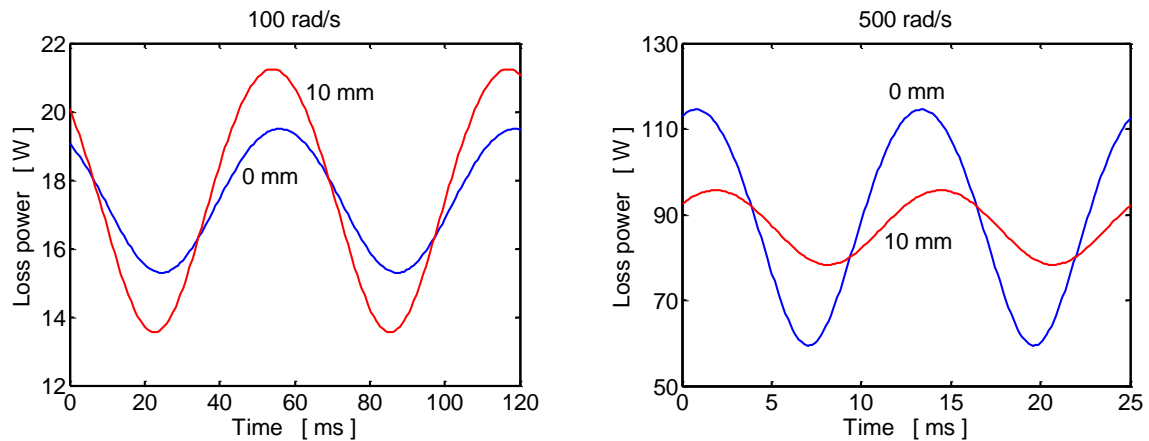


Fig. 3: The power loss in one bearing for speeds of 100 rad/s and 500 rad/s.

## 6. Conclusions

The carried out research work presents a study on the effect of controllable squeeze film dampers on reducing the energy losses in the rotor supports, which offers a new field of their application. The damping effect is controlled by shifting the outer damper ring in the axial direction, which reduces the damper land length. The developed mathematical model of the squeeze film damper is based on the classical theory of lubrication, the cavitation caused by sucking the air from the ambient space to the damper gap is implemented. The extension of the computational procedures, the evidence that a proper control of magnitudes of the damping forces makes it possible to minimize the energy losses in the bearing elements, and learning more on the influence of the controllable squeeze film dampers on the oscillatory motion of rigid rotors are the principle contributions of the work presented in this paper.

## Acknowledgement

This work was supported by the Czech Science Foundation 15-06621S and the National Programme of Sustainability project „IT4Innovations excellence in science - LQ1602“.

## References

- Bolek, A. and Kochman, J. (1989) Parts of machines, 1st volume, SNTL, Prague (in Czech).
- El-Shafei, A. and M. El-Hakim M. (2000) Experimental investigation of adaptive control applied to HSFD supported rotors, in: Trans. ASME J. Eng. Gas Turbines Power 122, pp. 685-692.
- Mu, C., Darling, J. and Burrows C.R. (1991) An appraisal of a proposed active squeeze film damper, in: ASME J. Tribol. 113, pp. 750-754.
- Olsson, K.O. (2004) Squeeze film damper with rigorous account of cavitation, in: Proc. 8th Int. Conf. Vibrations in Rotating Machinery, IMechE, Swansea, United Kingdom, pp. 55-65.
- SKF Rolling bearings catalogue, <http://www.skf.com/binary/56-121486/SKF-rolling-bearings-catalogue.pdf>.
- Zapoměl, J. (2007) Computer modelling of lateral vibration of rotors supported by hydrodynamical bearings and squeeze film dampers, VSB-Technical University of Ostrava, Ostrava (in Czech).
- Zapoměl, J., Ferfeckí, P. and Kozánek, J. (2013) Determination of the transient vibrations of a rigid rotor attenuated by a semiactive magnetorheological damping device by means of computational modelling, in: Applied and Computational Mechanics, 7, 2, pp. 223-234.

## DYNAMICS OF MOVEMENT IN SCISSOR-FINGER CUTTING ASSEMBLY

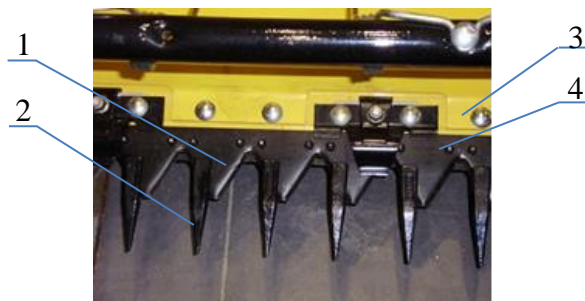
M. Zastempowski\*

**Abstract:** *The analysis of the dynamics of the shear-finger cutting assembly the drive of was performed by the rotating disc with a crank in asymmetric system is presented in this article. The conducted analysis as the only one in the generally available literature, describes thoroughly the dynamics of the working assembly by considering of all the components of the shear-finger cutting assembly. The analysis of the dynamics of the cutting assembly presented in the study makes it possible to determine the friction coefficient in the conditions of the real machine's operation.*

**Keywords:** Dynamics of the cutter bar's movement, Friction in the shear-finger cutting assembly, Cutting of plant materials, Shear-finger cutting assembly, Simulation calculations.

### 1. Introduction

The shear-finger cutting assembly is the basic assembly occurring in many working machines. The essence of its construction lies in the fact, that this assembly consists of a movable cutter bar and an immovable finger bar, and the rule of operation consists in the fact, that the knives riveted to the cutter bar make a to-and-fro motion, shifting in fingers' cut-outs which at the same time constitute a crosscut edge. The plant material between the side knife's edge and the finger is cut. In Fig. 1 there is presented a typical construction of a shear-finger cutting assembly.



*Fig. 1: Construction of the shear-finger cutting assembly in the example [own study]:  
 1-knife, 2-finger, 3-finger bar, 4-cutter bar.*

For the drive of the cutter bar making a to-and-fro movement (in and out) there are most of all used the asymmetric crank mechanisms. The existing constructional solutions of the cutting assemblies are characterised by a high energy-consumption of the cutting process, and what's connected with that – their power transmission systems are equipped with engines of high powers. It points out to the fact, that the known constructional solutions originated mainly based on a constructor's intuition. It is connected with the absence of a detailed analysis of the dynamics of the shear-finger movement's dynamics of the cutting assembly and the absence of mathematical models describing the cutting process of the shear-finger cutting assembly, on the basis of which there may be conducted simulation calculation, construction's optimization and the improvement of the improvement of functioning efficiency of the cutting assemblies. The authors then dealing with these issues were among the others Zastempowski and Bochat (2013, 2015). Other authors within the frames of machines construction, mainly dealt with the

---

\* Marcin Zastempowski, PhD.: Faculty of Mechanical Engineering, UTP University of Science and Technology, Poland.  
 Al. Prof. Kaliskiego 7, 85-796 Bydgoszcz, zastemp@utp.edu.pl



issues connected with the rules of design and analysis of construction's strength (Strzelecki et al., 2016), with the rules of use of MES and numerical analysis (Ligaj and Szala, 2014, Knopik et al., 2016) with mathematical modelling and construction's optimization (Keska and Gierz, 2011, Peszynski et al., 2016, Tomporowski, 2012 and Zastempowski et al., 2013, 2014, 2015).

## 2. Analysis of the issue

The analysis of operation of the shear-finger cutting assembly in the aspect of its dynamics is awkward because of the complexity of the whole system. In the cutting system the following components may be distinguished: a rotating disc with a crank, a connecting rod (pitman), a cutter bar and a finger bar with a slide bearing. On the basis of the energy model developed by the article's authors based on the results of the experiments it was found, that the resistances occurring most of all in the idle movements, which are connected with the necessity to overcome among the others the frictional resistance and amount up to 90 % of the total demand for power, have an essential share in the whole process's energy consumption. Due to that, the authors of the study have conducted the analysis of dynamics of the components' movement of the shear-finger cutting assembly. The model of that movement's dynamics has been developed with the following assumptions: the rotating disc rotates with the constant angle speed  $\omega$ , between the cutter bar and slide bearing there occurs the Coulomb's friction, frictional resistances in connection of the cutter bar with a connecting rod and of the connecting rod with a crank have been omitted. In Fig. 2 there is presented the diagram of the system driving the cutter bar taking into account the forces affecting the connecting rod and the cutter bar.

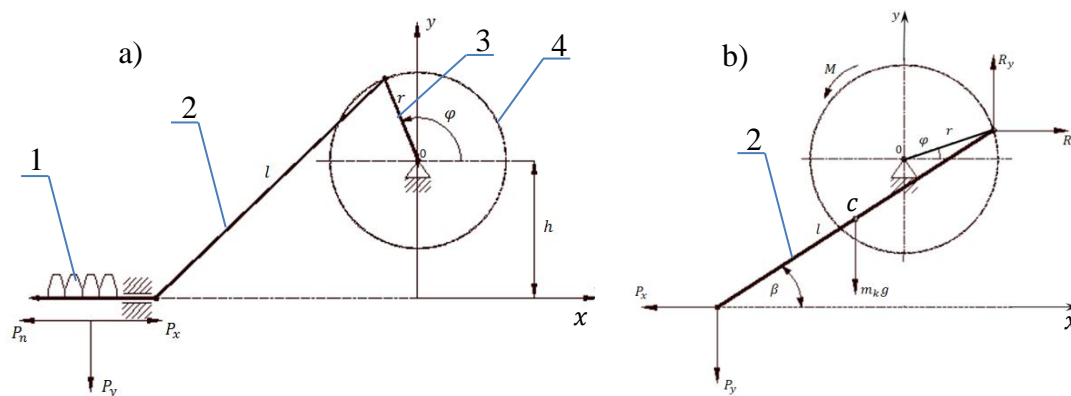


Fig. 2: Force system in the cutting assembly for the dead movement: a- force system for the cutter bar, b- system of forces on the connecting rod at the cutter bar's slide in; 1- cutter bar, 2- connecting rod, 3- crank, 4- rotating disc with a crank.

Process of the cutter bar's slide out is described by the following equations:

$$R_x r \sin \varphi - R_y r \cos \varphi = M, \quad (1)$$

$$-R_x + P_x = m_k a_x, \quad (2)$$

$$-R_y + P_y = m_k (a_y + g), \quad (3)$$

$$R_x \frac{l}{2} \sin \beta - R_y \frac{l}{2} \cos \beta + P_x \frac{l}{2} \sin \beta - P_y \frac{l}{2} \cos \beta = J_k \varepsilon_k, \quad (4)$$

where:

$a_x, a_y$  – acceleration of the connecting rod's centre of gravity,

$m_k$  – mass of the connecting rod,

$g$  – gravitational acceleration,

$\varepsilon_k$  – the connecting rod's angle acceleration,

$J_k$  – mass moment of the connecting rod's inertia.

The equations describing the process of the cutter bar's slide in are analogical to the above presented equations with consideration of the opposite movement's direction.

In order to determine the forces  $P_x$  i  $P_y$  influencing the cutter bar, following transformations of equations describing the process of sliding in and out of the cutter bar, the following matrix equation was received:

$$\begin{vmatrix} a_{11} & a_{12} \\ a_{21} & a_{22} \end{vmatrix} \begin{vmatrix} P_x \\ P_y \end{vmatrix} = \begin{vmatrix} M+b_1 \\ b_2 \end{vmatrix}. \quad (5)$$

The elements  $a_{ij}$  and  $b_{ij}$  have appropriately been accepted for the to-and-fro motion of the cutter bar.

Respectively for the sliding out:  $a_{11} = r \sin \varphi$ ,  $a_{12} = -r \cos \varphi$ ,  $a_{21} = l \sin \beta$ ,  $a_{22} = -l \cos \beta$  and for sliding in:  $a_{11} = -r \sin \varphi$ ,  $a_{12} = r \cos \varphi$ ,  $a_{21} = -l \sin \beta$ ,  $a_{22} = l \cos \beta$ .

Parameters  $b_1$  and  $b_2$  for a full revolution of a disc rotating with a crank takes the following values:

$$b_1 = \sin \varphi a_x - \cos \varphi (a_y + g), \quad b_2 = \sin \beta a_x - \cos \beta (a_y + g),$$

Solution of the equation (5) may be presented in the form:

$$P_x = M \frac{a_{22}}{W} + \frac{c_1}{W}, \quad (6)$$

$$P_y = -M \frac{a_{21}}{W} + \frac{c_2}{W}. \quad (7)$$

Expression describing the coefficients  $c_1$  and  $c_2$  and the determinant  $W$  are the following:

$$c_1 = b_1 a_{22} - b_2 a_{12}, \quad c_2 = b_2 a_{11} - b_1 a_{21}, \quad W = a_{11} a_{22} - a_{12} a_{21}.$$

Equation of the cutter bar's movement takes the form:

$$M(\varphi) \frac{a_{22}}{W} + \frac{c_1}{W} + \mu M(\varphi) \frac{a_{21}}{W} - \mu \frac{c_2}{W} = m_n a_n = 0. \quad (8)$$

Equation (8) describing the process of the cutter bar's sliding out may be presented in the following form:

$$M(\varphi) + F_{wy}(\varphi, \mu) = 0, \quad (9)$$

And the sliding in process in the form:

$$M(\varphi) + F_{ws}(\varphi, \mu) = 0, \quad (10)$$

$$\text{where: } F_{wy}(\varphi, \mu) = \frac{c_1}{f W} - \mu \frac{c_2}{f W} - \frac{m_n}{f} a_n, \quad F_{ws}(\varphi, \mu) = \frac{c_1}{f W} - \mu \frac{c_2}{f W} + \frac{m_n}{f} a_n, \quad f = \frac{a_{22}}{W} + \mu \frac{a_{21}}{W}.$$

Integrating the equation (9) in the interval of angles  $(\varphi_p, \varphi_k)$  and the equation (10) in the interval of angles  $(\varphi_k, 2\pi + \varphi_p)$ , and then adding them with sides, there was received the averaging equation of the cutter bar's movement, in the form:

$$M_{sr} + \frac{1}{2\pi} \int_{\varphi_p}^{\varphi_k} F_{wy}(\varphi, \mu) d\varphi + \frac{1}{2\pi} \int_{\varphi_k}^{2\pi + \varphi_p} F_{ws}(\varphi, \mu) d\varphi = 0. \quad (11)$$

where:

$\mu$  – friction coefficient,

$\varphi_p$  i  $\varphi_k$  – angles determining the extreme location of a cutter bar described with dependencies:

$$\varphi_p = \arcsin \frac{h}{l-r}, \quad \varphi_k = \pi + \arcsin \frac{h}{l+r}.$$

Equation (11) is a confounded dependency due to the friction coefficient  $\mu$  that is why its determination requires the use of numerical procedures used in case of solving of non-linear equations. The whole dynamic analysis of the shear-finger cutting assembly, together with determination of the friction coefficient  $\mu$  has been conducted on the basis of the author's computer programme. The dependence (11) makes it possible to determine the friction coefficient  $\mu$  for the given construction parameters of the shear-finger cutting assembly and for a given crank's angle speed. For the purposes of the friction coefficient's  $\mu$  determination, it is necessary to know the mean moment  $M_{sr}$  running on the crank, which has been determined on the basis of experiments. For the purposes of this study's performance, the experimental tests have been conducted. For these tests there has been used the test point with the shear-finger cutting assembly reflecting the real conditions of the machine's operation. The conducted tests are

presented in a separate publication (Zastempowski et al., 2014). The exemplary results of calculation of the friction coefficient  $\mu$  between finger bar and cutter bar are presented in Tab. 1.

*Tab. 1: Exemplary values of the friction coefficient calculated from the dependence (6).*

<i>Crank's angle speed <math>\omega</math> [rad/s]</i>	<i>Turning moment of the dead movement <math>M_{sr}</math> [Nm]</i>	<i>Friction coefficient <math>\mu</math></i>
30.92	22.80	1.48
47.57	23.36	1.19
103.70	28.44	0.28

Development of an innovative shear-finger cutting assembly's construction in which the impact of friction and inertial force were minimised (Zastempowski and Bochat, 2014) was an additional effect of the continuously conducted works at the Faculty of Mechanical Engineering UTP in Bydgoszcz.

### 3. Summary

The dynamic analysis of the shear-finger cutting assembly presented in the study, makes it possible to determine the friction coefficient  $\mu$  in the conditions of the real machine's operation. From the analysis of the obtained values of the friction coefficient  $\mu$  on the basis of dependencies (11) it results, that together with the increase of the crank's angle speed  $\omega$  its value decreases. The results of friction coefficient  $\mu$  occur directly from the operating conditions of the machine (dust, dirt, sand and plant material). During the literature's analysis, a similar approach has not been found. The values of the friction coefficient presented by other authors are based most probably on the experience conducted in the conditions of unnatural operation with slow movement of a batten and disassembled drive (Gach et al., 1991). The values of the friction coefficient terminated like that, are several times lower than the ones occurring in the conditions of the real operation of a machine and presented in the article.

### References

- Gach, S., Kuczewski, J. and Waszkiewicz, C. (1991) Agricultural machinery. SGGW Warszawa (in Poland).
- Keska, W. and Gierz, L. (2011) Mathematical modeling and computer simulation of sowing. 69th International Conference on Agricultural Engineering Land Technik AgEng, Hannover, Germany. pp. 459-464.
- Knopik, L., Migawa, K. and Kolber, P. (2016). Statistical analysis of parameters of rail vehicles. 22nd International Conference on Engineering Mechanics Location: Svratka, Czech Republic, pp. 286-289.
- Ligaj, B. and Szala, G. (2010) Experimental verification of two-parametric models of fatigue characteristics by using the tests of S55J0 steel as an example . Polish Maritime Research, 17, 1. pp. 39-50.
- Peszynski, K., Szmyt, W., Wawrzyniak, S. and Perczynski, D. (2016) Mathematical model of selected object thermal properties. 22nd International Conference on Engineering Mechanics Location: Svratka, Czech Republic, pp. 454-457.
- Strzelecki, P., Tomaszewski, T. and Sempruch, J. (2016) A method for determining a complete S-N curve using maximum likelihood. 22nd International Conference on Engineering Mechanics Location: Svratka, Czech Republic, pp. 530-533.
- Tomporowski, A. (2012) Stream of efficiency of rice grains multi-disc grinding. Eksploatacja i Niezawodnosc-Maintenance and Reliability. 2, 150. pp. 150-153.
- Zastempowski, M., Borowski, S. and Kaszkowiak, J. (2013) New solution in harvesting plants for power purposes. 5th International Conference TAE 2013. Trends in agricultural engineering, Prague, pp. 673-676.
- Zastempowski, M. and Bochat, A. (2014) Modeling of cutting process by the shear-finger cutting block. Asabe Applied Engineering in Agriculture. Vol. 30, No. 3, pp. 347-353
- Zastempowski, M. and Bochat, A. (2014) Scissor-finger cutting assembly for harvesting machines. Polish practical new-type patent RP 67617. Application number W.120954.
- Zastempowski, M., Bochat, A. and Korpala, K. (2014) Analysis of the possibility of stand tests of the cutting process plant material. Chemical Engineering and Equipment, 2/2014, pp. 133-135.
- Zastempowski, M. and Bochat, A. (2015) Mathematical model ling of elastic deflection of a tubular cross-section. Polish Maritime Research No.2 (86), Vol. 22, pp. 93-100.

## FRICTION FORCES AND FRETTING WEAR IN REACTOR CORE BARREL COUPLINGS

V. Zeman<sup>\*</sup>, Z. Hlaváč<sup>\*\*</sup>

**Abstract:** *The couplings key-groove between the lower part of core barrel and reactor pressure vessel in the nuclear VVER-type reactors show small assembling side clearances. Due to fretting wear the potential for increasing of the clearances exist. Reactor vibrations, caused by coolant pressure pulsations generated by main circulation pumps, produce impulse contact forces in the above mentioned couplings. These forces are used for calculation of friction forces in the slipping contact surfaces between the key and the groove and for their fretting wear prediction. Increasing of the clearances leads to decreasing of some reactor frequencies. Their changes present good tool for the interpretation of diagnostic measurements. The computational method with numerical results applied on VVER1000 type reactor is shown.*

**Keywords:** Nonlinear vibration, Nuclear reactor, Friction forces, Fretting wear.

### 1. Introduction

Vibration of VVER type nuclear reactors was investigated in previous author's research works and papers in co-operation with Nuclear Research Institut Řež on linear models with proportional damping. The original linearized spatial model of the VVER1000/320-type reactor (Fig. 1), intended for dynamic response calculation excited by pressure pulsations generated by main circulation pumps, was derived (Zeman, 2008) as linear clearance-free model with 137 DOF number in the form

$$\mathbf{M}\ddot{\mathbf{q}}(t) + \mathbf{B}\dot{\mathbf{q}}(t) + \mathbf{K}\mathbf{q}(t) = \sum_{j=1}^4 \sum_{k=1}^3 F_{PV}^{(k)} \mathbf{f}_j \cos k \omega_j t . \quad (1)$$

Due to excitation by coolant pressure pulsation, this linear model was used for calculation of spatial vibration of all main reactor components including nuclear fuel assemblies (Hlaváč, 2013). The excitation vector in (1) is expressed by means of amplitudes  $F_{PV}^{(k)}$  of  $k$ -th harmonic components of the hydrodynamic force acting on reactor pressure vessel generated by particular main circulation pumps with small different angular speeds  $\omega_j$ . The vectors  $\mathbf{f}_j$  of geometrical parameters correspond to main circulation loops  $j = 1, 2, 3, 4$ . The fluctuation of the pumps angular speeds is based on the measurement at NPP Temelín blocks.

The aim of this paper is an investigation of reactor nonlinear vibration, friction forces in the couplings key-groove between the lower part of core barrel (CB3) and reactor pressure vessel (PV) and fretting wear prediction in their contact surfaces in dependence on clearances.

### 2. Mathematical model of the reactor with clearances in couplings

The relative tangential displacement  $u_i$  (Fig. 3) of the one groove on CB3 from starting position compared to key on reactor PV can be written as

$$u_i = \mathbf{d}_i^T \mathbf{q}(t), \quad i = 1, 2, \dots, 8 , \quad (2)$$

---

<sup>\*</sup> Prof. Vladimír Zeman, DSc.: NTIS -New Technologies for Information Society, University of West Bohemia, Univerzitní 8; 306 14, Plzeň; CZ, zemanv@kme.zcu.cz

<sup>\*\*</sup> Assoc. Prof. Zdeněk Hlaváč, PhD.: NTIS-New Technologies for Information Society, University of West Bohemia, Univerzitní 8; 306 14, Plzeň; CZ, hlavac@kme.zcu.cz

where  $\mathbf{q}(t)$  is vector of generalized coordinates of dimension 137 detailed described in author's monograph (Hlaváč, 2013). Vector  $\mathbf{d}_i$  corresponding to coupling  $i$  is defined by the centre mass position of the CB3 in reactor (see Fig. 1) and by the coupling key-groove position after core barrel circumference

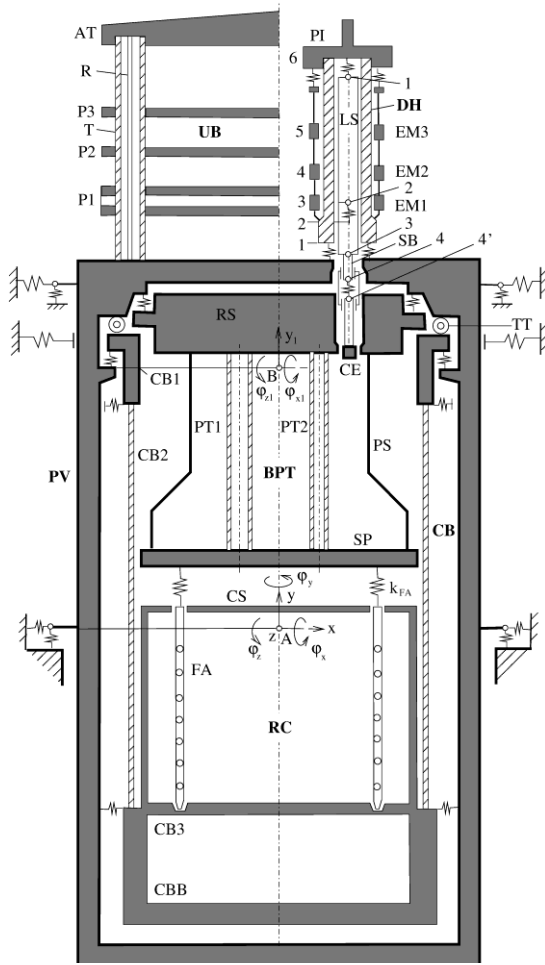


Fig. 1: Scheme of reactor model (PV- pressure vessel, CB3-lower part of core barrel).

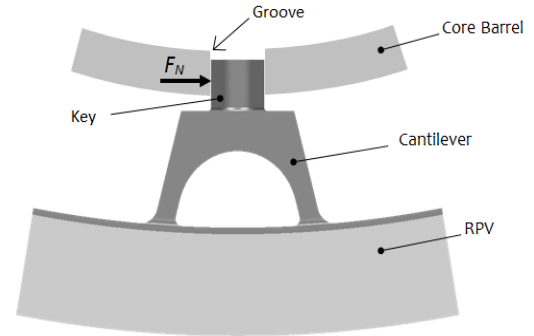


Fig. 2: Coupling key-groove between core barrel and reactor pressure vessel.

(radius  $r$  and angle  $\alpha_i$ ) depicted In Fig. 3. The tangential (normal) force transmitted by coupling  $i$  for general starting position of the CB3 centre relative to the reactor PV, defined by shift  $s$  in direction determined by angle  $\alpha$  (see Fig. 3), can be expressed in the form

$$N_i(u_i) = k \{ (u_i + \Delta_i - s_i) H(-u_i - \Delta_i + s_i) + (u_i - \Delta_i - s_i) H(u_i - \Delta_i - s_i) \}, \quad i = 1, 2, \dots, 8, \quad (3)$$

where  $k$  is contact stiffness in one clearance-free coupling and  $\Delta_i$  is half clearance in the corresponding coupling  $i$ . The small shift  $s_i$  of the groove with regard to key in tangential direction from starting position is

$$s_i = s \sin(\alpha + \alpha_i), \quad \alpha_i = \frac{\pi}{4}(i-1), \quad i = 1, 2, \dots, 8. \quad (4)$$

The Heaviside function  $H$  in (3) is zero when the key contact with groove in coupling is interrupted ( $|u_i| < \Delta_i - s_i$ ). The all coupling forces  $N_i(u_i)$  must be transformed in the reactor configuration space  $\mathbf{q}$  into mass centre CB3 and solid reactor PV. This operation has an effect on mathematical model (1) which is rearranged into reactor nonlinear model

$$\mathbf{M}\ddot{\mathbf{q}}(t) + \mathbf{B}\dot{\mathbf{q}}(t) + [\mathbf{K} - \mathbf{K}_c(t)]\mathbf{q}(t) = \sum_{j=1}^4 \sum_{k=1}^3 F_{PV}^{(k)} \mathbf{f}_j \cos k \omega_j t + \mathbf{f}(\mathbf{q}). \quad (5)$$

Elastic forces  $\mathbf{K}_c(0) \mathbf{q}(t)$  of all clearance-free coupling (for  $\Delta_i = 0$ ) in model (1) are replaced by the

nonlinear force vector

$$\mathbf{f}(\mathbf{q}) = -\sum_{i=1}^8 N_i(u_i) \mathbf{d}_i . \quad (6)$$

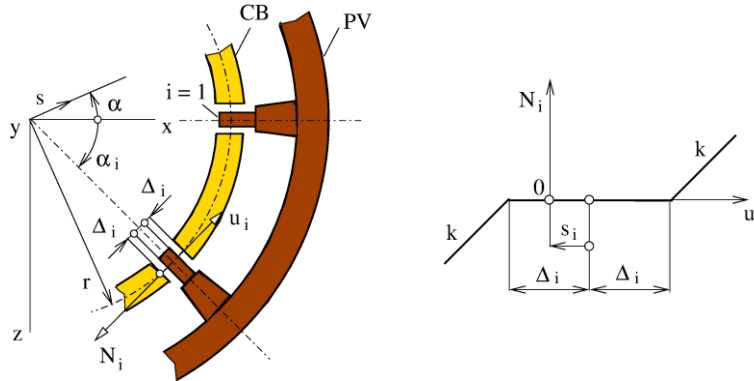


Fig. 3: The couplings between the lower part of core barrel (CB) and reactor pressure vessel (PV) and their stiffness characteristic.

### 3. Fretting wear of the contact surfaces

Due to fretting wear of the contact surfaces between the key and the groove the potential for increasing of the clearances there has been. For an assessment of this phenomenon the friction coefficient  $f$  and the fretting wear parameter  $\mu[g/J]$  (i.e. loss of mass in one contact surface generated by the work of friction force  $W=1[J]$  at the excited frequency  $\omega \approx \omega_j$ ) are experimentally obtained (Pečinka et al., 2016). The sliding velocity of the groove in the central contact points on radius  $r$  (see Fig. 3) as a result of CB3 and reactor PV vibration can be written by means of radial and axial components

$$c_{r,i} = \mathbf{d}_{r,i}^T \dot{\mathbf{q}}, \quad c_{ax,i} = \mathbf{d}_{ax,i}^T \dot{\mathbf{q}}, \quad i = 1, 2, \dots, 8 , \quad (7)$$

where vectors of geometrical parameters  $\mathbf{d}_{r,i}$  and  $\mathbf{d}_{ax,i}$  are defined by the centre mass position of CB3 in reactor model and by parameters  $r, \alpha_i$  corresponding to concrete coupling  $i$ . The criterion of the fretting wear of contact surfaces can be expressed using the work of friction forces (Zeman et al., 2016) during the representative time interval  $\langle t_1, t_2 \rangle$  as

$$W_i = \int_{t_1}^{t_2} |P_i(t)| dt, \quad P_i(t) = f N_i(u_i) \sqrt{c_{r,i}^2 + c_{ax,i}^2}, \quad i = 1, 2, \dots, 8 , \quad (8)$$

where  $P_i(t)$  is friction power. The fretting wear in grams in particular contact surfaces during the interval  $\langle t_1, t_2 \rangle$  can be expressed as

$$\Delta m_i = \mu \int_{t_1}^{t_2} |P_i(t)| dt, \quad i = 1, 2, \dots, 8 . \quad (9)$$

#### Application

The presented method has been applied to vibration analysis and fretting wear calculation of the side contact surfaces in couplings depending on clearances. The basic excitation frequency  $\omega$  corresponds to mean rotational speed of main circulation pumps  $n=996rpm$ , contact stiffness in one clearance-free coupling is  $k = 1.2 \cdot 10^9 \text{ N/m}$  and design values of clearances in all couplings  $2\Delta$  are in interval  $\langle 0,05; 0,17 \rangle mm$ . All geometrical parameters correspond to design parameters of VVER1000/320 type reactor. Reference values of the fretting wear parameters are  $f=1$  and  $\mu = 10^{-9} \text{ g/J}$ .

As an illustration, time behaviour of the normal contact force  $N_2$  and friction power  $P_2$  calculated according to (3) and (8) for same clearances  $\Delta_i = 75 \mu m$  in all eight couplings and for the central starting



position CB with respect to reactor PV ( $s_i = 0$ ) are shown in the Fig. 4. The time interval  $\langle 0;100 \rangle_s$  of numerical simulations includes the long period of the beating vibration caused by slightly different main circulation pumps revolutions (Zeman, 2008). Corresponding fretting wear of the side contact surfaces of coupling  $i = 2$  in this time interval, according to (9)  $\Delta m_2 = 3.014 \cdot 10^{-4} \text{ g}$ .

#### 4. Conclusion

The main objective of this contribution is to present the new basic method of fretting wear prediction in the reactor core barrel couplings with clearances. The method is based on mathematical remodelling of the original linear clearance-free reactor model into the nonlinear model and computer simulation of nonlinear vibration of the reactor and its components—reactor pressure vessel and lower part of core barrel linked by key-groove nonlinear couplings. The coolant pressure pulsations generate impulse forces between contact surfaces of key-groove and may result in fretting wear and increasing clearances. The developed software in MATLAB code is conceived in such a way that it enables to choose an arbitrary design clearances, starting position of core barrel with respect to reactor pressure vessel and operating mode of main circulation pumps. The presented method was applied for the VVER1000/320 type reactor in Czech NPP Temelín.

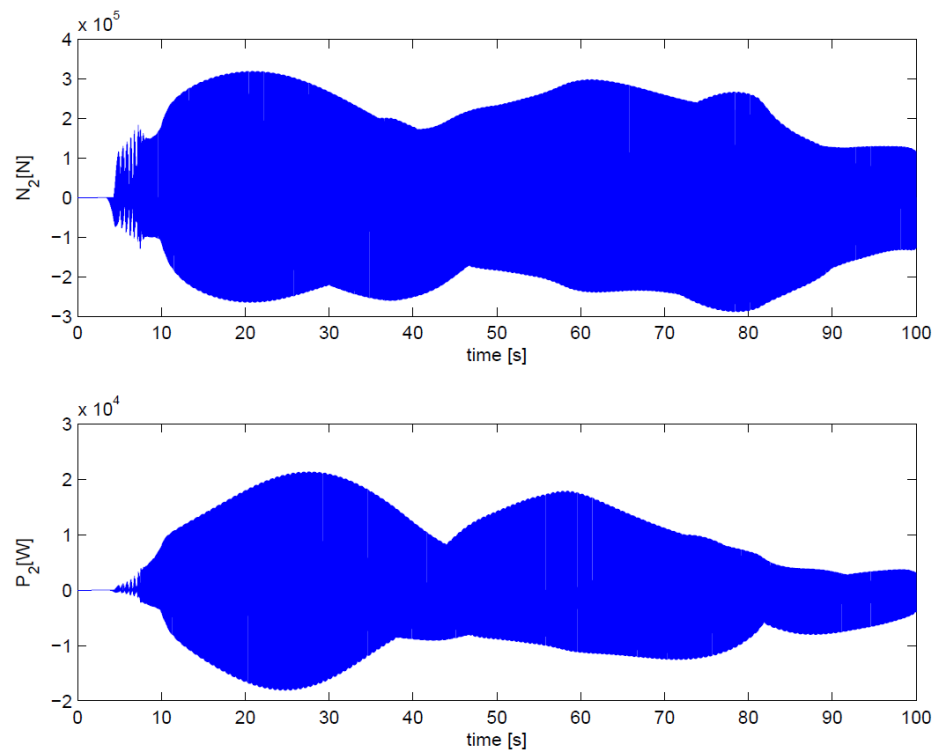


Fig. 4: Time behaviour of the normal contact force  $N_2$  and friction power  $P_2$  in coupling  $i = 2$  for clearances  $\Delta_i = 75 \mu\text{m}$ .

#### Acknowledgement

This study was supported by the project LO1506 of the Czech Ministry of Educations, Youth and Sports.

#### References

- Hlaváč, Z. and Zeman, V. (2013) Vibration of nuclear fuel assembly. LAP Lambert Academic Publishing, Saarbrücken.
- Pečinka, L., Svoboda, J. and Zeman, V. (2016) Friction and fretting wear coefficients between the key and the groove in the lower part of the WWER reactor pressure vessel, in: Extended Abstracts, 32nd conf. Computational Mechanics 2016, UWB Plzeň, pp. 97-98.
- Zeman, V. and Hlaváč, Z. (2008) Dynamic response of VVER1000 type reactor excited by pressure pulsations. Eng. Mech. 15, 6, pp. 435-446.
- Zeman, V., Dyk, Š. and Hlaváč, Z. (2016) Mathematical modelling of nonlinear vibration and fretting wear of the nuclear fuel rods. Arch. Appl. Mech. 86, 4, pp. 657-668.

## FREE VIBRATION ANALYSIS OF LAMINATED GLASS BEAMS USING DYNAMIC EFFECTIVE THICKNESS AND OTHER APPROACHES

A. Zemanová\*, J. Zeman\*\*, T. Janda\*\*\*, M. Šejnoha\*\*\*\*

**Abstract:** Effective thickness approaches are useful tools for a response prediction and the design of sandwich structures. In this contribution, we study their applicability to free vibration analysis of laminated glass beams – sandwich structures composed of glass layers connected with one or multiple compliant foils. These interlayers are made of polymer materials with frequency/temperature-dependent behavior. Here, the dynamic effective thickness approach, the modal strain energy method, and the Newton-type algorithm are applied to the complex eigenvalue problem for a three-layered laminated glass beam. The results of the modal analyses, in terms of natural frequencies and loss factors, are compared for all approaches. It is shown that the errors of the two simplified methods depend on the ambient temperature and the applied boundary conditions and that these errors can be large, especially for the loss factor.

**Keywords:** Laminated glass, Free vibration, Dynamic effective thickness, Modal strain energy method.

### 1. Introduction

Laminated glass structures are thin sandwich plates or beams composed of a few glass layers connected with one or more compliant foils, see Fig. 1. These interlayers are made of polymer materials with frequency-dependent and temperature-sensitive behavior. In this contribution, we focus on the modal analysis of such multi-layered structures composed of elastic and viscoelastic layers. A few approaches to the free vibration problem of a viscoelastically damped sandwich can be found in literature. Three of them, two numerical approaches and one semi-analytical method, are applied in this paper to the analysis of laminated glass beams.

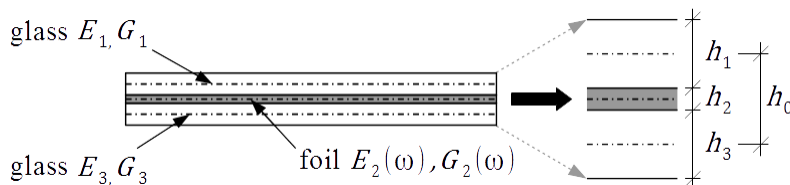


Fig. 1: Laminated glass sandwich's configuration.

### 2. Semi-analytical and numerical methods for free vibration analysis

The problem is introduced for a laminated glass beam with three layers (glass/interlayer/glass). The viscoelastic behavior of a polymer foil is described by a generalized Maxwell chain model and its damping behavior is accounted for through the complex shear modulus of the foil

$$G_2(\omega) = G_0 - \sum_{p=1}^P \left( G_p \frac{1}{\omega^2 \theta_p^2 + 1} \right) + i \sum_{p=1}^P \left( G_p \frac{\omega}{\omega^2 \theta_p^2 + 1} \right) = G_0 + G_\omega(\omega), \quad (1)$$

\* Ing. Alena Zemanová, PhD.: Department of Mechanics, Faculty of Civil Engineering, Czech Technical University in Prague, Thákurova 7, 166 29 Prague 6; CZ, alena.zemanova@fsv.cvut.cz

\*\* Assoc. Prof. Ing. Jan Zeman, PhD.: Department of Mechanics, Faculty of Civil Engineering, Czech Technical University in Prague, Thákurova 7, 166 29 Prague 6; CZ, jan.zeman@fsv.cvut.cz

\*\*\* Ing. Tomáš Janda, PhD.: Department of Mechanics, Faculty of Civil Engineering, Czech Technical University in Prague, Thákurova 7, 166 29 Prague 6; CZ, tomas.janda@fsv.cvut.cz

\*\*\*\* Prof. Ing. Michal Šejnoha, PhD., DSc.: Department of Mechanics, Faculty of Civil Engineering, Czech Technical University in Prague, Thákurova 7, 166 29 Prague 6; CZ, sejnomo@fsv.cvut.cz

where  $\omega$  is the complex value of an angular frequency (or its real part),  $G_0$  is the elastic shear modulus of the whole chain,  $P$  stands for the number of viscoelastic units,  $G_p$  denotes the shear modulus of the  $p$ -th unit,  $\theta_p$  is its relaxation time, and  $G_\omega(\omega)$  is the frequency-dependent part of the shear modulus. Therefore, the eigenvalue problem corresponding to the free vibration of a laminated glass beam is nonlinear and the eigenvalues and eigenvectors are complex. Three methods for this task are discussed in this paper: the dynamic effective thickness approach, the Newton-type algorithm for the complex eigenvalue problem, and the modal strain energy method. All methods were implemented into our MATLAB-based solver.

### 2.1. Dynamic effective thickness approach

To the best of our knowledge, a few effective thickness formulations can be found in literature for laminated glass beams and plates under static loading, whereas only one effective thickness approach exists for dynamic problems (López-Aenlle et al., 2014). The effective thickness is derived from the analytical model by Ross et al. (1959). The authors considered a three-layered, simply-supported beam with purely elastic face layers and a linearly viscoelastic core with a complex shear modulus. The shear strains in face layers are neglected, whereas only shear stresses are assumed in the core. The deflection is the same for all layers, and there is no slipping at layer-interfaces. Under these assumptions, the fourth-order differential equation of bending wave motion with the effective complex bending stiffness can be expressed. Then, the dynamic effective thickness for laminated glass beams, derived from the effective complex bending stiffness formulated in (Ross et al., 1959), is given by

$$h_{\text{eff}}(\tilde{\omega}) = \sqrt[3]{(h_1^3 + h_3^3) \left( 1 + Y \left( 1 + \frac{h_1}{g(\tilde{\omega})(h_1 + h_3)} \right)^{-1} \right)}. \quad (2)$$

In this approach, the effective thickness is a function of a real angular frequency  $\tilde{\omega}$ . The geometric parameter is provided by

$$Y = \frac{12h_0h_1h_3}{(h_1^3 + h_3^3)(h_1 + h_3)} \quad (3)$$

with the thicknesses  $h_1$  and  $h_3$  and the distance  $h_0$  introduced in Fig. 1. The shear parameter reads

$$g(\tilde{\omega}) = \frac{G_2(\tilde{\omega})}{E_3h_3h_2k^2} \quad (4)$$

and combines the complex shear modulus of the interlayer  $G_2(\omega)$ , the Young modulus of glass  $E_3 = E_1$ , the thicknesses of layers  $h_2$  and  $h_3$ , and the wavenumber  $k$ .

Due to the frequency-dependency, the problem is solved by an iterative algorithm. The initial frequency  $\tilde{\omega}_k = \tilde{\omega}_0$  is set to the average of the frequencies of two limiting cases: a monolithic glass beam with perfect interaction of glass layers and two independent monolithic glass layers with no interaction. The natural frequency  $f$  and the modal loss factor  $\eta$  follow from the equations (López-Aenlle et al., 2014)

$$\tilde{\omega}_{k+1}^2(1 + i\eta) = k^4 \frac{E_3h_{\text{eff}}^3(\tilde{\omega}_k)}{12\bar{m}}, \quad f = \frac{\tilde{\omega}}{2\pi}, \quad (5)$$

where  $\bar{m}$  is the mass per unit length. If the error of the new and the previous values of the frequency and the loss factor is out of the tolerance limit, the dynamic effective thickness is updated for the new frequency and the new values of the natural frequency and the loss factor are computed.

### 2.2. Complex-frequency approach using finite element method and Newton-type algorithm

Using the finite element discretization, the mass matrix  $\mathbf{M}$  of the laminated glass sandwich is real-valued and frequency-independent, whereas the stiffness matrix  $\mathbf{K}(\omega)$  is complex,

$$\mathbf{K}(\omega) = \mathbf{K}_0 + G_\omega(\omega)\mathbf{K}_{\text{const}}, \quad (6)$$

and consists of the frequency-independent part  $\mathbf{K}_0$  (corresponding to the glass layers and to the elastic part of the shear modulus of the foil  $G_0$ ) and the frequency-dependent part  $G_\omega(\omega)\mathbf{K}_{\text{const}}$  (corresponding to the frequency-dependent part of the foil shear modulus  $G_\omega(\omega)$ ;  $\mathbf{K}_{\text{const}}$  is a constant matrix), see for example (Daya et al., 2001).

The well-known natural vibration problem can be written in the form

$$(\mathbf{K}(\omega) - \omega^2\mathbf{M})\mathbf{U} = \mathbf{0}, \quad (7)$$

where  $\omega$  stands for a complex-valued angular frequency and the mode shape  $\mathbf{U}$  is a complex nodal vibration eigenvector. To be well-posed, the problem is complemented with the additional equation

$$\mathbf{U}_0^T(\mathbf{U} - \mathbf{U}_0) = 0, \quad (8)$$

where  $\mathbf{U}_0$  is the solution of the real-eigenvalue problem

$$(\mathbf{K}_0 - \omega_0^2 \mathbf{M})\mathbf{U}_0 = \mathbf{0} \quad (9)$$

obtained by a built-in MATLAB solver.

The system of nonlinear equations (7) and (8) can be solved by the Newton method starting from the real-eigenvalue solution of equation (9),  $\mathbf{U}_k = \mathbf{U}_0$  and  $\omega_k = \omega_0$ . Next, the mode shapes and the frequencies are updated

$$\mathbf{U}_{k+1} = \mathbf{U}_k + \delta\mathbf{U}_{k+1}, \quad \omega_{k+1} = \omega_k + \delta\omega_{k+1} \quad (10)$$

with increments  $\delta\mathbf{U}_{k+1}$  and  $\delta\omega_k$ . These increments result from the system of equations

$$\begin{bmatrix} \mathbf{K}(\omega_k) - \omega_k^2 \mathbf{M} & \left(\frac{\partial \mathbf{K}}{\partial \omega}(\omega_k) - 2\omega_k \mathbf{M}\right) \mathbf{U}_k \\ \mathbf{U}_0^T & 0 \end{bmatrix} \begin{bmatrix} \delta\mathbf{U}_{k+1} \\ \delta\omega_{k+1} \end{bmatrix} = - \begin{bmatrix} (\mathbf{K}(\omega_k) - \omega_k^2 \mathbf{M}) \mathbf{U}_k \\ \mathbf{U}_0^T(\mathbf{U}_k - \mathbf{U}_0) \end{bmatrix}. \quad (11)$$

We repeat this update until the norm of the right-hand side does not exceed a given tolerance. The eigenvalues and the eigenvectors are complex. The natural frequency  $f$  and the loss factor  $\eta$  are calculated from the complex value  $\omega$  according to

$$\omega^2 = \tilde{\omega}^2(1 + i\eta), \quad f = \frac{\tilde{\omega}}{2\pi}. \quad (12)$$

### 2.3. Real-frequency approach using finite element method and modal strain energy method

The complex eigenvalue solution can be expensive for larger problems. Therefore, the modal strain energy method was introduced by Johnson et al. (1982) to overcome this difficulty. The approximated value of modal loss factor of sandwich beams

$$\eta \approx \eta_m \Pi_2 / \Pi \quad (13)$$

involves the material loss factor of the core material (foil)

$$\eta_m = \text{Im}[G_2(\omega_k)] / \text{Re}[G_2(\omega_k)], \quad (14)$$

the elastic strain energy associated with the given mode shape  $\Pi$ , and the elastic strain energy attributed to the viscoelastic core  $\Pi_2$ , which are given by

$$\Pi = \frac{1}{2} \mathbf{U}_r^T \mathbf{K}_r(\omega_k) \mathbf{U}_r, \quad \Pi_2 = \frac{1}{2} \mathbf{U}_r^T \mathbf{K}_{r,2}(\omega_k) \mathbf{U}_r. \quad (15)$$

Here,  $\mathbf{U}_r = \text{Re}[\mathbf{U}]$  stands for the corresponding undamped mode shape and the matrix  $\mathbf{K}_r = \text{Re}[\mathbf{K}(\omega_k)]$  consists of the stiffness matrices of the glass layers and the real part of the stiffness matrix of the foil  $\mathbf{K}_{r,2} = \text{Re}[G_2(\omega)] \mathbf{K}_{\text{const}}$ . The natural frequencies and the mode shapes are determined iteratively by consecutive solutions of the undamped real-valued eigenproblem

$$(\mathbf{K}_r(\omega_k) - \omega_{k+1}^2 \mathbf{M}) \mathbf{U}_{r,k+1} = \mathbf{0}, \quad (16)$$

and the approximated loss factors are computed from (13).

## 3. Results

The results of modal analyses for the previous three approaches are compared for a simply-supported and a clamped-clamped laminated glass beam at ambient temperatures 20 °C and 40 °C. The dimensions of the beam are: the length 1 m, the width 0.1 m, and the thicknesses  $h_1/h_2/h_3 = 10/0.76/10$  mm of the glass/foil/glass layers. The material parameters are taken from (López-Aenlle et al., 2014).

In Tab. 1, the modal responses are compared in terms of natural frequencies and loss factors for both types of the boundary conditions and for both temperatures. The results for finite element approaches are computed for 100 elements per the beam length. The tolerance limit, set to  $10^{-5}$ , is used for all methods.

The dynamic effective thickness (DET) approach gives the natural frequencies with the errors less than 1 % compared with those from the Newton method (NM) for the simply-supported beam at both temperatures and also for the clamped-clamped beam at room temperature; the errors are less than 1 %.

However, the errors in natural frequencies are approximately 10 % for the clamped-clamped beam at 40 °C. The modal loss factors from the DET match the NM result only for simply-supported beam at 20 °C. In the other cases, the errors in loss factors are higher: 5 – 10 % for the simply-supported beam at 40 °C and 15 – 50 % for the clamped-clamped beam.

The modal strain energy (MSE) method gives the natural frequencies with the errors less than 1 % compared with those from the NM for both boundary conditions at 20 °C and 5 – 8 % for both beams at 40 °C. The results for the modal loss factor does not match those from NM. The errors are 5 – 15 % for the clamped-clamped beam and 10 – 50 % for the simply-supported beam.

*Tab. 1: Comparison of natural frequencies and loss factors provided by the dynamic effective thickness (DET) approach, the modal strain energy (MSE) approximation, and the Newton method (NM).*

temperature 20 °C	Mode	simply-supported beam			clamped-clamped beam		
		DET	MSE	NM	DET	MSE	NM
natural frequency	1	50.46	50.26	50.42	113.3	113.5	114.2
[Hz]	2	197.4	196.1	196.8	303.8	301.9	303.6
modal loss factor	1	1.22	1.53	1.22	1.74	3.78	3.31
[%]	2	2.22	2.43	2.21	2.88	4.51	4.23
temperature 40 °C							
natural frequency	1	44.66	41.76	44.77	95.16	80.80	85.43
[Hz]	2	160.3	148.0	160.7	241.4	214.2	226.6
modal loss factor	1	18.89	29.84	19.97	24.79	37.28	33.80
[%]	2	28.57	39.85	32.08	29.52	37.04	35.20

#### 4. Conclusions

For the natural vibration problem of a laminated glass beam with a viscoelastic interlayer foil, the results of two simplified methods were compared with the complex eigenvalue solution provided by the Newton-type algorithm. We made a comparison of natural frequencies and loss factors for a simply-supported and a clamped-clamped laminated glass beam at 20 °C and 40 °C.

The dynamic effective thickness approach combines an easy iterative algorithm with simple analytical equations for natural frequencies and loss factors. For frequencies, it gives very good results for simply-supported beam at both temperatures and for the clamped-clamped beam at 20 °C. For loss factors, the errors are under 1 % only for the simply-supported beam at 20 °C.

The modal strain energy method reduces the computational cost of the problem because it works only with the real parts of the mode shapes, the frequency, and the stiffness matrix. It provides very good results for frequencies of both beams at 20 °C. However, the errors in loss factors range from 5 % up to 50 % for the considered examples.

#### Acknowledgement

This work was supported by the Czech Science Foundation, grant No. 16-14770S.

#### References

- Daya, E.M. and Potier-Ferry, M. (2001) A numerical method for nonlinear eigenvalue problems application to vibrations of viscoelastic structures. *Computers and Structures*, 79, pp. 533-541.
- Johnson, C.D. and Kienholz, D.A. (1982) Finite element prediction of damping in structures with constrained viscoelastic layers. *AIAA Journal*, 20, 9, pp. 1284-1290.
- López-Aenlle, M. and Pelayo, F. (2014) Dynamic effective thickness in laminated-glass beams and plates. *Composites: Part B*, 67, pp. 332-347.
- Ross, D., Ungar, E.E. and Kerwin, E.M. (1959) Damping of plate flexural vibrations by means of viscoelastic laminate. In: *Structural Damping*, ASME, pp. 49-88.

## MODELLING OF VIRUS VIBRATION WITH 3-D DYNAMIC ELASTICITY THEORY

Z. Zhuravlova \*\*, D. Kozachkov \*\*, D. Pliusnov \*\*, V. Radzivil \*\*, V. Reut \*\*\*, O. Shpynarov \*\*,  
E. Tarasova \*\*, D. Nerukh \*, N. Vaysfel'd \*\*\*

**Abstract:** Elastic properties of virus shells (capsids) are important as they protect the virus genome and play important role in virus internalization (the process of virus entering the cell). These properties can also be measured experimentally by direct deformation of the capsid with a microscope's tip. A 3-D mathematical model of a virus under an external non-stationary load is proposed in this paper. The apparatus of the boundary value problems of mathematical physics was used during modeling. The stated initial boundary value problem of elasticity was solved with the help of the integral transformation method and the method of discontinuous solutions. As a result, the analytical solution of the problem was obtained in Laplace transformation domain. The numerical calculations of the virus elastic characteristics were illustrated for the case of a steady-state oscillation.

**Keywords:** Virus, Elastic hollow sphere, Acoustic medium, Wave potentials, Exact solution.

### 1. Introduction

Mesoscopic properties of viruses as elastic bodies are important biologically as they allow to investigate the physics of the virus particles in various biologically relevant processes. Establishing a virus mathematical model is necessary to represent the effect of parameters variation on the behaviour of the virus as a dynamical system. Such mathematical models based on the reasonable biological assumptions were obtained earlier using three main interdisciplinary approaches:

- 1) based on a hydrodynamic theory (Markestijn, 2014, Korotkin, 2016 and Scukins, 2015);
- 2) using the theory of numerical methods for solving hydrodynamic and elasticity non-linear problems (Polles, 2013 and Roos, 2010, Gibbons, 2007, Buenemann, 2007, Polles, 2013 and Zink, 2009);
- 3) based on the linear elasticity models (Zink, 2009, Buenemann, 2008 and Zandi, 2005).

These models allowed to obtain many important characteristics, but they could not fully describe the virus as a 3-D elastic object. In the proposed paper the authors first propose to use the full system of linear elasticity's motion equations for the virus wave field representation. It allows to take into consideration the virus 3-D structure and to obtain new qualitative characteristics of the virus stresses and displacements.

### 2. The statement of the problem

A virus PCV2 is modelled by an elastic hollow sphere occupying the area  $R_1 < r < R_2, 0 < \theta < 2\pi, -\pi < \varphi < \pi$  in the spherical coordinate system. The equations of motion are written with regard to the displacements  $u = u_r(r, \theta, \varphi, t), v = u_\theta(r, \theta, \varphi, t), w = u_\varphi(r, \theta, \varphi, t)$  (Nowacki, 1970). It is assumed that the virus is filled with an acoustic medium modelling the inside content of the virus composing of either the genome for the case of the real virus, or aqueous solution containing necessary ions in the case of an empty capsid (the so called Virus Like Particle). The virus is

---

\* Prof., DSc.: Aston University, Aston Triangle; B4 7ET, Birmingham; UK D.Nerukh@aston.ac.uk

\*\* PhD student: Aston University, Aston Triangle; B4 7ET, Birmingham; UK zhuravleva@te.net.ua

\*\*\* Prof., DSc.: Odessa I.I. Mechnikov National University, Dvoryanska, 1; 65082, Odessa; UA vaysfeld@onu.edu.ua



surrounded by the aqueous solution mimicking the cellular environment, which is also described by the ideal Newton liquid model. The wave potentials  $\Phi_i(r, \theta, \varphi, t)$  of the external ( $i = 2$ ) and the internal ( $i = 1$ ) acoustic media satisfy the wave equations (Guz, 1982). It is assumed that adhesion takes place at the contact of the surfaces of the virus and the surrounding acoustic media

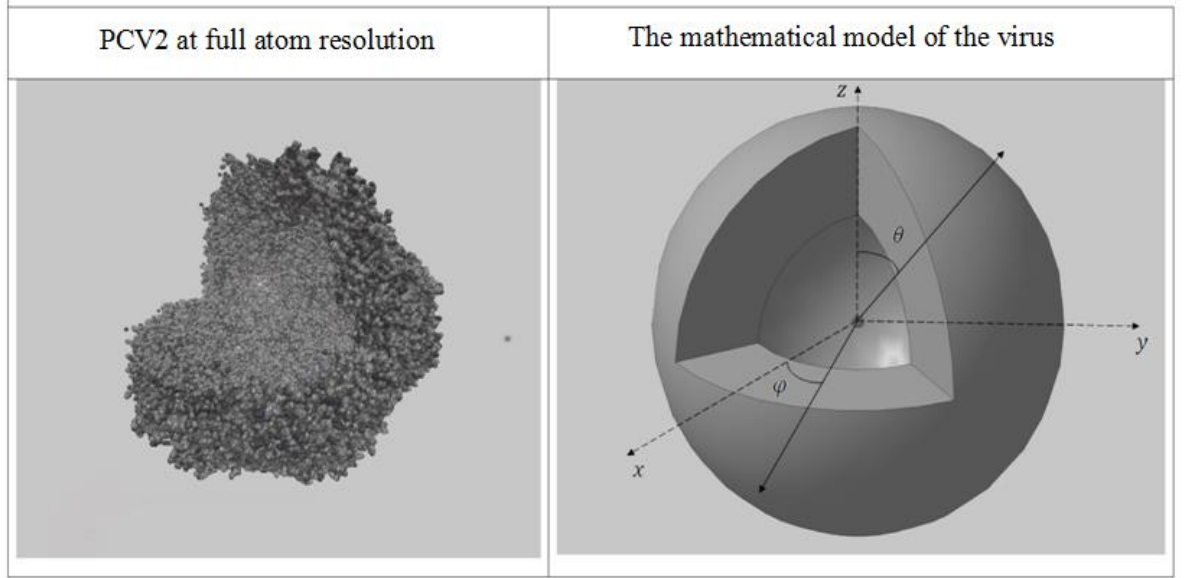


Fig. 1: The geometry of the problem.

$$\sigma_r|_{r=R_i} = -p_i(\theta, \varphi, t)|_{r=R_i} = \rho \frac{\partial \Phi_i}{\partial t} \Big|_{r=R_i}, \tau_{r\varphi}|_{r=R_i} = \tau_{r\theta}|_{r=R_i} = T_i(\theta, \varphi, t), i = 1, 2 \quad (1)$$

$$\begin{aligned} u_r|_{\theta=0, 2\pi} &= \frac{\partial u_r}{\partial \theta} \Big|_{\theta=0, 2\pi} = q_1(r, \varphi, t), u_\theta|_{\theta=0, 2\pi} = \frac{\partial u_\theta}{\partial \theta} \Big|_{\theta=0, 2\pi} = q_2(r, \varphi, t), \\ u_\varphi|_{\theta=0, 2\pi} &= \frac{\partial u_\varphi}{\partial \theta} \Big|_{\theta=0, 2\pi} = q_3(r, \varphi, t), u_r|_{\varphi=\pm\pi} = \frac{\partial u_r}{\partial \varphi} \Big|_{\varphi=\pm\pi} = g_1(r, \theta, t), \\ u_\theta|_{\varphi=\pm\pi} &= \frac{\partial u_\theta}{\partial \varphi} \Big|_{\varphi=\pm\pi} = g_2(r, \theta, t), u_\varphi|_{\varphi=\pm\pi} = \frac{\partial u_\varphi}{\partial \varphi} \Big|_{\varphi=\pm\pi} = g_3(r, \theta, t) \end{aligned} \quad (2)$$

All functions on the right hand sides of the equalities (1), (2) are known functions. It is possible also to formulate on a virus's surfaces as the boundary conditions of first main elasticity problem, so and the mixed boundary conditions (in last case the solution is solved with the method of boundary integral equations). Zero initial conditions are fulfilled. One has to determine the wave field under the influence of a spherical pressure wave  $\Phi_0(r, \theta, \varphi, t)$  falling on the virus external surface at the moment  $t = 0$ .

### 3. The methods of solution

Solution method is based on the application of the integral transformation method and the method of discontinuous solutions (Popov, 1982). The Laplace transformation with respect to the variable  $t$  and the finite Fourier transformation with respect to the variable  $\varphi$  are applied to the system of the equations of motion and the boundary conditions (1), (2). To construct the solution of the boundary value problem in the transformation domain one must use the discontinuous solutions of the motion equations for a spherical defect, which were constructed earlier in (Vaysfeld, 2002).

The transformations of the unknown functions are presented as a superposition of the functions  $u_{sn} = u_{sn}^1 + u_{sn}^2, v_{sn} = v_{sn}^1 + v_{sn}^2, w_{sn} = w_{sn}^1 + w_{sn}^2$ , where indexes  $s$  and  $n$  denote the parameters of the Laplace and the Fourier transformations respectively, the upper index 1 denotes the mechanical

characteristics, which are discontinuous on the interior surface of the sphere, the upper index 2 denotes the mechanical characteristics, which are discontinuous on the external surface of the spherical shell

$$\begin{aligned}\langle u_{sn} \rangle \Big|_{r=R_1} &= \langle u_{sn}^1 \rangle \Big|_{r=R_1} + \langle u_{sn}^2 \rangle \Big|_{r=R_1} = \langle u_{sn}^1 \rangle \Big|_{r=R_1} = -u_{sn}^1 (R_1 + 0, \theta), \\ \langle u_{sn} \rangle \Big|_{r=R_2} &= \langle u_{sn}^1 \rangle \Big|_{r=R_2} + \langle u_{sn}^2 \rangle \Big|_{r=R_2} = \langle u_{sn}^2 \rangle \Big|_{r=R_2} = u_{sn}^2 (R_2 - 0, \theta),\end{aligned}$$

where  $u \in \{u_r, u_\theta, u_\varphi, \sigma_r, \tau_{r\theta}, \tau_{r\varphi}\}$ .

Similar representations for the wave potentials are constructed. They lead to

$$\begin{aligned}\langle \Phi_{1sn} \rangle \Big|_{r=R_1} &= \Phi_{1sn} (R_1 - 0, \theta), \\ \langle \Phi_{2sn} \rangle \Big|_{r=R_2} &= -\Phi_{2sn} (R_2 + 0, \theta) + \Phi_{0sn} (R_2, \theta).\end{aligned}$$

The proposed solution method allowed to construct the representations for the wave potentials, displacements, and stresses of the elastic medium in terms of the Laplace transformations.

$$\begin{aligned}\Phi_{js} (r, \theta, \varphi) &= \frac{R_j^2}{2\pi} \left[ \int_{-\pi}^{\pi} \langle \Phi'_{js} (R_j, \tau, \phi) \rangle \int_0^{\pi} \sum_{n=-\infty}^{\infty} e^{in(\phi-\varphi)} K_n (\theta, \tau; r, R_j) \sin \tau d\tau d\phi - \right. \\ &\quad \left. - \int_{-\pi}^{\pi} \langle \Phi_{js} (R_j, \tau, \phi) \rangle \int_0^{\pi} \sum_{n=-\infty}^{\infty} e^{in(\phi-\varphi)} \frac{\partial}{\partial R_j} K_n (\theta, \tau; r, R_j) \sin \tau d\tau d\phi \right]\end{aligned}$$

where:  $K_n (\theta, \tau; r, R_j) = \sum_{k=|n|}^{\infty} \sigma_{k,|n|} \Gamma_{ik} (r, R_j) P_k^{|n|} (\cos \theta) P_k^{|n|} (\cos \tau)$ ,

$$\sigma_{k,|n|} = \frac{(k - |n|)! (k + 1/2)}{(k + |n|)!},$$

$$\Gamma_{ik} (r, R_j) = \frac{1}{\sqrt{rR_j}} \begin{cases} I_\nu (R_j q_i) K_\nu (rq_i), & r > R_j, \nu = k + 1/2 \\ I_\nu (rq_i) K_\nu (R_j q_i), & r < R_j, k = 0, 1, 2, \dots \end{cases},$$

$q_i^2 = \frac{s^2}{c_i^2}$ ,  $I_\nu (z), K_\nu (z)$  are modified Bessel functions,  $P_k^n (z)$  are associated Legendre functions.

$$\begin{aligned}u_s (r, \theta, \varphi) &= \frac{1}{2\pi\mu b^2} \sum_{n=-\infty}^{\infty} e^{in\varphi} \left\{ \sum_{k=|n|}^{\infty} \int_0^{\pi} P(n, k, \vartheta) \int_{-\pi}^{\pi} e^{-in\phi} \left\{ \sum_{j=1}^2 (-1)^{j+1} \Psi (R_j, \vartheta, \phi) \frac{\partial^2}{\partial R_j \partial r} \Gamma_{a,k} (r, R_j) P_\sigma (n, k, \theta) + \right. \right. \\ &\quad \left. \left. + \frac{1}{r} \frac{n^2}{\sin^2 \theta} \sum_{j=1}^2 (-1)^{j+1} \Psi (R_j, \vartheta, \phi) \Gamma_{b,k} (r, R_j) P_\sigma (n, k, \theta) - \frac{1}{r} \sum_{j=1}^2 (-1)^{j+1} \Psi (R_j, \vartheta, \phi) \Gamma_{b,k} (r, R_j) \frac{\partial^2}{\partial \theta^2} P_\sigma (n, k, \theta) - \right. \right. \\ &\quad \left. \left. - \frac{1}{r} \text{ctg} \theta \sum_{j=1}^2 (-1)^{j+1} \Psi (R_j, \vartheta, \phi) \Gamma_{b,k} (r, R_j) \frac{\partial}{\partial \theta} P_\sigma (n, k, \theta) \right\} d\phi d\vartheta \right\}\end{aligned}$$

where:  $P(n, k, \vartheta) = \sin \vartheta P_k^{|n|} (\cos \vartheta)$ ,  $P_\sigma (n, k, \theta) = \sigma_{k,|n|} P_k^{|n|} (\cos \theta)$ ,

$\Psi (R_j, \vartheta, \phi) = R_j^2 \rho \frac{\partial \Phi_j}{\partial t} (R_j, \vartheta, \phi)$ . The formulae for the displacements and the stresses are analogous.

#### 4. Numerical results

The obtained formulae were used to illustrate the case of steady-state oscillations, the homogeneous boundary conditions (2) and the conditions  $T_i(\theta, \varphi, t) = 0, i = 1, 2$ . The elastic constants of the virus, namely the Young module and the Poisson ratio, were determined with the help of LAMMPS Molecular Dynamics package. The sea water was selected as the external acoustic medium, and water was selected as the internal acoustic medium. The mechanical parameters of these liquids were taken for the modelling of the liquids inside and outside the virus. The stresses on the surfaces of the sphere were calculated. The analysis was conducted depending on the incident wave's angle.

## 5. Conclusions

1. 3-D mathematical model of a PCV2 virus was constructed on using dynamic elasticity boundary value problem. The elastic constants of the virus (the Poisson ratio, the Young module) were determined with the help of LAMMPS package.
2. Formulae determining the virus wave field under the acoustic pressure wave were obtained.
3. This model will serve as the first step in developing a more realistic models of viruses with varying density of the capsid, its geometry and, possibly, elastic properties.

## Acknowledgement

Erasmus+ Key Action 107- International Credit Mobility. Project number 2016-1-UK01-KA107-023724.

## References

- Buenemann, M. and Lenz, P. (2007) Mechanical limits of viral capsids. PNAS, 104, 24, pp. 9925-9930.
- Buenemann, M. and Lenz, P. (2008) Elastic properties and mechanical stability of chiral and filled viral capsids. PhysRevE.78.051924 PACS.
- Gibbons, M.M. and Klug, W.S. (2007) Nonlinear finite-element analysis of nanoindentation of viral capsids. PhysRevE.75.031901.
- Guz, A.N. and Kubenko, V.D. (1982) Theory of non-stationary aero-hydro-elasticity of shells. Naukova dumka, Kyiv.
- Korotkin, I., Nerukh, D., Tarasova, E., Farafonov, V. and Karabasov, S. (2016) Two-phase flow analogy as an effective boundary condition for modelling liquids at atomistic resolution. Journal of Computational Science.
- Markestijn, A., Karabasov, S., Scukins, A., Nerukh, D., Glotov, V. and Goloviznin, V. (2014) Concurrent multiscale modelling of atomistic and hydrodynamic processes in liquids. Phil. Trans. R. Soc. A 372, pp. 2021.
- May, E.R. and Brooks, C.L. (2012) On the Morphology of Viral Capsids: Elastic Properties and Buckling Transitions. J. Phys. Chem. B, 116, pp. 8604-8609.
- Nowacki, W. (1970) Theory of elasticity. Warszawa.
- Polles, G., Indelicato, G., Potestio, R., Cermelli, P., Twarock, R. and Micheletti, C. (2013) Mechanical and Assembly Units of Viral Capsids Identified via Quasi-Rigid Domain Decomposition. PLoS Comput Biol, 9, 11.
- Popov, G.Y. (1982) The elastic stress' concentration around dies, cuts, thin inclusions and reinforcements. Nauka, Moskow (in Russian).
- Roos, W.H., Gibbons, M.M., Arkhipov, A., Uetrecht, C., Watts, N.R., Wingfield, P.T., Steven, A.C., Heck, A.J.R., Schulten, K., Klug, W.S. and Wuite, G.J.L. (2010) Squeezing Protein Shells: How Continuum Elastic Models, Molecular Dynamics Simulations, and Experiments Coalesce at the Nanoscale. Biophysical Journal, 99, 4, pp. 1175-1181.
- Scukins, A., Nerukh, D., Pavlov, E., Karabasov, S. and Markestijn, A. (2015) Multiscale molecular dynamics/hydrodynamics implementation of two dimensional "Mercedes Benz" water model. European Physical Journal, 224, 12, pp. 2217-2238.
- Vaisfel'd, N.D. and Popov G.Y. (2002) Nonstationary dynamic problems of elastic stress concentration near a spherical imperfection. Mechanics of Solids. 37, 3, pp. 77-88.
- Zandi, R. and Reguera, D. (2005) Mechanical properties of viral capsids, Phys. Rev. E 72, 021917.
- Zink, M. and Grubmüller, H. (2009) Mechanical Properties of the Icosahedral Shell of Southern Bean Mosaic Virus: A Molecular Dynamics Study. Biophysical Journal, 96, 4, pp. 1350-1363.

## **POLYURETHANE COATINGS AND METHODS OF EXAMINATION OF THEIR PROPERTIES**

**J. Ziolkowska\***

**Abstract:** *The paper concerns problems of counteracting excessive wear of parts of mining machines. Key issues regarding tribology of polymer coatings are discussed. Methods of testing of properties of manufactured coatings on given elements are presented as well. Examples of utilization of polymer coatings are presented.*

**Keywords:** Coatings, Polyurethane, Mining, Abrasive wear, Tribology.

### **1. Introduction**

Brown coal is one of the most significant fuels. Such countries like Germany, China, United States and Poland are world leaders in terms of production of energy from brown coal. This fuel is excavated in open pit mines utilizing among others bucket wheel excavators and stackers. Their working conditions are extremely demanding as their parts are endangered to abrasive wear most of all. To lower this disadvantageous influence of rocks, enormous loadings and changeable weather conditions, polymer coatings, including polyurethane ones, are applied on surface layers of selected parts (Augustynowicz, 2002). Most important properties of such coatings are: thickness, hardness, adhesion to substrate, resistance to both scratches and abrasive wear.

### **2. Tribological aspects of usage of polymer coatings**

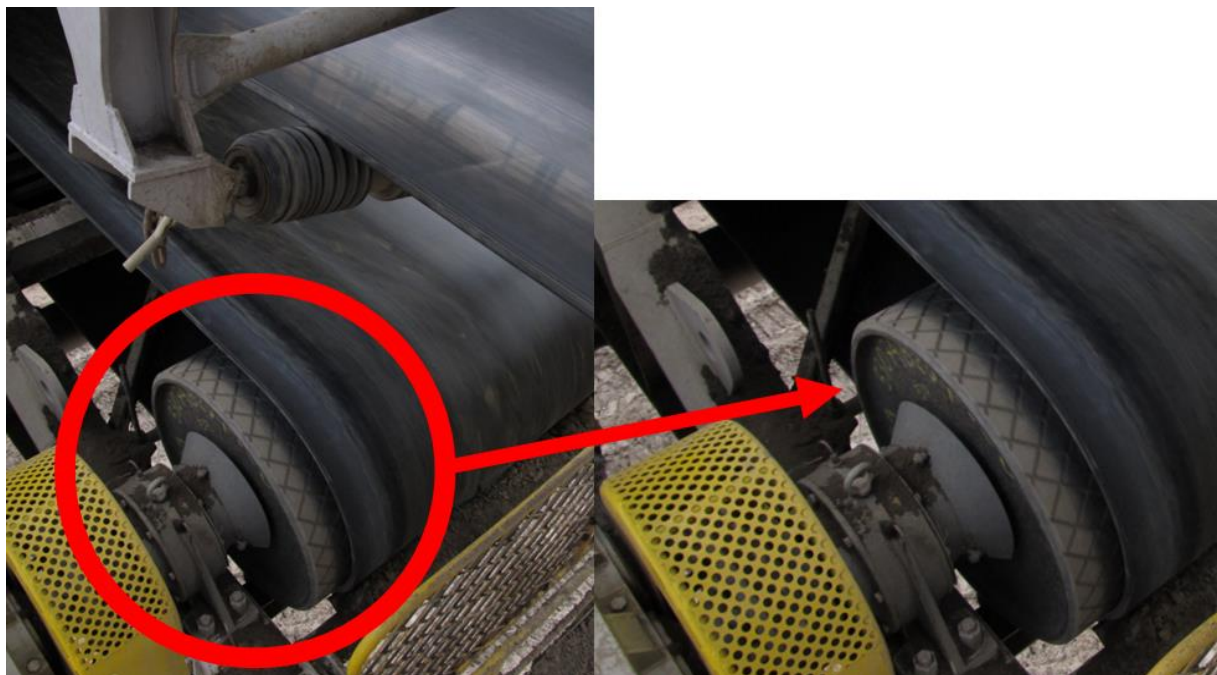
Wear resistance is a key parameter when analyzing operation of members of tribological pairs. Machines and devices in working conditions of a mine are especially endangered to disadvantageous influence of abrasive particles (abrasive wear) and environment (corrosion) most of all. Because of that special coatings are applied on tribological surfaces. Abrasion and cohesive wear are main mechanisms observed in polyurethane coatings (Mirhosseini et al., 2016). In (Kotnarowska, 2010) a study of process of wear of polymer coatings is done. It was found out that wear rate depends mainly on relative velocity between coating and particles which act as abrasive. Nonlinear character of this phenomena was observed. Also such parameters like residual strain which results from plastic deformation and ultimate elongation of a given coating influence wear resistance of polyurethane are crucial (Ashrafizadeh et al., 2016).

Key issue in terms of durability of coatings, including polyurethane ones, is to improve their wear resistance. To achieve this goal special nanofillers can be applied (Kotnarowska et al., 2011). It was found out that all of tested nanofillers had beneficial impact on wear resistance. It is worth noting that this is not a rule in case of other materials used for coatings, e.g. for epoxy coatings different dependency was observed.

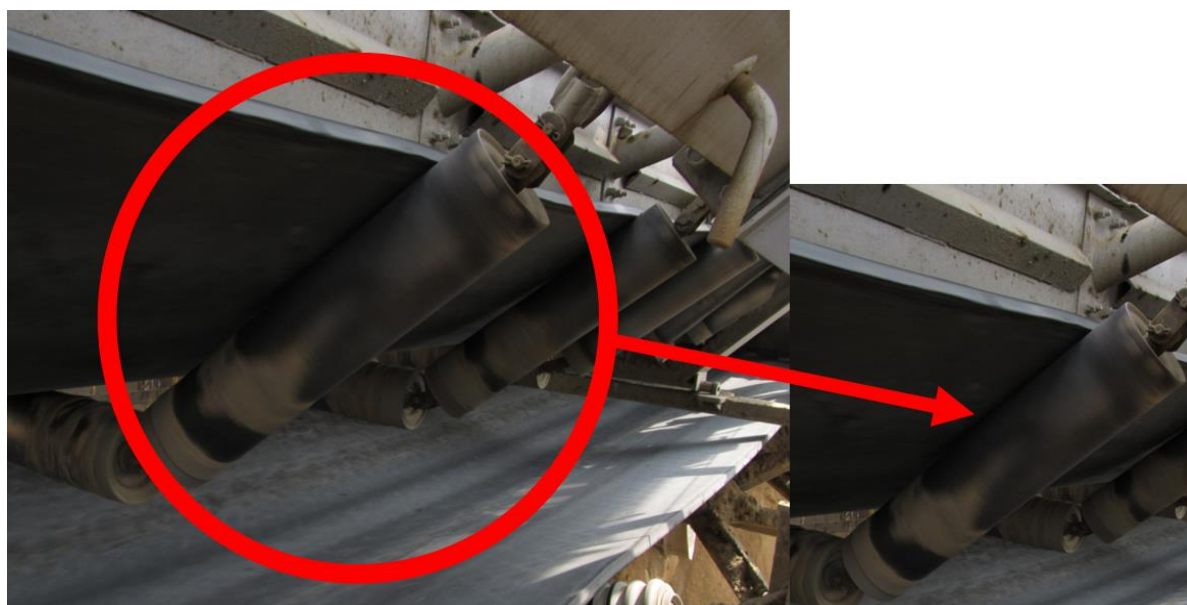
Polyurethane itself is considered as an excellent material for coatings in terms of wear resistance improvement (Ashrafizadeh et al., 2016). Those coatings are characterized by extremely advantageous mechanical parameters, thermal and chemical stability as well (Mirhosseini et al., 2016). Polyester polyoles as coatings improve wear resistance as a result of hydrogen bonding between soft and hard structures.

---

\* Justyna Ziolkowska, MSc. Eng.: Faculty of Mechanical Engineering, Wrocław University of Science and Technology, Łukasiewicza Street 4; 50-371 Wrocław; PL, justyna.ziolkowska@pwr.edu.pl



*Fig. 1: Examples of utilization of polymer coatings in real mining conditions. Coatings applied on driving wheel of belt conveyor.*



*Fig. 2: Examples of utilization of polymer coatings in real mining conditions. Coatings applied on rollers of belt conveyor (Author's archive).*

As mentioned earlier, environmental influence can be very adverse for parts of mining machinery, especially their surface layers. If there is a coating applied, this negative impact takes place in the structure of those additions. Roughness of coatings is the parameter which increases with time when coating is exposed to air influence (Kotnarowska, 2013). Main factors contributing to this process are: temperature and humidity changes and UV radiation. The latter is considered as the most significant climatic factors. This influence can in the long run lead to both physical and chemical destruction of a given coating, which can be revealed through corrosion which can be escalated by another phenomena. Among them is influence of aggressive media and microorganisms. If the process of ageing of coatings in such conditions lasts too long even loss of adhesion and following delamination and crumbling of fillers occur (Kotnarowska, 2013). All in all process of ageing of coatings results in deterioration of their protective function.

Wear resistance of coatings can be significantly improved due to formation of so-called interpenetrating polymer network based on polyurethane and epoxy. What is more, addition of nanodiamonds enables achieving similar results (Xia et al., 2014).

In open pit mining polyurethane is primarily applied for wheels and rollers of belt conveyors. Exemplary coatings are presented in Figs. 1 and 2.

### **3. Tests of selected polyurethane properties**

There are several types of measurements which are used to examine properties of already manufactured coatings. The most significant testing methods are discussed below.

#### **3.1. Thickness of coatings**

Depending on the method which was used, destructive or non-destructive methods can be utilized to evaluate thickness of a given coating (Kotnarowska and Wojtyniak, 2010):

- Using mechanical contact devices (can be used for flat surfaces only).
- Using microscopes (on a sample of a element with coating, on a coating separated from substrate or on a coating cut at a defined angle).
- Using magnetic gauges (gauges utilize magnetic induction or magnets). This method enables measurements of coatings applied on substrates with any shape. This method is very useful in mining conditions.
- Contactless method based on  $\beta$  particles dispersion or X-ray Fluorescence. This method is dedicated to cases when measuring device should not be in contact with examined surface.

#### **3.2. Adhesion to substrate**

There are 2 methods of testing of adhesion of a coating to substrate (Kotnarowska and Wojtyniak, 2010):

- Method of cuts meshwork. It consists in performing of 6 cuts in a coating (through entire thickness) in 2 perpendicular directions. Distance between cuts depends on coating thickness and type of the substrate. There should be 3 measurements made on all samples. After evaluation of examination results, one should attach a parameter described in a standard to the meshwork. The lower this value is, the better adhesion is (minimum value is 0 and maximum value is 5).
- Tear away method. It consists in tearing away a given coating perpendicularly to the substrate with a special device. A test stamp initially glued to the examined surface is torn away with increase of stress up to 1 MPa/s. The lowest values of tensile stress needed to separate the weakest boundary surface characterizes adhesion in this method. The results of this test are both the value of tensile stress and areas on which separation took place.

#### **3.3. Resistance to abrasive wear**

Resistance to abrasive wear is tested with flux of an abrasive material which strikes a given coating from a selected distance (Kotnarowska and Wojtyniak, 2010). The examination is carried out until a previously defined area of a substrate's surface with coating is unveiled. Artificial corundum is used (3,5 kg of mass) which strikes the tested surface from 1 m of height until entire thickness of the coating is worn. Subsequent portions of abrasive material are smaller until there is 0,5 kg of material left. The end of the examination is when elliptical hole in coating with bigger diameter of 3,6-3,7 mm is observed. Wear is proportional to used mass of the abrasive material and inverse to average thickness of the tested coating.

#### **3.4. Resistance to scratches**

This test is performed with a needle which scratches a substrate under some loading. The device is placed perpendicularly to the sample and is moved at 30 – 40 mm/s. The scratch must be continuous and have a length of 60 mm. During the test the loading is increased. The parameter which characterizes this resistance is the lowest value of loading which scratched the sample.



#### 4. Conclusions

Application of polymer coatings, including polyurethane ones, gives plenty of advantages. It improves primarily resistance to: corrosion, influence of chemical substances and abrasive wear of a part where it was used. There are different tests which enable verification whether an analyzed coating was manufactured correctly. A very disadvantageous process is when a coating structure is penetrated by micro-peaks of a mated elements' surface layer. It is more probable when the other element has higher hardness than the coating. If such a situation occur, strong dissolution and accelerated corrosion can be observed (Dobrowolska et al., 2015).

Additionally one can notice that tribological processes which include polymers are extremely complex. For these materials friction coefficient and wear data only are not sufficient to fully evaluate tribological properties of a pair in which these materials are used (Capanidis, 2007). Among needed parameters one can list characteristic of a material of a counterface and condition of both surface layers most of all. The latter includes such parameters as chemical composition, surface roughness, hardness of the sliding surfaces and information about producing technology as well (Capanidis, 2007).

#### References

- Ashrafizadeh, H., Mertiny, P. and McDonald, A. (2016) Evaluation of the effect of temperature on mechanical properties and wear resistance of polyurethane elastomers. *Wear*, 368, pp. 26-38.
- Augustynowicz, J. (2002) Development and implementation of a project of modification of friction nodes and elements supporting belt conveyors on bucket wheel excavators, stackers and belt conveyors systems. Report of Institute of Machine Design and Operation of Wroclaw University of Science and Technology, Wroclaw, (in Polish).
- Capanidis, D. (2007) Selected aspects of the methodology of tribological investigations of polymer materials. *Archives of civil and mechanical engineering*, 7(4), pp. 39-55.
- Dobrowolska, A., Kowalewski, P. and Ptak, A. (2015) Influence of the lubricating fluid on the changes on rubbing metallic biomaterials surface. *Colloids and Surfaces A-Physicochemical and Engineering Aspects*, Vol. 480, pp. 419-425.
- Kotnarowska, D. (2010) Effect of erosive particle velocity on the Intensity of polymeric coating wear. *Solid State Phenomena*. Trans Tech Publications, Vol. 165, pp. 91-96.
- Kotnarowska, D. (2013) Destruction of Epoxy Coatings Under the Influence of Climatic Factors. *Solid State Phenomena*. Trans Tech Publications, Vol. 199, pp. 581-586.
- Kotnarowska, D. and Wojtyniak, M. (2010) Methods of testing of protective coatings quality. Radom University of Technology, Radom, (in Polish).
- Kotnarowska, D., Przerwa, M. and Wojtyniak, M. (2011) Effect of epoxy and polyurethane coating modification with nanofillers on their resistance to erosive wear. *Journal of Vibroengineering*, 13(4), pp. 870-875.
- Mirhosseini, S.S., Razavi, R.S., Taheran, M. and Barekat, M. (2016) Wear behavior of polyurethane/carbon black coatings on 6061 aluminum alloy substrates. *Progress in Organic Coatings*, 97, pp. 37-43.
- Xia, S., Liu, Y., Zhang, L., Wang, D., Zou, W., Peng, J. and Cao, S. (2014) Tribological mechanism improving the wear resistance of polyurethane/epoxy interpenetrating polymer network via nanodiamond hybridization. *Journal of Applied Polymer Science*, 131(10).

## MATHEMATICAL MODEL OF ENGINE VALVE MECHANISM

T. Zvolský\*

**Abstract:** *The paper deals with mathematical modeling and numerical computing of valve mechanism. There is described the computing method for a specific combustion engine and valve mechanism. Model computes with real mass and stiffness of valve mechanism parts. Mathematical model reflects the stiffness of the roller finger follower and deals with follower oscillation and consequently oscillation of the valve. Valve bounce from its seat, axial compliance of valve and forces from the flue-gas acting on valve is not included in this model. Valve lift, velocity and acceleration are graphically shown.*

**Keywords:** Valve, Engine, Model, Stiffness, Lagrange.

### 1. Introduction

Car combustion engine can typically operate in a wide speed range. At low speed, the engine has low fuel consumption and at high speed, the engine has high power. At high engine speed, it is necessary to quickly open and close the valves of the engine. There is an extreme accelerations and stress of the valve mechanism parts. At the same time there are requirements for high reliability and durability of the valve mechanism. Therefore it is necessary to optimize the valve mechanism. Optimization is based on the mathematical model, but it is not included in this paper.

### 2. Methods

This publication deals with the valve mechanism simulation of the combustion engine VW 1.6 MPI, series EA211. Valve train layout is DOHC - Double Over Head Camshaft, which is characterised by two camshafts located within the cylinder head. One controls the intake valves and the other one controls the exhaust valves. The camshaft moves the valve through a roller finger follower (Scheidt, 2014). Return movement of the valve into its seat is ensured by the spring. Valve clearance is eliminated by hydraulic lash adjuster. Mathematical model reflects the stiffness of the roller finger follower and deals with follower oscillations and consequently oscillations of the valve. DOHC valve train configuration with roller finger followers is shown in Fig. 1.

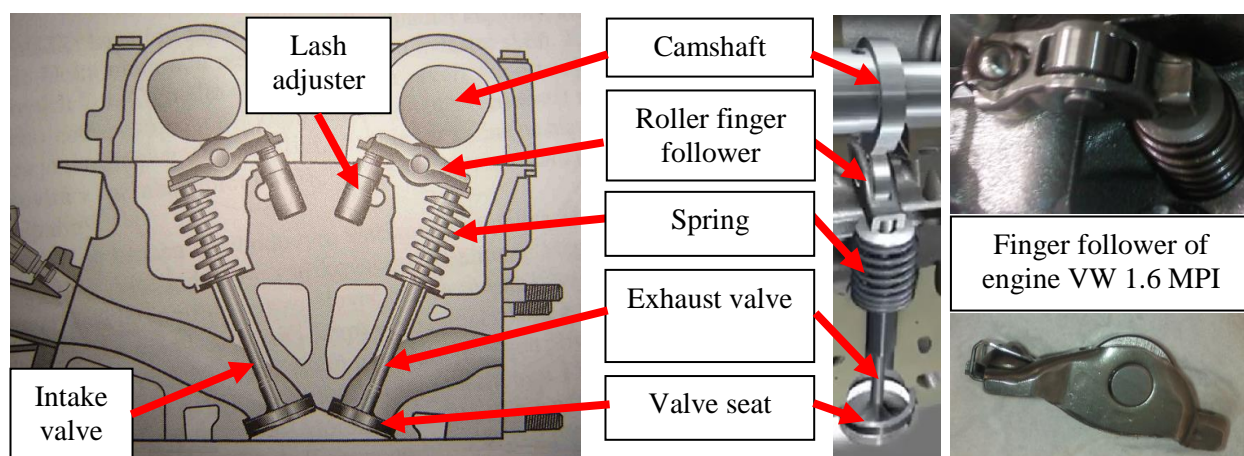


Fig. 1: Valve mechanism in combustion engine head.

\* Ing. Tomáš Zvolský: Technical University of Liberec, Studentská 2; 461 17, Liberec; CZ, tomas.zvolsky@tul.cz

## 2.1. Mathematical model of valve mechanism

Mathematical model was created from real model of valve mechanism of gasoline VW engine 1.6 MPI, series EA211, shown in Fig. 2.

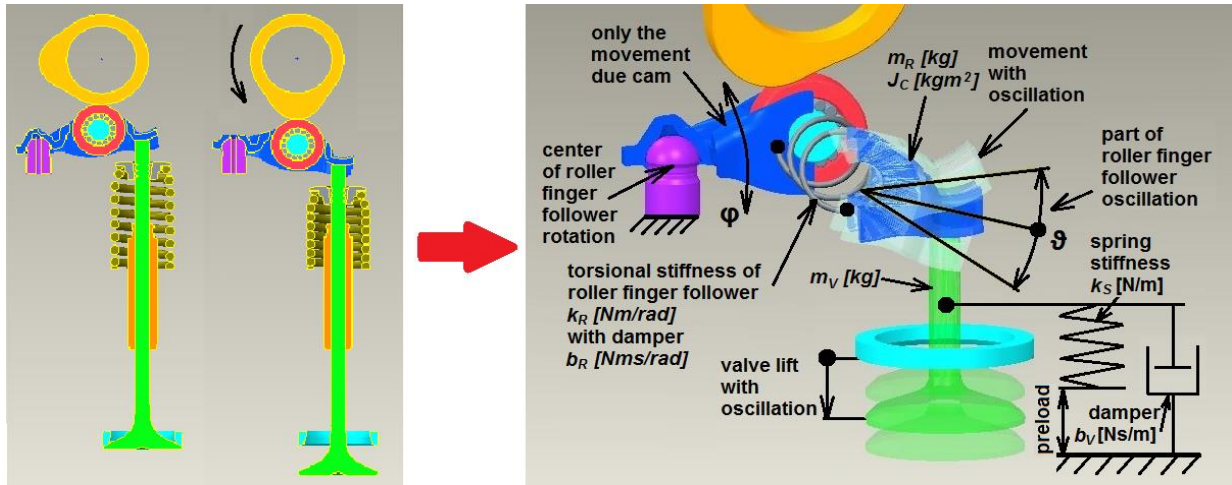


Fig. 2: Real and mathematical model of valve mechanism.

Roller finger follower is divided into two rigid parts that are elastically connected to each other. The first part of the finger follower is rotationally mounted to the spherical surface of the hydraulic lash adjuster and it includes a roller which is in contact with the cam. The second part of the finger follower is rotatable connected to the first part and can be deflected against it. Between both parts of the finger follower is inserted torsional stiffness  $k_R$ . The end of the finger follower is in contact with valve, which performs direct motion. Return movement of the valve is ensured by the spring. Stiffness of the spring is  $k_S$ . Masses  $m_V$  and  $m_R$ , moment of inertia  $J_C$  and stiffness of the finger follower  $k_R$  causes oscillation of the second part of the finger follower and consequently oscillations of the valve. The mathematical model is supplemented with natural damping  $b_R$  and  $b_V$ . Fig. 3 describes the dimensions of the valve mechanism and roller finger follower angular waveforms  $\phi$  and  $\vartheta$ . Angle  $\phi$  is an input value in the mathematical model and angle  $\vartheta$  is an output unknown variable.

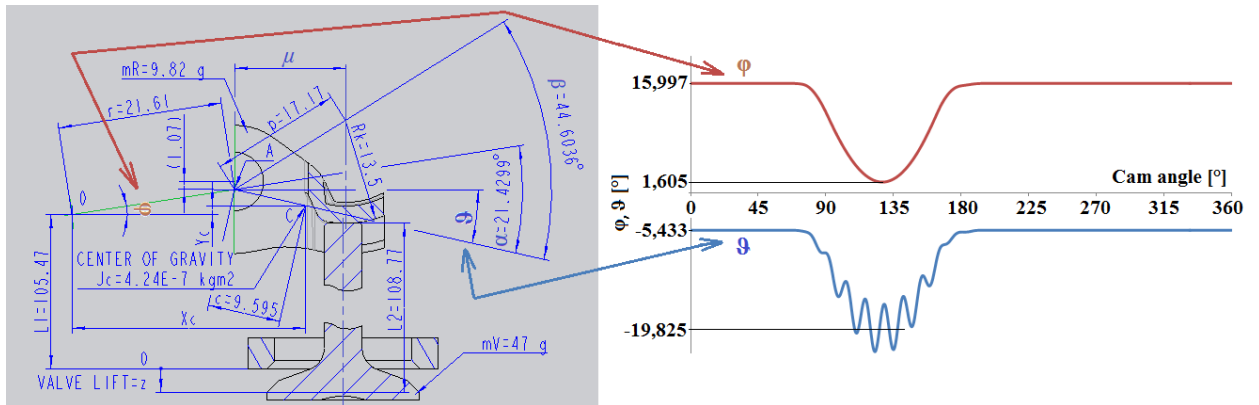


Fig. 3: Dimensions of valve mechanism with roller finger follower angular waveforms  $\phi$  and  $\vartheta$ .

Due to the cam rotation, the first part of the finger follower is deflected from the horizontal plane around point O by an angle  $\phi$ . Since the second part of the finger follower is elastically connected with the first part, the second part of the finger follower is deflected from the horizontal plane by different angle  $\vartheta$ . The second part of the finger follower can rotate around the point A. Point A also belongs to the first part of the finger follower and therefore trajectory of point A is a circle with center in point O and radius  $r$ . The second part of the finger follower has a center of gravity at point C, mass  $m_R$  and moment of inertia  $J_C$ . Valve mass, mass of fixing valve to the spring and 1/3 spring mass are included in  $m_V$ . Because this publication deals only with the valve oscillation, we do not need to specify the mass of the first part of the finger follower. It should be noted that permanent contact between cam and roller of finger follower is important assumption. Verification of this assumption is not described in this publication.

Stiffness of the finger follower was determined using the finite element method. The finger follower is considered as beam, which is constrained on two places - the first in the center of the spherical surface of hydraulic lash adjuster and the second in the center of roller. Load is placed to contact between finger follower and valve. Torsional stiffness of finger follower  $k_R$  can be calculated using bending stiffness  $k_O$

$$k_R = k_O \xi^2 = \frac{F}{\delta} \xi^2 \quad (1)$$

where  $F$  is load,  $\delta$  is displacement and  $\xi$  is distance between load position and center of roller.

## 2.2. Determining the equation of motion

Lagrange's equation of the second kind (Lanczos, 1986 and Julis, 1987) was used for solving this model. The angle  $\varphi(t)$  is specified as a time waveform. It is an input value in the mathematical model and period depends on the speed of the camshaft. The output angle  $\vartheta(t)$  is an unknown variable.

$$\frac{d}{dt} \left( \frac{\partial T}{\partial \dot{\vartheta}} \right) - \frac{\partial T}{\partial \vartheta} = - \frac{\partial V}{\partial \vartheta} - \frac{\partial D}{\partial \dot{\vartheta}} \quad (2)$$

The model has one degree of freedom. It is necessary to express total kinetic energy ( $T$ ), potential energy ( $V$ ) and Rayleigh dissipation function ( $D$ ) of the system through the angle  $\vartheta$  or its time derivatives. The kinetic energy of the second part of the finger follower consists of the translational and rotational parts.

$$\begin{aligned} T &= \frac{1}{2} m_R (\dot{x}_C^2 + \dot{y}_C^2) + \frac{1}{2} J_C \dot{\vartheta}^2 + \frac{1}{2} m_V \dot{z}^2 = \\ &= \frac{1}{2} m_R [r^2 \dot{\varphi}^2 + c^2 \dot{\vartheta}^2 + 2rc \dot{\varphi} \dot{\vartheta} \cos(\varphi - \vartheta)] + \frac{1}{2} J_C \dot{\vartheta}^2 + \frac{1}{2} m_V (r \dot{\varphi} \cos \varphi + \mu \dot{\vartheta})^2 \end{aligned} \quad (3)$$

The kinetic energy of linear motion of the valve is expressed as a function of the angle  $\vartheta$  using  $\mu$  function.

$$\mu(\vartheta) = p \cos(\vartheta + \beta) \quad (4)$$

Potential energy of the system is determined by the elasticity of the finger follower and the spring.

$$V = \frac{1}{2} k_R (\vartheta - \varphi + \alpha)^2 + \frac{1}{2} k_S (z + preload)^2 \quad (5)$$

where  $z$  is valve lift. Opening the valve represents a positive value of the valve lift.

$$z = R_K - L_1 + L_2 - r \sin \varphi - p \sin(\vartheta + \beta) \quad (6)$$

Rayleigh dissipation function is given by equation (7).

$$D = \frac{1}{2} b_R (\dot{\vartheta} - \dot{\varphi})^2 + \frac{1}{2} b_V \dot{z}^2 = \frac{1}{2} b_R (\dot{\vartheta} - \dot{\varphi})^2 + \frac{1}{2} b_V (r \dot{\varphi} \cos \varphi + \mu \dot{\vartheta})^2 \quad (7)$$

where  $b_R$  and  $b_V$  are damping coefficients. For natural damping we can use equations (8) and (9)

$$b_R = \frac{\ln 2}{\pi} \sqrt{k_R (J_C + m_R c^2)} = \frac{\ln 2}{\pi} \sqrt{k_R J_A} \quad (8)$$

$$b_V = \frac{\ln 2}{\pi} \sqrt{k_S m_V} \quad (9)$$

After expressing energy and calculating the relevant derivatives, we obtain differential equation.

$$\begin{aligned} (m_R c^2 + J_C + m_V \mu^2) \ddot{\vartheta} &= m_R r c \dot{\varphi}^2 \sin(\varphi - \vartheta) - m_R r c \ddot{\varphi} \cos(\varphi - \vartheta) - k_R (\vartheta - \varphi + \alpha) - b_R (\dot{\vartheta} - \dot{\varphi}) + \\ &+ m_V r \mu \dot{\varphi}^2 \sin \varphi - m_V r \mu \ddot{\varphi} \cos \varphi - m_V \mu v \dot{\vartheta}^2 + k_S \mu (z + preload) - b_V r \mu \dot{\varphi} \cos \varphi - b_V \mu^2 \dot{\vartheta} \end{aligned} \quad (10)$$

where  $v(\vartheta)$  is given by equation (11).

$$v(\vartheta) = -p \sin(\vartheta + \beta) \quad (11)$$

### 2.3. Solving the equation of motion

For solving the equation of motion was used Matlab software. The graphs below show lift, velocity and acceleration of the exhaust valve at camshaft speed 3250 rpm. This corresponds to the crankshaft speed 6500 rpm, which is the maximum motor speed. One complete rotation of the camshaft takes approximately 18.5 ms, but the graphs show only useful 7 ms. In those graphs are shown theoretical cam and real valve waveforms, specified in (Heisler, 1995).

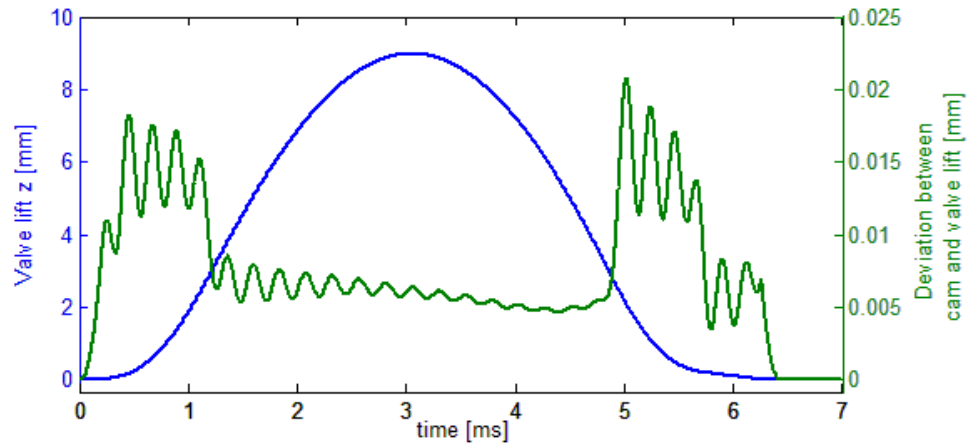


Fig. 4: Valve lift (blue) and deviation between theoretical cam lift and real valve lift (green).

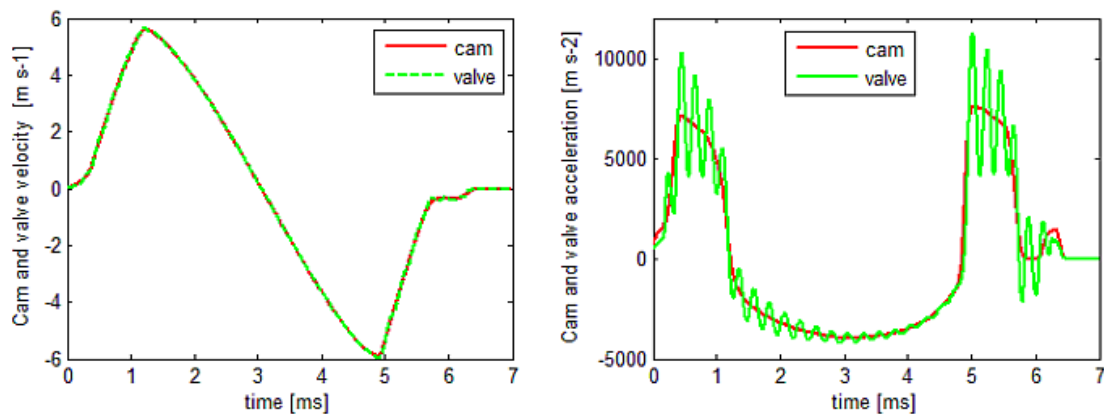


Fig. 5: Theoretical cam and real valve velocity and acceleration.

### 3. Conclusions

This publication deals with the valve mechanism simulation of the combustion engine 1.6 MPI, series EA211. Mathematical model reflects the stiffness of the roller finger follower and deals with follower oscillations and consequently oscillations of the valve. The stiffness of the finger follower is high and therefore frequency is relatively high, according to the simulation approximately 4000 Hz. Deviation between theoretical cam lift and real valve lift is greater than zero. This is important to keeping permanent contact between the valve and the finger follower. Theoretical cam velocity and real valve velocity are almost identical. Valve acceleration amplitude of oscillation is very significant.

### Acknowledgement

This publication was written at the Technical University of Liberec with the support of the Specific University Research Grant, as provided by the Ministry of Education, Youth and Sports of the Czech Republic in the year 2017.

### References

- Heisler, H. (1995) Advanced Engine Technology. SAE Technology, pp. 2-40.
- Julis, K. and Brepta, R. (1987) Mechanics part 2. Dynamics. SNTL, Praha (in Czech).
- Lanczos, C. (1986) The Variational Principles of Mechanics. Dover Publications Inc., New York, pp. 111-119.
- Scheidt, M. and Lang, M. (2014) Pure Efficiency. 10<sup>th</sup> Schaeffler Symposium, pp. 43-55.

## A DEVICE FOR AUTOMATIC ROBOT TOOL CENTER POINT (TCP) CALIBRATION ADJUSTMENT FOR THE ABB INDUSTRIAL ROBOTS

J. Zwierzchowski\*

**Abstract:** *In the process of serial welding, the one place to shorten the process for product finished is to shorten the preparatory process and diagnostic service. The preparatory process is largely to proper apply welded elements in welding devices. Diagnostic process is for example to make validation or calibration of so-called tool central point (TCP), which is attached to welding torch. When this point is incorrectly defined, the tool can wave during work and causes damage of the welding element. This phenomenon is particularly evident when the seam is made near the corner of welding profile, for example bent 90 degrees. In such cases, there are uncontrolled changes in distance contact between tip and work piece. The given phenomenon can be observed in welding arc. This article presents an automatic tool to validate the calibration tool. There are describes main assumptions like integrity with intuitional robots, easy to use, not expensive device, working in heavy environment. Robot program algorithm is also presented in this article.*

**Keywords:** TCP calibration, Industrial robots, Automatic TCP adjustment.

### 1. Introduction

To calculate position and orientation coordinates of manipulator in the industrial robot workspace is important to have information about the origin of the robot's tool. In this case, the robot user must conduct tool calibration. In this process operator usually sets only translation vector of the tool coordinates origin (TCP – tool center point) with respect to the last robot joint of the kinematic chain, where default tool is attached. In a few cases, user also indicates the orientation of the Z-axis of calibrating tool, after that the orientation of the other axes is the same as the default tool coordinate system.

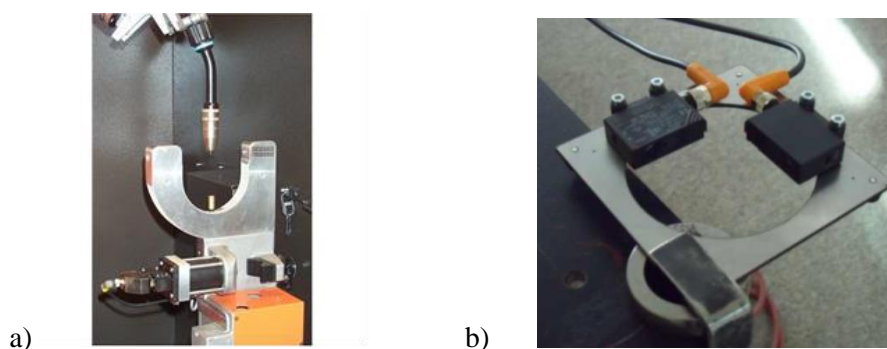


Fig. 1: Calibration devices: a) ABB Bulls Eye, b) device describe in the article.

Tool calibration is a very important issue in robotics, because it effects on accuracy of the programmed points in the robot program paths. Checking TCP repeatability is particularly important in robotic welding systems. In these cases, the TCP is attached to the end of the welding wire. Invalid eject, bent, unexpected move of the wire after the collision can result in interruption of the welding process, because there would be no arc weld setting up after scrapping, or seam would be forming in the wrong shift place. Those welding interruption, for example, in the middle of the path may cause the welded part becomes worthless.

---

\* Dr inż. Jarosław Zwierzchowski, PhD.: Faculty of Mechatronics and Mechanical Engineering, Kielce University of Technology, Al. Tysiąclecia Państwa Polskiego 7; 25 – 314 Kielce; PL, j.zwierzchowski@tu.kielce.pl



There are commercial solutions, which provide automatically checking position device of the TCP. For example, ABB devices called Bulls Eye is shown in Fig. 1a (1). In contrast, Fig. 1b shows the prototype described in this article. It is also important to mention that this device can be used in many other work (2-7).

## 2. Manual tool calibration and design of calibration device

Below is presented 4-points calibration method for ABB IRB1600 robot, which is described in instruction provided by the manufacturer (9). This calibration method is implemented to vast majority of industrial robots. The algorithm is as follows. Find reference fixed point in the robot workspace. Next, determine reference point on the tool. Normally it is end of the welding wire. Finally, indicate reference robot point from four different directions by moving manipulator tool, as shown in Fig. 1a (one position, four orientations). Reference robot point can be any sharp object for example steel rod. The robot control system calculates the TCP based on the different positions respected to robot mounting flange. It is important, that reference points should invade as close as possible to get the best accuracy.

Correctly defined TCP receives default coordinate system related to the previous one attached to the end of kinematic robot chain (in this case: the last robot joint). This is shown in Fig. 2b.

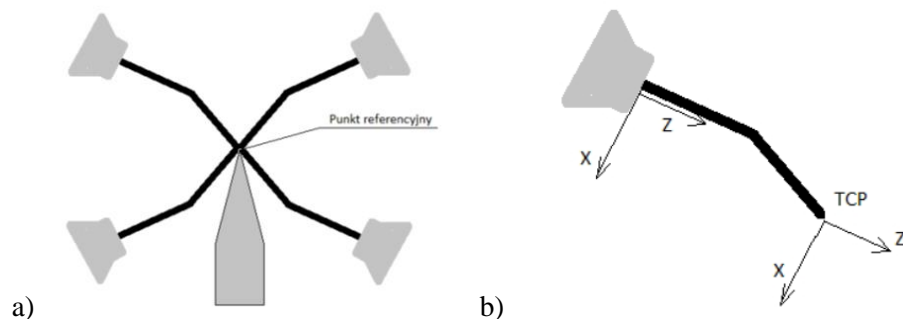


Fig. 2: a) manual 4 points calibration method, b) TCP location in welding torch.

Designed device for checking the accuracy of the calibration tool is composed of two laser sensors, in which the beam diameter does not exceed one millimeter. As mentioned in introduction, the device is mainly used in welding, where the thickness of welding wires is great or equal 0.8 mm. The second assumption was that the robot operator may run checking TCP process at any time, for example, between the free moving between welding paths.

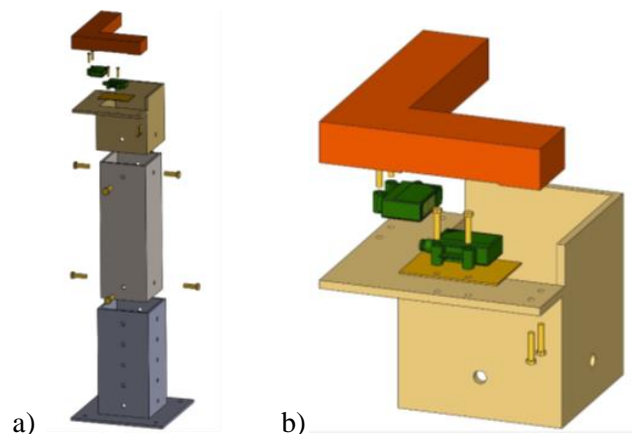


Fig. 3: Conception of calibration device: a) full view; b) laser location (green).

Third assumption was to obtain low cost device, so there had been chosen laser sensors from IFM Electronic, OJ5 laser type. These laser sensors use reflective diffusion. Beam receiver is located at the top of the lens, while beam transmitter in the lower one. The sensor range is in the range of 7 to 150 mm. Another objective was to design a structure, which can be working in a difficult operating environment and at the same time provides protection against laser beams. Appearance design, Figs. 3a and 3b.

### 3. Calibration device - principle of operation

In the first stage, should be determined positions and orientations of the calibration device. For this purpose, the robot need have properly calibrated TCP. Using TCP robot, indicate points 1, 2, 3 marked on Fig. 4a. This will allow to determine a straight line passing through the points 1 and 2, and then a straight line perpendicular to first one passing through point 3. The result will be origin of the coordinate system of calibrating device, which is placed in the intersection of the laser beams. Coordinates are calculated with respect to the base of the robot and stored in robot controller memory. These will be used as reference coordinates to calculate the correction values of the TCP. Next step, before first use of the device is also important. Operator must place the TCP in black marked place near the point *P*, as shown in Fig. 4b. The calibration device automatically operates as follows. Robot program moves the TCP along the device local *X* axis. During this movement, it intersects laser 2 beam and determines the *Y* coordinate (*p100.y*). Then the robot moves the TCP close to that intersection point and distances 15 mm from the laser beam 2 in direction of *-Y* axis. Next robot TCP searches the point of intersection with laser beam 1. In this manner, it calculates *X* coordinate (*p100.x*). This operation is performed repeatedly, each time robot moves the tool upward along the positive *Z* axis. This way can be searched for the end of the wire.

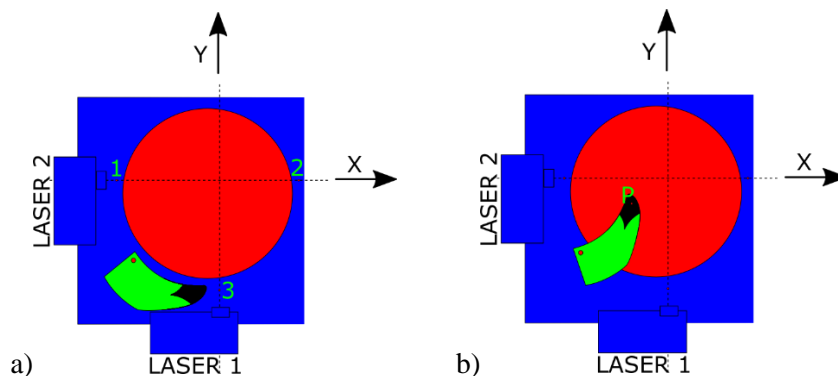


Fig. 4: a) Device calibrating procedure, b) Position *P* where the user should place robot TCP.

Below, in a few steps is shown program algorithm implemented into robot controller.

- User places the TCP at point *P* and stores it. It is done once – calibration procedure.
- Robot moves TCP down of 10 mm, because minimum welded wire eject is 17 mm. It is protection from tip hit of torch. ( $P[x, y, z-10]$ )
- Robot moves TCP along the *X* axis at distance of 15 mm. Calculates the average of 5 repetitions. ( $P[x, y, z-10] \rightarrow P[x+15, y, z-10]$ )
- Controller remembers *X* position, when the Laser 1 signal changed from logical 0 to 1.
- Robot moves the TCP to *X* - 15 mm position, but not more than 30 mm.
- Robot moves along *Y* axis by 15 mm. Calculates the average of 5 repetitions.
- Robot moves TCP to intersection point with the axis *Y*.
- Robot moves TCP upward along the axis *Z* + 0.5 mm, the system checks end of wire using signals for Laser 1. Waves no more than 50 mm in *Z* axis direction and in the range between  $\pm 2.5$  mm in *X* direction.
- Robot again searches end wire area along *Z* axis in distance  $\pm 0.5$  mm.
- Controller saves *Z* coordinate and enter tool correction only if the deviation of wire is lower than 5 %.

Positioning accuracy of designed device was tested in Kielce University of Technology in the station with ABB IRB1600 industrial robot. For the purposes of article were carried out 10 test series. Each series contained 20 test measurements. Before each series, the wire deviation was changed slightly. In this manner was changed the physical TCP compared with stored in the system tool values. Such approach simulated the work of the real welding torch. It should be noted that, the real wire ejects from the housing of the welding tip is not more than 27 mm. We tested this with 40 mm wire ejection, in case to increase the possible error. During research sought to ensure that the deviation is minor and direct only in one plane. Test robot speed was set to 1 mm/s and each laser intersecting movement was performed twice

(average). For each result was add value of 0.5 mm which is the value of half of thickness of the tested wire. Fig. 5 shows obtained results of X axis discrepancy. Other results were similar.

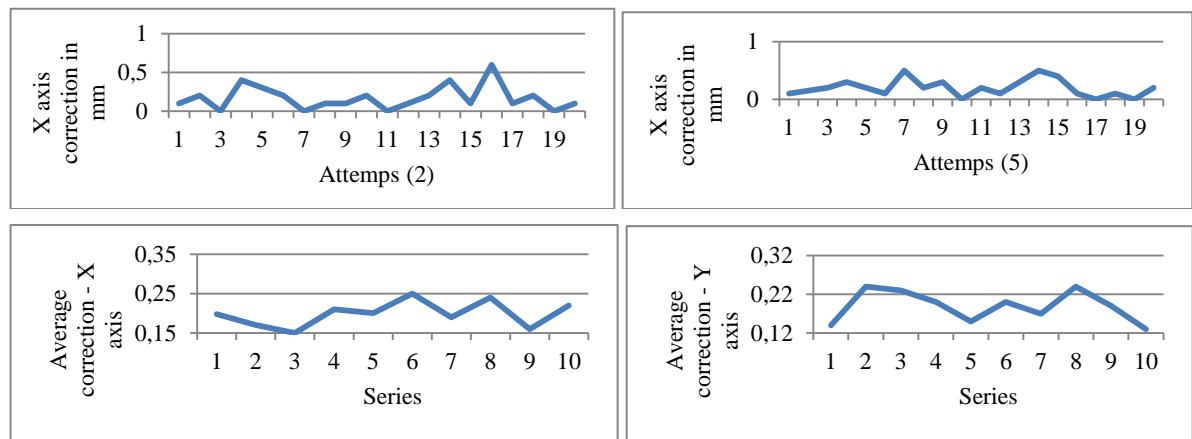


Fig. 5: The TCP X axis accuracy results calculated in calibrating device.

#### 4. Conclusions

Designed device always correctly detected the torch wire. Discrepancy of wire intersection position points were small and ranged on tenths of a millimeter. There was assuming, that the system is used to determine the adjustment of the welding wire, so results are better than expected. Only much wire deflection was a problem, that is above 10 degrees, because the wire extends beyond the boundaries of the vertical scan (search for tilting wire along the Z axis of the tool). However, each time in such situation system informed the user correctly and displayed measurement error. It should be noted that, if the wire deviation excides above 3 degrees, the system cannot make TCP adjustment. It can only display a message to the system operator of an invalid wire load. The operator should cut the wire and pull out it again to the required length.

#### References

- ABB BullsEye device <http://www.abb.com/product/seitp327/fa2dca58536be110c1257db0003c0fe3.aspx> (01.02.17).
- Blasiak, S., and Zahorulko, A.V (2016) A parametric and dynamic analysis of non-contacting gas face seals with modified surfaces, *Tribology International*, 94, pp. 126-137. doi:10.1016/j.triboint.2015.08.014.
- Laski, P.A. (2016) Proportional valve with a piezoelectric actuator, in: *Proceedings of the International Conference Experimental Fluid Mechanics 2016* (ed. Dancova, P.), Techn. Univ. Liberec, pp. 407-410.
- Pietrala, D.S. (2016) Parallel manipulator with pneumatic muscle drive, in: *Engineering Mechanics 2016* (eds. Zolotarev, I and Radolf, V.), Svrtaka, Czech Republic, pp. 458-461.
- Takosoglu, J.E. (2016) Experimental research of flow servo-valve, in: *Proceedings of the International Conference Experimental Fluid Mechanics 2016* (ed. Dancova, P.), Techn. Univ. Liberec, pp. 819-823.
- Janecki, D. and Zwierzchowski, J. (2015) A method for determining the median line of measured cylindrical and conical surfaces, *Measurement Science & Technology*, 26, 8. doi:10.1088/0957-0233/26/8/085001.
- Blasiak, M. (2016) Parametric analysis of piezoelectronic transducer used for signal processing, in: *Engineering Mechanics 2016* (eds. Zolotarev, I. and Radolf, V.), Svratka, Czech Republic, pp. 66-69.
- Nowakowski, L., Miesikowska M. and Blasiak M. (2016), Speech intelligibility in the position of CNC machine operator, in: *Engineering Mechanics 2016* (eds. Zolotarev, I. and Radolf, V.), Svratka, Czech Republic, pp. 422-425.
- Laski, P, Takosoglu, J. and Blasiak, S. (2014) A delta type closed kinematics chain with muscle actuator manipulator, in: *20th International Conference, Engineering Mechanics 2014*, (ed. Fuis, V.), Svratka, Czech Republic, pp. 360-363.
- Zwierzchowski, J. (2016) Industrial robot vision system for moving spherical elements, in: *Engineering Mechanics 2016* (eds. Zolotarev, I and Radolf, V.), Svrtaka, Czech Republic, pp. 626-629.

## Author Index

### A

Adamczak S.....	66, 70
Adámek V.....	246
Aizikovich S.....	74
Aleksandrowicz P. ....	78, 82, 490, 494
Andrlík V.....	278
Andryszczyk M. ....	1054
Andrzejewska A.....	1054
Anweiler S. ....	86, 782
Appel M. ....	90
Artemov M. A. ....	110
Augustín T.....	94
Awrejcewicz J. ....	346
Aydin E. ....	98

### B

Bachratý M.....	1002
Baka Z.....	450
Balasubramanian K.....	570
Baláž I. ....	102
Balcerzak M. ....	266
Balchanowski J. ....	974
Bang N. V. ....	106
Baranovskii E.....	110
Baranowski L. ....	114, 118
Bartoszewicz J.....	466
Bayer J.....	122
Bébarová M.....	750
Bęczkowski R. ....	126, 230
Bednář L.....	130

Benešovský M.....	134
Benýšek M. ....	226
Berezovski A.....	474
Bessegheir K.....	114, 138
Bezdekova J. ....	422
Bezděková J.....	454
Bialy L.....	994
Bieniek A.....	1058
Bienioszek G. ....	142
Blasiak M.....	146, 150
Blasiak S. ....	146, 150, 154, 158
Blatnická M. ....	162, 166
Blatnický M.....	162, 166
Bochat A. ....	170
Bochnia J. ....	174, 178
Bocian M.....	574
Bojczuk D. ....	186
Borák L. ....	190, 618
Borkowski K.....	194
Borowski S.....	198, 438
Borsuk G.....	202, 790, 1074
Borzovič V. ....	582
Bošanský M. ....	206
Brabec P.....	210
Bracha G. F. ....	778
Brezina L. ....	214
Brózda K.....	218
Brožek P.....	622
Bucci V.....	222
Bula V. ....	382, 942
Byrtus M.....	794

# C

Cabová K. ....	226
Cebulski J. ....	126, 230
Čečrdle J. ....	234
Cekus D. ....	238
Cerni P. ....	630
Černý M. ....	242
Červ J. ....	246
Chalupová M. ....	998
Chára Z. ....	1034
Chatys R. ....	250, 254, 918
Chen K.-S. ....	1022
Chlupová A. ....	434
Cho S. S. ....	474
Chojnacki J. ....	754
Christé G. ....	750
Chrzan M. ....	718
Ciałkowski M. ....	858
Cibulka J. ....	942
Cichański A. ....	922
Cienciala J. ....	258
Ćwiklak J. ....	262

# D

Dabrowski A. ....	266
Dalyak T. ....	866
Dekýš V. ....	950
Denk F. ....	818
Dindorf R. ....	270, 1066, 1070
Dižo J. ....	166
Dočkal K. ....	274
Dolgopyat D. ....	1050
Domański T. ....	846

Dorszewski P. ....	438
Drábková S. ....	314
Drahorádová L. ....	278
Duda S. ....	282, 878
Dudek D. ....	286
Dutkiewicz M. ....	98, 350, 354
Dvořák L. ....	318
Dvořáková E. ....	290
Dyk Š. ....	794
Dzierzek K. ....	294, 778
Dziopa Z. ....	298
Dzurilla M. ....	242

# E

Eliáš J. ....	302
Eliášová M. ....	802, 902
Elsner W. ....	826

# F

Ferfecki P. ....	1110
Fiedler J. ....	306
Fila J. ....	902
Filipiak J. ....	1106
Fillo E. ....	94
Fischer C. ....	310, 698
Florian Z. ....	618
Fojtášek J. ....	54
Fojtík F. ....	994
Frąckowiak A. ....	858
Frydryšek K. ...	258, 314, 318, 626, 670, 994
Fuis V. ....	406

## G

Gabriel D. ....	666
Gajdosova K. ....	322
Gałąska P. ....	966
Gapiński D. ....	326, 970
Gembalczyk G. ....	282
Gidlewski M. ....	330
Gierz Ł. ....	334, 838
Gilewski W. ....	338, 342
Goethel F. M. ....	346
Goga V. ....	682
Gogolewski D. ....	66, 70
Golebiowska I. ....	350, 354
Gonzalez J. G. ....	474
Grepl R. ....	90
Grzyb M. ....	358
Gucwa M. ....	126
Guz I. ....	650
Guzej M. ....	1078
Gzik M. ....	446, 1058

## H

Had J. ....	362
Hadaš Z. ....	534
Hájek P. ....	366
Hajžman M. ....	794
Halvonik J. ....	1026
Hamza J. ....	462
Hartl M. ....	274
Havelka J. ....	370
Hejnova M. ....	374
Hernandez Carrasco L. H. ....	898
Hlaváč Z. ....	1118

Hlinka J. ....	498
Hollý I. ....	378
Horáček J. ....	366, 382, 926, 1018
Horáčková L. ....	618
Horák M. ....	622
Horský J. ....	1078
Hospodář P. ....	798, 1050
Hoznedl M. ....	130
Hrabovský J. ....	682
Hrstka M. ....	806
Hubova O. ....	386
Hůlka J. ....	542
Hynek M. ....	638
Hynek P. ....	390, 666

## I

Ivankova O. ....	394, 398
------------------	----------

## J

Jaferník H. ....	262
Jamroziak K. ....	574
Janda T. ....	430, 850, 1122
Janecki D. ....	194
Janhuba L. ....	498
Janíček P. ....	402, 406
Janouchová E. ....	410
Jarzyna T. ....	414
Jebáček I. ....	42
Jegla Z. ....	418
Jelínek T. ....	702
Jemioł L. ....	330
Jíra A. ....	818



Jirásek M. ....	662
Jirásko J. ....	422
Juračka J. ....	46
Jureczko M. ....	426, 478
Jureczko P. ....	282, 426
Jurkojc J. ....	1058

## K

Kabele P. ....	1042
Kaczmarek W. ....	114, 138
Kadlíček T. ....	430
Kala Z. ....	1014
Kalduński P. ....	754
Karol' M. ....	434
Kasprowicz T. ....	50
Kaszkowiak J. ....	198, 438
Katrňák T. ....	442
Kawlewska E. ....	446
Kazala R. ....	286
Kciuk S. ....	142
Kebli B. ....	450
Keckstein T. ....	454
Keršner Z. ....	806
Kilinc O. ....	458
Klečková J. ....	462
Klíma J. ....	702
Kłosowiak R. ....	466
Klusák J. ....	806
Knižat B. ....	1030
Knopik L. ....	198, 470, 654, 658, 962
Kolber P. ....	658, 770, 886
Koleková Y. ....	102
Kolman R. ....	474, 666
Konecna L. ....	386, 398
Konfršt J. ....	1034

Konopelska A. ....	478
Kopačka J. ....	666
Kořínek T. ....	482
Koruba Z. ....	486, 530, 714, 970
Košina J. ....	382, 942
Kostek R. ....	490, 494
Košťal R. ....	498
Kotoul M. ....	862
Koudelka T. ....	306, 502, 710
Koukal M. ....	506
Kovář J. ....	510
Kowalczyk L. ....	1090
Kozachkov D. ....	1126
Kozánek J. ....	1038, 1110
Kozior T. ....	66, 70
Králik J. ....	514
Krasuski K. ....	262
Kraus P. ....	1002
Krejčí T. ....	502
Krejsa J. ....	518, 522, 1022
Kriváček J. ....	526
Kruis J. ....	502, 710
Kruml T. ....	434
Křupka I. ....	274
Krzysztofik I. ....	486, 530
Kšica F. ....	534
Kubiak M. ....	162
Kubík M. ....	538, 594, 830, 934
Kubík P. ....	542, 854
Kučera P. ....	54, 546
Kučerová A. ....	370, 410, 958
Kuchariková L. ....	998
Kucíková L. ....	550
Kukielka K. ....	554
Kukielka L. ....	554
Kukielka L. ....	754
Kulesza Z. ....	558

Kulhavý P. ....	562
Kuliński K. ....	602
Kumpán P. ....	566
Kupireddi K. K. ....	570
Kurzawa A. ....	574
Kutiš V. ....	682
Kwasniowski S. ....	1094, 1098
Kyncl M. ....	578

## L

Laco K. ....	582
Lamperová K. ....	898
Larysz D. ....	446
Laski P. A. ....	586, 778
Le J. -L. ....	302
Lepš M. ....	690
Ligaj B. ....	598, 986
Lišková N. ....	226
Löffelmann F. ....	590
Losak P. ....	214
Łukasik Z. ....	182

## M

Machacek J. ....	774
Macháček O. ....	538, 594, 830, 934
Machoczek T. ....	878
Maćkowiak P. ....	598
Mahdal M. ....	990
Majer Z. ....	862
Major I. ....	602
Major M. ....	218, 602
Makoviichuk M. ....	866

Malínek P. ....	606
Mališ M. ....	610
Mallick A. ....	614
Marcián P. ....	190, 618
Marino A. ....	222
Markiewicz-Patalon M. ....	438
Masák J. ....	666
Mašek J. ....	622
Mat'as M. ....	626
Matějů J. ....	42
Mattiazzo G. ....	222
Mauro F. ....	222, 630, 634
Max A. ....	422, 638
Mazánová V. ....	434
Mazůrek I. ....	538, 830
Mazurkiewicz A. ....	642, 646, 986
Menshykov O. ....	650
Menshykova M. ....	650
Meri D. ....	394
Michnik R. ....	718, 1058
Miczán M. ....	130
Mifsud L. ....	842
Migawa K. ....	470, 654, 658
Mikeš K. ....	662
Miko E. ....	726, 730, 734
Miśków G. ....	250
Míterka S. ....	986
Mitrin B. ....	74
Mrkvík M. ....	1030
Mlynár P. ....	1030
Mochar D. ....	666
Moravec J. ....	278
Morávková Z. ....	670
Mrózek L. ....	130
Mrozik D. ....	882
Mrozik Ł. ....	674
Mrozowski J. ....	346

Muraszkowski A. ....	678
Murín J. ....	682
Muscat C. ....	842
Musil M. ....	242, 686, 1002
Myšáková E. ....	690
Myśliwiec A. ....	718

## N

Nabergoj R. ....	630, 634
Nagireddy P. D. ....	694
Náprstek J. ....	310, 698
Návrat T. ....	134
Němec M. ....	702
Němec Z. ....	706
Němeček J. ....	710
Nerukh D. ....	1126
Neubauer A. ....	654
Nevrlý J. ....	706
Nocoń Ł. ....	714
Novák P. ....	594
Novotná P. ....	226
Novotný J. ....	834
Nowakowska K. ....	718, 1058
Nowakowski L. ....	730, 734
Nowakowski Ł. ....	722, 726
Nyckowski M. ....	298

## O

Obara P. ....	338
Olšiak R. ....	1030
Olszewski L. ....	50
Oravcová M. ....	998

Osadnik M. ....	1006
Osiński P. ....	738
Osowski P. ....	742, 1062
Öztürk B. ....	98

## P

Paczkowski T. ....	746
Palček P. ....	998
Panasiuk J. ....	114, 118, 138
Park K. C. ....	474
Pasek D. ....	126, 230
Pásek M. ....	750
Patyk R. ....	754
Patyk S. ....	754
Patzák B. ....	206, 290
Paulech J. ....	682
Pavlenko M. ....	758
Pawelec K. ....	270
Pejkowski Ł. ....	762
Pelant J. ....	578
Pelczyński J. ....	342
Perczyński D. ....	654, 770, 886, 962
Perepichka V. ....	866
Perz K. ....	766
Pešek L. ....	814, 942
Peszynski K. ....	50
Peszyński K. ....	470, 770, 882, 1082
Petříková M. ....	482
Petrů M. ....	562
Petruška J. ....	134, 542, 854
Pezowicz C. ....	966
Piatkowski T. ....	742, 1062
Pichal R. ....	774
Piernik K. ....	254
Pietrala D. S. ....	294, 778

Pikunov D. ....	266
Píštěk V. ....	54, 546
Piwowarski D. ....	782
Plánička S. ....	786
Plášek M. ....	314
Plešek J. ....	666
Pleva L. ....	994
Pliusnov D. ....	1126
Plonek T. ....	1106
Pochwala S. ....	202
Pochwala S. ....	790, 1074
Podešva J. ....	258
Polach P. ....	794
Popadyuk I. ....	870
Porteš P. ....	54
Prachař A. ....	798, 1050
Pravdová I. ....	802
Příhoda J. ....	930
Profant T. ....	806
Prokop A. ....	810
Prusaczyk P. ....	114, 138
Pruška J. ....	834
Půst L. ....	814
Pyka D. ....	574

## R

Radolf V. ....	382
Radzivil V. ....	1126
Rama R. ....	198
Ranjan R. ....	614
Rao Srinivasa Ch. ....	694
Raška J. ....	234
Rečko M. ....	294
Řehák K. ....	810
Řehounek L. ....	638, 818

Reichrt K. ....	210
Reppich M. ....	418
Reut O. V. ....	822
Reut V. ....	1126
Rewolińska A. ....	766
Ridzoň F. ....	1030
Romańczyk M. ....	826
Roupec J. ....	538, 830, 934
Rozehnal D. ....	106
Runt D. ....	834

## S

Sądej M. ....	838
Sadovský Z. ....	526
Šafařík P. ....	58
Sága M. ....	162
Sai Sudheer S. V. ....	570
Sandron C. ....	222
Sant Z. ....	842
Sapieta M. ....	846, 950
Sapietová A. ....	846, 950
Sawicki J. ....	746
Schmidt J. ....	850
Šebek F. ....	542, 854
Sedlár T. ....	682
Seifert A. ....	1050
Šejnoha M. ....	430, 550, 850, 1010, 1122
Selejdak J. ....	218
Semklo L. ....	858
Ševeček O. ....	862
Shatskyi I. ....	866, 870
Shpynarov O. ....	1126
Šidlof P. ....	1038
Sivý M. ....	686
Siwek M. ....	118

Siwulski T. ....	874
Skibicki D. ....	922
Skrobek D. ....	238
Skrzyniarz M. ....	726, 730, 734
Sławski S. ....	878
Šmilauer V. ....	946
Smolík L. ....	794
Smyk E. ....	50, 770, 882, 886
Sobotka J. ....	890
Sokół K. ....	894
Sokol M. ....	898
Sokol Z. ....	902
Sokolski M. ....	906
Sokolski P. ....	906, 910
Sołtysiak A. ....	658
Sonnenschein R. ....	322, 378
Sosnowski M. ....	914
Šperka P. ....	274
Šplíchal J. ....	610
Stefańska A. ....	918
Stefański K. ....	358, 918
Štěpán M. ....	1038
Stopel M. ....	922
Štorkán J. ....	926
Stosiak M. ....	738
Straczynski P. ....	286
Straka P. ....	930
Strecker Z. ....	538, 830, 934
Strmiska T. ....	934
Strzelecki P. ....	938
Šulc P. ....	942
Šulc S. ....	946
Šulka P. ....	846, 950
Šuránek P. ....	990
Švancara P. ....	366
Švec G. J. ....	366
Svoboda M. ....	166

Svojanovský T. ....	954
Sýkora J. ....	370, 410, 550, 958
Sýkora M. ....	518
Syrovátková M. ....	562
Szews M. ....	962
Szkoda K. ....	966
Szmidt P. ....	326, 970
Szrek J. ....	678, 974
Szteblelak W. ....	186

## T

Tajč L. ....	130
Takosoglu J. E. ....	978
Tańczuk M. ....	782
Tarasova E. ....	1126
Tomaszewski T. ....	982
Tomečková I. ....	670
Topolinski T. ....	986
Topoliński T. ....	1054
Trochimeczuk R. ....	558
Trtík L. ....	954
Tůma J. ....	990

## U

Učeň O. ....	994
Uhrčík M. ....	998
Ulbrich R. ....	782
Úradníček J. ....	1002
Urban F. ....	1030
Urbaniak R. ....	466
Usewicz B. ....	354
Uzny S. ....	1006

## V

Vágner J. ....	458
Valasik A. ....	398
Valentin J. ....	850
Valentová S. ....	1010
Valeš F. ....	246
Valeš J. ....	1014
Vampola T. ....	390, 926, 1018
Vasiliev A. ....	74
Vaysfeld N. ....	1126
Vechet S. ....	522, 1022
Velychkovych A. ....	870
Venglár M. ....	898
Vetiška J. ....	534
Vida R. ....	1026
Világi F. ....	1030
Vimr J. ....	786
Vlasák P. ....	1034
Vlček V. ....	1038
Vojtekova E. ....	394
Volkov S. ....	74
Vorel J. ....	550, 1010, 1042
Votápek P. ....	454
Votrubec R. ....	1046
Vrchota P. ....	798, 1050

## W

Wald F. ....	226, 946
Warzyńska U. ....	874

Wawrzyniak S. ....	470, 882, 886, 962
Wirwicki M. ....	1054
Wodarski P. ....	1058
Wolański W. ....	446
Wolski M. ....	742, 1062
Wos P. ....	270
Woś P. ....	1066, 1070
Wydrych J. ....	202, 790, 1074

## Z

Zachar M. ....	1078
Zachwieja J. ....	1082
Záda V. ....	1086
Zajac P. ....	1090, 1094, 1098
Žák J. ....	1102
Žak M. ....	966, 1106
Zapoměl J. ....	1110
Żardecki D. ....	330
Zarwańska M. ....	446
Zastempowski M. ....	170, 1114
Zeman F. ....	226
Zeman J. ....	958, 1122
Zeman V. ....	1118
Zemanová A. ....	1122
Zháňal L. ....	54
Zhuravlova Z. ....	1126
Ziolkowska J. ....	1130
Zmarzły P. ....	66, 70
Zolotarev I. ....	1038
Zvolský T. ....	1134
Zwierzchowski J. ....	194, 1138